IMPC ASIA PACIFIC 2022

22-24 August 2022
Melbourne, Australia

Conference Proceedings

CO-HOSTS

AusIMM

CSIRO

IMPC
INTERNATIONAL MINERAL PROCESSING COUNCIL

IMPC ASIA-PACIFIC 2022

22–24 AUGUST 2022
MELBOURNE, AUSTRALIA + ONLINE

The Australasian Institute of Mining and Metallurgy
Publication Series No 5/2022

Published by:
The Australasian Institute of Mining and Metallurgy
Ground Floor, 204 Lygon Street, Carlton Victoria 3053, Australia

All papers published in this volume were peer reviewed before publication.

ISBN 978-1-922395-08-5

ORGANISING COMMITTEE

Professor Robin Batterham
FAusIMM
International Mineral Processing Council Asia-Pacific 2022 Conference Chair

Dr Ralph Holmes
HonFAusIMM(CP)
IMPC Chair & IMPC Asia-Pacific 2022 Conference Co-Chair

Virginia Lawson
FAusIMM(CP)
IMPC Asia-Pacific 2022 Conference Co-Chair

Andrew Jenkin
MAusIMM

Bill Skinner
FAusIMM

Diana Drinkwater
FAusIMM

Eddie McLean
FAusIMM

Kevin Galvin

Louisa O'Connor
FAusIMM(CP)

Sandy Gray
FAusIMM

Steve Liddell
MAusIMM

AUSIMM

Julie Allen
Head of Events

Sarah Hallett-Patterson
Senior Manager, Events

Samara Brown
Conference Program Manager

REVIEWERS

We would like to thank the following people for their contribution towards enhancing the quality of the papers included in this volume:

Grant Ballantyne
Robin Batterham
Duncan Bennett
Pablo Brito-Parada
Craig Brown
Dave Deglon
Richard Dewhirst
Simon Dominy
Diana Drinkwater
Rod Elvish
Phillip Fawell
Yuqing Feng
Jim Finch
Silvia França
George Franks
Kevin Galvin
Lachlan Graham
Sandy Gray
Greg Harbort
Ralph Holmes
Shenggen Hu
Andrew Jenkin
Virginia Lawson
Steve Liddell
Robbie McDonald
Teresa McGrath
Edward McLean
Ellen Moon
Louisa O'Connor
Cyril O'Connor
Joe Pease
Zeljka Pokrajcic
Mark Pownceby
Pradip Pradip
Antonio Pucci
Chris Ritchie
Peter Scales
Phil Schwarz
Robert Seitz
William Skinner
David Stephenson
Anthony Stickland
San Thang
Andrew Tong
Yves van Haarlem
David Way
Grant Webber
Elaine Wightman
Zhenge Xu
Juan Yianatos
Max Zanin

FOREWORD

Dear peers in the minerals industry,

On behalf of the Conference Committee and the IMPC Council, I am delighted to welcome you to the International Minerals Processing Council Asia-Pacific 2022 Conference (IMPCAP22). The conference is co-hosted by AusIMM, CSIRO and the IMPC Council. It brings together delegates from Australia, the Asia-Pacifica and around the world to share best practice and knowledge in minerals processing from our region. This is the second regional minerals processing conference organised by the International Minerals Processing Council.

In keeping with the high standards set by the IMPC, all papers have been fully refereed and feature the latest innovations and thinking in the field of minerals processing. Environmental, social and governance (ESG) and innovation are key drivers for the resources sector. We look to industry, suppliers and researchers to drive open and rapid innovation, helping our industry meet the challenges of today and the future. Any organisation that is wanting to reach a target of net zero is going to rely heavily on minerals and their processing to reach it.

The conference will showcase an impressive range of speakers and topics, with over 160 technical sessions and nine keynote speakers spread over three days, highlighting leading innovations and research in minerals processing. Presentations will also be recorded and made available to all delegates following the conference to ensure the insights are captured.

I would like to thank all our speakers and authors who have prepared presentations, compiled technical papers and are travelling far and wide to participate in the conference. I would also like to thank the Organising Committee, paper reviewers, sponsors and exhibitors for their time and energy to make the conference a success.

Without our dedicated community and ongoing support this event would not be possible.

Yours faithfully,

Professor Robin Batterham

FAusIMM

IMPC Asia-Pacific 2022 Conference Organising Committee Chair

SPONSORS

Major Sponsor

BHP

Gold Sponsors

Ausenco

jord | IDEAS ENGINEERED

Metso:Outotec

SOLVAY
Progress beyond

Silver Sponsor

PROCESS IQ

Technical Session Sponsor

SEDGMAN

Lanyard and Name Badge Sponsor

120 Me Metcelerate

Keynote Speaker Sponsors

CSIRO

GEKKO

Networking Reception Sponsor

ARC Centre of Excellence for
ENABLING ECO-EFFICIENT
BENEFICIATION OF MINERALS

Catering Breaks Sponsor

WEIR
Minerals

Supporting Partner

IMPC
INTERNATIONAL MINERAL
PROCESSING COUNCIL

Student Supporting Partner

THE UNIVERSITY OF
MELBOURNE

CONTENTS

Advances in mineral processing – case studies

Advances in mineral processing – comminution

Advances in mineral processing – geometallurgy

Advances in mineral processing – hydrometallurgy

Advances in mineral processing – physical separation

Advances in mineral processing – physiochemical separation

Advances in mineral processing – pre-concentration and waste rejection

Advances in mineral processing – solid-liquid separation

Future operations – future mineral processing plants

Future operations – maximising separation at coarse particle sizes

Future operations – mine-to-mill intergration

Future operations – modelling and 'big data' utilisation

Future operations – net zero emissions

Future operations – waste processing and sustainable operation

Industry challenges – ensuring a sustainable future

Industry challenges – processing

Advances in mineral processing – case studies

Effect of alkaline roasting conditions on the dephosphorisation of high-phosphorus iron ore

A Batnasan[1], H Takeuchi[2], K Haga[3], A Shibayama[4], M Mizutani[5] and K Higuchi[6]

1. Project lecturer, Akita University, 1–1, Tegata-Gakuen-machi, Akita, 010–8502, Japan. Email: altansukh@gipc.akita-u.ac.jp
2. Graduate student (M2), Akita University, 1–1, Tegata-Gakuen-machi, Akita, 010–8502, Japan. Email: m6021211@s.akita-u.ac.jp
3. Associate professor, Akita University, 1–1, Tegata-Gakuen-machi, Akita, 010–8502, Japan. Email: khaga@gipc.akita-u.ac.jp
4. Professor, Akita University, 1–1, Tegata-Gakuen-machi, Akita, 010–8502, Japan. Email: sibayama@gipc.akita-u.ac.jp
5. Process Research Laboratories, Research and Development, Nippon Steel Corporation, Japan. Email: mizutani.9qc.moritoshi@jp.nipponsteel.com
6. Process Research Laboratories, Research and Development, Nippon Steel Corporation, Japan. Email: higuchi.t9g.kenichi@jp.nipponsteel.com

ABSTRACT

The main techniques for removing phosphorus as an impurity element in iron ores are physical separation (eg magnetic separation, flotation) and chemical separation (acid leaching, alkaline leaching and bioleaching) processes. When phosphorus occurs in iron ores as phosphate minerals (eg apatite), physical separation techniques are available to remove the gangue minerals from iron ores. On the other hand, chemical separation techniques are suitable for reducing phosphorus levels when phosphorus is associated with iron oxides and hydroxide minerals (eg hematite and goethite) in iron ores.

In this study, the dephosphorisation behaviour of high-phosphorus iron ore was investigated using a combined alkaline roasting and water washing route. Roasting experiments were conducted in a laboratory electric muffle furnace using various concentrations of sodium hydroxide (0–50 g/kg-ore) at different temperatures (100–800°C), varying prolonged roasting times (0–2 h), and different particle size fractions (-45 – -250 μm) of iron ore. Subsequent water washing experiments were employed at various pulp densities (30–1000 g/L) and different times (30 s – 60 min) at ambient temperature. Hematite and goethite were the main minerals in the high-phosphorus iron ore identified using X-ray diffraction (XRD) analysis. The iron ore assaying 63.40 mass % Fe (total), 0.240 mass % P, 4.53 mass % SiO_2, and 4.87 mass % Al_2O_3 were determined using X-ray fluorescence (XRF) analysis.

The results showed that the dephosphorisation rate of the iron ore was reached 40 per cent under roasting with 50 g/kg-ore NaOH at 300°C for 2 hours followed by water washing for 30 s with a pulp density of 300 g/L, reducing phosphorus level from 0.240 mass % to 0.142 mass %. At the same time, the iron grade was reduced from 63.4 per cent to 59.5 per cent, caused by an iron loss. Results suggest that the phase transformation of goethite induces the dephosphorisation of high-phosphorus iron ore under alkaline roasting conditions.

INTRODUCTION

Iron ore is a raw material for the iron and steelmaking industries. Nowadays, higher-grade iron ore reserves are depleting because of enormous iron and steel production growth. Therefore, high-impurity iron ore deposits are expected to be used as iron ores in the future (Baawuah *et al,* 2020; Löf *et al,* 2019). Reduction in the quality of iron ore due to high levels of impurities is a severe issue in iron and steel manufacturing processes. Typical major components in iron ore are magnetite (Fe_3O_4), hematite (Fe_2O_3) and goethite (FeO(OH)) as iron minerals, and impurity minerals containing silica (Si), aluminium (Al), phosphorus (P), and sulfur (S). Additionally, quartz and alumina occur in iron ore as kaolinite (clay), gibbsite, illite, and lateritic materials, while phosphorus presents as phosphate minerals and inclusions in iron oxides and hydroxides. The high impurities in iron ore affect energy consumption, CO_2 emissions, slag amounts, and slag viscosity throughout the steel production processing (Clout and Manuel, 2015; Park *et al,* 2021; Pownceby *et al,* 2019). Among

them, a high level (>0.1 wt.% P) of phosphorus causes detrimental effects on the quality of steel and the process costs associated with removing phosphorus from iron ore through steelmaking. The removal of phosphorus from iron ore is a vital process; mainly, phosphorus is a predominant phase into impurity components in iron ore (Ofoegbu, 2019; Bao *et al,* 2021). The main techniques for removing phosphorus as an impurity element in iron ores are physical separation (eg magnetic separation, flotation), chemical separation (acid leaching, alkaline leaching and bioleaching), and various combined techniques with thermal and physical separation (Xiao and Zhou, 2019; Pereira and Papini, 2015; Delvasto *et al,* 2008; Roy *et al,* 2020). Physical separation processes are suitable for removing phosphorus-containing minerals such as apatite in iron ore. Besides, chemical separation techniques are employed to remove phosphorus that adsorbs onto iron oxides and iron hydroxide minerals' surfaces. However, acid leaching and alkaline leaching techniques can adequately remove phosphorus that exists as phosphate in iron ore but cannot sufficiently remove phosphorus adsorbed in iron oxides and hydroxides (Yu *et al,* 2013; Mochizuki and Tsubouchi, 2019a; Zhang *et al,* 2019). Some authors used a combined thermal treatment and leaching process to investigate phosphorus removal from different iron ores. They found that the phosphorus adsorbed in iron oxide minerals' surfaces could leach out with aqueous solutions after the structural disruption of the iron minerals by thermal processing (Gooden *et al,* 1974; Fisher-White *et al,* 2013; Sanchez-Segado *et al,* 2015; Zhu *et al,* 2016; Mochizuki and Tsubouchi, 2019b).

In this study, the dephosphorisation behaviour of high-phosphorus iron ore was investigated using an alkaline roasting and water washing route. Various processing parameters, including sodium hydroxide concentration, roasting temperature, roasting time, particle size distribution, pulp density, and washing duration through roasting and water washing, were investigated to reduce phosphorus levels in the high-phosphorus iron ore.

EXPERIMENTAL

Materials

The high-phosphorus iron ore sample received from an iron ore producing company was used in this study. The iron ore sample was pulverised by crushing and milling it into powder. Then individual iron ore particles ranging between -45 µm and -500 µm in various size distributions were produced using sieving and classification (JIS Z 8801 sieves, IIDA Manufacturing Co, Ltd).

Reagent grade sodium hydroxide (NaOH) and distilled water were used in the alkaline roasting and water washing processes.

Methods

The high-phosphorus iron ore sample was roasted in an electric muffle furnace (Advantec, KM-160) after drying with an appropriate NaOH solution at 60°C for 24 hours. A process flow chart regarding the dephosphorisation of the high-phosphorus iron ore is represented in Figure 1.

In the roasting process, NaOH concentration (5–50 g/kg-ore), roasting temperature (100–800°C), prolonged roasting time at the target temperature (0–2 h), and particle size distribution (-45 – -500 µm) were studied. The roasted sample was cooled in a desiccator to room temperature and ground in a pestle with a mortar. Then the ground sample was washed with distilled water in a beaker at a pulp density of 100 g/L, washing time of 30 seconds at ambient temperature (20°C).

The pulp density (30–1000 g/L) and washing time (30 s – 60 min) were examined at ambient temperature through the water washing. After washing the sample, vacuum filtration was conducted to separate solid and liquid phases. Each experiment was performed in duplicate to confirm reproducibility.

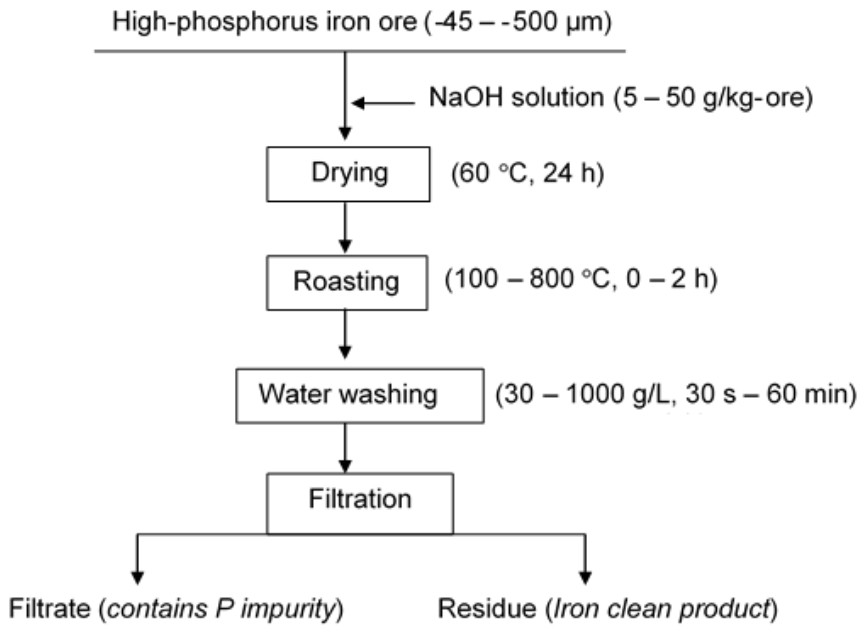

FIG 1 – A process flow for the dephosphorisation of the high-phosphorus iron ore.

Analytical

An electric muffle furnace (Advantec, KM-160) was used to roast iron ore samples. Temperature and agitation speed (revolutions per minute, rev/min) in water washing were controlled by an automatic multi-position magnetic stirring hot plate, HSH-6D (As One Corp).

The chemical constituents and mineral components in the initial iron ore samples, roasted samples, and washed residues were determined using an X-ray fluorescence spectrometer, XRF (Primus-II, Rigaku) and X-ray diffractometer, XRD (RINT–2200/PC, Rigaku), and scanning electron microscopy with energy dispersion spectroscopy, SEM-EDS (SU-70, Hitachi Hightech).

The dephosphorisation rate and iron loss through the processing of the high-phosphorus were calculated using the following equation (Equation 1).

$$R_{dephosphorisation/Fe\ loss}\,(\%) = 1 - \frac{T_{Fe/P}}{C_{Fe/P}} * 100 \quad (1)$$

Where:

- $C_{Fe/P}$ denotes the content of Fe and P in the initial iron ore sample used in this study.
- $T_{Fe/P}$ represents the content of Fe and P in the solid residue from the alkaline roasting and water washing.

RESULTS AND DISCUSSION

High-phosphorus iron ore sample characterisation

The chemical compositions of high-phosphorus iron ore samples with various particle size distributions are summarised in Table 1. The impurity components, namely phosphorus (P), silica (Si), alumina (Al), and sulfur (S) in the iron ore, range between 0.224–0.258 mass % for P, 9.18–10.9 mass % for SiO_2+Al_2O_3, and about 0.01 mass % for S, respectively (Table 1).

TABLE 1

Chemical constituents of the iron ore sample with various size distributions, mass %.

Particle size, (μm)	Fe, (total)	P	SiO_2	Al_2O_3	S
-500+250	63.24	0.230	4.48	4.84	0.009
-250+125 (head sample)	63.40	0.240	4.53	4.87	0.009
-125+90	62.55	0.224	4.34	4.84	0.007
-90+45	63.84	0.256	5.28	5.70	0.007
-45+38	63.62	0.258	5.11	5.55	0.008

The content of iron (Fe) in the iron ore is over 62.5 mass %, which is the iron content required from the ironmaking industries. The acceptable level of Fe, P, and the total amount of SiO_2 and Al_2O_3 (SiO_2+Al_2O_3) from iron- and steel-making industries should be higher than 60 per cent for Fe, and as low as 0.07 per cent for P, less than 5 per cent for SiO_2+Al_2O_3, and below 0.08 per cent for S, respectively (Clout and Manuel, 2015). It implies that the phosphorus level in the iron ore is several times higher than its acceptable level, while the SiO_2+Al_2O_3 level is about two times higher. It can be referred to as high-phosphorus iron ore because of its higher phosphorus content.

Hematite (Fe_2O_3) and goethite (FeO(OH)) are the main minerals in the high-phosphorus iron ore, as shown in Figure 2. Other minerals that contain phosphorus and aluminium were not identified by XRD analysis because of the low detection limits of these elements in the sample.

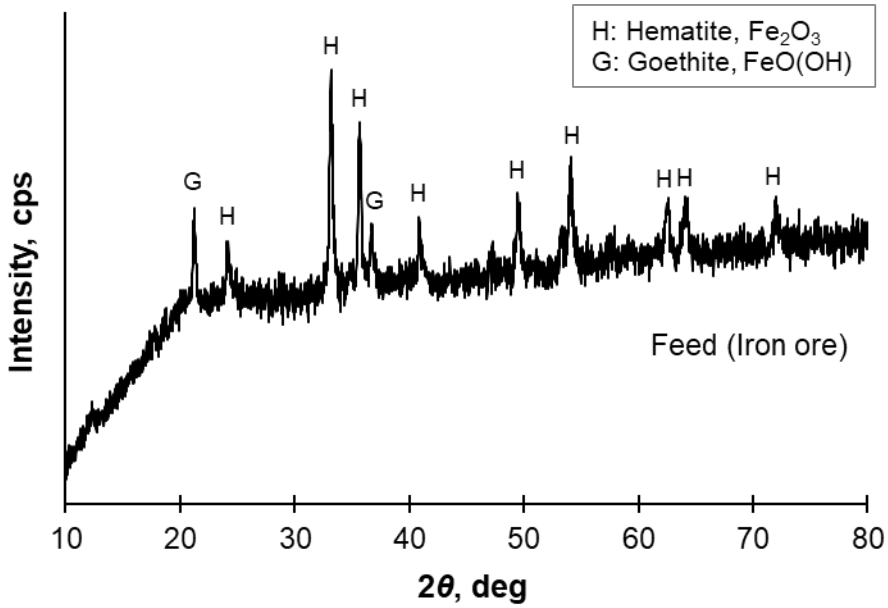

FIG 2 – XRD pattern of the high-phosphorus iron ore used in this study.

Alkaline roasting and water washing

The dephosphorisation of the high-phosphorus iron ore was investigated using alkaline roasting followed by a water washing route. The conditions determined for dephosphorisation of the iron ore through alkaline roasting and water washing were defined separately in the following sections.

Effect of NaOH concentration

Figure 3 shows a strong dependence of NaOH concentrations on the dephosphorisation of the high-phosphorus iron ore and iron loss through roasting at 300°C for 2 h.

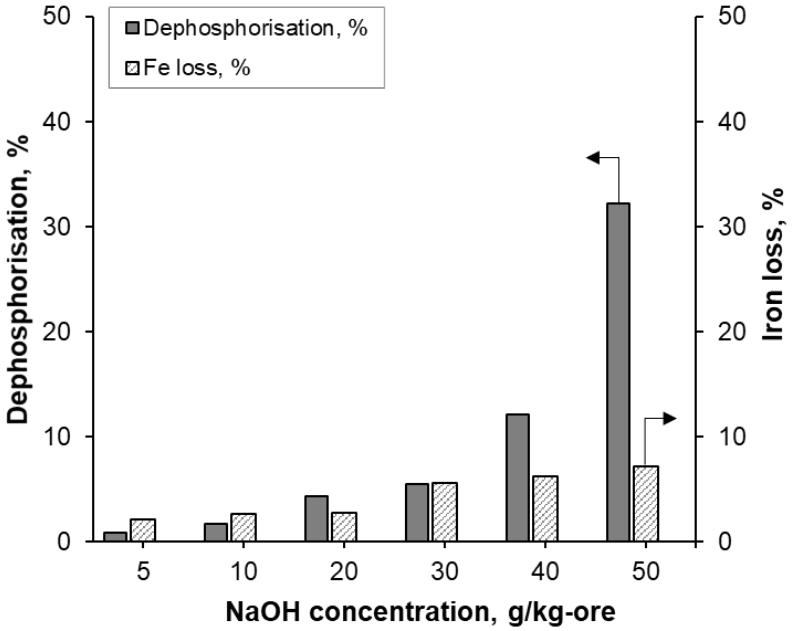

FIG 3 – Dependence of dephosphorisation and iron loss on NaOH concentration after heating at 300°C for 2 h.

Firstly, the dephosphorisation of the iron ore was increased from 1 per cent to 5.5 per cent with the increase in NaOH concentration from 5 g/kg-ore to 30 g/kg-ore and then increased drastically up to 32.2 per cent with further increases in NaOH concentration to 50 g/kg-ore. The iron loss increased in a straight line trend with the increase in the NaOH concentration. The minimum iron loss reached was 2.1 per cent with 5 g/kg-ore NaOH, while the maximum iron loss was 7.2 per cent with 50 g/kg-ore NaOH. It is unclear why the phosphorus removal rate and iron loss increase with an increase in NaOH concentration. It has been suggested that the appropriate amount of NaOH throughout the roasting process is crucial to removing phosphorus and controlling iron loss from the iron ore.

It is proposed that phosphorus-containing iron minerals (eg goethite) or phosphate minerals (eg apatite) in the iron ore may be converted to water-soluble compounds under high alkaline conditions. Some authors found that the phase transformation of goethite to hematite occurs at about 250°C (Liu H *et al,* 2013; Liu B *et al,* 2018).

Effect of roasting temperature

The dephosphorisation of the iron ore and iron loss associated with alkaline roasting temperature are presented in Figure 4. An increase in the roasting temperature from 100°C to 300°C in the presence of 50 g/kg-ore NaOH affects dephosphorisation which increases from 19.2 per cent to 32.2 per cent. Further increases in the roasting temperature to 500°C had no noticeable effect on the dephosphorisation of the iron ore. When the roasting temperature rises to 800°C, the highest dephosphorisation of 37.2 per cent was achieved. Moreover, the iron loss increases linearly from 4.2 to 7.2 per cent when the roasting temperature varies significantly from 100°C to 300°C under alkaline conditions, whereas there is no apparent change in the iron loss at 500°C. It can be seen that the iron loss decreased from 7.4 per cent to 4.3 per cent when the roasting temperature reached 800°C (Figure 4). Lowering the iron loss at the highest temperature (800°C) could correspond to a complete reduction of iron minerals.

It could be noted that the dephosphorisation of the iron ore is varied by temperature significantly of ≤ 100°C and ≥ 800°C, respectively, while no apparent variations at the temperatures between 300°C and 500°C. The roasting temperature of 300°C was selected for further studies due to economic reasons for high-temperature processing, which increases the energy consumption and other operating costs.

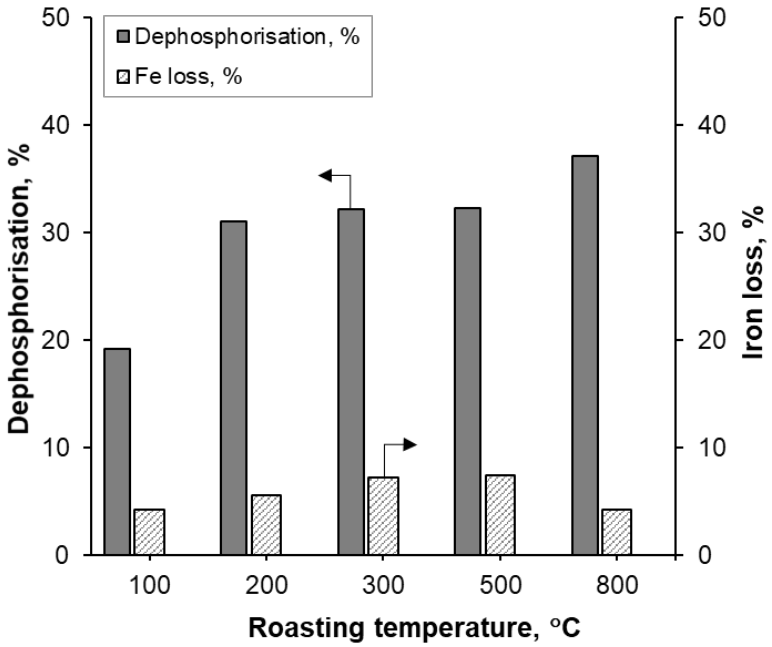

FIG 4 – Dependence of dephosphorisation and iron loss on roasting temperature (100–800°C) (NaOH concentration: 50 g/kg-ore, particle size: -250 µm, roasting time: 2 h).

Effect of roasting time

As shown in Figure 5, dephosphorisation and iron loss levels were varied depending on prolonged roasting times (0–2 h) under alkaline conditions (50 g/kg-NaOH) at 300°C. The prolonged roasting time was estimated after reaching the target temperature (300°C). The results show that when the roasting time extends from 0–2 hours, the dephosphorisation reduces from 39.2 per cent to 32.2 per cent.

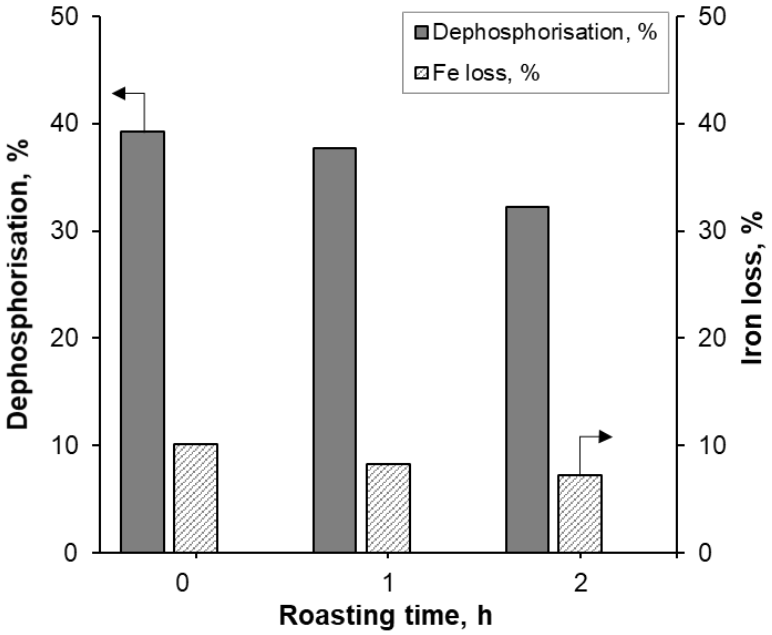

FIG 5 – Dependence of dephosphorisation and iron loss on roasting time (0–2 h), (NaOH concentration: 50 g/kg-ore, particle size: -250 µm, roasting temperature: 300°C).

Similarly, the iron loss at different roasting times decreases from 10.1 per cent to 7.2 per cent. It implies that the short roasting time has been beneficial for improving the dephosphorisation but detrimental to the iron loss compared to the extended roasting time (2 h). Except for the highest level of dephosphorisation, the lower iron loss is a crucial parameter for selecting applicable conditions for iron ore processing. At two hours of roasting, the dephosphorisation and the iron loss were

32.2 per cent and 7.2 per cent, respectively. Therefore, the prolonged roasting time of 2 h is selected as an optimal condition for further studies. These differences in the dephosphorisation and iron loss with roasting time could be related to the reaction behaviour of iron ore minerals with NaOH under the roasting temperature (300°C).

Effect of particle size distribution

The dephosphorisation and iron loss of the high-phosphorus iron ore with various particle size distributions throughout alkaline roasting followed by water washing are presented in Figure 6.

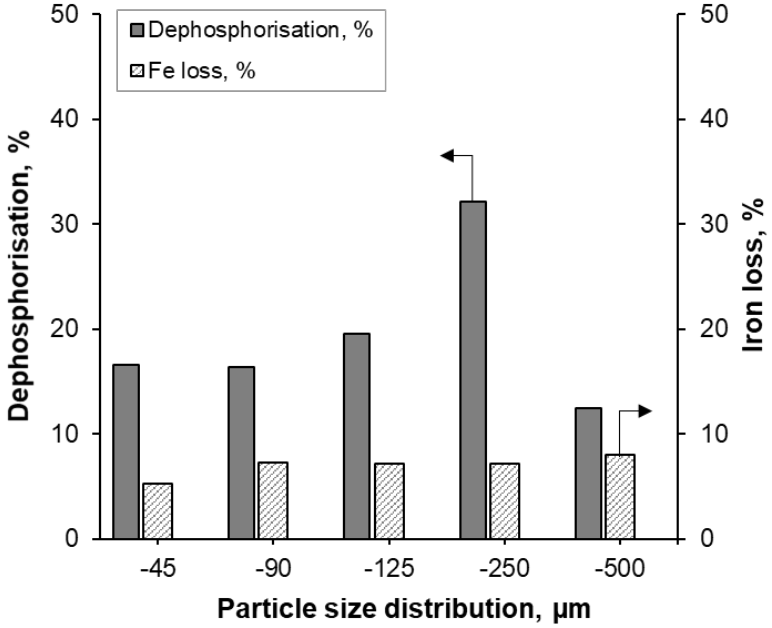

FIG 6 – Dependence of dephosphorisation and iron loss on the particle size distribution (-45 ~ -500 µm) (NaOH concentration: 50 g/kg-ore, roasting temperature: 300°C, roasting time: 2 h).

As can be seen in Figure 6, the level of dephosphorisation of the fine iron ore particles (-45 µm and -90 µm) was almost the same and increased from 16.4 per cent to 32.2 per cent with increasing the particle size from -90 µm to -250 µm. However, dephosphorisation is reduced in coarse iron ore particles and reaches 12.4 per cent as the particle size increases to -500 µm. Under the same conditions, the iron loss ranges between 5.3 per cent and 8 per cent. Notably, the iron loss is 5.3 per cent in the fine iron ore particles (-45 µm) throughout the alkaline roasting and water washing process. In comparison, about 7.2 per cent iron loss has occurred in a -90, -125 and -250 µm particle size interval, respectively. The iron loss is slightly higher as 8 per cent in the coarse iron ore particles (-500 µm).

It is observed that the phosphorus removal from the iron ore is size-dependent, while the iron loss is not much size-dependent. This observation may be related to the contact surface of the iron ore particles with various size distributions through the alkaline roasting followed by water washing.

Water washing

The ground iron ore sample from the alkaline roasting in a muffle furnace at the selected conditions (50 g/kg-ore NaOH, 300°C, 2 h) was washed with distilled water at different times (30 s – 60 min) and varying pulp densities (30–1000 g/L) at ambient temperature. The findings from the experiments mentioned above are discussed in the following session.

Effect of time

The levels of dephosphorisation and iron loss during the alkaline roasting followed by water washing at different times and an ambient temperature (20°C) are plotted in Figure 7. It can be seen that the levels of dephosphorisation are 32.2 per cent and 35.4 per cent during the water washing of the alkaline roasted samples for 30 s and 60 min, while the iron losses are 7.2 per cent and 7.0 per cent,

respectively. It indicates no significant differences in the dephosphorisation and iron losses between the short-term and long-term washing periods, such as 30 s and 60 min.

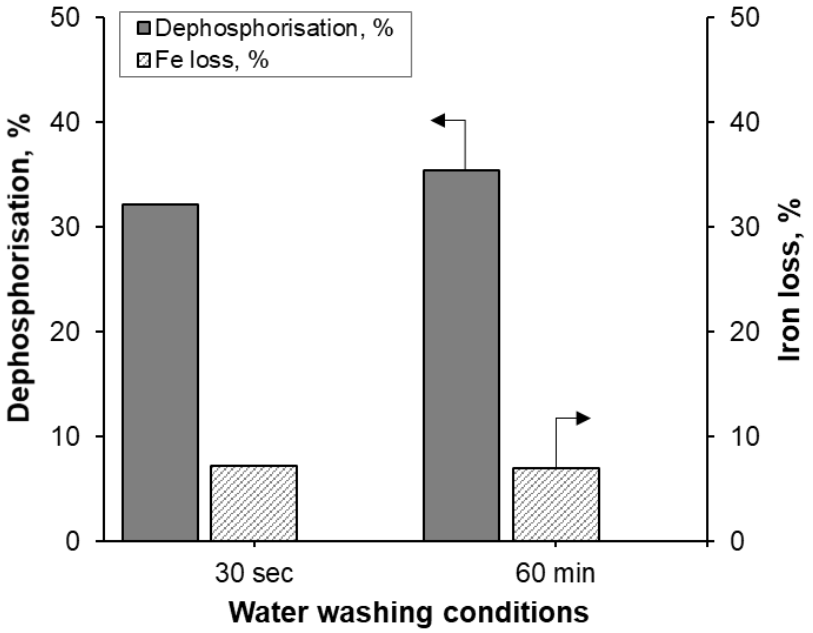

FIG 7 – Dependence of dephosphorisation and iron loss on washing time (30 s and 60 min), (Roasted conditions: 50 g/kg-ore NaOH, 300°C, 2 h; Washing conditions: H_2O, 100 g/L pulp density, 20°C).

This finding may be attributed to faster leaching kinetics of unstable phosphorus and iron species from the alkaline roasted iron ore. The shorter water washing time of 30 s is the best condition because of its economic efficiency.

Effect of pulp density

Figure 8 shows the influence of pulp density on the dephosphorisation and iron loss of the iron ore during the water washing after roasting. The pulp density effectively influences the phosphorus removal from the iron ore. Because the dephosphorisation is increased from 24.3 per cent to 40.6 per cent, increasing the pulp density from 30 to 400 g/L. However, a further increase in the pulp density to 1000 g/L reduces the phosphorus removal rate to 32.9 per cent. The maximum dephosphorisation of 40.6 per cent is achieved at a pulp density of 400 g/L, whereas the minimum dephosphorisation of 24.3 per cent at a 30 g/L pulp density. Results suggest that the dephosphorisation is efficient at slurry densities between 300 and 500 g/L (30–50 per cent solids). However, it is inefficient at lower (below 300 g/L) and higher pulp densities (above 500 g/L) depending on the mass transport phenomena in the water washing system. Generally, iron losses are slightly higher at low slurry density intervals between 30 g/L and 100 g/L than those at slurry densities above 100 g/L.

Whereas iron loss decreases with the pulp density increase, resulting in 5.9–7.3 per cent iron loss. The minimum iron loss was reached 5.9 per cent at a pulp density of 300 g/L, accompanied by 39.6 per cent phosphorus removal. It implies that the difference in the dephosphorisation rates and iron losses through the varying water washing conditions could be related to the specific gravity of solids and slurry viscosity caused by iron – and phosphorus-containing minerals.

Fisher-White *et al* (2013) reported that the phosphorus content of Australian goethite-hematite ores (Brockman ores) containing 0.146 per cent and 0.136 per cent P was reduced to 0.079 per cent and 0.095 per cent indicating phosphorus removal rates of 46.9 per cent and 35.2 per cent under the heating of 300°C followed by leaching with 20 per cent NaOH and a pulp density of 25 per cent at the balance point temperature (BPT) and 80°C, respectively.

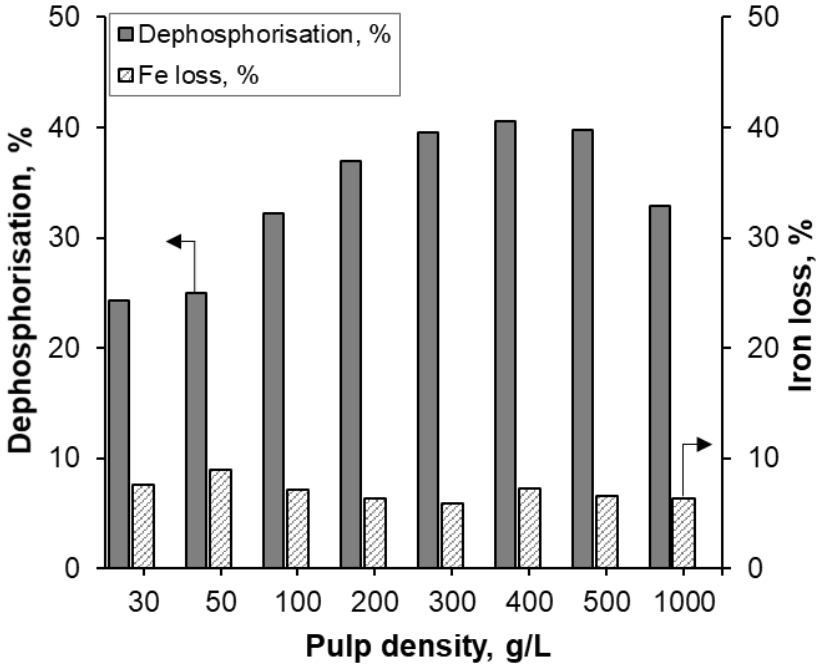

FIG 8 – Dependence of dephosphorisation and iron loss on the pulp density (30–1000 g/L), (Roasted conditions: 50 g/kg-ore NaOH, 300°C, 2 h; Washing conditions: H_2O, washing time: 30 s, 20°C).

As a result, the iron product that contains 59.5 mass % Fe and 0.145 mass % P could obtain from the high-phosphorus iron ore using a combined route consisting of alkaline roasting followed by water washing. The further challenging tasks in developing this proposed process are reducing iron loss and improving the phosphorus removal rate to produce a clean iron product containing over 60 per cent Fe and below 0.1 per cent P.

Mineral composition of the products

XRD patterns of iron ore samples before and after alkaline roasting and water washing are compared in Figure 9. The comparison of XRD patterns of the samples revealed the disappearance of diffraction peaks corresponding to the goethite from the iron ore sample after alkaline roasting at 300°C for 2 h. In contrast, the new diffraction peaks related to hydroxylsodalite as sodium aluminosilicate hydrate had appeared in samples after roasting and water washing (Figure 9). It can be seen that the mineral characterisation of the residue from water washing is almost similar to the roasted sample with NaOH in the roasting conditions. The result indicates that hematite is the major mineral phase in the final products from alkaline roasting and water washing processes.

The SEM-EDS analysis identified the variations in the morphology and compositional differences in impurity elements such as P in the initial iron ore sample, roasted sample, and residue, as shown in Figure 10.

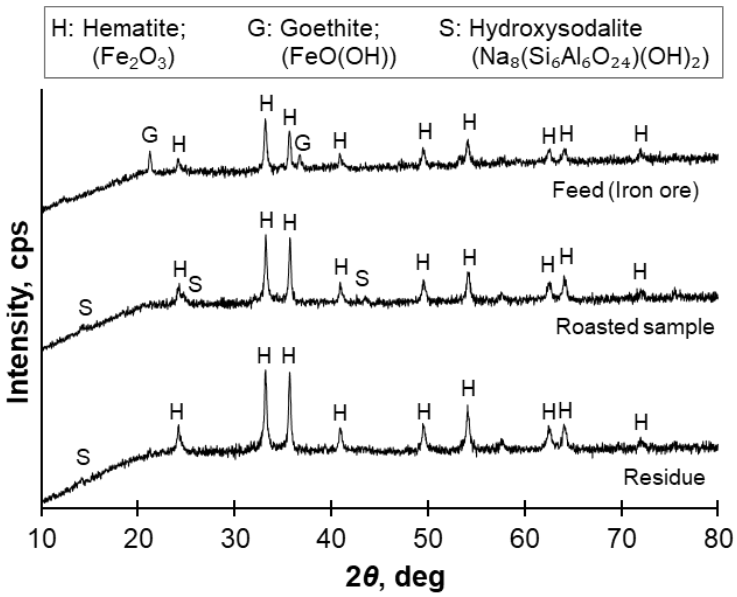

FIG 9 – XRD patterns of initial iron ore sample, roasted sample and residue from water washing, respectively (Roasting conditions: 50 g/kg-ore NaOH, 300°C, 2 h; Washing: H_2O, 100 g/L pulp density, 30 s, 20°C).

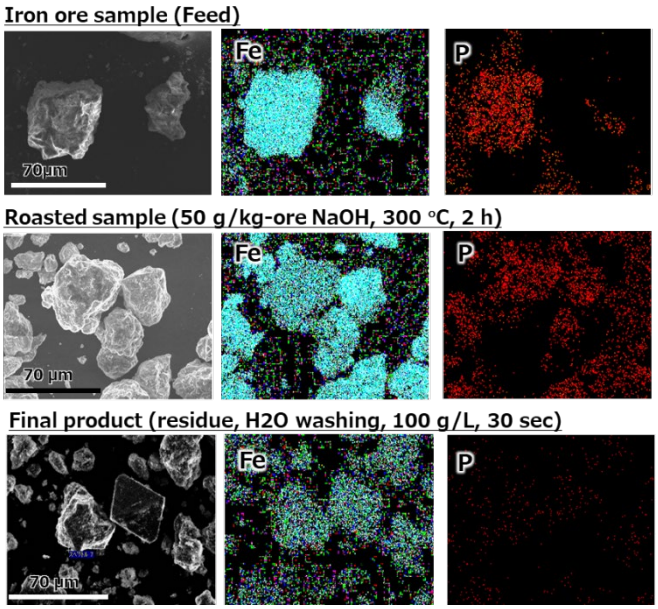

FIG 10 – SEM-EDS images of the iron ore samples: (A) initial iron ore sample; (B) roasted sample (50 g/kg-ore NaOH at 300°C for 2 h); (C) residue from water washing (pulp density of 100 g/L for 30 sec at 20°C).

CONCLUSIONS

The dephosphorisation of high-phosphorus iron ore was investigated using alkaline roasting followed by the water washing route throughout this study. Effects of various processing parameters in the roasting and water washing were examined to optimise the phosphorus removal from the iron ore.

Results showed that influential variables for achieving a higher dephosphorisation rate are NaOH concentration, temperature and duration through the roasting process, while pulp density in water washing. The phosphorus removal rate of the iron ore was increased with increased NaOH concentration and temperature through the roasting process and with pulp density in water washing. The maximum dephosphorisation of about 40 per cent was achieved from the high-phosphorus iron ore using the combined route of alkaline roasting and water washing under optimised conditions when the minimum iron loss was less than 6 per cent. The final iron product from the sequential processing contained 59.5 mass % Fe and 0.142 mass % P. It suggests that the dephosphorisation

of the iron ore could correspond to the phase transition of goethite to hematite or the decomposition of iron ore minerals containing phosphorus under alkaline roasting conditions.

ACKNOWLEDGEMENTS

This study was supported by the NEDO project (№19101845–0). The authors would like to acknowledge the Nippon Steel Corporation in Japan for providing iron ore samples and technical assistance in sample analysis and collaborative research.

REFERENCES

Baawuah, E, Kelsey, C, Addai-Mensah, J and Skinner, W, 2020. Economic and socio-environmental benefits of dry beneficiation of magnetite ores, *Minerals,* 10:955. doi:10.3390/min10110955.

Bao, Q, Guo, L and Guo, Z, 2021. A novel direct reduction-flash smelting separation process of treating high phosphorous iron ore fines, *Powder Technology*, 377:149–162. doi:10.1016/j.powtec.2020.08.066.

Clout, J M F and Manuel, J R, 2015. Mineralogical, chemical and physical characteristics of iron ore, in *Iron ore Mineralogy, Processing and Environmental Sustainability* (ed: Liming Lu), pp 45–84 (Woodhead Publishing, Elsevier Ltd).

Delvasto, P, Valverde, A, Ballester, A, Muñoz, J A, González, F, Blázquez, M L, Igual, J M, García-Balboa, C, 2008. Diversity and activity of phosphate bioleaching bacteria from a high-phosphorus iron ore, *Hydrometallurgy*, 92:124–129. doi:10.1016/j.hydromet.2008.02.007.

Fisher-White, M J, Lovel, R R, Sparrow, G J, 2013. Washington, B.M., Effect of temperature on removal of phosphorus from Australian goethitic iron ores, in *Iron ore 2013*. pp 373–380 (The Australasian Institute of Mining and Metallurgy: Melbourne).

Gooden, J E A, Walker, W M, Allen, R J, 1974. AMDEPHOS–A chemical process for dephosphorisation of iron ore, in *Proceedings of National Chemical Engineering Conference*, Queensland. pp 21–33.

Liu, B, Zhang, S, Chang, C, Volinsky, A A, 2018. Preparation and formation mechanism of monodisperse micaceous iron oxide from iron chromium grinding waste, *Powder Technology*, 329:401–408. doi:10.1016/j.powtec.2018.01.085.

Liu, H, Chen, T, Zou, X, Qing, C and Frost, R L, 2013. Thermal treatment of natural goethite: Thermal transformation and physical properties, *Thermochimica Acta*, 568:115–121. doi:10.1016/j.tca.2013.06.027.

Löf, A, Ericsson, M, Löf, O, 2019. Iron ore market review 2018, *CIS Iron and Steel Review*, 17:4–9. doi:10.17580/cisisr.2019.01.01.

Mochizuki, Y and Tsubouchi, N, 2019a. Removal of gangue components from low-grade iron ore by hydrothermal treatment, *Hydrometallurgy*, 190:105159. doi:10.1016/j.hydromet.2019.105159.

Mochizuki, Y and Tsubouchi, N, 2019b. Upgrading low-grade iron ore through gangue removal by a combined alkali roasting and hydrothermal treatment, *ACS Omega,* 4:19723–19734. doi:10.1021/acsomega.9b02480.

Ofoegbu, S U, 2019. Technological challenges of phosphorus removal in high-phosphorus ores: Sustainability implications and possibilities for greener ore processing, *Sustainability*, 11:6787. doi:10.3390/su11236787.

Park, T J, Kim, B C and Sohn, I, 2021. Effect of bonding area formation during sintering on the reaction characteristics of iron ores, *Steel Research Int*, 92:2100206. doi:10.1002/srin.202100206.

Pereira, A C and Papini, R M, 2015. Processes for phosphorus removal from iron ore – a review, *REM: R. Esc. Minas. Ouro Preto*, 68(3):331–335. doi:10.1590/0370–44672014680202.

Pownceby, M I, Hapugoda, S, Manuel, J, Webster, N A S, MacRae, C M, 2019. Characterisation of phosphorus and other impurities in goethite-rich iron ores – Possible P incorporation mechanisms, *Minerals Engineering*, 143:106022. doi:10.1016/j.mineng.2019.106022.

Roy, S K, Nayak, D, Rath, S S, 2020. A review on the enrichment of iron values of low-grade iron ore resources using reduction roasting-magnetic separation, *Powder Technology,* 367:796–808. doi:10.1016/j.powtec.2020.04.047.

Sanchez-Segado, S, Makanyire, T, Escudero-Castejon, L, Hara, Y and Jha, A, 2015. Reclamation of reactive metal oxides from complex minerals using alkali roasting and leaching – an improved approach to process engineering, *Green Chem*, 17: 2059–2080. doi:10.1039/C4GC02360A.

Xiao, J and Zhou, L, 2019. Increasing iron and reducing phosphorus grades of magnetic-roasted high-phosphorus oolitic iron ore by low-intensity magnetic separation–reverse flotation, *Processes*, 7:388. doi:10.3390/pr7060388.

Yu, J, Guo, Z and Tang, H, 2013. Dephosphorization treatment of high phosphorus oolitic iron ore by hydrometallurgical process and leaching kinetics, *ISIJ International*, 53(12):2056–2064. doi:10.2355/isijinternational.53.2056.

Zhang, L, Machiela, R, Das, P, Zhang, M, Eisele, T, 2019. Dephosphorization of unroasted oolitic ores through alkaline leaching at low temperature, *Hydrometallurgy*, 184:95–102. doi:10.1016/j.hydromet.2018.12.023.

Zhu, D, Guo, Zh, Pan, J and Zhang, F, 2016. Synchronous upgrading iron and phosphorus removal from high phosphorus oolitic hematite ore by high temperature flash reduction. *Metals. 6*(6):123. DOI: 10.3390/met6060123.

Integration of real-time, online, individual cyclone measurement at Cerro Verde – challenges and lessons learned

A Castillo[1], L Panduro Robles[2] and K Wiese[3]

1. Global Sales and Marketing, CiDRA Minerals Processing Inc, Wallingford CT 06042, USA. Email: acastillo@cidra.com,
2. Director Business Development Peru, SIMM S.A.C. Lima. Email: Peru.lpanduro@cidra.com
3. Metallurgy Superintendent, C2 Concentrator, Sociedad Minera Cerro Verde, Freeport McMoRan, Arequipa, Perú. Email: kwiese@fmi.com

ABSTRACT

For decades, organisations worldwide have been working to overcome challenges associated with new technology adoption while keeping up with rapid growth, development, and globalisation. In minerals processing, the challenges in developing and implementing solutions that contribute to the mining value chain are unique from other markets, as mining operations expect that world-class suppliers provide them solutions to gain a competitive advantage in their operation, production, performance as a financial asset, and as a long-term partner as we move into the future of mining. A simple shift in mindset is proven key to successful technology implementation. Change leaders must no longer think of their expertise in the area of application as their only responsibility; they must make a mental shift and see themselves in dual roles that strive to integrate the perspectives and needs of both developers and users. Successful change leaders must: (1) collaborate, seeking user involvement to ensure fit between product and operational needs, (2) demonstrate commitment to receive new technology, and (3) communicate to achieve an eventual shift of ownership from supplier to users that is seamless. Additionally, this strategy contributes to the mining value chain, as it allows developers and implementers to evaluate how change contributes to the asset's position both within the company and in the commodities market. This paper will explain the shift in perspective for new technology implementation in detail and provide recommendations that operations can emulate, using examples of real challenges and lessons learned during a commissioning of the CYCLONEtrac™ Particle Size Tracking (PST) system at Cerro Verde's C2 Concentrator. This concentrator has led technological change for plant optimisation, witnessed improved Net Metal Production (NMP), among other benefits with PST, the only technology in the market capable of providing real-time, online, and direct particle size measurement at the individual hydrocyclone level

INTRODUCTION

Hydrocyclone performance and particle size classification are crucial elements in the comminution process. The ability to measure particle size within individual cyclones is essential for grind circuit optimisation and for controlling product size sent downstream.

Current challenges

All cyclones within a cluster behave differently, yet until recently, operators were unable to measure the particle size from each individual cyclone. How can they ensure target size classification for optimal recovery? How is particle size variability controlled? In a macro economic environment where the demand for valuable mineral is outstripping the supply, how does a concentrator relax the grinding task, grind coarser, and increase throughput without violating the downstream process barrier? It is impossible to respond to industry challenges using conventional measurement technologies.

Innovative solutions

CiDRA's CYCLONEtrac™ Particle Size Measurement System (PST) with SMARTsensor™ technology is quickly becoming the industry standard for particle size measurement and is the only real time measurement system that directly measures and tracks particle size of individual cyclones every four seconds. The SMARTsensor is a waveguide that is inserted through the pipe wall on each overflow pipe. As the particles impact the waveguide, which is inserted in each hydrocyclone

overflow pipe, particles impinging on the wave guide create acoustic waves are generated, captured, and produce a frequency spectrum that is processed to determine particle size (Figure 1).

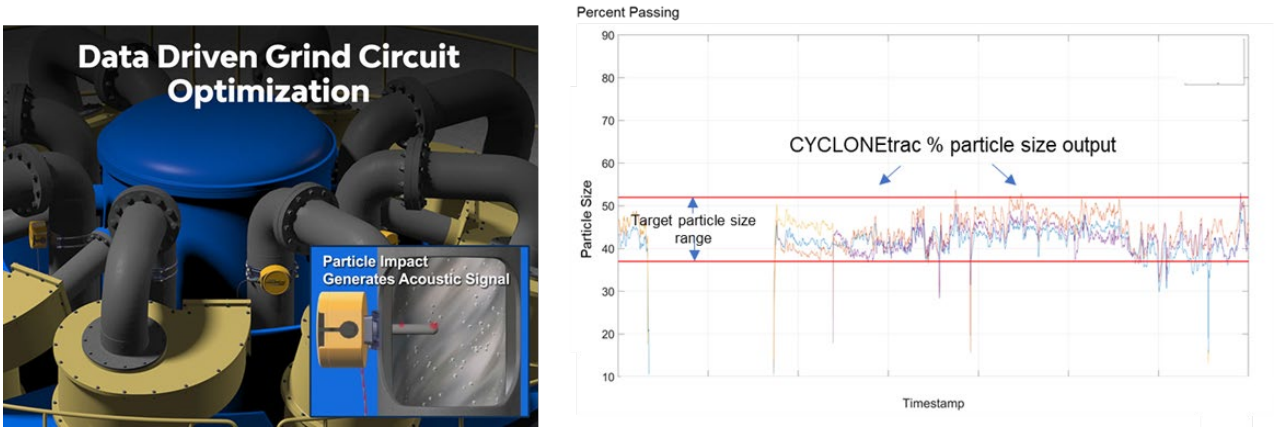

FIG 1 – Illustration of CYCLONEtrac Particle Size Measurement and Tracking System (PST) installed on a cluster of hydrocyclone overflow pipes together with a graph of five real time particle size measurements.

The paradigm shift

This unique technology allows minerals processing operations to make a step change from conventional particle size measurement analysers that take a periodic measurement from the *consolidated* overflow to a real-time measurement of *individua*l cyclones with the capability of providing up to five particle size measurements every four seconds. Operators can now make decisions that reduce particle size variability and achieve their target grind size (micro control strategy). CYCLONEtrac PST also enables a consolidated particle size measurement from all cyclones in the cluster to derive a P80 measurement for the control and optimisation of the grind circuit (macro control strategy).

The true shift in the paradigm is not achieved solely through implementing an innovative technology. The catalyst for the shift originates with internal 'change agents' with a shared vision and understanding how the new technology can bring increased and sustainable value to the enterprise. The change agents must also breakdown the barriers to adoption by working collaboratively with stakeholders. It's not just the challenge of having the organisation switch from one technology to another, the biggest challenges are changing the way we work (methods) and think about our jobs (culture).

CASE STUDY – CYCLONETRAC PST CHRONOLOGY AT CERRO VERDE MINING SOCIETY, PERU

2019

Cerro Verde identifies the CYCLONEtrac Particle Size Measurement and Tracking System (PST) as the technology for the optimisation at of its concentrators and the project begins.

2020

The PST technology was implemented on one cluster during the first quarter of the year and the CiDRA team together with Cerro Verde achieve all the quantifiable objectives established for the project. At the close of the project the Cerro Verde Project Management team and operations personnel shared their 'Lessons Learned' and in turn, the authors would like to share with our readers as it truly a handbook as to how to navigate and adapt to the application of a new technology. These thoughts are included at the end of this paper.

During the last quarter of 2020, using the data provided by the PST and the new knowledge provided, the next steps are analysed.

2021

During the first quarter, plant data was delivered to consultant Dr. Jaime Sepulveda for a Net Metal Production (NMP; Maron *et al*, 2019) study to evaluate the possibility of including his recommendations for an advanced, automated control strategy (see Table 1). The results follow:

- The data analysis confirms that by implementing the NMP strategy, the concentrator can expect results above concentrators of a similar size (benchmarking).
- The size of the flotation product (P80) significantly affects the yields of both the grinding stage and the flotation stage, so it is important to measure, and control said size around its ideal value that always maximises the NMP of the process, incorporating the real time PST real time particle size measurements to the corresponding Expert Control Strategy.
- The PST Technology, duly incorporated into the Expert Control System, also allows detecting and correcting the possible occurrence of total or partial blockages of the hydrocyclone discharges, thus avoiding harming the level of Recovery achievable in the subsequent Flotation stage.

TABLE 1

Net Metal Production benchmarking studies of concentrators in Peru and Chile performed by Dr. Jaime Sepulveda using actual plant data.

Benchmarking: Tonnage & Recovery vs. P80						
Operation	Average Capacity t/h	Product P80 µm	Capacity Increase %/10 µm	Recovery Reduction %/10 µm	NMP Increase %/10 µm	
Conc. A	2500	192	1.42	-0.60	0.81	⇗
Conc. B	2700	206	1.75	-1.00	0.73	⇗
Conc. C	7300	195	3.10	-0.26	2.83	⇗
Conc. D	2200	161	0.75	-0.16	0.59	⇗
Conc. E	2300	162	4.08	-1.53	2.49	⇗
Conc. F	1300	259	1.50	-0.92	0.57	⇗
Conc. G	6900	241	2.70	-1.18	1.49	⇗
Conc. H	4400	188	2.51	-0.62	1.87	⇗
Conc. I	6900	241	2.04	-0.19	1.85	⇗
Conc. J	4100	240	3.99	-0.48	3.49	⇗
Conc. K	2750	180	3.58	-1.31	2.22	⇗
Average			2.38	-0.69	1.67	⇗

2021

The results of the study and the expert's recommendations together with the performance of the CYCLONEtrac PST system are taken into account.

Cerro Verde lessons learned

Setting expectations for a new paradigm – challenges and opportunities

1. The site team should be encouraged to take inventory of current circuit physical constraints prior to implementing the PST System: flows, pressures, circulating loads, etc.

2. The entire execution team needs to challenge the operating paradigms and explore the entire range of operating conditions with ‘new eyes’ once the system is installed, with the mindset that new operating conditions may be found in previously ‘off limits’ territory.
    - Control system and operations understanding that they need to be there to back this up. The control room operator needs to be involved and know what to do if one cyclone is a bad actor during a stress test. (This is illustrated later in the appendix to this report).
3. Anticipate and reinforce at multiple stages that the PST shows you where opportunities are, but the site needs to take ownership to act on this information. Expect higher cyclone wear component replacement, call for cyclone changes, and that the follow up on process anomalies will be substantial. Ownership needs to come from all disciplines.
4. ‘The good news is that each individual cyclone’s performance can been seen. The bad news is that each individual cyclone´s performance can be seen.’ There is a wealth of new information that none of us have ever seen before regarding cyclone cluster operation. The challenge is to not allow this wealth of information to ‘vapor lock’ advancement on the project.
5. The key learning is the PST technology is powerful, but it is not ‘plug and play’. The stakeholder needs to roll up his sleeves to fully harness the benefits.
6. Expect much more than roping detection. If the client has been operating with minimal information on the ball mill product, prior supportive work should be done or revisited on optimal grind size (Bazin analysis, QEMSCAN lock/liberation profiles, tonnage/grind relationship analysis).

Concluding thought by Cerro Verde C2 Concentrator Metallurgy Supervisor ‘With the PST we are pushing more tonnage and producing more net valuable metal and that’s what counts.’

ACKNOWLEDGEMENTS

We would like to acknowledge and extend our sincere appreciation to the Cerro Verde Project and Management Teams together with the Operations, Instrumentation, Metallurgy and Process Engineers for their trust in CiDRA and its technology. We thank them their enduring commitment to the success of the program. A special thanks to Kyle Wiese who led the program with his talented team and for allowing us to share their ‘Lessons Learned’ thoughts and experiences in this paper.

REFERENCES

Maron, R, Sepulveda, J A, O’Keefe, C, Walqui, H, 2019. ‘Coarser Grinding: Economic Benefits and Enabling Technologies’, in *Proceedings of the MINEXCELLENCE 2019, 14th International Minerals Conference*, Santiago, Chile.

Sensors and automation – a unique opportunity to leverage real-time gold recovery data through data analysis and automation in gold processing

S Gray[1]

1. Technical Director, Gekko Systems, Mitchell Park VIC 3350. Email: sandyg@gekkos.com

ABSTRACT

Based on the 2021 Volume 5 *State of Play*™ mining survey of key executives and board members in the mining sector, the key responses to 'Which of the following technologies will have the biggest impact on mining in the next 15 years?', were 'Sensing and Data' followed by 'AI and Analytics'.

From the early 1970s it would have been unlikely to predict the level of sensing and automation introduced to the broad industrial sector. No better example is the automobile industry where the combination of technological advances and external drivers (such as emissions control) have driven an incredible rate of change.

The introduction of sensing, data, AI, and automation in the mining industry is just ramping up. Until now our energy efficiency, environmental footprint, labour shortage, skills, and safety have not been challenged by stakeholders in the way we are seeing market forces develop today. In order to address these challenges, we need to look back to the automobile industry and learn their lessons to accelerate our application of digital capability, analysis, AI and automation This is critical, particularly as access to skilled human resources becomes more difficult.

An example of how this can be achieved in a gold processing plant utilising the latest real-time sensing technologies is the 'Carbon Scout' developed by Curtin University, and OLGA developed by CSIRO, which are both online technologies, coupled together with Gekko's 'Neon' digital platform to achieve a fully automated real-time gold processing system.

Investigating industrial feasibility of utilising magnetising roasting for goethite ore

L Hosseini[1], R Hejazi[2], M Saghaeian[3], V Sheikhzadeh[4] and N Esmaeili[5]

1. Head of Metallurgy in R&D Department, Fakoor Sanat Tehran Company, Tehran Iran. Email: l.hosseini@fstco.com
2. Manager of R&D Department, Fakoor Sanat Tehran Company, Tehran Iran. Email: hejazi @fstco.com
3. Technical Vice Chairman, Fakoor Sanat Tehran Company, Tehran Iran. Email: saghaeian@fstco.com
4. Managing Director, Fakoor Sanat Tehran Company, Tehran Iran. Email: sheikhzadeh@fstco.com
5. Mineral Processing Expert, Fakoor Sanat Tehran Company, Tehran Iran. Email: n.esmaeili@fstco.com

ABSTRACT

Ore roasting has long been used for beneficiation and assay upgrading of different ores. In this process, which is mainly used for sulfide ores, the ore is heated to a high temperature. More specifically, it is a metallurgical process involving gas-solid reactions at elevated temperatures. Some types of Iron ore are weak in magnetic properties. Hematite, goethite and limonite are classified in this group. Unlike magnetite, which shows strong magnetic susceptibility, these ores are hard to beneficiate through magnetic separation route. Many researches have focused on gravity separation and flotation routes for upgrading these ores and these methods have also been utilised in the industry. One of the methods to whose industrial application less attention has been paid is magnetising roasting in which the non-magnetic iron ore is transformed to magnetite which is further beneficiated through magnetic separation. In this study, magnetising roasting tests have been performed on one goethite sample in order to check the feasibility of using this method for this specific ore in industrial scale. It is worth mentioning that high intensity magnetic separation have been performed on this sample before but the achieved results were not promising. Results have revealed that through magnetising roasting magnetite content of the ore could be increased from 1.7 per cent up to about 25 per cent. FeO content of the feed sample was increased from 1.03 per cent up to around 9.25 per cent. Also optimum size distribution for achieving the best results in magnetising roasting for this sample has been determined through this study. The best results were achieved when the ore size was 0–10 mm. The effect of coal ratio, time and temperature on the process have also be studied. A coal ratio of 5 per cent, time of 30 min and a temperature of 850°C were determined to be the optimum conditions. Finally, the technical feasibility of utilising magnetising roasting for this specific ore has been confirmed.

INTRODUCTION

In recent years, the rapid development of Iron and steel industry has led to a rapid decrease in high-grade magnetite iron ore deposits. Exhaustion and depletion of iron ore resources with strong magnetic properties has highlighted the importance of exploring methods for beneficiation and upgrading Fe content of iron ores with weak magnetic properties. As a result researchers have been looking into alternative resources of iron ore. Non-magnetic iron ores including hematite, goethite, limonite and siderite are usually hard to beneficiate as they lack strong magnetic properties. Therefore, alternative methods other than magnetic separation have to be used for upgrading the Fe content in these ores. Also, these ores often contain impurities and require some form of beneficiation in order to achieve the typical grades required for sale to downstream steel producers Nunna *et al* (2021). Magnetising roasting or reduction roasting followed by magnetic separation is an important method for the beneficiation of low-grade iron ores which are also weak in magnetic properties (Tang *et al*, 2019). Magnetising roasting is a process of converting a particle or substance from non/weak magnetic properties to high magnetic content at a critical temperature range of 500–900°C using a reducing agent considering the time duration. Below the critical temperature, conversion and reduction will be incomplete, but in the temperature above that, the formation of wustite which is paramagnetic will take place by fusion Ravisankar *et al* (2017).

Upgrading low-grade iron ores and tailings, often containing appreciable amounts of goethite, with magnetising roasting have been reported by many researchers. Yu *et al* (2017) demonstrated that through magnetising roasting followed by magnetic separation a high-grade concentrate containing 65.4 per cent iron can be achieved from an iron ore feed with Fe grade of 34.6 per cent. Nunna *et al* (2020) utilised magnetising roasting for recovering iron from an ore containing 57.0 wt per cent goethite and 31.1 wt per cent hematite.

As magnetising roasting has also been utilised for recovering iron bearing minerals from iron tailings as reported by Mitov *et al* (2021) and Yuan *et al* (2020b). Mitov *et al* (2021) showed that applying magnetising roasting followed by magnetic flocculation and magnetic separation on iron tailings results in an iron recovery of 88.00 wt per cent. They showed that the Fe per cent of the feed sample will increase from 45.72 per cent to 59.98 per cent. Yuan *et al* (2021) applied magnetising roasting to iron tailings with iron grade of 24.27 per cent containing hematite and magnetite. They demonstrated that iron concentrate with total iron content of 65.01 per cent and recovery of 89.07 per cent could be obtained.

Li *et al* (2018) reported successful application of magnetising roasting technology to recover iron oxides from red mud (bauxite residue). They showed that a magnetic concentrate with a total iron grade of 57.65 per cent and recovery of 90.04 per cent could be obtained from a red mud containing 44.32 per cent Fe. The same application was also reported by Yuan *et al* (2020a) who showed that the hematite and goethite phases in the red mud could easily be reduced to magnetite. They demonstrated that an iron concentrate with a total iron grade of 55.54 per cent and iron recovery of 95.22 per cent could be achieved from a red mud containing 47.67 per cent Fe. Samouhos *et al* (2013) also reported that a magnetic concentrate with an iron grade of 35.15 and 69.3 wt per cent metallisation could be recovered from a Greek red mud with 43.19 per cent Fe_2O_3.

In the present study, magnetising roasting was used for testing the feasibility of applying this method to samples received from a non-magnetic iron mine in Iran. This was done because processing this ore using conventional beneficiation methods comprising of gravity separation in combination with high gradient magnetic separation resulted in weight recovery, Fe and FeO grades of 41.86 per cent, 60.7 per cent and 2.43 per cent, respectively which were not suitable and acceptable. The effect of feed size distribution, coal ratio, time and temperature have also been studied in this article.

MATERIALS AND METHODS

Feed specifications

Iron ore received from mine in Iran named Badiz was used for this study. Iron and iron oxide grades of the feed sample were analysed through titration method. Iron and iron oxide grades of the feed were 39.56 per cent and 1.47 per cent, respectively. Fe/FeO ratio of the feed was 26.92 which shows the non-magnetic nature of the feed. X-ray Fluorescence analysis, results of which are shown in Table 1, was done on the feed sample to check the compounds and impurities associated with the feed.

TABLE 1

Results of XRF analysis for the feed.

SiO_2 (%)	Al_2O_3 (%)	BaO (%)	CaO (%)	Fe_t (%)	K_2O (%)	MgO (%)	MnO (%)	Na_2O (%)	P_2O_5 (%)	SO_3 (%)	TiO_2 (%)	LOI (%)
20.23	1.19	<	5.90	39.74	1.07	5.10	0.18	0.06	0.07	0.05	<	9.39

The specific gravity of the feed sample was also measured using a water pycnometer. The results show that the specific gravity of the feed was 3680 kg/m^3. The apparent density of the feed sample was measured to be 1890 kg/m^3.

Magnetising roasting tests

Magnetising roasting tests were performed on the feed sample. Coal was used as the reducing agent in the roasting tests. A muffle furnace was used for performing the roasting tests.

The effect of feed particle size distribution, coal addition ratio, roasting time and roasting temperature on magnetising roasting process were studied. Conditions in which the tests were performed are as mentioned in the following section.

Studying the effect of particle size distribution

For studying the effect of particle size distribution, the feed sample was divided into four fractions of 0–1 m, 1–4 mm, 4–10 mm and 0–10 mm. Chemical analysis of these different size fractions is as shown in Table 2. Roasting tests were done in the muffle furnace with a coal ratio of 5 per cent. In all of these test the temperature was set to 850°C. The duration of the tests was also set as 30 min.

TABLE 2

Chemical analysis of feed different size fractions.

Size distribution (mm)	Fe (%)	FeO (%)	Fe_3O_4 (%)
0–1	36.19	1.18	1.6
1–4	42.65	1.01	1.9
4–10	39.41	0.92	1.7
0–10	39.83	1.03	1.8

Studying the effect of coal addition ratio

For studying the effect of coal addition ratio to the feed, the result of determining the best particle size distribution were studied and these tests were done in the optimum feed size distribution which was confirmed to be 0–10 mm in the previous stage of tests. Roasting tests were done at coal ratios of 1, 3, 5, 7 and 9 per cent. In all the tests the feed size distribution was set as 0–10 mm, roasting temperature was set as 850°C and the roasting time was set as 30 min.

Studying the effect of roasting temperature

For studying the effect of roasting temperature, roasting tests were done at roasting temperatures of 550, 650 and 750°C. According to the results achieved from the previous stage, in these tests coal ratio was set to be 5 per cent. Similarly the feed size distribution was 0–10 mm. In these tests roasting time was 30 min.

Studying the effect of roasting time

Effect of roasting time on roasting process was also studied. The roasting time was set to be 15, 20, 25 and 30 minutes. The temperature in this stage was set according to the results achieved from the previous tests and was set to be 850°C. According to the results achieved from the previous stage, in these tests coal ratio was set at 5 per cent. Similarly the feed size distribution was 0–10 mm.

Satmagan tests

For determining the magnetite content of the feed and product in each of the roasting tests, Satmagan device was utilised.

X-ray diffraction tests

X-ray diffraction (XRD) tests were done on the feed sample and the sample roasted in optimised conditions. These tests were done to determine and compare the mineral phases present in the feed sample and the roasted sample and to compare them to better understand the effect of roasting process on the mineral phases change.

Davis tube tests

Davis tube tests at a magnetic field of 3800 Gauss was used to check the magnetic performance of ore roasted in the optimum conditions determined in each set of roasting tests. These tests were performed in two particle size distributions of K_{80} ~ 106 μm and K_{80} ~ 63 μm.

RESULTS AND DISCUSSIONS

Roasting tests results

Effect of feed particle size distribution on roasting test results

Results of the magnetising roasting tests performed on different particle size fractions are as shown in Figure 1. It can be seen in the graph that dividing the feed sample to different size fractions doesn't result in any significant difference in the roasting results. Therefore, the original feed size fraction of 0–10 mm was chosen as the optimum feed size fraction.

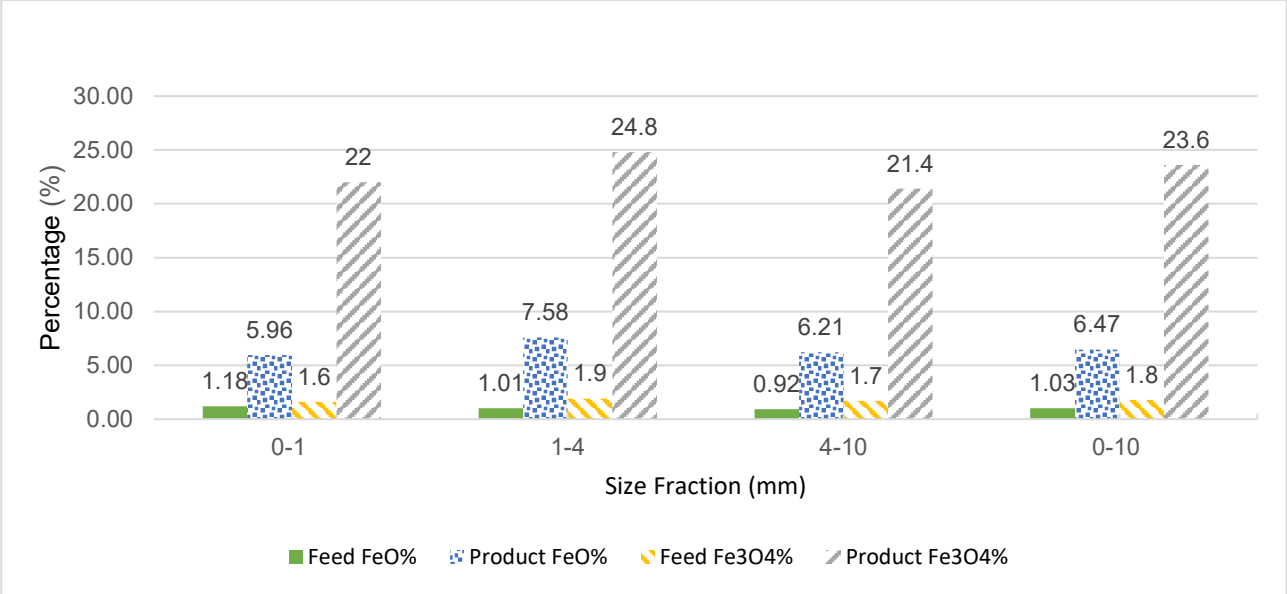

FIG 1 – Effect of feed particle size distribution on roasting product properties.

Effect of different coal ratios on roasting tests results

Results of varying the coal ratio are shown in Figure 2. These tests were performed on the optimum particle size fraction which is 0–10 mm and was determined in the previous stage of tests. As the graph in Figure 2 shows, as the coal ratio increases up to 5 per cent, FeO content and Fe_3O_4 content increase. This reveals that increasing the coal ratio up to 5 per cent results in an increase in magnetic susceptibility of the feed sample. The graph shows that further increasing the coal ratio to 7 per cent and 9 per cent doesn't result in any noticeable increase in the FeO and Fe_3O_4 contents. Hence, coal ratio of 5 per cent was chosen as the optimum coal ratio for performing further tests.

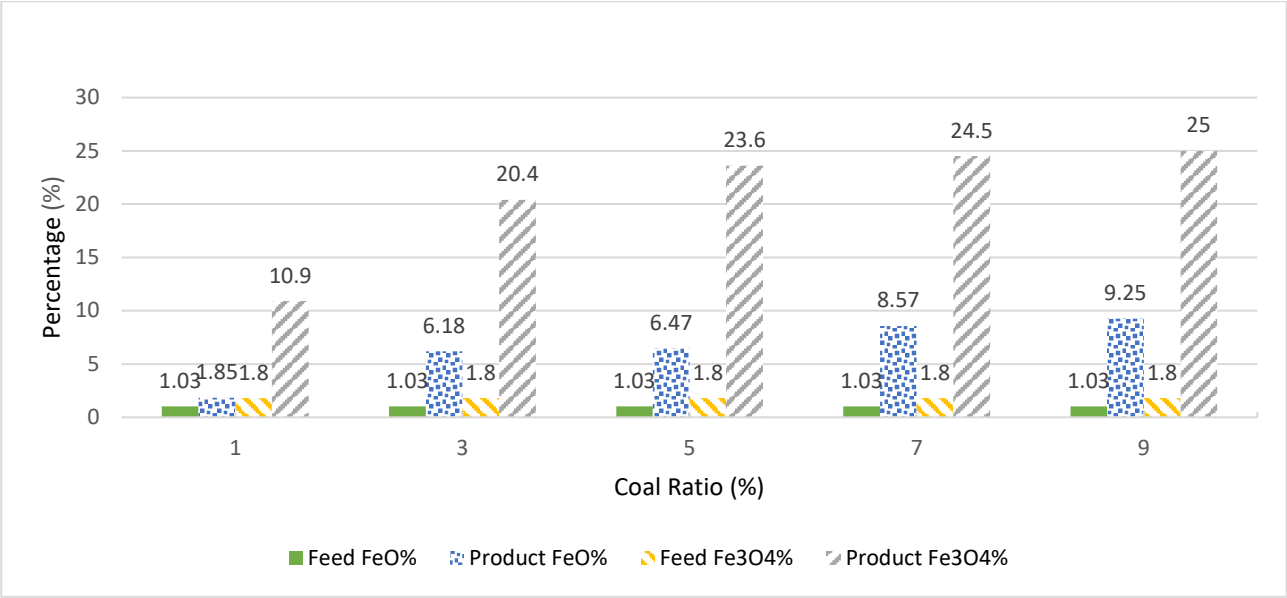

FIG 2 – Effect of coal ratio on roasting product properties.

Effect of roasting temperature on roasting tests results

Effect of roasting temperature on roasting product magnetic properties is as shown in Figure 3. As can be seen when the temperature is low and is 550°C, the roasting reactions do not take place. FeO content only increases ~0.8 per cent which is negligible. Fe_3O_4 content of the product is so low that is not detectable using Satmagan equipment. As the roasting temperature increases, the FeO and Fe_3O_4 contents of the product increase. It shows that at higher temperatures roasting reactions take place more easily and more quickly. Further increasing the temperature results in roasting reactions to proceed reversely. So the temperature of 850°C was chosen as the optimum roasting temperature.

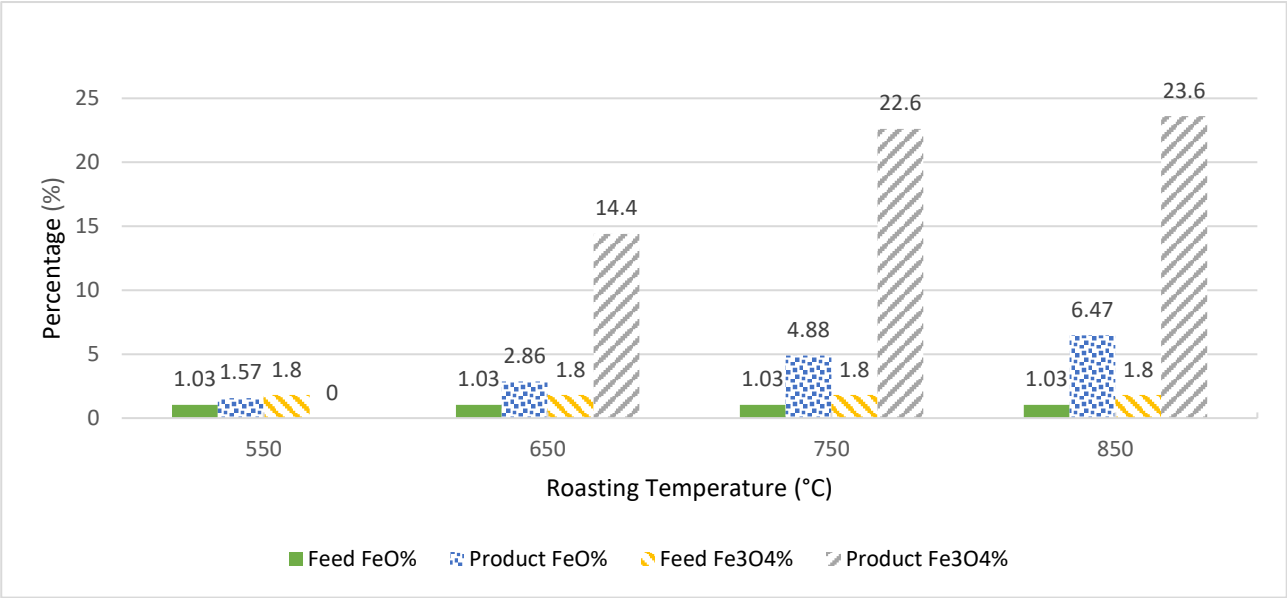

FIG 3 – Effect of roasting temperature on roasting product properties.

Effect of roasting temperature on roasting tests results

Effect of roasting time on roasting product magnetic properties is as shown in Figure 4. From the results we can see that increasing the roasting temperature from 15 min to 30 min has no significant effect on the FeO and Fe_3O_4 contents of the product.

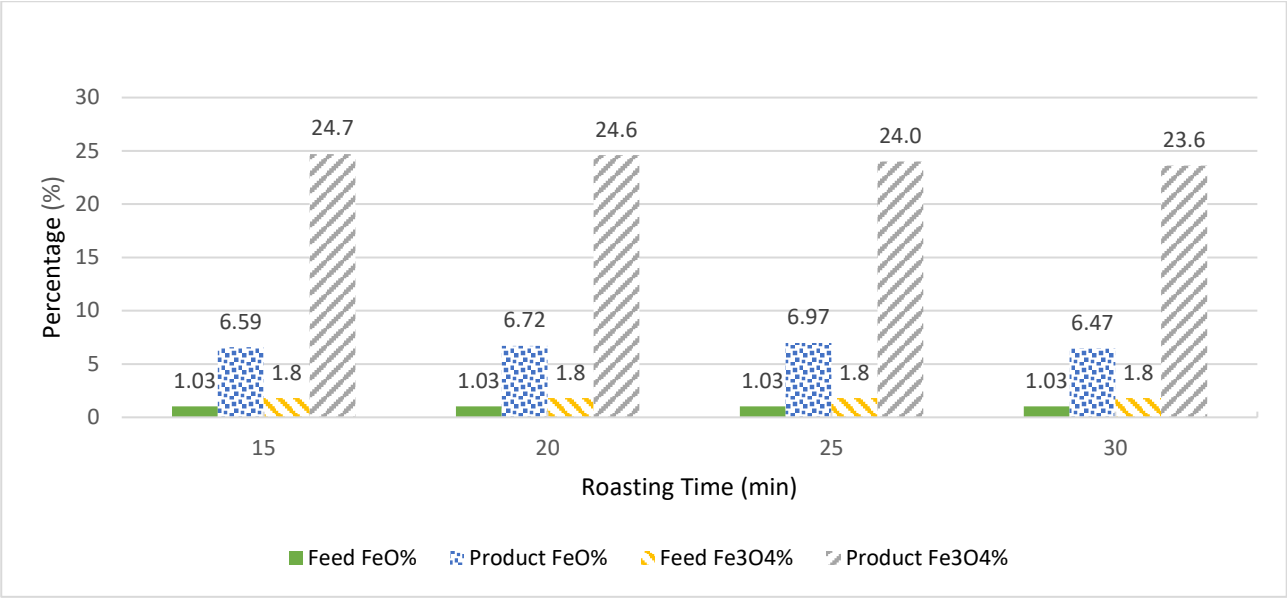

FIG 4 – Effect of roasting time on roasting product properties.

For further studying the effect of time on roasting reactions and the reactions accompanied with it, Fe content of the feed and product of the roasting tests were also measured. Table 3 illustrates the results of analysing the Fe contents of roasting feed and products.

TABLE 3

Fe content of roasting feed and product in different roasting times.

Roasting Time	Feed Fe (%)	Product Fe (%)
15	39.83	40.95
20	39.83	40.91
25	39.83	40.93
30	39.83	41.51

From the figures tabulated in Table 3 it can be seen that in all roasting times, iron content of the product increases compared with the iron content in the feed sample. We can also see that as the roasting time increases, iron in the product of the roasting process also increases. One of the reactions that take place when the temperature is elevated is evaporation of volatile materials called LOI (loss on ignition). This increase in Fe content is related to this LOI burn out. It can be seen from Table 3 that when the roasting time is short, this increase is almost negligible. As the roasting time increases, increase in Fe content also goes up. Therefore, it can be concluded that when the roasting time is short, time duration is not enough for complete LOI burnout. So, the roasting time of 30 min in which the maximum LOI burnout has taken place was chosen as the optimised roasting time.

X-ray diffraction test results

Results of XRD test performed on feed sample and the sample roasted in optimised conditions are as shown in Figure 5.

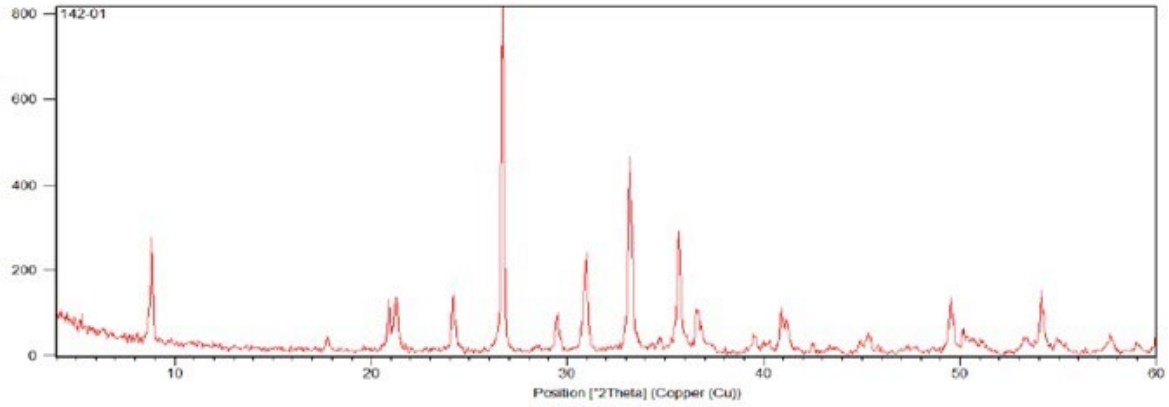

Sample	Phase(s)	Phase(s)
00-142-01	Quartz (33-1161) = 17%	Hematite (33-0664) = 41%
LAB: 142-01	SiO2	Fe2O3
Date :	Calcite (05-0586) = 5%	Goethite (29-0713) = 16%
4.2.2022	CaCO3	FeO(OH)
kV = 40	Dolomite (36-0426) = 12%	*Note: FeO Check*
mA = 30	CaMg(CO3)2	
Ka. = Cu	Mica - illite (26-0911) = 7%	
Fil. = Ni	K(Mg,Fe)3(Al,Fe)Si3O10(OH)2	

a. Feed sample

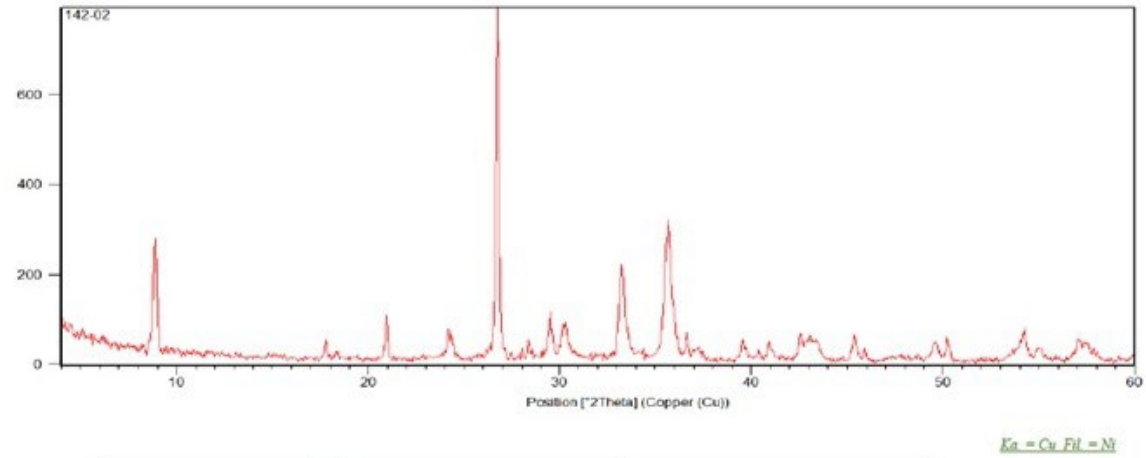

Sample	Phase(s)	Phase(s)
00-142-02	Quartz (33-1161) = 18%	Magnetite (19-0629) = 24%
LAB: 142-02	SiO2	FeFe2O4
Date :	Calcite (05-0586) = 9%	*Note: FeO Check*
4.2.2022	CaCO3	
kV = 40	Hematite (33-0664) = 37%	
mA = 30	Fe2O3	
Ka. = Cu	Mica - illite (26-0911) = 10%	
Fil. = Ni	K(Mg,Fe)3(Al,Fe)Si3O10(OH)2	

b. Product sample

FIG 5 – XRD analysis of (a) feed sample, (b) product sample roasted in optimised conditions.

Results of the XRD analysis show that Fe present in the feed sample is in the form of hematite (41 per cent) and goethite (16 per cent). It can be seen that there is no Fe in the form of magnetite present in the unroasted sample. Studying the XRD analysis of the roasted sample it can be seen that that the percentage of hematite has decreased slightly but goethite has been eliminated completely. Magnetite has been formed though the roasting process and its percentage in the roasting sample equals to 24 per cent. This shows that all the goethite and some part of the hematite present in the feed sample have been converted to magnetite.

Davis tube test results

Davis tube tests were performed on the product of the roasting test performed in optimum conditions which are particle size distribution of 0–10 mm, coal ratio of 5 per cent, roasting temperature of 850°C and roasting time of 30 min. Results of the Davis tube tests are as shown below.

Davis tube test results at K_{80} ~ 106 μm

- Concentrate: Fe= 60.12%, FeO= 9.28%, M-Wt= 60.33%, $Fe_{rec.}$= 88.04%
- Tailing: Fe= 12.42%, FeO= 3.19%, M-Wt= 39.67%, $Fe_{rec.}$= 11.96%

Davis tube test results at K_{80} ~ 63 μm

- Concentrate: Fe= 61.17%, FeO= 9.88%, M-Wt= 57.43%, $Fe_{rec.}$= 85.86%
- Tailing: Fe= 13.59%, FeO= 2.54%, M-Wt= 42.57%, $Fe_{rec.}$= 14.14%

From the results we can see that in both particle size distributions, Fe content of the magnetic product is more than 60 per cent and it can be predicted that in case the field intensity and particle size distribution be reduced, higher Fe grades in the product can be achieved.

CONCLUSIONS

Performance of magnetising roasting process in a laboratory muffle furnace with coal as the reducing agent was studied for a non-magnetic sample received from a mine in Iran. Effects of roasting conditions on different properties of the roasting product have been detailed. Optimum conditions for reduction roasting in laboratory scale were determined which can be used as the basis for pilot scale tests.

The feed sample contained 39.56 per cent and 1.47 per cent of iron and iron oxide, respectively. The results of studying the effect of different particle size distributions on roasted product properties showed that particle size distribution has no notable effect on the quality of the roasted product. As a result particle size distribution of 0–10 mm was chosen as the optimum size distribution for the roasting tests.

Studying the effect of different coal ratios on roasting product properties showed that increasing the coal ratio up to 5 per cent results in an increases the FeO content in the product sample. This shows that coal addition up to 5 per cent helps to promote the magnetic nature of the product sample. It was also seen that increasing the coal ratio to 7 per cent and 9 per cent doesn't result in any noticeable increase in the FeO and Fe_3O_4 contents. Therefore, coal ratio of 5 per cent was chosen as the optimised coal addition ratio.

The results of investigating the effect of roasting temperatures indicated that increasing the roasting temperature leads to improved magnetic properties of the roasting products. Roasting temperature of 850°C was the highest temperature tested and was chosen as the optimised roasting temperature.

FeO and Fe_3O_4 content of the product roasted at different time durations demonstrated that these two contents are not that much dependable on the roasting time duration. But it was seen that when the roasting time is short, the volatile materials in the sample don't have sufficient time for evaporation. Therefore, when the roasting time duration was short, the Fe content of the roasting product was confirmed to be lower. That being the case, roasting time of 30 min was determined to be the optimum time duration for magnetising roasting of this specific sample.

XRD analysis was performed on the feed sample and the roasting product roasted in optimised conditions. It was observed that Fe present in the feed sample is mainly in the form of hematite and goethite with percentages of 41 per cent and 16 per cent, respectively. No Fe is in the form of magnetite in the unroasted sample. XRD analysis results of the roasted sample revealed that the percentage of Fe in the form of goethite has been eliminated completely. Magnetite has been formed through the roasting process and its percentage in the roasting sample equals to 24 per cent. This shows that all the goethite and some part of the hematite present in the feed sample have been converted to magnetite.

Davis tube magnetic tests were performed on the sample roasted in optimised conditions which are particle size distribution of 0–10 mm, coal ratio of 5 per cent, roasting temperature of 850°C and roasting time of 30 min. It was concluded that in both particle size distribution of the sample used as the feed for Davis tube tests, which were K_{80}s of 106 μm and 63 μm, Fe content of the magnetic product is higher than 60 per cent. It can be foreseen that if the field intensity and particle size distribution be reduced, higher Fe grades in the product can be achieved.

Thereby, it's concluded that magnetising roasting is a feasible and suitable process for this sample and the results achieved in this study can be used as the basis for semi-industrial tests needed for conceptual design of a roasting plant for this specific iron ore mine.

ACKNOWLEDGEMENTS

The authors would like to thank Fakoor Sanat Tehran Company (FSTCo.) and Fakoor Sanat Tehran Test and Research Centre (FSTRC) for their help and support during this study project.

REFERENCES

Li, Y, Yuan, S, Han, Y, Zhang, S and Gao, P, 2018. Laboratory study on magnetization reduction of CO, *Journal of Mining and Metallurgy B: Metallurgy*, 54(3), 393–399.

Mitov, I, Stoilova, A, Yordanov, B and Krastev, D, 2021. Technological research on converting iron ore tailings into a marketable product, *Journal of the Southern African Institute of Mining and Metallurgy*, 121(5), 181–186.

Nunna, V, Hapugoda, S, Eswarappa, S G, Raparla, S K, Pownceby, M and Sparrow, G, 2020. Evaluation of dry processing technologies for treating low grade lateritic iron ore fines, *Mineral Processing and Extractive Metallurgy Review*, 1–17.

Nunna, V, Hapugoda, S, Pownceby, M and Sparrow, G, 2021. Beneficiation of low-grade, goethite-rich iron ore using microwave-assisted magnetizing roasting, *Minerals Engineering*, 166, 106826.

Ravisankar, V, Venugopal, R and Bhat, H, 2019. Investigation on beneficiation of goethite-rich iron ores using reduction roasting followed by magnetic separation, *Mineral Processing and Extractive Metallurgy*, 128(3), 175–182.

Samouhos, M, Taxiarchou, M, Tsakiridis, P E and Potiriadis, K, 2013. Greek "red mud" residue: A study of microwave reductive roasting followed by magnetic separation for a metallic iron recovery process, *Journal of hazardous materials,* 254, 193–205.

Tang, Z D, Gao, P, Han, Y-X and Guo, W, 2019. Fluidized bed roasting technology in iron ores dressing in China: A review on equipment development and application prospect, *Journal of Mining and Metallurgy B: Metallurgy*, 55(3), 295–303.

Yu, J, Han, Y, Li, Y and Gao, P, 2017. Beneficiation of an iron ore fines by magnetization roasting and magnetic separation, *International Journal of Mineral Processing*, 168, 102–108.

Yuan, S, Liu, X, Gao, P and Han, Y, 2020a. A semi-industrial experiment of suspension magnetization roasting technology for separation of iron minerals from red mud, *Journal of Hazardous Materials*, 394, 122579.

Yuan, S, Zhang, Q, Yin, H and Li, Y, 2021. Efficient iron recovery from iron tailings using advanced suspension reduction technology: A study of reaction kinetics, phase transformation, and structure evolution, *Journal of Hazardous Materials*, 404, 124067.

Yuan, S, Zhou, W, Han, Y and Li, Y, 2020b. Efficient enrichment of iron concentrate from iron tailings via suspension magnetization roasting and magnetic separation, *Journal of Material Cycles and Waste Management*, 22(4), 1152–1162.

Improving tungsten recovery through the reuse of mine wastewater

G Jing[1], D Liao[2], Z Shi[3], Q Chen[4], J Wang[5], S Ren[6], W Sun[7], S G Pooley[8] and Z Gao[9]

1. PhD Student, School of Mineral Processing and Bioengineering, Central South University, Changsha 410083, China. Email: gaoguijing@csu.edu.cn
2. Deputy Manager, Production Technology Department, Yuanjing Tungsten Industry Company Ltd, Hengyang 421165, China. Email: 254037459@qq.com
3. General Manager, Yuanjing Tungsten Industry Company Ltd, Hengyang 421165, China. Email: 675934493@qq.com
4. Technician, Yuanjing Tungsten Industry Company Ltd, Hengyang 421165, China. Email: 542323510@qq.com
5. PhD Student, School of Mineral Processing and Bioengineering, Central South University, Changsha 410083, China. Email: wangjianjuncsu@126.com
6. PhD Student, School of Mineral Processing and Bioengineering, Central South University, Changsha 410083, China. Email: renshuai@csu.edu.cn
7. Professor and Dean, School of Mineral Processing and Bioengineering, Central South University, Changsha 410083, China. Email: sunmenghu@csu.edu.cn
8. Visiting Professor, School of Mineral Processing and Bioengineering, Central South University, Changsha 410083, China. Email: stephen.pooley@csu.edu.cn
9. Professor and Vice Dean, School of Mineral Processing and Bioengineering, Central South University, Changsha 410083, China. Email: zhiyong.gao@csu.edu.cn

ABSTRACT

Yuanjing processing plant is a scheelite and wolframite plant in southern China. Water shortages and recent environmental regulations mean that the plant must reuse the wastewater that comes from the mining operation. This paper describes the efforts to reuse the mining and ore washing wastewater (MOW) in the processing plant.

Initial attempts to reuse the MOW in the strong magnetic separation were unsuccessful because the magnetic media pack was seriously fouled by the micro-fine precipitate generated. The focus changed to reuse the MOW in the scheelite flotation circuit, which includes one roughing, one cleaning and three scavenging steps. Laboratory batch tests showed this would likely be successful because using MOW reliably improved the flotation performance in the laboratory tests.

Then a 20 day industrial trial was run in the plant. The trial was very successful with the enrichment ratio of WO_3 increasing from 17.4 to 23.6, while the recovery remained around 79.2 per cent. The industrial trial was so successful the company immediately adopted the new scheme, which has remained in use ever since.

This technical solution not only alleviated serious water shortages, and satisfied environmental regulations but also improved the plant performance.

THE YUANJING DEPOSIT

The Yuanjing processing plant is located in a remote mountainous part of Hengyang, in Hunan Province, China and is owned by China Tungsten and Hightech Materials Co., Ltd. (CMT). The mining area in Hengyang has a complex geological structure with complete exposed strata of an important metallogenic belt for non-ferrous metals (Huang, 2011). Tungsten is main non-ferrous metal in the Henyang mining area but there are also significant deposits of tantalum-niobium ores, lead-zinc ores and iron ores.

THE YUANJING PROCESSING PLANT

The Yuanjing processing plant has daily processing capacity of around 3000 T. The rock obtained from the underground mine is mainly sandstone quartz vein type and slabstone quartz vein type. The most important mineral is scheelite, followed by wolframite. The deposit is described in more detail by Zheng (2008).

Figure 1 shows the summarised flow sheet of the Yuanjing plant. First, the run-of-mine ore is pre-treated by ore washing and screening to remove the slimes. The -22 mm size fraction is then classified using spiral classification and the oversize is transported to an ore bin. The fine portion flows into a thickening tank where the ore washing wastewater is produced. The +50 mm screen product from the ore washing is crushed and sent to an ore bin. And the -50 + 22 mm size fraction is processed by photoelectric separation, before also being sent to the ore bin. The ore from the ore bin is ground and classified to obtain a flotation feed with 65 per cent passing 74 μm.

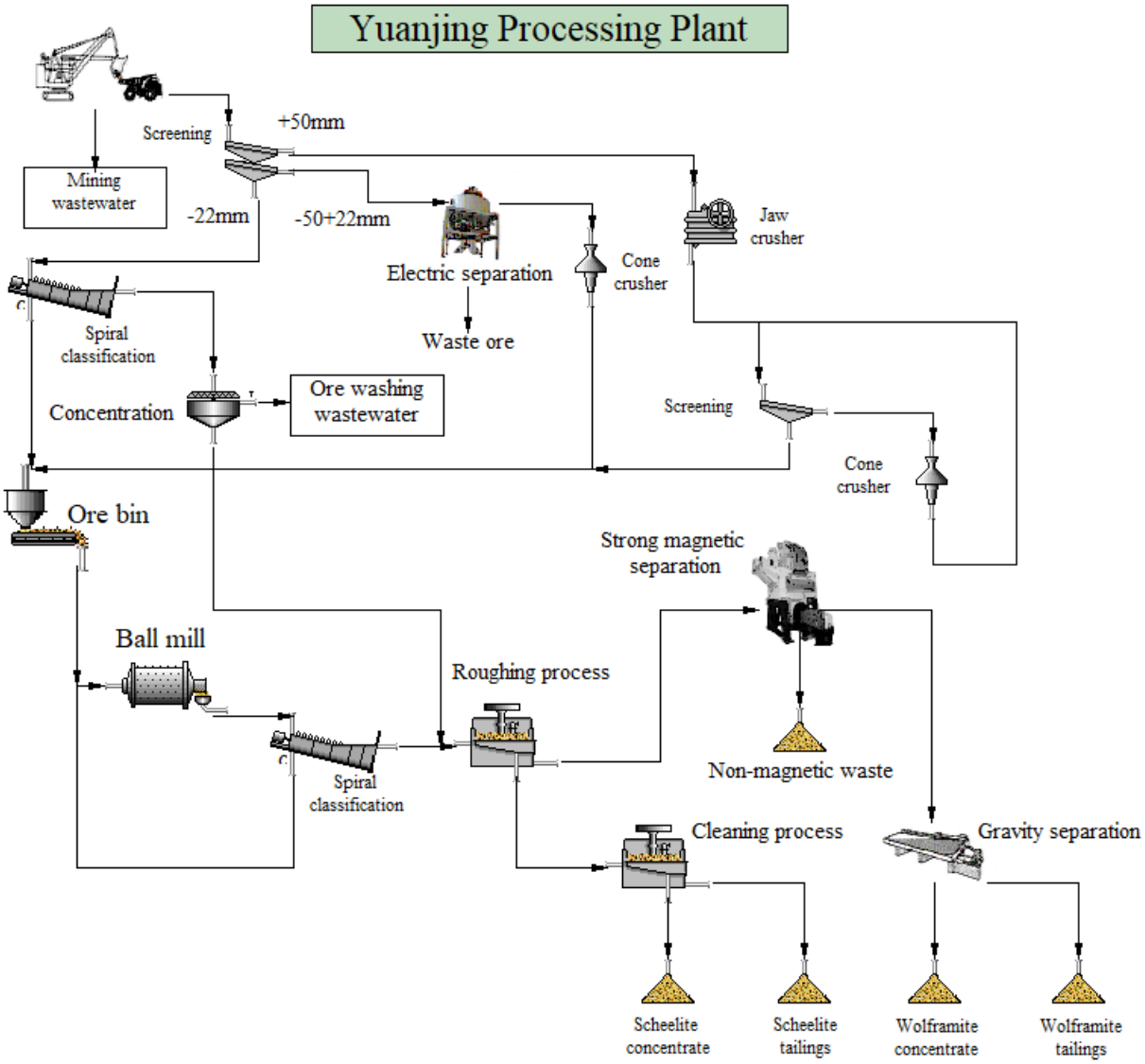

FIG 1 – Summarised flow sheet of the Yuanjing plant.

The scheelite concentrate is produced by using a roughing process followed by a cleaning process. The roughing process uses sodium carbonate to adjust pH, water glass (360 g/t) to depress floating gangue minerals and fatty acids to collect scheelite at ambient temperature. The cleaning process uses Petrov's process – water glass (50 kg/t) as a depressant at high temperature (around 90°C) to produce scheelite concentrate. The tailings of the roughing process are processed by magnetic separation and gravity separation to produce a wolframite concentrate.

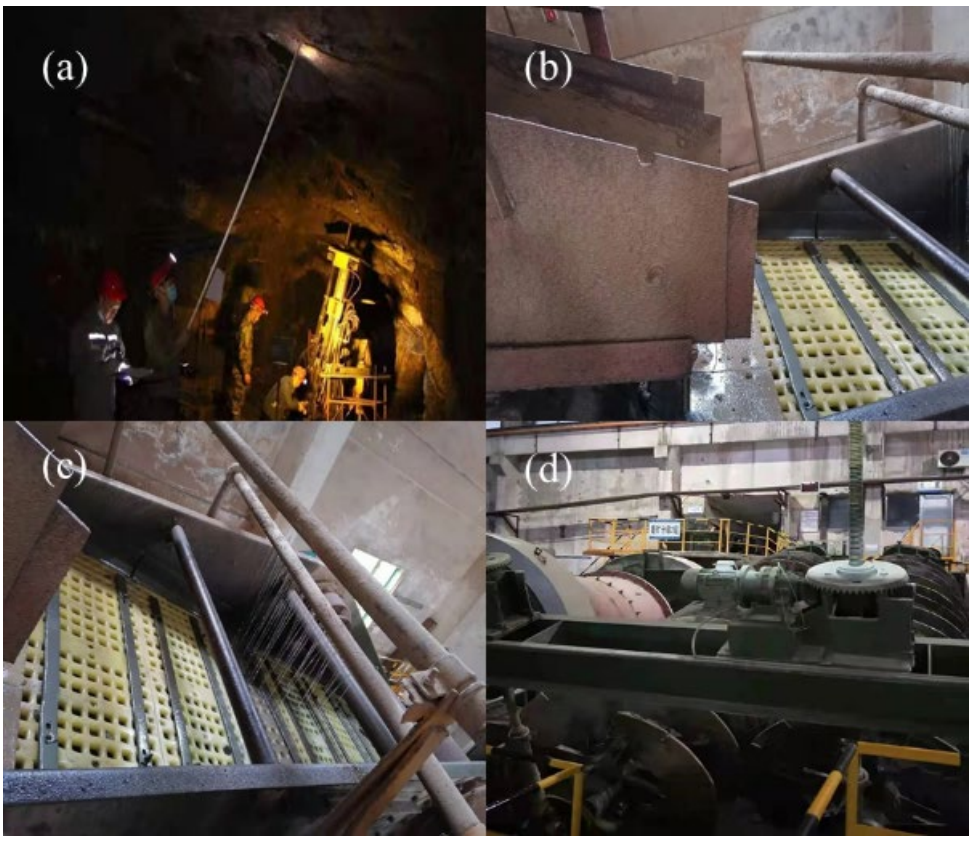

FIG 2 – The underground mine (a) ore-washing screen (b and c) and Grinding and Classification of the Scheelite Ore (d) at the Yuanjing Plant.

THE DRIVERS FOR WASTEWATER REUSE – WATER SUPPLY ISSUES AND REGULATORY CHANGES

The fresh process water used in the Yuanjing plant is mostly sourced from the Longxiqiao reservoir which is located 3 km south-west of the plant. However, the water level of the Longxiqiao reservoir changes seasonally. And when the water levels in the reservoir are low, the water supply to the plant is restricted. Relying so heavily on the water supply from this reservoir has been identified as a key production risk for the Yuanjing plant especially during the dry seasons. Because the Yuanjing plant is located in a remote mountainous region, obtaining freshwater from other sources is expensive. So it has become an urgent priority for the plant to ensure continuity of production by exploring new means of water supply or supplementation.

Considering that the wastewater from the mining operation and the ore washing wastewater produced by the plant were traditionally discharged to the surrounding environment, finding a way to reuse this wastewater in the plant became a key priority. Although of course, the wastewater reuse should not adversely affect mineral processing performance.

In addition to these economic drivers, there are also regulatory drivers impacting the use of the wastewater. The mining and ore washing wastewater (MOW) contains pollutants such as suspended solids (SS) and inorganic matter. Direct discharge of the MOW may pose a threat to the surrounding environment. And in recent years, the Chinese government has established rigorous standards for wastewater discharge to foster ecological conservation and sustainable development (Yang and Li, 2017). As a result, many Chinese mining companies are turning to recent advances in process chemistry to realise a zero discharge of wastewater, improve the water-use efficiency, and reduce net water consumption (Azevedo *et al*, 2018).

Based on these considerations, successful implementation of MOW reuse is not only beneficial to reduce operational costs, but also minimise environmental impact.

THE FIRST ATTEMPT TO REUSE MOW

Engineers at the Yuanjing mineral processing plant first attempted to reuse the MOW in the magnetic separation process. Magnetic separation is used to recover wolframite from the tailings of the scheelite roughing process, as shown in Figure 1. Magnetic separation is a physical separation process which is relatively simple compared to flotation (Meng *et al*, 2017). Because a significant amount of wash-water is required in magnetic separation, reusing the MOW in this process seemed to be a reasonable option. Before the MOW was reused, it was first treated to reduce the high suspended solids (SS: 674.5 mg/L) content. Carbide slag was used to treat the wastewater and followed by an inclined pipe settlement process. Carbide slag is an industrial waste residue which is readily available at a low price (Li and Zhang, 2010). So, using carbide slag to treat MOW is an environmentally-friendly treatment method that uses one waste to treat another. After the addition of carbide slag, the wastewater drains into the inclined tube settler to remove the suspended matter. The overflow from the inclined tube settler had an SS content of 42.5 mg/L in the treated MOW.

Unexpectedly, the yield of the wolframite concentrate gradually decreased over time after the introduction of the treated wastewater into the magnetic separation process. However, the gradual reduction of the yield meant that the cause remained hidden for some time. Ultimately, inspections of the magnetic media pack of the separator revealed that it was seriously blocked by a white precipitate. It was then postulated that this was due to a high Ca^{2+} concentration in the treated wastewater. Later detailed analysis at Central South University showed this precipitate to be $CaCO_3$. And detailed analysis of the treated wastewater revealed that during carbide slag treatment the Ca^{2+} concentration of the wastewater increased to 253.44 mg/L from 97.84 mg/L. This meant that the $CaCO_3$ fouling the media pack was likely caused by the interaction of Ca^{2+} in the reused wastewater and CO_3^{2-} in the roughing tailings pulp. The precipitate adhered and caused fouling in the spaces in the magnetic media pack and proved difficult to clear. The magnetic separator and some blocked magnetic media packs are shown in Figure 3. These results indicated that it was not feasible to use the treated water in the magnetic separation process.

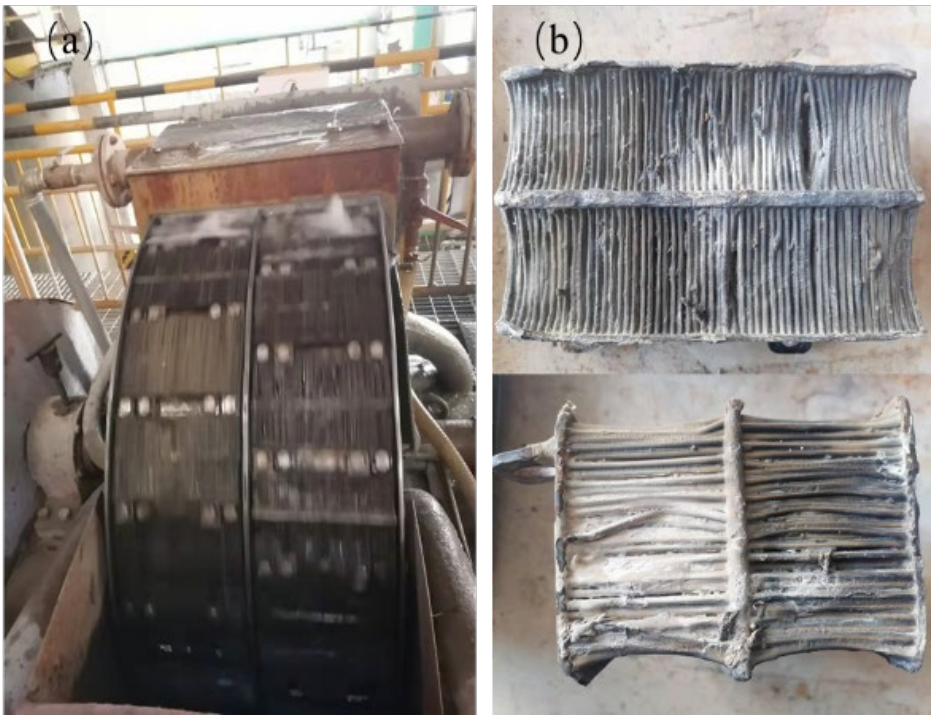

FIG 3 – The magnetic separator (a) and a fouled magnetic media pack (b).

REUSE OF MOW IN THE SCHEELITE ROUGHING PROCESS

Given that the reuse of the MOW in the magnetic separation process had proven infeasible, other approaches to reusing the wastewater were investigated. So the feasibility of reusing the MOW in the scheelite roughing process was explored. The performance of the scheelite flotation circuit is the main determinant of the economic benefits of the Yuanjing plant. So the effects of reusing MOW on

the WO_3 grade and recovery were carefully studied in the laboratory prior to conducting a plant trial. It was noted that the amount of water consumed by the roughing process was greater than the amount of wastewater being captured for reuse. This meant that to be used in the scheelite roughing process the MOW would need to be used as a supplement to the water from the Longxiqiao reservoir. So the effect of the MOW proportion (reused water/total process water) on the scheelite recovery was explored though a rigorous program of laboratory-scale flotation experiments using the existing reagent regime. The laboratory program and its surface chemistry have been discussed in detail elsewhere (Jing *et al,* 2022) but the key flotation results are presented here in Figure 4.

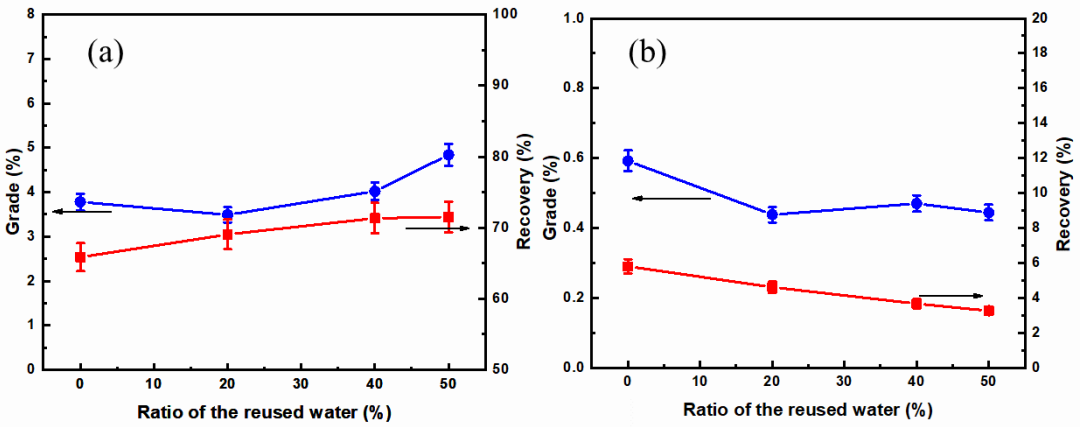

FIG 4 – Results of laboratory experiments using treated MOW in the rougher (a) and scavenger (b) processes (Rougher: Na_2CO_3 1500 g/t, water glass 1.0 kg/t, fatty acid 360 g/t; scavenger: fatty acid 120 g/t) (adapted from Jing *et al* (2022)).

It can be seen that the WO_3 grade and recovery are 3.78 per cent and 65.84 per cent respectively, in basic agreement with the recent production performance of the plant. The WO_3 recovery increased with increasing ratio of reused water/total process water. The WO_3 grade at the ratio of 20 per cent reused water is slightly lower than that using fresh process water but further increases in the percentage of reused water resulted in a significantly higher WO_3 grade. These results indicated that satisfactory results would be likely if the MOW were to be reused in the scheelite roughing process. The laboratory experiments showed no adverse effects on the recovery of scheelite and even better results could be obtained than using fresh process water. In the case of the scavenger flotation, the WO_3 grade and recovery of the obtained concentrate were 0.59 per cent and 5.80 per cent, which meant that most of the scheelite had been recovered by the roughing process. The WO_3 grade and recovery fluctuated slightly with increasing ratio of reused water/total process water.

As previously mentioned, the treated water is characterised by a high Ca^{2+} concentration. Previous studies have reported that the presence of Ca^{2+} will affect the flotation performance of several minerals such as fluorite and spodumene when sodium oleate is used as the collector (Fa *et al*, 2006; Wang *et al*, 2019). Classic activation theory explains that pre-adsorbed Ca^{2+} will increase the number of active sites on the mineral's surface, resulting in an increase of fatty acid adsorption (Gao *et al*, 2021). Another view is that the fatty acid and Ca^{2+} form metal-collector complexes first and are then strongly adsorbed on the mineral's surface. In scheelite flotation, the presence of Ca^{2+} is generally known to have a negative impact on scheelite recovery (Zhang *et al*, 2019). However, in this situation, the reuse of high Ca^{2+} containing wastewater had a significant positive impact on scheelite flotation, indicating that Ca^{2+} may exhibit different effects in different flotation systems. Presumably this is directly due to the high concentration of Ca^{2+}, but due to the complexity of the MOW, further research is needed to reveal the exact surface chemistry mechanism causing this improvement.

INDUSTRIAL TRIAL OF THE MOW REUSE IN THE SCHEELITE ROUGHING PROCESS

The laboratory-scale experiments were repeated several times to validate the results. Then an industrial trial was arranged at the plant. During the industrial trial, the ratio of the reused water fluctuated with the variability in the mining and ore washing processes but remained below

50 per cent. The scheelite roughing process consists of one rougher step, one scavenger step and three cleaner steps. The reused wastewater was used in the roughing process and the trail lasted 20 days. The performance of the roughing process for the 20 days immediately prior to the industrial trial was used as a baseline comparison. And in particular, the WO_3 grade, recovery and enrichment ratio were monitored. The concentrate obtained using fresh feed water before the industrial trial had an average WO_3 enrichment ratio of 17.41 and an average recovery of 79.17 per cent, while during the MOW reuse trial, an improved average WO_3 enrichment ratio of 23.61 at a similar recovery of 79.23 per cent was achieved. These results further confirmed the value of reusing the MOW in the roughing process and the plant immediately adopted this reuse strategy. And it has remained in place since. Reusing the MOW has also prevented subsequent water shortages at the Longxiqiao reservoir from limiting production at the Yuanjing plant. Effectively mitigating a key production risk. And it also has minimised any environmental impacts caused by the discharge of wastewater. More importantly, the authors believe that, based on these results and the subsequent scientific investigation into the surface chemistry (Jing *et al*, 2022), this method may be also feasible for other similar mineral processing plants.

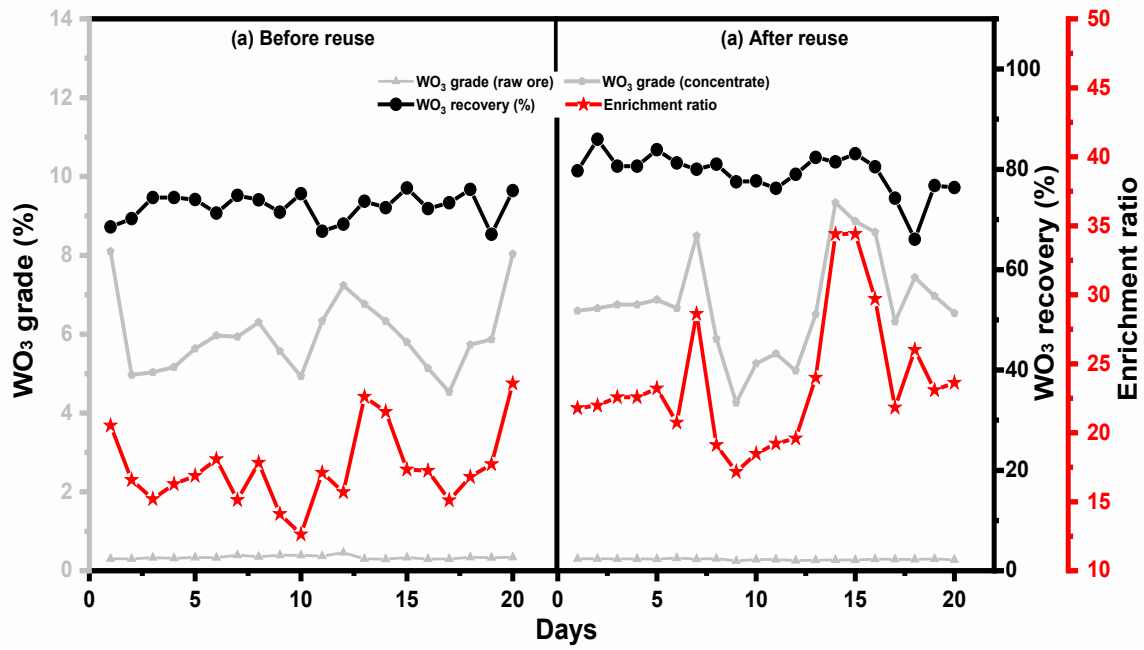

FIG 5 – Key results of the Industrial Trial of the MOW reuse – the WO_3 grade, recovery and enrichment ratio during the pre-trial comparison period (a) and during the industrial trial (b) (from Jing *et al* (2022)).

DISCUSSION AND FUTURE DIRECTIONS

As has been previously documented, wastewater reuse in mineral processing plants can be categorised into external reuse and internal reuse (Farrokhpay and Zanin, 2012; Shengo *et al*, 2016). To date, the authors are unaware of any other reuse of mining and ore washing wastewater in the processing plant. Our research indicates that carbide slag combined with an inclined pipe settlement process is an efficient method to remove suspended solids (SS) in the wastewater. However, the high concentration of Ca^{2+} introduced by carbide slag may influence the mineral separation processes and needs to be carefully investigated on a case-by-case basis. Using wastewater treated in such a way in a strong magnetic separation process will likely block the magnetic media pack, resulting in the decline production performance. This work has demonstrated that using the treated wastewater in a scheelite roughing process is feasible, and may even improve the recovery of scheelite. Not only has this process significantly alleviated the problems caused by water shortages at the Yuanjing plant, but it is also in accordance with the tenants of environmental protection and sustainable development. The authors presume that the improvement in the scheelite flotation is related to the high concentration of Ca^{2+}. However, due to the complex composition of the MOW, the further detailed studies are needed to conclusively reveal the relevant mechanisms.

ACKNOWLEDGEMENTS

The authors would like to thank Central South University Master's student Zichen Tang for using his JKSimMet skills to produce the flow sheet diagram of the Yuanjing processing plant.

REFERENCES

Azevedo, A, Oliveira, H A and Rubio, J, 2018. Treatment and water reuse of lead-zinc sulphide ore mill wastewaters by high rate dissolved air flotation. *Miner. Eng*, 127, 114–121.

Fa, K, Nguyen, A V and Miller, J D, 2006. Interaction of calcium dioleate collector colloids with calcite and fluorite surfaces as revealed by AFM force measurements and molecular dynamics simulation. *Int. J. Miner. Process*, 2006, 81(3), 166–177.

Farrokhpay, S and Zanin, M, 2012. An investigation into the effect of water quality on froth stability. *Advanced Powder Technology,* 2012, 23(4), 493–497.

Gao, J, Sun, W and Lyu, F, 2021. Understanding the activation mechanism of Ca^{2+} ion in sodium oleate flotation of spodumene: A new perspective. *Chemical Engineering Science*, 2021, 244, 116742.

Huang, M, 2011. Geochemical features of the ore-contral structures in Yanglin'ao Tuangsten deposit, Hunan province. *North China Geology (in Chinese),* 2011, 3(34), 1–5.

Jing, G, Liao, D, Shi Z, Chen, Q, Wang J, Ren, S, Lin, S, Sun, W, Pooley, S G and Gao, Z, 2022. Mine and ore washing wastewater reusability in scheelite flotation process. Unpublished Manuscript, 2022.

Li, Y and Zhang, X, 2010. Study on a Coal Washing Wastewater Treatment Process and Its Application with Carbide Slag and Polyacrylamide, In *2nd China Energy Scientist Forum*, Xuzhou, PEOPLES R CHINA, pp. 293–297.

Meng, Q, Feng, Q and Ou, L, 2017. Recovery Enhancement of Ultrafine Wolframite through Hydrophobic Flocs Magnetic Separation. *Mineral Processing and Extractive Metallurgy Review*, 2017, 38(5), 298–303.

Shengo, L M, Gaydardzhiev, S and Kalenga, N M, 2016. Malachite and heterogenite behavior during the locked-cycle recycling of process water in flotation of copper-cobalt oxide ores. *Int. J. Miner. Process*, 2016, 157, 152–162.

Wang, Z, Wang, L, Zheng, Y and Xiao, J, 2019. Role of of calcium dioleate in the flotation of powellite particles using oleate. *Miner. Eng,* 2019, 138, 95–100.

Yang, W and Li, L, 2017. Efficiency Evaluation and Policy Analysis of Industrial Wastewater Control in China. *Energies*, 2017, 10(8).

Zhang, Z, Cao, Y, Ma, Z, Liao, Y, 2019. Impact of calcium and gypsum on separation of scheelite from fluorite using sodium silicate as depressant. *Separation and Purification Technology*, 215, 249–258.

Zheng, P, 2008. Study on the ore-controlling structure of Yanglin'ao scheelite deposit in East Hengyang, Hunan province. *Central South University thesis (in Chinese).*

Ore variability and process plant performance – the impacts to revenue

A Millar[1] and B Wraith[2]

1. MAusIMM(CP), Senior Process Engineer, Sedgman Pty Ltd, South Brisbane Qld 4101. Email: andrew.millar@sedgman.com
2. MAusIMM, Principal Project Metallurgist, Bluestones Mines Tasmania JV, Zeehan Tas 7469. Email: ben.wraith@bluestonetin.com.au

ABSTRACT

Process plants are characterised by variability of performance over a wide range of time-scales; reflected in fluctuations in metal recovery, concentrate grade, plant throughput and reagent costs. In turn, these fluctuations impact financial metrics such as operating costs and revenue.

The primary cause of plant variability is variation in the physical, lithological and mineralogical characteristics of the ore fed to the plant. The variability of the ore is driven by the intrinsic heterogeneity of the geology and mineralogy of the orebody, the mining method and mine production plan, the capacity to stockpile and blend, as well as the plant flow sheet and the level of plant automation.

Whilst the impact of ore variability on process plants is universally recognised, it is rarely quantified in financial terms. Consequently, opportunities to reduce its impact are often overlooked due to the lack of a basis for a quantifiable cost-benefit analysis to justify improvement initiatives.

This paper will present case studies using production data from the Renison tin concentrator and a zinc concentrator. These case studies demonstrate that as the standard deviation of plant head grade increases (as a proxy for ore variability), plant metal recovery subsequently reduces. The metal recovery is then converted into plant revenue losses, to quantify the economic impact of ore variability.

The Renison case study demonstrated that whilst a very rare occurrence, revenue losses were as high as 34 per cent (relative to the baseline) when standard deviation was at its highest.

The zinc concentrator case study demonstrated that revenue losses were as high as 6 per cent (relative to the baseline) when standard deviation was at its highest.

Options are available for reducing and managing ore variability in the process plant. These options include changing mining practices so that the ore is fed to the plant with less variability, more advanced process plant control systems and the use of predictive geometallurgical models.

INTRODUCTION

Mineral processing plants are characterised by variability of performance over a wide range of time-scales. This variability is reflected in fluctuations in metal recovery, concentrate grade, plant throughput and reagent consumption. In turn, these fluctuations impact financial metrics such as operating costs and revenue.

The primary cause of performance variability is the variation in the physical, chemical and mineralogical characteristics of the ore fed to the plant. These characteristics that vary include head grade, ore hardness (which drives plant throughput), the mineralogy of the target commodity and gangue mineralogy. Variability is also a function of the mining method mining rate; the operations ability to stockpile and blend ore prior to being fed to the plant and the level of plant automation.

Whilst the impact of ore variability on process plants is universally recognised, it is rarely quantified in financial terms. Consequently, opportunities to reduce its impact are often overlooked due to the lack of a basis for a quantifiable cost-benefit analysis to justify improvement initiatives.

This paper will present case studies using production data from the Renison Bell tin concentrator and a zinc concentrator. These case studies demonstrate that as the standard deviation of plant feed grade increases (as a proxy for ore variability), plant metal recovery subsequently reduces. The metal recovery is then shown as plant revenue losses, to quantify the economic impact of ore variability.

THE CAUSES OF ORE VARIABILITY IN PROCESS PLANTS

The heterogeneity of orebodies

Orebodies are intrinsically heterogeneous in terms of their geology and mineralogy. David (2010) summarised orebodies as:

> *…naturally occurring phenomena with little consistency from location to location. Orebodies situated within a few hundred metres of each other can be as geologically different as orebodies on opposite sides of the earth. Within a single orebody it is possible have primary igneous rock sources, igneous intrusions, faulted zones, oxidised zones, alluvial accumulations and much more.*

Hoban and Brassnett (1978) described how the heterogeneity of the Mt Isa orebodies impacted the grinding and flotation circuits in the lead/zinc concentrator. This was due to the varying mineral textures from the Black Rock and Black Star orebodies that fed the lead/zinc concentrator.

Mining method and mine production rate

Ore variability in the process plant is also caused by the mining method, the mine production plan and the mining production rate.

The mining method will impact the head grades of the mined material. McCarthy (2015) observed that some underground mining methods, such as sublevel and block caving, allow no short-term control of product quality. Provided the ore is above the mining cut-off grade, in the short-term the ore is delivered to the surface as it presents from the drawpoints.

McCarthy (2015) also observed that there are physical limits to the rate that any orebody can be mined. High rates of mining are associated with greater day-to-day or month to month production volatility, with a tendency for dilution of the ore to become excessive at high rates as the pressure of production reduces the ability to mine more carefully and selectively. This volatility is demonstrated in Table 1.

TABLE 1

Monthly volatility of benchmarked mining operations of a 12 month period (McCarthy, 2015).

	Underground mines			Surface mines		
	Min (%)	Max (%)	Ave (%)	Min (%)	Max (%)	Ave (%)
Ore Mined (t)	6	34	14	11	62	25
Head Grade	5	28	11	3	22	9
Ore Processed (t)	3	32	13	4	22	10
Processed Grade	5	23	12	3	16	8

Impact of stockpiling and blending practices

Stockpiling and blending methods can also have a major impact on plant variability.

Where the mine is bottleneck of the operation, or where there is limited stockpiling footprint; the mine may have to supply ore directly to the plant so there is no ability to blend to reduce ore variability. Hoban and Brassnett (1978) described that as there was limited stockpile footprint, the ratio of the Black Star and Black Rock ores that fed the Mt Isa lead/zinc concentrator varied significantly which causes impacts on plant performance.

THE IMPACT OF ORE VARIABILITY ON PROCESS PLANT PERFORMANCE

Historically, the inability to sufficiently blend different ores would impact base metals concentrators which had limited automation and process control. Initially, the flotation circuit would be fed by a period of high-grade ore. The operators would increase air flow and reagent addition to the flotation banks to recover the ore. A period of low-grade ore would soon follow. Operating at plant settings

suited for high-grade ore would mean that the flotation circuit would operate with high mass pull, and in turn recover gangue minerals which would reduce concentrate grade. To compensate for this, the operators would reduce air flow and reagent addition to reduce the recovery of gangue minerals. The low-grade ore would soon be met with another period of high-grade ore. The plant settings, now set for low-grade ore, meant that some of the valuable minerals would not be recovered as there is insufficient air and reagent. The drop in recovery of valuable minerals would cause a reduction in revenue.

In gold cyanide leach plants, it is common for the plant to be fed from a different ore such as oxide, transitional and sulfide ores. If these ore sources are not sufficiently blended, the variable feed to the plant can cause plant problems. Flow sheets for gold plants where sulfide ore is treated typically includes a flotation circuit where the flotation concentrate reports to a regrind mill in closed circuit with hydrocyclones, ahead of a cyanide leach circuit. The plant may experience a period of sulfide ore feed where a flotation concentrate is produced. A period of oxide ore would follow, where only a minor flotation concentrate is produced. This variability in the production of flotation concentrate would cause poor classification in the regrind mill hydrocyclone circuit so that coarser material would report to the leach circuit. The coarse material may be insufficiently liberated and thus reduce gold recovery in the leach circuit.

CASE STUDIES

Introduction

The performance of the Renison tin concentrator and a zinc concentrator were examined to assess the impacts of ore variability on plant revenue.

The authors tested a theory that as standard deviation of plant head grade increases (as a proxy to ore variability) then plant recoveries, and subsequently revenue decreases.

Standard deviation of head grade was chosen as the selected variable for analysis, as plant feed grade is a variable that is commonly measured on an instantaneous level. Whereas other variables, such as mineralogy or lithology, are not instantly or consistently measured.

Case study 1 – Renison tin concentrator

The Renison tin mine is an underground tin mine located near Zeehan in Tasmania. Figure 1 shows that the Renison tin concentrator flow sheet is complex and consists of crushing, grinding, sulfide flotation, gravity separation, desliming, oxide flotation and concentrate leaching circuits.

The plant generates five separate tailings streams. Nominal throughputs are 0.9 to 1 Mt/a, with a typical overall tin recovery of 80 per cent at a tin concentrate grade of 57 per cent.

Each unit operation within the flow sheet serves a specific purpose and the performance in one section of the plant can significantly impact performance in another, both downstream and upstream. Many factors influence plant performance, but the focus of this case study is tin feed grade.

Variability in run-of-mine (ROM) ore treated, specifically the proportion of minerals presented, influences how the plant is operated. In order to operate the plant within the design criteria, efforts are made to minimise the variability through Mine to Mill scheduling and stockpile management. The tin metal units processed is further trimmed via manipulating the mill throughput rate. Process control systems and operator intervention further reduces process variability in order to achieve the key performance indicators of throughput, tin recovery and concentrate grade.

Unchecked variability in feed can lead to poor performance in both tin recovery and/or concentrate grade. The concentrator is equipped with a 24 stream on-stream analyser (OSA) to provide the operations team with regular assay updates on elements present. The stream data, combined with targets and accepted operating windows, provide guidance to the operations team.

The raw plant assay data, which was measured approximately every 9 to 18 minutes, was collated. The plant streams chosen for this analysis were Mill Feed (SFD), Tin Flotation Feed (CFF), Tin Flotation Concentrate (CFC) and Tin Flotation Tail. To minimise the impact of abnormal operation, various data points were removed from the data set. Utilising the two-product formula, a stage

recovery for the tin flotation circuit was generated. A 24-hour standard deviation of the mill feed data was normalised by dividing by the average tin grade for that time period.

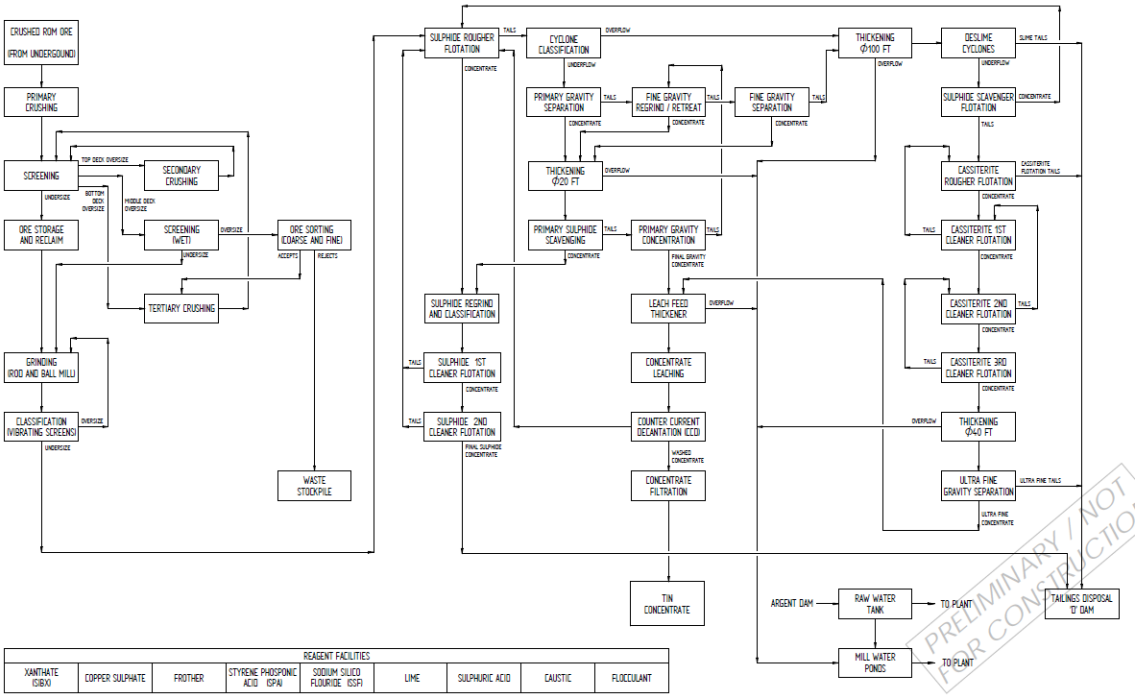

FIG 1 – Renison plant flow sheet.

Figure 2 depicts the tin stage recovery versus the normalised standard deviation in tin plant feed grade (Mill Feed). Of note is the decline in quantity of data points as the feed variability increases. The authors note that this thinning of the data set is due to the operational strategy of the plant, whereby high variability is minimised wherever possible to simplify the operation of the plant and sustain higher recovery.

FIG 2 – Tin flotation circuit tin stage recovery versus normalised StDev of plant tin feed grade.

The analysis highlights two main points. Firstly, the tin flotation circuit, in its current design and under current operating strategies, can withstand moderate variability in mill feed and upstream plant performance. Secondly, as the variability increases, a tipping point is reached and performance starts to fall away. In put a revenue value on the impact of the ore variability, Figure 3 depicts a filtered data set where data points of normalised plant tin feed standard deviation less than 25 per cent are omitted.

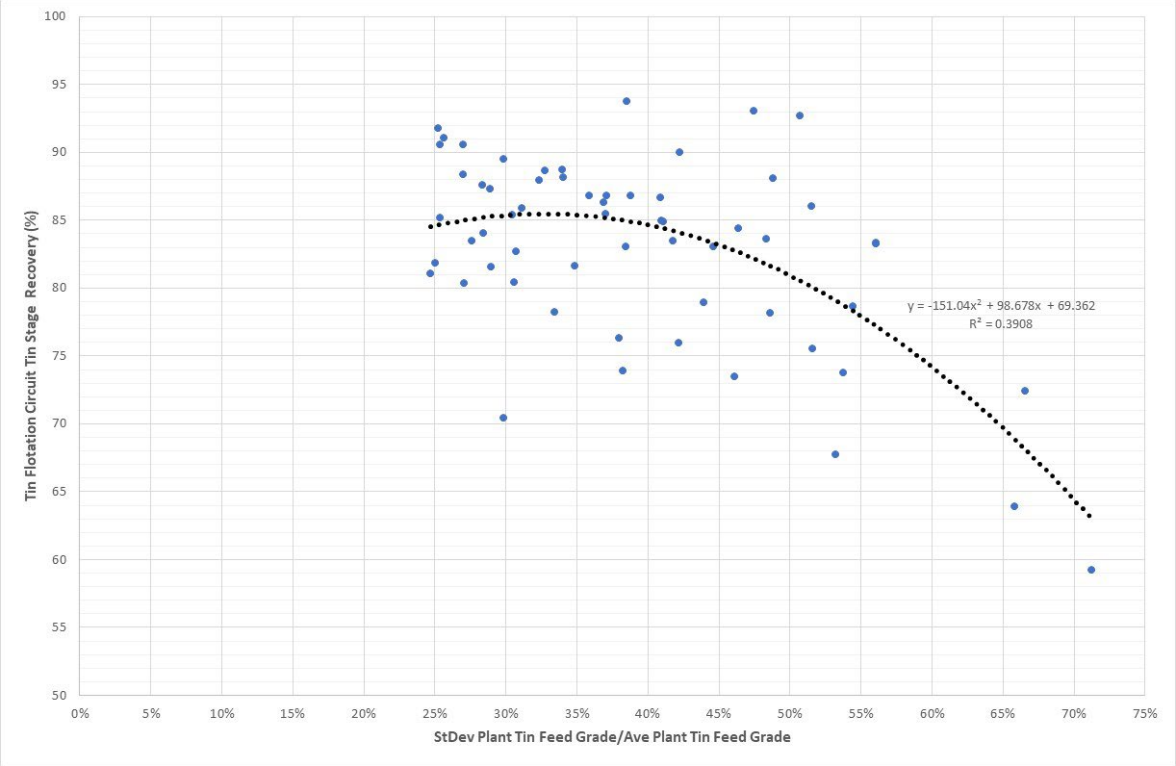

FIG 3 – Trimmed data of tin flotation circuit tin stage recovery versus normalised StDev of plant tin feed grade.

Figure 3 shows that there is a parabolic relationship, where after a normalised StDev of about 40 per cent, stage recovery tends to drop considerably.

A high-level economic analysis was performed utilising the nominal annual throughput, downstream tin recovery factors, typical tin feed grade and typical tin price. Figure 4 depicts the relative reduction in tin revenue versus the normalised standard deviation of plant tin feed grade (with a minimum of 25 per cent).

Figure 4 demonstrates that at the highest normalised standard deviation of 75 per cent, the relative reduction in revenue is 34 per cent.

Figure 4 highlights that if the controls used to mitigate feed grade variability were completely removed and the ore is treated in an un-optimised fashion, significant losses in revenue can occur.

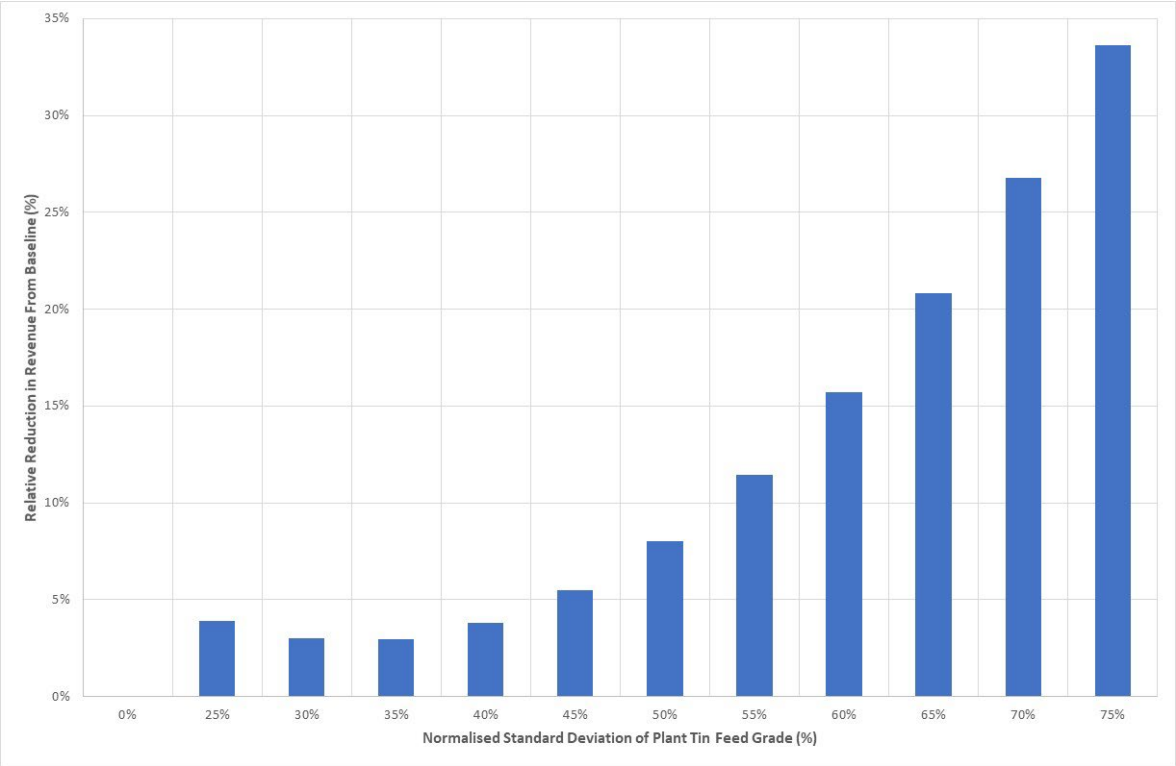

FIG 4 – Relative reduction in tin revenue versus normalised standard deviation of plant tin feed grade.

Case study 2 – Zinc concentrator

The zinc concentrator flow sheet, shown in Figure 5, had:

- a crushing circuit where the ROM stockpile feeds three stages of crushing before reporting to a coarse ore stockpile.
- a grinding circuit consisting of a ball mill operating in closed circuit.
- a zinc rougher/scavenger flotation circuit.
- a regrind mill circuit where the zinc rougher/scavenger concentrate is reground.
- three stages of zinc cleaner flotation to produce a final zinc concentrate.
- concentrate thickening and filtering of the zinc concentrate.
- flotation tailings thickening and disposal.

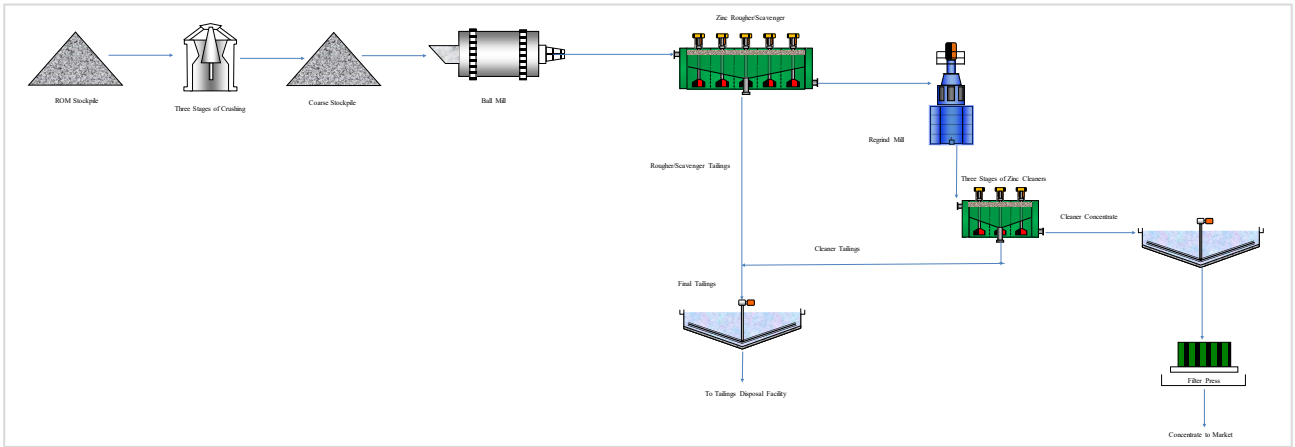

FIG 5 – Zinc concentrator flow sheet.

The zinc concentrator has a design throughput of 2 Mt/a and the target zinc concentrate grade was 50 per cent.

The concentrator has limited process control capabilities and relied on operators to change concentrator settings. There was also only minor stockpiling footprint, so the ability to blend ores was minimal.

A campaign was conducted on the concentrator to ascertain the impact of ore variability on plant recovery and revenue.

Two-hour sample composites were taken including plant feed, zinc concentrate and final tails. Daily zinc recoveries were calculated from the from the weighted average assays using the two-product formula. The standard deviation of plant zinc feed grade over the 24-hour period was then calculated from the 2-hour composite assays.

As was the case with the Renison production data, the standard deviation was divided by the average daily zinc feed grade to normalise the data.

The following data points were removed from the data set:

- To reduce the impact of high head grade on zinc recovery, the data was limited to zinc head grades of less than 5 per cent.
- Data points where the zinc concentrate grades were below 40 per cent, as these are well below the required marketing specifications.
- Data points where zinc recovery was less than 85 per cent were considered outliers and removed from the data set.

Figure 6 shows the daily zinc recovery versus the normalised standard deviation of daily concentrator zinc feed grade.

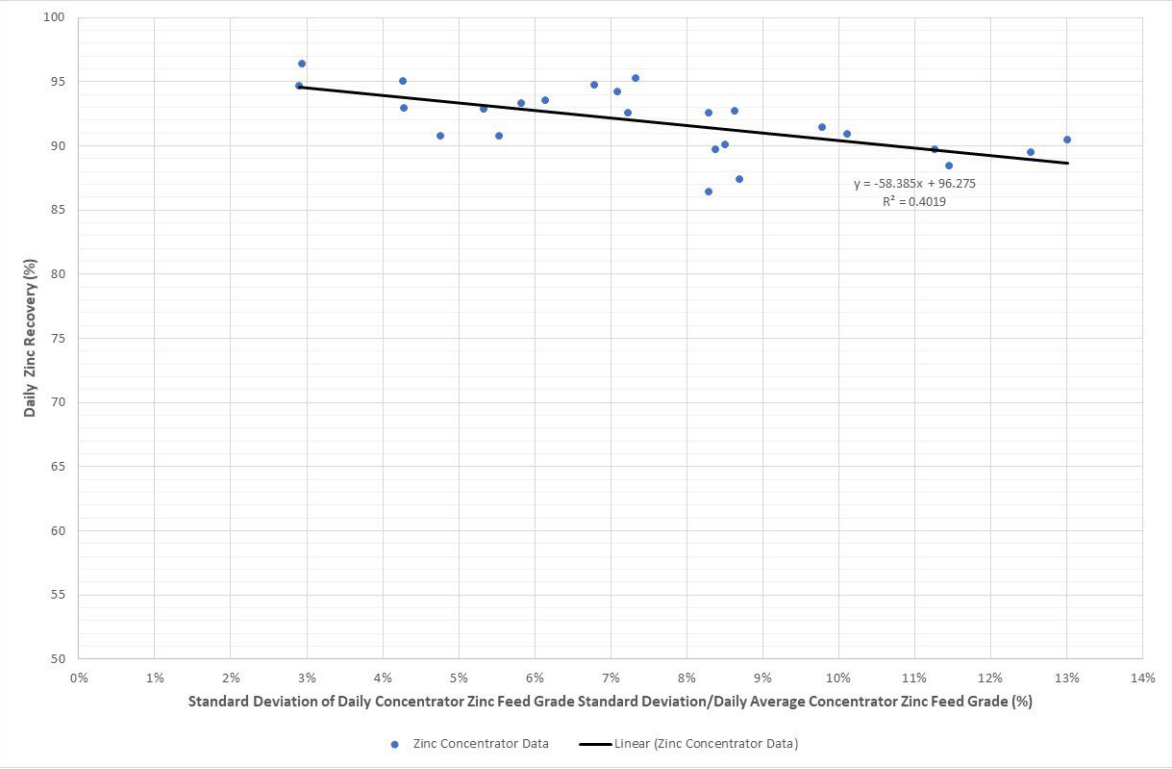

FIG 6 – Daily zinc recovery versus normalised standard deviation of daily concentrator zinc head grade.

The trend line in Figure 6 shows that there is a reasonable linear relationship that demonstrates as normalised StDev increases that zinc recovery tends to reduce. This produced a linear relationship where:

$$\text{Zinc recovery (\%)} = (-58.385 * \text{Normalised StDev}) + 96.275 \quad (1)$$

The correlation coefficient (R^2) of 0.4 is moderate, but the authors considered this to be reasonable given there are other parameters that may impact recovery other than just the standard deviation of head grade. These other parameters include the grain size of zinc sulfide minerals, macro textures of zinc minerals and quartz minerals (and subsequent liberation), amount of iron sulfides in the concentrator feed and the concentrator throughput (as this will impact flotation residence time).

Of intertest is that the range of normalised standard deviation (from 3 per cent to 14 per cent) was much lower than the Renison data range (up to 75 per cent) and this may be due to not having the number of data points that the Renison data set had.

A high-level economic analysis was performed. Equation 1 was used for calculating zinc recovery from the same range of normalised standard deviations as the data set. Zinc recovery was then converted into revenue.

The following inputs were used:

- A zinc price of US$3600/t.
- The zinc concentrator feed grade was kept constant at 4.2 per cent (which was the average zinc grade of the data set).

A normalised StDev of 3 per cent is considered the baseline as it was the lowest normalised StDev from the data set. The impact of normalised standard deviation on revenue is demonstrated in Figure 7.

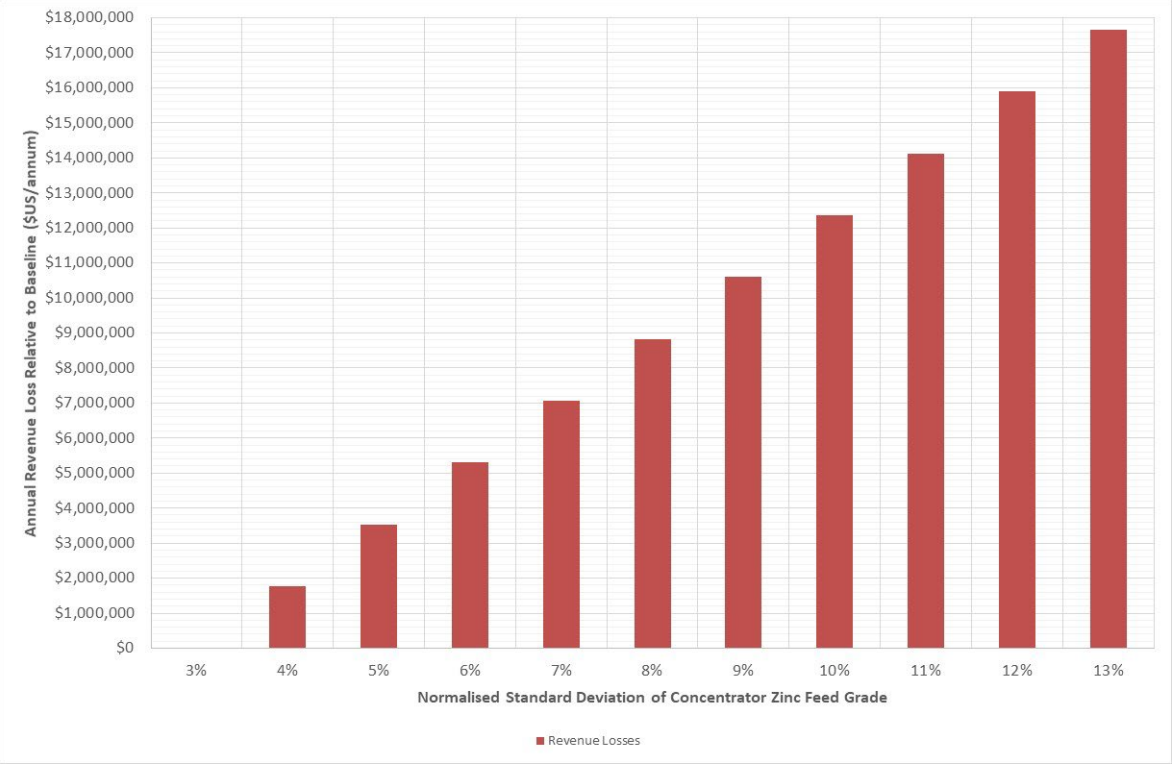

FIG 7 – Annual revenue loss (relative to the baseline) versus normalised StDev of concentrator zinc feed grade.

The revenue losses vary from US$1.8 million/a (at a normalised StDev of 4 per cent) to US$17.7 million/a (at a normalised StDev of 13 per cent). A StDev of 13 per cent is a 6 per cent reduction in revenue relative to the baseline.

OPTIONS FOR REDUCING THE IMPACT OF ORE VARIABILITY

Options are available for reducing and managing ore variability in the process plant. These options include changing mining practices so that the ore is fed to the plant with less variability, more advanced process plant control systems and the use of predictive geometallurgical models.

Mine planning and design

Changes to the mining practice can smooth out the variability of the ore delivered to the process plant. These changes can include mining method, mine production rate and the mine production plan. McCarthy (2015) observed that there is evidence that more selective mining is possible if it is designed into the process from the outset and the planned mining rate is adjusted downward to allow it to take place. A good example is the selective mining of acid-generating and benign waste from a pit, with the benign waste was used for capping.

Stockpiling and blending

Further focus should be put on stockpiling and blending to smooth out ore variances.

McCarthy (2015) recommended that the mine operation should be designed so that all stockpiles, including orepasses in an underground mine, have adequate capacity to smooth the short-term surges to a level acceptable for the system as a whole.

Process plant control

Flotation circuits can use process control systems for managing ore variability.

Rantala *et al* (2014) described an advanced control system at the Kevitsa nickel, copper and platinum group metal (PGM) concentrator in Finland. In the concentrator, an on-stream analyser (OSA) continually measures feed grades into the flotation circuit. As feed grades changes, the control system uses advanced algorithms to automatically change flotation circuit parameters such as froth speed, air flow rates and reagent additions to each flotation cell so that recovery and concentrate grade are optimised.

Plant flow sheet changes

Some process plants use an agitated storage tank after the grinding circuit and ahead of the downstream circuits to smooth out grade fluctuations (Wills, 2016, p 317). In flotation circuits, these tanks often have a pump with a fixed flow rate so that the flow to the flotation circuit is kept constant (and subsequently fluctuations to residence time are reduced).

An example of this was the Lone Tree gold plant in Nevada where agitated surge tanks (with 11 hours of capacity) were installed after the grinding circuit and ahead of the autoclave circuit to reduce variability to the autoclave circuit (Simmons, 1993).

Predictive geometallurgical models

Predictive geometallurgical models have become more common at mining operations. These models take the existing resource block models and populate each block with characteristics of the ore. These characteristics can include elemental data (both target commodity and gangue/deleterious elements), ore hardness data (such as A*b values taken from SMC tests) or mineralogical data.

When the mine is supplying ore directly to the plant, the information from the geometallurgical model allows the plant staff to be more proactive about changing plant settings prior to the ore reaching the plant to assist in plant optimisation. Compan *et al* (2015) expressed that the predictive geometallurgical model used at the Chuquicamata copper concentrator in Chile was able to predict plant copper recovery with acceptable accuracy.

ACKNOWLEDGEMENTS

The authors would like to acknowledge Dr Paul Greenhill for providing plant data to complete the analysis. The authors also thank Bluestone Mines for allowing them to use the Renison data.

REFERENCES

Compan, G, Pizarro, E and Videla, A, 2015. Geometallurgical model of a copper sulphide mine for long-term planning, *Journal of the Southern African Institute of Mining and Metallurgy*, vol 115, pp. 549–546.

David, D, 2010. *Flotation Plant Optimisation: A Metallurgical Guide to Identifying and Solving Problems in Flotation Plants*, first edn (The Australasian Institute of Mining and Metallurgy: Melbourne).

Hoban, M and Brassnett, T, 1978. Problems encountered in the control of Mount Isa Mine Concentrators, *The AusIMM North West Queensland Mill Operators' Conference*, Townsville, Qld, June 1978 (The Australasian Institute of Mining and Metallurgy).

McCarthy, P, 2015. Integrated Mining and Metallurgical Planning and Operation. *Proceedings of the Metallurgical Plant Design and Operating Strategies – MetPlant 2015* (The Australasian Institute of Mining and Metallurgy: Melbourne).

Rantala, A, Muzinda, I, Timperi, J, Cruickshank, C and Haavisto, O, 2014. Implementation of Advanced Flotation Control at First Quantum Minerals' Kevitsa Mine, *Proceedings of the 12th AusIMM Mill Operators' Conference* (The Australasian Institute of Mining and Metallurgy: Melbourne).

Simmons, G, 1993. Development of low temperature pressure oxidation at Lone Tree, *SME Annual Meeting,* February 15–18 1993.

Wills, B, 2016. *Wills' Mineral Processing Technology: An Introduction to the Practical Aspects of Ore Treatment and Mineral Recovery*, 8th edn (Butterworth-Heinemann: Oxford).

Real-time fluorine mineral sensor – taking research to prototype

T Payten[1], J Moffatt[2], L Teixeira[3], N Spooner[4], L A Balzan[5], G Wilkie[6] and G Tsiminis[7]

1. PhD Candidate, Institute of Photonics and Advanced Sensing, The University of Adelaide, Adelaide SA 5005. Email: thomas.payten@adelaide.edu.au
2. Postdoctoral Researcher, Institute of Photonics and Advanced Sensing, The University of Adelaide, Adelaide SA 5005. Email: jillian.moffatt@adelaide.edu.au
3. HDR Student, Institute of Photonics and Advanced Sensing, The University of Adelaide, Adelaide SA 5005; and Scantech International Pty Ltd, Camden Park SA 5038. Email: l.teixeira@scantech.com.au
4. Professor, Institute of Photonics and Advanced Sensing, The University of Adelaide, Adelaide SA 5005; and Weapons and Combat Systems Division, Defence Science and Technology Group, Edinburgh SA 5111. Email: nigel.spooner@adelaide.edu.au
5. Chief Technology Officer, Scantech International Pty Ltd, Camden Park SA 5038. Email: l.balzan@scantech.com.au
6. Research Manager, CRC for Optimising Resource Extraction, Kenmore Qld 4069; and The University of Adelaide, Adelaide SA 5005. Email: Gregory.wilkie@adelaide.edu.au
7. Postdoctoral Researcher, Institute of Photonics and Advanced Sensing, The University of Adelaide, Adelaide SA 5005; and Ziltek Pty Ltd, Email: Georgios.tsiminis@ziltek.com

INTRODUCTION

Fluorine is a penalty element due to its reactive nature. In acidic environments many fluorine minerals dissolve to form hydrofluoric acid (HF), changing processing conditions. When smelted HF can be released, causing negative effects to nearby people and the environment, as well as potentially damaging the smelter. Sale of ore with high fluorine levels elicit a financial penalty or are banned outright.

Real-time sensors create the opportunity for instantaneous decisions on ore processing due to changing conditions. A fluorine sensor would allow rises in fluorine concentration in a processing stream to be flagged, and decisions on processing conditions or diversion to stockpile before processing could be undertaken. As fluorine is a light element, it is difficult to detect with in-field XRF devices and does not work well with PGNAA. There are currently no existing sensors to quantify the presence of fluorine in real-time, and thus decisions based on fluorine grade cannot be made at minute- or even hour-scales.

Sensors designed to measure the presence of minerals that contain fluorine are a possible avenue to enable the real-time detection of this element. Mineral-based sensing may also give an added advantage of additional information about how the fluorine will react under different processing steps.

The authors were given a grant under CRC ORE II (project number P1–005) to search for mineral-specific signatures suitable for real-time analysis. The work focused on novel regimes and applications of fluorescence as a means to detect specific minerals. The aim was to exploit fluorescence responses unique to minerals of interest in mining systems in order to produce sensors that address gaps in existing capability. After the successful discovery of signatures specific to two major fluorine minerals an additional grant (P1–014) was funded to develop the research into a prototype on-belt sensor, in partnership with Scantech International Pty Ltd.

This paper details the development of a sensor package through multiple Technology Readiness Levels (TRLs) through collaboration with government/industry grant schemes, academics from university, and a sensor-focused Mining Equipment and Technology Services (METS) company. We give a brief description of the new sensor technique and provide a case study of multi-disciplinary collaboration.

PROJECT BACKGROUND

The CRC ORE II project P1–005 was funded to explore novel fluorescence signatures for real-time detection and identifications of minerals of economic significance. Fluorescence is a technique whereby a specific wavelength of light interacts with the sample of interest, which subsequently

produces a different target wavelength for detection. Conventional fluorescence utilises UV excitation; the induced fluorescence emission is observed in either longer-wavelength UV or in the visible waveband. ‘Novel Fluorescence’ mineral sensing is an emerging platform technology based on regimes of fluorescence that lie outside this limited conventional range of single-photon excitation/emission, and consequently have been understudied and generally overlooked. The utilisation of these ‘novel fluorescence’ modalities opens up the technique to more than the ‘classic’ fluorescence minerals, and can provide further advantages for sensing such as safer excitation wavelengths, lower noise backgrounds, and better separation between excitation and emission wavelengths.

An early win for the project was the observation of multiple signatures from two fluorine-bearing minerals. Many fluorine-containing crystals are known for their high propensity for fluorescence – both fluorine and fluorescence are named after the same fluoride mineral, fluorite/fluorspar. For a fluorescent signature to be useful for sensing, however, it needs to be present within all members of the mineral subset (this can be all of the naturally-grown mineral species, or all of the mineral present at a particular mine site, depending on the use-case.) Signal characterisation must therefore be conducted on a relevant subset of mineral samples as the origins of fluorescence may be due to variable mineral properties.

Many fluorescence signatures come from ion impurities within the mineral which may or may not be present in all samples across a mine site. Multiple mineral samples obtained as offcuts from museum specimens were tested to assess the ubiquity of the signatures. Three complex ore types were also tested to check for background signals from other common minerals. The two target minerals had fluorescence signals in a similar wavelength band that appeared to be common for all samples, and these were chosen as target signatures for the next stage of the project (Spooner, 2020). These signatures were excited in the visible part of the electromagnetic spectrum and emit in the infrared, which differs from the UV-to-visible regime that mineral fluorescence is commonly assumed to operate within. This allows safe excitation even at high powers, and minimises the overall background from sunlight and artificial lighting.

Collaboration with Scantech International enabled development of a prototype on-belt sensor for testing these target signatures in a more ‘lifelike’ scenario, funded by CRC ORE II project P1–014. A new targeted fluorescence platform was designed, and components were tested at the University of Adelaide before a full-scale prototype to measure belt widths up to 600 mm was assembled at Scantech International. The test planning followed methods standardised by Scantech and utilised for other similar on-belt analysis equipment. The prototype behaviour was characterised with initial tests conducted using museum-quality samples. Testing is ongoing and currently involves ore samples with known fluorine content in order to assess prototype behaviour under ‘realistic’ conditions and move the TRL of the system to 5.

An advantage of novel fluorescence as a mineral detection system is its adaptability. Once the initial prototype has been developed for a particular use-case (ie on-belt, handheld), only small changes need to be made to the system in order to make use of fluorescence signatures of other minerals. While the initial prototype focuses on signatures from fluorine minerals, continuation of the P1–005 project has found novel fluorescence signals of interest for other potential targets, including lithium minerals and heavy mineral sands.

SENSOR DESIGN CONSIDERATIONS

Fluorescence sensing requires an excitation source and a detector, and both must be considered when translating from a laboratory set-up to a field-deployable system. Detection and characterisation of mineral signatures in P1–005 were conducted using highly sensitive laboratory equipment that provide the high degree of flexibility required for a research environment but do not translate well into the field. A field-deployable device must take into account changes in temperature, dust and vibration, as well as the potential impact of ambient light conditions. Laboratory-style laser systems and sensitive detectors would have a very short operational life in a mining environment.

Light Emitting Diodes (LEDs) were chosen as the excitation source for the sensor prototype as these were readily available, commercial off-the-shelf (COTS) components with a high degree of reliability. Advantages over off-the-shelf lasers systems included an increased safety in a complex working

environment and the ability to excite a broad sample area instead of a small point. This allows greater sampling statistics and is more suitable for an on-belt application.

Detection devices on the initial prototype included a spectrometer for wavelength-dependent detection and a photodetector with specialised filters for intensity-dependent detection. This two-detector method was used to test each method and validate positive measurements. It was assumed that the process of using two detectors would remain for the set-up phase and for calibration for on-site conditions in the field, but that during steady-state operation only one detector system would be needed.

Design and construction of the prototype focused on scalability and modularity of components, in part to ensure laboratory tests could be conducted before construction of a full-scale prototype and also to allow for reconstruction to test different scenarios and scales of the on-belt sensor. Parts were limited to COTS equipment to ensure speed of construction and affordability of potential future beta-prototype and commercial products.

Lab-based sensor prototype

An initial small laboratory-based prototype was constructed to test both the detectors and the change of excitation source from high-powered pulsed laser source to continuous-wave LED. While in general Stoke's fluorescence has an easily extrapolated, linear excitation-to-emission dependence, nonlinear effects can occur, especially at high powers. Changes in heat deposition, and potential saturation of quenching effects at high powers had to be considered and tested before LEDs were confirmed as a suitable excitation source. Small, easily obtainable LEDs were used initially to test the target mineral's response to LEDs before higher powered LEDs suitable for the full-scale prototype were sourced.

The more rugged, COTS detectors were less sensitive than those in the P1–005 laboratory system, and the processing requirements needed to optimise their sensitivity to the target signatures were found and tested during this phase.

Scaling up from the lab to full-size

Once LEDs were confirmed to be suitable excitation sources, higher-powered LEDs used for industrial lighting were ordered and tested. Full optical systems were designed before construction of the prototype; these could not be tested beforehand as their optimum conditions were dependent on the sensor dimensions which was too large to test in a laboratory environment.

The full sampling area of the prototype was 600 mm × 1200 mm, with a maximum clearance of 1125 mm (see Figure 1). Clearance is likely to be smaller on a final product, with a corresponding distance-squared increase in signal detection (ie half the clearance distance results in a four-fold increase in signal intensity).

FIG 1 – The full-scale fluorine-mineral sensor prototype, showing the scale of the system, the LED arrays, and the detection optics (centre).

Validation tests at scale were conducted using a museum-grade sample of approximately 10 mm diameter. Emission detection over the full 'belt' width was confirmed. Optimal placement of excitation LEDs and detection optics depends on the final size and clearance of the final sensor product, so optimisation of these conditions was not finalised at this stage.

To aid in data collection and processing, specialist software was commissioned to synchronously run the detectors and excitation LEDs, as well as collect data from the detectors and from passive temperature and excitation level monitors. Through a Graphical User Interface (GUI) the operator of the sensor prototype was able to modify many parameters of the operation. The software also conducted real-time data analysis and output. The GUI was originally designed in the testing phase to output the data analysis in the form of a graph of detected intensity; in a field-deployable device that was correctly calibrated this output could instead be a live reading of fluorine grade or provide a 'traffic light' warning at threshold grades.

FLUORINE SENSOR TECHNOLOGY READINESS PROGRESS

Technology Readiness Levels (TRLs) provide an internationally agreed-upon standard to describe system development (see Table 1). Commercial Readiness Levels occur at the TRL stages 7–9 and beyond; before then sensor development must occur without a commercial product to produce cash flow or induce investment.

TABLE 1

Technology Readiness Levels and their definitions as per Australian Government guidelines.

TRL level	Definition
1	Basic Principles observed and reported
2	Technology concept and/or application formulated
3	Analytical and experimental critical function and/or characteristic proof of concept
4	Component/subsystem validation in laboratory environment
5	System/subsystem/component validation in relevant environment
6	System/subsystem model or prototyping demonstration in a relevant end-to-end environment
7	System prototyping demonstration in an operational environment
8	Actual system completed and qualified through test and demonstration in an operational environment
9	Actual system proven through successful operations

The CRC ORE II grant P1–005 started when the fluorine sensor was at TRL 2: fluorescence is a well-known and well-studied concept in other materials, and broad but limited fluorescence studies had been undertaken in the past on natural as well as synthetic minerals. Identifying and characterising the target signatures from fluorine minerals brought the TRL level to 3. CRC ORE II grant P1–014 progressed the TRL level through level 4.

Current work is aimed towards completion of TRL 5. To validate the system in a relevant environment, the system must be able to distinguish between ore with fluorine grades that differ by 100 ppm F, as discussions with end users suggest that this is the relevant benchmark for fluorine in Australian mining companies. The full-scale prototype was validated and characterised with museum-grade samples but has not yet been validated with natural crushed ore with fluorine minerals dispersed throughout the material, rather than concentrated in a discrete sample.

ISSUES ENCOUNTERED DURING THE TECHNOLOGY DEVELOPMENT

The lab-scale prototype was demonstrated to be effective on museum-grade samples and was able to detect to low fluorine levels in crushed museum samples blended to create a concentration series. A concern at this point in the project was that museum samples are selected for their ‘interest’, rather than their ‘typical-ness’, and this may bias observations of typical fluorescence efficiency, and therefore excitation power and detection time requirements. Construction of the full-scale prototype was delayed while typical industry samples were investigated in the lab-scale prototype. We recommend future sensor development by universities engage fully with industry partners as soon as possible, and quickly build full-scale prototypes of sensors for testing, for the following reasons:

- Target grades, especially for penalty elements, are generally quite low in ore samples. A full-scale prototype is therefore necessary to acquire relevant sampling statistics. Acquisition of enough data to allow for statistically relevant analysis of low-grade ore quickly becomes infeasible with laboratory-scale tests.
- It is difficult to acquire samples from mining partners in order to validate system response in target conditions. Industry partners are more likely to have contacts and mechanisms in place to acquire mine samples, in quantities relevant for sensor testing.

FURTHER IMPROVEMENTS AND LEARNINGS

Further improvements to the prototype are considered desirable in order to achieve TRL 5 for the target fluorine grade of 100 ppm. Natural background must be accounted for in intensity measurements – characterisation of typical background variability suggests background levels should be recalibrated every 1–5 seconds, and can in the current prototype only be sensed when

the excitation LEDs are off. LEDs capable of high pulse rates, or a continuous background monitoring system, would be a necessary addition to a new model of prototype.

Emission intensity is proportional to excitation power as well as target presence. The LEDs in the current prototype are typical in that their intensity is proportional to temperature – both ambient and self-generated. Temperature control or accurate excitation illumination monitoring are desirable to lower uncertainties in sensor output.

Signal-to-noise can be improved with greater excitation intensity at the sample; this can be achieved by lowering the clearance height, or by focusing the LED light to a narrow line across the belt width – as the sample will be moving along the belt, excitation coverage across the width of the belt matters for sampling statistics, but not length over the belt. This would also allow detection optics to be redesigned to focus on a narrower band of the belt, lowering background interference from other light sources.

Alternative applications of the technology

Alternative forms of fluorine-mineral sensors were discussed during the prototype design and development. Fluorescence has an advantage in that the technology is readily scalable and can be applied in many forms from hand-held to cross-belt. Hand-held mineral sensors utilising fluorescence are an alternative product development pathway being investigated.

Collaboration learnings

There is a well-known technology 'Valley of Death' in TRLs 3–5, where both universities and industry generally lack the funding and experience to take a proven idea to a prototype capable of demonstrating the idea to investors. CRC ORE's policy was not only to provide funding for projects at this level, but to facilitate collaboration between university and industry. Having a grant body with extensive experience at communicating to both academics and industry is rare, however, and learnings from our experience could prove valuable for future collaborations.

From the grant funding body

As a Co-operative Research Centre, CRC ORE's role was not only to fund research and development for improving the Australian mining industry, it also had a mandate to link Industry, METS and Research organisations to perform research in a co-operative framework. This builds deep connections between industry and researchers that can improve the success rate of low to mid TRL projects progressing through the 'Valley of Death'. This project has been an exemplar in the way that Co-operative Research can be performed in Australia and is a testament to the Co-operative Research Centre principles that is supported by the Australian Government.

A key learning from projects funded in this way is that the Co-operative Research Centre approach not only provided the funds but also the legal and communication framework to allow multiple parties to work together as each partner in the project had signed on to the common legal, commercial and Intellectual Property terms and conditions of CRC ORE. This greatly simplified the project proposal process as all parties were aligned to the same guiding principles. Execution of the project was also simplified as the interests of the Researchers, METS company and Industry representatives were aligned and communicated throughout the project delivery stage.

From the university

University research funding in Australia is funded in the main by grants, and thus the focus of research is to meet the deliverables of these grants. While CRC ORE was very good at communicating the requirements of these deliverables, especially of audience, length, and detail required for reports, it is good practice for a university to 'check in' with the detail of deliverable requirements between reports, in order to ensure research is moving along the right track.

The University and Scantech International had a previous relationship, which allowed good lines of communication between the two partners. This was vital for planning mitigation strategies to allow experimental work to continue through changing COVID-19 restrictions. While a global pandemic is a rare event, setbacks in a project are not, and developing a strong and honest relationship between collaborators as soon as possible is an important part of technology development in this space.

Research publications in peer-reviewed journals are major objectives for Universities and many grant funding bodies. This may be difficult when partnering to create new prototype systems. This project benefited from the support of the CRC ORE and Scantech International who were both keen to share the learnings, but publication may be a risk for other development partnerships.

From industry

A key benefit for industry partners is to gain access to cutting edge technological developments while being able to have initial R&D (prior to TRL4) completed at low cost. By partnering early, there is the possibility of influencing the approach and learning from any shortcomings in the early prototyping stages. With a demonstrated underlying technological base, commercialisation follows a straightforward path, involving additional prototyping, refinement for quality of results, quantification of limits on result accuracy, and ruggedisation of the equipment. It is also possible to obtain valuable market feedback on what the technical requirements are, such as performance accuracy and market interest, while the project is taking place. For a dynamic technology-focused company like Scantech, it is possible to move quickly and establish a market foothold, particularly through publication, which aligns well to university objectives.

CONCLUSION

This paper has discussed the development of a novel mineral-specific sensor technology in the innovation 'Valley of Death' at TRL3–5.

Design, construction and testing of a full-scale prototype encountered several issues, from unexpected power instability to the inability to obtain appropriate samples.

The fluorine-mineral sensor prototype is currently at TRL4–5, with planned improvements to enable very low detection limits and improved sampling of the belt surface. This sensor technology is the first real-time fluorine-mineral sensor, and the application of this sensor is not restricted to cross-belt scales. Further development of the cross-belt prototype will be undertaken parallel to alternative sensor scales.

ACKNOWLEDGEMENTS

The authors wish to acknowledge CRC ORE II, which funded this research and Scantech International who provided testing facilities and assistance. Resonate Systems designed and produced the software to run the full-scale prototype. The TATE Museum, School of Physical Sciences, The University of Adelaide; and the South Australian Museum provided samples for initial and further testing.

REFERENCES

Spooner, N S, Tsiminis, G, Moffatt, J E, Payten, T B, Teixeira, L de S, Klantsataya, L, de Prinse, T J, Smith, B W and Ottaway, D J, 2020. A novel fluorescence sensor for the detection of fluorine bearing minerals in base metal ores, in *Proceedings Preconcentration Digital Conference* (The Australasian Institute of Mining and Metallurgy: Melbourne), pp 303–308.

A geometallurgical approach towards the correlation between rock type mineralogy and grindability – a case study in the Aitik mine, Sweden

R Schmitt[1], M Parian[2], Y Ghorbani[3], I McElroy[4] and N J Bolin[5]

1. Emerald Master's student, Minerals and Metallurgical Engineering, Luleå University of Technology, SE-971 87 Luleå, Sweden. Email: raoul.s@web.de
2. Assoc. Professor, Minerals and Metallurgical Engineering, Luleå University of Technology, SE-971 87 Luleå, Sweden. Email: mehdi.parian@ltu.se
3. Assoc. Professor, Minerals and Metallurgical Engineering, Luleå University of Technology, SE-971 87 Luleå, Sweden. Email: yousef.ghorbani@ltu.se
4. Development Engineer, Division of Process Technology, Boliden AB, SE-936 81 Boliden, Sweden. Email: iris.mcelroy@boliden.com
5. Project Manager, Division of Process Technology, Boliden AB, SE-936 81 Boliden, Sweden. Email: Nils-Johan.Bolin@boliden.com

ABSTRACT

Aitik is a large copper porphyry type deposit located in northern Sweden, currently exploited at an annual rate of approximately 45 Mt. The ore's exceptionally low head grade of 0.25 per cent Cu and varying degrees of hardness across the entire deposit pose challenges to the two fully autogenous grinding lines, each of which comprises a primary autogenous mill in series with a pebble mill.

The variability in ore grindability frequently leads to fluctuations in mill throughput. Within the framework of a geometallurgical approach, the present study investigated the relationships between ore grindability and modal mineralogy. For this purpose, drill core samples from different lithologies were subjected to Boliden AB's in-house grindability tests. This fully autogenous laboratory-scale test generates a grindability index mainly related to abrasion breakage, which is a significant breakage mechanism within autogenous mills. The test results suggested divergent degrees of grindability within and across the selected rock types.

A combination of scanning electron microscopy, X-ray powder diffraction, and X-ray fluorescence analyses was performed for the grinding products and bulk mineral samples. The resulting mineralogical and elemental properties were subsequently correlated to the parameters from the grindability tests. It was shown that the main mineral phases, such as plagioclase, quartz, and micas, correlate well with the grindability indices. Similar correlations were found regarding the sample's chemical composition, attributable to the main mineral phases.

A further inverse correlation was established between the sample's calculated average Mohs hardness and the grindability indices. Moreover, mineral liberation information provided by scanning electron microscopy was associated with the parameters mentioned earlier. The identified relationships between grindability, modal mineralogy, and element grades may help Boliden develop a predictive throughput model for Aitik based on the mine's block model.

INTRODUCTION

As global resource demand rises, increasingly complex mineral deposits have to be exploited, implicating challenges such as declining head grades, orebody variability and ores that are more difficult to process (Dominy *et al*, 2018). A continuous decline in ore grades over time is indeed being observed in the copper mining sector (Guiomar *et al*, 2016). Karlsson (2020) reports a similar development for the Aitik copper open pit mine. These challenges lead to additional production risks and uncertainties for mining operations. Geometallurgy provides the ability to forecast mine production and economic variables (Rincon, Gaydardzhiev and Stamenov, 2019). This discipline can be understood as a cross-disciplinary approach integrating information from mineral processing, metallurgy, geology, and mining engineering, aiming to improve production forecasting, reduce production risks, and maximise a mining project's economic value (Dominy *et al*, 2018; Lishchuk *et al*, 2020).

Orebody variability can reduce plant throughput through fluctuations regarding ore hardness (Dominy *et al*, 2018). In the last decade, the Aitik mine underwent two major expansions to increase

its plant throughput to 45 Mt per annum from 2019 onwards, currently operating two fully autogenous grinding circuits. Variations in ore grindability have since long led to fluctuations in plant throughput and daily plant production (Westerlund, 2017). These circumstances impede meeting production targets and the scheduling of mining activities accordingly. The necessity arose to predict the grindability of Aitik's ore and consequently the mill throughput.

A well-known parameter influencing the performance of a comminution circuit, mainly throughput, is grindability (Shi *et al*, 2009), which is defined as an ore's resistance to breakage (Verret, Chiasson, and McKen, 2011). In the context of the present investigation, grindability is understood as the mass of fines generated due to abrasive grinding (Parian and Palsson, 2020). Since grindability is a variable parameter, it adds uncertainties and hinders the sound evaluation of a mining project's feasibility (Tungpalan *et al*, 2015). Laboratory-scale grindability tests are a standard tool to assess ore grindability and, depending on their suitability, may be used to map the variability of grindability throughout a mineral deposit (Mwanga, Rosenkranz and Pertti, 2017; Verret, Chiasson and McKen, 2011). Geometallurgical programs incorporate this type of mapping to predict metallurgical performance (Parian *et al*, 2015).

Traditionally, the design of AG mills is based on parameters derived from pilot-scale comminution tests performed on relatively large ore bulk samples (Verret, Chiasson and McKen, 2011). However, the collection and preparation of such bulk samples are expensive and time-consuming, and uncertainty remains regarding their ability to accurately represent the orebody (Morrell, 2004). Therefore, small-scale grindability tests have been developed over the past decades, some of which are suitable for geometallurgical mapping, characterised by their comparatively low cost, smaller required sample sizes, and ease of execution (Mwanga, 2016).

The principal objective of the presented study was to establish a link between grindability indices and rock type mineralogy. The methodology of the present study comprised a laboratory test method to assess the decomposition of large mineral particles by autogenous comminution developed by Boliden Mineral (grindability test, wear test). Different analysis techniques for chemical and mineralogical characterisation were implemented. Automated mineralogy provided additional information regarding mineral liberation. The geometallurgical approach of the project encompassed relating grindability indices to sample mineralogy, seeking to predict grinding performance through mineral grades as a proxy. The present paper reports on the results from the grindability tests and chemical and mineral characterisation.

Project site

The Aitik mine is one of two of Boliden Group's open pit mines (Boliden, 2020). The Cu-Au-Ag deposit is situated in Sweden's northernmost county, Norrbotten, approximately 10 km south-east of the town of Gällivare and 60 km north of the arctic circle (Karlsson, 2020). It is considered one of Europe's largest producers of Cu, Au, and Ag (Wanhainen *et al*, 2012). Since commencing production at Aitik with 2 Mt processed in 1968, the amount of processed ore has constantly risen and peaked at 41.6 Mt in 2020, while the average head grades of milled ore have constantly decreased (Karlsson, 2020). As compared to other copper producing open pit and underground mines whose ore grades average at around 1 per cent Cu (Guiomar *et al*, 2016), Aitik's average Cu-grade of 0.22 per cent is notably lower (Karlsson, 2020). Through a combination of strategic planning, automatisation, electrification, and digitalisation, Aitik has become one of the world's most productive open pit copper mines (Mackenzie, 2017; Beyglou, Schunnesson and Johansson, 2015; Boliden, 2020).

The deposit sits along a fault zone, with the hanging wall and footwall respectively constituting banded feldspar-biotite gneiss and feldspar-biotite-amphibole schist. The main ore zone is dominated by quartz-muscovite schist as well as biotite gneiss and biotite schist (Wanhainen *et al*, 2014). Furthermore, pegmatite dykes can be found within the deposit's ore zone and hanging wall. These dykes are generally mineralised within the ore zone and barren in the hanging wall (Wanhainen *et al*, 2014). Wanhainen *et al* (2012) suggests classifying Aitik as a hybrid deposit between both porphyry type and IOCG type deposit.

After blasting and crushing, the ore is conveyed to two parallel grinding lines, each of which comprises an Ø 11.6 m × 13.7 m primary autogenous mill in series with a Ø 8.1 m × 11.3 m

secondary pebble mill (Markström, 2012; McElroy *et al*, 2019). Each primary AG mill operates in a closed circuit with a cone crusher to crush salient pebbles aiming at increasing the AG mill's throughput (Hilden, Yahyaei and Powell, 2019). This set-up of the grinding lines indicates that the pebble fraction within the mill feed is a limiting factor for plant throughput.

Grindability

In general terms, grindability is defined as an ore's resistance to breakage. A well-known index to express an ore's grindability is the Bond Ball Mill Work Index (BWi) expressed in kWh/t, which indicates the specific energy requirement (kWh) to grind 1 t of ore to the desired target size (GMG, 2015). At Boliden, grindability is generally expressed as the mass of particles below 45 µm generated per kWh (Westerlund, 2017) and calculated according to Equation (1), where Out is the % <45 µm in the mill discharge, In the % <45 µm in the mill feed, and F and P respectively the feed rate (t/h) and mill power (kW).

$$Grindability = \frac{Out-In}{1000} * \frac{100*F}{P} = \frac{10(Out-In)}{Spec.Energy} \quad (1)$$

Boliden AB developed its laboratory grindability test in the 1970s to assess ore decomposition due to abrasive grinding and to be able to evaluate an ore's suitability for autogenous grinding by employing a grindability index k_s (Markström, 2018). The general idea was to compare and corroborate the results derived from the grindability tests with data from pilot plant tests and industrial mineral processing plants. Hence, this would allow appraising the grinding behaviour of a specific ore in an industrial grinding circuit on a laboratory scale (Borell and Lager, 1983). Other grindability tests developed to assess autogenous grinding are the SAG Mill Comminution test (Morrell, 2004), the MacPherson Autogenous Grindability Test (Macpherson, 1976) and the Advanced Media Competency Test (Morell, 2019).

Investigating the relationship between grindability and mineralogy

Recently, Rincon, Gaydardzhiev and Stamenov (2019) subjected nine ore samples from the Dundee Precious Metals' Chelopech mine in Bulgaria to grindability tests within a laboratory ball mill. The results suggested that grindability correlates positively with the sample's kaolinite content. To predict grinding performance at Aitik, Markström (2020) conducted a study aiming at indicating the relationship between ore mineral/element composition and plant performance. Belt-cut samples from the AG mill were subjected to SAG Mill Comminution Tests as well as Boliden's in-house grindability test method. No correlations were found between mineral, element grade, and AG mill grinding energy. In connection with the development of a predictive geometallurgical model at Hot Chili's Productora copper project in Chile, drill core samples were subjected to metallurgical tests for the determination of BWi and geochemical analysis for the determination of chemical composition (King and MacDonald, 2016). Subsequent regression analysis of the acquired data was aimed at using element concentrations as geometallurgical proxies. The BWi was best predicted by Al and K concentrations; hence, an equation for the calculation of BWi was developed based on this relationship.

MATERIALS AND METHODS

Samples

Sweden is a significant European mining region, with active iron oxide, sulfide, and precious metal mines situated in the mining districts of Norrbotten, Skelleftefältet, and Bergslagen. Regarding the amount of Cu in produced concentrates, Sweden accounts for approximately 11 per cent of the European Union's output (Norlin *et al*, 2020). Aitik is Sweden's largest sulfide mine (Wanhainen *et al*, 2012) and was responsible for 91 per cent of the country's production of Cu concentrates in 2020 (Norlin *et al*, 2020), underlining the mine's importance for the Swedish raw materials industry.

For this study, 11 ore samples in the form of drill cores were collected from four locations of the open pit mine (Figure 1) and according to the following classified rock types: Diorite (4), Mica Gneiss (3), and Sericite Schist (4). Mica Gneiss and Sericite Schist samples were retrieved from the deposit's main ore zone, whereas the Diorite samples originated from the footwall. Table 1 shows the collected samples with their respective logged textures and grain sizes of the mineral matrix.

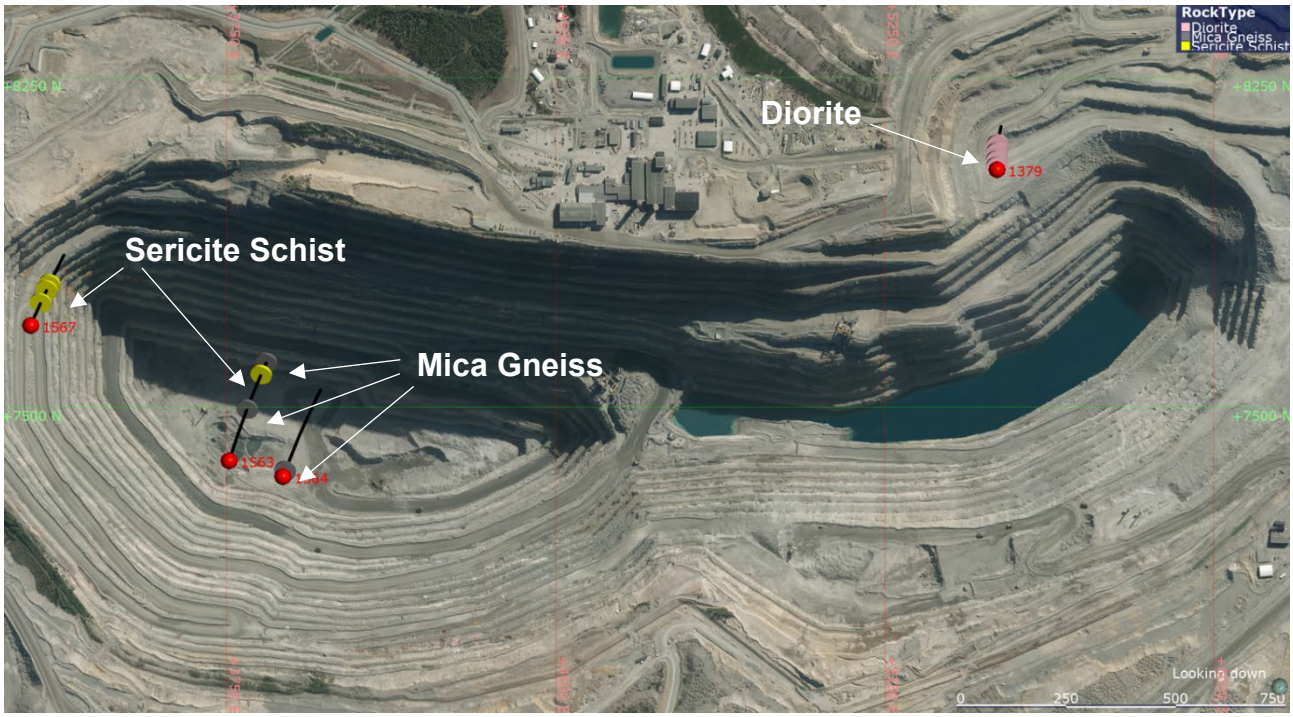

FIG 1 – Plan view of the Aitik open pit mine with the locations of the drill holes from which samples were retrieved. The disks are coloured according to the different rock types (red = Diorite, grey = Mica Gneiss, yellow = Sericite Schist) and illustrate the approximate depths of the samples.

TABLE 1

Ore samples with their corresponding rock type, depth at which the sample was taken, and information regarding texture and grain size of the mineral matrix.

Sample	Rock type	Texture	Matrix grain size	Type of sample	Depth (m)
1	Diorite	Phaneritic	Medium	Half drill core	84.0
2	Diorite	Phaneritic	Medium	Half drill core	10.0
3	Diorite	Phaneritic	Medium	Half drill core	44.0
4	Diorite	Phaneritic	Medium	Half drill core	122.0
5	Mica Gneiss	Porphyritic	Fine	Half drill core	206.0
6	Mica Gneiss	Porphyritic	Fine	Half drill core	24.7
7	Mica Gneiss	Porphyritic	Fine	Half drill core	388.7
8	Sericite Schist	Porphyroblastic	Fine	Half drill core	94.5
9	Sericite Schist	Porphyroblastic	Fine	Half drill core	173.9
10	Sericite Schist	Porphyroblastic	Fine	Half drill core	340.6
11	Sericite Schist	Porphyroblastic	Fine	Half drill core	150.0

Since the purpose of the present study was to investigate the relationship between grindability and rock type mineralogy, other parameters influencing grindability had to be isolated. The literature shows that an ore's grain size and texture influence grinding performance (Kekec, Ünal and Sensogut, 2006; Djordjevic, 2013; Mwanga, Rosenkranz and Pertti, 2017; Ghanei, 2020). Hence, these two variables were maintained uniform when collecting the ore samples of each rock type. Furthermore, it is important to mention that the number of selected samples was not sufficient to accurately represent the deposit's distribution of rock types or to map geometallurgical parameters such as grindability across the deposit. However, a larger number of samples would have exceeded

the study's scope. Geometallurgical studies typically require between 100 and 300 grindability tests and over 1000 mineralogical tests (Williams and Richardson, 2004).

After crushing and performing the grindability tests, the ore samples passed through different preparation steps according to the subsequent analyses. Representative portions of the grinding products were subjected to particle size distribution analyses. Consecutively, fine-grained parts of the grinding product in the ranges of 0–45, 45–90, and 90–180 µm were taken for the preparation of resin-mounted samples for automated mineralogy (quantitative evaluation of minerals by scanning electron microscopy, QEMSCAN). Furthermore, mineral bulk samples were prepared by pulverising crushed material in a ring mill and splitting it into representative portions for X-ray powder diffraction (XRD) and X-ray fluorescence (XRF) analyses.

Methods

X-ray powder diffraction in combination with Rietveld analysis

For mineral characterisation by XRD, a PANalytical Empyrean X-ray diffraction diffractometer equipped with a Cu LFF HR X-ray tube and a PIXcel3D detector at Luleå University of Technology's (LTU) department of chemistry was used.

As previously mentioned, 11 ore samples were pulverised by a ring mill at LTU's mineral processing laboratory to reduce the powder particle size and to provide for a random orientation of the mineral crystals (Alderton, 2021). The fine powder was then filled into Ø 26 mm back-loading holders. The diffractometer's scan axis was set to gonio-mode. The 2θ start and end positions were respectively set to 5° and 75° with a step size of 0.026° and a scan step time of 337 seconds, resulting in a scan time of approximately 60 minutes per sample.

Mineral phase quantification was accomplished by using Malvern PANalytical's XRD analysis software HighScore Plus in combination with the Inorganic Crystal Structure Database (ICSD), which at the time of the study contained 177 337 reference patterns for different inorganic crystal structures. During Rietveld refinement for improved phase-quantification in HighScore Plus, background corrections, specimen displacements, peak widths, and crystal lattice and peak shape parameters were considered.

Automated mineralogy – QEMSCAN

Automated mineralogy provides numerous methods for investigating mineral characteristics, amongst others the quantification of a sample's modal mineralogy and the measurement of grain size and shape, and the determination of the degree of mineral liberation (Parian *et al*, 2015).

For this study, modal mineralogy and mineral liberation information were decisive, since it was expected that this information would correlate well with the results of the grindability tests. Epoxy resin-mounted samples were prepared from ground ore samples of narrow size fractions (0–45, 45–90, and 90–180 µm) and bulk mineral samples. The latter allowed for a comparison between the measurement results from automated mineralogy and XRD.

The device implemented within this study was Boliden AB's FEI QEMSCAN® 650, equipped with a W-filament electron-gun, Energy Dispersive X-Ray Spectroscopy, and an electron backscatter detector. All analyses were processed using FEI company's iMeasure and iDiscover software suite (version 5.4), where the former was used for data collection and the latter for mineral identification. Particle Mineral Analysis (PMA) was the selected method of analysis, which enabled the determination of mineral abundance and mineral liberation. Boliden AB provided a custom-made species identification protocol (SIP) which was based on past mineralogical studies of the Aitik deposit. This database contained mineral phase definitions for mineral identification. The SIP was used as the starting point of the mineral characterisation procedure and modified by the author as required. Proportions of unknown mineral phases were minimised by applying two types of preprocessors: the touching particles and the boundary phase processor. The former allowed to split or filter touching particles, and the latter helped to mitigate falsely identified pixels (Warlo *et al,* 2019).

Chemical analyses

Chemical analyses of loose powder samples were performed at Boliden AB's mineral processing laboratory in Boliden according to the company's standardised techniques. XRF (SPECTRO XEPOS energy dispersive X-ray fluorescence) is routinely employed at the company's laboratory to determine the chemical composition of samples originating from its processing plants or pilot and laboratory-scale tests.

Representative portions of the samples prepared for XRD analyses were subjected to XRF analyses. These samples were previously pulverised in a ring mill to obtain a P_{80} <50 µm. Boliden's standard measurement setting for ore powder samples 'TQ Boliden Ore' was applied, which was configured to a measurement time of four minutes per sample. Results were reported as per cent by mass per detected element and imported into digital spreadsheets. Hence, no further data evaluation was required.

Grindability tests

Only half-core samples from Aitik mine were available for the grindability tests. The minimum sample mass for a single grindability test is approximately 15 kg (Markström, 2018). However, the required sample mass depends on how rapidly the ore decomposes in the grinding environment. The outcomes of the grindability tests performed throughout this study were used to generate a grindability index k_s based on the weight loss of a pebble charge over time due to wear. Hence, the grindability tests are also referred to as 'wear tests'.

Each grindability test requires a preparative step; broken and crushed drill cores are subjected to an autogenous grinding process in a Ø 284 mm laboratory mill (Sala Mill) over several hours at a low rotational speed of approximately 38 rev/min and under the addition of water and grinding sand. The autogenous grinding action at low rotational speed enforced the breakage mechanisms of attrition and chipping, which led to the removal of edges, asperities, and rough surfaces, producing well-rounded 'pebbles'. Subsequently, the mill discharge was cleaned and sized into fine, medium, and coarse size classes, which were used to assemble a pebble test batch of a specific weight.

For each wear test, a Ø 200 mm bench-top laboratory grinding mill was filled with a pebble test batch and combined with <1 kg of finely crushed material (<3.15 mm) of the same sample and water to reach a pulp density of approximately 10 per cent. Thus, the pebbles act as the grinding media and the finely crushed material as the mill charge. Sequentially, the mill charge was ground at 46 rev/min for 60, 90, and 150 minutes. Following each grinding process, the mill was emptied, and the weight loss of each of the test batch's size classes was measured and recorded. Before the next round of grinding, each size class was refilled with the amount of fresh material equal to the mass loss due to the grinding action. The k_s index was then determined by plotting the total percent weight loss of the test batch against the three grinding times. The slope of a straight line of best fit through these three points and the origin calculated using the least squared method is the wear index, expressed as % weight loss/(min*10^{-2}).

RESULTS

Grindability test results

The evaluation of the data from the grindability tests revealed disparities across k_s-values acquired from samples of different rock types (Figure 2). Likewise, the wear indices from samples of the same rock types show little congruency, except for Diorite 1 and 4 and Mica Gneiss 1 and 3. A high k_s-value implies a high mass loss of pebbles during grinding and thus a low resistance due to abrasive grinding. Sericite Schist samples experienced the highest mass loss during the grindability tests, whereas Diorite samples were less affected by the prevailing breakage mechanisms. K_s-values from Mica Gneiss samples lie intermediate between both other rock types.

The grindability indices derived from Sericite Schist samples diverge more strongly and appear to be between two to four times higher than those for Diorite and Mica Gneiss samples. In terms of grindability/resistance against abrasion, the test results suggest the following order: Diorite > Mica Gneiss > Sericite Schist. Hence, it becomes evident that different rock types from the Aitik mine vary in their comminution behaviour.

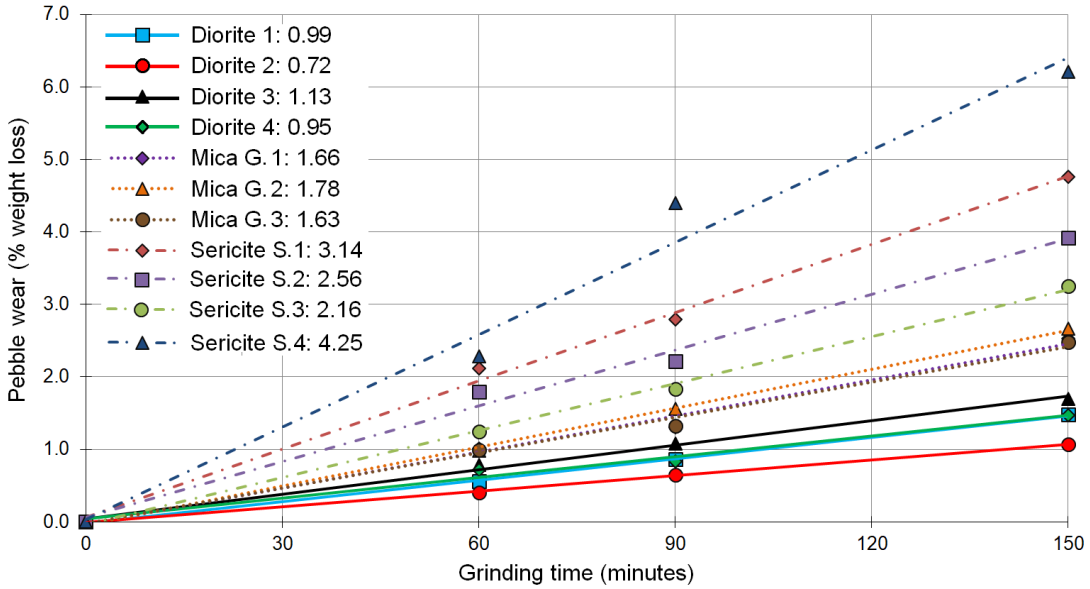

FIG 2 – Pebble wear as a function of grinding time for the different rock type samples. The legend shows the samples and their respective k_s-values.

The presented data allows for the following hypotheses: Texture and grain size of samples from the same rock type are equal (Table 1); Thus, differences in the mineral assemblage of the samples must be responsible for the varying grindability indices. Due to the low mass loss of Diorite samples observed during laboratory grindability tests, this rock type bears the potential of forming a critical size fraction during autogenous grinding. On the other hand, the Sericite Schist rock type may not provide suitable grinding media due to its relatively rapid decomposition.

Particle size distributions

Although the principal outcome of the grindability tests comprises the loss of mass of the pebble test batch, the particle size distribution (PSD) curves of the finely crushed <3.15 mm mill charge over time were investigated. The curves depicted in Figure 3 allow for the qualitative assessment of the PSD starting from the mill feed towards the final grinding product for the different samples of each rock type.

As for the mill feed (Figure 3a), different levels of coarseness are evident, which indicates a difference in crushability between the samples. The spread of the curves increases until 150 minutes of grinding time (Figure 3d). Analysing the order of the curves, it becomes apparent that the PSDs, from coarse to fine and grouped according to rock type, have obtained the following order: sericite schist > mica gneiss > diorite. This arrangement indicates that diorite samples generally generated higher proportions of fines, followed by mica gneiss and sericite schist samples. Hence, samples with high k_s-values, such as sericite schist, lead to a high % mass loss and a relatively coarse grinding product. Conversely, samples with low k_s-values lead to a low % mass loss and a finer grinding product.

To better comprehend the development of the fineness of the grinding product, the proportions of the -45 µm size fraction of the mill discharge were plotted against the grinding time (Figure 4). For long grinding times and as previously identified, samples with high k_s-values tend to generate proportionally less fines than samples with lower k_s-values. Thus, diorite samples presented the highest proportions of fines and sericite schist the least, whereas mica gneiss samples were positioned intermediate between the two. The inset plot of Figure 4 shows a correlation plot between the k_s-values and the proportions of the fine grinding product after 150 minutes of grinding time. Correspondingly, a correlation coefficient of -0.78 was found for a plot between the k_s-values and the proportion of fine grinding product after a grinding time of 90 minutes. The strong negative correlation coefficients indicate that the higher the k_s-values, the lower the proportions of generated fines and vice versa. However, such a relationship did not hold in the case of a grinding time of 60 minutes.

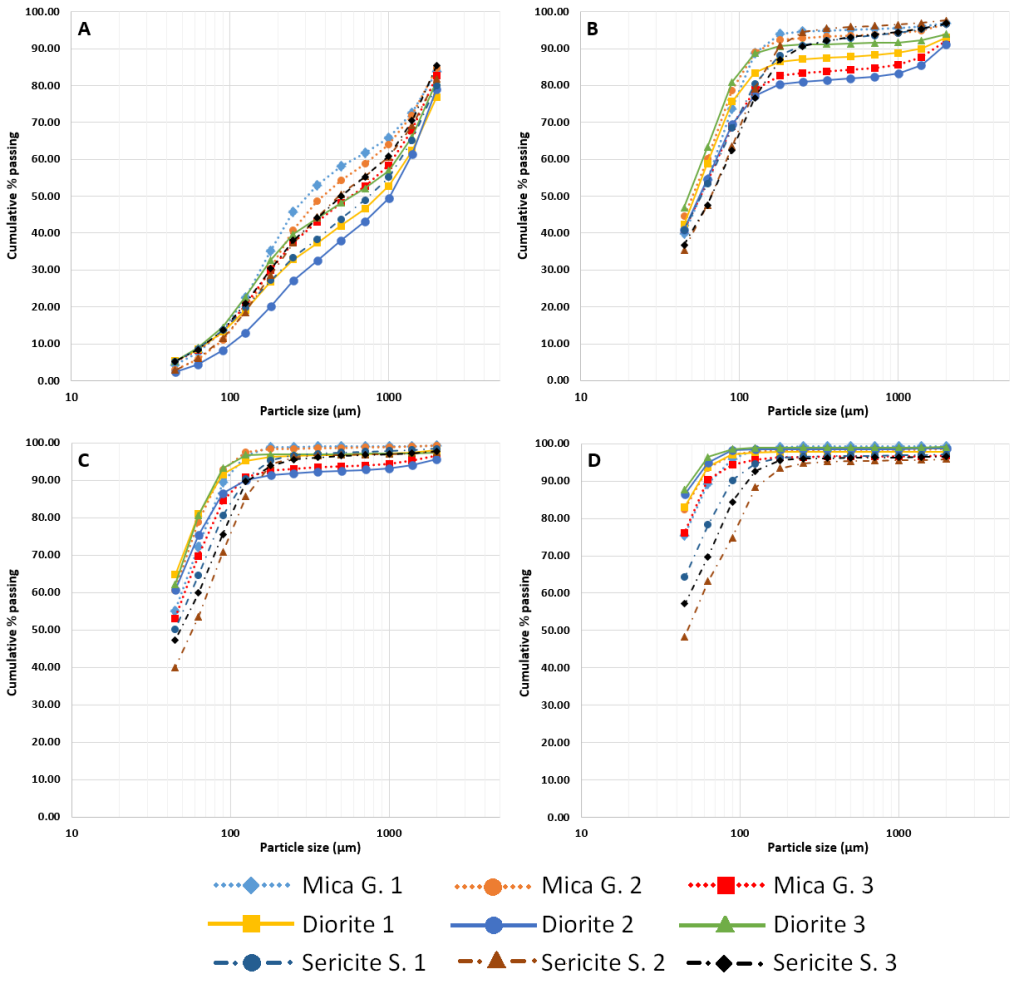

FIG 3 – Development of the particle size distribution of the mill feed (A), and after 60 (B), 90 (C), and 150 minutes (D) of grinding time.

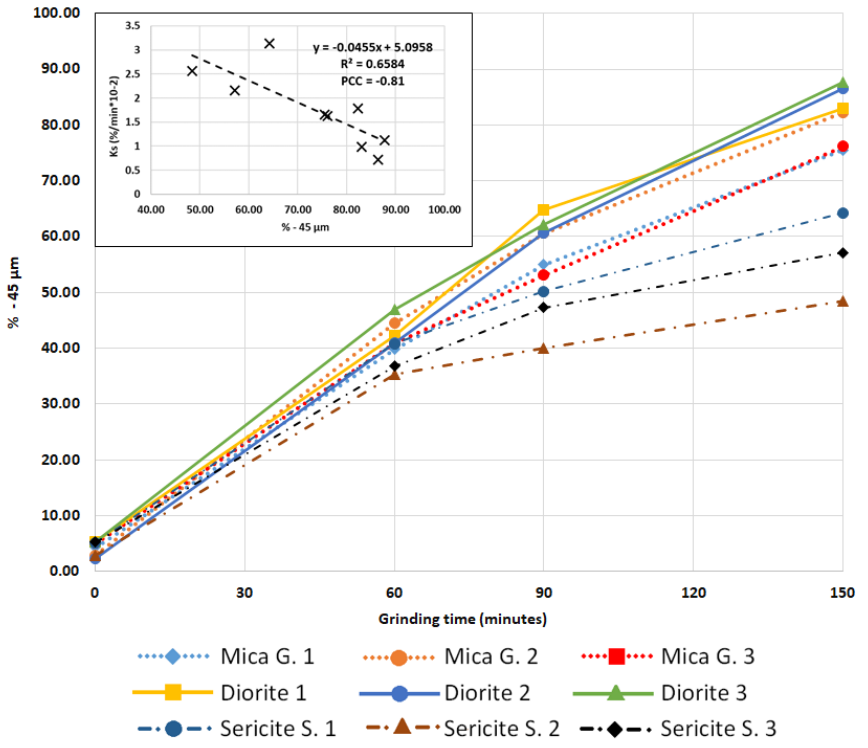

FIG 4 – Plot of grinding time versus fine grinding product (% -45 µm). The inset plot shows a correlation plot between the % -45 µm fraction and the k_s-values of the respective samples.

Mineral characterisation by XRD and QEMSCAN

Aiming at facilitating the comparison of the data acquired by mineralogical analyses and the subsequent correlation analyses between the identified mineral phases and the grindability indices, it was determined to bin the identified minerals into mineral groups (Table 2).

TABLE 2

Identified mineral phases and their corresponding mineral groups.

Mineral group	Identified mineral phases	
	X-ray diffraction	Automated mineralogy
Quartz	Quartz	Quartz
Plagioclase	Oligoclase	Albite, Anorthite, Oligoclase
Garnet	Spessartine	Spessartine, Almandine
K-Feldspar	Orthoclase	Orthoclase
Mica	Biotite, Muscovite	Biotite, Muscovite, Phlogopite
Amphibole	Actinolite	Actinolite
Clinopyroxene	Diopside	-
Chlorite group	Clinochlore	Clinochlore
Sulfides	Chalcopyrite, Pyrite, Pyrrhotite	Chalcopyrite, Pyrite/Pyrrhotite
Fe Oxides	Magnetite	Iron oxide
Others	-	Titanite, Barite, Apatite, <1 per cent by weight

Due to the different mineral characterisation techniques that were applied, not all identified mineral phases agreed. For example, the main plagioclase group mineral identified by XRD was oligoclase, whereas QEMSCAN analyses reported albite and anorthite as the main minerals of this group. However, Wanhainen, Broman and Martinsson (2003) and Frietsch (1980) confirmed the occurrence of both oligoclase and albite at Aitik. The mixed diffraction spectra of the natural samples subjected to XRD and the similar chemical composition of oligoclase and albite exacerbate the distinction of both minerals. The same applies to pyrite and pyrrhotite, which QEMSCAN can hardly distinguish.

Comparing the mineral assemblages obtained by XRD of the eleven bulk samples reveals the variations in mineral composition across the different samples and rock types (Figure 3). The mineral phases which occurred in the highest proportions are quartz, plagioclase, k-feldspars, and micas. Plagioclase is the main mineral phase in both diorite and mica gneiss samples. Its content is highest in diorite samples and decreases towards mica gneiss and sericite schist samples. The opposite is true for quartz: It is the main mineral phase in sericite schist samples and decreases towards mica gneiss and diorite.

Micas are most abundant in sericite schist samples, and their contents decline from mica gneiss towards diorite. K-feldspar is most abundant in mica gneiss samples and varies between approximately 10 to 25 per cent in diorite and sericite schist samples. Sulfides, chlorites, garnets, clinopyroxenes, and oxides were identified as the minor mineral phases (<3 per cent). Amphibole grades vary between 5 and 7 per cent in diorite samples.

When correlating the different mineral phases with each other, it was found that there are negative correlations between plagioclase and quartz, micas, and sulfides amongst others (Figure 5). Hence, as plagioclase content increases within the samples, quartz, mica, and sulfide contents tend to decrease. The unidentified mineral fractions reported by QEMSCAN are approximately 4–7 per cent. Compared to XRD, QEMSCAN analyses consistently yielded lower proportions of plagioclase and higher proportions of micas, meaning that the former is underestimated by QEMSCAN or

overestimated by XRD, whereas the opposite applies to the content of mica minerals. The sample preparation procedure and the plate-like shape of clay minerals, such as micas, may lead to the preferred orientation of the mineral crystals within the sample, hence intensifying XRD X-ray counts and introducing a measurement error (Lippmann, 1970; Hillier, 1999; Środoń *et al*, 2001). Similar issues were reported for minerals belonging to the plagioclase group, such as albite (Kleeberg, Monecke and Hillier, 2008).

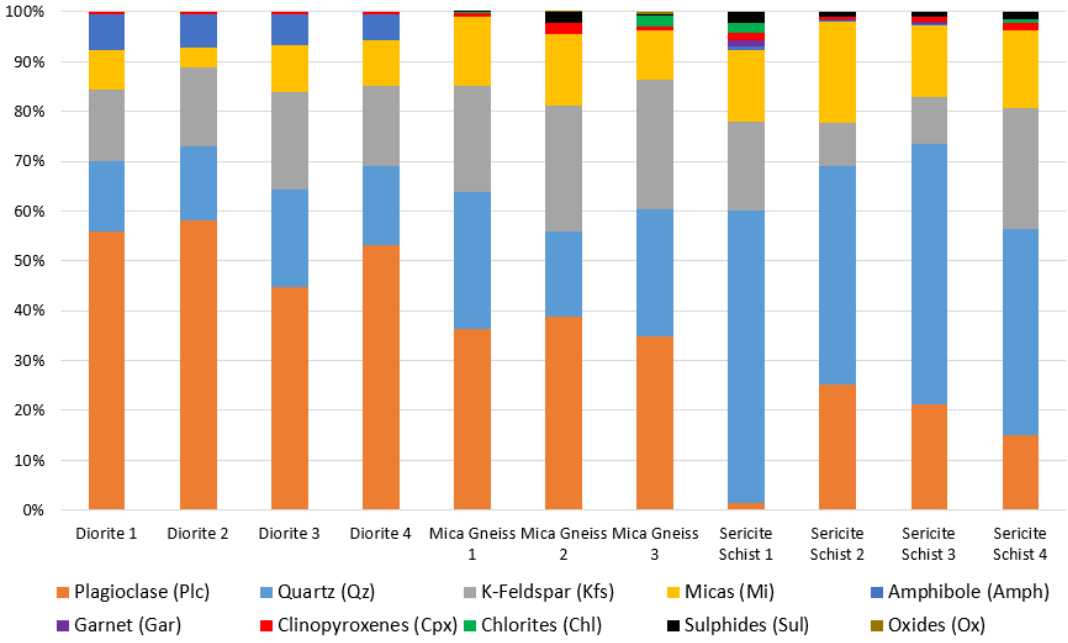

	Qz	Plc	Kfs	Mi	Amph	Gar	Cpx	Chl	Sul	Ox	Ks
Qz	1.00										
Plc	-0.94	1.00									
Kfs	-0.30	-0.03	1.00								
Mi	0.68	-0.74	-0.12	1.00							
Amph	-0.63	0.76	-0.27	-0.79	1.00						
Gar	0.76	-0.72	-0.24	0.30	-0.27	1.00					
Cpx	0.30	-0.49	0.42	0.37	-0.54	0.33	1.00				
Chl	0.35	-0.49	0.47	0.04	-0.41	0.44	0.11	1.00			
Sul	0.62	-0.77	0.17	0.65	-0.63	0.60	0.84	0.25	1.00		
Ox	-0.14	0.01	0.52	-0.13	-0.31	-0.17	-0.04	0.72	-0.11	1.00	
Ks	0.78	-0.89	0.14	0.73	-0.69	0.43	0.49	0.35	0.75	-0.09	1.00

FIG 5 – Modal mineralogy of the different rock type samples and Pearson correlation matrix of the identified mineral species. The results are according to XRD analyses from the bulk mineral samples.

Correlating grindability indices with mineralogy and chemical composition

Pearson correlation matrices were established to identify the strength of the linear relationship between modal mineralogy and grindability indices. The most relevant correlations were found for the bulk mineral samples.

Figure 6 shows the correlation plots of the most significant correlations between mineral phases identified by XRD and the respective k_s-values. Contrary to diorite and mica gneiss, the data points of sericite schist samples are spread around the regression lines. This disparity is a consequence of the greater spread in k_s-values reported for this rock type. The strongest Pearson correlation coefficient of -0.89 was found in the case of plagioclase (Figure 6b). Thus, with an increasing plagioclase content, the mass loss due to abrasion decreases. The opposite applies to quartz, mica, and the content of sulfides, which show positive correlations with their respective k_s-values. Hence an increase in the proportions of these minerals results in an increased mass loss due to wear. It is also worthwhile to mention that Pearson correlation matrices between the different mineral phases indicated negative correlations between plagioclase, quartz, mica, and the content of sulfides.

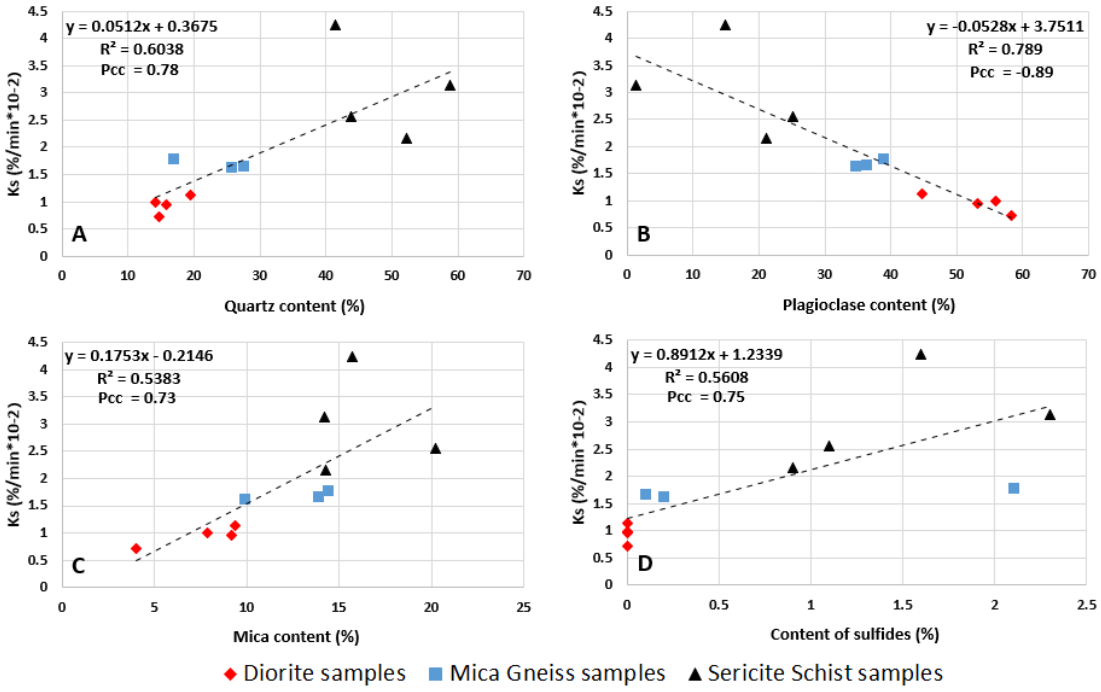

FIG 6 – Correlation plots between different mineral phases identified by XRD (bulk samples) and the respective k_s-values. In each case, the Pearson correlation coefficient (Pcc) and the model of a linear trendline with its respective R^2-value are given.

Relating the k_s-values to the proportions of the mineral phases of the three size classes analysed by QEMSCAN led to similar results (Figure 7). Strong positive and negative correlations were found between k_s-values and mineral phases across all size classes, particularly for the main mineral phases plagioclase, quartz, and sulfides. However, for the mica minerals, a Pearson correlation coefficient above 0.5 was only found within the 45–90 µm size fraction, which is due to the sericite schist 1 sample forming an outlier (Figure 7c), having approximately 50 per cent less mica content (Figure 5) as compared to the other sericite schist samples.

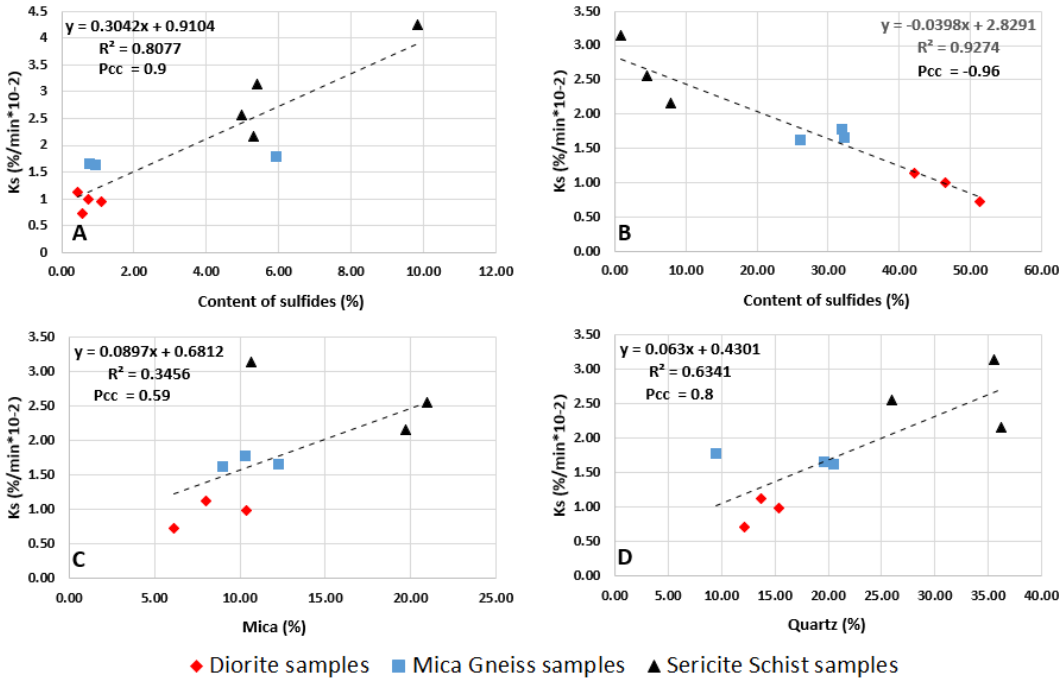

FIG 7 – Correlation plots between mineral phases identified by QEMSCAN and the respective k_s-values from different size fractions: Content of sulfides (bulk sample, A), plagioclase (90–190 µm, B), mica (45–90 µm, C) and quartz (0–45 µm, D).

Overall, the strongest correlation between mineral phase and k_s with a Pearson correlation coefficient of -0.96 was found for plagioclase in the 90–180 µm size class (Figure 7b). In the case of mineral phases such as K-feldspars and amphiboles, no significant correlations between mineral content and grindability indices were distinguished.

The chemical composition acquired by XRF powder analysis enabled the investigation of the relationship between grindability indices and the chemical composition of the bulk samples. Significant positive and negative correlations were observed between chemical data and k_s-values (Figure 8). The strongest correlations were found for Al_2O_3 and CaO, with Pearson correlation coefficients of -0.86. Negative correlations were detected in the cases of S and Fe. A further but less significant correlation was found for Al_2O_3 and CaO, resulting in a Pearson Correlation Coefficient of 0.64. As previously observed, the data points corresponding to sericite schist samples show more spread around the line of best fit.

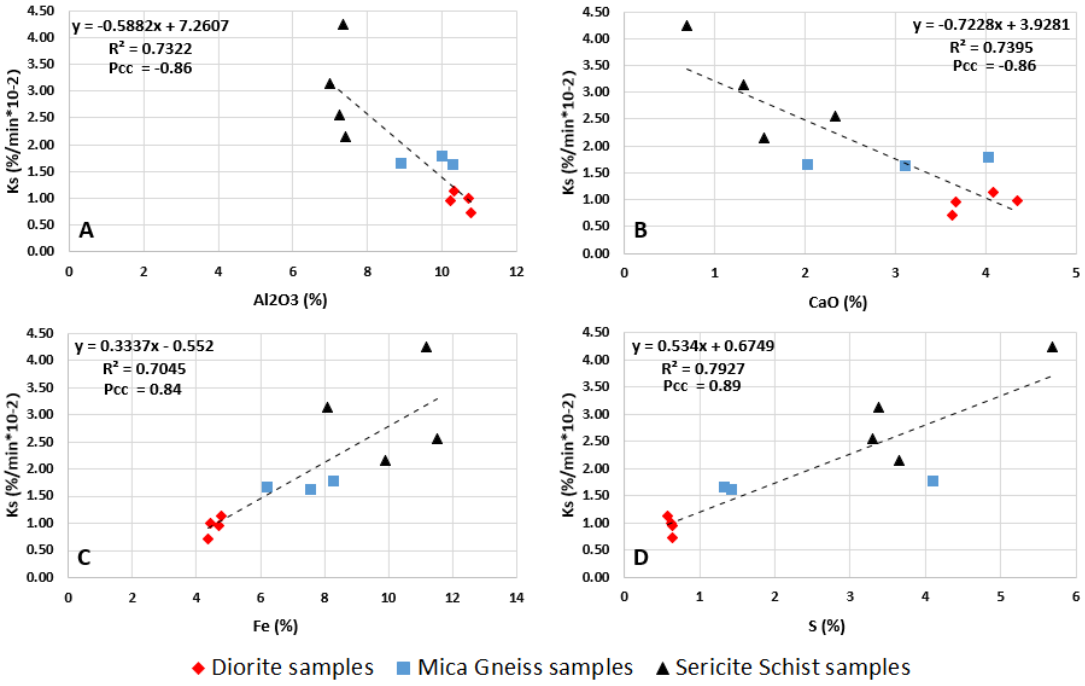

FIG 8 – Correlation plots between k_s-values and chemical data.

Mineral hardness and grindability

An approach from Mwanga (2016) was applied to calculate each sample's weighted average Mohs hardness based on the modal mineralogy acquired from XRD analyses. The hardness values for each mineral phase were obtained from the mineralogy database of webmineral.com and other relevant literature.

Aiming to investigate the relationship between k_s and Mohs hardness, the corresponding values for each sample were plotted in a correlation plot (Figure 9). The table embedded within Figure 9 lists the different mineral specimens with their respective k_s and Mohs hardness values. The negative correlation between the data indicates that an increasing average hardness leads to a decreasing mass loss regarding abrasion. Hence, and according to the information provided previously, the higher a sample's average Mohs hardness, the lower the percentage mass loss of the pebbles and the greater the proportions of generated fines within the grinding product. Since k_s and Mohs hardness are inversely correlated, the relationship between Mohs hardness and modal mineralogy is reciprocal. For example, the correlation between k_s and plagioclase content is negative, so the average Mohs hardness and plagioclase content are positively correlated. Consequently, average Mohs hardness increases with increasing plagioclase content.

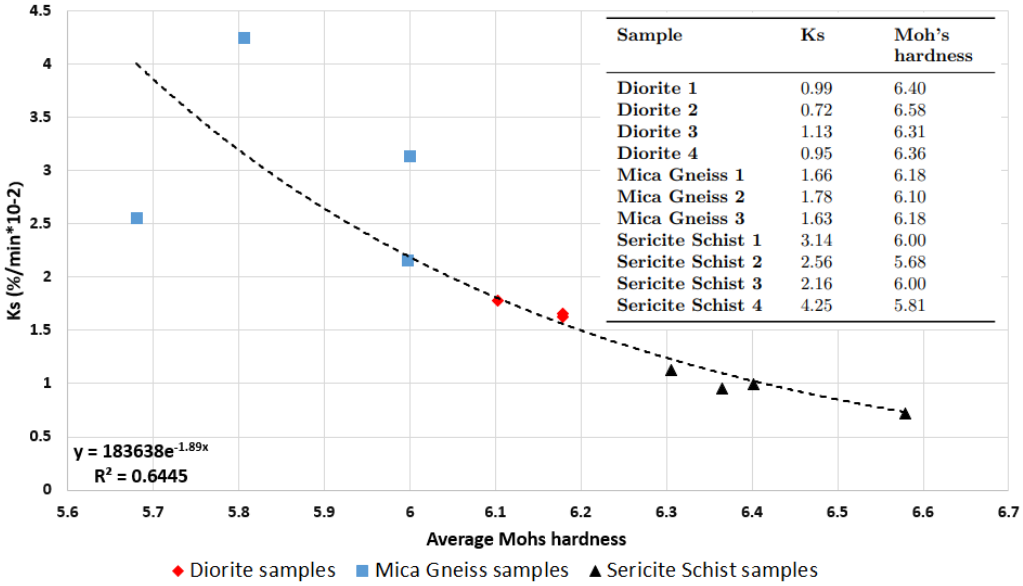

Sample	Ks	Moh's hardness
Diorite 1	0.99	6.40
Diorite 2	0.72	6.58
Diorite 3	1.13	6.31
Diorite 4	0.95	6.36
Mica Gneiss 1	1.66	6.18
Mica Gneiss 2	1.78	6.10
Mica Gneiss 3	1.63	6.18
Sericite Schist 1	3.14	6.00
Sericite Schist 2	2.56	5.68
Sericite Schist 3	2.16	6.00
Sericite Schist 4	4.25	5.81

FIG 9 – Scatterplot between k_s-values and average Moh's hardness calculated from mineral proportions reported by XRD.

Mineral liberation

A mineral liberation analysis was performed on the 0–45, 45–90, and 90–180 µm particle size fractions. Kumar *et al* (2021) considered particles with a liberation degree above 95 per cent as fully liberated. For the present study, this approach was adopted, and four liberation classes were created for the data obtained by QEMSCAN: >= 95 per cent, 80–95 per cent, 30–80 per cent, <=30 per cent.

At Aitik, as is the case for the majority of sulfide deposits, chalcopyrite frequently occurs in association with pyrite and pyrrhotite (Wanhainen, Billström, and Martinsson, 2006). Since the flotation process at Aitik aims at separating the chalcopyrite grains liberated from pyrite, pyrrhotite, and other main gangue minerals such as plagioclase, quartz, K-feldspars, and micas, the focus of the liberation study was set on these mineral phases.

It was observed that the proportions of fully liberated plagioclase and mica grains within sericite schist samples are generally lower across all size fractions when compared to diorite and mica gneiss samples (Figure 10). The liberation data showed that, in general, 92 per cent of pyrite/pyrrhotite and 91 per cent of quartz within the sampled size fractions were fully liberated, indicating approximately equal liberation within these size classes. The degree of liberation of chalcopyrite was the lowest in the 90–180 µm size class of the diorite samples. Fully liberated chalcopyrite grains with proportions of up to 90 per cent by mass were observed in the 0–45 and 45–90 µm size fractions of all samples, indicating that the liberation size of chalcopyrite grains is below 90 µm. However, on several occasions, the degree of liberation within the 45–90 µm size class was higher than in the 0–45 µm size class. However, the apparent higher degree of liberation within this size class may be due to touching particles in the sample.

For the gangue minerals plagioclase, K-feldspars, and quartz, a clear trend of increasing mineral liberation with decreasing particle size was distinguished, indicating that the liberation size of these mineral phases is below 90 µm. Attempting to scrutinise how mineral liberation, k_s-values, and mineral content affect each other, a correlation analysis was performed. Only a single significant positive correlation was detected between mineral content and liberation: the higher the plagioclase content, the higher the % mass of fully liberated plagioclase grains within the sample. This observation seems reasonable since the likelihood of liberated mineral grains increases with increased mineral content. Strong negative correlations between % fully liberated plagioclase grains and k_s-values suggest that as the material loss due to abrasion increases, the proportions of fully liberated mineral grains decrease (Figure 11). This relationship agrees with the general observation of sericite schist samples having a lower degree of liberation of the plagioclase mineral phase.

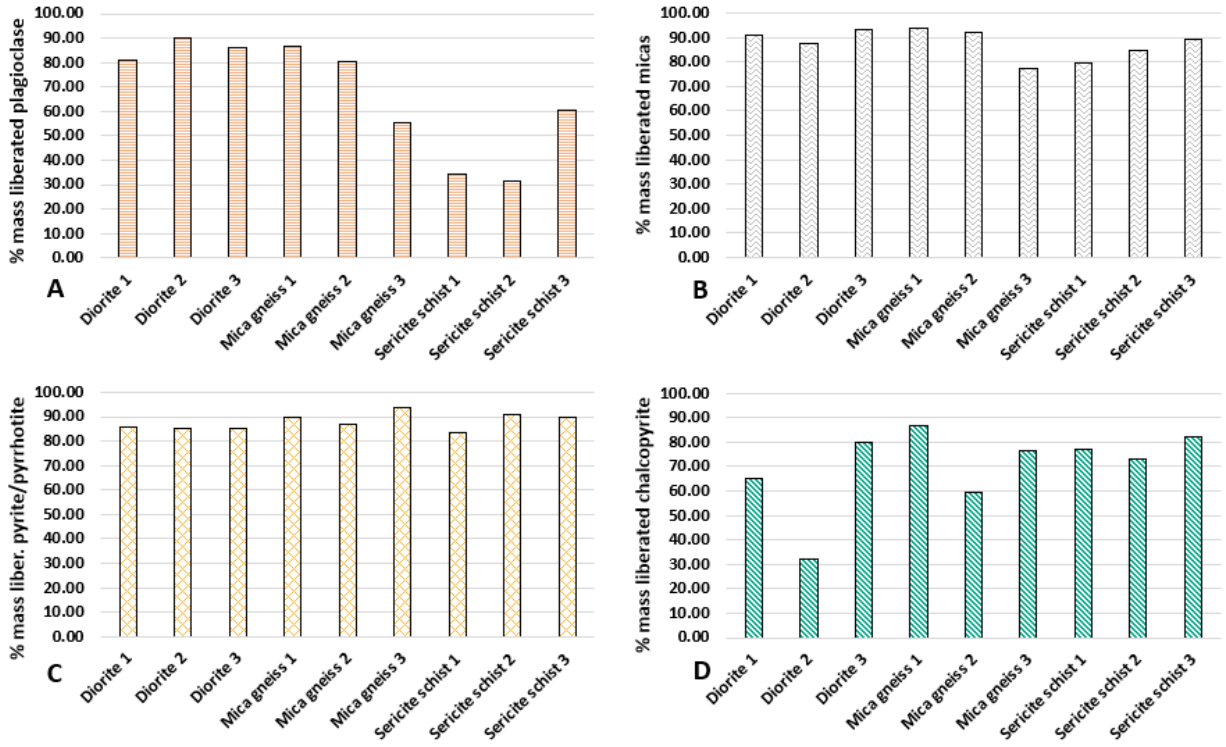

FIG 10 – % of fully liberated minerals grains of selected mineral phases: Plagioclase (90–180 µm, A), micas (45–90 µm, B), pyrite/pyrrhotite (0–45 µm, C), chalcopyrite (90–180 µm, D).

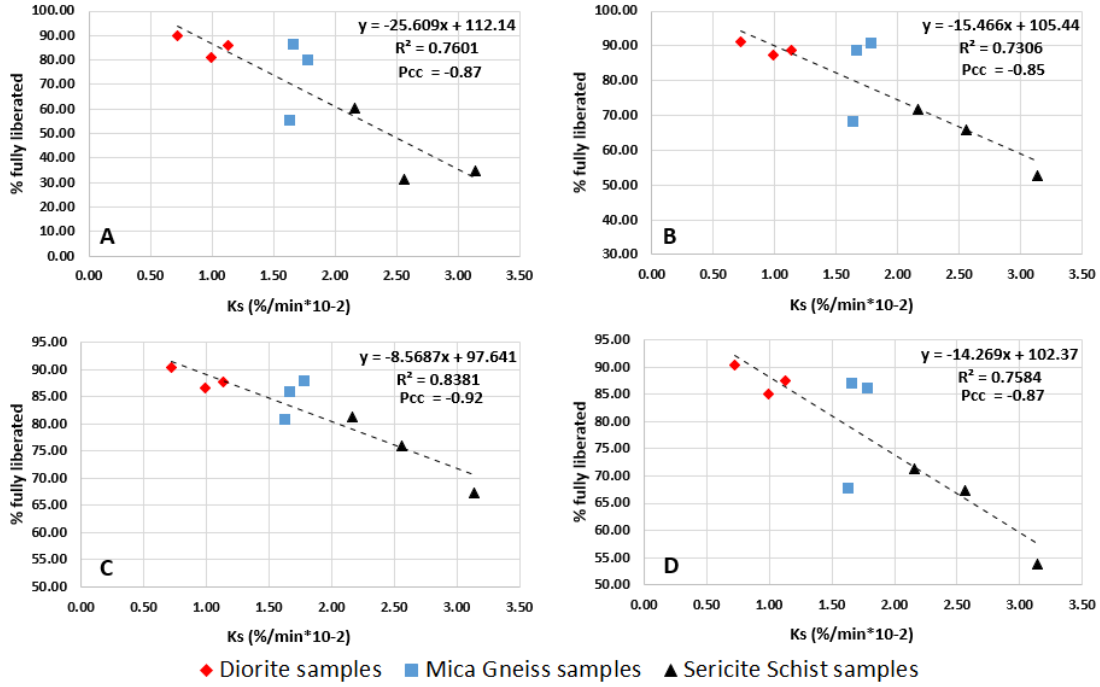

FIG 11 – Correlation plot between k_s-values and % fully liberated plagioclase particles in the 90–180 µm (A), 45–90 µm (B), and 0–45 µm (C) size classes and a combination of all size classes (D).

Preferential wear of mineral phases

The tendency of the mineral phases to accumulate in specific size classes was investigated. Accordingly, the modal mineralogy of the mill discharge after different grinding times and the bulk modal mineralogy were compared. Hence, any significant and systematic change in mineral composition within a particle size class may indicate preferential wear.

Considering the samples analysed with QEMSCAN, diorite 3, mica gneiss 2, and sericite schist 1 yielded the highest k_s-values (compare diagram inset of Figure 2). The elevated mass loss of these samples was expected to increase the likelihood of finding evidence for the preferential wear of mineral phases. Figure 12 shows the ratios between the mineral proportions after 150 and 60 minutes of grinding time and under consideration of the bulk mineral samples ordered by particle size classes. Generally, the mineral ratios are well below or above 1, indicating a notable difference in mineral composition after 150 minutes of grinding time (Figure 12a). The mineral ratios do not remain constant within the same size class, meaning the same mineral is deposited in different proportions. However, as for the 0–45 µm fractions, it was observed that the mineral ratios are approaching a value of 1, indicating that the mineral composition of the fine size fractions after 60 and 150 minutes of grinding are similar. Therefore, fine particles are abraded in a more homogenous and constant manner, resulting in comparable mineral compositions at different grinding times.

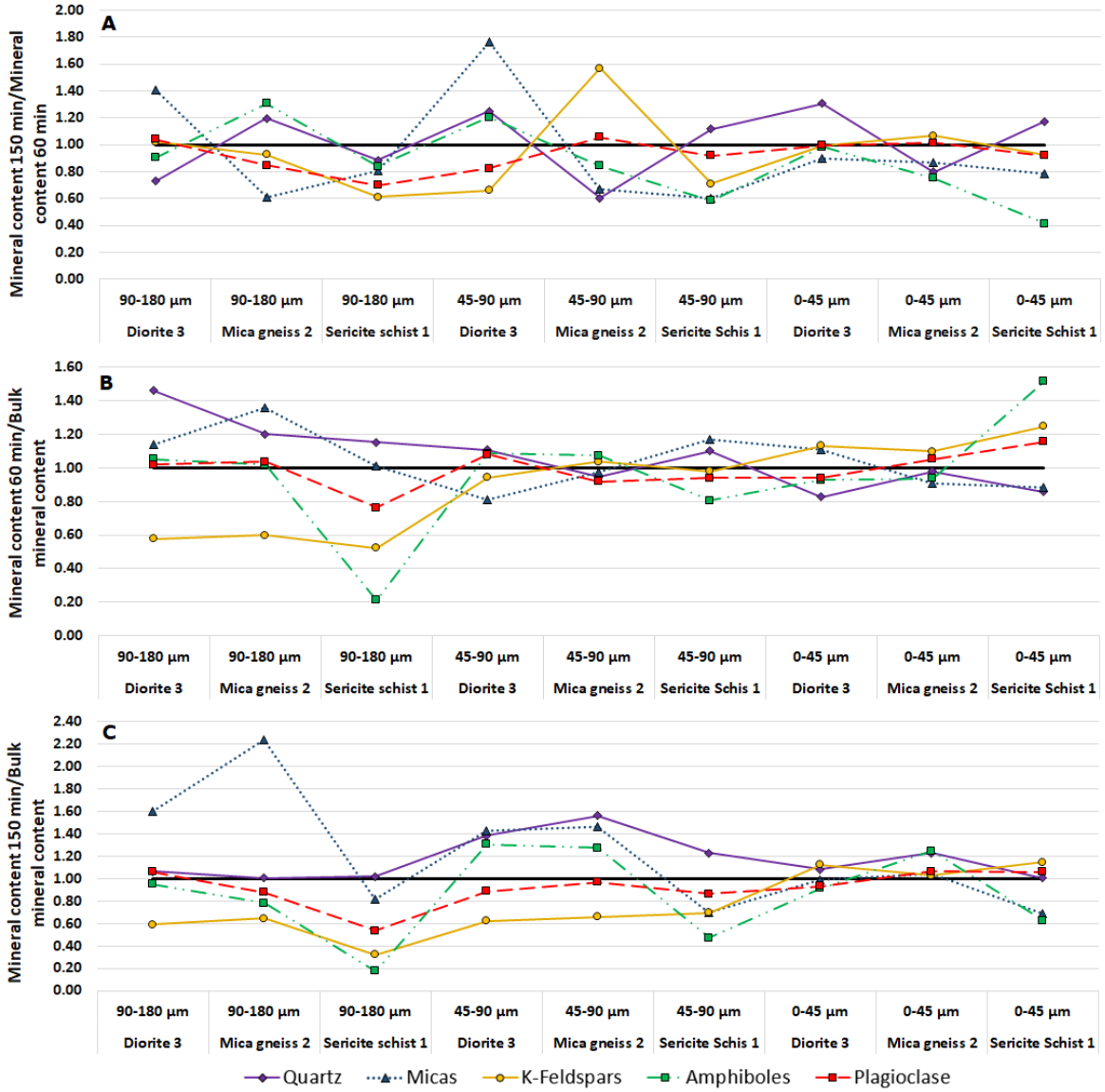

FIG 12 – Ratios of selected mineral phases: After 150 minutes versus 60 minutes of grinding (A), after 60 minutes of grinding versus bulk mineral content (B), and after 150 minutes of grinding versus bulk mineral content (C).

Concerning the mineralogy of the bulk samples (Figures 12b and 12c), the curves show ratios close to 1 for the medium and fine size classes. The divergence regarding the coarse size fractions is more pronounced. These results indicate that the grinding action leads to a constant and homogeneous abrasion of minerals so that the modal mineralogy approaches the bulk mineralogy. When comparing the mineral proportions resulting from different grinding times, it was indicated that K-Feldspars

preferentially compose the 0–45 µm size class. Contrastingly, micas became more abundant towards the coarse size fraction. The grade of chalcopyrite increased towards the 0–45 µm size fraction, whereas the opposite applied to pyrite/pyrrhotite. Considering that the mentioned mineral phases preferentially compose the same size fractions after 60 and 150 minutes of grinding time indicates a constant and homogeneous abrasion process.

DISCUSSION

For each rock type, the results of the wear tests show varying degrees of per cent weight loss over time, hence the visible spreads of the curves in Figure 2 result. Considering that sample texture and grain size were selected to be equal for each rock type, it is likely that differences in mineral composition are the main contributor. However, errors related to the test procedure and the impact of the sample's natural variability on the results cannot be eliminated. More grindability tests are necessary to obtain more accurate data. Even though samples were taken from three different rock types, considerable differences in mineral assemblage for samples from the same rock type may occur. Table 1 and Figure 1 indicate that the spatial distance between the chosen samples was relatively large. Thus, compositional differences regarding mineralogy are likely to influence grinding behaviour. In other words, the rock's resistance to abrasive grinding varies within and across Aitik's rock types. Likewise, the ore properties, in this case, the mineral composition, of samples 1 and 4 must be similar, as both samples exhibit very similar k_s-values of 0.99 and 0.95. Indeed, Figure 5 confirms the similar mineral composition of these samples. Considering that the invested grinding energy is equal for all samples and the similarity in texture and grain size, it is possible that other factors, such as a variation in mineral assemblage, impact grinding behaviour. A mechanism that may have influenced test results negatively is the pre-wear procedure: In case this procedure failed to remove the pebble's asperities and edges, the chipping breakage mechanism continued to be active during the wear tests releasing material and influencing the k_s-value. During grinding, the surface-specific wear rate of a particle decreases over time since the surface becomes increasingly rounded as the chipping and attrition breakage mechanisms remove edges and asperities (King, 2012). In other words, the mass loss of a particle due to chipping decreases with increasing grinding time. If sufficiently rounded pebbles are subjected to the wear tests, the abrasion mechanism becomes the dominant breakage mechanism. However, it was impossible to verify that all samples reached the required degree of roundness. Hence, k_s-values may have been influenced by this mechanism.

The grinding product's particle size distribution curves were used to investigate the relationship between k_s-values and particle size. The results showed that coarser particles are generated from samples with high k_s-values as grinding time increases. However, this observation relies on a relatively small sample population and only a few of the rock types present at Aitik. Furthermore, after 60 or even 150 minutes of grinding within the laboratory mill, over-grinding may occur, resulting in the unnecessary breakage of mineral particles (Kawatra, 2006). Thus, the significance of this observation is questionable, as the retention time inside Aitik's AG mill is between 7 and 10 minutes only (Isaksson, personal communication, February 12, 2021). Hence, in Aitik's comminution circuit, due to relatively short grinding times, certain rock types are possibly prone to producing increasingly coarse particles. However, since the target P_{80} of the feed for the flotation circuit of Aitik's processing plant is approximately 180 µm, no negative consequences are expected. Naturally, the proportions of generated fines increase with grinding time as particles are continuously reduced in size. While the coarse particles of the test batch increase in roundness due to abrasion, less material is abraded from their surfaces. Thus, the mineral surfaces become smoother, and eventually, less material is abraded over time. The material, which is abraded from the pebble's surfaces during the wear tests, is mixed with the -3.15 mm fraction that composes the mill charge. These circumstances tend to bias the test results. The fact that more material is abraded from sericite schist samples, while at the same time generating lower proportions of fines as compared to diorite and mica gneiss samples, indicates that the sample's mineral composition directly influences the smoothness of the pebble's surface. Thus, a smoother surface is less prone to being affected by abrasion. When conducting the laboratory tests, diorite samples exhibited a very smooth surface. Considering the relatively small number of samples selected for each rock type, no meaningful correlations between k_s-values and modal mineralogy were detectable. Thus, the data for all samples was plotted into a single diagram. Hence, as a result, it was not possible to make clear statements about the relationship between k_s

and the modal mineralogy of a specific rock type. However, Figure 6 depicts apparent rock type-specific trends for sericite schist and diorite. For example, taking into account only the data points of the mica gneiss samples in Figure 6b or Figure 7c, it seems as if the correlation between k_s and sulfide content is positive instead of negative. Nonetheless, additional data points for these rock types would be necessary to verify this observation.

Correlation analysis of the detected mineral phases and k_s-values showed that the major mineral phases govern the wear behaviour of the pebbles during autogenous grinding. Although the results derived from both techniques did not coincide entirely, similar correlations with the grindability indices were observed. These correlations seem reasonable, as some samples comprise >50 per cent of a single mineral phase. However, sulfides were shown to correlate with the grindability indices even though their proportions are generally below 5 per cent by weight. Strong negative correlations were observed between plagioclase, mica, quartz, and sulfides (Figure 5). Additionally, quartz, micas, and sulfides were shown to correlate positively with k_s, whereas plagioclase was found to have the strongest negative correlation with the k_s-values (Figure 5). This observation is reasonable since an increasing plagioclase content is accompanied by a decrease in the proportions of quartz and micas, amongst others, resulting in a decreasing k_s-value. Thus, plagioclase may be the actual steering force in terms of grindability. No correlations were observed for K-Feldspars in all size fractions. For some samples, high correlations of titanite, apatite, chlorites, and barite were detected. However, the mineral content of these phases is typically below 0.5 per cent. Hence, the influence of these mineral phases on grindability is unlikely. The correlations between k_s-values and the chemical composition of the samples (Figure 8) are meaningful. Elements such as Al or Fe occur in several minerals identified during this study. However, they cannot be related to a specific mineral. Fe, which positively correlates with k_s, is mainly present in biotite, amphiboles, and sulfides. Both micas and sulfides have shown positive correlations with the grindability indices, whereas amphiboles have shown no correlation. Therefore, the positive correlations between the grindability indices and Fe are likely due to the biotite and sulfide content. Sulfur has shown a positive correlation and is principally present in chalcopyrite, pyrite, and pyrrhotite, which, when grouped, have shown a positive correlation. Aluminium oxide (negative correlation) is, amongst several others, a compound of the minerals of the plagioclase and mica groups. However, considering that plagioclase is the main mineral phase within the samples, the negative correlation of aluminium oxide is probably attributed to the strong negative correlation between grindability indices and plagioclase. The negative correlation between plagioclase and micas supports this assumption. Calcium oxide occurs in plagioclase, amphiboles, and clinopyroxenes. However, amphiboles and clinopyroxenes are only minor mineral phases. Hence, the positive correlation of calcium oxide is possibly related to the negative correlation between plagioclase and grindability indices.

Mineral liberation encompasses random and non-random breakage (Gaudin, 1939, as cited in Guldris Leon, Hogmalm and Bengtsson, 2020). The former occurs due to the random formation and propagation of fractures within the mineral grain induced by comminution action, whereas the latter is associated with fracture propagation along the boundaries of the mineral. It is unknown which of the mentioned mechanisms was predominant during the wear tests conducted within this study. However, considering that abrasion constantly scrubs material off the pebble's surface, it is likely that random breakage prevails. In general terms, high proportions of fully liberated minerals were observed across all sampled size fractions. This observation may be linked to the relatively long grinding times of over 60 minutes, as mentioned further above, liberating most mineral grains. The data showed that the degree of liberation of plagioclase and mica is generally lower within sericite schist samples (Figure 11). This behaviour may be related to the high k_s-values of this sample type and the higher proportions of coarse particles generated during grinding. Hence, these coarse particles are less likely to be fully liberated. Plagioclase and mica minerals are known to have one plane of perfect cleavage, along which preferential breakage may occur. However, the tendency of less fully liberated particles was only observed for sericite schist and not for other samples containing these two mineral phases. In the case of chalcopyrite, the degree of liberation within the 45–90 µm size class was higher than in the 0–45 µm size classes. This occurrence may be due to chalcopyrite's liberation size falling within the 45–90 µm size class or fine particles from the 0–45 µm fraction sticking to the surface of liberated chalcopyrite grains. The latter would result in the QEMCAN-analysis not being able to identify these particles as liberated. The reasons why solely plagioclase content correlates with k_s are unknown.

Concerning the preferential wear of mineral phases, Figure 12 suggests that the observed mineral ratios change within the same size class, meaning that different proportions of minerals are deposited. For example, in the 45–90 µm fraction, after 150 minutes of grinding time, the quartz content of the diorite has increased, whereas it strongly decreased in the case of mica gneiss, only to rise once more for sericite schist (Figure 12a). However, this development may also be attributable to the mineral phases appearing in different proportions within the rock types. However, as for the 0–45 µm fractions, the mineral ratios are approaching one, indicating that the mineral composition of the fine size fractions after 60 and 150 minutes of grinding are more alike each other. Therefore, fine particles are abraded in a more homogenous and constant manner, resulting in similar mineral compositions at different grinding times.

CONCLUSIONS

The following conclusions can be drawn from the performed work:

- Abrasive grinding tests were performed on samples derived from rock types of the Aitik mine: diorite, mica gneiss, and sericite schist. Divergent degrees of grindability, expressed through the wear index k_s, were reported within and across the rock types. The abrasion resistance decreased from diorite over mica gneiss to sericite schist samples.
- Sieve analyses of the grinding products showed that particle size distribution varied according to rock type. High k_s-values generated a high % weight loss and a relatively coarse grinding product, whereas low k_s-values implied a low % weight loss and a finer grinding product.
- Results from XRD and QEMSCAN indicated the presence of similar mineral phases in the selected samples, though mineral content varied throughout the rock types. Plagioclase, quartz, K-Feldspars, and micas were identified as the main mineral phases, followed by minor amounts of amphiboles, chlorites, clinopyroxenes, and sulfides. Correlation analyses showed strong correlations between the main mineral phases and the k_s-values. It was determined that decreasing mica, quartz, and sulfides content and increasing plagioclase content result in a low k_s-value and vice versa. Plagioclase content is likely to dominate the response to abrasive grinding.
- The sample's chemical composition provided by XRF appeared to correlate with the respective k_s-values, supporting the findings mentioned above.
- A negative correlation between the weighted average Mohs hardness calculated from the sample's modal mineralogies and the grindability indices was found. Hence, it was proposed that a higher Mohs hardness results in a finer grinding product, oppositional to the k_s-values. Since k_s is interpretable as a measure of abrasiveness, it can be stated that an increase in sample hardness results in a lower abrasiveness and vice versa.
- There was little evidence for the preferential wear of specific mineral phases. However, it was observed that abrasive grinding results in a continuous and consistent removal of mineral particles from the sample's surface.
- The applied abrasion breakage mechanism leads to a high degree of liberation of gangue minerals and chalcopyrite. The only significant correlations between k_s and liberation parameters were found for plagioclase. With an increasing k_s-value, the liberation of plagioclase grains decreases.

ACKNOWLEDGEMENTS

The authors appreciate Boliden Mineral's provision of sample material from the Aitik mine and the financial support concerning sample analysis. Furthermore, the authors thank Boliden for granting access to the company's mineral laboratory for conducting wear tests and investigations by automated mineralogy. The assistance from Boliden's laboratory personnel concerning sample preparation is greatly appreciated. Thank you to Peter Karlsson from Aitik Boliden for assisting regarding sample selection and dispatching to Boliden.

REFERENCES

Alderton, D, 2021. X-Ray Diffraction (XRD), in *Encyclopedia of Geology*, Second Edition, (eds: D Alderton and S A Elias), pp. 520–531 (Oxford: Academic Press).

Beyglou, A, Schunnesson, H and Johansson, D, 2015. Face to surface – task 1: Baseline mapping of the mining operation in Aiti, Research report, Luleå University of Technology, Luleå.

Boliden, 2020. Annual and sustainability report 2020 [online], Available from: https://www.boliden.com/globalassets/about-boliden/corporate-governance/general-meetings/2021/ahr-2020-eng.pdf [Accessed: 06 June 2021].

Borell, M and Lager, T, 1983. Autogen malning – falltest, slitagetest: Resultatsammanattning, Technical Report TM 70/83 (unpublished), Boliden AB, Boliden.

Djordjevic, N, 2013. Image based modeling of rock fragmentation. *Minerals Engineering*, 46–47, 68–75.

Dominy, S, O'Connor, L, Glass, H, Parbhakar-Fox, A and Purevgerel, S 2018. Geometallurgy—A Route to More Resilient Mine Operations, *Minerals*, 8(12): 1–33.

Frietsch, R, 1980. Precambrian ores of the northern part of Norrbotten County, northern Sweden, Paris: *26th International Geological Congress*.

Gaudin, A, 1939. *Principles of mineral dressing* (1 ed.), (McGraw-Hill Book Company: New York).

Ghanei, J, 2020. '*Evaluation of the relation between ore texture and grindability*', Master thesis, Luleå University of Technology, Luleå.

GMG, 2015. Determining the bond efficiency of industrial grinding circuits [online], Available from: https://gmggroup.org/wp-content/uploads/2016/02/Guidelines%5C_Bond-Efficiency-REV-2018.pdf [Accessed: 29 June 2021].

Guiomar, C, Mudd, G, Valero, A and Valero, A, 2016. Decreasing Ore Grades in Global Metallic Mining: A Theoretical Issue or a Global Reality?, *Resources*, 5(4), 1–14.

Guldris Leon, L, Hogmalm, K and Bengtsson, M, 2020. Understanding Mineral Liberation during Crushing Using Grade-by-Size Analysis – A Case Study of the Penuota Sn-Ta Mineralization, Spain, *Minerals*, 10(2), 1–20.

Hilden, M, Yahyaei, M and Powell, M, 2019. Aitik survey report – grind curve surveys, Technical report (unpublished).

Hillier, S, 1999. Use of an air brush to spray dry samples for X-ray powder diffraction, *Clay Minerals*, 34(1): 127–135.

Karlsson, P, 2020. Boliden Summary Report, Resources and Reserves 2020 [online], Available from: <https://www.boliden.com/globalassets/operations/exploration/mineral-resources-and-mineral-reserves-pdf/2020/resources-and-reserves-aitik-2020–12–31.pdf> [Accessed: 05 June 2021].

Kawatra, S K, 2006. Design of iron ore comminution circuits to minimize overgrinding. In *Advances in comminution*, pp 309–320 (Society for Mining, Metallurgy, Exploration, Inc.: Englewood).

Kekec, B, Ünal, M and Sensogut, C, 2006. Effect of the textural properties of rocks on their crushing and grinding features, Journal of University of Science and Technology Beijing, *Mineral, Metallurgy, Material*, 13(5): 385–392.

King, G and MacDonald, J, 2016. The business case for early-stage implementation of geometallurgy – an example from the Productora Cu-Mo-Au deposit, Chile, In *Proceedings of the International Geometallurgy Conference 2016*, pp 125–133 (The Australasian Institute of Mining and Metallurgy: Melbourne).

King, R, 2012. Chapter 5 – Comminution operations, In *Modeling and simulation of mineral processing systems*, second edition (eds: C Schneider and E King), pp. 153–249 (Society for Mining, Metallurgy, Exploration, Inc.: Englewood).

Kleeberg, R, Monecke, T and Hillier, S, 2008. Preferred orientation of mineral grains in sample mounts for quantitative XRD measurements: How random are powder samples?, *Clays and Clay Minerals*, 56(4), 404–415.

Kumar, H, Luolavirta, K, Akram, S, Mehmood, H and Luukkanen, S. 2021. The Effect of Hydrodynamic Conditions on the Selective Flotation of Fully Liberated Low Grade Copper-Nickel Ore, *Minerals*, 11(328), 1–13.

Lippmann, F, 1970. Functions describing preferred orientation in flat aggregates of flake-like clay minerals and in other axially symmetric fabrics, *Contributions to Mineralogy and Petrology*, 25: 77–94.

Lishchuk, V, Koch, P H, Ghorbani, Y and Butcher, A 2020. Towards integrated geometallurgical approach: Critical review of current practices and future trends, *Minerals Engineering*, 145: 1–16.

Mackenzie, 2017. Wood Mackenzie: Metals cost benchmarking.

Macpherson, A 1976. A simple method to predict the autogenous grinding mill requirements for processing ore from a new deposit, SME-AIME Fall Meeting Exhibit (Society for Mining, Metallurgy and Exploration: Englewood).

Markström, S, 2012. Commissioning and operation of the AG mills at the Aitik expansion project (Canadian Institute of Mining, Metallurgy and Petroleum: Montreal).

Markström, S, 2018. Rapport jmf slitage-pilot, Technical Report TM_REP2018/xx (unpublished), Boliden AB, Boliden.

Markström, S, 2020. Aitik malbarhet idestudie 2019 – teknisk rapport, Technical Report TM_REP2020/031 (unpublished), Boliden AB, Boliden.

McElroy, A, Powell, M, Tillberg, J, Hilden, M, Yahyaei, M, Linna, M and Johansson, A, 2019. An assessment of the energy efficiency and operability of the world's largest autogenous grinding mills at Boliden's Aitik mine, Vancouver: *SAG Conference 2019*.

Morell, S, 2019. Testing and calculations for comminution machines, in *SME Mineral Processing, Extractive Metallurgy Handbook* (R Dunne, S Kawatra Komar and C Young, eds.), pp 529–565 (Society for Mining, Metallurgy and Exploration. Englewood).

Morrell, S, 2004. Predicting the specific energy of autogenous and semi-autogenous mills from small diameter drill core samples. *Minerals Engineering*, 17(3), 447–451.

Mwanga, A 2016. Development of a geometallurgical testing framework for ore grinding and liberation properties (PhD thesis), Luleå University of Technology, Luleå.

Mwanga, A, Rosenkranz, J and Pertti, L, 2017. Development and experimental validation of the Geometallurgical Comminution Test (GCT). *Minerals Engineering*, 108: 109–114.

Norlin, L, Åkerhammar, P, Hallberg, A, Hamberg, R, Westrin, P, Larsson, D, Norström, E, 2020. Bergverksstatistik 2020 – Statistics of the Swedish Mining Industry 2020, Geological Survey of Sweden (SGU), Uppsala.

Parian, M and Palsson, B, 2020. Review of autogenous grinding (AG) laboratory and pilot scale tests, Review Report Vinnova – 2019–05194 (unpublished). Luleå University of Technology, Luleå.

Parian, M, Lamberg, P, Möckel, R and Rosenkranz, J 2015. Analysis of mineral grades for geometallurgy: Combined element-to-mineral conversion and quantitative X-ray diffraction, *Minerals Engineering*, 82: 25–35.

Rincon, J, Gaydardzhiev, S and Stamenov, L, 2019. Coupling comminution indices and mineralogical features as an approach to a geometallurgical characterization of a copper ore, *Minerals Engineering*, 130: 57–66.

Shi, F, Kojovic, T, Larbi-Bram, S and Manlapig, E, 2009. Development of a rapid particle breakage characterisation device – the JKRBT [Special issue: Comminution]. *Minerals Engineering*, 22(7): 602–612.

Środoń, J, Drits, V A, McCarty, D K, Hsieh, J C and Eberl, D D, 2001. Quantitative X-ray diffraction analysis of clay-bearing rocks from random preparations, *Clays and Clay Minerals*, 49(6): 514–528.

Tungpalan, K, Manlapig, E andrusiewicz, M, Keeney, L, Wightman, E and Edraki, M, 2015. An integrated approach of predicting metallurgical performance relating to variability in deposit characteristics, *Minerals Engineering*, 71: 49–54.

Verret, F, Chiasson, G and McKen, A, 2011. Sag mill testing – an overview of the test procedures available to characterize ore grindability, Technical paper 2011–08, SGS Minerals Service.

Wanhainen, C, Billström, K and Martinsson, O, 2006. Age, petrology and geochemistry of the porphyritic Aitik intrusion and its relation to the disseminated Aitik Cu-Au-Ag deposit, northern Sweden, GFF, 128(4): 273–286.

Wanhainen, C, Broman, C, Martinsson, O and Magnor, B, 2012. Modification of a Palaeoproterozoic porphyry-like system: Integration of structural, geochemical, petrographic and fluid inclusion data from the Aitik Cu–Au–Ag deposit, northern Sweden. *Ore Geology Reviews*, 48: 306–331.

Wanhainen, C, Broman, C, Martinsson, O, 2003. The Aitik Cu-Au-Ag deposit in northern Sweden: A product of high salinity fluids. *Mineralium Deposita*, 38: 715–726.

Wanhainen, C, Nigatu, W, Selby, D, McLeod, C, Nordin, R and Bolin, N J, 2014. The distribution, character and rhenium content of molybdenite in the Aitik Cu-Au-Ag-(Mo) deposit and its southern extension in the northern Norrbotten ore district, northern Sweden. *Minerals*, 4(4): 788–814.

Warlo, M, Wanhainen, C, Bark, G, Butcher, A R, McElroy, I, Brising, D and Rollinson, G K, 2019. Automated Quantitative Mineralogy Optimized for Simultaneous Detection of (Precious/Critical) Rare Metals and Base Metals in A Production-Focused Environment. *Minerals*, 9: 1–19.

Westerlund, P, 2017. Actions to reach 45 mt capacity in the concentrator at Aitik, Memo DMS 1064126 (unpublished), Boliden Mineral, Boliden.

Williams, S and Richardson, J, 2004. Geometallurgical Mapping: A new approach that reduces technical risk, Technical Paper 2004–01, SGS Mineral Services.

Online FTIR analysis for improved efficiency in alumina production

J D Speed[1], S P Wood[2] and K Haroon[3]

1. Product and Applications Manager, Keit Spectrometers, Oxford, Oxfordshire, OX11 0RL. Email: jonathon.speed@keit.co.uk
2. Applications Scientist, Keit Spectrometers, Oxford, Oxfordshire, OX11 0RL. Email: stephanie.wood@keit.co.uk
3. Applications Scientist, Keit Spectrometers, Oxford, Oxfordshire, OX11 0RL. Email: kiran.haroon@keit.co.uk

ABSTRACT

Online analysis of continuous and batch processes has seen a dramatic increase in recent years, with examples ranging from petrochemicals to pharmaceuticals, to industrial biotechnology and food and drink. The particularly challenging environment of alumina processing has meant that instrumentation needs specific features and characteristics to be truly suitable, features such as: robustness, resistance to caustic conditions both in the analyte and the ambient environment, and reliability for long-term continuous use. Here we present the development of a novel FTIR spectrometer that achieves these requirements through the use of a static optics arrangement of mirrors, and stable diamond-tipped light-pipe probe.

Firstly we give a very brief explanation of spectroscopic analysis, and the difference between FTIR and other infrared methodologies. Next we outline the novel arrangement of mirrors required to produce an interferogram without moving mirrors, and compare the benefits and drawbacks of this approach instead of conventional designs.

We then share the results of laboratory analysis of synthetic Bayer liquors, with detection limits for aluminium hydroxide, sodium hydroxide, sodium carbonate and various sodium salts of organic acids. We then share the results of analysis on production samples, both in idealised laboratory conditions and then online in the process itself.

Lastly we present work on in situ ultrasonic descaling solutions to avoid scale build-up and provide continuous cleaning of the probe – preventing the need for probe removal and manual cleaning.

INTRODUCTION

Online process analytical technology (PAT) is an important area of development in a wide range of industrial processes (Bakeev, 2008; Chew and Sharratt, 2010) and a key element of Industry 4.0 – the commonly accepted fourth industrial revolution we are currently experiencing. Traditional instrumentation (such as pH and temperature probes) is being complimented with more advanced techniques such as spectroscopy.

Spectroscopy can be defined as the interaction of light with matter, and the wavelength and energy of the light absorbed determines the underlying interaction studied. A full explanation of all the different spectroscopic techniques and wavelengths is beyond the scope of this article and is available elsewhere (Atkins, De Paula and Keeler, 2006). The majority of PAT implementations make use of vibrational spectroscopy – namely near-infrared (NIR), Raman and mid-infrared Fourier transform (FTIR) spectroscopies. The work shown in this article uses a static optics FTIR spectrometer. A brief summary of conventional and static optics interferometers is explained below.

Conventional FTIR interferometer design

Conventional FTIR instruments make use of a Michelson interferometer (Michelson and Morely, 1887), as shown in Figure 1. The light is created by a light source (1), such as a silicon carbide infrared emitter. This light is shone onto a beam splitter (2) which sends half the light onto a stationary mirror (3) and the other half onto a moving mirror (4). The light that runs on the stationary path always has the same distance to travel, whilst the path length of the light on the moving mirror changes over time. The light is then recombined at the beam splitter (2) before interacting with the sample and finally landing on a detector (5). The detector is a single pixel of material such as lithium tantalite, deuterated triglycine sulfate or mercury cadmium telluride. The difference in path lengths (caused

by the moving mirror) creates an interference pattern that changes over time (as the mirror moves).This interference pattern is subjected to a Fourier transform (the ‘FT’ in ‘FTIR’) which ultimately creates a spectrum.

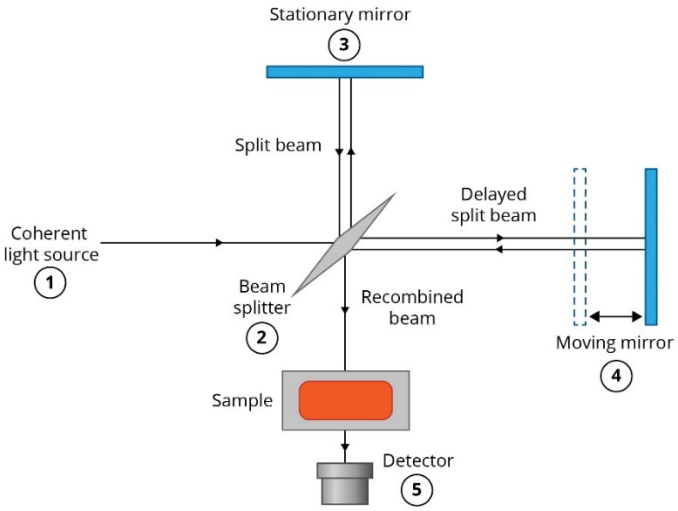

FIG 1 – A schematic of a Michelson interferometer showing light path from the light source through the pair of mirrors, the sample and eventually onto a single-pixel detector.

Static optics FTIR interferometer design

The static optics instrument design outline here makes use of a Sagnac interferometer (Sagnac, 1913), as shown in Figure 2. In this instance, the light (from a low powered source) runs through the sample first, before hitting a beam splitter (1). Half the light is reflected to run anti-clockwise through a pair of curved mirrors (2) whilst the other half is transmitted through the beam splitter to run clockwise through the pair of mirrors. Both beams of light are then incident onto a detector array (3) creating an interference pattern with respect to space directly onto the array. This interference pattern is subjected to the same Fourier transform mathematics as conventional designs.

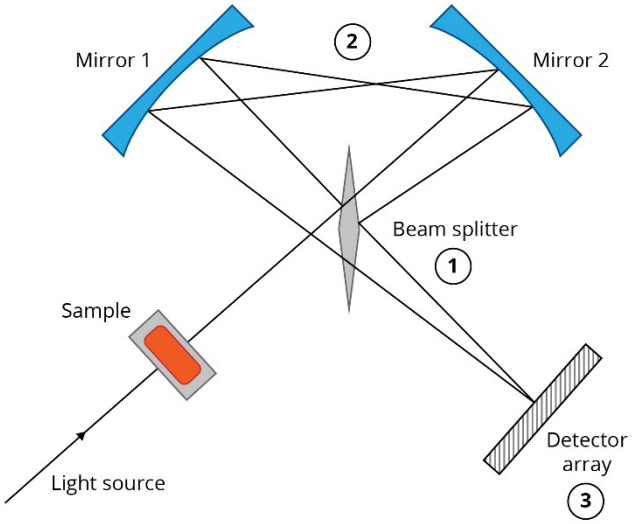

FIG 2 – A schematic of the modified Sagnac interferometer showing the light path through the sample, then the ‘Sagnac loop’ before the detector array.

The use of a ‘Sagnac loop’ of mirrors removes the need for moving mirrors and enables the use of secured mirrors onto an industrial baseplate. Ultimately this translates into a design that is significantly more resilient to vibration, as if one aspect of the optical design vibrates then the whole assembly vibrates – resulting in no change in the interference pattern and final spectrum.

RESULTS AND DISCUSSION

Detailed description of initial stage laboratory testing of synthetic Bayer liquors has been described previously (Speed and Wood, 2020). Briefly, a range of laboratory reference samples was made, and these were used to build a calibration curve using partial least squares (PLS) (Wold, Sjöström and Eriksson, 2001) methodology. Laboratory samples were prepared as follows: stock solutions of 607.5 g L^{-1} sodium hydroxide (NaOH), 75 g L^{-1} sodium carbonate (Na_2CO_3) and 155 g L^{-1} aluminium hydroxide ($Al(OH)_3$) dissolved in 328 g L^{-1} NaOH solution. These were mixed and diluted with additional water as appropriate to make a 'Design of Experiment' sample set for calibration.

A table of collated laboratory performance is shown below in Table 1. The results are reported as RMSECV (root mean squared error of cross validation) which is the average error during calibration. It is also a good approximation to limit of detection (LoD) for a calibration. It is highly affected by the absolute concentration range studied – in general higher concentration values have a higher RMSECV.

TABLE 1

Table of performance for laboratory calibrations of synthetic Bayer liquor.

Chemical name	RMSECV/g L^{-1}
Sodium hydroxide	7.38
Sodium aluminate	4.69
Sodium carbonate	1.36
Sodium oxalate	0.11
Sodium acetate	0.26
Sodium formate	0.27
Sodium succinate	0.31

Online process results

Following successful laboratory studies an online installation was performed directly into the spent liquor line in an alumina refinery in Europe. The instrument was installed using a welded flange directly into a side loop from the main process stream. This gives the ability to remove and inspect the instrument from time to time if required without affecting the daily production schedule of the refinery.

Spectra were recorded continuously with a 120 s averaging time, over one year. Calibrations were performed using spectra collected online from the instrument using reference data provided by the refinery, with primary laboratory quantitative analysis performed using a range of techniques such as ion chromatography (IC) and titration. Chemometric calibrations were built on the spectroscopic data using a combination of PLS and support vector regression (SVR) methods (Smola and Scholkopf, 1998).

A collated table of results for online process calibration using real world samples is shown below in Table 2. This table includes the RMSECV but also RMSEP (root mean squared error of prediction) which is a validation error – ie the average error predicting the concentration of samples not included in the calibration at all – and RPD (residual predictive deviation), defined as the standard deviation of reference data divided by the RMSEP. This allows the user to understand the capability of the calibration to be used for real-time control. Values greater than three are good for screening, greater than five show a strong and highly performing calibration suitable for quality control and above eight are good for analytical analyses (Conzen, 2014).

TABLE 2

Table of results for online calibration results.

Chemical name	RMSECV/g L^{-1}	RMSEP/g L^{-1}	RPD
Sodium hydroxide	1.76	1.12	1.97
Sodium aluminate	1.61	1.87	1.86
Sodium carbonate	1.07	0.36	6.33
Sodium oxalate	0.115	0.096	1.07
Sodium succinate	0.050	Not enough data	Not enough data
Sodium formate	0.067	0.10	Not enough data

The output of these calibrations for the inorganic compounds is shown below in Figure 3. The measurement is shown as a continuous line with the offline laboratory sampling overlaid. It is clear that the laboratory data shows good agreement with the majority of the online measurements, but there are several laboratory measurements that do not agree, and moreover do not agree with the trend of the measurement before or afterwards. Work is ongoing to determine whether these data points are in fact laboratory or human error, or whether the calibration needs refining to reflect these measurements.

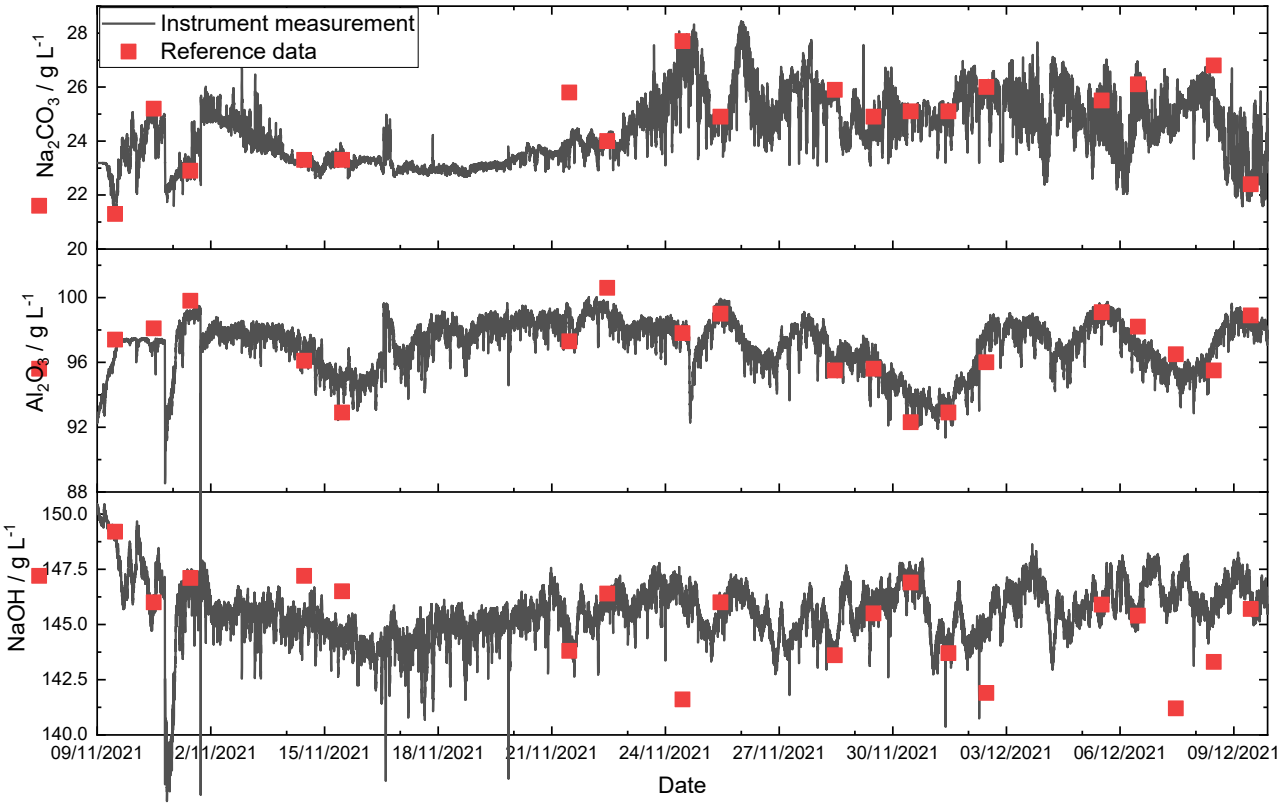

FIG 3 – Graph of spectrometer measurements over time overlaid with reference data from laboratory for inorganic compounds of interest for November and December 2021.

It should be noted that the 'spikes' seen in the data above are in fact real measurements caused by washing of the filters installed nearby to the instrument where periodic dilution of the liquor lasts for approximately 30 min. This appears as a 'spike' on the data above because of the timescale used.

The calibration for organic salts is shown below in Figure 4. It shows a good agreement between the oxalate reference values and instrument measurement, clearly highlighting the peaks and troughs in concentration over time. The succinate and formate concentrations are more stable, but increasing

succinate concentrations from January 20 through to 25 is clearly evident and would have been missed purely with offline sampling.

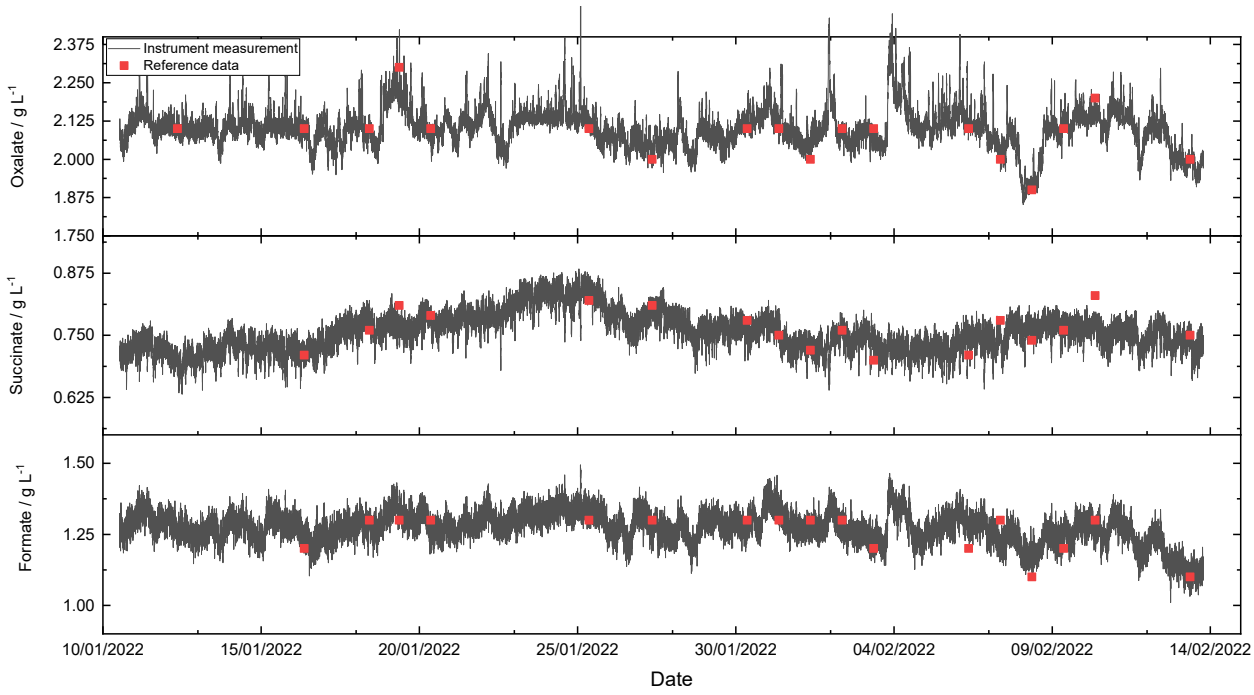

FIG 4 – Graph of spectrometer measurements over time overlaid with reference data from laboratory for organic compounds of interest for January 2022.

Preliminary descaling results

The spectrometer probe has been designed with an attenuated total reflectance (ATR) sensing tip that requires contact with the liquid to be studied. A potential issue with this is the formation of scale on the end of the probe, which could prevent the wetting of the diamond ATR element. The instrument presented here has been installed in a spent liquor stream for greater than 12 months without scale formation, but use in other locations in alumina refineries are highly likely to scale. Preliminary results have shown that scale can be removed from the end of the probe using an ultrasonic pulse. This is shown in Figure 5 – where the intensity of water, dissolved $Al(OH)_3$ and precipitated Gibbsite scale are measured before, during and after an ultrasonic pulse.

These results are very encouraging, but do require an ultrasonic generator strong enough to permeate through the pipework around the probe. Work by the author in the pulping sector has investigated the formation of pirssonite scale (a calcium, sodium carbonate mineral) on the end of the probe during use, and it is possible to identify its formation using FTIR spectroscopy, and then easily remove it using 1 M hydrochloric acid (HCl) solution in approximately 1 hr.

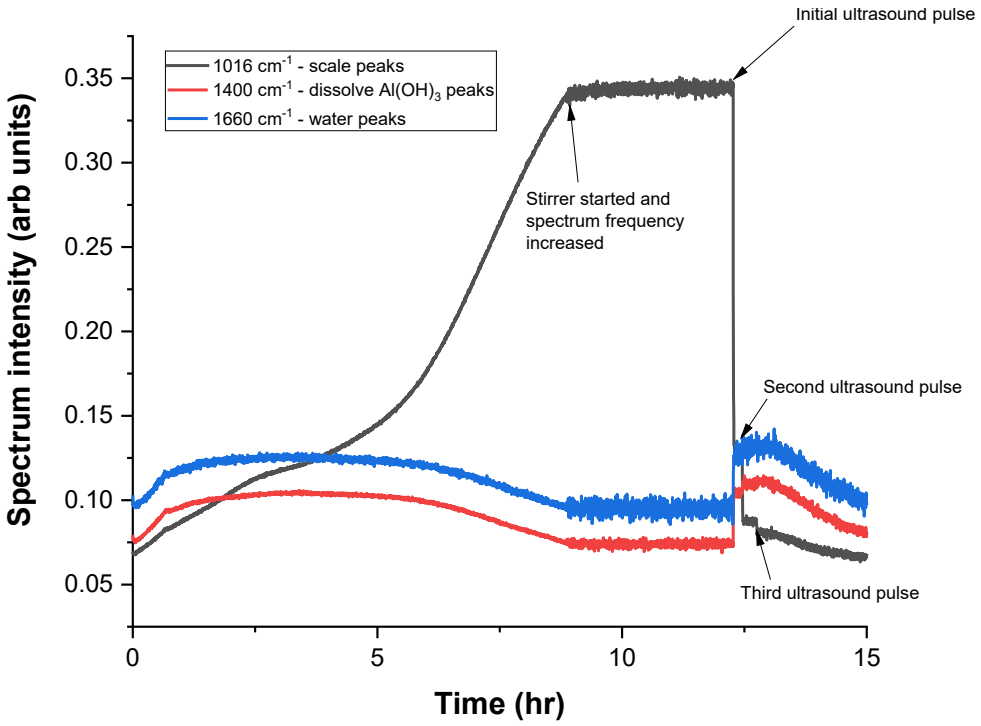

FIG 5 – Intensity of peaks for scale (1016 cm^{-1}), dissolved $Al(OH)_3$ (1400 cm^{-1}) and water (1660 cm^{-1}) at various stages throughout the experiment. (It can be seen that the scanning frequency is 10 s overnight and is increased to 1 s frequency during the ultrasound pulsing).

CONCLUSIONS

This work shows that FTIR spectroscopy is an effective tool for the measuring of alumina refining, and that robust and reliable measurements can be achieved when conventional interferometry is replaced with Sagnac interferometry. It is possible to measure dissolved alumina to an accuracy of 1.61 g L^{-1}, sodium hydroxide with 1.76 g L^{-1} and sodium carbonate to a level of 1.07 g L^{-1}. Moreover it is also possible to simultaneously measure different organic acids with the same instrument, with oxalic, formic and succinic acid measurements of 0.115, 0.067 and 0.050 g L^{-1} limits of detection respectively.

Lastly, the use of ultrasonic cleaning has been demonstrated to remove scale from the tip of the instrument with no damage or interference to the working of the instrument itself. However a 12 month installation in spent liquor has not resulted in any scale forming on the probe, showing that some applications are robust to scale formation and may not need any intervention.

REFERENCES

Atkins, P W, De Paula, J and Keeler, J, 2006. *Atkins' Physical Chemistry*. 8th edn. Oxford University Press. Available at: https://blackwells.co.uk/bookshop/product/Atkins-Physical-Chemistry-by-P-W-Atkins-author-Julio-De-Paula-author-James-Keeler-author/9780198769866 (Accessed: 7 September 2020).

Bakeev, K A (ed.), 2008. *Process Analytical Technology*. Oxford: Blackwell Publishing.

Chew, W and Sharratt, P, 2010. 'Trends in process analytical technology', *Analytical Methods*, 2(10), p. 1412. doi: 10.1039/c0ay00257g.

Michelson, A and Morely, E, 1887. 'On the Relative Motion of the Earth and the Luminiferous Ether', *American Journal of Science*, 34(203), pp. 333–345.

Sagnac, G, 1913. 'Regarding the Proof for the Existance of a Luminiferous Ether using a Rotating Interferometer Experiment', *Comptes Rendus*, 157, pp. 1410–1413.

Smola, A J and Scholkopf, B, 1998. 'A Tutorial on Support Vector Regression'. in NeuroCOLT2 Technical Report Series NC2-TR-1998-030, ESPRIT Working Group in Neural and Computaitonal Learning II, NeuroCOLT2 27150.

Speed, J D and Wood, S P, 2020. Online FTIR Analysis for Improved Efficiency in Alumina Production, in *Proceedings of the 38th International ICSOBA Conference*, 16–18 November 2020.

Wold, S, Sjöström, M and Eriksson, L, 2001. PLS-regression: A basic tool of chemometrics, in *Chemometrics and Intelligent Laboratory Systems*, pp. 109–130. doi: 10.1016/S0169–7439(01)00155–1.

Advances in mineral processing – comminution

A standardised method for the precise quantification of practical minimum comminution energy

S Ali[1], M S Powell[2], M Yahyaei[3], D K Weatherley[4] and G R Ballantyne[5]

1. PhD candidate, The University of Queensland, Sustainable Minerals Institute, Julius Kruttschnitt Mineral Research Centre, Indooroopilly Qld 4068. Email: shujaat.ali@uq.edu.au
2. FAusIMM, Emeritus Professor, The University of Queensland, Sustainable Minerals Institute, Julius Kruttschnitt Mineral Research Centre, Indooroopilly Qld 4068. Email: malcolm.powell@uq.edu.au
3. Associate Professor, The University of Queensland, Sustainable Minerals Institute, Julius Kruttschnitt Mineral Research Centre, Indooroopilly Qld 4068. Email: m.yahyaei@uq.edu.au
4. Senior Research Fellow, The University of Queensland, Sustainable Minerals Institute, Julius Kruttschnitt Mineral Research Centre, Indooroopilly Qld 4068. Email: d.weatherley@uq.edu.au
5. Director Technical Solutions – Global, Ausenco, South Brisbane Qld 4101. Email: grant.ballantyne@ausenco.com

ABSTRACT

This paper explores development of a novel ore characterisation method for the precise measurement of practical minimum comminution energy. A monolayer of particles with a narrow size distribution is broken using a precision rolls crusher (PRC); an ore characterisation device developed to overcome the shortcomings of conventional tests. For energy measurement, PRC uses two shaft-mounted rotary torque transducers. These transducers acquire precise torque and angular speed data in response to the load applied to the rotating shafts during breakage events, which is converted into energy. The test progressively crushes feed particles down to final product size in many controlled breakage stages. The generation of fines in each breakage stage is then plotted as a function of input energy. The inverse of the gradient of this plot provides the size specific energy (SSE) in kWh/t of material generated below a predefined marker size; -75 µm in this case. The PRC has potential to evolve as a geometallurgical ore characterisation test—it is simple, fast, requires small sample mass (200–300 g), covers a wide feed particle size range (10 mm to 115 µm), and provides ideal SSE measurements that can be used for the calibration of on-site production equipment.

INTRODUCTION

The endemic issue of not achieving the design throughput in comminution circuits relates to the selection of incorrect design criteria and the use of inaccurate models (Bueno *et al*, 2015). Incorrect design criteria include poor quality of test work, misinterpretation of results, and orebody variability. Orebody variability is based on spatial changes in geological structures and physical properties of the minerals present within the resource. Ore characterisation comes first in the design process, and it needs to be executed carefully as this underpins the entire circuit design. Since comminution is accountable on average for 37 per cent of mine energy consumption (Ballantyne and Powell, 2014), quality test work in ore characterisation is of significant importance. Ore characterisation provides useful information in understanding rock breakage behaviour and in establishing the relationship between input energy and size reduction. The traditional approach in ore characterisation involves testing representative reference samples across the orebody. Using geometallurgical principles, these reference samples can be used to establish spatial geometallurgical domains (Dunham and Vann, 2007; Lund, 2014). Combining these geometallurgical domains with the mine plan can provide a year-by-year estimate of the feed material that can be used for comminution circuit design. To allow for more extensive geometallurgical campaigns, ore characterisation needs to be fast, economical, and should have low sample requirements. Various characterisation methods have been developed to date. A comprehensive review has been reported by Mwanga *et al* (2015) and Chandramohan *et al* (2015) except for two recent developments by Böttcher *et al* (2021) and Bueno *et al* (2021). Widely used tests include the Bond work index test (Bond, 1952), drop weight test (DWT) (Napier-Munn, 1996), rotary breakage test (RBT) (Shi *et al*, 2006), SAG mill comminution (SMC) test (Morrell, 2004), Starkey SPI test (Starkey *et al*, 1994; Starkey and Dobby, 1996), and Starkey SAG design test (Starkey *et al*, 2006). These tests can be used to provide relatively risk-

free designs by using well-understood benchmarks developed over decades of operation. However, the required large sample size and test cost mean these tests are prohibitory in fully addressing ore variability, which can lead to results that are not representative for some ore types.

The fundamental comminution laws report an exponential increase in energy consumption at the fine particle size range (Hukki, 1961). Therefore, methods are required for accurate measurement of energy in the fines as it covers the major portion of energy consumption. However, the issue is the unavailability of a suitable method to quantify the energy requirements of individual, fine particles. In practice, many comminution models use values of A x b determined through DWT or RBT on the coarser particle size range, and Bond rod and ball milling tests in the fine end (Lane *et al*, 2013; Powell *et al*, 2014). Although various attempts have been made to measure the energy consumption of fine particles. These include micro compression testing of single particles by Farias *et al* (2014) and Romeis *et al* (2015), the application of the nano-indentation method to measure the fracture energy distribution of ultrafine particles by Schilde and Kwade (2012), Impact testing of particles beds by Barrios *et al* (2011), application of JK rotary breakage tester and Schonert device to determine size specific energy by Ballantyne *et al* (2015), and monolayer impact breakage using modified SILC test (Tavares and King, 1998) by Reja (2017) and using a mini drop weight by Yu *et al* (2019). However, all of these methods require tedious experimental work and extensive time, making their use impractical for geometallurgical sample testing.

Well-controlled single particle breakage under compression is the most effective way of determining primary fracture energy (Schönert, 1971) as it relates to the strain energy required for inducing bulk fracture within a particle (Tavares and King, 1998; Tavares, 2007; Tavares *et al*, 2020). However, this method is only proficient for coarse particles. Generally, single particle slow compression of small particles (<250 μm) is not suitable for industrial applications due to extensive cost and time requirements. Secondly, it provides limited information on the resulting progeny distribution. The recent application by Böttcher *et al* (2021) of breakage in monolayers based off the design of Powell, has shown promising results for particles below 150 μm. Particles were broken between a set of rigidly mounted rolls, and the breakage response was recorded as a profile of compression forces along the entire length of roll, referred to there as line load, expressed in N/mm. The line load was used to calculate compression stress that should be comparable to the particle strength measured by single particle compression testing, for instance measured by Schönert (1991).

The standard practice in the mining industry to determine the efficiency of a comminution unit is using a ratio between the operating work index and the Bond work index. The P_{80}-based methods have an underlying assumption that the feed and product distributions need to be parallel in log-log space (Bond, 1952). This makes application of the Bond test inappropriate for modern comminution equipment such as SAG mills, which produce considerably more fines relative to the P_{80} value than a ball mill; and stirred media mills, which produce a steeper size distribution with less reduction of the P_{80} size (Ballantyne *et al*, 2021). The test outcomes therefore can be misleading – an example is the incorrectly calculated inefficiency of the SAG mill relative to a ball mill when assessed using the Bond test.

Powell *et al* (2003–2010) proposed size specific energy (SSE) as an alternate method to measure ore competence. Size specific energy refers to the amount of energy consumed in generating material below a certain marker size (Powell *et al*, 2003–2010; Ballantyne *et al*, 2015). Typically, 75 μm is used as a standard marker size and SSE75 is measured. Musa and Morrison (2009) reported that for typical circuits that involve AG/SAG, HPGR, or ball milling, 75 μm material is a suitable marker size to benchmark equipment performance because material below this size contains 80 per cent surface area of the new surfaces generated. The application of SSE eradicates limitations of P_{80}-based tests and depends more on the generation of fines rather than P_{80}. The concept of size specific energy has been in use since the beginning of the 20th century when Davis (1919) used this method to measure the efficiency of the ball mill. Ballantyne *et al* (2015) established a linear relationship between specific energy and production of minus 75 microns material by breaking particles from a wide particle size range on JKRBT and Schonert devices. Reja (2017) applied the SSE method to determine minimum comminution energy by breaking a monolayer of particles using an impact load cell. And more recently, Ballantyne and Giblett (2019) reported that the SSE approach is an effective way to determine the efficiency of comminution circuits and individual equipment. However, determining SSE using single particle impact breakage, as in DWT

or JKRBT is still questionable. Studies in comminution testing and ore characterisation suggest that conventional single particle breakage tests such as the Drop Weight Tester (DWT) and the equivalent Rotatory Breakage Tester (RBT) have limited ability to provide a precise and accurate measure of the SSE. These devices are limited in a number of ways:

- inaccurate application and measurement of low energy impact
- insufficient generation of fines (sub 100 µm) for use in calculating the SSE
- inability to apply appropriate energies to small particles (below 5 mm)
- unable to achieve the ideal of primary fracture only.

Therefore, the development of a suitable method that employs the SSE method using single particle breakage and can be used to benchmark other lab-scale equipment, and industrial comminution devices and circuits is critical. This will allow the determination of practical minimum energy requirements for comminuting different types of ores on-site and will provide the opportunity to uplift the baseline performance of the comminution circuits by identifying underperforming units. Figure 1 shows a comparison between the specific energy measured on-site versus using bulk grindability tests, and single particle breakage for the same amount of material produced below 75 µm. The 'Missing data' in the graph represents the data gap that existing single particle breakage methods fail to populate.

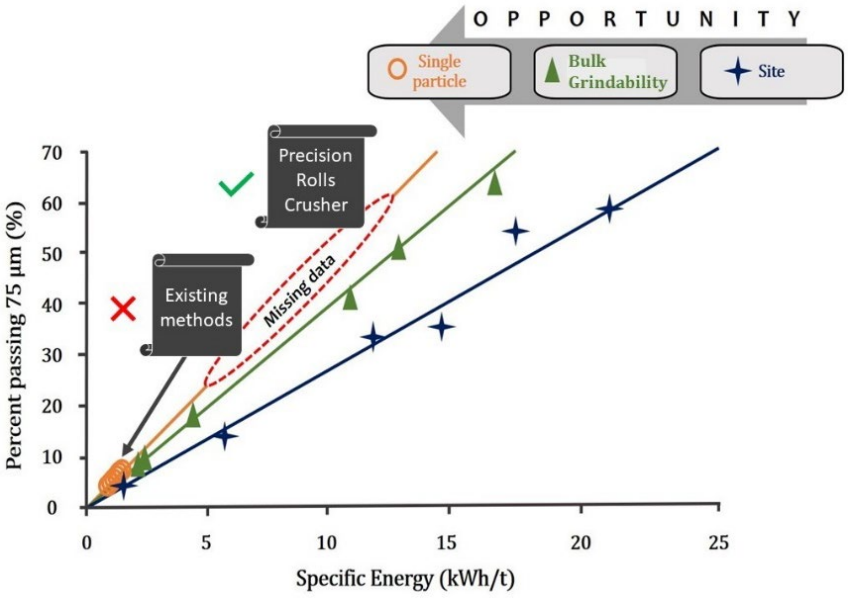

FIG 1 – Comparison of specific energy measured on-site versus specific energy measured using bulk grindability tests and single-particle breakage tests for the same generation of -75 µm material (modified from Reja, 2017).

This publication explores the development of a novel ore characterisation method that will provide practical minimum energy requirements in comminution. This method can potentially be used to benchmark operations, assess the energy efficiency of individual units and full-scale grinding circuits, and calibrate productivity improvements. Additionally, the method will be suited to characterising small samples for geometallurgy characterisation.

PRECISION ROLLS CRUSHER

The Precision Rolls Crusher (PRC) is a modern ore characterisation device being developed at the JKMRC, Sustainable Minerals Institute, The University of Queensland for the determination of practical minimum comminution energy. In 2017, a Buaermaeister rolls testing equipment, used in the food industry, was adopted as a prototype for testing the principle. Numerous modifications have been made in-house to make it suitable for comminution testing. Some preliminary test work was conducted internally to explore equipment suitability for ore characterisation. The equipment specifications are listed in Table 1. The concept of a rigidly mounted rolls mill was explored in the

1990s when Furstenau and his peers used similar equipment to study mathematical descriptions of single particle comminution, and for understanding particle interactions and energy dissipation (Fuerstenau *et al*, 1990, 1996; Gutsche *et al*, 1993).

TABLE 1

Specifications of precision rolls crusher.

Manufacturer	Bauermeister
Model	LRC250
Crusher dimensions (L × W × H)	1.4 m × 0.8 m × 1.4 m
Crusher weight	490 Kg
Power supply	415 volts (3 phase supply), 3 kW connected load (1.5 kW for each motor), 50 Hz power frequency
Roll diameter	250 mm
Roll width	80 mm
Roll speed	Individually controlled by frequency converter, 0–12 m/s (0–900 rev/min)
Motor	Induction motor (model 76646 manufactured by SEW-EURODRIVE, Germany)
Motor power frequency	50 Hz
Motor speed	1461 rev/min

A schematic of the PRC is shown in Figure 2. The PRC uses a set of counter-rotating stainless-steel rolls to crush rock particles. Each roll has a diameter of 250 mm and is 80 mm wide. The rolls have a smooth surface and can be controlled to a fixed gap using an adjustable gap assembly. The rolls are driven by 1.5 kW induction motors and are attached to each roll through shafts. Precise rotary torque sensors are installed on each shaft to record the response of rock breakage. The sensors were added with an additional feature of angular speed logging.

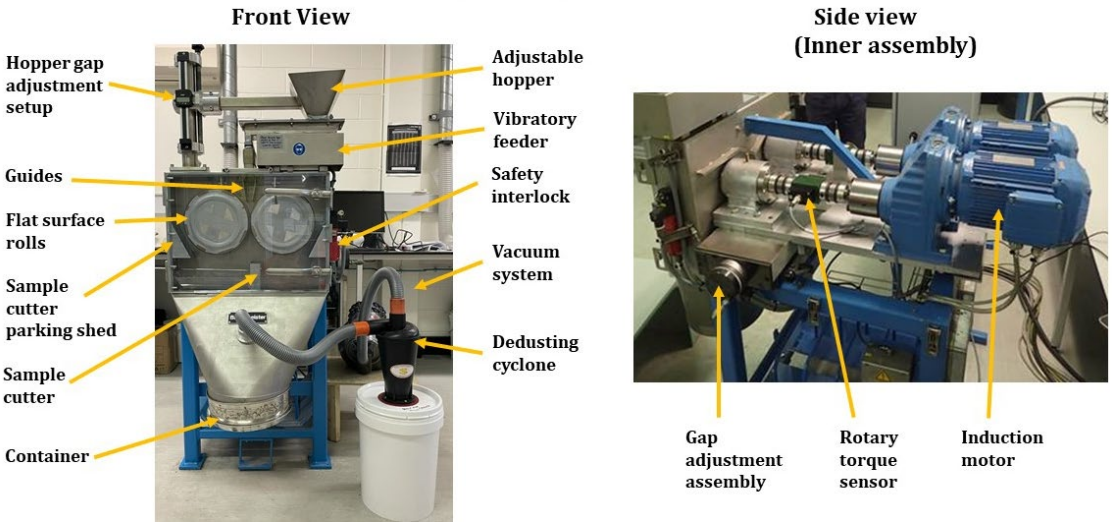

FIG 2 – Schematic of precision rolls crusher.

The Precision Rolls Crusher is fed with a small sample mass of approximately 200–300 g using a rectangular discharge hopper that sits on top of a vibratory feeder. The hopper gap height is adjusted by a dedicated digital hopper gap adjustment set-up to control the feed rate. The vibratory feeder is used to transport the ore particles to fall freely into the breakage zone. A pair of guides are installed to constrain the trajectory of any falling particles on the periphery of the flow and direct them towards

the centre of the rolls gap. The current dimensions of the guides limit the feed particles to below 11.5 mm. The crusher chamber has a plexiglass door that can be locked using a pair of cross-lock handles. A safety interlock is installed on the door that breaks the electrical circuit and stops the machine if the door is opened while the machine is functioning. This prevents the risk of injury. In addition, PRC also has an emergency stop button on the control panel. A sample cutter is installed underneath the set of rolls, to extract representative samples from the rolls product. The sample cutter stays under a parking shed when unattended. Another shed of the same dimension is installed on the opposite side for symmetrical airflow inside the mill chamber. On the inner side of the door, two plastic flaps are attached to the bottom to prevent sample loss when the door is opened for sample recovery. These flaps act as collection chutes and prevent fine dust on the door from spilling during cleaning. Air fines that are generated during breakage are collected using a dedusting cyclone set-up. The dedusting cyclone provides a sharp cut point of the rolls product and delivers almost 100 per cent of the air fines to the cyclone underflow, which allows convenient recovery of fines from the underflow bucket with minimal sample loss. The coarse breakage product is collected in a steel container attached to the bottom of the mill chamber.

A central control panel is used to operate the machine. The panel houses the electrical system of the PRC. It also has a graphic user interface that displays machine inputs. Rolls speed and feed rate are digital inputs to the control unit, while the gap width is adjusted manually. Gap adjustment is made by moving the moveable roll relative to the fixed roll. The moveable roll with its entire assembly is mounted on a sliding table that moves across by rotating a crank attached to the assembly. The changes in the gap can also be monitored on the control unit interface. A lever is used to lock the moveable roll at the desired gap width.

PRINCIPLES OF BREAKAGE

A standard test in the PRC is conducted using an appropriate reduction ratio (RR) between the gap width and particle top size that supplies adequate compression energy required to induce body fracture of individual particles. In practice, after the first pass, the RR is the ratio of rolls gap over the previous rolls gap. The breakage is achieved by testing a uniformly distributed monolayer of particles in a way that the gap is reduced progressively over sequential passes following a constant reduction ratio, and the product is recycled between passes. By doing so, the particles that are smaller than the gap pass through the rolls without breakage, while large particles break, and the breakage response is recorded in the form of torque and angular speed data. The recirculating material does not need screening between passes as was required to perform a similar kind of test work using impact breakage on JKRBT (Ballantyne *et al*, 2015). The test workflow is illustrated in Figure 3.

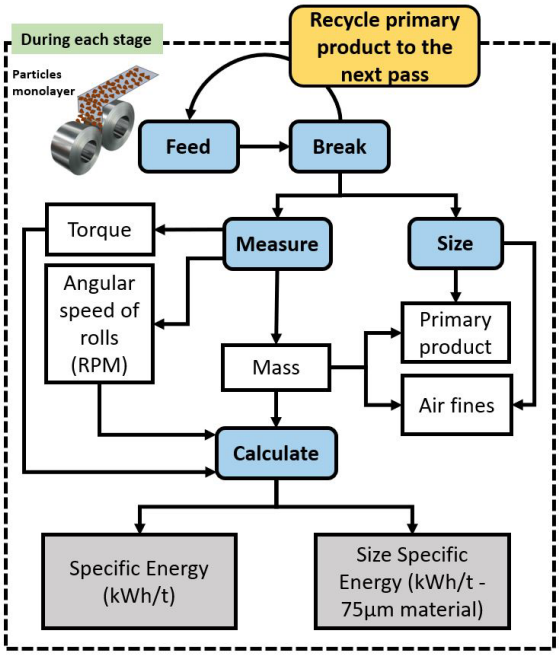

FIG 3 – Process flow in PRC.

A data logging program was developed in LabView 2017 software that takes user inputs to run the experiment, monitors the outputs such as torque and angular speed in real-time, and logs that data automatically to the desired location in computer memory. The data have been acquired at the sampling rate of 400 Hz using data acquisition devices manufactured by National Instruments. A MATLAB script was written to process the acquired data and convert that into energy in kWh. Equation 1 is used to calculate net torque energy during a breakage event. The area under the curve in the torque-time signal is integrated to get cumulative energy consumption during a breakage event (Figure 4). Before each experiment, torque data is logged for approximately 20 seconds at no-load. The average of that data gives no-load torque value that is subtracted from each torque measurement logged during the experiment. This allows discounting no-load torque from the acquired data. Adding cumulative energies for left and right rolls gives the overall energy consumption of a breakage event in the PRC. Dividing the torque energy by feed mass results in specific energy in kWh/t.

$$Net\ torque\ Energy(kWh) = \frac{\pi\left(\frac{\omega}{30}\right)\int_{t_0}^{t_1}[\tau(t)-\tau_0(t)]dt}{3600} \quad (1)$$

Where:

τ = Torque (Nm)

τ_0 = No-load torque

ω = Angular speed (rev/min)

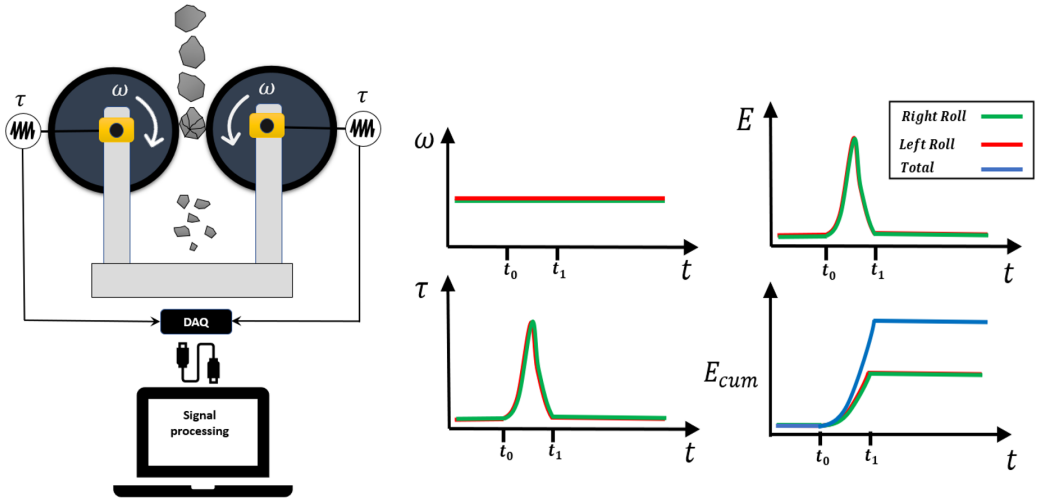

FIG 4 – Concept of breakage and energy logging in PRC.

The PRC employs the concept of SSE at 75 µm marker size. In addition to the accurate measurement of energy for SSE determination, it is equally important to effectively recover the mass of fines generated as both are inputs to SSE formulation ie SSE = Breakage Energy (kWh)/Fines generated below 75 microns (tons of -75 µm material). In a plot of specific energy versus percent new 75 µm generated, the inverse slope of the trend line forced to pass through zero gives SSE (Ballantyne *et al*, 2015).

Mass of material below 75 µm is measured both from the primary rolls product and from the air fines. Air fines that are generated inside the mill are collected during each pass of breakage by the dedusting cyclone and report to the cyclone underflow bucket at 100 per cent below 100 µm. These fines accumulate over a batch of three passes and are recovered after every third consecutive pass. Similarly, a sample from the primary product stream is cut every third pass, although it does not cumulate masses from the previous passes. The extracted sample mass of primary material in the cutter is not added back to the recycled mass, therefore, the extracted mass needs to be adjusted for specific energy calculations. Air fines collected in the vacuum are sized using a sonic sifter, a mechanical sizing method that is well suited to size small samples relatively quickly (Wolcott, 1977).

Breakage of particles in the PRC is analogous to testing particles between two flat parallel plates given that the feed rate is kept very low, and the particles are spread out uniformly along the roll

length to avoid interaction. The latter is achieved using an adjustable feed hopper that ensures a monolayer of particles leaves the feeder. Furthermore, the ratio of roll diameter to particle size is rather large which almost eradicates the effect of rolls curvature on particles and makes the concept similar to the compression of particles in a press. However, the strain rate in PRC cannot be controlled as in slow compression.

The validity of particle monolayer breakage relative to a single particle breakage was verified through a comparative analysis of specific energies and size distributions of the resulting progeny when particles were broken in the form of monolayer and singly on PRC (Figure 5). Particles of size class +6.7 mm -8 mm from a hard rock homogenous sample were chosen for the study. Results showed a match of specific energies within one standard deviation. Also, the resulting progeny distributions from both cases overlapped (Figure 5).

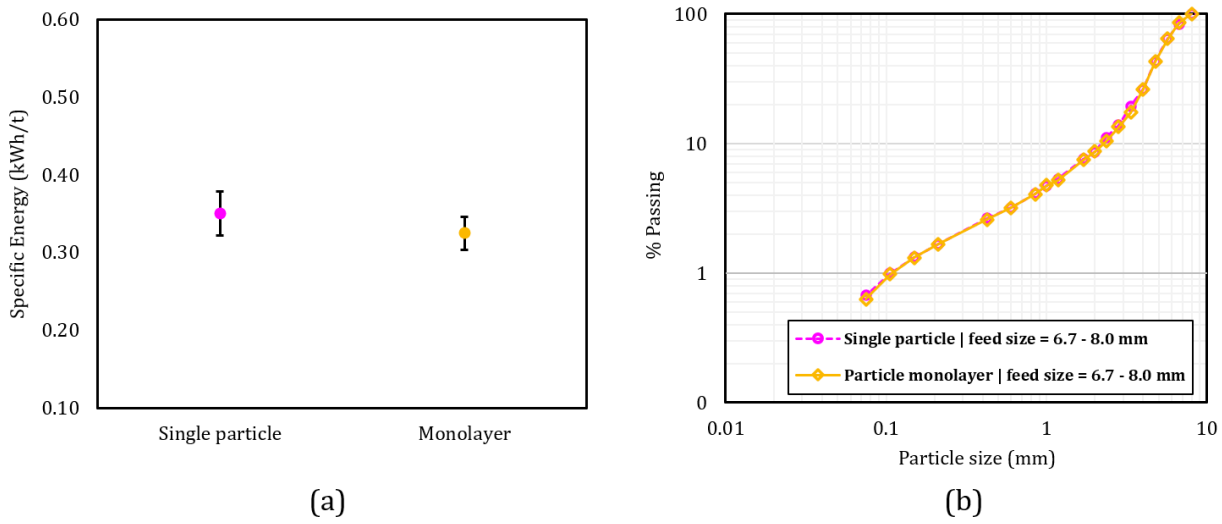

FIG 5 – (a) Comparison of specific energy measurement for the breakage of particle monolayer and single particles (b) Resulting progeny distributions.

Additionally, high-speed filming was used to ensure the breakage of particles singly, however, particles below 1.7 mm could not be captured by the camera due to the limitation of camera resolution. For coarse particles, ie >1.7 mm, it was observed that particles were falling individually in the breakage zone with little to no interaction with other particles. However, when the particles get smaller in size, their population density on the feeder increases which might result in particle interactions. This interaction seems to be random between particles of different sizes. Since knowledge of fine particle interactions in the breakage zone is relatively vague, it can however be hypothesised that generally a large population of particles smaller than the gap sweep through and leave behind a well spread-out layer of only those particles that then breaks normally. Nevertheless, it is still acknowledged that various factors may cause such interactions in the breakage zone, for instance, individual particle geometry, the mass difference between particles, surrounding distance from the other particles, collision during the free fall, etc.

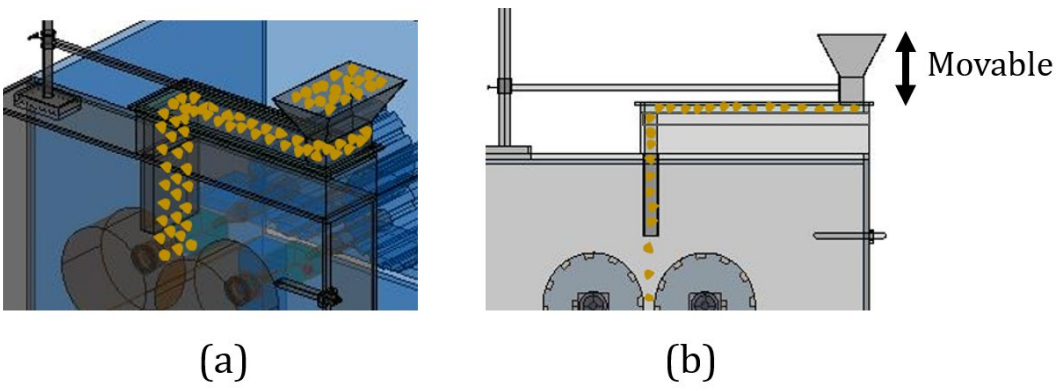

FIG 6 – Particles monolayer formation on the feeder (a) 3D view (b) Front view.

The effect of change in feed rate on specific energy was investigated by breaking particles from three different size fractions, at a range of feed rates that the equipment could reasonably be operated. The results show that breakage specific energy is independent of feed rate for the range tested for all the size fractions tested (Figure 7). The absolute specific energy for each size was dependent on the chosen reduction for that size, so holds no particular significance. High feed rates in the vibratory feeders increase vibrations and so the particle interactions. But since the monolayer was well controlled at hopper discharge (Figure 6), increased feed rates did not affect energy measurements that could otherwise have reflected particle interactions in the breakage zone. The independence from feed rate over almost an order of magnitude in sizes, gives confidence to this being the case for the finer feeds down to 150 µm.

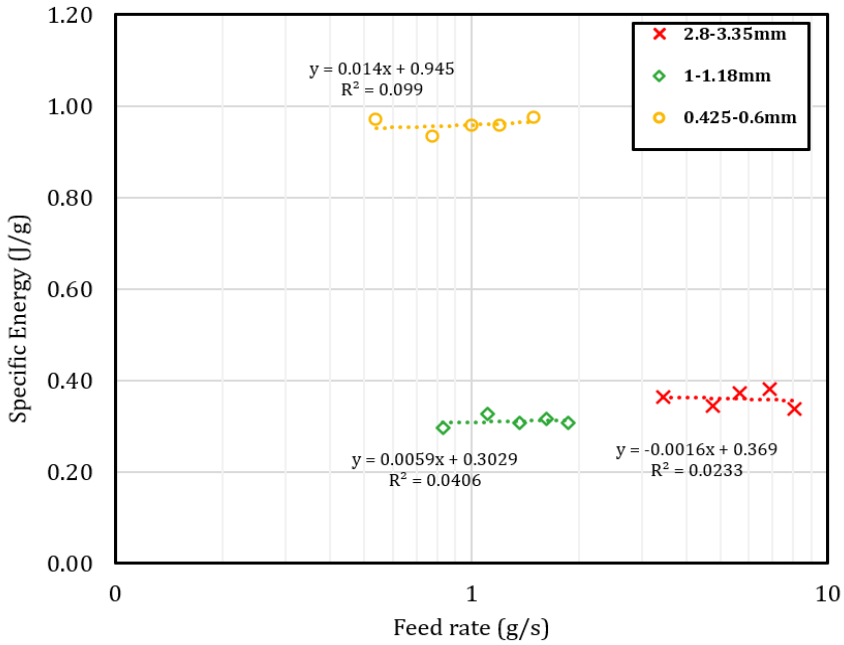

FIG 7 – Specific energy as a function of change in feed rate.

Based on the concern that slip between the particle and the rolls surface as the particle enters the nipping zone could induce an additional breakage mode of sliding abrasion, the influence of varying the speed of the rolls was investigated. The free-fall velocity of the particle was measured using a high-speed camera at a value of 2 m/s. A range of rolls surface speeds of 2–6 m/s was tested for two particle size ranges: +1.4 mm -1.7 mm and +4.00 mm -4.75 mm. Results presented in Figure 8 illustrate that there is no trend in the specific energy value across the range of rolls speed tested. Also, an overlap of corresponding progeny distributions was observed (Figure 8), which is evidence that the change in speed does not affect the breakage event. This indicates that particles most likely do not experience any significant slip due to static friction dominating as the particle enters the nipping breakage zone, as reported by Lieberwirth *et al* (2017). Although no sensitivity to rolls speed was measured, the tip velocity of the spinning rolls was set to the fall velocity of the particles to ensure that differential slip and attrition could be avoided. Additionally, a pair of guides were installed underneath the feeder fall point to direct particles to follow a path towards the centre of the rolls gap, avoiding undesirable bouncing of the particles which can lead to bypassing the breakage zone or interference with other particles.

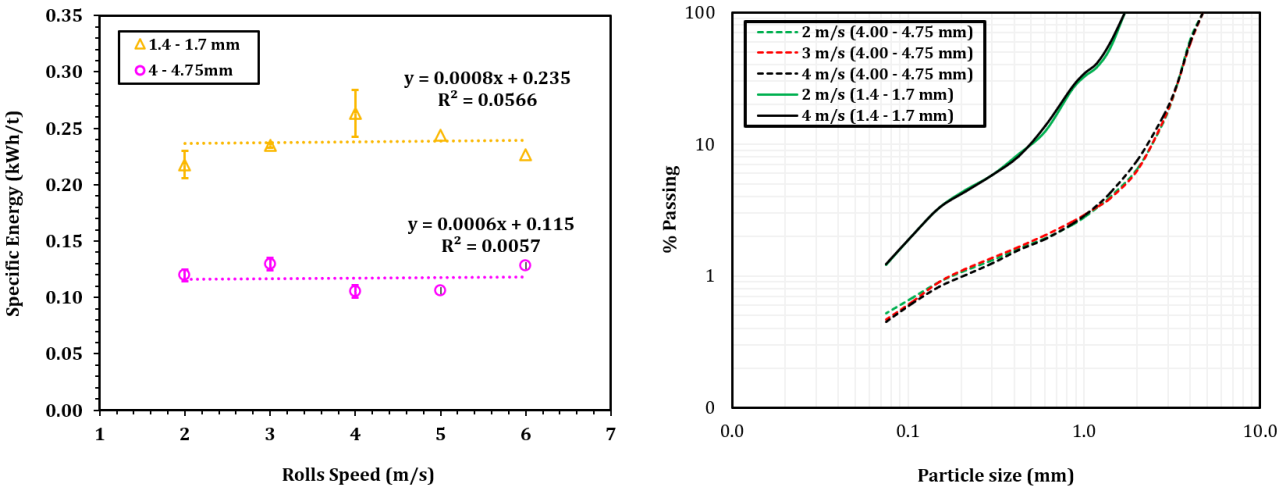

(a) (b)

FIG 8 – (a) Feed rate as a function of change in rolls speed (b) Progeny distributions at varying rolls speed.

In contrast to user-defined input energy for impact tests, the input energy is a response to the ore competence and degree of reduction in breakage. Thus for the PRC, the specific energy input is recorded as a response to breakage. This response varies depending on the intensity of compression which can be controlled by changing the gap between rolls for particles of fixed size. To test the influence of reduction ratio on breakage energy, progeny size, and SSE, a comparative trial was conducted against ideal single particle breakage.

The SILC uses double-sided impact to break a single particle at a time. A sample of at least 30 particles is selected from a narrow size class to provide a distribution of breakage energies, and the median energy E_{50} represents the energy at primary fracture (Tavares and King, 1998). The SILC was used to measure primary fracture energy and the corresponding progeny distribution was measured. Particles from the same ore type were broken in the PRC using various reduction ratios. The procedure was applied as illustrated in Figure 9 with the objective to find a reduction ratio where progeny distributions matched those from the SILC. Matching results would indicate that primary fracture was being achieved in the PRC.

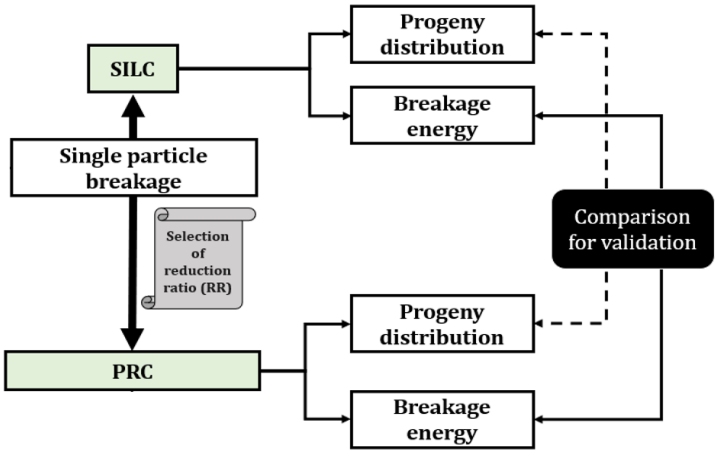

FIG 9 – Experimental approach for the selection of appropriate reduction ratio in PRC.

A rock sample from the size range +6.7 mm -8.0 mm was broken on both SILC and PRC. Results showed that the progeny distributions from PRC were similar to those of the SILC at RR = 0.8 (Figure 10), and close at the fine end below 500 µm. interestingly, the PRC product resulted in slightly steeper size distribution, potentially indicating that there is less secondary breakage than in the SILC device. Table 2 shows the corresponding gaps and nominal feed sizes for different

reduction ratios. The corresponding energy consumption of PRC at RR = 0.80 was slightly lower than SILC input energy, which is calculated using the potential energy of the ball related to the mass of the ball and drop height. The selection of input energy is entirely user-dependent; however, it is generally chosen to be the minimum required to repeatedly induce a bulk fracture of a particle. On the other hand, absorbed energy (E_{50}) is an absolute minimum measure of energy, calculated based on the first peak of the force-time profile captured from the SILC device, representing energy absorbed to first fracture. This does not include any subsequent breakage the rock may undergo.

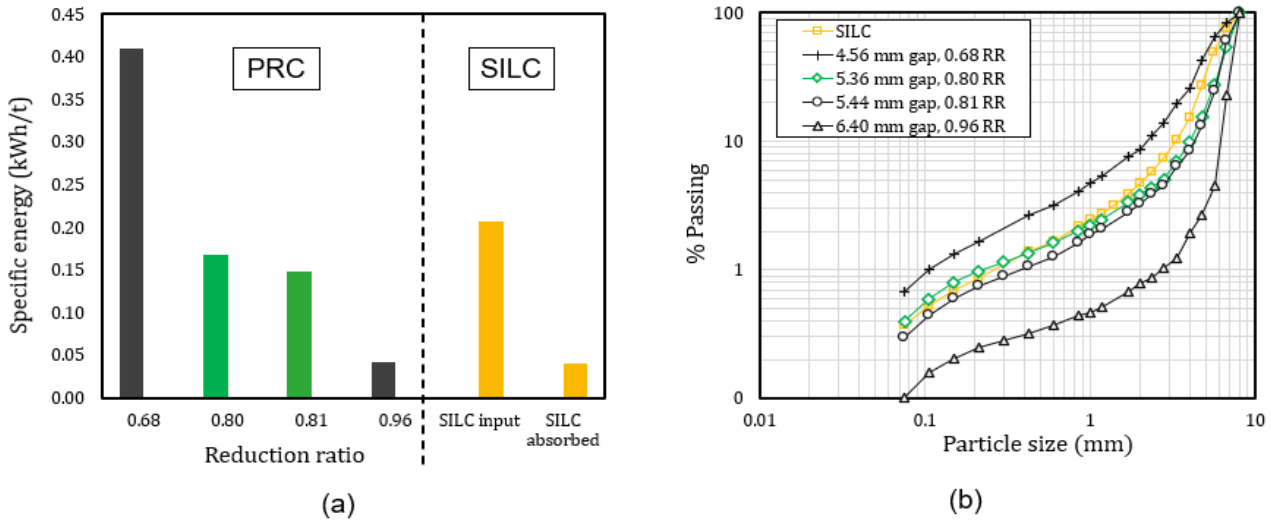

FIG 10 – Comparison of (a) specific energy and (b) resulting progeny distributions of single particle breakage in SILC versus single particle breakage in PRC at various reduction ratios.

TABLE 2

Reduction ratio and corresponding gap widths – PRC versus SILC.

Equipment	Nominal particle size (mm)	Reduction ratio (gap/particle size)	Gap width (mm)
SILC	6.7	NA	NA
PRC		0.68	4.56
		0.80	5.36
		0.81	5.44
		0.96	6.40

A similar kind of test work was conducted on a rock sample having flaky particles and the appropriate reduction ratio was found to be 0.74. As the RR is currently calculated on square-mesh screen size as opposed to the more appropriate minimum particle dimension, it is expected that the more flaky the particle the lower the reduction ratio value to achieve the same degree of compression.

Breaking a population of particles in PRC from a particular size fraction in the form of a monolayer provides statistically significant data on fracture energy considering that each particle is broken singly. The scale of energy measured in PRC is different from E_{50}. The impact load cell has a relative advantage of capturing the heterogeneity at the particle scale. This heterogeneity is acknowledged as the shape, mineralogy, and flaw density can affect the breakage energy of particles even within the same size class (Tavares and King, 1998; Tavares *et al*, 2020). In the PRC, the overall energy required to break a known mass of particles of the same size corresponds to the summation of fracture energies of individual particles. The resolution of measurements in PRC decreases for finer particle sizes. Therefore, the quality of sensors needs to be considered. A set of new torque sensors have been purchased and are being installed to achieve the required resolution.

EXPERIMENTAL

A homogenous hard rock sample was tested for the preliminary test work. Around 300 g of material from a mono-sized fraction of +6.7 mm -8 mm was progressively crushed down to a gap width of 115 µm. A standard operating procedure of the experiment is as follows:

- Equipment warmup – approximately 15 to 30 minutes.
- Setting up experimental parameters such as, gap width, feed rate, and rolls speed.
- Adjusting hopper gap to allow monolayer formation of feed particles on the feeder.
- Logging torque and rolls speed data during a breakage event, including no-load logging before and after, for approximately 20 seconds each.
- Extraction of samples from the primary product of rolls.
- Collection of air fines using a dedusting cyclone.
- Adjusting gap width for the next pass of sequential breakage, and recycling product from the last pass.
- Repeating the process for each progressive gap setting until the desired minimum gap is reached.

Since the method is still under development, the current methodology will be improved. Future improvements include automating the sample cutter which would reduce the dust loss that currently happens due to cleaning and transferring the material when the door is open. In addition, it would also speed up the process as the sample will be collected without the door being opened.

PRELIMINARY RESULTS AND DISCUSSION

The product generated from breaking a monolayer of particles in PRC resulted in a sequential parallel appearance function. Figure 11 illustrates the resulting percent passing as a function of progressive gap reduction. These distributions were calculated on the representative samples of primary products that were collected every third pass of sequential breakage. This appears to be an ideal primary breakage appearance function that can be directly implemented in mechanistic comminution models. Provided that the progeny distribution is parallel, the intermediate steps of sample extraction can be ignored in the future, and rather only the final product can be a focus. This will make the test relatively fast.

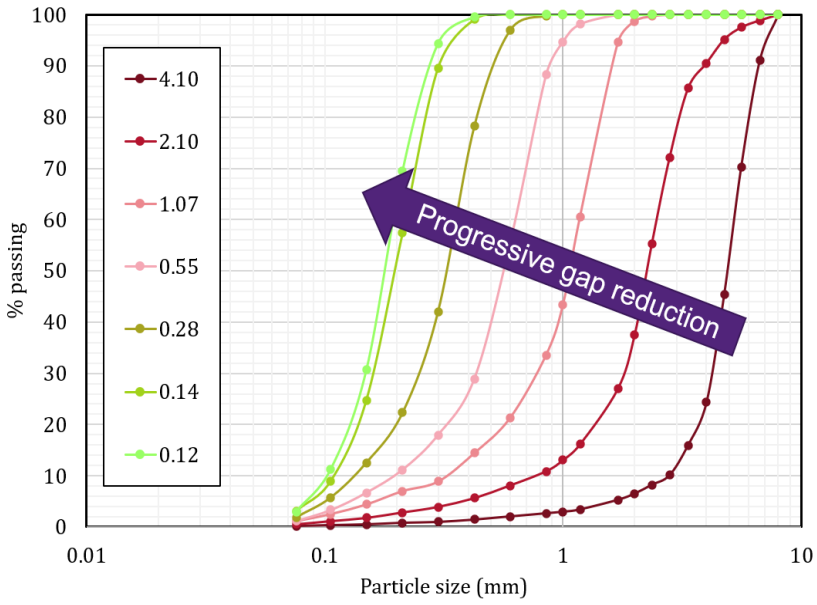

FIG 11 – Parallel progression in the appearance function as particle size or the corresponding gap width decreases.

Plotting gap width versus cumulative specific energy that was consumed to break the feed sample to the desired product size demonstrated an increase in energy consumption as a function of decreasing gap width (Figure 12). The plot fitted a logarithmic model that seems to be fitting reasonably well with an R^2 of 0.99; however, the underlying reason for the logarithmic model fit is still under investigation.

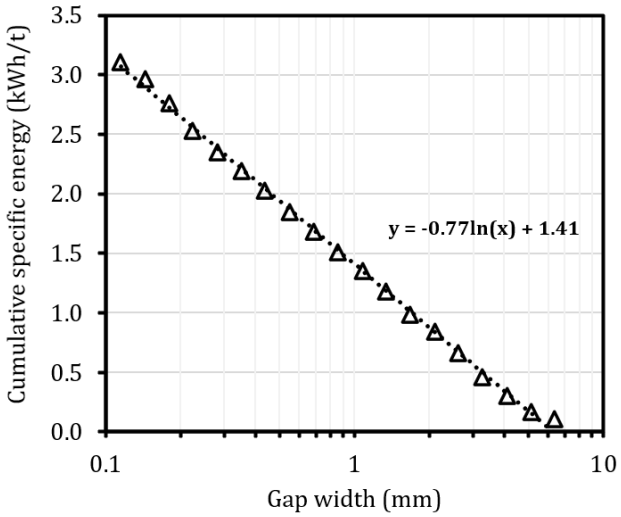

FIG 12 – Specific energy as a function of change in gap width. The dashed line represents logarithmic model fit.

Specific energy versus percent fines generated was plotted (Figure 13). The percent fines generated rather than 75 µm was plotted because the data was captured when the vacuum set-up was being installed and the cut point was not effectively set-up which resulted in some coarse material reporting to the dedusting cyclone underflow. However, it was observed that the amount of oversize (plus 75 µm) material reported to the fines was tiny, below 2 per cent of the fines content, and thus less than 1.5 per cent of the total fines product. Results in Figure 13 exhibited an increasing trend of energy consumption for the production of fines. As shown in Figure 1, a linear trend is typically expected when plotting fines generated versus cumulative specific energy. However, in these tests, this relationship is developed by progressively breaking single coarse particles down to fine particles. Therefore, feed particle size is impacting this relationship as the reduction ratio to produce -75 µm is greater for coarser particles.

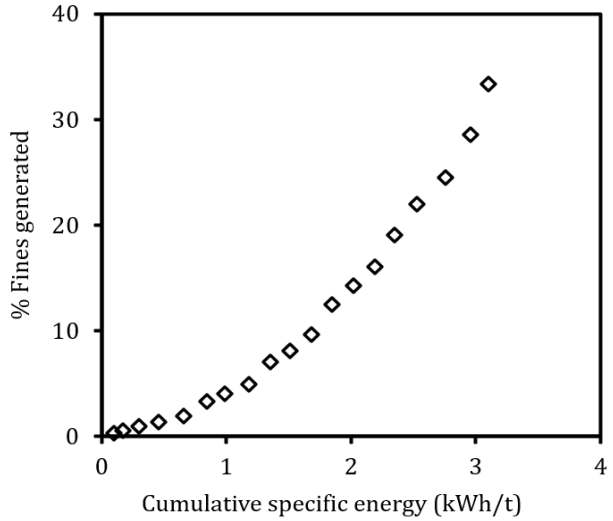

FIG 13 – Plot of specific energy versus percent passing fines generated.

The effect of initial feed size on size specific energy was investigated (Figure 14). The initial feed size was found to influence the size specific energy ie an increase in size specific energy with the

particle size was observed, which was more pronounced at the coarser end. The results are in agreement with a study conducted by Ballantyne *et al* (2015). The reason for this decrease in SSE for finer particle sizes is the lower reduction ratio.

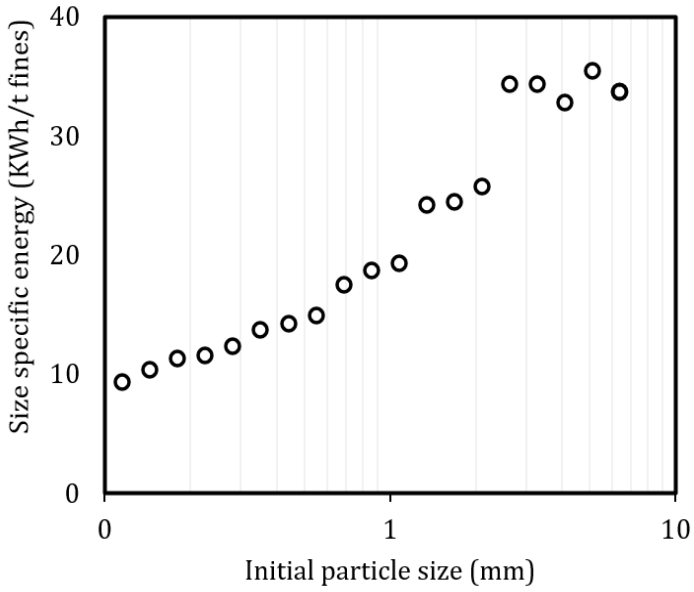

FIG 14 – Relationship between initial particle size and size specific energy.

CONCLUSIONS

The precision rolls crusher, a novel ore characterisation method that uses the concept of SSE to determine practical minimum comminution energy requirements was developed. The feasibility of monolayer breakage of particles that produces similar breakage results to single particle was proven. Also, the primary fracture of ore particles in PRC was targeted through the selection of an appropriate reduction ratio that generated relatively similar progenies as in breakage under impact to achieve primary fracture energy in the short impact load cell. In addition, the influence of various experimental variables such as feed rate and rolls speed was also investigated.

Even in its current initial set-up, the test is relatively fast, inexpensive, and requires a small sample of under 200 g, so has a potential to be used for geometallurgical variability programs. This can supplement recent developments such as Geopyora (Bueno *et al*, 2021), and the double roller mill used for fine particle characterisation. It is capable of capturing the primary ore characteristics, mostly independent of the grinding environment fairly similar to single particle breakage in compression and impact load cell. The ideal practical energy measurements are well suited to benchmark on-site equipment given the test is conducted on the same ore type. The stagewise product obtained from PRC can be used for liberation analysis, and the degree of liberation can therefore be linked to a robust energy measure ie SSE. The generation of ideal appearance function can be used directly in mechanistic comminution models. After some technological improvements to accelerate the testing rate, this device has a foreseeable future for being used in accurate ore characterisation for geometallurgical modelling of orebodies.

ACKNOWLEDGEMENTS

The authors would like to acknowledge the support of Julius Kruttschnit Minerals Research Centre management and pilot plant staff for providing support for this research.

REFERENCES

Ballantyne, G and Giblett, A, 2019. *Benchmarking comminution circuit performance for sustained improvement*. Paper presented at the SAG conference 2019, Vancouver Canada.

Ballantyne, G R and Powell, M S, 2014. Benchmarking comminution energy consumption for the processing of copper and gold ores. *Minerals Engineering, 65*, 109–114. doi:https://doi.org/10.1016/j.mineng.2014.05.017

Ballantyne, G, Foggiatto, B, Staples, P and Lane, G, 2021. *Coarse Vertical Stirred Mill Applications*. Paper presented at the AusIMM Mill Operators Conference, Brisbane, Australia.

Ballantyne, G, Peukert, W and Powell, M, 2015. Size specific energy (SSE)—Energy required to generate minus 75 micron material. *International Journal of Mineral Processing, 136*, 2–6. doi:https://doi.org/10.1016/j.minpro.2014.09.010

Barrios, G K P, de Carvalho, R M and Tavares, L M, 2011. Extending breakage characterisation to fine sizes by impact on particle beds. *Mineral Processing and Extractive Metallurgy, 120*(1), 37–44. doi:10.1179/1743285510Y.0000000002

Bond, F C, 1952. The third theory of comminution. *Trans. AIME*, 484–494.

Böttcher, A-C, Thon, C, Fragnière, G, Chagas, A, Schilde, C and Kwade, A, 2021. Rigidly-mounted roll mill as breakage tester for characterizing fine particle breakage. *Powder Technology, 383*, 554–563. doi:https://doi.org/10.1016/j.powtec.2021.01.055

Bueno, M, Foggiatto, B and Lane, G, 2015. *Geometallurgy Applied in Comminution to Minimize Design Risks*.

Bueno, M, Torvela, J, Chandramohan, R, Chavez Matus, T, Liedes, T and Powell, M, 2021. The double wheel breakage test. *Minerals Engineering, 168*, 106905. doi:https://doi.org/10.1016/j.mineng.2021.106905

Chandramohan, R, Lane, G, Foggiatto, B and Bueno, M, 2015. *Reliability of some ore characterization tests*.

Davis, E W, 1919. Fina crushing in ball mills. *Transactions of the American Institute of Mining Engineers, 61*, 250–297.

Dunham, S and Vann, J, 2007. Geometallurgy, Geostatistics and Project Value — Does Your Block Model Tell You What You Need to Know?

Farias, L R, Cordeiro, G, Toledo Filho, R and Tavares, L, 2014. Measuring the strength of irregularly-shaped fine particles in a microcompression tester. *Minerals Engineering, 65*, 149–155. doi:10.1016/j.mineng.2014.05.021

Fuerstenau, D W, Gutsche, O and Kapur, P C, 1996. Confined particle bed comminution under compressive loads. *International Journal of Mineral Processing, 44–45*, 521–537. doi:https://doi.org/10.1016/0301–7516(95)00063–1

Fuerstenau, D W, Kapur, P C, Schoenert, K and Marktscheffel, M, 1990. Comparison of energy consumption in the breakage of single particles in a rigidly mounted roll mill with ball mill grinding. *International Journal of Mineral Processing, 28*(1), 109–125. doi:https://doi.org/10.1016/0301–7516(90)90030–3

Gutsche, O, Kapur, P C and Fuerstenau, D W, 1993. Comminution of single particles in a rigidly-mounted roll mill Part 2: Product size distribution and energy utilization. *Powder Technology, 76*, 263–270.

Hukki, R T, 1961. Proposal for a solomnic settlement between the theories of von Rittinger, Kick and Bond. *Trans. AIME, 220*, 403–408. Retrieved from https://www.scopus.com/inward/record.uri?eid=2-s2.0–0011822505andpartnerID=40andmd5=0137b1724b7a5a3fcf1e26c9874fdebd

Lane, G, Foggiatto, B and Bueno, M, 2013. *Power-based comminution calculations using Ausgrind*.

Lieberwirth, H, Hillmann, P and Hesse, M, 2017. Dynamics in double roll crushers. *Minerals Engineering, 103–104*, 60–66. doi:https://doi.org/10.1016/j.mineng.2016.08.009

Lund, C, 2014. Geometallurgy – A tool for better resource efficiency. *European geologist, 37*, 39–43.

Morrell, S, 2004. Predicting the specific energy of autogenous and semi-autogenous mills from small diameter drill core samples. *Minerals Engineering, 17*(3), 447–451. doi:https://doi.org/10.1016/j.mineng.2003.10.019

Musa, F and Morrison, R, 2009. A more sustainable approach to assessing comminution efficiency. *Minerals Engineering, 22*(7), 593–601. doi:https://doi.org/10.1016/j.mineng.2009.04.004

Mwanga, A, Rosenkranz, J and Lamberg, P, 2015. Testing of Ore Comminution Behavior in the Geometallurgical Context—A Review. *Minerals, 5*(2), 276–297. Retrieved from https://www.mdpi.com/2075–163X/5/2/276

Napier-Munn, T J, 1996. *Mineral comminution circuits: their operation and optimisation* / (T J Napier-Munn, S Morrell, R D Morrison, T Kojovic). Indooroopilly, Qld: Julius Kruttschnitt Mineral Research Centre.

Powell, M, Hilden, M, Ballantyne, G, Liu, L and Tavares, L, 2014. The appropriate and inappropriate, application of the JKMRC t10 relationship. *IMPC 2014 – 27th International Mineral Processing Congress*.

Powell, M, Morrison, R, Djordjevic, N, Hilden, M, Cleary, P, Owen, P, ... Bbosa, L, 2003–2010. Eco-efficient liberation: outcomes and benefits (internal reports; JKMRC Sustainable Minerals Institute, University of Queensland). Brisbane, Australia: Centre for Sustainable Resource Processing (CSRP).

Reja, Y, 2017. *Development of a standard methodology for energy efficiency measurement in comminution processes,* Mineral processing MPhil Thesis. The University of Queensland, Brisbane, Australia.

Romeis, S, Paul, J, Herre, P, Hanisch, M, Taylor, R N K, Schmidt, J and Peukert, W, 2015. In Situ Deformation and Breakage of Silica Particles Inside a SEM. *Procedia Engineering, 102*, 201–210. doi:https://doi.org/10.1016/j.proeng.2015.01.128

Schilde, C and Kwade, A, 2012. Measurement of the micromechanical properties of nanostructured aggregates via nanoindentation. *Journal of Materials Research, 27*(4), 672–684. doi:10.1557/jmr.2011.440

Schönert, K, 1971. *The Role Of Fracture Physics In Understanding Comminution Phenomena*.

Schönert, K, 1991. Advances in comminution fundamentals and impacts on technology. *Aufbereitungs-Technik, 32*(9), 487–494.

Shi, F, Kojovic, T, Larbi-Bram, S and Manlapig, E, 2006. Development of a new breakage characterisation device. *AMIRA Project P9N Mineral Processing: 5th technical report*, 55–66.

Starkey, J and Dobby, G, 1996. Application of the MINNOVEX SAG Power Index at five Canadian SAG plants. Paper presented at the SAG 1996, Vancouver Canada.

Starkey, J, Dobby, G and Kosick, G, 1994. A new tool for SAG hardness testing. Paper presented at the Canadian Mineral Processor's Conference, Ottawa.

Starkey, J, Hindstrom, S and Nadasdy, G, 2006. SAG Design Testing – What it is and Why it works. Paper presented at the SAG 2006, Vancouver, Canada.

Tavares, L and King, R, 1998. Single-particle fracture under impact loading. *International Journal of Mineral Processing, 54*(1), 1–28.

Tavares, L, 2007. Breakage of single particles: quasi-static. *Handbook of powder technology, 12*, 3–68.

Tavares, L, de Carvalho, R M, Bonfils, B and de Oliveira, A L, R, 2020. Back-calculation of particle fracture energies using data from rotary breakage testing devices. *Minerals Engineering, 149*, 106263. doi:https://doi.org/10.1016/j.mineng.2020.106263

Wolcott, R T, 1977. Sieving Precision: Sonic Sifter Versus Ro-Tap.

Yu, P, Xie, W, Liu, L X and Powell, M, 2019. Applying Fréchet distance to evaluate the discrepancy of product size distribution between single particle and monolayer multi-particle breakage. *Powder Technology, 344*, 647–653. doi:https://doi.org/10.1016/j.powtec.2018.12.043

Comparison of dry VRM or HPGR circuits to wet milling circuits

G R Ballantyne[1] and G Lane[2]

1. Director Technical Solutions – Global, Ausenco, South Brisbane Qld 4101.
   Email: grant.ballantyne@ausenco.com
2. Chief Technical Officer, Ausenco, South Brisbane Qld 4101.

ABSTRACT

Dry milling circuits that include high pressure grinding rolls (HPGR) or vertical roller mills (VRM) and air classification have replaced dry ball milling in cement production, but how do they compare to wet milling and classification circuits in mineral processing plants? Two case studies are presented that compare the energy efficiency, wear, liberation and capital cost of dry and wet milling circuits. In both case studies the VRM and HPGR consume half the energy of a wet tumbling mill for the same duty. However, the dry classification system tends to significantly erode the energy benefits. A number of improvement opportunities are presented that have the potential to improve the energy and capital efficiency of dry milling circuits. These improvement opportunities focus on the dry classification system that consumes significant energy in heating and fan power requirements and requires a large proportion of the footprint.

INTRODUCTION

Designing the most cost-effective comminution circuit requires consideration of the ore characterisation, required capacity, power price, grind size and recovery drivers. Wet milling circuits utilising semi-autogenous (SAG), and ball mills are pervasive in the industry as they provide a low capital cost, low risk option that can be employed for a wide range of applications. Ball consumption can be reduced through autogenous (AG) and pebble milling circuits and power consumption can be reduced by using high pressure grinding rolls (HPGR). These technologies are well understood, provide acceptable risk and are known to add significant value given the right project conditions. Extending dry crushing via HPGR or vertical roller mills (VRM) to produce fine particle size distributions has the potential to further reduce power and media consumption. This paper describes the application of dry fine crushing in the minerals industry, how these technologies could be de-risked and the estimated value of these technologies through two case studies.

Fine dry crushing technologies are widely used in cement plants and other industrial minerals plants. However, until recently HPGRs were only considered in tertiary crushing applications prior to ball milling in mineral processing plants (Lane *et al*, 2019). In Australia in the last two years the West Musgrave project and the Iron Bridge project announced they will progress with dry fine crushing to final product size.

The West Musgrave project has partnered with Loesche to develop two parallel VRMs treating nominally 5 Mt/a each. Oz minerals stated that the decision to pursue VRMs in the feasibility study was due to a circa-15 per cent reduction in power consumption and a circa-2 per cent improvement in nickel recovery.

The 67 Mt/a Iron Bridge project (Fortescue, 2019), currently under construction, contains two stages of HPGR with the second stage closed with air classification (Figure 1). The dual HPGR circuit resulted in a 30 per cent reduction in energy consumption and wet tailings (Weir, 2019).

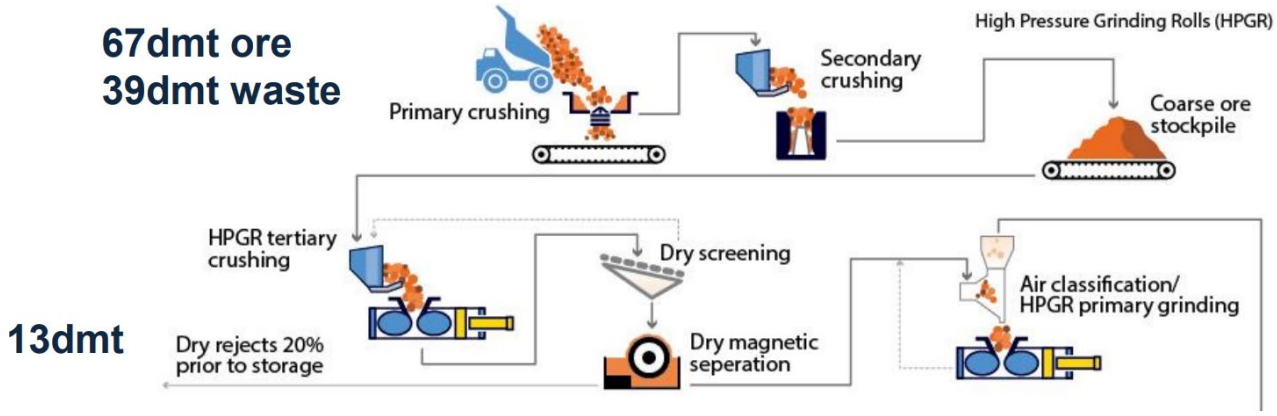

FIG 1 – Iron Bridge dual HPGR circuit configuration (Morrell, 2022).

The operating principal of the HPGR is two counter-rotating rolls compress the material inducing high pressure breakage. One roll is fixed while the other roll is subjected to a pressure and allowed freedom to move (Figure 2). The VRM is similar to a HPGR in that it is a dry compression crusher, the difference in breakage is largely related to the pressing force which is smaller in the VRM, Instead of the two driven opposing rolls of a HPGR, the VRM has a table that is pressurised against rotatable rolls that are not driven.

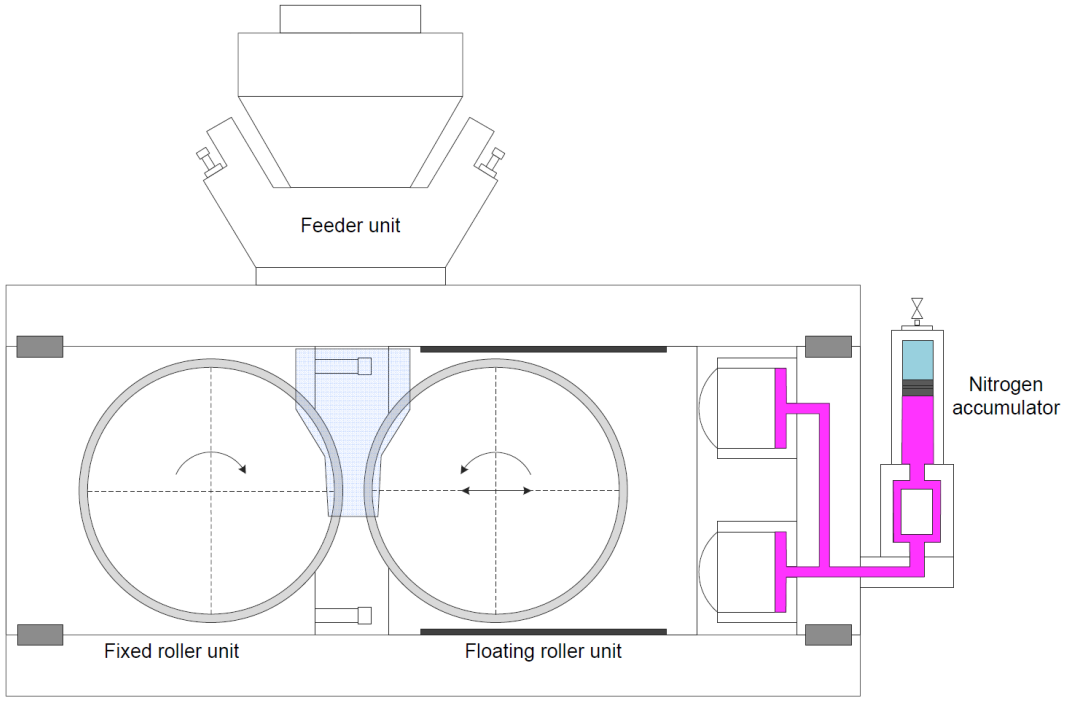

FIG 2 – HPGR schematic (Quist and Evertsson, 2012).

Air classification is required to produce the fine, dry products from both VRM and HPGR circuits. There are two types of air classification available: static and dynamic (Figure 3). Static classification is carried out in a cross-flow separator, where a stream of material cascading over plates is cross-swept by air flow, which removes the finer particles. In a dynamic classifier, the air flow loaded with fine ore particles is passed through the vane slots of a rotating cage wheel. Depending on the air flow and the rotational speed of the cage wheel, the coarser particles are thrown back and collected through a middlings outlet, whereas the fines are swept through the cage wheel with the air flow. The fines are then collected in a system of gas cyclones and dust collectors and form the final product of the classification operation.

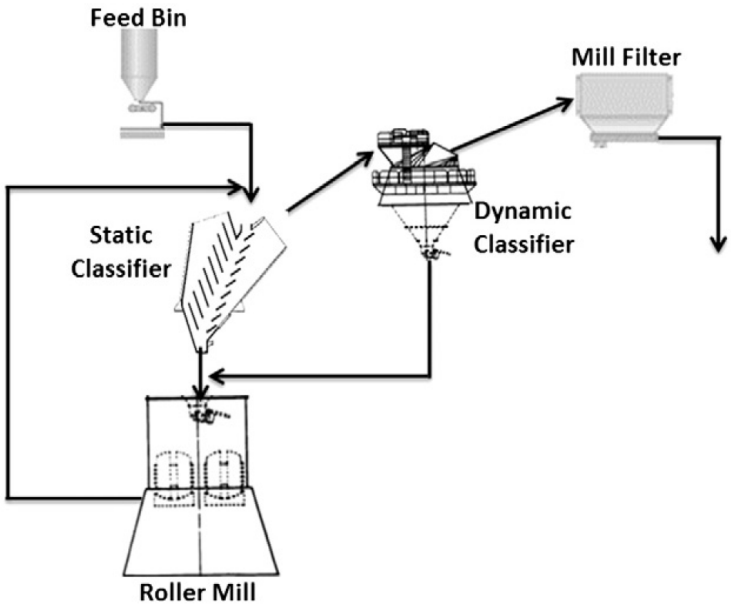

FIG 3 – Schematic of static and dynamic air classification in closed circuit with a VRM in overflow mode (Altun *et al*, 2015).

Both the HPGR and VRM can operate with a dry air classification system. In the case of the VRM the air classification is integral to the unit (Figure 4). The feed material is fed via a rotary star feeder and falls by means of an inclined chute onto the rotating grinding table. The grinding, drying and classification of the grinding material is performed inside the mill.

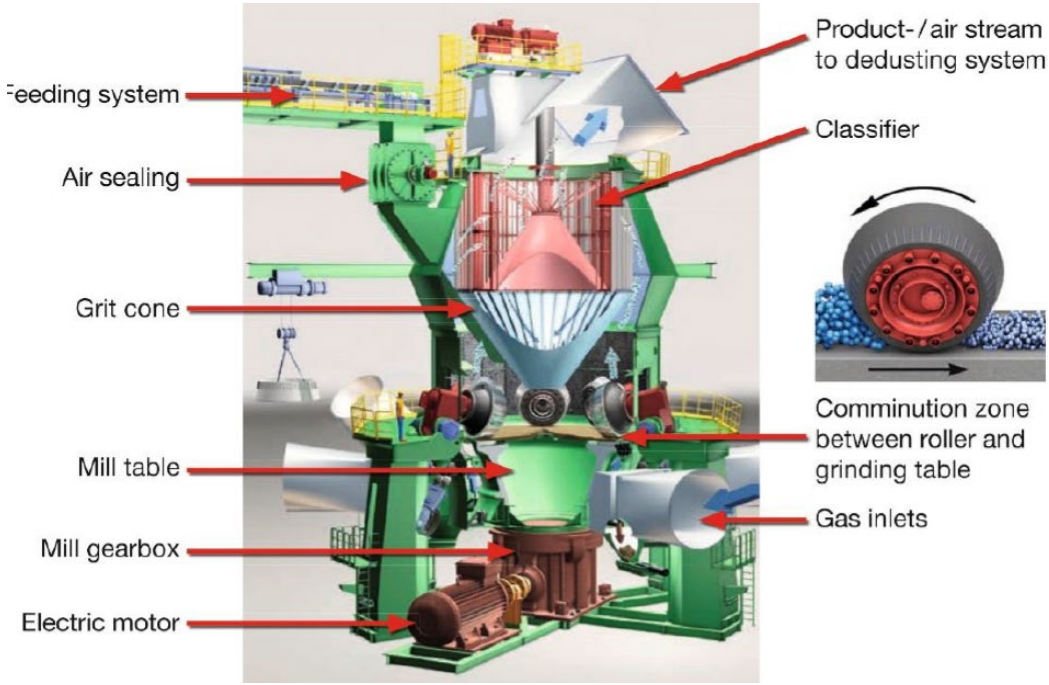

FIG 4 – VRM illustrating major milling components and control measures (Altun *et al*, 2018).

Many previous investigations have been completed that show the potential energy savings of dry fine crushing. Table 1 presents five case studies that have been published on the energy efficiency of VRM circuits. The efficiency of the circuits is presented in relation to the equivalent specific energy requirements calculated from the Bond work indices. The comminution specific energy for these case studies is between 56 per cent and 75 per cent of the Bond specific energy. Unfortunately, fewer case studies have been published related to dry fine crushing utilising a HPGR. However, it is anticipated that the energy efficiency factors will be similar considering the similar breakage and classification environments.

TABLE 1

Summary of previous studies into the energy efficiency of dry fine crushing. *reported HPGR circuit specific energy, not Bond Specific Energy as the base.

Parameter	Unit	Gamsberg (Airflow)	Gamsberg (Overflow)	Copper ore	Turkish Gold	Mogalakwena
Technology		VRM	VRM	VRM	VRM	VRM
Bond Work Index	kWh/t	14.0	14.0	11.2	18.1	23
F_{80}	mm	-	-	10.7	12	12
P_{80}	µm	65	65	45	45	45
Bond Specific Energy	kWh/t	14.3*	14.3*	16	25	32
Dry Fine Crushing Specific Energy	kWh/t	8	9	12	14	23
Bond Efficiency	%	56	62	75	57	70
Fan Specific Energy	kWh/t	5.6	2.5	7.2	-	-
Reference		(van Drunick *et al*, 2010)	(van Drunick *et al*, 2010)	(Altun *et al*, 2015)	(Altun *et al*, 2018)	(Altun *et al*, 2018)

CASE STUDY 1

Case study 1 considered a plant grinding very hard ore (Bond ball mill work index BWi of 33.5 kWh/t) from an F_{80} of 6.5 mm to a P_{80} of 75 µm. Three comminution technologies were reviewed in this study:

1. Wet ball milling.
2. Dry high pressure grinding roll (HPGR) and air classification.
3. Dry vertical roller mill (VRM) and air classification.

The ball mill sizing was based on the ore characterisation test work, specifically the Bond ball mill work index. There is no equivalent reliable small scale ore characterisation test that can be used for HPGR and VRM sizing. Therefore, the HPGR and VRM sizing was based on the pilot HPGR test results. A series of three locked cycle tests were conducted with an HPGR in closed circuit with air classification. The specific energy requirement for the HPGR circuit was calculated from the average operating work index for the three cycles. In comparison to the ball mill, the HPGR test work found that dry comminution required 45 per cent of the energy (Table 2). Due to the similarity in the breakage and classification mechanisms, the energy efficiency of the HPGR and VRM were assumed to be similar.

TABLE 2

Ball mill and HPGR/VRM design criteria.

Parameter	Unit	Ball milling	HPGR/ VRM
Bond ball mill work index	kWh/t	33.5	
Grinding circuit feed size, F_{80}	mm	6.5	
Grinding circuit product size, P_{80}	µm	75	
Specific comminution energy, design	kWh/t	35.0	15.7
Nominal circulating load	%	250	800

The large specific energy reduction was related solely to the comminution requirements. However, dry classification requires significant power for the fan to hydraulically transport the mill products to the classifier as well as the fine product to the product storage bin. In addition to the fan power, heating energy is required to ensure a low moisture feed to the classifier. For this case study, the required heating energy was extremely high due to the high (14 per cent by weight) moisture levels in the feed stock. The high moisture content is a substantial issue for dry milling as it increases capital cost and energy consumption. The high moisture is likely due to ice and snow collected from the uncovered stockpiles and may be able to be reduced in the comminution circuit design. Without design mitigation, a hot gas generator with an equivalent power of 147 kWh/t was required, effectively swamping the reduction in comminution energy.

The direct capital cost of the dry grinding scenarios was between 21 per cent and 68 per cent higher than the wet ball milling option. The HPGR and VRM options provided lower electrical energy consumption, improved storage prior to separation, modular design and the potential of increased recovery due to improved liberation, reduced surface oxidation and reduced density bias in classification. However, these strengths were not enough to outweigh the higher capital cost and higher risk associated with moisture levels and wear from metal components in the feed.

CASE STUDY 2

Case study 2 considered a high-capacity milling circuit (110 kt/d) treating competent (A*b ~ 30) hard (BWi ~15 kWh/t) ore. The study considered five comminution circuit options, this paper focuses on the outcomes from the SAG and ball mill circuit and the two-stage HPGR and dry classification circuit. Due to the ore hardness, the SAG-based circuit considered a secondary crushed feed to improve the capital and energy efficiency of the circuit (2CSAB).

The dual-stage HPGR circuit considers a primary gyratory crusher and coarse ore stockpile followed by closed-circuit secondary crushing and a fine ore stockpile. The coarse HPGR is closed with dry screens and the fine HPGR is closed with air classification prior to flotation (Figure 5). Although the HPGR circuit can be configured in a single stage, the fan energy and the classifier wear is reduced in the dual-stage configuration.

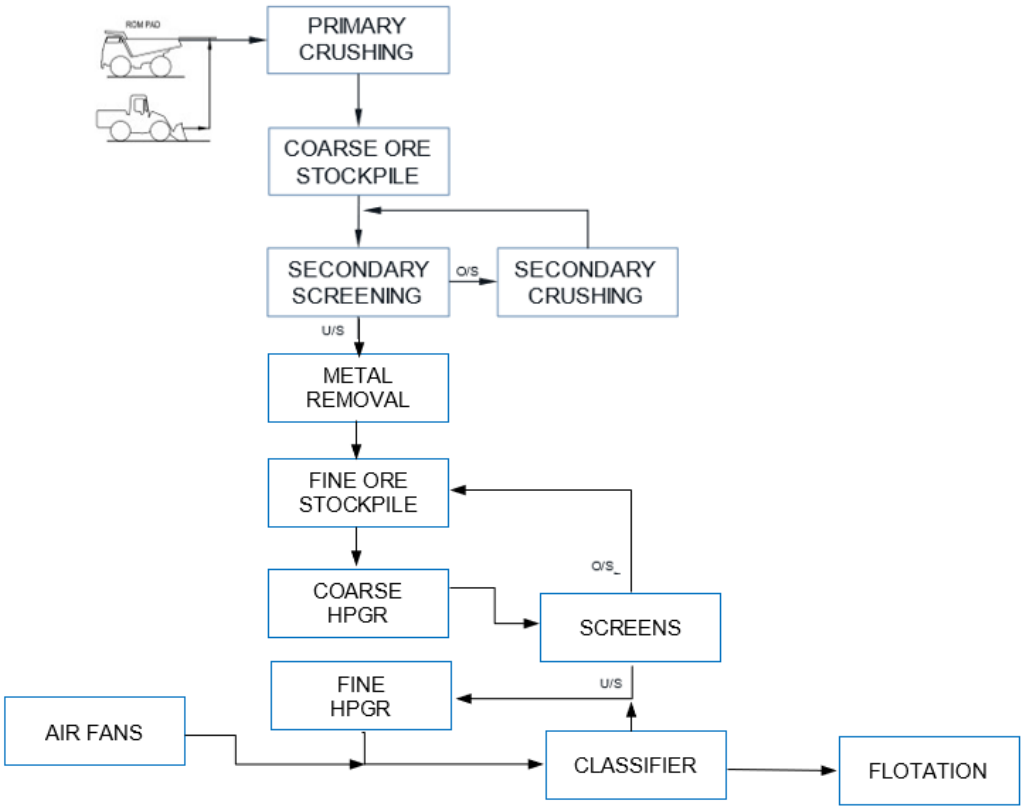

FIG 5 – Dual stage HPGR circuit considered for Case Study 2.

Order of magnitude economic analysis was completed for the two circuit configurations to determine which configuration should progress to the next stage of the study. The dual HPGR circuit reduced the energy consumption from the 2CSABC circuit by 36 per cent, inclusive of ancillary energy associated with fans, conveyors and pumps. The relative capital cost was 16 per cent higher for the dual HPGR circuit. However, due to the high price of electricity in this case study, the operating cost reduced by US$1.19/t for the dual HPGR circuit. This resulted in a very short payback period and showed that the dual HPGR circuit has the potential to add significant value to this project.

TABLE 3

2CSAB and HPGR design criteria.

Parameter	Unit	2CSAB	Dual HPGR
Grinding circuit feed size, F_{80}	mm	102	
Grinding circuit product size, P_{80}	µm	350	
Specific comminution energy	kWh/t	11.3	6.1
Specific ancillary energy	kWh/t	1.3	1.9
Total specific energy	kWh/t	12.6	8.0
Relative capital cost	%	0	+16
Relative operating cost	US$/t	0	-1.19

In addition to the financial analysis, the process/technology risk, the greenhouse gas emissions and readiness for the next study phase were evaluated. The collective result from this analysis was that the lower-risk HPGR ball milling circuit will progress to the next phase of the project as the economics were similar to the dual HPGR circuit, the risk was lower and the technology readiness was higher.

DISCUSSION

In comparison to SAG milling circuits, dry fine crushing circuits (HPGR and VRM) have the potential to almost halve the comminution energy. This power reduction is enhanced for competent, hard ores. However, the energy associated with ancillary equipment such as the fans and hot gas generation can significantly reduce the benefits in comminution energy reduction. Reducing the classification energy should be a major focus in dry fine crushing circuit design. However, this needs to be mindful of the fact that classification efficiency, fan energy consumption, comminution efficiency and downstream recovery performance are all interrelated.

Therefore, efficient size classification must be maintained while simultaneously reducing energy consumption. Some potential solutions to this problem are presented below:

1. For the VRM, the pressure drop can be reduced by operating in overflow mode, thereby not requiring the fan to pneumatically transport the coarse particles up to the classifier.
2. For dual stage circuits, the first stage can be extended finer by employing smaller aperture dry screens being developed by suppliers such as Derrick and Liwell.
3. Employing efficient wet classifiers such as screws and fine screens should be explored where the oversize product is 80–90 per cent solids by weight. With the dry new circuit feed, the % solids in the VRM/HPGR feed should be lower than 10 per cent and should not impact performance dramatically.

CONCLUSIONS

Dry fine crushing utilising High Pressure Grinding Rolls and Vertical Roller Mills should be explored for projects with hard ores and high electrical energy costs. The reduction in power and media consumption have the potential to significantly reduce operating cost and greenhouse gas emissions in compared to conventional tumbling mill circuits. The reduction in comminution energy has the potential to be eroded by high energy consumption in the classification circuit. However, this can be

reduced by utilising improved design principles. The benefit of dry fine crushing on recovery should be investigated and included in the economic benefit of the circuit configuration to obtain a more accurate economic analysis.

HPGR and VRM dry fine crushing circuits have similar comminution characteristics. However, the applications of the two systems are quite different and lend themselves to be applied in different project settings. The fully enclosed, modular VRM and classifier design will be most applicable to low-capacity projects such as the dual 5 Mt/a circuits at West Musgrave. On the other hand, the separate air classification and the large proven HPGR equipment design means these circuits are initially more applicable for higher capacity projects such as the 67 Mt/a Iron Bridge project. However, the development of these technologies over time will likely see the reduction of this differential.

ACKNOWLEDGEMENTS

Thanks to Ausenco for supporting the publication of this work and Ausenco's global comminution group for the collaborative, collegial technical discussions that have contributed to the outcomes of this work.

REFERENCES

Altun, D, Gerold, C, Benzer, H, Altun, O, Aydogan, N, 2015. Copper ore grinding in a mobile vertical roller mill pilot plant. *International Journal of Mineral Processing*, 136, 32–36.

Altun, D, Little, W, Benzer, H, Mainza, A, Becker, B, Gerold, C, 2018. Comparing Vertical Roller Mill Performance on Two Different Precious Metal Ores, In *Comminution 18*, Cape Town, South Africa.

Fortescue, 2019. Iron Bridge Project Approval, https://www.fmgl.com.au/docs/default-source/announcements/iron-bridge-project-approval.pdf?sfvrsn=8cdff6a3_4.

Lane, G, Hille, S, Pease, J, Pyle, M, 2019. Where are the opportunities in comminution for improved energy and water efficiency?, In *SAG conference*, Vancouver, Canada.

Morrell, S, 2022. Helping to reduce mining industry carbon emissions: A step-by-step guide to sizing and selection of energy efficient high pressure grinding rolls circuits. *Minerals Engineering*, 179.

Quist, J, Evertsson, M, 2012. Simulating pressure distribution in HPGR using the discrete element method, In *Comminution '12*. MEI, Cape Town.

van Drunick, W, Gerold, C, Palm, N, 2010. The Development of a Dry, Energy Efficient Grinding Circuit for Anglo American, In *Comminution 10*, Cape Town, South Africa.

Weir, 2019. Weir wins record £100 m order for Australian magnetite iron ore project, https://www.global.weir/newsroom/news-articles/iron-bridge/.

A HPGR pseudo-dynamic model approach integrated with real-time information for pressing iron ore concentrates in industrial-scale

T M Campos[1], H A Petit[2], R Olympio[3] and L M Tavares[4]

1. Research assistant, Department of Metallurgical and Materials Engineering, Universidade Federal do Rio de Janeiro, 21941–972. Email: tulio.campos@coppe.ufrj.br
2. Post-doctoral fellow, D.Sc, Department of Metallurgical and Materials Engineering, Universidade Federal do Rio de Janeiro, 21941–972. Email: hpetit@metalmat.ufrj.br
3. Engineer, M.Sc, Vale S.A, Complexo de Tubarão, 29090–860. Email: ricardo.olympio@vale.com
4. Professor, Ph.D., Department of Metallurgical and Materials Engineering, Universidade Federal do Rio de Janeiro, 21941–972. Email: tavares@metalmat.ufrj.br

ABSTRACT

Much practical experience has been gathered in the last 30 years of application of high-pressure grinding rolls (HPGR) integrated with ball milling in size reduction of fine iron ore concentrates. The company Vale S.A, in Complexo de Tubarão (Brazil), was one of the pioneers applying the technology prior to pelletisation with an outstanding size reduction energy efficiency in the circuit and a significant increment in the specific surface area of the product. Recent studies by the authors demonstrated benefits of modelling and simulation to improve the performance of HPGRs in this particular application, with the model being able to describe HPGR performance under different operating conditions and under variations of feed size distribution. Despite these important advances, this modelling approach has only been used offline and under steady-state conditions. The present work applies the modified Torres and Casali model proposed by the authors in pseudo-dynamic simulations. The ability of the model to predict the characteristics of the product in real-time is evaluated using data available online for the pellet feed preparation circuit. Results demonstrated the model capabilities to map the physical operation and give a realistic representation of the process. Additionally, the model is demonstrated to be able to support the pellet feed production by providing extended real-time information of the process, making it a useful tool for improvement of the operational strategies and process stability.

INTRODUCTION

High-pressure grinding rolls (HPGR) reached great popularity in the last 30 years of application in the minerals industry. The company Vale S.A, in the Complexo de Tubarão (Vitória, Brazil), was one of the pioneers using this technology for pressing iron ore concentrates in integrated circuits with ball milling (Van der Meer, 1997), where the HPGR usually operates in the regrinding prior to pellet formation in the so-called pellet feed preparation stage. The success of HPGRs in this type of application can be summarised by their capabilities to improve the Blaine specific surface area (BSA) coupled with a high throughput and low specific energy consumption (Van der Meer, 2010; Abazarpoor *et al*, 2018; Campos *et al*, 2019a). In this particular circuit configuration, the HPGR represents the interface between the end of the pellet feed preparation circuit and the beginning of the pellet formation process (Campos *et al*, 2019a), so that the technology occupies a key position in potentially absorbing disturbances caused in upstream operations and producing a qualified iron ore pellet feed to the downstream process.

Aiming to support operations, advances in the mathematical modelling describing HPGR performance followed, at least in parts, the improvement in the technology over the last 40 years (Rashidi *et al*, 2017). Among several works considering simplest and empirical modelling approaches (Chelgani *et al*, 2021), going through phenomenological models (Morrell *et al*, 1997; Torres and Casali, 2009; Dundar *et al*, 2013) and more in-depth descriptions with simulations using the discrete element method (Barrios and Tavares, 2016; Cleary and Sinnott, 2021; Rodriguez *et al*, 2021, 2022), improvements have been made possible in operations. New dynamic modelling approaches have been proposed, showing potential to be used as model predictive control in industrial-scale HPGRs (Numbi and Xia, 2015; Johansson and Evertsson, 2019; Vyhmeister *et al*, 2019) and to help improve understanding towards process integration. Nevertheless, the simplicity

of some of the descriptions and the very limited level of validation of some of these approaches raise several questions regarding their applicability. In the particular case of interest in the present work regarding pressing iron ore concentrates, published works by the authors (Campos *et al*, 2019b, 2021) proposed and demonstrated the validity of several modifications to the phenomenological HPGR model proposed by Torres and Casali (2009), applying it to both pilot – and industrial-scale HPGRs operating under a range of conditions. However, applications were limited to offline simulations and to steady state conditions.

Indeed, the new digital transformation in the minerals industry is shifting traditional operation towards new approaches that are able to correlate dynamic modelling with industrial demands from real-time simulations. Robust models providing rapid and accurate responses coupled with an integration into the plant network and real-time information between the physical operation and the digital models will, potentially, allow predicting variations within the process besides being the basis of a robust model-predictive control. Despite these potential improvements, several key challenges still remain when it comes to HPGR full process integration and multi-scale dynamic modelling within pellet feed preparation circuits for long periods.

The present work proposes a new modelling approach integrated with real-time information and uses it in pseudo-dynamic simulations of size reduction of iron ore concentrates in an industrial-scale HPGR. Model prediction is investigated in a period of a year of operation and applied to describe HPGR performance under different roll surface wear conditions. A new method is proposed and applied to improve model prediction when dealing with worn rolls.

MODELLING BACKGROUND

Among the main phenomenological mathematical models that are able to describe the HPGR performance (Morrell *et al*, 1997; Torres and Casali, 2009; Dundar *et al*, 2013), the approach proposed by Torres and Casali (2009) is able to predict power consumption and throughput on the basis of physical equations on the operations, besides describing the size reduction based on the population balance model. Recent works by the authors identified some limitations on the model when dealing with Brazilian iron ores and proposed some particular modifications to model equations with the aim of improving prediction (Campos *et al*, 2019b, 2021).

Briefly, the so-called modified Torres and Casali model (Campos *et al*, 2019b, 2021) relies on the plug flow model to calculate the HPGR throughput as:

$$Q = U_g L \chi_g \rho_g \left(\frac{100}{100 - \delta}\right) \tag{1}$$

where U_g is the material velocity, χ_g is the operating gap, *L* is the roll length, ρ_g is the flake density and δ is a parameter representing the proportion of material ejected by the edge of the rolls given by:

$$\ln\left(\frac{\delta}{\varphi}\right) = -\upsilon \frac{\chi_g}{D}\left(\frac{U}{U_{max}}\right)^{\tau} \tag{2}$$

where *D* is the roll diameter, *U* is the roll velocity, U_{max} is the maximum roll velocity allowed for the machine and φ, υ and τ are fitting parameters. The material velocity in Equation 1 is estimated as:

$$U_g = \frac{U \rho_a \chi_c}{\rho_g \chi_g} \tag{3}$$

where ρ_a is the bulk density and χ_c is the critical size given by $\chi_c = \chi_g + D\left(1 - \cos \alpha_{ip}\right)$.

The power consumption prediction is carried out based on the torque for both rollers multiplied by the angular roll velocity as:

$$P = 2F_m \sin\left(\frac{\kappa \alpha_{ip}}{2}\right) U \tag{4}$$

where α_{ip} is the nip angle, κ is a fitting parameter that allows adjusting the estimate of the nip angle and F_m is the compressive force applied to the particle bed (Torres and Casali, 2009):

$$F_m = p_m \frac{D}{2} L \tag{5}$$

where p_m is the hydraulic pressure.

Finally, the size reduction can be predicted from an analytical solution of the population balance model which allows to calculate the product size distribution ($w_{i,k}$) for N_b section along the axial roll position (Torres and Casali, 2009):

$$w_{i,k} = \sum_{j=1}^{i} A_{ij,k} exp\left(-\frac{S_{j,k}}{U_g} z^*\right) \tag{6}$$

where z^* is the distance between the beginning of the compression region and the extrusion zone (Torres and Casali, 2009) and $S_{j,k}$ is the breakage rate for each size class *j* and section *k*. The analytical solution uses the non-normalisable breakage function (King, 2001) and the specific selection function approach (Herbst and Fuerstenau, 1980) to solve the differential equations. The cumulative non-normalisable breakage function is given by:

$$\begin{aligned} B_{ij} &= \phi\left(\frac{x_i}{x_j}\right)^{\gamma} + (1-\phi)\left(\frac{x_i}{x_j}\right)^{\beta} \quad \text{for } x_i \geq \omega \\ B_{ij} &= \phi\left(\frac{x_i}{\omega}\right)^{\eta}\left(\frac{x_i}{x_j}\right)^{\gamma} + (1-\phi)\left(\frac{x_i}{x_j}\right)^{\beta} \quad \text{for } x_i < \omega \end{aligned} \tag{7}$$

where x_i is the particle size, γ, β, ϕ, ω and η are fitting parameters and b_{ij} is the distributed breakage function calculated from $b_{ij} = B_{i-1,j} - B_{ij}$. The breakage rate, on the other hand, is given by:

$$S_{i,k} = s_i^E \frac{P_k}{H_k} \Psi\left(\frac{P}{Q}\right) \tag{8}$$

where H_k is a constant Hold-up along the roll length, P_k is the power profile and s_i^E is the specific selection function:

$$\ln\left(s_i^E / s_1^E\right) = \xi_1 \ln(\hat{x}_i / \hat{x}_1) + \xi_2 [\ln(\hat{x}_i / \hat{x}_1)]^2 \tag{9}$$

where s_1^E, ξ_1 and ξ_2 are fitting parameters, $\hat{x}_i$ is the representative size calculated from $\hat{x}_i = \sqrt{x_i x_{i-1}}$ and $\hat{x}_1$ is a reference size given by the top size class.

The power profile in Equation 8 allows the model to predict the variation of the product size distribution along the roll length, which is a key feature in HPGR operations. The power profile is then given as:

$$P_k = 2F_m \sin\left(\frac{\kappa \alpha_{ip}}{2}\right) U \frac{P'_k}{\sum_{j=1}^{N_B} P'_j} \tag{10}$$

where P'_k is calculated on the basis of the Fourier Transform and allows the model to describe shape profiles that vary from trapezoidal to a parabolic (Campos *et al*, 2021):

$$P'_k = \frac{4}{\pi} \sum_{n=1}^{100} \frac{1 - \cos n\pi}{2n} e^{-\mu(n^2\pi^2)} \sin n\pi \bar{y}_k \tag{11}$$

where μ is a fitting parameter.

In order to account for the drop of energy efficiency when the specific energies are raised in HPGR operation, a damping parameter multiplying the breakage rate in Equation 8 was proposed (Campos *et al*, 2021):

$$\Psi(E_i) = exp\left[-\left(\frac{E_i}{E'}\right)^{\Lambda}\right] \tag{12}$$

where E_i is the specific input energy, E' is a parameter, called energy densification, and Λ is a second fitting parameter.

MATERIALS AND METHODS

HPGR operation

An industrial-scale HPGR from one of the pelletising plants from Complexo de Tubarão from Vale S.A (Vitória, Brazil) was selected as case study in the present work. The HPGR operates in an integrated circuit with ball milling and is at the boundary between the end of the pellet feed preparation stage and the beginning of the pellet formation process (Campos *et al*, 2021). The machine was connected to a process information management system (PIMS) in order to capture information on throughput, power consumption, operating pressure, roll peripheral velocity and operating gap. Operating gap was measured using a gap sensor positioned on both edges of the rolls.

Operation is often carried out with a feed moisture content of 8 ± 0.5 per cent, which is closer to the maximum that is tolerated for pressing iron ore concentrates (Van der Meer, 1997). Table 1 summarises the main HPGR settings and range allowed for the operating conditions. Given the large roll dimensions, this HPGR faces a particular issue operating below the designed capacity since the feed hopper does not allow to keep the HPGR operating in a choke fed condition and, therefore, drives the machine to operate under roll peripheral velocities lower than the original value allowed (Table 1).

TABLE 1

Summary of the main HPGR settings and operating ranges.

Variable	Value
Roll diameter (m)	2.25
Roll length (m)	1.55
Specific force (N/mm²)	0.5–5.5
Operating pressure (bar)	20–180
Roll velocity (m/s)	0.2–2.01
Operating gap (mm)*	5–15
Nominal throughput (t/h)	400–1200
Total power consumption (kW)	500–3600

As previous investigated by the authors (Campos *et al*, 2021), the HPGR is fed with a blend of four different iron ore concentrates mainly composed of hematite with minor amounts of quartz as contaminant. Specific gravity of the feed was measured by Helium Pycnometerry, being equal to 4.9 t/m³. The bulk density was determined from the ratio between the sample mass in a known volume after vibration and given as 3.0 t/m³, whereas the flake density was measured using preserved flakes from Archimedes principle and given as 3.54 t/m³.

In order to ensure a careful investigation about HPGR operation when machine is under different roll wear patterns, measurements of the distance between the top of the studs and a metal strip placed in the front of the rolls along the axial position were carried out as presented in Figure 1. This distance between the roll surface and the metal strip was measured periodically in 63 studs selected in both rollers using a digital calliper. It is worth mentioning that the authors recognise that recent works presented more reliable and accurate approaches to measure the wear pattern from online systems (Burchardt and Mackert, 2019), but the approach adopted in the present work was also used and already validated elsewhere (Rodriguez *et al*, 2021).

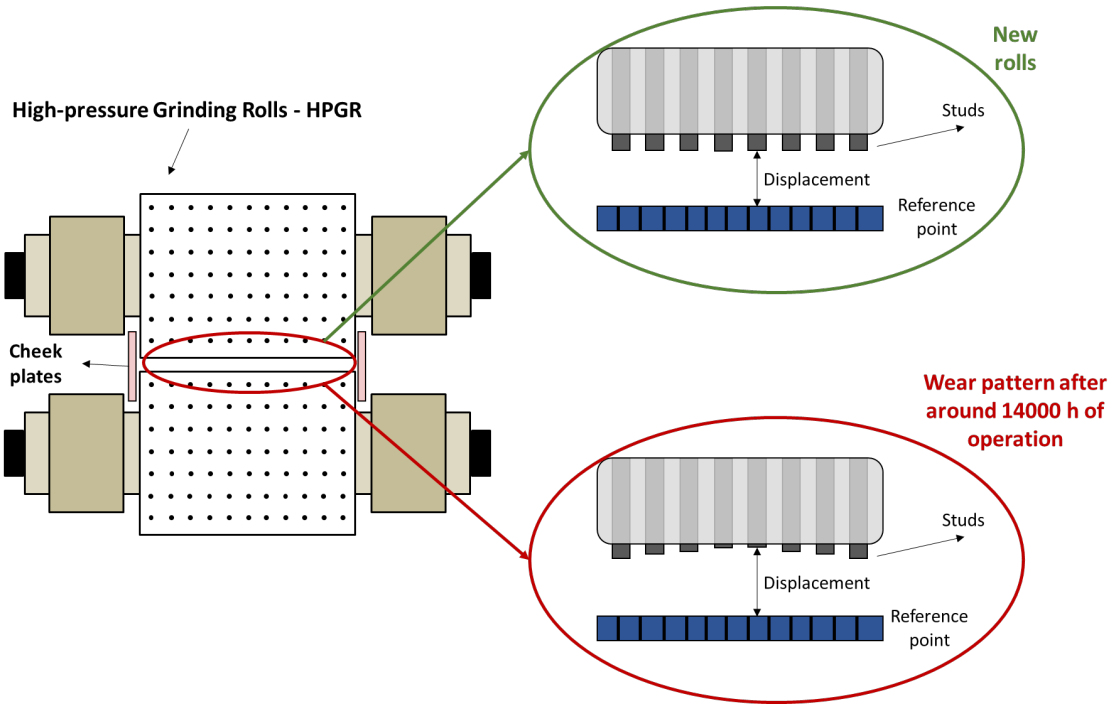

FIG 1 – Schematic diagram showing the experimental device used to measure the distance between a reference position and the top of 63 studs along the roll length. The green circle presents the rolls in the beginning of the wear life, whereas the red circle presents an illustration of the worn profile after 14 000 hours of operation, which is usually the total wear lifetime.

Data collection

A period of 12 months was selected with information recorded in a frequency of 5 min from PIMS, which corresponds to around 105 120 data points for a total of five variables in HPGR operation. Assuming no information about HPGR feed and product in real-time, samples were gathered from the process every four hours in the entire period evaluated. A sampler was used to collect material, whereas BSA was measured in laboratory using a PCBlaine-Star (Zünderwerke Ernst Brün GmbH). A total of 2190 points were recorded in this second data set.

To ensure that the data collected from the process was reliable, two steps were used in the present work. First, considering the lack of uniformity in the sampling rates between the PIMS data set and the laboratory data set, a regularisation between both was necessary. For this purpose, the BSA measurement was assumed as an average of the last four hours within the process and, therefore, its value repeated for these previous four hours considering the frequency of 5 min adopted in the PIMS data set. Considering the new regularised data, the second step relied on cleaning the data to avoid missing values, outliers, measurement disturbances and low accuracy in all process variables. Data deletion strategy was adopted to overcome missing values, which is a valid approach when the amount of missing data is only a negligible fraction of the entire data set. In order to remove outliers, a preliminary operation consisted of removing data when they do not satisfy physical conditions and usual operating ranges presented in Table 1. Outliers were also identified and removed when a value for a data point was more than three scaled median absolute relative deviations from the median (MAD). After data reconciliation and data cleaning a set of 65 193 data points for each HPGR variable was then used for modelling and simulation.

Model implementation

The modified Torres and Casali model (Campos *et al*, 2019b, 2021) was implemented in Matlab™ (version R2021b, Mathworks Inc) to perform all the simulations. A nonlinear optimisation method was used to calibrate the breakage parameters (Table 1), which basically relies in a function available in Matlab, called *fminsearch*, able to find the minimum of a multivariable scalar function using the Nelder-Mead method from an initial estimation. The objective function consisted of the sum of the differences of the logarithms of the experimental and the fitted values of the particle size distribution of a reference test (Base Case) in cumulative form using the least squares method:

$$f_{obj} = \sum_{i=1}^{N} \left[\log\left(W_{Calc}^{HPGR}(i)\right) - \log\left(W_{Exp}^{HPGR}(i)\right) \right]^2 \quad (13)$$

where N is the number of size classes, W_{Calc}^{HPGR} and W_{Exp}^{HPGR} are, respectively, the calculated and experimental fraction passing in size *i*. The objective function was proposed in the logarithmic form in order to ensure a more reliable description of the fine part of the size distribution, since the present work aims to quantify this part of the distribution accurately.

The online model structure relied on the application of the Modified Torres and Casali model coupled with real-time information about HPGR operating conditions and feed characteristics. Predictions are evaluated on the basis of the absolute relative deviation from measurements and from time series comparisons.

RESULTS

Process results

Data collected from PIMS and filtered following each step presented in the Section 'HPGR operation' was analysed in the entire period. Statistical analysis provided detailed information about operating conditions and HPGR performance variables, which were analysed in light of global variation in the entire period and local variations when dealing with each specific month.

Rolls wear patterns were carefully investigated in the entire period. Figure 2 shows wear profiles in the beginning, middle and end of rolls lifetime. A trapezoidal (also named 'bathtub') profile already discussed and investigated elsewhere (Gardula *et al*, 2015; Burchardt and Mackert, 2019; Rodriguez *et al*, 2021), is evident in the beginning, whereas a parabolic profile is reached when the HPGR is closer to 14 000 hours of operation, which is typically the maximum lifetime for the rolls in operation. Wear profiles were concave and more intensive wear occurred in the middle of the rolls, besides presenting modest wear on the edge region up to the middle lifetime and a significant edge effect when the parabolic wear profile was achieved in the end of its lifetime. Results are lined up with previous investigations carried out using DEM (Rodriguez *et al*, 2021) and from industrial-scale measurements for pressing iron ores (Nejad and Sam, 2017).

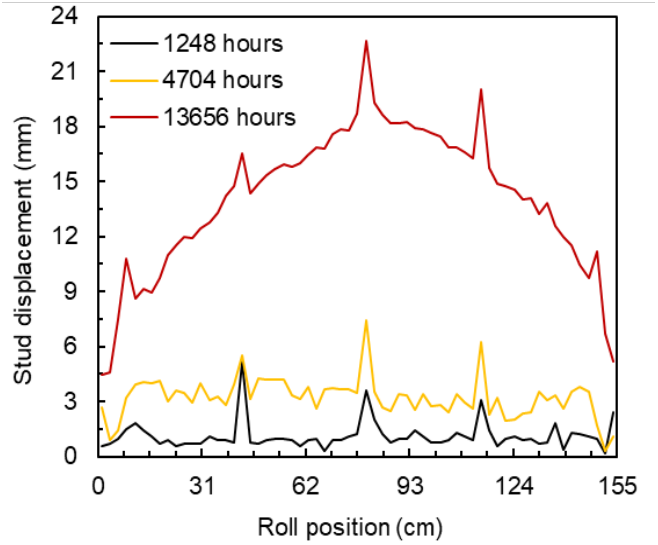

FIG 2 – Roll wear patterns registered from the beginning of operation up to the end of roll wear lifetime with nearly 14 000 hours of operation.

Figure 3 presents the average variation of operating pressure (a) and roll peripheral velocity (b) in the twelve months investigated, whereas vertical lines represent the standard deviation for each month. Figure 3a shows the minor global variation of the roll peripheral velocity, in which average values varied from 1.00 to 1.04 m/s. The very small standard deviation for each month (up to 0.04 m/s) also confirms that this process variable varies within a very narrow range of operating conditions. As discussed in Section 'HPGR operation', the HPGR investigated does not allow to

ensure a choke fed condition when dealing with high throughputs (higher than 650 t/h), thus imposing nearly constant roll velocities throughout its operation. Additionally, Figure 3a allows to conclude a potential improvement study in the HPGR performance since the roll velocity is a well-known controlled variable used to change throughput and power consumption of HPGRs (Johansson and Evertsson, 2019; Vyhmeister *et al*, 2019). Operating pressure, which is the key variable used to improve size reduction, presented monthly averages from 56.7 to 66.9 bar and standard deviations for each month up to 7.1 bar (Figure 3b). Local variation in the operating pressure in each month can be related to the control strategy adopted in order to maintain constant the torque in both rollers, besides potentially absorbing variations in the feed size distribution. A slight, but still important, global variation can be identified after the fifth month. Assuming the drop in size reduction caused by the worn rolls (Figure 2), the increase in operating pressure can be explained, at least in part, as an operational strategy used to overcome this issue.

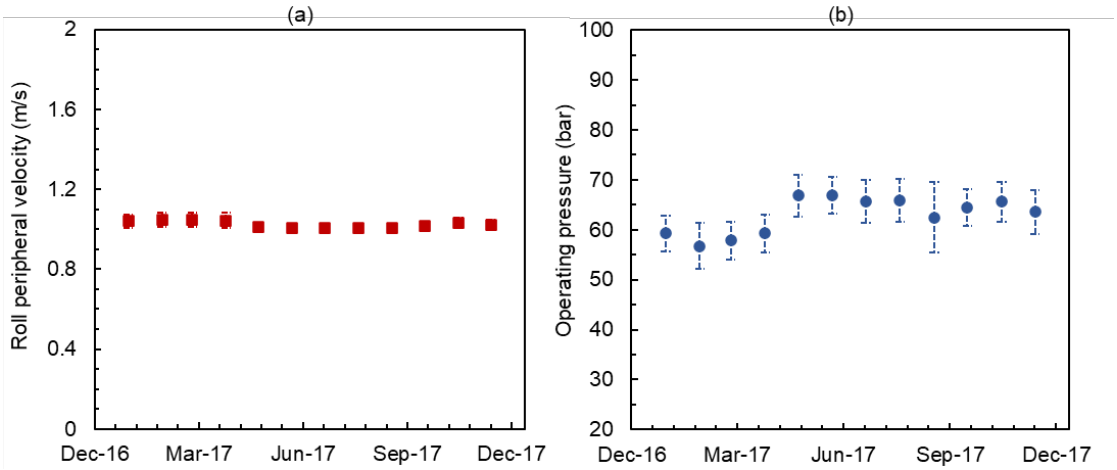

FIG 3 – Month-to-month variation of operating pressure (a) and roll peripheral velocity (b) over a period of 12 months. Markers are the average values for each month and vertical lines present the standard deviations within each month.

Variation of the average value of the measured operating gap in each month is presented in Figure 4. Results showed significant changes in the entire period with average values ranging from 13.0 to 5.1 mm. Unlike the well-known trend between operating pressure and operating gap (Daniel, 2002; Barrios and Tavares, 2016), the minor increase of pressure in Figure 3b does not have a clear relationship with the significant reduction in operating gap. In association to Figures 2 and 3b, the reduction of the operating gap and the poor relationship with operating pressure can be again explained on the basis of roll wear (Figure 2). Indeed, taking into account the approach used to determine the operating gap (Section 'HPGR operation') and the usual concave profile of the rolls (Figure 2), it is worth mentioning that measurements of operating gap are only associated to the distance between rollers in the edge, thus not accounting for the parabolic (or bathtub) profile in the centre region. Results from Figure 4 allow to state that operating gap is not a reliable variable in the process when dealing with worn rollers, although it remains valid as an indicator of roll condition.

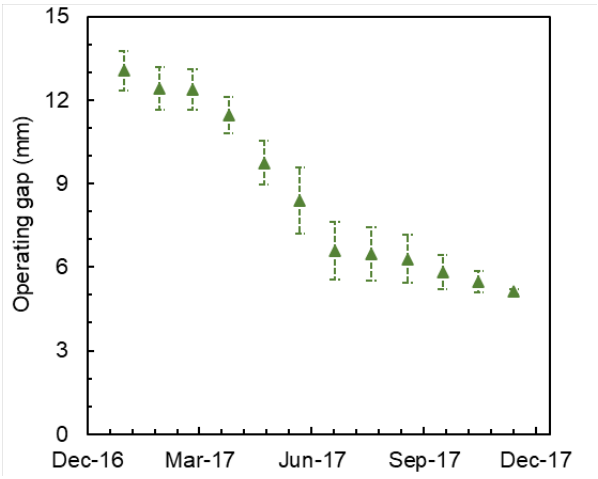

FIG 4 – Month-to-month variation of operating gap over a period of 12 months. Green triangles represent the average values and vertical lines present the standard deviations within each month.

Month-to-month variation of throughput and power consumption in the period investigated are shown in Figure 5. Minor global variations can be seen in the throughput with average values from 531 to 623 t/h. Standard deviation values for each month (vertical lines) reaching 52 t/h also demonstrate that the HPGR throughput varying within a narrow range of operating conditions. Results from Figure 5a are mainly governed by the roll peripheral velocity (Figure 3a), thus explaining its small changes.

On the other hand, Figure 5b presents both average values (from 1523 to 1483 kW) and standard deviations (up to 175 kW) for HPGR power with important variations. Comparing results from Figure 5b and Figure 3b it is possible to argue that power consumption for this HPGR is mainly determined by changes in operating pressure.

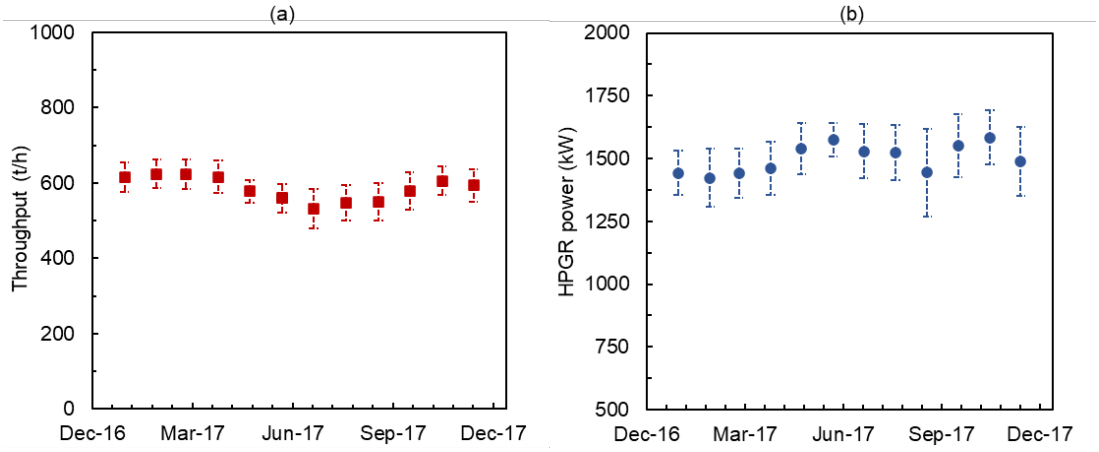

FIG 5 – Month-to-month variation of throughput (a) and power consumption (b) over a period of 12 months. Markers represent the average value, whereas vertical lines are the standard deviations within each month.

Data from laboratory analyses characterising the HPGR feed and product are presented in Figure 6. Important month-to-month variations are evident, with the average value for each month varying from 1550 to 1650 cm²/g in the HPGR feed and from 1770 to 1910 cm²/g in the HPGR product. Important variations within each month, evident from the high standard deviations, also demonstrate the significant changes in both feed and product size. Moreover, results from Figure 6 show that the product BSA is highly influenced by the feed BSA and, beyond the improvement in the product surface area, it is almost ever following the trend imposed by the feed.

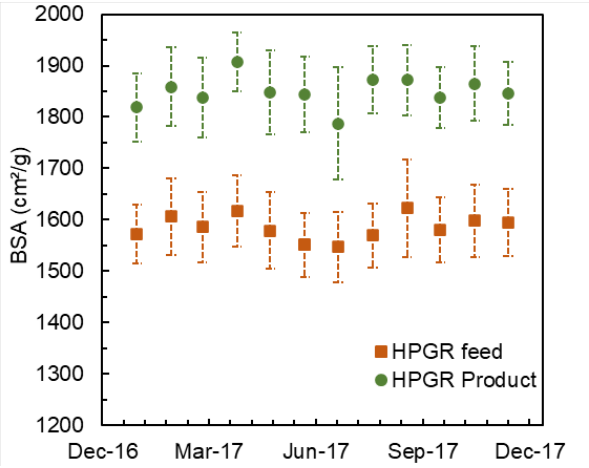

FIG 6 – Month-to-month variation of Blaine specific surface areas of the feed and product of the HPGR over a period of 12 months. Markers represent the average value, whereas vertical lines are the standard deviations within each month.

Power consumption and throughput predictions

Results from Figure 7 compare model predictions and experiments in the entire period assessed for power consumption (a) and throughput (b). Good agreement was reached for the first four months (close to 3000 hours of operation) with average absolute relative deviation from measurements up to 5.8 per cent for the throughput and 6.3 per cent for the power consumption. This period corresponds to the same period when the HGPR was operating from the beginning of lifetime until a point when the roll wear pattern reached a bathtub profile (Figure 2). Although already exhibiting a bathtub wear profile, results from Figure 7 demonstrate the ability of the model in providing good predictions of power and throughput. Under these conditions, the nip angle parameter (κ in Equation 4) was fixed in 2.75. On the other hand, in the case of the throughput model (Equation 2), two parameters were maintained equal to those previous calibration by the authors and given by $\varphi = 100$ and $\tau = 0.1$ (Campos *et al*, 2021), whereas the remaining parameter was fitted ($\upsilon = 550$).

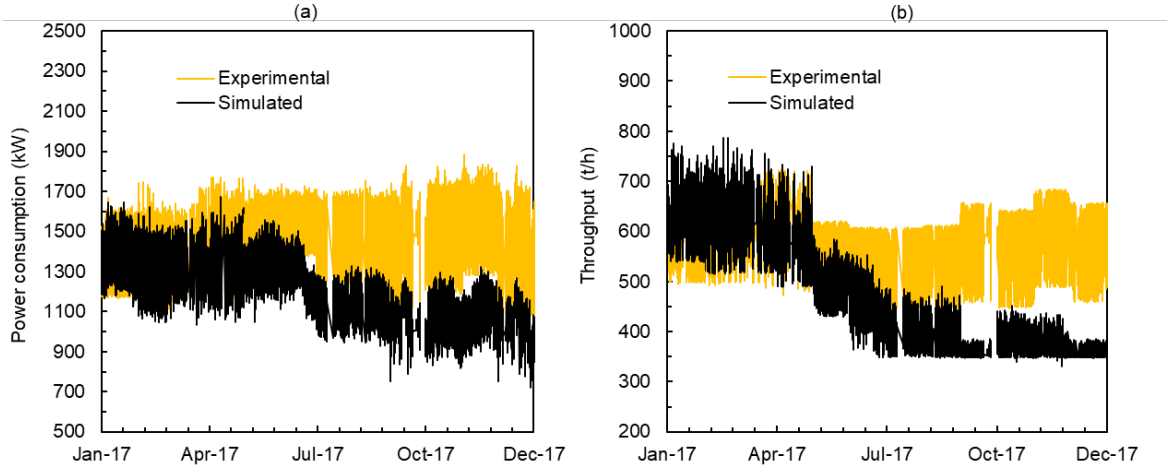

FIG 7 – Comparison of experimental and predicted values for power consumption (a) and throughput (b) in the twelve months investigated. Data is presented for every 5 min of operation.

With the aim of improving the model prediction when dealing with different roll wear patterns (briefly discussed in the Introduction), the present work proposes an algorithm to recalibrate selected parameters of the Modified Torres and Casali model. The step-by-step approach used to recalibrate the model is illustrated in Figure 8, which shows that it consists in a progressive analysis used to verify power consumption and throughput predictions, respectively. A value of absolute relative deviation from measurements of 10 per cent for both power and throughput is used as threshold for model accuracy. If the absolute relative deviation from measurements is higher than 10 per cent for more than one hour of operation, the approach allows the model to recalibrate selected model

parameters, as discussed previously. Parameter optimisation is performed from the difference between calculated and experimental values for a reference test selected in the previous hour of operation using the least square method. Parameter κ in Equation 4 was selected to be recalibrated in the power consumption model, whereas parameter υ was selected for the throughput model (Equation 2).

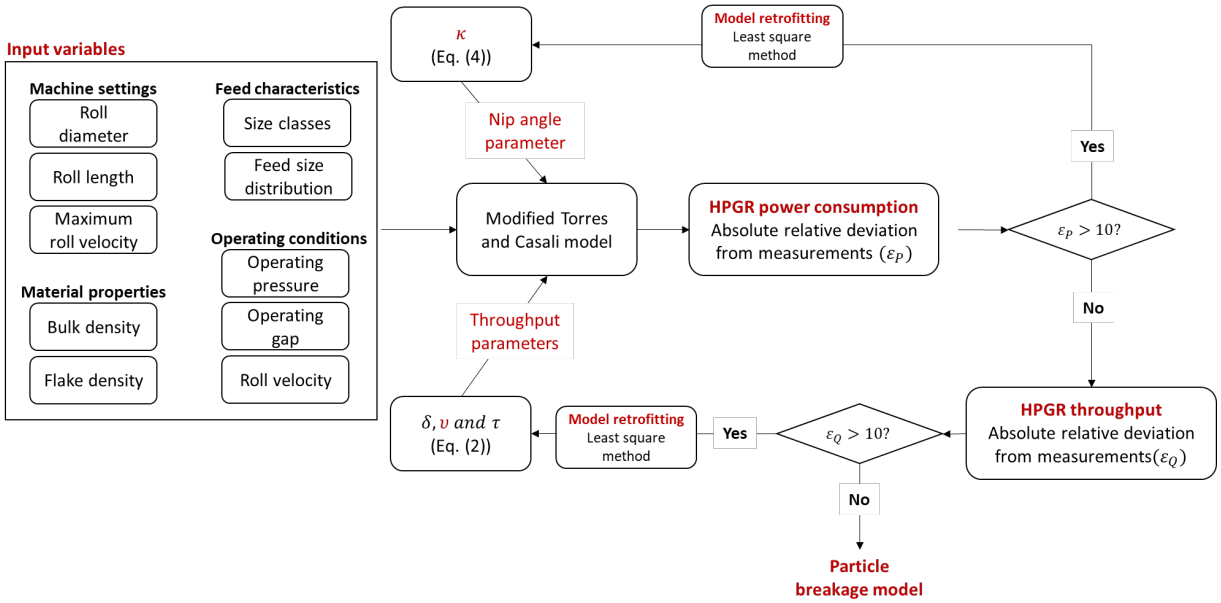

FIG 8 – Approach used to recalibrate model parameters based on the deviations in model prediction owing to roll wear. ε_Q and ε_P are the absolute relative deviation from measurements for the throughput and power consumption, respectively.

Figure 9 then presents the comparison between model and experiments when the approach presented in Figure 8 was applied. Results showed very good agreement over the entire period, with absolute relative deviations of simulations to measurements up to 4.8 per cent for power consumption and 6.0 per cent for throughput. The approach adopted seems to be able to circumvent the bias in the model prediction when dealing with worn rolls, as well as minor variations in feed competence. Nevertheless, results from Figure 9b shows the model limited the ranges of predicted values for HPGR throughput from October to December 2017. These poor predictions may be explained, at least in part, by the simplified assumption of recalibrating some model parameters to compensate the error of the operating gap measurement, which may be regarded as a disadvantage of the algorithm.

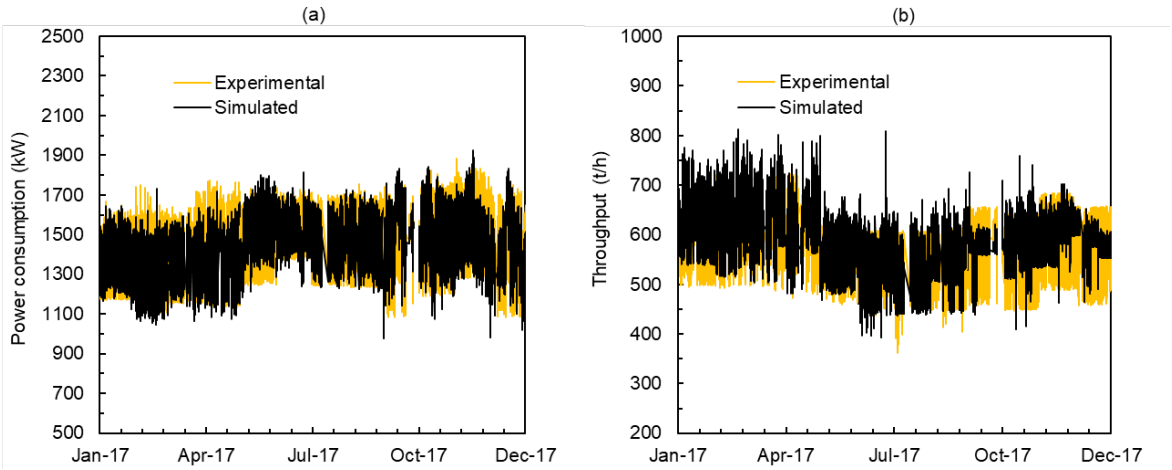

FIG 9 – Comparison between experimental and predicted power consumption (a) and throughput (b) in a period of twelve months assessed after applying the calibration approach depicted in Figure 8. Data is presented for every 5 min of operation.

Size reduction model

Feed size distribution prediction

To ensure a reliable assessment of the size reduction in the entire period, data from laboratory analyses were reconciled with supervisory system data. Reconciliation assumed that the measurement made of the BSA would be a process average over the last four hours, so that this value was repeated for the four hours prior to the measurement. Additionally, taking into account the key model requirement of using the complete feed size distribution as an input, the present work proposes that the feed sizes follows a Rosin-Rammler distribution function, given by:

$$P_i = 1 - exp\left[-\left(\frac{x_i}{x^*}\right)^{\alpha}\right] \quad (14)$$

where x_i is particle size (mm) and x^* is a 62.3 per cent passing size (mm). Based on an extended database containing 162 measurements of BSA and size distributions presented elsewhere (Campos *et al*, 2021), a relationship was then proposed to calculate the size parameter x^* as a function of the Blaine specific surface area. Figure 10 presents the relationship between these two variables for 80 per cent of the database, which was randomly selected as calibration data set. The clear linear relationship between this parameter and BSA suggests that simple linear equation to describe it, represented by:

$$x^* = 126.5 - 0.0412BSA_{Alim} \quad (15)$$

where x^* is given in μm and BSA_{Alim} is the Blaine specific surface area (cm²/g) from the HPGR feed gathered from laboratory measurements. The parameter α in Equation 14 was set to the optimal constant value of 0.97. Predictions made using Equation 14 were then compared to the respective experimental size distributions for both calibration data sets (80 per cent used for training) and validation data set (the remaining 20 per cent of the original data set) using Equation 13. Results demonstrate the good predictive capabilities of the model with average values for the objective function for calibration and validation data sets of 0.04 and 0.06, respectively. Figure 10 still presents the region bounds by the dotted red lines with relative deviations between model (black line) and fitted sizes (green circles) up to 10 per cent.

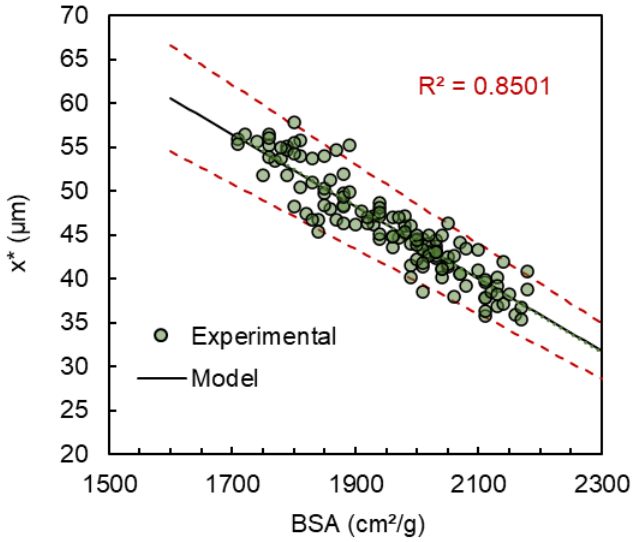

FIG 10 – Relationship between BSA for several measurements carried out elsewhere (Campos *et al*, 2021) and the critical size fitted in Equation 14. Green circles are values fitted from Equation 14 and the black line is the model fitting with Equation 15. The red dotted lines bound the region with relative deviations between black line and experiments up to 10 per cent.

Product BSA

In order to simulate the size reduction in the HPGR the breakage model was calibrated based on survey data. All five parameters from the breakage function (Equation 7) and two parameters from the selection function (Equation 9) were assumed to remain constant and equal to previous

calibration carried out by the authors (Campos *et al*, 2019b). The remaining parameter from the selection function (s_1^E) was then fitted on the basis of a reference test selected among the ones when the HPGR was operating under good wear conditions and in the beginning of roll life.

As such, considering the model presented in Equations 14 and 15 and the breakage parameter depicted above, Figure 11 presents the comparison between experimental and predicted values for the HPGR product BSA when considering a constant and average feed size distribution with 1550 cm²/g in a period of 740 hours of operation. This simplified assumption was adopted in order to check the real effect of the feed size distribution in the model prediction. Indeed, as discussed in Figure 6, there is a clear trend between both HGPR feed and product, being the second one strongly determined by the first. Analysing both results together allows to explain the poor agreement between model and experiments presented in Figure 11.

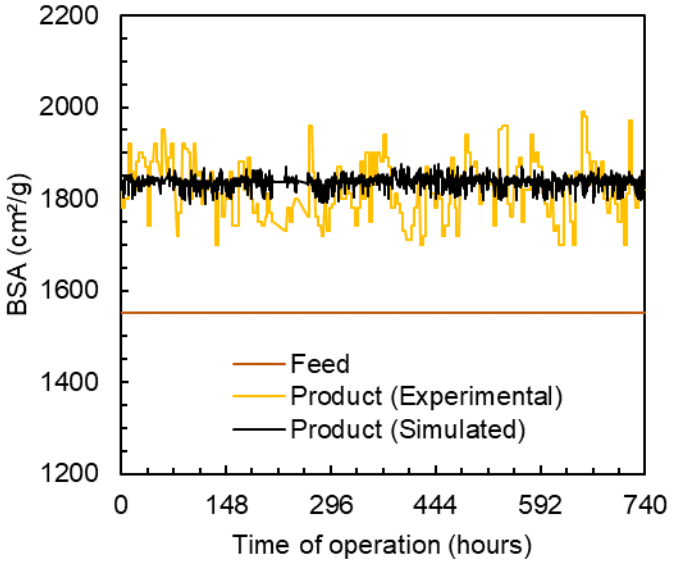

FIG 11 – Comparison between experimental and predicted value for the HPGR product BSA considering a fixed feed size distribution with 1550 cm²/g.

Figure 12 then presents a more complete version of the model dealing with the measured feed size distribution in real time. First it is worth highlighting the variation of the HPGR product over the entire period assessed following the trend imposed by the HPGR feed. Nevertheless, results from Figure 12 show the very good agreement between experimental and predicted values for the HPGR product BSA with average absolute relative deviation from measurements equal to 2.7 per cent. Results also allow to conclude that the model is able to capture key variations in the feed size distribution and accurately describe the HPGR product. Results for the twelve months assessed also presented good agreement with average absolute relative deviation from measurements of up to 5.3 per cent, but results were omitted for brevity. The predicted HPGR product BSA was calculated on the basis of the predicted product size distribution using a method proposed and calibrated previously by the authors (Campos *et al*, 2021).

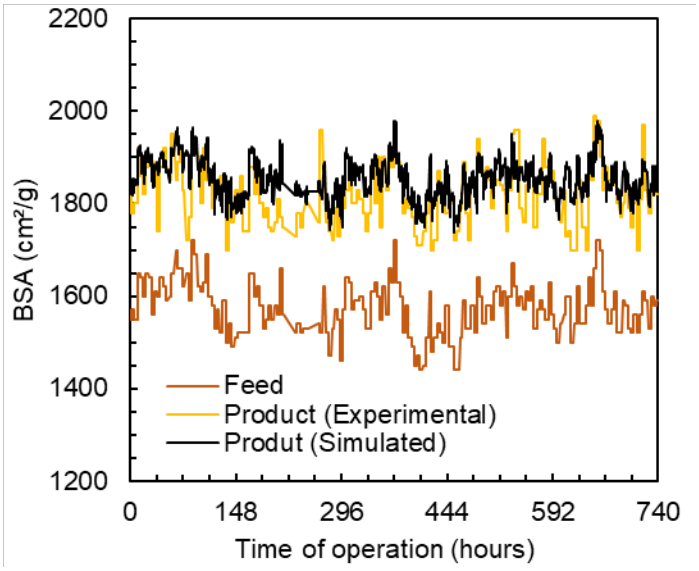

FIG 12 – Comparison of experimental and predicted values for the HPGR product BSA on the basis of the feed BSA measured every 4 hours.

CONCLUSIONS

The work relied on the application of the Modified Torres and Casali model as pseudo-dynamic approach to describe an industrial-scale HPGR pressing iron ore concentrates. Good agreement was reached to predict power consumption, throughput and product BSA when the HPGR was operating under good roll wear conditions.

Evidence of a bathtub wear profile and a wear parabolic profile after a period of 14 000 hours of operation was presented as a great challenge for model descriptions. Results highlighted an underestimation of power and throughput when the HPGR started operating under significant roll wear patterns. An algorithm was proposed to optimise selected model parameters with the aim of improving prediction for the HPGR with worn rolls which provided very good agreement between model and experiments.

A model was also proposed to convert the HPGR feed BSA into a cumulative feed size distribution. The model was validated under a wide range of measurements. Application of the breakage model using this new feature provided very good agreement between product BSA measured and predicted by the model.

Results showed feasibility of applying the model as a pseudo-dynamic model and coupled with real-time information to describe the HPGR performance in an industrial-scale plant pressing iron ore concentrates.

ACKNOWLEDGEMENTS

We thank you Vale S.A for the financial and technical support and the Brazilian agency CNPq for the additional financial support.

REFERENCES

Abazarpoor, A, Halali, M, Hejazi, R and Saghaeian, M, 2018. HPGR effect on the particle size and shape of iron ore pellet feed using response surface methodology. *Mineral Processing and Extractive Metallurgy*, 127(1), 40–48.

Barrios, G K P and Tavares, L M, 2016. A preliminary model of high pressure roll grinding using the discrete element method and multi-body dynamics coupling*, Int. J. Miner. Process*. 156, 32–42.

Burchardt, E and Mackert, T, 2019. HPGRs in minerals: what do more than 50 hard rock hpgrs tell us for the future? (Part 2–2019). *Proceeding of SAG Conference*, (2), 15–36.

Campos, T M, Bueno, G and Tavares, L M, 2021. Modeling comminution of iron ore concentrates in industrial-scale HPGR. *Powder Technology*, 383, 244–255.

Campos, T M, Bueno, G, Barrios, G K and Tavares, L M, 2019a. Pressing iron ore concentrate in a pilot-scale HPGR. Part 1: Experimental results. *Minerals Engineering*, 140, 105875.

Campos, T M, Bueno, G, Barrios, G K and Tavares, L M, 2019b. Pressing iron ore concentrate in a pilot-scale HPGR. Part 2: Modeling and simulation. *Minerals Engineering*, 140, 105876.

Chelgani, S C, Nasiri, H and Tohry, A, 2021. Modeling of particle sizes for industrial HPGR products by a unique explainable AI tool-A 'Conscious Lab' development. *Advanced Powder Technology*, 32(11), 4141–4148.

Cleary, P W and Sinnott, M D, 2021. Axial pressure distribution, flow behaviour and breakage within a HPGR investigation using DEM. *Minerals Engineering*, 163, 106769.

Daniel, M J, 2002. HPGR Model Verification and Scale-up, Masters Thesis. Julius Kruttschnitt Mineral Research Centre, University of Queensland, Brisbane.

Dundar, H, Benzer, H and Aydogan, N, 2013. Application of population balance model to HPGR crushing. *Minerals Engineering*, 50, 114–120.

Gardula, A, Das, D, DiTrento, M and Joubert, S, 2015. First year of operation of HPGR at Tropicana Gold Mine–Case Study. Cuprum: czasopismo naukowo-techniczne górnictwa rud, (2), 15–36.

Herbst, J A and Fuerstenau, D W, 1980. Scale-up procedure for continuous grinding mill design using population balance models. *International Journal of Mineral Processing*, 7(1), 1–31.

Johansson, M and Evertsson, M, 2019. A time dynamic model of a high-pressure grinding rolls crusher. *Minerals Engineering*, 132, 27–38.

King, R P, 2001. *Modeling and simulation of mineral processing systems*. Elsevier.

Morrell, S, Lim, W, Shi, F and Tondo, L, 1997. Modelling of the HPGR Crusher. *Comminution Practices*, 117–126.

Nejad, R K and Sam, A, 2017. Limitation of HPGR application. *Mineral Processing and Extractive Metallurgy*, 126(4), 224–230.

Numbi, B P and Xia, X, 2015. Systems optimization model for energy management of a parallel HPGR crushing process. *Applied Energy*, 149, 133–147.

Rashidi, S, Rajamani, R K and Fuerstenau, D W, 2017. A review of the modeling of high pressure grinding rolls. *KONA Powder and Particle Journal*.

Rodriguez, V A, Barrios, G K, Bueno, G and Tavares, L M, 2021. Investigation of Lateral Confinement, Roller Aspect Ratio and Wear Condition on HPGR Performance Using DEM-MBD-PRM Simulations. *Minerals*, 11(8), 801.

Rodriguez, V A, Barrios, G K, Bueno, G and Tavares, L M, 2022. Coupled DEM-MBD-PRM simulations of high-pressure grinding rolls. Part 1: Calibration and validation in pilot-scale. *Minerals Engineering*, 177, 107389.

Torres, M and Casali, A, 2009. A novel approach for the modelling of high-pressure grinding rolls. *Minerals Engineering*, 22(13), 1137–1146.

Van der Meer, F P, 1997. Roller Press Grinding of Pellet Feed. Experiences of KHD in the Iron Ore Industry. *AusIMM Conference on Iron Ore Resources and Reserves Estimation*, n. September, pp. 1–15.

Van Der Meer, F P, 2010. HPGR Scale-Up and Experiences. In *XXV International Mineral Processing Congress,* pp. 6–10.

Vyhmeister, E, Reyes-Bozo, L, Rodriguez-Maecker, R, Fúnez-Guerra, C, Cepeda-Vaca, F and Valdés-González, H, 2019. Modeling and energy-based model predictive control of high pressure grinding roll. *Minerals Engineering*, 134, 7–15.

Microwave heating behaviour of ores and its application to high-power microwave assisted comminution and ore sorting

J Forster[1], A Olmsted[2], X Tian[3], D Boucher[4], M Goldbaum[4], C A Pickles[2] and E R Bobicki[5]

1. University of Toronto, Toronto, ON, Canada. Email: john.forster@mail.utoronto.ca
2. Queen's University, Kingston, ON, Canada.
3. Sepro Mineral Systems Corp., Langley, BC, Canada.
4. University of Toronto, Toronto, ON, Canada.
5. University of Alberta, Edmonton, AB, Canada.

ABSTRACT

As the global demand for metal values expands, it becomes increasingly important to create more sustainable mining operations. Consequently, considerable research and technology development is required to produce processes which are both more energy efficient and have a minimal environmental impact. One potential technology is the utilisation of microwave pre-treatment to reduce the energy requirements in comminution. Microwaves can preferentially heat the valuable mineral phases in an ore and the resulting differential thermal expansion leads to the formation of microfractures along the grain boundaries. As a result of the preferential heating, ore competency is reduced, mineral liberation is enhanced, a coarser grind size can be employed, and plant throughput can be increased. Furthermore, microwave pre-treatment can be combined with advanced ore sorting, to decrease the quantity of gangue material processed downstream and hence reduce tailings production. Previous studies on the microwave treatment of ores over the last 30 years have mainly been limited to low power bench-scale studies and there is a paucity of information on pilot and/or commercial scale studies. In the present research, the microwave heating behaviours of over 40 ores have been studied at the bench-scale. These results were used to generate a database, from which a unique classification system was developed. This system was used to rank the amenability of any given ore for microwave pre-treatment. This knowledge can be employed to predict the performance of the ores in the high-power pilot scale tests and thus can be used as a pre-screening tool. The effects of high-power microwave pre-treatment on grindability and liberation were reported. Additionally, the ore sorting potential was evaluated using a combination of X-ray transmission (XRT) and microwave infrared (MW/IR).

INTRODUCTION

Conventional comminution circuits are extremely inefficient. A survey of three semi-autogenous grinding (SAG)/ball mill circuits by Bouchard *et al* (2019) revealed that 91 per cent of the energy input was lost, leaving only 9 per cent available for ore breakage. Given ever-increasing costs to mine depleting ore deposits coupled with more stringent environmental laws mandated by governments, it is exigent to develop more economic solutions. One possible solution is the application of microwaves for both assisted comminution and ore sorting (Bobicki *et al*, 2020; Forster *et al*, 2021; Olmsted *et al*, 2021).

In general, ores contain both valuable minerals and gangue (barren rock of little to no value). Many valuable minerals, such as sulfides and some metal oxides, heat very well in response to microwave irradiation. Typical gangue minerals, especially those containing large quantities of silica (SiO_2), are transparent to microwaves and do not heat. Selective heating causes differential thermal expansion, resulting in stress and strain across mineral grain boundaries, creating microfractures. It also generates distinctive heating patterns on the surfaces of the rocks. The three main benefits of microwave ore treatment are: ore competency reduction, increased liberation, and improved sortability, with significant variables being the frequency, power, temperature, dielectric properties, magnetic properties, load size, load mass, load position, and applicator type (Peng and Hwang, 2015).

Historically, the use of microwave energy to pre-treat minerals has focused on microwave-assisted comminution (Walkiewicz *et al*, 1991; Amankwah *et al*, 2005; Henda *et al*, 2005; Jones *et al*, 2005; Rizmanoski, 2011). Henda *et al* (2005) reported an uneconomical energy dose of 13 kWh/tonne from microwave pre-treatment and grinding. Here, the nickel and copper grades improved by 15 per cent

and 27 per cent, respectively, along with a recovery increase of 26 per cent. Therefore, although microwave pre-treatment and grinding alone may not be viable, downstream benefits may make a process worthwhile. The exploitation of the heat signature from microwave pre-treatment for ore sorting is more recent (eg Van Weert, Kondos and Gluck, 2009; Van Weert, Kondos and Wang, 2011; Ferrari-John *et al*, 2016; Batchelor *et al*, 2016, 2017; Naseh and Sam, 2019). Pioneering work by Van Weert and Kondos (2007) laid the foundation for this field by demonstrating that it is possible to use microwaves to readily heat sulfide ores and to use an infrared sensor as a sorting technique. However, one of their conclusions was that rocks shielded by surrounding rocks tended to heat up slowly. The authors recommended that scaling up requires the use of a belt instead of a shaft, which is contrary to a recent report from Holmes *et al* (2020), which suggested that a vertical system is appropriate for commercialisation. Despite the remarkable progress at the bench-scale (hundreds of studies), there is a lack of information regarding pilot and/or commercial scale studies on microwave-assisted comminution and sorting.

Three key parameters for successful application of microwave treatment at a larger scale are kinetics, penetration depth, and electronic control (Krieger, 1995). There is a trade-off between throughput and the energy input: a higher throughput reduces the energy input, but it also results in less grain boundary damage (Bradshaw *et al* (2011). Recently, a study has been conducted on the development and implementation of a continuous, pilot-scale, monomode microwave applicator that could deliver very high power (>100 kW) for very short times to produce ultra-low energy dosages of <0.7 kWh/t (Batchelor *et al*, 2017). This is because the electric field strength increases with microwave power. With this technique, for a copper porphyry ore, the same degree of liberation could be achieved at a grind size which was 50–60 µm greater than the untreated ore. Also the Ball mill work index was reduced by 3–9 per cent. Olmsted (2021) reported that high-power microwave pre-treatment of a gold sulfide ore improved gold recovery by 14 per cent after a leaching time of only 6 h. Anglo American PLC announced the development of a microwave-assisted comminution project at their Amandelbult platinum mine in South Africa, as part of their FutureSmart Mining™ program (Moore, 2021). In some of their preliminary test work, they reported hardness reductions of 5–25 per cent and 8–12 per cent for platinum and copper ores, respectively. The company is investigating installations at other facilities, starting with a pebble circuit at Los Bronces (Chile), followed by Mogalakwena (South Africa), Collahuasi (Northern Chile), and Quellaveco (Peru). This effort speaks very highly of the potential for microwave-assisted comminution in the mining industry.

The present work involves the study of the bench-scale heating behaviour of 42 unique ores to determine their amenability to microwave treatment. This test work resulted in a database, whereby a classification system was developed, which can be applied to rank any ore in one of four heating classes and determine its suitability for microwave pre-treatment. Select ores from this test program were tested at the pilot-scale using a 150 kW microwave system to determine the effects of microwaves on comminution, liberation of valuable minerals, and sorting potential.

MATERIALS AND METHODS

Materials

Table 1 presents the elemental analysis of the 42 ores investigated in the present study. There are many ore types including gold, silver, Ni/Cu, and Pb/Zn sulfides. Some of the oxide ores include chromite, and iron. There are also several silicate rich ores (Zn silicates, lithium, and kimberlite).

TABLE 1

Elemental composition of candidate ores from the Crush It! Challenge determined by inductively coupled plasma – optical emission spectrometry or X-ray fluorescence.

Ore ID	Ore Type	Element (wt.%)									
		Al	Ca	Co	Cu	Fe	Mg	Ni	S	Si	Zn
CA01	Au	3.34	3.55	0.00	0.06	5.73	1.60	0.03	0.80	31.4	0.02
CA02	Ni	3.65	2.24	0.10	1.97	31.9	1.62	4.73	19.0	10.7	0.02
CA03	Ni-Cu	5.53	3.00	0.03	1.27	21.6	1.41	1.51	10.5	18.3	0.03
CA04	Ag	7.70	1.68	0.01	0.05	4.00	0.88	0.02	0.48	28.0	0.64

CA05	Chromite	6.4	0.2	<0.1	<0.01	10.9	13.0	0.2	<0.1	6.6	<0.1
CA06	Magnetite-rich Fe	0.7	0.3	0.1	–	21.3	0.9	–	–	34.9	–
CA07	Hematite-rich Fe	0.6	0.7	<0.1	–	8.6	3.1	–	–	39.0	–
CA08	Cu-Au	7.06	4.17	0.00	0.22	4.79	2.93	0.01	1.02	24.3	0.07
CA09	Ovoid low-grade Ni	0.49	0.28	0.11	2.24	55.9	0.03	2.54	33.7	0.09	0.02
CA10	Ovoid high-grade Ni	6.93	5.52	0.02	0.19	11.9	7.11	0.25	2.13	19.2	0.02
CA11	Au-Cu	7.84	2.70	0.00	0.55	3.01	1.11	0.03	0.66	31.7	0.01
CA12	Au	7.55	2.32	0.00	0.83	3.07	0.99	0.02	1.41	31.6	0.02
CA13	Au	0.42	0.34	0.01	0.02	0.37	0.03	0.01	0.19	41.8	0.01
CA14	Au	4.92	3.87	0.01	0.00	12.6	1.48	0.02	1.25	21.6	0.02
CA15	Au	7.83	4.43	0.00	0.01	4.04	1.95	0.02	1.17	24.6	0.01
CA16	Au	7.33	3.80	0.01	0.06	6.92	2.77	0.01	0.84	26.4	0.02
CA17	Ni-Cu	5.89	3.94	0.03	0.81	17.8	2.39	0.94	6.90	20.6	0.02
CA18	Cu-Ni	7.11	3.35	0.01	0.61	6.60	1.62	0.15	0.41	26.9	0.01
CA20	Ultramafic Ni	0.81	0.67	0.01	0.01	5.41	23.80	0.22	0.75	18.3	0.01
CA21	Cu-Ni	6.67	4.10	0.02	0.63	13.6	2.04	0.56	3.71	23.0	0.02
CA22	Ultramafic Ni	0.88	0.71	0.02	0.04	8.96	20.27	0.48	1.97	16.25	0.02
CA26	Zn silicate	0.56	15.70	0.01	<0.005	4.05	9.97	<0.005	0.04	3.81	7.76
CA27	Zn silicate	0.18	19.00	<0.002	<0.005	2.91	10.80	<0.005	1.10	1.95	2.84
CA28	Zn silicate	3.37	8.58	0.01	0.01	3.59	5.53	<0.005	0.02	15.0	9.32
CA29	Massive sulfide	0.62	0.84	0.13	1.92	47.0	0.36	7.28	32.50	2.20	0.03
CA30	Net textured sulfide	1.07	1.86	0.09	1.36	30.3	8.36	4.50	19.10	9.01	0.01
CA31	Disseminated sulfide	1.46	0.84	0.05	0.58	16.6	15.20	1.88	7.56	14.7	<0.01
CA32	Argilite	9.40	0.92	0.00	0.03	4.69	2.25	0.07	0.70	28.9	<0.01
CA33	Peridotite	2.26	2.41	0.02	0.15	10.5	17.7	0.62	2.44	17.3	<0.01
CA34	Gabbro	8.06	8.20	0.00	0.01	7.13	4.63	0.01	0.15	23.5	<0.01
CA36	Au sulfide	9.63	0.88	–	–	5.86	1.50	–	0.62	26.4	–
CA37	Pb-Zn sulfide	0.90	0.46	0.00	0.02	6.40	0.12	<0.005	12.2	18.2	10.3
CA38	Net textured Ni-Cu sulfide	1.1	0.6	0.1	0.9	15.2	22.1	2.5	6.7	15.5	0.1
CA40	Cu-Ni sulfide	8.0	5.3	<0.1	0.2	10.5	2.8	0.2	1.1	26.5	0.1
CA41	Ni-Cu sulfide	7.79	2.92	–	1.03	7.53	1.87	0.32	1.20	25.54	–
CA42	Porphyry Cu	8.13	1.67	–	0.15	1.39	0.22	–	0.16	34	–
CA43	Ni sulfide	4.3	5.3	0.1	0.8	15.6	12.2	0.6	3.2	19.8	<0.1
CA44	Ni sulfide	4.6	5.7	<0.1	0.4	13.3	12.3	0.3	1.9	21.2	<0.1
CA45	Lithium	7.75	0.18	–	–	0.28	–	–	0.04	30.63	–
CA46	Ovoid low-grade Ni	11.83	6.24	–	0.24	10.37	4.35	0.23	1.45	21.59	–
CA47	Au sulfide	8.98	1.20	–	–	5.02	1.34	–	0.20	28.6	0.01
CA49	Kimberlite	5.97	4.41	–	–	5.50	9.23	–	0.17	26.36	–

Methods

Elemental composition

Inductively coupled plasma–optical emission spectrometry (ICP-OES) was used to determine the elemental composition of the head assays for the ore candidates and of selected rocks from sorting tests. For the head assays, representative crushed (2–3.35 mm) samples were pulverised into a fine powder and sent for analysis. For assays on rocks from the sorting tests, each rock was individually crushed and pulverised. All analyses were performed at XPS (Falconbridge, ON), where a subsample was split from the pulverised sample and digested via sodium peroxide fusion.

A Panalytical (Epsilon-1; 50 kV; Ag anode X-ray tube) XRF spectrometer was used to analyse the elemental composition of pulverised rock samples at Sepro Mineral Systems (Langley, BC). Each pulverised sample was riffled to between 10 and 15 g each, placed into a sample cup, and inserted into the system for analysis. The positive linear relationship with ICP-OES data was used to improve the accuracy of the XRF assays and to validate the methodology to be used for rapid XRF analysis of individual rocks in the pilot sorting tests.

Mineralogy and liberation

The SAG and BWI products form the grinding tests were sent for analysis using QEMSCAN. This technique allows for the determination of the mineralogy and liberation analysis of a sample. The samples of interest were split, mounted in epoxy, polished, carbon coated, and imaged. This analysis calculated the number, size, mineral composition, and associations of the particles. The liberation degree of target minerals (eg chalcopyrite, pentlandite, pyrrhotite, pyrite, sulfides, iron oxides) was represented as an area percent, indicative of the 2D surface fraction of the target mineral in a scanned particle. The particles observed on a single scan were grouped in liberation classes based on their area percent value as follows: locked (<30 per cent), low-grade middling (30–80 per cent), high-grade middling (80–95 per cent), liberated (>95 per cent) and free (100 per cent).

Bench-scale microwave heating behaviour tests

Microwave heating curves provide direct information on how a material responds to microwave irradiation. For each test, a 50 g sample of crushed (1.7–3.35 or 2–3.35 mm) ore was massed into a quartz crucible and placed into a BP-211 microwave oven (53.5 cm width × 25.1 cm height × 33 cm depth; Microwave Research and Applications, Illinois, USA). A top size of 3.35 mm was selected to match the feed size for typical ball mill grinding tests. Samples were exposed to 2450 MHz microwaves at 3.2 kW with time as the independent variable. After treatment, the quartz crucible was quickly removed from the microwave oven, and a Type-K thermocouple was inserted into the centre of the sample to measure the bulk temperature. Temperature was plotted against time to generate a microwave heating behaviour curve for each ore.

Pilot-scale microwave tests

The 915 MHz pilot-scale microwave system was designed and constructed by Thermowave (Danvers, MA, USA). It is equipped with two 75 kW transmitters. Multiple generators can provide a better excitation of modes yielding more uniformity compared to a single feed (Metaxas and Meredith, 1983). A water circulator dissipates any reflected microwave power, thereby preventing damage to the magnetron. The system is controlled via an HMI control panel equipped with an Allen Bradley PLC. The applicator is 1 m long, with a microwave transparent polypropylene bridge and a built-in arc sensor. The conveyor belt is made of microwave-transparent silicone/polyester and can reach speeds of up to 5 m/s. For all tests, the energy dosage in kWh/t was calculated prior to the test, and the tray packing, belt speed, and microwave power were varied to meet this value (eg 1–4 kWh/t electrical power). Immediately after processing, a FLIR A8300sc IR camera recorded a video of the sample trays and transferred the data via a Gigabit ethernet port connected to FLIR's Research IR software. In some of the monolayer sorting tests, the infrared videos were used to generate data for the ore sorting algorithm.

SAGDesign tests

Following microwave treatment, the sample was prepared for the SAGDesign test. Each ore required an initial reference grind (untreated material) before the microwave treated sample could be ground. The SAGDesign test was conducted using a laboratory SAG mill (Starkey, Hindstrom and Nadasdy, 2006). The grinding energy was determined for both a SAG mill (W_{SDT}) and a Bond Ball mill (S_d-BWI), both expressed in kWh/t. The W_{SDT} value estimates the energy consumption (kWh/t) of coarse grinding – SAG mill grinding from 80 per cent passing 152 mm to 80 per cent 1.7 mm. The BWI test (variability of ± 9 per cent) measured the energy required for fine grinding. The Bond mill used the ground product from the SAG mill test (T_{80} 1.7 mm) per the standard Starkey SAGDesign methodology.

RESULTS AND DISCUSSION

Bench-scale microwave heating behaviour of ores

The 42 ores tested were grouped into four classes (I–IV; Table 2) based on the bench-scale microwave heating behaviour (Figure 1). For the purposes of the current work, a formal definition of highly microwave amenable phases (HMAP)s is proposed. This includes the following minerals: bornite, chalcopyrite, galena, hematite, magnetite, molybdenite, pentlandite, pyrite, and pyrrhotite.

TABLE 2

Microwave heating classes, typical highly microwave-amenable phase (HMAP) content, and minimum, maximum, and mean initial (first 30 s) heating rates for 42 ores.

Heating Class		Typical HMAP Content (wt.%)	Initial Heating Rate (°C/min)		
			Minimum	Maximum	Mean
I	Poor	0–2	13	40	23
II	Fair	2–5	21	133	76
III	Good	5–20	105	339	159
IV	Excellent	>20†	150	829	559

† excluding massive sulfide ores

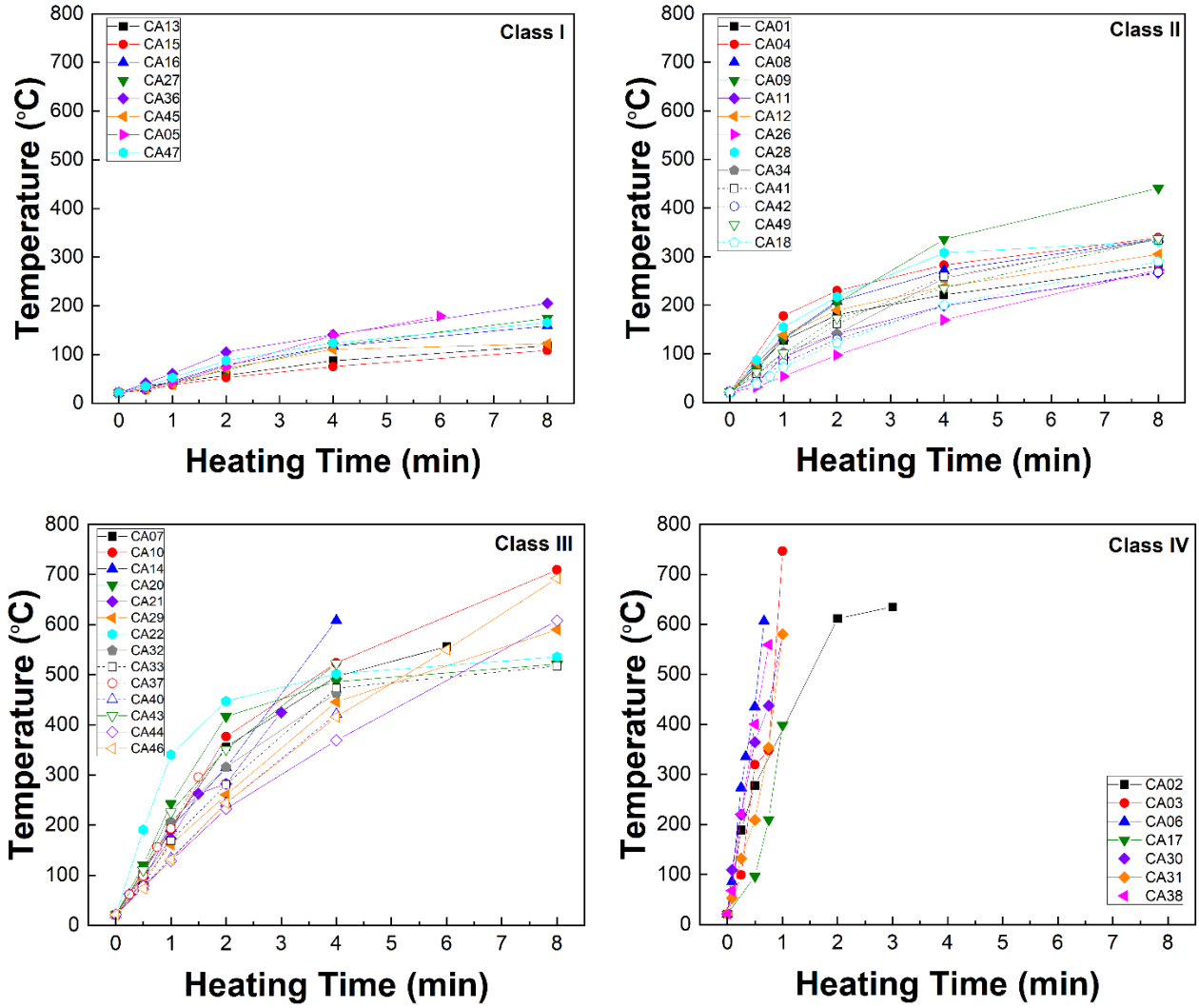

FIG 1 – Bench-scale heating behaviour curves for 50 g samples of 42 Class I–IV ores treated with 2450 MHz microwaves at 3.2 kW power; particle size 1.7–3.35 or 2–3.35 mm.

Class I ores showed limited heating, reaching a maximum temperature of roughly 200°C by 8 min. Despite this, grindability improvements are still possible. For example, Hredzak and Lovas (2005) reported that even relatively pure quartz (>99 per cent SiO_2) exhibited reductions in grindability after prolonged microwave heating. However, heating at low power (<5 kW) for a long period allows for thermal conduction between grains and particles. This additional heating mechanism reduces the temperature differential between grain boundaries of the various phases, thereby lessening the degree to which the ore will fracture. For comminution and ore sorting benefits, high heating rates are desirable. Hence, Class I ores are not ideal. Class II ores demonstrated moderate heating: most reached 250–300°C by 8 min. Class III ores exhibited high heating rates: most heated to >400°C after 4 min. Class IV ores had very high heating rates, with all ores reaching or exceeding 400°C within 1 min of treatment. However, none of these ores could be treated for the full 8 min due to thermal runaway and fusion of the samples. Furthermore, the power, particle size and the mass of the load will all affect the heating of any material. However, to achieve the maximum possible thermal gradient, the maximum power was applied. Future work will involve the exploration of these additional parameters.

In general, Class IV ores would be excellent candidates for pilot-scale microwave treatment. The very high heating rates would both initiate fractures in the ore (reducing competency and improving liberation) and provide a distinct thermal signature for sorting. Conversely, the low HMAP content of Class I ores would result in poor heat signatures. Class I ores are generally not amenable to the process. Class II and Class III ores can be expected to realise overall benefits, except ores with very conductive surfaces, which would reflect microwaves (eg massive sulfide ores). To facilitate comparison among the ores, the power was fixed at 3.2 kW for all the microwave heating behaviour tests. A lower power would have helped prevent thermal runaway (Huang and Lu, 2009) in some of the tests on the ores of a higher class. One of the major findings was that most of the gold sulfides are Class I ores (CA13, CA15, CA16, CA36, CA47), except for CA08 and CA14, which are Class II and Class III, respectively. CA08 contained roughly 2.4 wt.% iron sulfides (pyrite and chalcopyrite), and CA14 contained about 11 wt.% iron oxides. This proves that just a small increase in the amount of HMAP phases is enough to shift the curves to a higher class.

High-power microwave tests, comminution, and QEMSCAN of select ores

Ores CA30 (net textured sulfide ore), CA34 (gabbro rock), CA41 (Ni/Cu sulfide), and CA42 (Cu porphyry) were treated in the pilot-scale microwave system and subsequently tested using the grinding procedure according to the parameters in Table 3. The efficiency of conversion of electrical to microwave power was approximately 80 per cent which is on par with that reported by Tranquilla *et al* (1999). In many of the microwave assisted comminution tests, smaller particles (<25.4 mm) were added to the trays to mitigate arcing by reducing the void spacing between adjacent rocks. For the very soft copper porphyry ore (CA42), the W_{SDT} values of the microwave treated samples increased slightly after grinding, which may be indicative of improved breakage at the coarser particle size during grinding. A reduction in competency was not realised for this soft ore. Furthermore, the doubling of the electrical energy dose from 2 kWh/t to 4 kWh/t did not significantly reduce the ore competency either. However, improved liberation is still possible (see next section). In many of the grindability results presented, benefits are realised in the SAG portion of the SAGDesign test, as opposed to the Bond ball mill test (closing size based off process flow sheet).

TABLE 3

Microwave treatment parameters and SAGDesign comminution results for select ores.

Ore Class	Sample ID*	Electrical Energy Dose (kWh/t)	Power (kW)	W_{SDT} (kWh/t)	Reduction (%)	S_dBWI (kWh/t)	Reduction (%)	Bond Closing Size (µm)
II	CA34-Ref	N/A	N/A	23.2	N/A	14.7	N/A	106
	CA34-MW	2.0	150	17.6	24.1	14.0	4.6	106
	CA41-Ref†	N/A	N/A	16.7	N/A	16.5	N/A	106
	CA41-MW†	2.0	150	13.5	19.2	16.7	–1.4	106
	CA42-Ref1	N/A	N/A	7.6	N/A	16.3	N/A	106
	CA42-MW1	2.0	75	8.1	-6.6	17.0	-4.3	106
	CA42-Ref2	N/A	N/A	7.6	N/A	15.8	N/A	212
	CA42-MW2	4.0	75	8.0	-5.3	15.9	-0.6	212
IV	CA30-Ref	N/A	N/A	14.7	N/A	12.8	N/A	106
	CA30-MW	2.0	75	13.9	5.8	12.8	-	106

†Olmsted (2021); *Ref-Reference Sample; MW-Microwave Treated Sample

QEMSCAN

Ni/Cu sulfide ore (CA30)

QEMSCAN liberation analysis was carried out on the SAG test product and two size fractions from the BWI test: >106 and <106 µm. For the <106 µm products, considering the top two liberation classes (>95 and 100 per cent), the minimal improvement in pentlandite liberation from microwave treatment was mostly due to a slight improvement for the free (100 per cent liberated) class (Figure 2a). However, for chalcopyrite, the amount of liberated plus free material was more than 2.4 times higher for the microwave-treated (36.3 per cent) than for the reference samples (14.9 per cent; Figure 2b). It is possible that a greater proportion of the chalcopyrite is hosted within the gangue silicate matrix, whereas the pentlandite is preferentially combined with gangue pyrrhotite, which is a HMAP. Therefore, the chalcopyrite-silicate would experience more intergranular fracturing than the pentlandite-pyrrhotite system.

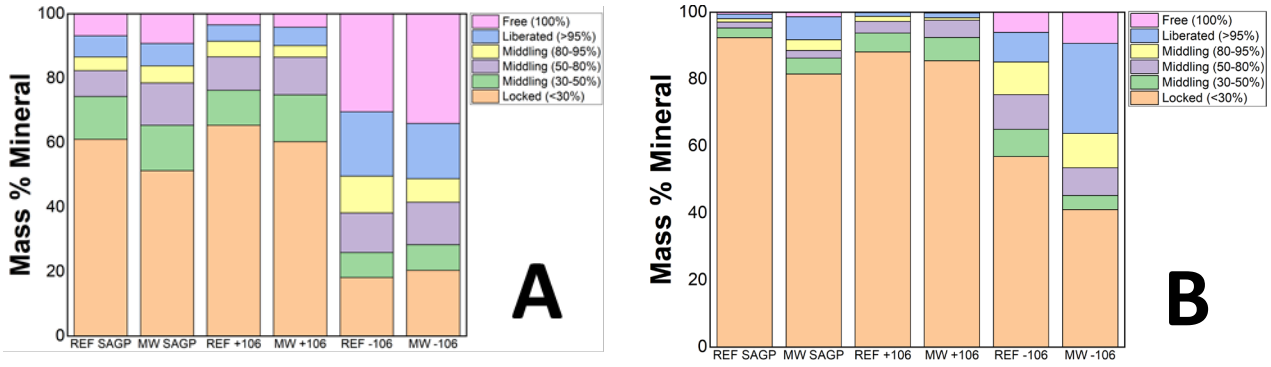

FIG 2 – Pentlandite (A) and chalcopyrite (B) liberation for reference (REF) and microwave-treated (MW) samples of CA30.

Copper porphyry ore (CA42)

Given the very low W_{SDT} for this ore (Table 3), microwave pre-treatment followed by comminution did not yield grinding energy savings. Instead, savings are expected to be realised in downstream flotation, where an improvement in the liberation of copper sulfide species should improve overall Cu recovery. Copper sulfide liberation (>95 per cent and 100 per cent) from the Bond ball mill

undersize products for Ref1 and 2 and MWT1 and 2 (Table 3) at both closing sizes showed a significant improvement after microwave pre-treatment (Figure 3). For the test with a closing size of 106 µm, microwave treatment increased liberation from 25 to 58 per cent. For the coarser closing size (212 µm), liberation was increased from 17 to 55 per cent.

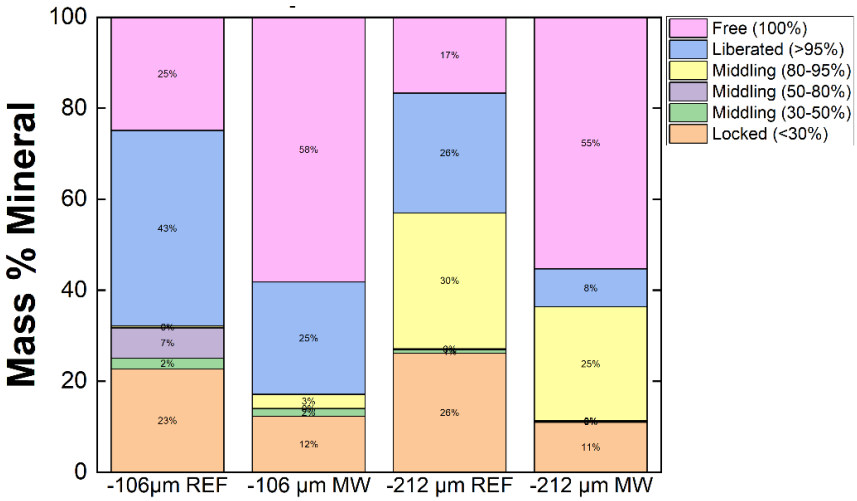

FIG 3 – Copper sulfide liberation analysis for reference and microwave treated samples at two closing sizes.

Monolayer sorting of nickel sulfide ore (CA30)/gangue rock (CA34) blend

CA30 and CA34 were from the same mine site, and therefore it was of interest to carry out a sorting test on a blend of these two materials. A 25.6 kg load comprising a 58/42 wt.% blend of CA30 (48 rocks)/CA34 (36 rocks) was treated at 75 kW power (2.2 kWh/t electrical energy dose). Many of the gangue rocks (white/grey) heated up, which is likely due to the larger penetration depth (Figure 4). Certain sections of the surfaces of the valuable rocks (darker in colour) were more conductive because they contained pentlandite, pyrrhotite, and chalcopyrite. Even if surface heating was high, there was less bulk heating for these rocks, given the lower penetration depths of their constituent sulfide minerals.

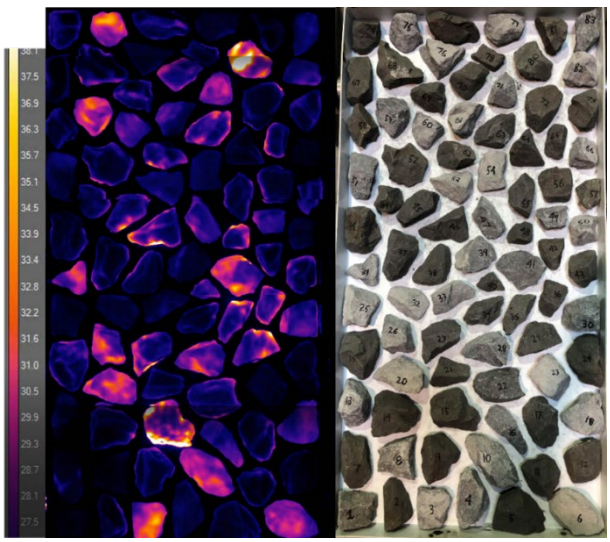

FIG 4 – Infrared and optical images of the sample tray of a 58/42 wt.% blend of CA30 (48 rocks) and CA34 (36 rocks) for the MWIR monolayer sorting test.

The infrared video was processed into multiple frames, and the pixels from the infrared heating pattern were then extracted and combined with the XRF and XRT analysis before being fed into a proprietary sorting algorithm which uses machine learning. Table 4 reports the mass split, recoveries, feed and product grades, and upgrade ratios for the nickel and copper. A mass rejection of 31.5 per cent yielded a nickel recovery of 98.7 per cent, and a corresponding upgrade ratio of

1.51. Mass rejection while maintaining high metal recovery directly translates into energy savings. A previous study by CanMicro found that the integration of ore sorting represents significant energy savings (Tian *et al*, 2021).

TABLE 4

Sorting analysis results for Ni/Cu (CA30) ore.

Component	Parameters	Value	Unit
Mass Split	Mass Rejected	34.50	%
	Mass Accepted	65.50	%
Nickel	Recovery	98.70	%
	Feed Grade	3.75	%
	Product Grade	5.65	%
	Upgrade Ratio	1.51	Ratio
Copper	Recovery	97.90	%
	Feed Grade	0.76	%
	Product Grade	1.13	%
	Upgrade Ratio	1.49	Ratio

CONCLUSIONS

A microwave heating behaviour database comprising of hundreds of bench-scale experiments on 42 ores was developed. Ores were classified into one of four heating behaviour classes, which is directly related to the wt.% of HMAP present in an ore: (poor, 0–2; fair, 2–5; good, 5–20; excellent, >20). This is the first comprehensive study on an array of ores spanning multiple commodities, especially sulfide ores.

Pilot-scale microwave tests were carried out on four selected ores. This involved treatment at high power (75 or 150 kW) for very short amounts of time. Appreciable reductions in the SAG W_{SDT} values were obtained on three out of the four ores. The ore (CA42) that did not achieve a reduction in grinding energy but still demonstrated substantial improvements in the liberation of the copper sulfide mineral species. This reveals that while comminution test work may not immediately show energy savings, this loss can be reclaimed in downstream unit operations, providing sufficient liberation has been attained.

Monolayer ore sorting results for a blend of a nickel sulfide ore and gangue rock demonstrated that if a discrete heat signature is captured then the combination of microwave pre-treatment with sorting has considerable potential.

ACKNOWLEDGEMENTS

Sepro Mineral Systems is thanked for providing support during the pilot-scale microwave tests. Elizabeth Whiteman from XPS is recognised for overseeing the ICP and QEMSCAN analysis. The authors would like to thank Corem for their assistance with the XRT analysis. Izzat Redza, Spencer Gulbrandsen, Byron Liang, Christine Yu, James Ambrose, and Trevor Kok are thanked for their efforts in the laboratory. Thank you to all the mining companies who supplied the ore samples for this research. Natural Resources Canada is thanked for sponsoring team CanMicro during the Crush It! Challenge.

REFERENCES

Amankwah, R K, Khan, A U, Pickles, C A and Yen, W T, 2005. Improved grindability and gold liberation by microwave pre-treatment of a free-milling gold ore, *Miner. Process. Extr. Metall. Trans. Inst. Min. Metall. C*, 114(1): 30–36.

Batchelor, A R, Buttress, A J, Jones, D A, Katrib, J, Way, D, Chenje, T, Stoll, D, Dodds, C, Kingman and S W, 2017. Towards large scale microwave treatment of ores: part 2-metallurgical testing, *Minerals Engineering*, 111: 5–24.

Batchelor, A R, Ferrari-John, R S, Dodds, C and Kingman, S W, 2016. Pilot plant microwave sorting of porphyry copper ores: Part 2-pilot plant trials, *Minerals Engineering*, 98: 328–338.

Bobicki, E R, Boucher, D, Forster, J, Pickles, C A and Olmsted, A, 2020. Canmicro: scaling up microwave technology for the mining industry, in *Proceedings of 59th Conference of Metallurgists*, pp 1568–1581.

Bouchard, J, LeBlanc, G, Levesque, M, Radziszewski, P and Georges-Filteau, D, 2019. Breaking down energy consumption in industrial grinding mills, *CIM Journal*, 10(4):157–164.

Bradshaw, S, Ali, A, Marchand, R and Barnard, A, 2011. Performance quantification of applicators for microwave treatment of crushed mineral ore, *Journal of Microwave Power and Electromagnetic Energy*, 45(1): 30–35.

Ferrari-John, R S, Batchelor, A R, Katrib, J, Dodds, C and Kingman, S W, 2016. Understanding selectivity in radio frequency and microwave sorting of porphyry copper ores, *International Journal of Mineral Processing*, 155: 64–73.

Forster, J, Olmsted, A, Pickles, C A, Boucher, D and Bobicki, E R, 2021. Multimode microwave assisted comminution of a sulfide ore: bench versus pilot-scale, in *Proceedings of 55th Annual Microwave Power Symposium (IMPI 55)*, pp 59–61.

Henda, R, Hermas, A, Gedye, R and Islam, M R, 2005. Microwave enhanced recovery of nickel-copper ore: comminution and floatability aspects, *Journal of Microwave Power and Electromagnetic Energy*, 40(1):7–16.

Holmes, T, Craig, D, Batchelor, A R, Dodds, C, Kingman, S W, Legault, E and Whetton, M, 2020. Selective heat ore treatment: shaking up the economics of mineral recovery, in *Proceedings of 59th Conference of Metallurgists*, pp 1689–1700.

Hredzak, S and Lovas, M, 2005. Influence of thermal pre-treatment on quartz crushability, *Acta Montanistica Slovaca*. 10(1): 60–66.

Huang, K and Lu, B, 2009. The precise condition of thermal runaway in microwave heating on chemical reaction, *Science in China Series E: Technological Sciences*, 52(2):491–496.

Jones, D A, Kingman, S W, Whittles, D N and Lowndes, I S, 2005. Understanding microwave assisted breakage, *Minerals Engineering*, 18: 659–669.

Krieger, B, 1995. Commercialization-steps to successful applications and scaleup, in *Proceedings of the Annual Meeting of the American Ceramic Society*, Cincinnati, pp 17–21.

Metaxas, A C and Meredith, R J, 1983. Industrial microwave heating. Peter Peregrinus Ltd, United Kingdom.

Moore, P, 2021. Anglo American says it is trialling insitu microwave pre-conditioning at Amandelbult platinum mine. [Online]. https://im-mining.com/2021/05/26/anglo-american-say-trialling-insitu-microwave-pre-conditioning-amandelbult-platinum-mine/. [Accessed: 26 May, 2021].

Naseh, R and Sam, A, 2019. Microwave infrared ore sorting of screen rejected rocks based on their iron and copper sulfide in Sarcheshmeh copper complex, Iran, Kerman, *Mineral Processing and Extractive Metallurgy*, 130(4): 416–424.

Olmsted, A, 2021. The effects of high-power microwaves on comminution and downstream processing, Master's Thesis, Queen's University, Kingston, ON.

Olmsted, A, Forster, J, Tian, X, Boucher, D, Bobicki, E R and Pickles, C A, 2021. The effects of pilot-scale microwave pre-treatment on the cyanidation of a canadian gold ore, in *Proceedings of 60th Conference of Metallurgists, pp 507–510*.

Peng, Z and Hwang, J, 2015. Microwave-assisted metallurgy, *International Materials Reviews*, 60(1):30–63.

Rizmanoski, V, 2011. The effect of microwave pre-treatment on impact breakage of copper ore, *Minerals Engineering*, 24: 1609–1618.

Starkey, J H, Hindstrom, S, Nadasdy, G, 2006. SAGDesign testing-what it is and why it works, in Proceedings of *SAG 2006*, *Vancouver, BC, October 2006*, pp 240–254.

Tian, X, Forster, J, Boucher, D and Bobicki, E R, 2021. Energy savings in microwave-assisted comminution: fact or fiction? *Presented at Comminution 2021, Online*.

Tranquilla, J M, Thompson, L, LaRochelle, W and Moritz, R, 1999. Advances in microwave metallurgical processes at EMR Microwave Technology Corporation: a case study in refractory gold ore, *Presented at CIM-New Brunswick Branch Annual Convention, September 1999*.

Van Weert, G and Kondos, P, 2007. Infrared recognition of high sulfide and carbonaceous rocks after microwave heating, In *Proceedings of the 39th Annual Meeting of the Canadian Mineral Processors, Ottawa, ON*, pp. 345–363.

Van Weert, G, Kondos, P and Gluck, E, 2009. Upgrading molybdenite ores between mine and mill using microwave/infrared (MW/IR) sorting technology, in *Proceedings of 41st Annual Meeting of the Canadian Mineral Processors*.

Van Weert, G, Kondos, P and Wang, O, 2011. Microwave heating of sulfide minerals as a function of their size and spatial distribution, *CIM* Journal, 2(3): 117–124.

Walkiewicz, J W, Clark, A E and McGill, S L, 1991. Microwave-assisted grinding. *IEEE Trans. Ind. Appl.,* 27:239–243.

In situ study of mineral liberation at the onset of fragmentation of a copper ore using X-ray micro-computed tomography

N Francois[1], Y Zhang[2], R W Henley[3], L Knuefing[4], R Cruikshank[5], M Turner[6], L Beeching[7], A Limaye[8], A Kingston[9], M Saadatfar[10] and M A Knackstedt[11]

1. ARC Training Centre for M3D Innovation, Research School of Physics, The Australian National University, Canberra ACT 2601. Email: nicolas.francois@anu.edu.au
2. ARC Training Centre for M3D Innovation, Research School of Physics, The Australian National University, Canberra ACT 2601. Email: yulai.zhang@anu.edu.au
3. Professor, ARC Training Centre for M3D Innovation, Research School of Physics, The Australian National University, Canberra ACT 2601. Email: richard.henley@anu.edu.au
4. ARC Training Centre for M3D Innovation, Research School of Physics, The Australian National University, Canberra ACT 2601. Email: lydia.knuefing@anu.edu.au
5. ARC Training Centre for M3D Innovation, Research School of Physics, The Australian National University, Canberra ACT 2601. Email: ron.cruikshank@anu.edu.au
6. ARC Training Centre for M3D Innovation, Research School of Physics, The Australian National University, Canberra ACT 2601. Email: michael.turner@anu.edu.au
7. ARC Training Centre for M3D Innovation, Research School of Physics, The Australian National University, Canberra ACT 2601. Email: levi.beeching@anu.edu.au
8. National Computational Infrastructure, The Australian National University, Canberra ACT 2601. Email: ajay.limaye@anu.edu.au
9. ARC Training Centre for M3D Innovation, Research School of Physics, The Australian National University, Canberra ACT 2601. Email: andrew.kingston@anu.edu.au
10. Associate-Professor, School of Civil Engineering, The University of Sydney, Sydney NSW 2006. Email: mohammad.saadatfar@sydney.edu.au
11. Professor, ARC Training Centre for M3D Innovation, Research School of Physics, The Australian National University, Canberra ACT 2601. Email: mark.knackstedt@anu.edu.au

ABSTRACT

A better understanding of ore fragmentation and the textural features of ore is a key to the energy efficient extraction of targeted minerals from low-grade ore deposits. In this study, X-ray microcomputed tomography (micro-CT) is employed to study mineral liberation during the tensile failure and onset of fragmentation of a copper ore. Our results show that X-ray micro-CT could inform new studies of ore micromechanics and fragmentation at the laboratory scale and may offer new avenues to address current challenges in the design of efficient comminution processes.

We present the results of experiments based on a high-pressure apparatus enabling micro-mechanical studies to be carried out *in situ* (inside a micro-CT scanner). This platform produces high-quality 3D images of the evolution of a sample of porphyry copper ore during an *in situ* fragmentation test. A sequence of tomographic images enables mapping in 3D of both the deformation of mineral phases and the fragmentation process. The fragmentation occurs quasi-statically through multiple stages starting with an initial tensile fracture splitting the ore diametrically, followed by tensile-activated nucleation and growth of multiple fractures producing a complex fracture network.

Coupling breakage with microstructural information enables quantitative determination of the impact of ore texture heterogeneity on fracture patterns and mineral liberation. This microstructural information can be compared to key measurements of the ore mechanical behaviour such as the global deformation energy, strain deformation field and the stress relaxation response. The latter allows one to identify interesting precursor signals of the tensile failure. The copper liberation, fragment size distribution and breakage patterns are statistically characterised and related to comminution mechanisms which are clearly identified in the sequence of tomographic images. The two dominant mechanisms are rock-rock friction/compression induced by fracture closing and compression-driven fragmentation at rock-crusher contact points.

INTRODUCTION

The mining industry uses diverse crushing and grinding methods to reduce lumps of ore into smaller fragments. This process of breaking a coherent orebody into many pieces, called comminution, is used to expose valuable minerals from the rock groundmass and to produce ore-concentrate. Ore comminution represents a substantial part of a mine's energy consumption. Energy-efficient comminution and optimal mineral extraction are key to the economics and sustainable development of critical mineral mining. Current research efforts to better understand the key factors governing geomaterials comminution reflect the need to rationalise empirical practices. Moreover, the increasing demand for minerals pushes the mining industry to exploit low-grade ore deposits. This trend challenges the usual modelling of comminution efficiency in terms of optimal liberation (resource efficiency) at minimal overgrinding (energy efficiency).

Failure and fragmentation of an ore lump involves a range of complex mechanisms at multiple length scales from microscopic crack openings, to the behaviour of large fractures interacting and producing broad distribution of fragment sizes (Jaeger, Cook and Zimmerman, 2007; Gueguen and Bouteca, 2004). In the context of mining applications, several questions on comminution are the subject of current and intense research efforts (Tavares, 2021; Ord, Blenkinsop and Hobbs, 2022). Typical questions are: What are the mechanisms of fragmentation of an ore with a given texture? Is there a dominant mechanism for a given crushing process? How is the prevalence of a fragmentation mechanism reflected in the final fragment size distribution? How is the coupling of breakage mechanisms with the ore texture heterogeneity impacting the efficient liberation of critical minerals?

Recent advances in X-ray microcomputed tomography (micro-CT) may offer new avenues to address these difficult questions and to inform studies of ore micromechanics and fragmentation at the laboratory scale (Cnudde and Boone, 2013; Noiriel, 2015; Viggiani *et al*, 2015), while providing the basis for development of energy-efficient liberation process streams. Indeed, high resolution X-ray scanners and micro-CT reconstruction techniques enable non-destructive observations of the inner structure of rocks, giving access to three-dimensional information on the crack density, mineral texture and heterogeneous structure of rocks. The capability of micro-CT to provide this structural information from microscopic to centimetre scale also makes it a remarkable tool for studying failure mechanisms in geomaterials (Cnudde and Boone, 2013; Noiriel, 2015; Ghamgosar *et al*, 2016; Viggiani *et al*, 2015). Over recent years, CT-based research efforts have focused on the realisation of *in situ* mechanical tests (Lenoir *et al*, 2007; Hurley *et al*, 2016; Saadatfar *et al*, 2012; Ando *et al*, 2013), whereby a rock is tested inside the scanner. This approach provides direct observations of the evolution of a rock microstructure as it deforms and fails. However, to date, the *in situ* study of hard rock failure remains extremely difficult and to our knowledge *in situ* tomography has been rarely exploited to study a rock on its path to fragmentation (Parapari *et al*, 2020; Jiang *et al,* 2021).

Here, we present the results of a model *in situ* experiment on mineral liberation during the failure and onset of fragmentation of a low-grade porphyry copper ore. This experiment is concerned with tensile activated rock failure which triggers fragmentation. We analyse *in situ* multiple stages of the ongoing fragmentation process starting with an initial tensile fracture splitting the ore diametrically, followed by tensile-activated nucleation and growth of multiple fractures producing a complex fracture network. During the mechanical test, high-resolution 3D images are acquired and the quasi-static fragmentation process is mapped sequentially. These 3D images enable tracking of the influence of ore texture on the local fracture mechanism and observing the interaction of multiple growing fractures in this heterogeneous rock. Moreover, tomographic data enables quantification of the copper liberation, the fracture density and the fragment size distribution.

ORE SAMPLE AND EXPERIMENTAL SET-UP

The objective of this experimental study was to explore the mechanical behaviour and fragmentation process of an ore sample subjected to a dominant tensile stress. For this pilot study, a 12 mm diameter 8 mm length subcore was used. It was extracted from a 45 mm diameter NQ3 drill core from the late Ordovician-early Silurian (~455–435 Ma) Northparkes porphyry copper mine in New South Wales (Australia). The geology of the deposit has been described in (Lickfold *et al,* 2003; Pacey *et al,* 2019). The deposit is made up of a cluster of intrusion-related porphyry copper orebodies centred on quartz monzonite porphyry intrusions and each has a copper core within potassium silicate altered intrusive and surrounding rocks (Pacey *et al,* 2019). The core sample used

here is from an altered volcaniclastic breccia that contains clasts of porphyritic andesitic volcanic lava and volcanic sediments ranging from bedded mudstones-siltstones to coarse sandstones and clast rich volcanic breccias.

Central to this study is a unique experimental platform: the X-ray micro-CT high-pressure apparatus (XCT-HP apparatus) which is part of the CTLab based at the Research School of Physics of the Australian National University. The design of the instrument grew out of research performed at the Australian National University for the last 15 years (Saadatfar *et al*, 2012; Sheppard *et al,* 2014). In the context of geomechanics, this instrument produces very high-quality 3D images which are pivotal to identifying key microscopic displacements and 3D microstructural changes during rock failure and fragmentation.

The XCT-HP apparatus is fully integrated to a cone-beam X-ray micro-CT instrument that was designed and built in-house at the ANU (Francois *et al*, 2022). Figure 1a and 1b show the main components of this instrumental platform, namely, the high-pressure cell, an X-ray source, an X-ray photon detector and a high precision sample manipulator consisting of a rotation stage and a vertical translation stage. Figure 1c shows the different components of the high-pressure cell. The design of the cell is based on two opposed pistons positioned at the extremities of a cylindrical confining chamber. The top piston is locked in position while the lower piston moves axially and is driven hydraulically by a syringe pump. The syringe pump is connected to a PID controller that enables an accurate control of the axial pressure applied to the moving piston. The pressure in the hydraulic loading line is measured using pressure transducers and simultaneously the piston displacement is measured by a Linear Variable Differential Transformer which provides an additional input to the PID control loop. These various transducers enable a control of pressure and piston displacement in a $\pm 1 \times 10^{-3}$ MPa and ± 0.5 µm range respectively.

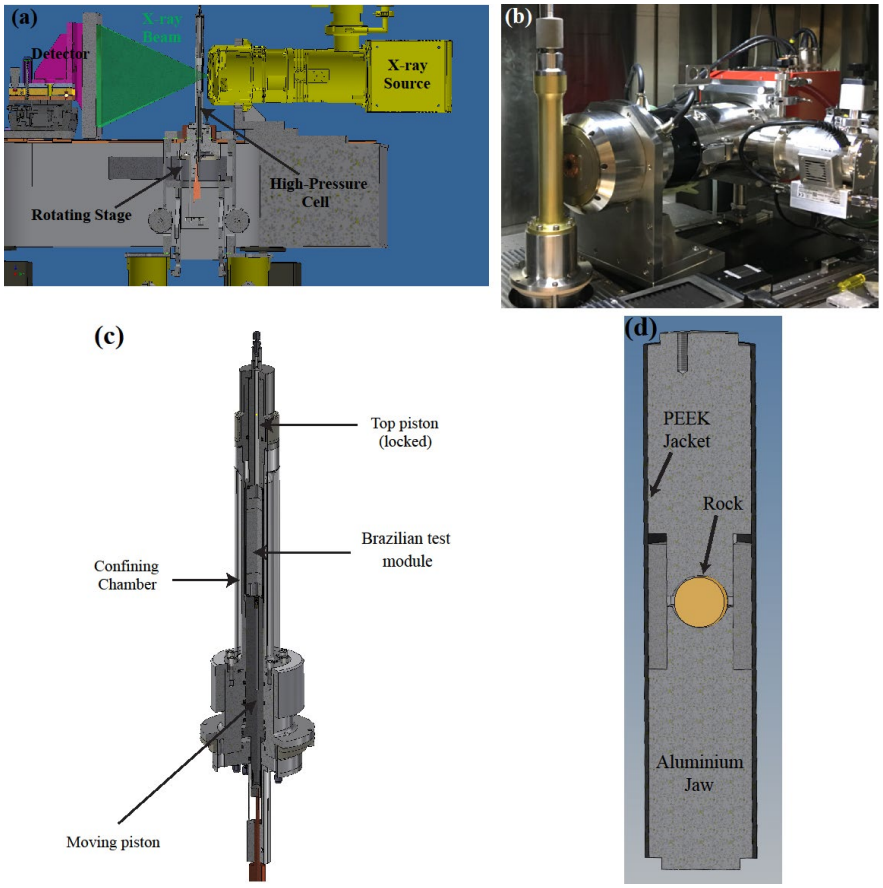

FIG 1 – (a) CAD drawings depicting the XCT-HP apparatus mounted on the high-resolution X-ray micro-tomography platform at the Australian National University. (b) Picture of the instrumental platform showing the confining chamber of the high-pressure cell and the X-ray source. (c) CAD drawing of the main components of the high-pressure cell. (d) Schematics of the crushing-test module. A disc-shaped rock sample is placed in the jaws of the rock-crusher device. The crushing device is placed in the confining chamber of the high-pressure cell.

To perform a tensile activated fragmentation test, we use an in-house designed crushing device. This crusher module is shown in Figure 1d, the loading configuration is based on that of Brazilian tensile tests (Li and Wong, 2013). It is composed of a pair of curved Aluminium jaws encapsulated in a cylindrical jacket made of PEEK. This module sits in the confining chamber of the high-pressure apparatus. A disc-shaped ore sample (diameter d = 12 mm, thickness t = 8 mm) is placed in the crusher. As the ore is compressed between the two jaws, a compressive stress is directed along the diameter of the rock while tensile stresses develop in the horizontal direction. The axial force F exerted by the hydraulic piston on the jaws may be converted to a tensile stress $\sigma_t = F/(d \times t)$ (Li and Wong, 2013). The strain ε_t is computed as $\varepsilon_t = \delta l/d$ where δl is the change in the gap distance between the jaws. Twelve high-resolution tomographic images were acquired at different stages of the mechanical test of the ore sample. The typical scanning time for an image is 17 hours. The image spatial resolution (ie the voxel size) is $9\ \mu$m. These images allow sequential quantitative tracking of the quasi-static failure and fragmentation of the ore. The loading protocol between each image consisted of a pressure ramp at a rate of 1.4×10^{-3} MPa/s followed by a 4-hour long relaxation period at fixed strain value before the image acquisition.

RESULTS

Figure 2a shows the stress-strain curve of the copper sulfide ore measured during a 15-day-long experiment. These mechanical measurements can be compared to tomographic sections of the rock obtained at increasing values of the tensile stress (see Figures 3a and 4a). These two figures clearly show how the rock undergoes successive tensile-activated failure and fragmentation. The images also reveal an interesting fact about the stress-strain curve shown in Figure 2a. An elastic deformation region seems to exist for a range of strain values extending up to $\varepsilon_t = 0.47$ per cent, however a large tensile-activated fracture (F1) occurred at a strain $\varepsilon_t = 0.26$ per cent, and a stress of 38 MPa. It was possible to load the ore beyond this failure point, and a linear relation between stress and strain was recovered until the rock sample could not sustain any further increase of the stress. This mechanical event is correlated to the emergence of a dense network of fractures, it occurred at a strain $\varepsilon_t = 0.47$ per cent, and a stress of 78 MPa. Figure 2b shows the fragmented rock after unloading from the high-pressure cell.

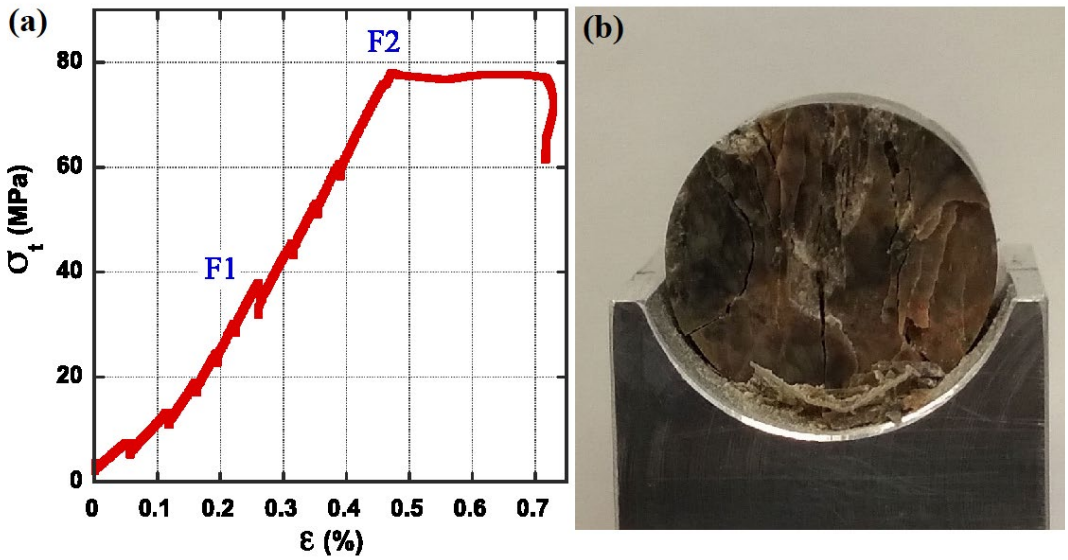

FIG 2 – (a) Stress-strain relation during the *in situ* tensile strength test performed on the copper sulfide ore. Indices F1 and F2 indicate the tensile failure and ultimate fragmentation. (b) Picture of the fragmented ore.

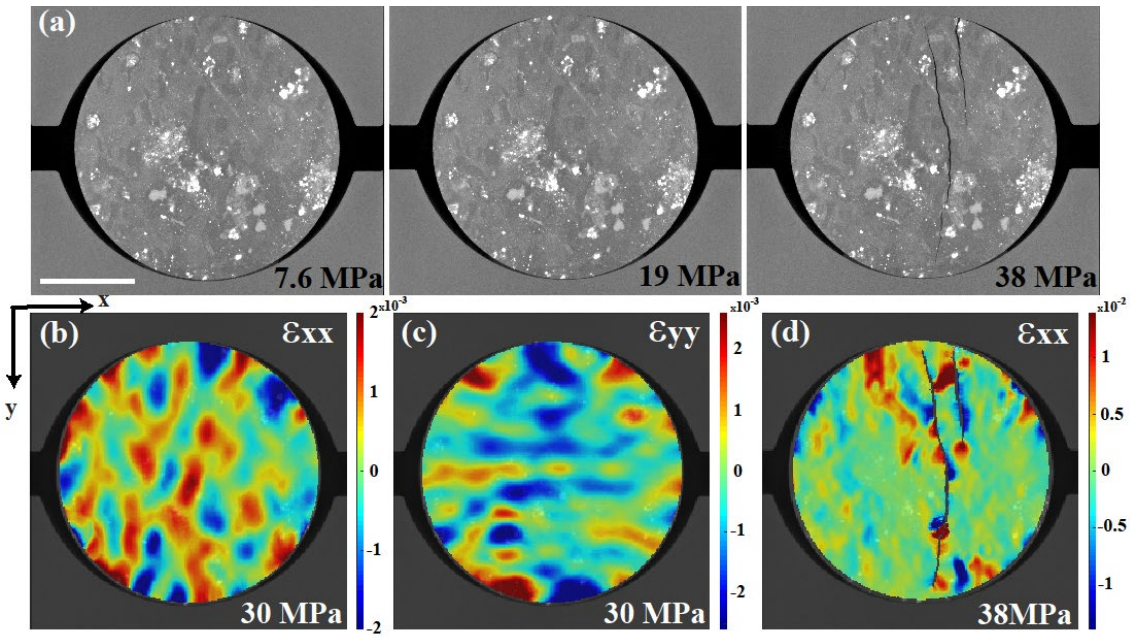

FIG 3 – (a) Midplane tomographic sections of the ore sample at increasing applied load until tensile failure occurs at $\sigma_t = 38$ MPa (Scale bar = 4.5 mm) (b–c) Maps of the strain components ε_{xx} and ε_{yy} measured for an increase of σ_t from 7.6 MPa to 30 MPa. (d) Strain map of ε_{xx} measured between the stressed state at $\sigma_t = 30$ MPa and the tensile failure at $\sigma_t = 38$ MPa.

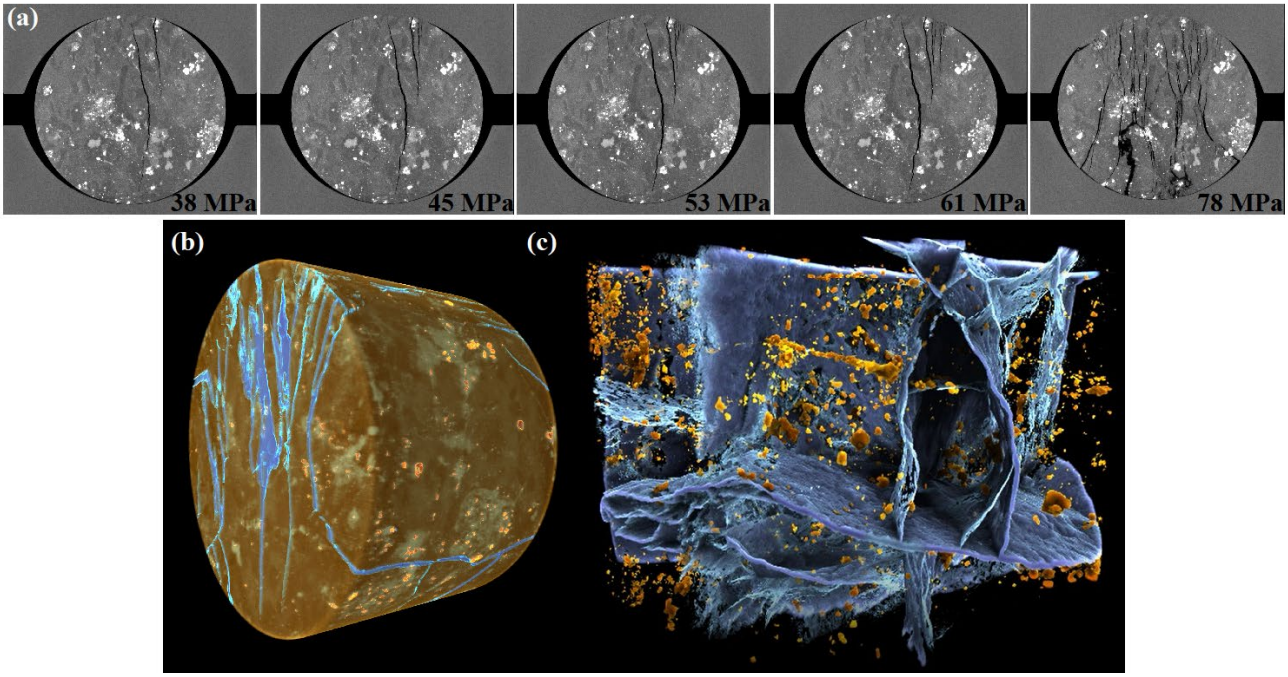

FIG 4 – (a) Midplane tomographic sections showing the ore undergoing successive failure ($\sigma_t = 38$ MPa) and fragmentation ($\sigma_t = 78$ MPa). (b) 3D reconstruction of the fragmented ore (at $\sigma_t = 78$ MPa): fractures (blue) and Cu-rich minerals (orange) are highlighted. (c) 3D visualisation of the fracture network and the Cu-rich grains.

The quantitative analysis of the tomographic images provides valuable information on many aspects of the breakage mechanism that leads to the rock fragmentation. For instance, the deformation field of the copper ore is mapped using digital image correlation technique in Figure 3 (Lenoir *et al*, 2007). Local strain amplitudes as low as 5×10^{-5} are measured using a 500-μm-diam interrogation window on a spatial grid with a mesh size of 50 μm. In Figure 3b and 3c, both tensile and compressive strains are observed on the maps of different components of the strain tensor. The spatial distribution of strain is quite different to that computed for homogeneous model rocks (Li and Wong, 2013); this

difference reflects the complex coupling between the ore heterogeneous structure and the deformation field. The maps in Figure 3b and 3c were computed by comparing a reference image with the image acquired at $\sigma_t = 30$ MPa just before the tensile failure. The axial strain component ε_{yy} shows an interesting structure with alternative compression and dilation bands along the vertical direction. The transverse strain component ε_{xx} shows the presence of tensile strain hot spots in particular in the central region and the region in contact with the top jaws. The locations of these hot spots are correlated with the opening of the three large fractures observed at $\sigma_t = 38$ MPa (shown in Figure 3a). Figure 3d shows a map of the strain component ε_{xx} measured at the tensile failure point when the first three fractures opened. As expected, there is a high tensile deformation at the tips of the different fractures. We also note the interesting interaction between the tips of the two central fractures which produces a region with both high tensile and compressive strains. The map also reveals the spatial distribution of compressive and tensile strain along the fracture contours.

The tomographic sections shown in Figure 4a illustrate the multiple stages that leads to the fragmentation of the ore. The initial large fracture splits the ore diametrically. As stress is further increased, we observe tensile-activated nucleation and growth of multiple fractures producing a complex fracture network. Remarkably the high-pressure apparatus and the PID controller enables us to stabilise the ore sample in a critical mechanical state, in a sense allowing to freeze the fragmentation process. Figure 4b shows a 3D *in situ* visualisation of the ore in its fragmented state. Taking advantage of this digital twin of the fragmented ore, segmentation techniques can be used to visualise the geometry of the fracture network while highlighting the locations of the copper clusters (see Figure 4c).

This microstructural information can be compared to different facets of the mechanical response of the ore to tensile stresses. Figure 5a shows the mechanical work done by the crushing jaws computed as $E_w = \int F\delta l$. A sharp change in the evolution of E_w occurs at $\delta l_t = 56\ \mu$m, marking two different regions. $\delta l = \delta l_t$ marks the onset of fragmentation. For $\delta l < \delta l_t$, E_w can be interpreted as a deformation energy of the ore sample which accounts for elastic and plastic deformations as well as fracture opening beyond the failure point F1. The ore fracturing occurs at $E_w = 0.12$ J and its fragmentation at $E_w = 0.42$ J. Beyond the threshold value δl_t, the ore is yielding and the mechanical response is dominated by the dynamics of the fractures. In this regime, the interpretation of the energy E_w becomes difficult because some large fractures are opening while some other are closing. The closing of a fracture is a highly dissipative process which impacts the ore comminution, this will be discussed below with reference to Figures 6 and 7.

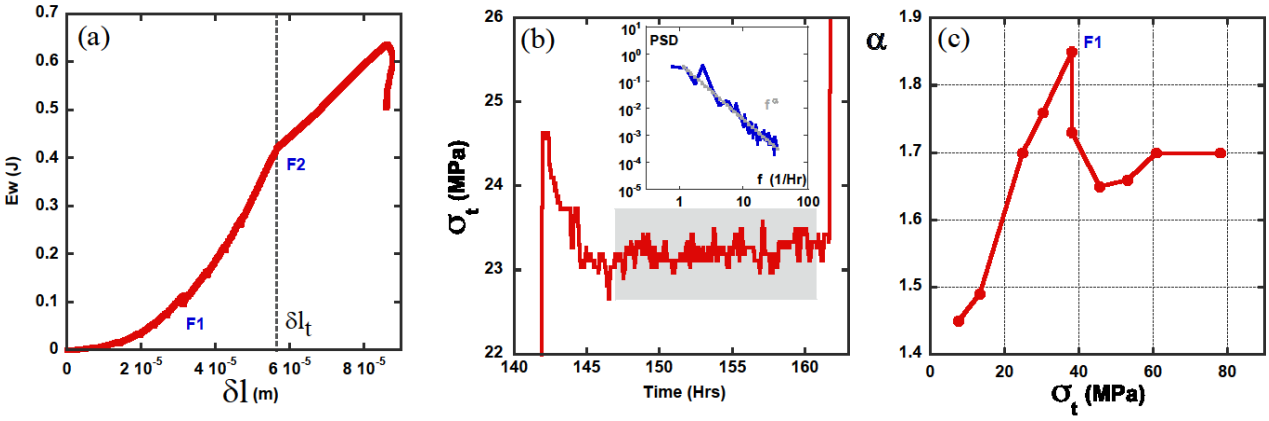

FIG 5 – (a) Mechanical work E_w done by the crushing jaws versus δl the reduction of the gap between the jaws. (b) Temporal fluctuations of the tensile stress measured at fixed strain during an image acquisition. The grey box indicates the time domain over which the spectral analysis is carried out. Inset: Typical frequency power spectrum of the stress fluctuations. The grey line shows the scaling law behaviour f^{α}. (c) Scaling law exponent α measured at various stages of the mechanical test.

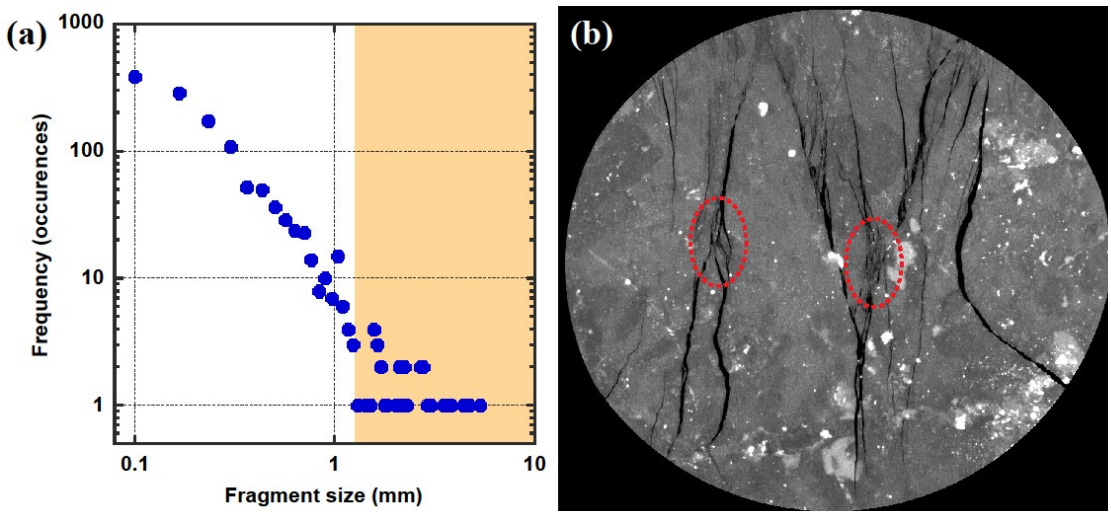

FIG 6 – (a) Fragment size distribution measured after the fragmentation point F2 at $\sigma_t = 78$ MPa. The fragment size l is computed as $l = \sqrt[3]{V}$ where V is the volume of the fragment. The orange area corresponds to the 50 largest fragments for which $l > 2\,m$m. (b) Tomographic section of the fragmented ore; regions of intense comminution are highlighted by red ellipses. In these regions, the closing of large fractures produces high compression and frictional stresses yielding small size fragments.

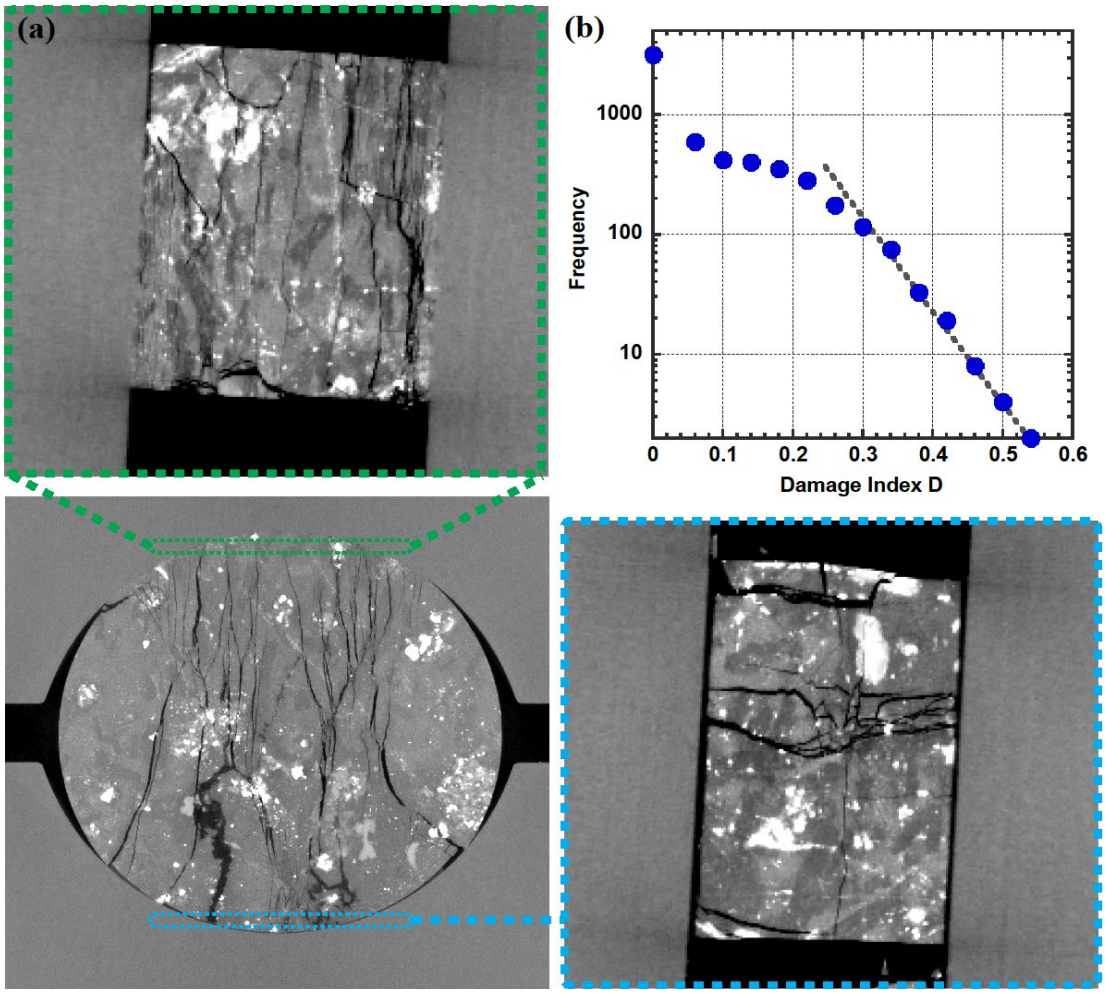

FIG 7 – (a) Vertical and horizontal tomographic sections showing regions of high comminution of the ore. Top and right panels show horizontal tomographic sections close to the contact regions between the rock and the aluminium jaws, where compressive stresses concentration produces a broad range of fragment size. (b) Damage index distribution computed on a 3D spatial grid with a mesh size of 0.5 mm.

The XCT-HP apparatus enables the study of the mechanical relaxation of the ore at different stages of the fragmentation process. The transient response to a change in mechanical deformation is an interesting phenomenon in geomaterials (Jaeger, Cook and Zimmerman, 2007). One typical transient experiment involves deforming a rock and observing the decay in stress over time under a constant strain level. In our experiment, the tensile stress is ramped up to a set value and after a conditioning stage, a tomographic image is acquired at fixed strain ε_t. During the day-long image acquisition, the relaxation of the tensile stress σ_t at fixed ε_t is continuously recorded. Figure 5b shows a typical time trace of σ_t measured over 17 hours. The fluctuations of σ_t are expected to be correlated to microstructural modifications occurring in the ore sample. To identify such correlations, we compute the frequency power spectrum of fluctuations of σ_t at different stages of the mechanical test.

These power spectra present a broad band with a scaling law behaviour where very low frequencies are excited (see inset Figure 5b). Figure 5c shows the measurement of the scaling law exponent α at increasing value of the tensile stress. Before fracture, the exponent α increases with the increase of σ_t, and peaks at the failure point, beyond which the exponent is saturating at a lower value $\alpha = 1.7$. These results suggest that the spectral analysis of the mechanical noise during stress relaxation could be used to predict the proximity to mechanical failure.

Tomographic data also enable precise measurement of two key descriptors of the ore comminution, namely, the fragment size distribution and the damage index. Figure 6a shows the distribution of fragment size as measured at the last stage of the mechanical test. The fragment size l is computed as $l = \sqrt[3]{V}$ where V is the volume of the fragment (note that the voxel size is $9\ \mu$m). Though the crushing of the ore is far from complete (the ore still withstands a tensile stress of $\sigma_t = 78$ MPa), the distribution of fragment size is already quite broad with a mean value at $\bar{l} = 250\ \mu$m. Quantitatively, the 50 largest fragments have a size $l > 2\ mm$ and represent 90 per cent of the ore volume, while the remaining 10 per cent of the ore volume is made of more than 1600 fragments. This large population of small fragments arise from two different breakage mechanisms:

1. As the ore yields beyond the fragmentation point F2, several large fractures are actually closing up and therefore producing high compressive and shear stresses (see regions highlighted by red ellipses in Figure 6b); the rock-rock friction and compression stresses when the two faces of a fracture come into contact produces small fragments with a broad range of sizes.
2. Other regions yielding many small fragments are located at the two rock-jaw contact points. Indeed, the geometry of the loading induces compressive stresses concentration at the contact point, this stress concentration is known to influence the failure process and to induce local damages (Li and Wong, 2013). In these locations, first damages appear after the initial fracture F1. As the loading increases, this process gives rise to a dense local fracture networks whose final state is shown in Figure 7a.

We should emphasise two challenges related to the measurements of the fragment size distribution. First, it relies on an accurate detection of the fracture location, such measurements are inherently dependent on the spatial resolution and the contrast level of the tomographic image. In this experiment, the voxel size was $9\ \mu$m, for future work we plan to use advanced image analysis method based on deep learning to improve the precision of our fracture measurements. Another difficulty is related to the segmentation of the ore image to identify its different fragments. We have used so-called grain partitioning methods which are very efficient in identifying the rounded grains of porous rocks. The application of these methods to fragmented ore is difficult because the ore fragments present a great diversity of size and shape.

To complement this quantitative description of the fragmented ore, we have also measured a damage index D. This descriptor is a popular measure of damage introduced by Kachanov (1958). It is based on a continuum mechanics approach to estimate the degree of damage from 2D sections of rocks. In 2D, the definition of the damage index D is given by $D = A_v/A$ where A is the surface area of the rock section and A_v is the area occupied by the cracks and fractures, also named the void area. In this study, we extend this definition to the 3D case, and compute the damage index as $D = V_v/V$ where V is the volume of the ore and V_v is the volume occupied by the fractures. In a sense, D quantifies the fracture density in the ore. When computed on the totality of the ore sample then $D_t = 0.072$. This descriptor can also be used to analyse the field of damage. To do so, local values

of D were computed on each unit of a 3D spatial grid with a mesh size of 0.5 mm. Figure 7b shows the distribution of the local value of D measured by using this approach. This distribution presents a strong peak at $D = 0$ corresponding to the undamaged parts of the ore. It also reveals a high probability of observing a damage index in the range $0.1 < D < 0.2$ that is associated with the fine cracks and the region of high comminution (such as those highlighted by red ellipses in Figure 6b). Finally, the distribution shows an exponential tail for large values of D that is related to the many fractures that are wide open.

A better characterisation of the coupling of the breakage statistics (fragments size distribution, local damage index D) with texture breakage and critical mineral liberation is key to improving current fragmentation models. In the recent study by Zhang and co-workers (Zhang *et al,* 2022), we have described a workflow integrating simultaneous 3D mapping of fracture locations and of the dominant mineral phases in an ore sample. Figure 8a shows such a texture map of the fragmented ore at $\sigma_t = 78$ MPa. This map has been computed by combining SEM_EDS data with the X-ray attenuation values of the tomogram. The ore texture is coarse-grained to present the dominant mineral phases only. Quantitatively the ore is made of: $67.2\ per\ cent$ of Alkali feldspar, $24.4\ per\ cent$ Plagioclase and $7.1\ per\ cent$ Epidote (expressed in volume fraction). Moreover, in our ore sample, there is $1.3\ per\ cent$ of copper sulfides (bornite and chalcopyrite). We emphasize that such estimations are not trivial, because it relies on the use of many experimental techniques, each bringing its own challenges as discussed in (Zhang *et al,* 2022). The fracturing of each phase can be clearly identified and quantified as the creation of new surface area compared to the unfractured state. In the fragmented state at $\sigma_t = 78$ MPa, $56\ per\ cent$ of the new surface area was produced in the feldspar phase, $39\ per\ cent$ in the plagioclase, $4.3\ per\ cent$ in the epidote and $0.7\ per\ cent$ in the copper.

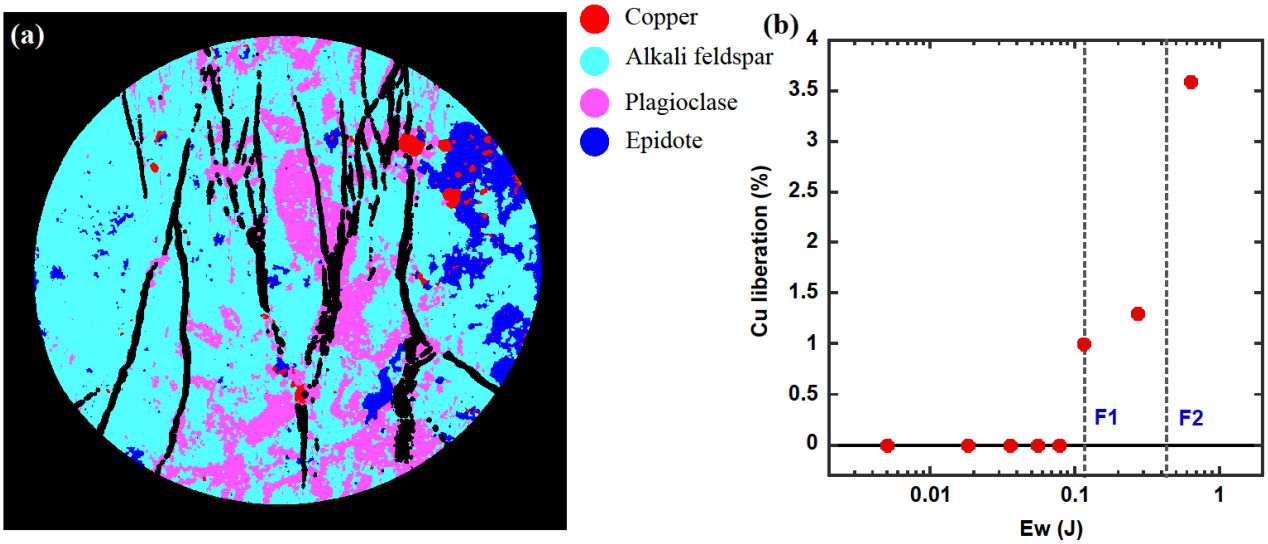

FIG 8 – (a) Texture map of the fragmented ore at $\sigma_t = 78$ MPa. The texture map has been computed by combining SEM_EDS data with X-ray attenuation values of the tomogram. In this section of the 3D map, the coarse-grained ore texture presents four main phases (Alkali feldspar, Plagioclase, Epidote and Copper sulfides), the fracture location is coloured in black. (b) Evolution of the Copper liberation versus the deformation energy.

The degree of liberation of copper (the proportion of copper exposed by fracturing) is shown in Figure 8b as a function of the deformation energy E_w. Two regimes of liberation are observed: after the rock fracturing (event F1), approximately $1\ per\ cent$ of the copper sulfides is freed from the gangue and this fraction increases weakly until the rock is fragmented (event F2). In the final fragmented state, the copper liberation increases substantially to $3.6\ per\ cent$. This evolution is consistent with three main features of the ore texture and breakage behaviour:

1. The copper sulfides grains are mainly embedded in the epidote and feldspar phases (with the highest contact preference with the epidote).
2. The plagioclase and feldspar are the most damaged phases during the fracturing and subsequent fragmentation.

3. The epidote is only substantially damaged beyond the onset of fragmentation.

The latter process explains the increase in the liberation of copper sulfides observed beyond the event F2. In this experiment, we only investigated the onset of ore fragmentation which explains the relatively low ($< 5\ per\ cent$) degree of liberation of the copper grains. Ongoing work focuses on measuring copper liberation at more advanced stages of the fragmentation process.

CONCLUSIONS

In summary, this experiment tackles a tensile-activated rock fracturing which triggers a substantial fragmentation of a porphyry copper ore. The results presented here show how high-resolution X-ray micro-CT has the potential to link breakage fundamentals and ore texture features such that this combined information may assist in the design of optimal processes for critical mineral liberation (Tavares, 2021; McKinnon and Ferguson, 2018; Ord, Blenkinsop and Hobbs, 2022).

This study shed light on the potential of *in situ* mechanical testing for empirical modelling of comminution processes as used in the mining industry. *In situ* data enable simultaneous quantification of mineral liberation, mechanical energy dissipation, fragment size distribution and of the coupling of local fracturing with the ore texture. Such data are needed to inform the modelling of optimal liberation (resource efficiency) at minimal overgrinding (energy efficiency).

In terms of rock mechanics, this example of an *in situ* fragmentation test, based on a simple loading configuration, opens up interesting opportunities to model in the laboratory complex breakage mechanisms. In this study, the focus was on comminution based on rock-rock friction induced by fracture closing and on fragment production at rock-metal compression contacts.

Ongoing work includes *in situ* investigation of more advanced stages of the fragmentation process with a focus on the relation between fragment size distribution and mineral liberation.

ACKNOWLEDGEMENTS

This work was supported by the Australian Research Council Training Centre M3D (ARC IC180100008).

REFERENCES

Ando, E, Viggiani, G, Hall, S A and Desrues, J, 2013. Experimental micromechanics of granular media studied by X-ray tomography: recent results and challenges, *Geotechnique Letters*, 3, 142–146.

Cnudde, V and Boone, M N, 2013. High-resolution X-ray computed tomography in geosciences: A review of the current technology and applications, *Earth Science reviews*, 123, 1–17.

Francois, N, Cruikshank, R, Herring, A, Kingston, A, Webster, S, Knackstedt, M and Saadatfar, M, 2022. A versatile microtomography system to study in-situ the failure and fragmentation in geomaterials. Accepted in *Review of Scientific Instruments*.

Ghamgosar, M, Erarslan, N and Williams, D J, 2016. Experimental investigation of fracture process zone in rocks damaged under cyclic loadings, *Experimental Mechanics*, 57, 97–113.

Gueguen, Y and Bouteca, M, 2004. *Mechanics of Fluid-Saturated Rocks*, Elsevier Academic Press, 2004.

Hurley, R C, Hall, S A, Andrade, J E and Wright, J, 2016. Quantifying interparticle forces and heterogeneity in 3D granular materials, *Phys. Rev. Lett.,* 117, 098005.

Jaeger, J C, Cook, N C W and Zimmerman, R W, 2007. *Fundamentals of Rock Mechanics*, Wiley-Blackwell publishing.

Jiang, S, Shen, L, Guillard, F and Einav, I, 2021. Characterisation of fracture evolution of a single cemented brittle grain using in-situ X-ray computed tomography, *International Journal of Rock Mechanics and Mining Sciences*, 145, 104835.

Kachanov, L M, 1958. Time of the rupture process under creep conditions, *IVZ Akad. Nauk, S.S.R. Otd Tech Nauk*., 8, pp 26–33.

Lenoir, N, Bornert, M, Desrues, J, Bésuelle, P and Viggiani, G, 2007. Volumetric digital image correlation applied to X-ray microtomography images from triaxial compression tests on argillaceous rock, *Strain*, 43, 193–205.

Li, D and Wong, L N Y, 2013. The Brazilian disc test for rock mechanics applications: review and new insights, *Rock Mech. Rock Eng.,* 46, 269–287.

Lickfold, V, Cooke, D R, Smith, S G and Ullrich, T D, 2003. Endeavour copper-gold porphyry deposits, Northparkes, New South Wales: Intrusive history and fluid evolution. *Economic Geology*, 98(8):1607–1636.

McKinnon, S D and Ferguson, G A, 2018. The role of research in cave mining, in Y Potvin and J Jakubec (eds), *Caving 2018: Proceedings of the Fourth International Symposium on Block and Sublevel Caving*, Australian Centre for Geomechanics, Perth, pp 499–510.

Noiriel, C, 2015. Resolving time-dependent evolution of pore-scale structure, permeability and reactivity using X-ray microtomography, *Reviews in Mineralogy and Geochemistry*, 80, 247–285.

Ord, A, Blenkinsop, T and Hobbs, B, 2022. Fragment size distributions in brittle deformed rocks, *Journal of Structural Geology*, 154, 104496.

Pacey, A, Wilkinson, J J, Owens, J, Priest, D, Cooke, D R and Millar, I L, 2019. The anatomy of an alkalic porphyry Cu-Au system: Geology and alteration at Northparkes mines, New South Wales, Australia. *Economic Geology*, 114(3): p. 441–472.

Parapari, P S, Parian, M, Forsberg, F and Rosenkranz, J, 2020. Characterization of ore texture crack formation and liberation by quantitative analyses of spatial deformation, *Minerals Engineering*, 157, 106577.

Saadatfar, M, Francois, N, Arad, A, Madadi, M, Cruikshank, R, Alizadeh, M, Sheppard, A, Kingston, A, Limay, A, Senden, T and Knackstedt, M, 2012. 3D mapping of deformation in an unconsolidated sand: A micro mechanical study, SEG Technical Program Expanded Abstracts, 1–6.

Sheppard, A, Latham, S, Middleton, J, Kingston, A, Myers, G, Varslot, T, Fodgen, A, Sawkins, T, Cruikshank, R, Saadatfar, M, Francois, N, Arns, C and Senden, T, 2014. Techniques in helical scanning, dynamics imaging and image segmentation for improved quantitative analysis with X-ray micro-CT, *Nuclear Instruments and Methods in Physics Research B*, 324, 49–56.

Tavares, L M, 2021. Editorial for Special Issue ‘Comminution in the Minerals Industry’, *Minerals*, 11, 445.

Viggiani, G, Ando, E, Takano, D and Santamarina, J C, 2015. Laboratory X-ray tomography: a valuable experimental tool for revealing processes in soils, *Geotechnical Testing Journal*, 38, 61–71.

Zhang, Y, Francois, N, Henley, R W, Knuefing L, Turner, M, Saadatfar, M, Brink, F, Knackstedt, M, 2022. A case study on the breakage behaviour of a porphyry copper ore sample using in-situ X-ray micro-CT and textural analysis, submitted.

Multicomponent modelling of ore blending in grinding circuits – a new model and case study

J J Hanhiniemi[1,2] and M S Powell[3]

1. MAusIMM, PhD Candidate, University of Queensland, SMI-JKMRC, Brisbane Qld 4068. Email: jeremy.hanhiniemi@uqconnect.edu.au
2. Head of Engineering, Weir Minerals, Artarmon NSW 2064. Email: jeremy.hanhiniemi@mail.weir
3. FAusIMM, Emeritus Professor, University of Queensland, SMI-JKMRC, Brisbane Qld 4068. Email: malcolm.powell@uq.edu.au

ABSTRACT

A 'Variable Blend and Rates' model is developed for SAG mills which extends upon the JKSimMet® Variable Rates Model. Similarly, a 'Variable Blend Residence Constrained Perfect Mixing' Ball Mill model is also introduced, also extending upon the existing JKSimMet® model. These models are used in conjunction with JKSimMet® while employing external technical programs. The technical model is then used to inform an economic model described elsewhere in Hanhiniemi and Powell (2022), which calculate operating and unit costs based on operating conditions, design, and ore characterisation.

The SAG and ball mill models include constraints beyond those in the JKSimMet® models. The SAG model constraints include Size Specific Energy (SSE) verification, charge weight limit, and assessment of the impact of media to ore composition in the charge using the SAG Charge SSE Model developed in this paper. The ball mill model includes residence time, volumetric capacity, and SSE verification constraints.

These models are applied to Cortez Gold Mine in the processing of two very different ore types and their blends; 'Horse Canyon' which is softer in coarser sizes and competent is fine sizes, and 'Wenban' which is competent at coarser sizes but softer in fine sizes than Horse Canyon. Horse Canyon also has a finer run-of-mine size distribution then Wenban. The application of the model at this site included undertaking five surveys at varying blends.

The behaviours of the blends and individual components is then studied in the SABC circuit. A non-linearity is observed with throughputs increasing with blending. The newly developed modelling approach captures these responses. Controlled blending based on ore competence-by-size and size distribution was implemented by the site, which then realised significant improvements in throughput without any capital cost (Ntiamoah *et al*, 2020).

The modelling developed in this paper is then compared to existing practice, and the new method was found to provide improved fidelity and utility. A three-dimensional surface is then developed using the model describing the SAG mill throughput capacity at varying conditions (speed-filling) versus varying blend. The change in throughput as a function of only the changing charge composition is presented. The result is nonlinear, and explanations are provided to describe this behaviour.

INTRODUCTION

Tumbling mills consume a significant portion of a concentrators operating expenditure, are capital intensive, and therefore often a bottleneck meriting careful attention. The performance of grinding circuits is also often impacted by processing differing blends of ore components with different physical properties and ROM size distributions, and this can result in throughput fluctuation, changing required transfer sizes between mills and variability in appropriate operating conditions (Mitchell and Holowachuk, 1996; Mkurazhizha, 2018; Bueno *et al*, 2011). Blending of components can thus have an important impact on financial performance. Controlled blending based on ore characteristics, competence-by-size, and feed size distribution in these cases offers the opportunity to increase overall throughput, reduce media and liner consumption, and balance utilisation across grinding stages (Powell *et al*, 2018; Ntiamoah *et al*, 2020). These blend effects are little understood and can be nonlinear with blend proportion. Existing technical modelling is not capable of simulating these effects.

A further issue with existing modelling is that of constraints and bottleneck identification. The JKSimMet® SAG and ball mill models are somewhat unconstrained with respect to comminution energy efficiency. The ball mill model is also unconstrained with respect to volumetric flow capacity and residence time and can produce results that are infeasible, as overfilling would have occurred in practice. Finally, the existing modelling does not include consumable models such as media and liner wear and life, and their response with operating, design, and ore characterisation.

This paper presents a multicomponent model of ore blending for Tumbling Mills and provides a Case Study detailing its application. The model first uses and expands upon the existing and well proven JKSimMet® models which are described in literature (Napier-Munn *et al*, 1996; Grimes and Keenan, 2015). It also incorporates energy, and volumetric/residence time constraints in the ball mill. Finally, it incorporates mechanistic consumable models and an overall operating and unit cost result. This grinding circuit model is one part of a wider comminution techno-economic model described in Hanhiniemi and Powell (2022).

OVERALL MODELLING STRUCTURE

The overall modelling structure is illustrated in Figure 1. Multiple JKSimMet® flow sheets, one per blend increment, form the basis of the model which employs the Variable Rates AG/SAG model and the Perfect Mixing Ball Mill models. Within each of these flow sheets the blends feed portion of each component is set using multiple feeders and splitters to achieve the combined feed particle size distribution of the blend, as each component has a different feed size distribution based on upstream conditions such as selective blasting, rock quality differences, etc.

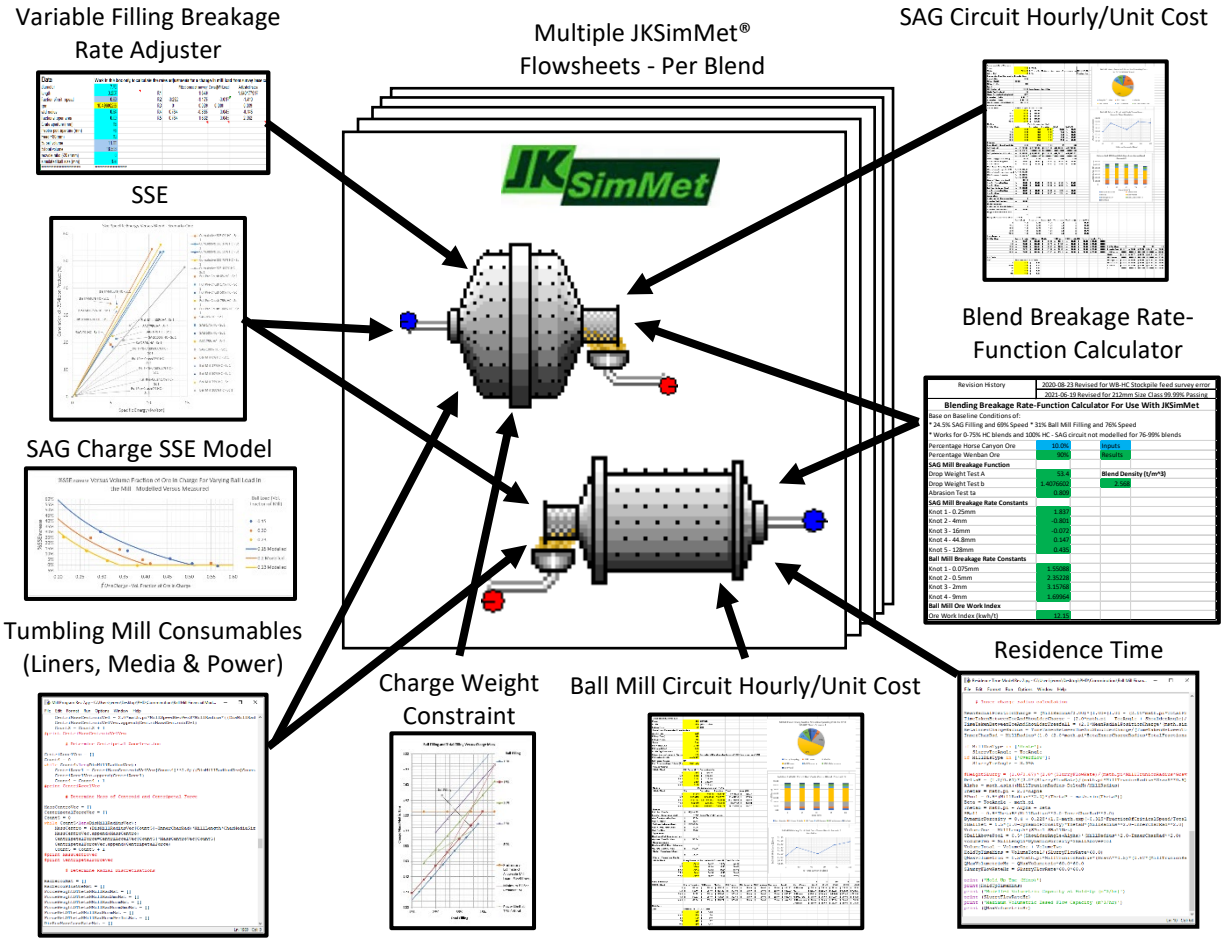

FIG 1 – Technical architecture.

Variable filling functionality for the SAG mill is achieved using Morrell (2001) by iteratively running JKSimMet® with the external 'Variable Filling Breakage Rate Adjuster' to determine adjusted breakage rates, until the filling in both closely agree. Only filling adjustments are made in this external calculation, and speed adjustments are made in JKSimMet®.

A 'Blend Breakage Rate-Function Calculator' model was developed and incorporated to provide the Breakage Rate response in the SAG and ball mills, including for blends of two components. It also provides a response to blend for the Breakage Function for the SAG mill, and the Bond Work Index in the ball mill, as well as providing the blends density, and is used in conjunction with JKSimMet®.

For ball milling, a constraint on the residence time is also applied based on the work of Shi (2016). This restricts unrealistic simulations where overfilling would be occurring. Further a basic volumetric flow constrain is also incorporated to ensure the volumetric capacity can be achieve in overflow ball mills. For the SAG mill, a charge weight constraint is applied based on total and media filling.

Size Specific Energy (SSE) calculations are performed across the circuit and Unit Processes to validate scenarios. This is done by measuring the percentage change in SSE from surveyed baseline for that blend, which is then interrogated against other measured changes in SSE in the literature. A SAG Charge SSE Model is also developed and applied to provide insight into the expected change in SSE with charge composition, as it is known that when media filling becomes the predominant volume fraction of the charge, there is a drop in SSE performance.

A Tumbling Mill model was also developed to capture consumable rates. In this media and lifter-liner life and consumption is modelled mechanistically, as described in Hanhiniemi and Powell (2019). Finally, integrated with all these technical models is an Operating and Unit Cost model for both SAG and ball mill circuit Unit Processes. The remainder of this paper will describe each of these elements in further detail (excluding consumables modelling, and operating and Unit Cost calculation for brevity) before describing their calibration and application in a Case Study.

BLEND BREAKAGE RATE-FUNCTION CALCULATOR

The various elements of the Breakage Rate-Function Calculator are now described.

Breakage function for blending

As described in Napier-Munn *et al* (1996) the breakage modelling for the SAG mill within JKSimMet® relies on the specific comminution energy (Ecs)-breakage index (t_{10}) relationship, which is fit to the following function from laboratory test data thus determining A and b constants for the ore type being treated:

$$t_{10} = A\left[1 - e^{(-b \times Ecs)}\right] \tag{1}$$

It is necessary to develop an approach to model the breakage characteristics *A* and *b* for any blend of the two ore types. The *A* value of this function is the asymptote, and this asymptote is typically fairly constant between most hard rock ores at approximately 50 (Napier-Munn *et al*, 1996) and pertains to high specific energy conditions which generally do not occur in horizontal tumbling mills. The *b* value is sensitive to ore competence differences and is sensitive in the range of specific comminution energies experienced in tumbling mills. Based on these observations above the *A* value can be set to the average of the any two ore types provided the measured values are not too dissimilar. A corrected *b* value, b_C, for each of the ore types was then determined by ensuring the as tested original *Axb* product of each ore type remained the same with the use of the averaged *A* value. The average *A* would be the mass weighted average of the ore blend:

$$A = \%w_{Ore\,1} \times A_{Ore\,1} + \%w_{Ore\,2} \times A_{Ore\,2} \tag{2}$$

$$b_{c_{Ore\,1}} = \frac{Axb_{Ore\,1}}{A} \tag{3}$$

$$b_{c_{Ore\,2}} = \frac{Axb_{Ore\,2}}{A} \tag{4}$$

Having established an averaged *A* for all blends, and two corresponding b_C values for pure blends of each ore, some means of adjusting the *b* value for varying blends was needed. As described by Bueno (2013) a weighted arithmetic average of these *Axb* values based on the respective mass portion in the blend is not believed to be representative of the breakage behaviour in mills for the blended mill contents. Instead, the inverse of the *Axb* for each ore was taken, *C*, and the weighted arithmetic average was taken on that based on the blend proportion. The resulting inversed *Axb* for

the blend was then inversed back to an *Axb* product. Finally, this allowed the determination of the *b* value for the blend by dividing the *Axb* product by the averaged *A* value. This is shown mathematically below.

$$C_{Ore\,1} = \frac{1}{Axb_{Ore\,1}};\ C_{Ore\,2} = \frac{1}{Axb_{Ore\,2}} \tag{5}$$

$$C_{Blend} = \%w_{Ore\,1} \times C_{Ore\,1} + \%w_{Ore\,2} \times C_{Ore\,2} \tag{6}$$

$$b_{Blend} = \frac{1}{AC_{Blend}} \tag{7}$$

Thus, the blends *Axb* has been established as a function of individual component Drop Weight Test results and the mass proportion of the blend and this was imbedded in the calculator. When the user enters the blend mass-proportion, the calculator returns the blends Breakage Function.

Blend breakage rates

To model the response in the SAG/AG and Ball Mills breakage rates with blend, multiple surveys of controlled blends were undertaken. The breakage rates were then model fitted for each blend at consistent knot sizes. As each of these surveys occur at different speeds and fillings in SAG/AG cases, adjustment had to be made to achieve a consistent filling and speed. Filling adjustment of the breakage rates was achieved using the Morrell (2001) model. Adjustments for speed were made using the Variable Rates model. The result was a model fitted set of breakage rates at consistent filling and speed, called the 'Adjusted Survey Simulation'.

A set of Bessel Spline functions were then fitted between the knot sizes versus blend fraction for this Adjusted Survey Simulation to predict their response between surveyed blends. This set of breakage rates versus blend data sets for both the SAG mill and Ball Mill were imbedded in the 'Blend Breakage Rates-Function Calculator' and used with the JKSimMet® modelling. When the user enters the blend mass-proportion, the calculator returns the breakage rates for SAG and Ball Mill knot sizes.

To remove the effect of the transport function in this breakage rate blend model, the SAG/AG discharge model was model fitted to consistent values across the blends surveyed and the simplifying assumption made that the discharge model did not vary with blend.

Other ore characterisation

The blended ore abrasion parameter is also needed. This was determined based on a weighted arithmetic mean value based on the proportion of ore mass in the blend. For Ball Milling the blended ore Bond Work index is needed. Similarly, this was estimated to also be the weighted arithmetic mean value based on the proportion by mass in the blend.

VARIABLE FILLING CALCULATOR

SAG mill breakage rates in the models above vary with mill filling. Once these rates are fitted to one filling condition, the change in these breakage rates with different fillings can be estimated using an external calculation to JKSimMet®. The modelling behind this external calculation has been developed and validated by Morrell (2001) and was employed in this work.

BALL MILL RESIDENCE TIME

The Ball Mill modelling in JKSimMet® is not constrained with respect to residence time or flow constraints (Shi, 2016). Shi states power modelling cannot offer an effective constraint as the power consumed is little effected by overfilling conditions in overflow Ball Mills. To address this a limit was determined on minimum residence time necessary to indicate effective Ball Mill operation. The method developed by Shi was adopted in this work. This calculates the residence time of slurry in the mill, and sets a minimum time of 2 minutes for mill with internal diameter below 5.9 m and 1 minute for mills larger than 5.9 m, based on industrial data sets. Below these residence times the risk of overfilling is deemed heightened. In this work this approach was coded in Python® and applied as a constraint over the modelling.

An absolute limit on volumetric flow out of the mill was also established based on the relation from (Morrell, 2016) derived from Bernoulli's equation, and is based on the allowable vertical height between the inlet invert and the discharge trunnion invert ($\Delta h_{Inverts}$), and the trunnion radius R_t, as follows:

$$Q_{Max_{Flow}} = 0.5\pi R_t g^{0.5}(0.67\Delta h_{Inverts})^{1.5} \quad (8)$$

SIZE SPECIFIC ENERGY

SAG milling

Figure 2 shows the result of laboratory scale testing of SSE and its relationship with volumetric fraction of media in the charge, and the mills volumetric filling of media after Powell *et al* (2015). Once a certain fraction is reached inefficiency begins to set in. This is thought to be due to the increase in media-on-media energy loss.

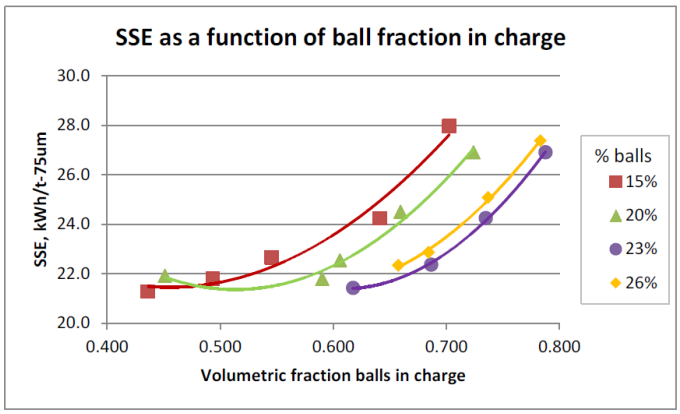

Figure 5 - SSE_{75} as a function of fraction of balls in the charge for different ball fillings

FIG 2 – Laboratory SSE versus volumetric fraction of media in the charge after Powell *et al* (2015).

A generalised function for this behaviour was sought so that any differences in SSE between simulations and measured results with different media and ore fillings could be compared for reasonableness. It was assumed that the results provided could be generalised across varying feed distributions, speeds and other conditions. The bounding case for this general function was that there would be zero increase in a baseline SSE due to high media composition in the case of AG milling, and conversely as the mill empties entirely of ore the inefficiency would rapidly rise to a vertical asymptote at no filling. The basic functional form that meets these bounds which was first employed is in Equation 9.

$$\%Increase_{SSE-75\mu m} = \frac{1}{f_{Ore_{Charge}}} - 1 \; for \; f_{Ore_{Charge}} < 1 \quad (9)$$

The *x* axis of Figure 2 was changed to present the fraction of ore in the charge $f_{Ore_{Charge}}$, and the vertical axis values were divided by the SSE at which all the cases appeared to asymptote at low media fraction in the charge, estimated to be 21.5 kWh/t -75 µm for this ore. This resulted in the vertical axis representing the percentage increase in SSE due to the media in the charge, $\%Increase_{SSE-75\mu m}$. It was assumed that having divided by this value, the resulting relative increase could be generally applied across other ores with varying competence.

The strength of the response in SSE increase versus the reduction in ore charge is varied by introducing a new calibration term, γ, which does not impact the $\%Increase_{SSE-75\mu m}$ intercept at 0 per cent with no media. It was further observed that the onset of this inefficiency does not appear immediately with media addition, but only when a certain threshold is reached. To account for this the relation above was modified to include an offset term, α, which is the fraction of ore in the charge when the inefficiency begins to manifest. This offset, α, appears to be a function of Ball Load in the mill. The data from Figure 2 was replotted using this new plane and equation and the data was fitted

to it. Each α was then estimated and plotted against each Ball Load expressed as a fraction of the total mill volume, $f_{Ball_{Mill}}$, and was found to fit the linear function below. Unfortunately, there is a coupling between the α and the γ terms, so γ was fitted individually. Once complete no relation of γ versus $f_{Ball_{Mill}}$ was obvious and fitted values ranged between 0.45–0.55 with an average of circa 0.5, therefore γ was set to 0.5. Therefore, the final relation is as follows:

$$\%Increase_{SSE-75\mu m} = \begin{cases} \frac{\alpha^{\gamma}}{f_{Ore_{Charge}}^{\gamma}} - 1, for\ f_{Ore_{Charge}} < \alpha \\ 0, f_{Ore_{Charge}} \geq \alpha \end{cases} \quad (10)$$

$$With: \alpha = -2.07 f_{Ball_{Mill}} + 0.82\ for\ 0.15 < f_{Ball_{Mill}} < 0.23\ and\ \gamma = 0.5 \quad (11)$$

The resulting generalised model and the measured results transposed from Figure 2 are illustrated in Figure 3. As the 26 per cent media filling was very high this was excluded. The model describes the behaviour of increasing inefficiency with low ore fraction in the charge, its onset, and its change with media filling, and fits 15 per cent and 23 per cent media well, with some inaccuracy at 20 per cent.

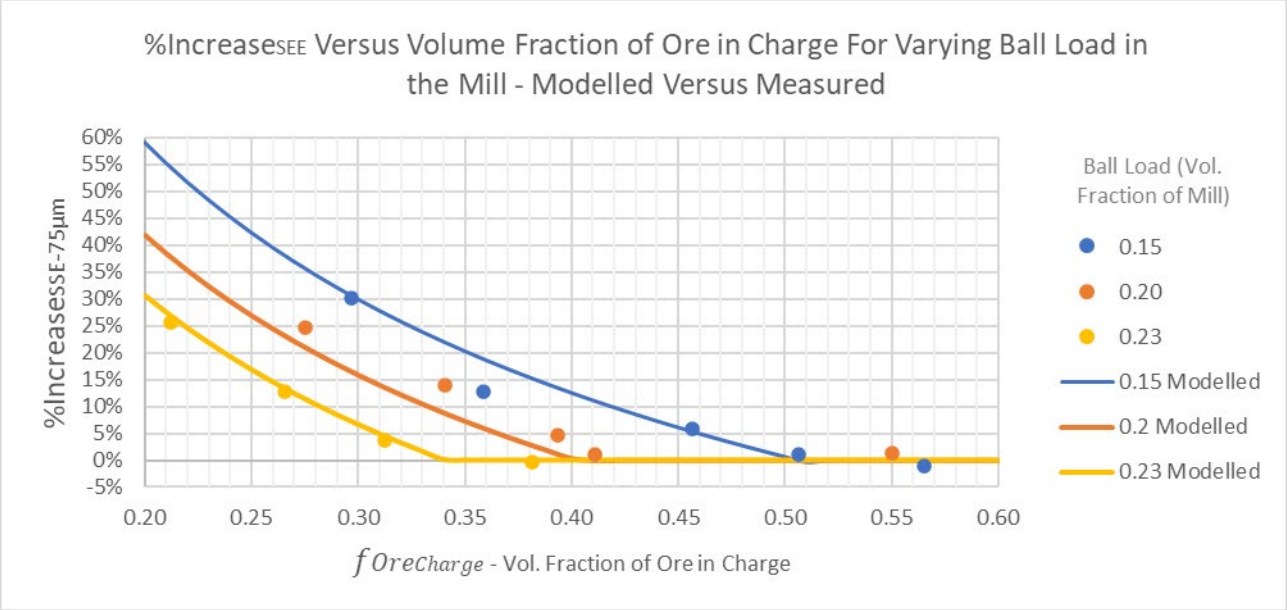

FIG 3 – Change in SAG SSE with charge composition.

In summary, the model developed above can be used as a guide to the differences in SSE between simulations and measured results with different media and ore fillings, and support evaluation of the reasonableness of simulated results. The data set employed is small and based on laboratory testing, however it is not used for predictive purposes, and supports the checking and validation of simulations.

CASE STUDY – CORTEZ MINE

Having described the modelling, it is now applied to a case study – Cortez Gold Mine. It is an open cut gold mine with an SABC circuit followed by CIP leaching. Two major ore components are mined together in the active pits – Horse Canyon and Wenban. Horse Canyon has an *Axb* 83.5 and a Bond Work Index (BWI) of 17.1 kW/t. Wenban has an *Axb* 74.3 and a BWI of 11.6 kW/t. Horse Canyon has a finer ROM distribution than Wenban, is softer in the larger size fractions, but harder in the finer fractions. This is illustrated by the lower *Axb* for Wenban indicating higher competence, with the Horse Canyon then having a markedly higher BWI. The site implemented controlled blending of these ores and increased overall throughput without any capital expenditure (Ntiamoah *et al*, 2020).

Two full surveys were taken of the circuit for Wenban and Horse Canyon including crash stop and grind out with surveyed streams shown in the top left figure by the stars. Three further snapshot surveys were taken of controlled blends of the two components. These five surveys were 0 per cent,

17 per cent, 50 per cent, 75 per cent and 100 per cent Horse Canyon. These were mass balanced, and model fitted and achieved convergence and were very successful.

SAG mill modelling

For SAG mill calibration breakage rates were fitted to the five blends. These surveyed were at different speeds and fillings however, and were thus converted back to a constant SAG filling and speed using the external Variable Filling Breakage Rate Adjuster and JKSimMet®. Similarly, the discharge function was fitted consistently across all blends. The blends breakage function was set by blend based on the approach previously described. The results were a set of breakage rates whose response is isolated from other considerations outside the blend composition. This condition is called the Adjusted Survey Simulation. The results are shown in Figure 4 at each knot versus blend and are relatively smooth.

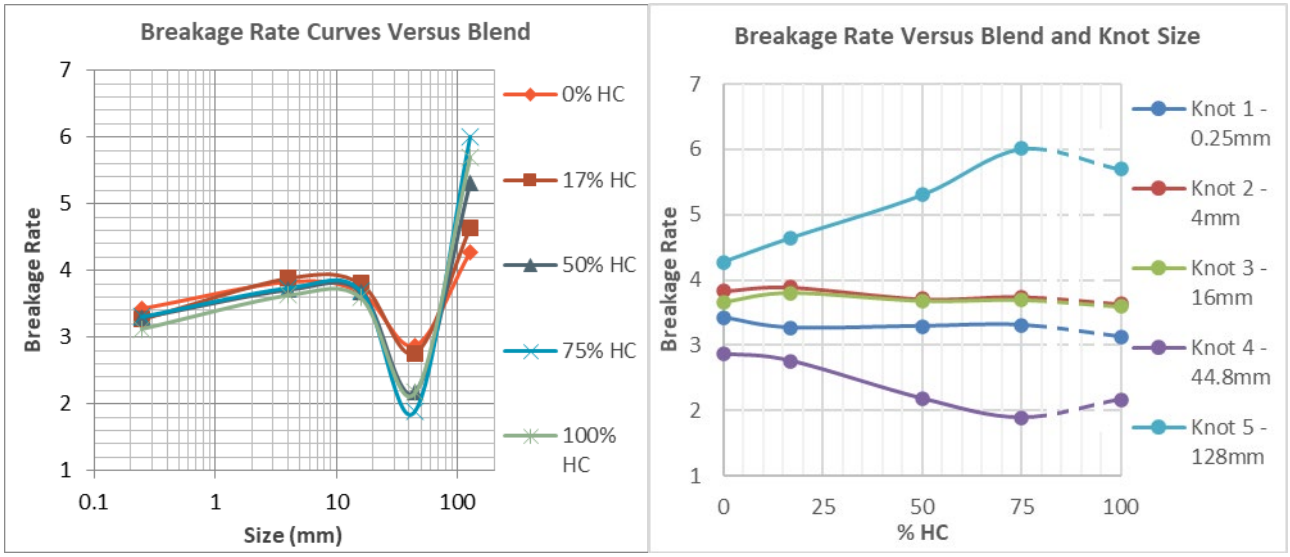

FIG 4 – SAG mill breakage rates versus size and blend – 24.5 per cent mill filling and 69 per cent speed.

To create the Blend Breakage Rate and Function Calculator, a spline was fitted to each of the corresponding rate constants for the baseline SAG filling and speed for any blend, as shown in Figure 5. A new regime (poor filling) was entered beyond 75 per cent HC – and transition from 75–100 per cent was not included in the spline as this transition may not be well modelled. The resulting spline function was added to the Blend Breakage Rate and Function Calculator.

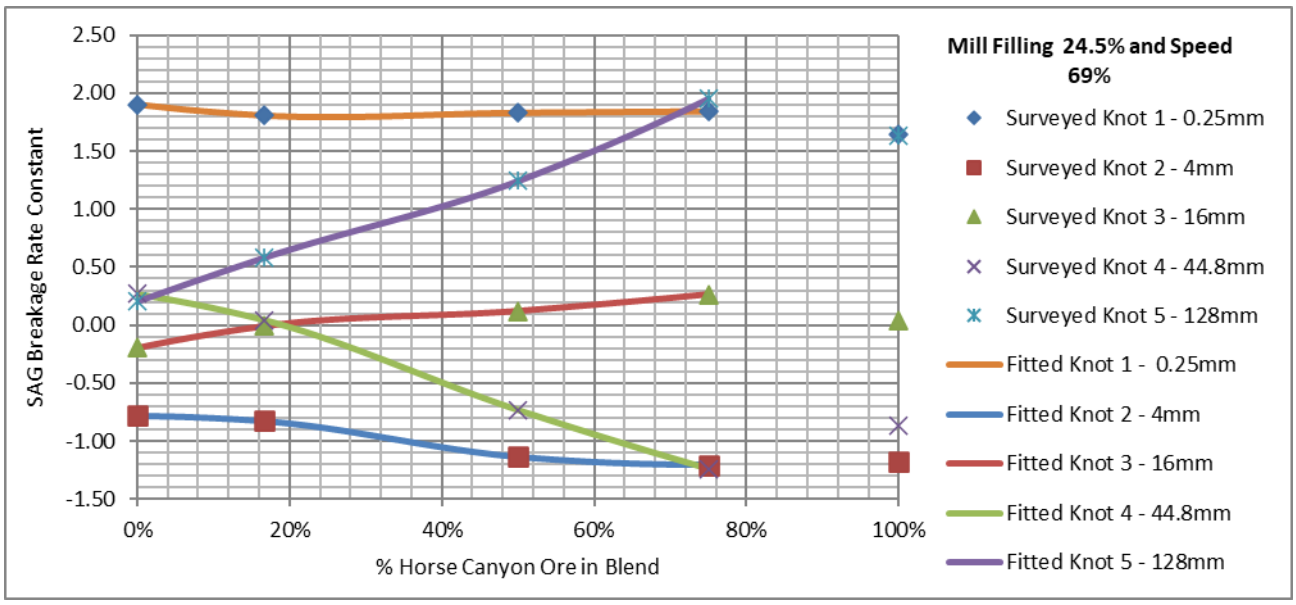

FIG 5 – SAG mill breakage rate constants versus knot size and blend.

The SSE was calculated for the SAG mill circuit for each blend and appears in Figure 14, baseline ('BL'). This was then used to evaluate the reasonableness of an example upgrade scenario below.

Ball mill modelling

A similar process as in the SAG was conducted for the Ball Mill. The five surveys were model fitted and the breakage rate curves versus blend are shown in Figure 6. The Ball Mill is simpler as surveyed filling and speed were consistent so no adjustment to consistent conditions was required. A spline was fitted to each of the corresponding breakage rate knot sizes versus blend, also shown in Figure 6, and this was employed in the Blend Breakage Rate and Function Calculator. BWI was also included and determined by the mass weighted average of the components. The resulting Blend Breakage Rate and Function Calculator interface is shown on the right in Figure 1.

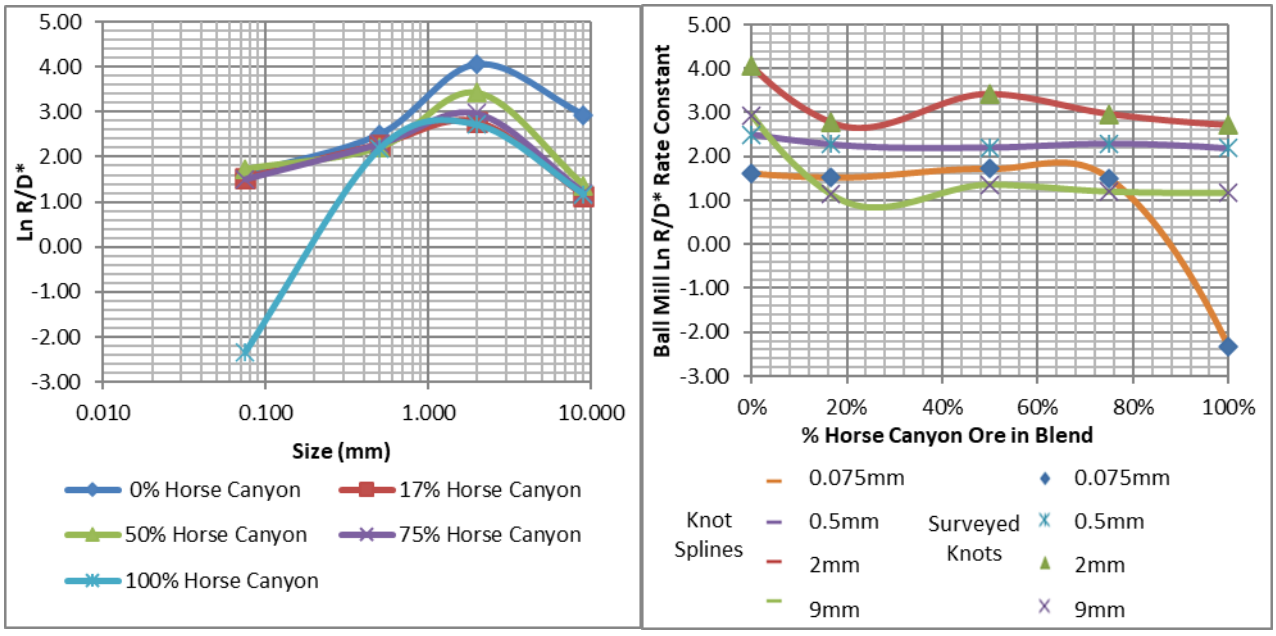

FIG 6 – Model fitted and spline ball mill breakage rates versus size and blend – 31 per cent filling and 76 per cent speed.

The maximum volumetric capacity of the ball mill was calculated. The ball mill is an overflow type, 8.66 m long, operates at 76 per cent speed, and has a filling of 31 per cent. Its trunnion diameter is 1.43 m and cone end length was estimated at 0.67 m. Its diameter is 4.67 m which is below 5.9 m,

therefore the minimum volumetric residence time is 2 minutes. The volumetric flow rate of this mill at this residence time was calculated at 1650 m^3/hr. All surveys were measured below this, and scenarios analysis was constrained below this limit.

Again, the SSE was calculated for the ball mill circuit also for each blend and appears in Figure 14, baseline ('BL'). This was again used to evaluate the reasonableness of an example upgrade scenario below.

DISCUSSION

Having introduces the modelling methodology, and then applied and calibrated it to the Cortez case study, we will now further explore the modelling capability. Comparisons to existing practice for modelling blending will be undertaken, and the modelling will be applied to evaluate an example upgrade scenario.

For the SAG mill the baseline model was then run for 11 blends and the resulting throughput is shown on the left in blue in Figure 9. Despite a constant SAG mill operating condition (filling and speed), and consistent discharge function, the throughput varies significantly based on the blend or ore. This figure is illustrating the effect of ore blend composition and characteristics in the mill in isolation. This result is thought to be explained by SAG composition as follows. In pure Horse Canyon there is a lack of adequate competent larger size material, and thus autogenous breakage is not promoted. With a small amount of Wenban ore added, a competent charge is established which promotes a higher frequency of autogenous breakage and attrition by having sufficiently large material available to act as media with sufficient energies to comminution the predominantly Horse Canyon charge which is soft in larger sizes. However, when this Wenban proportion increases to a higher proportion, the Wenban ore begins to dominate the charge content, and the effect of the higher frequency of larger particle comminuting smaller less competent ones is overtaken by more frequent more competent Wenban-on-Wenban ore breakage reducing overall breakage rate.

Conversely, in a charge that is all Wenban, more competent breakage events are occurring reducing throughput. Any addition of a small amount of soft-in-the-coarse Horse Canyon does not affect the charge content's ability to maintain load. Its finer distribution is ground by the Wenban pebbles in the charge, and its coarse sizes are broken at a high rate. This explains the improvement seen with small additions of HC ore to predominantly Wenban. Still however these explanations above fail to be reconciled with a dip in throughput at more even blends. This dip in middle blends is thought to be influenced by the selected speed-filling. Throughputs are known to peak at different speeds and fillings based on their ore properties, Grind-Curves refer (Van Der Westhuizen and Powell, 2006; Powell *et al*, 2009). This will now be further evaluated by extending the modelling to higher speed-filling conditions in the next section.

Extension to other SAG mill filling-speed conditions

The modelling was also extended further to a total of four speed-filling conditions. This modelling considered the SAG with screen and recycle crushing per the circuit in Figure 7, and it ignored recycle crushing and downstream constraints, to gain insight into the response of the SAG circuit in isolation at higher throughputs, speeds and fillings.

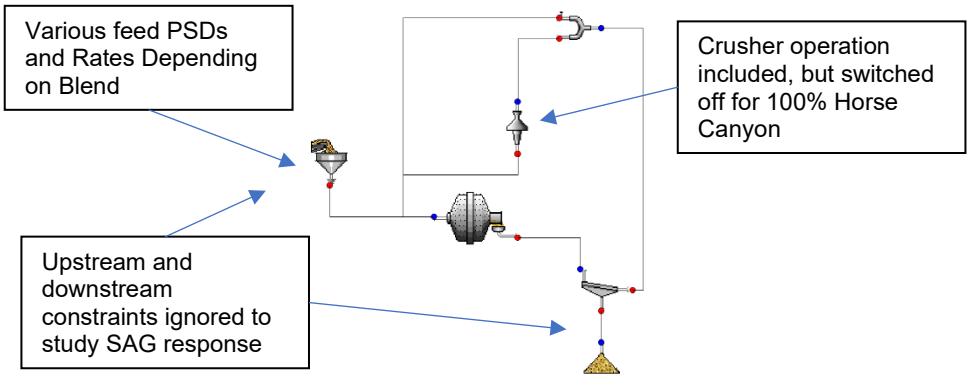

FIG 7 – Cortez SAG circuit isolated for model evaluation.

These SAG conditions were selected based on incrementally increasing speed. The filling for each speed was established by using MillTraj® and the existing liner design by determining what minimum filling was required to prevent ball-liner impact. The maximum speed-filling condition was set at the power limit of the mill. The resulting conditions were Case 1 as the baseline at 24.5 per cent mill filling and 69 per cent speed, then Case 2 at 27 per cent and 74 per cent, Case 3 at 30 per cent and 76 per cent, and Case 4 at 35 per cent and 78 per cent respectively.

The results are illustrated under 'New Methods' in Figure 8. As expected, each blend exhibits a varying Grind-Curve. Horse Canyon exhibits a peak and decline in throughput. Other blends appear to be still rising in throughput. A high throughput peak is observed at approximately 75 per cent Horse Canyon in Condition 4 that is higher than any other condition. The blends at which peak throughput performance is achieved varies at different speed-filling conditions. At the lower speed-filling conditions the peak occurs at between 20–30 per cent Horse Canyon.

Some comparison with measured results will now be made to support verification of the results. The same model results from the 'New Methods' surface of Figure 8 is also presented against measured throughput data in 'New Methods' in Figure 9 along with speed and filling. As seen in both the modelling and in measurements, blends produce throughputs larger than processing the ores separately. The peak at 75 per cent would have not been achieved in practice due to downstream constrains in ball milling with the high competent-in-the-fine-sizes Horse Canyon, and because these high fillings and speeds of condition 3 and 4 were not achieved in practice. Operation during measurements over the six month program being more like Condition 2, and here the modelling and measured results agree well for Wenban rich blends up to 67 per cent Horse Canyon. Beyond this the measured result drop below the model as expected from the known ball mill constraint treating Horse Canyon. The highest throughput blend measured in the survey, and also in a subsequent six month program of measurements, was at 33 per cent Horse Canyon. This is not too dissimilar to this peak shown by the model at between 20 per cent to 30 per cent.

The measured (but not fully surveyed) blend at 33 per cent shows close speed, filling and throughput agreement to the model. The 17 per cent, 50 per cent and 75 per cent surveyed throughput measurements agree with the model as indicated by their speed-filling condition lying between Condition 1 and 2, consistent with measurements. The model appears to somewhat underpredict the throughput for pure Wenban and Horse Canyon, despite being calibrated to include these. This is because the modelling reported was also part of a wider model which including blast modelling, so there were small differences in the baseline model feed distribution as compared to survey, due to model fitting differing to measurements.

Overall, the modelling was found to agree reasonably well with measured results. Where differences where identified, explanations have been identified. Therefore, the measured results have supported verification of the model. Next the existing methods of modelling blending will be undertaken and likewise compared against measured results.

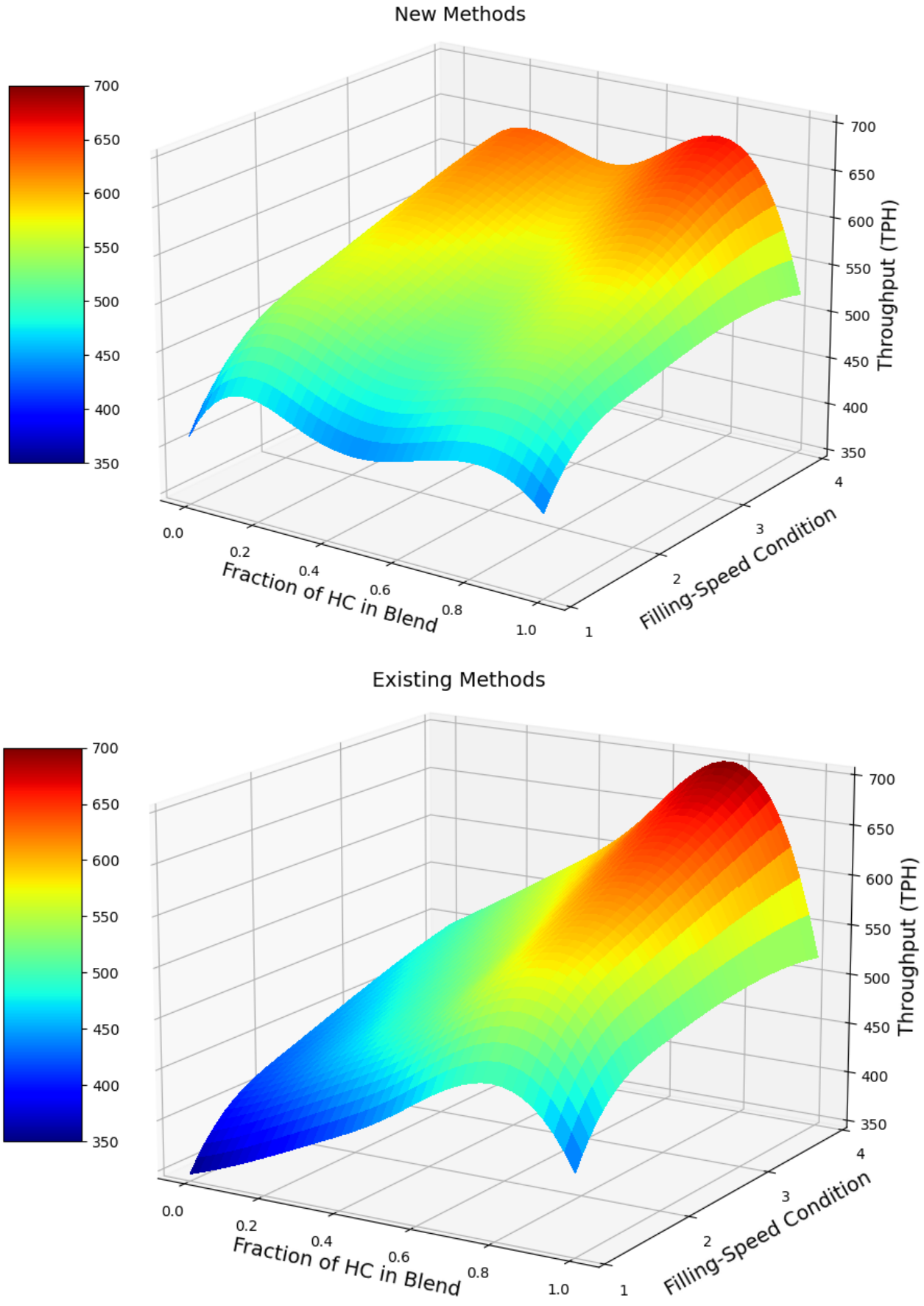

FIG 8 – Cortez baseline SAG mill throughput surface versus blend and filling-speed condition – new and existing methods.

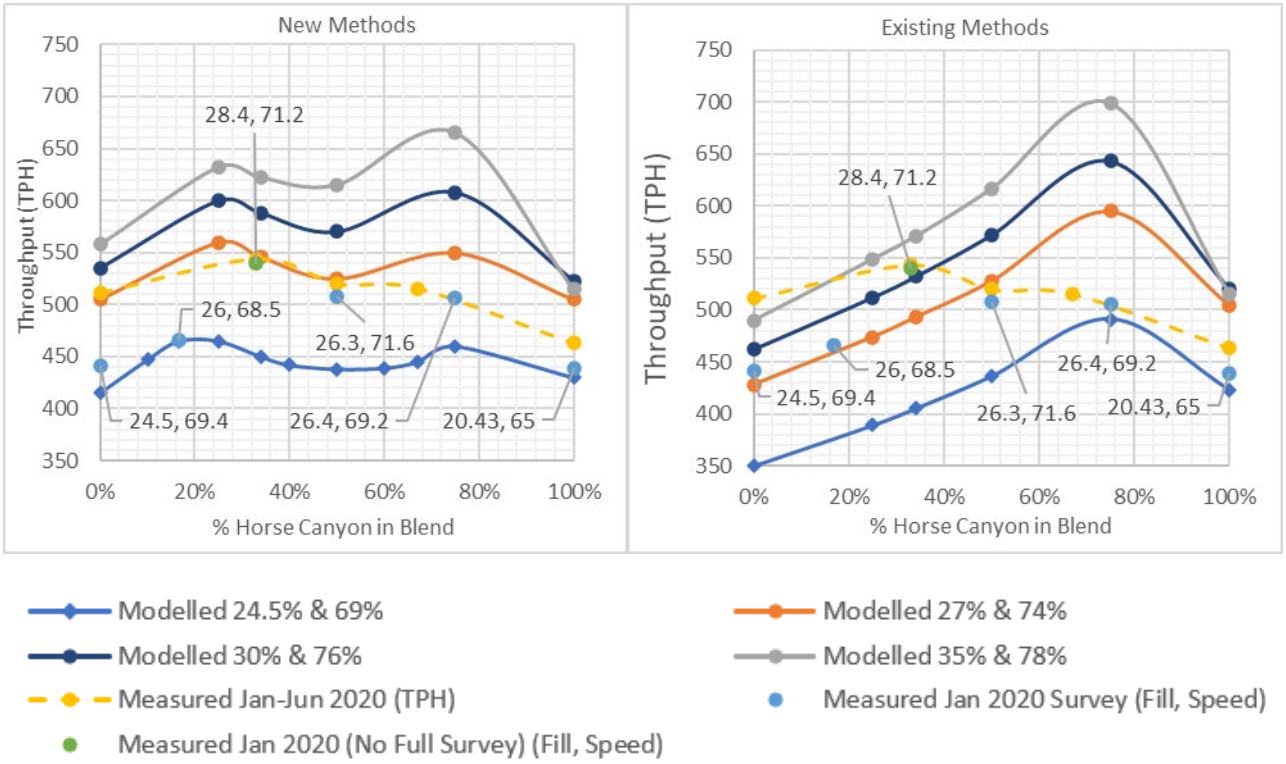

FIG 9 – Baseline SAG simulation throughput versus blend and speed-filling condition – new and existing methods.

Comparison with existing blend modelling practice in SAG mills

Existing practice for modelling SAG mill response is to survey at a single blend close to that most often processed in the mine plan, and to adjust to other blends based on mass weighted averages of the *Axb* and t_a. It is desirable to compare the new modelling approach described in this paper ('New Methods'), with this existing practice ('Existing Methods'), and to compare the fidelity of the two methods and any new utility achieved. The case study was used to do this using the same conditions to provide a direct comparison, and the single blend used for surveying and breakage rate fitting was selected at 50 per cent Horse Canyon.

The results are presented in Figure 8 ('Existing Methods'). The New and Existing Methods throughput versus blend and speed-filling surfaces are also overlayed in Figure 10 to provide a direct comparison. Comparing the two methods, the 100 per cent Horse Canyon blend is very similar between methods, as is 50 per cent as this was surveyed in both cases. The 75 per cent Horse Canyon blend has a higher result in Existing Methods, but interestingly the high throughput peak offered at this blend was identified by both models. This peak and subsequent drop at 100 per cent Horse Canyon may have been influenced by turning off the recycle crushing for this blend in both cases.

The other peak at 20–30 per cent Horse Canyon identified in the New Methods is not captured by the Existing Methods at all, and performance is underpredicted at these blends and for Wenban. This peak captured by the new method, and not by the existing methods, was demonstrated earlier as being real based on measured results.

As before, the same model results from the 'Existing Methods' surface of Figure 8 is also presented against measured throughput data in 'Existing Methods' on the right of Figure 9 along with speed and filling. As seen in both the modelling an in measurements, blends produce throughputs larger than processing the ores separately, as was also identified in New Methods.

The Existing Methods underpredict performance Horse Canyon to a worse degree than New Methods, and the performance of Wenban rich blends is grossly underpredicted with 0 per cent and 17 per cent blends having lower modelled throughputs at 27 per cent filling and 74 per cent speed compared to measured results at fillings of 24.5–26 per cent and 68.5–69.4 per cent speeds. The measured (but not fully surveyed) blend at 33 per cent shows that the model is predicting a

throughput commensurate with a filling and speed greater than 30 per cent and 76 per cent respectively, compared to the actual of 28.4 per cent and 71.2 per cent. This inaccuracy was not present in the New Methods, where modelled and measured speed, filling and throughput were in close agreement.

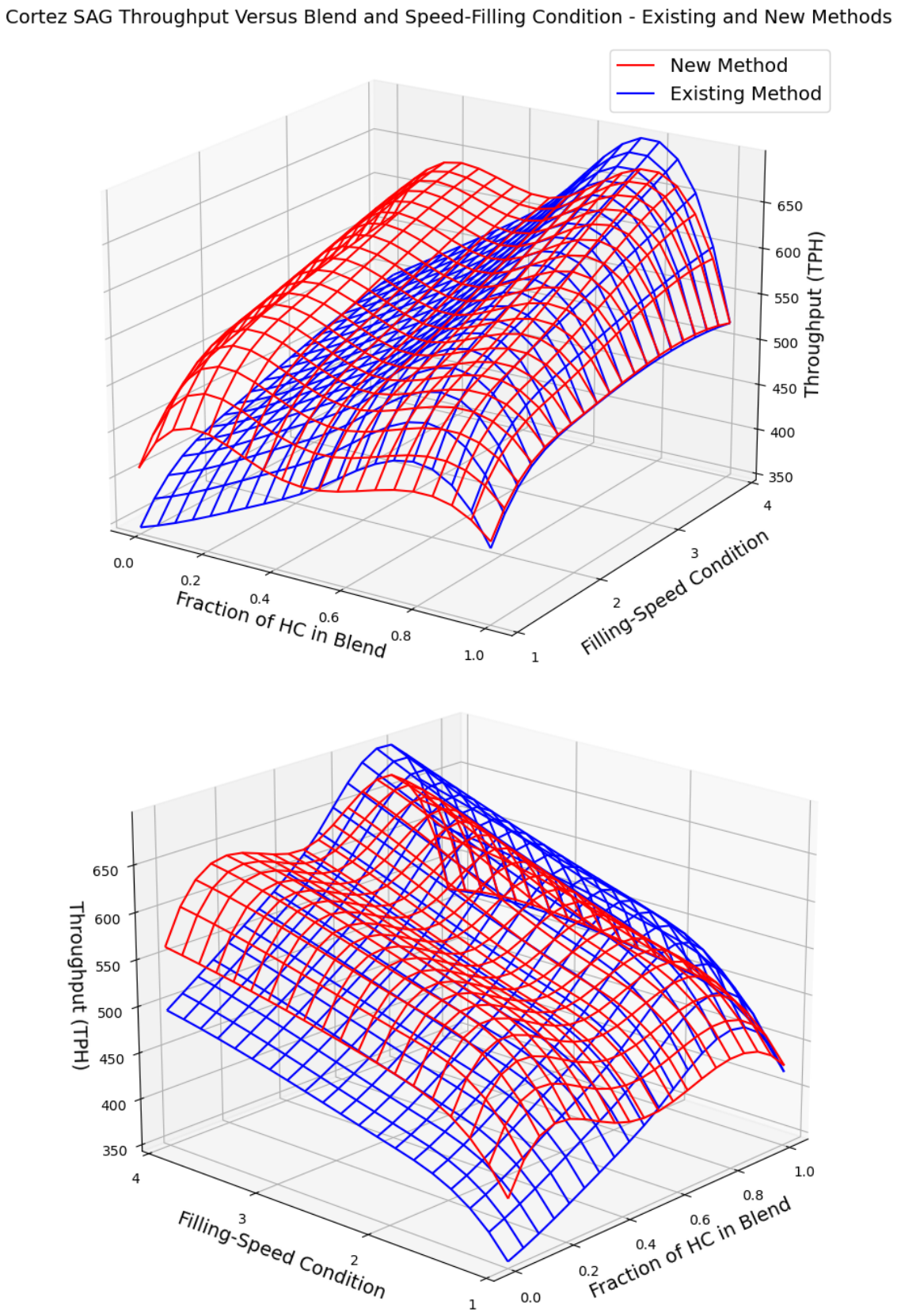

FIG 10 – Cortez SAG throughput versus blend and speed-filling condition – new and existing methods.

As described previously, operation during the measurements over the six month program would have been closest to Condition 2 of the 4 conditions, except for a drop off in predominantly Horse Canyon blends below the model resulting from the ball mill constraint treating highly competent-in-the-fine-sizes Horse Canyon. In the Existing Methods there is no close agreement between these measured results and the model. The highest throughput blend measured in the survey, and also in a subsequent six month program of measurements, was at 33 per cent Horse Canyon. This other peak is not captured at all, resulting in a completely different outcome when using Existing Methods, diverging from measured results.

The 17 per cent, 50 per cent and 75 per cent surveyed throughput measurements should, as indicated by their measured speed-filling condition, lie between Condition 1 and 2. The Existing Methods model fails this requirement at 17 per cent blend indicating performance above Condition 2 due the model's inability to identify the second throughput peak, but otherwise is consistent.

Overall, the Existing Methods modelling was found to agree reasonably well with measured results only close to where it was surveyed against. Its performance across blends was not as accurate as that achieved with the New Methods, and the non-linear behaviours arising with SAG composition were not captured, like the second peak in throughput at around 33 per cent blend. This has demonstrated improved fidelity and utility of the New Methods.

Scenario analysis and SSE

The modelling described in this paper was employed, along with wider modelling practice, to analyse an example potential upgrade option of Full Pre-Crushing ('Scenario 1'). Here the existing SABC circuit was upgraded with full pre-crushing, SAG discharge modifications, high media filling and reduced ball size, higher intensity Wenban blast design, and lower intensity Horse Canyon blast design, and increased number of operating cyclones with adjusted vortex and spigot sizes to promote coarser product. It is illustrated in Figure 11.

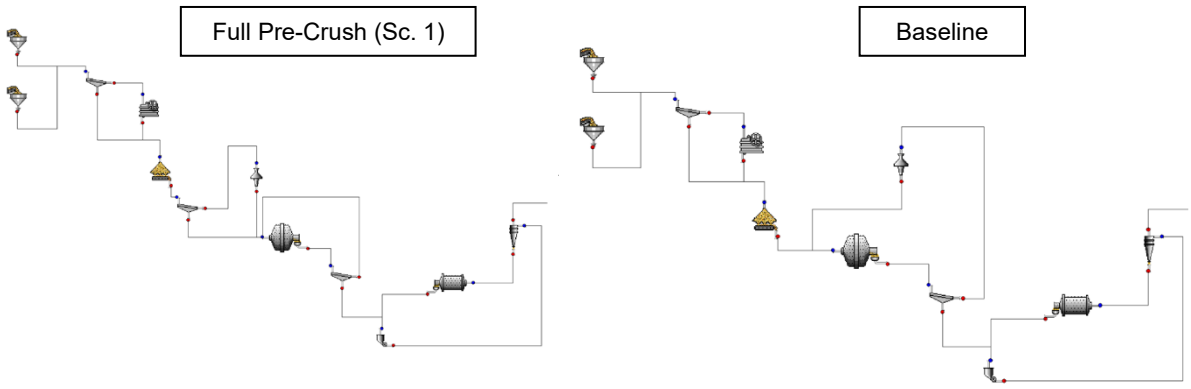

FIG 11 – Cortez upgrade scenario process flow diagrams.

The SAG Charge SSE model was used to support verification of the SAG circuit. The Baseline SAG circuit SSE was calculated and used along with total and media filling to back-calculate the SSE at no charge composition induced SSE increase ($\%Increase_{SSE-75\mu m} = 0$), thereby calibrating the SAG Charge SSE model at each blend. Then the calibrated model was used to calculate the expected $\%Increase_{SSE-75\mu m}$ per blend for Full Pre-Crush operation which generally had a higher media proportion in the charge. This was then compared to the JKSimMet® model produced SSE. The results are plotted in Figure 12.

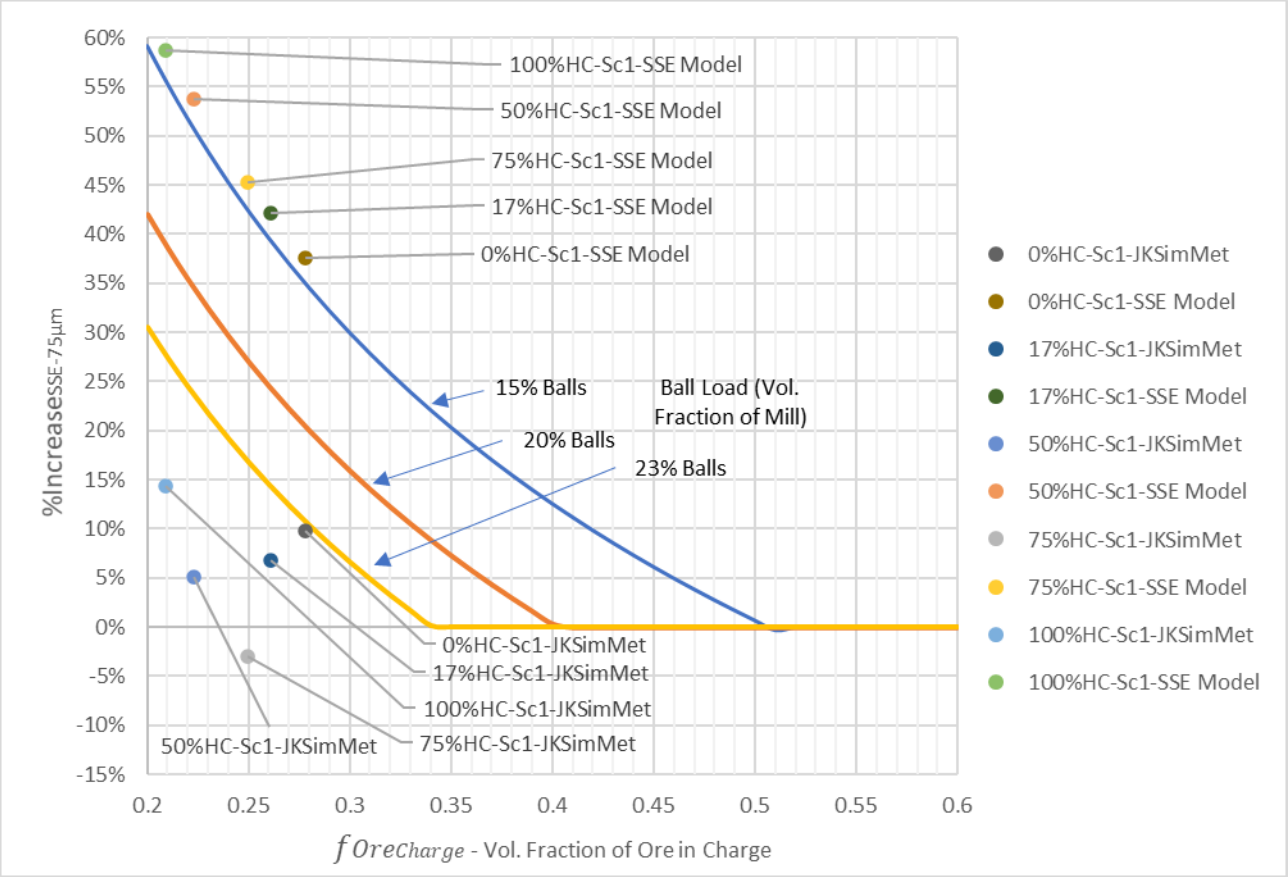

FIG 12 – Cortez SAG full pre-crush ('Sc 1')%Increase$_{SSE-75µm}$ versus volume fraction of ore in charge for varying ball fill – JKSimMet® modelled versus SAG charge SSE Model ('SSE Model').

The SAG Charge SSE model has been extended well beyond its very limited fitted data set, but it indicates JKSimMet® overpredicts performance of the full pre-crushing scenario by underestimating the SSE detriment from Barely Autogenous Grinding (BAG). JKSimMet® has little response to charge compositions by comparison. The data set from which the variable rates model was established has only up to 12 per cent ball load, and the form of the regressions used in its rate equations are provided in Grimes and Keenan (2015). These regressions do not include media to ore charge composition terms and given the low ball fraction limit in the fitted data set, it is not definitive JKSimMet® is providing any SSE increase response due to reducing ore charge fraction, as is clearly present in the SAG Charge SSE Model once a threshold composition fraction is reached.

The JKSimMet® derived SSE, SAG Charge SSE Model result, the relative difference between these, and also the as surveyed SSEs, are shown in Figure 13. A marked difference in SSE between the SAG Charge SSE Model and JKSimMet® models is shown. Little change occurs between the surveyed conditions and JKSimMet® results for the full pre-crush case due to its lack of response as described above.

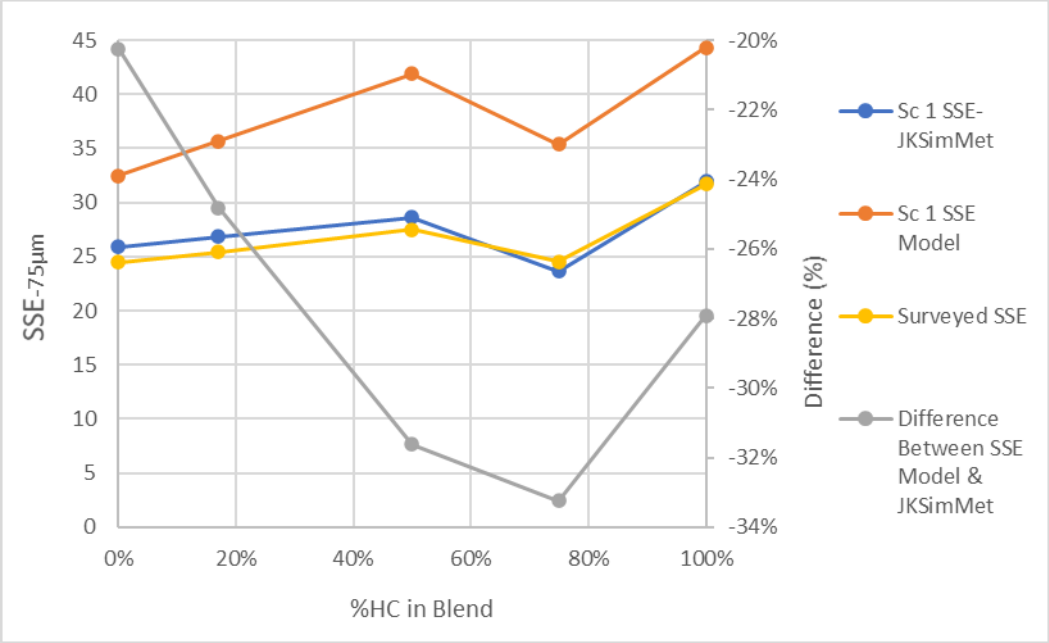

FIG 13 – Cortez full pre-crush (Sc 1) SAG SSE – surveyed, JKSimMet® and SAG charge SSE modelled results.

The SSE for the ball mill and whole comminution circuit was also calculated, to provide comparisons between the baseline and the full pre-crush case. Note the baseline is not quite the same as the as-surveyed because there was some variation from blasting through to cyclone overflow model fitting, and from employing consistent SAG speed-filling conditions across blends. The results show close agreement between the SAG SSE's as discussed above which is believed to be erroneous due to the different charge compositions.

The ball mill will now be evaluated. Ball mills can operate more efficiently with finer feeds which should be achieved with full pre-crushing, and so as expected the SSE has decreased for all blends with the finer feed. The degree of reduction is much larger than expected from prior experience however compared against typical changes in SSE measured at sites described in literature. Some of these cases will now be reviewed.

Ballantyne *et al* (2015) provides two data sets from two mines. In the first example SSE was found to be 32 per cent higher in one mill as compared to others. The cause was attributed to the recirculating load being higher than 450 per cent reducing classification efficiency, and possibly a bias in feed particle size between mills. In the second example poor classification is attributed to approximately 13 per cent increase in SSE. Powell *et al* (2018) provides a data set where a ball mill was underperforming with an approximate 8 per cent increase in SSE witnessed, determined by again employing the same methods. In this case the increase in SSE was attributed to the ball mill being overloaded and containing coarse rock. In summary potential differences in SSE have been reported in the literature of between 8–32 per cent due to a variety of factors including poor classification, overloading, and coarse feed.

Comparing this literature with the reduction in SSE of the ball mill from baseline to full pre-crush, it is suspected that the JKSimMet® model is overpredicting the performance of the ball mill circuit. This is likely exacerbated by the fact that the reduction in feed size to the ball mill might also be overpredicted by the SAG mill performance overprediction as previously described, resulting in a coarser than modelled feed size distribution.

The JKSimMet® overall circuit indicates reduced SSE for all blends in full pre-crush (Scenario 1) as compared to baseline SABC as shown in Figure 14, however this analysis has shown the opposite effect is expected, with pre-crushing and Barely Autogenous Grinding (BAG) expected to produce a less efficient result. The effect of this suspected inaccuracy in the modelling is that the product size is expected to be coarser than simulated, and the ball mill circuit may not be able to treat simulated throughput. In summary, the use of SSE for evaluating potential upgrade scenarios has been demonstrated. It should be noted that other scenarios were also run including partial pre-crushing of

critical size prior to SAG mill feed. This approach provided a more balanced ore-to-media charge composition reducing the expected inefficiency in the SAG mill, and the new SAG Charge SSE Model was able to indicate the benefits of this approach over full pre-crushing. These scenarios are further described in Hanhiniemi and Powell (2022).

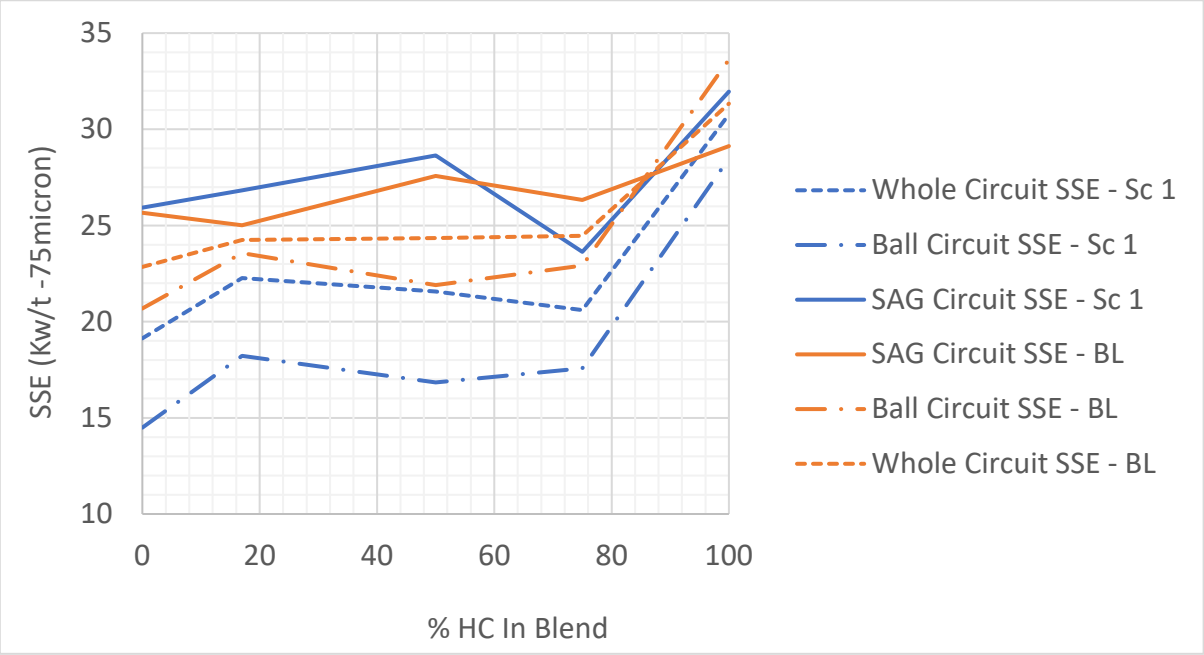

FIG 14 – JKSimMet® based SSE for full pre-crush (Sc 1) versus baseline (BL) – all blends.

CONCLUSIONS

A 'Variable Blend and Rates' model has been developed for SAG mills which extends upon the JKSimMet® Variable Rates Model primarily to capture blend response. Similarly, a 'Variable Blend Residence Constrained Perfect Mixing' ball mill model was introduced, also extending upon the existing JKSimMet® model, that captures blend response and residence time constraint. The generic approach of these models was applied to an example case study site to demonstrate their application. Comparisons with measured results showed improved fidelity of the new approach over current practice of blend modelling.

The use of SSE in validating simulation results was demonstrated. Further, a SAG Charge SSE Model which provides an indication on the impact on SSE with changing charge composition was developed, and then its application was demonstrated on a case study. This SAG Charge SSE model is based on a very small data set of pilot scale, and thus requires a larger data set. Several simplifying assumptions were made, such as assuming a consistent result irrespective of mill speed, mill size, and media size among others, and this requires validation or extension of the approach in future.

ACKNOWLEDGEMENTS

The authors would like to thank those involved in the survey including Marko Hilden, Vlad Jokovic, the Nevada Gold Mines Cortez team and the JKMRC. Nevada Gold Mines is also thanked for their permission to publish. This work was supported by the Australian Government Research Training Program (RTP).

REFERENCES

Ballantyne, G, Mainza, A and Powell, M, 2015. Using comminution energy intensity curves to assess efficiency of gold processing circuits. *World Gold.*

Bueno, M D P, 2013. Development of a multi-component model structure for autogenous and semi-autogenous mills. The University of Queensland, Sustainable Minerals Institute.

Bueno, M, Powell, M, Kojovic, T, Worth, J, Shi, F, Niva, E, Adolfsson, G, Henriksson, M, Partapuoli, A, Wikstrom, P, Tano, K and Fredriksson, A, 2011. The Dominance of the Competent. *SAG.* Vancouver.

Grimes, A and Keenan, C, 2015. JKSimMet Version 6.1 User Manual. *In:* LASKER, R. (ed.) *Steady State Mineral Processing Simulator.* JKTech Pty Ltd.

Hanhiniemi, J and Powell, M, 2019. Techno-Economic Modelling of Tumbling Mills: Economic Design and Operation. International Semi-Autogenous Grinding and High Pressure Grinding Roll Technology, 2019 Vancouver.

Hanhiniemi, J and Powell, M. 2022. Techno-Economic Modelling of Comminution Circuit Options. *International Mineral Processing Council Asia-Pacific.* Melbourne.

Mitchell, J and Holowachuk, N V, 1996. Ore Blending at Highland Valley Copper: Its Necessity, Effects, and Benefits. *SAG.* Vancouver.

Mkurazhizha, H, 2018. The effects of ore blending on comminution behaviour and product quality in a grinding circuit – Svappavaara (LKAB) Case Study. Iuleå, Sweden: Luleå University of Technology.

Morrell, S, 2001. Modelling of the Load-Throughput Response of AG/SAG Mills. *AMIRA P9M Project Fourth Progress Report.* Julius Kruttschnitt Mineral Research Centre.

Morrell, S, 2016. Modelling the influence on power draw of the slurry phase in Autogenous (AG), Semi-autogenous (SAG) and ball mills. *Minerals engineering,* 89, 148–156.

Napier-Munn, T J, Morrell, S, Morrison, R D and Kojovic, T, 1996. *Mineral comminution circuits: their operation and optimisation*, Indooroopilly, Qld.: Julius Kruttschnitt Mineral Research Centre.

Ntiamoah, K, Rader, L, Yalcin, E, Powell, M, Jokovic, V, Hilden, M and Hanhiniemi, J, 2020. The influence of ore blending on mill throughput – Cortez mine case study. *Nevada Mineral Processing Division Conference.* Reno.

Powell, M S, Mainza, A N, Hilden, M and Yahyaei, M, 2015. Full Pre-Crush To SAG Mills – The Case For Changing This Practice. SAG Conference, 2015 Vancouver.

Powell, M S, Van Der Westhuizen, A P and Mainza, A N, 2009. Applying grindcurves to mill operation and optimisation. *Minerals Engineering,* 22, 625–632.

Powell, M, Kanchibotla, S, Jokovic, V, Hilden, M, Bonfils, B, Musunuri, A, Moyo, P, Yu, S, Yong, J, Yaroshak, P, Yalcin, E and Gorain, B, 2018. Advanced Mine to Mill Application at the Barrick Cortez Mine. *14th AusIMM Mill Operators' Conference.* Brisbane.

Shi, F, 2016. An overfilling indicator for wet overflow ball mills. *Minerals engineering,* 95, 146–154.

Van Der Westhuizen, A P and Powell, M, 2006. Milling Curves as a Tool for Characterising SAG Mill Performance. *SAG Conference.* Vancouver.

An investigation of gyratory crusher liner wear at the Telfer Operation using non-operational streamlined modelling

J Harding[1], R A Bearman[2] and S Munro[3]

1. Mechanical – Technical and Maintenance, Newcrest Mining Ltd, Telfer Operation, WA 6762. Email: jason.harding@newcrest.com.au
2. Director, Bear Rock Solutions Pty Ltd, Melville WA 6956. Email: ted.bearman@bear-rock.com
3. Director, Met Dynamics Pty Ltd, Woodvale WA 6026. Email: scott.munro@metdynamics.com.au

ABSTRACT

Despite the importance of the primary crushing stage, performance optimisation is not well analysed with sufficient focus to give improvement opportunities.

At the Newcrest owned Telfer operation, liner life plays an important part in scheduling planned maintenance. Major consideration is given to monitoring crusher performance, as the highly abrasive nature of the feed significantly impacts the liner wear life.

A study was undertaken by the lead author which focused on establishing a strong baseline of accurate data pertaining to the performance of the crusher, in terms of, operating parameters, liner life and key machine design factors. As part of the study, mining feed materials were examined for a particular set of liners and this revealed that improved methods should be pursued.

Due to the competitive nature of the mining industry, the business solution to complex problems with long shutdown cycles should be streamlined to incorporate a non-operational modelling approach that is significantly more efficient than traditional online trial and error methods. In order to dramatically reduce the time and business risks, it was decided to engage services to model and simulate the liner life by varying main operational and mechanical factors.

The key to all simulation work is gathering high quality baseline data. Such data allowed deployment of the Kinematic Crusher Model and validation of the model against worn 2D wear liner profiles. The proven model was then successfully deployed to predict operational values that defined crusher performance.

To enhance the study, further investigation into a set of mechanical and operational simulations generated a sensitivity matrix measuring key performance parameters throughout the wear life of the liners. The study revealed throughput as a highly sensitive parameter and a change in eccentric throw provided the greatest improvement in extending liner wear life.

INTRODUCTION

Newcrest Telfer Operations uses a traditional front-end to the processing circuit (see Figure 1), which consists of two Metso 54–75 gyratory crushers operating in parallel. The crushers receive direct tip feed from the haul truck fleet, with the feed material varying in size and consistency. The characteristics of the ore lead to relatively high liner wear in the crushers, which impacts maintenance shutdown replacement strategies.

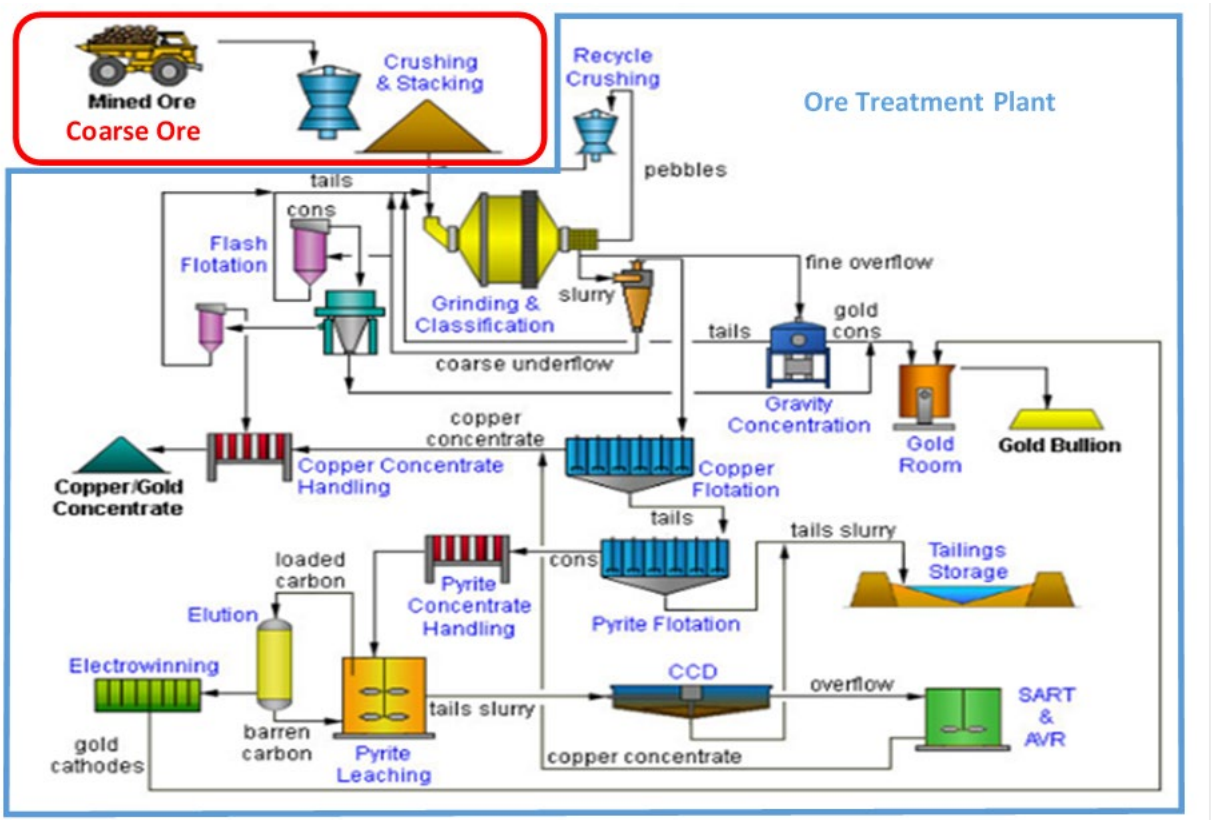

FIG 1 – Telfer: Single Train Processing Facility; simplified overview (Newcrest Mining Ltd, 2004).

In supporting the Newcrest vision to be 'Miner of Choice™', the Telfer Coarse Ore Maintenance team are constantly looking at innovative ways at reducing maintenance cost and improving plant reliability. The team identified that considerable value lies in extending liner life in the primary crushers. As an illustration of the fundamental issue, Table 1 shows the typical log of liner change-outs, with the repeating pattern of three mantles to one set of concave plates and the impact to the maintenance schedule from proposed liner life improvements.

Based on operational accounting data, if a 37.5 per cent increase in liner life cycle can be achieved, then an entire maintenance shutdown for a concave replacement can be removed from the schedule. The ability to remove one such shutdown equates to substantial savings through increased crusher availability and reduced maintenance costs. By utilising non-operational streamlined modelling, these savings can be realised over a shorter time frame, when compared with traditional trial and error approaches. The initial cost associated with modelling represents approximately 10 per cent of the estimated yearly savings and therefore represents a strong rate of return.

Currently the mantle and concave liners are replaced on cumulative throughput, due to liner wear influencing motor winding temperatures. Operating a maintenance strategy of three mantles per set of concaves, the Mainshaft Positioning System (MPS) showed that the average finished stroke height for each worn mantle in order is 58 per cent, 50 per cent and 40 per cent to achieve a cumulative throughput of 3 Mt of ore. By optimising mantle and concave liner wear profiles, this allows the opportunity to increase crusher runtime between scheduled shutdowns.

The study was designed to span two phases. Phase 1, which is the subject of this paper, was aimed at determining if simple and straightforward mechanical and operational changes resulted in positive improvement towards extending mantle liner life. Phase 2 is intended to examine, optimise and automate the design of crusher cavity profiles.

TABLE 1

Log of liner change-out events and the impact of achieving the target extension of liner life on the overall maintenance schedule.

Current

Timeline	(Weeks)	1	2	3	4	5	6	7	8	9	10	11	12	13	14	15	16
Concave life (Accumulative Tonnes)	M Tonnes	0.2	0.4	0.6	0.8	1	1.2	1.4	1.6	1.8	2	2.2	2.4	2.6	2.8	3	
Std Mantle (MPS Life Accumulative Tonnes)	M Tonnes	0.2	0.4	0.6	0.8	1	1.2										
1st Oversize (MPS Life Accumulative Tonnes)	M Tonnes							0.2	0.4	0.6	0.8	1					5 day shutdown
2nd Oversize (MPS Life Accumulative Tonnes)	M Tonnes												0.2	0.4	0.6	0.8	

Proposed

Timeline (Weeks)	(Weeks)	1	2	3	4	5	6	7	8	9	10	11	12	13	14	15	16	17	18	19	20	21	22	23
Concave life (Accumulative Tonnes)	M Tonnes	0.2	0.4	0.6	0.8	1	1.2	1.4	1.6	1.8	2	2.2	2.4	2.6	2.8	3	3.2	3.4	3.6	3.8	4	4.2	4.4	
Std Mantle (MPS Life Accumulative Tonnes)	M Tonnes	0.2	0.4	0.6	0.8	1	1.2	1.4	1.6															
1st Oversize (MPS Life Accumulative Tonnes)	M Tonnes									0.2	0.4	0.6	0.8	1	1.2	1.4	1.6							5 day shutdown
2nd Oversize (MPS Life Accumulative Tonnes)	M Tonnes																	0.2	0.4	0.6	0.8	1	1.2	

Approach to the study

From the outset of this project, the aim has been to deploy a method of investigation that allows key parameters to be tested in a non-operational setting. Basing the investigation in the virtual world removes the need for protracted trial periods and the possibility of introducing operational risk into a primary crushing installation.

The non-operational, streamlined modelling approach that has been used in this study has been underpinned by the generation of a high resolution data set, application of a structured investigation method and the use of detailed, mechanistic crusher modelling.

The following section provides details of the approach developed and deployed during this study, which leverages and combines methods from both maintenance and process engineering.

UNDERLYING PHILOSOPHY AND PROJECT STRUCTURE

Like all wearing components, the gyratory crusher operation requires a great deal of applied maintenance to ensure crushed ore is delivered on a regular and reliable basis. Setting and achieving targets to reduce the frequency of planned maintenance events leads to the maximisation of equipment utilisation and the extension of the life of wear components.

As previously noted, liner change-out at Telfer is based on a three mantle to one concave set strategy, ie for a single set of concave liners to reach a wear limit, three mantles – Standard, First Oversize and Second Oversize are required.

The three to one mantle to concave strategy is not optimal for all sites. Typically this ratio can vary from 2:1 to 5:1.

The ability to extend liner life, whilst maintaining process performance offers a value proposition that is compelling.

Given the mechanical nature of the study, the maintenance team at Telfer has led the efforts to understand what controls liner life and how it may be extended. In order to investigate the situation a Liner Management Strategy (LMS) has been developed.

LMS is based on standard approaches from asset management.

To methodically develop an LMS, the lead author looked to standard approaches commonly found in the maintenance community, namely:

- Dynamics Maintenance Strategy.
- Maintenance Business Process.
- Reliability Centred Maintenance.

Australian Standards (2004a), acknowledges a dynamic maintenance strategy as a non-scheduled task that utilises other maintenance tasks to assist in monitoring data collection and analysis to determine liner wear life. It is crucial in the case of the primary crusher, that an essential non-scheduled task involves monitoring liner wear profiles against feed type and rate (Bearman and Briggs, 1998). Such data can provide an overall picture of how the gyratory crusher is performing within its design limits (Posario, Hall and Maijer, 2004).

In combination, the Maintenance Business Process (MBP – see Figure 2) and Reliability Centred Maintenance (RCM – see Figure 3) have been the guiding principles for the investigation and the life cycle of events. The approaches recognise how system changes within organisations can allow the development of new ideas (Maintworld, 2013), while following a reliability process as per Australian Standards (2004b), that outlines the process to detect ‘failure modes’, which in this instance, is the point at which liners can no longer meet performance metrics.

The methodical gathering of data, in association with a structured investigation of the impact of crusher parameters, has been at the heart of the LMS development and the efforts to lower maintenance cost and increase productivity by minimising unscheduled downtime (Posario, Hall and Maijer, 2004; Metso, 2012; Major, 2002).

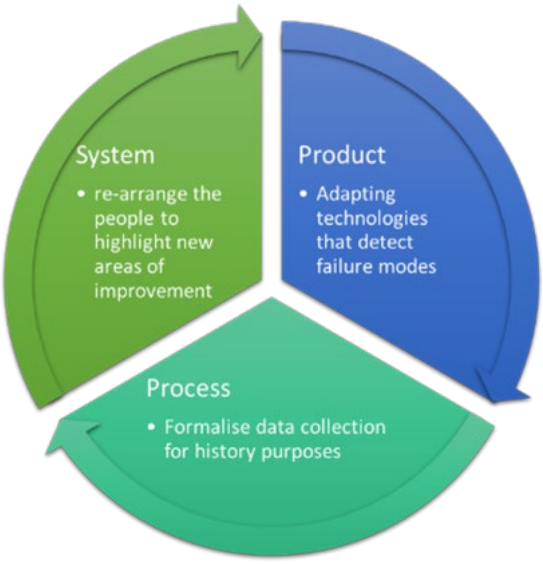

FIG 2 – MBP life cycle (Harding, 2018 after MaintWorld, 2013).

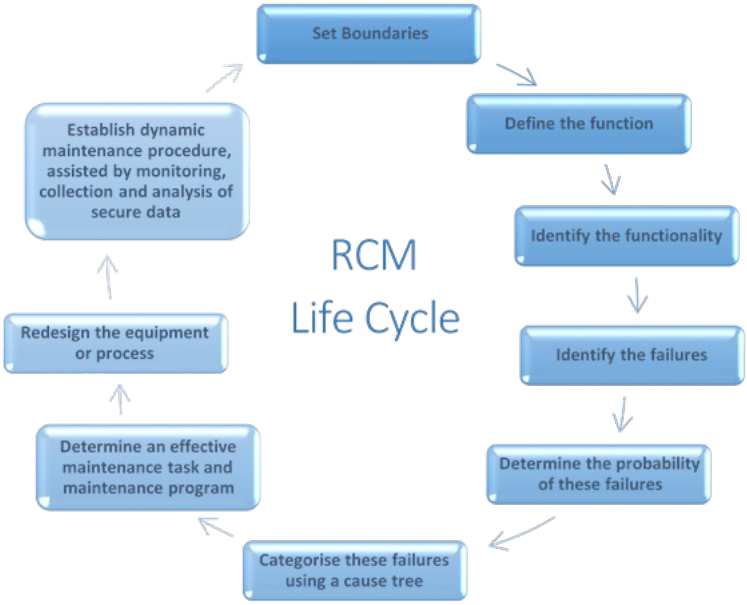

FIG 3 – RCM life cycle (Australian Standards, 2004b).

Embedded in the overall study approach are a series of sensitivity studies to determine the impact of mechanical crusher parameters. Within the study, this exercise was dubbed, a 'Matrix Evaluation'. In this part of the study key mechanical factors were varied to determine the impact on performance indicators.

The concept for the Matrix Evaluation comes from the One-Factor At a Time (OFAT) approach, which defines how to conduct a sensitivity analysis between input variables and directed output targets.

The approach is widely used, but as with many familiar concepts, some of the underlying principles can sometimes be overlooked. A sensitivity ('what-if') analysis is the most effective method to monitor and define the impact of behavioural change. The idea of sensitivity analysis is to monitor behavioural change of an input variable/s in respect to a single or multiple outputs within a set of boundary conditions (Saltelli, Chan and Scott, 2008). Monitoring large or small variations enables the sensitivity analysis to provide solutions, in terms of (Pannell, 2017):

- Understanding or quantifying, the relationship between each input factor and directed output targets.

- Model development, through testing of accuracy or validation, simplifying and calibrating, prioritising information and dealing with poor or missing data.
- Improved decision-making or recommendations, by knowing when and how to optimise the solution for changing circumstances.
- Communication of results, in logical format.

The OFAT approach investigates a single input in relation to multiple outputs, (Saltelli, Chan and Scott, 2008). The remainder of the input values stay the same allowing the analysis to evaluate each output factor in terms of its baseline value as a percentage.

Structure applied in the study

The overall philosophy of non-operational, streamlined modelling is to allow efficient testing of machine performance in a virtual environment, whereby production interruptions are removed from the investigative process.

In a typical case, the various phases involved in a physical process can lead to long and arduous projects. Figure 4 shows a typical, physical (online) process.

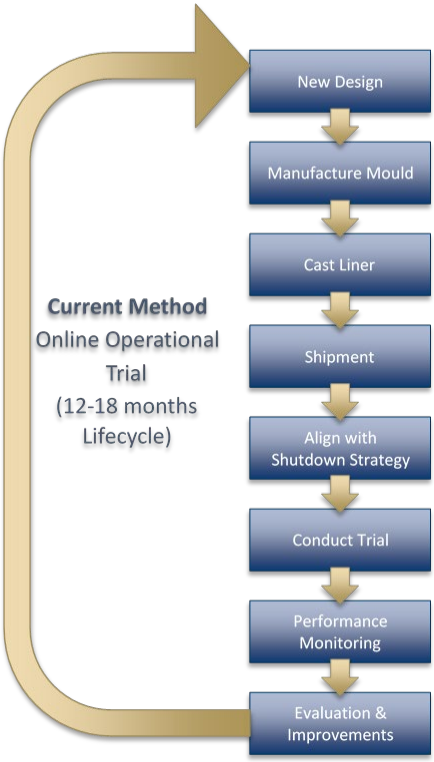

FIG 4 – Traditional, physical (online) liner evaluation process (Harding, 2018).

On top of the process of design, manufacture, operation and evaluation, there are other key factors to consider. The main areas are the data gathering requirements and associated personnel time, downtime of the crusher for performance testing and critically, the risk of an underperforming liner set.

The project that is the subject of this paper proposes to streamline the online physical process, by combining design, modelling and simulation to significantly short-cut the traditional process.

Figure 5 shows the offline streamlined process applied by Telfer Operations.

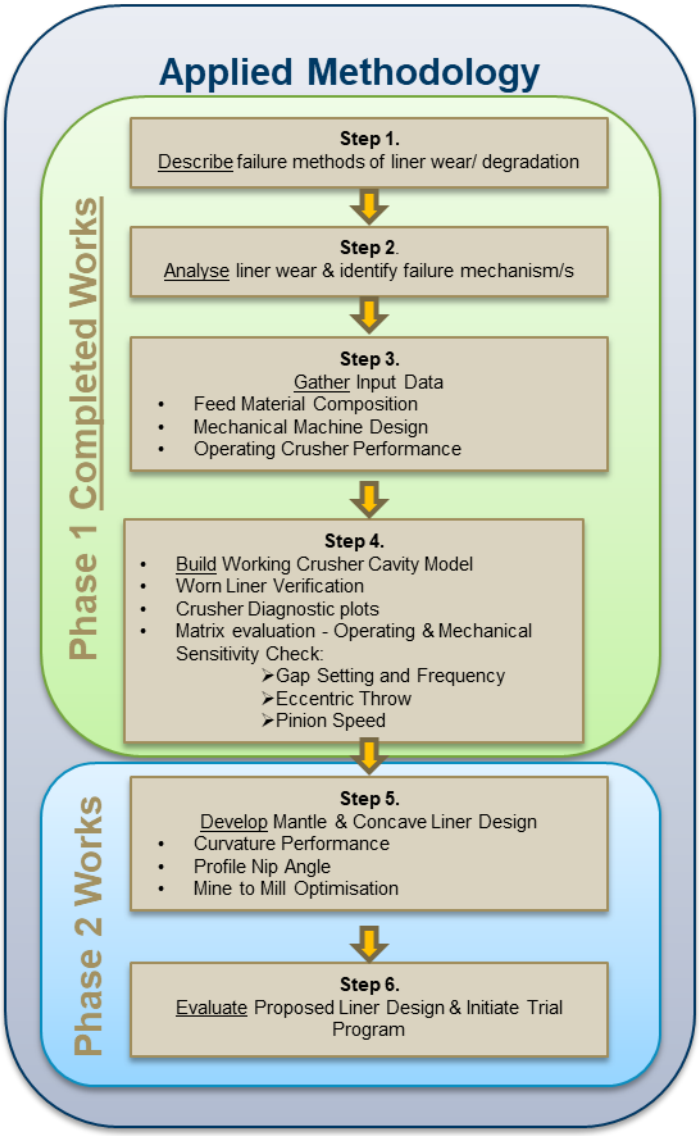

FIG 5 – Applied methodology for the non-operational streamlined modelling approach, with Phases 1 and 2 identified (Harding, 2018).

CRUSHER PERFORMANCE, DATA AND MODELLING

In terms of the project objectives, the target for Telfer Operations is illustrated in Figure 6.

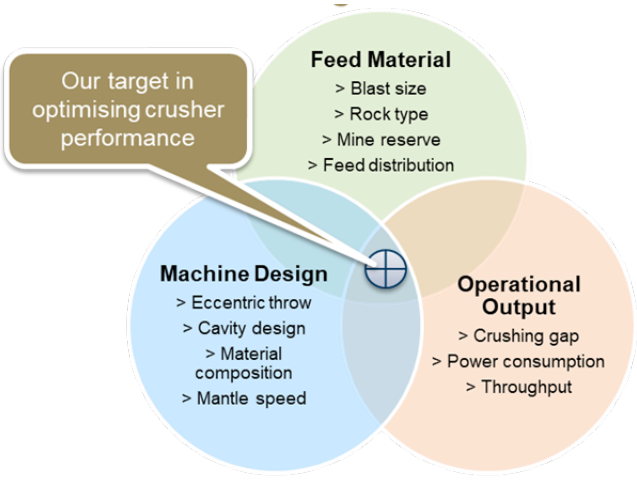

FIG 6 – Goal for primary crusher optimisation.

Factors impacting crusher performance

Various feed, operating and mechanical variables influence crusher performance and liner wear (see Figure 7), making it challenging to effectively optimise the crushing process and to develop a liner optimisation strategy.

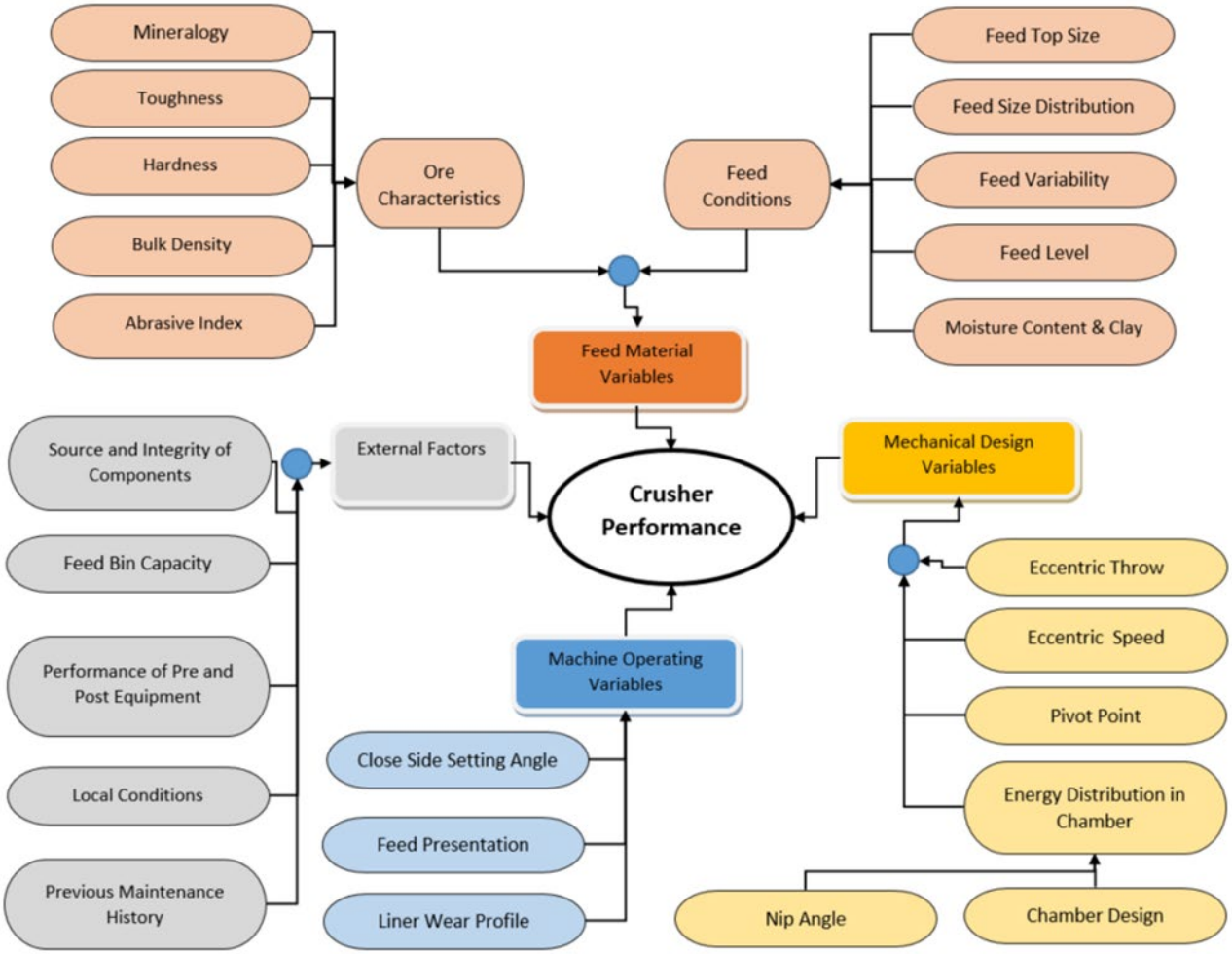

FIG 7 – Factors impacting crusher performance and liner wear (after Harding, 2018).

Any study requires a strong foundation and this relies on extensive and comprehensive data gathering and compilation. The factors shown on Figure 7 are split into:

- feed material variables;
- mechanical design variables;
- machine operating variables;
- external factors.

The categorisation is a deliberate decision by the lead author and it is based on work by Bearman (1994, 2019). The purpose of the delineation is to show that the crushing process is a combination of factors that relate to mechanical, maintenance, processing and feed and that all these need to be considered if a full study is to be undertaken.

Data gathering

A majority of the factors were gathered using available data from operational sources, vendor specifications and design documentation.

Where data was either unavailable or not current, efforts were made to gather new data using advanced technology. Two key exercises involved the lead author undertaking feed size distribution

measurement using a photogrammetry method and accurately measuring liner profiles using laser scanning technology.

To define the feed size distribution to the primary crushers, the PortaMetrics™ system from Motion Metrics was used (Motion Metrics, 2019a, 2019b). The system uses an optically based photogrammetry method, which uses 3D imaging and contributions from AI techniques to provide a size distribution, without the need for traditional screening methods. As with many electronic data collecting systems, results are based on quantity over quality leaving the finer particles to be manually sized. In this instance, Telfer was fortunate to have a database of historical feed size data and therefore the ore feed size distribution graphs incorporated both advanced and historical data to obtain the best result.

Accurate operational liner data relies on overlaying liner wear profiles of both new and worn liners across the full set of concaves, (ie three mantles to a single concave set).

Liner measurement in an operational environment, is often undertaken, but to match the level of modelling required, Telfer personnel embarked on a significant effort. The work was able to accurately generate worn profiles through all stages of mantle use and to also provide a full picture of wear around the circumference of the crushing chamber. The data for the mantles and concave plates was analysed and compiled, so that it could be presented in a number of ways. Figure 8 shows a screenshot from a master spreadsheet where it is possible to select from the full data set of liner profiles, spanning the entire life of the concave plates.

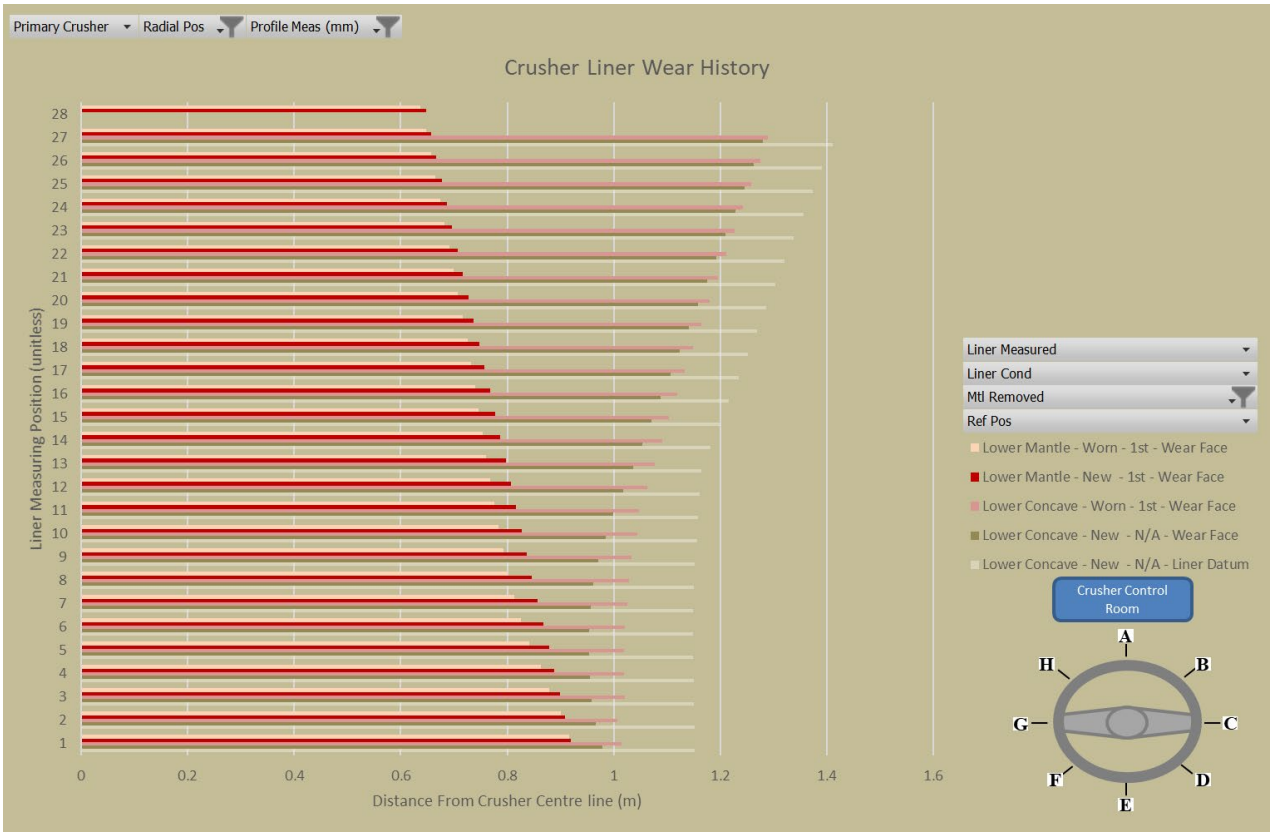

FIG 8 – Screenshot of the master graphic for the reporting of liner profile data.

Mechanistic crusher modelling

The ability to apply the virtual design and testing approach described in this study, relies on a model that is appropriate and comprehensive and can be shown to properly mimic physical processes.

The ability to virtually test potential modifications to liner profile, geometry and even material types, is particularly important in primary crushers.

On the basis of these functional and practical requirements for this project, Telfer decided to engage Bear Rock Solutions Pty. Ltd. (BRS) to provide independent advice and to deploy what is termed the Kinematic Crusher Model (KCM).

KCM was developed 10 years' ago as a joint project between BRS and Met Dynamics Pty. Ltd. The origin of the approach dates back to work by Bearman in the late 1980s (Bearman, 1991), whereby the need to combine breakage characteristics, processing parameters and mechanical crusher variables, was identified. In the prior, and intervening years, various workers (Karra, 1983; Whiten, 1984; Flavel *et al*, 1988; Evertsson and Bearman, 1997; Bearman and Briggs, 1998; Evertsson, 2000; Lindqvist, 2003) have advanced numerous methods and concepts, which have informed some of the approaches taken in KCM.

The KCM method is best described as a multi-component mechanistic model. It uses standard representations of geometry (see Figure 9) and feed characteristics, but then applies advanced techniques to generate material flow diagrams to determine both operating performance and mechanical wear of the crusher. KCM is tried and tested at many mine sites on a variety of both gyratory and cone crushers and has the ability to:

- Verify the machine specification against the required process duty (in both greenfields deployment and brownfields replacement scenarios).
- Align maintenance operating strategies by forecasting liner wear.
- Confirm mechanical and process changes, reducing business risk of long duration trials.

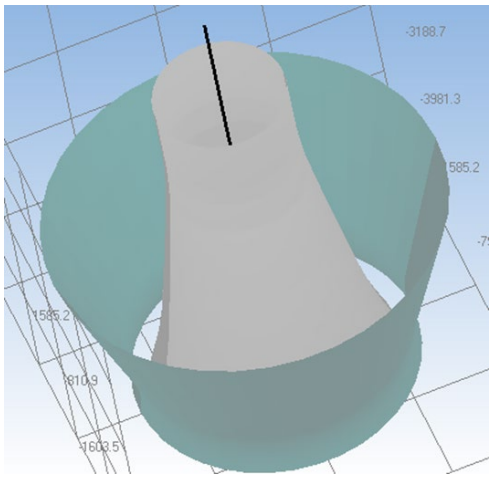

FIG 9 – Standard CAD coordinate plot in KCM showing liner geometry for a primary gyratory crusher.

Some of the plots generated (see Figure 10a, 10b) show obvious behaviour, which can easily be interpreted. Other plots are designed to supply information that can be used by experts in the diagnosis of crushing issues or in the re-design of liners. Some of the outputs that are specifically of use in more in-depth analysis, include:

- *Energy Distribution* enables us to illustrate the number of crushed rocks in a given area and directly link it to crushing throughput – Figure 10a.
- Impact of wear profile on the Mainshaft Positioning System (MPS) to determine the remaining life of a set of liners and the optimal change point for a move to an oversized replacement mantle – Figure 10b.
- Evaluating Compaction Behaviour forces to support Root Cause Analysis (RCA) investigations into bush failures, oil flow and temperature issues – Figure 10c.
- Fatigue management on Concave Plate Stresses used to prevent premature failures of liners and liner castings – Figure 10d.

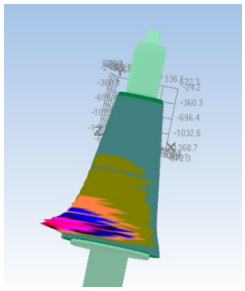

(a)

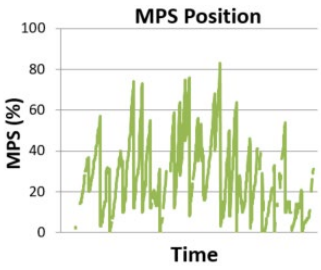

(b)

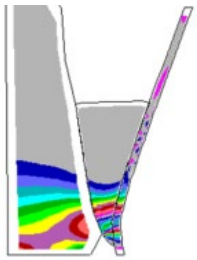

(c)

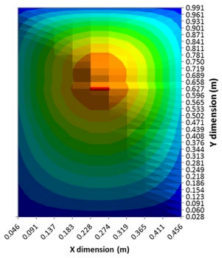

(d)

FIG 10 – Example plots from KCM and examples of subsequent analysis. (a) Energy distribution; (b) Mantle Positioning System; (c) Compaction behaviour; (d) Concave plate stress pattern.

Although there are several unique features of KCM, one of the most interesting, as it relates to primary crushers, deals with liner wear.

In the case of liner wear, the impact on throughput and power consumption, is seen every day in operations. For the Telfer operation and the requirements of this study, the ability to accurately predict wear was critical to success.

As detailed earlier, Telfer personnel took great care over data gathering and this included the measurement of liner wear.

As part of the evaluation of the utility of KCM, an early piece of work was to compare KCM wear predictions to measured mantle and concave profiles. Figure 11 shows the new profiles, with measured and KCM predicted profiles superimposed, at the end of the life of the Standard mantle and the second oversize mantle.

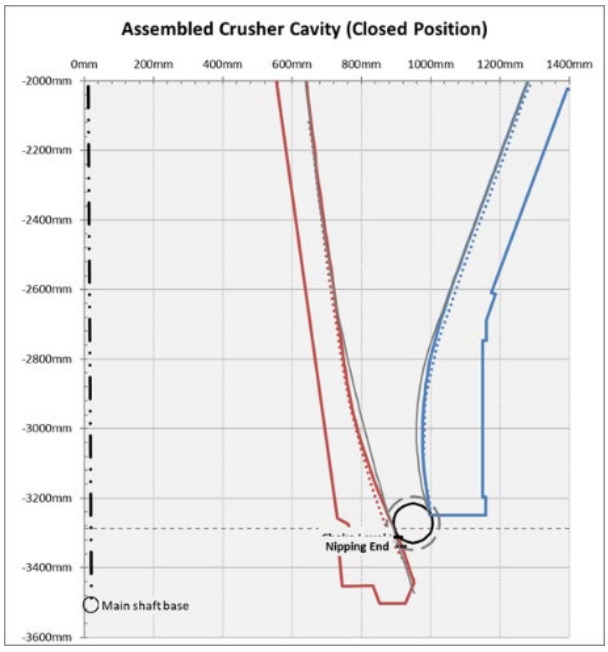

(a)

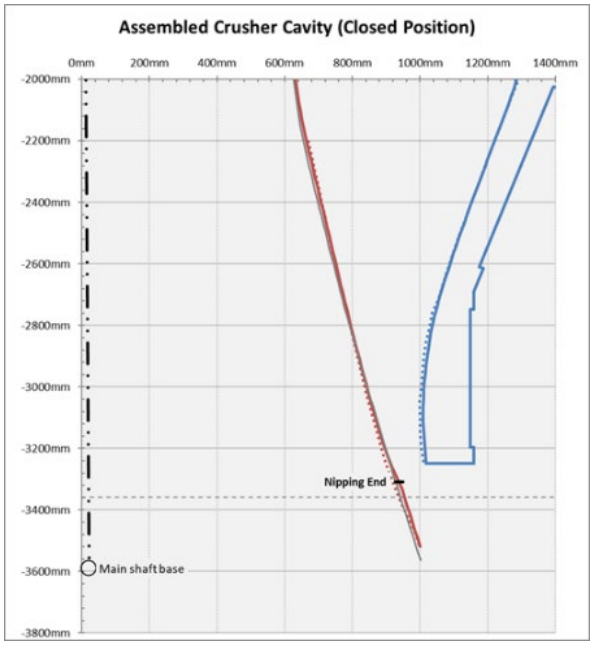

(b)

FIG 11 – Telfer wear analysis using KCM [Note: New liners (grey lines), measured profiles (solid red and blue) and KCM predictions (dotted red and blue)]. (a) Standard mantle – end of life; (b) Second oversize mantle – end of life.

The accuracy of the KCM predictions were acknowledged and determined to be a good basis for the crusher optimisation initiative at Telfer.

Study findings

The Telfer primary crusher study was aimed at defining if simple and straightforward mechanical and operational changes were likely to yield improvements in crusher performance. The crusher performance being mainly defined by the ability to extend liner life, but not at the expense of throughput, product size distribution or increased power draw.

In order to do this, the KCM system was set-up so that it was able to accept a range of inputs and run through the wear life of a mantle liner and vary the Open Side Setting (OSS), eccentric speed, and eccentric throw.

For every combination of input parameter, the model calculated outputs in the form of power consumption, mainshaft position (vertical) and product size distribution (P80).

The approach was internally referenced as a matrix evaluation.

Matrix evaluation

As previously noted, the matrix evaluation was designed on the basis of the OFAT approach. The work undertaken examined the crusher performance using original and new condition mantles and concave profiles, with these kept the same in the case of all changes to input parameters.

In this paper, the focus in Phase 1 was to look for simple improvements and validate the KCM model by examining variation in crusher parameters, before moving into Phase 2 to develop matched liner profiles.

The range of parameters used in this study are:

- OSS: 150, 175 and 200 mm;
- Eccentric Speed: Standard, +20 per cent and -20 per cent;
- Eccentric Throw: 36, 40 and 44 mm.

Figures 12, 13 and 14 refer to the second oversize mantle (end-of-life) and shows plots of the key output values with variation in input for OSS, eccentric speed and eccentric throw, respectively.

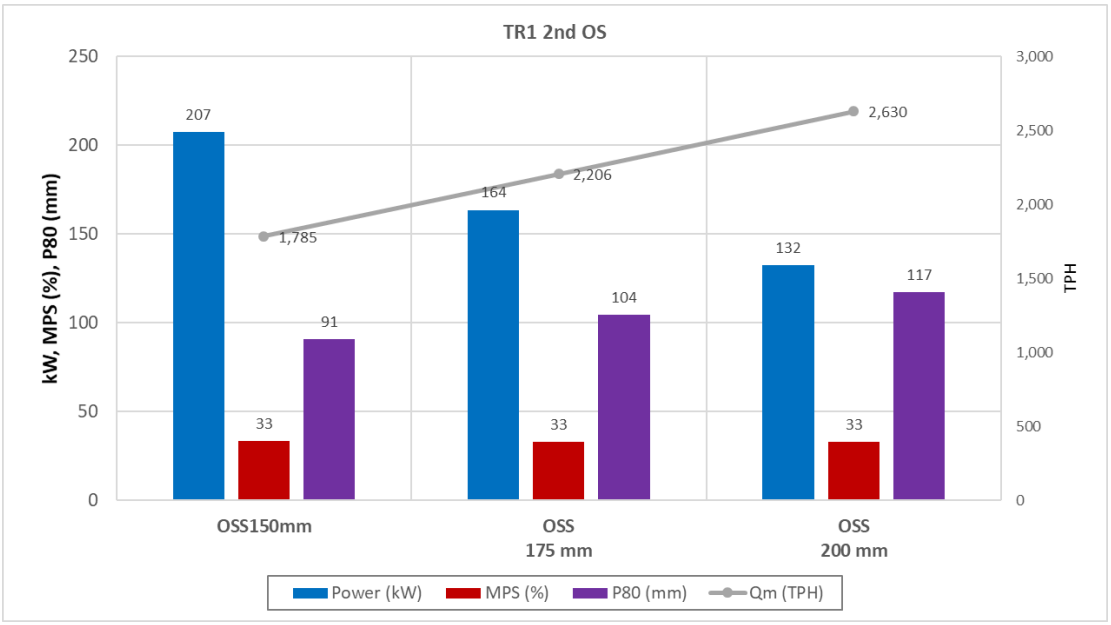

FIG 12 – Impact of changes in OSS.

In Figure 12 where the OSS is being varied, the plot shows the expected trends of increasing throughput and increasing product size, with increases in OSS. There is no change in the MPS value which shows that the same amount of liner use is required, compared to baseline.

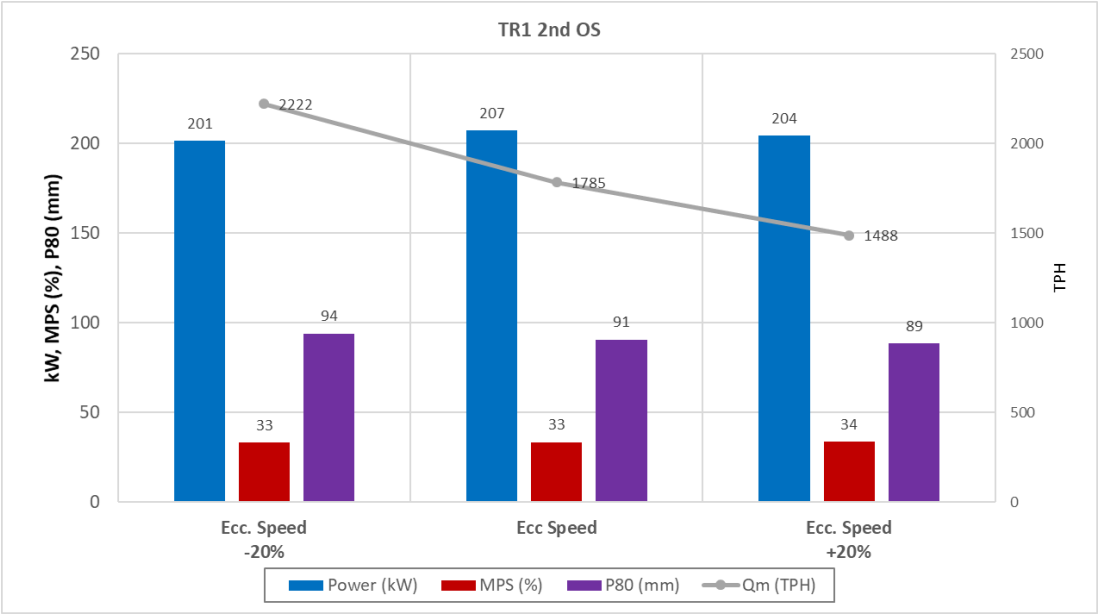

FIG 13 – Impact of changes to the eccentric speed.

In Figure 13, the impact of the eccentric speed is examined and the plot indicates that throughput decreases with increase in speed, which is commonly seen in primary gyratory crushers. Power consumption and MPS remains relatively consistent over the range of speed change.

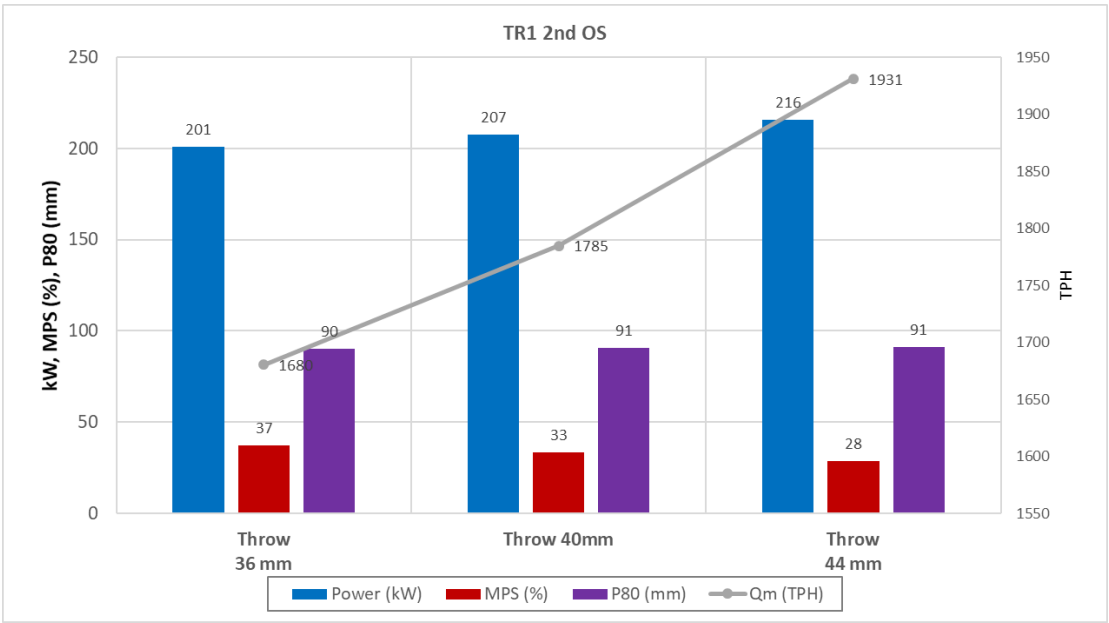

FIG 14 – Impact of changes to the eccentric throw.

For the same CSS, increasing the eccentric throw will provide more space at the discharge point of the crushing chamber, as the OSS is larger due to the increase in throw. Such a change, inevitably causes throughput to increase with throw, as seen in Figure 14. Similarly, power consumption rises as throw increases, primarily due to the increase in the flow of material. There is also a contribution from the fact that the throw increases the movement of the mantle and therefore the amount of compression applied to particles will be higher through the length of the chamber.

The most significant change that should be noted in Figure 14, is that the MPS value decreases with increasing throw. Essentially this shows that at the end of the nominal wear life of the liner set, the MPS movement required to achieve the desired setting is less than with the usual throw for this crusher, ie there is still mantle adjustment left that could be used and therefore the liner set could be operated for a longer period.

On the basis of the matrix evaluation, the move to a 44 mm eccentric throw was considered to offer the only significant benefit in the extension of liner life. Figure 15 shows the simulated changes in the key performance markers for crusher performance.

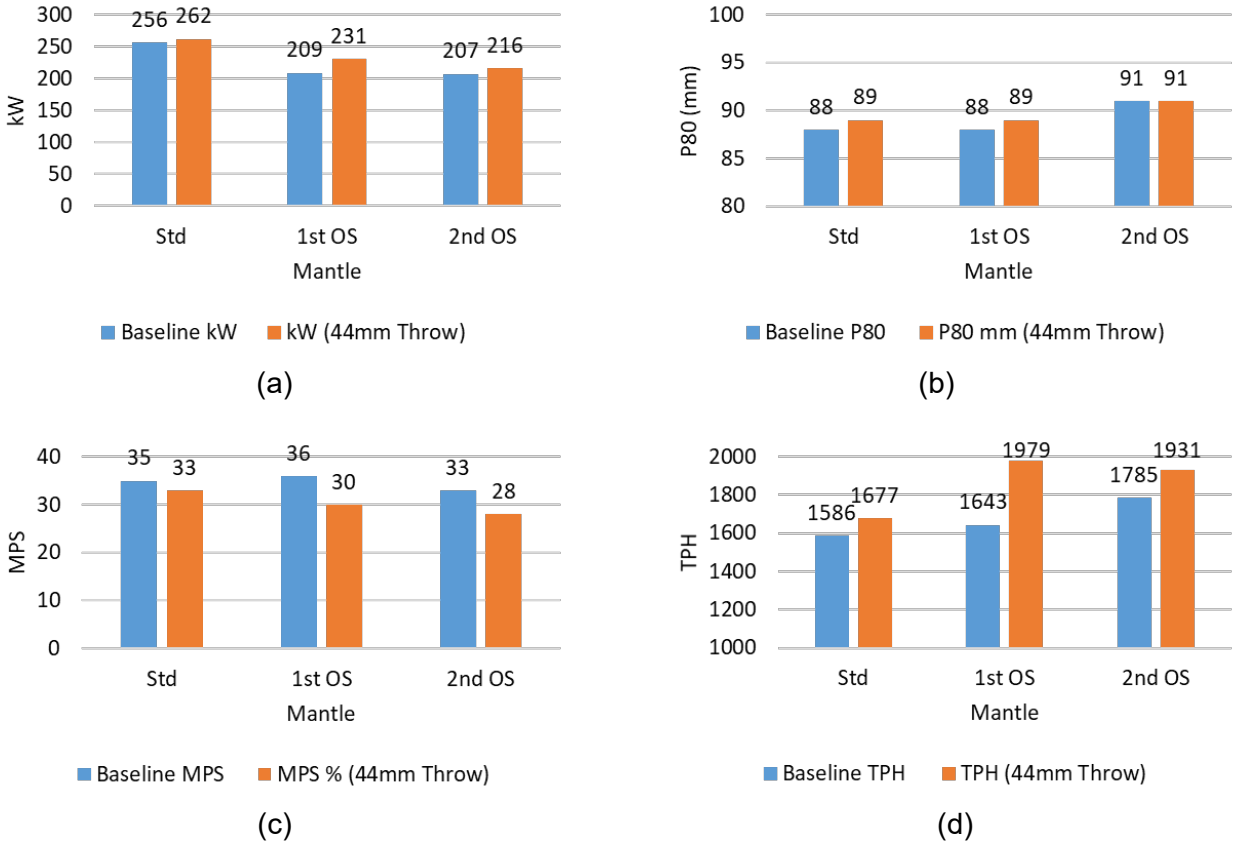

FIG 15 – Comparison of baseline crusher performance and simulated performance when a 44 mm eccentric is used. (a) Power Consumption; (b) Product P80; (c) Mainshaft Positioning System (%); (d) Throughput.

Figure 15 shows that in association with the positive change in MPS value (ie longer liner life), there were other changes that should be noted. The main points are that there is an increase in throughput and power is higher for all liner configurations. There is also a slight increase in the P80 size.

CONCLUSIONS AND FUTURE OPPORTUNITIES

The Phase 1 study reported in this paper, has shown that the non-operational, streamlined modelling approach can rapidly identify the areas influencing primary crusher performance. As such, the modelling is a system that builds trust between theory and reality, it can be used alongside physical adjustments to determine crusher parameters in order to manage business risk and develop life-long learnings.

The main technical finding points to increased eccentric throw as a way of lowering the MPS position and increasing throughput over the life of a set of liners. The associated slight increase in power consumption raises a concern for Telfer Mine site, as it currently experiences high motor winding temperatures. In addition, the impact of coarser product on downstream processing equipment needs to be carefully evaluated through modelling and simulation.

Given the success of the overall method applied in this study, the Phase 2 component (automated liner profile optimisation) is being evaluated in relation to operational considerations. As part of Phase 1, some initial work into semi-automated profile design was undertaken to build on the understanding of matched liner profiles.

Tables 2 and 3 show the results of semi-automated liner design between the existing profile and an alternate designed using the new method.

TABLE 2

New condition liners (first mantle and concave) – simulation of alternate liner set compared to current liners.

Liner set (no wear)	Power (kW)	Throughput	MPS (%)	P80 (mm)
Alternate (percentage change)	-3.6%	0%	0%	0%

TABLE 3

Worn condition liners (first mantle at end of life) – simulation of alternate liner set compared to current liners.

Liner set (worn)	Power (kW)	Throughput	MPS (%)	P80 (mm)
Alternate	-5.4%	+12.5%	-17%	0%

The results reported above are highly encouraging and they suggest that automated liner design may deliver significant performance benefits, in terms of liner life, power, throughput and control of product size.

In terms of the current status, the Liner Management Study has shown that rigour in gathering and consolidating baseline data has allowed development of an in-depth understanding that greatly assists in analysing crusher operating conditions and machine issues.

Phase 2 is now under consideration and the data, resourcing and funding requirements are being defined in readiness for management consideration.

REFERENCES

Australian Standards, 2004a. AS 60300.3.10 Application Guide – Maintainability. In: (A S Committee, ed.) Dependability Management. Sydney: Standards Australia.

Australian Standards, 2004b. AS 60300.3.11 Application guide – Reliability Centred Maintenance. In: (A S Committee, ed.) Dependability Management. Part 3.11 ed. Sydney: Standards Australia.

Bearman, R A and Briggs, C A, 1998. The Active Use of Crushers to Control Product Requirements. *Minerals Engineering,* 11(9):849–859.

Bearman, R A, 1991. The Application of Rock Mechanics Parameters to the Prediction of Crusher Performance. Ph.D. Thesis, Camborne School of Mines, CNAA, 1991.

Bearman, R A, 1994. Cone Crusher Design and Operation, *Proc. 1st CMTE Annual Conference*, Pinjarra Hills, Brisbane, July 20–22nd 1994, pp 56–59.

Bearman, R A, 2019. Gyratory and Cone Crushers, Chapter 3.4, SME Mineral Processing and Extractive Metallurgy Handbook, (R C Dunne, S K Kawatra, eds.), Pub. Society for Mining, Metallurgy and Exploration, pp. 391–416.

Evertsson, C M and Bearman, R A, 1997. Investigation of interparticle breakage as applied to cone crushing, *Minerals Engineering*, (10)2,(1997):199–214.

Evertsson, C M, 2000. Cone crusher performance, PhD thesis, Chalmers University of Technology, Gothenburg, Sweden.

Flavel, M D, Rimmer, H W, Woody, R N and Schmalzel, M O, 1988. The relevance of efficient crushing in comminution systems, Pre-Print 117th SME-AIME Annual Meeting, Jan. 25–28, 1988.

Harding, J, 2018. Increasing gyratory crusher liner wear life, B.Eng (Hons.) Thesis, Central Queensland University.

Karra, V K, 1983. Process performance model for cone crushers, *XIV International mineral processing congress*, CIM, Montreal, Que, Toronto, Canada, 1983, pp. 6.1–6.14.

Lindqvist, M, 2003. Prediction of worn geometry in cone crushers, *Minerals Engineering*, 16(12):1355–1361.

Maintworld, 2013. Continuous Improvement in Maintenance Strategies. [Online] Available at: https://www.maintworld.com/Asset-Management/Continuous-Improvement-in-Maintenance – Strategies [Accessed 31 July 2018].

Major, K, 2002. Types and Characteristics of Crushing Equipment and Circuit Flowsheets. In: (A L Mular, D N Halbe and D J Barratt, eds.), *Mineral Processing Plant Design, Practice and Control.* Vancouver: Society for Mining, Metallurgy and Exploration, pp. 566–605.

Metso, 2012. *Primary SUPERIOR® gyratory crushers, wear parts application guide.* [Online] Available at: https://www.metso.com/globalassets/saleshub/documents---episerver/application-guide-superior-series-2761-en-lowres.pdf [Accessed 10 July 2018].

Motion Metrics, 2019a. Advanced Monitoring Solutions for Mining Sites. [Online] Available at: https://www.mining-technology.com/contractors/communications/motion-metrics/#products [Accessed 18 March 2019].

Motion Metrics, 2019b. Porta Metrics. [Online] Available at: http://www.motionmetrics.com/portable/ [Accessed 18 April 2019].

Newcrest Mining Ltd, 2004. Telfer Treatment Plant Web, Internal Document, GRD Minproc Limited.

Pannell, D J, 2017. Sensitivity analysis: strategies, methods, concepts, examples [Online], Available from: http://dpannell.science.uwa.edu.au/dpap971f.htm, accessed: 8th February 2020.

Posario, P P, Hall, R A and Maijer, D M, 2004. Liner Wear and Performance Investigation of Primary Gyratory Crushers. *Minerals Engineering,* 17:1241–1254.

Saltelli, A, Chan, K and Scott, E M (eds.), 2008. *Sensitivity Analysis*, Wiley.

Whiten, W J, 1984. Models and control techniques for crushing plants, control 84. *Min. Metall. Process*. (February):217–225.

Quantification of HPGR energy efficiency effects on downstream grinding process

F Heinicke[1], H Lieberwirth[2] and M Pfeifer[3]

1. Köppern Aufbereitungstechnik, Freiberg, 09599. Email: F.Heinicke@koeppern.com
2. Institute for Mineral Processing Machines and Recycling Systems Technology, Technical University Bergakademie Freiberg, 09599. Email: H.Lieberwirth@iart.tu-freiberg.de
3. Köppern Aufbereitungstechnik, Freiberg, 09599. Email: M.Pfeifer@koeppern.com

ABSTRACT

HPGRs (high pressure grinding rolls) have been developed within the last decades for energy efficient processing of a wide variety of ores. Special interest has been raised by projects increasing the capacities of processing plants by installing HPGRs prior to ball mills. Bond ball mill tests have been used for decades as a base for ball mill dimensioning in mineral circuits. For final CAPEX-OPEX considerations of the processing circuit, one key question is about the level of grinding energy split between HPGR and downstream grinding stages. This is especially interesting if the downstream process comprises multiple grinding stages combined with separation steps.

The paper presents investigations on grinding energy consumption, size distribution and microfracturing of HPGR products, which affect the efficiency of the whole comminution and sorting process.

INTRODUCTION

The comminution process of High Pressure Grinding Rolls (HPGR) was discovered in the 1980s by the research work of the German Professor Schönert. Its main advantage is the high energy efficiency in comparison to ball mill grinding which has been the benchmark process in the cement industry by then (Schönert, 1988). Since then, a worldwide trend towards HPGR application has been established (Klymowsky *et al*, 2002), first in the cement industry but soon after also in ore processing.

Nevertheless, it has to be noted that the technology has its roots much earlier. Köppern, as one supplier of HPGR, has been working for more than 120 years on roller presses, starting with the formation of coal briquettes between two rollers. Subsequently, other fields of application, eg for fertilizer compaction, emerged (Schönert, 1966).

Even based on this history, it was a large step to transfer this process principle to minerals applications due to the much higher wear caused by the higher abrasivity of those materials. The first applications started in iron ore concentrate grinding. Meanwhile, with the optimisation of the roller surfaces using studs (Morely, 1995), the service life of the rollers substantially increased and the technology has been well established for ores and hard rock applications.

Figure 1 refers to a common installation of a HPGR for iron ore. Other set-ups with primary ball mills in circuit with cyclones which are prevalent in non-ferrous industries shall not be addresses in this paper. The material is pre-crushed to a feed size of 25 mm and then processed by HPGR within a pregrinding application in front of a primary ball mill (Morely, 1995). The HPGR is designed to work in open circuit in this case, with the transfer size to the ball mill being in the range of 80 per cent passing 7 mm. The primary ball mill is operated in a closed circuit with a screw classifier, followed by a magnetic separation stage. Tailings of this stage are reground in a ball mill hydrocyclone circuit for further processing.

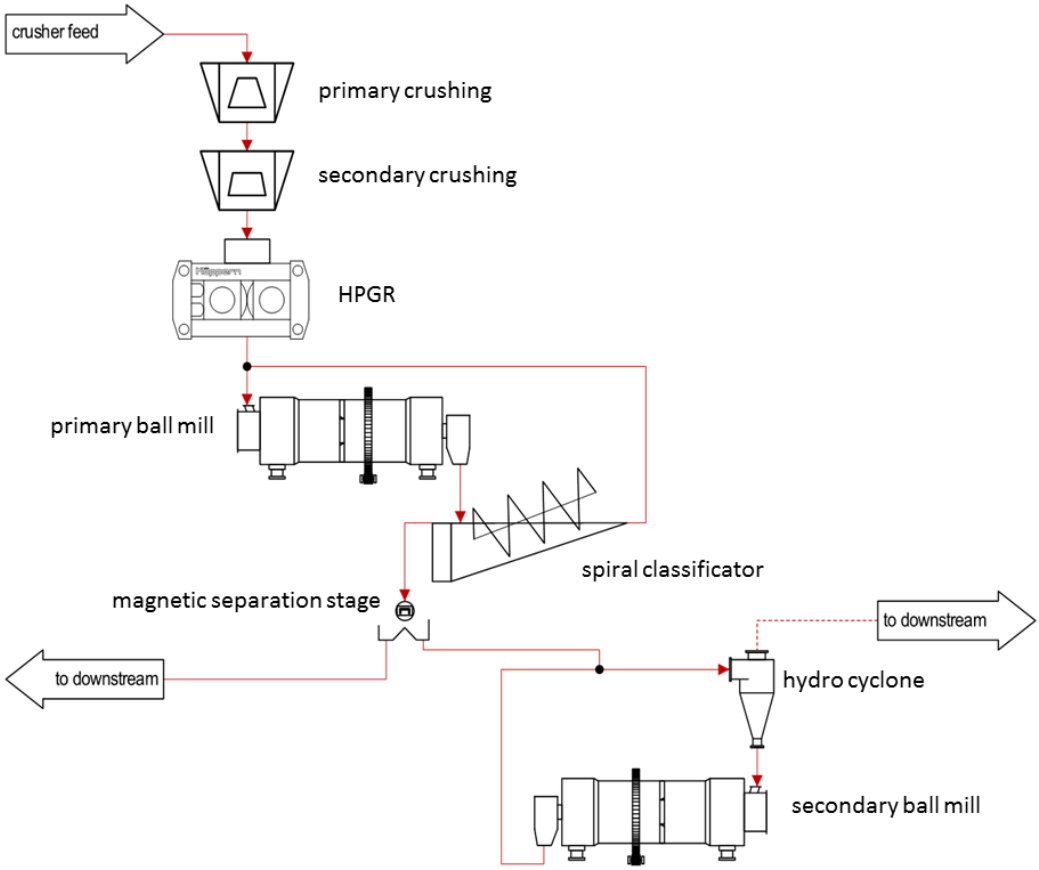

FIG 1 – Typical Flow sheet of HPGR processing in front of ball mill.

To achieve the best grinding efficiency, HPGR are available in a wide size range. Figure 2 shows a state-of-the art Köppern type HPGR. The key questions for sizing of such a machine are:

1. What throughput is to be processed by the machine?
2. What is the desired transfer size to the downstream process?
3. Which energy input shall be achieved?
4. How does the downstream flow sheet look like?
5. Which downstream effects shall be fostered, especially with regard to the subsequent ball mill grinding stage?

All those questions need to be answered in the process design phase, prior to selecting and sizing the key equipment.

FIG 2 – Typical example of a state-of-the-art HPGR.

SIZING KEY EQUIPMENT

The performance of HPGR primarily depends on the ore and its characteristics (Morley, 2006). Grinding tests are still indispensable to determine those characteristics and to predict the operational behaviour of the machine comminuting a certain material. The most important parameters are the specific throughput and specific energy consumption which allows selection of the appropriate HPGR for the required material and process parameters (Heinicke *et al*, 2016a; Gruendken *et al*, 2008). The specific energy consumption is a mass rate normalised value to describe the amount of energy transferred to the material in one single grinding pass.

$$W_{Sp,HPGR} = \frac{(P_{t,HPGR} - P_{i,HPGR})}{\dot{M}_{HPGR}} \quad (1)$$

where:

$W_{Sp,HPGR}$	mass specific energy consumption of HPGR
P_t	total power draw under load
P_i	idle power draw
$\dot{M}_{HPGR}$	total HPGR throughput equals fresh feed rate in open circuit operation

The Bond ball mill test (Bond, 1952) is a proven method to predict the performance of a ball mill. The power draw can be calculated respectively, using the following formula:

$$W_{Sp,BM} = W_i * k * \left(\frac{10}{\sqrt{P_{80}}} - \frac{10}{\sqrt{F_{80}}}\right) \quad (2)$$

where:

$W_{Sp,BM}$	power draw of ball mill
W_i	Bond work index as material specific parameter
k	product of correction factors according to Bond
P_{80}	80 per cent product size passing of ball mill
F_{80}	80 per cent feed size passing of ball mill

If the formula is analysed in an analytical way there are three influences to reduce the energy consumption which have different level of effect:

- reduce F_{80} at low impact
- reduce P_{80} at medium impact
- reduce work index at highest impact.

Figure 3 shows those effects on the throughput of a ball mill (varied parameters as per Table 1):

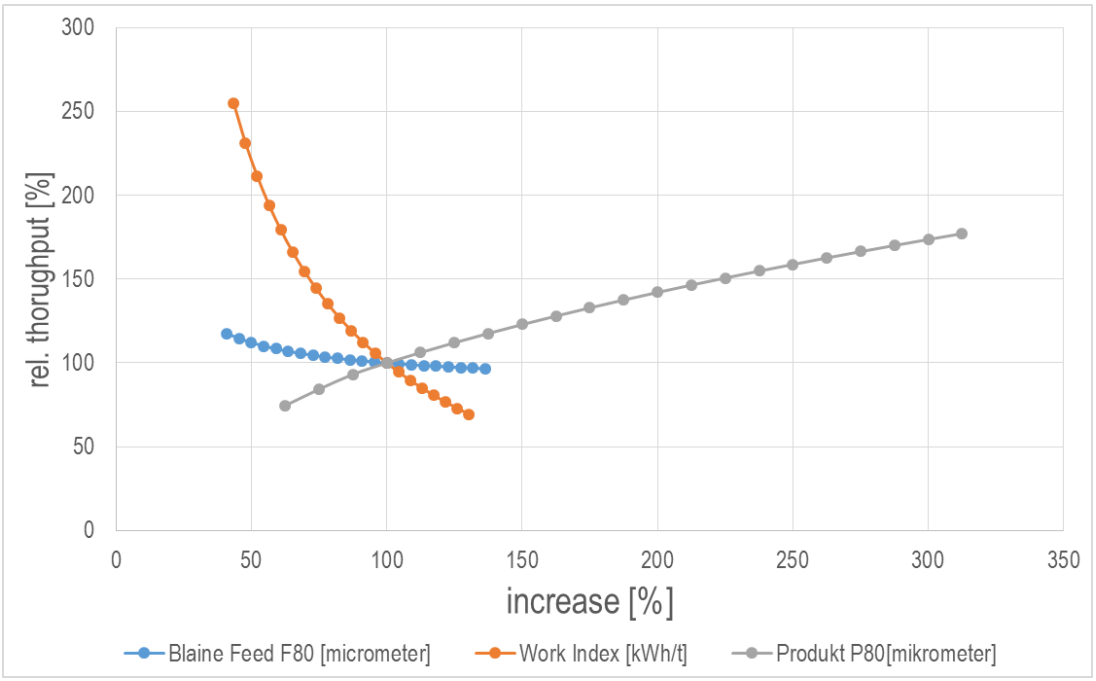

FIG 3 – Effect on throughput of Bond parameters.

TABLE 1

Input parameters for Bond variation graph of a brownfield plant (see also Povey *et al*, 2017).

Feed rate	466 t/h
Feed size F_{80}	11 mm
Product size P_{80}	0.181 mm
Mill power effective	3575 kW
Estimated Bond Wi	11.5 kWh/t

The total grinding energy according to the flow sheet shown in Figure 1 can be calculated as follows:

$$P_{TOTAL} = P_{HPGR} + P_{BM,1} + P_{BM,2} \quad (3)$$

where:

P_{Total} total grinding power consumption

P_{HPGR} power consumption of HPGR

$P_{BM,1/2}$ power consumption of primary (1) and secondary (2) ball mill

The combination of (1) and (3) results in (4):

$$P_{TOTAL} = W_{Sp,HPGR} * \dot{M}_{HPGR} + W_{Sp,BM,1} * \dot{M}_{BM,1} + W_{Sp,BM,2} * \dot{M}_{BM,2} \quad (4)$$

where:

$\dot{M}_{BM,1/2}$ total primary (1) and secondary (2) ball mill throughput

$W_{Sp,BM,1/2}$ primary (1) and secondary (2) ball mill work index

If a mass split of 50 per cent is assumed in the magnetic separation stage, the masses are related as follows:

$$\dot{M} = \dot{M}_{HPGR} = \dot{M}_{BM,1} = \dot{M}_{BM,2} * 2 \quad (5)$$

where:

$\dot{M}$ fresh feed rate

Thus, the combination of (2), (4) and (5) results in (6):

$$P_{TOTAL} = \dot{M} \left\{ \begin{array}{c} \left(P_{t,HPGR} - P_{i,HPGR}\right) + W_{i,1} * k * \left(\frac{10}{\sqrt{P_{80,\mathrm{BM1}}}} - \frac{10}{\sqrt{P_{80,\mathrm{HPGR}}}}\right) \\ +W_{i,2} * k * \left(\frac{10}{\sqrt{P_{80,\mathrm{BM2}}}} - \frac{10}{\sqrt{P_{80,\mathrm{BM1}}}}\right) * 0{,}5 \end{array} \right\} \quad (6)$$

where:

$W_{i,1/2}$ Bond ball mill work index as material specific parameter of primary (1) and secondary (2) ball mill

k product of correction factors

In a given brownfield application, the installed power of the ball mills is fixed which means that the product of specific energy and maximum attainable throughput has to be the same for each mill at all times. Also, the transfer size to the downstream process after second ball mill is defined by the material characteristics and respective specifications of the downstream process such as liberation size and throughput. The product size of the HPGR, however, can be adjusted by increasing the hydraulic piston pressure in the machine. Thus, also the feed size to the primary ball mill can be controlled. An increase of the hydraulic pressure in the HPGR leads to an increased power draw of the HPGR roll drives as well (see Figure 4).

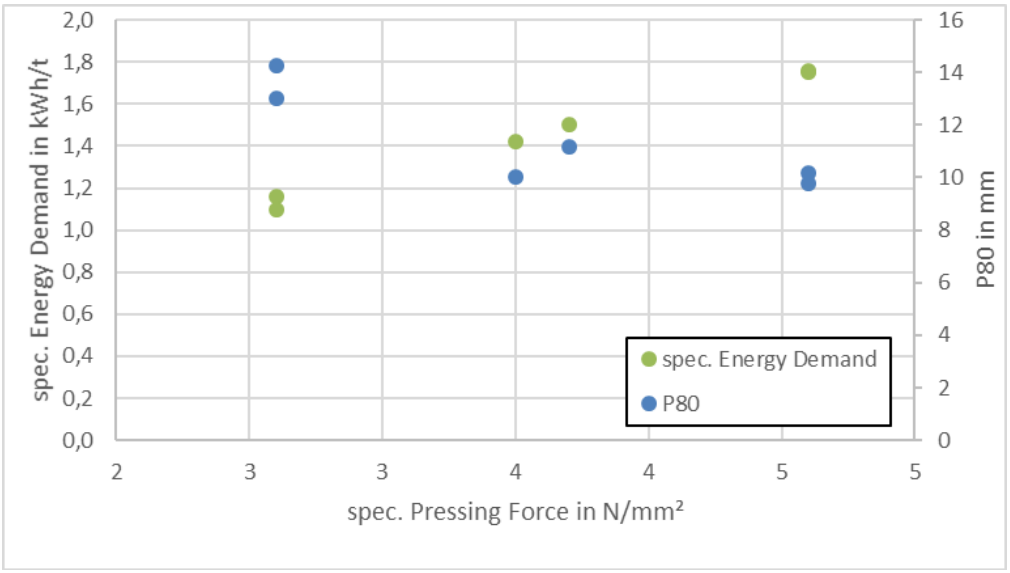

FIG 4 – Correlation of specific hydraulic pressure and specific energy demand from a test series with iron ore.

Moreover, the high pressure grinding regime leads to micro-fractures within the product as shown in Figure 5. Those micro-fractures reduce the strength of the ore fed to subsequent comminution machines. In the presented flow chart, they reduce the Bond ball mill work index of the material transferred from the HPGR to the primary ball mill. Thus, the throughput or the size reduction degree of the primary ball mill can be increased to fully exploit the installed power of the ball mill. It became clear that there is an optimisation potential between energy efficient grinding in the HPGR and downstream ball mill grinding.

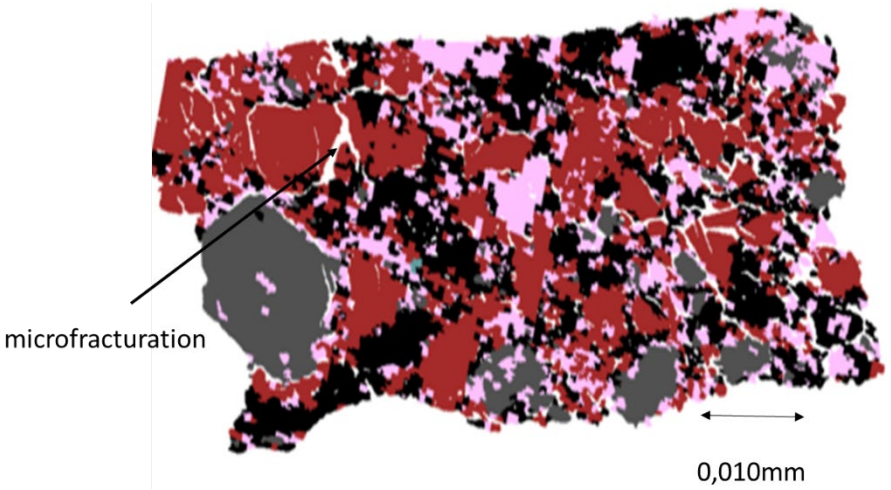

FIG 5 – Example of a micro-fractured particle of a HPGR.

Such an optimisation has to include the whole downstream process. An simple increase of the throughput in the primary ball mill would mean that the second ball mill would receive a higher feed rate as well. It can be assumed that the mircro-fracturing initiated by the HPGR will be exploited in the primary ball mill. Therefore, the secondary ball mill has to be designed considering a higher Bond ball mill work index than the primary one. The best way to avoid a potential overload of the secondary ball mill is to reduce the transfer size from primary ball mill. This affects the sorting behaviour and impacts the optimum process as well. The micro-fracturation of the particle is known to increase the liberation degree and therefore can influence the magnetic separation (Michaelis, 1995). Again the design of mass flows is influenced and need to be optimised. For this optimisation, it is essential to understand of the differences between ball mill grinding and HPGR grinding in view to the downstream energy efficiency effects.

INFLUENCES ON BOND WORK INDEX USING HPGR

To assess the energy efficiency effect of HPGR, various Bond ball mill test series were performed (see also Brüggemann, 2019), all of them following the stipulations of Bond. The feed material for the Bond tests was a medium grained granodiorite from Kindisch (Germany) with a compression strength of σ_D = 176 MPa, produced by a hammer mill with grate (HAZEMAG Unirotor 490/380), a single toggle jaw crusher (Retsch BB 250 XL) and an HPGR (Köppern HPGR 60/10–230 and HPGR 22/3), see Figure 6. In those three machines, the material is stressed in different ways, merely by compression in the jaw crusher and the HPGR or by blow and shear in the hammer mill.

Despite the upper limit of the feed size of the material for the tests was always the same (-3150 µm), the particle size distributions PSD vary significantly. The first mayor difference is the slope of the particle size distribution curve (see Figure 7). While the particle size curves distribution curves of the jaw crusher and hammer mill product in the respective size range show only minor differences, the slope of the HPGR product size distribution is shallower, which is a common observation for HPGR grinding (Heinicke, 2012).

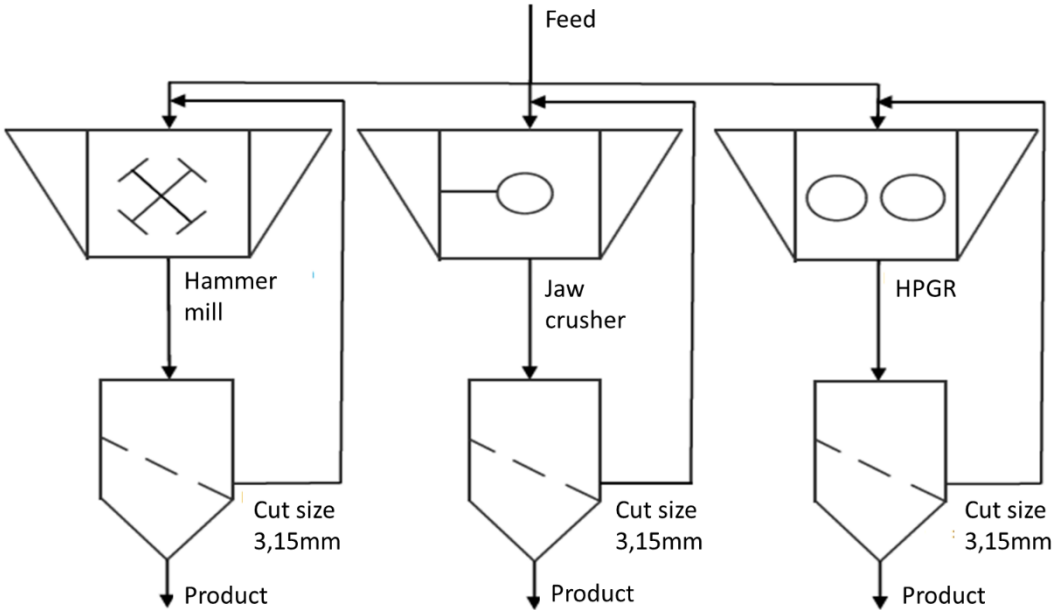

FIG 6 – Test work set-up for preparation of sample.

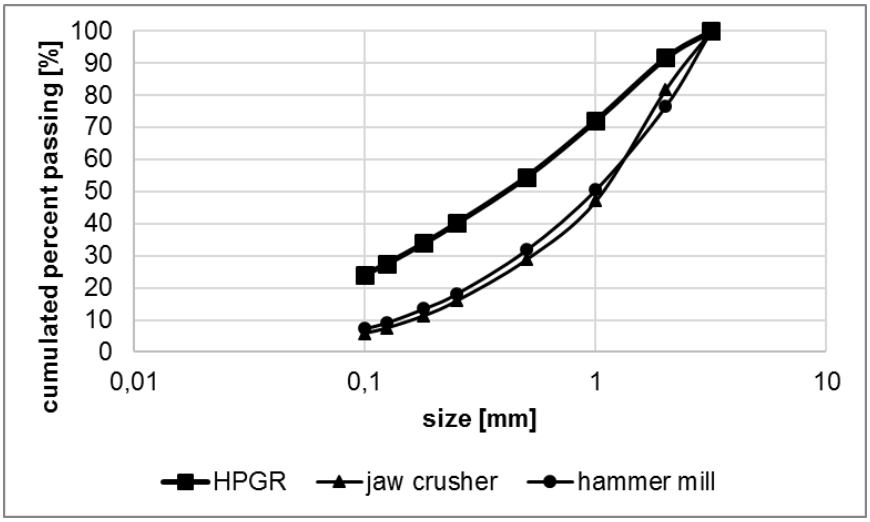

FIG 7 – Particle sizes for different preparations.

It has been well established, that among others the preparation of the feed material influences the results of the Bond test (Gonzáles, 2021; Weier and Chenje, 2018; Vizcarra and Wong, 2019) but the experimental error is usually small (Ballantyne and Giblett, 2019). The small experimental error was also confirmed in our own tests with the scatter of three repeated tests being around 0.4 per cent (±0.07 kWh/t of a medium 18.08 kWh/t). Therefore, the Bond test is used also in this paper to assess the influence of micro-fractures generated by HPGR onto the grindability. Initially the W_i values were assessed for the PSD of the materials as obtained by just screening at a cut size of 3150 µm, see Figure 7. The resulting values of the Bond test are given in Table 2. They showed a reduction of the Bond work index of up to 8 per cent for the material ground by the HPGR.

TABLE 2

Overview of Bond work index for different feed preparations.

Preparation aggregate	W_i [kWh/t]
Hammer mill	17.89
Jaw crusher	18.09
HPGR	16.79

This reduction included potential effects of micro-fractures caused by HPGR as well the difference of the three feed materials. To reduce the influence of the differing PSD distributions, the product materials of jaw crusher and hammer mill were screened and classified into eight size fractions between 0 and 3150 µm. For comparison, the same procedure was also conducted for the original fresh secondary crushed material from the quarry (fraction -3150 µm directly separated from original feed size -32 000 µm without further comminution). Afterwards, the mass per each fraction was adjusted to the shear of the respective fraction in the HPGR product. The modified fractions of each feed material were combined again and thoroughly blended and homogenised, finally well matching the particle size distribution of the HPGR product.

With the three modified feed materials, the Bond tests were repeated. The results are presented in Table 3. The reduction of the Bond work index increased even further to 15 per cent which indicates a remarkable effect for the power draw of a ball mill installed after the HPGR.

TABLE 3

Overview of Bond index for different feed preparations at same feed PSD.

Preparation aggregate	W_i [kWh/t]
Hammer mill screened to match HPGR	19.34
Jaw crusher screened to match HPGR	18.34
Fresh feed screened to match HPGR	18.32
HPGR	16.79

A further effect of an HPGR installation prior to ball milling in ore processing can be seen in the high comminution selectivity, as shown in Figure 8 (Kühnel, 2021). During size reduction in the sample preparation for the Bond tests deploying different machine types, the coarser particles report to the finer classes depending on their mineral content and the type of stressing introduced by the comminution machines. While selectivity in comminution is generally limited with machines such as jaw or cone crushers, machines deploying the confined bed comminution principle such as HPGRs may support such selectivity as shown in Figure 8. Here, the fine fractions (-1 mm) exhibit a remarkable reduced quartz content while the iron is enriched.

A sample collected from such material for the Bond test by just classifying the -3150 µm fraction would simply reflect the increased content of the softer iron containing minerals. Assessing such a sample in a Bond test may again result in overdesigning mills for a production process which do not account for the special comminution characteristics with an HPGR. This effect has not been quantified so far as the preparation method of material for the Bond tests is not further specified and typically does not reproduce the real production conditions appropriately for HPGR.

Those effects have to be carefully analysed for HPGR test work design. Typical vendors of HPGR have this ability and knowledge and will consult the individual clients accordingly for the individual ore type of the project (Heinicke *et al*, 2016b).

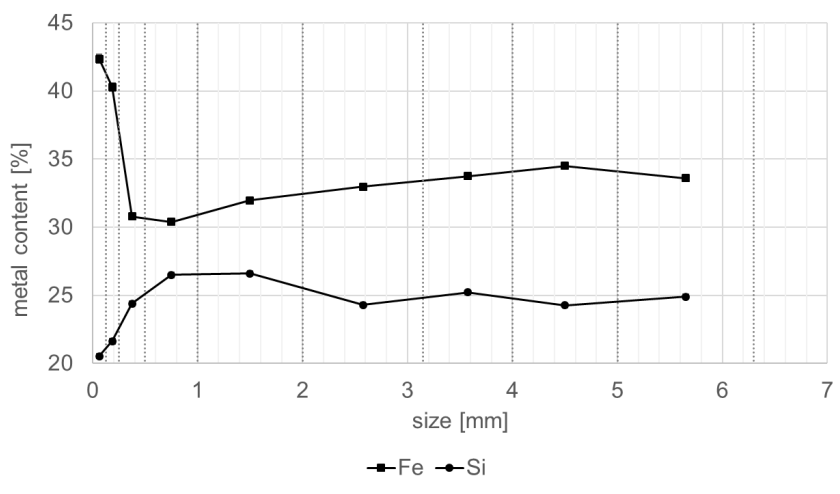

FIG 8 – Selective comminution effects in feed material processed by HPGR for an ore with high quartz and low iron contents.

CONCLUSIONS

The grinding with HPGR showed remarkable effects on the downstream energy efficiency in ore processing. To quantify those effects, common test routines according Bond may be oversate the actual specific energy consumption as they are influenced by size distribution, particle weakening and selective grinding effects of HPGR. A careful planning of HPGR test series has to be done to balance the effect to downstream processes correctly. As the ores will differ from project to project this procedure shall be addressed by client and vender for each individual project.

ACKNOWLEDGEMENTS

This work was funded by Köppern within a research cooperation with Technical University of Freiberg. The authors would like to thank Köppern for the right to publish this paper and Jonas Brüggemann for the excellent test work performed within his thesis.

REFERENCES

Ballantyne, G and Giblett, A, 2019. Benchmarking comminution circuit performance for sustained improvement. SAG Conference, Vancouver.

Bond, F C, 1952. The third theory of comminution. *Mining Engineering*, p. 484–494.

Brüggemann, J, 2019. Diskretisierung des Bondtest für GBWM Anwendungen. Masterarbeit. Technische Universität Bergakademie Freiberg.

Gonzáles, G G, Coello-Velazquez, A I, Fernandez, B, Menendez-Aguado, J, 2021. Multivariate Analysis of the Ball Mill Bond's Standard Test on 2 Tantalum Ore. *Metals*, 11, 1606.

Gruendken, A, Matthies, E, vanderMeer, F D, 2008. Flowsheet considerations for optimal use of high pressure grinding rolls. *Proceedings of Comminution 08*, pp 1–37.

Heinicke, F, 2012. Beitrag zur Modellierung der Zerkleinerung in Gutbettwalzenmühlen. Dissertation. Rheinisch-Westfälische Technische Hochschule Aachen.

Heinicke, F, Guenter, H, Kamptner, A, 2016a. How to avoid errors in HPGR product characterization. *Proceedings of Procemin*, in Santiago de Chile, pp 1–11.

Heinicke, F, Lieberwirth, H, Guenter, H, 2016b. Modelling of HPGR Edge recycling data with progressive grinding data. *Proceedings of Comminution*, pp 1–11.

Klymowsky, R, Patzelt, N, Knecht, J, Burchardt, E, 2002. Selection and sizing of High Pressure Grinding Rolls. *SME Handbook*, pp 1–40.

Kühnel, R, 2021. Untersuchungen zur trockenen Aufbereitung von Magnetiterzen unter besonderer Berücksichtigung des Trennverhaltens im Luftstrom. Dissertation. Technische Universität Bergakademie Freiberg.

Michaelis, H, 1995. Real and potential metallurgical benefits of HPGR in Hard Rock Ore Processing. *Randol Conference*, pp. 1–9.

Morley, C, 1995. The case for High Pressure Grinding Rolls. *Randol Conference*, pp. 1–16.

Morley, C, 2006. Flowsheets for HPGR. *SAG Conference*, pp. IV172-IV189.

Povey, B C, Nol, Lifanov, D, 2017. The introduction of HPGRs to the SGOK magnetite plant in Russia. *Proceedings of Metplant*, pp 1–19 (The Australasian Institute of Mining and Metallurgy: Melbourne).

Schönert, K, 1966. Einzelkorn-Druckzerkleinerung und Zerkleinerungskinetik. Untersuchungen an Kalkstein-, Quarz-, und Zementklinkerkörnern des Größenbereiches 0,1–0,3 mm. Dissertation. TH Karlsruhe.

Schönert, K, 1988. A first survey of grinding with high-compression roller mills. *International Journal of Mineral Processing* 22, pp 401–412.

Vizcarra, T, Wong, B, 2019. Testwork variabililty – implications for grinding circuit design. *SAG Conference*, Vancouver.

Weier, M L, Chenje, T, 2018. Accuracy of the Bond ball mill test and its implications. *14th International Mineral Processing Conference & 5th International Seminar on GeoMetallurgy*. Santiago, Chile, Procemin-Geomet.

Soft sensors for advanced process monitoring and control of comminution circuits

M Hilden[1], F Reyes[2], Z Ye[3], V Jokovic[4], G Forbes[5] and M Yahyaei[6]

1. Senior Research Fellow, University of Queensland, Indooroopilly Qld 4068. Email: m.hilden@uq.edu.au
2. Research Fellow, University of Queensland, Indooroopilly Qld 4068. Email: f.reyes@uq.edu.au
3. PhD Candidate, University of Queensland, Indooroopilly Qld 4068. Email: ziming.ye@uq.edu.au
4. Senior Research Fellow, University of Queensland, Indooroopilly Qld 4068. Email: v.jokovic@uq.edu.au
5. Senior Research Fellow, University of Queensland, Indooroopilly Qld 4068. Email: g.forbes@uq.edu.au
6. Associate Professor, University of Queensland, Indooroopilly Qld 4068. Email: m.yahyaei@uq.edu.au

ABSTRACT

Soft sensors offer several practical advantages for the process control of comminution circuits by combining multiple conventional sensors and other data sources with real-time analysis using mechanistic, phenomenological or machine learning models. While there has been a growth in the use of machine learning techniques for developing soft sensors in minerals processing applications, this paper describes advantages and challenges of using soft sensor models developed on the basis of process knowledge.

Recent experience with three new soft sensor technologies developed by the authors are discussed. The *Mill Filling Inference Tool* which has been implemented at several mine sites, compares SAG mill load cell and power draw measurements with outputs of a semi-mechanistic power model to estimate the mill ball and total filling in real time. The progressive wear of the mill liners is modelled, allowing the model to correct the load mass due to the mass loss automatically and to estimate the charge trajectory. This information enables the mill to be operated more confidently near its limits. A coarse-ore stockpile soft sensor as been recently developed using a 3D cellular automata-based model to track ore size throughout the pile, and estimating the live capacity and size at each stockpile feeder to the primary mills. Finally, a hydrocyclone soft sensor is being developed to monitor performance using available hydrocyclone models to estimate the size and flow balance around the cyclone in real time.

The model-based soft-sensor approach aims to synthesise and analyse existing data and provide operators and engineers with process- and model-relevant information that can facilitate making better process decisions. Maintenance data has proven useful for model development as it allows soft sensors to automatically adjust and compensate for the effect of progressive wear, for example for mill liners, thus helping the models to maintain calibration throughout the equipment life.

INTRODUCTION

Minerals processing plants rely on measured data from large numbers of physical sensors to monitor, control and operate the process. In many production environments, soft sensors (also known as software sensors, inferential sensors, virtual online analysers, adaptive estimators, state observers, or virtual sensors) are used to augment these process measurements. Soft sensors are mathematical models using data from physical sensors and other sources as inputs to calculate process parameters that may be impractical to measure directly or a redundant estimate to confirm physical measurements (Hodouin *et al,* 2001). Soft sensors can be capable of sensor fusion: synergistically combining multiple measurements with algorithms and models to provide the operator with deeper insights into the operating state of the process. Thus, soft sensors can range from relatively simple regression models to complex machine learning models potentially consisting of multiple submodels or even real-time simulations akin to a digital twin (Galan *et al,* 2021).

With the rise of the industrial internet of things and edge computing or smart sensor capabilities, physical sensors and virtual sensors can be combined using programmable microcontrollers

embedded into field devices, although soft sensor computation is more commonly performed on the DCS or a dedicated server. Performing some of the computation work locally can reduce latency and communication bandwidth requirements. Soft sensors have been used extensively, for example, in the chemical process industries (Kadlec, Gabrys and Strandt, 2009; Fortuna, Graziani and Rizzo, 2006), bioprocessing (Brunner *et al,* 2021), and minerals processing (Sbarbaro and del Villar, 2010; Hodouin *et al,* 2001) for a range of purposes. These include:

- Increasing the estimation frequency or reducing cost for parameters that can otherwise only be measured offline, which can then be used for process control.
- In parallel with hardware sensors for fault detection and to reconstruct sensor output in case of a fault (as a backup of the physical sensor).
- Monitoring and diagnosing process performance to detect process state and deviation from normal operation.
- Model-predictive process control.

Soft sensors may be primarily data-driven (black box) or model-driven (white-box), or a hybrid (grey box) (Kadlec, Gabrys and Strandt, 2009). These modelling approaches have pros and cons. The data-driven approach is based on a statistical analysis of historical performance specific to the process being modelled. This paradigm has become increasingly popular and is considered easier to implement as the degree of process knowledge required is much less. Various machine learning tools are employed, including deep learning, regression modelling (support vector regression, ARMAX, stepwise, principal component), artificial neural networks, fuzzy logic, case-based reasoning and clustering.

Model-driven solutions, on the other hand, incorporate process knowledge, for example, in the form of traditional engineering models. These can be more robust but are generally more costly to develop. An important advantage of the model-driven approach is the ability to embed existing knowledge of the process within the model. The complexity of real processes can be a barrier to model-based soft-sensors working reliably in practice, however. The industrial application of process models as soft sensors has long been an important focus of researchers. In fact, one of the earliest models developed at the Julius Krutchnitt Mineral Research Centre (JKMRC) by Rao (1966) was a site-specific soft sensor for hydrocyclone control. Since then, several soft sensor types have been reported for estimating hydrocyclone overflow size (eg P80 or minus 200#) (Casali *et al,* 1998b; Zhou, Lu and Chai, 2014; Karimi *et al,* 2010; Dai *et al,* 2016) and overflow solids concentration (Casali *et al,* 1998a).

Other examples of soft sensors in minerals processing include a dynamic weightometer soft-sensor for both fault detection and estimating conveyor weight from power draw and other measurements (Pan *et al,* 2003), estimation of ball mill overload (Forbes *et al,* 2021), monitoring of SAG mill filling (Gonzalez *et al,* 2008), and fault detection in hydrocyclones (Bazin *et al,* 2009). The reader is referred to Hodouin (2011) for a more comprehensive list of applications.

The soft sensor models in this paper adopt the model-based paradigm, and therefore the case for model-based soft sensors based on fundamentals and process knowledge is set out. Three soft sensor models are discussed as examples: a soft sensor for estimating the total and ball filling in SAG mills, a soft sensor for tracking ore flow in a coarse-ore stockpile, and a soft sensor for modelling the ball mill cyclones. Each of these soft-sensor models are designed to operate in real time to present additional information to the process control operator and production engineers. The advantages of the model-driven approach in minerals processing applications are discussed.

MILL FILLING INFERENCE TOOL

One of the most important factors affecting SAG mill performance is the filling level of the mill contents. Typically, mill control uses the mill weight (using a load cell) or the bearing pressure measurement (a proxy for mill weight) to maintain the desired filling. However, a complicating aspect for control is that the weight of the mill changes over the life of the mill liners due to wear. Furthermore, the mill contains both rock and steel balls as grinding media, and it is important to estimate the proportions of each.

The steel or composite rubber/steel liners in SAG mills are designed to lift the contents as the mill rotates as well as to protect the structural integrity of the mill. Liners are replaced every several months and, in many cases, on differing schedules due to wear rates varying in different parts of the mill. The 40' SAG mill at Cadia, for example, lost over 300 tons over the course of the 5-month liner life (Powell *et al,* 2012) relative to a typical load weight of around 750 tons. Hence the weight recorded by the load cells needs to be corrected for this change in mill weight. Given that laser scans are routinely performed for condition monitoring purposes at many sites, it is possible to use this data to create wear models, which can then be applied to automate the adjustment of the mill weight control set point.

A soft sensor developed by the authors combines multiple sensors and mathematical models to aid SAG and ball mill control. The system has been tested and is successfully operating at approximately 10 mine sites worldwide. The model, shown in Figure 1, incorporates:

- An estimate of the load mass, corrected for the change in liner weight, updated daily using a model of liner wear which is calibrated to historical data. Whether load cell or bearing pressure is used to estimate the mill weight, data are calibrated to measured filling levels obtained using crash-stop measurements.
- A version of Morrell's (1996) power model to back-calculate both the ball and total filling. Both power draw and load mass are required to estimate filling because a given load weight can be made of different combinations of ball and rock filling.
- Modelling of historical liner wear data to describe the shell lifter height and face angle, which is used with Powell's (1991) trajectory calculation to estimate the point of impact for the measured mill speed. This allows the mill speed to be controlled throughout the liner life in a way that avoids damaging shell impacts.
- A model of grinding media wear that provides an initial estimate of the ball filling. This is linked to the ball addition, whether added continuously or in batches.

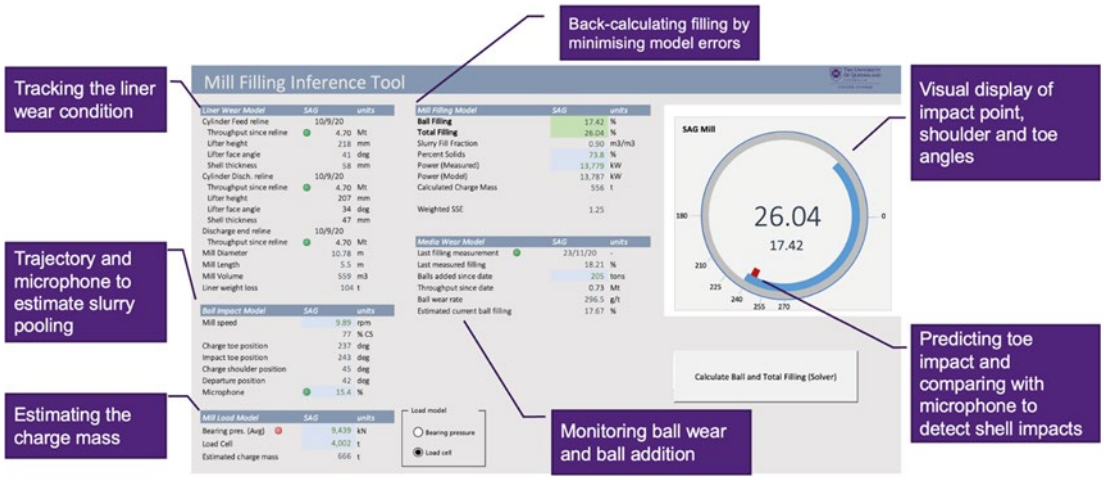

FIG 1 – A typical interface for the MillFIT SAG mill load analysis tool.

The objective of the sensor is to provide useful process information to the process control operator. Initially, this was via an Excel interface reading data from the plant historian system. More recent installations are being embedded directly in the DCS as the Excel-based solution is limited by a one or two minutes time lag before data appears in the historian system. The information provided by the soft sensor has several benefits for the operation and management of the SAG mill. The system provides an intuitive display of mill total and ball filling, making it easier to control the mill and prevent over or under-loading the mill. Likewise, the visual indicator of charge trajectory is useful for maintaining the optimal safe mill speed. Frequency of grind-outs can be reduced by estimating the ball load and tracking ball wear.

STOCKPILE SOFT SENSOR

Most milling circuits are fed from large coarse ore stockpiles that form a buffer between the mine and the plant. These piles typically contain several hours or perhaps up to a few days' worth of primary-crushed ore, which is drawn down to feed one or more SAG mills. The ore feeding the pile can vary in size and grade, and one of the functions of the stockpile is to blend the ore to reduce some of these variations. However, countering the blending function, granular materials with a broad particle size range can segregate by size within the pile resulting in product size variability. Various mechanisms contribute to segregation, although a dominant process is surface percolation which causes fines to settle between the gaps of larger particles while the particles are in motion.

Because stockpiles contain varying amounts of ore in the pile during operation, accurately quantifying storage volume is important for managing overall mine production. If the mine or primary crusher experience production delays, the mill can keep operating until the pile is emptied. Similarly, if the plant experiences downtime, the mine can continue production for some time, and the stockpile will continue to fill. Stockpile storage is measured using level sensors or photogrammetry. A soft sensor capable of estimating stockpile level was reported by Pan (2015) as a backup for existing ultrasonic or radar level sensors.

A mathematical model of the coarse ore stockpile has been developed at the JKMRC based on the continuous cellular automata approach. Details of the model are described elsewhere (Ye, 2022). The model (Figure 2) discretises the pile into a relatively coarse 3D grid of cells where the cells are in the order of 9 m^3 in size (cells are, however, permitted fractional filling), and therefore each cell represents many particles. This is necessary because particle-based methods such as DEM simulation would be too slow to permit real-time simulation with available computers.

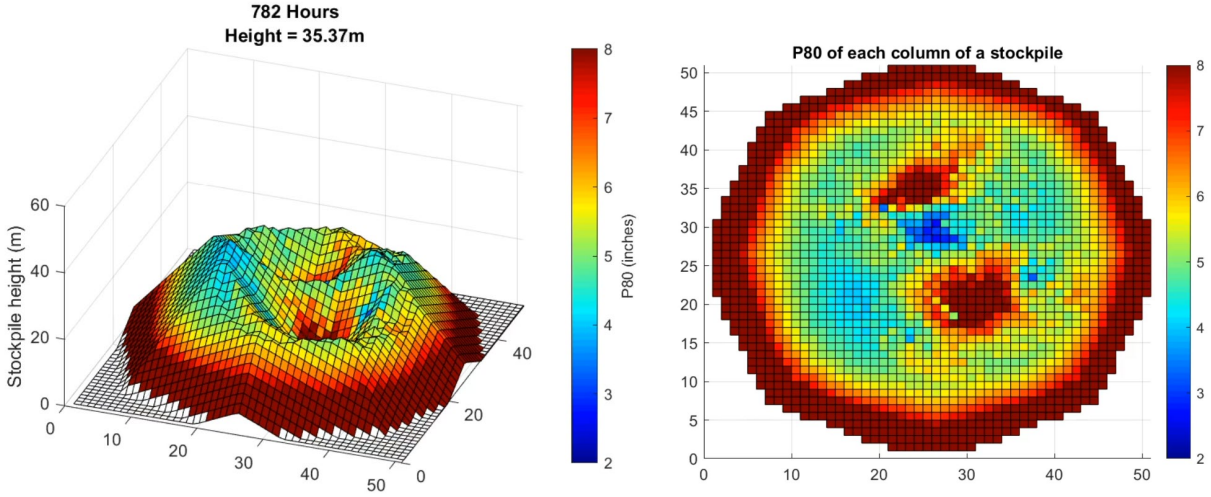

FIG 2 – Simulated coarse-ore stockpile showing significant size segregation of coarse particles to the edges of the pile (top view on right). Ore is extracted from up to eight drawpoints onto two product conveyors.

Each simulation timestep consists of four discrete processes:

1. New ore can be added to the grid at a position or positions corresponding to where a conveyor would throw the feed. This can be calculated using a conveyor trajectory model. The trajectory segregation mechanism can also be simulated in this step, separating the feed into a coarser portion to land on the pile slightly further from the conveyor position than the finer portion of the feed. Instrumentation from belt weighers, conveyor speed sensors and particle size cameras estimating the feed size can be used as soft sensor inputs to describe the properties of the ore being added to the pile.
2. Ore at the base of the pile can be removed at positions corresponding to the location of apron feeders. Multiple drawpoints can be assigned feeding one or more product conveyors. During the simulation, these feeders can start and stop or vary in feed rate. Data from the product conveyor belt weighers and, with the flow being characteirsed by the feeder speed and product.

3. Voids created at the base of the pile can propagate to the surface of the pile, allowing ore in the pile to migrate towards the drawpoints. The voids propagate vertically and laterally, eventually forming an inverted cone of flow towards the feeders (see Figure 2 near position (30,20,0)).
4. Material flows at the surface of the pile from higher columns to the lower neighbouring columns where the local slope exceeds the ore's angle of repose. The surface profile is continually perturbed by the feeding of new ore and the movement of the particles towards the discharge, causing new flow events. Size segregation takes place during flow events. This is modelled by dividing the volume of material located at the higher column into a coarser portion that flows to the lower column and a finer portion that remains at the higher column.

The soft sensor model incorporates many of the important mechanisms and behaviours observed in a coarse ore stockpile, albeit a simplification of the physics of granular process, which are still incompletely understood. The soft sensor model can report useful information about the operation of the pile in real time, including (Ye, Yahyaei and Hilden, 2021):

- Approximate surface profile and height of the stockpile that can be compared with measurements from photogrammetry and height sensors.
- Live volume of the pile that can be used for estimating remaining capacity for use in production planning, ore reconciliation and metal accounting.
- Particle size, grade and volume above each feeder that can be used for controlling the apron feeder speeds to control the feed size to the SAG mills.

CYCLONE SOFT SENSOR

Hydrocyclone soft sensors have been reported by numerous authors making use of existing empirical or semi-mechanistic hydrocyclone models designed for steady-state simulation (eg, Plitt, 1976 or Nageswararao, Wiseman and Napier-Munn, 2004), as noted earlier. Although in principle, empirical models can be used in soft sensor applications, naïve implementations of empirical hydrocyclone models in a real-time modelling application without also using a data-driven approach are typically not successful. For steady-state use, these empirical models contain parameters that have to be calibrated to experimental data collected during plant surveys. However, these parameters cannot be assumed to be constant for all operating conditions. Hydrocyclone performance is strongly affected by the feed particle size distribution, solids concentration and flow rate which are difficult to measure accurately in real time. Moreover, process dynamics also have to be considered.

Key process control variables that should be estimated by soft sensors are particle size distributions (especially the overflow P80) and solids concentrations. Plants typically have instrumentation to measure the cyclone feed flow rate and solids concentration, however these measures are rare for the cyclone underflow or overflow streams. Many plants have introduced particle size sensors on the overflow stream (for example, Metso Outotec PSI or Cidra PST), however these are not ubiquitous. A soft-sensor solution to measure these missing information would be an appropriate alternative. Additionally, it can be useful to develop fault detection algorithms or backup soft sensors for the physical instrumentation if they exist (Sepulveda *et al,* 2019).

A new hybrid hydrocyclone soft sensor (Figure 3) is under development at the JKMRC to model important operating parameters around the ball milling circuit. The developed system estimates the overflow P80, overflow solids concentration and circulating load.

Important features of the model are that it will:

- Estimate the cut size and flow rate for each cyclone in the cluster.
- Track the wear of key cyclone wear components, principally the spigot diameter and operating hours for each cyclone, as a means of automatically correcting the model for wear over time.
- Simulate hydrocyclone performance in the event of opening or closing one of the cyclones in the cluster to help with timing these control decisions.

- Warn of potential ball mill overloading when slurry accumulation in the ball mill circuit is detected.
- Estimate the operating work index and size-specific energy for detecting changes in ore properties.

FIG 3 – Dashboard of the JKMRC hydrocyclone performance soft sensor prototype. Online inference (yellow cells) of the feed properties, as well as the water and solids split, are provided using existing instrumentation (green cells).

DISCUSSION

As shown in the examples described in this paper, there are numerous challenges to developing soft sensors in minerals processing applications. However, the use of model-based or hybrid models can have advantages over pure data-driven or machine-learning models in soft-sensor applications.

Data quality

Data from sensors in minerals processing tend to be noisier than in many other industrial processes, sensors can be unreliable, missing values are common, and instrumentation faults can be frequent. Typically, subtle errors can take longer to detect compared with those that are grossly inaccurate (Pothina and Ganguli, 2020). However, soft sensors usually depend on having accurate data inputs. It is often necessary to apply signal conditioning (filters) and data reconciliation algorithms to validate the data before applying the models, whether they are data- or model-driven. Performing this processing work can require considerable manual effort and process knowledge to set-up.

The soft sensors described in this paper have been developed using offline data to fully develop the data preprocessing tools, and then transitioned to an online environment. Many of the data quality issues for a given process are identified during the offline processing stage.

Effect of Wear

An important factor affecting the performance of processes in minerals processing can be the wear of components over time. The aggressive wear environment due to handling large volumes of abrasive materials cause a progressive change in important equipment dimensions. Fortunately, the wear of many components follows a relatively predictable trend, and historical condition monitoring data can often be used to develop wear models. For example, the crusher gap can change appreciably on an hourly basis and typically needs daily adjustment. SAG mill liner and grate aperture wear is slower, with changes in performance occurring over weeks (Toor *et al*, 2013), causing grinding rates to change over the course of the liner life of several months. Cyclones, screen panels and pumps are other examples of components in a milling circuit that wear over time, affecting plant performance and efficiency.

Whether a soft sensor is data or model-driven, it should incorporate the effect of wear if it causes performance to change systematically over time. An advantage of the model-driven approach is that the effect of wear can be modelled separately and explicitly from the rest of the model. For example,

a wear model that tracks the change in apex diameter over the cyclone component life can be replaced with a different wear model if a component is changed, such as replacing rubber apex components with ceramic ones. An entirely new model may need to be developed in this scenario for a data-driven model.

Process knowledge

Data-driven soft sensors may sometimes be favoured because they do not rely on expert process knowledge for their development, however, in many cases, considerable process understanding is readily available. Existing mathematical models developed for simulating unit operations in minerals processing often have limitations including typically being designed to be used with process survey data rather than online data and ignore process dynamics. Many of the published steady-state models have inputs that require physical sampling, such as ore hardness, solids concentration and particle size distribution, which are usually difficult to measure in real time. There remains a lack of mechanistic or phenomenological models that are suited to use in soft sensors, and considerable research effort can be required for their development.

However, once developed, an advantage mechanistic models is that they can provide a physical interpretation that can help operators to make sense of the process and therefore lead to better process decisions. They can also be easily adapted to similar processes. For example, the mill filling model can be applied to any SAG mill design or the stockpile model to any coarse-ore stockpile without changing the model itself. Hence while process knowledge is indispensable for developing the model, applying it to other situations is relatively straightforward and no more difficult than for the data-driven approach.

Dynamics

Many of the simulation models for process equipment are based on steady-state process models. Although models need the ability to deal with dynamics, the transient effects occur over different time scales in different equipment. For example, hydrocyclones have a residence time in seconds, and therefore dynamic behaviour can be ignored for most purposes (Rajamani and Herbst, 1991). However, residence time in mills and stockpiles are typically tens of minutes and tens of hours, respectively, and therefore need to be considered. Both black- and white-box models need to incorporate the dynamic aspect into their architecture. White-box models do this by including the first-principle mass or energy conservation equations in form of ordinary differential equations that govern the underpinning processes in the equipment of interest. On the other hand, black-box models can include these dynamics by incorporating past values of the input variables into the regressions (Casali *et al,* 1998b; Zhou, Lu and Chai, 2014).

Process insights

Process plants are often described as data rich but information poor. Process control operators typically watch several monitors displaying operating status of hundreds of field equipment, numerous operating trends, alarms and more. A high level of complexity makes it difficult for control room operators to mentally analyse data and take the right corrective decisions (Li *et al,* 2011). Therefore, soft sensors should not be seen as simply providing more data in an already complex environment, but an opportunity to reduce the level of complexity and cognitive workload on process control operators. To that end, soft-sensors should be designed to synthesise data and present it in an intuitive, easy-to-understand form that helps the operator interpret the process state and to have a high degree of trust in the control system.

CONCLUSIONS

Wei and Craig (2009) conducted a series of interviews and surveys about automation in grinding circuits, and one of the main results that can be highlighted is the ‘instrumentation wish-list’ that the respondents from the industry specified. Particle size distribution, mill volumetric filling, cyclone overflow/underflow density and size distribution are within the main answers. In this article, three soft sensors that aim to fulfil this wish list are presented. Particle size distribution out of stockpile feeders can be inferred using a 3D white-box ‘digital twin’ of the stockpile that can predict size segregation. Mill volumetric filling (balls, rock and slurry) can be inferred using the well-established JKMRC MillFIT

which uses a semi-mechanistic power model to back-calculate these process unknowns. Finally, a prototype of a soft sensor for hydrocyclones is proposed to allow for online estimation of key process variables like circulating load, water split and product size to flotation.

All the above soft sensors are based on the white-box approach and rely mostly on well-understood process models. This approach, in contrast to black-box machine learning models, enables confidence in predictions and the behaviour of the sensor at the industrial scale, where signals can be faulty, noisy and inconsistent at times.

Further work is required to validate these sensors and to, in time, connect them directly into the plant's control system instead of being used as decision support tools for operators. All this work aims to bring more automation and autonomy to mineral processing plants, which tend to fall short in this aspect compared to other industries or even the operation of some mines—especially underground, where fully autonomous operations are becoming more common.

REFERENCES

Bazin, C, Mai Maiga, M, Renaud, M and Caron, S, 2009. Dynamic simulation of grinding circuits as an aid for the diagnosis of hydrocyclone malfunction, *Proc. of the Annual SME Meeting*, Denver, Colorado, Feb. 2009

Brunner, V, Siegl, M, Geier, D and Becker, T, 2021. Challenges in the Development of Soft Sensors for Bioprocesses: A Critical Review, *Front. Bioeng. Biotechnol*, 20 August 2021, https://doi.org/10.3389/fbioe.2021.722202

Casali, A, Gonzalez, G, Torres, F, Vallebuona, G, Castelli, L and Gimenez, P, 1998b. Particle size distribution soft-sensor for a grinding circuit. *Powder Technology*, 99(1), 15–21. https://doi.org/https://doi.org/10.1016/S0032–5910(98)00084–9

Casali, A, Vallebuona, G, Bustos, M, Gonzalez, G and Gimenez, P, 1998a. A soft-sensor for solid concentration in hydrocyclone overflow. *Minerals Engineering*, 11(4), 375–383. https://doi.org/https://doi.org/10.1016/S0892–6875(98)00015–6

Dai, W, Zhou, O, Zhao, D, Lu, S and Chai, T, 2016. Hardware in the loop simulation platform for supervisory control of mineral grinding process, *Powder Technology*, 288:422–434 https://doi.org/10.1016/j.powtec.2015.11.032

Forbes, G, Reyes, F, Hilden, M and Yahyaei, M, 2021. Data analytics guided by domain experts, a myth-busting tool. *Minería Digital 2021 – 8th International Congress of Automation, Robotics and Digitalization in Mining,* Santiago, Chile, 10–12 November 2021.

Fortuna, L, Graziani, S and Rizzo, A, 2006. Soft Sensors for Monitoring and Control of Industrial Processes, 292 p. Springer.

Galan, A, De Prada, C, Gutierrez, G, Sarabia, D and Gonzalez, R, 2021. Real-time reconciled simulation as decision support tool for process operation. *Journal of Process Control*, 100, 41–64. https://doi.org/10.1016/j.jprocont.2021.02.003

Gonzalez, G D, Miranda, D, Casali, A and Vallebuona, G, 2008. Detection and identification of ore grindability in a semiautogenous grinding circuit model using wavelet transform variances of measured variables. *International Journal of Mineral Processing,* 89(1–4), 53–59. https://doi.org/10.1016/j.minpro.2008.09.002

Hodouin, D, 2011. Methods for automatic control, observation and optimisation in mineral processing plants. *Journal of Process Control,* 21(2), 211–225. https://doi.org/10.1016/j.jprocont.2010.10.016

Hodouin, D, Jämsä-Jounela, S-L, Carvalho, M T and Bergh, L, 2001. State of the art and challenges in mineral processing control. *Control Engineering Practice*, 9(9), 995–1005. https://doi.org/10.1016/S0967–0661(01)00088–0

Kadlec, P, Gabrys, B and Strandt, S, 2009. Data-driven soft sensors in the process industry. *Computers and chemical engineering*, 33(4), 795–814. https://doi.org/10.1016/j.compchemeng.2008.12.012

Karimi, M, Dehgani, A, Neszamalhosseini, A and Talebi, S, 2010. Prediction of hydrocyclone performance using artificial neural networks, *J SAIMM*, 110, pp 207–212.

Li, X, McKee, D J, Horberry, T and Powell, M S, 2011. The control room operator: The forgotten element in mineral process control, *Minerals Engineering* 24(8), pp 894–902. https://doi.org/10.1016/j.mineng.2011.04.001

Morrell, S, 1996. Power draw of wet tumbling mills and its relationship to charge dynamics, part 1: A continuum approach to mathematical modelling of mill power draw, *Transcation of Institute of Mining and Metallurgy, Section C: Mineral Processing and Extractive Metallurgy,* 105, January-April 1996, pp. 43–53.

Nageswararao, K, Wiseman, D M and Napier-Munn, T J, 2004. Two empirical hydrocyclone models revisited. *Minerals Engineering,* 17(5), 671–687. https://doi.org/10.1016/j.mineng.2004.01.017

Pan, X W, Metzner, G, Selby, N, Visser, C, Letwaba, T and Coleman, K, 2003. Development of weightometer soft sensor, *Application of Computers and Operations Research in the Minerals Industries,* pp 261–266, South African Institute of Mining and Metallurgy.

Pan, X, 2015. Online smart sensor to measure stockpiles used in mineral processing, *International conference of mining*, 15 July 2015.

Plitt, L R, 1976. A mathematical model of the hydrocyclone classifier, *CIM Bulletin*, pp 114–123.

Pothina, R and Ganguli, R, 2020. Detection of subtle sensor errors in mineral processing circuits using data-mining techniques, *Mining Metallurgy and Exploration* 37(6).

Powell, M S, 1991. The effect of liner design on the motion of the outer grinding elements in a rotary mill, *International Journal of Mineral Processing,* 31 (1991), pp. 163–193.

Powell, M S, Hilden, M M, Weerasekara, N, Yahyaei, M, Toor, P, Franke, J and Bird, M, 2012. A more holistic view of mill liner management. *11th AusIMM Mill Operators' Conference 2012* (The Australasian Institute of Mining and Metallurgy: Melbourne).

Rajamani, R K and Herbst, J A, 1991. Optimal Control of a Ball Mill Grinding Circuit — I. Grinding Circuit Modelling and Dynamic Simulation, *Chemical Engineering Science*, 46 (3) (1991), pp. 861–870.

Rao, T C, 1966. The characteristics of hydrocyclones and their application as control units in comminution circuits, Ph.D. Thesis, University of Queensland (JKMRC).

Sbarbaro, D and del Villar, R, (eds), 2010. *Advanced Control and Supervision of Mineral Processing Plants,* Springer.

Sepulveda, J, Maron, R, Estrada, M and Bruna, R, 2019. Online detection of abnormal cyclone performance using particle size tracking (PST) technology, *Procemin-Geomet 2019*, Gecamin.

Toor, P, Franke, J, Powell, M S, Bird, M and Waters, T, 2013. Designing liners for performance not life, *Minerals Engineering,* 43–44, pp 22–28.

Wei, D and Craig, I K, 2009. Grinding mill circuits — A survey of control and economic concerns. *International Journal of Mineral Processing,* 90 (1–4), 56–66. https://doi.org/10.1016/j.minpro.2008.10.009

Ye, Z, 2022. Developing a 3-D dynamic stockpile/bin model with size segregation for dry comminution circuits. PhD Thesis. The University of Queensland, Brisbane, Queensland, Australia.

Ye, Z, Yahyaei, M and Hilden, M M, 2021. Application of a three-dimensional dynamic stockpile model for process optimisation. *Procemin-Geomet 2021*, Gecamin.

Zhou, P, Lu, S-W and Chai, T, 2014. Data-driven soft sensor modelling for product quality estimation using case-based reasoning and fuzzy-similarity rough sets, *IEEE Transactions on Automation Science and Engineering,* 11(4):992–1003, Oct. 2014, doi: 10.1109/TASE.2013.2288279

Measuring the effect of hybrid classification in a pilot-scale test

V Jokovic[1], K Barbosa[2], C Ndimande[3], M Hilden[4], K Runge[5] and M Yahyaei[6]

1. Senior Research Fellow, The University of Queensland, Sustainable Minerals Institute, Julius Kruttschnitt Mineral Research Centre, Brisbane Qld 4068. Email: v.jokovic@uq.edu.au
2. Postdoctoral Research Fellow, The University of Queensland, Sustainable Minerals Institute, Julius Kruttschnitt Mineral Research Centre, Brisbane Qld 4068. Email: k.barbosa@uq.edu.au
3. Postdoctoral Research Fellow, The University of Queensland, Sustainable Minerals Institute, Julius Kruttschnitt Mineral Research Centre, Brisbane Qld 4068. Email: c.ndimande@uq.edu.au
4. Senior Research Fellow, The University of Queensland, Sustainable Minerals Institute, Julius Kruttschnitt Mineral Research Centre, Brisbane Qld 4068. Email: m.hilden@uq.edu.au
5. Associate Professor, The University of Queensland, Sustainable Minerals Institute, Julius Kruttschnitt Mineral Research Centre, Brisbane Qld 4068. Email: k.runge@uq.edu.au
6. Associate Professor, The University of Queensland, Sustainable Minerals Institute, Julius Kruttschnitt Mineral Research Centre, Brisbane Qld 4068. Email: m.yahyaei@uq.edu.au

ABSTRACT

Classification devices provide a link between comminution and flotation. Basically, it determines which particles are diverted back for additional grinding and which ones pass to downstream flotation. Therefore, the classifiers play an important role in the performance of a mineral processing circuit.

Hydrocyclones are the most common classifiers used in wet grinding, despite being associated with poor classification efficiency. Hydrocyclones are widely used due to advantages related to low maintenance as well as reduced capital and operating cost. Other classifiers, such as fine screens, have much better classification efficiency compared to hydrocyclones. The major challenge of using screens in an operation, however, is their large footprint and increased maintenance requirements relative to hydrocyclones.

Some researchers have demonstrated that switching from hydrocyclones to screens, as the classifier device in a ball milling circuit, resulted in a 20 per cent increase in plant throughput and significant improvements in coarse particle recovery, resulting in a 6 per cent increase in overall flotation recovery. However, it is known that these benefits of improved classification are very much ore specific, ie depending on the ore response. Therefore, there is a need to estimate the benefits of improved classification in pilot scale testing before the plant could consider the potential classifier upgrade.

This paper presents the results of two pilot-scale grinding tests where the ore sample was processed using different classifiers: a traditional hydrocyclone and hybrid classification involving the use of a semi-inverted hydrocyclone followed by a screen. The size specific energy and circulating load were used to compare the performance of the grinding circuit. The grinding product was subject to mineral liberation analysis and the impact of classification efficiency on the mineral liberation is discussed in the paper.

INTRODUCTION

Mining companies require innovations that lead to new, better, and more efficient processes to achieve productivity improvements and more sustainable development. An area of interest to the mining industry is the ability to improve classification.

In wet grinding circuits, hydrocyclones became the dominant classifier in the 1950s, and despite its relatively poor process performance, it is often described as the workhorse of the mining industry and is used extensively for size separation (Dündar *et al,* 2014).

The importance of classification in a closed-circuit grinding circuit has been reported by many researchers (Hukki, 1968, 1979; McIvor, 1985, 2009; Dorr, 1929; Schlepp and Turner, 1990). Data from plant trials, where hydrocyclones were replaced by screens, indicate that lower bypass of fines and sharper separation can improve breakage rates and throughput (Dündar *et al,* 2014).

Frausto *et al* (2017, 2021) highlighted the potential benefits associated with improved classification. That work compared hydrocyclones and Derrick multi-deck screens at the Mexican mine Minera Saucito, where they could switch between cyclones and screens within their secondary ball milling stage. It was shown that the improved classification efficiency of screens resulted in a 20 per cent increase in throughput, and significant improvements in coarse particle flotation, resulting in a 6 per cent increase in overall lead flotation recovery. In this case, the improved classification was achieved by sharper separation, reduced bypass of fines back to the grinding circuit, and because the particle density does not influence how the screens classify material, which is not the case with hydrocyclones. Based on these findings, it can be concluded that the benefit of improved classification will also depend on the ore material that is being processed.

Currently, fine screens require massive floor space and are currently limited in application to low-capacity plants of a few hundred t/h. At high throughputs, screens are less efficient and attract high capital and running costs. Despite the reported benefits of improved classification of screens, not many plants have replaced hydrocyclones. This is because hydrocyclones have a relatively simple design (no moving parts), are robust and have a relatively small footprint for very high capacities compared to the screens.

Hybrid classification provides a potential solution, combining the benefits of both hydrocyclones and screens. A hybrid classification circuit consists of a hydrocyclone coupled with a screen that is used to scalp the coarse particles contained in the hydrocyclone overflow. The purpose of such a hybrid system is to take advantage of the high throughput attribute of the hydrocyclone in the first classification stage and the sharp separation characteristic of the screen in the second stage. A hybrid system addresses the limitations of these two classifiers. The poor classification performance of the hydrocyclone can be addressed by placing the screen in series with the cyclone. The tonnage to the screens is reduced because it is only fed the cyclone overflow and not the entire classification feed stream.

The hybrid classification strategy should ensure that less of the coarse low density particles report to the overflow, resulting in more of the particles fed to flotation being in the recoverable size fractions. The expected result is a higher recovery. Alternatively, the milling circuit grind could be coarsened achieving the same recovery level, and the circuit throughput increased.

The objective of this study is to measure the benefits of hybrid classification in a small pilot scale test program. The advantage of this approach is that it allows an evaluation of the effects of improved classification for an ore without the need for an expensive plant trial.

EXPERIMENTAL METHOD

In order to evaluate and demonstrate the performance of a hybrid screen-cyclone configuration, two pilot scale tests were conducted. One using a cyclone (base case, Figure 1) and the second using a hybrid screen-cyclone configuration as the classifier (hybrid classification, Figure 2). The aim was to conduct these tests with similar mill grinding parameters, in terms of the circulating load of 250 per cent and a targeted product P_{80} of 75 µm. The Size Specific Energy (SSE) and the degree of mineral liberation were then used to compare and assess the benefits of the hybrid classification and hydrocyclone classifier. The Size Specific Energy represents the energy required to generate a unit mass of material below a certain size. The Size Specific Energy of generating 75 µm material ($SSE_{-75\ \mu m}$) is commonly used for comparing the energy efficiency of grinding circuits.

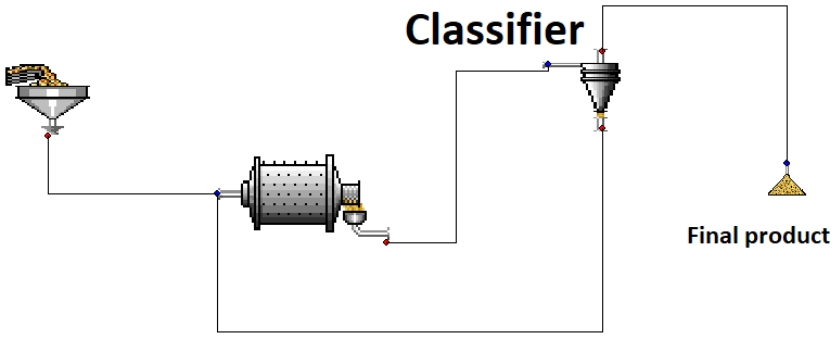

FIG 1 – The locked-cycle pilot test configuration which used a hydrocyclone as the classifier.

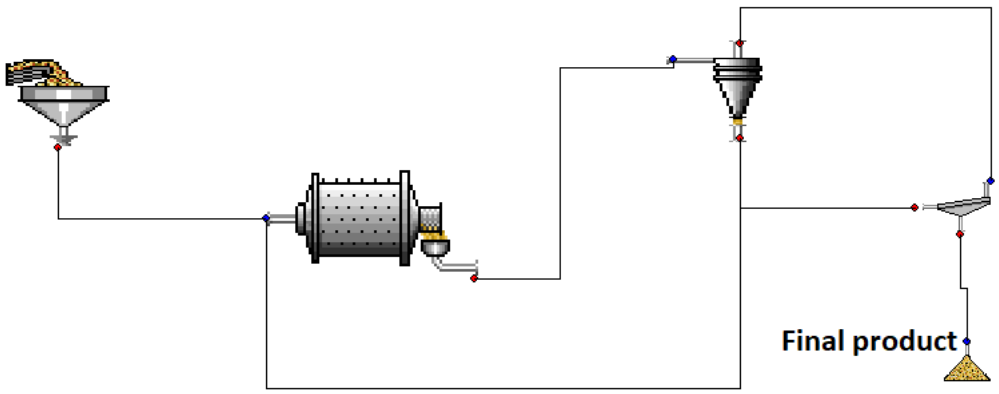

FIG 2 – The locked-cycle pilot test configuration which used a hydrocyclone and screen as the classifier.

Sample preparation

The sample used in this study was a base metal ore sample. The ore sample was crushed below 3 mm and representatively split into batches which was then used as mill feed material during testing. The specific density for the tested material was 2.8 t/m^3.

Initial simulations to determine the testing parameters

Prior to any testing, the pilot scale testing procedure was simulated using JKSimMet software to determine the required grind size for the mill discharge so the targeted circulating load could be achieved. In order to determine the grinding time required to achieve the required mill discharge P_{80}, an initial grinding test was conducted. The mill load was sampled at two grinding times, and these collected samples were sized. Using the measured P_{80}, F_{80}, the rock mass, the grinding time and the estimated mill power draw, the Operating Work Index (OWi) was calculated. The OWi values were then used to calculate the Specific Energy (SE) required to achieve the targeted grind size. Using the SE and the power draw, the required grinding time was calculated. The estimated grinding time was used in the locked-cycle pilot scale test as the initial grinding time.

The locked-cycle pilot scale testing procedure

Hydrocyclones cannot be easily scaled down and tested in the laboratory because the cut size is a strong function of the cyclone diameter. Small cyclones cut too fine. It is also difficult to operate a cyclone continuously at small scale because of the difficulties in matching the capacities of the mill and screen. But the performance of a hydrocyclone is dependent on the interaction with the grinding process. It is, therefore, very difficult to evaluate the improvements in performance (both in grinding and in flotation) of a change in hydrocyclone efficiency in the laboratory. However, JKMRC has a pilot scale 250 mm diameter hydrocyclone and a 1.8 m diameter mill that can be used in conjunction to study the grinding-classification interaction. However, it's not logistically possible to operate them together in a continuous mode. Instead, a locked-cycle methodology was adopted that allowed the de-coupling of the screen, cyclone and mill and thus allowed each equipment to be operated in batch mode.

The locked-cycle pilot testing procedure consisted of the following steps:

- Steel balls were added to the mill.
- 200 kg of ore was added to the mill.
- Sufficient water was then added to achieve a 70 per cent solids by weight.
- The mill was run for the calculated grinding time.
- The mill discharge was collected into drums with the aid of water to rinse the contents out of the mill.
- Steps 2–5 two were repeated until sufficient material was prepared for the hydrocyclone rig.
- The mill discharge was then placed into the cyclone sump.
- Classification was then used to split the mill discharge into coarse and fine material:
  - Using the cyclone as the classifier (base case as shown in Figure 1).
  - Using the cyclone-screen configuration as the classifier (hybrid classification as shown in Figure 2).
- The coarse material was dried and the dry mass measured.
- The grinding time for the next grinding stage (cycle) was then calculated.
- Fresh feed material was added to the coarse material to maintain the initial mass and then step 2 to 11 were repeated.
- The test was stopped after four or five locked-cycle tests had been completed.

The cyclone was operated in the semi-inverted position for the hybrid classification case as this allowed the achievement of a much coarser cut size.

The locked-cycle testing was performed for four cycles for the hybrid classification case and five times for the base case.

For the hybrid classification case, the cyclone overflow stream was collected and sized using Kason screens with a 100 µm screen aperture, Figure 2.

The final product (cyclone overflow stream for the base case and the screen undersize material for the hybrid classification) was sized using four sieve sizes and the material was sent for chemical assaying and MLA analysis. The feed and internal streams within the grinding circuits were sized using a root 2 series of screens.

RESULTS AND DISCUSSION

The locked-cycle testing

Although the locked-cycle laboratory test was conducted as a series of batch experiments, they were performed in such a way as to ‘simulate’ continuous operation. JKSimMet software was used to simulate this continuous mode operation to smooth and mass balance the experimental results. The grinding time and the mass of material were used to calculate the throughput for each stream. In order to match the throughputs of the feed and product streams, the mass of the product was used to calculate these throughputs. The results of mass balancing for both trials are presented in Figures 3 and 4. Note that the mass throughput and P_{80} for each stream is presented as a fraction of the feed values.

The experimental data was very similar to the mass balanced data, which indicates that the sampling and material sizing was conducted correctly.

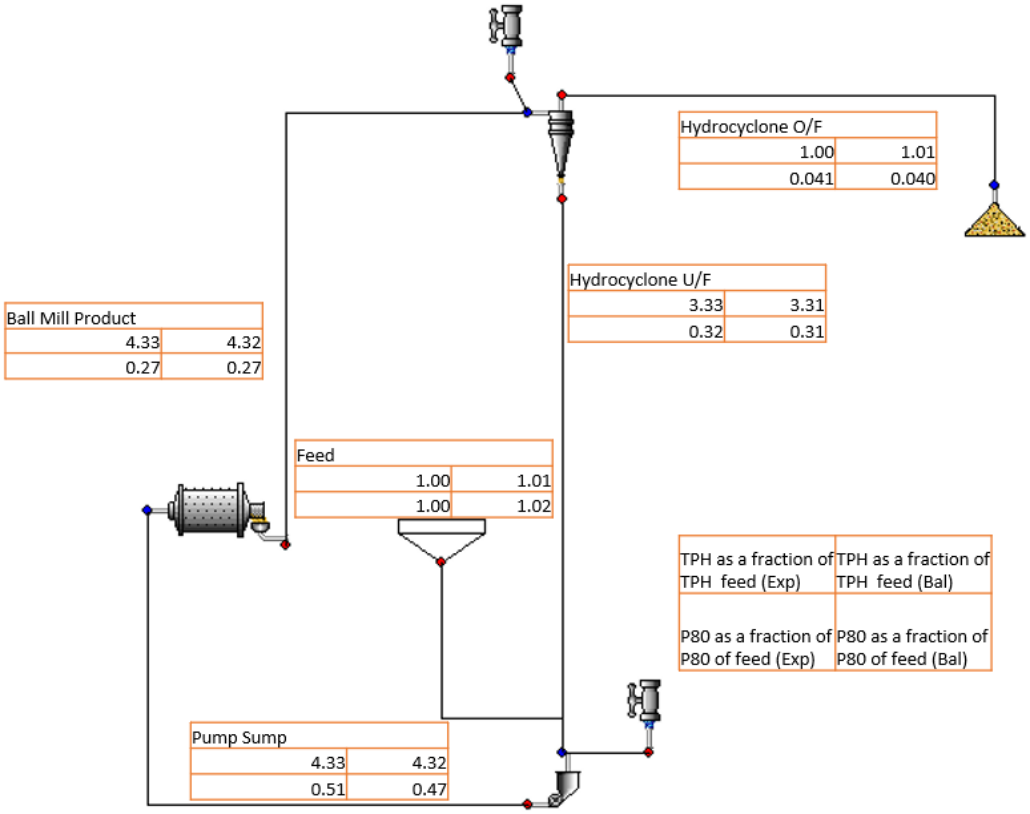

FIG 3 – Experimental and balanced data for the base case.

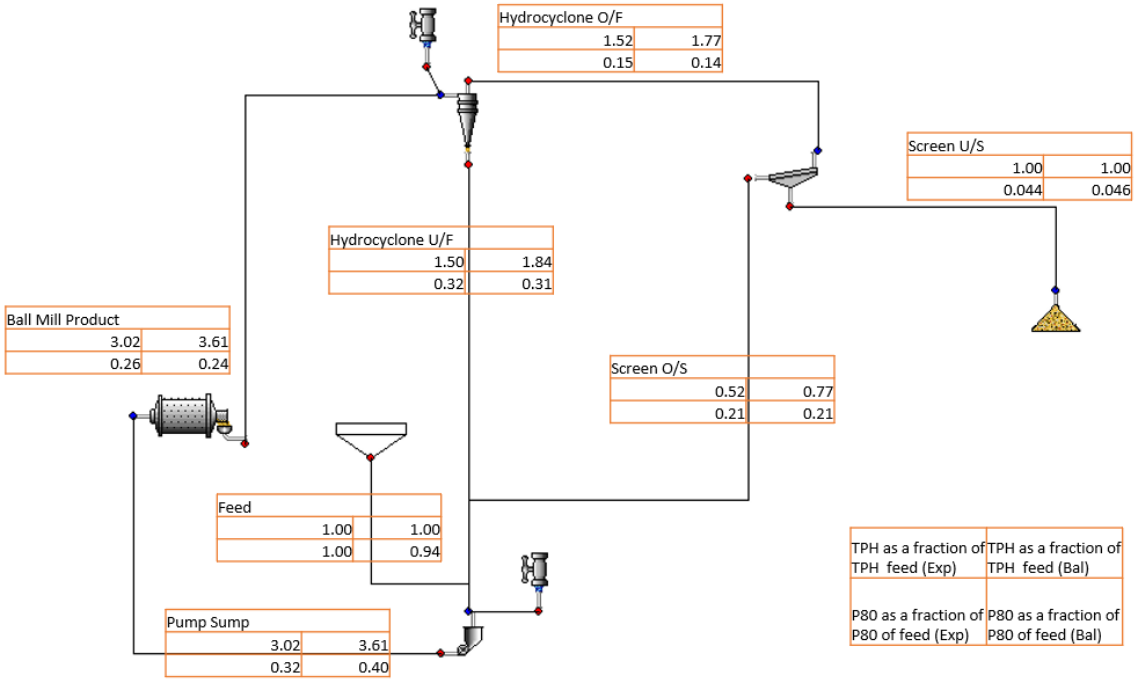

FIG 4 – Experimental and balanced data for the hybrid classification case.

The product size distributions achieved in the last cycle for the base case and the hybrid classification are presented in Figure 5. The measured P_{80} for the base case was lower by 4 µm than the P_{80} for the hybrid classification. Even though the P_{80} in both cases were similar, the product size distribution for the hybrid classification was sharper than for the base case and less fine material was generated.

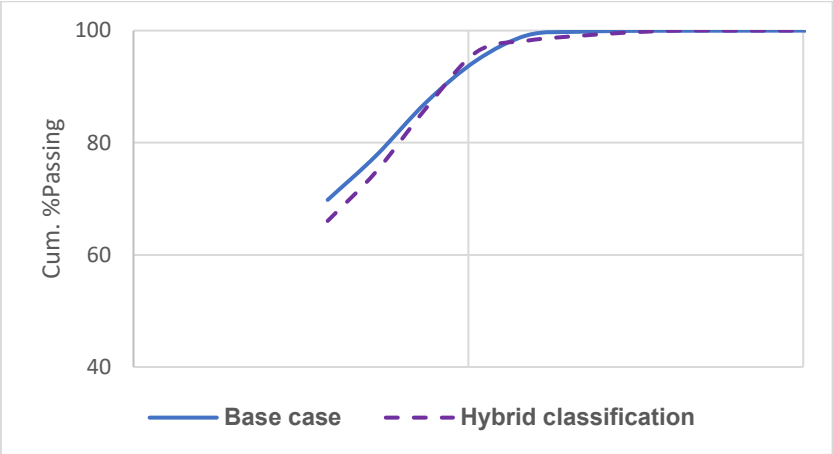

FIG 5 – The measured product size distribution for the base and hybrid classification cases.

The size-specific energy

The relative change in the $SSE_{-75\ \mu m}$ and circulating load for the hybrid classification case compared to the base case were calculated based on the measured data (batch mode) and the mass-balanced JKSimMet data (continuous mode); with the results presented in Table 1. These values, which are calculated based on the measured and balanced data, differ. However, in both cases, the hybrid classification produced a lower $SSE_{-75\ \mu m}$ (between 15–40 per cent) and a lower circulating load (21–39 per cent) compared to the base case. The results in Table 1 indicate that the hybrid classification pilot testing used up to 40 per cent less energy to generate material below 75 µm compared to the base case.

TABLE 1

The relative change of $SSE_{-75\ \mu m}$ and circulating load for the hybrid classification case compared to the base case calculated based on experimental data and JKSimMet mass balanced data.

Hybrid classification	Experiment	Balanced data
Δ $SSE_{-75\ \mu m}$ [%]	-40	-15
Δ Circulation Load [%]	-39	-21

The discrepancy between $SSE_{-75\ \mu m}$ values calculated based on the experimental and balanced data are due to the different amount of material in the feed and product during the batch mode experiment.

The size distribution of material sent back to the mill was found to be coarser and contain less fines in the hybrid classification case than in the base case (Figure 6). It can be concluded that hybrid classification reduces the misclassification of fine material, which is the reason why the circulating load is reduced compared to the base case.

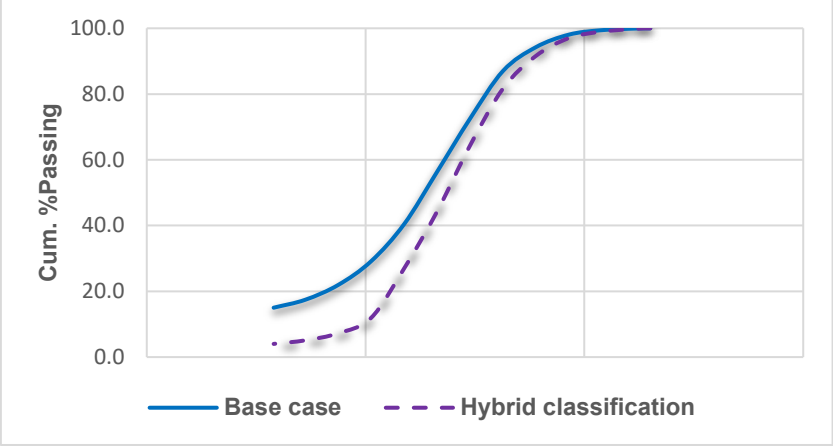

FIG 6 – The particle size distribution for the coarse stream (returned to the mill) for both trials.

MLA and assaying results

Differences in the circulating load and classification efficiency have been previously shown to modify or influence the resulting particle size distribution of the valuable minerals in the comminution product (or flotation feed) (Frausto *et al,* 2017).

Figure 7 shows the particle size distribution of the metal produced in the circuit product (ie flotation feed) by hybrid classification and the base (cyclone) case. The results indicate that hybrid classification produces a product with more metal in the coarser size fractions. This is even though the overall mass size distribution of the product from these two circuits is similar in terms of P_{80}, Figure 5.

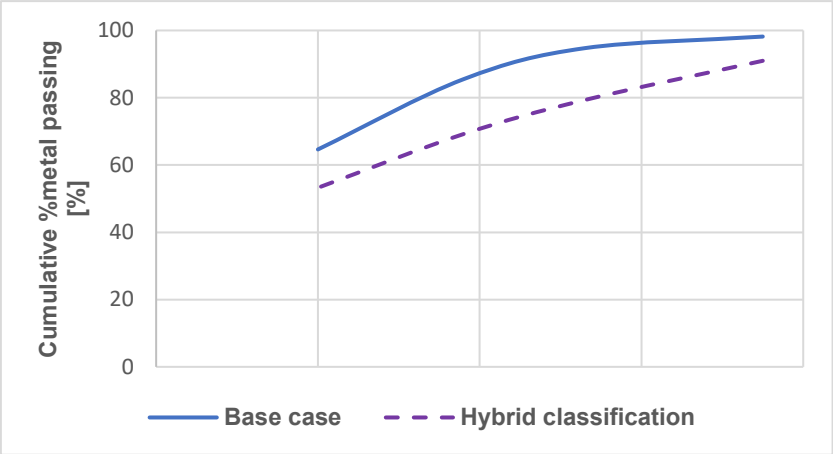

FIG 7 – The cumulative % passing of metal in the product of the cyclone classifier (base case) and the hybrid classification case.

The particle size distribution of the valuable mineral is much finer than the overall solids particle size distribution in the case of the cyclone, but that difference is much reduced in the hybrid classification scenario. The finer particle size of the valuable mineral, when classified using a hydrocyclone, is often observed in plant data. It is a consequence of the valuable mineral having a higher density. Therefore, particles containing the valuable mineral, especially those liberated, are heavier and preferentially report to the cyclone underflow. This increases their circulating load and a finer grind of the valuable mineral within the grinding circuit is the result.

However, for the hybrid classification case, the final stage of classification, which dictates whether a particle reports to downstream separation or is recycled for grinding, is a screen. Screens cut according to size only and therefore are not affected by particle density. Valuable minerals and gangue must achieve a particular size before they report to the screen undersize. Thus, their size distribution in the grinding circuit product is very similar. Any preferential grinding of a valuable mineral over gangue in the mill only affects the amount of each in the circulating load but does not affect the final product.

Another contributing effect may be the coarseness of the cut of the semi-inverted hydrocyclone in the hybrid circuit (in contrast to the hydrocyclone). Particles are less likely to be liberated in the coarser particle sizes, and therefore density differentials between particles will be reduced.

It is important to highlight that a change in preferential breakage caused by a classifier will not necessarily improve the flotation response (ie grade or recovery improvement), but it is likely to have an effect. This effect can be either negative or positive depending on the recovery by size relationship.

The MLA data were analysed to determine whether classification had a significant impact on the degree of liberation of minerals in the grinding circuit product.

Tables 2 and 3 show the mineral liberation distribution for different size classes in the grinding circuit product for the classification with cyclones and the hybrid classification case, respectively. Most of the metal is liberated for particles finer than the Size 4 class in both cases. However, what is very interesting is the improved liberation in the coarser particle sizes (Size 5) in the hybrid classification

scenario. Metal in the coarser sizes when classification conducted with cyclones (Table 2) exhibited a bimodal liberation distribution – it was either completely liberated or present in very poorly liberated classes. Poorly liberated mineral will be very difficult to recover in downstream flotation. However, the liberation of the coarser sizes in the hybrid classification scenario (Size 5 in Table 3) is much improved and isn't bimodal in nature.

TABLE 2

Valuable mineral liberation distribution per size class for the base case classification.

Base case	Very poorly liberated	Poorly liberated	Middlings	Highly liberated	Completely liberated
Size 5 (coarse particles)	30.55	12.78	6.02	2.45	48.2
Size 4	5.09	3.85	6.78	5.54	78.74
Size 3	1.26	2.12	2.61	6.95	87.07
Size 2	0.62	0.71	2.46	9.44	86.78
Size 1 (fines)	1.51	2.18	5.08	7.61	83.62

TABLE 3

Valuable mineral liberation distribution per size class for the hybrid classification.

Hybrid classification	Very poorly liberated	Poorly liberated	Middlings	Highly liberated	Completely liberated
Size 5 (coarse particles)	3.76	2.18	3.06	7.89	83.11
Size 4	2	2.35	5.11	7.47	83.06
Size 3	0.9	0.82	3.64	6.51	88.12
Size 2	0.45	0.64	1.82	13.67	83.43
Size 1 (fines)	1	2.2	2.58	7.87	86.34

Improved liberation when using screens in comparison to cyclones has been previously observed by Frausto Gonzalez (2020) in industrial scale trials. In this industrial work, the presented liberation distribution of the flotation feed was also bimodal in nature in the coarse size fractions when using cyclones whereas this did not occur when using screens. The density effect in cyclones does not only result in preferential deportment of valuable minerals to the underflow but also produces a bias in classification with respect to liberation. Valuable minerals in composite with gangue will be light and preferentially report to the overflow. Cyclones thus promote bypass of very poorly liberated minerals into the grinding circuit product, resulting in a bimodal liberation distribution. In the hybrid scenario, however, screening is the last stage of classification, and in this device, density does not play a role, and bypass of poorly liberated mineral to the grinding circuit product does not occur.

This improvement in liberation after grinding with hybrid classification will significantly positively impact downstream separation performance. Poorly liberated minerals are very difficult to float and, if recovered, bring a lot of gangue into the concentrate, reducing concentrate grade. Without the presence of poorly liberated classes in the feed, the grinding circuit product can be significantly coarsened whilst maintaining (or even improving) flotation recoveries.

The results of this study suggest that hybrid classification can produce the same benefits as observed with screening alone, as observed in the work of Frausto Gonzalez (2020). The hybrid classification has resulted in a significantly coarser metal size distribution (Figure 7), but the overall distribution of metal in the stream is largely in liberated classes (Table 3). Even though there is a significant amount of metal in the coarsest size fraction, it is largely liberated (Table 5). The degree

of liberation of the cyclone product is also high, but this is because most of the metal is located in finer sizes (Table 4).

TABLE 4

Valuable mineral liberation with respect to the entire sample for the cyclone base case.

Base case	Very poorly liberated	Poorly liberated	Middlings	Highly liberated	Completely liberated
Size 5 (coarse particles)	3.87	1.62	0.76	0.31	6.11
Size 4	0.45	0.34	0.60	0.49	6.98
Size 3	0.10	0.17	0.21	0.56	7.01
Size 2	0.07	0.08	0.29	1.13	10.38
Size 1 (fines)	0.88	1.27	2.97	4.45	48.89

TABLE 5

Valuable mineral liberation with respect to the entire sample for the hybrid classification.

Hybrid classification	Very poorly liberated	Poorly liberated	Middlings	Highly liberated	Completely liberated
Size 5 (coarse particles)	0.49	0.28	0.40	1.02	10.73
Size 4	0.26	0.30	0.66	0.96	10.72
Size 3	0.08	0.07	0.32	0.57	7.66
Size 2	0.05	0.07	0.21	1.56	9.55
Size 1 (fines)	0.54	1.19	1.39	4.25	46.66

Using the MLA data, it was possible to calculate the theoretical grade recovery curve achievable in the downstream separation process for the two grinding circuit scenarios (Figure 8). This is the grade and recovery achievable if the separation was perfect. In both classification cases, very high recoveries are achievable at a high-grade, and this is because most of the material has been ground to a size where it has been liberated. The hybrid classification scenario, though, is able to produce a marginally better grade versus recovery curve, even though the metal size distribution has a much coarser P_{80}. It is believed that much bigger differences will be observed between these two curves if a coarser grinding product had been produced.

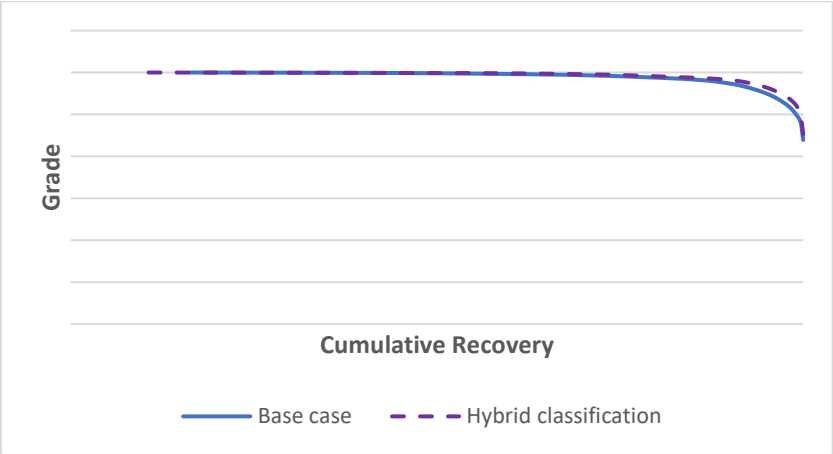

FIG 8 – Theoretical grade versus recovery curves calculated using the MLA data for the Cyclone and Hybrid Classification Regimes.

It is hypothesised that a coarser cyclone product would have resulted in much poorer liberation due to the presence of poorly liberated composites in the coarser sizes. This would translate into much larger differences in the theoretical grade versus recovery curves observed in this study. Unfortunately, this cannot be tested with the current size of the cyclone in the pilot equipment used in this study. Larger cyclones are required to achieve a coarser cut. However, running a larger cyclone would require a much large amount of sample and therefore would be logistically difficult to perform. To overcome these problems, the research team at the JKMRC is planning to develop a test involving the use of laboratory-scale mills tested in conjunction with laboratory screw classifiers and screens. A laboratory scale screw classifier can produce a density biased classification at coarser cut sizes than is possible with a small cyclone. The plan is to produce an experimental procedure that can be performed at a relatively small scale that can explore the difference in mineral and liberation of the flotation feed when operating with density biased classification, size alone based classification and hybrid classification. An ability to perform these types of laboratory experiments would enable mining operations to evaluate the likely effects of poor classification as a function of classifier cut size on the metal and liberation distributions of a grinding circuit product. The ability to do these types of evaluations is required for a mining operation to be able to justify a change in classification strategy.

CONCLUSIONS

In order to evaluate and demonstrate the performance of a hybrid screen-cyclone configuration, two locked-cycle pilot scale tests were conducted using the cyclone (base case) and the hybrid screen-cyclone configuration as a classifier. The experimental testing has produced the following findings:

- Even though the product P_{80} in both cases were similar, the product size distribution for the hybrid classification was sharper than for the base case and less fine material was generated.
- The hybrid classification pilot testing used between 15–40 per cent less energy to generate the -75 µm material compared to the base case.
- Hybrid classification reduces the misclassification of fine material, which is the reason why the circulating load is also reduced by 20–40 per cent compared to the base case.
- Differences in the circulating load and classification efficiency caused by the hybrid classification have modified the particle size and liberation distribution of the valuable minerals in the product (or flotation feed):
    - Hybrid classification produced a product with a coarser metal size distribution than when using hydrocyclones.
    - The change in classifier has had a significant impact on the degree of preferential breakage for the metal of interest.

- Because of improved coarser particle liberation, separability (measured using a theoretical grade versus recovery relationship) is not expected to deteriorate downstream when using hybrid classification, even though the valuable mineral is coarser.
- The cyclone produced a bimodal liberation distribution, and this was attributed to a bypass of poorly liberated mineral particles to the cyclone overflow. This bimodal liberation distribution was not observed when using hybrid classification.

As the benefits of improved classification are also ore dependent, there is a need for development of laboratory-scale continuous testing (for example, a small mill with a screw classifier and/or screen) that will enable measurement of these benefits over a wider range of conditions.

ACKNOWLEDGEMENT

The authors would like to acknowledge tremendous support during the pilot scale testing by students Marcelo Eduardo ávila Castillo, Zuo Meng Gan, Qi Wu and Yuxiang Chen.

REFERENCES

Dorr, J V N and Marriott, A D, 1929. Importance of Classification in Fine Grinding (With Discussion), *The American Institute of Mining, Metallurgical and Petroleum Engineers*: 46.

Dündar, H, Kalugin, A, Delgado, M, Palomino, A, Türkistanli, A, Aquino, B and Lynch, A, 2014. Screens and cyclones in closed grinding circuits, *The XXVII International Mineral Processing Congress – IMPC 2014*, Santiago, Chile, Gecamin.

Frausto Gonzalez, J, 2020. *The impact of classification efficiency on comminution performance and flotation recovery,* PhD, The University of Queensland, Julius Kruttschnitt Mineral Research Centre.

Frausto, J J, Ballantyne, G R, Runge, K, Powell, M S and Cruz, R, 2017. The Impact of Classification Efficiency on Comminution and Flotation Circuit Performance. *AusIMM Metallurgical Plant Design and Operating Strategies (MetPlant) Conference* (The Australasian Institute of Mining and Metallurgy: Melbourne).

Frausto, J J, Ballantyne, G R, Runge, K, Powell, M S, Wightman, E M, Evans, C L, Gonzales, P and Gomez, S, 2021. The effect of screen versus cyclone classification on the mineral liberation properties of a polymetallic ore. *Minerals Engineering* 169: 106930.

Hukki, R T, 1968. An Analysis of Mill and Classifier Performance in a Closed Grinding Circuit. Minerals Beneficiation, *The American Institute of Mining, Metallurgical and Petroleum Engineers* 7.

Hukki, R T, 1979. *Fundamentals Of The Closed Grinding Circuit – second operating handbook of mineral processing*, E/MJ Mining Information Services; McGraw Hill. 180: 102–109.

McIvor, R E, 1985. Classification Effects In Wet Ball Milling Circuits. Society for Mining, Metallurgy & Exploration, New York, *Society of Mining Engineers of AIME*.

McIvor, R E, 2009. The Importance Of Water Utilization For Maximizing Grinding Circuit Classification System Efficiency. *Society for Mining, Metallurgy & Exploration*, Denver, CO, SME.

Schlepp, D D and Turner, P A, 1990. Influence Of Circulating Load And Classification Efficiency On Mill Throughput. *SME Annual Meeting*. Salt Lake City, Utah, Society for Mining, Metallurgy & Exploration. 90–94: 10.

Incorporating wear into SAG mill dynamic modelling – implications for process control of grinding circuits

R Lage[1], F Reyes[2], V Jokovic[3] and M Yahyaei[4]

1. PhD candidate, The University of Queensland, Sustainable Minerals Institute, Julius Kruttschnitt Mineral Research Centre, Brisbane Qld 4068. Email: r.lage@uq.edu.com
2. Research Fellow, The University of Queensland, Sustainable Minerals Institute, Julius Kruttschnitt Mineral Research Centre, Brisbane Qld 4068. Email: f.reyes@uq.edu.au
3. Senior Research Fellow, The University of Queensland, Sustainable Minerals Institute, Julius Kruttschnitt Mineral Research Centre, Brisbane Qld 4068. Email: v.jokovic@uq.edu.au
4. Associate Professor, The University of Queensland, Sustainable Minerals Institute, Julius Kruttschnitt Mineral Research Centre, Brisbane Qld 4068. Email: m.yahyaei@uq.edu.au

ABSTRACT

Equipment wear is strongly related to the performance of grinding circuits. In particular, SAG mills are subjected to the wear of their shell liners and grates. Changes in lifter height and face angle impact mill performance, while classification at the mill discharge is also affected as grates wear out. Moreover, liner mass loss caused by wear affects how operators interpret readings of sensors such as load cells or bearings pressure. Automating and optimising grinding circuits under these constrain becomes challenging due to the nonlinear and dynamic nature of the system. The operation of SAG mill grinding circuits remains largely dependent on human intervention, which frequently results in inconsistencies in performance across shifts, reflecting the operator's personal preferences, experience, and other human factors. The influence of human factors can be reduced by careful training of operators as well as by automation using advanced supervisory control. The latter approaches could benefit from the development of dynamic process models that consider the effects of wear on the performance of equipment over time. This paper presents detailed industrial data showing the effects of wear on SAG mill performance. Additionally, a dynamic SAG mill model that accounts for these phenomena is proposed and demonstrated in a simulated environment. This model is shown to mimic the effect of wear on the performance of industrial scale mills and the operational constraints they are subject to, thus extending traditional SAG mill models. Incorporating wear into modelling and simulation platforms can improve the understanding of the effects that wear can have on the performance of key assets in comminution circuits and may allow the development of more robust model-based advanced process control strategies.

INTRODUCTION

Grinding circuits are energy inefficient, consuming 40 per cent of the energy in mineral processing operations (BCS, 2007). This scenario becomes even more challenging when paired with the expected surge in demand in the next decades for mineral resources (Watari, Nansai and Nakajima, 2020) and the increased complexity of ore bodies (Schodde, 2014). Therefore, the mineral processing industry needs to ensure that grinding circuits are operating at maximum efficiency, contributing in this way to sustainable development.

However, grinding circuits are dynamic systems that are complex to control and optimise. Their performance depends on factors that are changing over time, such as ore properties, delays in equipment responses, maintenance, and wear. Semi-Autogenous grinding mill, Ball mill, and Crusher (SABC) circuits are the most popular configuration of grinding circuits (Zhang, 2016), and the performance of SAG mills is importantly related to the performance of the ball mill circuit and the circuit as a whole.

Wear, in particular, changes the liner/lifter profile of SAG mills over time, as illustrated in Figure 1. These changes affect the charge movement inside the mill and, consequently, material breakage. Wear also changes grate aperture, influencing classification and discharge of material. Moreover, wear causes liners to lose mass continuously, influencing mill weight. The liner mass loss can be significant over time, as illustrated in Figure 2 for eight SAG mills at six different mine sites—mills can lose between 200–500 tons of weight over the liner life cycle. Inaccurate measurements of

charge mass can occur if liner mass loss is not considered when interpreting readings from load cells or bearing pressure.

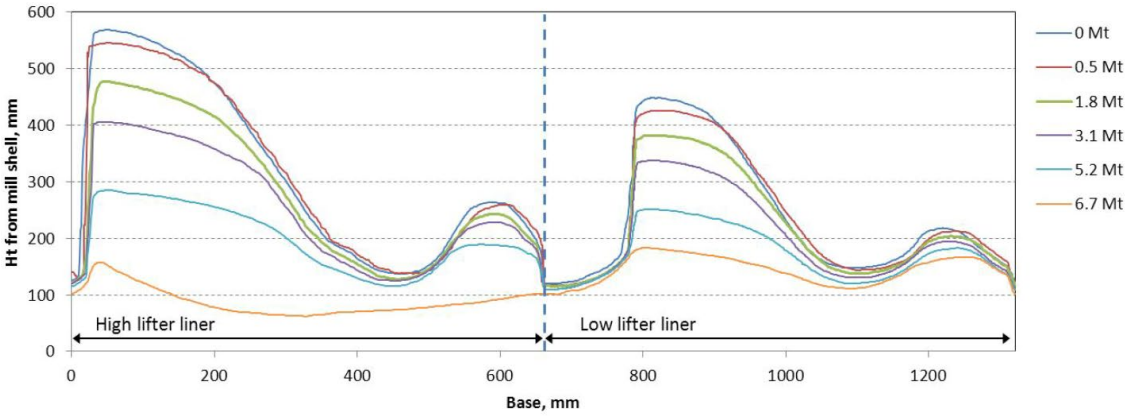

FIG 1 – Liner profile over cumulative tons (Bird, Powell and Hilden, 2011).

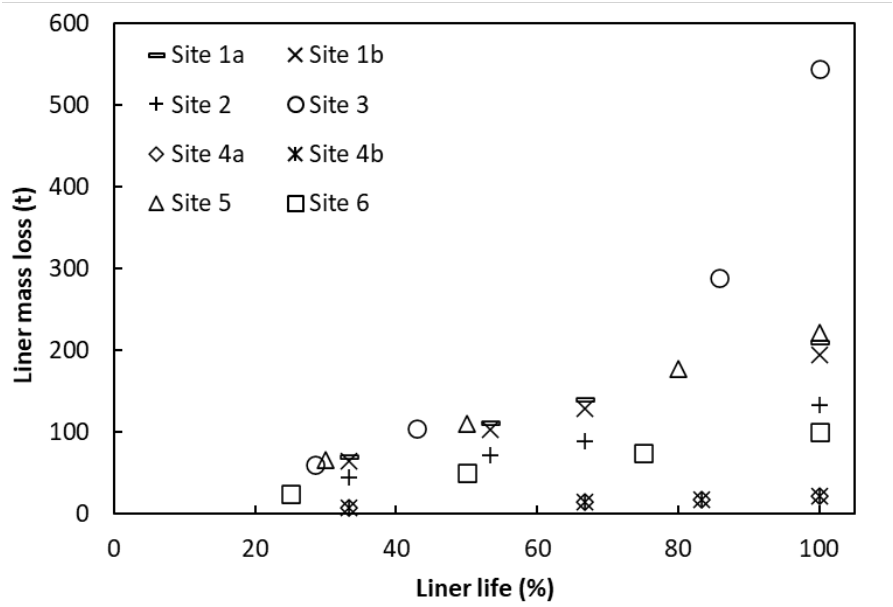

FIG 2 – Liner mass loss over liner life as a percentage of the design diameter. A liner life of 100 per cent corresponds to the moment just before the replacement of liners.

Moreover, the wear of the liner's profile also leads to an increase in the internal mill diameter, as illustrated in Figure 3, for the same mills as Figure 2. As an example, a 36-foot mill can increase its diameter by almost 200 mm over its liner life cycle. All these changes are part of the nonlinear environment of a SABC circuit. This nonlinearity makes automatic control and optimisation a challenging task, which results in regular human intervention in process control.

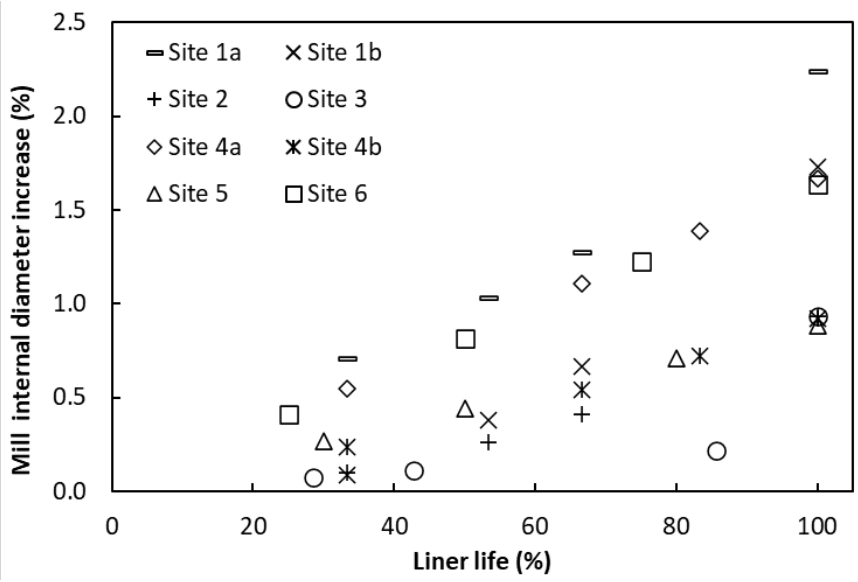

FIG 3 – SAG mills internal diameter increases at six mine sites over liner life. A liner life of 100 per cent corresponds to the moment just before the replacement of liners. Site 1 and Site 4 have two mills, labelled ‘a’ and ‘b’.

However, human decisions are subjected to levels of experience, personal preferences, and other factors that together create inconsistencies. Operator training and advanced supervisory control are options to reduce the effect of human factors on process control. These strategies can be enhanced through the development of dynamic models that can address the impact of wear on equipment performance over time. This article aims to contribute to the development of more accurate dynamic models for SAG mills with models that incorporate the changes described above.

MATERIALS AND METHODS

The investigation uses a SAG mill dynamic model available in a simulation platform that is being developed at JKMRC for design and control in mineral processing. The platform is built on MATLAB Simulink® and allows users to create simulations and process outcomes using a variety of applications. The flexibility of this platform enables the development and testing of dynamic models such as an expanded SAG mill model that includes wear.

A simple, single-stage, open-circuit SAG mill flow sheet was created in this simulation platform, consisting of just a feeder and a SAG mill so the effects of wear can be highlighted and isolated from other variables and equipment. Additional configuration and display blocks are added, as shown in Figure 4.

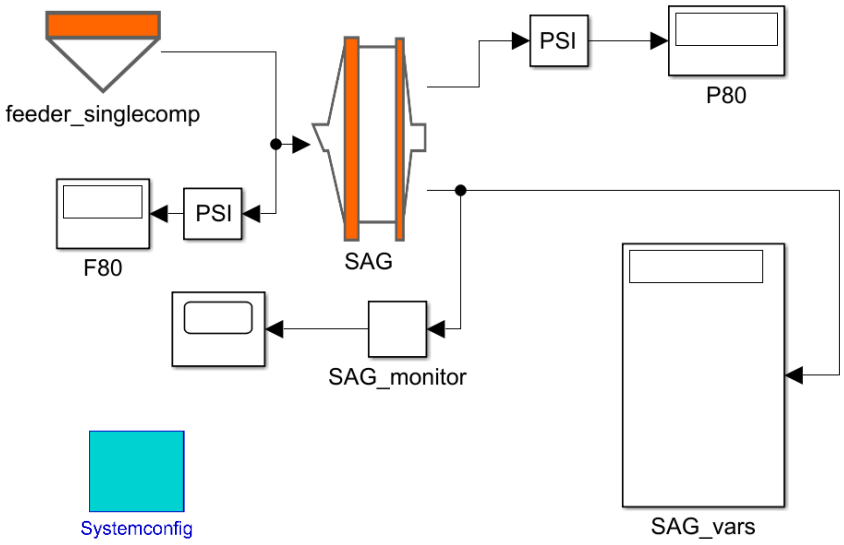

FIG 4 – Simple SAG mill flow sheet in JKMRC dynamic simulation platform.

The SAG mill dynamic model uses a population balance method based on Equation (1):

$$\frac{ds_i(t)}{dt} = f_i - p_i + \sum_{j=1}^{i} a_{ij} r_j s_i - (r_i s_i)$$**Error! Bookmark not defined.**(1)

$$p_i = d_i s_i$$

where:

$s_i(t)$	mass of material in size class *i* at time *t* in the mill
f_i	total flow rate of feed material in size class *i*
p_i	total flow rate of discharge in size class *i*
r_i	breakage rate of particles in size class *i*
a_{ij}	appearance function, which describes the fraction of material broken into size class *i* due to breakage of the size class *j*
d_i	discharge rate of size class *i*

The discharge, d_i, is the product of the transport to the grate and classification at the grate by the Equation (2):

$$d_i = D * c_i$$ (2**Error! Bookmark not defined.**)

where:

D	slurry total discharge rate
c_i	classification function value for size class *i*

The breakage rates model is based on the empirical function of Austin, Menacho and Pearcy (1987) in Equation (3):

$$K_i = \frac{aB\left(\frac{dp_i}{dp_1}\right)^{\alpha_B}}{1+\left(\frac{dp_i}{\mu_1}\right)^{\lambda_1}} + aS\left(\frac{dp_i}{dp_1}\right)^{\alpha S}$$ (3**Error! Bookmark not defined.**)

where:

dp_1	material top size
dp_i	representative *i*-ith size
$aB, \mu_1, \alpha_B, \lambda_1, aS, \alpha S$	model parameters to be fitted

Because operating conditions in the mill (speed, mill filling etc) affect material breakage, Ballantyne, Bonfils and Powell (2017) t_n-family appearance function, described in Equation (4) is used:

$$t_n = M\left[1 - e^{-fmat x^{\alpha}(E_{cs})}\right] \tag{4}$$

$$M = \left[\exp\left(-\frac{n}{437}\right) * \left(1 - \exp\left(-\frac{437^{0.13}}{n}\right)\right)\right]$$

$$fmat = \exp\left(-\frac{c}{\log(10.n)} - d\right)$$

where:

t_n	proportion of material passing through a screen with an aperture nth the geomean of the feed particles
M	saturation % passing (that is achieved at high energy impacts)
$fmat$	material dependent appearance function across the full range of size reduction
x	geomean of upper and lower sieve aperture to prepare the feed
α	Shape of the response of feed particle size and degree of breakage
E_{cs}	impact energy
n	relative progeny size
c and d	fitting parameters that ore-dependent

The main advantages of using Equation (4**Error! Bookmark not defined.**) are the direct calculation of the appearance function for any feed size and input energy and fewer fitting parameters. Impact energy is calculated using the potential energy of rocks and balls inside the mill shell. The drop height for its calculation uses the charge position inside of the mill in Equation (5):

$$Drop\ height = \left(\frac{\left(\frac{DM}{2} + CHSURA\right)}{2}\right) * (\sin(SHLDR) - \sin(TOE)) \tag{5}$$

where:

DM	mill diameter in metres
$CHSURA$	charge surface radius
$SHLDR$	charge shoulder angle
TOE	charge toe angle

The charge position characteristics are outputs of a power model based on Morrell (1993). The drop height is the input for the calculation of the potential energy of rocks and balls in the charge. The impact energy is then calculated by the sum of the potential energies of rocks and balls in each size class of the load. This allows the breakage model to respond to changes in the mill environment, including variations in mill diameter caused by wear.

The dynamic SAG mill model was adapted to account for the liner and grate wear, making the mill diameter, mill length, and grate aperture change over the cumulative tons processed. This affects the calculation of mill power, discharge classification function, appearance function, and population balance.

Moreover, the mill load cell reading was modified to account for the loss of mass due to wear in Equation (6). The liner mass loss is based on the decrease of the mill volume and assuming that liners are made of steel.

$$Load\ cell = charge\ mass + original\ mill\ mass - liner\ mass\ loss \tag{6}$$

The discharge calibration factor and breakage rates were adjusted to make the simulation generate reasonable mill outputs, although the model is not yet formally calibrated. Figure 5 shows the

adjusted breakage curve in the simulation, which resembles the typical shape of the curve for SAG mills.

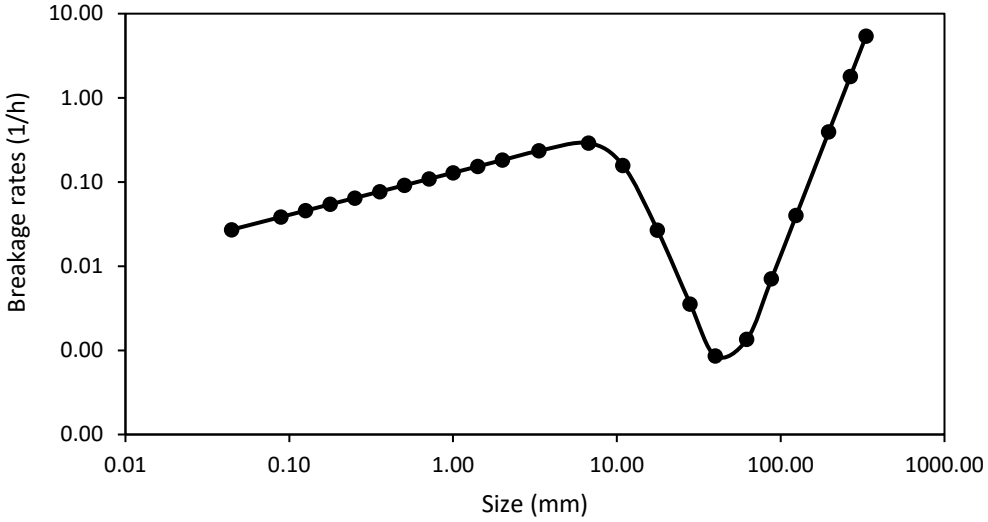

FIG 5 – Breakage rate curve of the SAG mill simulation.

Feed characteristics and mill operating parameters were kept constant in all simulation scenarios. It is worth noting that this is not how mills are operated in their normal liner life cycle, as discussed in the Introduction. In real plants, operators introduce changes in the operating parameters of the mills to compensate for liner wear or other circuit changes.

The simulations and results shown in the next Section are aimed to show the effect of wear, so they are run with wear being the only source of changes in mill performance. The simulations were stopped after the model reached a steady state. The effect of liner and grate wear on mill performance was investigated at different stages of liner life, from 0 per cent to 100 per cent. The 100 per cent liner life corresponds to the liner's state before relining. The SAG mill outputs analysed were power draw, load cell, total filling, void fill fraction, percentage of solids, and P80.

RESULTS AND DISCUSSION

Liner and grate wear models

The plant data from a mine in Chile was obtained to investigate the effect of liner and grate wear on the performance of a virtual mill. This data consisted of mill liner wear reports collected over four years. The grate and liner wear data are present in Figure 6, and the models are detailed in Table 1. The wear models for grate aperture, mill diameter, mill volume, and mill length are based on the percentage of liner life (%LL), assuming that 100 per cent liner life occurs when the mill is relined after processing 8 Mt of feed material. The adjusted R-squared values obtained after step-wise linear regression show that the models reasonably fit changes in grate aperture and mill dimensions over time. A similar approach can be conducted for any of the mine sites shown in Figures 1 and 2.

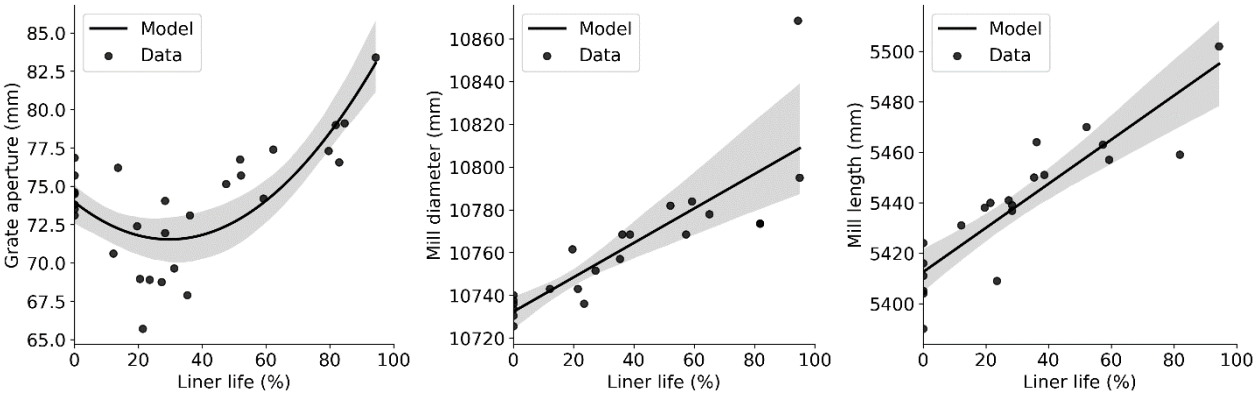

FIG 6 – Grate width, mill diameter, and mill length over the liner life. Grey areas show the 95 per cent confidence interval.

TABLE 1

Wear models for grate and mill dimensions.

Model	Equation	Adjusted R-squared
Grate aperture	$73.96 - 2.04 \times \mathrm{LL} + 0.43 \times \%\mathrm{LL}^2$	0.57
Mill diameter	$10732.43 + 9.98 \times \%\mathrm{LL}$	0.73
Mill length	$5412.51 + 10.93 \times \%\mathrm{LL}$	0.79
Mill volume	$528.02 + 2.84 \times \%\mathrm{LL}$	0.69

The behaviour of grate width over time can be associated with the grate design in Figure 7(a). The initial decrease in grate width is probably due to the charge wearing down the first part of the edges of the aperture, reducing it in Figure 7(b). Further wear of the grate consumes the second part of the edge in Figure 7(c), which start to increase in width. In this model, the difference between the smallest and largest grate aperture was approximately 18 per cent. Grates act as a classification mechanism, and an increase in grate aperture allows the passage of coarser particles, affecting the performance of the pebble crusher, mill throughput and product size. Models of grate aperture can increase the understanding of the effect of grate wear on mill performance.

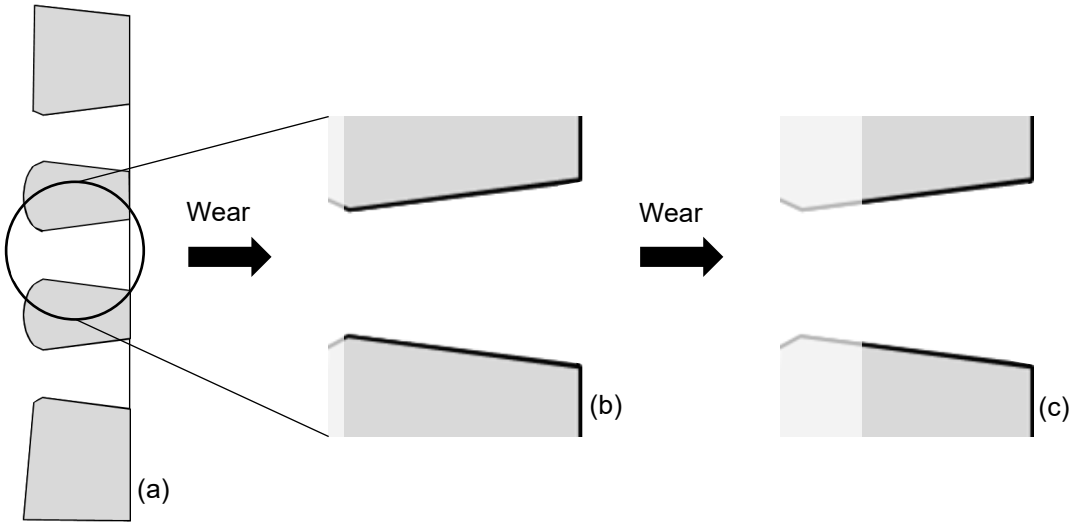

FIG 7 – Profile diagram of stages of the grate width over time. The grate (a) wears down, initially decreasing width aperture (b), and then increasing (c) until the grate is worn down or replaced.

The models in Table 1 also show a continuous increase in mill diameter and mill length over time. This is caused by the wear of liners due to the interaction with the charge, decreasing their profile

height over time and increasing mill internal dimensions. Changes in liner profile affect charge lifting inside of the mill and the amount of impact breakage and abrasion that the ore is subjected to. Thus, product particle size is directly affected, one of the main performance indicators of a SAG mill.

The increase in mill internal diameter and length causes an increase in mill volume. This leads to variations in mill filling and ball filling that can also affect the breakage of material, and impact product size distribution and throughput. Moreover, the change in mill internal dimensions is a result of liners losing mass due to wear. Accounting for this variation in mass leads to more accurate measurements of mill weight and better control decisions for the operator.

Mill performance over liner life

Mill simulation outputs show changes in performance indicators over the liner life, as illustrated in Figure 8. Noteworthy, this effect is not immediate, and substantial differences only occur over weeks. This contrasts with the rapid influence of changes in ore characteristics in mill performance. Mill power draw rose 2.3 per cent, and load cell readings decreased 12.5 per cent at the end of liner life. This is a significant change in the weight caused by liner mass loss, showing the importance to consider this for control and optimisation of a SAG mill, such as for mill filling.

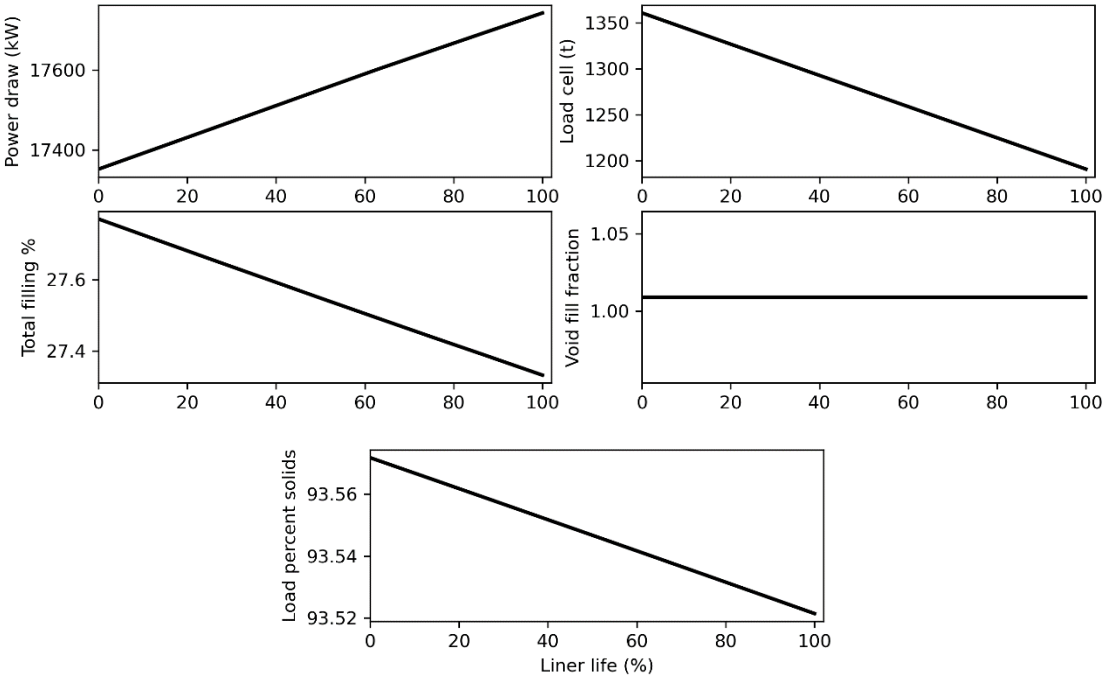

FIG 8 – Modelling outputs for the SAG mill over the percentage of liner life.

Total volumetric filling of the mill reduces 1.6 per cent along with liner life due to the increase in mill volume. Ball filling is constant since it is set as a percentage of the mill volume, creating an effect of virtually adding balls to the mill as the volume increases due to wear. Void Fill Fraction (VFF) is approximately constant over time at about 1. Mill percentage of solids also reduces over time, but less than 1 per cent compared to the initial value or new liners. These results imply that the mill's VFF and the load percent solids are not affected by the wear of the liners in this simulation.

The outputs illustrate the importance of liner wear in the performance of a simulated SAG mill using industrial data. Changes in some performance indicators can be associated with changes in liner profile and liner mass loss caused by wear. Liner wear modifies the behaviour of the charge inside the shell due to a decrease in lift or expansion in shell dimensions. Consequently, liner wear has an impact on the material breakage in the load and the particle size distribution and throughput of the mill. Moreover, mass loss due to wear influence the readings of the load cell that can change significantly over time.

Dynamic SAG mill models which consider liner wear could be used in testing different automated process control approaches and understanding how these strategies react, not only to the rapid

changes in the process but also to the slow changes caused by wear. This could lead to the development of improved control strategies for SAG mills, which contribute to the efficiency of the entire grinding circuit.

CONCLUSIONS

Liner wear affects the performance of SAG mills. This is a dynamic phenomenon that contributes to the nonlinearity of mills and grinding circuits, making automatic control challenging. Thus, human intervention in process control becomes the norm in the mineral processing industry at the cost of inconsistencies in performance between operators. Dynamic SAG mill models that account for wear can contribute to the development of novel controls that can decrease inconsistencies caused by human factors.

This paper illustrates the impact of liner wear on the performance of a virtual SAG mill. Industrial data shows a change in liner profile, grate aperture, and liner mass loss due to liner wear over time. The wear models were incorporated in a dynamic SAG mill simulation. Then, scenarios of progressive wear were simulated, showing its effect on some performance indicators of the mill and its importance for process control. Wear modelling can expand the current models for SAG mills and grinding circuits, opening opportunities for the creation of more robust model-based advanced process control strategies.

Future work involves a simulation of P80 over time, focusing on making the breakage rates change over time, as was discussed and shown by Toor (2013). After ensuring that all SAG mill outputs are reasonable, control strategies can be implemented to achieve the target product size and throughput.

ACKNOWLEDGEMENTS

The authors would like to thank The University of Queensland for sponsoring this research by providing the Higher Degree Research scholarship.

REFERENCES

Austin, L, Menacho, J and Pearcy, F, 1987. A general model for semi-autogenous and autogenous milling. *Proceedings of the 20th International Symposium on the Application of Mathematics and Computers in the Mineral Industries*.

Ballantyne, G R, Bonfils, B and Powell, M S, 2017. 'Evolution of impact breakage characterisation: Re-defining t-family relationship.' *International Journal of Mineral Processing,* 168: 126–135.

BCS, 2007. Mining Industry Energy Bandwidth Study, US Department of Energy [online]. Available from: https://www1.eere.energy.gov/manufacturing/resources/mining/pdfs/mining_bandwidth.pdf. Accessed: April 2022.

Bird, M, Powell, M S and Hilden, M, 2011. Adapting mill control to account for liner wear on the Cadia 40ft mill. *International Autogenous Grinding, Semiautogenous Grinding and High Pressure Grinding Rolls Technology*. Canada: Canadian Institute of Mining and Metallurgy: 25–28.

Morrell, S, 1993. *The prediction of power draw in wet tumbling mills*, University of Queensland Australia.

Schodde, R, 2014. The Global Shift to Undercover Exploration – How fast? How effective?, *Society of Economic Geologists*. Keystone, Colorado.

Toor, B, 2013. *Quantifying the Influence of Liner Wear on SAG Mill Performance Master of Philosophy*, The University of Queensland.

Watari, T, Nansai, K and Nakajima, K, 2020. 'Review of critical metal dynamics to 2050 for 48 elements.' *Resources, Conservation and Recycling,* 155.

Zhang, W, 2016. Optimising Performance of SABC Comminution Circuit of the Wushan Porphyry Copper Mine—A Practical Approach, *Minerals* 6(4): 127.

Assessment of lifter effect on tumbling mill dynamics using CFD-DEM coupling approach

A Mittal[1], K Mayank[1], M Narasimha[1], I Govender[2,3] and A N Mainza[4]

1. Department of Chemical Engineering, IIT Hyderabad, Kandi (V), Sangareddy (M), Medak, 502284, India. Email: ch18resch11001@iith.ac.in
2. Department of Chemical Engineering, University of Kwazulu-Natal, Rondebosch, Durban, South Africa. Email: indresan.govender@gmail.com
3. Center for Mineral Research, Chemical Engineering, University of Cape Town, Rondebosch, 7701, Cape Town, South Africa. Email: indresan.govender@gmail.com
4. Center for Mineral Research, Chemical Engineering, University of Cape Town, Rondebosch, 7701, Cape Town, South Africa. Email: aubrey.mainza@uct.ac.za

ABSTRACT

In mineral processing industries grinding is the most energy-consuming process. A tumbling mill is an essential grinding equipment widely used for particle size reduction. Power consumption, impact forces and trajectory paths are critical parameters for characterising a tumbling mill to determine grinding efficiency. The effect of lifters and mill speed plays a vital role in such parameters. However, most of the studies ignore the impact of the lifter and do not investigate the effect of slurry dynamics on charge motion. The focus of the present work is to prepare a computational model that can accurately predict the complex multi-phase dynamics of charge particles, air and slurry inside the mill using a model that couples computational fluid dynamics (CFD) and the discrete element method (DEM). The details of impact forces with lifter profiles and mill speed variations will be refined even further using the CFD-DEM coupling approach. The slurry-air free surface is modelled using the volume of fluid (VOF) method, and the charge motion is modelled using the DEM. The phases are coupled using the interface momentum exchange between the charge and the fluid slurry. The coupled model is validated against experimental results from the positron-emitting particle tracking (PEPT) data. The validated model compares the effect of slurry content on charge dynamics with the dry DEM model. The presence of slurry is observed to dampen the tangential and shear contact forces.

INTRODUCTION

Comminution, which includes crushing, grinding, and other controlled size reduction processes, is the first stage of mineral production (beneficiation). Crushing is the initial stage of comminution followed by grinding, where the particles are further reduced from small grits (<5 mm) to dust (<30 μm), which makes it the core of comminution. Tumbling mills are the most extensively used machine for grinding at the grain level. The feed to such mills consists of water and preprocessed ore particles. Grits breakdown into smaller particles due to the compressive forces and the frictional force between the particles and the mill shell. The water in the feed forms a slurry with the finer-sized particles, allowing the ground ore particles to exit the mill through a grate. The dynamics of particles in water/slurry would behave differently compared to dry grinding. It is believed that slurry consisting of fine particle fractions exhibits an increased viscosity in a wet tumbling mill, significantly affecting the grinding efficiency at higher particle load (Napier-Munn *et al,* 1996).

Although tumbling mills are extensively used in mineral industries, these mills are highly energy inefficient. According to Schönert's (1986) survey for copper production milling, out of 60 per cent of the total energy input, only less than 5 per cent is utilised for effective grinding. A thorough understanding of the charge and slurry dynamics can be of great help in energy-efficient mill design. However, none of the classical theories incorporated the effect of lifters on the mill power draw. The tumbling action inside a mill strongly depends on the size, shape, and number of lifters. Thus, to improve the economy of the tumbling mills, research on the tumbling mills configuration is crucial.

In comminution, Mishra and Rajamani (1992) were the first to develop code that understood the grinding mechanism of ball mills using discrete element method (DEM). Cleary (2001) investigated the effect of lifter patterns based on power draw in a 2D mill over various mill speeds. The lifter

pattern was found to be insensitive to mill speeds less than 70 per cent of the critical speed. Djordjevic *et al* (2004) made considerable progress using 3D DEM modelling and studied the effect of the number of lifters and its coefficient of friction on energy consumption in a tumbling mill. Makokha and Moys (2006, 2007) encountered that using cone shape lifters resulted in more cataracting events, which improved grinding efficiency and discharge rate. Powell *et al* (2011) used EDEM® software to produce a liner wear model based on collision energy distribution for mill liner design. Bian *et al* (2017) investigated the impact of mill speed, lifter height, and lifter number on particle trajectory and particle streamflow inside the mill. Mill speed and lifter height were found to significantly impact mill-work efficiency, whereas lifter numbers were found to have a notable impact on particle stream characteristics. Gutiérrez *et al* (2019) used DEM to simulate the material transport in a mill with different lifter profiles. They concluded that combining inclined lifters with helicoidal pulp lifters can effectively increase material flow at the mill's discharge, though they may be difficult to install. DEM simulations can significantly improve work efficiency and characterise particulate streams depending on the product output.

A large portion of the studies done in a tumbling mill has used the DEM strategy to get the particulate dynamics. To appropriately capture the dominant phenomena occurring in a multi-phase flow where gas or fluid interaction with particles is involved, computational fluid dynamics (CFD) coupled with DEM gives a detailed understanding of such issues. Using the CFD-DEM simulation approach on high speed stirred mills (IsaMill), Jayasundara *et al* (2011) investigated the flow properties in terms of particle velocity field and mill power draw, concluding that slurry density and viscosity have a significant impact on charge motion. They then compared it with the PEPT experiments for validation under similar conditions. Similar work was carried out by Mayank *et al* (2015a) to predict the charge motion in a tumbling mill but with a different coupling approach. Later, Mayank *et al* (2015b) developed a two-way coupled model to account for slurry's effect on solids and investigated the effect of different slurry concentrations on charge dynamics and vice versa. All the results were validated with an equivalent PEPT (Positron Emission Particle Tracking) experiment of lab-scale mills, and in some cases, an excellent agreement was found.

Cleary *et al* (2006), investigated slurry transport and other mill operational issues using smoothed particle hydrodynamics (SPH) coupled with DEM approach. Advection was observed to be perfect because in SPH, mass is discretised rather than the control volume. Many other researchers like Cleary (2015); Robinson *et al* (2014); Sun *et al* (2013), used the same SPH-DEM approach to study the solid-liquid flow in a tumbling mill. It was found that one of the few advantages of using Lagrangian methods is that they use straightforward convection models without the need to calculate fluxes. However, extremely fine resolution is required to reproduce precise fluid motion (ie the number of SPH particles). As a result, applying such a model for large scale practical system like industries is difficult.

The aim of this work is to evaluate the lifter effect on tumbling mill dynamics using a computational model capable of accurately predicting the complex multi-phase dynamics of charge, air, and slurry inside the mill by combining CFD and DEM. The dynamics of particle-particle collision forces were studied extensively using the CFD-DEM coupling approach, by varying lifter profiles and mill speeds. This model is compared to the dry DEM model to study the effect of slurry content on charge dynamics. The tangential velocity variation along the diametric line passing through the centre of circulation (COC) has been compared.

METHODOLOGY

The methodology used here is based on the work carried out by Mayank *et al* (2015b). The volume of fluid (VOF) approach is used to simulate the slurry-air free surface, and DEM is used to represent the charge particle motion. The interface momentum exchange between the charge and the fluids is used to integrate the phases. The flow is two-way coupled, with mutual effects between the fluxes of both phases, such that charge motion influences fluid phase motion and vice versa. The model accounts for the influence of slurry on solids in the tumbling mill. For more details, readers can refer to Mayank *et al* (2015b) work.

Experimental validation of the coupled CFD-DEM model

Using an advanced technique called Positron Emission Tracking (PEPT), developed by Parker *et al* (1997), comparable tests were done to validate the coupled model. Figure 1 compares the tangential velocity predicted by dry DEM, pure CFD, one-way and two-way coupled CFD-DEM models to PEPT data along the line passing through the mill's centre to the centre of circulation (COC) extended to the lifter assembly. The experimental PEPT results were shown to be overpredicted by the tangential velocity of the particles computed by the dry DEM model, because of the unaccounted shear damping effects due to the presence of slurry. Without a doubt, the pure CFD completely contradicted the experimentally anticipated tangential velocity profile. The two-way coupled model, on the other hand, has the best agreement with the experimental results because it can account for the slurry's drag as well as the slurry's shear damping effects on the particles while modelling.

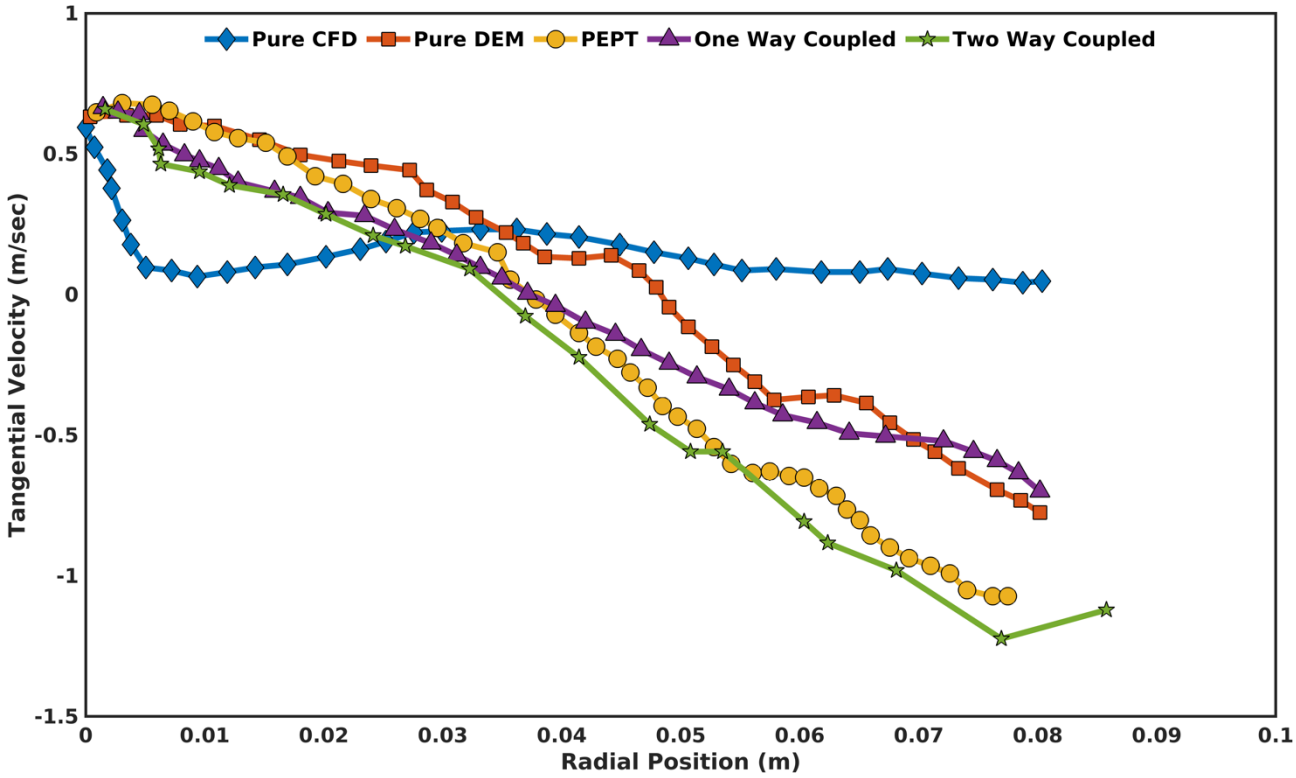

FIG 1 – Comparison of tangential velocity of charge particle predicted by different models against PEPT data.

Even a qualitative comparison of numerically predicted time-averaged solid concentration contours (Mayank *et al,* 2015b) for two-way CFD-DEM coupling model data to analogous experimental PEPT data for mill loading of 20 per cent by volume and 60 per cent critical speed, corresponding to a rotational velocity of 4.852 rad/sec, revealed the best agreement with the experimental results of all other models.

NUMERICAL SIMULATION

DEM model

Initial simulation validated the discrete element method to predict the charge motion inside a tumbling mill accurately. A set of dry DEM simulations were conducted, varying the speed of the mill. The particles were modelled as spherical balls of a diameter of 5 mm and density 2650 kg/m^3. The time step size for the simulation was chosen to be 1e-05 sec. Tumbling mill has a diameter of 300 mm and a length of 270 mm. The mill is equipped with 20 lifters uniformly spaced with a 20 mm height and varying lifter face angles (0°, 20° and 60°) as well as different mill speed (60 per cent, and 75 per cent of N_c). In addition, the simulated data is analysed using a coarse-grained temporal average approach (Artoni and Richard, 2015; Babic, 1997). After the simulation

reached steady-state, instantaneous DEM data were continually recorded at every 0.001 second for 1 second, which is roughly comparable to a drum revolution. Around ~59 000 particles were initialised position by filling a cylindrical corresponding to 31.25 per cent mill loading. Each particle was initially assigned to zero velocity. The commercial code LIGGGHTS® opensource software was used to solve the particle motion equations. The non-linear spring dashpot model inbuilt into the software was used to model the contact forces.

Pure CFD model

The pure CFD Model of the slurry-air system was also simulated to find the free surface profile. Two kinds of slurries were modelled as an incompressible fluid one with a density of 1103 kg/m^3 and viscosity 1.068e-06 N-sec/m^2 based on 15wt. per cent solid fraction and another with density 1332 kg/m^3 and viscosity 1.378e-06 N-sec/m^2 based on 40wt. per cent solid fraction. The viscosities are calculated using Ishii and Mishima (1984) model. The water level was kept constant at 21.67 per cent. The open-source CFD solver OpenFOAM® was used to solve the fluid flow governing equations. The slurry air multi-phase system was modelled using the volume of the fluid model. The $k-\epsilon$ model present in OpenFOAM® was used to model turbulence. A sliding mesh model was used to incorporate the rotation of the mill. The fluid flow governing equation was discretised using the finite volume method, where the pressure velocity coupling was done using the PISO algorithm.

Two-way coupled CFD-DEM model

A numerical model is developed using CFDEM® coupling, which uses a coupling to transfer momentum between the particles and the particles and fluid. CFDEM® coupling is open-source software for coupled CFD-DEM simulations. It uses the CFD framework of the open-source CFD code OpenFOAM® and the DEM framework of the open-source code LIGGGHTS®.

RESULTS AND DISCUSSION

Figure 2 shows the comparison between the fluid volume fraction for various mill configurations at 75 per cent of N_c with slurry containing 15wt. and 40wt. per cent solid fraction. The lifter face angle has a pronounced effect on the relative occupancy of the slurry. As observed in Figure 2, apart from the shear charge motion the presence of lifters seems to transport further the slurry resulting in a higher shoulder height. Therefore, the resultant region of occupancy of the slurry elongates with increasing lifter face angle at the expense of the occupancy near the centre of circulation.

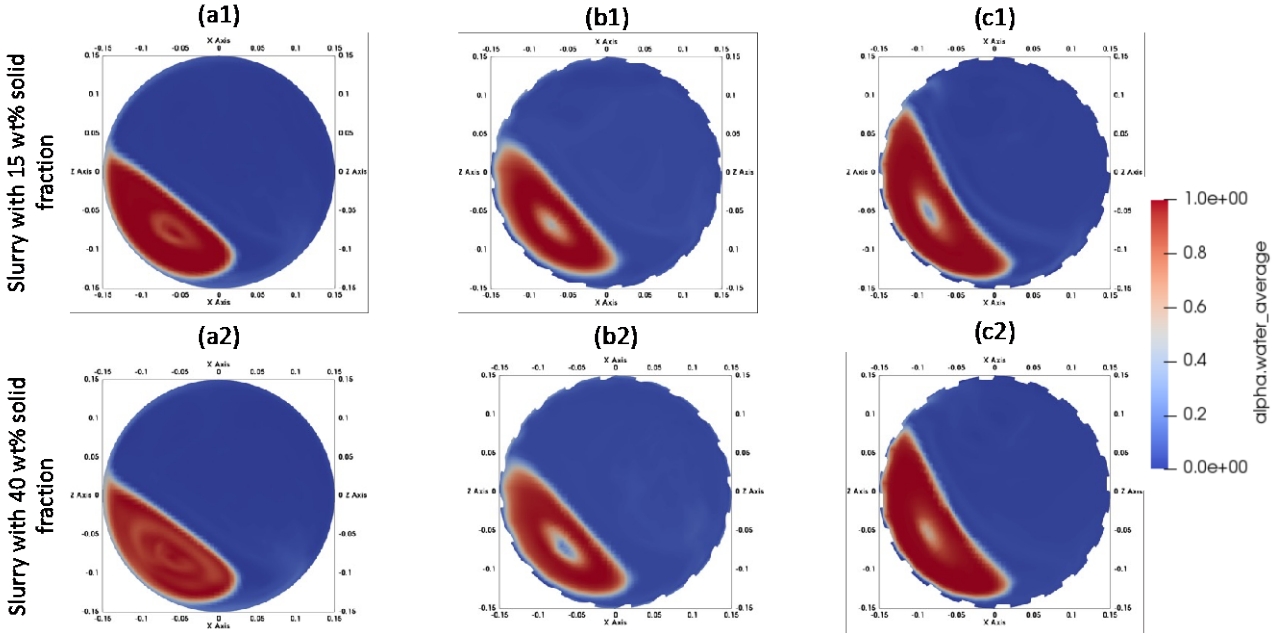

FIG 2 – Fluid volume fraction profile for various mill configurations: 0° lifter face angle (a1,a2); 20° lifter face angle (b1,b2); 60° lifter face angle (c1,c2) at 75 per cent of N_c.

The solid concentration profile is a critical metric for assessing flow energy dynamics and understanding the behaviour of the solids associated with the milling process. Figure 3 illustrates the charge particle solid concentration profile for various mill configurations at 75 per cent of N_c with a slurry containing 15wt. and 40wt. per cent solid fraction. The ascending region near the mill shell had a high solids content, which is a direct indication of high-pressure areas. Even the highest shear stress values are typically found near these regions. From Figure 3, the high solid content was observed to dilate with increasing lifter face angle. The particles are densely packed in the ascending part of the layer; however, as the lifter face angle increased, a gradual increase in porosity in the cascade region was observed. It occurs due to increased centrifugal force, which pushes particles further up from the shoulder, allowing them to fly freely under gravity's influence. From Figure 3, it is evident that the position of the charge particles (kidney-shaped region) does not vary considerably with slurry viscosity.

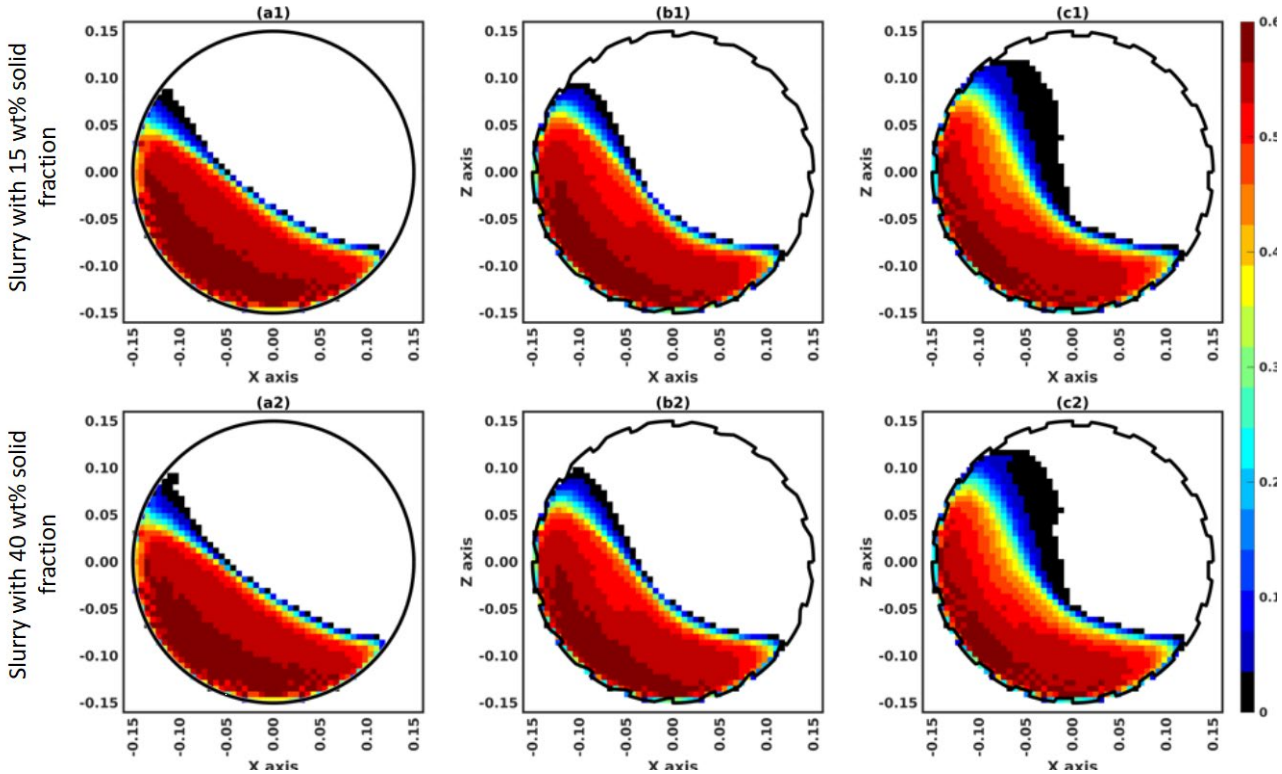

FIG 3 – Charge particle solid concentration profile for various mill configurations: 0° lifter face angle (a1,a2); 20° lifter face angle (b1,b2); 60° lifter face angle (c1,c2) at 75 per cent of N_c.

Figure 4 depicts the tangential velocity magnitude along the radial line for direct comparison between the dry DEM and two-way coupled CFD-DEM data. The tangential velocity at the mill shell was 20–25 per cent less than the mill speed in the absence of lifters. However, with lifters, tangential velocities were found to be nearly identical to mill speed for both coupled and dry DEM cases. For the 20° lifter profile, the difference was found to be 5–10 per cent whereas for the 60° lifter profile, 1–5 per cent difference was observed. Insignificant differences were observed in the tangential velocity near the mill shell between dry DEM and coupled CFD-DEM predictions for both slurries. Tangential velocity decreases linearly with distance as we approach the centre of circulation while remaining close to the mill shell. According to (Yamane *et al*, 1998), as the radial distance decreases, the charge particles slip, and the velocity deviates from linearity. However, in the case of dry DEM modelling, the velocity variation from linearity seems to differ marginally.

In the tumbling mill, the particles are densely packed in the ascending region of the layer (ie below the equilibrium surface), and porosity gradually develops in the cascade region, moving to a free surface where the cataract region becomes highly porous. The gradual evolution of porosity is primarily caused by an increase in free flight high-speed particles. The magnitude of high-speed particles is greater towards the mill centre in the absence of slurry than in the presence of slurry, resulting in an increasing cataracting profile without slurry. The dry DEM model overpredicts the charge particle path because shear forces from the slurry, which dampen particle motion, are not

considered. In the ascending region, the charge particle tangential velocity profile difference was significantly smaller. The presence of slurry appears to have little effect on the velocity of the charge particle due to the densely packed area, ie high packing density.

The cataracting profile appears to be completely dependent on the slurry rheology, and the effects become more prominent as the lifter face angle and mill speed increase. Figure 4(c2) shows a decrease in tangential velocity magnitude due to an increase in slurry viscosity. Although typically, the multi-phase effects need to be studied with respect to slurry fine fraction variation as the viscosity plays a vital role in charge particle motion.

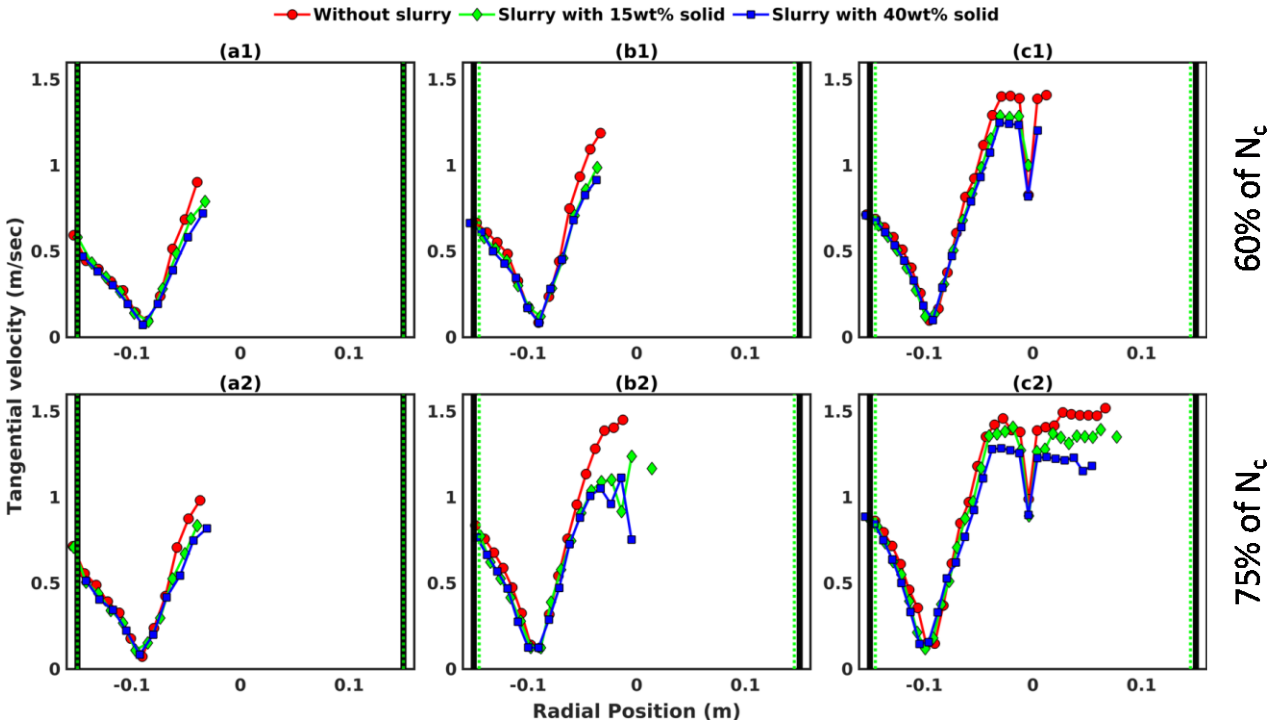

FIG 4 – Tangential velocity plot along the radial line connecting COC and Mill centre at 0° lifter face angle (a1,a2); 20° lifter face angle (b1,b2); 60° lifter face angle (c1,c2).

In Figure 5, the toe and shoulder angles of charge particles were plotted against variations in mill speed and lifter face angle for both scenarios. The lifter profile has no significant effect on the toe angle Figure 5b, but it substantially impacts the shoulder angle Figure 5a for both dry DEM and coupled CFD-DEM models. It is noteworthy that there is a significant change in the dynamics of granular flow as the mill speed increases. With increasing lifter face angle, a substantial number of particles were lifted to a sufficiently higher location, allowing maximum energy to be imported to the charge particles and thus higher grinding efficiency. Figure 5a and 5b show that the presence of slurry significantly reduced the shoulder angle, but only marginally reduced the toe angle. However, the charge particles' shoulder and toe angles do not appear to vary significantly with slurry viscosity.

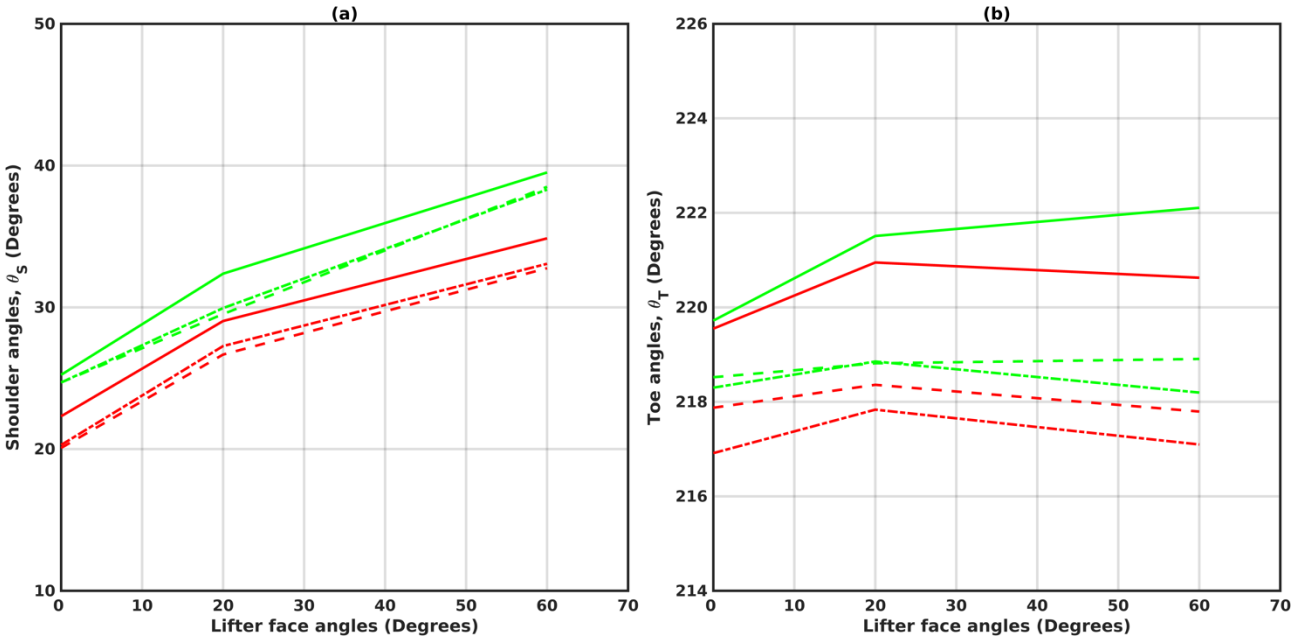

FIG 5 – Variation of the shoulder angle (left) and toe angle (right) with the lifter face angles.

The methodology for calculating power consumption was adopted from work by Bbosa (2013) based on the distribution of the mass of charge particles (simplify) and the average angular velocity. The spatially averaged mass and averaged angular velocity distribution was determined for each voxel to subsequently calculate the torque contribution of each voxel in the grid. Figure 6 depicts how the power consumption for the various mill critical speed ranges rise as the lifter face angle increases. The lifter face angle has a more decisive influence on mill speed. Without a doubt, the power consumption data for dry DEM must be larger than the coupled CFD-DEM simulation results, and the explanation is simple: there is slurry damping of particle motion.

The difference between the power draw values for 60 per cent of mill critical speed is significantly higher than other mill speeds. Typically, the motion occurring at 60 per cent of the mill critical speed is a nice blend of cascading and cataracting regimes that appear to be substantially influenced by slurry. In comparison, cascading and rolling regimes prevail at low mill speeds (50 per cent of N_c), whereas cataracting and centrifuging regimes dominate at high mill speeds (75 per cent of N_c). When comparing the two slurries used in the current study, a significant decrease in power draw was observed due to an increase in viscosity, indicating that the contribution from the slurry is well accounted for in the CFD-DEM model.

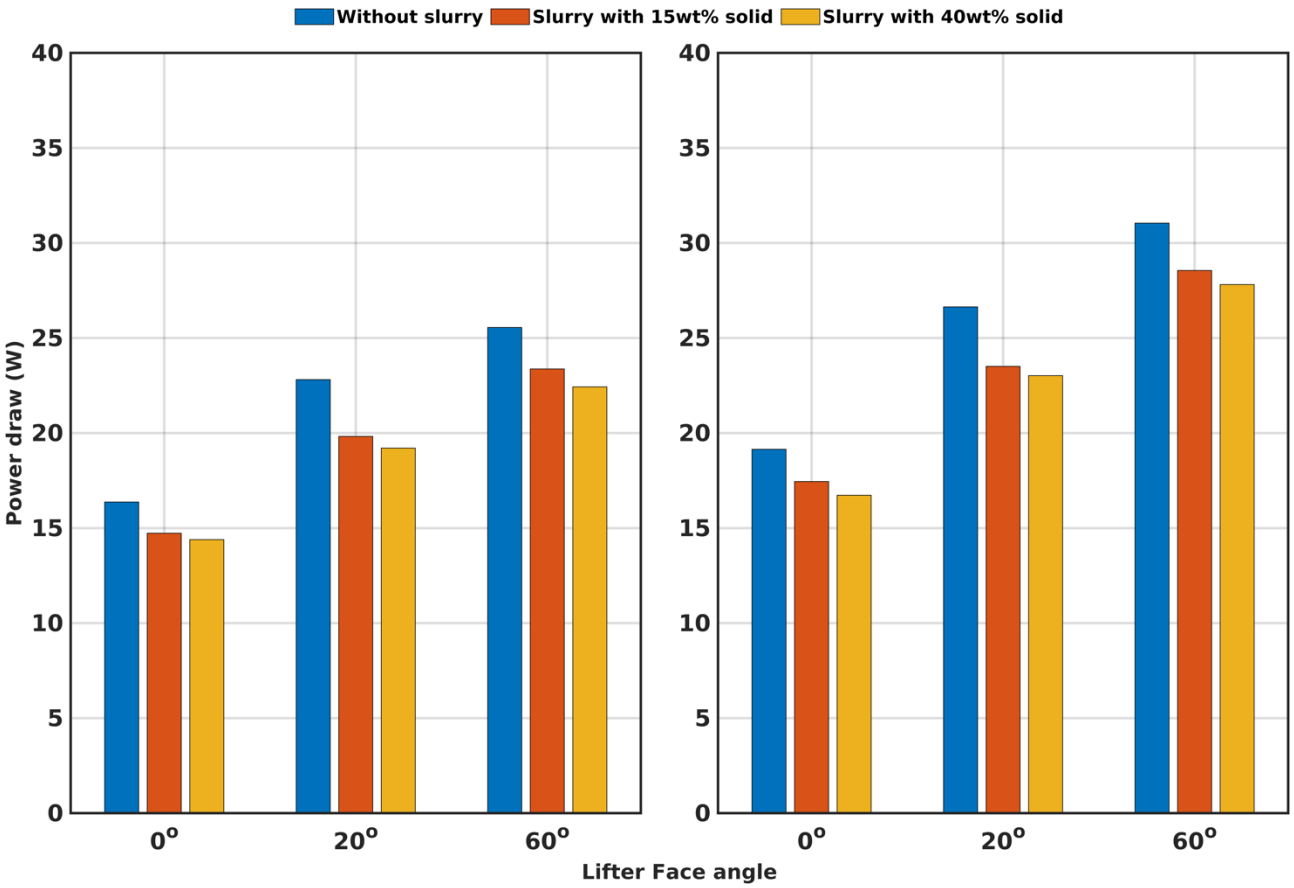

FIG 6 – Power consumption comparison between dry DEM and CFD-DEM coupled simulations data.

CONCLUSION

The coupled CFD-DEM approach is an excellent tool for accurately computing and characterising the charge particle dynamics inside a tumbling mill. On the contrary, the dry DEM model overpredicts particle dynamics because of the unaccounted effects of slurry shear forces. It was observed that raising the lifter face angle and mill speed made the particle streams denser and increased the number of high-speed particles in both scenarios with and without a slurry. Although in presence of slurry, the number of high-speed particles appears to decrease with increasing viscosity. Slurry appears to mitigate the dominant effect of high mill speed on solids concentration. The solids concentration appears to outweigh the dilating impact of speed at lower speeds. From no slurry to slurry, there was a 6–8 per cent shift in shoulder angle and a ~1 per cent shift in toe angle. In the presence of slurry, the shoulder and toe angles of the charge particles do not appear to vary significantly with slurry viscosity. At 60 per cent N_c, there is a ~16 per cent increase in the power draw of charge particles in the tumbling mill from no slurry to slurry, which is the most significant difference seen in all cases. The difference in power draw between the two slurries was approximately 3 per cent due to the dampen particle motion from the slurry. The current study successfully developed a computational model that accurately predicts the complex multi-phase dynamics of charge, air, and slurry inside the mill by combining computational fluid dynamics and the discrete element method.

ACKNOWLEDGEMENT

The authors would like to acknowledge the Indian Institute of Technology Hyderabad and the Science and Engineering Research Board for sponsoring, funding, and encouraging joint research on this project (DST No.: CRG/2020/006141).

REFERENCES

Artoni, R, Richard, P, 2015. Average balance equations, scale dependence, and energy cascade for granular materials. https://doi.org/10.1103/PhysRevE.91.032202

Babic, M, 1997. Average balance equations for granular materials. *International Journal of Engineering Science* 35, 523–548. https://doi.org/https://doi.org/10.1016/S0020–7225(96)00094–8

Bbosa, L, 2013. Probability based models for the power draw and energy spectra of a tumbling mill. PhD thesis. University of Cape Town.

Bian, X, Wang, G, Wang, H, Wang, S, Lv, W, 2017. Effect of lifters and mill speed on particle behaviour, torque, and power consumption of a tumbling ball mill: Experimental study and DEM simulation. *Minerals Engineering*. https://doi.org/10.1016/j.mineng.2016.12.014

Cleary, P W, 2001. Charge behaviour and power consumption in ball mills: Sensitivity to mill operating conditions, liner geometry and charge composition. *International Journal of Mineral Processing*. https://doi.org/10.1016/S0301–7516(01)00037–0

Cleary, P W, 2015. Prediction of coupled particle and fluid flows using DEM and SPH *Minerals Engineering* 73, 85–99. https://doi.org/10.1016/j.mineng.2014.09.005

Cleary, P W, Sinnott, M, Morrison, R, 2006. Prediction of slurry transport in SAG mills using SPH fluid flow in a dynamic DEM based porous media. *Minerals Engineering*. https://doi.org/10.1016/j.mineng.2006.08.018

Djordjevic, N, Shi, F N, Morrison, R, 2004. Determination of lifter design, speed and filling effects in AG mills by 3D DEM, in: *Minerals Engineering*. https://doi.org/10.1016/j.mineng.2004.06.033

Gutiérrez, A, Ahues, D, González, F, Merino, P, 2019. Simulation of Material Transport in a SAG Mill with Different Geometric Lifter and Pulp Lifter Attributes Using DEM *Mining, Metallurgy and Exploration*. https://doi.org/10.1007/s42461–018–0007–9

Ishii, M, Mishima, K, 1984. Two-fluid model and hydrodynamic constitutive relations. *Nuclear Engineering and Design* 82, 107–126. https://doi.org/https://doi.org/10.1016/0029–5493(84)90207–3

Jayasundara, C T, Yang, R Y, Guo, B Y, Yu, A B, Govender, I, Mainza, A, Westhuizen, A. van der, Rubenstein, J, 2011. CFD-DEM modelling of particle flow in IsaMills – Comparison between simulations and PEPT measurements. *Minerals Engineering* 24, 181–187. https://doi.org/10.1016/j.mineng.2010.07.011

Makokha, A B, Moys, M H, 2006. Towards optimising ball-milling capacity: Effect of lifter design. *Minerals Engineering*. https://doi.org/10.1016/j.mineng.2006.03.002

Makokha, A B, Moys, M H, 2007. Effect of cone-lifters on the discharge capacity of the mill product: Case study of a dry laboratory scale air-swept ball mill. *Minerals Engineering*. https://doi.org/10.1016/j.mineng.2006.07.010

Mayank, K, Malahe, M, Govender, I, Mangadoddy, N, 2015a. Coupled DEM-CFD Model to Predict the Tumbling Mill Dynamics. *Procedia IUTAM 15*, 139–149. https://doi.org/10.1016/j.piutam.2015.04.020

Mayank, K, Narasimha, M, Govender, I, 2015b. Two way coupled CFD-DEM model to predict tumbling mill dynamics, in: *SAG Conference*, Vancouver, Canada.

Mishra, B K K, Rajamani, R K, 1992. The discrete element method for the simulation of ball mills. *Applied Mathematical Modelling* 16, 598–604. https://doi.org/10.1016/0307–904X(92)90035–2

Napier-Munn, T J, Morrell, S, Morrison, R D, Kojovic, T, 1996. Mineral comminution circuits: Their operation and optimisation, *JKMRC monograph series in mining and mineral processing* (Julius Kruttschnitt Mineral Research Centre, University of Queensland: Indooroopilly).

Parker, D J, Allen, D A, Benton, D M, Fowles, P, McNeil, P A, Tan, M, Beynon, T D, 1997. Developments in particle tracking using the Birmingham Positron Camera. *Nuclear Instruments and Methods in Physics Research, Section A: Accelerators, Spectrometers, Detectors and Associated Equipment.* https://doi.org/10.1016/S0168–9002(97)00301-X

Powell, M S, Weerasekara, N S, Cole, S, Laroche, R D, Favier, J, 2011. DEM modelling of liner evolution and its influence on grinding rate in ball mills. *Minerals Engineering* 24, 341–351. https://doi.org/10.1016/j.mineng.2010.12.012

Robinson, M, Ramaioli, M, Luding, S, 2014. Fluid-particle flow simulations using two-way-coupled mesoscale SPH-DEM and validation. *International Journal of Multiphase Flow* 59, 121–134. https://doi.org/10.1016/j.ijmultiphaseflow.2013.11.003

Schönert, K, 1986. On the limitation of energy saving in milling. *World Congress Particle Technology*, Part II.

Sun, X, Sakai, M, Yamada, Y, 2013. Three-dimensional simulation of a solid-liquid flow by the DEM-SPH method. *Journal of Computational Physics* 248, 147–176. https://doi.org/10.1016/j.jcp.2013.04.019

Yamane, K, Nakagawa, M, Altobelli, S A, Tanaka, T, Tsuji, Y, 1998. Steady particulate flows in a horizontal rotating cylinder. *Physics of Fluids* 10, 1419–1427. https://doi.org/10.1063/1.869858

Evaluating rheological features inside tumbling mills using DEM data previously validated against PEPT measurements

T L Moodley[1] and I Govender[2,3,4]

1. Engineer, Mintek, Randburg, Gauteng, 2121, South Africa. Email: taswaldm@mintek.co.za
2. Group Executive: Mineral Processing and Characterisation, Mintek, Randburg, Gauteng, 2121, South Africa. Email: IndresanG@mintek.co.za
3. Professor of Particle Technology and Mineral Processing (Honorary), Discipline of Chemical Engineering, School of Engineering, University of KwaZulu-Natal, Durban, 4041, South Africa. Email: govenderi5@ukzn.ac.za
4. Professor of Chemical Engineering (Honorary), Department of Chemical Engineering, Centre for Minerals Research, University of Cape Town, Rondebosch, 7701, South Africa. Email: indresan.govender@uct.ac.za

ABSTRACT

Tumbling mills are grossly inefficient, using only 5 per cent of the total energy supplied for actual breakage. A significant proportion of this inefficiency is unavoidable owing to geometric limitations; rotating drum systems are prone to exhibiting certain regions (energy barriers) that resist particle entry thereby restricting the transfer of energy. Though such systems are inherently inefficient, improved modelling schemes may lead to slightly enhanced efficiency through better microscale predictions of key breakage drivers (stress, force). Central to achieving such incremental advances is the development of a universally accepted rheology for dense granular flows. Armed with a better understanding of these macro-scale ingredients, classical process modelling offers an efficient, spreadsheet friendly framework for recovering the spatial distributions of the comminution drivers. At this real-time level of process control, it should be possible to tune comminution operations towards more energy efficient configurations – the ultimate goal of this research. The present work employs validated DEM data to recover the full continuum field which will ultimately serve as a basis for calibrating process model outputs based on different rheological hypotheses. Such a continuum-based approach captures tensor properties like the shear stress and strain rate – both of which are necessary to developing a dense granular rheology. Moreover, DEM captures this data at the momentum transfer timescale of 10^{-6} s – no other measurement technique is capable of this level of spatial and temporal resolution. Importantly, the confidence in this DEM data is strengthened because it has been validated at the continuum scale using Positron Emission Particle Tracking (PEPT) kinematic measurements. Validated DEM data is derived from batch experiments conducted within a 300 mm ID laboratory drum using three and five millimetre glass beads at 60 and 75 percent critical speed; such mill speeds are typically encountered in the tumbling mill industry. Dimensional analysis is conducted using critical rheological parameters (shear rate, shear stress, granular temperature etc), which are key to not only developing a granular rheology but ultimately will be used to tune our mechanistic models.

INTRODUCTION

Researchers in the comminution industry have been trying for decades to optimise tumbling mill efficiency. Stemming from the fact that they consume about 4 per cent of the available electrical energy globally (Kolev *et al*, 2021), the slightest improvement in efficiency translates into significant cost savings. Being a complex multiphase phase flow that is difficult to describe using classical, fundamental physics, a significant proportion of the optimisation research in the tumbling mills community has been dedicated to the development of purely empirical models (Bbosa *et al*, 2011; Austin, 1990; Morrell, 1992). Such *black-box* models are extremely powerful provided they are applied within their domain of applicability – outside of this, their use is limited and can be detrimental to downstream processes. In addition, empirical models inherently lack detail concerning the internal dynamics within the mill which ultimately drive energy efficiency. These weaknesses necessitate the development of predictive fundamental models that explain the mechanisms of breakage and energy dissipation occurring within the mill – only then can one truly optimise the performance of tumbling mills.

This paper introduces a unique way to treat the data derived simulation and experiment. On the one hand, simulation provides the opportunity to obtain dynamic properties like shear stress, shear rate, power dissipation at the momentum transfer timescale of 10^{-6} s. At such a timescale, there is simply no experimental technique that can be used to validate these properties *in situ*. This has led experimentalists to argue the validity of the DEM data. Positron Emission Particle Tracking (PEPT) is a nuclear imaging technique capable of providing data (solids fraction, velocity) at a timescale of 10^{-3} s and spatial resolution of a millimetre. Clearly, this is too coarse a timescale to validate the dynamic data from DEM. Whilst it may be true that there is no way to experimentally validate this simulated data at the microscale, if the predictions are coarsened out to the mesoscale, then the DEM continuum fields can be validated using PEPT data. These DEM kinematic fields have been validated in the previous phase of work at the continuum scale using PEPT data (Moodley and Govender, 2020); the results from that study showed statistical agreement.

In order to develop a fundamental model that describes the underlying mechanisms that drive breakage, the relationship between shear stress and shear rate in a dense granular system must be known – such a relationship does not exist in the literature (Kumaran, 2004). In the absence of such a fundamental relationship, researchers resort to using dimensional analysis to characterise the system. There are two leading theories using dimensionless numbers that describe dense granular flows in three dimensions namely the μ(I) (Jop, Forterre and Poliquen, 2006) and modified – Pe number rheologies (Pähtz *et al*, 2019; Chialvo and Sundaresan, 2013); both require knowledge of fundamental properties like the shear rate, granular temperature and shear stress to be utilised.

The μ(I) rheology assumes that the granular medium behaves like an incompressible fluid and captures its behaviour locally. Based on a coulombic-like friction, it relates an effective friction coefficient μ (ie the ratio of the shear stress (τ) to the pressure (P)) to the dimensionless inertial number (I) in the following manner:

$$\mu(\mathrm{I}) = \left|\frac{\tau}{\mathrm{P}}\right| \text{ with } \mathrm{I} = \frac{|\dot{\gamma}|\mathrm{d}}{\sqrt{\mathrm{P}/\rho_m}} \tag{1}$$

where $\dot{\gamma}$ is the shear rate, $|\tau|$ is the magnitude of the deviatoric shear stress, *P* is the pressure, ρ_m the material density and *d* is the particle diameter. In essence, it compares the typical time scale of microscopic rearrangements to macroscopic deformation. Using an exhaustive experimental programme, the effective friction (μ) was determined to be related to I in the following manner:

$$\mu(I) = \mu_s + \frac{\mu_2 - \mu_s}{I_0/I + 1} \tag{2}$$

The exponential expression above implies that below a certain minimum friction (μ_s), no material flow occurs. Mathematically speaking, flow is possible if-and-only if $\left|\frac{\tau}{P}\right| > \mu_s$. The phenomenological nature of the model means that as the value of I increases (implying a shear dominant flow where $I \gg 1$), $\mu \approx \mu_s$. The parameters μ_s, μ_2 and I_0 are material specific and, in the case of spherical glass beads have been experimentally quantified as $\mu_s = \tan(20.9^0)$, $\mu_2 = \tan(32.76^0)$ and $I_0 = 0.279$. The solids fraction has been determined to decrease linearly with the inertial number:

$$\emptyset = \emptyset_{max} - \beth I \tag{3}$$

where $\emptyset_{max}$ is the maximum possible solids fraction ($\emptyset = {}^{\rho}/_{\rho_m}$ defined as the ratio of bulk to material density of the particulate flow) and ב is a positive constant usually equal to 0.2. Unfortunately, this equation is only valid for low values of I since if $I > {}^{\emptyset_{max}}/_{\beth}$, this will result in negatively valued solids fractions. Thus, the $\mu(I)$ rheology is restricted to the case of dense granular flows where the value of I is typically low. Apart from the obvious local dependence of the rheology *viz* does not account for long range effects prevalent in dense granular flows, an interesting omission from this rheology is the effect of velocity covariance (fluctuations). Such fluctuations influence the behaviour in granular beds in similar manner as they do in a gas through the thermodynamic temperature; thus it is aptly termed the granular temperature (T) and computed as follows:

$$\mathrm{T} = \frac{1}{3}\left(\langle \grave{U}_1^2 \rangle + \langle \grave{U}_2^2 \rangle + \langle \grave{U}_3^2 \rangle\right) \tag{4}$$

where $\langle \grave{U}_i^2 \rangle$ denotes the ensemble average (or root mean square) of the fluctuating velocity. Computing T allows for the prediction of particle movement which is particularly beneficial to mixing processes; such movement is underpinned by a gradient driving force principal where particles are more likely to flow from a region of high temperature to that of low temperature. Using DEM, we are able to obtain the binned granular temperature in each of the three principal directions as:

$$\langle \grave{U}_i^2 \rangle = \frac{\sum_1^N (U_i - \overline{U})^2}{N} \tag{5}$$

where U_i and $\overline{U}$ are the individual particle velocity and the mean velocity within each bin respectively. Despite some authors including the rotational degrees of freedom in the granular temperature calculation, this work is restricted to fluctuations due to translational particle velocity. It is generated as a result of the shear stress between particles and is diffused through the bed due to particle collisions and kinetic flux (Cleary, 2007). Researchers argue the validity of such a property (and kinetic theory in general) in a granular medium since in gases the collisions are perfectly elastic meaning the system is in equilibrium. In a granular medium, the collisions are dissipative in nature implying that the system in a constant state of non-equilibrium thus requiring a constant supply of energy to maintain fluidisation (Goldhirsch, 2008). Amidst these valid arguments, studies conducted by Goldhirsch (2001) and Khain (2007) have demonstrated the benefits of applying hydrodynamic and kinetic theories to granular flow. A rheology that incorporates this property is the modified Pe based rheology proposed by Pähtz *et al* (2019) which builds upon the original rheology proposed by Chialvo and Sundaresan (2013). Both of these rheologies are underpinned by a dimensionless number that is defined as follows:

$$\mathrm{Pe} \equiv \frac{\dot{\gamma} \mathrm{d}}{\sqrt{\mathrm{T}}} \tag{6}$$

where T is the granular temperature whilst the rest of the symbols have been previously defined. It can be interpreted as the ratio between the rates of macroscopic shearing motion ($\dot{\gamma}$) and kinetic rearrangements ($\frac{\sqrt{\mathrm{T}}}{\mathrm{d}}$). This differs from the $\mu(\mathrm{I})$ rheology that assumes the particle rearrangements are driven by pressure whereas, in this case, it is by the actual relative motion differences between particles. In addition, the authors propose that the coulombic friction (μ) scales with the Pe only according to the scaling parameter (C_μ) as follows:

$$\mu = C_\mu \sqrt{\mathrm{Pe}} \tag{7}$$

Equation 7 has been confirmed for both dilute and dense flow conditions except for scenarios where non-local effects dominate like sediment transport and gravity flows. The authors demonstrate that C_μ varies with the tangential friction coefficient and not the normal coefficient of restitution. This implies that μ encompasses the effects of anisotropies of the particle assembly (Pe) and the tangential contact force network (C_μ). In summary, the larger Pe number indicates a predominantly convective flow whilst a lower Pe indicates a diffusion dominated flow. Building upon the results of Chialvo and Sundaresan (2013), Pähtz *et al* (2019) introduced a dimensionless temperature gradient $\mathrm{M} \equiv \frac{\mathrm{d}|\nabla T|}{T}$ which accounts for the inhomogeneity associated with non-local effects whose effects are highlighted near the yield stress limit. Thus, the rheology makes use of either M for inhomogeneous flows or Pe for uniform flows in order to describe behaviour around a particular yield stress ($\mu_s{}^*$) which is dependent on the flow profile. The relationship between T and $\mu_s{}^*$ remains an open question.

Problem statement and objectives

The Discrete Element Method (DEM) has been used for decades now to simulate granular systems by discretising particles at a microscale resolution. Due to the computational limitations, DEM has been used to simulate the media charge in tumbling mills and infer probability of breakage. This time scale is ideal to characterise dynamic information like the shear stress, shear rate and granular temperature. Unfortunately, information at this scale is impossible to validate. This is because there is no experimental technique that can provide reliable information at the necessary spatial and temporal resolution. It is for this reason that researchers have questioned the validity of the predictions thereof. This paper serves to provide a solution to this dilemma. The kinematic DEM

outputs (velocity fields, solids fraction) have been previously validated at the mesoscale using Positron Emission Particle Tracking (PEPT). Upon applying advanced coarse graining schemes (Artoni and Richard, 2015; Babic, 1997) to discrete kinematic data, the resultant outputs yielded excellent statistical agreement between PEPT and DEM at the mesoscale. Such results support the hypothesis that there is more confidence in the DEM kinetic outputs (shear stress, shear rate, granular temperature) at the mesoscale because of the validated the kinematic data (solids fraction, velocity fields). This paper is organised in the following fashion:

1. The authors begin by detailing the experimental configuration of the DEM simulations.
2. Next, the methodology used to develop the continuum scale descriptions of the kinetic data is presented.
3. Thereafter, the kinetic data derived from the simulations (shear stress, shear rate, granular temperature) are presented. This data is subsequently combined to produce rheological predictions.
4. Finally, conclusions are drawn, and future work is suggested.

METHODOLOGY

DEM

A short methodology detailing DEM will now be presented; for further details, see Moodley (2022). ROCKY-DEM was used for the rotating drum particle simulations. The relatively large particle sizes (3 mm and 5 mm) operated in a dry, batch environment ensured that only gravity and inter-particle contact were relevant. The total contact force acting on a particle is broken up into the normal and tangential components with respect to the contact plane. The present work used the linear spring dashpot contact model (Cundall and Strack, 1979) to describe the normal component of the contact force: $F_n = K_{nl}S_n + C_n\dot{S_n}$ where K_{nl} is the normal contact stiffness, C_n is the normal damping coefficient, S_n is the contact normal overlap $\dot{S_n}$ is the time derivative of the contact normal overlap, ie velocity. For the tangential component of the contact force, the Linear-spring Coulomb limit model was selected. It is elastic in nature but also considers the frictional forces. The elastic component, at time *t*, is given by $F_{\tau,e}^t = F_\tau^{t-\Delta t} - K_\tau \Delta S_\tau$ where $F_\tau^{t-\Delta t}$ is the value of the tangential force at the previous time, ΔS_τ is the tangential relative displacement of the particles during the timestep (10^{-8} s this work) and K_τ is the tangential stiffness. The friction component of the model is introduced by assuming that the tangential force cannot exceed the Coulomb limit given by $F_\tau^t = \min\left(\left|F_{\tau,e}^t\right|, \mu F_n^t\right)\frac{F_{\tau,e}^t}{\left|F_{\tau,e}^t\right|}$, F_n^t is the contact normal force at time *t* and μ the friction coefficient. The Coulomb limit, μF_n^t, is the point at which the surface contact begins to shear and thus particles start to slide over one another. The Cauchy stress tensor is obtained directly from ROCKY-DEM and is based on the force generated by particle collisions. It is restricted to contact stress only because in granular matter with solid particles there is almost no random motion, therefore the kinetic stresses are negligible. Random motion is almost instantly killed in highly dissipative media like solid particles. It is only important for perfectly elastic collisions like for molecules of a gas. The 3D stress tensor $\left(\sigma_{ij}^p\right)$ is computed in the following manner:

$$\sigma_{ij}^p = \frac{1}{V_p}\sum_{c=1}^{N_p^c} x_i^c f_j^c \tag{8}$$

where V_p is the volume of the particle, x_i^c is the contact location of particle-particle pair *ij*, f_j^c is the contact force of pair *ij*, and N_p^c is the number of contacts of particle *p*. The nine component stress tensor consists of three normal and six deviatoric components. An important characteristic of this stress tensor is the requirement that all $\sigma_{ij} = \sigma_{ji}$ ie the deviatoric components are symmetric. The trace (or normal) components form the pressure (p) contribution whilst shear comprises of all deviatoric components and the overall stress tensor is expressed as $\sigma_{ij} = \left(\sigma_{ij}\right)_{\text{dev}} + \text{tr}\left(\sigma_{ij}\right)$ as follows:

$$\begin{pmatrix}\sigma_{11} & \sigma_{12} & \sigma_{13}\\ \sigma_{21} & \sigma_{22} & \sigma_{23}\\ \sigma_{31} & \sigma_{32} & \sigma_{33}\end{pmatrix} = \begin{pmatrix}(\sigma_{11}-\mathrm{p}) & \sigma_{12} & \sigma_{13}\\ \sigma_{21} & (\sigma_{22}-\mathrm{p}) & \sigma_{23}\\ \sigma_{31} & \sigma_{32} & (\sigma_{33}-\mathrm{p})\end{pmatrix} + \begin{pmatrix}\mathrm{p} & 0 & 0\\ 0 & \mathrm{p} & 0\\ 0 & 0 & \mathrm{p}\end{pmatrix} \quad (9)$$

where:

$$\mathrm{p} = \frac{1}{3}.(\sigma_{11}+\sigma_{22}+\sigma_{33}) \text{ and } \left(\sigma_{ij}\right)_{\text{dev}} = \tau_{ij} \quad (10)$$

The rotating drum was 300 mm in diameter, 270 mm long and fitted with 20 lifter bars. The rotating drum was drawn in AutoCAD™ and imported into the ROCKY-DEM platform. In each experiment, the drum consisted of either 60 000, 5 mm glass beads or 270 000, 3 mm glass beads with a particle density of ρ = 2500 kg/m^3. In either case, the particles occupied 31 per cent of the inner drum volume. The glass beads employed in the experimental work were first conditioned by rotating them in the drum for an extended period of time. This ensured that all rough edges, usually associated with new batches of beads, were thoroughly smoothed out. A natural and desirable consequence of conditioning is the evolution of a narrow size distribution which was measured to be normally distributed about the mean particle size with a maximum deviation of 0.5 mm. The narrow size distribution is known to prevent crystallisation in the packing structure. The problem of crystallisation can be significantly exacerbated in DEM simulations comprising of perfectly spherical particles with identical diameters. Accordingly, the measured distribution of particle size (and mass) was introduced into the simulation via a Gaussian distribution. Typical comminution speeds of 60 per cent and 75 per cent of critical speed (N_c) were investigated (Rose and Sullivan, 1957).

The standard material properties for the DEM simulations are given in Table 1 whilst the material interaction parameters are shown in Table 2. The frictional properties shown in Table 2 are the final values used (after systematically tuning the parameters against PEPT data) for each of the static μ_s, dynamic μ_d and rolling μ_r friction coefficients whilst C_r represents the coefficient of restitution (Chandramohan, 2005).

TABLE 1

Summary of material parameters for DEM simulations.

Item	Material	Density (kg/m^3)	Youngs modulus (GPa)	Poisson's ratio
Azimuthal wall	HDPE	950	0.8	0.46
Side wall	Perspex	1190	0.3	0.38
Lifter bars	Nylon	1200	3	0.4
Beads	Glass	2600	70	0.15

TABLE 2

Summary of contact interaction parameters.

Interaction pair	μ_s	μ_k	μ_r	C_R
Glass – HDPE	0.29	0.05	-	0.7
Glass – Nylon	0.53	0.1	-	0.28
Glass-Glass	0.9	0.4	0.01	0.66
Glass-Perspex	0.29	0.05	-	0.7

Data averaging process

To ensure an equitable comparison scale, we must convert the discrete particle data shown in Figure 1a, to average data per bin or voxel shown in Figure 1b. Only then can a coarse graining scheme can be employed to produce a smoother, more continuous field as shown in Figure 1c. We begin by explaining how particle level data in Figure 1a is converted to binned data in Figure 1b; this is the concept of data binning.

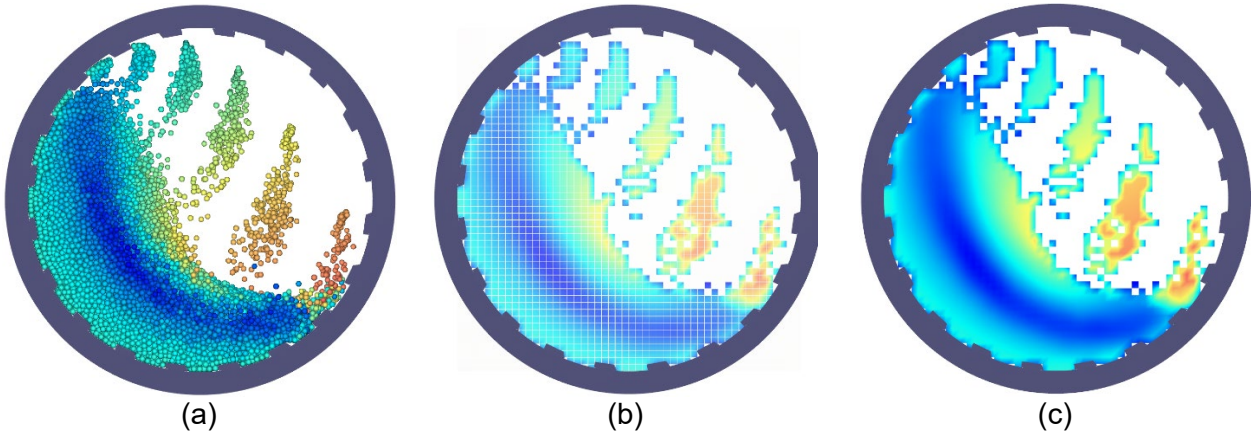

FIG 1 – Illustration of coarse graining process ranging from: (a) Discrete elements each coloured according to an arbitrary particle property ψ_p with colourmap values ranging from high to low (red to blue), (b) Binned particle properties coloured per voxel, (c) Continuous property after applying smoothing kernel.

Let's define $\psi_{\mathrm{p}}(\vec{x}_p)$ as a property of particle *p* flowing within a tumbling mill system operated at steady-state. We now seek the average particle property $\bar{\psi}$ at some probe point $\vec{x}$. The average property at the probe point can be thought of as the weighted contributions of nearby particles. To illustrate this effect, consider a data set *x* that is represented using the histogram shown in Figure 2.

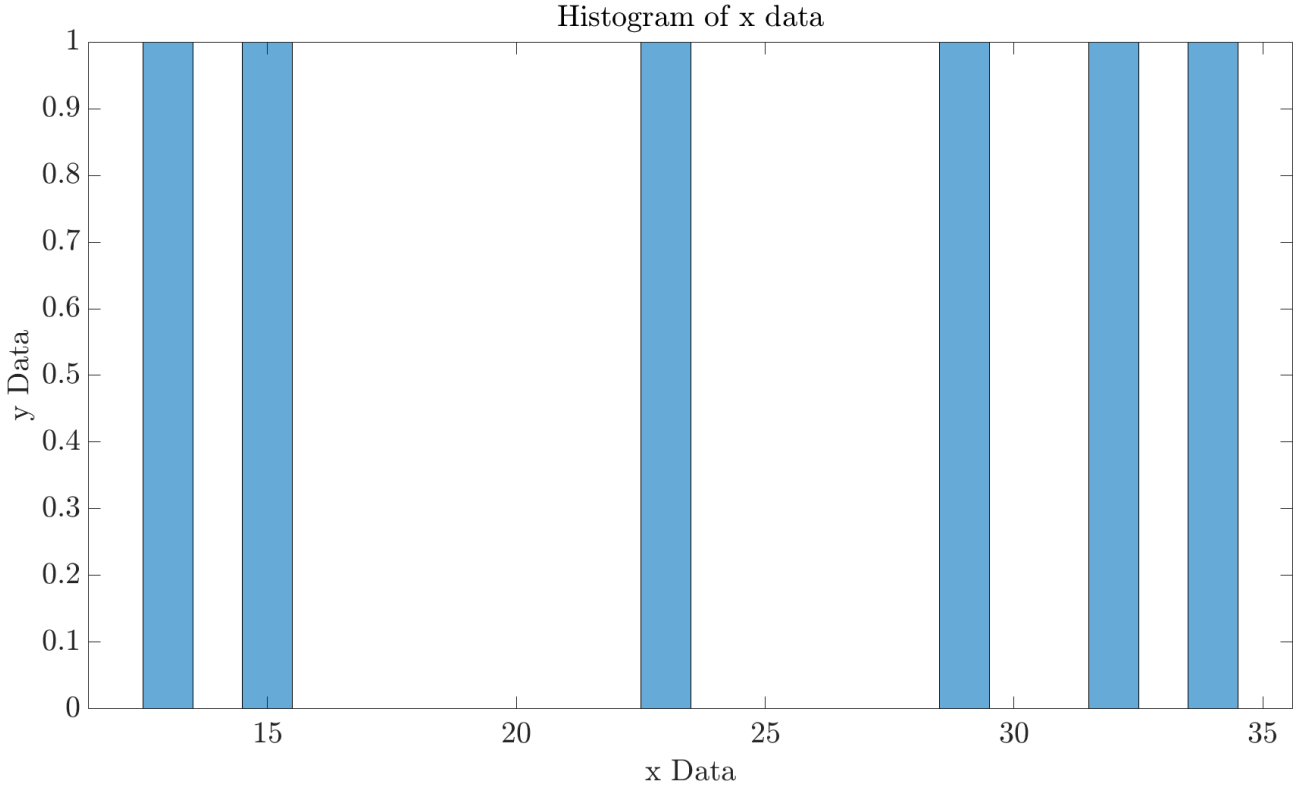

FIG 2 – Histogram of an arbitrary data set.

In this data set, there are several 'bins' wherein there is no data, for example the bins in between 15 and 23. However, we would still like to estimate the probability density at those points. In order to do so, we create a weighted average of the nearby points. This can be understood by considering the point corresponding to $x_0 = 17$. This lies in between 15 and 23 in our data set – bins that have data. We average these points nearby and count them as if they were present in this bin. In order to achieve this, a kernel function is overlayed onto each point in the histogram. We have utilised a

Gaussian function to serve as the basis for the weighted average. A 2D function which defines the kernel estimator of the probability density of any real values of *x* is shown in Equation 11:

$$\hat{f}_h(x) = \frac{1}{N.h}\sum_{i=1}^{N}\frac{K(x-x_i)}{h} \tag{11}$$

where x_i are random samples from an unknown distribution, *N* is the sample size, *K* is the kernel smoothing function, and *h* is the bandwidth or smoothing radius. The *h* represents how far away are we going to consider the effects of neighbouring data points on the point of interest. Using this kernel function estimator, we can approximate a probability density distribution as depicted in Figure 3.

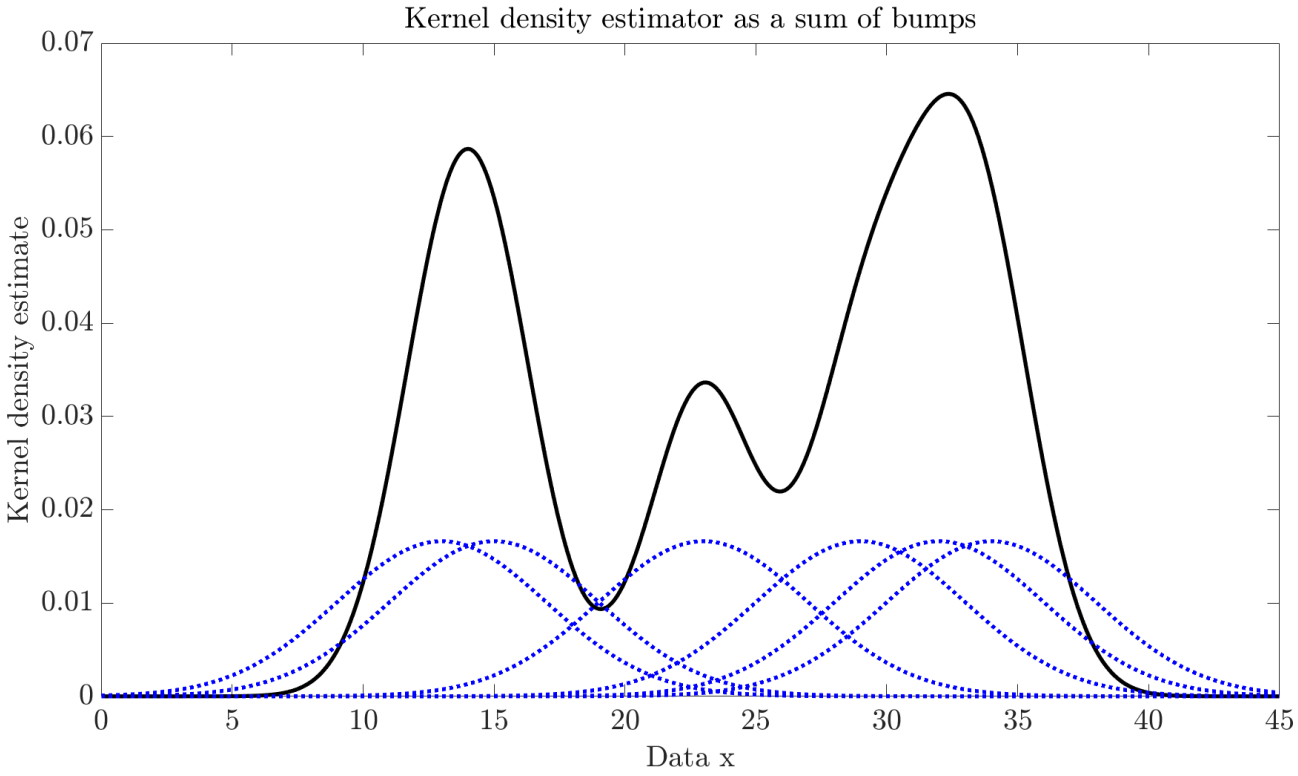

FIG 3 – Illustration of the benefit of using a kernel density estimate to replace missing data from bins.

The way to interpret Figure 3 is to consider a single point on the *x*-axis – say x_0 = 17 – and move your finger vertically upwards. Notice that since we chose a smoothing radius of 2 in this case, the Gaussian curves that intersect your finger are centred at x = 13, 15 and 23. Thus the kernel density estimate will be a weighted sum of these three values. In other words, this serves as an estimate of the frequency $\left[\hat{f}_h(x)\right]$ at the point x_0 = 17. In essence, we count these neighbouring points as being virtually present in the bin centered at x_0 = 17. A caveat of this kernel function is that all curves should satisfy the following relationship given by Equation 12.

$$\int_{-\infty}^{\infty} K(x - x_i)dx = 1 \tag{12}$$

Equation 2 means that we count every observation one time but we spread out how we count it over an area. In summary, a kernel allows us to take a finite set of data points and spread them apart over the *x*-axis. This enables data from one point to contribute to the calculation at various other points. So even Figure 3 only has six data points, we can see that the kernel centered over each data point spans the entire *x* range which enables us to estimate the density at any point. Now, this explains how kernel averaging is done statistically; unfortunately, in the case of granular systems, we must make some adjustments.

As depicted in Figure 3, to ensure that such averages are smoothly and uniformly computed at any probe point, we introduce a spatial smoothing function $G(\vec{x})$ that is continuous and differentiable. A popular form of the spatial smoothing function $G\left(\overrightarrow{\Delta x}\right)$ is built upon a Gaussian kernel $K\left(\overrightarrow{\Delta x}\right)$ such

that for each probe point $\vec{x}$ and particle centroid $\vec{x}_p$, the Gaussian smoothing function is given by Equation 13.

$$G(\overrightarrow{\Delta x}) = |W|^{-0.5} K(\overrightarrow{\Delta x}) \tag{13}$$

where $\overrightarrow{\Delta x} = \vec{x} - \vec{x}_p$ is the displacement between the probe point $\vec{x}$ (centre of a given voxel) and the centroid of particle $\vec{x}_p$;

$$W = \begin{bmatrix} w^2 & 0 & 0 \\ 0 & w^2 & 0 \\ 0 & 0 & \left(L/2\right)^2 \end{bmatrix}$$

and

$$K(\overrightarrow{\Delta x}) = \left(\frac{\pi}{4}\right)^{-3/2} \exp\left[-4\left(\frac{\overrightarrow{\Delta x}}{W^{0.5}}\right)^T \left(\frac{\overrightarrow{\Delta x}}{W^{0.5}}\right)\right]$$

denotes the spatial Gaussian kernel function where $\left(\frac{\overrightarrow{\Delta x}}{W^{0.5}}\right)^T$ reads the 'transpose of $\left(\frac{\overrightarrow{\Delta x}}{W^{0.5}}\right)$' and *W* is the bandwidth matrix where *w* is the smoothing length in the azimuthal plane while smoothing in the *z*-direction is over half the drum length *L*. The *w* in this equation is the same as the *h* in Equation 11. Using the previously defined coarse graining ingredients, the average particle property is then given by Equations 14 to 16.

$$\rho\bar{\psi} = \sum_p w_p m_p \psi_p \tag{14}$$

$$\rho(\vec{x}, t) = \sum_p w_p m_p \tag{15}$$

And:

$$w_p = K(\overrightarrow{\Delta x}, W) \tag{16}$$

where m_p is the mass of particle *p*, $\rho = \rho(\vec{x})$ is the average density at the probe point, and w_p a normalised weighting function (normalised spatial Gaussian kernel function) centered on the probe point $\vec{x}$. The property fluctuation $\tilde{\psi}_p$ is given by:

$$\tilde{\psi}_p = \tilde{\psi} - \tilde{\psi}_p(\vec{x}_p) \tag{17}$$

which is an improvement to the original work by Babic (1997).

Artoni and Richard (2015) showed that $\bar{\psi}_p(\vec{x}_p)$ can be approximated by:

$$\bar{\psi}_p(\vec{x}_p) \cong \bar{\psi}(\vec{x}) + (\vec{x}_p - \vec{x})\vec{\nabla}\bar{\psi}(\vec{x}) \tag{18}$$

So the property fluctuation, which is now said to be insensitive to coarse graining width, reduces to:

$$\tilde{\psi}_p = \tilde{\psi} - \bar{\psi}(\vec{x}) - (\vec{x}_p - \vec{x})\vec{\nabla}\bar{\psi}(\vec{x}) \tag{19}$$

Artoni and Richard (2015) also showed that the gradient of the average property (like, say, the shear rate) is:

$$\rho\vec{\nabla}\bar{\psi} = \sum_p(\vec{\nabla}w_p)m_p\psi_p - \bar{\psi}\sum_p(\vec{\nabla}w_p)m_p \tag{20}$$

The above methodology was used to calculate the smooth, average particle property distributions at each voxel within the azimuthal plane of interest. The basic properties include:

- Shear rate tensor: $\dot{\gamma}_{ij}$
- Granular temperature tensor: θ_{ij}

RESULTS AND DISCUSSION

The data is analysed for both three- and five-millimetre DEM data gathered over speeds of 60 and 75%N_c. We extract both the 2D azimuthal maps and perform analysis along centrally located radial lines taken perpendicular to the free surface. To extract the azimuthal profiles, we apply the following steps to the DEM data:

1. Discretise the azimuthal plane of the drum into voxels of dimensions ($d \times d \times \ell$) where d = 6 mm and ℓ = 285 mm is the drum length.
2. Bin the particle positions:
    - Once the simulation is running at steady state, the DEM data is binned at N = 1000 consecutive 10^{-3} s timesteps which is approximately a single revolution of the drum.
    - We apply coarse graining using a Gaussian smoothing kernel on the DEM data simply to smooth out the pixilation introduced by the bin edges. The effects of this convolution mediated smoothing are detailed in Moodley and Govender (2022).

Stresses

The stress field is an important entity in terms of the analysis of tumbling mills. It is a continuum representation of the average force per unit area of the contacting particles which ultimately drives fines production. The overall shear stress, deviatoric shear stress and pressure components are shown in Figure 4. Given that we were unable to validate the DEM data in the cataracting regime due to the poor PEPT tracer coverage, the profiles are necessarily truncated to the region below the free surface.

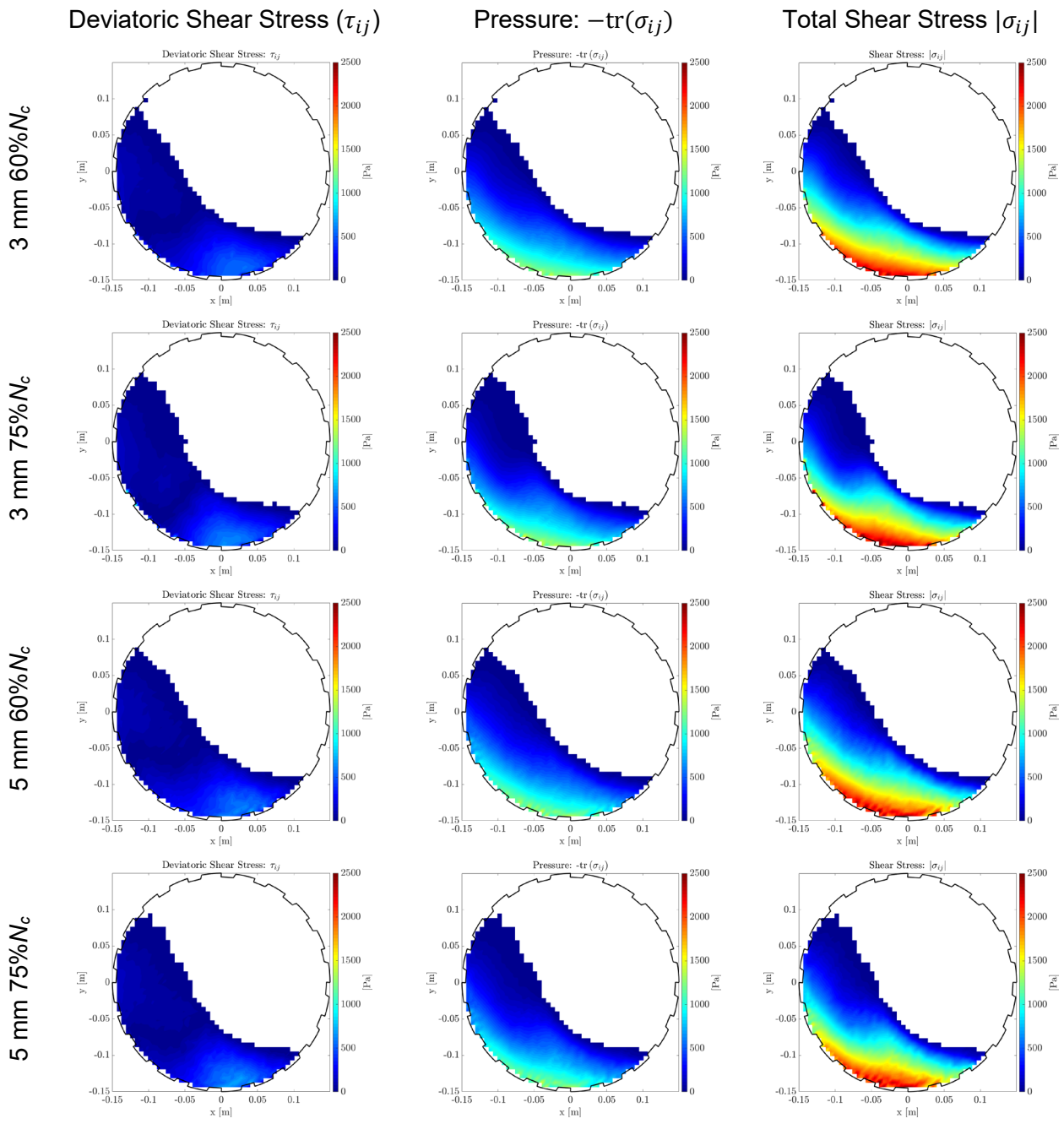

FIG 4 – Stress profiles.

The magnitude of the shear stress profiles range from 0 to 2500 Pa. The average pressure (or normal stress) dominates over the deviatoric stress by a factor of approximately two ie $2\langle\tau_{ij}\rangle \sim \langle P\rangle$; this relationship is similar to that reported by Govender and Pathmathas (2016). The stresses at the free surface are small, but non-zero. The maximum magnitude of the Total Shear Stress (denoted by the red hotspot) occurs near the toe region and in particular, along the mill shell. The deviatoric profiles exhibit a more concentrated smaller region of higher stress (light blue hotspot near the toe region) compared to the pressure. This implies that shear type contacts are more concentrated in a region and normal type contacts occur over a wider area. The particles near the free surface exhibit liquid like behaviour and therefore have a lower solids fraction compared to the particles towards the base of the bed which exhibit solid body rotation. In fact, these particles often form a rigid layer near the lifter bars. This implies that there is a higher probability of collisions near the base of the drum which is supported by the Pressure data. The deviatoric stress would rely on large velocity differences which is why is it predominantly concentrated near the turbulent toe region of the bed.

A radial analysis was undertaken for each of the 5 mm and 3 mm bead sets, in which centrally located slices were chosen and data along these slices binned. Thus, an error bar analysis, based

on the standard deviation, is introduced. The slices were taken perpendicular to the free surface. Being centrally located within the bed has its advantages, discussed by Govender (2016), which are that the properties are homogeneous, and the flow is unidirectional and fully developed with maximum thickness of the flowing layer. The slices taken from each of the corresponding solids fraction maps (Moodley and Govender, 2020) are shown in Figure 5.

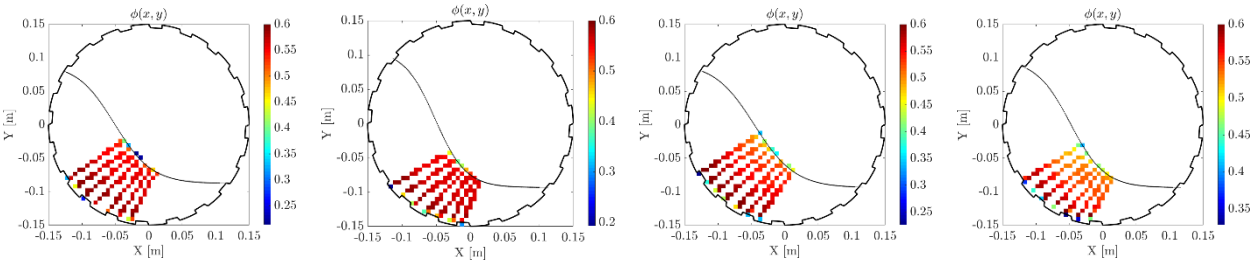

(a) 3 mm 60%N_c (b) 3 mm 75%N_c (c) 5 mm 60%N_c (d) 5 mm 75%N_c

FIG 5 – Centrally located slices taken from the solids fraction maps (Moodley and Govender, 2020).

The data from the slices in Figure 5 are subsequently collated to produce Figure 6.

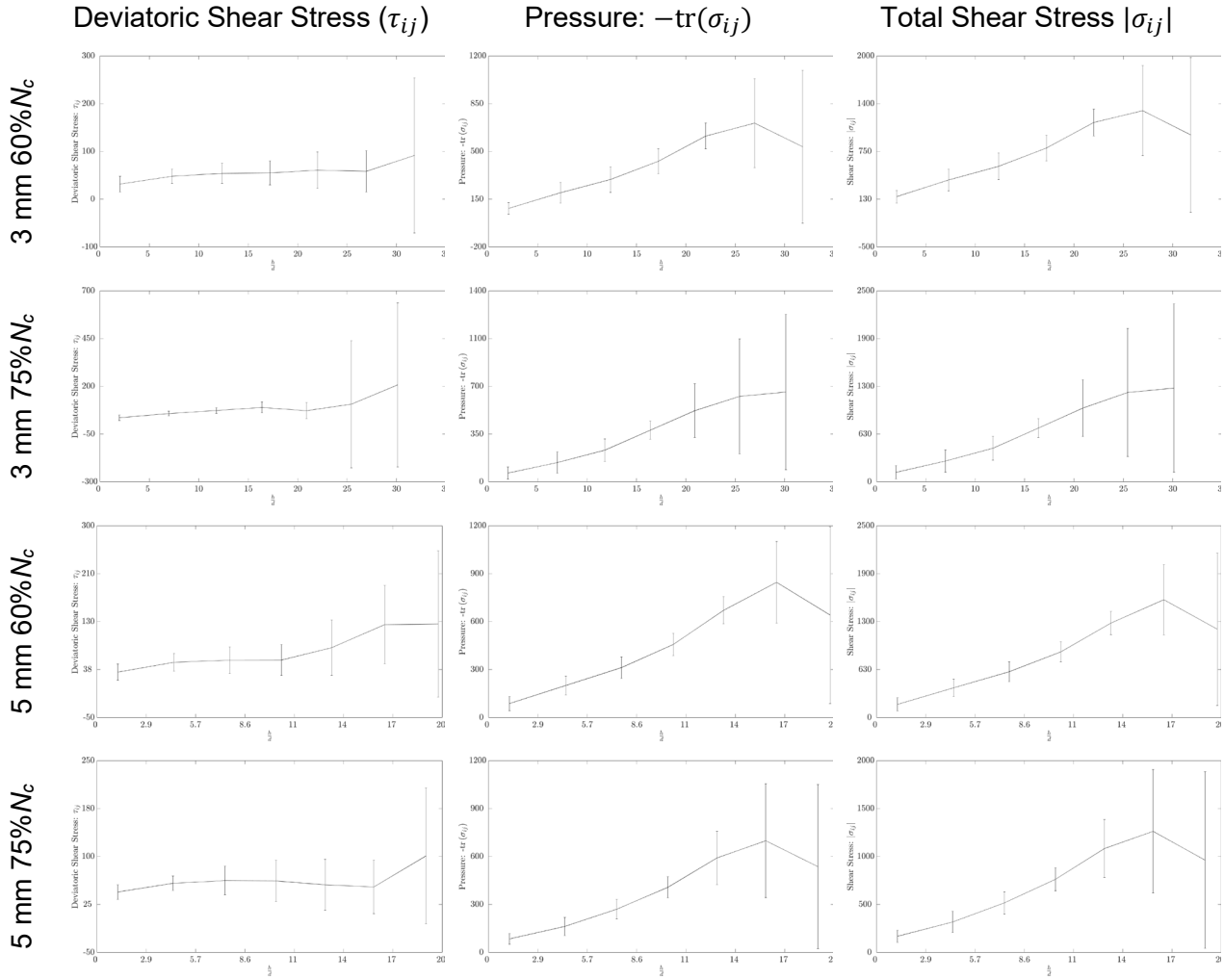

FIG 6 – Binned stress profiles.

The profiles in Figure 6 are generated by binning all the data in the respective bins arranged along with the bed depth where a value of $\mathrm{h/d} = 0$ corresponds to a location on the free surface. The error bars are more pronounced near the azimuthal walls indicating that we have low confidence of stress

in this region. This region corresponds to the hotspots of the deviatoric and pressure stresses seen in Figure 4. The fact that the profiles for the devaitoric shear stress are rather flat as we move from the free surface towards the middle of the bed indicates that it would be difficult to use these values to characterise the flow in these regions. The Pressure values show significant changes with depth which could be the reason it is incorporated in the $\mu(I)$ rheology. To a first order approximation, the pressure profile varies linearly with depth. It is interesting to note that for all experiments, except the 3 mm at 75%N_c, there is a drop-off in magnitude of the pressure near the azimuthal wall and seeming rise in deviatoric shear stress in this region. The effective friction profiles, $\mu(\mathrm{I}) = \left|\frac{\tau}{\mathrm{P}}\right|$, are given in Figure 7.

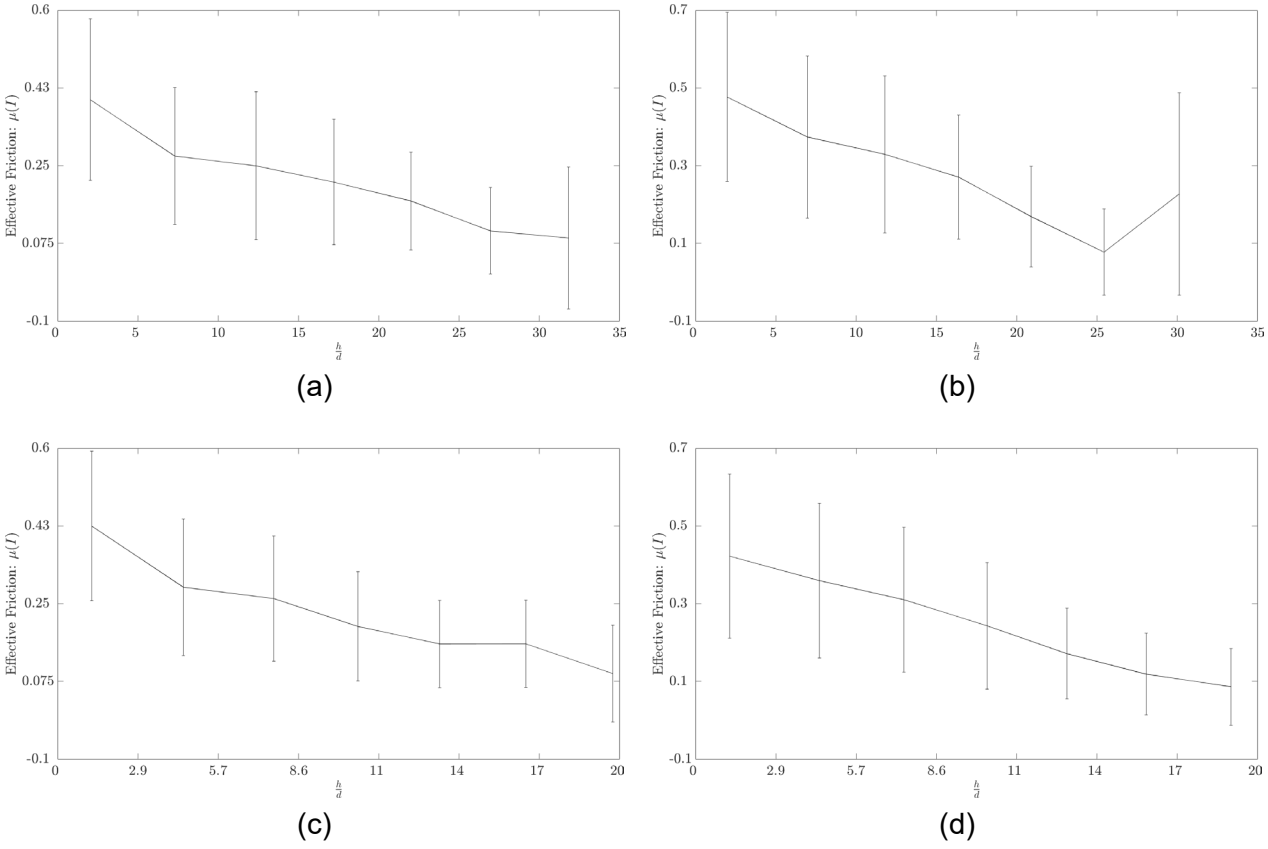

FIG 7 – Effective friction profiles. (a) 3 mm 60%N_c; (b) 3 mm 75%N_c; (c) 5 mm 60%N_c; (d) 5 mm 75%N_c.

The effective friction coefficient captures the relative contributions of shear and normal stresses to the $\mu(\mathrm{I})$ rheology. The values range from ≈ 0.5 at the free surface to ≈ 0.1 at the azimuthal shell. In the case of both bead sizes, we notice that the effective friction is directly proportional to the mill speed. To a first order approximation, the effective stress profile decreases linearly with depth. The 3 mm 75%N_c profile has a sudden increase in effective friction near the azimuthal shell. The reasons for this will have to be investigated but it is hypothesized that the region near the lifter bars may induce slip velocity.

Shear rate

Tumbling mills must produce consistent product grinds upfront or face potentially detrimental effects on downstream processes. Slurry transport through the mill is one of a variety of parameters that influence grinding efficiency. Accurate determination of the shear rate is vital to quantify the slurry viscosity – a key parameter in evaluating slurry transport. Figure 8 shows the magnitude of the shear rate, produced using the Artoni and Richard (2015) model, for the DEM data.

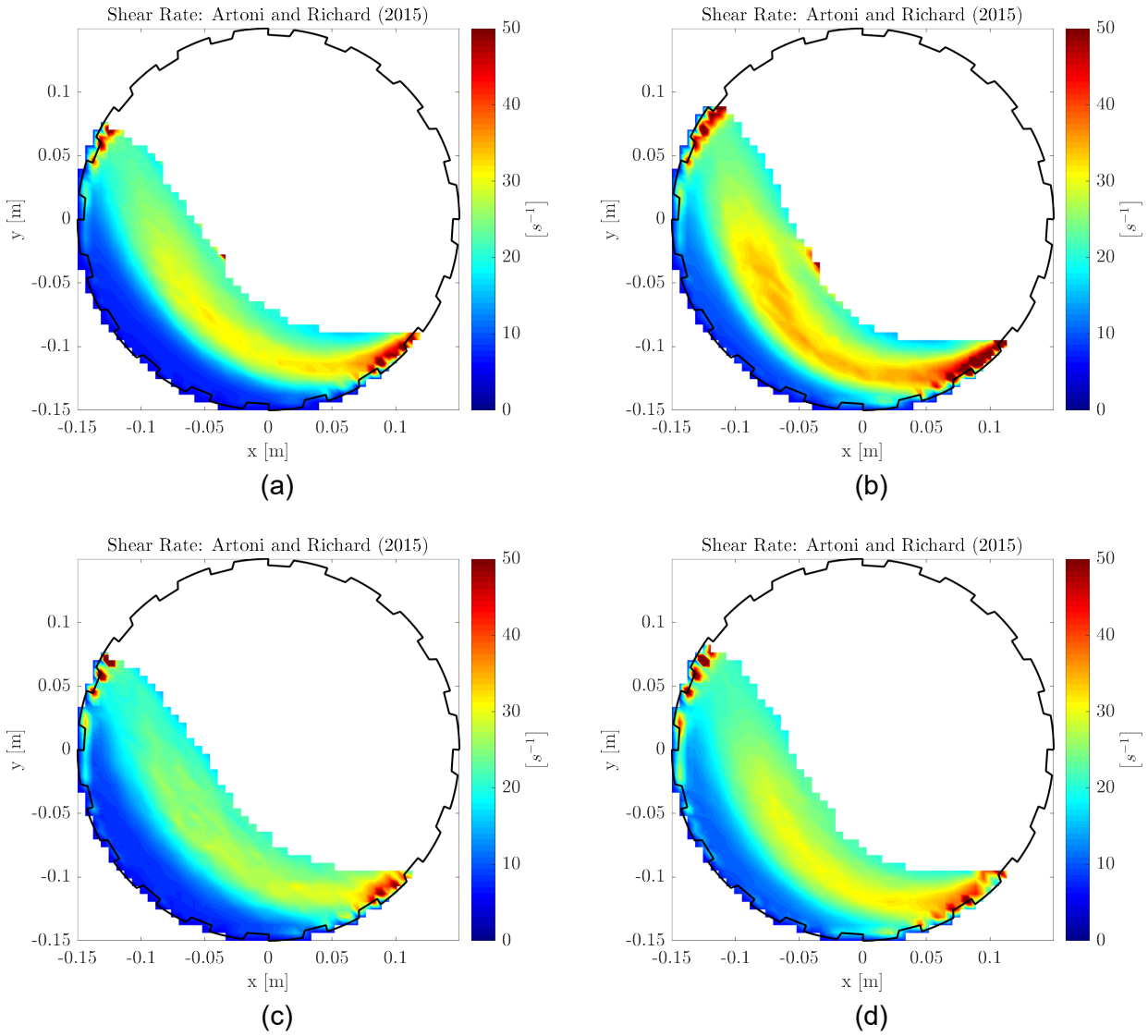

FIG 8 – Shear Rate profiles: (a) 3 mm 60%N_c; (b) 3 mm 75%N_c; (c) 5 mm 60%N_c; (d) 5 mm 75%N_c.

The shear rate varies between 0 and 50 s^{-1} for all configurations. It is also evident that the larger speeds produce larger shear rates, which is expected due to the increased particle velocities. The shear rate hotspot (red) is concentrated near the toe region across all configurations. The flow in this region is known to be highly turbulent and induces velocity fields which are highly chaotic; see *cf* Moodley and Govender (2020) for further details.

Figure 9 suggests that the shear rates are largest near the free surface $(\mathrm{h/d} = 0)$ and decrease steadily with depth. The higher speeds (75%N_c) result in slightly higher shear rate values for both glass bead sizes.

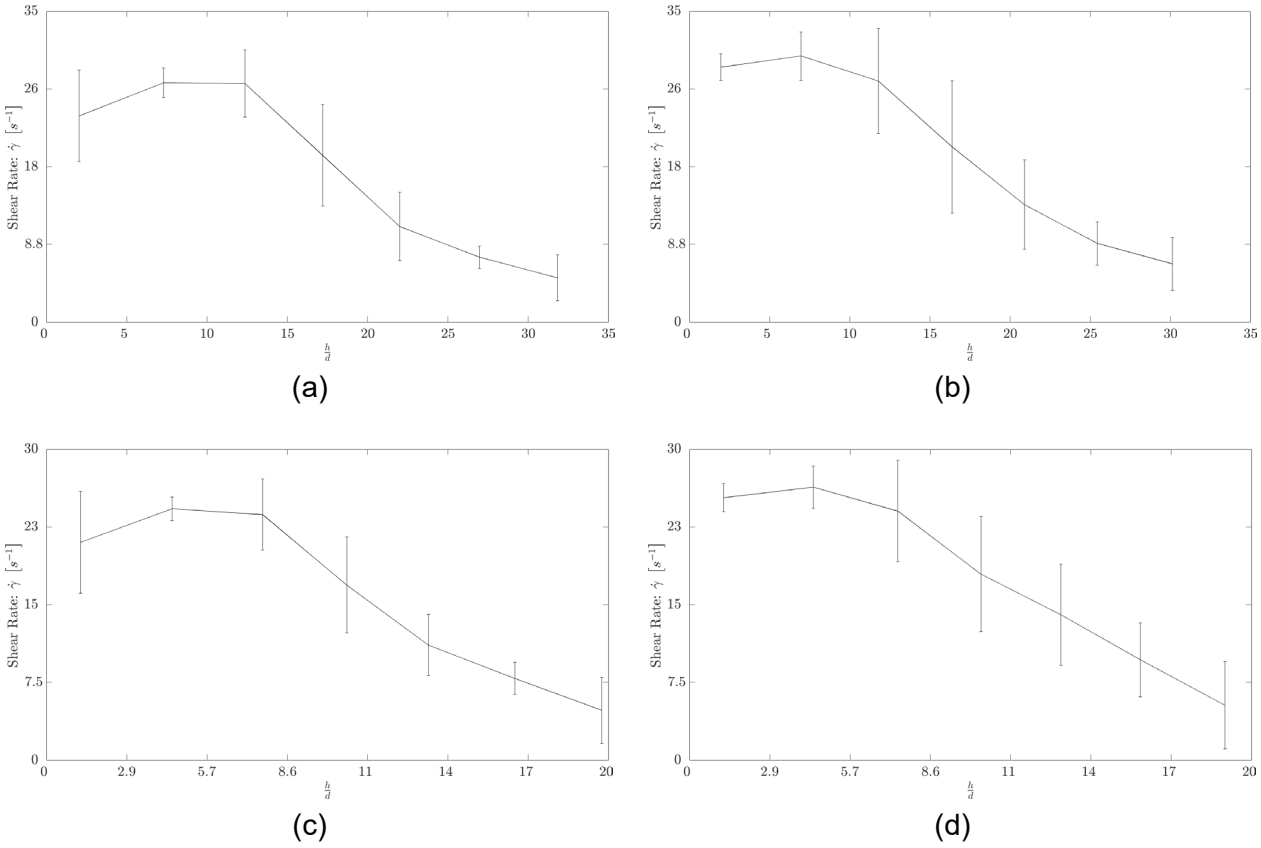

FIG 9 – Binned shear rate profiles. (a) 3 mm 60%N_c; (b) 3 mm 75%N_c; (c) 5 mm 60%N_c; (d) 5 mm 75%N_c.

Inertial number

Combining the shear rate and pressure profiles allows one to evaluate the inertial rheology of the system; the azimuthal Inertial number fields are shown in Figure 10.

The inertial number spans a range of $0.1 < \mathrm{I} < 0.7$. Figure 10 suggests that there is predominantly shear dominated flow (red hotspots) near the shoulder region of the free surface. This is expected due to the inertial regime that is characterised by high shear rates. This gradually reduces until it is replaced by low inertial numbers (pressure dominated flow) near the azimuthal wall as depicted by the relatively cooler (blue) colours.

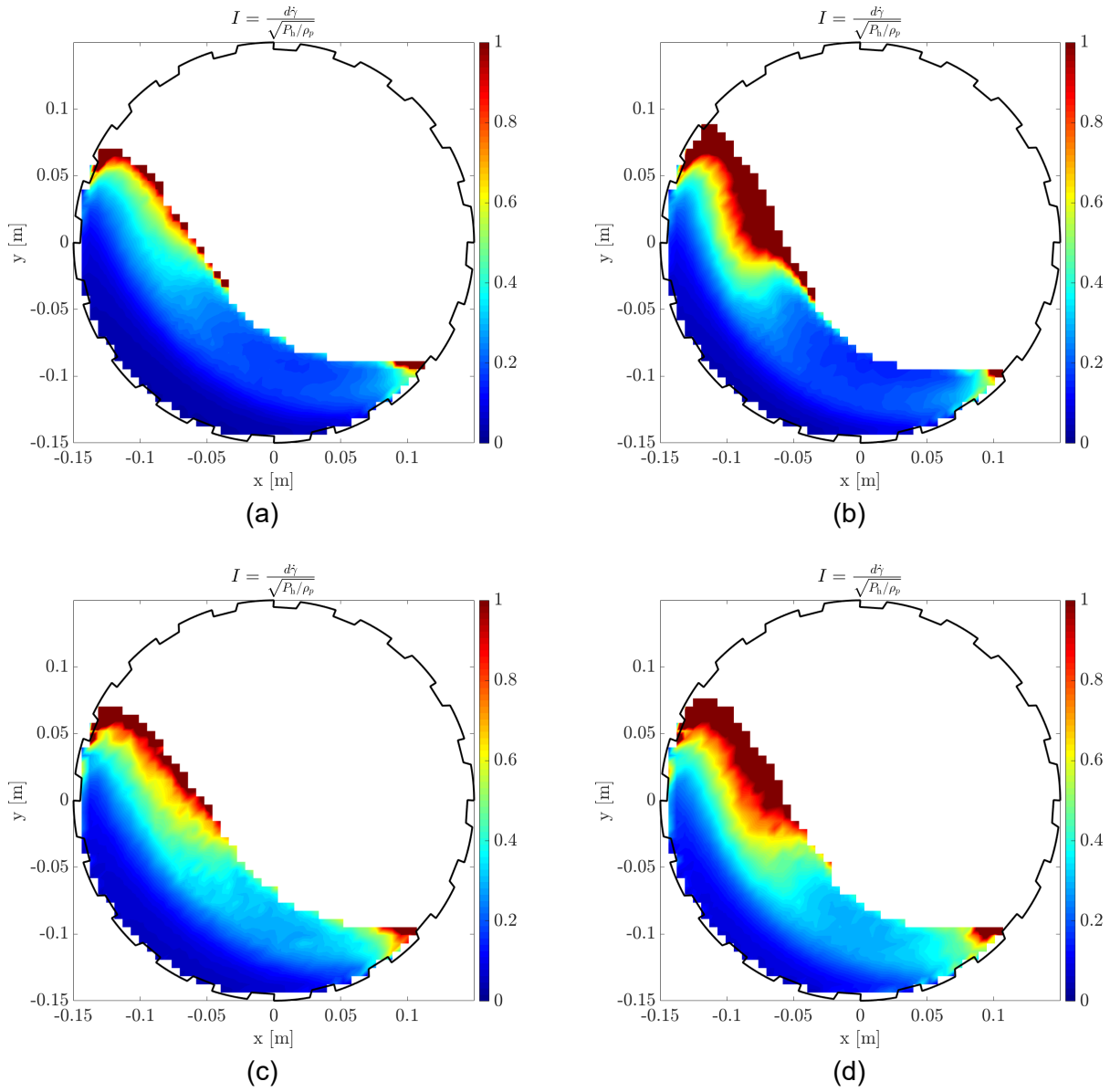

FIG 10 – Inertial Number profiles. (a) 3 mm 60%N_c; (b) 3 mm 75%N_c; (c) 5 mm 60%N_c; (d) 5 mm 75%N_c.

Visual inspection of Figure 11 suggests that the inertial number varies similarly for both bead sets. The higher speeds (75%N_c) result in slightly higher, but statistically insignificant, inertial number values. The inertial number drops exponentially from the free surface as the depth increases until it begins to remain relatively constant as it approaches the azimuthal wall (flattish profile). These flattish profiles near the azimuthal wall are expected since the bed exhibits a high solids fraction (≈ 0.6); this results in the formation of stress chains which is not accounted for in the rheology. The results indicate that the Inertial number rheology may only be used for modelling the dilute inertial regime near the free surface.

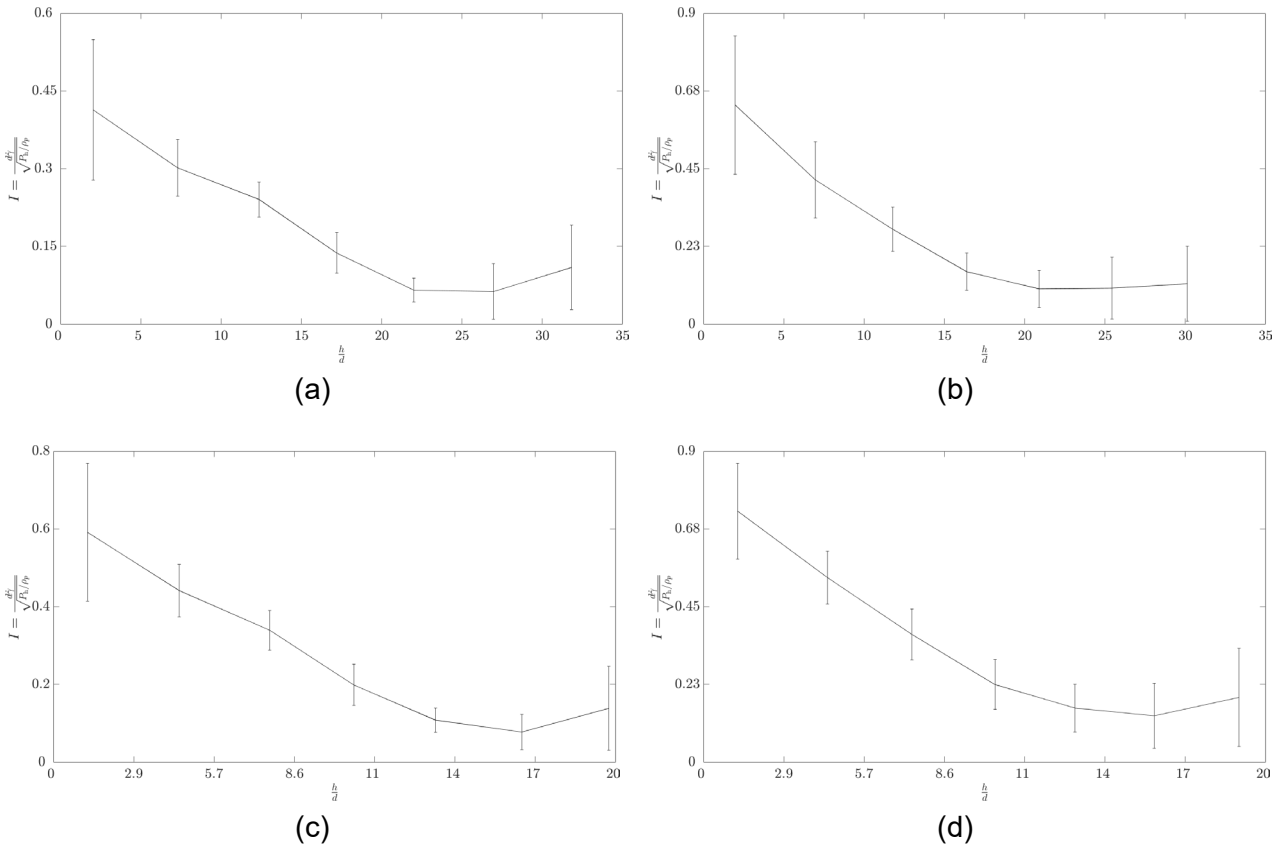

FIG 11 – Binned Inertial Number profiles. (a) 3 mm 60%N_c; (b) 3 mm 75%N_c; (c) 5 mm 60%N_c; (d) 5 mm 75%N_c.

Granular temperature

Figure 12 represents the granular temperature profiles across all configurations. There are large velocity fluctuations present in the toe region (red hotspots) probably due to the cataracting particles re-entering the charge in this highly turbulent, chaotic region. These hotspots are more pronounced at higher rotational speeds (75%N_c) owing to the increased particle velocity.

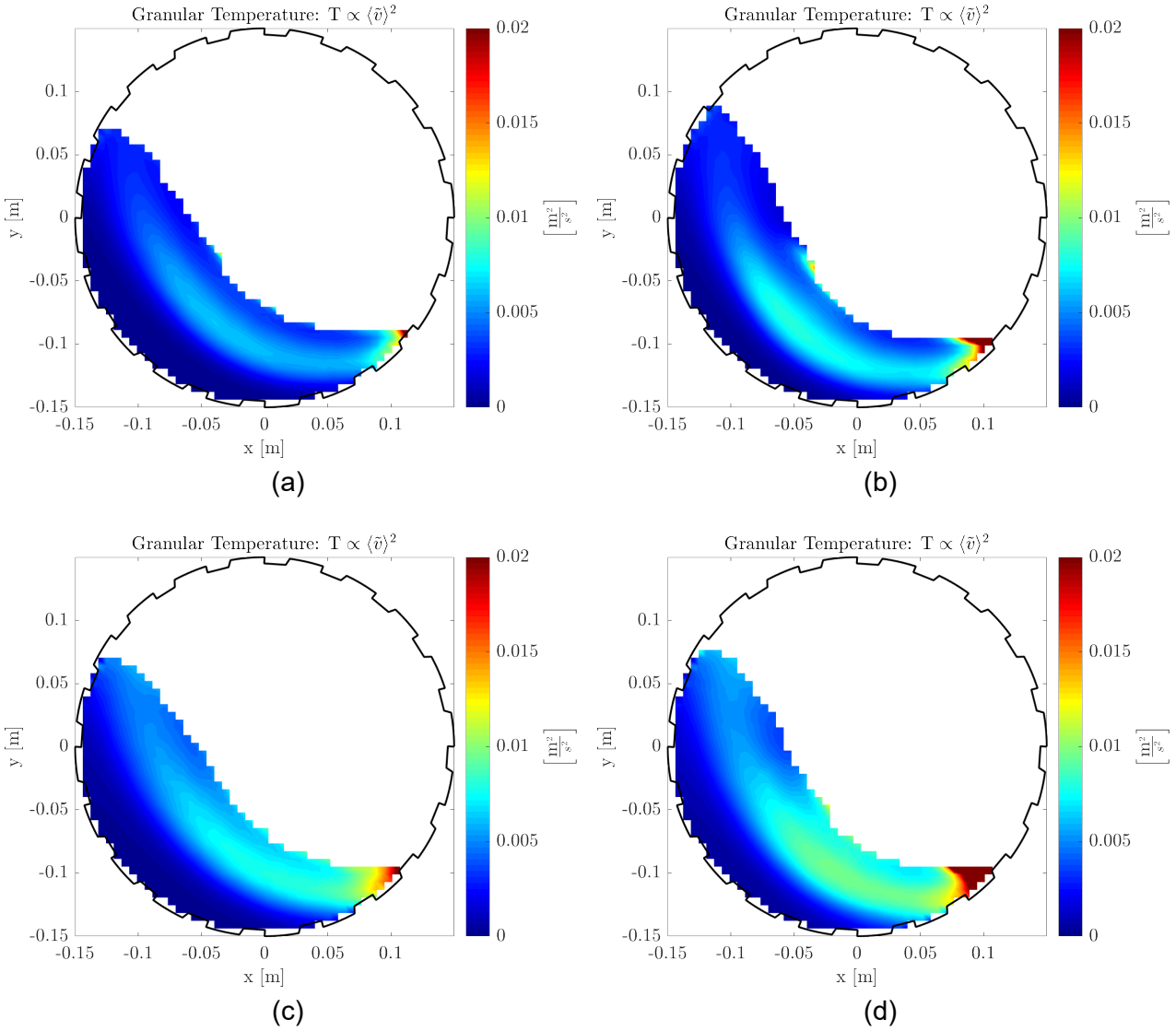

FIG 12 – Granular temperature profiles. (a) 3 mm 60%N_c; (b) 3 mm 75%N_c; (c) 5 mm 60%N_c; (d) 5 mm 75%N_c.

Visual inspection of Figure 13 suggests that the granular temperature varies similarly for both bead sets. The granular temperature ranges from 0.006 m^2/s^2 to 0.001 m^2/s^2. It initially rises just below the free surface $(\mathrm{h/d} = 3 \text{ to } 5)$ before decreasing exponentially with bed depth. Putting the information derived from the granular temperature, shear rate and shear stress data together enables one to investigate the modified – Pe number rheology.

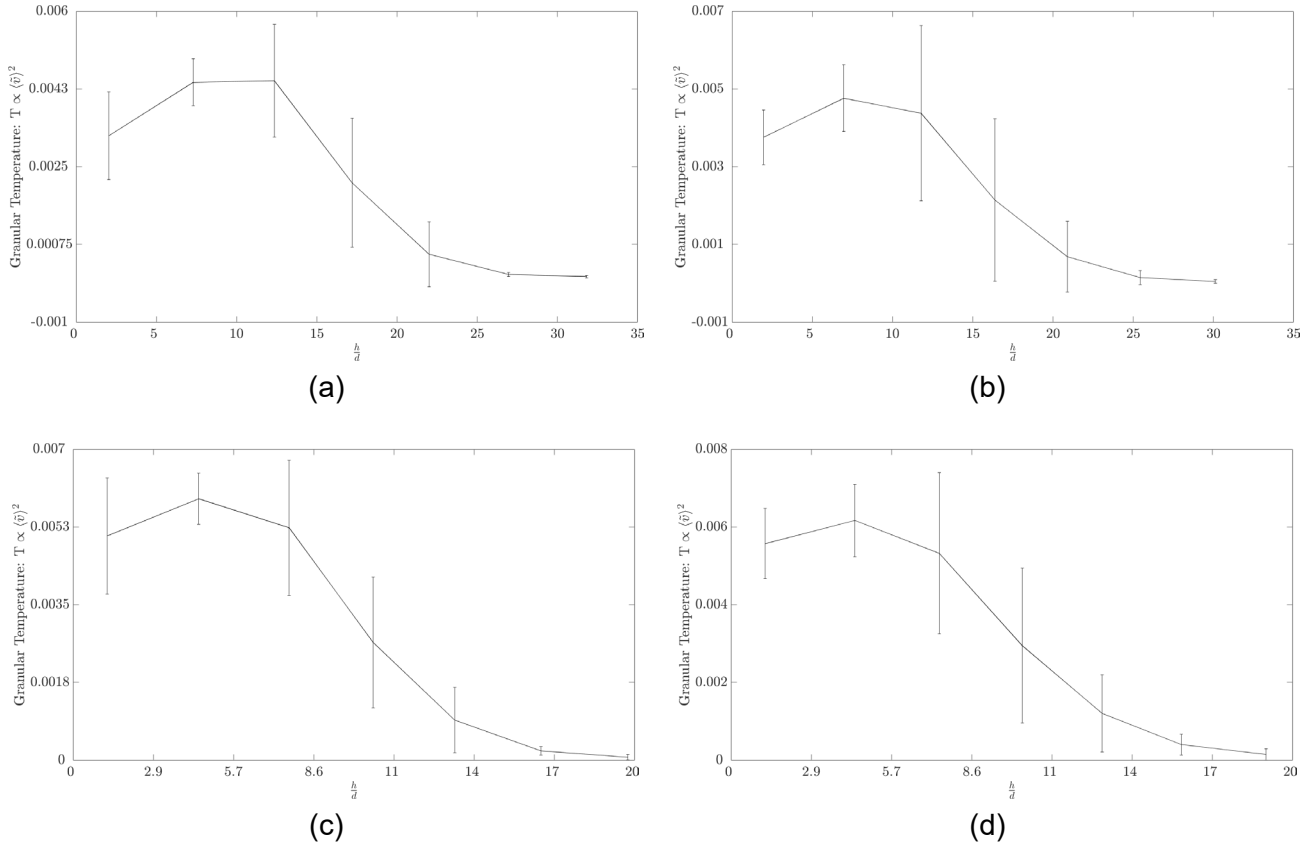

FIG 13 – Binned Granular Temperature profiles. (a) 3 mm 60%N_c; (b) 3 mm 75%N_c; (c) 5 mm 60%N_c; (d) 5 mm 75%N_c.

Modified Peclet number

Figure 14 represents the modified Peclet number profiles across all configurations. There is a relatively large region of large Pe values (red hotspots) lining the azimuthal wall all the way from the middle of the base of the drum towards the shoulder region. These hotspots correspond to regions of predominantly advective flow. On the other hand, lower values (cooler blue colours) which occupy an arguably larger proportion of the drum, correspond to a predominantly diffusive flow profile (Chialvo and Sundaresan, 2013).

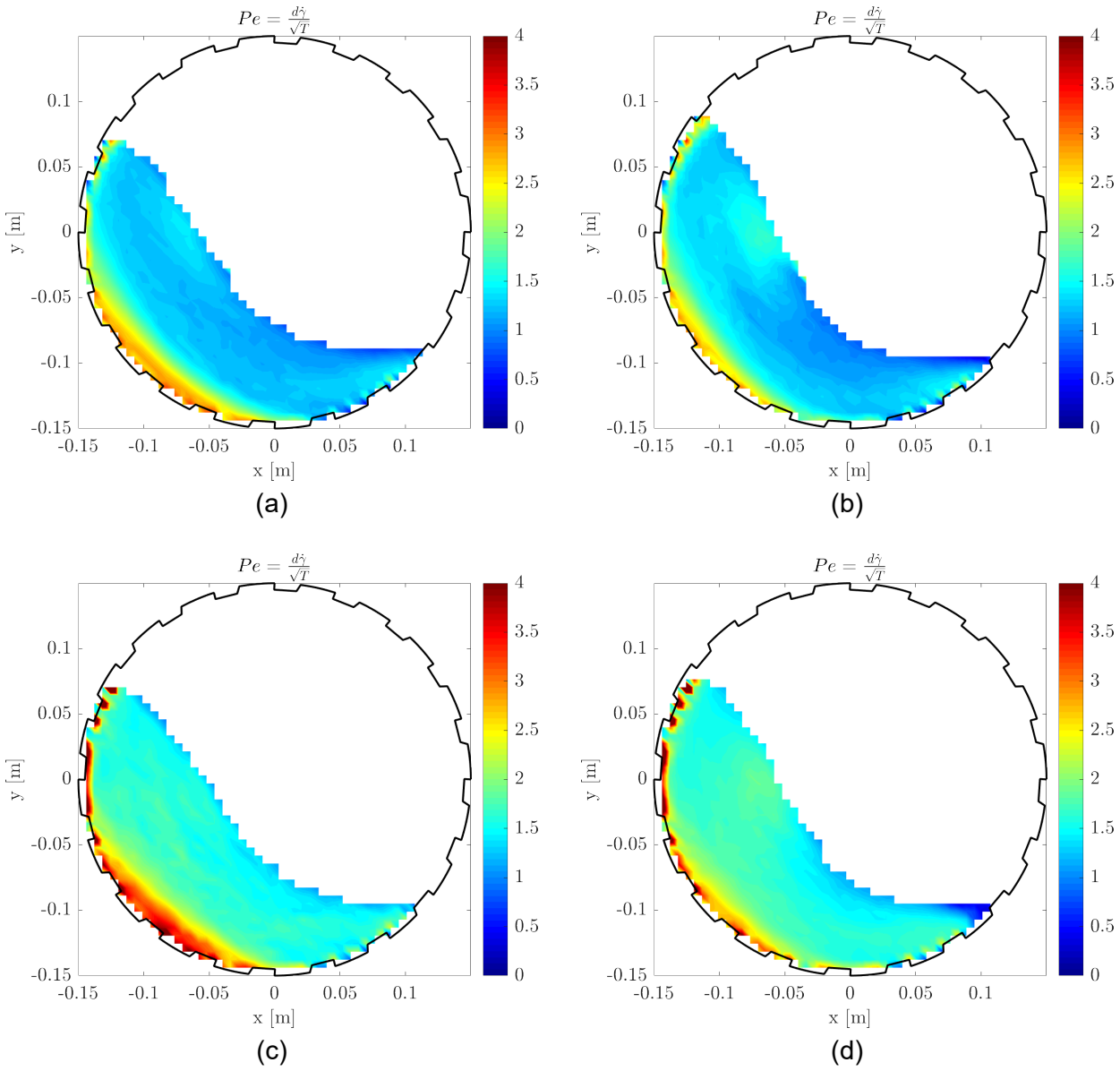

FIG 14 – Modified Peclet number profiles. (a) 3 mm 60%N_c; (b) 3 mm 75%N_c; (c) 5 mm 60%N_c; (d) 5 mm 75%N_c.

Visual inspection of Figure 15 suggests that the modified Pe number varies similarly for both bead sets. The modified Pe number ranges from 0.8 to 1.2. It is relatively constant between the free surface (h/d = 0) until approximately halfway through the bed. This implies that it is very difficult to delineate these regions based on the value of the Pe number – a fact that makes granular materials extremely complex to model. Thereafter it increases exponentially before steadying just before reaching the azimuthal shell. The higher speeds (75%N_c) result in slightly higher, but statistically insignificant, modified Pe number values.

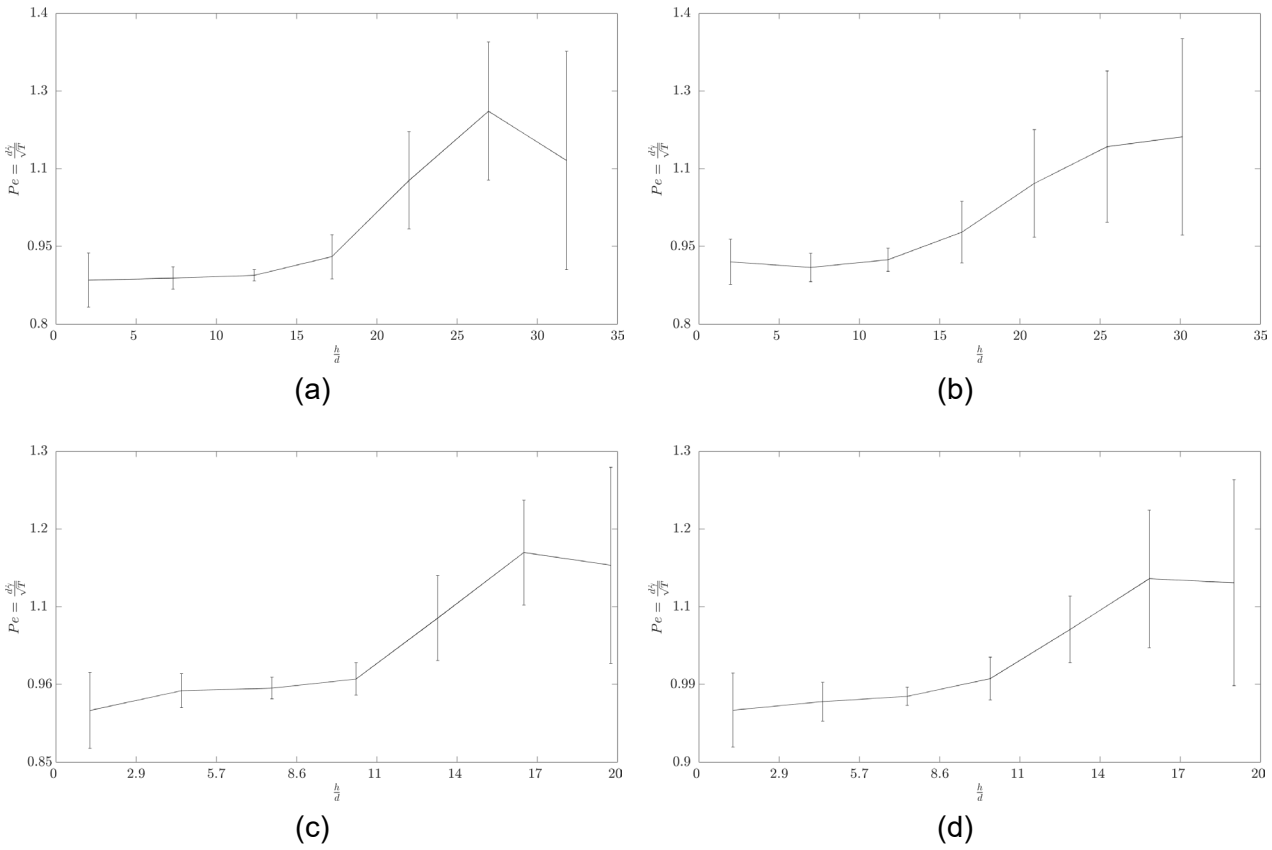

FIG 15 – Binned Modified Pèclet Number profiles.

CONCLUSIONS

The goal of this work was to investigate critical rheological parameters (shear rate, shear stress, granular temperature etc) which are key to not only developing a granular rheology, but will ultimately be used to tune our mechanistic models. The shear stress, comprising of both deviatoric and normal tensorial components, was found to vary between 0 to 2500 Pa. The maximum shear stress occurs along the base of the bed closest the azimuthal wall which is where the highest solids fraction is prevalent. These particles in this region have high probability normal collisions resulting in high values of Pressure in this region. In fact, the average pressure (or normal stress) dominates over the deviatoric stress by a factor of approximately 2 ie $2\langle\tau_{ij}\rangle\sim\langle P\rangle$. The effective friction $[\mu(\mathrm{I}) = \left|\frac{\tau}{\mathrm{P}}\right|]$, in the case of both bead sizes, is directly proportional to the mill speed and decreases linearly with increasing depth. The shear rate varies between 0 and 50 s^{-1} for all configurations. It is also evident that larger speeds produced larger shear rates, which is expected due to the increased particle velocities. Future work in this regard will involve the comparisons of the Povall *et al* (2021) derived granular temperature to those from Artoni and Richard (2015).The inertial number spans a range of $0.1 < \mathrm{I} < 0.7$ with shear dominated flow near the free surface and pressure dominated flow near the mill shell – a fact that is supported by the shear stress tensorial analysis. Due to the inertial number not accounting for the force chains prevalent towards the middle of the bed, the inertial number rheology may only be used for modelling the dilute inertial regime near the free surface. The granular temperature ranges from 0.006 m^2/s^2 to 0.001 m^2/s^2 with hotspots near the highly chaotic, turbulent toe region of the bed. Future work in this regard will involve the comparisons of the Artoni and Richard (2015) derived granular temperature to those from ROCKY-DEM. The modified Pe number ranges from 0.8 to 1.2 with a diffusive flow profile near the free surface region and an advective profile near the mill shell. The Pe number rheology showed a good ability to delineate behaviour near the mill shell but was poor in describing behaviour in the dilute inertial regime. Future work will involve incorporating the dimensionless temperature gradient $\mathrm{M} \equiv \frac{\mathrm{d}|\nabla T|}{T}$ which accounts for the inhomogeneity associated with non-local effects whose effects are highlighted near the yield stress limit. Ultimately, the relationship between T and μ_s*will be investigated.

ACKNOWLEDGEMENTS

The authors would like to extend their gratitude to fellow PTG members for their expertise in troubleshooting occasional coding irregularities. Finally, the authors are grateful for the continued financial support received from Mintek. The authors acknowledge ROCKY-DEM for the generous academic licensing of the DEM software.

REFERENCES

Artoni, R, Richard, P, 2015. Average balance equations, scale dependence and energy cascade for granular materials. *Physical Review E* 91, 032202.

Austin, L G, 1990. A mill power equation for SAG mills. *Minerals and Metallurgical Processing*, 57–63.

Babic, M, 1997. Average balance equations for granular materials. *Int. J Eng. Sci*. 35, 523–548.

Bbosa, L S, Govender, I, Mainza, A N and Powell, M, 2011. Power draw estimations in experimental tumbling mills using PEPT, *Minerals Engineering, 24*, 319–324.

Chandramohan, R, 2005. *Measurement of particle interaction properties for the incorporation into Discrete Element Methods*. MSc. thesis. University of Cape Town.

Chialvo, S and Sundaresan, S, 2013. A modified kinetic theory for frictional granular flows in dense and dilute regimes. *Physics of Fluids*, 25(7), p. 070603.

Cleary, P W, 2007. Granular flows: Fundamentals and applications, in *Granular and Complex Materials*, World Scientific Lecture Notes in Complex Systems, vol. 8, edited by T Aste, T Di Matteo and A Tordesillas, pp. 141–168, World Sci. Publ, Singapore.

Cundall, P A, Strack, O D L, 1979. A discreate numerical model for granular assemblies. *Geotechnique* 29, 47–65.

Goldhirsch, I, 2001. Granular gases: Probing the boundaries of hydrodynamics. In *Granular gases,* pp. 79–99, Springer, Berlin, Heidelberg.

Goldhirsch, I, 2008. Introduction to granular temperature. *Powder Technology*, *182*(2), pp. 130–136.

Govender, I and Pathmathas, T, 2016. A positron emission particle tracking investigation of the flow regimes in tumbling mills. *Journal of Physics D: Applied Physics*, *50*(3), p.035601.

Govender, I, 2016. Granular flows in rotating drums: A rheological perspective. *Minerals Engineering*, *92*, pp. 168–175.

Jop, P, Forterre, Y and Pouliquen, O, 2006. A constitutive law for dense granular flows. *Nature*, 441(7094), pp. 727–730.

Khain, E, 2007. Hydrodynamics of fluid-solid coexistence in dense shear granular flow. *Physical Review E*, *75*(5), p. 051310.

Kolev, N, Bodurov, P, Genchev, V, Simpson, B, Melero, M G and Menéndez-Aguado, J M, 2021. A Comparative Study of Energy Efficiency in Tumbling Mills with the Use of Relo Grinding Media. *Metals*, 11(5), p. 735.

Kumaran, V, 2004. Constitutive relations and linear stability of a sheared granular flow. *Journal of Fluid Mechanics* 506, 1–43.

Moodley, T L and Govender, I, 2022. Experimental validation of DEM in rotating drums using Positron Emission Particle Tracking, *Mechanics Research Communications.*

Moodley, T L, 2022. Experimental validation of DEM in rotating drums using Positron Emission Particle Tracking, *PhD thesis,* University of Kwazulu-Natal.

Moodley, T L, Govender, I, 2020. Experimental Validation of DEM in rotating drums using Positron Emission Particle Tracking, in: *XXX International Minerals Processing Conference, IMPC 2020*.

Morrell, S, 1992. Prediction of grinding-mill power. *Transactions of the Institution of Mining and Metallurgy Section C: Mineral Processing Extraction and Metallurgy, 101*(January-April), C25-C32.

Pähtz, T, Durán, O, De Klerk, D N, Govender, I and Trulsson, M, 2019. Local rheology relation with variable yield stress ratio across dry, wet, dense and dilute granular flows. *Physical review letters*, 123(4), p. 048001.

Povall, T M, Govender, I and McBride, A T, 2021. Dense granular flows in rotating drums: A computational investigation of constitutive equations. *Powder Technology*, *393*, pp. 238–249.

Rose, H, Sullivan, R, 1957. A treatise on the Internal Mechanics of Ball, Tube and Rod mills. Constable, London.

Effect of pebbles on collisional environment in a ball mill using composite media (balls/pebbles)

S Nkwanyana[1] and I Govender[2,3,4]

1. Engineer, Mintek, P/Bag X3015, Randburg, Gauteng, 2121, South Africa. Email: sandilen@mintek.co.za
2. Group Executive: Mineral Processing and Characterisation, Mintek, Randburg, Gauteng, 2121, South Africa. Email: IndresanG@mintek.co.za
3. Professor of Particle Technology and Mineral Processing, Discipline of Chemical Engineering, School of Engineering, University of KwaZulu-Natal, Durban, 4041, South Africa. Email: govenderi5@ukzn.ac.za
4. Professor of Chemical Engineering, Department of Chemical Engineering, Centre for Minerals Research, University of Cape Town, Rondebosch, 7701, South Africa. Email: indresan.govender@uct.ac.za

ABSTRACT

Batch experiments in a 0.6 m diameter mill have shown that improvements of about 13 per cent in the efficiency of energy utilisation can be realised in ball mills by replacing 25 per cent of the ball charge by an equivalent volume of cost-free critical size pebbles from AG/SAG mills.

For a mill of a given size, speed and charge filling, the rate of size reduction of ore particles depends on (i) the frequency of grinding media collisions (ii) the probability of capture of ore particles between the colliding grinding media (iii) the probability of fracture of the captured particles. The probability of fracture depends on the magnitude of collision energy. The distribution of collision energy into shear and impact events determines the relative strengths of attrition breakage and impact breakage. The efficiency of energy utilisation depends on which of the two mechanisms of breakage is more desirable in a particular milling stage.

In this paper collision data from a series of DEM simulations of a mill charged with steel media and a mixture of steel media and pebbles is presented in energy spectra and spatial distribution maps. The data provides the necessary detail to elucidate the improvements in the efficiency of energy utilisation in ball mills when using a mixture of pebbles and steel media.

INTRODUCTION

Most mineral processing concentrators are now treating low-grade, more competent and complex ores than before. To remain profitable ways of reducing operating costs are sought. It is estimated that comminution contributes 30–50 per cent to the total cost of mineral processing (Zhang, 2016; Clermont and De Haas, 2010; Jankovic *et al*, 2006). Key to the cost of comminution is energy consumption and grinding media consumption.

The conventional grinding circuit for processing hard ores (eg copper-gold ores) typically consists of semi-autogenous grinding (SAG) primary mills, followed by one or two parallel ball mills per primary mill. Most research has been focused on stabilising and expanding throughput in SAG mills. The research has led to the inclusion pre-crushers before mills, operating the mills with very high steel ball loads and pebble crushing. It has been reported that pebble crushing can expand throughput by more than 15 per cent (Powell *et al*, 2015).

Ball milling is considered to be a well-understood grinding method. Most optimisation studies on ball milling are site-specific, where variables such as mill speed, ball filling level, ball top-up size, liner-lifter design and pulp density are optimised for varying feed properties (eg size distribution, hardness and mineralogy) to achieve an acceptable product size distribution. Ball mills are known to be costly to operate because of the cost of ongoing ball replacement. This cost can be as much as the cost of mill power consumption (Daniel *et al,* 2010).

Pebble milling is an alternative to ball milling. The main advantage of pebble milling is the cost-free grinding media. However, larger mills are required to draw an equivalent power and the availability of sufficient competent pebbles, particularly large ones, can be a concern.

Nkwanyana and Loveday (2018, 2017) reported on experimental work, which explored the use of the critical-size pebbles from a SAG mill as grinding media in ball mills (ie replacing a proportion of steel balls by an equivalent volume of pebbles). This provides the freedom to adjust the proportion of pebbles if the availability of pebbles varies. The data showed that any proportion of pebbles up to 25 per cent could be used in the ball mills, with no change in throughput and product size distribution, and the process is referred to as 'composite milling' in this paper.

The experimental results were a pleasant surprise, given that production of fines is normally considered to be proportional to power draw (or specific energy input) (Hilden and Suthers, 2010; Musa and Morrison, 2009; Levin, 1992). In this paper, it is contended that the production of fines in a mill is proportional to power draw if the following conditions hold:

- The distribution of power into dissipation through media collisions and dissipation through viscous stresses in the slurry remains the same when power draw changes.
- The distribution of the power dissipated in media collisions into head-on impacts (impact power) and shear (shear power) remains the same when power draw changes.

The distribution of the power dissipated in media collisions is influenced by the operating conditions such as speed, media filling level, and lifter-liner design (Cleary and Owen, 2019a; Djordjevic *et al,* 2004; Powell, 2001). It is also influenced by the shape and size distribution of media (Cleary and Owen, 2019b; Cleary, 2019; Weerasekara *et al*, 2016).

The shape and size distribution of critical size pebbles from SAG/AG mills are variable and inherently different from that of steel balls used in ball mills. The charge bed can be expected to dilate when steel balls and irregular shaped pebbles are mixed (Sinnott *et al,* 2011). Therefore, when comparing the production of fines from ball milling and composite milling, it should not be simply expected to be proportional to mill power draw; it is necessary to analyse the relative strengths of head-on impacts and shear events, and the charge packing.

This paper presents data from DEM simulations of a mill charged with steel balls and a mixture of steel balls and pebbles. The objective is to explain the experimental results reported in Nkwanyana and Loveday (2018, 2017). This paper is limited to an analysis to shear power, and makes the assumption that attrition is linked to shear power, and it is the dominant mechanism for the production of -75 µm material in a mill processing feed of size F_{80} <1 mm. It is acknowledged that head-on impacts also contribute to the production of -75 µm material. Future work will explore the contribution of both the mechanisms.

DEM SIMULATIONS

Overview

It is hypothesized that a 25/75 mixture of pebbles and balls results in the same production rate of fines as a load of steel balls only, despite a reduction in the specific energy input. This is because the shape of pebbles in a 25/75 mixture alters the distribution of collision power, in such a way that the shear power is comparable to that in a mill loaded with steel balls only.

For a mill of a given size, speed and charge filling, the rate of size reduction of ore particles depends on: (i) the frequency of grinding media collisions; (ii) the probability of capture of ore particles between the colliding grinding media; (iii) the probability of fracture of the captured particles. The probability of fracture depends on the magnitude of collision energy (shear/impact). DEM simulations of a mill give insight into this type of information. ROCKY-DEM®, a commercial software package, was used to carry out the simulations.

The first set of simulations briefly investigated the effect of shape, material and size grinding media on the distribution of collision power. The second set of simulations was set-up to replicate the regrind mill experiments and the secondary stage mill experiments described in Nkwanyana and Loveday (2018, 2017). The third set of simulations investigated the effect of mill diameter, mill speed and filling level on the distribution of collision power when changing from ball milling to composite milling.

Table 1 shows the set-up of the simulations. Table 2 shows the seasoned size distributions of media used in the first set of simulations. The seasoned loads simulate steady state size distributions in a mill topped-up with 37.5 mm and 75 mm media (assuming the wear of media can described by the surface area model (Vermeulen *et al,* 1983)).

TABLE 1

Simulation set-up.

	First set of simulations	**Second set of simulations**	**Third set of simulations**
Mill dimensions (D × L)	1.2 m × 0.3 m	0.6 m × 0.5 m	1.2 m × 0.3 m
Mill speed	29 rev/min (75% *Nc*)	38 rev/min, 43 rev/min (69% *Nc*, 75% *Nc*)	26 rev/min, 29 rev/min 32 rev/min (68% *Nc*, 75% *Nc*, 83% *Nc*)
Mill filling	33%	25%, 33%	28%, 33%, 40%

TABLE 2

Media size distribution for the first set of simulations.

Size (mm)	**Seasoned Load 1 mass (%)**	**Seasoned Load 2 mass (%)**
-75.00 + 65.00	-	43.62
-65.00 + 53.00	-	31.51
-53.00 + 37.50	-	19.03
-37.50 + 26.50	78.34	4.48
-26.50 + 19.00	15.71	1.03
-19.00 + 13.20	5.95	0.32

For the second and third set of simulations, the steel balls were spheres and the rounded pebbles were an equal mixture (on mass basis) of four shapes shown in Figure 1. The size distribution of the media used in the second set of simulations is shown in Table 3. For the third set of simulations, the size distribution of steel balls and pebbles were set-up to be the same as that of steel balls in secondary stage mill shown in Table 3.

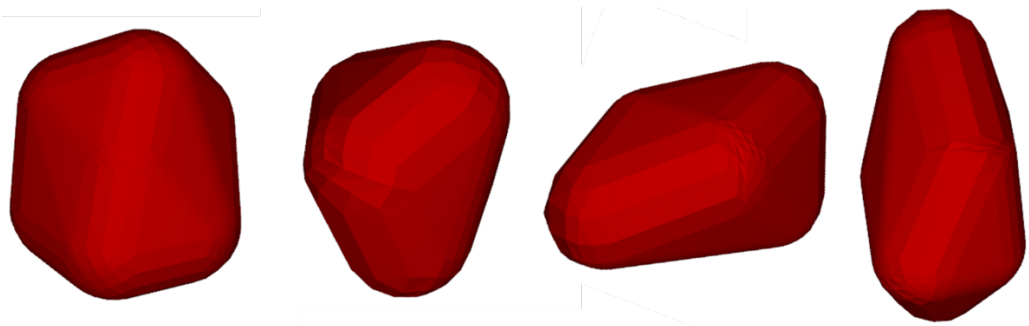

FIG 1 – Rounded pebble shapes.

TABLE 3

Media size distribution for the second and third set of simulations.

Size (mm)	Steel balls for regrind mill	Pebbles for regrind mill	Steel balls for secondary stage mill	Pebbles for secondary stage mill
-75.00 + 63.00	-	7.65	13.26	7.54
-63.00 + 53.00	-	12.10	24.34	22.36
-53.00 + 37.50	-	29.22	47.76	37.48
-37.50 + 26.50	78.34	23.02	11.25	21.27
-26.50 + 19.00	15.71	23.68	2.59	9.06
-19.00 + 13.20	5.95	4.33	0.81	2.30

Mill geometry

Figure 2 shows the 1.2 m diameter mill (left) and 0.6 m diameter (right). The material property of the mills was defined by three parameters, which were the density = 7850 kg.m^{-3}, Young's modulus = 1 × 10^{11} N.m^{-2} and Poisson's ratio = 0.3.

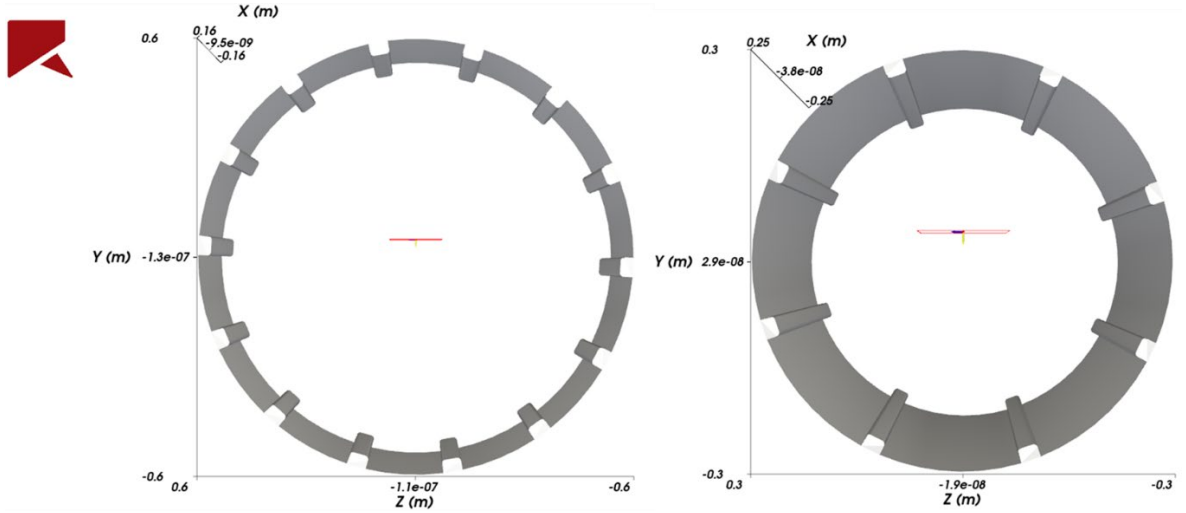

FIG 2 – Mill geometries used in the simulations.

Material contact parameters

The Hertzian spring-dashpot law was chosen to model normal contact force, and the Mindlin-Deresiewicz law was chosen to model the tangential contact force. These contact force laws have been used widely in simulation studies which had energy dissipation as a parameter of interest (Weerasekara *et al*, 2016; Bbosa *et al,* 2016; Carvalho, 2013; Sarracino *et al,* 2004). Table 4 shows the material interaction parameters used in the simulations.

TABLE 4

Material interaction parameters.

Contact type	Coefficient of friction	Coefficient of restitution
Steel-Steel	0.2	0.3
Steel-Rock	0.25–0.3	0.3
Rock-Rock	0.35–0.4	0.2

The choices of the coefficient of restitution were based on the following research work: Carvalho and Tavares (2013); Tavares and Carvalho (2010); Weerasekara and Powell (2010); Kulya (2008); Dong and Moys (2002), which used the same contact model as that used in the simulations. The coefficient of friction for steel-rock and rock-rock was adjusted between the ranges shown, such that the power draw (calculated by the torque method) and the power dissipation (calculated from collision energy losses) were comparable, and similar to the power draw measured from the 0.6 m diameter mill loaded with media only. This adjustment had a negligible effect on the distribution of power between shear and impact events.

RESULTS AND DISCUSSION

The effect of media shape, size and material

The simulations investigated the effect of shape, size distribution and material of grinding media, on the distribution of power which is dissipated in media collisions. Figure 3 shows the snapshots of the charge in motion (colour-coded by translational speed, dark blue corresponding to almost 0 m/s and orange corresponding to highest speed of ~4.6 m/s).

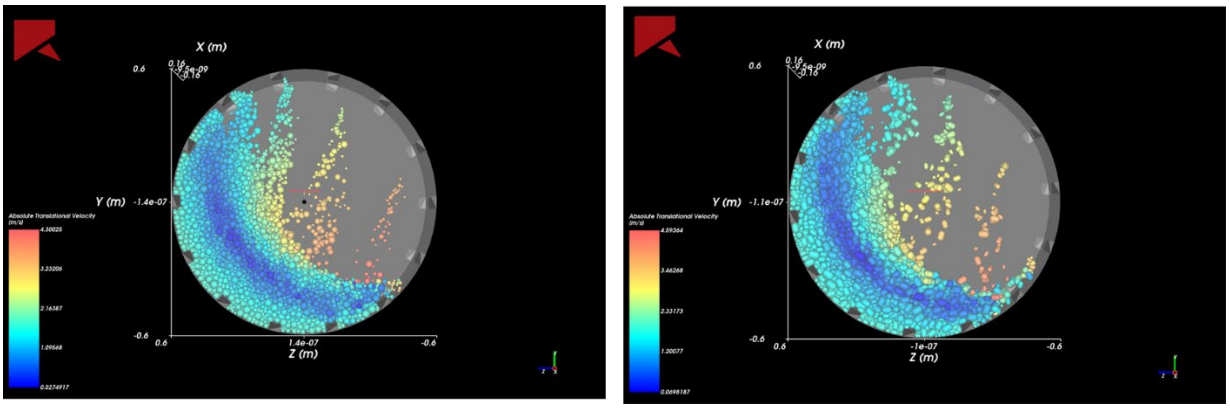

FIG 3 – Snapshot of the charge in motion (Left: spheres, Right: sphero-cylinders).

The primary source of energy dissipation during a collision is related to the inelastic nature of the contact force (F_c). The dissipation work done by this force (W^{diss}) and power (P^{diss}) are calculated using Equations 1 and 2. The integral is defined over the entire collision interval (loading and unloading):

$$W^{diss} = -\int F_c . v_c^{rel} dt \tag{1}$$

$$P^{diss} = \frac{\sum_{k=1}^{k}(W^{diss})}{\Delta t_{out}} \tag{2}$$

where v_c^{rel} is the instantaneous relative velocity at the contact point, *k* is the number of collisions occurring within the time interval Δt_{out}. The total contact force is given by Equation (3):

$$F_c = F_n . \hat{n}_c + F_t \tag{3}$$

where F_n and F_t are, respectively, the normal and tangential components of the contact force, calculated by contact models mentioned in section 2.3. Additionally, $\hat{n}_c$ is the normal unit vector of the contact.

The shear work (W^{shear}) is calculated using Equation (4):

$$W^{shear} = -\int F_t . ds_t \tag{4}$$

where ds_t is the sliding distance, that is, the displacement parallel to the tangential plane of the contact. The integral is defined over the entire collision interval. The difference of Equations 1 and 4 gives the impact work.

Figures 4 and 5 show the variation in the distribution of power when the shape of media is changed from spheres to sphero-cylinders.

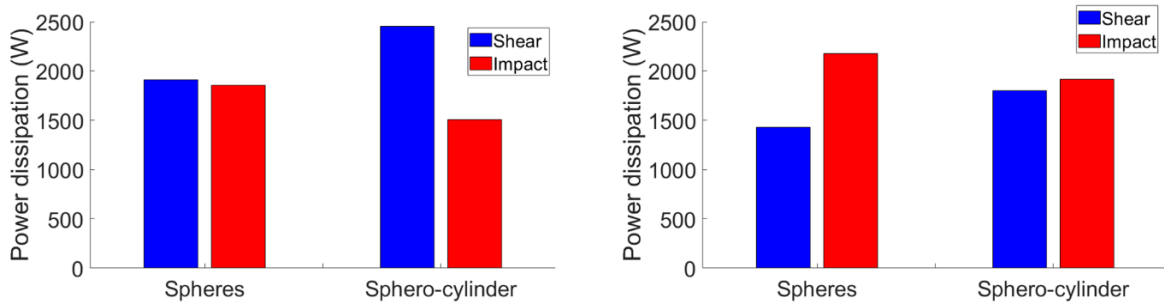

FIG 4 – Power dissipation of steel media: 37.5 mm top-up size (left) and 75 mm top-up size (right).

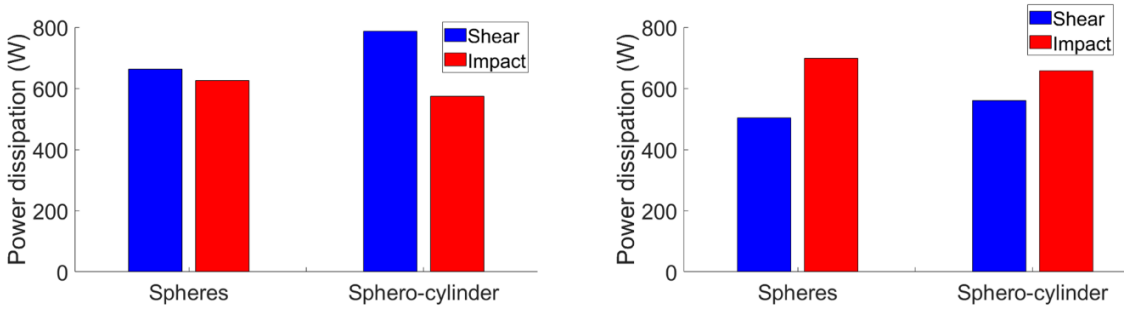

FIG 5 – Power dissipation of rock media: 37.5 mm top-up size (left) and 75 mm top-up size (right).

It is evident in Figures 4 and 5 that the shape of media has a notable influence on the distribution of power. For simulations of steel media with top-up size of 37.5 mm, changing from sphere to sphero-cylinder increased the proportion of shear power from 51 per cent to 62 per cent. For simulations of steel media with top-up size of 75 mm, changing from sphere to sphero-cylinder increased the proportion of shear power from 40 per cent to 48 per cent. The impact component reduced proportionately. Similar trends can be deduced from the simulations of rock media.

The non-spherical media are not able to rotate as easily as the spherical ones, which causes them to slide rather than rolling. The increase in the proportion of shear power in Figures 4 and 5 reflects the increase in the incidences of sliding contacts instead of rolling contacts within the load; similar results have been observed by Cleary (2019).

The effect of grinding media shape on specific breakage rates has been studied experimentally by the following authors: Simba and Moys (2014); Ipek (2006); Shi (2004); Kelsall *et al* (1973). The differences in specific breakage rates, resulting from different media shapes, have been attributed to the changes in the contact surface area. The data presented in Figures 4 and 5 demonstrate that, in addition to the changes in the contact surface area, the differences in specific breakage rates are caused by the changes in the relative strengths of grinding mechanisms (ie head-on impacts versus shear events).

It is evident in Figures 4 and 5 that the size of media also has a notable influence on the distribution of power. For simulations of spherical steel media, changing the top-up size from 37.5 mm to 75 mm reduced the proportion of shear power from 51 per cent to 40 per cent. For simulations of sphero-cylinder steel media, changing the top-up size from 37.5 mm to 75 mm reduced the proportion of shear power from 62 per cent to 48 per cent. The impact component increased proportionately.

Additional simulations using steel media of mono-sizes of 60 mm, 50 mm, 40 mm, 30 mm and 20 mm (and seasoned loads simulating topping up with these sizes) were carried out. The simulations are not reported here, but it can be mentioned that the data showed similar trends, the proportion of impact increases with media size.

The effect of media size on specific breakage rates is detailed in Austin *et al* (1984); and other authors, eg Katubilwa and Moys (2009); Teke *et al* (2002); Herbst and Lo (1989), have demonstrated similar effects. Comparing media of same shape and material, the data presented in Figures 4 and 5 demonstrate that the response of specific breakage rates of ore particles to changes in media size is also a result of changes in the relative strengths of grinding mechanisms.

It is evident in Figures 4 and 5 that the grinding medium material has a marginal influence on the distribution of power. For simulations of spheres with top-up size of 75 mm, changing medium material from steel to rock increased the proportion of shear power from 40 per cent to 42 per cent. For simulations of sphero-cylinders with top-up size of 75 mm, changing medium material from steel to rock reduced the proportion of shear power from 48 per cent to 46 per cent.

The data in in Figures 4 and 5 suggests that in composite milling there may be a complex interrelationship between grinding medium size, shape and material, and the distribution of the power dissipated in collisions. The following sections explore this interrelationship.

Ball milling versus composite milling – power dissipation

Lab-scale mill (0.6 m diameter) simulations

The simulations replicated the experiments in terms of media filling level, mill rotational speed, and medium size distribution and material (described in Nkwanyana and Loveday (2017, 2018)). The simulations did not include the slurry. The following assumptions were made prior to the analysis of the simulation data:

- The slurry does not change the flow behaviour of the grinding media significantly, as mentioned by Cleary *et al* (2006) and observed by Katubilwa and Moys (2011).
- The ratio of shear power to impact power in a simulation that includes the slurry is approximately the same as that in a simulation that does not include the slurry; ie the drag force from the viscous slurry only dampens the collisions.
- The influence of media shape on the distribution of power into dissipation through media collisions and viscous stresses in the slurry is negligible.

Figures 6 and 7 show the distribution of power dissipated in collisions in ball milling and composite milling. The data used to construct the plots is from simulations which set-up were using the coefficients of restitution listed in Table 4. However, similar trends were also observed using the following coefficients of restitutions: steel-steel = 0.5, steel-rock = 0.5, 0.4, and rock-rock = 0.3, and are reported elsewhere (Nkwanyana, 2021).

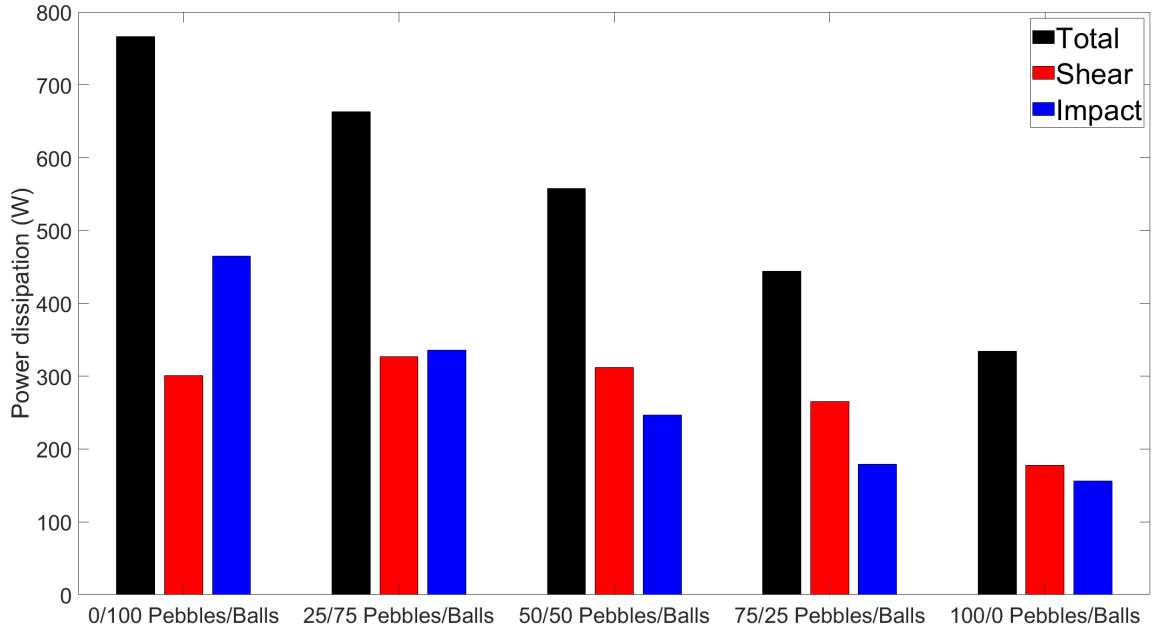

FIG 6 – Regrind ball mill simulations.

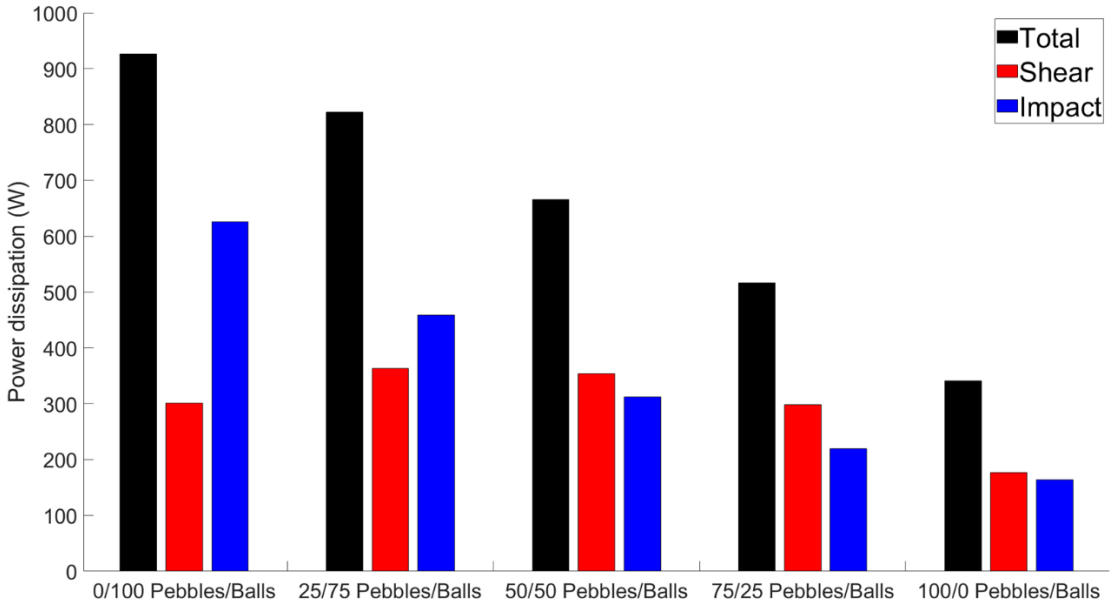

FIG 7 – Secondary ball mill simulations.

It can be deduced from Figures 6 and 7 that changing from ball milling to composite milling resulted in decline in the total power dissipated. This was expected since the bulk density of the charge decreases when steel balls (7850 kg/m^3) are substituted by an equivalent volume of pebbles (3280 kg/m^3 in regrind mill and 2644 kg/m^3 in secondary stage mill).

It is evident from Figures 6 and 7 that, in addition to a decline in total power dissipated, changing from ball milling to composite milling results in a redistribution of the collision power. In Figure 6 the proportion of shear power increased from 39 per cent to 49 per cent on a 25/75 blend, and to 56 per cent on a 50/50 blend. The redistribution of the dissipated power results in the shear power in composite milling being comparable to (or slightly more than) that from ball milling.

The data presented in Figures 6 and 7 suggest that when a fraction of the steel balls load is replaced by an equivalent volume of pebbles, there is a change in the balance of grinding mechanisms, with increasing relative contribution of attrition.

The amount of fines generated by shear events in ball milling and composite milling can be expected to be similar if the ore particles are sufficiently broken by attrition, and if the following hold:

- The shear energies dissipated in ball milling and composite milling are within the same collision energy level.
- The spatial location and area of regions of high shear energy dissipation in ball milling and composite milling are similar, and the energies dissipated in these regions are similar.

Collision energy spectra plots and spatial maps of collision energies are useful for exploring if these conditions hold.

Pilot-scale mill (1.2 m diameter) simulations

A 1.2 m diameter mill was simulated in DEM to investigate the effect of mill diameter, speed and filling level. Figures 8–10 shows the distribution of collision power from the simulations. For these simulations the size distribution of steel balls and pebbles was the same, this was done to ensure that the effect of size of pebbles on the distribution of power was eliminated. It was important to do this in order to show that the redistribution of power in composite milling is mainly a result of pebble shape, especially because in real applications the size distribution of pebbles will be variable.

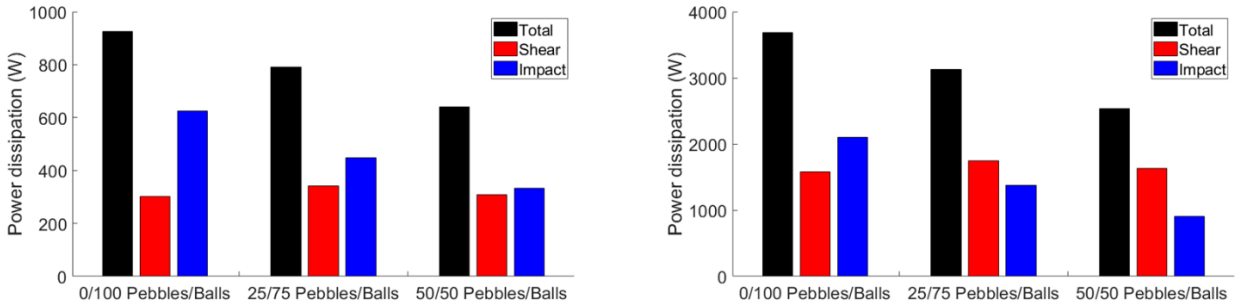

FIG 8 – Effect of mill diameter using a 33 per cent fill level and a speed of 75 per cent *Nc*. Left: 0.6 m diameter mill, Right: 1.2 m diameter mill.

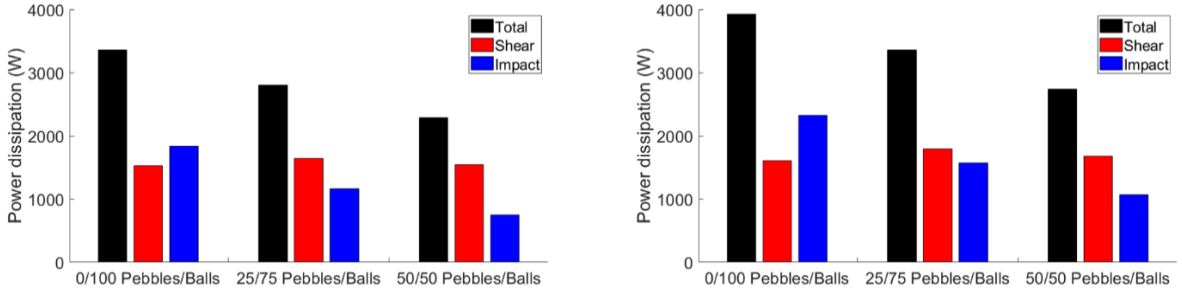

FIG 9 – Effect of mill speed using a 1.2 m diameter mill filled up 33 per cent level. Left: 68 per cent *Nc*, Right: 83 per cent *Nc*.

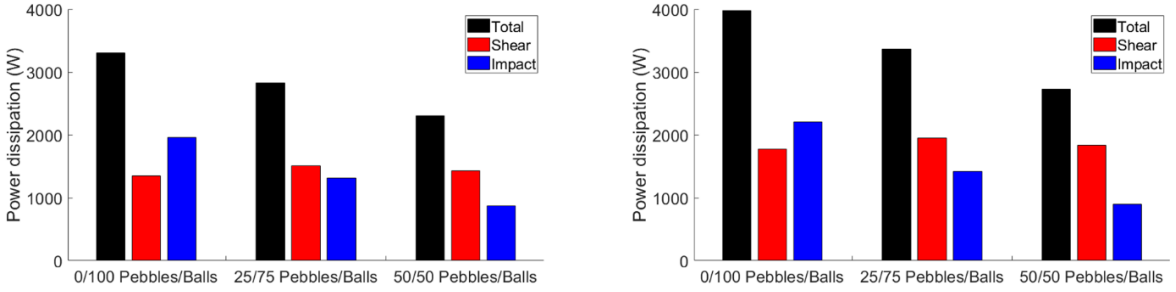

FIG 10 – Effect of mill fill level using a 1.2 m diameter mill operated at 75 per cent *Nc*. Left: 28 per cent fill, Right: 40 per cent fill.

Figure 8 shows a notable difference in the distribution of collision power in the two mills simulated. Comparing the ball milling cases, in the 0.6 m diameter mill the shear component is 32 per cent, whereas in the 1.2 m diameter mill it is 43 per cent. A similar mill size effect has been reported in Weerasekara *et al* (2016).

As expected, Figure 9 shows that the proportion of shear is lower for the high speed, and Figure 10 shows that it is higher for the high fill level. Comparing 25/75 mixture cases, the proportion of shear for the mill rotating at 68 per cent *Nc* is 59 per cent, whereas at 83 per cent *Nc* it is 53 per cent. Comparing the 50/50 mixture cases, the proportion of shear for 28 per cent filling level is 62 per cent, whereas at 40 per cent fill level it is 67 per cent.

Figures 8–10 show that the redistribution of the collision power when changing from ball milling to composite milling was evident in both mills, across all speeds and filling level, and independent of media size distribution. For an example, in Figure 9 (left) the proportion of shear increased from 46 per cent to 59 per cent in 25/75 mixture, and to 67 per cent on 50/50 mixture.

Ball milling versus composite milling – energy spectra

The data presented in Figures 4–10 show the total power resulting from all collision events (ball-ball, ball-pebble, ball-liner and pebble-liner) in the normal and tangential directions. It is also important to compare the probability distribution of power and collision frequencies in all possible collision energy

levels. Figures 11–12 show the energy spectra plots for shear events (truncated at 1 × 10^{-4} J), which are of interest in this paper.

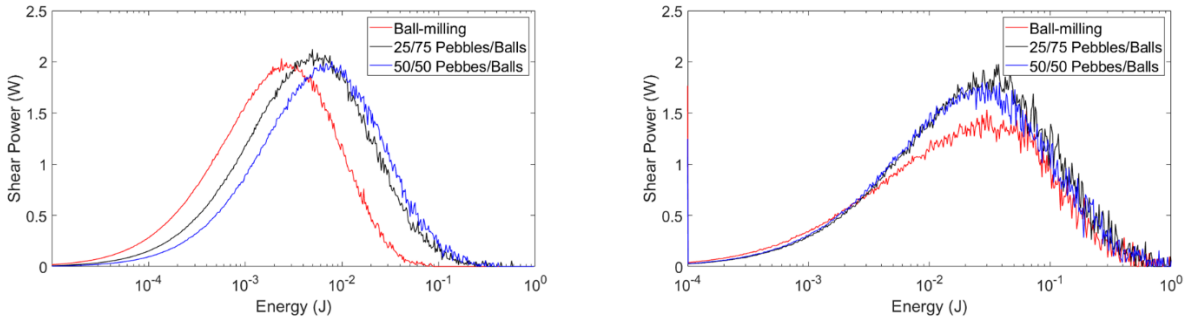

FIG 11 – Shear power dissipation. Left: Regrind ball mill, right: Secondary ball mill.

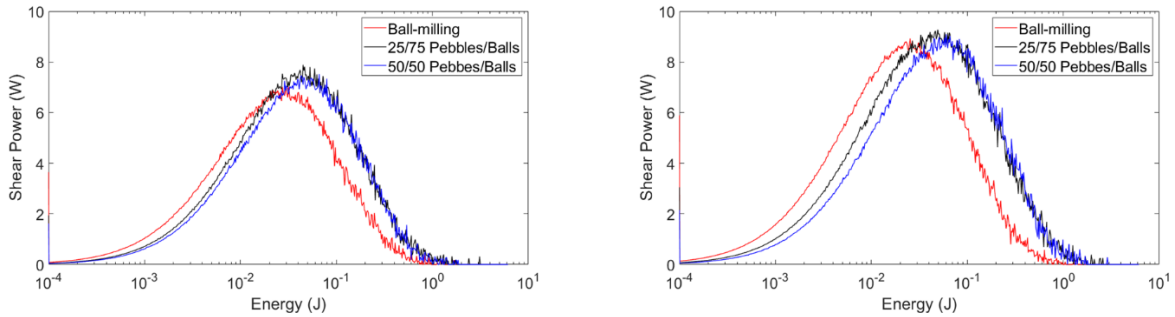

FIG 12 – Shear power dissipation (1.2 m diameter mil, effect of fill level). Left: 28 per cent, Right: 40 per cent.

Figure 11 left shows that for simulated charge filling, mill speed and media size distributions, in composite milling the energy spectra shift to the right. The energy spectra reveal that the total shear power (shown in Figure 6) in composite milling (25/75 and 50/50 mixtures) is comparable to that in ball milling because of higher energy shearing events.

Figure 11 right shows that for the simulated charge filling, mill speed and media size distributions, in composite milling the energy spectra shifts upwards. The energy spectra reveal that the shearing events in ball milling and composite milling (25/75 and 50/50 mixtures) are similar in energy intensity.

Figure 12 show that for the simulated charge filling, mill speed and media size distributions, in composite milling the energy spectra shift slightly upwards and to the right. The energy spectra reveal that the total shear power (shown in Figure 10) in composite milling (25/75 and 50/50 mixtures) is comparable to that in ball milling because of higher energy shearing events.

As mentioned earlier, introducing non-spherical media changes the local contact interactions from predominantly rolling to sliding. This information can be deduced from a collision frequency plot. Figures 13 and 14 show the collision frequency plots corresponding to Figures 11 and 12.

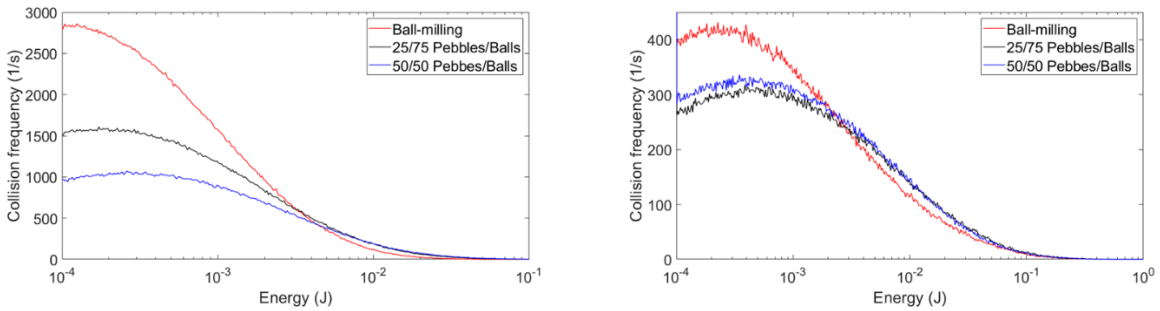

FIG 13 – Collision frequency. Left: regrind ball mill, right: Secondary ball mill.

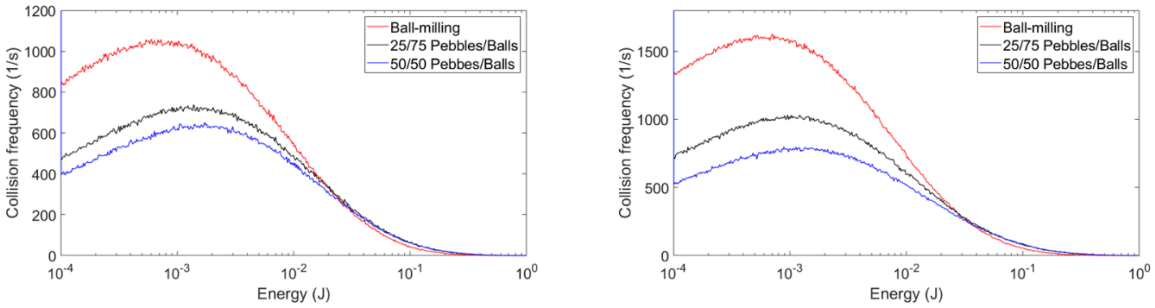

FIG 14 – Collision frequency (1.2 m diameter mil, effect of fill level). Left: 28 per cent, Right: 40 per cent.

It is evident in Figures 13 and 14 that on the higher end of the energy spectra (>10^{-2} J), the frequency of collisions in composite milling are slightly higher than in ball milling. However, on the lower energy end the frequency of collisions in composite milling are significantly less. One can expect rolling to be a low energy shearing event compared to sliding. Therefore the high frequency of low energy collisions in ball milling can be attributed to the fact spherical media roll with ease, but dissipates less energy in the tangential direction.

Ball milling versus composite milling – spatial maps of collision energy

Spatial distribution maps can be used to locate the regions where the energy dissipated is high ('hot-spots'), and by inference the regions where the probability of ore particle breakage is high (Ndimande *et al,* 2019; Nordell and Potapov, 2015; Powell and McBride, 2004). Figure 15 shows the spatial distribution of cumulative shear energy dissipated in collisions over a period of 10 seconds after the simulation has reached steady state, and the average volume fraction. The spatial maps shown are for the 1.2 m diameter mill filled up to 40 per cent level and rotating at 75 per cent *Nc*. Similar trends have been observed from maps of all the other simulations described in this paper.

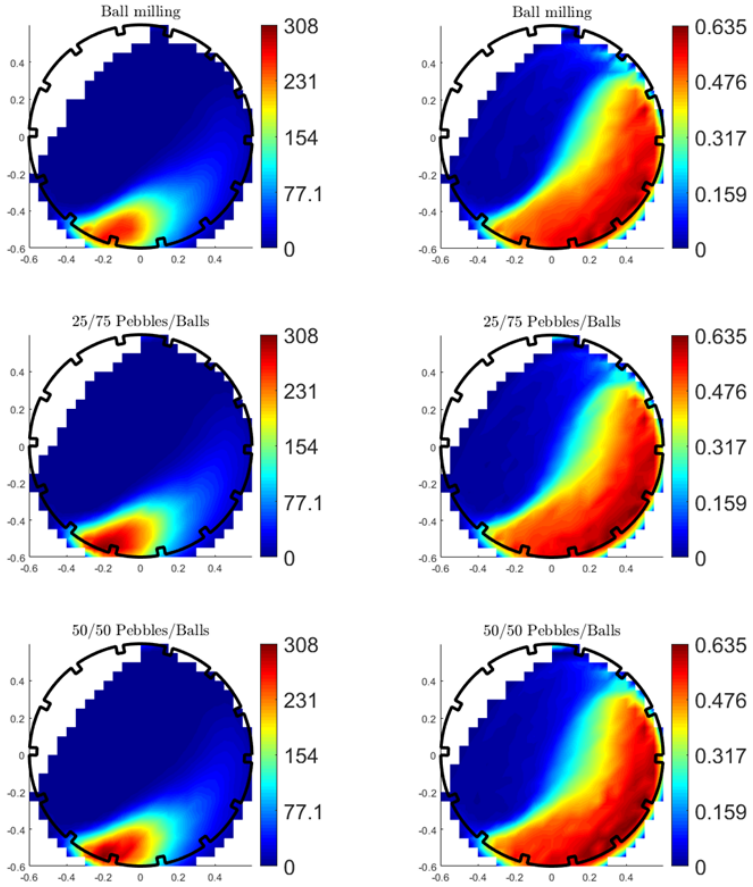

FIG 15 – Spatial distribution maps. Left: Cumulative shear energy dissipation, Right: Volume fraction.

High shear energy dissipation occurs in regions where the pressure and shear rates are high. The pressure and shear rates can be expected to be high starting from the bulk toe region, and moving inwards into bulk of the charge. In this region there is high turbulence, the cataracting streams and the cascading streams converge and change flow direction. The pressure is also high in this region due to the weight above the charge. The location of the 'hot-spots' in Figure 15 are in agreement with the description given here.

From a qualitative standpoint, it appears that the area of the 'hot-spots' (the red, yellow, green and light blue hues) are comparable. The cumulative shear energies dissipated in the hot-spots are also comparable (with a slight increase as the volume of pebbles increases). There is no significant difference in the volume fraction maps of composite milling and ball milling. This implies that the irregular shapes of pebbles may not compromise the probability of capture of ore particles between the colliding media in composite milling.

If the collision energies covered by the energy spectra shown in Figures 11–14 exceed the threshold required to cause catastrophic (body) breakage of the ore particles captured, the maps shown in Figure 15 suggest that one can at least expect the size distribution of the progenies produced from attrition when using 25/75 and 50/50 mixtures will be similar to that from ball milling.

The effect of the reduction in impact energy (refer to Figures 6–10) on the overall fines production depends on the contribution of impact breakage. Literature does not provide a clear weighting of attrition and impact breakage on the overall fines production from a secondary stage or regrind ball mill. However, intuitively one can imagine that if the feed material has a considerable mass of coarse and hard particles, the reduction in impact energy can be detrimental to fines production.

If only the shear power was important, then a ball mill charged with only spherical steel balls and a ball mill charged with a 50/50 mixture will produce the same amount of fines per unit time. The experimental data reported in Nkwanyana and Loveday (2018, 2017) showed that this is not the case, a loss in the production of fines was incurred when a 50/50 mixture was used. Therefore, there is an unknown weighted contribution of shear and impact events on the production rate of fines, but in this paper it is assumed that the shear contribution dominates. At high pebble volumes the effect of reduction in impact energy becomes evident.

CONCLUSIONS

- There is a complex interrelationship between grinding medium size, shape and material and the distribution of the energy dissipated in collisions. The interrelationship results in a redistribution of collision energy (shear: impact) when a portion of spherical steel balls is replaced by irregular shaped rounded pebbles in a ball mill.
- The redistribution was evident on 0.6 m and 1.2 m diameter mills, at 68 per cent, 75 per cent and 83 per cent of critical speed, and at 28 per cent, 33 per cent and 40 per cent filling.
- There is an unknown weighted contribution of shear and impact on the production rate of fines in a ball mill processing fine feeds (F_{80} <1 mm). In this paper it was assumed that the shear contribution dominates.
- Based on the shear power dissipation it can be postulated that attrition grinding in ball milling and composite milling (25/75 and 50/50) would yield progenies of similar size distribution.
- The shear power in a mill loaded with steel balls only and in mill loaded with a 25/75 mixture are comparable, this is a probable reason for the comparable production rate of fines (-75 µm material) reported in Nkwanyana and Loveday (2018, 2017).

ACKNOWLEDGEMENTS

The authors wish to thank and acknowledge Mintek for financial support and permission to publish this paper.

REFERENCES

Austin, L, Klimpel, R and Luckie, P, 1984. *Process Engineering of Size Reduction: Ball Milling*, Society of Mining Engineers. AIME, pp. 112–113.

Bbosa, L, Govender, I and Mainza, A, 2016. Development of a novel methodology to determine mill power draw, *International Journal of Mineral Processing*, 149, pp. 94–103.

Carvalho, R and Tavares, L, 2013. Predicting the effect of operating and design variables on breakage rates using the mechanistic ball mill model, *Minerals Engineering*, 43, pp. 91–101.

Carvalho, R, 2013. 'Mechanistic modeling of semi-autogenous grinding', PhD thesis, Universidade Federal do Rio de Janeiro, UFRJ/COPPE, Brazil.

Cleary, P and Owen, P, 2019a. Effect of operating condition changes on the collisional environment in a SAG mill, *Minerals Engineering*, 132, pp. 297–315.

Cleary, P and Owen, P, 2019b. Effect of particle shape on structure of the charge and nature of energy utilisation in a SAG mill, *Minerals Engineering*, 132, pp. 48–68.

Cleary, P, 2019. Effect of rock shape representation in DEM on flow and energy utilisation in a pilot SAG mill, *Computational Particle Mechanics*, 6 (3), pp. 461–477.

Cleary, P, Sinnott, M and Morrison, R, 2006. Prediction of slurry transport in SAG mills using SPH fluid flow in a dynamic DEM based porous media, *Minerals Engineering*, 19 (15), pp. 1517–1527.

Clermont, B and De Haas, B, 2010. Optimization of mill performance by using online ball and pulp measurements, *The Journal of The Southern African Institute of Mining and Metallurgy,* 110 (3), pp. 133–140.

Daniel, M, Lane, G and McLean, E, 2010. Efficiency, economics, energy and emissions– emerging criteria for comminution circuit decision making, in *Proceeding of XXV International Mineral Processing Congress,* pp. 3523–3531.

Djordjevic, N, Shi, F and Morrison, R, 2004. Determination of lifter design, speed and filling effects in AG mills by 3D DEM, *Minerals Engineering,* 17 (11–12), pp. 1135–1142.

Dong, H and Moys, M, 2002. Assessment of discrete element method for one ball bouncing in a grinding mill, *International Journal of Mineral Processing*, 65 (3–4), pp. 213– 226.

Herbst, J and Lo, Y, 1989. Grinding efficiency with balls or cones as media, *International Journal of Mineral Processing,* 26 (1–2), pp. 141–151.

Hilden, M and Suthers, S, 2010. Comparing energy efficiency of multi-pass high pressure grinding roll (HPGR) circuits, in *Proceedings of the XXV International Mineral Processing Congress*.

Ipek, H, 2006. The effects of grinding media shape on breakage rate, *Minerals Engineering*, 19(1), pp. 91–93.

Jankovic, A, Valery, W, Maloney, K and Markovic, Z, 2006. Improving Overall Concentrator Performance with Stirred Milling, in *Proceedings of the 23rd International Mineral Processing Congress*.

Katubilwa, F and Moys, M, 2009. Effect of ball size distribution on milling rate, *Minerals Engineering*, 22 (15), pp. 1283–1288.

Katubilwa, F M and Moys, M H, 2011. Effects of filling degree and viscosity of slurry on mill load orientation, *Minerals Engineering*, 24(13), pp. 1502–1512.

Kelsall, D, Stewart, P and Weller, K, 1973. Continuous grinding in a small wet ball mill. Part V. A study of the influence of media shape, *Powder Technology*, 8 (1–2), pp. 77–83.

Kulya, C, 2008. 'Using discrete element modelling (DEM) and breakage experiments to model the comminution action in a tumbling mill', MSc. Thesis, University of Cape Town, Cape Town.

Levin, J, 1992. Indicators of grindability and grinding efficiency, *The Journal of The Southern African Institute of Mining and Metallurgy*, 92 (10), pp. 283–290.

Musa, F and Morrison, R, 2009. A more sustainable approach to assessing comminution efficiency, *Minerals Engineering*, 22(7–8), pp. 593–601.

Ndimande, C, Cleary, P, Mainza, A and Sinnott, M, 2019. Using two-way coupled DEM-SPH to model an industrial scale Stirred Media Detritor, *Minerals Engineering*, 137, pp. 259–276.

Nkwanyana, 2021. 'An exploration of the benefits of using a mixture of critical size pebbles (from semi-autogenous mills) and steel balls in secondary ball-mills', PhD thesis, University of Kwa-Zulu Natal, Durban.

Nkwanyana, S, Loveday, B K, 2017. Addition of pebbles in a ball-mill to improve grinding efficiency, *Minerals Engineering*, 103–104, pp. 72–77.

Nkwanyana, S, Loveday, B K, 2018. Addition of pebbles in a ball-mill to improve grinding efficiency – Part 2, *Minerals Engineering*, 128, pp. 115–122.

Nordell, L and Potapov, A, 2015. Novel comminution machine may vastly improve crushing-grinding efficiency, in *Proceedings of the International Conference on Autogenous and Semi-autogenous Grinding Technology 2015*.

Powell, M and McBride, A, 2004. A three-dimensional analysis of media motion and grinding regions in mills, *Minerals Engineering*, 17 (11–12), pp. 1099–1109.

Powell, M, 2001. Liner selection—a key issue for large SAG mills, in *Proceedings of the International Conference on Autogenous and Semi-autogenous Grinding Technology 2001*.

Powell, M, Mainza, A, Hilden, M and Yahyaei, M, 2015. Full pre-crush to SAG mills – the case for changing this practice, in *Proceedings International Conference on Autogenous Semiautogenous Grinding Technology 2015*.

Sarracino, R, McBride, A and Powell, M, 2004. Using particle flow code to investigate energy dissipation in a rotary grinding mill, Numerical Modeling in Micromechanics via Particle Methods-2004, in *Proceedings of the 2nd International PFC Symposium*, pp. 111–118.

Shi, F, 2004. Comparison of grinding media—Cylpebs versus balls, *Minerals Engineering*, 17 (11–12), pp. 1259–1268.

Simba, K and Moys, M, 2014. Effects of mixtures of grinding media of different shapes on milling kinetics, *Minerals Engineering*, 61, pp. 40–46.

Sinnott, M, Cleary, P and Morrison, R, 2011. Is media shape important for grinding performance in stirred mills?, *Minerals Engineering*, 24 (2), pp. 138–151.

Tavares, L and Carvalho, R, 2010. A mechanistic model of batch grinding in ball mills, in *Proceedings of the XXV International Mineral Processing Congress*.

Teke, E, Yekeler, M, Ulusoy, U and Canbazoglu, M, 2002. Kinetics of dry grinding of industrial minerals: calcite and barite, *International Journal of Mineral Processing*, 67 (1–4), pp. 29–42.

Vermeulen, L, Howat, D and Gough, C, 1983. Theories of ball wear and the results of a marked-ball test in ball milling, *The Journal of the Southern African Institute of Mining and Metallurgy,* 83 (8), pp. 189–197.

Weerasekara, N and Powell, M, 2010. Exploring the breakage environment in mills with discrete element methods, in *Proceedings of the XXV International Mineral Processing Congress*.

Weerasekara, N, Liu, L and Powell, M, 2016. Estimating energy in grinding using DEM modelling, *Minerals Engineering*, 85, pp. 23–33.

Zhang, Z-X, 2016. *Rock fracture and blasting: theory and applications*, Butterworth-Heinemann.

Enhancing energy efficiency and reducing water consumption in TowerMill circuit through design and optimisation

S Palaniandy[1] and H Ishikawa[2]

1. Global Product Manager, Nippon Eirich Co. Ltd., Willawong Qld 4110. Email:samayamutthirian@nippon-eirich.com
2. Senior Technical Officer, Nippon Eirich Co. Ltd., Nagoya Aichi Prefecture 451–0045 Japan. Email:ishikawa.hidemasa@nippon-eirich.co.jp

ABSTRACT

The gravity-induced stirred mill such as the TowerMill is an energy-efficient grinding solution used in secondary, tertiary, and regrinding duties in the mineral processing concentrator. The interest in this technology is emerging, with more than 300 mills installed globally in various grinding duties and commodities for the last 30 years. Although the technology is matured, there are still opportunities for improvement and the development of new knowledge to improve its circuit energy efficiency and reduce water consumption. Recent studies show that a combination of stress intensity, ore hardness, slurry density, and mill feed configuration can be used to evaluate the performance of the grinding circuit. A recent pilot-scale TowerMill test work at various stress intensities shows that a lower operating work index and size-specific energy were achieved at higher agitator tip speed and using medium size grinding media. These outcomes were confirmed through several site trials. A smaller 17 mm grinding media has reduced the operating work index and size-specific energy by 18 per cent and 11 per cent, respectively, compared to the 20 mm in a magnetite concentrator. Moreover, the conversion from top feed to bottom feed configuration has reduced the operating work index and size-specific energy by 13 per cent and 37 per cent, respectively. The circulating load was reduced by 34–38 per cent, leading to a reduction in the dilution water consumption in the hydrocyclone feed sump by 20 per cent. A variable frequency drive offers flexibility to change the stress intensities on the TowerMill, where a 35 per cent reduction in specific energy was achieved when the ore became soft. This paper explores the potential design and operating strategies that can be implemented to enhance the energy efficiency, reduce water consumption and reduce CO_2 emissions in the circuit and finally evaluate its impact on the total cost of ownership.

INTRODUCTION

The mining industry has been facing challenges such as depleting orebody grades, increase in hardness as the mine goes deeper, and finely disseminating valuable minerals in the orebodies. All these challenges have led to the building of large energy and water-intensive concentrator to meet the targeted concentrate grade and productivity for a profitable operation. These concentrators were equipped with large autogenous/semi-autogenous grinding mills and ball mills to grind and liberate the valuable minerals from the gangue. These comminution devices consume 50–70 per cent of the energy in the concentrator that making grinding an energy-intensive process. On top of these challenges, our industry is also facing increasing pressure to reduce carbon emissions to secure a global net-zero by 2050 and keep a maximum of 1.5°C of warming within reach.

Energy-efficient equipment such as the stirred mills and high-pressure grinding rolls (HPGR) have been introduced to the comminution circuit to address the above-mentioned challenges specifically to reduce specific energy consumption (the kWh/t) and water consumption. This paper will focus on the application of the stirred mill in the circuit specifically the TowerMill – a gravity-induced stirred mill. The TowerMill was developed in Japan in the 1950s for fine grinding duty. In the 1980s, this technology was introduced in the mineral processing concentrator for rougher concentrate regrind duty to improve the concentrate grade. The ability of the TowerMill to grind efficiently down to 13–15 µm at a lower specific energy consumption has attracted many concentrators to install this technology in the regrind duty. Over the last 15 years, the TowerMill technology has been introduced to the coarse grinding application by partially replacing the secondary and tertiary ball mill duties. The ability of the TowerMill to receive feed up to 6 mm (100 per cent passing) has attracted applications that partially replace the ball mills. Recently, the Eirich TowerMill has been chosen for

a coarse grinding duty of soft hematite ore (F100 = 6 mm) to produce a pellet feed with Blaine number of 1800–2000 cm^2/g.

The technology is mature and has been well accepted in the industry but, with the new challenges, there are still opportunities to further improve in terms of equipment, circuit design, and operations. These improvements will reduce the energy and water consumption in the circuit hence reducing the carbon emission as well. This paper will present some new knowledge that has been developed through laboratory experiments and site trials that reduces energy and water consumption.

GRINDING DUTIES OF TOWERMILL IN THE CONCENTRATORS

The TowerMill has been used in mineral processing concentrators for the last 40 years in various grinding duties and commodities such as copper-gold, silver-lead-zinc, hematite, magnetite, and PGMs. Its grinding duties include secondary, tertiary, and regrinding of concentrate and tailings. Its ability to receive feed up to 6 mm (top size) and produce a circuit product down to 13 µm has enabled this technology for a wide range of grinding duties in the mineral processing concentrators. This section will discuss the application of TowerMill in secondary and tertiary grinding duties.

Secondary grinding duty

The TowerMill has been installed for secondary grinding duty receiving the feed from the autogenous or semi-autogenous mill replacing the ball mill. Figure 1 shows the simplified comminution circuit flow sheet of a magnetite concentrator in West Asia – one of the lines out of 14 lines. The primary grinding was carried out in an autogenous mill and the rougher magnetic separator (RMS) concentrate was ground in a TowerMill down to 35 µm and followed by a cleaner magnetic separator (CMS) to produce the final concentrate. One of the advantages of this circuit is the application of an autogenous mill that eliminates the use of grinding media in the primary grinding stage and energy-efficient TowerMill in the secondary grinding duty. Typically the secondary grinding duty is being carried out in a ball mill. A comparison in terms of specific energy consumption, dilution water addition to the circuit (that can be translated to water consumption for the secondary grinding duty), and CO_2 emission were compared for the existing TowerMill circuit and equivalent ball mill circuit. The CO_2 emission was calculated based on the CO_2 emissions for electricity generation and grinding media manufacturing. Morrell (2022) mentioned that the CO_2 emission for electricity generation and grinding media manufacturing were 556 g/kWh and 2.3 kg per kg of steel ball consumed. The specific energy consumption for the ball mill was determined through the Levin Test. The circulating load for the ball mill circuit and TowerMill circuit were 380 per cent and 270 per cent respectively. Table 1 shows the specific energy consumption, dilution water requirement, and CO_2 emission for the existing TowerMill circuit and the simulated ball mill circuit. The specific energy consumption, dilution water requirement, and CO_2 emission for the TowerMill circuit are lower compared to the ball mill circuit. The grinding efficiency through attrition in the TowerMill has contributed to the lower specific energy and grinding media consumption hence reducing the CO_2 emission. Moreover, the lower circulating load helps to reduce the dilution water requirement. The hydrocyclone feed slurry density is maintained below 50 per cent (w/w). In general, the application of TowerMill technology in the secondary grinding duty has more benefits compared to the ball mill in the secondary grinding duty in a magnetite concentrator.

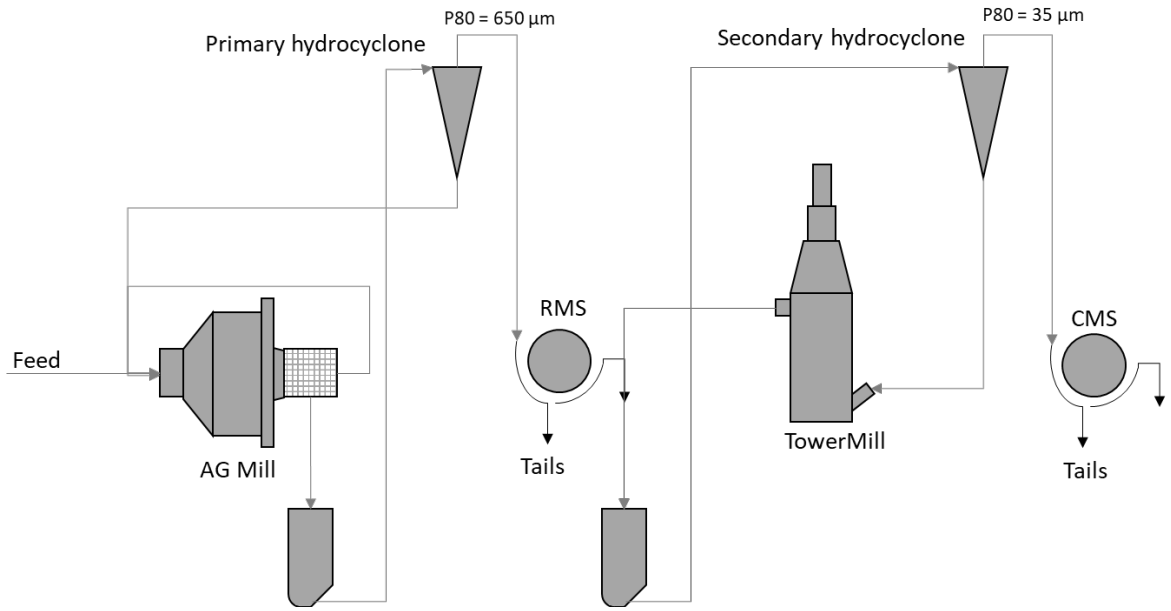

FIG 1 – Simplified comminution circuit of a magnetite concentrator.

TABLE 1

Comparison between the ball mill and TowerMill circuit in the secondary grinding duty in a magnetite concentrator.

Circuit	Ball Mill	TowerMill	% reduction
F80 (µm)	460	460	-
P80 (µm)	34	34	-
Throughput (t/h)	133	133	
No of Mills	1	1	
Power requirement in the mill (kW)	2558	1968	
Hydrocyclone feed pump power (kW)	211	166	
Total power requirement in the circuit	2783	2050	
Installed power in the mill (kW)	2984	2050	
Specific energy consumption (kWh/t) – Mill only	21.3	16.4	23.1
Specific energy consumption (kWh/t) – Circuit	23.2	17.8	23.3
Dilution water requirement (m^3/h)	360	308	12.0
CO_2 emission per tonne of ore ground (kg/t-of ground ore)	15.3	10.7	30.0

Tertiary grinding duty

A similar analysis was carried out to compare the ball mill and TowerMill in a tertiary grinding duty in a Cu-Au concentrator where the front-end grinding circuit was a semi-autogenous-ball mill-pebble crusher (SABC). The circuit product of SABC circuit product ranged between 150–180 µm. The ore is considerably hard with a Bond ball mill work index of 18 kWh/t. The site decided to reduce the rougher flotation feed to 85 µm to enhance the liberation and recovery. Two grinding technologies were compared ie ball mill and TowerMill during the study phase. Finally, the TowerMill was chosen due to its lower specific energy consumption and minimal space requirement as space was limited for this brownfield expansion. After the installation, the TowerMill circuit performance was audited and the results are shown in Table 2. The same data (F80 and P80) was used along with the Bond Ball Mill Work Index to determine the specific energy requirement for a tertiary ball mill circuit. Table 2 summarises the comparison data between the existing tertiary TowerMill circuit and the simulated ball mill circuit. In general, the TowerMill circuit exhibits lower specific energy consumption, dilution

water requirement, and CO_2 emission. Similar to the abovementioned secondary grind circuit, the TowerMill circuit exhibits superiority compared to the ball mill circuit in the tertiary grinding circuit.

TABLE 2

Comparison between the ball mill and TowerMill circuit in the tertiary grinding duty in a Cu-Au concentrator.

Circuit	Ball Mill	TowerMill	% reduction
F80 (μm)	155	155	-
P80 (μm)	85	85	-
Circuit feed rate (t/h)	335	335	
Specific energy consumption (kWh/t)	5.07	3.15	37.8
Power (kW) – Mill	1697	1055	
Power (kW) – Pump	212	166	
Power (kW) – Total	1909	1221	
Installed Power (kW)	1865	1120	
No. of mill	1	1	
Dilution water requirement (m^3/h)	330	178	46.1
CO_2 emission per tonne of ore ground (kg/t of ground ore)	3.63	2.19	39.6

TOWERMILL CIRCUIT PRODUCES A NARROW PRODUCT SIZE DISTRIBUTION

The TowerMill circuit produces a narrow product size distribution. Figure 2 shows the particle size distribution of the secondary grinding TowerMill circuit feed and the product in a magnetite concentrator (Figure 1). The circuit product exhibits narrow product size distribution with an excellent top particle size reduction for magnetite particle liberations. Both particle size distributions were fitted to the Rosin-Rammler model to determine their slopes. The circuit feed and product size distribution slopes were 0.75 and 1.02 respectively. These numbers indicate that the TowerMill circuit produces a sharper product size distribution which aids mineral recovery and dewatering processes. The slurry zone on top of the grinding zone in the TowerMill shell acts as a classification zone – especially in coarse grinding applications. The coarse particles that enter the slurry build-up zone will be returned to the grinding zone, while the slurry current will push the fines out from the mill. The slurry build-up acts as an internal classifier. In this case, those particles that reached the targeted grind size will be classified immediately thus reducing the over-grinding in the mill grinding chamber hence reducing the circulating load in the hydrocyclone. The combination of internal classifications in the mill and hydrocyclone produces a narrower circuit product size distribution. This effect is common in TowerMill circuits for all grinding duties.

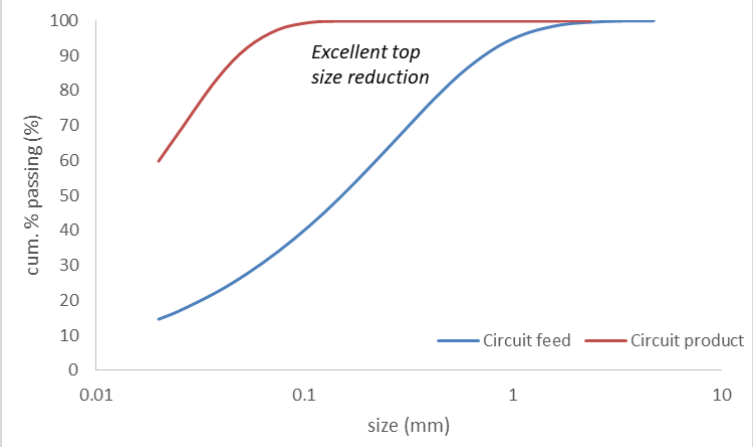

FIG 2 – Particle size distribution of TowerMill circuit feed and product.

TOWERMILL DESIGN, OPERATING VARIABLES, AND STRESS INTENSITY CONCEPT

Despite the maturity of the technology and the advantages mentioned, there is still opportunities for improvement to operate the mill more efficiently and maximise its capability. This section will evaluate the design and operating variables that affect the grinding efficiency and later relate it to the stress intensity concept. The TowerMill model available ranged from ETM 20 (15 kW) to ETM 2000EX (1865 kW). The design concept of the TowerMill includes gap (distance between mill shell and the tip of the screw), agitator screw design, and agitator screw tip speed (if the mill is installed with a DOL main drive motor), mill feed configuration, and the application of the coarse classifier. The operating variables include specific energy consumption, grinding media size, grinding media density, % solids, and tip speed (if the main drive motor is operated with a variable frequency drive). Table 3 shows the summary of the design and operating variables.

TABLE 3

Summary of design and operating variables.

Variables		**Description**
Design	Application of coarse classifier	The coarse classifier is recommended for coarse grinding application when the particle size is above 1–1.5 mm to classify and recycle the coarse particle to the high grinding efficiency region at the bottom of the mill. Typically, the coarse classifier is installed at the mill discharge launder.
	Mill feed configuration	Top feed → low reduction ratio regrinding duty Bottom feed → large reduction ratio grinding duty – secondary, tertiary, and regrind
	Agitator screw tip speed (for DOL main drive motor)	Typical screw agitator speed ranged from 3.5–4.0 m/s
Operating	Specific energy consumption	This is the main operating variable as a function of motor power draw and circuit feed rate that determines the fineness the of grind.
	Grinding media size	12.7–25 mm
	Grinding media density	Typically, the steel Hi-Cr grinding media with a density of 7800 kg/m^3 is used but recently there are the application of ceramic media in the TowerMill to eliminate the iron contamination. The ceramic media density ranged from 3600–6000 kg/m^3.
	Mill content % solids (w/w)	50–74% depending on the specific gravity of the feed.
	Agitator screw tip speed (if the main drive motor is operated with a variable frequency drive)	The agitator tip speed can be an operating variable if a variable frequency drive is installed to the main drive motor. It is not recommended to operate below 2.0 m/s as it affects the grinding efficiency.
	Amount of grinding media in the mill	The amount of grinding media inside the mill affects the power draw.

Design variables

Two design variables that are useful during the circuit design stage will be discussed in this section ie mill feed configuration and application of coarse classifier for secondary grinding duty. Mill feed

configurations are an important design variable for the TowerMill. The TowerMill can be fed either from the top or bottom. The choice of top or bottom feed configuration depends on the feed size distribution and reduction ratio. The bottom-feed configuration is preferred for a board feed size distribution and requires a large reduction ratio such as a particle size distribution shown in Figure 2. Meanwhile, the top feed configuration is preferred for fine feed with narrow particle size distribution and requires a low reduction ratio grinding duty. EIRICH TowerMill is designed with both feed ports – top and bottom, that offer flexibility for the circuit design. Table 4 shows the summary of the mill feed configuration based on the grinding duties that enable circuit modification when the ore changes. The effect of mill feed configuration on grinding efficiency can be tested only at the site using the production scale mill. The authors have experience in conducting site trials comparing the effect of top and bottom feed configuration. The results of this study will be discussed in the latter part of this paper.

TABLE 4

Summary of mill feed configuration according to the TowerMill grinding duty.

Mill feed configuration	**Grinding duty**
Top	Tertiary (for fine feed and/or low reduction ratio) Regrind
Bottom	Secondary Tertiary Regrind (flash flotation concentrate + flotation concentrate)

Previously, the TowerMill was designed with a fixed speed (DOL motor) and this was considered a design variable. In the last five to seven years most of the TowerMills are being installed with a variable frequency drive. This upgrade or advancement has offered operational flexibility to the mill, especially when grinding ore with high variability. This upgrade has changed the tip speed from a design variable to an operating variable.

The EIRICH TowerMill is suitable for coarse grinding applications as it can receive feed up to 6 mm (100 per cent passing). A purpose-designed coarse classifier is fitted to the mill discharge stream to classify the coarse particles and return them to the bottom of the mill (high grinding intensity region) to efficiently grind the coarse particles. Figure 3a shows the coarse classifier attached to the ETM 1500 TowerMill and Figure 3b shows the particle size distribution of all three streams of the coarse classifier in one of the coarse grinding hematite applications. The α value (sharpness of cut) of the coarse classifier ranges from 0.6 to 1.5 depending on the operating condition of the mill. Although this is considered a rough classification, it helps to reduce the circulating load in the hydrocyclone by 20–35 per cent. The reduction in the hydrocyclone circulating load helps to reduce the capital expenditure (smaller hydrocyclone cluster and hydrocyclone feed pump) and operating expenditure (smaller slurry pumping energy requirement).

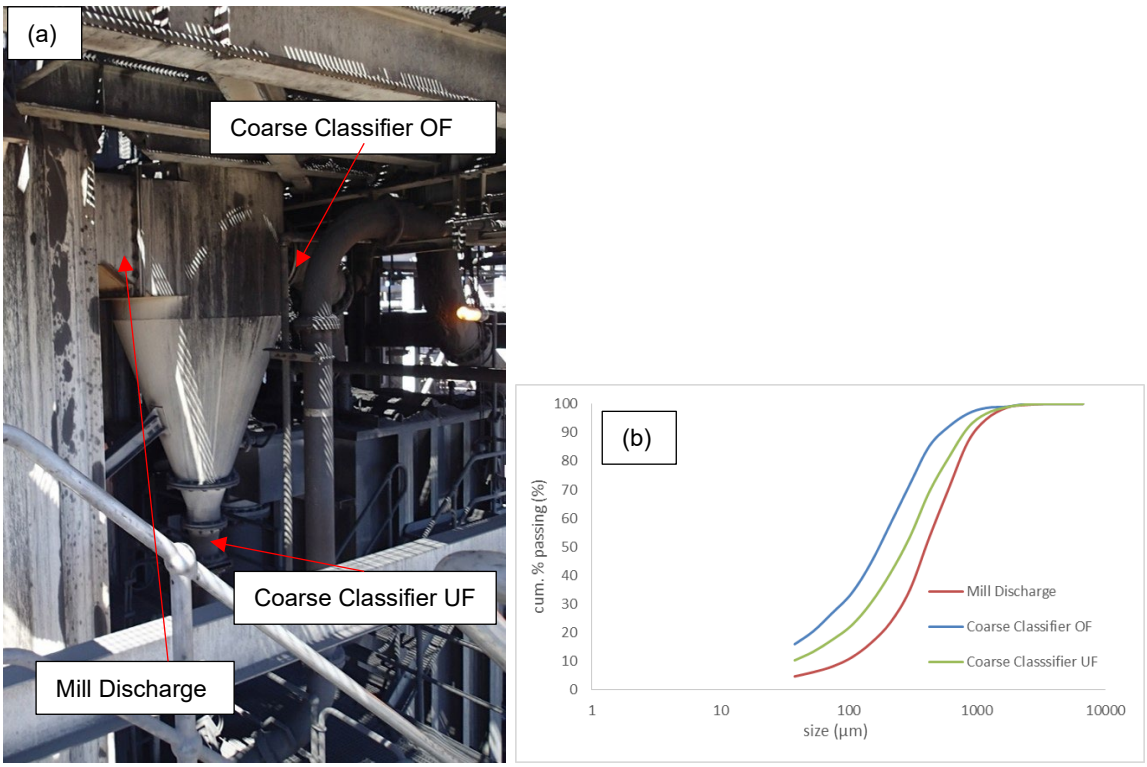

FIG 3 – (a) EIRICH TowerMill Coarse Classifier attached to Mill discharge; (b) Particle size distribution of the coarse classifier streams.

Operating variables

The main operating variables in the EIRICH TowerMill circuit are specific energy consumption, grinding media size, grinding media density, % solids, and screw agitator tip speed (for variable speed main drive motor). The specific energy consumption which is measured in kWh/t is the electrical energy consumed to grind one tonne of material from a designated F80 to a targeted P80. For TowerMill, the power draw is dictated by three main factors, ie the amount of grinding media in the mill, tip speed, and grinding media density. Figure 4 shows the TowerMill power draw as a function of the amount of grinding media in the mill and agitator screw rotational speed. This trial was carried out during ETM 1750 TowerMill commissioning installed for regrind duty at a gold concentrator. In general, as the amount of grinding media and screw rotational speed increases, the mill power draw increases. Table 5 shows the pilot-scale TowerMill power draw when using two different grinding media, ie steel and ceramic. The ceramic media, which has a lower density, draws less power compared to the steel grinding media. Although 98 per cent of the TowerMill applications are using steel media, some concentrators have shifted to using ceramic media in the TowerMill to avoid iron contamination that affects the flotation performances. These results indicate that three main levers can be optimised/manipulated to achieve a certain power draw in the mill.

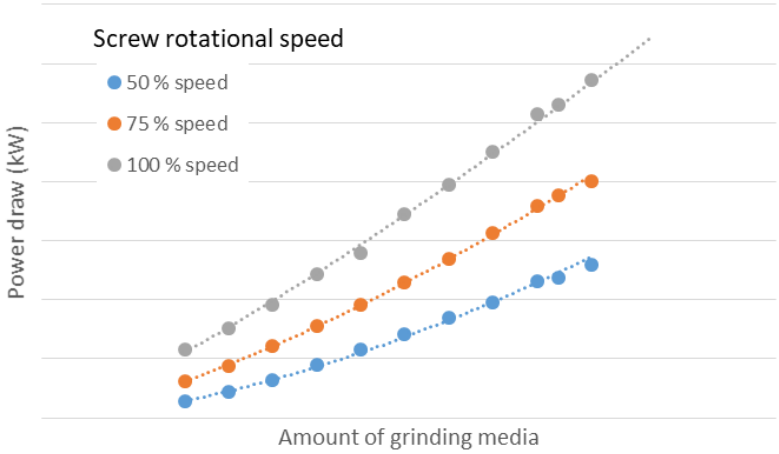

FIG 4 – Effect of grinding media addition and agitator screw rotational speed on power draw for an ETM 1750 EIRICH TowerMill.

TABLE 5

Effect of grinding media density on TowerMill power draw.

Grinding media material	Hi-Cr Steel media	Alumina Ceramic media
Density (t/m^3)	7.8	3.6
Pilot TowerMill Power draw (kW)	1.05	0.44

The effect of grinding media size, screw rotational speed and mill content % solids were tested in a pilot-scale TowerMill. A Cu-Au ore (sampled from a ball mill feed stream) was used for this experimental work. The feed size was 450 µm (at 80 per cent passing). The ore specific gravity was 2.81. Table 6 shows the operating variables range of the pilot-scale TowerMill experiments. The experiments were carried out at three levels. The following section will discuss the piloting results.

TABLE 6

Operating variables range of the pilot-scale mill experiments.

Operating variables	**Range**		
Media size (mm)	12.7	20	25
Solids (% w/w)	50	60	70
Screw tip speed (%)	2.0	2.5	3.0

Effect of screw rotational speed

As mentioned in the previous section, the recent TowerMills are being installed with a variable frequency drive that offers flexibility to adjust the power draw by adjusting screw rotational speed. Three grinding tests were carried out by varying the screw rotational speed at constant % solids and media size. Figure 5 shows the particle size distribution and breakage function at three different screw tip speeds. In general, a higher screw rotational speed results in a higher breakage rate that produces a finer particle size distribution.

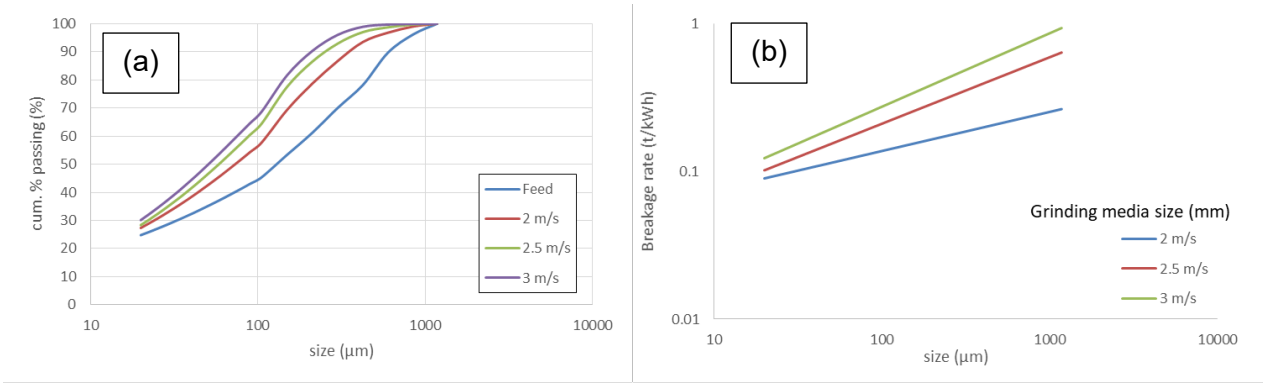

FIG 5 – (a) Particle size distribution and (b) breakage rate at different screw rotational speeds.

Effect of grinding media size

Three grinding media tests were carried out by varying the grinding media size at constant screw rotational speed and mill content % solids. Figure 6 shows the particle size distribution and the breakage rate for three different grinding media sizes. The highest breakage rate was obtained with 15 mm grinding media while the lowest breakage rate was observed with 12.7 mm grinding media. Choosing the appropriate grinding media size is essential for optimum breakage in the mill. The rule of thumb is to choose the grinding media size that can break the top particle size. In this test work, the 12.7 mm grinding media exhibited a lower grinding efficiency to break the coarse particles. Typically smaller grinding media have a higher surface area which leads to higher grinding efficiency but in this case, it has a lesser ability to break the top particle sizes. The 20 mm grinding media has a lesser surface area compared to the 15 mm, and shows lower grinding efficiency comparatively. This test work shows that selection of grinding media size is of utmost importance for a given grinding duty.

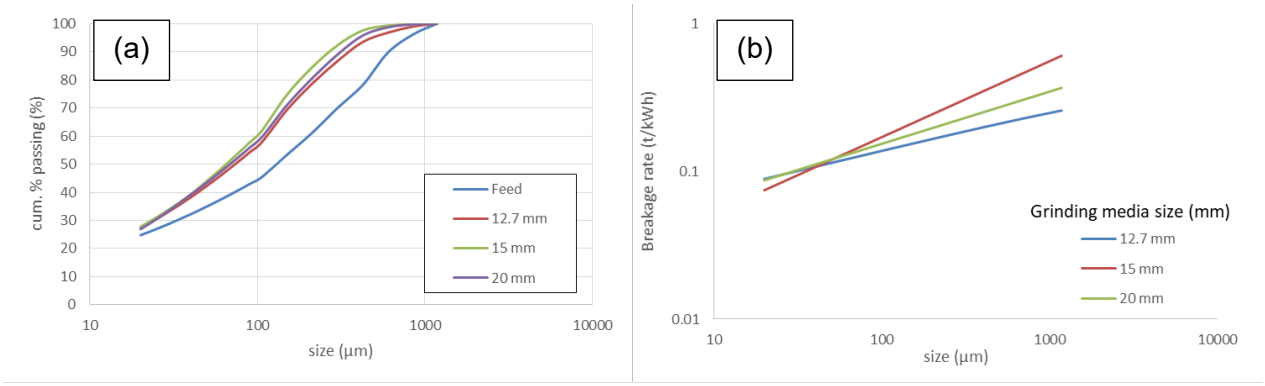

FIG 6 – (a) Particle size distribution and (b) breakage rate at different grinding media size.

Effect of mill content slurry density

The effect of slurry density was tested at three different levels, ie 50 per cent, 60 per cent and 70 per cent. Typically the TowerMill operates comfortably between 50 per cent to 68 per cent solids for ore with a specific gravity of 2.65 to 2.80. Meanwhile, for high specific gravity ore such as magnetite and lead concentrate, the TowerMill mill content % solids ranged from 70 per cent to 80 per cent. Figure 7 shows the particle size distribution and breakage rates at three different levels of mill content slurry density. The breakage rate at 50 per cent and 60 per cent solids were similar; meanwhile, the breakage rate reduced when the per cent solids increased to 70 per cent. This result indicates that the grinding efficiency drops at higher % solids due to the increase in the slurry viscosity. On a separate note, operating the TowerMill below 40 per cent solids will increase the interaction between media to media and media to the liner which will escalate the wear rate of the grinding balls and screw liner. In this case, it is not advisable to operate the mill with a slurry density (mill content) below 40 per cent solids.

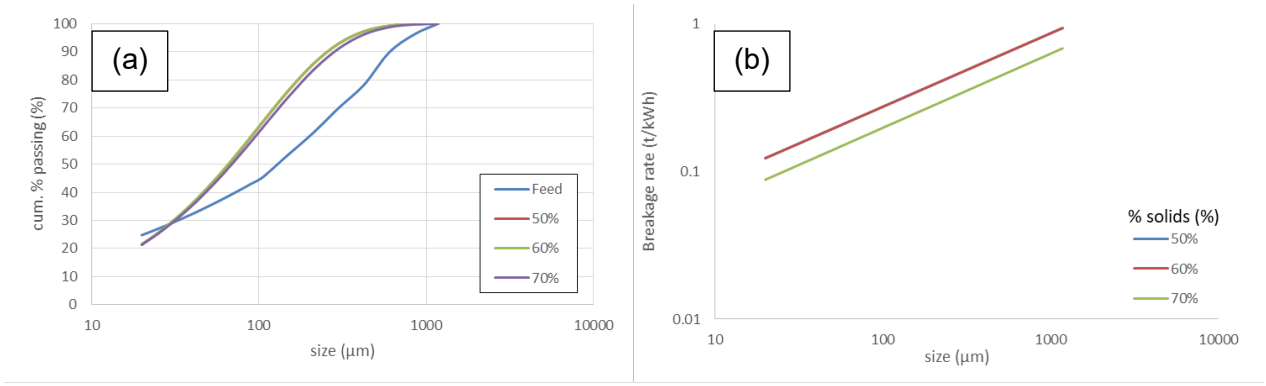

FIG 7 – (a) Particle size distribution; and (b) breakage rate at different mill content slurry density.

The pilot test work indicated that grinding media size, agitator screw rotational speed and mill content slurry density affect grinding efficiency in the TowerMill. In general, a higher screw rotational speed, and an appropriate choice of grinding media according to the feed top size and % solids around 65–68 per cent exhibits optimum grinding efficiency for the TowerMill. There is another concept, ie media stress intensity that co-relates media size, media density and tip speed. It is worth investigating as this analysis will exhibit the optimum media stress intensity to achieve the targeted grind size. The following section will use the test work data and evaluate the optimum media stress intensity required to achieve the targeted grind size.

Media stress intensity to understand the optimum grinding condition

The main particle breakage mode in the TowerMill is predominately attrition. The attrition breakage takes place at the annular region – the gap between the tip of the screw and mill shell. Equation 1 shows the grinding media stress intensity model which is a function of grinding media diameter, density, and tip speed.

$$SI_{GM} = d_{GM}^3 * \rho_{GM} * v_t^2 \quad (1)$$

where:

SI_{GM} stress intensity due to centrifugal force

d_{GM} grinding media diameter

ρ_{GM} density of grinding media

v_t agitator screw tip speed

Figure 8 shows the product particle size (P80) as a function of stress intensity. The results show that there is an optimum stress intensity value to reach the minimum product size. The stress intensity is a measure of pressure acting on the particles by the grinding media. In a typical grinding application, the media size, media density, and tip speed are fixed. For a given feed size and specific energy consumption, the stress intensity controls the product size distribution. For a given specific energy, the stress intensity can be manipulated by varying the media size, media density, and tip speed. In this work, the stress intensity of 0.8 Nm is optimum where a targeted product size of P80 150 µm was achieved. Table 7 shows that a similar stress intensity can be achieved in two different conditions. This analysis clearly shows that the screw rotational speed needs to be changed when the grinding media size is changed in the TowerMill. The recent development by using variable frequency drive type main motor is the way to move forward to achieve optimum grind size.

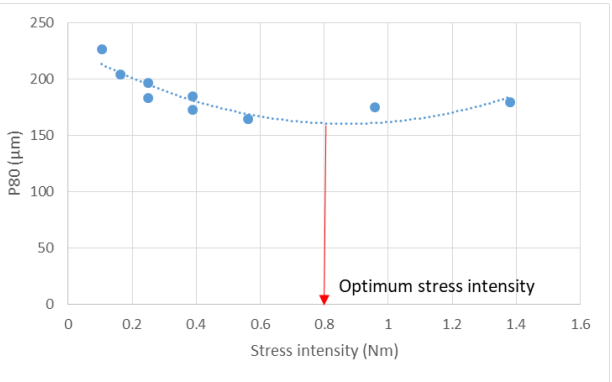

FIG 8 – P80 as a function of stress intensity.

TABLE 7

Grinding media stress intensity.

Media size (mm)	15	20
Media density (kg/m^3)	7800	7800
Tip speed (m/s)	5.5	3.6
SI (Nm)	0.80	0.81

The pilot TowerMill specific energy for the abovementioned two conditions were 14.8 and 12.1 kWh/t, calculated based on an empirical model. The difference in the specific energy was mainly contributed by the screw rotational speed. A basic calculation of carbon emission for a hypothetical feed rate of 100 t/h to reduce the particle size from 450 µm to 100 µm was done based on these two conditions. The CO_2 emissions were 8.23 and 6.73 kg/t of ground ore respectively for the 15 and 20 mm grinding media.

The pilot test work analysis has developed new knowledge in looking at the operating condition of the TowerMill. It is worth incorporating the stress intensity concept together with the operating condition such as grinding media size, and screw tip speed to identify the optimum grinding condition at lower CO_2 emission. The challenge is to scale this concept for the production scale TowerMill where the stress intensity due to gravity plays an important role.

PRODUCTION SCALE TOWERMILL ON-SITE TRIAL

The authors have carried out several trials at the site on the production scale TowerMill such as the ETM 1500 and ETM 1750. The results of such trials have been reported in several technical papers (Palaniandy *et al*, 2017, 2018, 2021). This section will discuss the effect of mill feed configurations, ball size, and screw rotational speed that was carried out in a magnetite concentrator in Western Australia and a gold concentrator in the United States. The details of these trials can be referred to in the abovementioned technical papers. Additionally, the CO_2 emission in each trial after the improvement will be calculated and compared as part of this paper.

Modification of mill feed configuration that improves grinding efficiency

A plant trial was carried out at a magnetite site in Western Australia to compare the top and bottom mill feed configuration. The trial was motivated by the changes in the circuit feed that are coarser than the design particle size as the Derrick Screen in front of the TowerMill circuit was bypassed. Initially, the circuit was designed with a top mill feed configuration. When the Derrick screen was bypassed, the top size (F99) increased from 100 µm to 1180 µm. Based on Nippon Eirich's experience, the authors recommended changing the mill feed configuration from top to bottom feed configuration. Table 8 shows the results of the site trial comparison between the top and bottom feed configuration. The Bond operating work index and the size-specific energy at 35 µm represent the grinding efficiency at coarse and fine particle sizes. Indicators showed a reduction of 30 and 50 per cent respectively. Meanwhile, the circulating load was reduced by 34 per cent. In general, the

modification from the top feed to the bottom has improved the overall grinding efficiency in the mill which requires lesser specific energy to achieve the same targeted grind size.

TABLE 8

Comparison of top and bottom mill feed configuration (Palaniandy *et al*, 2017).

Mill feed configuration	Top	Bottom
Circuit Specific energy (kWh/t)	3.0	2.9
Bond Operating work index (kWh/t)	14.2	9.90
Size specific energy at 35 µm (kWh/t)	55.0	27.6
Circulating load (%)	185	122

Improving grinding efficiency using slightly smaller grinding media

The ETM 1500 installed at the Western Australian magnetite concentrator was using 20 mm grinding media. As part of the process improvement program, one of the mills was loaded with 17 mm grinding media and its performance were compared to another mill with 20 mm grinding media. The specific energy consumption of both mills was similar during the survey. The total surface area of the 17 mm and 20 mm grinding media was 7139 and 6088 m^2 respectively. The 3 mm reduction in the grinding media size has increased the total surface area by 15 per cent. Table 9 shows the performances of the 17 and 20 mm grinding media. In general, the grindability improves by 18 per cent and 11 per cent at coarse and fine particle sizes plus a 33 per cent reduction in the circulating load. The 17 mm grinding was chosen as it can break the top particle sizes and at the same time, the increase in the surface area helps the attrition breakage. Although the smaller grinding media such as 12.7 mm will improve the fines generation through attrition, it will not have the ability to break the top particle sizes. The choice of 17 mm grinding media was a balance for efficiently breaking the top particle sizes and attrition of fine particles generation.

TABLE 9

Comparison of 17 and 20 mm grinding media (Palaniandy *et al*, 2018).

Grinding media size (mm)	20	17
Circuit Specific energy (kWh/t)	2.94	3.00
Bond Operating work index (kWh/t)	30.8	25.2
Size-specific energy at 35 µm (kWh/t)	22.6	20.2
Circulating load (%)	106	71

Reducing specific energy consumption by adjusting screw rotational speed

The ETM 1750 in a gold mine was installed with a variable frequency drive main motor that allows operating the mill at different screw rotational speeds. The targeted grind size was 25 µm. Table 10 shows the operating conditions at two different screw rotational speeds. At 100 per cent speed, the circuit product was finer than the design as the plant was receiving softer ore. This site is experiencing a high ore variability. The second survey was carried out by reducing screw rotational speed to 75 per cent that reducing the specific energy consumption by 36 per cent. As the specific energy reduces, the Bond ball mill work index and the size-specific energy reduce as well indicating improved energy utilisation for grinding to achieve the design product size. The reduction in the specific energy has increased the circulating load by 19 per cent but the value was still below 200 per cent. The ability to adjust the mill power draw by changing the screw speed is beneficial when grinding ore with high variability to achieve the targeted grind size plus optimising the operating expenditure (possible reduction in energy and wear part consumption).

TABLE 10

Comparison of specific energies by adjusting the screw rotational speed.

Screw speed (%)	100	75
Circuit Specific energy (kWh/t)	25.4	16.2
F80 (µm)	99	106
P80 (µm)	22	25
Bond Operating work index (kWh/t)	18.1	12.9
Size-specific energy at 20 µm (kWh/t)	57.2	41

Implementations that reduce water consumption and CO_2 emission

The implementation of process improvements has helped to reduce the dilution water consumption and the CO_2 emission. The reduction in the dilution water is achieved due to the reduction in circulating load and maintaining the hydrocyclone feed slurry density. Based on the process improvement implemented at the magnetite and gold concentrator, the dilution water requirement and CO_2 emission were calculated. Table 11 shows the dilution water requirement at the hydrocyclone feed sump and the CO_2 emission per tonne of ground ore. The implementation of bottom feed configuration and the use of smaller grinding media (17 mm) reduces the dilution water requirement and CO_2 emission.

TABLE 11

Reduction in water consumption and carbon emission after implementation of process improvement.

	Magnetite Concentrator			**Gold concentrator**	
Condition	Base case	Bottom Feed	Smaller media	Base case	Reduce speed
Dilution water addition (m^3/h)	702	523	529	13.9	21.2
CO_2 emission per tonne of ore ground (kg/t-of ground ore)	1.67	1.16	1.37	14.6	11.5

These analyses indicate that a small step-by-step improvement on one unit operations in the whole concentrator helps to reduce water consumption and CO_2 emission. It is important to understand the fundamentals behind the technology that helps to improve the overall process.

REDUCTION IN TOTAL COST OF OWNERSHIP

The improvement in the design and operating strategies will also reduce the overall circuit's total cost of ownership. For example, smaller units of pumps, sumps, hydrocyclone, foundations, and electrical items are required. These items can contribute towards lower capital expenditure hence also reducing operating expenditure through lower energy, water, grinding media, and liner consumption for future circuit design.

A total cost of ownership analysis was carried out using the data from the above-mentioned magnetite concentrator. This analysis includes capital expenditures (equipment prices, foundation, and installation costs) and operating expenditures (power, grinding media, screw liner, and maintenance costs). An internal rate of return and price escalation of 8 per cent and 4 per cent were taken into consideration in this analysis. The operational data was used to select the equipment model as shown in Table 12. In general, the pump, and hydrocyclone cluster became smaller for the optimised condition.

TABLE 12

Equipment model selection for the base case and optimised condition.

Condition	Base case	Optimised
No of 15' hydrocyclone in the cluster	12	10
Hydrocyclone feed pump model	14 × 12	12 × 10

The difference in the capital expenditure is around A$0.4 million but there is a huge difference in terms of operating expenditure. The difference in net present value operating expenditure for fifteen years of operation is approximately A$13 million and offers a shorter payback period of six months. The cost per tonne calculated based on 15 years of productivity is A$1.19 and A$0.87 for the base case and optimised scenarios respectively. This is a significant difference between these two conditions with a 27 per cent difference. This analysis shows that improvement in the design and operation of the TowerMill circuit has a significant contribution to the total cost of ownership of the circuit.

CONCLUSIONS

The EIRICH TowerMill technology has been used in the mineral processing concentrators since the 1980s for regrind duty. For the last 10–15 years, this technology has been used to partially replace the ball mill in secondary and tertiary grinding duties. The TowerMill circuit consumes lesser energy/water and emits less CO_2 compared to the ball mill circuit for all the above-mentioned grinding duties. Although this technology is mature and well accepted in the mining industry, there are opportunities for improvement in terms of design and operating strategies when processing challenging ores. Implementation of new design concepts and optimising operating conditions such as mill feed configurations, application of coarse classifiers in a coarse grinding application, agitator screw rotational speed, media size, and mill content slurry density improved the overall grinding efficiency. The media stress intensity concept helps to evaluate the best combinations of circuit operating conditions to achieve the target efficiently – low energy and water consumption and lower CO_2 emission. The CO_2 emission can be implemented as one of the mill operators' key performance indicators (KPI). This paper has shown the importance of continuous design improvement and operating strategies that reduced the specific energy/water consumption and CO_2 emission by 20–30 per cent. Nippon Eirich is committed to achieving this goal.

ACKNOWLEDGEMENTS

The authors acknowledge and thank Nippon Eirich Co. Ltd for approving this paper to be published.

REFERENCES

Morrell, S, 2022. Helping to reduce mining industry carbon emissions: A step-by-step guide to sizing and selection of energy-efficient high pressure grinding rolls circuits. *Minerals Engineering*. 179. 107431.

Palaniandy, S, Carr, D, Johns, J and Williams, N, 2021. Installation, commissioning, operation and performance review of TowerMill at OceanaGold Haile Gold Mine, South Carolina. *Proceedings of AUSIMM Mill Operators' Conference 2021* (The Australasian Institute of Mining and Metallurgy: Melbourne).

Palaniandy, S, Halomoan, R and Ishikawa, H, 2018. Shifting the comminution workload from the primary ball mill to TowerMill circuit. *Proceedings of 14th AUSIMM Mill Operators' Conference 2018* (The Australasian Institute of Mining and Metallurgy: Melbourne).

Palaniandy, S, Spagnolo, M, Halomoan, R, Zhou, H and Ishikawa, H, 2017. Fine grinding circuit process improvement at the Karara Mine concentrator. *Proceedings of Metallurgical Plant Design and Operating Strategies – Worlds Best practice (MetPlant 2017)*. pp 101–120 (The Australasian Institute of Mining and Metallurgy: Melbourne).

An attempt to a full energy balance for a pilot-scale stirred media mill

B I Pålsson[1], M Parian[2], S Larsson[3] and P Jonsén[4]

1. Senior Lecturer, Minerals and Metallurgical Engineering, Luleå University of Technology, Luleå SE-97187, Sweden. Email: Bertil.Palsson@ltu.se
2. Associate Professor, Minerals and Metallurgical Engineering, Luleå University of Technology, Luleå SE-97187, Sweden. Email: Mehdi.Parian@ltu.se
3. Associate Lecturer, Division of Solid Mechanics, Luleå University of Technology, Luleå SE-97187, Sweden. Email: Simon.Larsson@ltu.se
4. Professor, Division of Solid Mechanics, Luleå University of Technology, Luleå SE-97187, Sweden. Email: Par.Jonsen@ltu.se

ABSTRACT

The question of effective energy utilisation in grinding mills is not new. There are several conflicting arguments about tumbling mills, whether the efficiency is around 1 per cent or maybe 10 per cent, or even much lower. The energy not used is assumed to be lost as heating of the pulp, the grinding mill body, the charge, generation of shock waves and vibrations, etc. Stirred media mills on the other hand are generally considered to have better energy utilisation, but their energy efficiency is still not that clear. To shed some light on this a pilot-scale, wet stirred media mill was investigated over a range of operating conditions.

The wet stirred media mill is a Drais PMH 5 TEX pearl mill fitted with an electric motor at 11 kW. It has been investigated over a range of operating conditions to try to balance the dissemination of the input energy in forms of the net grinding energy, mechanical energy losses, and the heating transferred to the pulp, the mill, the charge, and the cooling water.

It is found that approximately 20–40 per cent of the input energy accounts for the grinding process. Also, that the difference between gross and net input electrical energy is mainly disseminated as heating of the pulp and cooling water. Mechanical energy losses appear to be much smaller than the heating effects. The use of a dispersant seems to mainly influence the heating effect.

INTRODUCTION

The question of effective energy utilisation in grinding mills is not new. There are several conflicting arguments about tumbling mills, whether the efficiency is around 1 per cent or maybe 10 per cent, or even much lower (Wills and Finch, 2016). They cite Lowrinson (1974), who calculated the efficiency as 1 per cent by multiplying the created increase in surface area by the surface tension of the material ground. Fuerstenau and Abuzeid (2002) on the other hand, arrived at an efficiency of 15 per cent for ball mill grinding of quartz.

The energy not used for particle breakage is assumed to be lost as heating of pulp, the grinding mill body and charge as well as elastic deformation of particles and initial creation of micro-cracks (Wills and Finch, 2016).

Stirred media mills are generally considered to have better energy utilisation than ball mills (Shi *et al*, 2009). However, their energy efficiency is still not that clear. To shed some light on this a pilot-scale, wet stirred media mill was investigated over a range of operating conditions.

EXPERIMENTAL

The wet stirred media mill is a Drais PMH 5 TEX pearl mill fitted with an electric motor at 11 kW. It has a horizontal design, a double-walled water-cooled grinding chamber with an inner diameter of 149 mm and a length of 415 mm. A central shaft with discs is used to rotate the grinding charge. The mill is described in more detail in Gao and Forssberg (1992, 1993) and the current experimental set-up in Larsson *et al* (2020).

It has been used in several investigations on grinding of mineral fillers and mineral coatings. Basic parameter studies were presented already in 1992 and 1993 by Gao and Forssberg. The influence of rheology effects were reported for quartzite (He and Forssberg, 2007a) and limestone (He and

Forssberg, 2007b). Recently, the whole mill was simulated in a new approach with the particle finite element method (Larsson *et al,* 2020). During the latter investigation, the idea that it might be possible to also use the mill for a primitive energy balance emerged.

Testing

The test material is a commercial dolomite filler (myanite 0–70) from Björka Mineral AB in Sweden. The solid density is measured to be 2.87 g/cm³ with a helium pycnometer (micromeritics Accupyc II 1340). For every test, a sack with 25 kg dolomite filler was used. While stirring, it was slowly emptied into a 50 L plastic bucket prefilled with the amount of water required for each test. The resulting slurry was kept in suspension with a mechanical stirrer driven by a compressed air motor.

Tests were conducted at three suspension concentrations: 60, 65 and 70 weight% solids. To the feed pulp at 65 and 70 weight% a liquid dispersant, Dispex® AA 4140 from BASF was added. This dispersant is a solution of a sodium salt of an acrylic polymer in water. It was added at 0.5 per cent of the solids mass in a test ie approximately 125 g. For each suspension concentration, two separate tests were run at approximately feed rates 1 and 2 L/min respectively. A test run was started with the preparation of the suspension, it was then pumped (Pass 1) through the mill into another, receiving 50 L bucket until the feed bucket was nearly empty. Thereafter, the receiving bucket became the new feed bucket, and the suspension was pumped back (Pass 2) into the now cleaned first bucket. Samples for particle size measurements were collected in 0.5 L plastic bottles: from the first feed bucket and from the mill discharge pipe close to the end of each pass. Particle size distributions were obtained by wet laser diffraction (Cilas 1064), *cf* Figure 1.

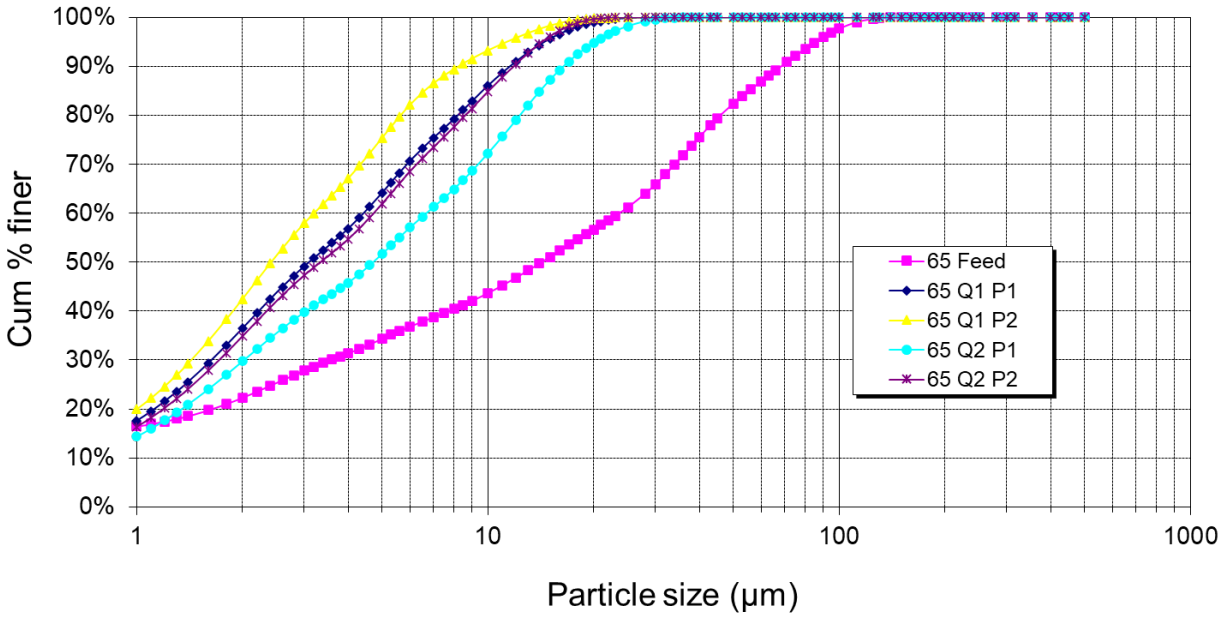

FIG 1 – Particle size distribution for test with 65 weight% solids. Q1 1 lpm, Q2 2 lpm, P1 Pass 1, P2 Pass 2.

Temperatures of pulp and cooling water, as well as the cooling water flow was manually measured at intervals throughout each pass. For temperature, a digital contact thermometer was held in the pulp flow and cooling water flow until a stable reading was obtained. Cooling water flow and pulp flow were estimated by taking the time to fill a 1 L graded beaker. An example of temperature measurements is in Figure 2.

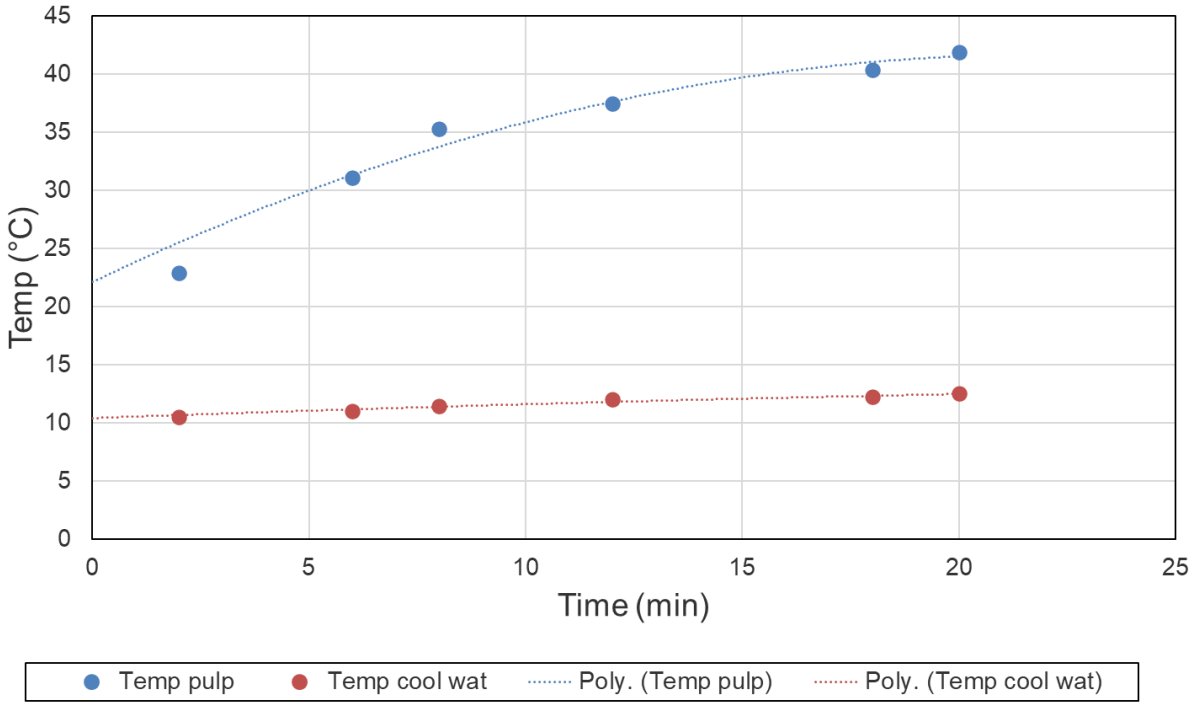

FIG 2 – Temperature curves for test with 65 weight% solids. Dotted lines for second order polynomial fits.

Traditional grinding parameters

The mill is investigated in two ways: firstly, the traditional approach with measurement of supplied electrical energy resulting in a decrease of particle size, and from this, several grinding efficiency indices may be calculated; secondly by comparing the supplied electrical energy to the heating of pulp and cooling water, and then an estimate of energy efficiency can be obtained.

The active power was measured by an energy metre (Micro VIP from ELCONTROL). It was found that the mill idling power with water in the mill was approximately 3 kW, and the working power varying between 4 and 5 kW. Knowing input power, feed rate, dilution ratio, and pulp density, it is possible to calculate the amount of net energy spent per mass unit of solid feed. Here, the mechanical efficiency is taken as the quotient between net and gross power. The size reductions were estimated from the particle size distributions (Figure 1), and then an apparent Bond work index, and grindabilities (kg <size/kWh net energy) could be calculated. An example for a test with 65 weight% solids and 1 L/min feed rate is shown in Table 1.

TABLE 1

Compilation of grinding data for test with 65 weight% solids, feed rate 1 L/min.

Dolomite filler 0–70 µm	Feed	Pass 1	Pass 2
Amount of material [kg]		25.08	25.08
Pulp feed rate [lpm]		1.04	1.05
Pulp wt-% solids		65.08%	65.08%
Dilution ratio		0.54	0.54
Solids flow [kg/s]		0.020	0.020
Gross power [kW]		4.5	4.0
Idling power [kW]		3.1	3.2
Mechanical efficiency [%]		31.1%	20.0%
Net power [kW]		1.4	0.8
Specific net energy in each step [kWs/kg]		71.48	40.46
Specific net energy in each step [kWh/tonne]		19.86	11.24
Cumulative specific net energy [kWh/tonne]	0.00	19.86	31.09
d_{80} [µm]	45.0	8.5	5.6
< 20 µm [%]	56.68	98.97	99.84
< 10 µm [%]	43.71	86.05	93.25
< 5 µm [%]	34.36	64.20	75.42
Grindability [kg <10 µm/kWh_{net}]		21.3	6.4
Av. Grindability [kg <10 µm/kWh_{net}]		21.3	15.9
Grindability [kg <5 µm/kWh_{net}]		15.0	10.0
Av. Grindability [kg <5 µm/kWh_{net}]		15.0	13.2
Apparent BWI [kWh/tonne]		10.24	14.12
Average app. BWI [kWh/tonne]		10.24	11.37

Energy parameters

Knowing the gross and net power of the mill in combination with the heating of the pulp and the cooling water allows for doing a rough energy balance for the mill under the following assumptions:

- Net energy comes from the difference between working and idling power, and that the calculations are done per second.
- Temperatures at the end of a run have approximately reached steady state. This is seen in Figure 2.
- Heating of internal parts at the end of a run are at steady state, and then the heat capacity and heating of these parts may be neglected in the calculations.

The results for a test with 65 weight% solids, and pulp flow 1 L/min are presented in Table 2. In most tests, the net energy for the second pass is lower than in the first. This is interpreted as a grinding limit effect that the smaller particle size makes for less efficient grinding. This is also supported by the fact that the heating of the pulp is larger in the first step. To calculate the heating of pulp the specific heats for limestone 0.84 kJ/kg·K and water 4.18 kJ/kg·K are used in combination with the respective flows of solids and water. In the same way, the heating of the cooling water comes from the knowledge of temperature increase and water flow. These three heating values taken together

become the sum of heating, or loss of energy to heating. It is interesting to note that sum of heating is approximately 2/3 of the idling energy.

TABLE 2

Energy values for test with 65 weight% solids, and flow 1 L/min.

Pass	**Gross power (kW)**	**Gross energy (Ws) or (J)**	**Net power (kW)**	**Net energy (J)**	**Idling energy (J)**		
P1	4.5	4500	1.4	1400	3100		
P2	4	4000	0.8	800	3200		
Pass	**Pulp flow (lpm)**	**Solids (kg/s)**	**ΔT_{solids} (K)**	**$Heating_{solids}$ (J)**	**Water (kg/s)**	**ΔT_{water} (K)**	**$Heating_{water}$ (J)**
P1	1.04	0.02	19.8	332.64	0.011	19.8	910.40
P2	1.05	0.02	10.2	171.36	0.011	10.2	469.00
Pass	**Cooling (lpm)**	**Cooling (kg/s)**	**$\Delta T_{cooling}$ (K)**	**$Heating_{cooling}$ (J)**	**Sum of heating (J)**		
P1	5.56	0.093	2.1	813.43	2056.47		
P2	5.56	0.093	3.6	1394.45	2034.80		

RESULTS AND DISCUSSION

A summary of all the results is presented in Table 3. In the left part of the table are the traditional grinding efficiencies: grindability at 5 and 10 μm, and the apparent Bond Work Index. Grindability is a fair indicator of overall grinding efficiency since it connects a grinding result fineness with a measured energy input. The Bond Work Index is included for comparison since it is an industry standard, but it is hardly applicable in this low particle size range. In the present case, the net energy is the active energy as measured with an energy metre, and with the idling energy deducted. In this way, it is found that approximately 20–40 per cent of the input gross energy is used for the grinding process, and this is in fair agreement with the data found by Shi *et al* (2009). It does not say, however, that this is the real energy used for breaking the particles since the energy connected to the elastic deformation of particles and creation of micro-cracks cannot be distinguished. Therefore, the net energy and grinding efficiencies presented here are practical limits that can be had in full-scale operations.

The idling energy, the difference between gross and net input electrical energy, is always larger than the calculated heating of the pulp and the cooling water. The difference between them, is energy not measurable in the experimental set-up. However, it may be assumed that this is mainly mechanical energy losses in the transmission.

The table also reveals that most of the grinding takes place during the first pass through the mill, as can be seen from the grindability values. There is no clear effect of the use of a dispersant on the grindability, but the measured heating is lower if a dispersant is added to the pulp. However, this cannot in this experimental set-up be separated from the effect of increasing the solids concentration.

For the two lower solids concentrations, there is a patten that the higher flow rate (Q = 2 L/min) gives a better grinding efficiency. This seems not to be true for the highest solids concentration (70 weight% solids) that corresponds to 44.3–44.9 volume% solids. The grinding efficiency in this case is generally worse, especially at the high flow rate. At the same time, the heating is lower. A likely interpretation is that what is seen is a flow resistance effect, due to the high volumetric solids concentration. A possible explanation is that the charge is mostly rotated as a viscous body inside the mill, without the free movement of grinding bodies. The free movement and rotation of grinding balls is a necessity for attrition grinding. It should also be noted that the measured idling energy is lower at the highest flow rate, and this might indicate an experimental error. This also results in apparent, but not likely, better usage of energy for the highest solids concentration and flow rate.

TABLE 3

Summary of grinding and energy efficiencies.

Grinding				Energy					
Identity	Grindability		App BWI	Gross energy	Net energy	Idling energy	Heating	Dispers.	Used for grind.
	(kg <10 µm/ kWh)	(kg <5 µm/ kWh)	(kWh/ton)	(J)	(J)	(J)	(J)	(% of solids)	
60Q1P1	18.4	13.8	11.32	4200	1200	3000	2847	0	29%
60Q1P2	6.9	11.3	14.39	4000	1000	3000	2883	0	25%
60Q2P1	34.4	17.5	6.38	4100	800	3300	2596	0	20%
60Q2P2	17.5	18	8.89	4200	900	3300	2181	0	21%
65Q1P1	21.3	15	10.24	4500	1400	3100	2056	0.51%	31%
65Q1P2	6.4	10	14.12	4000	800	3200	2035	0.51%	20%
65Q2P1	28.2	17.2	7.44	4400	1300	3100	2277	0.50%	30%
65Q2P2	15.1	12.3	14.42	4200	1100	3100	1506	0.50%	26%
70Q1P1	19	13.2	11.48	5000	1900	3100	2611	0.50%	38%
70Q1P2	10.6	15.3	10.72	4000	800	3200	1939	0.50%	20%
70Q2P1	*12*	*8*	*18.48*	*5200*	*2400*	*2800*	*1930*	*0.50%*	*46%*
70Q2P2	*8.4*	*7.3*	*24.07*	*4400*	*2000*	*2400*	*1397*	*0.50%*	*45%*

The relationships between the different energies are also described in Figure 3 with the example of the runs with 65 weight% solids and flow rate 1 L/min. Here, the gross energies are set as 100 per cent, and the others as part of this. The net energy, defined as the difference between the supplied gross energy and the idling energy, is in this case between 20 and 30 per cent. The idling energy may be split between the energy related to heating of pulp and cooling water, and a difference that is here called Idling-Heating (Idling minus Heating). This energy difference probably mostly contains mechanical losses, but also any heating of the gearbox and motor.

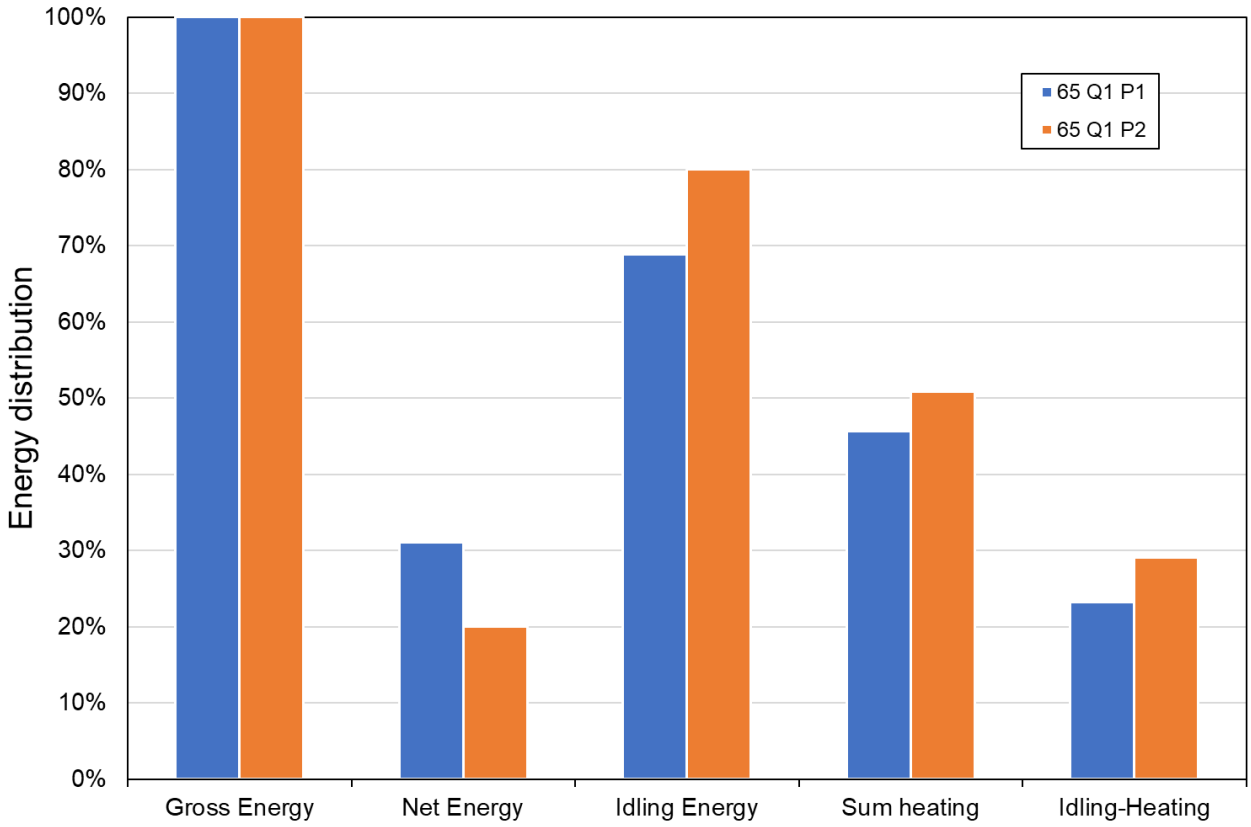

FIG 3 – Energy distributions in test with 65 weight% solids, and pulp flow 1 L/min.

CONCLUSIONS

The actual useful grinding energy is the estimated net energy, and this accounts for 20-40 per cent of the applied electrical energy to the stirred media mill. This is far more than what was estimated by Lowrinson (1974), but slightly higher than found by Fuerstenau and Abouzeid (2002), who worked with ball mill grinding. This is a reasonable difference since stirred media grinding is normally assumed to be more efficient than ball mill grinding.

It is not certain that the net energy is the effective energy for size reduction since it is not known to what extent any elastic effects in the deformation of the solids are accounted for. However, it is the most effective measure from an industrial perspective.

Any estimation of an approximate grinding energy balance should be simple even on an industrial scale:

- Run the mill with no feed to get an estimate of the idling power, and then measure the power draw with normal feed rate. This will work for stirred media mills, but maybe not for tumbling mills since a low feed rate will move the charge centre of gravity outwards.
- Measure the temperature difference between feed pulp and discharge pulp at steady-state operation to calculate the heating energy.

Heating of pulp and cooling water accounts for most of the idling energy, the rest is mechanical losses and heating in motor and gearbox that are not caught by the experimental set-up.

The addition of a dispersant seems not to directly affect the net grinding efficiency but lowers the losses to heating. Thus, a dispersant is indirectly beneficial.

ACKNOWLEDGEMENTS

The work presented here was done within the Vinnova project 2017–05463, ‘Stirred media mill performance and grinding wear prediction’.

REFERENCES

Fuerstenau, D W, Abouzeid, A-Z M, 2002. The energy efficiency of ball milling in comminution. *Int. J. Miner. Process.* 67:161–185.

Gao, M W and Forssberg, E, 1992. Increasing the specific surface area of dolomite by stirred ball milling, in: *Comminution–Theory and Practice*, (ed: S Komar Kawatra), pp. 153–170 (Society for Mining, Metallurgy and Exploration: Littleton, CO, USA).

Gao, M W and Forssberg, E, 1993. A study on the effect of parameters in stirred ball milling. *Int. J. Miner. Process.* 37:45–59.

He, M and Forssberg, E, 2007a. Influence of slurry rheology on stirred media milling of quartzite. *Int. J. Miner. Process.* 84:240–251.

He, M and Forssberg, E, 2007b. Rheological behaviors in wet ultrafine grinding of limestone. *Minerals and Metallurgical Processing*, 24(1):19–29.

Larsson, S, Pålsson, B I, Parian, M and Jonsén, P, 2020. A novel approach for modelling of physical interactions between slurry, grinding media and mill structure in wet stirred media mills. *Minerals Engineering*, 148:1–11.

Lowrinson, G C, 1974. Crushing and grinding: the size reduction of solid materials. CRC Press.

Shi, F, Morrison, R, Cervellin, A, Burns, F, and Musa, F, 2009. Comparison of energy efficiency between ball mills and stirred mills in coarse grinding. *Minerals Engineering*, 22:673–680.

Wills, B A and Finch, J A, 2016. Chapter 5.4 Comminution efficiency, *Wills' mineral processing technology: an introduction to the practical aspects of ore treatment and mineral recovery*. Butterworth-Heinemann.

XCT investigation on the generation of fatigue in autogenous grinding pebbles and its contribution to pre-weakening before fracture

M Parian[1], B I Pålsson[2] and J Kuva[3]

1. Associate professor, Minerals and Metallurgical Engineering, Luleå University of Technology, Luleå SE-97187, Sweden. Email: mehdi.parian@ltu.se
2. Senior lecturer, Minerals and Metallurgical Engineering, Luleå University of Technology, Luleå SE-97187, Sweden. Email: bertil.palsson@ltu.se
3. Senior scientist, Geological survey of Finland, PO Box 96, Espoo, FI-02151, Finland. Email: jukka.kuva@gtk.fi

ABSTRACT

One of the main factors affecting the suitability of an ore for autogenous grinding is the ore's competency, ie providing enough critical stones for the grinding process. Several experimental test routines exist and are used for assessing the viability of the ore for autogenous grinding. However, very little attention is given to the generation of fatigue in large stones experiencing repeated shocks in the mill. To investigate this, large pebbles sampled from an industrial autogenous grinding mill running hard and soft ores were categorised based on the grinding energy.

From the pebbles, small drill core samples were prepared and went through a series of fatigue cycle tests. Both hard and soft ores showed similar average resistance to failure in compression tests, but the hard ore had a consistent resistance with lower variations. The cores were scanned by XCT before and in-between fatigue tests at the highest reachable resolution, 1.5 µm voxel size. The outcome showed that a higher number of micro-cracks were visible in the soft ore compared to the hard ore. The frequency of micro-crack development in the soft ore may be the reason for its lower specific grinding energy compared to the hard ore.

It is obvious that for realistic conditions in an autogenous grinding mill, stones are pre-weakened by fatigue before they fracture. Therefore, shortcut methods focusing only on running tests on fresh and small samples may operate in unrealistic conditions by ignoring the fatigue phenomenon. This is even more important for ores that are on the borderline to be considered as competent for autogenous milling.

INTRODUCTION

Comminution is the process for liberation and size reduction of ores prior to separation processes. Generally, in mineral processing, grinding is done using rod, ball, autogenous, or semi-autogenous mills. Fully autogenous grinding (AG) is the most cost- and process-efficient grinding, benefiting from eliminating steel grinding media. It is also a superior choice for downstream processes such as flotation, since some sulfide minerals are sensitive to the reducing conditions caused by iron chipped away from the steel media.

The dominant loadings on particles in autogenous mills are impact and attrition. Successful impact of large stones on particles directly relates to an ore's competency and hardness. On the other hand, fines generation in the mill is often related to abrasion resistance of the ore. During mill tumbling, the large stones self-break after some cycles and generate smaller and sometimes critical stones. The motion of the charge and sliding of the particles inside the mill leads to abrasion breakage. This is known for quite some time and applied also for developing empirical and mathematical models for AG mills (Stanley, 1974).

The general idea of designed tests for autogenous grinding originated from how the breakage may occur inside the mill. This is principally divided into impact and attrition tests also known as low and high energy breakage (grinding) tests. Many small-scale test methods were developed and used over the years for AG milling design and estimating the ore response to AG grinding. These include, for example, the Macpherson test (Macpherson, 1977), Bond work indices (Barratt and Allan, 1986), the Drop Weight Test (Lynch, 2015), the SAG Power Index (Starkey and Dobby, 1996), the SAGDesign test (Starkey, Hindstrom and Nadasdy, 2006), the SAG Variability Test, Advanced

Media Competency Testing (Mcken and Williams, 2006), the Hardness Index Tester (Bergeron *et al*, 2017) and a couple of other instrumented tests based on similar principles.

A large number of small-scale test methods ignore realistic mill conditions corresponding to the generation of fatigue in stones during grinding cycles. The current study presents an experimental procedure and results from fatigue tests on two samples, corresponding to two ores described as soft and hard ores. The generation and growth of micro-cracks during fatigue cycles contribute to weakening the stones prior to breakage, therefore, X-ray computed tomography (XCT) scanning with the highest resolution was used to observe these phenomena (Parapari *et al*, 2020).

EXPERIMENTAL WORK

The experimental part is focused on investigating the generation of fatigue in large stones (coarse fraction of the AG mill feed) that happens under realistic mill conditions. Fatigue, the accumulated stress in stones, makes them more prone to fracture. It is believed that the generation of micro-cracks (in size of microns) and their growth during loading cycles are the main contributors to this phenomenon. Therefore, XCT scanning at best resolution (1–2 µm) may potentially reveal the frequency of micro-cracks in the micron range. As high resolution XCT scanning works best on extremely small samples, drill cores with dimension of ϕ4.5 × 7.0 mm were produced. To perform loading on such a small drill core, a special sample holder was designed and manufactured. Loading on the samples was done at the Geological Survey of Finland (GTK) and followed by XCT scanning at their facilities.

Samples and sample preparation

The samples for the experimental work were received from Boliden Mineral AB. The samples named soft and hard ores were the <100 mm fractions of the ores. The specific grinding energy required for the soft and hard ore was 17 and 9 kWh/t respectively in an autogenous grinding circuit in the plant. To evaluate the fatigue of large stones in AG grinding, a coarse fraction from both ore types was selected for preparing small drill cores. The samples were washed and cut into 2 cm slices (Figure 1), drilled using a diamond bit, and trimmed to obtain ϕ4.5 × 7.0 mm drill cores.

FIG 1 – Sliced large stones for preparation of small drill cores.

Instrumental set-up for failure and fatigue tests

To generate fatigue in the cores, a special sample holder for conducting the Brazilian loading test (Bieniawski and Hawkes, 1978) was designed and manufactured at the workshop of Luleå University of Technology. The sample holder outer dimension was set to match the dimensions of the loading machine (Figure 2) and the inner gap matched the cores of diameter 4–8 mm.

The Deben CT5999 Tec unit at GTK was used for the compression tests. The device can deliver up to 5000 N loading. For the experiments, a 0.1 mm/min displacement rate was selected as the ore material is brittle and generally has very low elastic behaviour.

FIG 2 – Deben CT5000 TEC unit at GTK used for compression tests. The Brazilian loading test apparatus is on top of the loading cell.

Failure tests

Before starting the fatigue tests, it is important to know the range of resistance that the ores may have to avoid breaking the cores too early. Therefore, to find the range of failure points for both ores, ten failure tests were performed on each ore type. The test procedure for all the test runs was identical.

In general, both ore types had similar average failure points of around 433–435 N (Table 1). However, the soft ore showed larger variability (Standard deviation 114 compared to 73) and is often accompanied by initial breakage (or chipping) before breakage. The minimum and maximum resistances for the hard ore were 303 N and 570 N and for the soft ore were 284 N and 673 N. In general, the hard ore showed more consistent resistance to compression load.

TABLE 1

Failure points for hard and soft ores and the average values.

Sample	Hard ore	Soft ore
	Failure load [N]	Failure load [N]
1	303	542
2	410	673
3	570	485
4	366	323
5	501	409
6	459	431
7	438	284
8	447	338
9	395	402
10	464	445
Average	435	433
Standard deviation	73	114

Fatigue tests

To ensure that the samples will not break prematurely during fatigue test experiments, a safe loading force, 200 N, and 0.1 mm/min displacement rate was used for the first cycle of fatigue tests. For the

second stage of fatigue tests, the load was increased to 300 N with a 0.1 mm/min displacement rate. Each fatigue stage consists of ten loadings and ten releases of the force at a 0.1 mm/min displacement rate (Table 2). During running the first and second fatigue stages none of the cores broke. The cores were saved for XCT analysis and new cores were selected for higher load tests. For the new cores, the fatigue test run was ten cycles of 400 N loading at 0.1 mm/min displacement rate. Therefore, the first set of samples went through the first two stages of fatigue runs (in Table 3, A1 and B1 samples) and the second set of samples underwent only the third stage of fatigue runs (Table 3, A2 and B2 samples).

TABLE 2

Fatigue test stages on each ore type core.

Stage	Sample state	Fatigue test condition
0	no fatigue	No cyclic load
1	1st fatigue run	10 cycles at 200 N
2	2nd fatigue run	10 cycles at 300 N
3	3rd fatigue run	10 cycles at 400 N

TABLE 3

XCT scans on samples using the microfocus tube.

Scan	Core	Ore type	Fatigue state
1	A1	Hard	No fatigue
2	A1	Hard	10 cycles at 200 N
3	A1	Hard	10 cycles at 200 N and 10 cycles at 300 N
4	A2	Hard	10 cycles at 400 N
5	B1	Soft	No fatigue
6	B1	Soft	10 cycles at 200 N
7	B1	Soft	10 cycles at 200 N and 10 cycles at 300 N
8	B2	Soft	10 cycles at 400 N

At 400 N loading, the hard ore remained completely intact once in three different core repetitions. Other tests had some chipping and failure before the end of the ten cycles. At the same load, the soft ore broke all the time before the end of the cycles. In one of the test runs, the sample (B2) broke without catastrophic failure.

XCT Scanning

In total, eight XCT scans were conducted on the samples according to Table 3. The samples were scanned using the 180 kV microfocus tube in focus mode 2 with an accelerating voltage of 100 kV and a tube current of 260 µA, for a total tube power of 26 W. No beam filter was used. There were 2700 angle steps, and at each angle, the camera first waited for a single exposure time and then took an average of over three exposures. The single exposure time was 2000 ms for a total imaging time of 6 hours per sample. The voxel resolution was 1.53 µm in the final images.

RESULTS AND DISCUSSIONS

The reconstructed volume from the XCT images has shown many micro-cracks in both the hard and soft ore samples even before the fatigue tests. The micro-cracks in XCT slices are visible as dark spots or hair shapes depending on the orientation of the cracks in the images (Figures 3 and 4).

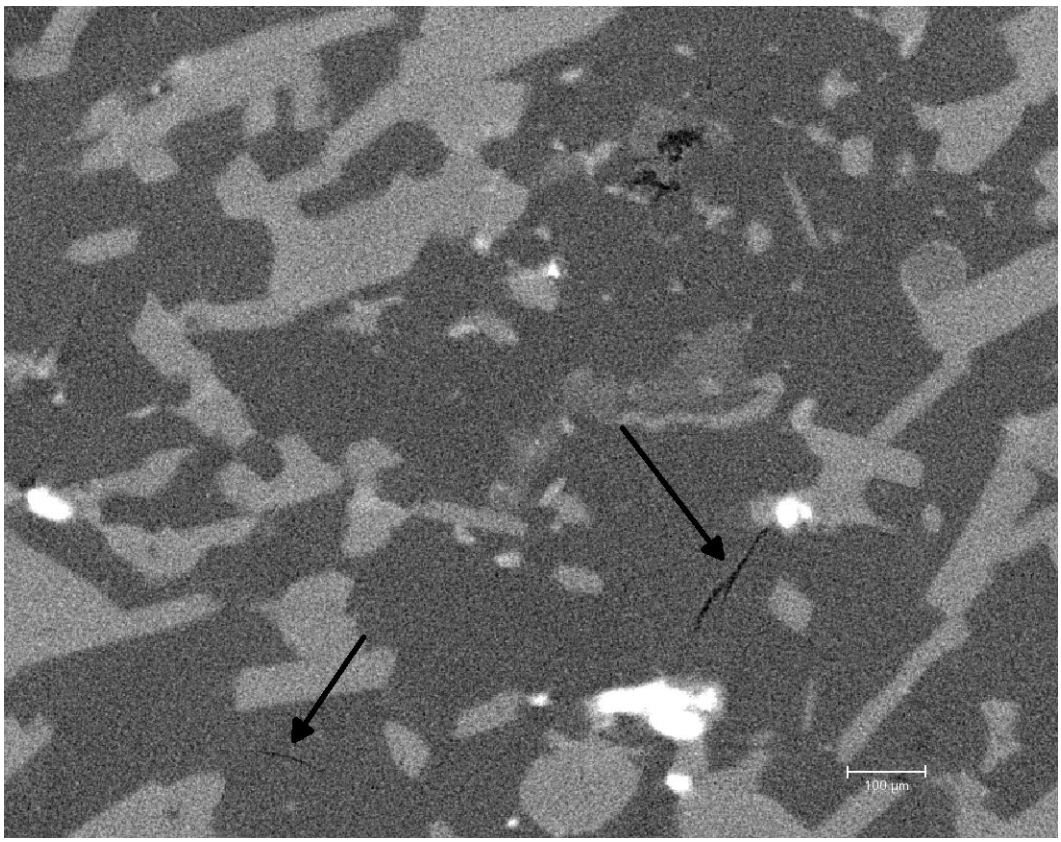

FIG 3 – A slice image of reconstructed volume of drill core A1, hard ore, after the second stage (10 × 200 N and 10 × 300 N cycles) fatigue loading. Dark spots and hair shapes are micro-cracks with different orientations.

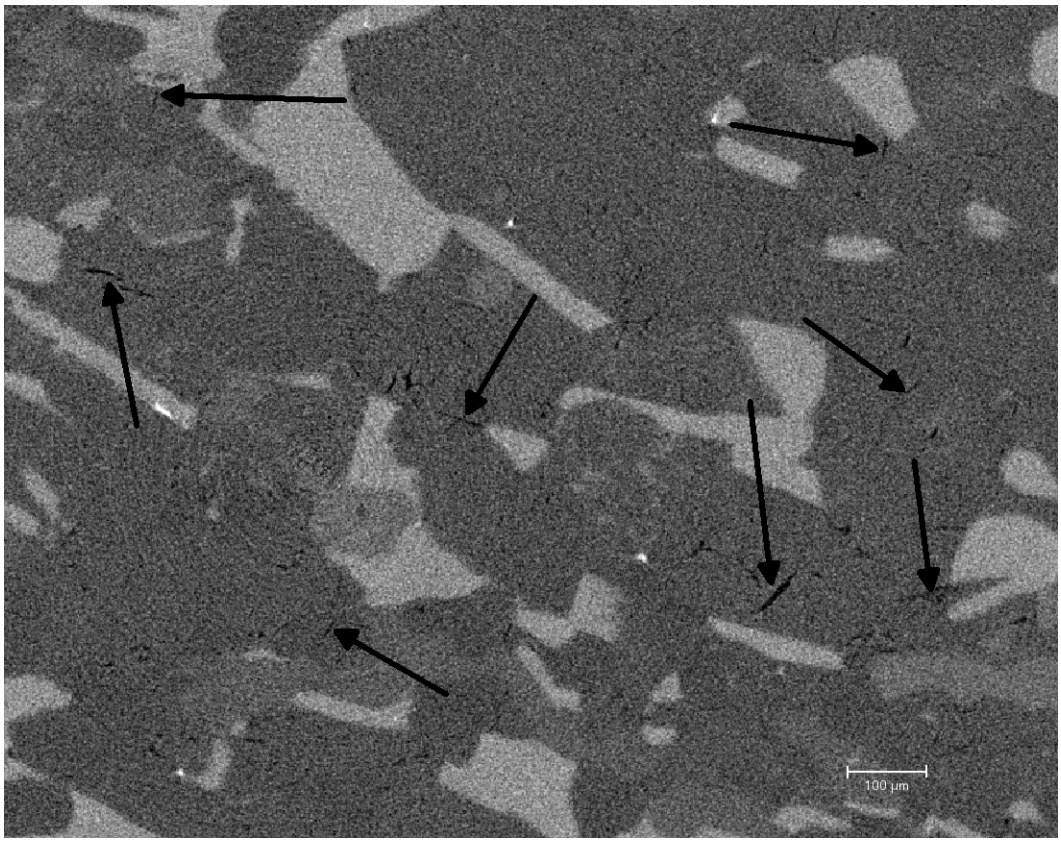

FIG 4 – A slice image of reconstructed volume of drill core B1, soft ore, after the second stage (10 × 200 N and 10 × 300 N cycles) fatigue loading. Dark spots and hair shapes are micro-cracks with different orientations.

After the first stage of the fatigue tests on both samples, the number of micro-cracks in the soft ore increased, however, no apparent increase of micro-cracks was visible in the hard ore. A similar pattern was seen after the second stage of fatigue tests.

The fatigue test at 400 N loading on hard ore (A2) did not result in any fractures visible in the XCT images. But in the process of investigating the images, holes and void volumes were found accumulated in some regions of the samples. Theoretically, they are weak spots for growing cracks, but apparently the 400 N loading cycles were not enough to generate fracture. The soft ore (B2) partially fractured during the 400 N loading cycle tests, but the sample as a whole stayed together and resisted the ten cycles.

In the soft ore, the progressive increase of micro-cracks after each fatigue test and eventually fracturing in the higher load indicate that the critical stones are likely consumed faster compared to the hard ore. This is also reflected in the specific grinding energy of each ore type where they correlate well with the frequency of micro-cracks observed in each ore. To further investigate this, conducting single breakage tests on intact and fatigue-induced samples may give some insights on the magnitude of the pre-weakening effect of fatigue.

In term of crack size, the soft ore has longer visible cracks. It is worthwhile to note that, to view the true size and length of micro-cracks, it is best to be observed under loading when cracks are opened due to tensile stress. However, for such a small sample with loading apparatus close to the objective, this was not achievable.

The XCT scanning of the ore at this resolution (1.53 µm) is providing a lot of details about micro-structure of the rock including cracks. However, this comes with limitation on the sample size and quality of the images. The sample must be in a size of a few millimetres and the results often accompanied by artifacts and irregularities in illumination of image slices. The later makes it difficult to extract volume information digitally. Therefore, the data evaluation in this case was only done qualitatively by comparing two distinctive ores namely the soft and hard ores.

CONCLUSIONS

Two samples corresponding to soft and hard ore according to grinding energy were used to evaluate their behaviour in response to fatigue. Both samples showed relatively similar average resistance to failure in Brazilian compression tests, however, the hard ore had a consistent resistance with lower variations. The soft ore often displayed initial chipping before reaching failure. XCT scans of the cores after each stage of fatigue cycles showed that more micro-cracks were visible in the soft ore compared to the hard ore. The frequency of micro-cracks development in the soft ore may be the reason that it requires lower grinding energy compared to the hard ore.

It is obvious that for realistic conditions in an AG mill, stones are pre-weakened by fatigue before fracture. Therefore, the shortcut methods focusing only on running tests on fresh and small samples may operate under unrealistic conditions by ignoring fatigue. This is even more important for ores that are on the borderline to be considered as competent for AG milling.

ACKNOWLEDGEMENTS

The work presented here was done within the Vinnova project 2019–05194, ‘AG-Test; Small scale tests for autogenous grinding scale-up’. X-ray tomography analysis was funded by the Academy of Finland through the RAMI infrastructure project (293109). Assistance in providing the samples by Boliden Mineral AB is appreciated.

REFERENCES

Barratt, D J, Allan, M J, 1986. Testing for autogenous and semi autogenous grinding: A designer’s point of view. Mining*, Metallurgy and Exploration,* 3(2), 65–74.

Bergeron, Y, Kojovic, T, Gagnon, M-D-N, Okono, P, 2017. Applicability of the Hit for Evaluating Comminution and Geomechanical Parameters from Drill Core Samples-the Odyssey Project Case Study. *COM2017 The Conference of Metallurgists.*

Bieniawski, Z T, Hawkes, I, 1978, Suggested methods for determining tensile strength of rock materials, *Int. J Rock Mech. Min. Sci. Geomech. Abstr,* 15 (1978), pp. 99–103.

Lynch, A, 2015. *Comminution handbook*.

Macpherson, A R, 1977. A Simple Method To Predict The Autogenous Grinding Mill Requirements For Processing Ore From A New Deposit. *Transactions of the AIME*, 262, 236–240.

Mcken, A, Williams, S, 2006. An overview of the small-scale tests available to characterise ore grindability. *Autogenous and Semi-Autogenous Grinding Technology Conference,* 8–11.

Parapari, P S, Parian, M, Forsberg, F, Rosenkranz, R, 2020, Characterization of ore texture crack formation and liberation by quantitative analyses of spatial deformation, *Minerals Engineering*, 157, 106577.

Stanley, G G, 1974. Mechanisms in the Autogenous Mill and Their Mathematical Representation. *Journal of The South African Institute of Mining and Metallurgy,* 75(4), 77–98.

Starkey, J, Dobby, G. 1996. Application of the Minnovex Sag Power Index At Five Canadian Sag Plants. *Autogenous and Semi-Autogenous Grinding,* 345–360.

Starkey, J, Hindstrom, S, Nadasdy, G, 2006. SAGDesign testing–What it is and why it works. *International AG and SAG Grinding Technology*, 240–254.

The irrefutable value of introducing a dynamic transport term into mill modelling

M S Powell[1], I Govender[2], A N Mainza[3], D K Weatherley[4] and L M Tavares[5]

1. FAusIMM, Emeritus Professor, University of Queensland, SMI-JKMRC, Indooroopilly Qld 4068. Email: malcolm.powell@uq.edu.au
2. Professor and Group Executive, Mintek, Randburg, Gauteng, 2121, South Africa. Email: indresang@mintek.co.za
3. Head of Department, Professor, CMR – Dept of Chemical Engineering, University of Cape Town, Rondebosch, 7700, South Africa. Email: Aubrey.mainza@uct.edu.za
4. Senior Research Fellow, University of Queensland, SMI-JKMRC, Indooroopilly Qld 4068. Email: d.weatherley@uq.edu.au
5. Professor, Department of Metallurgical and Materials Engineering, Universidade Federal do Rio de Janeiro, COPPE-UFRJ, Rio de Janeiro, Brazil. Email: tavares@metalmat.ufrj.br

ABSTRACT

It is understood that rocks do not instantaneously transport along a grinding mill and are consequently not perfectly mixed, but this is conveniently overlooked in mill modelling. A lack of understanding of the transport phenomenon and the difficulty of modelling realistic transport in a complex tumbling system, contribute to this.

Visual observation of segregation in AG and SAG mills and measured lag time of mill response to changes in feed provide evidence of the influence of axial transport within mills. Incorporating this lag in dynamic models should underpin dynamic simulation of milling circuits for design and for model-based control. Limitations and errors in predicting the influence of increased power via mill length versus diameter, inability to predict pebble production, and a lack of the differential in residence time across rock sizes and competences, all contribute to inadequate design prediction that can be especially acute for large Autogenous mills. Examples of dramatically under – and over-loaded pebble regrind circuits and the inability to predict pebble load in AG milling discouraging the application of this energy-efficient option, point to the need for predictive modelling of breakage by competence linked to transport through and out of mills.

Incorporating progress in granular flow and mixing, coupled to computational advances enable models to be based on complex breakage and transport models at high spatial resolution. This allows mechanistic models to simulate thousands of times faster than real time, opening the door to more accurate mill design, including dynamics in process simulation and to live simulation for process control – all with advanced mechanistic models. The value of grasping this opportunity is not easily refuted.

INTRODUCTION

It is understood that rocks do not instantaneously transport along a grinding mill and thus the contents are not necessarily perfectly mixed, but this is omitted from mill modelling. A lack of understanding of the transport phenomenon and the difficulty of modelling realistic transport in a complex tumbling system with a wide size range of rocks, contribute to this. The discussion focuses on industrial SAG and AG mills with a wide range of rock size distribution and considerable length, that are most affected by axial transport effects.

As a workhorse for size reduction in the minerals industry for over 100 years, the understanding of the grinding action in the tumbling mill is remarkably poor. Underlying this is the challenge that as simple as it appears in principle, the grinding action in a mill is a genuinely complex problem. The lifting and cascading or cataracting of a mixture of steel balls and rocks was first described in simple mathematical terms by White (1905) and then Davis (1919). Greater insight was provided by Powell and Nurick (1996a, 1996b, 1996c) through filming the internals of a model mill with X-ray cameras to elucidate the motion of grinding balls. This was refined and extended in the work of Govender, Powell and McBride (2004) which provided more quantitative measurement of the charge motion,

leading to a more formal description of the structure of the charge described by Powell and McBride (2004). The description is illustrated in Figure 1.

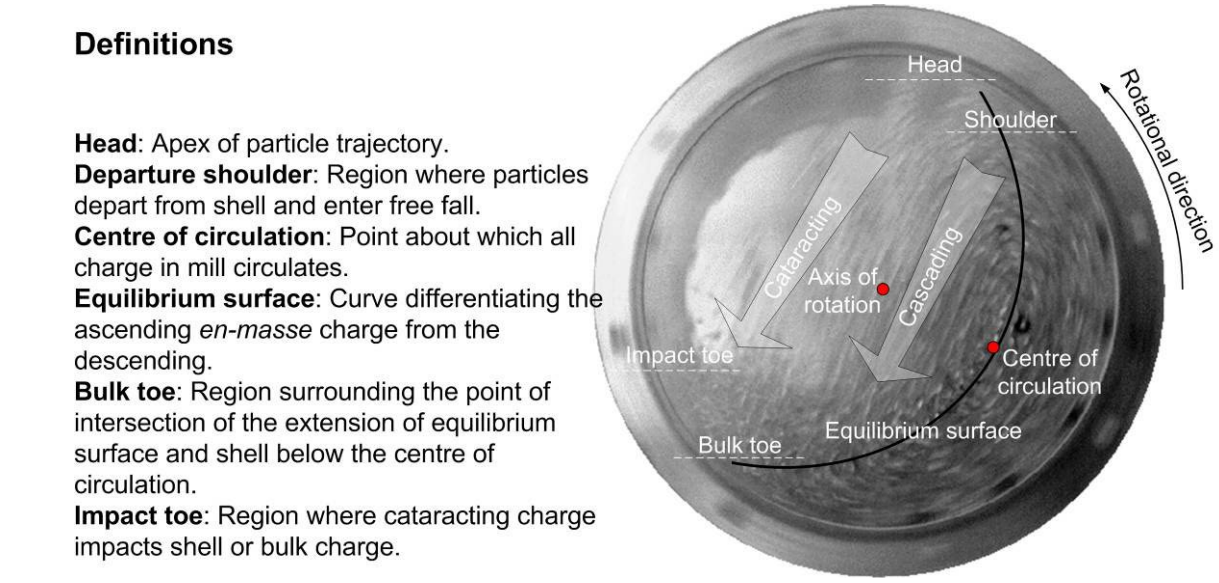

FIG 1 – Description of the charge rotation motion in a tumbling mill (Powell and McBride, 2004).

Although useful, the vertical slice view of charge motion does not provide input to the axial transport phenomenon. Powell measured axial motion of balls (Powell and Nurick, 1996b), but this was presented as qualitative data due to issues of location accuracy of the tracked particle. The work of Govender (Govender, Powell and McBride, 2004) developed improved particle tracking methods that allowed this axial motion to be tracked over many revolutions of the mill, such as that in Figure 2. This shows a strong and quantifiable drifting of a particle over time, which is clear evidence of axial transport and mixing. The particle can take 1 to 3 minutes to travel the length of the mill operated in batch mode. Superimposed upon this will be the average flux of particles being transported along a continuously fed and discharging production mill.

Insights into transport in mills have been gained from radioactive and conductivity tracer studies (Faria, Rajamani and Tavares, 2019; Fuerstenau, Abouzeid and Swaroop, 1986; Gardner, Verggese and Rogers, 1978; Hassanzadeh, 2017; Kelsall, Reid and Restarick, 1970; Makokha, Moys and Bwalya, 2011; Rogers, Bell and Hukki, 1982; Vinnett *et al,* 2018; Weller *et al*, 2000; Yianatos *et al,* 2005). However, very often these studies are either limited to studying either the fluid or very fine particles (Faria, Rajamani and Tavares, 2019; Makokha, Moys and Bwalya, 2011; Hassanzadeh, 2017). Although allowing to confirm the common assumption in assumption of the similar behaviour of those very fine particles to that of the fluid, they offer no insights on the behaviour of coarser particles, which are critical in Autogenous and Semi-Autogenous mills. Only very few studies have been conducted with relatively coarse particles that act as grinding media, in particular in Autogenous and Semi-Autogenous mills (Vinnett *et al,* 2018). Unfortunately, analysis of data has been often only limited to fitting theoretical residence time distribution models for population balance model formulations. Yet, Vinnett *et al* (2018) demonstrated that coarser particles presented twice the residence time of fines, thus demonstrating the important differences in their transport in the mill.

The present work analyses critically transport of coarse particles in mills, with emphasis to AG and SAG mills, analysing practical observations in industrial mills, principles of a modelling approach that can potentially describe it mechanistically and finalising by analysing implications of incorporating transport in dynamic and mechanistic models.

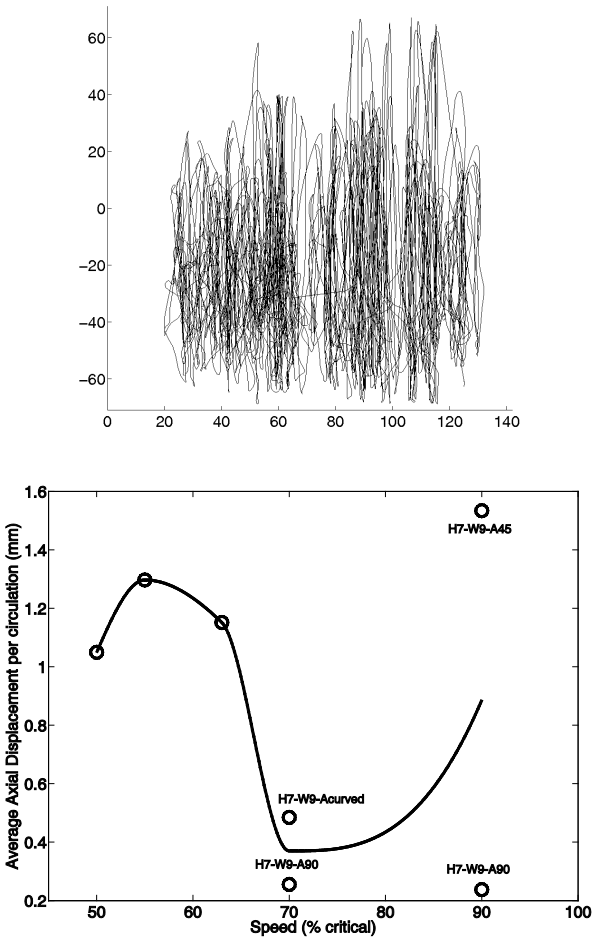

FIG 2 – Measured axial motion in the laboratory mill (Govender, Powell and McBride, 2004). (a) Axial view of tracked particle; (b) Average axial displacement per circulation with mill speed.

PRACTICAL OBSERVATIONS

One of the strongest motivations for incorporation of transport in mills can be provided by the simple path of observation. It is usual to crash stop a mill in order to conduct accurate measures of mill filling. The concurrent stopping of ore feed, inlet water, recycle streams (crushed pebbles and sometime cyclone underflow) and switching off the mill power provide a snapshot of the mill internals. The high inertial force of the mill contents ensure the mill rapidly decelerates to a stop in less than one rotation, thus not allowing any significant flow along the mill. A few examples are shown to illustrate how significant the transport and segregation is in mills. The images in Figure 3 provide clear visual evidence of segregation by size and ball fraction along a SAG mill. The fraction of balls increases along the length of the mill while the mid-size rocks are sparse and there are fewer large rocks.

FIG 3 – Segregation from feed to discharge end of a 32 ft diameter, 16 ft long SAG mill (left: feed end; right: discharge end).

The segregation in a SAG mill treating a relatively soft ore is well illustrated in Figure 4, with almost no rock visible at the discharge end.

FIG 4 – SAG mill 21 per cent filling, 11 per cent balls.

A large autogenous mill provides an extreme case shown in Figure 5. This 22 MW, 38 ft diameter mill provides an illuminating study of the transport of the large rocks along the length of the mill, crowding near the discharge. Understating the transport time along with the breakage abrasion rate of the large rocks becomes central to predicting the overall performance of this mill.

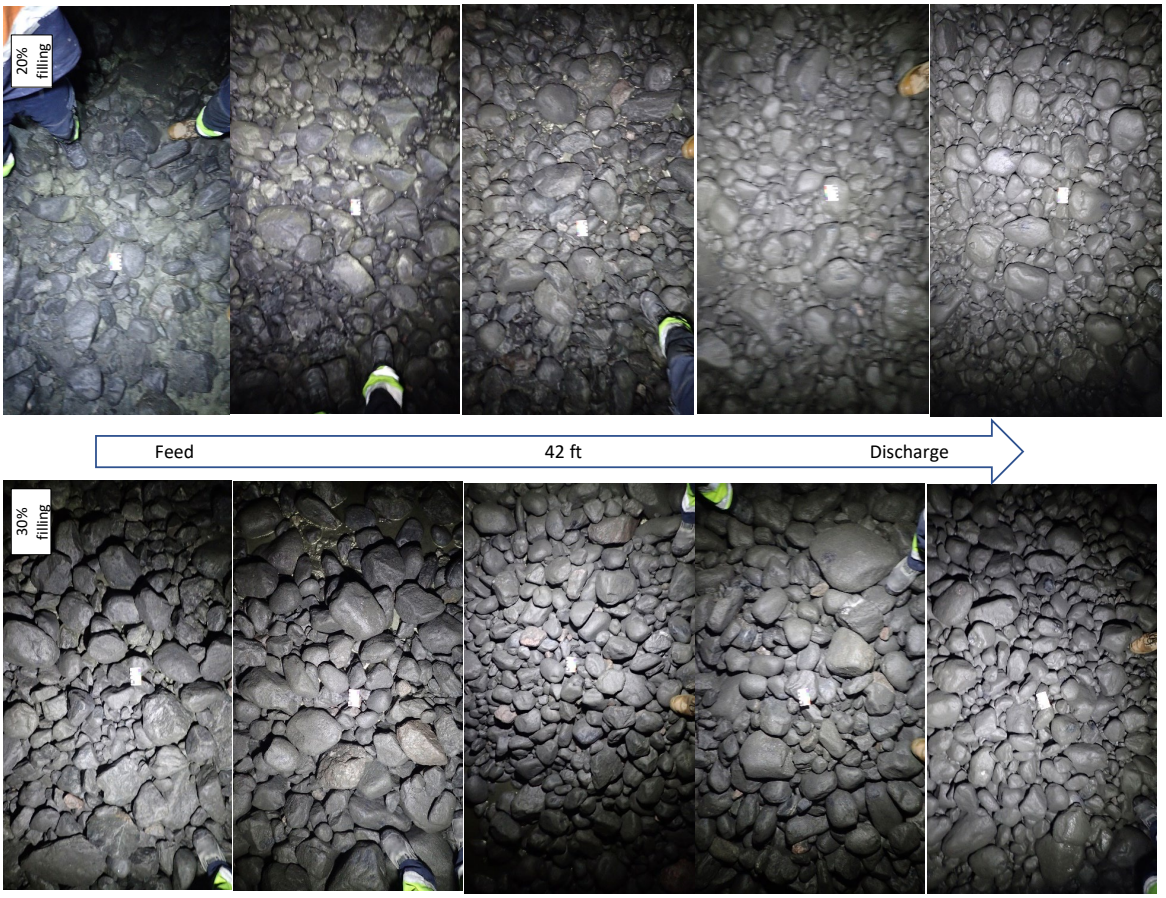

FIG 5 – Survival of large rocks in the Aitik Boliden 42 ft long (12 m internal length) AG mill.

Although indirect, the influence of transport on mill operation is also demonstrated quite differently through the dynamic lag in mill response. The method of developing grindcurves, as evolved by Powell and Mainza (2006), implemented by Powell, van der Westhuizen and Mainza (2009), and extended by Powell, Perkins and Mainza (2011), provides excellent data on control lag. The method of incrementally increasing feedrate in small steps over an extended period prevents pulsing of the mill contents. When applied, this results in a distinct signature of the lag between a control change and mill response, such as in Figure 6.

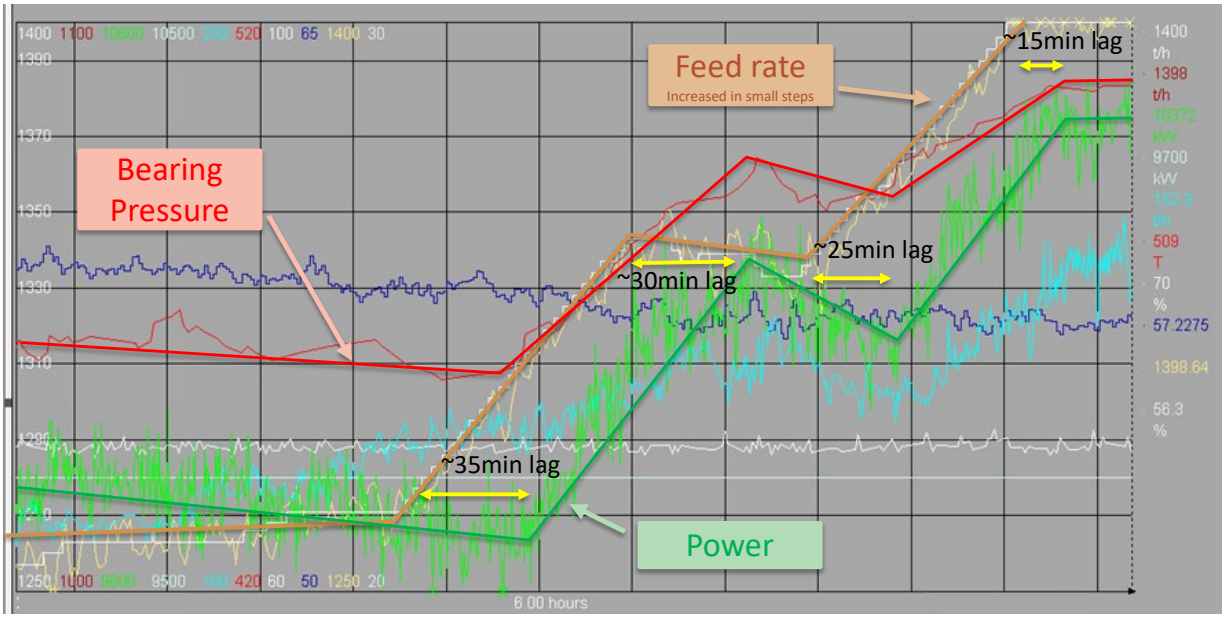

FIG 6 – Response lag time measured in a SAG mill.

For this 12 MW mill, the mill filling is indicated by bearing pressure. The gradual 2 t/h per 2 minute rate of increase in mill feed shows no effect on the mill load and power for 35 minutes at the start of the test, noting that the mill had been gradually losing load and power prior to this feed increase. The feedrate is then held relatively stable for an hour, yet the mill continues to increase in filling for another 30 minutes. The subsequent reduction in filling and power indicate that the discharge has overtaken the new stable feedrate. A further gradual step-wise increase in feedrate turns the mill filling in 25 minutes. The final stabilisation of feedrate brings the mill into a stable operation for the last data point.

The consistent measurement of these lags in mill response point towards the discharge end of the mill being ignorant to the change in feed. The classification of the discharge for the earlier feed remains consistent and the discharge rate is maintained to match the increasing feedrate, as the content at the discharge end has had a longer residence time, consistent with the original feedrate. Gradually the coarser product associated with the higher feedrate reaches the discharge end and begins to build-up and affect the internal transport, leading to the strong ramp-up in mill filling.

No perfectly mixed model or steady state model can predict such behaviour. The so-called model-based control systems rely on extreme step tests for calibration. Large changes do pulse the mill contents and force a rapid, and easily measured, response. However, such a calibration method is inappropriate for a granular system with significant transport time in the system. It is the position of the authors, that this forces calibration leads to over-reactive control systems. Rather than a control that dampens out perturbances these approaches can amplify disturbances through over-control. It is not uncommon to observe cyclic mill operation, with swings in power of up to 10 per cent with a consistent period in the region of an hour. These are control-induced, as easily proven by overriding any control system or operator input and leaving the mill to stabilise, a practice successfully applied by the authors on mills around the world.

Incorporating this lag in dynamic models should underpin dynamic simulation of milling circuits for design and for model-based control. If there is not a realistic, size dependent transport term in a mill model, especially significant for SAG/AG mills, then it cannot be mechanistic or dynamic – highlighting falsely claimed dynamic models in process control.

The analysis of Powell, Morrell and Latchireddi (2001) highlighted the influence of mill aspect ratio (ratio of diameter to length) on grinding performance. As a consequence of longer residence time, which is an outcome of granular flow and transport, the longer mills produce a finer product. A long mill cannot be forced to produce a coarse product and thus design engineers had fallen into the trap of an imbalance between SAG and ball mill power when specifying longer SAG mills.

The work of Mwansa and Powell (2004) and Powell, Mwansa and Condori (2006) provided further impetus to understand transport. In this study, the contents of a small production SAG mill (3.5 m diameter by 4.7 m long) was emptied out as four separate slices, including careful pre-draining of the slurry. The particle size distribution of the feed and content from the four slices along the mill are shown in Figure 7 and the corresponding data for the size passing 80 per cent of the material is given in Figure 8. There is segregation of the material in the mill with the content at the feed end exhibiting more coarse particles. The material was shown to become progressively finer from the feed end to the discharge end of the mill. This agrees with observations made by Hogg and Rogovin (1982) from their segregation studies in an overflow laboratory mill. The unique feature with the high steel load SAG mills, or RoM ball mills are they are sometime referred to, is that the content is depleted of particles in a certain size range represented by the portion where the particle size distribution is constant. Mwansa and Powell (2004) carried out ore breakage characterisation tests on the feed and material from each of the four slices and analysis from the Drop Weight and Bond ball tests indicated the rocks near the discharge end were significantly more competent than that at the feed end. The feed material has a wide distribution of competence, particularly in the UG2 ore in this trial. Since material that is not competent grinds down easily, the fraction of competent rocks increases progressively from the feed end to the discharge end. The Bond work index increased from 15.2 kWh/t for the feed sample to 18.2 kWh/t for the material in the slice just before the discharge (Figure 9), demonstrating that this increase in competence appeared over the whole size spectrum of particles in the mill. Shoji, Hogg and Austin indicated that there is less segregation at high ball load and high filling operations. This would imply that the segregation observed in high steel

ball load SAGs like the example given in this study is less than what would be encountered in conventional SAG mills and AG mills.

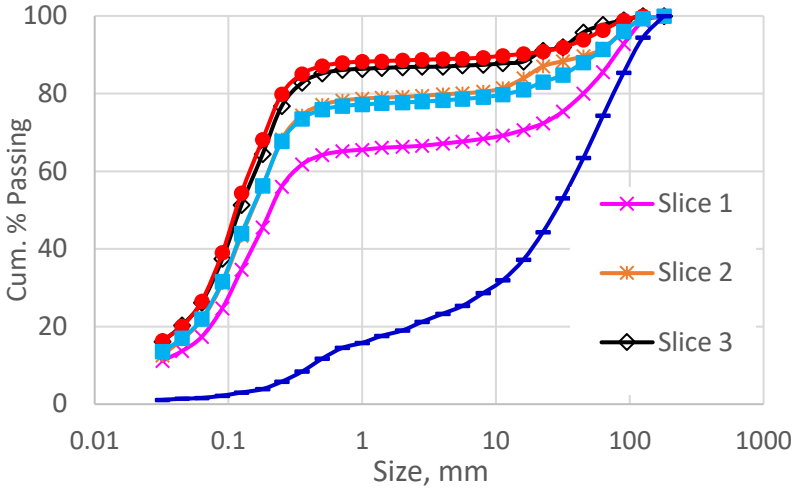

FIG 7 – Particle size distributions for the feed and mill content slices.

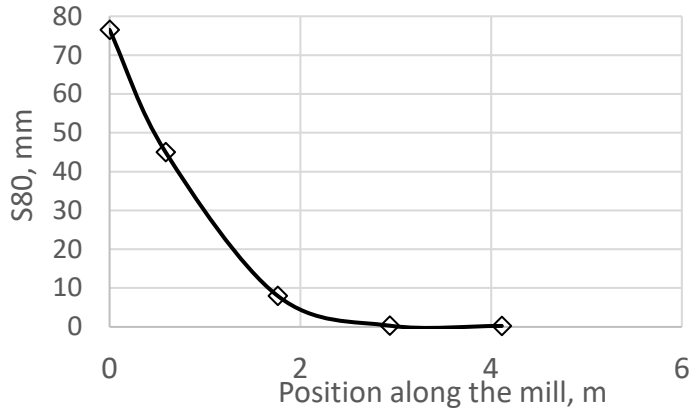

FIG 8 – The 80 per cent passing size of the feed and mill content slices.

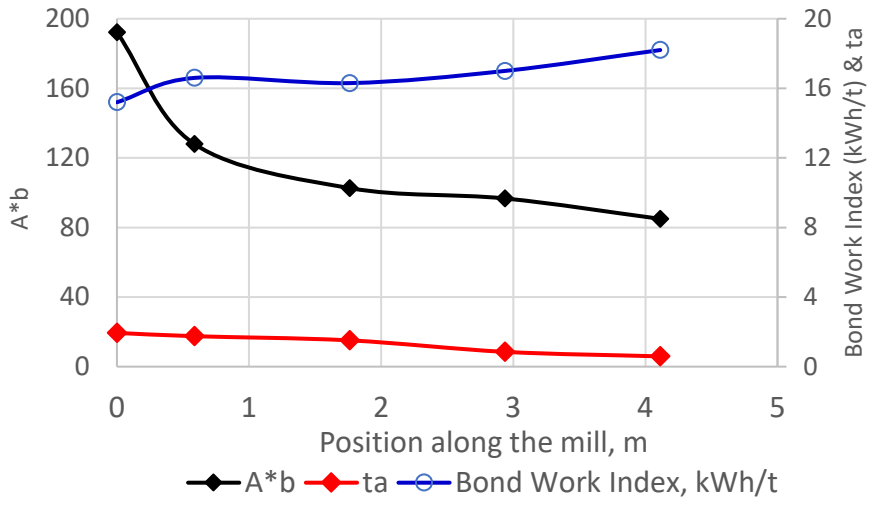

FIG 9 – Ore competence measurements obtained for the feed and mill content slices.

In one hand, these results are consistent with recent approaches that describe breakage in mills mechanistically, since more brittle rocks are preferentially broken (Tavares and Carvalho, 2009; Carvalho and Tavares, 2011), with more competent particles being able to survive and, as such, being transported axially towards the discharge of the mill. On the other hand, results such as these demonstrate the need for understanding and modelling rock segregation in mills, which is not achievable as a single parameter. The combination of the transport rate by size and the competence of the rocks (their survivability) determined the outcome. This led to the initiation of an extended study of transport in tumbling mills and drums led principally by Govender, such as in the work of Tupper *et al* (2016).

An inability to predict pebble production rate is directly related to the assumption of equal residence time for all particle classes – size and competence. This issue becomes acute in modelling large autogenous mills, in terms of predicting the hold-up of competent grinding media and what fraction should be withdrawn for crushing. Uncertainty in pebble discharge has been an ongoing stumbling block in designing SAG circuits with recycle crushing, with evidence of circuits globally that have excess or inadequate recycle crusher capacity.

The science of granular flow dynamics in mixing and segregation is well advanced in other fields, such as pharmaceuticals. Incorporating this progress in understanding mixing, transport and diffusion along mills, coupled to computational advances enable models to be based on complex breakage and transport models at high spatial resolution. This allows mechanistic models to simulate thousands of times faster than real time, opening the door to more accurate mill design, including dynamics in process simulation and to live simulation for process control – all with advanced mechanistic models. The value of grasping this opportunity drives the work of the authors in understanding and applying transport phenomena in mill modelling.

GRANULAR FLOW DYNAMICS

The granular (rocks and balls) porous network through which slurry is transported in a tumbling mill is arguably the primary driver for any pressure-driven slurry transport model. The standard Ergun equation (1952) is well known to describe flow-through a static bed, while the dynamic Ergun equation (Tupper *et al,* 2016) accounts for the granular velocity and includes a Reynolds dependent permeability. In the interest of mathematical tractability, most of these models assume a uniform porosity and granular concentration throughout the drum when effecting a solution. However, rotating drum flows are well known to exhibit radial (Powell and Nurick, 1996b, 1996c; Sherritt *et al,* 2003) and axial (Hajra and Khakhar, 2005; Khakhar *et al,* 1997) granular mixing.

There are numerous studies of segregation in rotating drums and mills but most of these are confined to radial segregation (Rogers and Clements, 1971; Donald and Roseman, 1962; Cleary, 1998) ranging from computational modelling to residence time studies. According to Savage and Lun (1988), radial mixing in rotating drums is governed by two basic mechanisms: Kinetic Sieving (or percolation) and Squeeze expulsion. Shearing layers give rise to voids (sieve-like holes) that are neither fixed in size nor location, ie they are randomly seeded. The appearance rate and structure of the sieves are reported by Gray (2018) to be directly dependent on the shear rate encountered by the granular layer making up the sieve. Gravity pulls particles from the upper layer towards the sieve and the voids regulate whether they go through, with the probability being higher for smaller particles. Contact force imbalances quickly develop to balance the mass differential, resulting in particles being squeezed out to restore the mass balance. For slowly rotating drums, the net effect results in larger particles rising towards the surface of the bed while smaller particles are driven towards the centre of circulation of the bed (De Klerk, Govender and Mainza, 2019). Consistent with basal friction rheological theories on granular flow (Andreotti, Forterre and Pouliquen, 2013), smaller particles have a relatively higher number of contacts than an equivalent volume of larger particles. Accordingly, smaller particles experience a greater flow resistance than their larger counterparts. Lower (respectively, higher) flow resistance reduces (respectively, increases) the probability of larger (respectively, smaller) particles being ‘captured’ by the sieves before reaching the toe region of the bed, thereby reinforcing the radial segregation effect that is commonly referred to as the Brazil Nut Effect (BNE). Interestingly, and somewhat counter-intuitively, above a certain drum speed the segregation pattern can completely reverse (Hong, Quinn and Luding, 2001). Such complex granular flows are commonly found in industry.

Initial reports of segregation in mills were by Oyuma in 1939 who developed a theory to explain axial segregation in terms of surface flow and successfully modified an effective diffusion equation which accounted for reverse effects. In addition to radial segregation, experimental evidence of axial banding is also reported in the literature, such as that of Hill, Caprihan and Kakalios (1997). Most of the experiments for axial segregation involve obtaining particle residence time data and examples of these are the studies by Khakhar *et al* (1997) and Kelsall (1969). The results from residence time studies performed by Khakhar *et al* (1997) using irradiated feed material of varying sizes and by Kelsall using non-breakable (alumina) tracers yielded inconclusive results. They alluded to the coarseness of the tracers as the reason for inconclusive results. Various theoretical models such as Gupta, Khakhar and Bhatia (1991), and computational simulations (Matuttis, Luding and Herrmann, 2000; Newey *et al,* 2004; Rapaport, 2007; Taberlet, Losert and Richard, 2004) have subsequently emerged to explain the time-dependent banding phenomenon. Axial dispersion models comprising convection and diffusion to describe transport in mills have been used in several studies indicating that transport in mills arise from the convective component defined by an axial velocity and a diffusion term defined by a concentration gradient with an appropriate diffusion coefficient. The most practical of the various theories is the axial diffusion model of Zik *et al* (1994) for binary mixtures that was recently extended by Ahmed, Govender and Mainza (2021) to describe the time evolution of ternary and quaternary mixtures while also proposing a general result for any number of particle species. These works argue that spontaneous, localised fluctuations in concentration seed alternating bands along the length of the drum. Figure 10 illustrates three adjacent bands in a batch operation. Consistent with the basal friction theories on granular flow, the relatively higher slices (two outer bands) are richer in high friction particles (less mobile with relatively higher flow resistance) than the lower central slice that is dominated by low friction particles (more mobile with relatively lower flow resistance). The height difference between adjacent bands sets up a natural gravity slope that drives particles down the local axial gradient. Clearly the more mobile (low friction) species flow more readily down the gravity slope than their less mobile counterparts (high friction species), resulting in the depletion of low friction species from the higher bands that accumulates in the central lower band. The slope region also becomes richer in low friction species. Friction-limited mobility acts like a positive feedback mechanism that reinforces the depletion of low friction species from the outer higher bands while simultaneously replenishing the central lower band with low friction species. Accordingly, the alternating banding pattern is reinforced.

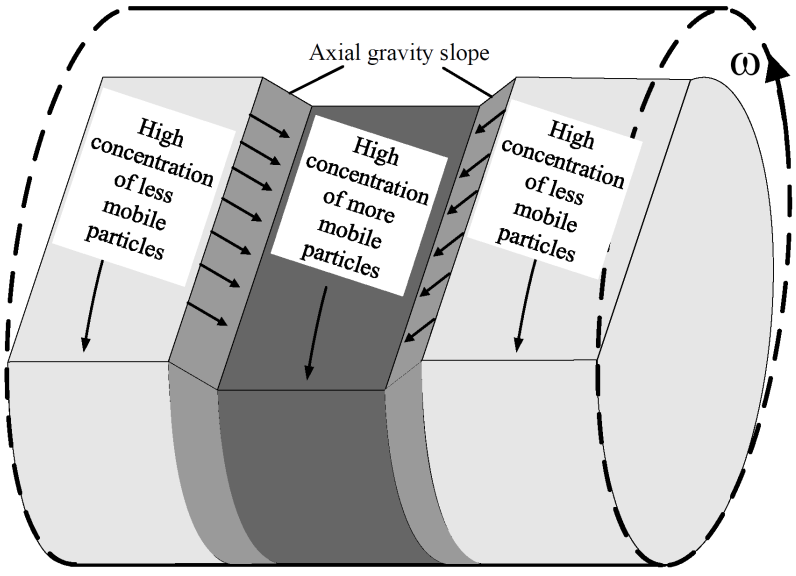

FIG 10 – Development of banding through granular flow.

The governing differential equations of axial segregation is derived from a material balance between flux down the gravity slope and a corresponding back flux occurring deep within the granular bed. Ahmed, Govender and Mainza (2021) showed this derivation for two, three, four frictional species, and illustrated the resulting banding patterns that result in the long-time limit. The result for n-species was also derived. Equation (1) illustrates the governing partial differential for *j*th species in a *n*-species mixture.

$$\frac{\partial C_j}{\partial t} = D\frac{\partial}{\partial z}\left[\left|C_j\right|\sum_{n=1}^{n-1} C_j\left(\mu_j - \mu_m\right) + \left|C_j\left(\mu_m - \mu_j\right)\right|\frac{\partial C_j}{\partial z}\right] \quad (1)$$

Where μ_j is the friction coefficient associated with the *j*th species, μm is the highest friction coefficient of the *n*-species mixture and C_j is the time dependent concentration of the *j*th species along the drum axis. *D* denotes a diffusion coefficient such that model resembles a non-linear diffusion equation for relative concentrations along the axial direction of the mill, which is given by:

$$D = \frac{P_0^3}{3\eta(\rho g)^2}\left[1 + y_x^2\right]\left[\frac{y_{C_j}}{y_x}\right] \quad (2)$$

The diffusion coefficient is physically driven by the lithostatic pressure P_0, viscosity η, material density ρ, acceleration due to gravity g, spatial gradient $y_x = \frac{\partial y}{\partial x}$, and a coupling gradient $y_{C_j} = \frac{\partial y}{C_j}$. The present work does not explore the physical dependencies of the diffusion coefficient and solves the diffusion problem for n-species along the drum length.

Incorporation of this theory into the modelling of transport in tumbling mills presents a pathway to enabling size-dependent segregation to be integrated into mill modelling.

INITIAL MEASURES AND MODELLING

A simplified Surface cascade model based off the theory of Ahmed, Govender and Mainza (2021) leads to some interesting and scalable transport phenomena. With granular friction being lower for larger rocks, based on their ability to flow across a surface, and diverge along the mill due to random collisions.

The work on pilot tracer tests conducted by Powell *et al* (2022) provides novel data upon which to base the development of a model of rock transport in a continuously operating mill. In analysing this data, it was found that the measured transport rates and distribution along the mill in the tests conducted for in-mill segregation demonstrated the dominance of the surface cascading flow phenomena.

The conceptual model is built off four subprocesses (as this stage), namely:

- Advection – bulk flow along the mill. This corresponds to the transport rate of the finer material, taken as 1–10 mm in the first implementation. This can be calculated based on superficial residence and thus transport rate of the measured mass of this size range in the mill load. When estimating this, it aligned with the water flow velocity, providing a pointer to calibrating this in future modelling.
- Bulk diffusion. This is classic diffusion within the granular, stirred media, with particles shifting into available spaces that are formed during the mixing process. It is inferred from the experimental data to be a low rate.
- Cascade diffusion created by the flow of particles down the cascading surface of the descending charge. This is strongly size-dependent, with larger particles having a larger cascade angle and thus displacement, plus the fraction exposed to cascade is greater for larger particles.
- Discharge grate. This hinders discharge of particles, allowing zero above grate size and increasing to a maximum for small particles below about 10 per cent of grate aperture. The hinderance to flow forces particles to crowd and then backflow through diffusion.

The outcome of the cascade concept is illustrated in Figure 11. The model predicts that for a 6 ft (1.7 m) diameter by 1.4 m long pilot mill the maximum transport velocity ranges from 0.016 to 0.025 m/s from 1 to 150 mm particles, a difference of about 50 per cent. For a large 13 m diameter by 12 m long mill the range is reduced to less than 20 per cent. Notably, the model predicts a maximum velocity of about ten-fold for the large mill compared to the pilot mill, related to the long cascading region for this large diameter. Additionally, the maximum velocity is predicted to be more than 10 per cent higher for lower fillings due to the increase exposure of the rocks to the surface cascade zone.

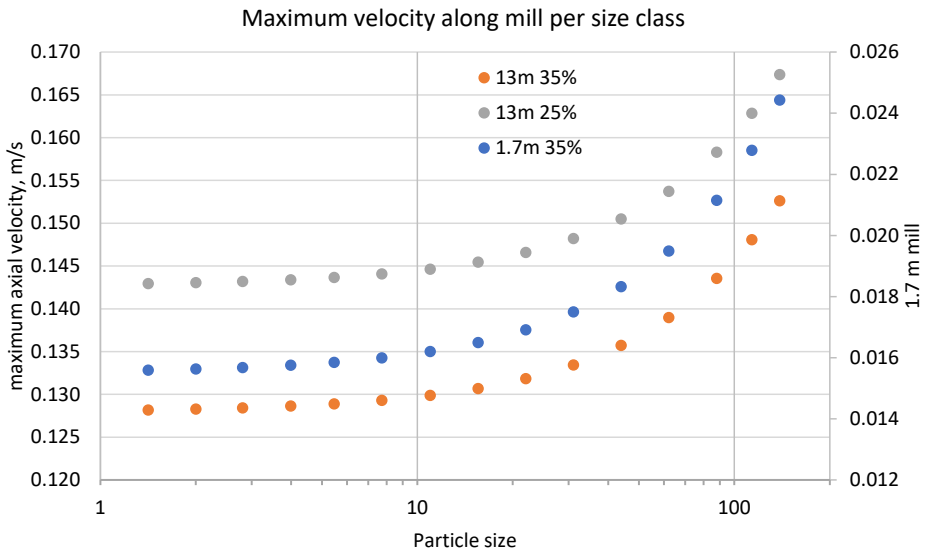

FIG 11 – Differential transport speed by particle size predicted through a conceptual surface cascade model.

This concept cascade model has not been validated and is still a work in progress, but serves to illustrate the effects that can be predicted and then incorporated in models that allow for transport.

For a model to incorporate such transport and diffusion effects, it intrinsically has to be dynamic. The approach taken is that of a discretised time model with conceptual 'slices' along the mill that provide sufficient resolution to capture the transport effects.

IMPLICATIONS OF INCORPORATING TRANSPORT IN MILL MODELLING

Besides breakage rates, breakage distribution and internal classification, transport is another subprocess that is required in a realistic tumbling mill model. However, simplifying assumptions in regard to how particles move axially through the mill by assuming, for instance, that either the entire mill contents or significant parts of it are perfectly mixed have led to challenges in decoupling some of these subprocesses.

Incorporation of size-dependent transport allows the observed accumulation of larger and more competent rocks at the discharge – thereby changing residence time and product size distribution in the modelled mill. Cumulation of larger rocks at the discharge will allow a higher than expected discharge rate, due to their high concentration at the discharge grate.

Indeed, the current SAG models, such as the variable rates model of the JKMRC (Napier-Munn, 1996) suffer from an anomaly for the coarse breakage. The well-known breakage rates curve drops off from a size of around 10 mm, reaching a minimum around 44 mm, then rising steeply to high breakage rates for the large rocks. Such a rise is against the understanding and measurement of breakage of large rocks in mills, which in fact have a low probability of breakage. The large rocks tend to 'wear out' through abrasion, which leads to the build-up of a critical size in the mill and motivates pebble porting to extract rocks for crushing. This apparent high breakage rate in the models is a result of back-fitting rates to satisfy a population balance model that is based on an assumption of equivalent residence time for all sizes of particles. However, the large rocks actually have a far longer residence time than fine particles, hence the back-fitted rates are exaggerated to compensate for this inadequacy of the modelling method. Incorporation of transport and differential residence time for particles by size will address such anomalies and provide improved predictive capability, especially for non-standard operations, ie outside of fitted databases.

In reality, the discharge from a grate-ended mill is only from the 'layer' exposed to the discharge grate. Only particles that are directly exposed to the slots of the discharge grate can flow out of the mill. Currently, a discharge function is used that is calculated based on the probability of the total mill contents leaving the mill. This simplification results in an artificial discharge function based on perfect mixing and incorporating a hidden differential of transport by size through the charge and along the mill. Referring back to the illustrations in Figures 3 to 5, it is clear that the calculated discharge must

be false due to the population at the end of the mill being quite different to the average contents. The discharge function will have to be artificially modified to fit identical mills with different degrees of rock segregation along the mill. This will lead to incorrect predictions of mill performance under changing conditions.

So-called mechanistic mill models, which rely on collision energy spectra from simulations of the charge using the discrete element method (DEM) (Weerasekara *et al,* 2013) and microscale descriptions of particle breakage using special population balance model descriptions, allow the prediction of preferential breakage of the more brittle particles and, therefore, survival of the tougher ones (Carvalho and Tavares, 2011). While this makes them amenable to, potentially, reproduce some of the practical observations observed in low diameter-length mills, these models require proper collision energy spectra along the mill and a realistic description of axial transport of coarse particles.

An example of the direct consequence of the lack of understanding and incorporation of transport in SAG mills is the poor utilisation and inconsistent loading of recycle crushers across the industry (Powell, Evertsson and Mainza, 2019). As blast fragmentation size, ore competence, variability in competence within the ore and the application of pre-crushing varies, the load on recycle crushers varies considerably, with idle or overloaded crushers a common issue. Extensive experimentation with pebble discharge ports is generally conducted over years to address this, but the chosen design can become inefficient with new feed characteristics. At the other extreme the common trend to pre-crushing can lead to unexpected loss of mill load and consequent negative impacts on mill and liner performance. The ability to more accurately and reliably predict the build-up and discharge potential of competent rock for the intrinsic competence distribution found in orebodies is expected to lead to more reliable and consistent circuit design. Site data collected by the authors shows loss of total circuit power utilisation in the range of 2 to 16 MW (Powell *et al,* 2021). Recapturing such large losses of available milling energy, should be highly motivating to the industry to improve this area of poor understanding and predictive modelling.

Example of applying diffusive transport terms

Diffusive transport terms have been incorporated in a dynamic mill model under development. The bulk flow is calculated as an advection term. A standard bulk diffusion term is applied and a diffusive term incorporated to capture the surface cascade mode described above. This was applied to a 2 m diameter mill being filled from empty at a fixed 1 t/h feedrate. Constant breakage and discharge functions were used for three sets of simulations with advection only, then bulk diffusion added, then cascade diffusion added. The transport of a set of tracer rocks is shown in Figure 12 as time to discharge from the mill (a) and the location within the mill after 2 minutes (b). The substantial difference in transport speed is clear with the addition of diffusion, providing considerably higher degree of mobility to the larger rocks (51–76 mm in this example).

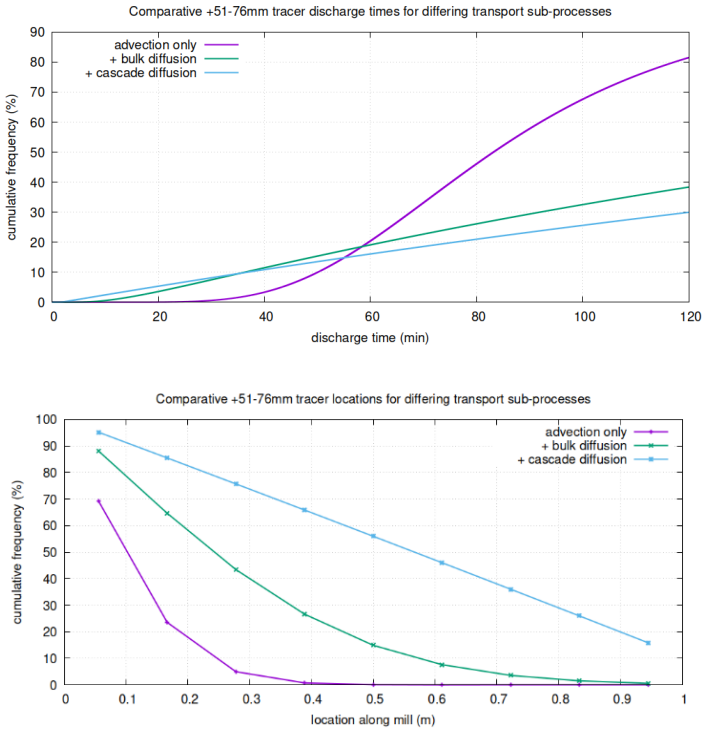

FIG 12 – Discharge time and distance travelled along the mill for tracer rocks.

The mass hold-up and resulting content size in the mill are shown in Figure 13. The case with no diffusion results in a considerably higher hold-up as the large rocks transport at the same rate as the bulk finer material. This also leads to a coarser mill content for the diffusion cases.

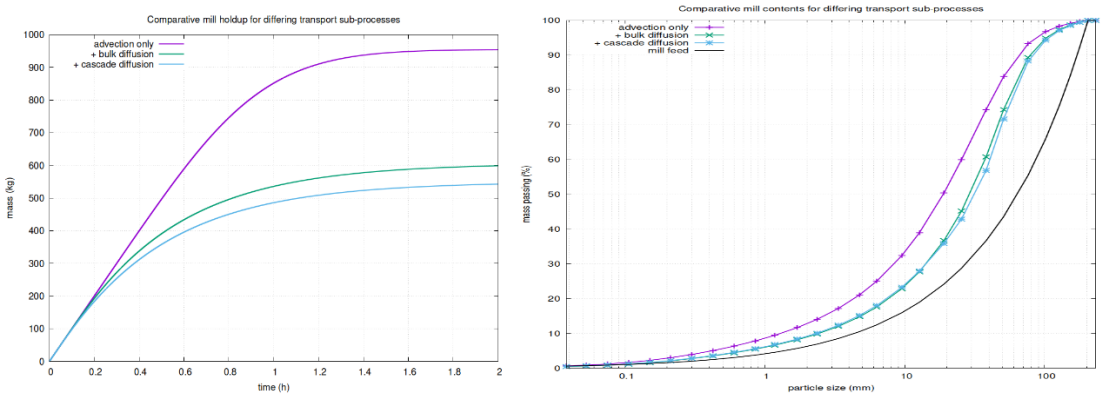

FIG 13 – Hold-up and content size distribution for different diffusive transport.

Although only a concept study, this example illustrates the substantial influence that differential transport by size through diffusive transport phenomena can have on the milling conditions. Currently this is hidden in bulk rates curves and discharge functions to compensate for this discrepancy, but these provide incorrect outcomes when feed or operating conditions change from the calibrated baseline.

Experimental tracer tests of a range of rock sizes conducted in a 1.7 m diameter by 1.4 m long pilot mill support these modelling outcomes (Powell *et al,* 2022).

CONCLUSIONS

The review presented here, and some initial simulation outcomes point to the value of making an effort to fully model the milling system with transport. The explicit prediction of pebble survival and discharge in AG mills needing pebble retention contrasting with the controlled discharge in SAG mills with a need for high pebble discharge, present a clear need for a transport function in mill modelling to capture these required outcomes. It is reasonable to state that the realistic modelling of the

mechanics within mills lags behind progress in understanding the micro-processes in breakage, thus diminishing the value for predictive mill modelling of such understanding.

Elements of a description of axial segregation in mills, based on granular flow dynamics with a meaningful definition of diffusion coefficient, demonstrates its great potential to describe size-dependent segregation to be integrated in more realistic mill models.

There is a clear influence on mill contents when incorporating transport and size-dependent diffusive terms in modelling outcomes. The dynamic structure of a model that includes transport allows future modelling of transients, such as pulses in feed, unstable feed rate, changes in feed type, mill speed, etc. This will be of considerable value in predicting the dynamics of the mill with variable feed and how the system responds to different control strategies, leading future incorporation of genuinely model based control.

These methods will be applied to recent tracer test work for subsequent presentation.

This widespread group of researchers within the global Comminution Collaborative (GCC), have for over 15 years been steadily building the tools and understanding to take this forward. Transport is one of the key elements to dynamic, mechanistic mill modelling. With the emphasis on improving the efficiency, especially in terms of energy use, while maximising use of the largest capital equipment on the mine site (where power utilisation has been measured to be up to 16 MW below available), the industry should be well-motivated to underwrite the final push to a fully-implemented dynamic model that can be used to explore future milling options. The improved modelling tools and outcomes are seen as a strong motivator to accelerate this work to the point of useful uptake.

REFERENCES

Ahmed, A M E, Govender, I, Mainza, A N, 2021. Axial segregation of polydisperse granular mixtures in rotating drum flows. *Minerals*, Vol. 11, No. 915, pp. 1–12.

Andreotti, B, Forterre, Y, Pouliquen, O, 2013. *Granular Media: Between Fluid and Solid*. Cambridge University Press.

Carvalho, R M, Tavares, L M, 2011. Leaping forward in SAG and AG mill simulation using a mechanistic model framework. *International Autogenous Grinding, Semi-Autogenous Grinding and High-Pressure Grinding Roll Technology*, pp. 1–26.

Cleary, P W, 1998. Predicting charge motion, power draw, segregation and wear in ball mills using discrete element methods. *Minerals Engineering*, Vol. 11, No. 1, pp. 1061–1080.

Davis, E W, 1919. Fine crushing in ball mills. *AIME Trans*, Vol. 61, pp. 250–296.

De Klerk, D N, Govender, I, Mainza, A N, 2019. Geometric features of tumbling mill flows: A positron emission particle tracking investigation. *Chemical Engineering Science*, Vol. 206, pp. 41–49.

Donald, M B and Roseman, B, 1962. Mixing and de-mixing of solid particles. I. mechanisms in a horizontal drum mixer. *British Chemical engineering*, Vol. 7, No. 10, pp 749 -753.

Ergun, S, 1952. Fluid flow through packed columns. *Chemical Engineering Progress*, Vol. 48, pp. 89–94.

Faria, P, Rajanani, R K, Tavares, L M, 2019. Optimization of solids concentration in iron ore ball milling through modeling and simulation. *Minerals*, Vol. 9, No. 366, pp. 1–17.

Fuerstenau, D W, Abouzeid, A Z M, and Swaroop, S H R, 1986. Material transport in ball mills: Effect of discharged design. *Powder Technology*, Vol. 46, pp. 273–279.

Gardner, R P, Verggese, K, and Rogers, R S C, 1978. The on-stream determination of large scale ball mill residence distributions with short-lived radioactive tracers. *Transactions SME-AIME*, pp. 422–431.

Govender, I, Powell, M S and McBride, A, 2004. Improved Experimental Tracking Techniques for Validating Discrete Element Method Simulations of Tumbling Mills. *Journal of Experimental Mechanics*, Vol. 44, No. 6, pp. 593–607.

Gray, J M N T, 2018. Particle segregation in dense granular flows. *Annual Review of Fluid Mechanics*, Vol. 50, pp. 407–433.

Gupta, S D, Khakhar, D, Bhatia, S, 1991. Axial segregation of particles in a horizontal rotating drum. *Chemical Engineering Science*, Vol. 46, pp. 1513–1517.

Hajra, S K, Khakhar, D V, 2005. Radial mixing of granular materials in a rotating cylinder: Experimental determination of particle self-diffusivity. *Physics of Fluids*, Vol. 17, pp. 013101.

Hassanzadeh, A, 2017. Measurement and modeling of residence time distribution of overflow ball mill in continuous closed circuit. *Geosystem Engineering*, Vol. 20, pp. 251–260.

Hill, K M, Caprihan, A, Kakalios, J, 1997. Bulk segregation in rotated granular material measured by magnetic resonance imaging. *Physical Review Letters*, Vol. 78, pp. 50–53.

Hogg, R and Rogovin, Z, 1982. Mass transport in wet overflow ball mills. *XIV International Mineral Processing Congress* (IMPC), Canadian Institute of Mining and Metallurgy (CIM), October 17–23, 1982. Toronto, Canada, pp I-7.1 -I-7.19.

Hong, D C, Quinn, P V & Luding, S, 2001. Reverse Brazil nut problem: Competition between percolation and condensation. *Physical Review Letters*, Vol. 86, No. 15, pp. 3423–3426.

Kelsall, D F, Reid, K J, Restarick, C J, 1969. Continuous grinding in a small wet ball mill. Part III A study of distribution of residence time. *Powder Technology*, Vol. 3 (1969–1970), pp. 170–178.

Khakhar, D V, McCarthy, J J, Shinbrot, T, Ottino, J M, 1997. Transverse flow and mixing of granular materials in a rotating cylinder. *Physics of Fluids*, Vol. 9, pp. 31–43.

Makokha, A B, Moys, M H, Bwalya, M M, 2011. Modeling the RTD of an industrial overflow ball mill as a function of load volume and slurry concentration. *Minerals Engineering*, Vol. 24, pp. 335–340.

Matuttis, H G, Luding, S, Herrmann, H J, 2000. Discrete element methods for the simulation of dense packings and heaps made of spherical and non-spherical particles. *Powder Technology*, Vol. 109, pp. 278–292.

Mwansa, S, Powell, M S, 2004. Measuring particle segregation along SAG mills. *Mineral Processing '04*. Cape Town, 5–6 Aug. 2004. Abstracts Published by SAIMM, Western Cape Branch. pp. 101–102.

Napier-Munn, T J, 1996. Mineral comminution circuits: their operation and optimisation / T J Napier-Munn, S Morrell, R D Morrison, T Kojovic. Indooroopilly, Qld: Julius Kruttschnitt Mineral Research Centre.

Newey, M, Ozik, J, van der Meer, S M, Ott, E, Losert, W, 2004. Band-in-band segregation of multidisperse granular mixtures. *Europhys. Letters*. 66, 205.

Oyama, Y, 1939. Studies on mixing of solids, *Bull. Inst. Phys. Chem. Res. Japan*, Report No. 5, 18: 600–639.

Powell, M S, Chiasson, G, Vien, A, Mular, M, Brissette, M, Weatherley, D K, 2022. Measurement of size-dependent transport in a pilot AG mill. *Proc. 17th European Symposium on Comminution & Classification* (ESCC 2022).

Powell, M S, Evertsson, C M and Mainza, A N, 2019. Redesigning SAG mill recycle crusher operation. *Proceedings International autogenous and semi-autogenous grinding and high pressure grinding roll technology 2019*, Sep. 23–26, Ed. Staples *et al,* Published CIM.

Powell, M S, Mainza, A N, 2006. Extended grinding curves are essential to the comparison of milling performance. *Minerals Engineering*, Vol. 19, no. 15, pp 1487–1494.

Powell, M S, McBride, A T, 2004. A three-dimensional analysis of media motion and grinding regions in mills. *Minerals Engineering*, Vol. 17, No. 11, pp. 1099–1109.

Powell, M S, Morrell, S, Latchireddi, S, 2001. Developments in the understanding of South African style SAG mills. *Minerals Engineering,* Vol. 14, No. 10, pp. 1143–1153.

Powell, M S, Mwansa, S, Condori, P, 2006. Charge segregation and slurry transport in long SAG mills. *XXIII International Mineral Processing Congress*, 3 – 8 Sep. 2006. Istanbul, Turkey.

Powell, M S, Nurick, G N, 1996a. A Study of charge motion in Rotary Mills. Part 1 – Extension of the theory. *Minerals Engineering*, Vol. 9, No. 2 pp 259–268.

Powell, M S, Nurick, G N, 1996b. A Study of charge motion in Rotary Mills. Part 2 – Experimental Work. *Minerals Engineering*, Vol. 9, No. 3, pp 343–350.

Powell, M S, Nurick, G N, 1996c. A Study of charge motion in Rotary Mills. Part 3 – Analysis of Results. *Minerals Engineering*, Vol. 9, No. 4, pp 399–418.

Powell, M S, Perkins, T, Mainza, A N, 2011. Grind curves applied to a range of SAG and AG mills. *Proceedings International Autogenous and Semiautogenous Grinding Technology 2011*, Sep. 25–28, Ed. Flintoff *et al,* Published CIM.

Powell, M S, van der Westhuizen, A P, Mainza, A N, 2009. Applying grind curves to mill operation and optimisation. *Minerals Engineering*, Vol. 22, pp. 625–632.

Powell, M S, Yahyaei, M, Mainza, A N, and Tavares, L M, 2021. The endemic issue of ball mill overload in SABC circuits. *Proc 15th Mill Operators conference 2021* (The Australasian Institute of Mining and Metallurgy: Melbourne).

Rapaport, D C, 2007. Simulated three-component granular segregation in a rotating drum. *Physics Review* E, Vol. 76, 041302.

Rogers, A R and Clements, J A, 1971. The examination of segregation of granular materials in a tumbling mixer, *Powder Technology*, Vol. 5, pp. 167–178.

Rogers, R S C, Bell, D G, Hukki, A M, 1982. A short-lived radioactive tracer method for the measurement of closed circuit ball mill residence time distributions. *Powder Technology*, Vol. 32 (2), pp. 245–252.

Savage, S B, Lun, C K K, 1988. Particle size segregation in inclined chute flow of dry cohesionless granular solids. *Journal of Fluid Mechanics*, Vol. 189, pp. 311–335.

Sherritt, R G, Chaouki, J, Mehrotra, A K, Behie, L A, 2003. Axial dispersion in the three-dimensional mixing of particles in a rotating drum reactor. *Chemical Engineering Science*, Vol. 58, pp. 401–415.

Taberlet, N, Losert, W, Richard, P, 2004. Understanding the dynamics of segregation bands of simulated granular material in a rotating drum. *Europhysics Letters*, Vol. 68, pp. 522–528.

Tavares, L M, Carvalho, R M, 2009. Modeling breakage rates of coarse particles in ball mills. *Minerals Engineering*, Vol. 22, pp. 650–659.

Tupper, G B, Govender, I, de Klerk, D N, Richter, M C, Mainza, A N, 2016. Testing of a new dynamic Ergun equation for transport with positron emission particle tracking. *AIChE Journal*, Vol. 62, No. 3, pp. 939–946.

Vinnett, L, Contreras, F, Lazo, A, Morales, M, Díaz, F, Waters, K E, 2018. The use of radioactive tracers to measure mixing regime in semi-autogenous grinding mills, *Minerals Engineering*, Vol. 115, pp. 41–43.

Weerasekara, N S, Powell, M S, Cleary, P W, Tavares, L M, Evertsson, M, Morrison, R D, Quist, J and Carvalho, R M, 2013. The contribution of DEM to the science of comminution, *Powder Technology*, 248, pp. 3–24. DOI: 10.1016/j.powtec.2013.05.032

Weller, K R, Spencer, S J, Gao, M W, Liu, Y, 2000. Tracer studies and breakage testing in pilot-scale stirred mills. *Minerals Engineering*, Vol. 13, pp. 429–458.

White, H A, 1905. The theory of the tube mill. *The Journal of the Chem, Metall. and Min. Soc. Of S A*, pp. 290–305, May.

Yianatos, J, Bergh, N, Bucarey, R, Rodríguez, J, Díaz, F, 2005. The effect of fines recycling on industrial grinding performance. *Minerals Engineering*, Vol. 18, pp. 1110–1115.

Zik, O, Levine, D, Lipson, S G, Shtrikman, S, Stavans, J, 1994. Rotationally induced segregation of granular materials. *Physics Review Letters*, Vol. 73, pp. 644–648.

Practical measures of process efficiency and opportunity

M S Powell[1], M Evertsson[2], A N Mainza[3] and G R Ballantyne[4]

1. FAusIMM, Emeritus Professor, University of Queensland, SMI-JKMRC, Indooroopilly Qld 4068. Email: malcolm.powell@uq.edu.au
2. Professor, Department of Industrial and Materials Science Rock Processing Systems, Chalmers University of Technology Göteborg, Sweden. Email: magnus.evertsson@chalmers.se
3. Head of Department, Professor, CMR – Dept of Chemical Engineering, University of Cape Town, Rondebosch, 7700, South Africa. Email: Aubrey.mainza@uct.edu.za
4. Director Technical Solutions – Global, Ausenco, South Brisbane Qld 4101. Email: grant.ballantyne@ausenco.com

ABSTRACT

Quantifying the performance of a comminution circuit relative to the potential that can be achieved is a standard requirement in justifying operating practice (the stick) and seeking operational upside (the carrot). Historic measures tend to focus on performance relative to laboratory design tests that provide a direct measure of specific grinding energy, such as the Bond Work index; or use drop-weight breakage tests calibrated to a substantial database of operating sites, such as the SMC methodology.

Although of value, such approaches are flawed in significant aspects. The assumption is that the laboratory prediction is correct and the single sample it is based on is representative. The database benchmarking methods are, by definition, locked into current average operating practice. These approaches do not illuminate upside; can 'punish' operations that are actually more efficient, such as grinding finer than standard operation; and reward poor operation that may comfortably produce a coarser grind than optimal for recovery or excess slimes that reduce recovery and increase water consumption and tailings volume.

The authors present a set of established and easily applied measures, that draw together daily operation, highlight areas of opportunity and inefficiency, use simple samples and data, and can be used to provide the 'size of the prize' in pursuing specific areas of process improvement. These tools include size specific energy (SSE), overall operating effectiveness (OEE) which includes product quality, theory of constraints, and links this to the end objective – maximising the efficient production of valuable metals. Feeds into objective function driven by economics – financial return, energy, environment.

INTRODUCTION

'It is necessary to measure performance in order to improve', is a well-known concept. However, application in practice is not straightforward. The types of measurements should be appropriate to the application, dictated by the objectives and drivers. The measures should also be reliable and provide direction as to how to improve the performance.

In mineral processing the emphasis tends to be on throughput and product size relative to targets. The efficiency of the process tends to be judged against standard measures, so as to provide a benchmark of performance and target for improvement. For example, what is the measured specific energy (SE), kWh/t of ore processed, versus the expected SE? Such measures allow the performance to be quantified, providing a quantifiable gap for improvement, such as the measured SE is 14.8 kWh/t against the expected SE based the ore characterisation and associated models of 13.2 kWh/t, therefore for a given available power, the throughput should be 12 per cent higher. The benchmark tends to be the stick to drive operations to higher production, with the predicted value being the carrot of operational upside.

Historic measures tend to focus on performance relative to laboratory design tests that provide a direct measure of specific grinding energy, such as the Bond Work index; a relative grinding energy such as the SPI or updated SAG grindability test (Starkey *et al* 2015); or use drop-weight breakage tests calibrated to a substantial database of operating sites, such as the SMC methodology (Morrell, 2009); or one or two of a number of other measures. The use of these measures are further

compounded by their inclusion in geometallurgical models that use statistical modelling to calibrate measured performance to the breakage properties mapped into the orebody. The processing plant can then be held to matching the throughput, grind, recovery predicted from the geomet model, and process efficiency measured against this.

Industrial process performance can be measured through a number of methods such as comprehensive survey(s), a quick check on product, operating data assessed via online measures along with automated or manual product shift samples. Although of value in highlighting potential upside in performance, such approaches are flawed in significant aspects. There are a number of assumptions that these comparisons are based on, and limitations that arise from these.

Laboratory test methods:

- The laboratory prediction is assumed to be correct. However, all are proxies for the real system and involve a model, scale-up factors, databases etc to predict the real circuit. They also do not include natural variability and the fact that the circuits are continuous not batch processes.
- The single sample, or few samples, the prediction is based on are assumed representative. This is of course unlikely, especially as the orebody is never equivalent throughout. The natural variability leads to fluctuating performance and thus not an ideal stable performance.
- Variable blending of different parts of an orebody or ore types in the deposit lead to non-linear responses that the ore tests do not predict. To overcome this limitation, the performance needs to be calibrated at the different blends.
- The mode of breakage captured in the laboratory test is assumed to represent the entire comminution circuit, yet some capture only the fine end, some only the coarse impact breakage, and others focus around abrasion milling.

Scale-up:

- Database benchmarking is assumed to represent the optimum performance. Whereas, using a database, by definition, locks into current average operating practice linked to data over the past 20 years or so.
- A laboratory energy value cannot capture the complexity of a circuit process, so the circuit performance has to be assumed to be fixed relative to a simple batch test.
- The scale-up calculations are calibrated to capture the difference in performance between the laboratory test and full-scale operations. Usually this is averaged over a number of calibrated data sets based on surveys of operating plants. These operating plants are by definition assumed to represent good operation, which is flawed in a few respects:
    - How is the absolute performance of the database calibrated?
    - What of the outliners? Where they good or poor or actually a measure of different performance not predicted by the laboratory test in question?
    - Is the distribution of the database reported and used in the ultimate comparison?

Plant performance measurement:

- Averaged daily operating data provides good power and throughput measures, which with the shift samples can be used to calculate SE and assess product against target size. In many ways this is the correct measure to use, for it is the ongoing production performance that matters to profitability. However, they can be misleading in terms of actual efficiency, such as:
    - Inclusion of inappropriate operating periods, such as when the feed is depleted due to delivery issues, fluctuations as ore type changes, variation in feed size with stockpile level and mine operation, and similar external influences.
    - Averaging performance with varying blends when throughput and grind are non-linear with blends by competence.
    - Single point of final production sample to assess overall circuit performance.

    - Lack of reliability and consistency of manual process samples and potential bias in both manual and automated samplers.
- Surveys are a good method to provide a more accurate snapshot of performance than the average daily operation and a basis of measuring operating efficiency under known conditions. However, their limitations are:
    - They do not highlight issues with the plants longer term operation.
    - They tend to be expensive and are thus seldom performed.
    - The final data and reporting is often long removed from the survey period.
    - They apply to the specific feed of the time.

Incorrect scaling with size distribution:

The calibration tests and scaling equations applied to compensate for changes in feed and product size are approximations of the response. As circuits produce a wide range of product sizes, the scaling equations are used in most assessments. The limitations in these include:

- The calculated measures can 'punish' operations that are actually more efficient, such as grinding finer than standard operation thereby moving up the Hukki curve (Hukki, 1962) but predicting a Bond style square root of P80 response.
- They can reward poor operation that may comfortably produce a coarser grind than optimal for recovery, delivering a low SE and low operating work index.
- The SMC method does have improved compensation for this size effect, although it is an average ore dependence whereas the gradient of the Hukki energy curve is ore-dependent.
- The operation may be meeting a simple P80 or SE objective but produce excess slimes that reduce recovery and increase water consumption and tailings volume.

Not quantifying upside:

- The generally applied measures of performance measurement do not illuminate potential upside when the 'expected' performance is met. Noting that this reflects average industry performance over a number of decades, continents, operators, ore types etc, the operations should be aiming to exceed the calibrated average performance of the past.
- The system measure hides where areas of low efficiency lie, such as in the SAG mill, crushers, ball mill, classification circuit, or control method.
- The single measures are not appropriate across the range of equipment, thus if they are applied through appropriate measure across-sections of a circuit, can incorrectly apportion poor performance, such as using Bond work index across the SAG mill (Ballantyne, Peukert and Powell, 2015; Powell *et al,* 2014).

An aspect that is actually central to measuring process efficiency is the appropriate product in terms of mineral liberation for recovery, the real objective function of mineral processing being to recover minerals not to grind rock. Although this aspect won't be addressed in the current paper, it is the basis for directing the operation of a comminution circuit. The improvement of recovery and reduction in water usage, tailing, pollutants should be passed up to the objective function of the comminution product.

The objective of the authors has been to overcome many of the listed limitations and bring quantifiable performance measures closer to operations in a manner that is both correct and meaningful.

THE BASIS OF OPERATING MEASURES

The calculation of efficiency requires input data, measures of operation, a calculation technique, and some comparative measure.

Data measures

Collecting data is fraught with error and uncertainty. A few standard sampling points with good automated or manual access can fulfil every criteria. For ongoing assessment of operating efficiency, the data should be standard measures, such as feed conveyor, equipment power, product sizes from automated samplers. To obtain greater value and discrimination from the measures, it is likely that additional sample access points will need to be engineered, such as crusher product (camera system), SAG product (bespoke sampling system), and even cyclone feed or ball mill product. These can be routine or accessed on a regular basis, such as a weekly check or during good or poor periods of operation.

Calculation of efficiency

The calculation methods should also meet the above criteria. A method that is dependent on complex models suffers from a number of drawbacks such as:

- The outcome is opaque to the site personnel, data into a black box with an output. This can lead to incorrect use and to dismissal of the outcomes.
- The value of the outcome is dependent on the quality and validity of the model. For example, the use of drop weight numbers relies on the use of a bespoke SAG mill model or crusher model.
- Calibrated models, such as the SMC indices, are locked into the database upon which they were developed, thus assuming average performance characteristics. They also tend to have hidden calibration parameters, such as the calculation of the internal indices.
- Geometallurgical models are far more fraught with uncertainty and bias, such as using SPI values to model the throughput and product size by using a multi-parameter empirical back-fit of SPI and assay data to correlated performance.
- The use of uncertainty and variability in the calculated outputs, even through simple standard deviation values, is often not available let alone used.

Comparative measure

The calculation of efficiency tends to be by comparison with the predictions of laboratory tests based on ore samples. These intrinsically suffer from the sampling issue:

- The samples are tiny compared to the production volumes.
- The samples are unlikely to be representative of the entire process stream under comparison.
- Measures are often inappropriately linearly averaged or Kriged between the spatial sample points to provide expected averages for the operating regime.
- Even production samples taken at the time of surveys tend by necessity to be only a single sample at the end of a trial, rather than representative over the trial period.

Additionally, the limitations outlined earlier apply.

Proposed methods

Some key points that are desired in assessing operating performance are that they should be:

- simple
- accurate
- relevant
- achievable
- reliable
- reproducible.

These objectives are interrelated, and consideration of the suite can provide some elegant solutions to assessment. ‘Simple’ refers to both the method of measure and the analysis thereof.

Based on decades of conducting rigorous sampling campaigns, the methods outlined above are not the favoured approach of the authors. In general, the effort and cost associated with the rigour were aimed at development of process models, rather than assessing processing efficiency. In this period of intensive site work, covering possibly 200 plant surveys across the authors, many lessons on technique and value have been learned. For example, based on the ‘blind’ nature of walking onto a plant and expecting to conduct a stable survey within a day or two, the value of first assessing the circuit response was highlighted, as described in the development of grinding curves by Powell and Mainza (2006), and later extended to the Grindcurves methodology (Powell, van der Westhuizen and Mainza, 2009).

In grappling with the issue of more appropriate measures to apply across circuits, Powell (2014) developed the concept of size specific energy (SSE). This method is based off the successful application of this measure at the fine end of product size that had been extensively used in the South African mining industry for over a hundred years (Davis, 1919) and applied to a laboratory testing technique by Levin (1992). Hilden and Suthers (2010) more recently demonstrated the linearity over a range of laboratory equipment, Musa and Morrison (2009) provided improved justification to the theory through analysis of the production of surface area at fine product sizes. The SSE was measured for the first time through single particle breakage testing down to final product sizes by Ballantyne, Peukert and Powell (2015). This has led to ongoing development of the laboratory measurement of SSE by Ballantyne *et al* (2015), Böttcher *et al* (2021) and Ali *et al* (2022). In parallel the use of SSE as a direct measure of energy efficiency on operating sites has evolved over sets of site survey work Powell *et al* (2018, 2021).

The inappropriate nature of standard measures when applied across different types of circuits grinding to a wide range of product size distributions has also been extensively studied, such as in the work of Powell *et al* (2014). The development of a method to more accurately gather measures of energy use in comminution process was developed by Ballantyne, Powell and Tiang (2012) and extended in the continuing study of Ballantyne and Powell (2014). This led to the evolution of measures of process efficiency, captured as ‘Efficiency curves’ by Ballantyne and Powell (2014) and Ballantyne, Mainza and Powell (2015) in order to benchmark relative performance of circuits processing a range of ores to required product sizes. One of the measures used in these curves is the SSE, based on its readily calculated value from production data (Ballantyne and Powell (2014), Ballantyne *et al* (2015), CEEC (2022).

An aspect that these energy measures lacked, was a measure of the effective use of equipment. Thus, a crusher could be run most efficiently in terms of energy use, but be only utilised for a small fraction of the time, thus rendering its overall effectiveness in production as low. The work of Evertsson had identified this need in assessing crushing plants in aggregate production, where utilisation is of primary importance on production of high volume products. To this end he adopted the Overall Equipment Effectiveness (OEE) measure developed in the car industry (Dal, Tugwell and Greatbanks, 2000).

Based on these range of readily utilised measures, the authors have been evolving a standard suite of measures to be of practical use in assessing comminution circuit efficiency. Their application and calculation are described.

SSE

Size specific energy (SSE) is a useful measure of ore competence for changing ores, or of circuit efficiency for a given ore. The concept is illustrated in Figure 1. As energy is cumulatively added to the circuit, the production of the fine final product, generally taken at 75 µm, is linear with the specific energy, in kWh/t. This is irrespective of the comminution equipment, as the efficiencies are similar. However, if one piece of equipment is operating at below the efficiency of the others in the circuit, it will fall below the line. Thus, a simple plot of % – 75 µm versus specific energy across the circuit, will highlight a poorly performing ball mill.

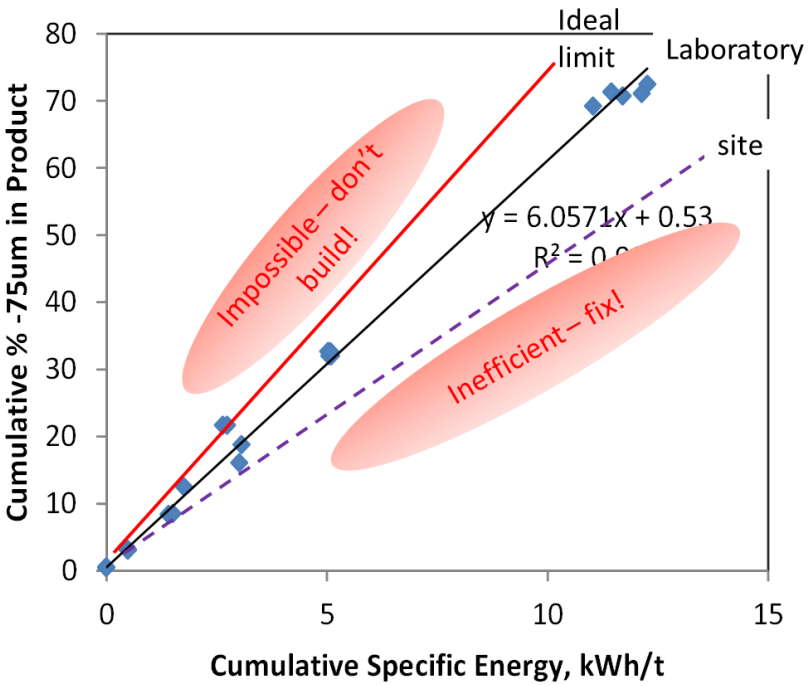

FIG 1 – Illustration of the SSE concept.

The methodology for calculating the SSE for individual comminution equipment within a circuit is described below to facilitate the use of this simple tool.

1. Segment circuit into individual components containing the minimum number of comminution devices either in parallel or series being careful to apply the system boundaries correctly to conserve mass.
2. Record comminution equipment power consumption and the mass flow rate through the subcircuit.
3. Calculate the flow rate of 75 µm (or alternative relevant marker size) material for the feed and product of each comminution device within the subcircuit.
4. Calculate specific energy (kWh/t) and the % new 75 µm generated within the subcircuit by dividing the production rate (t/h) of 75 µm by the total circuit throughput.
5. The size specific energy (SSE) is the specific energy divided by the new 75 µm expressed as a proportion.

Although not ideal and given there is no currently valid alternative, the Bond test results can provide an indication of ore competence in terms of SSE. This is simply done by obtaining the raw Bond test results and following the following process:

1. Use the calculated work index along with the test F80 and P80 to back calculate the assumed specific energy of the test using the Bond equation: $W = 10*Wi*(P80^{-0.5} - F80^{-0.5})$.
2. Calculate the % new 75 µm (or alternative relevant marker size) generated in the Bond test.
3. Calculate the equivalent SSE for the Bond test using the equation: SSE = W/% new 75 µm.

This value for the Bond SSE provides similar results as the Bond work index when the feed and product size distributions are parallel in log/log space. However, they can vary when the feed or product size distribution are relatively fines devoid or have excessive fines. The Bond SSE value can be used to provide a relative efficiency value for individual equipment, or to provide a relative efficiency at different points in time.

Overall equipment effectiveness (OEE)

OEE gives a single-figure measure of the utilised versus available production capability in equipment, based on the following relationship (Dal, Tugwell and Greatbanks, 2000):

OEE%= Availability × Performance × Quality × 100

Availability = actual operating time/planned operating time

Performance = actual rate of production/possible rate of production

Quality = fraction of acceptable product

For a crushing operation the standard manufacturing measures are not necessarily applicable, so equivalent available measures are used:

- Availability: time crusher switched on, ie drawing power/planned total availability (ie total hours – planned hours of maintenance). Thus planned maintenance is excluded, but should also be reviewed for potential production gains, as excessive planned maintenance give an optimistic OEE value.
- Performance: integral of the power draw over the operating time/peak practical capacity (the maximum continuous power that can be used, a reasonable value is 90 per cent of installed power).
- Product quality – percentage of product below desired top size is suitable.

An example of OEE method application taken from a ties operating data is shown in Figure 2. This example shows the OEE plot for a SAG mill circuit equipped with three pebble crushers. In this example, only power draw was analysed, as the product quality is not measured online. Often, online measurement of recycle crusher product is not available; however, it is preferable to include product quality as a parameter to be analysed.

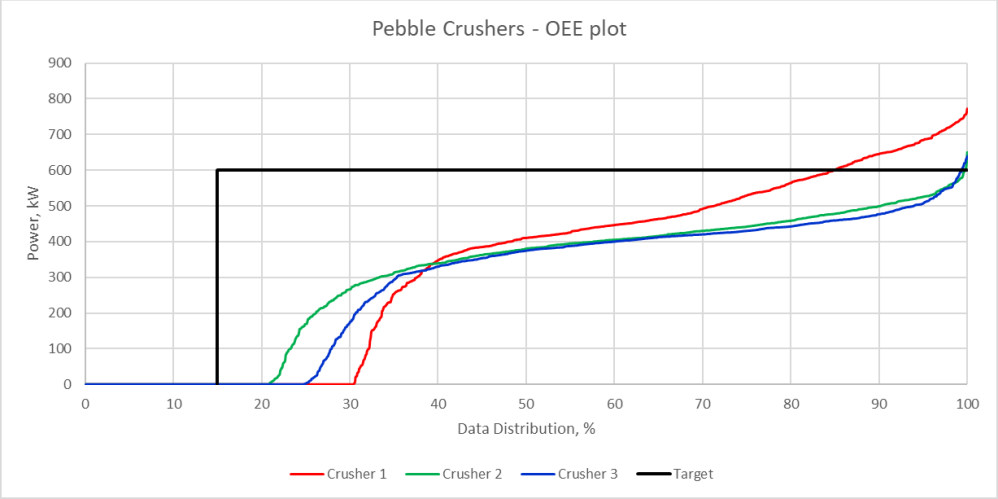

FIG 2 – OEE of a set of three recycle crushers.

The operating data is logged at reasonable resolution representative of the operation, at least five minute intervals, over a few months of operation. All non-numeric and out-of-range values need to be removed from the data. The data is sorted by power from lowest to highest value, then plotted as a cumulative distribution.

The planned availability is 85 per cent, and the power draw achieved is 600 kW for two of the three crushers, so this was set as the power target. The area under the black line gives the 100 per cent target, on which is based the OEE of each crusher. Figure 2 gives the OEE figures for the three crushers, clustered around 60 per cent. In addition to the OEE, the simple idle time can be used, which is given by the data from the OEE that falls below the idle power of the crushers, in this case 140 kW. Unusually, the idle time does not show up on the plots in Figure 2, a power plateau would be expected for a small percentage of operating time.

Unused available time is the difference between the budgeted downtime for mechanical maintenance and the actual idle time. By using the idle time average of 42 per cent and the sites budgeted 15 per cent maintenance time, it is shown that there is 27 per cent available operating time available that the crushers are idle. Another useful indicator is ramp-up time, the period the crusher

is receiving feed but not yet drawing operating power. For these crushers they are only operating in a semi-choke-fed condition from above 340 kW power draw. The difference in operating time between the minimum operating power and idle power gives the ramp-up time of the crusher over the monitored period.

PRACTICAL EXAMPLES

The authors have collected examples from dozens of operations when conducting research and when consulting for process improvement. A few are presented to illustrate the use of these simple measures. A key value of measuring energy efficiency is in how to improve it, so the measures should point to inefficiencies, the magnitude of potential improvement and where to address the issues.

Inefficient parts of a circuit

Total circuit assessment misses out on informing the operation of where a poor area of operation is, such as the SAG mill, ball mill, recycle crushers, unequal feed size distribution, or poor cyclone operation. The SSE method can be used to breakup the circuit into sections, provided good quality samples are taken between sections of the circuit. This can be notoriously difficult, such as SAG circuit product being quite inaccessible, but can usually be addressed with good engineering design and some investment of time and money.

Examples of how this data can be used are presented in Ballantyne, Mainza and Powell (2015), Ballantyne *et al* (2015), and Powell *et al* (2018). Figure 3 shows a circuit where the ball mills were at a lower efficiency than the SAG mill. If the operating issues of the ball mills are addressed, this offers a 10 per cent throughput gain or 5 per cent finer 75 µm product size for improved recovery.

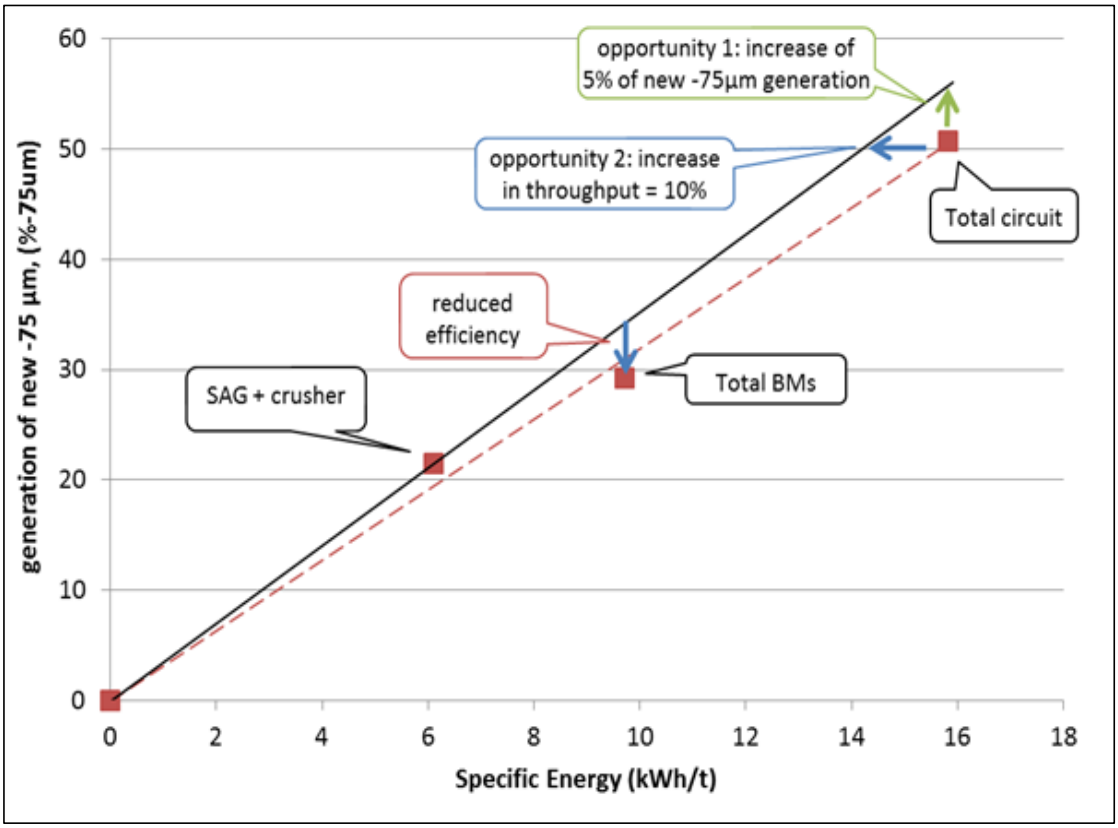

FIG 3 – Differential SSE across a circuit.

Figure 4 presents an example of an SABC circuit where ball mill 1 was markedly less efficient than the rest of the circuit, while ball mill 2 was by far the most efficient. This was tracked down to a biased split of the SAG mill sump product sending the coarser particles to ball mill 1 feed pump. Ball mill 1 was suffering from overload of oversize, while mill 2 was spared this. The impact on the ball mill performance is discussed in the work of Powell *et al* (2021).

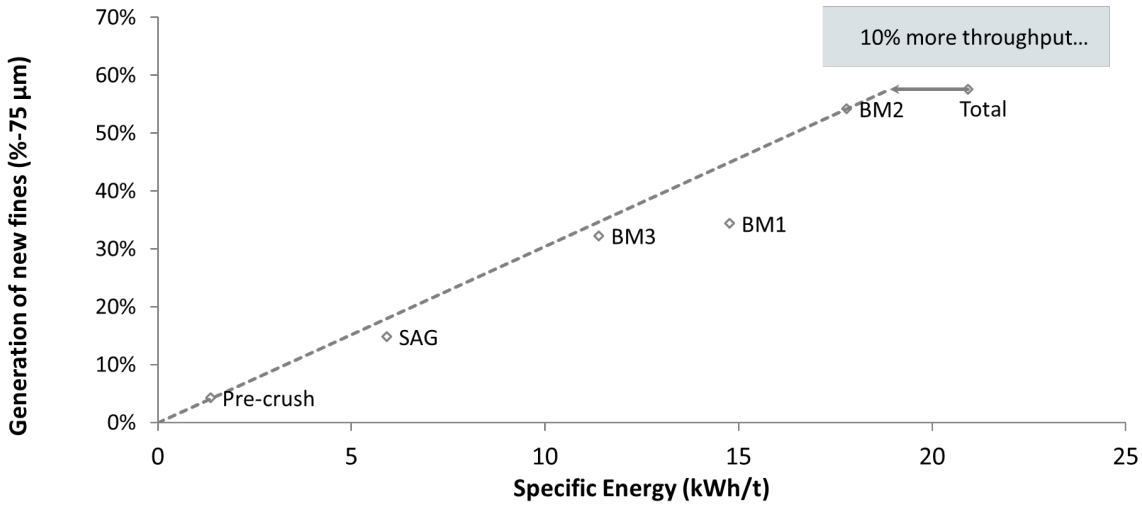

FIG 4 – SSE across a SABC circuit.

Large Cu-Porphyry operation

This comminution circuit has two SAG mills, three recycle crushers and two ball mills, with a total installed power of 80 MW. Table 1 summarises the performance over a year period. The presented OEE is actually optimistic, as this does not include product quality. This is tricky to apply when there is no measure of size between the SAG and ball mill circuits, but can be applied to overall circuit performance.

TABLE 1

Summary of energy efficiency indictors.

SAG Mill No		1	2	Average
OEE,%		85.3	87.7	86.5
Total% Idle		20.2	14.8	17.5
Unused Available%		15.2	9.8	12.5
Ball Mill No		1	2	Average
OEE,%		92	92	92
Total% Idle		9.4	9.0	9.2
Unused Available%		4	4	4
Crusher No	1	2	3	Average
OEE,%	51.7	49.2	42.5	47.8
Total% Idle	32.1	32.1	37.7	34.0
Unused Available%	22.1	22.1	27.7	24.0
Ramp-Up%	7.6	9.9	8.7	8.7

It can be seen from Table 1 and Figure 5 that SAG mill 2 consistently outperforms SAG mill 1, in terms of OEE, utilisation and feedrate, with distribution of feedrate showing a difference of about 10 per cent, despite a close match in mill load (total value of loadcell readings). This points to a need for the site to fucus on the differential, aiming to elevate SAG mill 1 to match the achieved performance of number 2 – clearly an achievable target. The wide range in power from 20 to 24 MW indicates that there is not a consistent target in power draw, which would show up as a plateau in the distribution of data. Upon further investigation it was found that, contrary to expectation of the site personnel, the less efficient SAG mill had a finer feed, lacking adequate rock grinding media in the mill. The control system was found to be dramatically over-responsive, cycling the mill load and

power with control responses at short intervals of 2 to 5 minutes, when the mill response lag is around 20 minutes. Switching off the control system on one mill and leaving on manual feedrate, the feed was steadily increased by 300 t/h with stable operation. The advice to site was that the control system should be replaced, which was actioned with considerable improvement in mill performance. It was also found that the control cap on power was below installed power, at 21 MW on these 24.5 MW motors. Some investigation pointed back to early limits applied by the motor supplier, so this limit was lifted over time to release the milling potential of the circuit.

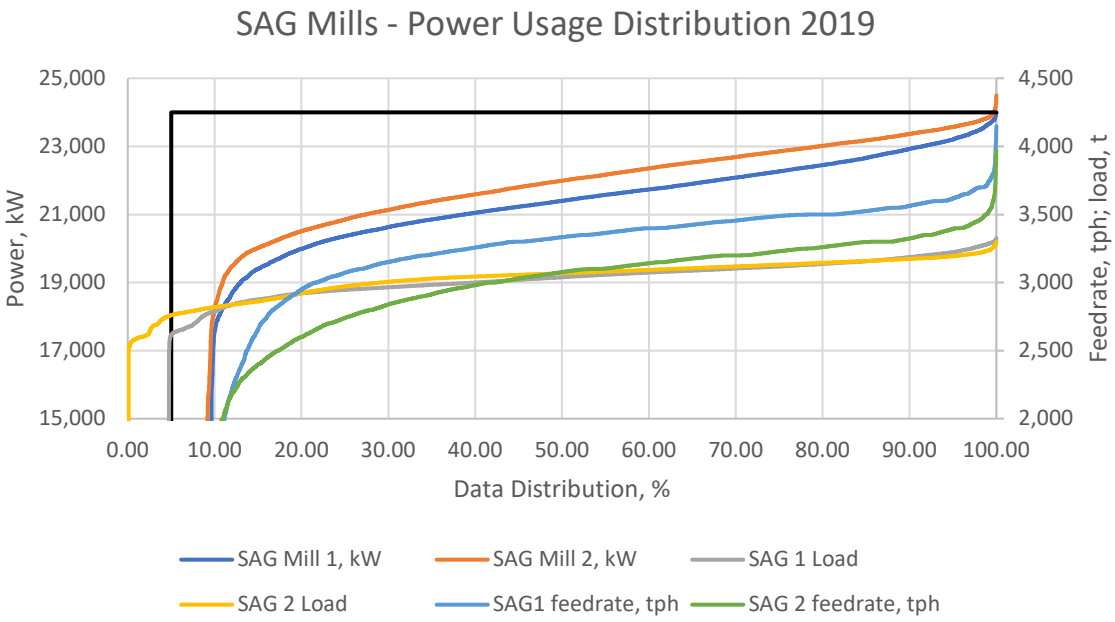

FIG 5 – Distribution of SAG mills performance.

The underutilisation of the balls mills was not as severe, at 8 per cent available capacity, but it is relatively simple, and desirable, to operate ball mills at maximum power. The distribution in load of 200 t, as shown in Figure 6, which was found to arise from the ball mills being overloaded and operating over the power peak, which leads to a drop in power. This had arisen from coarsening of the feed due to the SAG mill screen being opened up, as described in the work of Powell *et al* (2021).

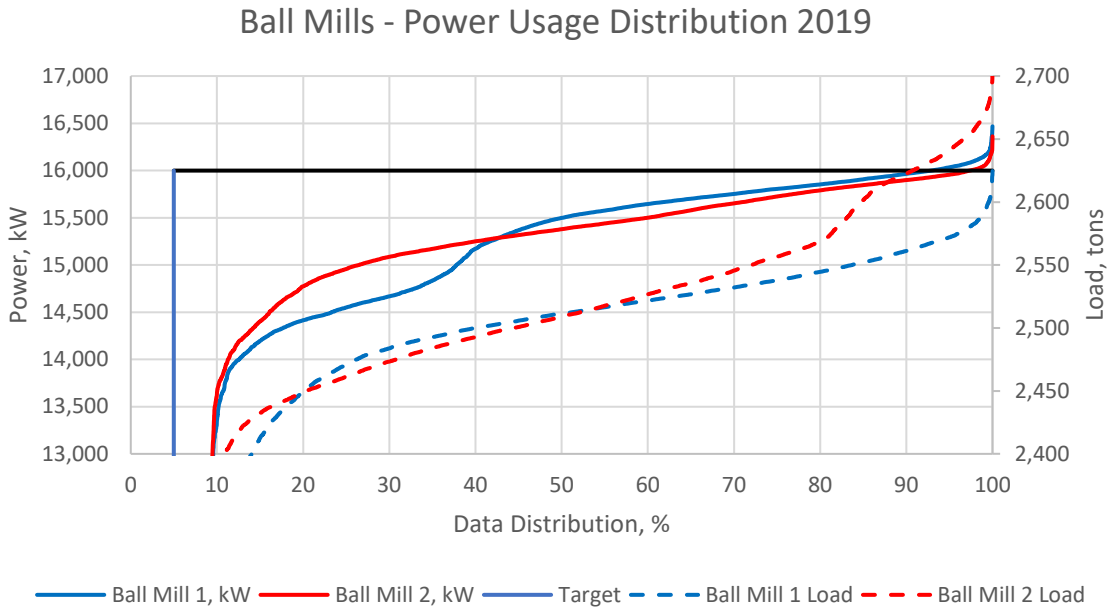

FIG 6 – Distribution of ball mill performance.

The pebble mills suffer from dramatic underutilisation, with an OEE under 50 per cent, with the distribution of utilisation plotted in Figure 7. The crushers have both a low utilisation, at below 70 per cent, and low power draw, ranging from 300–600 kW of the installed 750 kW. The low power draw was linked to excessive time between gap resetting, incorrect chamber design and biased feed distribution. This results in poor use of the available power and a coarse crusher product. This simple illustration also helped avert the commitment to a quite unnecessary fourth crusher that an engineering company was recommending. More information on this common underutilisation of recycle crushers is presented in the work of Powell, Evertsson and Mainza (2019).

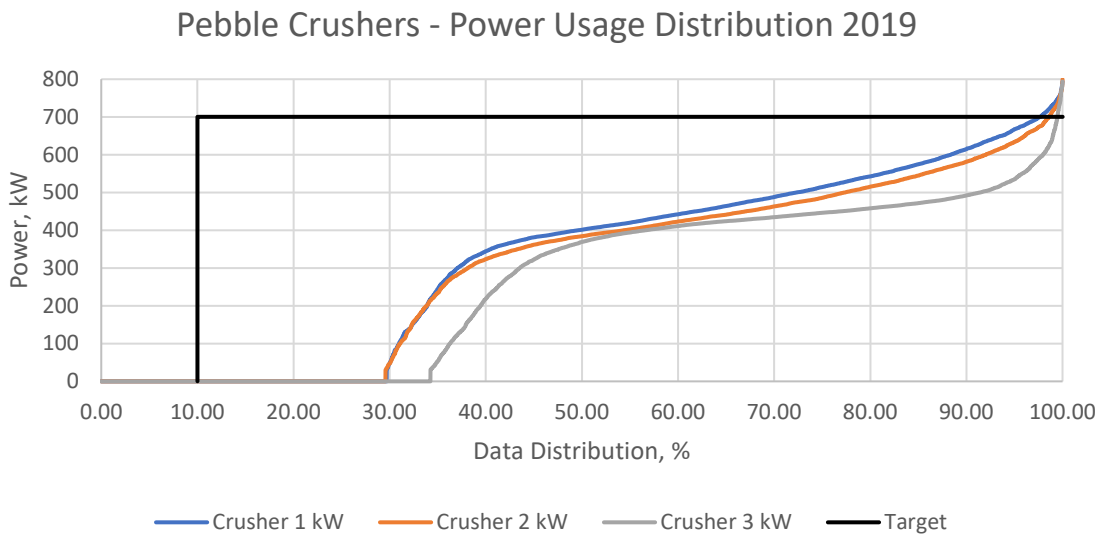

FIG 7 – Distribution of recycle crusher performance.

The SSE based on 230 µm produced was used to analyse the circuit, as this is the standard marker size recorded by the online sampler. The power is the total circuit utilisation (SAG, ball and crusher) averaged over an hour for each separate circuit. The data is filtered for extremes and bad readings. Figure 8 shows the overall trend of the two circuits.

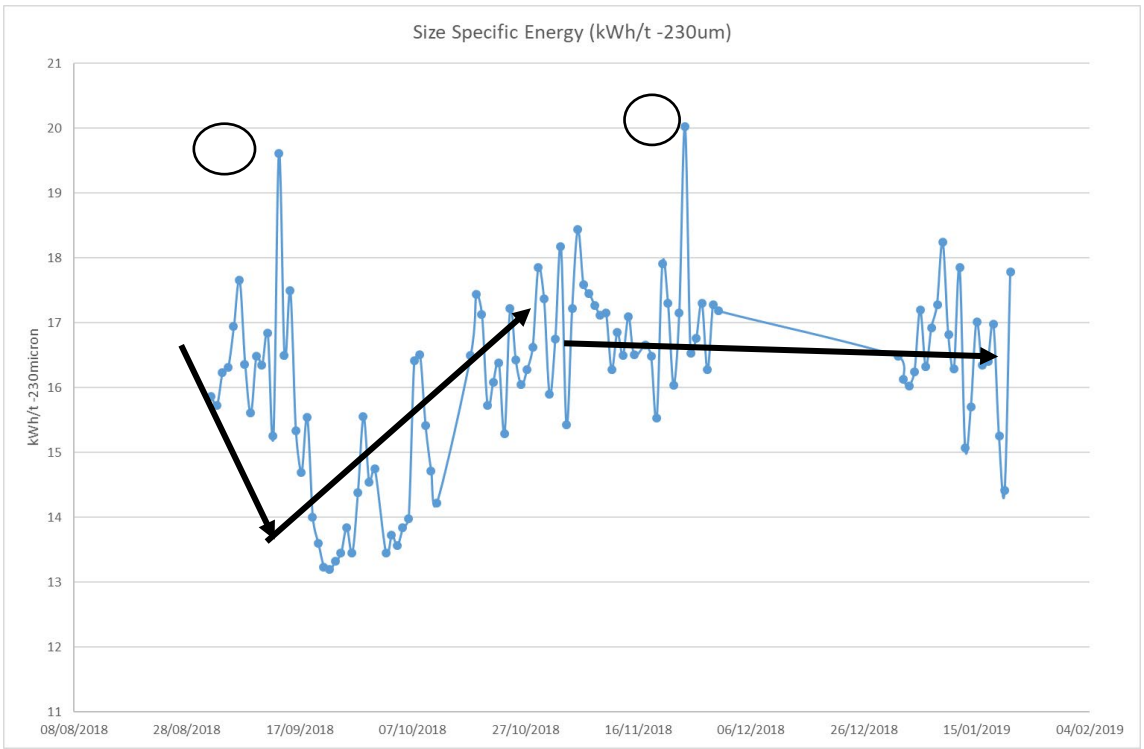

FIG 8 – Size specific energy for the entire comminution circuit over 6 months.

The steadily decreasing trend in SSE through August to September results in a substantial decrease from 16.5 to 14 kWh/t - 230 µm. This rises backup to 17 by November. Such a gross change reflects a markedly softer ore being processed. The extreme outliers arise from periods of low throughput, which drives up the SSE as the ball mills continue to draw full power without the equivalent benefit in reduced grind size, showing up the wasted energy (and ball consumption) in these periods. Superimposed on this are consistent fluctuations of ±1 kWh/t - 230 µm on a daily basis. As it is unexpected that such consistent strong changes in ore competence would be experienced, the cause of such fluctuations should be tracked down. This could point to the need for more consistent blending or control issues that result in fluctuating efficiency of the milling plant.

The SSE distributions in Figure 9, support the conclusion that circuit 2 has a lower efficiency or has more competent feed. Circuit 1 has about 20 per cent of periods with a decidedly softer ore, likely the periods of high fines feed, shown by the excessively low SSE values below 15 kWh/t - 230 µm. The extended shoulders of the distributions, above the indicator lines, also highlight the periods of excessively high energy use for about 10 per cent of operational time. Analysing the operational conditions during these periods should highlight some of the causes of the low efficiency.

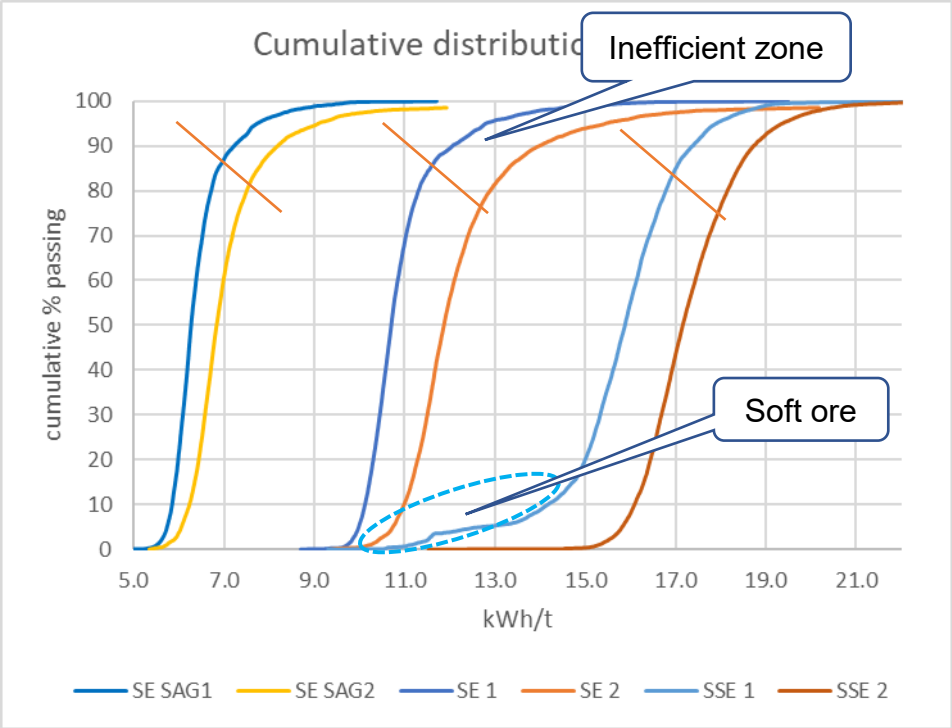

FIG 9 – Cumulative distribution of SE and SSE Dec–Jan 2019.

Small gold operation

For a smaller operation reviewed, the OEE of the SAG mill was exceedingly low at 72 per cent, as shown in Figure 10. This reflects periods of non-use arising from circuit reliability issues and poor liner life. Additionally, the wide variation in power draw shown in Figure 11, point to why the power use is so low.

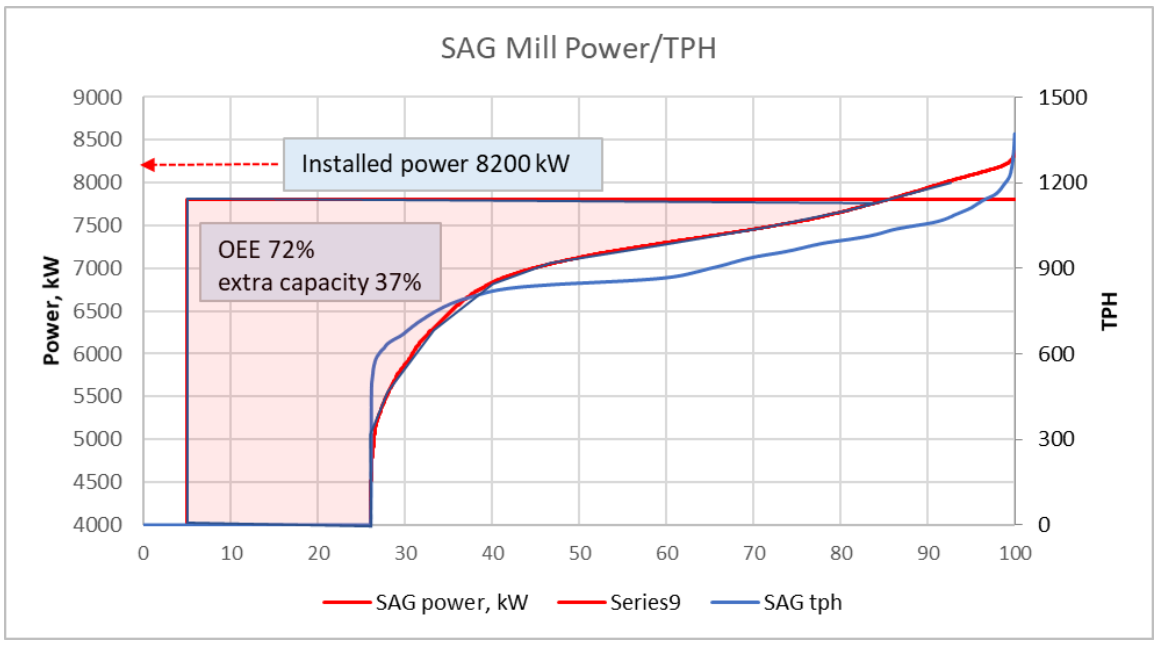

FIG 10 – OEE of a small SAG mill.

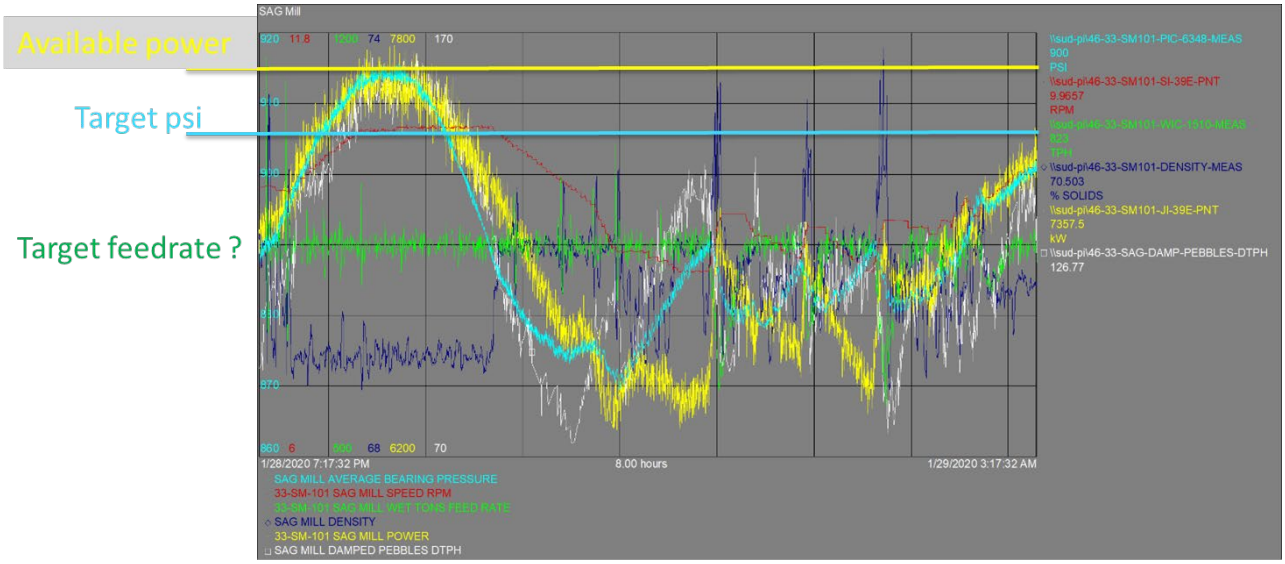

FIG 11 – Process trends for the SAG mill over 8 hours.

As shown in Figure 11, for a random 8 hour period during the site visit, the power varied by 1.3 MW (yellow trend), the load indicator of bearing pressure (blue line) by 45 psi (target window 905 ± 5 psi), while mill speed and water addition were used to try and hold the target feedrate of 850 t/h. The pebble discharge rate varies from 80 to 160 t/h and the product size will be highly variable with the change in power, speed and water addition.

This wide variation in performance was tracked back to lack of control or tracking of the ore dumping and storage in the feed bin, that receives ore from multiple sources. The fluctuation in feed was amplified by an over-responsive control system. The combination of the OEE curves and demonstrated variability in short-term performance provide the basis a business case to address the option of ore tracking and blending.

Iron ore operation

With the increased need to process Magnetite and fine-grained iron ores, the energy-efficient grinding of these relatively soft ores has an increasing importance. A critical aspect of grinding is to minimise the production of slimes that are lost to slimes washing prior to concentration. For this operation there are seven parallel milling streams with a tripper distributing feed between the process

lines. The minus 100 µm fines are washed to slimes on fine screens, representing direct loss of recovery. The distribution of the desired product range being fed to each recovery plant is plotted in Figure 12. Line 7 has a decided lower fraction at 10 per cent lower than lines 2 and 3.

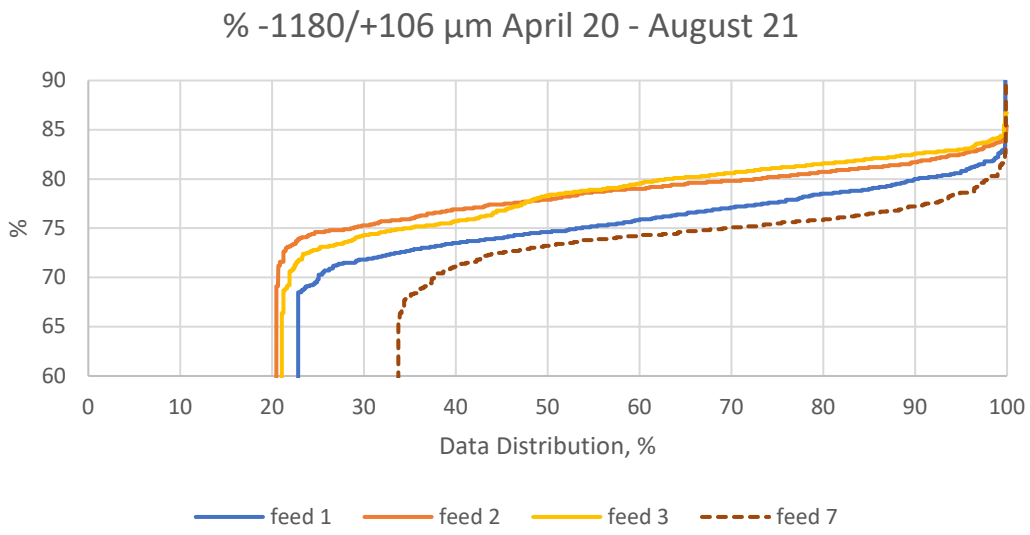

FIG 12 – Distribution of the % of desired product size.

The distributions of SSE are about 4 kWh/t 106 µm higher for lines 7 and 3 compared to the more efficient lines, as shown in Figure 13. This is a difference of around 20 per cent, which bears investigation. The site were encouraged to conduct a detailed comparison of operating conditions between lines 1, 2 and 7 to identify the causes of poor efficiency, with the performance of line 2 as the achievable target.

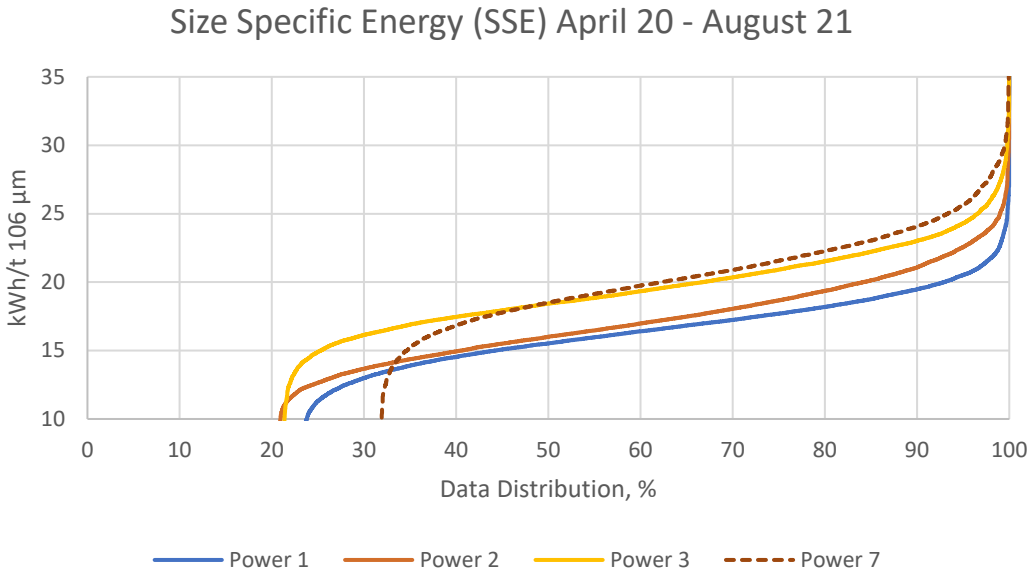

FIG 13 – Distribution of SSE for four milling lines.

CONCLUSIONS

Some alternative options for simple assessments of process efficiency are presented. These are relatively simple to apply with logged process data and supplemented by some more careful sampling. A key aspect that is often overlooked, and tends to only be captured in long and expensive surveys, is the transfer size distribution across-sections of a circuit, such as separate feed size to grinding lines, product size from the SAG mill circuit and recycle crushers. These separate measures are required to identify good and poor performing parts of a circuit.

The authors encourage measures that are easily accessed by site, identify where inefficiencies lie and point to realistically achievable goals – such as the best performing part of a circuit. Caution should be applied in benchmarking against inadequate, often single, feed samples tested at laboratory scale. Additionally, the value of laboratory tests is dependent upon the energy scaling relationships associated with them. It is also noted that all the data benchmarking methods are aspiring to the average performance over the past 20 years, not to future targets the industry should be striving to achieve.

The few measures presented here are only part of the techniques that should be regularly applied in ongoing process improvement and addressing the pressure to focus on efficient energy utilisation. This is an ongoing process where a toolbox of a limited set of valid and achievable measures can be utilised.

Effort is being applied to developing more precise and generally applicable tests that provide a more accurate and reliable measure of performance against what is achievable with current equipment. A target within this is to be able to test a statistically significant number of feed samples against which to compare plant performance. A laboratory test method under development is presented in the work of Ali *et al* (2022). The Geopyörä test presented by Bueno *et al* (2021) and Chavez Matus *et al* (2021) has also been recently developed to better fill this gap. Importantly, such measures are aimed at setting the realistic goals for the energy efficiencies of future circuits.

REFERENCES

Ali, S, Powell, M S, Yahyaei, M, Weatherley, D K and Ballantyne, G R, 2022. A standardised method for the precise quantification of practical minimum comminution energy. *Proceedings of the IMPC Asia-Pacific 2022,* pp 78–92 (The Australasian Institute of Mining and Metallurgy: Melbourne).

Ballantyne, G R and Powell, M S, 2014. Benchmarking comminution energy consumption for the processing of copper and gold ores. *Minerals Engineering* vol. 65, pp. 109–114

Ballantyne, G R, Mainza, A N and Powell, M S, 2015. Using comminution energy intensity curves to assess efficiency of gold processing circuits. *Proceedings World Gold 2015*, 29 Sep. to 1 Oct, Johannesburg, South Africa. Published SAIMM.

Ballantyne, G R, Peukert, W and Powell, M S, 2015. Size Specific Energy (SSE) – Energy Required to Generate Minus 75 Micron Material. *International J, Mineral Processing* vol. 139, pp. 2–6.

Ballantyne, G R, Powell, M S, Bonfils, B, Yahyaei, M, 2015. Simple energy measures for assessing total circuit efficiency. *Proceedings International autogenous and semi-autogenous grinding and high pressure grinding roll technology 2015*, Sep. 20–23, Published CIM.

Ballantyne, G, Powell, M S and Tiang, M, 2012. Proportion of energy attributable to comminution. *Proceedings 11th Mill Operators conference* (The Australasian Institute of Mining and Metallurgy: Melbourne).

Böttcher, A C, Thon, C, Fragnière, G, Chagas, A, Schilde, C and Kwade, A, 2021. Rigidly-mounted roll mill as breakage tester for characterizing fine particle breakage. *Powder Technology*, 383. https://doi.org/10.1016/j.powtec. 2021.01.055

Bueno, M, Trovella, J, Chandramohan, R, Chavez Matus, T, Liedes, T and Powell, M S, 2021. The double wheel breakage test. *Minerals Engineering* 168.

CEEC, 2022. https://www.ceecthefuture.org/energy-curve-program

Chavez Matus, T, Bueno, M, Powell, M S, Michaux, S and Luukkanen, S, 2021. The Geopyörä Breakage test for geometallurgy. *Proceedings of the IMPC 2020: XXX International Mineral Processing Congress*, Cape Town, South Africa, 18–22 oct, 2020. SAIMM.

Dal, B, Tugwell, P and Greatbanks, R, 2000. Overall equipment effectiveness as a measure of operational improvement – A practical analysis. *International Journal of Operations and Production Management*, Volume 20 No. 12, pp. 1488–1502. https://doi.org/10.1108/01443570010355750

Davis, E W, 1919. Fine crushing in ball mills. *Transactions of AIME Mining Engineering*, 61, 250.

Hilden, M and Suthers, S, 2010. Comparing energy efficiency of multi-pass high pressure grinding roll (HPGR) circuits. *XXV International Mineral Processing Congress 2010, IMPC 2010*.

Hukki, R T, 1962. Proposal for a Solomonic settlement between the theories of von Rittinger, Kick and Bond. *AIME Transactions (Mining)*, 223, 403–408.

Levin, J, 1992. Indicators of grindability and grinding efficiency. *Journal of South African Institute of Mining and Metallurgy* 92, 283–290.

Morrell, S, 2009. Predicting the overall specific energy requirement of crushing, high pressure grinding roll and tumbling mill circuits, *Minerals Engineering*, Volume 22, Issue 6, May, Pages 544–549

Musa, F, Morrison, R, 2009. A more sustainable approach to assessing comminution efficiency. *Minerals Engineering* 22, 593–601.

Powell, M S and Mainza, A N, 2006. Extended grinding curves are essential to the comparison of milling performance. *Minerals Engineering*, Vol. 19, no. 15, pp 1487–1494. DOI: 10.1016/j.mineng.2006.08.004

Powell, M S, 2014. *Eco-Efficient Liberation, outcomes and Benefits*, CSRP, Julius Kruttschnitt Mineral Research Centre.

Powell, M S, Evertsson, C M and Mainza, A N, 2019. Redesigning SAG mill recycle crusher operation. *Proceedings International autogenous and semi-autogenous grinding and high pressure grinding roll technology 2019*, Sep. 23–26, Published CIM.

Powell, M S, Hilden, M M, Ballantyne, G, Liu, L and Tavares, L M, 2014. The appropriate and inappropriate, application of the JKMRC t10 relationship. *Proceedings of the XXVII IMPC*, Santiago, Oct. Paper 767.

Powell, M S, Kanchibotla, S S, Jokovic, V, Hilden, M H, Bonfils, B, Musunuri, A, Moyo, P, Yu, S, Young, J, Yaroshak, P, Yalcin, E and Gorain, B, 2018. Advanced Mine to mill application at the Barrick Cortez mine. *Proceedings of the 14th Mill Operators conference* (The Australasian Institute of Mining and Metallurgy: Melbourne).

Powell, M S, van der Westhuizen, A P and Mainza, A N, 2009. Applying grindcurves to mill operation and optimisation. *Miner. Eng*. Vol. 22, pp. 625–632. doi:10.1016/j.mineng.2009.01.008

Powell, M S, Yahyaei, M, Mainza, A N and Tavares, L M, 2021. The endemic issue of ball mill overload in SABC circuits. *Proceedings of the 15th Mill Operators conference 2021* (The Australasian Institute of Mining and Metallurgy: Melbourne).

Starkey, J, Hedderson, J, Reeves, S and Brissette, M, 2015. Tenth anniversary of SAGdesign testing: production successes and development. *Proceedings International autogenous and semi-autogenous grinding and high pressure grinding roll technology 2015*, Sep. 20–23, Published CIM.

Multicomponent modelling and simulation of the Minas Rio iron ore grinding circuit

B K N Rocha[1], T M Campos[2], L P Alves[3], J Silva[4], H D G Turrer[5], J Lichter[6] and L M Tavares[7]

1. Research assistant, Department of Metallurgical and Materials Engineering, Universidade Federal do Rio de Janeiro, 21941–972. Email: brena.nrocha@metalmat.ufrj.br
2. Research assistant, Department of Metallurgical and Materials Engineering, Universidade Federal do Rio de Janeiro, 21941–972. Email: tulio.campos@coppe.ufrj.br
3. Research assistant, Department of Metallurgical and Materials Engineering, Universidade Federal do Rio de Janeiro, 21941–972. Email: luciana.engminas@gmail.com
4. Engineer, Anglo American, Iron Ore Brazil, 35860–000. Email: julio.silva@angloamerican.com
5. Engineer, Anglo American, Iron Ore Brazil, 35860–000. Email: henrique.turrer@angloamerican.com
6. Engineer, Head of Comminution at Anglo American. Email: Jens.Lichter@angloamerican.com
7. Professor, Department of Metallurgical and Materials Engineering, Universidade Federal do Rio de Janeiro, 21941–972. Email: tavares@metalmat.ufrj.br

ABSTRACT

The depletion of the richest ore deposits and the increase in number of mining projects involving deposits with complex mineralogy, higher competence and lower grade has led to an eminent need for improving understanding on multicomponent behaviour in mineral processing. One particularly relevant case is the ball milling of itabirite iron ores fed to the processing plant of Minas-Rio operation in Brazil. Dealing with the two main mineralogical components of the ore, namely hematite and quartz, the operation faces some challenges to improve understanding on how the two components behave in the process. Mathematical models have showed potential to give support in this task, but its applications to describe this type of industrial-scale grinding is still missing. The present work demonstrates the application of a multi-component ball mill model to simulate a closed ball mill circuit with hydrocyclones using the commercial software Integrated Extraction Simulator (IES). Model was calibrated on the basis of bench-scale tests and industrial surveys. Multi-component simulation results are then compared to those considering a single component in the feed, demonstrating the value and great insights that can be achieved by using the former in optimising plant operation.

INTRODUCTION

The complex and heterogenous composition of orebodies is a well-known challenge in comminution operations. Yet, it is common to assume that the orebody responds as a single component to the various comminution and size separation operations. However, it is worth mentioning that, when the ore is ground in large tonnages, a proper understanding on how the different components behave individually and interact with each other is key to improve operations from the point of view of size reduction and liberation (Venkataraman and Fuerstenau, 1984).

Indeed, the current increase in metal demand coupled with significant depletion of the richest ore deposits are placing mineral processing plants in a delicate position to provide a rapid solution when dealing with the so-called multicomponent environment. Direct consequences of these are the growing of ore competence and hardness in the run-of-mine (ROM), the reduction of wear lifetime of parts and machines and the lower ore grade.

With the aim of overcoming the challenges presented above, several studies have been proposed to investigate in-depth the multicomponent behaviour in size reduction. For instance, some authors have performed experimental works to assess performance of AG and SAG milling (Mainza *et al*, 2011; Bueno *et al*, 2011), multicomponent ball milling (Dündar and Benzer, 2015) and component interaction inside hydrocyclone classifiers (Padhi *et al*, 2021). Aligned to the experimental works, advances in the mathematical modelling for multicomponent environments have proven to be a potential solution for process optimisation. Fuerstenau and co-workers (Venkataraman and Fuerstenau, 1984; Fuerstenau and Kapur, 1995) were the pioneers to propose ball mill models relying on multi-component feeds using the population balance model. They partially validated the modelling approach with laboratory experiments but did not report application at industrial-scale.

Additionally, the poor description of ore breakage behaviour and the narrow range of application of these models have limited its appropriate use as a predictive tool.

One type of ore that is facing the challenges of increasing competence and reduced grades is iron ore, which stands out also for the large throughputs processed around the world. One particular and relevant example is the itabirite iron ore in the Minas-Rio operation, from Anglo American (Brazil). In short, the wet part of the circuit consists of primary ball milling in close circuit with hydrocyclones, which processes the ore which may be represented as a binary mixture of Iron Minerals (mostly hematite, with minor amounts of goethite and magnetite) and Gangue (mostly quartz). A recent work reported several challenges to map the presence of different mineralogical components in an iron ore, besides a detailed investigation of its liberation, but also the feasibility of describing it as a binary system in the realm of ball milling (França *et al*, 2020).

The present work proposes a modelling approach describing the industrial-scale closed ball milling circuit processing an itabirite iron ore as a multicomponent mixture. The circuit is simulated in processing a binary mixture of Iron Minerals and Gangue. The multicomponent ball mill model is calibrated on the basis of batch grinding tests and results are validated with industrial survey data. Multicomponent simulations are then compared to those considering a single component in the feed, demonstrating the value and great insights that can be gained when using the multicomponent approach.

MODELLING BACKGROUND

To describe size reduction and classification in an integrated circuit when dealing with a multicomponent approach, the following sections present a multicomponent ball mill model and a multicomponent classification model.

Multicomponent ball mill model

The multicomponent ball mill model is based on the Herbst and Fuerstenau ball mill model (Herbst and Fuerstenau, 1980) with modifications to account for the different breakage responses of different components in the feed.

The model developed by Herbst and Fuerstenau (1980) is based on the population balance model that considers a mass balance for the material in the size class i according to the specific energy (E) applied. Description of size reduction relying on a multicomponent environment follows a similar approach depicted elsewhere (Venkataraman and Fuerstenau, 1984) and is given by:

$$\frac{d[w_i(E_k)]}{d\overline{E}} = -\kappa_{i,k} s^E_{i,k} w_{i,k}(E_k) + \sum_{j=1}^{i-1} b_{ij,k} \kappa_{j,k} s^E_{j,k} w_{j,k}(E_k) \quad (1)$$

where $s^E_{i,k}$ is the specific breakage rate in size class i for component k (t/kWh), $w_{i,k}$ is the mass fraction in size class i for component k, $b_{ij,k}$ is the breakage function in density form for each component k and $\kappa_{i,k}$ is the energy split factor for each component k and size class i that allows to divert breakage for a component when ground in a mixture (Kapur and Fuerstenau, 1988). The specific energy input to the mill for each component k (E_k) is obtained from the ratio between the mill power and the solids feed rate (t/h), being the mill power for each component determined according to its average volumetric fraction in the feed. Volumetric component distribution is simply obtained from the weight component distribution and the measured specific gravities for each component. A key simplifying assumption of the model at this point is the assumption that both components follow the same residence time distribution within the mill. As such, from a feed size distribution given by w_0, an analytical solution for Equation 1 can be stated as follows:

$$w_{f,k} = \left(T_k J_k {T_k}^{-1}\right) w_0 \chi_k \quad (2)$$

where $w_{f,k}$ is the mass fraction in each size class in the product of each component k, w_0 is the mass fraction in each size class in the feed and χ_k is the weight distribution for each component k. The matrixes *T* and *J* may be found elsewhere (Herbst and Fuerstenau, 1980).

The energy split factor ($\kappa_{i,k}$), which allows preferable breakage for one component over the other (Kapur and Fuerstenau, 1988) in a mixture, is calculated as:

$$\kappa_{i,k} = \kappa_{0,k}\hat{x}_i^{\sigma_k} \tag{3}$$

where $\kappa_{0,k}$ and σ_k are fitting parameters for each component κ and $\hat{x}_i$ is the geometric mean size given by $\hat{x}_i = \sqrt{x_i x_{i-1}}$.

In order to solve the model in a continuum operation, the residence time distribution is calculated on the basis of *N* perfect mixers in series model, in which the number of perfect mixers may be estimated by (Austin and Concha, 1994):

$$N = \frac{0.26R_e^{\frac{L_m}{D_m}}}{\sqrt{U_{cs}}} + 1.3 \tag{4}$$

where L_m is the mill length (m), D_m is the mill diameter (m), U_{cs} is the fraction of the critical mill speed and R_e is the Reynolds number.

In order to solve the system of differential equations, the model relies on the non-normalisable breakage function (King, 2001) and the specific selection function (Herbst and Fuerstenau, 1980). The cumulative breakage function is calculated as:

$$B_{ij,k} = \phi_k\left(\frac{x_i}{x_j}\right)^{\gamma_k} + \left(1-\phi_k\right)\left(\frac{x_i}{x_j}\right)^{\beta_k} \text{ for } x_i \geq \omega_k$$

$$B_{ij,k} = \phi_k\left(\frac{x_i}{\omega_k}\right)^{\eta_k}\left(\frac{x_i}{x_j}\right)^{\gamma_k} + \left(1-\phi_k\right)\left(\frac{x_i}{x_j}\right)^{\beta_k} \text{ for } x_i < \omega_k \tag{5}$$

where x_i is the particle size and ϕ_k, γ_k, β_k, ω_k and η_k are fitting parameters for each component k and $b_{ij,k} = B_{i-1,j,k} - B_{i,j,k}$.

On the other hand, the specific selection function is calculated as:

$$\ln\left(s_{i,k}^E/s_{1,k}^E\right) = \xi_{1,k}\ln(\hat{x}_i/\hat{x}_1) + \xi_{2,k}[\ln(\hat{x}_i/\hat{x}_1)]^2 \tag{6}$$

where $\xi_{1,k}$, $\xi_{2,k}$ and $s_{1,k}^E$ are selection function parameters for each component k. The current model takes into account that the $\hat{x}_1$ (reference size) in Equation 6 is equal to 1 mm. Finally, the breakage rates can be described as:

$$S_{i,k} = \frac{P_{Mill,k}}{H_k}s_{i,k}^E \tag{7}$$

where $S_{i,k}$ is the breakage rate for each size class and component k, H_k is the holdup for each component (t) and $P_{Mill,k}$ is the power for each component calculated based on the average volumetric composition of each component (kW).

Aiming to simulate the mill in processing the feed as a single component, the same model is suitable, by considering k = 1.

Multi-component classification model

To describe the classification in the multi-component environment, the proportion of material reported to the oversize (c_{dp}) is then defined for each component as:

$$c_{dp} = 1 - C_{ov}\frac{exp(\alpha_k)-1}{exp\left(\alpha\frac{\hat{x}}{d_{50_k}}\right)+exp(\alpha_k)-2} \tag{8}$$

where d_{50_k} is the size where the probability of going to the oversize is equal to 50 per cent for each component k in the corrected curve, C_{ov} is the water split to the overflow and α_k is a fitting parameter for each component k. Model assumes C_{ov} constant and equal for both components.

METHODOLOGY

The following sections present the experimental work conducted and the modelling and simulation approach. After defining the flow sheet to be studied, industrial surveys were carried out to characterise the plant performance from collecting samples and operational information from the circuit. Samples were characterised through bench-scale tests, through which data was used to

calibrate the mathematical models. Details about model implementation and simulation are also presented.

Since operations of interest consist of ball milling and classification in hydrocyclones, the components defined are Iron Minerals (mostly hematite) and Gangue (mostly quartz). The description used here considers a simplified assumption that both components are fully liberated in the mixture, even though Iron Mineral particles with sizes above about 200 μm may be regarded as locked, with around 80 per cent of hematite and 20 per cent quartz.

Experimental

Industrial survey

A survey was carried out in the Minas-Rio circuit from Anglo American (Brazil). The survey was carried out in the ball milling and classification circuit. Information about operating conditions was recorded from the supervisory system, whereas samples were collected in the fresh feed, ball mill product and both hydrocyclone products. Remaining streams were obtained by mass balance reconciliation. The ball mill investigated has 7.92 m in diameter and 12.8 m in length, whereas the hydrocyclone cluster is composed by eight cyclones with 33 inches of diameter. Ball milling was operating under 27 per cent of mill filling, 76 per cent of critical speed and 70 mm of make-up ball size.

In the lab, samples were subjected to dry sieving in Rotap® sieve shaker until the 75 μm sieve, with the material passing being subjected to wet sieving until the 20 μm sieve. Samples of individual fractions were then ground below 75 μm and analysed in an energy dispersive X-ray fluorescence spectrometer Simutix 14 (Rigaku) for chemical composition, besides analyses of loss on ignition. The fresh feed solids rate was 2856 t/h, whereas the average component composition was 53 per cent Iron Minerals and 47 per cent Gangue in weight, corresponding to 37 per cent Fe. Specific gravity of each component was measured using Helium pycnometry.

Batch grinding tests

Batch grinding tests were carried out with individual components in the narrow size ranges 1.18–0.60 mm and 2.36–1.18 mm. Each component was prepared by dry high-intensity magnetic separation carried out in multiple stages in the device presented elsewhere (André *et al*, 2019) with fresh mill feed samples collected in the industrial survey. Two products generated in magnetic separations were used for each test, namely the Iron Minerals, containing about 85 per cent of hematite and goethite, and the Gangue, with more than 95 per cent of quartz. Batch grinding tests were performed in a ball mill with 30 cm in diameter and 30 cm in length, equipped with six shell lifters. A torque sensor allowed to accurately estimate the mill power consumption. Grinding times of 2, 4 and 10 minutes were used. Tests considered a solids concentration in the slurry by volume equal to 57 per cent. A summary of the conditions used in the grinding experiments is presented in Table 1.

Additional tests with the original samples collected in the fresh feed of the ball milling circuit were also performed. The test relied on a feed size distribution with a top particle size of 19 mm. These tests were carried out with in a bench-scale ball mill with a diameter of 58 cm and a length of 24 cm. The mill was equipped with eight shell lifters and a torque sensor able to record the torque during grinding. Solids concentration by volume was also maintained at 57 per cent, corresponding to a solids concentration by weight of 83 per cent, whereas top size ball diameter was equal to 63 mm. Five grinding times were used (1, 2, 4, 8 and 16 minutes) in order to cover specific energies below and above the one usually observed in the industrial-scale grinding operation, equal to 1.7 kWh/t. A summary of the main grinding conditions, which were selected to mimic the industrial-scale grinding operation, are presented in Table 1.

All feed and product size distributions from each test were analysed using the same approach used to deal with the samples from the industrial survey.

TABLE 1

Summary of the conditions used in the batch grinding tests.

	Single component (composite ore)	Multicomponent (Iron minerals, gangue and mixture)
Mill diameter (cm)	58.0	30.5
Mill length (cm)	24.0	30.5
Mill filling (%)	27.0	24.0
Top ball size (mm)	63.0	36.5
% Critical speed	76.0	76.0
Mill speed (rev/min)	44.2	61.4
Interstitial filling (%)*	100	100

*Estimated from industrial surveys.

Model implementation and parameter fitting

Fitting of parameters in the breakage and selection functions (Equations 5 and 6) from the multi-component ball mill model (section 'Modelling background') was performed using a nonlinear constrained optimisation method able to find the minimum of a multivariable scalar function using the Nelder-Mead method from an initial estimation. Initially this parameter fitting was conducted with batch grinding tests at different grinding times and the objective function was defined from the differences between the experimental and calculated cumulative product size distribution using the least-square method. Breakage parameters for a single-component approach were calibrated with batch grinding data carried out with the complete feed size distribution in the 58 cm diameter batch ball mill (section 'Batch grinding tests'). On the other hand, for a multicomponent approach, parameters from Iron Minerals and Gangue were calibrated from batch grinding tests with material in the narrow size ranges 1.18–0.60 mm and 2.36–1.18 mm.

Integrated simulations

The ball mill model presented in the 'Modelling background' section was implemented in the Integrated Extraction Simulator (IES) as part of the present work to simulate the operation in integrated circuits. Open-circuit and closed-circuit ball mill simulations were carried out following the operating conditions listed in 'Industrial surveys' section. The flow sheet of this ball milling and classification circuit implemented in IES is presented in Figure 1.

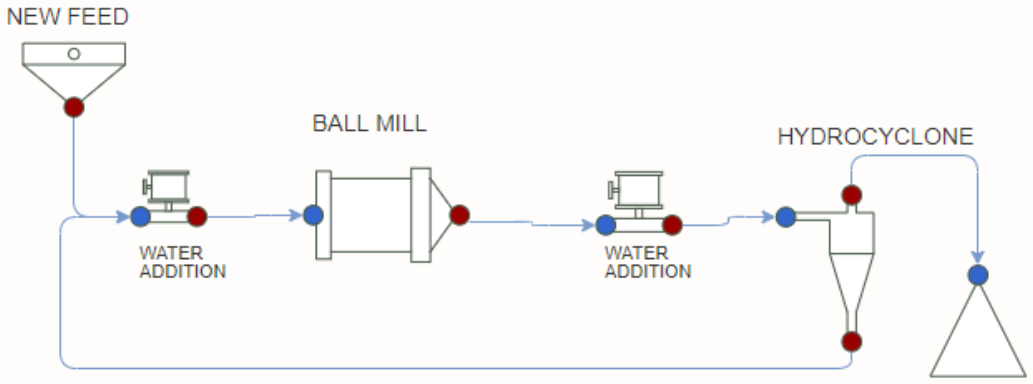

FIG 1 – Flow sheet of the ball milling and classification circuit implemented in IES for simulation.

RESULTS AND DISCUSSION

Experimental results

Evidence of the multicomponent behaviour of the itabirite iron ore processed in the grinding circuit was observed with a careful analysis of size distribution and chemical composition of samples collected in the industrial survey. Figure 2a presents the component distribution by weight in each size class for the underflow of the hydrocyclone cluster, which demonstrates the high iron content throughout the size classes. Results from Figure 2a may be explained by the high specific gravity of the Iron Minerals (4.75 t/m³), which are responsible for their higher tendency to concentrate in the circulating load to the mill. On the other hand, when analysing the component distribution in the hydrocyclone overflow (Figure 2b), the limited proportion of Iron Minerals in the coarser size ranges that report to the desliming stages. These results demonstrate the importance of describing separately the different components in the ore in the hydraulic classification stage.

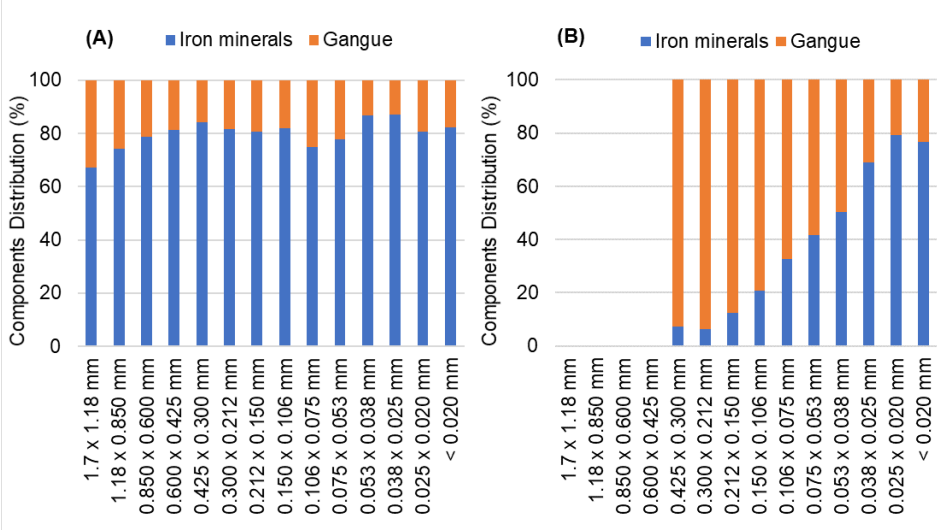

FIG 2 – Component distribution by weight obtained by X-ray fluorescence analysis for the hydrocyclones: (a) underflow; and (b) overflow.

Model calibration

The optimisation of parameters from breakage and selection functions on the basis of batch grinding data when considering the fresh feed as a single component is presented in Figure 3, where very good agreement between fitted and experimental values is evident. These results indicated a small proportion of material remaining in the coarser size classes after 2 min of grinding time (approximately 1 kWh/t), whereas a small but progressive shift was observed in the fine part of the size distribution as grinding progresses. Fitted breakage and selection functions are presented in Figure 4.

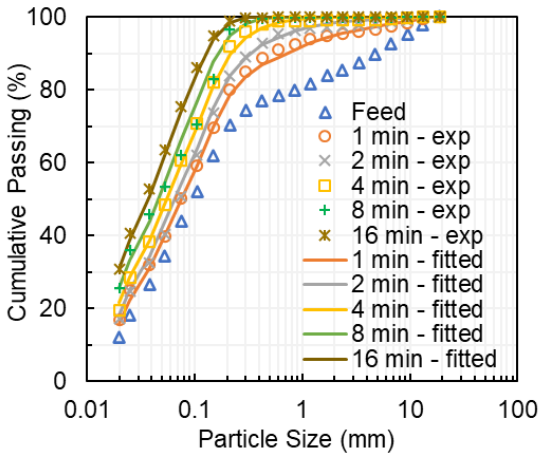

FIG 3 – Comparison between fitted and experimental values for the batch grinding tests carried out with the fresh feed in five different grinding times.

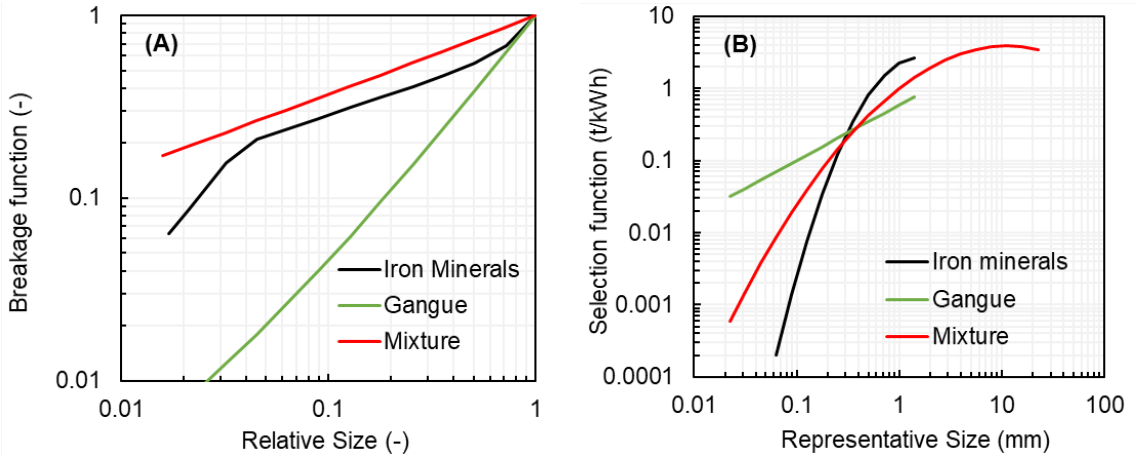

FIG 4 – Comparison of breakage functions (A) and specific selection functions (B) fitted from the batch grinding tests when considering both single and multicomponent approaches.

Parameter optimisation was also carried out for the multicomponent approach when dealing with each component separately in the narrow size ranges of 1.18–0.60 mm and 2.36–1.18 mm, with results presented in Figure 5. Results in Figure 5a demonstrate the well-known behaviour of Brazilian iron ores with a non-normalisable progeny size distribution in respect to the parent particle size for the Iron Minerals component. Beyond the good agreement in Figure 5a, it is also worth mentioning the inflexion point in the size distribution around 53 µm, which is in line with other observation by the authors (Faria *et al*, 2019; Campos *et al*, 2019). On the other hand, progeny size distribution for the Gangue component presented a linear trend in log axes with very good agreement between fitted and experimental values. Additional analyses of results in Figure 5 allows to demonstrate the greater amenability of the Iron Minerals to breakage, being the percent passing the 75 µm sieve equal to 54.4 per cent for Iron Minerals and 20.6 per cent for Gangue after 10 min of grinding. Comparison between fitted and experimental values for the narrow size range of 2.36–1.18 mm was omitted for brevity.

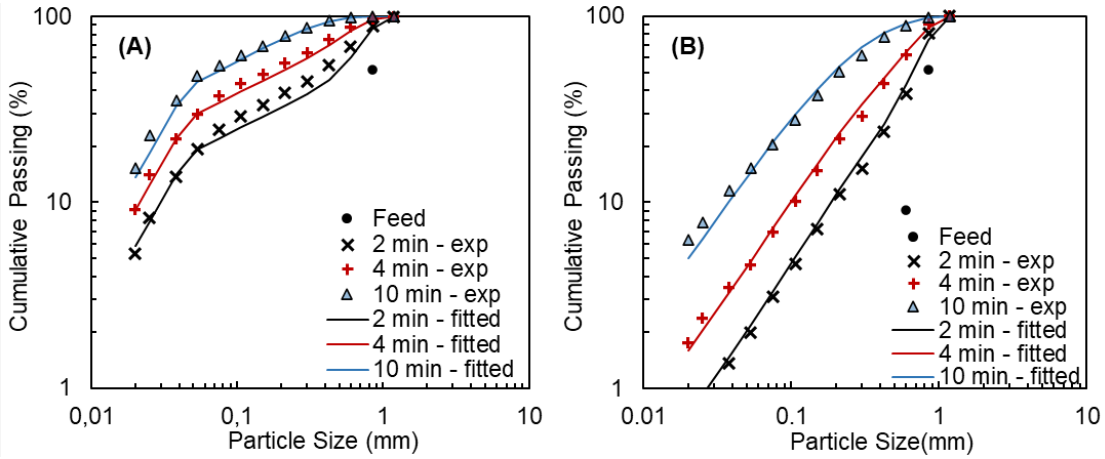

FIG 5 – Comparison between fitted and experimental size distributions from the batch grinding tests carried separately with the: (a) Iron Minerals component; and (b) the Gangue component in the narrow size range of 1.18–0.60 mm.

Breakage and selection functions for each component fitted in Figure 5 are presented in Figure 4 with a comparison between them and the ones fitted in Figure 3 for the fresh feed sample as a single component. Results shown a finer breakage function when considering the ore as a single component (Figure 3), whereas the breakage rate for the ore assumed intermediate values between the Iron Minerals and the Gangue components. Breakage function for the single component approach did not require a non-normalisable breakage behaviour to describe the progeny size distribution. This may be, at least in part, explained by the very large proportion of fines shown in Figure 3, thus dampening the particle segregation effect in these selected size classes.

Beyond the ball mill model calibration, results from the mass balance reconciliation of the survey data showed good results and relative deviations from measurements up to 1 per cent for the mass flow rates and solids concentration. These results were also used to calibrate the classification model (Equation 8). Mass balanced results from each stream were then used to calculate partition data and a comparison between fitted and experimental size distributions is presented in Figure 6 for the single component model (a), as well as when considering the multicomponent model with Iron Minerals (b) and Gangue (c).

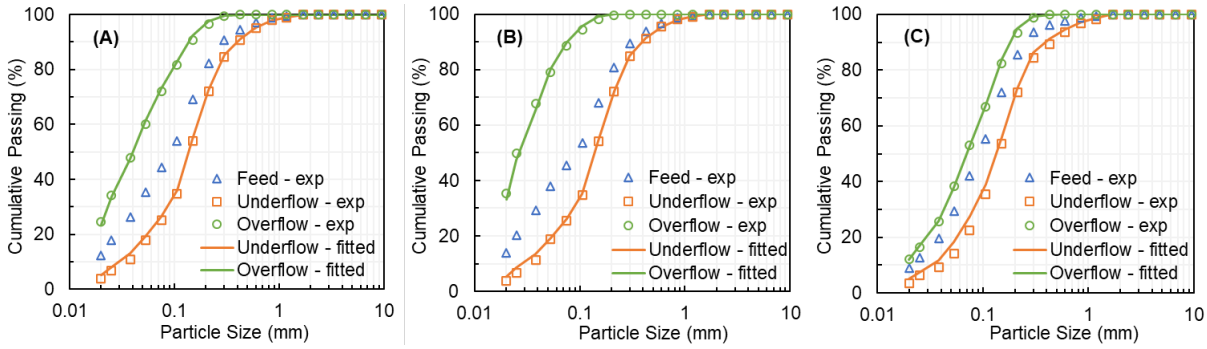

FIG 6 – Measured size distributions from streams around the hydrocyclone cluster and fitted results using a partition curve model considering a single component approach (a), and for both Iron Minerals (b) and Gangue (c) in a multicomponent approach.

For optimisation, the d_{50c} and water split to undersize (C_{ov}) were gathered from experimental analyses, while the remaining parameter (α) was fitted in the IES platform. As shown in Figure 6, very good agreement was reached for the three curves. In addition to Figure 6, results showing the proportion of solids reported to the oversize are then presented in Figure 7. These results indicated a high proportion of Iron Minerals reporting to the hydrocyclone underflow with a d50c of 64 μm and α of 2.1, while the Gangue component presenting a d50c of 214 μm and α of 1.9. The water split to the undersize was constant for both components and equal to 0.77. Fitted results for the mixture in the average between each component demonstrated the good agreement between data used.

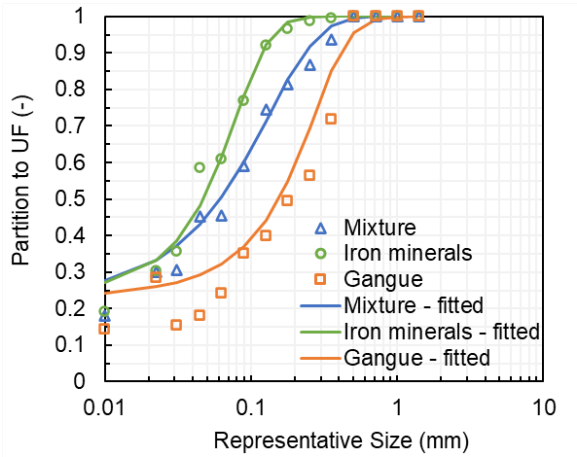

FIG 7 – Partition curve to the underflow (oversize) of the Iron Minerals, the Gangue, and the mixture.

Model validation

Validation of the models was carried out by performing simulations of the industrial grinding circuit operation. Figure 8 shows a comparison between experiments and model predictions when dealing with the ball mill as an open circuit unit, where Figure 8a describes the model prediction when dealing with a single component model and Figure 8b shows the multicomponent one. Very good agreement was reached between experiments and predictions made through both modelling approaches. Parameters fitted for each component separately, even though using narrow size ranges, demonstrated the feasibility to describe the particle breakage behaviour of the ore. An additional point should be raised regarding the single component model: it required a minor adjustment of the s_1^E parameter (Equation 6) fitted from the batch-grinding test in order to describe the industrial-scale results. This adjustment may be explained, at least in part, by conditions in the batch grinding tests (Table 1) that differed from the industrial-scale.

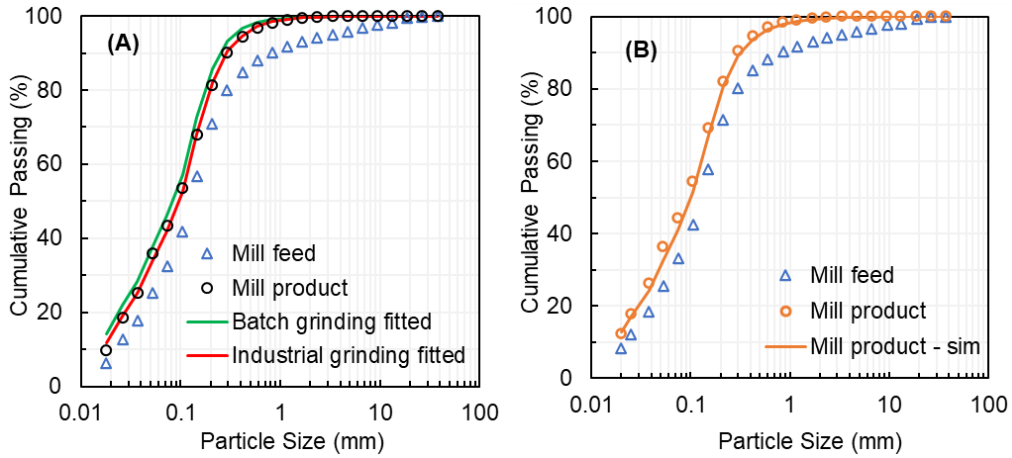

FIG 8 – Comparison between model predictions and experiments for the industrial-scale ball mill analysed in open circuit using the single component model (a) and the multicomponent model (b).

Figure 9 shows the comparison between experimental and predicted product size distributions for each component for the case of the ball mill operating in open circuit. Very good agreement was reached for Iron minerals component, whereas the Gangue product presented good agreement in the fine part of the size distribution and an underestimation in the coarser size classes. This may be explained by the assumption that Gangue is fully liberated in the coarser size classes (section 'Component definition'), which is not entirely valid. Indeed, experimental evidence up to this point indicates that quartz composing the locked particles (coarser size classes) presented higher amenability to breakage in comparison to its behaviour when ground fully liberated. Unfortunately, no mathematical description of this different behaviour has been used in the present work.

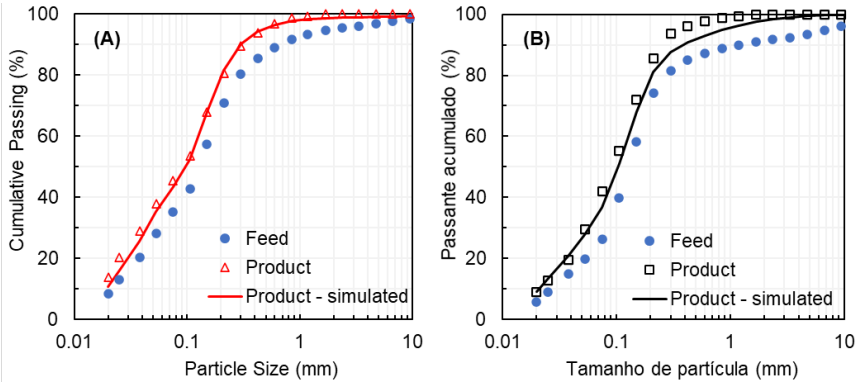

FIG 9 – Experimental and simulated particle size distributions of Iron Minerals (a) and Ganga (b) in the mill product.

Integrated simulations

The multicomponent model was applied to describe the closed ball mill circuit. A comparison is shown in Figure 10 between model and experiments on the ball mill discharge (Figure 10a) and the hydrocyclone products (Figure 10b). Relatively good agreement was achieved is some streams when using the multicomponent model to describe the size reduction, but significant underestimations also became evident. Poor agreement in the coarser size classes for the Gangue component (Figure 9b) was responsible for limiting these predictions. Description of the closed-circuit ball mill performed considering a single component model was very good and is shown in Figure 10c and 10d. Nevertheless, it is worth mentioning that the multicomponent modelling approach justifies its used by the strong capability of mapping the proportion valuable and deleterious components in the mixture, thus allowing to propose changes in the operational strategy or circuit configuration to overcome, for instance, overgrinding of liberated Iron Minerals.

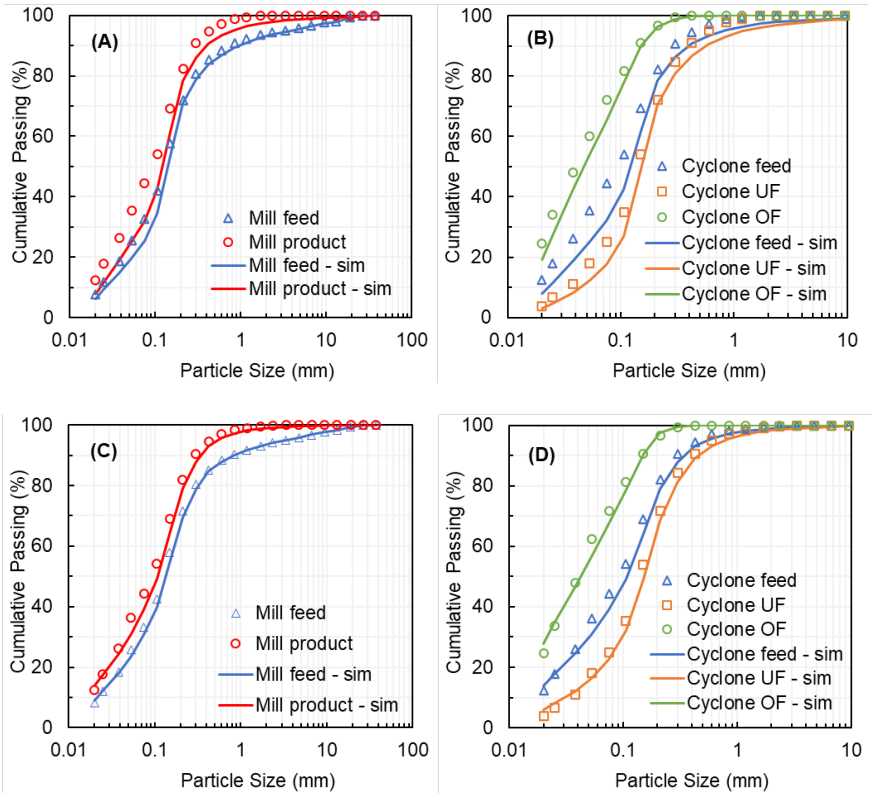

FIG 10 – Comparison between model and experiments for the mill product (a) and the hydrocyclone products (b) using a multicomponent modelling approach (top), whereas comparison between model and experiments for the mill discharge (c) and the hydrocyclone products (d) using a single component modelling approach (bottom).

Table 2 presents a comparison between some performance variables obtained through the multicomponent simulation and during the industrial survey. Results showed some important deviations in the circulating load and in solids feed rate to the mill feed, even though model being able to accurately predict the component content in each stream evaluated, clearly demonstrating the enrichment of Iron Minerals in the hydrocyclone underflow.

TABLE 2

Comparison between the main performance variables obtained during the industrial survey and from the multicomponent simulation.

Performance parameter		Iron minerals		Gangue	
		Experimental	**Simulated**	**Experimental**	**Simulated**
Ball mill	Composite feed rate (t/h)	4760	6421	2096	2856
	Composite feed component content (%)	69.4	69.2	30.6	30.8
	Composite feed F_{80} (μm)	297	265	281	579
	Composite P_{80} (μm)	208	204	186	355
Cyclones	Product passing 75 μm sieve (%)	35.4	27.3	26.3	21.3
	Circulation load ratio (%)	217	328	58	115
	Underflow content (%)	81.0	76.3	19.0	23.7
	Overflow content (%)	53.0	53.0	47.0	47.0

CONCLUSIONS

The present work investigated an industrial-scale ball milling and classification circuit from standpoint of multicomponent response. Definition of components resulted in characterising the iron ore as a binary mixture composed by Iron Minerals and Gangue.

Hydrocyclone classification survey results were used to describe the behaviour of each component, where substantial enrichment of the Iron Minerals component was observed in the hydrocyclone underflow.

A multicomponent modelling approach was used to simulate the industrial-scale ball mill circuit. Calibration of the model on the basis of batch grinding tests showed feasibility to describe the component breakage behaviour, with results being partially validated in industrial-scale. Limitation when describing the Gangue component was reported and associated to the simplified assumption that particles are fully liberated in the entire size classes. The underestimation of size reduction of the Gangue component had direct effects on the prediction of the mixture when the model was not able to properly predict the closed ball mill circuit.

A comparison between single and multicomponent approaches to describe the same industrial-scale circuit showed similar results between them, with single-component approach presenting closer predictions to measure results when applied to simulate stream size distributions in the closed circuit. Nevertheless, the ability of the multicomponent model to map the component within the circuit was demonstrated and provided insights, which suggests that it can serve as the basis for investigating different operation strategies so as to, for instance, prevent regrinding or fully liberated hematite.

ACKNOWLEDGEMENTS

We thank you Anglo American S.A for the financial and technical support and the Brazilian agencies CAPES and CNPq for the additional financial support.

REFERENCES

André, F P, Miceli, H, Moura, L C, Neumann, R and Tavares, L M, 2019. Upgrading a manufactured fine aggregate for use in concrete using dry rare-earth magnetic separation. *Minerals Engineering*, 143, 105942.

Austin, L G and Concha, F, 1994. Diseño y simulación de circuitos de molienda y clasificación. CYTED. Programa Iberoamericano de Ciencia y Tecnología para el Desarrollo. Subprograma de Tecnología Mineral. Red de Fragmentación XIII-A.

Bueno, M, Shi, F, Kojovic, T, Powell, M S, Sweet, J, Philips, D and Plint, N, 2011. Multi-component autogenous pilot trials. *Proceedings of SAG conference.*

Campos, T M, Bueno, G, Barrios, G K and Tavares, L M, 2019. Pressing iron ore concentrate in a pilot-scale HPGR. Part 1: Experimental results. *Minerals Engineering*, 140, 105875.

Dündar, H and Benzer, H, 2015. Investigating multicomponent breakage in cement grinding. *Minerals Engineering*, *77*, 131–136.

Faria, P, Rajamani, R K and Tavares, L M, 2019. Optimization of solids concentration in iron ore ball milling through modeling and simulation. *Minerals*, *9*(6), 366.

França, J R, Barrios, G K, Turrer, H D and Tavares, L M, 2020. Comminution and liberation response of iron ore types in a low-grade deposit. *Minerals Engineering*, *158*, 106590.

Fuerstenau, D W and Kapur, P C, 1995. Newer energy-efficient approach to particle production by comminution. *Powder Technology*, *82*(1), 51–57.

Herbst, J A and Fuerstenau, D W, 1980. Scale-up procedure for continuous grinding mill design using population balance models. *International Journal of Mineral Processing*, 7(1), 1–31.

Kapur, P C and Fuerstenau, D W, 1988. Energy split in multicomponent grinding, *International Journal of Mineral Processing*, 24(1-2), 125–142.

King, R P, 2001. *Modeling and simulation of mineral processing systems*. Elsevier.

Mainza, A N, Kojovic, T, Katsande, E, Seerane, K, Khumalo, R and Seke, D, 2011. AG milling with and without pebbles recycle – Effect on multi-component ore deportment and throughput. *Proceeding of SAG Conference*.

Padhi, M, Mangadoddy, N, Mainza, A N and Anand, M, 2021. Study on the particle interaction in a hydrocyclone classifier with multi-component feed blend at a high solids content. *Powder Technology*, *393*, 380–396.

Venkataraman, K S and Fuerstenau, D W, 1984. Application of the population balance model to the grinding of mixtures of minerals. *Powder technology*, *39*(1), 133–142.

Research on the throughput of inertia cone crusher using orthogonal experimental method

X Wang[1], X Xia[2], T Song[3], F Ma[4] and G Liang[5]

1. BGRIMM Technology Group, Beijing 100160, China; State Key Laboratory of Mineral Processing, Beijing 102628, China. Email: wang_xu@bgrimm.com
2. BGRIMM Technology Group, Beijing 100160, China; State Key Laboratory of Mineral Processing, Beijing 102628, China. Email: xiaxo@bgrimm.com
3. BGRIMM Technology Group, Beijing 100160, China; State Key Laboratory of Mineral Processing, Beijing 102628, China. Email: songtao@bgrimm.com
4. School of Mechanical Engineering, University of Science and Technology Beijing, Beijing 100083, China. Email: yeke@ustb.edu.cn
5. School of Mechanical Engineering, University of Science and Technology Beijing, Beijing 100083, China. Email: b20170255@xs.ustb.edu.cn

ABSTRACT

Inertia cone crushers have found applications mostly in steel slag crushing operations in China. Compared with conventional eccentric cone crushers, the crusher has an obvious advantage in reducing product size. In addition, they are mostly used in two-stage open circuit crushing flow sheet, which simplifies the crushing process. However, inertia cone crushers are not widely used in the mineral processing industry due to their low crushing capacity. In this paper, the throughput performance of the inertia cone crusher was investigated in a laboratory-scale inertia cone crusher and relationships between operational parameters were identified. Iron ore was crushed using orthogonal experimental method under different machine parameters and operational conditions. The crusher throughput and product size distributions were determined. The effects of parameters such as eccentric speed, discharge gap, eccentric mass and eccentric distance on product mass flow and product size were investigated. The results of this study can help reduce the feed size of the mill in order to reduce total energy consumption of comminution.

INTRODUCTION

Inertia cone crusher (Vaisberg, Zarogatsky and Turkin, 2004) was designed by the former Soviet Union based on the vibration theory. The biggest difference between inertia cone crusher and eccentric cone crusher is that the motion of the moving cone is excited by a vibrator (unbalanced rotor) rather than the eccentric sleeve. The vibrator is fixed on the sliding bearing around the shaft of the moving cone. The moving cone swings around the centre of the spherical support under the inertial centrifugal force generated by the vibrator. The main body is located on the rubber shock absorber. The structure diagram of the inertia cone crusher is shown in Figure 1.

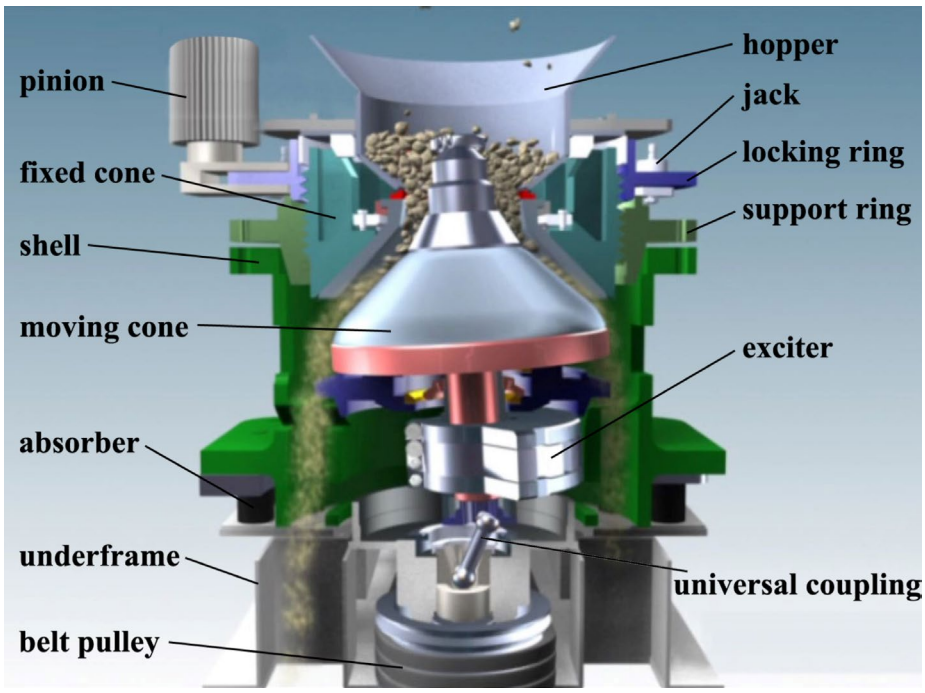

FIG 1 – Structure diagram of inertia cone crusher.

In conventional cone crushers, the motion of the moving cone is independent of the loading of the crusher. The eccentricity and the stroke amplitude are constant (Evertsson, 2000). In order to achieve interparticle breakage, choke fed conditions are recommended. In inertia cone crushers, the stroke amplitude of the moving cone is unconstrained (Blekhman, 2000). The crushing force of the inertia cone crusher is influenced by the eccentric speed, eccentric mass, eccentric distance, the chamber geometry and the material property. The concept of the discharge gap which is called 2S is different from the closed side setting (CSS) in eccentric cone crushers. Particles are more likely to be compressed into a compact state, leading to interparticle breakage (Vaisberg and Zarogatskii, 2003). Due to this characteristic, choke fed conditions are required at all times (Xia *et al,* 2009). Starved feeding conditions will cause severe damage to the crusher.

The power input of the inertia cone crusher is successively transmitted to the crushing mechanism through the universal transmission device and the sliding bearing. The centrifugal rotational motion of the vibrator is not limited by the spatial position of the moving cone. Since there is no rigid connection, when the oscillating motion of the moving cone is stopped by an uncrushable body in the chamber, the mechanical transmission keeps running around the sliding bearing. Due to this feature, the inertia cone crusher is suitable for tramp iron conditions. In addition, the particles undergo more crushing times under the high-frequency vibration crushing process, and the final products have fine particle size. Compared with conventional eccentric cone crushers, the crusher has an obvious advantage in reducing product size. Based on the above two advantages, inertia cone crushers have found applications mostly in steel slag crushing operations in China (Xia and Luo, 2015). It can be well applied to iron-containing materials, better realise the dissociation of slag and iron, recover metal and produce steel slag micropowder at the same time. In addition, due to the high proportion of fines in the product, closed circuit crushing and sieving flow sheet are usually not required. They are mostly used in two-stage open circuit crushing flow sheet, which simplifies the crushing process. However, inertia cone crushers are not widely used in the mineral processing industry due to the low crushing capacity. Due to the low-grade of the ore, more ores need to be processed in order to obtain sufficient metal. The production scale of the mineral processing industry is usually large, which leads to higher requirements for the processing capacity of the crushing equipment. It is necessary to increase the processing capacity of the inertia cone crusher while maintaining the product size to meet the crushing demand of the mineral processing industry. Because the grinding operation consumes more energy than the crushing operation, inertia cone crushers will help reduce the feed size of the mill and reduce the total energy consumption of comminution.

EXPERIMENTAL

Laboratory-scale GYP100 inertia cone crusher

The equipment used in the experiment is a laboratory-scale GYP100 inertia cone crusher. The bottom diameter of the moving cone is 100 mm. It can be used to crush brittle materials such as ores, refractories, abrasives, ceramics and so on. The structure diagram of the GYP100 inertia cone crusher is shown in Figure 2.

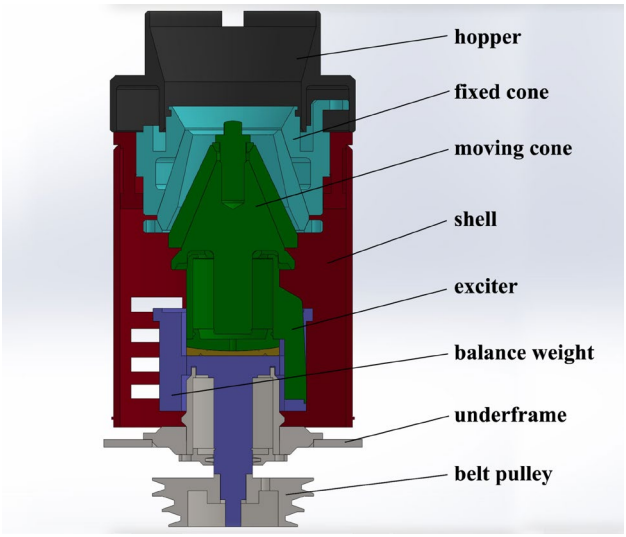

FIG 2 – Laboratory-scale GYP100 inertia cone crusher.

Experimental conditions and procedures

Crusher throughput, product size distribution and working current were investigated under different equipment parameters and operating conditions. Unlike previous experiments, this experiment introduces how the centripetal force component (m*r) works. Eccentric mass (m) is composed of an eccentric body and several counterweights installed on different locations. It is changed by adjusting the number of counterweights. Eccentricity (r) is influenced both by the number of counterweights and their installation location on the eccentric body. Their values are automatically calculated by 3D drawing software. The vibrator diagram with eccentric body and all nine counterweights is shown in Figure 3, which is displayed in bottom orientation.

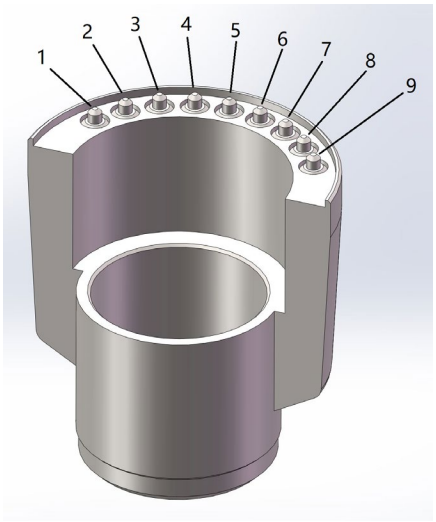

FIG 3 – Vibrator diagram with an eccentric body and 9 counterweights.

The experimental conditions include eccentric speed (ω), discharge gap (2S) and centripetal force component. Each condition has three values according to the structural parameters, operating

instructions and limitations. Different eccentric speeds are obtained based on the belt pulley design of the crusher. The crusher gives three standard eccentric speeds by changing the belt transmission ratio. The discharge gap of the equipment called 2S should not exceed 6 mm.

The materials used in the experiment are iron ore with a magnetic iron content of around 3.5 per cent. Ore minerals are mainly magnetite and pyrite, with a small amount of hematite and limonite. Gangue minerals include quartz, plagioclase, potassium feldspar and biotite. The feed size of the GYP100 inertia cone crusher should not exceed 12 mm. The minerals used in the experiment were mainly in the size range of 2–8 mm.

In order to reduce the number of tests and to cover all parameter combinations to the greatest extent, the orthogonal test method was used. Orthogonal experimental design is a method of scientific analysis by rationally arranging multi-factor experiments using orthogonal tables. According to the number of factors and levels, the orthogonal table was selected. The header design of the orthogonal table with three factors and three levels was completed. Nine experimental combinations (No. 1–9) were obtained. The above experiments include the effect of the centripetal force component under different conditions. However, counterweight and eccentricity affect the crushing force ($m*r*\omega^2$) in different ways. In order to study the effect of counterweight and eccentricity, six groups of supplementary experiments (No. 10–15) were carried out. The experimental conditions and results are shown in Table 1. Installation location corresponds to the circular holes arranged in order in Figure 3.

TABLE 1

Experimental conditions and parameters for crushing tests.

Test #	ω (rpm)	2S (mm)	m*r (g*mm)	m (g)	r (mm)	Number of counter-weights	Installation location	Through-put (g/min)	Current (A)
No. 1	1609	2	34.2	1.798	19.0	2	19	162.9	2.13–2.24
No. 2	1609	4	35.7	1.841	19.4	3	129	172.9	2.29–2.42
No. 3	1609	6	37.1	1.884	19.7	4	1289	398.9	2.14–2.16
No. 4	2299	2	35.7	1.841	19.4	3	129	169.3	2.74–2.95
No. 5	2299	4	37.1	1.884	19.7	4	1289	291.1	2.41–2.65
No. 6	2299	6	34.2	1.798	19.0	2	19	345.7	2.05–2.13
No. 7	2840	2	37.1	1.884	19.7	4	1289	265.3	3.14–3.43
No. 8	2840	4	34.2	1.798	19.0	2	19	391.4	3.16–3.29
No. 9	2840	6	35.7	1.841	19.4	3	129	258.8	2.83–3.06
No. 10	2299	4	34.2	1.798	19.0	2	19	177.9	2.99–3.08
No. 11	2299	4	34.2	1.755	19.5	1	5	247.4	2.58–2.67
No. 12	2299	4	35.7	1.841	19.4	3	129	235.7	2.66–2.92
No. 13	2299	4	35.7	1.798	19.9	2	37	311.1	2.63–2.74
No. 14	2299	4	35.1	1.798	19.5	2	28	271.4	2.5–2.64
No. 15	2299	4	36.1	1.798	20.1	2	46	240.7	2.29–2.36

In each experiment, the weight of the crushed material was about 1 kg and the crushing time varied between 3 and 5 minutes. The current was measured throughout the crushing process. Products were gathered when the equipment was working steadily. After the crushing test, the materials were sieved with a vibrating screen and weighed separately. All of these tests were performed under choke fed conditions. The crushing process and product characteristics were measured under different equipment parameters and operating conditions. The experimental process is shown in Figure 4.

FIG 4 – The experimental process.

Through the record of the crushing time and weight of the product, the crusher throughput and current of 15 groups of parameters combination were obtained.

RESULTS AND DISCUSSION

Crusher throughput

First, the crusher throughput of the first nine groups of orthogonal experiments was analysed. In order to study the effect of each factor on the experimental results, an intuitive analysis is carried out, which is also called range analysis. The larger the range, the more important the corresponding factor. The purpose of the range analysis is to determine the order of primary and secondary factors in order to select a better parameter. In order to visualise the range analysis results, a trend graph (effect curve graph) was drawn as shown in Figure 5. These data were calculated from the first nine groups of orthogonal test results (No. 1 to No. 9) by using range analysis calculation method.

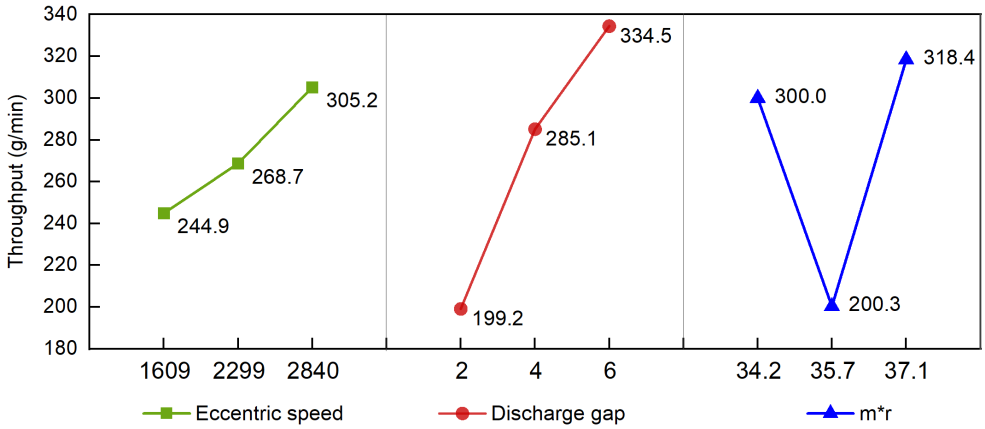

FIG 5 – Effect plot for range analysis of test No. 1 to No. 9.

The range analysis results show that the discharge gap has the greatest impact on crusher throughput, followed by the centripetal force component and finally the eccentric speed. The largest and smallest values differ by a factor of 1.68, and the change is faster and the curve is steeper. From the overall trend of curves, except for the centripetal force component, the crusher throughput is proportional to eccentric speed and discharge gap. It is large at both ends and small in the middle of the centripetal force component. A larger discharge gap provides a larger swing range of the moving cone. More crushing force is generated by a larger vibrator rotation radius. The space between the mantle and concave increases at the same time. These cause more

crushing to occur and rapid vertical flow-through the crushing chamber, resulting in higher throughput. In terms of eccentric speed, there is a contradiction with the results of previous papers (Wang *et al,* 2021). The difference is that all nine counterweights were installed in the previous experiment. In this experiment, most of the counterweights were removed. Three installation methods were used in the orthogonal test with only 2–4 counterweights. Less counterweights reduce the centripetal force component and affect the inertial force. For some of the tests there wasn't enough crushing force to break the feed, so the results are in two bands – before there wasn't enough force, and after there was enough force. The previous work always applied enough force to be in the 'ideal crushing phase', which means the feed is always broken with enough crushing force during the steadystate downward movement.

The current value fluctuates within a certain range when the crusher is working. The current value and amplitude range can be used as a reference for power consumption. The relationship between current and throughput under different centripetal force components is shown in Figure 6.

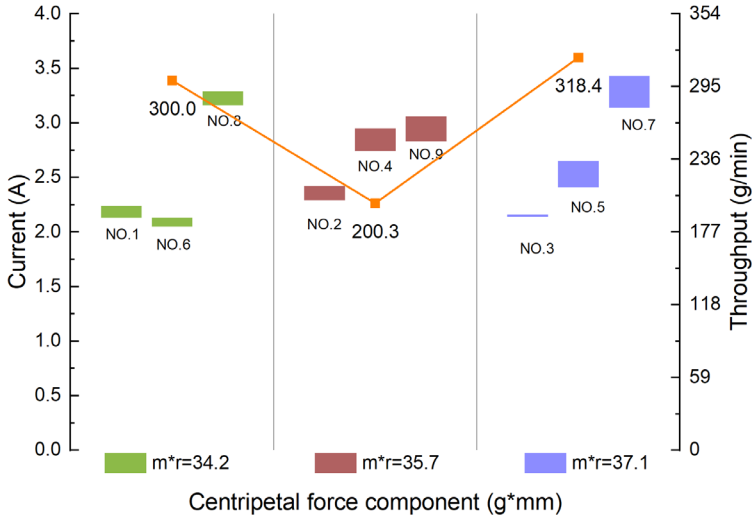

FIG 6 – Relationship between current and throughput under different centripetal force component.

When the centripetal force component increases, both the current value and the amplitude range increase. The greater centripetal force component requires more power to drive. In the case of less counterweights, the eccentric excitation force is not enough to meet the force threshold required for material crushing. The crusher throughput is limited by the crushing force. When the inertial force exceeds the force threshold required for material crushing, the crusher throughput is limited by the volume space of the crushing chamber. From this moment on, the crusher throughput decreases with the increase of the eccentric speed. Therefore, in addition to the traditional method of adjusting the discharge gap, selecting the appropriate eccentric speed and vibrator installation method is an important way to adjust crusher throughput. Above all, the first step is to find the 'ideal crushing phase' when facing materials with different mechanical properties and to make sure the crusher operates in that phase.

Second, the influence of different installation methods under the same centripetal force component is analysed. Two groups of experiments were selected for analysis, and the results are shown in Figure 7.

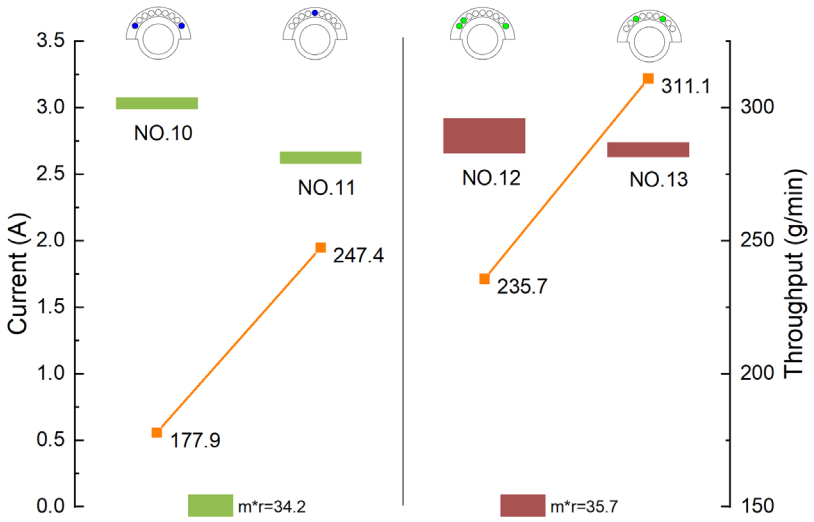

FIG 7 – Results showing the effect of changing counterweight installation location under the same centripetal force component with 34.2 and 35.7 respectively.

By comparing the two groups of experiments, it can be seen that the crusher throughput is larger when less counterweights are concentrated in the middle than that when more counterweights are evenly distributed on both sides.

Finally, the variation of eccentricity is analysed under the same counterweight condition. The results of four test data are shown in Figure 8.

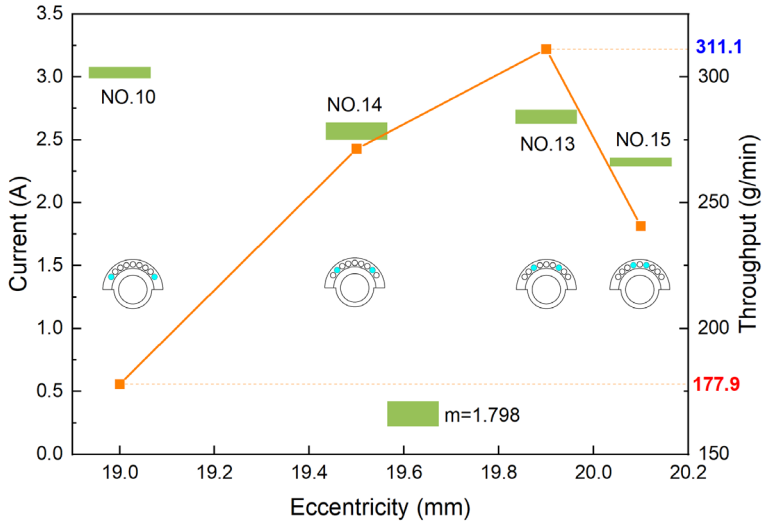

FIG 8 – Results showing the effect of different eccentricity under the same eccentric mass of 1.798.

Maximum throughput occurred at test No. 13 with 311.1 g/min and minimum throughput occurred at test No. 10 with 177.9 g/min. When the current fluctuation is not much different (in the range of 2.63–3.08 A), the crusher throughput is nearly 1.75 times different. The data in Figure 7 and Figure 8 are from the last six groups (No. 10 to No. 15) of experiments, which belong to single factor and multi-level experiments. There are some contradictions with the previous orthogonal test results of three factors and three levels in terms of crusher throughput. The difference is that the crusher throughput varies at both ends with the change of the centripetal force component. This may be because the single factor experiment results are insufficient. Under multi-factor and multi-level conditions, they cannot fully cover all the data. This phenomenon will be further tested at other levels by single factor experiments.

Product size distributions

There are 15 groups of tests, all of which use the same material as the feed. To represent the feed size, three samples were randomly selected from the raw materials. The sieving results of the feed materials are represented in Figure 9 by the dashed lines. The product size distributions of nine groups of products in the orthogonal tests were first analysed, as shown in Figure 9.

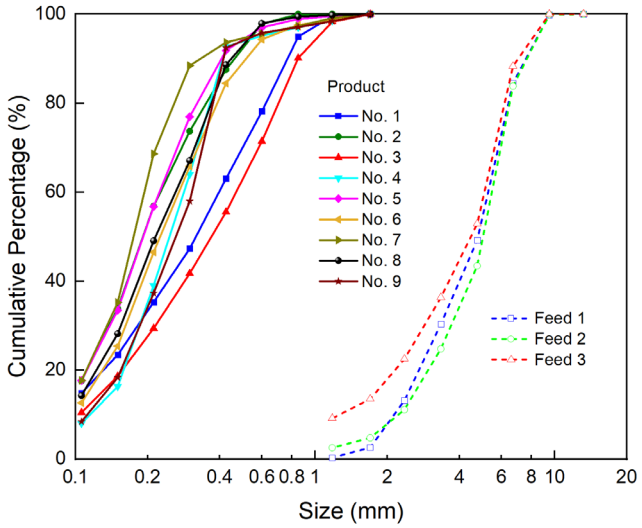

FIG 9 – Feed and product particle size distribution in orthogonal test.

The P_{80} product size in all nine groups of experiments is below 0.8 mm. The coarse and fine ends of the curves correspond to test No. 3 and No. 7. Test No. 3 uses the minimum eccentric speed, the maximum discharge gap and the maximum centripetal force component. Test No. 7 uses the maximum eccentric speed, the minimum discharge gap and the maximum centripetal force component. The eccentric speed controls the period of the precession of the compression zone around the concave circumference of the crusher. This in turn determines the duration of the compression of the particles when the bed is in the compression phase and the time available for particles to move lower during the expansion phase of the crusher cycle. High eccentric speed shortens the expansion phase of the crusher motion, which leads to a reduced vertical downward displacement per rotation cycle. More crushing frequency increases the chance of particles being broken, which leads to an increase in breakage, resulting in a finer product. The increase in the discharge gap creates more space for particles to flow-through the crusher chamber per unit time, and bigger particles are more likely to be discharged. As a result, the product size becomes coarser.

The two coarser products of test No. 1 and No. 3 in the curves use the minimum eccentric speed. In test No. 1, the inertial force is insufficient because the centripetal force component is small and the discharge gap is small, resulting in a low degree of breakage. In test No. 3, although the crushing force is increased, the degree of breakage will still decrease due to the increase in the discharge gap. In terms of influence on product size, the eccentric speed is the highest, the discharge gap is the second, and the centripetal force component is the lowest.

Figure 10 shows the product size distribution of the last six groups of tests, which are single factor and multi-level experiments. The effect of the centripetal force component on product size is studied. From the density of the curve distribution, the particle sizes of the last six groups of products are relatively closer to the results in the orthogonal tests. The best product comes from test No. 15, which uses the maximum centripetal force component. This result is consistent with the orthogonal test result. Under the four test conditions shown in Figure 7, with the same centripetal force component and relatively the same current, the crusher throughput varies greatly, but from Figure 10, the product size does not change significantly. The results show that reasonable parameter matching can effectively increase crusher throughput while keeping product size stable without increasing power consumption. It also shows that when the parameter settings are unreasonable, less energy is used for crushing operations and more energy is used for internal mechanical transmission, vibration and friction loss. A typical example in industrial applications is

the direct impact and wear between two liners. This conclusion can also be proved from the product size distribution of test No. 10 and No. 13 in Figure 8. The particle size is relatively close, but the crusher throughput differs by a factor of nearly 1.75. In addition, the power consumption is higher in the case of low crusher throughput. The kinetic motion of the equipment consumes more energy than the crushing operation. Inertia cone crushers are generally heavier than eccentric cone crushers under the same diameter of the moving cone and consume more energy in terms of equipment dynamics. Future work includes optimising the parameters of rigid body and bulk material coupling vibrating crushing system to achieve a reasonable distribution of crushing energy. Two-way coupled simulation using discrete element method and multi-body dynamics is an effective way to achieve this goal.

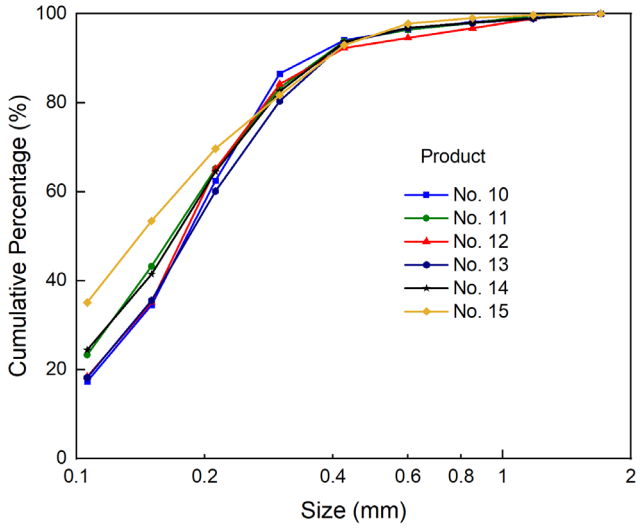

FIG 10 – Feed and product size distribution in the last six groups of tests.

CONCLUSIONS

A laboratory-scale GYP100 inertia cone crusher was investigated by orthogonal test method. The effects of changes in mechanical parameters and operating conditions on product characteristics were investigated. The main conclusions can be summarised as follows:

- The discharge gap has the greatest impact on crusher throughput, followed by the centripetal force component, and finally the rotational speed.
- The eccentric speed has the greatest impact on product size, followed by the discharge gap, and finally the centripetal force component.
- Whether the crusher throughput is limited by the power or the volume of the crushing chamber depends on whether the eccentric excitation system can provide enough crushing force required for material crushing.
- Reasonable parameters matching can effectively increase the crusher throughput while keeping the product size stable without increasing the power consumption. Parameter design directly affects whether energy consumption is used for crushing or mechanical transmission loss to a large extent.

ACKNOWLEDGEMENTS

This work was supported by the National Key R&D Program of China (Grant No. 2020YFE0201100), and the Key Projects of Department of Science and Technology in Gansu Province (Grant No. 20ZD7WC010). The authors would like to thank Beijing Kaite Crusher Ltd. for permission to publish a portion of the results on this research effort.

REFERENCES

Blekhman, I I, 2000. Vibrational mechanics: nonlinear dynamic effects, general approach, applications, (World Scientific: Singapore).

Evertsson, C M, 2000. Cone crusher performance, PhD thesis, Chalmers University of Technology, Sweden.

Vaisberg, L A and Zarogatskii, L P, 2003. Foundations of optimal mineral disintegration, *Journal of Mining Science*, 39(1): 87–93.

Vaisberg, L A, Zarogatsky, L P and Turkin, V Y, 2004. Vibrating crushers, Foundations of Calculation, Designing and Technological Application.

Wang, X, Song, T, Xia, X and Luo, X, 2021. Experimental study on influencing factors of product characteristics of inertia cone crusher, *Nonferrous Metals Mineral Processing Section*, 2: 123–128.

Xia, X and Luo, X, 2015. *Inertia cone crusher*, Metallurgical Industry Press: Beijing.

Xia, X, Sun, X, Tang, W and Luo, X, 2009. Interparticle comminution, more crushing & less grinding and inertia cone crusher, *Metal Mine*, 7: 79–83, 89.

Investigation of silica reduction effects on HPGR operation condition in case of iron ore increasing specific surface area

M Zare[1], R Hejazi[2], M Saghaeian[3] and V Sheikhzadeh[4]

1. Head of Mineral processing, R&D Department, Fakoor Sanat Tehran Company (FSTCO), Tehran, Iran, 1586633118. Email: M.Zare@fstco.com
2. R&D Manager, Fakoor Sanat Tehran Company (FSTCO), Tehran, Iran, 1586633118. Email: Hejazi@fstco.com
3. Vice Chairman Technical, Fakoor Sanat Tehran Company (FSTCO), Tehran, Iran, 1586633118. Email: Saghaeian@fstco.com
4. Managing Director, Fakoor Sanat Tehran Company (FSTCO), Tehran, Iran, 1586633118. Email: Sheikhzadeh@fstco.com

ABSTRACT

High-Pressure Grinding Roll (HPGR) is one of the efficient methods for increasing the specific surface area (SSA) of iron ore concentrate for pellet feed production. HPGR grinding mechanism implies that material should compressed between the two rolls, therefore layer of material must be able to resist required pressure for achieving suitable grinding conditions. In this study, by doing SSA increasing tests with pilot HPGR, the effects of silica reduction on SSA increasing results were investigated. For this purpose, HPGR tests were performed on an Iranian magnetite concentrate before and after reverse flotation silica reduction tests. Based on the laboratory test results, silicates have been concentrated in two fraction sizes of the sample comprises coarser than 150 microns in form of quartz and finer than 7 microns in form of iron silicates. These silicates have been effected on reduction of concentrate bed pressure resistance by creating a pasty and sticky mud. In this condition, HPGR cannot work properly and operation results are not acceptable. According to flotation silica reduction tests, with 90 per cent weight recovery, concentrate Fe grade is increased from 67.8 per cent to 69.5 per cent and SiO_2 content is reduced from 1.98 per cent to 0.9 per cent and especially for lower than 7 microns fraction size, as a critical fraction, SiO_2 content decreased from 4.45 per cent to 2.35 per cent. HPGR tests were performed on 8 per cent moisture in 4 N/mm^2 specific force and according to the results after silica reduction HPGR operation conditions are optimised. Results showed that the working gap increased from 7 to 10.5 mm and specific throughput of material raised from 180 ts/hm^3 to 250 ts/hm^3, and SSA increased by 300 cm^2/gr in a single pass.

INTRODUCTION

The formation of high-quality pellets depends on the preparation of fines defined by both size distribution and specific surface area (SSA) (Van Der Meer, 2015) therefore, mostly iron ore concentrate SSA increased in a grinding circuit for produce pellet feed.

Before feeding to pelletising plants, iron ore concentrate, is generally grinding by two methods of High pressure grinding roll (HPGR) or dry grinding circuit by ball mill. These methods' results are different, and the shape of particles from HPGR would be more angular as compared to ball mill products (Bleifuss, 1997). These features together with a high proportion of fines would allow an HPGR product to be suitable for pelletising at a lower Blaine value from a presumed better packing and density in generated pellets (Van Der Meer, 2015). Additionally, stronger pellets were produced from the HPGR products, with a lower binder requirement (Ehrentraut and Ramachandra Rao, 2001). Using HPGR pre-treatment on magnetite concentrate, it was found better quality pellets would be produced at lower bentonite consumption rates (Zhu *et al*, 2004).

HPGR increases the specific surface area (eg Blaine cm^2/g) as a result of compression grinding and attrition or abrasion of the particle surfaces. The size reduction and associated increment in the specific surface area depend on the size distribution and specific surface area of the HPGR feed (Van Der Meer, 2015). Based on HPGR grinding mechanism, the materials layer between the rolls should be able to resist the required pressure for optimal grinding. Main parameter for optimal performance and material compressing in HPGR is resistance required pressure with the optimal working gap, effect of working gap on HPGR specific throughput and capacity are shown in following

Equations 1 and 2. Specific throughput is a parameter frequently used for sizing HPGR capacity (Van Der Meer and Gruendken, 2010).

$$m° \ (ts/hm^3) = Q / (D \times L \times v) \quad (1)$$

$$Q \ (t/h) = s \times L \times v \times \rho \times 3.6/1000 \quad (2)$$

- m° specific throughput
- Q HPGR capacity
- D roll diameter
- L roll length
- v roll speed
- s working gap
- ρ material density between the gap

If material pressure resistance was low, material does not able to tolerate the required pressure for suitable grinding and product Blaine value will be decreased. Moreover, HPGR working gap will be low and based on the formula, HPGR capacity will be decreased.

Pressure resistance depends on condition and material specifications such as particle size distribution, moisture, particle shape, surface texture and fines and clay content, therefore by reducing impurities, material pressure resistance and HPGR operating results were (are) improved.

Chemical/traditional flotation is one of the most effective methods for separating valuable particles from waste minerals, which is used in most mineral processing industries. In the iron ore processing industry, the major impurities present in iron ore concentrate include sulfur, silica and phosphorus (Xiong *et al*, 2015), which are often carried out by reverse flotation methods for the removal of sulfide and oxide impurities (Araujo *et al*, 2005; Ma, 2012; Frommer, 1967).

Generally, silica impurities of iron concentrates are of two types: quartz-containing minerals and silicate minerals such as pyroxene, clinopyroxene, amphibole and the like. Often, when quartz is the main mineral that forms silica of the sample, the silica flotation process is easily carried out by amine collectors. But, when the iron silicates are typical of the siliceous main minerals, the process of flotation is often complicated and the efficiency of the method is also relatively low (Frommer, 1967; Filippov *et al*, 2010; Houot, 1983).

This study was performed on an industrial case, that's final concentrate (filter cake) specific surface area increased by HPGR. Operation results showed that HPGR working gap was the same as zero gap and HPGR capacity was very low. Material was very pasty and sticky and could not go between the rollers gap. HPGR capacity was reduced by half compared to the design, without a very noticeable change in feeding moisture. Material analysis showed that due to the increasing clay minerals (SiO_2, Al_2O_3) content in plant feed (crushed ore), produced concentrate SiO_2 content increased more than 380 per cent compared to the design value (Table 1). Thus, silica reduction as an optimisation plan was investigated.

TABLE 1

Feed and concentrate specification compared to design value.

Sample name	Specification	Design	Actual	Difference
Feed (crushed ore)	Fe (%)	54.8	53.02	-3%
	FeO (%)	22.51	20.44	-9%
	SiO_2 (%)	6.47	8.50	**+31%**
	Al_2O_3 (%)	1.37	1.91	**+39%**
	CaO (%)	2.6	2.99	**+15%**
Concentrate (studied sample)	Fe (%)	70.5	68.06	-3%
	FeO (%)	26	27.54	+6%
	SiO_2 (%)	0.41	1.98	**+383%**

The purpose of this study was to investigate the silica reduction effect on HPGR operation conditions and improved SSA increasing results. For this purpose HPGR regrinding tests were performed on industrial concentrate sample, before and after reverse silica reduction flotation test and HPGR main effective parameters such as specific throughput (m dot), working gap and amount of SSA increasing was compared.

MATERIALS AND METHODS

In this study, flotation and regrinding tests with HPGR were performed on the prepared samples in FSTCO Mineral Processing and Metallurgy Research Centre (FSTRC).

Sample characteristic

The sample used in the experiments included magnetite concentrate which was prepared from one of the iron beneficiation plants in Iran. Screen analysis showed that in the studied samples, D99 and D80 were around 500 and 110 microns, respectively. Also sample Fe grade was 68.06 per cent and SiO_2 content was 1.98 per cent.

Flotation tests

Flotation test was performed with the silica reduction purpose. In order to perform reverse flotation tests, the chemical modifiers were used including sodium carbonate as a dispersion of impurities containing silica and starch with the aim of depressing iron minerals. Meanwhile, the Flotigam EDA was used as a collector. Flotation tests were carried out at pH values of 8.5 to 9.5. The device used for traditional flotation experiments included the DENVER Pilot Mechanical Flotation Machine with six cells and each cell volume was 25 L.

HPGR regrinding tests

HPGR regrinding tests were performed by pilot HPGR, with the aim of increasing concentrate specific surface area in the FSTCO Mineral Processing and Metallurgy Research Centre (FSTRC). The device was manufactured by Koppern consist of a roll diameter of 1030 mm and 250 mm widths, motors with power of 2 × 132 kW and adjustable roll speed of 6.2 to 31 rev/min. Tests were performed in four moisture levels from 6–9 per cent, with 4 kN/m^2 pressing force in an open circuit. To investigate the silica reduction effect, HPGR regrinding tests were performed on concentrate before and after of flotation tests.

RESULTS AND DISCUTION

Sample metal screen analysis – before flotation

The variation in the weight percentage of particles at different fractions in addition to iron and silica content of each fraction was measured individually and shown in Table 2.

TABLE 2

Screen metal analysis of concentrate sample – before flotation.

Size (micron)	Weight (%)	Fe (%)	SiO_2 (%)
> 150	8.4	62.50	6.02
106–150	14.08	67.25	2.61
75–106	13.80	68.35	1.75
53–75	14.76	69.10	1.10
38–53	12.01	69.69	0.90
25–38	6.24	69.68	0.83
19–25	9.08	70.12	0.36
13–19	5.45	69.96	0.58
9–13	4.24	69.34	1.27
7–9	3.39	69.22	1.33
< 7	8.54	64.34	4.45
Total		68.06	1.98

Distribution evaluation of iron and silicate minerals at different fractions showed that in coarse (>150 micron) and fine (<7 micron) fractions, Fe content was low and silica content was high. In fact, silica impurities were concentrated in both coarse and fine fractions. Silica impurities in the coarse fraction were in form of quartz but in the fine fraction is silicate minerals such as pyroxene, clinopyroxene and amphibole.

Silica reduction tests by flotation

In order to silica reduction, reverse flotation tests performed on concentrate. Tests results showed that, with 90.72 per cent weight recovery, SiO_2 content reduced from 1.98 per cent to 0.9 per cent and Fe content of the product increased from 68.06 to 69.16 per cent.

Sample metal screen analysis – after flotation

After flotation tests, screen and chemical analysis were performed on the concentrate to compare silica contents and to investigate the flotation effect on silica reduction. The variation in the weight percentage of particles at different fractions In addition of iron and silica content of each fraction was measured individually and shown in Table 3.

Results showed that Fe grade in the concentrate was increased from 68.06 per cent to 69.5 per cent and SiO_2 content was reduced from 1.98 per cent to 0.9 per cent. Especially for lower than 7 microns fraction size, as a critical fraction, SiO_2 content decreased from 4.45 per cent to 2.35 per cent.

TABLE 3

Screen metal analysis – flotation product.

Size (micron)	Weight (%)	Fe (%)	SiO_2 (%)
> 150	14.04	65.25	2.55
106–150	8.06	68.65	1.10
75–106	17.54	69.55	0.75
53–75	17.49	70.31	0.58
38–53	11.77	70.58	0.51
25–38	7.73	70.85	0.11
19–25	8.29	70.41	0.10
13–19	4.15	70.35	0.12
9–13	3.23	69.96	0.20
7–9	2.58	69.85	0.34
< 7	5.12	65.81	2.35
Total		69.16	0.90

HPGR regrinding tests result

HPGR regrinding test was performed on studied sample, before and after flotation tests, regrinding tests condition and the results are presented in Table 4.

TABLE 4

HPGR regrinding test.

		Before Silica Reduction				After Silica Reduction			
Test No.	**Unit**	**1**	**2**	**3**	**4**	**5**	**6**	**7**	**8**
Static gap	mm	5				5			
Spec. press force	kN/m^2	4				4			
Feed SSA (Blaine method)	(cm^2/g)	1050				980			
Feed Moisture	%	6	7.0	8.0	9.0	6	7.0	8.0	9.0
Working gap	Mm	10.3	7.2	6.9	5.1	14.7	11.7	10.5	6.5
$W_{spec.}$	kWh/t	1.1	1.1	1.5	0.9	0.9	1.0	1.3	1.45
m-dot	ts/hm^3	265	220	180	60	310	280	250	165
Product SSA (Blaine method)	(cm^2/g)	1450	1380	1350	1320	1459	1410	1398	1330
SSA Increasing (Blaine method)		400	330	300	270	478	429	417	349

According to regrinding test results, before silica reduction, only at 6 per cent moisture, HPGR specific throughput was more than 250 ts/hm^3 and the working gap was obvious. In 7 per cent working gap was very low and this situation was not suitable for perfect operation. In 8 per cent and 9 per cent moisture, the material was completely sticky and the working gap was the same as zero gap. Therefore specific throughput was very low and HPGR did not work properly. After flotation tests, specific throughput in each moisture increased. Results showed that better working condition can be obtained by HPGR. Additionally, results revealed that in 8 per cent moisture after flotation tests and reduced SiO_2 content, HPGR working gap increased up to 10.5 mm and specific throughput increased from 180 ts/hm^3 to 250 ts/hm^3.

Comparison tests result

HPGR regrinding test result on concentrate samples showed that at moisture content between 7 to 9 per cent, HPGR have not significant working gap and specific throughput was very low. Moreover, chemical analysis of HPGR feed sample showed SiO_2 content of studied sample increased more than 380 per cent compared to the design value. SiO_2 content was concentrated on two fraction size, coarser than 150 microns metre and finer than 7 microns. Generally, silica impurities of iron concentrates are of two types: quartz-containing minerals in coarse fraction and silicate minerals such as pyroxene, clinopyroxene, amphibole and the like, in the fine fraction. Basically, fine silicate minerals have a higher water absorption capability. By increasing silicate minerals in the fine fraction, the layers of material could not be able to resist the required pressure for achieving suitable grinding conditions and the material was sticky and unsuitable for HPGR feeding.

Therefore silica reduction as an optimisation plan was performed on the studied sample, compared results are shown in Figure 1. As it can be seen, flotation tests have a suitable effect on silica reduction, Based on the results, in the coarse fraction SiO_2 content decreased from 6.02 to 2.55 per cent. In the fine fraction, especially for lower than 7 microns fraction size, as a critical fraction, SiO_2 content decreased from 4.45 per cent to 2.35 per cent.

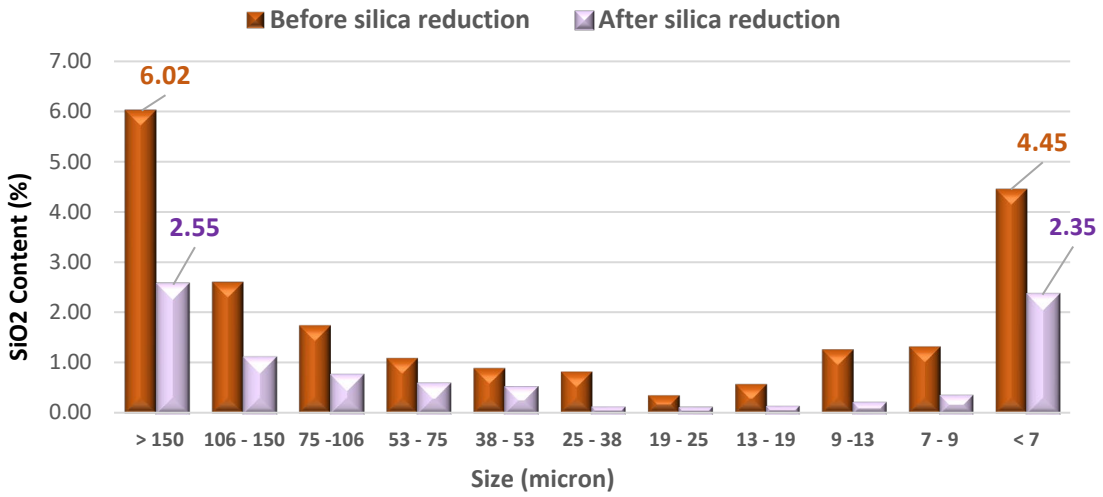

FIG 1 – SiO_2 content before and after flotation test.

Finally, after flotation tests, SiO_2 content of the studied sample reduced from 1.98 to 0.9 per cent and especially in the fine fraction dropped significantly from 4.45 per cent to 2.35 per cent. HPGR tests were performed on the studied samples before and after of flotation test, compared results show in Figure 2. According to results, after flotation test and reduction in SiO_2 content, HPGR working gap and specific throughput increased, as a results in same condition material bed ability to pressure resistance were increased. Results showed that before silica reduction, in 8 per cent moisture as a design value, HPGR working gap was very low and material could not go through the roller gap, therefore specific throughput was lower than 200 ts/hm^3. However, after silica reduction, HPGR working gap had significant changes and increased from around 7 mm to 10.5 mm. According to this changes after silica content reduction, specific throughput increased from 180 ts/hm^3 to 250 ts/hm^3, HPGR can be worked with this material and operating condition optimised.

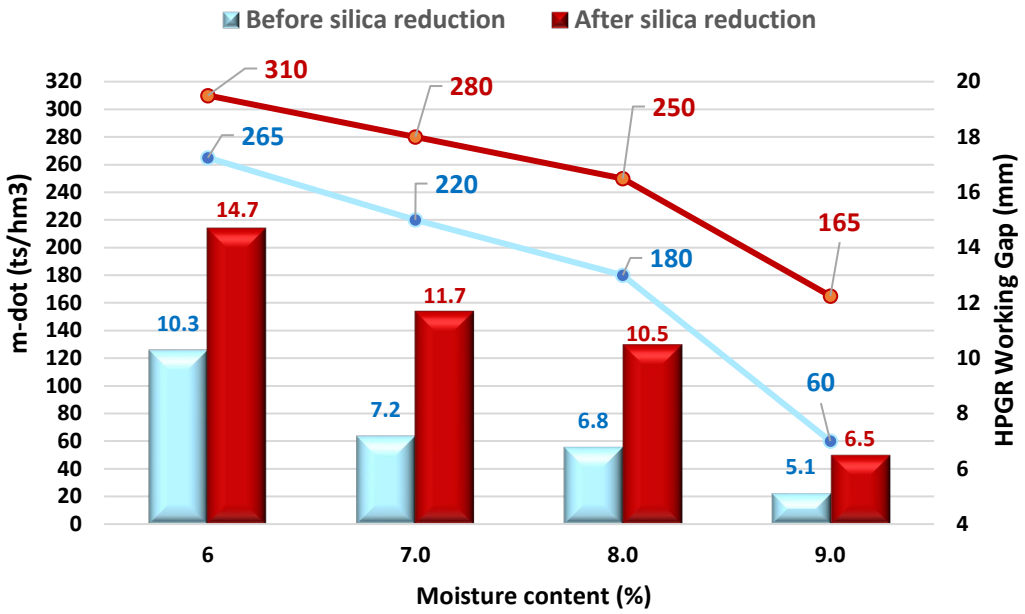

FIG 2 – Comparative results of HPGR tests.

CONCLUSIONS

HPGR grinding mechanism implied that, in the aim of suitable grinding conditions, the material should be able to resist required pressure to compress between two rolls. Also clay minerals content such as silicate minerals especially in the fine fraction, reduced material bed pressure resistance.

In this study, silica reduction effect on HPGR working conditions was investigated. Result showed that flotation tests had a suitable effect on silica reduction and with 90 per cent weight recovery, Fe grade in the concentrate increased from 67.8 per cent to 69.5 per cent and SiO_2 content reduced from 1.98 per cent to 0.9 per cent. Especially for lower than 7 microns fraction size, as a critical fraction, SiO_2 content decreased from 4.45 per cent to 2.35 per cent.

Compared results of HPGR test showed that due to silica reduction, material bed ability to resist the required pressure was increased and HPGR operation condition was optimised. As a result, in 8 per cent moisture the working gap increased from 7 to 10.5 mm and specific throughput of material raised from 180 ts/hm^3 to 250 ts/hm^3, and SSA increased 300 cm^2/gr in a single pass.

ACKNOWLEDGEMENTS

The authors would like to acknowledge the financial and technical support of Fakoor Sanat Tehran Company (FSTCO), as well as the research and development department and Mineral Processing and Metallurgy Research Center (FSTRC) for the technical and operational assistances.

REFERENCES

Araujo, A, Viana, P and Peres, A, 2005. Reagents in iron ores flotation. *Minerals Engineering,* 18, 219–224.

Bleifuss, R, 1997. MBR Pellet Feed Investigations. *Internal Reporting of KHD & Coleraine Minerals Research Laboratory*.

Ehrentraut, G and Ramachandra Rao, T, 2001. Betriebserfahrungen mit einer Rollerpresse in der Pelletieranlage der Kudremukh Iron Ore Company Ltd. *AT. Aufbereitungs-Technik,* 42, 469–476.

Filippov, L O, Filippova, I V and Severov, V, 2010. The use of collectors mixture in the reverse cationic flotation of magnetite ore: The role of Fe-bearing silicates. *Minerals Engineering,* 23, 91–98.

Frommer, D W, 1967. Iron ore flotation: Practice, problems, and prospects. *Journal of the American Oil Chemists Society,* 44, 270–274.

Houot, R, 1983. Beneficiation of iron ore by flotation—review of industrial and potential applications. *International Journal of Mineral Processing,* 10, 183–204.

Ma, M, 2012. Froth flotation of iron ores. *International Journal of Mining Engineering and Mineral Processing*, 1, 56–61.

Van Der Meer, F P and Gruendken, A, 2010. Flowsheet considerations for optimal use of high pressure grinding rolls. *Minerals Engineering,* 23, 663–669.

Van Der Meer, F P, 2015. Pellet feed grinding by HPGR. *Minerals Engineering*, 73, 21–30.

Xiong, D, Lu, L and Holmes, R, 2015. Developments in the physical separation of iron ore: magnetic separation. *Iron Ore.* Elsevier.

Zhu, D, Pan, J, Qiu, G, Clout, J, Wang, C, Guo, Y and Hu, C, 2004. Mechano-chemical activation of magnetite concentrate for improving its pelletability by high pressure roll grinding. *ISIJ international,* 44, 310–315.

Advances in mineral processing – geometallurgy

Powerful laboratory and real time examination tools for copper porphyry exploration

C Bauer[1], R Wagner[2], B Orberger[3,4], C Garcia-Piña[5], J A Meima[6], M Firsching[7], S Merk[8], L Rybok[9], R Hyypiö[10], C Wagner[11], O Boudouma[12], K Siahcheshm[13], C Kaminski[14], H Lindström[15] and M Alamäki[16]

1. Scientist, Fraunhofer Institute for Integrated Circuits IIS, Division Development Center X-Ray Technology, 90768 Fürth, Germany. Email: christine.bauer@iis.fraunhofer.de
2. Scientist, Fraunhofer Institute for Integrated Circuits IIS, Division Development Center X-Ray Technology, 90768 Fürth, Germany. Email: rebecca.wagner@iis.fraunhofer.de
3. President, Catura Geoprojects, 75014 Paris, France. Email: beate.orberger@catura.eu
4. Associate Professor, GEOPS Université Paris Saclay, 91405 Orsay, France. Email: beate.orberger@universite-paris-saclay.fr
5. Geologist, DMT GmbH & Co. KG, 45307 Essen, Germany. Email: carlos.garcia-pina@dmt-group.de
6. Scientist, Federal Institute for Geosciences and Natural Resources (BGR), 30655 Hannover, Germany. Email: Jeannette.Meima@bgr.de
7. Senior Scientist, Fraunhofer Institute for Integrated Circuits IIS, Division Development Center X-Ray Technology, 90768 Fürth, Germany. Email: markus.firsching@iis.fraunhofer.de
8. Data Scientist R&D, LTB Lasertechnik Berlin GmbH, 12489 Berlin-Adlershof, Germany. Email: sven.merk@ltb-berlin.de
9. Scientist, J&C Bachmann GmbH, 75179 Pforzheim, Germany. Email: lry@jcbachmann.de
10. Principal R&D Engineer, Timegate Instruments Oy, FI-90590 Oulu, Finland. Email: risto.hyypio@timegate.com
11. Associate Professor, Sorbonne Université, ISTeP, 75005 Paris, France. Email: christiane.wagner_raffin@sorbonne-universite.fr
12. Research Engineer, Sorbonne Université, ISTeP, 75005 Paris, France. Email: omar.boudouma@upmc.fr
13. Associate Professor, Department of Earth Sciences, University of Tabriz, Tabriz 51368, Iran. Email: kl_siahcheshm@tabrizu.ac.ir
14. Mechanical Engineer, DMT GmbH & Co. KG, 45307 Essen, Germany. Email: Christian.Kaminski@dmt-group.com
15. Engineer, VTT Technical Research Centre of Finland, Kaitoväylä 1, 90570 Oulu, Finland. Email: hannu.lindstrom@vtt.fi
16. Physicist, VTT Technical Research Centre of Finland, Kaitoväylä 1, 90570 Oulu, Finland. Email: markku.alamaki@vtt.fi

ABSTRACT

Copper porphyries represent complex alteration zones, hosting variable grades of Cu- (Au-Mo), but also Pb, Zn, Te, Bi and Ag. Moreover, environmental harmful elements, such as As or Cd are present. It is therefore crucial that mining companies get reliable chemical and mineralogical drill core data from the earliest exploration state on to avoid project failure and to obtain three-dimensional models for mine and processing planning. Systematic sensor-based drill core logging and material sorting coupled with smart data evaluation is the ideal solution for accurate in-field and in-plant real time decision-making to reduce waste and anticipate dysfunction during metal production. Risks and operational costs can be reduced while increasing resource efficiency.

In this paper, as an example, specific alteration zones of the Niaz porphyry copper (Mo)-deposit in north-western Iran were investigated by laser-induced breakdown spectroscopy (LIBS), X-ray Fluorescence (XRF), time-gated Raman spectroscopy, dual energy X-ray transmission (DE-XRT), multi energy X-ray transmission (ME-XRT) and X-ray computed tomography (CT). Most of these instruments were combined in the European Institute of Innovation and Technology (EIT) RawMaterials project ANCORELOG. The sensor results were compared and evaluated against laboratory results obtained by scanning electron microscopy (SEM) coupled with energy dispersive spectroscopy (EDS), and optical microscopy for calibration.

Fast LIBS, Raman and XRF core-scanner instruments clearly allow to distinguish the alteration zones: The potassic-phyllic alteration zone is characterised by two differently mineralised rock types: (i) the Cu-mineralised quartz diorite where the key minerals are chlorite and barite, quartz, albite/oligoclase, muscovite and the major ore mineral is chalcopyrite; (ii) the Cu-Mo-mineralised monzonite, where carbonates, orthoclase and albite/oligoclase are the key minerals. Ore minerals are molybdenite and chalcopyrite. The propylitic alteration zone is characterised by a coarse-grained diorite. Key minerals are orthoclase, epidote, sphene and apatite. Molybdenite is the major ore mineral. The phyllic-argillic mineralised zone is represented by a microgranular quartz-diorite. Key minerals are kaolinite-dickite, quartz, albite, muscovite-sericite and apatite. The major ore mineral is chalcopyrite. The peripheral part of the porphyry is a coarse-grained skarn with andradite, calcite, tremolite and epidote as key minerals. The major ore mineral is chalcopyrite. LIBS elemental mapping clearly reflects the ore mineralogy and texture. Analysis of reconstructed three-dimensional CT volume data revealed structural information as well as two to three different groups of grey values. After calibration, eg by SEM or LIBS, mine-geologists can assign these grey values to minerals or elements with low (eg Al, Si), medium (eg Fe, Cu), and high (eg Mo) effective atomic numbers. Our study shows that sensor-based characterisation of successive alteration zones and Cu-Mo mineralised zones is possible for unknown samples. XRF, Raman spectroscopy, LIBS and XRT can be used and adapted in-field on mine and exploration sites as well as in plants. Selected samples of drill cores can then be sent for CT analysis and detailed LIBS imaging.

INTRODUCTION

Porphyry systems (Cu, Mo, Au) are intensively drilled to be efficiently explored, modelled, and mined. Orebody modelling, exploration and mine planning must rely on a solid and reliable data basis, which can be achieved by systematic chemical and/or mineralogical logging using analytical sensors. These data can then feed three-dimensional (3D) geological modelling and/or design appropriate beneficiation. The EIT RawMaterials projects ANCORELOG and T-REX (EIT RawMaterials, 2022a, 2022b, both until 2021) provide the basis to bring a modular drill core scanner to the market. X-ray fluorescence (XRF), Raman spectroscopy and laser-induced breakdown spectroscopy (LIBS) were upscaled and adapted for use in exploration and mining. These methods were combined with dual energy (DE) and multi energy (ME) X-ray transmission (XRT) as well as X-ray computed tomography (CT). However, the optimal use of these instruments requires the definition of smart mineralogical and chemical parameters to reach real time accurate decision-making for optimal exploration campaigns, mine planning and processing methodology.

Porphyry deposits together with iron-oxide-copper-gold (IOCG) deposits account for more than 60 per cent of the global primary copper production. Moreover, globally, 100 per cent of the molybdenum production, 10 per cent to 15 per cent of uranium, and an important part of gold production are provided by these ore deposit types. Giant porphyry systems are Grasberg (Indonesia), La Escondida (Chile), Rio Blanco (Peru), Continental (Arizona, USA), Butte (Montana, USA), El Teniente (Chile) ending up with the supergiant Chuquicamata (Chile) deposit. Copper grades range from 0.3 per cent to about 2 per cent. These grades are low to moderate; therefore, the size makes it profitable (Ayuso *et al*, 2010 and references therein). All these deposits are drilled at several ten thousand of drill core metres per annum. They are mainly manually logged and stored.

The definition of mineralogical and chemical logging parameters considers major and minor ore minerals, typical associated silicates and metals, environmental harmful metals to avoid soil, atmosphere, and hydrosphere contamination, but also contaminating metals for the commercial products (eg Cd, Pb, As, Hg, U and Th; Tabelin *et al*, 2021). The main characteristics of Cu porphyry deposits are disseminated Cu bearing minerals in the rocks, Cu minerals in veins and fractured rocks distributed in large rock volumes. They form high tonnage (>100 Mt) of low to moderate grade ores. The host rocks are composed of granitoids, and adjacent rocks are altered at various degrees (Ayuso *et al*, 2010; Chang *et al*, 2011; Seedorff *et al*, 2005).

Cu porphyry systems can be closely related to skarns (Ayuso *et al,* 2010; Taghipour *et al,* 2013 and references therein). A famous example is the Grasberg deposit in Indonesia (Sillitoe, 2010 and references therein). These types of deposits are usually high-grade, but relatively small and patchy. They can contain red garnets, green pyroxenes, and amphiboles. Cu (and Mo) grades can be locally

very high and heterogeneously distributed. This heterogeneous ore-distribution makes skarn-related Cu porphyries challenging for mining and processing.

For processing, these rocks are very hard and thus have high milling costs (Michaud, 2014). Efficient and early separation of barren from economic valuable materials needs planning and testing at the exploration stage to ensure a constant Cu production over time while reducing waste production at each stage of processing. Leaving the barren material in the ground will also reduce hazardous waste, as Cu-Mo-Au ores may host harmful metals (Pb, Hg, As and U; Tabelin *et al,* 2021, and references therein). High density drilling combined with systematic data acquisition as well as material sorting in valuables, hazardous and non-hazardous barren fractions from the exploration stage on will reduce processing costs mainly driven by energy and water consumption.

The samples studied here belong to the skarn type porphyry deposits, coming from the Niaz porphyry in north-west Iran (Hassanpour *et al*, 2015; Omrani *et al*, 2008). This deposit is a Cu and Mo porphyry. The samples cover the major alteration zones (potassic-phyllic, propylitic, phyllic-argillic and the peripheral skarn, Figure 1). These alteration zones, corresponding to spatial and temporal hydrothermal and supergene events, are used to vector the Cu-Mo mineralisation during exploration drilling.

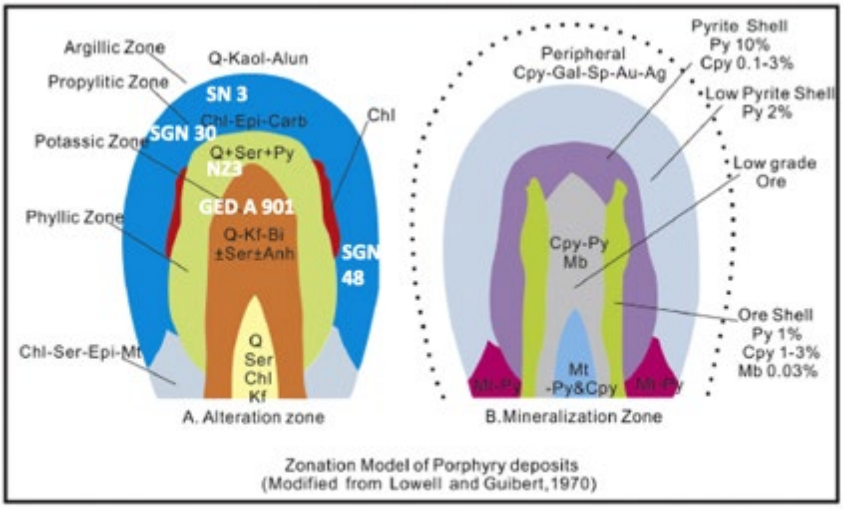

Chl-Chlorite; Kaol-Kaolinite; Epi-Epidote Alun-Alunite; Carb-Carbonate; Bi-Biotite
Q-Quartz; Ser-Sericite; Kf-Potassium Feldspar; Py-Pyrite; Cpy-Chalcopyrite;
Gal-Galena;Sp-Sphalerite; Au-Gold; Ag-Silver; Mb-Molybdenite; Anh-Anhydrite

FIG 1 – Cu-Mo porphyry deposits scheme. Left: The sample locations on the alteration zones and the major vectoring minerals; Right: Alteration zones showing the major mineralisations from high-grade Cu and Mo to low-grade Pb, Zn, Au and Ag ores (modified from Lowell and Guilbert, 1970).

The five samples, which are characteristic for porphyry alteration zones, have previously been examined with scanning electron microscopy (SEM, at ISTeP, Sorbonne Université, Paris, France), DE-XRT, ME-XRT and CT (at Fraunhofer IIS, Fürth, Germany) to quantify the fractions of elements with low and high atomic numbers, which are correlated roughly to waste and valuables (Bauer *et al*, 2021b). This work's objective is to demonstrate the potential of these methods in combination with XRF and Raman spectroscopy of the ANCORELOG core scanner (DMT, Essen, Germany) and LIBS (BGR, Hannover, Germany). The combination allows to correlate regions of low and high atomic number elements to minerals. A calibration of XRT data with the other methods enables the in-field definition of alteration zones as well as Cu-Mo-Zn-Pb mineralisations and strengthens the data set from other sensors, so that real time sorting of waste from ore can be achieved.

ANALYTICAL METHODS

ANCORELOG – Raman spectroscopy and X-ray fluorescence

ANCORELOG (Analytical Core Logger) is a multi-sensor scanner which can be applied to drill cores and/or loose materials (crushed, milled etc). It can be modularly equipped with several analytical sensors. It allows data acquisition through spatial sensor co-registration. All data from the different

sensors are combined into a dedicated database. Machine learning algorithms applied on the multi-sensor data enable a classification of rock-types and/or material into site-specific geological domains, waste, and valuable material.

The ANCORELOG's semi-automated scan process is presently designed to scan drill core samples with a high scan rate of up to 14 mm/s depending on the chosen sensor combination and the required accuracy and resolution. The sensor combination of ANCORELOG used in this study consists of an XRF and a Raman sensor.

XRF spectroscopy is a non-destructive analytical method that measures characteristic X-ray emission spectra from a sample while being excited by a primary X-ray source. The emitted spectra are composed of intensity peaks in certain energy lines that are characteristic for the elemental composition of the measured sample. Handheld XRF devices are widely used in the exploration and mining industry for predicting the elemental composition of rock samples. ANCORELOG's XRF sensor is a special adaptation of J&C Bachmann's TEXAS device designed for both, single point measurements and continuous profile measurements along a defined scan path. The XRF measurements were performed in the profile scan mode, moving the sensor over the sample surface at a speed of 1 mm/s. This results in a continuous measurement profile of 5 mm width over the complete sample length as indicated by the red frame in Figure 2. The emission signal was integrated over the complete profile to a single measurement for each sample. The results are obtained as counts normalised to 120 s integration time for each element peak area after background signal subtraction and thus indicating a qualitative estimation of elemental concentrations. A conversion into quantitative elemental concentrations would require a site-specific sensor calibration against representative samples.

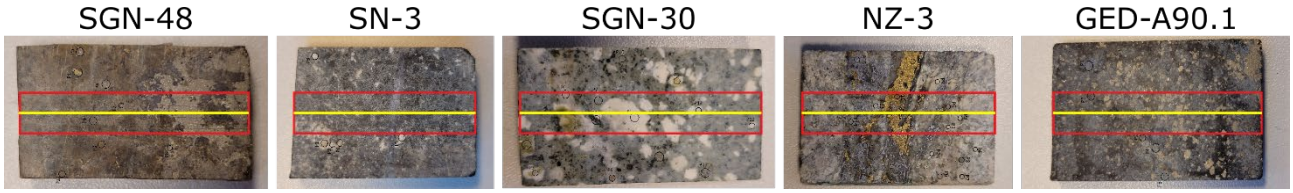

FIG 2 – Block samples analysed in this study. From left to right: SGN 48 (peripheral skarn); SN 3 (phyllic-argillic alteration zone); SGN 30 (propylitic alteration zone), NZ 3 and GED-A90.1 (potassic-phyllic alteration zone). Red frames indicate the measurement area of the XRF sensor. Yellow lines indicate the measurement profile of the time-gated Raman sensor. Sample height is approximately 2.5 cm.

Raman spectroscopy is a spectroscopic analytical method that detects energy shifts of photons emitted from a monochromatic excitation source, in this case a 532 nm pulsed picosecond range laser, caused by an interaction with primarily molecular vibrations in the measured sample. By detecting the characteristic energy shifts of molecules, typical Raman shift fingerprints allow the determination of the mineralogical sample composition.

The Raman technology used in ANCORELOG is a time-gated Raman sensor (T-REX, Timegated Raman for Exploration, special adaptation of Timegate Instruments' PicoRaman device). The time-gated Raman measurements were conducted in a combination of profile and single point scan mode. In the continuous profile scan mode, the Raman sensor moved over the sample at a speed of 5 mm/s resulting in a 160 µm wide profile line at the centre of each sample as indicated by the yellow line in Figure 2. The measurement has been integrated over the complete profile length resulting in one mixed Raman spectrum per sample profile. Additionally, several randomly selected single points have been measured on each sample. Characteristic peaks in the measured spectra have been automatically compared to reference spectra of given target minerals from the RRUFF™ database (Lafuente *et al*, 2015). Due to the different Raman signal intensities the detectability of target minerals with low signal intensities such as pyrite or chalcopyrite by the time-gated Raman sensor is limited when analysing a mixed spectrum. The technical specifications of both sensors are summarised in Table 1.

TABLE 1

Technical specifications of the XRF and time-gated Raman sensors used in this study.

XRF sensor specification		Timegated Raman sensor specifications	
X-ray source	RTW MCB 65C-0,2 Mo, run at 30kV and 300 µA	Laser Excitation Wavelength	532 nm
		Laser Repetition Rate	250 kHz
X-ray detector	Amptek DP5-X 25 mm^2 SDD, 8192 energy channels	Laser Power	230 mW max.
		Gating Adjustment Resolution	10 ps

Laser induced breakdown spectroscopy

LIBS is a multi-elemental technology for application in core scanner and industrial instrumentation to investigate compositional variations in rocks and sediments (eg Kuhn *et al*, 2016; Rifai *et al*, 2020). The technology is based on atomic emission spectroscopy, in which the excitation of the atomic species occurs *in situ* on the sample surface using a highly energetic pulsed laser. Excellent reviews are presented by eg Hahn and Omenetto (2012) and Harmon and Senesi (2021). In this study, imaging LIBS was applied, which yields detailed information on the spatial distribution of the different target elements on the sample surface, reflecting spatial variation in mineral chemistry.

The GeoLIBScanner (LTB, 2021) was used in this study, which is a device for fast, high resolution (both spectral and spatial) LIBS-scanning of drill cores in one or two dimensions (1D or 2D). It has the capability to be loaded with core boxes, without the need to manipulate the actual drill cores within. Prior to the actual LIBS scanning, an overview image is taken, and a morphological scan of the sample's topography is performed. This allows for the precise on-the-fly focal adjustment during the LIBS-scan. Both hyperspectral LIBS images and fast depth profile scans with configurable numbers of repetitions are the scope of the instrument. The system is equipped with a Nd:YAG laser at 1064 nm, emitting 25 mJ at 100 Hz (M NANO, Montfort Laser GmbH, Austria) and a high-resolution echelle spectrometer with a spectral range of 200 nm to 1000 nm and a resolving power above 4000 (Aryelle-150, LTB Lasertechnik Berlin GmbH, Germany) especially chosen for general purpose scanning of unknown geological material. The detector is an Evolve 512 Delta EMCCD camera (Photometrics, USA) capable of taking up to 67 full frames per second. Spectra can be either stored to disc or analysed on the fly. The results are then visualised and mapped on top of the photographic image of the core box.

Imaging LIBS measurements on the complete sample surfaces were performed using single-pulse measurements, a laser spot size of about 50 µm, a step size of 50 µm, and air suction to keep dust particles away from the spot area. The intensity of several characteristic emission lines for rock-forming elements as well as for sulfide-forming elements was calculated using an integration window of 0.1 nm (ultraviolet-visible region) or 0.2 nm (infrared region). The software ENVI version 5.3 (by Exelis Inc) was applied for visualisation of intensity distribution images. Normalisation with respect to the total intensity was applied for the emission lines of Si to highlight quartz minerals which generally have very weak emission properties. The results presented here are qualitative. A conversion into elemental concentrations would require a site-specific sensor calibration against representative samples.

X-ray transmission

While XRF detects fluorescence from elements close to the sample surface, XRT measures the intensity of X-rays transmitted through a sample. The detected signal is determined by the X-ray attenuation that the radiation experienced along the beam path. The resulting radiograph is therefore a projection of the X-ray attenuation of the sample into 2D space.

One drawback of XRT is that a high *Z* material with low density can lead to the same grey value in an X-ray projection as a low *Z* material with high density, ie no material information is gained by XRT. This disadvantage can be eliminated by making use of the energy dependence of the X-ray attenuation. By combining radiographs recorded with different X-ray spectra, information on the

chemical sample composition can be obtained. Both DE-XRT and ME-XRT were applied in this study as described below.

Dual energy X-ray transmission

The DE-XRT set-up consists of an X-ray source (Comet MXR-225HP/11) and a line detector with 0.8 mm pixel pitch (DT X-Scan 0.8iL-410 DE-USB-C2). This detector is a sandwich detector made of two layers. The first layer records mainly the low energy (LE) photons transmitted through the sample. Thereby it acts as a prefilter for the second detector layer that mainly records the high energy (HE) photons. The difference between both layers is enhanced by an additional filter of 0.6 mm Cu between both layers. An X-ray tube voltage and current of 220 kV and 2.2 mA and a 0.5 mm Cu prefilter were used for the measurements. A linear manipulation system moved the samples between source and detector at 340 mm/s while X-ray projections were recorded with 2.67 ms per line.

The two spectrally different projections were analysed by basis material decomposition (BMD) (Firsching *et al*, 2011). When applied to two known pure materials, this method reveals their respective areal densities (mass per area). For complex materials it yields the areal densities of two groups of elements with (effective) atomic number close to the chosen basis materials (here: Cu with $Z = 29$ und quartz glass with $Z_{eff} = 11.65$, Wagner *et al*, 2022; Bauer *et al*, 2021a, 2021b). In combination with methods like XRF or LIBS, these groups can be correlated with chemical elements or minerals.

Multi energy X-ray transmission

The ME-XRT set-up uses the same source as the facility for DE-XRT. The main difference between both machines is the line detector. The MultiX ME100 multi energy detector with 0.8 mm pixel pitch collects X-ray photons between 20 keV and 160 keV in 128 energy channels. The measurements were performed with 160 kV tube voltage, 0.5 mA tube current and 1 mm Ti as prefilter. Samples were moved between source and detector with 40 mm/s and the exposure time was 20 ms per line.

The data were analysed with a method published in (Alvarez, 2011, 2016). It requires calibration measurements with the materials of interest in different thicknesses. Here, quartz glass, Cu and W were used for calibration. Like DE-XRT analysis, the result gives the areal density of groups of elements with similar effective atomic number. Here, these are low-Z ($Z \approx 12$), medium-Z ($Z \approx 29$) and high-Z elements ($Z \approx 74$), which can be further assigned to single elements or minerals in combination with other methods. The analysis requires combining the 128 energy channels into three energy bins. These three bins were chosen to contain channels 1 to 44, 45 to 80 and 81 to 128, respectively. The first bin boundary corresponds approximately to the K-absorption edge of W. Along the direction of sample movement a 3 × 1 median filter was applied to the detected X-ray attenuation in all energy bins.

The flexibility of the energy binning, which can be adapted to the application, and the possibility to distinguish more than two materials if an absorption edge is present in the detected energy range are the advantages of ME X-ray detectors, which are currently not as well established as DE detectors.

Computed tomography

While XRT scans result in one projection of the sample's X-ray attenuation into 2D space, CT requires several projections from different directions. These radiographs can be reconstructed into a 3D volume data set. This volume can be sliced virtually into arbitrary directions to gain insight into the internal sample structure. The grey value in the volume is correlated with the X-ray attenuation, leading to a brighter colour of areas that consist of high-Z materials and/or have high density.

The CT set-up is equipped with an Yxlon FXE-225.99(48) microfocus X-ray source. A PerkinElmer XRD 1621 flat panel detector with CsI scintillator and 200 µm effective pixel pitch was used. Measurements were performed with 220 kV tube voltage and a current of 140 µA. A helical scanning trajectory was chosen (Kalender *et al*, 1990), where the sample rotated between source and detector and at the same time moved parallel to its rotational axis. The prefilter, exposure time and number of projections were adapted to the sample attenuation: 2.5 mm Cu, 1000 ms and 1600 projections

per 360° rotation were used for NZ-3, 1 mm Cu, 555 ms and 1200 projections per 360° rotation were applied for the other four samples. The voxels of the reconstructed volume have an edge length of 36 µm. To obtain the fraction of materials with similar grey values, which correspond to materials with similar Z_{eff} and attenuation, blob analysis was used. For details of this method, see Bauer *et al* (2021a, 2021b).

SAMPLE DESCRIPTION

The Niaz porphyry Cu-Mo deposit is located in the Arasbaran metallogenic belt of north-western Iran. It presents the northern part of the 2000 km north-west–south-east trending Cu-porphyry belt system which is about 50 km wide (Omrani *et al*, 2008, and references therein). It is low-grade Cu-Mo-porphyry with grades varying from 0.1 wt. per cent to 0.4 wt. per cent of Cu, and 50 ppm to 200 ppm of Mo (Hassanpour *et al*, 2015). More details about the samples are described in Bauer *et al* (2021b).

The major Niaz porphyry rock types are microdiorite, monzonite and granodiorite. They show porphyritic to microcrystalline porphyry textures. The rocks are cut by several generations of quartz-sulfide, quartz-oxide, and sulfide veinlets of different sizes. It represents a typical stockwork texture.

Five samples representative of four temporally and spatially distinguishable alteration zones were studied (Figure 2): (1) peripheral skarn (SGN-48), (2) phyllic-argillic (SN-3), (3) propylitic alteration (SGN-30) and (4) potassic-phyllic (NZ-3, GED-A90.1).

RESULTS

Mineralogy

Optical microscopy and scanning electron microscopy

All samples were studied by transmitted and reflected light microscopy, and SEM (ZEISS Supra 55 VP in Backscattered Electron (BSE) mode coupled to Energy Dispersive Spectroscopy (EDS)) at ISTeP (Sorbonne Université, Paris, France). The methodology and results were described in Bauer *et al* (2021b). These results are the base for reliable interpretation of the subsequent results from Raman spectroscopy, XRF (core scanner), LIBS, ME-XRT, DE-XRT, and CT measurements. The mineralogy of each sample is reported in Table 2 in comparison to the mineralogy found by the time-gated Raman spectrometer.

The petrology and detailed mineralogy of the studied samples was already presented in Bauer *et al*, 2021b. Here, relevant data which are necessary for sensor calibration and mineralogical interpretation are presented.

The peripheral part of the porphyry is represented by sample SGN-48. The sample is greenish and coarse-grained, cross-cut by a centimetre-thick white vein. It is a skarn composed of garnet (andradite) and tremolite, actinolite, chlorite, epidote, calcite, phosphates, and ilmenite. Ore minerals are pyrite, chalcopyrite, magnetite, sphalerite (ZnS) and galena (PbS), as inclusions in pyrite and chalcopyrite, and Ag-sulfides and TeBi, forming clusters. Scheelite ($CaWO_4$) is also observed.

The phyllic-argillic mineralised zone in quartz diorite is represented by sample SN-3. It is light grey, fine-grained, and cross-cut by a white vein. This sample is composed of 35 per cent albite, 30 per cent orthoclase, 15 per cent biotite and hornblende, sericite, clay minerals, and minor apatite, magnetite, and rutile. The ore minerals Cu-sulfides, barite, monazite (rare earth elements phosphate), thorite $(Th,U)SiO_4$ and galena (PbS) occur in the rock matrix. The vein hosts quartz and carbonate $(Ca,Fe,Mg)CO_3$.

The propylitic alteration zone in diorite is represented by sample SGN-30. It is light-grey, whitish coarse-grained rock. The mineralogy is orthoclase, amphiboles and epidote, minor calcite, apatite (Ca-phosphate), zircon ($ZrSiO_4$), sphene ($CaTiSiO_5$), and ilmenite ($FeTiO_3$). The mineralisation comprises disseminated pyrite with molybdenite MoS_2, PbS and TeBi inclusions. Rare sphalerite (ZnS) is observed.

TABLE 2

Mineralogy of the studied samples using optical microscopy (M), SEM combined with EDS (S) (data from Bauer *et al*, 2021b), and time-gated Raman spectroscopy (R). Target minerals which can be assessed by time-gated Raman are marked in grey.

	Sample	**SGN-48**		**SN-3**		**SGN-30**		**NZ-3**		**GED-A90.1**	
	Matrix	**Peripheral skarn**		**Phyllic-argillic**		**Propylitic**		**Potassic-phyllic**			
	Minerals	**R**	**M-S**	**R**	**M-S**	**R**	**M-S**	**R**	**M-S**	**R**	**M-S**
Target-Minerals	Quartz			x	x			x	x	x	x
	Orthoclase			x	x	x	x	x	x		
	Plagioclase (albite (a)/ oligoclase (o))			(a)	(a)			(a) (o)	(a)	x	x
	Muscovite/sericite			x	x				x	x	x
	Biotite				x				x		x
	Amphibole (tremolite (t)/actinolite (l))		(t) (l)				x		x		
	Chlorite	x	x					x	x	x	x
	Garnet (andradite (r))	(r)	(r)								
	Sphene					x	x				
	Epidote	x	x			x	x				
	Clay-minerals (dickite P10 (d), kaolinite (k))			(d)	(k)						
	Carbonates (calcite (c)/ ankerite (n))	(c)	(c)	(n)	(n)	(c)	Minor (c)	(c)	(c) (n)		
	Barite			x	x				x	x	x
	Apatite	x	x	x	x	x	x	x			
	Monazite				x						
	Thorite				x						
	Zircon						x				
Ore mineralogy	Pyrite		x				x		x		x
	Cu-sulfides (chalcopyrite (ch))		(ch)		(ch)				(ch) CuS		(ch)
	Molybdenite						x	x	x		
	Galena				x		x		x		x
	Ilmenite		x				x				x
	Rutile/Anatase			x	x			x			
	Magnetite		x		x					x	x
	Sphalerite		x				x				
	Ag-Te-Bi minerals		x				x		x		
	Scheelite		x								

Two samples represent the potassic-phyllic alteration zone in the inner part of the porphyry system: (i) the Cu-Mo-mineralised in monzonite is represented by sample NZ-3. The sample is light grey to green. It hosts albite, orthoclase, muscovite, sericite, quartz, chlorite, biotite and hornblende. Carbonates (calcite ($CaCO_3$) and ankerite (Ca, Mg, Fe)CO_3) and barite ($BaSO_4$) also occur. The ore minerals occur in veinlets. They are Cu-sulfides (major $CuFeS_2$), pyrite (FeS_2), molybdenite (MoS_2) (millimetric size). Molybdenite is cross-cut by micrometric veins, which are filled with galena (PbS), Cu-Bi and Cu-sulfides hosting Cd, Sb and As.

(ii) the Cu-mineralised quartz diorite, represented by sample GED-A90.1. This sample is dark grey, finer grained than sample NZ-3 with large white minerals. It is composed of about 40 per cent plagioclase (albite), 25 per cent biotite, minor muscovite and 25 per cent quartz as veinlets. Ore minerals comprise 10 per cent of pyrite, Cu-sulfides, and magnetite. Chalcopyrite is also associated with barite ($BaSO_4$). Pyrite hosts chalcopyrite, pyrrhotite (FeS) and galena (PbS). Furthermore, ilmenite (Fe,Mn)TiO_3 is present.

Figure 3 represents SEM-BSE mosaic images of the whole sample surface showing the repartition of the ore and matrix minerals in SGN-30 and SGN-48. Figure 4 shows SEM-BSE pictures of matrix and ore mineral associations at higher resolution (A: NZ-3, B: GED-A90.1).

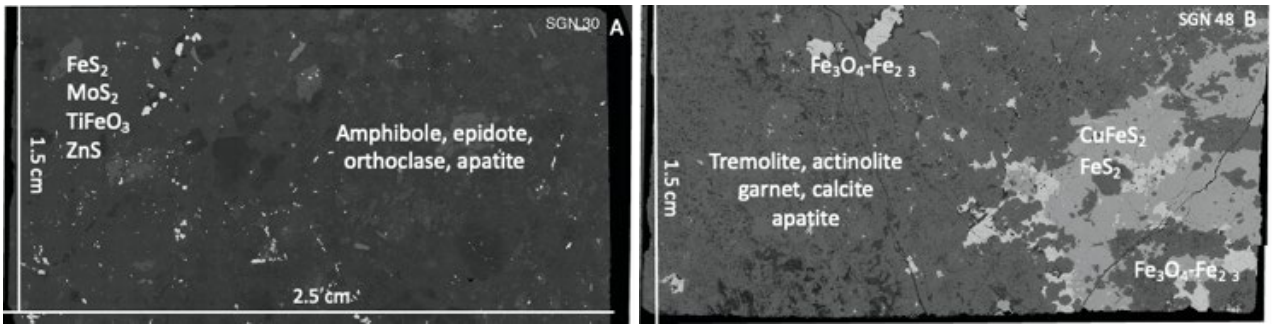

FIG 3 – SEM-Mosaic images showing the ore mineral and silicate-carbonate distribution at the entire sample surface scale (A: SGN-30; B: SGN-48).

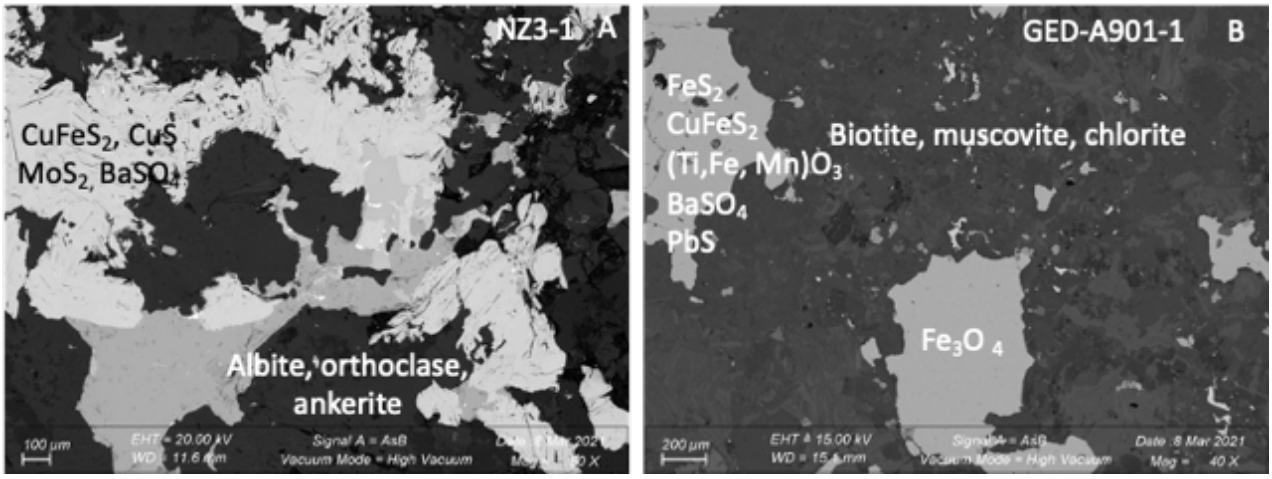

FIG 4 – SEM micrographs. A: NZ-3, Matrix silicates and carbonates and ore minerals (chalcopyrite, CuS and molybdenite), B: GED-A90.1, Matrix silicates and ore mineral association (modified from Bauer *et al*, 2021b).

Table 2 shows (i) the minerals which can be used as exploration tools, such as orthoclase, amphiboles, micas, clay-minerals, carbonates, sulfates, garnets, epidote and sphene, and (ii) the ore minerals, in this case Cu-sulfides and molybdenite.

Time-gated Raman

The spectra obtained from profile and single point time-gated Raman measurements were analysed with the aim of extracting characteristic intensity peaks of the minerals identified by means of optical

microscopy and SEM combined with EDS. The mixed spectra from the profile measurements contain the signature of several minerals as exemplarily shown in Figure 5.

FIG 5 – Feature extraction from mixed Raman spectra: The blue line shows the mixed spectrum from a profile measurement. The green line shows a reference spectrum of a mineral found in the mixed spectrum. The red line shows a reference spectrum of a mineral that is not identifiable in the mixed spectrum.

The occurrence of minerals with high Raman signal intensities may obstruct the signatures of minerals with lower Raman intensities and therefore a software tool dedicated to extract mineralogical signatures from mixed Raman spectra by comparison with mineralogical reference spectra was used in this study. The software was developed within the ANCORELOG project. Spectra from the RRUFF™ database (Lafuente *et al*, 2015) were used as a reference. Single point measurements can also lead to mixed spectra depending on grain sizes of the samples taking into consideration a measurement spot size of 160 µm.

The minerals identified by the time-gated Raman sensor are listed in Tables 2 and 3.

TABLE 3

Minerals and their characteristic Raman peaks observed in the measurement spectra.

Mineral	Raman Peaks [cm^{-1}]	Sample
Quartz	~466, ~355, ~207, ~128	SN-3, NZ-3, GED-A90.1
Orthoclase	~512, ~285, ~157	SN-3, SGN-30, NZ-3
Albite	~508, ~479, ~291	SN-3, NZ-3 and GED-A90.1
Chlorite	~683, ~552, ~357	SGN-48, NZ-3, GED-A90.1
Andradite	~874, ~843, ~816, ~516, ~493, ~371, ~352, ~174	SGN-48
Sphene	~910, ~857, ~615, ~545, ~468	SGN-30
Epidote	~1087, ~983, ~917, ~604, ~572, ~514, ~455, ~350	SGN-48, SGN-30
Dickite	~915, ~749, ~460, ~434, ~336, ~270, ~247, ~131	SN-3
Calcite	~1085	SGN-48, NZ-3
Ankerite	~1092	SN-3
Molybdenite	~408, ~382	NZ-3
Magnetite	~670, ~560	GED-A90.1

Figure 6 shows an extract of detected mineral signatures with their respective reference spectra from the RRUFF™ database.

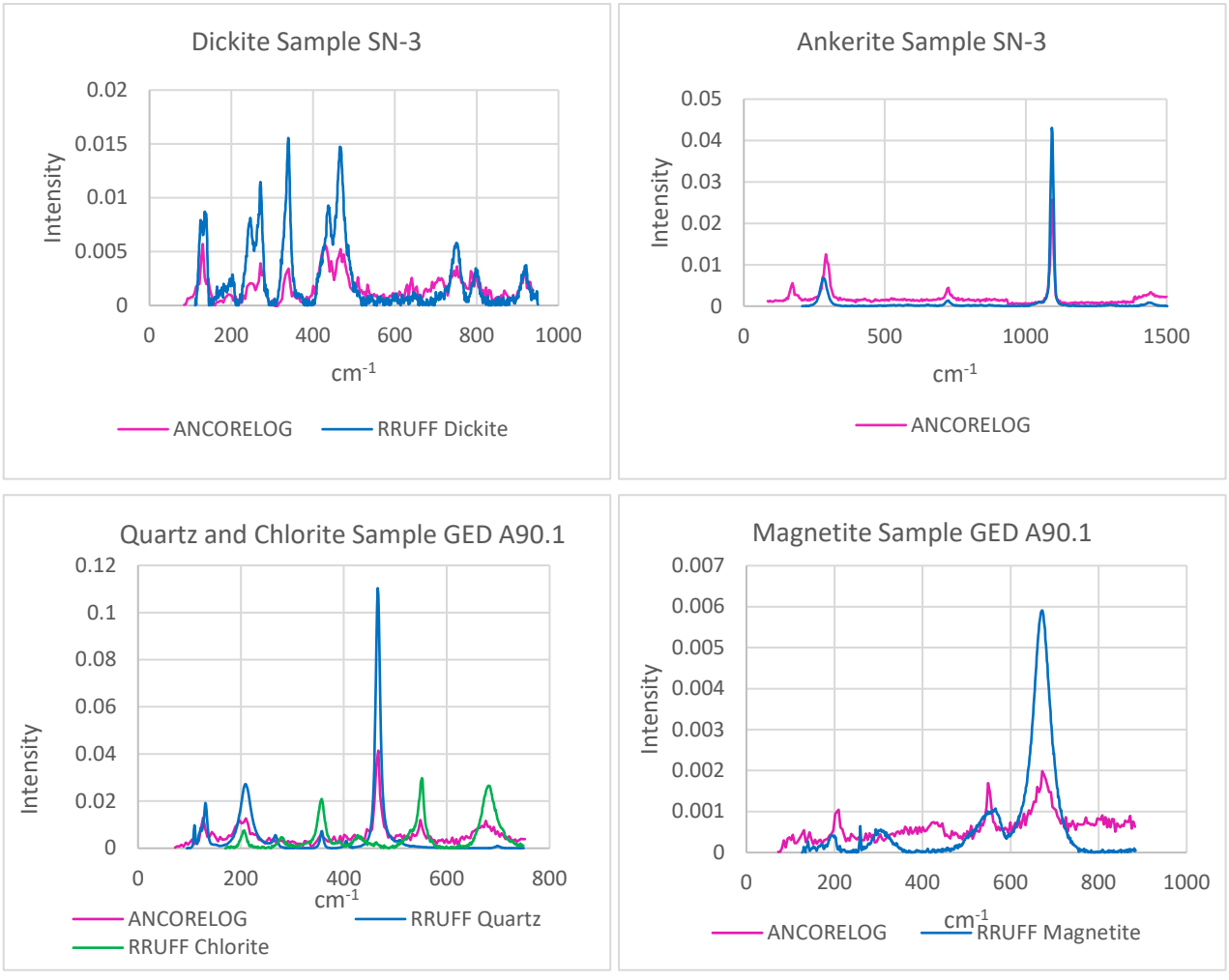

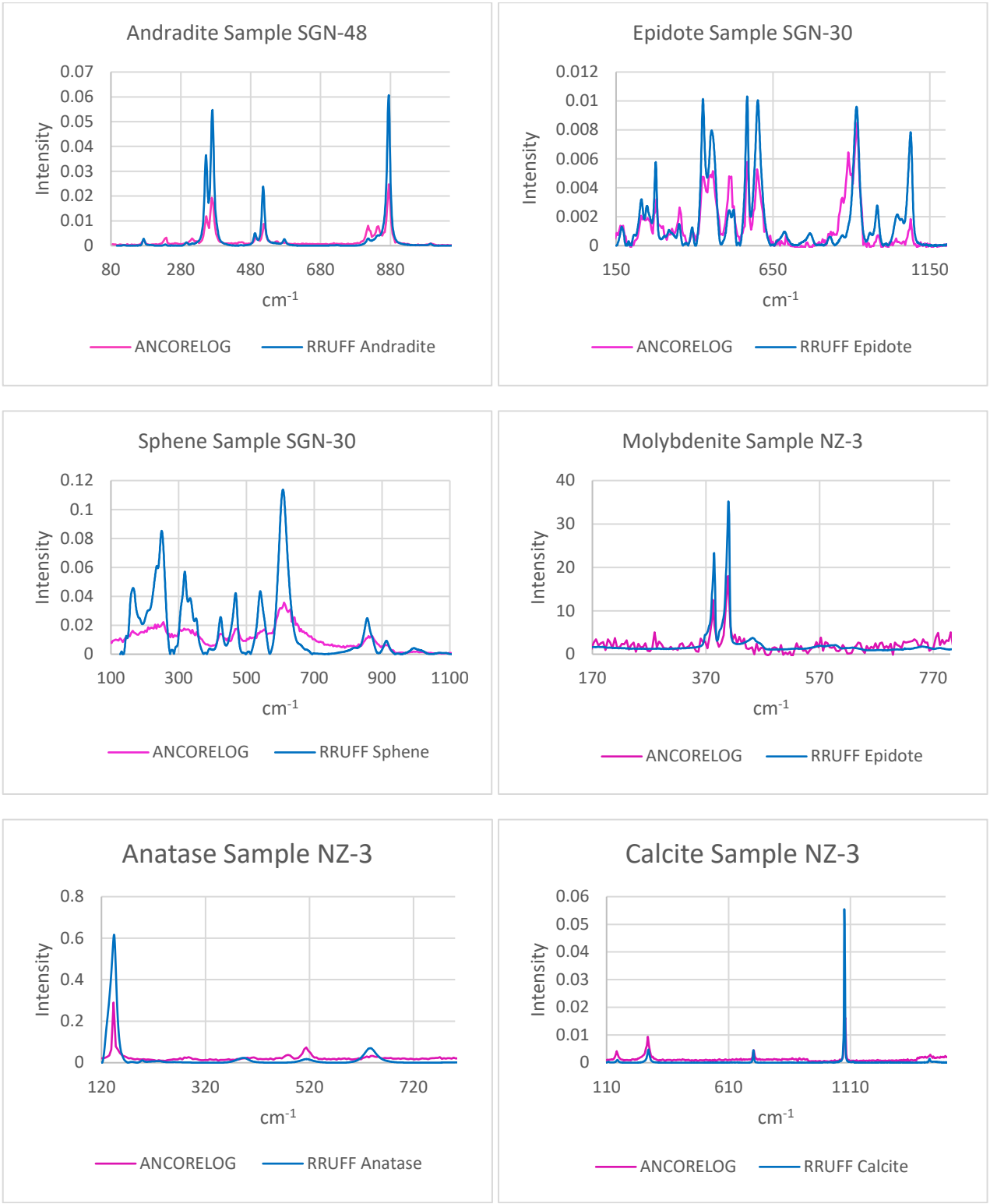

FIG 6 – Extracted mineral signatures from ANCORELOG's time-gated Raman measurements matched with reference spectra from the RRUFF database.

Geochemistry

Laser induced breakdown spectroscopy

Figure 7 shows LIBS-based intensity distribution images (heat maps) of characteristic emission lines for major rock-forming and sulfide-forming elements. The upper graphs represent the distribution of the major rock-forming elements Si, Al, Na, K, Ca, and Mg. The bottom graphs represent the distribution of the sulfide-forming elements Fe, S, Cu, Mo, and Zn. The data reflect the extreme heterogeneity of the sample sections. Please note that the relationship between LIBS intensity and

element concentration is often not linear because of matrix effects (eg Hahn and Omenetto, 2012). An advantage of LIBS compared to XRF is that light elements (Na, Mg, Al: Figure 7) can be measured as well. Furthermore, following appropriate calibration routines, LIBS can also be used for quantitative analysis (eg Kuhn *et al*, 2016; Rifai *et al*, 2020; Harmon and Senesi, 2021).

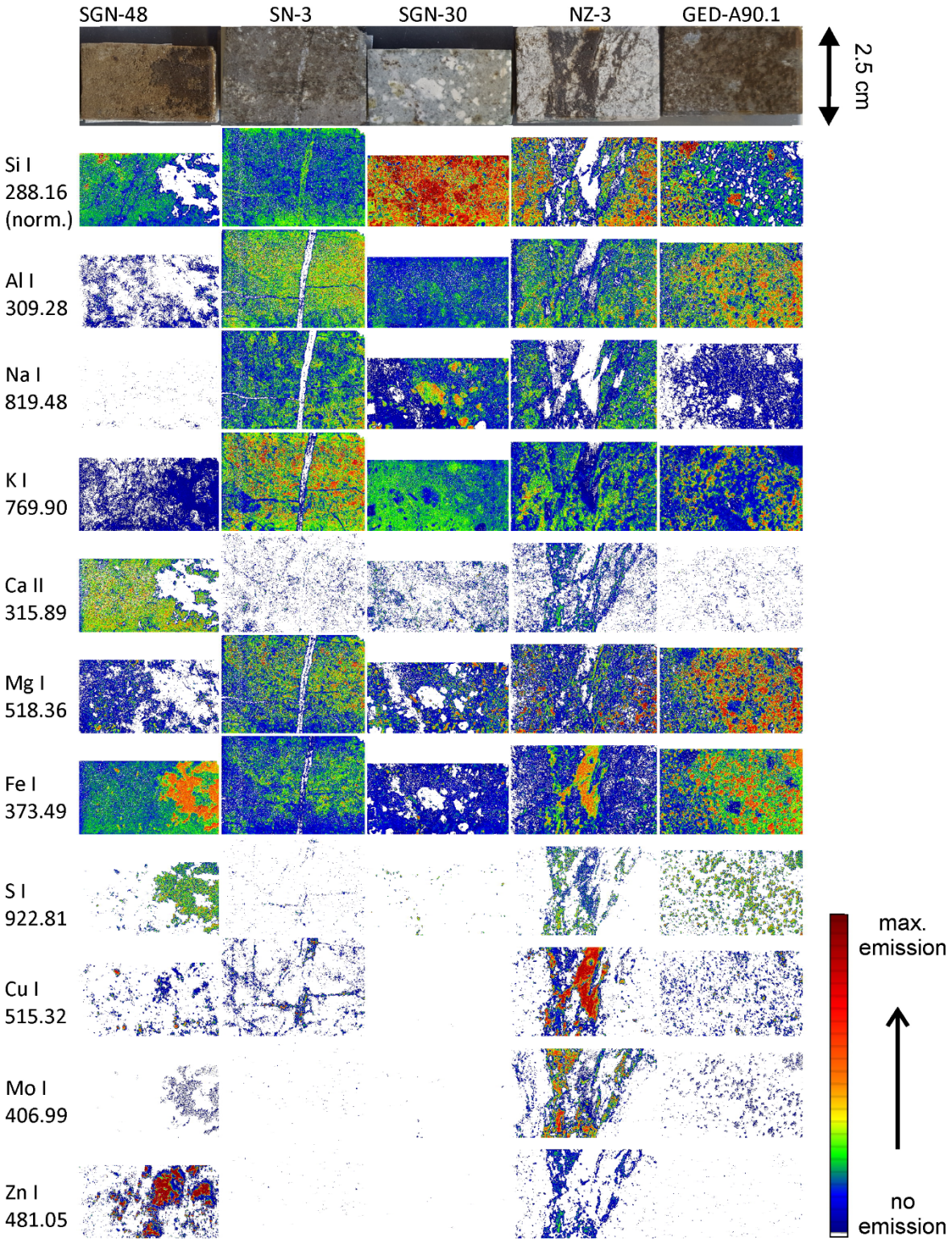

FIG 7 – LIBS-based intensity distribution images (heat maps) of characteristic emission lines of major rock-forming and sulfide-forming elements. The colour bar at the bottom right was scaled for each emission line individually according to the maximum observed intensity. Please note that the relationship between LIBS intensity and element concentration is often not linear because of the matrix effects. Left: (SGN 48) peripheral skarn, right: GED-A90.1, the potassic-phyllic zone in the centre of the porphyry.

The location of the mineralisation is clearly visible in sample SGN-48 (Zn, Fe, S, and small spots of Cu), in sample SN-3 (Cu and S in veins), in sample NZ-3 (Cu, Mo, Fe, S), and in sample GED-A90.1 (Fe, S, and small spots of Cu). Furthermore, the Cu enrichments show different Cu/Fe intensity ratios, possibly pointing to Cu minerals with different Fe content.

The heat maps for the major rock-forming elements can be used to deduce the position of specific minerals based on the presence or absence of specific elements. For example, biotite will show high emission of both Mg and K, whereas orthoclase and muscovite will show low emission of Mg and high emission of K. Calcite will show high emission of Ca only. C could not be detected in the spectra. Quartz minerals are characterised by the absence of emission lines for most elements except for Si. For automatic mineral classification, a mineral library can be built, and supervised classification algorithms applied. The methodology for imaging LIBS is described by Meima and Rammlmair (2020) and several geological applications are reviewed by Harmon and Senesi (2021).

The data in Figure 7 are in good correspondence with the microscopic results (Table 2) and results from other sensor technologies (see below). However, the LIBS-based emission intensities for the minor elements Pb, As, and Ti seem not to be consistent with the other data. With respect to Pb, small Pb-rich spots were detected in sample SGN-48 and NZ-3 with LIBS. The LIBS spectra, however, did not show any S emission at these spots, which would be expected for galena (PbS). With respect to As, the LIBS spectra show increased intensities for multiple characteristic emission lines of As in sample NZ-3, although As minerals have not been found during microscopic analysis and the presence of As could not be confirmed with XRF. With respect to Ti, not only a Ca-rich Ti phase was detected with LIBS in sample SGN-30 (which could be sphene according to Table 2), but also a very large amount of spots in sample NZ-3 show strongly increased Ti emission. These discrepancies may be explained by interferences in the LIBS spectra that could not be resolved with the applied spectrometer system. A spectrometer system with a higher resolution would be advantageous but would significantly reduce the speed of measurement. Proper calibration, eg based on a multivariate approach, could prevent such discrepancies, but could also introduce new artefacts. This example well demonstrates the advantages of a multi-sensor approach: it offers complementary information (eg chemistry, mineralogy) and offers potential for in-line quality control by automatic cross-validation of results.

X-ray fluorescence

Energy line intensities in counts per second (cps) for selected elements from the XRF analysed samples are displayed in Figure 8. The Fe Kα line shows high intensities for samples SGN-48 (>15 kcps) and GED-A90.1 (>11 kcps), medium intensities for samples SN-3 and NZ-3 (both >5 kcps) and lower intensities for sample SGN-30 (<3 kcps). Sample SGN-48 shows the highest Ca Kα line intensity (1.4 kcps) and the lowest K Kα line intensity (<10 cps) among the samples. The highest K Kα line intensity (>300 cps) is found in sample SGN-30 and may reflect the occurrence of K-feldspars (orthoclase). The Cu and Mo Kα line reach the highest intensities in sample NZ-3 (both >3 kcps) whereas the highest Zn Kα line intensity occurs in sample SGN-48 (3.5 kcps). Zr Kα line intensities are low in all samples reaching the highest value in sample SGN-30 (69 cps) coinciding with the occurrence of the mineral zircon. Ti Kα line intensities range between 100 cps and 150 cps for all samples except SGN-48 (<20 cps). The occurrence of Ti is probably related to sphene, ilmenite and rutile/anatase mineralisation.

In general, trends in the elemental distribution within the samples can be derived from the XRF measurements. Cross validation with other sensors is an important approach for improved data consistency and reliability. A site-specific sensor calibration on reference samples with known elemental compositions would further improve the information and lead to an estimation of quantitative elemental concentrations.

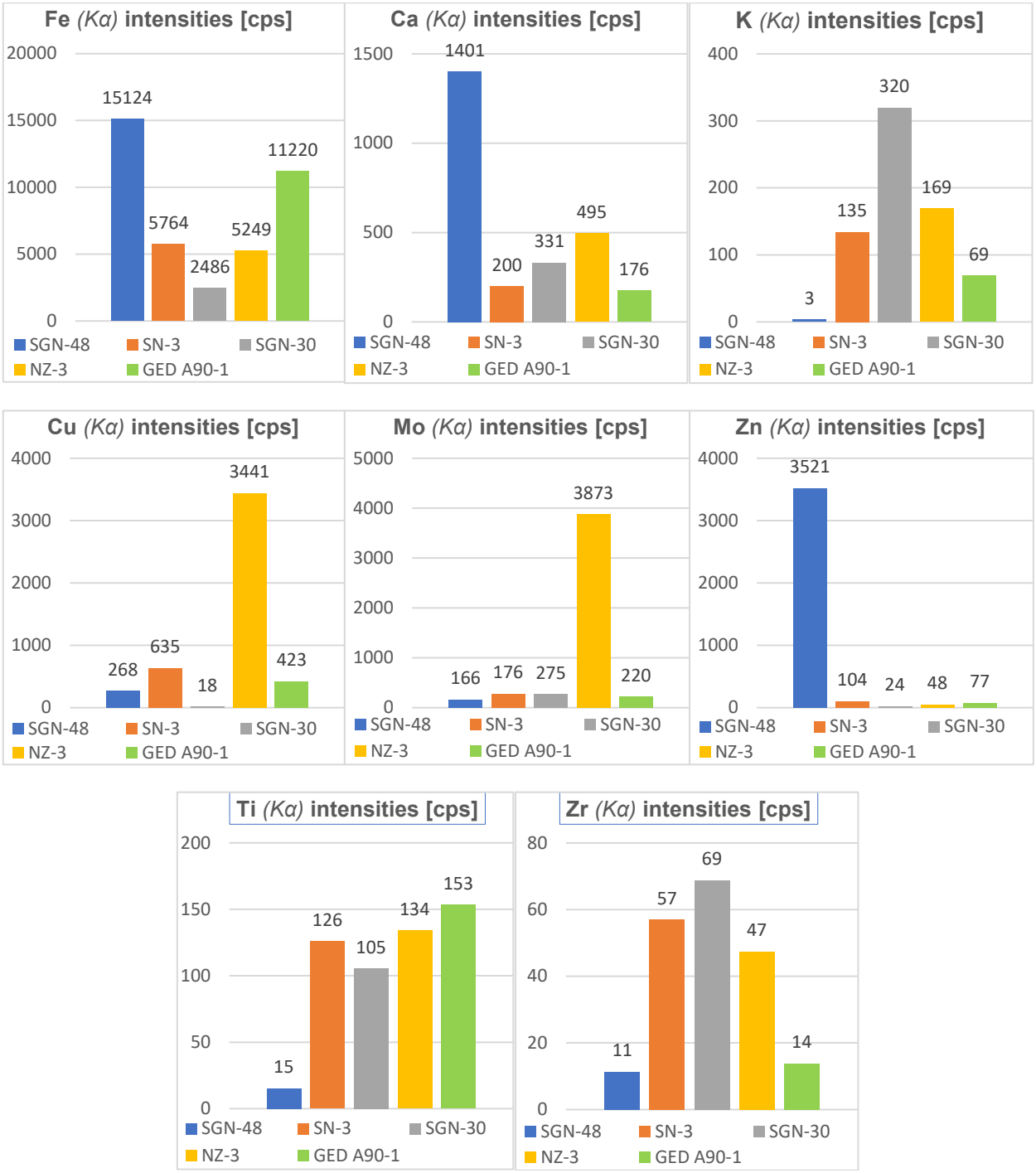

FIG 8 – ANCORELOG XRF measurements – energy line intensities in counts per second of selected elements.

X-ray transmission and computed tomography

In contrast to LIBS and XRF, DE-XRT does not reveal chemical elements but the content of groups of elements with effective atomic numbers, in our case Z_{eff} around 12 and around 29. Figure 9a and b show exemplarily the results obtained for sample NZ-3. It can be compared to the imaging LIBS results in Figure 7. This comparison shows that the low-*Z* group corresponds to Si, Al and Na, the medium-*Z* group to Fe, Cu and Zn. The same is true for ME-XRT with the difference that a third group, consisting of high-*Z* elements with *Z* around 74, is also distinguished (Figure 9d, 9e, 9f). The amount of high-*Z* elements is low and only slightly increased in the region with high medium-*Z* element concentration. A similar observation was made for sample SGN-48, where W was also observed with SEM. A search for W with LIBS to confirm the ME-XRT results will be executed in the future.

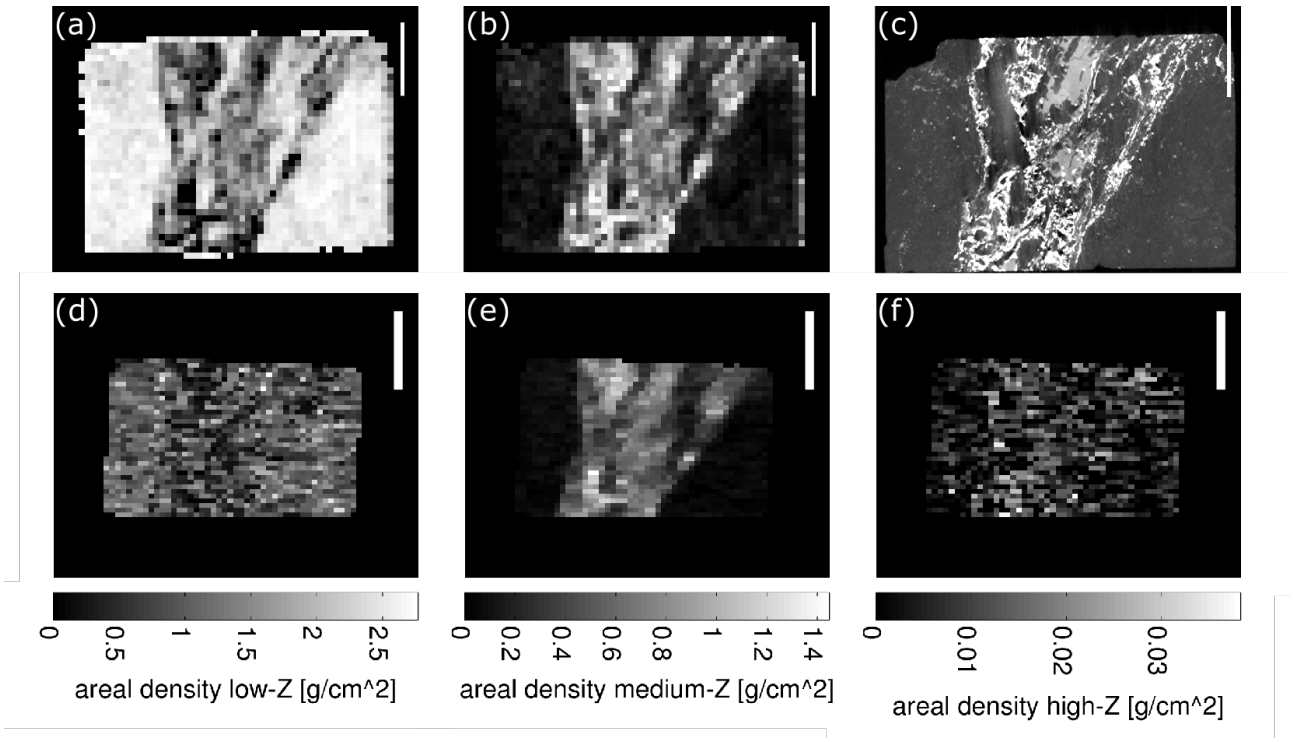

FIG 9 – (a) Low-*Z* and (b) medium-*Z* concentration for sample NZ-3 obtained by DE-XRT. Black and white correspond to concentration 0 per cent and 100 per cent, respectively. (c) Virtual cross-section through CT volume data. Areas of highest X-ray attenuation have the lightest colour. (d) Areal density of low, (e) medium and (f) high-*Z* elements obtained from ME-XRT. The meaning of the colours is indicated by the colour bars. All scale bars are 10 mm. Adapted from Bauer *et al* (2021b).

A virtual cross-section through the reconstructed CT volume allows to recognise three different grey values (Figure 9c). These correspond to elements with different attenuation. Comparison to Figure 7 shows that the darkest regions are formed of low-*Z* elements like Si, Al and Na, medium grey areas consist of Fe and Cu, the brightest regions contain highly absorbing elements like Mo.

Also for the other samples, agreement of imaging LIBS results with those obtained by DE-XRT, ME-XRT and CT was found. Figure 10 shows the medium-*Z* areal density of all samples found by ME-XRT. The comparison to the LIBS results (Figure 7) shows a similar spatial distribution of the corresponding elements. This indicates that the surface data obtained by imaging LIBS are representative for the whole volume, ie there are no relevant hidden internal structures that would only be visible with XRT or CT. The results also show that LIBS can be used to calibrate XRT and CT data. Further DE- and ME-XRT, as well as CT images of the other samples can be found in Bauer *et al* (2021b).

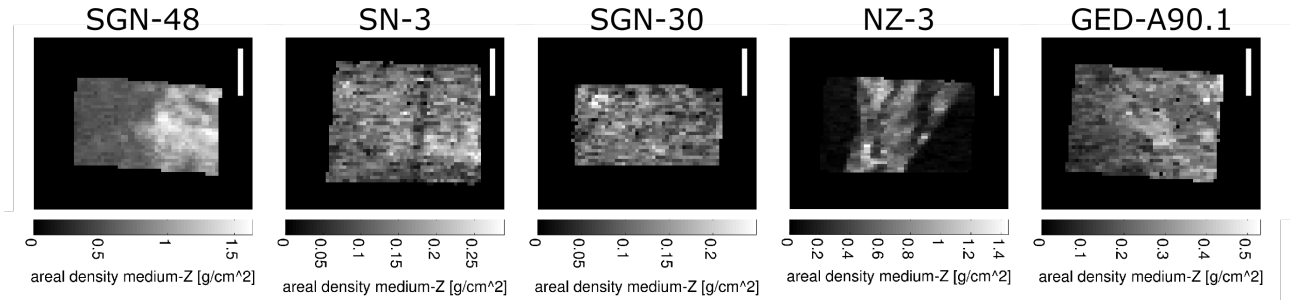

FIG 10 – Areal density of medium-*Z* elements obtained from ME-XRT. Adapted from Bauer *et al* (2021b).

The XRT and CT results can be used to estimate the fractions of the material classes with different atomic numbers Z_{eff} (Bauer *et al*, 2021a, 2021b). The results are given in Table 4. They indicate that

the content of medium-*Z* elements like Fe, Cu and Zn is highest in SGN-48 from the peripheral skarn, followed by samples GED-A90.1 and NZ-3 from the potassic-phyllic zone. The lowest content is found in samples SN-3 and SGN-30 from the phyllic-argillic and propylitic zones. The fraction of high-*Z* elements with $Z \approx 74$, like W, is low in general, which is in agreement with expectation.

TABLE 4

Fractions of material classes with different atomic numbers Z_{eff} found by DE-XRT, ME-XRT and CT. The sum of the peak areas of Fe-, Cu- and Zn-peaks of XRF spectra show approximately the same trend like the medium-*Z* elements groups found by DE- and ME-XRT.

Sample	SGN-48	SN-3	SGN-30	NZ-3	GED-A90.1
Alteration Zone	peripheral skarn	phyllic-argillic	propylitic	potassic-phyllic	potassic-phyllic
DE-XRT Median for Medium-Z Elements	26.6%	6.9%	6.5%	20.9%	17.8%
ME-XRT Median for Medium-Z Elements	20.8%	5.6%	5.4%	17.5%	13.3%
ME-XRT Median for High-Z Elements	1.1‰	1.3‰	1.2‰	3.7‰	0.7‰
CT Medium- and High-Z Elements	20.4%	7.8%	7.4%	17.5%	15.1%
XRF sum of Fe, Cu and Zn, Signal in counts per s	18 913	6504	2527	8737	11 720

The fraction of medium-*Z* elements correlates approximately to the trend shown by the total XRF signal measured for Fe, Cu and Zn. An exception are the samples from the potassic-phyllic zone NZ-3 and GED-A90.1. One reason is presumably that XRT and CT measure the whole volume, while the XRF signal was recorded only from a part of the surface.

DISCUSSION

Advantages of multisensor-based core and material scanning

The here applied methods provide useful information during exploration and mining. Moreover, they allow parameter definition for ore processing. Exploration campaigns are tightly scheduled. In remote areas, it is time consuming and costly to go back to the laboratory if information is missing. Sensor-based in-field measurements accompanied by an experienced field geologist will bring out systematic mineralogical and chemical data. Coupled with deep learning software, decisions can be made during the drilling campaigns. Ore body modelling can be successively fine-tuned. During the mining phase, in-mine measurements allow to characterise the ore feed for the plant, to anticipate dysfunction during processing related to ore anomalies (grain size, composition), and thus to define parameters for beneficiation in real time.

The multisensor approach yields complementary information, including geochemistry (XRF, LIBS), mineralogy (Raman), as well as the propagation of specific textures in 3D (XRT, CT). The here applied methods, the time-gated Raman spectrometer, LIBS, XRF and DE- and ME-XRT devices can be used in-field on mine sites on drill cores and/or crushed material on conveyor belts (moving at up to 3 m/s depending on device). Here, Raman spectroscopy, XRF and LIBS can be applied for fast line scans, while DE- and ME-XRT can image the whole sample. CT and imaging LIBS are time consuming and must be performed on selected samples which are specific objectives of the project,

based on ‘core scanner/conveyor belt’ results. The sensors can be configured and adapted to the particular ore deposits and material matrices at DMT, Essen, Germany and related companies. Imaging LIBS can be performed in the field, samples for CT measurements must be shipped to laboratories like Fraunhofer IIS, Fürth, Germany.

The ANCORELOG cross-method approach – optimising the characterisation of Cu-porphyry alteration zones

Our findings show that in-field instruments such as time-gated Raman spectroscopy, XRF and LIBS, when coupled, perfectly allow to recognise the alteration zones (here studied samples) based on prior calibration by SEM-EDS of the Niaz porphyry. The mineralised zone can be characterised in terms of volumes of samples.

Performance of Raman spectroscopy for Cu-porphyry material classification

Little studies were carried out with Raman spectroscopy on mineralogical compositions in Cu porphyry alteration zones (Abrol and Layne, 2021). These authors show that hydrous minerals such as chlorite, alunite and mica can be used to characterise hydrothermal alteration zones. Test analyses with a robust field Raman spectrometer instrument mounted on the Mars rover were performed in the Tabernas desert in Spain (Veneranda *et al*, 2021). Reliable results are reported for feldspar, carbonate, and organic compounds characterisation, in particular using point analyses on crushed material. The latter result shows the performance of Raman spectroscopy for processed materials on conveyor belts.

Our study using a time-gated Raman spectrometer shows that Raman spectroscopy is powerful for skarn-type porphyries: (1) Minerals, such as clay minerals, chlorite, hornblende, sphene and epidote can be detected. Raman is also powerful to distinguish dickite from kaolinite. This feature is particularly important to decipher hypogene argillic alteration zones (eg Chang *et al*, 2011). (2) In skarn-type porphyries, garnet (andradite) is the indicator when the porphyry is reached top-down. Raman perfectly detects this key mineral. Titanium is often a harmful element during hydrometallurgical processing (Kologrieva *et al*, 2022). Time-gated Raman allows to detect sphene, rutile and anatase to eliminate these minerals/element in the earliest stage of the processing chain. The distinction of anatase and rutile impacts the density estimation at high Ti contents. Anatase (3.79 g cm^{-3}) has a lower density than rutile (4.13 g cm^{-3}). Most importantly Raman perfectly detects molybdenite in the ore horizon. However, chalcopyrite and pyrite cannot be measured. As vector mineral by Raman spectroscopy orthoclase can be used. For efficient use of the time-gated Raman spectrometer, calibration is necessary and key spectral lines can be defined in the software.

Performance of the ANCORELOG XRF for Cu-porphyry material classification

Portable XRF is used for Cu-porphyry samples and helps significantly classifying the alteration zones and the mineralisation (eg Gray and Van Rythoven, 2020 and references therein). The ANCORELOG XRF can be particularly configured for sulfide mineralisations. In this study the skarn can be classified clearly by Fe, Ca and Zn. Cu rich, Cu and Mo rich zones are also rich in K, and can thus be clearly distinguished from non-mineralised zones. Ti-rich and poor zones can be rapidly characterised and attributed to Ti-minerals detected by Raman.

Performance of LIBS for Cu-porphyry material classification

A LIBS line scan allows to determine the spatial distribution of ore forming metal bearing phases (Cu, Mo, Zn, Fe, S) and additionally light elements (Al, Si, K, Na, Mg) to clearly locate the major silicates and carbonates (Ca, Mg). The data are qualitative or (semi)-quantitative and can also be used for identification of minerals with distinct chemistry (eg Kuhn *et al*, 2016; Meima and Rammlmair, 2020; Harmon and Senesi, 2021). Applied in core scanner or industrial instrumentation, LIBS is very fast, eg up to 1000 measurements per second are possible as shown by Rifai *et al* (2020).

Performance of DE-XRT and ME-XRT for Cu-porphyry material classification

The strength of DE-XRT and ME-XRT is that these methods allow the fast analysis of the whole volume of all samples (Bauer *et al*, 2021a, 2021b; Firsching *et al*, 2011; Wagner *et al*, 2022).

However, they do not allow the identification of elements or minerals. Thus, while they can be used to determine the volume fraction of groups of elements with similar atomic numbers, they require calibration by other methods for an assignment of these groups to elements or minerals. This calibration can be done by SEM-EDS, LIBS, Raman spectroscopy and XRF measurements on the sample surface. To ensure that the sample surface is representative for the whole sample volume, CT can be useful as it allows a fully 3D visualisation of the internal sample structure. Thus, the volume distribution of minerals in the sample can be determined. Furthermore, it allows to investigate the structural features, such as fractures.

While mapping elements or minerals on the whole surface of a sample by LIBS, Raman spectroscopy or XRF is too time consuming for a sorting application, scans along some lines or measurements of a few spots (diameters of up to 400 µm) per sample are possible. These could be combined with the XRT results to increase their accuracy. The spatial density of measurement spots necessary to obtain a realistic characterisation of the samples has to be derived from the laboratory analyses. For homogeneous samples, one or a few spots may be sufficient, but more measurements are required for heterogeneous rocks.

CONCLUSION

This study shows that a combined sensor approach is an efficient way to classify alteration zones and associated mineralisation (Cu, Mo, Zn etc). Core scanner instruments must be configured based on laboratory measurements and core-scan tests on representative samples (barren, economic, differently altered etc). Therefore, in a first phase prior to routinely material scanning, a team of instrument developers and geologists, ideally also including a process engineer, elaborate the baselines for the upcoming industrial use. Adjustments can then be performed during material scanning.

The ANCORELOG approach reduces drilling costs as drilling campaigns can be directly adapted on the results and adjacent material models (orebody, feedstock for plants etc). It also reduces operational costs during hauling, crushing, milling and further processing, as prior sorting implies that less waste material enters the processing chain. Combined or single sensors from the ANCORELOG scanner can be configured and adapted to all type of processing materials.

OUTLOOK

The ANCORELOG sensors and scanner are currently tested on VMS-type deposits and materials in southern Spain. Further materials such as bauxites (Meima *et al*, 2021; Orberger *et al*, 2022) and process materials from TiO_2 pigment production and Al-production will be tested.

ACKNOWLEDGEMENTS

The authors would like to thank the European Institute of Innovation and Technology (EIT), a body of the European Union under the Horizon 2020, the EU framework Program for Research and Innovation, for funding sensor developments in the projects ANCORELOG (Grant N°17028) and T-REX (N° 19122). The authors would also like to thank the French Iranian TRIGGER project for funds for the laboratory SEM and microprobe analyses.

REFERENCES

Abrol, C and Layne, G D, 2021. Raman Spectroscopy coupled with Reflectance Spectroscopy as a tool for the characterization of key hydrothermal alteration minerals in epithermal Au-Ag systems: utility and implications for mineral exploration. *Applied Spectroscopy*, 75(12): 1475–1496.

Alvarez, R E, 2011. Estimator for photon counting energy selective X-ray imaging with multibin pulse height analysis, *Med Phys*, 38(5): 2324–2334.

Alvarez, R E, 2016. Efficient, Non-Iterative Estimator for Imaging Contrast Agents with Spectral X-ray Detectors, *IEEE Trans Med Imaging*, 35(4): 1138–1146.

Ayuso, R A, Barton, M D, Blakely, R J, Bodnar, R J, Dilles, J H, Gray, F, Graybeal, F T, Mars, J L, McPhee, D, Seal II, R R, Taylor, R D and Vikre, P G, (ed: John, D A), 2010. Porphyry copper deposit model: chapter B in mineral deposit models for resource assessment, No. 2010–5070-B, US Geological Survey.

Bauer, C, Wagner, R, Orberger, B, Firsching, M, Ennen, A, Garcia Pina, C, Wagner, C, Honarmand, M, Nabatian, G and Monsef, I, 2021a. Potential of Dual and Multi Energy XRT and CT Analyses on Iron Formations, *Sensors*, 21(7): 2455.

Bauer, C, Wagner, R, Orberger, B, Firsching, M, Wagner, C, Boudouma, O and Siahcheshm, K, 2021b. Dual and Multi Energy XRT and CT Analyses Applied to Copper-Molybdenum Mineralizations in Porphyry Deposits, *Mater Proc*, 5(1): 27.

Chang, Z, Hedenquist, J W, White, N C, Cooke, D R, Roach, M, Devell, C L, Garcia, J, Gemell, J B, McKnight, S and Cuison, A L, 2011. Exploration Tools for Linked Porphyry and Epithermal Deposits: Example from the Mankayan Intrusion-Centered Cu-Au District, Luzon, Philippines, *Economic Geology*, 106(8):1365–1398.

European Institute of Innovation and Technology (EIT) RawMaterials, 2022a. ANCORELOG: Analytical Core Logging System [online]. Available from: <https://eitrawmaterials.eu/project/ancorelog/> [Accessed: 28 March 2022].

European Institute of Innovation and Technology (EIT) RawMaterials, 2022b. T-REX: Timegated Raman for Exploration [online]. Available from: <https://eitrawmaterials.eu/project/t-rex/> [Accessed: 28 March 2022].

Firsching, M, Nachtrab, F, Uhlmann, N and Hanke, R, 2011. Multi-Energy X-ray Imaging as a Quantitative Method for Materials Characterization, *Adv Mater*, 23:2655–2656.

Gray, C A and Van Rythoven, A D, 2020. A comparative study of porphyry-type copper deposits mineralogies by portable X-ray fluorescence and optical petrography. *Minerals*, 10(5): 431.

Hahn, D W and Omenetto, N, 2012. Laser-Induced Breakdown Spectroscopy (LIBS), Part II: Review of Instrumental and Methodological Approaches to Material Analysis and Applications to Different Fields. *Applied Spectroscopy*, 66(4): 347–419.

Harmon, R S and Senesi, G S, 2021. Laser-Induced Breakdown Spectroscopy – A Geochemical Tool for the 21st Century. *Applied Geochemistry*, 128: 104929.

Hassanpour, H, Alirezaei, S, Selby, D and Sergeev, S, 2015. SHRIMP zircon U–Pb and biotite and hornblende Ar–Ar geochronology of Sungun, Haftcheshmeh, Kighal, and Niaz porphyry Cu–Mo systems: evidence for an early Miocene porphyry-style mineralization in northwest Iran, *Int J Earth Sci*, 104: 45–59.

Kalender, W A, Seissler, W, Klotz, E and Vock, P, 1990. Spiral volumetric CT with single breath-hold technique continuous transport and scanner rotation, *Radiology*, 176(1):181–183.

Kologrieva, U, Volkov, A, Krasnyanskaya, I, Stulov, P and Waistein, D, 2022. Hydrometallurgical Methods for obtaining vanadium concentrates from the waste by chemical production of vanadium pebtoxide. *Materials*, 15(3): 938.

Kuhn, K, Meima, J A, Rammlmair, D and Ohlendorf, C, 2016. Chemical Mapping of Mine Waste Drill Cores with Laser-Induced Breakdown Spectroscopy (LIBS) and Energy Dispersive X-Ray Fluorescence (EDXRF) for Mineral Resource Exploration. *J Geochem Explor,* 161: 72–84.

Lafuente, B, Downs, R T, Yang, H and Stone, N, 2015. The power of databases: the RRUFF project in *Highlights in Mineralogical Crystallography*, (ed: T Armbruster, R M Danisi), pp 1–30 (De Gruyter, Berlin, Germany).

Lowell, J D and Guilbert, J M, 1970. Lateral and Vertical Alteration-Mineralization Zoning in Porphyry Ore Deposits. *Economic Geology*, 65(4):373–408.

Meima, J A and Rammlmair, D, 2020. Investigation of compositional variations in chromitite ore with imaging Laser Induced Breakdown Spectroscopy and Spectral Angle Mapper classification algorithm. *Chemical Geology,* 532: 119376.

Meima, J A, Orberger, B, García Piña, C, Prudhomme, A and Dittrich, C, 2021. Increasing Resource Efficiency of Bauxites Using LIBS. *Mater Proc*, 5(1): 81.

Michaud, D, 2014. Ore Hardness Testing -SAG Mill Tonnage Estimation Method [online]. Available from: <https://www.911 metallurgist.com/blog/ore-hardness-testing-grinding-measurement> [Accessed: 28 March 2022].

Omrani, J, Agard, P, Whitechurch, H, Benoit, M, Prouteau, G and Jolivet, J, 2008. Arc-magnetism and subduction history beneath the Zagros Mountain, Iran: A new report of adakites and geodynamic consequences, *Lithos*, 106(3–4): 380–398.

Orberger, B, Garcia-Pina, C, de Waard, B, Rybo, L, Hyypiö, R, Prudhomme, A, Capar, L, Lindström, H, Uusitalo, S, Alamäki, M, Kaminski, C, Meima, J A and Merk, S, 2022. LIBS, XRF and Raman sensors for optimal bauxite sorting, in *Proceedings of the IMPC Asia-Pacific 2022*, pp 437–461 (The Australasian Institute of Mining and Metallurgy: Melbourne).

Rifai, K, Michaud Paradis, M-C, Swierczek, Z, Doucet, F, Özcan, L, Fayad, A, Li, J and Vidal, F, 2020. Emergences of New Technology for Ultrafast Automated Mineral Phase Identification and Quantitative Analysis Using the CORIOSITY Laser-Induced Breakdown Spectroscopy (LIBS) System. *Minerals*, 10(10): 918.

Seedorff, E, Dilles, J H, Proffett, J M, Einaudi, M T, Barton, M, Zurcher, L, Stavast, W J A and Johnson, D A, 2005. Porphyry deposits: Characteristics and origin of hypogene features, *Economic Geology*, 100th Anniversary Vol, 251–298.

Sillitoe, R H, 2010. Porphyry copper systems, *Economic geology*, 105(1):3–41.

Tabelin, C B, Park, I, Phengsaart, T, Jeon, S, Villacorte-Tabelin, M, Alonzo, D, Yoo, K, Ito, M and Hiroyoshi, N, 2021. Copper and critical metal production from porphyry ores and E-wastes: A review of resource availability,

processing/recycling challenges, socio-environmental aspects and sustainability issues, *Resources, Conservation and Recycling*, 170:105610.

Taghipour, B, Moore, F, Macizadeh, M A and Taghipour, S, 2013. Hydrothermal garnet in porphyry copper related skarn deposits, Ali-Abad, Yazd Province, Iran, *Iranian Journal of Science and Technology (Sciences),* 37(A1):11–22.

Veneranda, M, Lopez-Reyes, G, Manrique-Martinez, J, Sanz-Arranz, A, Medina, J, Pérez, C, Quintana, C, Moral, A, Rodriguez, J A, Zafra, J, Nieto Calzada, L M and Rull, F, 2021. Raman spectroscopy and planetary exploration: testing the ExoMars/RLS system at the Tabernas Desert (Spain). *Microchem J*, 165: 106–149.

Wagner, R, Bauer, C, Firsching M and Leisner J, 2022 (in prep). From Food to Mining: Dual Energy XRT Applications, in *Advances in Sensors: Reviews*, 8.

Throughput forecast modelling over the Life-of-Mine

L Brennan[1], W Valery[2], Y Quan[3], B Bonfils[4], T Farmer[5], R Hayashida[6], A Jankovic[7] and K Duffy[8]

1. Process Engineer, Hatch, Brisbane Qld 4000. Email: lachlan.brennan@hatch.com
2. Global Director – Consulting and Technology, Hatch, Brisbane Qld 4000. Email: walter.valery@hatch.com
3. Process Engineer, Hatch, Brisbane Qld 4000. Email: ying.quan@hatch.com
4. Senior Process Engineer, Hatch, Brisbane Qld 4000. Email: benjamin.bonfils@hatch.com
5. Mining Engineer, Hatch, Brisbane Qld 4000. Email: thomas.farmer@hatch.com
6. Senior Mining Consultant, Hatch, Brisbane Qld 4000. Email: rodrigo.hayashida@hatch.com
7. Principal Consultant, Hatch, Brisbane Qld 4000. Email: alex.jankovic@hatch.com
8. Senior Process Engineer, Hatch, Brisbane Qld 4000. Email: kristy.duffy@hatch.com

ABSTRACT

Hatch has developed forecast models for predicting Life-of-Mine (LOM) circuit throughput for a number of operations worldwide. These models can be used to predict variations in future operating throughput arising from changes in ore characteristics, mine planning, blending strategies, and operating strategies, thereby improving process stability and helping to maximise profit over the LOM. In this paper, Hatch shares three case studies of throughput forecast modelling and discusses the main results, model precision, and associated challenges with the methodology, and provides a comparison of predicted plant performance with operational data.

Hatch's forecasting methodology considers the effect of ore characteristics and blast fragmentation on the entire feed particle size distribution (PSD) to the comminution circuits. Site-specific Morrell power-based models are also used to capture the key factors contributing to plant throughput. These include the proportion of each ore type in the feed blend, the characteristics of each ore type (hardness and breakage characteristics), product size targets, and equipment specifications.

Data is then collected (often during Mine-to-Mill (M2M) optimisation projects) and used to validate the power-based throughput forecast model against historical observed ore hardness and plant throughput. Outputs from site geological and geotechnical/geometallurgical block models, such as the distribution of the various ore types and their hardness, plus mine planning information are then used to predict the throughput on an annual basis over the LOM. The power-based equations that predict comminution circuit specific energy are also tuned to reflect the recommended mine and plant optimisation strategies, thus the model can reflect not only current practices, but also be used to investigate potential optimisation opportunities.

INTRODUCTION

In any operation, a certain level of variability in plant throughput is inevitable. Changes in the *in situ* ore characteristics (strength and structure) associated with different ore types or domains yield different run-of-mine (ROM) PSDs under a given set of drill and blast parameters. Changes in the hardness and breakage characteristics provide an additional source of variability once the ore reaches the plant. Differences in mineralogy and liberation characteristics may also necessitate changes in the target grind size to maintain the performance of downstream separation processes, adding yet another layer of complexity. The ability to anticipate and control the resulting variation in throughput is critical to achieving consistent, stable operation, which is a necessary precondition for process optimisation and maximising profit over the LOM.

Members of Hatch's Mining and Minerals Processing group have developed throughput forecast models to predict LOM circuit throughput for several operations globally (see Bennet *et al,* 2017; Burger *et al,* 2006; Farmer *et al,* 2021) using a methodology based on established power-based approaches, and incorporating site-specific factors and constraints. These models consider the proportion of the different ore types present in the feed blend, and where available leverage detailed ROM fragmentation models to link the blend composition to the feed size seen by the plant. Combined with ore hardness data and inputs for available comminution power and target grind size, conventional power-based models can be applied to predict the LOM throughput. With many mining companies having invested significant effort in recent decades into the development of detailed

geometallurgical models, which integrate geological, mining, and processing aspects (Alruiz *et al*, 2009), many of the required inputs can now be sourced from the one location.

Hatch's methodology is described in detail in the section that follows, with three case studies provided thereafter. While the use of similar models has been described elsewhere (Misle *et al,* 2013; Farmer *et al,* 2021), the case studies in this paper are intended to provide examples of the sort of challenges which can be encountered when applying this methodology – and the approaches needed to overcome them – as well as the flexibility of the methodology to consider future circuit changes.

METHDOLOGY OVERVIEW

At its core, Hatch's approach to throughput forecasting involves the application of power-based methods to determine the achievable throughput over the LOM, considering the available grinding power. The methodology for determining the total circuit specific energy, and the specific energy of the AG/SAG mill – proposed by Morrell (2004a, 2004b) and accepted as industry standard (Global Mining Guidelines Group, 2021) – is used to calculate the throughput over a given period, with the final forecast and the limiting grinding stage determined based on the lower of the two values. The key equations for total and SAG/AG specific energy are as follows:

$$Morrell\ Total\ Specific\ Energy\ \left(\frac{kWh}{t}\right) = 4M_{ia}\left(750^{f(750)} - F_{80}^{f(F_{80})}\right) + 4M_{ib}\left(P_{80}^{f(P_{80})} - 750^{f(750)}\right) \quad (1)$$

$$SAG/AG\ \ Specific\ Energy\ \left(\frac{kWh}{t}\right) = K\ \times\ {F_{80}}^{a} \times DWi^{b} \quad (2)$$

Where:

M_{ia}	coarse grinding work index (kWh/t)
M_{ib}	fine grinding work index (kWh/t)
F_{80}	80 per cent passing size (µm) of the grinding circuit feed
P_{80}	80 per cent passing size (µm) of the grinding circuit product
f(x)	defined functions of F_{80} and P_{80}, as per Morrell (2004a, 2004b)
DWi	drop weight index (kWh/m^3) of the ore
K, a & *b*	site-specific factors, calibrated to production data

Much of the value of Hatch's approach, however, comes from combining data from typically available sources (the LOM plan or geometallurgical model) and other models (blast fragmentation models and mechanistic process models) to best define the inputs to the power-based model, and to augment it where the impact of certain changes cannot be accurately captured by power-based approaches alone.

When developing a throughput forecast model, Hatch typically draws upon the LOM plan or geometallurgical model to provide the proportion of feed ore originating from the various ore sources or defined domains over time. The LOM plan or geometallurgical model will also contain data for the typical indicators of comminution characteristics (eg DWi, Axb, BBWi, M_{ia}, M_{ib}) for each of the ore sources, with the level of definition dependent on the maturity of the geometallurgical program at a particular site.

The proportion of the different ore types and DWi (or an equivalent parameter, from which DWi can be determined) in the LOM plan allows for a weighted average AG/SAG specific energy to be calculated for a given period. Similarly, the information within the LOM plan can be used to calculate the total specific energy via the Morrell method, provided a given feed size (F_{80}) and product size (P_{80}). While product size is a process target informed by the mineralogical and liberation characteristics of a given ore, feed size is often less well understood, particularly insofar as how it is influenced by drill and blast practices and *in situ* ore characteristics. Defining the F_{80} is critical for any power-based throughput forecasting, and it is here where detailed ROM fragmentation modelling is particularly useful, such as that completed by Hatch during a M2M study.

In a M2M study, blast domains are defined based on the *in situ* characteristics of the ore, specifically its structure (typically measured in terms of *in situ* block size) and strength (unconfined compressive strength, determined via point load testing). These two parameters respectively dictate the coarse and fine end of the ROM PSD under a given set of blast conditions. Defining these domains and conducting a controlled blast audit provides the basis for developing ROM fragmentation models, which are then used to establish drill and blast guidelines for each domain. The ultimate objective of these guidelines is to provide a ROM PSD which maximises plant throughput, while avoiding indiscriminate or unilateral increases in drill and blast cost. More energy is typically applied to harder and less naturally fractured domains, while less energy is applied in softer or more fractured domains where it is not required. The detailed fragmentation models and simulations used in a M2M study to identify the optimal blast design provide a link between ore characteristics, drill and blast practices, and ROM fragmentation, which can be captured and integrated into a forecast model. Within the forecast model this takes the form of a family of functions which together describe the ROM F_{80} in terms of drill diameter and powder factor for each of the different domains. The SAG/AG F_{80} can then be estimated in turn, based on tuned mechanistic models of the crushing stage.

Where a M2M project has not been completed, and no blast fragmentation model is therefore available, an alternative approach is required. In that scenario, data from online camera systems (eg *Ore3D*® or *Split Online*®) is often used to derive general relationships between SAG/AG feed F_{80} and blend composition.

Once the expected F_{80} is determined, the total and AG/SAG specific energy is then calculated, using Equations 1 and 2. Throughput is then calculated based on the AG/SAG and total specific energies, and the grinding power available in the AG/SAG mill and the overall circuit. By comparing the two throughput figures, a realistic estimate can be made, considering the 'rate limiting step' in the grinding process. Extending this to a full LOM forecast, useful information is provided regarding not only throughput, but also how the limiting step may shift over time, which can assist in strategic planning for long-term plant expansions or upgrades.

For a throughput forecast prepared in conjunction with a M2M study, the same blast fragmentation models used to determine ROM F_{80} also provide details regarding the increase in fines generation associated with optimised blast conditions. Mechanistic models of the grinding circuit (such as those in *JKSimMet*) and analysis of historic operating data and surveys are used to estimate the throughput increase associated with these additional fines. Of course, the effect of these fines is not captured by the power-based approaches, whether that be the total specific energy method (which considers only F_{80} as a feed size indicator) or calculations of AG/SAG specific energy, which are tuned to historic data with the 'pre-optimisation' blast conditions. When developing a throughput forecast model, Hatch incorporates the estimated impact of the added fines by applying a correction factor to the calculated throughput, linked to a toggle for the user to specify baseline or optimised blast conditions.

Where possible, validation of the increase in fines production associated with the M2M blast may help to further refine the blast model, as well as the throughput forecast. Caution should be applied, however, using online image analysis systems for this purpose, or integrating their output into the model directly. As noted by Contreras Bravo and Morales (2017), these systems are effective for measuring the F_{80} (at least when properly calibrated and maintained), however are often more prone to error at fine sizes.

Finally, an effective throughput forecast model needs to account for site specific factors or constraints, beyond those set by the feed conditions and installed power of the grinding circuit. Where such constraints are identified, Hatch's approach is to incorporate them into the model via 'constraint ON/OFF' toggle, allowing an immediate and flexible means by which to evaluate the benefit associated with relieving the issue or bottleneck. The case studies in this paper include an example where this approach has been applied.

CASE STUDY 1

Operation description

The operation in Case Study 1 is an open pit copper/molybdenum operation, with the major ore minerals being chalcocite, chalcopyrite, and bornite. Ore at this site is classified into three hardness domains (soft, medium, and hard) according to Axb and BBWi values, and six geometallurgical units, referred to as UGM 1 through 6. The comminution circuit consists of three parallel grinding lines, fed by primary crushed ore. Two of the three lines feature identical SAG and secondary ball mill circuits. The third line features a larger SAG mill, with two secondary ball mills.

SAG trommel oversize from all three lines is classified over common pebble screens; undersize from those screens reports to the ball mills in the third line, while oversize is crushed. Crushed pebbles are distributed between the two smaller grinding lines in an 80/20 split, with none of the crushed pebbles reported to the larger grinding line.

Forecast model

Hatch were engaged to complete a M2M optimisation project, and develop a throughput forecast model in parallel. Audited blasts and plant surveys were completed for the soft and medium ore types, allowing for the development of calibrated blast fragmentation models for these ores, as well as models of the crushing and grinding processes in JKSimMet. Hard ore was modelled based on the medium models, with adjustments made with reference to historical data. For the purposes of the blast fragmentation models, the soft domain was divided further into coarse and fine structural subdomains, based on the variability in *in situ* block size. Once the blast fragmentation models were developed, a range of drill and blast design conditions were simulated, with a view towards improving fragmentation in the medium and hard domains by increasing blasting intensity, while reducing operating costs and complexity in the soft domains by relaxing the blast. The prescribed blast guidelines were forecast to yield a 6 per cent increase in fines generation in the soft fine domain, 4 per cent in the medium domain, and 7 per cent in the hard domain, as well as improvements at the coarse end (reduced P_{80} and top size). In the soft fine domain, only marginal improvement in terms of fines production was possible, however some reduction in ROM P_{80} was predicted. ROM fragmentation for the simulated base cases and guidelines is shown in Figure 1.

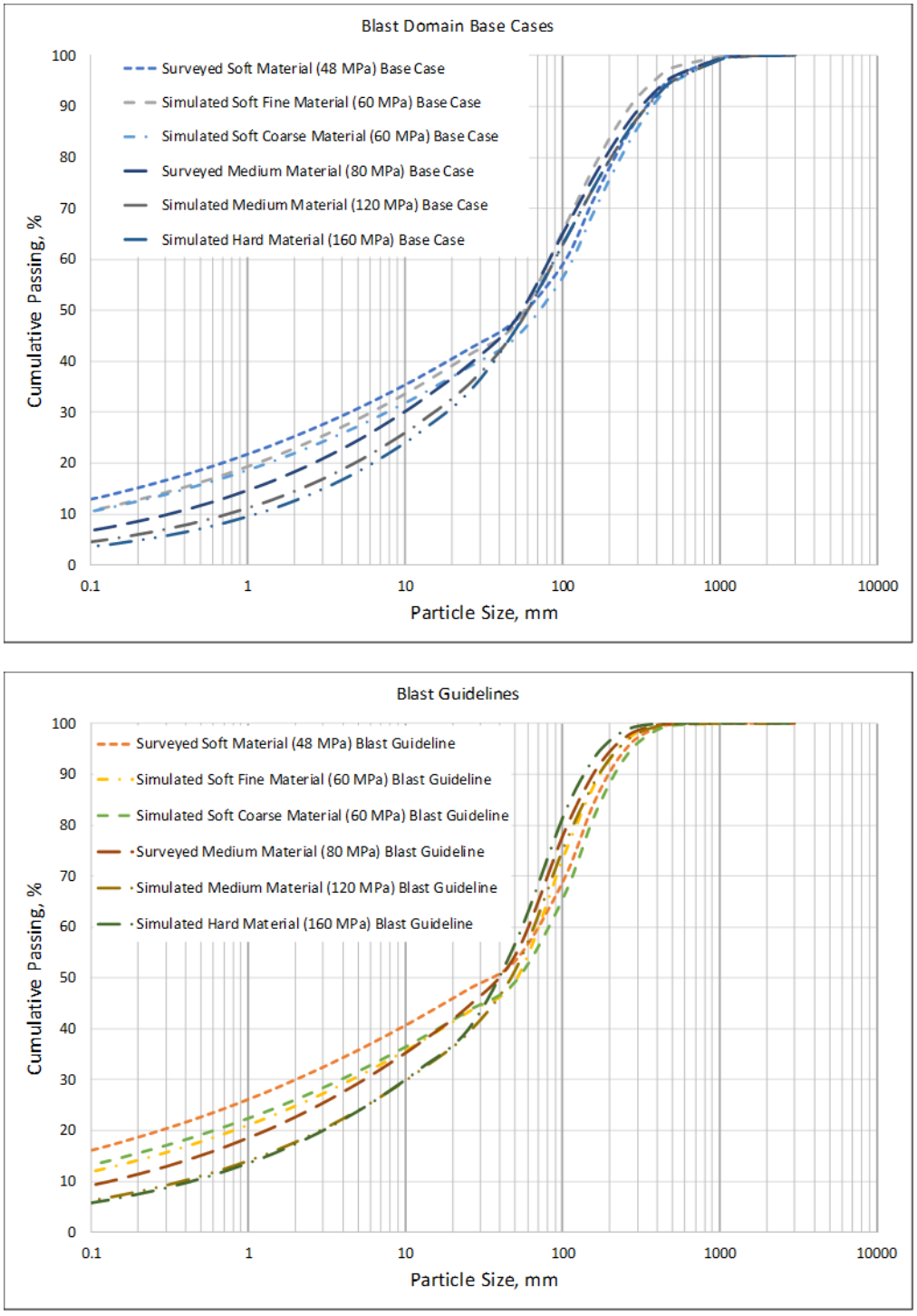

FIG 1 – ROM fragmentation for base case and optimised blast conditions in each of the blast domains defined as part of the M2M study.

Moving downstream, opportunities to optimise the crushing and grinding circuits were also identified. These included:

- improving power utilisation in the two smaller SAG mills via increasing the mill speed and ball load.
- leveraging the finer ROM fragmentation from the optimised blast by tightening the primary crusher gap, thereby providing a finer SAG feed top size.
- optimising the grate and pulp lifter designs to increase pebble production and better utilise the installed pebble crusher capacity, while simultaneously reducing the risk of slurry pooling.

The total throughput benefit of the optimised blast fragmentation and the changes in the process plant was forecast as between 10 and 12 per cent, depending on ore type. A potential opportunity to reject barren pebbles by integrating the existing pebble screens into an ore sorting circuit – and thereby free up capacity in the milling circuit, while also improving the feed grade to the downstream separation process – was also identified for further review.

Along with the M2M study, a throughput forecast model was developed. Site had an existing model, based on the Morrell power-based equations, however an updated model was required to capture the impact of the improved blast fragmentation associated with the M2M recommendations. Input data required for the LOM forecast model was drawn from sites' existing geometallurgical model. Extensive ore characterisation – including Axb, DWi, BBWi, and UCS – sits within the geometallurgical model, allowing the development of a high-quality throughput forecast. Whereas the M2M study considered the three hardness classifications, the throughput forecast was based on the six previously mentioned geometallurgical units, which provided a higher level of definition. The modelled blasting behaviour (based on the hardness domains) was captured via a correlation between F_{80} and Axb, which could then be applied to the geometallurgical domains to estimate the F_{80} to the plant for a given blend. Figure 2 shows the annual average Axb values for each UGM over the LoM. A reasonable level of variation can be seen, with values varying between approximately 40 (moderately hard) and 100 (soft) for the most part for the period out to 2036. Test work for ores to be processed beyond 2036 was not available at the time of the forecast being developed.

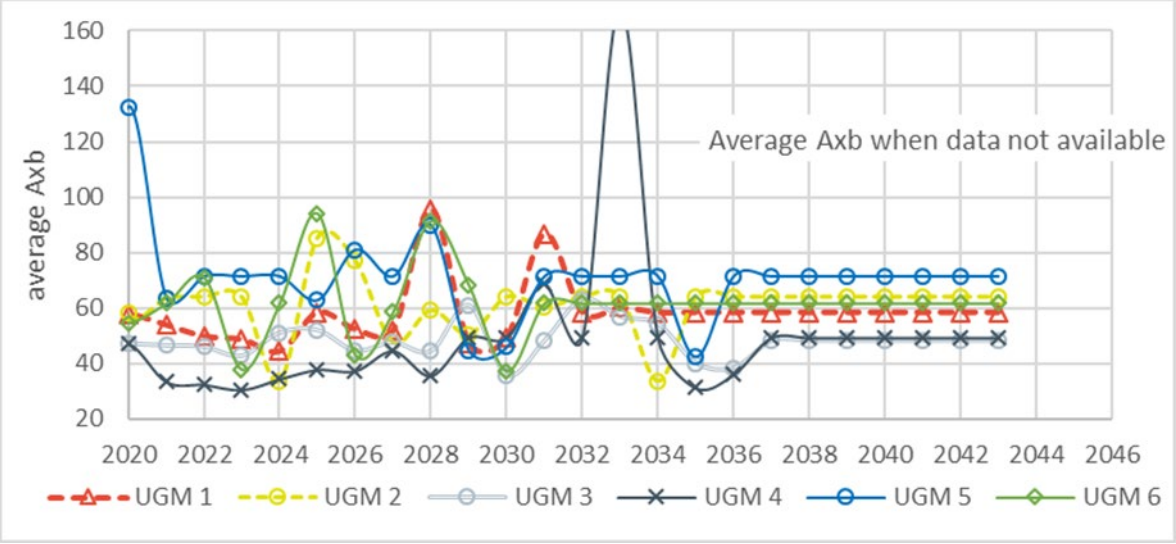

FIG 2 – Axb of the various UGMs from Case Study 1.

These data, along with the BBWi data also in the geometallurgical model, are used to calculate the M_{ia} and M_{ib} indices used in the Morrell specific energy calculations. Together with the estimated F_{80}, and the user-specified grind size target, this allows the calculation of the specific energy for each UGM. It is important to note that the specific energies used for the final throughput calculations are based on a weighted average specific energy, derived from the individual specific energies calculated for each UGM. This allows for the differing F_{80} associated with each UGM to be accurately accounted for and avoids incorrectly averaging the non-additive Axb values. Once the weighted average specific energy is calculated, throughput is calculated based on the available grinding power in each line, and the final estimate calculated by comparison against the throughput calculated based on SAG specific energy. Calibration factors were also applied to account for differences between the lines, specifically the consistent trend of lower specific energy in Lines 1 and 2, compared with Line 3.

Finally, the model features optionality allowing the user to predict ROM fragmentation for different drill and blast scenarios, being either the base case 'as is' blast design, or under conditions in line with the recommendations of the M2M study. Calculated throughput in the M2M cases is adjusted by reducing the specific energy in inverse proportion to the expected throughput gain determined from the detailed process modelling. The overall model structure is shown in Figure 3.

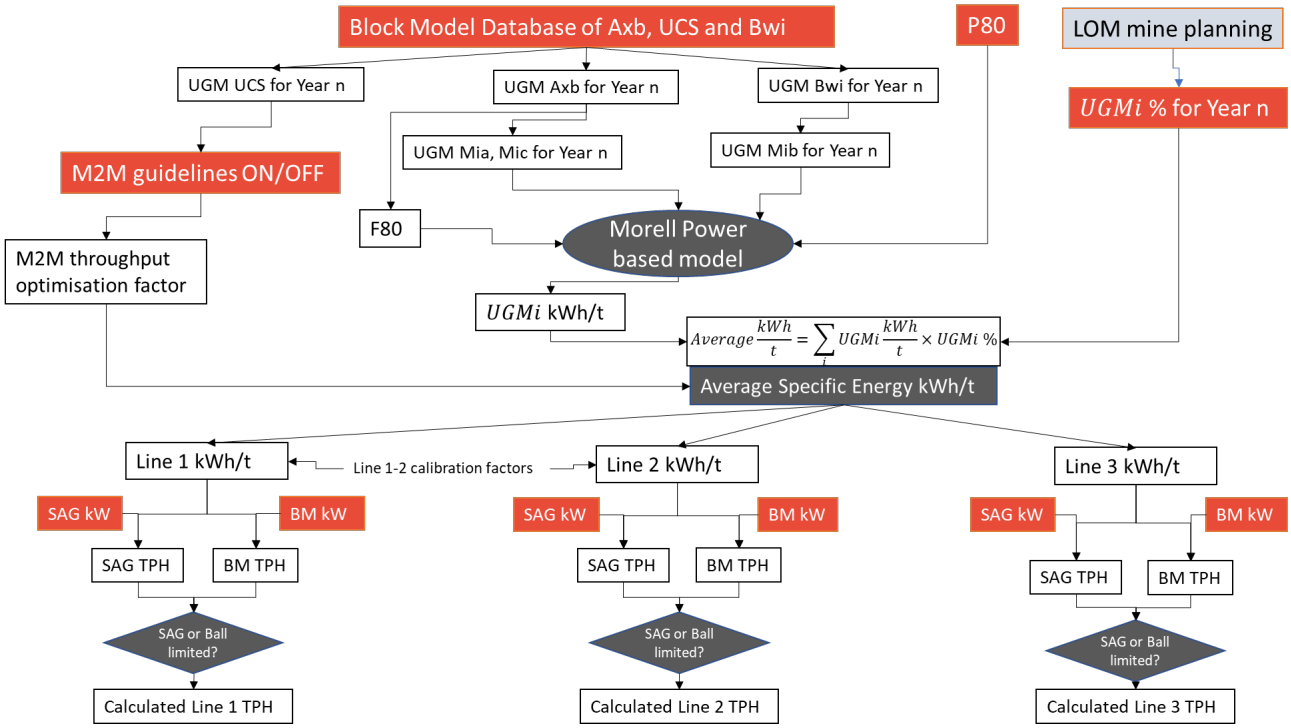

FIG 3 – Overall forecast model structure for Case Study 1. Note the on/off toggle available to the user for the M2M guidelines.

The model was validated against one years' worth of production data, covering the 2018 calendar year. Recorded power and product size were used as inputs, and the model predicted throughput was compared against the actual throughput. Model standard error equated to 9.8 per cent of the average total throughput (Line 1 + Line 2 + Line 3) on a monthly basis. Standard error for each individual line equated to 9.3 per cent, 5.8 per cent, and 11.2 per cent of the average, corresponding to confidence intervals of between 12–25 per cent of the line average throughput at a 95 per cent confidence level.

CASE STUDY 2

Operation description

Case Study 2 takes places at another large open pit copper/molybdenum operation. Copper mineralisation occurs primarily in the form of chalcopyrite and chalcocite. Recovery is via two flotation stages, with the bulk Cu-Mo concentrate from the first stage reporting to the molybdenum circuit, with the molybdenum concentrate subject to hydrometallurgical treatment also on-site. Minor silver content provides an additional by-product credit.

Comminution at the site takes place in a conventional SAG-ball-crusher (SABC) flow sheet. Primary crushed material feeds a large SAG mill in primary grinding duty. Discharge from the SAG mill is classified via a trommel and incline screen, with the circuit closed with two cone crushers. Product from the SAG circuit feeds the secondary grinding stage, consisting of two parallel ball mills, each of which is closed by two cyclone clusters. A second grinding line had been recently commissioned and was in the process of ramp-up at the time the throughput forecast model was being developed. While not the focus of this discussion, a preliminary forecast model for the new grinding line was also provided, based on the assumption that it would operate in the same manner as the existing line.

Throughput forecast model

The throughput forecast model for this operation had a similar overall structure to that described in Case Study 1, however with some key differences. As was the case in the earlier example, the LOM planning (covering the period from 2020 out to 2044) was drawn upon to define the proportion of the various ore types in the feed blend. Here, the LOM plan defined six different lithologies, five of which

occurred in significant proportion over the LOM, with the sixth being present in the plant feed in only a handful of years, and in very small proportion. The model therefore considered the five main lithologies as its basis. The proportion of the different lithologies in the plant feed over the LOM is shown in Figure 4.

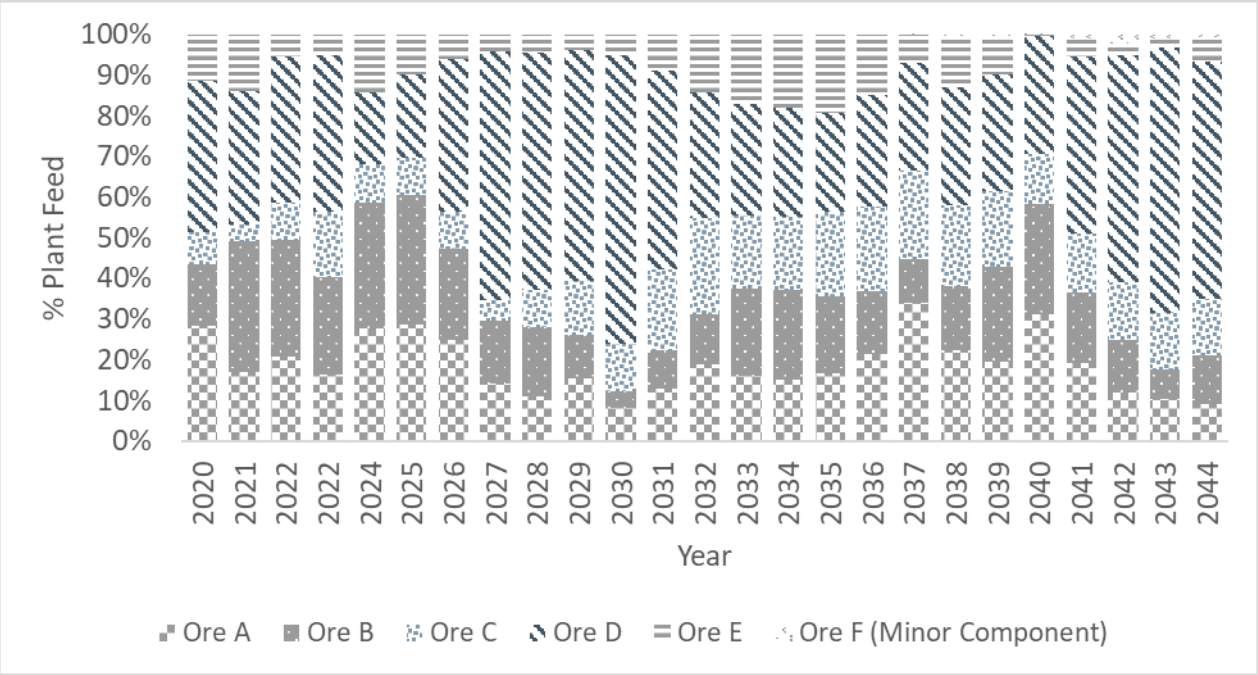

FIG 4 – Bar chart showing the proportion of each of the different lithologies in the feed blend, on an annual basis.

Where the site covered in Case Study 1 had a detailed geometallurgical model, the extent of the test work conducted at the site in Case Study 2 was much more modest. Some Macon crushability index and BBWi data was available, however the number of samples was quite limited. Based on this, a single impact hardness (DWi) and grinding hardness (BBWi) value was assigned to each lithology, with the model assuming the characteristics of the ore from each lithology will not change in future, only the proportion of the feed drawn from each. Considering this, the model was configured to allow the user to adjust the ore hardness inputs in the future, when additional test work becomes available and the variation in the hardness of each lithology is better understood. The assigned values are shown in Table 1.

TABLE 1

Assigned ore characterisation data for each of the lithologies in Case Study 2.

Ore Type	Estimated Axb	BBWi (kWh/t)
Ore A	36.7	15.28
Ore B	70.2	9.74
Ore C	50.1	13.62
Ore D	37.4	15.07
Ore E	34.7	17.60

In this case, Hatch did not have the benefit of having already completed a full M2M project for this operation. Calibrated drill and blast models to define the ROM fragmentation were therefore not available. Fortunately, the SAG feed belt at the site is equipped with an image analysis system (*Split Online).* Data from the image analysis system was cross referenced with daily production records, which provided the proportion of each ore type in the feed. Multi-linear regression was carried out,

and an equation to predict F_{80} as a function of the feed blend composition type was derived. The equation took the following form, where a, b, c, d, and e are fixed coefficients:

$$F80 = (a \times \%\ Ore\ A) + (b \times \%\ Ore\ B) + (c \times \%\ Ore\ C) + (d \times \%\ Ore\ D) + (e \times \%\ Ore\ E) + Constant \quad (3)$$

While analysis of variance (ANOVA) indicated there was a statistical significance to each of the coefficients, and that the overall regression was significant, there is a degree of scatter in the data due to operational variability and error associated with the image analysis. This is reflected in Figures 5 and 6.

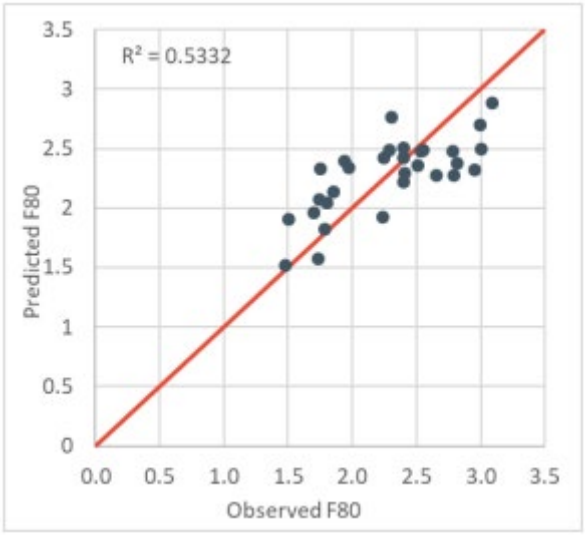

FIG 5 – Parity chart of predicted and observed (online camera) SAG feed F_{80}.

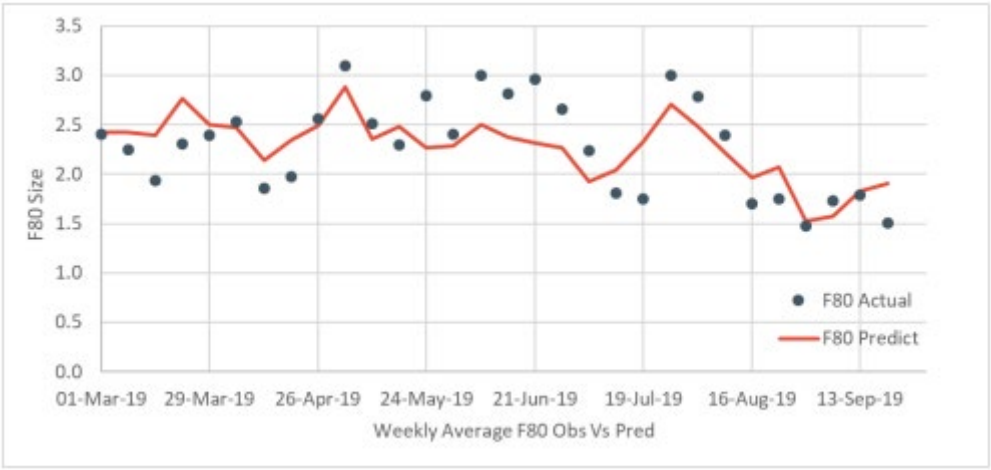

FIG 6 – Timeseries plot of predict and observed SAG feed F_{80} (weekly average).

Finally, the model development was complicated further by specific conditions which occurred when Ore B was present in high amounts. Being the softest of the five main ore types, the power-based model was predicting a reduction in the required specific energy as the proportion of Ore B increased, with a corresponding increase in the predicted throughput. The initial model, however, was shown to be systematically overestimating during these periods. Based on this, it became evident that there was an operational/practical factor at play, which was not being captured in the model.

Discussions with site indicated that this ore, along with Ore C, had been causing issues in the downstream thickener. These issues compelled the operators to manually reduce throughput when these ores were present in significant amounts. In the case of Ore B, the particularly soft nature of the ore meant that the SAG mill struggled to maintain a rock charge once the operator reduced the throughput, leading to a reduced power draw. The relationship between the proportion of Ore B in the feed and SAG mill power draw is shown in Figures 7 and 8. This relationship was incorporated

into the throughput forecast model to capture the ‘reduced SAG mill power’ operating state, with the option to disable this function once the thickener issues are resolved.

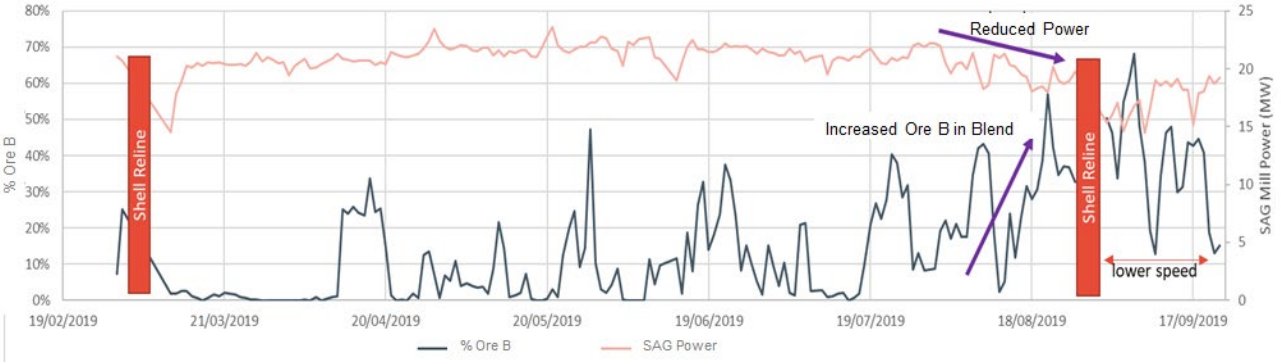

FIG 7 – Timeseries plot of SAG power alongside the proportion of Ore B in the feed blend.

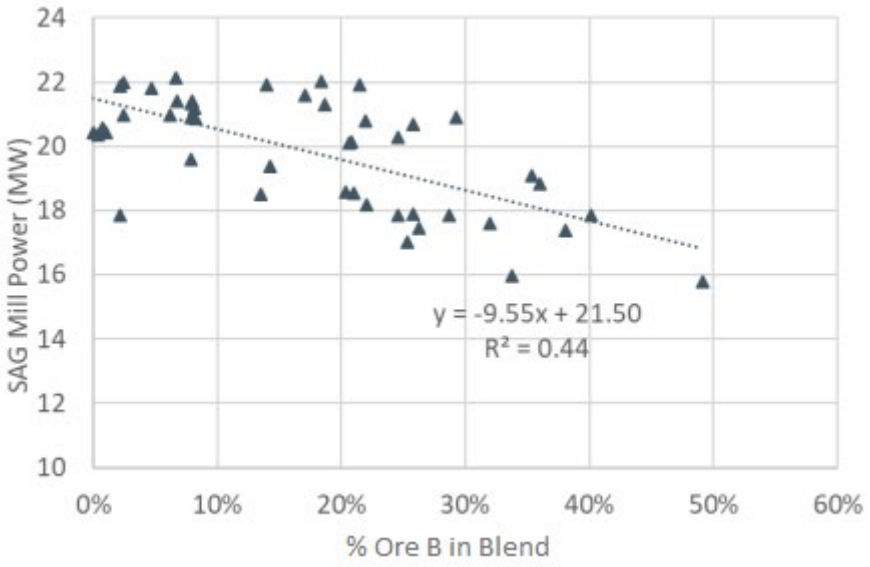

FIG 8 – Regression of SAG mill power as a function of the proportion of Ore B in the feed.

While production data covering the period from March 2019 to September 2019 was used to calibrate the forecast model (specifically, the calibration constants for SAG specific energy), data for the subsequent six months was used to validate the model predictions. Blend composition data over that period was averaged at daily, weekly, and monthly intervals, and provided as the input to the model. Figures 9–11 shows the comparison of the actual and predicted plant throughput at each time scale, with the red line separating the calibration and validation periods.

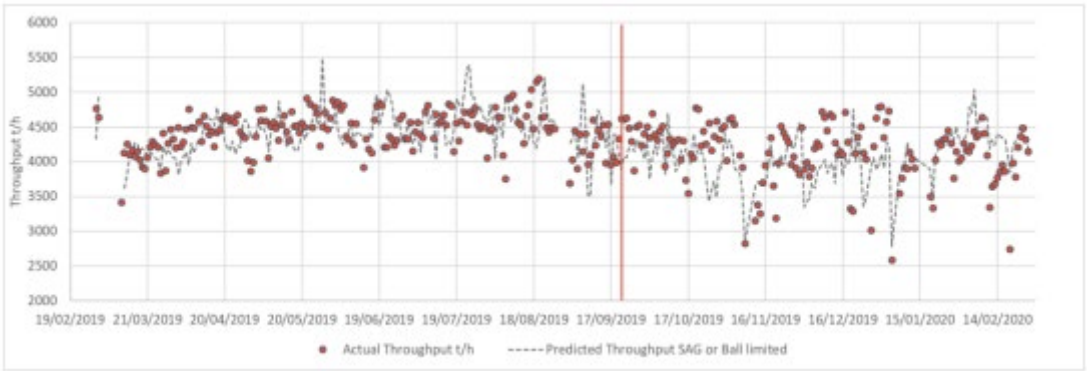

FIG 9 – Timeseries plot showing actual and predicted model throughput, on a daily timescale. Area to the left of the red line is the data used for calibration, area to the right is the validation period.

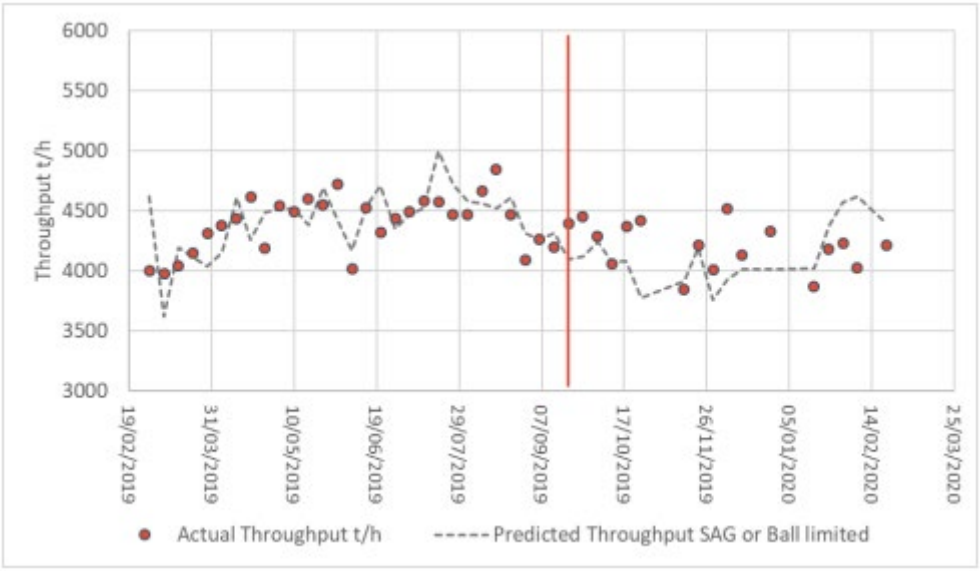

FIG 10 – Timeseries plot showing actual and predicted model throughput, on a weekly timescale.

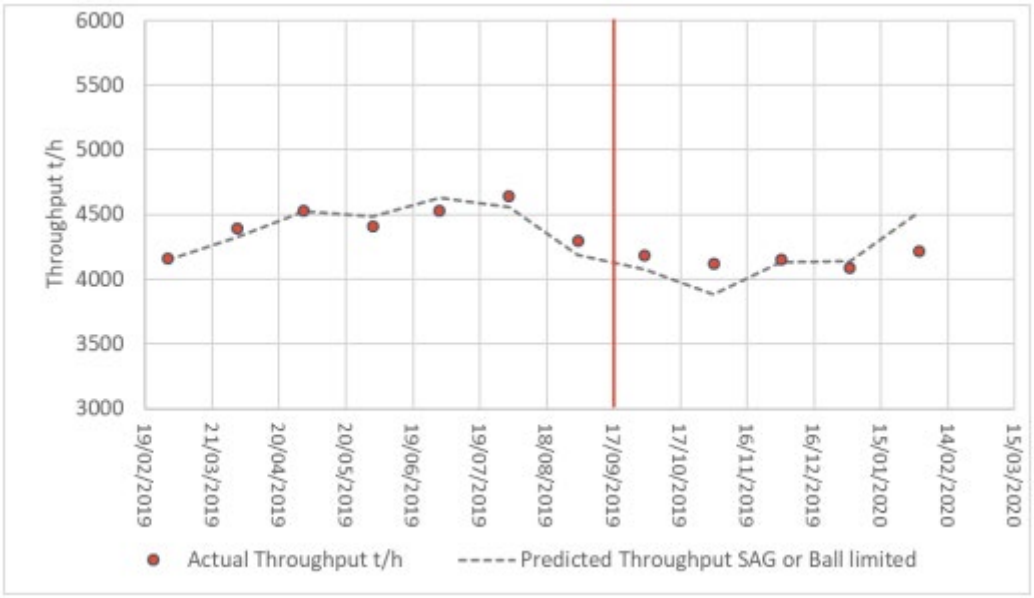

FIG 11 – Timeseries plot showing actual and predicted model throughput, on a monthly timescale.

Model standard error at each time scale was determined, along with the 95 per cent confidence interval. Standard error equated to 10.9 per cent, 7.5 per cent, and 4.4 per cent on a daily, weekly, and monthly basis, corresponding to confidence intervals of 21.5 per cent, 15.8 per cent, and 11.4 per cent respectively. While some apparent outliers can be seen in the graphs in Figures 9–11, these confidence intervals represent a good level of accuracy, particularly at a weekly and monthly timescale.

CASE STUDY 3

Operation description

Case Study 3 concerns an open pit polymetallic operation. Ore at the site is sourced from three pits, with ROM material processed first through two parallel crushing lines. The first crushing line consists of a jaw crusher receiving feed scalped over a grizzly, while the second consists of an in-pit gyratory crusher, product from which is scalped over another grizzly, with oversize reporting to a mineral sizer. Primary grinding takes place in a 34' SAG mill, which operates in closed circuit with two pebble crushers. Undersize from the SAG screen reports to a cluster of primary cyclones for pre-classification ahead of the secondary ball mill circuit. Undersize from those cyclones feeds directly

into the 24’ ball mill, along with undersize from the ball mill closing cyclones. Overflow from the two cyclone stages reports to flotation, which produces a bulk concentrate, which is sold without further selective flotation.

Forecast model

Hatch, in conjunction with the site’s explosive supplier, completed a M2M optimisation project at the site from December 2019, which concluded with the delivery of the final report and recommendations in July 2020. The M2M project identified several opportunities – including improved drill and blast practices, and optimised operating parameters of the primary and pebble crushers, SAG and ball mills, and cyclones – which were predicted to provide a 13–22 per cent uplift in throughput if implemented in full, while maintaining the product size to flotation. While the implementation of the M2M recommendations was underway, Hatch were engaged to support site in the development of a geometallurgical and throughput forecasting model.

Historically, there had been a small number of comminution tests conducted for the main lithologies in each of the three pits on-site. The test work program included impact testing conducted by external groups, and point load testing (PLT) conducted by the site geology department. A campaign of full Drop Weight (DWi and Axb) and BBWi testing was also completed shortly prior to Hatch’s engagement with site, with the same samples also subject to testing using the Hardness Index Tester (HIT) breakage device. At the time of delivering the model, a campaign of HIT tests on exploration drill core samples was underway, with the intent of further improving orebody definition and the understanding of hardness variability. HIT results representing ores to be processed in 2021 and 2022 were used to predict the throughput for those and subsequent years, with the data for later years to be updated once additional test results become available.

The model itself was based on the general structure described earlier. As in Case Study 1, a site-specific feature was incorporated to capture the impact of the increased fines (-10 mm) in the plant feed associated with the recommended M2M blasting conditions. Once again, this correction involved reducing the calculated specific energy in inverse proportion to the throughput increase predicted for the relevant domain in the M2M study.

A site-specific adjustment was also added to accommodate a proposed partial pre-crushing circuit. The model treats the pre-crushed material as a separate component in the feed with its own required specific energy in the grinding circuit, similar to how each of the different ore types are treated. To calculate the contribution of this stream to the required grinding specific energy, and therefore the overall throughput, an estimate of the pre-crushing circuit throughput and usability is required.

Model validation was completed using process data from 2020 and 2021, which was compared with the throughput forecast model predictions on daily, weekly, monthly, and annual timescales.

Partway through the period of data considered in the model validation, a change to the SAG mill internals occurred, which saw a bi-directional liner design and radial pulp lifters installed, replacing the single-direction configuration which had been in place at the time of the M2M survey. The bi-directional liners and pulp lifters were later removed. The total period for which they had been installed amounted to around 4 months, from a total of 18 months in the validation data set. While changes to SAG mill internals, and particularly the discharge assembly (grates and pulp lifters) can have an impact on mill performance, the model appears to be robust during this period. This is not entirely unsurprising, given details of these components are not inputs into the specific energy calculation. Where care would need to be taken, however, would be in a scenario where significant changes to the grate design are planned, for example to build a larger rock charge to promote fine grinding in the SAG mill and relieve the secondary circuit. In this scenario, drawn power may differ from expectations, while the calibration factors used to estimate SAG specific energy may need to be re-established under the new conditions. Alternatively, where changes are needed to alleviate slurry pooling issues, the subsequent increase in power draw may impact the assumed power draw used for forecasting, as well as the overall grinding efficiency and SAG specific energy relationship.

A second period in the validation data set saw the circuit operated under single-stage SAG conditions. The model was not designed to predict the throughput in this mode of operation and would need to be adjusted to do so. This period was therefore excluded from the validation process.

Those considerations aside, the model predictions showed good agreement with the observed throughput. The relative standard error was approximately 11.8 per cent of the average value on a daily basis, 7.3 per cent on a weekly basis, and 4.9 per cent on a monthly basis. These figures correspond to confidence intervals of 23.1 per cent, 14.6 per cent, and 10.5 per cent respectively, at a 95 per cent confidence level.

CONCLUSION

This paper has presented three case studies from recent throughput forecast projects completed by Hatch. The forecast models described provide the respective sites with a powerful tool for both short – and long-term planning, which can ultimately assist in maximising operational efficiency and profits over the Life-of-Mine. Hatch's methodology combines detailed drill and blast modelling (when available) with widely accepted power-based methodologies for grinding circuit throughput estimation, to provide a model with the flexibility required to assess trade-offs along the full value chain. While not covered here, these models also lend themselves to use alongside models of the downstream separation processes, giving an insight into the impact of changes in the drill and blast or the installation of additional comminution capacity on the overall economics of the operation.

REFERENCES

Alruiz, O M, Morrell, S, Suazo, C J and Naranjo, A, 2009. A novel approach to the geometallurgical modelling of the Collahuasi grinding circuit. In *Minerals Engineering*, 22(12):1060–1067.

Bennet, D, Crnkovic, I, Walker, P, Hoyle, A, Tordoir, A, La Rosa, D, Valery, W and Duffy, K, 2017. Process development and throughput forecasting at the Phu Kham copper-gold Operation, Laos PDR. In *We are Metallurgists, Not Magicians,* Spectrum Series (The Australasian Institute of Mining and Metallurgy: Melbourne).

Burger, B, McCaffery, K, Jankovic, A, Valery, W and McGaffin, I, 2006. Batu Hijau Model for Throughput Forecast, *Mining and Milling Optimisation and Expansion Studies* (Society for Mining, Metallurgy and Exploration).

Contreras Bravo, F and Morales, M, 2017. Reconciliation Methodology for Model Improvement and Process Evaluations: Throughput (Part I). *Proceedings of Minexcellence 2017: 2nd International Seminar on Operational Excellence in Mining*.

Farmer, T, Valery, W, Holtham, P and Duffy, K, 2021. Improving, Sustaining and Forecasting Performance for the Life of Mine. *Life of Mine Conference 2021 Proceedings,* pp. 40–43 (The Australasian Institute of Mining and Metallurgy: Melbourne).

Global Mining Guidelines Group, 2021. The Morrell Method to Determine the Efficiency of Industrial Grinding Circuits (revised, first published in 2016). Available at: https://gmggroup.org/wp-content/uploads/2021/12/GUIDELINE_The-Morrell-Method-to-Determine-the-Efficiency-of-Industrial-Grinding-Circuits_2021.pdf

Misle, J, Jimenez, J, Diaz, P and Luer, D, 2013. SAG specific energy consumption prediction model. *Proceedings of the 10th International Mineral Processing Conference – Procemin 2013.*

Morrell, S, 2004b. An Alternative Energy-Size Relationship to That Proposed By Bond For The Design and Optimisation Of Grinding Circuits. In *International Journal of Mineral Processing*, 74:133–141.

Morrell, S. 2004a. Predicting the Specific Energy of Autogenous and Semi-autogenous Mills from Small Diameter Drill Core Samples. In *Minerals Engineering*, 17(3):447–451.

The thin line between accuracy and bias in characterisation of ore grindability

F Faramarzi[1,4], R Morrison[2] and T G Vizcarra[3]

1. Global Senior Mining Industry Consultant, Dassault Systemes, Brisbane Qld 4000. Email: farhad.faramarzi@3ds.com
2. Honorary Professor, JKMRC, The University of Queensland, Brisbane Qld 4068. Email: r.morrison@uq.edu.au
3. Senior Consultant, JKTech Ltd Pty, Brisbane Qld 4068. Email: t.vizcarra@jktech.com.au
4. Alumnus, JKMRC, The University of Queensland, Brisbane Qld 4068. Email: f.faramarzi@uq.net.au

ABSTRACT

In comminution, grindability or 'hardness' indices are used to describe ore resistance to ball milling. The most commonly used measure is the Bond ball mill work index (BBMWi). The implicit assumption underlying this test is that the distribution of mineral hardness within the sample is uniform, or at least falls within a narrow range of variation. This paper considers cases where that assumption is not valid.

In actual industrial practice, feed is subjected to multiple breakage mechanisms and several stages of classification. These may introduce biases in the hardness of material that is actually processed by the ball mill. That is, the actual hardness of feed presented to the ball mill may differ from the fresh circuit feed, especially when transition/weathered ore types are processed. Such ore types tend to exhibit variable breakage characteristics, and separation of their different hardness components is likely during different stages in comminution processes. The result is that harder minerals will tend to concentrate in the ball mill recirculating load. Another example is when crushed SAG pebbles (which are generally comprised of harder minerals) are diverted to the ball milling stage with the aim of improving SAG mill throughput. In this case, ball mills will process material which may be significantly harder than the circuit feed. In both cases, the ball milling stage may become an operational bottleneck. For these milling strategies, results from standard test work conducted on fresh ore samples should be treated with caution.

In addition to proposing a model for describing attrition breakage behaviour, this paper also tests one approach to measuring the extent and impact of ore hardness variability not reflected in standard test work protocols. It presents the results and discusses implications from a laboratory test method, developed at the Julius Kruttschnitt Mineral Research Centre (JKMRC), to investigate the distribution of hardness within samples that would each otherwise be considered 'uniform'. The results from testing three different samples characterised by standard and modified Bond ball tests confirmed that up to a 10 per cent under-estimation in evaluating ore grindability is possible. Under-estimation of ball milling feed hardness increases the risk of ball mills with limited capacity during periods of processing transitional ore domains or when a modified circuit configuration is required for debottlenecking and improvement purposes.

INTRODUCTION

Review of literature

In mining and mineral processing, particle size reduction commences with drilling and blasting operations, continuing through to the comminution circuit where rocks are subjected to different types of breakage environments. The breakage environment depends on the objectives of rock breakage, which varies from transportation in mining, to liberation in milling.

The intrinsic variability of an ore can cause instability in SAG mill throughput (Faramarzi *et al*, 2018, 2019) and inefficient classification, ultimately compromising grind size and recovery (Putland, 2006). To mitigate these risks, comminution characterisation can be undertaken to spatially model the hardness of different regions in a deposit.

In general, comminution characterisation can be conducted as single – or multi-particle test work. The former refers to tests in which individual particles are broken separately at pre-defined levels of energy; these include the JK Drop Weight (Brown, 1992, personal communication; Napier-Munn *et al*, 1996) and SMC tests (Morrell, 2004). The latter refers to tests that require batches of material to be processed in pilot or laboratory mills. Some widely-used batch test examples are the JK abrasion mill test (Leung, 1988), the Bond tumbling mill tests (Bond, 1952), the MacPherson autogenous grindability test (MacPherson and Turner, 1978), and the SAG power index test (Starkey *et al*, 2006). It is important to note that these tests usually are undertaken on 'fresh' circuit feed.

The focus of this paper is to highlight the possibility of problematic changes in ore hardness between the fresh circuit feed and the ball mill feed, that are not necessarily detected with standard testing procedures. Depending on the mineralogical composition of the ore, minerals of higher resistance to grinding would likely accumulate in the ball milling recirculating load (Maxson *et al*, 1933). However, in variable ore types, it is likely that SAG milling preferentially disintegrates softer minerals in the ore which would in turn preferentially exit the grinding circuit, further exacerbating the accumulation of hard minerals in the ball milling recirculating load. It is expected that this effect would be most prominent in weathered ores, which often exhibit the largest degrees of hardness variability in a deposit. But since standard test protocols are applied to fresh circuit feed, this phenomenon would likely remain undetected during comminution test work programs.

The Bond ball mill work index (BBMWi) is the industry-standard measurement of resistance to ball mill grinding. However, low-energy attrition events are applied to the feed during stages as early as crushing, and remain significant contributors to size reduction in both SAG and ball milling. In this context, the review of the literature focuses on the understandings gained from batch attrition test work studies, and how this impacts subsequent grindability.

Implications from attrition breakage characterisation

Previous workers have undertaken experiments to identify key variables in low-energy breakage events, often with a view to incorporating these modes of breakage into comminution models.

Bemrose and Bridgwater (1987) categorise some variables affecting attrition into particle-related and environment-related properties:

- Particle properties include size, shape, surface, porosity, hardness and cracks.
- Breakage environment properties include time, velocity, pressure, shear and temperature.

It has been observed that the rate of attrition decreases with time (Dietz, 1979; Forsythe and Hertwig, 1949). This phenomenon may be due to the initial loss of mass in the form of fines, and then gradual smoothing of particles which are less susceptible to attrition (Bemrose and Bridgwater, 1987).

The importance of this topic in mineral processing has encouraged some researchers to investigate breakage characteristics of ores at low levels of energy, conventionally called 'abrasion' or 'chipping'. Austin *et al* (1986) defined abrasion as the steady removal of relatively small progenies broken from the particle surface as it tumbles in the mill. They conducted dry tests using -63 + 53 mm material, tumbled over a period of 35 minutes in a 600 mm diameter mill. In their experiments, the undersize was screened out and replaced with the same weight of fresh feed at pre-defined time intervals. Test results were plotted as percent weight in the top size fraction versus grinding time, from which the following conclusions were made:

- At the beginning of the test, the rate of mass loss for the fresh feed is high, leading to a steep downward slope. This is probably due to initial chipping and rapid removal of asperities from particle surfaces.
- Percent mass in the oversize decreases gradually as the coarse particles are further abraded over time. This reduces the slope as the test progresses.

Tests at low-energy levels produce a bimodal size distribution that is typical of attrition. Leung (1988) conducted extensive experiments to obtain low-energy appearance functions from bimodal product size distributions by designing two types of tumbling tests (multi-particle and single-particle tumbling tests). It was observed that the product size distributions generated in either test regime were identical. Additionally, he conducted a series of low impact-energy (2.4×10^{-4} kWh/t) tests. The

results of this comparative program, applied to samples from four different mines, indicated that product size distributions from individually tumbled particles, multi-particle tumbling, and low-energy impact tests, were effectively identical.

These experiments also showed that the amount of fine product mainly depends on grind time, mass of charge and the particle size of the charge. Leung's findings formed the basis of the now-standard JK abrasion test that measures the abrasiveness of a given rock sample, expressed in terms of a 't_a' parameter (Napier-Munn *et al*, 1996).

Later, Devasahayam (2013) adopted the standard JK abrasion mill testing approach to investigate the effect of grind time and particle size on the produced bimodal product size distributions. Three kg of -55 + 37.5 mm, -37.5 + 26.5 mm, -26.5 + 22.4 mm and -22.4 + 16 mm size fractions from five different rock samples were prepared. Tests were run up to 10 minutes, and results largely aligned with the findings of Leung (1988) – specifically, that a longer grind time and a smaller size fraction produces a finer product, while the relative shape of the product size distributions remains identical. Devasahayam (2013) concluded that the shape factor of the particles was also a key parameter in abrasion, which varied with particle size and rock type.

Faramarzi (2020) argued that the current abrasion tests, being dry experiments, do not capture the likely effect of water upon attrition or low-energy breakage events that predominate in SAG milling. It is likely that water has an important role in low-energy comminution especially when milling highly altered or weathered ores, which are generally rich in aluminosilicate minerals (eg clays) that can more readily deteriorate in water. Additionally, several other testing issues were highlighted:

- The standard JK abrasion mill test is a dry procedure.
- The test scrubs the surface of the particles for a short period of time, and quantifies rock attrition with a single 't_a' value after 10 minutes of tumbling. Therefore, time-dependencies are not considered in the procedure.

Faramarzi (2020) developed an extended attrition mill testing approach with the aim of capturing the role of ore variability in ore breakage behaviour under low-energy levels in dry and wet modes. The experiments were conducted on eight rock types, and showed that different rock types exhibit different attrition characteristics in wet compared to dry environments. To an extent, this reflected the degree of alteration or weathering of the rock. Preliminary results showed that the role of water might either improve or suppress attrition, depending on the rock type. The outcomes of the attrition tests in wet vs. dry environments led to a suite of experiments that tested the hardness of actual ball milling circuit feed, which was shown to sometimes be harder than fresh circuit feed.

The point is further discussed in the following sections of this paper.

Implications from grindability characterisation

The Bond ball mill test is a batch laboratory test in which the circuit is closed with a limiting screen, to simulate the effect of hydrocyclones that are commonly used to classify ball milling discharge. It is the industry-standard measure of ore grindability, and ultimately is used in ball mill design and geometallurgical modelling. The interaction between the ball mill and classifier drives the material composition in the mill, with harder minerals accumulating in the re-circulating load. The Bond test targets a 250 per cent re-circulating load which is a typical value in conventional ball milling circuits (Man, 2002).

The Bond ball mill has smooth liners to facilitate emptying the mill after each cycle. Additionally, liner packing is avoided with the use of smooth liners. Conversely, most industrial ball mills have lifters and rotate at typical speeds ~72–76 per cent (Morrell, 1996). The charge motion inside the laboratory mill must attain a profile similar to its industrial analogues, and thus with smooth liners the test is undertaken at 91 per cent critical speed.

Blending is common practice to improve feed consistency during production. Yan and Eaton (1994) tested whether the average of grindability of different components is a reliable indicator for ore blends. They carried out experiments on samples of hard rock, soft rock and three differing blends of the two components. It was observed that ore blend grindabilities were weighted more heavily

towards the harder rocks. This suggests that the harder components were accumulating in the circulating load.

Fuerstenau and Venkataraman (1988) showed that minerals of different hardness interact with each other, with harder minerals improving the breakage rates of softer minerals, and with their own breakage rates decreasing with time. It has also been reported that in grinding multi-component feeds, the breakage rate functions of individual minerals change with variations in the composition of the mill hold-up (Fuerstenau and Venkataraman, 1988; Yan and Eaton, 1994).

Yan and Eaton (1994) asserted that in grinding a blend of hard and soft components in closed-cycle, the harder components break at slower rates and eventually predominate in the recirculating load. Accumulation of the harder components in the mill was evident during the Bond ball tests as well. They concluded that Bond ball testing may not be appropriate on ores of widely differing grindability, since the composition of the mill hold-up material may not represent the composition of the starting blend. This finding is analogous to the changes in composition that can take place between SAG milling and ball milling.

Implications from the extended attrition mill tests

Details of the extended attrition mill testing are provided in the Appendix A of this paper. The 'M10' variable (%) is the amount of material passing 1/10th of the geometric mean size of the original size interval (Faramarzi, 2020). Figure 1, shows the samples tested as well as the colour of their progenies after a comminution test; Table 1 summarises their comminution properties as a reference.

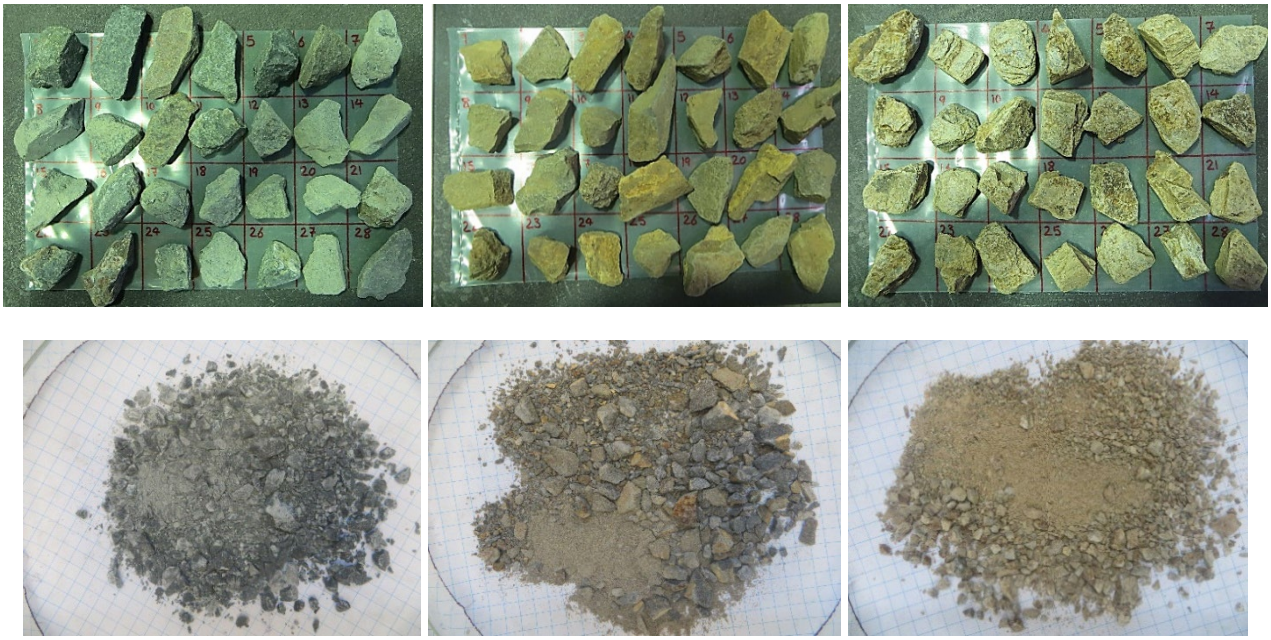

FIG 1 – Left to Right (Top): Sample A: Cadia Block Caved Gold Mine; Sample B: Maaden Gold Mine; Sample C: Weathered JK Site Rock; Left to Right (Bottom): Progenies for Samples A, B and C.

TABLE 1

Standard comminution and physical properties of tested samples.

Description	ta*	A×b	BBMWi (kWh/t)	Density (t/m^3)
Sample A	0.23	30	19.7	2.74
Sample B	0.30	30	12.7	2.70
Sample C	0.91	71	11.9	2.55

*Abrasion ore parameter.

Figure 2 shows the results of the extended attrition mill test for the three samples. The rate of mass loss for Sample A is low and is similar in both dry and wet modes. The rate of mass loss for Sample B is higher and the difference between dry and wet modes is more evident. Figure 3 shows that the rate of mass loss is very high for Sample C in both dry and wet modes.

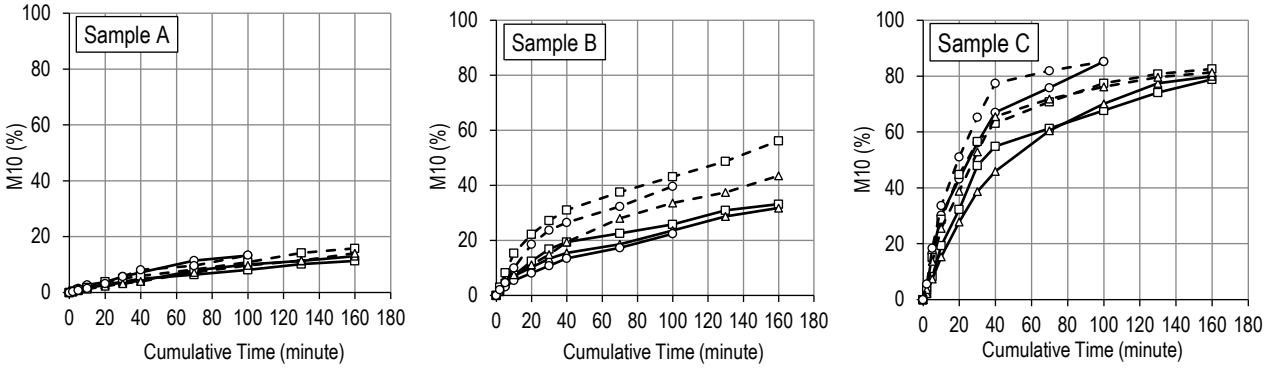

FIG 2 – Experimental results for three samples, with each sample tested three times (solid line for dry and dashed line for wet experiments).

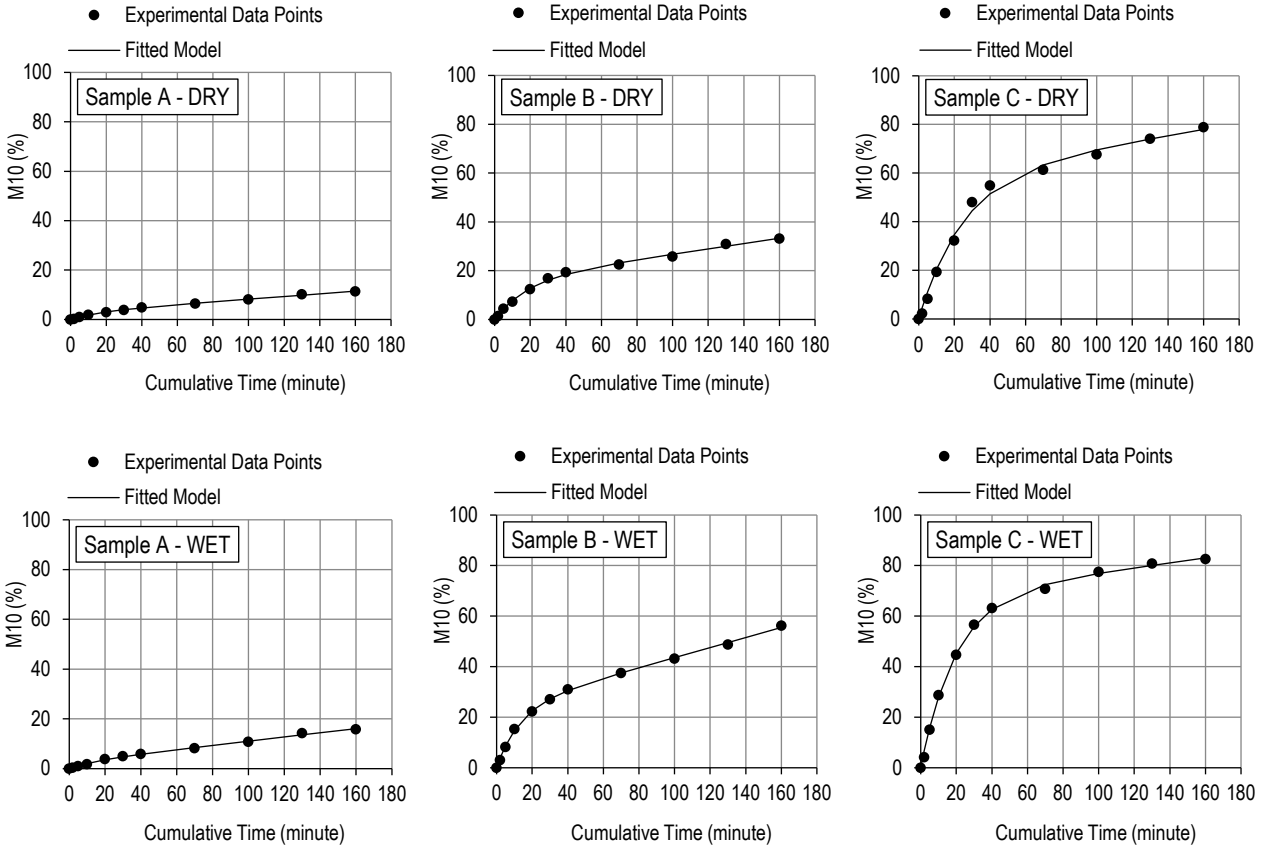

FIG 3 – Equation 2 fitted to the experimental data points of Test 1 – as an example.

The observed difference between dry and wet modes for Samples B and C may have been a consequence of their altered or weathered nature. Figure 2 shows that as expected, a rapid rounding and smoothing process occurs first followed by an almost constant rate of mass loss while the grinding environment remains more or less constant. It also indicates that water can promote the effect of low-energy breakage events.

Faramarzi (2020) used an exponential model which provided a good description of the rapid mass loss phase. However, we can combine the two relationships for a wider range estimate of M10 at time t minutes:

$$M10 = C + mt - C(1 - \exp(-Tt)) \quad (1)$$

where *m* is the slope of the linear processes, that is the rate of mass loss and *C* is the projected intercept at *t* = 0. The second term is an exponential decay which is equal to – *C* at *t* = 0. The rate of decay T controls how quickly the rounding process occurs and is the rate constant.

The model can be further simplified:

$$M10 = mt + C(1 - \exp(-Tt)) \quad (2)$$

Figure 3 shows that this model is a good match to the measured data. Tables 2 and 3 show the derived parameters and the standard error of the model fit or the estimate.

TABLE 2

Parameter estimates from model fitting and standard error – Dry mode.

Description	Test 1			Test 2			Test 3		
	m	***C***	***T***	***m***	***C***	***T***	***m***	***C***	***T***
Sample A	0.055	2.739	0.060	0.000	18.967	0.007	0.000	18.993	0.012
SE	0.173			0.302			0.378		
Sample B	0.109	15.936	0.055	0.141	9.612	0.085	0.151	7.209	0.073
SE	0.704			0.508			0.360		
Sample C	0.125	58.117	0.040	0.096	66.355	0.025	0.215	63.663	0.052
SE	2.598			0.853			2.098		

*SE: Standard Error of the estimate = $\sqrt{SS/_{N-3}}$ where N is the sample size.

*SS: Sum of Squares of difference = $\sum_{i=1}^{n}(M_i - P_i)^2$ where M and P are measured and predicted values of i.

TABLE 3

Parameter estimates from model fitting and standard error – Wet mode.

Description	Test 1			Test 2			Test 3		
	m	***C***	***T***	***m***	***C***	***T***	***m***	***C***	***T***
Sample A	0.083	2.727	0.061	0.050	8.496	0.008	0.027	14.226	0.013
SE	0.333			0.179			0.729		
Sample B	0.200	23.559	0.077	0.155	18.558	0.032	0.160	23.194	0.050
SE	0.585			0.907			1.014		
Sample C	0.097	67.597	0.051	0.034	75.564	0.039	0.000	86.340	0.048
SE	1.257			2.122			2.141		

*SE: Standard Error of the estimate = $\sqrt{SS/_{N-3}}$ where N is the sample size.

*SS: Sum of Squares of difference = $\sum_{i=1}^{n}(M_i - P_i)^2$ where M and P are measured and predicted values of i.

Observations based on the model parameters

Sample A which is appreciably harder than samples B and C shows very similar parameters for wet and dry attrition. The intercept C at 2.7 per cent suggests that only a small amount of rounding and smoothing occurs.

The grinding rate *m* for Sample A is much lower than for Sample B. Surprisingly *m* for Sample C is lower again. However, that may be because with a *C* value of 58 per cent, the intensity of the grinding environment will have been substantially reduced.

Sample B has a much lower *C* value of 15.9 per cent and should enjoy a more constant grinding environment. However, an *m* which correlates better with mill performance may need to be normalised with an estimated or measured mill power draw.

The Bond test overcomes these issues by using a well-controlled ball charge and restoring the ore loading before each cycle.

The initial rapid wear phases enjoy a much more similar grinding environment and should offer more valid comparisons. The two harder ores A and B have similar dry rate constants *T*, but the altered Sample C has a much lower value. As noted earlier, fresh ore Sample A shows similar parameters, but oxidised/altered Samples B and C show appreciably increased rates of initial loss and intercept when milled wet.

Overall, this model provides a way to estimate M10 over time and to compare how quickly and how much rounding will occur. However, as noted earlier, the *m* parameter may need to be normalised against power draw to be useful for prediction of attrition in other environments.

As the Bond test is based on grams of new product per revolution, the presence of or absence of -106 µm material in the feed sample makes little difference.

The modified feed does allow a little more of the new volume for grinding – about 25 per cent, but as the volume of feed is matched to the interstitial ball space, it does not make much difference.

Concluding remarks on attrition breakage behaviour

The rounding of Sample A is just that and does not imply a multicomponent feed. This is consistent with the C value of 2.7 per cent wet and dry, which suggests that ore A is also highly uniform with respect to hardness. The measured work indices overlap at less than two standard deviations.

Samples B and C have much broader distributions of hardness losing around 30 per cent of the soft feed hardness distribution as -425 µm. Hence the remaining feed material should be harder on average than the standard feed as suggested by the C values of 16 and 58 per cent respectively for Samples B and C. Their measured work indices do not overlap at two standard deviations.

Some other key observations during the test work were:

- The slow rate of attrition for the hard rock samples in dry and wet modes, producing more rounded particles. The colour of the product after each cycle was similar to the final product in both the dry and wet modes.
- The fast separation and disintegration of the soft components (likely to be clays and oxides) from the hard components (probably quartz) during the early stages of tumbling, particularly when wet. This was especially the case for Sample C (see Figure 2).
- Changes to the colour of the product in dry and wet modes. For example, in the case of Sample C, as the test proceeded the product colour changed from dark brown to light brown, ending with an almost white, silica-rich material.
- Decreasing viscosity of the slurry product in the wet tests, probably due to further removal of the clay minerals from the original sample after each cycle. This was particularly the case for Sample C.

The outcomes from this suite of experiments formed the basis of the hypothesis in the next section.

Statement of problem

The results of the extended attrition mill test in dry and wet modes lead to the following question and hypothesis:

- When a typical SAB or SABC circuit processes a transition ore type, a considerable amount of the softer material grinds out the SAG mill and reports directly to the hydrocyclone overflow; consequently, the harder (and coarser) material with a truncated particle size distribution (PSD) is introduced to the ball mill which accumulates in the recirculating load and ultimately constrains milling capacity.

  This potentially results in a change in BBMWi between the fresh circuit feed hardness, and the actual hardness introduced to the ball mills (see Figure 4).

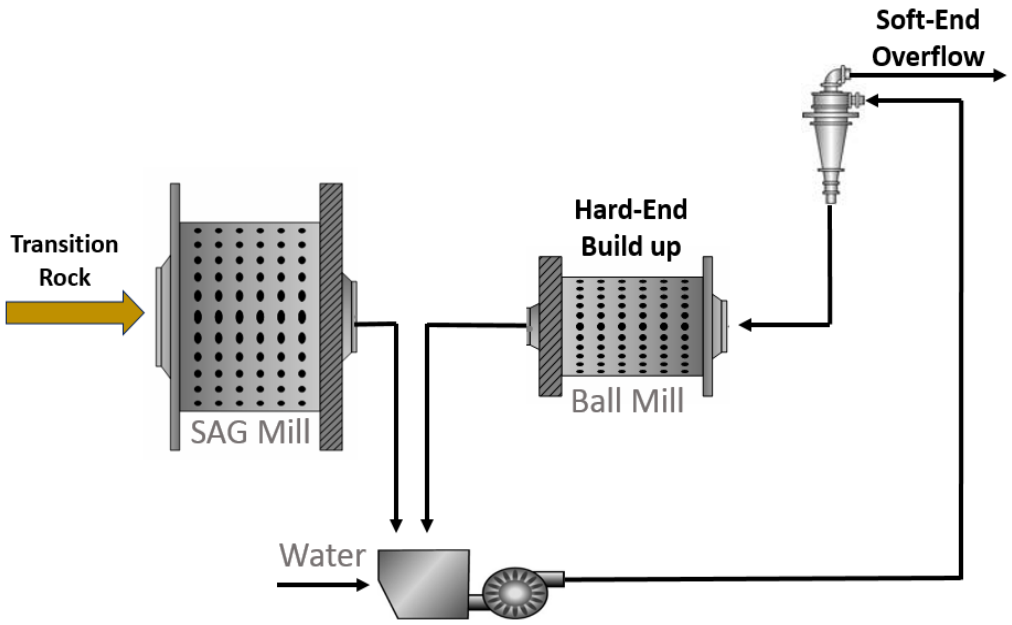

FIG 4 – Typical SAG – ball milling circuit configuration.

EXPERIMENTAL DESIGN

A test work program was designed to mimic the effect of attrition of rocks prior to introduction into ball milling circuits. It was assumed that scrubbing the material in a wet environment would remove some soft minerals in the feed, similarly to what occurs inside SAG mills. Additionally, a classification stage was introduced to mimic the duty of a hydrocyclone and generate a 'truncated' feed size distribution. The sample preparation process was as follows:

1. Material was crushed to -3.35 mm.
2. 4000 g of -3.35 mm material was fed to the JK abrasion mill (300 mm diameter × 300 mm length with four 10 mm lifter bars).
3. 1.5 L fresh water was added to the mill.
4. The mill was operated for 20 minutes at 53 rev/min.
5. The mill was emptied, and the product wet-sieved on a 425 µm screen.
6. The +425 µm material was oven-dried, and the undersize discarded.
7. After drying, the +425 µm material was re-sieved on a 425 µm screen to ensure good separation of fines.
8. This process was repeated several times to collect sufficient -3.35 mm + 425 µm material.
9. The standard Bond ball mill test was undertaken on the prepared samples.

For each ore type (shown in Figure 1), three samples were prepared based on the modified approach and three samples were prepared with the standard Bond procedure.

The closing screen sizes for Sample A were 106 µm for four experiments, and 150 µm for the other two which is reflected in a coarser product PSD for 'modified tests 1 and 2' shown in Figure 5. All experiments on Samples B and C were conducted with a closing size of 150 µm. The feed and product PSDs show good consistency in the experimental work.

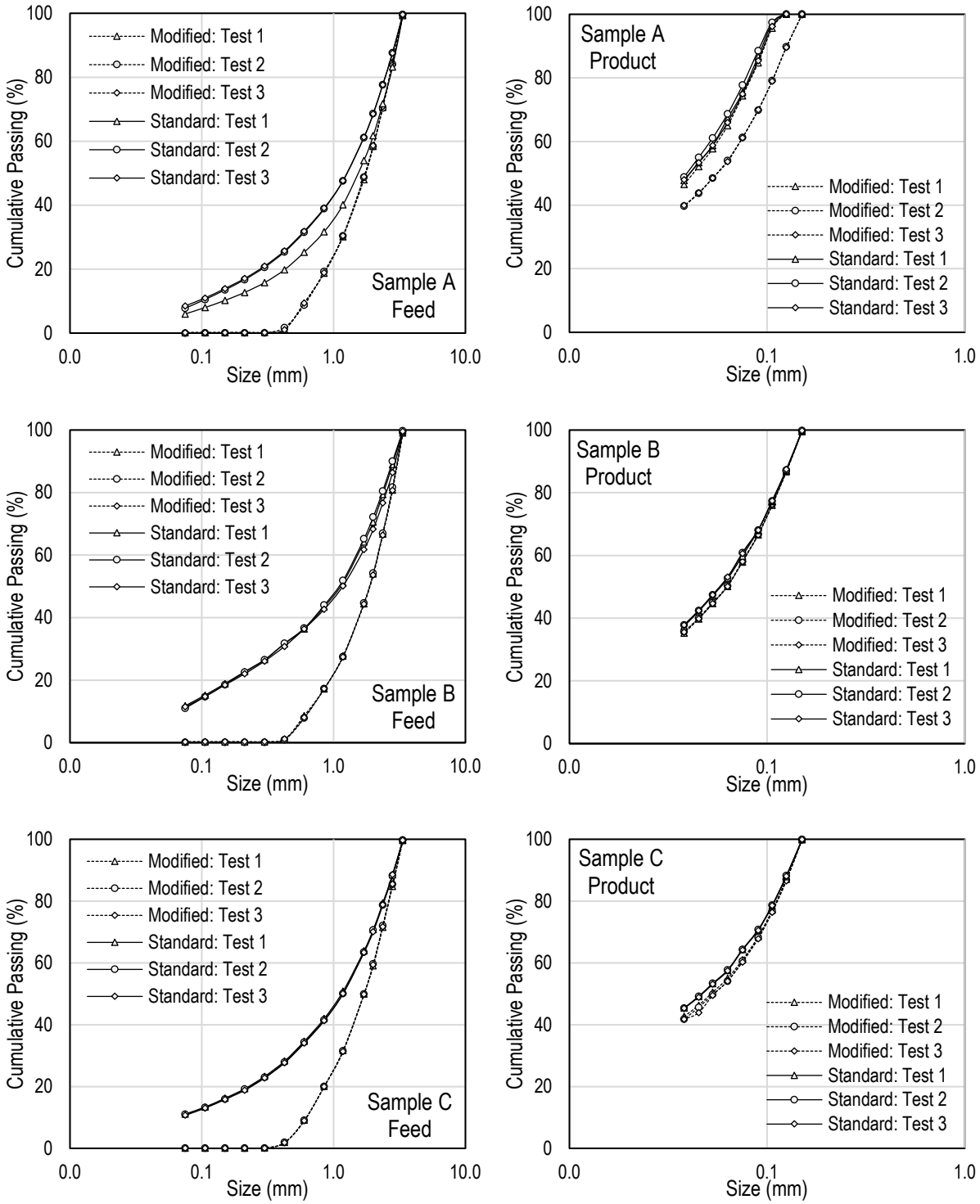

FIG 5 – Feed and product size distributions for all Bond ball mill tests.

RESULTS AND ANALYSIS

The Bond ball mill experiments (Standard versus Modified sample preparations) were undertaken three times on each sample. The measured BBMWi values as well as confidence limits (CL) are reported in Table 4.

The BBMWi values measured by the standard and modified Bond ball experiments are illustrated in Figure 6.

TABLE 4

Summary statistics of Bond ball mill tests (Standard versus Modified sample preparations).

Type of Test	Bond Ball Mill Test (Standard Sample Prep)			Bond Ball Mill Test (Modified Sample Prep)		
Measurable	BBMWi (kWh/t)			BBMWi (kWh/t)		
Sample	Sample A	Sample B	Sample C	Sample A	Sample B	Sample C
Test 1	19.8 (CS=106um)	12.8 (CS=150um)	11.9 (CS=150um)	20.6 (CS=106um)	14.0 (CS=150um)	13.1 (CS=150um)
Test 2	19.7 (CS=106um)	12.5 (CS=150um)	11.9 (CS=150um)	20.7 (CS=150um)	13.9 (CS=150um)	13.0 (CS=150um)
Test 3	19.6 (CS=106um)	12.7 (CS=150um)	11.9 (CS=150um)	21.0 (CS=150um)	13.9 (CS=150um)	13.4 (CS=150um)
Mean	19.7	12.7	11.9	20.8	13.9	13.2
SD	0.10	0.15	0.00	0.21	0.06	0.21
95% CL	0.25	0.38	0.00	0.52	0.14	0.52

SD: Standard Deviation, CL: Confidence Limit, CS: Closing Screen.

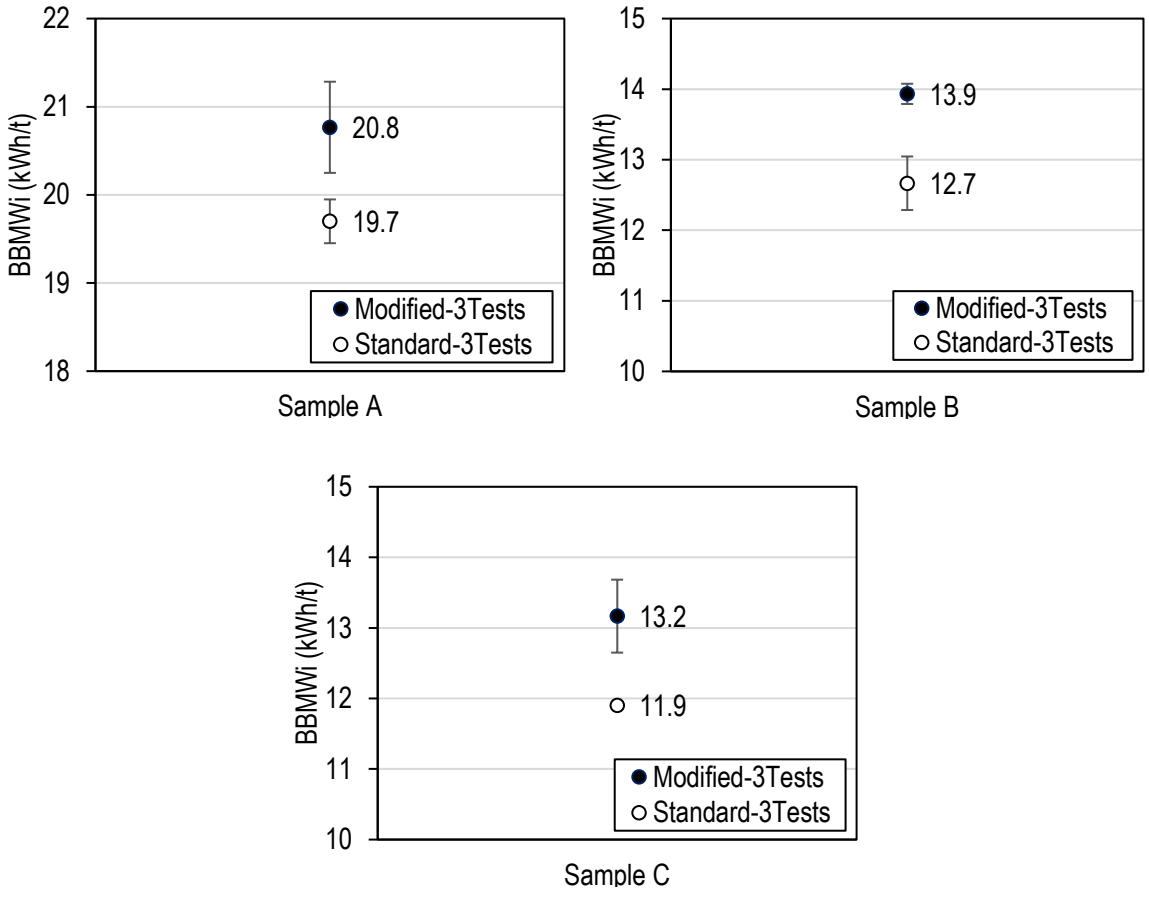

FIG 6 – Comparison of standard and modified BBMWi values.

In each test, the modified procedure resulted in 'harder' BBMWi results. While the magnitude of this change differed between each sample, all increases in BBMWi from the baseline standard procedure to the modified procedure were statistically significant.

The differences in the BBMWi values between the standard and modified testing procedures are likely to be driven by ore mineralogy and texture, and to some degree the removal of the -425 µm fines. That is, in the case of variable ores, the feed prepared through the modified sample preparation is concentrated in harder minerals following the removal of softer minerals. However, the circulating load in the BBMWI test is truncated as the closed-circuit size as part of the standard test. This factor will reduce the sensitivity to using a truncated feed.

Figure 7 compares the grindability of all samples during the experiments. For Sample A (a fresh, competent, less heterogeneous rock type) it was difficult to differentiate between grindability rates of the standard (Mean = 0.863 g/rev) and modified (Mean = 0.876 g/rev) experiments. However, Sample B (a competent but more variable rock type) shows a significant difference in grindability between the standard (Mean = 1.547 g/rev) and modified (Mean = 1.785 g/rev) tests. Sample C (a weathered, soft and variable rock sample) shows similar patterns between the standard (Mean = 1.629 g/rev) and modified (Mean = 1.864 g/rev) tests.

As shown in Figure 7, the grindability rates for Sample A show no significant difference between standard and modified tests, which is characteristic of a competent ore type. It is interesting to note that for Samples B and C, standard and modified feeds resulted in significantly different grindability rates at all stages. A possible reason would be the presence of higher concentrations of hard minerals in the modified feed. That is, the attrition process in wet environments results in preferential disintegration and separation of 'softer' minerals from the initial feed. Mineralogical analysis is required for confirming possible changes in composition in these ore samples, which should be considered in future investigations.

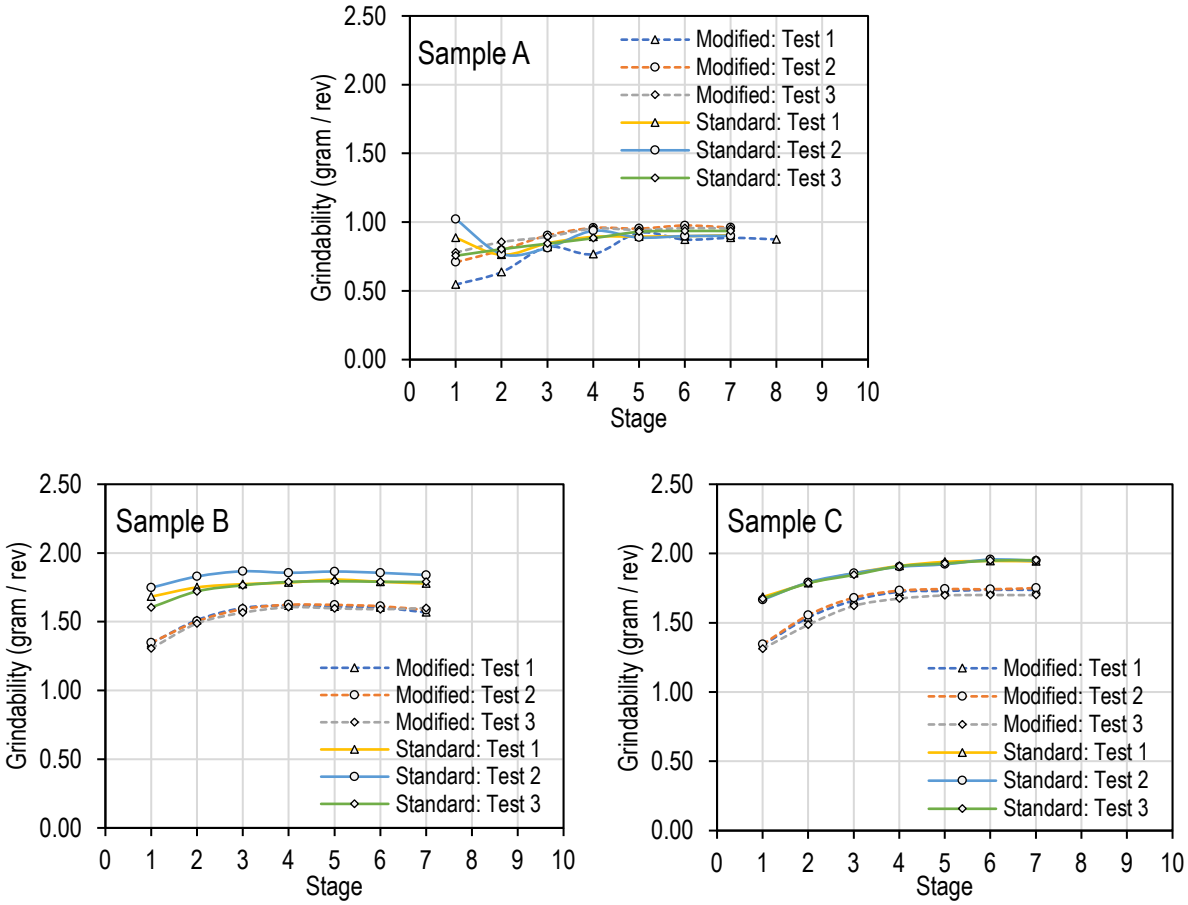

FIG 7 – Grindability rate per stage for all Bond ball mill tests.

DISCUSSION

A simple model of the process has been developed. The model parameters provide quantitative characterisation of the rounding phase and the more uniform rate of attrition phase after removal of asperities and altered material.

To further understand the implications of ore variability, the possibility of hardness/grindability changes through the comminution-classification process was examined by developing a suite of novel laboratory experiments. The outcomes are considered indicative and should assist future investigations in improving ore testing procedures.

Although standard 'average-based' comminution tests provide indicative measurements of ore hardness properties, not accounting for possible changes in material hardness at different stages of

a flow sheet could render standard test outcomes as misleading. At worst, this may result in the selection of a ball mill which is too small.

The attrition tumbling mill testing approach in dry and wet modes characterises the amenability of rock samples to attrition. The difference between wet and dry attrition parameters to some extent indicates the degree of alteration or weathering of the rock (eg clay-rich samples). The indications from these experiments suggest that it would be beneficial if standard testing methods are improved to obtain more information on ore breakage behaviour on a stage-by-stage basis, particularly before and after classification steps where removal of fine particles from the circuit could bias the composition of recirculating loads towards harder minerals.

The results of this study suggest that it is likely that comminution characteristics (ie BBMWi) of fresh, competent ore types (eg Sample A) remain largely consistent through the milling process. That is, the BBMWi of fresh feed will be representative of ball milling feed. Conversely, for weathered samples where soft minerals are susceptible to rapid deterioration in the presence of water (eg Samples B and C), size reduction and classification processes might bias ball milling feed grindability towards harder minerals.

It is worth noting that this effect can, in other ways, offset the benefit of strategies that are otherwise intended to improve circuit performance. One example is when crushed SAG pebbles (which are generally comprised of larger percentages of hard minerals when compared to fresh feed) are diverted to the ball milling stage with the aim of improving SAG mill throughput. This can overload ball mills with material that may be significantly harder than the circuit feed.

Overall, the results of this study suggest that depending on the ore characteristics, ball mill feed hardness could increase by 10 per cent compared to fresh circuit feed, which is otherwise tested in conventional test work programs. This difference might be exacerbated with different circuit configurations, and should be investigated in future research.

CONCLUSIONS

The standard ore hardness test work procedures assume reasonably homogeneous feed. The test work approach detailed in this paper provides a way to quantify variability arising from non-homogenous feed. High variability will most likely increase the required ball milling power compared with traditional design techniques. Hence one way to reduce risk associated with high variability would be to increase contingency in ball mill selection.

The novel tests undertaken in this study showed that, depending on the degree of alteration/weathering of an ore, the rates of attrition in dry versus wet environments could differ, due to the preferential breakage (and removal from the grinding circuit) of soft minerals prior to ball milling. This has implications for the subsequent grindability of these types of rocks, as measured with Bond work index testing.

Key conclusions from this study are as follows:

- The results from this initial suite of experiments suggest that, depending on ore properties, up to a 10 per cent difference in hardness between circuit feed and the actual ball mill feed is possible. However, the difference may become more pronounced for highly variable ore types.
- Higher BBMWi values for samples prepared with the modified procedure are likely to be driven by ore mineralogy.
- Therefore, for orebodies of highly variable mineralogy, the standard Bond ball mill results should be treated with caution; for design purposes, higher risk factors should be considered when sizing mills.

Future experiments could compare Bond test results on circuit feed samples versus samples obtained from the hydrocyclone underflow of a full-scale production plant. Correlating these differences with mineralogical data will help operations better refine production strategies when dealing with highly variable/multicomponent ore types.

ACKNOWLEDGEMENTS

The authors express their sincere appreciation to Prof. Sarma S Kanchibotla for his guidance during this PhD research work as well as his never-ending support as the first author's principal advisor. Additionally, the authors would like to acknowledge The University of Queensland and JKTech Pty Ltd. for sponsoring this research. Support from Dassault Systemes, The 3DEXPERIENCE® Company, is acknowledged, which made it possible for the authors to present this paper at IMPC Asia Pacific 2022. Last but not least, the IMPC Council and AusIMM are acknowledged for their effort in putting the IMPC Asia Pacific 2022 conference together in Australia.

REFERENCES

Austin, L G, Barahona, C A and Menacho, J M, 1986. Fast and slow chipping fracture and abrasion in autogenous grinding. *Powder technology*, 46(1), 81–87.

Bemrose, C and Bridgwater, J, 1987. A review of attrition and attrition test methods. *Powder Technology*, 49(2), 97–126. https://doi.org/https://doi.org/10.1016/0032–5910(87)80054–2

Bond, F C, 1952. The 3rd theory of comminution. *Transactions of the American Institute of Mining and Metallurgical Engineers*, 193(5), 484–494.

Devasahayam, S, 2013. Abrasion characteristics of ores. *Mineral Processing and Extractive Metallurgy Review*, 34(2), 114–129.

Dietz, V, 1979. Determination of the attrition resistance of granular charcoals.

Faramarzi, F, 2020. The measurement of variability in ore competence and its impact on process performance. The University of Queensland.

Faramarzi, F, Jokovic, V, Morrison, R and Kanchibotla, S S, 2018. Quantifying variability of ore breakage by impact–Implications for SAG mill performance. *Minerals Engineering*, 127, 81–89.

Faramarzi, F, Kanchibotla, S S and Morrison, R, 2019. Simulating the impact of ore competence variability on process performance – Case study of a large copper mine, *SAG Conference*, Vancouver, Canada.

Forsythe, W and Hertwig, W, 1949. Attrition characteristics of fluid cracking catalysts. *Industrial and Engineering Chemistry,* 41(6), 1200–1206.

Fuerstenau, D and Venkataraman, K, 1988. The comminution of multicomponent feeds under batch and locked-cycle conditions: kinetics, simulation and energy distribution. *International Journal of Mineral Processing*, 22(1–4), 105–118.

Leung, K, 1988. An energy based, ore specific model for autogenous and semi-autogenous grinding mills.

MacPherson, A R and Turner, R R, 1978. Autogenous grinding from test work to purchase of a commercial unit. *Mineral processing plant design*, 279–305.

Man, Y, 2002. Why is the Bond Ball Mill Grindability Test done the way it is done? *European journal of mineral processing and environmental protection*, 2(1), 34–39.

Maxson, W, Cadena, F and Bond, F, 1933. Grindability of various ores. *Transactions American Institute of Mining and Metallurgical Engineers*, 112, 130.

Morrell, S, 1996. Power draw of wet tumbling mills and its relationship to charge dynamics. Part 2: An empirical approach to modelling of mill power draw. *Transactions of the Institution of Mining and Metallurgy Section C-Mineral Processing and Extractive Metallurgy*, 105, C54-C62.

Morrell, S, 2004. Predicting the specific energy of autogenous and semi-autogenous mills from small diameter drill core samples. *Minerals Engineering*, 17(3), 447–451. https://doi.org/http://dx.doi.org/10.1016/j.mineng.2003.10.019

Napier-Munn, T J, Morrell, S, Morrison, R D and Kojovic, T, 1996. Mineral comminution circuits: their operation and optimisation, Vol. 2. Julius Kruttschnitt Mineral Research Centre, University of Queensland.

Putland, B, 2006. Comminution circuit selection–key drivers and circuit limitations. Department of mining engineering, university of British Columbia.

Starkey, J, Hindstrom, S and Nadasdy, G, 2006. SAGDesign testing–What it is and why it works. *International AG and SAG Grinding Technology,* 4, 240–254.

Yan, D and Eaton, R, 1994. Breakage properties of ore blends. *Minerals Engineering*, 7(2), 185–199. https://doi.org/http://dx.doi.org/10.1016/0892–6875(94)90063–9

APPENDIX A

The testing procedure is illustrated in Figure A1. The extended attrition mill testing approach steps are as follows (Faramarzi, 2020):

- A 300 mm diameter × 300 mm long tumbling mill with four 10 mm lifter bars.
- The mill speed is 53 rev/min.
- Sample requirement is 4000 ± 30 g.
- Particles suitable for this testing approach can be in either of -63 + 53 mm, -53 + 45 mm, -45 + 37.5 mm, -37.5 + 31.5 mm and -31.5 + 26.5 mm or a combination of two successive size fractions. However, it has to be noted that the experiments were conducted by using 4000 ± 30 g particles in the size range of -63 + 45 mm (2000 ± 15 g of -63 + 53 mm and 2000 ± 15 g of -53 + 45 mm). It was aimed to use very coarse particles, assuming that they should contain more elements of intrinsic variability.
- Accumulative grind time is 100 minutes. It includes time intervals/cycles at which tumbling stops to measure mass loss at a defined size criterion. In this study, the accumulative grind time was extended to 160 minutes for several experiments to further investigate the effect of time on attrition behaviour of the tested samples.
- The testing approach includes two separate experiments in the wet and dry modes. In the wet mode, 1.5 litre fresh water is used in the first cycle as well as each of the time intervals.

The measurable is mass loss at a certain size criterion at the end of each cycle. Therefore, two 'characteristic' sizes were chosen as size criteria as below:

- M2 size: It is used to separate the product at 1/2nd of the geometric mean size of the upper and lower apertures of the original size interval. All the particles smaller than M2 size are removed and coarser particles will be present in the next cycle.
- M10 size: The M10 variable expressible in percent is the amount of material passing 1/10th of the geometric mean size of the upper and lower apertures of the original size interval. This variable is used in the modelling.
- Additionally, mass of the particles that are still falling in the original size range is measured in each cycle. This variable shows percentage of mass loss within the original size range after each cycle.

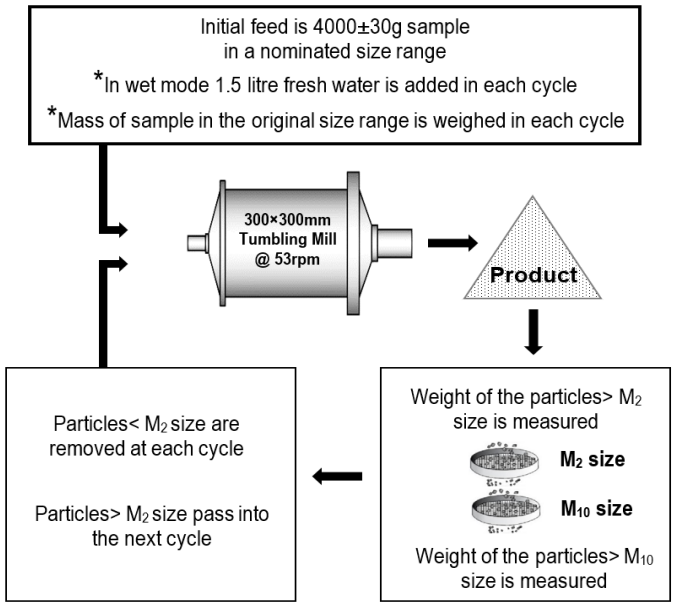

FIG A1 – The extended attrition mill testing approach procedure (Faramarzi, 2020).

Digitalisation of conveyed ore flows and using real time composition data to improve process performance

H Kurth[1]

1. Chief Marketing Officer, Minerals Consultant, Scantech International Pty Ltd, Underwood Qld 4119. Email: h.kurth@scantech.com.au

ABSTRACT

Advanced sensing technologies are used to measure conveyed flow composition in real time in many commodities to provide data for improved process control. The most reliable data is supplied by continuous, fully penetrative sensing techniques that representatively measure material in timely increments. Parameters measured in conveyed flows include elemental content, moisture and mineralogy using different methods. Quantitative techniques include high specification Prompt Gamma Neutron Activation Analysis (PGNAA) proven to provide multi-elemental content at high precisions, Magnetic Resonance (MR) proven to measure a range of minerals, and microwave transmission proven to be effective for moisture measurement. These techniques are largely independent of particle size, belt speed, segregation, dust, or matrix effects. Other techniques have generally proven to be qualitative by sensing only parts of the surface of conveyed material. These provide less compositional certainty due to high sampling error. Measuring conveyed flows over short time increments provides high selectivity as each decision can be made on a relatively small mass. This higher resolution provides opportunities for ore and waste separation between the mine and mill to upgrade ore and reduce waste entering the process. The higher measurement precisions also provide greater confidence in responses to the data. Data can be customised to suit ore tracking, ore blending, bulk diversion (bulk sorting), ore reconciliation, feed forward control, and metal accounting. While proven in many of these applications in the case studies outlined in the paper, further benefits are available through increased use of advanced analytics and digital twin modelling to relate composition fingerprinting to process performance. Process performance improvements can be modelled and implemented as each ore type is received for processing. Geometallurgical parameters that affect process performance are used at multiple stages in processing to optimise performance and examples are provided.

INTRODUCTION

It seems obvious to say that measurement is a requirement for quality management and process improvement, yet few mining operations implement proven, representative measurement technologies early in the bulk material flows between the mine and processing operations. The opportunity to improve many aspects of the operations using this data is therefore commonly overlooked. These opportunities include the digitalisation of the ore and waste quality to provide high precision, real time data considered by many sites as essential to manage and improve their performance (Arena and McTiernan, 2011; Balzan *et al,* 2016; Kurth and Balzan, 2017; Matthews and du Toit, 2011; Patel, 2014). Applications include:

- feedback of actual mined material quality to the mining and geology teams for reconciliation,
- active grade (quality) control through ore blending and/or bulk diversion (bulk sorting),
- feed forward of ore quality data to process operations to enable responses to process impacting parameters, and
- metal accounting to help processing operations reconcile metal content in feed with product and discard flows.

The paper discusses some of the representative sensing technologies that have been proven for conveyed flows and how the data they produce, presented via case studies, can benefit existing mining operations.

Conveyed flows provide continuous movement of materials in relatively predictable configurations which are ideal for sensor applications. Existing measures of flow variability via belt scales or

volumetric flow measurement are utilised as inputs to penetrative sensing systems to enable representative measurement through tonnage weighted compositional data.

HETEROGENEITY

Segregation is common in mining and most ores and waste materials display obvious heterogeneity due to mineralogical characteristics that include; density variation, brittleness, predisposition to break with preference for finer fractions where material is friable, or larger particles if massive and competent. It is common for the grade by size analysis to show preferences for fines to be higher grade in some commodities and lower grade in others. Every orebody is sufficiently different in composition and structure that few can be considered the same when it comes to application of sensing technologies for broken rock measurement. The segregation is further complicated by bulk material handling processes which may mix materials and therefore early measurement is essential to take advantage of quality variability. Heterogeneity is always present at some scale despite multiple handling stages (see Figures 1 and 2). This affects which technologies can be considered. Process feed variability has a major effect on process performance (Goodall, 2021) and should therefore be measured and managed. A ten percent reduction in metal recoveries due to increased feed quality variability can be the difference between profit and loss for a mining operation.

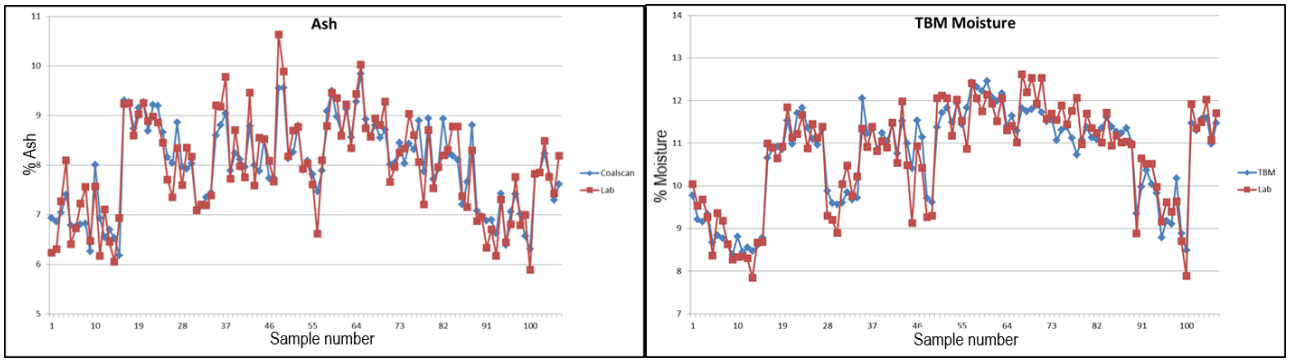

FIG 1 – Typical heterogeneity of ash and moisture content in coal.

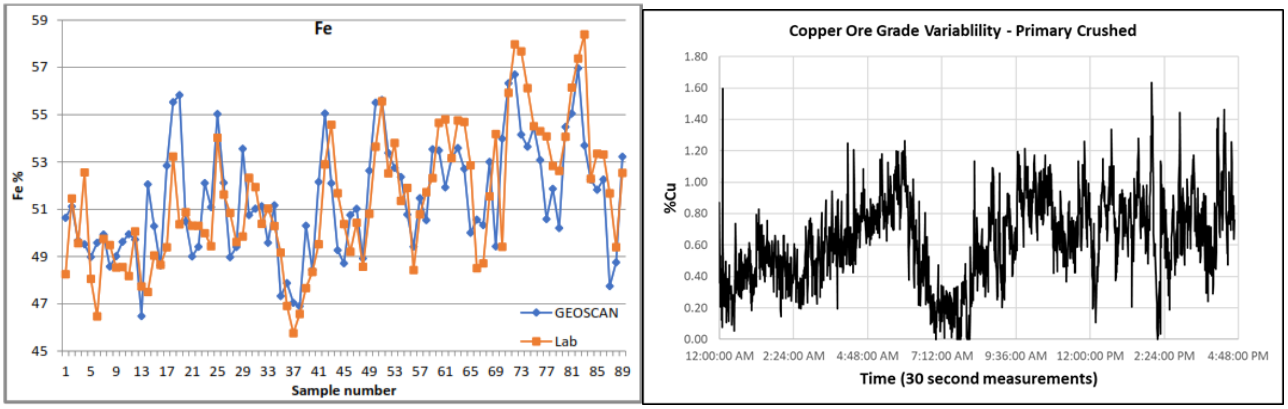

FIG 2 – Typical heterogeneity in iron ore and porphyry copper-gold run-of-mine ore.

The impact of plant feed quality variability has been studied by many companies when major changes in process performance needed to be explained retrospectively. Figure 3 is an example of the impact on metal recovery where variable feed quality was present but with the same average grade. A reduction in metal recovery of 15 percent is financially disastrous for any operation, but can be avoided through better ore quality management.

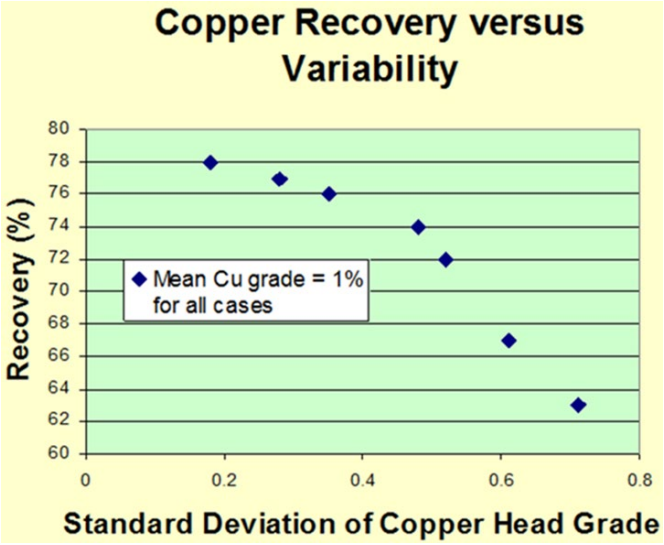

FIG 3 – An example of the effect of ore quality variability on metal recoveries (Codelco, 2007).

SENSING TECHNOLOGIES

The focus of the paper is on technologies providing timely, representative measurement. There are not many commercially available technologies for ore and waste measurement that have proven to provide unbiased results when evaluated against intensive sampling and sub-sampling of a measured interval or increment.

Representative measurement

Representative measurement occurs when the data generated is unbiased, which requires that all material has an equal probability of influencing the measurement outcome without preference to any specific component. It implies that any characteristic of the material that prevents this will result in a bias in the measurement. The heterogeneity of materials will change at some scale through handling. Heterogeneity between particles increases as they are reduced in size and ultimately reaches its maximum when all minerals are liberated, usually after fine grinding. The mineralisation style will influence how heterogeneous the particles may be in a flow. What has been clear through decades of measurement experience with Scantech analysers is that all commodities exhibit heterogeneity including coal, iron ore, bauxite, phosphate rock, porphyry copper-gold and many more, some of which appear to be considered more homogeneous due to the disseminated nature of the minerals, but which at smaller scales (several tonnes) are shown to contain significant variability.

To be considered representative the sensing should be transmissive through the full material depth and not biased by any physical characteristics such as particle size, movement speed, physics of the sensing technology, segregation of material, matrix effect changes, effect of the conveyance type, or other aspect. There is not a single technology that can provide every parameter of interest for a complete solution for elemental (chemical) content, moisture, mineralogy, particle size distribution, ore texture, mineral form (crystallography), hardness, abrasiveness and other parameters that influence processing performance. It is therefore appropriate to utilise whichever sensing techniques can be applied to provide representative analysis and to use further data as proxies, where strong correlations exist, for parameters that can’t be directly measured.

Techniques that have proven to provide representative measurement include high specification prompt gamma neutron activation analysis (PGNAA) for elemental analysis, microwave transmission for free moisture measurement, and magnetic resonance for mineral sensing. Magnetic resonance (MR) can be applied to conveyed flows to measure the response of certain minerals, but each analyser can only be configured to measure one mineral, so if there are multiple minerals of interest then multiple units are required or assumptions need to be made, which introduces errors. The MR is fast and penetrative, making it representative, though somewhat limited in its application as few sites are fully dependent on only one mineral for their overall process performance. Grade is calculated from the direct measurement of one mineral only, hence this technique has numerous limitations.

The through belt moisture (TBM) transmission microwave technology is effective in measuring free moisture content in conveyed flows utilising the dielectric properties of the material relative to those of water. Attenuation and group delay in microwave signals penetrating the full conveyed flow continuously indicate the amount of free moisture present, when proportioned to the mass flow provide a percent free moisture content.

High performance PGNAA for high precision, multi-elemental analysis over conveyed increments of 30 seconds to two minutes uniquely provides representative analysis of conveyed composition irrespective of the atomic arrangement of the elements contained in the flow. The chemical analysis can be reported in the form of total by element typical for metal content, or as common oxides of elements, or as elemental ratios, or in the form of mineralogy depending on how the stream of digital data is intended to be utilised. PGNAA utilises a small neutron source, typically Californium-252, to expose the conveyed material to the neutrons at a rate of over 100 million neutrons per second. Elemental nuclei capture neutrons and emit unique prompt gamma signatures which are detected allowing a combined spectral response to be accumulated over each analysis time increment. The finger print of each element's response is used to identify the proportion present in the spectral response and any variation in mass flow is used to weight the responses over the measurement time interval.

PROCESS PERFORMANCE BENEFITS

Representative moisture measurement is useful for dry tonnage determination for ore reconciliation and metal accounting, management of dust, filter and dryer control, and provides information on material handling impacts for some ore types. Changes in moisture content can reflect changes in mineralogy, for example clay content. The continuously measured moisture content replaces the moisture factors commonly applied for mill feed. The factors are determined through one-off reconciliation exercises and applied continuously irrespective of ore sources, weather conditions (rain) and seasonal changes.

Barrick's digital transformation program at Cortez (Bozbay and Moyo, 2019) included process objectives to address:

- reduction of manual tasks that pose a high risk to employees (specifically sampling from conveyor belts in hazardous areas such as reclaim tunnels),
- collecting field data that would lead to process optimisation (availability of timely data), and
- targeting best operating practices (not stopping conveyors to take samples and interrupt production).

An increase in ore throughput of three percent was achieved within two months of implementing a moisture analyser (Figure 4). This ensured compliance with the site's dry tonnage processing permit and increased the value of contained gold in plant feed by USD 75 million per annum based on USD 1500 per ounce.

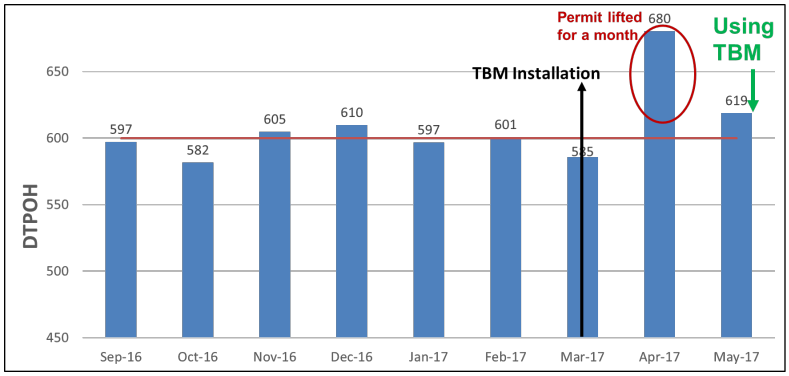

FIG 4 – Benefit of moisture measurement over moisture factor on ore feed (after Bozbay and Moyo, 2019).

The high specification PGNAA technique has proven highly reliable for 30 second measurement intervals and has enabled high confidence in diversion (bulk ore sorting) decisions and minimised misallocation of material evident in lower specification systems and unrepresentative measurement technologies. Kurth (2022) showed that the magnitude of the difference between sensing system precisions is significant in metal recovered to the mill feed using a copper bulk ore sorting example. Analyser precision directly affects material allocation efficiency. The additional contained metal recovered to the ore stream when using more precise measurement in operations processing 1000–1500 t/h is valued at tens of millions of dollars per annum.

Figure 5 shows a mobile ore sorting plant configuration incorporating a high specification PGNAA GEOSCAN analyser that measures each 30 seconds of conveyed flow with a precision of about 0.03 per cent Cu. Anglo American (2019) was quoted in International Mining in July 2019 saying that:

> *at El Soldado, we are sorting in four tonne packages. …. Being able to remove an orebody above the cut-off grade alongside waste tonnages and upgrade the latter has led to an effective lift in head grade. It has been enabled by new sensing technology with a particular type of neutron sensor. What we have seen in early results has surprised us on the upside. We thought we would see a 5% uplift in head grade, but in fact we have seen about 20% – to qualify that, it's in its early stages.*

FIG 5 – GEOSCAN analyser in a copper ore bulk sorting plant at El Soldado, Chile (source: Hillyer, 2019).

The benefits accumulate as bulk sensing of a conveyed flow provides a set of digital measurements that can be used immediately for active control of the quality by means of bulk diversion but also by feedback to adjust ore blends where that flexibility exists from stockpiles or mine sources. The same data can be used to feed forward to the process operators to warn of quality changes and also to adjust process settings. These include adjustments to mill feed rate based on ore quality and other process impacting parameters such as ore hardness, clay content etc (Kurth, 2018). Changes in ore type or quality can also be used to adjust reagent addition, particularly where variations in deleterious content can lead to contamination of concentrate if not addressed. Many of the characteristics of the ore can be measured, calculated or determined from the composition measurement before processing. Sepon process operators utilised the real time data for copper ore blending, pyrite proportioning to feed a ferric leach process, and determination of acid consuming gangue content and moisture for pH control (Balzan *et al,* 2016). They also achieved a 0.4 per cent metal accounting error.

Benefits of real time, high quality elemental and moisture measurement data in iron ore are exemplified through the applications at Assmang Khumani (Matthews and du Toit, 2011) where a detailed understanding of the ore types at multiple mines feeding a beneficiation plant have realised many benefits. This application is seen as a successful implementation of operation geometallurgy.

Ore chemical composition enabled different categories (Table 1) to be defined and utilised through conveyed material sensing. Material considered ‘on-grade’ on the overland conveyors is determined to be of product quality not requiring beneficiation through the jig plant and increments meeting these compositional criteria are diverted to bypass the jigs. The five million tonnes per annum bypassing the plant saves upwards of AUD 6 million per annum in beneficiation costs alone and represents 30–35 per cent of total product.

TABLE 1

Algorithms used for run-of-mine classification (after Matthews and du Toit, 2011).

	%Fe	%Al_2O_3	%K_2O+%Na_2O	%SiO_2	%Estimated yield
On-grade	>=65.3	<=1.8	<=0.25	<=2.5	>91
Just barely off spec	>=65.3	>1.8 & <=2.2	>0.25 & <=0.35	>2.5 & <=4.5	>80
Off-grade high	<65.3 & >60	>2.2 & <=3.2	>0.35 & <=0.40	>4.5 & <=6.5	>60 & <80
Off-grade low	<65.3 & >60	>3.2	>0.40 & <=0.54	>6.5 & <=12	>45 & <60
Waste1	<60 & >=39		>0.54	>12	
Waste2	<39				

Material classified as ‘off-grade’ continues to the plant to be processed. There are multiple ore types and each has a target upgrade quality which is used to optimise recovery using analysers installed on jig feed and jig product conveyors. Discard and three product types are also measured as is the train load out from each of the product stockpiles. The application of analysers throughout the plant allows for high confidence in production reporting and effective real time elemental balance to be determined.

Benefits of sensor fusion

Combining data from multiple sensor types is a proven way to increase the knowledge of plant feed material as there are no single sensors that can provide all the necessary information required to completely characterise plant feed in real time at full production rates. Ash and moisture measurement for coal was used in the 1980s to help power stations determine the energy value for conveyed coal feeding boilers. Different coal sources were blended to achieve optimal and consistent feed quality. Elemental analysers were used from the 1990s with moisture measurement to provide more precise energy value determination and further improve efficiencies in power station performance. In minerals processing, operators mostly rely on offline ore characterisation and ore tracking methods to determine which material is in plant feed and how to best process it based on prior metallurgical bench scale test work. Ore tracking is the real time component of the system, rather than any online analysis from a sensor on conveyed feed which started to occur in the 2000s. There had been systems in place for decades on slurry sample measurement but these did not help the plant decide which ore to process and how to proactively manage blends from different ore sources and ore quality feeding the stockpiles and mill.

The relatively recent development and application of representative measurement technologies has enabled the combination of elemental and moisture data with qualitative fragmentation and mineralogy data derived from surface sensing. The processing power of data from geological and chemical assay databases and the integration of plant performance data has resulted in greater predictability and better management of process plant performance to maximise metal recoveries and product quality and consistency. Operational geometallurgy uses real time sensing data to promptly identify ore type changes, variation in deleterious content in plant feed and trends in ore quality that cannot be predicted with high confidence from geological block model and mine planning data.

Each site needs to assess the potential benefits of multiple sensors and their data, whether it is representative, qualitative or indicative to determine synergies (Scott *et al,* 2020). Sites that benefit

most are those with a comprehensive understanding of their ore and waste types, their process characteristics, process sensitivities, and the ability to collect useful, timely data to optimise their recoveries and process efficiencies.

CONCLUSIONS

Utilising high performing representative measurement technologies for conveyed flows in plant feed can provide multiple benefits. Mining and processing operations with a detailed understanding of ore and waste characteristics and sensitivities of the process plant to these and their variability will derive immense benefits and very short paybacks when implementing suitable sensors and combinations of sensor technologies appropriate to their orebody and flow sheet.

The paper has discussed some key representative technologies suitable for elemental and moisture measurement and given examples of process performance improvements achieved when high quality sensor data are timely and successfully integrated into mining and processing operations. There are many more benefits to be achieved as geology and mineral processing professionals develop a better understanding of the benefits of real time data from digitalising the material flows between the mine and the mill.

ACKNOWLEDGEMENTS

The author acknowledges the work of many Scantech staff who have been instrumental in developing unique measurement capabilities, the customers who have shared their experiences and benefits in published papers, and Scantech for approval to publish.

REFERENCES

Anglo American, 2019. FutureSmart Mining overcoming hurdles, *International Mining*, July 2019, pp. 8–9. https://im-mining.com/2019/06/07/anglo-americans-futuresmart-mining-way-tangible-technology-results/

Arena, T and McTiernan, J, 2011. On-belt analysis at Sepon Copper operation, in *Proceedings Metallurgical Plant Design and Operating Strategies (MetPlant 2011)*, pp 527–535 (The Australasian Institute of Mining and Metallurgy: Melbourne).

Balzan, A, Jolly, T, Harris, A and Bauk, Z, 2016. Greater use of Geoscan on-belt analysis for process control at Sepon copper operation, in *Proceedings XXVIII International Mineral Processing Congress* (Canadian Institute of Mining, Metallurgy and Petroleum: Quebec).

Bozbay, C and Moyo, P, 2019. Conveyor Belt Online Moisture Analyzer at Cortez, presentation at *CIM 2019* (Canadian Institute of Mining, Metallurgy and Petroleum: Quebec).

Codelco, 2007. [Presentation], 1 February 2007, Austmine Networking Event, Brisbane, Queensland.

Goodall, W, 2021. Understanding what is feeding your process: how ore variability costs money. *Process Mineralogy Today*, March 10, 2021. https://minassist.com.au/understanding-what-is-feeding-your-process-how-ore-variability-costs-money/

Hillyer, L, 2019. Mining Automation – Mine Smarter, Load Quicker & Ore Sorting, MMD presentation, *Future of Mining Conference* (Aspermont Media: UK). https://www.youtube.com/watch?v=2NJ3HhphJc4

Kurth, H and Balzan, L, 2017. Assessing bulk sorting suitability at the New Afton Mine. *Proceedings Metallurgical Plant Design and Operating Strategies (MetPlant 2017)*, pp 315–323 (The Australasian Institute of Mining and Metallurgy: Melbourne).

Kurth, H, 2018. Role of real-time elemental analysis using PGNAA in operational geometallurgy, in *Proceedings SAIMM Geometallurgy Conference 2018*, Cape Town, 7–8 August 2018.

Kurth, H, 2022. Ore quality measurement and control using Geoscan-M PGNAA real time elemental analysis, in *Proceedings International Mining Geology Conference 2022*, pp 338–345 (The Australasian Institute of Mining and Metallurgy: Melbourne).

Matthews, D and du Toit, T, 2011. Validation of material stockpiles and roll out for overall elemental balance as observed in the Khumani iron ore mine, South Africa, in *Proceedings Iron Ore Conference*, pp 297–305 (The Australasian Institute of Mining and Metallurgy: Melbourne).

Patel, M, 2014. On-belt elemental analysis of lead-zinc ores using Prompt Gamma Neutron Activation Analysis. *Proceedings XXVII IMPC 2014*, 20–24 October 2014 Santiago, Chile. Gecamin.

Scott, M, Rutter, J, du Plessis, J and Alexander, D, 2020. Operational deployment of sensor technologies for bulk ore sorting at Mogalakwena PGE Mine, in *Proceedings Preconcentration 2020* (The Australasian Institute of Mining and Metallurgy: Melbourne).

A new classification method of gold-bearing sulfide by automated mineralogy – evaluation of gold refractory degree

J Li[1] and C Gianatti[2]

1. Principal Geometallurgist, AXT PTY LTD, Belmont WA 6104. Email: jing.li@axt.com.au
2. Senior Project Metallurgist, KCGM, Northern Star Resources Limited, Kalgoorlie WA 6433. Email: cgianatti@nsrltd.com

ABSTRACT

Quantification of submicroscopic gold is one of the critical ore characteristics in evaluating the refractory degree of gold ores. This is because submicroscopic gold cannot be leached until the sulfide carriers have been oxidised. The variation of the submicroscopic gold in different types of pyrite has challenged the quantitative evaluation for the gold industry. Although previous studies have proved the relationship between morphological types of pyrite and the amount of submicroscopic gold, the classification was conducted under optical microscopes by experienced mineralogists.

With the automated mineralogy system development, high-resolution scanning electron microscope and multiple factor particle categoriser have become a new tool for classifying gold carriers. This paper is a case study of quantifying the ore characteristics inhibiting gold leaching and investigating the correlation between gold and arsenic for various ore domains at KCGM. Diagnostic leaching tests showed that most of the un-leachable gold was locked in sulfide phases. The mineralogical study quantified the distribution of gold locked in sulfides, including submicroscopic gold, Au (Ag) and Au-Te inclusions, combined with the grain size distribution of gold inclusions, explaining the different leaching performance of each sample. High-resolution SEM scanning indicated that arsenic mainly occurred as micro arsenopyrite inclusions (1–5 μm) or crystal lattice replacement in pyrite rather than coarse arsenopyrite. Au-bearing pyrite has been classified into four morphological types by automated mineralogy categoriser tools in TIMA. LA-ICP-MS measurement showed that submicroscopic gold concentration gradually decreased from pyrite with micro – arsenopyrite inclusions, to porous pyrite, to fine-grain pyrite, to coarse pyrite and arsenopyrite. The positive correlation between arsenic and gold concentrations in pyrite was verified in this study, which aligned with the previous study by other microprobe analyses. The Au/As ratio was recommended as one of the geometallurgical indexes to estimate the gold leachability for flotation concentrates in the Fimiston ore system. The objective and high-speed classification method by automated mineralogy could benefit more gold projects.

INTRODUCTION

Submicroscopic gold, named as invisible gold (Bürg, 1930), is identified as solid-solution and colloid gold locked in sulfides and iron oxides (Chryssoulis and Cabri, 1990; Zhou, Jago and Martin, 2004) because it is invisible under the optical microscope and scanning electron microscope (SEM). Due to the rare probability of being exposed to the cyanide solution by the ultrafine grinding process, the quantification of submicroscopic gold became the critical ore characteristic in evaluating the refractory degree of gold ores and selecting pre-oxidation techniques. However, the analytical method was challenged by the inhomogeneous amounts of gold among sulfide particles.

The quantitative submicroscopic gold study method based on secondary-ion mass spectrometry (SIMS) analysis and morphological classification as coarse pyrite, porous pyrite, fine-grained pyrite and microcrystalline pyrite was reported by Cook and Chryssoulis (1990) and Zhou, Jago and Martin (2004). The morphological classification and statistics of pyrite were usually conducted under optical microscopes by extensively experienced mineralogists.

The morphological classification is necessary because of the various amounts of submicroscopic gold in sulfide particles, changing from less than one ppm to ten thousand ppm. As the most common gold carrier, the morphological features of pyrite pertaining to gold were studied on various types of gold ores, referring to solid-solution gold is strongly enriched in the fine-grained sulfides (Cook and

Chryssoulis, 1990; Arehart, Chryssoulis and Kesler, 1993; Simon *et al*, 1999; Reich *et al*, 2004; Zhou, Jago and Martin, 2004).

This paper is a case study of the refractory degree of ores from Kalgoorlie Consolidated Gold Mines (KCGM) in Western Australia. KCGM operations include the Fimiston open pit (Super Pit), Mt Charlotte underground mine and the Fimiston and Gidji Processing Plants. The Super Pit is Australia's largest open pit gold mine processing refractory gold in which most of the gold is locked in sulfides. The processes undertaken in the Fimiston processing plant include crushing, grinding, and flotation. The flotation concentrate is then transported to the Gidji Processing plant for ultrafine grinding and carbon-in-leach (CIL). This study focused on the features of flotation concentrate affecting the following CIL.

METHODOLOGY AND SAMPLES

A series of quantitative mineralogical studies were conducted on flotation concentrate samples, including the mineral abundance, locked microscopic gold study and submicroscopic gold study. Scanning electron microscopy (SEM) with an automated mineralogy system (TIMA: TESCAN Integrated Mineral Analyzer) was used for mineral composition and microscopic gold scanning. The specific sulfide morphological categoriser for KCGM ore was developed through high-resolution SEM scanning and the TIMA system to provide objective classification results. A new type of gold-bearing pyrite was identified in this study, which enriched the highest gold among all the categories. Laser ablation inductively coupled plasma mass spectrometry (LA-ICP-MS) was applied for the *in situ* gold and arsenic analysis on various types of pyrite and arsenopyrite. Agilent7700 ICP-MS and ESL NWR213 laser were used for submicroscopic gold measurement, with spot size 10 μm, repetition rate 10 Hz, laser energy 3.6 J/cm^2.

Sixteen flotation concentrates were studied by the same method, with eight of them from different domains of the metallurgical feasibility study for deposit S and another eight from the current Fimiston flotation concentrate. Samples of flotation concentrate collected prior to processing at the Gidji Processing plant were selected where they subsequently achieved a 90 per cent gold recovery in August, and compared against those that achieved a 95 per cent gold recovery in July (Table 1).The metallurgical tests results for Deposit S samples proved the high refractory degree of several domains, such as FS-03, FS-06, FS-07 and FS-09 (Table 1). All of the leaching results were processed on ultrafine ground concentrates.

TABLE 1

Sample assay and mineral abundances.

Sample		Au ppm	As ppm	Au leaching recovery/%	Pyrite %	Arsenopyrite %	Non-sulfides %
Deposit S Feasibility study	FS-01	36.1	1420	87.80	52.45	<0.01	47.46
	FS-03	11.2	2495	65.98	31.37	<0.01	68.43
	FS-04	34.1	1930	85.92	50.57	<0.01	49.34
	FS-05	27.4	1730	84.51	50.01	0.01	49.90
	FS-06	18.9	3075	68.43	35.18	0.05	64.68
	FS-07	13.1	1015	71.31	38.96	0.02	60.97
	FS-08	40.9	1060	88.35	47.76	0.02	52.14
	FS-09	19.7	2800	78.29	36.66	0.14	63.13
Plant July	22/07	31.3	959	95.80	56.82	0.02	41.39
	23/07	48.1	1520	95.40	61.20	0.04	36.73
	25/07	32.95	1150	95.30	55.91	0.03	42.21
	27/07	31.15	1110	95.00	57.00	0.03	40.70
Plant August	05/08	48.5	1950	90.60	59.89	0.09	37.40
	06/08	37.6	1690	90.80	48.94	0.06	47.97
	07/08	40.2	1560	90.80	59.56	0.12	38.00
	09/08	41.5	1510	91.00	50.90	0.10	47.55

RESULTS AND DISCUSSION

Bulk mineralogy

The flotation concentrates were composed of 30–61 per cent sulfide and 37–68 per cent non-sulfide minerals (Table 1). Sulfide minerals included mainly pyrite, with a trace amount of pyrrhotite and arsenopyrite. Most of the arsenic occurred as the impurity in pyrite, including isomorphism and micro arsenopyrite inclusions (1–5 μm). Au leaching recovery of Deposit S samples came from metallurgical tests, while the recovery of plant samples was the average recovery of the operation day. All of the leaching results were processed on ultrafine ground concentrates.

Locked microscopic gold study

Microscopic gold is one of the main gold occurrences in Fimiston ores. The designed flotation concentrate targets a P80 passing 180 μm. As exposed gold in the concentrates is leachable, this study paid attention to the characteristics of locked gold. Mineral speciation is one of the mainly mineralogical factors affecting gold leachability because some gold-bearing minerals known to have a slow kinetic leaching rate. The grain size of locked gold is another parameter since the <4 μm grains reduced the probability to be exposed by the ultrafine grinding at P80@11 μm. Microscopic gold was measured through high-resolution, bright phase searching tools in TIMA with a pixel size of 0.5 μm. High-resolution gold scanning was conducted on one resin block per sample, and a totally of 822 enclosed gold grains were observed, 98 per cent of which grains were locked in pyrite.

Gold minerals observed in KCGM samples are native gold, electrum, calaverite ($AuTe_2$), petzite (Ag_3AuTe_2) and sylvanite ($(Au,Ag)_2Te_4$). Because gold tellurides were reported as slow leaching minerals, the microscopic gold inclusions were sorted into gold-silver alloy (Au(Ag)) and gold telluride (Au-Te). Table 2 shows the relative gold distribution in the two types of microscopic gold inclusions. Most of the microscopic gold inclusions in the current Fimiston flotation concentrate occurred as native gold or electrum, with various amounts of gold telluride. Some samples from Deposit S contained a high component of gold tellurides, especially FS-07, which affected the leaching performance. Whilst other occurances of lower than expected recovery could not be explained by the presence of telluride minerals.

TABLE 2

Relative gold distribution of locked microscopic gold by speciation.

	Deposit S feasibility study							
Speciation	**FS-01**	**FS-03**	**FS-04**	**FS-05**	**FS-06**	**FS-07**	**FS-08**	**FS-09**
Au(Ag) %	58.08	79.48	78.75	74.38	70.81	18.95	38.4	41.74
Au-Te %	41.92	20.52	21.24	25.62	29.19	81.05	61.59	58.26
	Fimiston Plant July				**Fimiston Plant August**			
Speciation	**22/07**	**23/07**	**25/07**	**27/07**	**05/08**	**06/08**	**07/08**	**09/08**
Au(Ag) %	96.23	84.79	70.96	93.83	78.76	79.99	94.26	91.73
Au-Te %	3.77	15.21	29.04	6.17	21.24	20.01	5.74	8.27

Since the flotation concentrates will be ground to 11 μm before the leaching process, the exposing probability of gold inclusions was controlled by the grain size, in which +7 μm grains would have more chance to be exposed to cyanide solution based on industry experience. Figure 1 shows the grain size distribution of locked gold inclusions in concentrates. Most of the locked microscopic gold in Deposit S samples was smaller than 10 μm. Especially in FS-03, FS-06 and FS-09, more than 85 per cent of the locked gold grains were smaller than 4 μm, which challenged exposure by grinding. On the other hand, the locked gold was much coarser in the current plant ores from July and August, with 52 per cent and 50 per cent smaller than 10 μm individually. Aligning with the excellent leaching performance in July (Table 1), the results indicated that the grain size of locked microscopic gold was one of the crucial factors for the refractory degree.

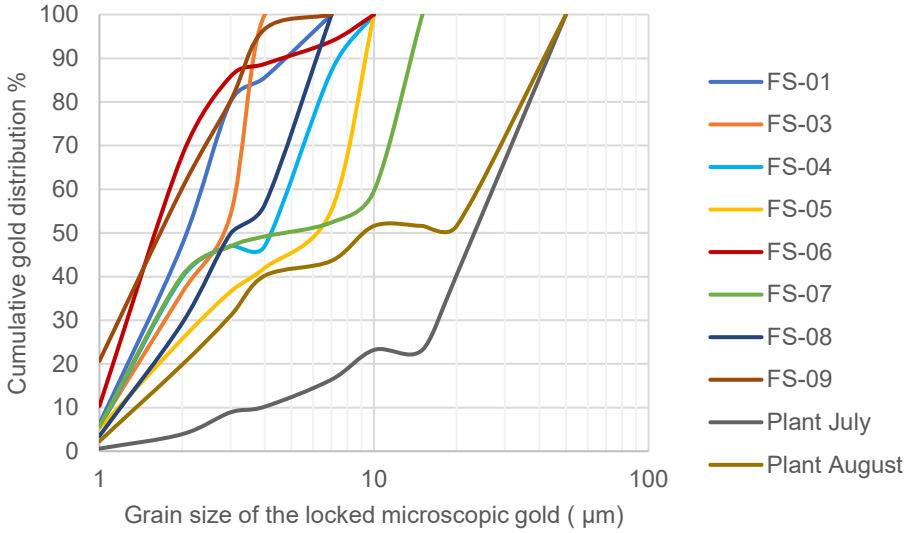

FIG 1 – Grain size distribution of the locked microscopic gold.

Submicroscopic gold study

Submicroscopic gold usually occurs as a solid-solution or colloidal gold. Solid-solution gold refers to gold atomically distributed in the crystal lattice of sulfide minerals like pyrite and arsenopyrite, which is non-leachable without oxidation of sulfides. Colloidal gold is a submicron gold inclusion in sulfide minerals, with a size between 5–500 nm, which is able to be detected by SIMS (Chryssoulis, Cabri and Salter, 1987) and imaged and analysed by high-resolution transmission electron microscopy (HR-TEM) (Bakken *et al*, 1989). However, the possibility to expose the colloidal gold in natural pyrite by ultrafine grinding is very low. LA-ICP-MS was used in this study to measure submicroscopic gold with the laser spot at 10 μm, so the results included solid-solution gold and colloidal gold.

Morphological identification and classification of pyrite

The morphological classification of pyrite was conducted by 1 μm pixel size SEM scanning and particle categoriser tool by TIMA system. A specific type of pyrite was identified and sorted in this study which is pyrite (Py) with micro arsenopyrite (Apy) inclusions. The detectable arsenopyrite inclusions were 1–5 μm locked in the crystal zone of pyrite (Figure 2e) or in the centre of the particle (Figure 2d). This type of pyrite was proved as the most robust submicroscopic gold carrier in the Fimiston ore deposit (Table 3). Therefore, the morphology of pyrite pertaining to gold was classified into four types for Fimiston ore deposit, including pyrite with micro arsenopyrite inclusion, porous pyrite, fine-grained pyrite and coarse pyrite (Figure 2 and Table 3).

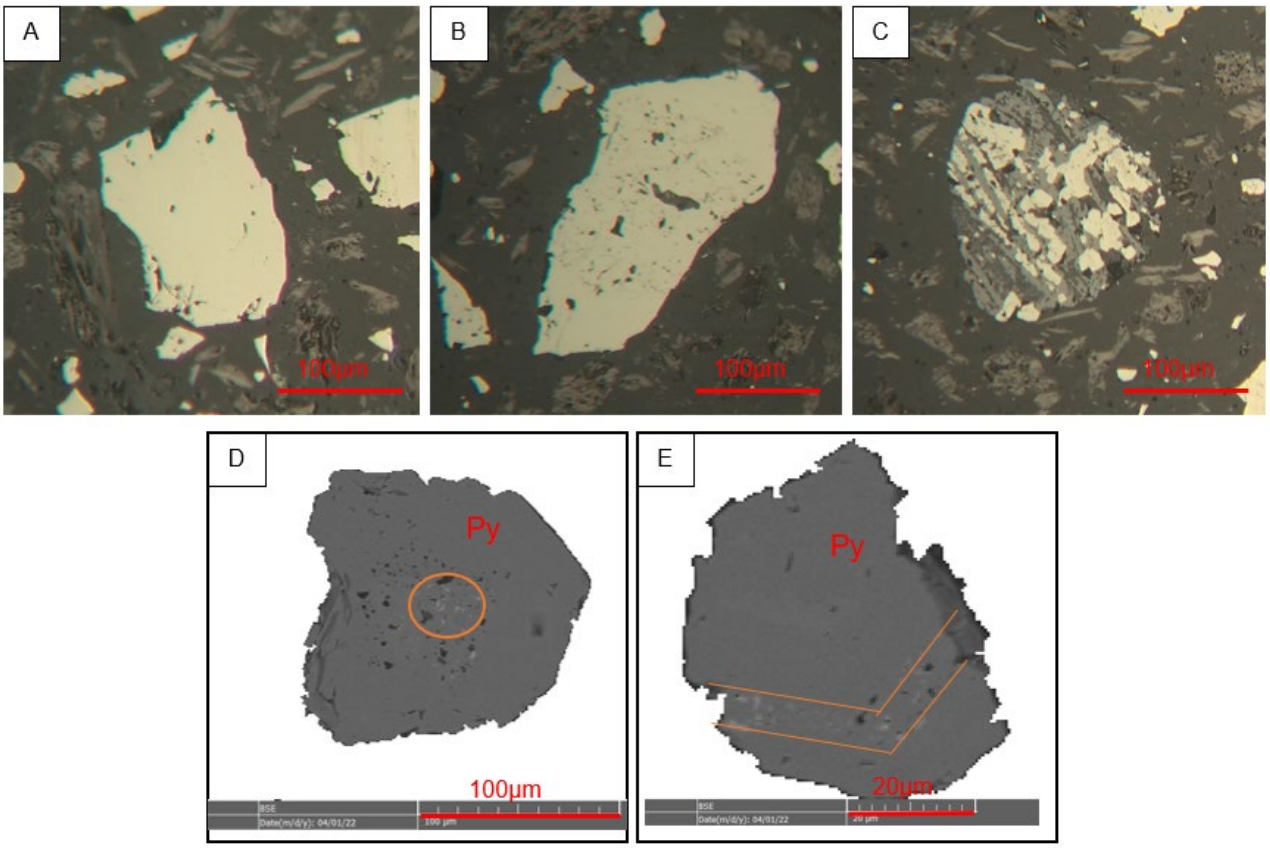

FIG 2 – Pyrite morphological types for submicroscopic gold study. A, B, C are reflective optical microscope images; D and E are SEM BSE images. A: coarse pyrite; B: porous pyrite; C: fine-grained pyrite D: Py with micro Apy inclusions hosted in the middle of the grain (bright spots in the orange circle); E: Py with micro Apy inclusions hosted in the growth zone (bright spots between the orange line).

The morphological sorting results show (Table 3) that pyrite from current plant ores was mainly coarse pyrite, secondly porous pyrite, with a minor amount of fine-grained pyrite and pyrite with micro arsenopyrite inclusions. For Deposit S samples, the mass of fine-grained Py and Py with Apy inclusions (Table 3) increased with the arsenic abundances in the samples, such as samples FS-03, FS-06 and FS-09. For plant July and plant August samples, only the mass of Py with Apy inclusions particles increased in August samples, while the mass of the other three types of pyrite stayed at the same level (Table 3).

Gold concentration in various types of pyrite particles

The concentration of submicroscopic Au in different morphological types of pyrite (Table 3) was measured by LA-ICP-MS. Totally 153 pyrite and seven arsenopyrite particles were measured in this study. The counts over time graph (Figure 3) of each particle showed S, Fe, As, Au concentrations with the depth profile during 30 seconds acquisition time. The particles with stable counts of gold contents (Figure 3 left) were used to quantify submicroscopic gold, while the graph with plateaued S, Fe and As but strongly disturbed Au curve (Figure 3 right) indicated that gold inclusions were detected under the surface, which was not used for the submicroscopic gold statistic. So 45 pyrite and seven arsenopyrite from Deposit S samples, 32 pyrite particles from Fimiston plant July and 41 pyrite particles from Fimiston plant August were applied to calculate the concentrate of submicroscopic gold in various morphological types of pyrite.

TABLE 3

The quantification of submicroscopic gold in pyrite.

Morphological type		Py with micro Apy inclusions			Porous Py			Fine-grained Py			Coarse Py			Total Sub-microscopic gold ppm per head
		Type abundance %	Au conc*. ppm	Au carried ppm	Type abundance %	Au conc*. ppm	Au carried ppm	Type abundance %	Au conc*. ppm	Au carried ppm	Type abundance %	Au conc*. ppm	Au carried ppm	
Deposit S Feasibility study	FS-01	1.6	Avg. 29.3 Range: 16.2–48.3	0.25	29.32	Avg. 11 Range: <0.1–93.0	1.69	7.3	Avg. 6.1 Range: 0.7–32.2	0.23	61.78	Avg. 0.2 Range: <0.1–0.4	0.06	2.24
	FS-03	3.96		0.36	32.44		1.12	6.79		0.13	56.81		0.04	1.65
	FS-04	1.99		0.29	30.66		1.71	7.68		0.24	59.67		0.06	2.30
	FS-05	1.71		0.25	21.18		1.17	8.15		0.25	68.94		0.07	1.73
	FS-06	12.06		1.25	25.17		0.98	16.03		0.34	46.6		0.03	2.60
	FS-07	0.6		0.07	27.29		1.17	5.69		0.14	66.38		0.05	1.43
	FS-08	3.15		0.44	30.48		1.6	13.65		0.40	52.68		0.05	2.49
	FS-09	7.83		0.84	30.14		1.22	27.59		0.62	34.05		0.03	2.71
	No	6			19			15			5			45
Plant July	22/07	0.25	Avg. 14.4 Range: 0.3–56.4	0.02	13.34	Avg. 0.8 Range: <0.1–2.3	0.06	0.78	Avg. 1.9 Range: 0.4–9.6	0.01	85.63	Avg. 0.1 Range: <0.1–0.9	0.05	0.14
	23/07	1.02		0.09	24.61		0.12	0.88		0.01	73.49		0.04	0.26
	25/07	0.66		0.05	19.83		0.09	1.62		0.02	77.89		0.04	0.20
	27/07	0.76		0.06	18.15		0.08	1.62		0.02	79.47		0.04	0.20
	No	6			7			7			12			32
Plant August	05/08	3.27	Avg. 23.1 Range: 0.1–83.6	0.44	18.60	Avg. 1.3 Range: 0.1–6.7	0.14	1.49	Avg. 4.7 Range: 0.1–31.7	0.04	76.63	Avg. 0.2 Range: <0.1–1.2	0.11	0.74
	06/08	2.18		0.24	18.26		0.12	1.41		0.03	78.15		0.09	0.48
	07/08	1.36		0.18	20.94		0.16	1.30		0.04	76.40		0.11	0.49
	09/08	1.84		0.21	21.78		0.15	1.55		0.04	74.83		0.09	0.49
	No	8			6			15			12			41

*conc. = concentration.

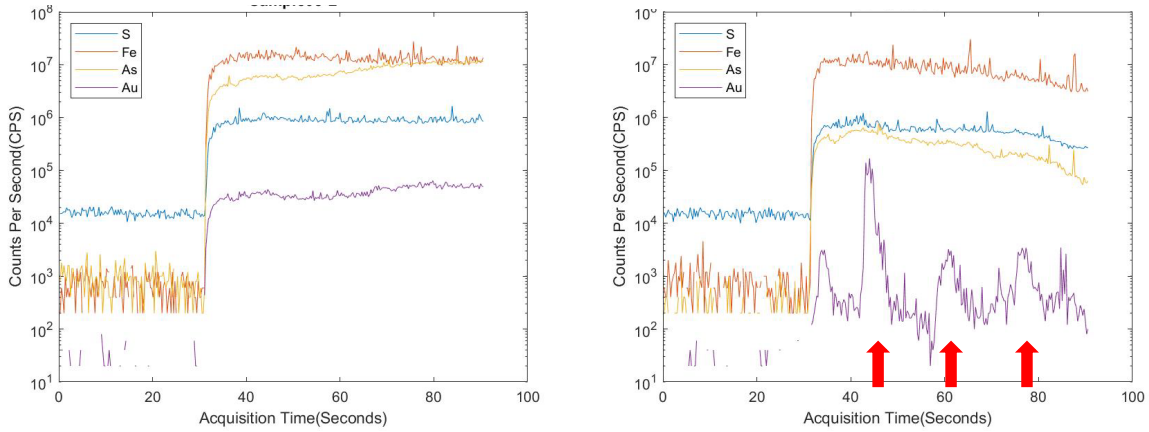

FIG 3 – LA-ICP-MS counts over time graph.

Generally speaking, submicroscopic gold was typically strongly enriched in the pyrite with arsenopyrite inclusions, secondly in fine-grained pyrite or porous pyrite, traced in coarse pyrite or coarse arsenopyrite (Table 3). The gold concentration hosted in Py with Apy inclusions was 14.4–29.3 ppm which can be identified as high gold carriers, while it was usually 0.8–11 ppm in porous Py, 1.9–6.1 ppm in fine-grained Py and only 0.1–0.2 ppm in coarse Py.

Quantification of submicroscopic gold

Submicroscopic gold was quantified based on the mass% of different pyrite types and the average gold concentration in each type (Table 3).

For samples from plant July or plant August, the gold concentrations in fine-grained Py were greater than that in porous Py. However, the high mass of porous pyrite (18.15–24.61 per cent) contributed more submicroscopic gold to the sample than that from fine-grained Py. Relatively higher mass of Py with Apy inclusions and the increasing of gold concentration in Py with Apy inclusions, porous Py and fine-grained Py in plant August samples were the crucial features for submicroscopic gold compared to July samples, which affected the leaching performance.

Several samples from Deposit S displayed various refractory related characteristics. Obviously, more high gold pyrite carriers, such as Py with Apy inclusions, were observed in the lower recovery samples, such as FS-03, FS-06 and FS-09. The abundance of fine-grained Py and porous Py also increased.. Moreover, the gold concentrations in the three types of pyrite except coarse Py were higher than that from the current plant samples. Extremely high gold contents in porous Py particles with the mass of this type provided more than 70 per cent of the submicroscopic gold in the Fimiston south samples. The abundances of arsenopyrite were less than 0.2 per cent (Table 1), which occurred as coarse particles and micro inclusions in pyrite. The average gold concentration of seven coarse arsenopyrite was 0.1 ppm, which indicated that the submicroscopic gold was not enriched in coarse arsenopyrite particles. However, the total amount of submicroscopic gold (Table 3) did not show a linear relation with the gold recovery.

The parameters that can be used to estimate the refractory degree will be discussed below.

DISCUSSIONS

Correlation between as and submicroscopic gold in pyrite particles

The positive correlation between arsenic and gold concentrations in pyrite was recognised early in the course of routine determinations of solid-solution gold in pyrite by SIMS, in which the solubility of gold was found as a function of arsenic content in pyrite, and the function was various among different ore types (Chryssoulis and Cabri, 1990; Reich *et al*, 2004).

In this study, arsenic and gold were measured by LA-ICP-MS at the same time for each particle. The correlation of submicroscopic gold and arsenic on 118 pyrite particles in four morphological groups was displayed, overlapping the gold versus arsenic plot for pyrite that was modified from Reich *et al* (2004) (Figure 4). The results from this study were located in the same area as the previous study,

with most of the spots sitting in the solid-solution gold area, which verified the reliability and high quality of the method in this study and also proved the positive correlation between arsenic and submicroscopic gold in pyrite particles.

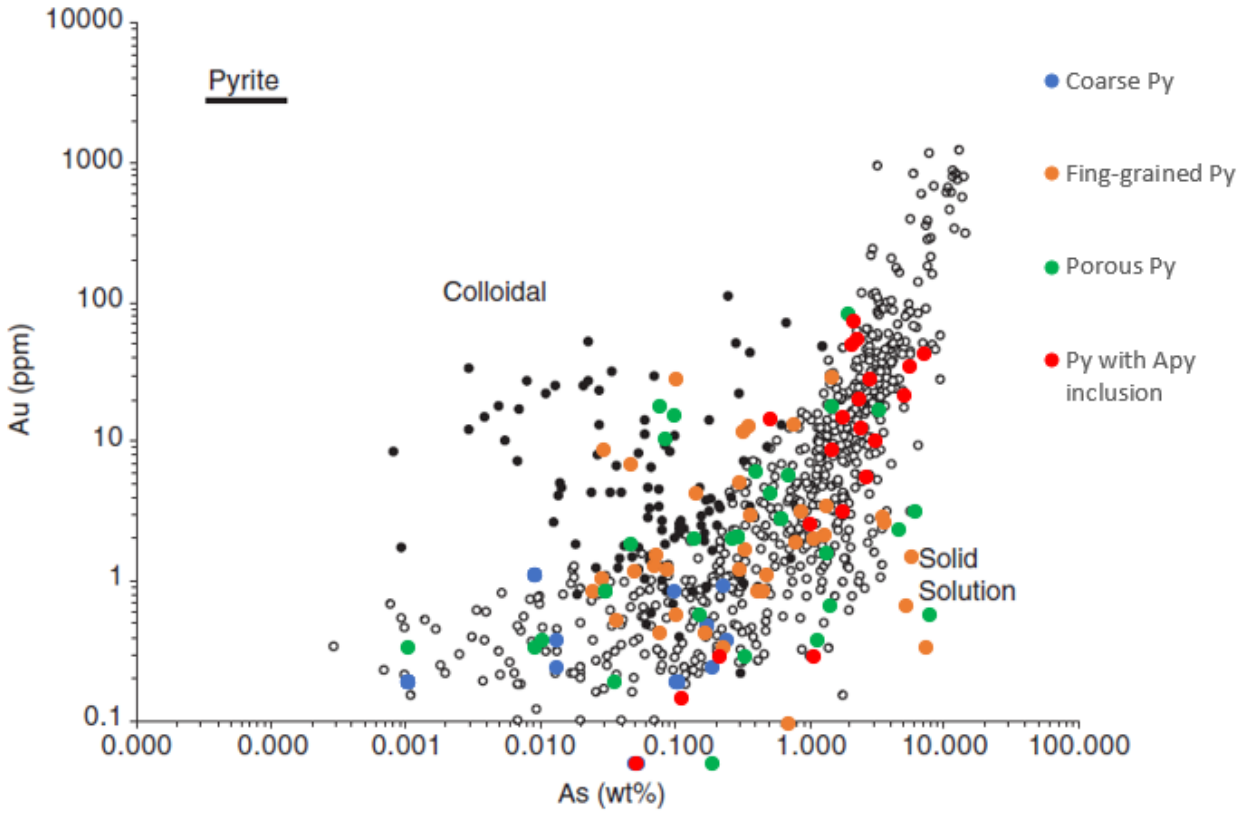

FIG 4 – Correlation of submicroscopic gold and arsenic in the morphological types of pyrite (colour spots from this study), modified from Reich *et al* (2004) (solid-solution gold (○) and colloidal size gold (●)).

Py with Apy inclusions type (Figure 4) hosted the highest gold concentrations (10–100 ppm), most of which were solid-solution gold. This type of high gold carrier in the Fimiston gold deposit has not been detected previously. Fine-grained pyrite (Figure 4 orange spots) contained 0.03 per cent-8 per cent arsenic, with mainly solid-solution gold and minor colloidal gold. Porous pyrite (Figure 4 green spots) carried a wide range of As and Au, including both types of submicroscopic gold as well. Coarse pyrite (Figure 4 blue spots) usually carried less than one ppm solid-solution gold with arsenic less than 0.3 per cent.

Geometallurgical factors evaluating the refractory degree

Although it is known that the increase of arsenic content negatively affects the gold leaching recovery, it is not a linear relationship between arsenic abundance and gold. To evaluate the refractory degree, understanding the refractory gold ore-forming process is necessary.

Based on an Au versus As plot of over 1000 microprobe analyses of pyrites of all morphological types (Figure 4), Reich *et al* (2004) found that the maximum solubility of gold in pyrite in epithermal and mesothermal gold ores was calculated as a function of arsenic content in pyrite as:

$$C_{Au} = 0.02\ C_{As}$$

Where C is the concentration of As, Au in mol%. When gold abundance in the ore-forming fluid was more than the maximum solubility, gold would occur as colloidal gold, micro gold inclusions, and even coarse gold minerals. The more gold exceeded the solubility, the lower the proportion of refractory gold in the ore. Therefore, the refractory degree of gold ore was determined by the relative amounts of arsenic and gold in the same ore deposit, regardless of other detrimental elements, such as tellurium and antimony. Figure 5 showed a good correlation between As/Au ratio and the gold leaching recovery of the samples in this study which can be explained by the theory of refractory

gold ore-forming studies until now. Therefore, As/Au ratio would be recommended as one of the geometallurgical factors to evaluate the refractory degree for KCGM and to understand the leaching performance affected by arsenic. Another important detrimental factor that affects gold leachability is tellurium. The significant presence of gold telluride, especially in FS-07 (Table 2), will result in slow leaching kinetics and explains the decrease in gold recovery for some samples. As the samples in this study were limited, research on more samples will be required to develop an accurate geometallurgy index for refractory degree estimation.

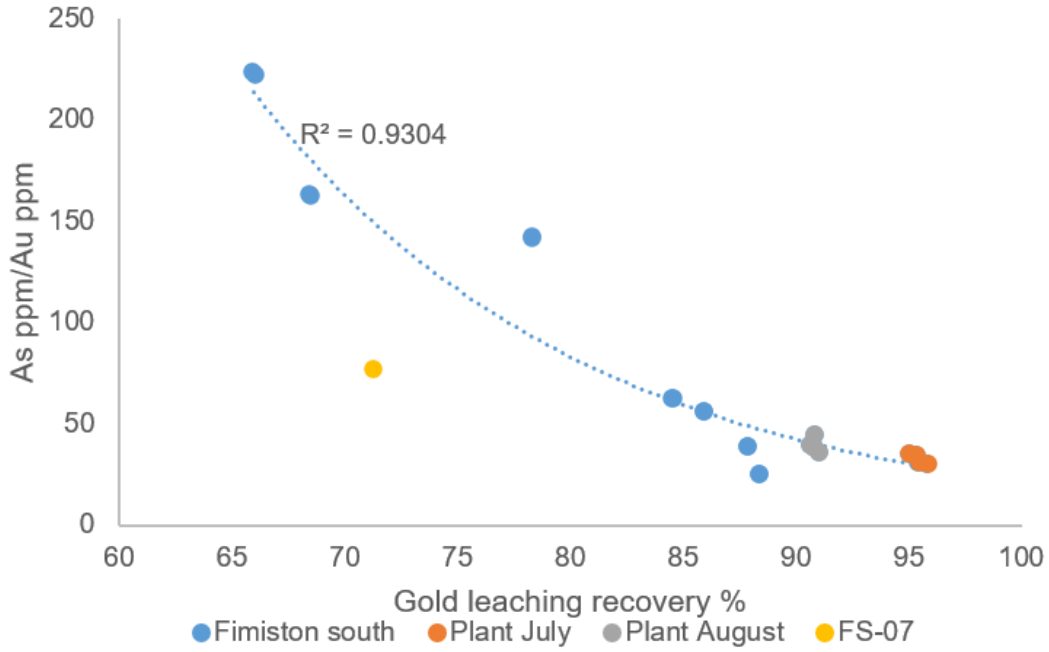

FIG 5 – Correlation between submicroscopic gold and As/S ratio.

CONCLUSIONS

High-resolution SEM scanning and automated mineralogy software (TIMA) combined with LA-ICP-MS were applied for the refractory gold deportment study for KCGM samples. The ore characteristics affecting the gold leachability were studies on flotation concentrates with various leaching performances. The morphological classification of pyrite was successfully conducted by an automated mineralogy categoriser tool. The pyrite with arsenopyrite inclusions was identified as a new pyrite type which was identified as the most vital gold carrier type in Fimiston and Fimiston south deposits. The arsenopyrite inclusions indicated that arsenic was oversaturated in pyrite under the ore-forming condition and generated high gold solubility in pyrite, resulting in the refractory nature of the ore. Most Py with Apy inclusion type particles hold more than 1–10 per cent As and 3–100 ppm Au, in which the gold occurred primarily as solid-solution gold. The amounts of this type of pyrite increased obviously with the rising arsenic content in the samples. The relatively high arsenic content also generated more fine-grained pyrite particles or porous pyrite particles, which were significant gold carriers as well. The positive correlation between arsenic and gold concentrations in pyrite was verified in this study. The Au/As ratio was recommended as one of the geometallurgical indexes to estimate the gold leachability for flotation concentrates in the Fimiston ore system.

ACKNOWLEDGEMENT

The authors thank AXT PTY LTD and KCGM, Northern Star Resources Limited, for permission to publish this paper. The first author is also grateful to Mr Joe Zhou for his assistance in the study of pyrite morphological classification. LA-ICP-MS analysis was conducted at Bureau Veritas Perth.

REFERENCES

Arehart, G, Chryssoulis, S and Kesler, S, 1993. Gold and arsenic in iron sulfides from sediment-hosted disseminated gold deposits: implications for depositional process. *Econ. Geol*. 88, pp 171–185.

Bakken, B, Hochella Jr, Marshall, A and Turner, A, 1989. High-resolution microscopy of gold in unoxidised ore from the Carlin mine. *Nev. Econ. Geol*. 84, pp 171–179.

Bürg, G, 1930. Die Sichtbarmachung des feinverteilten goldes in goldhöffingen Erzen un ihre wirtschaftliche Bedentung. *Metall. Erz* 27 (13), pp 333–338.

Chryssoulis, S and Cabri, L, 1990. Significance of gold mineralogical balances in mineral processing. *Trans. Inst. Min. Metall. (Sect. C: Mineral. Process. Extr. Metall.)* 99, pp C1-C9.

Chryssoulis, S, Cabri, L and Salter, R, 1987. Direct determination of invisible gold in refractory sulfide ores. In: Salter, R.S., Wyslouzil, D.M., McDonald, G.W. (Eds.), *Proceedings of International Symposium on Gold Metallurgy*, Winnipeg, Canada. Pergamon Press, New York, pp 235–244.

Cook, N and Chryssoulis, S, 1990. Concentrations of 'invisible' gold in common sulfides. *Can. Mineral*. 28, pp 1–16.

Reich, M, Kesler, S, Utsunomiya, S, Palenik, C, Zaoju, Y, Chryssoulis, S and Ewings, R, 2004. SIMS, EPMA and HRTEM investigation of arsenian pyrite: implications for the solubility and chemical state of 'invisible' gold. *Geochim. Cosmochim. Acta* 69 (11), pp 2781–2796.

Simon, G, Huang, H, Penner-Hahn, J, Kesler, S and Kaol, S, 1999. Oxidation state of gold and arsenic in gold-bearing arsenian pyrite. *Am. Mineral*. 84 (7–8), pp 1071–1079.

Zhou, J, Jago, B and Martin, C, 2004. Establishing the process mineralogy of gold ores. In: Abols, J. (Ed.), Proceedings 2004: 36th CMP Meeting, Ottawa. CIM, Montreal, pp 199–226.

Not all outliers are bad – the Olympic Dam example

Y Li[1], V Liebezeit[2], K Ehrig[3], B Pewkliang[4], M Smith[5] and E Macmillan[6]

1. AAusIMM, Senior Geometallurgist, BHP Olympic Dam, Adelaide SA 5000.
   Email: yan.li@bhp.com
2. MAusIMM, Principal Geometallurgist, BHP Olympic Dam, Adelaide SA 5000.
   Email: vanessa.liebezeit@bhp.com
3. FAusIMM(CP), Superintendent Geometallurgy, BHP Olympic Dam, Adelaide SA 5000.
   Email: kathy.ehrig@bhp.com
4. MAusIMM(CP), Senior Geometallurgist, BHP Olympic Dam, Adelaide SA 5000.
   Email: benjamath.pewkliang@bhp.com
5. Lead Geoscience Data Management, BHP Olympic Dam, Adelaide SA 5000.
   Email: michelle.smith@bhp.com
6. MAusIMM(CP), Senior Geometallurgist, BHP Olympic Dam, Adelaide SA 5000.
   Email: edeltraud.macmillan@bhp.com

ABSTRACT

Like many data sets, test results generated from geometallurgical test work inevitably contain outliers. There are many causes for outliers. A common practice during any model development is to exclude outliers to avoid a biased or skewed model. Outlier removal is a critical step in geometallurgical model development since the decision we make at this stage has significant impact on final output. Will deleting all outliers result in a better prediction?

All data tells a story – a small group of data points behaving significantly different from the majority doesn't necessarily mean they are erroneous and quite often they are telling us something that we don't already know. This paper uses examples at Olympic Dam to describe how outliers in the flotation tails leach acid consumption model triggered us to review the compositional variability of the chlorite group of minerals in the deposit and the way we cluster them. This exercise led to improved understanding of how different subtypes of the mineral chlorite have distinct behaviours during tails leach and that chlorite mineral composition varies widely across the deposit, which was also linked to another 'abnormal' ore behaviour in tails leach process. Understanding the spatial distribution in mineral characteristics supported our decision to retain the data points that were initially classified as statistical outliers but were, in fact, genuine test results. As we sampled and tested those areas more, the number of 'outlier' results increased, hence suggesting they were not outliers. A different case study is uranium leach extraction where early samples showed unexpected extraction results but as more samples from the same area were tested they started to show a new trend. This approach enabled us to group data more sensibly and make better predictions for plant production.

INTRODUCTION

The Olympic Dam iron-oxide copper gold (IOCG) deposit is hosted by the 1.6 billion year old Roxby Downs Granite. Mineralisation is associated with intense, texturally destructive hematite and sericite alteration and brecciation of the primary host rock units, including Roxby Downs Granite, bedded clastic facies rocks, and mafic-ultramafic dykes (Ehrig, McPhie and Kamenetsky, 2012). The vast majority of the rock mass (>90 per cent) is comprised of gangue minerals with less than 10 per cent of deposit mass as sulfide minerals. While the recovery of the sulfide minerals and uranium is obviously critical, the behaviour of the ore through the concentrator and hydrometallurgical circuit is controlled by the gangue mineralogy and therefore its characteristics and abundance are important in a geometallurgy context.

Ore is mined using a sublevel open stoping method underground. Ore from different stopes are mixed on the run-of-mine stockpiles on the surface. There are 5 to 10 stopes online at one time and about 60 stopes are mined each year. Ore is then treated in the fully integrated processing plant to produce copper cathode, uranium oxide concentrate, and gold and silver bullion. Ore is milled in one of the two autogenous grinding mills to expose sulfide minerals from gangue minerals. Bulk sulfide flotation separates the copper sulfide concentrate from the tailings stream. The copper sulfide

concentrate is leached using sulfuric acid to further reduce uranium, fluorine and a portion of hematite gangue. The leached concentrate is smelted in the copper smelter before electrolytic refining to produce copper cathode, Anode slimes are sent to the gold room to produce gold and silver bullion. The majority of the uranium reports to flotation tailings stream which is treated in an atmospheric sulfuric acid leach then concentrated by solvent extraction. About three quarters of the revenue are from copper, with the remaining 20 per cent from uranium and 5 per cent from gold and silver.

Geometallurgy

The driver behind geometallurgy at Olympic Dam is to reduce the technical risk to the current operations and future expansions caused by unexpected mining and process performance issues due to variable ore properties (Ehrig, 2017). The following three objectives of Olympic Dam geometallurgy:

- Develop metallurgical performance predictors that reliably describe the process performance of different ore types and spatially distribute these into the resource block model for use as a fundamental input into mine planning.
- Identify any ores which may be 'problematic' to the current plant, and provide variability data of suitable quality for process plant design and future plant optimisations.
- The chemical, mineralogical, physical property, and 'recovery models', collectively called the geometallurgical model, provide the data required to support the JORC Code 'modifying factors'.

Since the beginning of geometallurgy program in 2006 over 2000 samples have gone through extensive metallurgical tests, all of which carries sufficient information to tag them back to a spatial location in the orebody. Each head sample is assayed for more than 50 elements, and analysed for mineralogy via both Mineral Liberation Analysis (MLA) and quantitative X-ray diffraction (QXRD). Other tests include specific gravity by pycnometer, comminution, flotation and tailings leach conducted on flotation tails generated from flotation. As Liebezeit *et al* (2020) pointed out even though this is a data-rich set from the metallurgical viewpoint, the sample support is far too low to allow the use of traditional geostatistical estimation techniques in Olympic Dam's 20-million block resource block model. Therefore, each geometallurgical relationship (ie metallurgical performance predictor, for example tailings leach acid consumption) is expressed as a function of variables geostatistically estimated in the block model (eg elements, minerals calculated from elements and density). Hence metallurgical performance is predicted on every block in the resource model.

Tailings leach

Flotation tailings are thickened and pumped to a series of leach tanks and the slurry flows through them by gravity. Sulfuric acid and sodium chlorate are added to maintain targeted levels of free acid and oxidation-reduction potential. As an essential reagent, part of the required acid is produced in the acid plant from smelter off-gases and sulfur, and additional acid requirements are transported by road to Olympic Dam. Therefore, prediction of acid consumption is critical to manage the acid balance on-site and manage acid import requirements. Since the main purpose of tailings leach is to extract uranium from flotation tailings, uranium extraction has direct impact on downstream uranium production.

Outliers

As with any data set, we regularly encounter outliers during the geometallurgy test work and in the process of model development. Depending on the underlying reason for their classification as outliers, they should be treated differently. However, how the outliers are handled can have significant impact on the final outcome. According to Napier-Munn (2014):

> *Outliers are values which appear to stand apart from the rest of a dataset in some way. If some mistakes can be identified in the way the outlier(s) were collected then of course they should be excluded because they will unreasonably distort the properties of the data. If not then careful consideration should be given to whether or*

not they should be excluded, because it is possible that they are conveying useful information and are a legitimate part of the data.

This paper includes three case studies from the Olympic Dam tailings leach circuit where outliers were not caused by mistakes, and in fact they were telling us something that we didn't already understand. Hence outlier rejection needs to be investigated so that potentially valuable information is not lost.

CASE STUDY 1 – TAILINGS LEACH ACID CONSUMPTION MODEL

Tailings leach acid consumption model

The primary acid consuming minerals at Olympic Dam include chlorite, sericite and carbonate (ie siderite, with lesser amounts of ankerite and dolomite). The geometallurgy acid consumption model inputs are simply the concentrations of those minerals. Since acid consumption is also a function of the solubility rates of the minerals and tailings leach conditions, coefficients for those minerals varies. Table 1 contains the gross acid consumption model based on mineralogy derived from different methods (ie QXRD, MLA, calculated) for tails leach operated at 70°C for 10 hours at a free acid concentration of 12 gpl and oxidant addition of a minimum of 1 kg/t sodium chlorate. This is the standard leach condition in the geometallurgy program and will be referred to as LFT in this paper. It includes the acid remaining in the liquor at the end of the leach and the acid required to convert sodium chlorate oxidant.

TABLE 1

Summary of the latest acid consumption models under LFT condition.

Model input	Model format	R^2_{adj} (%)	Total # of data used	# of outliers
QXRD*	acid consumption (kg/t) = 28.9 + 19.5 *%chlorite + 4.7 *%carbonate	97	1389	102
MLA*	acid consumption (kg/t) = 28.9 + 18.1 *%chlorite + 5.8 *%carbonate	95	1639	127
Calculated mineralogy	acid consumption (kg/t) = 15.2 + 12.7 *%chlorite + 5.4 *%siderite + 0.6 *%sericite	93.5	1520	144

*QXRD: model input mineralogy measured by quantitative X-ray diffraction.

*MLA: model input mineralogy measured by Mineral Liberation Analysis.

All three models have reasonably good predictive ability but there are some samples that the model statistics show just couldn't predict their acid consumption correctly (outliers in Table 1). This could be caused by:

1. Actual acid consumption for the leach test could be wrong due to operation error or equipment failure
2. Model input for those samples were incorrect. In this case measured or calculated mineralogy might not be accurate
3. There is something else that influence acid consumption but is not explained by the model

The first and second causes could be combined together since they are both caused by errors during the data collection process and if that is the case those sample results should be excluded from model development until the affected test was repeated correctly. On checking all the related information and if all of them are correct, then those data points might deserve extra attention since they are telling a story.

Chlorite measurement

In the original MLA results there are 61 minerals in total and this is referred to as the ungrouped mineral list. For various purposes minerals that behave similarly for the process of interest are grouped together to create a simplified mineral list for that particular purpose and they are referred to as the condensed mineral list. In the ungrouped mineral list there are three types of chlorite. They all belong to the chlorite group but with different endmembers. Chlorite2 is the Fe-rich endmember. Chlorite3 is the Mg-rich endmember and chlorite1 is in between chlorite2 and chlorite3. The nominal chemical formula for each chlorite type can be found in Table 2, although there is still considerable compositional variation.

TABLE 2

chemical formula for different types of chlorite.

Mineral	Formula
Chlorite1	$(Mg,Fe,Al)_3(Al,Si)_4O_{10}(OH)_2$
Chlorite2	$(Fe,Al)_3(Al,Si)_4O_{10}(OH)_2$
Chlorite3	$Mg_2(Al,Fe)_3Si_3AlO_{10}(OH)_8$

Chlorite content represented in the resource block model is calculated from drill core assays and we don't have the ability to differentiate different types of chlorite. Chlorite measured by QXRD is also the total of all types of chlorite.

As more and more samples from new mining areas have undergone geometallurgy testing, we started to see more Mg-rich chlorite samples and this triggered us to investigate how different types of chlorite will affect acid consumption during tails leach. It was also noticed that Mg-rich chlorite samples are all sourced from a localised area (refer to as Area A in the rest of this paper) in the orebody and that area was included in the mine plan for the first time in 2016.

Figure 1 compares predicted acid consumption by MLA model during standard LFT with actual acid consumption. Orange colours are for samples with chlorite3 >4 per cent. The MLA model tends to over predict acid consumption for samples with high chlorite3. In other words, those samples with high chlorite3 consume less acid than predicted by the model. The MLA acid consumption model is based on all geomet samples and the vast majority of them have no or very low chlorite3. The handful of new samples with dominant chlorite type being chlorite3 have been excluded from model development because they don't behave the same as the bulk of the samples so not meet expectation. Also, the model uses the condensed mineral list so all three types of chlorite are aggregated into one.

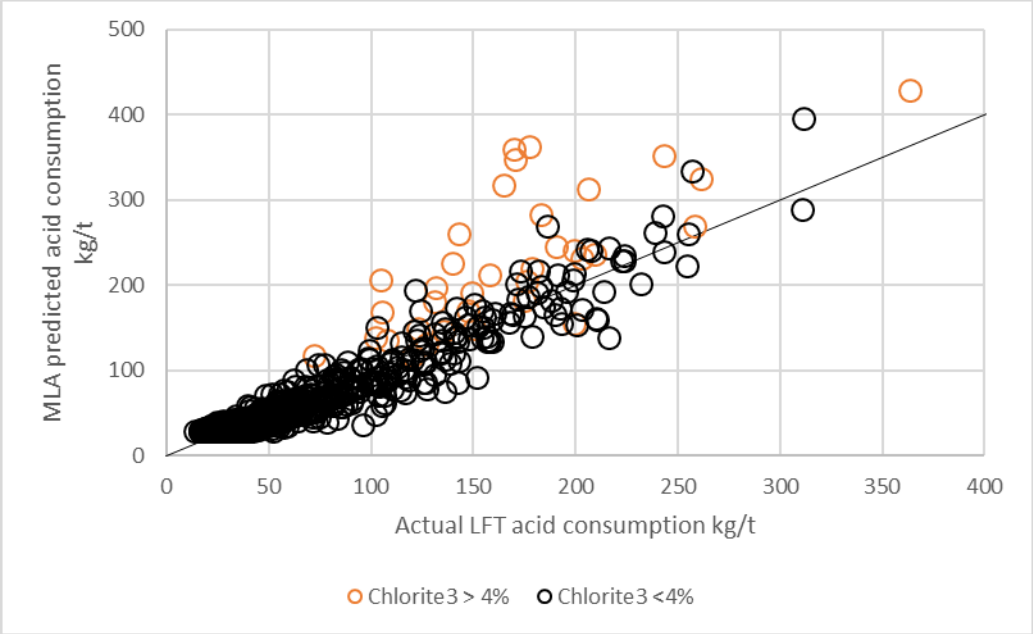

FIG 1 – MLA predicted acid consumption versus actual acid consumption.

In order to understand how chlorite3 consumes acid differently, MLA acid consumption models for Area A and all areas were created using the ungrouped mineral list. As shown in Table 3 both the area specific model and general model suggested that chlorite1 and chlorite2 consumes nearly double the amount of acid chlorite3 consumes. Please note Area A doesn't contain any carbonates so carbonates don't appear in the model.

TABLE 3

LFT acid consumption models using ungrouped mineral list.

LFT acid consumption model	**Model format**
Area A model	Acid consumption (kg/t) = 30 + 19.7 *%Chlorite1 + 20 *%Chlorite2 + 10 *%Chlorite3
All area model	Acid consumption (kg/t) = 29.4 + 15.5 *%Chlorite1 + 20.4 *%Chlorite2 + 12.8 *%Chlorite3 + 9.5 *%Carbonate + 5.6 *%Siderite

Another way to look at this is to group the samples according to their head total chlorite content by 1 per cent intervals and then separate samples with similar total chlorite by dominant chlorite type. For example, if more than 50 per cent of total chlorite is chlorite1 then the sample was classified as a 'chlorite1 dominated' sample. Figure 2 plots the LFT acid consumption kinetic curve for samples with total chlorite at different levels. It shows chlorite2 dominant samples consume more acid than samples with similar total chlorite but dominated by chlorite1 or chlorite3. Chlorite1 dominated samples consume slightly higher or similar acid to clorite3 dominated samples depending on the total chlorite group. Charts for total chlorite at all levels were created but not included here. They all show very similar trend.

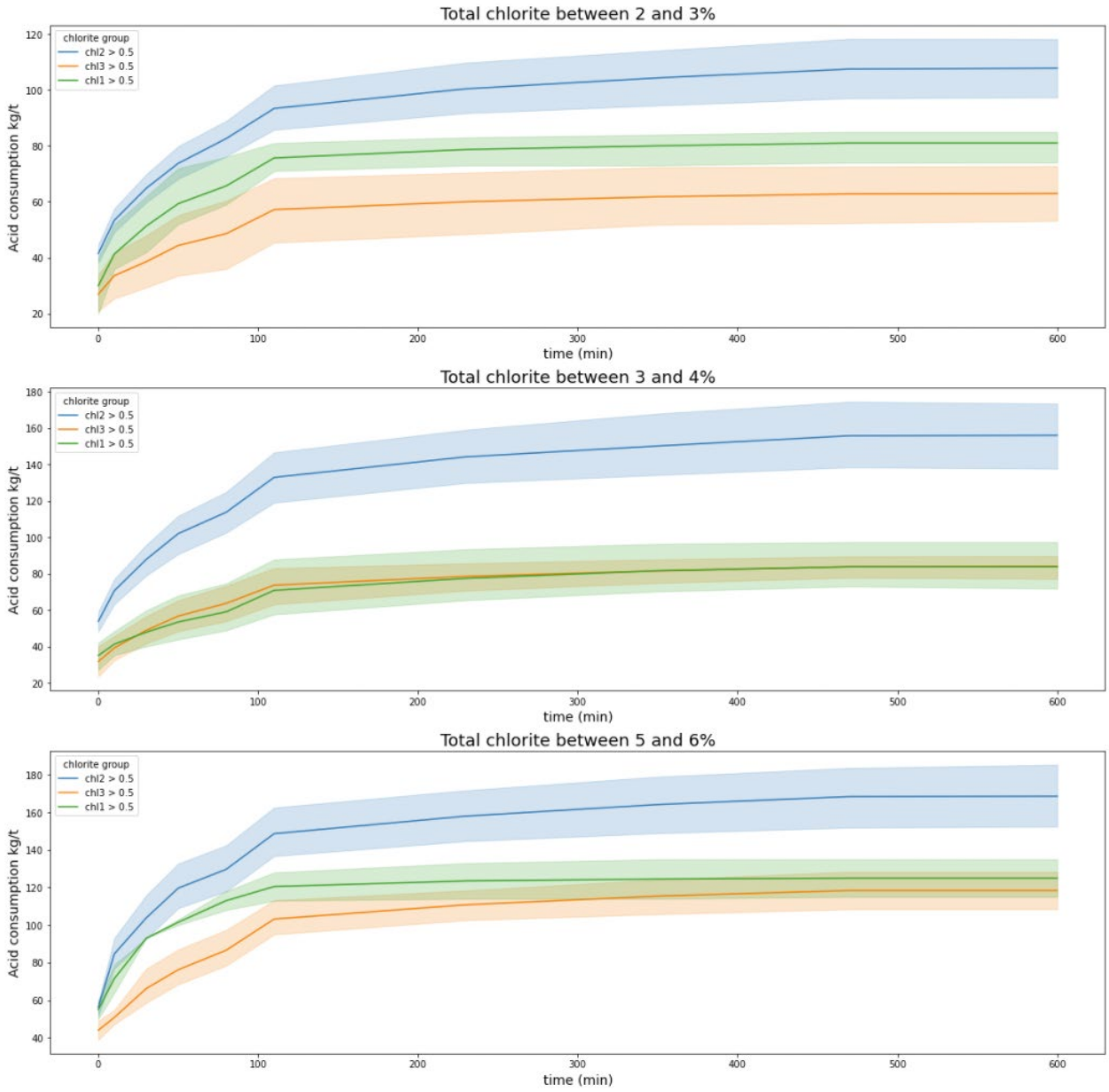

FIG 2 – LFT acid consumption kinetic chart for samples with various total chlorite. Solid line for average, shading represents range of results.

This discovery didn't result in updating the current acid consumption model with ungrouped mineral list at this stage because the current acid consumption based on the condensed mineral list is fit for purpose. There are limited geometallurgy samples (~5 per cent) with head chlorite3 greater than 3 per cent and it will not have material impact on the final model. However, it is used to modify the local estimates of acid consumption for stopes in Area A, which means that this effect is accounted for in short to medium term predictions. However if more chlorite3 rich material became mill feed in the future, this discovery will explain why actual acid consumption is not aligning well with modelled value and the model can be modified accordingly.

CASE STUDY 2 – GELLING POTENTIAL REVIEW

Chlorite content versus gelling

The first gelling event in OD happened on 1st May 2004 when the tailings leach process came to a halt as the easy-flow slurry in the tailings leach tank turned into a gel that could not be pumped nor dewatered. Gelling occurs when silica in solution (sourced from the leaching of chlorite) forms long chain polymers, instead of remaining in solution or precipitating (Ehrig *et al*, 2019). A gelling event

could have a profound impact on uranium production, and if not controlled in a timely manner, it could stop the production of the whole plant and have significant financial implication on the business. Ehrig *et al* (2019) stated mitigating the potential to gel is the primary reason why OD continues to support an ongoing geometallurgy program.

Apart from being a significant acid consumer, numerous studies have demonstrated that chlorite is the main cause of gelling from source material's point of view. As a risk mitigation measure, a chlorite concentration limit of less than 2–3 per cent is placed on the ore sent to the processing plant. Leach conditions also affects the probability of gelling with the same ore more likely to gel under high intensity conditions than a low intensity leach.

Gelling potential against chlorite content was analysed and is plotted in Figure 3. Low intensity leach (LIL) test conditions are 60°C for 10 hours at a free acid concentration of 8gpl and oxidant addition of a minimum of 1 kg/t sodium chlorate. Unlike LFT, LIL test is not conducted on all samples in the geometallurgy program but selected ones. So the LIL data set is smaller than LFT but all samples with a LIL result also has a paired LFT test. Under LFT conditions, gelling starts at 2 to 3 per cent chlorite while LIL tests have slightly higher gelling onset at 3 to 4 per cent chlorite. For both types of leach tests, gelling potential rises with the increase of chlorite concentration for sample with medium to high chlorite then drops for samples with over 8 per cent chlorite. The drop in gelling potential for high chlorite samples was attributed to the small number of leach test conducted on samples in those groups and was not considered a likely behaviour in the plant.

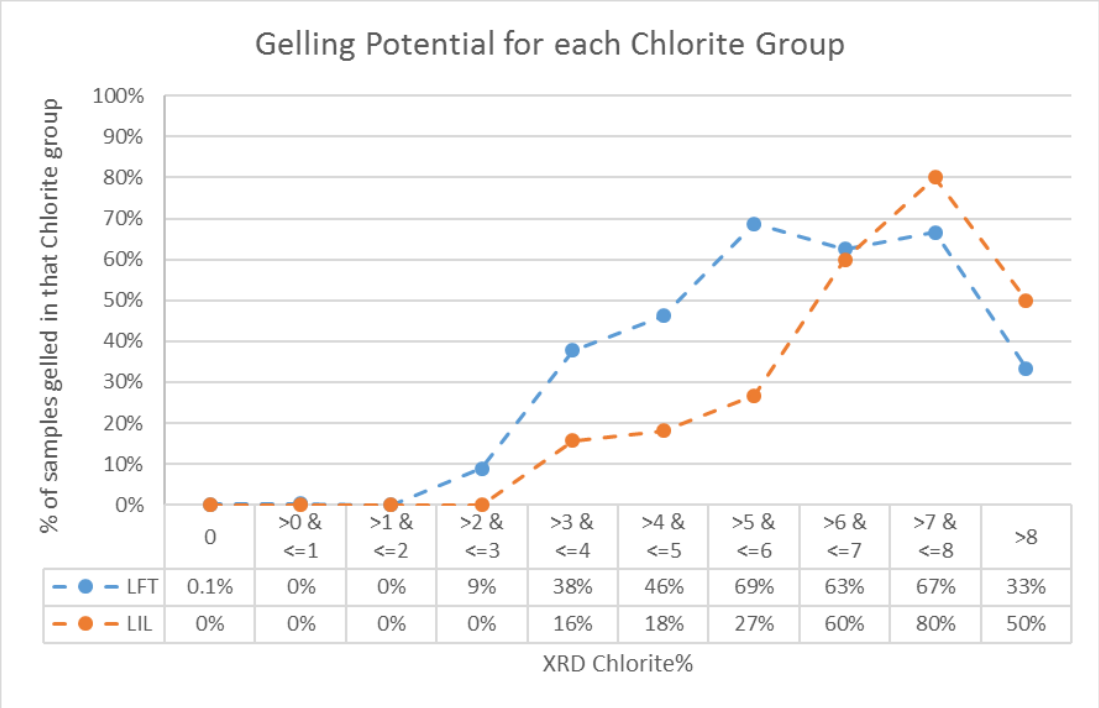

	0	>0 & <=1	>1 & <=2	>2 & <=3	>3 & <=4	>4 & <=5	>5 & <=6	>6 & <=7	>7 & <=8	>8
LFT	0.1%	0%	0%	9%	38%	46%	69%	63%	67%	33%
LIL	0%	0%	0%	0%	16%	18%	27%	60%	80%	50%

FIG 3 – gelling potential for each chlorite group under LFT and LIL.

Table 4 lists the total number of LFT and LIL tests conducted in each chlorite group and it is evident that the number of leach test reduces with the increase of chlorite content. There are several hundred leach tests conducted on samples with no or less than 1 per cent chlorite and only a handful of tests in the >8 per cent chlorite group but is small sample number really the cause of the problem here?

TABLE 4

LFT and LIL sample numbers in each XRD chlorite group

XRD chlorite%	Total # of LFT sample in each chlorite group	Total # of LIL sample in each chlorite group
0	670	269
Between 0 and 1	311	153
Between 1 and 2	112	74
Between 2 and 3	56	45
Between 3 and 4	53	51
Between 4 and 5	26	22
Between 5 and 6	16	15
Between 6 and 7	8	5
Between 7 and 8	6	5
Above 8	9	8

High chlorite = gelling?

Due to the importance of gelling behaviour, gelling is recorded for each geometallurgy sample during laboratory leach test. Technicians observe the settling and thickening status of the slurry throughout the test and record their observations in the data file as ‘gelling rank’. Since visual observation can be subjective to the technician’s experience, the geomet team conducted a series of yield stress measurement during leach tests using a Haake Viscometer 550 to quantitatively measure gelling. Yield stress measurements were compared with gelling results derived from traditional observations. The good comparison indicates gelling results based on visual observations are valid. The use of yield stress measurement does add time and cost to the leach test, and could compromise the uranium extraction result since the slurry does change temperature during the yield stress measurement when it is removed from the hotplate. Therefore yield stress measurement is just used to validate visual observation for gelling rank and has not been part of the standard leach protocol.

For the yield stress measurement work, a range of samples with different chlorite levels and gelling behaviours were selected to have a good representation of existing samples. In the sample selection process, it came to our attention that there are some samples with elevated chlorite (up to 15 per cent) but the gelling rank based on visual observation indicates they didn’t gel. Considering that tailings leach (in the plant) starts gelling at 2–3 per cent chlorite and the laboratory leach observation showing similar gelling onset levels, our previous experience meant we thought it was almost impossible for have a sample with confirmed 15 per cent chlorite and no gelling. To our surprise, yield stress test work on those samples confirmed the visual observation and those samples didn’t gel.

It is unclear what is preventing the high chlorite material from gelling. One hypothesis is that there are some natural occurring substances (eg minerals, or cations/anions) in those samples that can prevent gelling from happening. A composite sample was created by mixing a high chlorite non-gelling sample with an equally high chlorite gelling sample. Yield stress measurement results on the composite sample show the blended composite sample did gel. Chlorite in the non-gelling sample will contribute to gelling when mixed with other gelling samples from other areas.

Unusual gelling behaviour of chlorite3

Further investigation showed all the high chlorite3 non-gelling samples came from a localised area (area A) and they are high in Mg-rich chlorite3. So it was hypothesized that chlorite3 is less likely to cause gelling than the other types of chlorite at the same concentrations.

Figure 4 plots different types of chlorite versus total chlorite for all samples with both LFT and MLA data. Open circle indicates sample didn't gel during LFT and triangle represents gelled sample during LFT. Blue are for samples from Area A while black is for samples from the rest of the orebody. Samples that are high in chlorite2 are most likely to gel (top right chart) while samples that are high in chlorite1 are slightly less likely to gel than high chlorite2 samples (top left chart). Samples with a high amount of chlorite, all as chlorite3, are much less likely to gel under the same condition (bottom left chart). This chart also confirmed that all samples containing chlorite3 (blue symbols) are sourced from Area A.

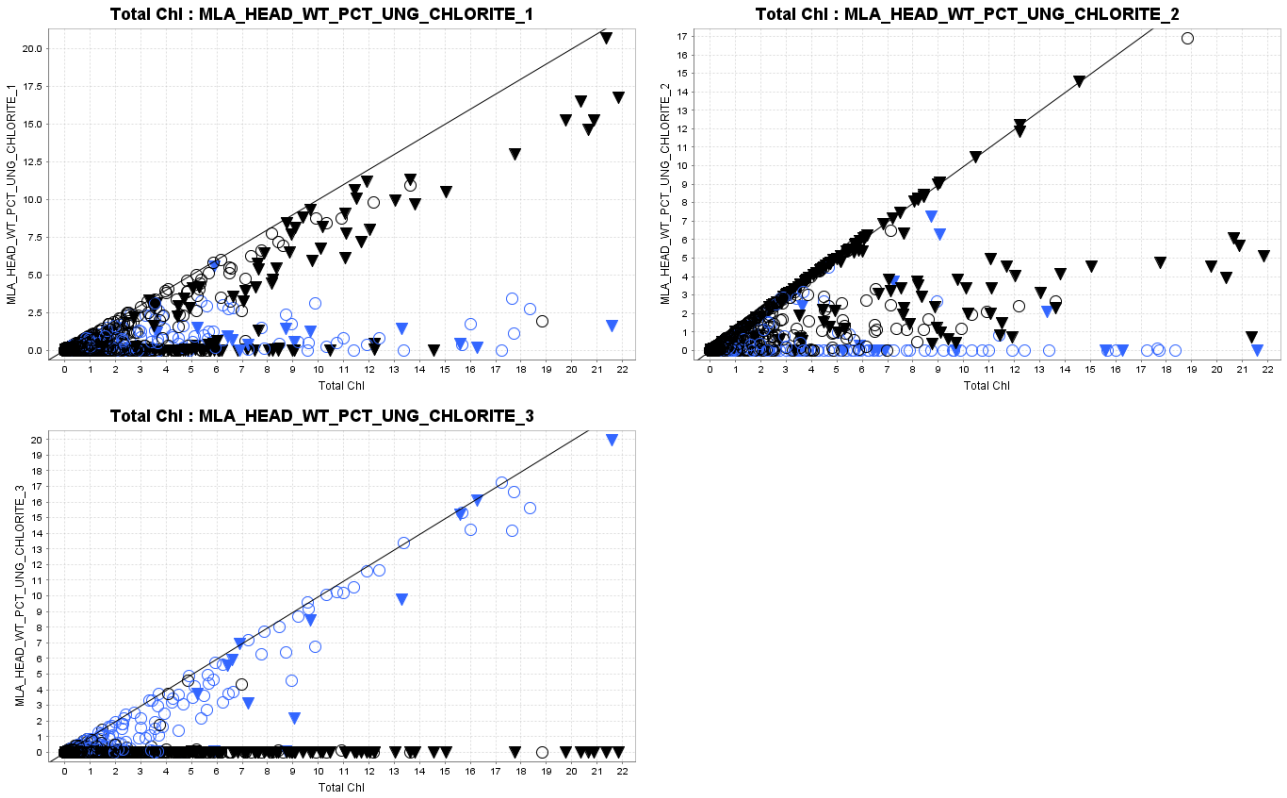

FIG 4 – different types of chlorite versus total chlorite.

This observation ties in nicely with the Case 1 observation. Chlorite3 consumes less acid at a slower rate, which suggests it slowly releases less silica into the leach liquor and hence it is less likely to cause gelling than the other two types of chlorite at the same abundance. It also explains why gelling potential dropped for samples with total chlorite >8 per cent in Figure 3. Actually 80 per cent of the non-gelling samples with chlorite >8 per cent are chlorite3 rich samples with more than 90 per cent of chlorite being chlorite3.

But is that all?

There are some samples containing only chlorite3 which gelled, even though they were a small proportion of the chlorite3 sample population. Are the results just inconvenient that should be ignored or is there something else that we don't know yet? We further extended the analysis to understand why two samples with the same type of chlorite and chlorite content had completely different gelling status by examining different types of chlorite by abundance with all other minerals in the head sample. Particular attention was paid to the minerals which the literature (Tan, Skinner and Addai-Mensah, 2013) has identified as playing a role in gelling. Figure 5 plots head chlorite3 versus fluorite and it shows samples with high chlorite3 (>4 per cent), none of them with fluorite below 2 per cent gelled. Samples with high chlorite3 (>4 per cent) and fluorite >2 per cent have a much higher chance of gelling. This is indicating that chlorite3 on its own without fluorite (or very little fluorite) is very unlikely to result in gelling.

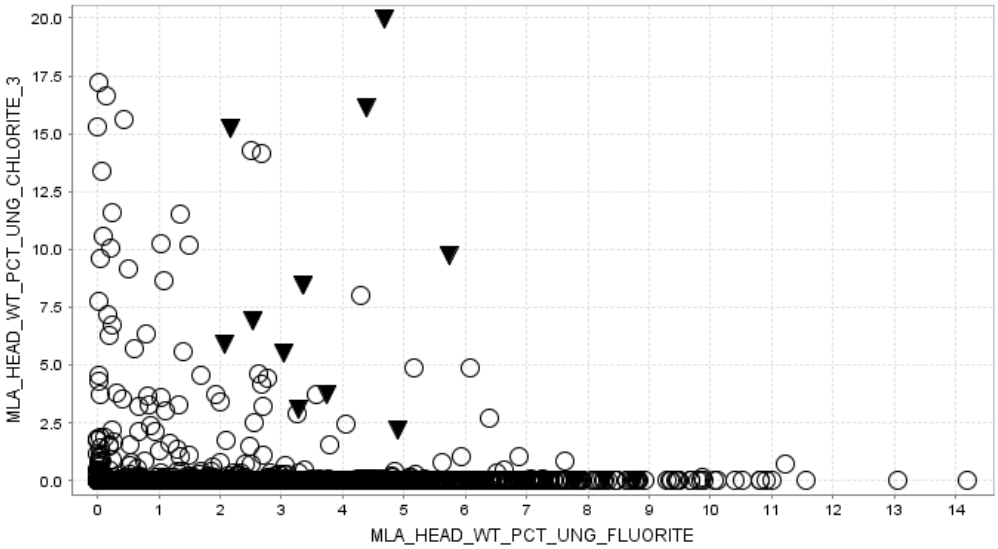

FIG 5 – Head chlorite3 versus fluorite for all samples. Triangle: gelled during LFT; Circle: didn't gel during LFT.

To further verify this theory, leach residue fluorite versus leach feed fluorite are plotted in Figure 6 and samples with head fluorite >2 per cent and chlorite3 >4 per cent were highlighted by different colours depending on if it gelled or not. Gelling samples are orange and non-gelling samples are green. Regardless of head fluorite and chlorite3 contents, gelling samples have a higher amount of fluorite dissolved in liquor during leach than non-gelling samples with triangles located further away from the parity line while circles closer to y=x line. This indicates that fluorine in leach liquor is key for high chlorite3 (and only chlorite3) samples to gel.

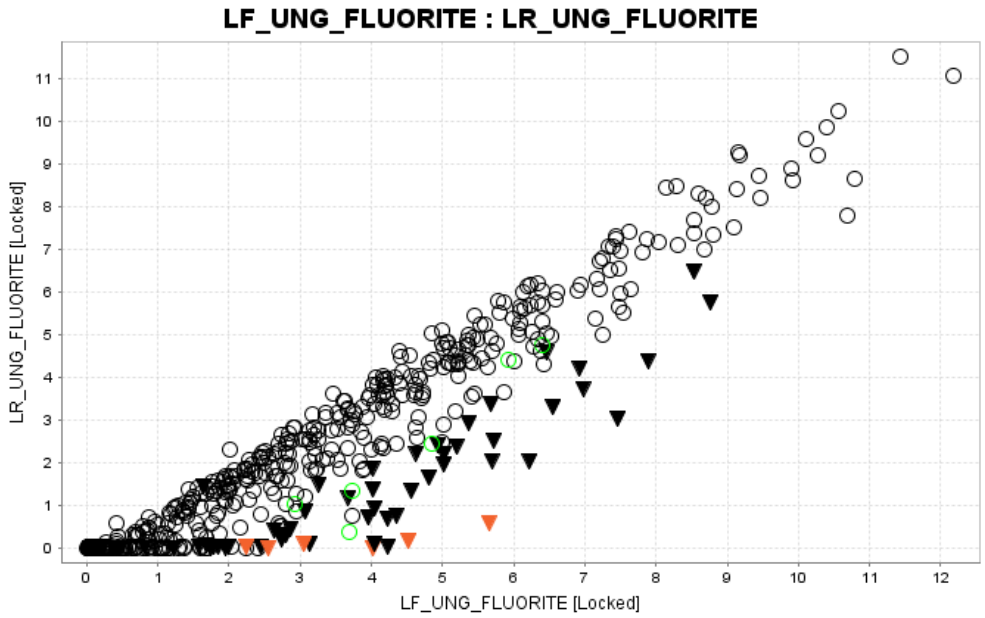

FIG 6 – leach residue fluorite versus leach feed fluorite.

Currently this observation cannot benefit plant production since mill feed is a blend of multiple stopes plus a small portion of development on any given day and fluorite content is well above 2 per cent all the time. However, it does provide direction for further research into the gelling phenomenon in tails leach.

CASE 3 – URANIUM EXTRACTION

As a critical production metric, uranium extraction during tailings leach and uranium grade in leach residue is measured in all geomet samples. As the first results became available in 2006, the leach

residue uranium grades were compared with plant data. At that time plant leach residue U_3O_8 grade was around 150 ppm. The first geomet sample had leach residue under the same leach conditions with more than double the amount of U_3O_8 at 370 ppm. The next couple of samples dropped slightly to about 300 ppm but still much higher than what the plant was getting. Figure 7 shows the leach residue box and whiskers chart of plant and the first 30 geomet samples. It is obvious that the distribution of those two populations are markedly different from each other.

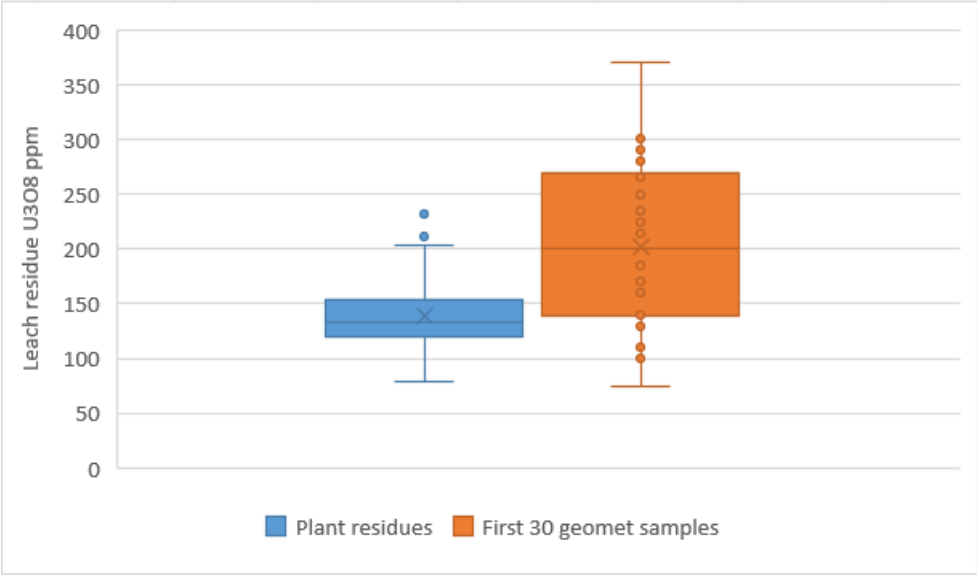

FIG 7 – comparison of leach residue U_3O_8 grade between plant data and the first 30 geomet samples.

There was clearly something going on with those results and the following actions were taken to trouble shoot the issue:

- Leach residue samples were split into several subsamples and sent to different laboratories for assaying. They came back on the same level as original results
- Plant material was leached under the same conditions by the same laboratory and the same leach residue grade as plant was achieved
- Leach test under the same condition on the same sample was conducted by a different laboratory and the same leach residue as the original laboratory was received

Those check results gave us high confidence in the data by eliminating the possibility of sample splitting error, assay error and test error and also confirmed that the leach test is a good representation of plant operation. Since there was no mistake in the data generation process, we cannot remove them just because they are dramatically different from what we expected or where the bulk of the samples are. The unusually high leach residue uranium grade must be associated with the sample itself. The geomet team continued on testing new samples with the same method while investigating the root cause of low uranium extraction during tailings leach. It turned out that all geometallurgy samples at the beginning of the geometallurgy program were sourced from the Southern Mine Area (SMA) as future material, but the processing plant had only processed ore from the Northern Mine Area (NMA) up to that time. It happens that the relative proportions and absolute concentrations of the uranium minerals in the SMA are significantly different from the NMA. The SMA ores have a smaller proportion of the easy leaching uraninite as illustrated in Figure 8. Liebezeit *et al* (2020) explained the leach characteristics for various uranium minerals in more detail.

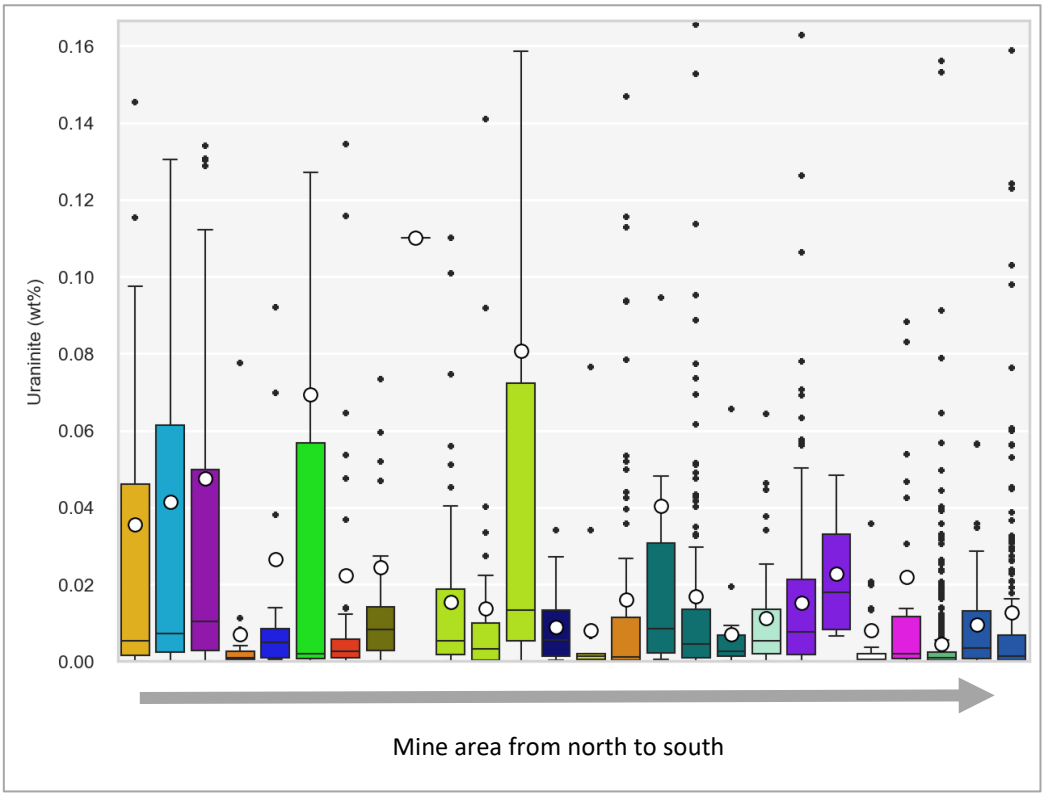

FIG 8 – weight percent of uraninite in head from north to south.

This is an excellent example of the reason for geometallurgy – that future material doesn't necessarily have similar behaviour as past material. Geometallurgy tests on future material enables us to predict potential processing issues that the plant would face in the future and allows time to make adjustments accordingly to avoid any negative impact on production. Those 'anomaly' geomet samples informed us of increase in leach residue uranium and drop in uranium extraction for SMA ores and equipped us with the right information to adjust our prediction of uranium in leach residue when SMA material came online. Figure 9 plots the plant feed and leach residue U_3O_8 since 2006 and the dotted line indicates when the plant started processing SMA ores. Straight away there was an upward shift in leach residue uranium grade. Since we forecast this would happen due to the different composition of SMA uranium mineralogy, it was not a shock when leach residue uranium grade jumped as SMA ores hit the mill. This actually validated our prediction.

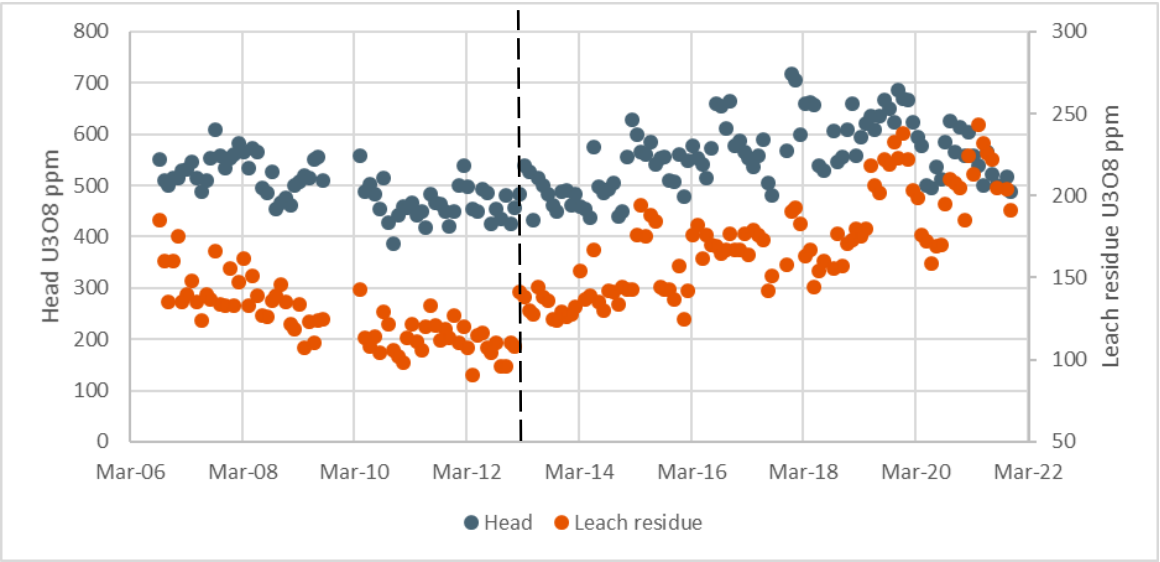

FIG 9 – Plant feed and leach residue U_3O_8 grade since 2006.

CONCLUSIONS

Outliers are inevitable during data collection and model development but they shouldn't be excluded just because they returned unexpected results or are minorities that sit outside the 'normal' range. Thorough investigation should be conducted to rule out the possibility of any mistakes during sample preparation. If they are caused by mistakes or errors during the test process then they should be removed from the data set since including them will unavoidably skew the data set. However, if there is high confidence in the results, 'outliers' may deserve extra attention as they are trying to tell a different story and further investigation quite often broadens our knowledge on the subject.

ACKNOWLEDGEMENTS

The authors appreciate the support from BHP Olympic Dam to publish this paper.

REFERENCES

Ehrig, K, 2017. Geometallurgy – what do you really need to know from exploration through to production?, in *Proceedings We are Metallurgists, Not Magicians 2017*, pp. 33-36.

Ehrig, K, Liebezeit, V, Smith, M, Pewkliang, B, Li, Y and Macmillan, E, 2019. Effect of Gangue Mineralogy on Flow Sheet Design and Plant Operation – Olympic Dam, in *Proceedings MetPlant 2019*, pp 15–27 (The Australasian Institute of Mining and Metallurgy: Melbourne).

Ehrig, K, McPhie, J and Kamenetsky, V S, 2012. Geology and Mineralogical Zonation of the Olympic Dam Iron Oxide Cu-U-Au-Ag Deposit, South Australia, in *Geology and Genesis of Major Copper Deposits and Districts of the World: A Tribute to Richard H. Sillitoe* (eds: Hedenquist, J W, Harris, M and Camus, F), Society of Economic Geologists Special Publication 16, pp 237–268.

Liebezeit, V, Ehrig, K, Li, Y, Macmillan, E, Pewkliang, B and Smith, M, 2020. Mineralogy and Modelling – Predicting Uranium Leach Extraction at Olympic Dam, in *Proceedings of the 4th International Uranium Conference, U2020* (The Canadian Institute of Mining, Metallurgy and Petroleum: Montreal, QC).

Napier-Munn, T, 2014. *Statistical methods for mineral engineers – How to design experiments and analyse data*, (Julius Kruttschnitt Mineral Research Centre: Queensland), 640p.

Tan, H, Skinner, W and Addai-Mensah, J, 2013. Influence of fluorite on the isothermal leaching and rheological behaviours of chlorite mineral pulps at low pH: International Journal of Mineral Processing, v 123, pp 1–8.

Operational geometallurgy for mass mining

B Newcombe[1] and G T Newcombe[2]

1. Principal Metallurgist, OptiFroth Solutions Pty Ltd, Orange NSW 2800.
   Email: biancanewcombe@hotmail.com
2. Director, OptiFroth Solutions Pty Ltd, Orange NSW 2800.
   Email: geoffreynewcombe@gmail.com

ABSTRACT

The development of geometallurgical programs for the prediction of future ore performance (recovery) can be a complex balancing act. Significant front end engineering and assumptions on future revenue streams rely on geometallurgy study programs. The scope of these study programs are frequently dictated by financial constraints that affect both the number of samples and the amount of test work that is able to be completed. This paper provides practical insights for those working in mass-mining operations on key aspects of predictive geometallurgy to make the most of these samples including:

- sample selection methodology – grade profiles, mineralogy, host rock lithology
- sample number requirements – development of orebody specific sample selection methods
- metallurgical test work flow sheet development
- primary variable determination and analysis
- integration with geology and mine planning departments
- integration with financial modelling for life-of-mine.

Practical examples are presented on the methodologies used. The intention is to leave the reader with an informed starting point when embarking on a future ore test work program.

INTRODUCTION

Orebodies, by their very nature, are rare and are required to be assessed on limited data capture. Conversion of discoveries to projects requires careful planning of resource definition (res-def) drilling that is most often carried out in a way that is aligned to meeting JORC geology reporting standards.

The definitions around the requirements of metallurgical assessment lags a long way behind geological assessment, however this is likely to change in coming years with many companies taking steps to ensure the projects they have coming online in the near term are compliant with the standardised metallurgical assessment requirements.

This paper considers the sampling methods used by the lead author for mass-mining (large scale developments) to ensure adequate sample coverage. The development of appropriate test work programs with a view to the end user requirements (mine planning) is discussed. Data usage in Life-of-mine (LOM) systems and the inherent risks and errors associate with this is also considered.

What is Geometallurgy? According to Wikipedia…..

> *Geometallurgy relates to the practice of combining geology or geostatistics with metallurgy, or, more specifically, extractive metallurgy, to create a spatially or geologically based predictive model for mineral processing plants.*

The practical reality of working as a geometallurgist involves working within multi-disciplinary teams (geology, processing, mining and environment). Future ore studies work is generally managed within the mining department (mine planning or mining studies). The primary deliverable of a geometallurgical study is typically ore processing plant recovery models for valuable metals in future ore sources. To ensure compatibility with mine planning systems, simple, head-grade based models that are spatially discrete (within a mine planning block model) are required. Final models should be developed around variables that are measured consistently across the orebody and with sufficient data density to ensure propagation of error does not cause issues. Secondary deliverables include

mill throughput forecasting (utilising hardness test work data); the impact of grind size on recovery (using targeted test work at multiple P80s), concentrate grade forecasting, consumables optimisation for OPEX evaluation, and tailings management (including cyanide detox requirements).

Geological domains do not necessarily correlate with observed metallurgical performance and determining a definitive 'geometallurgical domain' cannot be undertaken by either geology or metallurgy in isolation. The process of developing a site specific geometallurgical system involves defining amongst the entire team (geology, mining and metallurgy) the domains that are meaningful to performance, not geological formation alone. Key questions requiring consideration:

- Do the geological domains correlate to metallurgical domains?
- Do the chosen domains separate key mine planning requirements?
- Are the domains easily identifiable using either, or a combination of:
  - spatial location (can the orebody be zoned?)
  - lithological properties
  - head grade (of one or more elements) or
  - mineralogically driven.

Host rock lithology types do not necessarily drive the recovery of target payable elements, different lithology types can report similar metallurgical performance. To successfully determine relevant recovery domains, mineralogy is key for success, and textural changes in the ore should be part of the mineralogical assessment process. In order to relate mineralogical measurements to the *in situ* properties of the ore, a coarser size class is required for analysis (as opposed to mill discharge sized material).

Ore samples are characterised using detailed mineralogical methods and hardness testing. Ore performance is assessed on the response observed using a standardised hydrometallurgical (flotation and/or leaching and/or gravity etc) test work procedure. This procedure should provide a meaningful reflection of anticipated performance of a processing route at the full plant scale (testing for each major unit operation).

When performed correctly, geometallurgical characterisation of ores allows a profile of expected ore performance to be developed across an orebody for use in long-term forecasting and planning. The type of test program discussed here is not intended to be used for short-term production planning, but is suitable for determining long-term economic assessment and planning. This paper will discuss the methods developed to gather and interpret primary sampling and data types for use in long-term modelling of ore performance of large deposits (>200 Mt) or ore zones (50–200 Mt). Details of ore specific recovery modelling will be presented in a subsequent paper.

SAMPLE SELECTION

Appropriate sample selection is critical for successful modelling of key metallurgical variables. Traditionally geological lithology types are used in conjunction with the grade distribution of target elements within the block model. The number of samples required and the spatial distribution of these samples is often dependent on the level of study the results are being used for. Typically, in a desk top or pre-feasibility study there will be limited drill holes available to select from and the generated data is used for a high-level overview assessment of anticipated performance. If the ore performs well on these samples, then a targeted drilling program (geomet drilling) is undertaken to ensure coverage of ore types and grade distributions. To have a successful geomet campaign there are a number of key questions to consider:

- How many host rock lithologies are there?
- How does the grade vary of recovery targets?
- Variations in the presence of deleterious elements (possible preg robbing, smelter penalty elements etc)?

- Will mineralogical domain sampling be used (eg. high pyrite versus low pyrite; bornite versus chalcopyrite, tellurides, which depends on the nature of the orebody)?
- Differences in application of processing routes.
- Metallurgical sample size requirements.

The sampling method used is dictated by the size and style of deposit. In large scale mass mining operations where hundreds of millions of tonnes are expected to be mined, the application of a traditional approach can result in an economically crippling number of samples required to be metallurgically assessed to meet corporate orebody evaluation guidelines and 'matching' of statistical distributions of the grade of target elements with the distributions of these elements within the ore reserve block models. In addition to this statistical matching, the samples must be spatially distributed across the ore zone to ensure all regions are covered and there are no 'blind spots' for estimation of recovery forecasts. Figures 1 and 2 shown the distribution of two key elements within an ore deposit using data from the block model. Both elements are payable and require recovery forecasting to LOM. For the purposes of the discussion here these two target elements will be known as X and Y. Typically, the distribution of these elements in the head grades of metallurgical samples should be as close as possible to the distributions within the block model.

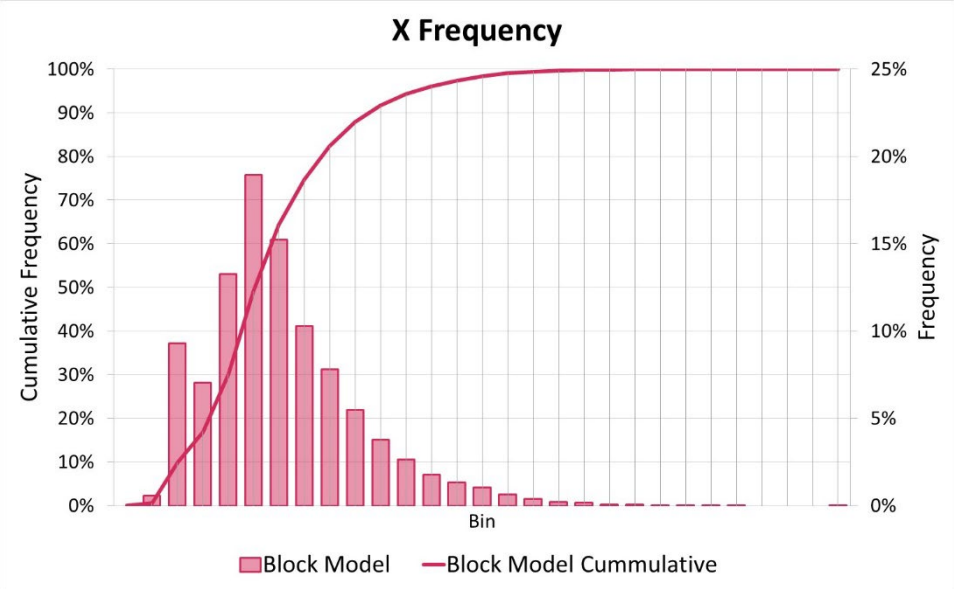

FIG 1 – Distribution of element X within the block model.

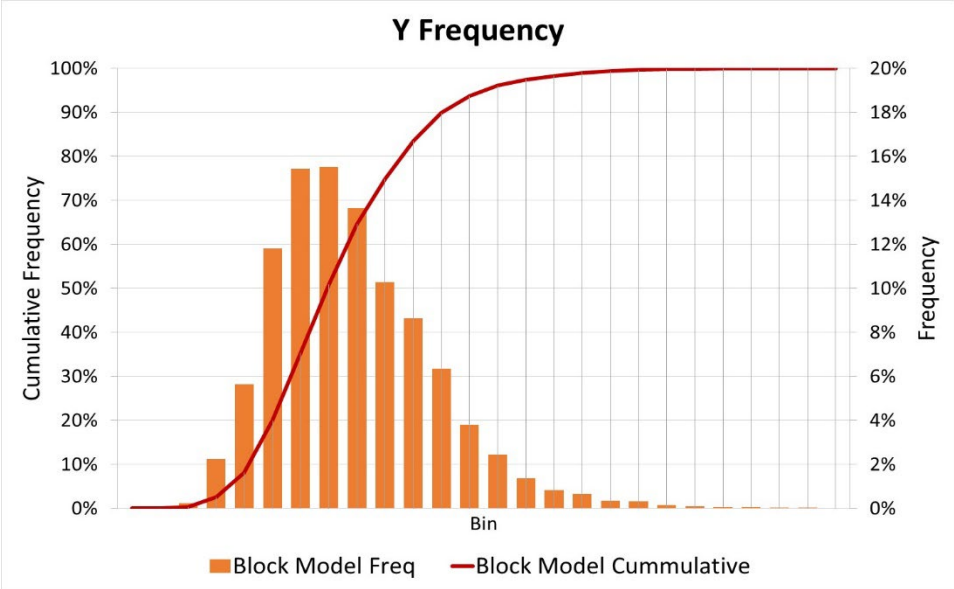

FIG 2 – Distribution of element Y within the block model.

Both elements X and Y provide the economic basis of the operation, they are processed together, recovered together and consequently sold together. The use of the separate distributions (Figures 1 and 2) to select samples for metallurgical testing can make sample selection a time-consuming process as drill hole intervals are individually assessed and reassessed in an attempt to match the metallurgical sample set distribution with that of the block model. Where this approach has been applied to large ore zones a spatial bias is often observed.

A different approach has been developed by the author[1] in which samples within large ore zones (>200 Mt) are taken at regular spatial intervals to ensure there is no bias from one area of the orebody to another. This method is not applicable to small or narrow deposits where other considerations must be taken into account. The spacing of the samples (in a grid format) is determined by the expected number of samples required and the analysis of key elemental data in combination (as opposed to individual elemental histograms). This approach has been successfully applied to a number of discrete ore zones in mass mining applications. Reverse analysis of input data has shown that the approach provides excellent statistical matching of elemental distributions while ensuring appropriate spatial coverage and weighting of all samples. This further ensures the consequent metallurgical models are not spatially biased towards one area of the ore zone.

Application of this method involves placing a 3D grid over the ore zone and selecting a single sample from a hole within each 3D space. In very large deposits, the grid layers could be 100–200 m apart in vertical height (Z direction) and 50–100 m apart in width and depth directions (X and Y directions within mining systems). The scaling will depend on the geometry of the deposit under consideration. Holes should be as close to vertical as possible so height (Z) within the ore zone can be isolated for modelling purposes.

Sample weight is a critical requirement to determine the length of core to be used. In programs managed by the author of this paper (Newcombe), a run of 30 m of half HQ core generally provides sufficient material for a full set of metallurgical analyses (approximately 100 kg). This requirement must be achieved by all samples to ensure they are all equally spatially weighted for modelling purposes. For this approach to be successful, each sample must be metallurgically tested individually. Any compositing of samples will not allow for spatial models to be developed.

Each block of ore contains both element X and Y together. Analysis of elemental data from the block model shows the range of grades of X and Y within each individual block. Figure 3 presents this data graphically, where each data point is semitransparent (darker colour = more data points). The average grade of all blocks is highlighted in blue.

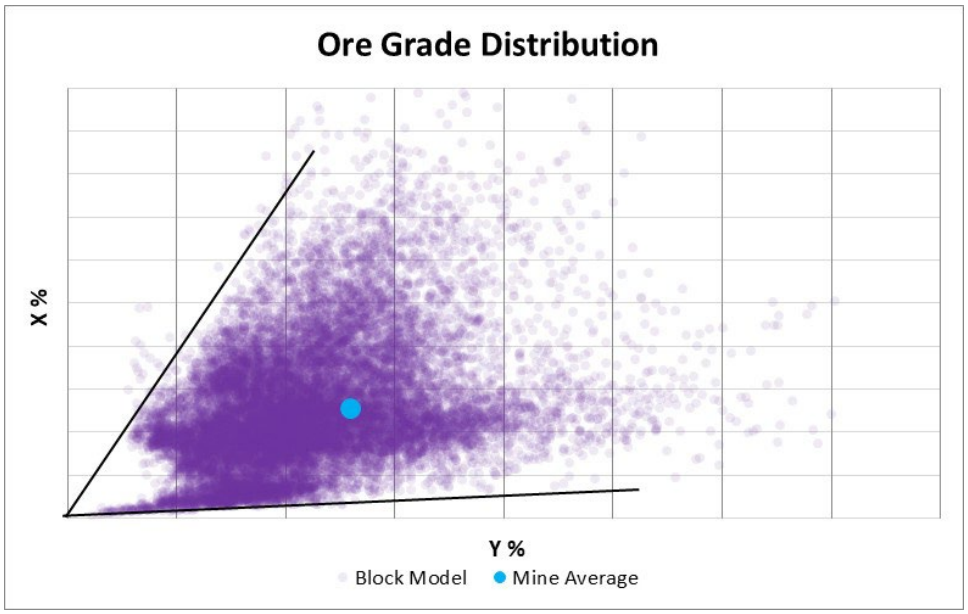

FIG 3 – Block model output for elements X and Y.

Each block will be mined at a given time based on the mine plan. Mine planning can estimate when each block will present to the mill. Mining simulation and scheduling programs such as PCBC,

Deswick, XPack, DataMine or Whittle can estimate the average grade of material to be presented to the mill. Mixing occurs within the mining process itself and as ore is moved from the pit or underground. Don't forget stockpile mixing! An output of expected daily head grades and source material type (lithology or ore zone classification) should be produced by mine planning to allow an estimate of material likely to be presented to the processing facility.

Figure 4 shows the expected daily average mine output for LOM of the material in Figure 3. Mill feed material is generally within the 'triangle'.

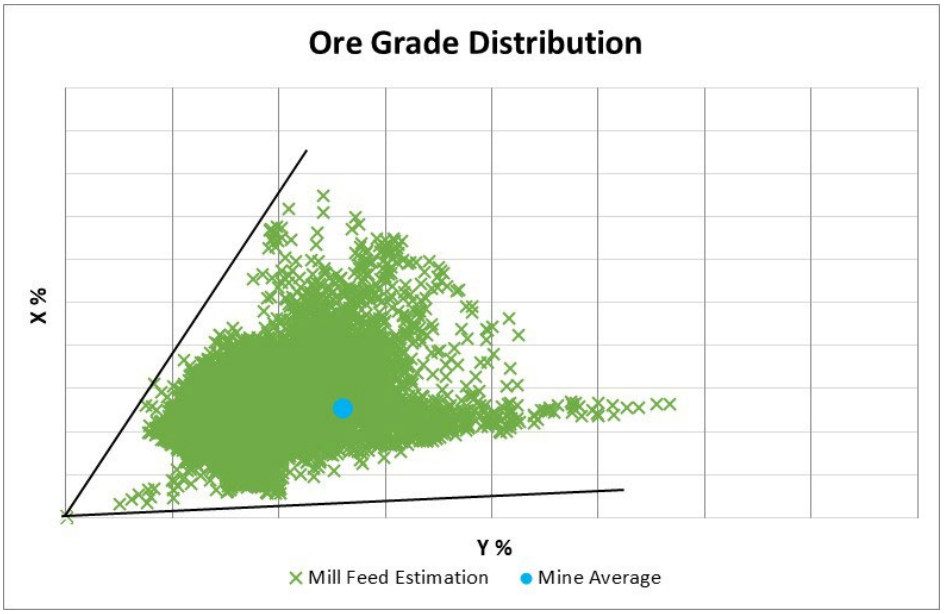

FIG 4 – Mine plan output mill feed grade estimate of element X and Y.

Similarities are observed between the two data sets; however, the extremities of the block model data have now been effectively blended out by the mining process. This ore zone has been sampled using the grid approach, with samples selected indicated on Figure 5 in red. Figure 5 also includes the backdrop of data from Figures 3 and 4 for comparative purposes. The average grade of the sample set is indicated in yellow and is observed to be very close to the orebody average grade (blue).

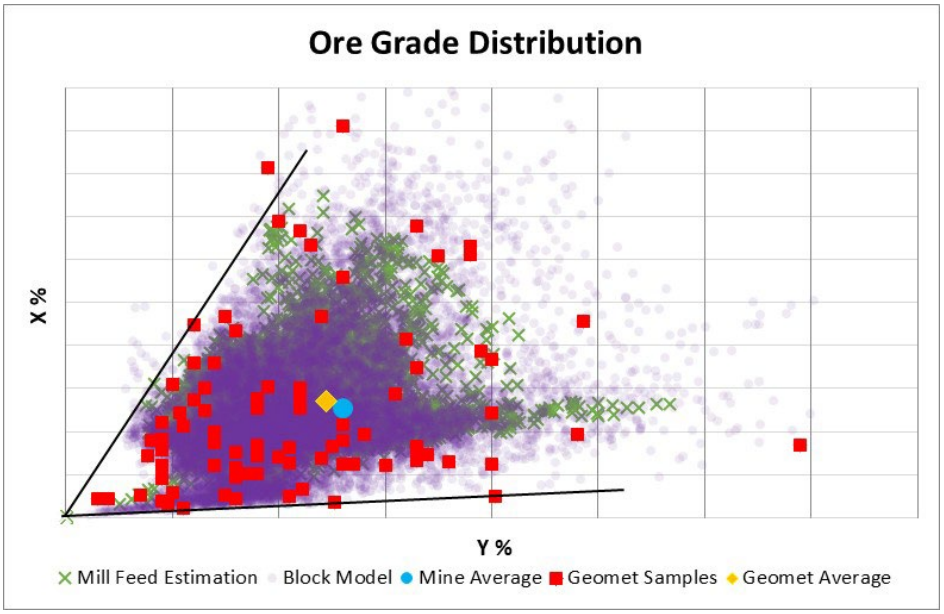

FIG 5 – Combined sample analysis.

When the distribution of the head grades of the samples used are directly compared with both the block model and mine plan output (Figures 6 and 7), the similarities in the grade distributions are clearly observed. This indicates that the sampling method (spatially weighted grid-based approach) has covered the combination of X and Y grades satisfactorily and has also incorporated the extremities of behaviour (very high or very low-grades). Further analysis shows that in addition to good spatial coverage, all relevant lithology and mineralogical types have been analysed. The implementation of this approach to sampling has allowed the successful development of recovery algorithms that have been in use for forecasting plant performance for many years at the operation under consideration. These forecasting models track within ±2 per cent of actual plant performance.

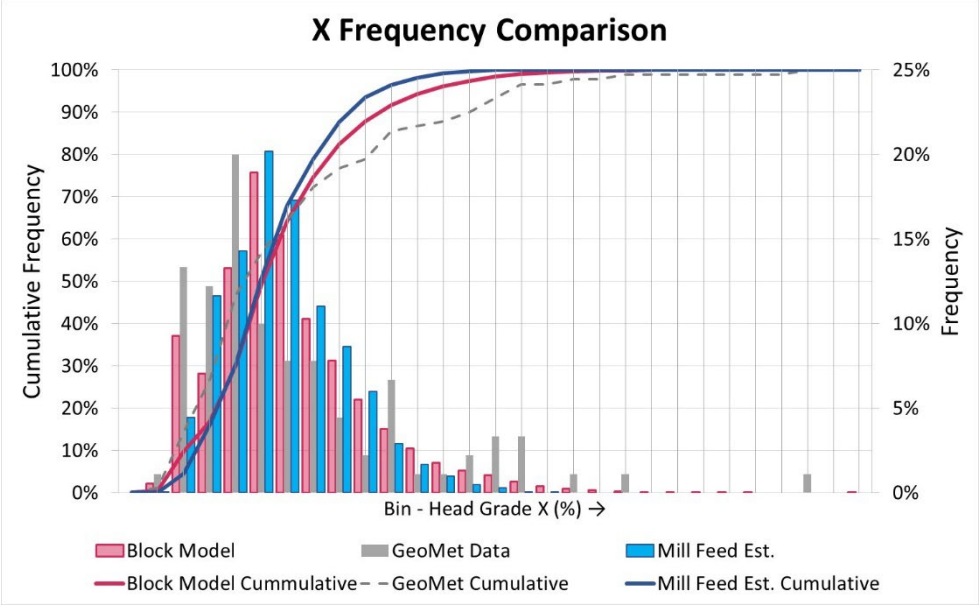

FIG 6 – Comparative distributions of element X.

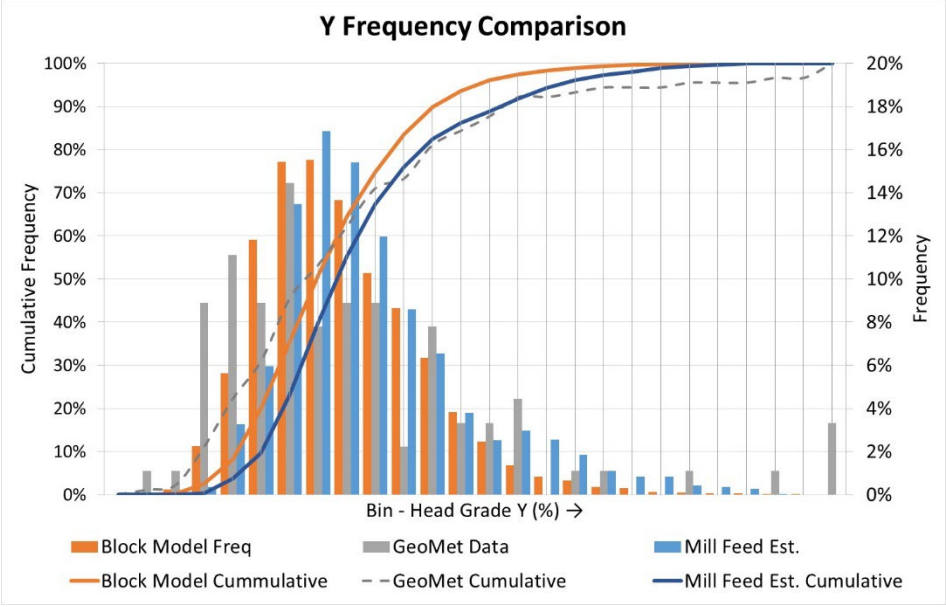

FIG 7 – Comparative distributions of element Y.

STANDARDISED TEST WORK PROGRAMS

Once sample selection has been completed, the individual composites require metallurgical testing. In existing operations the site standard test that represents plant recovery should be used. In new deposits where no current standard is in place, a test work regime should be established that best represents the likely unit operations and processing route for the anticipated plant. A standard test work regime would typically incorporate the following elements:

- Sample geo-chemistry (full multi-element analysis).
- Modal mineralogy assessment for ore texture.
- XRD for clays or targeted Au deportment work for Au deposits.
- Hardness testing with a view to mill simulation. Must include as a minimum:
  - SMC (SAG Mill Comminution) Test.
  - BBWi (Bond-Ball Work Index).
- Further hardness testing should consider:
  - CWi (Crusher Work Index).
  - BRWi (Bond-Rod Work Index).
  - Ai (Abrasion Index).
- Standard set of tests for each major unit operation of the plant including (as appropriate):
  - Flotation testing.
  - Leaching methods.
  - Gravity (GRG) and Au, Ag, Cu diagnostics.
- Targeted testing including (flow sheet dependent):
  - slurry rheology.
  - flotation cleaner circuit configuration.
  - grind sensitivity (both primary grind and regrind).
  - reagent consumption.
  - recycle stream impact.
  - site water impact.
  - environmental impacts (acid mine drainage, tailings properties).

There may be other tests required dependent on the nature of the deposit under consideration. An example of a test work flow sheet is presented in Figure 8.

If possible, a point load test (PLT) should be included on a full core sample taken prior to and after the end of the 30 m of geomet core and a segment in the middle (15 m). PLT is used by structural geologists and mining engineers in their structural evaluation of deposits. It is recommended that wherever possible PTL is incorporated into the geomet program to allow comparison between the geotechnical and geometallurgical data sets. It is important to note that PLT must be done on a piece of whole core and that the test is considered destructive, ie the material used for the PTL cannot be used again for any other type of hardness evaluation. The PLT needs to be incorporated into the core processing procedure to ensure that samples are managed correctly. Once the core has been cut lengthways, the PLT is no longer possible.

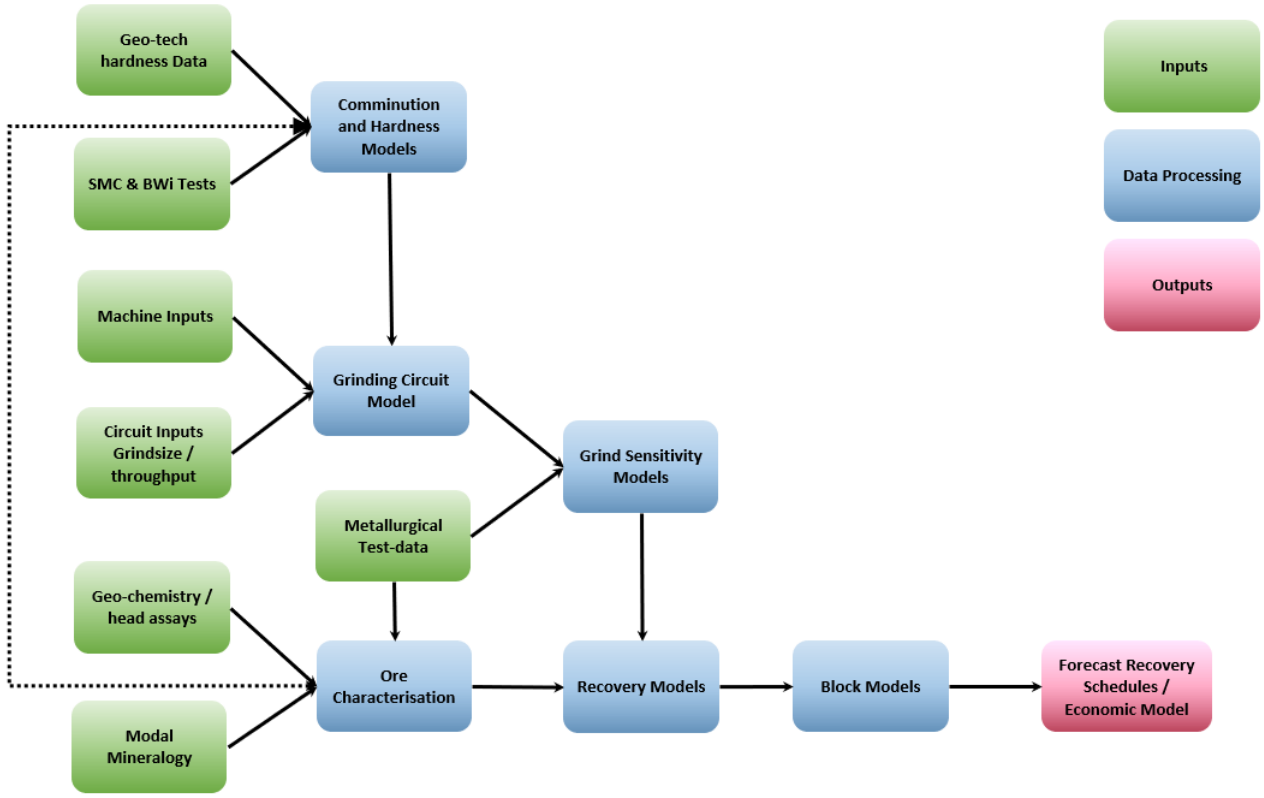

FIG 8 – Example geomet testing flow chart to produce data ready for scheduling and recovery forecasting.

The final destination of the geomet work is the recovery models used for the economic evaluation of a deposit. This output must be compatible with the data existing in both the block model and the mine planning system. This usually dictates that any recovery algorithm should be based on universally measured elemental head assays. The metallurgical algorithms developed should also reflect the different metallurgical domains, with each domain having its own algorithm as required. Ore characterisation work then becomes a primary consideration to the segregation of ores within the block model. Figure 9 shows how the recovery models are used in conjunction with mineralogical evaluation and primary ore hardness characteristics to culminate in the final set of recovery algorithms for an ore zone. Note that there is interaction between hardness models (for circuit simulation), ore characterisation (various mineralogical inputs and lithology considerations) and the recovery models themselves. The process of finalising the recovery models is iterative between these three major inputs as they each affect the other and the consequent final result that is used by mine planning. In the authors' experience, ores are regrouped several times before metallurgical domains can be finalised.

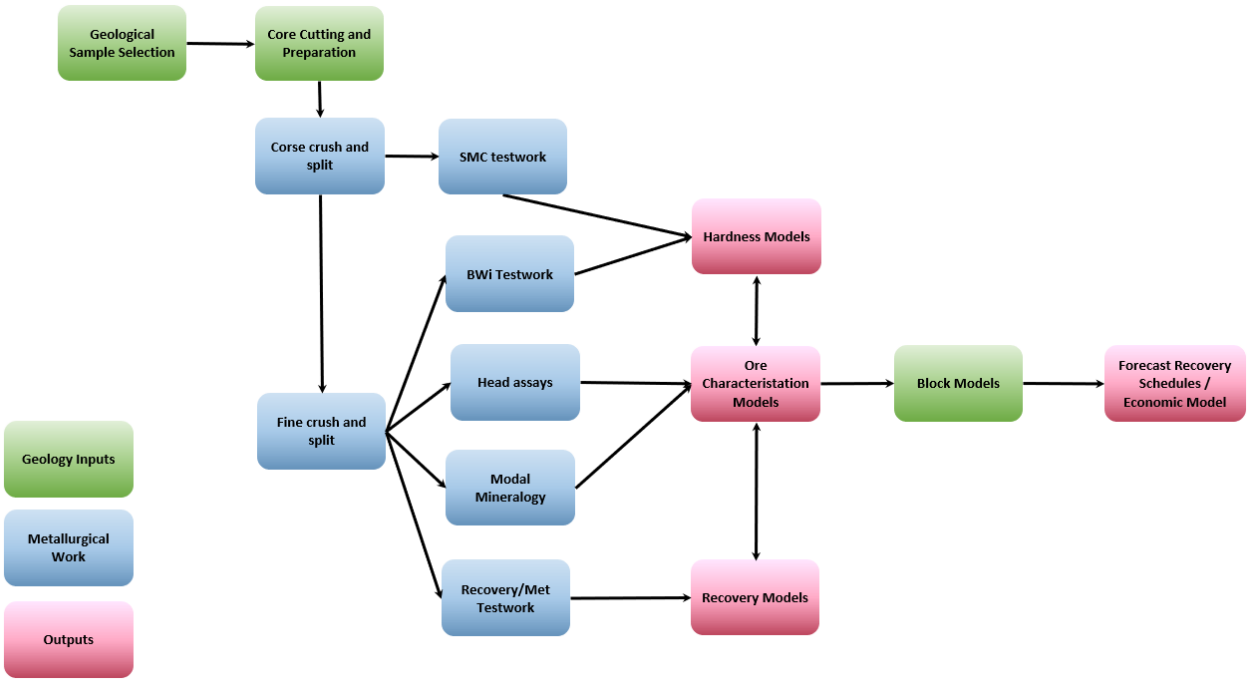

FIG 9 – Geometallurgical modelling process flow chart.

DATA EVALUATION

Large amounts of data are generated by complex metallurgical evaluation. Mineralogy data is used in combination with metallurgical response data in an iterative process to determine whether grouping of samples is achievable and appropriate.

Comminution data

An example of hardness data modelling using mineralogical inputs is presented in Figure 10. The original data set in this case is for Ore A, which was modelled using key minerals for their impact on ore hardness properties. A subsequent data set from a neighbouring ore zone (Ore B) was generated and tested against the Ore A data set to determine if any measurable change in comminution properties could be observed which may change the mill output P80 to hydrometallurgical processing. The mineralogy data indicates that these two ores should process in a similar way through the plant.

The hardness parameters must be relatable to a universally measured variable in the mine planning system to allow an output of data over time. In this case spatial location and elemental head assays were available to be used. In this case the Ore A BWi is mineralogically related to quartz, sphene and chlorite. Regression analysis of elemental data and spatial tags allowed a model to be developed that uses Fe assays for BWi and Dwi, with DWi found to be spatially related to height within the ore zone. Note that these models will be bounded based on their source data set.

$$\text{Ore A BWi (kWh/t)} = 18.2 + 0.797 \times \text{Fe\%} \quad (1)$$

$$\text{Ore A DWi (kWh/m}^3\text{)} = 25.2 + 0.438 \times \text{Fe (\%)} - 0.0037 \times \text{Z (m)} \quad (2)$$

The BWi model was validated with Ore B, which also showed strong correlation to quartz and sphene.

$$\text{Ore B BWi} = 18.593 + 0.564 \times \text{Fe (\%)} \quad (3)$$

The similarities between the relationships for BWi and statistical equivalence testing indicated that these two adjacent ore zones will have similar properties in processing through the mill. At the time of writing, DWi data for Ore B was not available.

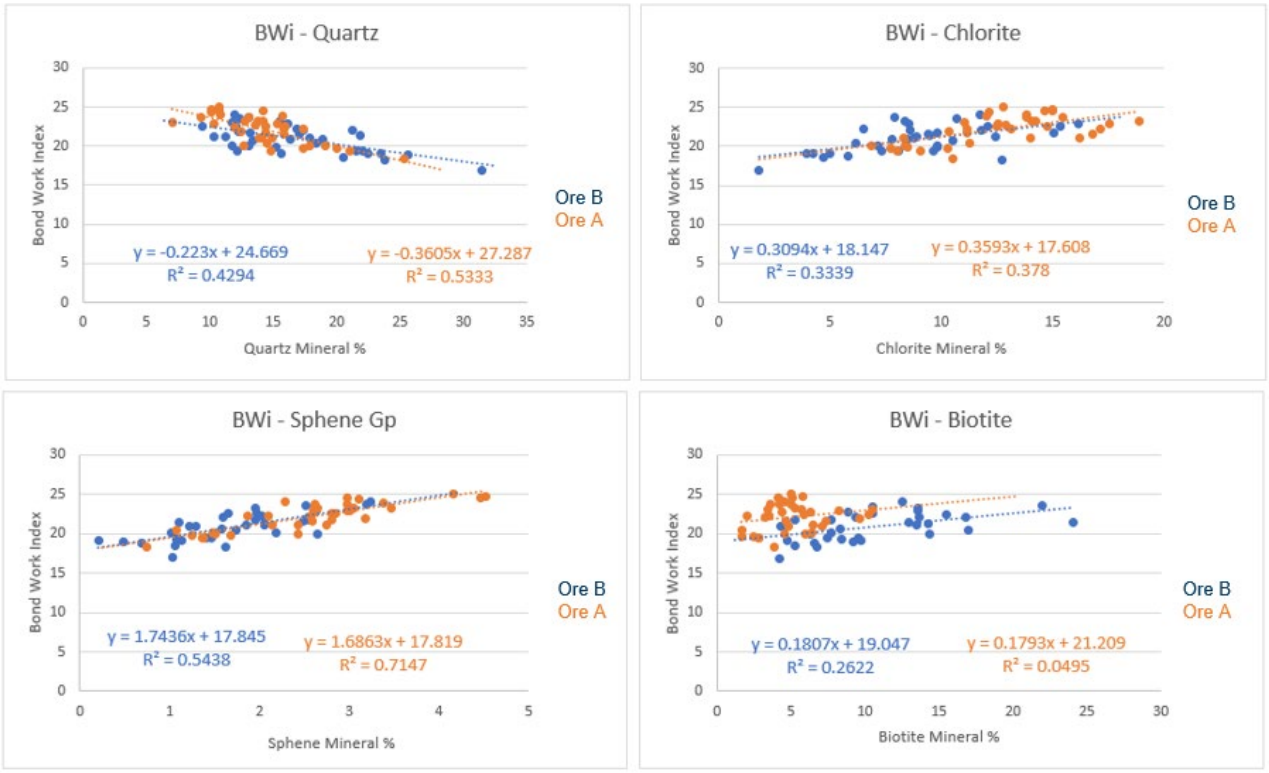

FIG 10 – Hardness parameter and mineralogical relationship development.

The data generated by modelling of hardness parameters allows an annualised estimate of key variables that can subsequently be used in mill throughput simulations. An example of this output data is presented in Figure 11. Any stockpiled material that is going to be part of the mill feed plan should be included in this type of work.

How this data may be utilised in comminution simulations is presented in Figure 12. This provides estimates of mill throughput based on the ore input data from all known sources as per the mine plan. Using the comminution data generated for each ore type in combination can provide estimates of wet plant feed P80 (milling circuit product) and power requirements. Simulations can be performed to evaluate the impact of running the comminution circuit with various ore feed blends and circuit operating conditions (maximum power draw versus target throughput etc).

A key output for metallurgical circuit financial modelling is the P80 grind-size produced by the primary milling circuit (flotation or leach feed P80 μm). Grind sensitivity test work allows the recovery impact of target elements to be determined. An example of grind sensitivity data is present in Figure 13. The slope of the P80-recovery curve provides an estimate of the per cent recovery loss per micron increase in grind-size, this is often referred to as the *Delta* recovery loss. Delta recovery loss with P80 can then be applied to the P80 prediction from comminution simulation data to provide an adjustment to the overall recovery calculations for financial modelling work.

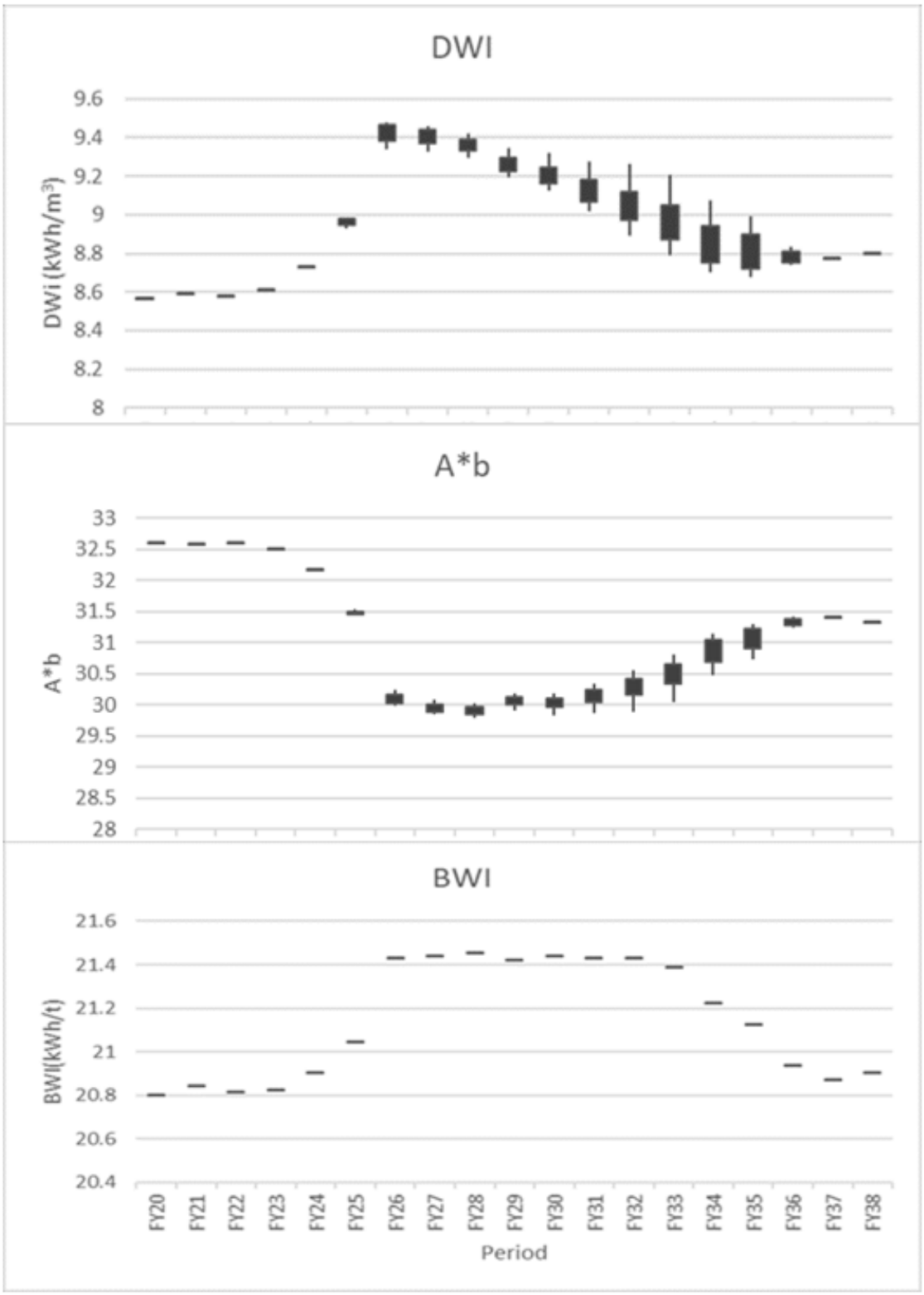

FIG 11 – Example of annualised hardness parameters DWi, A*b and BWi.

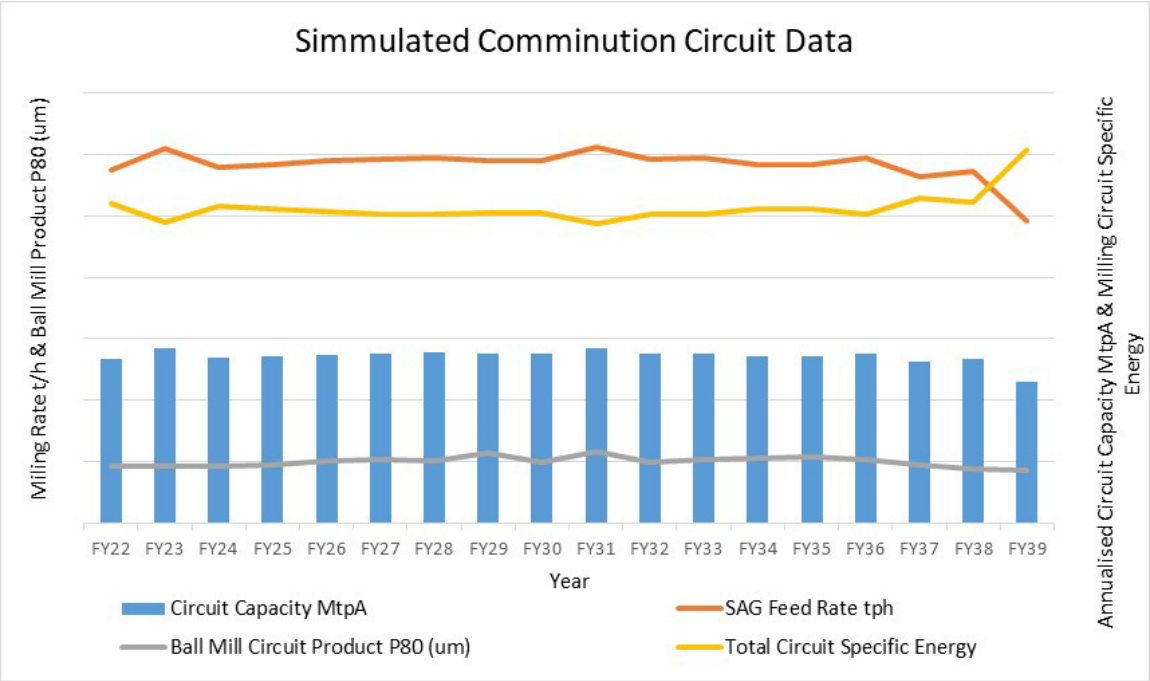

FIG 12 – Example of annualised comminution circuit simulation data.

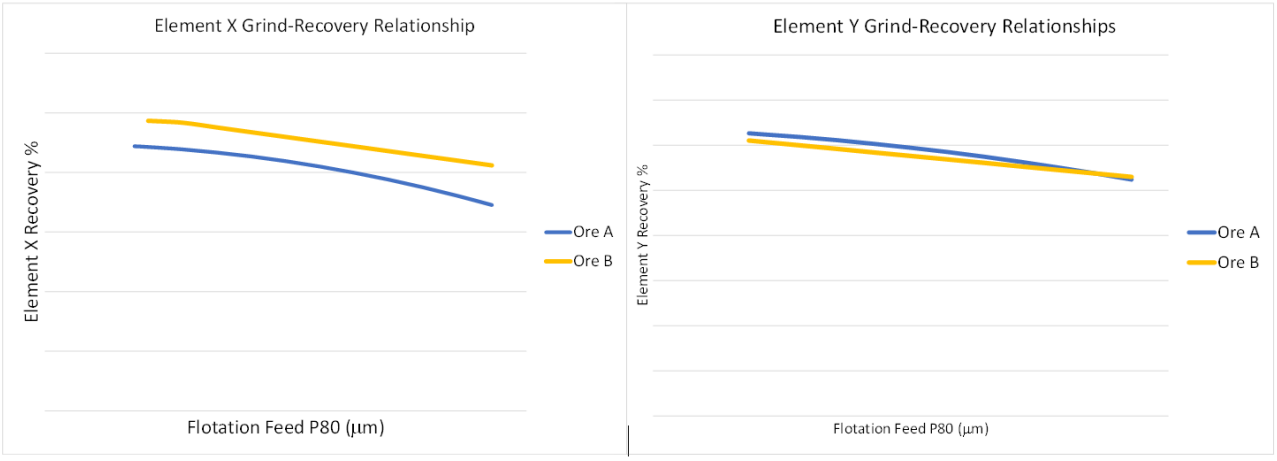

FIG 13 – Example of grind sensitivity estimation for elements X and Y.

Recovery modelling

Effective financial evaluation of an ore relies on the recovery models to be a good representation of all types within a deposit. Key questions which must be considered are:

- How many target value elements for recovery modelling are within the ore? (What do we get paid for?) Au, Ag, Zn, Pb, Cu, Ag, Ni or Mo? Or any combination of these or others.
- What will impact recovery? In the case of Au leaching, preg-robbing contaminants must be considered. What is the mineral liberation size and grind sensitivity.
- What else is being recovered? Penalty elements that will cause financial impacts need to be considered.

Metallurgical data is evaluated in conjunction with sample mineralogy using an iterative approach to establish groups of samples based on both metallurgical response and feed mineralogy. Host rock modal mineralogy, grain size data, and mineral association data is utilised. Spatial location is modelled to determine if there is regional variability and if ore zones can be established and bounded with their own recovery models. The modelling method used is multivariable regression analysis (generally non-linear). The process of modelling is in itself a complex process and will be discussed in detail in a subsequent paper.

The culmination of modelling work results in recoveries for each ore type or domain to be calculated (Figure 14). The algorithms for each ore type are used within the mine planning system in conjunction with grind sensitivity adjustments to estimate output metal units and average recovery for the processing facility on an annualised basis (Figure 15).

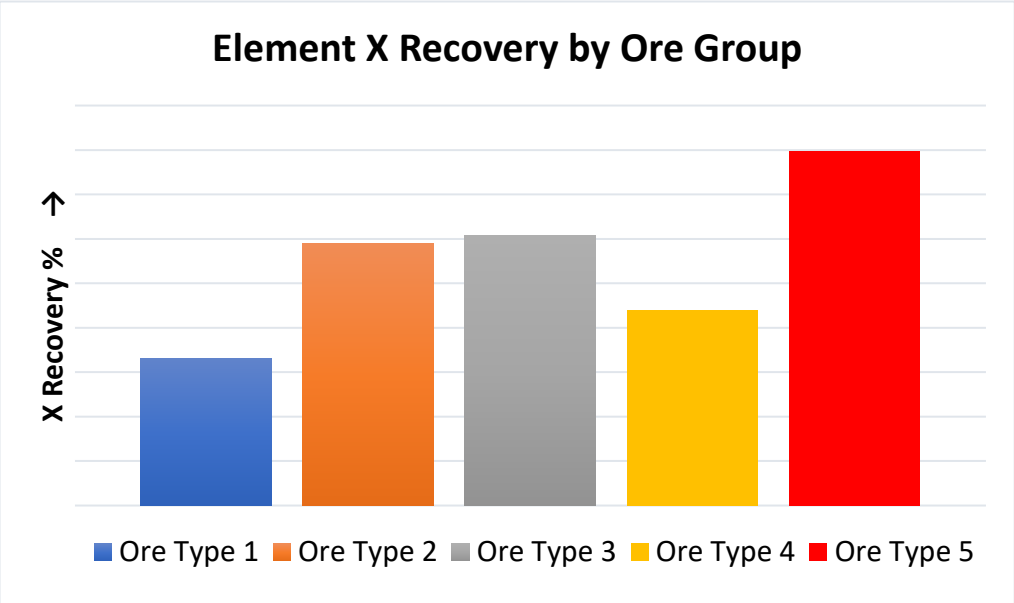

FIG 14 – Example of ore type recovery average variability.

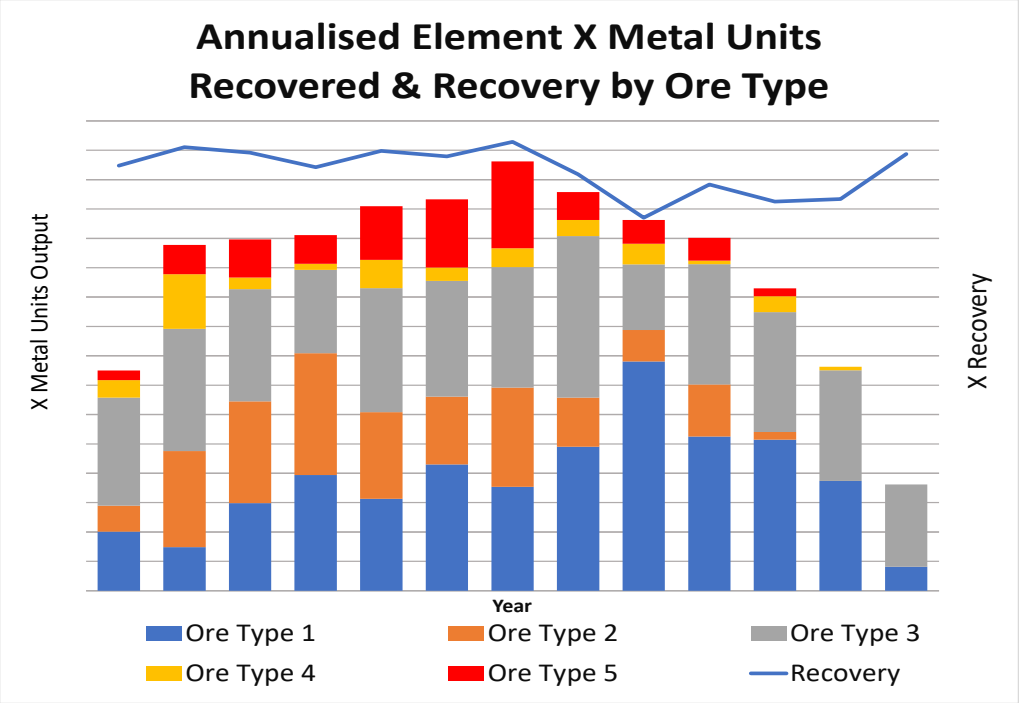

FIG 15 – Example of application of ore type recovery data to estimate average metal production and recovery.

INTEGRATION ACROSS LIFE-OF-MINE PLANNING

As described in previous sections, geometallurgical test work can unlock significantly more for a mining project than just recovery functions. The key to successful integration of the full suite of orebody knowledge (OBK) requires two key elements:

1. Knowing your orebody with well understood spatially captured data; and
2. A system that allows people to integrate knowledge and develop this into practical plans.

The first step for an organisation to know its orebody is to have a well-defined drilling program with good QAQC and data capture within a database. A carefully constructed program can add significant value. Understandably, the first focus of exploration teams is the identification of valuable elements and minerals. However, it is the authors' experience that significant business value (and time) is lost when other parts of the planning process are not considered in follow up drilling once a target has been identified as prospective.

Once a target is identified the definition of needs for a drilling program expands to:

- Further definition of the geological setting and valuable elements;
- The geotechnical setting as it relates to the mining method (rock mass characteristics, stress regime, and factors important to excavation stability) and hydrogeology information.
- The geometallurgical factors such as head grades, mineralogy, hardness and key mineralogical properties such as grain size and mineral association.

These form the basis of the data required for full orebody knowledge and the ability to define the best Mine to Mill plan. The requirements for each operation will be unique and influenced by the orebody itself as well as the organisation conducting the work. The ability to create meaningful test work programs that have quality outputs for planning integration comes from a well-defined drilling and data collection program.

Once test work programs and modelling is complete, the process of bringing the data generated together into a mine production model is the role of the mine planning team. Although traditionally this is an area of speciality for mining engineers, larger operations and those operations with complex orebodies are increasingly using teams comprising of geologists and metallurgists to extract the best from the planning process.

The key elements of a good mine production model for mass mining are:

- A valuation field parameter within the spatial block model to enable economic planning.
- The ability to calculate and output parameters that matter to the ore treatment planning process, including parameters that impact on rate, grind size and 'red flag' elements that can result in significant impacts to processing.
- The ability to provide feedback loops to enable team members to collaborate on key drivers of the success of the project.

In determining the value of each block, the team will need to consider:

- Head grade of economic elements
- Geometallurgical domains for accurate recovery estimates and interaction planning where domain interaction issues exist.
- Orebody parameters that affect the saleable value of the operations product (deleterious elements and expected concentrate quality)
- Geotechnical factors that affect input costs, including poor ground conditions, drill and blast performance characteristics, caving performance and water ingress.
- Mill performance characteristics that increase or decrease costs and throughput rates and adjusting the value of a block to account for these.

Bringing the elements of the plan together in one 3D space with the impact of each OBK field transparently shown allows an understanding of the entire value chain for each member of the planning team. With an increasing focus on the use of AI tools in the mine planning industry, the correct assignment of this value field is of even greater importance.

Other important elements of the mine production plan are also brought together into the model at the same time as the creation of the valuation field. This process can be as simple as aggregating other models, whilst at other times it can require software to interpret or calculate results. Once created, the full OBK model can then be used to create the mine and processing plans. Figure 16 presents an example of an OBK flow sheet for Mine to Mill planning purposes.

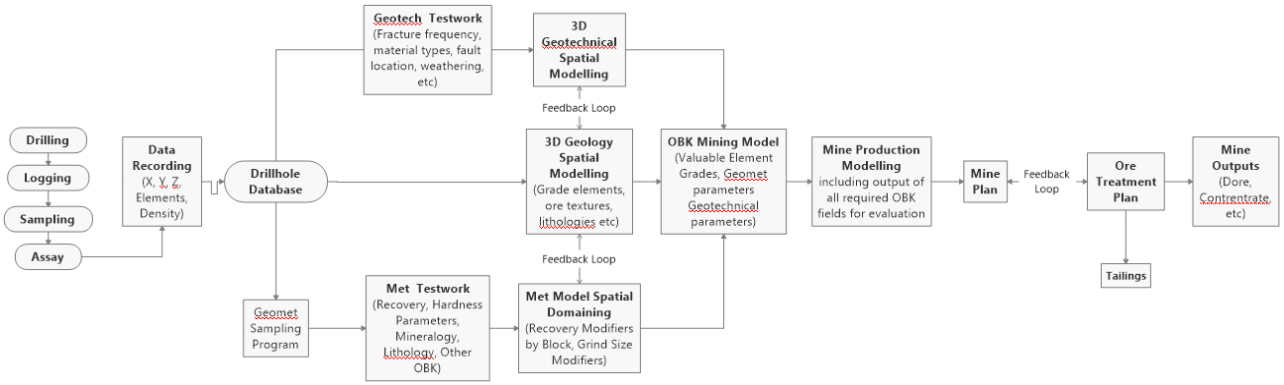

FIG 16 – Typical OBK Mine to Mill planning flow sheet.

Quite often at this point, the question is asked by management 'Why is this the answer?'. The answer is almost invariably in a drill hole interpretation or a model created by a technical expert. By bringing the orebody knowledge together in one central mine planning model, the answer to this question can be more clearly articulated, investigated and tested. This allows better decision-making and operational responses to upcoming issues before they become today's problems.

CONCLUSION

In large scale mining operations, a grid-based sample selection process is proposed for feasibility study level deposit evaluation. This method has been successfully applied to a number of ore zones and deposits.

Appropriate spatial coverage is essential. Samples must have equal spatial weighting within the overall ore zone to allow integration of spatial models with mining systems – this means no mixtures. Ore interaction test work can be undertaken as part of an additional program to check for any issues that may be caused by mixing of different ore types.

Feed material evaluation should include multi-element assay and mineralogical analysis. The metallurgical test work requirements are dictated by the expected processing route of the ore.

Modal mineralogy is required to determine measurable links to both geology and key metallurgical performance parameters.

Defining a 'geometallurgical' domain is only possible when the observed metallurgical response is supported (or explained) by both the mineralogy and the geology of a system.

LIBS, XRF and Raman sensors for optimal bauxite sorting

B Orberger[1,2], C Garcia-Piña[3], B de Waard[4], L Rybok[5], R Hyypiö[6], A Prudhomme[7], L Capar[8], H Lindström[9], S Uusitalo[10], M Alamäki[11], C Kaminski[12], J A Meima[13] and S Merk[14]

1. President, CATURA Geoprojects-Géosciences Conseil, 75014 Paris, France. Email: beate.orberger@catura.eu
2. Associate Professor, GEOPS, Université Paris-Saclay, 91405 Orsay, France. Email: beate.orberger@universite-paris-saclay.fr
3. Geologist-Business Developer, DMT GmbH and Co.KG, 45307 Essen, Germany. Email: carlos.garcia-pina@dmt-group.de
4. Researcher, SPECTRAL Industries, Delft, Netherlands. Email: waard@spectral-i.com
5. Scientist, J&C Bachmann GmbH, 75179 Pforzheim, Germany. Email: lry@jcbachmann.de
6. Principal R&D Engineer, Timegate Instruments Oy, FI-90590, Finland. Email: risto.hyypio@timegate.com
7. Exploration Geologist, ERAMET, 78190 Trappes, France. Email: antoine.prudhomme@eramet.com
8. Researcher, BRGM, 36009 45060 Orléans Cedex 2. Email: l.capar@brgm.fr
9. Engineer, VTT Technical Research Centre of Finland, 90570 Oulu, Finland. Email: hannu.lindstrom@vtt.fi
10. Dr. Tech, VTT Technical Research Centre of Finland, 90570 Oulu, Finland. Email: sanna.uusitalo@vtt.fi
11. MSc. Physics, VTT Technical Research Centre of Finland, 90570 Oulu, Finland. Email: markku.alamaki@vtt.fi
12. Engineer, DMT GmbH and Co. KG, 45307 Essen, Germany. Email: christian.kaminski@dmt-group.com
13. Scientist, Federal Institute for Geosciences and Natural Resources (BGR), 30655 Hannover, Germany. Email: Jeannette.Meima@bgr.de
14. Data Scientist R&D, LTB Lasertechnik Berlin GmbH, 12489 Berlin. Email: sven.merk@ltb-berlin.de

ABSTRACT

Bauxite, bauxite residues (BR) and Bayer Liquor are important resources for Al, Sc, V and Ga. Bauxite is currently the solely source for primary aluminium. At global scale about 80 plants produce alumina. From these resources, about 1–1.4 t of bauxite residues are generated per tonne of alumina (Ujaczki *et al,* 2018). Bauxites present heterogeneous grades at lateral and vertical scale, variable mineralogy, and chemistry. Therefore, it is important to localise most precisely minerals hosting valuable metals for Al, Sc, V and Ga, but also hazardous minerals/metals for processing such as reactive silica (aluminosilicates), TiO_2 (rutile, anatase), and minerals generating moisture (phyllosilicates). This must be done at the beginning of the value chain on mine sites to reduce transport and processing costs, and BR volumes. In this study, different types of sensors were applied to major lithologies of the karst bauxite deposits of SODICAPEI (Villeveyrac, Southern France), for optimal bauxite sorting. Therefore, the applicability of Laser-Induced Breakdown Spectroscopy (LIBS) was investigated with an industrial LIBS system and a LIBS core scanning system. Furthermore, first time-gated Raman and XRF spectroscopic analyses were performed with the multi-sensor ANCORELOG system. Our results, obtained in the frame of the EIT ANCORELOG and T-REX projects, show that LIBS is powerful to precisely define the bottom and top layer of bauxite ores and define the bauxite types by measurement of major and trace elements (Al, Mg, K, Na, Ca, C, Si, Ti, Fe, S). Furthermore, LIBS can access the critical parameters crucial for bauxite processing. XRF gives semiquantitative data for Mn, Fe, Cr, Ti, V, Ca, K while time-gated Raman spectroscopy allows deciphering clay minerals, Ti-minerals, boehmite and carbonates, all allowing defining bauxite on and offset.

INTRODUCTION

Bauxite production and bauxite residues

Bauxite is the most important raw and feed material for alumina (Al_2O_3) production worldwide with the major producers Australia, China, Brazil, Guinea, and India, and further reserves in Vietnam, Jamaica, and Indonesia (USGS, 2021). Bauxite is a tropical soil formed on Al-rich rocks with variable morphologies and topographies, and therefore ore grades are heterogenous at vertical and horizontal scale. About 85 per cent of the bauxite is converted into alumina through the Bayer process, then into aluminium metal through the Hall-Heroult process, while 10 per cent of Al is used for non-metal products, and 5 per cent in refractory and abrasive materials.

In 2021, primary aluminium production globally amounts to 5747 kt at a daily rate of 185.4 kt. Western and Central Europe produced 279 kt, while Russia and Eastern Europe produced 350 kt. A yearly increase of about 5.2 per cent of Al production was noted based on July 2021-data (https://international-aluminium.org/july-2021-global-primary-aluminium-production/). Until 2030, a 4 per cent-increasing Al demand is expected. Bauxite residues are the world-largest industrial by-products estimated at around >4 Bt with an annual growth of 120 Mt (bauxite.world-aluminium.org). This reflects approximately 1–1.4 t of bauxite residues (BR) generated per tonne of alumina produced (Ujaczki *et al,* 2018). Bauxite residues represent an excellent resource for scandium, vanadium, gallium, and titanium (Vind *et al,* 2018).

Why do we need analytical sensors to optimise separation of bauxite ore from waste?

We must reduce the annual growth of about 120 million t of BR and the associated environmental impact of bauxite processing. Bauxite processing including mining, refining, anode production, electrolysis, and casting, emits 16.1 t of CO_2 per tonne of Al. Considering global CO_2 emissions, primary Al production accounts for 92 526 kt of CO_2/a (https://international-aluminium.org/july-2021-global-primary-aluminium-production/).

Europe produces only 10 per cent of the total bauxite which is needed for Al production. For that reason, bauxite ores are imported from eg Australia and Guinea, and transported at high cost to feed the EU processing plants.

A first step to leave low-grade and most waste material in the ground, requires efficient mining, based on detailed geomodels. Moreover, a second step of sorting should occur at different processing steps, starting with sorting rare metal bearing BRs hosting eg Sc, V, Ga from ‘barren’ materials. The latter are suitable for eg cement additives.

Bauxite from different regions have variable chemical and mineralogical compositions (eg Guinean deposits: Schulte and Foley, 2013; Barry *et al,* 2021). The feed materials are crushed, grinded and homogenised at the plant. For Bayer processing, a constant chemical composition must be ensured (https://www.removal-project.com/wp-content/uploads/2021/09/removal-policy-report-20210923.pdf). Therefore, the monitoring of the feed with analytical sensors will contribute to anticipating dysfunction in processing and further process optimisation.

Solutions for sensor-based material sorting

Laser induced breakdown spectroscopy (LIBS) is more and more used in the mining and processing industries (Pedarnig *et al*, 2021; Noll *et al*, 2018). It performs multi-element chemical analyses with minimal destruction, using a highly energetic pulsed laser for *in situ* excitation of the atomic species at the sample surface (Cremers and Radziemski, 2006; Hahn and Omenetto, 2012). This multi-elemental technology can be applied as well-aimed point measurements, as line scan, or as imaging tool (Pedarnig *et al*, 2021; Rifai *et al*, 2020; Jolivet *et al*, 2019). LIBS measurements are fast (eg Rifai *et al*, 2020), can operate under harsh conditions (Pedarnig *et al*, 2021; Noll *et al*, 2018), and can also access the light elements (Harmon and Senesi, 2021).

However, quantitative use of LIBS on rocks, soils, and processing materials (muds and slurries) is challenging, as the plasma strongly responds to physical and chemical variations on the sample surface (eg Harmon and Senesi, 2021). Moreover, when analysing slurries, the detected LIBS signal

is weakened because part of the light energy is absorbed by water (Khajehzadeh *et al,* 2016). In general, calibrated LIBS data can be considered as semi-quantitative when compared to conventional laboratory analyses. Thereto, several different calibration and classification methods for LIBS applications have been developed (eg Harmon and Senesi, 2021; Galbács, 2015).

A wide variation in LIBS instruments exists, of which many are customised for particularly applications. The optimal specification of the different components (laser, spectrometer, optical components) of a LIBS system depends on the application. Commercial LIBS instruments include portable handheld instruments (Rakovský *et al*, 2014), industrial instruments for various sorting, quality control, or routine analysis applications (Pedarnig *et al*, 2021), drill core scanner, as well as imaging LIBS instruments:

- Raman Spectroscopy, a well-known non-destructive method to analyse and identify minerals, has been further developed for use in portable equipment or for being installed on Mars Rovers for Martian surface exploration (Veneranda *et al*, 2021). Time-gated (TG) or time-resolved (TR) Raman spectrometers have been developed to obtain fluorescence-free Raman spectra with only a single laser as source of excitation (Kögler and Heilala, 2020; Beyssac, 2020). Furthermore, the hardware is miniaturised so that the instruments can be used in-field on Earth and planetary applications (Veneranda *et al,* 2021 and papers therein). Time-gated Raman spectroscopy suppresses the fluorescence and disturbing signals. Time-gated Raman is essentially used in sensing industrial processing, followed by mineralogical applications (Kögler and Heilala, 2020). The Timegate Instruments (copyright) developed a Raman instrument specifically dedicated to the entire value chain from exploration, processing to recycling of materials (www.timegate.com). For Raman-based mineral identification, open access mineral libraries are available (eg RUFF Lafuente *et al*, 2015); USGS spectral library (Kokaly *et al*, 2017) or the Raman Open database ROD (El Mendili *et al*, 2020), which can be adapted and extended to the target materials.
- Portable XRF (pXRF) is a non-destructive and well-established method, which is widely used in the mining and processing industries for obtaining reliable Quality Assurances/Quality Control (QA/QC) validated by laboratory analysis (Lemière, 2018; Duée *et al*, 2019). Such analyses can be performed as line and or point analyses. Several XRF scanners are in operation such as the Minalyzer (https://minalyze.com/), combining XRF, high resolution photography and topography, designed for the mining and processing industries, while others, such as Avaatech (www.avaatech.com), are designed for sedimentary and marine applications. JC Bachmann (www.jcbachmann.com) developed an XRF device within the ANCORELOG project for a combined analytical expert system for chemical logging and monitoring drill cores and production processes.

In the frame of the EIT projects ANCORELOG and T-REX (https://www.dmt-group.com/ancorelog-1.html) a modular combined analytical sensor system with X-Ray Fluorescence (XRF), time-gated Raman spectroscopy, and short wave-infrared spectroscopy (SWIR) was developed.

This paper demonstrates the performance of in-field sensors on an artificially composed bauxite drill core profile which is typical for Karst environments, as present in Southern France, or South-eastern Europe. A typical drill core profile from the Southern France bauxite presents the top sedimentary rocks, various bauxite ore and grades, and the bottom dolomitised limestone. Results from In-field instruments (XRF, LIBS, pIR, Raman) is compared to those from laboratory XRF, LIBS and X-Ray Diffraction (XRD). Recommendation for industrial use of sensor combination based on this study are presented.

SAMPLE MATERIALS

The samples used in this study come from the karst-type bauxite deposit, SODICAPEI, close to Villeveyrac in Southern France. The lithologies of the samples comprise from right to left (Figure 1): bottom dolomitised limestone (karst), pisolitic bauxite, red bauxite, pisolitic bauxite, pisolitic bauxite conglomerate, red clay with bauxite, the marker horizon composed of black shale, marl, and sandy shale. The black shale marker horizon indicates the proximity of the onset of the bauxite. This layer is oxidised in some parts of the ore deposit to red shale.

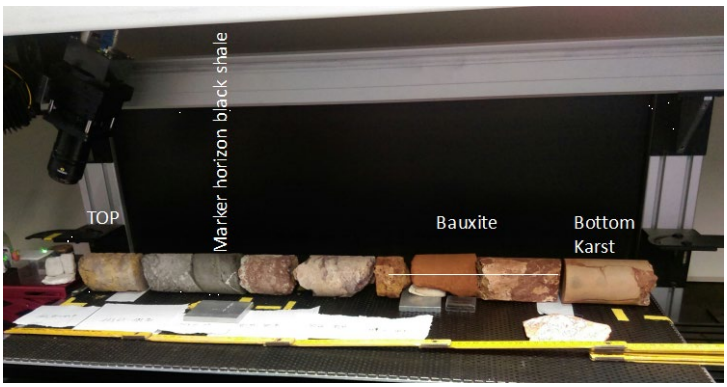

FIG 1 – LIBS measurement configuration of the composite bauxite profile for a line scan with the LTB core scanner from 2011 (from Meima *et al*, 2021).

ANALYTICAL METHODS

Portable infrared spectroscopy

For accessing mineralogy, was applied with an ASD Fieldspec 3® (Panalytical) at the BRGM (Orléans, France). Prior to measurements, the signal was calibrated on the white reference material, Spectralon®. Each spectrum is composed of averaged 250 consecutive acquisitions to decrease the background noise. The measurement window is 1.7 cm in diameter. The device can acquire a total of 2150 spectral bands and has its own halogen light source. For each sample, we selected the pIR measurement points considering colour and texture parameters. Spectra are Hull-corrected (Phang *et al,* 2006).

X-Ray Diffraction analyses

For determining mineralogical compositions, were performed at ERAMET IDEAS, Trappes, France. An X'Pert Pro Panalytical diffractometer with CuKα radiation at 450 kV and 40 mA was used on (<80 microns)-agate-milled samples. The analytical conditions of the diffractometer were 3–80 °2 Theta with counting times 188 s every 0.0167° in an Al-rotating sample holder. The COD (http://www.crystallography.net/cod/) database and high SCORE software was used for diffractogram interpretation.

X-Ray Fluorescence analyses

For accessing major and minor elements**,** were performed with a Panalytical Axiosm AX-WD XRF (X-ray tube SST-m AX Rh, 4 kW) at ERAMET IDEAS, TRAPPES, France. The samples were milled (<100 microns, dried at 105°C for 24H prior to fusion with LiBr flux at 1050°C for 30 min.

Laser Induced Breakdown Spectroscopy

for fast screening of spatial distributions of major and minor elements was performed with three different LIBS instruments (Table 1). The instruments are very different from each other, which mainly manifests in the intensity and resolution of the LIBS spectra, the speed of measurement, and tolerance with respect to sample morphology. The instruments will be referred to as LIBS core scanner and LIBS industrial. Their specifications can be found in Table 1. For a more detailed description of the core scanner instruments, the reader is referred to Kuhn *et al* (2016) and Bauer *et al* (2022).

TABLE 1

Specifications of LIBS instruments applied in this study.

Specification	LIBS core scanner	GeoLIBScanner	Industrial LIBS system
Manufacturer	LTB, 2011	LTB, 2021	Spectral Industries, 2021
Application (this paper)	Line scan	Imaging LIBS	Line scan
Laser	Nd:YAG Q-switched 1064 nm, 35 mJ, 20 Hz	Nd:YAG Q-switched 1064 nm, 25 mJ, 100 Hz	Nd:YAG Q-switched 1064 nm, 1 mJ, 10 kHz
Spot size	~ 200 µm	~ 50 µm	~200 µm
Detector system	Echelle spectrograph and CCD	Echelle spectrograph and CCD	Czerny-Turner and CCD
Spectral range	285–960 nm	210–1000 nm	180–450 nm
Spectral resolution	0.021–0.070 nm	0.047–0.222 nm	0.09–0.11 nm
Working distance	25 cm	2 cm (autofocus using morphology scan)	19 cm
Measurement speed	2 spectra / second	Up to 50 spectra / second	Up to 300 spectra / second
Other	XY stage (2.5 × 100 cm), air suction	XY stage (60 × 110 cm), air suction	

A prototype LIBS core scanner (LTB, Berlin) was used for a line scan across the composite bauxite profile as shown in Figure 1. For a detailed description of these measurements, the reader is referred to Meima *et al* (2021). In summary, a step size of 200 µm was applied, and each single LIBS measurement consisted of one cleaning shot and three accumulated measurement shots. Additionally, another prototype LIBS core scanner (geoLIBScanner, LTB) was used for detailed imaging LIBS on the core section ‘pisolitic bauxite’ and ‘red bauxite’ to visualise the spatial variation in mineral chemistry. Thereto, single-pulse measurements, and a step size of 50 µm were applied. All spectra were processed by calculating the intensity of multiple emission lines for each of the target elements. Measurements that were out of focus were removed from the data set. Further processing included normalisation to reduce normal shot-to-shot variation. The data were plotted as a function of core length or as 2D images to visualise compositional variations within and between samples. For classification purposes, the supervised classification algorithm Spectral Angle Mapper was applied. A calibration of the LIBS data was not attempted in this study, because it was the objective of this study to investigate whether similarities and/or differences between samples can be recognised in the raw LIBS data.

Measurements with a commercial industrial LIBS system (Spectral Industries) where undertaken in the SPECTRAL Industries laser lab facility in Delft, Netherlands. The specifications of the instrument are shown in Table 1. Samples were placed within focus of the laser on a linear translation stage. The position of the sample was fine-tuned using a manual translation stage until optimal LIBS signal was achieved. The translation stage moves the core at a speed of 5 mm/s. During this continuous translation, the non-gated LIBS measurements are performed. With the applied integration time of 2 ms, each recorded spectrum is an accumulation of 20 individual plasmas generated over a length of roughly 2.5 µm of core. The main benefit of integration over multiple plasmas is that the fraction a scan that is actively ablated (and therefore sampled) is much higher as compared to single-shot spectra. On the other hand, the summation of multiple plasmas also introduces some form of averaging which makes it more difficult to detect minor trace elements or very small scale heterogeneity. The spot size of the laser at focal was not considered in this study. However, it is

expected that this spot size is significantly larger (100 to 200 µm), than the resolution mentioned above. After basic pre-processing steps, the intensities of emission lines from common elements such as K, Si, Al, Ti, C, Ca, S, and Fe were extracted.

ANCORELOG (Analytical Core Logger) is a multi-sensor drill core scanner that can be modularly equipped with several analytical sensors (Raman spectroscopy, X-Ray Fluorescence, hyperspectral cameras, LIBS). The sensors are mounted on a high-precision linear moving stage that is steered by a programmable logic controller (PLC) and allows data acquisition through spatial sensor co-registration. Data from different sensors are stored into a dedicated database where machine-learning algorithms can be applied to classify drill core samples into site-specific geological domains, waste, and valuable material. ANCORELOG's semi-automated scan process is designed to scan drill core samples with a high scan rate of up to 14 mm/s depending on the chosen sensor combination and the required accuracy and resolution. This allows its use in industrial scale drilling campaigns. For this study a combination of an XRF and a time-gated Raman sensor was used. ANCORELOG's XRF sensor, a special adaptation of J&C Bachmann's TEXAS device, was used in a continuous profile scan mode measuring a profile of 5 mm width along the complete sample length at a speed of 1 mm/s. Emission signals were integrated over the complete profile length resulting in one single measurement for each sample. The results were obtained as counts per second (cps) normalised to 120 s integration time after background signal subtraction and thus indicating a qualitative estimation of elemental concentrations. A conversion into quantitative elemental concentrations would require a site-specific sensor calibration against representative samples. ANCORELOG's Raman sensor, T-REX (Time-gated Raman for Exploration) is a special adaptation of Timegate Instruments' PicoRaman device. A precise synchronisation in the range of picoseconds between the pulsed laser excitation source and the sensitive and fast detector allows the rejection of sample-induced fluorescence emission, which has a longer delay. The time-gated Raman measurements were conducted in a combination of profile and single point scan mode. The profile scans were measured at a speed of 5 mm/s resulting in a 160 µm-wide profile line over each sample while integrating the measurement over the complete sample length. Randomly selected single spots were measured on each sample additionally. An automated matching of the obtained mixed Raman spectra with reference spectra of given target minerals from the RRUFF™ database (Lafuente *et al*, 2015) was conducted using a software module developed within the ANCORELOG project. The technical specifications of both sensors are summarised in Table 2.

TABLE 2

Technical specifications of the XRF and time-gated Raman sensors used in this study.

XRF Sensor Specification		**Time gated Raman Sensor Specifications**	
X-ray source	RTW MCB 65C-0,2 Mo	Laser Excitation Wavelength	532 nm
X-ray detector	Amptek DP5-X 25 mm^2 SDD	Laser Repetition Rate	250 kHz
		Laser Power	**230 mW max**
		Gating Adjustment Resolution	10 ps

RESULTS

An overview of the results obtained with the different sensors used in this study is presented in Tables 3 (mineralogy) and 4 (chemistry).

TABLE 3

Mineralogy determined by ANCORELOG time-gated Raman spectroscopy, laboratory XRD and portable Infrared spectroscopy; pIR: portable Infrared Spectroscopy; XRD: X-ray-diffraction (Prudhomme, 2018); RAMAN Timegate (TG): this study; x: low amount; xx medium amount, xxx high amount; Al: Aluminium; RA: Raman.

		TOP SEDIMENTARY ROCKS (SR)									BAUXITE																		BOTTOM DOLOMITISED LIMESTONE					
	Mineralogy/ Method	RA	XRD	pIR	RA	XRD	pIR	RA	XRD	IR	RA	XRD	pIR	RA	XRD	pIR	RA	XRD	pIR	RA	XRD	pIR	RA	XRD	pIR	RA	XRD	pIR	RA	XRD	pIR	RA	XRD	pIR
	Lithology	Sandy shale			Marls			Carbonated black shales			Marls, pisolotic bauxite			Red clay with bauxite			Pisolitic bauxite conglomerate			Pisolitic red bauxite			Pisolitic bauxite			Red bauxite			Dol limestone+ bauxite clasts			Dol limestone (karst)		
	Sample number	ER-SD00–0108			ER-SD00–0107			ER-SD00–0106			ER-SD00–0105			ER-SD00–0104			ER-SD00–0103			ER-SD00–0102			ER-SD00–0101			ER-SD00–0100			ER-SD00–0100			ER-SD00–0099		
SR	Quartz	x	xxx		xxx	xxx			x					x	x																			
SR	Kaolinite		x			xx	x		xxx			xx	x		xx	x		xx	x		xxx	x		xx	x		xxx	x		xxx	x			x
SR	Illite			x?		xx	x			x			x			x			x			x												
SR	Vermiculite/ smectite		xx			xx																												
SR	Gypsum		xx						x																									
SR	Zircon																						x	?										
Marker horizon	Pyrite								x																									
Al ore	Goethite			x								xx	x		x			x	x		xx	x		xx	x			x			x			x
Al ore	Hematite			?								xx	x			x		x	x		xx	x		x	x		xx	x		xx	x			x
Al ore	Rutile													x	x	x		x			x			x		xxx	xx							
Al ore	Anatase										x	x		x	x			x		xx	x		xxx	x		xxx	x		x	x				
Al ore	Boehmite																x	xx					xxx	xxx		xxx	xxx							
Karst	Calcite		x	?	xxx	xxx		xxx	xxx		xx	xxx	x	xx	xxx	x					xxx						?		xxx	xxx	x	xxx	xxx	x
Karst	Dolomite																					?	x?		?									

TABLE 4

Chemical analyses by different sensors: XRF laboratory, XRF ANCORELOG (AL), LIBS core scanner and industrial LIBS; XRF Lab: Laboratory XRF (ERAMET IDEAS, Trappes, Prudhomme, 2018); XRF AL: XRF developed in the EIT ANCORELOG-project: semiquantitative; LIBS lab: Specifications see Table 1; LIBS ind: specifications see Table 1; n.a.: not analysed; n.v. not visible D.L.: Detection Limit: Pis: pisolitic; Cb: carbonated; Co: conglomerate: dol: dolomite; Bx: bauxite; O.R. out of spectral range.

	Lithologies	Sandy shale	Marls	Cb.black shales	Marls – pis. bauxite	Red clay+bauxite	Pis bauxite co.	Pis red bauxite	Pis bauxite	Red bauxite	Limestone+Bx	Limestone
Analytical method	**Sample number**	ER-SD00–0108	ER-SD00–0107	ER-SD00–0106	ER-SD00–0105	ER-SD00–0104	ER-SD00–0103	ER-SD00–0102	ER-SD00–0101	ER-SD00–0100	ER-SD00–0100	ER-SD00–0099
XRF Lab (wt.%)	**SiO_2**	69.80	56.20	60.80	19.00	18.40	16.80	34.70	4.34	7.99	5.41	1.44
XRF AL	**Si**	n.a.	n.a.	n.a.	high error	high error	high error	high error	high error	high error	high error	high error
LIBS corescan	**Si**	xx	xx	xx	n.a.	x	x	x	x	x	x	n.a.
LIBS ind	**Si**	n.a.	n.a.	n.a.	n.a.	n.a.	xxx	n.a.	xx	n.a.	x	x
XRF Lab	**Al_2O_3**	10.40	14.40	5.60	13.80	14.30	39.60	29.40	50.30	55.00	4.46	1.09
XRF AL	**Al**	n.a.	n.a.	n.a.	high error	high error	high error	high error	high error	high error	high error	high error
LIBS corescan	**Al**	x	x	x	n.a.	x	x	xxx	xxx	xxx	x	n.a.
LIBS ind	**Al**	n.a.	n.a.	n.a.	n.a.	n.a.	xxx	n.a.	xxx		x	x
XRF Lab (wt.%)	**Fe_2O_3**	4.43	1.91	5.35	4.02	1.61	30.40	13.70	31.70	22.70	2.03	0.45
XRF AL (counts/s)	**Fe**	n.a.	n.a.	n.a.	3893	1227	22 753	10 986	25 625	17 334	2423	925
LIBS corescan*	**Fe**	<D.L.	<D.L.	<D.L.	n.a.	x	<D.L.	xx	xx	xx	-	n.a.
LIBS ind**	**Fe**	n.a.	n.a.	n.a.	n.a.	n.a.	?		?		xx	x
XRF Lab (wt.%)	**CaO**	6.01	12.10	11.80	32.50	34.2	<D.L.	6.30	0.12	0.36	48.90	54.80
XRF AL	**Ca**	n.a.	n.a.	n.a.	4237	4157	14	428	16	27	7040	6705
LIBS lab	**Ca**	x	xx	xx	n.a.	xx	xxx	<D.L.	<D.L.	<D.L.	xxx	n.a.
LIBS ind	**Ca**	n.a.	n.a.	n.a.	n.a.	n.a.	x	n.a.	x	n.a.	xxx	xxx
XRF Lab (wt.%)	**MgO**	0.63	0.85	0.31	0.84	0.53	0.12	0.18	<D.L.	0.09	0.51	0.54
XRF AL	**Mg**	n.a.	n.a.	n.a.	high error	high error	high error	high error	high error	high error	high error	high error
LIBS corescan	**Mg**	x	x	x	n.a.	x	x	x	x	<D.L.	x	n.a.
LIBS ind	**Mg**	n.a.	n.a.	n.a.	n.a.	n.a.	x	n.a.	x	n.a.	xxx	xxx
XRF Lab (wt.%)	**MnO**	0.04	<D.L.	0.04	0.07	0.06	0.04	0.25	0.07	0.08	0.1	0.07
XRF AL (cps)	**Mn**	31	12	25	72	43	28	213	39	48	91	61
LIBS corescan	**Mn**	x	<D.L.	x	n.a.	x	<D.L.	x	x	x	-	n.a.
LIBS ind	**Mn**	n.a.	n.a.	n.a.	n.a.	n.a.	<D.L.	n.a.	<D.L.	n.a.	<D.L.	<D.L.
XRF Lab (wt.%)	**K_2O**	0.57	1.15	0.20	<D.L.	<D.L.	<D.L.	0.16	<D.L.	0.11	<D.L.	<D.L.
XRF AL (cps)	**K**	153	243	52	22	18	12	55	4	28	8	8
LIBS corescan	**K**	x	x	x	n.a.	x	x	x	x	x	x	n.a.
LIBS ind	**K**	n.a.	n.a.	n.a.	n.a.	n.a.	<D.L.		<D.L.	n.a.	<D.L.	<D.L.

	Lithologies	Sandy shale	Marls	Cb.black shales	Marls – pis. bauxite	Red clay+bauxite	Pis bauxite co.	Pis red bauxite	Pis bauxite	Red bauxite	Limestone+Bx	Limestone
XRF Lab (wt.%)	**P_2O_5**	0.02	0.061	0.088	0.03	<D.L.	0.21	0.14	0.36	0.24	0.03	<D.L.
XRF AL (cps)	**P**	high error	high error	high error	high error	high error	high error	high error	high error	high error	high error	high error
LIBS corescan	**P**	<D.L.	<D.L.	<D.L.	n.a.	<D.L.	<D.L.	<D.L.	<D.L.	<D.L.	<D.L.	n.a.
LIBS ind	**P**	n.a.	n.a.	n.a.	n.a.	n.a.	O.R.	n.a.	O.R.	n.a.	<D.L.	<D.L.
XRF Lab (wt.%)	**TiO_2**	0.63	0.68	0.37	0.70	0.88	2.28	1.74	2.64	2.59	0.24	0.04
XRF AL (cps)	**Ti**	192	211	61	202	259	712	318	948	808	46	34
LIBS corescan	**Ti**	<D.L.	x	x	n.a.	x	x	xx	xx	xxx	<D.L.	n.a.
LIBS ind	**Ti**	n.a.	n.a.	n.a.	n.a.	n.a.	xxx		xxx	n.a.	x	x
XRF Lab (wt.%)	**S**	0.93	0.10	3.69	0.02	0.01	0.01	0.01	0.01	0.01	0.03	0.04
XRF AL (cps)	**S**	n.a.	n.a.	n.a.	n.a.	n.a.	n.a.	n.a.	n.a.	n.a.	n.a.	n.a.
LIBS corescan	**S**	x	<D.L.	xx	n.a.	<D.L.	<D.L.	<D.L.	x	<D.L.	<D.L.	n.a.
LIBS ind	**S**	n.a.	n.a.	n.a.	n.a.	n.a.	n.v.	n.a.	O.R.	n.a.	n.v.	n.v.
XRF Lab	**Zr**	n.a.	n.a.	n.a.	n.a.	n.a.	n.a.	n.a.	n.a.	n.a.	n.a.	n.a.
XRF AL (cps)	**Zr**	n.a.	n.a.	n.a.	n.a.	n.a.	n.a.	n.a.	n.a.	n.a.	n.a.	n.a.
LIBS corescan	**Zr**	n.a.	n.a.	n.a.	n.a.	n.a.	n.a.	n.a.	n.a.	n.a.	n.a.	n.a.
LIBS ind	**Zr**	n.a.	n.a.	n.a.	n.a.	n.a.	n.v.		n.v.	n.a.		
XRF Lab	**C**	n.a.	n.a.	n.a.	n.a.	n.a.	n.a.	n.a.	n.a.	n.a.	n.a.	n.a.
XRF AL (cps)	**C**	n.a.	n.a.	n.a.	n.a.	n.a.	n.a.	n.a.	n.a.	n.a.	n.a.	n.a.
LIBS corescan	**C**	x	?	x	n.a.	x	x	<D.L.	x	<D.L.	?	n.a.
LIBS ind	**C**	n.a.	n.a.	n.a.	n.a.	n.a.	x	n.a.	x	n.a.	xx	xxx
XRF AL (cps)	**Zr**	n.a.	n.a.	n.a.	n.a.	n.a.	n.a.	n.a.	n.a.	n.a.	n.a.	n.a.
LIBS corescan	**Zr**	n.a.	n.a.	n.a.	n.a.	n.a.	n.a.	n.a.	n.a.	n.a.	n.a.	n.a.
LIBS ind	**Zr**	n.a.	n.a.	n.a.	n.a.	n.a.	n.v.		n.v.	n.a.		
XRF Lab	**C**	n.a.	n.a.	n.a.	n.a.	n.a.	n.a.	n.a.	n.a.	n.a.	n.a.	n.a.
XRF AL (cps)	**C**	n.a.	n.a.	n.a.	n.a.	n.a.	n.a.	n.a.	n.a.	n.a.	n.a.	n.a.
LIBS corescan	**C**	x	?	x	n.a.	x	x	<D.L.	x	<D.L.	?	n.a.
LIBS ind	**C**	n.a.	n.a.	n.a.	n.a.	n.a.	x	n.a.	x	n.a.	xx	xxx

All samples were studied by laboratory XRF and XRD (ERAMET IDEAS, Trappes, France Prudhomme, 2018) and portable infrared (BRGM, Orléans, France) as part of the H2020 SOLSA project. The mineralogy of the analysed samples has previously been described in Meima *et al* (2021). Sandy shales and marls are composed of calcite ($CaCO_3$), kaolinite ($Al_2Si_2O_5(OH)_4$), illite ($(K,H_3O)(Al,Mg,Fe)_2(Si,Al)_4O_{10}$), vermiculite ($(Mg,Ca)_{0.7}(Mg,Fe,Al)_6(Al,Si)_8O_{22}(OH)_{4.8}H_2O$) and/or smectite ($A_{0.3}D_{2-3}[T_4O_{10}]Z_2 \cdot nH_2O$), quartz ($SiO_2$), and gypsum ($CaSO_4{\cdot}2H_2O$). In addition, the sandy shale contains goethite (FeO(OH)). In carbonated black shales, the marker horizon, similar in composition as sandy shale and marls, vermiculite, smectite and goethite are absent, but pyrite (FeS_2) and organic carbon are present. The bauxite layers start with marls and pisolitic bauxite with similar composition as the previous lithologies. Bauxite layers are rich in boehmite (AlO(OH)), hematite (Fe_2O_3), rutile (stable TiO_2), and anatase (metastable TiO_2) and may host zircon ($ZrSiO_4$). The bottom layer carbonate is mainly composed of calcite ($CaCO_3$), dolomite ($(Ca,Mg)(CO_3)_2$), hematite, goethite, and kaolinite (Table 3).

LIBS

Figure 2 shows the results of the line scan across the composite bauxite profile measured with the LIBS core scanner. These results previously published in Meima *et al* (2021), show that the different facies can be well distinguished with LIBS. The black shale horizon is easily characterised by the increased S emission. The bauxite/karst boundary is recognised by a sudden increase in Ca and decrease in Al emission. The brecciated bauxite shows already Ca. Other target elements (eg Si, Fe, Ti, Mg, Na, K, Li, C) support these observations and/or provide additional data.

Indeed, the LIBS spectra from the four key horizons (black shale, marl, red bauxite, bottom limestone) are very different from each other. The LIBS spectra of the black shale horizon are dominated by the many Fe emission lines, but also show relatively strong emission of Al, Ca, S, and occasionally C. The marl horizon is dominated by Ca emission lines, and additionally shows emission lines for eg Al, Fe, and Ti. Emission lines of Al, Ti, and Fe dominate the red bauxite horizon, and emission lines of Ca dominate the bottom carbonate horizon.

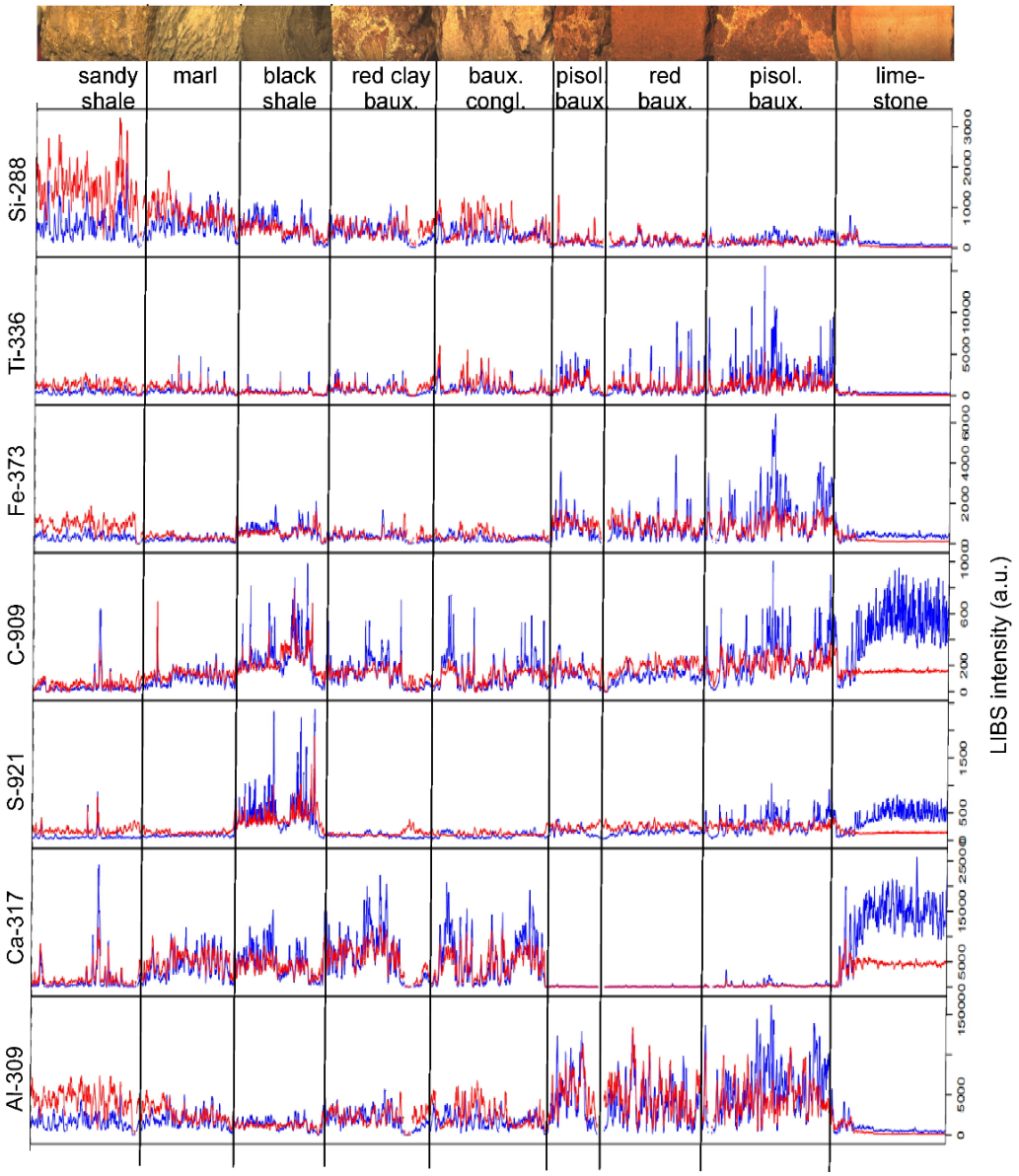

FIG 2 – Uncalibrated LIBS intensities for the composite bauxite profile as measured with the LIBS core scanner. Red lines represent normalised data, blue lines not-normalised data. A running average filter of five was applied to reduce noise and small-scale variations in the data. Unfiltered data are shown for S-921, C-909, and Ti-336 above intensity-thresholds of 500, 500, and 2500, respectively (from Meima *et al*, 2021). Please note that the relationship between LIBS intensity and element concentration is often not linear because of matrix effects.

Figure 2 also shows Ti enrichments in the brecciated bauxite, possibly representing rutile/anatase. Anatase is a heavy mineral, and it may be due to gravity that it is enriched in the brecciated part. Titanium and Ti-minerals are valuable materials to recover for its use in titanium industries. Titanium is generally easily detected with LIBS due to its many moderate and strong emission lines. A LIBS-based image of pisolitic bauxite (ER-SD00–0101) showing both distinct and diffuse Ti and Fe enrichments is shown in Figure 3.

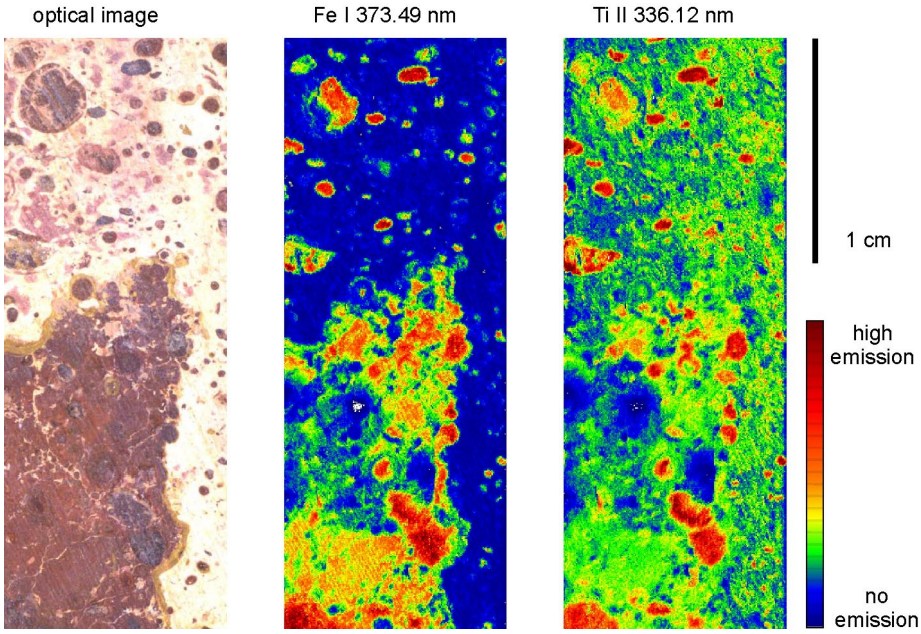

FIG 3 – LIBS-based Fe and Ti intensity distribution images (heat maps) for sample ER-SD00–0101 (pisol. baux.). The colour bar at the bottom right was scaled for each emission line individually according to the maximum observed intensity. Please note that the relationship between LIBS intensity and element concentration is often not linear because of matrix effects.

The results of the line scans obtained with the industrial LIBS system are shown in Figure 4. Due to the more limited spectral range, it was not possible to measure the C-909 line and the S-921 line. The C-193 emission in the UV was selected as a replacement for this. Unfortunately, S does not have a non-interfering emission line in the available spectral range and was therefore not included in these results.

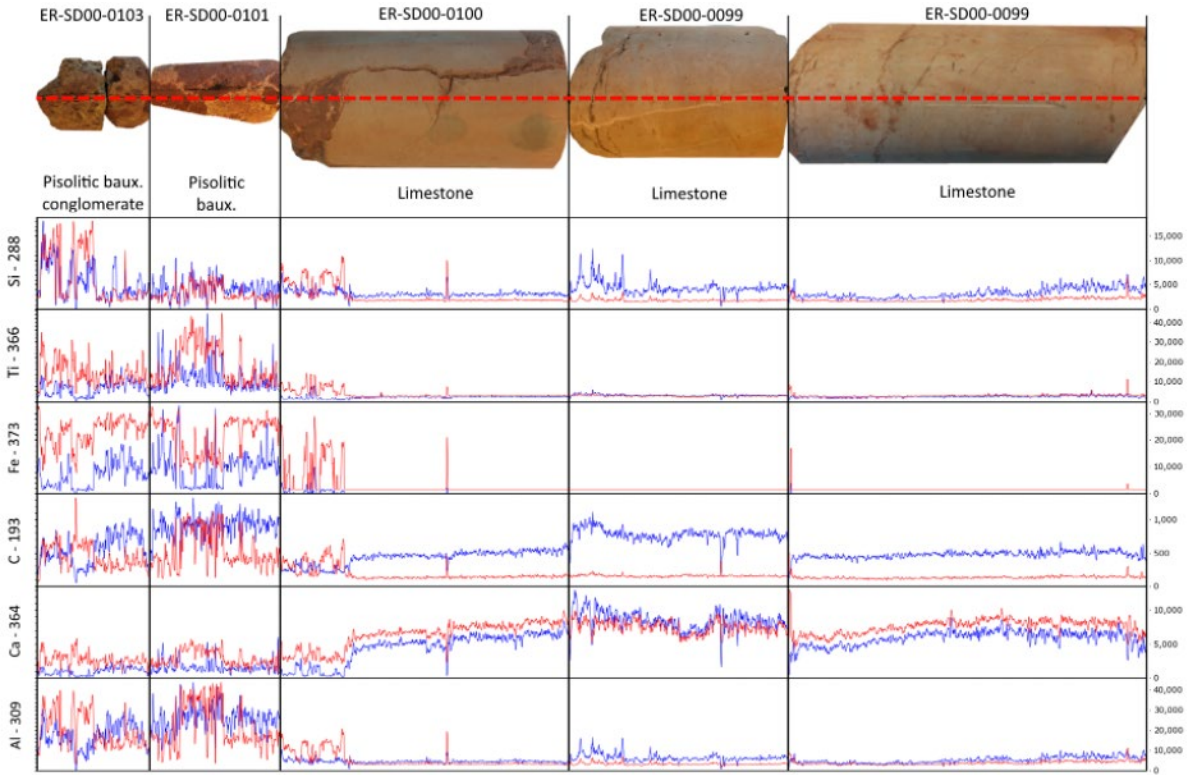

FIG 4 – LIBS line-scan results from the measurement using the industrial LIBS system (SPECTRAL) for the bottom part of the composite bauxite profile. The blue line corresponds to the intensity value of extracted peaks before normalisation, and the red line corresponds to normalised intensity.

It is important to note the following points regarding the results in Figure 4:

- The prominent spike/gap detected in the middle of the third limestone piece is caused by the crack that crosses the lines-can and defocuses the laser. This prominent feature therefore has no meaning regarding any of the measured elements.
- There might be slight differences in absolute intensity between the different samples. These changes are mostly related to differences in the laser focus position when placing the samples within the motorised stages. This difference is most prominent for example when comparing the first limestone with the second.
- The Ca I 364.xx nm emission line of Ca was selected instead of the Ca II 317.93 nm emission line used in Figure 2. This was related to the frequent saturation of the Ca II 317.93 nm line (and many of the other intense Ca lines) in the measurements with the industrial LIBS system. To prevent interference by saturation, a less intense line of Ca had to be selected.

Furthermore, most emissions used, do not show any significant overlap or interference with neighbouring peaks. Only the carbon line at 193.09 nm is occasionally partially overlapped by an Al line at 193.58 (Figure 5). This overlap is particularly present in the pisolitic bauxite samples, because these samples host both significant quantities of Al and C. The actual intensity of the C emission of those two samples is lower than the intensity presented in Figure 5.

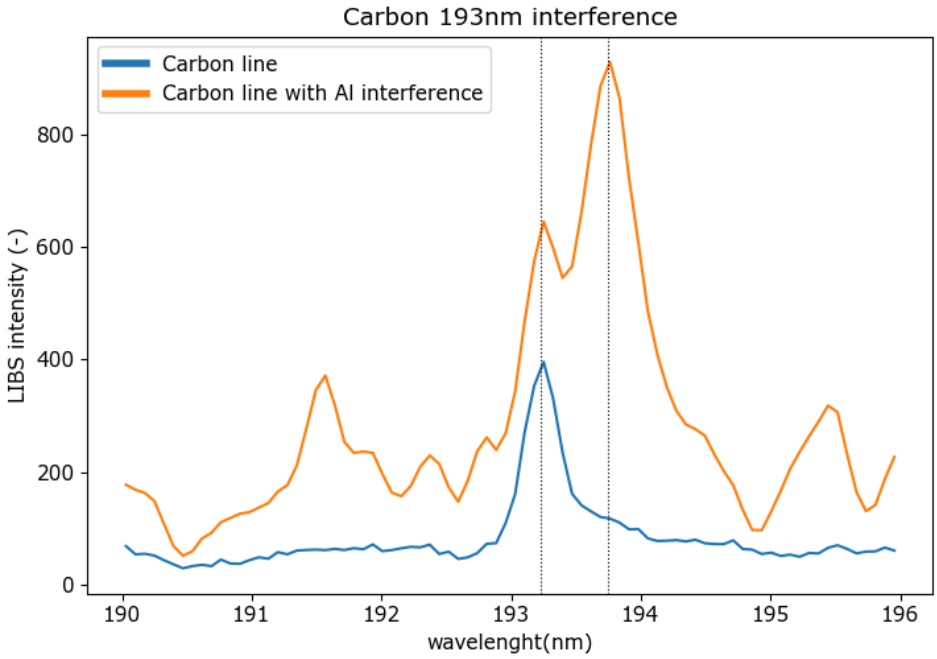

FIG 5 – Comparison of the C I 193.09 nm emission line for two samples measured with the industrial LIBS system, one without low Al contents (limestone) and one with increased Al contents (pisolitic bauxite). Shown spectra are an average of each sample. Note that there can be a slight dislocation of the measured peak due to calibration inaccuracies of the spectrometer.

LIBS-based classification of bauxite

In order to study how LIBS scan can be used to discriminate automatically against the two rock types within this sample set, a Principle Component Analysis (PCA) was performed on the data shown in Figure 4. From each sample, ten random spectra were selected and using algorithms from the python package 'Scikit-Learn' (Pedregosa *et al,* 2011). Additional pre-processing steps were performed such as normalisation, baseline correction, and removing frequently saturated wavelengths. After that, the full spectra were used as input to the algorithms.

The results from this PCA are presented in Figure 6, displaying the scores, and explaining variance and loadings of the PCA results. First of all, the elbow plot in Figure 6b displays how many Principle Components (PC's) are required to capture the variance within the data set. It shows that after only

two PC's, the explained variance does not increase strongly. These two PCs are sufficient to explain nearly 90 per cent of all variances.

The loadings presented in Figure 6c explain which variables, in this case wavelength positions, are used by the PCA to capture the variance in the data set. When using LIBS spectra, the most 'loaded' variables often correspond to emission lines of specific elements. The data show that the first two PCs are mostly based on Ca, Mg, Ti, and Al. PC1 has strong positive loadings for Ca and Mg lines and negative loadings for Al and Ti. While PC2 has strong positive loadings for Al and Ti but slightly negative loadings for Ca and Mg.

Figure 6a shows the calculated scores of each randomly selected spectrum on the first two PCs. Two clusters correspond well to the host rocks of the bauxite horizon. The limestones below the horizon score strongly on the first PC while the bauxite score is very low on this PC. This is clearly related to the high Ca and Mg content of the dolomitised limestones. There is one small cluster of datapoints from limestone (ER-SD00–100) right in between the two previously described clusters. This cluster corresponds perfectly to the top part of the sample that is the transition between limestones and bauxites.

The bauxite cluster scores universally low on PC1, but as a widespread within the second PC. This means that within the bauxites there is a strong heterogeneity regarding the Al and Ti contents.

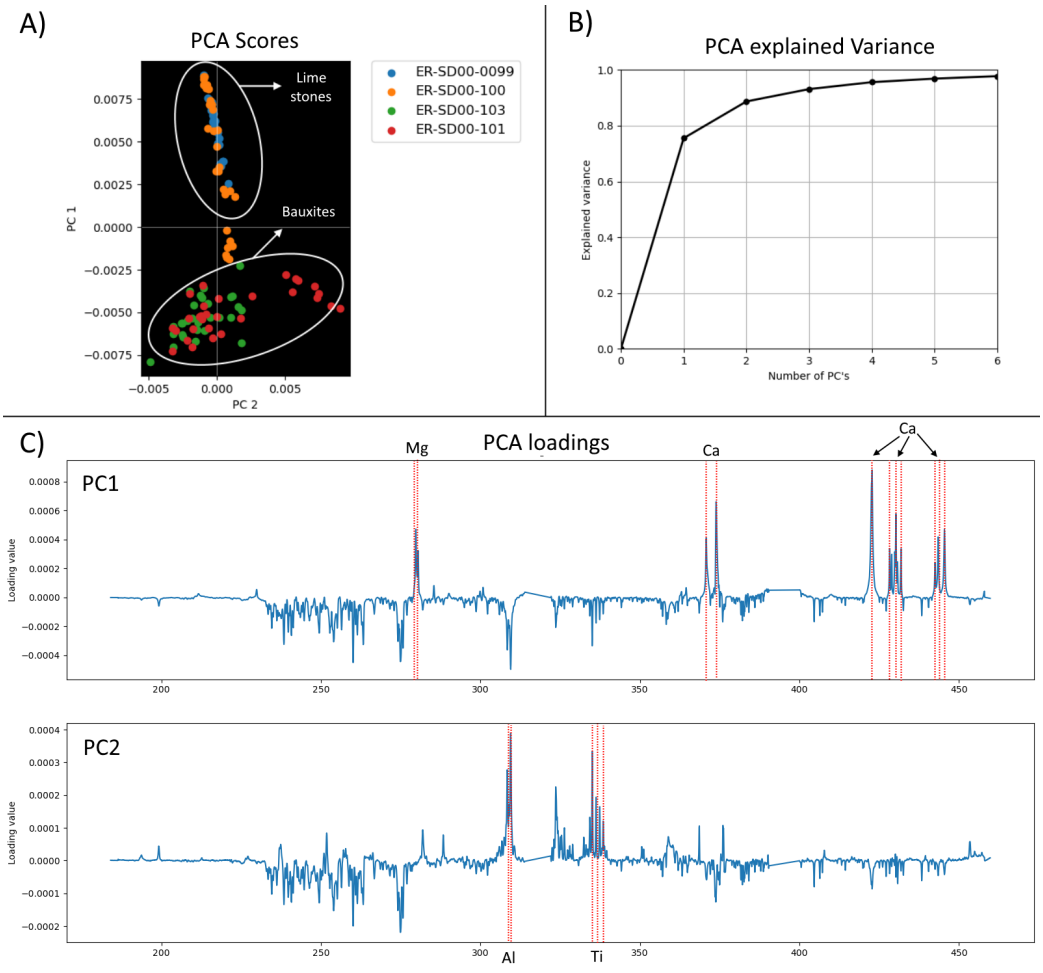

FIG 6 – Results of the PCA analysis based on the LIBS data collected with the Industrial LIBS sensor. (a) A scatterplot of the calculated Principle Component (PC) scores based on ten randomly selected spectra per sample. The y-axis indicates the score for PC1 and the x-axis indicates PC2. (b) Elbow plot of the PCA explained variance. (c) Plot of the loadings for the first two principal components.

Table 5 shows a confusion matrix with classification results for the identification of all nine lithologies based on the LIBS core scanner measurements shown in Figure 2. Thereto, a spectral database was built using the average LIBS spectra of each core piece as a reference spectrum. Best results

were obtained with several characteristic emission lines for the target elements, rather than with the full LIBS spectrum. The supervised classification algorithm Spectral Angle Mapper was then used to calculate the spectral similarity between the reference spectra in the database and all subsequent averaged spectra (n=10) from the line scan. Table 5 shows that each of the lithologies is statistically correctly classified. However, due to the heterogeneity of the sample material, correct classification will require a few measurements, preferably on different parts of the sample. In case of the limestone, for example, three spectra were classified as pisolitic bauxite, which corresponds to spectra representing the transition between limestone and bauxite (see also Figure 5). Sample heterogeneity can also be seen in the fluctuation of the LIBS intensities on the line scans (Figures 2 and 4) and in the mapping (Figure 3) as well as in the optical appearance of the sample. However, because LIBS is very fast (Table 1 industrial LIBS system with 300 spectra per second), it should be no problem to perform the required number of measurements. In conclusion, classification of LIBS data may be used to identify key horizons to separate bauxite from waste rock.

TABLE 5

Confusion matrix with classification results for the nine lithologies based on the measurements with the LIBS core scanner. Explanations in the text below.

		Predicted								
		sandy shale	marl	black shale	red clay baux	baux congl	pisol baux	red baux	pisol baux	lime stone
Actual	sandy shale	45	4	0	0	0	0	0	0	1
	marl	16	27	1	0	0	0	0	0	0
	black shale	3	1	31	4	1	0	0	0	0
	red clay baux	11	4	0	21	14	0	0	5	0
	baux congl	6	1	0	14	23	0	1	4	0
	pisol baux	0	0	0	0	0	16	0	8	0
	red baux	3	0	0	0	0	8	37	10	0
	pisol baux	2	2	0	5	0	2	22	28	3
	limestone	0	0	0	0	0	0	0	0	43

X-Ray fluorescence

Roof rocks, bauxites, and bottom limestone can be clearly classified by chemistry (Table 3). According to the laboratory XRF results, roof rocks contain 56–69 wt. per cent SiO_2, whereas bauxites have significantly lower SiO_2 (<20 wt. per cent), except for one pisolitic bauxite which shows about 35 wt. per cent SiO_2. Bottom limestone contains <7 wt. per cent SiO_2. Al_2O_3 successively increases towards the bauxite horizon with a maximum value of 50 wt. per cent Al_2O_3, then, in the bottom limestone, it decreases below 5 wt. per cent. Similar trends are observed for Fe_2O_3, reaching up to 32 wt. per cent in the bauxite horizon. TiO_2 reflects the rutile/anatase content and is also highest in the bauxites reaching 2.6 wt. per cent. Phosphorus shows highest values in the bauxites (0.36 wt. per cent) and correlates with highest Fe_2O_3 contents. Sulfur characterises the black shales marker horizon with 3.7 wt. per cent.

Results of ANCORELOG's continuous XRF measurement profiles are plotted together with the laboratory XRF results in Figure 7. The results in cps of element specific emission lines are divided by 1000 (Fe, Mn), 200 (K, Ti) and 100 (Ca) for a better comparative presentation with laboratory results in wt. per cent. The qualitative results from ANCORELOG's profile scans reproduce the elemental concentration values derived from laboratory measurements and thus fulfill the requirements for a calibration against reference analytics on a larger sample and data set.

The increasing content of Fe and Ti towards the bauxite horizon is clearly reflected in the measurements (samples ER-SD00–0100 to ER-SD00–0103).

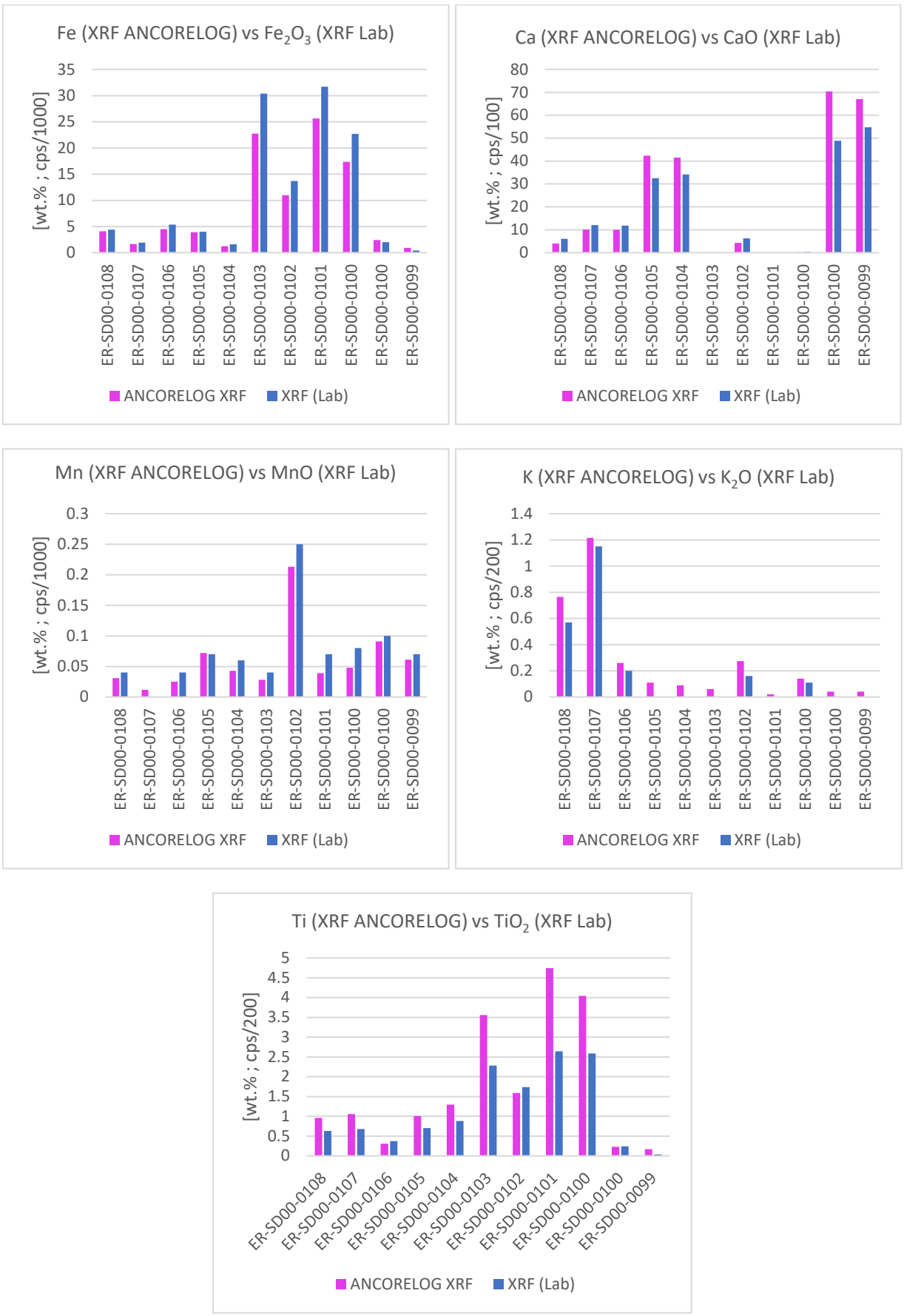

FIG 7 – ANCORELOG qualitative XRF results versus quantitative laboratory XRF results. ANCORELOG XRF values in cps are divided by 1000 (Fe, Mn), 200 (K, Ti) and 100 (Ca) for a better comparative presentation with laboratory results.

Time-gated RAMAN spectroscopy

Profile and single point measurement spectra were analysed to extract major characteristic peaks of target minerals detected by XRD and pIR reference measurements (Figure 8).

FIG 8 – Feature extraction from mixed Raman spectra: The blue line shows the mixed spectrum from a profile measurement. The green line shows a reference spectrum of a mineral found in the mixed spectrum. The red line shows a reference spectrum of a mineral that is not identifiable in the mixed spectrum. Y-axis: intensities (counts); X-axis wavelength shift (cm^{-1}).

The minerals identified by the time-gated Raman sensor in the different sample sections are listed Table 3 and characteristic Raman peaks identified in the measured spectra are listed in Table 6. Example Raman spectra from the measurements representing different minerals are shown in Figure 9. Quartz shows clear Raman peaks at ~466 cm^{-1}, ~355 cm^{-1}, ~207 cm^{-1} and ~128 cm^{-1} in samples ER-SD00–0104, ER-SD00–0107 and ER-SD00–0108. Anatase presents clear Raman peaks at ~143 cm^{-1} and ~638 cm^{-1} in samples ER-SD00–0100, ER-SD00–0101, ER-SD00–0102, ER-SD00–0104 and ER-SD00–0105. Boehmite peaks located at ~498 cm^{-1} ~362 cm^{-1} are present in the spectra of samples ER-SD00–0100, ER-SD00–0101 and ER-SD00–0103. Rutile shows Raman peaks at ~610 cm^{-1}, and ~445 cm^{-1} in samples ER-SD00–0100 and ER-SD00–0104. Calcite peaks at ~1089 cm^{-1}, ~710 cm^{-1}, ~279 cm^{-1}, and ~155 cm^{-1} occur in samples ER-SD00–0099, ER-SD00–0104, ER-SD00–0105, ER-SD00–0106 and ER-SD00–0107.

TABLE 6

Raman peaks of characteristic minerals i.

Mineral	Raman Peaks [cm^{-1}]	Sample
Quartz	~466 cm^{-1}, ~355 cm^{-1}, ~207 cm^{-1}, ~128 cm^{-1}	ER-SD00–0104, ER-SD00–0107, ER-SD00–0108
Anatase	~143 cm^{-1}, ~638 cm^{-1}	ER-SD00–0100, ER-SD00–0101, ER-SD00–0102, ER-SD00–0104, ER-SD00–0105
Boehmite	~498 cm^{-1}, ~362 cm^{-1}	ER-SD00–0100, ER-SD00–0101, ER-SD00–0103
Rutile	~610 cm^{-1}, ~445 cm^{-1}	ER-SD00–0100, ER-SD00–0104
Calcite	~1089 cm^{-1}, ~710 cm^{-1}, ~279 cm^{-1}, ~155 cm^{-1}	ER-SD00–0099, ER-SD00–0104, ER-SD00–0105, ER-SD00–0106, ER-SD00–0107

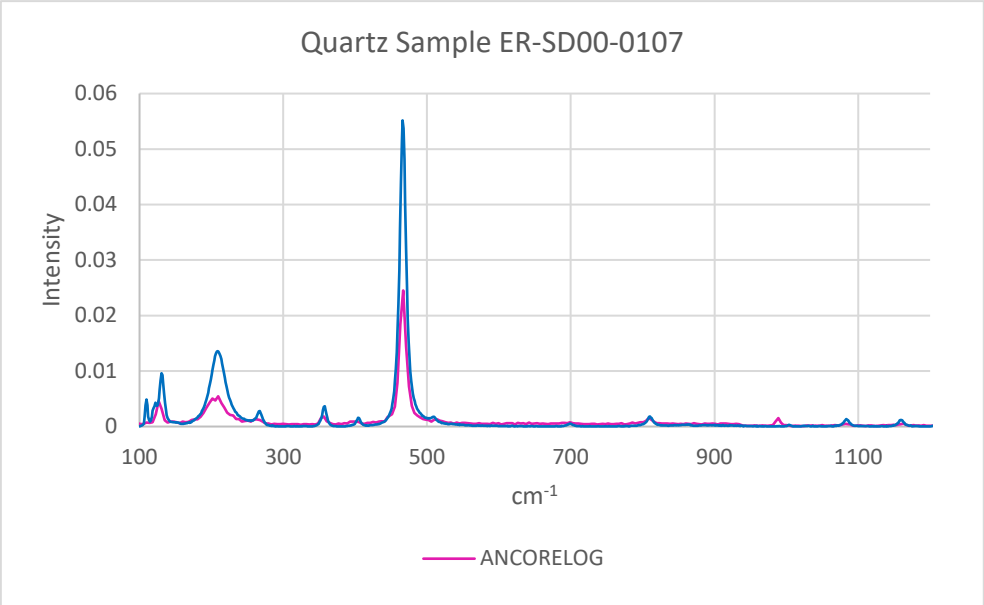

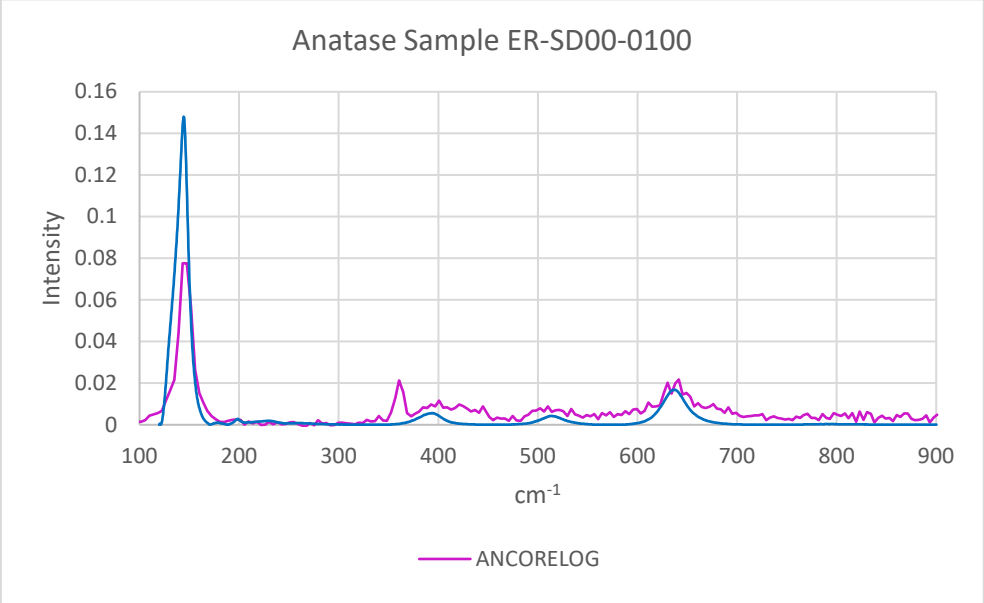

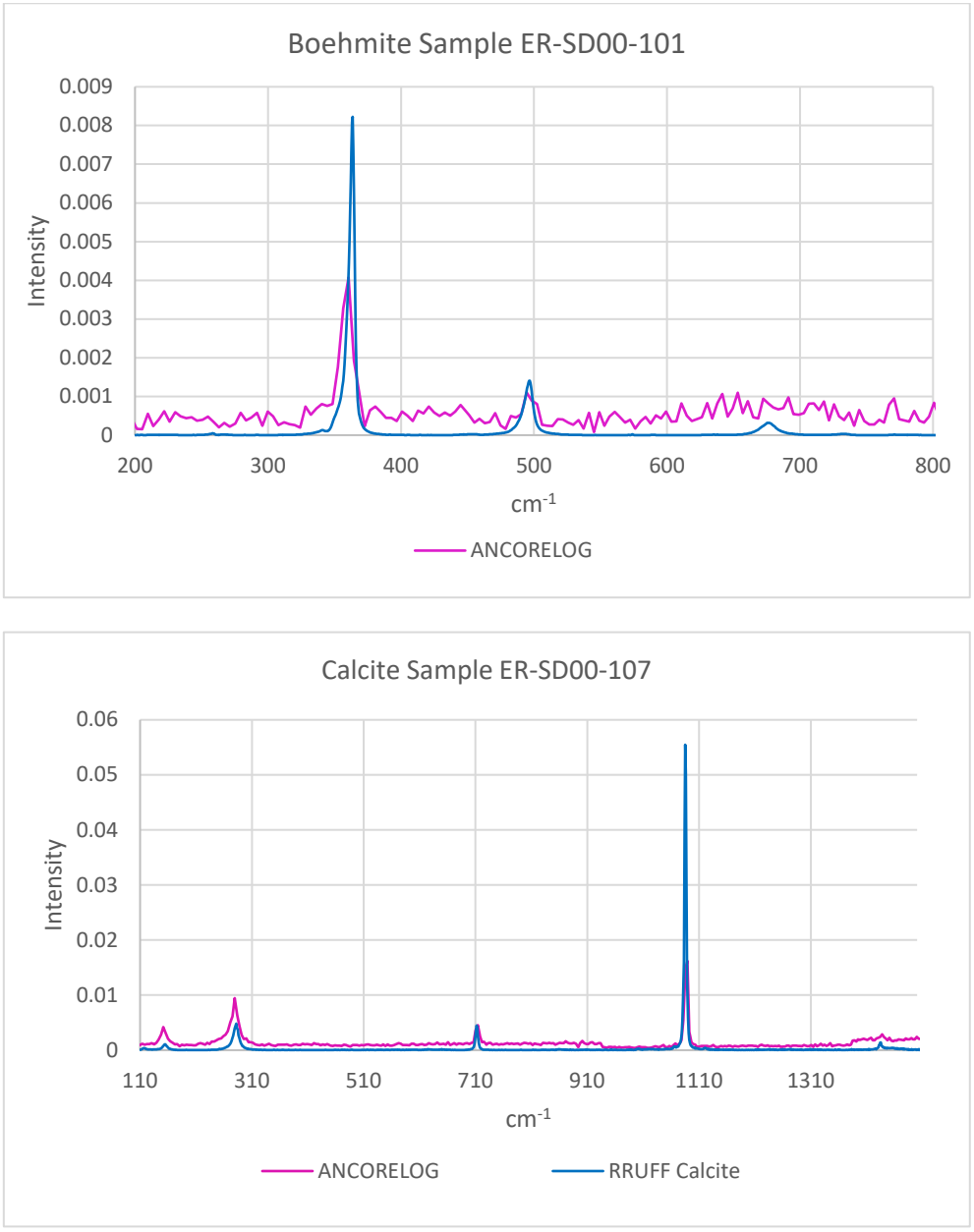

FIG 9 – Raman spectra from selected minerals. Blue line: reference spectra from the RRUFF™ database. Red line: extracted spectra from ANCORELOG measurements. X-axis: wavelength shift.

Portable Infrared spectroscopy (pIR)

Analyses were performed on each sample on characteristic features. The analytical window is 1.76 mm in diameter. Therefore, the pIR analyses/spectra represent a mixture of phases. With this field spectrometer, phyllosilicates, and iron oxyhydroxides (goethite, hematite) can be identified. Carbonates, normally present in the thermal infra-red region, were detected with the spectral line at 2333–1990 nm. Kaolinite is represented by the double peak at 2157 and 2203 nm, and the peak at 1910 (water molecule). The characteristic form of a 'shoulder' between 600 nm and 900 nm, with a peak at 876 nm in the VNIR region, indicates the presence of hematite and goethite. The measurements on all samples are summarised (Table 3).

In the bottom limestone, pIR detects mainly calcite, kaolinite, hematite, and goethite. Kaolinite, hematite, and goethite is mainly found in veins. The bauxite samples host kaolinite, hematite, and goethite. Two samples show peaks corresponding to dolomite. In the upper part of the bauxite, illite is detected. Ilite also appears to be present in lighter areas of the samples. It is important to note that Al-oxyhydroxides, such as boehmite (γ-AlO(OH), could not be detected by pIR. Rutile was detected in one single bauxite sample by pIR, but no anatase.

In the roof rocks, calcite was detected in all samples, but also illite, kaolinite, hematite and goethite are present. The 'black shale' maker horizon shows low reflectance, and hosts kaolinite, calcite, illite, hematite and goethite.

Classification by pIR of the bauxite horizon is ambiguous. The only mineral which may allow to classify bauxite from host rocks in this study, is hematite. Hematite is however also present in the lower part of the barren roof rocks (Table 3).

X-Ray Diffraction (XRD) results

The XRD results are presented in Table 3. The bottom-limestones contain mostly calcite. The bauxite samples host hematite, goethite, rutile and anatase. Calcite is detected in all samples in which boehmite is not detected. Kaolinite is detected in all bauxites and roof rocks. The roof rocks consist of quartz, clay minerals (illite, or inter-stratified illite-smectite).

DISCUSSION

Sorting of bauxite-waste by LIBS and XRF

LIBS

The results of the PCA performed on the LIBS data from the industrial LIBS sensor show that it is very feasible to distinguish the limestone-bauxite horizon using LIBS measurements alone. The horizon between bottom karst limestones and bauxites is very pronounced. Moving from the bottom limestone into the bauxites, Fe, Al, and Ti intensity rises drastically while the Ca intensity drops. In this small data set used, it is possible to make a perfect separation by setting a hard boundary only on Principle Component 1. The fact that such a classification can be made using a relatively lightweight analysis method displays the high potential of LIBS for fast classification applications. Furthermore, the confusion matrix with classification results for all nine lithologies (Table 5) shows that LIBS data can be used to identify all key horizons to separate bauxite from waste rock. Correct classification, however, will require a few LIBS measurements, preferably on different parts of the sample. This is because of sample heterogeneity. Because LIBS is very fast (Table 1 industrial LIBS system with 300 spectra per second), it should be no problem to meet this requirement.

Different LIBS systems have been tested in this study and the results can be used for the recommendation of appropriate LIBS components for industrial use on bauxite characterisation applications. Most notable fundamental differences between the tested LIBS instruments are the type of laser and type of spectrometer. The core scanner system utilises a relatively high power laser of 25 mJ that operates at 100 Hz compared to the laser used in the industrial system that operates at 1 mJ and 10 kHz. The ablation and sampling characteristics of both systems will therefore be intrinsically different. Due to the high laser power of the core scanner laser, ablation will be better for that set-up. However, the sampling properties of the industrial system are much better due to the very high repetition rate of the laser. This allows for faster scanning of core, which is often required for feasibility in industrial applications. However, when evaluating minor/trace elements or small-scale heterogeneity, a core scanner system will be of advantage. Furthermore, a high-resolution spectrometer is also of advantage when analysing minor or trace elements. This is especially relevant for bauxite, because valuable elements such as V and Sc are oft associated with iron or titanium minerals, and both iron and titanium show a very large number of emission lines in the same spectral window as eg vanadium. The spectral resolution of the core scanner system has been shown to be high enough to separate characteristic V emission lines from the titanium and iron emission lines.

ANCORELOG XRF

Portable XRF, eg provided by Olympus were tested on bauxites. Although light elements reveal low detection limits, Al_2O_3, reactive SiO_2, TiO_2 and Fe_2O_3 can be reliable analysed (https://www.olympus-ims.com/fr/portable-xrd-for-bauxite-exploration-mining-and-extraction/).

ANCORELOG's fast XRF profile scan allows for mapping of elemental concentrations and thus detecting lithological boundaries. Due to the limited number of samples in this study, a calibration of

ANCORELOG's XRF results against laboratory reference measurements has not been conducted. With a larger number of samples and a data calibration on reference samples against laboratory results would enable a quantitative estimation of elemental concentrations. Light elements with an atomic number Z<18 are difficult to measure by XRF due to, among other reasons, the Auger effect that constitutes a non-radiative transition or internal conversion of K series photons or the fact that the energy of the emission lines is low. So, the photons are easily absorbed and generate a weak signal (Laperche and Lemière, 2021). Choosing a different set-up of components and measurement geometry enables a more precise measurement of Si, Al, and S, but also impedes the usage in an industrial environment with high production rates as required in exploration drill core logging campaigns.

Mineralogical information of bauxite-waste by Raman-pIR

Laboratory micro-Raman spectroscopy was carried out on drill core parts from laterite profiles. Although perfect results were obtained, micro-Raman it is too time consuming for online-real time analyses. However, it can be used on selected samples in the mine workshop (eg Duée *et al,* 2019; El Mendili *et al,* 2019; Secchi *et al*, 2018). Bauxite mineralogy from Northern Brazil mines was investigated by micro-Raman spectroscopy (Leite Faulstich *et al,* 2011). Results show that gibbsite, clay minerals, Ti-oxides, ironoxhydroxides, and quartz were detected. Greek bauxites were investigated by micro-Raman showing the performance for analysing polymorphe diaspore and boehmite (Gamaletsos *et al,* 2007).

The ANCORELOG time-gated Raman spectroscope is the first which will operate as an online mineral analyser on a drill core logger (Havisto *et al,* 2021). The time-gated Raman sensor used in the ANCORELOG system allows fast and automated profile core scanning with scan rates of up to 20 mm/s. In this study we clearly demonstrated that the target minerals boehmite, anatase and rutile, typical for the bauxite horizon, can be identified. Iron oxyhydroxides could not be detected. The mineralogy determined by the Timegate Raman spectrometer is coherent with the mineralogy determined by laboratory XRD and pIR. Therefore, we exclude phase transformation related to instrumental configuration such as laser power (El Mendili *et al,* 2010), or matrix effects to the fine-grained soil material.

Algorithms dedicated to unmixing the measurement spectra and thus identifying characteristic mineral signatures must be adapted to specific site requirements and become more precise with a growing number of samples and data.

Infrared spectroscopy as portable instruments or hyperspectral core scanner (SWIR, VNIR) is used since some years on drill cores (eg malvernpanalytical.com; corescan.com). Some tests on bauxite with VNIR-SWIR were performed in field on drill cores from the Villeveyrac bauxite deposit (Orberger *et al,* 2019). However, mineral databases which are adapted to the material to be analysed and smart software to rapidly interpret the data are crucial (eg Bui *et al,* 2018 and papers therein). In this study, pIR covering the VNIR and SWIR spectra, was used. This method is powerful to detect the clay minerals kaolinite and illite, goethite, and hematite. The presence of hematite mainly in the bauxite samples can be used to classify the ore samples. However, a cross-method approach using time-gated Raman in addition to detect Ti-minerals and Al-hydroxides (here boehmite) is necessary to complete pIR results.

Recommendation for mining and processing industries

Table 7 summarises the performance of each sensor on bauxite material. For brownfield exploration, beneficiation, and further processing (hydro and pyrometallurgy), a concept study must be performed in tight collaboration with the industrial partner. This study would be composed of laboratory mineralogy and chemistry, followed by test analyses using the in-field instruments on the target material(s). Then, the sensor combination, sensor configuration, and sensor calibration for the specific materials will be defined. A suitable mineral database will be established. For the case study here, Table 7 shows the performances and final recommendations.

TABLE 7

Sensor performances for bauxite and waste material sorting.

Sensor evaluation or bauxite - waste material classification and sorting							
Parameter	**LIBS**		**XRF**		**RAMAN ind**	**pIR ind**	**XRD lab**
	LIBS ind.	LIBS corescan	XRF ANCORELOG	XRF lab	ANCORELOG		
Speed	eg. 300 spectra/s	eg. 50 spectra/s	1mm/s to 10 mm/s high	low	1mm/s to 10 mm/s high	high	low
Sample preparation	no	no	no	yes	no	no	yes
Spot size	200 microns	200 microns	5mm continuous profile	100s microns on glass disc	160 microns, continuous profile	1.7 cm	powder analyses
Target Metals	Al, Si, Mg, C, S, Ca, Ti, V, Mn, Fe, Cr	Al, Si, Mg, C, S, Ca, Ti, V, Mn, Fe, Cr	Ca, Ti, Fe, Mn, Cr	major and minor elements	-	-	-
Target Minerals	-	-	-	-	clay minerals, quartz, rutile, anatas, calcite	clay minerals, goethite, hematite, calcite	crystalline minerals
Quantitative	-	-	-	x	-	-	-
Qualitative	x	x	x		x	x	x
Semiquantitative	x	x	x				x
Recommendation for bauxite sorting							
In field combination	x	?	x	-	x		-
Lab validation				x			x

For the here studied karst bauxite profile, during drilling, the bauxite on and offset can be defined by chemistry using Al, Si, Mg, Fe, Ti, Ca, C and S. All elements are detectable by LIBS; XRF will allow to do semiquantitative analyses for the metals Ti, Fe, Mn, Ca, K in Karst bauxites. Cr is present (eg Greek bauxites, Vind *et al,* 2018). For process design, mineralogy is important. Time-gated Raman spectroscopy will detect the Ti-bearing minerals, Al-hydroxides (eg boehmite) calcite, quartz and clay minerals, while pIR will enhance the knowledge on iron-oxyhydroxides. As iron-oxyhydroxides are the main phosphorus carrier, they can be used as proxy for targeting lab analyses. This classification method can be used for primary sorting of bauxite from waste. On selected samples, LIBS mapping more focused on trace elements accumulation, and/or XRT and CT analyses can be performed (Bauer *et al,* 2022).

CONCLUSIONS

1. Rapid and efficient bauxite characterisation is possible through industrial LIBS. ANCORELOG Profile scans with the XRF and time-gated Raman spectrometer can clearly distinguish between bauxite horizons, and the top and bottom Al-barren sedimentary rocks. Target minerals for the bauxite horizon are boehmite, anatase, rutile, goethite, and hematite. Calcite and dolomite indicate the bottom Karst.
2. Chemical tracing by XRF is possible using increasing Fe contents from the top sedimentary rocks, from low to high Al bearing bauxites and decreasing Fe contents in the dolomitised limestones. Titanium is another key element which can easily determine the Al-rich horizons, as Ti and Al are positively correlated in this study.
3. Our study shows that time-gated Raman is an important tool also for defining titanium minerals, in exploration, mining and processing. Anatase, rutile and ilmenite can be distinguished (see also Bauer *et al,* 2022).
4. The use of analytical sensors on raw materials for early quality evaluation can help significantly to reduce the environmental impact of mining and processing. Most waste can be left in place, and an efficient parameter definition for ore sorting during crushing and beneficiation on mine sites will contribute to reducing transport costs. Thus, CO_2 emissions will be reduced, less waste is entering the aluminium production, also saving energy, water, and gas emissions.

OUTLOOK

- Sensor-calibration must be performed on bauxite materials to obtain semi-quantitative data. Raman spectroscopy, XRF and LIBS must be performed on bauxite of different origins to establish a solid database for efficient and reliable data interpretation.
- Scandium, V and Ga will be extracted in the future at the end of the KIC EIT projects Scaleup (www.scale-technology.eu and VALORE. Several processing steps are involved needing a QA/QC as do the final commercial products Sc-hydroxides, oxides and fluorides, or V-pentoxides, salts, nitrates, or Ga. A sensor-based approach could be successful here as well.

For example, LIBS and XRF can detect Sc in Sc-extraction products, although it could not be detected in bauxite (Meima *et al,* 2021). Furthermore, V und Sc can be detected with LIBS and XRF.

As outlined by Abe Mitchell (2022; EXXON Mobil, USA), Industry 4.0 brought and is still bringing analytical sensors to the mining and processing industries. Industry 5.0 must shift from the technological data assess level to a holistic data-understanding and goal setting, human-centered approach. The core must be people from the mining and processing industries (geologists, technicians, mine and plant managers, operators), to better understand all these data, and convert them into actionable insights.

ACKNOWLEDGEMENTS

We thank the EIT RawMaterials projects: ANCORELOG (N°17028), the EIT T-Rex project (N°19122), the ScaVanger (N°20093), Scaleup projects (N°21013), VALORE (N°21018) and the H2020 project SOLSA (N°689868) for financial support of this project.

REFERENCES

Barry, A N, Cisse, M, Parfait, M M, Hallarou, M M, 2021. Mineralogical and geochemical characteristics of the Sangaredi Bauxite deposit, Bike Region, republic of Guinea. *Environmental and Earth Sciences Research Journal,* 8(1):11–22. https://doi.org/10.18280/eesrj.080102.

Bauer, C, Wagner, C, Orberger, B, Garcia Piña, C, Meima, J A, Firsching, M, Merk, S, Rybok, R L, Hyypiö, R, Wagner, C, Boudouma, O, Siahcheshm, K, Kaminski, C, Lindström, H, 2022. Powerful laboratory a real time examination tools for copper porphyry exploration, in *Proceedings of the IMPC Asia-Pacific 2022* (The Australasian Institute of Mining and Metallurgy: Melbourne).

Beyssac, O, 2020. New Trends in Raman Spectroscopy: From High-Resolution Geochemistry to Planetary Exploration. *Geosciences World*, hal-03049557.

Bui, T, Orberger, B, Blancher, S, Mohamed-Djafari, A, Pillière, H, Salaün, A, Bourrat, X, Maubec, N, Lefevre, T, Rodriguez, C, Grazulis, S, Duée, C, Harang, D, Wallmach, T, Chateigner, D, Le Guen, M, 2018. Building a Hyperspectral library and its incorporation into sparse unmixing for mineral identification. *Proceedings ICARSS (International Remote Sensing conference)*, Valencia Spain, July; IGARSS 2018–2018 IEEE International Geoscience and Remote Sensing Symposium, 2018, pp. 4261–4264.

Cremers, D A, Radziemski, L J, 2006. *Handbook of Laser-Induced Breakdown Spectroscopy*, 1st ed.; Wiley: Chichester.

Duée, C, Orberger, B, Maubec, N, Laperche, V, Capar, L, Bourguignon, A, Bourrat, X, El Mendili, Y, Chateigner, D, Gascoin, S, Le Guen, M, Rodriguez, C, Trotet, F, Kadar, M, Devaux, K, Ollier, M, Pillière, H, Lefèvre, T, Harang, D, Eijkelkamp, F, Nolte, H, Koert, P, 2019. Impact of heterogeneities and surface roughness on pXRF, pIR, XRD and Raman analyses: challenges for on-line, real-time combined mineralogical and chemical analyses on drill cores and implications for 'high speed' _Ni-laterite exploration. *J. Geochem. Explor*. 198, 1–17.

El Mendili, Y, Bardeau, J F, Riandrianantoandro, N, Gourbil, A, Grenèche, J M, Mercier, A M, Grasset, F, 2010. New evidence of in situ laser irradiation effects on g-Fe2O3 nanoparticles: a Raman spectroscopic study. *J. Raman Spectrosc*., 42, 239–242.

El Mendili, Y, Chateigner, D, Orberger, B, Gascoin, S, Petit, S, Bardeau, J F, Duée, C, Le Guen, M, Pillière, H, 2019. Mineralogical textural and chemical quantification of serpentinized harzburgite from Népoui mine in New Caledonia combined XRF-XRD, SEM EDS and Raman analyzes. *ACS Earth and Space Chemistry,* 3(10):2237−2249.

El Mendili, Y, Vaitkus, A, Merkys, A, Grazulis, S, Chateigner, D, Mathevet, F, Gascoin, S, Petit, S, Bardeau, J F, Zanatta, M, Secchi, M, Mariotto, G, Lumar, A, Vassetta, M, Lutterotti, L, Borobin, E, Orberger, B, Simon, P, Hehlen, B, Le Guen, M, 2020. Raman Open database: first interconnected Raman-X-ray diffraction open-access resources for material identification. *J. Appl. Cryst.,* 52, 618–625.

Galbács, G, 2015. A Critical Review of Recent Progress in Analytical Laser-Induced Breakdown Spectroscopy. *Anal. Bioanal. Chem. 407*, 7537–7562, doi:10.1007/s00216–015–8855–3.

Gamaletsos, P, Godelitsas, A, Chatzitheodoridis, E, Kostopoulos, D, 2007. Laser micro-Raman investigations of Greek bauxites from the Parnassos-Ghiona active mining area. Bulletin of Greece, *Proceedings of the 11th International Congress*, Athens, May, pp 736–746.

Hahn, D W, Omenetto, N, 2012. Laser-Induced Breakdown Spectroscopy (LIBS), Part II: Review of Instrumental and Methodological Approaches to Material Analysis and Applications to Different Fields. *Appl. Spectrosc*, *66*, 347–419, doi:10.1366/11–06574.

Harmon, R S, Senesi, G S, 2021. Laser-Induced Breakdown Spectroscopy—A Geochemical Tool for the 21st Century. *Appl. Geochem.*, *128*, 104929, doi:10.1016/j.apgeochem.2021.104929.

Havisto, J, Lindström, H, Uusitalo, S, Heilala, B, Muller, S, Pons Peres, J M, Garcia Pina, C, 2021. Time-gated Raman spectroscopy as mineral analysis tool in multi-sensor Ancorelog drill core logger. *11th International Conference on advanced Vibrational Spectroscopy*, p. 198.

Jolivet, L, Leprince, M, Moncayo, S, Sorbier, L, Lienemann, C-P, Motto-Ros, V 2019. Review of the recent advances and applications of LIBS-based imaging. *Spectrochimica Acta Part B: Atomic Spectroscopy* 151, 41–53. https://doi.org/10.1016/j.sab.2018.11.008.

Khajehzadeh, N, Haavisto, O, Koresaar, L, 2016. On-stream and quantitative mineral identification of tailing slurries using LIBS technique. *Minerals Engineering* 98, 101–109. https://doi.org/10.1016/j.mineng.2016.08.002

Kögler, M, Heilala, B, 2020. Time-gated Raman spectroscopy – a review. *Measurements Science and Technology,* 32, 1–17.

Kokaly, R F, Clark, R N, Swayze, G A, Livo, K E, Hoefen, T M, Pearson, N C, Wise, R A, Benzel, W M, Lowers, H A, Driscoll, R L and Klein, A J, 2017. USGS Spectral Library Version 7: U.S. Geological Survey Data Series 1035, 61 p, https://doi.org/10.3133/ds1035.

Kuhn, K, Meima, J A, Rammlmair, D, Ohlendorf, C, 2016. Chemical Mapping of Mine Waste Drill Cores with Laser-Induced Breakdown Spectroscopy (LIBS) and Energy Dispersive X-Ray Fluorescence (EDXRF) for Mineral Resource Exploration. *J. Geochem. Explor.*, *161*, 72–84, doi:10.1016/j.gexplo.2015.11.005.

Lafuente, B, Downs, R T, Yang, H, Stone, N, 2015. The power of databases: the RRUFF project. *In: Highlights in Mineralogical Crystallography*, T Armbruster and R M Danisi, eds. pp 1–30 (https://rruff.info/).

Laperche, V, Lemière, B, 2020. Possible Pitfalls in the Analysis of Minerals and Loose Materials by Portable XRF, and How to Overcome Them. *Minerals 2021*, 11, 33. https://doi.org/10.3390/min11010033.

Leite Faulstich, F R, Castro, H V, Cappa de Oliveira, L F, Neumann, R, 2011. Raman spectroscopy analysis of real samples: Brazilian bauxite mineralogy. *Spectrochimica Acta Part A*: molecular and biomolecular Spectroscopy, 80, 1, pp 102–105.

Lemière, B, 2018. A review of pXRF (field portable X-ray fluorescence – applications for applied geochemistry. *J. Geochemial Exploration*, 188, pp. 350–363. https://doi.org/10.1016/j.gexplo.2018.02.006.

Meima, J, Orberger, B, Garcia Pina, C, Prudhomme, A, Dittrich, C, 2021. Increasing resource efficiency of bauxites using LIBS. *Mater. Proc.* 5 (81), https:// doi.org/10.3390/materproc2021005081.

Mitchell, A, 2022. The power of people. *Global Mining Review,* 5 (2) 24–27.

Noll, R, Fricke-Begemann, C, Connemann, S, Meinhardt, C, Sturm, V, 2018. LIBS analyses for industrial applications – an overview of developments from 2014 to 2018. *Journal of Analytical Atomic Spectrometry* 33, 945–956. https://doi.org/10.1039/C8JA00076J

Orberger, B, Le Guen, B, Bui, T, Kanzari, K, Rodriguez, C, Prudhomme, A, Nolte, H, Teerlink, T, Koert, P, Pillière, H, Lefevre, T, El Mendili, A, Delchini, S, Grybauskas, A, Merkys, A, Vaitkus, A, Borovin, E, Lutterotti, L, Marchand, E, 2019. Sonic drilling coupled with on-line-on-mine-analyses: field tests at the Villeveyrac bauxite deposit (Southern France). *15th SGA Biennial Meeting on Life with Ore Deposits on Earth*, Aug 2019, Glasgow, United Kingdom.

Pedarnig, J D, Trautner, S, Grünberger, S, Giannakaris, N, Eschlböck-Fuchs, S, Hofstadler, J, 2021. Review of Element Analysis of Industrial Materials by In-Line Laser—Induced Breakdown Spectroscopy (LIBS). *Applied Sciences* 11, 9274. https://doi.org/10.3390/app11199274.

Pedregosa, F, Varoquaux, G, Gramfort, A, Michel, V, Thirion, B, Grisel, O, Blondel, M, Prettenhofe, P, Weiss, R, Dubourg, V, Vanderplas, J, Passos, A and Cournapeau, D*,* 2011. Scikit-learn: Machine Learning in Python, JMLR 12, pp. 2825–2830.

Phang, C, Williams, S, Munday, T, Waldron, T, 2006. Reflectance spectroscopy of regolith pulps and chips: implications for the detection of alteration mineralogy in the lower saprolite. *Regolith 2006*. Consolidation and Dispersion of Ideas. 274–278.

Prudhomme, A, 2018. Characterization of a Bauxite Core Using Several Field and Laboratory Methods. *Master Thesis*, Université Paris Saclay-ERAMET, p. 20.

Rakovský, J, Čermák, P, Musset, O, Veis, P, 2014. A review of the development of portable laser induced breakdown spectroscopy and its applications. *Spectrochimica Acta Part B: Atomic Spectroscopy* 101, 269–287. https://doi.org/10.1016/j.sab.2014.09.015.

Rifai, K, Michaud Paradis, M C, Swierczek, Z, Doucet, F, Özcan, L, Fayad, A, Li, J, Vidal, F, 2020. Emergences of New Technology for Ultrafast Automated Mineral Phase Identification and Quantitative Analysis Using the CORIOSITY Laser-Induced Breakdown Spectroscopy (LIBS) System. *Minerals* 10, 918. https://doi.org/10.3390/min10100918.

Schulte, R F, Foley, N K, 2013. Compilation of gallium resource data for bauxite deposits. Open-file report 2013–1272. 9 p.

Secchi, M, Zanatta, M, Borovin, E, Bortolotti, M, Kumar, A, Giarola, M, Sanson, A, Orberger, B, Daldasso, N, Gialanella, S, Mariotto, G, Montagna, M, Lutterotti, L, 2018. Mineralogical investigations using XRD, XRF and Raman spectroscopy in a combined approach. *J. Raman Spectrosc*, 1–8. https://doi.org/10.1002/jrs.5386.

Ujaczki, É, Feigl, V, Molnár, M, Cusack, P, Curtin, T, Courtney, R, Lenz, M, 2018. Re-using bauxite residues: benefits beyond (critical raw) material recovery. *Journal of Chemical Technology & Biotechnology*, *93*(9), 2498–2510.

USGS, 2021. Global Bauxite Reserves, Bauxite and Alumina Mineral Commodity Summaries. Available online: https://minerals.usgs.gov/minerals/pubs/commodity/bauxite/ (accessed on 16 June 2021).

Veneranda, M, Manrique, J A, Garcia-Prieto, C, Sanz-Arranz, A, Saiz, J, Lalla, E, Konstantinidis, M, Moral, A, Medina, J, Rull, F, Nieto, L M and Lopez-Reyes, G, 2021. Raman semi-quantitification on Mars: ExoMars RLS system as a tool to better comprehend the geological evolution of Martian crust, *Icarus*, 367, 114542.

Vind, J, Malfilet, A, Bonomi, C, Paiste, P, Sajo, I E, Blanpai, B, Takczyk, A H, Vassiliadou, V, Panias, D, 2018. Modes of occurrences of scandium in greek bauxite and bauxite residue. *Mineral Engineering*, 123, 35–48.

Digital geometallurgy – let data do the work

Z Pokrajcic[1] and P C Stewart[2]

1. Technical Director, PETRA Data Science, Melbourne Vic 3000.
   Email: zpokrajcic@petradatascience.com
2. CEO, PETRA Data Science, Brisbane Qld 7000. Email: pstewart@petradatascience.com

ABSTRACT

Geometallurgy is a very valuable and insightful practice that links geology characteristics to mineral processing performance. The aim being to predict the behaviour of the ore during processing using only geological properties such as geochemistry, rock type and mineralogy. These predictions of downstream performance are populated into the geological block model for more informed mine planning and can assist in optimised mineral processing design. It requires thousands of samples of drill core from across the orebody to undergo various metallurgical characterisation tests. The results of which are used to build prediction models showing the ore's response to mineral processing unit operations such as grinding, flotation and leaching. The final stage is this the distribution of these responses throughout the geological block model using suitable geostatistical techniques.

A complement to the proven and well documented geometallurgy practice is a digital approach using only the information in the geological block model and historical operating data. It involves integration of masses of historical data and information from all stages of the mining value chain from geology to mineral processing, through (1) a data fusion technique where the ore is tracked from the mine through all stages of the operation using mathematical validation methods and (2) application of machine learning for generation of superior prediction models. The process is called orebody learning.

Orebody learning converts spatial geological data into a time series geological data (fused geological data) suitable for machine learning modelling of downstream processes such as dig rate, load and haul, crushing, milling, and separation. Orebody knowledge acquired through data fusion ore tracking and machine learning is based on tens to hundreds of millions of tonnes of ore data and its actual response to processing.

Two case studies demonstrate how orebody knowledge is translated into operational insights by adding new 'operational experience' variables to the block model. This provides accurate inputs to mine planning and scheduling and employs predictions that are based on actual plant operating data rather than empirical models.

The first case study relates to Ban Houayxai, a gold operation located in northern Laos.

During its operation, the Ban Houayxai CIL (carbon-in-leach) gold plant experienced extended periods of very low gold recovery, less than 50 per cent gold recovery. The losses, high gold content in tails, were thought to be a result of gold locked in silicates and sulfides and to limited to fresh, unweathered rocks (Carpenter *et al,* 2018). Internal petrographic and geochemical studies failed to clearly identify problematic zones in the orebody and the reason for high gold losses.

Orebody learning and data fused ore tracking was implemented using two years of operating data. This is equivalent to the tracking of ten million tonnes of ore from the pit to waste dumps and to the plant. The data was merged and collated to produce a digital representation of the operation from pit to plant. This digital representation included periods of low gold recovery pertaining to the processing of fresh unweathered ore.

The application of machine learning techniques to CIL predict gold tail grade (Au g/t) using only variables in the geological block model enabled gold tail grade to be spatially linked to information in the geological block model, referred to as orebody learning. Block-by-block predictions of gold tail grade were added to the geological block models as new block model variables.

Orebody learning using data fusion for ore tracking and machine learning prediction models identified potentially problematic high tails blocks in the LOM (Life-of-mine) block model and allowed planning and scheduling engineers to proactively either stockpile or blend this material to avoid previous high tail grade excursions (Figure 1).

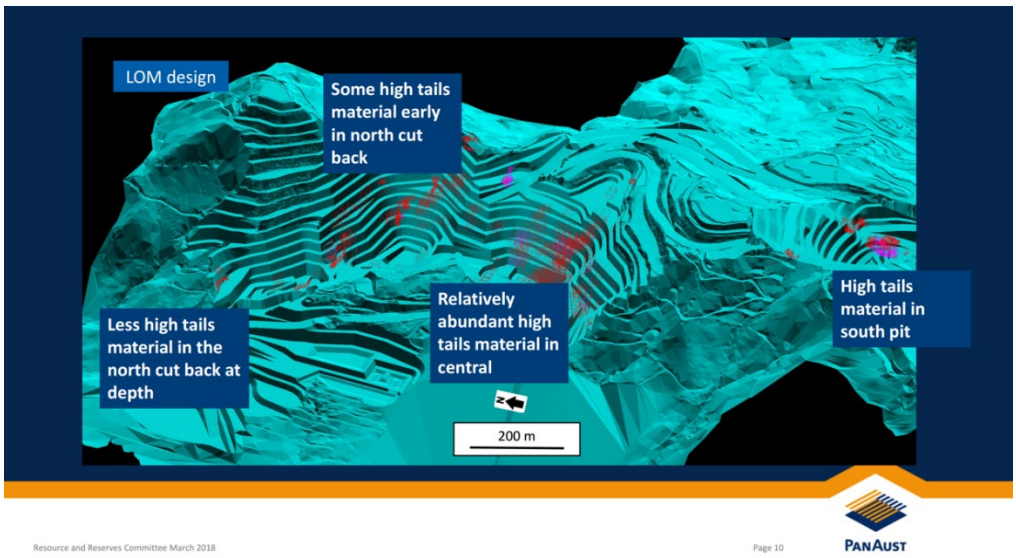

FIG 1 – Identification of problematic (high tail grade) blocks in the Life-of-mine block model using orebody learning (a combination of data fused ore tracking and machine learning).

The second case study relates to a very large magnetite plant consisting of multiple process trains, at the head of which are AG mills. The throughput of these mills dictates the capacity and production of the operation.

The aim was to develop a prediction model for AG mill throughput using only variables from within the geological block model. This facilitated a collaboration between mining and process engineers for proactive planning for variations in ore type and properties.

Mining, loading, primary crusher as well as coarse ore stockpile (COS) data was fused to create digital representation of the whole value chain. In this instance, the COS proved the most challenging part of the system to model and track material through. This was overcome by the use of virtual stockpiles and an iterative modelling methodology to verify the movement of ore through the stockpile. This amounted to tracking 17.2 Mt of ore from the pit, through the primary crushers, the COS and the AG mills.

Machine learning was used to generate an AG mill throughput prediction model. In total 25 variables were used in the algorithm used to predict AG mill throughput. In house validation of the AG mill throughput prediction indicated less than 5 per cent deviation on a month-on-month basis to actual throughput rates.

The overall performance of machine learning prediction model using unseen test data, data not used in the model building, is shown below in Figure 2.

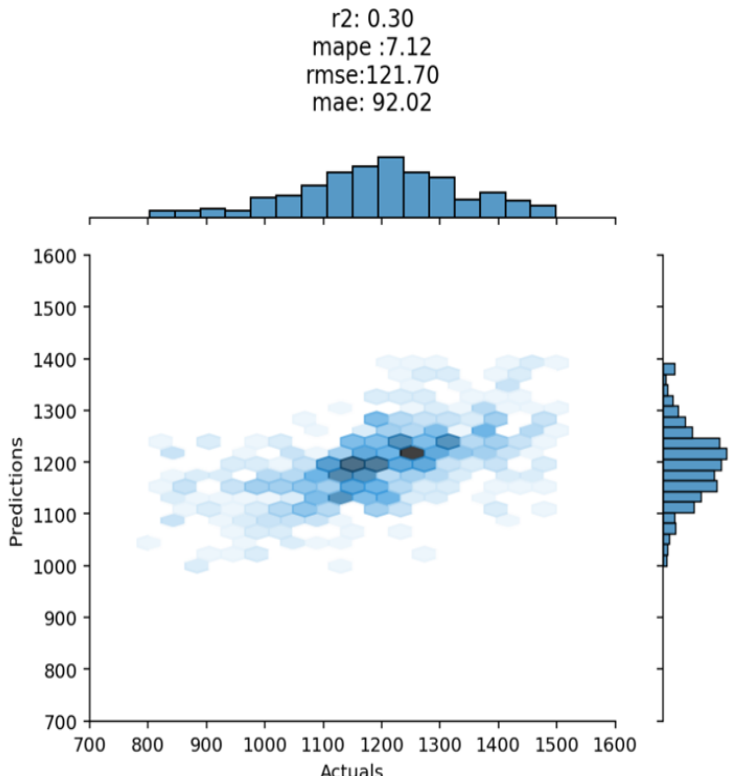

FIG 2 – Machine learning model accuracy (unseen data) for AG mill throughput.

Machine learning predictions for AG mill throughput were populated into the geological block model on a block-by-block basis. A visualisation of the AG mill throughput prediction for each block using Vulcan software is shown in Figure 3.

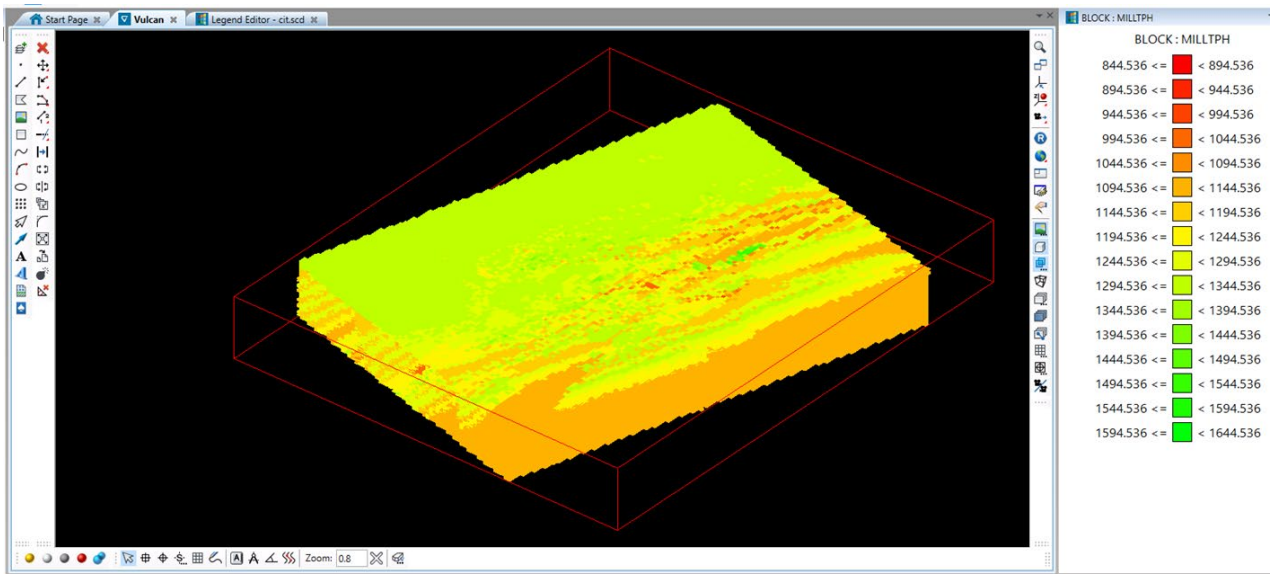

FIG 3 – Machine learning model AG mill throughput populated in geological block model.

In conclusion, geometallurgy is holistic approach to understanding processing characteristics as a function of ore type and ore variability. Orebody learning through the use of data fused ore tracking and machine learning prediction models is a complementary yet alternative approach to conventional geometallurgy. It avoids the extensive and repeated sampling, characterisation test work and statistical and empirical modelling. Rather involves integration of masses of data from all stages of the mining value chain from geology to mineral processing and builds machine learning prediction models based on tens to hundreds of millions of tonnes of ore data and its actual response to processing.

Orebody learning facilitates strengthening of the ties between the connected mining disciplines by sharing and merging data, no matter the source of the data. The case studies presented provide examples of accurate inputs for plant design decisions, mine planning and life-of-mine optimisation.

REFERENCE

Carpenter, J, Cowie, S, Stewart, P, Jones, E and Offer, A, 2018. Machine learning at a gold-silver mine: a case study from the Ban Houayxai Gold-Silver Operation. Abstract submitted to *Complex Orebodies 2018*, Brisbane 2018.

Geometallurgical proxies for HPGR comminution – comparison of packed bed test with SMC and Bond Ball Mill tests

R Vargas[1], R Valenta[2] and C Evans[3]

1. PhD Candidate, W H Bryan Mining and Geology Research Centre, University of Queensland, Brisbane Qld 4068. Email: r.vargassoto@uq.edu.au
2. Director, W H Bryan Mining and Geology Research Centre, University of Queensland, Brisbane Qld 4068.
3. Senior Research Fellow, W H Bryan Mining and Geology Research Centre, University of Queensland, Brisbane Qld 4068.

ABSTRACT

Comminution is the most energy-intensive stage in mining and the design of an effective and efficient comminution circuit requires knowledge of the machine-specific ore hardness from the early stages of the development of an ore deposit. Geometallurgy seeks to quantify the impact of variability in ore characteristics such as comminution response on the net present value of the deposit. A typical geometallurgical program aims to maximise operational potential by integrating measures of mining and processing attributes into 3D orebody models that reflect the economic value and allow mining companies to manage technical and operational risk and uncertainty (Keeney, 2010; Dominy and O'Connor, 2016). To understand the processing behaviour and its variability at a deposit scale, and aid the prediction of metallurgical performance, measures of intrinsic ore properties are integrated with processing parameters quantified using small-scale physical testing, and the resulting data is combined with geological and mining information which place it in a spatial context (Keeney, 2010; Dobby *et al*, 2004).

High-Pressure Grinding Rolls (HPGR) technology has been introduced to metal mining as a tertiary, quaternary, and pebble crusher, after many years of application in the cement and diamonds industry (Davaanyam, 2015). With its application in base and precious metal mining, many questions arise on the performance of this device in the context of the heterogeneity of ore deposits.

The industry-standard laboratory tests for comminution characterisation include the SMC test (Morrell, 2004) and the Bond Ball Mill Work Index (BBMWi) test (Bond, 1961). While the indices A*b and BBMWi resulting from these tests are accepted to characterise the size reduction of materials in SAG mills and ball mills, there is no equivalent widely-accepted laboratory-scale test for the HPGR. Despite suggestions in the literature about its greater energy efficiency, this device has not been widely adopted in metal mining. The absence of studies analysing the effect of ore variability in the context of compression breakage, the mechanism of rock breakage in the HPGR, could be one of the reasons for this. Some approaches have been developed to use the piston and die test (PDT) as a small-scale laboratory test, but most of these have focused on the development of a method for sizing HPGR units (eg Davaanyam, 2015; McClintock, 2018).

This study compares the results of widely-accepted small-scale comminution tests on ore samples from a porphyry Cu-Au deposit in Chile with results from the Packed Bed Test (PBT) used to characterise HPGR breakage response and explores the relationships between them. Specifically, the metallurgical data for comminution characterisation consisted of the results of the HRC™Packed Bed Test (Herbst *et al*, 2011), the SMC test, and the Bond Ball Mill Work Index test performed on 115 samples from 21 drill holes.

The Packed Bed Test uses a piston-and-die press configuration to compress a relatively small mass of sample under tightly-controlled test conditions, capturing the force applied and the resulting displacement of the piston. In order to identify an index of compressibility at the scale of geometallurgical modelling, several parameters were estimated from the test results. These included the reduction ratios R_{50} and R_{80}, Bed Height Reduction, Bed Compaction ratio and Bed Porosity Reduction.

The parameter R_{80} derived from the PBT, which represents the ratio between the 80 per cent passing sizes in the feed and the product (F_{80}/P_{80}), shows a very strong correlation with the A*b index obtained from SMC Tests, displaying higher values for the softer ores. The relationships of this

variable with the energy variables DWi (Drop Weight index), Standard circuit specific energy (SCSE) and Mih (HPGR ore work index) resulting from the SMC Test are strong, negative and nonlinear. However, there are no significant correlations between the PBT and SMC results and the BBMWi results.

Some of the differences between the results of the tests are explained by the different breakage mechanisms employed in each of the tests since the PBT uses compression, the SMC test uses impact and the BBMWi test uses impact and abrasion. Another potential reason is that the size fractions examined in each test differ: the PBT and SMC test are performed on a feed size range between 10 and 30 mm, and the BBMWi feed must be 100 per cent finer than 3.35 mm and for these samples has an average F_{80} of 2.16 mm.

Analysis of the mineralogical characteristics of the ores identified the main ore characteristics controlling the breakage response, which are similar for the SMC and PBT. The comminution test results of the PBT and the SMC tests show several moderate to strong correlations with the mineralogical characteristics of the ore measured using quantitative X-ray diffraction and QEMSCAN. The comminution variables also show moderate to strong relationships with geochemistry. The variability of the PBT and SMC test results agree in the spatial and geological context. The relationships identified were used as inputs for the development of predictive models of hardness across the deposit.

The similarities between the PBT and SMC test results support its use in geometallurgy to assess ore hardness in compression breakage. Additionally, the mineralogical controls identified for the ore tested can be used as proxies for ore hardness at a deposit scale where the results of physical tests are not available. For many early-stage projects, where only limited amounts of drill core samples exist, the possibility to use small-scale compression tests will, in turn, facilitate the early consideration of HPGR technology in the flow sheet design and will allow the use of geometallurgical information to characterise the operational risk due to ore heterogeneity.

ACKNOWLEDGEMENTS

This work is part of a research project funded by NuevaUnión SpA and the Sustainable Minerals Institute International Centre of Excellence Chile. The University of Queensland is acknowledged for its funding through the UQ Research Training Scholarship and the Complex Orebodies Program. Thanks are extended to staff from NuevaUnión SpA, Teck Resources Limited and Newmont Corporation for their continued support and comments throughout the project, and the approval to publish this work. SMI BRC and JKMRC staff are also acknowledged for their valuable comments during this research.

REFERENCES

Bond, F C, 1961. Crushing and Grinding Calculations Part I and II, *British Chemical Engineering*, 6(6; 8).

Davaanyam, Z, 2015. *Piston Test Procedures for Predicting Energy-Size Reduction of High Pressure Grinding Rolls.* Doctoral dissertation, University of British Columbia.

Dobby, G, Bennett, C, Bulled, D and Kosick, X, 2004. Geometallurgical Modelling – The New Approach To Plant Design And Production Forecasting/Planning, And Mine/Mill Optimization. In *Proceedings of the 36th Annual Canadian Mineral Processors Conference*, Ottawa.

Dominy, S C and O'Connor, L, 2016. Geometallurgy – Beyond Conception, In *3rd AusIMM International Geometallurgy Conference* (The Australasian Institute of Mining and Metallurgy: Melbourne).

Herbst, J A, Mular, M A, Pate, W T and Qiu, X, 2011. Detailed Modeling of an HPGR/HRC for Prediction of Plant Scale Unit Performance, *Proceedings of the International conference on autogenous grinding, semiautogenous grinding and high pressure grinding roll technology*, (Paper #46). Vancouver, BC, Canada.

Keeney, L, 2010. *The Development of a Novel Method for Integrating Geometallurgical Mapping and Orebody Modelling.* PhD Thesis, Sustainable Minerals Institute, The University of Queensland.

McClintock, M, 2018. *Validation Of Methodologies For Sizing A High Pressure Grinding Roll*. Master Of Applied Science. The University of British Columbia.

Morrell, S, 2004. Predicting The Specific Energy Of Autogenous And Semi-Autogenous Mills From Small Diameter Drill Core Samples, *Minerals Engineering*, vol 17/3, pp 447–451.

Selection and application of the main mineralogy techniques for mineral processing

J Zhou[1,2], H Yang[3] and L Tong[4]

1. Principal Consultant, Joe Zhou Mineralogy Ltd, Peterborough, Ontario, K9L 2A6.
2. Concurrent Professor, Northeast University, Shenyang, Liaoning, 110819, China.
   Email: joe.zhou.mineralogy@gmail.com
3. Professor, Northeast University, Shenyang, Liaoning, 110819, China.
   Email: yanghy@smm.neu.edu.cn
4. Associate Professor, Northeast University, Shenyang, Liaoning, 110819, China.
   Email: tongll@smm.neu.edu.cn

ABSTRACT

Mineral processing of various ores is largely driven by mineralogical factors, making mineralogical characterisation a significant part of a mineral processing project at any stage in the mine value chain. As more low-grade and complex ores are being discovered and developed, mineral processing engineers require more comprehensive and accurate information on the ores and metallurgical products being processed in order to understand the ore better during process development and plant operation. There is a variety of conventional and advanced techniques used in research and commercial mineralogy laboratories. Based on their features and capabilities, mineralogy techniques used in a process mineralogy laboratory can be classified into five categories: qualitative, semi-quantitative, quantitative mineral analysis, quantitative elemental analysis and mineral surface analysis. Each of the techniques has its advantages and limitations and has to be selected and applied primarily based on its merit when considering a mineralogy program to ensure the information obtained is reliable and accurate.

INTRODUCTION

It is well known that geological and mineralogical characteristics and parameters of an orebody such as grade, bulk mineralogy, metal deportment, ore texture and hardness often vary vertically and laterally within an orebody, and such variability has a direct impact on mineral processing and extractive metallurgy. It is important for mineral processors to understand the characteristics and variability of the ore to be processed during flow sheet development and mill operation. As an important part, mineralogy plays a critical role in ore characterisation of a mineral program. To ensure the information acquired in a mineralogy program is reliable and accurate, selecting the right tool(s) is extremely important and a standard operating procedure must be followed in any mineralogy program related to mineral processing. Without using the right tool, mineralogy data can be discounted or even misleading.

There is a variety of mineralogy techniques employed in mineral research and commercial labs (Table 1). These techniques are mainly based on the availability of existing instrument platforms and on the need for information required for mineral processing. Each of the mineralogy techniques has its advantages and limitations, and has to be selected and applied primarily based on its features/capabilities when considering a mineralogical program. Conventional analytical techniques such as optical microscopy, SEM and XRD are still being used in many mineralogical laboratories for their easy-operating and/or low-cost features, while automated mineralogy techniques have been widely used in recent years for their robust and rapid analytical capabilities to provide information on model mineralogy including grain size distribution, liberation and association of target minerals. D-SIMS and LA-ICP-MS have been used in quantifying trace metals (such as Au, Ag and PGE) carried in sulfide minerals of refractory ores. TOF-SIMS and XPS are mainly used for mineral surface analysis to detect and quantify surface adsorbent such as the chemicals used in sulfide flotation and the gold adsorbed on the surface of carbonaceous matter by preg-robbing. More often, a combination of conventional and advanced techniques are required for characterising the complex ores.

TABLE 1

Main techniques used in process mineralogy.

Category	Technique	Abbreviation	Application	Feature
Qualitative Mineral Analysis	Stereoscopy	SS	Mineral identification and sample preparation	10 μm LR
	Microscopy	MS	Mineral identification and semi-quantitative analysis of bulk material	0.5–1 μm LR
Semi-Quant Mineral Analysis	Automated Digital Image System	ADIS	Mineral identification and semi-quantitative analysis of bulk material	1 μm LR
	X-ray Diffraction	XRD	Mineral identification and semi-quantitative analysis of bulk material	0.5 wt% MDL
	Scanning Electron Microscopy	SEM	Mineral identification and semi-quantitative analysis of bulk material	0.5% MDL, 0.5 μm LR
Quantitative Mineral Analysis	Mineral Liberation Analyser	MLA	Mineral identification, quantitative analysis and imaging of bulk material	0.5% MDL, 0.5 μm LR
	Quantitative Evaluation of Materials by Scanning Electron Microscopy	QEMSCAN		
	Advanced Mineral Identification and Characterisation System	AMICS		
	TESCAN Integrated Mineralogical Analyser	TIMA		
Quantitative Elemental Analysis	Electron Probe Microanalysis	EPMA	Quantitative elemental analysis and imaging of individual particles	200 ppm MDL, 1 μm LR, 1–2 μm DR
	Proton-induced X-ray Emission	PIXE		10–100 ppm MDL 25–100 μm LR 15–50 μm DR
	Dynamic Secondary Ion Mass Spectrometry	D-SIMS		100–500 ppb MDL, ≥1 μm LR
	Laser Ablation Inductively Coupled Plasma Mass Spectrometry	LA-ICP-MS		ppm-ppb
	Time of Flight Laser Ion Mass Spectrometry	TOF-LIMS		1–100 ppm MDL, 2 μm LR, 100–300 Å DR
Mineral Surface Analysis	Time of Flight Resonance Ionisation Mass Spectrometry	TOF-RIMS	Surface analysis and imaging of bulk and individual particles (TOF-LIMS inorganic, TOF-SIMS inorganic and organic)	10 ppb MDL
	Time of Flight Secondary Ion Mass Spectrometry	TOF-SIMS		500 Å LR, 10 Å DR
	X-ray Photon Spectrometry	XPS		0.01–1 wt% MDL

Modified from Zhou *et al* (2004) and AMTEL (2022). Note: LR: Lateral Resolution; DR: Depth Resolution; MDL: Minimum Detection Limit.

This paper reviews the advantages and limitations of the five categories of techniques and discusses how to select and apply these techniques to acquire the reliable and accurate information required for a mineral processing program. Considering the importance of sampling and sample preparation in mineralogical study, a brief introduction to the techniques commonly used in mineralogy labs is also provided. Examples will be presented where applicable.

SAMPLE PREPARATION AND PRECONCENTRATION

The importance of sampling and sample preparation can never be overemphasized. Typically, the focus of laboratory results is on the analytical method, and sampling is pretty much taken for granted.

However, sampling is the major source of error in the analytical process, potentially, is an overwhelming source of error for any metallurgical project. The selection of the actual sample preparation procedures depends on the type and size of the sample, the mineralogy, and the analytical and budgetary constraints (LeVier, 2019). Actually, the quality of all analyses is dependent on the quality of sampling and sample preparation no matter how advanced the analytical technique is. It is not possible to obtain quality mineralogical information without quality samples. Therefore, standard sample preparation procedures must be followed in any analytical and mineralogical study program to ensure sample representativity and to avoid cross-contamination. In any case, it is highly recommended: (1) to get the sample preparation done in a dedicated area; (2) to split each sample using a riffler; (3) to start from low-grade samples towards high-grade samples; and (4) to clean the working area and used tools thoroughly after each use (Zhou *et al*, 2004).

Sample preparation

As with any analytical technique, sample preparation is crucial to obtaining reliable information. Samples used for a process-related mineralogical study may include large hand specimens, drill cores, rock chips, run-of-mine ores, flotation concentrate and tailings, leach residue and other metallurgical products. Usually, these samples need to be prepared before analysed using selected sample preparation techniques. More information on sample preparation and some standard procedures can be found in the references (Stanley and Laflamme, 1998; Zhou *et al*, 2004; Aylmore, 2019).

Mineralogy sample preparation usually starts from crushing and then going through grinding, screening (dry and wet), splitting for various test work and chemical analysis, pre-concentration, preparation of granular samples for surface analysis, preparation of polished thin sections and blocks for microscopic examination, and preparation of polished grain mounts for microscopic examination and instrumental analysis. Size distribution is critical for mineral processing. To avoid over-grinding, stage-crushing is highly recommended for all mineralogy samples. Trial grinding should be conducted prior to grinding of real samples to get an estimation of the time required for the test samples. Ground material needs to be screened after each run with coarse fraction going back to further grinding. Same as sample crushing and grinding, extra caution should be taken during polishing of grain mounts and over-polishing should always be avoided. This is particularly important for samples containing gold and silver minerals due to their softness. Samples for surface analysis (Figure 1a and 1b) should be kept at low temperature after it is taken in the lab or plant and analysed soon after preparation to avoid any surface oxidation or contamination. When conducting quantification of trace elements using EPMA, D-SIMS, LA-ICP-MS or other microbeam techniques, it is recommended to have mineral particles pre-selected to ensure data representativity and instrument efficiency. It is well known that gold-bearing sulfide (typically pyrite and arsenopyrite) often occur in three or four morphological types and gold in each variety may vary greatly. It is highly recommended to pre-select the sulfide particles under a microscope based on the morphological types and abundance of each type (Figure 1c). Random selection of target mineral particles should be avoided due to poor representativity.

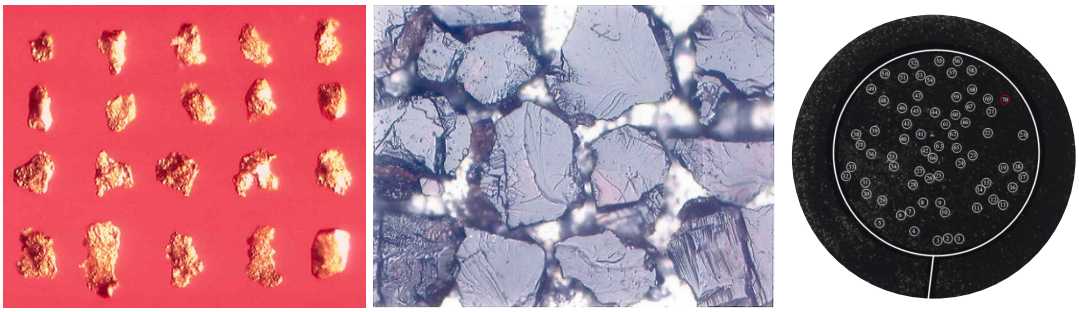

FIG 1 – Mineralogy samples prepared under stereoscope and optical microscope. (a) Individual -20 μm gold particles picked out from tailings for surface analysis; (b) sphalerite grains cluster prepared for surface analysis; (c) sulfide mineral particles selected in a polished section for quantification of submicroscopic gold using D-SIMS.

Pre-concentration

Most of the elements with economic value occur in low to extremely low abundance in the earth's crust and require pre-concentration prior to mineralogical characterisation to make the data acquired more representative and meaningful. This is particularly important for any mineralogy program of precious metals, critical metals and some other trace elements. For bulk mineralogy analysis using optical microscopy and/or automated instruments, common practice is to prepare one or more polished sections of unconcentrated material for direct analysis (screened size fractions may be required for certain samples to acquire better data quality). However, it is difficult (if not impossible) to get quality data on unrepresentative samples in metal deportment study programs because most mineralogy programs only use a few grams material if preconcentration is not involved. Thus, for any metal deportment study program, particularly for low-grade ores or tailings, large subsamples (one kilogram or more per sample depending on the grade) split from well-mixed as-received material using standard rifflers are highly recommended.

The pre-concentration techniques and equipment commonly-used in process mineralogy laboratories may include Knelson concentrator, shaking table, heavy liquid separation (HLS) and superpanner. These techniques use gravity to separate and concentrate minerals based on specific gravity difference of various minerals without changing the shape, grain size and surface properties except HLS (some labs use chemical-based heavy liquid products such as Sodium polytungstate or Methylene iodine as heavy media which may alter the mineral surface chemistry).

Superpanner is a unique and highly recommended preconcentration device for mineralogy labs. It is usually used to further concentrate the Sink fraction generated from heavy liquid separation, but can also be used to concentrate any other samples containing heavy minerals. After working for 20–30 minutes, heavy minerals and silicates are separated in decreasing S.G. of major minerals in the sample and a small amount of highly concentrated 'tip' (in case of a gold sample, tip contains all liberated gold particles and other heavy minerals), a 'clean' sulfide fraction and silicate fraction will be obtained for instrumental analysis and assayed for elements of interest (Figure 2). For gold deportment study, one or more polished sections are made from each product for gold scanning using microscope or automated mineral analyser, to determine the gold mineral species, size distribution, association, and for quantitative analysis by the electron microprobe to determine the mineral chemistry. Work completed by the senior author showed that the recovery of heavy minerals using this technique is ~99 per cent and the total amount of liberated gold and attached gold (both directly cyanide leachable) determined by this method is much closer to the gold recovery by cyanide leaching (Zhou *et al*, 2004).

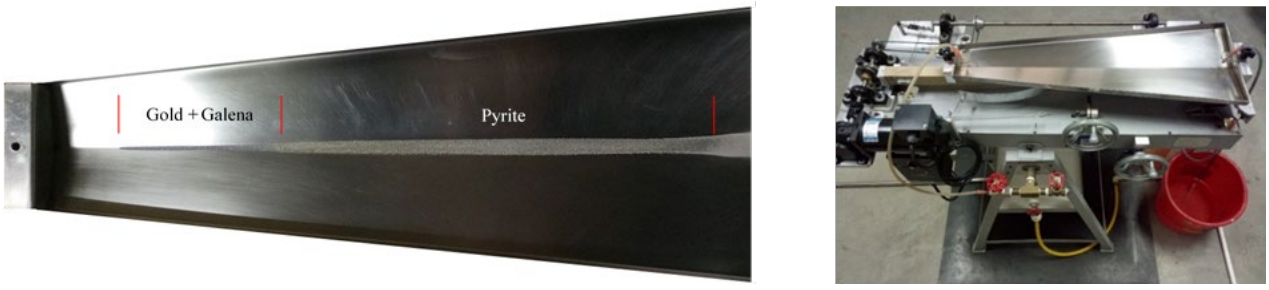

FIG 2 – Photographs showing the separation of a sulfide gold ore (left) by superpanner (right) Gold, galena, pyrite and silicate fraction were well separated.

TECHNIQUES FOR QUALITATIVE ANALYSIS

Qualitative techniques in this paper refer to those conventional mineralogy techniques such as stereoscopy and optical microscopy. Both microscopic techniques are commonly used for mineral identification, grain size measurement, liberation assessment and sample preparation for advanced instrumental analysis (Craig and Vaughan, 1994; Petruk, 2000; Zhou *et al*, 2004). The minimum detection limit (MDL) for both techniques are 1 μm and 10 μm lateral resolution (LR), respectively. In addition to mineral identification and morphological study, stereoscopy is often used for grain sample preparation for microbeam analysis such as TOF-LIMS and TOF-SIMS analysis which requires individual mineral particles (Figure 1a and 1b) and for quality check of final products generated by preconcentration techniques such as heavy liquid separation and superpanning. It is

also used for diamond selection in mineralogy labs and for quality check of the gravity or flotation concentrate in mineral processing labs. Optical microscope is also used for particle selection in some mineralogy labs which conduct instrumental analysis of individual mineral particles using EPMA, SIMS and LA-ICP-MS (Figure 1c), although it is mainly used for examination of polished thin section under transmitted light and polished section under reflected light for mineral identification, texture description, alteration classification, particle size measurement, and liberation and association determination of target minerals (Figure 3). Sample preparation for instrumental analysis is critical for any mineralogical program and will be discussed in detail in the next sections. Without quality samples, it would not be possible to produce quality results.

The advantages of stereoscopy and optical microscopy are that these techniques are fast and cost-effective, easy to operate and require low capital investment. They also offer excellent visual images (Figures 1 and 3). The limitations are that stereoscopy and microscopy only offer qualitative or semi-quantitative results. They are operator-dependent and it can be difficult to get the reliable data when the ore is complex and/or the sample is fine (<20 μm). However, stereoscopy and microscopy remain critical in many mineralogical studies and will not be replaced by advanced techniques in the foreseeable future. They are good for use in lab and at mine site.

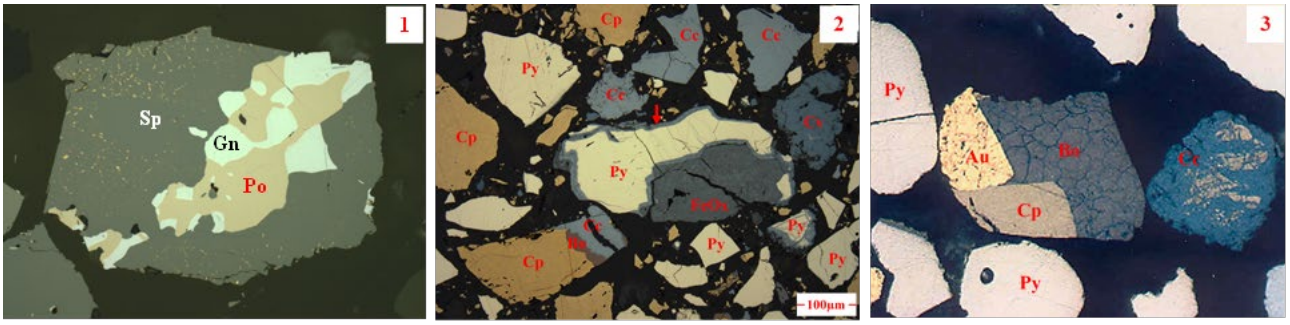

FIG 3 – Reflected light photomicrographs showing mineralogical composition, grain size, liberation and association of target minerals in tails and concentrate samples. (1) A composite particle of sphalerite (Sp) with locked galena (Gn), pyrrhotite (Po) and chalcopyrite (tiny green dots) from an Ag-Pb-Zn flotation tail; (2) Chalcopyrite (Cp), bornite (Bo), chalcocite (Cc), covellite (Cv), pyrite (Py) and iron oxide (FeOx) in a copper concentrate; (3) gold (Au), chalcopyrite (Cp), bornite (Bo), covellite (blue vein in Bo), pyrite (Py) and chalcocite (Cc) with Cp (greenish microinclusions) in a copper-gold concentrate.

TECHNIQUES FOR SEMI-QUANTITATIVE ANALYSIS

Information on mineral speciation, quantity and texture of mineral of interest is required for each ore being developed and processed. At the early stage of a development project or during processing of non-refractory ore, semi-quantitative analysis may provide the essential mineralogical information required for project evaluation or plant operation. Automated Digital Image System (ADIS), X-ray Diffraction (XRD) and Scanning Electron Microscopy (SEM) are the three major semi-quantitative techniques commonly used in mineralogy labs for identification and quantification of minerals in common ore samples.

Automated Digital Image System (ADIS)

ADIS is an optical microscopy system with imaging capability. Image analysis techniques have been described in detail by Petruk (1988, 2000), Lastra *et al* (1994, 2016) and Berry *et al* (2008). These techniques, if applied properly, can be more productive and provide better quality results than optical methods. Sized ore samples can be examined optically using an ore microscope equipped with an automated digital imaging system (ADIS). ADIS assigns imaging thresholds based upon colour and intensity to individual mineral species. Minerals with distinctive colour under reflected light such as chalcopyrite, bornite, chalcocite, covellite, galena, sphalerite, magnetite, hematite, pyrrhotite and pyrite are easily measured. Silicate minerals are grouped as non-opaque gangue minerals and are differentiated from the epoxy background using a coating technique. Same as optical microscopy, ADIS is fast and cost-effective, easy to operate and require low capital investment. In addition to excellent statistics, ADIS also offers quality visual images and information on mineral grain size and

liberation characteristics, making the system a great tool for lab and mine use. Available information and the senior author's experience showed that it is difficult for the system to differentiate minerals with the same or similar reflected colours. It is also ineffective and inaccurate for analysing complex ores.

X-ray Diffraction (XRD)

XRD is a powerful tool in minerals and materials studies and offers both qualitative and semi-quantitative results. Rietveld method is the most commonly used methodology to achieve quantitative phase analysis of crystalline materials. XRD uses X-ray (0.05–0.25 nm) to identify minerals through analysing their crystal structures and is considered to be most accurate technique in mineral identification because each mineral is unique in its crystal lattice. 10–40 μm powder material of ore sample is commonly used in XRD analysis and results are presented in two forms, a pattern showing the mineral species and qualitative/semi-quantitative data showing bulk mineralogy and mineral content in the sample analysed (MDL is about 0.5 wt per cent for semi-quantitative analysis depending on crystallinity of minerals present in the samples).

XRD is commonly used in mineralogy labs to determine the mineralogical composition of feed and metallurgical products on a daily basis. It is a preferred tool for speciation and quantification of clays, pyrrhotite and some other minerals. Actually, it is the only technique that can accurately distinguish the two types of pyrrhotites and has been used in characterising a number of pyrrhotite ores (Becker *et al*, 2008, 2010; Multani *et al*, 2018).

Structurally, there are two types of pyrrhotite, hexagonal pyrrhotite (Fe_9S_{10}, 47.37 per cent Fe) is weakly magnetic or nonmagnetic, while monoclinic pyrrhotite (Fe_7S_8, 46.7 per cent Fe) is highly magnetic. Different crystalline forms of pyrrhotite behave differently in beneficiation circuits, and carefully constructed and controlled processes, eg flotation units, are thus required to achieve good separation of pentlandite and hexagonal pyrrhotite. Monoclinic pyrrhotite is readily removed by drum magnets, but hexagonal pyrrhotite is almost unaffected. Under many conditions, hexagonal pyrrhotite has similar flotation kinetics to pentlandite.

In addition to minerals analysis, XRD is also used in analysis of metals, polymers, catalysts, pharmaceuticals, plastics, thin-film coatings, ceramics and semiconductors. In terms of unit cost and turnaround time, XRD is relatively cost-effective and fast if ore is simple. It is generally operator-independent due to sophisticated software. Application of XRD is limited in mineral quantification due to its higher detection limit. It is not accurate for low abundance minerals (1–3 per cent DT) and not suitable for detection and quantification of trace minerals such as gold, silver and PGMs. Some X-ray spectra may overlap and hard to evaluate. No textural information (grain size/liberation) available from XRD analysis is another disadvantage of the XRD analysis. When textural information is required, optical microscopy, SEM or automated mineralogy techniques are recommended.

SEM has been used in many mineralogy labs for different purposes. The advantages and limitations are discussed in the next section in conjunction with automated mineralogy techniques.

TECHNIQUES FOR QUANTITATIVE MINERAL ANALYSIS

Among the mineralogical factors affecting mineral processing, liberation, grain size distribution and association of target minerals are the three most important ones impacting various processes. In most ores, target minerals must be liberated or exposed prior to processing to achieve acceptable recovery and concentrate grade, although target minerals in some ores may not need complete liberation for concentration. For example, gold in a sulfide ore is often recovered by gravity, flotation, cyanidation or a combination of these techniques after milling, while gold in a copper-gold ore is usually recovered into a copper concentrate by flotation as liberated or binary particles. In the UG2 PGE ore, fine-grained PGMs (~10 μm) associated with sulfide minerals are recovered by flotation as composite particles to avoid loss of liberated fine PGMs. Therefore, it is important to have the information on liberation, grain size and association of target minerals during process development and plant operation.

In the past three decades, SEM-based automated mineralogy gained significant progress due to rapid development of analytical technologies and instrument hardware. Several advanced mineral analysis systems have been developed and widely used in the mining industry for their robust and

rapid analytical capabilities to provide information required for mineral processing (Gregory *et al*, 2013; Gu, 2003; Gu *et al*, 2014; Zhou and Gu, 2016; Multani *et al*, 2018; Aylmore *et al*, 2018a, 2018b; Aylmore, 2019). These techniques include Mineral Liberation Analyser (MLA), Quantitative Evaluation of Materials by Scanning Electron Microscopy (QEMSCAN), Advanced Mineral Identification and Characterisation System (AMICS), Tescan Integrated Mineralogical Analyser (TIMA), INCAMineral and BGRIMM Process Mineralogy Analyser (BPMA). The information that can be obtained from automated SEM systems includes: (1) modal mineralogy (the percentage of each mineral in the sample); (2) grain size distribution (distribution of grain sizes of target mineral in the sample); (3) mineral liberation (the liberation degree of the mineral of interest based on exposed surface area of particles; (4) mineral locking (a measure of target mineral enclosed in other minerals based on exposed surface area of the mineral of interest; (5) mineral association (a measure of the relationship of target mineral with the host mineral(s) in the sample.

Automated mineralogy techniques offer excellent statistics for major, moderate and minor minerals with quantitative analysis down to 0.1 per cent level. It also provides textural information (grain size, liberation, locking and association). The systems are generally operator-independent for simple ores. Figure 4 presents the information on modal mineralogy and sulfide liberation characteristics of five head samples from a sulfide gold ore. Modal mineralogy shows that the head samples are mainly composed of pyrite, siderite with moderate amounts of quartz, silicate, iron oxides and minor amounts of arsenopyrite and jarosite. Pyrite is the primary sulfide mineral in the head samples, accounting for 18.3 per cent in #3 Head to 36.3 per cent in #5 Head. Pyrite liberation data indicate that liberated pyrite and middling particles accounted for over 90 per cent in all five head samples. In addition to modal mineralogy and liberation data of target minerals, automated mineralogy techniques can also create cumulative grain size distribution curves to guide grinding and mineralogically limiting grade-recovery curves to predict correlation between concentrate grade and recovery (Aghamirian *et al*, 2012). Automated mineralogy techniques have the following limitations: (1) cannot detect and quantify elements in solid solution and do not provide real image for automated analysis; (2) fine particles can be missed at lower magnification (the minimum particle size for gold minerals can be detected and measured at 400X is ~0.6 μm); (3) statistics for trace minerals can be poor if preconcentration was not conducted; (4) cost-wise, they are moderately expensive to expensive for multi-size fractions; (5) operator-dependent when mineralogy is complex; and (6) not suitable for ores containing minerals with similar chemistry such as magnetite and hematite, pyrite and marcasite, and enargite and tennantite (classification or speciation can be wrong due to similar mineral chemistry). Like SEM, when used for bright phase (such as gold, silver and PGM) search, automated mineralogy techniques will take a considerably longer time if the sample contains a large amount of minerals with high backscatter signals such as galena, native silver and native tellurium. If this is the case, it is recommended that an optical microscope be used for bright phase search under the guidance of an experienced mineralogist. It is also recommended that a brief observation of polished sections under optical microscope is taken prior to instrument analysis to gain some knowledge of the samples for better setting up the instrument operating conditions. When analysis of iron oxide (such as magnetite, hematite and goethite) is required, it is suggested that quantification of the total Fe-oxide content be done by automated instrument and determination of the proportion of the different Fe-oxides by optical microscope.

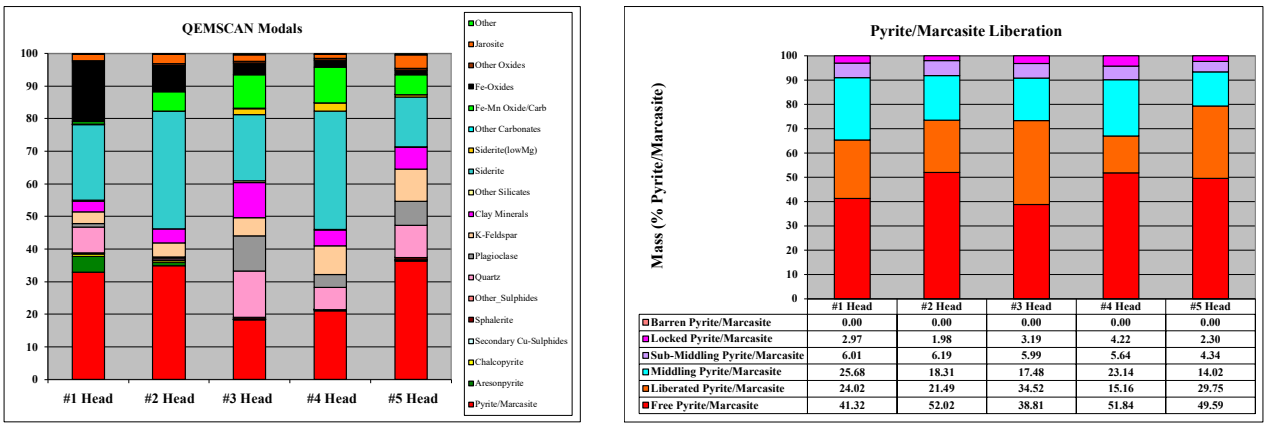

	#1 Head	#2 Head	#3 Head	#4 Head	#5 Head
Barren Pyrite/Marcasite	0.00	0.00	0.00	0.00	0.00
Locked Pyrite/Marcasite	2.97	1.98	3.19	4.22	2.30
Sub-Middling Pyrite/Marcasite	6.01	6.19	5.99	5.64	4.34
Middling Pyrite/Marcasite	25.68	18.31	17.48	23.14	14.02
Liberated Pyrite/Marcasite	24.02	21.49	34.52	15.16	29.75
Free Pyrite/Marcasite	41.32	52.02	38.81	51.84	49.59

FIG 4 – QEMSCAN modal mineralogy and sulfide liberation data of a sulfide gold ore. Left: Modal mineralogy of five head samples. Right: Liberation characteristics of pyrite/marcasite in head samples.

TECHNIQUES FOR QUANTITATIVE ELEMENTAL ANALYSIS

Mineral chemistry and concentration of trace element in host minerals are important to mineral processing because they often controls the target metal recovery and concentrate grade and often impact process selection and plant operation, and need to be quantitatively determined in a mineralogy program. The quantification of major constituents of a mineral is commonly done by electron probe microanalysis (EPMA), while the quantification of trace elements (such as Au, Ag, PGE and some critical metals) in host minerals is commonly done by Dynamic Secondary Ion Mass Spectrometry (D-SIMS), Laser Ablation Inductively Coupled Plasma Mass Spectrometry (LA-ICP-MS), Proton-induced X-ray Emission (PIXE) or other microbeam techniques.

Electron Probe Microanalysis (EPMA)

EPMA offers quantitative analysis of major and minor elements and also distribution of elements of interest in many metallic and non-metallic minerals. The minimum detection limit (MDL) is generally considered to be 0.02 per cent or 200 ppm for most elements. It is suitable for quantification of Au and Ag in native gold and electrum, Ag in dyscrasite, freibergite and other silver minerals, Fe in sphalerite and spodumene, Ni in pentlandite and pyrrhotite, As in pyrite and marcasite, and Ag in galena among other elements. EPMA is cost-effective comparing to other microbeam techniques. However, EPMA is standard dependent and not suitable for trace element analysis.

Sphalerite (ZnS) is the world's primary source of Zn. It is commonly formed with impurities such as Fe, Cu, Cd, Ga, In, Ge and Mn among others (Lepetit *et al*, 2003; Cook *et al*, 2009). It is well known that iron in sphalerite varies between deposits in different locations and in some cases between single samples from a given deposit, and has an impact on sphalerite floatability. Boulton *et al* (2005) investigated the effect of iron in sphalerite on the froth flotation of sphalerite at alkaline pH. It was found that a critical copper sulfate concentration exists where sphalerite recovery is maximised, above which the recovery of sphalerite then decreases. The presence of iron in sphalerite is detrimental to the rate of sphalerite flotation and hence its recovery, with the coarser particles being more affected than the fines. The presence of iron reduces the activation of sphalerite by copper, which in turn results in a reduction in collector adsorption. Yu *et al* (2019) found that the floatability of sphalerite from the Huize lead-zinc mine in China varied greatly with the iron impurity content. The flotation experiments conducted on the three types of sphalerites with iron content of 2.30 wt. per cent, 3.20 wt. per cent and 4.66 wt. per cent showed that the flotation recovery increased with the increase in iron impurity content. Therefore, the iron content in sphalerite needs to be quantified using a mineralogy tool for each deposit or each of the ore types in a given deposit. This type of analysis is commonly done in a mineralogy lab using EPMA.

The Dumont deposit is a large (1066 Mt probable reserve) low-grade (0.27 per cent Ni) nickel sulfide deposit in Canada. During the pre-feasibility study from 2010 to 2012, a detailed mineralogical program including 1980 QEMSCAN samples and 7260 electron microprobe points were undertaken to increase the understanding of the nickel deportment in the various recoverable and non-recoverable phases in a spatial context across the deposit (Muinonen *et al*, 2013). Disseminated

ultramafic-hosted nickel mineralisation is characterised by disseminated blebs of pentlandite ((Ni, Fe)$_9$S$_8$), heazlewoodite (Ni$_3$S$_2$), and the ferro-nickel alloy, awaruite (Ni$_{2.5}$Fe), occurring in various proportions throughout the sill. Nickel can also occur in the crystal structure of several silicate minerals including olivine and serpentine. Quantifying the difference in the nickel deportment between metallic and silicate phases is critical in understanding metallurgical response in different areas of the deposit. Electron microprobe analyses were performed to quantify the variability of nickel content (tenor) in key minerals of interest for samples from locations throughout the Dumont deposit. All minerals analysed showed low variability in nickel tenor throughout the sill except for pentlandite and serpentine. Pentlandite shows the most variability of the metallic minerals and exhibits a bimodal population. For samples where nickel tenor in pentlandite is lower, the lower nickel values are mostly associated with an increase in iron. The lower tenor pentlandite, averaging 27 per cent Ni, is highly correlated with the areas of higher Fe Serpentine. The pentlandite outside these areas has an average Ni tenor of 34 per cent. Fe-serpentine is correlated to higher nickel in silicates. This understanding of the differences in the high Fe-serpentine area was a key breakthrough used to define the Pn-rich domains. Obviously, nickel deportment will impact nickel recovery and concentrate grade.

Lac des Iles platinum-group elements deposit located in north-west Ontario, Canada is the only known palladium ore in the world. In an early study conducted by Zhou using EPMA on the deportment of PGE in a flotation concentrate from Lac des Iles plant indicated that Pd-bearing minerals account for 91 per cent in the concentrate, including vysotskite ((Pd, Pt, Ni)S), stillwaterite (Pd$_8$As$_3$), kotulskite (Pd(Te,Bi)), isomertieite (Pd$_{11}$Sb$_2$As$_2$), merenskite ((Pd, Pt)(Te,Bi)$_2$, sperrylite (PtAs$_2$) and a minor amounts of other PGE-carriers in the order of decreasing abundance (Zhou, 2007).

Dynamic Secondary Ion Mass Spectrometry (D-SIMS)

D-SIMS and LA-ICP-MS are the two most common techniques that have been used in quantifying trace elements contained in other minerals such as submicroscopic gold carried by sulfide minerals in refractory ores and trace critical elements present in solid solution in Zn-bearing ores. Zhou *et al* (2004) and Chryssoulis and McMullen (2016) used a comprehensive approach including D-SIMS in gold deportment studies.

D-SIMS is one of a few most important microbeam techniques applied in minerals studies because of its unique quantification and mapping capabilities. It has been used in quantifying Au and other trace elements for more than three decades (Chryssoulis and Cabri, 1990; Chryssoulis and McMullen, 2016; Zhou *et al*, 2004; Zhou and Fleming, 2007). Theoretically, it can detect and measure all the elements in the periodic table in concentration from ~1 per cent to 10 ppb and has the ability to discriminate between the isotopes of many elements. The element and isotope contents can be measured with a sensitivity that is as high as the sensitivity of bulk analysis methods, such as atomic absorption (McMahon and Cabri, 1998). Its exceptional operational capabilities include: (1) small beam size: 15–20 μm; (2) quantitative analysis with low detection limit (0.3–0.5 ppm for Au); (3) shallow beam sampling depth (0.5–1 μm); (4) individual particle analysis; (5) depth concentration profiling; and (6) element mapping.

High sensitivity makes SIMS an excellent analytical tool for the quantification of trace elements in a variety of materials. It is considered to be the best technique for quantification of submicroscopic gold in sulfides. The SIMS in-depth concentration profiling is used to discriminate colloidal gold and solid solution gold. Colloidal gold (0.02–0.1 μm) can be identified from the ‘spikes’ and ‘bumps’ in the in-depth concentration profiles of gold, whereas solid solution gold is characterised by ‘flat’ in-depth profiles (Figure 5a and 5b). SIMS mapping is used to show the location and distribution of submicroscopic gold in host minerals (Figure 5c).

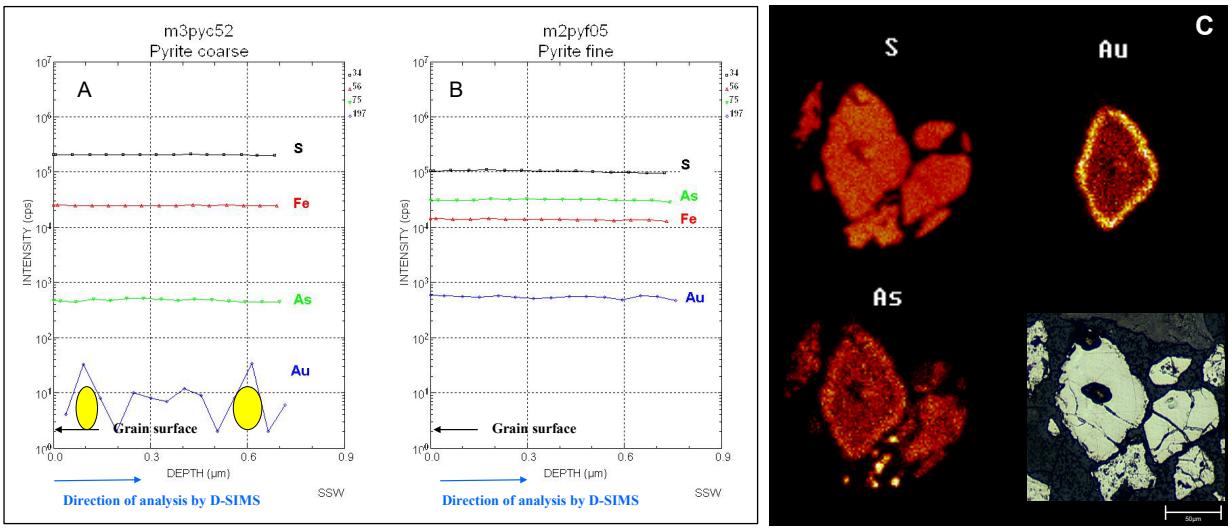

FIG 5 – SIMS in-depth concentration profiles (a and b) and elemental maps (c). (a) Colloidal gold (3.10 ppm, ~0.1 μm in size) in coarse pyrite; (b) solid solution gold (220.7 ppm) in fine pyrite; (c) SIMS elemental maps showing the distribution of Au, As and S in an Au-bearing zoned pyrite. Au concentration in the outer accretion zone (323 ppm, shown in golden yellow) is much higher than that in the core (143 ppm). The lower right optical picture shows the grain size of pyrite particle (Figure 5c was adapted from Zhou and Fleming, 2007).

As discussed earlier, sample preparation and particle selection are very important steps in a SIMS study. During the study, the mineralogist should work closely with the SIMS operator to ensure that the standard study procedure is followed.

It is worth pointing out that D-SIMS is not suitable for major elements analysis and non-sulfide minerals. It is standard dependent and moderately expensive comparing to EPMA and LA-ICP-MS.

Laser Ablation Inductively Coupled Plasma Mass Spectrometry (LA-ICP-MS)

LA-ICP-MS was first used in 2003 to determine whether Au is distributed homogeneously in sulfides, particularly arsenopyrite, or is contained as micronuggets in the Lodestar prospect in eastern Newfoundland (Hinchey *et al*, 2003). Since then, the technique has been widely used in mineralogical and geochemical studies, mostly in quantification and distribution of trace elements such as Au, Ag, As, Bi, Cd, Co, Cu, Fe, Ga, Ge, In, Mn, Mo, Ni, Pb, Sb, Se, Sn and Tl in geological samples and metallurgical products (Cabri *et al*, 2008, 2010, 2017; Cook *et al*, 2011; Gregory *et al*, 2013; Liu *et al*, 2013; Raimondo *et al*, 2017; Gao *et al*, 2019; Xu *et al*, 2021). Available information has shown that LA-ICP-MS offers excellent potential in trace element analysis through significantly improved detection limits for *in situ* analysis, and the ability to generate profiles through minerals by progressive ablation. The system is capable of determining, with good accuracy, a large suite of trace elements in various mineral hosts including silicates, carbonates, phosphates, oxides, and sulfides. Limits of detection vary from a few ppm to a few ppb depending upon a number of operating variables, such as pit size and number of elements determined. Sampling resolution better than 10 μm can be achieved, although ablation pits on the order of 40 μm are usually used, when grain size allows, to provide better precision and detection limits. Like D-SIMS, LA-ICP-MS has imaging capability in addition to *in situ* analysis.

Sphalerite is an important host mineral for a wide range of minor and trace elements. Cook *et al* (2009) used LA-ICP-MS to investigate the distribution of Ag, As, Bi, Cd, Co, Cu, Fe, Ga, Ge, In, Mn, Mo, Ni, Pb, Sb, Se, Sn and Tl in samples collected from 26 ore deposits, including specimens with wt. per cent levels of Mn, Cd, In, Sn and Hg. The results showed that the technique provided accurate trace element data, confirming that Cd, Co, Ga, Ge, In, Mn, Sn, As and Tl are present in solid solution. The concentrations of most elements vary over several orders of magnitude between deposits and in some cases between single samples from a given deposit. Sphalerite was characterised by a specific range of Cd (typically 0.2–1.0 wt. per cent) in each deposit.

The Kevitsa Ni–Cu–PGE deposit is a low-grade, disseminated sulfide deposit, which resides in the upper ultramafic unit of the Kevitsa intrusion. Commissioning of the Kevitsa operation began in 2012. A Cu–Ni sequential flotation circuit produces two concentrates, a Ni–PGE concentrate and a Cu–Au concentrate, with some Au, Pt and Pd. Earlier studies had reported trace concentrations of platinum-group elements in several minerals using the electron microprobe. In an effort to evaluate PGE and Au recovery performance in more detail and identify opportunities to improve recovery, a heavy mineral concentrate from a processed stream of 'run-of-mine' mill feed containing elevated levels of PGE and Au was studied using laser ablation inductively coupled plasma mass spectrometry (LA-ICP-MS), which has much lower limits of detection, to target potential carrier minerals (sulfide, sulfarsenide, and arsenide) as part of a process mineralogy study of the ore, with the data used to determine the deportment of the precious metals. Trace precious-metal data were obtained on pentlandite, pyrite, gersdorffite, maucherite, and nickeline for Rh, Pd, Os, Ir, Pt, and Au. A unique feature of the data was the new discovery that nickeline is a significant carrier of Au (up to 74.1 ppm), in addition to Rh, Pd, Os, Ir, and Pt. The unexpected concentration of gold in nickeline demonstrates the versatility of LA-ICP-MS analysis when using an appropriate calibration standard and established protocols (Cabri *et al*, 2017).

TECHNIQUES FOR MINERAL SURFACE ANALYSIS

Surface issues can affect flotation and leaching performance and need to be analysed and assessed for improving the plant operation. TOF-SIMS and XPS are the two main techniques among others used for surface analysis to detect and quantify surface adsorbent such as the chemicals used in sulfide flotation and the gold adsorbed on the surface of carbonaceous matter by preg-robbing.

Time of Flight Secondary Ion Mass Spectrometry (TOF-SIMS)

TOF-SIMS uses a pulsed, primary ion beam to desorbs and ionise species from a sample surface. It is a non-destructive technique offering comprehensive inorganic and organic surface analysis. The minimum detection limits are in the low ppm to ppb range. It possesses imaging capabilities with spatial resolution down to 0.3 μm and features elemental depth profiling. It is one of few techniques available for both individual mineral particle and cluster surface analysis with detection limits in the low ppm/ppb concentrations.

Applications of TOF-SIMS include identification of collectors on individual mineral particles from plant samples; measurements of collector loadings on mineral grains from flotation circuit at plant concentration levels. Practical detection limits are less than 1 g/t; identification of activators and depressants on mineral particles – comparative analysis on the degree of activation or depression of mineral phases during flotation; characterisation and mapping of surface coatings on gold grains from cyanide leach residues; and evaluation of preg-robbing capability of carbonaceous matter and quantification of adsorbed gold (Chryssoulis and McMullen, 2016; Dimov and Hart, 2017). In a gold deportment study conducted by the senior author on a carbonaceous ore containing total carbonaceous matter (TCM) and disseminated TCM, TOF-SIMS quantitative analysis showed substantial concentrations of preg-robbed surface gold (59 ppm) on the carbonaceous material. The preg-robbed surface gold was present in two different forms: metallic gold and gold compound $Au(CN)_2$, accounting for 14 per cent and 86 per cent, respectively (Zhou, 2011).

SUMMARY

Mineral processing of various ores is largely driven by mineralogical factors and requires mineralogical information at each stage of a mineral project. Mineralogists use a variety of conventional and advanced techniques to characterise the ore and metallurgical products and provide solution to mineral processers in supporting project development and plant operation. Each of the mineralogy techniques is designed or borrowed based on metallurgical needs and has its advantages and limitations. Selection of the mineralogy techniques must be based on the capability of each technique and the information being sought for mineral processing. During the exploration or at the early stage of a development project, qualitative and semi-quantitative mineralogy techniques will provide the information required for target identification and project evaluation. During project development, a large amount of mineralogical information acquired through advanced mineralogy techniques will be required to support process selection and flow sheet development. After commissioning, mineralogy information will still be required for production prediction and

trouble-shooting, and selection of mineralogy techniques will be based on the nature of the ore to be processed and the issues encountered in the plant. In many cases, a set of mineralogy techniques are required for a comprehensive geometallurgy program during project development and plant operation.

When considering a mineralogical program, it is always good to understand what kind of the information is required and which instrument is good for such analysis. Selecting a qualified laboratory and an experienced mineralogist for the mineralogical program is critical for getting the best quality. Instrument provides data, mineralogist provides solution.

ACKNOWLEDGEMENT

The authors wish to acknowledge the anonymous AusIMM reviewers for their reviews and constructive comments, which helped to improve the quality of this paper.

REFERENCES

Aghamirian, M, Mohns, C, Grammatikopoulos, T, Imeson, D, Pearse, G, 2012. An overview of spodumene of beneficiation. In: *Proceedings of the 44th Annual Meeting of Canadian Mineral Processors Operators, 2012,* pp. 141–153 (CIM: Ottawa).

AMTEL, 2018. Analytical Techniques [online]. Available from: <http://www.amtel.ca/index-7.html> [Accessed: 3 June 2022]

Aylmore, M G, 2019. Automated Mineralogy, in: *Mineral Processing and Extractive Metallurgy Handbook* (ed: R Dunn), Chapter 1.3, pp 43–68 (SME: Englewood).

Aylmore, M G, Merigot, K, Quadira, Z, Rickard, W, Evans, N, McDonald, B, Catovic, E and Spitalny, P, 2018. Applications of advanced analytical and mass spectrometry techniques to the characterisation of micaceous lithium-bearing ores. *Miner. Eng.* 116:182–195.

Aylmore, M G, Merigot, K, Rickard, W, Evans, N, McDonald, B, Catovic, E and Spitalny, P, 2018. Assessment of a spodumene ore by advanced analytical and mass spectrometry techniques to determine its amenability to processing for the extraction of lithium. *Miner. Eng.* 119:137–148.

Becker, M, de Villiers, J and Bradshaw, D, 2010. The mineralogy and crystallography of pyrrhotite from selected nickel and PGE ore deposits, *Economic Geology,* 105: 1025–1037.

Becker, M, de Villiers, J R R and Bradshaw, D, 2008. Evaluation of pyrrhotite from selected Ni and platinum group element (PGE) ore deposits and the influence of its mineralogy on flotation performance, in *Proceedings of Ninth International Congress for Applied Mineralogy,* pp 401–409 (The Australasian Institute of Mining and Metallurgy: Melbourne).

Berry, R, Walters, S G and McMahon, C, 2008. Automated mineral identification by optical microscopy, in *Proceedings of Ninth International Congress for Applied Mineralogy,* pp 91–94 (The Australasian Institute of Mining and Metallurgy: Melbourne).

Boulton, A, Fornasiero, D, Ralston, J, 2005. Effect of iron content in sphalerite on flotation. *Minerals Engineering,* 18(11)1120–1122.

Cabri, L J, Choi, Y, Nelson, M, Tubrett, M and Sylvester, P J, 2010. Advances in precious metal trace element analyses for deportment using LAM-ICP-MS, in *Proceedings of the 42nd Annual Meeting of The Canadian Mineral Processors,* pp. 182–196 (CIM: Ottawa).

Cabri, L J, Kelvin, M, Yang, Z, Jackson, S E and Altun, O, 2017. Application of LA-ICP-MS trace-element analysis for precious metal deportment: a case study of the Kevitsa mine, Finland. *Eur. J Mineral,* 2017:29:635–644.

Cabri, L J, Rudashevsky, N S and Rudashevsky, V N, 2008. Current approaches for the process mineralogy of platinum-group element ores and tailings, in *Proceedings of Ninth International Congress for Applied Mineralogy,* pp 9–17 (The Australasian Institute of Mining and Metallurgy: Melbourne).

Chryssoulis, S L and Cabri, L J, 1990. Significance of gold mineralogical balances in mineral processing. *Trans. Instn. Min. Metall. (Sect. C: Mineral Process. Extr. Metall.),* 99, January-April 1990, pp. C1-C10.

Chryssoulis, S L and McMullen, J, 2016. Mineralogical Investigation of Gold Ores, in *Gold Ore Processing* (ed: M Adams) (2nd edn), 2016, 15, pp. 57–93.

Cook, N J, Ciobanu, C L, Pring, A, Skinner, W, Shimizu, M, Danyushevsky, L, 2009. Trace and minor elements in sphalerite: A LA-ICPMS study. *Geochim. Cosmochim. Acta,* 73:4761–4791.

Cook, N J, Ciobanu, C L, Williams, T, 2011. The mineralogy and mineral chemistry of indium in sulphide deposits and implications for mineral processing. *Hydrometallurgy,* 108 (3–4) 226–228.

Craig, J R and Vaughan, D J, 1994. *Ore Microscopy & Ore Petrography,* Second Edition, 434 p (John Wiley & Sons, Inc.: New York).

Dimov, S S and Hart, B R, 2017. Applications of microbeam analytical techniques in gold deportment studies and characterization of losses during the gold recovery process. *Surf. Interface Anal,* 49:1404–1415.

Gao, F, Du, Y, Pang, Z, Du, Y, Xin F and Xie, J, 2019. LA-ICP-MS Trace-Element Analysis of Pyrite from the Huanxiangwa Gold Deposit, Xiong'ershan District, China: Implications for Ore Genesis. *Minerals,* 9:157.

Gregory, M J, Lang, J R, Gilbert, S and Hoal, K O, 2013. Geometallurgy of the Pebble Porphyry Copper-Gold-Molybdenum Deposit, Alaska: Implications for Gold Distribution and Paragenesis. *Economic Geology,* 108:463–482.

Gu, Y, 2003. Automated scanning electron microscope based mineral liberation analysis. *Miner. Mater. & Charact. Eng,* 2(1):33–41.

Gu, Y, Schouwstra, R P and Rule, C, 2014. The value of automated mineralogy. *Miner. Eng,* 58: 100–103.

Hinchey, J G, Wilton, D H C and Tubrett, M N, 2003. A LAM-ICP-MS study of the distribution of gold in arsenopyrite from the Lodestar prospect, Newfoundland, Canada. *Can. Mineral,* 41(2) 353–364.

Lastra, R and Paktunc, D, 1994. Determining association of unliberated minerals in ground products by image analysis, in: *Proceedings of the 26th Annual Meeting of Canadian Mineral Processors,* Paper 3, p10 (CIM: Ottawa).

Lastra, R and Paktunc, D, 2016. An estimation of the variability in automated quantitative mineralogy measurements through inter-laboratory testing. *Miner. Eng,* 95:138–145.

Lepetit, P, Bente, K, Doering, T, Luckhaus, S, 2003. Crystal chemistry of Fe-containing sphalerites. *Phys. Chem. Miner,* 2003, 30, 185–191.

LeVier, M D, 2019. Analytical Testing. In: *Mineral Processing and Extractive Metallurgy Handbook* (ed: R Dunn), Chapter 1.2, pp 19–42 (SME: Englewood).

Liu, Y, Hu, Z, Li, M and Gao, S, 2013. Applications of LA-ICP-MS in the elemental analyses of geological samples. *China Sci Bull,* 58(32):3863–3878.

McMahon, G and Cabri, L J, 1998. The SIMS technique in ore mineralogy, in *Modern Approaches to Ore and Environmental Mineralogy,* Short Course Series Vol 27 (L J Cabri and D J Vaughan, eds.), Chapter 8, pp 199–224 (Mineralogical Association of Canada: Ottawa).

Muinonen, J, Sciortino, M, Korczak, J and St-Jean, A, 2013. Geometallurgical modelling of the Dumont deposit, in *Proceedings of the 45th Annual Meeting of Canadian Mineral Processors Operators,* pp. 15–27 (CIM: Ottawa).

Multani, R, Marrs, G, Deredin, C, Coffin, J, Lawson, V, Muinonen, M and Fragomeni, D, 2018. Pyrrhotite rejection at the Strathcona Mill, in *Proceedings of the 50th Annual Canadian Mineral Processors Operators Conference*, pp 225–237 (CIM: Ottawa).

Petruk, W, 1988. Automatic image analysis to determine mineral behaviour during mineral beneficiation, in *Applied Mineralogy VII* (eds. D J T Carson and A H Vassiliou), pp 347–357 (Warrendale, PA: TMS).

Petruk, W, 2000. *Applied Mineralogy in the Mining Industry,* 268 p (Elsevier: Amsterdam).

Raimondo, T, Payne, J, Wade, B, Lanari, P, Clark, C, Hand, M, 2017. Trace element mapping

Stanley, C and Laflamme, J H G, 1998. Preparation of specimens for advanced ore-mineral and environmental studies, in: *Modern Approaches to Ore and Environmental Mineralogy,* Short Course Series Vol 27 (Editors: L J Cabri and D J Vaughan), Chapter 3, pp 111–121 (Mineralogical Association of Canada: Ottawa).

Xu, J, Ciobanu, C L, Cook, N J, Slattery, A, Li, X F, Kontonikas-Charos, A, 2021. Phase relationships in the system ZnS-$CuInS_2$: insights from nanoscale study of indium-bearing sphalerite. *American Mineralogist,* 106: 192–205.

Yu, J, Wu, X, Zhao, Z, Zhu, Y and Luo, S, 2019. Effect of a small amount of iron impurity in sphalerite on xanthate adsorption and flotation behavior. *Minerals,* 9:687.

Zhou, J and Fleming, C, 2007. Gold in tailings: mineralogical characterization and metallurgical implications, in *Proceedings of the World Gold Conference,* pp. 311–317 (The Australasian Institute of Mining and Metallurgy: Melbourne).

Zhou, J and Gu, Y, 2016. Geometallurgical characterization and automated mineralogy of gold ores, in: *Gold Ore Processing: Project Development and Operations* (ed: M D Adams), Chapter 6, pp. 95–111, Elsevier B V.

Zhou, J, 2007. Deportment of PGE in a flotation concentrate from Lac des Iles plant (unpublished data).

Zhou, J, 2011. Deportment study of gold and characterization of carbonaceous matter in head and process products (unpublished report).

Zhou, J, Jago, B and Martin, C, 2004. Establishing the process mineralogy of gold ores. In: *Proceedings of the 36th Annual Meeting of Canadian Mineral Processors,* pp. 199–226 (CIM: Ottawa) (Also published in CIM Bulletin, 3/4, 2006).

Advances in mineral processing – hydrometallurgy

Sensitivity of coupled dissolution – precipitation reactions to brine chemistry during copper sulfide heap leaching

E O Ansah[1], A Jyoti[2], J R Black[3] and R R Haese[4]

1. PhD student, University of Melbourne, Melbourne Vic 3001. Email: eaowusu@student.unimelb.edu.au
2. Research Fellow, University of Melbourne, Melbourne Vic 3001. Email: apoorv.jyoti@unimelb.edu.au
3. Lecturer/Research Fellow, University of Melbourne, Melbourne Vic 3001. Email: jay.black@unimelb.edu.au
4. Professor, University of Melbourne, Melbourne Vic 3001. Email: ralf.haese@unimelb.edu.au

ABSTRACT

Copper (Cu) is a critical metal in the transition to a low-carbon power supply. Presently, low-grade copper sulfide ores account for almost 80 per cent of the global reserves. Large amounts of water are required to process these low-grade copper ores. The mining industry utilises lixiviants from recycled water from different sources to conserve water, whilst enhancing Cu recovery. Some utilise intermediate to pregnant leach solutions, sea water, and processed water from electrowinning circuits with highly variable concentrations of ions. Previous studies have highlighted the formation of precipitates that passivate the surfaces of minerals in these low-grade copper ores and/or block flow paths for lixiviant during heap leaching. In this study, we utilised concepts of phase replacement to devise an innovative means of controlling precipitation and increasing copper recovery using industrial brine as opposed to freshwater. We propose the formation of Al-rich phases (such as $AlSO_4^+$ or alunite) to replace iron sulfate and iron hydroxysulfates (such as jarosite) during the chalcopyrite dissolution-precipitation mechanism. The rationale is to have available Fe^{3+} throughout the chalcopyrite leaching process. We tested this method by carrying out various batch experiments using $CaCl_2$, $AlCl_3$, and NaCl industrial brine types compared to freshwater and explored the capacity to leach Cu from chalcopyrite. There is higher Cu recovery during oxidative leaching of chalcopyrite in industrial brine with 91 per cent recovery using $AlCl_3$-rich brine, 84 per cent with NaCl-rich brine, and 56 per cent with $CaCl_2$-rich brine as compared to 35 per cent recovery using freshwater. In the absence of Al^{3+}, various forms of iron sulfates, and jarosite are formed, reducing the availability of Fe^{3+} for chalcopyrite dissolution. The introduction of Al^{3+} leads to the formation of $AlSO_4^+$ species, thus lowering sulfate activity and the tendency for K-jarosite formation.

INTRODUCTION

Copper (Cu) is a critical metal in the transition to low-carbon-based electrification. This shift towards a greener economy will require sustainable copper mining. Leaching of low-grade ores for copper results in high processing costs and a large volume of tailings. Also, these low-grade ores require large volumes of water to process (Dunne, 2012 and references therein). Water resources are particularly scarce in remote and arid environments (such as the Atacama Desert of Chile and the iron oxide copper-gold (IOCG) deposits of Australia) where mining often occurs. It is estimated that by 2025, as water scarcity intensifies, more countries will be severely short of water (Dunne, 2012 and references therein). The mining industry utilises lixiviants from recycled brine from different sources to conserve water whilst enhancing copper (Cu) recovery. Some of these sources are intermediate to pregnant leach solutions, sea water, and processed water from electrowinning circuits with highly variable concentrations of major and minor cations (eg K, Na, Mg, Mn, Cu, Fe etc), and anions (mostly sulfate and chloride). In the present study, we show how industrial brine can be utilised in processing low-grade porphyry copper minerals. We utilised concepts of coupled dissolution-precipitation and mineral replacement to minimise precipitation at the surface of Cu-bearing minerals (passivation) and to increase copper recovery using industrial brine as opposed to freshwater.

Past research (Hernández *et al,* 2018, 2020; Velásquez-Yévenes *et al,* 2018; Watling *et al*, 2014) including our ongoing study highlighted that there is higher copper recovery when using sea water/brine as compared to freshwater for copper leaching. However, there is hydroxysulfate,

hydroxide, silicate, and oxide precipitation during porphyry copper heap leaching with highly concentrated brines. These precipitates tend to either passivate the surface of minerals in these low-grade copper ores and/or block flow paths for lixiviant in leaching heaps. This in turn leads to reduced mineral-lixiviant contact and subsequently low copper recovery. Our study points to iron hydroxide and hydroxysulfate formation as major inhibitors for chalcopyrite dissolution, but the passivation of the chalcopyrite surface by precipitates such as iron hydroxide or iron hydroxysulfate (eg jarosite) might not be the main hindrance to efficient chalcopyrite dissolution. If the water chemistry favours the formation of hydrous precipitates such as aluminium sulfate minerals as opposed to jarosite, Cu recovery may still proceed at a high rate. In effect, we propose that the main hindrance to chalcopyrite dissolution is not necessarily passivation by jarosite but the decrease in available Fe^{3+} for oxidative leaching of chalcopyrite.

To control iron hydroxysulfate (such as jarosite) passivation during heap leaching, past research has proposed: (1) the application of highly active thermophiles (D'Hugues *et al,* 2002); (2) the use of additives such as silver (Ag) or other external electrode materials as a catalyst; (3) physical processes for the removal of jarosite; and (4) pH control to minimise the formation of jarosite (Yang *et al*, 2018 and references therein). Our proposed method differs from the above, in that, we propose the formation of Al-rich precipitates to replace jarosite during the chalcopyrite dissolution-precipitation mechanism. The rationale is to have available Fe^{3+} throughout the chalcopyrite leaching process. The results of test work undertaken using $CaCl_2$, $AlCl_3$, and NaCl industrial brine types as compared to freshwater for leaching low-grade porphyry copper sulfide ore are the subject of this paper. Watling *et al* (2014) remark NaCl as a primary source of chloride for cupric-cuprous chloride complexation during chalcopyrite leaching. The use of $CaCl_2$ (Faine *et al*, 2009) as patented in the CuproChlor® process for chalcopyrite leaching highlights the formation of gypsum for agglomeration and chloride source as merits. In this study, we report for the first time on the $AlCl_3$ leaching of chalcopyrite.

Coupled dissolution – precipitation reactions during chalcopyrite dissolution

Proton promoted dissolution of chalcopyrite occurs as (Kimball *et al*, 2010):

$$\mathrm{CuFeS_{2(s)} + 4H^{+}_{(aq)} = Cu^{2+}_{(aq)} + Fe^{2+}_{(aq)} + 2H_2S_{(aq)}} \quad (1)$$

In the presence of oxygen and ferric ions, chalcopyrite dissolves respectively as (Kimball *et al*, 2010):

$$\mathrm{CuFeS_{2(s)} + 4O_{2(aq)} = Cu^{2+}_{(aq)} + Fe^{2+}_{(aq)} + 2SO^{2-}_{4(aq)}} \quad (2)$$

$$\mathrm{CuFeS_{2(s)} + 16Fe^{3+}_{(aq)} + 8H_2O = Cu^{2+}_{(aq)} + 17Fe^{2+}_{(aq)} + 2SO^{2-}_{4(aq)} + 16H^{+}_{(aq)}} \quad (3)$$

There is jarosite precipitation during the dissolution of chalcopyrite as:

$$\mathrm{CuFeS_{2(s)} + 4O_{2(aq)} + K^{+}_{(aq)} + 6H_2O + 2Fe^{3+}_{(aq)} = Cu^{+}_{(aq)} + KFe_3(SO_4)_2(OH)_{6(s)} + 6H^{+}_{(aq)}} \quad (4)$$

Also, in this study, we propose alunite precipitation during chalcopyrite dissolution as:

$$\mathrm{CuFeS_{2(s)} + 4O_{2(aq)} + K^{+}_{(aq)} + 6H_2O + 3Al^{3+}_{(aq)} = Cu^{+}_{(aq)} + KAl_3(SO_4)_2(OH)_{6(s)} + Fe^{3+}_{(aq)} + 6H^{+}_{(aq)}} \quad (5)$$

According to Sequeira *et al* (2008), chalcopyrite can undergo a phase replacement reaction as:

$$\mathrm{CuFeS_{2\,(s)} + CuSO_{4(aq)} = 2CuS_{(s)} + FeSO_{4(aq)}} \quad (6)$$

followed by the oxidation-reduction couple as:

$$\mathrm{6CuS_{(s)} + 3CuSO_{4(aq)} + 4H_2O = 5Cu_{1.8}S_{(s)} + 4H_2SO_{4(aq)}} \quad (7)$$

MATERIALS

Ore sample

The low-grade porphyry copper sulfide sample was obtained from the ORE Research and Exploration Pty Ltd, Bayswater, Melbourne – Australia. The samples were pulverised, homogenised, and resampled for X-ray diffraction (XRD) analysis at the Land and Water division of CSIRO in Adelaide (Table 1). The BET surface area of the pulverised sample was measured using a Micromeritics surface analyser at the School of Engineering, the University of Melbourne (Table 1).

TABLE 1

Mineralogical and surface area characteristics of crushed low-grade porphyry copper sulfide with a particle size between 0.45–1.00 mm.

BET	Quartz	Chlorite	Mica	Chalcopyrite	Hematite	Orthoclase	Albite	Bornite	Anhydrite
(m^2/g)	(%)	(%)	(%)	(%)	(%)	(%)	(%)	(%)	(%)
0.25	15.9	0.60	7.70	0.50	0.40	36.5	34.3	2.20	1.90

Chemical reagents

All chemicals used in this study were analytical grade.

METHODS

Brine preparation

The calculated masses of the various salts were added to known masses of 18.2 mΩ MilliQ water (DI) at 25°C. The pH was adjusted with 1 M NaOH and 2 M HCl. Subsequently, $FeCl_3$ was added to provide ferric ion (Fe^{3+}) as an oxidant in some experiments. The pH was rechecked and readjusted before measuring Eh. It is important to note that the Eh value was mainly influenced by Fe^{3+}. The solution was filtered through a membrane filter with a 0.45 µm pore size and transferred into Nalgene bottles. The Eh and pH were rechecked and pH readjusted, if needed, before the start of the experiment. pH standards of 1, 4, and 7 were used throughout. The pH and Eh were measured with the Metrohm 902 Titrando. Note that there is a possibility of a pale yellow thin-film precipitate formation on the walls of the leaching bottles, especially during the preparation and storage of solutions with $FeCl_3$. To resolve this, it is recommended that Na_2SO_4 be weighed and dissolved first before adding the other salts.

Near-equilibrium batch test

Two different series of near-equilibrium batch experiments were conducted using DI and artificially prepared industrial brine. The industrial brines were classified as $CaCl_2$-dominated brine, NaCl-dominated brine, and $AlCl_3$-dominated brine. Table 2 shows the compositions of the various reagents used in this study. In all the tests, 5 g of 0.45–1.00 mm granulated ore sample was utilised in a 100 mL of brine held in a Nalgene bottle. We were able to conduct five tests in parallel in a water bath utilising an in-house continuously stirred experimental set-up. Before the experiment, the sample was sonicated and rinsed in DI, acetone, and DI for each step lasting 15 minutes, respectively. The aim was to remove any fines and possibly oxidised phases at the surface of the ore material. The experiments were conducted over a 12-to-72-hour period.

TABLE 2

Conditions of the near-equilibrium batch test. All tests were acidified with 0.2 M HCl, except for BB2, BB15A, BB3A, and BB15B, which were acidified with 0.5 M H_2SO_4. Unit for all ions is in mol/L.

ID	Fe^{3+}			Cl^-	SO_4^{2-}	Comment
Fresh Water						
BB1	0.10			0.30		pH 2; 25°C
BB2	-			-	0.50	pH 2; 25°C

$CaCl_2$	Fe^{3+}	Ca^{2+}	K^+	Mg^{2+}	Na^+	Cl^-	SO_4^{2-}	Comment
BB15A	-	2.6				5.20	0.50	pH 1.5; 25°C
BB17	0.10	0.06	0.50	0.14	1.00	1.20	0.50	pH 1.5; 25°C

NaCl	Fe^{3+}		K^+	Mg^{2+}	Na^+	Cl^-	SO_4^{2-}	Comment
BB3A	-				2.60	2.60	0.50	pH 1.5; 25°C
BB11	0.10		0.50	0.14	3.60	3.68	0.50	pH 1.5; 45°C
BB12	0.10		0.50	0.14	3.60	3.68	0.50	pH 1.0; 25°C

$AlCl_3$	Fe^{3+}	Al^{3+}	K^+	Mg^{2+}	Na^+	Cl^-	SO_4^{2-}	Comment
BB15B	-	0.87				2.61	0.50	pH 1.5; 25°C
BB19	0.10	1.60	0.50	0.14	1.00	5.88	0.50	pH 1.0; 25°C
BB22	0.10	0.87	0.50	0.14	1.00	3.69	0.50	pH 1.5; 45°C

Chemical and data analysis

A 1.5 mL volume of solution was sampled from each test at times 2, 4, 6, 8, 12, 24, 48, and 72 hours. The solution samples were filtered through a membrane filter with a 0.25 µm pore size. Ions were analysed with ICP-OES (Agilent Technologies 5100) against aqueous standards in 2 per cent ultra-pure nitric acid (HNO_3). Eh and pH were measured in untreated samples after allowing the solution to stand for a while for consistent duplicate measurements. To determine mineral stability under the given experimental conditions, stability diagrams were derived using the Geochemist Workbench (GWB) software (version 15.0).

RESULTS

Changes in fluid composition are presented for the NaCl, the $CaCl_2$, the $AlCl_3$-dominated brines, and the freshwater leaching experiments.

Leaching in fresh water system

The copper recovery with 0.1 mol/L Fe^{3+} (BB1) reached 40 per cent as compared to less than 5 per cent for the case without (BB2) (Figure 1). This shows that for higher copper dissolution, copper sulfide leaching is via oxidation coupled to Fe^{3+} reduction as opposed to proton dissolution. The higher recovery is also positively related to the higher Eh observed in the ferric promoted leaching. There is a decline in the total sulfur (as sulfate, SO_4^{2-}) concentration, suggesting the likely precipitation of sulfate phases, possibly together with Fe, Cu, or other metals. The increase in copper dissolution positively correlates to a decrease in total iron (Fe) concentration for the ferric-promoted leaching mechanism. In the case of proton-promoted leaching, there is no significant variation in the total iron or sulfate concentration over the leaching period.

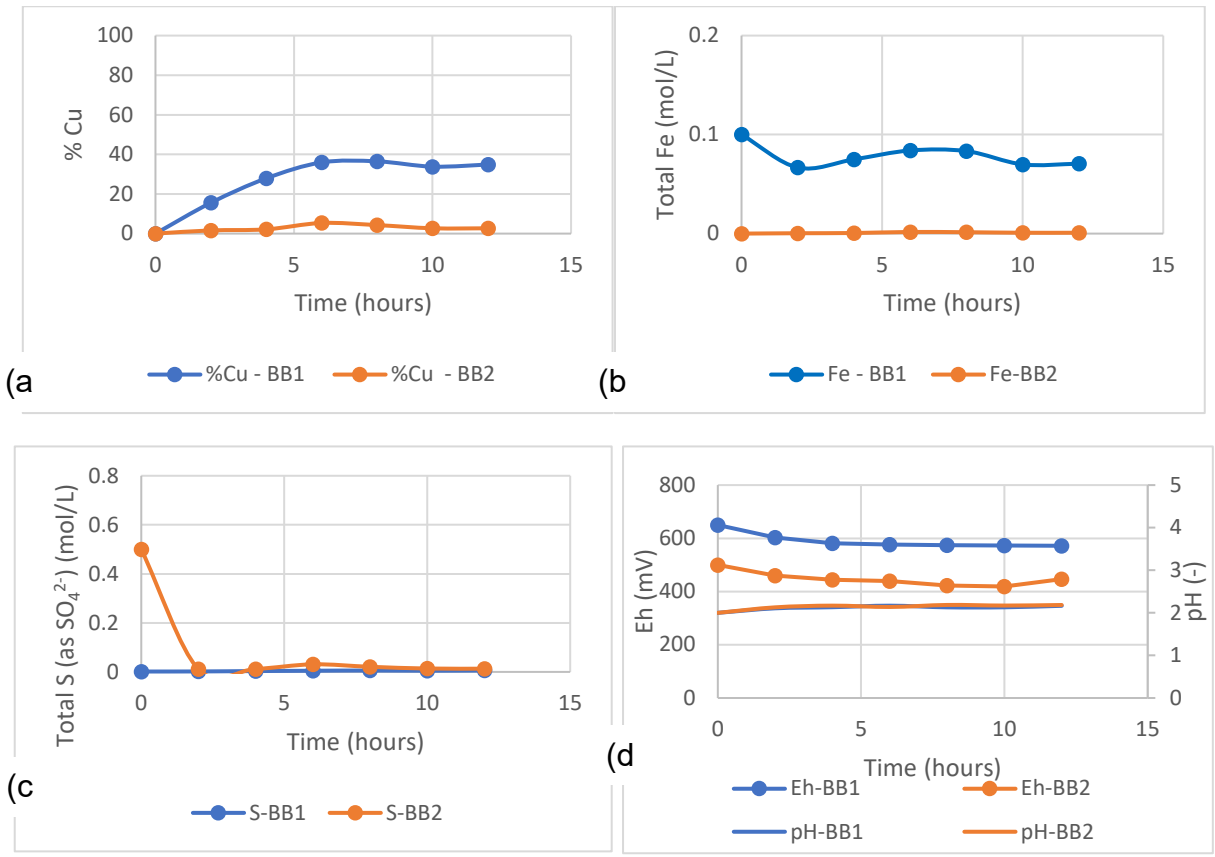

FIG 1 – Leaching in freshwater (a) % copper recovery (b) total Fe (mol/L) (c) total S (as SO_4^{2-}) (mol/L) (d) Eh – pH with oxidant (BB1) at 25°C and without oxidant at 25°C (BB2).

Leaching in $CaCl_2$ brine

We investigated $CaCl_2$ as a reagent for the dissolution of low-grade copper sulfides with (Fe-BB17) and without (Fe-BB15A) Fe^{3+} as an oxidant (Figure 2). Without Fe^{3+}, copper recovery is lower (at ~10 per cent) with possible sulfate precipitation at higher pH (~pH 4), whereas copper recovery reaches almost 60 per cent due to the reaction of ferric initially added at higher Eh (~530 mV) and lower pH (~1.5). Faine *et al* (2009) highlighted the formation of gypsum during the leaching of copper sulfides in $CaCl_2$ lixiviant. Gypsum is known to form hydration bonds that aid very fine particles to cluster together during agglomeration to form near-uniform large particles, hence, reducing local fluid flow due to segregation and possible fines migration during ion transport in a heap leach. In our study, it was observed that the instantaneous formation of a gelatinous mixture involving $CaCl_2$ would not be practicable for heap leaching, as pumping such a mixture would prove difficult.

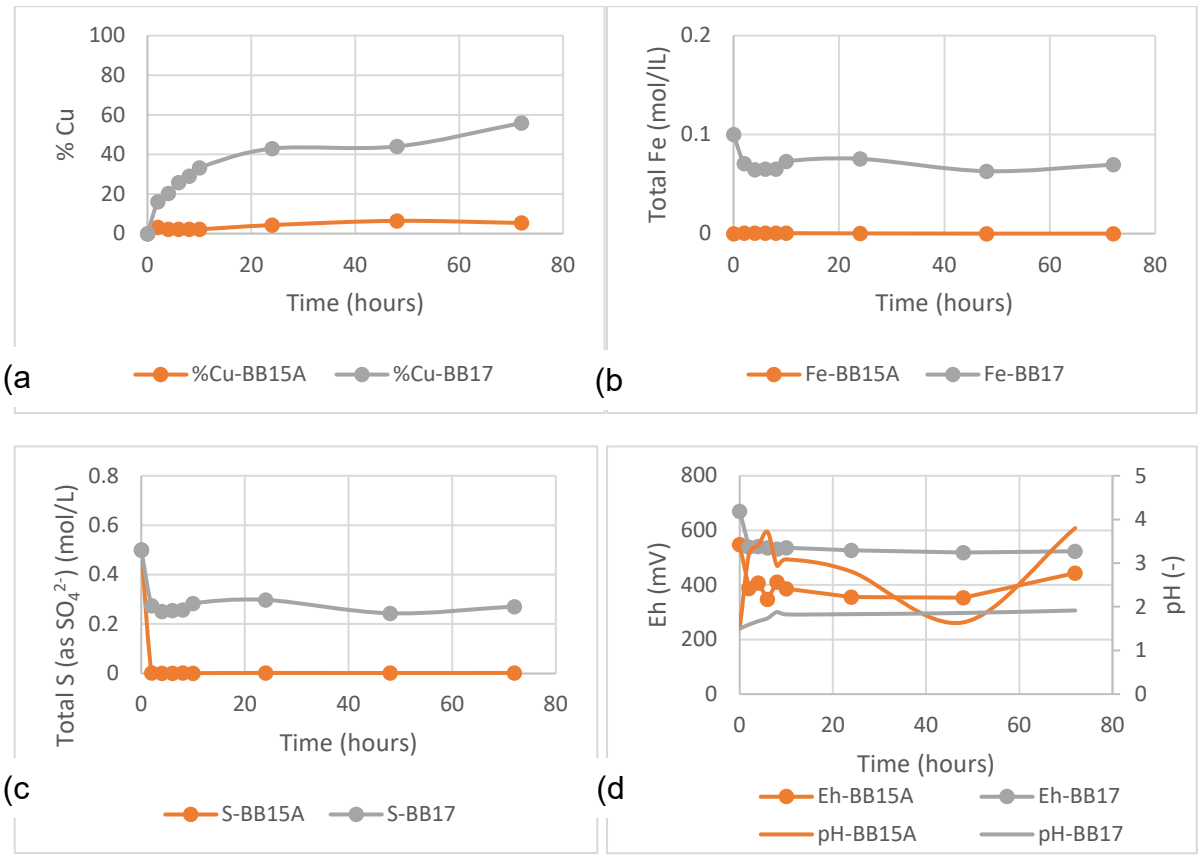

FIG 2 – Leaching in $CaCl_2$ saturated brine (a) % copper recovery (b) total Fe (mol/L) (c) total S (as SO_4^{2-}) (mol/L) (d) Eh – pH with oxidant (BB17) at 25°C and without oxidant (BB15A) at 25°C.

Leaching in NaCl brine

In this study, the goal is to optimise copper recovery utilising high chloride (~5 M) brine due to the scarcity of freshwater for mining. In almost all NaCl brine leaching tests of copper sulfide, we observe a sudden rise (initial 2 hours of leaching) and drop before a continuous increment in copper recovery (Figure 3). This will likely be correlated with pH and the precipitation-dissolution of basic copper salts. Dissolved iron (Fe) declines immediately while total sulfur (as SO_4^{2-}) requires some time to reach a new steady-state concentration. The experiment involving NaCl-rich brine, without ferric iron as an oxidant, demonstrates that the presence of chloride and low pH (~1.5) alone does not lead to high Cu recovery, even in the presence of oxygen (Exp. BB3-A, Figure 3). Leaching in the presence of ferric (Fe^{3+}) and at higher Eh accelerate the copper recovery. This is further increased and influenced by temperature: the highest copper recovery of ~84 per cent was reported at 45°C (BB11). In a low concentration NaCl medium, copper recovery reached 25 per cent, whereas the recovery increased further to 60–88 per cent in the presence of a high chloride concentration. This is expected because high chloride concentration results in high cuprous and cupric chloro complex formation (Brugger *et al*, 2001). Also, high chloride ensures the stability of the various copper ions in the solution during the period of dissolution. The formation of chloride bridges between solution complexes and the surface of the reacting sulfide minerals facilitates electron transfer (Senanayake and Muir, 2003). The availability of high Fe^{3+} concentrations drives the oxidation of cuprous to cupric copper.

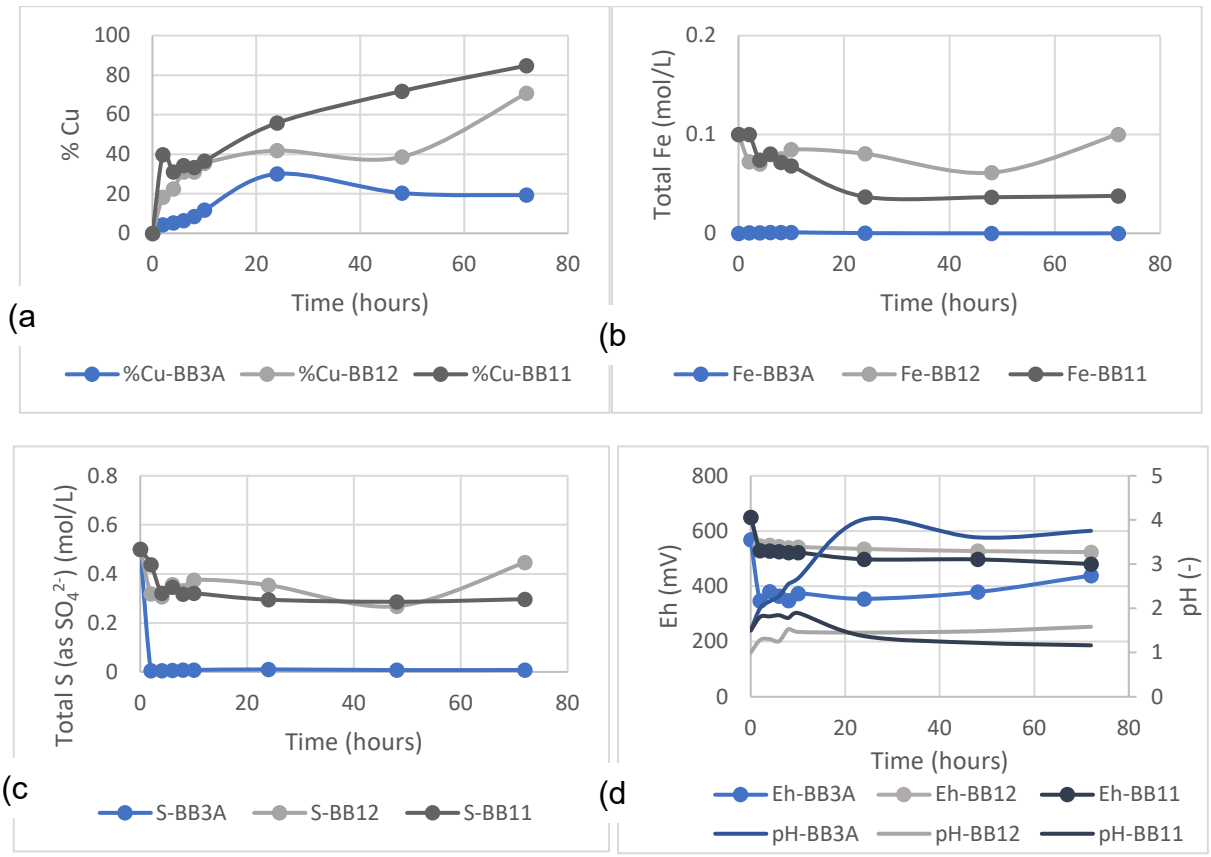

FIG 3 – Leaching in NaCl saturated brine (a) % copper recovery (b) total Fe (mol/L) (c) total S (as SO_4^{2-}) (mol/L) (d) Eh – pH with oxidant (BB12) at 25°C, with oxidant at 45°C (BB11) and without oxidant (BB3A) at 25°C.

Leaching in $AlCl_3$ brine

In this study, we propose the use of $AlCl_3$ in place of NaCl to favour (i) potential mineral replacement reactions where primary copper sulfides (chalcopyrite and bornite) may form easily leachable forms such as chalcocite; (ii) the formation of aluminium sulfates over iron hydroxysulfates (eg jarosite) to increase the availability of Fe^{3+} and a high Eh for enhanced copper recovery; (iii) the presence of $AlCl_3$ as a Lewis acid results in extremely low pH and (iv) a coagulation ability of the Al-rich precipitate to form hydration bonds and adhere to the mineral surface thereby limiting solution, fine particle, and ion transport. As found for the other brine media (NaCl and $CaCl_2$), the absence of ferric (Fe^{3+}) leads to the lowest copper recovery (20 per cent) (Figure 4). The highest copper recovery is reported for the case with the highest temperature and the presence of ferric iron. At 45°C, 35°C and 25°C, the Cu recovery was 90 per cent, 70 per cent and 60 per cent, respectively. At ambient temperature, an increase in copper recovery is maintained for a consistently high sulfate concentration. Similarly, despite the initial sharp decrease at 45°C, high copper recovery was found for consistently high total iron concentration. The sharp decrease and recovery in Fe concentration indicate a rapid reaction with regeneration that will require an oxidant, most likely oxygen. Clearly, in all experiments involving $AlCl_3$ and Fe^{3+} (added as $FeCl_3$ and from the ferrous ion generated which is re-oxidised to generate the ferric ion oxidant), there is a continuously high availability of ferric iron required for chalcopyrite dissolution as indicated by a high Eh of approximately 580 mV (Figure 4d). Also, there is iron sulfate precipitation, which may lead to surface passivation of chalcopyrite. There may also be some form of aluminium sulfates or aluminium hydroxysulfate phases, however, these phases are hydrous and less stable (Bigham and Nordstrom, 2000) as compared to iron hydroxysulfate formed in NaCl brine. The pH for the case without Fe^{3+} rises to almost pH 2.5, whereas the case with Fe^{3+} maintains a lower pH <1.3 (Figure 4d).

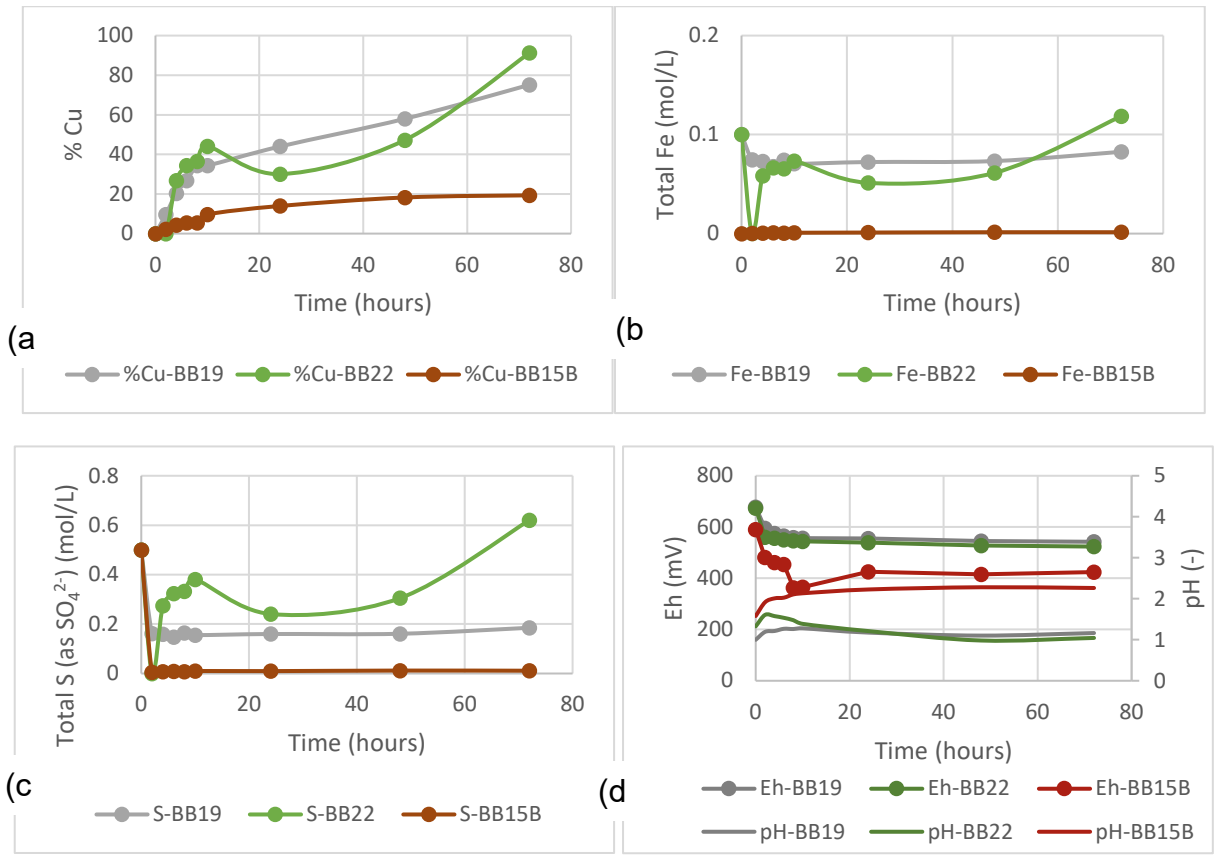

FIG 4 – Leaching in $AlCl_3$ saturated brine (a) % copper recovery (b) total Fe (mol/L) (c) total S (as SO_4^{2-}) (mol/L) (d) Eh – pH with oxidant (BB19) at 25°C, with oxidant at 45°C (BB22), and without oxidant (BB15B) at 25°C.

Discussion

Why $AlCl_3$ for low-grade porphyry copper sulfide leaching?

Almost all copper recovery experiments show that leaching in $AlCl_3$-dominated brine with an initial ferric ion concentration of 0.1 mol/L is the most effective (Figures 3 and 4). Aluminium leads to a higher Eh (above 530 mV) due to an increase in the availability of Fe^{3+} with little or no jarosite formation. At a relatively high pH of 1.5, there is 56 per cent copper recovery for NaCl, while a maximum Cu recovery of 50.5 per cent was observed for the $AlCl_3$-dominated brine. As the pH decreases to pH 1.0, the recovery of copper increases to 75 per cent for $AlCl_3$-dominated as compared to 70 per cent for NaCl-dominated brine.

Mineralogically, it can be suggested that in the absence of Al^{3+}, there is the formation of forms of iron sulfate, sodium sulfate, hydronium sulfate, and jarosite which decrease the available Fe^{3+} for chalcopyrite dissolution (Figure 5a). In contrast, the introduction of Al^{3+} leads to the formation of $AlSO_4^+$ species, thus lowering sulfate activity and the tendency for K-jarosite formation. As a result of this, the K-jarosite region of stability shrinks in the presence of Al^{3+} (Figure 5b). More research is being conducted to evaluate the mineralogical changes occurring during experiments to test some of these observations in changing thermodynamic stability. Bigham and Nordstrom (2000) noted that Al remains predominately dissolved at pH<4.5, that is, pH values below the first hydrolysis constant for Al (pK = 5.0).

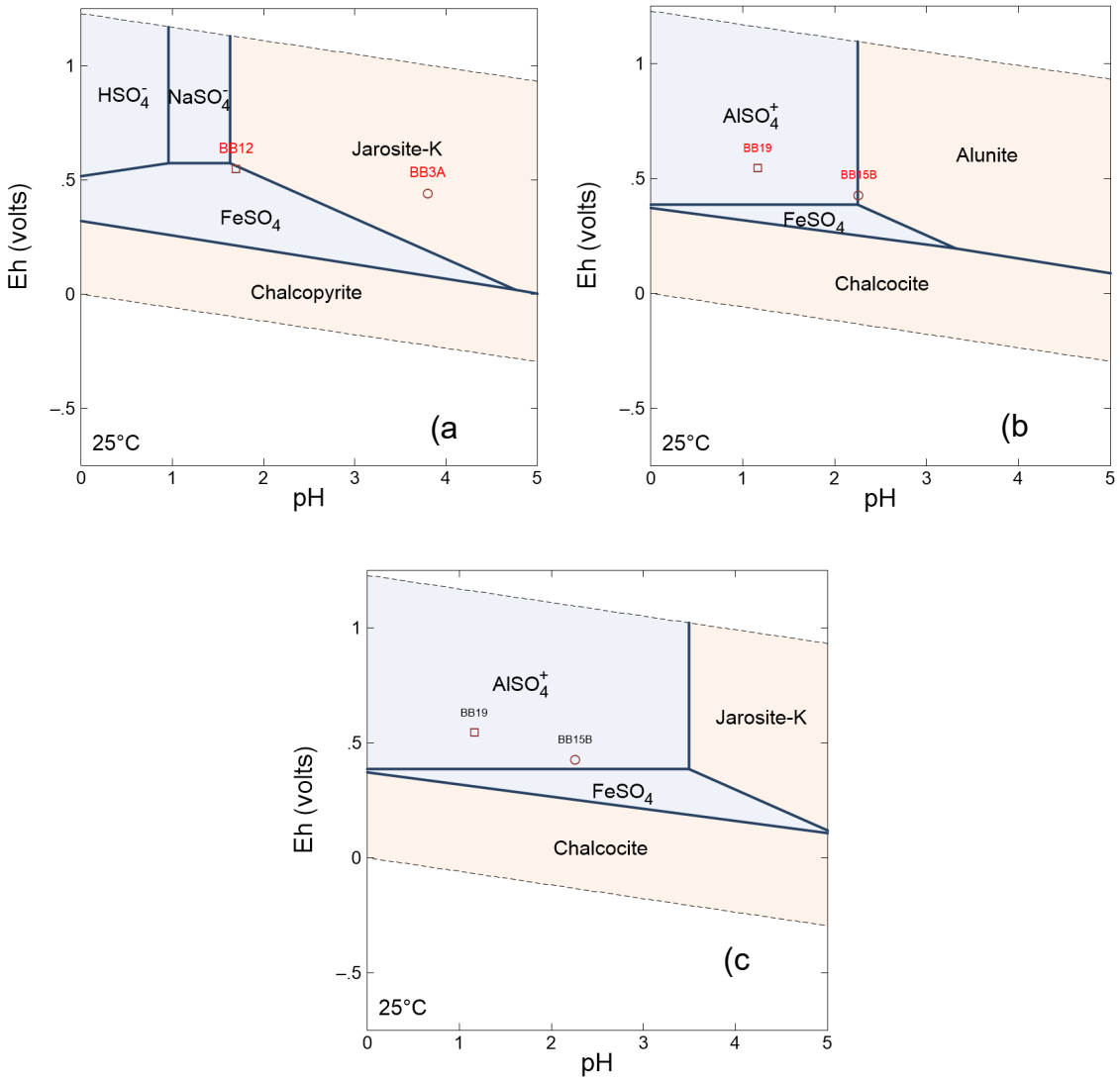

FIG 5 – These plots utilised the final effluent ionic composition, Eh, and pH from the indicated tests (BB12, BB3A, BB19, and BB15B). (a) SO_4^{2-} stability diagram for NaCl brine leaching system, T = 25°C, P = 1.013 bars, a[Fe^{3+}] = $10^{-4.47}$, a[H2O] = 1, a[Cu^{2+}] = $10^{-3.06}$, a[K^+] = $10^{-0.57}$, a[Na^+] = $10^{0.34}$, a[Cl] = $10^{0.38}$, a[SO_4^{2-}] = $10^{-1.33}$. (b) SO_4^{2-} stability diagram for $AlCl_3$ brine leaching system, T = 25°C, P = 1.013 bars, a[Fe^{3+}] = $10^{-4.29}$, a[H2O] = 1, a[Cu^{2+}] = $10^{-3.05}$, a[K^+] = $10^{-0.63}$, a[Na^+] = $10^{0.33}$, a[SO_4^{2-}] = $10^{-2.64}$, a[Cl] = $10^{0.39}$, a[Al^{3+}] = $10^{-0.89}$. (c) Same as Figure 5b with Alunite suppressed.

CONCLUSIONS

This study investigates the performance of different industrial brine types for Cu recovery from a low-grade copper sulfide ore. The study is motivated by an increase in the global demand for copper. The main findings are:

1. In our experiments, industrial brines lead to a Cu recovery of 56–91 per cent, as opposed to a Cu recovery of 35 per cent in freshwater.
2. Ferric iron (at a concentration of 0.1 mol/L) serves as a strong oxidant and leads to higher copper recovery. Dissolved chloride and a low pH alone cannot dissolve copper sulfide mineral fully even in the presence of oxygen.
3. According to thermodynamic predictions, the introduction of Al^{3+} may lead to the formation of $AlSO_4^+$ species, thus lowering sulfate activity and the tendency for K-jarosite formation. Therefore, phase replacement concepts such as $AlSO_{4+}$ and alunite formation to replace iron hydroxysulfates (such as jarosite) can be applied to increase copper recovery.
4. The presence of Al^{3+} suppresses the formation of stable iron hydroxysulfate and jarosite and thus ensures the continuous availability of Fe^{3+} for chalcopyrite dissolution as Eh and pH vary.

ACKNOWLEDGEMENTS

The Melbourne Research and George Lansell Memorial Scholarships provided funding for this study. The analytical instrumentation used in this study was provided by the University of Melbourne's Trace Analysis for Chemical, Earth, and Environmental Sciences (TrACEES) Platform. Much appreciation to Dr. Kodjo Afewu and the anonymous IMPC reviewer for their discussions and comments on this paper.

REFERENCES

Bigham, J M and Nordstrom, D K, 2000. Iron and aluminium hydroxysulfates from acid sulfate waters. *Reviews in mineralogy and geochemistry*, 40(1), pp 351–403.

Brugger, J, McPhail, D C, Black, J and Spiccia, L, 2001. Complexation of metal ions in brines: application of electronic spectroscopy in the study of the Cu (II)-LiCl-H_2O system between 25 and 90°C. *Geochimica et Cosmochimica Acta*, 65(1), pp 2691–2708.

D'Hugues, P, Foucher, S, Galle-Cavalloni, P and Morin, D, 2002. Continuous bioleaching of chalcopyrite using a novel extremely thermophilic mixed culture. *International Journal of Mineral Processing*, *66*(1–4), pp 107–119.

Dunne, R, 2012. Water water everywhere and not a drop to drink, nor do I know its whereabouts. *Water in Mineral Processing*, 1.

Faine, J R, Alfaro, F A, Jullian, R M and Gutierrez, A B, Minera Michilla SA, 2009. Procedure to leach copper concentrates, under pressure and at ambient temperature, by forming a reactive gel in a sulfate-chloride medium. *US Patent* 7,491,372.

Hernández, P C, Taboada, M E, Herreros, O O, Graber, T A and Ghorbani, Y, 2018. Leaching of chalcopyrite in acidified nitrate using seawater-based media. *Minerals*, 8(6), p 238.

Hernández, P, Dorador, A, Martínez, M, Toro, N, Castillo, J and Ghorbani, Y, 2020. Use of seawater/brine and caliche salts as clean and environmentally friendly sources of chloride and nitrate ions for chalcopyrite concentrate leaching. *Minerals*, 10(5), p 477.

Kimball, B E, Rimstidt, J D and Brantley, S L, 2010. Chalcopyrite dissolution rate laws. *Applied Geochemistry*, 25(7), pp 972–983.

Senanayake, G and Muir, D M, 2003. Chloride processing of metal sulphides: review of fundamentals and applications. *Hydrometallurgy 2003 – Fifth International Conference in Honor of Professor Ian Ritchie*, Vol. 1, TMS, Warrendale, pp 517–531.

Sequeira, C A C, Santos, D M F, Chen, Y and Anastassakis, G, 2008. Chemical metathesis of chalcopyrite in acidic solutions. *Hydrometallurgy*, 92(3–4), pp 135–140.

Velásquez-Yévenes, L and Quezada-Reyes, V, 2018. Influence of seawater and discard brine on the dissolution of copper ore and copper concentrate. *Hydrometallurgy*, 180, pp 88–95.

Watling, H R, 2014. Chalcopyrite hydrometallurgy at atmospheric pressure: 2. Review of acidic chloride process options. *Hydrometallurgy*, 146, pp 96–110.

Yang, I, Choi, S and Park, J, 2018. Passivation of chalcopyrite in hydrodynamic-bioleaching. *Episodes Journal of International Geoscience*, *41*(4), pp 249–258.

Process mineralogy of Tarkwaian paleo placer gold deposit in Ghana

M Beyuo[1], E A Agorhom[2], C Owusu[3] and I Quaicoe[4]

1. Technical Instructor, University of Mines and Technology, Tarkwa, Ghana, +223. Email: mbeyuo@umat.edu.gh.
2. Senior Lecturer, MAusIMM, University of Mines and Technology, Tarkwa, Ghana, +223. Email: eagorhom@umat.edu.gh.
3. Senior Lecturer, University of Mines and Technology, Tarkwa, Ghana, +223. Email: mbeyuo@umat.edu.gh.
4. Senior Lecturer, University of Mines and Technology, Tarkwa, Ghana, +223. Email: cowusu@umat.edu.gh.

ABSTRACT

Understanding the mineralogy and liberation of gold particles in an ore is key to the development and optimisation of gold processing operations, being cyanidation or gravity separation. This can be achieved through basic historic geological information, gold deportment studies, chemical speciation and metallurgical test works. The present study assessed the nature of the occurrence of gold particles (mineralogical composition, liberation, associations and surface chemistry) and its effect on the process route (cyanidation and gravity separation) of a typical paleo placer gold ore deposit within the Tarkwaian Rock system. The investigative approach used involved chemical assay, quantitative X-ray diffraction (QXRD) and quantitative evaluation of minerals using scanning electron microscopy (QEMSCAN). The ore samples (A, B, C, D, E, F) used were obtained from six active pits of a gold mine working on this orebody. The results of the mineralogical analysis revealed that the ore is highly oxidised and comprised quartz (>80 per cent) and Muscovite mica (>6 per cent) as the major mineral phases in all the samples. Trace amounts of hematite, kaolinite and todorokite were also identified in all the samples. The chemical analysis showed presence of gold (Au) in all the samples with samples B (3.62 g/t) and C (3.96 g/t) containing the highest concentrations. Trace amounts of copper (Cu), iron (Fe), sulfur (S), aluminium (Al), arsenic (As) were also detected in all the ores. The QEMSCAN mineralogical liberation and gold association results revealed that the gold grains were relatively coarser in all samples (P_{80} > 80 µm Au in size) except F (P_{80} < 32 µm Au in size). Gold grains were highly liberated especially in sample B with the majority of the locked gold grains forming complex associations. All the samples responded well to cyanidation and gravity separation except samples C and F, respectively.

INTRODUCTION

Historically, gold production in Ghana is believed to date back over 2500 years, with Ghana, formerly called the Gold coast (Pigois *et al,* 2003; Fisher, Dagdelen and Turner, 2005). Primarily, the gold has been mined from two sources:

1. Hematite-and-magnetite-bearing, modified paleo placer deposits in Tarkwaian quartz-pebble conglomerates (Sestini, 1973; Strogen, 1988; Hirdes and Nunoo, 1994; Hirdes, Senger and Adjei, 1994; Fisher, Dagdelen and Turner, 2005).
2. Structurally controlled, epigenetic lode, or orogenic gold deposits hosted in rocks of the Birimian Supergroup (Milési *et al,* 1992; Appiah, 1991; Mumin, Fleet and Chryssoulis, 1994; Blenkinsop *et al,* 1994; Groves *et al,* 1998, 2000; Allibone *et al,* 2002a, 2002b; Pigois *et al,* 2003).

Until recently, there was considerable debate over whether the paleo placer deposits in the Banket Series of the Tarkwaian System were derived from the lode deposits hosted in Birimian rocks or whether they predated the deformation events in which the Birimian-hosted gold lodes formed (Kesse, 1985; Hirdes, Davis and Eisenlohr, 1992; Milési *et al,* 1991, 1992; Pigois *et al,* 2003). Whilst much attention has been given to the assessment of the regional geological structures and origin of the gold, especially in paleo placer deposit, little is known about their chemistry, mineralogy and metallurgical characteristics that are necessary for designing processing route and/or optimising gold processing operations.

Designing, developing and optimising gold processing operations depend on comprehensive gold (Au) deportment studies such as physical, chemical, mineralogical and metallurgical assessments. This is done to obtain a full understanding of the nature and variability of gold in the ore and its respond to metallurgical extraction.

The most efficient gold extraction processing route is directly related to the inherent mineralogical features of the gold ore being processed (Zhou and Cabri, 2004; Chryssoulis and Cabri, 1990; Marsden and House, 2006; Chryssoulis and McMullen, 2005; Agorhom, Skinner, and Zanin, 2012, 2013; Agorhom *et al,* 2012). It is therefore necessary to accurately characterise the mineralogical nature of the ore to be processed, thus, characterisation of the gold metal phases, grain size, speciation, liberation, association and the associated gangue minerals. This information can be obtained using automated mineralogical analytical techniques such as quantitative evaluation of minerals by scanning electron microscopy (QEMSCAN) and mineral liberation analyser (MLA).

Although these techniques are able to provide the necessary information required to optimise gold extraction, the trace occurrence of gold in most ores makes them difficult to analyse. Therefore, the results of Au deportment studies are affected by representivity (representativeness) of the samples being analysed and the variation in gold grade (Coetzee *et al,* 2011).

Studies have shown that information gleaned from the mineralogical and Au deportment analyses provide the grounds for the extractability of gold from the ore to be tested using metallurgical techniques such as direct cyanidation, gravity separation, flotation and diagnostic leaching (Lorenzen and Tumilty, 1992; Lorenzen and Van Deventer, 1993; Lorenzen, 1995; Marsden and House, 1992; Henley, Clarke and Sauter, 2001; Goodall, Scales and Ryan, 2005; Celep *et al,* 2009; Botha *et al,* 2004; Tshiongo, Mbaya and Maweja, 2011; Esmkhani *et al,* 2013; Kasaini *et al,* 2008; Agorhom *et al,* 2012; Agorhom, Skinner and Zanin, 2013). This study makes use of bulk chemical assay, quantitative X-ray diffraction (QXRD) and QEMSCAN for the identification and characterisation of gold-bearing minerals in paleo placer gold ore of the Tarkwaian system of Ghana. The aim of the study was to conduct gold mineralogical, liberation and association to better understand and forecast possible leaching and recovery challenges.

MATERIALS AND METHODS

Materials

The paleo placer gold ore samples were obtained from six active pits at different reefs of a gold mining company operating within the Tarkwaian belt of Ghana. The samples from the six pits were designated as sample A, B, C, D, E and F respectively. Approximately 360 kg of rock samples in total was taken, crushed and milled to 80 per cent passing 106 µm.

The milled ore was blended and split into 3 kg representative subsamples due to the variable nature of gold in the ore (Figure 1). During the blending and splitting process, 200 g subsamples were taken from each pit samples for head grade elemental and QXRD analyses.

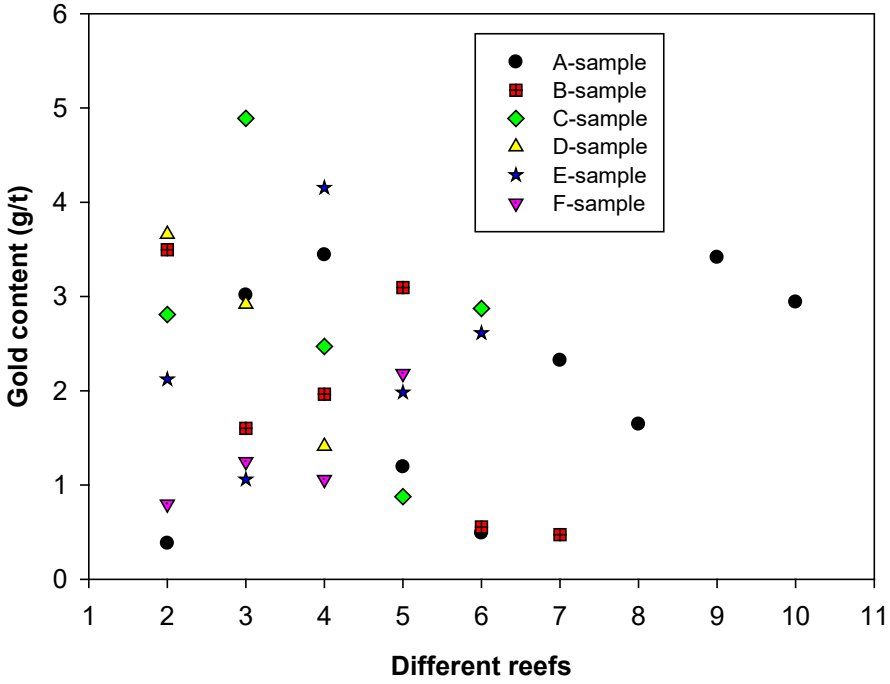

FIG 1 – Gold content (g/t) in the samples at different reefs of the different pits.

Methods

Elemental analysis

The elemental compositions of the ore samples were determined using bulk chemical assay and acid digestion with atomic absorption spectrometry (AAS), Inductively Coupled Plasma (ICP) optical emission spectrometry (OES) (S, Al, Ca, Fe, K, Mg, P, Si) and inductively coupled plasma (ICP) mass spectrometry (Ag, As, Cu, Pb, Sb, Te) finishing.

Quantitative X-ray diffraction analysis (QXRD)

Quantitative XRD identifies all detectable crystalline phases and their abundance is quantified and expressed as a table of normalised mineral abundances. The samples from pits A to F were micro milled for 10 minutes, with ethanol as the grinding liquid. The resultant sample was lightly pressed into a back-packed sample holder. The XRD trace was collected under the following instrument conditions (Table 1):

TABLE 1

X-ray diffraction analysis conditions.

XRD system	PANalytical X'Pert Pro PW3040 diffractometer, 40 kV, 40 mA
Filter	Iron
Radiation	CoKa (I = 1.789 Å)
Angular range	5° to 80° 2θ
Angular speed	0.04426° 2θ/second
Step size	0.0167°
Divergence Slit	¼°
Anti-scatter Slit	½°
Spinning	0.50 second per revolution

Mineral identification was undertaken using the X'Pert High Score Plus search/match software. Rietveld quantitative analysis was performed on the XRD data using the commercial package, SIROQUANT™ V3 from Sietronics Pty Ltd.

Quantitative evaluation of minerals by scanning electron microscopy (QEMSCAN)

QEMSCAN analysis using particle mineral analysis (PMA) and trace mineral search (TMS) mode of analysis was conducted on the panned concentrate as shown in Figure 2. Twenty five (25) kilograms of each sample was subjected to two-stage gravity concentration (Knelson concentration followed by hand panning) to upgrade gold particle for easy identification and statistical analysis using TMS. Eight polished sections were prepared from each panned concentrate (heavy pan fraction).

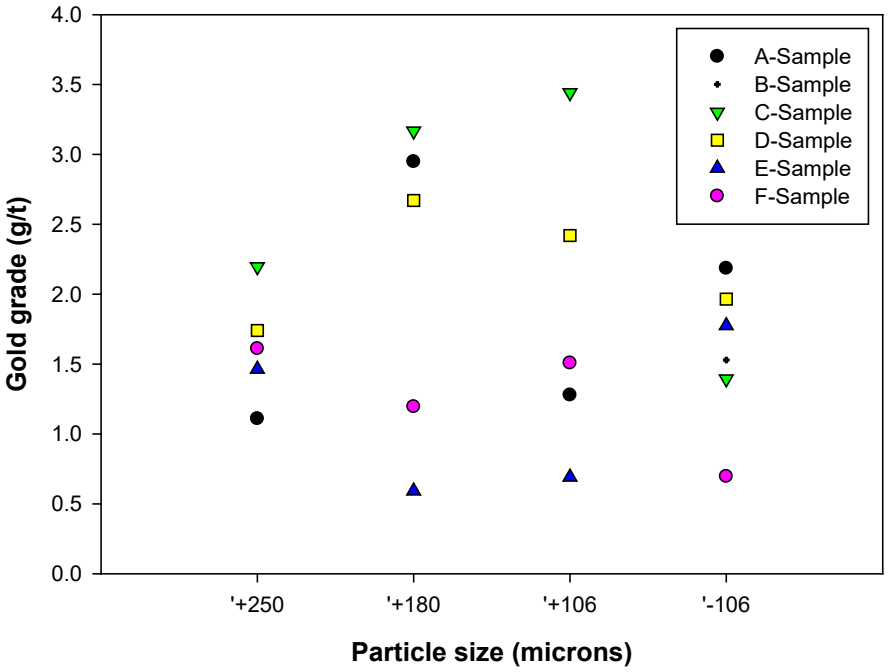

FIG 2 – Variation of gold grades in the ore samples from the different pits (A-F).

The block was ground, polished and coated with carbon prior to QEMSCAN analysis. QEMSCAN PMA and TMS modes were used on the samples and the 'Gen v3' SIP used to classify the data.

Modification were made to the SIP to account for Thorium and metals detected in the samples. The data was processed using iDiscover v.5.3 'Field stitching', 'Particulator', Area>1 filter, 'touching particles' and 'Boundary phase' processors were applied.

QEMSCAN data was used to display the grain size distribution curve of a mineral (eg Au) or group of minerals (eg Au/Ag mineral). A particle comprises of mineral grains. QEMSCAN average particle and grain size is an estimate of the diameter of the particle in a population. PMA was used for particle size estimation while TMS was used for estimating the grain size of the trace minerals or elements, gold and silver or Au/Ag minerals.

Laboratory Cyanidation test

A laboratory cyanidation test program was conducted to investigate the impact of the different gold mineralogy on Au leaching and recovery as well as the process route for the different ore samples. 1 kg each of the composite samples and the Knelson gravity tails for the different pits at approximately 80 per cent passing 106 µm were leached. Each sample was put into a 5 L leach bottle and Tarkwa tap water was added to prepare a pulp of 54 wt. per cent solids. The pulp power of hydrogen (pH) was adjusted to 10.5 with lime and initial free cyanide (CN) strength set to 250 ppm. Leaching was conducted for 24 h with the bottle rolling to agitate and aerate the pulp. No further reagents (lime and CN) were added during the leaching period. At completion, the sample was filtered and pregnant solution sampled and assayed for Au. Residue solids were washed and assayed for Au as well.

RESULTS AND DISCUSSION

Elemental composition

Gold (Au), which is the metal of interest, occurs in all the ores with concentrations within the ranges of 0.88–3.96 g/t. Whilst samples from pits B and C recorded the highest concentrations of 3.62 g/t and 3.96 g/t, respectively, the ore from pit F contained the lowest gold concentration, 0.88 g/t. Gangue elements/metals such as copper (Cu), sulfur (S), aluminium (Al), iron (Fe), arsenic (As) are also present in trace amount whilst silicon (representing silicate minerals) element occurs in high concentration in the ores from all the pits.

The high amount of silicon is linked to the high amount of quartz often reported in the Tarkwaian ore zone (Pigois *et al*, 2003; Fisher, Dagdelen and Turner, 2005). Studies have shown that the presence of these gangue elements, especially, Cu, S and Fe, significantly affect gold cyanidation process by increasing the consumption of cyanide and oxygen (Habashi, 1967; Dai and Jeffrey, 2006).

These base metals were consistently low in all the samples suggesting that cyanide consumption due to the speciation of these metals would be low under standard leaching conditions.

Size-by-size Au Analysis

The results for the size-by-size Au analysis for the all the samples obtained from the six active pits indicate that Au occurs in all size fractions, particularly in the -106 µm for all the samples, on the average of 70 per cent. A plot of Au grade and the particle size (Figure 2) indicates that Au grade varies across all size ranges regardless of the sample type.

It can be clearly seen that there does not exist a strong correlation between gold content and the particle size for the different samples. For example, sample B contains high Au grades in all size fractions except in the -106 µm where sample A had the highest grade. The variations of Au grades in all the samples indicate that proper blending procedure is required if a consistent feed grade is to be ensured in plant feed material. Otherwise, a gravity separation may be required to provide a consistent feed grade to the carbon-in-leach (CIL) circuit.

Mineralogical characterisation

Quantitative mineralogy of the ore samples (QXRD analysis)

The XRD was used to determine and quantify the general mineralogical composition of the ore samples from all the six active pits.

The XRD analysis was conducted on the composite head samples from the different reefs within each pit and the results are presented in Table 2. The results show that all the samples predominantly consist of quartz, varying between 83 and 90 wt. per cent.

TABLE 2

Quantitative modal mineralogy of the samples using QXRD.

Mineral (wt.%)	Composition	A	B	C	D	E	F
Quartz	SiO_2	88	90	90	90	83	89
Hematite	Fe_2O_3	2	2	3	3	2	2
Mica	$K(Fe^{2+},Mg)_3Al(Si_3Al)O_{10}(OH)_2$	8	8	7	6	12	9
Kaolinite	$Al_2Si_2O_5(OH)_4$	2	0	<1	1	3	<1
Todorokite	$(Na,Ca,K)Mn_6O_{12}$ 3-4.5H_2O	0	0	1	1	0	<1
Total		100	100	100	100	100	100

Muscovite mica is the most dominant phyllosilicate gangue mineral constituting between 6 and 12 wt. per cent. Kaolinite also varied between 1–3 wt. per cent and its presence is an indication of

the degree of superficial weathering of the orebody. This is particularly significant for the ore sample from pit E. The higher amounts of muscovite mica and kaolinite in sample E may pose rheological problems during processing. Fe-oxides, predominantly hematite is the most common non-silicate gangue mineral identified in all the ore samples, varying between 2 and 3 wt. per cent. Trace amount of todorokite was detected in all the samples (maximum 1 wt. per cent). The gangue mineralogy of the samples from the various pits is consistent and shows a true reflection of Tarkwaian sediment composition (Pigois *et al*, 2003; Fisher, Dagdelen and Turner, 2005).

Gold mineralogy, liberation and associations (QEMSCAN analysis)

The grades of Au in all the samples were quite low and highly variable, varying between 0.88 g/t (sample F) and 3.96 g/t (sample D) (Figure 2).

Au deportment and statistical identification analysis for low-grade Au ores are often problematic due to the difficulty in identifying statistical significant number of Au grains (Goodall, Scales and Ryan, 2005; Agorhom, Skinner, and Zanin, 2012). Moreover, presence of high amount of coarse Au grains also makes it difficult and this was the case in this study. Therefore, for easy identification of Au particles/grains, all the samples were upgraded through two-stage gravity concentration before subjecting the samples to QEMSCAN analysis.

Particle and grain size distribution

The particle sizes of the identified minerals were all below 200 µm in all the samples. Eighty per cent (80 per cent) of the identified minerals varied between 166 and 197 µm with sample B showing the smallest mineral particle size (ie P_{80} = 166 µm).

Gold grain size analysis performed using TMS showed that the 80 per cent of all the Au grains varied between 32 and 109 µm. For samples A to E, majority (>55 per cent) of the gold grains were higher than 40 µm. Gold grains higher than 40 µm are 69 per cent, 58 per cent, 55 per cent, 75 per cent and 0 per cent for samples A, B, C, D, E, and F, respectively. Fine Au grains were found in the pit F ore sample (<40 µm). This shows that gravity circuit may be required to enhance gold recovery by providing consistent gold grade, stable reagent consumption and management, and minimise high gold in process and hence faster leaching kinetics at the CIL circuit (Henley, 1975).

Au/Ag mineral liberation and locking studies

The liberation results showed that 67 per cent of the identified Au grains was completely (over 100 per cent) liberated in ore sample B (Table 3). However, in all the samples, the liberation of the gold grains varied between 44 and 94 per cent. Highest liberation was achieved in ore sample B while ore sample F showed the lowest Au grains liberation. The level of Au grains liberation increased at the targeted grind size (P_{80} = 106 µm) in the order of:

Sample F < Sample A < Sample C < Sample D < Sample E < Sample B.

The locking/mineral association analysis is shown in Table 4. The locking or association of the Au/Ag minerals showed that Au grains in pit A and F samples show a bimodal distribution. That is, between 58 and 44 per cent of the Au grains were fully liberated whereas 41 and 51 per cent formed complex aggregates with other mineral phases. This shows that finer grind may be required to increase liberation of gold from the association minerals in these ore samples for enhanced direct cyanidation. About 1 to 5 per cent of the identified Au grains were either associated or locked in Fe-Ox/OH or titano Fe-Ox/OH mineral phases (Table 4).

TABLE 3

Liberation of Au/Ag Minerals (TMS Analysis).

Mass %	A	B	C	D	E	F	
=100%	15	67	14	7	12	44	Liberated
90–100%	43	27	52	68	65	0	
80–90%	1	1	9	7	16	0	High Middling
70–80%	22	0	9	2	0	0	
60–70%	1	0	0	7	0	0	
50–60%	0	0	0	0	0	0	Low Middling
40–50%	1	0	0	0	0	0	
30–40%	0	0	0	0	0	0	
20–30%	0	0	0	0	0	0	Locked
10–20%	0	0	11	2	0	0	
0–10%	17	5	5	7	7	56	
TOTAL	100	100	100	100	100	100	

TABLE 4

Locking and association analysis of Au/Ag minerals (TMS analysis).

Mass %	A	B	C	D	E	F
Liberated	58	94	66	75	77	44
Bn Qtz	1	0	6	3	0	0
Ter Fe/OxOH + Ti Fe Ox	0	1	2	5	1	3
Ter Fe/OxOH + Qtz	0	0	0	1	0	2
Complex	41	6	26	16	22	51
Total	100	100	100	100	100	100

Gold surface chemistry

The surface chemistry speciation of the gold grain identified in the various samples was also examined using SEM/EDX. Generally, about 8 to 11 gold grains were scanned for the surface chemistry analyses as shown in Figure 3. The speciation of gold particles in the ore is simple as majority of the identified Au particles were relatively pure Au-alloy chemistry (above 90 per cent) (Figure 3).

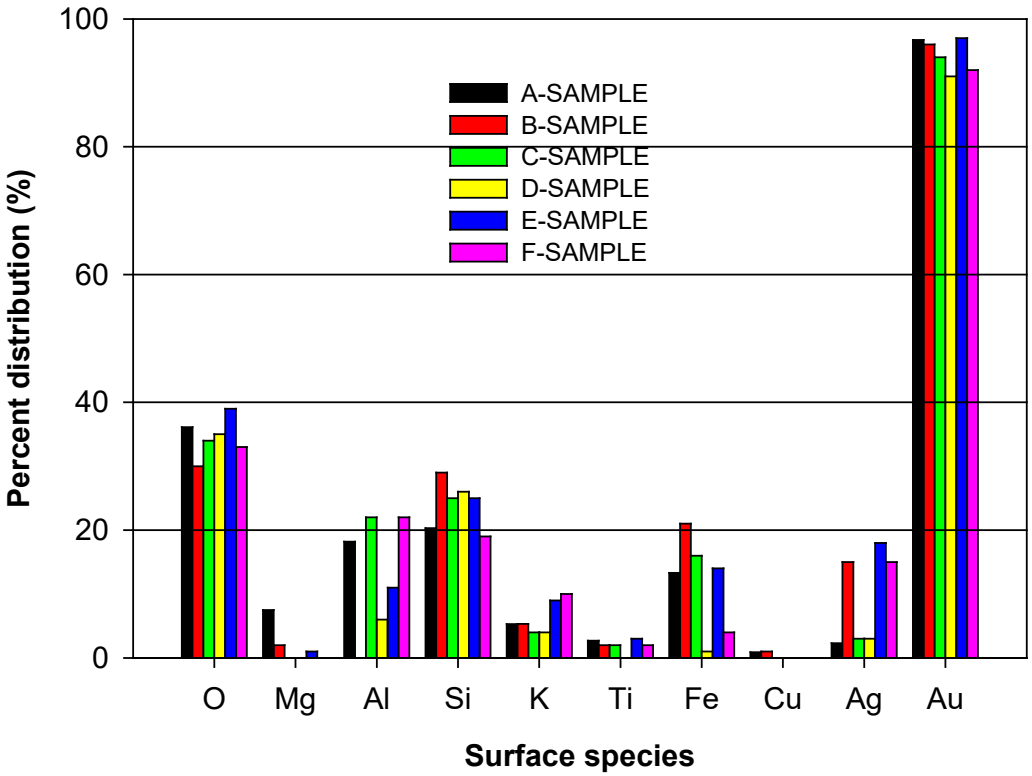

FIG 3 – Surface chemistry speciation of the identified gold grains in the ore as identified by SEM/QEMSCAN.

The relatively coarse gold particles exhibit pure Au-alloy while the fine particles exhibit variable Au-chemistry comprising O, Mg, Si, Al, K, Ti, Fe, Cu and Ag. This is because most of the relatively fine gold particles occur as fine inclusions within complex aggregates of Fe Ox/OH, Ti-Fe Ox/OH and silicates.

In terms of sample-by-sample analysis, the Au particles found in the ore sample from pit F were highly contaminated compared to the other samples. Some amounts of Ag, alumina-silicates and iron oxide/hydroxides were identified as the main Au surface contaminants, especially for the fine gold particles. The nature of the gold particles in the F ore sample as fine, low liberation and highly variable surface chemistry indicate that Au cyanidation will be difficult for this ore (Venter, Chryssoulis and Mulpeter, 2004). It is therefore recommended that the proportion of this ore in the leach feed should always be low compared to the others.

Gold leaching and recovery

Based on the mineralogical and liberation results obtained, gold extraction and leaching behaviour was studied for all the samples using gravity separation and cyanidation. Table 5 highlights the results for both gravity concentration and cyanidation test works.

TABLE 5

Gold recovery data for both the gravity separation and cyanidation using 250 ppm CN for 24 h.

Sample ID	Gravity concentration (1)		Gravity tails CN (2)		(1) + (2) = (3)	4
	Au Rec (%)	Con Au (g/t)	Au Rec (%)	Tails Au (g/t)	Overall, Au Rec (%)	Direct CN Au Rec (%)
A	55.0	65.05	90.4	0.04	95.7	91.4
B	49.0	46.99	90.8	0.05	95.3	91.9
C	33.4	39.29	89.8	0.09	93.2	96.9
D	43.2	52.42	88.0	0.12	93.2	94.9
E	51.1	74.24	89.4	0.06	94.8	94.0
F	51.2	24.94	88.5	0.06	94.4	86.8

CN – cyanidation.

The results show that the gravity concentration achieved between 33.4 per cent and 55.0 per cent of gold recovery for all the samples at the grind size of 106 µm. Notably, Sample A produced the highest gold recovery of 55 per cent almost the same as the amount of gold liberated (Table 5) whilst sample E yielded the highest gold concentrate grade of 74.24 g/t. Additionally, the cyanide leaching of the gravity tails also produced a very good recovery for all the samples studied (88–90 per cent).

For the direct cyanidation, it was found that Au recovery in all the samples varied between 88.6 per cent and 96.9 per cent (Table 5). The Au leaching in all the samples gave recovery efficiency in the order of C (96.9 per cent) > D (94.9 per cent) > E (94.0 per cent) > B (91.9 per cent) > A (91.4 per cent) > F (86.9 per cent) which is consistent with the nature of Au liberation and association in the samples. For example, the low Au recovery exhibited by sample F can be attributed to the low liberation and high locking of the Au particles (Table 5) coupled with varied surface chemistry of the identified gold particles in the sample. Overall, direct cyanidation of the ore from the pits A, B and F achieved lower recoveries compared to the two-stage extraction route (ie gravity concentration of the samples followed by cyanide leaching of the gravity tails). However, for pits C, D and E there was no appreciable change in gold recovery under the tested conditions.

CONCLUSIONS

Paleo placer Au ore process mineralogy through basic elemental analysis and quantitative mineralogy complimented with gravity concentration and direct Au cyanidation has been conducted. The grades of gold in all the samples were erratic, hence blending is required to maintain consistent plant feed grade. Over 88 per cent of the ore samples composed of quartz as the major gangue minerals with muscovite mica and hematite as the minor gangue minerals. Trace amounts of kaolinite and todorokite were also detected. Although sulfide minerals were rarely detected in both the head composite and QEMSCAN samples, small amounts of Cu (17–25 ppm) and S (50–150 ppm) were identified in all the ore samples. Majority of the identified Au particles were relatively coarse in all samples except F (particles less than 32 µm). Au particles were highly liberated (66–94 per cent) in the ore from pits B, C, D and E samples than the A and F samples.

The remaining gold grains form complex aggregates with silicates and iron oxide minerals. The coarse gold particles were relatively pure (Au > 90 per cent) as compared with the fine gold particles (Au > 32 µm), especially for the pit F sample. Key Au surface contaminants such as silver, copper, alumina-silicates and iron oxides were detected by the SEM/EDX scan. Cyanidation of the composite sample from each of the pits (@ 250 ppm, 24 h) showed recoveries varying between 86.9 and 96.9 per cent, with pit F sample giving the lowest recovery (86.9 per cent). Pit C sample gave the highest recovery of 96.9 per cent. A comprehensive gravity concentration gold leaching kinetics based on blending these pit samples should be considered.

It must however be emphasized that good use of mineralogical characterisation techniques (XRD and PSD), to assist with flow sheet development are not 'new' but, this study provides a good basis for early stage project assessment and would be of benefit at the conceptual/scoping study level and process optimisation.

ACKNOWLEDGEMENTS

The authors acknowledge the support received from (Catherine Diko, Nelson Fordjour, Kwaku Owusu Boateng and Redeemina Comfort Bonnah) during ore sampling and laboratory sample preparation.

REFERENCES

Agorhom, E A, Skinner, W and Zanin, M, 2012. Upgrading of low-grade gold ore samples for improved particle characterisation using Micro-CT and SEM/EDX. *Advanced Powder Technology*, *23*(4), pp 498–508.

Agorhom, E A, Skinner, W and Zanin, M, 2013. Influence of gold mineralogy on its flotation recovery in a porphyry copper–gold ore. *Chemical Engineering Science*, *99*, pp 127–138.

Agorhom, E A, Swierczek, Z, Skinner, W and Zanin, M, 2012. *Combined QXRD-QEMSCAN mineralogical analysis of a porphyry copper-gold ore for the optimization of the flotation strategy* (Doctoral dissertation, International Mineral Processing Council/Indian Institute of Mineral Engineers/Indian Institute of Metals).

Allibone, A H, McCuaig, T C, Harris, D, Etheridge, M, Munroe, S, Byrne, D, Amanor, J and Gyapong, W, 2002b. Structural controls on gold mineralization at the Ashanti deposit, Obuasi, Ghana.

Allibone, A, Teasdale, J, Cameron, G, Etheridge, M, Uttley, P, Soboh, A, Appiah-Kubi, J, Adanu, A, Arthur, R, Mamphey, J and Odoom, B, 2002a. Timing and structural controls on gold mineralization at the Bogoso gold mine, Ghana, West Africa. *Economic Geology*, *97*(5), pp 949–969.

Appiah, H, 1991. Geology and mine exploration trends of Prestea goldfields, Ghana. *Journal of African Earth Sciences (and the Middle East)*, *13*(2), pp 235–241.

Blenkinsop, T, Schmidt Mumm, A, Kumi, R and Sangmor, S, 1994. Structural geology of the Ashanti gold mine. *Geologisches Jahrbuch D*, *100*, pp 131–153.

Botha, J A, Smit, F S, Heins, R and Colvin, P, 2004. Improved Gold Recovery Economics at Target Gold Mine, South Africa. *Proceedings, Gravity Concentration*, *4*.

Celep, O, Alp, İ, Deveci, H and Vicil, M, 2009. Characterization of refractory behaviour of complex gold/silver ore by diagnostic leaching. *Transactions of Nonferrous Metals Society of China*, *19*(3), pp 707–713.

Chryssoulis, S L and Cabri, L J, 1990. Significance of gold mineralogical balances in mineral processing. *Trans. Inst. Min. Metall*, *99*, pp C1-C10.

Chryssoulis, S L and McMullen, J, 2005. Mineralogical investigation of gold ores. *Developments in Mineral Processing*, Vol. 15, pp 21–71.

Coetzee, L L, Theron, S J, Martin, G J, Van der Merwe, J D and Stanek, T A, 2011. Modern gold deportments and its application to industry. *Minerals Engineering*, *24*(6), pp 565–575.

Dai, X and Jeffrey, M I, 2006. The effect of sulfide minerals on the leaching of gold in aerated cyanide solutions. *Hydrometallurgy*, *82*(3–4), pp 118–125.

Esmkhani, R, Ghobadi, B, Amirkhani, A and Rezadust, S, 2013. The effect of increasing capacity on gold recovery and optimization of cyanidation parameters in Aghdarreh gold ore plant. *Australian Journal of Basic and Applied Sciences*, *2*(7), pp 702–708.

Fisher, T R, Dagdelen, K and Turner, A K, 2005. Modelling 3D grade distributions on the Tarkwa paleo placer gold deposit, Ghana, Africa. In *Geostatistics Banff 2004* (pp 439–448). Springer, Dordrecht.

Goodall, W R, Scales, P J and Ryan, C G, 2005. Applications of PIXE and diagnostic leaching in the characterisation of complex gold ores. *Minerals Engineering*, *18*(10), pp 1010–1019.

Groves, D I, Goldfarb, R J, Gebre-Mariam, M, Hagemann, S G and Robert, F, 1998. Orogenic gold deposits: a proposed classification in the context of their crustal distribution and relationship to other gold deposit types. *Ore geology reviews*, *13*(1–5), pp 7–27.

Groves, D I, Goldfarb, R J, Knox-Robinson, C M, Ojala, J, Gardoll, S, Yun, G Y and Holyland, P, 2000. Late-kinematic timing of orogenic gold deposits and significance for computer-based exploration techniques with emphasis on the Yilgarn block, Western Australia. *Ore Geology Reviews*, *17*(1–2), pp 1–38.

Habashi, F, 1967. *Kinetics and mechanism of gold and silver dissolution in cyanide solution* (pp 1–42). Butte: Montana College of Mineral Science and Technology.

Henley, K J, 1975. Gold ore mineralogy and its relation to metallurgical treatment, *J Minerals Science and Engineering* (1975) 289–312.

Henley, K J, Clarke, N C and Sauter, P, 2001. Evaluation of a diagnostic leaching technique for gold in native gold and gold ± silver tellurides, *Miner. Eng,* 14(1):1–12.

Hirdes, W and Nunoo, B, 1994. The Proterozoic paleo placers at Tarkwa gold mine, SW Ghana: sedimentology, mineralogy and precise age dating of the Main Reef and West Reef and bearing of the investigations on source area aspects. *Geologisches Jahrbuch D*, *100*, pp 247–311.

Hirdes, W, Davis, D W and Eisenlohr, B N, 1992. Reassessment of Proterozoic granitoid ages in Ghana on the basis of U/Pb zircon and monazite dating. *Precambrian Research*, *56*(1–2), pp 89–96.

Hirdes, W, Senger, R and Adjei, J, 1994. Explanatory Notes for the Geological Map of Southwest-Ghana 1: 100 000.

Kasaini, H, Kasongo, K, Naude, N and Katabua, J, 2008. Enhanced leachability of gold and silver in cyanide media: Effect of alkaline pre-treatment of jarosite minerals. *Minerals Engineering*, *21*(15), pp 1075–1082.

Kesse, G O, 1985. *The rock and mineral resources of Ghana*. AA Balkema, Rotterdam, Netherlands, 610 p.

Lorenzen, L and Tumilty, J A, 1992. Diagnostic leaching as an analytical tool for evaluating the effect of reagents on the performance of a gold plant. *Minerals Engineering*, *5*(3–5), pp 503–512.

Lorenzen, L and Van Deventer, J S J, 1993. The identification of refractoriness in gold ores by the selective destruction of minerals. *Minerals Engineering*, *6*(8–10), pp 1013–1023.

Lorenzen, L, 1995. Some guidelines to the design of a diagnostic leaching experiment. *Minerals Engineering*, *8*(3), pp 247–256.

Marsden, J and House, I, 1992. *The chemistry of gold extraction*, Ellis Horwoord Limited, England, pp. 488–505.

Marsden, J O and House, C I, 2006. *The chemistry of gold extraction*, Society for Mining, Metallurgy and Exploration. Inc. (SME), Littleton, Colorado, USA, *80127*, p 619.

Milési, J P, Ledru, P, Ankrah, P, Johan, V, Marcoux, E and Vinchon, C, 1991. The metallogenic relationship between Birimian and Tarkwaian gold deposits in Ghana. *Mineralium Deposita*, *26*(3), pp 228–238.

Milési, J P, Ledru, P, Feybesse, J L, Dommanget, A and Marcoux, E, 1992. Early proterozoic ore deposits and tectonics of the Birimian orogenic belt, West Africa. *Precambrian Research*, *58*(1–4), pp 305–344.

Mumin, A H, Fleet, M E and Chryssoulis, S L, 1994. Gold mineralization in As-rich mesothermal gold ores of the Bogosu-Prestea mining district of the Ashanti gold belt, Ghana: remobilization of 'invisible' gold. *Mineralium Deposita*, *29*(6), pp 445–460.

Pigois, J P, Groves, D I, Fletcher, I R, McNaughton, N J and Snee, L W, 2003. Age constraints on Tarkwaian paleo placer and lode-gold formation in the Tarkwa-Damang district, SW Ghana. *Mineralium Deposita*, *38*(6), pp 695–714.

Sestini, G, 1973. Sedimentology of a Paleo placer: The Gold-bearning Tarkwaian of Ghana. In *ores in sediments,* pp 275–305. Springer, Berlin, Heidelberg.

Strogen, P, 1988. The sedimentology, stratigraphy and structure of the Tarkwaian, Western Region and its relevance to gold exploration and development. In *Proc Int Conf Geology of Ghana with special emphasis on Gold, Accra*.

Tshiongo, N, Mbaya, R K K and Maweja, K, 2011. Leaching kinetics of Cu, Co, Zn, Pb and Fe from copper smelting slags cooled in different ways after tapping. In *The Southern African Institute of Mining and Metallurgy 6th Southern African Base Metals Conference*.

Venter, D, Chryssoulis, S L and Mulpeter, T, 2004. Using mineralogy to optimize gold recovery by direct cyanidation. *JOM*, *56*(8), pp 53–56.

Zhou, J Y and Cabri, L J, 2004. Gold process mineralogy: Objectives, techniques, and applications, *Journal of Minerals, Metals & Materials Society*, 56(7), pp. 49–52.

The effect of energy impacts on the leaching performance of eudialyte concentrate and selective recovery of zirconium and REE from pregnant solutions

V A Chanturia[1], V G Minenko[1], I Zh Bunin[1], A L Samusev[2] and M V Ryazantseva[1]

1. Institute of Comprehensive Exploitation of Mineral Resources Russian Academy of Sciences (ICEMR RAS), Moscow 111020, Russia.
2. ICEMR RAS, Moscow 111020, Russia. Email: Andrey63vzm@mail.ru

ABSTRACT

A promising source for the extraction of rare metals and REEs in Russia is the eudialyte ores of the Lovozero deposit, which do not contain active uranium components. The eudialyte ore reserves of the Lovozero Massif are considered virtually unlimited and therefore have the potential to become a primary source of a number of rare and rare earth metals.

The goal of this study was to comprehensively examine the effect of the parameters of high-power nanosecond electromagnetic pulses (HPEMP) and dielectric barrier discharge (DBD) on the leaching performance of eudialyte concentrate and the selective separation of zirconium and REEs from productive solutions.

Using scanning electron microscopy and infrared spectroscopy, the mechanism behind the intensification of acidic dissolution of eudialyte as a result of pretreatment with energy impacts was described. During the HPEMP treatment, weakening and destruction of the eudialyte surface was observed, which at the substructural level is expressed in the deformation and local destruction of $Si_{10}O_{27}$, Si_9MO_{30} resulting in formation of microcracks. During the DBD treatment, the formation of characteristic defects was observed in the form of imprints of dielectric breakdown microchannels and individual mineral fragments.

Pretreatment of eudialyte concentrate using HPEMP made it possible to increase the recovery of zirconium into the pregnant solution of leaching by 3.4–4.3 per cent (from 86.6 per cent to 90.9 per cent) and by 4.1 per cent (from 86.6 per cent to 90.6 per cent) when using DBD. The increase in the total recovery of REEs was 1.2–1.8 per cent (from 87.7 per cent to 89.2 per cent).

The effect of pH values, solution temperature, initial concentrations of valuable components on the successive recovery performance of zirconium and REEs from the pregnant solutions nitric from the acid leaching of eudialyte concentrate by chemical precipitation was examined. The possibility of selective separation of the zirconium product and rare earth elements with a zirconium recovery of 99.95 per cent and a REE recovery of 87.5 per cent was established. REE loss with the zirconium product was 8.0 per cent and 4.5 per cent with the spent pregnant solution.

INTRODUCTION

The eudialyte ores of the Lovozero deposit in Russia's Murmansk Region are a promising mineral resource for the production of zirconium and rare earth metals (REE) (Kryukov *et al*, 2012; Samsonov and Semyagin, 2014). Multiple pyro- and hydrometallurgical processing options for eudialyte concentrates have been proposed in the literature based on multistage decomposition by acids and alkalis (Zakharov *et al*, 2005, 2011a, 2011b; Lebedev, 2003; Lebedev *et al*, 2003; Davris *et al*, 2017). The central challenges involved in the hydrometallurgical processing of eudialyte are associated with the significant (40–60 per cent) share of silicon (Johnsen *et al*, 2003; Bogatyreva *et al*, 2018a, 2018b). During acid leaching, silicon passes into solution in the form of silicic acid, which undergoes a polycondensation process with the formation of polymers of various composition and structure, including stable gels, which reduces the recovery of valuable components, decreases the filtration performance, and complicates the further processing of solutions by extraction and sorption-based methods (Jha *et al*, 2016; Ma *et al*, 2018a, 2018b). Potential solutions to the challenges involved in the hydrometallurgical processing of ores high in silicon include exposing mineral suspensions to energy impacts (ultrasound, high-voltage pulses, plasma and electrochemical treatment etc), which improves the unlocking and breakage performance of fine-grained mineral complexes and the recovery of non-ferrous and precious

metal micro – and nanoparticles in the downstream ore processing circuits (Chanturia *et al*, 2019a, 2019b).

The zirconium and REE grades of the resulting leaching pregnant solutions of eudialyte concentrate do not exceed 1–10 g/L (Vaccarezza and Anderson, 2018; Voßenkaul *et al*, 2016; Johnsen *et al*, 2003), in which connection the study of the method of sequential chemical deposition of zirconium and REEs, characterised by its process simplicity and low operating costs, is highly relevant. This method makes it possible to obtain precipitates of Zr and REEs readily soluble in slightly acidic solutions, suitable for further processing.

The goal of this study was to comprehensively examine the effect of the parameters of high-power nanosecond electromagnetic pulses (HPEMP) and dielectric barrier discharge (DBD) on the structural and chemical properties of the eudialyte surface and the leaching performance of eudialyte concentrate and the selective separation of zirconium and REEs from pregnant solutions.

EXPERIMENTAL

Materials

The studies were carried out on samples collected from an experimental eudialyte concentrate batch from the Lovozero Mine and Concentrator with a particle size of -630+63 μm (97.7 per cent), containing 8.34 per cent of zirconium oxide and 2.5 per cent of REE oxides. The main impurities in the concentrate are individual grains of feldspar, nepheline, loparite, aegirine, and intergrowth thereof (up to 10 per cent). The share of twin loparite crystals, fragments thereof, and golden brown lamprophyllite crystals is substantially lower (~3 per cent). Accessory minerals include secondary zeolites (natrolite, gonnardite) (Chanturia *et al*, 2019a).

Experimental conditions

Eudialyte concentrate was leached in a reactor, which is the key unit of the lab-scale plant designed by IPKON RAS for unlocking concentrates of non-ferrous, rare, and rare-earth metals through the use of thermal, electrochemical, and ultrasonic impacts on the mineral suspension (Chanturia *et al*, 2020). Leaching conditions were as follows: temperature — 80 (40)°C, exposure — 1 hour, S:L ratio — 1:20, agitation intensity — 550 min^{-1}, nitric acids — 450 g/L.

After leaching, the suspension was filtered, the precipitate was washed with distilled water and dried. The composition of the precipitate was analysed using the inductively coupled plasma mass spectroscopy (ICP-MS) (ICPE-9000, Shimadzu) and X-ray fluorescence (XRFA) (ARL ADVANT'X, Thermo Scientific) methods; the solutions were analysed using the inductively coupled plasma atomic emission method (ICP-AES) (Elan-6100, PerkinElmer). Surface micromorphology of the eudialyte was examined by analytical scanning electron microscopy (SEM) (LEO 1420VP, Carl Zeiss). X-ray diffraction analysis (XRD) of the concentrate was carried out using an ADP-2 diffractometer (NPO Burevestnik). To record the IR spectra of eudialyte mineral particles, a Fourier spectrometer (IRS) (IR-Affinity, Shimadzu) and a diffuse reflection add-on unit (DiffuseIR, Pike Technologies) were used. Changes in the elemental composition of the eudialyte surfaces were examined by X-ray photoelectron spectroscopy (XPS) using a Versa Probe II spectrometer (ULVAC-PHI). AFM measurements were made in the air under standard conditions with 256×256 points resolution at Ntegra Prima scanning probe microscope (NT-MDT, Zelenograd). Polished mineral sections of 10×10×4.5 mm were fixed with conducting duplex scotch in order to prevent generation of an uncontrollable static surface charge. In all the measurements it was imperative to scan an initial specimen to detect surface alterations acquired in the course of specimen preparation and to exclude artifacts in data processing.

The recovery (Zr, REEs, and impurities) was calculated by the Equations 1–2.

$$\varepsilon_{i,L} = \frac{C_{i,N} \times V_N + C_{i,W} \times V_W}{C_{i,L} \times V_L} \times 100\% \quad (1)$$

$$\varepsilon_{i,S} = (1 - \frac{C_{i,P} \times m_P}{C_{i,L} \times V_L}) \times 100\% \quad (2)$$

Where $\varepsilon_{i,L}$, $\varepsilon_{i,S}$ is the recovery of the component during precipitation, calculated for the liquid and solid phases, respectively; $C_{i,L}$, $C_{i,N}$, $C_{i,W}$ are the grade of the component in the initial pregnant solution, solution after neutralisation, and wash solution, respectively; V_L, V_N, V_W are the volume of the initial pregnant solution, solution after neutralisation, and wash solution; $C_{i,P}$ is the grade of the neutralisation precipitate; m_P is the mass of the precipitate. All experiments were repeated three times, and the results were averaged with a relative error of ±3 per cent. The calculations were verified by the mass balance of each element in the solid phase and liquid phase with a relative error of ±5 per cent.

The mineral samples were treated with high-power nanosecond electromagnetic pulses (HPEMP) and low-temperature dielectric barrier discharge (DBD) plasma in air under standard conditions using dedicated experimental set-ups (IPKON RAS, NPP FON LLC, Ryazan), consisting of high-voltage pulse generators and electrode systems (discharge cells). In the HPEMP generator, a voltage converter converts 220V AC (50 Hz) to DC to charge the capacitive energy storage device of the nanosecond pulse generator. When treating the samples with HPEMP, the following pulse parameters were set: video impulse type; pulse leading edge duration ~3–8 ns; pulse duration ~30–50 ns; pulse voltage amplitude not less than 70 kV; electric field strength in the interelectrode space not less than 10^7 V/m; distance between electrodes 7 mm; pulse frequency 375 Hz; sample treatment time (t) 30, 60, and 90 s. Before the electromagnetic treatment, the mineral samples were moistened with distilled water at a S:L ratios of 6:1.

Mineral sample treatment by low-temperature pulsed (sub-nanosecond) dielectric barrier discharge plasma in air at atmospheric pressure was carried out under standard conditions for the following parameters using discharge-initiating pulses: pulse leading edge duration 250–300 ns; pulse duration 8 μs; voltage amplitude on the electrodes in the barrier discharge cell 20 kV; pulse frequency 16 kHz; sample treatment time (t) 10–90 s, eudialyte concentrate sample treatment time 30 s. The dimensions the DBD discharge cell significantly exceeded the length of the interelectrode gap, which was ~5 mm. The gas temperature in the impact area of the discharge cell did not exceed the temperature of the dielectric barrier and remained of the order of room temperature during the treatment.

RESULTS AND DISCUSSION

The effect of energy impacts

Based on the SEM data, the original eudialyte grains have a conchoidal fracture characteristic of this mineral, forming a concave profile of smooth surface areas separated by sharp uneven edges (Figure 1a). The non-thermal action of HPEMP caused damage to the surface of a significant share of the mineral grains with the formation of new relief forms: depending on the treatment time (t), from parallel-fractured at t = 30 s (Figure 1b) to polygonal-fractured at t = 60 s and 90 s (Figure 1c and 1d).

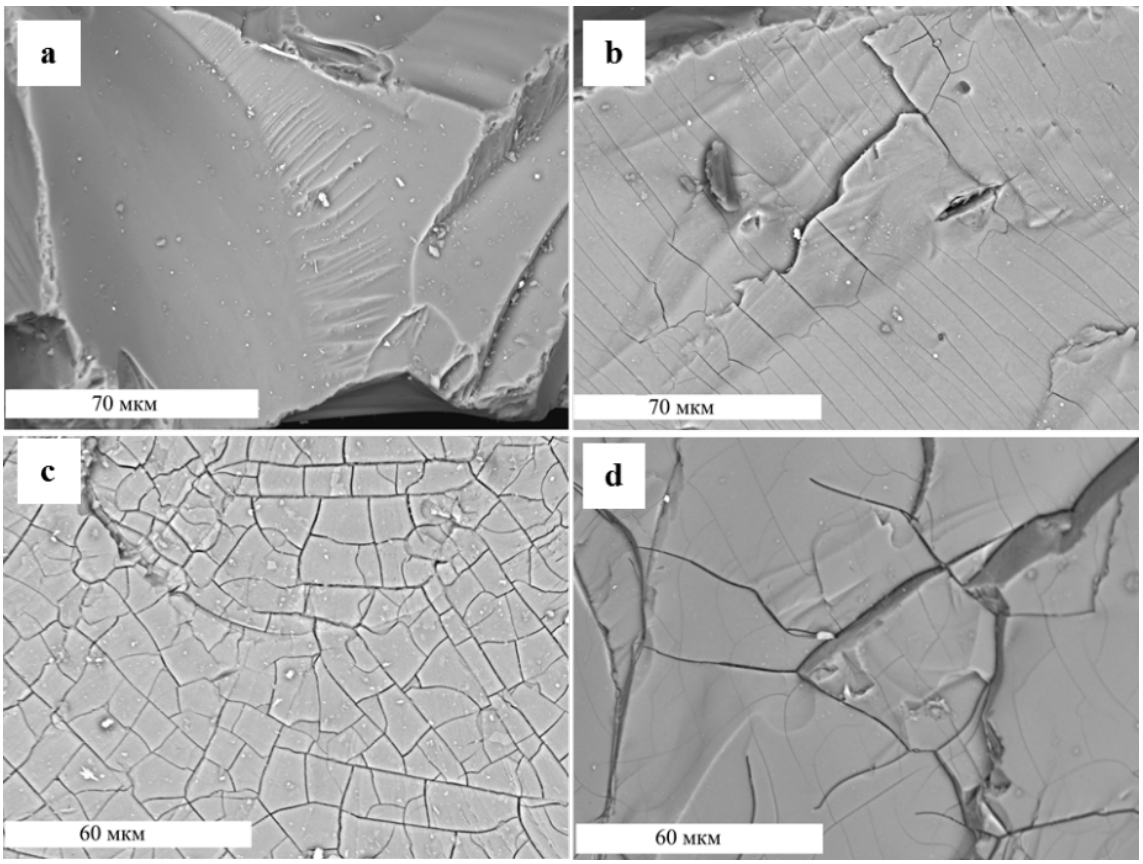

FIG 1 – SEM images of the eudialyte original grain (a) and the mineral surface after HPEMP treatment for t = 30 s (b), 60 s (c) and 90 s (d).

A distinctive feature of the micromorphology of eudialyte grains after treatment under DBD conditions under all conditions applied is the formation of a different number of imprints from electrical breakdown microchannels no larger than 3–4 μm (Figure 2). Despite the fact that, in most of the grains, there are only single manifestations thereof, among the studied samples, individual particles containing a significant number of such defects were found (Figure 2a). Surface microfracturing, typical of samples after exposure to HPEMP, is less developed or practically absent when exposed to a barrier discharge.

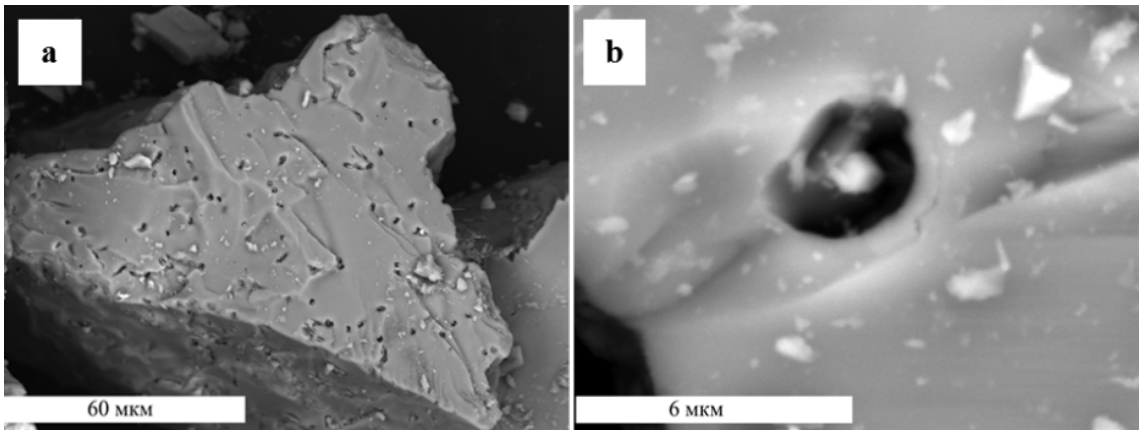

FIG 2 – Electrical breakdown microchannel imprints on the eudialyte surface after DBD treatment.

A detailed study of the areas between the microchannel imprints made it possible to reveal a modified, compared to the original (Figure 3), mineral surface, composed of closely adjacent new formations sized 400 nm or less.

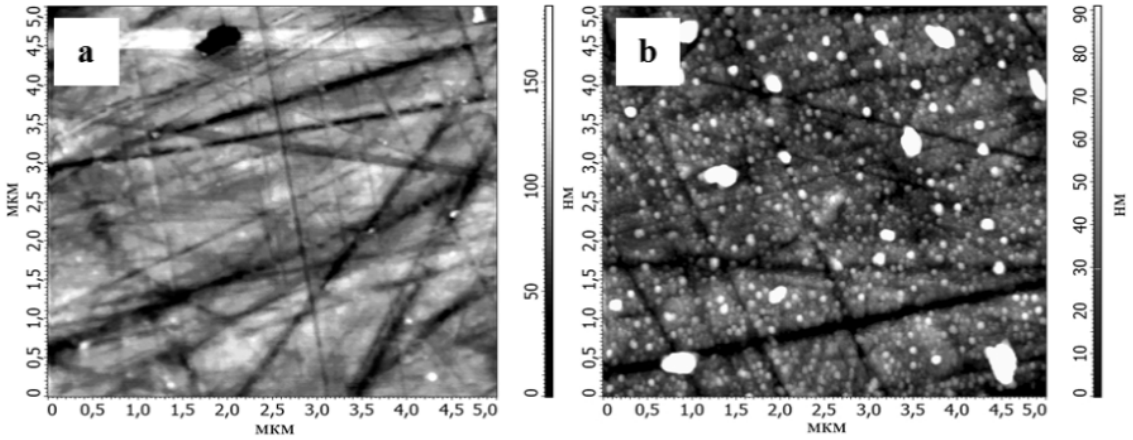

FIG 3 – AFM images of the original eudialyte surface (a); and that after a DBD treatment (t = 60 s) (b).

The interaction of eudialyte grains with a nitric acid solution after preliminary exposure to HPEMP leads to a smoothing of the surface upon dissolution, initially, of the surface cracked layer. As a result, the appearance of the particles becomes close to the original.

Our observations are in good agreement with those described in Chanturia *et al* (2019a) in terms of the predominantly tangential (layered) mineral dissolution mechanism in a HNO_3 solution. The findings of our morphological study of the grains after exposure to DBD and interaction with a HNO_3 solution are, in general, similar to those under exposure to HPEMP. Nevertheless, an insignificant number of eudialyte grains with deep cracks was observed, including separation of entire mineral fragments.

The IR spectral signatures of the original and electromagnetic pulse treated (HPEMP and DBD) eudialyte are presented in Figure 4. Our examination of the obtained spectral signatures showed that in the region of stretching vibrations of the Si–O bond of the initial sample, five absorption bands were identified: 940 cm^{-1}, 980 cm^{-1}, 1010 cm^{-1}, 1070 cm^{-1} and 1135 cm^{-1}. In the sample treated with HPEMP for t = 30 s, the 940 cm^{-1} band is smoothed, and at a longer exposure (t = 60, 80–90 s) transforms in a shoulder at about 900 cm^{-1}, and a mild shoulder appears at 1100 cm^{-1}.

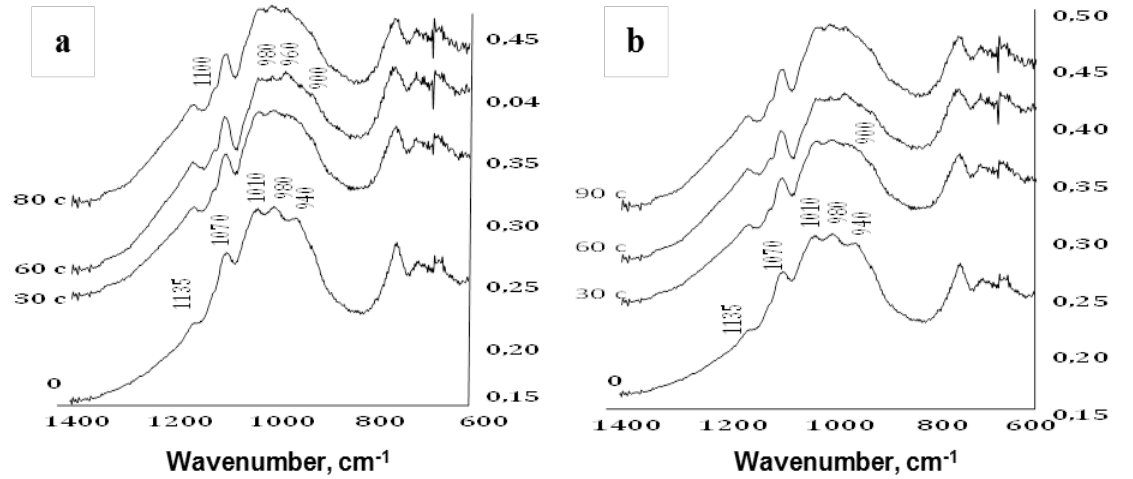

FIG 4 – IR spectra of eudialyte before and after (a) HPEMP and (b) DBD treatments.

As reported in Rastsvetaeva *et al* (2020), the presence of a band at 940 cm^{-1}, indicates a high content of ten-membered $Si_{10}O_{27}$, Si_9MO_{30} clusters in the structure of the mineral. Taking this into account, the observed changes in the spectral signatures can be associated with destruction of the silicon-oxygen bonds.

Thus, it can be assumed that when the surface of mineral particles interacts with high-intensity pulsed electric fields, the surface of eudialyte undergoes structural changes, which are manifested in the IR spectra of the mineral, and are the result of deformation and/or local destruction of eudialyte's silica-oxygen lattice.

High-power electromagnetic pulses have a significant destructive effect on the structural state of the eudialyte surface, which causes the activation of the process of dissolution of mineral particles in nitric acid and improves the performance of acid leaching of eudialyte concentrate, based on a chemical analysis of cakes and calculation of leaching indicators taking into account the material balance (Table 1).

TABLE 1

Effect of the high-power electromagnetic pulse impact parameters on the nitric acid leaching performance of eudialyte concentrate.

Treatment conditions	REE recovery, %						
	Zr	Ce	Hf	La	Nd	Y	∑REE
No treatment	86.6	87.5	84.9	86.2	88.4	89.7	87.7
HPEMP (30 s)	89.9	88.4	89.9	87.2	89.9	92.4	89.5
HPEMP (60 s)	90.9	88.2	90.7	85.7	90.1	92.8	89.4
HPEMP (90 s)	90.2	87.6	89.5	85.8	89.4	92.3	88.9
DBD (30 s)	90.6	87.9	89.4	85.9	89.9	92.8	89.2

In general, pre-treatment with HPEMP made it possible to increase the recovery of zirconium into the pregnant leach solution by 3.4–4.3 per cent, while with the use of DBD, the increase in recovery was 4.0 per cent. The maximum increase in zirconium recovery (4.3 per cent) was achieved as a result of treating the concentrate with HPEMP for t = 60 s, which is comparable to the performance obtained with a short-term (t = 30 s) exposure to a barrier discharge (4.1 per cent). The increase in the total recovery of rare earth elements was 1.2–1.8 per cent.

Selective recovery of zirconium and REE from pregnant solutions

The chemical composition of the resulting pregnant solution is characterised by a zirconium grade of 2.6 g/L and a REE grade of 0.6 g/L, where the dominant REEs are Ce, Y, La, and Nd. Together with valuable components (Zr and REE), Na, Ca, Fe, Al, Mn, Sr, Ti, Mg and K pass into solution when leaching the eudialyte concentrate.

Separation of Zr and REE with neutralisation of the pregnant solutions was carried out in two stages – at the first stage, neutralisation of nitric acid with the recovery of Zr with Al and Fe impurities was achieved by increasing the solution pH from -0.74 to 4.8–5.0 using calcium carbonate. In the second stage, precipitation of the *REE* from the solution was achieved by increasing the pH of the solution to 6.0–6.4 using sodium carbonate.

Figure 5 shows the relationship between the recovery of Zr, Al, Fe into the solid precipitate and the pH of the environment under isothermal conditions (20°C). It can be seen from the presented results that the precipitation performance increases with increasing pH, and at a pH of 4.0, 99.9 per cent of zirconium, 100 per cent of aluminium, and 43.8 per cent of iron is precipitated. It was found that the recovery of other impurities (Na, Mn, Sr, Ti, Mg and K) did not exceed 15–35 per cent, and the total loss of rare earth elements to the precipitate was approximately 8 per cent.

A further increase in pH to 4.8–5.0 leads to a sharp increase in REE loss to 40.0 per cent due to co-precipitation with Zr, which is probably associated with the onset of precipitation in the form of carbonates. At the same time, due to a decrease in the solubility of $CaCO_3$, its specific consumption increased by a factor of 1.6 from 375 to 600 g/L.

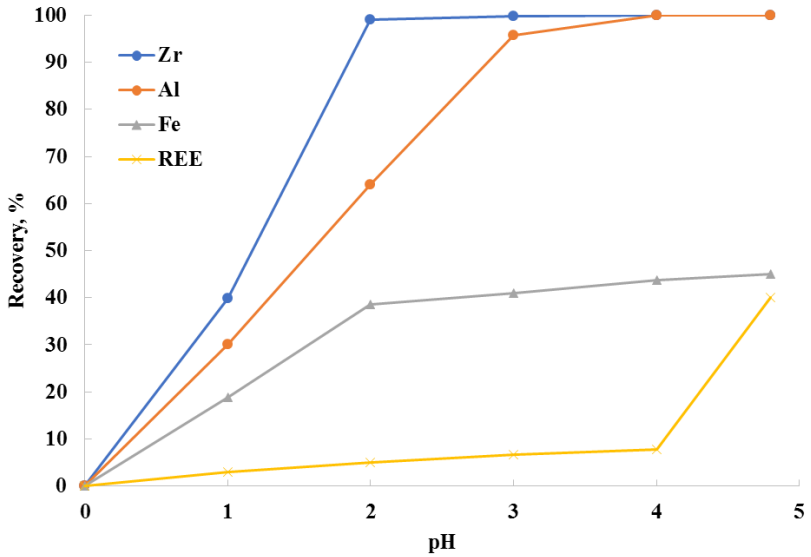

FIG 5 – Effect of (a) the solution pH on element recovery to residue and (b) specific consumption of calcium carbonate on the solution pH. Solution temperature was 20°C.

Thus, the separation of zirconium from REE occurred at pH 4.0. Further chemical precipitation of REE compounds should be carried out using more soluble compounds, such as sodium carbonate and sodium hydroxide.

The results of the second stage of the experiment showed that at a specific consumption of sodium carbonate of 6 g/L (pH 6.1), the highest REE recovery of 95.5 per cent into the solid phase was achieved. When the pH of the pregnant solution is increased to 6.0 using sodium hydroxide, the highest REE recovery into the precipitate was at 59.1 per cent, which suggests the recovery of a significant share of the REEs into the solid phase in the form of carbonates.

Table 2 shows the results of chemical analysis of residues performed by the X-ray fluorescence method. High content of CaO (30–40 per cent) is confirmed by the SEM and IR spectroscopy data on the predominance of calcium carbonates in the residue. Significant losses on ignition (up to 53.5 per cent) are due to the predominance of both calcium carbonates and calcium nitrate tetrahydrate in the residues. The content of ZrO_2 and total REE oxides in first stage residue is 6.96 and 0.06 per cent respectively, second stage residue – 0.21 and 2.82 per cent, which is consistent with the data on the efficiency of valuable component recovery from the liquid phase. Note that relatively low contents of Zr and REE are associated with both their low concentrations in the primary pregnant solution and a significant amount of residues. However, unlike the original eudialyte concentrate, the residues are readily soluble in weakly acidic solutions, which makes it possible to produce solutions with a high concentration of valuable components for subsequent processing.

TABLE 2

Chemical composition of the solid phase of I and II deposition stage.

Component	Content, %		Component	Content, %	
	I stage	II stage		I stage	II stage
CaO	30.50	40.29	SrO	0.09	0.18
Na_2O	0.17	4.01	ZrO_2	6.96	0.21
Al_2O_3	2.26	0.59	HfO_2	0.09	< 0.02
K_2O	0.04	0.08	∑REE oxides	0.06	**2.82**
TiO_2	1.20	< 0.02	Cl	0.04	0.07
SiO_2	0.26	0.18	LOI (400°C)	24.08	11.67
Fe_2O_3	3.49	0.21	LOI (950°C)	53.55	50.02

Since the temperature of the pregnant solution in the process of nitric acid leaching is 80°C, the effect of the initial temperature of the pregnant solution on the performance of zirconium and REE precipitation at the first stage was examined. Theoretically, temperature should have a significant effect on the rate of chemical reactions, for example, according to the Van't Hoff empirical rule, for every 10°C increase in temperature, the rate constant of a homogeneous elementary reaction increases by a factor of 2 to 4. However, the analysis of our results showed that the initial temperature of the solution in the range of 20 to 80°C did not affect the precipitation of valuable components, and the recovery of zirconium into the precipitate was 99.84–99.99 per cent, that of REEs 7.61–7.93 per cent. This fact is probably due to the initially high rate of the chemical reaction of neutralisation and the long duration of the treatment (2 hours), during which the temperature is reduced to 30–35°C.

It was found that the recovery of zirconium does not depend on the initial content in the studied concentration range and was 99.64–99.97 per cent. At the same time, an increase in the initial REE grade from 0.15 g/L to 1.2 g/L increased the loss to the precipitate from 0.29 per cent to 8.48 per cent, which is most likely due to the co-precipitation of REEs with impurity metals, whose concentrations also increase. The results obtained are consistent with those reported in the literature (Soltani *et al*, 2018; Chen *et al*, 2020).

CONCLUSIONS

According to SEM and IR spectroscopy results, the mechanism behind the intensification of the acid dissolution of eudialyte as a result of pretreatment with HPEMP and DBD is associated with the disintegration and breakage of the mineral surface and is expressed at the substructural level as the local disintegration of $Si_{10}O_{27}$, Si_9MO_{30} structural units with subsequent formation of microcracks, as well as the direct formation of characteristic defects in the form of electrical breakdown current microchannel imprints and individual mineral fragments.

Our results showed the fundamental possibility of using high-power electromagnetic pulsed impacts (HPEMP and DBD) to intensify the acid leaching of eudialyte concentrate with relatively low electricity consumption (0.1–1.0 kW*h/t). Pre-treatment of mineral samples with HPEMP made it possible to increase the recovery of zirconium into the pregnant leach solution by 3.4–4.3 per cent, and by 4.1 per cent when using a DBD treatment. The increase in the total REE recovery was 1.2–1.8 per cent.

The study demonstrated the high performance of chemical sequential precipitation of zirconium and REEs from a pregnant solution resulting from nitric acid leaching of eudialyte concentrate.

It was established that an increase to 4.0 in the pH value of the initial pregnant solution at the first stage of precipitation with calcium carbonate supports a zirconium recovery of 99.95 per cent into the solid phase with the associated recovery of impurity metals – aluminium (100 per cent) and iron (43.8 per cent). The total loss of REEs to the zirconium product did not exceed 8 per cent. The subsequent increase of pH to 6.1 using sodium carbonate enables a REE recovery of 87.5 per cent into the solid phase, while the total recovery from the solution was 95.5 per cent.

Valuable components in the resulting precipitates are concentrated mainly as complex hydroxides and carbonates, giving 6.96 per cent of ZrO_2 and 2.82 per cent of REE oxides. The resulting products are easily soluble in weakly acidic solutions, making downstream processing possible, which will be the focus of our research in the future.

ACKNOWLEDGEMENTS

The authors are grateful to Candidate of Geology and Mineralogy E.V. Koporulina for her assistance in carrying out the experimental studies.

FUNDING

This work was supported by the Ministry of Science and Higher Education of the Russian Federation, project no. 13.1902.21.0018, agreement no. 075–15–2020–802.

REFERENCES

Bogatyreva, E V, Chub, A V, Ermilov, A G, Khokhlova, O V, 2018a. The efficiency of alkaline-acid method of complex leaching of eudialyte concentrate. Part 1, *Tsvetnye Metally*, 7:57–61. (in Russian).

Bogatyreva, E V, Chub, A V, Ermilov, A G, Khokhlova, O V, 2018b. The efficiency of alkaline-acid method of complex leaching of eudialyte concentrate. Part 2, *Tsvetnye Metally*, 8:69–74. (in Russian).

Chanturia, V A, Chanturia, E L, Minenko, V G, Samusev, A L, 2019a. Acid leaching process intensification for eudialyte concentrate based on energy effects, *Obogashchenie Rud*, 3:29–36. (in Russian).

Chanturia, V A, Minenko, V G, Samusev, A L, Chanturia, E L, Koporulina, E V, Bunin, I Zh, Ryazantseva, M V, 2020. The effect of energy impacts on the acid leaching of eudialyte concentrate, *Mineral Processing and Extractive Metallurgy Review*, 42(7):12.

Chanturia, V A, Minenko, V G, Koporulina, E V, Ryazantseva, M V, Samusev, A L, 2019b. Influence of Acids on Extraction Efficiency of Zirconium and Rare Earth Metals in Eudialyte Concentrate Leaching, *J. Min. Sci.,* 55(6):984–994.

Chen, Sh, Huang, X, Feng, Z, Xu, Y, Wang, M, Xia, C, Zhao, L, 2020. Behavior of Rare Earth, Iron, and Phosphorus during Purification of Rare Earth Sulfate Leach Solution Using Magnesium Oxide, *J. Hydrometallurgy*, 105377.

Davris, P, Stopic, S, Balomenos, E, Panias, D, Paspaliaris, I, Friedrich, B, 2017. Leaching of rare earth elements from eudialyte concentrate by suppressing silica gel formation, *Minerals Engineering*, 108:115–122.

Jha, M K, Kumari, A, Panda, R, Kumar, J R, Yoo, K, Lee, J Y, 2016. Review on Hydrometallurgical Recovery of Rare Earth Metals, *Hydrometallurgy*, 161:77.

Johnsen, O, Ferraris, G, Gault, R, Joel, D G, Kampf, A, Pekov, I, 2003. The Nomenclature of Eudialyte-Group Minerals, *The Canadian Mineralogist*, 41:785–794.

Kryukov, V A, Tolstov, A V, Samsonov, N Yu, 2012. Strategic importance of rare earth metals in the world and in Russia, *ECO*, 11:5–16. (in Russian).

Lebedev, V N, 2003. Sulfuric Acid Technology of Eudialyte Concentrate, *Zhurn. Prikl. Khim.*, 76(10):1601–1605. (in Russian).

Lebedev, V N, Shchur, T E, Mayorov, D V, Popova, L A, Serkova, R P, 2003. Features of Acid Decomposition of Eudialyte and Some Rare Metal Concentrates of the Kola Peninsula, *Zhurn. Prikl. Khim.*, 76(8):1233–1237. (in Russian).

Ma, Y, Stopic, S, Gronen, L, Friedrich, B, 2018b. Recovery of Zr, Hf, Nb from Eudialyte Residue by Sulfuric Acid Dry Digestion and Water Leaching with H_2O_2 as a Promoter, *Hydrometallurgy*, 181:206–214.

Ma, Yi, Stopic, S, Gronen, L, Milivojevic, M, Obradovic, S, Friedrich, B, 2018a. Neural network modeling for the extraction of rare earth elements from eudialyte concentrate by dry digestion and leaching, *Metals*, 267(8).

Rastsvetaeva, R K, Chukanov, N V, Pekov, I V, Varlamov, D A, 2020. Structural features of potential new mineral of eudialyte group from the Lovozero massif, Kola Peninsula, *Vestnik Geonauk*, 1:3–7. (in Russian).

Samsonov, N Yu, Semyagin, I N, 2014. World and Russian rare earth market survey, *ECO*, 2:45–54. (in Russian).

Soltani, F, Abdollahy, M, Petersen, J, Ram, R, Becker, M, Koleini, S J and Moradkhani, D, 2018. Leaching and Recovery of Phosphate and Rare Earth Elements from an Iron-Rich Fluorapatite Concentrate, Part I: Direct Baking of the Concentrate, J. *Hydrometallurgy*, 177:66–78.

Vaccarezza, V, Anderson, C, 2018. Beneficiation and leaching study of norra kärr eudialyte mineral. *In: Kim H. et al. (eds) Rare Metal. Techn., TMS 2018, The Minerals, Metals and Materials Series. Springer, Cham.*

Voßenkaul, D, Birich, A, Müller, N, Stoltz, N, Friedrich, B, 2016. Hydrometallurgical processing of eudialyte bearing concentrates to recover rare earth elements via low-temperature dry digestion to prevent the silica gel formation, *J. Sustain. Metal.*, 3;79–89.

Zakharov, V I, Maiorov, D V, Alishkin, A R, Matveev, V A, 2011b. Causes of insufficient recovery of zirconium during acidic processing of Lovozero eudialyte concentrate, *Izvestiya Vysshikh Uchebnykh Zavedeniy. Tsvetnaya Metallurgiya*, 5:26–31. (in Russian).

Zakharov, V I, Skiba, G S, Solovyov, A V, Lebedev, V N, Mayorov, D V, 2011a. Some aspects of eudialyte acid processing, *Tsvetnye Metally*, 11:25–29. (in Russian).

Zakharov, V I, Voskoboinikov, N B, Skiba, G S, Solov'ev, A V, Mayorov, D V, Matveev, V A, 2005. Development of Hydrochloric Acid Technology for Complex Processing of Eudialyte, *Zap. Gorn. Inst.,* 165:83–85. (in Russian).

An electrochemical and spectroscopic study of the leaching mechanisms of enargite and chalcopyrite in sulfuric acid

M Chen[1], Y L Ma[2] and W Bruckard[3]

1. Senior Principal Research Scientist, CSIRO Mineral Resources, Clayton South, Vic 3169. Email: miao.chen@csiro.au
2. Research Scientist, CSIRO Mineral Resources, Clayton South, Vic 3169. Email: yalong.ma@csiro.au
3. Group Leader, CSIRO Mineral Resources, Clayton South, Vic 3169. Email: warren.bruckard@csiro.au

ABSTRACT

With the extensive exploitation and gradual depletion of high-grade copper reserves, the mining industry is paying more and more attention to the hydrometallurgical extraction of copper from low-grade and arsenic bearing copper ores. Hydrometallurgical processing, such as heap leaching, column leaching and bioleaching, provide a viable alternative to the traditional pyrometallurgy due to its harmony with the environment, moderate capital investment, and low operating costs. However, the slow leaching kinetics of enargite (Cu_3AsS_4) and chalcopyrite ($CuFeS_2$) remain problematic for commercial leaching practice. The formation mechanism and the nature of the passivating layers during leaching is still a matter of debate in hydrometallurgical research. In this study, the dissolution mechanism of enargite and chalcopyrite in sulfuric acid solution was investigated using a range of electrochemical and spectroscopic analysis methods. Electrochemical oxidation of enargite demonstrated an obvious passivation region from 500 to 750 mV (Ag/AgCl). The formed passivation film was found a n-type semiconductor behaviour, which is different from the original enargite with a p-type behaviour. The results of X-ray photoelectron spectroscopy (XPS) suggested that a nonstoichiometric film $Cu_{(3-x)}As_{(1-y)}S_4$ (x>>y) accumulated on the electrode surface, which accounted for the obvious decrease in current density in the passive potential region. For chalcopyrite, three important potentials of 550, 680 and 730 mV which are related to the formation and dissolution of passivation film were observed based on the cyclic voltammetry (CV) and potentiodynamic polarisation. Raman and X-ray absorption near edge structure (XANES) spectra studies of the chalcopyrite electrodes after being treated under these three potentials indicated a metal-deficient sulfide of $Cu_{1-x}Fe_{1-y}S_2$ (y>>x) might be responsible for the passivation phenomenon. Hence, it is concluded that the passivation of enargite and chalcopyrite are similar which are caused by metal-deficient sulfide surfaces although the compositions of the metal-deficient sulfide are different.

INTRODUCTION

Currently, it has been estimated that around 80 per cent of copper was produced by pyrometallurgy, however, this processing method requires ores with high-grade. With the gradual decreasing trend of high-grade copper ores and the more complex ore mineralogy, it will become more difficult to process low-grade and complex copper ores by the traditional pyrometallurgy. For example, chalcopyrite ($CuFeS_2$), the most abundant copper sulfide on the earth's crust, has become one of the most important copper sources with the extractive method transforming from traditional pyrometallurgy to hydrometallurgical methods due to the gradual depletion of high-grade ores and the need for processing low-grade ores. Meanwhile, many of the low-grade copper ores contain arsenic-bearing sulfide phases, for example, enargite (Cu_3AsS_4), which is commonly found in the copper deposits of some mining countries. Although, pyrometallurgy can efficiently extract copper from high-grade copper ores, it is unsuitable for processing the low-grade and arsenic-bearing copper ore because of the high energy cost and emissions of environmentally toxic arsenic gas during smelting.

Hydrometallurgy has been proved to be more advantageous than pyrometallurgy for processing the low-grade and complex copper ores (Safarzadeh *et al*, 2013). Additionally, aqueous arsenic species are more controllable by precipitated and stabilised methods in hydrometallurgical processing. However, the refractory character of chalcopyrite and enargite during leaching poses a major challenge for researchers (Hackl *et al*, 1995; Viramontes-Gamboa *et al*, 2010). Chalcopyrite and

enargite are more refractory in acidic media as compared to other copper sulfides, such as bornite and chalcocite in various acid systems with or without bacteria during which the leaching kinetics of copper is extremely low (Corkhill *et al*, 2008; Li *et al*, 2013; Padilla *et al*, 2010; Riveros and Dutrizac, 2013). The slow leaching behaviour of chalcopyrite and enargite is related to the formation of a passivating layer whose composition and formation mechanism are still unknown (Lattanzi *et al*, 2008; Watling, 2013). Elemental sulfur (S^0), jarosite and a metal-deficient surface layer have been suggested to be responsible for the slow leaching kinetics.

It has been suggested that the oxidative dissolution of metal sulfides in solutions occurs via an electrochemical mechanism by several researchers (Ghahremaninezhad *et al*, 2010; Guo *et al*, 2017; Karimi *et al*, 2017; Liu *et al*, 2017; Tu *et al*, 2017). Various electrochemical techniques have been used to gain a better understanding of the mechanism underlying the leaching process of metal sulfides, such as chalcopyrite, pyrite, and sphalerite. In the present study, electrochemical methods were employed to systematically investigate the oxidation of chalcopyrite and enargite in 0.1 mol/L sulfuric acid. Meanwhile, the oxidised surface chemistry was studied by various surface analytical techniques with the hope to provide complementary information for interpretation of the passivation mechanism.

EXPERIMENTAL

Electrodes preparation

High-quality natural enargite and chalcopyrite obtained from Wright's Rock Shop (USA) were used for electrode fabrication. The ores were cut into approximately cubic shapes and connected to copper wire by silver paint on the back. The electrode contacts were protected from the solution by mounted in epoxy, leaving only one face of the electrode with an area of approximate 0.25 cm^2 exposed to the solution.

Electrochemical experiments

The electrochemical experiments were carried out using a PARSTAT 2273, Princeton Applied Research (USA) on a conventional three-electrode electrolytic cell at approximately 20°C. An Ag/AgCl, KCl (sat.) electrode (0.204 V versus SHE at 20°C) was used as the reference electrode and all further potentials quoted in this study are with respect to it if not otherwise mentioned. A Pt wire was used as the auxiliary electrode. All solutions were prepared in 18 MΩ water (MilliQ, Millipore) and deaerated by bubbling high-purity N_2. Cyclic voltammetry, potentiodynamic curves, chronoamperometric polarisation and Mott-Schottky were performed to study the behaviours of the electrodes. EIS tests at different potentials were conducted in the frequency range of 10^{-2} to 10^4 Hz with a peak-to-peak amplitude of 10 mV. ZSimpWin 3.20 (2004) software was used to fit the impedance data.

Surface chemical analysis methods

XPS measurements of the oxidised electrodes were performed using a Kratos Axis ULTRAX-ray photoelectron spectrometer (Kratos Analytical Ltd., UK) incorporating a monochromatic Al Kα X-rays (1486.6 eV) at 150 W (15 kV, 15 mA). Survey (wide) scans were obtained at a pass energy of 160 eV over 1060−-40 eV binding energy (BE) range with 1.0 eV steps and a dwell time of 100 ms. Multiplex (narrow) high-resolution scans were carried out at a pass energy of 40 eV with 0.05 eV steps and a 250 ms dwell time. Base pressure in the analysis chamber was $<5.0 \times 10^{-7}$ Torr during sample analysis. Spectra analysis and peak fitting were carried out using CasaXPS software (Version 2.3.14).

Raman spectrometry was performed using a RenishAW Invia Raman Microscope (USA) with a 514 nm laser source. The spectrometer was calibrated using silicon as a standard before the test. To protect the sample from being damaged by the laser, a low laser intensity of 1 mW was used throughout the experiment. The Raman data was collected in the wavenumber range between 800 and 100 cm^{-1}, with a step width of 0.1 cm^{-1}.

The S K-edge XANES spectra were collected at beam-line 4B7A, Beijing National Synchrotron Radiation Facility (BSRF) using fluorescence mode. The spectrum was scanned in the energy region

between 2450 to 2520 eV at a step width of 0.1 eV. Freshly polished enargite, elemental sulfur, covellite and jarosite were used as standards materials. XANES data was processed with the ifeffit software package.

RESULTS AND DISCUSSION

Electrochemical study of enargite and chalcopyrite

Potentiodynamic polarisation, Mott-Schottky and EIS of enargite

Potentiodynamic curve and Mott-Schottky plot of a freshly polished enargite electrode in 0.1 mol/L sulfuric acid solutions are shown in Figure 1. It can be seen from Figure 1 that a passive region was evident from the 0.50 to 0.75 V at a scan rate of 0.5 mV/s, which is related to the formation of a passivation surface layer (Equation 1) (Ásbjörnsson *et al*, 2004; Lattanzi *et al*, 2008). In this region, the electrode current increased slowly and even decreased with the increase of the applied potential above 0.5 V. When the potential increased from 0.75 V to 0.90 V, the electrode transferred into a trans-passive state. Within this small potential window, the measured current started to increase gradually, which is likely related to the partial dissolution of the passive film shown as Equation 2 (Elsener *et al*, 2007). As the anodic potential reached 0.90 V, the surface layer dissolved completely and the electrodes entered an active area Equations 3 and 4 (Lattanzi *et al*, 2008).

$$\mathrm{Cu_3AsS_4} \rightarrow \mathrm{Cu_{(3-x)}As_{(1-y)}S_4} + x\mathrm{Cu^{2+}} + y{\mathrm{AsO_3}}^{3-} + 2x\mathrm{e^-} + 3y\mathrm{e^-}\ x >> y \quad (1)$$

$$\mathrm{Cu_{(3-x)}As_{(1-y)}S_4} \rightarrow \mathrm{As_{(1-y-z)}S_4} + (3-x)\mathrm{Cu^{2+}} + z{\mathrm{AsO_3}}^{3-} + (3z+6-2x)\mathrm{e^-} \quad (2)$$

$$\mathrm{As_{(1-x-z)}S_4} \rightarrow 4\mathrm{S^0} + (1-\mathrm{y}-z){\mathrm{AsO_4}}^{3-} + 3(1-y-z)\mathrm{e^-} \quad (3)$$

$$\mathrm{Cu_3AsS_4} + 4\mathrm{H_2O} \rightarrow 3\mathrm{Cu^{2+}} + {\mathrm{AsO_4}}^{3-} + 4\mathrm{S^0} + 8\mathrm{H^+} + 11\mathrm{e^-} \quad (4)$$

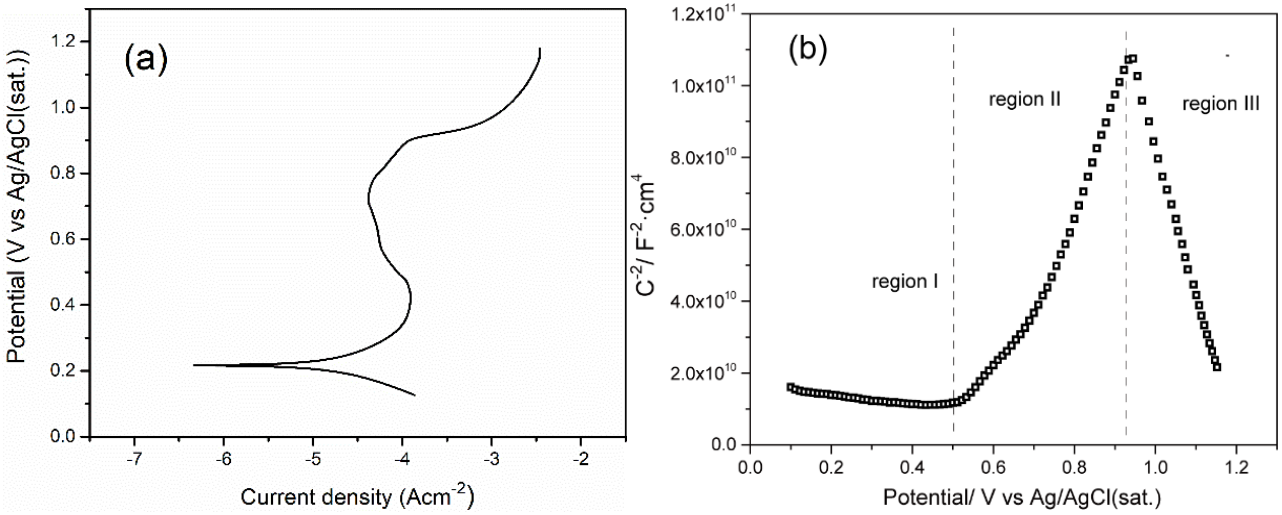

FIG 1 – Potentiodynamic polarisation of enargite electrode (scan rate: 0.5 mV s^{-1}) and Mott-Schottky plots for enargite electrode in 0.1 mol/L sulfuric acid.

The Mott-Schottky plot demonstrates three typical regions, regions I, II and III with different slopes. The negative slopes in regions I and III are attributed to p-type behaviour, while the positive slope in region II is indicated to the n-type behaviour of the passive films (Fattah-alhosseini and Vafaeian, 2015). For the potential region II, the potentiodynamic curve presented in the previous section show a thick passive film formed on the surface of the electrode when the applied potential higher than 400 mV. The positive slope in region II corresponding to the formation of passive film indicating this passive film is an n-type semiconductor thus explains the break of Mott-Schottky plot at 500 mV. It has already been mentioned from the above potentiodynamic study that enargite actively dissolved in the potential above 900 mV as suggested by Equation 4. Thus, the observed p-type semiconductor of enargite electrode in Figure 1b in the potential region of above 900 mV is directly associated with the properties of the enargite.

Figure 2 shows the measured and fitted Nyquist plots at different potentials obtained by the corresponding equivalent circuits. The fitted value of the elements in the equivalent circuit of Figure 2b and 2c are shown in Table 1. It can be seen from Figure 2a that the EIS spectrum obtained at OCP and 400 mV demonstrated a flattened semicircle followed by a straight line which is related to the existence of a Warburg impedance. Thus a circuit of R(QR)(C(WR))) shown in Figure 2b was used to fit the measured data at OCP and 400 mV. With an increase of applied potential to 600 mV, the electrochemical impedance increased significantly, indicating a passive film formed and the thickness of this passive layer increased according to Equation 1. It is also worth mentioning that the diffusion process characterised by a Warburg impedance disappeared at the potential of 600 mV shown in Figure 2a, which might be associated with the dense passive layer formed under this potential inhibiting the diffusion of oxidation products away from the enargite electrode. Thus a circuit of R(QR)(CR) shown in Figure 2c was used to fit the measured data at 600 mV. For the enargite oxidation at 800 mV, the electrode entered a trans-passive region. The acquired impedance spectra under this potential decreased significantly compared with that at 600 mV. The substantially different impedance values at these two potentials imply that different faradic processes were occurred. The results can be explained by the oxidation model of the $Cu_{(3-x)}As_{(1-y)}S_4$ layer being oxidised to another surface layer due to the increasing depletion of surface copper as suggested by Equation 2.

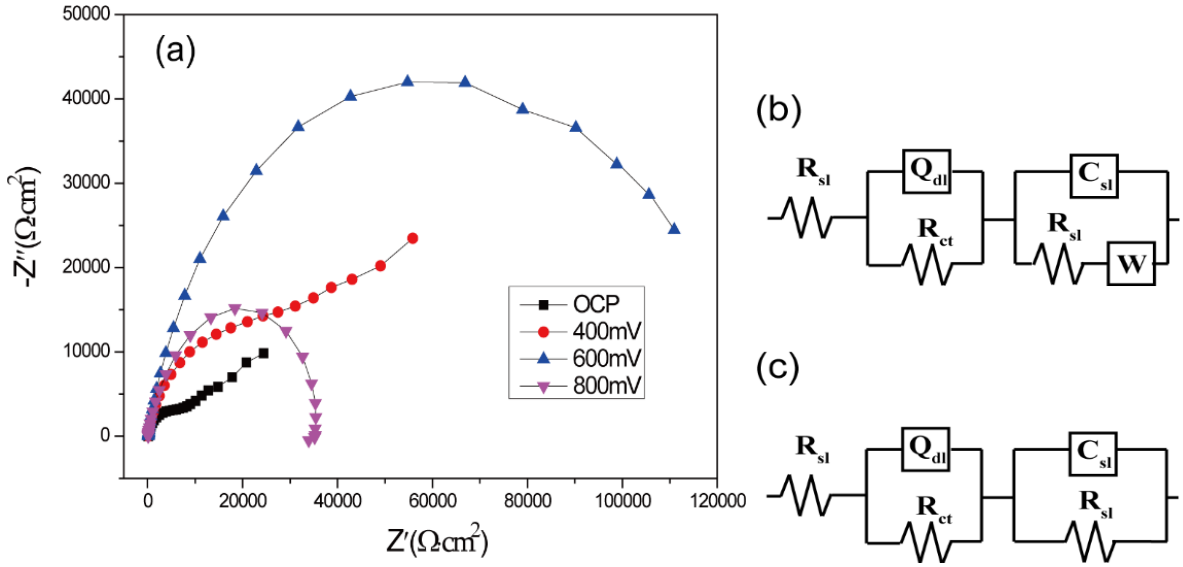

FIG 2 – The measured and calculated Nyquist plots (a) and the equivalent circuits of enargite electrodes in 0.1 mol/L sulfuric acid at OCP and different anodic potentials of 400, 600 and 800 mV, (b) the equivalent circuit applied to fit the obtained experimental data under OCP, (c) the equivalent circuit applied to fit the obtained experimental data under applied potentials of 400, 600 and 800 mV.

TABLE 1

Model parameters for the equivalent circuit of Figure 2.

Potential	Rs ($\Omega \cdot cm^2$)	Q_{dl}		Rct ($k\Omega \cdot cm^2$)	W ($S\ s^{0.5}\ cm^{-2}$)	C_p	Rp ($k\Omega \cdot cm^2$)	χ2
		$10^{-5}\ Y_0$ ($\Omega \cdot s^{-n}$)	n			$10^{-5}\ Y_0$ ($\Omega \cdot s^{-n}$)		
OCP	108	2.21	0.92	19	2.56×10^{-5}	0.15	3.4	0.007
400 mV	108	4.18	0.72	44	1.94×10^{-5}	0.21	8.0	0.002
600 mV	108	1.13	0.83	110	-	4.24	29.4	0.006
800 mV	109	0.92	0.83	8	-	0.11	27.1	0.0004

CV and potentiodynamic polarisation of chalcopyrite

The results of CV and potentiodynamic polarisation are shown in Figure 3. Four anodic peaks and two cathodic peaks were detected (Figure 3a). The peak A1 may be due to the initial dissolution of

iron from the crystal lattice of chalcopyrite (Equation 5) to form $Cu_{1-x}Fe_{1-y}S_2$ (y >> x) and it has been confirmed by several researchers that iron is more preferentially dissolved than copper from the crystal lattice of chalcopyrite (Ghahremaninezhad *et al*, 2013; Nava *et al*, 2008; Yang *et al*, 2015). A2 around 700 mV could be ascribed to partial oxidation of chalcopyrite as shown Equation 6 and/or the oxidation of the surface layer of $Cu_{1-x}Fe_{1-y}S_2$ (y >> x) (Equation 7) (Ghahremaninezhad *et al*, 2013; Yang *et al*, 2015). The formed surface layers of $Cu_{1-x}Fe_{1-y}S_2$ and $Cu_{1-x-z}S_2$ are suggested to be responsible for the passivation of chalcopyrite dissolution. When the potential further increased to over 0.8 V, this layer dissolved with the oxidation of ferrous iron to ferric iron and the oxidation of sulfur to sulfuric acid (Equation 8) (Ghahremaninezhad *et al*, 2010).

$$CuFeS_2 \rightarrow Cu_{1-x}Fe_{1-y}S2 + xCu^{2+} + yFe^{2+} + 2(x + y)\, e^- \; y >> x \quad (5)$$

$$Cu_{1-x}Fe_{1-y}S_2 \rightarrow Cu_{1-x-z}S_2 + zCu^{2+} + (1 - y)\, Fe^{2+} + 2(z + 1 - y)\, e^- \quad (6)$$

$$CuFeS_2 \rightarrow 0.75CuS + 1.25S^0 + 0.25Cu^{2+} + Fe^{2+} + 2.5e^- \quad (7)$$

$$CuFeS_2 + 8H_2O \rightarrow Cu^{2+} + Fe^{3+} + 2SO_4^{2-} + 16H^+ + 17e^- \quad (8)$$

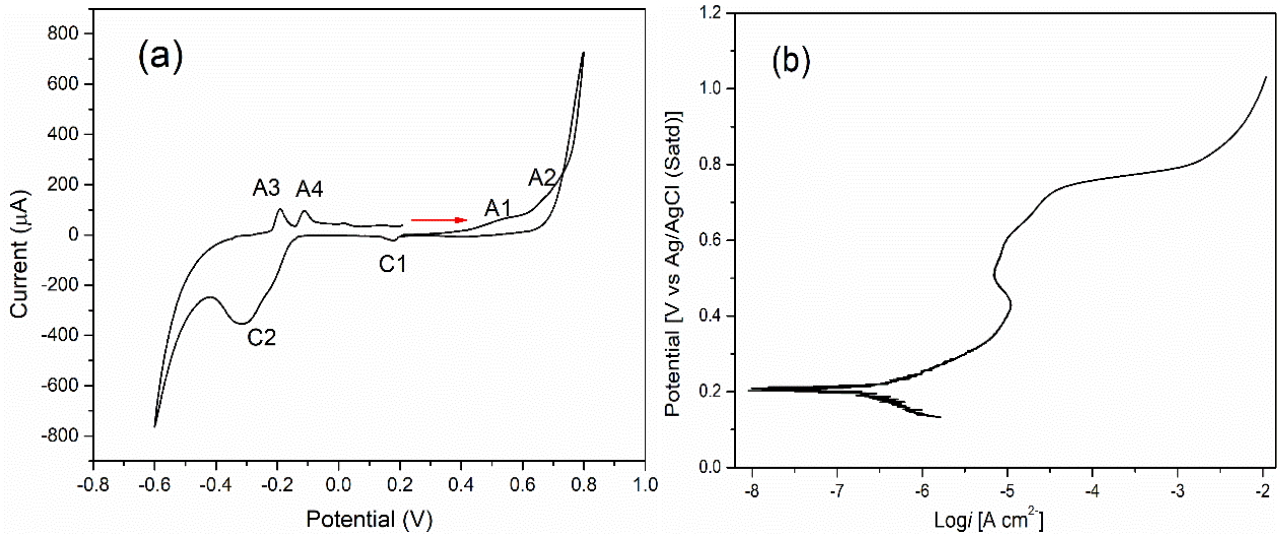

FIG 3 – (a) Cyclic voltammograms of chalcopyrite electrode (The scan was initiated from $E_{OC}P$ (0.215 V) in the positive direction at a scan rate of 10 mV s^{-1}) and (b) potentiodynamic polarisation of chalcopyrite electrode (scan rate: 0.5 mV s^{-1}) in 0.1 mol/L H_2SO_4 solution.

In the inverse scan, C1 may be attributed to the reaction of cupric ions with CuS or elemental sulfur, producing chalcocite (Liang *et al*, 2011). When the potential value was lower than −100 mV, peaks C2 observed. The peak C2 possibly is related to the reduction of covellite and/or chalcopyrite. Thus, the anodic peaks of A3 and A4 might be corresponded to the oxidation of the reduced products of peaks C1 and C2. Further explanation of these peaks is not in the scope of this study because these peaks are irrelevant to the dissolution and passivation of chalcopyrite.

Figure 3b shows the result of potentiodynamic curve of chalcopyrite at a scan rate of 0.5 mV s^{-1}. The result shows that the potentiodynamic profile is similar to that observed by Ghahremaninezhad *et al* (2010). A passive region is evident from the OCP to 630 mV. In this region the current was low and surface reaction was very slow. According to the CV curve, it is assumed that some nonstoichiometric or secondary metal sulfide mineral formed in this region as shown in Equation 5. From 630 to 700 mV, the current rose rapidly with the increase of potential. In this region, the surface reaction was fast due to the oxidation of the formed surface layer (Equation 6) and the partial oxidation of chalcopyrite (Equation 7).

Surface chemical analysis of enargite and chalcopyrite

XPS of electrochemical oxidised enargite surface

The spectra of S 2p of the oxidised enargite electrodes with the increase of applied potential in Figure 4 show significant differences compared with the freshly polished enargite. The spectra of

S 2p were fitted to interpret the sulfur oxidation states and to identify the oxidation products. The fitted analysis results are presented in Table 2.

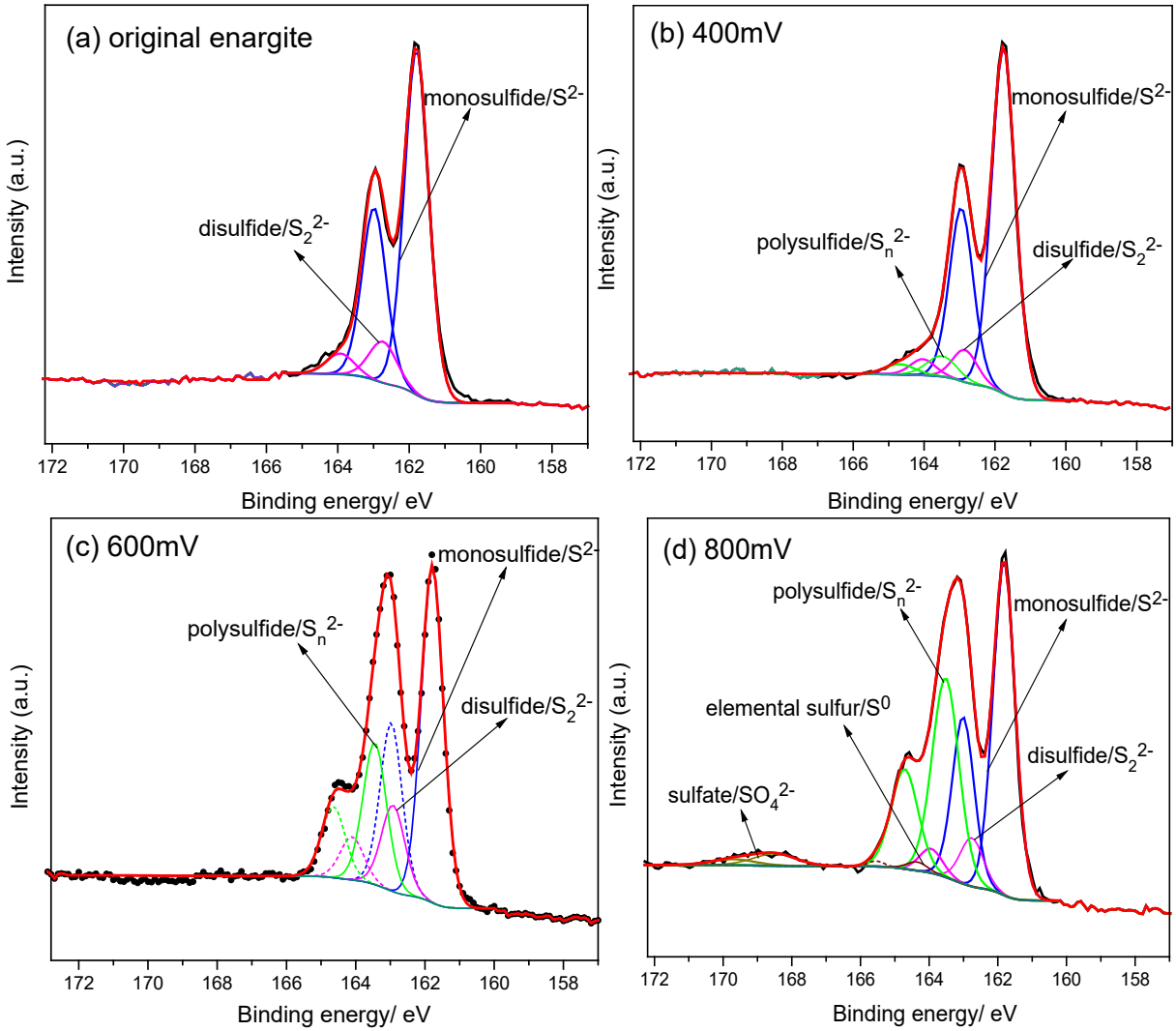

FIG 4 – S 2p XPS spectra for freshly polished enargite electrode surface (a) and the electrodes obtained after dissolution at 400 (b), 600 (c) and 800 mV (d).

TABLE 2

XPS analysis of the relative proportion of different sulfur species present on the enargite electrode.

	S^{2-}	S_2^{2-}	S_n^{2-}	S^0	SO_4^{2-}
Original	88.1	11.9	-	-	-
400 mV	87.2	8.4	4.4	-	-
600 mV	64.7	7.7	27.6	-	-
800 mV	58.2	9.1	28.6	1.3	2.8

Figure 4c illustrates the S 2p XPS spectra of freshly polished enargite surface, with the peak at 161.8 eV and 162.9 eV corresponding to the S $2p_{3/2}$ and S $2p_{1/2}$ peaks for monosulfide sulfur (S^{2-}) in enargite. Compared to the untreated enargite, it is clear that sulfur species with higher oxidation states formed on the surface of the electrode after oxidation with the increasing potential. Examining the spectra for S 2p at potentials of 400 and 600 mV revealed the presence of three distinct sulfur species: the S $2p_{3/2}$ peaks located at 161.8, 162.8, and 163.5 eV. An additional peak has been fitted at 164.4 eV for the S $2p_{3/2}$ at the potential of 800 mV. The S $2p_{3/2}$ species at 161.8 and 162.8 eV corresponds to the monosulfide (S^{2-}) and disulfide (S_2^{2-}) in enargite. Assignment of the S $2p_{3/2}$ peaks

identified at 163.5 and 164.4 eV is not straightforward. However, analysis based on binding energy suggests it would appear reasonable for the peak at 163.4 eV to be assigned to metal deficient sulfide or polysulfides (S_n^{2-}) that, for the latter, fall in the range 162.0−163.6 eV and the peak at 164.4 eV is likely due to S^0.

Raman spectroscopy and XANES of chalcopyrite

Raman spectroscopy was applied to study the sulfur species of chalcopyrite electrode surface after being electrochemical oxidation under different potentials. Based on the previous CV and potentiodynamic polarisation studies, chalcopyrite electrodes were subjected to chronoamperomatic treatment under three important potentials: 550, 680 and 730 mV which are related to the formation and dissolution of passivation films. Raman spectra of original and oxidised chalcopyrite are shown in Figure 5. The Raman spectra of original chalcopyrite displayed three peaks of 292, 319 and 353 cm^{-1}, which resulted from lattice vibrations. At 550 mV, a broad peak around 470 cm^{-1} was found in the spectra, which could be assigned to a S–S bond of covellite (Yang *et al*, 2015). Furthermore, the broad shoulder shows the presence of polysulfides (Mycroft *et al*, 1990). The evidence of polysulfides and covellite supported Equations 5 and 6. The spectra of electrode oxidised at 680 mV shows several new peaks of 272, 415 and 452 cm^{-1} which are similar to the previous study by Parker *et al* (2008). They suggested that these peaks were produced by the irradiation of the oxidised surface which was a Raman-inactive phase with laser light. The photo-induced product yielded a Raman spectrum consistent with polymeric sulfur (S_μ) and they concluded that the parent compound is a metal-deficient sulfide having a remnant chalcopyrite lattice structure which further supported the Equations 5 and 6. At higher potential of 730 mV, more intensive peaks at 152, 220 and 474 cm^{-1} were observed, suggesting the accumulation of crystalline elemental sulfur (S_8) (Equation 7).

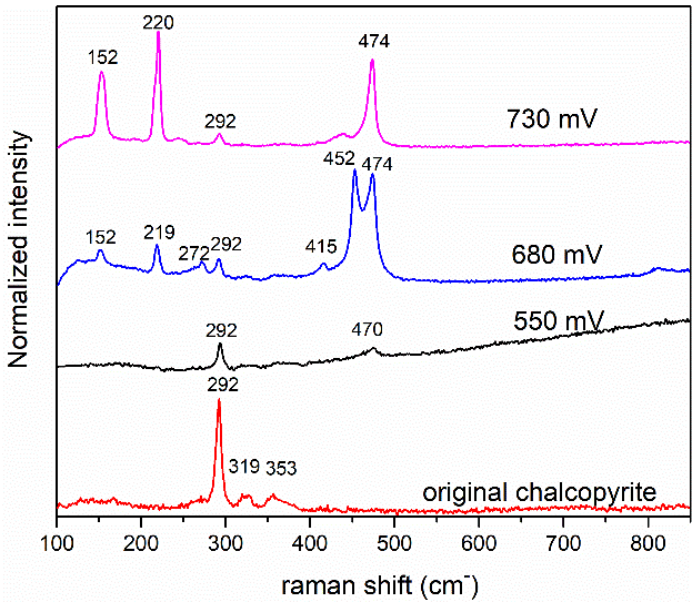

FIG 5 – The Raman spectra of original chalcopyrite surface and oxidised chalcopyrite electrode surfaces after chronoamperometry treatment at different potentials.

The S K-edge XANES spectra are shown in Figure 6. The original chalcopyrite shows a sharp absorption edge at 2.4698 KeV, which decreased as the increase of potential. On the other hand, a peak 2.4722 KeV, which suggests the oxidation of electrode surface, appeared after electrochemical oxidation, and rose with the increasing potential. According to the literature, this peak is higher than that of FeS_2 (S_2^{2-}) but slightly lower than that of elemental sulfur (S_8) (Xia *et al*, 2010). Coupled with the results of XPS study, it can be inferred that this peak indicates the formation of polysulfide (S_n^{2-}) and/or S_8 which are in line with the previous results of Raman spectroscopy.

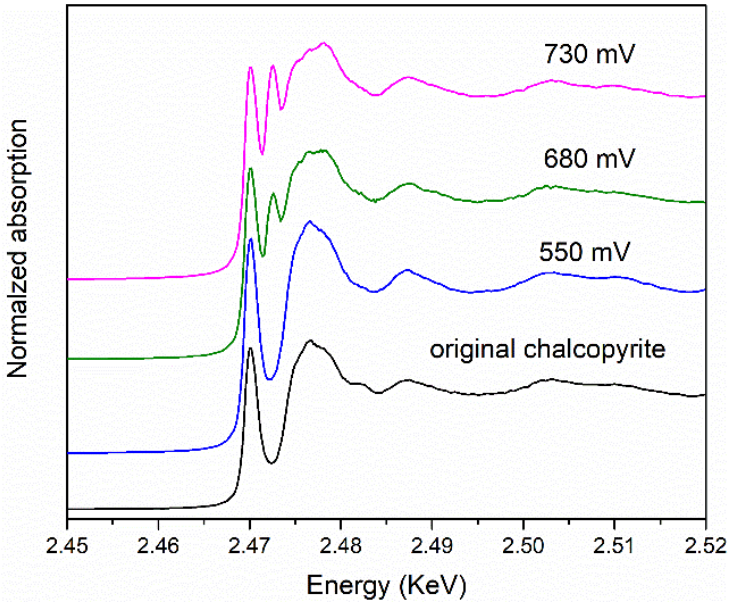

FIG 6 – The S K-edge spectra of the unreacted enargite and oxidised enargite electrode surfaces after chronoamperometry treatment at different potentials.

CONCLUSIONS

Electrochemical and surface analytical techniques were employed to investigate the oxidation of enargite and chalcopyrite in 0.1 mol/L sulfuric acid. Electrochemical oxidation of enargite demonstrated an obvious passivation region from 500 to 750 mV. A nonstoichiometric film $Cu_{(3-x)}As_{(1-y)}S_4$ (x>>y) likely accumulated on the electrode surface, which accounted for the obvious decrease in current density in the passive potential region. Results of XPS have shown a substantial change in the oxidation state of sulfur species on the surface of enargite at the passive and trans-passive region. For chalcopyrite, three important potentials of 550, 680 and 730 mV which are related to the formation and dissolution of passivation film were observed based on the CV and potentiodynamic polarisation. Raman and S K-edge XANES spectra studies of the chalcopyrite electrodes after being treated under these three potentials indicated a metal-deficient sulfide of $Cu_{1-x}Fe_{1-y}S_2$ (y >> x) might be responsible for the passivation phenomenon. Hence, it is concluded that the passive and transpassive dissolution of enargite and chalcopyrite are similar which are caused by metal-deficient sulfide surfaces although the compositions of the metal-deficient sulfide are different for these two cases.

ACKNOWLEDGEMENTS

The authors would like to thank the support from the Australian Research Council Linkage grant (ARC LP160101760). The authors also acknowledge the staff of Beijing National Synchrotron Radiation Facility (BSRF) for their help to collect XANES spectra.

REFERENCES

Ásbjörnsson, J, Kelsall, G H, Pattrick, R A D, Vaughan, D J, Wincott, P L and Hope, G A, 2004. Electrochemical and surface analytical studies of enargite in acid solution, *Journal of the Electrochemical Society*, 151(7): E250-E256.

Corkhill, C, Wincott, P, Lloyd, J and Vaughan, D, 2008. The oxidative dissolution of arsenopyrite (FeAsS) and enargite (Cu_3AsS_4) by *Leptospirillum ferrooxidans*, *Geochimica et Cosmochimica Acta*, 72(23): 5616–5633.

Elsener, B, Atzei, D, Fantauzzi, M and Rossi, A, 2007. Electrochemical and XPS surface analytical studies on the reactivity of enargite, *European Journal of Mineralogy*, 19(3): 353–361.

Fattah-alhosseini, A and Vafaeian, S, 2015. Comparison of electrochemical behavior between coarse-grained and fine-grained AISI 430 ferritic stainless steel by Mott–Schottky analysis and EIS measurements. *Journal of Alloys and Compounds,* 639: 301–307.

Ghahremaninezhad, A, Asselin, E and Dixon, D G, 2010. Electrochemical evaluation of the surface of chalcopyrite during dissolution in sulfuric acid solution, *Electrochimica Acta,* 55(18): 5041–5056.

Ghahremaninezhad, A, Dixon, D G and Asselin, E, 2013. Electrochemical and XPS analysis of chalcopyrite ($CuFeS_2$) dissolution in sulfuric acid solution, *Electrochimica Acta,* 87: 97–112.

Guo, Y, Guo, X, Wu, H, Li, S, Wang, G, Liu, X and Wang, D, 2017. A novel bio-oxidation and two-step thiourea leaching method applied to a refractory gold concentrate, *Hydrometallurgy*, 171: 213–221.

Hackl, R P, Dreisinger, D B, Peters, E and King, J A, 1995. Passivation of chalcopyrite during oxidative leaching in sulfate media, *Hydrometallurgy*, 39(1): 25–48.

Karimi, S, Ghahreman, A, Rashchi, F and Moghaddam, J, 2017. The mechanism of electrochemical dissolution of sphalerite in sulfuric acid media, *Electrochimica Acta*, 253: 47–58.

Lattanzi, P, Da Pelo, S, Musu, E, Atzei, D, Elsener, B, Fantauzzi, M and Rossi, A, 2008. Enargite oxidation: A review, *Earth-Science Reviews*, 86(1–4): 62–88.

Li, Y, Kawashima, N, Li, J, Chandra, A P and Gerson, A R, 2013. A review of the structure and fundamental mechanisms and kinetics of the leaching of chalcopyrite, *Adv Colloid Interface Sci,* 197–198: 1–32.

Liang, C, Xia, J, Yang, Y, Nie, Z, Zhao, X, Zheng, L, Ma, C and Zhao, Y, 2011. Characterization of the thermo-reduction process of chalcopyrite at 65°C by cyclic voltammetry and XANES spectroscopy, *Hydrometallurgy*, 107(1–2): 13–21.

Liu, Q, Chen, M and Yang, Y, 2017. The effect of chloride ions on the electrochemical dissolution of chalcopyrite in sulfuric acid solutions, *Electrochimica Acta*, 253: 257–267.

Mycroft, J, Bancroft, G, McIntyre, N, Lorimer, J and Hill, I, 1990. Detection of sulphur and polysulphides on electrochemically oxidized pyrite surfaces by X-ray photoelectron spectroscopy and Raman spectroscopy, *Journal of Electroanalytical Chemistry and Interfacial Electrochemistry*, 292(1–2): 139–152.

Nava, D, González, I, Leinen, D and Ramos-Barrado, J R, 2008. Surface characterization by X-ray photoelectron spectroscopy and cyclic voltammetry of products formed during the potentiostatic reduction of chalcopyrite, *Electrochimica Acta*, 53(14): 4889–4899.

Padilla, R, Rodríguez, G and Ruiz, M C, 2010. Copper and arsenic dissolution from chalcopyrite–enargite concentrate by sulfidation and pressure leaching in H_2SO_4–O_2, *Hydrometallurgy*, 100(3–4): 152–156.

Parker, G K, Woods, R and Hope, G A, 2008. Raman investigation of chalcopyrite oxidation, *Colloids and Surfaces A: Physicochemical and Engineering Aspects*, 318(1–3): 160–168.

Riveros, P A and Dutrizac, J E, 2013. The Leaching of Tennantite, Tetrahedrite and Enargite in Acidic Sulphate and Chloride Media*, Canadian Metallurgical Quarterly*, 47(3): 235–244.

Safarzadeh, M S, Moats, M S and Miller, J D, 2013. Recent Trends in the Processing of Enargite Concentrates, *Mineral Processing and Extractive Metallurgy Review*, 35(5): 283–367.

Tu, Z, Wan, J, Guo, C, Fan, C, Zhang, T, Lu, G, Reinfelder, J R and Dang, Z, 2017. Electrochemical oxidation of pyrite in pH 2 electrolyte, *Electrochimica Acta*, 239: 25–35.

Viramontes-Gamboa, G, Peña-Gomar, M M and Dixon, D G, 2010. Electrochemical hysteresis and bistability in chalcopyrite passivation, *Hydrometallurgy*, 105(1–2): 140–147.

Watling, H R, 2013. Chalcopyrite hydrometallurgy at atmospheric pressure: 1. Review of acidic sulfate, sulfate–chloride and sulfate–nitrate process options, *Hydrometallurgy*, 140: 163–180.

Xia, J, Yang, Y, He, H, Zhao, X, Liang, C, Zheng, L, Ma, C, Zhao, Y, Nie, Z and Qiu, G, 2010. Surface analysis of sulfur speciation on pyrite bioleached by extreme thermophile *Acidianus manzaensis* using Raman and XANES spectroscopy, *Hydrometallurgy*, 100(3): 129–135.

Yang, Y, Harmer, S and Chen, M, 2015. Synchrotron-based XPS and NEXAFS study of surface chemical species during electrochemical oxidation of chalcopyrite, *Hydrometallurgy*, 156: 89–98.

Development of a comprehensive methodology for *in situ* characterisation of sulfide minerals during leaching

M Chen[1,2], Y Yang[3], Y L Ma[4] and W Bruckard[5]

1. Senior Principal Research Scientist, CSIRO Mineral Resources, Clayton Vic 3169. Email: Miao.Chen@csiro.au
2. Professor, RMIT University, Melbourne Vic 3001. Email: Miao.Chen@rmit.edu.au
3. Research Fellow, RMIT University, Melbourne Vic 3001. Email: Yi.Yang@csiro.au
4. PhD Candidate, RMIT University, Melbourne Vic 3001. Email: Yalong.Ma@csiro.au
5. Research Group Leader, Process Engineering and Chemistry, CSIRO Mineral Resources, Clayton Vic 3168. Email: Warren.Bruckard@csiro.au

ABSTRACT

To improve the understanding of the reactions and mechanisms occurring during the leaching of sulfide ores at high temperatures a range of advanced characterisation and sensing tools have been combined to provide a sophisticated and powerful methodology to examine sulfide leaching systems. These include advanced electrochemical methods, surface chemistry and materials characterisation techniques such as synchrotron X-Ray Absorption Spectroscopy (XAS), X-Ray Photoelectron Spectroscopy (XPS), Scanning Electrochemical Microscopy (SECM), and *in situ* X-ray diffraction (XRD), together with new robust solid state chemical sensors for *in situ* real time monitoring of key aqueous chemical parameters. The methodology was employed to investigate various sulfide mineral leaching processes. For example, oxidation of arsenopyrite at elevated temperature involves complicated multiple reactions and the process is strongly influenced by the solution conditions, component speciation and mineralogy. The methodology was used to study this system both *ex situ* and *in situ* to gain a detailed understanding of the complex chemical reaction mechanisms operating. These mechanisms are discussed in terms of the observed leaching efficiency. The application of this methodology enables complex sulfide leaching systems to be understood more fully such that process efficiency can be improved.

METHODS

The *in situ* XAS study was carried out in X-ray Absorption Spectroscopy (XAS) beamline at Australian synchrotron. The experiment set-up is shown as in Figure 1 (Chen *et al*, 2018). The solid sample and solution was filled in the quartz capillary with an OD of 1 mm and wall thickness of 0.1 mm. The position of capillary was controlled by a motor and accurately adjusted to fit in the X-ray path. For each leaching experiment the pressure of leaching was set as 28 bar using oxygen or air and the system was heated from room temperature to 200–225°C and then the cooled down to room temperature. A set of XAS data were collected at different temperatures during the heating-up and cooling down stages.

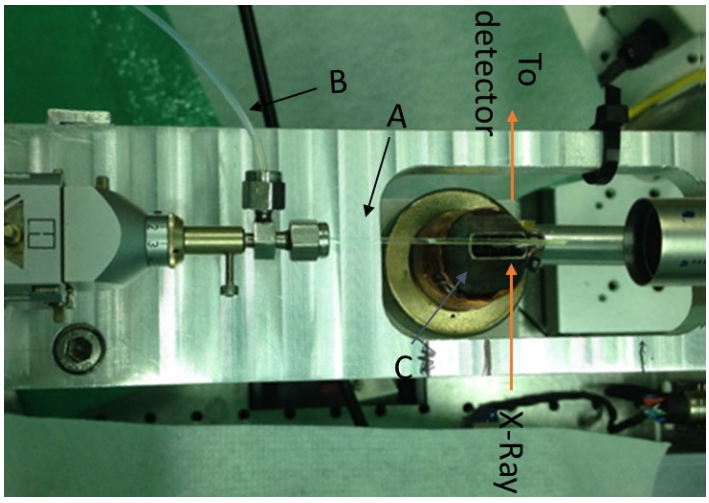

FIG 1 – The set-up of *in situ* XAS experiment (A: quartz capillary; B: gas line; C: hot air blower).

RESULTS AND DISCUSSION

The evolution of As solution species in arsenopyrite pressure leaching with oxygen is shown in Figure 2. At room temperature, the As k edge XANES spectra show a single strong peak at 11874.8 eV (Testemale *et al*, 2004), which indicated the presence of As(V) species. In Figure 2a with the increase of temperature, the spectra showed a clear trend of change. Increasing the temperature up to 80°C, the spectra showed similar features to that at room temperature, which indicated only As(V) was in the solution. When the temperature raised to 100°C, a dramatic change of spectra was seen. At 100°C, a peak at 1171.3 eV appeared which is corresponding to that of As(III) species (Ona-Nguema *et al*, 2010). With the further increase of the temperature, the As(V) peak decreased to a shoulder at 160°C and disappeared at 200°C. At the same time, the As(III) peak was increasing and became the only detectable peak at 200°C or above.

In the cooling phase, a reversed evolution of As speciation was seen (Figure 2b). The As(III) was the only As species in the solution at 220°C and 160°C. When the temperature was decreased to 100°C, a shoulder appeared which possibly indicated the presence of As(V). A clear presence of As(V) occurred at 50°C and most of the As presented as As(V) at room temperature.

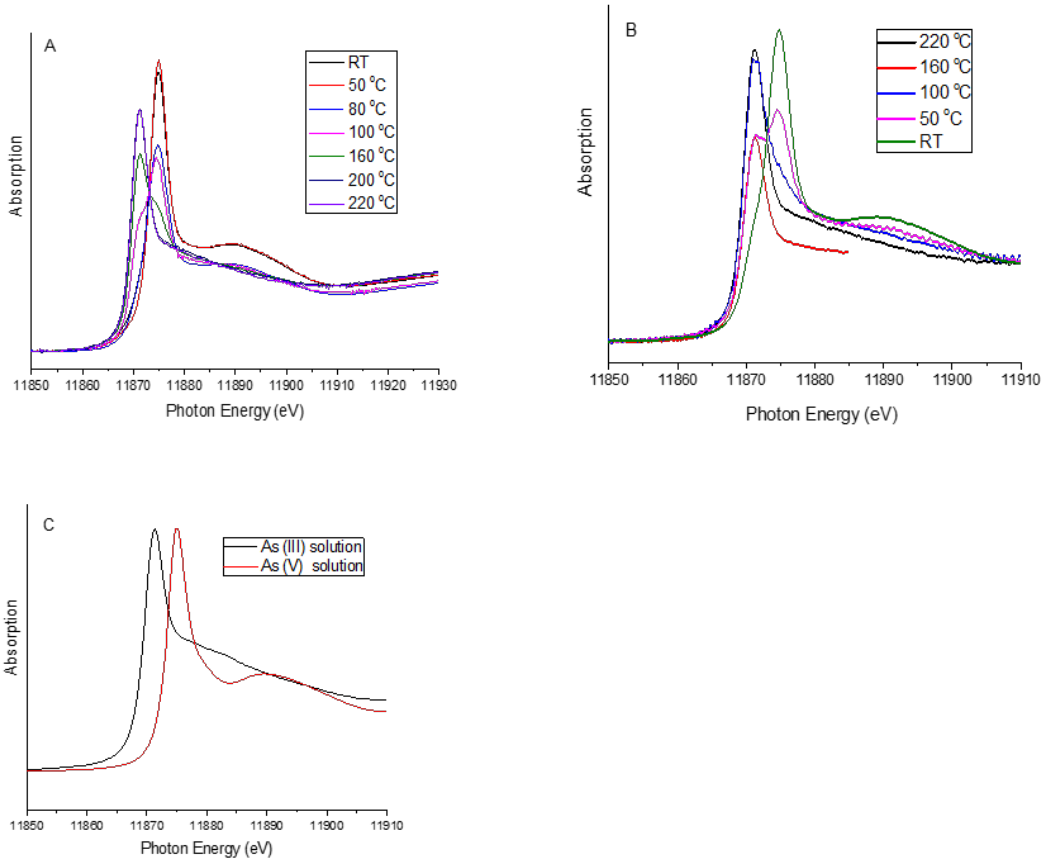

FIG 2 – The As K edge XANES spectra of arsenopyrite leaching solution at 28 bar oxygen (A, heating; B, cooling; C, As(III) (dissolved As_2O_3 in 0.5 M sulfuric acid) and As(V) (sodium arsenate standard solution).

To quantify the As(V)/As(III) ratio in the solution, the spectra was deconvoluted by curve fitting using arctangent curve representing absorption step and Lorentzian curve representing the As(V) or As(III) species (Takahashi *et al*, 2003). The As(V)/As(III) ratio could be directly represented by the area of the corresponding Lorentzian curve. In either heating phase or cooling phase, the curve fitting results are in line with the above qualitative interpretation. The fitting results show that As(V) was the only solution As species up to 80°C. At 100°C, the proportion of As(III) to As(V) was 31.7 per cent to 68.3 per cent, which then increased to 84.2 to 15.2 at 160°C. Only As(III) was found in solution at temperate at 200°C or above. During cooling, as only As(V) first showed up at 100°C, accounting to 12.3 per cent of the solution As and quickly increased to 50.5 per cent, when temperature lowered

to 50°C. At room temperature, As(V) returned to the predominant As species and comprised of 80.3 per cent of total solution As.

The arsenic species in solution during the arsenopyrite pressure leaching with the co-existence of pyrite or pyrrhotite have been also investigated. *In situ* XAS has confirmed that the arsenic in solution was present mostly as As(V) at low temperatures and As(III) at elevated temperatures, and the As(III) can be re-oxidised to As(V) during cooling process. The addition of pyrrhotite facilitated the reduction of As(V) and increased the stability of As(III) in the solution, which is possibly explained by the faster oxidation of pyrrhotite that created a more reductive environment, which was further confirmed by the S k-edge XANES study on the leached residue (Yang *et al*, 2020). On the other hand, the addition of pyrite favoured the presence of As(V) in the solution, which could be explained by the relatively slower oxidation rate or/and the catalysing reaction of pyrite on As(III) oxidation.

ACKNOWLEDGEMENTS

The authors would like to thank the support from the Australian Research Council grant (ARC LP160101760), CSIRO Research plus postdoctoral scheme and Zijin Mining Group. The *in situ* XAS study of arsenic species was carried out on the XAS beamline at the Australian Synchrotron, part of ANSTO, Victoria, Australia. The S k-edge XANES data were collected in the Beijing Synchrotron Radiation Facility (BSRF), Beijing, China. The authors appreciate the support provided by the beamline scientists and staff of the Australian Synchrotron and Beijing Synchrotron Radiation Facility.

REFERENCES

Chen, M, Yang, Y, Liu, W, Wang, C and Johannessen, B, 2018. An in-situ synchrotron XAS study on the evolution of aqueous arsenic species in acid pressure leaching, *Hydrometallurgy*, 175:11–19.

Ona-Nguema, G, Morin, G, Wang, Y, Foster, A L, Juillot, F, Calas, G and Brown, G E, 2010. XANES Evidence for Rapid Arsenic(III) Oxidation at Magnetite and Ferrihydrite Surfaces by Dissolved O_2 via Fe^{2+}- Mediated Reactions, *Journal of Environmental Science and Technology,* 44:5416–5422.

Takahashi, Y, Ohtaku, N, Mitsunobu, S, Yuita, K and Nomura, M, 2003. Determination of the As(III)/As(V) ratio in soil by X-ray absorption near-edge structure (XANES) and its application to the arsenic distribution between soil and water, *Analytical Sciences*, 19:891–896.

Testemale, D, Hazemann, J L, Pokrovski, G S, Joly, Y, Roux, J, Argoud, R and Geaymond, O, 2004. Structural and electronic evolution of the As(OH)(3) molecule in high temperature aqueous solutions: An x-ray absorption investigation, *The Journal of Chemical Physics*, 121:8973-8982.

Yang, Y, Chen, J, Liu, W, Zhong, S, Ma, Y, Gao, X and Chen, M, 2020. The impacts of pyrite/pyrrhotite on aqueous arsenic species in arsenopyrite pressure leaching: An XAS study, *Minerals Engineering*, 155:106447.

Separation and enrichment of copper, nickel and cobalt from acidic leach solution of smelter slag using solvent extraction and selective precipitation

L L Godirilwe[1], K Haga[2], G Danha[3] and A Shibayama[4]

1. PhD candidate, Akita University, Akita, Japan 010–0852. Email: llgodirilwe@gmail.com
2. Associate Professor, Akita University, Akita, Japan 010–0852. Email: khaga@gipc.akita-u.ac.jp
3. Associate Professor, Botswana International University of Science and Technology, Palapye. Email: danhag@biust.ac.bw
4. Professor, Akita University, Akita, Japan 010–0852. Email: sibayama@gipc.akita-u.ac.jp

ABSTRACT

The hydrometallurgical separation and enrichment processes provide an effective way to selectively recover metals from relatively dilute multicomponent sulfuric acid leach solutions. The multicomponent leach solution utilised in this study contained 0.3 g/L Cu, 0.34 g/L Ni, 0.13 g/L Co, and 2.96 g/L Fe, which was obtained after high-pressure oxidative acid leaching (HPOAL) of the copper-nickel smelter slag. The solvent extraction (SX), precipitation, and xanthate complexation processes were employed to recover and upgrade Cu, Ni, and Co from the leach solution. Batch SX tests were carried out using a countercurrent two-stage mixer settler extraction column, and LIX 984N (10 per cent v/v) as a copper extractant. Fundamental parameters influencing the extraction process such as pH, mixing speed, H_2SO_4 concentration, and organic/aqueous (O/A) phase ratio were investigated. For copper enrichment in solution, a combination of two extraction stages and two stripping stages were employed. Copper was successively separated from Fe, Ni, and Co under optimised extraction conditions (pH 2, 400 rev/min, O/A 0.25, and 20 min contacting) and stripping conditions (175 g/L H_2SO_4, 400 rev/min, O/A 4, and 20 min contacting). About 97 per cent of copper was extracted with low co-extraction of Fe, Ni, and Co of about 5.90 per cent, 1.47 per cent, and 2.53 per cent, correspondingly. A final Cu-rich solution containing 23 g/L Cu was obtained with a very low Fe concentration of 0.05 g/L. Additionally, for iron removal from the Ni/Co raffinate solution, more than 99 per cent of iron was precipitated at pH 4 by the addition of a calcium carbonate ($CaCO_3$) suspension, with low co-precipitation of nickel and cobalt of around 3.68 per cent and 2.27 per cent, respectively. Furthermore, about 83.6 per cent of nickel and 99.4 per cent cobalt were co-precipitated from the solution by potassium amyl xanthate (PAX) solution at pH 6. The Ni and Co xanthate complexes were thermally decomposed and recovered as cobalt oxide (CoO) and nickel sulfide (NiS) solids.

INTRODUCTION

Hydrometallurgical processes have recently been playing an efficient role in the extraction of valuable metals from metallurgical waste, low-grade ores, and complex ore materials. This includes the high-pressure leaching of slag waste from pyrometallurgical operations to recover the entrained valuable metals such as nickel, copper, and cobalt. Even though the high-pressure leaching of slag has comprehensive metal recoveries (Baghalha, Papangelakis and Curlook, 2007; Huang *et al,* 2015; Li, Perederiy and Papangelakis, 2008), due to the low metal content in the waste material, the generated leach solutions are relatively dilute in metals concentrations. Consequently, this necessitates multiple metal enrichment stages and impurity removal steps to obtain an industrial standard solution suitable for electrowinning. Furthermore, in a multicomponent leach solution, several metal separation processes in sequence may be necessary to realise the maximum value of each metal. The separation of metal ions and the removal of impurities from leach solutions is very important in enabling efficient operation in the upstream processes to achieve high purity metals by electrowinning.

Acidic pressure leaching solutions of copper-nickel smelter slags commonly contain low content of Cu, Ni, and/or Co, with impurities of Fe, Ca, and/or Mg. The solvent extraction process is generally used in the selective extraction of copper from leach solutions. Hydroxyoxime extractants, such as LIX 984N (aldoxime-ketoxime mixture) are often used for the extraction of copper from the solution because of their high stability and excellent copper selectivity properties (Schlesinger *et al,* 2011;

Shakibania *et al,* 2020). The separation of nickel and cobalt is commonly done by solvent extraction utilising organic extractants such as Cyanex 272 (bis(2,4,4-trimethylpentyl) phosphinic acid), and D2EHPA (di-2-ethylhexyl phosphoric acid). However, increased content of impurities in solution has been noted to cause difficulties in the separation of nickel and cobalt (Huang, Li and Chen, 2007; Kursunoglu, Ichlas and Kaya, 2017). Therefore, alternative methods for the separation of nickel and cobalt are currently being explored. Shirayama and Uda (2015) utilised the difference in Ni and Co oxidation/reduction rate to selectively reduce Ni and separate it from Co in an acidic aqueous solution. Vakylabad, Darezereshki and Hassanzadeh (2021) selectively extracted nickel and cobalt from the leach solution by a xanthate complex at room temperature, owing to the strong hydrophobic properties of nickel and cobalt xanthates.

Several other studies have investigated a combination of different techniques to separate and enrich metals from multicomponent leach solutions (Banza, Gock and Kongolo, 2002; Huang, Li and Chen, 2007; Keber *et al,* 2020; Kursunoglu, Ichlas and Kaya, 2017; Parhi and Sarangi, 2008; Sridhar and Verma, 2011). Huang, Li and Chen (2007) developed a technique for the recovery of copper, nickel, and cobalt from leach solutions, employing solvent extraction for the separation of Cu, and used the Na_2S precipitation method to further recover Ni and Co in solution. Selective precipitation is known to have good selectivity for metal removal and fast reaction rates (Godirilwe *et al,* 2021; Perez *et al,* 2020). Banza, Gock and Kongolo (2002) also incorporated the iron precipitation method in between sequential solvent extractions of Cu followed by that of Ni and Co. Therefore, a combination of separation processes has proven to be effective for the recovery of valuable metals from a multi-component solution.

This study is focusing on the processing of the acidic pressure leaching solution to recover Cu, Ni, and Co from the solution. Three hydrometallurgical processes of solvent extraction (SX), precipitation, and xanthate complexation processes were used to selectively separate and enrich metal ions of Cu, Ni, and Co, and remove the Fe impurity from the pregnant leach solution (PLS). The solvent extraction method using a countercurrent two-stage mixer settler extraction column and LIX 984N as a copper extractant was employed to separate copper from other metals (Ni, Co) and Fe impurity as well as upgrade the copper concentration in the PLS. A multistage counter-current extraction column has been proven to effectively extract metals from dilute solutions (Takahashi and Nii, 1999). Iron impurity in the raffinate solution, which is known to have detrimental effects on the upstream processes, was removed by precipitation using calcium carbonate ($CaCO_3$) emulsion from the solution prior to nickel and cobalt recovery. In this study, the xanthate complexation method using potassium amyl xanthate (PAX) displays an effective route to recover nickel and cobalt from the solution.

EXPERIMENTAL

Reagents and material

Solvent extraction and stripping of copper were carried out using a simulated pregnant leach solution (PLS) obtained from the optimised high-pressure leaching of copper-nickel slag. The metal concentration in the PLS is displayed in Table 1, showing dilute metal concentrations of nickel, copper, and cobalt. The multicomponent leach solution contained 0.3 g/L Cu, 0.34 g/L Ni, 0.13 g/L Co, and 2.96 g/L Fe and was used for optimisation tests during solvent extraction experiments. The simulated sulfate solution was prepared by dissolving analytical grade salts of $NiSO_4 \cdot 6H_2O$ (99 per cent purity), $CuSO_4 \cdot 5H_2O$ (99 per cent purity), $CoSO_4 \cdot 7H_2O$ (98 per cent purity), and $Fe_2(SO_4)_3 \cdot nH_2O$ (78 per cent purity) all from Nacalai Testique, Inc, Japan, in distilled water. The pH adjusting solutions were prepared by dissolving analytical grade sodium hydroxide pellets (97 per cent purity, Nacalai Testique, Inc) in distilled water, and diluting concentrated sulfuric acid (98.08 per cent purity, Nacalai Testique, Inc) with distilled water. A commercial-grade LIX 984N (BASF, Ireland) and diluent Isoper M were used in this study. An analytical grade $CaCO_3$ powder (98 per cent purity, Nacalai Testique, Inc) was dissolved in water to prepare the emulsion used for iron removal. A 28 per cent analytical grade ammonia solution (NH_3) (FUJIFILM Wako Pure Chemical Co., Ltd, Japan) was used for washing the Ni/Co xanthate precipitate. Chemical-grade PAX (Potassium amyl xanthate, $C_5H_{11}OCSSK$) from Wako Chemicals, Japan, was dissolved in distilled water to be used for the complexation of nickel and cobalt.

TABLE 1

Metal concentration in the simulated pregnant leach solution from the HPOAL stage.

Element	Fe	Ni	Cu	Co
Concentration, g/L	2.96	0.34	0.30	0.13

Procedure

Solvent extraction of copper

Batch solvent extraction tests were carried out using a countercurrent two-stage mixer settler extraction column illustrated in Figure 1. Copper was selectively extracted using LIX 984N (10 per cent v/v) with Isoper M as a diluent. The initial pH of the PLS was measured to be 1.0, and the pH was adjusted between 1.0–2.5 using a 1 M NaOH solution. For each extraction test, 400 ml of solution and 100 ml of diluted extractant (O/A = 0.25) were simultaneously fed by a pump into the extraction column at about 15 ml/s. The agitation speed was adjusted to the desired set point. Once the extractant has been filled into the extraction column, the respective pump was stopped to avoid air bubbles in the extraction column. The mixing and settling were allowed for 20 minutes to achieve steady-state and clear phase separation. The copper-loaded organic phase was then collected at its respective outlet leaving behind the copper barren aqueous phase (raffinate), which was collected afterward at the aqueous phase outlet. The raffinate solution was analysed using MP-AES to determine the metal concentration and compute the extraction efficiency. Fundamental parameters influencing the extraction process such as pH and mixing speed were investigated.

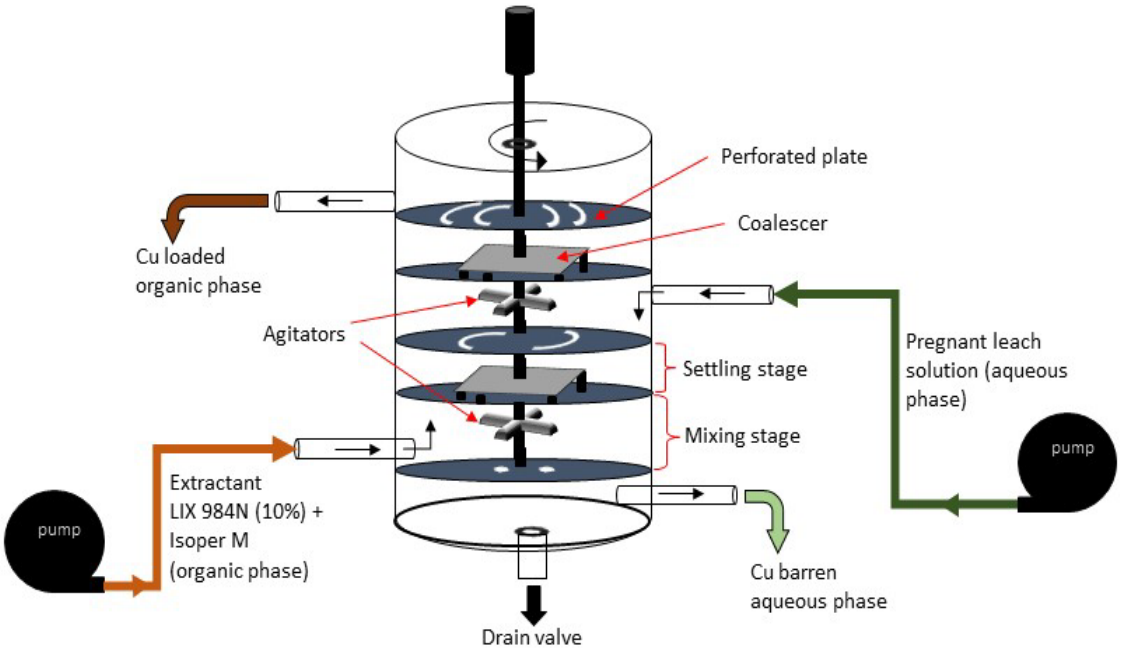

FIG 1 – Experimental set-up of a 2-stage mixer-settler extraction column.

The copper-loaded organic was subjected to stripping experiments using a sulfuric acid solution. The stripping column had a similar set-up as the extraction column. A desired volume of the sulfuric acid solution (50–175 g/L H_2SO_4) and the copper loaded organic was pumped into the stripping column at 15 ml/s and mixed at an agitation speed of 400 rev/min. After 20 minutes contacting, the barren organic and the stripped solution were collected separately from their respective outlets. The strip solution was analysed using MP-AES for copper concentration and determination of the stripping efficiency. Fundamental parameters influencing the stripping efficiency of copper such as H_2SO_4 concentration, and organic/aqueous (O/A) phase ratio were investigated. For copper enrichment in solution, a combination of two extraction stages and two stripping stages were employed. An illustration of the extraction and stripping procedure is shown in Figure 2.

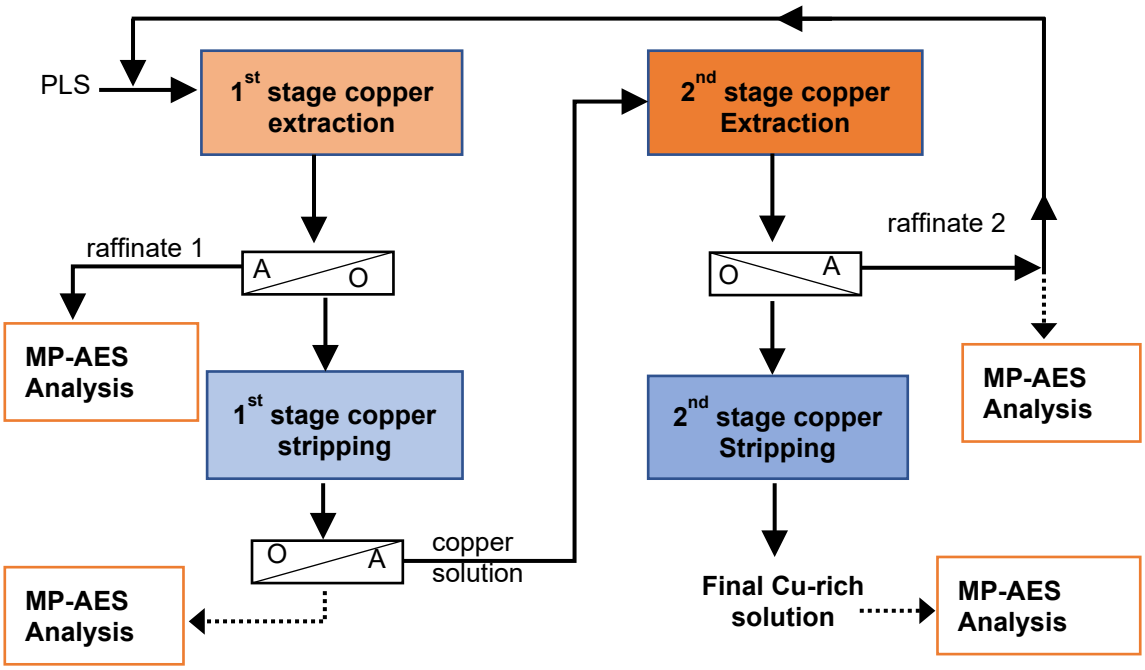

FIG 2 – An illustration of the extraction and stripping procedure of the pregnant leach solution obtained from high–pressure oxidative acid leaching of slag.

Iron removal

The raffinate solution obtained from the first extraction stage contained 0.303 g/L nickel, 0.125 g/L cobalt, and 2.52 g/L iron and was further processed for iron removal. A prepared calcium carbonate emulsion of 200 g/L was added to the raffinate solution in a dropwise manner, to achieve a pH of 4. The raffinate solution was then heated to 65°C using a magnetic stirrer operating at 500 rev/min. Once the temperature reached 65°C the reaction time was set to 20 minutes. The resulting precipitate and the residual solution were cooled and filtered, and the solution was taken for MP-AES analysis for the elemental analysis to determine the precipitation efficiency. The Fe precipitate solids were dried and analysed for mineral composition using XRD while part was dissolved using aqua regia for chemical analysis of the precipitated solids.

Complexation of nickel and cobalt

A PAX solution of 55g/L was prepared and added in a dropwise manner to the 50 ml solution of the raffinate. The pH was investigated between 5.5–8.0, from the initial pH of the raffinate solution (pH 4). The solution mixture was then heated to 50°C using a magnetic stirrer operating at 400 rev/min. The complexation reaction was allowed to proceed for 2 h, after which the solution was cooled and filtered. The residual barren solution was analysed using MP-AES to determine the amount of nickel and cobalt remaining in the solution and accordingly calculate the complexation efficiency. The Ni/Co xanthate precipitate was dried overnight, weighed, and roasted in a muffle furnace at 220°C for 1.5 hrs. After the calcination process was complete, the calcined products were removed and cooled to room temperature before being analysed using XRD for mineral identification. Part of the calcined product was dissolved using aqua regia and analysed for elemental composition using MP-AES.

Separation of nickel and cobalt

The Ni/Co xanthate precipitate was washed with 10 ml of ammonia solution and shaken for 15 minutes using a shaker at room temperature. The solution was filtered and taken for MP-AES analysis to determine the amount of nickel dissolved, while the remaining cobalt xanthate was dried before the calcination process. The cobalt xanthate precipitate was roasted in a muffle furnace at 220°C for 1.5 hrs. After the calcination process, the products were cooled to room temperature and analysed using XRD for mineral identification. Part of the calcined product was dissolved using aqua regia and analysed for elemental composition using MP-AES.

RESULTS AND DISCUSSIONS

Solvent extraction of copper

Effect of stirring speed

The stirring speed was investigated in the range of 200–400 rev/min to find the optimal operating conditions for the extraction of copper from the pregnant leach solution. The results are displayed in Figure 3, showing that as the stirring speed of the column extractor is increased, the copper extraction also increases, with the highest percentage extraction of 98.28 per cent at 400 rev/min. A high stirring speed increases the contact between the organic phase and the aqueous phase thus resulting in the formation of the Cu–LIX984N complex and thus enhancing the extraction of copper from the leach solution. Takahashi and Nii (1999) also noted that the mass transfer coefficient of the organic phase is dependent on the agitation speed. On the other hand, iron carryover to the organic phase had an increasing trend as the stirring speed was increased, which is mostly by entrapment in the organic phase (Schlesinger *et al,* 2011).

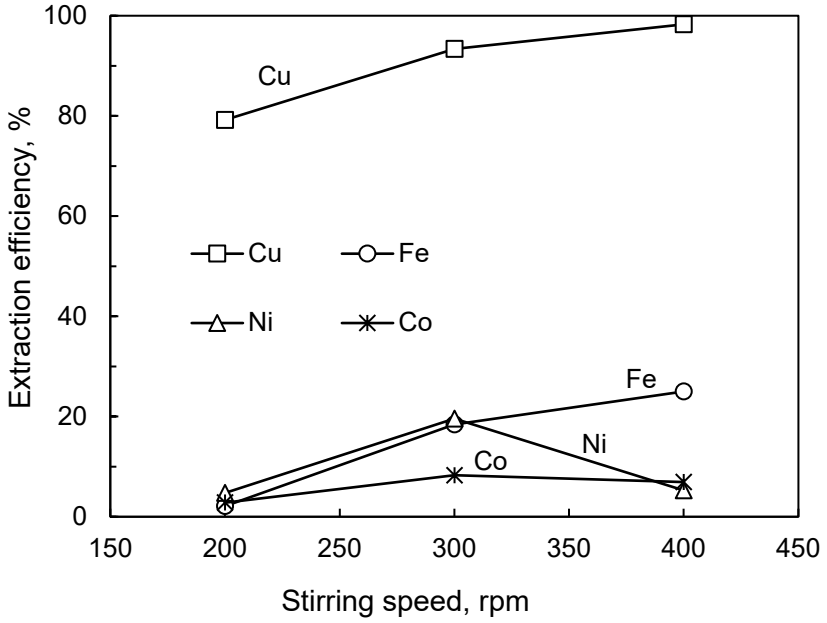

FIG 3 – The extraction behaviour of metals versus the stirring speed. Conditions: O/A ratio 0.25 (100 ml to 400 ml), pH 2.5, solutions flow rate 15 ml/s, and residence time 20 min).

Effect of pH on copper extraction

The pH was investigated in the range of 1–2.5 on metal extractions, and the results are displayed in Figure 4. As the pH was increased, the amount of copper extracted from the pregnant leach solution likewise increased, reaching a high of 98.28 per cent when the pH was 2.5. Banza, Gock and Kongolo (2002) also found that the favourable pH for copper selectivity using LIX 984 was 2.5. The amount of Fe extracted with copper remained below 6 per cent when the pH was 2 or lower, however, when the pH was increased to 2.5, the amount of Fe co-extracted with copper sharply increased from 5.90 per cent to about 25 per cent which is undesirable due to the consequential effects iron has in the upstream processes such as in the electrowinning process. Co-extractions of cobalt and nickel remained low at all the investigated pH values at 2.53 per cent and 1.47 per cent respectively. Therefore, a pH of 2 was chosen as the optimal condition for the extraction of copper (97 per cent) from the pregnant leach solution due to the good separation efficiency of copper from iron, nickel, and cobalt.

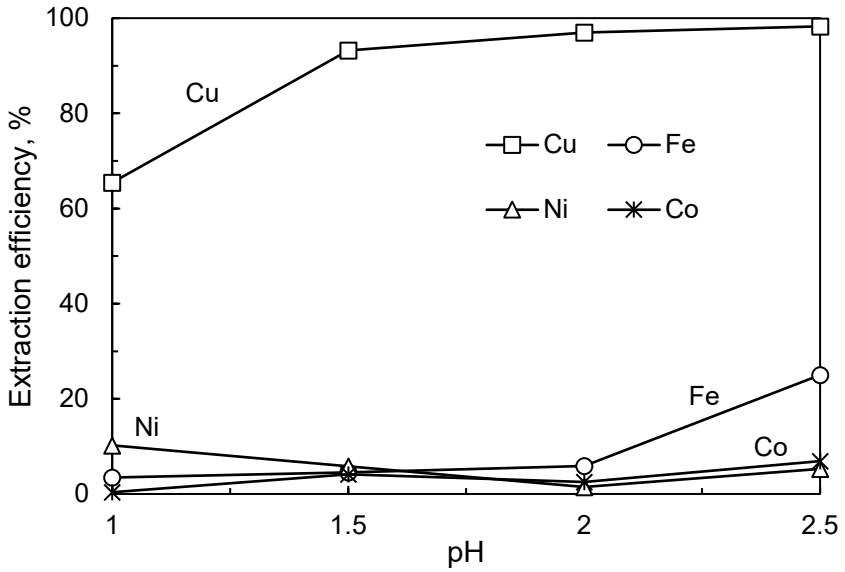

FIG 4 – The extraction behaviour of metals as a function of pH. Conditions: O/A ratio 0.25 (100 ml to 400 ml), agitating speed 400 rev/min, solutions flow rate 15 ml/s, and residence time 20 min).

Effect of sulfuric acid concentration on stripping

The effect of sulfuric acid on the stripping of copper from the organic phase was investigated in the range of 50 g/L to 175 g/L H_2SO_4 concentration (Figure 5). At lower acid concentration, 50 g/L H_2SO_4, copper stripping efficiency was low, and only 66 per cent was recovered from the organic phase while the amount of iron stripped from the organic phase was high at 89 per cent. As the concentration of sulfuric acid increased, so as the separation efficiency between copper and iron. Utilising a sulfuric acid concentration of 175 g/L, a high copper stripping efficiency of 97.28 per cent was achieved, with a lower iron stripping efficiency at 15.63 per cent, yielding a separation efficiency of 81.65 per cent between copper and iron. Therefore 175 g/L sulfuric acid was selected as the optimum conditions for efficient copper stripping from the organic phase.

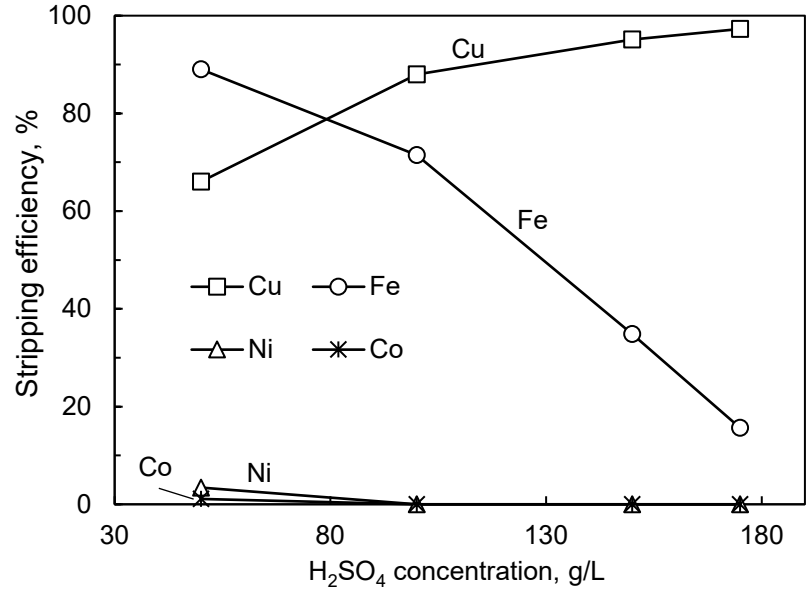

FIG 5 – The copper stripping behaviour of metals as a function of sulfuric acid concentration. Conditions: O/A ratio 0.25 (100 ml to 400 ml), stirring speed 400 rev/min, solutions flow rate 15 ml/s, and residence time 20 min).

Effect of organic/aqueous (O/A) ratio

The organic/aqueous (O/A) ratio was investigated to achieve a higher copper concentration in the stripped solution and the results are displayed in Figure 6. The copper concentration increased from

0.26 g/L to 4.18 g/L as the O/A ratio was increased from 0.25 to 4.0. The concentration of iron slightly increased as the O/A ratio was increased, reaching a high of 1.27 g/L at an O/A ratio of 4. The stripping efficiency of copper was not significantly affected by the increase in the O/A ratio but maintained a stripping efficiency above 86 per cent.

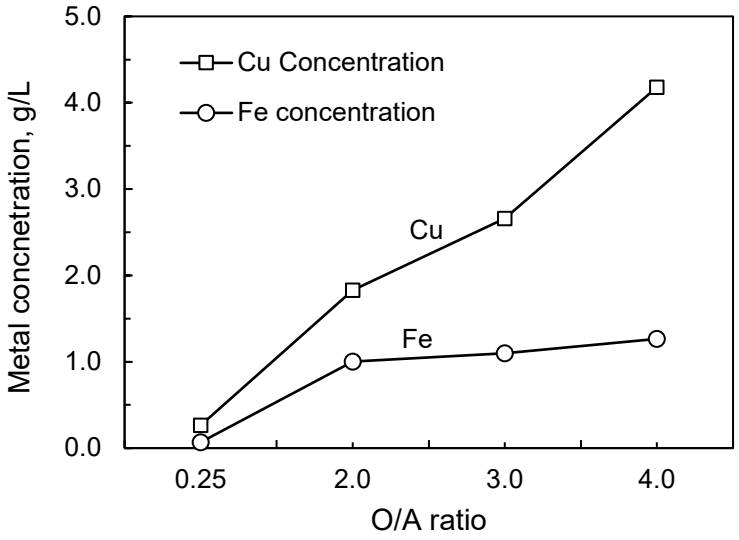

FIG 6 – The effect of the organic/aqueous (O/A) ratio on the concentration of metals in the stripped copper solution. Conditions: H_2SO_4 concentration 175 g/L, stirring speed 400 rev/min, solutions flow rate 15 ml/s, and residence time 20 min).

Two stages of copper extraction and stripping

Two stages of copper extraction and 2 stages of copper stripping were employed to further upgrade the copper concentration in the final stripped solution. The stripped solution obtained under the optimal copper stripping conditions (O/A ratio 4, H_2SO_4 concentration 175 g/L, stirring speed rev/min, solutions flow rate 15 ml/s, and residence time 20 min) was further contacted with a fresh LIX 984N extractant to carry out the second stage of extraction and stripping stages. The conditions of extraction and stripping in the second stages were kept the same as in the first extraction and stripping stages. The copper concentration was successfully upgraded from 4.18 g/L in the first extraction and stripping stages to 22.9 g/L in the second extraction and stripping stages. Moreover, iron concentration was further minimised in the final stripped solution, decreasing from 1.27 g/L to 0.05 g/L in the first and second stripped solution, respectively. The metal concentration of the raffinate (0.4 g/L Cu, 1.57 g/L) obtained from the second stage of copper extraction had a comparable copper concentration to the PLS, therefore it can be recycled back to be blended with the initial PLS feed.

Iron removal

The raffinate solution obtained from the first extraction stage contained 0.303 g/L nickel, 0.125 g/L cobalt, and a higher concentration of iron at 2.52 g/L. Before recovery of nickel and cobalt from the raffinate solution, iron was removed using a calcium carbonate precipitating reagent at a pH of 4. Excellent removal of iron (99.99 per cent) from the solution was achieved, with no residual iron detected by MP-AES. Low co-precipitation of nickel and cobalt was obtained at 3.68 per cent and 2.27 per cent, respectively. The precipitation of iron using calcium carbonate may form iron carbonate solids or a mixture of calcium-iron hydroxides (Bhattacharjee *et al,* 2005). An XRD analysis of the obtained precipitates was carried out and the result is displayed in Figure 7. The main mineral component is shown to be gypsum, while the iron mineral component could not be detected by XRD, indicating that the iron precipitate formed may exist in a colloidal structure, not in a crystalline structure. The precipitate was chemically analysed to contain about 12 wt% Fe.

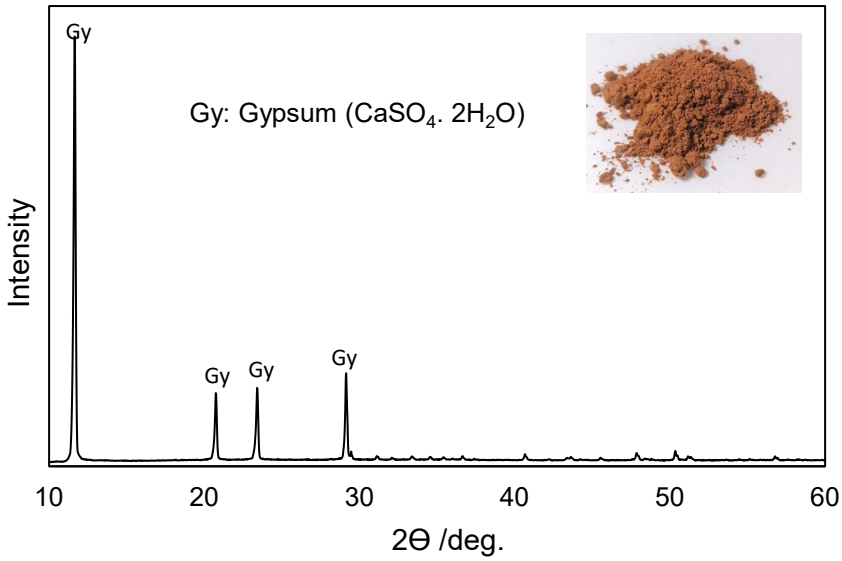

FIG 7 – An XRD pattern of the precipitate obtained after iron removal.

Xanthate complexation of nickel and cobalt

For the recovery of nickel and cobalt from the raffinate solution obtained from the first stage of copper extraction, a xanthate complexation method was used. Potassium amyl xanthate, PAX (potassium-O-pentyl dithiocarbonate), was used as a complexing agent to form complexes of nickel and cobalt xanthates. Nickel and cobalt xanthates form insoluble metal xanthates which are hydrophobic (Yamasaki *et al,* 1963), making it possible to remove nickel and cobalt as xanthate precipitates from the solution. The xanthates' solubility product constant (K_{sp}) is an essential physicochemical parameter affecting the selective extraction of metals in hydrometallurgical methods (Darezereshki *et al,* 2021). Therefore, factors such as the solution pH significantly influence the K_{sp}. Figure 8 shows the complexation behaviour of nickel and cobalt under different pH conditions using PAX as a complexing agent.

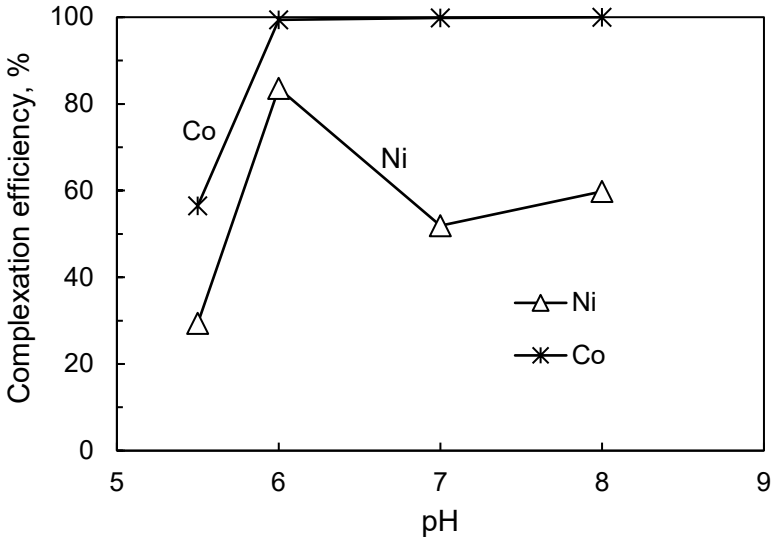

FIG 8 – The effect of pH on the Ni/Co complexation using PAX. Conditions: 50°C, 2 h, 400 rev/min.

The results show that as pH was increased beyond 6, cobalt was completely complexed out of the solution forming cobalt xanthate precipitate. The highest complexation efficiency of nickel achieved was 83.6 per cent at a pH of about 6, while a further increase in pH resulted in a decline in the formation of nickel xanthate. At high pH values, hydroxide ions have been noted to compete with xanthates for metal ions (Zhang *et al,* 2018), and since nickel xanthate is less stable than cobalt xanthate due to its lower K_{sp}, it can easily dissociate resulting in a lower complexation efficiency. Therefore, pH of 6 was selected as the optimum condition for effective complexation of nickel and

cobalt using PAX reagent. The complexation of cobalt and nickel from solution using PAX is suggested to follow reactions (1) and (2) (Vakylabad, Darezereshki and Hassanzadeh, 2021). The balanced reactions (1) and (2) indicate that a PAX dosage corresponding to a xanthate/(Ni+Co) molar ratio of 2 is required to achieve comprehensive complexation of Ni and Co from solution.

$$Ni^{2+} + 2CH_3(CH_2)_4OCS_2K \rightarrow Ni(CH_3(CH_2)_4OCSS)_2 + 2K^+ \quad (1)$$

$$Co^{2+} + 2CH_3(CH_2)_4OCS_2K \rightarrow Co(CH_3(CH_2)_4OCSS)_2 + 2K^+ \quad (2)$$

Separation of nickel and cobalt

For the separation of nickel and cobalt, the difference in their solubility product (K_{sp}) was explored. Since nickel xanthate has a lower solubility product (K_{sp}) than cobalt xanthate (Co (1.0 × 10–13) and Ni (1.4 × 10–12)) (Vakylabad, Darezereshki and Hassanzadeh, 2021), nickel xanthate can therefore be easily dissolved. Additionally, nickel is known to form stable complexes with ammonia (Yang *et al,* 2020), therefore, ammonia solution (NH_3) was used to selectively leach the nickel xanthate complex while cobalt xanthate remained in solid form. The dissolution of nickel xanthate complex using ammonia solution was anticipated to follow the reaction (3). Cobalt was not detected in the wash solution by MP-AES analysis, confirming that almost all cobalt xanthate remained in solid form due to its higher K_{sp}. However, the leaching efficiency of nickel xanthate was marginal, showing only 51 per cent nickel xanthate dissolution when washed with ammonia solution, yielding a nickel ammine solution of 1.6 g/L Ni. The low leaching efficiency of nickel is attributed to the easy hydrolysis of NH_3 to NH_4^+ in an aqueous solution, thereby resulting in insufficient ammonia complexation with Ni^{2+} in the solution (Yang *et al,* 2020).

$$Ni(CH_3(CH_2)_4OCSS)_{2\,(s)} + 6NH_{3(aq)} \rightarrow Ni(NH_3)_6{}^{2+}{}_{(aq)} + 2CH_3(CH_2)_4OCSS^-{}_{(aq)} \quad (3)$$

Thermal decomposition of cobalt xanthate precipitate was carried out in a muffle furnace at 220°C for 1.5 hrs. The XRD pattern of the calcined product is shown in Figure 9. Cobalt xanthate decomposed to form cobalt oxide (CoO) product, which was chemically analysed to be 25 wt% Co. Due to a high nickel carry-over from the ammonia washing stage, nickel xanthate was transformed into nickel sulfide (NiS) as detected by XRD. The nickel content in the calcined product was chemically analysed to be 10.5 wt% Ni.

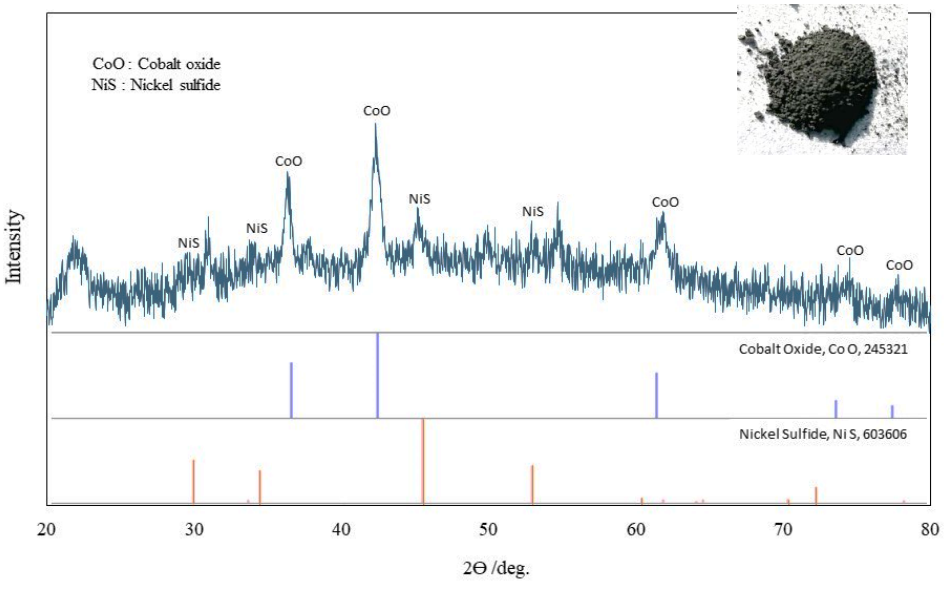

FIG 9 – An XRD pattern of the calcined product obtained after nickel and cobalt xanthates thermal treatment.

CONCLUSION

This study presents a combination of various separation techniques to selectively separate metal ions from the pregnant leach solution (PLS) and upgrade the content of the metals from the dilute PLS. The general findings obtained from the three main processes (solvent extraction, precipitation, and xanthate complexation) investigated can be concluded as follows:

1. Solvent extraction
    - About 97 per cent of copper can be selectively extracted from the PLS at pH 2, with minimum co-extractions of Fe, Ni, and Co, using LIX 984N (10 per cent v/v) extractant. A 175 g/L sulfuric acid solution can effectively strip copper from the organic extractant.
    - Utilising a combination of two extraction stages and two stripping stages, copper concentration in the PLS was remarkably upgraded from 0.3 g/L Cu to 23 g/L Cu with a very low impurity content concentration of 0.05 g/L Fe and no Ni and Co co-extraction in the second stage.
2. Iron removal
    - More than 99 per cent of iron was precipitated at pH 4 by the addition of a calcium carbonate ($CaCO_3$) suspension, with low co-precipitation of nickel and cobalt of around 3.68 per cent and 2.27 per cent, respectively.
3. Xanthate complexation
    - Utilising potassium amyl xanthate (PAX) solution, a pH of around 6 can effectively complex about 83.6 per cent of nickel and 99.4 per cent cobalt from the raffinate solution forming stable Ni and cobalt xanthate precipitates.
    - Due to a higher solubility constant (K_{sp}) of cobalt xanthate, more than 99 per cent Co successfully remained as cobalt xanthate precipitate during the selective dissolution of nickel xanthate using ammonia solution.
    - Thermal treatment of nickel and cobalt xanthate precipitates at 220°C for 1.5 h converted Ni and Co to be recovered as CoO and NiS solids.

This study demonstrates that dilute leach solutions obtained after the extraction of valuable metals from waste materials or low-grade materials can be significantly upgraded by employing various hydrometallurgical processes to qualify them for upstream processing. Therefore, the utilisation of waste materials, such as smelter slag, as a secondary source of valuable metals can be considered viable. More so in the future, as the demand for base metals continues to increase, similarly the metal prices will significantly increase, making the processing of waste and/or low-grade metal sources economically feasible.

ACKNOWLEDGEMENTS

The authors are grateful for the financial support of the Program for Leading Graduate Schools ‘New Frontier Leader Program for Rare Metals and Resources’ and Akita University Support for Fostering Research Project.

REFERENCES

Baghalha, M, Papangelakis, V G and Curlook, W, 2007. Factors affecting the leachability of Ni/Co/Cu slags at high temperature. *Hydrometallurgy,* 85:42–52.

Banza, A N, Gock, E and Kongolo, K, 2002. Base metals recovery from copper smelter slag by oxidizing leaching and solvent extraction. *Hydrometallurgy,* 67:63–69.

Bhattacharjee, S, Gupta, K K, Chakravarty, S, Thakur, P and Bhattacharyya, G, 2005. Separation of Iron, Nickel, and Cobalt from Sulfated Leach Liquor of Low Nickel Lateritic Oxide Ore. *Separation Science and Technology,* 39:413–429.

Darezereshki, E, Vakylabad, A B, Hassanzadeh, A, Niedoba, T, Surowiak, A and Koohestani, B, 2021. Hydrometallurgical Synthesis of Nickel Nano-Sulfides from Spent Lithium-Ion Batteries. *Minerals,* 11.

Godirilwe, L L, Magwaneng, R S, Sagami, R, Haga, K, Batnasan, A, Aoki, S, Kawasaki, T, Matsuoka, H, Mitsuhashi, K, Kawata, M and Shibayama, A, 2021. Extraction of copper from complex carbonaceous sulfide ore by direct high-pressure leaching. *Minerals Engineering,* 173.

Huang, F, Liao, Y, Zhou, J, Wang, Y and Li, H, 2015. Selective recovery of valuable metals from nickel converter slag at elevated temperature with sulfuric acid solution. *Separation and Purification Technology,* 156:572–581.

Huang, K, Li, Q-W and Chen, J, 2007. Recovery of copper, nickel and cobalt from acidic pressure leaching solutions of low-grade sulfide flotation concentrates. *Minerals Engineering,* 20:722–728.

Keber, S, Brückner, L, Elwert, T and Kuhn, T, 2020. Concept for a Hydrometallurgical Processing of a Copper-Cobalt-Nickel Alloy Made from Manganese Nodules. *Chemie Ingenieur Technik,* 92:379–386.

Kursunoglu, S, Ichlas, Z T and Kaya, M, 2017. Solvent extraction process for the recovery of nickel and cobalt from Caldag laterite leach solution: The first bench scale study. *Hydrometallurgy,* 169:135–141.

Li, Y, Perederiy, I and Papangelakis, V G, 2008. Cleaning of waste smelter slags and recovery of valuable metals by pressure oxidative leaching. *J Hazard Mater,* 152:607–15.

Parhi, P and Sarangi, K, 2008. Separation of copper, zinc, cobalt and nickel ions by supported liquid membrane technique using LIX 84I, TOPS-99 and Cyanex 272. *Separation and Purification Technology,* 59:169–174.

Perez, I D, Anes, I A, Botelho Jr, A B and Espinosa, D C R, 2020. Comparative study of selective copper recovery techniques from nickel laterite leach waste towards a competitive sustainable extractive process. *Cleaner Engineering and Technology,* 1.

Schlesinger, M E, King, M J, Sole, K C and Davenport, W G, 2011. *Extractive Metallurgy of Copper,* The Netherlands, Elsevier.

Shakibania, S, Mahmoudi, A, Mokmeli, M and Rashchi, F, 2020. The effect of the chloride ion on chemical degradation of LIX 984N extractant. *Minerals Engineering,* 159.

Shirayama, S and Uda, T, 2015. Separation of Nickel and Cobalt Utilizing Selective Reduction of Nickel in Acidic Aqueous Solution. *Materials Transactions,* 56:340–347.

Sridhar, V and Verma, J K, 2011. Extraction of copper, nickel and cobalt from the leach liquor of manganese-bearing sea nodules using LIX 984N and ACORGA M5640. *Minerals Engineering,* 24:959–962.

Takahashi, K and Nii, S, 1999. Behaviour of multistage mixer-settler extraction column. *Memoirs of the School of Engineering, Nagoya University,* 51.

Vakylabad, A B, Darezereshki, E and Hassanzadeh, A, 2021. Selective Recovery of Cobalt and Fabrication of Nano-Co3S4 from Pregnant Leach Solution of Spent Lithium-Ion Batteries. *Journal of Sustainable Metallurgy,* 7:1027–1044.

Yamasaki, T, Shimoiizaka, J, Sasaki, H and Ohyama, T, 1963. Utilization of Xanthate as a Selective Precipitant for Nickel and Cobalt Ions (2nd Report). *Journal of the Mining Institute of Japan,* 79:97–104.

Yang, Y, Liu, F, Song, S, Tang, H, Ding, S, Sun, W, Lei, S and Xu, S, 2020. Recovering valuable metals from the leaching liquor of blended cathode material of spent lithium-ion battery. *Journal of Environmental Chemical Engineering,* 8.

Zhang, Y-H, Wu, L-M, Huang, P-P, Shen, Q and Sun, Z-X, 2018. Determination and application of the solubility product of metal xanthate in mineral flotation and heavy metal removal in wastewater treatment. *Minerals Engineering,* 127:67–73.

Flow sheet development for treatment of rare earth ores

M S Henderson[1], R D Alorro[2] and L G Dyer[3]

1. Post-graduate Research Student, Western Australia School of Mines: Minerals, Energy and Chemical Engineering, Curtin University, Kalgoorlie, WA 6430. Email: Mark.S.Henderson@student.curtin.edu.au
2. Senior Lecturer, Western Australia School of Mines: Minerals, Energy and Chemical Engineering, Curtin University, Kalgoorlie Campus, WA 6430.
3. Associate Professor, Western Australia School of Mines: Minerals, Energy and Chemical Engineering, Curtin University, Kalgoorlie, WA 6430. Email: Laurence.Dyer@curtin.edu.au

ABSTRACT

An alternative leaching system for rare earth element recovery from monazite is under development. The initial stage utilises oxalic acid to convert the rare earth phosphate into an oxalate salt through dissolution and reprecipitation and it is the efficiency of this stage that governs the overall recovery achieved. It has previously been proposed that lixiviant consumption is the primary limitation in this process.

This work further investigates a range of conditions in an attempt to further elucidate the factors influencing the achievable conversion in this stage. It has been shown that the pH may be governed by multiple reactions both consuming and producing acid (thus the mild change over time). The importance of proper mixing and potential to operate at lower temperature with only moderate impact on kinetics has also been demonstrated. Staged/sequential leaching is more effective in fresh solution as opposed to restoring the lixiviant concentration with subsequent reagent addition, suggesting some impact of solution composition. However, contrary to previous findings, subjecting the leach residue to fresh solution resulted in significant decline in leach rate and overall dissolution. This may be because a greater proportion of conversion was achieved in stage 1 in this work than in previous investigation. This may indicate that eventual passivation or the presence of some more refractory REE minerals limits dissolution. Iron dissolution was relatively consistent upon exposure to fresh solution, displaying the ability of the solution to continue to leach the goethite component of the concentrate.

INTRODUCTION

Rare earth elements (REEs) are a crucial component of many technologies, particularly those relating to renewable energy generation (Baolu *et al*, 2017). As such the demand is growing rapidly and is projected to continue growing into the future as these technologies become more prevalent in society. These elements are considered critical not only because of their utilisation, but the risk to supply given the vast majority of global reserves and production originates from China (Chen *et al*, 2018). As such, exploitation of resources outside China have received significant attention. Increasingly, alternatives to conventional processes are being considered for challenging orebodies and waste streams to maximise REE resource utilisation.

Studies conducted at Curtin University have considered the use of various organic acids for disintegration of phosphate mineralisation containing the rare earth elements (REE) (Lazo *et al,* 2017). These minerals are attacked and disintegrated by treatment with these acids, with oxalic acid showing considerable promise in this regard, offering the potential to provide an alternative option for REE production. While investigations have centred on treatment of existing concentrates that are amenable to conventional sulfuric acid bake and water leach technology, the ultimate objective for this process is more likely a niche application where ore or concentrate that is not particularly suited or responsive to conventional treatment or where significant non-recoveries are experienced.

Oxalic acid treatment attacks and breaks down rare earth phosphate mineral structures, releasing phosphorus to solution. The reaction indicated, using RE to signify rare earth element, was proffered as that given in Equation 1 (Lazo *et al*, 2017).

$$2REPO_{4\,(s)} + 3H_2C_2O_4\,(aq) \longrightarrow RE_2(C_2O_4)_{3\,(s)} + 2H_3PO_{4\,(aq)} \quad (1)$$

The insolubility of REE oxalates results in precipitation and collection with the mineral residue. Phosphoric acid is also generated in this reaction.

The solids once separated from the acidic solution are further processed to recover REE, which in this case has successfully used ethylene diamine tetra acetic acid (EDTA) with solution pH elevated to around ten to achieve solubilisation. The use of EDTA alone without the oxalic acid treatment was claimed to not significantly solubilise REE components. It is worth noting that the extent of REE solubilisation in EDTA closely corresponded with the degree of solubilisation of phosphorus in the oxalic acid treatment step. Hence, phosphate concentrations provided a reasonable predictor for the degree of REE release from phosphate mineralisation in the previous endeavours.

Testing also demonstrated that insoluble rare earth hydroxides can then be formed and these, once resolubilised, would be suitable as feed to conventional solvent extraction. A high-level overview of proposed processing has been developed (Lazo *et al*, 2018), but significant efforts are required to develop a processing flow sheet upon which technical and economic valuation could be based.

A key finding from reviewing the initial endeavours is the complex nature of the oxalic acid leach system. Oxalic acid attacked the phosphate mineral at all temperatures. Iron was also dissolved from iron oxides during the oxalic acid treatment. At 25°C the reactions proceeded slowly with only about 13 to 14 percent phosphorus release over 24 hours, with very little iron reporting to solution. At 65°C, a greater extent of phosphorus was released than at 25°C, rising to approximately 30 percent, and iron dissolution too was far greater, closing in on 22 percent dissolution. A notable result was achieved at 85°C, with far greater iron dissolution near 39 percent but less phosphorus release than at 65°C. Overall, the initial results indicated only around 30 percent of the phosphate mineral was attacked by the oxalic acid solution in a single contacting in these series of tests. Iron dissolution increased in line with increased temperature.

Phosphorus and iron are the two major components identified as dissolved by the oxalic acid treatment. In the initial work, iron dissolution reactions were not put forward, but such could be contemplated as provided in Equations 2 and 3.

$$2Fe_2O_{3\,(s)} + 3H_2C_2O_{4\,(aq)} \longrightarrow Fe_2(C_2O_4)_{3\,(aq)} + 2H_2O \quad (2)$$

$$2FeOOH_{\,(s)} + 3H_2C_2O_{4\,(aq)} \longrightarrow Fe_2(C_2O_4)_{3\,(aq)} + 4H_2O \quad (3)$$

These imply an acid consumption response which should lead to increasing solution pH levels. Interestingly, changes in solution pH were less at 65°C and 85°C than at 25°C. Contrary to expectations, the greatest increase in solution pH occurred at the lower temperature of 25°C, the testing with the lowest extent of iron release to solution. Hence, the only minor changes in acidity did not conform particularly well with the iron reactions presented.

The complexity of the system requires greater attention to the mechanisms that limit recovery, these could be soliubility limits of dissolved species, consumption of the lixiviant, passivation through REE reprecipitation, pH alterations or a combination thereof.

OTHER INVESTIGATIONS USING OXALIC ACID OR PHOSPHORIC ACID

The complex nature of the oxalic acid leach system implied by the response in the initial testing directed the need to investigate and establish the types of reactions and behaviours of other minerals seen in other works with this acid. As phosphoric acid is an implied product of the oxalic acid leach, it was deemed appropriate to also investigate the use of this acid in other mineral processing applications. An assortment of materials have been subjected to experimentation using these acids, with some of these investigations as listed in Tables 1 and 2 for oxalic acid and phosphoric acid respectively.

TABLE 1

Oxalic acid investigations treating other materials.

Resource	Investigation	References
Clay	Fe removal	Lee *et al*, 2006*,* 2007; Taran *et al*, 2015
Kaolin	Fe removal	Martinez-Luevanos *et al*, 2011
Feldspar	Fe removal	Pariyan *et al,* 2019
Silica sands	Fe removal	Veglio *et al*, 1999
Red mud	Fe removal	Yu *et al,* 2012
Manganese ores and residues	Mn recovery	Sahoo *et al*, 2001; Deng *et al*, 2018; Baba *et al*, 2020; Soner, 2020
Uranium ore	U recovery, Mn and REE release	Xu *et al*, 2019
Phosphate rock	P, REE recovery	Bakry *et al*, 2020
Coal	V recovery	Hu *et al*, 2017
Magnet scrap	REE recovery	Liu *et al,* 2020; Sinha *et al*, 2017
Spent batteries	Li, Ni, Co and Mn recovery	Zeng *et al*, 2015; Refly *et al*, 2020

TABLE 2

Phosphoric acid investigations treating other materials.

Resource	Investigation	Reference
Phosphate rock	P, REE recovery	Stone *et al*, 2016; Jin *et al*, 2017; Liang *et al*, 2017; Soltani *et al,* 2019; Bandara and Senanayake*,* 2019; Wu *et al*, 2019a, 2019b; Li *et al*, 2021
Iron oxides	Response to phosphoric acid	Beltran *et al*, 2009
Kaolin	Fe removal	Hernandez-Hernandez *et al*, 2015
Quartz sands	Fe removal	Zhang *et al*, 2012
Red mud	Fe removal	Pepper *et al*, 2016
Magnet scrap	REE recovery	He *et al*, 2021

A common theme relating to phosphoric acid treatment of phosphate rock was reprecipitation of phosphorus from solution as temperature was elevated. This is a proposed procedure for recovery of REE. Elevation of temperatures from ambient to around 90°C was described as a route for isolation of REE, either by concentration to mineral residue for subsequent recovery (Bandara and Senanayake*,* 2019; Li *et al*, 2021; Soltani *et al*, 2019; Stone *et al*, 2016) or by direct precipitation from solution as an isolated REE residue (Wu *et al,* 2019a*,* 2019b). Re-formation of REE phosphates, essentially reversing the phosphorus dissolution implied in Equation (1) was the proffered explanation. A representation of such re-precipitation is provided in a simplistic reaction (Equation 4).

$$RE^{3+} + H_3PO_4 \longrightarrow REPO_{4\,(s)} + 3H^+ \quad (4)$$

Phosphoric acid solution is also capable of attacking iron oxides with formation of both ferric and ferrous phosphate complexes (Hernandez-Hernandez *et al*, 2015). Both ferrous and ferric ions are

typically soluble in phosphate solution, with a range of compounds and complexes possible, such as $FePO_4$, $FeHPO_4^+$ and $FeH_2PO_4^{2+}$, or $Fe_3(PO_4)_2$ and $Fe(H_2PO_4)_2$ for instance. Dissolution of iron oxides in phosphoric acid solution could be expected to be acid consuming reactions.

Iron oxide reactions in oxalic acid have also been investigated. A pertinent finding was that hematite in oxalic acid solution, typically at elevated temperatures, results in a reductive leach reaction described by Equation 5 (Lee *et al*, 2006*,* 2007).

$$H^+ + Fe_2O_3 + 5HC_2O_4^- \longrightarrow 2Fe(C_2O_4)_2^{2-} + 3H_2O + 2CO_2 \quad (5)$$

Disintegration of the iron oxide resulted in ferrous oxalate as well as the generation of carbon dioxide, thus destroying oxalate. It was indicated that both hematite and maghemite reacted in this manner, while goethite and lepidocrocite reacted through acid consumption and generation of soluble ferric ion. The reductive leach would result in ferrous ion formation and ferrous oxalate is typically described as insoluble. However, the authors predictive modelling indicated soluble ferrous oxalate with iron concentrations up to 0.1 M in solutions with pH less than 2.

The potential for acid generation from iron dissolution, ferrous ion formation and stable ferrous oxalate solution species was also identified in other sources (Veglio *et al*, 1999). These results speak to the observed pH changes during oxalic acid leaching of the samples in question, as well as highlighting the complexation and reprecipitation of iron oxalate species as possible limitations to REE dissolution, along with oxalate loss as carbon dioxide. The array of metals dissolved in the process of converting the REE phosphate to oxalate may also play a role in oxalic acid consumption, limiting access of the leach solution to remaining monazite in the sample or modification of the pH and Eh.

This paper further investigates the impact of temperature, additional oxalic acid entering the system over time and monitors other metals in solution in an attempt to elucidate the reactions occurring in the system.

EXPERIMENTAL

The approach to flow sheet development has been to conduct experiments that centre on examination of the response of the two main components, phosphorus and iron, which are solubilised in the oxalic acid contacting step. These have examined the influence of temperature on the reactions occurring, residence time and the degree of agitation provided, as measured by dissolution of these two components.

In the first instance, the same flotation concentrate as used in Lazo *et al* (2017) was treated in the work presented here. This was done to allow correlation with the previous results and provide an initial sample with consistent composition (given in Table 3).

TABLE 3

Elemental composition of concentrate as stated in Lazo *et al* (2017).

Element	Grade (wt%)
Ce	14.36
Fe	16.25
La	8.65
Nd	3.32
P	7.24

Leaching experiments were conducted in a 2.5 L stainless steel, baffled reactor with a water jacket to achieve and maintain temperature. A three blade impeller was driven by overhead stirrer at 550 rev/min, unless otherwise stated, was used to suspend the solids and ensure effective solid/liquid mixing. Standard experiments utilised a pH of 1, oxalic acid concentration of 0.8 M, solids concentration of approximately 100 g/L and reaction time of 24 hours. Experiments involved varying

several conditions: temperature (ambient to 65°C), stirrer speed (up to 705 rev/min), and retention time (up to 96 h).

Staged/sequential leaching experiments were also conducted, these involved two modes: introducing additional oxalic acid to the current leach solution and collecting a dry residue from one stage of leaching and subjecting it to fresh oxalic acid with the same initial conditions. These were used to examine whether the limitation is due to the solution factors (solubility limits of dissolved species or reagent consumption) or solid factors (passivation). Samples were collected over time and immediately filtered upon collection, these were analysed with ICP-OES using an Agilent Technologies 5100 instrument.

RESULTS AND DISCUSSION

Leaching of two main components, phosphorus and iron, obtained in the previous test work with a flotation concentrate are presented in Figure 1. The values for the earlier results have been extrapolated from the original graphs (Lazo *et al*, 2017). These curves are presented along with the results of the first test conducted in this series of experiments. All the work was conducted on flotation concentrate reportedly having particle size P_{80} of 83 µm.

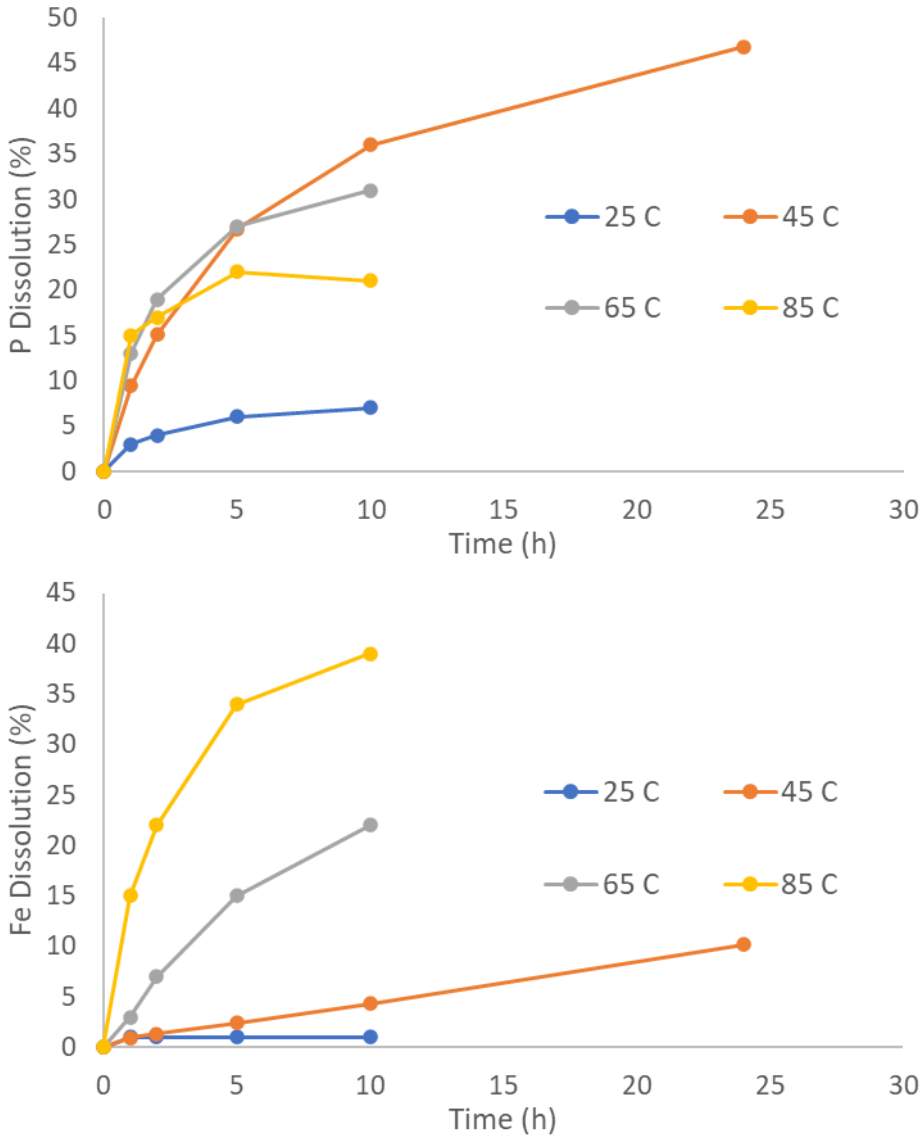

FIG 1 – Results from initial test with baffled tank reactor, 45°C, compared with previous results using different reactors at 25°C, 65°C and 85°C.

These results demonstrate that the baffled tank reactor is suitable for conducting the oxalic acid leaching process. Interestingly, the 45°C results for phosphorus dissolution in the initial two hour

window of operation were comparable to those achieved at both 65°C and 85°C in a different unbaffled reactor. After approximately five hours, the results demonstrated superior phosphorus release to solution than previously achieved at the two higher temperatures. The stalling of the reaction at 85°C in the initial test work after about four hours is evident.

While not initially as rapid, the P dissolution achieved at 45°C was comparable or surpassed that previously reached at both 65°C and 85°C. It's likely that the improved mixing in the baffled tank contributes to this result. Interestingly, while iron dissolution in the current experiment is much lower than seen at higher temperatures, it also continues linearly over an extended period of time rather than a decline in reaction rate over time previously observed. This suggests the rate controlling step is not affected in 96 hours at 45°C be that a reagent consumption or solubility-related phenomenon.

The next series of experiments were conducted with the intention of identifying the influence of temperature on the reaction, the potential to increase phosphorus release through the use of longer residence times, and to also have a preliminary understanding of the influence of the degree of agitation on leach performance. Results of this work are summarised in Table 4.

TABLE 4

Phosphorus and iron release from flotation concentrate in treatment with oxalic acid.

Test	rev/min	Hour	P Dissolution	Fe Dissolution
C1 45°C	545	1	10	1
		2	15	1
		5	27	2
		10	36	4
		24	47	10
C2 65°C	545	1	18	3
		2	26	5
		5	39	14
		10	45	26
		24	50	45
C3 45°C	551	1	9	1
		2	15	1
		5	26	2
		24	45	10
		48	51	18
		72	52	23
		96	55	29
C4 45°C	705	1	10	1
		2	14	1
		5	27	2
		24	45	9
		48	50	18
		72	51	24

These experiments further demonstrate the superior performance of the baffled reactor, achieving better recoveries again at 65°C, however increasing stirring speed had no additional benefit to the outcome. Over the extended time period, again the initial rapid kinetics at 65°C the P dissolution slowed rapidly and converged with the 45°C reaction extent. This may be that the equilibrium limiting reaction extent is reached more rapidly, or that the much greater extent of iron dissolution (more than four times faster) limits leaching to a greater extent. Without data for a much greater period of time this is unknown.

Subsequent experiments were conducted to understand the impact of oxalate availability to the reaction over time. Conducting the leach at 30°C, additional solid oxalic acid was added to the system in excess to determine whether this was an appropriate method for continuing the leach. This was conducted commencing with a concentration of 0.8 M acid, adding a further 0.75 M after 24 hours and then another 0.5 M equivalent after 48 hours of reaction. These are presented in Figure 2 as subsequent stages at 30° (ie Stage 1: 0–24 h @ 0.8 M, Stage 2: 24–48 h @0.8 + 0.75 M and Stage 3: 48–72 h @ 0.8 + 0.75 + 0.5 M).

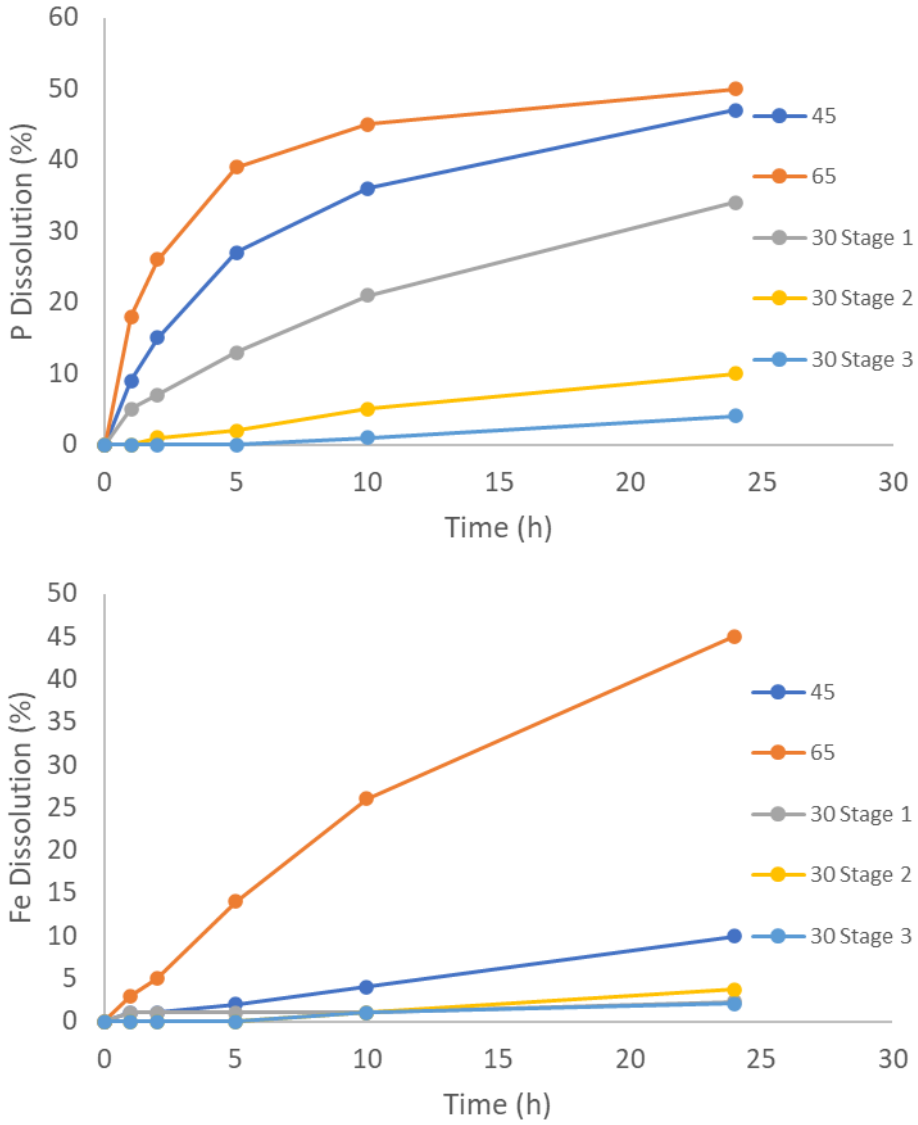

FIG 2 – Oxalic acid leaching at different temperatures and three stages at 30°C.

As anticipated, the leach at 30°C was slower again than that at 45°C and thus was more linear in rate over the 24 h. However, when additional oxalic acid was added, the subsequent 24 h periods showed significantly decreased reaction rates only achieving an additional 10 and 4 per cent P dissolution respectively. There are multiple potential reasons for this, the first being that saturation of the solution with respect to oxalic acid (solubility of ~1 M at ambient conditions) actually slows the

reaction, possibly through precipitation of other phases. Another possibility is the increasing dissolved ions in solution over time decreased the reaction extent, perhaps approaching solubility limits. However, if this is the case, then reactions at higher temperatures should have reached maximum recoveries faster and at lower overall P concentrations in solution.

A similar approach was conducted using the residue from prior tests at 45°C by re-immersing them in collected filtrate with additional make-up oxalic acid (0.8 M). This was again conducted multiple times (Figure 3). The major difference being that due to losses in solid-liquid separation the solids loading of each subsequent step decreased notably. These were effectively 100 g/L in stage 1, 75 g/L in stage 2 and 50 g/L in stage 3. While the premise of the experiment was the same the lower solids loading may promote a greater degree of leaching.

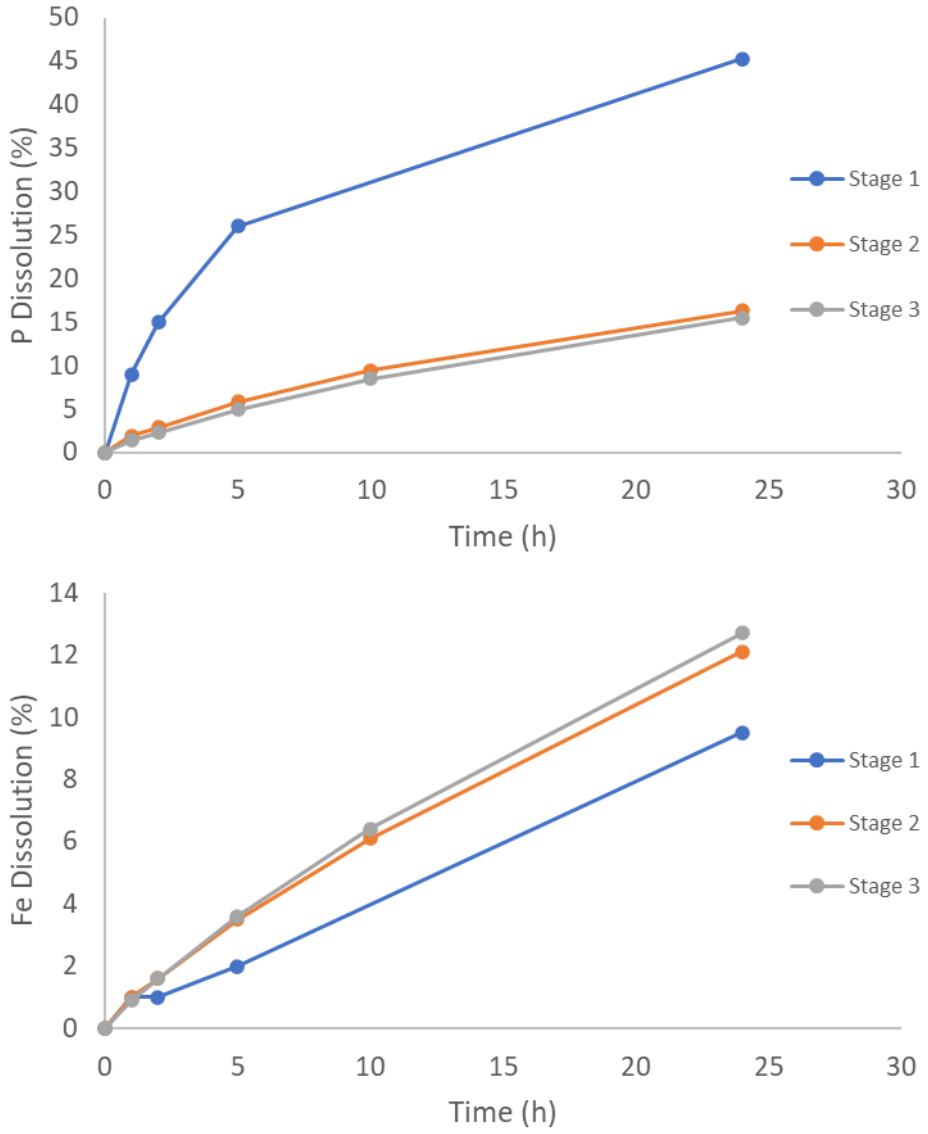

FIG 3 – Oxalic acid leaching in three stages at 45°C.

While a similar trend was observed in that there was a large decline in the P dissolution rate from stage 1 to stage 2, the further drop to stage 3 was minimal. As mentioned, this may be due to solids loading, or the elevated temperature. The overall P release achieved was in excess of 75 per cent, suggesting the 47 per cent reached in three stages at 30°C was unlikely due to increasing concentrations of dissolved ions. It may be somewhat related to the oxalate saturation, however, as the higher temperature promotes more rapid consumption of the lixiviant. This is underlined by the iron dissolution which is several times greater than that at 30°C. Interestingly, the iron dissolution rate increased marginally between the stages, again most likely due to the lower solids concentration of the slurry.

To further understand the impact of solids concentration, a single test was conducted at 200 g/L solids at 45°C (Figure 4). As expected, and in line with previous findings, the leach rate as a proportion of the P present in the sample mass decreased as did iron after some time. This aligns with the observation above regarding improved leach performance with lower solids loading.

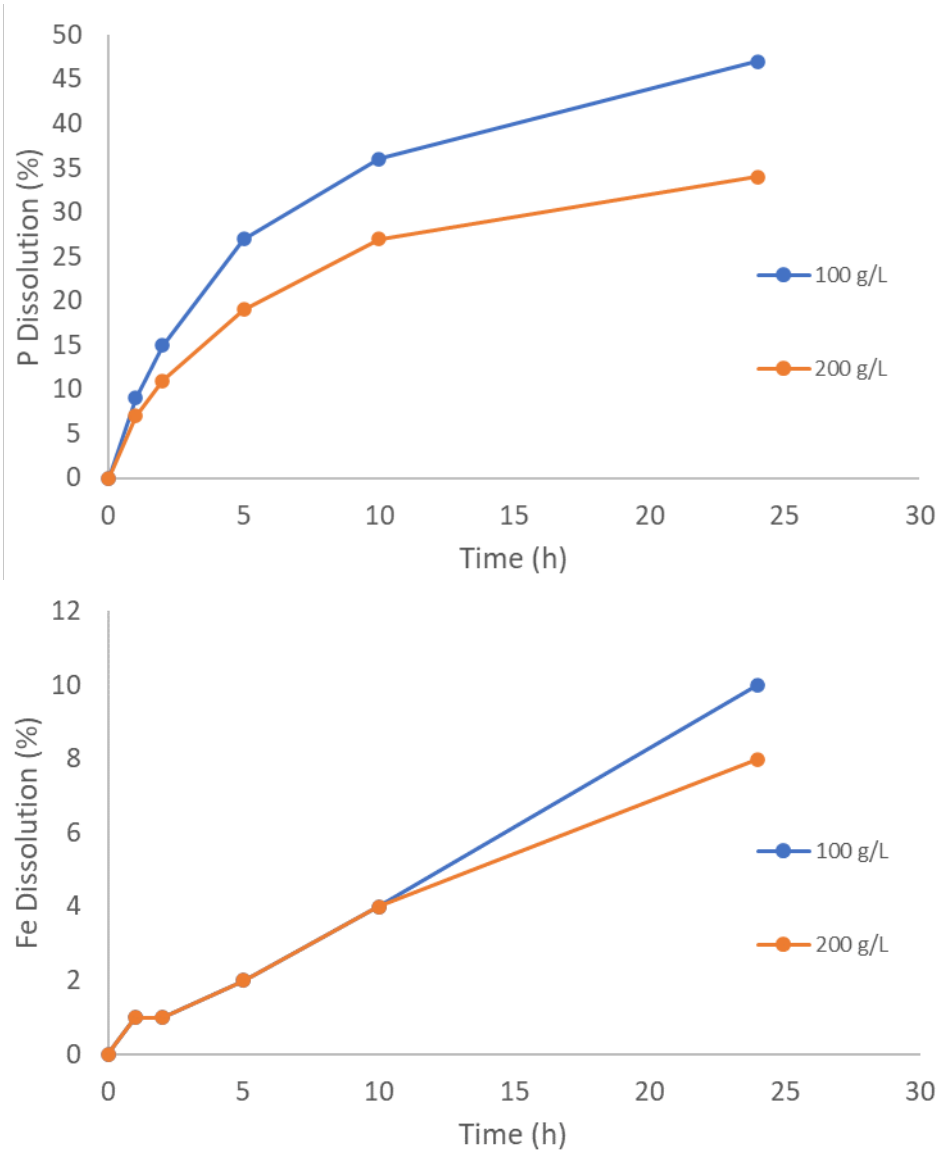

FIG 4 – Single stage oxalic acid leaching at different solids loadings at 45°C.

One aspect of leaching of interest that was observed during this work were the solution pH values. In these tests, once concentrate was added, the pH typically dropped and then tended to increase over time as the test continued. While problems were experienced in obtaining properly buffered values and drift commonly occurred between samples so that only the trends should be noted, the results are consistent with an acid generation type reaction occurring, this potentially relatable to iron dissolution as proffered above. Results are provided in Table 5. The largest pH decrease can be seen relating to the 65°C test, this having the greatest degree of iron dissolution.

TABLE 5

Solution pH trends during oxalic acid treatment.

Test	Hour					
	0	1	2	5	10	24
45°C C1 Stage I	1.0	0.9	0.9	0.9	0.9	1.1
65°C C2 Stage I	0.9	0.8	0.8	0.8	0.8	0.7
45°C C3 Stage I	1.0	0.9	0.9	0.9	1.0	1.0
45°C C4 Stage I	1.1	1.0	1.1	1.0		1.0
45°C C5 Stage II	1.0	0.9	0.9	0.9	0.9	1.0
30°C C6 Stage I	1.1	1.2	1.2	1.1	1.2	1.0
30°C C6 Stage II	1.0	0.9	1.2	1.1	1.2	0.9
30°C C6 Stage III	0.9	0.9	1.1	1.1	1.1	0. 9
45°C C7 Stage II	0.9	0.9	0.9	0.9	0.9	0.9
45°C C9 Stage III	1.0	1.0	1.1	1.0	1.1	1.1
45°C C8 Stage I	0.8	0.8	0.9	0.9	0.9	1.2

The zero hour pH measurement was prior to addition of concentrate.

REE concentrations in the oxalic acid solutions used in these tests remained at low levels. Maximums of around 20 ppm were seen for lanthanum and cerium in the 65°C test, otherwise they were typically less than 10 ppm. This is in line with the previous observations that REE oxalate precipitates were formed. Testing is underway with EDTA to confirm resolubilisation occurs and that the use of phosphorus concentrations are indicative of REE phosphate mineral disintegration through the oxalic acid contacting.

The results for several other elements in the first stage oxalic leach were obtained. Given the limited testing to date, some caution is warranted in examining the values presented, but there are interesting trends. These can be seen in Figure 5.

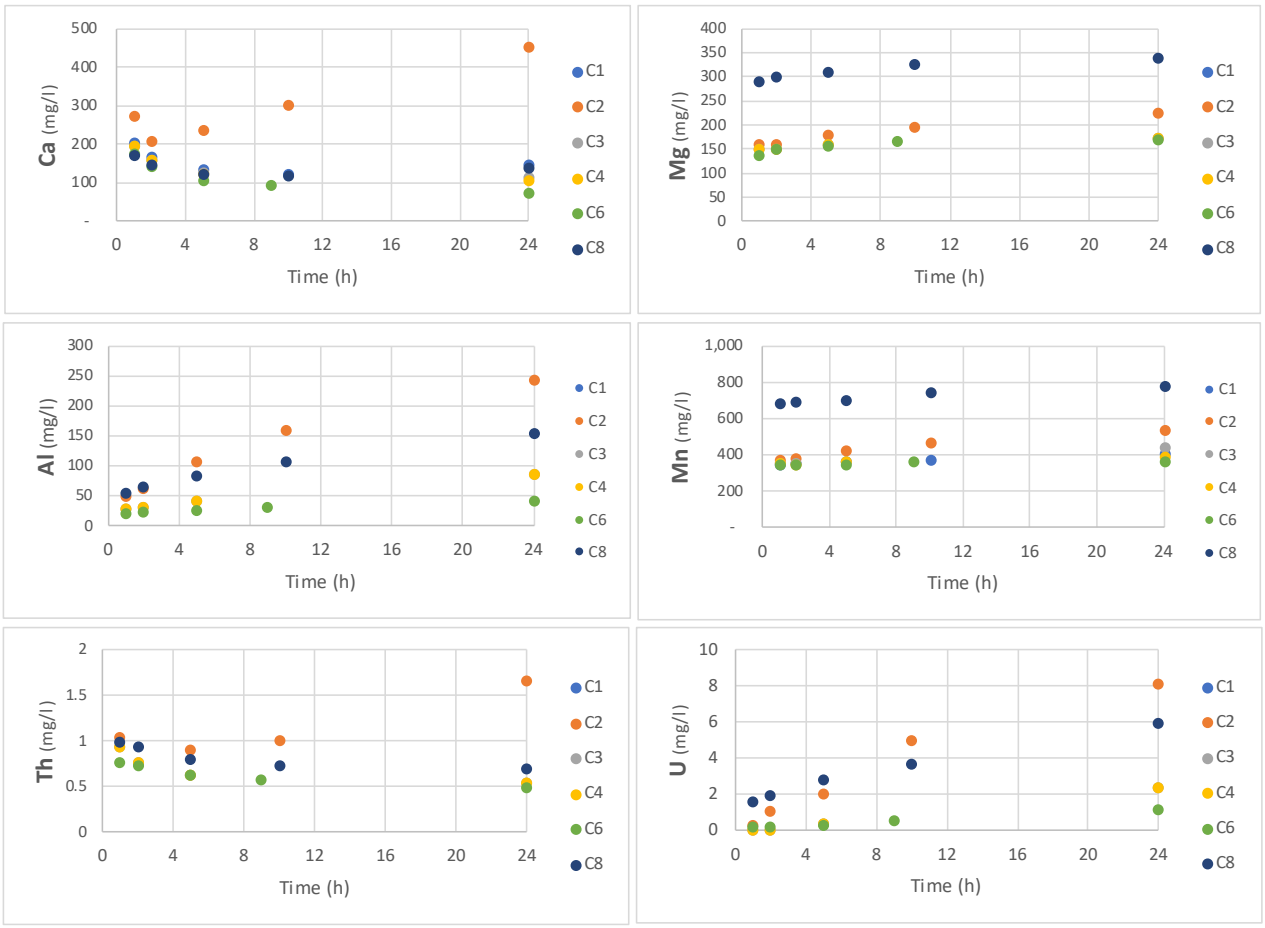

FIG 5 – Concentrations of various other elements in solution.

Calcium, magnesium and thorium rapidly reached moderate levels and then plateaus which agrees with the solubilities of their respective oxalate salts. Manganese displayed similar behaviour but should be moderately soluble in weak acids. There was a slight increase in dissolution over time suggesting a proportion of the Mn is being exposed slowly during leaching of other components of the concentrate, perhaps the iron phases. In any case, available Mn is rapidly leached in this system.

Aluminium dissolves relatively slowly but quite linearly over the leach duration in a similar vein to iron. Uranium display similar behaviour but at very low levels, indicating that the radioactive components may actually behave quite differently in the leach systems. While these present limited insight into rare earth conversion and phosphate dissolution, they are very important for environmental and safety concerns around radioactive material and impurity separation and byproduct generation as the overall composition of the leach solution wil govern how effective those approaches are.

CONCLUSIONS

Oxalic acid is capable of dissolving REE phosphate mineralisation present in a REE flotation concentrate, releasing phosphorus to solution while the REE remain in the residue. An operating temperature of 45°C produced favourable results with the experimental apparatus used here, essentially matching and in some cases bettering results achieved at higher temperatures in earlier work with an unbaffled reactor, at least for a single stage of leaching.

Results to date have been consistent with the requirement to operate with a multi-staged cross-flow leach approach, but have only realised around 77 percent overall phosphorus mineral decomposition as measured by phosphorus concentrations in solution. Efforts are underway to evaluate whether further improvements can be achieved.

Potential phosphorus release mechanisms and solubility limitations relating to temperature and phosphorus (phosphate) concentrations are in accord with findings elsewhere. Similarly, iron

dissolution through a combination of acid consumption and acid generation mechanisms appears to account for the reaction response, where this is in accord with results obtained in other works by various investigators.

ACKNOWLEDGEMENTS

This research is supported by an Australian Research Training Program (RTP) Scholarship.

Special thanks go to personnel at Curtin University, Western Australia School of Mines (WASM), including Associate Professor Laurence Dyer for advice, equipment supply and technical assistance, and to Mujesira Vukancic for obtaining necessary experimental apparatus and completion of the ICP-OES solution analyses.

REFERENCES

Baba A A, Abdulkareem A Y, Raji M A, Adebayo S A, Alabi A G A, Ghosh M K, Hariprasa D, Adeyemi C O, 2020. Quantitative reductive leaching of a low-grade spessartine ore in acidic media. *Int. J. of Environmental Analytical Chemistry Volume 100, No. 6* (2020) 635–646.

Bakry A R, Hashima M D, Elwya A M, 2020. Thermodynamic and Kinetic Studies of Uranium and REEs Leaching by Oxalic Acid from Abu-Tartur Phosphate Rock, Western Desert, Egypt. *Radiochemistry Vol. 62, No. 3* (2020), 359–367.

Bandara A M T S, Senanayake G, 2019. Dissolution of calcium, fluoride and rare earth elements (REEs) from a disc of natural fluorapatite mineral (FAP) in perchloric, hydrochloric, nitric, sulphuric and phosphoric acid solutions: A kinetic model and comparative batch leaching of major and minor elements from FAP and RE-FAP concentrate. *Hydrometallurgy 184* (2019) 218–236.

Baolu, Z, Zhongxue, L, Congcong, C, 2017. Global potential of rare earth resources and rare earth demand from clean technologies, *Minerals*, 7(11), 203.

Beltran J J, Novegil F J, García K E, Barrero C A, 2009. On the reaction of iron oxides and oxyhydroxides with tannic and phosphoric acid and their mixtures. *Springer online*, published 10 November 2009, retrieved 15 October 2021 from DOI 10.1007/s10751–009–0110-x

Chen, J, Zhu, X, Liu, G, Chen, W, Yang, D, 2018. China's rare earth dominance: The myths and the truths from an industrial ecology perspective, *Resources, Conservation and Recycling*, 132, 139–140.

Deng B, Wang B, Su S, Ding S, Sun W, 2018. Recovery of Iron from Pyrolusite Leaching Slag by a Lab-Scale Circulation Process of Oxalic Acid Leaching and Ultraviolet Irradiation. *Metals 8* 2018, 8.

He L, Xu Q, Li W, Dong Q, Sun W, 2021. One-step separation and recovery of rare earth and iron from NdFeB slurry via phosphoric acid leaching. *Journal of Rare Earths* (pre-publication paper).

Hernandez-Hernandez R A, Garcia F L, Hernandez-Cruz L E, Jacuinde B, 2015. Bleaching by leaching using phosphoric acid solutions. *J Mex. Chem. Soc 59(3)* (2015) 198–202.

Hu P, Zhang Y, Liu T, Huang J, Yuan Y, Zheng Q, 2017. Highly selective separation of vanadium over iron from stone coal by oxalic acid leaching. *J. of Industrial and Engineering Chemistry 45* (2017) 241–247.

Jin H X, Wu F Z, Mao X H, Wang M L, 2017. Leaching isomorphism rare earths from phosphorite ore by sulphuric acid and phosphoric acid. *Rare Metals 36(10)* (2017) 840–850.

Lazo, D E, Dyer L G, Alorro R D, Browner R, 2017. Treatment of monazite by organic acids I: Solution conversion of rare earths. *Hydrometallurgy 174* (2017) 202–209.

Lazo, D E, Dyer L G, Alorro R D, Browner R, 2018. Treatment of monazite by organic acids II: Rare earth dissolution and recovery. *Hydrometallurgy 179* (2018) 94–99.

Lee S O, Tran T, Jung B H, Kim S J, Kim M J, 2007. Dissolution of iron oxide using oxalic acid. *Hydrometallurgy 87* (2007) 91–99.

Lee S O, Tran T, Park Y Y, Kim S J, Kim M J, 2006. Study on the kinetics of iron oxide leaching by oxalic acid. *Int. J Mineral Processing 80* (2006) 144–152.

Li Z, Xie Z, He D, Deng J, Zhao H, Li H, 2021. Simultaneous leaching of rare earth elements and phosphorus from a Chinese phosphate ore using H3PO4. *Green Processing and Synthesis 10* (2021), 258–267.

Liang H, Zhang P, Jin Z, DePaoli D, 2017. Rare-earth leaching from Florida phosphate rock in wet-process phosphoric acid production. *Minerals & Metallurgical Processing Vol. 34, No. 3*, (2017), 146–153.

Liu Q, Tu T, Guo H, Cheng H, Wang X, 2020. High efficiency simultaneous extraction of rare earth elements and iron from NdFeB waste by oxalic acid leaching. *Journal of Rare Earths 39* (2021) 323–330.

Martinez-Luevanos A, Rodriguez-Delgado M G, Uribe-Salas A, 2011. Leaching kinetics of iron from low grade kaolin by oxalic acid solutions. *Applied Clay Science 51* (2011) 473–477.

Pariyan K, Hosseini M R, Ahmadi A, Zahiri A, 2019. Optimization and kinetics of oxalic acid treatment of feldspar for removing the iron oxide impurities. *Separation Science and Technology, Volume 55, No. 10* (2019) 1871–1882.

Pepper R A, Couperthwaite S J, Millar G J, 2016. Comprehensive examination of acid leaching behaviour of mineral phases from red mud: Recovery of Fe, Al, Ti and Si. *Minerals Engineering 99* (2016) 8–18.

Refly S, Floweri O, Mayangsari T R, Sumboja A, Santosa S P, Ogi T, Iskandar F, 2020. Regeneration of LiNi1/3Co1/3Mn1/3O2 Cathode Active Materials from End-of-Life Lithium-Ion Batteries through Ascorbic Acid Leaching and Oxalic Acid Coprecipitation Processes. *ACS Sustainable Chem. Eng 8 (*2020) 16104−16114.

Sahoo R N, Naik P K, Das S C, 2001. Leaching of manganese from low-grade manganese ore using oxalic acid as reductant in sulphuric acid solution. *Hydrometallurgy 62* (2001) 157–163.

Sinha M, Pramanik S, Kumari A, Sahu S, Prasad L, Jha M, Yoo K, 2017. Recovery of value added products of Sm and Co from waste SmCo magnet by hydrometallurgical route. *Separation and Purification Technology 179* (2017) 1–12.

Soltani F, Abdollahy M, Petersen J, Ram R, Koleini J, 2019. Leaching and recovery of phosphate and rare earth elements from an iron-rich fluorapatite concentrate: Part II: Selective leaching of calcium and phosphate and acid baking of the residue. *Hydrometallurgy 184* (2019) 29–38.

Soner T, 2020. Separation of Fe and Mn from Manganiferous Iron Ores via Reductive Acid Leaching Followed by Magnetic Separation. *Mining, Metallurgy & Exploration 37* (2020) 297–309.

Stone K, Bandara A M T S, Senanayake G, Jayasekera S, 2016. Processing of rare earth phosphate concentrates: A comparative study of pre-leaching with perchloric, hydrochloric, nitric and phosphoric acids and deportment of minor/major elements. *Hydrometallurgy 163* (2016) 137–147.

Taran M, Aghaie E, 2015. Designing and optimization of separation process of iron impurities from kaolin by oxalic acid in bench-scale stirred-tank reactor. *Applied Clay Science 107* (2015) 109–116.

Veglio F, Passariello B, Abbruzzese C, 1999. Iron removal process for high-purity silica sands production by oxalic acid leaching. *Ind. Eng. Chem. Res. 38* 1999, 4443–4448.

Wu S, Zhao L, Wang L, Huang X, Zhang Y, Feng Z, Cui D, 2019a. Simultaneous recovery of rare earth elements and phosphorus from phosphate rock by phosphoric acid leaching and selective precipitation: towards green process. *Journal of Rare Earths 37* (2019) 652–658.

Wu S, Zhao L, Wang L, Huang X, Zhang Y, Feng Z, Cui D, 2019b. Precipitation-dissolution behaviors of rare earth ions in H3PO4-Ca(H2PO4)2 solutions. *Journal of Rare Earths 37* (2019) 520–527.

Xu L, Yang H, Liu Y, Zhou Y, 2019. Uranium leaching using citric acid and oxalic acid. *J. of Radioanalytical and Nuclear Chemistry 321* (2019) 815–822.

Yu Z L, Shi Z X, Chen Y M, Niu Y J, Wang Y X, Wan P Y, 2012. Red-mud treatment using oxalic acid by UV irradiation assistance. *Trans. Nonferrous Met. Soc. China 22* (2012) 456–460.

Zeng X, Li J, Shen B, 2015. Novel approach to recover cobalt and lithium from spent lithium-ion battery using oxalic acid. *Journal of Hazardous Materials 295* (2015) 112–11.

Zhang Z, Li J, Li X, Huang H, Zhou L, Xiong T, 2012. High efficiency iron removal from quartz sand using phosphoric acid. *International Journal of Mineral Processing 114–117* (2021) 30–34.

The importance of the curing stage in the fixation of arsenic in pressure oxidation

W S Ng[1], Y Liu[2] and M Chen[3,4]

1. Research Fellow, RMIT University, Melbourne Vic 3001. Email: will.ng@rmit.edu.au
2. PhD Candidate, RMIT University, Melbourne Vic 3001. Email: S3765625@student.rmit.edu.au
3. Professor, RMIT University, Melbourne Vic 3001. Email: miao.chen@rmit.edu.au
4. Senior Principal Research Scientist, CSIRO, Clayton Vic 3169. Email: miao.chen@csiro.au

INTRODUCTION

In the processing of refractory gold-bearing sulfides, pressure oxidation (POX) is commonly known for its role in liberating the gold in solid-solution via oxidation of the sulfide occlusions. For deposits that contain arsenic-bearing species including arsenian pyrite and arsenopyrite, POX serves an important secondary function in the fixation of arsenic, via the hydrothermal precipitation of stable arsenates such as scorodite and basic ferric arsenate sulfate (BFAS). There have been various investigations on the impact of different POX conditions on arsenic precipitation and the stability of the formed phases, but less is known about the changes to the arsenic carrier that occur in the curing stage, which follows directly from POX.

The primary function of curing is to coax the dissolution of sulfates to reduce lime consumptions during cyanide leaching, and the slurry is kept at elevated temperatures near 100°C to achieve this. While the arsenic-bearing phases are expected to undergo transformation during this stage, there has thus far been limited experimental evidence. In this study, the effect of curing time and curing temperature on the arsenic-bearing species and arsenic deportment in the POX product has been investigated. Leaching of the curing products was also conducted to examine the stability of the arsenic species in the solid precipitates.

METHODS

The synthetic feeds used in this study were prepared using mixtures of pyrite (FeS_2; ~98 per cent purity) obtained from Crystal World and arsenopyrite (FeAsS; ~93 per cent purity) obtained from the Renison Bell mine. Prior to curing, POX was first conducted for synthetic mixtures of pyrite and arsenopyrite at varying compositions to target iron-to-arsenic ratios between 1:1 to 10:1. This was performed to examine the different effect of curing on varying ore feeds. During POX, the samples were reacted for one hour under pure oxygen at a total pressure of 30 bar at varying temperatures between 180–220°C at pH 1.5. For each run, the POX product was cooled to the designated curing temperatures and the reaction vessel was depressurised before being cured as-is. A modified toxic characteristic leaching procedure (TCLP) was used as a simple measure of the stability of arsenic for comparison between the precipitates formed under the studied conditions.

RESULTS AND DISCUSSION

Effect of curing time

The effect of curing between 0 to 24 h at 90°C following POX was investigated for synthetic feeds with iron-to-arsenic rations between 1:1 to 10:1, with the product characteristics as shown in Table 1. Based on X-ray diffraction (XRD) studies, the POX temperature appeared to have no effect on the phases of the mineral product exiting the stage and entering curing. For the POX feeds with iron-to-arsenic ratios of 1:1 (pure arsenopyrite) and 2:1, BFAS was found to be the major product following POX prior to curing. For the 1:1 samples, BFAS remained as the major product following curing up to 18 h, after which scorodite was observed to be the major product up to a curing time of 24 h. The evolution of the arsenic-bearing species over 24 h of curing can be seen from Figure 1. This suggests that the formation of scorodite may proceed via transformation from BFAS rather than precipitation from solution, though the transition to scorodite was also associated with a significant increase in arsenic precipitation from solution. BFAS remains as a minor product, indicating that the transformation is incomplete and expected to continue at extended curing times. This transformation

was absent in the 2:1 samples studied here, with BFAS being detected as the major solid phase at up to 24 h of curing.

TABLE 1

Summary of the characteristics of the POX product under varying feed Fe:As ratios, POX temperatures, curing times and curing temperatures.

Feed Fe:As	POX temperature (°C)	Curing time (h)	As in solids product (%)	As in solution product (ppm)	As in TCLP extractant (ppm)
1:1	180	0	39.5	1207	12.4
		1	38.1	1733	9.8
		24	38.7	1290	4.5
	200	0	36.2	1784	12.5
		1	32.4	2126	15.1
		24	41.2	1186	5.4
	220	0	38.1	2192	10.2
		1	36.4	1624	7.0
		6	40.5	2299	6.6
		18	42.0	596	5.1
		24	41.4	391	6.6
		24 at 60°C	40.7	1594	5.2
		24 at 120°C	41.6	513	4.2
2:1	180	0	26.4	209	14.0
		1	26.5	483	6.1
	200	0	25.1	72	9.3
		1	22.8	216	4.4
		24	25.4	564	5.1
	220	0	27.7	130	12.2
		1	28.8	244	8.6
		24	24.4	812	3.2
4:1	180	1	15.2	342	14.1
	200	1	16.6	215	33.1
	220	1	17.8	181	140.8
10:1	180	1	9.1	177	220.7
	200	1	6.4	169	409.0
	220	1	9.7	122	304.5
		24	12.1	508	354.0

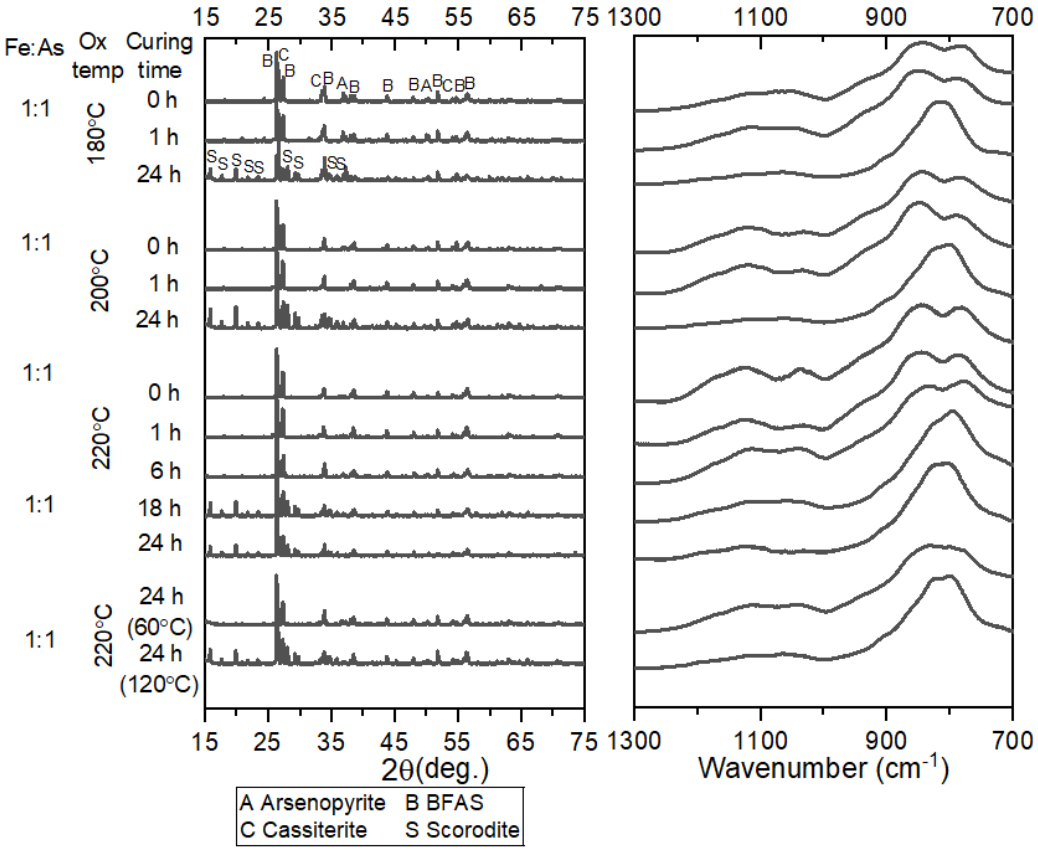

FIG 1 – XRD and normalised FTIR spectra for the product formed after curing at 0–24 h, following pressure oxidation of pure arsenopyrite (Fe:As of 1:1) at 180–220°C. Unless indicated otherwise, curing was conducted at 90°C.

An arsenic-bearing mineral could not be identified in the solids phase for most of the 4:1 samples and all 10:1 samples, potentially due to the low concentrations of the arsenic-bearing phases. X-ray photoelectron spectroscopy (XPS) suggests that the arsenic in these samples is present as adsorbed As_2O_5 species. There might also be low incorporation of the arsenic in hematite, as well as in sulfate minerals via substitution with arsenate groups. While curing for one hour did not result in any apparent changes to the arsenic-bearing phase, a general increase in the dissolved arsenic was observed, suggesting the dissolution of weakly-adsorbed arsenic species or unstable precipitates in the first hour.

Effect of curing temperature

The impact of curing at 60°C and 120°C was investigated for the 1:1 samples, at a curing time of 24 h. The formation of scorodite was observed following curing at 120°C, similar to 90°C, but the product remained as BFAS at 60°C after 24 h, as shown in Figure 1. Despite the absence of scorodite, the Fourier-transform infrared (FTIR) spectra for the sample after curing at 60°C is clearly different from the other BFAS samples, resembling a transformation in progress. While arsenical ferrihydrite is known to form near 70°C, this is unlikely here due to the low pH conditions. As the temperature regime would dictate the phase stability and rate of transformation, the formation of scorodite might occur at lower time scales at 120°C, though a follow-up study has yet to be conducted.

Arsenic stability

The formation of scorodite under extended curing times not only results in increased arsenic precipitation, but also improved the stability of the arsenic carrier. The arsenic extracted from the TCLP studies drops from approximately 10–15 ppm for the BFAS product to around 5 ppm following the transformation into scorodite, as shown in Table 1. This also suggests that the BFAS may be moderately crystalline, as other studies have achieved TCLP results below 5 ppm for BFAS. The extracted arsenic for the samples cured for 24 h at 60°C to 120°C were similar, with the 60°C sample

exhibiting low extractability despite the absence of scorodite. The TCLP arsenic extract for the 10:1 samples were substantially higher at 220–410 ppm despite initially containing less arsenic in the POX feed, suggesting that high feed ratios of arsenic-to-iron may be necessary to encourage the formation of stable precipitates.

ACKNOWLEDGEMENTS

The authors acknowledge the financial support provided by Zijin Mining and the Australian Research Council Linkage Project grant LP160101760 for this work. The authors are thankful to Nadia Zakhartchouk, Zahra Homan, Stephen Grist, Bebeto Lay, Sandro Longano, Susan Holden, Billy Murdoch, the Centre for Advanced Materials and Industrial Chemistry high-pressure research facility and the RMIT Microscopy and Microanalysis Facility. Special thanks to Selvakannan Periasamy, Ylias Sabri and Lydon Alexandrou for their assistance at various stages of this study.

The MTM copper process

R W Shaw[1]

1. FAusIMM, Director, Minetometal Pty Ltd, Melbourne 3054 Vic. Email: rwshaw3050@gmail.com

ABSTRACT

The MTM Process targets treating lower grade and/or problem concentrates that are not attractive to smelters. The process has been developed at laboratory scale for copper and is based on a related development for zinc that has been extensively developed both in the laboratory and through pilot testing.

The basis of the process is novel ammonia-ammonium chloride leach chemistry adapted to give high copper extraction whilst being selective over iron, arsenic and many other elements. The preferred flow sheet depends on location, especially infrastructure and utilities. These impact upon the leach and crystallisation stages more than copper reduction.

The drivers behind the development have been:

- Minimising CAPEX – no SX-EW steps, no acid plant.
- Flexibility on concentrate grade and impurities.
- Inert residue:
  - Sulfur fixed as calcium sulfate not acid or elemental sulfur.
  - Iron as iron oxide.
  - Arsenic as calcium arsenate and/or ferric arsenate.
- Break point in product at site – can be C.
- copper oxide and/or copper metal.
- Flexibility in energy source – can be any combination of wind:
  - Solar thermal and solar photovoltaics.
  - Biomass.
  - Coal.
  - LNG and/or natural gas.
- Recovery of gold and silver as well as copper.
- Suitable for smaller scale (<50,000 t/a) operations.

A process design for a 50 000 t/a plant has been developed sufficient to enable estimates for the CAPEX and OPEX. The CAPEX estimate of ~US$4060/installed annual tonne suggests the process will be lower CAPEX than alternative hydrometallurgical processes being developed for copper concentrates. This stems from having a much simpler leach circuit and through not requiring solvent extraction and electrowinning. The OPEX cost of ~US$517 is comparable to other hydrometallurgical processes and of the same order as historical treatment and refining charges.

Minetometal doubts that the process will be competitive with existing smelters for high quality concentrates but has niche opportunities for deposits which struggle to make readily marketable concentrates. The process chemistry has been confirmed at laboratory scale, but considerably more laboratory and pilot scale development are needed to bring the process to being ready for commercialisation. Minetometal aims to continue development and reach the commercial ready stage within the next 2–3 years.

INTRODUCTION

The MTM Copper Process has been developed to enable more economic copper production from a range of copper materials including sulfides. The process is particularly suited to problem deposits

where it has proven difficult to produce the high-quality concentrates required by conventional smelters. The process can treat low-grade concentrates and/or concentrates with problem impurities such as arsenic and radionuclides.

The current dominant process for producing copper metal from sulfide ores is to make a copper concentrate via comminution and flotation and then smelt the concentrates at high temperatures to make an impure blister copper. This is then electro refined to give high purity metal and to recover other valuable components especially gold and silver. The sulfur is converted to sulfuric acid for sale or for use in heap leaching.

The economics of the process are very dependent on the costs for building the smelter and the cost of transporting the concentrate to the smelter. The CAPEX of smelters is high, and these are invariably large installations which benefit from economies of scale. The transport costs and penalties imposed by the smelters for impurities and low copper grade are restrictive on the miners and force them to produce high-grade, high purity concentrates which may not be ideal for the overall deposits being mined.

There have been many attempts over the last 50 years to find an alternative low temperature process capable of making copper metal from a range of ores and concentrates without the high CAPEX needed for building a large smelter. These processes have also targeted processing problem ores and/or concentrates which are high in toxic heavy metals such as arsenic which many of the existing smelters will not accept as feed material.

Despite these concerted efforts none of the processes developed to date have achieved significant commercialisation. There has been some success with two medium scale plants being used to treat chalcocite which is the most readily leached of the copper sulfide minerals. Chalcopyrite is much more refractory and difficult to leach and to date there have only been a few small tonnage demonstration plants built.

The processes developed have mainly focused on using an oxidative acidic leach to dissolve the copper. A major drawback of these acid systems is that the iron also dissolves and must be precipitated. Another drawback is that the sulfur present most commonly reports as a sulfate which needs precipitation with lime to form an insoluble calcium sulfate that can be separated into the residue. This precipitation step is difficult and often consumes more than the stoichiometric lime requirement especially where the lime also precipitates acid required for the leach step.

Other challenges facing these processes is that solvent extraction followed by electrowinning are needed and these are both high CAPEX and OPEX operations. They are well established technology and widely used for heap leach operations where the costs are offset by not requiring a concentrator and the lack of choice as producing a concentrate is not possible.

Apart from the acid systems there have also been some attempts to use ammonia leaching over the past 100 years. A commercial plant was built using the Arbiter Process and another using a variation of this for partially leaching chalcocite concentrate at Escondida. These were not commercially successful and were uncompetitive with smelting. Their major challenges were the need for the high-cost solvent extraction – electrowinning steps and issues with ammonia recovery and managing sulfate build-up in the system.

OVERVIEW OF THE MTM COPPER PROCESS

The key to the process is using an ammonia-ammonium chloride lixiviant to selectively dissolve copper and then precipitating out high purity copper containing crystals. The crystals can then be reduced to copper metal by a hydrogen containing gas at quite modest temperatures. The process is based on known chemical reactions which have been reported previously and combining those into an overall cost-effective process. The advent of reverse osmosis for managing the water balance and increased use of plastics in construction are important advantages that were not available to many of the earlier workers.

Copper is known to be highly solubility in ammonia-ammonium chloride liquor and depending on the liquor concentration can reach over 100 g/L (Wei *et al,* 2010a). Figure 1 shows laboratory solubility data determined by Minetometal for different concentrations of ammonia in 50 g/L ammonium chloride liquor as a function of temperature.

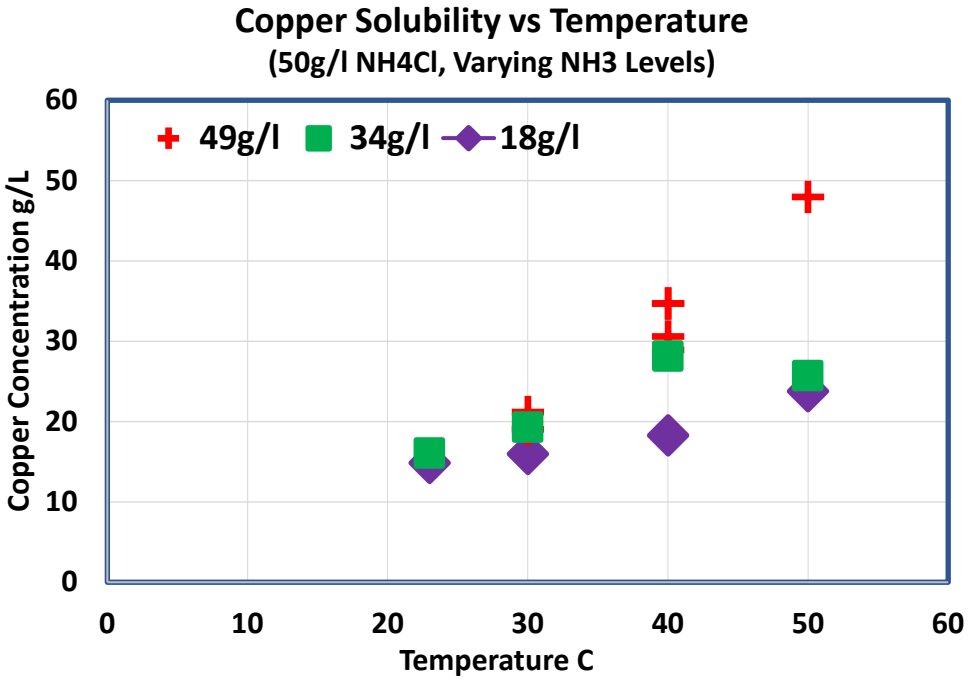

FIG 1 – Copper solubility at varying temperatures and liquor compositions.

The liquor dissolves oxidised copper minerals (Wei *et al,* 2010b; Yartasi and Copur, 1996; Ekmekyapar and Oya, 2003) but copper sulfides and copper metal do not dissolve without an oxidation step either prior to or during the leach (Dixon and Madigan, 1972).

Once dissolved the copper can be precipitated from the liquor by stripping off part of the ammonia and/or cooling to give copper containing crystals. These crystals are either cupric oxide or are suitable for conversion to cupric oxide which is readily reduced to copper metal at temperatures above 200°C (Bond and Clark, 1960).

Minetometal developed two conceptual flow sheets for the MTM Process to utilise the known chemistry for producing copper metal from sulfide concentrates. The two flow sheets shown in Figure 2 have a common crystallisation – reduction section but differ in their approach to oxidising the sulfides to enable their leaching.

A laboratory program has been carried out to confirm the chemistry behaves as reported by others to firm up the flow sheets and provide data for a first pass economic evaluation.

The two options for the sulfide oxidation are:

- Roasting at around 650–720°C in air to convert the copper sulfide to a copper sulfate – copper oxide mixture without the formation of refractory copper ferrites.
- Leaching the sulfide concentrates with oxygen injection such that the sulfides oxidise during the leach.

The choice between the two options depends on a mix of the concentrate composition, the availability and cost of energy and reagents and the target production tonnage.

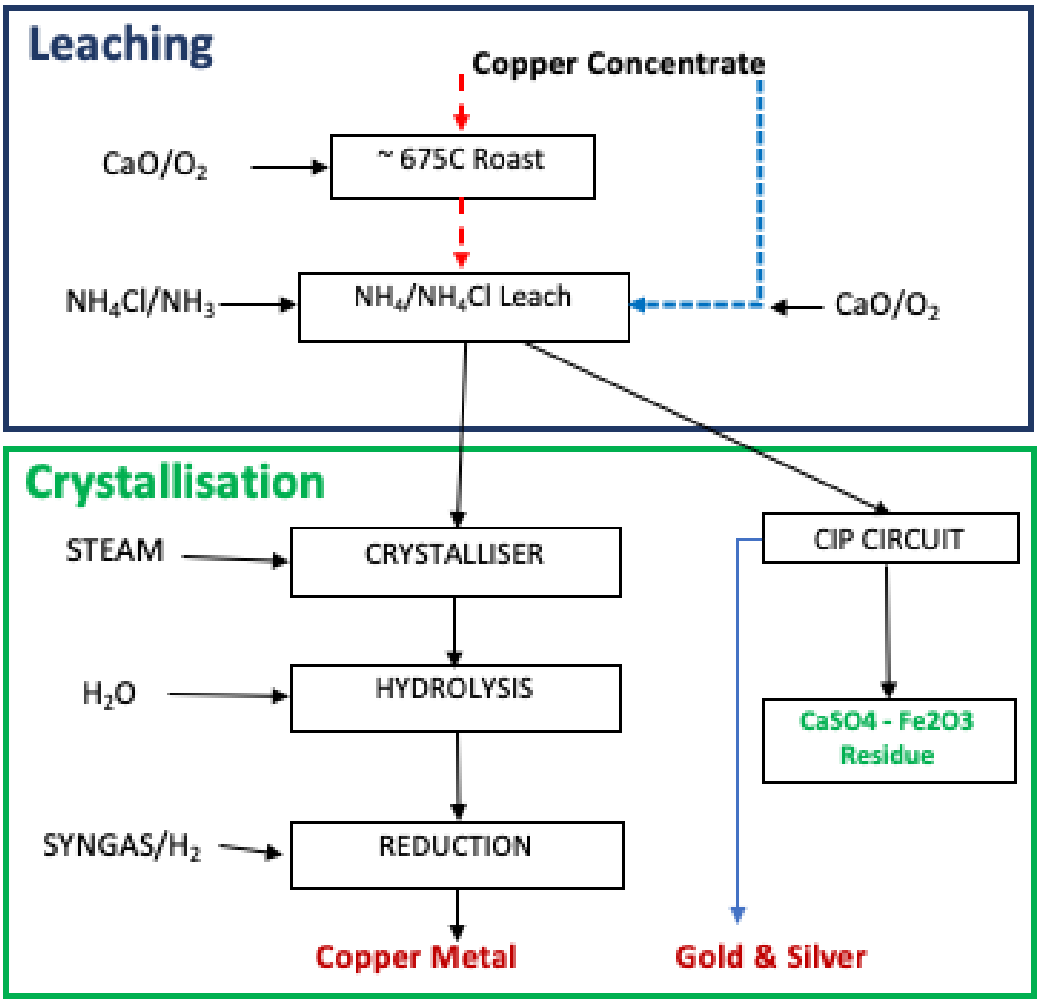

FIG 2 – The MTM process flow sheet.

DEVELOPMENT OF THE MTM COPPER PROCESS

Roasting

Thermodynamically copper sulfides are very difficult to dead roast to copper oxide without the formation of copper ferrites. Complete removal of the sulfur requires roasting at temperatures above 720°C where copper ferrite formation starts to occur. At temperatures below 720°C roasting gives calcine with a mix of copper sulfate and copper oxide. It is not possible to have all the copper report as copper sulfate (Guntner and Hammerschmidt, 2012).

Both copper oxide and copper sulfate are readily leached by the ammonia-ammonium chloride liquor so it is not critical to removal all the sulfur during roasting. The iron is not leached which avoids the problems of the acid systems working from calcine feed. The roasting can be carried out to either generate a high sulfur dioxide off-gas suitable for making acid or as a lime roast where a calcium source such as lime or limestone is added to the roaster to capture the sulfur as calcium sulfate (Bartlett and Haung, 1973).

The lime roast is preferred where the concentrate has a Cu:S ratio above 1 and/or where there is no suitable outlet for sulfuric acid. At Cu:S above 1 the sulfur dioxide of the off-gas is too low for sulfuric acid production with air roasting and even oxygen enrichment struggles to make it an economically attractive acid feed (Guntner and Hammerschmidt, 2012). Laboratory lime roasting at 650°C oxidised almost all the sulfides to sulfate as shown in the X-Ray Diffraction (XRD) analysis for the feed and calcine in Table 1.

TABLE 1

Mineralogy of Concentrate, Calcine and Leach Residue by XRD.

Mineral	Formula	Concentrate	Calcine	Leach residue
Chalcopyrite	$CuFeS_2$	33.5		
Bornite	Cu_5FeS_4	31.1	2.1	
Pyrite	FeS_2	10.5		0.9
Hematite	Fe_2O_3	16.8	27.2	22.5
Quartz	SiO_2	4.8	1.4	0.7
Covellite/Digenite	CuS/Cu_9S_5	3.4		
Chalcocyanite/Brochanite	$CuSO_4$		23.2	
Anhydrite/Gypsum	$CaSO_4$		38.8	73.1
Lime	CaO		2.7	
Tenorite	CuO		3.6	2.6

Leaching the calcine

The copper in the calcine as both copper oxide and copper sulfate leaches in less than two hours in the ammonia-ammonium chloride liquor. The conditions are chosen to give a target copper level rather than by the needs of the leach step. The preferred leach liquor has around 50 g/L ammonium chloride which gives 50 g/L copper in solution and a delta copper across the leach of ~30 g/L. The leach is quite selective for copper over iron and most other impurities such as arsenic.

The sulfate level in the liquor is controlled by dissolving some lime in the spent liquor which then precipitates the sulfate as gypsum as shown in Table 1. Having the calcium in solution prior to the leach avoids the difficulty of reacting solid lime particles with sulfate.

Direct oxidative leaching of concentrates

An alternative approach to obtaining the copper rich pregnant liquor is to leach the concentrate directly in the liquor under an oxygen atmosphere at moderate temperature and pressure. Warman filed a patent (Dixon and Madigan, 1972) outlining the leaching behaviour under a range of conditions and showed that all the sulfide minerals can react reasonably quickly. The sulfur can report as either the sulfate and/or a mix of elemental sulfur and sulfate depending mainly on the temperature, time and ammonia-ammonium chloride ratio (Dixon and Madigan, 1972; Filmer, 1978).

In the MTM Process we prefer to oxidise all the sulfur to sulfate and precipitate it as gypsum rather than leave elemental sulfur in the residue. Forming elemental sulfur requires less oxygen and lime but recovering a marketable sulfur product is difficult and the residue is not well suited to cyanide gold recovery. The elemental sulfur can form AMD (Litke, 2019) so dumping it has environmental issues and the inert gypsum residue is much more acceptable. The lime is soluble in the spent liquor and reacts with the sulfate as it forms avoiding the complex neutralisation circuits such as those in BIOX plants.

Crystallisation

The pregnant liquor from either the calcine leach or the direct oxidative leach typically contains around 50 g/L copper. As the solubility of the copper depends on the ammonia concentration for a set ammonium chloride concentration stripping off the ammonia causes copper containing crystals to precipitate. A process using this approach was patented (Bartlett, 1993) but it was never developed through to a commercial operation. Our work has also found the solubility to have significant temperature dependence such that cooling also causes precipitation.

The MTM Process removes part of the ammonia by steam stripping and then uses indirect cooling to drop the liquor temperature below 30°C. This enables around 60 per cent of the copper in the

liquor to be recovered into crystals while the remainder recycles in the spent liquor which typically contains ~20 g/L copper.

The copper concentration can be reduced further by stripping off more ammonia, but the energy needed per tonne of copper increases and the amount removed depends largely on the local energy cost for the steam generation. In the roasting based flow sheet heat recovery from the roaster supplies a substantial part of the energy required.

The composition of the crystals depends mainly on the ammonium chloride concentration and can be any one or a combination of diamine copper chloride, copper hydroxy chloride and cupric oxide. (Limpo, Luis and Cristina, 1995; Wei *et al,* 2010a, 2010b). Diamine copper chloride is difficult to convert to cupric oxide and/or copper metal and the liquor conditions are controlled such that this does not form. The crystals are usually ammonia free copper hydroxy chloride (atacamite) and/or cupric oxide (tenorite). These can both be reduced to copper metal in a hydrogen containing gas at temperatures above around 250°C.

Reduction

Two alternatives are still being considered for the reduction of the crystals to copper metal and further development work is underway. The choice will in part depend upon the presence of trace impurities in the crystals. The most likely option is to hydrolyse any chloride containing crystals by reacting them with a dilute ammonia solution to convert them to cupric oxide and leave the chloride in solution as ammonium chloride. Laboratory testing has shown this occurs readily with <10 g/L ammonium hydroxide liquor. Trace impurities present in the crystals also dissolve leaving high purity cupric oxides.

An alternative is to place the crystals in the furnace at 250°C without the hydrolysis step and decompose the copper hydroxy chloride to copper oxide (Sharkey and Lewin, 1972) and reduce this to copper metal while simultaneously volatilising the chloride present as hydrochloric acid vapour. This removes the need for the hydrolysis step but requires using materials that can withstand aqueous hydrochloric acid vapour. It also only removes impurities that form volatile chlorides and subsequent purification may be required when the copper powder is melted.

Water balance

All hydrometallurgical processes face issues of managing the water balance to both minimise losses of valuable metals in residues through insufficient washing and to avoid the need for complex bleed streams. The MTM Process makes extensive use of reverse osmosis to internally recycle water between the steps. This adds costs but is an essential part of the process. The liquor chemistry is controlled such that reverse osmosis can readily be applied. The process benefits from the major advantages in reverse osmosis over the past 20 years which have significantly reduced the CAPEX and OPEX of these systems.

DEVELOPMENT STATUS

The process has been developed at laboratory scale for all steps excepting the final copper reduction. This work has proven that the chemistry behaves as expected and has provided data to enable the basic design of a commercial plant. Much of the process is the same as the MTM Zinc technology for producing zinc oxide powder which has been extensively tested and developed through to a 50 t/a pilot scale. A prefeasibility study has been conducted for the zinc technology and the engineering design and cost data from that has been applied to the copper process.

CONCEPTUAL DESIGN OF A COMMERCIAL PLANT

To enable first pass costing and test the practicality of the process a conceptual design has been developed for a 50 000 t/a copper metal plant treating a high-grade concentrate with 33 per cent copper and 22 per cent sulfur. The design uses roasting with added lime for the oxidation step. A simplified Process Flow Diagram showing the main steps, but not internal recycles, is shown in Figure 3.

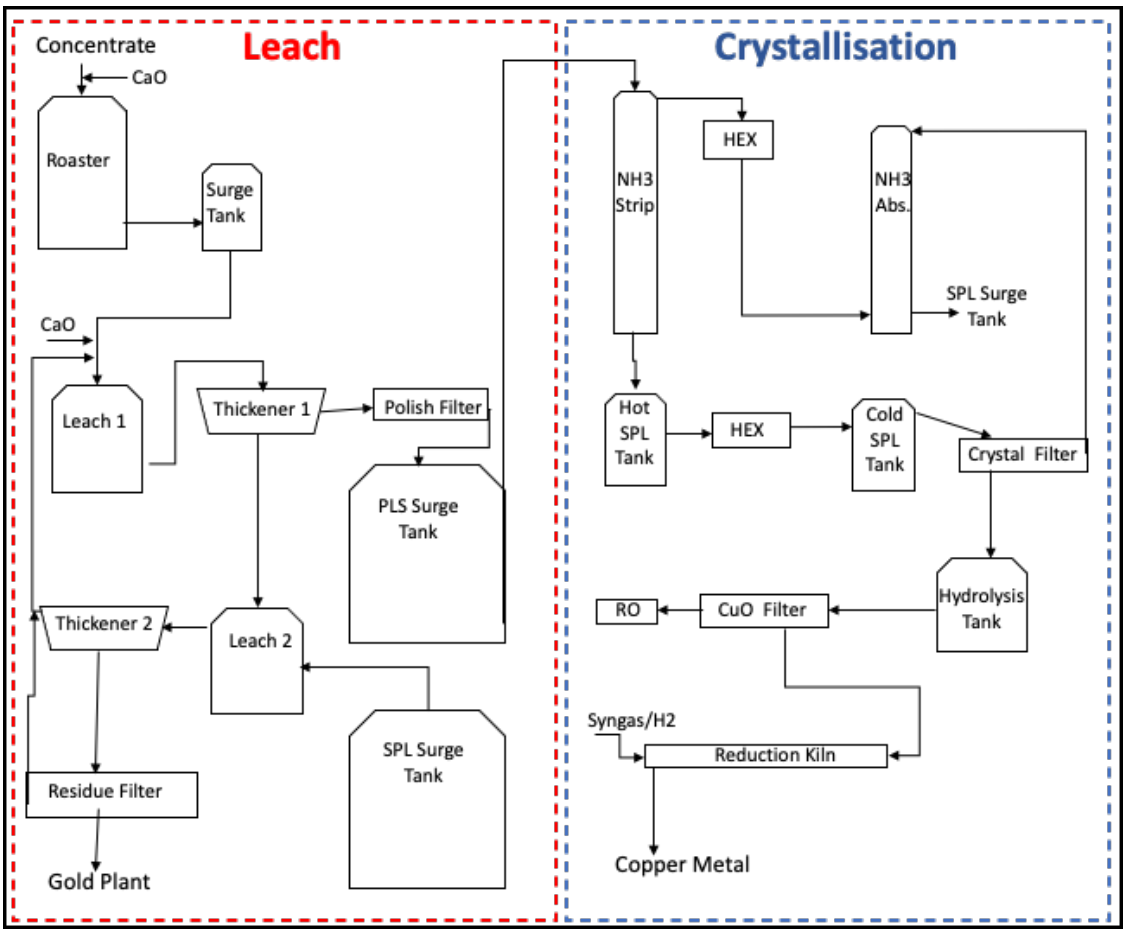

FIG 3 – Simplified process flow diagram for the MTM process.

The concentrate is mixed with lime and fed to a 7 m diameter circulating fluid bed and roasted at 680°C to convert all the sulfide to sulfate with >90 per cent of the sulfur remaining in the calcine as a mix of calcium sulfate and copper sulfate. The low sulfur dioxide off-gas is scrubbed with lime which is recycled to the roaster. The roast reactions are strongly exothermic and water additions are used to control the temperature and ensure there are no excursions leading to copper ferrite formation. The heat from the roaster off-gas is captured and used to provide steam for the ammonia stripping.

The calcine is leached in ammonia-ammonium chloride to dissolve the copper. The leach reaction is quite rapid, and a total residence time of two hours is sufficient. The current preference is to use a simple two stage counter current leach at 60°C to ensure complete leaching of the copper. Unreacted lime in the calcine is supplemented by lime added to the spent liquor to provide a small excess of calcium such that the sulfate present precipitates as gypsum. For 50 000 t/a copper two 300 m^3 leach tanks are sufficient for the leach stage.

The leach slurry is filtered and extensively washed to remove entrained copper and sent to a conventional gold plant. The residue at PH ~10 with minimal reactive copper or sulfur is suitable for the Carbon in Pulp (CIP) and Carbon-in-leach (CIL) processes.

The pregnant liquor from the first leach stage thickener overflow passes through a polishing filter to remove any solids and is then fed to the crystallisation circuit. Around 40–50 per cent of the ammonia is stripped off in a column which is of the order of 3.5 m diameter by 10 m high. Direct steam injection is used to heat the liquor to boiling point and drive off the ammonia. The steam is partly generated from heat recovered from the roaster and part from a conventional steam boiler fired by natural gas. The total energy requirement from the boiler is not large being of the order of 3–5 GJ/t of copper.

The ammonia depleted liquor is then cooled using indirect heat exchangers to below 30°C causing more crystals to precipitate. The liquor does not supersaturate, and the crystallisation rate is quite rapid so the residence time through the crystallisation circuit is quite low typically being <15 minutes

apart from time in the holding tank after cooling. The crystals are filtered off, washed on the filter and transferred to a stirred tank to undergo hydrolysis in dilute ammonium hydroxide liquor.

The cooled spent liquor is pumped to an ammonium absorption column to contact the stripped ammonia – water gas to recapture the ammonia. A cooling circuit is incorporated into the absorption column to maintain the capture liquor at around 30–35°C. The cooling is by indirect heat exchange with liquor circulating through a conventional cooling tower.

The crystals are held in a 100 m^3 hydrolysis tank for around 30 minutes at ~60°C to ensure any copper hydroxy chloride crystals are hydrolysed to cupric oxide and that trace amounts of impurities are leached out. After hydrolysis the crystals are filtered, washed and fed to a rotary kiln operating at 250°C with syngas being passed through to reduce the oxide to metal. The preferred gas is hydrogen but unless green hydrogen is available syngas produced from natural gas is used on both environmental and cost grounds. The copper metal powder can either be briquetted and sold in that form or more probably melted and cast into either ingot or directly into finished products such as wire or tubing.

Having to thoroughly wash the residue and product, and provide clean water for the steam boiler, requires considerable clean water which far exceeds the only outlets which are with the residue and from the reduction furnace. The water balance is maintained using reverse osmosis on selected streams and using the permeate from this for wash water and hydrolysis. The streams selected are those with little free ammonia present as reverse osmosis has quite limited selectivity for free ammonia.

ECONOMICS

The conceptual engineering design for a 50 000 t/a plant has been used to estimate CAPEX and OPEX. Where possible published data for related technologies has been used to supplement the cost data for a prefeasibility study on the related MTM Zinc technology.

CAPEX

A first pass estimate has been carried out for the plant outlined in Figure 3 treating the high-grade copper concentrate using a roaster to oxidise the sulfur and fixing the sulfur as gypsum. The residue is treated in a conventional CIP plant to recover the precious metals. The main costs centres are shown in Table 2. The CAPEX is estimated at US$4060 per installed annual tonne of copper which includes a 40 per cent contingency given the early stage of the development and the generic nature of the estimate.

TABLE 2

CAPEX and OPEX estimates for a 50 000 t/a MTM process plant.

CAPEX	US$	OPEX	US$/t Cu
Roaster	42	Natural Gas	45
Leach – Crystallisation	62	Electricity	35
Reduction Kiln	13	Lime	168
Melt and Cast	16	Reagents	44
Gold Plant	12	Labour	138
Total Installed Cost	145	Maintenance	87
Contingency (40%)	58	**Cost / tonne Copper**	**517**
Total	203		
Cost / t Copper Capacity	**4060**		

The process steps are all high intensity requiring much less equipment than processes such as those using bio-oxidation which require long residence time leaching, separate neutralisation and solvent extraction and electrowinning. The process uses conventional hydrometallurgical equipment all of

which is in operation albeit in different combinations in existing plants. There are no high pressure or temperature steps.

Ammonium chloride is corrosive to most common metals and so the plant is largely designed using plastics with titanium for heat exchangers and impellors. The inclusion of the roaster adds CAPEX, but it also provides significant usable energy for the crystallisation step. It also avoids the need for oxygen injection into the leach tanks. The process is quite suitable for smaller scale plants as the individual steps can readily operate at low tonnages.

OPEX

In common with other proposed hydrometallurgical processes for copper concentrates the operating costs are dominated by the cost of fixing the sulfur as gypsum, the energy cost for producing the metal and labour. The MTM Process avoid the high electricity cost for electrowinning but does require energy for ammonia stripping and gaseous reductant for the copper oxide reduction.

The roaster typically provides around 50–75 per cent of the steam needed for ammonia stripping and this must be supplemented by either solar thermal or fossil fuels. The preferred fossil fuel is natural gas rather than coal due to its lower carbon emissions and CAPEX cost. Solar thermal heating can also be used if the local conditions are suitable. The copper reduction step uses syngas from natural gas unless cost affective green hydrogen is available.

The direct operating costs of the process excluding any transportation or marketing expenses have been estimated for a generic plant using lime for the sulfur fixation and natural gas as the primary energy source for ammonia stripping and for generating the syngas needed for the reduction step. The costs are included in Table 2. With the limited number of processes steps the plant is well suited to automation and a labour force of ~80 operators should be sufficient to run the 50 000t/a plant.

The exact OPEX is location dependent but for a coastal site with direct access to natural gas the cost is likely to be around US$517/t of copper. The main location sensitivities are the availability and cost of labour and of natural gas. Lime is a globally traded commodity with the cost largely fixed by the world market. There may be scope to reduce the costs if there is a local source of highly active limestone that can replace the lime in the roasting step.

COMPARISON TO ALTERNATIVE TECHNOLOGIES

The process is potentially much lower CAPEX than alternative hydrometallurgical technologies through using high intensity simple steps. The leach stage is much simpler than Pressure Oxidation and much smaller than BIOX and there is no complex neutralisation stage. Replacing the high cost SX-EW stage which typically has CAPEX of over US$4000/t of Cu capacity (Stinn and Allanore, 2020; BioMore, 2018) by crystallisation and reduction more than offsets the inclusion of the roaster for the initial oxidation.

The OPEX costs are expected to be higher than current smelter costs but similar, or lower, than other hydrometallurgical processes. The higher cost of using lime rather than limestone for fixing the sulfur is offset by lower overall energy costs from not having electrowinning or the need for injecting oxygen and/or air into the leach for the sulfide oxidation.

The OPEX costs for the process are comparable to the historical Treatment and Refining charges (TC/RC) from smelters but well above those currently on offer. Even allowing for TC/RC increases, payment for more of the contained metal, and lower transportation costs the revenue margin for the MTM Process is insufficient to justify the CAPEX expenditure for a clean medium – high-grade concentrate which has ready access to the smelter market.

CONCLUSION AND FUTURE PLANS

The MTM Copper Process has the potential to be a low-cost hydrometallurgical process for treating sulfide concentrates. The process struggles to compete with smelting for high quality concentrates and Minetometal's target in developing the technology is to apply it to niche opportunities where the concentrate is not well suited to smelting. The primary focus is on concentrates which have difficult grade – recovery curves and/or have problem impurities especially arsenic and/or radionuclides.

Another opportunity is for concentrates that have valuable levels of other recoverable metals such as cobalt and/or rare earths.

Minetometal is continuing to develop the technology in parallel with our related work on zinc oxide technology. The next step in the development of the MTM Copper Process is further laboratory work addressing the purity of the metal and the recovery of other metals. In conjunction with that pilot plant testing is required to fully prove the process and provide data for more rigorous engineering and costing.

REFERENCES

Bartlett, R W and Huang, H H, 1973. The lime-concentrate-pellet roast process for treating copper sulfide concentrates. *Journal of Metals,* December pp 28–34.

Bartlett, R W, 1993. Recovery of non-ferrous metals from smelter flue dusts and sludges. *US Patent* 5,234,669.

BioMore, 2018. Report for European Grant Agreement 642456.

Bond, W E and Clark, W C, 1960. Reduction of Cupric Oxide by Hydrogen – Fundamental Kinetics. *Oak Ridge National Laboratory Report* ORNL – 2815.

Dixon, P and Madigan, D C, 1975. A Hydrometallurgical Process for Recovering Metals from Sulfide Ores by Oxidation with Air or Oxygen in Ammoniacal Solutions. *US Patent* 3,927,170.

Ekmekyapar, A, Oya, R and Kunkul, A, 2003. Dissolution kinetics of an oxidised copper ore in ammonium chloride solution. *Chem. Biochem. Eng Q*. 17: pp 261–266.

Filmer, A O, 1978. Oxidation of Copper Sulfides in Aqueous Ammonia, PhD (Murdoch Uni.).

Guntner, J and Hammerschmidt, J, 2012. Sulfating roasting of copper-cobalt concentrates. *The Journal of the South African Institute of Mining and Metallurgy* 112:, June pp 455–460.

Limpo, J L, Luis, A and Cristina, M C, 1995. Hydrolysis of cupric chloride in aqueous ammoniacal ammonium chloride solutions. *Rev. Metal. Madrid,* 31 (3): pp 150–155.

Litke, S, 2019. An Investigation into Determining the Source of Elevated Metals in Seepage at Mount Polley Mine, (Unpublished) M APP Sci Thesis, University of British Columbia.

Sharkey, J B and Lewin, S Z, 1972. Thermochemical properties of the copper (II) hydroxychlorides. *Thermochemica Acta* 3: pp 189–201.

Stinn, C and Allanore, A, 2020. Estimating the Capital Costs of Electrowinning Processes, *The Electrochemical Society Interface,* 29, 2 (June 2020): 44.

Wei, L, Tang, M T, Tang, C B, Jing, H E, Yang, S H and Yang, J G, 2010b. Dissolution kinetics of low grade copper ore in ammonia-ammonium chloride solution. *Trans. Nonferrous Met. Soc. China*, 20: 910–917.

Wei, L, Tang, M T, Tang, C B, Jing, H E, Yang, S H, Yang, J G and Yongming, C, 2010a. Thermodynamic Research of Leaching Copper OXIDE Materials with Ammonia-ammonium chloride-water Solution. *Canadian Metallurgical Quarterly,* 49:2: 131–145.

Yartasi, A and Copur, M, 1966. Dissolution kinetics of copper (II) oxide in ammonium chloride solutions. *Journal of Minerals Engineering*, Vol 9: 639–698.

Synergistic defoaming/anti-foaming in zinc leaching with surfactant and silicone based defoamers

Q Zhou[1], W Wang-Geissler[2] and H Nordberg[3]

1. Technical Service Manager, Nouryon, Bridgewater, NJ 08807 USA.
   Email: Peter.Zhou@Nouron.com
2. Sr. Research Chemist, Nouryon, Brewster, NY 12533 USA.
   Email: Wan.Wanggeissler@Nouryon.com
3. Section Manager, Nouryon, Stenungsund, 444 85, Sweden.
   Email: Henrik.Nordberg@nouryon.com

INTRODUCTION

Efficiently controlling foam/froth within mineral processing continues to pose a challenge to the mining sector. The foaming characteristics of aqueous solutions for two-phase systems of air/liquid are well-studied with theories and mechanisms proposed to describe and predict foam formation and stability. The types and structures of reagents that either promote or prevent foaming/froth formation and stability are well-defined in these studies and practiced across various applications. Three-phase systems of air/liquid/solid, such as froth from mineral slurries, however, pose a challenge with the presence of a large quantity of relatively fine mineral particles. Theories and mechanisms that rationalise the effects of chemical additives as a defoamer or foaming agent in aqueous can be applied as a general rule, but do not provide the most effective solution for mineral slurry systems.

Silicone-based defoamers, particularly their O/W emulsions, have been widely and successfully used at various stages of mineral processing to efficiently control the mineral slurry foaming properties. However, their foaming control ability could be significantly impacted by different processing aids used during the upstream process. In a zinc-rich mineral system, a silicone-based defoamer starts losing the properties necessary to effectively control foaming in the leaching circuit when throughput is increased. In this study, the synergistic defoaming/anti-foaming effects from surfactants and silicone-based defoamers are discussed to effectively control foaming/froth in the zinc leaching circuit, even with lower total defoamer dosage. Improvements during mineral processing can also lead to a cleaner mineral grade by reducing waste.

EXPERIMENTS

The zinc concentrate and associated leaching liquor are obtained from a zinc mine in Central America. The leaching liquor has a pH of less than 1.0 and over 1 per cent electrolytes by weight. A silicone/polydimethylsiloxane-based (polysiloxane) defoamer, is currently being used in the zinc leaching circuit at this mine. Nouryon provided Propomeen® T/12, Berol® 3100 and Ethylan® 1005 surfactant defoamers to compare with the product currently in use.

To simulate plant operation, lab-scale foaming and foam stability tests are done in a Denver D12 laboratory flotation machine with a 1.5 L plexiglass cell. Zinc concentrate and leaching liquor are conditioned in the cell to be uniform, then air is injected continuously and the height of the froth in the cell is measured to monitor froth stability at intervals of 1, 3 and 5 minutes. The froth height is observed to increase over time. About 800 mL of the slurry at ~13 per cent (solid per cent) is used in each test, and the tests are done at elevated temperatures of 40–45°C. By comparison, any observation of froth formation at more than 1.0 cm high in the cell is considered excessive foaming. Measurements of the static stability of the foam from the same slurry are also taken by vigorously shaking the slurry in a graduated test tube without external air injection.

RESULTS AND DISCUSSIONS

In the lab bench tests, without the addition of a defoamer, zinc slurry exhibits excessive foaming of more than 5 cm high foam in the cell within 1 minute (Table 1). When both the polysiloxane defoamer and the Propomeen® T/12 defoamer are used alone at a dosage up to 1.2 kg/ton, each shows a reduction in the amount of foam formed but the zinc slurry still yields excessive foaming. It is worthwhile to note the difference of physical appearance and particle accumulation of the froth when each defoamer product is used alone. The froth from the polysiloxane defoamer is dark in colour

with many fine mineral particles, while the froth from the Propomeen® T/12 defoamer is nearly colourless with almost no mineral particles present.

TABLE 1

Foam height and stability of zinc slurry with application of different defoamer systems.

Defoamer Used	Dosage (kg/ton)	Foam Height (cm)		
		1 min	3 min	5 min
Blank		> 5		
Reference polysiloxane defoamer	0.65	3.5	> 5	
	1.24	2.5	> 5	
Propomeen® T/12	0.63	5	> 5	
	1.30	4	> 5	
Defoamer 10 + Propomeen® T/12	0.21	1	1	2
	0.41	0	0.5	0.5
	0.61	0	0	0
Berol® 3100	0.25	0	0.5	0.5
Ethylan® 1005	0.28	0	0	0

From Table 1, when the Propomeen® T/12 surfactant defoamer and the polysiloxane-based defoamer are used together in this zinc slurry, significant defoaming synergism is observed. Not only is the height of the foam drastically reduced, but also the total dosage of defoamer is decreased to less than 50 per cent. It is suspected that when the Propomeen® T/12 defoamer and the polysiloxane defoamer are used together in this zinc slurry, the Propomeen® T/12 defoamer will modify the surface of zinc ore so it is less prone to entrainment. This results in a relatively clean froth and the polysiloxane defoamer effectively controls the froth height. Here, polysiloxane defoamer is believed to mainly function by reducing the local surface tension of the foam and causing bubbles to burst, while Propomeen® T/12 defoamer destroys the elasticity of the foam film, causing bubbles to burst and more importantly renders the mineral particles for fast drainage from foam films.

In addition to the Propomeen® T/12 defoamer, a propoxylated fatty amine surfactant, additional cationic surfactants with a similar chemical structure are tested in blends with the polysiloxane defoamer in the same zinc slurry system. Test results suggest that surfactant derivatives from propoxylation on fatty amines provide better foaming control than derivatives from ethoxylation on fatty amines. Further, both too high and too low hydrophobic lipophilic balance (HLB) of the surfactant derivatives tend to reduce the foaming control ability, whereas surfactant derivatives with a mid-range HLB value appear to provide the best foaming control. This seems to suggest that the blended defoamer system will show synergistic effects only when the polysiloxane defoamer is used together with cationic surfactants of necessary HLB range.

Blends of the polysiloxane defoamer with other types of low-foaming surfactants, namely branched alcohol ethoxylates such as the Berol® 3100 and Ethylan® 1005 defoamers, are also tested on this zinc slurry, observing no synergistic defoaming effects. In fact, the Berol® 3100 and Ethylan® 1005 defoamers work very well for foaming control when used alone in this zinc slurry, even at relatively lower dosages than the blends of the polysiloxane defoamer and the Propomeen® T/12 defoamer (Table 1).

Switching from ethoxylation to propoxylation on alcohols typically promotes the defoaming properties of chemicals within aqueous solutions, so alcohol propoxylates were incorporated in the foaming tests performed on this zinc slurry system. Contrary to initial expectations, the alcohol propoxylates alone result in worse foaming/froth control ability than the alcohol ethoxylates in the mineral system studied. Interestingly, when the alcohol propoxylates are used together with the polysiloxane-based defoamer, significant synergistic defoaming from the blend is observed. No synergistic defoaming is

observed from blending the polysiloxane defoamer with corresponding alcohol ethoxylates. Further studies will be needed to illustrate the mechanisms of how structural changes from surfactant defoamers affect their defoaming properties in mineral slurry systems.

Whether the Propomeen® T/12 surfactant defoamer is added to the polysiloxane defoamer or the Berol® 3100 and Ethylan® 1005 defoamers are used in zinc slurry, it seems that a lower dosage of chemicals is required to produce cleaner and more controlled froth. This is especially meaningful where operations are working to achieve environmental sustainability objectives.

ACKNOWLEDGEMENTS

The authors wish to acknowledge and thank Nouryon for the support of this work and the permission to publish these results.

Advances in mineral processing – physical separation

Flow field investigation of high gravity spirals using experimental and CFD techniques

P Ankireddy[1], P Sudikondala[2], N Mangadoddy[3], S K Tripathy[4] and R M Yanamandra[5]

1. Research Scholar, Indian Institute of Technology Hyderabad, Hyderabad Telangana 502284, India. Email: ch19resch01001@iith.ac.in
2. Research Scholar, Indian Institute of Technology Hyderabad, Hyderabad Telangana 502284, India. Email: ch18resch01005@iith.ac.in
3. Professor, Indian Institute of Technology Hyderabad, Hyderabad Telangana 502284, India. Email: narasimha@che.iith.ac.in
4. Principal Researcher, Iron and Ferroalloys Research Group, Tata steel Ltd, Jamshedpur Jharkhand 831001, India. Email: sunilk.tripathy@tatasteel.com
5. Principal Researcher, Iron and Ferroalloys Research Group, Tata steel Ltd, Jamshedpur Jharkhand 831001, India. Email: yrama.murthy@tatasteel.com

ABSTRACT

Spiral concentrator is one of the most commonly used gravity concentration devices in mineral processing. The particles are classified based on their specific gravity and size. The present work analyses the experimental and numerical investigations of the water flow field, such as fluid depth and free surface primary velocity of two high gravity spiral concentrators at different flow rates. The measurement techniques use a flow depth gauge and flow visualisation technique adapting lycopodium powder as the tracer. Flow features in terms of liquid depth and primary velocity at the free surface of the flow are captured across the trough in two different high gravity spirals. A high-speed motion camera with an imaging frequency of 5400 frames per second and 768 × 768 pixel resolution is utilised to track the tracer particles in the liquid flow on the dark surface background. Further, the two-phase flow is studied numerically on high gravity spirals based on the volume of fluid (VOF) approach utilising the RNG k-ε model and Reynolds Stress Model (RSM) for predicting the fluid flow on trough surfaces such as water depth and free surface primary velocity. The CFD predictions of the flow field for the two spirals are attempted to validate against experimental data. The high gravity spiral concentrators show lower flow depths and free surface primary velocities but steep velocities on the outer trough zone compared to that of low gravity spiral concentrators (conventional coal spirals). Among the computationally tested high gravity spirals, higher pitch and higher secondary slope design shows greater flow characteristics.

INTRODUCTION

Spiral concentrators are widely used for processing beach sands, iron ore, rutile, gold, ilmenite, glass sands, high ash coal and chromite ore. A spiral concentrator consists of an open trough that extends vertically downwards in a helix configuration around a central axis (Napier-Munn and Wills, 2005). Complex mechanisms, including the combined effects of gravitational and centrifugal forces (among others), differential settling rates, interstitial trickling and Bagnold shear forces, affect the stratification of particles (Sivamohan and Forssberg, 1985). Large and dense particles migrate towards the near column zone of the spiral trough and are recovered as concentrates. Fine and lighter particles migrate towards the outer edge of the spiral trough and are collected as tailings. Spirals exhibit one of the most complex flow patterns among gravity separators. These flow patterns allow for dilation of the particle bed and provide an opportunity for separating mechanisms to operate. The primary flow is that of the slurry descending the inclined portion of the trough. The primary circulation is the result of primary slope (α), which varies from 0.2 to 0.5 and remains constant for a particular helix on the spiral. Because of the presence of mixed laminar, transitional, and turbulent flow regimes, particles on the spiral are subjected to a medley of randomly fluctuating, transient and steady force fields that act in a particular manner to generate a unique flow pattern called secondary circulation (Kapur and Meloy, 1998). The secondary water flows, which develop perpendicular to the primary flow and frictional drag effects, contribute to the mineral separation processes taking place on the spiral trough.

In the last few decades, researchers have attempted to examine the fluid flow patterns on spiral concentrators (Holtham, 1990; Holland-Batt and Holtham, 1991; Loveday and Cilliers, 1994; Ye *et al,* 2019; Meng *et al,* 2021). The spiral concentrator consists of primary and secondary circulation, which prevails in a lesser fluid depth in the inner zone and greater fluid depth in the outer zone (Holland-Batt, 1989). Holtham (1990) demonstrated the visualisation of secondary flow on the LD9 spiral by filming the dye streamline on the trough surface. Secondary circulation consists of an inward flow at the trough base and an outward flow at the free surface (Holtham, 1990). It is observed that secondary flow has a significant role in particle transport. The fluid flow can be considered fully developed only after the first two turns. The flow rate has no significant influence on fluid depths and primary velocities in the inner trough region but affects abruptly in the outer trough region (Doheim *et al*, 2008). The gauge measurements have shown that the flow depths normal to the spiral trough are in the order of 1–2 mm in the inner column region and can reach up to 12 mm on the outer edge region (Holtham, 1992). The mean primary velocities are less than 0.1 m/s in the inner zone and more than 2 m/s in the outer edge of the trough (Holtham, 1992). However, limited details are available on the water flow field in spiral concentrators.

Matthews *et al* (1998) developed and validated a computational fluid dynamics (CFD) model using Volume of Fluid (VOF) and formulations for predicting the fluid flow characteristics on the LD9 spiral. Doheim *et al* (2008) presented a computational model based on the volume of Fluid (VOF) approach, RANS turbulence models, namely k-ε, RNG k-ε, SST k-ω, and RSM models, were adopted and compared the predictions with the experimental measurements of LD9 spiral. Comparisons indicate that the Reynolds stress model (RSM) is the most accurate model for predicting the fluid flow on spirals. Ye *et al* (2019) demonstrated the influence of structural parameters such as pitch, flow rate, and transverse angle on the water flow field in LD9 spiral concentrator computationally. Meng *et al* (2021) computationally investigated the effects of cross-sectional geometry of laboratory spiral, which takes the trough profile of parabolic equation of the form $|x|=m|y|^n$.

From the literature, it is noted that most of the experimental and numerical investigations have been undertaken on conventional coal (LD9) spirals. Virtually no research is focused on the fluid and particle flow phenomenon of high gravity spirals. The aim of the present work is to measure the fluid film depth of high gravity spirals using a depth gauge and determine the primary free surface velocity of high gravity spirals experimentally using the tracer imaging technique. Once measurements are made, the flow field is simulated using the CFD model and validated against in-house experimental data on high gravity spirals. The measurement techniques use a flow depth gauge and high-speed camera for fluid flow measurements. The numerical approach incorporates the VOF method and RNG k-ε, RSM turbulence models for modelling the free surface transport on high gravity spiral concentrators.

EXPERIMENTAL METHODOLOGY

The study is performed on two vertically installed high gravity spiral concentrators with the same inlet feed provision, as shown in Figure 1. The geometrical parameters of the spirals are listed in Table 1. Both are single start wash waterless spirals. Compared to spiral 2, spiral 1 has a higher pitch and higher transverse slope. Both spirals have the same inner radii. The outer radius and trough width of spiral 2 is larger than spiral 1.

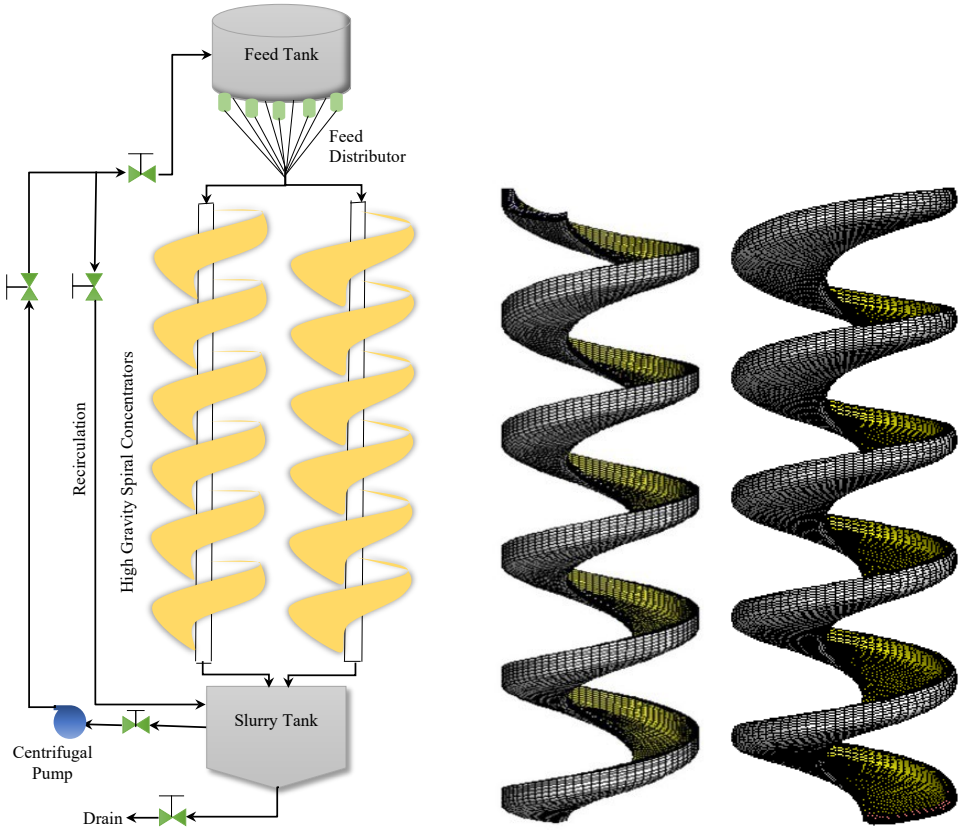

FIG 1 – Schematic of the experimental set-up and computational grids of high gravity spirals.

TABLE 1

Geometrical parameters of high gravity spiral concentrators.

Variable	Symbol	Spiral 1	Spiral 2
Inner radius (mm)	r_i	57	57
Outer radius (mm)	r_o	295	330
Trough width (mm)	W	238	273
Pitch (mm)	u	440	390
Primary slope (°)	α	7–32	10.65–42.81
Transverse slope (°)	β	3–26.5	1–25.46
Number of turns	n	7	6.5

The experimental rig comprises of two high gravity spiral concentrators, as shown in Figure 2. They are fed with clear water by a 5 HP centrifugal pump to the inlet feed tank at the top of the spiral rig. As the fluid flow is fully developed after the first two turns, the flow field measurements are taken at the fifth turn of the spirals for stabilised flow conditions. The depth gauge probe is mounted on a vertical stand at the top of the water-free surface perpendicular to the trough surface. It is submerged manually from the tip of the water-free surface at different radial locations to the trough base to measure the fluid depth. A high-speed motion camera (Photron FASTCAM SA 1.1) is used to measure the fluid free surface velocities by utilising lycopodium powder as the tracer particles. The utilised resolution is 1024 pixels × 512 pixels with a frame rate of 5400 frames per second (fps) and an exposure time of 10 µs. It is supported by a tripod stand and positioned normal to the spiral trough to reduce the distortion view of the trough. The experiments are carried out at the flow rates of 3, 4 and 5 m^3/hr.

(a) (b)

FIG 2 – Projection of (a) depth gauge and (b) high speed camera on trough surface.

Numerical model

The Reynolds average approach is typically suitable for solving the Navier-Stokes equation in most flow dynamics problems in fluid mechanics. The Volume of Fluid (VOF) method was used for modelling the free-surface flow on both spiral concentrators. The method is solved implicitly. In this study, the liquid phase is considered as the continuous phase using the RNG k-ε and Reynolds stress model (RSM). The semi-implicit method for pressure linked equations (SIMPLE) algorithm was applied for pressure-velocity coupling. The conservation equations are discretised using Quadratic Upwind Interpolation (QUICK) scheme for the momentum, turbulent kinetic energy equations, and turbulent dissipation rate.

Computational domain

The computational model has been applied to five turns of both high gravity spiral concentrators. The domain consists of multiple blocks with cells in 3D hexahedral control volumes. The grid for five turns of the spiral units is shown in Figure 1. The cells in a depth-wise direction are clustered towards the solid walls until the control volumes capture the thin films of the fluid medium. The analysis for grid independence is carried out with cells varying from 125 120 to 415 880 for spiral 1 and 243 200 to 420 600 for spiral 2, respectively. It is found that 314 240 cells for spiral 1 and 334 400 cells for spiral 2 are optimum to predict the flow field in spiral units.

Boundary conditions

At the inlet of the domain, the two-phase inflow velocity boundary condition. At the outlet plane, the pressure-out conditions were specified. The trough wall has a no-slip boundary condition, whereas the upper wall has a free-slip boundary condition.

RESULTS AND DISCUSSIONS

Comparisons are made based on the flow field characteristics such as water depth and free surface velocity on high gravity spiral concentrators. Figure 3 shows fluid depth and primary free surface velocity radial profiles (r/R = 0 represents the column centre and r/R = 1 represents the outer edge) obtained at 4 m^3/hr. The results show that fluid depths increase radially outward with shallow depths in the inner section and increase abruptly in the outer section. A similar trend is observed for primary free surface velocities. High centrifugal forces associated with the outer section cause the water surface elevation and create the circulation of secondary currents.

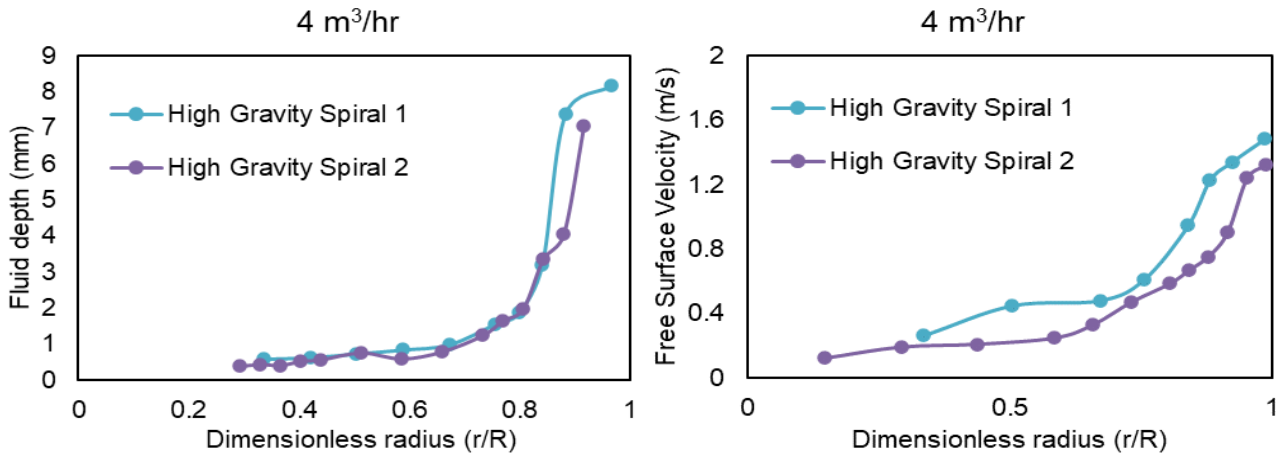

FIG 3 – Experimental measurements of fluid depth and primary free surface velocity profiles of high gravity spirals at 4 m^3/hr (fifth turn).

Figure 3 shows that the fluid depths and primary free surface velocities of spiral 1 are greater than spiral 2. High gravity spiral concentrators are designed with steep pitches and compound slopes. From the geometrical description in Table 1, spiral 1 has a higher pitch and higher transverse slope than spiral 2. The high pitch transforms the gravitational potential energy into kinetic energy and raises the elevation of the fluid level at the outer edge, 6. The steep pitch spirals were able to separate particles of specific gravity <~3 to the outer region. For low pitch spirals such as coal spirals, the differential specific gravity is ~2. The mineral ores having concentration criteria (CC) values greater than 2.5 are easily separable, and less than 1.5 are difficult to separate. Spiral 2 has a less acute slope (flat bottomed) at the inner trough and greater curvature at the outer trough than spiral 1. Flat profile (flat in the first section and low inclination in the second section) spirals with a lowered pitch should function effectively with very fine particles of similar densities because of the low velocities that exist. This design is beneficial in separating heavy mineral ores (<100 µm).

Fluid depth

The water flow on high gravity spirals will be directed outwards, causing an increment in depths radially along the trough can be seen in Figure 4. The flow down the spiral trough experiences very shallow depths (<1 mm) in the inner zones, and the depth of the fluid increases gradually towards the outer zone (15 mm and more). When the spirals were being monitored at 3, 4 and 5 m^3/hr, no significant increase in depths was observed at the inner zone, while the depth level at the outer zone increased abruptly with an increase inflow rate. With finite differences in primary slope, transverse slope, and pitch, the high gravity spirals exhibit different flow depth distributions in the radial direction. Spiral 1 experiences greater fluid depth at inner and outer sections than spiral 2 at all flow rates. The lowering of the pitch and the transverse angle decreases the fluid depth in the outer section as the trough profile makes it difficult for fluid to move outward. Figure 5 shows the comparisons of experimental and numerical predictions of fluid depths on respective spiral concentrators at 3, 4 and 5 m^3/hr. Both RNG k-ε and RSM turbulence models are qualified enough to capture the fluid depth in high gravity spiral concentrators. The outermost region of the spiral trough reflects the air entrainment caused by turbulent eddies, which is likely to increase the fluid depth by 15–20 per cent (Matthews, Holtham and Golab, 1998). The spiral 2 design creates intense turbulence flow at the outer edge region and causes air entrainment, for which the model prediction deviates from the actual parameter. Hence the numerical predictions show a significant deviation from the experimental results in the outer zone than the inner zone. The RSM model gives a more accurate prediction for the flow field in the outer and inner zones than the RNG k-ε model.

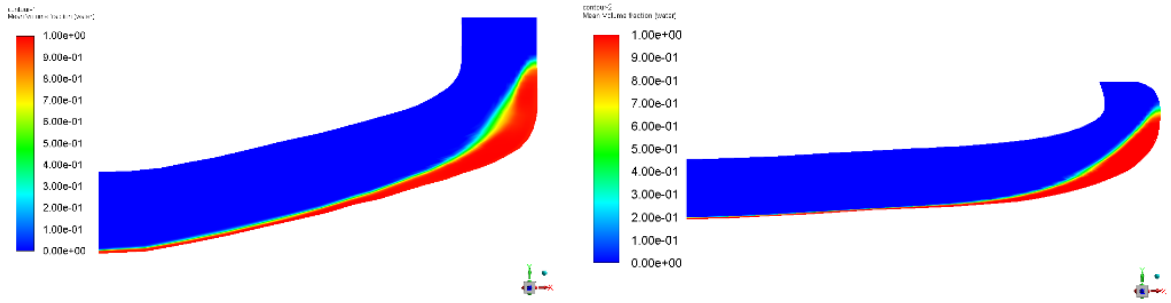

(a) (b)

FIG 4 – Fluid depth contours of the high gravity spirals at the end of the fifth turn at 4 m^3/hr; (a) Spiral 1; (b) Spiral 2.

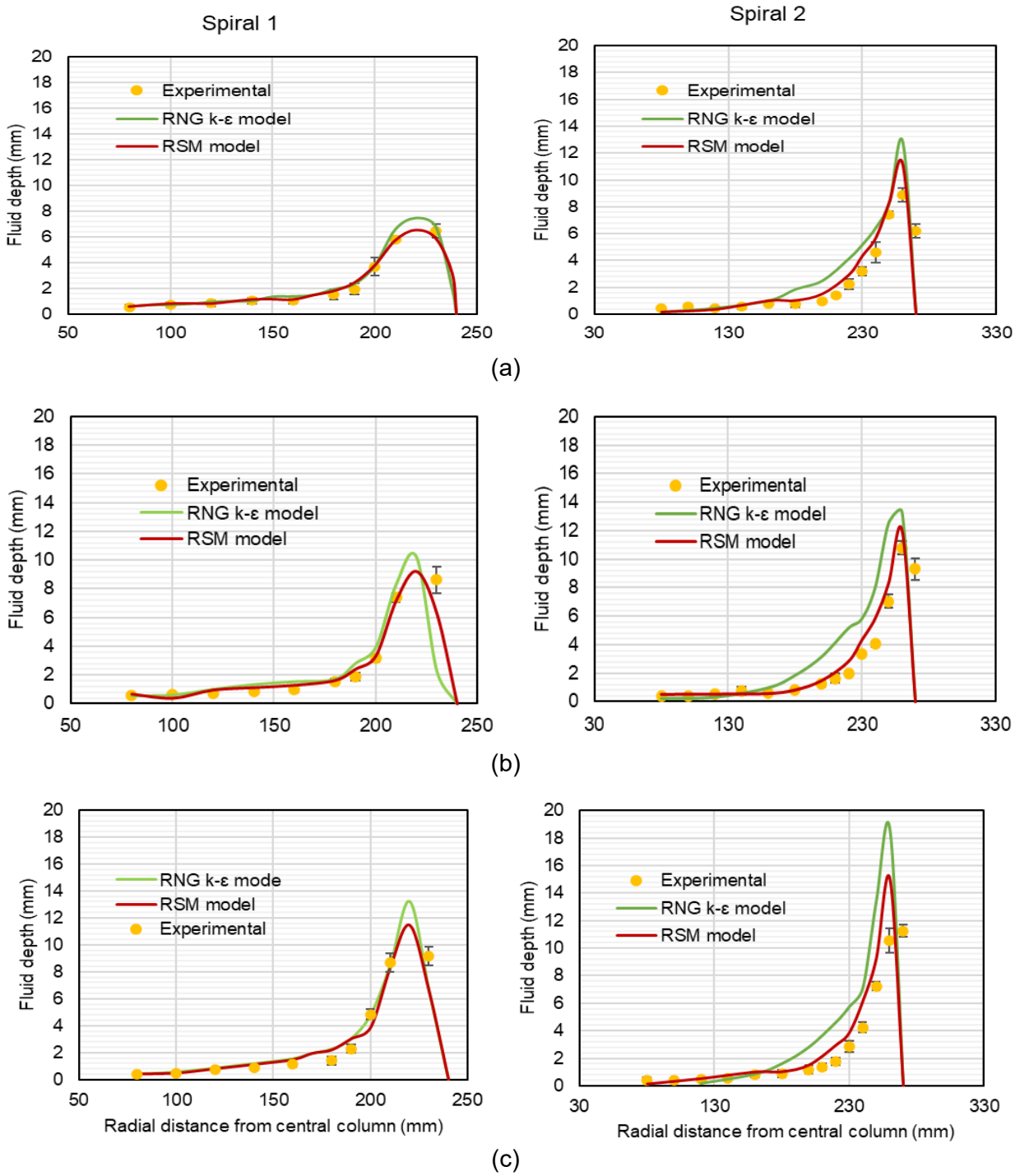

FIG 5 – Experimental and numerical predictions of fluid depth in spiral 1 and spiral 2 at: (a) 3 m^3/hr, (b) 4 m^3/hr and (c) 5 m^3/hr.

Free surface velocity

Free surface velocities also follow a similar trend with fluid depths across the trough. The free surface velocity increases evenly with radial distance at a given flow rate. With an increase inflow rate, there is an increment in free surface velocity as well. The pitch and flow rate have a more significant influence on the primary velocity in the outer zone (Holtham, 1992; Ye *et al,* 2019). At 3, 4 and 5 m^3/hr, the free surface velocities in spiral 1 are higher than in spiral 2 (Figure 6). The fluid velocity in a spiral concentrator with a higher pitch is greater than that of a lower pitch because the high pitch transforms the gravitational potential energy into kinetic energy. A comparison of velocity profiles among RNG k-ε and RSM turbulence models shows that the RSM model gives the best predictions at a free surface. It is noted that a maximum velocity of 1.75 m/s is observed for spiral 1 and 1.44 m/s for spiral 2.

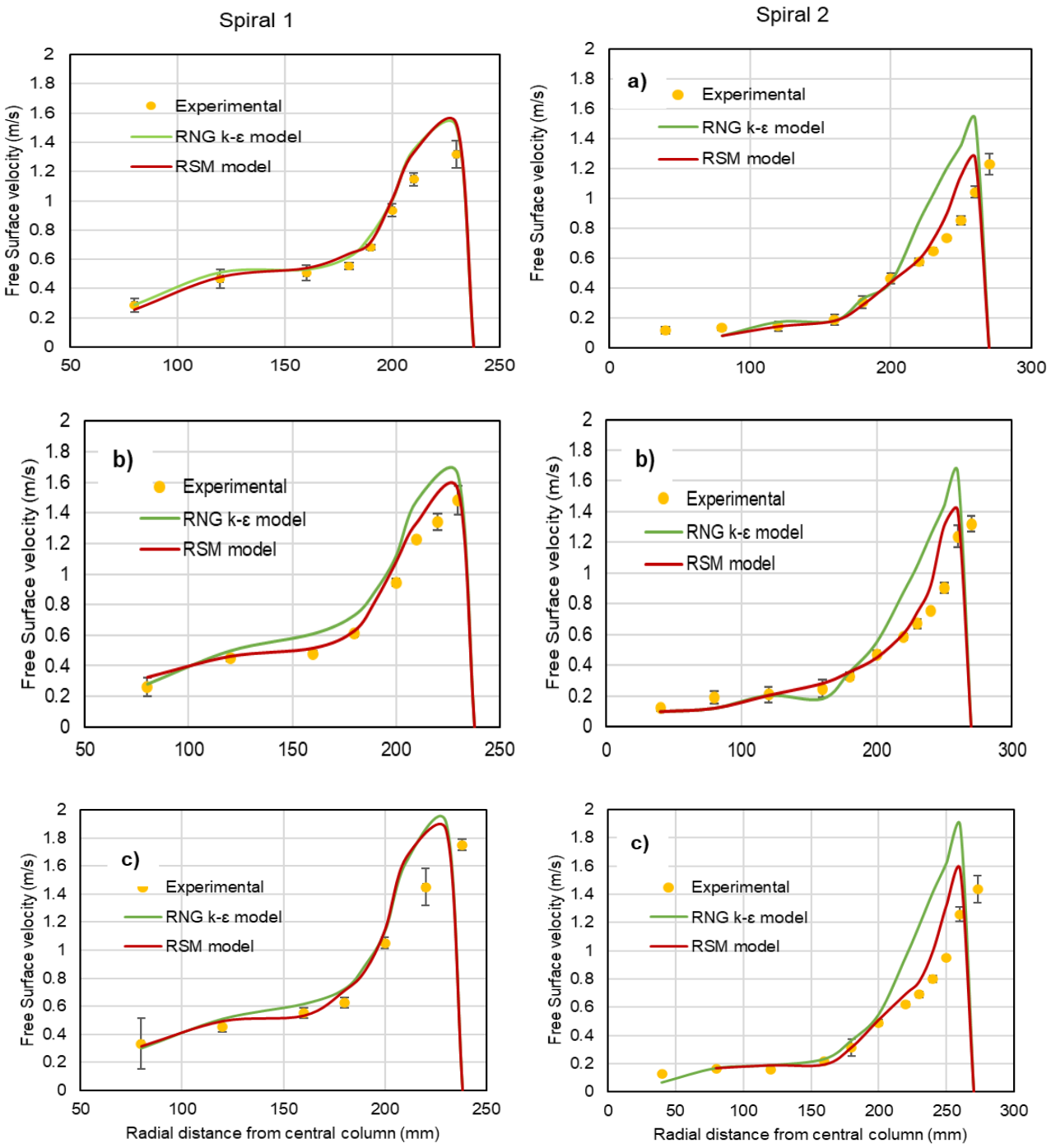

FIG 6 – Experimental and numerical predictions of Free surface velocity in spiral 1 and spiral 2 at: (a) 3 m^3/hr, (b) 4 m^3/hr, and (c) 5 m^3/hr.

CONCLUSIONS

The flow field measurements have been explored on the high gravity spiral concentrators, and the main conclusions can be drawn as follows:

- The flow field in LD9 coal spirals is greater compared to high gravity spirals because of finite differences in trough geometry, transverse slope, and pitch.
- The experimental and numerical studies with variations inflow rates are performed to understand the fluid flow phenomenon on high gravity spiral concentrators. An increase inflow rate leads to increased fluid depth and free surface velocity along the trough surface in the outer zone.
- The standard error for the measured fluid depths ranges from 0.01 to 0.08 and 0.004 to 0.03 for the free surface velocities at 3, 4 and 5 m^3/hr flow rates.
- The mean absolute percentage error between RSM and RNG k-ε models of fluid depth is 17.83 and 21.72 for spiral 1 and 23.32 and 35.95 for spiral 2, respectively.
- The mean absolute percentage error between RSM and RNG k-ε models of free surface velocity is 24.94 and 28.01 for spiral 1 and 16.34 and 35.75 for spiral 2, respectively.
- The error analysis shows that the RSM turbulence model gives a more accurate prediction for the flow field than the RNG k-ε turbulence model.

ACKNOWLEDGEMENTS

The authors would like to acknowledge the Indian Institute of Technology Hyderabad, the management of R&D TATA Steel and Uttatchhar Aviskar Yojana (UAY)-MHRD, Govt. of India for sponsoring, funding, and encouraging joint research of this project.

REFERENCES

Doheim, M A, Abdel Gawad, A F, Mahran, G M A, Abu-Ali, M H and Rizk, A M, 2008. 'Computational Prediction of Water-Flow Characteristics in Spiral Separators: Part II, the Primary and Secondary Flows', *JES Journal of Engineering Sciences*, 36(4), pp. 951–961. doi:10.21608/jesaun.2008.118512.

Holland-Batt, A B and Holtham, P N, 1991. 'Particle and fluid motion on spiral separators', *Minerals Engineering*, 4(3–4), pp. 457–482. doi: 10.1016/0892–6875(91)90147-N.

Holland-Batt, A B, 1989. 'Spiral separation: theory and simulation', *Institution of mining and metallurgy transactions. Section C Mineral Processing and Extractive Metallurgy*, 98.

Holtham, P N, 1990. 'Flow visualisation of secondary currents on spiral separators', *Minerals Engineering*, 3(3–4), pp. 279–286. doi: 10.1016/0892–6875(90)90123-S.

Holtham, P N, 1992. 'Primary and secondary fluid velocities on spiral separators', *Minerals Engineering*, 5(1), pp. 79–91. doi: 10.1016/0892–6875(92)90007-V.

Kapur, P C and Meloy, T P, 1998. 'Spirals observed', *International Journal of Mineral Processing*, 53(1–2), pp. 15–28. doi: 10.1016/s0301–7516(97)00053–7.

Loveday, G K and Cilliers, J J, 1994. 'Fluid flow modelling on spiral concentrators, Threaded rod Radial arm Levelling support Slurry surface Spiral trough Splitter blades', *Minerals Engineering*, 7(2–3), pp. 223–237.

Matthews, B W, Holtham, P and Golab, K, 1998. 'Computational and Experimental Investigation of Spiral Concentrator Flows', *Coal Operators Conference*, (February 2019), pp. 415–421.

Meng, L, Gao, S, Wei, D, Cui, B, Shen, Y, Song, Z and Yuan, J, 2021. 'Effects of cross-sectional geometry on flow characteristics in spiral separators', *Separation Science and Technology*, 56(17), pp. 2967–2977. doi: 10.1080/01496395.2020.1853169.

Napier-Munn, T and Wills, B A, 2005. *Wills' Mineral Processing Technology*, *Wills' Mineral Processing Technology*. doi: 10.1016/B978–0-7506–4450–1.X5000–0.

Sivamohan, R and Forssberg, E, 1985. 'Principles of spiral concentration', *International Journal of Mineral Processing*, 15(3), pp. 173–181. doi: 10.1016/0301–7516(85)90033-X.

Ye, G, Ma, L, Alberini, F, Xu, Q, Huang, G and Yu, Y, 2019. 'Numerical studies of the effects of design parameters on flow fields in spiral concentrators', *International Journal of Coal Preparation and Utilization*, 42(1), pp. 67–81. doi: 10.1080/19392699.2019.1579200.

Air-core imaging in a hydrocyclone using non-invasive ERT Technique – effect of reconstruction algorithms

S Diddi[1], P Jampana[2] and N Mangadoddy[3]

1. Research Scholar, Indian Institute of Technology Hyderabad, Hyderabad Telangana 502284, India. Email: ch20resch01002@iith.ac.in
2. Associate Professor, Indian Institute of Technology Hyderabad, Hyderabad Telangana 502284, India. Email: pjampana@che.iith.ac.in
3. Professor, Indian Institute of Technology Hyderabad, Hyderabad Telangana 502284, India. Email: narasimha@che.iith.ac.in

ABSTRACT

The study of air-core dynamics in hydrocyclone operation is essential for predicting separation efficiency in mineral processing. Electrical resistance tomography (ERT) allows non-invasive measurements of hydrocyclone internal flow dynamics. Existing regularisation methods such as Gauss-Newton and TV norms rely on optimisation techniques which have very high computational cost for very fine meshes. In contrast, the monotonicity method has much lower computational cost as it does not solve such minimisation problems. In this paper, results from the monotonicity method, Gauss-Newton (GN) (Tikhonov) and Total-Variation (TV) norm-based minimisation methods for estimating the air-core diameter in hydrocyclones are compared. We study these methods on the laboratory hydrocyclone experimental two-phase flow data. The results obtained are validated against High-speed video (HSV) imaging and Computational Fluid Dynamics (CFD) results. The results on different mesh sizes, in particular for very fine meshes with the number of cells ranging from 30 000 to above 100 000 are also investigated. The data used in this study is obtained from ITS Z8000 ERT system. This system does not measure the voltages on the current carrying electrodes. Since these voltage values are required for the monotonicity method, we implement an interpolation method to compute them. The results show that the monotonicity method provides a closer approximation of the interface between air and the water phases.

INTRODUCTION

The hydrocyclone, one of the fast-processing devices in the mineral processing industries, is used to separate particles from multiphase processing fluids. It works on the principle of centrifugal sedimentation in which particles separate according to size and density from processing fluid by centrifugal force (Rakesh *et al*, 2014). It consists of four main parts: the tangential feed inlet, cylindrical cone, spigot, and vortex finder. The tangential inlet of feed into the cyclone body creates an outer and inner vortex flows. The outer vortex moving in the downward direction carries the coarse size particles whereas the inner vortex moving in the upward direction carries the fine sized particles (Williams, 1995). Due to inner vortex formation, a low-pressure area prevails along the axis, responsible for forming air-core, which determines the separation efficiency. Careful control of the air-core in the process achieves the required efficiency in the separation. The initial ERT work in Hydrocyclone by (Ilyas *et al*, 1995) analysed air-core dynamics through a sensitivity density coefficient algorithm. Later literature (Dyakowski and Williams, 1996; Gutiérrez *et al*, 2000) reported air-core size estimation. Deoiling hydrocyclone operation with ERT analysis was provided in (Bennett and Williams, 2004). Recent studies of algorithm comparison in air-core dynamics have been analysed in (Rakesh *et al*, 2014) for Gauss-Newton (GN), Total Variation (TV) and Modified Sensitivity Back Projection (MSBP) for up to 6400 mesh elements. Later (Vakamalla *et al*, 2014) examined the air core variation with studies of inclined hydrocyclone through the linear back-projection algorithm.

To improve the sharpness of the interface, in this paper, we consider a relatively recent monotonicity-based method for reconstructing ‘binary’ conductivity profiles (Harrach, 2015). The monotonicity method relies on the full voltage data, ie voltages at the current carrying electrodes are also needed. Since these were not available for the experimental system ITS Z8000 for which the studies are conducted, we implement two interpolation schemes (geometric and linear) to estimate these missing values (Harrach, 2015). We compare the results of the monotonicity

method with that of the existing algorithms such as GN (Adler *et al*, 2007) and TV norm (Borsic *et al*, 2010) methods. The monotonicity method does not perform optimisation and hence is very fast compared to both GN, TV methods. Due to the small computational cost, the current work explores fine mesh elements ranging from thousands to one lakh for the monotonicity method.

The paper is organised into several sections. In section II, the ERT inverse problem is presented. This section also contains the discussion of optimisation-based techniques and the monotonicity method. In section III, reconstruction results of laboratory hydrocyclone experimental two-phase flow data. Concluding remarks are given in section IV.

ERT Inverse Problem

In ERT, a set of currents through adjacent electrodes are used as inputs whereas the outputs/solutions of the forward problem are u (the potential in the domain Ω) and U where $U^k = (U_1, U_2, \cdots, U_{L-1}, U_L)$ (the vector of voltages on the electrodes) for the kth current pattern. In experimentation, only U is measured L^2. These voltages can be rearranged into an $L \times L$ matrix for the L current patterns where each column vector is $U^k, k = 1,2, \cdots, L$. This matrix is denoted by V. For a numerical implementation, the domain is discretised into cells/pixels using a meshing algorithm. In this study, the meshing and the solution to the forward problem are implemented in MATLAB using the EIDORS toolbox. In the Sheffield measurement protocol, the potential differences between adjacent electrodes except at the current carrying ones are measured. The ITS Z8000 ERT system on which the current studies are done is based on this protocol and provides $L(L-3)/2$ independent voltage measurements. For $L = 16$ electrode set-up a total of $n = 16 * 13/2 = 104$ voltages are obtained.

Reconstruction of the conductivity profile from ERT data has been studied extensively in the literature (Borsic and Adler, 2012; Cheney *et al*, 1999; Tamburrino *et al*, 2000). The data obtained from the experiment is the difference of voltages $\Delta V = V - V_0$ where V, V_0 are respectively the true and the reference voltage matrices as defined above. The reference voltage matrix V_0 corresponds to the case where the domain Ω is filled with water. Let σ_0 be the reference conductivity and $F(\sigma)$ denote the solution of the forward problem. In other words, given a conductivity profile (σ) and some fixed current vector, $F(\sigma)$ equals the $L \times L$ matrix, V as discussed above. Then, by definition, we have $\Delta V = V - V_0 = F(\sigma) - F(\sigma_0) \approx F'(\sigma_0)(\sigma - \sigma_0)$ where $F'(\sigma_0)$ is the Frechet derivative $F'(\sigma_0)$.

Optimisation based algorithms

Most of the existing algorithms are based on the following minimisation problem:

$$\hat{\kappa} = argmin_{\kappa} \|Y - G\kappa\|^2_a + \|L\kappa\|^2_b \quad (1)$$

where the a, b refer to different choices of norms, Y is the difference voltage data (ΔV) for the various current patterns, G is the Jacobian/Sensitivity matrix, κ is the vector of conductivity differences and L is a fixed prior matrix. For example, $a = b = 2$ corresponds to the Tikhonov regularisation and with Laplacian prior, this is implemented in the Gauss-Newton One Step method of EIDORS. Another choice is $a = 2, b = TV$, ie when the TV norm is used for the regularisation term. The solution to the Tikhonov problem can be obtained analytically leading to a simpler and computationally efficient solution. In contrast, the TV norm results in a convex optimisation problem whose solution is relatively costlier to compute. It may be stressed that the goal of these methods is to obtain the conductivity difference κ_i at each mesh cell/pixel.

Monotonicity method

We now describe a recent method for inclusion detection in ERT, namely the monotonicity method. In contrast to the methods described before, the goal of this technique is to find the support of the conductivity change κ, ie to find the pixels where κ is non-zero. The monotonicity method assumes that the conductivity values of continuous phase (σ_0) and the air-core (σ_1) are known *a priori*. In the studies considered in this paper, the continuous phase is water with conductivity $\sigma_0 = 430\mu S$ and the conductivity of air is considered to be a very low value $\sigma_1 = 10^{-9} S$. Therefore, inside the air-core, the conductivity change is given by $\kappa = \sigma_1 - \sigma_0$ whereas outside the air-core $\kappa = \sigma_0 - \sigma_0 = 0$. Therefore, by finding the locations of the non-zero values of κ the approximate

diameter of the air-core can be computed. Assuming that the contact impedance vector z does not vary for the reference and the true measurements, the monotonicity relation can be written as (Harrach, 2015):

$$\int_{\Omega} \frac{\sigma_0}{\sigma}(\sigma_0 - \sigma)|\sum_{i=1}^{L} I_i \nabla u_0{}^i|^2 dx \geq I^T V I \geq \int_{\Omega}(\sigma_0 - \sigma)|\sum_{i=1}^{L} I_i \nabla u_0{}^i|^2 dx \text{ for any vector } I \in R^m \quad (2)$$

where $u_o{}^k$ is the solution to the current pattern I^k for the reference conductivity σ_0. The domain is discretised using a mesh generator and the cells (pixels) are represented as $P_i, i = 1,2,\cdots,N$, where N is the total number of cells in the mesh. Therefore, $\cup_{i=1}{}^{N} P_i \approx \Omega$, where the approximation is due to the curved parts of the boundary which may not be exactly covered by the triangular elements obtained from the mesh generator. From the discussion above, it is clear that if the cell P_i is inside the air-core, $\sigma_0 - \sigma = \sigma_0 - \sigma_1$, otherwise $\sigma_0 - \sigma = 0$.

In either case, $\sigma_0 - \sigma \geq 0$ in Ω. The monotonicity relation then provides the following. Let $\beta \geq 0$ and assume that $\beta \chi_{P_i} \leq \sigma_0 - \sigma$, then:

$I^T V I \geq \int_{\Omega}(\sigma_0 - \sigma)|\sum_{i=1}^{L} I_i \nabla u_0{}^i|^2 dx \geq \beta \int |\sum_{i=1}^{L} I_i \nabla u_0{}^i|^2 dx \geq -\beta I^T S_i I$ which shows that:

$V + \beta S \geq 0$, ie $V + \beta S$ is positive semi-definite. The monotonicity method computes,

$\beta_i = max\{\beta \geq 0; V + \beta S_i \geq 0\}$ and approximates the support of κ by the function $\sum_i \beta_i \chi_{P_i}$. Here χ_A represents the indicator function of the set A.

RESULTS AND DISCUSSION

The above section described the image reconstruction algorithms used in this study from a theoretical perspective. In this section, the spatial accuracy of these algorithms with respect to change in the mesh density has been studied on experimental data from a hydrocyclone. Two interpolation methods namely, geometric, and linear, are utilised to estimate the full voltage data in the monotonicity method. The ERT experiments were conducted using hydrocyclone with a diameter of 75 mm for gas and water phase studies. Sixteen equidistance and circular surfaced electrodes were placed to acquire the voltages. The electrodes were made of stainless steel. Air core is estimated for two phase flow experiments in the hydrocyclone with various operating pressures. The hydrocyclone was operated with 12.5 mm of spigot diameter and 25 mm of vortex finder diameter.

Figure 1 provides the tomograms and surface profiles for an operating pressure of 20 psi.

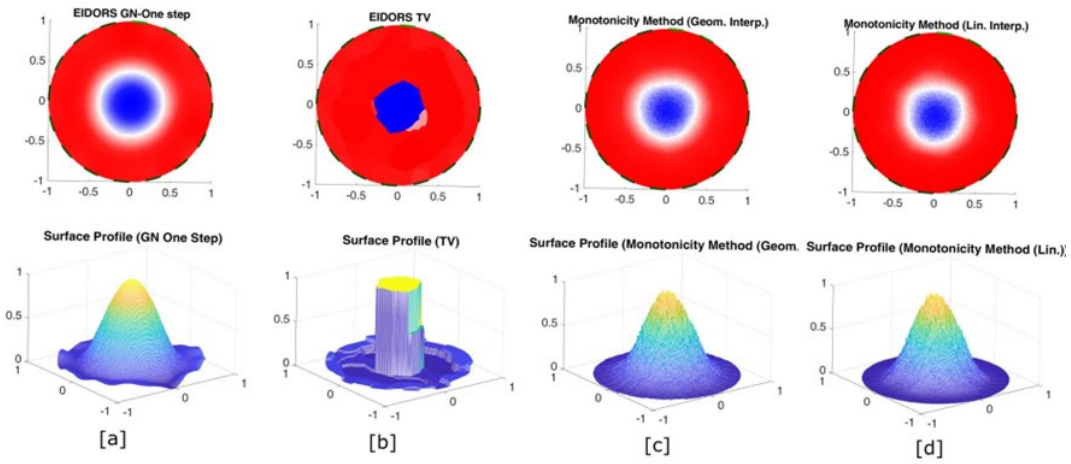

FIG 1 – Air core variation tomograms and profile shapes on 20 psi.

Compared with the other two algorithms, the TV norm method results in a sharper boundary separation between phases. However, we note that GN one-step and monotonicity methods do not provide a sharp interface. To obtain a good separation, we use a threshold on the tomogram values.

In this study, a variable threshold level in the range of 0.1 to 0.9 has been explored for each of the three methods. For each threshold level, the estimated diameter is compared with the diameter

obtained from image processing from a high-speed video (HSV) camera. Then, an optimal threshold for each of the methods is chosen. It may be noted that the threshold for each method is dependent on the operating pressure of the hydrocyclone.

Figure 2 shows the results after applying the optimal thresholds for different operating pressures. For the GN one-step method, the optimal threshold was found to be approximately 80 per cent whereas the TV norm method overestimated the air core diameter for all the thresholds in the above range. To get better comparisons with high-speed video camera (HSV) results a threshold of 98 per cent was calculated for the TV method. The Monotonicity method required a 75 per cent threshold to give estimates closest to the diameter estimated from HSV. Figure 2 also gives the predicted diameter from computational fluid dynamics simulations (CFD). GN one step exhibits a maximum error of 28 per cent with HSV data and 13 per cent with CFD predictions. The TV norm estimates resulted in a maximum error of 31 per cent with HSV and 16 per cent with CFD. Monotonicity with geometric interpolation has a maximum error of 26 per cent of error with HSV and 14 per cent with CFD predictions whereas with linear interpolation, the maximum error is 31 per cent with HSV and 15 per cent with CFD predictions. Therefore, overall, the monotonicity method with geometric interpolation showed a closer approximation with the CFD and HSV results than the GN and TV methods.

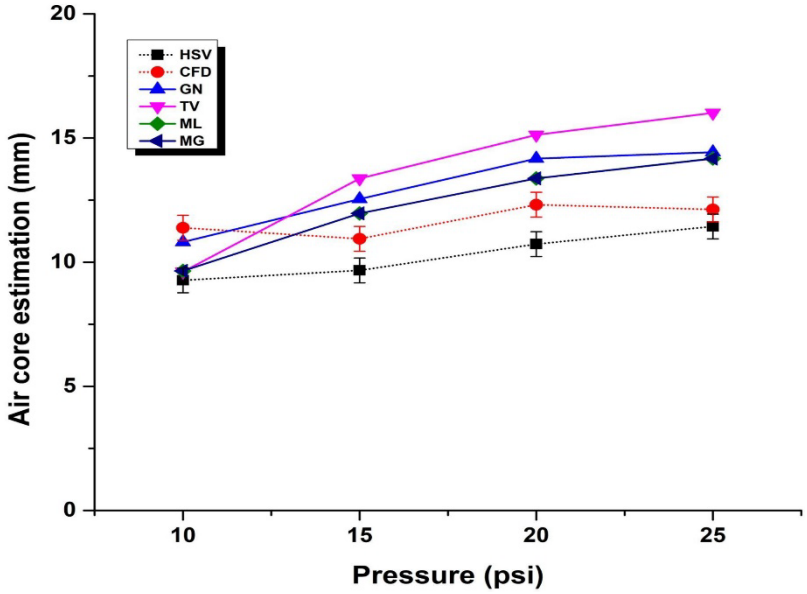

FIG 2 – Air-core diameter validation with HSV and CFD results.

We also evaluated the computational cost of each algorithm for mesh elements ranging from 4448 to 9091 elements. It can be seen that the monotonicity method is much faster. Figure 3 shows this comparison. Beyond these, we have also studied the computational time for each method individually for large meshes. The TV norm method proved to be the costliest algorithm in terms of computational time, about 36 minutes for 14 306 mesh elements. The GN-one step method took a maximum time of five minutes for 47 306 mesh elements. The evaluation time for the monotonicity method is 16 minutes for 127 191 mesh elements.

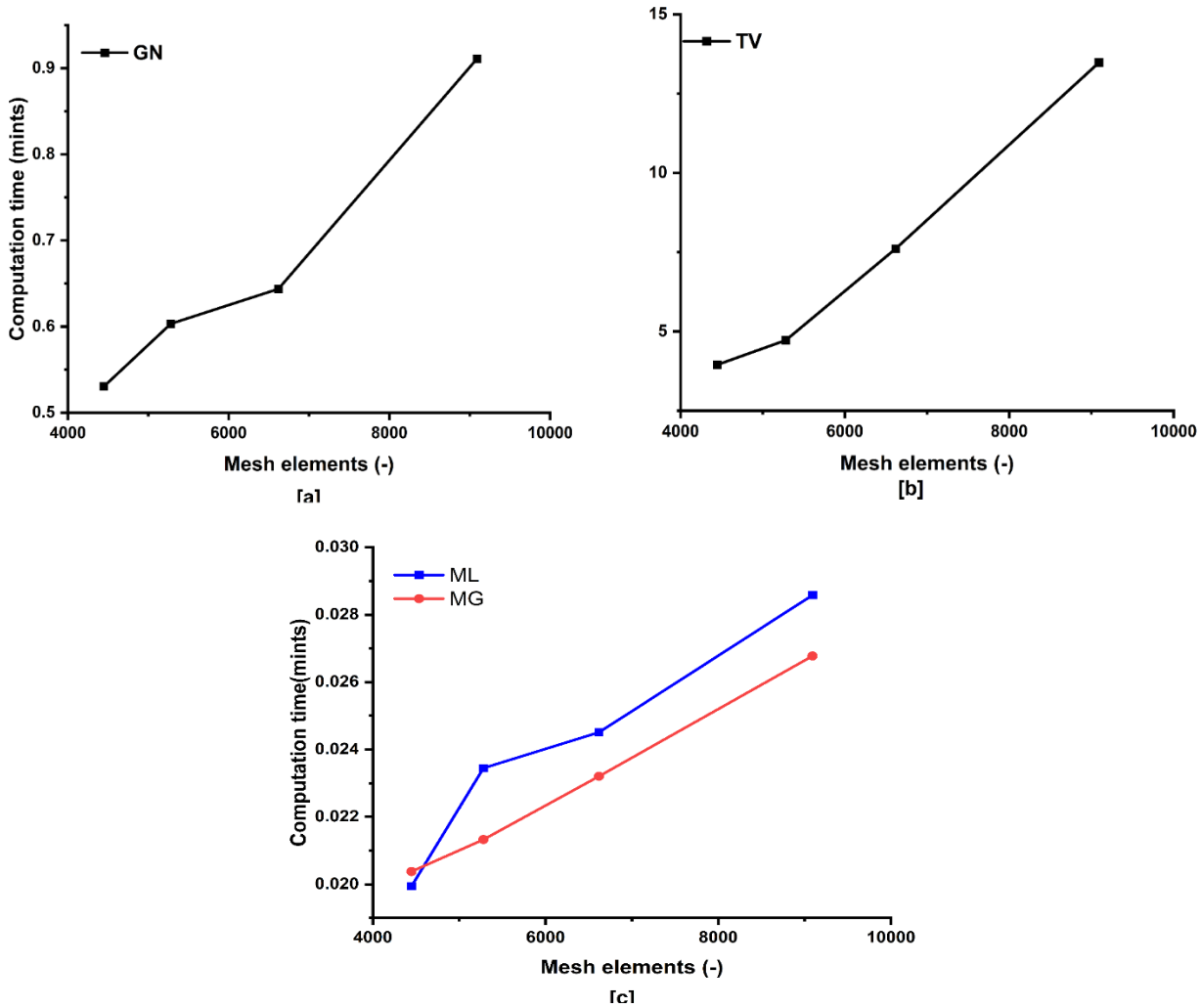

FIG 3 – Simulating time profiles for different image reconstruction algorithms with respect to mesh elements (a) GN-one step (b) TV norm (c) Monotonicity.

CONCLUSIONS

Comparison studies of image reconstruction algorithms have been performed to estimate the air core diameter for hydrocyclone operated with air-water flows. This work evaluated the monotonicity method and compared it to TV norm and GN one-step algorithms. The computational cost of GN one-step, TV, and monotonicity methods with varying number of mesh elements has also been studied. Monotonicity method gives the fastest reconstruction which is about 470 times faster than the TV norm and 26 times faster than the GN one-step for reconstructing 9091 mesh elements. Though TV performs well on shape and boundary sharpness, it is also the most computationally expensive, which could be impractical for finer meshes. The GN one-step and the monotonicity methods result in a diffusive tomogram; an appropriate threshold enables these methods to estimate the target with better accuracy and consume significantly less time compared to the TV norm method. To improve the accuracy, a thresholding method has been adopted. The overall percentage of error with HSV and CFD after thresholding is the smallest for the monotonicity method with geometric interpolation. Finally, we note that the threshold is dependent on the pressure. We are currently exploring other algorithms which can provide a radius independent threshold.

ACKNOWLEDGEMENTS

The authors would also like to thank the IITH for providing necessary facilities for the work and SERB project, DST (CRG/2018/004892) Govt.of India for funding the research work.

REFERENCES

Adler, A, Dai, T and Lionheart, W R B, 2007. Temporal image reconstruction in electrical impedance tomography. *Physiological Measurement*, *28*(7). https://doi.org/10.1088/0967–3334/28/7/S01

Bennett, M A and Williams, R A, 2004. Monitoring the operation of an oil/water separator using impedance tomography. *Minerals Engineering*, *17*(5), 605–614. https://doi.org/10.1016/j.mineng.2004.01.021

Borsic, A and Adler, A, 2012. A primal-dual interior-point framework for using the L1 or L2 norm on the data and regularization terms of inverse problems. *Inverse Problems*, *28*(9). https://doi.org/10.1088/0266–5611/28/9/095011

Borsic, A, Graham, B M, Adler, A and Lionheart, W R B, 2010. In vivo impedance imaging with total variation regularization. *IEEE Transactions on Medical Imaging*, *29*(1), 44–54. https://doi.org/10.1109/TMI,2009.2022540

Cheney, M, Isaacson, D and Newell, J C, 1999. Electrical Impedance Tomography. In *Society for Industrial and Applied Mathematics,* Vol. 41, Issue 1. http://www.siam.org/journals/sirev/41–1/33361.html

Dyakowski, T and Williams, R A, 1996. Prediction of high solids concentration regions within a hydrocyclone. *Powder Technology*, *87*(1), 43–47. https://doi.org/10.1016/0032–5910(95)03075–1

Gutiérrez, J A, Dyakowski, T, Beck, M S and Williams, R A, 2000. Using electrical impedance tomography for controlling hydrocyclone underflow discharge. *Powder Technology*, *108*(2–3), 180–184. https://doi.org/10.1016/S0032–5910(99)00218–1

Harrach, B, 2015. Interpolation of missing electrode data in electrical impedance tomography. *Inverse Problems*, *31*(11). https://doi.org/10.1088/0266–5611/31/11/115008

Ilyas, O M, Dyakowski, T and Williams, R A, 1995. Air Core Imaging in Cyclonic Coal Separators using Electrical Resistance Tomography. *Coal Preparation*, *15*(3–4), 149–163. https://doi.org/10.1080/07349349508905293

Rakesh, A, Kumar Reddy, V T S R and Narasimha, M, 2014. Air-core size measurement of operating hydrocyclone by electrical resistance tomography. *Chemical Engineering and Technology*, *37*(5), 795–805. https://doi.org/10.1002/ceat.201300672

Tamburrino, A, Ventre, S and Rubinacci, G, 2000. Reconstruction techniques for electrical resistance tomography. *IEEE Transactions on Magnetics*, *36*(4 PART 1), 1128–1131. https://doi.org/10.1109/20.877639

Vakamalla, T R, Kumbhar, K S, Gujjula, R and Mangadoddy, N, 2014. Computational and experimental study of the effect of inclination on hydrocyclone performance. *Separation and Purification Technology*, *138*, 104–117. https://doi.org/10.1016/j.seppur.2014.10.013

Williams, R A, 1995. Tomographic imaging for modelling and control of mineral processes. *The Chemical Engineering Journal and The Biochemical Engineering Journal*, *59*(1), 71–85. https://doi.org/10.1016/0923–0467(95)03008–5

Flotation machine gas characterisation – *v*ariation between different types of flotation machines

G J Harbort[1] and D Felipe[2]

1. General Manager, Geometecon, Rosewood Qld 4340.
   Email: greg.harbort@geometecon.com.au
2. Process Specialist, JKTech Pty Ltd, Indooroopilly Qld 4068. Email: d.felipe@jktech.com.au

ABSTRACT

In the past 40 years substantial changes have occurred in flotation machines. This has included increases in mechanical cell size to 630 m^3, significant changes to flotation column aeration design and widespread use of the Jameson cell and other pneumatic flotation cells. Over the corresponding period there has been increased used of machine characterisation measurements to benchmark and optimise flotation circuit performance.

JKTech maintains a database of industrial flotation machine characterisation measurements. The database contains over 4000 entries and includes gas dispersion measurements, such as bubble size, gas hold-up and superficial gas velocity, cell dimensions and impeller tip speeds. Data comes from numerous operating sites and commodity groups, including gold, copper, molybdenum, nickel, palladium, lead-zinc, platinum, silica, phosphate, coal and iron ore. Flotation duties registered include flash flotation, preflotation, roughing, scavenging and cleaner circuits.

Measurements have been conducted on a wide range of flotation machines from different manufacturers. This includes forced air machines, such as Outotec and Dorr Oliver, and self-aerated machines, such as Denver and Wemco. The database also includes substantial flotation column entries, such as the Microcel, Eriez/CMT Slamjet and Jameson cell.

This paper describes the flotation machine characterisation database and discusses the variation between different types of industrial flotation machines, in operating production circuits.

INTRODUCTION

The study of flotation hydrodynamics that is commonly referred to as flotation machine gas characterisation dates back to research conducted in the 1980s, at McGill University and the University of Newcastle (Jameson and Allum, 1984; Dobby and Finch, 1986). This extended into the 1990s where research at the Julius Kruttschnitt Mineral Research Centre (JKMRC) by Barun Gorain provided a link between gas characterisation and flotation kinetics (Gorain, Franzidis and Manlapig, 1995a, 1995b, 1996, 1997, 1999; Gorain *et al,* 1998).

In the following 20 years flotation machine gas characterisation became a critical mainstay of flotation machine and circuit evaluation. There are numerous publications on its use in industrial flotation plants, including reviews by Deglon, Egyah-Mensah and Franzidis (2000), Nesset *et al* (2006), Power and Franzidis (2000), Gomez and Finch (2002, 2007), Fournier *et al* (2015), Lopez-Saucedo *et al* (2012), Gorain (2000) and Hernandez-Aguilar *et al* (2006).

Key gas dispersion measurements include bubble size (d_b), gas hold-up (ε) and superficial gas rise velocity (Jg), These measurements characterise the hydrodynamic conditions in the pulp phase of a particular flotation cell. Gas dispersion is defined as how well the air entering a flotation cell is dispersed throughout the volume of the cell and is heavily dependent on the air flow rate and impeller speed. Numerous sensors have been developed for gas characterisation measurements and continue to evolve. These sensors include devices by McGill University (Canada), the JKMRC (Australia), the University of Capetown (South Africa), the University of Santa Maria (Chile), the Helsinki University of Technology (Finland) and Anglo Platinum (South Africa). Reviews of gas dispersion devices have been published by Gomez and Finch (2002), Harbort and Schwarz (2010) and Grau and Heiskanen (2003).

This paper uses a similar format to that of the seminal presentation by Schwarz and Alexander (2006) at the Centenary of Flotation Conference. It makes uses of an extensive database of measurements from operating sites to determine typical operating conditions. The authors acknowledge that

flotation and gas charcterisation are complex processes, with multiple interacting factors (Harbort, Schwarz and Nguyen, 2018). Fundamental research measurements are excluded from the database and readers interested in these areas are referred to various other publications including Shabalala *et al* (2011), O'Connor, Randall and Goodall (1990), Finch, Gélinas and Moyo (2006), Grau, Laskowski and Heiskanen, (2005), Cappuccitti and Finch (2008), Cappuccitti and Nesset (2010).

DATABASE

Sources of information

Data included in the database was initially sourced from the AMIRA P9 project, utilising measurements taken by students from the JKMRC, McGill University and the University of Cape Town. With the introduction of JKTech, data sets collected from conducting plant optimisation studies were also incorporated. The last 15 years has seen multiple measurements taken by various groups including equipment manufacturers, research institutes, consultants and operating sites.

A requirement for inclusion in the database is that data can be independently verified. Some studies reported in literature have been excluded due to lack of sufficient verification information.

The database focuses on operating sites with solid-water-air systems. Measurements undertaken in laboratory flotation cells are generally not included, nor are measurements conducted in air-water systems.

As shown in Figure 1, most flotation cell entries were undertaken in the period 2006 to 2009. In recent years, a concerted effort has been untaken by the authors to collate measurements from operating sites and literature for database inclusion.

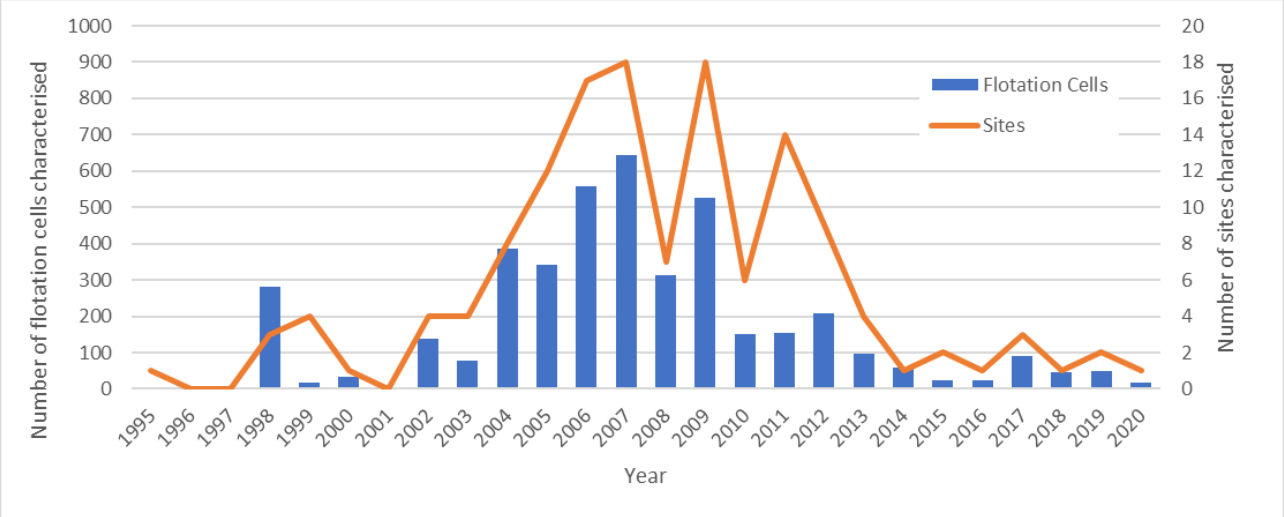

FIG 1 – Characterisation measurements per annum.

Measurements

The database currently contains hydrodynamic measurements from over 4200 flotation cells. The information included is dependent on the scope of gas characterisation surveys conducted, resulting in varying totals for different types of measurement. Measurements recorded include:

- Superficial gas rise velocity – 4092 entries.
- Air hold-up – 3264 entries.
- Bubble diameter – 3276 entries.

Calculations of bubble surface area flux (Sb) within the pulp zone are also included. The bubble surface area flux is a measure of the rate of bubble surface area rising through a flotation cell per unit cross-sectional area. This parameter combines the superficial gas velocity and bubble size into a single quantity, according to the following equation:

$$Sb = \frac{Jg \cdot 6}{d_b}$$

Sb is an important parameter as it links gas dispersion to flotation performance, being directly proportional to the kinetic rate.

An estimate of the bubble surface area flux can also be obtained using measurements of the superficial gas velocity, impeller speed (Ns), impeller design–characterised by the ratio of height to diameter (aspect ratio, As) and the particle size of the feed entering the cell (P_{80}). There are 1142 sets of data entry relating to these measurements.

Flotation cell geometry relating to froth area and lip length is also included. In instances where a gas characterisation survey is accompanied by a mass balancing survey this allows carrying rates per lip length or froth area to be conducted. In addition, residence times per cell calculations are also conducted.

In cases where a full flotation modelling survey is conducted the froth recovery can also be conducted. There are currently 743 froth recovery entries in the database.

Figures 2 to 4 give an indication of the variability in air hold up, superficial gas velocity and bubble size. Air hold-up measurements averaged 12.1 per cent across all cells measured. The majority of air hold-up measurements were between 7.0 per cent and 14.5 per cent. There were only a few measurements above 40 per cent, and the reasons behind these high values are likely due to ore viscosity properties at specific sites and ultrafine bubble sizes due to excessive frother addition. Superficial gas velocity averaged 1.3 cm/s. In operating cells with values less than 1 cm/s, it was recommended to investigate increasing the air flow rates to improve the pulp kinetics. However, values greater than 3 cm/s indicated possible flooding (pulp recovered in the concentrate) and it was recommended decreasing the air flow rates to improve the froth performance (increase stability and decrease entrainment). Bubble size measurements averaged 1.6 mm across all cells measured. The majority of bubble size measurements were between 1.1 mm and 1.9 mm.

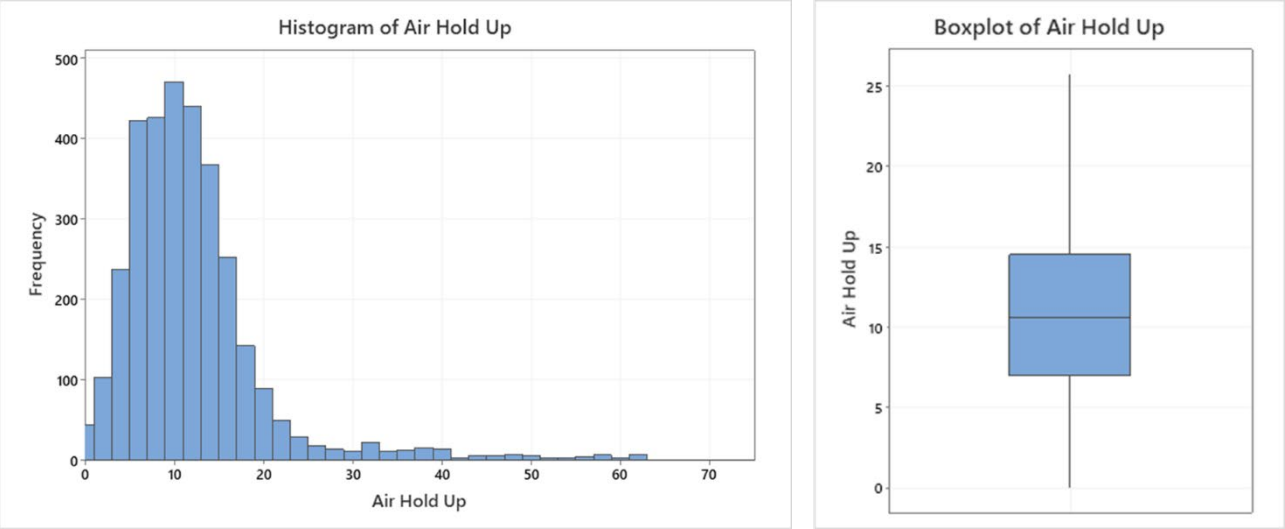

FIG 2 – Air hold up measurement histogram and box plot.

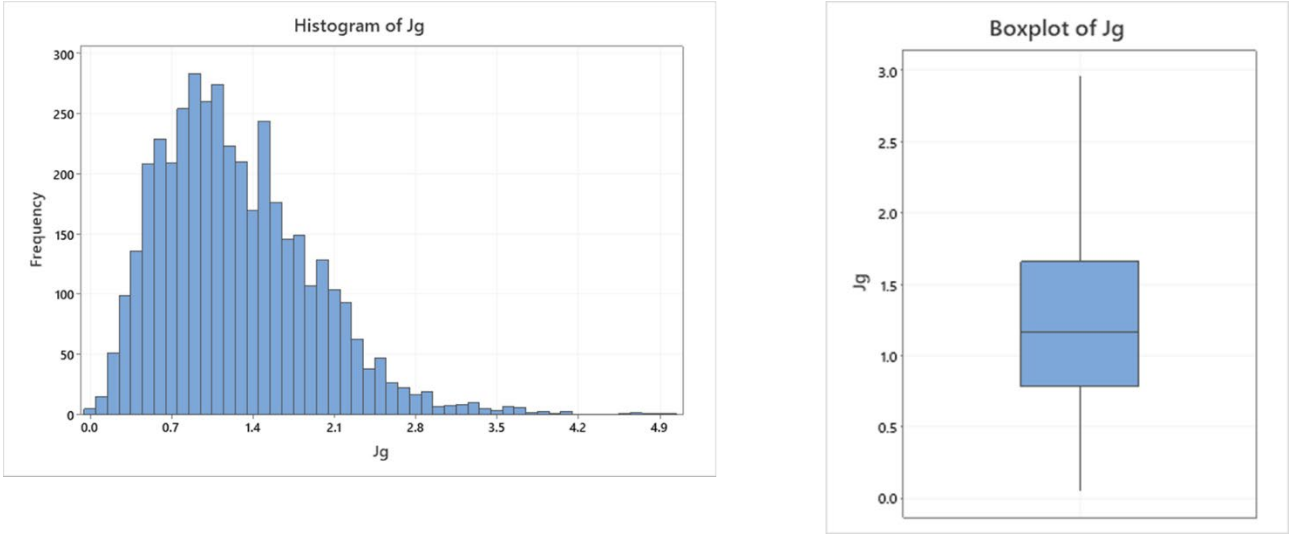

FIG 3 – Superficial gas velocity measurement histogram and box plot.

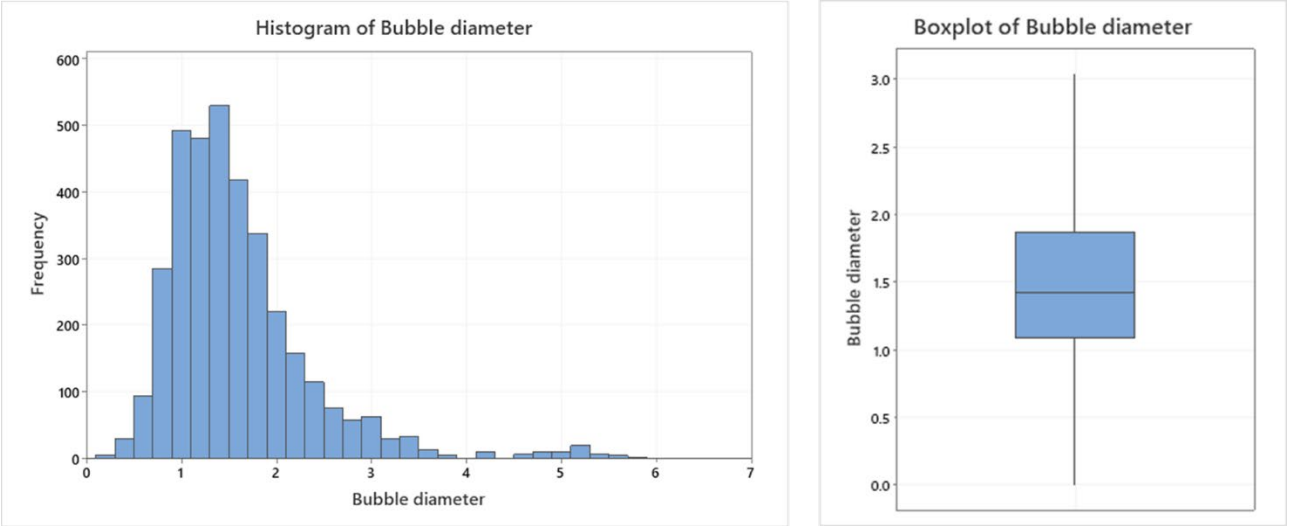

FIG 4 – Superficial gas velocity measurement histogram and box plot.

Flotation cell location and commodity

Gas characteristic measurements formed an integral part of the Australian Mineral Industries Research Association (AMIRA) P9 project, between 2000 and 2010. Measurements were conducted initially by researchers from the Julius Kruttschnitt Mineral Research Centre (JKMRC), McGill University and the University of Capetown (UCT), as well as JKTech, in the operating sites of P9 sponsor companies. This resulted in an emphasis on base metals (ie copper, lead and zinc) and precious metals (gold and platinum group metals). Table 1 shows this trend has continued, although in the last ten years there has been a number of characterisation measurements conducted in iron ore and phosphate operations. In 2005 the database geographic scope was limited, with 75 per cent of the total measurements from sites in. In the intervening years, gas characterisation measurements have become widespread, with 23 countries now represented.

TABLE 1

Database entry by commodity and cell location.

Commodity	Number of cells	Cell location	Number of cells
Copper	1492	Australia	1415
Platinum Group Metals	607	South Africa	594
Zinc	509	USA	414
Lead	412	Chile	283
Gold (pyrite)	366	Canada	259
Nickel	295	PNG	169
Molybdenum	214	Indonesia	151
Coal	127	Peru	143
Iron ore	90	Brazil	112
Other (including kaolin, palladium, phosphate, silica, talc)	157	Other (including Bolivia, China, Fiji, India, Iran, Ireland, Laos, Mexico, New Zealand, Portugal, Sweden, Tanzania, Zambia, Zimbabwe	712

Flotation cell duty

The database initially described flotation cell duty in terms of the operating site terminology. This resulted in multiple descriptions for cell duty, even when duties were similar. It has since been updated to summarise flotation duties as either flash flotation, prefloat, roughing, scavenging, cleaning, or cleaner scavenging. Although roughing-scavenging and cleaner flotation cells dominate Table 2, there are numerous entries for less common applications such prefloat and flash flotation.

TABLE 2

Database entry by flotation cell duty.

Flotation cell duty	Number of cells
Rougher	1868
Scavenger	678
Prefloat	32
Flash flotation	29
Cleaner	1509
Cleaner scavenger	149

Flotation cell size

The flotation capacity details for mechanical flotation cells are recorded in m^3. The cataloguing of flotation columns includes both short and tall columns, sparged columns, externally aerated columns and pneumatical flotation cells (Harbort, 2019; Harbort and Clarke, 2017).

A summary of data entry by flotation cell size is given in Table 3. Approximately 50 per cent of mechanical flotation cells entries are less than 20 m^3 in volume, with the remainder up to 300 m^3. There are a number of manufacturer data sets for 530 m^3 flotation cells they have not been independently verified and have not been included in the database. Flotation column entries are more evenly spread from 0.5 m diameter to greater than 5.0 m diameter.

TABLE 3

Database entry by flotation cell size.

Mechanical cell volume (m^3)	Number of cells	Flotation column diameter (m)	Number of cells
<20	1925	<0.5	90
20 to 50	824	0.5 to 1.0	55
50 to 100	185	1.0 to 2.0	29
100 to 150	417	2.0 to 3.0	63
150 to 300	289	3.0 to 4.0	77
>300	71	4.0 to 5.0	75
		>5.0	82

Flotation cell equipment type

The database currently catalogues 32 different flotation machine types. Entries commonly refer to the generally accepted industry name for a flotation machine, rather than the manufacturer name. A summary of the different equipment types is given in Table 4.

TABLE 4

Database entry by flotation cell equipment type.

Flotation cell	Number of cells
Outotec	1604
Wemco	1228
Dorr-Oliver	314
Agitair	280
Slamjet Column	113
Microcel	101
Denver	96
Bateman	84
Metso/Sala/Svedala	66
Other mechanical	99
Other column	168

Sufficient data exists to allow an evaluation of variation in flotation machine gas characterisation for Outotec, Wemco, Agitair, Dorr-Oliver, Jameson, Microcel and SlamJet column flotation machines. Miscellaneous columns were also grouped together for evaluation.

An effective way to increase flotation cell kinetic rate is to increase bubble surface area flux, either by increasing air addition (hence increasing superficial gas velocity) or decreasing bubble size. The most common method used in day-to-day operating is by variation in air addition.

Figure 5 provides a comparison of Jg with bubble size for the eight flotation machine types evaluated. Error bars represent one standard deviation. The data indicates that all the flotation machines have an increase in bubble size with Jg. Below a Jg of 1.5 cm/s bubble size variability, even in multiple plants with multiple duties and commodities is relatively small. Above a Jg of 1.5 cm/s bubble size variability increases.

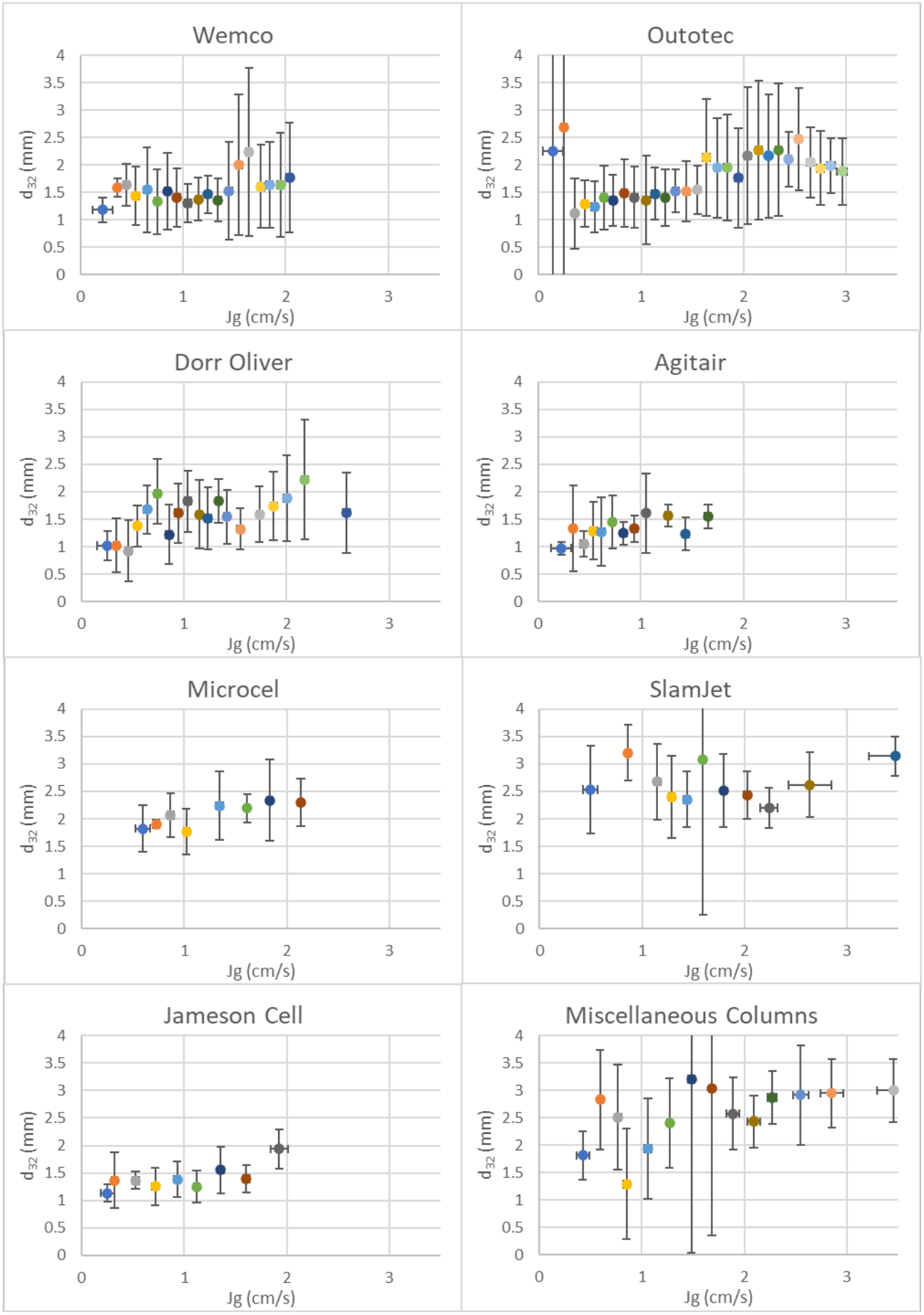

FIG 5 – Relationship between Jg and bubble sizes for various types of flotation machines.

The relationship between Jg and bubble size indicates that Jg and Sb do not form a linear relationship. This is evident in Figure 6 where each type of flotation machine has a maximum limiting Sb, or kinetic rate, based on gas characteristics.

The flotation machines can be catalogued into two groups base on the rate that Jg is converted into Sb, (ie the effectiveness of air addition to increase kinetic rate). The first group consists of Wemco, Outotec, Agitair, Dorr-Oliver and the Jameson Cell. These types of flotation machines could be considered more effective bubble surface are flux generators. The second group consists of the Microcel, SlamJet column and the miscellaneous column grouping. These types of flotation machines could be considered less effective bubble surface are flux generators.

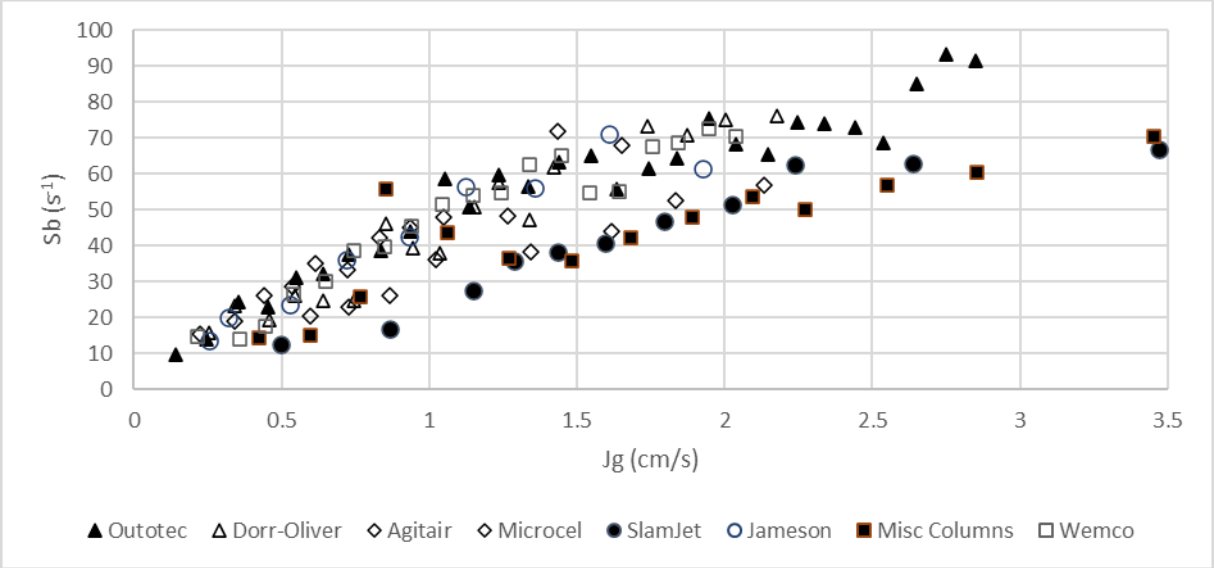

FIG 6 – Relationship between Jg and Sb for various types of flotation machines.

If the data is treated as a first order rate reaction, then k, the rate that Jg is converted into Sb, and $Sb_{max,}$ can be calculated. A summary of k and Sb_{max} values are given in Table 5. This indicates that the Jameson Cell and Agitair flotation cell are the most efficient bubble surface area flux generators, with k values of 1.64 and 1.61. They both achieved similar Sb_{max} values of ~72 m^{-1}. The Wemco, Outotec and Microcel had very similar Sb generation efficiency, with k values between 1.45 and 1.47. The Microcel however had a significantly lower Sb_{max} value of ~60 m^{-1}, compared to ~73 m^{-1} for the Wemco flotation cell an ~73 m^{-1} for the Outotec flotation cell. Of the mechanical flotation cells evaluated the Dorr-Oliver cell was the least efficient bubble surface are flux generator, with a k value of 1.31. It did however have the highest Sb_{max} value of ~80 m^{-1}. The SlamJet flotation column and miscellaneous columns group had the lowest bubble surface are flux generation efficiency, with k values of 0.84 and 1.61.

TABLE 5

k and Sb_{max} values for various types of flotation machine types.

Flotation machine type	k	Sb_{max}
Wemco	1.47	73
Outotec	1.47	75
Dorr-Oliver	1.31	80
Agitair	1.61	72
Microcel	1.45	60
SlamJet	0.85	72
Jameson	1.64	72
Misc Columns	0.80	74

Several observations can be drawn from this data, including:

- Wemco and Outotec flotation cells would require similar residence times to achieve the same performance.
- The Agitair flotation cell in a typical operating range would require less residence time to achieve the performance of Wemco and Outotec cells.
- The Dorr-Oliver flotation cell in a typical operating range would require more residence time to achieve the performance of Wemco and Outotec cells.
- The SlamJet column in a typical operating range would require notably more residence time to achieve the performance of Wemco and Outotec cells.
- At maximum stable Jg the Dorr-Oliver cell would require less residence time to achieve the performance of Wemco and Outotec cells.

CONCLUSIONS

A database has been generated using data collected from many types and sizes of industrial flotation cells over the past 27 years. The database currently contains gas dispersion measurements, such as bubble size, air hold-up and superficial gas velocity, for over 4200 cells and is continually growing with ongoing pulp phase investigations.

A review of data relating to different types of flotation machines indicates:

- the Jameson Cell and Agitair flotation cell are the most efficient bubble surface are flux generators.
- the Wemco, Outotec and Microcel had very similar Sb generation efficiency.
- of the mechanical flotation cells evaluated the Dorr-Oliver cell was the least efficient bubble surface are flux generator.
- the SlamJet flotation column and miscellaneous columns group had the lowest bubble surface are flux generation efficiency.

ACKNOWLEDGEMENTS

This paper is dedicated to the late Dan Alexander, who together with Sarah Schwarz was instrumental in setting up the flotation machine gas characterisation database.

The authors would like to thank JKTech and Geometecon for permission to publish the paper.

REFERENCES

Cappuccitti, F and Finch, J A, 2008. Development of new frothers through hydrodynamic characterization, *Minerals Engineering* 21 (12–14), pp 944–948.

Cappuccitti, F and Nesset, J E, 2010. Frother and Collector Effects on Flotation Cell Hydrodynamics and Their Implication on Circuit Performance, *Proceedings of the 42nd Annual Meeting of the Canadian Mineral Processors* (Canadian Institute of Mining and Metallurgy).

Deglon, D A, Egyah-Mensah, D and Franzidis, J P, 2000. Review of hydrodynamics and gas dispersion in flotation cells on South African platinum concentrators, *Minerals Engineering* 13, pp 235–244.

Dobby, G S and Finch, J A, 1986. Particle collection in columns – gas rate and bubble size effects, *Can Metall Q*, 25(1), pp 9–13.

Finch, J A, Gélinas, S and Moyo, P, 2006. Frother-related research at McGill University, *Minerals Engineering* 19, pp 726–733.

Fournier, J, Hardie, C, Torrealba, J and Nesset, J E, 2015. A review of gas dispersion studies in flotation plants, *47th Annual Canadian Mineral Processors Operators Conference,* (Canadian Institute of Mining and Metallurgy).

Gomez, C O and Finch, J A, 2002. Gas dispersion measurements in flotation machines, *CIM Bull*, Vol 95 (1066), pp 73–78, (Canadian Institute of Mining and Metallurgy).

Gomez, C O and Finch, J A, 2007. Gas dispersion measurements in flotation cells, *Int J Miner Process*, Vol 84, pp 51–58.

Gorain, B K, 2000. Selection of cell operating conditions to optimise performance of flotation circuits with large cells, *Proceedings of the Seventh Mill Operators Conference* (The Australasian Institute of Mining and Metallurgy), pp 179–187.

Gorain, B K, Franzidis, J P and Manlapig, E V, 1995a. Studies on impeller type, impeller speed and air flow rate in an industrial scale flotation cell. Part 1: Effect on bubble size distribution, *Minerals Engineering* 8 (6), pp 615–635.

Gorain, B K, Franzidis, J P and Manlapig, E V, 1995b. Studies on impeller type, impeller speed and air flow rate in an industrial scale flotation cell. Part 2: Effect on gas hold-up, *Minerals Engineering* 8 (12), pp 1557–1570.

Gorain, B K, Franzidis, J P and Manlapig, E V, 1996. Studies on impeller type, impeller speed and air flow rate in an industrial flotation cell – part 3: effect on superficial gas velocity, *Minerals Engineering*, 9, pp 639–654.

Gorain, B K, Franzidis, J P and Manlapig, E V, 1997. Studies on impeller type, impeller speed and air flow rate in an industrial scale flotation cell – Part 4: Effects of bubble surface area flux on flotation kinetics, *Minerals Engineering*, 10(4), pp 367–379.

Gorain, B K, Franzidis, J P and Manlapig, E V, 1999. The empirical prediction of bubble surface area flux in mechanical flotation cells from cell design and operating data, *Minerals Engineering* 12, pp 309–322.

Gorain, B K, Napier-Munn, T J, Franzidis, J P and Manlapig, E V, 1998. Studies on impeller type, impeller speed and air flowrate in an industrial scale flotation cell. Part 5: validation of k–Sb relationship and effect of froth depth, *Minerals Engineering* 11, pp 615–626.

Grau, R A and Heiskanen, K, 2003. Gas dispersion measurements in a flotation cell, *Minerals Engineering* 16, pp 1081–1089.

Grau, R A, Laskowski, J S and Heiskanen, K, 2005. Effects of frothers on bubble size, *International Journal of Mineral Processing,* 76, pp 225–233.

Harbort, G and Clarke, D, 2017. Fluctuations in the popularity and usage of flotation columns – An overview, *Minerals Engineering*, Volume 100, January 2017, pp 17–30.

Harbort, G and Schwarz, S, 2010. Characterisation measurements in industrial flotation cells, *Flotation Plant Optimisation* (C J Greet, ed), pp 95–106 (The Australasian Institute of Mining and Metallurgy: Melbourne).

Harbort, G J, Schwarz, S and Nguyen, T, 2018. Chapter 6 – Characterisation Measurements in *Industrial Flotation Cells in Flotation Plant Optimisation: A Metallurgical Guide to Identifying and Solving Problems in Flotation Plants*, Edition 2, pp 171–199 (The Australasian Institute of Mining and Metallurgy: Melbourne).

Harbort, G, 2019. Pneumatic flotation, Chapter 7.3, *SME Mineral Processing and Extractive Metallurgy Handbook*, (Society for Mining, Metallurgy & Exploration), (Eds. R C Dunne, S Komar Kawatra), pp 931–957.

Hernandez-Aguilar, J R, Thorpe, R and Martin, C J, 2006. Experiences in using gas dispersion measurements to understand and modify metallurgical performance, *38th Annual Meeting of the Canadian Mineral Processors*, (Canadian Institute of Mining and Metallurgy).

Jameson, G and Allum, P, 1984. A Survey of Bubble Sizes in Industrial Flotation Cells, Report Prepared for AMIRA Ltd.

Lopez-Saucedo, Uribe-Salas, F A, Perez-Garibay, R and Magallanes-Hernandez, L, 2012 Gas dispersion in column flotation and its effect on recovery and grade, *Canadian Metallurgical Quarterly*, 51 2, pp 111–117.

Nesset, J E, Hernandez-Aguilar, J R, Acuna, C, Gomez, C O and Finch, J A, 2006. Some gas dispersion characteristics of mechanical flotation machines, *Minerals Engineering* 19, pp 807–815.

O'Connor, C T, Randall, E W, Goodall, C M, 1990. Measurement of the effects of physical and chemical-variables on bubbles size, *International Journal of Mineral Processing*, 28(1–2), pp 139–149.

Power, A and Franzidis, J P, 2000, The characterization of hydrodynamic conditions in industrial flotation cells, *Proceedings AusIMM 7th Mill Operators Conference*, pp 243–255 (The Australasian Institute of Mining and Metallurgy: Melbourne).

Schwarz, S and Alexander, D, 2006. Gas dispersion measurements in industrial flotation cells, *Minerals Engineering* 19, pp 554–560.

Shabalala N Z, Harris, M Leal Filho and Deglon, D A, 2011. Effect of slurry rheology on gas dispersion in a pilot-scale mechanical flotation cell, *Minerals Engineering* 24, pp 1448–1453.

Estimation of bubble size distribution and local turbulence in a bubbly flow system

M M Hoque[1], A Wang[2], P Ireland[3], G Evans[4] and S Mitra[5]

1. Research Associate, ARC Centre of Excellence for Enabling Eco-Efficient Beneficiation of Minerals, The University of Newcastle, Callaghan NSW 2308. Email: mohammad.hoque@newcastle.edu.au
2. Research Associate, ARC Centre of Excellence for Enabling Eco-Efficient Beneficiation of Minerals, The University of Newcastle, Callaghan NSW 2308. Email: ai.wang@newcastle.edu.au
3. Senior Lecturer, ARC Centre of Excellence for Enabling Eco-Efficient Beneficiation of Minerals, The University of Newcastle, Callaghan NSW 2308. Email: peter.ireland@newcastle.edu.au
4. Conjoint Professor, ARC Centre of Excellence for Enabling Eco-Efficient Beneficiation of Minerals, The University of Newcastle, Callaghan NSW 2308. Email: geoffrey.evans@newcastle.edu.au
5. Research Associate, ARC Centre of Excellence for Enabling Eco-Efficient Beneficiation of Minerals, The University of Newcastle, Callaghan NSW 2308. Email: subhasish.mitra@newcastle.edu.au

ABSTRACT

This work presents an experimental study of flow dynamics in a bubble column system (cross-section: 100 mm × 100 mm) using a non-intrusive optical technique with targeted application in a novel REFLUX™ Flotation Cell. The study had two aims – measurement of the bubble size distribution (BSD) and local energy dissipation rate in the system due to bubble motions over a low range of gas flux varied from 0.02 to 0.08 cm/s without impairing the visibility of the system. A central bubble plume was generated by injecting compressed air through a sintered glass distributor in quiescent liquid. Highspeed shadowgraphy imaging was performed to determine the BSD in the presence of surfactant (Sodium Dodecyl Sulfate (SDS) concentration ~ 10 ppm). The BSD exhibited a unimodal shape at different locations of the column for all gas flux cases. A non-intrusive particle image velocimetry (PIV) technique was used to quantify the flow field generated by the bubble motions, which was used to estimate the local energy dissipation rate. The local energy dissipation rate exhibited an increasing power-law dependency on the gas flux.

INTRODUCTION

The REFLUX™ flotation cell (RFC) is a novel flotation system that is capable of accommodating both fine and coarse particles and offers fast hydrodynamics and higher throughput than conventional mechanical flotation cells. The upper part of the cell is operated as an inverted fluidised bed of bubble-particle aggregates rising against the downflowing wash water in absence of any froth zone, and an array of parallel inclined channels in the bottom section for efficient segregation of bubbles from the tailings. Previous studies have analysed the operating principle of this system based on drift-flux analysis (Dickinson and Galvin, 2014); and demonstrated its superior desliming performance (Galvin and Dickinson, 2014; Galvin *et al* 2014).

The hydrodynamic characteristics, ie flow regimes, gas holdup, bubble size distribution, and local energy dissipation rate are some of the critical design parameters for evaluating the performance of the RFC system. However, these hydrodynamic parameters have not been extensively investigated for RFC system. Among the aforementioned parameters, bubble size plays a key role in governing gas holdup and bubble velocity. Ahmed and Jameson (1985) reported that a first-order rate equation could describe the removal of particles. They found that bubble size strongly influences the flotation rate constant (k), which is a complex function of the particle properties and the hydrodynamic conditions in the cell. However, bubble size has rarely been studied in lab-scale flotation cells, probably due to the fact that bubble size determination in aerated stirred vessels and particularly in three-phase systems (gas-liquid-solid) is complex. Tucker *et al* (1994) examined the influence of physical and chemical variables on bubble size in a modified 3 dm^3 Leeds flotation cell. Later, Laskowski *et al* (2003) extensively studied the influence of several commercial frothers on bubble

size in a 1 dm^3 open-top Leeds flotation cell using the University of Cape Town (UCT) bubble sizer technique.

Only a few studies have reported bubble size measurements in industrial cells which could be attributed to the complexities involved associated with such measurements and the lack of any standard methods. Jameson and Allum (1984) measured bubble size in operational cells using a photographic technique and reported that Sauter mean (d_{32}) bubble diameters in the range of 0.5–1.8 mm. Gorain *et al* (1997) reported values measured with the UCT (University of Cape Town) bubble sizer technique, in a 2.8 m^3 portable cell, in the range of 0.7–1.8 mm. While Deglon *et al* (2000), using the UCT method, found that d_{32} values varied over the range of 1.2–2.7 mm in industrial mechanical cells.

There are various intrusive and non-intrusive techniques are available for analysis the bubble size distribution (Adetunji and Rawatlal, 2017; Azizi *et al*, 2017; Guan and Yang, 2017; Hernandez-Alvarado *et al*, 2017; Lau *et al*, 2018a, 2018b; Möller *et al*, 2017; Murgan *et al*, 2017; Nedeltchevet al., 2017). The intrusive measurement technique tends to influence the fluid-structure, while the non-intrusive method does not affect the flow field in the system, which has attracted research attention in recent years (Wen *et al*, 2018).

The aims of the present study were two-fold – developing a non-intrusive technique to determine bubble size distribution that can be applied to RFC system and local energy dissipation rate in the system due to bubble motions. Experiments were performed in a rectangular bubble column of cross-section (100 × 100 mm^2) similar to a pilot plant scale RFC unit. High-speed imaging was performed, and an image processing algorithm was developed to quantify bubble size distribution. Additionally, local turbulence was characterised by energy dissipation rate at different bubble surface fluxes using the non-intrusive particle image velocimetry (PIV) technique.

EXPERIMENTAL DETAILS AND APPROACH

Apparatus

A schematic representation of the rectangular column is illustrated in Figure 1. The column is made of acrylic with dimension of 100 (L) × 100 (W) × 300 (H) mm^3. Compressed air and reverse osmosis (RO) water were used to generate the bubbly flow system. Gas was introduced into the column through a sintered disc type distributor located at the centre of the column. The pore size of the distributor varied in the range from 16 to 40 µm. The gas flow rate was varied between 0.1 to 0.5 L/min and monitored by measuring with a rotameter (Cole Parmer). The corresponding gas flux ranged from 0.02 to 0.08 cm/s. Before generating the bubbles, ~10 ppm Sodium Dodecyl Sulfate (SDS) was added to liquid to lower the surface tension and facilitate smaller size and spherical shape bubble generation. For all experimental conditions, the liquid level was kept at a height of 220 mm from the base of the column.

Experimental methodology

High-speed shadowgraphy imaging was performed to capture the motion of the bubbles in the presence of surfactant using a Phantom v311 camera (Figure 1a). The images (640 × 600 pixels) were captured at a frame rate of 2000 fps with an exposure time ~180 µs and stored in a computer. The experiments were carried out at two different locations in the column, (a) zone 1, located 80 mm above the gas distributor and (b) zone 2, located 20 mm below the free surface. An in-house image processing algorithm was developed and implemented in the open source tool *ImageJ* to determine the bubble size distribution.

In a separate set of experiments, high-speed particle image velocimetry (PIV) measurement (Figure 1b) was performed using a Nd:YLF laser system (Litron LDY303, wavelength: 527 nm, Dantec Dynamics, Denmark) involving 15 µm fluorescent seeding particles (Kanomax, Japan). Raw velocity data were processed using a combination of the adaptive PIV and average filtering algorithm to generate the velocity field. For the details of the PIV procedure readers are referred to Hoque *et al* (2018).

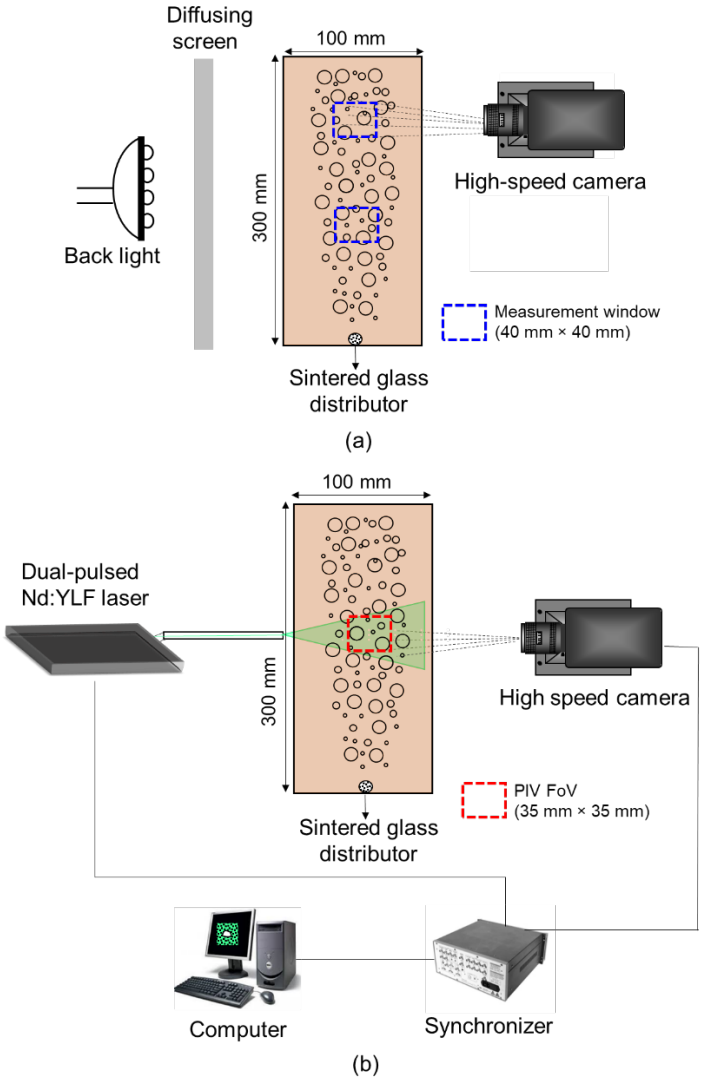

FIG 1 – Schematic arrangement of the experimental set-up with the measurement windows (a) bubble column with shadowgraphy technique and (b) PIV set-up for flow measurement inside the bubble column.

Image processing

The bubble properties that can be obtained from an image are the projected area and shape. Subsequently, from these quantities the centroids and equivalent diameter can be calculated. To acquire these values, a number of operations were performed using an in-house image processing algorithm in *ImageJ* (see overview in Figure 2). Starting with the raw image, the background was first removed using local area thresholding in conjunction with a median filter. Subsequently, a global threshold was applied to create a binary image, separating the bubbles from the background. After these filters have been applied, the detected objects were divided into individual bubbles and overlapping/clustering bubbles on the basis of the roundness.

The roundness is defined as:

$$Ro = \frac{S}{\sqrt{4pA}} \tag{1}$$

where S and A represent the surface perimeter and area of the bubble, respectively.

The criteria to distinguish isolated bubbles is $0.8 \leq Ro \leq 1.0$ pixels, was determined by applying the image processing algorithm to an initial set of image data. Finally, the area of each segregated bubble object was counted and converted from pixel to metric values using a predetermined

calibration factor (1 pixel ~ 61 μm). From the measured area, the equivalent bubble diameter was calculated as follows:

$$d_e = \sqrt{\frac{4A}{p}} \tag{2}$$

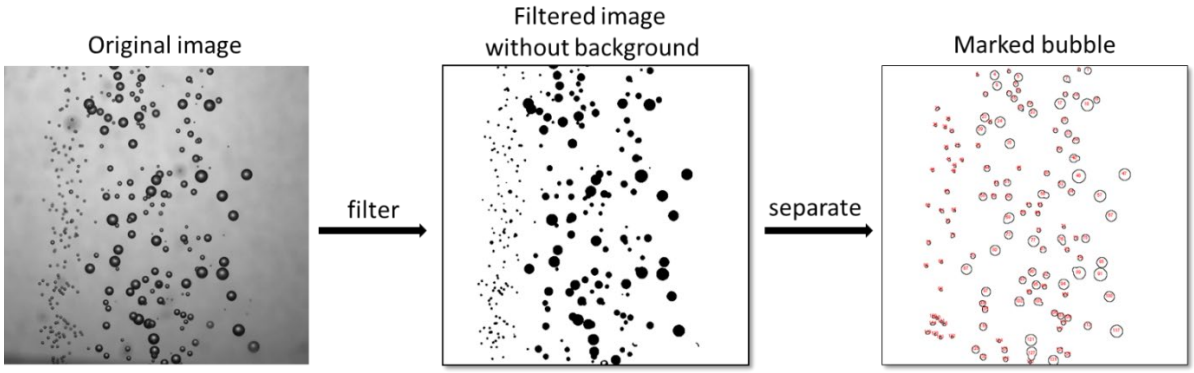

FIG 2 – Image processing sequences to determine the bubble size distribution.

Examples of the detected bubbles at different gas fluxes are shown in Figure 3. It can be observed that the algorithm marked different sizes of individual bubbles from the images leaving the aggregates of potential coalescence. The measured bubble size distributions (BSD) are expressed in the form of a number-based probability density function (PDF).

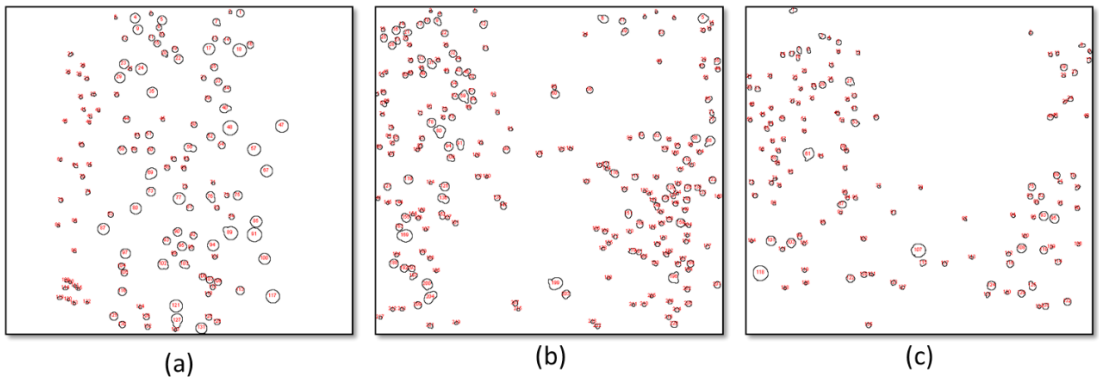

FIG 3 – Example images of detected bubbles at various gas flux (a) window 1: 0.02 cm/s (b) window 1: 0.05 cm/s and (c) window 1: 0.08 cm/s.

RESULTS AND DISCUSSIONS

Measurements were performed for initial liquid heights 220 mm with gas flux ranging from 0.02 to 0.085 cm/s for an air-water system. The measurement zones are shown in Figure 1. Samples of the obtained shadowgraphy images at zone 1 and zone 2 for different gas fluxes are demonstrated in Figures 4 and 5, respectively. At low gas flux of 0.02 cm/s (see Figure 4a), the bubbles appear to be similar in size at the different regions of the column (see Figure 5b). The bubbles rose upward in vertical chains in a homogeneous fashion without many interactions. When gas flux is increased to 0.03 cm/s (see Figures 4b and 5b), coalescence and breakup of bubbles start to play a role.

For a gas flux of 0.07 cm/s (see Figures 4c, and 5c), a bubble plume becomes more evident, which creates a strong liquid recirculation near the walls. A plume is a dynamic region within the bubble column, where the bubbles rise with a higher velocity. Bubble size in this dynamic region increases due to increased interactions among the bubbles, which lead to coalescence. The smaller bubbles accumulate close to the side walls and are dragged down by the down-flow of the liquid. Small vortical structures are also formed close to the side wall regions. At high gas flux of 0.08 cm/s (see Figures 4d and 5d), high bubble rise velocity is observed and the down-flow of smaller bubbles at the side walls is clearly visible. A large number of small bubbles were formed due to intense bubble breakup. The bubbly flow was very chaotic, which made visual observation very difficult.

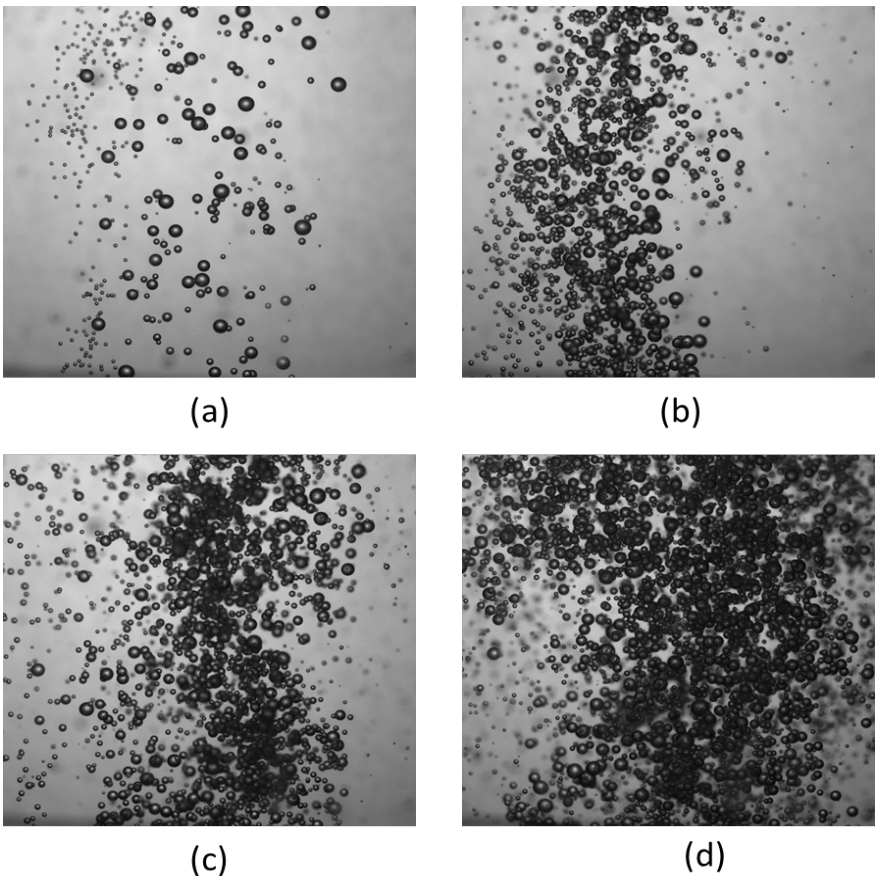

FIG 4 – Highspeed camera images of the bubbly flow at zone 1 for different gas flux: (a) 0.02 cm/s, (b) 0.03 cm/s, (c) 0.07 cm/s and (d) 0.08 cm/s.

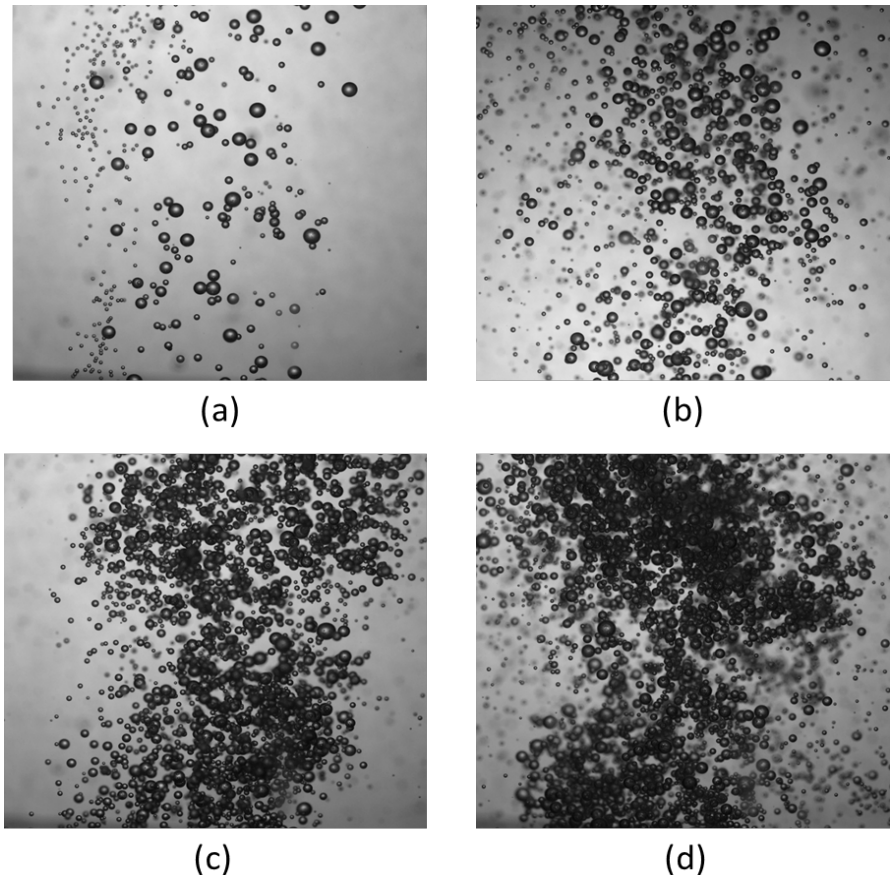

FIG 5 – Highspeed camera images of the bubbly flow at zone 2 for different gas flux: (a) 0.02 cm/s, (b) 0.03 cm/s, (c) 0.07 cm/s and (d) 0.08 cm/s.

The bubble size distributions for different flow rate at zones 1 and 2 are illustrated in Figures 6 and 7, respectively. A normal distribution curve was fitted to the experimental bubble size distribution to estimate the mean bubble diameter with standard deviation. For similar liquid heights, the trends (ie PDF has a unimodal shape) are the same and the bubble size distribution at zone 1 of the column prevails at the upper zone 2. There is an equilibrium between bubble coalescence and breakup along the height of the column, and the gas flux solely determines this equilibrium. To illustrate the effect of the gas flux on the BSD, the mean bubble diameter and corresponding standard deviation are listed in Table 1. It shows that the increase of gas flux decreases the mean bubble diameter with the corresponding standard deviation. The mean bubble diameter of zone 1 was approximately 8 per cent smaller than the bubble diameter of zone 2.

TABLE 1

The mean and standard deviation of the detected bubbles for different flow rate.

Gas flux (cm/s)	Zone 1		Zone 2	
	Mean bubble diameter d_b (mm)	Standard deviation	Mean bubble diameter d_b (mm)	Standard deviation
0.01	0.601	0.267	0.657	0.340
0.03	0.561	0.245	0.622	0.279
0.05	0.541	0.224	0.570	0.236
0.07	0.511	0.225	0.528	0.237
0.08	0.509	0.217	0.512	0.230

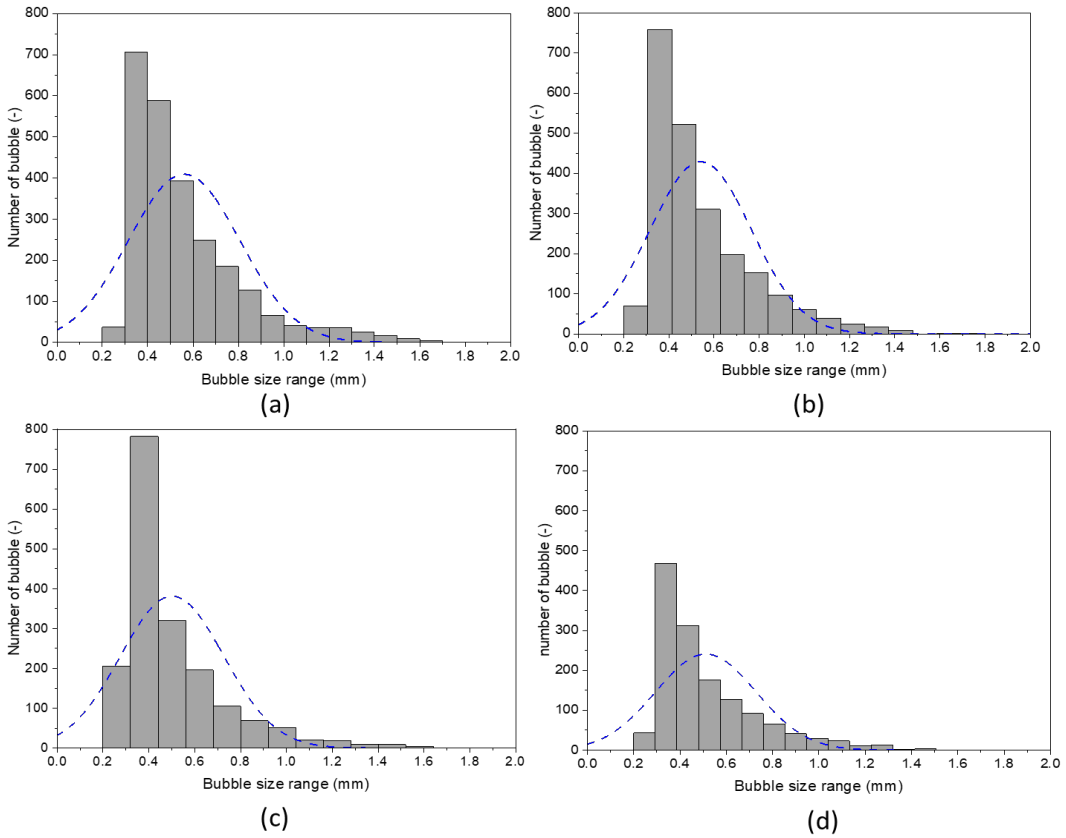

FIG 6 – Bubble size distribution at zone 1 for different gas flux: (a) 0.02 cm/s, (b) 0.05 cm/s, and (c) 0.07 cm/s and (d) 0.08 cm/s. The blue dotted curve represents the normal distribution.

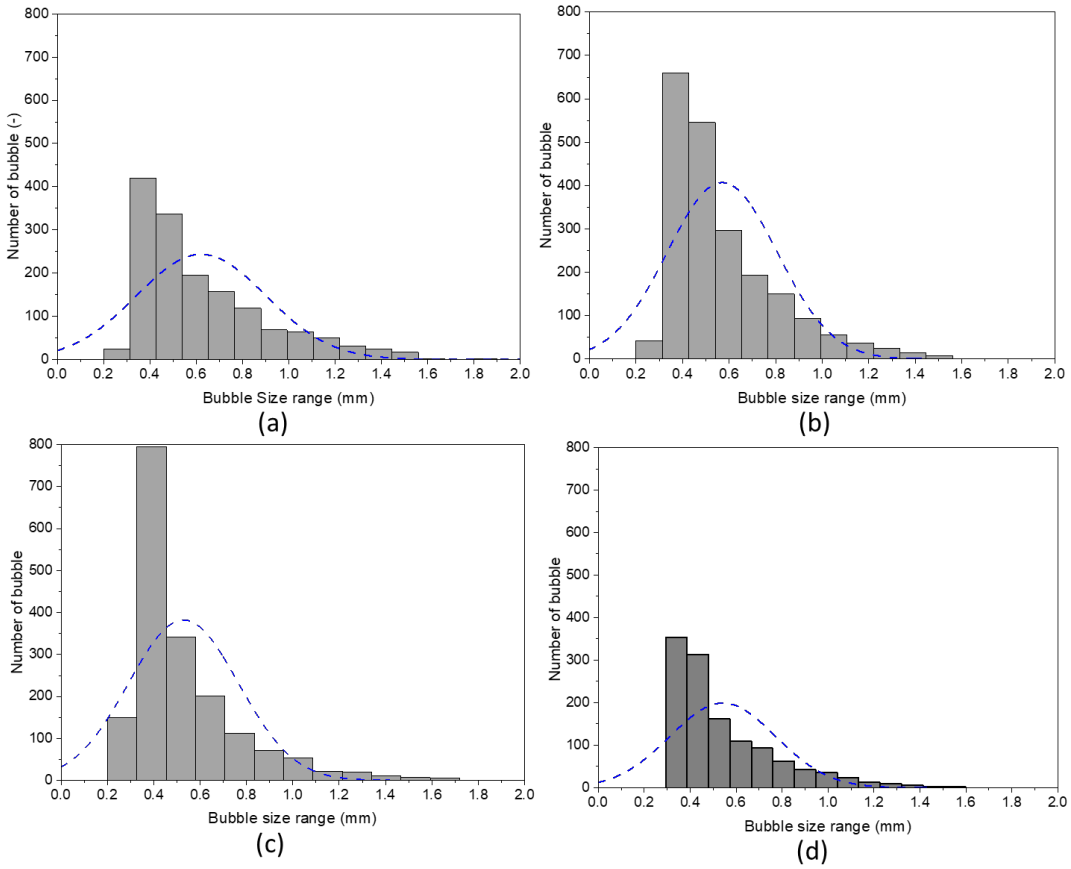

FIG 7 – Bubble size distribution at zone 2 for different gas flux: (a) 0.02 cm/s, (b) 0.05 cm/s, and (c) 0.07 cm/s and (d) 0.08 cm/s. The blue dotted curve represents the normal distribution.

It was interesting to carry out the PIV experiments in the bubble column to quantify the spatial distribution of the local energy dissipation rate. In the present study, the local turbulence energy dissipation rate was determined using the two-dimensional velocity gradient method and can be written as (Hoque *et al*, 2015):

$$\varepsilon = \nu\left(2\overline{\left(\frac{\partial u}{\partial x}\right)^2} + 3\overline{\left(\frac{\partial v}{\partial x}\right)^2} + 3\overline{\left(\frac{\partial u}{\partial y}\right)^2} + 2\overline{\left(\frac{\partial v}{\partial y}\right)^2} + 2\overline{\left(\frac{\partial u}{\partial y}\frac{\partial v}{\partial x}\right)}\right) \tag{3}$$

where u and v represent the fluctuating velocity components along the x and y directions, respectively.

Figure 8 compare the spatial distribution of energy dissipation rate for two different gas fluxes such as 0.02 and 0.08 cm/s, respectively. It can be observed that the local energy dissipation rate is high close to the bubble plume region. More specifically, the local energy dissipation rate could be seen concentrated near the bubble interface, the effect of which decreases further away from the interface. Serizawa and Kataoka (1990) mentioned two different effects of the bubble plume on the local energy dissipation rate: (a) an increase in the specific energy dissipation rate due to the higher velocity gradients near the bubble interface and (b) an energy dumping effect due to bubble deformation. The flow acceleration by bubbles and suppression of the coherent structures could also be responsible for a higher local energy dissipation rate (Zhang *et al*, 2015).

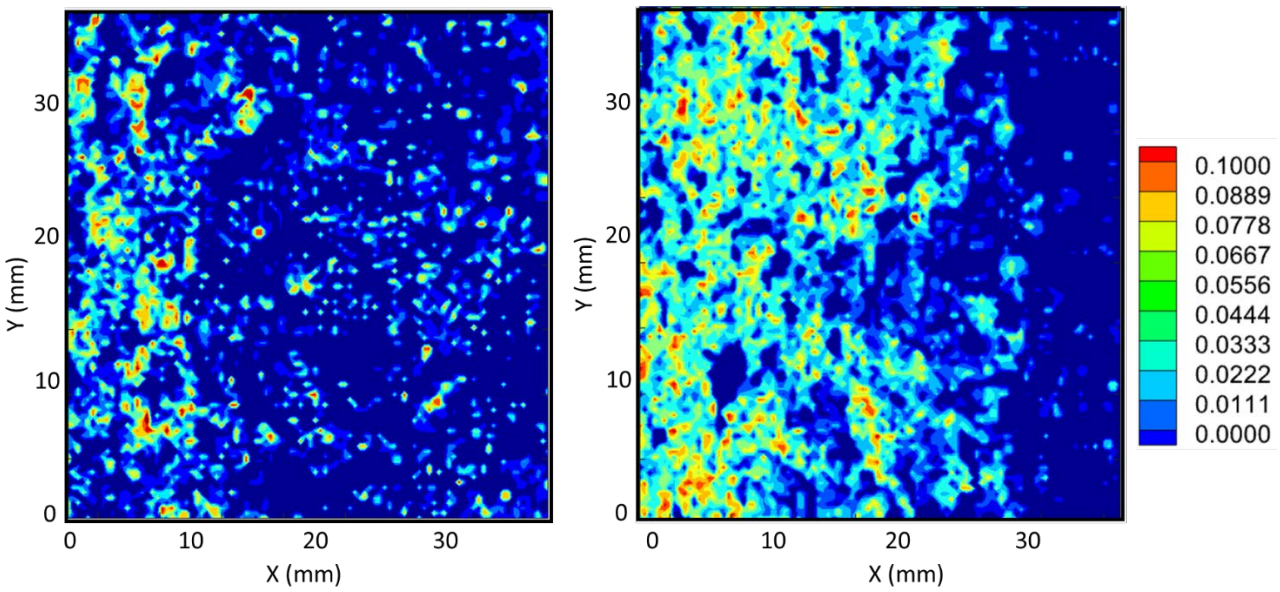

FIG 8 – Contours of local energy dissipation rate at different gas flux: (a) 0.02 cm/s and (b) 0.08 cm/s.

Figure 9 shows the time-averaged energy dissipation rate as a function of different gas flux. It can be observed that the value of ε increases with an increase in the gas flux, which can be attributed to more interfacial momentum exchange by the bubbles with the surrounding liquid leading to breakup and coalescence. The trend suggests a power-law dependency of local energy dissipation rate (R^2 ~ 0.99) and yields an exponent of 15.23 over the gas flux range studied.

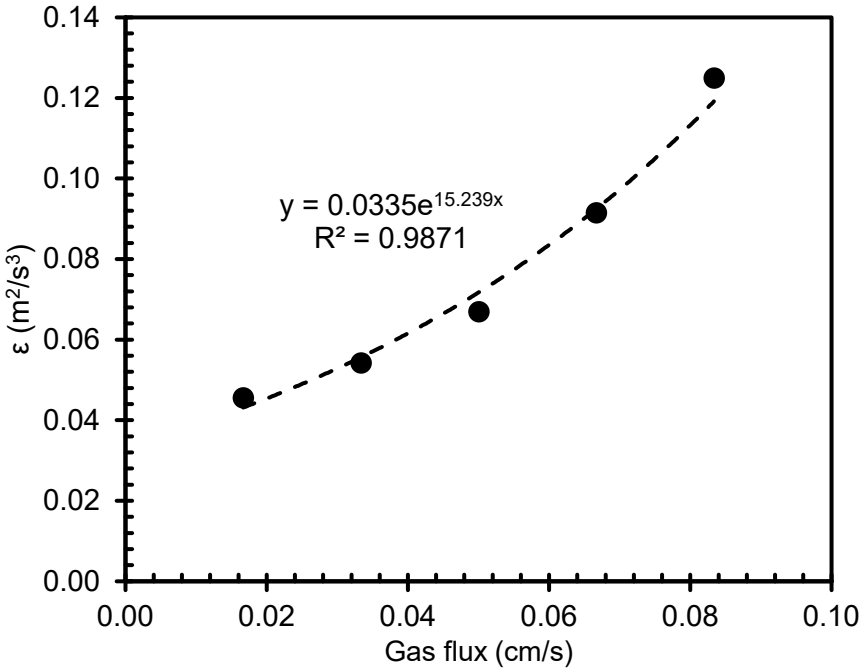

FIG 9 – Local energy dissipation rate as a function of gas flux.

CONCLUSIONS

In the present study, an image processing framework was proposed to optically measure bubble size distributions (BSD) in a bubble column system similar to the top section of a RFC system with potential application to a pilot plant scale RFC system soon. The algorithm was tested over the gas flux range from 0.02 to 0.08 cm/s to consistently isolate individual bubbles from the background interferences. The system showed increased heterogeneity with increased gas flux exhibiting bubble coalescence and breakups. Bubble size measured at the two locations (mid column and near the

free surface) showed similar distributions exhibiting reduction in mean bubble size at increasing gas flux. The local energy dissipation rate due to momentum transfer from bubbles to surrounding liquid was found to be positively correlated to the gas flux and showed a power-law dependency.

ACKNOWLEDGEMENTS

The authors acknowledge the funding support from the Australian Research Council (ARC) Centre of Excellence for Enabling Eco-Efficient Beneficiation of Minerals (grant number CE200100009).

REFERENCES

Adetunji, O, Rawatlal, R, 2017. Estimation of bubble column hydrodynamics: image-based measurement method. *Flow Measurement and Instrumentation*, 53:4–17.

Ahmed, N, Jameson, G, 1985. The effect of bubble size on the rate of flotation of fine particles. *International Journal of Mineral Processing*, 14(3):195–215.

Azizi, S, Yadav, A, Lau, Y M, Hampel, U, Roy, S, Schubert, M, 2017. On the experimental investigation of gas-liquid flow in bubble columns using ultrafast X-ray tomography and radioactive particle tracking. *Chemical Engineering Science*, 170:320–331.

Deglon, D A, Egya-Mensah, D and Franzidis, J P, 2000. Review of hydrodynamics and gas dispersion in flotation cells on South African platinum concentrators, *Minerals Engineering*, 13 (3):235–244.

Dickinson, J E, Galvin, K P, 2014. Fluidized bed desliming in fine particle flotation – Part I *Chemical Engineering Science*, 108:283–298.

Galvin, K P, Dickinson, J E, 2014. Fluidized bed desliming in fine particle flotation – Part II: Flotation of a model feed. *Chemical Engineering Science*, 108:299–309.

Galvin, K P, Harvey, N G, Dickinson, J E, 2014. Fluidized bed desliming in fine particle flotation – Part II: Flotation of difficult to clean coal. *Mineral Engineering*, 66–68:94–101.

Gorain, B, Franzidis, J, Manlapig, E, 1997. Studies on impeller type, impeller speed and air flow rate in an industrial scale flotation cell. Part 4: effect of bubble surface area flux on flotation performance. *Minerals Engineering*, 10(4):367–379.

Guan, X, Yang, N, 2017. Bubble properties measurement in bubble columns: from homogeneous to heterogeneous regime. *Chemical Engineering Research and Design*, 127, 103–112.

Hernandez-Alvarado, F, Kalaga, D V, Turney, D, Banerjee, S, Joshi, J B, Kawaji, M, 2017. Void fraction, bubble size and interfacial area measurements in co-current downflow bubble column reactor with microbubble dispersion. *Chemical Engineering Science*,168:403–413.

Hoque, M M, Mitra, S, Evans, G M, Sathe, M J, Joshi, J B, 2018. Modulation of turbulent flow field in an oscillating grid system owing to single bubble rise. *Chemical Engineering Science*, 185:26–49.

Hoque, M M, Sathe, M J, Mitra, S, Joshi, J B, Evans, G M, 2015. Comparison of specific energy dissipation rate calculation methodologies utilising 2D PIV velocity measurement. *Chemical Engineering Science*, 137:752–767.

Jameson, G, Allum, P, 1984. A survey of bubble sizes in industrial flotation cells, AMIRA Limited report.

Laskowski, J S, Tlhone, T, Williams, P, Ding, K, 2003. Fundamental properties of the polyoxypropylene alkyl ether flotation frothers. *International Journal of Mineral Processing*, 72 (1–4): 289–299.

Lau, Y, Hampel, U, Schubert, M, 2018a. Ultrafast X-raytomographic imaging of multiphase flow in bubble columns-Part 1: image processing and reconstruction comparison. *International Journal of Multiphase Flow*, 104:258–271.

Lau, Y, Möller, F, Hampel, U, Schubert, M, 2018b. Ultrafast X-ray tomographic imaging of multiphase flow in bubble columns–Part 2: characterisation of bubbles in the dense regime. *International Journal of Multiphase Flow*, 104, 272–285.

Möller, F, Seiler, T, Lau, Y, Weber, M, Weber, M, Hampel, U, Schubert, M, 2017. Performance comparison between different sparger plate orifice patterns: hydrodynamic investigation using ultrafast X-ray tomography. *Chemical Engineering Journal,* 316:857–871.

Murgan, I, Bunea, F, Ciocan, G D, 2017. Experimental PIV and LIF characterization of a bubble column flow. *Flow Measurement and Instrumentation*, 54:224–235.

Nedeltchev, S, Hampel, U, Schubert, M, 2017. Extraction of information and reconstruction entropies from ultrafast X-ray tomography data in a bubble column. *Chemical Engineering Science*,170,225–233.

Serizawa, A, Kataoka, I, 1990. Turbulence suppression in bubble two-phase flow. *Nuclear Engineering and Design*, 122:1–16.

Tucker, J P, Deglon, D A, Franzidis, J P, Harris, M C, O'Connor, C T, 1994. An evaluation of a direct method of bubble size distribution measurement in a laboratory batch flotation cell. *Minerals Engineering*, 7(5–6): 667–680.

Wen, J, Sun, Q, Sun, Z, Gu, H, 2018. An improved image processing technique for determination of volume and surface area of rising bubble. *International Journal of Multiphase Flow*, 104:294–306.

Zhang, A, Yokomine, T, Kunugi, T, 2015. Turbulence modulation of the upward turbulent bubbly flow in vertical duct. *Nuclear Engineering and Technology*, 47:513–522.

An investigation into maximising the product grade and recovery of dense minerals in a single-stage REFLUX™ Classifier

C P Lowes[1], J Bijzet[2], C Bezuidenhout[3], J Zhou[4], J L Sutherland[5], L Crompton[6] and K P Galvin[7]

1. Research Associate, ARC Centre of Excellence for Enabling Eco-Efficient Beneficiation of Minerals, Newcastle Institute for Energy and Resources, University of Newcastle, Callaghan NSW 2308. Email: callan.lowes@newcastle.edu.au
2. Technology Development Specialist, Anglo American, Johannesburg, 2001, South Africa. Email: joani.bijzet@angloamerican.com
3. Principal Engineer: Technology Open Forum, Anglo American, London, UK. Email: chandon.bezuidenhout@angloamerican.com
4. Senior Research Associate, ARC Centre of Excellence for Enabling Eco-Efficient Beneficiation of Minerals, Newcastle Institute for Energy and Resources, University of Newcastle, Callaghan NSW 2308. Email: james.zhou@newcastle.edu.au
5. Research Assistant, ARC Centre of Excellence for Enabling Eco-Efficient Beneficiation of Minerals, Newcastle Institute for Energy and Resources, University of Newcastle, Callaghan NSW 2308. Email: joshua.sutherland@newcastle.edu.au
6. PhD Candidate, ARC Centre of Excellence for Enabling Eco-Efficient Beneficiation of Minerals, Newcastle Institute for Energy and Resources, University of Newcastle, Callaghan NSW 2308. Email: luke.crompton@uon.edu.au
7. Director, ARC Centre of Excellence for Enabling Eco-Efficient Beneficiation of Minerals, Newcastle Institute for Energy and Resources, University of Newcastle, Callaghan NSW 2308. Email: kevin.galvin@newcastle.edu.au

ABSTRACT

Platinum Group Metal (PGM) bearing ores from the Upper Group 2 (UG2) reef often contain significant concentrations of chromite which can potentially be upgraded to produce a saleable product. A common approach is to implement gravity separation on the PGM flotation circuit tailings. However, where the particle size range of interest is broad and the lower size limit ultra-fine, the challenge is how to maximise the recovery at a saleable product grade without compromising throughput. This study was concerned with the performance of a REFLUX™ Classifier for beneficiation of a PGM bearing chromite ore and the benefits of size classification. The sample had a nominal top size of 0.5 mm and was processed over the complete size range and in two discrete size classes following classification at 106 µm. The primary goal was to produce a concentrate exceeding 40 wt. per cent Cr_2O_3, ideally approaching 42 wt. per cent Cr_2O_3, with minimal PGM losses above 106 µm. A major challenge was to process at the required solids throughput in a single stage with the feed pulp density constrained to a nominal upper limit of 30 wt. per cent solids. It was found that varying the controller density set point of the REFLUX™ Classifier produced strong control of the product grade. Products as high as 41.1 wt. per cent Cr_2O_3 were produced at 78.6 per cent recovery for the +106 µm material, while in the −106 µm portion the product grade was as high as 41.4 wt. per cent Cr_2O_3 at 83.2 per cent recovery. Processing the feed in discrete size classes enabled the volumetric feed and fluidisation rates to be optimised for a given application; hence, superior performance was achieved at the finer sizes. This work has demonstrated the value in considering feed preparation as well as technology selection in developing a robust process solution.

INTRODUCTION

The world's largest deposits of Platinum Group Metals (PGM) exist within three South African orebodies: the Merensky reef, the Upper Group 2 (UG2) reef and the Platreef. The UG2 reef is unique in that the most abundant gangue is chromite ($FeO{\cdot}Cr_2O_3$) which can contribute to up to 75 per cent of the ore by mass (Hay and Roy, 2010). The concentration of chromite, as represented by a Cr_2O_3 assay, must be limited to 2.5–3.0 wt. per cent Cr_2O_3 in the final PGM flotation concentrate to avoid issues in smelting (Ross, 2018). However, additional value can be added to the operation by upgrading the PGM flotation tailings which can be sold as a separate concentrate exceeding 40 wt. per cent Cr_2O_3. The most common approach used within the industry has been gravity separation (Dawson, 2010; Engelbrecht, 2012).

There has been recent interest from the industry in the potential of a gravity separator known as the REFLUX™ Classifier for the recovery of chromite, primarily motivated by the need to process down to very fine sizes to extract maximum value. The REFLUX™ Classifier is the combination of a fluidised bed and a set of parallel inclined channels which is configured as shown in Figure 1. Feed material enters below the inclined channels and is fluidised by water delivered through the base to establish a suspension. The fluidisation rate is kept as close to the minimum as possible, promoting a high suspension density which provides a mechanism for an autogenous dense medium effect (Galvin *et al,* 2016). Here, low-density particles can be expelled from the bed and transported to the inclined channels where they readily report to the overflow. Conversely, high-density particles can settle onto the upwards facing inclined surface of the channel and slide back into the vertical section, eventually migrating to the underflow. Narrow channels provide enhanced settling area for retaining very fine high-density particles while simultaneously promoting stronger velocity gradients for re-suspending the relatively coarse gangue (Galvin *et al,* 2020).

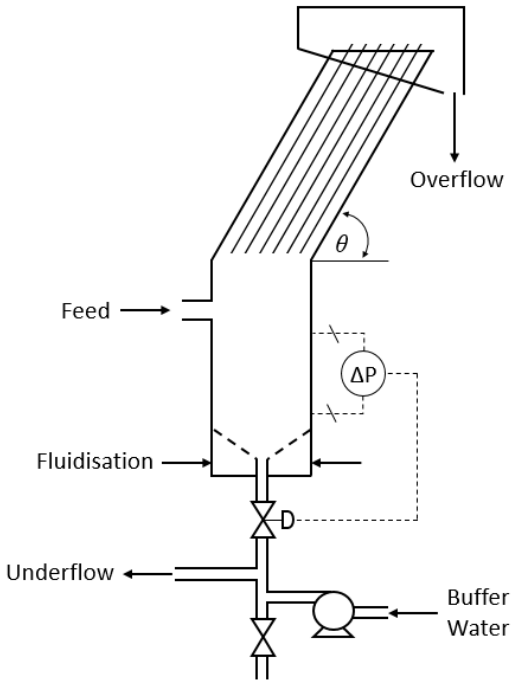

FIG 1 – Schematic of the laboratory-scale REFLUX™ Classifier.

The present study focuses on the beneficiation of a UG2 chromite sample of nominal top size 0.5 mm. The sample was processed over the complete −500 + 0 µm size range and in two discrete size classes following classification at 106 µm. In view of a proposed plant design, the −500 + 106 µm material needed to be processed at around 80 t/h in a full-scale system, while the finer fraction required only 20 t/h, with the feed pulp density constrained to a maximum of roughly 30 wt. per cent solids. These separations pose a significant challenge given the ultra-fine lower size limit and dilute nature of the feed which dictates high volumetric feed rates to achieve the desired solids throughput. In a conventional spirals plant the solution would likely be to increase the number of spiral starts and/or add additional processing stages. The approach outlined in this paper, however, is based on a single-stage of separation and therefore represents a significant simplification on current industry practice.

This paper outlines an investigation into maximising the product grade and recovery of dense minerals in a single-stage REFLUX™ Classifier, and the benefits of size classification in achieving this goal. A series of laboratory-scale experiments were conducted according to the above conditions and processing constraints, the objective being to produce a 40 wt. per cent Cr_2O_3 product grade at the highest recovery achievable. The data indicates that the performance of the separator is highest when the volumetric feed and fluidisation rates are optimised for a given size range.

MATERIALS AND METHOD

The feed was a UG2 chromite-bearing PGM ore of nominal top size 0.5 mm. The head grade of the −500 + 106 µm portion of the feed was around 32 wt. per cent Cr_2O_3 and 1.2 g/t 2E (Pt + Pd), for the −106 + 0 µm portion 30 wt. per cent Cr_2O_3 and 7 g/t 2E, and for the −500 + 0 µm sample 28 wt. per cent Cr_2O_3 and 7.9 g/t 2E. Note that the samples were received pre-classified. For each experiment, the feed solids were concentrated in a 300 L mixing tank and discharged into a series of buckets. The pulp density of the highly concentrated buckets was measured during preparation, allowing the concentrated feed slurry and a known volume of water to be added to the mixing tank to prepare the feed to the target pulp density, in this case nominally 30 wt. per cent.

As illustrated in Figure 1, the continuous separation experiments were conducted using the RC100, a laboratory-scale REFLUX™ Classifier with a horizontal cross-section of 100 mm × 100 mm. Both sections of the unit were 1000 mm long, though the upper section was positioned at an angle of 70° relative to the horizontal. The perpendicular inclined plate spacing was 3 mm. Fluidisation was supplied via mains tap water and delivered through an inverted square shaped pyramid chamber positioned below the vertical section. The underflow buffer system situated at the underflow discharge provided stability in the system control (Galvin *et al,* 2016).

Tables 1 and 2 summarise the process parameters for the experiments conducted on the −500 + 106 µm and −106 + 0 µm material, respectively, in order of increasing set point. Assuming a 3.1 m^2 RC2000 unit for full-scale implementation, the target solids throughput for the −500 + 106 µm experiments needed to be 26 t/(m^2 h), and for the −106 + 0 µm experiments roughly 7 t/(m^2 h). The final experiment, effectively Run 8, was for the −500 + 0 µm material and was processed using conditions equivalent to Run 1 in Table 1 to allow for comparison with a narrower size range at the same top size.

TABLE 1

Summary of the process parameters used for the −500 + 106 µm experiments in order of increasing set point.

Run	Feed pulp density	Feed rate	Solids throughput	Fluidisation rate	Set point	Channel spacing
(-)	(wt.%)	(L/min)	t/(m^2 h)	(L/min)	(kg/m^3)	(mm)
2	26.6	13.0	29.4	2.1	2650	3.0
3	31.6	13.0	34.5	2.1	2680	3.0
1	25.6	13.0	28.5	2.1	2750	3.0
4	30.9	13.0	31.0	2.1	2800	3.0

TABLE 2

Summary of the process parameters used for the −106 + 0 µm experiments in order of increasing set point.

Run	Feed pulp density	Feed rate	Solids throughput	Fluidisation rate	Set point	Channel spacing
(-)	(wt.%)	(L/min)	t/(m^2 h)	(L/min)	(kg/m^3)	(mm)
6	31.4	4.0	9.44	0.20	2500	3.0
7	30.6	4.0	9.20	0.20	2550	3.0
5	32.0	4.0	9.15	0.18	2600	3.0

The REFLUX™ Classifier control system was driven by a feedback PID control loop. The difference in pressure between two probes positioned 60 and 440 mm above the flange of the fluidisation chamber was used to infer the average suspension density. The position of the underflow valve was

regulated based on the measured value in comparison to the target suspension density, referred to as the set point. The set point is a major factor determining the mass yield for the separation.

The experiments were run for at least 60 min (often 180 min for the fine size range) to ensure steady-state had been reached before sampling the underflow and overflow streams simultaneously. Following this, a feed sample was taken. These run samples were then dried to determine the pulp density and solids rate of each stream before being combined and subdivided into smaller representative samples using a riffle splitter. The size distributions of each stream were then determined by de-sliming one subsample (chosen at random) at the low sieve size and sieving using a √2 series. The full set of sieves used were 500, 425, 300, 212, 150, 106, 75, 53 and 38 µm. The sized samples were then sent to an external laboratory for assay analysis to determine the concentration of Cr_2O_3 using XRF and Pt + Pd using fire assay with ICP-MS finish. A mass-balance reconciliation was then performed to provide a consistent basis for calculating the yield and recovery using the two-product formula (Wills and Finch, 2016).

RESULTS AND DISCUSSION

−500 + 106 µm experiments

The approach was taken to vary the controller density set point of the REFLUX™ Classifier to examine the relationship between the product grade and recovery achievable. Table 3 summarises the results from the experiments while Figure 2 plots the product grade as a function of recovery.

TABLE 3

Summary of the results for the −500 + 106 µm experiments in terms of Cr_2O_3 (mass-balanced data).

Run	Feed grade	Underflow-grade	Overflow-grade	Mass yield	Upgrade ratio	Cr_2O_3 recovery
(-)	(wt.% Cr_2O_3)	(wt.% Cr_2O_3)	(wt.% Cr_2O_3)	(wt.%)	(-)	(%)
2	30.8	39.2	2.6	76.9	1.3	98.1
3	32.6	40.2	4.4	78.9	1.2	97.2
1	32.6	41.1	18.5	62.3	1.3	78.6
4	31.9	41.4	28.6	25.9	1.3	33.6

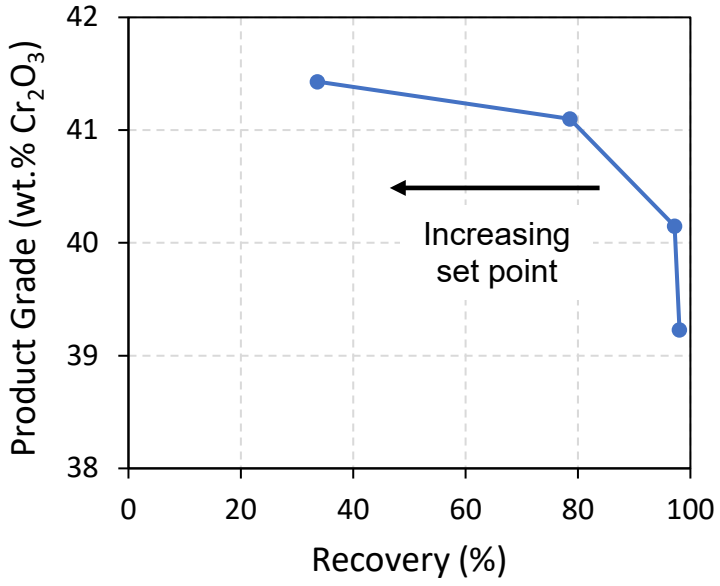

FIG 2 – Cr_2O_3 product grade as a function of recovery for the −500 + 106 µm experiments. The set point values of the experiments range from 2800 kg/m^3 (left) to 2650 kg/m^3 (right).

In Run 3, an underflow product just exceeding the minimum for metallurgical grade chromite (40 wt. per cent Cr_2O_3) was produced with a remarkably high recovery of 97.2 per cent. By increasing the set point, the product grade has increased to as high as 41.4 wt. per cent Cr_2O_3, though Run 1 is considered a better result given the product grade was only marginally lower at 41.1 wt. per cent Cr_2O_3 with a significantly higher recovery of 78.6 per cent. This sharp drop in recovery for a very similar product grade reflects the liberation characteristics of the material where it becomes difficult to build very high suspension densities without incurring some losses. Clearly, however, the density set point provides a robust method for controlling the product grade to achieve the maximum recovery possible.

High PGM recovery in this size class could be considered problematic given the PGM's are unlikely to be liberated such that the overflow could be re-ground once stripped of chromite. However, as shown in Table 4, the PGM recovery was 23.4 per cent in Run 1, reaching as high as 25.6 per cent in Run 3. This is not considered an issue given this means that effectively 75 per cent of the PGMs reported to the overflow. In fact, there has been an effective upgrade of PGM into the overflow stream by a factor of roughly 3 in Runs 2 and 3 which may help justify the option of regrinding.

TABLE 4

Summary of the results for the −500 + 106 µm experiments in terms of PGM (mass-balanced data). Note that the 2E Recovery refers to the percentage of the PGM in the feed which reported to the underflow stream.

Run	Feed grade	Underflow-grade	Overflow-grade	Mass yield	2E recovery
(-)	(g/t 2E)	(g/t 2E)	(g/t 2E)	(wt.%)	(%)
2	1.12	0.25	3.92	76.3	17.0
3	0.80	0.26	2.75	78.4	25.6
1	0.72	0.27	1.47	62.5	23.4
4	1.06	0.26	1.34	25.9	6.4

−106 + 0 µm experiments

The second size class provided was much finer but only needed to be processed at the equivalent of 20 t/h in a full-scale unit, equivalent to ~7 t/(m^2 h). Again, the approach was taken to vary the controller density set point. Table 5 summarises the key results from this program of experiments.

TABLE 5

Summary of the results for the −106 + 0 µm experiments in terms of Cr_2O_3 (mass-balanced data).

Run	Feed grade	Underflow-grade	Overflow-grade	Mass yield	Upgrade ratio	Cr_2O_3 recovery
(-)	(wt.% Cr_2O_3)	(wt.% Cr_2O_3)	(wt.% Cr_2O_3)	(wt.%)	(-)	(%)
6	30.8	41.0	5.9	70.8	1.3	94.4
7	30.8	41.1	14.0	62.0	1.3	82.8
5	29.4	41.4	12.1	59.1	1.4	83.2

The performance for the finer separations was once again strong, with product grades exceeding 41 wt. per cent Cr_2O_3 produced at recoveries as high as 94.4 per cent. The recovery at the highest set point was 83.2 per cent so there may still be scope to push the product grade even higher at a loss in recovery by increasing the set point above 2600 kg/m^3.

Figure 3 shows the recovery and product grade as a function of the geometric mean particle size for Runs 5–7. Note that the +106 µm and −38 µm size fractions were assigned geometric mean sizes of 106 and 38 µm, respectively. It is evident from Figure 3a that very high recoveries have been

achieved for all sizes greater than 38 µm. For the −38 µm size fraction, the recovery in Run 6 is still reasonable at roughly 60 per cent, particularly considering this includes particles below 10 µm.

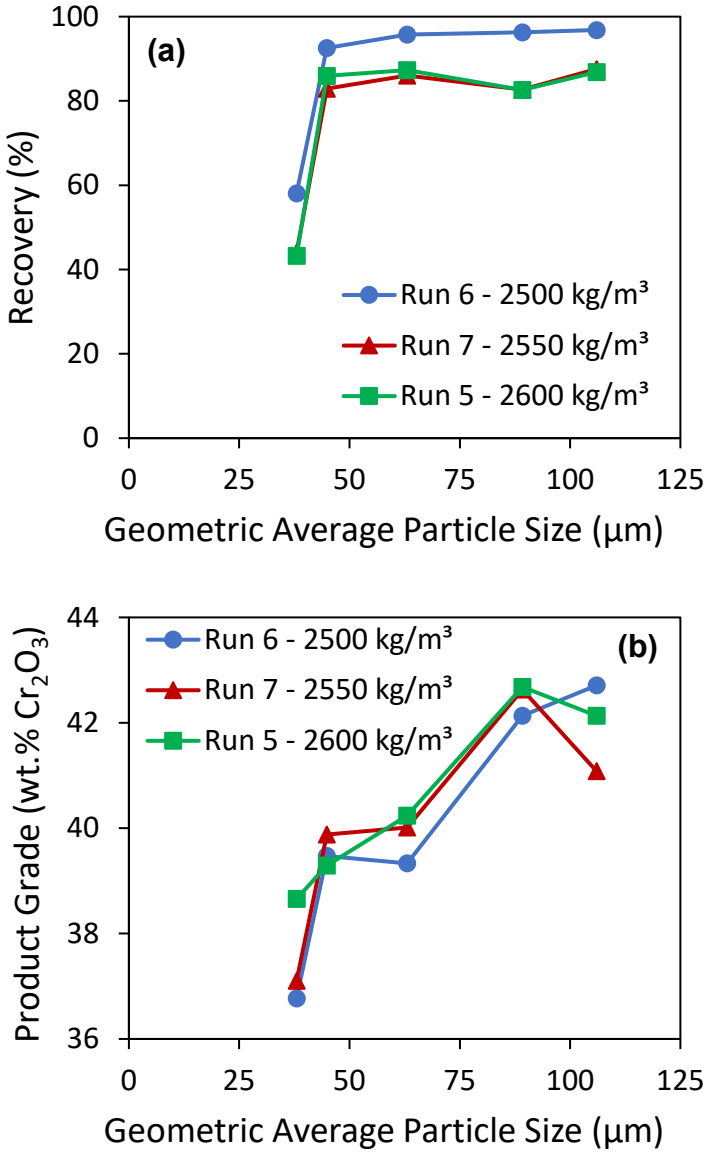

FIG 3 – (a) recovery and (b) product grade as a function of geometric mean particle size for the −106 µm experiments based on Cr_2O_3 (mass-balanced data).

−500 + 0 µm experiments

The target parameters for the −500 + 0 µm experiment were the same as Run 1 where the set point was 2750 kg/m^3 and the fluidisation rate 2.1 L/min. The feed pulp density was 21 wt. per cent solids which was slightly lower than expected, delivering a solids throughput of 20.3 t/(m^2 h). The volumetric feed rate was roughly three-fold higher than that used in the −106 µm work. Table 6 shows the mass-balanced mass percent and Cr_2O_3 assay data as a function of particle size for the feed, underflow and overflow.

TABLE 6

Mass percent and Cr_2O_3 assay data as a function of particle size for the −500 + 0 µm experiment (mass-balanced data). Note that data in red font was assumed in the mass-balance reconciliation because there was insufficient mass for an assay.

Size Range (µm)	Feed		Underflow		Overflow		Yield (wt.%)	Recovery (%)
	Mass (wt.%)	Assay (wt.% Cr_2O_3)	Mass (wt.%)	Assay (wt.% Cr_2O_3)	Mass (wt.%)	Assay (wt.% Cr_2O_3)		
+500	1.25	27.0	5.79	32.1	0.26	2.32	82.9	98.5
−500 + 425	2.35	31.9	10.8	38.2	0.51	3.17	82.2	98.2
−425 + 300	7.85	31.0	30.4	41.5	2.93	7.26	69.4	92.8
−300 + 212	11.5	29.6	30.6	44.9	7.32	15.6	47.7	72.4
−212 + 150	16.6	28.3	18.1	42.3	16.2	24.9	19.6	29.3
−150 + 106	16.9	28.2	4.09	43.7	19.7	27.4	4.36	6.77
−106 + 75	12.7	27.6	0.26	44.1	15.4	27.6	0.36	0.58
−75 + 53	10.8	26.3	0.0	48.1	13.1	26.3	0.05	0.08
−53 + 38	2.91	25.1	0.0	43.3	3.54	25.0	0.05	0.09
−38	17.3	22.5	0.0	44.2	21.0	22.5	0.09	0.18
Head Grade		27.3		41.9		24.1	17.9	27.5

Table 6 shows that a 41.9 wt. per cent Cr_2O_3 product was produced. The recovery by size data indicated that reasonable recovery was obtained as fine as 212 µm, with some recovery down to 106 µm, though the overall mass yield was only 17.9 wt. per cent. Given the mass yields in the earlier experiments were at least 60 wt. per cent when high recovery was achieved, the set point for this composite separation was clearly far too high.

It is noted that 56.3 per cent of the feed was coarser than 106 µm. In Run 1, which used the same set point to process the +106 µm feed, the recovery was 78.6 per cent. Thus, based on the entire −500 µm feed, the Run 1 recovery was effectively 0.563 × 78.6 ~ 44 per cent which is significantly higher than the recovery value of 27.5 per cent achieved here on the overall feed. While a modest shift in set point would likely match the Run 1 result, this work does suggest advantages in operating in parallel instead of series by classifying the feed prior to the gravity separation.

The recovery effectively drops to zero below 106 µm. This behaviour is a result of the high fluidisation velocity required to facilitate fluidisation of the 500 µm top size, roughly an order of magnitude higher than that required in the −106 µm work. The net result is that it becomes increasingly difficult to recover fines as the particle size range broadens. Therefore, the best approach is to classify the feed upfront so that a lower fluidisation rate can be used for the fine separation.

CONCLUSIONS

A series of REFLUX™ Classifier experiments have been conducted on size classes of −500 + 106 µm, −106 + 0 µm, and −500 + 0 µm. A product grade as high as 41.1 wt. per cent Cr_2O_3 was produced at 78.6 per cent recovery for the −500 + 106 µm material, while in the −106 + 0 µm portion the product grade was as high as 41.4 wt. per cent Cr_2O_3 at 83.2 per cent recovery. Varying the controller density set point provided strong control of the product grade and recovery, with recoveries exceeding 94 per cent produced at saleable grade for both discrete size classes. For the −500 + 0 µm experiment, the recovery declined significantly below 106 µm, largely due to the high fluidisation and volumetric feed rates required. The improved performance for the discrete particle size ranges demonstrates the benefits of classifying the feed so that the volumetric feed and fluidisation rates can be optimised for the application.

ACKNOWLEDGEMENTS

The authors acknowledge the support of Anglo American in funding this research, and the additional support from the Australian Research Council for the ARC Centre of Excellence for Enabling Eco-Efficient Beneficiation of Minerals, grant number CE200100009.

REFERENCES

Dawson, N F, 2010. Experiences in the production of metallurgical and chemical grade UG2 chromite concentrates from PGM tailings streams. *The Journal of the Southern African Institute of Mining and Metallurgy, 110*, 683–690.

Engelbrecht, J, 2012. Potential changes in the physical beneficiation processes that can improve the recovery grade or costs for the platinum group metals. *Proceedings of the Fifth International Platinum Conference: A Catalyst for Change.* Sun Citry, South Africa.

Galvin, K P, Iveson, S M, Zhou, J and Lowes, C P, 2020. Influence of inclined channel spacing on dense mineral partition in a REFLUX™ Classifier. Part 1: Continuous steady state. *Minerals Engineering, 146*, 106112.

Galvin, K P, Zhou, J, Price, A J, Agrwal, P and Iveson, S M, 2016. Single-stage recovery and concentration of mineral sands using a REFLUX™ Classifier. *Minerals Engineering, 93*, 32–40.

Hay, M P and Roy, R, 2010. A case study of optimising UG2 flotation performance. Part 1: Bench, pilot and plant scale factors which influence Cr_2O_3 entrainment in UG2 flotation. *Minerals Engineering, 23*, 855–867.

Ross, V, 2018. Improved PGM-chromite selectivity in a pneumo-mechanical flotation cell. *Proceedings of the XXIX International Mineral Processing Congress.* Moscow, Russia.

Wills, B A and Finch, J A, 2016. *Will's Mineral Processing Technology: An Introduction to the Practical Aspects of Ore Treatment and Mineral Recovery* (8th ed.). Amsterdam: Butterworth-Heinemann (Elsevier).

Evolution of the modern surge-bin in mineral processing plants with highly variable feeds

D MacHunter[1], J Lyons[2], D Pepper[3] and S Baker[4]

1. Senior Principal Process Engineer, Mineral Technologies, Carrara Qld 4211.
   Email: dolf.machunter@mineraltechnologies.com
2. Principal Design Specialist, Mineral Technologies, Carrara Qld 4211.
   Email: john.lyons@mineraltechnologies.com
3. Engineering Projects – Lead, Mineral Technologies, Carrara Qld 4211.
   Email: dustin.pepper@mineraltechnologies.com
4. Senior Mechanical Engineer – WA, Mineral Technologies, Carrara Qld 4211.
   Email: sam.baker@mineraltechnologies.com

ABSTRACT

Mineral processing plants require a storage buffer to bridge differences in production rates between mining and processing. Where coarse ores are processed, such as coal or hard rock, this buffer may be an ore stockpile or silo.

For wet-mining processes, eg dredging or hydraulic mining, or where fine ores are slurried close to the mining face, a surge-bin is used to contain the plant feed and smooth out the variations in mining rates. These bins have gradually evolved from simple storage vessels to units that are now frequently part of the mineral separation process itself, such as providing a desliming function to remove deleterious ultrafine gangue. This feed conditioning is often essential to achieve the levels of plant performance required in times of declining ore grades and or where inherent ore characteristics make separations harder to achieve.

To achieve these dual roles requires careful consideration of bin design factors such as geometry and lining selection and increased use of instrumentation and advanced, or remotely supervised, control systems. All this ensures they provide capacity to smooth out variations in mining rates and guarantees that when conditioning ores or adjusting slurry densities ahead of the plant it is achieved without loss of valuable minerals.

This paper examines the evolution of the modern surge-bin from a simple, so called, constant density tank with its inherent mass-flow compromises, limited feed preparation and beneficiation abilities, and footprint penalty, to a current state-of-the-art surge-bin, the LFCU, with a control system which provides demonstrable steady outputs, while conditioning and in some cases beneficiating the ROM material and all from a highly compact unit.

It further discusses their use in other applications around the world, for example providing the necessary security for long distant high-density pumping systems; constant high density, low water usage, tailings disposal pipelines and high capacity ultrafine iron ore beneficiation.

INTRODUCTION

In the mineral processing industry, even the simplest of processing units requires a method of introducing material into the process which bridges the different production rates between mining and processing. For coarse ores, typically greater than say 5 to 10 mm the required buffer can be a stockpile or silo which are invariably dry or low moisture storage units. The stockpile or silo discharge can then be regulated to the desired feed rate and with water added to the required density provide the process plant with the optimum feed conditions.

For fine ores where wet mining is utilised, eg dredging or hydraulic mining, or where the ROM material is slurried close to the mining face and pumped to the processing plant, a surge bin is utilised to smooth out the mining rate fluctuations and provide a steady feed rate, in terms of solids rate and slurry density, to the process by varying its contained solids volume according to the balance between the input and output. That is the solids level in the bin will rise should the mining rate exceed the bin output rate and vice versa when the mining rate is less than the discharge rate. This type of surge bin is the subject of this paper.

PROCESS REQUIREMENTS

In the traditional sense the surge bin is designed to carry out two functions:

1. To smooth out variations in input flows so that stable output flows can be maintained which, in turn, allows downstream equipment to be adjusted to operate at optimum conditions.
2. To provide a storage of material so that output flows can be maintained during short interruptions to input flows.

In the first instance, so long as input flows do not exceed the maximum design input flows to the extent, or for sufficient time, such that the amount of material added to the bin would exceed its capacity and overflow the surge bin, the surge bin can operate effectively providing steady output flows in perpetuity. The target range of the surge bin capacity or level in operation is therefore set by the degree of 'safety margin' the operator wishes to maintain to avoid bin overflows in the event of occasional severe and short-term spikes.

Where long-term input and outflows are reasonably matched and input flow spikes are reasonably infrequent, short-lived and/or not extreme, the bin level can be set at almost any level. In this scenario, residence or retention time is largely immaterial.

The more frequent, extreme and/or sustained are any input flow spikes, the more defensively the notional operational bin level may need to be set.

To fulfill its second duty then, the surge bin target operating level should be set close to the maximum design capacity so that, in the event of an unforeseen loss or reduction of input flow, downstream operation is maintained for as long as required before the input flow recommences and presumably catches up over time. If a known input flow downtime is approaching, the surge bin can be run to full design capacity just prior to the input flow interruption to maximise the volume retained in the bin and hence maintain downstream operation for as long as possible.

Clearly, maximum benefit from the surge bin is achieved when the input supply and output demands are reasonably matched over the medium or longer term and input spikes are not the result of very extreme flows or sustained operation above output flow rate.

Should the surge bin be set-up with a continuous overflow it will provide additional de-sliming of the ROM feed material.

CONSTANT DENSITY TANK TO SURGE BIN

Perhaps the original slurry surge bin concept followed the dry storage silo principle where a volume of slurry was held at or marginally higher density than the discharge density required. This type of surge bin acted somewhat like a large transfer hopper and generally were typified by operating without an overflow. Without an overflow no additional de-sliming of the feed occurs.

In addition, the CD tank without overflow does not take advantage of the natural consolidation property of the material to optimise the solids surge volume that consequently limited the available capacity to smooth out input variations. For example (Table 1), at 800 t/h bin discharge rate, a CD tank with some 250 m^3 bin surge volume a CD tank would provide 10 minutes of surge capacity. Compared to the modern surge bin, taking advantage of the consolidation properties of the feed material, would provide some 50 per cent more surge time (15 minutes) for the same volume and although the modern surge bin has a conical bottom section and the CD tank is cylindrical, they would be similar in overall dimensions (~7 m Ø × ~7 m tall).

TABLE 1

CD tank versus surge bin**.**

Parameter	Unit	CD Tank	Surge Bin
Discharge Rate	t/h	800	800
Surge Capacity	minutes	10	15
Surge Mass	t	135	203
Surge Material Density	% solids (w/w)	40	80
Surge Material Density	% solids (v/v)	20	30
Surge Material Slurry Volume	m^3	253	203
Surge Material Water Volume	m^3	253	51

As the material consolidates in the modern surge bin, an up-current of liquid occurs that reports to the bin overflow which carries with it slimes (ultra-fine material) in a process Mineral Technologies refers to as ‘autogenous’ classification. This has the benefit of providing additional desliming of the feed to the downstream process and in some cases can replace a second stage of desliming hydrocyclones.

It is noted that as the surge volume contained in the CD tank is very sensitive to all but relatively minor feed fluctuations, particularly in regard to feed density, its application in most mining operations and certainly for dredging operations is not recommended nor appropriate.

MAXIMISING CONSOLIDATION IN THE MODERN SURGE BIN

Conventional surge bins were design as large tanks, under the assumption that simply storing a large volume of feed would even out fluctuations in feed rate and feed density to downstream equipment (Lyons *et al,* 2009). Typically, these conventional surge bin had sidewall angles of around 45 degrees above the horizontal and designed without consideration of the flow properties of the material.

In the past, surge bins were not designed to promote mass flow and instead operated with funnel flow (Figure 1) with a rat-hole in the centre of the bin allowing the incoming feed to pass straight through the bin. Interruptions in feed caused the consolidated material hanging up on the bin sides to slough off, sending high density slugs forward to the processing plant (Lyons *et al*, 2009).

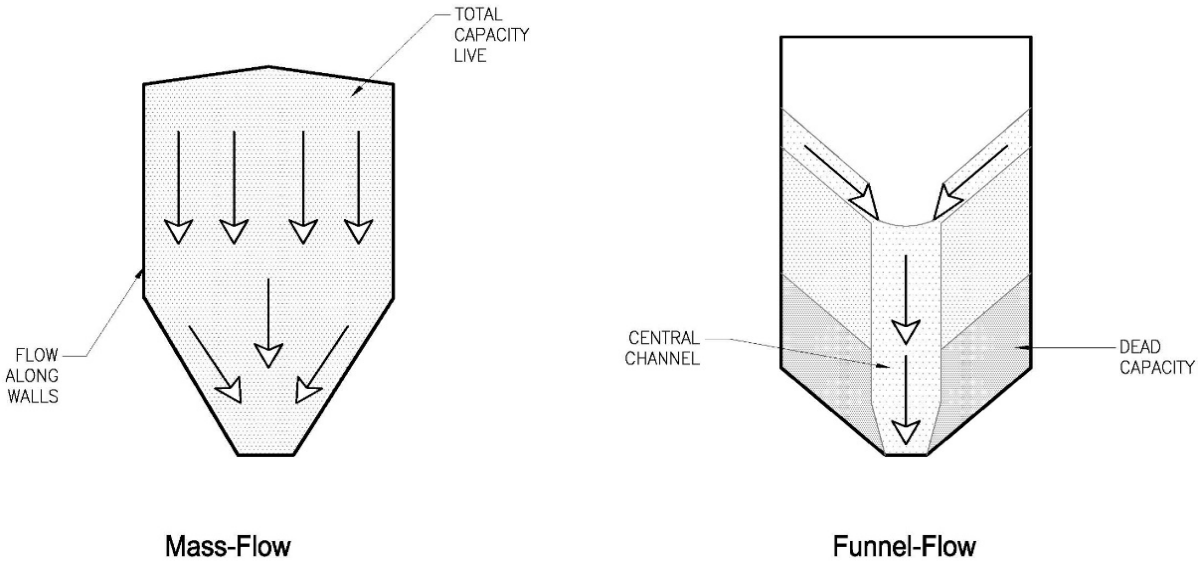

FIG 1 – Mass flow versus funnel flow.

To overcome some of these material flow problems, surge bins were designed with 60° sidewall and agitation water was injected near the pump suction point to fluidise the material. In some later surge bins, system was added to draw water from the top of the bin and inject into the underflow pump suction point. Underflow density could be controlled by throttling the waterflow through this bypass using valves. These surge bins operated reasonably well within a narrow range of solids levels inside the bin, but outside this range the pressure differential between the slurry suction and the bypass suction made density control difficult (Lyons *et al*, 2009).

A change of thinking started slightly more than 10 years ago: the slurry in the surge bin is considered as a consolidated bulk solid in saturated conditions instead of a viscous liquid. The surge bin is then designed more like a silo than a slurry tank.

It has been shown (Lecreps and Wiche, 2013) that Jenike's (1964) design principles can be applied to the design of modern surge bins handling slurries if the test work is conducted in a submerged condition. In other words, when designing bins to treat water and mineral ore slurry mixtures, the mixture is should be considered a bulk solid under saturated conditions, rather than as a viscous liquid.

One major benefit of the modern surge bin design is the capability to handle very high density material (>80 per cent w/w) by achieving mass flow-through adherence to Jenike's (1964) design principles. Storing the surge bin feed at higher density increases the solids storage capacity of the tank. Furthermore, the process of consolidating the feed displaces a large volume of liquid in a rising current that can be used to achieve a separation, or desliming step. In some cases, a beneficiation process can be achieved (Hasan *et al,* 2021).

MODERN SURGE BIN OPERATING STRATEGY

By way of an extreme example demonstrating how the modern surge bin coupled with an optimised production strategy manages a highly variable mining operation (by a floating dredge) and provides a very stable and consistent feed to the wet plant, a simulation of an African mineral sands operation is presented below. The operation has a name plate design capacity of 500 t/h and consists of a floating dredge supplying a floating wet concentrator spiral plant.

Dredge operation

The dredge in this operation would be considered somewhat oversized for optimum synchronisation between the dredge output rate and the WCP feed rate, which tends to make the output in terms of the solids rate extremely variable and difficult to regulate. This factor tests the surge bin operation and clearly demonstrates its effectiveness. It is noted that the dredge volume output is well regulated.

The dredge output for the simulation has been based on actual data gathered from the operation data logging system and is tabulated (Table 2).

TABLE 2

Dredge output.

Parameter	Unit	Value
Upper Push Rate	t/h	1200
Upper Reduced Rate	t/h	1000
Minimum Rate	t/h	10
Maximum Volume Rate	m^3/h	1600
Minimum Volume Rate	m^3/h	1400
Bin Level Reduced Rate Trigger	t	100
Bin Level Push Rate Trigger	t	50

The 'Upper Push Rate' is the maximum instantaneous production rate derived from the plant SCADA system and is triggered when the surge bin reaches the minimum operational level, while the 'Upper

Reduced Rate' is a notional reduction or easing off in the maximum production rate which is triggered when the surge bin reaches the maximum operational level.

Surge bin

The surge bin in this operation is primarily provided to stabilise the dredge output rate as feed to the WCP. The relevant surge bin design data and simulation parameters are tabulated in Table 3.

TABLE 3

Surge bin design parameters.

Parameter	Unit	Value
Total Maximum Live Capacity	t	125
Maximum Rougher Spiral Feed Rate	t/h	520
Minimum Rougher Spiral Feed Rate	t/h	480
Maximum RSF Volume Rate	m^3/h	880
Minimum RSF Volume Rate	m^3/h	860

Simulation

The simulation output is depicted in Figure 2.

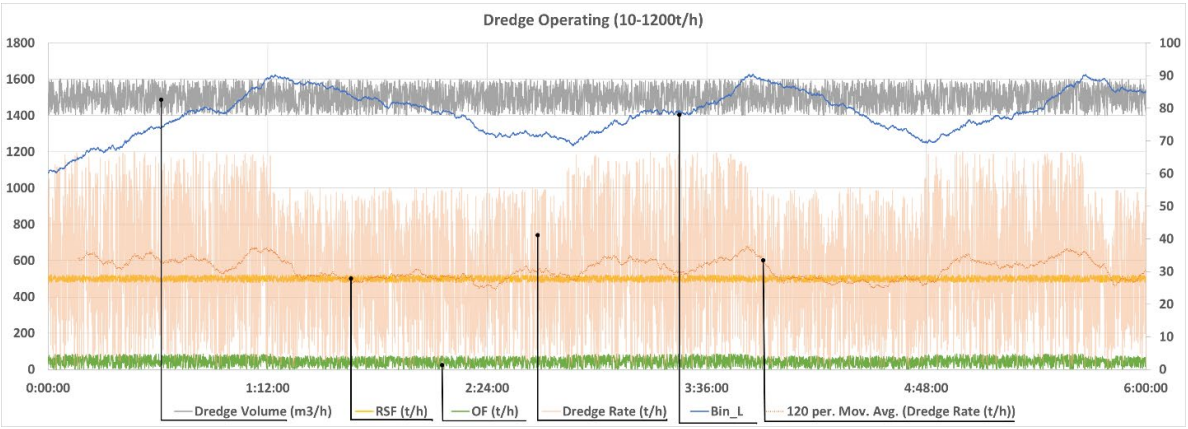

FIG 2 – Simulation output.

Figure 2 clearly indicates that incorporating a push and reduced maximum dredge output rates (t/h) that are triggered by the minimum and maximum bin levels stable rougher spiral feed can be sustained.

Although this strategy has not been adopted it is useful to note that as depicted in Figure 3 similar stability of the rougher spiral feed is being achieved.

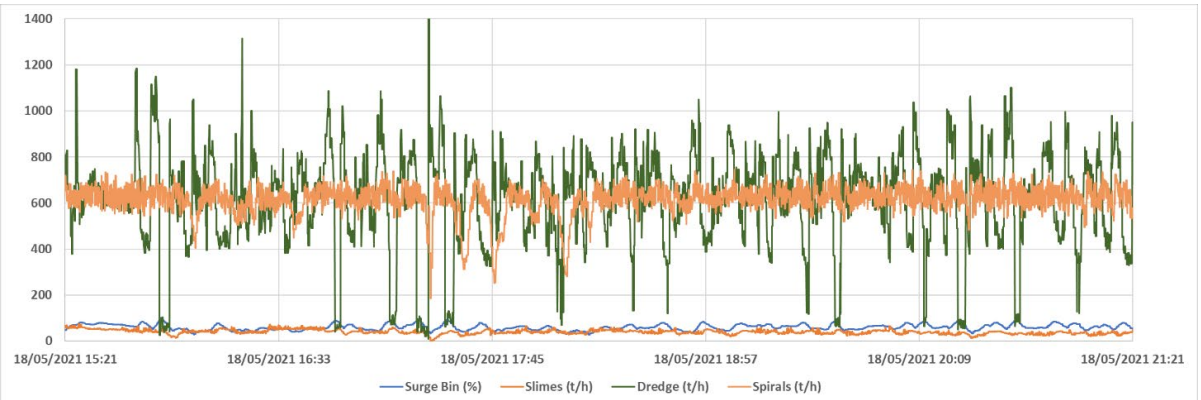

FIG 3 – Actual plant trend data.

BENEFICIATION IN A MODERN SURGE BIN

Mineral Technologies (MT) worked with a prominent Australian iron ore producer over five years (starting in 2017) to implement gravity separation technology based on the modern surge-bin design for the beneficiation of ultrafine magnetite.

Extensive laboratory and pilot-scale test work has shown that, when well liberated, the magnetite can be efficiently separated from the gangue material using a modern surge-bin design referred to as Lyons Technology. Four Lyons Units, with a combined throughput capacity of 4500 t/h solids, reduce the SiO_2 content by a factor of approximately 2.2 (from 19.7 per cent to 9.0 per cent) whilst upgrading the magnetite Fe content by a factor of approximately 1.2 (from 53.7 per cent to 63.6 per cent Fe) (Hasan *et al*, 2021).

Figures 4 and 5 show these results graphically, whilst Figure 6 provides a qualitative visual illustration of the upgrade.

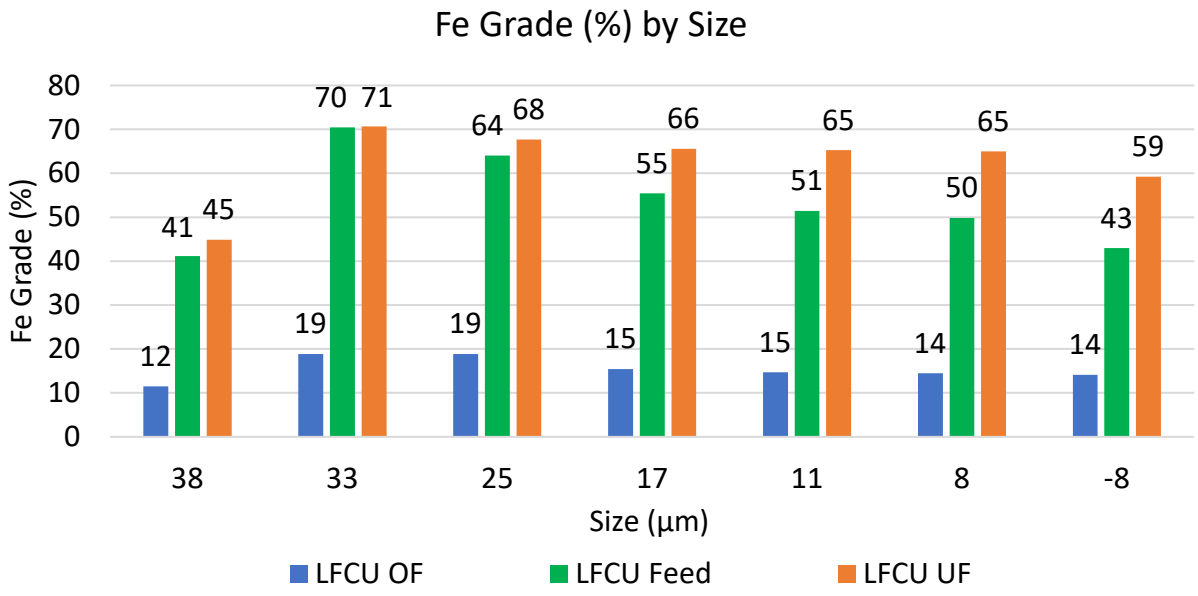

FIG 4 – magnetite beneficiation results using modern surge-bin technology, Fe grade by size.

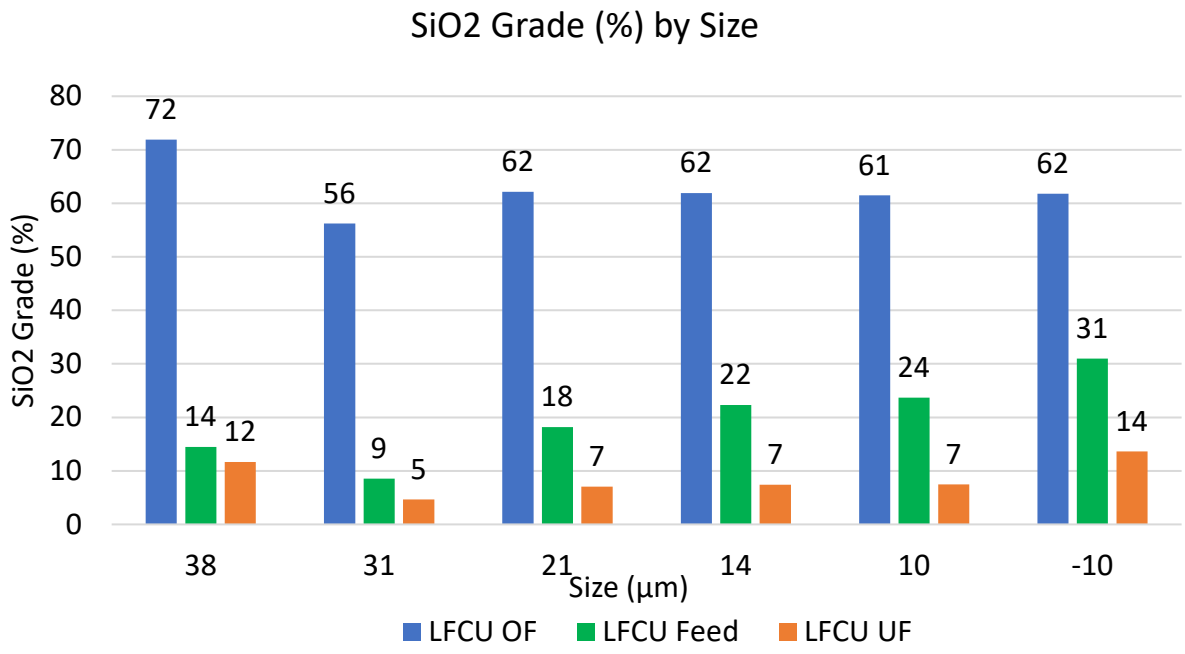

FIG 5 – Magnetite beneficiation results using modern surge-bin technology, SiO_2 grade by size.

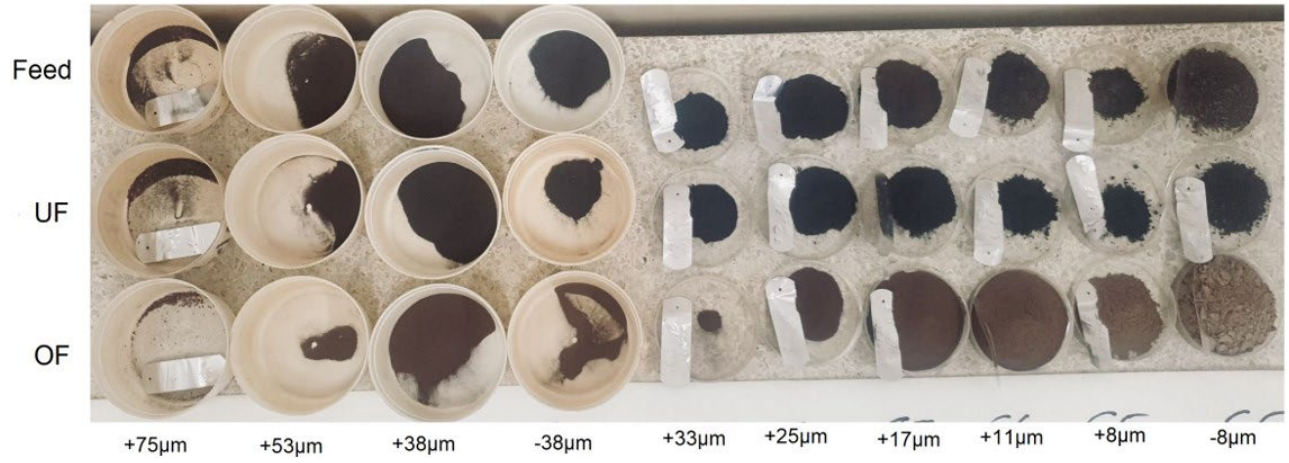

FIG 6 – Magnetite beneficiation results using modern surge-bin technology.

CONCLUSIONS

The modern surge bin:

- copes with extreme variations in mining rates
- provides the necessary stability of feed (rate and density) to downstream process stages to ensure they can operate optimally
- ensures continuity of feed to downstream processes during mining disruptions
- will provide additional de-sliming function
- can provide beneficiation of heavy values to the bin discharge.

ACKNOWLEDGEMENTS

The management of Mineral Technologies is thanked for their support in publishing this paper.

REFERENCES

Hasan, M, Pepper, D, Lyons, J and Vadeikis, C, 2021. A Novel Application of Gravity Separation Technology to Beneficiate Ultrafine Iron Ore, *Iron Ore 2021 Conference Proceedings* (The Australasian Institute of Mining and Metallurgy: Melbourne).

Jenike, A W, 1964. Storage and Flow of Solids. *Bulletin 123* Utah Engineering Experiment Station, University of Utah, Utah.

Lecreps, I and Wiche, S, 2013. Design Principles for Wet Solids Concentrator Vessels. *International Conference for Bulk Materials Handling*.

Lyons, J, Hill, G, Vadeikis, C and Wiche, S, 2009. Innovative Surge Bin Design for Mineral Sands Processing Plant.

Multi-phase CFD modelling of spiral concentrator – Prediction of particle segregation and separation performance

P Sudikondala[1], M Kumar[2], S K Tripathy[3], R M Yanamandra[4] and N Mangadoddy[5]

1. Research Scholar, Indian Institute of Technology, Hyderabad, Sangareddy, Telangana State, India, 502285. Email: ch18resch01005@iith.ac.in
2. Research Scholar, Indian Institute of Technology, Hyderabad, Sangareddy, Telangana State, India, 502285. Email: ch15resch02001@iith.ac.in
3. Principal Researcher, Research and Development Division, Iron and Ferroalloys Research Group, Tata Steel Ltd., Jamshedpur 831 001, India. Email: sunilk.tripathy@tatasteel.com
4. Principal Researcher, Research and Development Division, Iron and Ferroalloys Research Group, Tata Steel Ltd., Jamshedpur 831 001, India. Email: yrama.murthy@tatasteel.com
5. Professor, Indian Institute of Technology, Hyderabad, Sangareddy, Telangana State, India, 502285. Email: narasimha@iith.ac.in

ABSTRACT

Spiral concentrators are one of the flowing film gravity concentration devices used to beneficiate coal and mineral ores. The aim of the current study is to understand the particulate flow and separation performance of an LD9 spiral concentrator using a multi-phase Computational Fluid Dynamics (CFD) model. The CFD model utilises the Algebraic slip mixture model to simulate particulate flows. The model employs the Renormalisation group (RNG) k-ε turbulence models to resolve the fluid turbulence. Initially, the volume of fluid method was adopted to track the water-air interface. Simulations were then carried out at low (0.3 and 3 wt.%) and moderate (15 wt.%) solids concentrations. Multiple particle-phase representing particles of poly sizes (75–1400 μm) and multi-densities (1450–2650 kg/m^3) were simulated to study the particle segregation on the spiral trough surface. The numerical predictions are compared with the literature performance data at a diluted pulp flow rate of 6 m^3/hr. The results were found in close agreement. Further, the same CFD model is used to study the change in pulp velocity, streamflow rates, and separation performance at increasing solids concentration. For the same density particles, Fine particles mostly show higher volume concentration in the middle and outer trough regions, whereas coarse particles show higher volume concentration in the interior and central trough regions. It implies that the fine particles mostly segregate towards the outer region, and dense particles segregate towards the axial column.

INTRODUCTION

The usage of gravity separation as a mineral concentration technique has increased significantly in the past few decades. The separation of minerals using the gravity concentration method has widely been considered a cost-effective, eco-friendly process, absence of reagents usage and less operating costs due to lower power consumption. Spiral concentrators are flowing film gravity separation devices that can efficiently separate minerals in size range of 75 μm to 3 mm. However, for coal beneficiation, the size of particles in the feed is 200 μm to 850 μm is recommended (Fuerstenau and Han, 1979). The spiral concentrator is simple in structure, and it has a helical sluice of an altered semi-circular cross-section wrapped around a central supporting cylindrical column (Matthews, Fletcher and Partridge, 1998). Since their widespread commercial introduction over 80 years ago, spiral concentrators have been simple, metallurgically efficient, low-cost, and less energy-consuming devices. Each spiral concentrator has a distinctive trough profile with constant or variable pitch and features. Spirals have gone through continuous improvement over the last couple of decades for specialist applications and the availability of high-capacity spirals. Each spiral concentrator is used for specific and sometimes diverse processing requirements to ensure efficient separation. Spirals are used to process fine coal, silica sands, heavy mineral sands, sulfide minerals, tungsten, chromite ore, and gold ores.

As the prepared feed slurry mixture flows into the spiral trough surface through the feed box, gravitational and centrifugal forces act on the flowing slurry to radially segregate the particles on the trough surface based on density and size. Segregation of particles occurs, where fine

suspended minerals move to the outer trough region, and dense particles settle and travel to the inner trough region under the influence of secondary circulations. Medium-sized particles are segregated across the trough in close ratios (Wills and Napier-Munn, 2005; Bazin *et al,* 2014). The higher the concentration criterion needed, the easier separation of two minerals is.

Researchers (Holland-Batt, 1989, 1995; Holland-Batt, 1994; Tripathy *et al,* 2012; Sadeghi, Bazin and Renaud, 2014, 2016) have investigated separation theory and conducted experiments to understand the particle segregation in the spiral trough. Boucher used the PEPT technique to understand the mineral particles motion in a fluid flow (Boucher *et al,* 2014, 2016). Fluid flow in a spiral has primary and secondary flow components, where secondary flow superimposes the primary flow (Holland-Batt, 1989).

The water depth increases in a radial direction. Researchers (Holtham, 1990, 1992; Jain and Rayasam, 2017) have captured the generation of secondary circulations using colour dye on the trough surface and revealed that the secondary flow plays a crucial role in particle separation across the spiral trough. However, limited details were measured using experiments. Wang and Andrews (1994) initiated the development of a fluid flow mechanistic model of the spiral operation. His model was used to predict the flow fields for simplified rectangular spiral sections (Wang and Andrews, 1994). Ye *et al* (2019) simulated the interaction between the design variables and the water flow field distribution for the LD9 coal spiral concentrator using the VOF method (Ye *et al,* 2019). Four turbulence models are used to find the best suitable model for simulation studies. Much of simulation studies (Matthews *et al,* 1999; Doheim *et al,* 2008; Ye *et al,* 2019) are carried out CFD modelling of the two-phase (water and air) flow in an LD9 spiral concentrator. Matthews, Fletcher and Partridge (1998) simulated the dilute particulate (coal and quartz) flow in a spiral by the Lagrangian method, VOF approach and Renormalisation group k-ε turbulence modelling (Matthews, Fletcher and Partridge, 1998). Doheim *et al* (2013) initiated the simulation of a dilute particle flow in a spiral based on the Eulerian approach and turbulence modelling (Doheim *et al,* 2013).

The key drawbacks of previous particulate flow studies are that the dynamics of particulate flow in a spiral concentrator at industrial solid concentration have not been studied. Fluid flowing on a spiral trough surface consists of various phases, including water and particles of different densities and sizes. As a result, a suitable multi-phase model is essential for accurate modelling. Very limited studies on particulate flow have been carried out using the discrete phase model (DPM) and eulerian model (Matthews, Fletcher and Partridge, 1998; Matthews, Holtham and Golab, 1998; Doheim *et al,* 2013). DPM is not appropriate for feed solids concentrations over 10 wt.% because of the absence of particle concentration effect on the fluid medium and the inability to consider the interaction between particles (Ansys Fluent, 2013). A full Eulerian-Eulerian model is more accurate but computationally expensive due to solving more number of transport equations (Ansys Fluent, 2013). To overcome the above limitation, a simplified Eulerian approach, ie the Algebraic slip mixture model, is employed in various mineral processing applications to numerically simulate the multi-phase flows. The ASM model solves fewer transport equations compared with the full EE approach and is computationally efficient. Multi-phase simulation studies using a standard ASM model can predict the experimental data at dilute feed solids concentration. No studies on particulate flow dynamics have been carried out using the algebraic slip mixture (ASM) model. The present study uses the standard ASM model to study the particulate flow dynamics such as particle radial segregation, pulp velocity and stream flow rate at a low and medium concentration of solids. The predicted results are validated against experimental results (Holtham, 1997).

METHODOLOGY

Identification of a better CFD model for spiral concentrators is helpful for designers and operators. It helps design the various spiral concentrators and reduces the expense of real experimental models. These are also beneficial for operators to decrease time usage and the expense of trials to get better operating conditions. The current study predicts flow field characteristics of an LD9 spiral concentrator using ANSYS Fluent 19.2 software by solving the continuity and Navier-stokes equations in 3D cartesian coordinates by the finite volume method. The initial step in the multi-phase modelling is to identify the water profile on the spiral trough. Following that, the second step in the spiral concentrator simulation is to model particulate flow. The Renormalisation group (RNG)

k-ε turbulence model has been employed to resolve the laminar to turbulence transition across the spiral trough surface. The VOF model, coupled with the RNG k-ε turbulence model, is used for the initial tracking of the interface between the water and air. The coal, quartz and glass beads particles are modelled using the Algebraic slip mixture model (Manninen and Taivassalo, 1996). In industrial practice, spiral concentrators can operate from 10 to 40 wt.% of solids. An increase in feed solids concentration leads to an extra generation of stresses because of particle to fluid and particle to particle interactions and also increases the slurry viscosity. The present work aims at evaluating a standard ASM model by incorporating these extra formulations.

Algebraic slip mixture (ASM) model

Before introducing distinct size range particles to the converged two-phase CFD simulations as secondary phases, the multi-phase model was changed from the VOF scheme to the ASM model. The ASM model enables the interpretation and movement of the phases at different velocities. It solves the continuity, the Navier-stokes equations for the mixture, and the volume fraction equation for the dispersive phases (Manninen and Taivassalo, 1996). The solid particle phases are introduced in the ASM model by enabling the granular option in ANSYS's Fluent (Ding and Gidaspow, 1990).

The continuity equation:

$$\frac{\partial}{\partial t}(\rho_m) + \nabla.(\rho_m \vec{v}_m) = 0$$

Here ρ_m is the mixture density and $\vec{v}_m$ is the mass averaged velocity.

$$\vec{v}_m = \frac{\sum_{k=1}^{n} \alpha_k \rho_k \vec{v}_k}{\rho_m}$$

Here n indicates the number of phases.

$$\sum_{k=1}^{n} \alpha_k = 1$$

$$\rho_m = \sum_{k=1}^{n} \alpha_k \rho_k$$

The momentum conversation equation is

$$\frac{\partial}{\partial t}(\rho_m \vec{v}_{m,i}) + \frac{\partial}{\partial x_j}(\rho_m \vec{v}_{m,i} \vec{v}_{m,j}) = -\frac{\partial p}{\partial x_i} + \frac{\partial}{\partial x_j}\left(\mu_m\left(\frac{\partial \vec{v}_{m,i}}{\partial x_j} + \frac{\partial \vec{v}_{m,j}}{\partial x_i}\right)\right) + \rho \vec{g}_i + \frac{\partial}{\partial x_j}\left(\sum_{k=1}^{n} \alpha_k \rho_k \vec{v}_{dr,ki} \vec{v}_{dr,kj}\right)$$

where $\vec{v}_{dr,k}$ the secondary phase drift velocity, μ_m is the mixture viscosity and expressed as

$$\mu_m = \sum_{k=1}^{n} \alpha_k \mu_k$$

$$\vec{v}_{dr,k} = \vec{v}_k - \vec{v}_m$$

The secondary phase volume fraction is

$$\frac{\partial}{\partial t}(\alpha_p \rho_p) + \nabla.(\alpha_p \rho_p \vec{v}_m) = -\nabla.(\alpha_p \rho_p \vec{v}_{dr,p})$$

where p is the secondary phase.

$$\vec{v}_{pq} = \vec{v}_p - \vec{v}_q$$

where $\vec{v}_{pq}$ is the slip or relative velocity. It is defined as the secondary phase (p) velocity relative to the primary phase (q) velocity. This is modelled by the Manninen and Taivassalo model (1996).

The air slip velocity is disabled and set to zero (Schiller and Naumann, 1935). The present multi-phase model is applicable at dilute feed solids concentration.

Boundary conditions and numerical treatment

The LD9 spiral concentrator is used in the current study to conduct the multi-phase CFD simulations. The details of the spiral are shown in Figure 1a. The LD9 spiral concentrator geometry and mesh are generated by ANSYS's ICEM tool. For CFD simulations, a 3D unstructured grid of the LD9 spiral concentrator is utilised (Figures 1b and 1c). The grid independence study is performed using six different sizes and is tested and presented elsewhere (Sudikondala *et al*, 2022). The optimum grid size utilised for better flow field predictions in the CFD simulations is 404 k. The given domain has an inlet, outlet, and solid walls as the boundaries. In the inlet section, the desired velocity and volume fraction of solids are assigned for the slurry. At the outlet boundary, pressure out conditions is chosen. No-slip and no penetration conditions are recommended for water in the trough wall boundary. The trough wall roughness coefficient was fixed to 0.5. The top wall was considered to be the free slip condition. The details of the primary and secondary phases, together with their properties, are shown in Table 1. All the phases considered in the simulation studies have constant physical properties. The SIMPLE scheme was used for pressure velocity coupling. The momentum, turbulent kinetic energy and turbulent dissipation rate equations were discretised using a QUICK scheme. Body Force Weighted opted for a pressure interpolation scheme. Compressive was chosen for the discretisation of the volume fraction equation. The model of particulate flow uses a time-dependent formulation, and equations were solved using an unsteady solver. Residuals of all variables were fixed to 0.00001 to attain the convergence criterion. The complete details about the RNG k-ε turbulence model and the Volume of Fluid model are presented elsewhere (Sudikondala *et al,* 2022). The reason for choosing the RNG k-ε model is that it is most suitable for experimental velocity profiles at low swirls (Escue and Cui, 2010). The current spiral concentrator simulations are performed using ANSYS Fluent 19.2 software (Ansys Fluent, 2013).

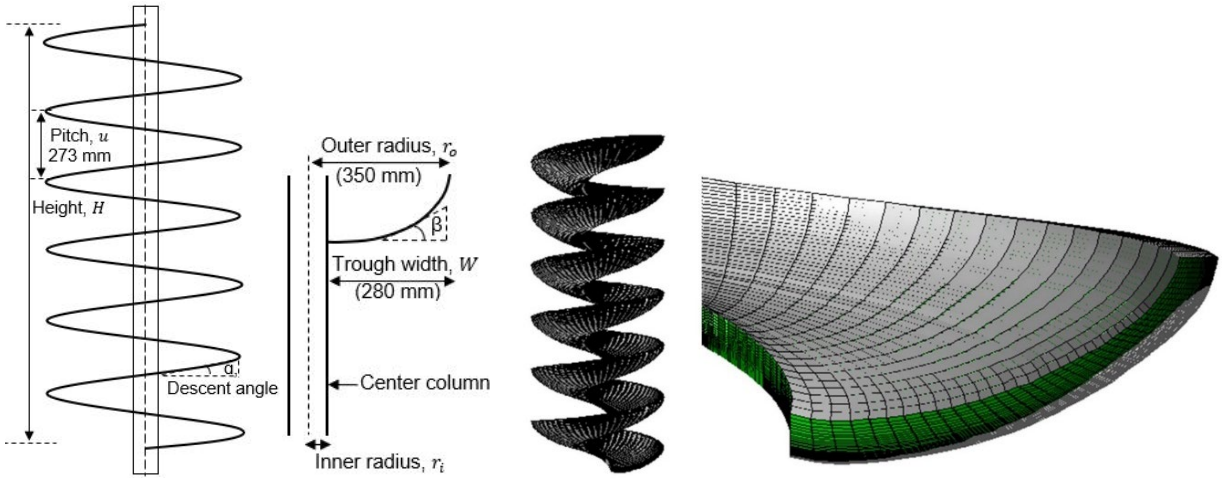

FIG 1 – (a) Detailed schematic of a spiral concentrator (Kapur and Meloy, 1998); (b) computational grid; (c) refined mesh on the trough surface (Sudikondala *et al*, 2022).

TABLE 1

Properties of the fluids utilised in CFD simulations.

S. No.	Phases	Density in kg/m^3	Viscosity, kg/ms	Size in μm
1	Water	1000	0.0009	-
2	Air	1.225	1.7894×10^{-05}	-
3	Coal	1450	0.004	75, 530
4	Glass beads	2440	0.004	75, 530
5	Quartz	2650	0.004	75, 530, 1400

RESULTS AND DISCUSSIONS

Numerical predictions of particulate flow at 0.3 wt.% solids

The current CFD simulations of particle flow in the LD9 spiral concentrator are conducted at 0.3 per cent feed solids and a flow rate of 6 m^3/hr. The predicted numerical results are validated against the experimental measurements (Holtham, 1997). All simulation studies use a highly accurate turbulence model for spirals, ie the RNG group k-ε model (Doheim *et al,* 2013; Mahran *et al,* 2015). At 0.3 wt.% feed solids, the model uses glass beads (75, 530 μm) and quartz (1400 μm) particles having densities of 2440 kg/m^3 and 2650 kg/m^3, respectively, and the ratio of a mix among the three sizes is 1:1:1. The particulate flow parameters, such as particle distribution, pulp velocity, and flow rate, are discussed below. The converged multi-phase flow simulations are used to analyse the particulate flow parameters.

Radial segregation of particles

Predicting the distribution of particles with varying sizes across the trough surface helps in fixing the splitter location on the spiral trough. Figure 2 shows the cumulative weight percentage of particle distribution across the trough surface at 0.3 wt.% of solids. For a better understanding of the CFD model predictions across the trough surface, the spiral trough surface has been divided into three regions, namely the inner region (0–116 mm), middle (116–195 mm) and outer region (195–280 mm). The present model predictions reveal that the 75 μm glass beads particles show the 41.78, 25.45 and 32.77 wt.% distribution in the inner, middle, and outer trough regions. Glass beads particles of size 530 μm are majorly reported in the inner radii, and it shows 97.20 wt.% distribution in the inner region. Finally, 1400 μm quartz particles are distributed across the trough surface, and it shows 46.84, 23.89 and 29.27 wt.% distribution in the inner, middle, and outer trough regions. Numerical predictions show satisfactory agreement with the experimental data. The present model underpredicts the results near the inner radii.

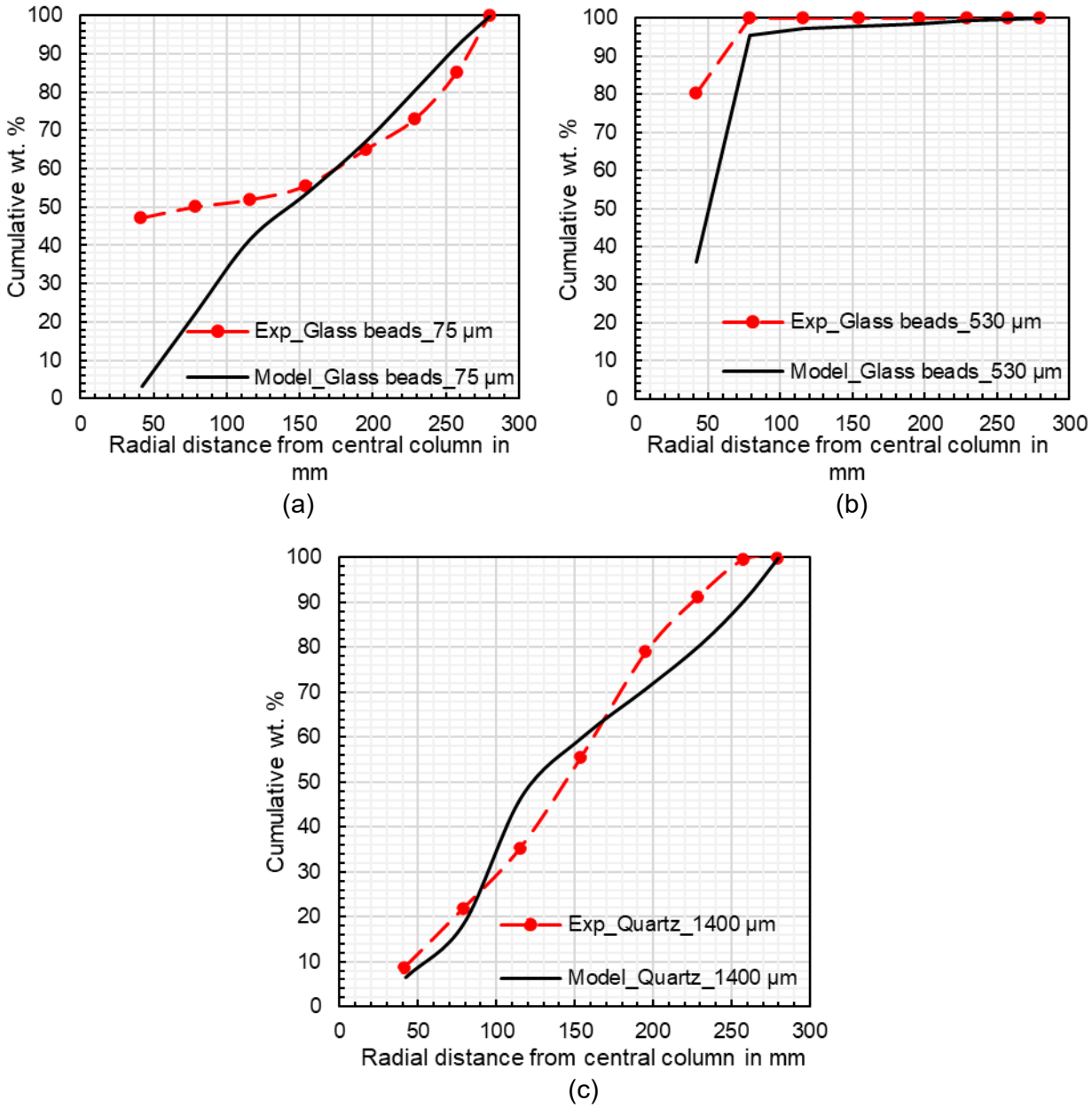

FIG 2 – Numerical prediction of (a) glass beads, 75 µm (b) glass beads, 530 µm and (c) quartz, 1400 µm particles radial distribution on the trough surface at 0.3 per cent of solids (Holtham, 1997).

Pulp velocity and streamflow rate

The experimental measurements of pulp velocity on the trough surface are presented as mean stream velocity, which implies that the spiral concentrator trough surface is separated into eight streams by employing seven splitters (Holland-Batt and Holtham, 1991) (Figure 3a). Figure 3b shows the contour map of pulp velocity across the spiral trough. It increases continuously in the outward direction from the centre of the cylinder column due to an increase in centrifugal force dominance over the gravitational force (see Figure 4a). Figure 4b shows the numerically predicted results of the stream flow rate. The flow rate in different streams varies with the cross-section area and the velocity of the flowing pulp in individual streams.

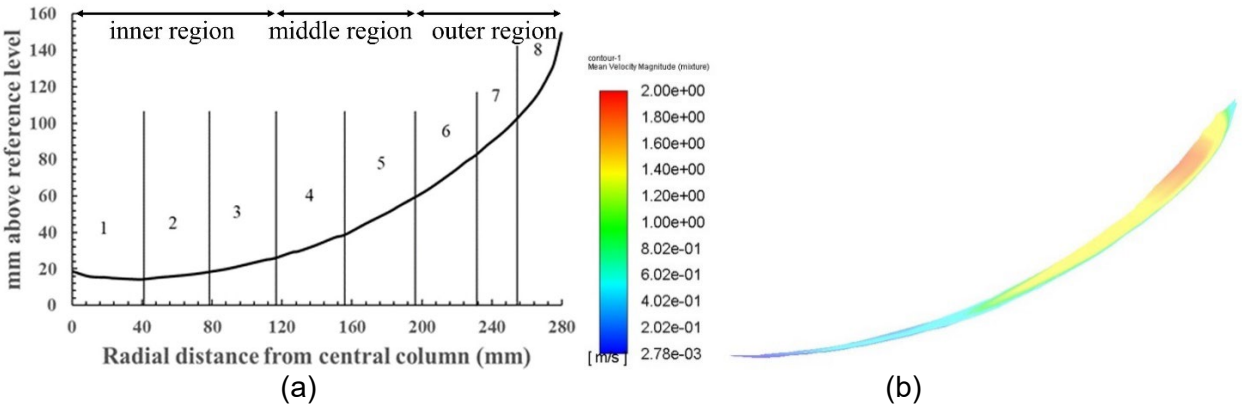

FIG 3 – (a) Sampling streams employed on the LD9 spiral concentrator (b) The pulp velocity contour map at 0.3 wt.% of solids.

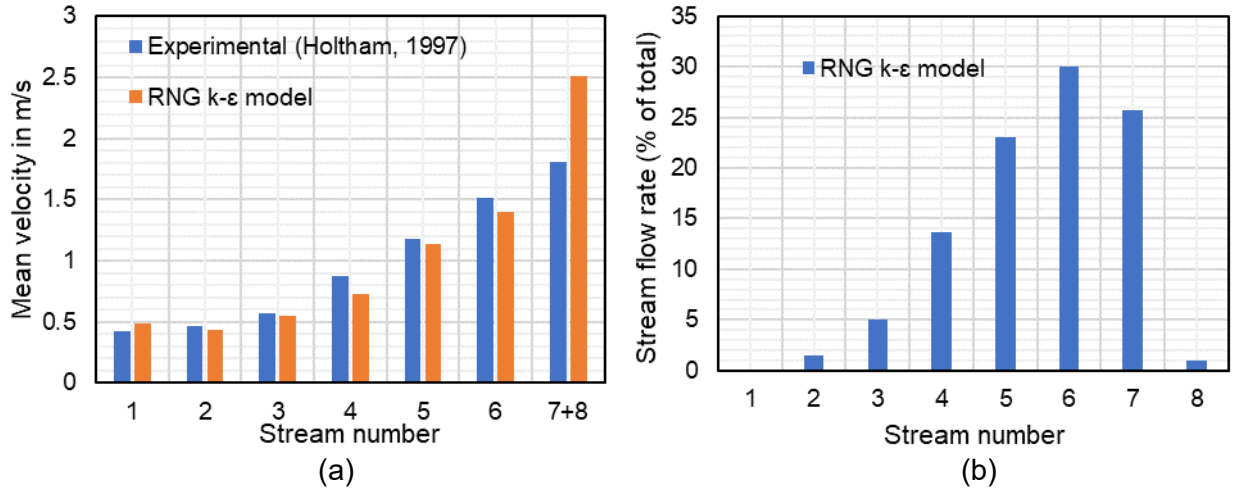

FIG 4 – Predicted values of (a) mean pulp velocity and (b) flow rate in different streams at 0.3 per cent solids.

Numerical predictions of particulate flow at 3 and 15 wt.% feed solids

The current study of particulate flow was extended from dilute feed solids content (0.3 wt.%) to medium feed solids content (3 and 15 wt.%) at a flow rate of 6 m^3/hr. In the case of 3 wt.% of feed solids content, the current model uses glass beads particles (2440 kg/m^3) of sizes 75 and 530 µm at an equal mix ratio. The details of the particles at 15 per cent by weight are shown in Table 2. Figure 5 shows the cumulative volume percentage distribution of particles of various sizes across the spiral trough at 3 and 15 wt.% of solids, respectively. Table 3 shows the predicted results of various particle volume per cent distribution in three regions at 3 and 15 wt.% of solids. In the case of 3 wt.% of solids, 75 µm glass beads particles are mostly distributed in the middle and outer trough regions, whereas 530 µm glass beads particles are majorly distributed in the inner and middle trough regions (see Table 3). In the case of 15 wt.% of feed solids content, 75 µm coal particles are mostly distributed in the middle and outer trough regions, whereas the 75 µm quartz particles are majorly distributed in the middle region. Both coal and quartz particles of 530 µm size are distributed in all three regions (Table 3). In both cases, fine particles move to the outer radii, and coarse particles move to the inner radii. Pulp velocity increases towards the outer radii of the LD9 spiral trough due to an increase in centrifugal force dominance over the gravitational force (Figure 6).

TABLE 2

Particles used at 15 wt.% of solids.

S. No	Particle type	Density in kg/m^3	Size in µm	Mix ratio
1	coal	2440	75	2
2	coal	2440	530	2
3	quartz	2650	75	1
4	quartz	2650	530	1

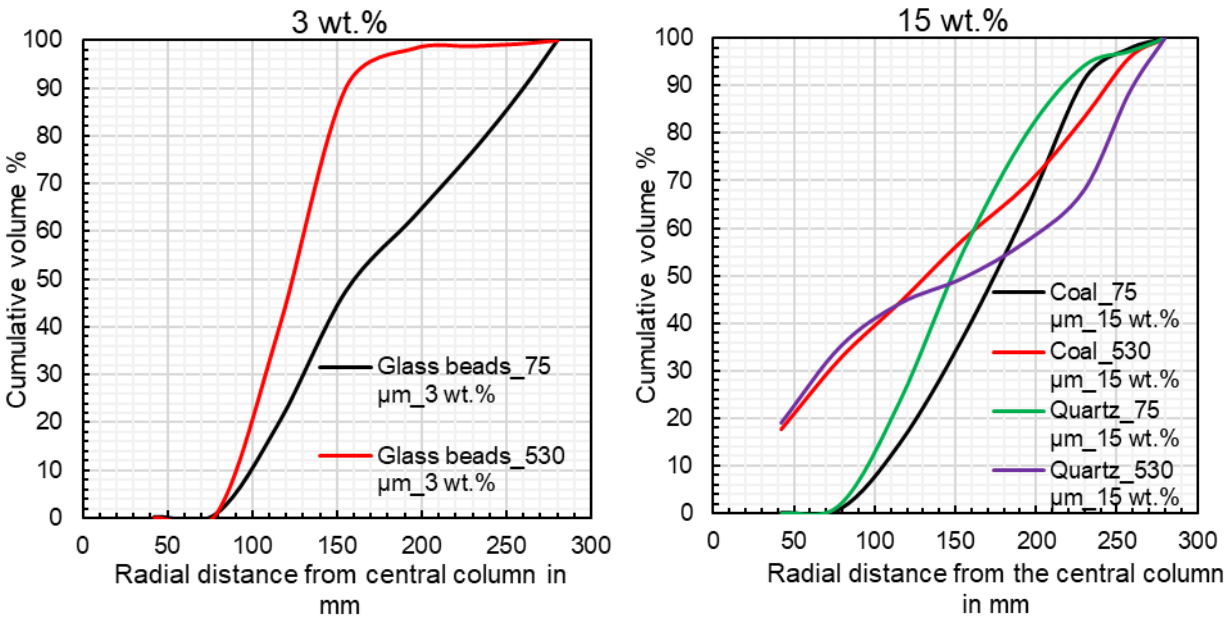

(a) (b)

FIG 5 – Numerical prediction of (a) glass beads and (b) coal and quartz particles distribution across the spiral trough at 3 and 15 wt.% solids.

TABLE 3

CFD predicted volume percent distribution in different regions at 3 and 15 wt.% of solids.

	Glass beads 75 µm	Glass beads 530 µm	Coal 75 µm	Coal 530 µm	Quartz 75 µm	Quartz 530 µm
Region	**Volume% distribution (% of total)**					
Inner	20.27	40.22	14.88	44.43	23.98	44.20
Middle	42.68	58.07	49.60	24.90	56.36	13.22
Outer	37.05	1.71	35.52	30.67	19.66	42.58

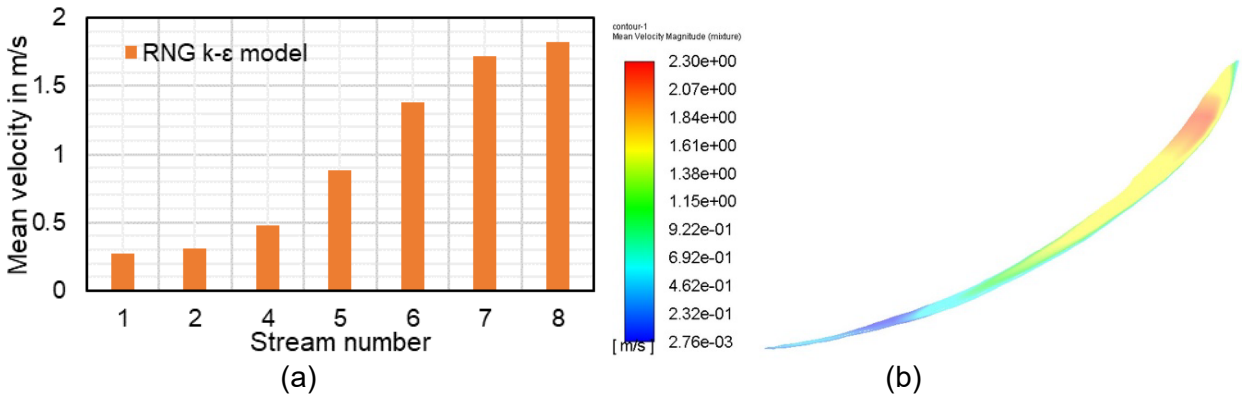

FIG 6 – Predicted values of (a) mean stream pulp velocity and (b) contour map at 3 wt.% solids.

CONCLUSIONS

Numerical prediction of particle flow in an LD9 spiral concentrator has been studied using the ASM model at low (0.3 and 3 wt.%) and medium (15 wt.%) solids concentrations. The numerical predictions of particulate flow at 0.3 wt.% of solids showed better validation with experimental results using the RNG k-ε turbulence model. The maximum pulp velocity of 2.5 m/s was observed in streams numbers 7 and 8 together. In the particulate flow model predictions at 3 per cent of feed solids, the 75 µm glass beads particles distribute in the middle and outer regions, and it shows the 20.27, 42.68 and 37.05 vol. per cent distribution in the inner, middle, and outer trough regions. Glass beads particles of 530 µm size distribute in the inner and middle regions and show the 40.22, 58.07 and 1.71 vol. per cent distribution in the inner, middle, and outer trough areas. The final implemented CFD model aids in designing the various spiral concentrators operating at moderate feed solids with different components. Future work will model the particulate flow in spiral concentrators at a high solids concentration using various turbulence models.

ACKNOWLEDGEMENTS

The authors wish to thank the management of R&D TATA Steel, IIT Hyderabad and Uchchatar Avishkar Yojana (UAY)-MHRD, Govt. of India for funding and resource support to undertake the present work.

REFERENCES

Ansys Fluent (2013) 'Ansys Fluent 15.0 – Theory Guide', *ANSYS Inc., USA*, 15317 (November), pp. 724–746.

Bazin, C, Sadeghi, M, Bourassa, M, Roy, P, Lavoie, F, Cataford, D, Rochefort, C and Gosselin, C, (2014) 'Size recovery curves of minerals in industrial spirals for processing iron oxide ores', *Minerals Engineering*. Elsevier Ltd, 65, pp. 115–123. doi: 10.1016/j.mineng.2014.05.012.

Boucher, D, Deng, Z, Leadbeater, T W, Langlois, R and Waters, K E, (2016) 'Speed analysis of quartz and hematite particles in a spiral concentrator by PEPT', *Minerals Engineering*. Elsevier Ltd, 91, pp. 86–91. doi: 10.1016/j.mineng.2015.09.014.

Boucher, D, Deng, Z, Leadbeater, T, Langlois, R, Renaud, M and Waters, K E, (2014) 'PEPT studies of heavy particle flow within a spiral concentrator', *Minerals Engineering*. Elsevier Ltd, 62, pp. 120–128. doi: 10.1016/j.mineng.2013.12.022.

Ding, J and Gidaspow, D, (1990) 'A bubbling fluidization model using kinetic theory of granular flow', *AIChE Journal*, 36(4), pp. 523–538. doi: 10.1002/aic.690360404.

Doheim, M A, Abdel Gawad, A F, Mahran, G M A, Abu-Ali, M H and Rizk, A M, (2013) 'Numerical simulation of particulate-flow in spiral separators: Part I Low solids concentration (0.3% & 3% solids)', *Applied Mathematical Modelling*. Elsevier Inc., 37(1–2), pp. 198–215. doi: 10.1016/j.apm.2012.02.022.

Doheim, M A, Abdel, A F, Mahran, G M A, Abu-Ali, M H and Rizk, A M, (2008) 'Computational prediction of water-flow characteristics in spiral separators: Part I, Flow depth and turbulence intensity', *Engineering Sciences*, 36(4), pp. 935–950.

Escue, A and Cui, J, (2010) 'Comparison of turbulence models in simulating swirling pipe flows', *Applied Mathematical Modelling*. Elsevier Inc., 34(10), pp. 2840–2849. doi: 10.1016/j.apm.2009.12.018.

Fuerstenau, M C and Han, K N, (1979) *Principle of Mineral Processing*, The Society for Mining, Metallurgy, and Exploration Inc: Littleton.

Holland-Batt, A B and Holtham, P N, (1991) 'Particle and fluid motion on spiral separators', *Minerals Engineering*, 4(3–4), pp. 457–482. doi: 10.1016/0892–6875(91)90147-N,

Holland-Batt, A B, (1989) 'Spiral separation: theory and simulation', *Transactions of the Institution of Mining and Metallurgy, Section C: Mineral Processing and Extractive Metallurgy*, pp. 46–60.

Holland-Batt, A B, (1994) 'The effect of feed rate on the performance of coal spirals', *Coal Preparation*, pp. 199–222. doi: 10.1080/07349349408905234.

Holland-Batt, A B, (1995) 'Some design considerations for spiral separators', *Minerals Engineering*, pp. 1381–1395. doi: 10.1016/0892–6875(95)00104-X,

Holtham, P N, (1990) 'Flow visualisation of secondary currents on spiral separators', *Minerals Engineering*, 3(3–4), pp. 279–286. doi: 10.1016/0892–6875(90)90123-S,

Holtham, P N, (1992) 'Primary and secondary fluid velocities on spiral separators', *Minerals Engineering*, 5(1), pp. 79–91. doi: 10.1016/0892–6875(92)90007-V,

Holtham, P N, (1997) 'Vol.1 Experimental Validation of a Fundamental Model of Coal Spirals' Australian Coal Association research program (ACARP)'.

Jain, P K and Rayasam, V, (2017) 'An analytical approach to explain the generation of secondary circulation in spiral concentrators', *Powder Technology*. Elsevier B V, 308, pp. 165–177. doi: 10.1016/j.powtec.2016.11.040.

Kapur, P C and Meloy, T P, (1998) 'Spirals observed', *International Journal of Mineral Processing*, 53(1–2), pp. 15–28. doi: 10.1016/s0301–7516(97)00053–7.

Mahran, G M A, Doheim, M A, Abdel Gawad, A F, Abu-Ali, M H and Rizk, A M, (2015) 'Numerical simulation of particulate flow in Spiral Separators (15% Solids)', *AFINIDAD LXXII, 571*, pp. 223–229.

Manninen, M and Taivassalo, V, (1996) 'On the mixture model for multi-phase flow', *VTT Publications*, (288), pp. 3–67.

Matthews, B W, Fletcher, C A J and Partridge, A C, (1998) 'Computational simulation of fluid and dilute particulate flows on spiral concentrators', *Applied Mathematical Modelling*, 22(12), pp. 965–979. doi: 10.1016/S0307–904X(98)10030–6.

Matthews, B W, Fletcher, C A J, Partridge, A C and Vasquez, S, (1999) 'Computations of Curved Free Surface Water Flow on Spiral Concentrators', *Journal of Hydraulic Engineering*, 125(11), pp. 1126–1139. doi: 10.1061/(asce)0733–9429(2001)127:7(629).

Matthews, B W, Holtham, P N and Golab, K, (1998) 'Computational and Experimental Investigation of Spiral Concentrator Flows', *Coal Operators Conference*, (July), pp. 415–421.

Sadeghi, M, Bazin, C and Renaud, M, (2014) 'Effect of wash water on the mineral size recovery curves in a spiral concentrator used for iron ore processing', *International Journal of Mineral Processing*. Elsevier B V, 129, pp. 22–26. doi: 10.1016/j.minpro.2014.04.006.

Sadeghi, M, Bazin, C and Renaud, M, (2016) 'Radial distribution of iron oxide and silica particles in the reject flow of a spiral concentrator', *International Journal of Mineral Processing*. Elsevier B V, 153, pp. 51–59. doi: 10.1016/j.minpro.2016.06.003.

Schiller, L and Naumann, A, (1935) 'A drag coefficient correlation', *Zeitschrift des Vereins Deutscher Ingenieure*, (77), pp. 318–320.

Sudikondala, P, Mangadoddy, N, Kumar, M, Kumar Tripathy, S and Yanamandra, R M, (2022) 'CFD Modelling of Spiral Concentrator – Prediction of Comprehensive Fluid Flow Field and Particle Segregation', *Minerals Engineering*. Elsevier Ltd, 183(May), p. 107570. doi: 10.1016/j.mineng.2022.107570.

Tripathy, S K, Ramamurthy, Y, Tathavadkar, V and Denys, M B, (2012) 'Efficacy of Multi Gravity Separator for Concentrating', *Journal of Mining and Metallurgy*, (1), pp. 39–49.

Wang, J and Andrews, J R G, (1994) 'Numerical simulations of liquid flow on spiral concentrators', *Minerals Engineering*, 7(11), pp. 1363–1385.

Wills, B A and Napier-Munn, T, (2005) *Wills' Mineral Processing Technology*, *Wills' Mineral Processing Technology*. doi: 10.1016/B978–0-7506–4450–1.X5000–0.

Ye, G, Ma, L, Alberini, F, Xu, Q, Huang, G and Yu, Y, (2019) 'Numerical studies of the effects of design parameters on flow fields in spiral concentrators', *International Journal of Coal Preparation and Utilization*. Taylor & Francis, 2699, pp. 1–15. doi: 10.1080/19392699.2019.1579200.

New sensor development for hydrocyclone overflow particle cumulative percent passing size online monitoring – a preliminary experimental investigation under dry condition

D Tang[1], L Chen[2], L Yang[3] and E Hu[4]

1. Research Associate, The University of Adelaide, Adelaide SA 5005. Email: difan.tang@adelaide.edu.au
2. Senior Lecturer, The University of Adelaide, Adelaide SA 5005. Email: lei.chen@adelaide.edu.au
3. Ph.D. Candidate, The University of Adelaide, Adelaide SA 5005. Email: lin.yang@adelaide.edu.au
4. Associate Professor, The University of Adelaide, Adelaide SA 5005. Email: eric.hu@adelaide.edu.au

ABSTRACT

Online monitoring of particles cumulative percent passing (PCPP) for a target size at hydrocyclone overflow, compared with traditional offline methods, provides PCPP feedback in real time, and is advantageous in enabling energy-efficient comminution, increasing downstream flotation efficiency, and improving upstream resource knowledge. However, existing online approaches are generally costly and bespoke, and some are sensitive to operational changes. Therefore, this study proposes a new low-cost alternative based on accelerometer measurement for online PCPP monitoring in the overflow of hydrocyclones and provides a preliminary experimental investigation under dry condition. The proposed method uses a sensing probe inserted into the overflow pipe of a hydrocyclone to receive particle impact from the incoming slurry, with accelerometers attached to the probe and mounting frame outside the pipe for particle-probe impact detection. As a preliminary investigation before studying particle-probe impact events in slurry, tests under dry condition without fluids were conducted using dry sand particles in free fall from a fixed height. Accelerometer measurements are analysed in both time and frequency domains through root-mean-square (RMS) and fast Fourier transform (FFT). Results show that accelerometer measurements are useful in estimating mass flow rates, which are correlated to the accelerometer output amplitude RMS values in time domain, in a non-linear mapping. Different particle size classes can be identified by examining the accelerometer output amplitude at a known mass flow rate. Different particle size classes feature their distinct signature frequencies (SFs) that can be examined via FFT and the SF is found to be independent of the mass flow rate. The results imply that any PCPP changes can be detected by the change in the accelerometer output amplitude as well as a shift in SF, which demonstrates the effectiveness of using accelerometers to gauge changes in PCPP. Based on the current findings in dry condition, future work will investigate particle-probe impact events in slurry.

INTRODUCTION

Hydrocyclones play an important role in classification process within a grinding circuit, where fine or light particles are directed to the overflow and sent to flotation while coarse or dense particles are classified to the underflow and fed back for regrinding. Oversized particles reduce flotation efficiency while over-grinding wastes energy (Wills, 2006; Maron, O'Keefe and Sepulveda, 2018). Therefore, online monitoring of particles cumulative percent passing (PCPP) for a target size at hydrocyclone overflow is crucial to maintaining effective and energy-efficient grinding and flotation (Blasco and Kongas, 2011). A majority PCPP monitoring procedures are performed offline via methods such as sieving analysis (International Organization for Standardization, 1988), sedimentation and elutriation (Heywood, 1958), microscopic sizing and image analysis (Allen, 1997), electrical impedance (Hogg and Coulter, 1967) and laser imaging (Napier-Munn *et al,* 1996), resulting in additional labour cost as well as hours of delay (Wills, 2006). A conservative measure to maintain acceptable PCPP otherwise leads to increased margin, either between the actual percent passing size (eg P80) and a target dimension, or between the actual PCPP and the desired PCPP of a target size. This means extended grinding task and higher energy consumption as a result (Maron, O'Keefe and Sepulveda, 2018).

Camera-based online imaging technique has been proposed for monitoring PCPP for the underflow of hydrocyclones (Aldrich, Uahengo and Kistner, 2015), which however, is inapplicable to the overflow due to considerably smaller sizes of overflow particles. It has been shown that particle size analysis via laser diffraction can also be used online (Norris and Kongas, 2011) and further improvements to measurement accuracy have been made in the work of Tabuchi *et al* (2019). A most common disadvantage of laser-based methods is that slurry needs to be diluted prior to analysis. Instead of using laser, solid concentration and PCPP can also be estimated via measuring the ultrasonic velocity and the attenuation spectrum in slurry (Hathaway and Guthnals, 1976). Variants among ultrasonic approaches have arisen in recent decades to deliver more accurate measurement results (Coghill, Millen and Sowerby, 2002; Xue *et al,* 2009; Coghill and Millen, 2012; Greenwood, 2012). However, an additional sampler is inevitable for slurry treatment prior to PCPP analysis. Another interesting direction towards online PCPP estimation is based on analysing acoustic emissions from particles impacting a sensing probe (Pecorari, 2013; Sun *et al,* 2014; Wang *et al,* 2019a; Nsugbe *et al,* 2019; Zhang *et al,* 2019). The size detection range by acoustic emission sensing is nevertheless limited towards the finer side, compared to laser and ultrasonic methods. It is also worth noting that the aforementioned online PCPP monitoring methods can all incur high cost for application on hydrocyclone overflow given that every individual overflow pipe needs to be monitored (Maron, O'Keefe and Sepulveda, 2018) and normally there are dozens of or more hydrocyclone units at a mineral processing plant.

A relatively low-cost alternative for online PCPP estimation can be based on particle impact force measurement (Gao *et al,* 2013; Sun *et al,* 2014; Wang *et al,* 2019a*,* 2019b), where piezoelectric sensors are used to detect vibrations resulted from particle impact on a sensing medium. These methods were tested in airflow with particles of sizes down to 400 μm at low concentrations, allowing every single particle-probe impact event to be individually identified and counted. However, it remains unclear whether force sensing can be applied to the overflow of hydrocyclones where the majority of particles are smaller than 400 μm and the solid concentration is significantly higher.

Particle-probe impact forces normally present themselves in the form of vibration, which could be better captured via accelerometers which are also potentially cost-effective. Vibration sensing via accelerometers has been used in combination with acoustic emission methods for measurement of bubble solids mass loading at Jameson cell (Spencer *et al,* 2012). The application of accelerometers on hydrocyclones can be seen in the work of Nayak *et al* (2019) where vibration signals are found useful in online choking detection. A comprehensive review on online vibration sensing for monitoring hydrocyclone performance is given by Mishra and Majumder (2022), and corresponding applications are found limited to roping and choking detection. In general, there has been no work related to the use of accelerometers for PCPP measurements at hydrocyclone overflow.

Therefore, this paper explores the feasibility of utilising accelerometers for capturing particle size dependent vibrations to perform online PCPP estimation at the overflow of hydrocyclones and provides a preliminary experimental investigation in dry condition without fluids.

METHOD

Proposed prototype

The proposed vibration measurement unit (VMU) prototype is shown in Figure 1, which consists of a probe and two miniature single-axis accelerometers. The probe is inserted into the overflow pipe to capture particle-probe impact events on the probe head that is interchangeable and can vary in shapes. In this paper, a triangular prism is used for the probe head. The vibration movements on the probe rod caused by particle-probe impact events are passed onto the accelerometer installed on the probe rod outside the pipe at a position between the external pipe wall and the fixture mount. The second accelerometer is installed on the VMU mounting frame to capture non-impact related vibrations. It is worth noting that the proposed VMU installation is not restricted to the vertical set-up in Figure 1 but can also be installed at multiple possible locations along the overflow pipe including horizontal placement.

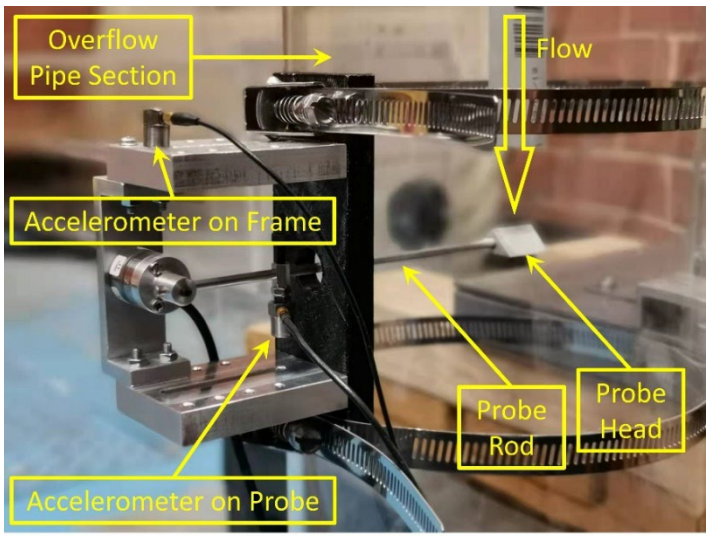

FIG 1 – Proposed VMU prototype.

Laboratory experiment set-up

In this paper, as a preliminary investigation, only the partible-probe impact events on the probe head under dry condition (without fluids) is considered, with the experiment set-up shown in Figure 2. The overall configuration is given in Figure 2a, where dry particles are placed in the computer-controlled particles disperser for release in free fall through the guide tube, with the VMU installed on a vertically placed transparent pipe section and positioned under the guide tube to receive impacts. As illustrated in Figure 2b, the release of dry particles is controlled by the opening between the motorised plug conical tip and the hopper bottom aperture. The opening is finely adjusted via computer by lifting the plug vertically with position feedback, which guarantees consistence in the resulting mass flow rate. A 6-axis force/torque transducer is used to measure the weight change of the entire hopper unit containing dry particles. The mass flow rate can then be readily acquired by calculating the rate of weight reduction.

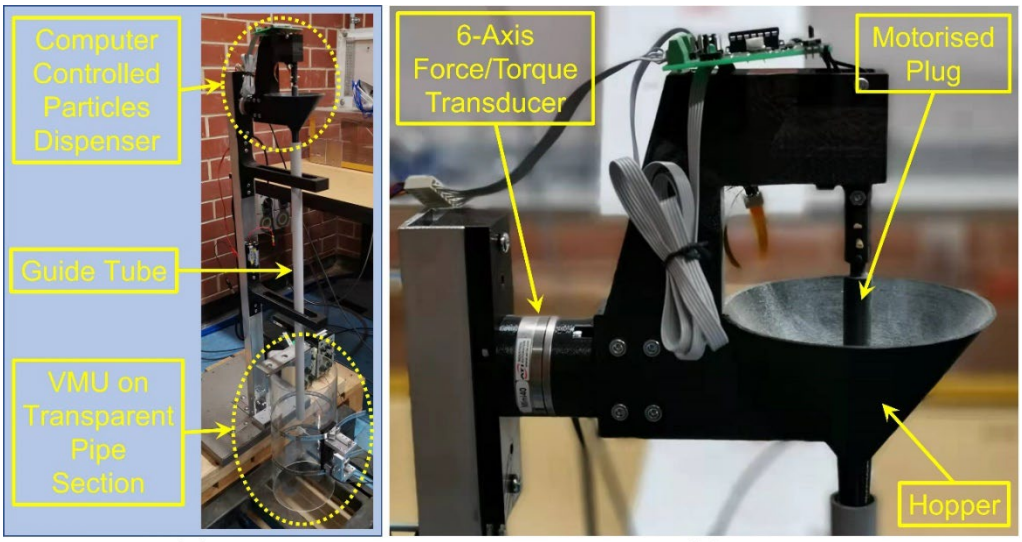

FIG 2 – Laboratory experiment set-up.

Experiment procedures

Particles used in experiments were dry sand sieved into four size classes in micrometres: 150–212, 212–300, 300–425, and 425–600. The mass flow rate was monitored at a rate of 1000 Hz, while particle-probe impact events were sampled at 3×10^5 Hz. The mass flow rates for each size class were varied from 0.5 g/s to 3.5 g/s with 0.2 g/s increment and was maintained constant for every

single test lasting over 12 s. Data were recorded from the start of releasing sand till 10 s in each test. Background noises, that is, conditions under no loading, were also recorded for reference.

To obtain clean data that only contains particle-probe impact events (excluding transient responses before and after impact events), data between 3 s and 7 s were analysed. Scattered data points of accelerometer output amplitudes against mass flow rates are fitted with second order polynomials to give a clean representation of trends. Data are analysed in both time domain and frequency domain.

Root-mean-square (RMS) is adopted to evaluate the time response of particle-probe impact events in terms of the resulted accelerometer output amplitudes. Given that in time domain vibrations of different frequencies are mixed and overlapped, further investigation is conducted in frequency domain via fast Fourier transform (FFT). To reveal non-background signals, background noises are first subtracted from measurements that contain particle-probe impact events. To identify vibrations exclusively associated with particle-probe impact events, FFT of the accelerometer on the probe and the accelerometer on the VMU frame are compared. According to the Hertz impact theory (Hertz, 1881) which establishes the relation between contact time and particle size during an elastic impact, there exists a signature frequency (SF) corresponding to any particle size during a particle-probe impact event, and there exists a generalised SF for different particle size classes as a whole. Therefore, accelerometer output amplitudes and their corresponding frequencies are key variables under investigation.

RESULTS AND DISCUSSION

As an illustration of how particle-probe impact events are determined, Figure 3 shows the responses of the two accelerometers installed on the VMU in a test using 150–212 μm size class at 0.1 g/s flow rate. Instead of using acceleration unit, the accelerometer output in the form of voltage (V) is used for ease of explanation. Under laboratory environment, it is expected that the accelerometer attached on the probe should pick up stronger vibrations than those captured by the accelerometer installed on the VMU frame. This can be confirmed in Figure 3a where significantly higher output amplitudes are present for the accelerometer on the probe. In an *in situ* case where the VMU is mounted on an overflow pipe of a hydrocyclone unit, structural vibrations can also pass onto the accelerometer on the VMU frame and may cause stronger vibrations than those from particle-probe impact events. However, the latter case does not affect signal analysis since frequency components related to structural vibrations can be readily identified in frequency domain. As can be seen from Figure 3b, frequency components associated with measurements from the accelerometer on the VMU frame are dominant at low frequency regime ($< 2.5 \times 10^4$ Hz), whereas most high-frequency components are from the accelerometer on the probe. The amplitude peaks at high-frequency regime are related to significant vibration modes of the probe, which are indirectly linked to particle-probe impact events, as will be shown in Figures 4 and 5.

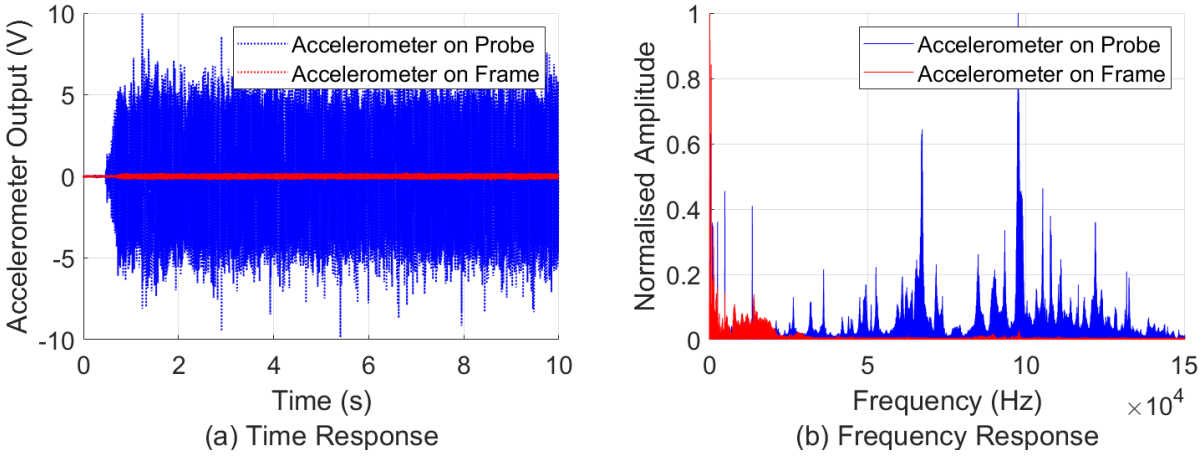

FIG 3 – Responses of accelerometers under particle-probe impact events with 150–212 μm size class at 0.1 g/s flow rate.

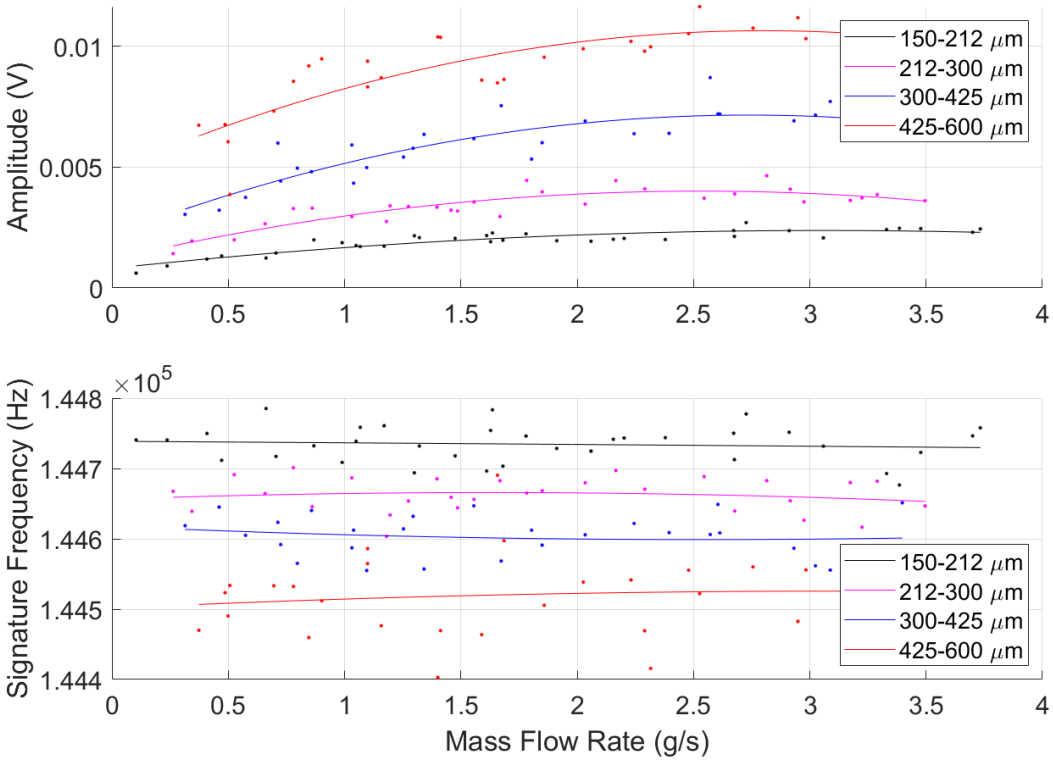

FIG 4 – VMU probe frequency response around 1.446×10^5 Hz.

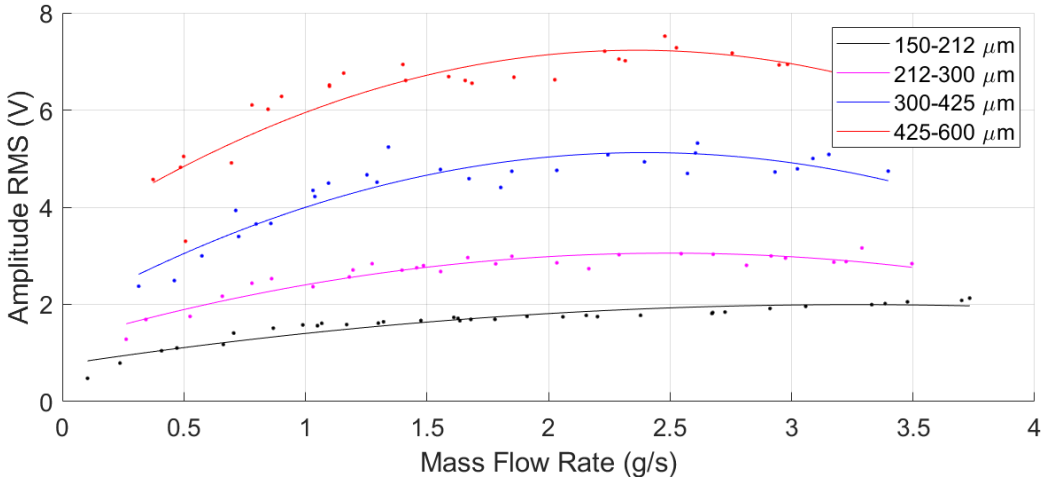

FIG 5 – Output amplitude RMS against mass flow rate for accelerometer on probe in time domain.

Due to the presence of low-frequency noises (as shown in Figure 3b), SF can be better captured at high-frequency regime ($> 2.5 \times 10^4$ Hz). Figure 4 illustrates the conditions evaluated at a frequency of 1.446×10^5 Hz, where vibrations due to particle-probe impacts are examined in accelerometer output amplitudes (V) and corresponding frequencies (Hz), and three main findings can be identified as follows.

Firstly, in the top subfigure, as the mass flow rate increases, the vibration amplitude gradually rises and then starts to decline after a particular mass flow rate. The specific mass flow rate after which the vibration amplitude starts to decline depends on the particle size class. These indicates a useful correlation between particle size classes and mass flow rates.

Secondly, the scattered data points associated with different particle size classes are nicely spaced and separated vertically in group in terms of accelerometer output amplitude, clearly distinguishing the different size classes from each other. It can be seen that particle-probe impact events of larger particles have higher vibration amplitudes than those of smaller particles. This reveals a correlation between vibration amplitudes and particle sizes.

Thirdly, and most importantly, despite the change in mass flow rate, the SF of each particle size class remains constant, and smaller size is associated with higher SF. This finding agrees with the Hertz impact theory (Hertz, 1881) mentioned in *Experiment procedures*. As contact time increases with particle size, the corresponding SF lowers, and vice versa. Therefore, the SF is an important measure to distinguish particles of different size classes given that it is independent of mass flow rates.

When accelerometer output amplitudes are evaluated in the form of RMS in time domain, results are given in Figure 5. Correlations similar to Figure 4 can be observed in terms of vibration amplitudes against mass flow rates. Again, larger particles correspond to higher vibration amplitudes and there exists a maximum value in amplitude for each size class along its fitted curve as the mass flow rate increases. This confirms the first finding from Figure 4.

CONCLUSIONS

Results show that accelerometer measurements are useful in estimating mass flow rates, which are nonlinearly correlated to the accelerometer output amplitude RMS values in time domain. Different particle size classes can be identified by evaluating the accelerometer output amplitude at a known mass flow rate, which can be either the absolute amplitude at a particular SF or the RMS value in time domain. The SF associated with a particular particle size class can be revealed and examined via FFT and is found to be independent of the mass flow rate. Particle samples of narrow size classes can be identified by their distinct SFs, where a larger size features a lower SF. The results imply that whenever the PCPP changes, it can be detected by the change in accelerometer output amplitude as well as a shift in SF. This demonstrates the effectiveness of using accelerometers to gauge changes in PCPP. On the basis of the current findings under dry condition, future work will investigate particle-probe impact events in slurry.

ACKNOWLEDGEMENTS

This research has been supported by the SA Government, end-users partner BHP, and translation partners Manta Control and Rockwell Automation, through the PRIF RCP Mining Consortium ‘Unlocking Complex Resources through Lean Processing’.

REFERENCES

Aldrich, C, Uahengo, F D L and Kistner, M, 2015. Estimation of particle size in hydrocyclone underflow streams by use of multivariate image analysis, *Minerals Engineering,* 70: 14–19.

Allen, T, 1997. *Particle Size Measurement (5th edition) – Volume 1: Powder Sampling and Particle Size Measurement,* (Chapman and Hall: London).

Blasco, A and Kongas, M, 2011. Automated on-line particle size measurement for efficient minerals processing, *AusIMM Bulletin,* (5): 26–29.

Coghill, P J and Millen, M, 2012. Calculation of particle size distributions from ultrasonic measurements: A mineral slurry case study, *Particle & Particle Systems Characterization,* 29(1): 43–52.

Coghill, P J, Millen, M J and Sowerby, B D, 2002. On-line measurement of particle size in mineral slurries, *Minerals Engineering,* 15(1): 83–90.

Gao, L, Yan, Y, Carter, R M, Sun, D, Lee, P and Xu, C, 2013. On-line particle sizing of pneumatically conveyed biomass particles using piezoelectric sensors, *Fuel,* 113: 810–816.

Greenwood, M S, 2012. Particle size and density of a slurry from ultrasonic backscattering measurements at a solid interface, *Review of Scientific Instruments* [Online], 83(9). Available from: <https://doi.org/10.1063/1.4748520> [Accessed: 24 November 2020].

Hathaway, R E and Guthnals, D L, 1976. Continuous measurement of particle size in fine slurry processes, *CIM Bulletin,* 69(766): 64–71.

Hertz, H, 1881. Über die berührung fester elastischer Körper, *Journal für die reine und angewandte Mathematik,* 92: 156–171.

Heywood, H, 1958. *Fundamental Principles of Subsieve Particle Size Measurement,* (IMM: London).

Hogg, W R and Coulter, W, 1967. Apparatus and method for measuring a dividing particle size of a particulate system, *United States Patent* 3557352.

International Organization for Standardization (ISO), 1988. ISO 2591–1: 1988 – Test sieving – Part 1: Methods using test sieves of woven wire cloth and perforated metal plate, December 1988.

Maron, R, O'Keefe, C and Sepulveda, J, 2018. Methodology for assessing the benefits of grind control using particle size tracking technology for true on-line particle size measurement, *Journal of the South African Institute of Mining and Metallurgy,* 118(11): 1149–1154.

Mishra, S and Majumder, A K, 2022. Online techniques for performance and condition monitoring of hydrocyclone: Present status and the future, *Mineral Processing and Extractive Metallurgy Review* [Online], 43(4). Available from: <https://doi.org/10.1080/08827508.2022.2047042> [Accessed: 30 March 2022].

Napier-Munn, T J, Morrell, S, Morrison, R D and Kojovic, T, 1996. *Mineral Comminution Circuits – Their Operation and Optimisation (Appendix 3),* (JKMRC, The University of Queensland: Indooroopilly, Queensland).

Nayak, D K, Das, D P, Behera, S K, Das, S P and Sadangi, J K, 2019. Prevention of hydrocyclone choking through detection of sub-Hz frequency shift of vibration signal, *Journal of Vibration Engineering & Technologies,* 8(4): 517–528.

Norris, R and Kongas, M, 2011. Analysing slurry size online, *The Mining Magazine,* 202(5): 54–55.

Nsugbe, E, Starr, A, Jennions, I and Ruiz-Carcel, C, 2019. Estimation of online particle size distribution of a particle mixture in free fall with acoustic emission, *Particulate Science and Technology,* 37(8): 953–963.

Pecorari, C, 2013. Characterizing particle flow by acoustic emission, *Journal of Nondestructive Evaluation,* 32(1): 104–111.

Spencer, S J, Bruniges, R, Roberts, G, Sharp, V, Catanzano, A, Bruckard, W J, Davey, K J and Zhang, W, 2012. An acoustic technique for measurement of bubble solids mass loading: (b) Monitoring of Jameson cell flotation performance by passive acoustic emissions, *Minerals Engineering,* 36–38: 21–30.

Sun, D, Yan, Y, Carter, R M, Gao, L, Lu, G, Riley, G and Wood, M, 2014. On-line nonintrusive detection of wood pellets in pneumatic conveying pipelines using vibration and acoustic sensors, *IEEE Transactions on Instrumentation and Measurement,* 63(5): 993–1001.

Tabuchi, T, Bando, K, Kondo, S, Tomita, H, Shiobara, E, Hayashi, H, Kato, H, Nakamura, A, Matsuura, Y and Kondo, K, 2019. Real-time measurement of exact size and refractive index of particles in liquid by flow particle tracking method, *IEEE Transactions on Semiconductor Manufacturing,* 32(4): 460–464.

Wang, K, Liu, G, Li, Y, Qin, M, Wang, J, Wang, G and Mei, D, 2019a. Vibration and acoustic signal characteristics of solid particles carried in sand-water two-phase flows, *Powder Technology,* 345: 159–168.

Wang, K, Liu, G, Li, Y, Wang, G, Feng, K and Yi, L, 2019b. Vibration sensor approaches for experimental studies of sand detection carried in gas and droplets, *Powder Technology,* 352: 386–396.

Wills, B A, 2006. *Wills' Mineral Processing Technology: An Introduction to the Practical Aspects of Ore Treatment and Mineral Recovery (7th Edition),* (Butterworth-Heinemann: Oxford).

Xue, M, Su, M, Dong, L, Shang, Z and Cai, X, 2009. An investigation on characterizing dense coal-water slurry with ultrasound: Theoretical and experimental method, *Chemical Engineering Communications,* 197(2): 169–179.

Zhang, G, Yan, Y, Hu, Y and Zheng, G, 2019. On-line size measurement of pneumatically conveyed particles through acoustic emission sensing, *Powder Technology,* 353: 195–201.

Breakthrough in elliptical motion screen trial delivers significant performance gains

D Teyhan[1] and J Kirsch[2]

1. Product Expert – Screening, Schenck Process Australia, Beresfield NSW 2322.
   Email: d.teyhan@schenckprocess.com
2. Vice President Technology, Schenck Process Australia, Beresfield NSW 2322.
   Email: j.kirsch@schenckprocess.com

ABSTRACT

Traditionally, most Australian iron ore mining operations have been surface-based. Processing plants were designed to handle dry ores. In recent years mining operations in the Pilbara have progressively moved below the water table exposing wet, sticky ores which have caused lost efficiency in screening operations as particles tend to agglomerate and adhere, blinding screening media.

Miners and vibrating screen manufacturers have experimented with a shift from linear motion to elliptical motion screens. Elliptical motion conveys and lifts particles. Effective on flat deck (horizontal and inclined) or sloping decks it can be configured to provide a controlled transport rate, applying pressure in all directions to maximise screening efficiency. In practice, elliptical motion screens have proven to be effective in dislodging sticky particles from screening media, reducing blinding rates and improving screen efficiency.

Moisture and clay content change during the life of a mine. These changes are sometimes the effect of seasonal rainfall, in other cases due to increased groundwater and clay content as mining operations go deeper. To compensate for such changes and optimise screen efficiency, changing the 'shape' of elliptical screen motion is required. This has traditionally required shutting down processing plants and making mechanical screen adjustments. Plant downtime is costly and machine adjustment has been a 'trial and error' practice.

This paper will explore the results of a field trial that is currently underway in Brazil of a next generation elliptical motion screen design that allows operators to make changes to exciter rotational direction, speed and screen stroke angle, through electronic drive phase control. The machine's electronic drive system synchronisation is enhanced for stability with a unique mechanical timing system. Operating at up to 6 g, screen adjustments can be made on the fly without stopping production. Early trial results are showing up to 50 per cent improvement in screen efficiency compared with traditional elliptical motion machines under certain feed conditions.

INTRODUCTION

The earliest form of screening in mineral processing took place in the form of manual sizing. 'Breaker boys' would sit above the product stream and manually sort and size the large lumps as required by the process. Later, static screens were developed where the product was manually manipulated over apertured plate or bars with lateral spacing matching the sizing cut point as required by the process application. Typically, these were aggressively sloped from feed to discharge end to promote the material flow. With the introduction of electric motors to the mineral processing industry, some of the earliest forms of mechanised screening took place in the form of crank driven reciprocating shaker screens and simple spring mounted single shaft circular motion screens which are still used in some applications today (Figure 1). Where shaker screens had significant limitations in terms of capacity and adhesion (having little to no perpendicular acceleration component to the apertured deck), the circular motion mechanised screens facilitate both elevation of the product and transportation of the product from feed to discharge end.

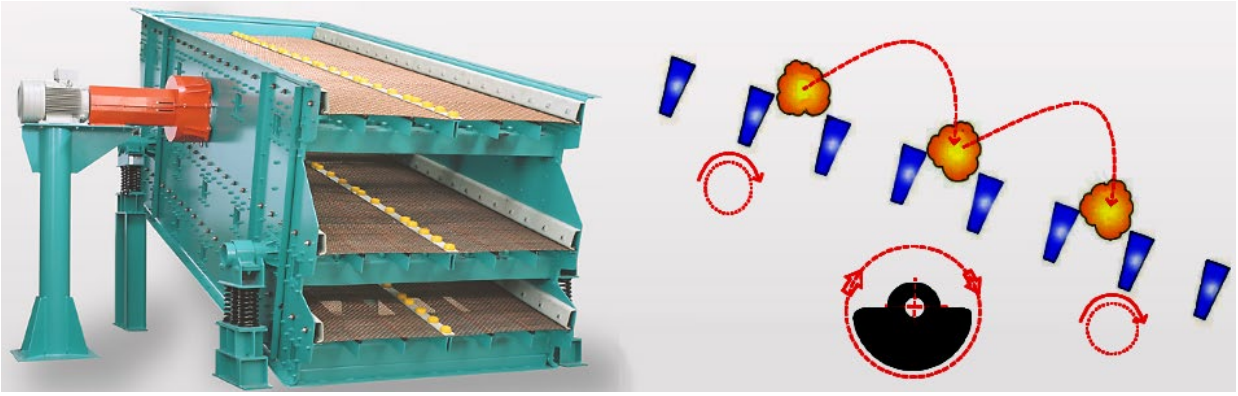

FIG 1 – Single shaft circular motion screen showing motion pattern and particle trajectory.

Circular motion screens are mounted on soft springs and are excited by a forcing function that generates a motion pattern which is essentially an orbital system between the screen body and the counterweight based on momentum principals. Due to the interaction between the particle trajectory of the bed of material and the screen panel apertures on circular motion screens, a very specific range of operating speed and acceleration are required to ensure that the product flow is not over energised resulting in a reduction in probability of separation and reduced overall efficiency, or under energised resulting in retarding the flow of product, increased bed depth, and a reduction in overall efficiency. A typical operating characteristic for circular motion screens would be 3.5 g acceleration at a speed close to 850 rev/min, and the theoretical feed material single particle trajectory from these operating characteristics can be seen in Figure 2. As demonstrated, the feed material particle trajectory with these operating characteristics results in impact with the apertured deck each cycle with the impact occurring somewhere between the maximum velocity of screen vertical motion, and the theoretical point of separation of particles from the apertured deck. It should be noted that particle interaction at the maximum vertical velocity point will result in no horizontal impact component being imparted on the particle, and that interaction at a velocity vector significantly greater than 45° from horizontal will result in under-energisation of the vertical velocity component. For this reason, the operating characteristics selected for circular motion screens need to be highly specific, and the decks need to be inclined to promote material flow. A pegged or adhered particle will however have force components applied in all directions.

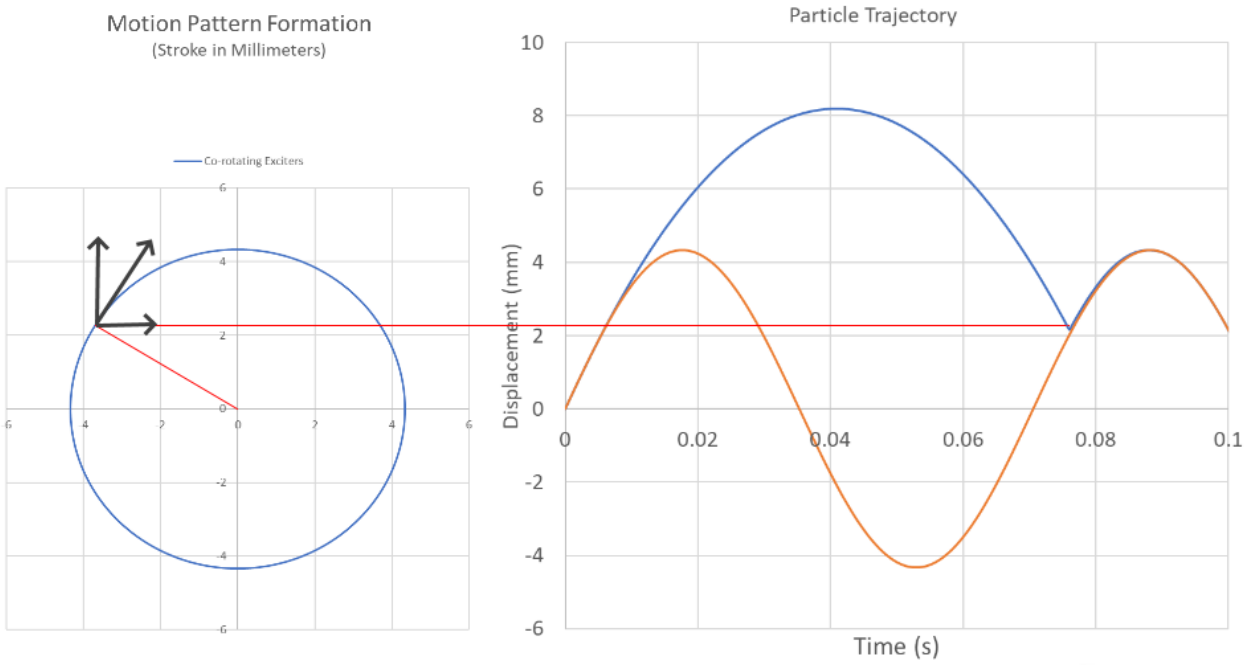

FIG 2 – Theoretical single particle vertical trajectory based on 8.7 mm stroke at 850 rev/min (3.5 g).

One of the benefits of the traditional circular motion screen is the acceleration component imparted on the particle in the plane of the apertured panel. This in plane motion is highly effective at dislodging near size and/or sticky particles when pegged in the apertures. Among the disadvantages are the specific operating characteristic requirements, and the difficulty in controlling flow velocity of larger particles down the deck of the screen. Using simple mathematical models of single particle trajectories to predict probabilities of separation based on operating characteristics of the screen alone, ignores particle on particle interactions and interparticle cohesion (Cleary, Wilson and Sinnot, 2018). A causal link between a simple particle trajectory calculation and material transport velocity and bed depths can be observed in practise. However, this has not necessarily translated to better particle size stratification or process efficiency.

Following from the development of the circular motion vibrating screen was the linear motion flat deck screen (Figure 3). The development of linear motion screening by utilising pairs of counter-rotating eccentric mass shafts addressed some of the issues associated with the requirement for highly specific operating characteristics. This meant that regardless of the speed and stroke length selected, there would always be a velocity component of the screen to lift the particle, and a component transporting the particle from feed to discharge end. Linear motion screens have the advantage of a horizontal velocity component to their stroke which conveniently allowed designers to achieve controlled transport velocities of feed material without needing to incline the screen decks. This facilitated lower overall build heights which allowed for more compact processing plants, and lower overall production power requirements due to the reduction in potential between the feed and discharge points of the screen. Whether appropriate for the application or not, a line of stroke at 45° was assumed as the industry standard as this provided equal vertical and horizontal velocity components.

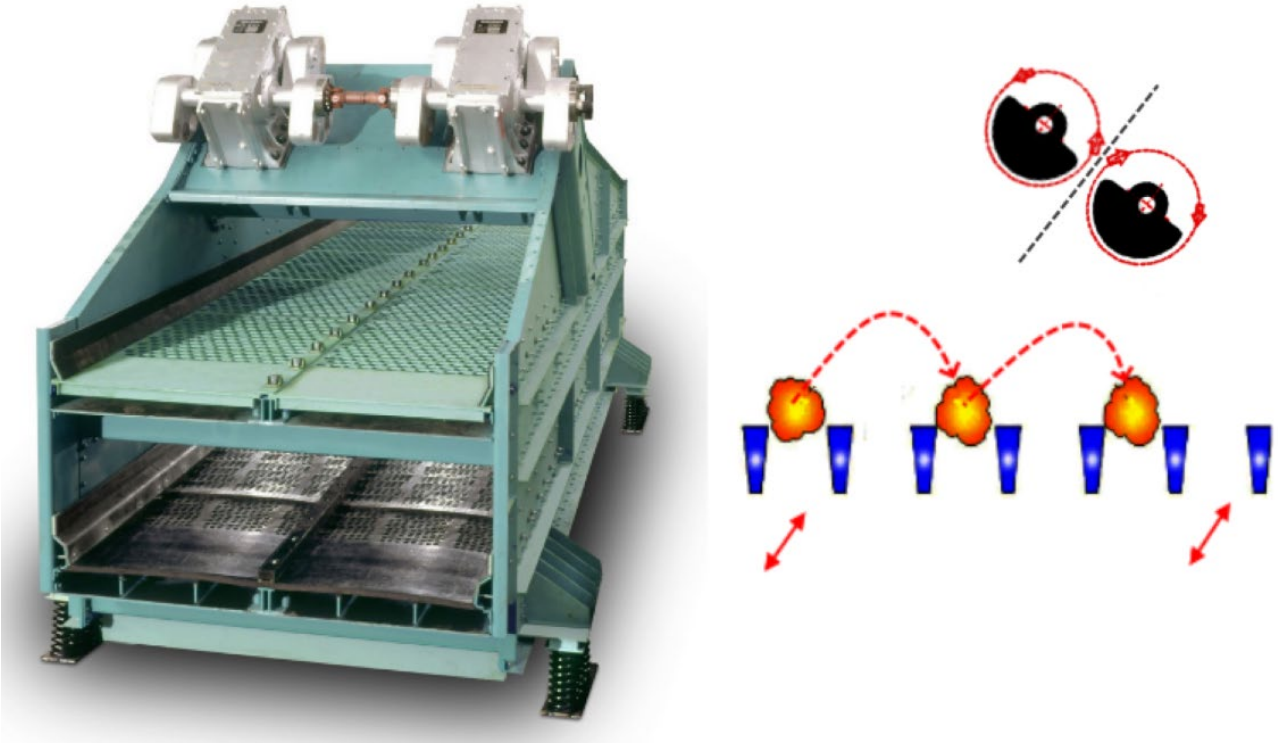

FIG 3 – Counter-rotating mass linear motion screen showing motion pattern and particle trajectory.

Despite having a completely different set of material interaction characteristics to circular motion screens, with the introduction of linear motion screens the nominal speed and maximum acceleration perpendicular to the screening panels of circular motion screens was maintained. For horizontal flat deck screens, this results in a peak acceleration of approximately 5 g along the line of stroke of 45° from horizontal. The theoretical feed material single particle trajectory can be seen in Figure 4.

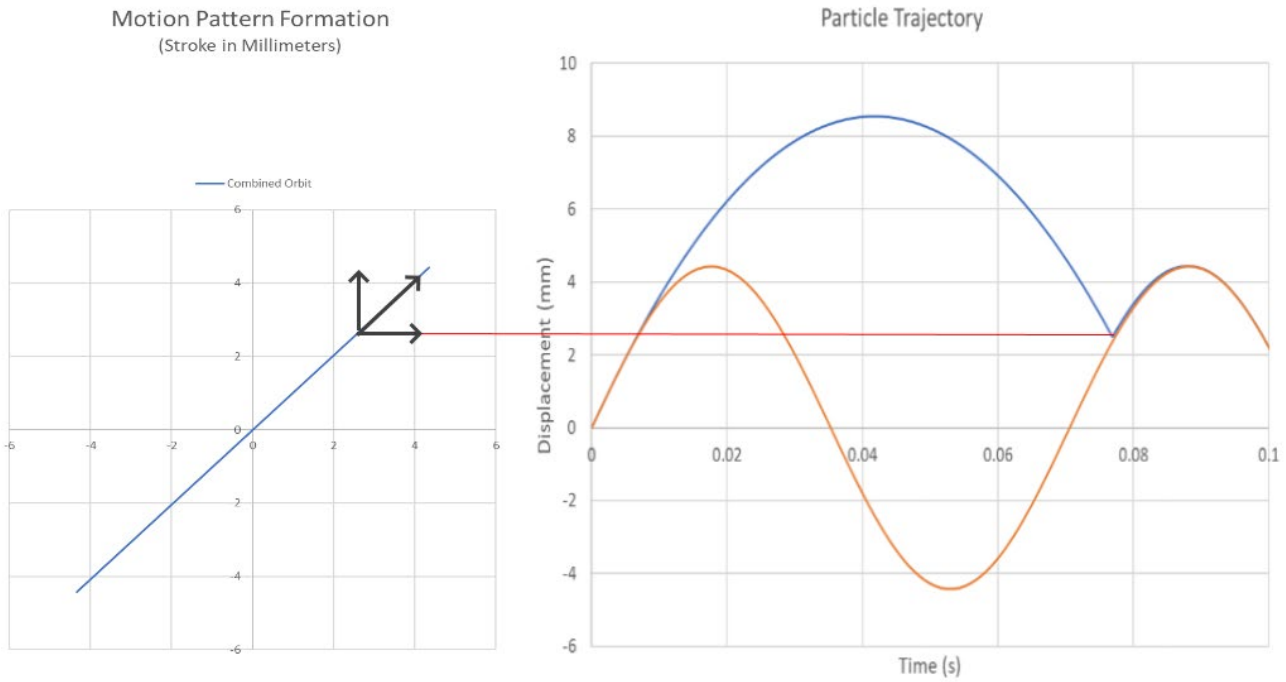

FIG 4 – Theoretical single particle vertical trajectory based on 12.4 mm stroke at 850 rev/min (5 g).

Alongside the benefits of the new linear motion screening concept was the limitation on structural capacity due to lower deck inclination and lower transport velocities of feed material. Previous studies undertaken on the phenomenon of particle separation using numerical methods (specifically DEM – Cleary *et al*, 2009; Shen and Tong, 2020) have identified several mechanisms for separation including:

- Energisation of the bed to create interstitial gaps.
- Percolation of finer particles through the bed of coarser material.
- Particle on particle interactions.
- Aperture penetration.

Little information is available in these studies on the segregation phenomenon due to the different levels of mobility of particles in the high velocity feed zone of aggressively sloped screen decks, whereby the higher transport velocity of the larger and less inhibited particles results in segregation, leading to larger particles transporting to the top of the material bed. This contribution to stratification is lost in the feed zone of horizontal flat deck screens. Flat deck screens are sometimes inclined up to 10° from horizontal to circumvent this problem, however in these cases the benefit of low potential between the feed and discharge points of the screen are lost. Pegging of feed material particles in the screening panel apertures of horizontal flat screens with high near size particle fractions in the particle size distribution is also common and strongly related to particle shape and adhesion characteristics. Pegged or adhered particles in linear motion screening only experience forces applied in one direction with fluctuating and completely opposing vectors.

In the last 30 years, the use of multi-slope ‘banana screens’ has become increasingly common for high-capacity screening for both wet and dry applications. Banana screens are constructed with an aggressively sloped feed end section which becomes progressively shallower in inclination toward the discharge end. Whilst some circular motion banana screens have been built, banana screens are predominantly driven by the same type of linear motion exciters as flat deck linear motion screens. Curved Banana screen decks introduce the benefit of high ore feed velocity at the feed end of the machine. The elevated transport velocity of the feed material up to 4 m/s results in a thinning of the bed depth, allowing for larger particle spacing of the larger lump fraction which facilitates liberation of more fines. The larger particles being unconstrained from high bed depth pressures are freer to mobilise down the deck at higher transport velocities than the fines fraction, assisting effective stratification at the discharge end. Relatively higher levels of shearing flow at the feed end

in comparison to horizontal flat deck screens coupled with progressive reduction in transport velocity due to particle interactions provides an effective means for larger particles to liberate agglomerated fines without relying solely on the machine's operating characteristics. Finally, pressure on the near size particles at the discharge end from the stratified bed with low transport velocity gives higher probabilities of separation.

Wet screening of slurries on banana screens is also effective despite interphase drag having a normalising effect on the particle size related and slurry velocity distributions (Cleary, Wilson and Sinnot, 2018). This effectiveness is due to the ready percolation of fines entrained in slurry through the dilute phase in the feed end bed depth. Despite the high proportion of the fines fraction in the feed material which passes through the apertures in the feed end of the screen, the lower transport velocity of the discharge end and greater number of cycles experienced by the feed material over the discharge stages is important for the screens to achieve the process efficiency target (refer to Figure 5).

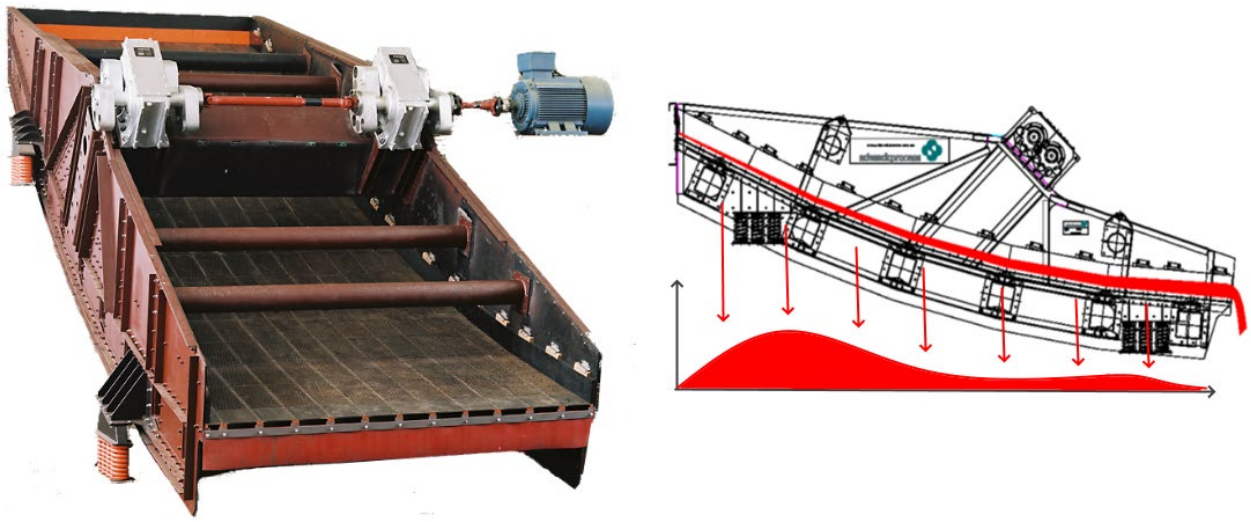

FIG 5 – Counter-rotating mass linear motion banana screen showing typical feed material distribution.

Elliptical motion screen concepts have been in existence since the 1970s but gained market traction over the past two decades as more ore producers have been attempting to mine product below water table or to screen product with natural moisture. The concept of elliptical motion screens is to develop a screen stroke with an orbit path that provides both the reliable transport velocity of a linear motion screen, but with the multi-directional force components of a circular motion screen. The aim is to provide sufficient energisation of the bed of material to maximise stratification by creation of interstitial gaps between larger particles, and to provide a multi-directional excitation to de-peg near size particle blockages of apertures and adherent material. Elliptical motion screens have been built in flat deck designs (both horizontal and inclined), and more recently in multi-slope banana style designs. Several techniques have been used for generating elliptical motion, including:

- Two counter-rotating single shaft exciters with differing eccentric mass positioned at distances from the screen centre of gravity inversely proportional to the eccentric masses.
- Utilising three single shaft exciters with the same or different eccentric masses, two exciters co-rotating and one counter-rotating.
- Mounting a series of single shaft or double shaft exciters on perpendicular axes and controlling their phase relationship to generate elliptical motion.

In dry coarse sizing, elliptical motion screens have consistently demonstrated the capacity for more efficient separation. Elliptical motion has already been applied to sticky or difficult to screen materials where the empirically derived formulas for screen sizing and efficiency are of questionable validity. This paper presents the findings of a field trial of a 2.5 m × 6.4 m Double Deck Banana Elliptical Motion Screen for natural moisture screening of coarse iron ore.

DESIGN DEVELOPMENT

The Schenck Process elliptical motion screen utilised in the trial was developed to fit the existing footprint of a South American iron ore producer and was designated the model name SED2564. The screen was designed to be driven by six Schenck Process VZ501 circular motion exciter cells closely spaced about the centre of gravity of the screen and mounted in three laterally opposed pairs connected with intermediate shafts spanning the screen. The screen was designed to be driven by three independent direct drive electric motors via universal shafts, with each motor being independently electronically synchronised. The product designation represents a double deck multi-slope elliptical machine with a 2.5 m wide and 6.4 m long apertured section, with this particular machine being designed for deck angles from 20° to 8° on the top deck.

The preliminary design stage commenced with the sizing of the screen using traditional proprietary calculation methods by modifying the moisture factor of the material. It should be noted for iron ore with significant fines fraction, feed material with surface moisture content exceeding 8 per cent of the product mass will typically suffer from adhesion of fines to the lump fraction. The adhesion of fines makes separation more difficult as the finer particles have a tendency to carry over to discharge from the machine with the coarser particles. Moreover, the particle size distribution (PSD) related transport velocity differential, which aides in stratification, in the feed end of multi-slope banana screens is present to a lesser extent. Historically, sizing and machine capacities have been determined by an empirically derived formula which treats the process parameters as being independent, for example:

$$C = B \times I \times D \times Sh \times So \times A \times Oa \times W \times Y \times M \times Z \times E$$

Where:

C	is tonnes/square metre
B	is base capacity
I	is inclination factor
D	is deck number
Sh	is % passing half the separation (cut) size
So	is % of oversize in feed
A	is the aperture shape factor
Oa	is the Open Area factor of the deck
W	is Bulk density of the feed material
Y	is Wet Screening. Water added as spray or in feed
M	is moisture content of the feed material – If screening is to be dry screening
Z	is Particle Shape factor
E	is Efficiency Factor

Shen and Tong (2020) identified that under varying material and operating characteristics, there was a noticeable degree of interdependencies between the process application variables. Since at the design stage of this project these interdependencies were unknown, an unmodified traditional application sizing approach was used.

The outputs of the application sizing calculations were required in order to determine worst case retained product loads for the upper and lower deck of the screen. These were dependent on maximum and minimum process efficiencies of the top deck based on both wet and dry season material conditions. The worst case retained deck loads were used for preliminary sizing of the deck components based on hand calculations of cross beam bending stress. Conservative permissible fatigue design stress acceptance criteria were applied according to the recommendations of BS7608–2014 Fatigue design and assessment of steel structures.

Following the basic sizing of the screen components, a bounding envelope for a side plate was defined and a mass estimate developed. Appropriate sizing of the exciters was then conducted to

ensure that 6 g of acceleration could be achieved within the bearing capacity limits. At this stage, the screen was modelled in Autodesk Inventor, and Finite Element Analysis (FEA) model produced. Given the primary objective of the screen to be adaptable to the process without shutting the machine down, one aim of the analysis was to achieve a separation between the operating speed and the closest modal frequencies of the screen body structure to permit operation of the screen between 850 rev/min and 950 rev/min. Since acceleration of the screen is a function of the square of the operating speed, with variable speed control in this operating frequency range the screen would be capable of delivering an ellipse with a major axis of between 4.8 g and 6.0 g acceleration without the requirement to change the eccentric mass of the exciter cells. The screen design was extensively analysed with the preliminary FEA focused on the mass and stiffness distribution to ensure the primary flexural natural frequency modes were significantly above the operating frequency so as not to adversely affect the operating characteristics. The FEA then focused on determining the suitability of the component selection under a number of exciter phasing positions and inertia load case combinations. Principal stress load case combinations were used for fatigue design purposes.

In tandem with the screen body structural design, the PLC control logic for phase adjustment between the exciter cells was developed. In order to test the control logic prior to the screen being built, a small-scale workshop test bed weighing 120 kg and driven by three Uras KEE-3-6WK vibrator motors was developed to prove the stroke predictions and test the stability of the control logic. Three operating configurations were tested as detailed in Figure 6.

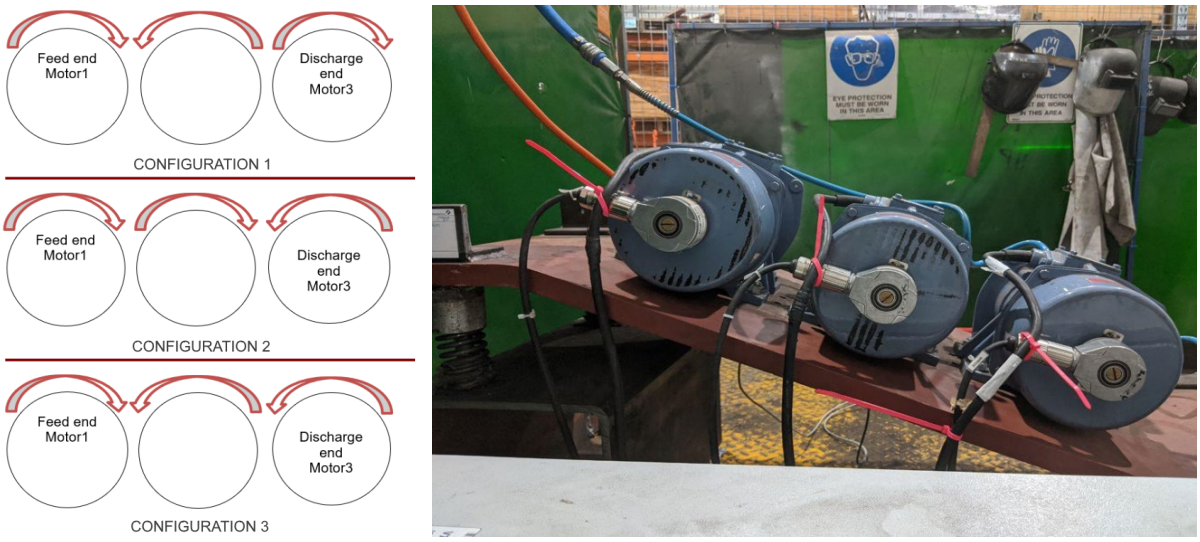

FIG 6 – Operating configurations tested on the scaled test bed.

For each design operating configuration, three intended weights setting (25 per cent, 75 per cent, and 100 per cent) at different phase angles and combinations of rotational directions were tested. For each direction of rotation the operating data of speed, torque, and position were recorded and plotted.

Consistent across all test results, design rotation Configuration 1 (both outer exciter pairs co-rotating) was shown to be the most stable. It performed better in terms of maximum and minimum possible phase angle adjustment, and synchronisation stability for different parameters of speed and eccentric weights. It was observed that a configuration with a 75 per cent eccentric mass setting and an initial 20° phase angle from horizontal, broke synchronisation stability at 70° phase angle from horizontal. It was further observed at the stability limits of the system that motors 1 and 3, whilst trying to achieve the command velocity, suffered significant signal disturbance in the actual velocity data. There was a torque spike which indicated that the control was suffering some degree of overshoot and a general divergence in the torque demand of motors 1 and 3 as seen in Figure 7. It was not established whether this was due to saturated control, control lag, or inertia torque effects. The same characteristic was not observed on motor 2. This indicated that the development of higher rotational inertia by use of flywheels and developing external synchronisation of co-rotating elements by mechanical means would be effective in eliminating system instability but would still permit complete angular control of the elliptical motion through changing the phasing relationship between

co-rotating and counter rotating elements by electronic means. To remove the inertia torque effects from the motor torque demand and make a more stable electronic synchronisation, mechanical connection of motor 3 and motor 1 with a timing belt system was proposed, developed, and tested on the small-scale test bed. A full-scale synchronisation system was developed for the SED2564 machine and was implemented for the duration of a six-month site trial. The synchronisation system development has a Patent Pending.

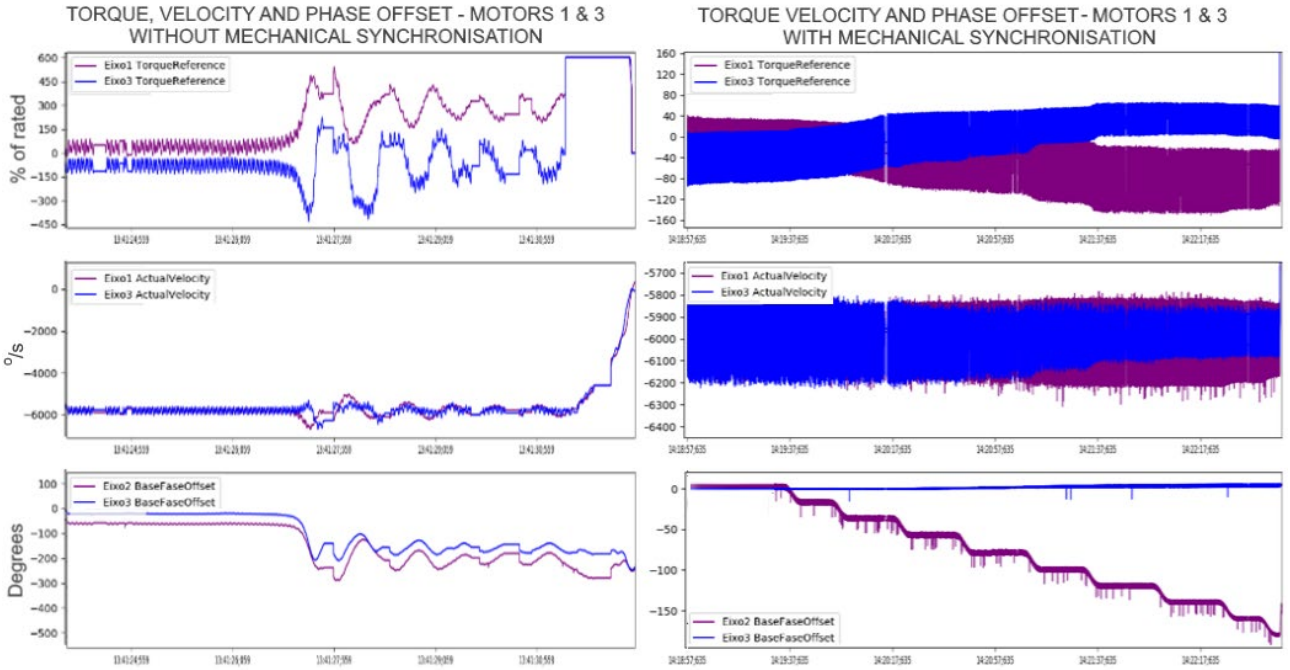

FIG 7 – Torque demand, instantaneous angular velocity, and phase relationship of elliptical test bed with and without mechanical synchronisation between co-rotating elements.

Data collected on the scaled elliptical test bed demonstrated that the system stability was determined by the two outer co-rotating motors due to inertia torque effects. The centre counter-rotating motor appeared not to be affected by inertia torque to the same extent. An actuation of phase angle relationship between the co-rotating and counter-rotating motors resulted in loss of synchronisation at a stroke angle of 70° from horizontal without the mechanical synchronisation system. The same configuration with mechanical synchronisation between co-rotating elements reduced the peak torque demand and permitted full control of the major axis of the ellipse through 180° by electronic synchronisation. Furthermore, a series of tests were run where a step input disturbance was introduced to the scaled test bed by dropping the weighted end of a 4 lb (~1.8 kg) mallet (with parabolic rubber buffer) a distance of 200 mm onto the end of the test bed adjacent to motor 1. In all cases without mechanical synchronisation the system lost synchronisation stability, but with mechanical synchronisation was capable of retaining synchronisation stability at all phasing angles. This indicated that the full-scale system with mechanical synchronisation would be more stable under transient dynamic events, which typically occur under on-feed and off-feed conditions.

The full-scale screen was built in the Schenck Process workshop in Taubate, Brazil, and tested under 6 g acceleration with a series of operating speeds between 850 rev/min and 950 rev/min. Strain gauge data was collected to verify the design, and some fine tuning to the intermediate shafts between exciters was conducted to improve modal separation from torsional resonance of the drive system. The screen was despatched for field trial in a wet season natural moisture iron ore screening application.

APPLICATION OVERVIEW

The scope of the machine development was to design a 2.5 × 6.4 m double deck multi-slope banana screen capable of screening a nominal 1200 t/h at less than 8 per cent surface moisture content (dry season) or 735 t/h of high moisture iron ore (up to 13 per cent surface moisture content – wet

season), but also capable of being adapted between the wet and dry season screening conditions. The material properties and operating requirements included:

- Bulk Density – 2.7 t/m^3.
- Specific Gravity – 4.7.
- Maximum Lump size – 120 mm.
- 76 per cent of the feed PSD <6 mm (approximately 1/3 the bottom deck cut point).
- 90 per cent operational availability.
- Operating acceleration requirement of between 5 g and 6 g.

The high fines content and seasonally high surface moisture content make the application a very challenging process to achieve with a vibrating screen. This is mainly due to adhesion of fines to the lump fraction, but also the cohesion between fines, and the adhesion of the fines to the screening panels. It was understood that this would further be challenged by a significant reduction in stratification caused by the normalising of particle size related transport velocity differences. It was hypothesised that some combination of operating speed between 850 and 950 rev/min, acceleration between 5 and 6 g, and some operating angle of the major axis of the ellipse between 20° to 70° from horizontal with operating direction either with material flow or counter material flow at the top of the ellipse, would provide a process efficiency and screen capacity advantage. The exciter configuration to achieve the adjustable elliptical operation can be seen in Figure 8.

FIG 8 – SED2564 electronic synchronisation testing in Tabaute workshop.

The trial of process performance was set at six months to ensure a good seasonal variation of surface moisture content dependent on performance and a target availability of 90 per cent set over the course of the trial. Process performance requirements were for a bottom deck discharge with less than 25 per cent sub 4 mm particles, and a bottom deck undersize with 0 per cent lump over 19 mm in particle size.

FIELD TRIAL RESULTS

The SED2564 6 g electronically synchronised elliptical motion screen was installed for field trials carried out in the period from 01 December 2020 to 31 May 2021. During the field trial, a significant variation in feed material characteristics was experienced based on differences in surface moisture content. Various operating characteristics of the screen were trialled with each feed material type. Figure 9 demonstrates the operating characteristics with low moisture content (approximately 8 per cent) from data collected between 25 November 2020 to 30 November 2020 in the initial commissioning stages of the project. At the time, the screen was operating at a nominal 500 t/h for commissioning purposes, with fines fraction high enough that no appreciable bed depth was forming on the discharge stage. Detail 'A' from Figure 9 demonstrates operation with a 6 g acceleration 60° major axis from horizontal with an ellipse aspect ratio of 3:1 with rotation direction of co-rotating exciters with the direction of material flow over top centre. Visual observations of the live operating characteristics clearly demonstrated over energisation of particles with high amplitude particle bouncing, and clearly visible interaction with the screen deck every second cycle. Whilst the general direction of transport was toward the discharge, there were an appreciable number of particles being projected backward during this operating characteristic. It was also evident that the fines carry over at the discharge end was relatively low, and well below the target of 25 per cent. Utilising the theoretical particle trajectory as a basis for comparison, the 0.5× subharmonic observed during operation was supported by the theoretical particle trajectory, and the low transport velocity and random particle directions were supported by the theoretical point of interaction with the deck panels having a vector almost vertical in orientation. The opportunity to trial the performance of the screen with these operating characteristics and a more heavily formed bed of material has not yet been negotiated with site personnel. Proposals for further testing have been developed.

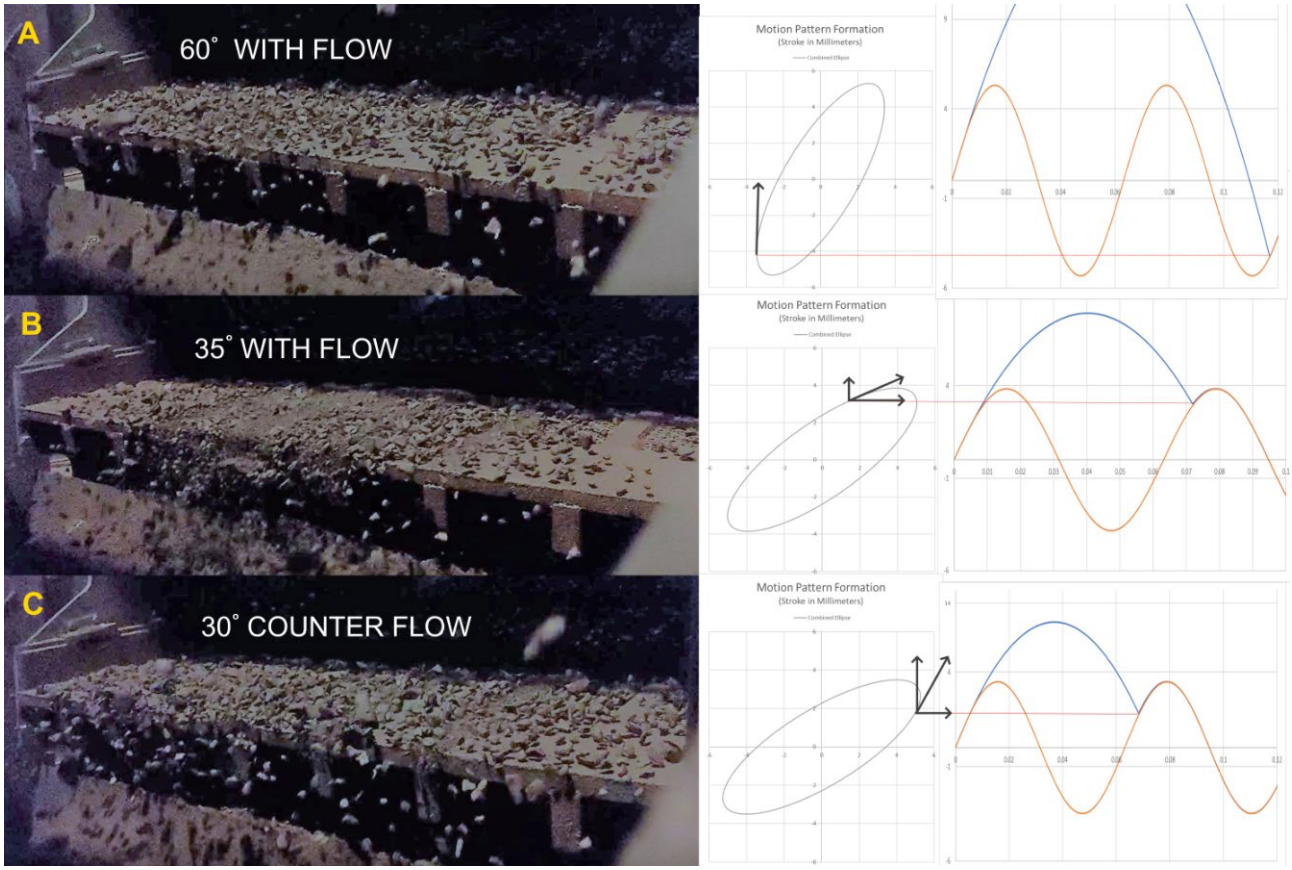

FIG 9 – Observed material conditions and associated theoretical material interaction with the screen deck.

Figure 9 Detail 'B' shows the operation with a 6 g 35° major axis from horizontal with an ellipse aspect ratio of 3:1 with rotation direction of co-rotating exciters with the direction of material flow over top centre. The material was visually under energised in the vertical direction resulting in mostly horizontal motion. The transport velocity was high, and fines carry over significantly higher than that

seen with operating major axis angle at 60°. The single particle theoretical trajectory also supported the under energisation seen in the actual material flow, and the excessive transport velocity and fines carry over was consistent with the theoretical vector of interaction with the screen deck panels being largely horizontal.

Figure 9 Detail ‘C’ was a trial run with the direction of co-rotating exciters counter flow over top centre with a major axis at 6 g 30° from horizontal. The aspect ratio of the ellipse was again 3:1 and visual observations were characterised by a good well controlled transport velocity, reasonable levels of particle energisation with a regular steady state impact period coinciding with the screen deck every cycle. Fines carry over was low and comparable to that seen with 60° major axis in the co-rotation direction. The main source of fines carry-over in this configuration was seen as material tracking along the blank join line between panels. This characteristic was not evident with the higher angle of major axis seen in Detail ‘A’.

Periodic fortnightly bucket samples of product PSD and moisture content failed to capture the true variance of PSD and moisture content observed in the performance of the screen. At times the fines fraction was seen to be a thick, muddy paste indicating surface moisture content at or above 12–13 per cent. Under these circumstances, operation with a low angle of the major axis and counterflow rotation even at 6 g acceleration allowed the bed at the discharge end to form large slabby cakes of agglomerated material. Under these material conditions operation with 60° major axis from horizontal with rotation direction with flow appeared to break up the slabby cakes and allow a significantly larger proportion of fines to pass the bottom deck apertures. Balls of agglomerated fines captured from the undersize fraction during this high moisture operating condition can be seen in Figure 10.

FIG 10 – Agglomerated fines obtained from the undersize of the screen whilst operating with high surface moisture content.

CONCLUSIONS

The development of the elliptical motion for the SED2564 machine demonstrated that phasing stability of the system was limited by the co-rotating exciters. When operating near stability limits, small perturbations to the system caused the scaled screen to lose synchronisation. The development of a mechanical synchronisation system linking the co-rotating exciter cells only, allowed complete phase stability throughout 360° of phasing actuation regardless of eccentric mass, acceleration, or introduced perturbations.

The loss of one of the main mechanisms of stratification with high moisture screening results in significantly restricted tonnage throughput. With surface moisture content between 8–10 per cent, the feed characteristics are such that elliptical motion with a traditional operating angle of 45° results

in poor efficiency performance. Two operating characteristics provided beneficial results on efficiency with these feed materials, operation with a 3:1 ellipse at 6 g acceleration and a major axis at 60° from horizontal and direction of rotation of co-rotating exciters with the direction of flow over top centre, and operation with a 3:1 ellipse at 6 g acceleration with a major axis 30° from horizontal and direction of rotation of co-rotating exciters against the direction of feed material flow over top centre. At feed surface moisture content above 10 per cent, the formation of slabby cakes of consolidated fines required the high vertical acceleration of 'with' flow rotation and 60° major axis from horizontal to break the material up enough to liberate fines that were capable of passing the bottom deck screen aperture.

ACKNOWLEDGEMENTS

Octavio Leardine Neto – Engineering Coordinator, Schenck Process Brazil.

Duguai Braga – Technical Director Engineering, Schenck Process Brazil.

Alf van Dijk – Former Head of R&D, Schenck Process Australia.

Gordon Ashley – Former Product Expert Vibrating Screens, Schenck Process Australia.

REFERENCES

Cleary, P W, Fernandez, J, Morrison, R and Sinnot, M D, 2009. Using DEM to Model Industrial Banana Screens, XXV International Mineral Processing Congress (IMPC 2010) (The Australasian Institute of Mining and Metallurgy: Melbourne).

Cleary, P W, Wilson, P and Sinnot, M D, 2018. Effect of particle cohesion on flow and separation in industrial vibrating screens, CSIRO.

Shen, G and Tong, X, 2020. Particle stratification of a vibrating screen with translation-swing composite motion, School of Mechanical Engineering and Automation, Huaqiao University.

Advances in mineral processing – physiochemical separation

Effects of anglesite on the flotation of sphalerite in complex sulfide ores and a method to suppress sphalerite floatability

K Aikawa[1], M Ito[2], A Kusano[3], S Jeon[4], I Park[5] and N Hiroyoshi[6]

1. PhD Student, Hokkaido University, Sapporo Japan 060–8628. Email: k-aikawa@frontier.hokudai.ac.jp
2. Associate Professor, Hokkaido University, Sapporo Japan 060–8628. Email: itomayu@eng.hokudai.ac.jp
3. Master's Student, Hokkaido University, Sapporo Japan 060–8628. Email: kusano.atsuhiro.z2@elms.hokudai.ac.jp
4. Assistant Professor, Hokkaido University, Sapporo Japan 060–8628. Email: shjun1121@eng.hokudai.ac.jp
5. Assistant Professor, Hokkaido University, Sapporo Japan 060–8628. Email: i-park@eng.hokudai.ac.jp
6. Professor, Hokkaido University, Sapporo Japan 060–8628. Email: hiroyosi@eng.hokudai.ac.jp

ABSTRACT

In mineral processing of complex sulfide ores containing copper (Cu), lead (Pb), and zinc (Zn), flotation has been commonly used. Typical Pb mineral in the ores is galena (PbS), while some types of the ores contain anglesite ($PbSO_4$). This article reviews our recent studies on the effects of coexisting $PbSO_4$ on the flotation of complex sulfide ores, and a method to suppress the floatability of sphalerite (ZnS) in the presence of $PbSO_4$ was proposed.

Comparison of flotation experiments for different types of model samples showed that $PbSO_4$ makes the separation of Zn from Cu difficult; that is, for the model sample containing PbS without $PbSO_4$, Zn could be separated from Cu, while when the model sample containing $PbSO_4$, Zn was recovered together with Cu as froth. Solution analysis and thermodynamic calculation suggested that Pb^{2+} was released from $PbSO_4$ and reacted with ZnS to form PbS, acting as an adsorption site for the flotation collector, xanthate. This would be the main reason for high floatability of ZnS in the presence of $PbSO_4$.

As a method to suppress ZnS floatability for the ores containing $PbSO_4$, a pre-treatment of the ores to remove $PbSO_4$ prior to flotation was proposed. The results of model experiments using mixture of ZnS and $PbSO_4$ showed that ~97 per cent of $PbSO_4$ was dissolved within 30 minutes of pre-treatment using ethylenediaminetetraacetic acid (EDTA) as extractant, and thus ZnS floatability was markedly suppressed. Moreover, Pb^{2+} extracted from $PbSO_4$ during the pre-treatment could be recovered as zero-valent Pb by the cementation using zero-valent Fe as a reductant. The details of ZnS flotation in the presence of $PbSO_4$ and the effects of the pre-treatment are discussed based on the results of surface analysis like XPS.

INTRODUCTION

The demand for critical metals (eg, copper (Cu), lead (Pb), zinc (Zn) etc) is projected to be continuously increased in the future to achieve a carbon-neutral society (Nansai *et al,* 2014). In 2015, 193 governments adopted 17 sustainable development goals (SDGs) aiming to eradicate poverty, protect the planet and ensure peaceful and prosperous lives for everyone by 2030 (Hák *et al,* 2016; Tabelin *et al,* 2021). To keep up with the high demand for critical metals as following SDGs, mine developments should be in harmony with environment. Complex sulfide ores are one of the most important sources of critical metals because they are typically composed of several metal-sulfide minerals like chalcopyrite ($CuFeS_2$), galena (PbS), and sphalerite (ZnS). In mineral processing of complex sulfide ores, flotation has been commonly used to produce concentrates of each mineral for smelting. Typical Pb mineral in the ores is galena (PbS), while some types of the ores contain anglesite ($PbSO_4$) (Aikawa *et al,* 2021; Zeng *et al,* 2021). In a typical flotation method of complex sulfide ores, Cu-Pb-Zn sulfide minerals are processed via a two-stage flotation process whereby Cu- and Pb-sulfide minerals are recovered as froth in the first stage, followed by the recovery of Zn-sulfide minerals as froth in the second stage (Woodcock *et al,* 2007). This typical two-stage flotation process may be difficult to be applied to complex sulfide ores containing $PbSO_4$ because ZnS would

be activated and recovered in the froth together with Cu- and Pb-sulfide minerals in the first stage (Aikawa *et al,* 2021). In addition, $PbSO_4$ is typically distributed to flotation tailings because it has poor affinity with collector (eg xanthate) (Fuerstenau *et al,* 1987; Rashchi *et al,* 2005). When $PbSO_4$ is disposed of into the tailings dam, it would cause lead pollution to the surrounding environment (Schindler *et al,* 2021; Silwamba *et al,* 2022). Therefore, $PbSO_4$ would cause not only the difficulties in separation of ZnS from Cu- and Pb-sulfide minerals, but also lead pollution in the surrounding environment of tailings dam when $PbSO_4$ is contained in complex sulfide ores. In this article, our recent studies on the effects of coexisting $PbSO_4$ on the flotation of complex sulfide ores were reviewed, and a method for enhanced depression of ZnS by extracting $PbSO_4$ and recovery of extracted Pb^{2+} as zero-valent Pb by cementation using zero-valent Fe was proposed.

EFFECTS OF COEXISTING ANGLESITE ON THE FLOTATION OF COMPLEX SULFIDE ORES

Typical Pb mineral in complex sulfide ores is PbS, while some types of the ores contain $PbSO_4$. When $PbSO_4$ is contained, Pb^{2+} is readily released from $PbSO_4$ during flotation due to its higher solubility than that of PbS (K_{sp} of $PbSO_4$ and PbS are $10^{-7.79}$ and $10^{-26.77}$, respectively) (Ball and Nordstrom, 1991). When Pb^{2+} is released from $PbSO_4$ during flotation, lead activation of ZnS is known to occur as illustrated in the following equation (Aikawa *et al,* 2021; Laskowski *et al,* 1997; Trahar *et al,* 1997):

$$ZnS_{(s)} + Pb^{2+} = PbS_{(s)} + Zn^{2+} \quad (1)$$

Comparison of flotation experiments for different types of model samples showed that $PbSO_4$ makes the separation of Zn from Cu difficult; that is, for the model sample containing PbS without $PbSO_4$, Zn could be separated from Cu, while when the model sample containing $PbSO_4$, Zn was recovered together with Cu as froth (Figure 1). Solution analysis and thermodynamic calculation suggested that Pb^{2+} was released from $PbSO_4$ and reacted with ZnS to form PbS, acting as an adsorption site for the flotation collector, xanthate. This would be the main reason for high floatability of ZnS in the presence of $PbSO_4$. Moreover, $PbSO_4$ can cause lead pollution in the surrounding environment of tailings dam because it has poor affinity with collector (eg, xanthate) and would be distributed into tail in flotation (Fuerstenau *et al,* 1987; Rashchi *et al,* 2005). Therefore, a method to depress ZnS floatability and prevent lead pollution caused by the presence of $PbSO_4$, is necessary for mineral processing of complex sulfide ores containing $PbSO_4$.

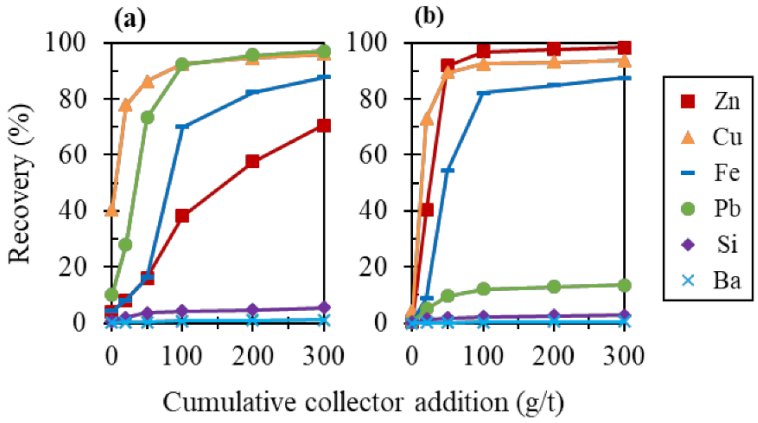

FIG 1 – Flotation results of (a) PbS-type model sample and (b) $PbSO_4$-type model sample with increasing potassium amyl xanthate (KAX) dosage (conditions: 20 µL/L methyl isobutyl carbinol (MIBC, frother), 20 kg/t of sodium sulfite (pyrite depressant), pH 6.5, 25°C, pulp density 5 per cent, air introduction rate 1 L/min, impeller speed 1000 rev/min) (Aikawa *et al,* 2021).

A proposed method for enhanced depression of sphalerite by extracting anglesite and recovery of extracted lead ion as zero-valent lead by cementation using zero-valent iron

For developing a sustainable process flow sheet covering both the improved flotation separation of complex sulfide ores as well as the detoxification of solid/solution wastes contaminated with Pb

species like $PbSO_4$, the authors have proposed a method for enhanced depression of ZnS by extracting $PbSO_4$ and recovery of extracted Pb^{2+} as zero-valent Pb by cementation using zero-valent Fe (Aikawa *et al,* 2022).

Two types of minerals were used: sphalerite (ZnS, Kamioka Mine, Japan) and lead sulfate ($PbSO_4$, 98 per cent purity, FUJIFILM Wako Pure Chemical Corporation, Japan). A mineral specimen of ZnS was characterised using X-ray fluorescence spectroscopy (XRF) and X-ray powder diffraction (XRD). Based on the XRF result, ZnS is composed of 55.7 per cent Zn, 6.2 per cent Fe, 0.2 per cent Pb, 21.3 per cent S, and 8.4 per cent Si. The XRD pattern of ZnS implied that ZnS is relatively pure based on the absence of peaks from common minerals like quartz (Aikawa *et al,* 2022).

Extraction of anglesite using EDTA

In flotation of complex sulfide ores containing $PbSO_4$, ZnS floatability increased due to lead activation of ZnS, resulting in the difficulties in separation of ZnS from Cu- and Pb-sulfide minerals. To address the above-mentioned problems caused by the presence of $PbSO_4$ (ie, un-wanted activation of ZnS and lead contamination), its extraction prior to flotation was investigated. Among the extractants, EDTA was chosen in this study because of its ability to extract metal ions from sulfates like $PbSO_4$, without dissolving metal sulfides (eg PbS and ZnS) (Aikawa *et al,* 2021; Bicak, 2019; Grano *et al,* 1988; Kant *et al,* 1994; Rumball and Richmond, 1996). Figure 2 shows effects of EDTA concentration and time on extraction of $PbSO_4$. Almost of all $PbSO_4$ was extracted When the stoichiometric ratio of EDTA/$[Pb]_{tot}$ was >1, ~97 per cent of $PbSO_4$ was extracted within 30 min with 500 mM of EDTA. These results indicate that EDTA pre-treatment can extract almost of all $PbSO_4$, thus preventing lead pollution in the surrounding environment of tailings dam by extracting environmentally hazardous minerals before flotation.

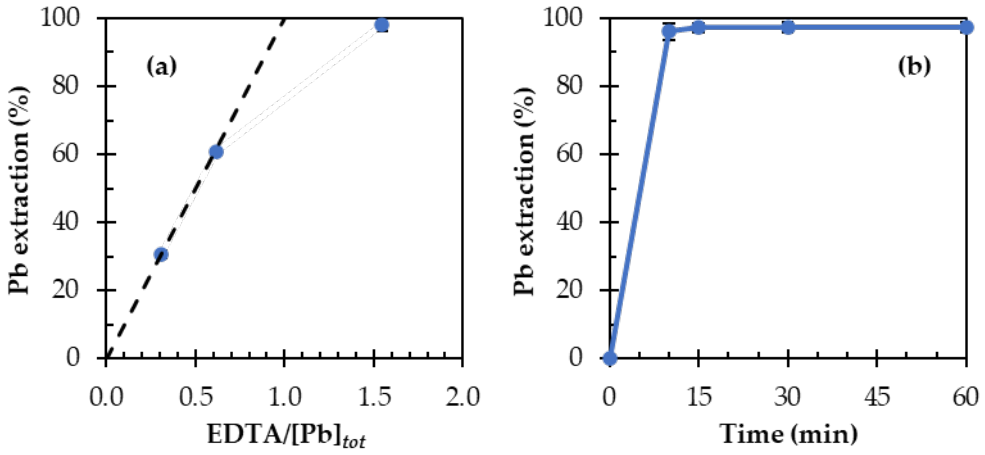

FIG 2 – (a) The extraction efficiency of $PbSO_4$ after 24 h with different concentrations of EDTA (100, 200, or 500 mM) and (b) effects of time on $PbSO_4$ extraction with 500 mM EDTA. Note that the dotted line in Figure 3a corresponds to the ratio of EDTA/$[Pb]_{tot}$ (conditions: $PbSO_4$ 1 g/10 mL of EDTA, shaking speed 120 rev/min, amplitude 40 mm, 25°C) (Aikawa *et al,* 2022).

Recovery of extracted Pb^{2+} as zero-valent Pb by cementation

After EDTA pre-treatment, recovery of Pb^{2+} from the leachate will not only add economic value but also protect the environment. Cementation is one of the effective methods to reductively recover metal ions as metals (Jeon *et al,* 2020). In this method, the metal ion (B^{b+}) receives electrons from a reductant, metals (A^0), via its dissolution and is deposited on the surface of A^0 as B^0 as illustrated in Equation 4 (Choi *et al,* 2021).

$$n\ A^0 + m\ B^{b+} \rightarrow n\ A^{a+} + m\ B^0\ (na = mb) \quad (4)$$

To recover the extracted Pb^{2+} as zero-valent Pb (Pb^0) from EDTA leachate, cementation experiments were carried out using zero-valent iron (ZVI, Fe^0) powder as a reductant. Figure 3 shows effects of ZVI amount and time on the recovery of extracted Pb^{2+} from the leachate after $PbSO_4$ extraction using 500 mM of EDTA for 30 min (solid/liquid ratio: $PbSO_4$ 1g/10 mL of EDTA). Almost of all extracted Pb^{2+} (~97 per cent) was recovered within 24h using 1 g/10 mL of ZVI. To confirm the

recovery of Pb^0 on ZVI, the residue of the cementation experiments using 1 g/10 mL ZVI for 24 h was analysed using SEM-EDS and the deposition of Pb on ZVI powder was observed (Figure 4), suggesting that extracted Pb^{2+} was reductively deposited via cementation reaction:

$$Pb(EDTA)^{2-} + 2e^- = Pb^0 + EDTA^{4-} \quad (5)$$

Figure 5 shows the XRD pattern of the residue of the cementation experiments. The peaks of Fe^0, Pb^0, PbO, and Fe_2O_3 were detected, indicating that Pb^{2+} was reductively deposited as Pb^0 on the surface of ZVI as illustrated in Equation 5. The presence of PbO and Fe_2O_3 is due most likely to the oxidation of Pb^0 and ZVI surface (Silwamba *et al,* 2020).

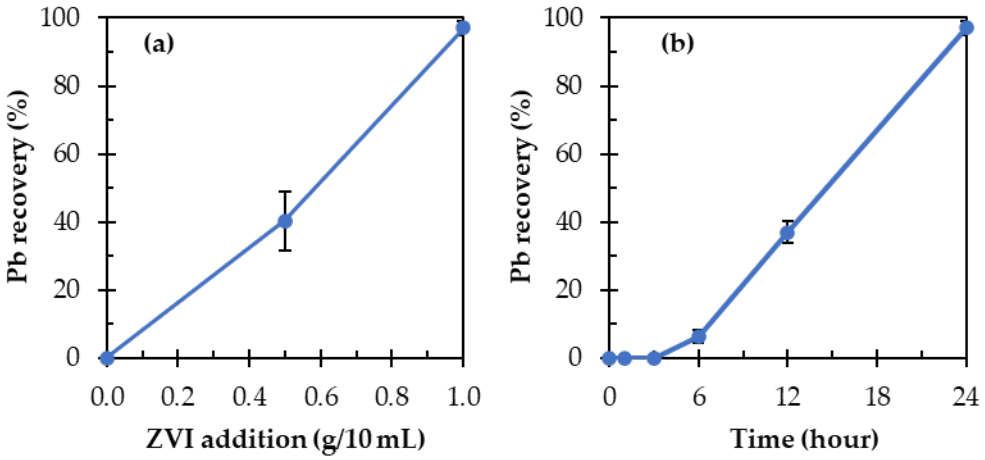

FIG 3 – (a) effects of ZVI amount on the recovery of extracted Pb after 24 h in the leachate after $PbSO_4$ extraction using 500 mM of EDTA for 30 min and (b) effects of time on the recovery of extracted Pb^{2+} using 1 g/10 mL ZVI in the leachate after EDTA pre-treatment using 500 mM EDTA for 30 min (conditions: shaking speed 120 rev/min, amplitude 40 mm, 25°C, purging with ultrapure nitrogen) (Aikawa *et al,* 2022).

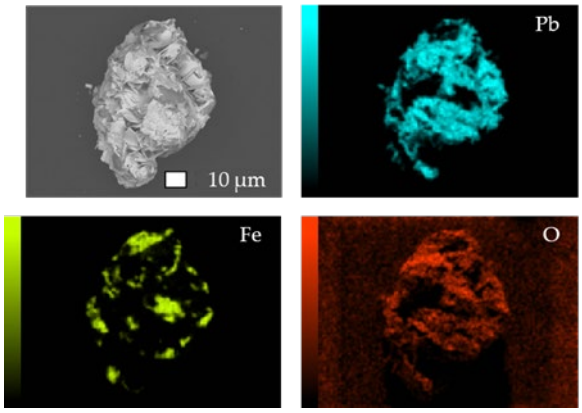

FIG 4 – SEM photomicrograph of the residue of the cementation experiment using 1 g/10 mL ZVI for 24 h with the corresponding elemental maps of Fe, Pb, and O (Aikawa *et al,* 2022).

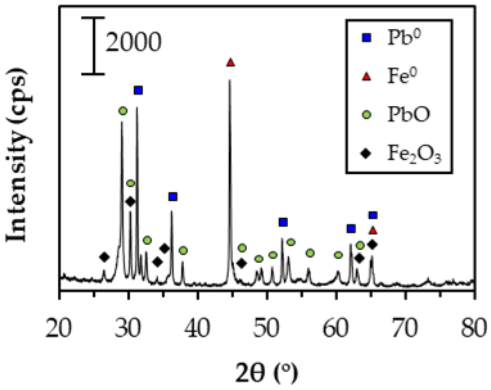

FIG 5 – The XRD pattern of the residue of the cementation experiment using 1 g/10 mL ZVI for 24 h (Aikawa *et al,* 2022).

Effects of EDTA pre-treatment on ZnS depression in flotation

As described above, almost of all $PbSO_4$ was extracted with EDTA. The effects of EDTA pre-treatment on ZnS depression in flotation was investigated. Flotation experiments of model samples containing ZnS and $PbSO_4$ with and without EDTA pre-treatment were conducted (Figure 6). Prior to flotation experiments, the mixture of 15 g ZnS and 5 g $PbSO_4$ was treated with 200 mL of 500 mM EDTA in 500 mL Erlenmeyer flasks for 30 min where the extraction efficiency of $PbSO_4$ was 99.8 per cent, and then flotation experiments were conducted with ~5 kg/t $ZnSO_4$ (100 ppm Zn^{2+}) and 1 kg/t Na_2SO_3 as depressants. Figure 6 shows the flotation results and the floatability of Zn was clearly depressed from ~82 per cent to ~30 per cent when EDTA pre-treatment was applied. Cementation experiments using the leachate of EDTA pre-treatment were also conducted to recover extracted Pb^{2+}, and 99.7 per cent of extracted Pb^{2+} was recovered as Pb^0 using 1 g/10 mL ZVI. To confirm depression of ZnS floatability after EDTA pre-treatment, pre-treated sample reacted with zinc sulfate for 3 min, ~5 mL of aliquot of the pulp was collected, and the filtrate and the residue were analysed by ICP-AES and XPS, respectively.

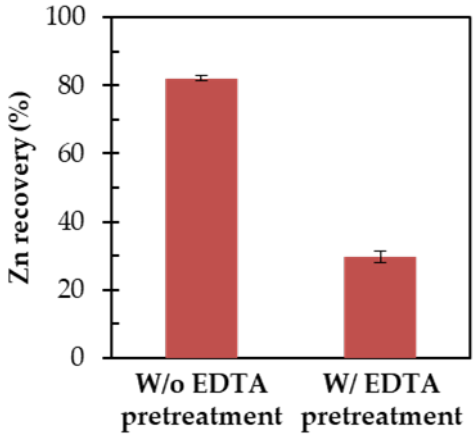

FIG 6 – Effects of $PbSO_4$ extraction on the floatability of ZnS in the presence of $PbSO_4$ (conditions: 20 µL/L MIBC (frother), 20 g/t KAX (collector), ~5 kg/t zinc sulfate (100 ppm Zn^{2+}, sphalerite depressant), 1 kg/t sodium sulfite (sphalerite depressant), pH 6.5, 25°C, pulp density 5 per cent, air introduction rate 1 L/min, impeller speed 1000 rev/min) (Aikawa *et al,* 2022).

The concentrations of Pb^{2+} in the filtrate with and without EDTA extraction showed 5.3 ppm Pb^{2+} without EDTA pre-treatment and 0.2 ppm Pb^{2+} with EDTA pre-treatment, indicating that Pb^{2+} concentration decreased by EDTA pre-treatment due to extraction of $PbSO_4$. The concentrations of Zn^{2+} in the filtrate with and without EDTA extraction showed 101 ppm Zn^{2+} without EDTA pre-treatment, 99.4 ppm Zn^{2+} with EDTA pre-treatment since 100 ppm of Zn^{2+} (zinc sulfate) was added as a depressant.

Based on thermodynamics calculation using Equation 6, the possibility of lead activation of ZnS (Equation 1) could be evaluated using the measured values of Pb^{2+} and Zn^{2+} (Aikawa *et al,* 2021; Basilio *et al,* 1996; El-Shall *et al,* 2000). In this study, the changes in free energy were calculated using the above measured value of Pb^{2+} and Zn^{2+}. Table 1 shows the calculated results of the changes in free energy based on the equilibrium constants of lead activation of ZnS (Equation 1). The change in free energy without EDTA pre-treatment was negative while that with EDTA pre-treatment was positive. When the change in free energy is positive, the backward reaction of lead activation (Equation 1) would occur spontaneously, indicating that lead activation would be limited by EDTA pre-treatment. These results support the flotation results that the depression of ZnS floatability was achieved by the pre-treatment which decreases Pb^{2+} concentration during flotation by extraction of $PbSO_4$.

$$\Delta G = -RT \ln K + \ln(\mathrm{Zn}^{2+}/\mathrm{Pb}^{2+}) \quad (6)$$

$$K = \frac{K_{sp}^{ZnS}}{K_{sp}^{PbS}} \quad (7)$$

TABLE 1

The calculation results of the change in free energy with and without EDTA pre-treatment (Aikawa *et al,* 2022).

K	ΔG (kJ/mol) Without EDTA pre-treatment	ΔG (kJ/mol) With EDTA pre-treatment
1000[a]	–6.9	1.8
704[b]	–6.1	2.7
1059[c]	–7.1	1.7
1127[d]	–7.2	1.5

[a] The equilibrium constant was referred from El-Shall *et al* (2000).

[b, c, d] The equilibrium constants were calculated using EQ 7 by the reported K_{sp} values of ZnS and PbS from Helgeson (1969), Latimer (1952), and Leckie and James (1974), respectively.

To confirm whether the lead activation of ZnS was limited by the extraction of $PbSO_4$ using EDTA, untreated ZnS as well as $ZnSO_4$-pretreated ZnS/$PbSO_4$ mixtures with and without EDTA pre-treatment were analysed by XPS (Figure 7). The $Pb4f_{7/2}$ core-level spectra of the samples are shown in Figure 7, and the corresponding curve fitting parameters are summarised in Table 2. Since the Zn3s peak is overlapping with the $Pb4f_{7/2}$ signals, the spectrum has been resolved by curve fitting to subtract the area due to the Zn3s peak (Basilio *et al,* 1996; Liu *et al,* 2020). As illustrated in Figure 7b and 7c, the deconvoluted XPS spectra of the residues with and without $PbSO_4$ extraction showed two types of Pb species: (1) Pb^{2+}–S of PbS (143.6 and 138.6 eV), and (2) Pb^{2+}–SO_4 of $PbSO_4$ (144.7 and 139.8 eV), while the deconvoluted XPS spectrum of untreated ZnS showed no Pb species (Figure 7a) (Aikawa *et al,* 2020; Hernan *et al,* 1995). The decrease in the intensity of Pb^{2+}–SO_4 is in a good agreement with the extraction efficiency of $PbSO_4$ using EDTA for ZnS/$PbSO_4$ mixture (~99.8 per cent). When EDTA pre-treatment was applied prior to flotation experiments, the peak intensity ratio of PbS/ZnS decreased from 2.3 to 0.2, indicating that EDTA pre-treatment is effective in limiting lead activation of ZnS. This is in line with the calculated results of the change in free energy based on thermodynamics (Table 1).

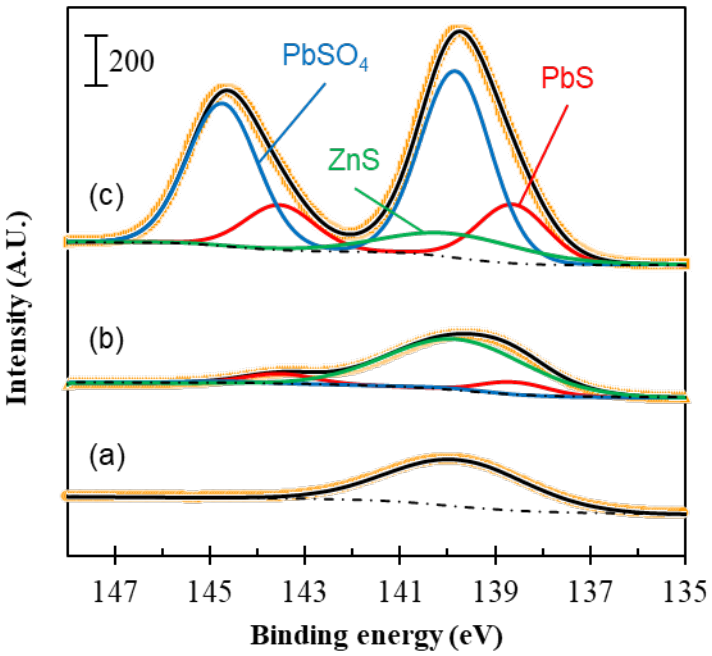

FIG 7 – XPS Pb4f$_{7/2}$ spectra of (a) raw ZnS, (b) ZnS/PbSO$_4$ mixture with EDTA pre-treatment, and (c) ZnS/PbSO$_4$ mixture without EDTA pre-treatment (Aikawa *et al,* 2022).

TABLE 2

XPS peak parameters for Pb4f$_{7/2}$ spectra and the relative abundances of Pb species (Aikawa *et al,* 2022).

Binding energy (eV)	FWHM	Assignments	Contents (at.%)		
			Untreated[a]	w/EDTA[b] pre-treatment	w/o EDTA[a] pre-treatment
138.6±0.05 143.5±0.05	1.7	PbS	0	17.1	21.5
139.8±0.05 144.7±0.05	1.7	PbSO$_4$	0	8.8	48.4
139.8±0.05	3.4	ZnS	100	80.5	9.5

[a] The binding energies of photoelectrons were calibrated using C1s (285 eV) for charge correction.

[b] The binding energies of photoelectrons were calibrated using Zn2p$_{3/2}$ (1022.0 eV) for charge correction.

SUMMARY

Complex sulfide ores are important sources for critical metals like Cu, Pb, and Zn; however, when PbSO$_4$ is contained, its processing remains challenging due to the presence of easily soluble PbSO$_4$ that releases Pb^{2+} and activate ZnS, making the separation of Cu-Pb-Zn sulfide minerals difficult to accomplish. The results of this article have significant implications not only for understanding of how the presence of anglesite in the complex sulfide ores affects the floatability of ZnS but also for proposing a sustainable process flow sheet covering both the improved flotation separation of complex sulfide ores as well as the detoxification of solid/solution wastes contaminated with Pb species. Firstly, the presence of anglesite might have a detrimental impact on flotation separation of complex sulfide ores due to unwanted lead activation of ZnS that improved its floatability which could not be depressed with ZnSO$_4$ – the conventional depressant for ZnS. Secondly, EDTA pre-treatment could extract almost all PbSO$_4$ from ZnS/PbSO$_4$ mixture, and consequently, the floatability of ZnS decreased due to the limited amount of PbS-like compound formed on the ZnS surface by lead activation. Finally, cementation using ZVI could recover Pb^{2+} extracted from PbSO$_4$ during EDTA pre-treatment as Pb^0, which will not only add economic value but also protect the environment.

Based on the findings of this study, a sustainable process flow sheet for complex sulfide ores is proposed (Figure 8). In this proposed flow sheet, $PbSO_4$ is first extracted by EDTA pre-treatment before flotation. The residue obtained after EDTA pre-treatment is fed to a flotation stage where ZnS floatability is effectively depressed by the conventional depressant for ZnS due to the decrease in the ratio of Pb^{2+}/Zn^{2+} of the flotation pulp. Meanwhile, the leachate obtained from EDTA pre-treatment is rich in Pb^{2+} that can be recovered via cementation using ZVI as Pb^0. To keep up with the high demand for critical metals as following SDGs, mine developments should be in harmony with environment. This proposed flow sheet can achieve enhanced selective flotation of complex sulfide ores (depression of ZnS floatability) while preventing lead pollution in the surrounding environment of tailings dam (removal of toxic $PbSO_4$ before flotation) and maximising the recovery of critical elements by cementation (recovery of Pb^0 using ZVI).

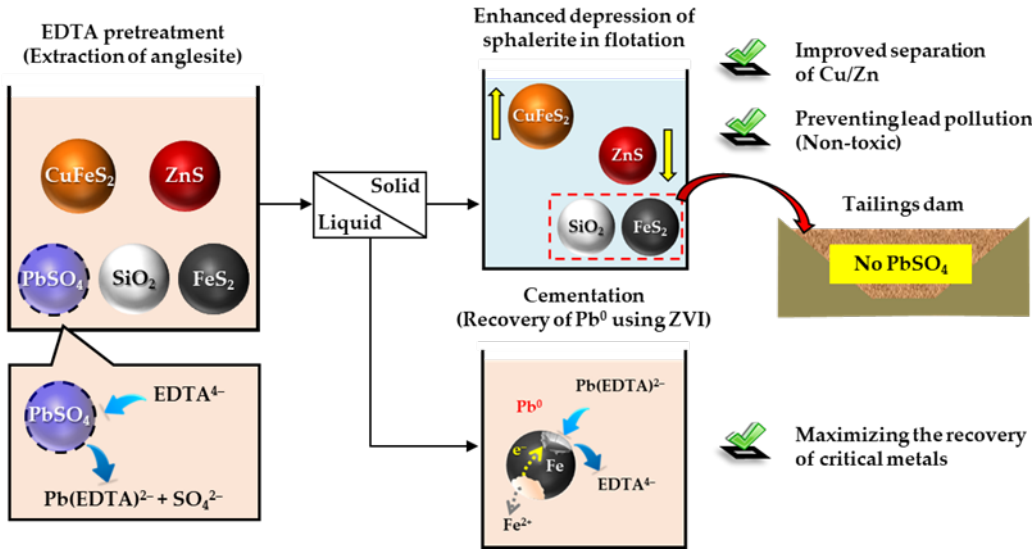

FIG 8 – Proposed enhanced depression of ZnS by extracting $PbSO_4$ using ethylene diamine tetra acetic acid (EDTA) and recovery of extracted Pb^{2+} as zero-valent Pb (Pb^0) by cementation using zero-valent Fe (ZVI) (Aikawa *et al,* 2022).

ACKNOWLEDGEMENTS

This work was supported by JSPS KAKENHI Grant Number JP21J20552.

REFERENCES

Aikawa, K, Ito, M, Kusano, A, Jeon, S, Park, I and Hiroyoshi, N, 2022. Development of a sustainable process for complex sulfide ores containing anglesite: Effect of anglesite on sphalerite floatability, enhanced depression of sphalerite by extracting anglesite, and recovery of extracted Pb2+ as zero-valent Pb by cementation using zero-valent Fe, *Minerals*.

Aikawa, K, Ito, M, Kusano, A, Park, I, Oki, T, Takahashi, T, Furuya, H and Hiroyoshi, N, 2021. Flotation of Seafloor Massive Sulfide Ores: Combination of Surface Cleaning and Deactivation of Lead-Activated Sphalerite to Improve the Separation Efficiency of Chalcopyrite and Sphalerite, *Metals*, 11, 253.

Aikawa, K, Ito, M, Segawa, T, Jeon, S, Park, I, Tabelin, C B and Hiroyoshi, N, 2020. Depression of lead-activated sphalerite by pyrite via galvanic interactions: Implications to the selective flotation of complex sulfide ores, *Minerals Engineering*, 152, 106367.

Ball, J W and Nordstrom, D K, 1991. User's manual for WATEQ4F, with revised thermodynamic data base and text cases for calculating speciation of major, trace, and redox elements in natural waters, *U.S. Geological Survey Water-Resources Investigations Report*, Reston, VA, USA.

Basilio, C I, Kartio, I J and Yoon, R-H, 1996. Lead activation of sphalerite during galena flotation, *Minerals Engineering*, 9: 869–879.

Bicak, O, 2019. A technique to determine ore variability in a sulfide ore, *Minerals Engineering*, 142, 105927.

Choi, S, Jeon, S, Park, I, Tabelin, C B, Ito, M and Hiroyoshi, N, 2021. Enhanced cementation of Cd2+, Co2+, Ni2+, and Zn2+ on Al from sulfate solutions by activated carbon addition, *Hydrometallurgy*, 201, 105580.

El-Shall, H E, Elgillani, D A and Abdel-Khalek, N A, 2000. Role of zinc sulfate in depression of lead-activated sphalerite, *International Journal of Mineral Processing*, 58: 67–75.

Fuerstenau, M C, Olivas, S A, Herrera-Urbina, R and Han, K N, 1987. The surface characteristics and flotation behavior of anglesite and cerussite, *International Journal of Mineral Processing*, 20: 73–85.

Grano, S R, Ralston, J and Johnson, N W, 1988. Characterization and treatment of heavy medium slimes in the Mt. Isa mines lead-zinc concentrator, *Minerals Engineering*, 1: 137–150.

Hák, T, Janoušková, S and Moldan, B, 2016. Sustainable Development Goals: A need for relevant indicators, *Ecological Indicators*, 60: 565–573.

Helgeson, H C, 1969. Thermodynamics of hydrothermal systems at elevated temperatures and pressures, *American Journal of Science*, 267: 729–804.

Hernan, L, Morales, J, Sanchez, L, Tirado, J L, Espinos, J P and Gonzalez Elipe, A R, 1995. Diffraction and XPS Studies of Misfit Layer Chalcogenides Intercalated with Cobaltocene, *Chem. Mater*, 7: 1576–1582.

Jeon, S, Tabelin, C B, Takahashi, H, Park, I, Ito, M and Hiroyoshi, N, 2020. Enhanced cementation of gold via galvanic interactions using activated carbon and zero-valent aluminum: A novel approach to recover gold ions from ammonium thiosulfate medium, *Hydrometallurgy*, 191, 105165.

Kant, C, Rao, S R and Finch, J A, 1994. Distribution of surface metal ions among the products of chalcopyrite flotation, *Minerals Engineering*, 7: 905–916.

Laskowski, J S, Liu, Q and Zhan, Y, 1997. Sphalerite activation: Flotation and electrokinetic studies, *Minerals Engineering*, 10: 787–802.

Latimer, W M, 1952. *The oxidation states of the elements and their potentials in aqueous solutions*, 2nd ed, pp 72, 152, 169 (Prentice-Hall, Inc.: Upper Saddle River)

Leckie, J O and James, R O, 1974. *Aqueous Environmental Chemistry of Metals* (ed: A J Rubin), pp 1–76, (Ann Arbor Science Publishers: Ann Arbor).

Liu, J, Ejtemaei, M, Nguyen, A v, Wen, S and Zeng, Y, 2020. Surface chemistry of Pb-activated sphalerite, *Minerals Engineering*, 145, 106058.

Nansai, K, Nakajima, K, Kagawa, S, Kondo, Y, Suh, S, Shigetomi, Y and Oshita, Y, 2014. Global Flows of Critical Metals Necessary for Low-Carbon Technologies: The Case of Neodymium, Cobalt, and Platinum, *Environmental Science & Technology*, 48: 1391–1400.

Rashchi, F, Dashti, A, Arabpour-Yazdi, M and Abdizadeh, H, 2005. Anglesite flotation: a study for lead recovery from zinc leach residue, *Minerals Engineering*, 18: 205–212.

Rumball, J A and Richmond, G D, 1996. Measurement of oxidation in a base metal flotation circuit by selective leaching with EDTA, *International Journal of Mineral Processing*, 48, 1–20.

Schindler, M, Santosh, M, Dotto, G, Silva, L F O and Hochella, M F, 2021. A review on Pb-bearing nanoparticles, particulate matter and colloids released from mining and smelting activities, *Gondwana Research*.

Silwamba, M, Ito, M, Hiroyoshi, N, Tabelin, C B, Fukushima, T, Park, I, Jeon, S, Igarashi, T, Sato, T, Nyambe, I, Chirwa, M, Banda, K, Nakata, H, Nakayama, S and Ishizuka, M, 2020. Detoxification of lead-bearing zinc plant leach residues from Kabwe, Zambia by coupled extraction-cementation method, *Journal of Environmental Chemical Engineering*, 8, 104197.

Silwamba, M, Ito, M, Hiroyoshi, N, Tabelin, C B, Hashizume, R, Fukushima, T, Park, I, Jeon, S, Igarashi, T, Sato, T, Nyambe, I, Nakata, H, Nakayama, S and Ishizuka, M, 2022. Alkaline Leaching and Concurrent Cementation of Dissolved Pb and Zn from Zinc Plant Leach Residues, *Minerals*, 2022, 12, 393.

Tabelin, C B, Park, I, Phengsaart, T, Jeon, S, Villacorte-Tabelin, M, Alonzo, D, Yoo, K, Ito, M and Hiroyoshi, N, 2021. Copper and critical metals production from porphyry ores and E-wastes: A review of resource availability, processing/recycling challenges, socio-environmental aspects, and sustainability issues, *Resources, Conservation and Recycling*, 170, 105610.

Trahar, W J, Senior, G D, Heyes, G W and Creed, M D, 1997. The activation of sphalerite by lead — a flotation perspective, *International Journal of Mineral Processing*, 49: 121–148.

Woodcock, J T, Sparrow, G J, Bruckard, W J, Johnson, N W and Dunne, R, 2007. Plant Practice: Sulfide Minerals and Precious Metals in *Froth flotation A century of innovation* (ed: M C Fuerstenau, G J Jameson and R H Yoon), pp 781–843 (Society for Mining, Mettallurgy, and Exploration Inc: Colorado)

Zeng, Z, Chen, Z and Qi, H, 2021. Two Processes of Anglesite Formation and a Model of Secondary Supergene Enrichment of Bi and Ag in Seafloor Hydrothermal Sulfide Deposits, *Journal of Marine Science and Engineering*, 10, 35.

Investigation of silica removal by reverse flotation to improve quality of mixture concentrates produced through spiral gravity separation and Slon-VPHGMS process

A H Baladastian[1], A Dehghani Ahmadabadi[2], R Hejazi[3], M Saghaeian[4] and V Sheikhzadeh[5]

1. Process Engineer, Fakoor Sanat Tehran Company. Email: Baladastian@fstco.com
2. Senior Process Engineer, Fakoor Sanat Tehran Company. Email: dehghani@fstco.com
3. R&D Manager, Fakoor Sanat Tehran Company. Email: Hejazi@fstco.com
4. Technical Chairman, Fakoor Sanat Tehran Company. Email: Saghaeian@fstco.com
5. Managing Director, Fakoor Sanat Tehran Company. Email: Sheikhzadeh@fstco.com

ABSTRACT

This research was done to reduce silica from mixed hematite concentrate of Barfkar Iron Ore Sample and increase Fe grade using reverse flotation method (Depressing Hematite and floating Silica). The used sample in the reverse flotation tests was a mixture containing two types of hematite concentrates (Spiral cleaner concentrate and Slon-VPHGMS cleaner concentrate) with the percentage of 16 per cent and 84 per cent, respectively. Fe grade of two samples was 59.31 per cent and 57.52 per cent and SiO_2 grade was 5.83 per cent and 6.71 per cent, respectively. After mixing, the Fe and SiO_2 grade of the mixed sample was measured at 58.10 per cent and 6.20 per cent. For flotation tests, effect of variable operational parameters including feed size distribution (d_{80} = 130 microns and d_{80} = 53 microns), pulp solidity (25 per cent and 30 per cent w/w), pH (9.70, 10.20 and 11), Sodium silicate as a dispersant (500, 1000 and 2000 g/ton), Starch as a depressant (500, 1000, 2000 and 3000 g/ton) and EDA as a collector (180, 300, 400 and 500 g/ton) were investigated. For evaluating the influence of Sodium silicate and Starch dosage, initial flotation tests were performed on the main sample (d_{80} = 130 microns). These two parameters had no significant effects on the yield, Fe, and SiO_2 grade of flotation concentrate based on test results. In the next step, screen analysis was carried out on the main sample for mineralogical studies. Accordingly, the suitable size distribution for releasing Fe and SiO_2 particles was smaller than 53 microns. Therefore, the sample was crushed until d_{80} = 53 microns. Then, supplementary tests were performed on the crushed sample for studying the pH range, pulp solidity, and EDA collector dosage. After doing silica removal flotation tests based on the designed pattern and comparison of the results, the conditions consisting of size distribution d_{80} = 53 microns, pulp solidity 25 per cent, pH 10.20, Sodium silicate 1000 g/ton, Starch 1000 g/ton, and EDA 500 g/ton was selected as optimum values. In the last test, Fe and SiO_2 grade was measured at 60.00 per cent and 3.93 per cent, respectively, and Fe recovery was obtained at 74.93 per cent.

INTRODUCTION

Impurities in iron ore are divided into useful and harmful parts. Useful impurities mainly contain lime or manganese compounds. The presence of these impurities improves the properties and increases the iron ore concentrate price (Forsmo *et al,* 2008). The most important harmful impurities in iron ore concentrate processing plants are silica, phosphorus, sulfur, and titanium. The existence of more than permissible amounts of them causes problems in downstream processes of iron and steel production. Other impurities are commonly found with iron ore that their grade is lower than the four mentioned cases, but if we do not use appropriate methods to remove them, they will result in many problems in downstream processes, especially steel production (Xie *et al,* 2021). These impurities mainly include copper, chromium, molybdenum, tin, and vanadium. For example, more silica in the concentrate (The permissible percentage is less than 5 per cent for the blast furnace method and less than 2 per cent for the direct reduction method) increases the amount of produced slag in the melting stage. Usually, for every kilogram of SiO_2 in iron ore that enters the furnace, about 3 to 4 kg of slag per ton of steel is produced. In the direct reduction method, due to the sensitivity of the process to the presence of silica impurities, the content of SiO_2 should be as low as possible in the pellets and consequently in the iron ore concentrate to avoid the production of excess slag and probable problems during the process (Lima, Valadao and Peres, 2013). On the other hand, illegal amounts of silica content in the produced concentrate also decline quality and lower product prices. Also, the presence of some impurities leads to the growth of undesirable gases in the environment.

These elements are generally chlorine, fluorine, arsenic, sodium oxide, potassium oxide, lead, and zinc. Therefore, it is necessary to remove these elements to the optimal level using appropriate and conventional methods (Sahoo *et al,* 2016).

One of the essential parameters for specifying the quality of produced iron ore concentrate is the ratio of CaO to SiO_2 so increasing this ratio decreases the consumption of melting materials and makes the conditions and costs of the melting process more favourable. Also, the ratio of Fe to SiO_2 is another effective parameter. Iron ore concentrate with Fe to SiO_2 ratio about seven is considered unsuitable, and with a ratio higher than 12, it is approximately proper concentrate (Filippov, Severov and Filippova, 2014).

Reverse flotation is one of the most important and widely used methods for eliminating silica from magnetite or hematite iron ore concentrates. Using suitable chemicals, at first iron is depressed in the sample. After adjusting other parameters such as pH, solidity, optimal size distribution of the sample, determining the surfactants, and the preparation time of each of them, a flotation test is performed. Chemical depressants of iron, such as Starch, Sodium silicate, and other chemicals, depress iron in the flotation feed sample and prevent its flotation (Houot, 1983). In the next step, after making the necessary adjustments, using a suitable collector such as EDA Flotigam, Armac C, or Armac D, conditions are provided for the flotation of silica particles with a proper liberation degree (Silva *et al,* 2021). Depending on the type of silica present in iron ore concentrate (Silica is usually present in form of ferrous silicate lattice or separate quartz particles in iron ore concentrate, which can be very difficult to omit from the concentrate in the first case and in contrast, simple in the second case) and also other particles or impurities, it may be necessary to use additional chemicals such as dispersants, activators or other surfactants (Aarab *et al,* 2021). For example, in samples containing a high percentage of clay mineral Particles, it is needed to disperse them utilising a dispersing agent such as Sodium silicate and then perform flotation of silica particles.

MATERIALS AND METHODS

The sample used in this study was a mixture of concentrate produced from spiral gravity separation, and Slon electromagnetic separation (VPHGMS) that have performed on the samples of Kooh Barfkar mine located in Iran, Kerman province, Zarand. At first, a gravity separation test was carried out on the sample using a spiral as a rougher and cleaner stage. Then, the produced middle and tailing samples of the rougher and cleaner stages were mixed with a defined weight percentage, and then Slon electromagnetic separation was done on a mixed sample as a rougher and cleaner stage. Based on the results of total yield by gravity and electromagnetic tests, two types of concentrate samples were blended with a weight percentage of 16 per cent and 84 per cent, respectively. The Fe grade of the spiral and Slon concentrate were 59.31 per cent and 57.52 per cent, respectively. After mixing the samples, the Fe grade of the mixed concentrate was 58.10 per cent. Also, the SiO_2 grade of two samples was 5.83 per cent and 6.71 per cent, respectively, which was obtained after mixing 6.20 per cent and of course was 6.20 per cent after mixing both of them. For determining the size distribution of the sample, sieve analysis was performed by a wet method, and d_{80} = 130 microns were obtained. Table 1 shows the physical and chemical specifications of the flotation feed sample, including the size distribution diagram and also Fe, and SiO_2 grade of concentrate.

TABLE 1

Physical and chemical specifications of the flotation feed sample (size distribution, Fe and SiO_2 grade).

Chemical specifications	
Fe (%)	58.10
SiO_2 (%)	6.20
Al_2O_3 (%)	1.60
CaO (%)	0.22
MgO (%)	0.18
P_2O_5 (%)	0.17
K_2O (%)	0.12
Na_2O (%)	0.02
TiO_2 (%)	0.14
SO_3 (%)	0.04
LOI (%)	6.75

Size distribution diagram

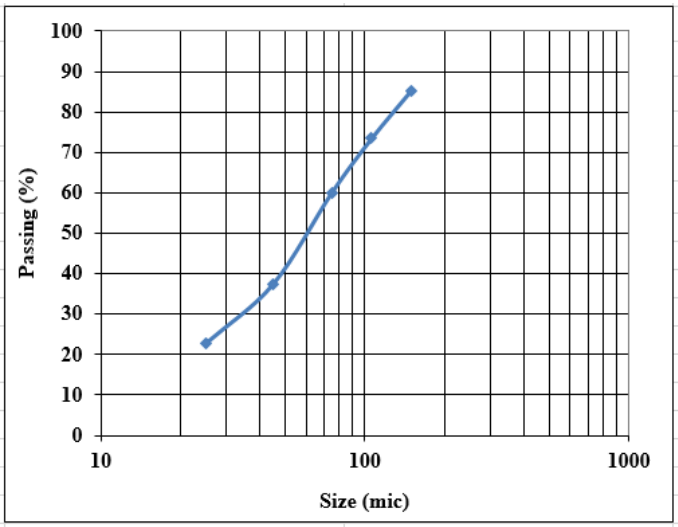

For experiments, operational parameters containing feed size distribution (d_{80} = 130 microns, d_{80} = 53 microns), pulp solidity (25, 30, and 35 per cent w/w), pH (9.70, 10.20, and 11), Sodium silicate dosage as a dispersant of clay mineral particles (500, 1000 and 2000 g/ton), Starch dosage as an iron depressant (500, 1000, 2000 and 3000 g/ton) and collector dosage EDA (180, 300, 400 and 500 g/ton) were selected. Also, all experiments were operated using Denver mechanical flotation cell with 2 L cell volume. Constant Experimental parameters in this study were stirring speed of 1200 rev/min, preparation times of Sodium silicate, Starch and EDA collector 5, 5 and 2 minute, respectively, Combination ratio 9 to 1 of pH regulator including Na_2CO_3 and NaOH and finally seven steps of adding chemicals and frothing stages. The effects of Sodium silicate and Starch were investigated on the original sample with a size distribution of d_{80} = 130 microns. After obtaining the data of the initial tests, sieve analysis was performed to determine the liberation degree, type of mineralogy, and SiO_2 grade in each fraction of the sample. Also, microscopic mineralogical studies were determined on each fraction separately. Examine the effect of collector dosage and pH changes on the crushed sample (Crushing sample to investigate the effect of liberation degree of Fe and SiO_2 particles) were performed up to d_{80} = 53 microns. Results of tests were analysed, and the optimal level of each parameter was obtained. Then supplementary tests were experimented with appropriate amounts of each chemical.

RESULTS AND DISCUSSIONS

Initial flotation tests

Effect of Sodium silicate dosage

For investigating the effect of Sodium silicate dosage on the removing silica from concentrate, flotation test conditions consist of different dosages 500, 1000, 2000 g/ton in constant conditions such as d_{80} = 130 microns, solidity 30 per cent, Starch dosage 500 g/ton, collector EDA dosage 180 g/ton and pH about 9.70 were considered. The results (Figure 1) showed that yield decreased with increasing the Sodium silicate dosage, but significant changes were not obtained in the Fe and SiO_2 grade of concentrate. On the other hand, the insignificant effect of this chemical dosage on variation of Fe and SiO_2 grade indicates that the dispersing of clay mineral particles doesn't have an important role on the efficiency of the removal silica reverse flotation. In this part, the fractional reduction of Fe and SiO_2 grade was measured at about 0.30 per cent and 1 per cent, respectively.

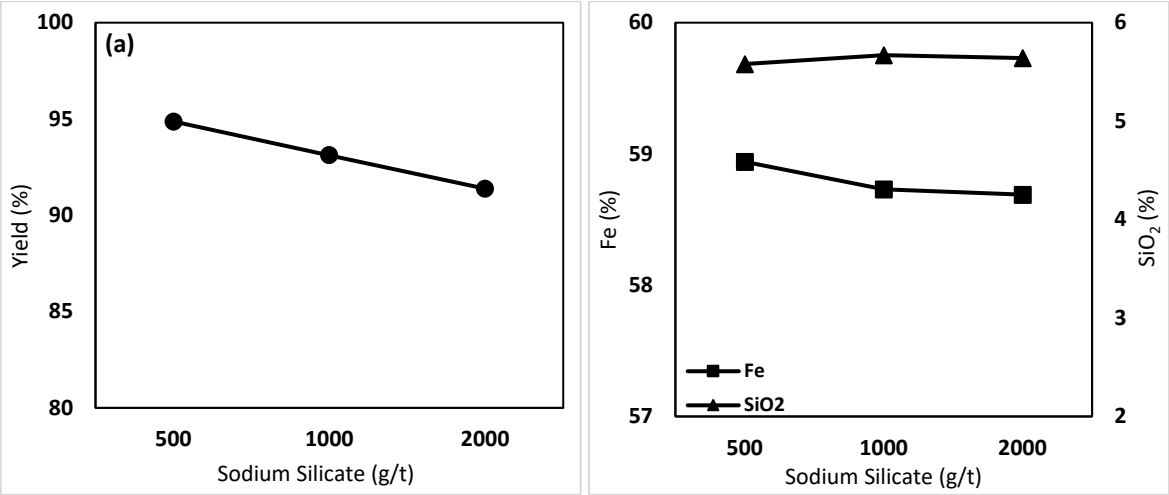

FIG 1 – Changes of (a) Yield, (b) Iron and silica grade versus Sodium silicate dosage (g/ton).

Effect of Starch dosage

In order to study the influence of Starch dosage on the omitting silica from concentrate, amounts of dosages 500, 1000, 2000, 3000 g/ton in constant conditions such as d_{80} = 130 microns, solidity 30 per cent, 500 g/ton of Sodium silicate, collector EDA dosage of 180 g/ton and pH about 9.70 were considered. The results are shown in Figure 2. By getting bigger of Starch dosage, the flotation concentrate yield decreases. The slope of yield decreasing is reduced, too. In fact, it can be predicted that if the experiments continue at values above 3000 g/ton of Starch, yield declining gradually disappears, and its amount will reach to a constant value. Furthermore, results revealed that changes in this parameter have an inconsiderable effect on the Fe and SiO_2 grade of concentrate in the flotation test. It had the same performance as the changes of Sodium silicate dosage.

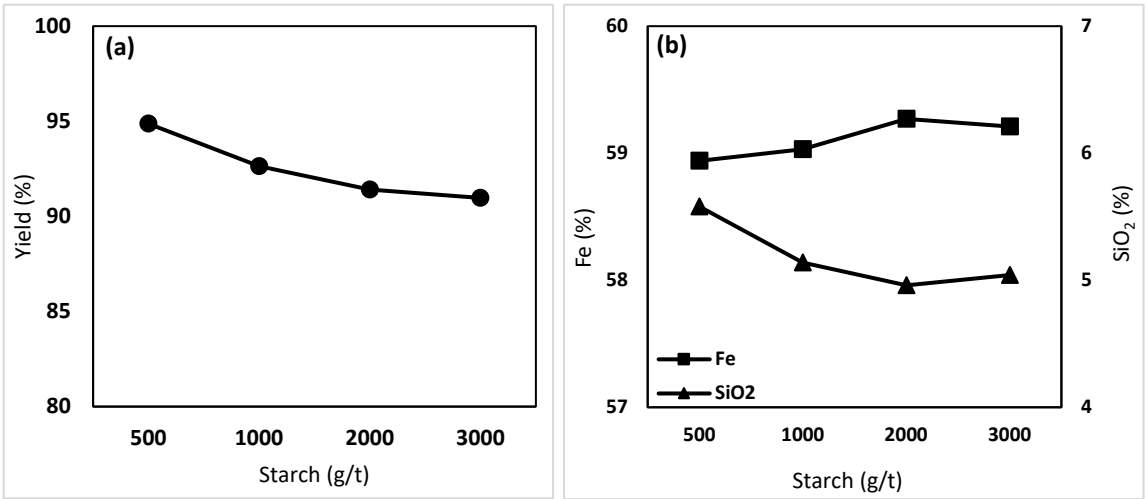

FIG 2 – Changes of (a) yield, (b) Fe and SiO_2 grade versus Starch dosage.

Flotation feed mineralogy

Based on the results of the initial tests and the lack of significant effect on the Sodium silicate and Starch dosage, which were done on the main sample (d_{80} = 130 microns), Sieve analysis was performed on the sample to determine the association and dispersion of silica in each fraction of sieving. Fractional chemical analysis of SiO_2 grade separately was done, too. Also, microscopic mineralogy was performed separately on polished sections and thin blades of each fraction. For fractions smaller than 75 microns, silica accumulation is less than larger fractions. On the other hand, in accordance with mineralogical observations, it was found that more than 80 per cent of the silica is ferrous silicate minerals that causes difficulty in removing silica by the flotation method. Also, less than 20 per cent of silica is quartz that had a suitable liberation degree in fractions smaller than 75 microns. In all fractions, the major tailings minerals in terms of abundance were quartz, calcite,

chlorite, biotite, and muscovite, and the main stocking of ferrous minerals were silica and chlorite. Accordingly, to create a suitable liberation degree especially for iron and silica particles and perform supplementary flotation tests, the sample was crushed up to d_{100} = 75 microns and d_{80} = 53 microns.

Supplementary flotation tests

Effect of pH

Supplementary flotation tests were performed to investigate the effect of pH on the flotation concentrate specifications for the crushed sample, with pH ranges of 9.70, 10.20, and 11 in constant conditions such as d_{80} = 53 microns, pulp solidity 30 per cent, Sodium silicate dosage 500 g/ton, Starch dosage 500 g/ton and collector EDA 180 g/ton. Results are shown in Figure 3. Based on the results, the concentrate yield increases by mounting the pH range. Also, the SiO_2 grade in concentrate decreased by about 1.66 per cent (removing approximately 28 per cent, relatively). Increasing the pH leads to more and better depression of iron particles in the flotation method, and also, it does not affect the flotation of silica with EDA. On the other hand, based on the graph of changes of Fe grade versus pH range, growing this parameter has caused a reduction of Fe grade in the concentrate. However, this reduction was not noticeable and only happened by 1 per cent, which indicates that the pH in the studied range (9.70 to 11) does not influence on the Fe grade of the flotation concentrate specifications.

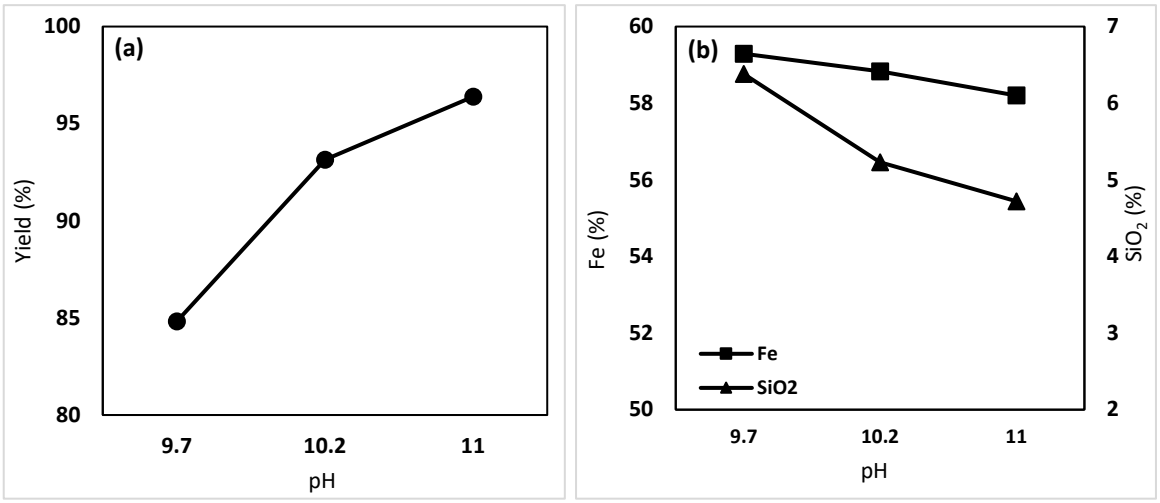

FIG 3 – Changes of (a) yield, (b) Fe and SiO_2 grade versus pH range.

Effect of pulp solidity

Supplementary flotation tests were performed to evaluate the pulp solidity on the properties of flotation concentrate. Therefore, three flotation tests were operated with pulp solidity 25 per cent, 30 per cent, and 35 per cent in constant conditions such as d_{80} = 53 microns, Sodium silicate dosage of 500 g/ton, the Starch dosage of 500 g/ton, pH range of 10.20, and collector EDA 500 g/ton. Results are shown in Figure 4. The results indicate that enhancing the pulp solidity increased the concentrate yield. Increasing this parameter resulted in lock and engage of inside the cell making difficult for particles to float and rise. Based on the diagrams, it is clear that the pulp solidity did not have a significant effect on the Fe and SiO_2 grade of the sample; because this factor does not cause any change in the main and fundamental properties of the sample, especially the surface physicochemical properties of the particles that play a significant role in the flotation process.

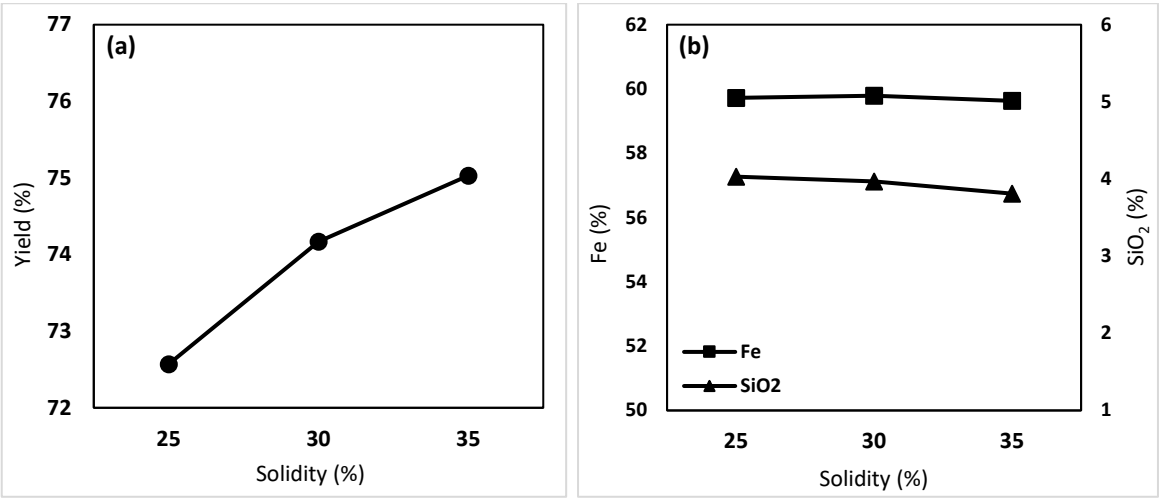

FIG 4 – Changes of (a) yield, (b) Fe and SiO_2 grade versus pH range.

Effect of EDA collector dosage

Supplementary flotation tests to investigate collector dosage (EDA) was performed at amounts of 180, 300, 400, and 500 g/ton and in constant conditions such as d_{80} = 53 microns, solidity 25 per cent, Sodium silicate dosage of 500 g/ton, Starch dosage of 500 g/ton and pH range 10.20. Test results are shown in Figure 5. Based on the results, increasing the collector dosage caused a decrease in concentrate yield. The increasing amount of this chemical causes it to be absorbed on silica particles higher locked with iron particles. This issue leads to transfer of a large part of low-grade silica particles to the tailing. On the other hand, changing the amount of EDA has not significantly affected the iron content of flotation concentrate. Based on this, the changes of Fe grade concentrate are only about 0.50 per cent. With the increasing dosage of this chemical, the SiO_2 grade in concentrate has decreased by about 16 per cent, relatively. Therefor EDA is one of the best chemicals for proper silica removal, and whatever the consumption of this chemical increases, absorption on the surface of silica particles and their flotation is better, which will result in a decline of this material grade related to flotation concentrate.

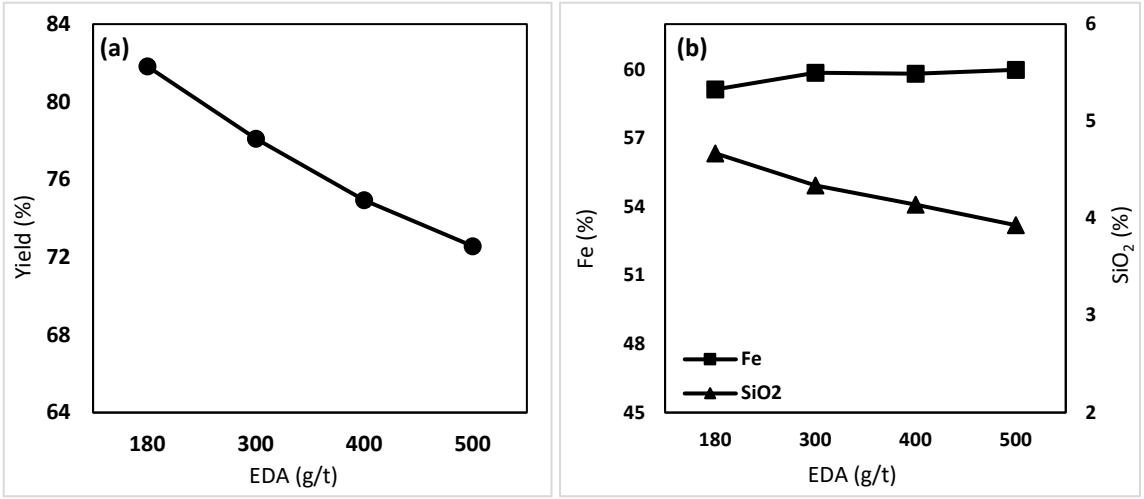

FIG 5 – Changes of (a) yield, (b) Fe and SiO_2 grade versus collector EDA dosage.

CONCLUSIONS

In this study, for producing hematite concentrate with appropriate grade and recovery from Kooh Barfkar sample and removing its impurities, especially silica, reverse flotation tests were designed and performed on a mixed concentrate of spiral gravity separation and Sloan electromagnetic test. Important Parameters, in this case, were feed size distribution, pulp solidity, pH, Sodium silicate (dispersant of clay mineral particles), Starch (depressant of iron particles especially hematite), and EDA collector (floating silica particles). Dependent variables were yield, Fe grade, and SiO_2 grade

of concentrate and effect of each independent parameter was investigated on them. Based on results, optimal test conditions were d_{80} = 53 microns, pH range about 10.20, Sodium silicate dosage 500 g/ton, Starch dosage 500 g/ton, and EDA collector dosage 500 g/ton. In this test, flotation concentrate yield was 72.57 per cent and Fe and SiO_2 grade was 60 and 3.93 per cent, respectively. Also, Fe recovery was 74.93 per cent. The most effective parameter was EDA collector dosage that caused significant changes on dependent variables such as yield, Fe, and SiO_2 grade of concentrate. Finally, due to the crystallisation of silica particles in the form of ferrous silicate crystals, using the flotation method, in order to reduce the silica content of this sample, was not suitable. On the other hand, the parameter with the most negligible effect was the pulp solidity that had an insignificant role on Fe and SiO_2 grade of concentrate. We can use Gravity methods such as Multi Gravity or spiral separation to achieve better results.

ACKNOWLEDGEMENTS

The authors would like to thank from management and personnel of FST Company and its R&D test centre, especially Mr. Ali Sheikhzadeh, Mr. Ali Dehghani, Mr. Mostafa Abolhassani, and Mr. Asghar Noor Mohammadi for comprehensively supporting this research project.

REFERENCES

Aarab, I, Derqaoui, M, Amari, K E, Yaacoubi, A, Abidi, A, Etahiri, A and Bacaoui, A, 2021. Influence of surface dissolution on reagents' adsorption on low-grade phosphate ore and its flotation selectivity, *J. Colloids and Surfaces A: Physicochemical and Engineering Aspects*, vol 631, 127700.

Filippov, L O, Severov, V V and Filippova, I V, 2014. An overview of the beneficiation of iron ores via reverse cationic flotation, *International Journal of Mineral Processing*, vol 127, pp. 62–69.

Forsmo, S P E, Forsmo, S E, Bjorkman, B M T and Somskog, B O, 2008. Studies on the influence of a flotation collector reagent on iron ore green pellet properties, *J. powder Technology*, vol 182, pp 444–452.

Houot, R, 1983. Beneficiation of iron ore by flotation – Review of industrial and potential applications, *International Journal of Mineral Processing*, vol 10, pp. 183–204.

Lima, N P, Valadao, G E S and Peres, E C A, 2013. Effect of amine and starch dosages on the reverse cationic flotation of an iron ore, *J. Minerals Engineering*, vol 45, pp. 180–184.

Sahoo, H, Rath, S S, Rao, D S, Mishra, B K and Das, B, 2016. Role of silica and alumina content in the flotation of iron ores, *International Journal of Mineral Processing*, vol 148, pp. 83–91.

Silva, K, Filippov, O L, Picarra, A, Filippova, V I, Lima, N, Skliar, A, Faustino, L and Filho, L L, 2021. New perspectives in iron ore flotation: Use of collector reagents without depressants in reverse cationic flotation of quartz, *J. Minerals Engineering*, vol 170, 107004.

Xie, L, Wang, J, Lu, Q, Hu, W, Yang, D, Qiao, C, Peng, X, Peng, Q, Wang, T, Sun, W, Liu, Q, Zhang, H and Zeng, H, 2021. Surface interaction mechanisms in mineral flotation: Fundamentals, measurements and perspectives, *J. Advances in Colloid and Interface Science*, vol 295, 102491.

Investigating the influence of the electrochemical environment on the flotation of a mixed sulfide mineral system of bornite and chalcocite

K C Corin[1], T P Tafirenyika[2] and C T O'Connor[3]

1. Associate Professor, Centre for Minerals Research, University of Cape Town, Cape Town, South Africa, 7700. Email: kirsten.corin@uct.ac.za
2. Centre for Minerals Research, University of Cape Town, Cape Town, South Africa, 7700. Email: tfrtan001@myuct.ac.za
3. Professor, Centre for Minerals Research, University of Cape Town, Cape Town, South Africa, 7700. Email: cyril.oconnor@uct.ac.za

INTRODUCTION

There is a growing demand for copper driven by its applications in renewable energy and electric vehicles. Sulfide ores are an important source of copper. Flotation is a critical front-end process used to remove gangue minerals and concentrate the copper minerals. The electrochemical activity of sulfide minerals contributes to their overall activity in the flotation pulp. The mineral rest potential dictates how collectors interact with the mineral surface, and hence ultimately on the flotation response. Dissolved oxygen, (DO), pH, redox potential (Eh) and water composition and ionic strength are also significant in controlling flotation performance. The aim of this investigation was to determine the influence of the electrochemical environment both during milling and flotation on the flotation behaviour of bornite and chalcocite. For this investigation, the interactions of collector with bornite and chalcocite were studied using synthetic plant water (SPW1) and deionised water (DIW) at 5 different pH levels. Sodium isobutyl xanthate (SIBX) was used both in microflotation, collector adsorption and zeta potential tests.

MATERIALS AND METHODS

To investigate the surface chemistry of bornite and chalcocite individually and when mixed, experiments were conducted at pH 3, 5, 7, 9 and 11, under 2 different water qualities, Deionised water (DIW) and UCT Synthetic Plant Water (SPW1) (Wiese, Harris and Bradshaw, 2005).

Mineralogy

Bornite and chalcocite samples were analysed using XRD. The purity of the samples showed that the bornite (42 per cent) sample contained large portions of gangue minerals and chalcocite (62 per cent) had significant portions of marcasite (FeS_2) and pyrite (FeS_2) which are iron containing minerals, which makes differentiating between them when in a mixture complex.

Microflotation

The water type being used was adjusted to the required pH by adding HCl or NaOH. three g of the mineral was weighed in a beaker and the adjusted pH water added to create a slurry. The pH was adjusted to maintain the desired pH and dosed with SIBX collector at a dosage of 0.5 pseudo monolayer which is 493 g/ton for chalcocite and 386 g/ton for bornite. Microflotation was conducted using a standard procedure. Four concentrates were collected over 20 minutes.

Adsorption studies

Adsorption tests were carried out on the pure mineral samples and the concentration determined using UV/Vis spectroscopy (ƛ= 301 nm).

Zeta potential studies

Zeta potential tests were conducted using a Malvern ZetaSizer 4.

RESULTS AND DISCUSSION

Figure 1 shows that bornite recovery between pH 5 and 11 was generally the same, while pH 3 recorded the lowest recovery and recovery in SPW1 was lower compared to DIW. Chalcocite in

DIW had two distinct flotation recovery regions, one below 50 per cent recovery (pH 5 and 7) and recoveries above 50 per cent at pH 3, 9 and 11. Chalcocite in SPW1 showed a slight drop in recovery compared to DIW. The highest recovery was at pH 3 while pH 5 had the lowest recovery.

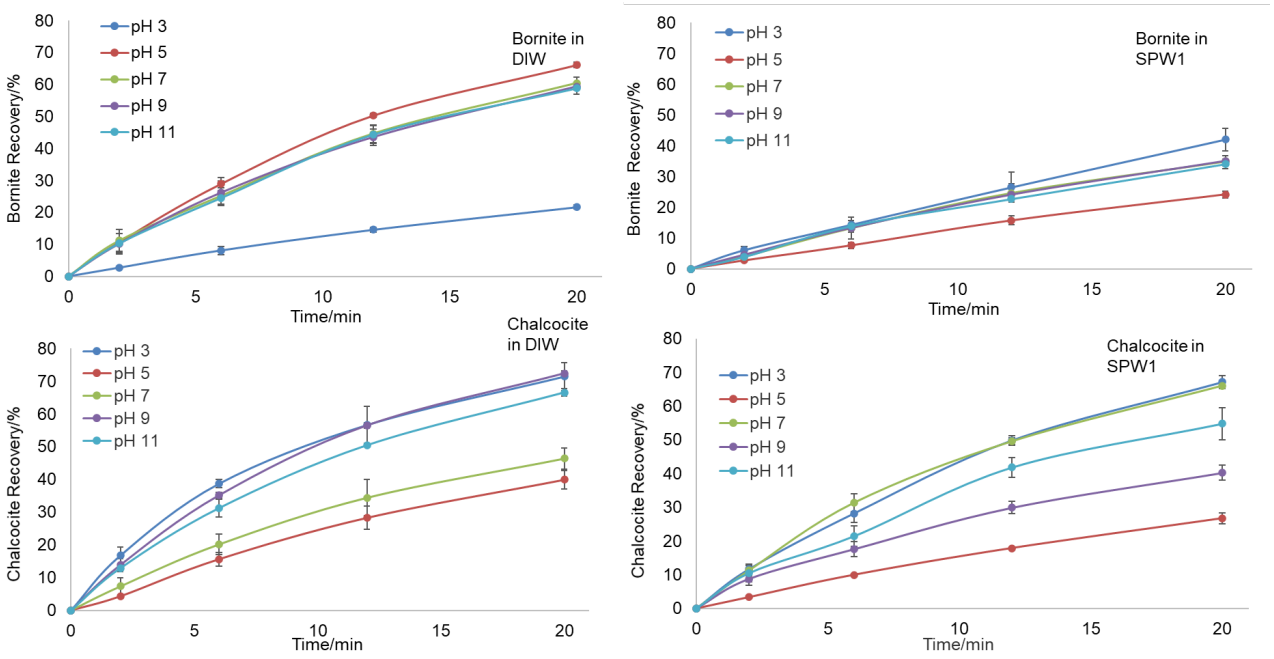

FIG 1 – Recovery versus time for bornite and chalcocite under DIW and SPW1 at pH 3, 5, 7, 9 and 11.

Figure 2 showed that there is distinctly better adsorption of SIBX onto the surface of chalcocite compared to bornite at all conditions. The key difference likely lies in the presence of iron in bornite and the lack thereof in chalcocite. There was also higher residual collector concentration when using 1 monolayer versus 0.5 monolayer collector dosage. For bornite the residual collector concentration decreased as the pH increased from 3 to 7 with the minimum residual concentration observed at pH 7 for all dosages and water types. From pH 7 to 11, the concentration steadily increased. Hence most of the collector was adsorbed at the mineral surface. There was higher residual collector concentrations in the DIW compared to SPW1 for the 1 monolayer dosage in bornite (except for pH 11). At 0.5 monolayer dosage, there was higher residual concentration in SPW1 at pH 3 to 7 whereas under alkali conditions there was higher residual concentration in DIW. Chalcocite generally showed a high adsorption rate, particularly using the 0.5 monolayer dosage where all pH values showed minimal residual collector concentration. The differences in collector adsorption are regulated by the pH, which dictates the specific collector mineral interactions, and the xanthate species formed under the given conditions. The collector mineral interactions are dictated by the pulp potential, which is heavily influenced by the pH of the system.

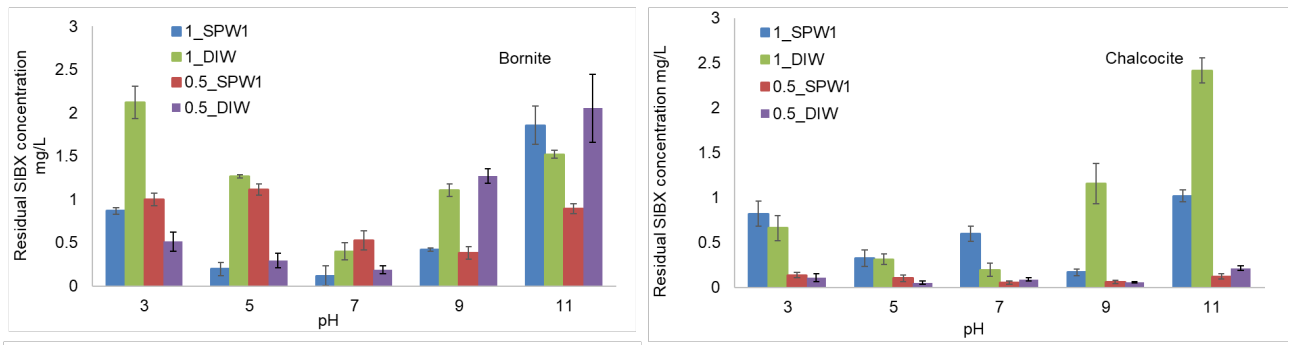

FIG 2 – Residual xanthate in solution after contacting bornite and chalcocite with 0.5 pseudo-monolayer and 1 pseudo-monolayer dosages of SIBX under DIW and SPW1 at pH 3, 5, 7, 9 and 11.

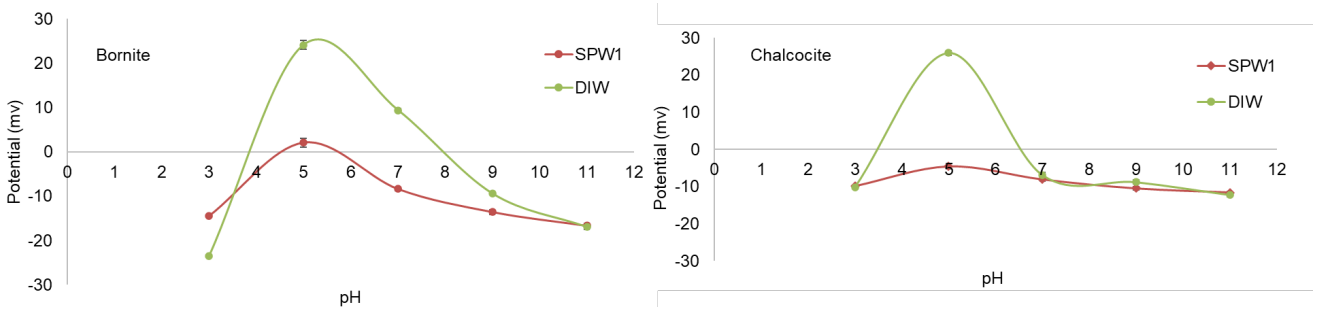

FIG 3 – Zeta Potential profiles for bornite and chalcocite under DIW and SPW1 at pH 3–11.

It is interesting to note that for DIW both bornite and chalcocite have quite similar zeta potential profiles. And that both bornite and \ exhibit 2 isoelectric points and higher potentials than in SPW1. Under SPW1, the profiles of both minerals are quite similar.

CONCLUSIONS

The purity of the minerals may have mitigated against the validity the results of this study although it could be argued that they may be more typical of real ore samples. In evaluating the flotation results in the context of collector adsorption and the zeta potential data it is possible to make reasonable deductions about the behaviour of these minerals in a flotation process.

ACKNOWLEDGEMENTS

South Africa/China Joint Research Centre sponsored by the South African Department of Science and Innovation.

REFERENCES

Wiese, J, Harris, P and Bradshaw, D, 2005. The Influence of the Reagent Suite on the Flotation of Ores from the Merensky Reef, *Reagents'04,* 18(2), 189–198.

Considering the action of water quality on the electrochemical response of Galena

K C Corin[1], N Ndamase[2] and M Tadie[3]

1. Associate Professor, University of Cape Town, Cape Town, South Africa, 7700. Email: kirsten.corin@uct.ac.za
2. University of Cape Town, Cape Town, South Africa, 7700. Email: ndmnol002@myuct.ac.za
3. Stellenbosch University, Cape Town, South Africa, 7700. Email: mtadie@sun.ac.za

INTRODUCTION

Mining operations in arid regions are compelled to reduce their consumption of fresh water. Closed water circuits are an attractive solution and, in addition to reducing freshwater consumption, have the added benefit of reducing reagent consumption as well as the environmental impact by eliminating effluent discharge. Accumulating ionic species have been shown to hinder collector adsorption which reduces the recovery of valuable minerals.

Numerous studies have investigated the effect of degrading water quality on collector adsorption however there is very limited understanding as to how this takes place from an electrochemical perspective. This study therefore aims to investigate how the presence of accumulating ionic species at varying concentrations affects the electrochemical adsorption of sodium ethyl xanthate onto galena. The synthetic plant water used in this study comprised of single salt solutions to isolate the effects of the ionic species of interest. The ionic strengths were varied between 0.0242 M, 0.0727 M, 0.1212 M and 0.2426 M which correspond to University of Cape Town (UCT) Centre for Minerals Research (CMR) synthetic plant waters of 1, 3, 5 and 10SPW, respectively. Mineral rest potentials indicated how changing water quality affected xanthate-mineral interactions. Microflotation observed the impact of changing water quality on mineral floatability.

MATERIALS AND METHODS

Synthetic plant water

In order to consider changes in water quality within flotation, the UCT CMR developed a synthetic plant water (SPW) recipe (Wiese, Harris and Bradshaw, 2005). The accumulation of ions in process water owing to on-site recycling impact the redox reactions taking place. These reactions can be considered through electrochemistry experiments. Single salt synthetic plant water solutions were generated to isolate the effects of specific ions. Sulfur chemistry is paramount to the flotation of sulfide minerals; thus, the ions of interest are SO_4^{2-} and $S_2O_3^{2-}$. The salt solutions were prepared in ultra-pure water with sodium as the counterion: $Na_2S_2O_3$ and Na_2SO_4. Table 1 shows the ionic composition of the waters.

TABLE 1

Composition of synthetic plant waters (adapted from Wiese, Harris and Bradshaw, 2005; Manono, Corin and Wiese, 2018; Ndamase, Tadie and Corin, 2020).

Water type	SO_4^{2-} (ppm)	$S_2O_3^{2-}$ (ppm)	Ionic strength (M)
1SPW	2325	2714	0.0242
3SPW	6984	8152	0.0727
5SPW	11 642	13 589	0.1212
10SPW	23 304	27 202	0.2426

Electrodes

A pure galena mineral electrode acted as the working electrode. The galena electrode was made and prepared for measurement as described by Tadie *et al* (2015). Ag/AgCl (3 M KCl) was used as

the reference electrode. Platinum was used to monitor the standard potential throughout. The electrodes are shown in Figure 1.

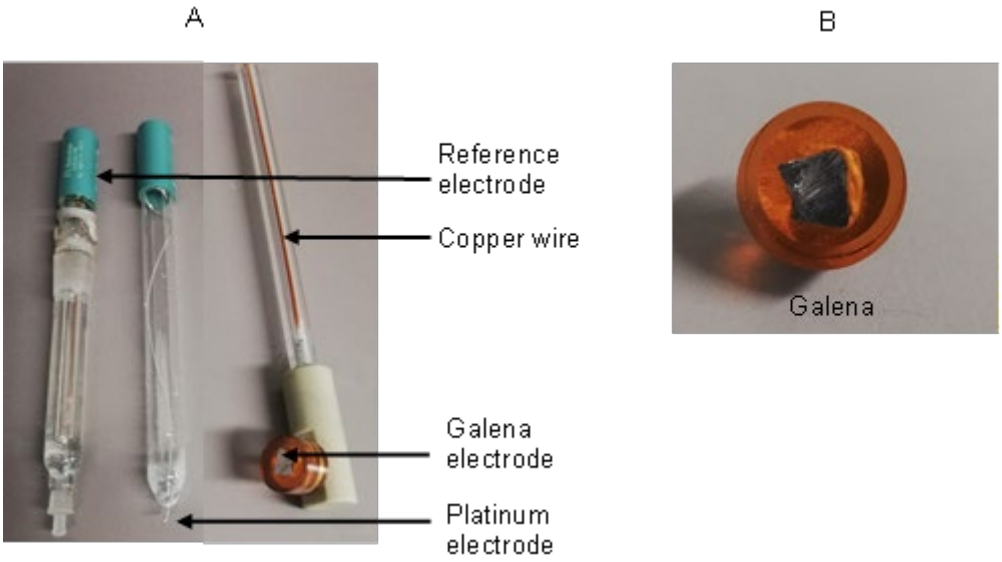

FIG 1 – (A) Electrodes used for electrochemistry measurements (B) Galena electrode (Ndamase, Tadie and Corin, 2020).

Collector

The collector, sodium ethyl xanthate (SEX), provided by AECI Mining Chemicals, was used at a concentration of 6.24×10^{-4} M in the electrochemistry studies. This concentration was chosen to be able to compare to other electrochemical studies (Chimonyo *et al,* 2017; Tadie *et al,* 2015). Microflotation tests were conducted at 50 g/t SEX, intended to be low enough for partial surface coverage in order to be able to see changes in flotation responses.

Rest potential

A 500 ml double walled glass electrochemical cell was used for rest potential measurements. The cell temperature was maintained at 25 ± 1°C using a water bath. The cell was filled with 450 ml of the SPW of interest, agitated with a magnetic stirrer, and the electrodes were suspended in the solution. A Gamry 600 potentiostat connected to a computer recorded the measured potentials using the Gamry Framework software. Initial rest potentials of the mineral was conducted for 600 seconds, after which collector (SEX at 6.24×10^{-4} M) was dosed and another 600 seconds was allowed for measurements. Tests were conducted in duplicate.

Microflotation

A 250 ml UCT microflotation cell (Bradshaw and O'Connor, 1996) was used to determine mineral floatability. Three grams of pure galena was mixed with 50 ml of the SPW of interest to form a slurry, the slurry was sonicated for 5 minutes to disperse fine particle agglomerates. The cell was filled to the desired volume with the SPW of interest. 50 g/ton SEX collector was dosed. The slurry was agitated with a peristaltic pump at 65 rev/min and a microsyringe controlled the air flow rate of 7 ml/min. Concentrates were collected after 2, 4, 6 and 8 minutes, allowing a total of 20 minutes. The concentrates and tailings filtered, dried and weighed to determine the mineral recovery. Microflotation tests were performed in duplicate.

RESULTS AND DISCUSSION

Figure 2 shows the rest potential profiles of galena with changing ionic strength. The equilibrium potential, 0.15 V, of xanthate oxidation at 6.24×10^{-4} M has been determined elsewhere (Tadie *et al,* 2015; Chimonyo *et al,* 2017). Note that the starting potential of each solution is different owing to the different concentrations of the SPW single salt used. Figure 2 indicates that galena surface is susceptible to changes in water chemistry. The measured potentials for both species and at all concentrations were below the equilibrium potential of xanthate oxidation, indicating that

only the metal xanthate would likely be formed. Further, the potentials with $S_2O_3^{2-}$ were all negative.

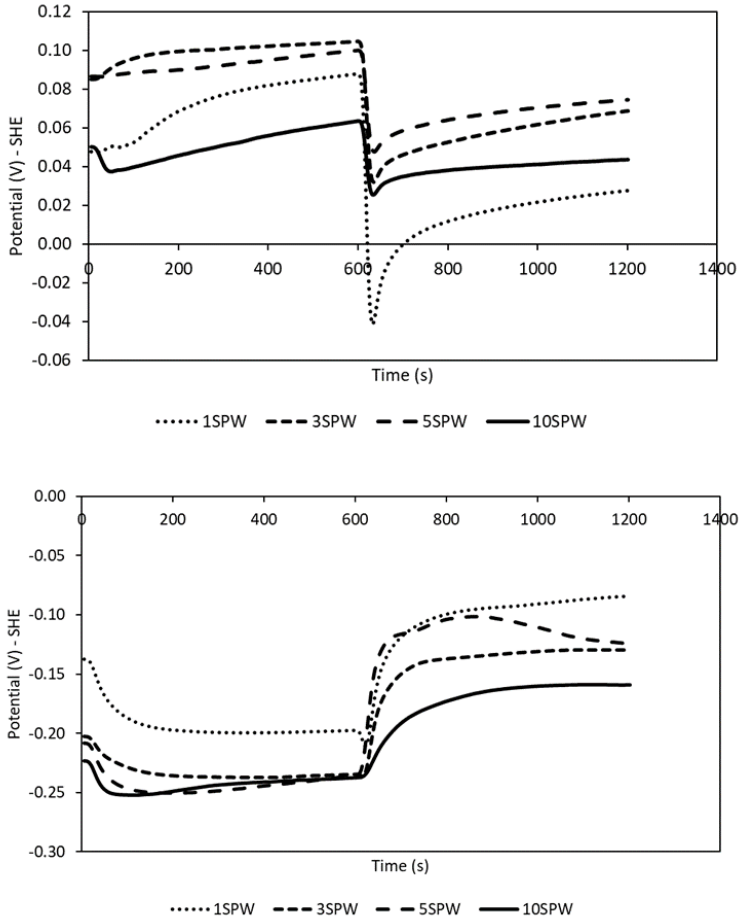

FIG 2 – PbS rest potential profile in Na_2SO_4 (left) and $Na_2S_2O_3$ (right) at varying ionic strengths.

The rest potential measurements provide further insight by predicting the extent of collector-mineral interaction. This can be observed by looking at the difference between the average rest potentials before and after collector addition. Consequently, the lower the difference the lower the extent of collector-mineral interaction. Figure 3 compares the first concentrate recovery to the extent of collector-mineral interaction predicted by electrochemistry. It should be noted that both Na_2SO_4 and $Na_2S_2O_3$ showed the formation of metal xanthate under all conditions. For Na_2SO_4 the change in potential showed an inverse trend to the recovery. While initial recoveries were very low with $Na_2S_2O_3$, this is complemented with negative changes in potential, indicating that the interaction between the mineral and the collector was not straightforward under these conditions and there may be a species generated at the mineral surface other than the metal xanthate.

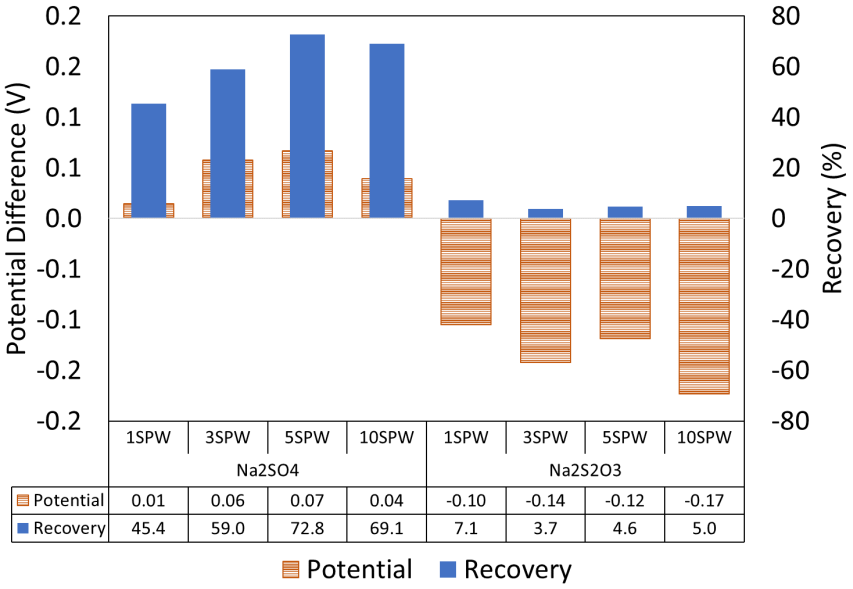

FIG 3 – 1st concentrate recovery versus average potential difference before and after collector addition.

CONCLUSIONS

This study investigated the effect of the presence of SO_4^{2-} and $S_2O_3^{2-}$ on the performance of galena flotation from an electrochemical perspective. Electrochemical techniques are able to show whether the mineral surface is impacted by changes in the water chemistry and can indicated possible flotation responses. In this case, the presence of ions such as SO_4^{2-} and $S_2O_3^{2-}$ has a significant impact on flotation performance with $S_2O_3^{2-}$ having a depressing effect on galena flotation, an indication that operations should be aware of ions such as this and where possible monitor their presence.

ACKNOWLEDGEMENTS

This work has received funding from the European Union H2020 program under grant agreement No 730480, ITERAMS.

REFERENCES

Bradshaw, D J and O'Connor, C T, 1996. Measurement of the sub-process of bubble loading in flotation, *Minerals Engineering* 9(4):443–448.

Chimonyo, W, Wiese, J, Corin, K and O'Connor, C, 2017. The use of oxidising agents for control of electrochemical potential in flotation, *Minerals Engineering* (109):135–143.

Manono, M S, Corin, K C and Wiese, J G, 2018. Water quality effects on a sulfide PGM ore: Implications for froth stability and gangue management, *Physiochemical Problems of Mineral Processing,* 54(4):1253–1265.

Ndamase, N, Tadie, M and Corin, K C, 2020. Considering the action of degrading water quality on the electrochemical response of sulphide minerals, *IMPC 2020: XXX International Mineral Processing Congress Proceedings*, 18–22 October 2020.

Tadie, M, Corin, K C, Wiese, J G, O'Connor, C T and Nicol, M, 2015. An investigation into electrochemical interactions between platinum group minerals and xanthate: Voltammetric study, *Minerals Engineering,* 70:148–155.

Wiese, J G, Harris, P J and Bradshaw, D J, 2005. The influence of the reagent suite on the flotation of ores from the Merensky reef, *Minerals Engineering*, 18(2):189–198.

The effects of operational parameters on HydroFloat® performance in a metalliferous application

K Demir[1], A J Morrison[2], K Runge[3], C Evans[4] and J Kohmuench[5]

1. Research Officer, Julius Kruttschnitt Mineral Research Centre, Sustainable Minerals Institute, The University of Queensland, Brisbane Qld 4109. Email: k.demir@uq.edu.au
2. Senior Research Fellow, Julius Kruttschnitt Mineral Research Centre, Sustainable Minerals Institute, The University of Queensland, Brisbane Qld 4109. Email: angus.morrison@uq.edu.au
3. Principal Research Fellow, Julius Kruttschnitt Mineral Research Centre, Sustainable Minerals Institute, The University of Queensland, Brisbane Qld 4109. Email: k.runge@uq.edu.au
4. Senior Research Fellow, WH Bryan Mining and Geology Research Centre, Sustainable Minerals Institute, The University of Queensland, Brisbane Qld 4109. Email: c.evans@uq.edu.au
5. Vice President International, Eriez Manufacturing Company, Erie, PA, USA. Email: jkohmuench@eriez.com

ABSTRACT

The Eriez HydroFloat® is a flotation device capable of recovering significantly coarser and less-liberated particles than is possible using a conventional mechanical flotation cell. Originally developed for industrial and bulk mineral beneficiation, the HydroFloat® is attracting increasing interest as a means of increasing the required grind size for metalliferous ore flotation. Doing so would reduce the costs of processing complex ores, either by decreasing the energy required to grind the flotation feed or by increasing the throughput achievable with a given comminution circuit. Processing coarser particles would also result in coarser waste streams, potentially improving the mechanical and hydraulic performance of the waste dams that they are sent to. Recent work at pilot – and industrial-scale has proven the potential of the HydroFloat® technology to achieve these gains in metalliferous applications. However, in order to realise the full potential of the HydroFloat® technology, it is necessary to understand not just its performance but also the drivers for that performance. Doing so will allow the design and operation of HydroFloat® devices to be optimised for different ores and applications. For this work, a HydroFloat® pilot rig was deployed to a copper-gold plant in Australia and was used to investigate the effect of stream and operating conditions for treating the tailings stream of one of the plant's rougher flotation cells. Under each set of operating conditions, samples were taken of the HydroFloat® feed, tailings and concentrate streams, and processed to yield the grade and recovery achieved by the device. At the same time, the bubble size and bed behaviour inside the device were measured. This paper presents preliminary relationships observed between the operating conditions and the performance of the HydroFloat® cell, and thus suggests a range of possible drivers for the measured coarse particle flotation performance.

INTRODUCTION

Flotation is a unit operation that separates valuable minerals from gangue by using particle surface properties. Flotation is a size dependant process. Gaudin *et al* (1931) presented the particle size effect on the flotation process that showed higher recoveries are typically achieved between 50 µm and 120 µm. With advances in flotation since this time, high recoveries are now achieved down to 5 µm particles. Coarse particle flotation recoveries, however, are still typically low in industrial plants for +120 µm particles. There would be many advantages to increasing coarse particle recovery, enabling increases in overall recoveries at a particular grind size or enable the grind size to be coarsened to enable increases in throughput or decreases in energy use in the preceding comminution process.

Eriez identified the opportunity of using a fluidised bed for flotation, potentially increasing coarse particle recovery. The HydroFloat® cell concept was patented in 2002 (Mankosa and Luttrell Gerald, 2002). The Eriez HydroFloat® is a flotation device capable of recovering significantly coarser and less-liberated particles than is possible using a conventional mechanical flotation cell. Originally developed for industrial and bulk mineral beneficiation, the HydroFloat® is attracting increasing interest as a means of increasing the required grind size for metalliferous ore flotation. By doing so,

it would reduce the unit processing cost of complex ores, either by reducing the required energy input to a grinding circuit or by increasing the overall throughput achievable with an existing comminution circuit. In addition to this, coarse processing of the ore would also result in coarser waste streams, potentially improving mechanical and hydraulic performance of the recycled water recovery from the tailings thickeners and tailing storage facilities (TSF).

The HydroFloat® cell can be divided into three regions, as depicted in Figure 1. First is a freeboard region which is located at the top of the cell where the feed pipe is located. The feed is fed through this pipe into the centre of the vessel. Particles in this region are exposed to hindered settling conditions due to the upward flowing fluidisation water. Particles can be attached by air bubbles in this region and directly report to concentrate. Flotation therefore starts in this region. The second region is called the fluidised bed region, where the density is much higher than the freeboard region, resulting in particles becoming more buoyant once they attach to a bubble. In this region, interaction between phases is maximised and it is envisaged that this facilitates attachment of particles to bubbles. Finally, there is a dewatering cone region where no flotation occurs. This section has a conical shape designed for dewatering of the tailing stream. Fluidisation water and air is added through a manifold located above the cone region. Because of the restrictive nature of the dewatering cone, the fluidisation water moves upwards, which in conjunction with the buoyancy of the bubbles, facilitates the upward movement of air particle aggregates which overflow into the concentrate launder.

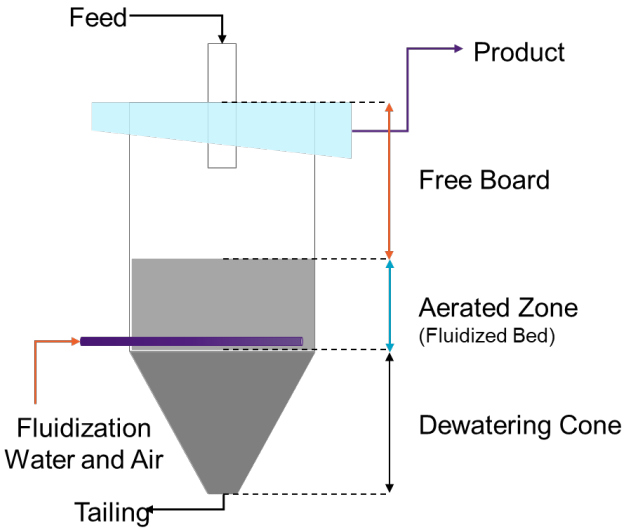

FIG 1 – Simplified schematic drawing of HydroFloat®.

The HydroFloat® has many features which make it more suitable for coarse particle flotation than a conventional mechanical cell. These include a low degree of turbulence because it does not require an impeller to keep particles in suspension. This will likely reduce the probability of bubble particle detachment. The fluidised bed promotes a high degree of interaction between the bubbles and particle, likely increasing the probability of particle bubble attachment. The upward flowing fluidisation water promotes the lifting of coarse heavier particles upwards into the concentrate launder. It also does not have a froth region, where coarse particle detachment is often observed to occur (Rahman *et al*, 2012).

The feed to the HydroFloat®, however, does need to be deslimed with the finer material removed before being fed to the device, This is because fines disrupt the formation of a stable fluidisation bed and also result in lower grades as they are unselectively entrained into the concentrate. Most industrial applications of the HydroFloat® to date have used a CrossFlow teeter bed for desliming. The CrossFlow is similar in design and operation to the HydroFloat® but without air addition.

Recent work published in the literature has proven the potential of the HydroFloat® cell to achieve the above-mentioned gains in metalliferous applications (Kohmuench *et al*, 2018; Seaman and Vollert, 2017; Vollert *et al*, 2019). However, in order to realise the full potential of the HydroFloat® technology, it is necessary to understand not just its performance but also the key drivers for that

performance. By doing so, it will allow the design and operation of the HydroFloat® cells to be optimised for different circuit options and orebodies. For this work, a pilot HydroFloat® plant has been designed, manufactured and deployed to a copper-gold plant in NSW, Australia. A site campaign has been performed using the JKMRC's pilot HydroFloat® rig to investigate the effect of operating conditions and determine the optimal operating conditions for treating the tailings stream of one of the plant's rougher flotation banks. Under each set of operating conditions, samples were taken of the HydroFloat® feed, concentrate and tailings streams and processed to yield the grade and recovery achieved by the device.

This paper presents the details of the testing program performed using the HydroFloat® rig and preliminary relationships and trends observed between performance and cell operating conditions. A range of possible drivers to explain the measured trends in flotation performance are proposed.

EQUIPMENT AND MATERIAL

JKMRC's pilot HydroFloat® rig

A modular, compact, pilot scale HydroFloat® rig has been designed and manufactured at the JKMRC. This rig is operated using a central automation and control system. The rig consists of a feed buffer tank, two process tanks, a CrossFlow (XF-101), a HydroFloat® cell (HF-150–152 mm diameter), slurry and dosage pumps, flow metres, sensors and actuated valves, configured as shown in the simplified process flow diagram given in Figure 2.

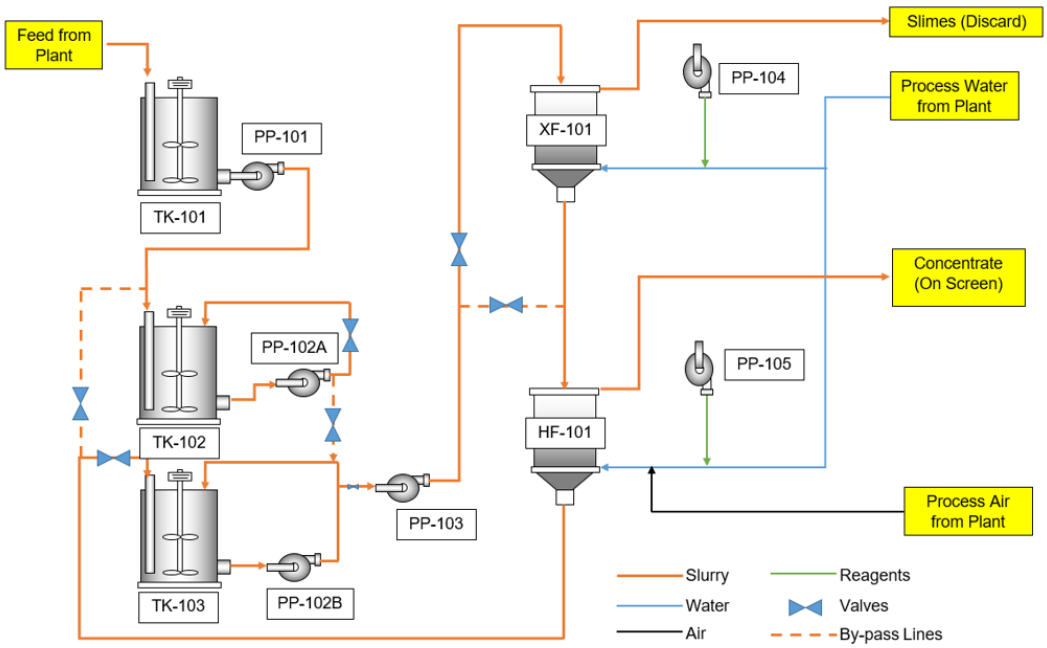

FIG 2 – Simplified process flow diagram of the JKMRC's pilot HydroFloat® rig.

TK-101 is the feed buffer tank, which is used to minimise the effect of process fluctuations on the experiments by collecting and storing the volume of sample required for the planned day of test work at the start of the day. The required sample required for each test is pumped from TK-101 to one of the process tanks (TK-102103). Pumps (PP-102A/B) are used to circulate the slurry to prevent segregation in the tanks. From the selected process tank, feed material for each test is pumped to XF-101 or directly to HF-101 by a Variable Speed Drive (VSD) controlled pump (PP-103). The CrossFlow is used for feed preparation desliming and collector conditioning prior to the slurry being pumped to the HydroFloat®. Processed tailings can be collected in the other process tank or be discarded. Note that with the rig design shown the Tailings can be reprocessed repeatedly. The aim of reprocessing the tails is to be able to test the operation of multiple units in series. In addition, when the feed is already deslimed, the CrossFlow can be bypassed with the feed directly routed to the HydroFloat® unit. Additionally, VSD controlled PP-103 can be used to set the throughput at different flow rates to investigate the throughput/residence time effect on the performance. In the study

outlined in this paper, the rig was operated in a configuration where the feed was sent first to XF-101, with the underflow sent to HF-101. The tailings were discarded.

In the test program performed for this study, collector (and promoter) were introduced through the XF-101 teeter water line (with water). The frother was added through the HF-101 teeter water and air manifold.

During the test program, fluidisation and dilution water flow, airflow and reagent flow rates were monitored continuously. In addition to these online measurements, pressure transmitters were used to determine the pressure within the fluidised bed at two heights. This information can be used to indirectly determine HF-101's bed height and bed porosity. For the CrossFlow, XF-101, a pressure transmitter was used to indirectly determine bed height only.

The JKMRC's Pilot HydroFloat® Rig has its own automation and control system which enables the operator to monitor and control the whole pilot rig by a computer (Figure 3). It also enables collection of measurements from each sensor as a report at the end of each test.

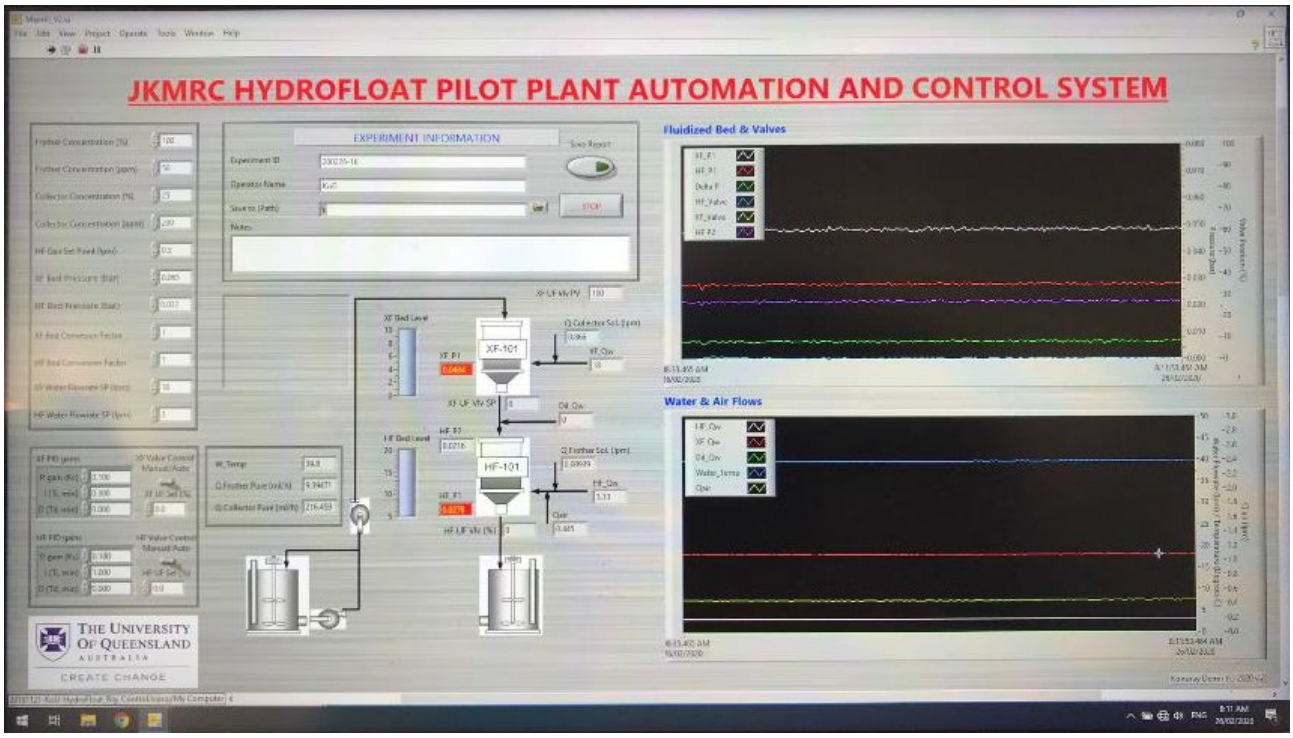

FIG 3 – JKMRC's Pilot HydroFloat® rig automation and control system.

Material tested

The sample used for the pilot testing in this study was sourced from one of the rougher tail streams of a copper-gold plant in NSW, Australia by using an auto-sampler pump. As outlined in the introduction, fines are not desirable in the feed material. Therefore, the CrossFlow incorporated in the rig was used to deslime the feed prior to HydroFloat® testing. Typical CrossFlow and HydroFloat® feed particle size distributions are given in Figure 4.

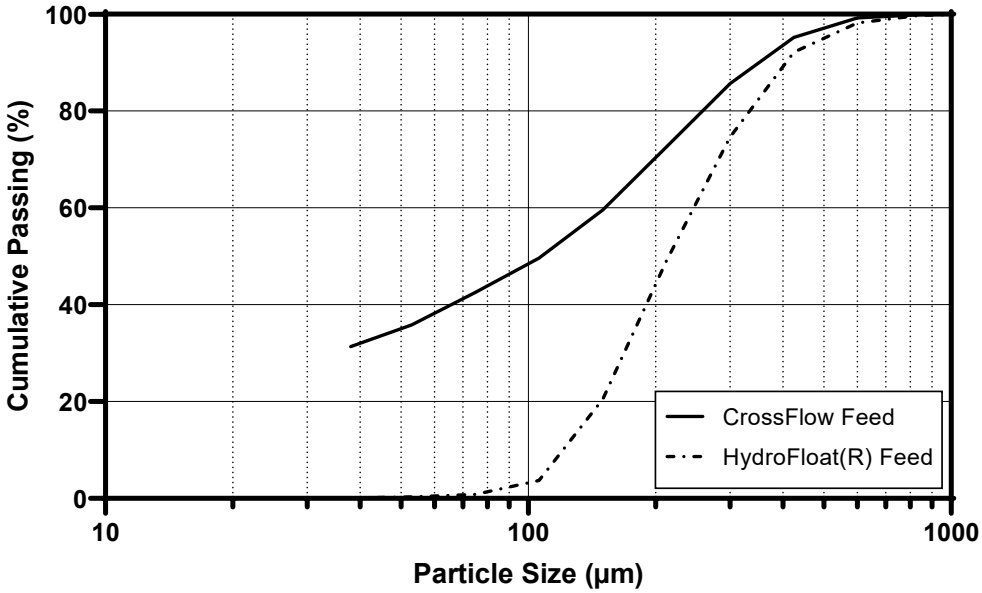

FIG 4 – CrossFlow and HydroFloat® feed particle size distributions.

The typical head assays measured in the streams feeding the CrossFlow and HydroFloat® are given in Table 1. It should be noted that the rougher tails test material was found to exhibit a consistent grade throughout the test campaign. Also, it should be noted, that the only feed material to the HydroFloat® was deslimed rougher tails and no other solid material was used to dilute the feed.

TABLE 1

Typical chemical assay measured in the feed streams.

	Al_2O_3	CaO	Cu	Fe_2O_3	K_2O	MgO	S	SiO_2
CrossFlow Feed	16.25	4.11	0.07	6.20	3.57	3.81	0.27	58.40
HydroFloat® Feed	16.30	3.33	0.13	5.10	3.41	3.08	0.19	60.50

METHODOLOGY

A series of statistically designed experimental programs were developed to investigate the effect of operational parameters and stream properties on HydroFloat® performance using the JKMRC's HydroFloat® pilot rig.

The operational variables varied during these tests included:

- fluidisation water flow rate (Q_w)
- air flow rate (Q_a)
- freeboard height (H_b).

In addition to these parameters, different feed particle size distributions have also been tested.

Each parameter was tested at three different levels within the factorial designs. Each test condition was also performed at a minimum of three throughput values. Changing the throughput was performed to enable an assessment of the effect of residence time and to potentially enable calculation of particle flotation rate at each test condition. The JKMRC's pilot HydroFloat® rig is a continuous, rather than a batch, system. It is not suitable for sampling at different time intervals to obtain a conventional mineral recovery by time curve. Thus, residence time was varied instead to enable this relationship to be determined.

Residence time is best varied in a fluidised bed system by changing the mass flow rate through the HydroFloat®. All other operational parameters and volumetric flow rates were kept constant.

For each test, HydroFloat® feed, concentrate and tailing streams were sampled and the time of collection recorded. Samples were then weighed wet and dry. This information was used to calculate the mass flow and solid concentrations for each stream. All dry samples were then divided into representative subsamples for analysis. One was used to determine the head assay. One was used for size analysis and the other kept in reserve. Sizing involved firstly wet sieving at 38 µm, then dry sieving from 850 µm down to 38 µm using a root 2 series of screens. Size fractions were also submitted for assay analysis.

Stream data was then mass balanced to make the data consistent and to enable calculation of balanced elemental grades and recoveries.

The following additional measurements were also performed during each test:

- fluidisation water flow rate
- air flow rate
- bed height
- differential pressure through the fluidised bed
- bubble size (*in situ*)
- pH, temperature
- reagent addition rates.

Replicate tests were performed throughout the test campaign, as part of the experimental design. Repeat testing was also performed prior to commencement of the work to ensure repeatability of the test procedure. These preliminary repeats comprised of four different tests. Two were aimed at investigating whether the reagent, which was typically collected fresh once a week on a Monday or Tuesday, would degrade and cause a change in performance. To do this investigation, one test was performed on Tuesday using freshly collected reagent and the other one was performed on the Friday just before discarding the reagent. The other two tests were performed on the same day but at different times (am/pm) to investigate whether surface oxidation that might occur as the sample was mixed within the feed buffer tank during the course of a day would result in a change in performance.

The recovery values measured in these four repeat tests are shown in Figure 5. For all of these tests throughput was maintained constant at about 40 to 45 kg/h (2.26 to 2.55 t/h/m^2). The operating conditions were Q_w = 6 lpm; Q_a = 1 lpm, H_b = 20 cm. The error bars shown on this graph represent the standard deviation (1σ) of the results of twelve tests performed within the main test program which were performed using the same operating conditions.

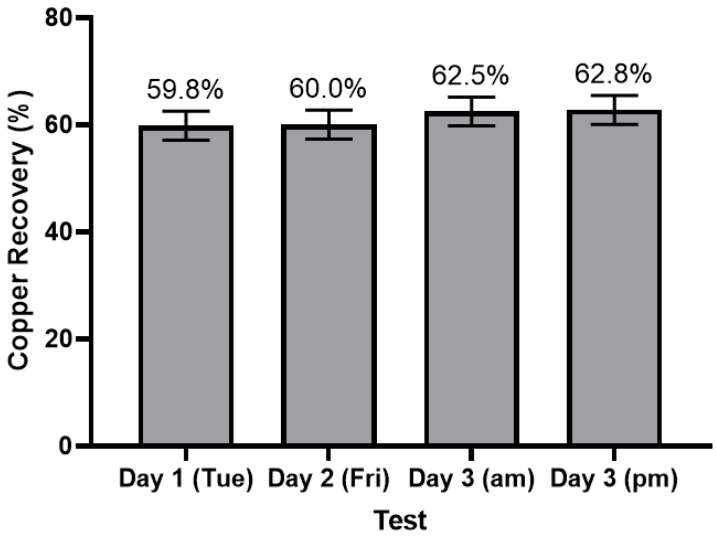

FIG 5 – Preliminary repeatability test results.

It is concluded from the preliminary testing that reagent degradation or surface oxidation during the day, did not result in an appreciable change in copper recovery. The results were within the error of the results produced during the test program.

RESULTS AND DISCUSSION

Effect of residence time

In flotation, residence time plays a critical role in unit operation performance. However, the extent to which this occurs in the fluidised bed flotation system is unknown. To change residence time in the continuously operating HydroFloat®, throughput was varied and the residence time was estimated at each condition by dividing the solids holdup estimated in the cell by the solids volumetric flow rate. Solids holdup at various conditions was estimated by dumping the cell contents at different operating conditions and developing a regression model between solids holdup and cell operation. The relative error for this solids holdup model is 5.9 per cent.

Figure 6 shows the copper recovery measured as a function of the estimated cell residence time at a range of different operating conditions. Increasing throughput (which would decrease particle residence time in the cell) resulted in a decrease in copper recovery. For higher retention times, recovery increases and asymptotes to a constant value as is typically observed in conventional flotation.

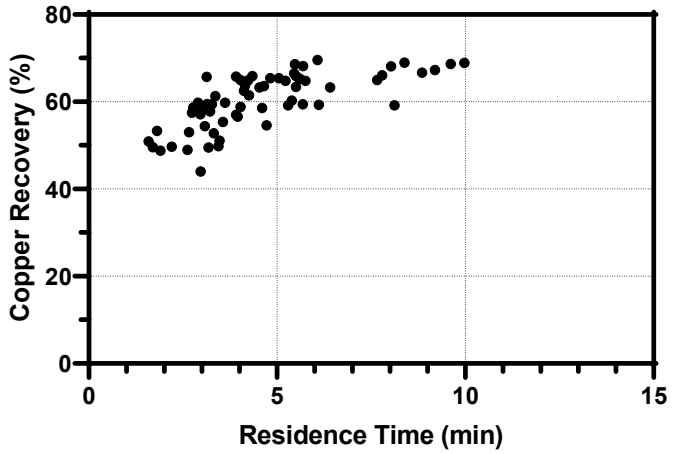

FIG 6 – Effect of residence time on HydroFloat® cell copper recovery.

An additional observation was that the extent to which residence time affects copper recovery is a function of the cell operating variables. When operating the cell under aggressive conditions which result in higher recoveries, there is very little difference between short and long residence time operation. In contrast, gentler operation where low recoveries and high-grades are typically achieved, larger variation in results with residence time are observed. This is demonstrated in Figure 7 (below) which shows the effect of residence time on copper recovery for three different fluidisation water flow rates. Higher water flow rates can be considered as more aggressive operation.

Effect of fluidisation water flow rate

An increase in fluidisation water was found to result in an increase in copper recovery (Figure 7). This increase in recovery was expected as it results from the increased flow of water upwards which increases the upward forces on the bubble-particle aggregates.

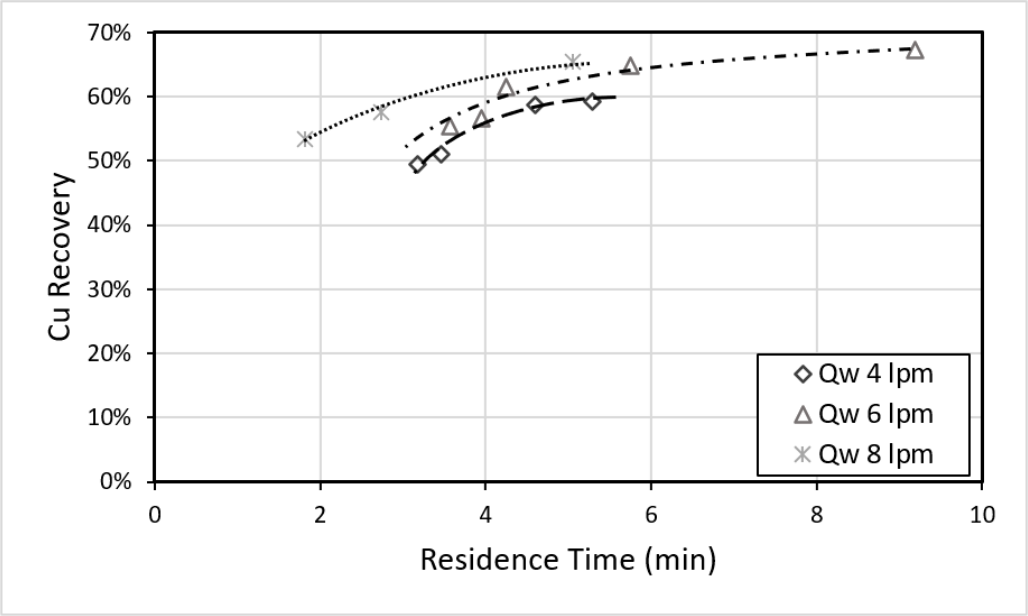

FIG 7 – Effect of residence time on HydroFloat® cell copper recovery at different fluidisation water flow rates.

Effect of air flow rate

Air is mixed into the fluidisation water and added via the fluidisation manifold. The air flow rate is an important operational parameter and it was also investigated during this test program. Tests were conducted during one day of testing at 0, 0.5, 1.0 and 1.5 L/min of air addition. Fluidisation bed height (H_b 20 cm) and fluidisation water flow rate (Q_w 6 lpm) were kept constant. Figure 8 shows the measured relationship between the air flow rate and the copper recovery. In this figure, vertical error bars represent the standard deviation of each point (calculated via repeat tests of the same condition); horizontal error bars represent the standard deviation of the air flowmeter readings for each flow rate.

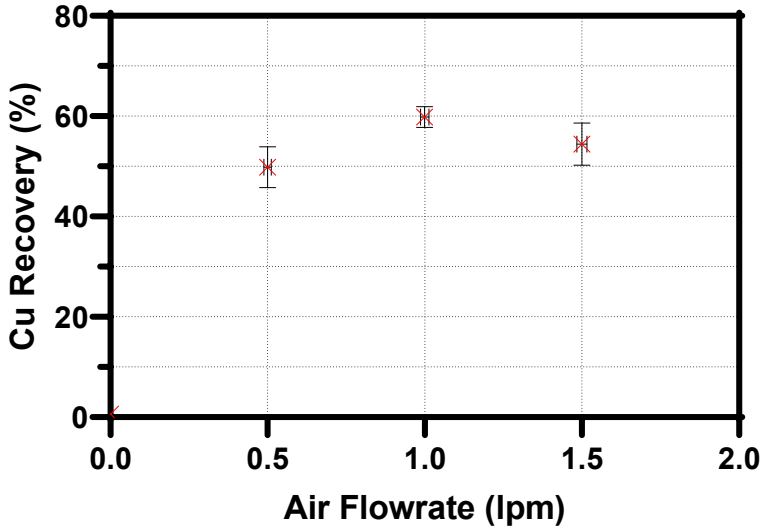

FIG 8 – Effect of air flow rate on HydroFloat® cell copper recovery.

The test performed at zero air rate was conducted to understand the hydraulic entrainment when no air is added to the cell. Air flow was cut, and only entrained material was collected as concentrate. The copper recovery is really low (0.6 per cent). It can therefore be concluded that entrainment recovery is minimal under the conditions tested.

At increasing values of air flow, copper recovery was found to increase and then decrease. It is found that there is an optimum air flow rate for the HydroFloat® with this point being in the order of 1 lpm (1/6 Q_a/Q_w ratio) under the conditions tested.

This shape of relationship is an indication that competing mechanisms exist in the system. Presumably, recovery increases in the low air region because an increase in air flow results in more bubbles and greater probabilities of recovery. Increasing air rate, however, must also be associated with another mechanism that decreases recovery and this mechanism becomes dominant in the high air flow rate region. High air flow rates may destabilise the fluidised bed or result in changes in bubble size that decrease recoveries. An analysis of bubble size and the bed properties is hoped to provide better insight into the actual mechanisms involved.

Previous researchers that have investigated the effect of air rate in conventional cells have also reported a peak in performance at intermediate air rates (Barbian *et al*, 2006; Hadler and Cilliers, 2009; Hadler *et al*, 2010). They showed that initial increases in airflow resulted in an increase in air recovery to concentrate, followed by a significant drop in air recovery at higher airflow rates. Hadler and Cilliers (2009) also showed that cell recovery was optimised when the airflow rate was at the point where peak air recovery was observed. They hypothesized that this trend was a consequence of changes in froth stability and mobility as air rate varied. However, the HydroFloat® cell does not have a thick froth layer but nevertheless also exhibits a peak with air. This suggests that the mechanism by which high air adversely affects recovery, at least in the case of the HydroFloat®, is not in the froth phase per se but is related to changes in the pulp or detachment at the pulp air interface. Could this mean that low recoveries in a conventional cell at high air rate are also a result of changes in the pulp phase or detachment at the pulp froth interface? Further studies are needed to clarify the reason for the observed phenomenon.

Effect of freeboard height

The third operating parameter tested in this work was freeboard height, which is the distance between the overflow lip and the top of the fluidised bed. The effect of freeboard height on recovery was investigated at two different fluidisation water flow rate conditions. The results are shown in Figure 9 which includes error bars that represent the standard deviation of each point (calculated using repeat tests of the same condition). A higher freeboard height equates to a lower fluidised bed height which is inherently harder to stabilise, and operation was observed to fluctuate more than at other conditions. This contributes to the higher standard deviation value for this point. The high SD value is also a consequence of the relatively small number of repeat tests performed at these conditions (N = 3).

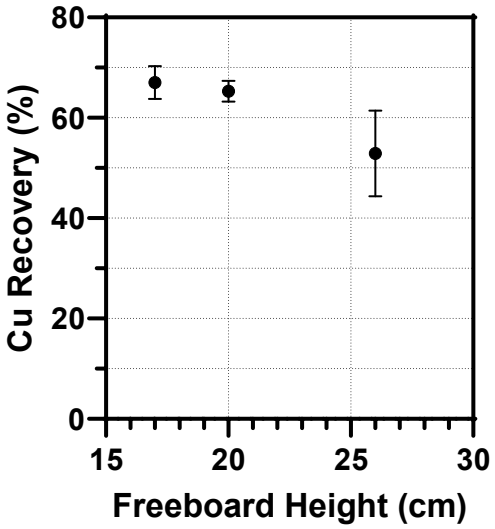

FIG 9 – Effect of Freeboard height on HydroFloat® cell copper recovery.

Decreasing the freeboard height results in higher recoveries. Presumably, this is because as the distance to reach the overflow lip for bubble-particle aggregates decreases, there is less chance for particle detachment. Smaller distances correlate with a greater probability of reaching the concentrate launder. As height increases, however, the magnitude of this effect diminishes. In addition to this, decreasing freeboard height, increases the fluidised bed height, and thus increases the residence time. It has been shown above that the residence time affects the recovery and presumably, it has an effect for this aspect as well.

Effect of the feed particle size distribution

In addition to the operating parameters, the feed particle size was varied to the HydroFloat® cell by manipulating operation of the upstream CrossFlow unit. The resulting three HydroFloat® feed particle size distributions are shown in Figure 10. Although the P80 values of the three feed size conditions are reasonably close, there are significant differences in the proportion of fines. The amount of material below 150 µm are 23.1 per cent for Fine, 17.2 per cent for Nominal, and 2.25 per cent for the Coarse case. Fine particles are considered to have a significant effect on HydroFloat® operation as they will alter the characteristics of the fluidised bed. Fines may also exhibit better liberation and therefore be easier to recover.

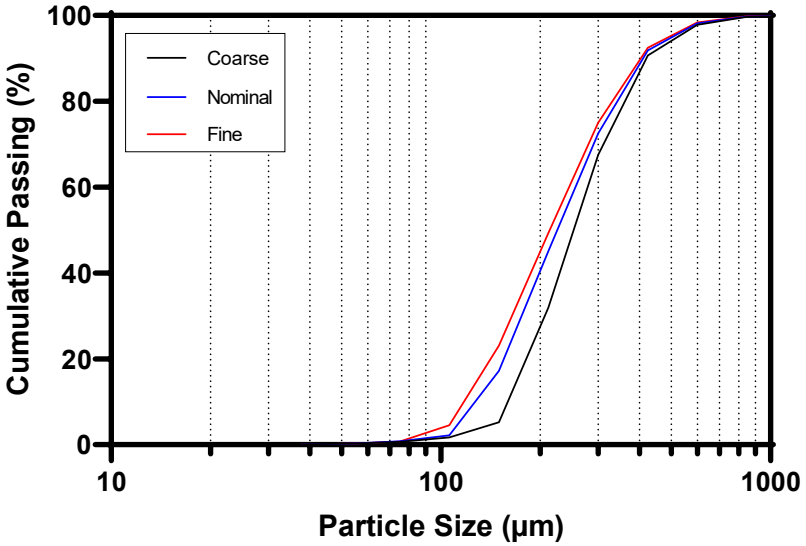

FIG 10 – Feed particle size distributions for three different feed conditions.

Feed particle size distribution was found to have a significant effect on HydroFloat® recovery (Figure 11). Copper recovery decreases as the feed particle size decreases. The magnitude of this effect varies depending on the operating parameters (ie how aggressively the cell is operated). The test conditions for the results shown on Figure 11 are listed in Table 2.

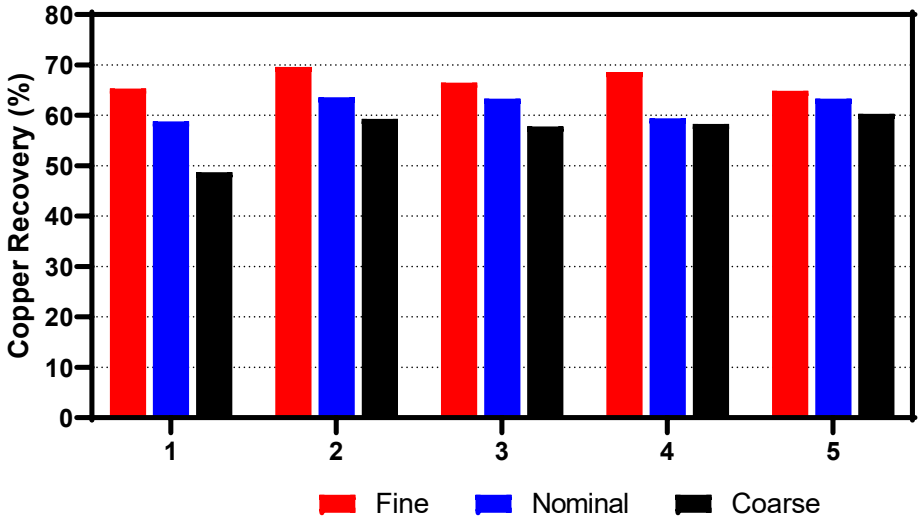

FIG 11 – Recovery values for different feed material under different test conditions.

TABLE 2

Operating conditions used in the different tests performed to investigate the effects of particle size distribution.

Test	Run Order	Q_w (lpm)	Q_a (lpm)	H_b (cm)
1	5	4.50	0.75	20.00
2	2	4.75	1.25	14.00
3	1	6.00	1.00	17.00
4	4	7.50	0.75	14.00
5	3	7.50	1.25	20.00

Gentle operation results in a much greater recovery difference between the feed sizes. In Figure 11, test condition 5 is an aggressive operation and it results in a minimal recovery change, with a change in feed size. On the other hand, test condition 1, which is a relatively gentle operating condition, results in large differences in the recoveries observed for the different feed PSDs values.

CONCLUSION

Within this study, the effect of operational parameters and particle size on HydroFloat® cell's performance was investigated. For this purpose, a comprehensive on-site test campaign was successfully carried out using a newly constructed JKMRC pilot HydroFloat® rig which was shown to be able to produce repeatable results. The results showed that recovery is affected by throughput, presumably because of its effect on particle residence time. Fluidisation water flow rate was found to have a positive correlation with copper recovery. There is an optimum recovery observed with the air flow rate setting within the range of operating conditions investigated. It is also observed that the freeboard height is inversely correlated with recovery. Particle size distribution has an effect on the cell performance, with a coarser particle size distribution exhibiting lower cell recoveries. However, this effect is minimised when operating under aggressive operating conditions such as higher fluidisation water and air flow rates. Aggressive operating conditions also resulted in less variation in HydroFloat® performance with retention time.

The experimental work in this study was performed using a series of statistical experimental designs, and the next stage of analysis will involve the use of statistical techniques to determine the extent to which the operating variables effect cell performance in comparison to each other. The analysis, which will be performed with respect to both overall recovery and size by size recovery, will also determine if there are any interactions occurring in the system.

Bubble size is a parameter which is expected to affect flotation performance because of its effects on the probabilities of particle attachment, detachment and the bubble/particle buoyancy. Future work will use the bubble sizes measured *in situ* during the test program to determine whether performance can be correlated to the bubble size produced in the cell. How operating conditions such as teeter bed water flow rate, air rate and bed height affect bubble size will also be investigated.

REFERENCES

Barbian, N, Hadler, K, Cilliers, J J, 2006. The froth stability column: Measuring froth stability at an industrial scale. *Minerals Engineering*, 19(6): 713–718.

Gaudin, A M, Groh, J O, Henderson, H B, 1931. Effect of Particle Size on Flotation. *Class B Milling and Concentration*, 35(414): 3–23.

Hadler, K, Cilliers, J J, 2009. The relationship between the peak in air recovery and flotation bank performance. *Minerals engineering*, 22(5): 451–455.

Hadler, K, Smith, C D, Cilliers, J J, 2010. Recovery vs. mass pull: The link to air recovery. *Minerals engineering*, 23(11): 994–1002.

Kohmuench, J, Wasmund, E, Seaman, B, Vollert, L, 2018. HydroFloats Running at Cadia. *Engineering and Mining Journal*, 219(12): 53.

Mankosa, M J, Luttrell Gerald, H, 2002. Air-assisted density separator device and method.

Rahman, R M, Ata, S, Jameson, G J, 2012. The effect of flotation variables on the recovery of different particle size fractions in the froth and the pulp. *International Journal of Mineral Processing*, 106–109: 70–77.

Seaman, B A, Vollert, L, 2017. Recovery of coarse liberated gold particles using pneumatically assisted fluidized bed flotation, *7th International World Gold Conference*, Vancouver, B C. Canada.

Vollert, L, A B, Seaman, B, Kohmuench, J, 2019. Newcrest's Industry First Application of Eriez HydroFloat(R) Technoclogy for Copper Recovery from Tailings at Cadia Valley Operations, *Copper 2019*, Vancouver.

An electrochemical investigation on the mechanisms of interfacial interactions of a xanthate collector on PGM mineral surfaces in the presence of ions

L Dzinza[1], M Tadie[2] and K C Corin[3]

1. PhD candidate, University of Cape Town, Cape Town South Africa 7701. Email: dznluc001@myuct.ac.za
2. Senior Lecturer, Stellenbosch University, Stellenbosch South Africa 7600. Email: mtadie@sun.ac.za
3. Associate Professor, University of Cape Town, Cape Town South Africa 7701. Email: kirsten.corin@uct.ac.za

ABSTARCT

The recycling of process water comes with increased electrolyte concentrations that affect water quality, which may in turn affect the flotation performance of valuable minerals (Hirajima *et al*, 2016). Electrolytes such as Ca^{2+}, SO_4^{2-}, Mg^{2+} and $S_2O_3^{2-}$ have been surmised to have an impact on the action of flotation reagents such as collectors (Ikumapayi *et al*, 2012). Xanthate collectors are known to play a significant role in imparting hydrophobicity on mineral surfaces to enhance their flotation. The interaction between minerals and xanthates is well known to be electrochemical in nature. Such redox processes may be elucidated by electrochemical techniques. Since the mechanisms involving the interactions between electrolytes in process water with sulfide minerals and the subsequent adsorption kinetics of collectors are not well understood, this study therefore aims to provide fundamental knowledge to unpack the mechanisms involved when electrolytes interact with Platinum Group Minerals (PGMs) and how these interactions may affect xanthate adsorption.

The interaction of sodium iso-butyl xanthate (SIBX) in the presence of electrolytes at increasing ionic strength was investigated by rest potential measurements, to explain the impact of electrolytes on the adsorption of SIBX on PGMs in the flotation process. Rest potential measurements for $PdTe_2$ and PdS were conducted in an air saturated 0.05 M di-sodium tetraborate decahydrate solution, in the absence and presence of SIBX and electrolytes. It was found that the existence of sulfide and telluride on palladium affects the mechanisms in which electrolytes interact with Pd mineral surfaces. An increase in the ionic strength of $Na_2S_2O_3$, $CaCl_2$ and $MgCl_2$, increased the interaction between the salts and PdS, thus decreasing the extent to which SIBX interacted with PdS. An increase in ionic strength for $Na_2S_2O_3$ increased the interaction between $Na_2S_2O_3$ and $PdTe_2$ and therefore decreased the extent to which SIBX interacted with $PdTe_2$. Other salts investigated in this study increased the rate of oxidation of $PdTe_2$ with an increase in ionic strength thereby enhancing the interaction of SIBX and $PdTe_2$. This study has shown that mineral type, electrolyte type and concentration all have an impact on the mechanisms that result in the adsorption of SIBX on PGMs.

INTRODUCTION

The Bushveld Complex in South Africa is a well-known source of a substantial proportion of platinum and palladium in the world. PGMs associated with telluride minerals, moncheite ($PtTe_2$) and merenskyite ($PdTe_2$) contribute about 20–45 per cent of the PGMs present in the Platreef ore (Shackleton, Malysiak and O'Connor, 2007). Alternatively, the UG-2 and Merensky Reef are dominated by PGM sulfides (cooperate, braggite and vysotskite), which are considered as the most common minerals in a Pt-Pd-S system (Verryn and Merkle, 1994). This study will investigate the palladium minerals PdS and PdTe2.

PdS and $PdTe_2$ have been determined to possess tetragonal and hexagonal crystal structures, respectively (Berlincourt, Hummel and Skinner, 1981). Te has been reported to have a stronger σ-donation characteristic that renders it a greater trans influence than that of S, hence the bond lengths for Pd-S and Pd-Te have been found to be 2.268 Å and 2.492 Å, respectively (Singh *et al*, 1999). The strength of bonds within a crystal structure determines the reactivity of a mineral. The lower polarisability of Te than that of S is attributed by its larger ionic radius, consequently resulting in stronger intra-molecular bonds for PdS than PdTe (Westland, 1981).

The reactivity of PGM sulfides is almost similar to reactions of base metal sulfides, therefore it is valuable to understand the reactions of base metal sulfides. The oxidation of base metal sulfides (Equation 1), with regards to the flotation process has been extensively studied to determine the effects of oxidation products on flotation recoveries. However, there is very limited work in literature on the oxidation of PGMs (Elvy and Williams, 1996).

$$MS + xH_2O \rightarrow M(H_2O)_x^{2+} + S^- + e^- \quad (1)$$

The initial oxidation of PdS in alkaline conditions at pH 9, has been proposed by Westland (1981) as shown in Equation 2.

$$PdS + 4H_2O \leftrightarrow Pd + SO_4^{2-} + 8H^+ + 6e^- \quad (2)$$

Very limited work has been reported on the oxidation of PGMs with tellurides. Elvy and Williams (1996) proposed that the most stable species formed after the initial oxidation of PdTe is tellurite (Equation 3).

$$PdTe_2 + xO_2 \rightarrow PdTe_{1-x} + xTeO_2 \quad (3)$$

$PdTe_2$ is a novel transition-metal with an as-cleaved surface which possesses a surface termination comprised of an atomic layer of Te. Their surface stability is determined by the lone pair of electrons on the Te atoms. The Te termination has been determined to evolve into TeO_2 upon exposure to air, with the thickness of TeO_2 estimated to be 2.2±0.4 Å after 10 minutes exposure and was observed to remain in the subnanometric range of 8.8±0.5 Å after 1 year of exposure (D'Olimpio *et al*, 2019). The incongruent oxidation of $PdTe_2$ to palladium tellurite was initially established by Elvy and Williams (1996), who observed formation of the oxide layer covering the palladium enriched substrate. The order of reactivity of palladium minerals has been considered to be PdTe < PdTeBi < PdBi, where PdTe is the least reactive relative to other palladium minerals.

Research work on the flotation of PGMs in the past decades has mainly focused on the flotation of base metal sulfides due to their good association with PGMs. However, Penberthy, Oosthuyzen and Merkle (2000) disputed this assumption with the findings of their comprehensive study on recoveries of PGMs. It was found that though PGM grains are usually smaller than 10 µm in diameter, milling to 80 per cent <75 µm would successfully liberate about 50 per cent of the PGMs from the matrix. The PGMs associated with liberated base metal sulfides were established to be the fastest-floating species. It was also observed that the response of liberated PGMs to flotation was dependent upon the type of mineral and grain size. Therefore, the findings of this work make it of great importance to understand the flotation behaviour of PGMs.

Froth flotation is a water-intensive process, in which water represents about 80–85 per cent of the pulp phase. The most ideal media for the process is fresh water, however, due to the scarcity of fresh water, mining operations are required to reduce freshwater consumption by making use of alternative sources such as the use of relatively impure primary water supplies or recycled process water. Alternative sources of fresh water come with increased ionic strength of electrolytes such as magnesium, sulfate, thiosulfate, chlorides, calcium etc, which consequently affect the flotation performance of valuable minerals (Boujounoui *et al*, 2015; Manono, Corin and Wiese, 2016; Li *et al*, 2018; Sinche-Gonzalez and Fornasiero, 2021).

Previous studies have shown that ions found in process water may either have a beneficial or detrimental effect on flotation recoveries of sulfide minerals (Hodgson and Agar, 1989; Kirjavainen, Schreithofer and Heiskanen, 2002; Elizondo-Álvarez *et al*, 2017). At 0.0242 M of Ca^{2+} and Mg^{2+} ions, it has been reported that the presence of divalent ions can increase frothability and alternatively reduce solids recoveries (Manono, Corin and Wiese, 2016). Similarly, it has been reported that an increase in the ionic strength of process water may result in an increase in water recoveries due to increased frothability (Corin *et al*, 2011). Furthermore, low concentrations of Ca^{2+} ions at 186 mg/l and SO_4^{2-} ions at 153 mg/l have been found to have a detrimental effect on the flotation of galena (Ikumapayi *et al*, 2012). Sea water is known to have concentrations of Ca^{2+} and Mg^{2+} ions at approximately 0.01 M and 0.05 M, respectively (Mewes *et al*, 2014). These have been observed to depress the flotation of chalcopyrite due to the adsorption of Mg and Ca hydroxyl complexes on the mineral surfaces, therefore giving rise to less hydrophobic mineral surfaces (Hirajima *et al*, 2016; Li *et al*, 2018). Divalent ions such as Ca^{2+}, SO_4^{2-} and $S_2O_3^{2-}$ were found to be significantly surface-active ions on both pentlandite and pyrrhotite surfaces at normal process water pH (Hodgson and

Agar, 1989). Ca^{2+} ions have been postulated to adsorb on the sulfur sites of a pyrrhotite mineral surface, with the SO_4^{2-} adsorbing onto the Fe sites. The $S_2O_3^{2-}$ ions were presumed to coordinate to the mineral surface via an oxidised Fe site of $Ca(S_2)$ product. Ultimately, adsorbed $S_2O_3^{2-}$ ions were determined to reduce mineral hydrophobicity by reducing its selectivity.

The presence of ions in process water has been found to interfere with the adsorption of surfactants on mineral surfaces (Kirjavainen, Schreithofer and Heiskanen, 2002; Ikumapayi *et al*, 2012; Chang, Chen and Peng, 2018). Ions may enhance the adsorption of surfactants by increasing the active sites on the mineral surface or alternatively depress the adsorption of surfactants by competitive adsorption on a mineral's active sites.

Surfactants such as collectors are used in the flotation process to modify the surface wettability of mineral particles to enhance their hydrophobicity (Wills and Napier-Munn, 2006). The polar regions of collectors adsorb onto selective sites on the mineral surface with their non-polar hydrophobic hydrocarbons protruding into the bulk, thereby rendering the mineral surface hydrophobic. Sulfydryl collectors such as xanthates have been used in the effective flotation of base metal sulfide minerals (Usul and Tolun, 1974; Leppinen, 1990; Wang and Forssberg, 1991; Herrera-Urbina and Sotillo, 1999). The interactions between xanthates and base metal sulfide minerals are believed to occur through a mixed potential mechanism, where the anodic oxidation reaction involves transfer of charge from the xanthate collector onto the mineral surface and a simultaneous cathodic reaction involves the reduction of oxygen (Equation 4). The oxidation of xanthates has been established to occur in three different ways, the first mechanism involves the chemisorption of a xanthate collector on the mineral surface as shown in Equation 5. The second mechanism involves the chemisorption of a xanthate ion onto a mineral surface to form a metal xanthate. The latter equation may occur as a single step (Equation 6) or through separate surface oxidation and ion exchange processes (Equations 7 and 8). Additionally, the third mechanism involves the formation of dixanthogen (Equation 9).

Cathodic reaction, reduction of oxygen:

$$O_2 + 2H_2O + 4e^- \leftrightarrow 4OH^- \tag{4}$$

First mechanism, chemisorption of xanthate:

$$X^- \leftrightarrow X_{ads} + e^- \tag{5}$$

Second mechanism, formation of a metal xanthate – single step:

$$2X^- + MS + 4H_2O \rightarrow MX_2 + SO_4^{2-} + 8H^+ + 8e^- \tag{6}$$

Or through separate surface oxidation:

$$MS + 4H_2O \rightarrow MSO_4 + 8H^+ + 8e^- \tag{7}$$

And ion exchange:

$$MSO_4 + 2X^- \rightarrow MX_2 + SO_4^{2-} \tag{8}$$

Third mechanism, formation of dixanthogen:

$$2X^- \rightarrow X_2 + 2e^- \tag{9}$$

It has been reported in literature that the presence of Ca^{2+} and $S_2O_3^{2-}$ ions may enhance the flotability of copper sulfides in the presence of a potassium ethyl xanthate collector (Kirjavainen, Schreithofer and Heiskanen, 2002). Floatability was observed to increase steadily with an increase in ionic strength. Ca^{2+} ions were proposed to increase xanthate adsorption on copper sulfides whereas on the contrary $S_2O_3^{2-}$ ions were proposed to decrease xanthate adsorption. The effect of $S_2O_3^{2-}$ ions was aligned to the ability of the ions to reduce the effect of hydrophilic species formed on sulfide mineral surfaces than the actual activation effect caused by Ca^{2+}. The effect of Ca^{2+} and SO_4^{2-} ions on the flotation of galena was investigated by Ikumapayi *et al* (2012) and it was observed that the presence of the two divalent ions reduced xanthate adsorption. Furthermore, it was reported that in the presence of calcium ions, there was a decrease or disappearance of surface oxidised products probably due to the formation of soluble calcium complexes with sulfoxy species and surface carbonate. High concentrations of NaCl have been reported to inhibit xanthate adsorption on sphalerite particle surfaces due to competitive adsorption between the NaCl ions and xanthate ions

on the mineral surface. Additionally, Ca^{2+} and Mg^{2+} ions have been presumed to adsorb on mineral surfaces and thus play an important role in the bubble-particle interaction (Wang *et al*, 2015). This observation could be ascribed to the ion valence and ion type that play an important role in depressing the chemical adsorption of collectors on mineral surfaces. Moreover, the presence of ions may also change the structure and morphology of adsorbed xanthate collector layers primarily by screening the electrostatic repulsive forces between the polar groups which oppose aggregation (Chang, Chen and Peng, 2018).

Though the effects of ions on the flotation of base metal sulfides using bench-scale flotation techniques have been well documented, their mechanisms of interaction are not well understood. However, due to the good PGM textural association with base metal sulfides, previous studies have centred their work on the flotation of base metal sulfides. Furthermore, the assumption made on PGMs was challenged by the work of Penberthy, Oosthuyzen and Merkle (2000), who conducted an extensive study on the recoveries of PGMs from UG2 and found that approximately 50 per cent of PGMs were liberated during milling. The subject on the effect of ions found in process water and/or xanthate collectors on PGMs has been neglected. It is therefore essential to understand the interactions of ions in recycled process water with PGMs and their subsequent effects on the adsorption of xanthate collectors.

Therefore, this study makes use of electrochemical techniques to understand the mechanisms of interactions of single ions at increasing ionic strength on the adsorption of SIBX on $PdTe_2$ and PdS mineral surfaces.

METHODOLOGY

Material

PdS and $PdTe_2$ minerals used in this study were synthesized at the Anglo-American Research laboratories as described by Shackleton, Malysiak and O'Connor (2007). The mineral compositions are shown in Table 1.

TABLE 1

Palladium telluride and sulfide composition.

Mineral	Stoichiometric composition selected	Product purity
Merenskyite ($PdTe_2$)	$Pd_{1.00}Te_{2.00}$ (20g Pd, 40g Te)	60g @ 68.7% purity
Vysotskite (PdS)	$Pd_{6.00}S_{6.00}$ (30.74g Pd, 9.26g S)	40g @ 97.4% purity

Due to the small size and scarcity of PGMs, the minerals were synthetically prepared to reflect on the behaviour of naturally occurring minerals (Vermaak, Pistorius and Venter, 2005; Shackleton, Malysiak and O'Connor, 2007).

The xanthate collector, SIBX, was supplied by Senmin (Pty) Ltd as yellow pellets. The chemical salts used in this study sodium thiosulfate ($Na_2S_2O_3$), sodium chloride (NaCl), calcium chloride ($CaCl_2$), magnesium chloride ($MgCl_2$) and magnesium sulfate ($MgSO_4$), were supplied by Merck. The sodium tetraborate decahydrate ($Na_2B_4O_7.10H_2O$) was supplied by Sigma-Aldrich Co. 0.05 M $Na_2B_4O_7.10H_2O$ buffer solution was prepared with ultra-distilled water to maintain a pH of 9.2.

SIBX was prepared prior to each run with ultra-distilled water to a dilution of 1 per cent, which was dosed at a volume that would bring the final concentration of SIBX to 6.24×10^{-4} M in the electrochemical cell.

The salts were prepared in order of increasing ionic strengths to represent different water qualities such as 1 synthetic plant water (1 SPW), 3 SPW, 5SPW and 10SPW which are equivalent to 0.0242 M, 0.0727 M, 0.1212 M and 0.2426 M, respectively (Wiese *et al*, 2005; Corin *et al*, 2011; Manono, Corin and Wiese, 2016).

All solutions used in the experimental work were prepared with analytical grade salts, diluted with ultra-distilled water and prepared prior to experiments.

Electrochemical measurements

Rest potential measurements were performed using a Gamry Instruments Reference 600™ Potentiostat. All reactions were performed in a double-wall glass reactor with a two-electrode system, Ag/AgCl reference electrode and a mounted working electrode. All potentials were measured against the standard Ag/AgCl reference electrode, which was filled with a 3 M KCl electrolyte, with a potential of +0.207 V against the standard hydrogen electrode (SHE). The mineral was embedded in a non-conductive epoxy resin, with a portion of the mineral exposed.

All rest potentials measurements were conducted at 25°C (±1°C). Prior to each test, the surface of each palladium mineral was freshly prepared by wet polishing using 1 µm, 0.3 µm and 0.05 µm alumina powder suspensions. The electrode was subsequently rinsed with ultra-distilled water and dabbed lightly with paper towel after which it was quickly transferred to the electrochemical cell for measurements (Tadie *et al*, 2015).

The measurements were performed in the absence and presence of salts and SIBX. The measurements were executed by dosing each salt solution at a specific ionic strength at 300 seconds (blue bars in Figures 1 and 2) after which SIBX was dosed at 600 seconds (orange bars in Figures 1 and 2). The total time for all the runs was 1200 seconds.

RESULTS AND DISCUSSION

Equilibrium potential of SIBX

Table 2 shows the equilibrium potential for the xanthate/dixanthogen couple for SIBX at 6.24×10^{-4} M which was measured to be 80 mV.

TABLE 2

Equilibrium potentials for xanthate/dixanthogen couple (SIBX).

Conc. of SIBX (M)	E/(mV versus SHE)		E^0/(mV versus SHE)	
	Buswell (1998)	Experimentally Measured	Buswell (1998)	Calculated
1×10^{-3}	49	**68**	-127	**-109**
6.24×10^{-4}	-	**80**	-128	**-110**
1×10^{-4}	108	**126**	-128	**-110**

The Nernst equation is considered as an important equation in electrochemistry that relates the reduction potential of an electrochemical reaction to the standard electrode potential, temperature and activities of chemical species undergoing reduction and oxidation reactions.

For unit activity X_2, the Nernst equation predicts that:

$$E = E^0 - {}^{RT}/_{2F.In[X^-]^2} \quad (10)$$

Where E represents cell potential, E^0 represents standard cell potential, R represents universal gas constant, T represents temperature in Kelvin, F represents Faraday constant and X represents xanthate.

The Nernst equation (Equation 1) predicts a 59 mV increase in equilibrium potential for every order of magnitude decrease in xanthate concentration (Buswell, 1998). A 58 mV change was obtained both in this work and by Buswell (1998). The results obtained in this work agree with the prediction from the Nernst's equation. E^0 values for each concentration of SIBX as shown in Table 1, were calculated using the Nernst's equation. The work of Allison *et al* (1972) determined that all systems in which dixanthogen is formed, have their rest potentials above the equilibrium potential of the

dixanthogen/xanthate couple, whereas systems with rest potentials below the equilibrium potential will most likely form metal xanthate as the principal product.

In this work, rest potential differences (Ndamase, Corin and Tadie, 2020) for salts and SIBX have been defined as the difference in rest potential between the potential obtained immediately upon adding the salt and SIBX and the potential obtained prior to adding SIBX and after adding SIBX, respectively. Figures 1 and 2 show rest potential differences for PdS and $PdTe_2$, respectively in the absence and presence of single salts and SIBX. The changes in potential are indicative of reactions occurring at the mineral surfaces. The difference in rest potentials can be used to interpret the extent of interactions between PGM mineral surfaces with salts and xanthate collectors.

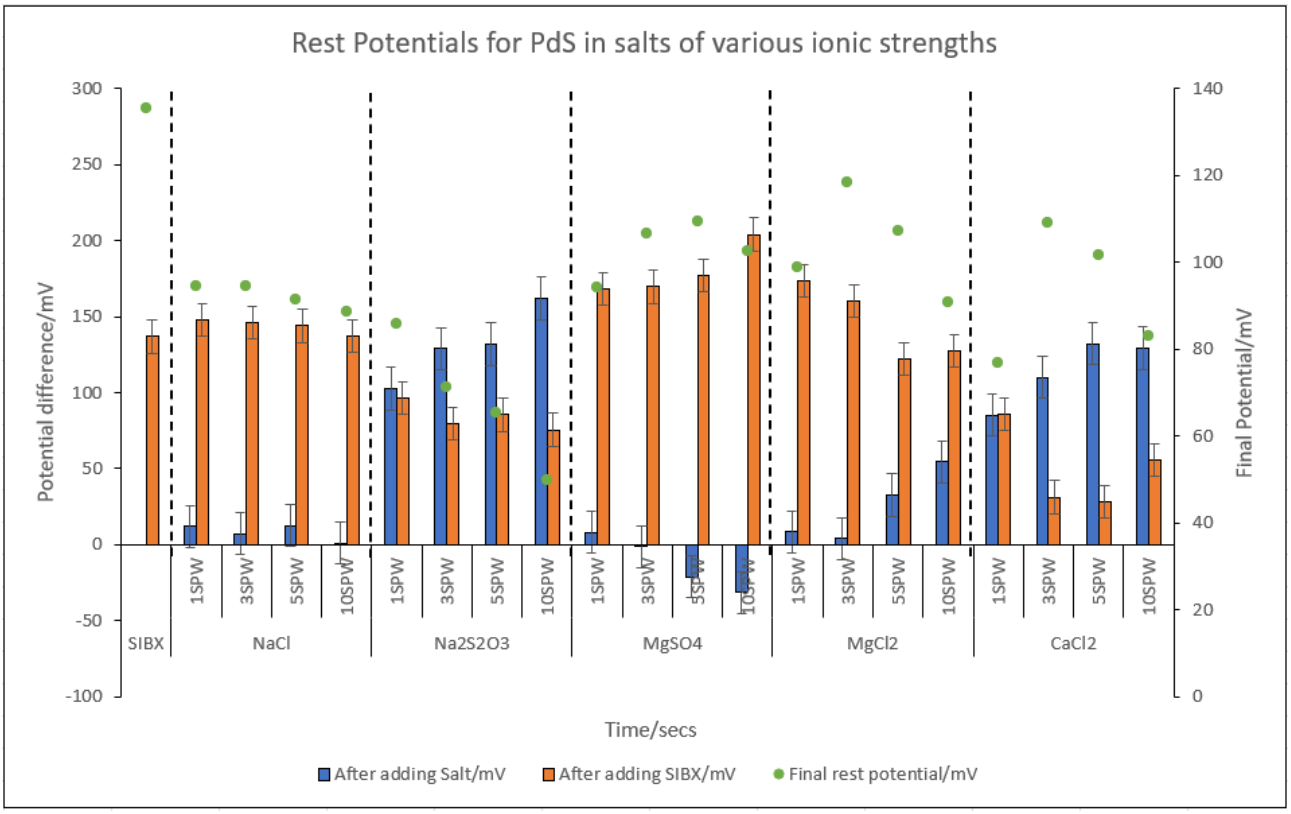

FIG 1 – Final rest potentials and rest potential differences for PdS in the presence and absence of SIBX and single salts at various ionic strengths at pH 9.2 and 25°C.

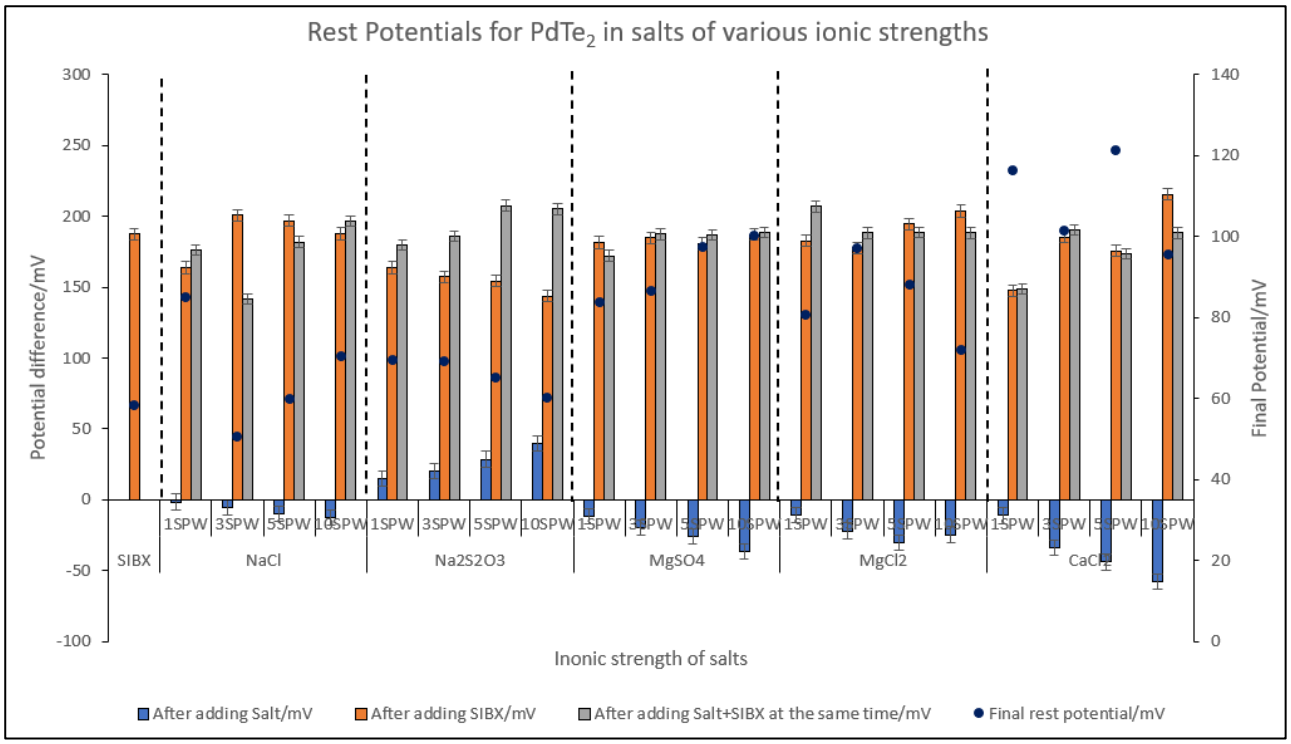

FIG 2 – Final and differences in rest potentials for $PdTe_2$ in the presence and absence of SIBX and single salts at various ionic strengths at a pH of 9.2 and 25°C.

Figures 1 and 2 show differences in rest potentials and final rest potentials for PdS and $PdTe_2$. For conditions where the final rest potentials were higher than the equilibrium potential of the xanthate-dixanthogen couple of SIBX (80 mV), the oxidation of SIBX most likely favoured the formation of dixanthogen (Equation 9). Alternatively, lower final rest potentials than the equilibrium potential of the xanthate-dixanthogen couple of SIBX imply that it is likely that the oxidation of SIBX favours the chemisorption reaction (Equation 5) or the formation of a metal-xanthate species (Equations 6 or 7 and 8). It is shown in Figure 1 that the final rest potential in the absence of salts is higher than the potential for dixanthogen formation. The oxidation of SIBX in this case favours the formation of dixanthogen. On the other hand, it is shown in Figure 2 that in the absence of salts the final rest potential is lower than the potential for dixanthogen, denoting that the formation of dixanthogen is not favoured. Therefore, the oxidation of SIBX favours either the chemisorption reaction or formation of a metal xanthate species. An electrochemical investigation of similar PGMs by Tadie *et al* (2015) shows that the opposite is true in the case of sodium ethyl xanthate. A comparison between this work and observations reported by Tadie *et al* (2015) shows that despite similar minerals, concentration of xanthate collectors and test conditions, collector type plays a significant role in defining the mechanism by which the collector oxidises at a mineral surface.

Effect of $S_2O_3^{2-}$ ions

$Na_2S_2O_3$ was observed to interact more with both PdS and $PdTe_2$ minerals than other salts investigated in this study. An increase in interaction with both PdS and $PdTe_2$ was observed with an increase in ionic strength. This implies an increase in the rate of reduction of both minerals as the ionic strength of $Na_2S_2O_3$ increases. Subsequently, the interaction between SIBX and both minerals decreased, thereby indicating a lower rate of reduction of both mineral surfaces with an increase in ionic strength of $Na_2S_2O_3$. The final rest potential of PdS in the presence of $Na_2S_2O_3$ at 1 SPW is higher than the potential for dixanthogen formation. This implies that dixanthogen may be formed on the mineral surface under these conditions. However, higher ionic strengths of 3 SPW, 5 SPW and 10 SPW $Na_2S_2O_3$ in the presence of PdS resulted in final rest potentials that were lower than the potential for dixanthogen formation. This indicates that the dixanthogen species should not form under these conditions. Similarly, it was observed that final rest potentials for $PdTe_2$ in the presence of $Na_2S_2O_3$ at all ionic strengths investigated were lower than the equilibrium potential for dixanthogen formation. Since the formation of dixanthogen did not contribute to the rest potential

differences under these conditions, two alternative reactions possibly occurred on the mineral surfaces. A chemisorption reaction (Equation 5), which is thermodynamically favoured in the interaction between xanthates and sulfide minerals and therefore occur at lower potentials than the formation of the corresponding dixanthogen (Buckley and Woods, 1997). The lower rest potentials may also indicate the formation of the less hydrophobic metal xanthates species. Metal xanthate species may be formed through a single step reaction (Equation 6) or through a surface oxidation and ion exchange mechanism (Equations 7 and 8). This study proposes that a chemisorption reaction (Equation 5) most likely occurred or the formation of metal xanthate (Equations 6 or 7 and 8) in the case of $PdTe_2$ at all ionic strengths of $Na_2S_2O_3$ investigated. It is possible that a Te-xanthate formed in addition to Pd – xanthate (Tadie *et al*, 2015). The increase in interaction of $Na_2S_2O_3$ which subsequently decreases the interaction of SIBX is proposed to reduce the hydrophobic nature of PdS and $PdTe_2$ in a real flotation system. It is possible that in this study, the thiosulfate ion might have interacted readily with Pd to form a Pd – thiosulfate complex on the mineral surface (Eliseev and Kirbitova, 1984; Petrus *et al*, 2012). An investigation by Petrus *et al* (2012) presumed the formation of a copper thiosulfate complex in the presence of thiosulfate on both chalcopyrite and tennantite mineral surfaces. The copper thiosulfate complex formed was proposed to inhibit the adsorption of diethyl dithiophosphate collector, thereby depressing the flotation of both minerals. The findings of this study also agree with the observation made by Kirjavainen, Schreithofer and Heiskanen (2002), where a reduction in xanthate adsorption and adsorption rate was observed in the presence of $S_2O_3^{2-}$ ions on nickel and copper sulfide ores.

Effect of Ca^{2+} ions

Figures 1 and 2 show the different mechanisms in which $CaCl_2$ interacts with the two minerals. With regards to PdS, an increase in ionic strength of $CaCl_2$ increases the extent to which PdS interacts with $CaCl_2$. This observation implies that the rate of reduction of the PdS mineral surface is increased in the presence of $CaCl_2$ at increased ionic strengths. Subsequently, this decreases the rate of reduction of PdS in the presence of SIBX. Possibly, the presence of the $CaCl_2$ creates steric hindrance, thus preventing SIBX from interacting directly with the metal sites on the mineral surface. Higher concentrations of calcium ions have been reported to have a detrimental effect on the flotation recovery of chalcopyrite due to the adsorption of calcium hydroxyl precipitates on the mineral surface thereby giving rise to a less hydrophobic surface (Hirajima *et al*, 2016; Li *et al*, 2018). Previous work have ascribed a decrease in xanthate adsorption in the presence of Ca^{2+} ions to the chemisorption of calcium ions on the active sites in the case of galena. This observation was presumed to prevent the ion-exchange between xanthate-sulfate, xanthate-carbonate and xanthate-hydroxyl, therefore causing a decrease in hydrophobicity of galena and consequently decreasing its flotation recovery (Ikumapayi *et al*, 2012; Elizondo-Álvarez *et al*, 2017).

Alternatively, this study has shown that an increase in ionic strength of $CaCl_2$ increases the rate of oxidation of $PdTe_2$ and subsequently increases the extent of interaction between $PdTe_2$ and SIBX. Increasing the interaction of SIBX and $PdTe_2$ indicates an increase in the rate of reduction of $PdTe_2$ in the presence of SIBX. Furthermore, it has been shown that in the case of PdS, higher rest potentials were obtained relative to the potential required to form the dithiolate, at higher ionic strengths of 3 SPW, 5 SPW and 10 SPW $CaCl_2$. This work proposes that under these conditions, the reaction responsible for the changes in potential observed after adding SIBX, was most likely the formation of dixanthogen (Equation 9). The initial reaction could be the chemisorption of SIBX as in (Equation 5). The chemisorption reaction is most likely followed by a second reaction (Equation 9), which is the oxidation of the adsorbed xanthate species to dixanthogen. In the presence of $CaCl_2$ at 1 SPW, a lower final rest potential than the potential for dixanthogen formation was obtained with SIBX. As proposed above, the chemisorption reaction may have occurred (Equation 5) or alternatively the formation of a metal xanthate through Equations 6 or 7 and 8. Additionally, it is observed that the rate of dixanthogen formation decreased from 3 SPW to 10 SPW.

With regards to $PdTe_2$, for all conditions, the presence of $CaCl_2$ resulted in higher final rest potentials relative to the potential for dixanthogen formation. This denotes that under these conditions the changes in potential were due to the oxidation of the xanthate collector through the chemisorption reaction (Equation 5) and formation of dixanthogen (Equation 9).

Overall, the effect of concentration of Ca^{2+} ions plays a significant role in the interactions of xanthate collectors with mineral surfaces. Previous work has shown that at 3× and 6× less calcium compared to this study, calcium ions enhance the adsorption of xanthate on both nickel and copper sulfides (Kirjavainen, Schreithofer and Heiskanen, 2002). These findings were attributed to the decrease in adsorption of oxidation products formed on the sulfide minerals by calcium ions. At very low calcium concentrations of 9×10^{-3} mol/L (22× less than 1SPW), it was found that calcium ions have 7 times higher affinity for chalcopyrite than for galena, thus depressing the flotation of chalcopyrite and promoting the flotation of galena (Liu and Zhang, 2000).

Effect of SO_4^{2-} ions

It is shown in Figures 1 and 2 that $MgSO_4$ interacts in the same mechanism with both PdS and $PdTe_2$. This study has shown that an increase in ionic strength of $MgSO_4$, increases the rate at which PdS and $PdTe_2$ minerals are oxidised. Oxidising environments render sulfide minerals sulfur rich creating non-polar surfaces thereby enhancing hydrophobicity, hence improving the adsorption of xanthate collectors (Buckley and Woods, 1984; Hamilton and Woods, 1984). This work proposes that $PdTe_2$ goes through the same mechanism as PdS in the case of $MgSO_4$. The increase in the rate of oxidation of both palladium minerals in the presence of $MgSO_4$ increases the extent of interaction of SIBX and the minerals, implying an increase in the rate of reduction of PdS and $PdTe_2$ in the presence of SIBX. The changes in potential in the presence of SIBX for both minerals, favour the formation of dixanthogen as indicated by the higher final rest potentials than the potential for dixanthogen formation. This work therefore proposes the possibility of the thermodynamically favoured chemisorption reaction (Equation 5) and the subsequent formation of dixanthogen as shown in Equation 9 for both PdS and $PdTe_2$. It has been shown that an increase in ionic strength of $MgSO_4$ results in an increase in the greater driving force for the formation of dixanthogen on both palladium minerals (Khan and Kelebek, 2004).

The interaction of $MgSO_4$ on the active sites of oxidised palladium minerals may be influenced by the electrostatic charge on the mineral surface. Both of which are governed by the concentration and intrinsic binding affinities of the SO_4^{2-} ions (Wu *et al*, 2002; Lefevre and Fedoroff, 2006). Considering the high interactions of SIBX with both PdS and $PdTe_2$, in the presence of $MgSO_4$, it is likely that the conditions used in this study could result in improved flotation recoveries. This assumption is due to the cleaning effect of sulfate ions on mineral surfaces. Previous studies have proposed that the presence of sulfate ions result in the formation of heavy metal sulfite salts which are slightly soluble (Boujounoui *et al*, 2015). This could be the case in this study as palladium is considered a heavy metal. Contrary to the findings of this study, a recent publication by Sinche-Gonzalez and Fornasiero (2021) suggested that the presence of sulfate ions led to the oxidation of the mineral surface which resulted in hydrophilic mineral particles and thus lower recoveries. These two contradictory findings may be related to the rate of oxidation of the mineral surfaces in the presence of SO_4^{2-} ions which will subsequently affect the rate of reduction of mineral surfaces in the presence of xanthate ions. The mechanisms which are likely controlled by the concentration of sulfate ions in a particular system and the crystal structure of the mineral under investigation. Metal ions can interact differently with sulfate ions, thus resulting in the formation of different surface species thereby impacting the flotation recoveries obtained therein (Bulut and Yenial, 2016).

Effect of Mg^{2+} ions

Figures 1 and 2 show that $MgCl_2$ interacts with PdS and $PdTe_2$ through different mechanisms. This work has shown that an increase in ionic strength for $MgCl_2$ increases the extent of interactions between the $MgCl_2$ and the PdS mineral surface. Consequently, this interaction decreases the extent of interaction between SIBX and PdS. This denotes the increase in the rate of reduction on PdS as the ionic strength of $MgCl_2$ increases, thereby reducing the rate of reduction of PdS. Figure 1 shows a decrease in the rate of dixanthogen formation with an increase in ionic strength of $MgCl_2$ (from 3 SPW to 10 SPW). In the case of PdS, this study proposes a decrease in flotation recoveries with an increase in the ionic strength of Mg^{2+} ions in a real flotation system. Previous studies have reported a decrease in flotation recoveries with an increase in ionic strength of $MgCl_2$ owing to the formation of $Mg(OH)_2$ precipitates at the mineral surface (Hirajima *et al*, 2016; Li *et al*, 2017). In this study, the presence of $MgCl_2$ at all ionic strengths investigated, resulted in higher final rest potentials relative to the potential for dixanthogen formation. This implies that the oxidation of SIBX favoured

the formation of the dixanthogen species. This work proposes the oxidation of SIBX to occur in series through a chemisorption reaction (Equations 5), following the formation of dixanthogen (Equation 9). Alternatively, with regards to $PdTe_2$, the presence of $MgCl_2$ with increasing ionic strength, increases the rate of oxidation of $PdTe_2$. This effect consequently increased the interaction between SIBX and $PdTe_2$, denoting an increase in the rate of reduction of $PdTe_2$ with an increase in ionic strength. The oxidation of SIBX favoured the formation of dixanthogen through a chemisorption reaction (Equation 5) and the formation of a dithiolate (Equation 9) at lower ionic strengths (1 SPW, 3 SPW and 5 SPW). This is possible evidence of two reactions occurring in series. Chemisorption (Equation 5) or formation of a metal-xanthate (Equations 6 or 7 and 8) are presumed to be the favoured reactions at the highest ionic strength. In the case of $MgCl_2$ at 1 SPW. It is interesting to note that the final rest potential is almost the same as the equilibrium potential of SIBX.

Effect of Na^+ ions

Both Figures 1 and 2 show that the interaction of Na^+ ions with PdS and $PdTe_2$ is insignificant. However, NaCl has been observed to interact with both minerals in different mechanisms. Figure 1 shows that the rate of reduction of PdS in the presence of NaCl is insignificant such that it does not interfere with the interaction of SIBX with PdS. It is observed that the oxidation of SIBX for all ionic strengths of NaCl favours the chemisorption reaction (Equation 5) which possibly occurs in series with the formation of dixanthogen (Equation 9). However, a slight decrease in the rate of formation of dixanthogen is observed with an increase in ionic strength.

With regards to $PdTe_2$, Figure 2 shows that an increase in the ionic strength of NaCl slightly increases the rate of oxidation of $PdTe_2$. This observation resulted in an insignificant effect on the extent to which SIBX interacted with $PdTe_2$. It is interesting to note that the final rest potentials obtained in the presence of NaCl at 1 SPW were higher than the potential for dixanthogen formation. It is proposed that for NaCl at 1 SPW, the mechanisms favoured were the formation of dixanthogen possibly through a chemisorption reaction (Equation 5), followed by the formation of a dithiolate (Equation 9). On the other hand, lower final rest potentials were obtained in NaCl at 3 SPW, 5 SPW and 10 SPW, which are proposed to favour the chemisorption reaction (Equation 5) or formation of metal-xanthate (Equations 6 or 7 and 8). Overall, this study has shown that the effect of Na^+ ions in both PdS and $PdTe_2$ systems is insignificant. In agreement with the findings of this study, previous studies have reported that Na^+ ions slightly affect flotation recoveries owing to their insignificant effect on surface charge, adsorption behaviour and contact angle (Moudgil and Ince, 1991; Bakalarz, Duchnowska and Luszczkiewicz, 2017).

Previous work has also observed that the presence of NaCl enhances the adsorption of anionic surfactants, owing to the compensation of a negative mineral surface charge by Na^+ ions and thus reducing electrostatic repulsion between the mineral surface and xanthate ions (Nevskaia, Guerrero-Ruiz and Lopez-Gonzalez, 1998; Potapova *et al*, 2010; Hirajima *et al*, 2016). It Is proposed in this study that the presence of Na^+ ions slightly increased the positive charge on the positively charged palladium metal ions, therefore slightly increasing the electrostatic forces between the mineral surface and negatively charged xanthate ions, thus the high interactions of SIBX with the palladium minerals and high rates of reduction of the palladium minerals in the presence of SIBX.

This study postulates that due to the small size of the Na^+ ion, it could enter the layer spacing of a mineral surface and increase the dipole-dipole forces between the mineral surface and the collector ions, thereby improving the interaction between the collector and the mineral surface and hence high flotation recoveries. Overall, NaCl has been reported to have a ‘salt effect’ on anionic collectors which could possibly promote the flotation of valuable minerals (Chaojun *et al*, 2020).

CONCLUSION

- This study has shown that electrochemical techniques such as rest potential measurements can be used to predict mechanisms that occur in flotation systems. Rest potential measurements have proven to provide useful information on the interactions of ions and xanthates with PGMs and the rates of formation of xanthate species at specific conditions.

- This study shows the pivotal role played by S and Te bonded to the Pd metal ion. It is clear that different crystal structures of Pd that form as a result S and Te result in different mechanisms with ions present in process water.
- Thiosulfate ions interacted more or competed more with xanthate ions for active sites on Pd surfaces than other ions investigated, thus reducing the extent to which SIBX interacts with Pd mineral surfaces.
- In the case of PdS, as the ionic strength of $Na_2S_2O_3$, $CaCl_2$ and $MgCl_2$ increased, the interaction between the salts and PdS increased, thus subsequently decreasing the extent to which SIBX interacted with PdS. $MgSO_4$ enhanced the adsorption of SIBX on the PdS minerals surface whereas NaCl did not have a significant effect in the manner at which SIBX interacted with PdS.
- In the case of $PdTe_2$, as the ionic strength of $Na_2S_2O_3$ increased, the interaction between $Na_2S_2O_3$ and $PdTe_2$ increased thereby decreasing the extent to which SIBX interacted with the mineral surface. However, $MgSO_4$, $MgCl_2$, NaCl and $CaCl_2$ increased the rate of oxidation of $PdTe_2$ with an increase in ionic strength therefore permitting the SIBX to interact more with $PdTe_2$.
- Mineral type, ion type and concentration all have proven to have an impact on the mechanisms that result in the adsorption of SIBX on PdS and $PdTe_2$.
- It is essential to monitor concentrations of thiosulfate ions in flotation systems of sulfides and tellurides. Calcium ions showed a more detrimental effect on sulfides than tellurides, where they proved to enhance the adsorption of SIBX. Sulfate ions enhance the interaction of SIBX on both PdS and $PdTe_2$. Magnesium and calcium ions have been observed to interact with PdS and $PdTe_2$ by different mechanisms owing to the decrease and increase in rest potentials, respectively. Sodium ions have been observed to play an insignificant role on both Pd mineral surfaces.

ACKNOWLEDGEMENTS

The authors wish to express appreciation for funding received from South African Minerals to Metals Research Institute (SAMMRI) and the South African Department of Science and Innovation (DSI).

REFERENCES

Allison, S A, Goold, L, Nicol, M and Granville, A, 1972. A determination of the products of reaction between various sulfide minerals and aqueous xanthate solution, and a correlation of the products with electrode rest potentials. *Metallurgical and materials transactions A Physical metallurgy and materials science*, 3, 2613–2618.

Bakalarz, A, Duchnowska, M and Luszczkiewicz, A, 2017. The effect of process water salinity on flotation of copper ore from Lubin mining region (SW Poland). *E3S Web of Conferences,* 18.

Berlincourt, L E, Hummel, H H and Skinner, B J, 1981. Phases and Phase Relations of the Platinum-Group Elements. In: (L J Cabri, ed.) *Platinum – Group Elements: Mineralogy, Geology, Recovery*. Canadian Institute of Mining and Metallurgy, 23, 19–45.

Boujounoui, K, Abidi, A, Bacaoui, A, Amari, K E and Yaacoubi, A, 2015. The influence of water quality on the flotation performance of complex sulfide ores – case study at Hajar Mine, Morocco. *The Journal of the Southern African Institute of Mining and Metallurgy,* 115, 1243–1251.

Buckley, A N and Woods, R, 1984. X-ray photoelectron spectroscopic investigation of the surface oxidation of sulfide minerals. *International Symposium on Electrochemistry in Mineral and Metal Processing*, Cincinnati. Electrochemical Society, 286–302.

Buckley, A N and Woods, R, 1997. Chemisorption – the thermodynamically favoured process in the interaction of thiol collectors with sulfide minerals. *International Journal of Mineral Processing,* 51, 15–26.

Bulut, G and Yenial, U, 2016. Effects of major ions in recycled water on sulfide minerals flotation. *Minerals and Metallurgical Processing,* 33, 137–143.

Buswell, A M, 1998. *Buswell Andrew Mark. An electrochemical investigation into the floatability of pyrrhotite.* Master's degree, University of Witwatersrand.

Chang, Z, Chen, X and Peng, Y, 2018. The adsorption behavior of surfactants on mineral surfaces in the presence of electrolytes – A critical review. *Minerals Engineering,* 121, 66–76.

Chaojun, F, Yu, S, Peng, H, Dneg, X and Wan, G, J, 2020. Ionin effect of NaCl and KCl on the flotation of diaspore and kaolinite using sodium oleate as collector. *In:* (A Tomsett, ed.) *TMS Annual Meeting and Exhibition.* San Diego, CA: Springer.

Corin, K C, Reddy, A, Miyen, L, Wiese, J G and Harris, P J, 2011. The effect of ionic strength of plant water on valuable mineral and gangue recovery in a platinum bearing ore from the Merensky reef. *Minerals Engineering,* 24, 131–137.

D'Olimpio, G, Guo, C, Kuo, C N, Edla, R, Lue, C S, Ottaviano, L, Torelli, P, Wang, L, Boukhvalov, D W and Politano, A, 2019. PdTe2 Transition-Metal Dichalcogenide: Chemical Reactivity, Thermal Stability and Device Implementation. *Advanced Functional Materials,* 30, 1–12.

Eliseev, N I and Kirbitova, N V, 1984. Chalcopyrite and pyrite depression with a mixture of hyposulfite and copper sulfate. *Sov. J Non-Ferrous Met,* 125–126.

Elizondo-Álvarez, M A, Flores-Álvarez, J M, Dávila-Pulido, G I and Uribe-Salas, A, 2017. Interaction mechanism between galena and calcium and sulfate ions. *Minerals Engineering,* 111, 116–123.

Elvy, S B and Williams, P A, 1996. XPS evidence for the incongruent surface oxidation of minerals in the Pd-Te-Bi system. *Surface and Interface Analysis,* 24, 641–646.

Hamilton, I C and Woods, R A, 1984. Voltammetric study of the surface oxidation of sulfide minerals International Symposium on Electrochemistry in Mineral and Metal Processing, Cincinnati. Electrochemical Society.

Herrera-Urbina, R and Sotillo, F J, 1999. Effect of sodium sulfide additions on the pulp potential and amyl xanthate flotation of cerussite and galena. *International Journal of Mineral Processing,* 55, 157–170.

Hirajima, T, Suyantara, G P W, Ichikawa, O, Elmahdy, A M, Miki, H and Sasaki, K, 2016. Effect of Mg 2+ and Ca 2+ as divalent seawater cations on the floatability of molybdenite and chalcopyrite. *Minerals Engineering,* 96–97, 83–93.

Hodgson, M and Agar, G E, 1989. Electrochemical Investigations into the Flotation Chemistry of Pentlandite and Pyrrhotite: Process Water and Xanthate Interactions. *Canadian Metallurgical Quarterly,* 28, 189–198.

Ikumapayi, F, Makitalo, M, Johansson, B and Rao, K H, 2012. Recycling of process water in sulfide flotation: Effect of calcium and sulfate ions on flotation of galena. *Minerals Engineering,* 39, 77–88.

Khan, A and Kelebek, S, 2004. Electrochemical aspects of pyrrhotite and pentlandite in relation to their flotation with xanthate. Part 1: Cyclic voltammetry and rest potential measurements. *Journal of Applied Electrochemistry,* 34, 849–856.

Kirjavainen, V, Schreithofer, N and Heiskanen, K, 2002. Effect of calcium and thiosulfate ions on flotation selectivity of nickel copper ores, 15, 1–5.

Lefevre, G and Fedoroff, M, 2006. Sorption of sulfate ions onto hematite studied by attenuated total reflection-infrared spectroscopy: Kinetics and competition with other ions. *Physics and Chemistry of the earth,* 31, 499–504.

Leppinen, J O, 1990. FTIR and flotation investigation of the adsorption of ethyl xanthate on activated and non-activated sulfide minerals. *International Journal of Mineral Processing,* 30, 245–263.

Li, W, Li, Y, Xiao, Q, Wei, Z and Song, S, 2018. The Influencing Mechanisms of Sodium Hexametaphosphate on Chalcopyrite Flotation in the Presence of MgCl2 and CaCl2. *Minerals,* 8.

Li, Y, Li, W, Xiao, Q, He, N, Ren, Z, Lartey, C and Gerson, A, 2017. The Influence of Common Monovalent and Divalent Chlorides on Chalcopyrite Flotation. *Minerals,* 7.

Liu, Q and Zhang, Y, 2000. Effect of calcium ions and citric acid on the flotation separation of chalcopyrite from galena using dextrin. *Pergamon,* 13, 1405–1416.

Manono, M S, Corin, K C and Wiese, J G, 2016. The influence of electrolytes present in process water on the flotation behaviour of a Cu-Ni containing ore. *Minerals Engineering,* 96–97, 99–107.

Mewes, A, Langer, G, De Nooijer, L J, Bijma, J and Reichart, G J, 2014. Effect of different seawater Mg(2+) concentrations on calcification in two benthic foraminifers. *Mar Micropaleontol,* 113, 56–64.

Moudgil, B M and Ince, D, 1991. Effect of sodium chloride on flotation of dolomite from apatite. *Minerals and Metallurgical Processing*, 139–143.

Ndamase, N, Corin, K C and Tadie, M, 2020. Considering the action of degrading water quality on the electrochemical response of galena. *IMPC 2020: XXX International Mineral Processing Congress Proceedings.*

Nevskaia, D M, Guerrero-Ruiz, A and Lopez-Gonzalez, J D D, 1998. Adsorption of polyoxyethylenic nonionic and anionic surfactants from aqueous solution: Effects induced by the addition of NaCl and CaCl2. *Journal of Colloid and Interface Science,* 205, 97–105.

Penberthy, C J, Oosthuyzen, E J and Merkle, R K W, 2000. The recovery of platinum-group elements from the UG-2 chromitite, Bushveld Complex – a mineralogical perspective. *Mineralogy and Petrology,* 68, 213–222.

Petrus, H T B M, Hirajima, T, Sasaki, K and Okamoto, H, 2012. Effects of sodium thiosulfate on chalcopyrite and tennantite: An insight for alternative separation technique. *International Journal of Mineral Processing,* 102–103, 116–123.

Potapova, E, Grahn, M, Holmgren, A and Hedlund, J, 2010. The effect of calcium ions and sodium silicate on the adsorption of a model anionic flotation collector on magnetite studied by ATR-FTIR spectroscopy. *J Colloid Interface Sci,* 345, 96–102.

Shackleton, N J, Malysiak, V and O'Connor, C T, 2007. Surface characteristics and flotation behaviour of platinum and palladium tellurides. *Minerals Engineering,* 20, 1232–1245.

Sinche-Gonzalez, M and Fornasiero, D, 2021. Understanding the effect of sulfate in mining-process water on sulfide flotation. *Minerals Engineering,* 165, 1–10.

Singh, A K, Amburose, C V, Misra, M and Butcher, R J, 1999. trans influence of Telluro and Thio-ether donor sites: First palladium complex, $PdCl_2$[{4-$MeOC_6H_4TeCH_2CH_2SEt$}], showing their Relative Magnitude in the Same Molecule. *J Chem. Research*, 716–717.

Tadie, M, Corin, K C, Wiese, J G, Nicol, M and O'Connor, C T, 2015. An investigation into the electrochemical interactions between platinum group minerals and sodium ethyl xanthate and sodium diethyl dithiophosphate collectors: Mixed potential study. *Minerals Engineering,* 83, 44–52.

Usul, A H and Tolun, R, 1974. Electrochemical study of the pyrite-oxygen-xanthate system. *International Journal of Mineral Processing,* 1, 135–140.

Vermaak, M K G, Pistorius, P C and Venter, J A, 2005. Electrochemical and Raman spectroscopic studies of the interaction of ethyl xanthate with Pd–Bi–Te. *Minerals Engineering,* 18, 575–584.

Verryn, S M C and Merkle, R K W, 1994. Compositional variation of cooperite, braggite and vysotskite from the Bushveld Complex. *Mineralogical Magazine.* Pretoria, South Africa.

Wang, J, Xie, L, Liu, Q and Zeng, H, 2015. Effects of salinity on xanthate adsorption on sphalerite and bubble–sphalerite interactions. *Minerals Engineering,* 77, 34–41.

Wang, X-H and Forssberg, K S E, 1991. Mechanisms of pyrite flotation with xanthates. *International Journal of Mineral Processing,* 33, 275–290.

Westland, A, 1981. Inorganic chemistry of the platinum-group elements. Platinum Group elements: Mineralogy, geology, recovery. *Canadian Institute of Mining, Metallurgy and Petroleum, Special,* 23, 5–18.

Wiese, J G, Harris, P J and Bradshaw, D J, 2005. The influence of the reagent suite on the flotation of ores from the Merensky reef. *Minerals Engineering*, 18, 189–198.

Wills, B A and Napier-Munn, T, 2006. *An introduction to the Practical Aspects of ore treatment and mineral recovery,* Elsevier Science and Technology Books.

Wu, C-H, Kuo, C-Y, Lin, C-F and Lo, S-L, 2002. Modeling competitive adsorption of molybdate, sulfate, selenate and selenite using Freunndlich-type multi-component isotherm. *Chemosphere,* 47, 283–292.

Selective flocculation of hematite and silica

J C Eardley[1,4], C A Thomas[2,4] and G V Franks[3,4]

1. PhD Candidate, Chemical Engineering, University of Melbourne, Melbourne Vic 3010. Email: jeardley@student.unimelb.edu.au
2. Research Fellow, Chemical Engineering, University of Melbourne, Melbourne Vic 3010. Email: casey.thomas@unimelb.edu.au
3. Professor, Chemical Engineering, University of Melbourne, Melbourne Vic 3010. Email: gvfranks@unimelb.edu.au
4. ARC Centre of Excellence for Enabling Eco-Efficient Beneficiation of Minerals.

INTRODUCTION

As valuable minerals are more disseminated, there is a need for low-grade ores to be finely ground to liberate these valuable minerals. However, this has a negative impact on ultrafine mineral recovery as conventional separations processes such as gravity separation are no longer effective. Instead, fine particles can be recovered by froth flotation. Various novel reagents have been introduced along with development in flotation cell designs such as Jameson cell and column cells to improve performance and recovery of ultrafine valuables. This study, on the other hand, aims to recover the fines using a combination of commercially available reagents to selectively flocculate the valuables, so they are large enough to be recovered via conventional froth flotation cells. This technique if successful can be implemented in many existing industries that continue to use mechanical flotation cells that require particle sizes to be 50–150 μm for effective recovery (Ralston, 1992; Batterham and Moodie, 2005). Selective flocculation is not widely implemented in industries mainly due to the inability to float the aggregates ones they are formed and gangue entrapment within the aggregates which consequently affects the grade of concentrate recovered (Forbes, 2011). The major goal is to aggregate the minerals and float the aggregates unlike the more common industrial technique such as reverse flotation of hematite, where the aggregates itself is not recovered via flotation.

MATERIALS AND METHODOLOGY

Hematite and silica used for the study have a median particle size, D_{50} of 0.77 μm and 1 μm respectively. The isoelectric point of hematite lies around pH 9.7 whereas the isoelectric point of silica is below pH 2. This study utilises the difference in surface charge to selectively flocculate one material while the other remains suspended in 0.01 M KCl electrolyte. A combination of anionic dispersant and commercial high molecular weight charged polyacrylamide are used to selectively aggregate hematite and silica. The anionic dispersant, sodium hexametaphosphate (Na-HMP) is used to disperse the fine material specially to prevent heterocoagulation when the two material have high opposite surface charges. Initial experiments were carried out in glass jars for simplicity followed by controlled shear experiments in stirred baffle reactors that are set-up to mimic shear conditions in general mechanical flotation cells. The set-up follows the method suggested by Forbes (2011) and Ng *et al* (2017) where the shear conditions can be determined and compared to typical power input values in mechanical flotation cells that Deglon *et al* (2000) reviewed.

RESULTS

High molecular weight anionic polyacrylamides with a range of charge densities successfully aggregated hematite whereas cationic polyacrylamides aggregated silica at pH 5 to form flocs that settle rapidly in individual mineral suspensions. The general trend in Figure 1 indicates the dosage of polymer required to aggregate particles and produce clear supernatant decreases with increase in charge density of polymer.

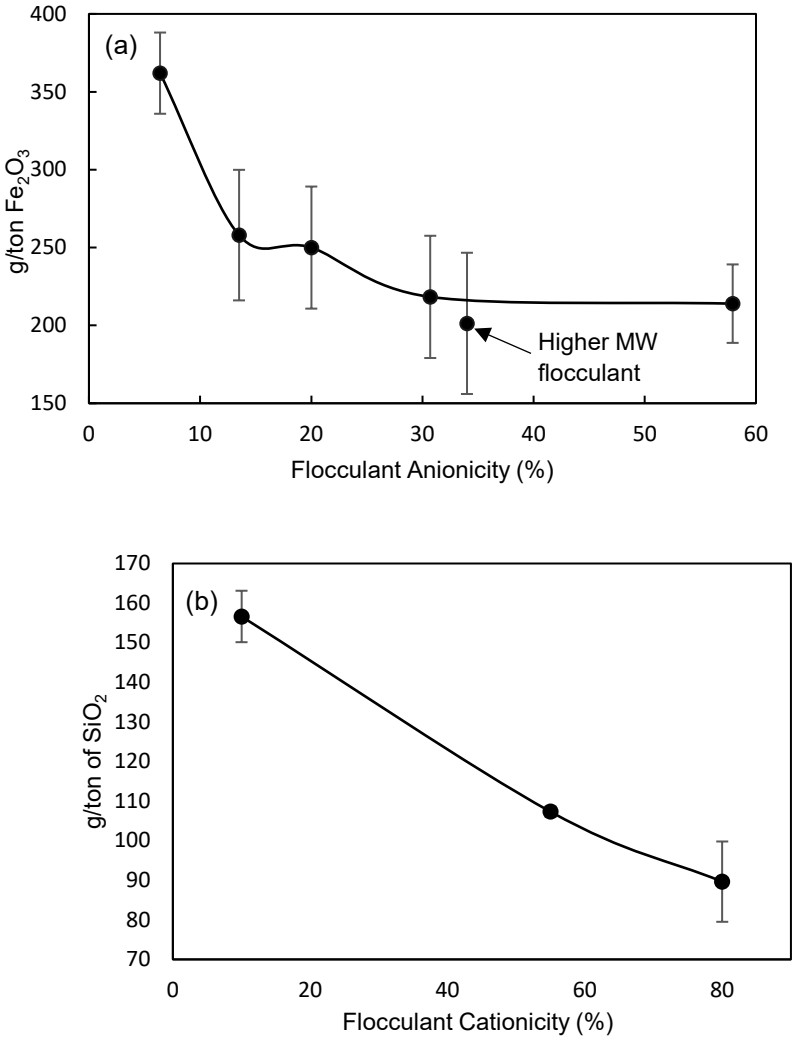

FIG 1 – Effect of charge density on minimum dosage of (a) anionic polyacrylamide to aggregate hematite (b) cationic polyacrylamide to aggregate silica, at pH 5 in 0.01 M KCl.

The two materials coagulate when mixed at pH 5, hence why selective flocculation is also carried out under pH 10 and involving anionic Na-HMP. Above the isoelectric point of hematite, both materials have negative surface charges which enhances dispersion due to electrostatic repulsion. Selectivity towards hematite improves at pH 10 when dispersant (Na-HMP) is added as seen in Figure 2 as it increases the negative surface charge of both materials but has a higher affinity towards the less negative material, hematite. The change in surface charges with dispersant dosage is analysed via zeta potential measurements. However, excess dispersant also hinders the selectivity towards hematite. The interactions between the polymer and hematite surfaces are different to when individual mineral flocculation is carried out at pH 5 mainly due to the change in surface characteristics once pH is adjusted to 10 and dispersant is added. The selectivity towards slightly negative surfaces of hematite under these conditions is possibly due to hydrogen bonding between the surface hydroxyl groups of hematite and carboxyl groups of the polyacrylamide as suggested in literature. The highly negative silica repels the negatively charged polyacrylamides, hence why selective flocculation is achieved. However, this mechanism is still rather unclear (Read, 1972; Bagster and McIlvenny, 1985; Khangaonkar and Subramani, 1993).

The white colour of the suspended solids in Figure 2 after sedimentation of the aggregates for the case with Na-HMP shows that the separation is better than when there is no dispersant where the pink colour of the suspended solids indicates both silica and hematite remain in suspension. When cationic polyacrylamide is added instead, silica is selectively aggregated as shown in Figure 3 with Na-HMP as aggregates that settle is much lighter in colour and majority of hematite remains suspended. The extend of selectivity of charged flocculant towards hematite and silica under varied dispersant dosages is analysed using X-Ray fluorescence. The optimum dispersant dosage is where

majority of one material remains highly dispersed in the supernatant while the other settle as aggregates. However, the challenge with handling fines is the entrapment of unwanted material within the aggregates which is also analysed.

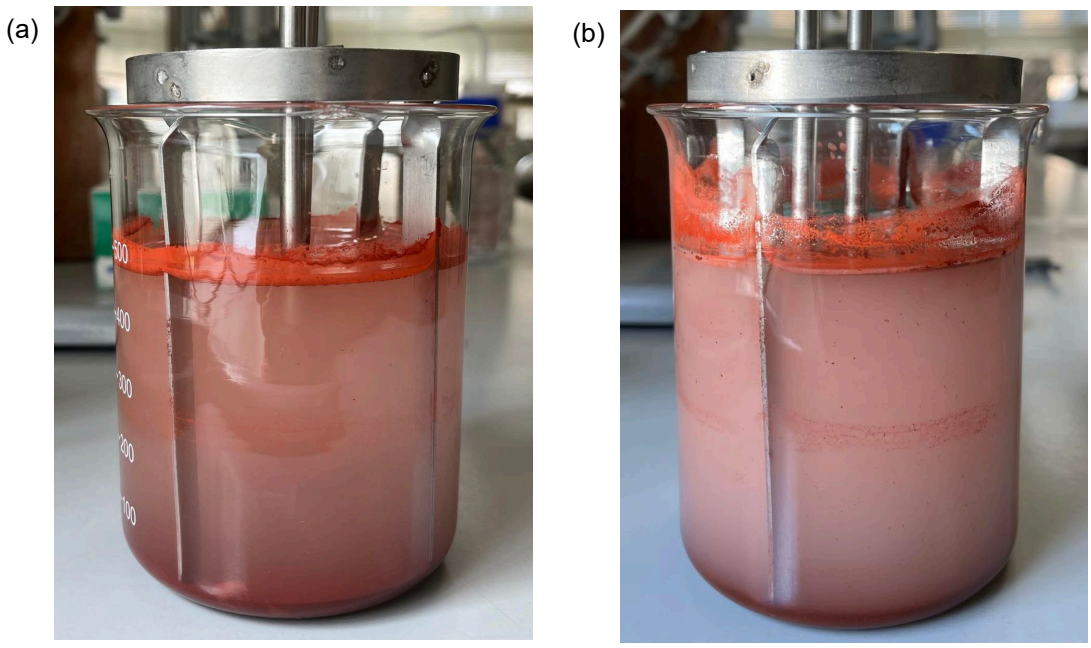

FIG 2 – Selective flocculation of hematite using anionic flocculant when dispersant dosage of (a) 0; (b) 300 Na-HMP/t Fe_2O_3 is used for 1 wt per cent suspension containing 5:5 hematite and silica in 0.01 M KCl at pH 10.

FIG 3 – Selective flocculation of silica using cationic flocculant when dispersant dosage of 300 Na-HMP/t SiO_2 is used for 1 wt per cent suspension containing 1:9 hematite and silica in 0.01 M KCl at pH 10.

CONCLUSION

The ultrafine hematite is selectively flocculated using high molecular weight anionic polyacrylamides in the presence of ultrafine silica. Anionic sodium hexametaphosphate increases the negativity of hematite and silica surface charges to disperse the fines, while the difference in the negative charges facilitates the selective flocculation. Selectivity in flocculation is potentially due to hydrogen bonding

between surface hydroxyl groups of hematite and hydrolysed carboxyl groups of polyacrylamides at pH 10, and not due to electrostatic forces. The negative charges of the polyacrylamide repel the highly negative silica, leaving it suspended in the supernatant. However, when cationic flocculant is added, silica is selectively flocculated instead under the same conditions.

ACKNOWLEDGEMENTS

The author would like to acknowledge the funding support from Australian Research Council for the ARC Centre of Excellence for Eco-Efficient Beneficiation of Minerals, grant number: CE200100009. The author would also like to thank Liza Forbes for her guidance on this project and thank Solvay and SNF for the polymers being used in this study. Finally, the author would like to appreciate the Melbourne Research Scholarship offered by the University of Melbourne.

REFERENCES

Bagster, D F and McIlvenny, J D, 1985. Studies in the Selective Flocculation of Hematite from Gangue using High Molecular Weight Polymers. Part 1: Chemical Factors, *International Journal of Mineral Processing*, 14, pp. 1–20.

Batterham, R and Moodie, J P, 2005. Flotation in the Minerals Industry-Some Observations, Centenary of Flotation Symposium, pp. 3–5.

Deglon, D A, Egya-Mensah, D and Franzidis, J P, 2000. Review of hydrodynamics and gas dispersion in flotation cells on South African platinum concentrators, *Minerals Engineering*.

Forbes, E, 2011. Shear, selective and temperature responsive flocculation: A comparison of fine particle flotation techniques, *International Journal of Mineral Processing*, pp. 1–10. doi:10.1016/j.minpro.2011.02.001.

Khangaonkar, P R and Subramani, K J B, 1993. Flocculation of Hematite Fines by Anionic Polyacrylamide Polymers, *Minerals Engineering*, 6(7), pp. 765–774.

Ng, W S, Connal, L A, Forbes, E, Mohanarangam, K and Franks, G V, 2017. In situ investigation of aggregate sizes formed using thermo-responsive polymers: Effect of temperature and shear, *Journal of Colloid and Interface Science*, 494, pp. 139–152. doi:10.1016/j.jcis.2017.01.067.

Ralston, J, 1992. The influence of particle size and contact angle in flotaton, in In: Laskowski, J S, Ralston J (eds), *Colloid Chemistry in Minerals Processing*. Amsterdam: Elsevier, pp. 203–224.

Read, A D, 1972. The Use of High Molecular Weight Polyacrylamides in the Selective Flocculation Separation of a Mineral Mixture, *Br. Polym. J.*

Investigation of flotation behaviours of fine particles in a complex ore consisting of various copper minerals

Y Ebisu[1], J V Satur[2], K Mitsuhashi[3], K Aikawa[4], T Suto[5], I Park[6], M Ito[7] and N Hiroyoshi[8]

1. Senior Metallurgist, Nittetsu Mining Co. Ltd., Nishitama-gun, Tokyo 190–0182. Email: y-ebisu@nittetsukou.co.jp
2. Senior Metallurgist, Nittetsu Mining Co. Ltd., Nishitama-gun, Tokyo 190–0182. Email: jv-satur@nittetsukou.co.jp
3. Manager, Nittetsu Mining Co. Ltd., Nishitama-gun, Tokyo 190–0182. Email: mituhasi@nittetsukou.co.jp
4. PhD Student, Hokkaido University, Sapporo-shi, Hokkaido 060–8028. Email: k88a28_tennis@eis.hokudai.ac.jp
5. Master's Student, Hokkaido University, Sapporo-shi, Hokkaido 060–8028. Email: sutotomo214@gmail.com
6. Assistant Professor, Hokkaido University, Sapporo-shi, Hokkaido 060–8028. Email: i-park@eng.hokudai.ac.jp
7. Associate Professor, Hokkaido University, Sapporo-shi, Hokkaido 060–8028. Email: itomayu@eng.hokudai.ac.jp
8. Professor, Hokkaido University, Sapporo-shi Hokkaido 060–8028. Email: hiroyosi@eng.hokudai.ac.jp

ABSTRACT

Copper concentration using flotation is becoming more difficult, because of an increase in ore complexity accompanied by smaller grain sizes of copper minerals than usual, requiring finer grinding in order to liberate them. Project Arqueros, located at the mid northern part of Chile, is a copper mine project with an orebody consisting of various sulfides such as chalcopyrite, chalcocite, and bornite. Some of the copper minerals in Arqueros show low floatability mainly because of their fine grain size and resulted fine grinding size, and also because of the complex mineralogical composition. For example, chalcopyrite in Arqueros floats less than the other copper sulfide minerals.

In this study we carried out some kinetic flotation tests with the Arqueros ore using a laboratory-scale forced air type flotation machine by varying the regrinding size. The products were assayed and mineralogically analysed to compare the minerals in their flotation behaviour with respect to size classes and liberation classes. The results were compared with a model calculation according to bubble size measurement.

From the flotation testing and mineralogical analysis, it was found that copper minerals of the same size and liberation class floated at the same rate even with different regrinding size. At the same time the comparison between experiment and calculation showed that the fine particles of less than 5 μm size floated faster in actual than in the model applied. These results suggested that interactions among minerals of different species and of different sizes had positive impacts on the flotation rate of the fine particles. It indicates that this phenomenon can be applied to improve copper recovery in the project.

INTRODUCTION

In recent years in the mining area of metal resources, the low-grade and the fineness of the valuable minerals in the ore are becoming a big problem. The easily exploitable mines are either currently operating or have already been closed while the remaining mines characterised by low-grade and fineness of the minerals of interest have difficulty of development due to the scarcity of the infrastructure or the depth of the resources, etc. Flotation is one of the most applied methods to separate precious minerals from unnecessary ones using the difference in hydrophobicity (or hydrophilicity). In the flotation method, the air is fed to a cell filled with the pulp of crushed ore and agitation is implemented to introduce air and generate bubbles. The hydrophobic particles float along with the bubbles and the hydrophilic particles remain in the pulp.

To recover the fine valuable minerals locked in the gangue minerals, the ore has to be ground until the valuables are liberated from the gangue, because poor liberation results in weak hydrophobicity and low floatability (Jameson, 2017; Miettinen *et al*, 2010). However, the recovery of fine particles is usually poor due to their low probability of collision with bubbles (Grano *et al*, 1994; Tao, 2004; Hassanzadeha *et al*, 2016; Rahman *et al*, 2014; Shahbazi *et al,* 2010) and lack of kinetic energy to displace the water film (Hewitt *et al*, 1993; Chipfunhu *et al*, 2012). In addition, in the flotation of fine particles, not only the fineness of the mineral of interest impairs the flotation but also the fineness of the gangue minerals (Leistner *et al*, 2017).

In industrial flotation plants there usually is a regrinding stage to regrind rougher concentrates in order to liberate enough the minerals of interest to obtain the final concentrate of required grade. Consequently, in the following cleaner flotation stage, fine minerals are to be recovered. Actually, in previous studies with laboratory-scale tests on Arqueros ore, some of the copper minerals in Arqueros showed low floatability mainly because of their fine grain size and resulted fine grinding size, and also because of the complex mineralogical composition. And we also found that chalcopyrite floats slower than bornite and chalcocite. This suggests that the chalcopyrite in Arqueros ore exists as finer grain which negatively impacts chalcopyrite flotation. Therefore, analysing fine particles' behaviour in Arqueros flotation is useful to improve the Cu recovery in the project.

In this study we carried out a few cleaner-scavenger flotation tests following regrinding and analysis of their products to reveal the fine particles' behaviour. If a phenomenon that increases or decreases the flotation rate of fine particles is observed, clarifying the mechanism and applying it to the actual process may lead to an increase in actual recovery.

MATERIALS AND METHODS

Ore sample and preparation

As the ore sample, we used the drill core from Chile, which contains bornite, chalcopyrite, and chalcocite as copper minerals. The main gangue minerals are calcite, orthoclase, albite, and quartz. The ore sample was crushed and ground with a jaw crusher and a ball mill to a P_{80} of 70 µm and analysed chemically with Atomic Absorption Spectroscopy (Cu), Inductively Coupled Plasma – Optical Emission Spectrometry (Fe, Ca) and Combustion-Ion Chromatography (S), as well as mineralogically with MLA (Mineral Liberation Analyzer) for characterisation. The composition of the sample is shown in Figure 1 and Table 1.

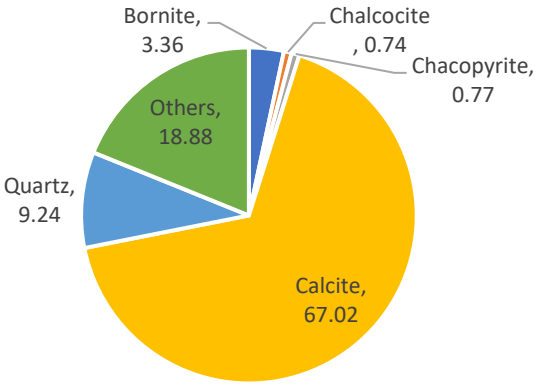

FIG 1 – Modal mineralogy of the ore sample.

TABLE 1

Assay of the ore sample.

Cu (wt%)	Fe (wt%)	S (wt%)	Ca (wt%)
1.02	1.07	0.36	31.8

Flotation flow sheet

In this study we focused on fine particle flotation after regrinding. Feed sample preparation process was conducted before the main flotation stage (highlighted in the flow sheet shown in Figure 2). The test conditions are listed below.

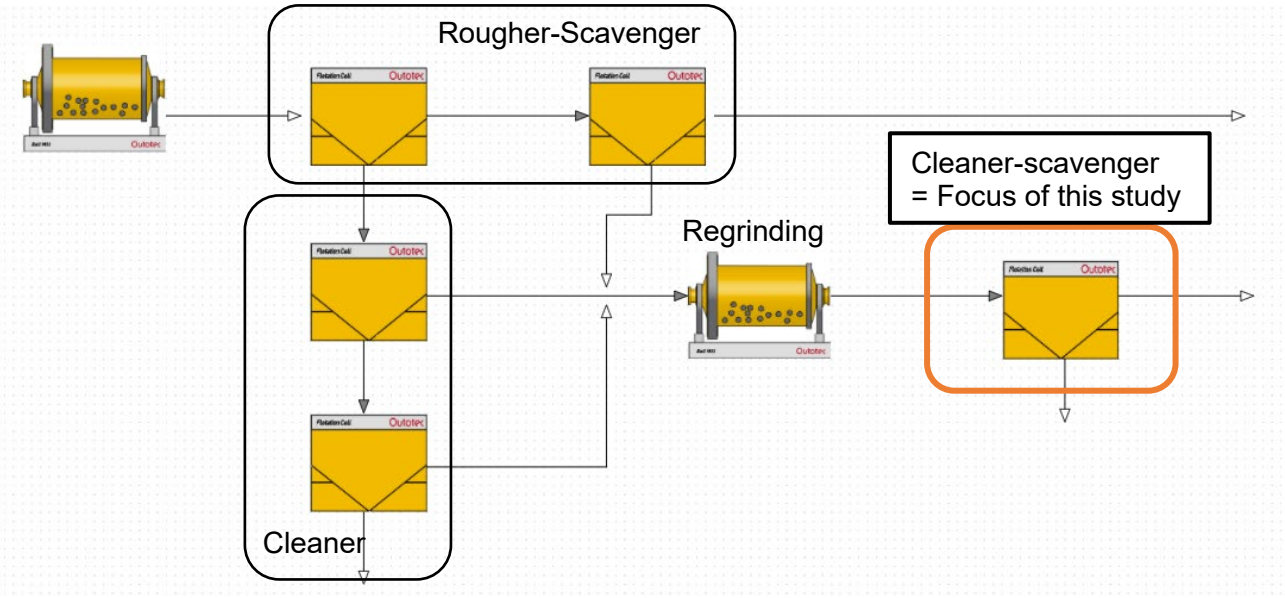

FIG 2 – Flow sheet of flotation tests.

Flotation feed sample preparation

The rougher-scavenger flotation tests were carried out with the conditions below.

Flotation machine:	Essa FTM101 (FLSmidth)
Cell size:	1.75 L
Air flow rate:	5.0 L/min
Pulp density:	37 wt%
Flotation time:	6 min (rougher stage) + 36 min (scavenger stage)
Reagents:	Dithiophosphate: Aero 3477 (collector) = 81 g/t
	NaHS (activator) = 151 g/t
	MIBC (frother) = 20 g/t

In order to produce sufficient amount of concentrate to carry out the cleaner test, the rougher-scavenger test was repeated four times. The rougher concentrate of the first 6 minutes (mixture of four rougher tests' concentrates) was reported to the cleaner stage with the conditions below. On the other hand, the scavenger concentrates of the succeeding 36 minutes (mixture of four scavenger tests' concentrates) were reported to the regrinding stage.

The cleaner tests consist of two stages, wherein the concentrate of the first stage was fed to the second stage. The tailings of the two stages were reported to the regrinding stage.

Flotation machine:	FW type (Yoshida Seisakusho)
Cell size:	800 mL
Pulp density:	10 wt%
Flotation time:	10 min (1st cleaner) + 7 min (2nd cleaner)
Reagents:	MIBC (frother) = 10 g/t

The regrinding tests were carried out with the feed sample, that is the mixture of the rougher-scavenger concentrates and the cleaner tailings. Their conditions and grinding times for required particle size were as follows.

Grinding mill:	Ball and rod mill 1140-A-S (Yoshida Seisakusho)
Pulp density:	30 wt%
Particle size analysis:	Microtrac MT3300 II (MicrotracBel)
Regrinding time:	8 min 56 sec (P_{80} = 20 μm), 21 min 25 sec (P_{80} = 10 μm)

Cleaner-scavenger flotation tests

The flotation tests on the regrinding products were carried out with the below-listed conditions.

Flotation machine:	Essa FTM101 (FLSmidth)
Cell size:	1.75 L
Air flow rate:	5.0 L/min
Pulp density:	20 wt%
Flotation time:	30 min
Reagents:	Dithiophosphate: Aero 3477 (collector) = 30 g/t
	MIBC (frother) = 10 g/t

Flotation products analysis

The products (concentrates and tailings) were dried in an oven at 90°C, weighed, and assayed with AAS (Cu), ICP-OES (Fe, Ca) and C-IC (S). Mineralogical analysis with MLA was also conducted on the products and the flotation behaviour of fine particles was analysed.

Bubble size measurement

Bubble size was measured to calculate the model-based flotation rate of particles. Bubbles were introduced into the measurement cell, dozens of pictures were taken using a high-speed camera, and the bubble diameters (equivalent circle diameters) were measured by image processing. The conditions of the flotation machine were set to be similar with those of the actual flotation test, but water was used instead of sample pulp for the bubble measurement.

Flotation machine:	Essa FTM101 (FLSmidth)
Cell size:	1.75 L
Air flow rate:	5.0 L/min
Reagents:	MIBC (frother) = 4.8 mg
Measurement cell:	Acrylic cell
High-speed camera:	HAS-U2 (Detect)
Image processing:	ImageJ

First-order kinetic model

The batch flotation process was assumed in the flotation tests. The suspension in the flotation tank contains several types of particle groups with different compositions and particle sizes. Here we consider a particular particle group i of these. The recovery rate R_i of particle group i that attaches to the bubbles and is collected in the froth increases with the flotation time t. The first-order kinetic model of flotation assumes that the recovery rate dR_i/dt is proportional to the fraction of particles remaining in suspension at that time, $1 - R_i$, as follows.

$$\frac{dR_i}{dt} = k_i(1 - R_i)$$

The k_i is the flotation rate constant, and the recovery R_i is expressed as a solution of this differential equation as,

$$R_i = 1 - e^{-k_i t}$$

Kinetic constant considering bubble-particle collision

We considered the case where the bubble diameter $D_b[m]$ is sufficiently large compared to the particle diameter $D_i[m]$ and the settling velocity of the particles is slow and negligible compared to the bubble's rising velocity $v_b[ms^{-1}]$. In this case, the kinetic constant k_i is expressed as the product of the number of bubbles per unit volume in the flotation cell (bubble numerical density) $n_b[m^{-3}]$, the volume swept by one bubble rising in the flotation tank in unit time $V_s[m^3 s^{-1}]$, and the collision coalescence probability $P[-]$ of bubbles and particles (Hornn *et al*, 2020).

$$k_i = n_b \times V_s \times P$$

The number density of bubbles, n_b can be calculated by the following equation.

$$n_b = \frac{G\tau_b}{\frac{\pi}{6}D_b^3} = \frac{Q/V}{\frac{\pi}{6}D_b^3 v_b/L}$$

where:

air supply per unit volume of the flotation cell $G := Q/V$

volume per bubble = $(\pi/6)\, D_b^3$

average residence time $\tau_b[s] := L/v_b$ ($L[m]$: water depth of the flotation tank)

The swept volume is expressed as the product of the cross-sectional area of the bubble and the rate of rise by the following equation.

$$V_s = \frac{\pi}{4} v_b D_b^2$$

The collision and coalescence probability $P[-]$ of bubbles and particles is expressed as follows using the bubble-particle collision probability P_c, the probability of particle attachment to a bubble P_A, and the probability for the detachment of a particle from a bubble P_D.

$$P = P_c P_A (1 - P_D)$$

The collision probability P_c is expressed by the following equation using the ratio of particle diameter to bubble diameter D_i/D_b and the Reynolds number of the bubble $Re_b = v_b D_b \rho/\mu$ (ρ: water density, μ: water viscosity coefficient) (Yoon and Luttrel, 1989).

$$P_c = \mathrm{C}\left(\frac{D_i}{D_b}\right)^2, C = \frac{3}{2} + \frac{4{Re_b}^{0.72}}{15}$$

Now, if the hydrophobicity of a particle is sufficient, the probability of attachment $P_A = 1$ and the probability of desorption $P_D = 0$. Therefore, the kinetic constant k_i is expressed as follows.

$$k_i = \frac{3G}{2D_b/L} \times P_c P_a (1 - P_d) = \frac{3Q/V}{2D_b/L} \times \left[\frac{3}{2} + \frac{4{Re_b}^{0.72}}{15}\right]\left(\frac{D_i}{D_b}\right)^2$$

RESULTS AND DISCUSSIONS

Cleaner-scavenger flotation tests results

The flotation curves are shown in Figure 3. As known in the previous studies the Cu recovery of P_{80} = 20 µm flotation was as low as 88.6 per cent. The reason for this may be that the copper minerals are so fine that the liberation remains low even when ground to 20 µm. The flotation rate of 10 µm sample was faster than that of 20 µm sample even though it is of finer particle size. This indicates that a very fine grinding size of 10 µm may be suitable when the mineral grains are fine in size.

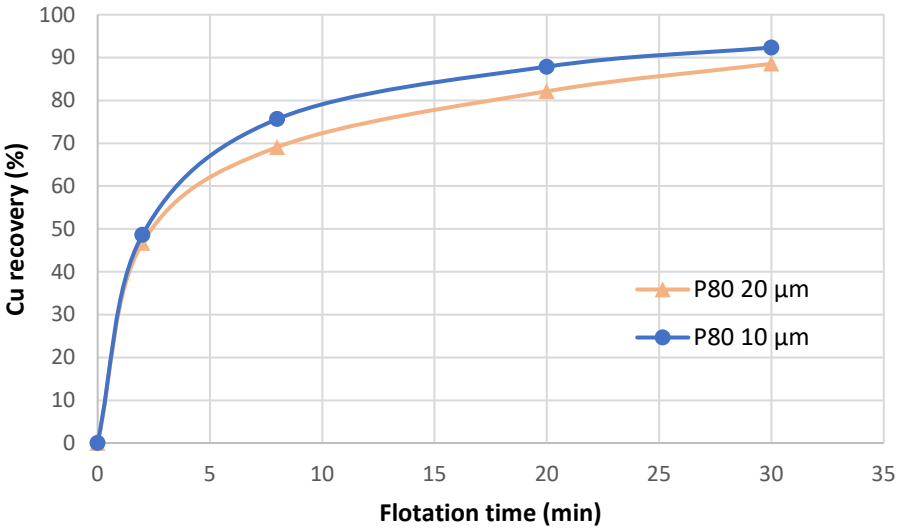

FIG 3 – Flotation rate comparison by regrinding size.

Flotation rate calculation by size-liberation class

The MLA results were analysed and flotation rates were calculated separately according to the size and liberation class. We classified the particles into five liberation classes and seven size classes, so that we got 35 classes in total. The flotation rates and maximum recovery for each class were calculated fitting the curve of next equation. The results were shown in Tables 2 to 5.

$$R(t) = R_{max}(1 - e^{-kt})$$

TABLE 2

Flotation rate constants $\boldsymbol{k}$ (min^{-1}) by size-liberation class (P_{80} = 20 µm).

Liberation (%)	Particle size (µm)						
	-5	-7.5	-10	-15	-20	-35	+35
100	0.36	0.59	0.65	0.78	0.64	4.92	---
-100+70	0.35	0.50	0.61	0.62	0.60	0.49	0.51
-70+30	0.28	0.31	0.34	0.32	0.29	0.27	0.27
-30+0	0.21	0.15	0.15	0.13	0.13	0.08	0.12
0	0.20	0.17	0.12	0.09	0.12	0.05	0.09

TABLE 3

Flotation rate constants $\boldsymbol{k}$ (min^{-1}) by size-liberation class (P_{80} = 10 µm).

Liberation (%)	Particle size (µm)						
	-5	-7.5	-10	-15	-20	-35	+35
100	0.35	0.54	0.74	0.74	5.60	5.60	---
-100+70	0.38	0.55	0.54	0.56	0.35	0.25	---
-70+30	0.27	0.32	0.32	0.31	0.17	0.27	---
-30+0	0.20	0.15	0.11	0.13	0.11	0.14	0.24
0	0.20	0.17	0.10	0.10	0.08	0.11	0.00

TABLE 4

Maximum recovery $\boldsymbol{R_{max}}$ (%) by size-liberation class (P_{80} = 20 μm).

Liberation (%)	Particle size (μm)						
	-5	**-7.5**	**-10**	**-15**	**-20**	**-35**	**+35**
100	92.70	97.25	97.68	95.41	98.70	100.00	---
-100+70	94.38	97.49	97.60	97.26	96.28	95.52	100.00
-70+30	88.12	86.08	89.69	92.28	96.04	87.55	93.60
-30+0	81.16	76.66	73.64	73.43	85.95	84.48	63.41
0	88.24	73.91	65.15	47.51	21.81	46.00	63.73

TABLE 5

Maximum recovery $\boldsymbol{R_{max}}$ (%) by size-liberation class (P_{80} = 10 μm).

Liberation (%)	Particle size (μm)						
	-5	**-7.5**	**-10**	**-15**	**-20**	**-35**	**+35**
100	94.91	95.74	98.16	98.76	100.00	100.00	---
-100+70	95.31	95.80	94.90	96.22	96.64	100.00	---
-70+30	91.10	91.67	91.54	84.62	99.59	82.11	---
-30+0	88.40	81.49	80.98	77.39	76.21	77.23	90.72
0	91.46	81.43	80.87	70.79	73.66	44.31	---

We found that particles of the same size-liberation class showed similar flotation behaviour even though the regrinding size was different. For the next step the average flotation curve of the two regrinding sizes was calculated for each class to obtain the flotation parameters common in the two conditions (Tables 6 and 7). Comparing the rate constant values of the fully liberated particles, we can find that smaller particles floated slower because of their low probability of collision. This tendency is consistent with the theory.

MLA analysis also provided us with the Cu distributions among the 35 classes of the two conditions (Tables 8 and 9).

TABLE 6

Flotation rate constants $\boldsymbol{k}$ (min^{-1}) by size-liberation class (average of both P_{80}s).

Liberation (%)	Particle size (μm)						
	-5	**-7.5**	**-10**	**-15**	**-20**	**-35**	**+35**
100	0.35	0.56	0.69	0.76	0.99	4.92	---
-100+70	0.36	0.53	0.57	0.59	0.47	0.33	---
-70+30	0.28	0.32	0.33	0.31	0.21	0.27	---
-30+0	0.20	0.15	0.13	0.13	0.12	0.10	0.19
0	0.20	0.17	0.11	0.09	0.08	0.08	0.01

TABLE 7

Maximum recovery R_{max} (%) by size-liberation class (average of both P_{80}s).

Liberation (%)	Particle size (μm)						
	-5	**-7.5**	**-10**	**-15**	**-20**	**-35**	**+35**
100	93.80	96.48	97.91	97.09	99.23	100.00	---
-100+70	94.86	96.64	96.24	96.73	96.11	98.24	---
-70+30	89.61	88.88	90.62	88.45	97.76	84.83	---
-30+0	84.78	79.08	77.14	75.41	81.04	79.51	75.65
0	89.85	77.67	72.78	59.15	47.67	42.29	---

TABLE 8

Cu distribution in each class (%) (P_{80} = 20 μm).

Liberation (%)	Particle size (μm)						
	-5	**-7.5**	**-10**	**-15**	**-20**	**-35**	**+35**
100	11.27	3.59	1.84	2.02	1.02	0.09	0.00
-100+70	3.28	4.80	4.33	6.87	4.08	4.65	1.06
-70+30	3.90	4.12	3.09	4.89	3.39	3.40	1.65
-30+0	0.85	1.75	2.00	4.81	3.05	6.46	3.79
0	1.81	0.24	0.16	0.40	0.33	0.83	0.20

TABLE 9

Cu distribution in each class (%) (P_{80} = 10 μm).

Liberation (%)	Particle size (μm)						
	-5	**-7.5**	**-10**	**-15**	**-20**	**-35**	**+35**
100	16.26	5.78	2.74	2.03	0.44	0.23	0.00
-100+70	4.24	6.15	5.65	7.77	3.59	1.36	0.00
-70+30	4.94	5.36	3.83	4.92	2.34	2.43	0.00
-30+0	0.99	2.04	2.03	3.31	2.42	3.06	3.08
0	1.97	0.28	0.13	0.20	0.13	0.19	0.10

Then we calculated the time-recovery relationship using the average parameter set and the different Cu distributions to compare it with the experimental results. As shown in the Figure 4 the calculation expressed well the difference between the two regrinding sizes. This indicates that even when the P_{80} of the ground ore is as fine as 10–20 μm, the increase in flotation rate due to improved liberation may outweigh the decrease in flotation rate due to finer grinding size. And it is suggested that bubble-particle collision model considering liberation can be established and may predict well flotation behaviour.

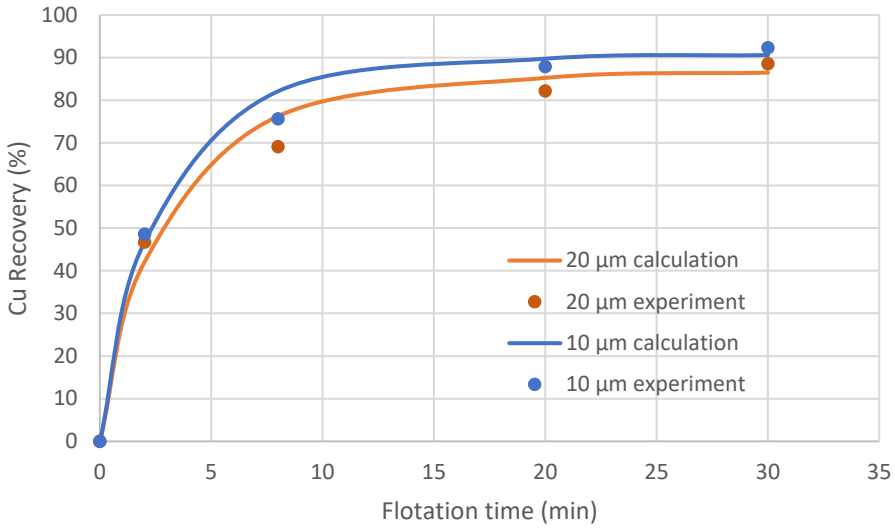

FIG 4 – Comparison of experimental results and calculation.

Model calculation of flotation rate of fully liberated Cu

From the bubble size measurement using high speed camera and image analysis we got the representative values of D_{20} = 0.38 mm, D_{50} = 0.71 mm, and D_{80} = 1.22 mm. Given the bubble size, the flotation rate was calculated according to the bubble-particle collision model. In this study, the bubble size of 0.71 mm (= D_{50}) was used in the model calculation. On the other hand, from the MLA results we calculated the flotation rate of fully liberated Cu sulfide particles. It can be considered that they have the attachment probability of 100 per cent because of their totally hydrophobic surface, so that they are supposed to float theoretically. In Figure 5 the comparison of model calculation and experimental results (P_{80} = 10 µm) is shown. The particles larger than 5 µm showed similar flotation behaviour with the model, but those of less than 5 µm floated faster than calculation. This means that the negative impact of finer regrinding size is not so significant as the bubble-particle collision model indicates. The possible factors that caused this phenomenon are hydrophobic agglomeration of sulfide particles and interaction among sulfide particles and gangue particles. If this is the case, we believe that a confirmatory test should be conducted, as their applications could improve flotation results.

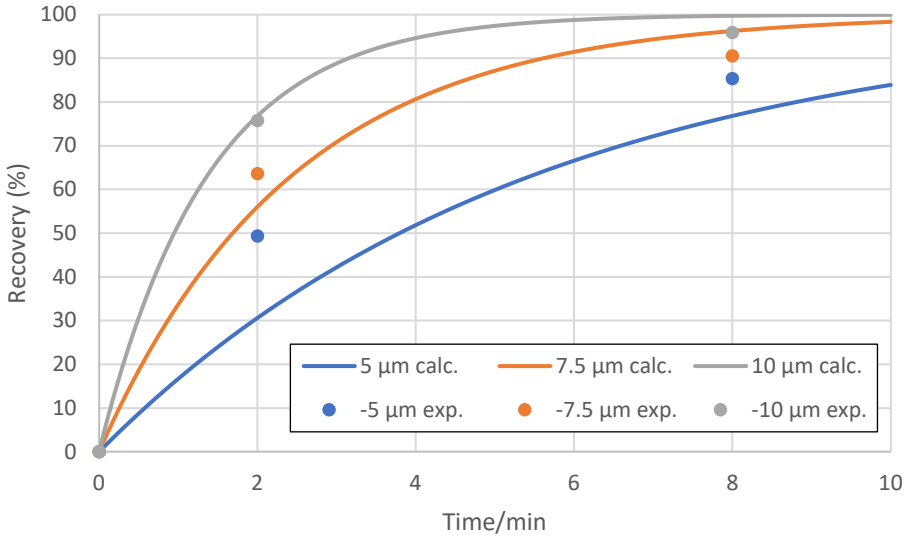

FIG 5 – Comparison of model calculation and experimental results for fully liberated Cu sulfide particles.

CONCLUSIONS

This study investigated the flotation behaviour of fine particles and compared it with first-order kinetic model calculation. Also bubble size measurement was carried out for the model-based flotation rate calculation. The results of the flotation tests and MLA analysis of their products revealed the following.

- Particles of the same size and same liberation floated at the same speed even if they have different regrinding sizes.
- The time-recovery relationship using the averaged parameter set for the 35 size-liberation classes and the different Cu distributions fitted with the experimental results.
- These facts suggest that bubble-particle collision model considering liberation can be established and may predict well flotation behaviour.

Theoretical flotation rate considering bubble-particle collision probability in the present experimental system was calculated by measuring bubble diameters. Flotation rate of fully liberated Cu minerals, which are considered to behave theoretically because their attachment probability is 100 per cent, was compared to the model calculation. The results were as follows.

- The model-based calculation fitted well the experimental results for particles larger than 7.5 μm.
- The particles of <5 μm floated faster in the experiment than calculation.

The possible factors that caused this phenomenon for particles of <5 μm are hydrophobic agglomeration of sulfide particles and interaction among sulfide particles and gangue particles. If this is the case, their applications could improve flotation results of Cu ores that are difficult to process because of their fine Cu grains like Arqueros.

ACKNOWLEDGEMENTS

The authors would like to thank the Nittetsu Mining Co., Ltd. and Hokkaido University for supporting this research and approval to publish.

REFERENCES

Chipfunhu, D, Zanina, M and Grano S, 2012. Flotation behaviour of fine particles with respect to contact angle. *Chem. Eng. Research and Design.* 90. 26–32.

Grano, S R, Wong, P, Skinner, W, Johnson, N W and Ralston, J, 1994. The effect of autogenous and ball mill grinding on the chemical environment and flotation of the copper ore of Mt. Isa Mines Ltd. *III Latin-America Cong. on Froth Flotation* (Univ. of Concepcion Publ.), 351–388.

Hassanzadeha, A, Hassas, B V, Kouachi, S, Brabcova, Z and Celik, M S, 2016. Effect of bubble size and velocity on collision efficiency in chalcopyrite flotation, *Colloids and Surfaces A: Physicochem. Eng. Aspects* 498, 258–267.

Hewitt, D, Fornasiero, D and Ralston, J, 1993. Aqueous film drainage at quartz/water/air interface. *J. of Chem. Society, Faraday Transactions,* 89, 817–822.

Hornn, V, Ito, M, Yamazawa, R, Shimada, H, Tabelin, C B, Jeon, S, Park, I and Hiroyoshi, N, 2020. Kinetic Analysis for Agglomeration-Flotation of Finely Ground Chalcopyrite: Comparison of First Order Kinetic Model and Experimental Result, *Mater. Trans.* 61, 10, 1940–1948.

Jameson, G J, 2017. Bubble movement in a rotating eddy: The implications for particle-bubble detachment. *Chem. Eng. Sci.* 161–6, 329–340.

Leistner, T, Peuker, U A and Rudolph, M, 2017. How gangue particle size can affect the recovery of ultrafine and fine particles during froth flotation. *Mining Eng*. 1–9.

Miettinen, T, Ralston, J and Fornasiero, D, 2010. The limits of fine particle flotation. *Minerals Eng*. 23, 420–437.

Rahman, A, Ahmad, K D, Mahmoud, A and Maoming, F, 2014. Nano-microbubble flotation of fine and ultrafine chalcopyrite particles, *Int. J. of Mining Sci. and Tech*. 24, 559–566.

Shahbazi, B, Rezai, B and Javad Koleini S M, 2010. Bubble–particle collision and attachment probability on fine particles flotation, *Chem. Eng. and Processing*. 49, 622–627.

Tao, D, 2004. Role of bubble size in flotation of coarse and fine particles – a review. *Separation Sci. and Tech*. 39, 4, 741–760.

Yoon, R H and Lutttrell, G H, 1989, The effect of bubble size on fine particle flotation. *Miner. Process. Extr. Metall. Rev*. 5, 101–122.

New perspectives in iron ore flotation – from fundamental studies to on-site pilot testing

L O Filippov[1], K Silva[2], N P Lima[3], A Piçarra[4] and I V Filippova[5]

1. Professor, Université de Lorraine, CNRS, GeoRessources, 54000 Nancy, France. Email: lev.filippov@univ-lorraine.fr
2. Université de Lorraine, CNRS, GeoRessources, 54000 Nancy, France; Engineer, VALE S.A., Mineral Processing Development Department, Nova Lima CEP 34.006–200, MG, Brazil. Email: klaydison.silva@vale.com
3. Engineer, VALE S.A., Mineral Processing Development Department, Nova Lima CEP 34.006–200, MG, Brazil. Email: neymayer.lima@vale.com
4. Engineer, Université de Lorraine, CNRS, GeoRessources, 54000 Nancy, France. Email: alex.m.picarra@gmail.com
5. Senior Scientist, Université de Lorraine, CNRS, GeoRessources, 54000 Nancy, France. Email: inna.filippova@univ-lorraine.fr

ABSTRACT

The reverse cationic flotation using the starch as depressor of iron oxides is the most efficient upgrading process when is applied to the simple systems composed by hematite/magnetite and quartz. The fundamental studies performed with iron ore samples from different deposits over the world (Brazil, Russia, Mexico) confirmed the inefficiency of starch when the silica content in the concentrate is controlled by Fe/Mg-bearing minerals. The main approaches for solving these issues focused on using new collector formulations or new depressants. However, the alternative depressants tested inhibited flotation of quartz or were less efficient as iron oxide depressant. In this work, a comparison between new amidoamine collector with conventionally used etheramine and oleate collectors in the flotation of pure minerals and actual iron ore samples was performed. The electrophoretic mobility, contact angle and infrared spectroscopy measurements allowed to deduce the hindrance effect as main mechanism of selective adsorption of the amidoamine on the quartz surface compared to hematite and kaolinite. Molecular modelling studies revealed that this steric hindrance effect can be explained by the combination of the "shield" formed by the coordinating water molecules on the (001)-D2 hematite surface and the large volume of the amidoamine head group. The amidoamine tested as collector without use of a depressant showed excellent flotation selectivity allowing the total flotation of quartz from a mixture with hematite. High collector performance and selectivity were confirmed during reverse flotation of quartz using continuous flotation column (D = 500 mm; H = 4000 mm) and allowed to produce the iron concentrates with more than 60 per cent of iron from the rejected slimes samples of Vargem Grande 2 processing plant (Iron Quadrangle, MG, Brazil). The new collector allowed to develop flexible flotation flow sheets to process the iron ore with a complex gangue mineralogy and unlock the old altered tailings and slimes product as new resources.

INTRODUCTION

The iron ore mining industry in the Iron Quadrangle, Brazil, is currently at the stage called by some authors '*The Third Wave'*, that means, due to the ore characteristics, the most suitable concentration process is the reverse cationic flotation with amine as collector and starch as depressant. It is known that the presence of slimes in this type of flotation causes some problems such as increased consumption of reagents, issues related to froth stability and selectivity in the concentration process. Thus, a desliming stage is necessary to removal the slimes before the flotation.

An important loss of iron minerals (mainly hematite and goethite) in the slimes occurs on the desliming process by hydrocyclones. These slimes are disposed in tailings dams, increasing the environmental impacts related to the iron ore mining industry. A negative aspect, considering the impacts caused by the mineral activity, is the 'NIMBY syndrome' (acronym in English for the expression Not In My Back Yard), which, in the case of mining, means: 'You can mine anywhere, but not in my yard' (Gomes, 2017) and the presence of tailings dams is an important factor that can potentiate this 'NIMBY syndrome'.

A survey prepared by Gomes (2017) showed that, in 2014, there were 15 mines in the Iron Quadrangle and about 111 million tons of tailings were produced. Mining companies are looking for a way to increase the sustainability of their operations by improving mineral recovery by implementing new tailings concentration routes and replacing dams with tailings piles (adopting tailings filtration or, recently, developing the dry concentration process). Among the tailings, the material that presents the greatest processing challenges is the ultrafine tailings (slimes).

This article presents a summary of the recent works performed (Filippov *et al*, 2021; Silva *et al*, 2021, 2022; Matiolo *et al*, 2020; Lima *et al,* 2020) in the area of development of iron ore treatment processes at Vale S.A, together with the University of Lorraine and support from CETEM (Mineral Technology Center, Brazil), aiming at the development of a collector and new flotation routes for the processing of iron ore slimes, without the use of starch. These collaborations works were performed as part of Vale S.A.'s R&D initiatives, which also includes the PhD thesis programs between Vale's Process Engineers and the University of Lorraine.

CHEMICAL AND SIZE DISTRIBURION CHARACTERISTICS OF BRAZILIAN IRON ORE SLIMES

The deleterious effect of the slimes in the iron ore concentration process is quite widespread, but the understanding of the interaction mechanism of slime with ore is not unanimous in the literature and has been the subject of extensive debate (Marques, 2013). The granulometric range of the feed of a conventional iron ore flotation plant in the Iron Quadrangle is, generally, constituted by particles in size fraction -150+10 μm. The slimes fraction below 10 μm are previously removed in the desliming process by hydrocyclones. Due to the slime characteristics and the low efficiency of the hydrocyclones separation process, a high amount of hematite ultrafine particles are removed with the slimes (Aguiar, 2013).

According to Wolff *et al* (2011), the amount and content of iron in Brazilian iron ore slimes varies from mine to mine and depends on the characteristics of the ore. For example, in 2011, the slimes from Vargem Grande 2 plant constituted about 19 per cent of the ROM, representing a mass of 546 t/h of material containing about 42 per cent Fe (Guimarães, 2011). Wolff *et al* (2011) collected nine slimes samples from seven mines located in the Iron Quadrangle and Carajás regions (state of Pará – northern Brazil). The results (Table 1) showed that the iron content in the Iron Quadrangle slimes ranged from 44.3 per cent to 56.3 per cent (the slimes from Carajás presented 64 per cent iron).

TABLE 1

Chemical analysis and D80 of some slimes from Brazilian iron ore plants (Wolff *et al*, 2011).

Sample/Mine	Fe (%)	Al (%)	Mn (%)	P (%)	D80 (μm)
Brucutu	44.8	3.1	0.2	0.16	15
Córrego do Feijão I	56.3	1.3	4.6	0.27	10
Córrego do Feijão II	46.5	2.0	1.1	0.11	22
Conceição	44.3	1.0	1.9	0.11	27
Cauê	45.6	1.1	2.1	0.12	25
Fábrica Nova	53.4	1.1	0.3	0.17	14
Alegria I	51.8	2.4	0.2	0.21	13
Alegria II	48.6	1.2	0.4	0.17	16
Carajás	64.0	0.8	0.9	0.08	10

ISSUES THAT HINDER THE SELECTIVE ACTION OF STARCHES IN THE IRON ORE CATIONIC REVERSE FLOTATION PROCESS

In the Iron Quadrangle mines, the reverse cationic flotation of iron ore is possible due to the action of the collector/depressor system (Filippov *et al*, 2014). This means that it is not possible to obtain

high quality concentrates with high metallurgical recovery without the adoption of a depressant. Therefore, currently, the starch (depressor) is as essential as the amine (collector) in this type of process in the Iron Quadrangle plants.

Starches are the universal iron oxides depressants (Araujo *et al,* 2005). Corn starch is the most used depressant in the reverse flotation of iron ore due to its availability, cost and low environmental impact (Shrimali and Miller, 2016). The starch adsorption on quartz and hematite surfaces are different not merely in terms of the magnitude, but also in terms of the bonding strength. This is because the polysaccharides adsorption on the iron oxides and Fe-bearing silicates is mainly controlled by their chemical bonding with the iron in the mineral structure (Weissenborn *et al,* 1995; Filippov *et al,* 2014); however, hydrogen bond is the main adsorption mechanism on the quartz surface (Severov *et al*, 2013). Thus, amine collectors can replace the starch molecules on the quartz surface because of their stronger electrostatic interactions with the negatively charged quartz surface.

Starch adsorbs extensively on hematite and to a lesser extent on quartz, but in some cases, the adoption of starch is not sufficient to obtain satisfactory selectivity in the flotation process. The role of clay minerals on the starch-hematite interaction cannot be ruled out (Rath and Sahoo, 2020). Another important issue that influences the effectiveness of starch as a selective depressant is the presence of Fe-Mg-Al bearing silicates in the ore (Filippov *et al*, 2010).

Filippov and co-workers demonstrated that the starch cannot be considered as a selective depressant for magnetite at pH of approximately 10 in the iron ores reverse cationic flotation when the Fe–Mg–Al-bearing silicates as amphiboles are present in the system (Filippov *et al*, 2014; Veloso *et al* 2018). The flotation process separation efficiency decreases because the surface properties of these silicates are similar to those of iron oxides, resulting in the non-selective action of depressants, such as starch, due to a strong chemical complex of the metal ions on the mineral surface with starch molecules (Turrer and Peres, 2010; Filippov *et al,* 2010, 2014; Veloso *et al*, 2020).

Detailed studies on reverse cationic flotation with iron ore samples from different deposits over the world (Brazil, Russia, Mexico) performed by Filippov and co-workers confirmed this inefficiency of starch when the silica content in the concentrate is controlled by Fe-/Mg-bearing minerals such as amphiboles, epidote, chamosite, and diopside (Filippov *et al,* 2010; Severov *et al,* 2013; Veloso *et al*, 2018). The studies suggest that starch attaches to the Fe-Mg silicates not only by hydrogen bonding with the surface hydroxyls, but also by the formation of a surface chemical complex with metal atoms. Thus, the chemical complexation adsorption mechanism can explain the strong depression effect of the starch during the magnetite and Fe–Mg–Al-bearing amphibole flotation (Severov *et al,* 2013; Veloso *et al*, 2020).

Iron ore slimes from Brazil contains clay minerals such as kaolinite. Considering that kaolinite is the main Al_2O_3 mineral in Brazilian iron ore slimes, the presence of slimes can affect quartz flotation by depression of kaolinite with corn starch, impairing hematite depression. As the main interaction mechanism of collector in quartz cationic reverse flotation is electrostatic, lack of depression can cause hematite flotation, decreasing the selectivity of the process. The collector can also adsorb on the kaolinite surface and, due to the high specific surface of these clay mineral and their anisotropy, high consumption of reagents can occur without satisfactory kaolinite flotation.

Table 2 shows the recovery of Al_2O_3 in the underflow from the sedimentation tests with a typical Brazilian iron ore slime. It is possible to notice that, increasing the starch dosage, the percentage of Al_2O_3 also increases. Table 3 shows that a higher percentage of Al_2O_3 in the flotation feed negatively affected the quality of the concentrate.

TABLE 2

The effect of corn starch dosage on the recovery of Al_2O_3 to the underflow on the sedimentation tests with on iron ore slime (copied from Lima *et al* (2020)).

Corn Starch (g/t)	Recovery of Al_2O_3 to the Underflow
0	16.5
100	43.3
250	62.9
500	84.7

TABLE 3

Results of bench scale flotation tests with the products of the sedimentation tests of the iron ore slime (copied from Lima *et al* (2020)).

Al_2O_3 Concentrate%	Fe Concentrate%	SiO_2 Concentrate%
1.01	65.24	1.51
2.21	61.91	3.34
2.75	59.39	5.14
3.24	56.87	6.93

The Al sites of the kaolinite seems to interact with the starch while the Si sites can be free to interact with the collector. This behaviour can reduce the floatability of quartz particles.

The investigations on new flotation collectors, more selective, without the use of depressor, may contribute toward unlocking new iron ore resources related to primary deposits with complex gangue mineralogy (ie Fe-bearing silicates, kaolinite), processing of old tailings with high degrees of alterations and also to recover the Fe minerals in the slimes.

DEVELOPMENT OF SELECTIVE COLLECTORS

Development approach

Some authors have demonstrated that the steric hindrance could improve the selectivity of a collector in the cationic flotation process. For example, the high selectivity to float quartz in a mixture with magnesite, without depressor, due to the steric hindrance in the molecular structure of some collectors was demonstrated by Liu *et al* (2020). The authors used surface tension measurements, molecular dynamics simulations and density functional theory to investigate the effects of introducing an isopropanol substituent in amine collectors in the flotation process for a mineral system composed by quartz and magnesite. The results showed that introducing this isopropanol substituent in dodecyl amine weakened the electrostatic repulsion of the polar groups and increased the cross-sectional size of these groups; this can decrease the electrostatic effect and increase steric hindrance, thereby improving the selectivity of the reagent, providing a high floatability of the quartz and low floatability of the magnesite.

Budemberg (2016) analysed and compared some different structures of amidoamines with commercial amines used in the flotation of iron ore. The studies were carried out using the iron ore from the Alegria mine in the Iron Quadrangle region. One of the amidoamines tested was the N-[3(dimethylamino)propyl]dodecanamide and, according to the author, this amidoamine is conducive to steric hindrance phenomena, resulting from the bonding between the methyl and amine groups (Figure 1). The analysis carried by Budemberg (2016) considered the starch as depressant therefore, it was not possible to verify if, adopting the amidoamine in the absence of starch, it would be possible to obtain good selectivity without significantly reducing the quartz floatability.

The structure of the N-[3(dimethylamino)propyl]dodecanamide molecule (molecular formula: $C_{17}H_{36}N_2O$ is presented below (Figure 1):

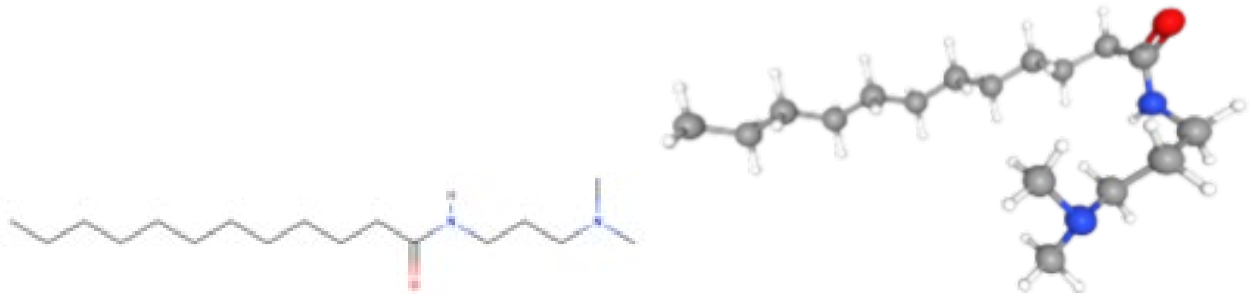

FIG 1 – Structure of N-[3(dimethylamino)propyl]dodecanamide molecule (p. https://pubchem.ncbi.nlm.nih.gov/compound/lauramidopropyldimethylamine).

Lab scale flotation studies with the amidoamine N-[3(dimethylamino)propyl]dodecanamide

Lab scale flotation tests were carried out to verify the scientific hypothesis that amidoamine N-[3(dimethylamino)propyl]dodecanamide could present adequate selectivity in the iron ore slimes flotation, even without the adoption of depressants.

The measurements of the contact angle on the hematite surface demonstrated that this amidoamine presents similar contact angle values with and without starch, while etheramine presents an important variation at similar experimental conditions (Figure 2).

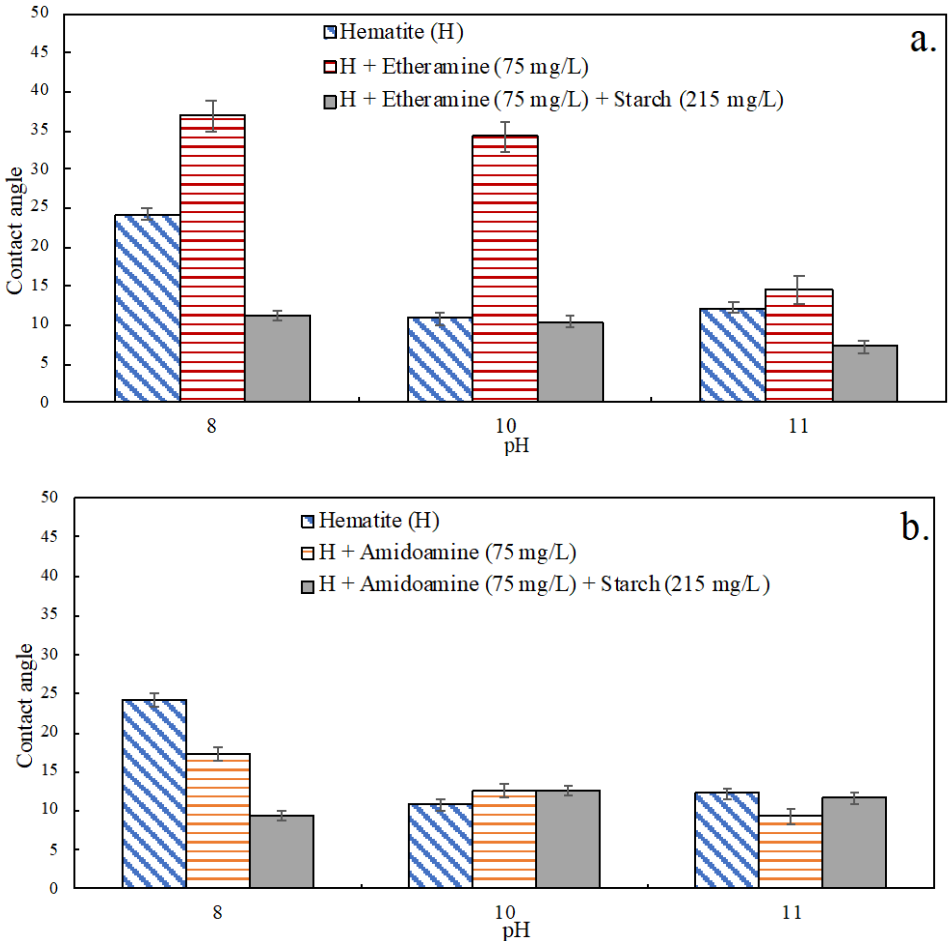

FIG 2 – Contact angle measurements on hematite with SD estimated based on three experiments. (a) Without reagents, in an aqueous solution of etheramine with and without starch. (b) Without reagents, in an aqueous solution of amidoamine with and without starch. Dosage: 215 mg/L of starch, 75 mg/L collector) (copied from Silva *et al* (2021)).

Regarding quartz, the contact angle values related to etheramine were higher than with amidoamine but both, etheramine and amidoamine presented contact angle values sufficient to float quartz.

Pure minerals bench scale flotation tests (Figures 3 and 4) confirmed the results obtained by the contact angle measurements.

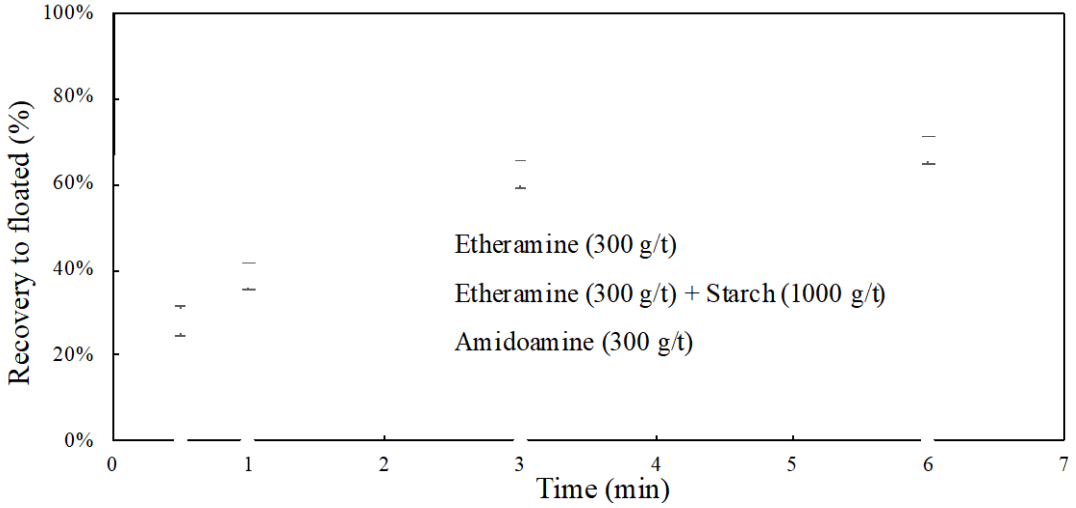

FIG 3 – Hematite recovery in bench-scale tests using etheramine, etheramine with starch, oleate and amidoamine at pH 10.

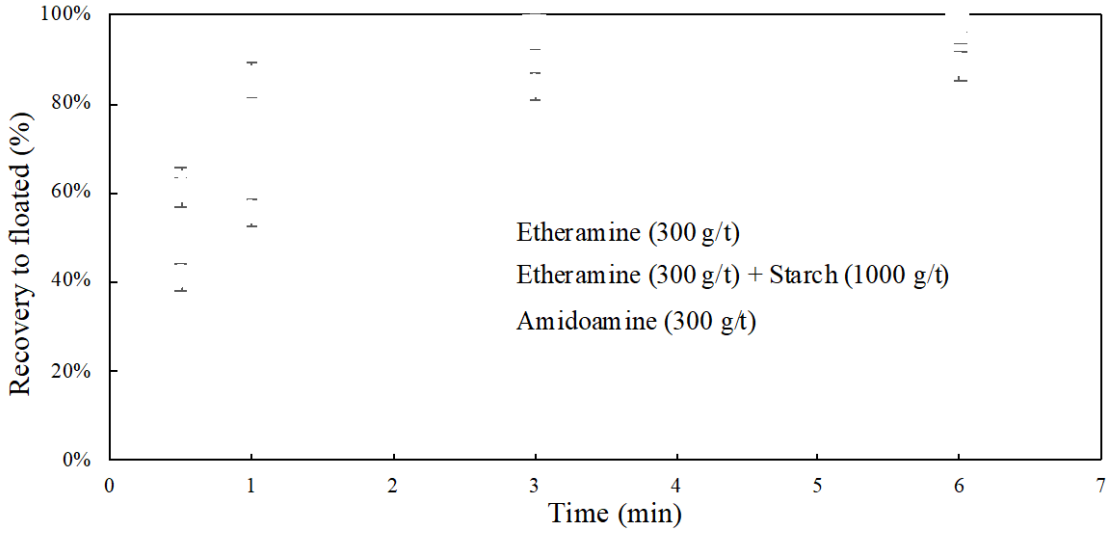

FIG 4 – Quartz recovery in bench-scale tests with etheramine, etheramine plus starch, and amidoamine.

Bench scale flotation tests with pure kaolinite and kaolinite mixed with hematite were also performed. The presence of kaolinite appears to inhibit the cationic flotation of hematite by the etheramine. A suitable hypothesis for these results is that SiO_4 face on kaolinite is capable of adsorbing etheramine, but the flotation of kaolinite is hampered by an anisotropy in its structure.

Interaction mechanism of amidoamine collectors on the silicates and iron oxides

Infrared measurements of the amidoamine on the hematite, quartz and kaolinite surfaces at three different dosages showed no difference in the adsorption behaviour of the amidoamine collector at a low concentration (10^{-4} M/L) (Figure 5). However, the peaks intensity increases significantly on the quartz and kaolinite for the concentration of 5 10^{-3} M/L of the collector (Figure 6), pointing to a higher quantity of adsorption of the collector on silicate minerals, such does not occur for hematite. This difference in adsorption behaviour is responsible for the selective flotation of quartz from hematite.

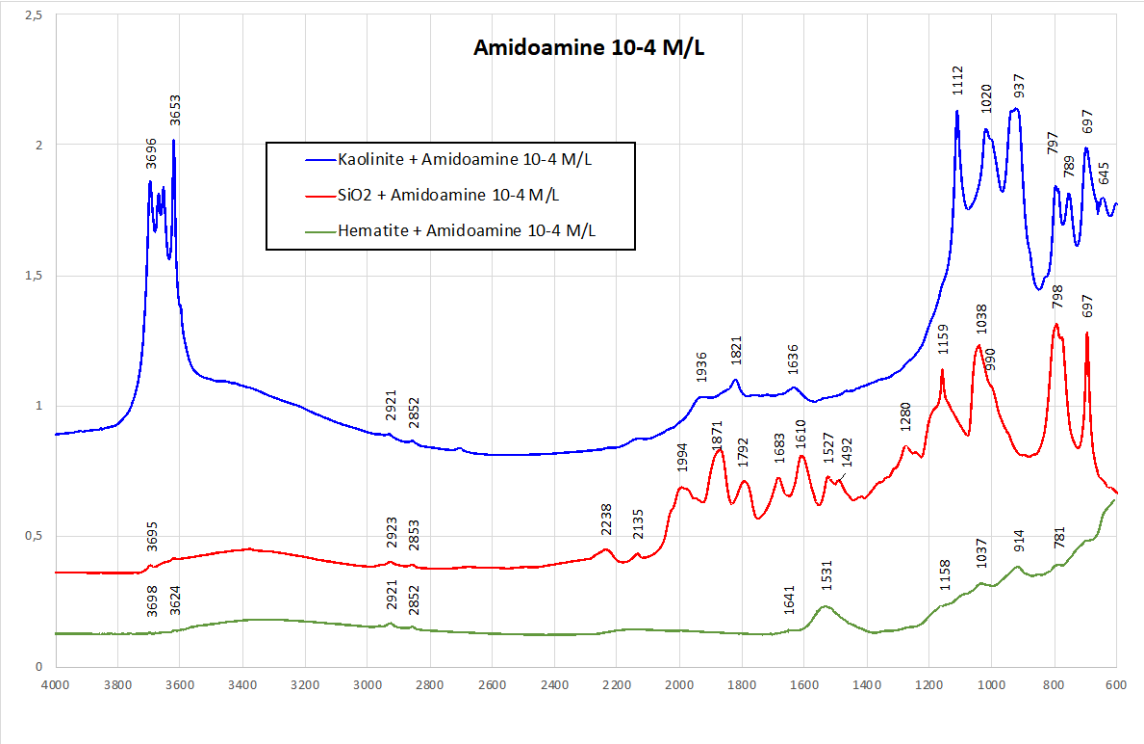

FIG 5 – FTIR spectra of hematite, quartz and kaolinite after interaction with amidoamine at the concentration of 10^{-4} M/L.

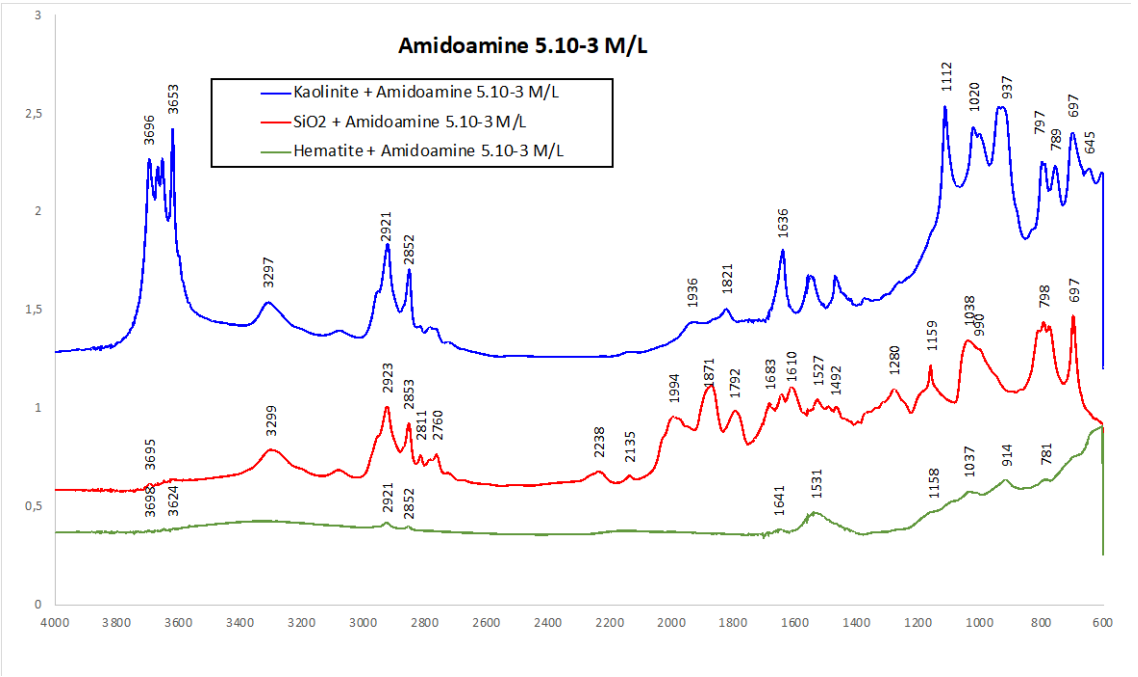

FIG 6 – FTIR spectra of hematite, quartz and kaolinite after interaction with amidoamine at the concentration of 5 10^{-3} M/L.

For quartz and kaolinite, the more intense peaks may be explained by the specific adsorption on the more negatively charged silicate minerals surface defined by the silica tetrahedron. Additionally, a shift of the amidoamine peak at 3307 cm^{-1} to 3297 cm^{-1} on the kaolinite and 3299 cm^{-1} on the quartz was observed due to the specific adsorption of the NH – group on the surface of silicates minerals while any shift was not observed on the hematite surface (Figure 6).

Since for the amidoamine collector the structure of the adsorption layer is controlled by the collector concentration, there is a hindrance effect for hematite. An increase in collector concentration leads

to the increased quartz recovery due to the increased quantity of the collector deduced from the higher peak intensity, while the flotation of hematite does not occur or is very low.

The flotation behaviour of kaolinite is similar to those of hematite while the CH_3 and CH_2 peaks intensity is similar to the spectrum of quartz. The high specific surface area coupled with double sheet structure may be an explanation for this behaviour (Ma and Bruckard, 2010; Xu *et al*, 2015).

Molecular modelling

Molecular modelling studies were carried out to compare the adsorption of etheramine and the amidoamine N-[3(dimethylamino)propyl]dodecanamide on the quartz and hematite surfaces aiming to explain the cause for the hindrance effect related to the amidoamine adsorption on the hematite surface, even without depressor. Figure 7 shows the structures built (hematite and quartz surfaces and etheramine and amidoamine molecules) to carry out the molecular modelling studies. Only the main mineral surfaces of quartz and hematite were evaluated in this work. The pKa of amidoamine was determined and the value was evaluated at about 8.23 (Silva *et al*, 2022), while the pKa of etheramine considered in molecular modelling was at 10.5.

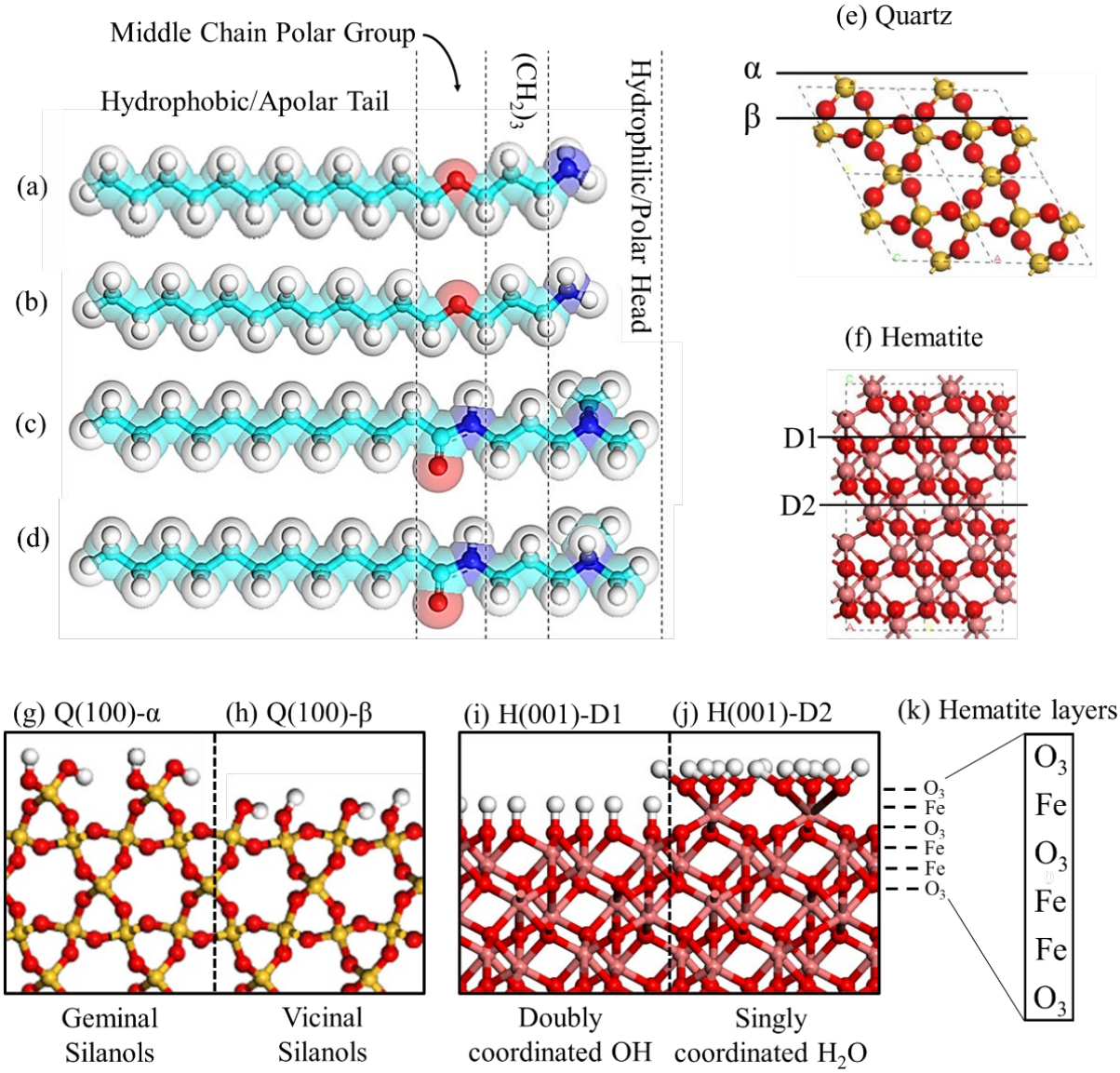

FIG 7 – Molecular and crystal structures of: (a) Etheramine, (b) Etherammonium, (c) Amidoamine, (d) Protonated Amidoamine, (e) Quartz unit cell, (f) Hematite unit cell, (g) Quartz (100)-α surface, (h) Quartz (100)-β surface, (i) Hematite (001)-D1 surface, (j) Hematite (001)-D2 surface, (k) Order of hematite layers. Atom colour code: hydrogen – white, oxygen – red, nitrogen – blue, carbon – cyan, silicon – yellow, iron – pink (copied from Silva *et al* (2022)).

The results showed that amidoamine has a much higher affinity for quartz than for hematite, indicating selectivity. The amidoamine N-[3-(dimethylamino)propyl]dodecanamide, in the neutral state (pH 10.5), presents sufficient mineral-collector interaction energy to start the adsorption process on the quartz surface. The amide group in this collector structure plays important role for the hydrogen bonding stabilisation of the adsorption layer, thus the collector-collector interaction energy contributes to organise the amidoamine on the quartz surface.

Concerning the hematite, it was demonstrated that for the surface (001)-D2, the selectivity behaviour for the quartz-hematite flotation system with amidoamine can be explained by the combination of the 'shield' formed by the coordinating water molecules on this surface with the large molecular volume of amidoamine head group, due to the methyl bonded to nitrogen in the tertiary amine (Figure 8), generating steric hindrance and impairing the adsorption on this surface, even considering the protonated amidoamine (pH 8.5). Hematite-D1 barely shows any collector affinity when comparing to the other surfaces.

In relation to etheramine, the neutral collector adsorption is impaired by the coordinating water on the hematite-(D2) surface, but the protonated molecule (etherammonium) can penetrate and bind on this surface due the electrostatic driving force.

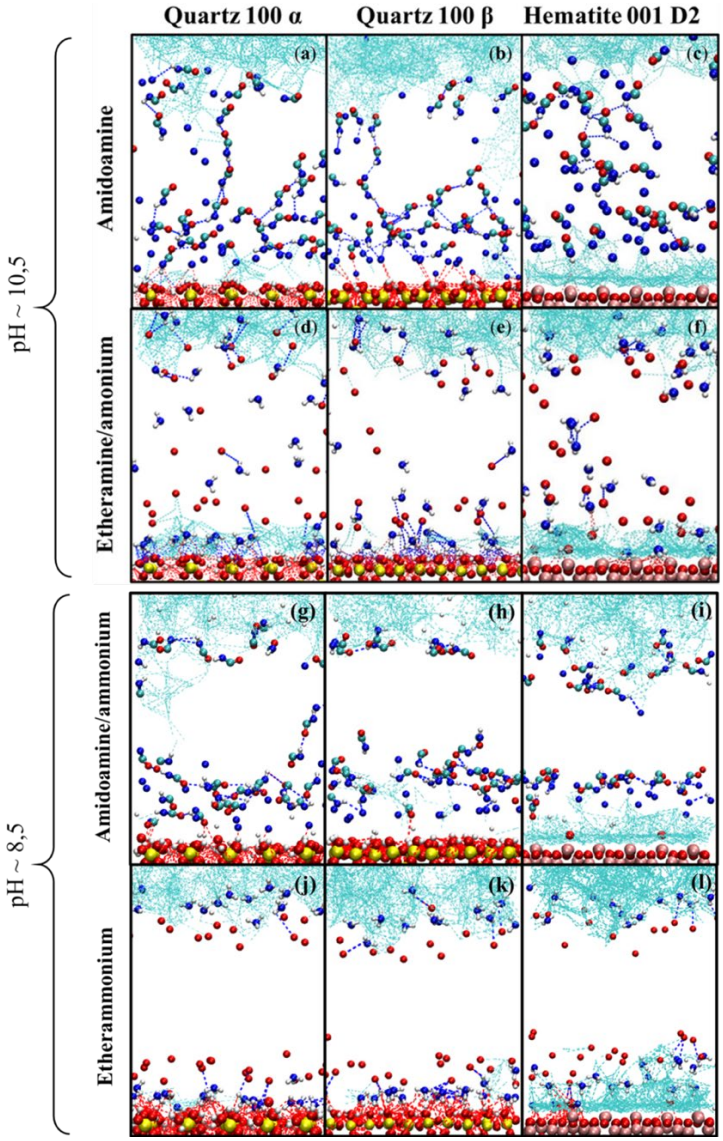

FIG 8 – Snapshots of the hydrogen bonds observed in the simulation systems. For clarity, only the collectors' hydrogen bonding functional groups are shown, as well as surface atoms. Hydrogen bonds colour code by HB donor: water – cyan; non-water: oxygen – red, nitrogen – blue. Atom colour code: hydrogen – white, oxygen – red, nitrogen – blue, carbon – cyan, silicon – yellow, iron – pink (copied from Silva *et al* (2022)).

PILOT TESTS

Pilot column flotation tests were carried out to verify the feasibility of adopting the amidoamine N-[3-(dimethylamino)propyl]dodecanamide as a collector in an industrial plant aiming at the concentration of iron ore slimes.

Initially, two slimes samples supplied by Vale SA were collected in two different plants of the Iron Quadrangle and tested in the CETEM pilot plant (Figure 9). Both Sample 1 and Sample 2 were collected from the underflow of the slime thickener. The D50 of the sample 1 was 10 μm and the D50 of the Sample 2 was 11 μm. Other characteristics of the samples are presented in the Tables 4 and 5.

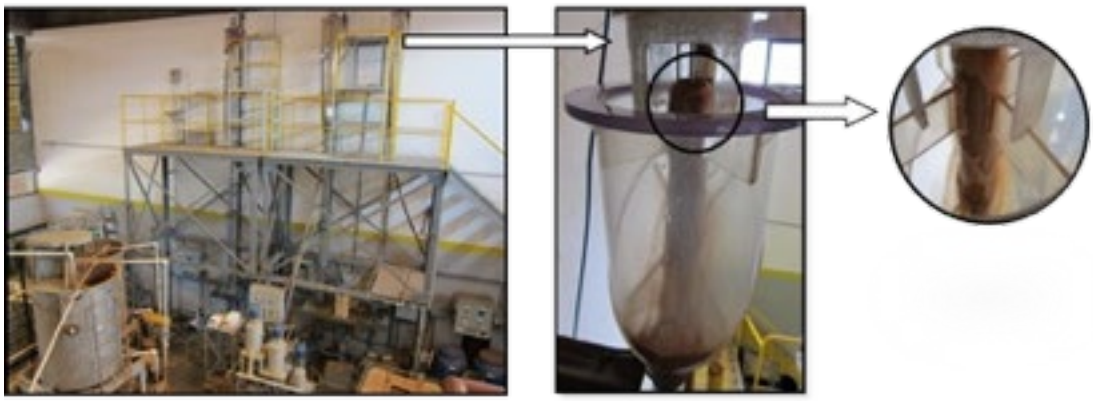

FIG 9 – General view of the columns at CETEM's pilot plant (a) and 2″ column flotation 2″.

TABLE 4

Chemical analyses of the slime samples.

Sample	Fe	SiO_2	P	Al_2O_3	Mn	TiO_2	CaO	MgO
1	45.2	28.6	0.09	3.1	0.09	0.13	0.05	0.06
2	39.6	33.4	0.09	5.1	0.4	0.10	0.20	0.70

TABLE 5

Mineralogical composition of the slime samples (copied from Matiolo *et al* (2020)).

Sample	Hematite	Goethite	Quartz	Kaolinite	Others
1	51.5	13.3	27.9	4.6	2.7
2	54.6	6.4	28.9	6.4	3.7

For each slime sample, experiments were performed in different scales using flotation columns with internal diameter of 2″ and 6″ (height of 6.0 metres). Flotinor 5530 (commercial name of the amidoamine N-[3-(dimethylamino)propyl]dodecanamide from Clariant) and Flotigam EDA-C (supplied by Clariant) were used as collectors. The flotation tests were carried out with the pulp at about 20 per cent solids by weight.

The results indicated that it was possible to produce iron concentrates with grades higher than 60 per cent, SiO_2 content below 5 per cent and Al_2O_3 at 3 per cent from only the Sample 1. The collector type had a great impact on the flotation results. The best results with Sample 1 were achieved with the amidoamine instead of the classical etheramine collector extensively applied in the iron ore plants in Brazil.

As demonstrated by laboratory-scale studies, the presence of kaolinite can impair the results of iron ore slime flotation and, perhaps, this may be the main reason for the better results obtained in the flotation tests of Sample 1, since this sample has lower kaolinite content than Sample 2.

Sample 1 came from the Vargem Grande mine; therefore, a pilot flotation plant was installed next to the slime thickener in Vargem Grande plant (Figures 10 and 11) with the objective of carrying out long-term pilot tests to evaluate the effects related to variability of ore.

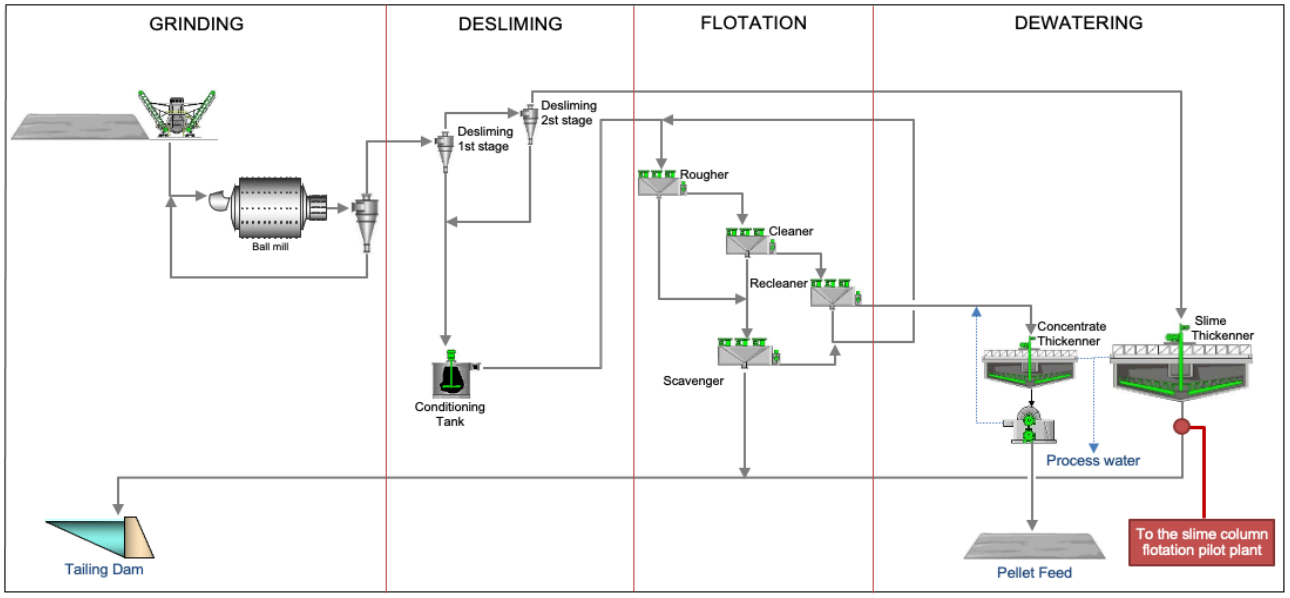

FIG 10 – Simplified flow sheet of Vargem Grande 2 industrial plant (copied from Filippov *et al* (2021)).

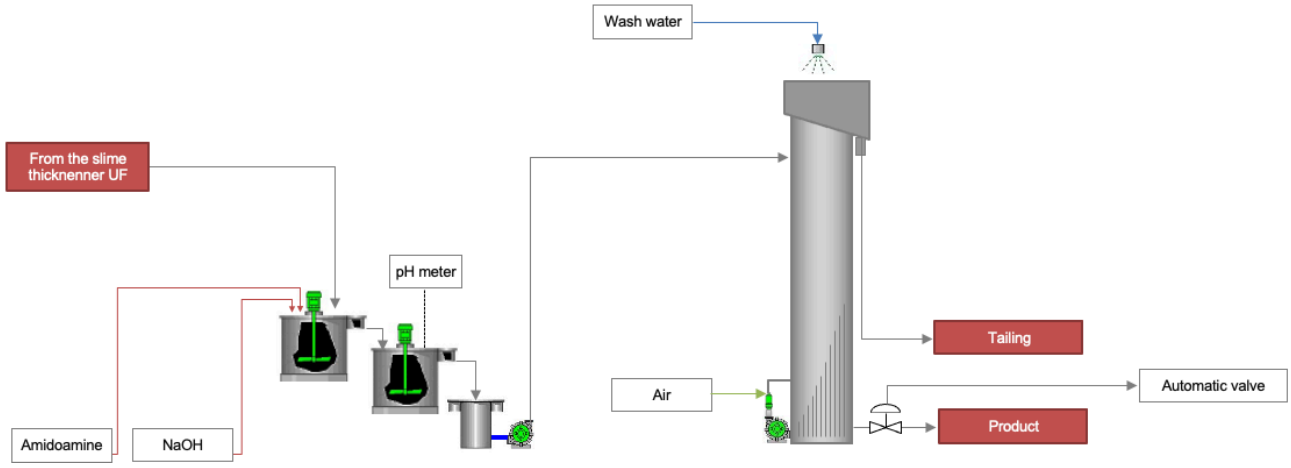

FIG 11 – Flotation pilot plant flow sheet.

The tests were performed using a pilot flotation column of 500 mm diameter and 4000 mm height with a cavitation tube system for bubbles generation. Amidoamine N-[3-(dimethylamino)propyl]dodecanamide (Flotinor 5530) was used as a collector at a dosage of 152–160 g/t in the absence of depressant. The flotation tests were performed at pH 10.5.

The results presented in the Table 6 need to be evaluated at the first slime concentration stage (Rougher) where the product could feed a cleaner stage. The median values were: 44.6%Fe in the feed, 52.6%Fe in the concentrate and 14.1%Fe in the tailing. In addition to adopting only one concentration step in the pilot tests, the collector dosage was kept almost constant, so these factors may be contributing to the results related to the iron content in the concentrate, however it is important to notice the values for the recovery of iron in the concentrate were above 86 per cent, which demonstrate the high selectivity of the amidoamine used as a collector.

TABLE 6

Summary of results for 67 pilot tests.

ID	%Fe Feed	%Fe Product	%Fe Tailing	Mass Recovery	Fe Recovery Product	SiO_2 Recovery Froth
Average Value	44.5	53.3	15.2	76.9	91.5	53.1
90th percentile	47.1	59.6	21.6	89.1	97.7	78.5
Median	44.6	52.6	14.1	76.8	92.4	51.2
10th percentile	41.7	48.6	8.4	62.8	86.1	30.0

From the pilot test campaign, it was possible to conclude that the loss of iron in the tailings was correlated with entrainment effect, thus the adjustment of the specific collector dosage and the relationship between the washing water and the froth volume are important factors to control the flotation performance as was mentioned in (Filippov *et al*, 2021). The implementation of automatic control systems regarding these parameters will improve the performance of an eventual slimes flotation industrial application.

The increased values of the carrying rate decreases the SiO_2 content in the iron concentrate to the detriment of the increased losses of iron in the froth product (tailings). Thus, there is no guarantee to reach high iron metallurgical recovery and low SiO_2 content in the concentrate, adopting only one column flotation stage during an industrial operation.

The iron content in the product varies according to the mineralogical characteristics of the slimes and, for high LOI values in the concentrate, there is a tendency to obtain low iron content in the nonfloated product.

MAGNETIC CONCENTRATION AS CLEANER STAGE

To improve the iron content in the concentrate, a cleaner stage was introduced. Exploratory studies showed that the synergy between two distinct processes (flotation and magnetic concentration) was the most appropriate option to ensure less iron loss in the tailings and higher iron content in the concentrate. This article does not aim to detail these exploratory studies, but only to show some results obtained.

After comparative tests between WHIMS (Wet High Intensity Magnetic Separator) and VPHGMS (Vertically Pulsed High Gradient Magnetic Separator), the VPHGMS was the most suitable to be tested as the cleaner stage in the magnetic concentration of iron ore slimes from the Vargem Grande 2 plant (Figure 12).

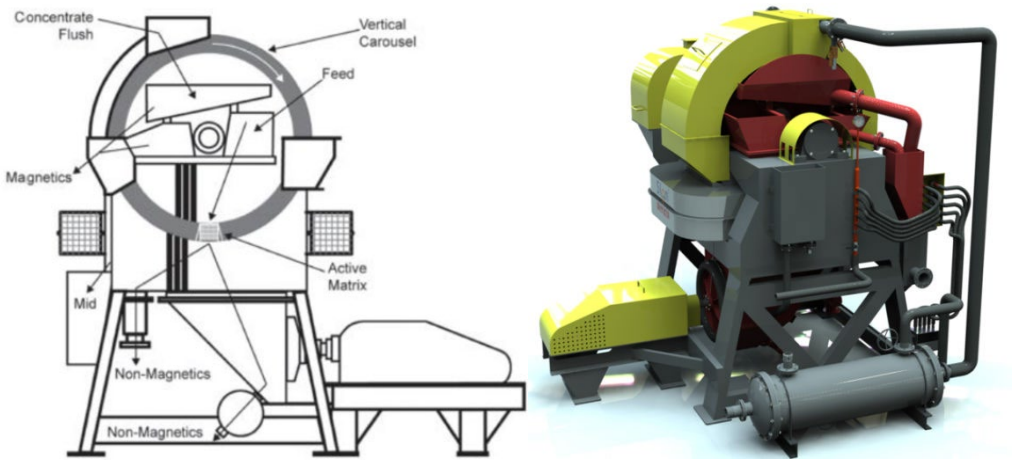

FIG 12 – Schematic of the magnetic separator used (VPHGMS) (Altin *et al*, 2016; www.slonmagnetics2020.en.made-in-china.com).

According to Altin *et al* (2016), the VPHGMS allows the processing of fine and weakly magnetic particles through the combined magnetic force field, pulsation in the separation zone, gravity and vertical rotating ring.

Several pilot tests were carried out and Figure 13 shows that, by adopting the VPGHMS as the cleaner stage, it was possible to stabilise the quality of the concentrate.

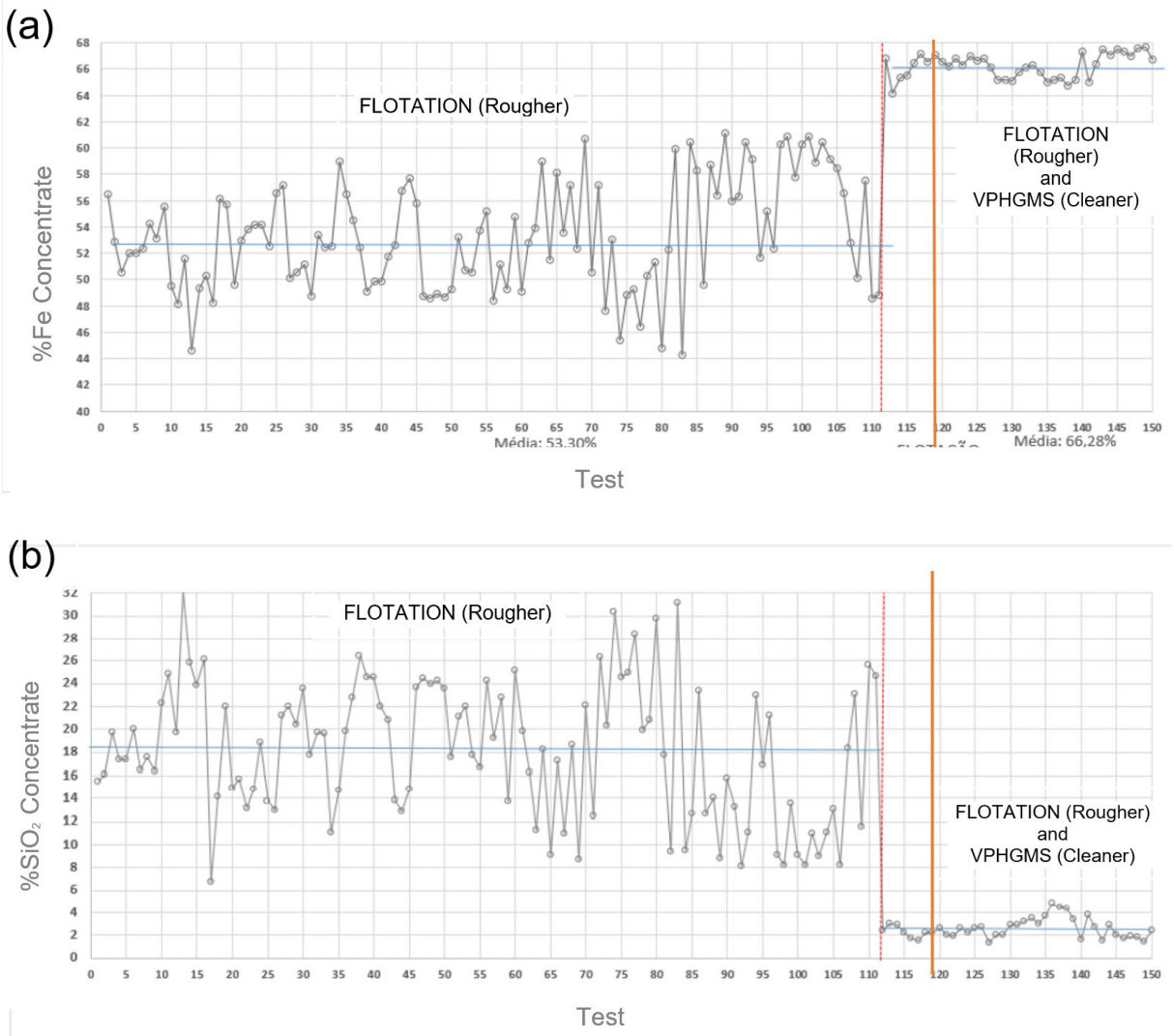

FIG 13 – Fe content (a) and SiO_2 content (b) for pilot test adopting flotation as rougher stage and flotation +VPHGMS as rougher/cleaner stages.

Through the pilot tests, the mass balance was determined for three different circuit configuration options to concentrate de slimes from Vargem Grande 2, considering a project with 45.86%Fe in the industrial plant slimes (Table 7).

TABLE 7

Flotation + VPHGMS simplified flow sheet and mass balance.

Flow sheet configuration	Product	Mass%	Fe, %	SiO_2, %	Al_2O_3, %	P, %	LOI, %
Flotation	Feed	100.00	45.86	30.42	2.33	0.060	1.53
	Concentrate	70.53	57.75	13.67	1.91	0.077	0.66
	Tailing	29.47	17.41	70.50	3.33	0.019	1.22
VPHGMS	Feed	100.00	45.86	30.42	2.33	0.060	1.53
	Concentrate	52.38	65.01	3.88	0.97	0.066	1.25
	Tailing	47.62	24.75	59.61	3.83	0.054	1.94
Flotation + VPHGMS	Feed	100.00	45.86	30.42	2.33	0.060	1.53
	Concentrate	47.99	67.22	2.47	0.45	0.050	0.85
	Tailing	52.01	26.15	56.21	4.06	0.069	2.16

It can be deduced from the Table 6, that in an industrial project, it is possible to design a flexible circuit to operate according to the characteristics of the slimes and the specific objectives (improve mass recovery or improve the quality of the concentrate, for example) adopting the configuration including flotation and magnetic separation or the options to bypass column flotation or the magnetic concentration.

CONCLUSIONS

The new amidoamine collector was able to promote a selective flotation of quartz from hematite without a depressant agent, such as starch. Therefore, this reagent can be an advantageous alternative to conventional amines, currently used in reverse cationic flotation of iron ores. The contact angle and infrared spectroscopy measurements showed that amidoamine has a much higher affinity for quartz than for hematite, indicating selectivity. The amide group in this collector structure plays important role for the hydrogen bonding stabilisation of the adsorption layer, thus the collector-collector interaction energy contributes to organise the amidoamine on the quartz surface. The structure of the adsorption layer of the amidoamine collector is controlled by the collector concentration. Thus, the adsorption on the hematite is limited by a hindrance effect on the mineral surface. The concentration of iron-bearing minerals from the slimes samples from two different industrial plants at Vale (Quadrilátero Ferrífero – MG) was evaluated at pilot scale considering the application of column flotation (reverse configuration), starch as a depressant and two kinds of silicates collector without previous desliming. It was possible to produce iron concentrates with grades higher than 60 per cent, SiO_2 below 5 per cent and Al_2O_3 at 3 per cent from only one of the two samples studied because of high amount of kaolinite. In the other hand, the significant fluctuations of the feed and concentrate grades were observed during continuous on-site pilot test campaign. The combination of the column flotation and high gradient magnetic separation allowed to stabilise the grade of the iron concentrate at 67 per cent with the silica content below 2.5 per cent.

ACKNOWLEDGEMENTS

The authors are grateful to the industrial partner Vale for the financial support and permission to publish this work.

REFERENCES

Aguiar, F L, 2013. Redução do Impacto Ambiental Através da Recuperação dos Ultrafinos de Minério de Ferro Redução do Impacto Ambiental Através da Recuperação dos Ultrafinos de Minério de Ferro, Monografia. Belo Horizonte (Minas Gerais): Universidade Federal de Minas Gerais, 2013.

Altin, G, Inal, S, Alp I, Lekili, M E, 2016. Recovery of chromite from processing plant tailing by vertical ring and pulsating hight-gradient magnetic separation, *International Black Sea Mining and Tunnelling Symposium*, 2016, 2–4 novembre, Trabzon-Turkey.

Araujo, A, Viana, P, and Peres, A, 2005. Reagents in iron ores flotation. *Miner. Eng.* 18(2):219–224.

Budemberg, G, 2016. Síntese de coletores para flotação de minério de ferro, Dissertação de Mestrado (unpublished). Lorena(São Paulo): Universidade de São Paulo. Escola de Engenharia de Lorena.

Filippov, L O, Filippova, I V, and Severov, V V, 2010. The use of collectors mixture in the reverse cationic flotation of magnetic ore: The role of Fe-bearing silicates. *Minerals Engineering,* 23(2):91–98.

Filippov, L O, Silva, K, Piçarra, A, Lima, N, Santos, I, Bicalho, L, Filippova, I V, Peres, A E C, 2021. Iron Ore Slimes Flotation Tests Using Column and Amidoamine Collector without Depressant, *Minerals*, 11(7): 699.

Filippov, L, Severova, V, and Filippova,., 2014. An overview of the beneficiation of iron ores via reverse cationic flotation. *International Journal of Mineral Processing*, 127:62–69.

Gomes, A C F, 2017. Estudo de Aproveitamento de Rejeito de Mineração, Dissertação de Mestrado (unpublished). Belo Horizonte (Minas Gerais): Universidade Federal de Minas Gerais, 2017.

Guimarães, N C, 2011. Filtragem de rejeitos de minério de ferro visando a sua disposição em pilhas, Dissertação de Mestrado (unpublished). Belo Horizonte(Minas Gerais): Universidade Federal de Minas Gerais, 2011.

Lima, N P, Silva, K, Souza, T, Filippov, L, 2020. The Characteristics of Iron Ore Slimes and Their Influence on The Flotation Process. *Minerals*, 10:675.

Liu, W, Peng, X, Liu, W, Wang, X, Zhao, Q, Wang. B, 2020. Effect mechanism of the iso-propanol substituent on amine collectors in the flotation of quartz and magnesite. *Powder Technology*, 360:1117–1125.

Ma, X and Bruckard, W, 2010. The effect of pH and ionic strench on starch-kaolinite interactions. *Int. J. Miner. Proc.,* 94:111–114.

Marques, M, 2013. Comportamento de minérios de ferro na concentração por flotação na presença de lamas, Dissertação de Mestrado (unpublished). Belo Horizonte (Minas Gerais): Universidade Federal de Minas Gerais, 2013.

Matiolo, E, Couto, H J B, Lima, N, Silva, K, 2020. Improving recovery of iron using column flotation of iron ore slimes. *Miner. Eng.* 158:106608.

Rath, S S, and Sahoo, H, 2022. A Review on the Application of Starch as Depressant in Iron Ore Flotation. *Mineral Processing and Extractive Metallurgy Review*, 43:122–135.

Severov, V, Filippova, I, Filippov, L, 2013. Floatability of Fe-bearing silicates in the presence of starch: adsorption and spectroscopic studies. *J. Phys. Conf. Ser.* 416(1):012017.

Shrimali, K, and Miller, J, 2016. Polysaccharide Depressants for the Reverse Flotation of Iron Ore. *Trans Indian Inst Met*, 69:83–95.

Silva, K, Filippov, L O, Piçarra, A, Filippova, I V, Lima, N, Skliar A, Faustino L, Leal Filho, L, 2021. New perspectives in iron ore flotation: use of collector reagents without depressants in reverse cationic flotation of quartz, *Minerals Engineering*, 170:107004.

Silva, K, Silva, L, Pereira, A, Bastos, L, Correia, J, Piçarra, A, Bicalho, L, Lima, N, Filippova, I V, Filippov, L O, 2022. Comparison between etheramine and amidoamine (N-[3-(dimethylamino)propyl]dodecanamide) collectors: Adsorption mechanisms on quartz and hematite unveiled by molecular simulations, *Minerals Engineering*, 180:107470.

Turrer, H, and Peres, A, 2010. Investigation on alternative depressants for iron ore flotation. *Miner. Eng.,* 23:1066–1069.

Veloso, C H, Filippov, L O, Filippova, I V, Ouvrard S, Araujo A C, 2020. Adsorption of polymers onto iron oxides: Equilibrium isotherms. *J Mater. Res. Technol*., 9(1):779–788.

Veloso, C, Filippov, L, Filippova, I, and Araujo, A, 2018. Investigation of the interaction mechanism of depressants in the reverse cationic flotation of complex iron ores. *Minerals Engineering* 125:133–139.

Weissenborn, P, Warren, L, Dunn, J, 1995. Selective flocculation of ultrafine iron ore. 1. Mechanism of adsorption of starch onto hematite*. Colloids and Surfaces – A: Physicochemical and Engineering Aspect*, 99:11–27.

Wolff, A P, Costa, G M, and Dutra, F, C, 2011. A comparative study of ultra-fine iron ore tailings from Brazil. *Mineral Processing and Extractive Metall. Rev*., 32:47–59.

Xu, L, Hu, Y, Dong, F, Jiang, H, Wu, H, Zhen, W, Liu, R, 2015. Effects of particle size and chain length on flotation of quaternary ammonium salts onto kaolinite. *Mineral. Petrol*., 109:309–316.

Techno-economic implications of implementing novel reagents to improve fines recovery in mineral flotation

G V Franks[1,7], S Lowjun[2,7], C A Thomas[3,7], E Forbes[4,7], K Runge[5,7] and I Verster[6,7]

1. Professor, Chemical Engineering, University of Melbourne, Vic 3010.
   Email: gvfranks@unimelb.edu.au
2. Student, Chemical Engineering, University of Melbourne, Vic 3010.
   Email: slowjun@student.unimelb.edu.au
3. Research Fellow, Chemical Engineering, University of Melbourne, Vic 3010.
   Email: casey.thomas@unimelb.edu.au
4. Senior Research Fellow, JKMRC, The University of Queensland, Indooroopilly, Qld 4068.
   Email: l.forbes@uq.edu.au
5. Associate Professor, JKMRC, The University of Queensland, Indooroopilly, Qld 4068.
   Email: k.runge@uq.edu.au
6. Senior Research Fellow, JKMRC, The University of Queensland, Indooroopilly, Qld 4068.
   Email: l.verster@uq.edu.au
7. ARC Centre of Excellence for Eco-Efficient Beneficiation of Minerals

INTRODUCTION

Fine (<20 μm) valuable mineral particles are difficult to recover in conventional flotation circuits. (Trahar and Warren, 1976; Jameson, Nguyen and Ata, 2007; Kohmuench *et al*, 2018). This leads to a loss of valuable fine mineral particles to tailings. Recovering these particles would be of economic benefit. Novel reagents, including temperature responsive polymers, for example, are being developed to improve recovery of fine valuable mineral particles by froth flotation (Ng *et al*, 2018a, 2018b). The approach involves selectively aggregating the valuable fine particles and making these aggregates hydrophobic, resulting in hydrophobic aggregates of appropriate size (in order of 100 microns) being amenable to recovery by froth flotation. The polymers developed have been produced at laboratory scale but not a full scale yet. The exact cost of producing such novel polymers is currently unknown, but they are likely to be more expensive than conventional reagents.

APPROACH

This work involves preliminary techno-economic analysis of the impact of implementing such reagents in processing of copper and nickel ores. The influence of the cost of the reagent, other operating costs and additional capex requirements are considered. The value of the additional valuable mineral recovered is estimated. Analysis is conducted on some typical copper and nickel mineral processing flow sheets based on similarity to some actual operations. As shown in Figure 1, two scenarios are considered: 1) treating the tailings for the existing operation and 2) splitting the feed by size into different streams and treating the fines in parallel to the majority of the ore.

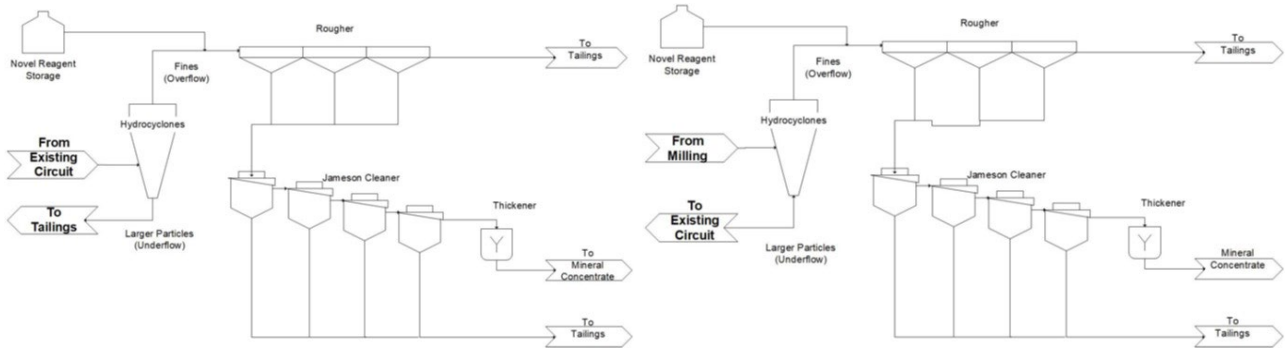

FIG 1 – Block flow diagrams of schemes for (left) processing the tailings and (right) splitting the feed and processing the fines and coarse fractions separately.

PRELIMINARY RESULTS

The split processing is generally more economically viable than the tailings processing. Also, the efficiency of the novel reagents in recovering fines is a significant factor in determining the economic viability of implementing novel reagents in a particular operational scenario. The assumption used in the current work is that the novel reagent can recover 90 per cent of the valuable fine particles. The confidence in the actual effectiveness of such reagents in full scale industrial operation is low since only lab scale tests have been conducted to date. The novel reagents may or may not add value to operations, depending on various factors such as the feed grade, the original plant recovery and amount of lost valuables in the fines. In general, novel reagents can provide value for operations where the overall recovery is below about 60 or 70 per cent, particularly where that loss is mainly in the fine fraction. The economic viability of the process looks more promising when the cost of the reagents required is assumed to be similar to the cost of currently used commercial flocculants.

CONCLUSIONS

Preliminary techno-economic analysis has been conducted to improve understanding of the types of operations which could benefit from implementation of novel reagents that improve recovery of fine particles by flocculation/flotation mechanism. The approach can provide benefit in cases when the amount of fines lost to tailings is currently high and if the cost of the reagents can be reduced to similar to the cost of current commercial flocculants.

ACKNOWLEDGEMENTS

Thanks to The Australian Research Council (ARC) Centre of Excellence (CoE) for Enabling Eco-Efficient Beneficiation of Minerals Grant No. CE200100009 for supporting this research.

REFERENCES

Jameson, G J, Nguyen, A V and Ata, S, 2007. The flotation of fine and coarse particles, in *Froth Flotation, A Century of Innovation*, Eds., M C Fuerstenau, G J Jameson, and R-H Yoon, (Society for Mining, Metallurgy and Exploration, Littleton CO, USA).

Kohmuench, J N, Mankosa, M J, Thanasekaran, H and Hoebert, A, 2018. Improving coarse particle flotation using the HydroFloat™ (raising the trunk of the elephant curve), *Minerals Engineering*, 121, 137–145.

Ng, W S, Connal, L A, Forbes, E and Franks, G V, 2018a. A review of temperature responsive polymers as novel reagents for solid-liquid separation and froth flotation of minerals', *Minerals Engineering*, 123, 114–159.

Ng, W S, Cooper, L, Connal, L A, Forbes, E, Jameson, G J and Franks, G V, 2018b. Tuneable collector/depressant behaviour of xanthate-functional temperature-responsive polymers in the flotation of copper sulfide: Effect of shear and temperature, *Minerals Engineering*, 117, 91–99.

Trahar, W J and Warren, L J, 1976. The flotability of very fine particles – A review. *International Journal of Mineral Processing,* 3, 103–131.

Assessing flotation circuit efficiencies using the liberation characteristics of particles in the circulating load

M Gupta[1], K Huang[2], R H Yoon[3] and A Noble[4]

1. Graduate Research Assistant, Virginia Tech, Blacksburg, Virginia, USA 24061. Email: mgupta07@vt.edu
2. Research Associate, Virginia Tech, Blacksburg, Virginia, USA 24061. Email: hkaiwu91@vt.edu
3. University Distinguished Professor, Virginia Tech, Blacksburg, Virginia, USA 24061. Email: ryoon@vt.edu
4. Associate Professor, Virginia Tech, Blacksburg, Virginia, USA 24061. Email: aaron.noble@vt.edu

INTRODUCTION

Froth flotation is the most commonly used separation technology in the mineral industries. Given the complexity of the pulp and froth phases as well as the multitude of operational parameters that influence flotation performance, purely fundamental models with strong predictive capacity are limited. As a result, accurately modelling modifications to an existing flotation circuit are challenging, particularly when using empirically-derived models from a different operating configuration. Despite these complexities, a recent publication by the authors (Huang *et al*, 2022) has shown that flotation rates can be accurately predicted from a first-principles model that incorporates hydrodynamic parameters (eg pulp density, superficial gas velocity, feed flow rates etc), surface chemistry parameters (eg contact angle, zeta potentials and surface tension), and size-by-class liberation data. Circuit simulations using this model were shown to be effective in predicting experimental grade-recovery curves from the size-by-class mineral liberation matrix. Since the model is derived from fundamental characteristics of the flotation system, it can be used to simulate alternative circuit configurations with varying degrees of recycle.

Conventional flotation circuits are operated in a closed-circuit configuration by routing the cleaner scavenger tails (CST) back to the rougher feed to provide an additional opportunity to recover the slow-floating particles. This widely-used flotation strategy has been under constant debate, and several researchers have provided evidence that open circuit configurations provide higher separation and better circuit control (Konigsman, 1985; Bulatovic *et al*, 1998; Thompson, 2016). Recently, Finch and Tan (2021), used linear circuit analysis to show that open circuit configurations have a fundamental advantage when stage recoveries are high. Given the limitations of these prior studies, the objective of the current work is to further evaluate the merits of the open circuit configuration through a detailed circuit analysis and simulation study incorporating the first principles model described above.

Experimental

Plant audit data, namely including the size-by-class mass liberation matrix (m_{ij}), were collected for both the fresh feed and CST from an operating copper flotation plant. The rougher circuit consisted of five flotation cells and the rougher-cleaner circuit was run in a standard closed-circuit design with the CST being recirculated to the roughers feed tank. The recirculation from the CST constituted 11.6 wt per cent of the rougher feed, with the remainder being fresh feed from the grinding circuit. The fresh feed Cu grade was 0.24 per cent while the CST grade was 0.29 per cent. XRD analysis confirmed chalcopyrite as the major copper bearing mineral in the feed, and as such, a binary model consisting of chalcopyrite and gangue minerals were chosen for simulation.

Results

Model validation

The mineral-liberation data was used to determine the mean contact angles (θ_{ij}) by assigning contact angle of 72° and 8° for free chalcopyrite minerals and gangue particles respectively. θ_{ij}, a thermodynamic parameter, was used to determine the hydrophobic force constants, a kinetic parameter, using K_{131} versus θ developed by Pazhianur and Yoon (2003). Hydrophobic force plays

an important role in determining the energy barrier for bubble-particle attachment and thereby, helps in accurately predicting the flotation rate constants as has been shown by Huang *et al* (2022). Using the modelling approach described in that paper, the flotation rate constants were predicted for each size-by-liberation class and were then used to calculate the cell-by-cell recoveries. For the rougher circuit, the simulated recovery was determined to be 85.4 per cent, while the corresponding recovery measured in the plant was 85.4 per cent, an error of just 1.2 per cent. Similarly, the Cu grade obtained from simulation was 2.96 per cent, while the plant data showed a rougher concentrate grade of 2.5 per cent.

Effect of recirculating load

When the CST stream is continually recycled to the roughers, there is an increased probability of oxidation, due to the increased surface area of the fine particles that are exposed to highly aerated cleaner cells. This oxidation inhibits the hydrophobicity of the recycled materials, thus reducing the floatability relative to that of similarly sized materials in the fresh feed. In order to account for this oxidation, the free chalcopyrite mineral present in the CST is assigned a contact angle of 60° rather than the higher 72° assigned to that of the fresh feed. While the contact angle difference is not large, the effect of oxidation on the rate constants is very profound as the energy barrier for bubble-particle attachment is strongly dependent of mineral contact angle (Figure 1).

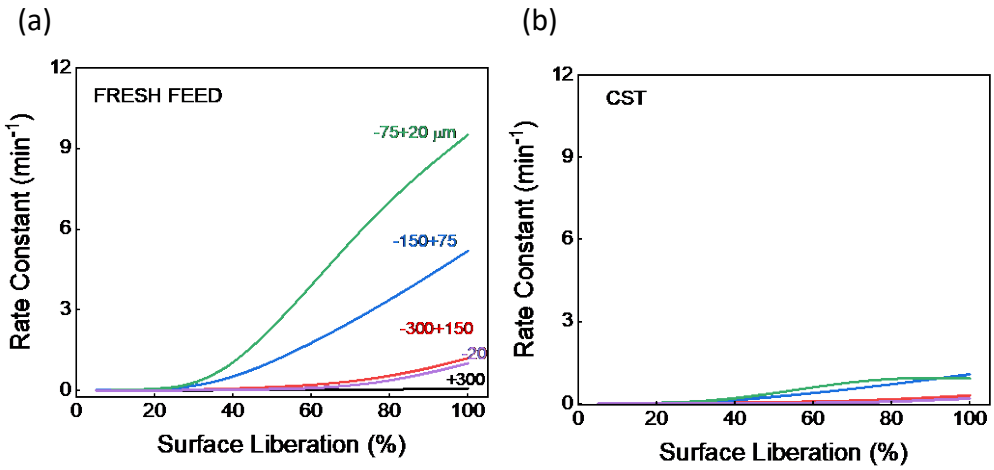

FIG 1 – Comparison of the rate constants for the fresh feed and CST with different size by class liberation. (a) feed with a maximum contact angle of 72°; (b) CST with a maximum contact angle of 60°.

To investigate the influence of the recycled CST on the performance of the rougher cells, a series of simulations were conducted varying the ratio of the CST to that of the fresh feed in the rougher feed. Values in the simulation ranged from 80 per cent fresh feed (by volume) to 100 per cent fresh feed, effectively representing a fully open circuit. As the portion of CST in the rougher feed was increased, the overall recovery decreased owing to the lower mean contact angle and lower mean particle size. Interestingly, this effect was particularly pronounced for coarse particles. Moving from the 88 per cent fresh feed / 12 per cent CST condition to the fully open circuit condition prompted a 5 per cent increase in the copper recovery of the -300+150 µm fraction

In addition, the fresh feed usually has a higher solids density (~40–45 per cent) compared to that of the CST (10–20 per cent). As a result, the recycling of CST reduces the retention time in the rougher and negatively impacts the circuit performance. To demonstrate this effect, the solids density of the feed was changed during the circuit simulation in conjunction with the change in the CST makeup. An economic analysis was also conducted assuming a feed throughput of 5000 t/h. This result indicates that both the recoveries and revenue can be increased by reducing the CST contribution to the roughers feed (Figure 2).

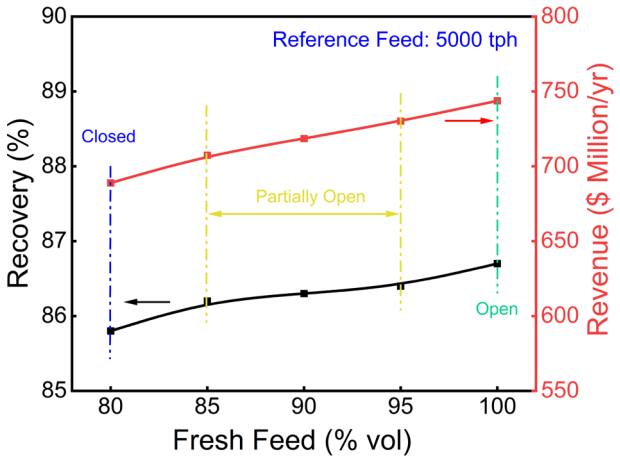

FIG 2 – Simulation results showing the effect of increasing the portion of fresh feed versus CST in the combined rougher feed. Economic results were computed assuming a reference feed of 5000 t/h and a copper price of $4.20/lb.

CONCLUSIONS

Liberation data from an operating copper flotation plant were used to validate a novel flotation simulator. The inclusion of the chemical parameters in the simulator allows it to predict grade and recovery for a circuit with low error. The size-by-class flotation rate constants computed using the simulator were significantly lower for CST in comparison to the fresh feed. This reduction can be associated with the lower particle size and oxidation of the CST particles during recirculation. The slow-floating CST particles therefore, reduces the kinetics of the feed to the roughers leading to reduction in the overall plant performance. Open circuits can provide a more efficient way to improve the plant performance. Alternatively, the slow-floating CST can be recovered in separate flotation circuit in order to maximise the Cu recovery.

REFERENCES

Bulatovic, S M, Wyslouzil, D M and Kant, C, 1998. Operating practices in the beneficiation of major porphyry copper/molybdenum plants from Chile: Innovated technology and opportunities, a review, *Miner. Eng*., 11(4), 313–331.

Finch, J A and Tan, Y H, 2021. A comparison of two flotation circuits. *Miner. Eng*., 170, 107002.

Huang, K, Keles, S, Sherrell, I, Noble, A and Yoon, R H, 2022. Development of a flotation simulator that can predict grade vs. recovery curves from mineral liberation data, *Miner. Eng*., 181, 107510.

Konigsman, K V, 1985. Flotation techniques for complex ores, In: A D Zunkel (ed.), *Complex Sulphides: Processing of Ores, Concentrates and By-products*, Pennsylvania, USA, pp. 5–19.

Pazhianur, R and Yoon, R H, 2003. Model for the origin of hydrophobic force, *Min. Metall. Explor.*, 20(4), 178–184.

Thompson, P, 2016. Laboratory testing for sulfide flotation process development, *Miner. Metall. Process.*, 33, 200–213.

α-Tocopherol based small molecules and RAFT polymers as novel collectors for mineral beneficiation

T Hsia[1], B Fan[2], T Perera[3] and S Thang[4]

1. Research Fellow, Monash University, School of Chemistry, Clayton Vic 3800. Email: tina.hsia@monash.edu
2. Research Fellow, Monash University, School of Chemistry, Clayton Vic 3800. Email: bo.fan@monash.edu
3. PhD candidate, Monash University, School of Chemistry, Clayton Vic 3800. Email: tammitage.perera@monash.edu
4. Professor, Monash University, School of Chemistry, Clayton Vic 3800. Email: san.thang@monash.edu

ABSTRACT

Minerals are valuable resources and critical elements for a broad range of biological and technological applications, including technological developments to improve energy efficiency and the global movement to promote a low-carbon economy. However, in order to extract these critical metals, large amounts of waste and toxic chemicals are generated, as well as the use of high energy and large amounts of water consumption. Froth flotation is one of the most commonly used processes to separate and collect high-value minerals, but it still has some limitations, including low flotation efficiency performances using existing collectors and other reagents. Therefore, there is an urgent need to design and develop new metal-specific collectors to more efficiently separate and recover valuable minerals and to allow bulk water recovery from flocculated tailings. In this research, we propose to use our newly designed and synthesised novel collectors derived from a type of vitamin E (α-tocopherol), a relatively inexpensive and non-toxic natural molecule. As a potential collector-building block, α-tocopherol has a long hydrophobic carbon chain that facilitates the attachment to air bubbles during the froth flotation process. In addition, the phenol group of this molecule can be easily modified to incorporate various functional groups for targeting different types of minerals. Furthermore, α-tocopherol can be converted into a monomer for polymerisation by the reversible addition-fragmentation chain-transfer (RAFT) process, which can provide us with polymer based-collectors with high precision control of molecular weight and architecture. So far, small-scale qualitative experiments on α-tocopherol-based collectors have been performed with good results, which indicates the feasibility of these compounds as novel collectors for improved froth flotation processes.

INTRODUCTION

Froth flotation is a versatile and facile technology used in mineral beneficiation processes for collecting high-value minerals (Liu *et al*, 2017; Prakash *et al*, 2018). Although froth flotation has been used for over a century, it still has some limitations, such as the generation of large amounts of waste (including unbound minerals) and toxic chemicals during the metal recovery process as well as the use of high energy and a large volume of water consumption (Mesa and Brito-Parada, 2019; Xie *et al*, 2021). Globally, more than 100 Bt of mining waste is generated each year, and that number is likely to grow as high-grade and easily processed ores are depleted and lower-grade resources are increasingly utilised (Tayebi-Khorami *et al*, 2019). The global movement towards a low-carbon economy is driving the mining industry's transition to a circular economy system and the reprocessing of mining waste into valuable products (Norgate and Haque, 2010; Tayebi-Khorami *et al*, 2019). However, the minerals industry is facing serious challenges as there are three main types of mining and refining wastes: i) mining wastes, ii) processing wastes and iii) metallurgical wastes, which have different characteristics such as particle size, pH and poor mineral liberation (Whitworth *et al*, 2022). Existing collectors exhibit low flotation efficiency in recovering these refractory ores. Therefore, new flotation methods need to be developed to maintain the sustainability of the metal resources.

The current use of advanced grinding techniques means that low-grade mineral deposited can be economically exploited (Farrokhpay *et al*, 2021). This has allowed researchers to focus on improving

flotation efficiency in particular towards fine and ultrafine particles. Several studies have been carried out to further explore the nature of the flotation process. These studies include capturing of solid particles by air bubbles according to their surface hydrophobicity and hydrophilicity in aqueous media (Prakash *et al*, 2018). Three strategies have been proposed: i) increasing the probability of particle-bubble collision by increasing particle size through aggregation or lowering bubble size; ii) using vacuum or pressure-release flotation in which the gas is precipitated on the particles to be floated; and iii) using selective chemisorbing collectors. Recently, the use of polymer collectors has gained a lot of attention, especially for fine and ultrafine particles. Polymer collectors, depending on their molecular weight, can improve fine particle recovery by aggregating them into particles with larger sizes (high molecular weights) that are more suitable for flotation or flocculant tailings.

This research focuses on the selective separation, as well as the bulk water recovery from flocculated tailings, which can be achieved through the design and development of new metal-specific collectors (both small molecules and macromolecules) derived from a type of vitamin E (α-tocopherol). In addition to the use of economically and environmentally friendly α-tocopherol-based small molecule collectors, this research will also use the reversible addition-fragmentation chain-transfer (RAFT) polymerisation (Chiefari *et al*, 1998) to design polymeric collectors with high precision ratios of hydrophobic and hydrophilic components, as well as polymers designed to accommodate various complex structures (block, brush, comb, star-shaped polymers etc) to improve flotation efficiency, which is difficult to achieve in small molecules.

The design of α-tocopherol collectors

Typically, flotation collectors consist of two parts; the polar group that exhibits a strong affinity to the mineral surface and the non-polar hydrocarbon chain that attaches to the air bubbles, with emphasis on the longer hydrocarbon chain that tends to adhere better to the air bubble (Liu *et al*, 2022). The natural source α-tocopherol consists of an aromatic ring as well as a sixteen-carbon aliphatic chain that provides an ideal hydrophobic portion of the collector (Figure 1). The phenolic functionality can be easily modified to incorporate various functional groups for targeting different types of minerals.

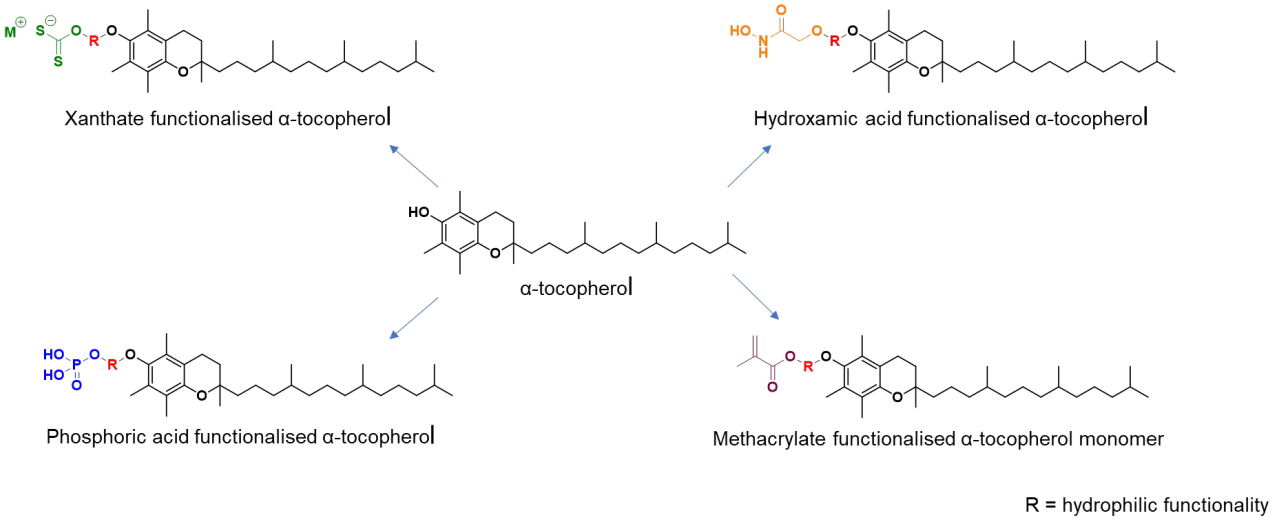

FIG 1 – α-tocopherol derived collectors and monomers.

The α-tocopherol-based collectors was designed by incorporating the common chelating functionalities: xanthate, phosphate and hydroxamic acid (Lee *et al*, 2009; Marion *et al*, 2020). Through modification of the phenol site of the α-tocopherol (Figure 1), a series of hydrophobic collectors was synthesized. Furthermore, hydrophilic functionality was also incorporated into the α-tocopherol collectors as shown in Figure 1, and by increasing the length of the hydrophilic linker (R group), these α-tocopherol collectors exhibit surfactant-like properties and allow the generation of stable foams. For example, by tunning the hydrophilic linker length, the α-tocopherol collectors with the xanthate group exhibited different water solubility, ranging from insoluble compound to easily dispersed surfactant that produces stable foam for up to several hours (Figure 2).

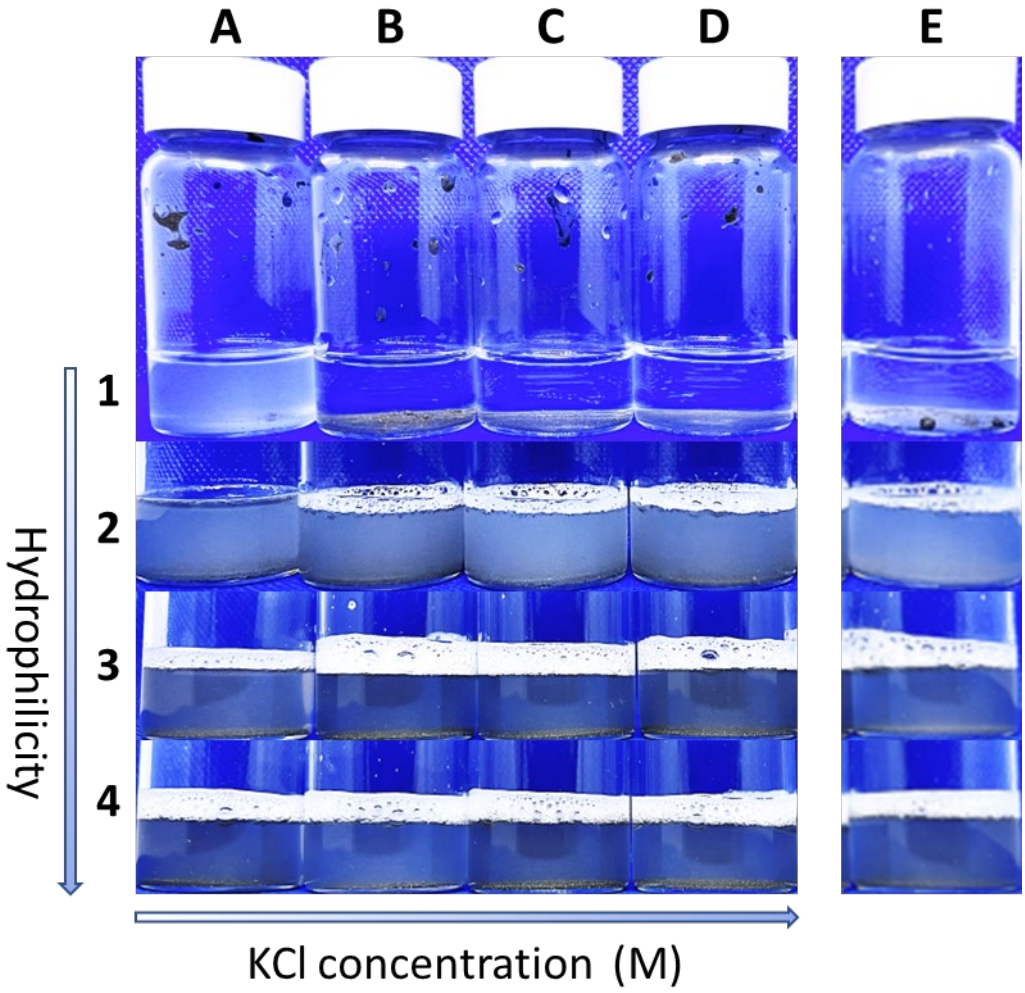

FIG 2 – α-tocopherol-based xanthate collectors with chalcopyrite at different salt concentration with: column A: H_2O; column B: 0.01M KCl; column C: 0.1M KCl; column D: 1.0M KCl; column E: addition of silica in 0.1M KCl.

A series of laboratory-scale experiments were conducted with α-tocopherol xanthate collector, where chalcopyrite was added with the collector at different saline concentrations and then shaken vigourously to mimic the insertion of air bubbles. Photographs were taken after allowing the samples to settle for 5 minutes (Figure 2). The α-Tocopherol xanthate collectors with different hydrophilic properties were used to test their performance as chalcopyrite collectors at different saline concentrations. The saline concentration ranged from 0.1M potassium chloride (KCl) to 1.0M KCl solution to mimic the different saline water used at various mining sties. As shown in Figure 2, when the hydrophilicity of the collector increased, the collector acquired surfactant-like properties and was able to behave like a foaming agent. When comparing the same collector at different saline concentrations, it was observed that as the saline concentration increased, it helped to stabilise the foam (Wang and Peng, 2014), which was evident in the second row of collectors. The collector selectivity was examined by samples containing chalcopyrite and silica (column E, Figure 2). It was observed that in the presence of hydrophobic α-tocopheryl xanthate collector, chalcopyrite aggregates with the collector, and when the hydrophilicity of the α-tocopheryl xanthate collector increases, chalcopyrite particles were seen to float to the foam surface while silica particles remained settle at the bottom of the vial.

In addition, α-tocopherol can be converted into monomers, which can be polymerised through the environmentally friendly RAFT process and provides us with α-tocopherol polymer-based collectors with predetermined molecular weights and low dispersity as well as various functional units for modulating hydrophobic and binding properties (Figure 1). To demonstrate this, a RAFT block copolymer was synthesized using α-tocopherol monomers representing hydrophobic domain that

attach to air bubbles and xanthate-functionalised hydrophilic domain with collector properties. Similar tests were also conducted with α-tocopherol-based polymeric collectors, which have an affinity for mineral surfaces and prolonged foam stability compared to small-molecule-based α-tocopherol collectors. These results indicate the feasibility of these compounds as novel collectors and/or flocculants for the improved froth flotation processes.

CONCLUSIONS

The use of naturally sourced α -tocopherols to design mineral collectors offers great insight into improving mineral beneficiation. The α-tocopherol derivative collectors with foaming properties can reduce the use of chemical reagents, providing an economical and environmentally friendly option. By designing α-tocopherol derivative collectors and using RAFT polymerisation, we can explore small molecule collectors, low molecular weight polymer collectors as well as high molecular weight flocculants to effectively separate different types of minerals.

ACKNOWLEDGEMENTS

The authors acknowledge the funding support from the Australian Research Council Centre of Excellence for Enabling Eco-Efficient Beneficiation of Minerals (CE200100009).

REFERENCES

Chiefari, J, Chong, Y K, Ercole, F, Krstina, J, Jeffery, J, Le, T P T, Mayadunne, R T A, Meijs, G F, Moad, C L, Moad, G, Rizzardo, E and Thang, S H, 1998. Living Free-Radical Polymerization by Reversible Addition−Fragmentation Chain Transfer: The RAFT Process. *Macromolecules,* 31, 5559–5562.

Farrokhpay, S, Filippov, L and Fornasiero, D, 2021. Flotation of Fine Particles: A Review. *Mineral Processing and Extractive Metallurgy Review,* 42, 473–483.

Lee, K, Archibald, D, Mclean, J and Reuter, M A, 2009. Flotation of mixed copper oxide and sulphide minerals with xanthate and hydroxamate collectors. *Minerals Engineering,* 22, 395–401.

Liu, G, Yang, X and Zhong, H, 2017. Molecular design of flotation collectors: A recent progress. *Adv Colloid Interface Sci,* 246, 181–195.

Liu, M, Yu, H, Zhang, H, Wang, K, Tan, X and Liu, Q, 2022. Roles of the hydrophobic and hydrophilic groups of collectors in the flotation of different-sized mineral particles. *Colloids and Surfaces A: Physicochemical and Engineering Aspects,* 637.

Marion, C, Li, R and Waters, K E, 2020. A review of reagents applied to rare-earth mineral flotation. *Adv Colloid Interface Sci,* 279, 102142.

Mesa, D and Brito-Parada, P R, 2019. Scale-up in froth flotation: A state-of-the-art review. *Separation and Purification Technology,* 210, 950–962.

Norgate, T and Haque, N, 2010. Energy and greenhouse gas impacts of mining and mineral processing operations. *Journal of Cleaner Production,* 18, 266–274.

Prakash, R, Majumder, S K and Singh, A, 2018. Flotation technique: Its mechanisms and design parameters. *Chemical Engineering and Processing – Process Intensification,* 127, 249–270.

Tayebi-Khorami, M, Edraki, M, Corder, G and Golev, A, 2019. Re-Thinking Mining Waste through an Integrative Approach Led by Circular Economy Aspirations. *Minerals,* 9.

Wang, B and Peng, Y, 2014. The effect of saline water on mineral flotation – A critical review. *Minerals Engineering,* 66–68, 13–24.

Whitworth, A J, Forbes, E, Verster, I, Jokovic, V, Awatey, B and Parbhakar-Fox, A, 2022. Review on advances in mineral processing technologies suitable for critical metal recovery from mining and processing wastes. *Cleaner Engineering and Technology,* 7.

Xie, L, Wang, J, Lu, Q, Hu, W, Yang, D, Qiao, C, Peng, X, Peng, Q, Wang, T, Sun, W, Liu, Q, Zhang, H and Zeng, H, 2021. Surface interaction mechanisms in mineral flotation: Fundamentals, measurements and perspectives. *Adv Colloid Interface Sci,* 295, 102491.

Traversing the Valley of Death – upscaling the REFLUX™ flotation cell

S M Iveson[1], J L Sutherland[2], M J Cole[3], D J Borrow[4], J Zhou[5] and K P Galvin[6]

1. Research Academic, ARC Centre of Excellence for Enabling Eco-Efficient Beneficiation of Minerals, Newcastle Institute for Energy and Resources, University of Newcastle, Callaghan NSW 2308. Email: simon.iveson@newcastle.edu.au
2. Research Associate, ARC Centre of Excellence for Enabling Eco-Efficient Beneficiation of Minerals, Newcastle Institute for Energy and Resources, University of Newcastle, Callaghan NSW 2308. Email: joshua.sutherland@newcastle.edu.au
3. Research Associate, ARC Centre of Excellence for Enabling Eco-Efficient Beneficiation of Minerals, Newcastle Institute for Energy and Resources, University of Newcastle, Callaghan NSW 2308. Email: Matt.Cole@newcastle.edu.au
4. Research Associate, ARC Centre of Excellence for Enabling Eco-Efficient Beneficiation of Minerals, Newcastle Institute for Energy and Resources, University of Newcastle, Callaghan NSW 2308. Email: daniel.j.borrow@newcastle.edu.au
5. Senior Research Associate, ARC Centre of Excellence for Enabling Eco-Efficient Beneficiation of Minerals, Newcastle Institute for Energy and Resources, University of Newcastle, Callaghan NSW 2308. Email: james.zhou@newcastle.edu.au
6. Laureate Professor, ARC Centre of Excellence for Enabling Eco-Efficient Beneficiation of Minerals, Newcastle Institute for Energy and Resources, University of Newcastle, Callaghan NSW 2308. Email: kevin.galvin@newcastle.edu.au

ABSTRACT

New technologies can easily take around ten years to commercialise. Strong research support is needed in parallel with the process of innovation and commercialisation, in building a deeper understanding of the underpinning physicochemical and hydrodynamic forces that deliver the separations, in achieving improvements, in the deployment of a new technology, and in expanding the innovation platform to create new IP. External investment beyond the research, derived from the genuine value proposition of transformational change, funds the pathway for traversing the so-called Valley of Death.

INTRODUCTION

The invention of the REFLUX™ Flotation Cell (RFC™) (Galvin, 2021), filed as a provisional patent in 2011, was originally motivated by an industrial need to recover and concentrate high value cenospheres from fly ash. The research soon expanded to address the far greater need for a better flotation cell, confirming the potential for delivering process intensification and extreme levels of product cleaning. That research is continuing as part of multiple CoEMinerals projects. The technology TRL of 6–7 finally increased to 8 in 2021 following a successful full-scale trial on a mine site, having survived the proverbial near-death experience multiple times!

SECURING FUNDING FOR A FULL-SCALE TRIAL

Efforts to secure funding to investigate up-scaling of the RFC™ commenced many years earlier, such is the nature of the commercialisation journey. Following one failed attempt for a NSW government grant in 2015, a sum of $1 M was secured in 2016 from the Australian Government's new Global Innovation Linkage (GIL) scheme, along with initial support of $0.7 M from the licensee, FLSmidth, $0.3 M from ACARP and $0.2 M from the University of Newcastle.

NEAR DEATH EXPERIENCES

Once the project commenced, the host site chose to invest its own funds towards a plant six times larger than required for the trial. While this confidence was encouraging, their design incorporated significant contingency in the form of an allowance to revert, if necessary, back to the conventional technology, making the entire proposition too expensive. This diversion took the project to its **first near-death experience**, costing over 12 months of project time, and leaving just four weeks to re-assemble an entirely new proposition.

A new site was identified within a week, and MoU between six organisations secured, and contract with an SME signed, leaving just a few days spare. A two-stage cascading RFC™ system, over 20 m high, underwent detailed design. There was bad news when it was discovered the foundations under the existing concrete slab would need to be excavated and re-engineered at considerable cost. And following the tender it was discovered the cost of the facility was well beyond the budget. This was the **second near-death experience**.

In parallel with the detailed design work, new research confirmed the viability of replacing the two-stage system with a single-stage RFC™ separator. The new goal was to operate at about five times the feed rate of a conventional cell, while achieving product cleaning well beyond that currently possible. Laboratory work led to the development of two skid-mounted pilot plants, one for the Americas, and one for Australia, both funded by partner FLSmidth.

The full-scale facility was re-designed as a single-stage separator at ground-level (Figure 1). If we had known that wind-loads had triggered the need for excavation of the site in the previous design, this ground-level approach would have been adopted sooner, saving significant time and money. The new single-stage ground-level design was, in fact, a blessing, a considerable reduction in the complexity and cost, hence a vastly more attractive solution for industry. **There are benefits from the Valley of Death after all!**

FIG 1 – Photograph of the skid-mounted single-stage separator installed on-site.

With the project funds depleting with time, however, it became clear following a new tender that even this solution was too expensive. **The project was now firmly on death row.** The timing was not good for FLSmidth either, so we needed a way to keep the project moving. The solution was to establish a Phase I and a Phase II objective, by securing an alternative feed source in the plant to reduce the costs. FLSmidth's local engineering group undertook the installation, greatly de-risking the project from the pitfalls of 'variations'. These changes made it possible for the University to commit the project funds, guaranteeing a facility would be produced. New funds from FLSmidth were secured in the following year to complete Phase II; the final project cost was $4.5 M cash and in-kind.

In addition to meeting mine site compliance, there were further delays due to catastrophic bushfires in 2019–2020, the NSW lock-down in early 2020, and floods. Following initial commissioning, a plug of sediment that formed within the main water pipe over the pre-ceding months travelled through the circuit causing significant damage, costing two more months.

Finally, prior to Easter 2021, the facility was ready for its first experiment. However, the absence of a single pipe bracket support delayed commencement by two more days, after which we discovered the plant feed was no longer available that week. Pre-Easter plans were abandoned. This was a considerable blow as the site was also closed for two weeks after Easter for maintenance. The completion date of the government funding was June 30; there would be no more extensions as we had already been granted a 12 month COVID extension in the previous year! **Could a single pipe bracket become the proverbial 'straw that breaks the camel's back'?**

OUTCOMES

In May 2021 we seized the opportunity to commence the experiments despite the facility requiring more engineering improvements. The goal was to achieve a turn-key commencement by applying the settings established from the laboratory program. Once the reagent settings were confirmed, the turn-key performance was secured. The system was sustained at elevated feed fluxes with a strong focus on the intermediate throughput of 220 m^3/h, ie 1.9 cm/s. The five runs had an average feed ash of 60.9 wt%, product ash of 12.7 wt%, and reject ash of 81.8 wt% across the period. The investigation was benchmarked in multiple ways, confirming the grade-recovery response had outperformed the Tree-Curve and Coal Grain Analysis flotation predictions (Iveson *et al*, 2022).

The technology had been de-risked! After completing the engineering improvements, a new road was installed near the facility preventing site access for a month. Then, NSW went into lockdown for four more months. **A single $100 pipe bracket could have terminated a $4.5 M project.**

CONCLUSIONS

This project was ultimately successful. The goal was 'not to deliver a pre-conceived process design', but rather 'to de-risk a new technology'. This meant there needed to be flexibility in the pathway, coupled with a preparedness to redefine the meaning of success.

ACKNOWLEDGEMENTS AND DISCLAIMERS

The University of Newcastle holds international patents on the REFLUX™ Flotation Cell and has a Research and Development Agreement with FLSmidth Pty Ltd. One of the report authors, K P Galvin, is the inventor of the REFLUX™ Flotation Cell and is a beneficiary of the University's intellectual property policy.

This research was funded by an Australian Government Global Innovation Linkage grant (GIL53761) and the Australian Coal Association Research Program (ACARP Project C23045). The upscaling of the technology also is aligned with the research programs of the ARC Centre of Excellence for Enabling Eco-Efficient Beneficiation of Minerals (Grant CE200100009). A number of companies also contributed valuable support to this project:

- FLSmidth fabricated and installed the REFLUX™ Flotation Cell and provided commissioning and maintenance support.
- We thank the site for access to their flotation feed and electrical supply. We particularly thank the site managers, engineers, operators, electricians and other site staff and contractors who patiently gave their time to help us install, modify, and operate the facility.
- Nalco provided the frother and the reagent dosing system used in this work.
- Advitech provided in-kind support during the design of the facility.

REFERENCES

Galvin, K P, 2021. Method and Apparatus for Separating Low Density Particles from Feed Slurries (US Patent No. 11,066,312 B2), U.S. Patent and Trade Mark Office. https://patentsgazette.uspto.gov/week29/OG/Cpc-c.html

Iveson, S M, Sutherland, J L, Cole, M J, Borrow, D J, Zhou, J and Galvin, K P, 2022. Full-Scale Trial of the REFLUXTM Flotation Cell. *Minerals Engineering*, 179, 107447. https://doi.org/10.1016/j.mineng.2022.107447

Enhanced fine particle recovery with the Concorde Cell

G J Jameson[1], N M L Kupka[2], P G Bourke[3] and A Yáñez[4]

1. FAusIMM, Laureate Professor, University of Newcastle, Callaghan, Australia.
   Email: graeme.jameson@newcastle.edu.au
2. Senior metallurgist – Flotation, Metso Outotec Finland Oy, Espoo, Finland.
   Email: nathalie.kupka@mogroup.com
3. FAusIMM Group Metallurgist – Flotation, Metso Outotec Australia Ltd, Perth WA 6000.
   Email: peter.bourke@mogroup.com
4. Product Manager – Concorde Technology, Metso Outotec Finland Oy, Espoo, Finland.
   Email: alejandro.yanez@mogroup.com

INTRODUCTION

The kinetics of fine and ultrafine particles in conventional mechanical flotation cells are limited (Feng and Aldrich, 1999; Trahar, 1981; Wang *et al*, 2016). Accordingly, even limited recoveries with such machines require long residence times. Theoretical investigations into the rate of capture of fine particles by flotation, have indicated that a key parameter is the rate of shear in the fluid surrounding the bubbles and the particles. Achieving fast flotation rates of ultrafines requires a new method of bringing the particles and bubbles into contact, utilising the beneficial properties of highly dissipative flows to break through the water boundary layer.

In 2010, a new type of flotation cell known as the Concorde Cell was described, in which bubbles and particles are brought together in a sonic shock wave (Jameson, 2010). Earlier research had shown that when a dispersion of fine bubbles in liquid passed through a converging nozzle at the local speed of sound, the resulting shock wave downstream generates a mass of even finer bubbles in the flow as it passes through the shock wave. The fluid within the shock wave is highly turbulent, and an environment is created that is very favourable to particle-bubble collision and capture.

In this paper, we briefly describe the Concorde Flotation Cell and give examples of its use.

FLOTATION WITH THE CONCORDE CELL

The Concorde Cell is an enhanced forced-air pneumatic flotation technology. It was launched as a product by Metso Outotec on 1 November 2021 (MetsoOutotec, 2021). The feed to the Concorde Cell is introduced at the top of a vertical jet, the 'Blast Tube', where it mixes under pressure with a stream of air bubbles. The slurry then travels down the Blast Tube, which is maintained under pressure. The aerated mixture reaches the speed of sound where the flow diameter is smallest at the throat of the bottom choke. As the discharging stream from the Blast Tube reaches the cell tank, the flow reverts to subsonic conditions to match the pressure within the tank slurry volume, generating a shock wave. The stream strikes against an impingement bowl, where vortex rings form, allowing particles multiple passes through the high-shear collection zone before the slurry is radially dispersed throughout the cell volume. Overall, particle-bubble contacting can occur in three zones: in the plunging jet inside the Blast Tube, in the shock waves generated after the choke or within the impingement bowl.

Recovery can be enhanced by recycling some of the tails back through the Blast Tube. This increases the total residence time of the valuable particles in the Blast Tube and giving them a renewed opportunity to be collected.

Lab-scale experiments were conducted on a graphite ore with a d_{100} of 27 µm at different air-to-pulp ratios (APR). Recovery can be improved by using high APR, one of the characteristics of the Concorde Cell being that it can operate at higher APR than other pneumatic technologies. In this case, froth washing was applied to minimise entrainment and improve concentrate grade. The results are plotted against the number of passes through the Blast Tube in Figure 1. As the cell was operated batch-wise, the tailings were entirely recirculated to the feed until the test ceased, ie float to extinction.

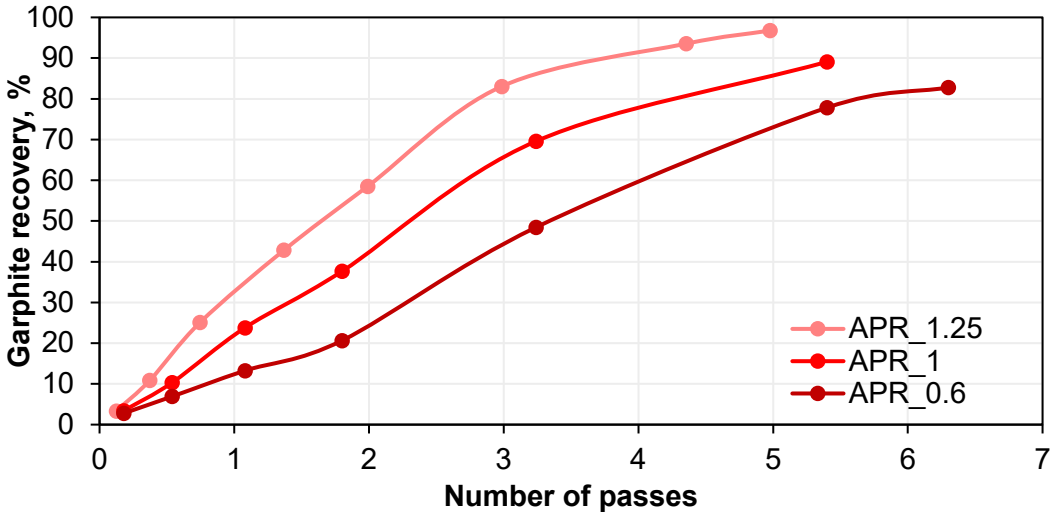

FIG 1 – Graphite recovery depending on the air-to-pulp ratio as well as the number of passes of particles through the Concorde Cell.

Figure 1 shows that as expected, a higher APR increases the graphite recovery, with 96.8 per cent recovery at 1.25 APR compared to 82.8 per cent at 0.6 APR. Flotation kinetics increase with increasing APR. As expected, the results also indicate that the recycling ratio of the tailings can be beneficial.

The effect of recycle ratio was further investigated in a continuous pilot-scale Concorde Cell test using a feed from the slimes circuit of a complex nickel operation with a head grade of 0.37 per cent and a d_{100} of 75 µm. The nominal feed capacity of the cell was 43 L/min (2.6 m^3/h), with at 1 APR a superficial velocity of 1 cm/s in the Cell, a value that is typical of base-metal flotation cells (Gorain *et al*, 1996; Schwarz and Alexander, 2006; Vinnett *et al*, 2014; Yianatos *et al*, 2001).

The Concorde Cell was tested against a single column and six mechanical cells at different tailings recycle ratios of 1:1, 2:1 and 4:1 at an APR of 0.6 without froth washing. Figure 2 shows that nickel recovery significantly increases with tailings recycle, clearly outperforming the column and producing with a single Concorde Cell unit the equivalent performance to six mechanical cells.

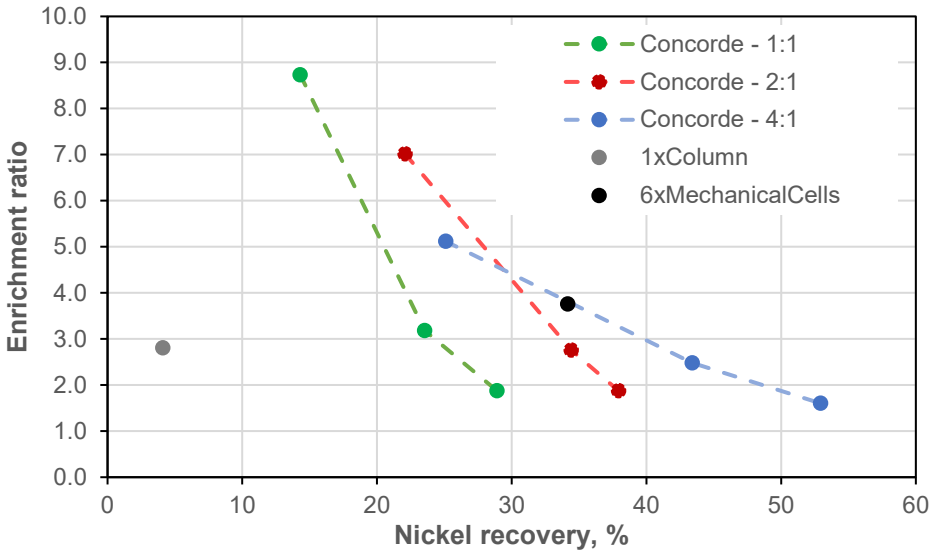

FIG 2 – Effect of recycle ratio on the nickel grades and recoveries, lines to guide the eye.

The recovery increases with increasing recycle ratio as expected, with a gain of up to 15 per cent in recovery for the same enrichment ratio. In addition, it was observed that there was a shift in the grade-recovery curves. It appears that with each pass through the Blast Tube, the surfaces of the

particles became more polished, and slime coatings were removed. Also, floc formation, typical in this ore and which would prevent valuable particles from making contact with bubbles, was reduced.

CONCLUSION

The Concorde Cell is a pneumatic flotation technology device dedicated to the flotation of fine and ultrafine particles. High recoveries of said particles are obtained thanks to the higher shear rate and finer bubbles in the Concorde Cell. As was shown in this paper in two examples at lab and pilot scales, air-to-pulp ratio and recycle ratio are critical components of this novel technology, allowing a strong increase in recoveries and kinetics of the particles. Recycling part of the tailings into the feed of the Concorde Cell can lead to a better conditioning of the slime particles for their second pass in the Blast Tube, improving their collection probability.

ACKNOWLEDGEMENTS

The authors gratefully acknowledge Berivan Tunc and Danish Bilal for conducting the Concorde Cell lab-scale experiments and Joshua Sovechles and Lonn Cooper for their support with Concorde Cell test work.

REFERENCES

Feng, D and Aldrich, C, 1999. Effect of particle size on flotation performance of complex sulphide ores. *Minerals Engineering*, *12*(7), 721–731. https://doi.org/10.1016/S0892–6875(99)00059-X

Gorain, B K, Franzidis, J P and Manlapig, E V, 1996. Studies on impeller type, impeller speed and air flow rate in an industrial scale flotation cell. Part 3: Effect on superficial gas velocity. *Minerals Engineering*, *9*(6), 639–654. https://doi.org/10.1016/0892–6875(96)00052–0

Jameson, G J, 2010. New directions in flotation machine design. *Minerals Engineering*, *23*(11), 835–841. https://doi.org/10.1016/j.mineng.2010.04.001

MetsoOutotec, 2021. *Metso Outotec launches innovative Concorde Cell flotation technology for fine and ultra-fine particle recovery*. Metso: Outotec. Retrieved 31.01.2022 from https://www.mogroup.com/corporate/media/news/2021/11/metso-outotec-launches-innovative-concorde-cell-flotation-technology-for-fine-and-ultra-fine-particle-recovery/

Schwarz, S and Alexander, D, 2006. Gas dispersion measurements in industrial flotation cells. *Minerals Engineering*, *19*(6), 554–560. https://doi.org/10.1016/j.mineng.2005.09.022

Trahar, W J, 1981. A rational interpretation of the role of particle size in flotation. *International Journal of Mineral Processing*, *8*(4), 289–327. https://doi.org/https://doi.org/10.1016/0301–7516(81)90019–3

Vinnett, L, Yianatos, J and Alvarez, M, 2014. Gas dispersion measurements in mechanical flotation cells: Industrial experience in Chilean concentrators. *Minerals Engineering*, *57*, 12–15. https://doi.org/10.1016/j.mineng.2013.12.006

Wang, L, Runge, K, Peng, Y and Vos, C, 2016. An empirical model for the degree of entrainment in froth flotation based on particle size and density. *Minerals Engineering*, *98*, 187–193. http://dx.doi.org/10.1016/j.mineng.2016.08.025

Yianatos, J, Bergh, L, Condori, P and Aguilera, J, 2001. Hydrodynamic and metallurgical characterization of industrial flotation banks for control purposes. *Minerals Engineering*, *14*(9), 1033–1046. https://doi.org/10.1016/S0892–6875(01)00109–1

The effect of soluble cations on monazite flotation

M Jung[1], B Tadesse[2], B Albijanic[1] and L G Dyer[1]

1. Western Australian School of Mines, Curtin University, Kalgoorlie WA 6430.
2. Western Australian School of Mines, Curtin University, Kalgoorlie WA 6430.
   Email: bogale.tadesse@curtin.edu.au

ABSTRACT

The presence of high concentrations of dissolved ions in groundwater, sea water or recycled water may alter the water structure, particle surface wettability and colloidal interactions between bubbles and particles and can have a significant effect on mineral flotation. While the impact of water quality on the flotation of precious and base metal minerals is well established, no relevant published study exists currently regarding the effect of water salinity on the flotation of rare earth bearing minerals.

This paper attempts to quantify the effect of water quality variation on flotation recovery and grade of rare earth minerals and gain an understanding on which ions existing in saline water affect flotation behaviour. Specifically, it is aimed at investigating the effects of water quality on the flotation of monazite in the presence of cations such as Ca^{2+}, Mg^{2+}, K^{+}, and Na^{+}. Flotation tests, zeta potential measurements, and adsorption tests were performed to explain the flotation behaviour. It was found that monovalent ions such as Na^{+} and K^{+} have negative impact on rare earth minerals recovery and grade. The result of single mineral flotation tests showed that the floatability of monazite was significantly depressed in the presence of Ca^{2+} and Mg^{2+}. The result of single mineral flotation test showed varying depression levels in the presence ions in the order of $Ca^{2+} > Mg^{2+} > Na \sim K$.

INTRODUCTION

Froth flotation is a widely used technique for the beneficiation of monazite (Kanazawa and Kamitani, 2006; Ferron *et al*, 1991; Guy *et al*, 2000; Jordens *et al*, 2013; Li and Yang, 2014; Pavez and Peres, 1993). It is well known that the water quality is an important factor for the better performance in froth flotation. However, it has been reported that the flotation of sulfide minerals has been successfully operated with hyper saline water (Laskowski and Castro, 2015). Whereas the flotation performance of rare earth minerals was negatively affected when using the saline water for their operation (Wang *et al*, 2020a, 2020b; Espiritu *et al*, 2018). This makes necessary to purify water sources to minimise the detrimental effects on monazite flotation performance for rare earth mineral process plants.

There are a few studies to investigate the effect of water quality on rare earth mineral flotation. For example. Wang *et al*, (2020a, 2020b) investigated the effects of dissolved ions from gangue minerals (barite and fluorite) on bastnasite flotation using sodium oleate collector. It was found that the ions dissolved from gangue minerals such as Ca^{2+}, F^{-} and Ba^{2+} reduce the recovery of bastnasite because of the depletion of free oleate ions by the formation of insoluble precipitate with the ions. Zhang *et al* (2016) and Zhang and Honaker (2018) studied the monazite flotation using hydroxamic acid collector in the presence of different ions dissolved from calcite. It was suggested that the negative effects on flotation performance of Ca^{2+} were probably caused by adsorption of calcium hydroxide on monazite, leading to less adsorption of collector on the surface. Espiritu *et al* (2019) also found that the adsorption of calcium and magnesium hydroxide on monazite surface can reduce the floatability of monazite in addition to the precipitation of calcium and magnesium oleate. However, the experiment investigation of monazite flotation using sodium oleate collector in the presence of different cations was hardly found. In this study, it was aimed at investigating the flotation behaviour of monazite using sodium oleate in the presence of different cations such as Ca^{2+}, Mg^{2+}, Na^{+}, and K^{+} using microflotation experiments, zeta potential measurements and adsorption density measurements.

MATERIALS AND METHODS

Materials

Monazite ore was received from Western Australia, which having 67 per cent of purity. Monazite sample was ground manually using mortar and pestle, and -75 +38 µm size fraction was collected by screening for microflotation experiments, zeta potential measurement and adsorption test. The

XRD spectrum was shown in Figure 1 and XRF analysis showed that the contents of major rare earth elements in monazite were 25.86 per cent CeO_2, 13.2 per cent La_2O_3, 10.91 per cent Nd_2O_3, 2.81 per cent Pr_6O_{11}, 1.28 per cent Sm_2O_3 and traces (ie less than 0.5 per cent) of other rare earth elements such as praseodymium, samarium and yttrium.

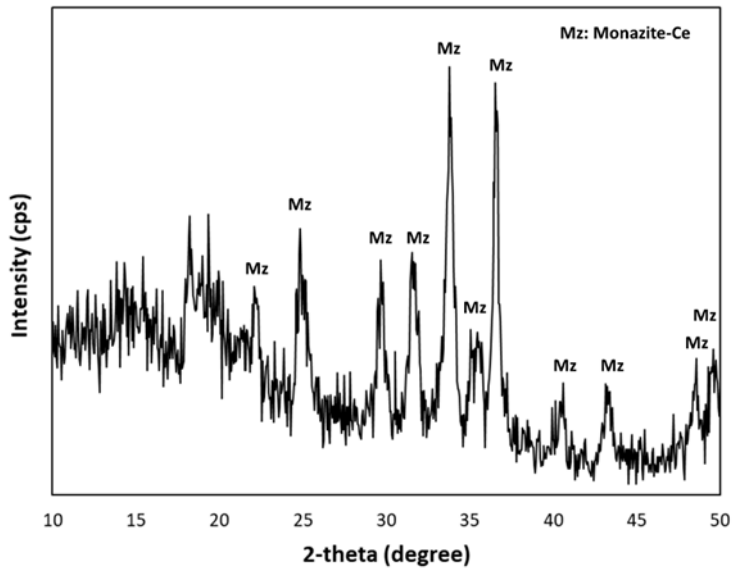

FIG 1 – The XRD spectrum of monazite ore.

Methods

Flotation experiments

Flotation experiments were carried out using microflotation cell (90 ml of volume), illustrated in Figure 2. For conditioning, one weight percent of solid sample was dispersed in solution with magnetic stirring and pH of solution was adjusted with diluted HCl and NaOH solution. The reagents were added in the order of metallic salts ($CaCl_2$, $MgCl_2$, NaCl and KCl), sodium silicate depressant (98 per cent purity, Redox Pty Ltd), and sodium oleate collector (99 per cent purity, TCI America) with the 2 minutes of conditioning time, respectively, followed by adding 30 ppm MIBC frother (98 per cent purity, Orica Limited) with 1 minute of conditioning. The prepared solution was transferred to the micro-flotation cell and final pH was measured. The bubble was generated through the fritted glass filter disk at the bottom of the cell with the compressed air and air flow rate was maintained at 50 ml/min. At all experiments, mild magnetic stirring was employed to ensure the suspension of particles in the solution. The concentrates were collected after 3 min of flotation time. Each experiment was repeated three times with the standard deviation of less than 5 per cent. These experiments were conducted at 22±1°C.

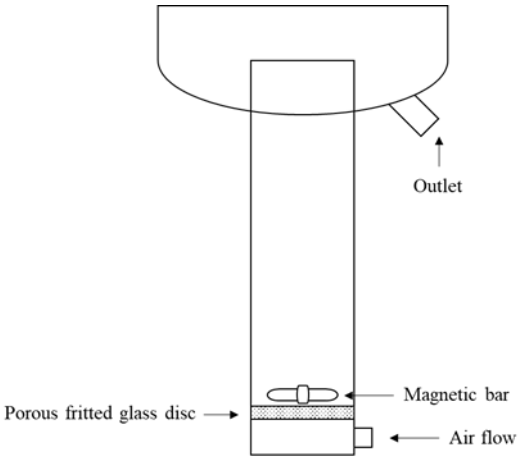

FIG 2 – Mircroflotation cell.

Zeta potential experiments

A solid concentration of 0.1 wt.% was used for conditioning for zeta potential measurement. The samples were fully dispersed in the solution for 5 minutes and conditioned for every 5 minutes after addition of electrolytes, sodium silicate, and collector in the presence of 1×10^{-3} M NaCl as a background electrolyte. After conditioning, the suspension was allowed to settle down large particles for 30 minutes and the clear supernatant was used for analysis. The pH of the solution was adjusted with 0.1 M hydrochloric acid and 0.1 M sodium hydroxide and the final pH was noted down right before the zeta potential analysis. The measurement of zeta potential was conducted using a Malvern NanoZ zeta sizer (Malvern, UK) under the room temperature. All the tests were carried out for three times, and the mean value of measurement was used for further analysis.

Adsorption experiments

Adsorption tests were performed with 1 per cent solid ratio using -75/+38 μm of monazite sample. The conditioning of sample was similar to the procedure for micro-flotation tests. After conditioning, the solution was centrifuged or 10 minutes with 4000 rev/min and 25 ml of clear supernatant was transferred to test tube. The solution for colorimetric analysis was prepared by Gregory method (Gregory, 1966), where the concentration of oleate is proportional to the maximum absorbance at 435 nm wavelength from UV-Vis measurement. The residual fatty acid concentration in solution was determined using UV-Vis spectroscopy (Lambda35, PerkinElmer, USA) under room temperature. Based on the maximum absorbance values, the calibration curve was determined as seen in Figure 3. The adsorption kinetics using the monazite-oleate system showed that the adsorption equilibrium was achieved after 2 min as seen in Figure 4. Thus, the duration of all the adsorption experiments using monazite was 2 min. The specific surface area for monazite was 0.1028 m^2/g.

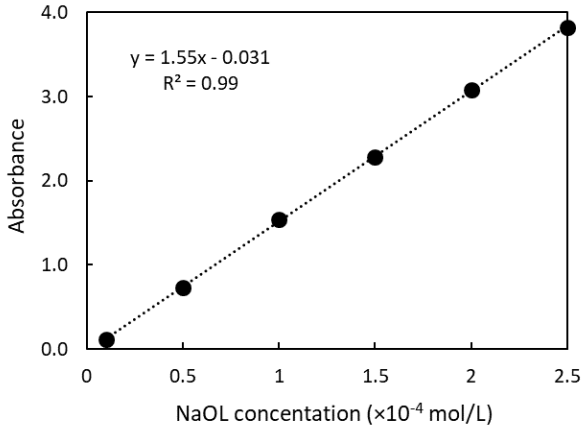

FIG 3 – Standard curve fitting using the absorbance at 435 nm wavelength of different concentration of oleate solutions.

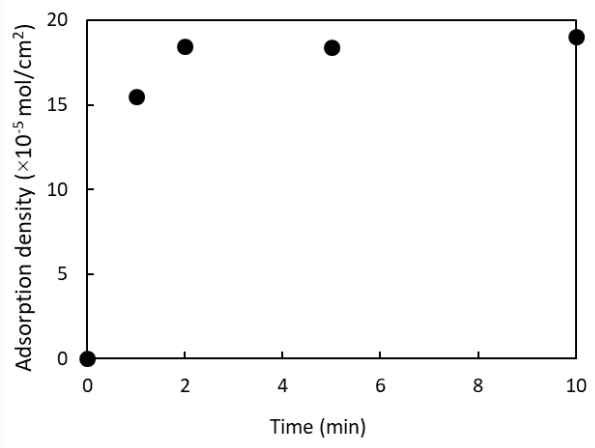

FIG 4 – Adsorption kinetics tests of monazite using 2×10^{-4} mol/L sodium oleate.

RESULTS AND DISCUSSIONS

Microflotation of monazite

Effect of pH and sodium silicate

Microflotation experiments were carried out to investigate the effects of pH and the concentration of sodium silicate (Figure 5). As seen in Figure 5a, the recovery of monazite was maximum at pH 8, which agrees well with the results obtained by some authors (Abeidu, 1972; Pavez and Peres, 1993; Cheng *et al*, 1993; Espiritu and Waters, 2018). Thus, all the experiments were conducted at pH 8. Figure 5b shows the influence of the concentration of sodium silicate; sodium silicate is added typically during rare earth flotation to depress oxide minerals and thus this chemical was also used in this work to simulate the chemical conditions during flotation of monazite from its ore (Pavez and Peres, 1993). The recovery of monazite decreased slightly with increase of the sodium silicate concentration to 0.006 mol/L, and that of monazite was depressed noticeably above 0.006 mol/L of sodium silicate dosage. Therefore, further experiments were carried out in the presence of 0.006 mol/L of sodium silicate concentration.

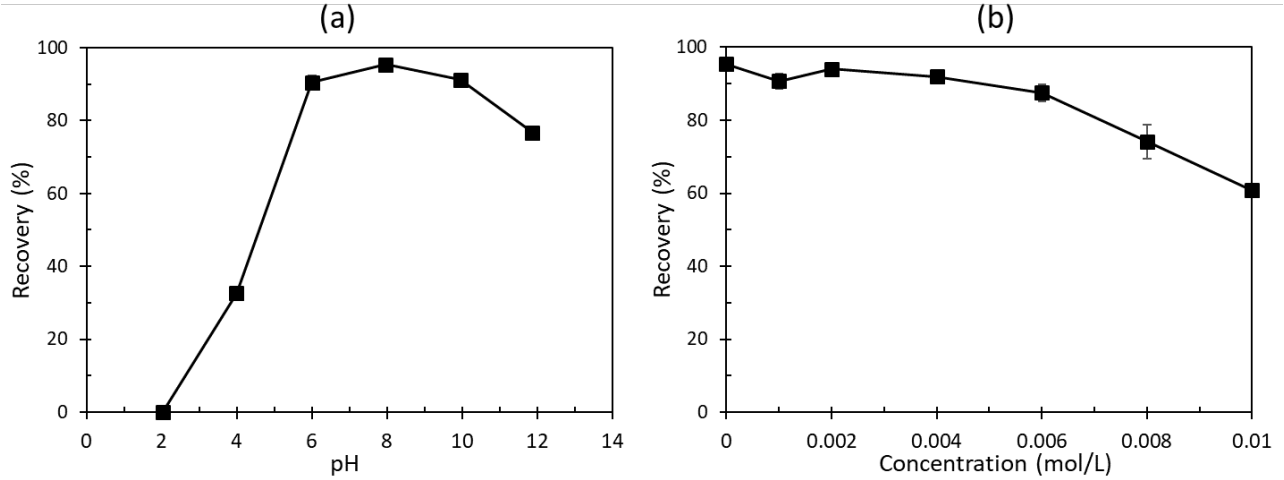

FIG 5 – Effect of (a) pH and (b) sodium silicate at pH 8 on the recovery of monazite in the presence of 2×10^{-4} mol/L sodium oleate.

Effect of Ca^{2+}, Mg^{2+}, K^{+} and Na^{+}

The flotation experiments were carried out to investigate the effects of different cations such as Ca^{2+}, Mg^{2+}, Na^{+} and K^{+} using sodium oleate collector in the presence of sodium silicate depressant (Figure 6). Figure 6a showed that the recovery of monazite was significantly depressed in the presence of Ca^{2+} ions. This is probably because the free oleate ions were depleted from solution by forming insoluble precipitate with Ca^{2+} ions, leading to the decrease of oleate adsorption on monazite surface. The result of solution chemistry experiment as seen in Figure 14 can support this hypothesis. Similarly, Mg^{2+} ions also depressed the monazite recovery, but it was less detrimental than Ca^{2+} ions as shown in Figure 6b.

Monovalent ions such as Na^{+} and K^{+} also had a negative impact slightly on recovery as seen in Figure 6c and 6d. This might be also related to the free oleate concentration in solution, and the free oleate concentration did not changed with the increase of Na^{+} and K^{+} concentration (see Figure 14).

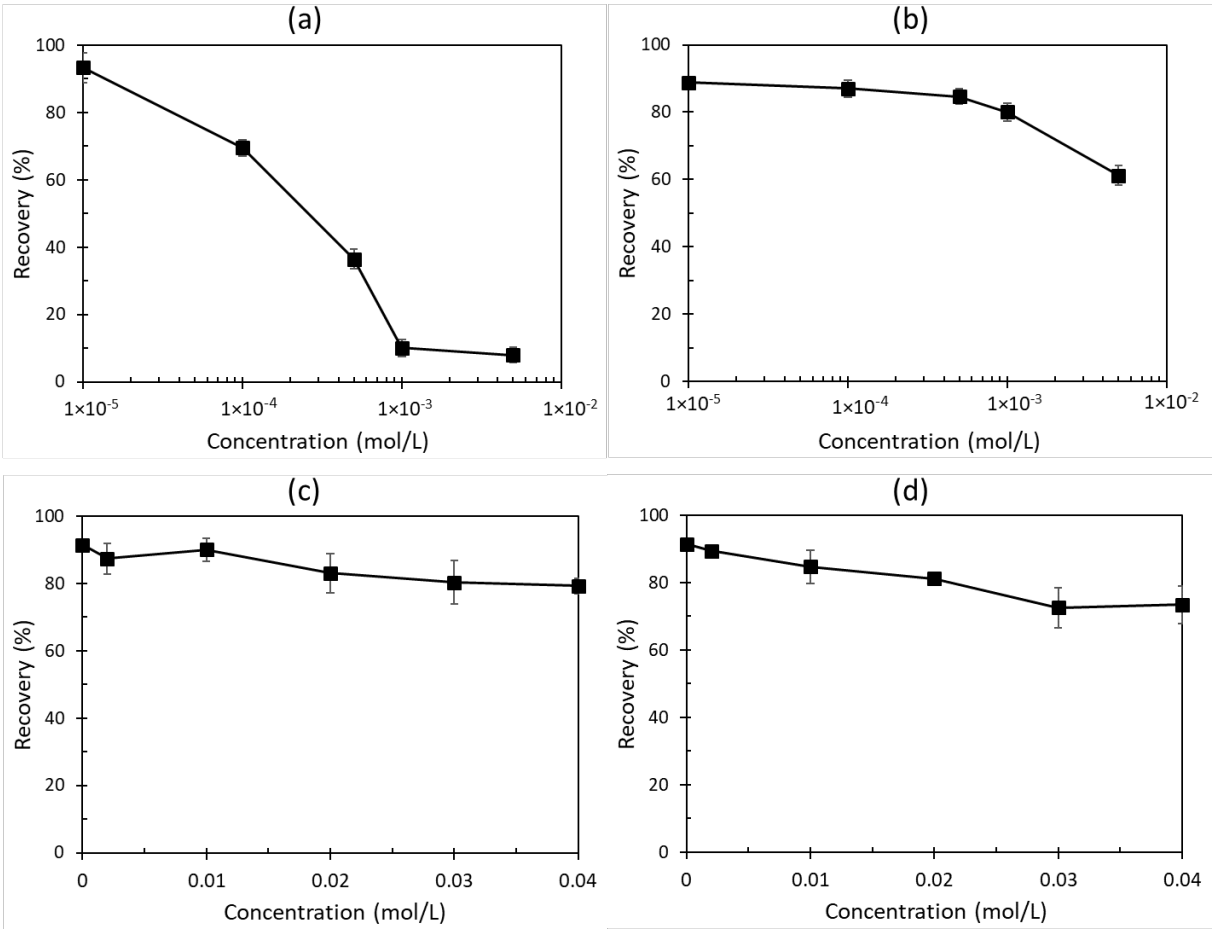

FIG 6 – Effect of (a) Ca^{2+}, (b) Mg^{2+}, (c) Na^{+} and (d) K^{+} ions on the recovery of monazite in the presence of 6×10^{-3} mol/L sodium silicate and 2×10^{-4} mol/L sodium oleate at pH 8.

Zeta potential measurement

Zeta potential of monazite was studied in the different condition. As shown in Figure 7, IEP (isoelectric point) located at pH 7.5. It was found that sodium silicate and sodium oleate shifted the IEP to around pH 5 and 3.5, which indicating both sodium silicate and sodium oleate can adsorb on monazite surface. However, in the presence of both reagents, the zeta potential of monazite surface was same with that in the presence of sodium oleate only. This indicate the adsorption of oleate ions was more significant than that of silicate ions on monazite surface, and the adsorption of oleate was not interfered by the presence of silicate ions.

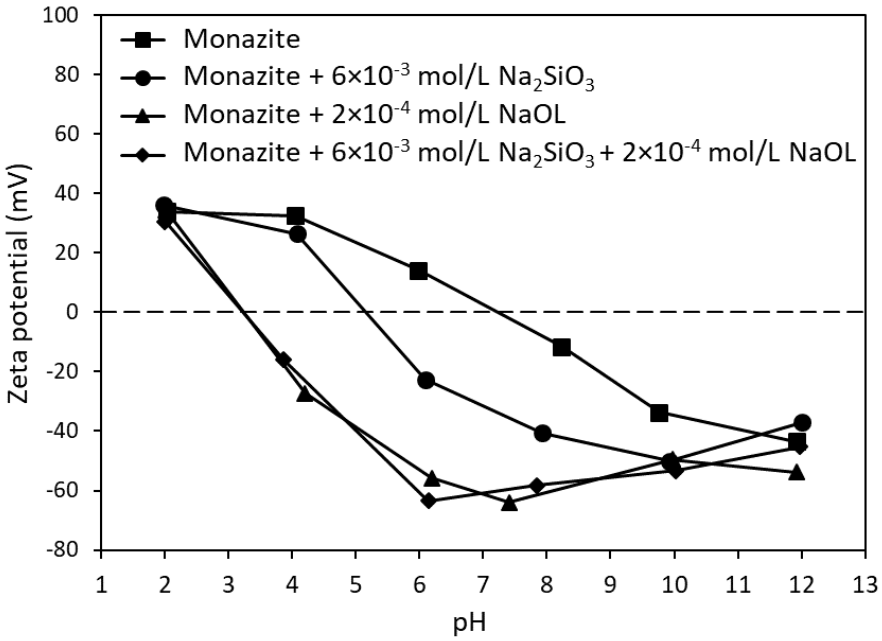

FIG 7 – Zeta potential of monazite as a function of pH before and after conditioning in 2×10^{-4} mol/L NaOL and 6×10^{-3} mol/L Na_2SiO_3, respectively.

Figures 8 to 11 shows the influence of different cations on the surface charge of monazite. As seen in Figures 8 to 11, zeta potential of monazite surface become less negative with the increase of the concentration of each ion. In case of divalent ions, it may be due to the adsorption of Ca^{2+} and Mg^{2+} metal ions or their hydroxide compound as shown in Figure 12. Monovalent ions do not form any precipitates, thus it is probably because of the compression of electrical double layer.

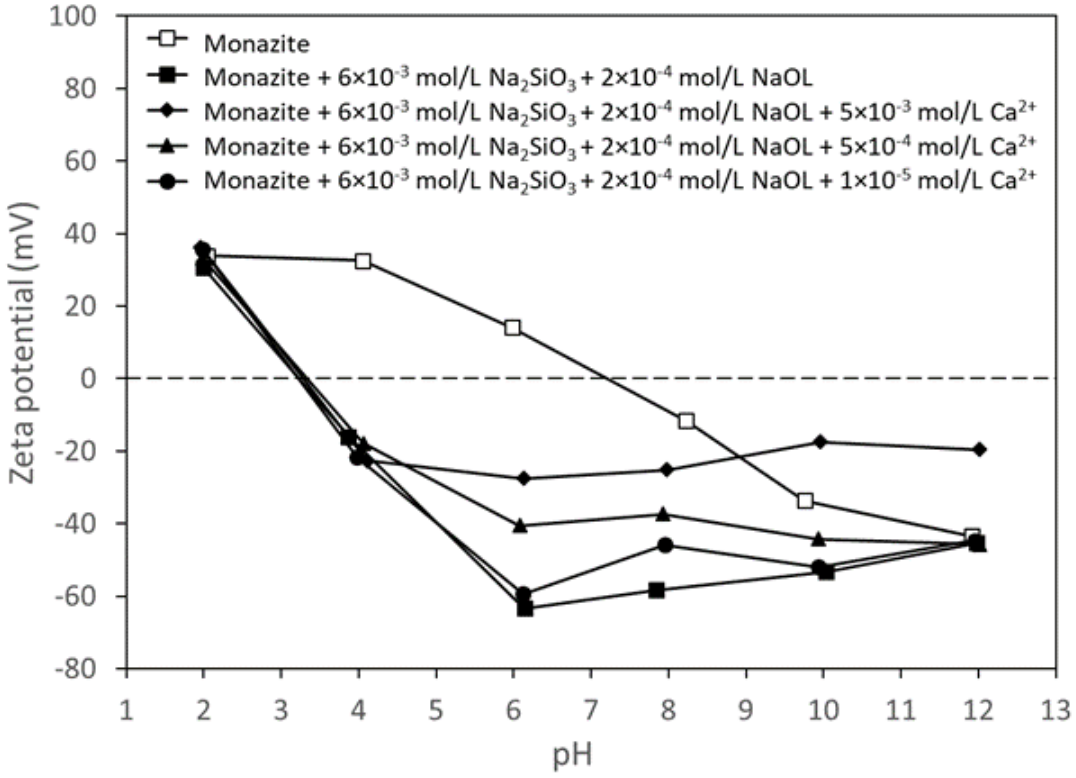

FIG 8 – Zeta potential of monazite particles in the difference concentration of Ca^{2+} ions.

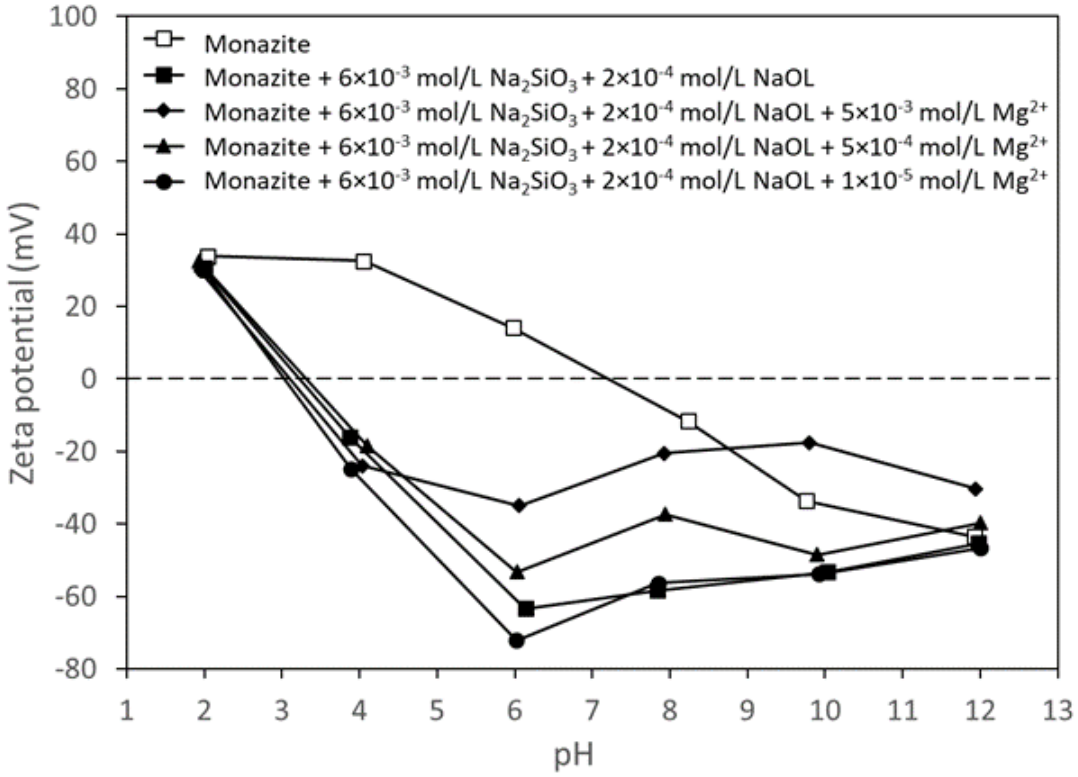

FIG 9 – Zeta potential of monazite particles in the difference concentration of Mg^{2+} ions.

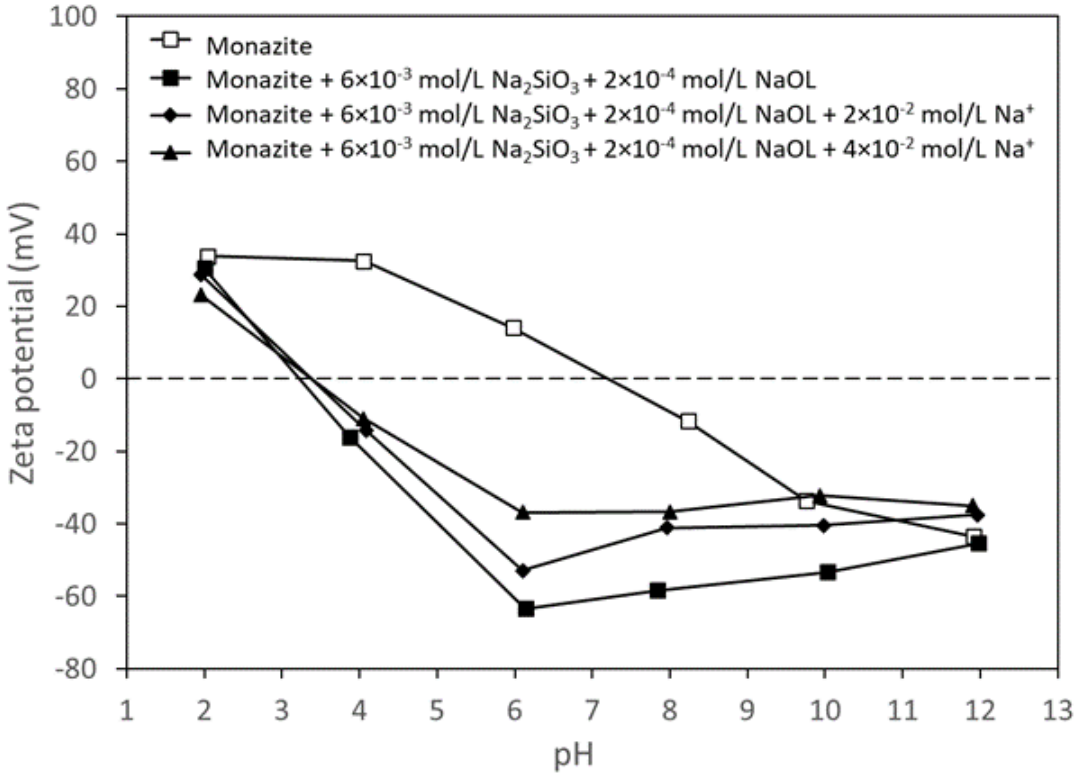

FIG 10 – Zeta potential of monazite particles in the difference concentration of Na^{+} ions.

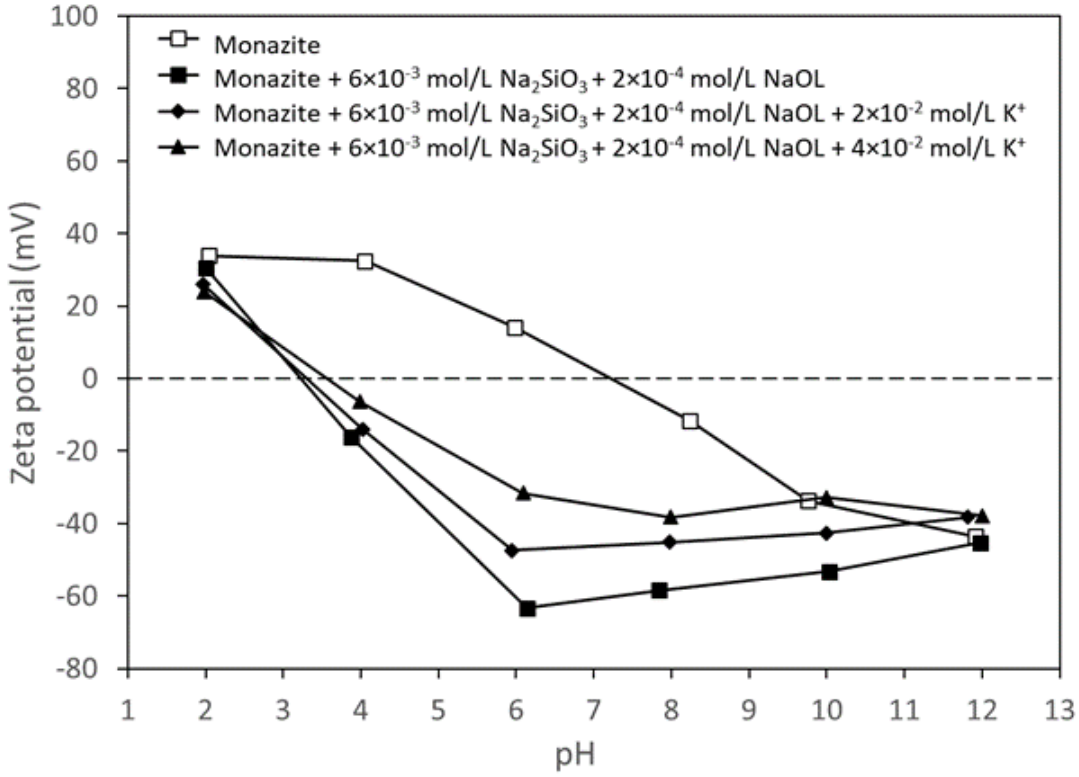

FIG 11 – Zeta potential of monazite particles in the difference concentration of K^+ ions.

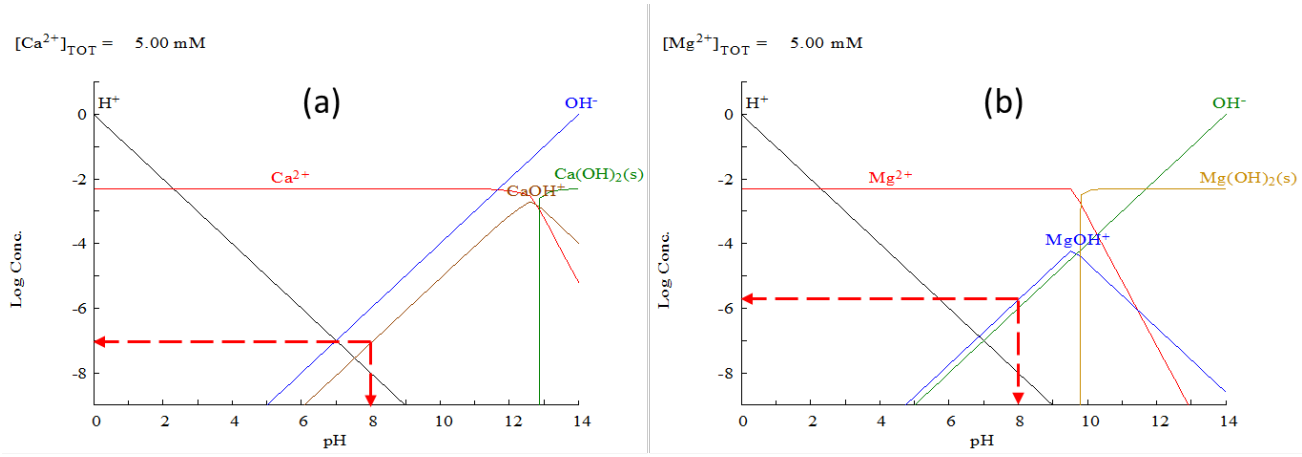

FIG 12 – LogC-pH diagram of (a) calcium and (b) magnesium species; the calculations were performed using Medusa open-source software.

Adsorption of oleate on monazite

Figure 13 illustrates the effects of Ca^{2+}, Mg^{2+}, Na^+, and K^+ ions on the adsorption density change on monazite particle. The adsorption density of sodium oleate collector significantly decreased with the increase of Ca^{2+}, and the increase of Mg^{2+} concentration reduced the adsorption density of oleate collector as well but not significant as much as Ca^{2+} (Figure 13a and 13b). This is probably due to the formation of insoluble calcium oleate and magnesium oleate, thus the amount of available oleate for adsorption reduced with the increase of Ca^{2+} and Mg^{2+} ions concentration. Monovalent ions (Na^+ and K^+) did not affect the adsorption density because the oleate ions did not form any precipitates with monovalent ions (Figure 13c and 13d).

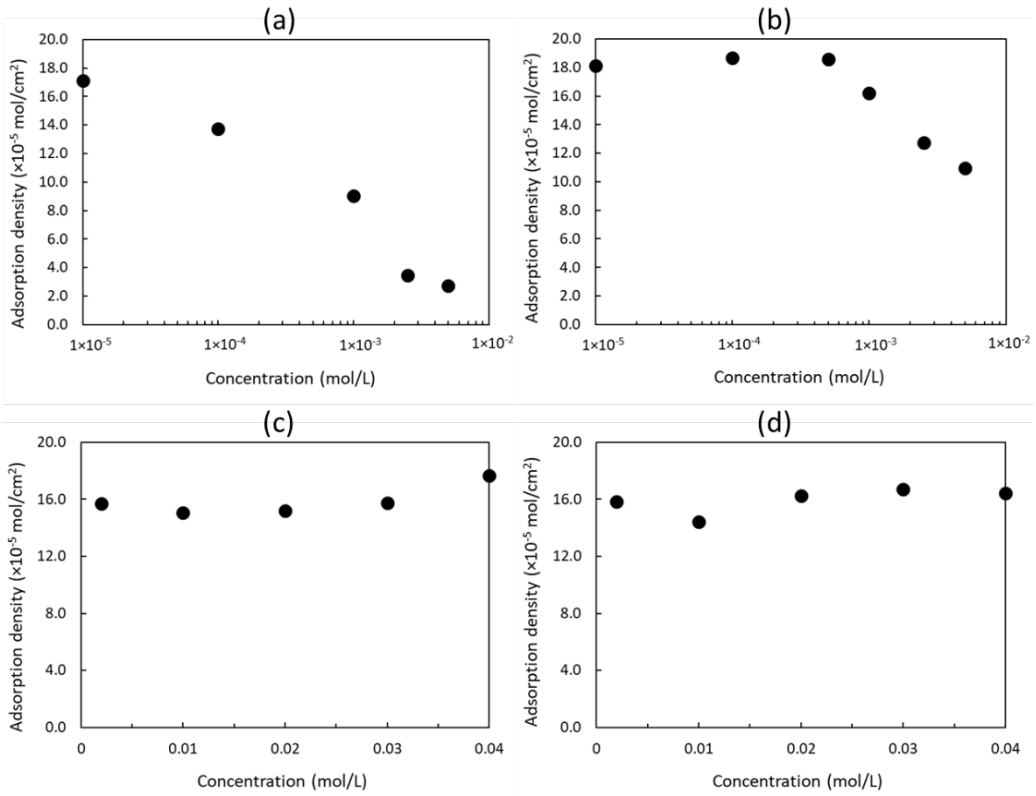

FIG 13 – Effects of (a) $CaCl_2$, (b) $MgCl_2$, (c) NaCl, and (d) KCl on the adsorption density of oleate on monazite in the presence of 2 × 10^{-4} mol/L sodium oleate and 6 × 10^{-3} mol/L sodium silicate.

Solution chemistry of oleate in the presence of Ca^{2+}, Mg^{2+}, Na^+ and K^+

It is important to understand the behaviour of reagents in flotation solution. For this reason, the concentration change of the oleate collector in the solution was measured in the presence of different concentration of metallic ions without the monazite particles. As seen in Figure 14, the concentration of oleate was significantly reduced in the presence of Ca^{2+} and Mg^{2+}, however, that of oleate did not decrease in the presence of Na^+ and K^+ ions. This might indicate the oleate was consumed by Ca^{2+} and Mg^{2+} ions by forming the insoluble precipitate, but not with Na^+ and K^+. The further studies are required to investigate the interaction between metallic ions, oleate ions, and silicate ions in the solution at pH 8.

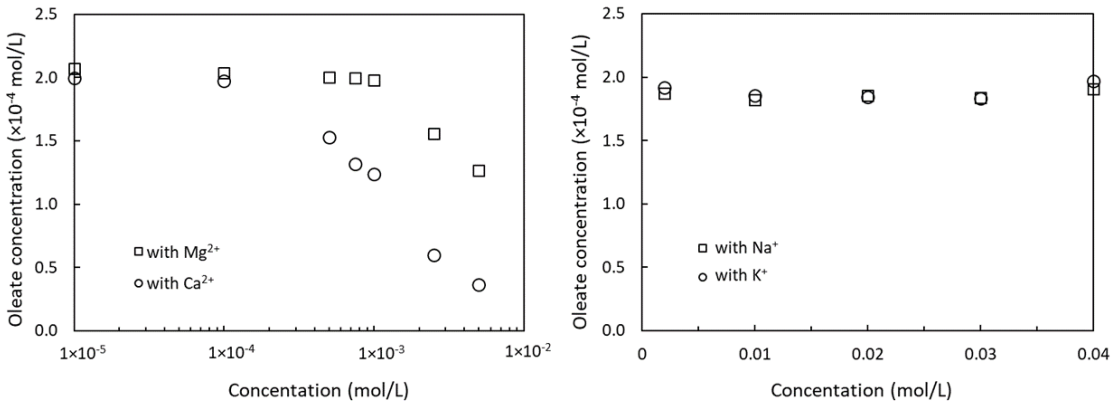

FIG 14 – Oleate concentration in the presence of Ca^{2+}, Mg^{2+}, Na^+ or K^+ and 6 × 10^{-3} mol/L sodium silicate.

CONCLUSIONS

The effects of different ions (Ca^{2+}, Mg^{2+}, Na^+ and K^+) on the monazite flotation mechanism with a sodium oleate collector were investigated in this study. It was found that Ca^{2+} and Mg^{2+} ions had

negative impacts on monazite flotation behaviour because the oleate ions form insoluble precipitates with Ca^{2+} and Mg^{2+} ions. This lead to decrease of the available oleate ions for adsorption on mineral surface, thus reduce the flotation recovery. The monovalent ions such as Na^{+} and K^{+} also reduced the flotation recovery of monazite slightly even though the oleate ions were not consumed by such as the formation of precipitates. These results were confirmed by microflotation experiments, zeta potential measurements and adsorption density measurements. A further work is required to understand the mechanism why the ions depress the monazite flotation recovery, which includes the investigation of change of surface characteristics, thermodynamic calculations, solution chemistry studies, and etc.

ACKNOWLEDGEMENTS

The authors gratefully acknowledge the financial support from the MRIWA, Curtin University and Lynas Rare Earth Ltd.

REFERENCES

Abeidu, A M, 1972. The separation of monazite from zircon by flotation. *J. Less Common Metals* 29, 113–119. https://doi.org/10.1016/0022–5088(72)90181–6

Cheng, T W, Holtham, P N and Tran, T, 1993. Froth flotation of monazite and xenotime. *Miner. Eng*. 6, 341–351. https://doi.org/10.1016/0892–6875(93)90014-e

Espiritu, E R L and Waters, K E, 2018. Flotation studies of monazite and dolomite. *Miner. Eng*. 116, 101–106. https://doi.org/10.1016/j.mineng.2017.02.010

Espiritu, E R L, Silva, G R da, Azizi, D and Larachi, F, Waters, K E, 2018. The effect of dissolved mineral species on bastnäsite, monazite and dolomite flotation using benzohydroxamate collector. *Colloids Surfaces Physicochem. Eng. Aspects* 539, 319–334. https://doi.org/10.1016/j.colsurfa.2017.12.038

Espiritu, E R L, Silva, G R da, Azizi, D, Larachi, F and Waters, K E, 2019. Flotation behavior and electronic simulations of rare earth minerals in the presence of dolomite supernatant using sodium oleate collector. *J. Rare Earth* 37, 101–112. https://doi.org/10.1016/j.jre.2018.04.016

Ferron, C J, Bulatovic, S M and Salter, R S, 1991. Beneficiation of Rare Earth Oxide Minerals. *Mater. Sci. Forum* 70–72, 251–270. https://doi.org/10.4028/www.scientific.net/msf.70–72.251

Gregory, G R E C, 1966. The determination of residual anionic surface-active reagents in mineral flotation liquors. *Analyst* 91, 251–257. https://doi.org/10.1039/an9669100251

Guy, P J, Bruckard, W J and Vaisey, M J, 2000. Beneficiation of Mt weld rare earth oxides by gravity concentration, flotation, and magnetic separation, in *Proceedings of the Seventh Mill Operators' Conference*, pp. 197–205 (The Australasian Institute of Mining and Metallurgy: Melbourne).

Jordens, A, Cheng, Y P and Waters, K E, 2013. A review of the beneficiation of rare earth element bearing minerals. *Miner. Eng*. 41, 97–114. https://doi.org/10.1016/j.mineng.2012.10.017

Kanazawa, Y and Kamitani, M, 2006. Rare earth minerals and resources in the world. *J. Alloy Compd*. 408, 1339–1343. https://doi.org/10.1016/j.jallcom.2005.04.033

Laskowski, J and Castro, S, 2015. Flotation in concentrated electrolyte solutions. *Int. J. Miner. Process*. 144, 50–55. https://doi.org/10.1016/j.minpro.2015.09.017

Li, L Z H I and Yang, X, 2014. China's rare earth ore deposits and beneficiation techniques, *1st European Rare Earth Resources Conference*, 26–36. Available at: http://www.eurare.eu/docs/eres2014/firstSession/XiaoshengYang.pdf.

Pavez, O and Peres, A E C, 1993. Effect of sodium metasilicate and sodium sulphide on the floatability of monazite-zircon-rutile with oleate and hydroxamates. *Miner. Eng*. 6, 69–78. https://doi.org/10.1016/0892–6875(93)90164-i

Wang, Z, Wu, H, Xu, Y, Shu, K, Fang, S and Xu, L, 2020a. The effect of dissolved calcite species on the flotation of bastnaesite using sodium oleate. *Miner. Eng*. 145, 106095. https://doi.org/10.1016/j.mineng.2019.106095

Wang, Z, Wu, H, Xu, Y, Shu, K, Yang, J, Luo, L and Xu, L, 2020b. Effect of dissolved fluorite and barite species on the flotation and adsorption behavior of bastnaesite. *Sep. Purif. Technol*. 237, 116387. https://doi.org/10.1016/j.seppur.2019.116387

Zhang, J, Zhao, B and Schreiner, B, 2016. *Separation Hydrometallurgy of Rare Earth Elements.* https://doi.org/10.1007/978–3-319–28235–0

Zhang, W and Honaker, R Q, 2018. Flotation of monazite in the presence of calcite part II: Enhanced separation performance using sodium silicate and EDTA. *Miner. Eng*. 127, 318–328. https://doi.org/10.1016/j.mineng.2018.01.042

Unravelling the adsorption modes of flotation reagents by atomistic simulations

J Lainé[1], Y Foucaud[2], C Veloso[3], A C de Araujo[4], and M Badawi[5]

1. PhD Candidate, Laboratoire de Physique et Chimie Théoriques, UMR CNRS 7019, Université de Lorraine, Vandœuvre-lès-Nancy 54500, France; and Arcelor Mittal Global Research and Development, Voie Romaine, Maizières-lès-Metz 57280, France. Email: juliette.laine@univ-lorraine.fr
2. PhD, Université de Lorraine, CNRS, GeoRessources Laboratory, F-54000 Nancy, France. Email: yann.foucaud@univ-lorraine.fr
3. PhD, ArcelorMittal Global Research and Development, Voie Romaine, Maizières-lès-Metz 57280, France. Email: carlos.veloso@arcelormittal.com
4. PhD, ArcelorMittal Global Research and Development, Voie Romaine, Maizières-lès-Metz 57280, France.
5. Associate Professor, Laboratoire de Physique et Chimie Théoriques, UMR CNRS 7019, Université de Lorraine, Vandœuvre-lès-Nancy 54500, France. Email: michael.badawi@univ-lorraine.fr

INTRODUCTION

Flotation is the one of the most used techniques for the mineral separation of non-ferrous ores worldwide. However, the increase of the complexness along with the decrease of ores liberation sizes ought to become important challenges for mineral processing, including flotation. It now appears necessary to better understand the fundamentals of the flotation process, particularly the adsorption of flotation reagents at the liquid/mineral interfaces, to propose further improvements.

Flotation relies on different phenomena: surfactants adsorption, on one hand, and collision, adhesion, and transport of particles with bubbles, on the other hand. For acknowledging the reagents adsorption mechanisms, molecular modelling tools borrowed from chemical and material sciences, are increasingly used. Atomistic simulations were successfully applied to study the flotation reagents interaction with various mineral surfaces, eg of two common minerals from iron ores, kaolinite, and magnetite surfaces, or with fluorite surface, a tungsten ores common gangue mineral.

Modelling techniques allow predicting surface reactivity and properties that are difficult to investigate by experimental techniques due to the aqueous phase. Most of them have been intensively employed in other domains, like catalysis (Badawi *et al*, 2011) or depollution (Lainé *et al*, 2022), demonstrating their reliability. Introduced in 1927, it was only in the 1960s that Hohenberg and Kohn formalised Density Functional Theory (DFT) to solve Schrödinger's equation (Hohenberg and Kohn, 1964). DFT relates the total energy to the electron density functional, allowing the determination of the ground-state energy. A thorough description of the dispersion interactions, playing a non-negligible role in organic molecules adsorption on minerals surfaces, is necessary. The use of dispersion correction schemes combined to the PBE functional (Perdew *et al*, 1996) allows a good compromise between time and accuracy (Foucaud *et al*, 2021; Hounfodji *et al*, 2021; Lainé *et al*, 2022). However, only Molecular Dynamics (MD) can account for pressure and temperature – therefore, ions movements, absent from DFT calculations – that considerably influence the adsorption process. Those simulations are based on solving Newton's law of motion, in which ions trajectories are related to the forces at stake. In *Ab Initio* MD (AIMD), forces are described using DFT calculations, allowing an accurate description of reactivity (bond formation and breakage), as well as oxido-reduction and acid-base processes, but on limited number of atoms and simulation time. On the other hand, the use of classical MD (CMD), in which the forces are derived from force fields, allow the description of large systems evolution (over thousandth of atoms) during large simulation time, allowing the description of entropic effects without considering reactivity. The combination of these types of calculations can give access to the flotation reagents adsorption mechanisms onto mineral surfaces.

Prior studying reagents adsorption, minerals hydration is thoroughly investigated as it can significantly modify surface properties. Indeed, many oxides like magnetite or quartz have partly hydroxylated surfaces, creating different adsorption sites with different adsorbents affinities.

Kaolinite – clay mineral formed by aluminosilicates alteration – is almost always present in fine/ultrafine particles that generally hinder flotation processes due to particles coating, reagents overconsumption, or mechanical entrainment. Kaolinite, as many phyllosilicates, presents two dominant basal surfaces: the aluminol-terminated octahedral surface, and the siloxane-terminated tetrahedral surface. Experimentally, differentiating both surface is almost impossible. Using static DFT and AIMD, we showed that, at neutral pH, water molecules do not dissociate on both basal surfaces (Figure 1a). The Al-terminated surface interacts with a single water molecule (ΔE_{ads} = -62 kJ.mol^{-1}) more strongly than the Si-terminated surface (ΔE_{ads} = -38 kJ.mol^{-1}). When the surface coverage is increased, water molecules form structured layers on kaolinite surfaces: on the Al-terminated surface, it forms stable ice-like hexagonal shapes (Figure 1b) while the structure is less organised on top of the Si-terminated surface. Opposite to what was proposed in the literature, only two structured layers of water molecules are formed on both surfaces (Figure 1c).

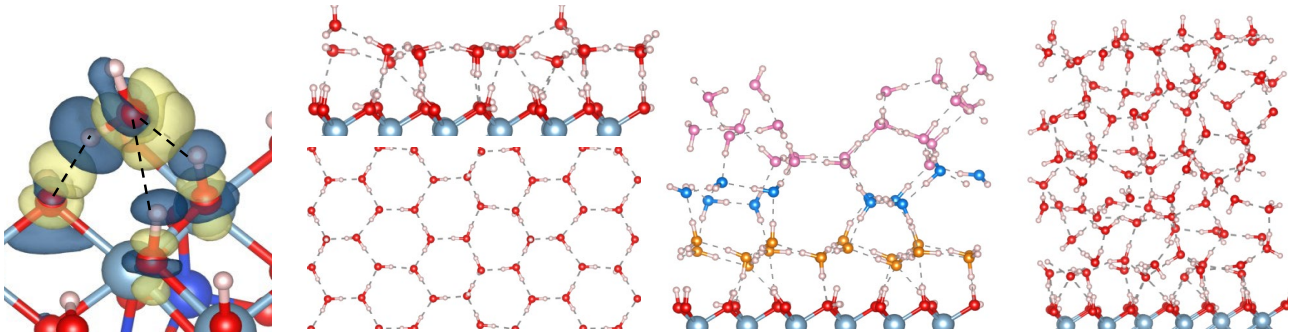

FIG 1 – Snapshots of (a) the adsorption of a single water molecule and the corresponding calculated electron density variations, (b) a monolayer of water molecules, seen from side (top) and from top (bottom), (c) three layers of water seen from side, and (d) a full hydrated model of water, seen from side. In (a), the yellow and blue represent the increase and decrease of the electron density during the water molecule adsorption, respectively.

Besides, on magnetite (111) surface, water dissociates to form surface hydroxyl groups. Mixed water adsorption can happen through dissociation and through the adsorption *via* surface hydroxyl groups. Therefore, this surface is like kaolinite Al-terminated surface, with a significant degree of hydroxylation.

Since amines are common collectors in iron ores reverse flotation, the adsorption mechanisms of dodecylamine (DDA) on both kaolinite basal surfaces were investigated using DFT and MD simulations. To complete modelling results, adsorption isotherms were acquired at three temperatures (Figure 2, left). We demonstrated that the adsorption of DDA mainly occurs through electrostatic and hydrogen bonding, while the chlorine counter-ion doesn't influence the adsorption mechanism (Figure 2, right). Meanwhile, CMD will be used in a next step as they can allow simulating larger systems at larger time scales, allowing the investigation of the formation of collectors' layers.

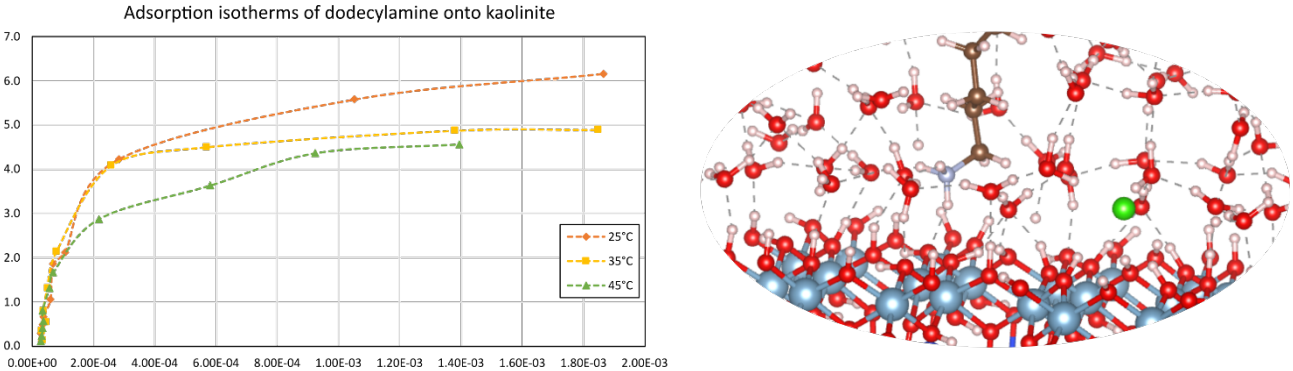

FIG 2 – *Left* – adsorption isotherms of chloride DDA onto kaolinite powder at 25, 35, and 45°C. *Right* – Snapshot after 40 ps of AIMD simulation of DDA adsorption onto kaolinite.

To fully exploit properties obtained by MD simulations, comparisons were made between simulated and experimental infrared spectra. It unravelled fatty acids adsorption modes onto fluorite which were of two natures: mixed bidentate and monodentate modes. Also, for the first time, the importance of the counterion role for the adsorption layer formation was highlighted (Foucaud *et al*, 2021).

To conclude, atomistic simulations have been applied to understand the hydration mechanisms of kaolinite basal surfaces. We demonstrated a non-dissociative adsorption of water molecules, which form stable ice-like structured multilayers, while water molecules readily dissociate onto magnetite. The study of amine collectors' adsorptions on kaolinite demonstrates that mechanisms involve electrostatic and hydrogen bonding. The authors hope to exhibit the value of modelling for flotation processes and for the improvement of existing operations to tackle future challenges.

ACKNOWLEDGEMENTS

This work was granted access to the HPC resources of TGCC under the allocations 2020-A0080810169 and 2021-A010081433 by GENCI -EDARI project.

REFERENCES

Badawi, M, Paul, J-F, Cristol, S, Payen, E, 2011. Guaiacol derivatives and inhibiting species adsorption over MoS2 and CoMoS catalysts under HDO conditions: A DFT study. *Catal. Commun*. 12, 901–905. https://doi.org/10.1016/j.catcom.2011.02.010.

Foucaud, Y, Lainé, J, Filippov, L O, Barrès, O, Kim, W J, Filippova, I V, Pastore, M, Lebègue, S, Badawi, M, 2021. Adsorption mechanisms of fatty acids on fluorite unraveled by infrared spectroscopy and first-principles calculations. *J. Colloid Interface Sci*. 583, 692–703. https://doi.org/10.1016/j.jcis.2020.09.062.

Hohenberg, P, Kohn, W, 1964. Inhomogeneous Electron Gas. *Phys. Rev*. 136, B864–B871. https://doi.org/10.1103/PhysRev.136.B864.

Hounfodji, J W, Kanhounnon, W G, Kpotin, G, Atohoun, G S, Lainé, J, Foucaud, Y, Badawi, M, 2021. Molecular insights on the adsorption of some pharmaceutical residues from wastewater on kaolinite surfaces. *Chem. Eng. J.* 407, 127176. https://doi.org/10.1016/j.cej.2020.127176.

Lainé, J, Foucaud, Y, Bonilla-Petriciolet, A, Badawi, M, 2022. Molecular picture of the adsorption of phenol, toluene, carbon dioxide and water on kaolinite basal surfaces. *Appl. Surf. Sci*. 585, 152699. https://doi.org/10.1016/j.apsusc.2022.152699.

Perdew, J P, Burke, K, Ernzerhof, M, 1996. Generalized Gradient Approximation Made Simple. *Phys. Rev. Lett*. 77, 3865–3868. https://doi.org/10.1103/PhysRevLett.77.3865.

Managing the flotation response of pyrrhotite from Cu-Ni-PGM ores using process water of a degrading quality

M S Manono[1] and K C Corin[2]

1. Senior Lecturer, Centre for Minerals Research, Department of Chemical Engineering, Faculty of Engineering and the Built Environment, University of Cape Town, Rondebosch 7700, South Africa. Email: malibongwe.manono@uct.ac.za
2. Associate Professor, Centre for Minerals Research, Department of Chemical Engineering, Faculty of Engineering and the Built Environment, University of Cape Town, Rondebosch 7700, South Africa. Email: kirsten.corin@uct.ac.za

ABSTRACT

The optimisation and process developments surrounding the beneficiation of Cu-Ni-PGM ores is of fundamental importance when considering the continued rise in global demand for these precious metals. The selective sequential flotation of these ores is accompanied with various processing challenges such as the successful separation of the Cu-Ni-PGMs from non-sulfide naturally floatable gangue and pyrrhotite. Reagents such as sodium iso-butyl xanthate (SIBX) and sodium carboxymethyl cellulose (CMC) have proven to significantly improve the selectivity of the flotation process in their respective roles. The use of recycled water with abnormal inorganic electrolyte concentrations can modify the selectivity of these reagents, as ions may adsorb onto minerals such as pyrrhotite, thereby hindering or promoting the hydrophocity and floatability of pyrrhotite. Process water quality effects on the behaviour of pyrrhotite may have negative or positive influence on the recovery and grades of the wanted Cu-Ni-PGMs as valuable minerals associated with pyrrhotite such as pentlandite may be affected in like manner. Thus, the impact of concentrator process water quality on the behaviour of pyrrhotite needs to be determined. In this study synthetic process water at various ionic strengths was investigated against various CMC dosages to understand the behaviour of pyrrhotite during the flotation of a Cu-Ni-PGM Merensky ore in a batch flotation cell. This study showed that pyrrhotite grades increased with an increase in CMC dosage for fixed ionic strengths whereas the recoveries of pyrrhotite increased with an increase in ionic strength until 3SPW, then a trend of a decrease in recoveries was seen with 5SPW resulting in the lowest pyrrhotite recoveries. Furthermore, this study showed that moderate CMC dosages of 100 g/t resulted in the highest pyrrhotite recovery for all four ionic strengths of synthetic process water tested. It can be said that to maximise value recovery from Cu-Ni-PGM ores, understanding the behaviour of pyrrhotite against degrading water quality and reagent suites could be of paramount importance given the sensitivity of pyrrhotite to oxidising chemical conditions.

INTRODUCTION

Platinum group metals (PGMs) are precious metals which are used in catalysis, automotive, medical and industrial manufacturing processes due to their purity, high melting points, unique catalytic properties and high corrosion resistance (Hochreiter *et al*, 1985). The mining of these PGMs is a crucial part of the South African economy, as the country boasts the world's largest PGMs deposit, located in the Bushveld Igneous Complex (BIC). Moreover, the BIC is explored for other valuable metals such as nickel and copper as these metals occur in association with the PGMs as base metal sulfides (BMS), namely, chalcopyrite ($CuFeS_2$) and pentlandite ($Fe_9Ni_9S_8$) (O'Connor and Alexandrova, 2021; Schreithofer *et al*, 2011). However, the presence of pyrrhotite ($Fe_{(1-x)}S$) within these ore deposits provides a challenge for mineral concentrators during liberation processes such as comminution and flotation (Allison and O'Connor, 2011; Becker *et al*, 2009; Wiese *et al*, 2005). During the flotation of these ores, there is a challenge of a decrease in concentrate grades. This is mainly attributed to the recovery of naturally floatable non-sulfide gangue, such as talc as well as pyrrhotite's affinity or association with pentlandite and other value bearing minerals (Becker *et al*, 2009). Consequently, there exists a need to understand the behaviour of pyrrhotite during the flotation of Cu-Ni-PGM ores. Furthermore, the scarcity of water in mining regions has resulted in the need to recycle water and use recycled water during froth flotation so as to reduce the demand on fresh water (Corin *et al*, 2011; Rao and Finch, 1989). Given that water is both a reagent and transport

medium in flotation, changes in its quality can significantly affect flotation performance through electrolyte-reagent-mineral interactions (Manono *et al*, 2018).

This study involved conducting a series of batch flotation tests under various ionic strengths of process water and depressant dosages, using sodium carboxy methyl cellulose (CMC) to assess the behaviour of pyrrhotite under degrading water quality during the flotation of a Cu-Ni-PGM ore from the Merensky reef. A careful mass balance was carried out to determine pyrrhotite recoveries and grades. This was made possible by analysing the % grade and recovery of elemental copper, nickel, and sulfur and thus deducing the recovery of pyrrhotite, and the amount of non-sulfide gangue recovered by entrainment and true flotation.

MATERIALS and METHODS

A Merensky reef Cu-Ni-PGM ore obtained from one of the PGM concentrators in Rustenburg, South Africa was crushed, blended, and riffled. The ore fragments were then split into 1 kg samples by using a rotary splitter. A flotation slurry was then prepared by milling the 1 kg ore samples in synthetic plant water of the required ionic strength (see Table 1) at 66 per cent solids. A thiol collector, sodium isobutyl xanthate (SIBX) supplied by AECI (Senmin) was added to the mill at a dosage of 150 g/t. The collector solution was added to the mill because Wiese *et al* (2005) had shown this to be beneficial in sulfidic Cu-Ni-PGM ore flotation. A laboratory scale stainless steel rod mill was used to achieve a grind of 60 per cent passing 75 µm. The slurry was then transferred to a 3 L Barker flotation cell fitted with a variable speed drive and a manual pulp level. The volume of the slurry in the cell was made up to 3 L with the addition of the required synthetic plant water to produce about 35 per cent solids and the rest being water. The impeller speed was set to 1200 rev/min. A polymeric depressant in the form of Depramin 267 (supplied by AKZO Nobel Functional Chemicals), a CMC was added to the cell before the start of flotation. The CMC was added at dosages of 0, 100 and 500 g/t. 40 g/t of DOW 200 was added to the cell as the frother supplied by Betachem. After all reagents were added, an air flow rate of 7 L/min into the cell was applied and the froth height was allowed to build-up to 2 cm. Both air flow rate and froth height were kept constant. Four concentrates were collected at 2, 6, 12 and 20 min (denoted as C1, C2, C3 and C4 respectively) by scraping the froth into a collecting pan every 15 s. Feed and tailing samples were taken before and after each flotation test. The amount of water recovered with each of the four concentrates was measured. All the tests were performed in duplicate, and reproducibility was found to be within 5 per cent mass recovery standard error. The samples were filtered, dried, and weighed before analysis. This also allowed for the determination of the total solids and water recovered at the end of flotation for each experimental condition.

TABLE 1

Ion concentration, TDS, and *I* in synthetically prepared plant water.

Water type	Ca^{2+} (mg/l)	Mg^{2+} (mg/l)	Na^{+} (mg/l)	Cl^{-} (mg/l)	SO_4^{2-} (mg/L)	NO_3^{-} (mg/L)	NO_2^{-} (mg/L)	CO_3^{2-} (mg/L)	TDS mg/L	*I* [m]
1SPW	80	70	153	287	240	176	–	17	1023	0.0242
3SPW	240	210	459	861	720	528	–	51	3069	0.0727
5SPW	400	350	765	1435	1200	880	–	85	5115	0.1212
10SPW	800	700	1530	2870	2400	1760	–	850	10230	0.2426

To determine pyrrhotite recoveries and grades from the recovered concentrate samples, copper and total nickel analyses were conducted using a Bruker X Ray Fluorescence (XRF) S4 Explorer Spectrometer. Sulfur analysis was carried out using a LECO DR423 sulfur analyser. Assuming the stoichiometries for chalcopyrite and pentlandite to be $CuFeS_2$ and $(FeNi)_9S_8$ respectively, the recovery of iron sulfides (including pyrrhotite) was estimated from the copper, nickel, sulfur values for each concentrate.

Standard synthetic plant water was used as the base water quality (1SPW) and the levels of the ions was increased three, five and ten times for the higher ionic strength flotation tests as shown in Table 1. All the chemical salts used to make up the synthetic plant water solutions were supplied by Merck and were of analytical grade.

RESULTS

The effect of ionic strength and CMC dosage on pyrrhotite recoveries and grades

Figure 1 shows the relationship between pyrrhotite grade and recovery for all experimental conditions. It can be seen that in the absence of CMC, the recovery of pyrrhotite increased with an increase in the ionic strength of synthetic plant water (1, 3 and 10SPW) except for 5SPW which resulted in the lowest pyrrhotite recoveries. A similar trend was seen for a CMC dosage of 500 g/t. However, for a CMC dosage of 100 g/t, the recovery of pyrrhotite showed a general increase with increasing ionic strength of plant water in the order 10SPW>5SPW>3SPW>1SPW. It is also interesting to note that for a given water type, pyrrhotite recovery increased upon the addition of CMC at 100 g/t compared to 0 g/t, however a deep occurred at the addition of 500 g/t CMC. Figure 1 also shows that, for a given water type, pyrrhotite grade increased upon an increase in CMC dosage. In the absence of CMC, there seems to be no observable difference in pyrrhotite grade for 1SPW, 3SPW and 10 SPW, however in 5SPW, pyrrhotite grade was the lowest. A similar trend is seen for a CMC dosage of 100 g/t, except that pyrrhotite grade shows no apparent difference for all water types. For a CMC dosage of 500 g/t, the grade is in the following order 10SPW<5SPW<1SPW<3SPW.

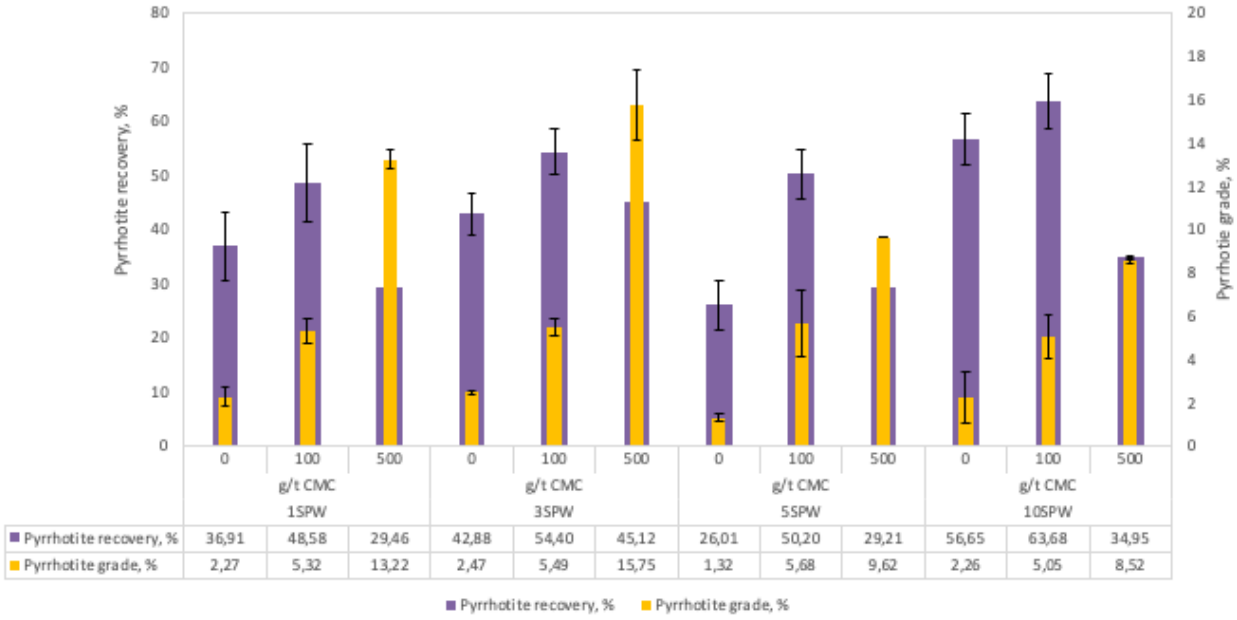

FIG 1 – Total pyrrhotite recoveries and grades for all tested conditions.

Figure 2 shows the recovery of pyrrhotite as a function of the amount of water recovered for the different water types and CMC dosages. It is important to clarify that the number on the right side of the water type denotes the dosage of CMC (eg 1SPW 100 simply means that the experiment was conducted using 1SPW in the presence of CMC at a dosage of 100 g/t).

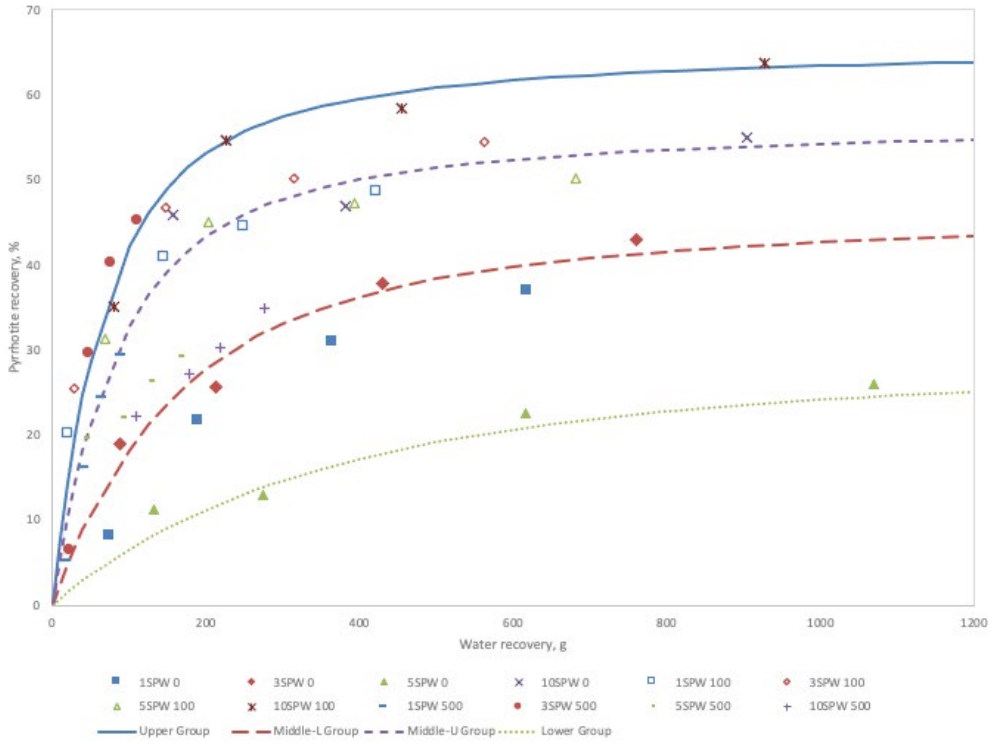

FIG 2 – Pyrrhotite recovery versus water recovery with fitted first order models.

The experimental data presented in Figure 2 were fitted into a modified first order equation shown in Equation 1.

$$R = R_{\infty}(1 - e^{-km_t}) \quad (1)$$

R presents the accumulated recovery after time t for a given recovered amount of water in g (m_t), R_{∞} is the maximum (or equilibrium) recovery that might be reached at infinite time, and k is the first order water recovery specific constant (g^{-1}). The model results were such that the experimental data fitted into four different first order models, denoted as Upper Group, Middle-Lower Group, Middle-Upper Group, and Lower Group. The k values for these models are presented in Table 2.

TABLE 2

First order water recovery specific constant calculated from Equation 1.

Model category	Experimental conditions	k (g^{-1})
Upper Group	3SPW 500	0.0255
	10SPW 100	
Middle-U Group	10SPW 0	0.0205
	1SPW 100	
	3SPW 100	
	5SPW 100	
	1SPW 500	
Middle-L Group	1SPW 0	0.0108
	3SPW 0	
	5SPW 500	
	10SPW 500	
Lower Group	5SPW 0	0.0051

It can be seen from Figure 2 and the *k* values in Table 2 that 5SPW in the absence of CMC resulted in the lowest pyrrhotite recoveries per unit water whilst 3SPW 500 and 10SPW 100 resulted in higher pyrrhotite recoveries per unit water.

Relating the effect of ionic strength and CMC on pyrrhotite to solids and water recoveries

Figure 3 show the effects of CMC dosage and ionic strength of plant water on the recovery of solids and water. The recovered solids are split into four categories, namely, non-sulfide entrained gangue, floating gangue, pyrrhotite and other sulfides. Figure 3 displays, for 0 g/t and 100 g/t CMC, a directly proportional trend between solids and water recovery with increasing ionic strength of plant water except for what seems to be an anomaly with 5SPW. It is interesting to note that from, generally for each water type, increasing CMC dosage from 0 g/t to 100 g/t resulted in an increase in the mass of pyrrhotite recovered, however an increase in CMC dosage from 100 g/t to 500 g/t gave rise to a decrease in pyrrhotite being pulled to the concentrate. However, the mass of pyrrhotite particles for a CMC dosage of 500 g/t in comparison to the 0 g/t CMC, seemed to have had no general trend.

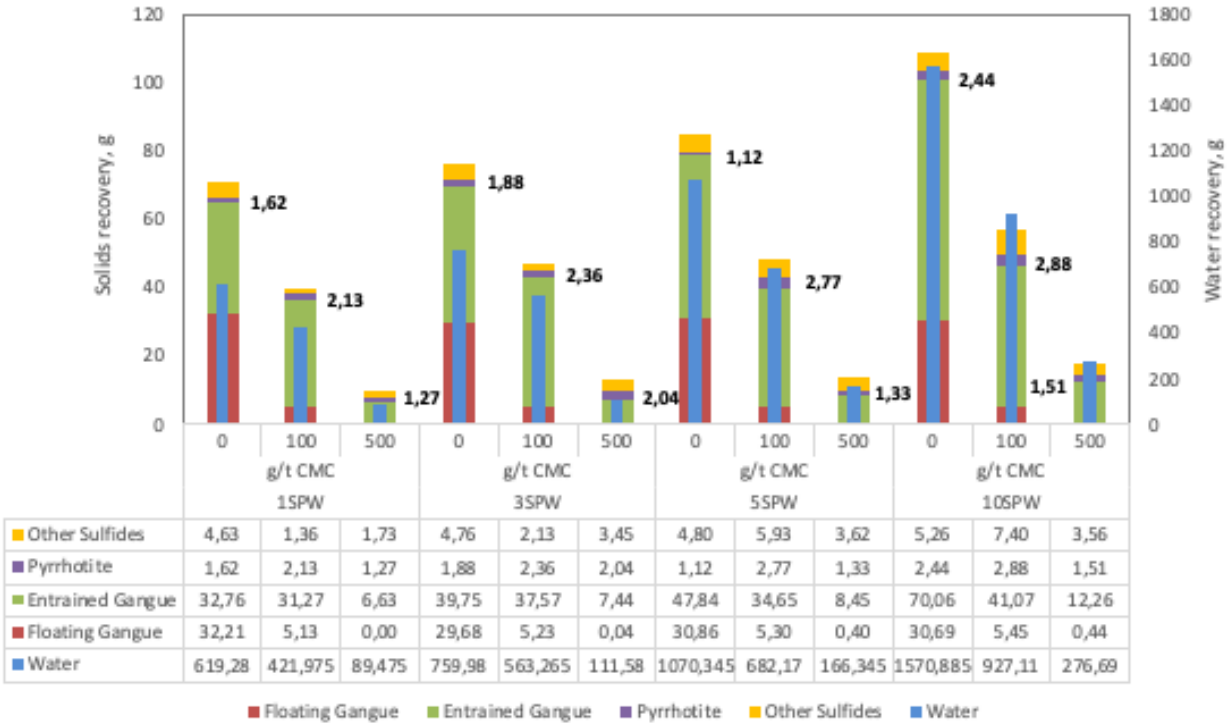

FIG 3 – Total solids and water recovery for all tested conditions.

It is interesting to note that the recovery of pyrrhotite neither followed the trend seen with non-sulfide entrained gangue nor that scene with floating gangue in relation to the changes in the ionic strength of plant water and CMC dosages. A more apparent trend of an increase in pyrrhotite recoveries with increasing ionic strength of plant water is seen in 0 g/t and 100 g/t of CMC, thus corresponding well with the trends seen with the non-sulfide entrained and floating gangue.

DISCUSSION

The results from this investigation have shown that entrained gangue, floating gangue, and water recoveries increased with an increase in the ionic strength of plant water and decreased with an increase in CMC dosages. It must be mentioned that the resulting increase in total solids and water recoveries in increasing strength of plant water can be attributed to a an increase in. froth stability (Corin and Wiese, 2014; Manono *et al*, 2013, 2012). Observations from this work on entrained gangue and floating gangue correlated well the water recovery trend and were therefore in agreement with the fact that increases in the ionic strength of plant water, increase the stability of the froth whereas increases in CMC dosages are known to decrease the stability of the froth

(Schreithofer *et al*, 2011; Wiese *et al*, 2007). Pyrrhotite recoveries, however, were not easily comparable to the trends seen on entrained gangue, floatable gangue, and water recoveries and thus could not be correlated with the impact the ionic strength of plant water and CMC dosage on the stability of the froth. The trend scene on entrained and floatable gangue can thus be attributed to the rise in froth stability as well as the activation of gangue particles which occurs in the presence of inorganic electrolytes, thus causing surface hydration of naturally hydrophobic minerals to decrease (Manono, 2018). In the presence of hydrophobic non-sulfide naturally floatable gangue minerals and pyrrhotite, a metallic conductor, highly prone to oxidation resulting in flotation due to the production of hydrophobic sulfur species but the same oxidation could result in sites on the pyrrhotite surface that are more hydrophilic and therefore prone to depression along with non-sulfide gangue minerals. Yoon and Sabey (1989) suggested that an ionic strength increase results in a further increase in hydrophobicity, this could explain the increase in the recovery of pyrrhotite with increasing ionic strength of plant water for 0 g/t and 100 g/t CMC conditions. This phenomenon can be attributed to inorganic electrolytes which reduce repulsive forces between bubbles and pyrrhotite particles by decreasing the zeta potential as was shown in (October *et al*, 2019, 2021). Moreover, this study did not show any apparent relationship between the ionic strength of plant water and CMC dosage on the recovery of pyrrhotite per unit water as seen in the results in Figure 3 and Table 2 thus showing no apparent link between the behaviour of pyrrhotite and froth stability. From these results, it can be deducted that the behaviour and floatability of pyrrhotite in ionic strength and CMC dosages cannot be simply correlated to the behaviour of non-sulfide naturally floatable gangue and entrained gangue which can be directly correlated with the impact on the stability of the froth. However, fundamental studies need to be conducted to further understand the behaviour of pyrrhotite in terms of its floatability and recovery per unit water. Future investigative work should also consider how a CMC dosage of 100 g/t resulted in better pyrrhotite recoveries compared to 0 and 500 g/t, this could be done by examining the floatability of pyrrhotite with more CMC dosages in between 100 and 500 g/t.

Thus, it can be said that the ionic strength of plant water and CMC dosage electrolytes are important variables to consider when tracking the behaviour of pyrrhotite from BMS-PGM ore flotation. With the activity of the CMC depressant being affected by interactions between the non-sulfide naturally floatable gangue, entrained gangue, pyrrhotite and other sulfides in the pulp, it is even more important to examine the behaviour seen from the results of this work. Table 3 summarises the effects of ionic strength and CMC dosages seen on pyrrhotite flotation.

TABLE 3

Effects of increasing ionic strength and CMC dosages on pyrrhotite flotation.

Response	Variable	Effect on Response
Total Pyrrhotite Recovery	Increasing Ionic Strength of SPW	Increases
	Increasing CMC Dosage	Increases between 0 and 100 g/t, then decreases between 100 and 500 g/t
Pyrrhotite Recovery per Unit Water	Increasing Ionic Strength of SPW	No definitive trend
	Increasing CMC Dosage	No definitive trend

CONCLUSIONS

The findings of this work showed that an increase in ionic strength results in an increase in pyrrhotite recoveries. This finding corresponds well with the general trend of an increase in the recoveries of non-sulfide entrained gangue and floating gangue for 0 and 100 g/t CMC. Increasing the depressant dosage of CMC from 0 to 100 g/t resulted in an increase in the recovery of pyrrhotite. However, a further increase in CMC dosage from 100 g/t to 500 g/t resulted in a decrease in pyrrhotite recoveries. 5SPW resulted in the poorest pyrrhotite recoveries compared to 1, 3 and 10SPW. The recovery of pyrrhotite per unit water did not give a definitive trend.

ACKNOWLEDGEMENTS

The authors would like to acknowledge support from the University of Cape Town and members of the Reagent Research Group (RRG) in the Centre for Minerals Research (CMR). This work was supported in part by the National Research Foundation (NRF) of South Africa (SA) (Grant numbers 99262). Any opinions, findings, conclusions, or recommendations expressed in any publication generated by NRF supported research is that of the authors, and the NRF accepts no liability whatsoever in this regard.

REFERENCES

Allison, S A, O'Connor, C T, 2011. An investigation into the flotation behaviour of pyrrhotite 98 (3–4), *Miner. Eng*. 98, 202–207.

Becker, M, Harris, P J, Wiese, J G, Bradshaw, D J, 2009. Mineralogical characterisation of naturally floatable gangue in Merensky Reef ore flotation. *Int. J Miner. Process*. 93, 246–255. https://doi.org/10.1016/j.minpro.2009.10.004.

Corin, K C, Reddy, A, Miyen, L, Wiese, J G, Harris, P J, 2011. The effect of ionic strength of plant water on valuable mineral and gangue recovery in a platinum bearing ore from the Merensky reef. *Miner. Eng*. 24, 131–137. https://doi.org/10.1016/j.mineng.2010.10.015.

Corin, K C, Wiese, J G, 2014. Investigating froth stability: A comparative study of ionic strength and frother dosage. *Miner. Eng.* 66, 130–134. https://doi.org/10.1016/j.mineng.2014.03.001.

Hochreiter, R C, Kennedy, D C, Muir, W, Woods, A I, 1985. Platinum in South Africa (Metal Review series No.3). *J South. African Inst. Min. Metall. African Inst. Min. Metall.* 85, 165–185.

Manono, M S, 2018. *Investigating Electrolyte-Reagent-Mineral Interactions in Response to Water Quality Challenges in the Flotation of a PGM Ore*. PhD Thesis. University of Cape Town.

Manono, M S, Corin, K C, Wiese, J G, 2012. An investigation into the effect of various ions and their ionic strength on the flotation performance of a platinum bearing ore from the Merensky reef. *Miner. Eng*. 36–38. https://doi.org/10.1016/j.mineng.2012.03.035.

Manono, M S, Corin, K C, Wiese, J G, 2013. The effect of ionic strength of plant water on foam stability: A 2-phase flotation study. *Miner. Eng.* 40. https://doi.org/10.1016/j.mineng.2012.09.009.

Manono, M, Corin, K, Wiese, J, 2018. Perspectives from literature on the influence of inorganic electrolytes present in plant water on flotation performance, *Physicochemical Problems of Mineral Processing*, 54(4), 2018, 1191–1214. https://doi.org/10.5277/ppmp18157.

O'Connor, C, Alexandrova, T, 2021. The geological occurrence, mineralogy, and processing by flotation of platinum group minerals (PGMs) in South Africa and Russia. *Minerals* 11, 1–15. https://doi.org/10.3390/min11010054.

October, L L, Manono, M S, Corin, K C, Schreithofer, N, Wiese, J G, 2021. The Influence of Specific Ions and Oxyhydroxo Species in Plant Water on the Bubble-Particle Attachment of Pyrrhotite. *ACS Omega* 6, 28496–28506. https://doi.org/10.1021/acsomega.1c01152.

October, L, Corin, K, Schreithofer, N, Manono, M, Wiese, J, 2019. Water quality effects on bubble-particle attachment of pyrrhotite. *Miner. Eng*. 131. https://doi.org/10.1016/j.mineng.2018.11.017.

Rao, S R, Finch, J A, 1989. A review of water re-use in flotation. *Miner. Eng*. 2, 65–85.

Schreithofer, N, Wiese, J, McFadzean, B, Harris, P, Heiskanen, K, OConnor, C, 2011. Frother-depressant interactions in two and three phase systems. *Int. J Miner. Process*. 100, 33–40. https://doi.org/10.1016/j.minpro.2011.04.008.

Wiese, J, Harris, P, Bradshaw, D, 2005. The influence of the reagent suite on the flotation of ores from the Merensky reef. *Miner. Eng*. 18, 189–198. https://doi.org/10.1016/j.mineng.2004.09.013.

Wiese, J, Harris, P, Bradshaw, D, 2007. The response of sulphide and gangue minerals in selected Merensky ores to increased depressant dosages. *Miner. Eng.* 20, 986–995. https://doi.org/10.1016/j.mineng.2007.03.008.

Yoon, R H, Sabey, J B, 1989. Coal flotation in inorganic salt solutions, in: Botsaris, G D, Glazman, Y M (Eds.), *Interfacial Phenomena in Coal Technology*. *Surfactant Science Series*, pp. 87–114.

Application of water-soluble polymers as flotation reagents for the extraction of gold from finely ground products

T N Matveeva[1], V A Chanturia[2], V V Getman[3] and A Yu Karkeshkina[4]

1. Deputy Director for Research, Institute of Comprehensive Exploitation of Mineral Resources Russian Academy of Sciences (ICEMR RAS), Moscow 111020, Russia. Email: tmatveyeva@mail.ru
2. Chief Research Associate, ICEMR RAS, Moscow 111020, Russia. Email: vchan@mail.ru
3. Senior Research Associate, ICEMR RAS, Moscow 111020, Russia. Email: viktoriki.v@gmail.com
4. Research Associate, ICEMR RAS, Moscow 111020, Russia. Email: ankatrin06@mail.ru

ABSTRACT

The development and application of new effective environmentally friendly reagents for the flotation of thin and ultrathin mineral components is an urgent task. The analysis of the nomenclature of chemicals, including flotation reagents and flocculants, showed that water-soluble polymers (WSP) might be used in flotation separation of fine grinding products containing non-ferrous and precious metals. Water-soluble polymers that are responsive to temperature changes are the most attractive as reagents during flotation. These are the thermo-responsive polymers or thermomorphic polymers. The presence of nitrogen and oxygen atoms in the polymer molecule contributes to the formation of a coordination bond with non-ferrous and precious metals. A research conducted at the ICEMR RAS within the framework of the scientific school of Academician of the Russian Academy of Sciences Chanturia helped to develop a method of flotation of finely ground mineral particles containing valuable components using modified thermomorphic polymers. The paper focuses on the experimental study of poly (vinyl caprolactam) (PVC) as a flotation reagent for gold recovery from finely ground mineral products. PVC is a ready-made water-soluble thermosensitive polymer that does not require complex synthesis. PVC has a high ability to form complexes in an aqueous environment when heated. According to experimental data, the polymer interacts with gold nanoparticles, contributing to the extraction of gold from fine mineral products and the tailings that makes it perspective as an additional flotation agent for the processing of gold-containing ores.

INTRODUCTION

The aim of the paper is to study the application of water-soluble thermosensitive polymer poly (vinyl caprolactam) (PVC) as an additional selective collecting reagent for the flotation recovery of finely grinded mineral products containing noble metals.

Water-soluble polymers that are sensitive to temperature variation and change the aggregate state from soluble to solid are attractive as flotation reagents. These are the so-called thermosensitive (TSP) or thermomorphic polymers (TMP). Nitrogen and oxygen atoms in the polymer structure contribute to the formation of complex compounds with non-ferrous and noble metals. IPKON RAS has developed a technique for the flotation separation of finely dispersed mineral particles containing valuable components in the presence of modified thermomorphic polymers (Chanturia and Getman, 2015; Chanturia *et al*, 2016, 2009). When the pulp heated to the phase transition temperature (Tf.r.), the polymer changes its molecular structure, hydrophilicity/hydrophobicity parameters and aggregate state from liquid to solid. After heating the mineral pulp, fine particles of valuable metals, primarily fixed on the polymer in aqua solution, are concentrated in a throth flotation product.

Poly (vinyl caprolactam) (PVC) – a water-soluble polymer that has thermal sensitivity properties was chosen for the research (Verezhnikov *et al*, 2006; Fu *et al*, 2018). PVC is a ready-made polymer that does not require complex synthesis; it is widely used in medicine, biology and biotechnology. It is a viscous translucent liquid, highly soluble in water and organic solvents. According to preliminary data, the polymer interacts with gold nanoparticles, contributing to the additional extraction of gold from tailings, that makes it possible to use PVC as an additional flotation reagent for extracting gold from complex ores and poor finely divided mineral products.

EXPERIMENTAL

PVC solution thermal sensitivity was studied by kinetic photometry on Shimadzu 1700 UV spectrophotometer in the visible part of the spectrum at λ = 500 nm. A PVC solution of variable concentration (1.0 per cent, 0.1 per cent and 0.02 per cent) analysed after heating to 35°C.

The interaction between PVC and gold studied by analytical scanning electron microscopy (SEM) on a LEO 1420VP microscope equipped with an INCA 350 X-ray energy-dispersive microanalyser. Polished sections of natural pyrite sample and artificially enriched with gold pyrite sample were prepared for microscopy tests (Chanturia *et al*, 2010; Chanturia and Getman, 2015). Artificially enriched with gold pyrite sample was prepared using H [$AuCl_4$] solution with a concentration of 5 mg/l.

Flotation studies carried out on monomineral fractions of natural pyrite and Au-bearing pyrite samples grinded to -0.16 + 0.063 mm. A sample weighing 1 g mixed with PVC solution, and then slow heating carried out to 35°C with constant stirring. The suspension was transferred to the flotation cell (V = 25 ml), butyl potassium xanthate PBX (2.5 mg/l) was added and agitated for 1 minute; MIBC (15 mg/l) was used as a froth agent. Flotation time was 1 minute to obtain a concentrate and tailings.

Hydrophobic and flotation properties of poly (vinyl caprolactam) (PVC) were studied on a sample of gold-bearing ore from the Olimpiada deposit. The ore sample is a gold-bearing arsenopyrite carbonate-silicate ore with impregnations of pyrrhotite, pyrite, arsenopyrite, and antimonite. The chemical composition: Au – 3.07 ppm, Ag – 0.416 ppm, S – 2.10 per cent.

RESULTS AND DISCUSSION

Study of PVC physical and chemical properties

PVC is a viscous translucent liquid, highly soluble in water, as well as in organic solvents, has a high absorption capacity. PVC has high biocompatibility and low toxicity, that allows to use it in medicine (drug delivery and encapsulation), biology (permeability controlled membranes), and biotechnology (sensors). PVC has a high ability to form complex compounds in an aqueous medium when heated, depending on the concentration and molecular weight (MW). Structural formula of PVC (Figure 1):

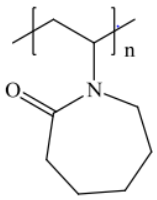

FIG 1 – Structural formula of PVC.

The temperature-sensitive properties of a water-soluble polymer (PVCL) based on the balance between two interactions: PVC-water and PVC-PVC (Figure 2). On the one hand, PVC chains undergo solvation of a solute and a solvent in water. On the other hand, there are hydrophobic interactions between the chains of PVC molecules. In the result of heating, its structure becomes like a sponge that upon further heating is capable of pushing out ‘extra molecules’ of water.

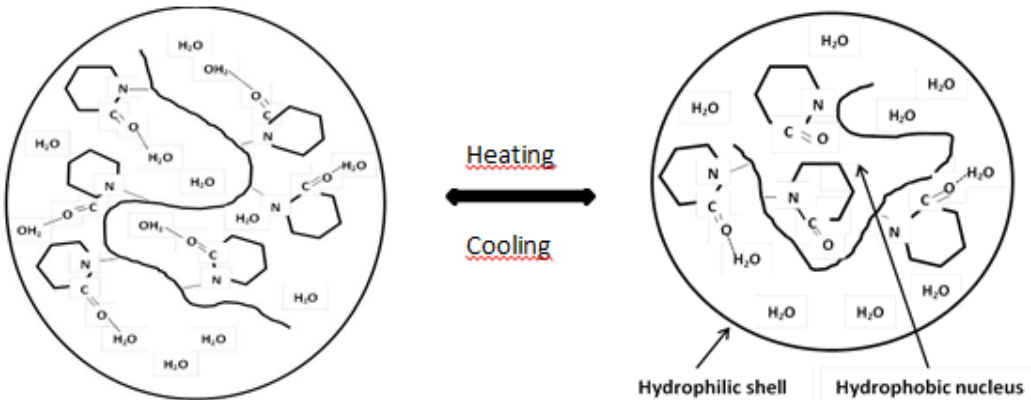

FIG 2 – Interaction between PVC and water in solution.

The phase transition temperature of the polymer strongly depends on the molecular weight of the polymer because an increase in MW will contribute to a decrease in solvation and a decrease in Tf.r.

PVC thermos-sensitivity studied visually by changing the state of aggregation of the solution (1 per cent) with fixing the phase separation temperature (Figure 3). With an increase in the phase transition temperature, an abundant separation of the dispersed phase and a sharp increase in turbidity occur. Cooling the solution leads to a clarification of the solution to the initial state of aggregation, which indicates the reversibility of the process.

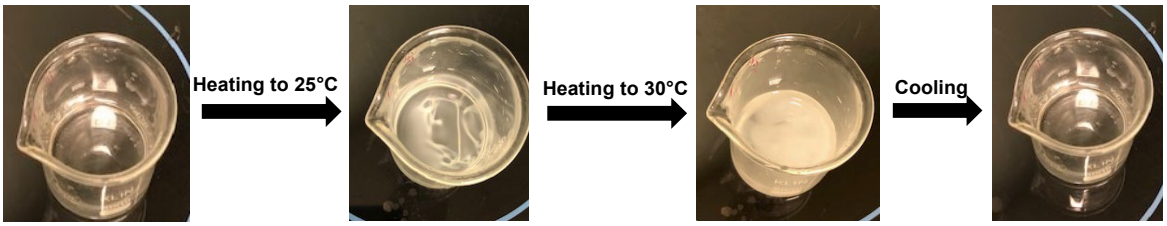

FIG 3 – Changes in aggregation state of PVC solution (1 per cent).

Taking into account the reversibility of the process of transition from one aggregation state to another, the thermosensitive properties of PVC (1 per cent) studied using kinetic photometry. In the experimental result it was found (Figure 4) that after 300 seconds there was a sharp increase in the amount of light transmission (T, %), ie PVC solution becomes transparent on cooling.

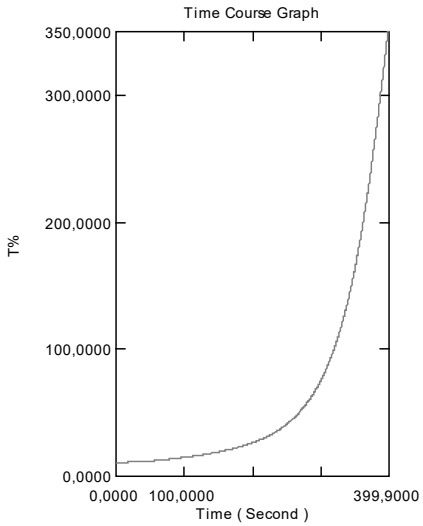

FIG 4 – Curve of the change in light transmission of the PVC solution (1 per cent) via time of cooling.

A series of experiments carried out to determine the thermal sensitivity for PVC solutions of variable concentration 1.0 per cent, 0.1 per cent and 0.02 per cent (Table 1). The tested PVC solution was

slowly heated from 20 to 450°C on a water bath with Tf.r. value fixation. Upon cooling to room temperature, the solutions passed into the initial state of aggregation (became transparent). It is determined that PVC Tf.r. value decreases with an increase in the polymer concentration in solution.

TABLE 1

Dependence of the phase transition temperature from polymer concentration.

Polymer	Concentration, %	Tf.r., °C
PVC solution	1.0	30
	0.1	29
	0.02	27

Results of SEM studies of the PVC adsorption on the mineral surface

An analysis of images of the surface of polished sections of pyrite sample with gold after interaction with a PVC solution (Figure 5) showed that dark spots of PVC are clearly visible on the surface of pyrite directly in areas with of gold particles accumulation (Figure 5b). The X-ray spectrum of this area (Figure 5c) showed a carbon peak characteristic of PVC and a gold peak.

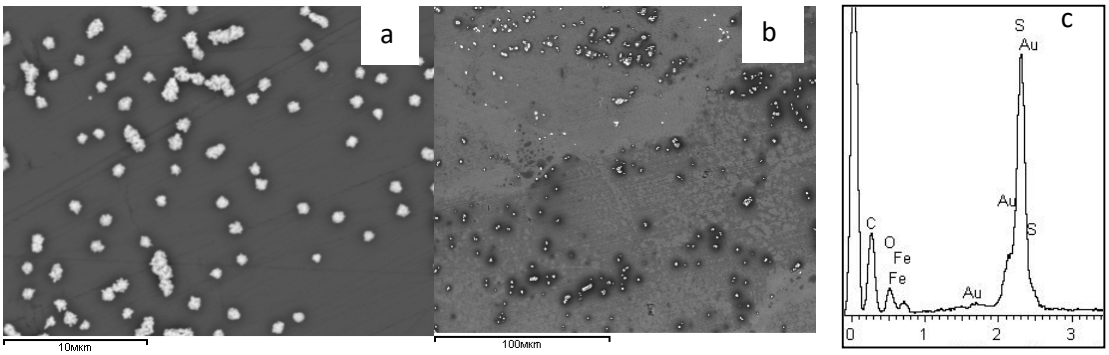

FIG 5 – SEM micrograph of polished section of pyrite with gold before contact with PVC solution (a), after contact with a 0.1 per cent PVC solution (b), X-ray spectrum (c).

Results of the flotation studies

Comparative monomineral flotation of natural pyrite and pyrite with gold carried out using the PVC reagent as an additional collector for gold together with PBX (Figure 6). PVC concentration varied from 0 to 7.5 mg/L.

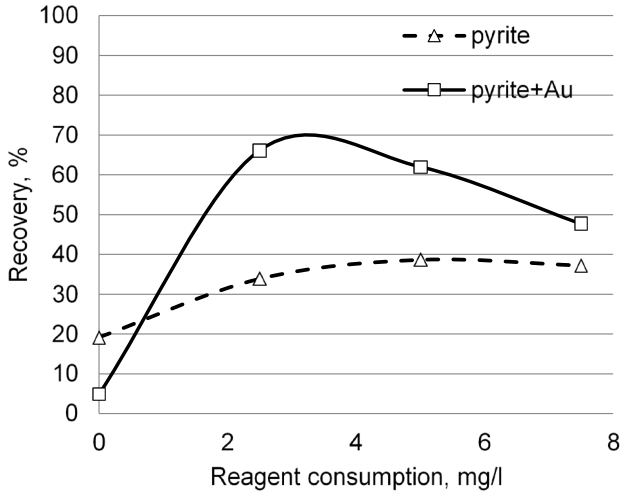

FIG 6 – Results of comparative mono-mineral flotation of pyrite and Au-pyrite by PVC (0 to 7.5 mg/l).

The flotation yield of Au-pyrite is much higher (68 per cent) than the yield of natural pyrite (45 per cent). Moreover, the maximum floatability of Au-pyrite is achieved at a low concentration of PVC (3 mg/L) than that of natural pyrite (5 mg/L).

Study of the hydrophobic properties of PVC on finely ground products containing non-ferrous and noble metals

The hydrophobic properties of poly (vinyl caprolactam) (PVC) were studied on a sample of gold-bearing ore from the Olimpiada deposit. To study the flocculating properties of PVC, a series of experiments was carried out on a finely ground ore sample 96.5 per cent -0.071 mm.

Flocculation was studied by sedimentation method in a gravitational field, according to the mass of sediment settling over a certain period of time. Finely ground ore (pulp) (500 ml) was placed into a wide beaker with a volume of 1 L, thoroughly mixed with an overhead stirrer. Then, the pulp was heated to the required temperature (40°C). Under static conditions, the solid particles of the pulp settled, in 5 minutes the liquid part was decanted. The precipitate and overflow were dried and weighed. The results and conditions of the experiments are in Table 2.

TABLE 2

Results of the study of PVC flocculation properties.

Test number	Tests conditions	Solid particles content, %	
		In drain	In sludge
1	Without pulp heating (t = 21°C)	18.80	81.20
2	Pulp heating (t = 40°C)	15.83	84.17
3	Pulp heating (t = 40°C) PVC 10 g/t	12.92	87.08
4	Pulp heating (t = 40°C) PVC 20 g/t	12.07	87.93
5	Pulp heating (t = 40°C) PVC 30 g/t	11.37	88.63
6	Pulp heating (t = 40°C) PVC 40 g/t	9.87	90.13

Without heating the pulp and without a reagent, 18.8 per cent of solid particles are detected in the drain (test 1), and as it is heated, the content of solid particles in the drain decreases by 2.97 per cent (test 2). The addition of PVC (10 g/t) reduces the solids content in the overflow by an additional 2.91 per cent. An increase in PVC consumption to 40 g/t (test 6) leads to decrease in solid particles in the drain to 9.87 per cent, while the content of solid particles in the sludge is 90.13 per cent, which is 8.93 per cent more than in test 1. A graphical dependence of the content of solid particles in the flocculation products, depending on the concentration of PVC shown in Figure 7. When heated, the polymer promotes the aggregation of solid fine particles, which indicates the flocculating properties of PVC.

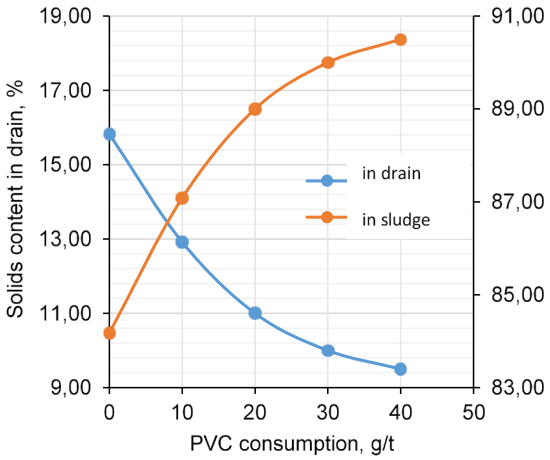

FIG 7 – Dependence of the solid particles content in flocculation products via the initial PVC concentration.

Ore flotation

A series of flotation experiments in an open cycle in one stage carried out with obtaining concentrate and tailings. As a baseline test, a traditional reagent for flotation of sulfide ores, potassium butyl xanthate (PBX 200 g/t), was used. A water-soluble polymer, poly (vinyl caprolactam) (PVC), was used as an additional collector for gold. $CuSO_4$ 100 g/t used as activator, MIBC 100 g/t as a froth agent. Technological indicators presented in Table 3.

TABLE 3

Technological indicators of Olimpiada ore flotation.

Test	Reagent mode, g/t	Product	Yield, %	Content Au, ppm	Recovery Au, %
1	PBX 200	Concentrate	12.31	19.92	78.59
		Tailings	87.69	0.76	21.41
		Ore	100.00	3.12	100.00
2	PVC 10 PBX 200	Concentrate	12.64	18.77	77.00
		Tailings	87.36	0.81	23.00
		Ore	100.00	3.08	100.00
3	PVC 20 PBX 200	Concentrate	12.28	22.04	87.60
		Tailings	87.72	0.44	12.40
		Ore	100.00	3.09	100.00
4	PVC 30 PBX 200	Concentrate	13.19	21.61	91.65
		Tailings	86.81	0.30	8.35
		Ore	100.00	3.11	100.00

PBX (200 g/t) dosage as the main collector makes it possible to obtain a concentrate with a yield 12.31 per cent, Au content 19.92 ppm and Au recovery 78.59 per cent (test 1). The dosage PVC 10 g/t together with PBX 200 g/t do not provide better flotation results. An additional PVC dosage leads to an increase in the quality of the Au concentrate and Au recovery. At PVC consumption 20 g/t (test 3), the gold content is 22.04 ppm and Au extraction 87.6 per cent. An increase in PVC consumption up to 30 g/t (test 4) gold recovery raises to 91.65 per cent that is 13.06 per cent higher than in the test with single PBX. In those conditions, the quality of the Au concentrate is 1.5–1.7 ppm higher than that in baseline test.

CONCLUSIONS

For the first time, the application of a water-soluble polymer, poly (vinyl caprolactam) (PVC), as a flotation reagent for the extraction of finely ground Au-containing mineral products has been proposed and scientifically substantiated.

PVC adsorption on gold-bearing pyrite has been identified by scanning analytical microscopy. PVC interacts with fine gold particles, contributing to the additional Au recovery from tailings, and makes it possible to recommend PVC as an additional flotation reagent for the complex extraction of gold from finely ground ores.

Studies of PVC hydrophobic and flocculation properties has demonstrated that PVC promoted the aggregation of fine Au-containing mineral particles, that helped to achieve high flotation indicators in laboratory tests of processing of Au ore.

The introduction of PVC into the flotation process as an additional collector to potassium butyl xanthate (PBX) increased the recovery of gold into the flotation concentrate, thereby reducing the loss of gold with tailings in 2.5 times. Au content in flotation tailings decreased from 0.76 to 0.3 ppm.

REFERENCES

Chanturia, V A and Getman, V V, 2015. Experimental investigation of interaction between modified thermomorphic polymers, gold and platinum in dressing of rebellious precious metal ore, *Journal of Mining Science*, 51(3):580–85.

Chanturia, V A, Ivanova, T A and Koporulina, E V, 2010. Method for assessing the effectiveness of the interaction of flotation reagents with gold-bearing pyrite, *Tsvetnye Metally*, 8:16–19.

Chanturia, V A, Ivanova, T A, Getman, V V and Koporulina, E V, 2015. Methods of minerals modification by the micro – and nanoparticles of gold and platinum for the evaluation of the collector's selectivity at the flotation processing of noble metals from the fine ingrained ores, *Mineral Processing and Extractive Metallurgy Review*, 36 (5): 288–304.

Chanturia, V A, Matveeva, T N, Ivanova, T A, Getman, V V, 2016. Mechanism of interaction of cloud point polymers with platinum and gold in flotation of finely disseminated precious metal ores, *Mineral Processing and Extractive Metallurgy Review*, 37(3):187–195.

Chanturia, V A, Nedosekina, T V, Ivanova, T A, Getman (Stepanova), V V, Nedosekin, D A, 2009. Method for flotation of precious metals, Patent of the Russian Federation 27/2368427.

Fu, X, Hosta-Rigau, L, Chandrawati, R and Cui, J, 2018. Multi-stimuli-responsive polymer particles, films and hydrogels for drug delivery, *Chem*, 4: 2084–2107.

Verezhnikov, V N, Plaksitskaya, T V, Poyarkova, T N, 2006. PH-thermosensitive properties of (co)polymers of N, N-dimethylaminoethyl methacrylate and N-vinyl caprolactam, *High Molecular Compounds*, 48 (8): 1482–1487.

Decoupling the pulp and froth effect of ultrafine particles on Itabirite iron ore flotation

B McFadzean[1], N P Lima[2] and D A Deglon[3]

1. Associate Professor, Centre for Minerals Research, University of Cape Town, Rondebosch, Cape Town 7700. Email: belinda.mcfadzean@uct.ac.za
2. Specialist Engineer, Vale S.A.; Av. Dr. Marco Paulo Simon Jardim, 3580, Bairro Piemonte, Nova Lima, CEP: 34.006–200, MG, Brasil. Email: neymayer.lima@vale.com
3. Professor, Centre for Minerals Research, University of Cape Town, Rondebosch, Cape Town 7700. Email: david.deglon@uct.ac.za

ABSTRACT

The reverse flotation of Itabirite iron ore is typically performed after a desliming step in which most of the sub-10 µm particles are removed. This is done to limit processing problems such as poor flotation recovery of SiO_2 due to slime coatings and increased slurry viscosities, unmanageable froths and increased losses of hematite particles due to entrainment. However, the rejection of ultrafine particles contributes to large losses in iron recovery and may contribute to the instability of tailings dams. The aim of this study is to decouple the effects of ultrafine particles in the pulp and froth phases to better understand the processing capabilities of the fines fraction.

The flotation test work was performed in a special-purpose continuously operated laboratory flotation cell that has a deep froth section to simulate plant-scale froth conditions. Five conditions of fines addition were investigated at three different froth heights and a solids concentration of 50 per cent.

The behaviour of the pulp and the froth were decoupled using froth stability and froth recovery tests. This showed that, even though there is an exponential increase in froth stability at increasing fines quantities, the performance of the pulp has the overriding effect on the overall SiO_2 recovery. Pulp zone, froth zone and overall SiO_2 recoveries showed that overall recoveries increased by about 3.6 per cent for every 1 per cent decrease in fines content. This meant a large increase of 20 per cent in SiO_2 recovery when going from undeslimed to deslimed feed. This was driven largely by increases in the pulp zone recoveries, which were about 4 per cent for every 1 per cent decrease in fines content. The froth recoveries, on the other hand, decreased by between 0.75 per cent and 2.5 per cent for every 1 per cent decrease in fines content, depending on froth height. This paper explores further insights into iron ore flotation processing at different slimes concentrations.

INTRODUCTION

Reverse flotation of Itabirite iron ore is traditionally performed with the inclusion of desliming cyclones prior to rougher flotation to remove most of the sub-10 µm particles, due to the processing challenges that the fines fraction presents. These include poor quartz flotation due to factors such as poor collision/attachment efficiencies and slimes coating, excessively stable froths and large iron losses due to entrainment. However, there is an increasing drive to be able to include these fines in the flotation circuit to limit iron losses, which can represent up to 15 per cent of the total iron, and to limit the amount of fines discarded to tailings dams.

The effects of decreasing particle size on the sub-processes of true flotation and entrainment are well known. Very fine particles are detrimental to the collision and attachment efficiencies (Ralston, 1999; Ralston *et al,* 1999), while the entrainment of fine particles increases exponentially at ultrafine particle sizes (Zheng *et al,* 2006). Finer particles also require increased reagent dosages due to higher surface areas. Previous studies have shown that the inclusion of ultrafine particles in the feed to reverse iron ore flotation results in poor selectivity of the process (Lima *et al,* 2012), likely due to poor SiO_2 recovery and Fe entrainment. Split flotation circuits for fine (-45 µm) and coarse particles (45–150 µm) yielded an overall greater recovery of Fe by 3 per cent, as well as lower reagent consumption and higher grade than when size fractions were floated together in a batch flotation cell (Lima *et al,* 2013).

Not only do fine particles affect the sub-processes whereby particles report to the concentrate, but they also affect the properties of the slurry itself. Decreasing particle size and increasing solids

concentration result in an increase in slurry viscosity (Shi and Napier Munn, 1996). This may be especially problematic at the high solids concentrations typically used in reverse iron ore flotation of about 50 per cent by mass. In addition, this will be exacerbated by the presence of phyllosilicate minerals, which also increase slurry viscosity by particle aggregation of their oppositely charged surfaces (Ndlovu *et al,* 2014). High viscosities negatively affect bubble-particle collision and gas dispersion (Shabalala *et al,* 2011) and can be severely detrimental to flotation performance.

Dilution of slurry densities is a simple way to reduce pulp viscosity. Gao *et al* (2018) found that reducing the pulp density from 40 wt per cent to 20 wt per cent increased nickel and copper recoveries in a nickel-copper sulfide ore that was artificially spiked with between 5 and 30 wt per cent serpentine. Mowla *et al* (2008) found a similar increase in separation efficiency in the flotation of hematite from silica at decreasing solids concentrations of between 40 and 20 wt per cent. Conversely, Luo *et al* (2016) found that there was an approximately linear increase in lead recovery of a Pb-Cu ore from 60 per cent to 80 per cent when increasing solids concentration from 27.5 per cent to 50 or 55 per cent. However, the flotation was performed in a self-aerated flotation cell and this may account for the increase in recovery, since the air flow rate is directly related to the hydrostatic head, which will be influenced by the pulp density.

The effect of the froth phase should not be discounted when performing this type of test work. The froth recovery in a batch flotation cell can be extremely high, depending on scraping rate and froth depth (Amelunxen *et al,* 2014). This is in contrast to plant-scale cells, which operate at equilibrium and generally have longer froth residence times and much deeper froths. This factor is often ignored in laboratory test work and the interpretation thereof. An interesting study undertaken by Runge *et al* (2012) investigated the effect of solids concentration on flotation performance of a copper ore taken from various streams in an operating plant and routed to a 3 m^3 flotation cell. They decoupled the pulp and froth phase recoveries and found that an increase in solids concentration from 20 per cent to 35 per cent had a negative impact on the pulp zone performance, but a positive impact on froth phase recovery. This was further impacted by particle size, with finer particles being more severely negatively affected than coarser particles.

The research presented in this paper investigates the effects of incrementally adding increasing amounts of iron ore fines to the feed to assess the effects on the flotation performance. The main difficulty in assessing these effects is trying to mimic froth effects in the laboratory. This was achieved by designing a special-purpose continuously operated flotation cell, with a bottom-driven impeller-stator and having a series of deep froth sections (100 to 300 mm). This paper reports on the effect that increasing fines contents and decreasing the solids concentrations have on the flotation performance of an Itabirite iron ore.

EXPERIMENTAL DETAILS

Ore

Itabirite iron ore was collected as slurry from the feed to the plant desliming cyclone. This slurry was separated into a fine and coarse fraction in a laboratory-scale cyclone, as shown in Figure 1 and Table 1. BET surface area analysis was done on the fine and coarse fractions. Here, the coarse and fine fraction had a specific surface area of 0.28 m^2/g and 9.56 m^2/g respectively, representing a 34 times difference.

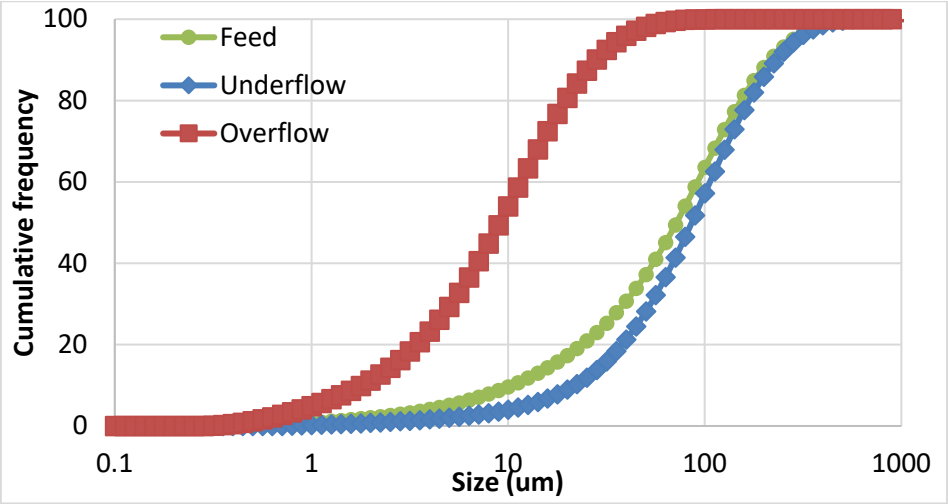

FIG 1 – Particle size distribution of cyclone feed, overflow and underflow determined by laser light scattering.

TABLE 1

Mass percent of -10 µm, 10–25 µm and +25 µm in the feed, underflow and overflow determined by laser light scattering.

	-10 µm (%)	**10–25 µm (%)**	**+25 µm (%)**
Feed	9.64	10.71	79.65
Underflow/Coarse	4.04	7.89	88.07
Overflow/Fine	53.97	33.41	12.62

Figures 2 and 3 show the grade of Fe_2O_3, SiO_2 and Al_2O_3 by size class for the underflow and overflow respectively. This shows that in the underflow the SiO_2 grade generally increased with particle size, culminating in the highest grade in the +106 µm size class (91 per cent). The grade of Fe_2O_3, on the other hand, was between 67 per cent and 84 per cent up to 75 µm, whereafter it dropped and there was only 10 per cent Fe_2O_3 in the +106 µm size class. There was less than 0.5 per cent Al_2O_3 present in all size classes except for the -10 µm size fraction, where there was 3 per cent Al_2O_3. In the overflow there was only mass up to the +25 µm size class and all grades were relatively consistent across these size classes (47–55 per cent for Fe_2O_3 and 33–41 per cent for SiO_2). However, there was markedly more Al_2O_3 present in the overflow, with between 4 and 6 per cent in all size classes.

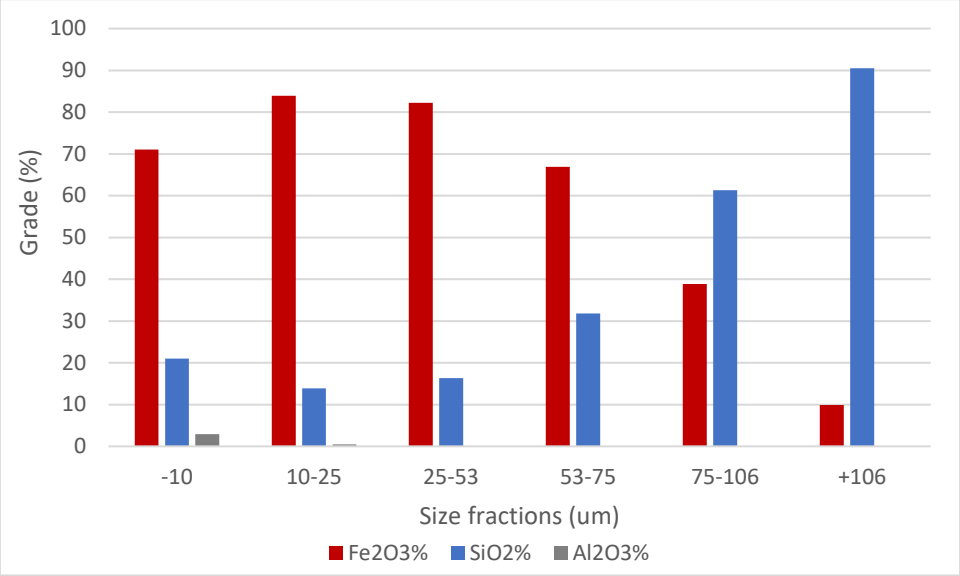

FIG 2 – Mass fraction of Fe_2O_3, SiO_2 and Al_2O_3 by size class for the underflow/coarse.

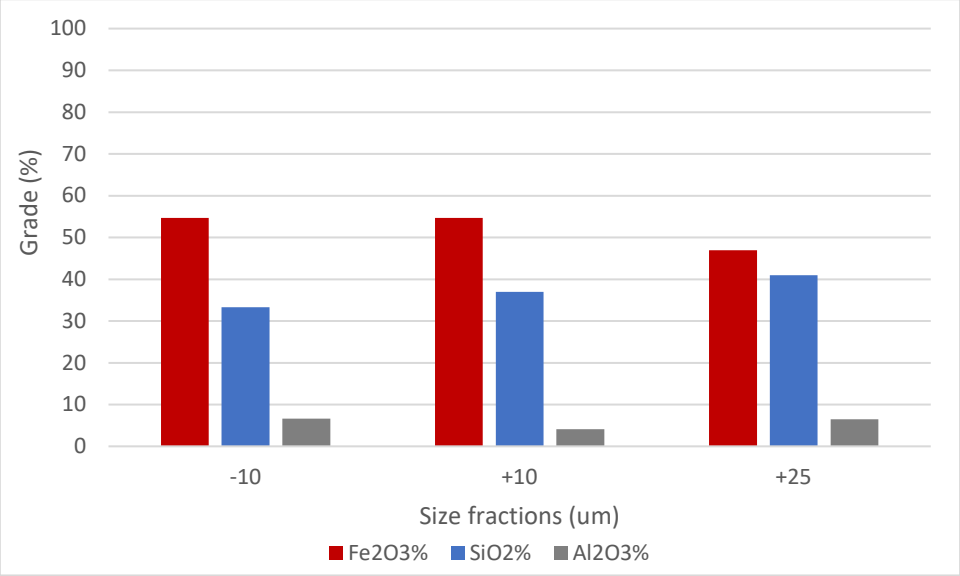

FIG 3 – Mass fraction of Fe_2O_3, SiO_2 and Al_2O_3 by size class for the overflow/fine.

Flotation cell

A special-purpose laboratory flotation cell developed at the Centre for Minerals Research was used for this test work, as shown in Figure 4. The cell was designed to have the same hydrodynamic and energy inputs as a standard batch flotation cell. However, the key differences are that the cell is continuously operated and has a large adjustable froth section. Continuous operation means that the pulp and froth sections can reach dynamic equilibrium These differences are designed to mimic, as closely as possible, the froth characteristics of a full scale flotation cell. The interchangeable froth sections have diameters of 200 mm and heights of 100 mm, 200 mm and 300 mm, which are deep enough to allow for froth drainage and give more realistic entrainment recoveries than a 20 mm batch flotation froth. The 200 mm froth diameter is large enough to limit preferential water drainage down the walls of the vessel (Geldenhuys and McFadzean, 2018). The froth area is 314 cm^2. Froth stability was measured using the same cell, with the addition of a 1 m non-overflowing froth section. Froth stability (s) is defined as the maximum froth height (cm) divided by the superficial gas velocity (cm/s).

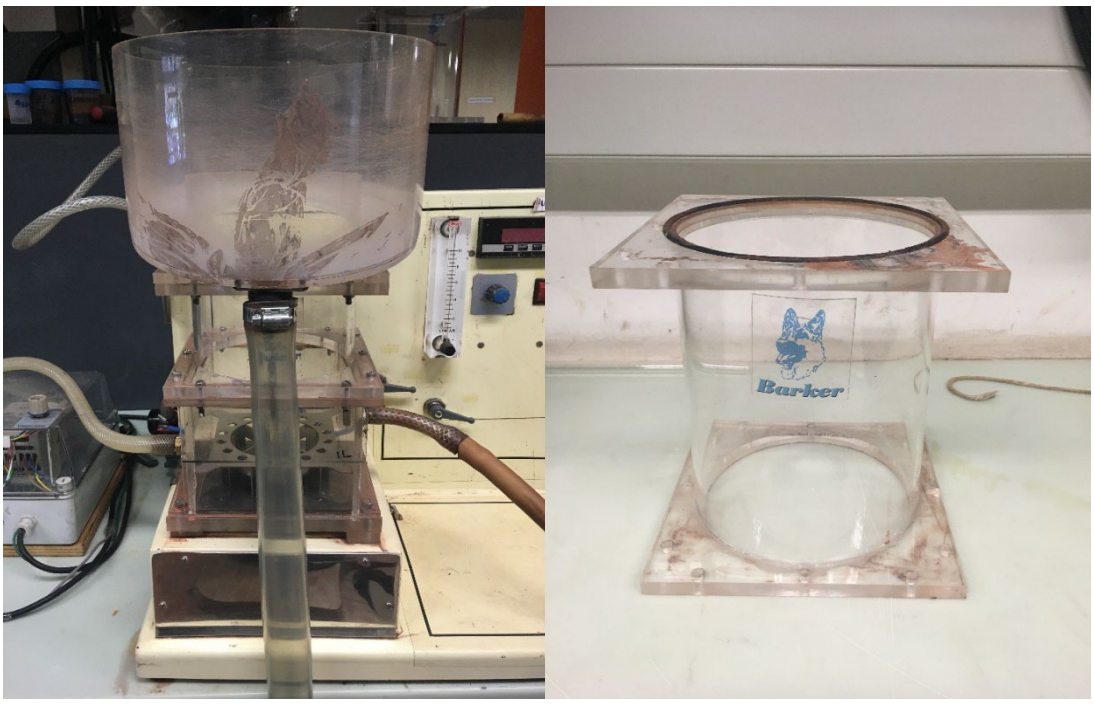

FIG 4 – Continuous laboratory scale hybrid flotation cell, with interchangeable froth heights.

Test conditions

Tests were performed at increasing amounts of fines, from completely deslimed (the underflow in Table 1), through increasing amounts of fines, until the flotation feed had the composition of an undeslimed feed (the feed in Table 1). These tests were performed at 30, 40 and 50 per cent solids concentrations and 100, 200 and 300 mm froth heights. Residence time was approximately 0.5 minutes. The test work was done at standard plant reagent types and dosages. Collector was EDA supplied by Clariant and dosed at 80 g/t. Depressant was corn starch from Sigma-Aldrich dosed at 400 g/t. pH was maintained at 10.5 using NaOH. The objective was not to obtain the optimum set of operating conditions, but to operate in a region where differences in performance would be evident at the different fines conditions. Feed and tails were collected and analysed by size for Fe_2O_3, SiO_2 and Al_2O_3. The tests used a large amount of feed material and were relatively time consuming. Therefore, repeats were not done on all tests. Repeatability was tested by doing four repeats on five different tests. Average standard error was shown to be 6.93 per cent and this is reported as error bars in the graphs.

Feed particle size distribution

The flotation tests were performed at five different fines concentrations as shown in Table 2. A mass fraction of one indicates that this is the deslimed condition where the feed is 100 per cent from the underflow of the desliming cyclone. Fines from the overflow of the desliming cyclone were added in 2 per cent increments until the undeslimed condition was reached. This condition is the same as the feed composition to the plant before the desliming cyclone and corresponds to the '0.92' or 9.26 per cent <10 µm. Even though the mass percent increased between the undeslimed and deslimed conditions appears to be small, in that there is only about a 4 per cent increase in the amount of -10 µm in the feed, the surface area of the particles increases by almost four times.

TABLE 2

Particle size distribution and surface area of feed to flotation tests.

	Mass fraction in flotation feed			Surface area of feed (m^2/min)		
Mass fraction of underflow	**-10 µm (%)**	**+10–25 µm (%)**	**+25 µm (%)**	**50% solids**	**40% solids**	**30% solids**
1	5.13	8.98	85.90	1451	712	448
0.98	6.16	9.43	84.41	2345	1224	731
0.96	7.19	9.88	82.93	3149	1762	1039
0.94	8.23	10.33	81.44	4120	2184	1284
0.92	9.26	10.78	79.96	4843	2806	1720

Froth recovery

Froth recovery was measured using the method of varying froth heights as described by Vera *et al* (2002). Froth recovery, R_f, is defined as the recovery to the concentrate of particles entering the froth zone, from the collection zone, attached to gas bubbles. It can be calculated as the total rate of transfer from the pulp to the concentrate, k, divided by the rate of transfer from the pulp to the froth phase, k_c, where k and k_c are first order rate constants. In this investigation the total SiO_2 rate constant was plotted against three different froth heights, 100 mm, 200 mm and 300 mm. The straight line so obtained was extrapolated back to the y-intercept to obtain the pulp zone rate constant, k_c. R_f is then obtained by dividing the rate constant at the froth height of interest by k_c.

Rheology

Rheology measurements were performed using an AR1500EX TA rheometer with vane spindle geometry. The tests were conducted at 30 per cent, 40 per cent, 50 per cent and 60 per cent solids concentrations by mass and at each increment of fines addition. A pre-shear step was included to suspend the solids in solution. Once the samples were equilibrated, the shear stress was recorded at pre-defined shear rates, in continuous ramp settings. The shear stress was recorded at 200 sample points between shear rates of 10/s to 400/s for a duration of 2 minutes. The temperature of the experiment was maintained at 22°C to avoid the influence of temperature changes on the rheology readings. The Bingham model was then applied to the linear portion of the rheology data, the slope of which was taken as the Bingham viscosity.

RESULTS AND DISCUSSION

Please note that throughout this paper preference will be given to a mechanistic interpretation of the data (floatable species and entrained species) rather than conventional reverse flotation terminology. Therefore, reference will be made to recovery to the froth product or recovery to the pulp product. If concentrate and tailings are mentioned, then this will be in the context of reverse flotation terminology, where concentrate refers to the pulp product and tailings refers to the froth product.

SiO_2 flotation performance at different solids concentrations

Initially it was found that when operating at the standard operating solids concentration of 50 per cent, there was a dramatic decrease in the SiO_2 recovery to the tailings as the amount of fines in the feed increased, from recoveries of around 67–75 per cent at 5 per cent <10 µm to around 36–48 per cent at 9.3 per cent <10 µm, depending on froth depth, as shown in Figure 5. This translated to between a 7 to 8 per cent decrease in SiO_2 recovery for every 1 per cent increase in -10 µm material that was reintroduced to the feed.

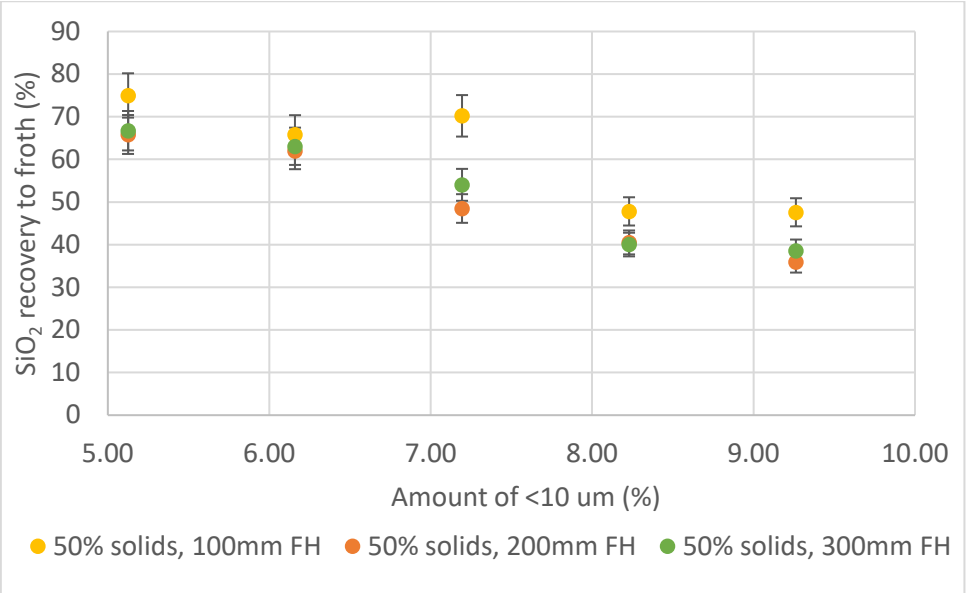

FIG 5 – SiO_2 recovery to the froth product as a function of the amount of fines in the feed at 100 mm, 200 mm and 300 mm froth height and 50 per cent solids concentration.

The poor performance at high fines contents may be treated by reducing the solids concentration (Gao *et al,* 2018; Mowla *et al,* 2008; Runge *et al,* 2012) and this remedy was attempted as shown in Figures 6 and 7. The unexpected outcome of this was that there was a reduction in the recoveries at lower percent solids. Figure 6 shows the SiO_2 recovery as a function of solids concentration at 100 mm froth height for all fines concentrations. This shows that, for the deslimed feed (5 per cent <10 µm), recovery drops from 75 per cent at 50 per cent solids to 16 per cent at 30 per cent solids. The undeslimed feed (9.3 per cent <10 µm) has a very poor recovery even at 50 per cent solids (48 per cent), goes through a maximum at 40 per cent solids (52 per cent) and finally decreases to 26 per cent recovery at 30 per cent solids. This shows that the difference between the recoveries at 30 per cent or 40 per cent and 50 per cent are not as marked for the highest amount of fines, whereas when the ore is deslimed, there is a significant decrease in recovery at lower solids concentrations.

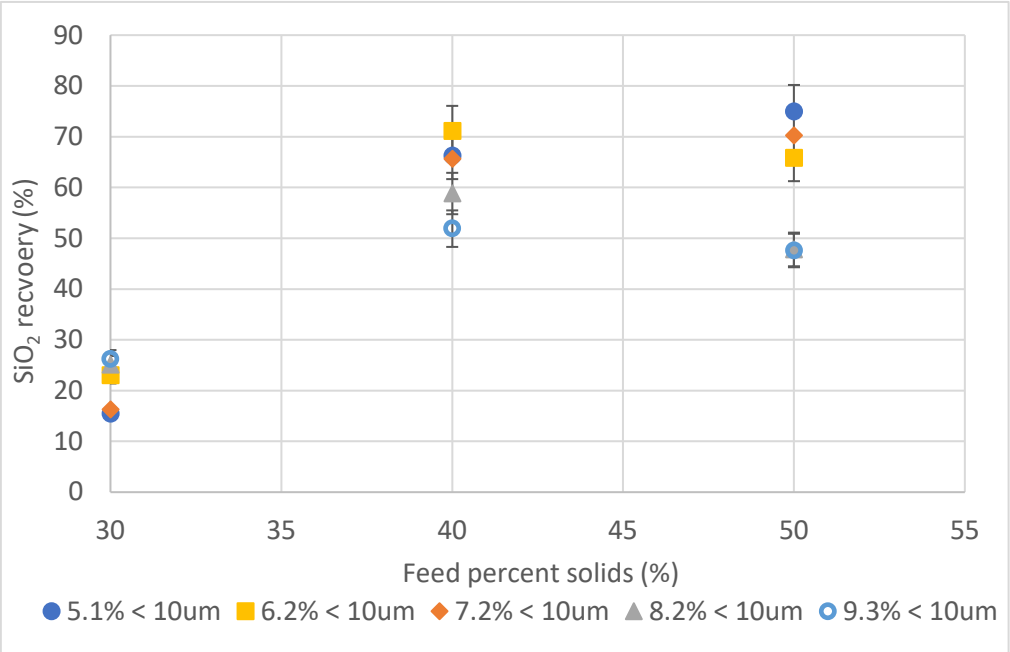

FIG 6 – SiO_2 recovery to the tailings (froth product) as a function of solids concentration at increasing fraction of fines and 100 mm froth height.

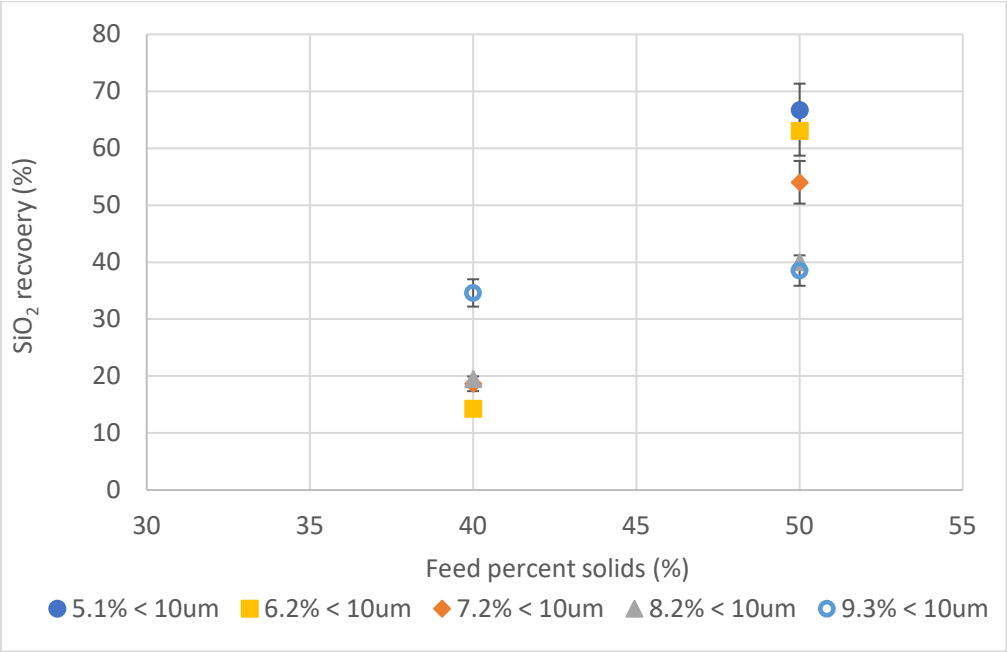

FIG 7 – SiO_2 recovery to the tailings (froth product) as a function of solids concentration at increasing fraction of fines and 300 mm froth height.

Figure 7 shows similar data for the 300 mm froth height condition. In this case, no flow could be obtained at 30 per cent solids, which is why only 40 per cent and 50 per cent solids data are shown. Once again, it is clear that there is a substantial decrease in overall SiO_2 recovery to the froth product at lower pulp solids concentrations, contrary to the expected increase in recovery. Again, this decrease is far less for the undeslimed condition (9.3 per cent <10 µm) than the deslimed condition (5 per cent <10 µm).

Decoupling SiO_2 pulp and froth zone performance

To better investigate the causes of the decrease in SiO_2 recovery with decreasing solids concentration, the pulp and froth zone recoveries were decoupled by the method outlined in the experimental section. This revealed some interesting insights. Focusing firstly on the pulp zone recoveries in Figure 8 (yellow squares), it can be seen that when the solids concentration is decreased from 50 per cent (a) to 40 per cent (b), the pulp zone recovery increases slightly, which was predicted. The trend for each solids concentration shows the true problem of attempting to process the fines fractions, which is the decrease in pulp zone recoveries as the fines concentration increases. There is a 30 per cent reduction in recovery at 50 per cent solids and slightly less reduction of 23 per cent at 40 per cent solids.

Focusing then on the froth zone recoveries (blue circles), it can be seen that at 50 per cent solids (a) the froth recoveries are far higher than at 40 per cent solids (b), especially at the deslimed condition (5 per cent <10 µm). This explains the root cause of the overall SiO_2 recovery decrease at low solids concentrations ie the froth recovery is compromised at low solids concentrations. For example, the froth recovery at 40 per cent solids and the coarsest particle condition, reduced the pulp zone recovery of 78 per cent down to an overall recovery of just 14 per cent.

Another interesting point to note with respect to froth recoveries is that froth recovery increases with increasing fines concentrations, unlike the pulp recovery, which decreases. At 40 per cent solids, the increase in froth recovery is significant, from 5 per cent at low fines contents to 43 per cent at high fines contents.

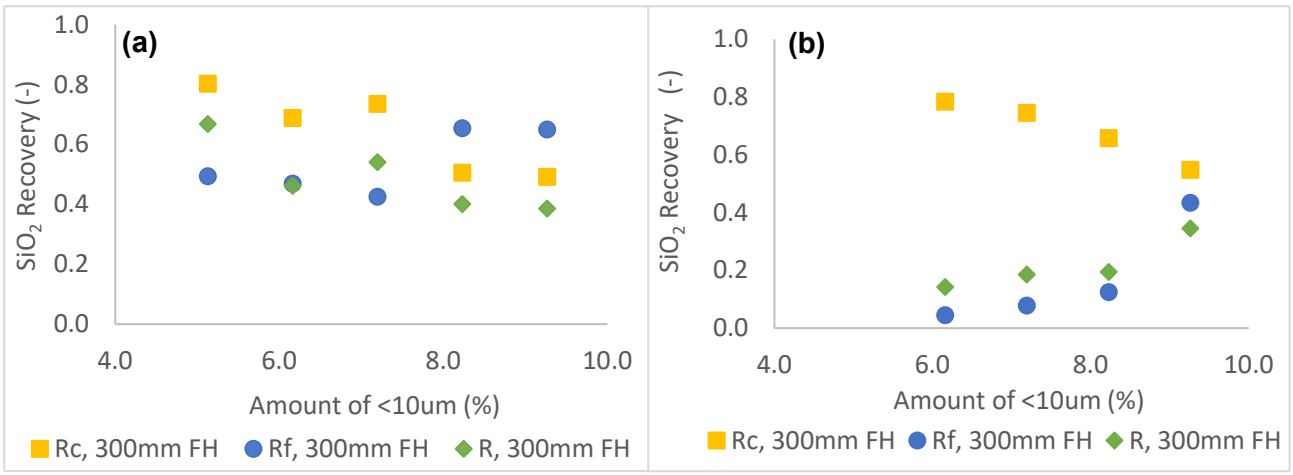

FIG 8 – Pulp, R_c, Froth, R_f, and overall recoveries, R, at 300 mm froth height and (a) 50 per cent solids and (b) 40 per cent solids.

Figure 9 shows similar data to that in Figure 8 for the 100 mm froth height condition. This supports the previous data. Pulp recoveries are very similar to those shown in Figure 8, as expected since froth height will not substantially affect the pulp zone performance. Once again, pulp recoveries at 40 per cent solids (b) are slightly higher than those at 50 per cent solids (a), as expected. In this case, the froth recoveries are far higher for both solids concentrations since the froth residence time is shorter at lower froth depths and there is less time for drainage and bubble bursting to take place. At 100 mm froth height, it is mostly the pulp recoveries that are dictating the overall recovery. Thus, overall recoveries are similar to the pulp recoveries and are not substantially reduced by low froth recoveries as they were at 300 mm froth height. It is self-evident but might be worth stating, that overall recoveries can never be higher than pulp recoveries, with pulp recoveries simply being moderated by the froth recoveries. This is captured in the two-compartment mass transfer model shown in Equation 1 (Vera *et al,* 2002):

$$R = \frac{R_c R_f}{R_c R_f + (1 - R_c)} \quad (1)$$

Therefore, because froth recoveries are close to 100 per cent in Figure 9a, the overall recoveries are almost the same as the pulp recoveries. Whereas in Figure 8b, the very low froth recoveries have clearly undone the good recoveries that were achieved in the pulp zone.

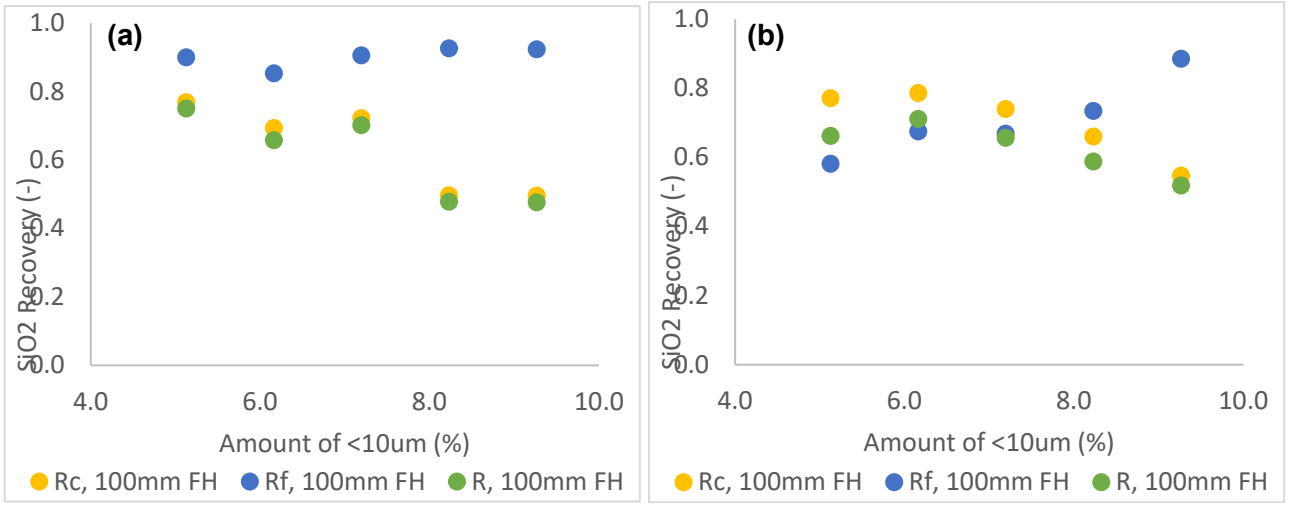

FIG 9 – Pulp, R_c, Froth, R_f, and overall recoveries, R, at 100 mm froth height and (a) 50 per cent solids and (b) 40 per cent solids.

Froth stability

Froth stability measurements were conducted in the same equipment as the flotation experiments, simply with the addition of a 1 m non-overflowing column. Figure 10 shows that there is a strong dependence on solids concentration, which increases with increasing fines concentration in the feed. This combined dependence on particle size and concentration has previously been discussed in a paper by McFadzean *et al* (2016), which showed that froth stability was dependent on particle surface area rather than the individual effects of size and hydrophobicity. The froth stability at 50 per cent solids is between 7.5 and 3.7 times as great as that at 30 per cent solids, depending on fines concentration. This accounts for the poor froth recoveries at low solids concentrations since froth recovery is positively correlated to the froth stability (Barbian *et al,* 2005).

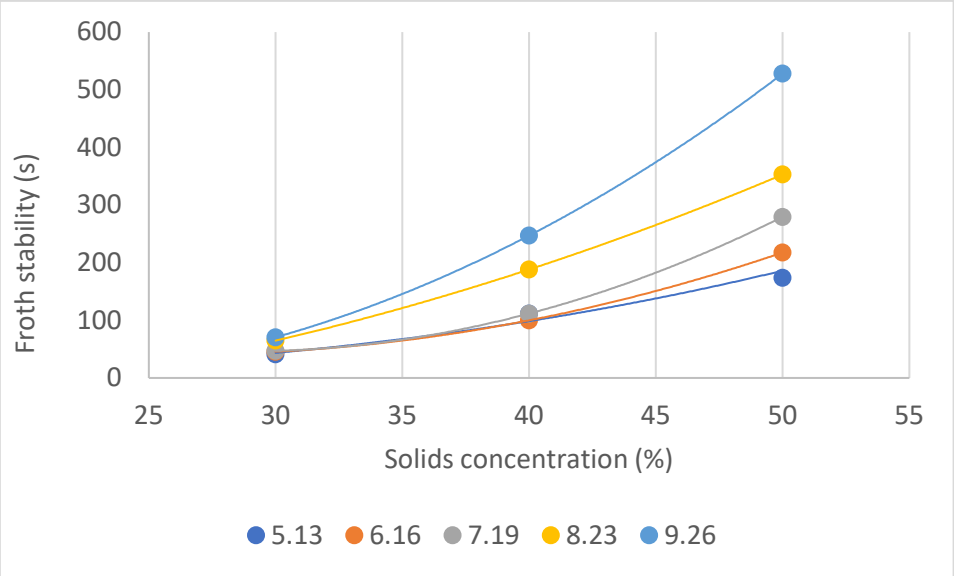

FIG 10 – Froth stability as a function of solids concentration at increasing fines amounts given in percentage -10 µm particles in the feed. The lines are a guide to the eye.

Preliminary remediation steps

Although this study was mostly focused on mechanisms behind the overall flotation performance of the iron ore, there were some preliminary efforts made at remediation at high fines contents. Since the froth zone performance was shown to actually improve with increasing fines concentrations, it was the pulp zone performance that required improvement. The initial hypotheses with regards to poor performance related to collector concentration, slimes coatings and increased viscosity-related problems at higher particle surface areas. Viscosity was measured at solids concentrations between 30 and 60 wt per cent and at all fines concentrations. It was found that the amount of fines had very little effect on the viscosity and that variations appeared to be due to experimental error, as shown in Figure 11. It was the solids concentration that had the overwhelming effect on the viscosity. This was confirmed when a dispersant, sodium metasilicate, was added to the undeslimed ore at 50 per cent solids and SiO_2 recovery suffered a large decrease. This was due to the fact that no benefit was realised with respect to viscosity problems, since there were not any there to start with, and because of a reduction in froth stability which has been shown to be detrimental to iron ore flotation performance.

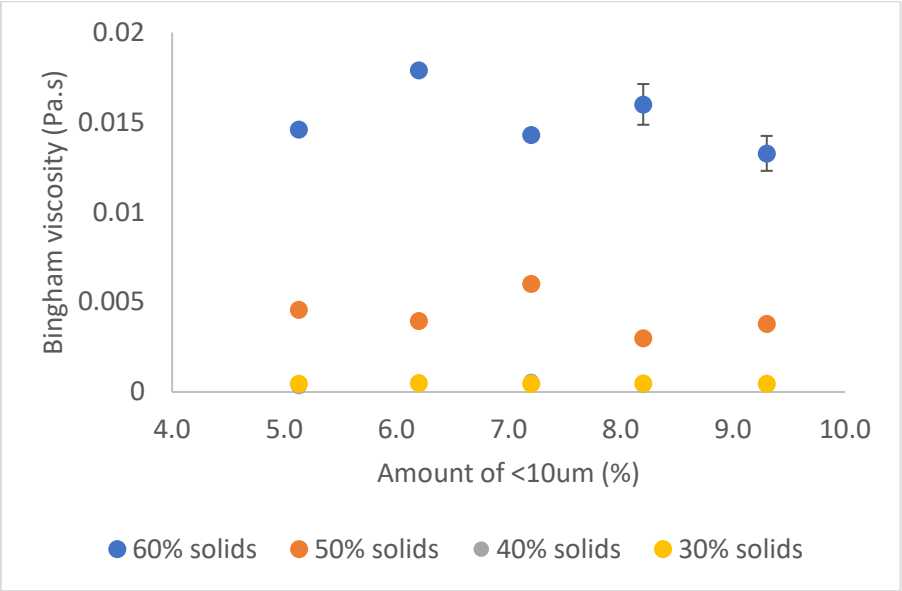

FIG 11 – Apparent viscosity of feed slurry at 30–60 wt per cent solids concentration and increasing fines concentration.

Secondly, collector concentration was increased proportionally to the increase in surface area of the undeslimed feed, which was 3.6 times the surface area of the deslimed feed. The standard collector dosage was 80 g/t and this was gradually increased to 290 g/t. The test condition was the undeslimed feed at 50 per cent solids and 100 mm froth height. Figure 12 shows that the initial increase to 150 g/t collector had little effect on SiO_2 recovery. In fact, recovery decreased slightly. Thereafter, recovery increased to a final recovery of about 50 per cent at 290 g/t. The rate constant increased from 1.1 min^{-1} at 80 g/t collector to 1.9 min^{-1} at 290 g/t collector. Therefore, it appears that increasing the collector dosage, or using a stronger collector, may be a partial remedy for poor recoveries at undeslimed conditions.

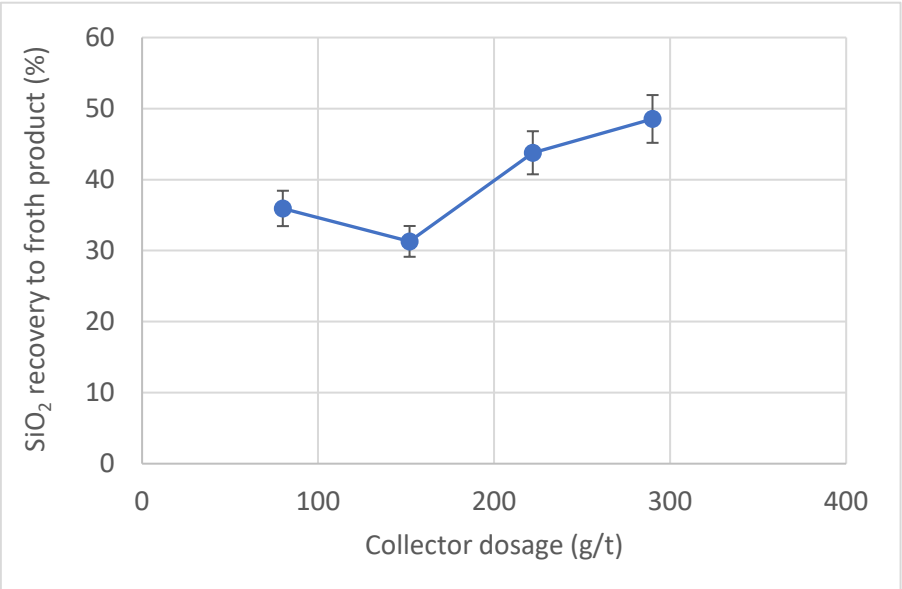

FIG 12 – SiO_2 recovery to the froth product at increasing collector dosage. 9.3 per cent <10 µm, 50 per cent solids and 100 mm froth height.

CONCLUSIONS

This paper investigated the effect of ultrafine particles on the flotation behaviour of an Itabirite iron ore. Progressive amounts of ultrafine particles were added to a deslimed feed at various solids concentrations. Pulp and froth effects were decoupled using froth stability and froth recovery tests. From this study one may conclude that, although there is an exponential increase in froth stability at

increasing fines quantities, the performance of the pulp has the overriding effect on the overall SiO_2 recovery. Pulp zone, froth zone and overall SiO_2 recoveries showed that overall recoveries increased by about 3.6 per cent for every 1 per cent decrease in fines content. This meant a large increase of 20 per cent in SiO_2 recovery when going from undeslimed to deslimed feed. This was driven largely by increases in the pulp zone recoveries, which were about 4 per cent for every 1 per cent decrease in fines content. The froth recoveries, on the other hand, decreased by between 0.75 per cent and 2.5 per cent for every 1 per cent decrease in fines content, depending on froth height. Low solids concentrations improved pulp zone recoveries but had an adverse effect on froth recoveries. Attempts at mitigating the decrease in SiO_2 recovery with increasing fines content showed that rheology is not a factor but that significantly increased collector dosage can result in an improvement in overall recovery. This paper has illustrated the importance of measuring froth effects and taking the froth zone into account when performing laboratory-scale flotation experiments. The overall objective of treating undeslimed ores was found to be very difficult in practise since, even at lower solids concentrations, the inclusion of all the ultrafine material in the feed resulted in a 23 per cent loss in overall recovery. It appears that the best option would be a partial desliming step, combined with working at intermediate solids concentrations (~40 per cent), shallow froth depths and a higher collector dosage.

ACKNOWLEDGEMENTS

The authors would like to extend their thanks to Vale S.A. for funding this work and their approval to publish the paper.

REFERENCES

Amelunxen, P, Sandoval, G, Barriga, D, Amelunxen, R, 2014. The implications of the froth recovery at the laboratory scale. *Minerals Engineering*, 66–68, 54–61.

Barbian, N, Hadler, K, Ventura-Medina, E, Cilliers, J J, 2005. The froth stability column: linking froth stability and flotation performance. *Minerals Engineering*, 18, 317–324.

Lima, N P, Peres, A E C, Marques, M L S, 2012. Effect of slimes on iron ores flotation. *International Journal of Mining Engineering and Mineral Processing*, 1(2), 43–46.

Lima, N P, Valadao, G E S, Peres, A E C, 2013. Effect of particles size range on iron ore flotation. *REM – International Engineering Journal*, 66(2), 251–256.

McFadzean, B, Achaye, I, Wiese, J, Chidzanira, T and Harris, M, 2016. The effect of particle properties on froth stabilities of different ores. *XXVIII International Mineral Processing Congress*, Quebec City, Canada.

Ndlovu, B, Forbes, E, Farrokhpay, S, Becker, M, Bradshaw, D, Deglon, D, 2014. A preliminary rheological classification of phyllosilicate group minerals. *Minerals Engineering*, 55, 190–200.

Ralston, J, 1999. Controlled flotation processes: prediction and manipulation of bubble-particle capture. *The Journal of the South African Institute of Mining and Metallurgy*, Jan/Feb 1999, 27–34.

Ralston, J, Fornasiero, D, Hayes, R, 1999. Bubble-particle attachment and detachment in flotation. *International Journal of Mineral Processing*, 56, 133–164.

Shabalala, N Z P, Harris, M, Leal Filho, L S, Deglon, D A, 2011. Effect of slurry rheology on gas dispersion in a pilot-scale mechanical flotation cell. *Minerals Engineering*, 24, 1448–1453.

Shi, F N and Napier-Munn, T J, 1996. A model for slurry rheology. *International Journal of Mineral Processing*, 47, 103–123.

Vera, M A, Mathe, Z T, Franzidis, J-P, Harris, M C, Manlapig, E V, O'Connor, C T, 2002. The modelling of froth zone recovery in batch and continuously operated laboratory flotation cells. *International Journal of Mineral Processing*, 64, 135–151.

Zheng, X, Johnson, N W, Franzidis, J-P, 2006. Modelling of entrainment in industrial flotation cells: Water recovery and degree of entrainment. *Minerals Engineering*, 19, 1191–1203.

Modification and adsorption of triazine collectors onto pyrite surfaces

P P Mkhonto[1], X Zhang[2], L Lu[3], W Xiong[3], Y Zhu[3], L Han[3] and P E Ngoepe[4]

1. Materials Modelling Centre, University of Limpopo, Sovenga 0727, South Africa. Email: peace.mkhonto@ul.ac.za
2. State Key Laboratory of Mineral Processing, BGRIMM Technology Group, Beijing 102600, China. Email: zhxr1984@126.com
3. State Key Laboratory of Mineral Processing, BGRIMM Technology Group, Beijing 102600, China.
4. Materials Modelling Centre, University of Limpopo, Sovenga 0727, South Africa.

ABSTRACT

The triazine molecules have not been given much attention and they are potential collectors that may positively impact the mineral processing industry. The adsorption of triazine as collectors such as sodium 2,6-dithio-4-butylamino-1,3,5-triazine (SDTBAT) on pyrite form a basis in design of flotation collectors that may be applicable in a wide range of sulfide minerals. The SDTBAT collector was compared with the sodium normal butyl xanthate (SNBX) and sodium normal butyl dithiocarbamate (SNBDTC). All collectors were adsorbed in their neutral form containing sodium on the pyrite (100) surface. The computational calculations found that the adsorption energies followed the order: SDTBAT (-300.35 kJ/mol) > SNBX (-186.10 kJ/mol) > SNBDTC (-163.78 kJ/mol). It was observed that the SNBX and SNBDTC adsorbed through the S atoms, while the SDTBAT adsorbed through the S atoms and N atoms onto Fe atoms. It is clear that the SDTBAT had a strong binding energy which is attributed to the presence of the triazine group that is electron depositing to the active S atoms compared to the SNBX which possessed the oxygen that is electron withdrawing. Moreover, the SDTBAT collector was found to bind stronger than the xanthate. This was complimented by microflotation tests that showed fast floating and higher recoveries of pyrite when using the SDTBAT collector than the xanthate and DTC. This clearly demonstrated that the SDTBAT is a potential collector to replace the xanthate collector due to its high selectivity and flotation power.

INTRODUCTION

Design of collectors is one of the major challenges in the field of mineral processing and requires fundamental understanding to attain a well performing collector that can recover minerals efficiently. One major challenge is to design and synthesise a collector that can perform better than the well-known xanthate collectors, which have high collecting power but low selectivity (Adkins and Pearse, 1992). The search for new chemical reagents having strong affinity and better selectivity for certain metal ions has received attentions (Yekeler and Yekeler, 2006). However, this presents a number of experimental challenges in securing the desired reagents and running a large number of time-consuming and expensive tests. Molecular modelling is an attractive option to screen potential collector molecules using minimal time and resources prior to beginning full laboratory testing. However, the flotation process is extremely complex, with many contributing factors that are not easily probed using computational methods. Therefore it is desirable to measure the computational outputs against experimental outputs to check for congruency.

Previously a study on comparisons of xanthate, dithiocarbamate and thiophosphate on pyrite and galena had been conducted using computer modelling and microcalorimetry method (Chen, Lan and Chen, 2013). Recently, the density functional theory (DFT) method adsorption energies had been compared with the experimental flotation recoveries using oxycarbonyl thiocarbamate for chalcopyrite and demonstrated good correlation between the two methods (Mkhonto *et al*, 2021). Furthermore, the DFT and experimental flotation recoveries methods were used to investigate the separation of chalcopyrite and pyrite using O-isopropyl-N-ethyl thiocarbamate (IPETC), O-isopropyl-N-diethyl-thionocarbamate (IPDETC) and S-allyl-N-diethyl-dithiocarbamate (ADEDTC) and also described their adsorption mechanisms (Mkhonto *et al*, 2022). It is therefore clear that measuring computational outputs against experimental outputs is the best method to screen different reagents. Other collectors such as 2-mercaptobenzoxazole (MBO) for chalcocite (Cu_2S), 2-mercaptobenzothiazole (MBT) for galena (PbS) and 2-aminothiophenol (ATP) for sphalerite

(ZnS) have been studied and have advantages since they can be used in neutral pH and show good selectivity (Maier and Dobias, 1997). It has been reported that the heterocyclic compounds can form hydrophobic complexes with many metals such as iron, copper, cobalt and nickel (Feng *et al*, 2006). This suggested that the presence of a benzene ring or mercapto ring in collector reagents produces a highly selective collector.

The triazine compounds which are a class of nitrogen-containing heterocycles with a molecular formula of $C_3H_3N_3$ have not been explored as collector for separation of minerals and are potential collector molecules for sulfide minerals. The available literature that explored these type of molecules was an investigation of crosslinking of poly(vinyl chloride) fibres with 2-dibutylamino-4,6-dimercapto-1,3,5-triazine in the presence of sodium hydroxide and tetra-n-butylammonium bromide (TBAB) in water (Jando and Mori, 1990) and investigation of sorption and adsorption of 2,4,6-tri(20-pyridyl)-s-triazine (TPTZ) complexes with iron(II) and ruthenium(III) on silica gel (Yacoub, El-Kourashy and Al-Hajjaji, 2013). Another study used DFT+U to investigate the mechanical, structural, electronic and magnetic properties of s-triazine sheet (C_6N_6) with embedded Mn atom ($Mn–C_6N_6$) under the influence of external environment (symmetric deformation and perpendicular electric field) (Abdullahi *et al*, 2017). Furthermore, a DFT study was also conducted on adsorption of CO_2, O_2, NO and CO on s-triazine-based g-C_3N_4 surface which demonstrated that the adsorption affinity of these gas molecules followed the order of $CO_2 > O_2 > NO > CO$ (Zhu *et al*, 2019). A theoretical study of Di-Amino-Triazine (DAT, $C_{64}H_{68}N_{10}$), 1,4-bis(4-(2,4-diaminotriazine) phenyl)-2,3,5,6-tetrakis(4-tert-butyl phenyl) benzene adsorption on Cu(110) and Au(111) surfaces was also previously performed (Benjalal and Ghanjaoui, 2016). It is clear that the triazine compound have not been applied in mineral processing studies.

In the current research work, we have used the computational DFT dispersion (DFT-D) to design and screen the sodium 2,6-dithio-4-butylamino-1,3,5-triazine (SDTBAT) collectors through adsorption on pyrite (100) surfaces. The collector thereafter was synthesised and tested on pyrite minerals through experimental microflotation. The SDTBAT collector was compared to the performance of sodium normal butyl xanthate (SNBX) and sodium normal butyl dithiocarbamate (SNBDTC). The adsorption energies were also calculated to determine the affinity of the collectors with pyrite mineral surface. These approaches offer a platform to design and test collector reagents and describe their adsorption behaviour which is beneficial in the identification of well-performing and selective collectors for sulfide minerals.

MATERIALS AND METHODOLOGY

Computational methods

We carried out DFT-D3 study of the pyrite bulk and (100) surface interaction with SDTBAT, SNBX and SNBDTC. All calculations were performed using the Vienna *Ab-initio* Simulation Package (VASP) code (Kresse and Hafner, 1993; Kresse and FurthermÜller, 1996), where the ion–electron interactions were represented by the projector augmented wave (PAW) method (Kresse and Joubert, 1999). The electron-exchange correlations were represented by the generalised gradient approximation (GGA) with the Perdew–Wang functional (PW91) (Perdew *et al*, 1992), employing the spin interpolation formula of Vosko, Wilk and Nusair (1980). All the calculations include the long-range dispersion correction approach by Grimme, Ehrlich and Goerigk (2011), with Becke-Jonson damping. The valence states were expanded in a plane-wave basis set with a cut-off at 450.0 eV for the kinetic energy, which was sufficient to converge the total energies during relaxations to within 0.2 meV.atom^{-1}. The initial magnetic moments were described with low-spin distributions in Fe on both bulk and (100) surface. We employed Monkhorst–Park grids of 8 × 8 × 8 k-points for bulk model and 3 × 3 × 1 k-points for (100) surface, which ensures electronic and ionic convergence (Monkhorst and Park, 1976). We used the Hubbard-*U* approximation for an accurate treatment of the electron correlation in the localised Fe d-orbitals (Dudarev *et al*, 1998). This improves the description of localised states in this type of system where standard local density approximation (LDA) and GGA functionals fail. We followed the approach used by Dudarev *et al*, 1998 and varied different values of the *U*-parameter (0–2.5 eV) on pyrite bulk Fe atoms and compared the resulting band gap and lattice parameters to the experimental vales for pyrite. We found that the U = 1.7 eV produced a band gap of 0.96 eV (0.95 eV) (Ennaoui *et al*, 1993; Ennaoui and Tributsch, 1986) and a lattice vector of a = 5.406 eV (5.417 eV) (Choi *et al*, 2021), which were

in agreement with the experimental values in parenthesis. The geometries of all stationary points were obtained with the conjugate-gradient algorithm and considered converged when the force on each ion dropped below 0.02 eV.Å^{-1}, whereas the energy threshold, defining self-consistency of the electron density, was set to 10^{-6} eV. In order to improve the convergence of the Brillouin-zone integrations, the partial occupancies were determined using the Methfessel-Paxton smearing with a set width for all calculations of 0.2 eV.

Now, in order to calculate reaction energies, the optimisation of SDTBAT, SNBX and SNBDTC models were performed in a cubic cell of 40 Å, which was enough to minimise spurious mirror-image interactions between collector molecules in adjacent supercells. The PAW potential, cut-off energy at gamma point (1 × 1 × 1 k-points) and other precision parameters as in the surface calculations were employed. Note that we have included the sodium ions (Na^+) in the simulation of the collector to neutralise the negative charge on the S^- atoms on the collector polar site. It has been reported that there is greater association of the Na^+ with S^- of collectors such as MBT^- (Galvao *et al*, 2016).

The surface energy is computed using Equation 1:

$$E_{surface} = \frac{[E_{slab} - (n_{slab})(E_{bulk})]}{2A} \quad (1)$$

where E_{slab} is the energy of the surface, E_{bulk}/atom is the energy of the bulk per total number of atoms in the bulk and n_{slab} is the number of atoms of the surface and *A* is the surface area.

The adsorption energies ($E_{ads.}$) of the collector molecules on the surfaces were calculated from the difference in total energy between the collector-surface ([S + C]) and the sum of the collector ([C]) and surface ([S]) models, as expressed in Equation 2:

$$E_{ads.} = E_{[S+C]} - (E_{[S]} + E_{[C]}) \quad (2)$$

In the adsorption energy calculations a negative value shows an exothermic favourable reaction between the collector molecules and the surface, whereas a positive value reveals the opposite.

In this study, all of the reported adsorption energies were corrected by addition of the vibrational frequency zero-point energy (ΔZPE), calculated as the difference between the ZPE correction of the collector molecule on the surface and in the gas phase (ie isolated collector in a cubic box = 40 Å), according to Equation 3 (Dzade and de Leeuw, 2018):

$$\Delta ZPE = \left(\sum_{i=1}^{3n} \frac{hv_i}{2}\right)_{S+C} - \left(\sum_{i=1}^{3n} \frac{hv_i}{2}\right)_{Gas(C)} \quad (3)$$

Experimental methods

Materials and reagents

Pyrite was obtained from Hubei Province in China and it was characterised using X-ray diffraction (XRD) to ensure that the samples were single phases. The pure minerals were collected by handpicking, pulverised in a ceramic ball mill, crushed in a porcelain mortar and dry sieved to get particle sizes between 38−74 µm fractions before being used for microflotation. The purities of pyrite was calculated using the chemical assays of S as shown in Table 1 and the theoretical grade of S (53.33) according to Equation 4 and are approximately 97.10 per cent and also on the basis of XRD (Figure 1). The pyrite samples were stored in a vacuum desiccator in a refrigerator at approximately 5°C.

TABLE 1

Pyrite minerals key element contents (wt%).

Element	Cu	Fe	S	Zn	Ca	Mg	Al
Pyrite	<0.05	46.15	51.77	0.12	0.06	<0.05	0.07

$$\text{Mineral purity} = \frac{\text{Chemical assay}}{\text{Theoretical grade}} \times 100\% \quad (4)$$

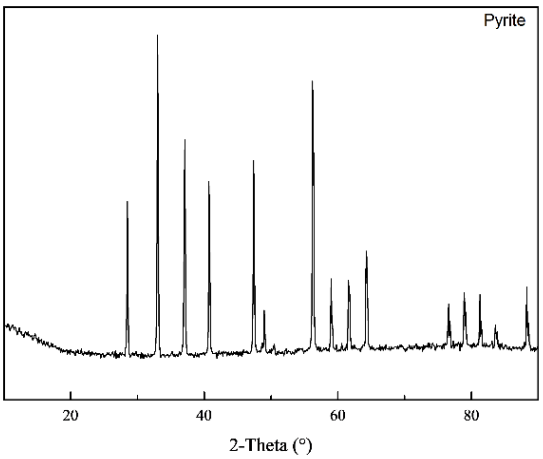

FIG 1 – X-ray diffraction (XRD) patterns of pyrite.

The SDTBAT collector reagent was synthesized in BGRIMM Technology Group lab by adding equivalent n-butylamine to the dispersion of 1,3,5-trichloro-2,4,6-triazine in crushed ice at 0~5°C with strong agitation for 1~2 h; then two times of NaSH was added in batches at 25~30°C for 2 h and 85°C for 3 h and then acidified the reaction mixture to precipitate the product, which yielded purity of 95.3 per cent as illustrated in Figure 2. Methyl isobutyl carbinol (MIBC) was chosen as the frother and was purchased from Sinopharm Chemical Reagent Co., Ltd., China. All water used in the experiments was distilled.

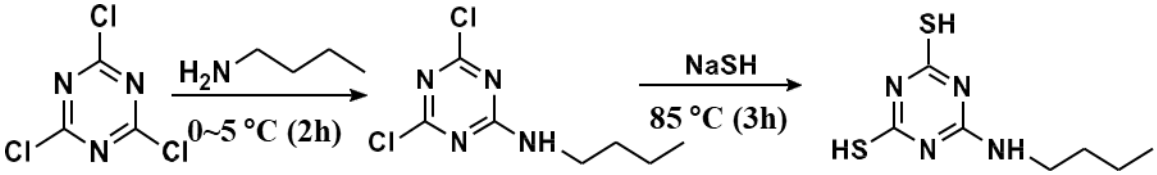

FIG 2 – Synthetic route for the SDTBAT collector.

Microflotation

In this section, we describe the microflotation experiments that were carried out to investigate the flotation tests of the SNBX, SNBDTC and SDTBAT collectors for pyrite. The microflotation flow chart is displayed in Figure 3. In the flotation process, the pulp pH was adjusted to approximately 9.0 with dilute NaOH solutions, and MIBC was selected as the frother with a dosage of 20 mg.L^{-1}. The microflotation test for single pyrite minerals was performed in an XFG5–35 flotation machine with a 40 mL plexiglass cell. The agitation speed was controlled at 1752 r.min^{-1}. The collector and MIBC frother were added to the slurry with 2 mins of stirring.

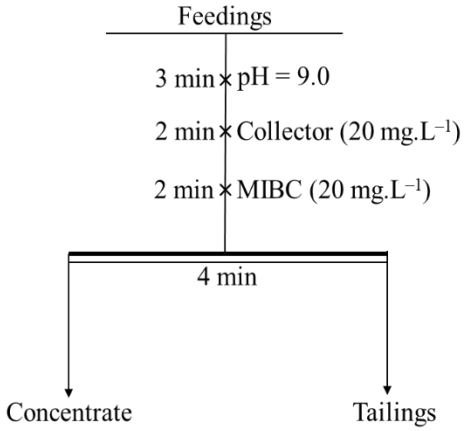

FIG 3 – Pyrite microflotation flow chart.

The mineral recoveries were determined over 4 min. The recovered concentrates were collected and dried in an oven and thereafter weighed and the percent recoveries were obtained from Equation 5:

$$\text{Recovery (\%)} = \frac{\text{Mass of mineral in concentrate}}{\text{Mass of mineral in feed}} \times 100\% \quad (5)$$

Finally, the recovery of the froth products was used to evaluate the flotation power of the collectors for the minerals.

RESULTS AND DISCUSSION

Pyrite bulk and (100) surface models

The 2 × 2 (100) surface (Figure 4b) was obtained from the relaxed bulk structure of pyrite (FeS_2) with space group symmetry of *Pa-3*, which possesses rock-salt type structure with Fe^{2+}:[Ar]$3d^6$ cations at the face-centred of the cubic cell and S^{1-}:[Ar]$3s^2 3p^5$ forming dimers (S_2^{2-}) centred about the anion positions as shown in Figure 4a. Pyrite is defined as a low-spin with the d-orbital splitting occupied in the order of t_{2g}^6 and e_g^0, which is adopted in this study.

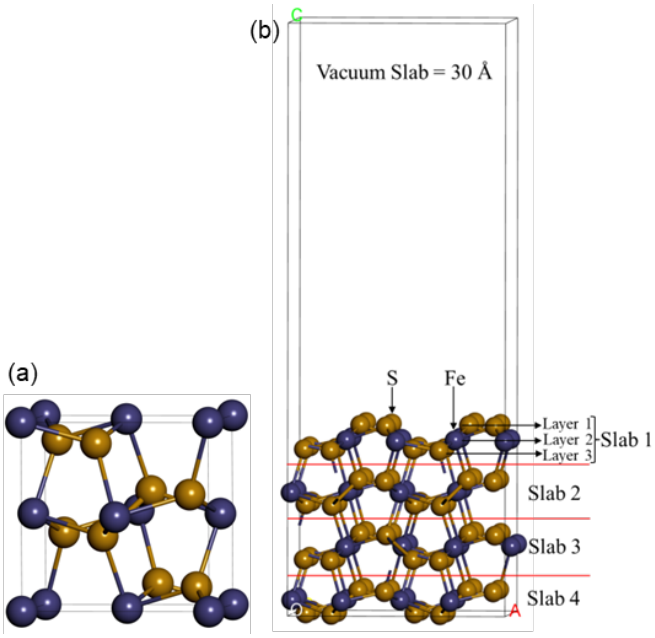

FIG 4 – (a) Relaxed FeS_2 bulk and (b) 2 × 2 (100) surfaces models.

The surface terminations were determined on the basis of minimal surface dipole. The 2 × 2 (100) surface model is composed of 12 atomic layers and the periodic cells of 10.811 × 10.811 × 39.352 Å was used and possessed a vacuum slab separation of 30 Å in order to avoid interaction between the collectors and the mirror image surface (Figure 4b). In the adsorption system the bottom six layers (6L) were kept fixed to bulk coordinate, while the top six layers (6L) were relaxed and allowed to interact with the collectors. In Table 2 we show the calculated surface energy for pyrite (100) surface and it is clear that the surface energy is lower compared to our previous calculated surface energy (Mkhonto *et al*, 2022), which illustrate the effect of the DFT-D3 and U-parameters.

TABLE 2

Surface coordination and surface energies for pyrite (100) surface.

Surfaces	Surface coordination		Surface energies
	Fe	S	J.m^{-2}
Bulk	6	4	–
(100) Surface	5	3	1.17

Triazines, Xanthate and DTC molecular geometries

The relaxed bond lengths for the minimum energy geometries of the SNBX, SNBDTC and SDTBAT models are shown in Table 3. Note that we focus on the centre of reactivity C–S group atoms of the collectors. As shown in Figure 5, the C4–S1 possesses a double bond and the C4–S2 possesses a single bond on SNBX and SNBDTC. In addition the C–S bonds of SDTBAT are single bonds. The negative charge on the S atoms forming single bonds is neutralised by the sodium (Na^+) cation.

TABLE 3

The selected polar sites bond lengths and angles on relaxed geometry of isolated triazine, xanthate and DTP collectors.

Bonds	SNBX	SDBDTC	SDTBAT
C4/C6–S1	1.705	1.721	1.726
C4/C2–S2	1.710	1.727	1.725
C4–O/N	1.352	1.349	1.376
S1–C4–S2	127.25	126.09	–

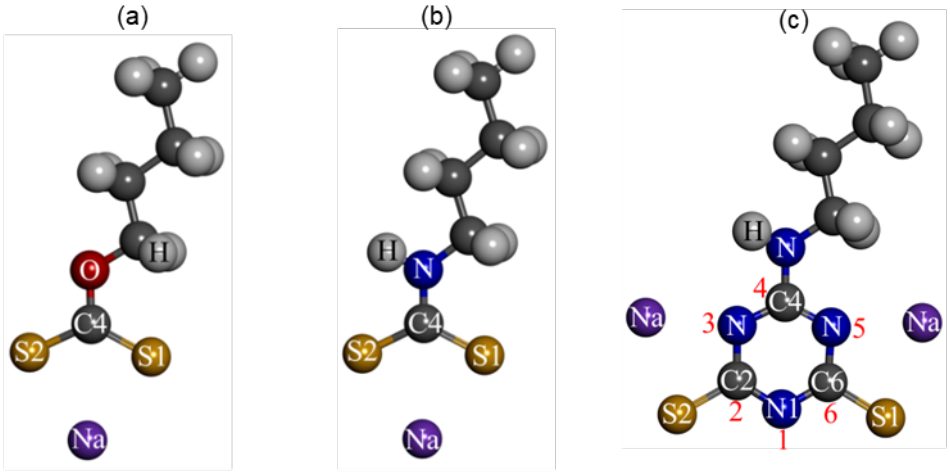

FIG 5 – The relaxed molecular geometries of the collectors: (a) SNBX, (b) SNBDTC and (c) SDTBAT.

Table 3 shows that the C4–S1 and C4–S2 bond lengths in SNBX are shorter thus more stable than those in SNBDTC, which suggests that SNBDTC may be more reactive than SNBX. The C4–S2 bond is longer than the C4–S1 bonds, showing the effect of double and single bonds. The C–S bond lengths in SDTBAT are similar to those of SNBDTC and longer than those of SNBX. In particular the SDTBAT C–S bond lengths are almost equal to that of C4–S2 single bond for SNBDTC, which shows the effect of nitrogen atoms in the C–S bonds. It is suggested that SDTBAT will be more reactive than SNBDTC due to the slight longer C–S bonds. The N atoms are responsible for the strong reactivity of SDTBAT. This effect is due to the presence of N atoms that donates electron density towards the C atom, while the O atom withdraws electron density from the C atom. This phenomenon is a result of oxygen atoms being stronger electron acceptors than N atoms. As such, since SDTBAT contains more N atoms than the SNBDTC, it may be a more reactive collector.

Collector adsorption on pyrite (100) surface

The adsorption of the collectors was initiated by positioning the collectors S atoms at approximately 2.00 Å on the Fe atoms of pyrite (100) surface as the preferred stable adsorption site. The adsorption energies are displayed in Table 4 and depicted in Figure 6. We observed that the collector preferentially chemisorbed on the Fe atoms and formed stable six-membered Fe complexes, as shown in Figure 7. Interestingly, we noted that for SDTBAT adsorption the N atom

also formed bonds with Fe atom. The bond lengths and angles for collector adsorption on the pyrite (100) surface clearly illustrated a strong Fe2–S2 bond for SDTBAT (2.257 Å). The SNBX had a larger Fe2–S2 bond (2.297 Å) than SNBDTC (2.290 Å). However, the SDTBAT had a larger Fe1–S1 bond (2.320 Å), which is ascribed to the stretch of the collector molecule to form the Fe–N1 bond of 2.140 Å. This bonding behaviour clearly demonstrated the strong binding of the SDTBAT collector on pyrite surface.

TABLE 4

The relaxed bond lengths and angles geometry of charged and neutral xanthate adsorbed on pyrite (100) and (111) surfaces.

Bonds	SNBX	SDBDTC	SDTBAT
Fe1–S1	2.309	2.305	2.320
Fe2–S2	2.297	2.290	2.257
Fe–N1	–	–	2.140
S1–C4–S2	132.69	132.07	–

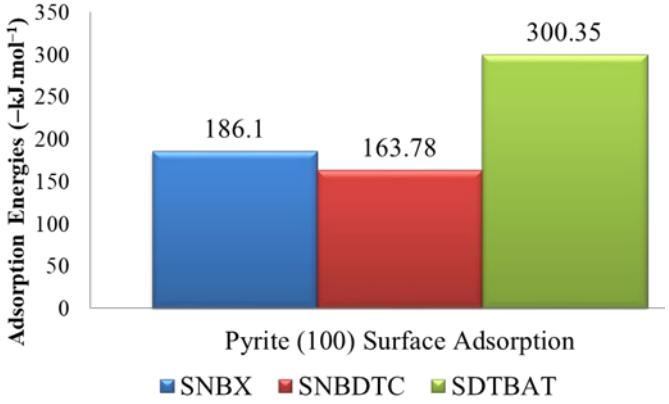

FIG 6 – Bar graph displaying the adsorption energies trend of SNBX, SNBDTC and SDTBAT collectors on pyrite (100) surface.

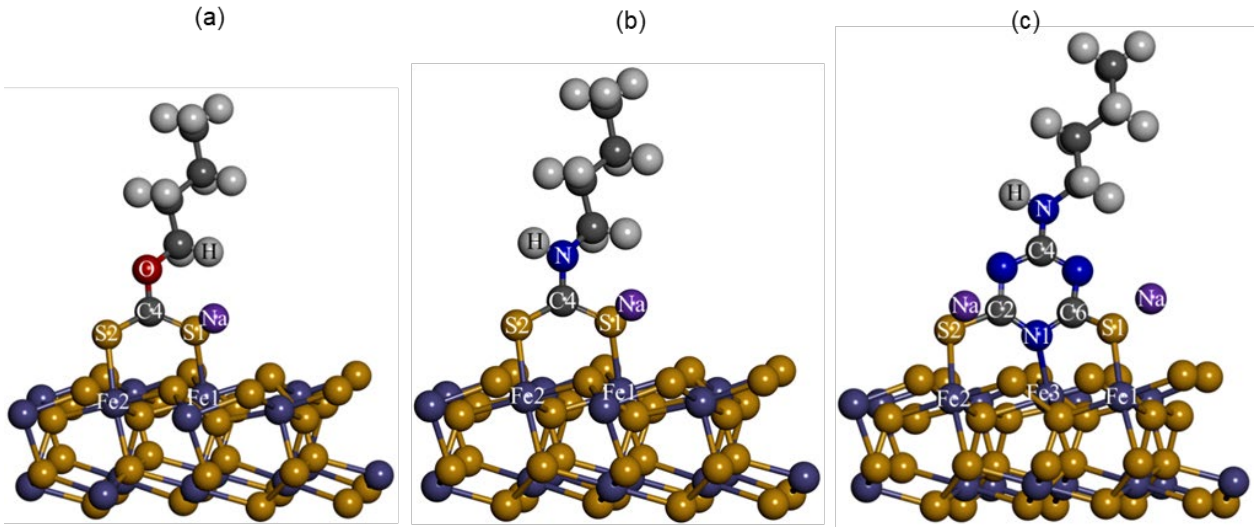

FIG 7 – Relaxed geometries of collectors' adsorption on (100) surface: (a) SNBX, (b) SNBDTC and (c) SDTBAT adsorptions.

The binding strengths of the collectors on the pyrite (100) surface are given in Table 5 and displayed in Figure 6. The adsorption energy of SDTBAT (–300.35 kJ/mol) was more exothermic than that of SNBX (–186.10 kJ/mol) and SNBDTC (–163.78 kJ/mol) (Table 5). These results indicated that the triazine group of SDTBAT resulted in an improved adsorption performance on

the pyrite surface. Furthermore, the SDTBAT was found to be a better collector than the SNBDTC collector, which is attributed to the presence of more N atoms that are electron dense and deposited towards the C atom. This suggested that SDTBAT may be highly selective and powerful in the flotation of pyrite.

TABLE 5

Adsorption energies for charged xanthates and neutral xanthate collector adsorption on pyrite (100) surface, calculated according to Equation 2.

Adsorbates	Adsorption	E_{S+C} (eV)	E_C (eV)	E_S (eV)	ΔZPE (eV)	$E_{Ads.}$ (kJ.mol^{-1})
SNBX	Fe-Bridge	-627.2115	-96.6183	-528.8531	-0.1888	-186.10
SNBDTC	Fe-Bridge	-633.1206	-102.5774	-528.8531	-0.0074	-163.78
SDTBAT	Fe-Bridge	-679.3127	-147.6702	-528.8531	-0.3236	-300.35

Microflotation tests

Microflotation was performed for each collector, and the final recoveries were calculated according to Equation 5 as displayed in Figure 8. The recoveries demonstrated the flotation performance of the SNBX, SNBDTC and SDTBAT collectors for pyrite mineral at the pH = 9.0. We found that the trends of the recoveries were consistent with the predictions based on the DFT adsorption energies. We observed that SDTBAT exhibited better performance with high pyrite recoveries of almost 90 per cent, particularly at 20.0 mg/L dosage. However, at 5.0 mg/L, SNBX had higher pyrite recoveries than SNBDTC and SDTBAT. Significantly, at 10 mg/L the SDTBAT increased in recovery to above 60 per cent and almost matched that of SNBX, while that of SNBDTC was around 11 per cent recovery. This demonstrated that at higher dosages the SDTBAT surpass the SNBX in performance. Although the DFT adsorption energies and prediction showed that SDTBAT is more reactive and adsorb stronger compared to SNBX on pyrite, the flotation experiment revealed the flotation power of xanthates at low dosages, in particular at dosage of 5.0 mg.L^{-1}. This indicated that in order to validate the computational work, experiments are crucial. The SDTBAT was found to be a better collector than SNBX and SNBDTC, which is ascribed to the triazine group. This suggested that all collectors required higher dosages to float pyrite to above 60 per cent, although SNBDTC performance was poor, with recoveries of up to 30 per cent. This showed that SNBDTC had high selectivity but poor flotation power. The SDTBAT was found to have both high selectively and flotation power and is the best collector to compete with the low selectivity of xanthate that has high flotation power capacity.

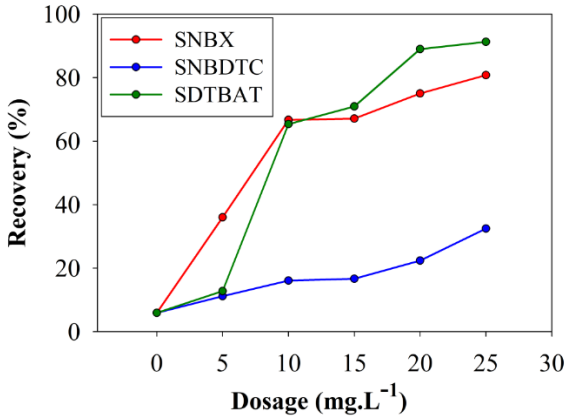

FIG 8 – Microflotation recoveries of pyrite using the SNBX, SNBDTC and SDTBAT collectors at pH 9.0.

CONCLUSIONS

In this study we used DFT-D3 and experimental methods to design and synthesised a novel SDTBAT collector and investigate its interaction with pyrite mineral surface. The SDTBAT molecule is a potential collector that may positively impact the mineral processing industry. The SDTBAT

collector was compared with SNBX and SNBDTC collector to determine the best collector. The microflotation experiment was also conducted to determine a well performing collector in the flotation of pyrite mineral. The adsorption of triazine collectors (SDTBAT) on pyrite formed a basis in design of flotation collectors that may be applicable in a wide range of sulfide minerals. The collectors were adsorbed in their neutral form containing sodium on the pyrite (100) surface. The computational calculations found that the adsorption energies followed the order: SDTBAT (-300.35 kJ/mol) > SNBX (-186.10 kJ/mol) > SNBDTC (-163.78 kJ/mol). It is clear that the SDTBAT had a strong binding energy which is ascribed to the presence of the triazine group that is electron depositing to the active S atoms compared to the SNBX which possessed the oxygen that is electron withdrawing. It was observed that the SNBX and SNBDTC adsorbed through the S atoms, while the SDTBAT adsorbed through the S and N atoms onto Fe atoms. The bond lengths of adsorption of the collectors were found to be shorter for SDTBAT compared to the SNBX and SNBDTC. This indicated that SDTBAT had a strong adsorption on pyrite surface. Moreover, the SDTBAT collector was found to bind stronger than the xanthate. This was complimented by microflotation tests that showed fast floating and higher recoveries of pyrite when using the SDTBAT collector than the xanthate and DTC. This clearly demonstrated that the SDTBAT is powerful and highly selective collector to can potentially replace the xanthate collectors.

ACKNOWLEDGEMENTS

This work is in collaboration with the Materials Modelling Centre at the University of Limpopo and China-South Africa Joint Research Centre on the Development and Utilization of Mineral Resources and China-South Africa Belt and Road Joint Laboratory on Sustainable Exploration and Utilization of Mineral Resources at BGRIMM Technology Group. Financial support was received from the Department of Science and Innovation (DSI) and National Research Foundation (NRF) of South Africa in the Young Scientist Exchange Program (YSEP) and the National Key R&D Program of China (Grant No. 2020YFE0202800) from Ministry Of Science and Technology (MOST) of China and the National Natural Science Foundation of China (Grant No. 51974030). The computational work benefited from supercomputing resources at the Centre for High Performance Computing (CHPC).

REFERENCES

Abdullahi, Y Z, Leong, Y T, Halim, M M, Hashim, Md R, Leng, L T, Uebayashi, K, 2017. Adsorption of atoms and molecules on s-triazine sheet with embedded manganese atom: First-principles calculations, *Phys Lett A*, 381:3664–3674.

Adkins, S J, Pearse, M J, 1992. The influences of collectors chemistry on kinetics and selectivity inbase-metal Sulphide flotation, *Miner Eng*, 5:295–310.

Benjalal, Y, Ghanjaoui, M E A, 2016. Theoretical study of Di-Amino-Triazine adsorption on Cu(110) and Au(111) surfaces, *J Mater Environ Sci*, 7(5):1531–1537.

Chen, J-H, Lan, L-H, Chen, Y, 2013. Computational simulation of adsorption and thermodynamic study of xanthate, dithiophosphate and dithiocarbamate on galena and pyrite surfaces, *Miner Eng*, 46–47:136–143.

Choi, H, Seo, J Y, Uhm, Y R, Sun, G M, Kim, C S, 2021. Crystalline structure and magnetic properties of pyrite FeS_2, *AIP Adv*, 015131, 11:1–5.

Dudarev, S L, Botton, G A, Savrasov, S Y, Humphreys, CJ, Sutton, AP, 1998. Electron-energy-loss spectra and the structural stability of nickel oxide: An LSDA+U study, *Phys Rev B*, 57:1505–1509.

Dzade, N Y, de Leeuw, N H, 2018. Adsorption and desulfurization mechanism of thiophene on layered FeS(001), (011), and (111) surfaces: A dispersion-corrected density functional theory study, *J Phys Chem C*, 122:359−370.

Ennaoui, A, Fiechter, S, Pettenkofer, Ch, Alonso-Vante, N, Büker, K, Bronold, M, Höpfner, Ch, Tributsch, H, 1993. Iron disulfide for solar energy conversion, *Sol Energy Mater Sol Cells*, 29:289–370.

Ennaoui, A, Tributsch, H, 1986. Energetic characterization of the photoactive FeS2 (pyrite) interface, *Sol Energy Mater*, 14(6):461–474.

Feng, Y, Chen, S, Zhang, H, Li, P, Wu, L, Guo, W, 2006. Characterization of iron sulphide modified by 2-mercaptobenzothiazole self-assembled monolayers, *Appl Surf Sci*, 253:2812–2819.

Galvao, T L P, Kuznetsova, A, Gomes, J R B, Zheludkevich, M L, Tedim, J, Ferreira, M G S, 2016. A computational UV-Vis spectroscopic study of the chemical speciation of 2-mercaptobenzothiozole corrosion inhibitor in aqueous solution, *Theor Chem Acc*, 135(78):1–11.

Grimme, S, Ehrlich, S, Goerigk, L, 2011. Effect of the damping function in dispersion corrected density functional theory. *J Comput Chem*, 32:1456–1465.

Jando, T, Mori, K, 1990. Crosslinking of poly(vinyl chloride) fibers with 2-dibutylamino-4,6-dimercapto-1,3,5-triazine in Water. *Polymer J*, 22(9):793–802.

Kresse, G, FurthermÜller, J, 1996. Efficient iterative schemes for ab-initio total-energy calculations using a plane-wave basis set, *Phys Rev B*, 54:11169–11186.

Kresse, G, Hafner, J, 1993. Ab initio molecular dynamics for liquid metals, *Phys Rev B*, 47:558–561.

Kresse, G, Joubert, D, 1999. From ultrasoft pseudopotentials to the projector augmented-wave method, *Phys Rev* B, 59:1758–1775.

Maier, G S, Dobias, B, 1997. 2-mercaptobenzothiazole and derivatives in the flotation of galena, chalcocite and sphalerite: A study of flotation, adsorption and microcalorimetry, *Miner Eng*, 10(12):1375–1393.

Mkhonto, P P, Zhang, X, Lu, L, Xiong, W, Zhu, Y, Han, L, Ngoepe, P E, 2022. Adsorption mechanisms and effects of thiocarbamate collectors in the separation of chalcopyrite from pyrite minerals: DFT and experimental studies, *Miner Eng*, 107318, 176:1–14.

Mkhonto, P P, Zhang, X, Lu, L, Zhu, Y, Han, L, Ngoepe, P E, 2021. Unravelling the performance of oxycarbonyl-thiocarbamate collectors on chalcopyrite using first-principles calculations and micro-flotation recoveries, *Appl Surf Sci*, 150332, 563:1−13.

Monkhorst, H F, Park, J D, 1976. Special points for Brillouin-Zone integrations, *Phys Rev B*, 13:5188–5192.

Perdew, J P, Chevary, J A, Vosko, S H, Jackson, K A, Pederson, M R, Singh, D J, Fiolhais, C, 1992. Atoms, molecules, solids, and surfaces: applications of the generalized gradient approximation for exchange and correlation, *Phys Rev B*, 46:6671–6687.

Vosko, S H, Wilk, L, Nusair, M, 1980. Accurate spin-dependent electron liquid correlation energies for local spin density calculations: a critical analysis, *Can J Phys*, 58:1200–1211.

Yacoub, E-S A K, El-Kourashy, A-G, Al-Hajjaji, M A, 2013. Sorption of iron(II) and ruthenium(III)-triazine complexes on silica gel and its analytical applicability, *Arabian J Chem*, 6:111–114.

Yekeler, M, Yekeler, H, 2006. A density functional study on the efficiencies of 2-mercaptobenzoxazole and its derivatives as chelating agents in flotation processes, *Colloids and Surf A: Physiocochemical Eng Aspects*, 186:121–125.

Zhu, B, Wageh, S, Al-Ghamdi, A A, Yang, S, Tian, Z, Yu, J, 2019. Adsorption of CO_2, O_2, NO and CO on s-triazine-based g-C_3N_4 surface, *Catalysis Today*, 335:117–127.

Computational density functional theory study of triazine adsorption on sperrylite (100) surface

B Nemutudi[1], S Pikinini[2], P P Mkhonto[3], B McFadzean[2], X Zhang[4] and P E Ngoepe[3]

1. Materials Modelling Centre, University of Limpopo, Sovenga 0727, South Africa. Email: bradleynemu@gmail.com
2. Centre for Minerals Research, University of Cape Town, Rondebosch 7701, South Africa.
3. Materials Modelling Centre, University of Limpopo, Sovenga 0727, South Africa.
4. State Key Laboratory of Mineral Processing, BGRIMM Group, Beijing 102600, China.

ABSTRACT

There is still a huge challenge in efficiently recovering the arsenides minerals that are largely concentrated in the Platreef Bushveld Complex which constitutes about 21 per cent of the platinum group minerals (PGMs). Therefore new collectors are required to improve the recovery separation of hard to float minerals, in particular sperrylite. The triazine modifications are promising reagents for mineral flotation and have not been given much attention in minerals processing. The adsorption of sodium 2,6-dithio-4-butylamino-1,3,5-triazine (SDTBAT), sodium 2,6-ditrithiocarbonate-4-butylamino-1,3,5-triazine (SDTTCBAT) and sodium normal butyl xanthate (SNBX) on sperrylite (100) surface were performed to identify a well performing collector molecule. We observed that the triazine collectors preferred to bridge on surface As and Pt atoms through the S atoms. We found that the adsorption energies were in the order: SDTTCBAT > SDTBAT > SNBX, indicating that the SDTTCBAT had strong exothermic adsorption on sperrylite and pyrite. These results showed that the ditrithiocarbamate had a great influence in the adsorption strength on the sperrylite surface. Importantly it was found that the triazine collector had stronger adsorption than the xanthate, which portrayed a promising replacement of xanthate collector. These results paved a way for design of novel collector for sperrylite and other chalcogenide minerals to improve their recovery.

INTRODUCTION

South Africa has the largest deposits of platinum group elements (PGEs) in the world. The PGEs consist of platinum (Pt), palladium (Pd), rhodium (Rh), ruthenium (Ru), iridium (Ir) and osmium (Os). These metals are often concentrated together geologically due to their similar geochemical characteristics (Jones, 2005). The deposits are located in the Bushveld igneous complex (BIC) in the north of the country and have been commercially mined since 1925 (Matthey, 2014).

There are three main reefs found in the Bushveld, namely Merensky reef, Platreef and UG2 reef. The Platreef hosts the third largest amount of platinum group minerals in the world. This reef is composed of approximately 21 per cent sperrylite ($PtAs_2$) which is particularly slow floating, whereas the platinum sulfides are recovered relatively easily (O'Connor and Shackleton, 2013). The UG2 reef on the other hand, consists mainly of chromitite disseminated by finer grains of both BMS and platinum group minerals (PGMs) mineralisation (Penberthy and Merkle, 1999).

The mining, recovery and processing of PGEs from their ores is a multibillion dollar industry. One of the greatest challenges associated with this industry is to separate the relatively low-abundance PGMs from the vast excess of commercially worthless rock (Waterson *et al*, 2016). The most widely applied separation process employed is froth flotation, a method that separates mixtures of solids on the basis of their relative hydrophobicities (Kelly and Spottiswood, 1982). Control of chemistry occurring within the flotation process can allow enhancing the recovery of a particular mineral over others. This is achieved by the addition of collector ligands, which are small organic molecules that adsorb preferentially on the surfaces of targeted minerals (Liu and Norskov, 2001). Shackleton *et al* (2007) suggested that when sperrylite sample have been well recovered in flotation experiments, it is more likely to do with platinum blebs in the crystal structure, which have high affinity for the collectors. Vermaak (2005) suggests that this is not due to an inability of the collectors to adsorb onto the mineral surface, but due to particle size effects. However, Shackleton goes on to suggest that the adsorption of hydroxyl on the sperrylite at elevated pH significantly depresses the recovery.

The xanthate collectors have been the industrial workhorse of the mineral processing industry for many years (Nagaraj and Ravishankar, 2007). They have been extensively used in the flotation of sulfides minerals that contain PGEs (Nyambayo, 2014). It has been reported that the flotation of certain PGMs resulted in low recovery when using traditional xanthates. This was attributed to the poor recovery of platinum arsenides that were not amenable to flotation (O'Connor and Shackleton, 2013). Therefore, novel collectors may show promise in order to improve the recovery of slow floating arsenide minerals. The novel collectors such as triazine and their modifications for mineral flotation have not been given much attention. Nonetheless, computational methods offer a cost-effective method to screen collector molecules and their adsorption. The triazine collectors offer hope in improving the recovery of arsenides minerals. Previously, the triazines have been investigated on tin (Sn) metal and alloy surfaces by the solution dipping method (Hirai *et al,* 2017).

In this study we investigated the interaction and binding energies of sodium normal butyl xanthate (SNBX), sodium 2,6-dithio-4-butylamino-1,3,5-triazine (SDTBAT) and sodium 2,6-ditrithiocarbonate-4-butylamino-1,3,5-triazine (SDTTCBAT) on sperrylite mineral surface using computational and microcalorimetry methods. Similar interactions are shown for pyrite as comparison. In a PGM ore, pyrite is not necessarily a gangue mineral since PGM's may be associated with base metal sulfide minerals.

MATERIALS AND METHODOLOGY

Computational methods

All calculations were carried out using the plane-wave density functional theory (DFT) code Cambridge Serial Total Energy Package (CASTEP) (Clark *et al,* 2005). The generalised gradient approximation of Perdew-Burke-Ernzerhof (GGA-PBE) (Perdew, Burke and Ernzerhof, 1996) exchange-correlation functional was used, along with a plane-wave basis set with an energy cut-off of 500 eV, which demonstrated convergence to within 0.2 meV/atom. A k-point grid of 6×6×6 and 4×4×1 was generated for the bulk and surface based on the Monkhorst-Pack (Monkhorst and Pack, 1976) scheme, respectively. The convergence tolerances for force, ionic displacement and energy were 0.02 eVÅ^{-1}, 0.015 Å and 0.01 meV/atom, respectively. The same method was adopted for pyrite adsorption, however, the cut-off of 450 eV and 4×4×1 k-points were used for the pyrite surface study.

In order to calculate reaction energies, the optimisation of SNBX, SDTBAT and SDTTCBAT models were performed at gamma point (k-points = 1×1×1) in a cubic cell of 40 Å, which was enough to minimise spurious mirror-image interactions between collector molecules in adjacent supercells. The ultrasoft pseudopotential, cut-off energy at gamma point and other precision parameters as in the surface calculations were employed. Note that we have included the sodium ions (Na^+) in the simulation of the collector to neutralise the negative charge on the S^- atom/s on the collector polar site. It has been reported that there is greater association of the Na^+ with S^- of collectors such as MBT^- (Galvao *et al,* 2016).

The surface energy is computed using Equation 1:

$$E_{surface} = \frac{[E_{slab} - (n_{slab})(E_{bulk})]}{2A} \quad (1)$$

where E_{slab} is the energy of the surface, E_{bulk}/atom is the energy of the bulk per total number of atoms in the bulk and n_{slab} is the number of atoms of the surface and *A* is the surface area.

The adsorption energies ($E_{ads.}$) of the collector molecules on the surfaces were calculated from the difference in total energy between the collector-surface ([S + C]) and the sum of the collector ([C]) and surface ([S]) models, as expressed in Equation 2 (Mkhonto *et al,* 2022)::

$$E_{ads.} = E_{[S+C]} - \left(E_{[S]} + E_{[C]}\right) \quad (2)$$

In the adsorption energy calculations a negative value shows an exothermic favourable reaction between the collector molecules and the surface, whereas a positive value reveals the opposite.

Experimental methods

Isothermal titration calorimetry

Isothermal titration calorimetry tests were carried out to measure the adsorption enthalpies at 25°C using the TAM III isothermal titration microcalorimeter. This technique measures the heat consumed or released during a reaction of the minerals with a given ligand. The synthetic sperrylite sample of mass 0.2 ± 0.0005 g was weighed into an ampoule and 0.7 ml of distilled water was added into each ampoule and sonicated for 3 minutes to disperse the slurry. It was not possible to control and adjust the pH of the slurry after loading the ampoules into the titration channel, hence all the tests were carried out at the natural pH of the slurry, which was around 6.3. The ampoules were loaded into the calorimeter and the titration syringe was loaded with the collector solution. Time was given for the machine to stabilise and full calibration of the machine against a known power input was carried out before each run. The machine was then programmed to run and to add 2 µL of the collector every hour once the selected conditions were met. The 2 µL collector solution was precalculated based on the BET results of the -38 µm sperrylite sample to cover approximately 0.25 pseudo-monolayers of the mineral surface. Ten titrations that amounted to 2.5 pseudo-monolayers collector coverage were carried out for each run.

The area under the peaks that result from the mineral-collector interactions was integrated to obtain the specific enthalpies of adsorption per injection. Heats of dilution per injection of a collector were also carried out for each collector and subtracted from the mineral-collector heats of adsorption. In this study, data from four titrations that amount to 1 pseudo-monolayer collector coverage heats of adsorption were calculated and reported.

SDTBAT and SDTTCBAT collectors were synthesised at BGRIMM and SNBX was purchased commercially as a pure powder. $PtAs_2$ mineral was synthesised by the method of Shackleton *et al* (2007). SDTBAT and SDTTCBAT required dissolution in high pH solution. The interaction of the hydroxide ions was taken into account when processing the calorimetry data and was a reference value which was subtracted from the collector-mineral interaction value.

RESULTS AND DISCUSSION

Sperrylite bulk and (100) surface models

The 2×2 (100) surface (Figure 1b) was obtained from the relaxed bulk structure of sperrylite ($PtAs_2$) with space group symmetry of *Pa-3 (205)* (Cabri, Laflamme and Stewart, 1977), which possesses rock-salt type structure with Pt^{4+}: $[Xe]4f^{14}3d^6$ cations at the face-centred of the cubic cell and As^{2-}:$[Ar]3d^{10}3s^23p^1$ forming dimers (As_2^{4-}) centred about the anion positions as shown in Figure 1a. Sperrylite is defined as a low-spin with the d-orbital splitting occupied in the order of t_{2g}^6 and e_g^0, which is adopted in this study. The full structural relaxation of the bulk model was performed and we found that the bulk relaxed lattice parameters was 5.967 Å, which was in agreement with the experimental value of 5.970 Å (Aminoff and Parsons, 1928).

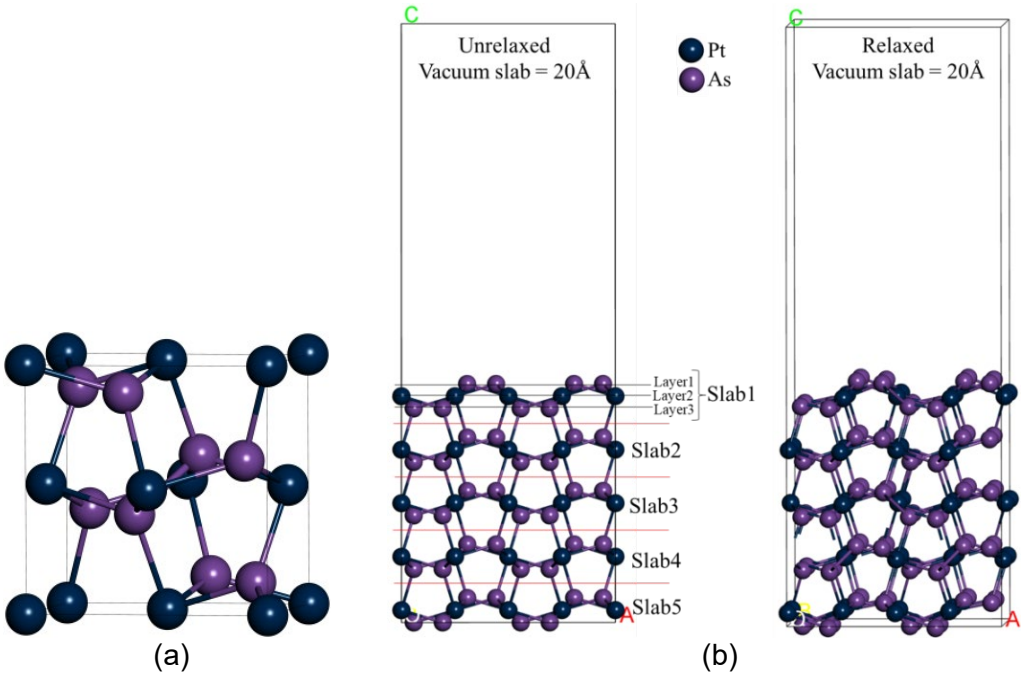

FIG 1 – The relaxed bulk structure of sperrylite ($PtAs_2$) and the un-relaxed and relaxed (2×2) $PtAs_2$ (100) surface.

The surface terminations were determined on the basis of minimal surface dipole. To ensure that the results of the calculations accurately represent an isolated surface, the vacuum regions must be wide enough. This is because the faces of adjacent crystal slabs do not interact across the vacuum region, and the crystal slab must be thick enough so that the two surfaces of each crystal do not interact through the bulk crystal. Therefore we adopted a 2×2 (100) surface model composed of 15 atomic layers with the periodic cell of 10.746×10.746×32.004 Å, which possessed a vacuum slab separation of 20 Å in order to avoid interaction between the collectors and the mirror image surface. In the adsorption system the bottom six layers (6L) were kept fixed to bulk coordinate, while the top nine layers (9L) were relaxed and allowed to interact with the collectors. Gibbs (1928) developed the concept that the equilibrium structure of a crystal will possess the minimum possible excess energy for a given volume, and as volume and surface area are inseparably linked, the crystal face with the lowest surface energy will predominate. However, finding the surface structure with the lowest surface energy for each metal or mineral under study offers the best chance of defining a broadly representative working surface. In Table 1 we show the atoms coordination and calculated surface energy for sperrylite bulk and cleaved (100) surface. The (100) surface had the lowest positive surface energy value, thus most stable. This is in agreement with the previous reports by Waterson *et al* (2015) and Ntoahae *et al* (2005).

TABLE 1

Surface coordination and surface energies for sperrylite (100) surface.

Surfaces	Surface coordination		Surface energies
	Pt	As	$J.m^{-2}$
Bulk	6	4	–
(100) Surface	5	3	1.05

Collectors molecular geometries

The relaxed bond lengths for the minimum energy geometries of the SNBX, SDTBAT and SDTTCBAT models are shown in Table 2. Note that we focus on the centre of reactivity C–S group atoms of the collectors. As shown in Figure 2, the C4/C3/C1–S1/S3 possesses a double bond and the C4/C3/C1–S2/S4 possesses a single bond on SNBX and SDTTCBAT. In addition the C2–S2

and C6–S1 bonds of SDTBAT are single bonds. The negative charge on the S atoms forming single bonds is neutralised by the sodium (Na^+) cation.

TABLE 2

The selected polar sites bond lengths (in Å) and angles (in deg) on relaxed geometry of isolated triazine and xanthate collectors.

Bonds	SNBX	SDTBAT	SDTTCBAT
C6/C4/C1–S1	1.708	1.715	1.709
C4/C2/C1–S2	1.705	1.734	1.682
C4–O/N	1.355	1.370	1.356
C3–S3	–	–	1.682
C3–S4	–	–	1.711
S1–C4/C3/C1–S2	127.77	–	128.77
S3–C3–S4	–	–	128.82

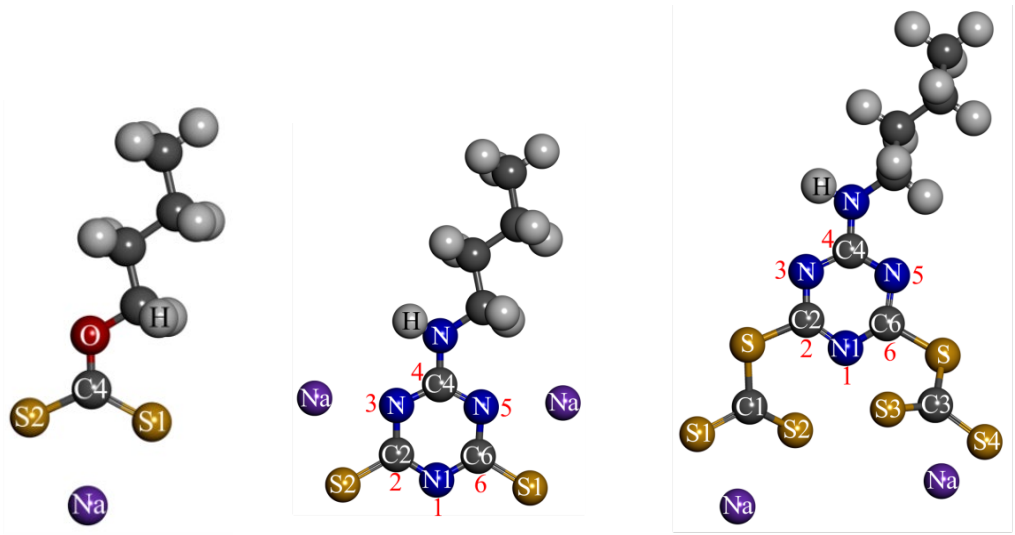

(a) (b) (c)

FIG 2 – The relaxed molecular geometries of the collectors: (a) SNBX, (b) SDTBAT and (c) SDTTCBAT.

The optimised organic collector geometries of SNBX, SDTBAT and SDTTCBAT are shown in Figure 2 and their geometries are given in Table 2. We noted that the C4–S2 and C3–S3 with single bonds on SNBX and SDTTCBAT were shorter than the C4–S1 and C3–S4 with double bonds. The C2–S2 and C6–S1 bond length for SDTBAT were larger thus less stable, which suggests that SDTBAT may be more reactive. The SNBX had C4–O bond length of 1.355 Å whereas the SDTBAT had a C4–N bond length of 1.370 Å, which is larger than the SDTTCBAT bond length of 1.356 Å. The bond angles of 127.77° for SNBX and 128.77° and 128.82° for SDTTCBAT were also obtained. However, the N atoms are responsible for the reactivity of SDTBAT and SDTTCBAT being predicted to be stronger than that of SNBX. This effect is due to the presence of N atoms that donates electron density towards the C atom, while the O atom withdraws electron density from the C atom. This phenomenon is a result of oxygen atoms being stronger electron acceptors than N atoms. As such, the SDTBAT and SDTTCBAT contain more N atoms suggesting that they may be the most reactive collectors.

Collector adsorption on sperrylite (100) surface

The adsorption of the collectors was initiated by positioning the collectors S atoms at approximately 2.00 Å at different adsorption sites on the sperrylite (100) surface. The addition of

collector on the mineral surface during flotation that results in attachment to the mineral surface is the method used to test the collecting power on the surface. However, the highest heat of adsorption indicates that the collector resides at the most exothermic preferred sites on the mineral surface. The tested sites for all the collectors were bridging two sulfurs (S) atoms and nitrogen (N) atom addressing different sites on Pt and As atoms on the surface. The adsorption energies are displayed in Table 4. We observed that the collectors preferentially chemisorbed on the Pt and As atoms and formed stable six-membered Pt and four-membered As complexes, as shown in Figure 3a, 3b and 3c. Interestingly, we noted that for SDTBAT adsorption, the N atom also formed bonds with As atom. We described the parameters (bond lengths and bond angles) for the three collectors as shown in Table 3. The SNBX appeared to form two bonds with the surface. The bond lengths and angles for collector adsorption on the sperrylite (100) surface clearly illustrated a strong Pt1–S1 bond for SNBX (2.390 Å). The SDTBAT had a larger Pt1–S1 bond (2.550 Å). Moreover, the SDTTCBAT also had a larger Pt2–S2 bond (2.477 Å). The Pt1–S4 (2.371 Å) for SDTTCBAT is ascribed to the stretch of the collector molecules as shown in Figure 3c. The SDTBAT formed a bond length of As–N = 1.997 Å. The SDTTCBAT formed As1–S1 and As2–S3 bond lengths of 3.300 Å and 2.349 Å, which As2–S3 bond is shorter than the As2–S2 = 2.371 Å bond for SNBX. A small bond angle of 129.13° for SNBX than 136.06° and 134.91° for SDTTCBAT were also obtained. This bonding behaviour clearly demonstrated the strong binding of the SDTBAT and SDTTCBAT collectors on sperrylite surface.

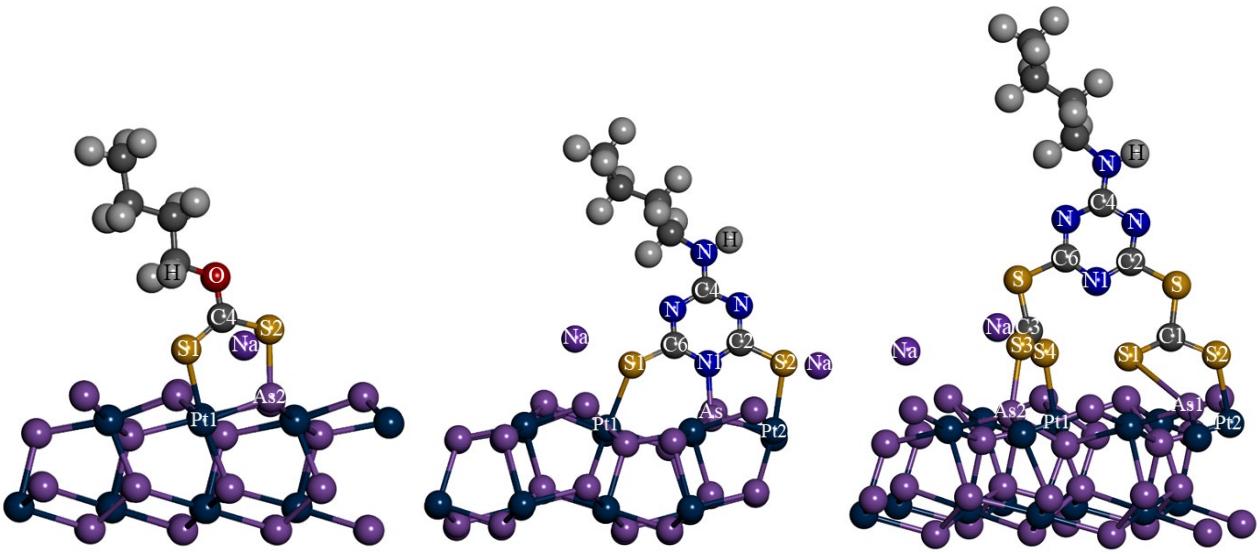

FIG 3 – Relaxed geometries of collector's adsorption on (100) surface: (a) SNBX, (b) SDTBAT and (c) SDTTCBAT adsorptions.

TABLE 3

The relaxed bond lengths (in Å) and angles (in deg.°) geometry of charged and neutral xanthate and triazine collectors adsorbed on sperrylite (100) surface.

Bonds	SNBX	SDTBAT	SDTTCBAT
Pt1–S1/S4	2.390	2.550	2.469
As1–S1		–	3.300
As2–S2/S3	2.371	–	2.349
Pt2–S2	–	2.474	2.477
As–N	–	1.997	–
S1–C4/C1–S2	129.13	–	136.06
S3–C3–S4		–	134.91

TABLE 4

Adsorption energies for charged xanthates and neutral xanthate collector adsorption on sperrylite (100) surface, calculated according to Equation 2.

Adsorbates	Adsorption	E_{S+C} (eV)	E_C (eV)	E_S (eV)	$E_{Ads.}$ (kJ.mol^{-1})
SNBX	Pt-As-Bridge	–45770.69842	–3216.989492	–42551.96229	–168.53
SDTBAT	Pt-As-Bridge	–48050.3659	–5496.018211	–42551.96229	–230.16
SDTTCBAT	Pt-As-Bridge	–49470.46927	–6915.819617	–42551.96229	–259.29

The binding strengths of the collectors on the sperrylite (100) surface are given in Table 4 and displayed in Figure 4. The adsorption energy of SDTTCBAT (–259.29 kJ/mol) was more exothermic than that of SDTBAT (–230.16 kJ/mol) and SNBX (–168.53 kJ/mol) (Table 4). These results indicated that the triazine group of SDTTCBAT and SDTBAT resulted in an improved adsorption performance on the sperrylite surface. Furthermore, SDTTCBAT was found to be a better collector than the SDTBAT collector, which is attributed to the addition of CS_2 group. The SDTTCBAT and SDTBAT were better collectors than SNBX due to more N atoms that are electron dense and deposited towards the C atom. This suggested that SDTTCBAT and SDTBAT may be highly selective in improving the flotation of the slow floating sperrylite mineral.

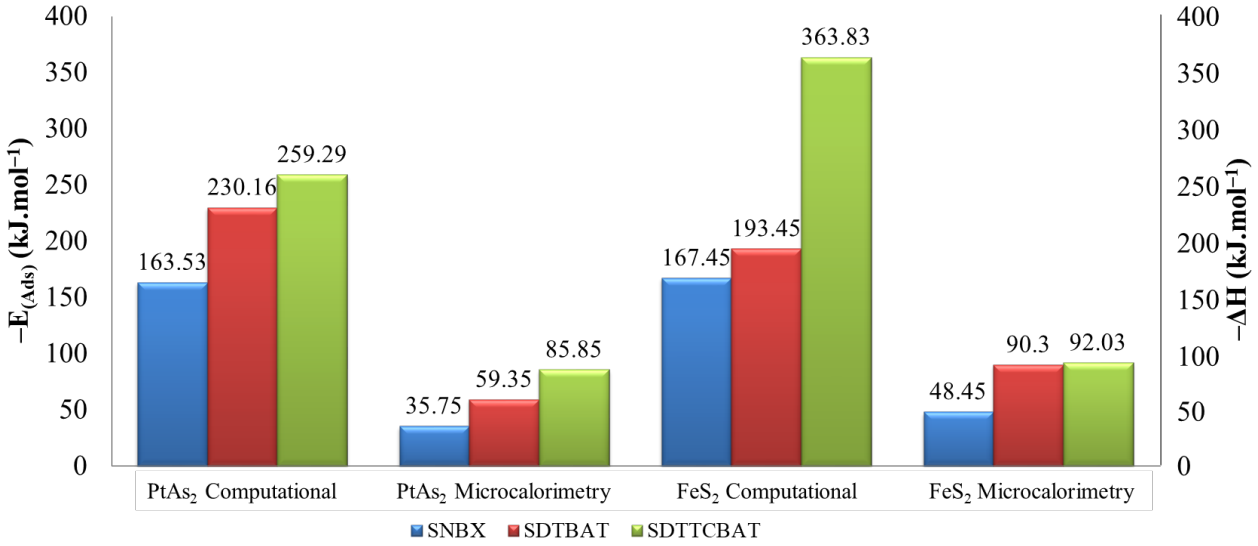

FIG 4 – Computational adsorption energies and microcalorimetry enthalpy of adsorption of sperrylite using the SNBX, SDTBAT and SDTTCBAT collectors.

Microcalorimetry tests

Microcalorimetry titration was performed for each collector, and the enthalpies of adsorption are displayed in Figure 4, in comparison with the computational adsorption energies. The adsorption energies of the SNBX, SDTBAT and SDTTCBAT were –35.75 kJ/mol, –59.35 kJ/mol and –72.70 kJ/mol for sperrylite, respectively. The results follow the same trend that was obtained from the molecular modelling computations making both techniques suitable to deduce the binding energies of the collectors onto sperrylite. However, the molecular modelling binding energies are higher than those determined using the titration isothermal calorimetry where tests are carried out in the presence of water. In addition, molecular modelling computations give the binding energy of one collector molecule while isothermal titration calorimetry gives the binding energy for one monolayer coverage. This would introduce steric effects unique to the structure of the collector molecules when they bind to the mineral. Greater steric hindrances affect the orientation of the collector molecules to a greater extent, resulting in lower overall binding energies. The sperrylite binding energies were compared to pyrite which has the same structure as shown in Figure 4. The adsorption energies of the SNBX, SDTBAT and SDTTCBAT on pyrite were –48.45 kJ/mol, –

90.30 kJ/mol and –92.03 kJ/mol, respectively. These also followed the same trend as predicted by computational modelling. It interesting that the SDTTCBAT had a much stronger binding on pyrite of about –363.83 kJ/mol. It is evident that the collectors have a strong binding on pyrite compared to sperrylite. A significant phenomenon is that the triazine collectors portray a strong binding on both minerals compared to xanthate. The SDTTCBAT was found to give superior binding, which demonstrated that the modification of the SDTBAT greatly improved the binding active site. This strong binding is attributed to the presence of two CS_2 groups that bind on the surface. This indicated that the triazines are potential replacement of xanthate collectors.

CONCLUSIONS

The aim of this work was to use computational chemistry and microcalorimetry methods to study the adsorption of flotation collector molecules on sperrylite mineral surface. This study investigates the comparison of sodium normal butyl xanthate (SNBX), sodium 2,6-dithio-4-butylamino-1,3,5-triazine (SDTBAT) and sodium 2,6-ditrithiocarbonate-4-butylamino-1,3,5-triazine (SDTTCBAT) adsorptions on sperrylite mineral using computational density functional theory approach and microcalorimetry method. It was observed that the calculated and experimental lattice parameters were in good agreement. The calculated surface energy indicated that the (100) surface was the most stable surface plane, with the lowest positive surface energy. During adsorptions, different adsorption sites were varied in order to find the most stable exothermic site and bonding mode of the collector ligands on sperrylite mineral surface. The adsorptions of SNBX, SDTBAT and SDTTCBAT were found to prefer to bridge on the Pt and As atoms through the S and N atoms. These findings showed that the collector adsorbs on the surface through both Pt and As atoms and indicated that the As atoms were significantly active in the adsorptions.

We found that the adsorption energies were in the order: SDTTCBAT > SDTBAT > SNBX, indicating that the SDTTCBAT had strong exothermic adsorption on sperrylite and pyrite. This trend was replicated in the experimental adsorption energies. However, the absolute values were lower than the computational energies. These results showed that the ditrithiocarbamate had a great influence in the adsorption strength on the sperrylite surface. Significantly it was found that the triazine collector had stronger adsorption than the xanthate, which portrays a promising replacement of xanthate collector. These findings suggest that the use of triazine collectors and their modifications as collectors may improve the floatability of sperrylite mineral.

ACKNOWLEDGEMENTS

The authors would like to thank and appreciate Materials Modelling Centre (MMC), University of Limpopo and Centre for Minerals Research (CMR), University of Cape Town for collaboration in this work. The computational work was performed at the Materials Modelling Centre in University of Limpopo and also benefited from supercomputing resources at the Centre for high Performance Computing (CHPC). The experimental work was carried out at the Centre for Minerals Research in University of Cape Town. Also, many thanks to International Mineral Processing Congress (IMPC) for the opportunity to share our work.

REFERENCES

Aminoff, G and Parsons, A L, 1928. The crystal structure of sperrylite, *Canadian Mineralogy*, 27:5–10.

Cabri, L J, Laflamme, J H G and Stewart, J M, 1977. Platinum group minerals from the onverwacht, *Platarsite, a new sulfarsenide platinum*, 15:385–388.

Clark, S J, Segall, M D, Pickard, C J, Hasnip, P J, Probert, M J, Refson, K and Payne, M C, 2005. First principles methods using CASTEP, *Zeitschrift für Kristallographie*, 220:567–570.

Galvao, T L P, Kuznetsova, A, Gomes, J R B, Zheludkevich, M L, Tedim, J and Ferreira, M G S, 2016. A computational UV-Vis spectroscopic study of the chemical speciation of 2-mercaptobenzothiozole corrosion inhibitor in aqueous solution, *Theoretical Chemistry Accounts*, 135:1–11.

Gibbs, J W, 1928. *The collected works of J. Willard Gibbs*, pp 58–73 (Longmans: New York).

Hirai, A, Sang, J, Aisawa, S and Hirahar, H, 2017. Adsorption of triazine thiol on Sn metal and alloy surfaces by the solution dipping method, *Journal of the Japan Society of Colour Material*, 90:161–167.

Jones, R T, 2005. An overview of Southern African PGM smelting, *44th Annual Conference of Metallurgists*, 147–178.

Kelly, E G and Spottiswood, D J, 1982. *Introduction to mineral processing*, pp 48–57 (Wiley: New York).

Liu, P and Norskov, J K, 2001. Ligand and ensemble effects in adsorption on alloy surfaces, *Physical Chemistry Chemical Physics*, 3:3814–3818.

Matthey, J, 2014. The Bushveld Complex, *Platinum Metals Review*, 58:2–5.

Mkhonto, P P, Zhang, X, Lu, L, Xiong, W, Zhu, Y, Han, L and Ngoepe P E, 2022. Adsorption mechanisms and effects of thiocarbamate collectors in the separation of chalcopyrite from pyrite minerals: DFT and experimental studies, *Minerals Engineering*, 176:1–14.

Monkhorst, H J and Pack, J D, 1976. Special points for brillouin-zone integrations, *Physical Review B*, 13:5188–5192.

Nagaraj, D R and Ravishankar, S, 2007. A flotation reagants – a critical overview from an industry perspective, *A century of Innovation*, 375–424.

Ntoahae, P S, Pettifor, D G and Ngoepe, P E, 2005. *Application of computer simulation methods to the study of platinum group minerals*, PhD thesis, University of Limpopo, Polokwane.

Nyambayo, C K, 2014. *The use of mixed thiol collectors in the flotation of Nkomati sulphide ore*, MSc Dissertation, University of Cape Town, Cape Town.

O'Connor, C T and Shackleton, N J, 2013. Investigations into the recovery of platinum group minerals from the platreef ore of the Bushveld Complex of South Africa, *Platinum Metals Review*, 57:302–309.

Penberthy, C J and Merkle, R K, 1999. Lateral variations in the platinum-group element content and mineralogy of the UG2 Chromitite layer, Bushveld complex, *South African Journal of Geology*, 102:240–250.

Perdew, J P, Burke, K and Ernzerhof, M, 1996. Generalized gradient approximation made simple. *Physical Review Letters*, 77:3865–3868.

Shackleton, N J, Malysiak, V and O'Connor, C T, 2007. Surface characteristics and flotation behaviour of platinum and palladium arsenides, *International Journal of Mineral Processing*, 85:25–40.

Vermaak, M K G, 2005. *Fundamentals of the flotation behaviour of palladium bismuth tellurides*, PhD thesis, University of Pretoria, Pretoria.

Waterson, C N, Tasker, P A and Morrison, C A, 2015. *Design, synthesis and testing of reagents for high-value mineral collection*, PhD thesis, The University of Edinburgh, Edinburgh.

Waterson, C N, Tasker, P A., Farinato, R, Nagaraj, D R, Shackleton, N and Morrison, C A, 2016. A computational and experimental study on the binding of dithio ligands to sperrylite, pentlandite and platinum, *The Journal of Physical Chemistry C,* 120:22476–22488.

Considering the effects of milling media and water chemistry in the flotation of selected base metal sulfides

S N Nyoni[1], K C Corin[2] and C T O'Connor[3]

1. PhD. Student, Centre for Minerals Research, University of Cape Town, Cape Town, South Africa, 7700. Email: NYNSAN007@myuct.ac.za
2. Associate Professor, Centre for Minerals Research, University of Cape Town, Cape Town, South Africa, 7700. Email: Kirsten.Corin@uct.ac.za
3. Professor, Centre for Minerals Research, University of Cape Town, Cape Town, South Africa, 7700. Email: Cyril.OConnor@uct.ac.za

INTRODUCTION

Considering future water scenarios, as influenced by the increasing scarcity of water and the move towards sustainable process engineering etc, the closed water circuit becomes an important point of study in metallurgical operations, such as in milling and flotation. However, a deterrent in the use of recycled process water is often a lack of understanding of the effects of the accumulation of dissolved ions and other process chemicals. Recovery of the valuable minerals may be impacted by the concomitant complex mineral-pulp chemistry interactions. Literature indicates that these interactions are not necessarily antagonistic to process outcomes. Wet milling using steel media results in the dissolution of Fe from the media, the rate of which is dependent, inter alia, on the type of media and the chemical conditions of the aqueous environment in the mill. The pulp-phase interactions of dissolved ions with sulfide minerals may result in significant changes to the chemical conditions in the mill, which may subsequently impact negatively on the flotation recoveries. To understand the effect of these interactions in the context of the processing of sulfide minerals, this study seeks to consider the effect of three factors, *viz* mineral type – pyrite (Py) and galena (Gn) -, milling media of different compositions – forged steel (FS), 21 per cent high chrome and ceramic media -, and water chemistry, *viz*, deionised water (DI) and synthetic plant water (SPW). Ceramic media and galena are used for the respective control cases where the milling media and sulfide mineral contribute no Fe species. Using DI as a control case, a high ionic strength case is used to mimic the changes in water chemistry for a closed water circuit. Batch flotation tests are used as a diagnostic tool to determine the effects of these media-water-mineral interactions to investigate correlations between the chemical reactions occurring and chemical species present during the milling process and the ultimate flotation performance.

EXPERIMENTAL

Milling was initially performed in the absence of ore to determine the standalone dissolution effects of the mill shell and the different media types. Next, Py and Gn were obtained from Mineral World, Cape Town, South Africa, and analysed by X-ray diffraction (XRD) to confirm the absence of other sulfide minerals and their purity, which was 95.1 and 78 per cent, respectively. Then, using a Magotteaux Mill (Greet *et al*, 2004), operating at 55 rev/min and with a targeted grind size of 60 per cent passing 75 µm, parallel experiments were carried out using FS, 21 per cent Cr, and ceramic media. With regards to the water type, DI and 5SPW were used (Corin *et al*, 2011; Manono *et al*, 2018; Wiese *et al*, 2005). After milling, the slurry was transferred to a 4.5 L bottom driven Magotteaux flotation cell, operating at 1100 rev/min. The amount of ethylenediaminetetraacetic acid (EDTA) extractable iron in the slurry entering the flotation cell was determined by Inductively Coupled Plasma Optical Emission Spectroscopy (ICP-OES). Reagents added to the cell included 100 g/t sodium isobutyl xanthate (SIBX) collector and 60 g/t DOW 200 frother. Aeration was initiated at 12 L/min, and concentrates were collected after 2, 6, 12, and 20 min: with the systematic scraping of loaded froth at 15 sec intervals. Fe/Pb in the dried and weighed feed, concentrates and tailings solids was measured by X-ray Fluorescence Spectroscopy (XRF). The error values associated with the experiments for each media type were determined and presented accordingly as error bars.

RESULTS AND DISCUSSION

Solids and water analysis

Figure 1 compares solids to water recovery for pyrite and galena under all milling conditions.

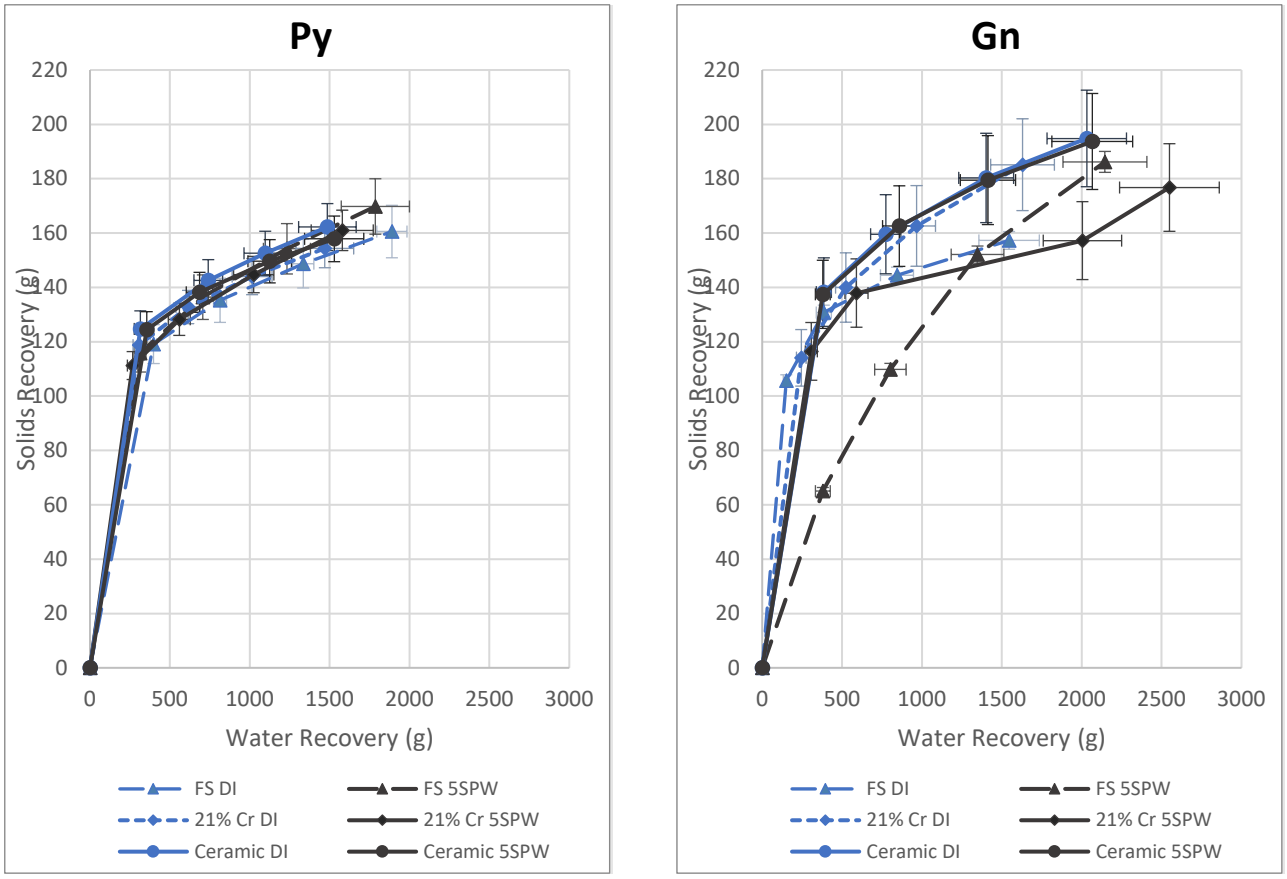

FIG 1 – Comparison of solids to water recovery in the flotation of Py versus Gn for different media and water types.

While slight variance is noted for the solids and water recoveries in Py flotation, more water is recovered when milling with FS under both water types. In the case of Gn, FS at 5SPW shows distinctly lower solids and water recoveries at the beginning of flotation. The higher ionic strength, 5SPW, impacts overall water recoveries for all milling media types.

Concentrate grade and recovery analysis

The water sustainability of the process lies in recycling water into the system, starting in the mill. However, there must be evidence that the recovery of values is not affected to consider such. Figure 2 shows the grades versus recoveries for Py and Gn; Py indicates an impact of milling media type on recovery and, to a lesser extent, grade. Ceramic media gave the best recovery and grade regardless of water type. Gn shows that as one increases the nobility of the media, the recovery increases and the grade shows the same trend, except at 5SPW, where both 21 per cent Cr and ceramic media show the same final grade.

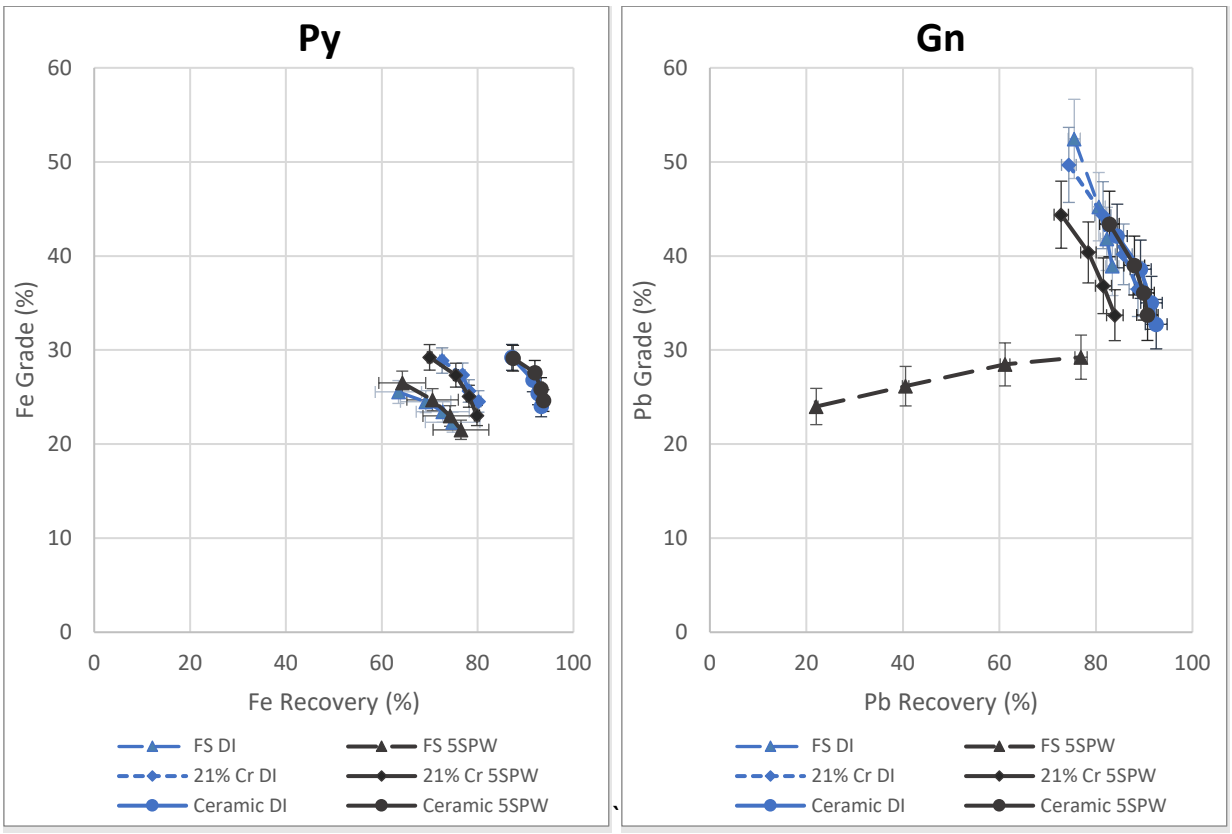

FIG 2 – Grade-recovery plots for Py and Gn.

Dissolution of Fe into the water phase

Fe in the aqueous phase may originate from dissolution reactions related to the mill shell, media, and minerals. No-ore milling tests using ceramic media estimated the mill shell contribution, while no-ore tests using 21 per cent Cr and FS estimated the mill shell and media contributions. The first was deducted from the second to determine media-related Fe dissolution for FS and 21 per cent Cr media. The contribution of the minerals to the dissolved Fe could then be calculated from ore-inclusive tests. Figure 3 shows the EDTA extractable Fe in the aqueous phase versus media type for no-ore, Py and Gn cases. Such accumulation must be checked as the presence of Fe may adversely impact flotation (Bruckard *et al*, 2011; Greet, 2009; Liao *et al*, 2020; Song *et al*, 2018; Xia *et al*, 2017).

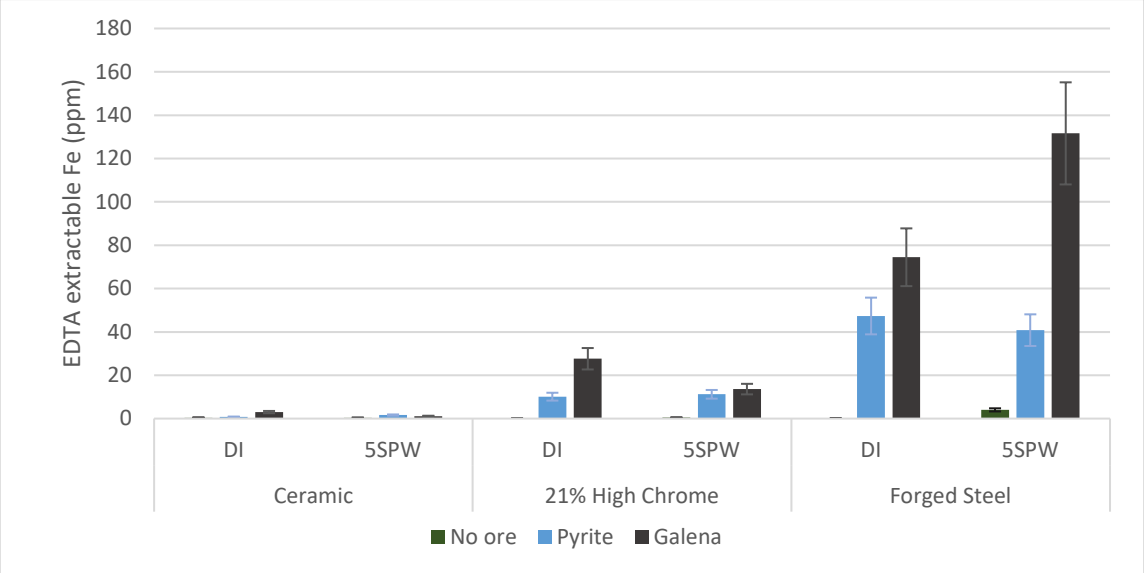

FIG 3 – Plot of EDTA extractable Fe versus media type.

The plot shows that, according to media type, susceptibility to Fe dissolution increases in the order ceramic<21 per cent Cr<FS, a trend that concurs with the decreasing media nobility. A comparable and anticipated trend is observed when milling with Py. However, media dissolution is unexpectedly highest when Gn is milled, even though it is not Fe-bearing. This observation applies across all media types, but the most significant variance is observed in runs using FS media. Figure 3 thus suggests that the presence of Pb in the system promotes Fe dissolution into the aqueous phase, and an increase in the ionic strength of the process water enhances this effect.

CONCLUSIONS

For both Py and Gn, true recovery decreased with increasing reactivity in the milling media, the rate of Fe/Pb recovery decreased, and Fe dissolution into the milling media increased. For Gn, using high ionic strength process water, 5SPW, negatively affected Pb recovery, which coincided with increased susceptibility to Fe dissolution. Therefore, further study is necessary to determine the effect of associated galvanic interactions, chemical species present (particularly Fe species), and potential contributions from mineralogy.

REFERENCES

Bruckard, W J, Sparrow, G J and Woodcock, J T, 2011. A Review of the Effects of the Grinding Environment on the Flotation of Copper Sulphides. *International Journal of Mineral Processing*, *100*(1), 1–13. https://doi.org/10.1016/j.minpro.2011.04.001

Corin, K C, Reddy, A, Miyen, L, Wiese, J G and Harris, P J, 2011. The effect of ionic strength of plant water on valuable mineral and gangue recovery in a platinum bearing ore from the Merensky reef. *Minerals Engineering*, *24*(2), 131–137. https://doi.org/10.1016/j.mineng.2010.10.015

Greet, C J, Small, G L, Steinier, P and Grano, S R, 2004. The Magotteaux Mill®: Investigating the Effect of Grinding Media on Pulp Chemistry and Flotation Performance. *Minerals Engineering*, *17*(7), 891–896. https://doi.org/10.1016/j.mineng.2004.03.003

Greet, C, 2009. The Significance of Grinding Environment on the Flotation of UG2 Ores. *Journal of the Southern African Institute of Mining and Metallurgy*, *109*(1), 31–37.

Liao, N, Wu, C, Xu, J, Feng, B, Wu, J and Gong, Y, 2020. Effect of Grinding Media on Grinding-Flotation Behavior of Chalcopyrite and Pyrite. *Frontiers in Materials*, vol *7*, p 176. https://doi.org/10.3389/fmats.2020.00176

Manono, M, Corin, K and Wiese, J, 2018. Perspectives from Literature on the Influence of Inorganic Electrolytes Present in Plant Water on Flotation Performance. *Physicochemical Problems of Mineral Processing*, *54*.

Song, Z G, Corin, K C, Wiese, J G and O'Connor, C T, 2018. Effect of Different Grinding Media Composition on the Flotation of a PGM Ore. *Minerals Engineering*, *124*, 74–76. https://doi.org/10.1016/j.mineng.2018.05.014

Wiese, J, Harris, P and Bradshaw, D, 2005. The Influence of the Reagent Suite on the Flotation of Ores from the Merensky Reef. *Reagents'04*, *18*(2), 189–198. https://doi.org/10.1016/j.mineng.2004.09.013

Xia, L, Hart, B, Chen, Z, Furlotte, M, Gingras, G and Laflamme, P, 2017. A TOF-SIMS Investigation on Correlation Between Grinding Environments and Sphalerite Surface Chemistry: Implications for Mineral Selectivity in Flotation. *Surface and Interface Analysis*, *49*(13), 1397–1403.

Further investigations into the relationship between the non-ideal behaviour of a particle-collector aggregate as determined using partial molar excess Gibbs energy and its hydrophobicity

C T O'Connor[1] and K C Corin[2]

1. Professor, Centre for Minerals Research, Department of Chemical Engineering, University of Cape Town, Cape Town 7701, South Africa. Email: Cyril.oconnor@uct.ac.za
2. Associate Professor, Centre for Minerals Research, Department of Chemical Engineering, University of Cape Town, Cape Town 7701, South Africa. Email: Kirsten.corin@uct.ac.za

ABSTRACT

In recent years it has been shown that the concept of using partial molar excess Gibbs energy ($\bar{G}^{ex}$) to explain the behaviour of collectors in the recovery of minerals can be usefully applied to explain flotation performance. Fundamentally this is because hydrophobicity of a mineral particle on which a collector is adsorbed may be strongly related to the fact that the alkyl chain associated with the collector behaves in the same way as any hydrocarbon would in an aqueous medium. This hydrocarbon-water system represents a classical non-ideal mixture, and such mixtures are quantified thermodynamically by determining the activity coefficient of the hydrocarbon moiety of the collector and hence its $\bar{G}^{ex}$ in the mixture. It has been shown that $\bar{G}^{ex}$ is a more rigorous indicator of the contributions of various alkyl groups of a collector than HLB (Corin and O'Connor, 2014) and was also able to explain aspects of froth behaviour (Harris and O'Connor, 2017) and hydrophobicity (O'Connor, 2021). The present paper is aimed at extending the above concepts in two different ways. Firstly, a study is undertaken of a range of results previously reported in which various reagents containing different alkyl groups were analysed in terms of their effect on contact angle and their performance as flotation reagents in terms of recovery. These results sustain the previous observations that there is a robust positive relationship between hydrophobicity as indicated by flotation recovery and contact angle and $\bar{G}^{ex}$ of the alkyl group associated with the collector. Secondly, on the basis of the observation that increases in $\bar{G}^{ex}$ are indicative of increases in the hydrophobicity of the mineral particle-collector aggregate, a study was undertaken to examine the effect of ions typical of electrolytes in water as well as the effect of the presence of alcohols and of pH on $\bar{G}^{ex}$ of the collector alkyl group. In the former two instances the absence of any correlation between $\bar{G}^{ex}$ and recoveries supported the proposition of the respective authors of these studies that the major effect of these electrolytes and added alcohols may be on particle–bubble attachment rather than on the hydrophobicity of the mineral/collector in the aqueous system. On the other hand, the effect of pH on $\bar{G}^{ex}$ correlated reasonably well with changes reported in the literature on the effect of pH on recovery and contact angle.

INTRODUCTION

As is well known the main purpose of using a collector in the flotation of ores is to render the mineral particles which are to be recovered hydrophobic. Classically contact angle has been used to indicate hydrophobicity and there is voluminous literature on the measurement of contact angles as well as the relationship between contact angle and recovery (eg Fuerstenau, Harper and Miller, 1970; Bogdanov *et al*, 1957). However, it has been pointed out (Nagaraj and Ravishanker, 2007) that although contact angles in single mineral systems have been correlated with mineral flotation, they are poor predictors of flotation performance in real systems with complex mineralogy. There have also been attempts to use the concept of the hydrophilic-lipophilic balance (HLB) number to characterise the hydrophobicity imparted by reagents (eg Zhang *et al*, 2012; Laskowski, 2003; Pugh, 2007). The HLB number represents an empirical numerical correlation of the emulsifying and solubilising properties of different surface-active agents (Davies, 1957). However, in its original context the HLB number was an early attempt to show how the molecular structure is related to hydrophobicity. Modern thermodynamics is now far advanced in this regard through the determination of the activity coefficient or $\bar{G}$ex as the more appropriate way in which to define the behaviour of molecules in a non-ideal solution. In that regard the hydrocarbon associated with the collector adsorbed onto the mineral particle in a pulp and its water environment represents a classical non-ideal solution (Corin and O'Connor, 2014).

In a previous set of publications (Harris and O'Connor, 2017; O'Connor, 2021) the authors have shown how the use of thermodynamics to determine the behaviour of a non-ideal solution as indicated by $\overline{G}^{ex}$ of, for example, a frother molecule or of the hydrocarbon moiety of a collector is related to the behaviour of a frother or collector-mineral aggregate in a flotation system. The present paper further interrogates the hypothesis that it is the non-ideality of the hydrocarbon-water system, as indicated by the $\overline{G}$ex of the hydrocarbon moiety of the collector, which provides the driving force to transfer the mineral particle, on which the collector is adsorbed, from the water (liquid phase) to the bubble (gas phase) and the greater the $\overline{G}^{ex}$ the greater is that driving force. Given that the hydrophobicity of the particle, especially in a microflotation cell, is reflected in its recovery there should be a robust relationship between $\overline{G}^{ex}$ and recovery. This paper has also investigated the extent to which the $\overline{G}^{ex}$ is affected by factors such as pH, presence of other species such as electrolytes or alcohols in the water, and whether these changes can be used to interpret previously reported results on the influence these factors have on flotation recoveries.

METHODS TO ESTIMATE ACTIVITY COEFFICIENTS AND PARTIAL MOLAR EXCESS GIBBS ENERGY

As indicated above the hydrocarbon associated with a collector molecule adsorbed onto a mineral particle when located in an aqueous environment represents a classical thermodynamically non-ideal solution. Such non-ideal solutions are quantified by determining the activity coefficient, and subsequently the $\overline{G}^{ex}$ of the hydrocarbon at a given molar concentration. The collector molecule is adsorbed onto the mineral particle via a chelating ligand such as typically represented by a thiol end group. The hydrocarbon is associated with the collector in many instances via an oxygen atom (eg xanthates, aminothiophenol etc) and thus using the alcohol of the relevant alkyl group is an appropriate proxy for the behaviour of the hydrocarbon group of the collector.

There are many methods described in the literature to estimate activity coefficients. Of the more modern methods the UNIFAC (Uniquac Functional-group Activity Coefficient) method (eg Fredenslund, Gmehling and Rasmussen, 1977; Sandler, 2006) has been widely used. More recently the COSMO-SAC model (Xiong, Sandler and Burnett, 2014) has been used. There are numerous papers in the literature comparing these approaches and some suggest that COSMO-SAC may be slightly superior for aqueous systems (eg Gerber and Soares, 2010). In any event the activity coefficient is an indicator of the combined effects of properties such as total molecular surface area, molecular volume, molar volume and molecular weight of the constituent functional groups for each of the compounds. In determining activity coefficients using COSMO-SAC the temperature was set at 298 K, total pressure at 0.1 MPa and, unless otherwise stated, the mole fraction of the collector at 0.0001 which equates fairly well to typical concentrations used in industrial flotation plants. The activity coefficient in turn is used to determine the $\overline{G}^{ex}$, the excess value being the difference between the value for a real as opposed to an ideal mixture. The most useful excess thermodynamic property is the $\overline{G}^{ex}$ since this term incorporates the enthalpic and entropic contributions. The $\overline{G}^{ex}$ is calculated using its relationship to the activity coefficient, γ_i, *viz*.

$$\overline{G_i}^{ex} = RT \ln \gamma_i (T,P,\underline{x}) \quad (1)$$

where R is the universal gas constant and T is the absolute temperature. It is important to note that the $\overline{G}^{ex}$ is not the same as the surface free energy (eg van Oss and Good, 1988) or the free energy of collector adsorption as expressed by, for example, the Stern-Grahame equation (eg Fuerstenau, Harper and Miller, 1970).

As mentioned in the introduction the various experimental values used in this investigation were obtained from the published literature. The source of the data is indicated in the references in the relevant sections. Unless otherwise stated the flotation recovery data were obtained in microflotation cells.

RESULTS AND DISCUSSION

Further evidence that partial molar excess Gibbs energy ($\bar{G}^{ex}$) is indicative of hydrophobicity as indicated by flotation recovery

As previously reported (O'Connor, 2021) flotation recovery in a microflotation cell is an excellent indicator of the extent to which a mineral particle has been rendered hydrophobic since it allows for all the variables resulting from a complex mineralogy of the particle and simply indicates the propensity of the collector-particle aggregate to attach to a bubble and ultimately to report to the concentrate. McFadzean, Castelyn and O'Connor (2012) in a study of the flotation of galena using various thiol collectors have shown that, in the case of xanthates, sodium ethyl xanthate showed recovery of 52.5 per cent and the iso-butyl equivalent a recovery of 85.0 per cent. Similar tests using ethyl and iso-butyl dithiophosphate had recoveries of 51.8 per cent and 72.0 per cent respectively. The $\bar{G}$ex for the ethyl and isobutyl chains are 4.65 kJ/mol and 12.06 kJ/mol respectively. These results again provide evidence that the increase in recovery can be related to the increased hydrophobicity imparted by the iso-butyl compared to the ethyl hydrocarbon as indicated by the greater values of $\bar{G}^{ex}$ or the greater degree of non-ideality of the hydrocarbon-water system. Similar effects have been shown in a study of the flotation of pyrite using, respectively, ethyl, isobutyl and amyl xanthates (Yang *et al,* 2018).

Sahoo *et al* (2016) reported on the flotation of quartz using ionic liquids with different functional groups and varying alkyl chain lengths. They concluded that the flotation results imply that the alkyl chain length plays a major role in determining the floatability of the quartz compared to the interaction pattern of the ionic liquid with the quartz. This can be confirmed by applying the concept of $\bar{G}^{ex}$ to the flotation results. Table 1 shows the values of the $\bar{G}^{ex}$ for the respective alkyl groups for each ionic liquid (as determined for the alcohol of that alkyl group) and the recoveries of quartz (Figure 1).

TABLE 1

Correlating quartz recovery and $\bar{G}^{ex}$ for various ionic liquids.

Reagent	Activity coeff.	$\bar{G}^{ex}$ (kJ/mol)	Quartz recovery (est. from Figure 3 of reference)
1-methyl-3-octyl imidazolium chloride	123	11.92	20
1-n-decyl-3-methyl imidazolium tetrafluoroborate	273	13.89	68
1 n hexyl 3 methyl imidazolium chloride	47	9.54	12
Cetyl pyridinium bromide	1393	17.93	100

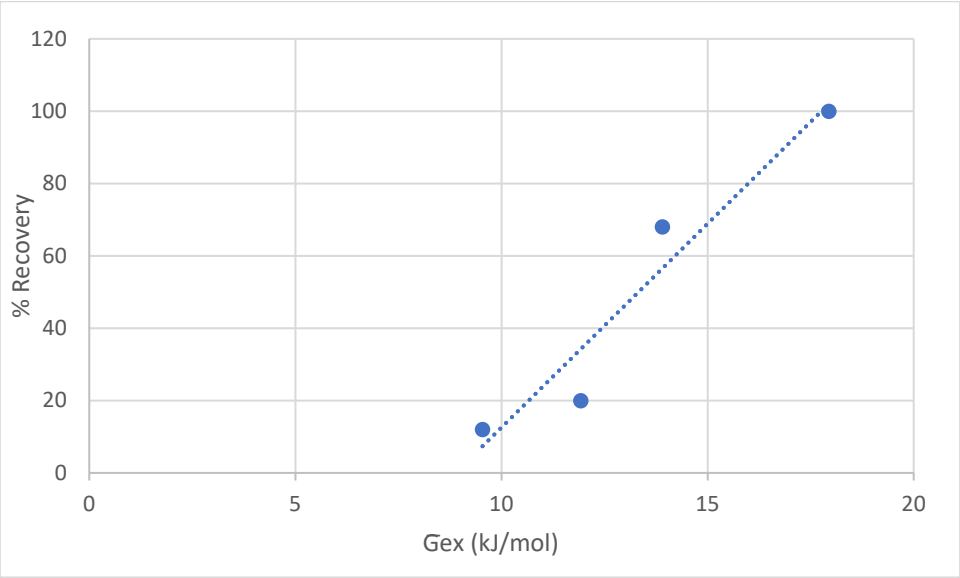

FIG 1 – Quartz recovery (per cent) versus $\bar{G}^{ex}$ (kJ/mol) for various ionic liquids used in flotation (R^2 = 0.93) (Sahoo *et al*, 2016).

In a similar context it is of interest to use results reported by Marabini *et al* (2007) studying the effect of changing structures of various collectors, on the recoveries of Zn (mainly smithsonite) and Pb (mainly cerrusite). In one set of studies the effect of changing the alkyl group on aminothiophenol reagents for which the core structure is shown in Figure 2 and the variations in the alkyl group, R, bonded to the oxygen atom. Reagents in which the alkyl group R ranged from methoxy (CH_3O) to hexyloxy ($C_6H_{13}O$) were used in the flotation tests.

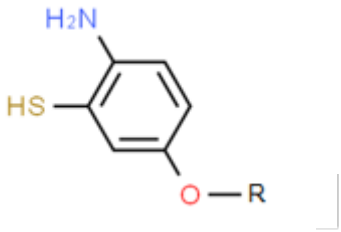

FIG 2 – Basic structure of aminothiophenol ion (Marabini *et al,* 2007).

The flotation tests were carried out in a standard laboratory batch flotation cell which, for the present purposes, is less ideal than using a microflotation cell. The results of Zn recoveries are shown in Figure 3.

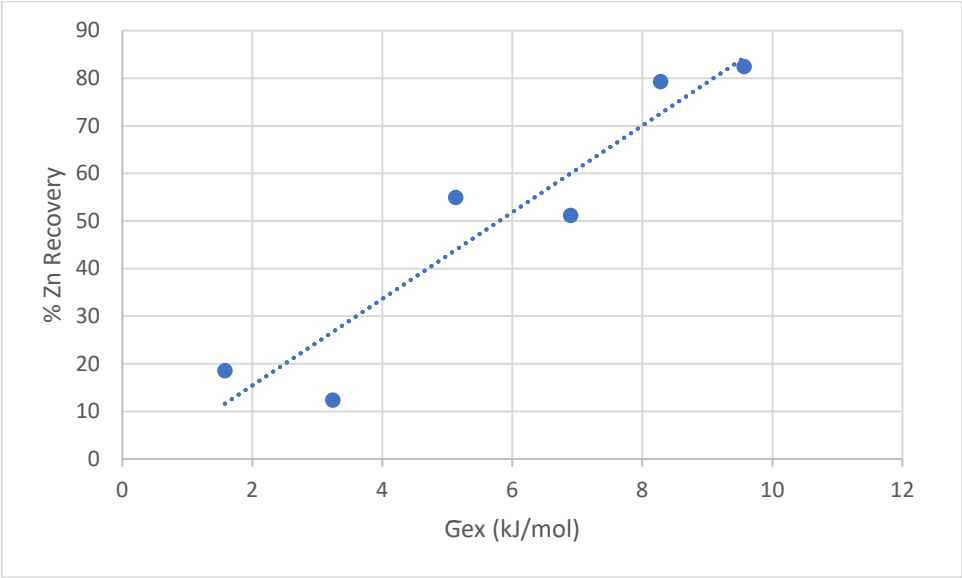

FIG 3 – Relationship between Zn recoveries using C1 to C6 alkoxy aminothiophenols and the $\bar{G}^{ex}$ of the respective alkoxy groups (R^2 = 0.88) (Marabini *et al,* 2007).

Figure 3 shows that there is a clear trend in the relationship between the recovery of Zn and the $\bar{G}^{ex}$ of the various alkoxy chain lengths. It must be emphasised that the chelating action of the backbone structure (Figure 2) of the aminophenol on the Zn mineral is a constant in all cases.

Further investigations into the relationship between contact angle and partial molar excess Gibbs energy ($\bar{G}^{ex}$)

In order to investigate further the previously reported relationship between $\bar{G}^{ex}$ and contact angle, two other studies were considered. Han *et al* (2020) in reporting on the effect of alkyl chain length on bubble particle attachment using galena as a model mineral presented results of the contact angles obtained using ethyl, propyl, butyl and amyl xanthates. Correlating these values (65°, 71°, 77° and 86°) with their equivalent $\bar{G}^{ex}$ (3.23, 5.12, 6.74, 8.28 kJ/mol respectively) gave a linear relationship with an R^2 value of 0.98. Fosu, Skinner and Zanin (2015) have provided contact angles for SIPX and PAX (60°, 67°) using sphalerite as a test mineral which have almost the same relative relationship as the $\bar{G}^{ex}$ values (7.47, 8.28 kJ/mol).

Effect of electrolytes on partial molar excess Gibbs energy ($\bar{G}^{ex}$)

As shown above, as well as in studies previously referred to, it now appears to be reasonable to hypothesize that $\bar{G}^{ex}$ is a good indicator of the hydrophobicity of a mineral-collector aggregate both in terms of recovery, especially in a microflotation cell, and of contact angle. On that basis it was decided to investigate whether the presence of electrolytes had any significant effect on $\bar{G}^{ex}$. If such an effect was observed, it could be deduced that changes in flotation recovery in the presence of such electrolytes could be due to their effect on the non-ideal behaviour of the alkyl group of the collector in the aqueous environment. It should be noted that in this section the activity coefficient of the electrolyte or of the solvent, water, is not being calculated but rather its influence on the activity coefficient and $\bar{G}^{ex}$ of the hydrocarbon associated with the collector molecule.

To investigate this hypothesis, data generated by October *et al* (2020) on the effect of the presence of electrolytes on flotation recoveries as well as on bubble-particle attachment was used. In this study it was reported that the presence of nitrate and sulfate ions resulted in a significant increase in recovery of both galena and chalcopyrite.

The effect of the presence of these ions on $\bar{G}^{ex}$ was investigated by using H_2SO_4 (sulfate ions) and HNO_3 (nitrate ions) at constant concentration for a range of xanthates from ethyl to pentyl. The effect of the presence of these ions on $\bar{G}^{ex}$ is shown in Table 2.

Table 2

Effect of presence of HNO_3 and H_2SO_4 on $\bar{G}^{ex}$ of various alkyl groups represented by their respective alcohols.

Alkyl group of xanthate	$\bar{G}^{ex}$ (kJ/mol) in presence of HNO_3	$\bar{G}^{ex}$ (kJ/mol) in presence of H_2SO_4	$\bar{G}^{ex}$ (kJ/mol) in absence of acid
Ethyl	4611	4616	4650
Propyl	7725	7736	7774
1 butyl	10 718	10 732	10 774
2-butyl	11 865	11 881	11 908
isobutyl	11 988	12 021	12 058
1-pentyl	13 877	13 904	13 950

As expected, the values of $\bar{G}$ex in the absence of acid increased as the alkyl chain length increased as has been previously reported. However, it is clear that the presence of SO_4^{2-} and NO_3^- ions had hardly any effect on the values of $\bar{G}^{ex}$ thus implying, in terms of the underlying hypothesis, that these ions hardly affected the hydrophobic character of the mineral-collector aggregate. These results are therefore consistent with the proposition by these authors that the main effect of the presence of the electrolytes was on the extent of bubble-particle attachment.

Effect of pH on partial molar excess Gibbs energy ($\bar{G}^{ex}$)

In a manner similar to the behaviour of the electrolytes the role that pH has on hydrophobicity and hence recovery can be investigated using $\bar{G}^{ex}$. In a study of the effect of pH on the contact angle and recovery in a quartz/dodecylamine (DDA) system it was shown that as pH increased from 2 to 10 the contact angle increased from about 20° to >80° (Fuerstenau, 1957) In order to investigate whether this effect was also observed in the values of $\bar{G}^{ex}$, $\bar{G}^{ex}$ values for DDA were determined at increasing mole fractions of H_2SO_4 of 0.15, 0.1, 0.05 and 0.005 while maintaining a constant mole fraction of DDA at 0.05. These changes in acid concentrations equate to pH changes of approximately 3.4, 3.6, 3.9 and 4.9. At these pH and acid concentrations the values of $\bar{G}^{ex}$ are 9.69, 12.93, 13.56 and 15.07 kJ/mol respectively. The increase in the values of $\bar{G}^{ex}$ as pH increased are consistent with increasing hydrophobicity (microflotation recovery) and contact angles reported in the reference above. Although this result does not explain fundamentally the effect of changing pH, *viz* H^+ / OH^- ratio, on the behaviour of the alkyl group it does infer that, in terms of the underlying hypothesis, changes in pH do seem to have a direct impact on the hydrophobicity of the mineral-collector aggregate.

Effect of alcohol species on partial molar excess Gibbs energy ($\bar{G}^{ex}$)

It has been previously shown that many of the functions of a frother such as their effect on froth height, surface tension and critical coalescence concentration respectively are strongly related to the $\bar{G}^{ex}$ of the alkyl groups associated with the reagent. It was demonstrated that it was possible to reasonably predict the performance of frothers based on the value of their $\bar{G}^{ex}$ (Harris and O'Connor, 2017). Frothers are usually alcohols and there are numerous reports on the role which the addition of frothers may have on flotation behaviour. Hence it is of interest to investigate whether the presence of an alcohol may influence the $\bar{G}^{ex}$ of the collector being used given that the hypothesis proposed in the present paper is that the absence of such an effect would point to the role of the alcohol being other than influencing the hydrophobicity of the collector. In the present instance data generated by Pienaar *et al* (2019) on the effect of adding hexanol to SEX on the recovery of galena in a batch flotation cell showed that the effect of adding hexanol was to increase the first order flotation rate constant from 0.091 min^{-1} to 0.190 min^{-1} with the recovery after 6 min increasing from ~40 per cent to 69 per cent. This addition of hexanol, not surprisingly, resulted in a decrease in $\bar{G}^{ex}$ of the ethyl group from 3.23 kJ/mol to 1.23 kJ/mol since hexanol as the third phase in this non-ideal solution is more amenable to the presence of the ethyl group associated with the SEX. It can therefore be deduced that this reduction in $\bar{G}^{ex}$ on the addition of hexanol suggests that the hydrophobicity is, if

anything, reduced and that hence the increase in recovery when hexanol was present is arguably related to its effect on particle-bubble attachment phenomena at the air-water interface as was indeed proposed by these authors.

CONCLUSIONS

Previous publications by the authors and colleagues have suggested that, given that a mineral particle, on which a collector containing a hydrocarbon moiety is adsorbed, when present in an aqueous system such as a flotation pulp, such a system represents thermodynamically a classical non-ideal system. Such systems are characterised by activity coefficients and hence $\overline{G}^{ex}$. This led to the hypothesis that there could be a relationship between the $\overline{G}^{ex}$ of the hydrocarbon moiety associated with the adsorbed collector and its hydrophobicity as indicated by, for example, recovery in a microflotation cell or contact angle. The present paper provides further evidence that continues to sustain this hypothesis. It is shown that the effect of pH on hydrophobicity as indicated by $\overline{G}^{ex}$ is consistent with previously reported contact angle and recovery results in a quartz/DDA system. In a further development of this hypothesis, it has been shown that when factors such as the presence of electrolytes or alcohols in the flotation pulp are investigated there was no indication that there was any increase in the hydrophobicity of the mineral-collector aggregate as indicated by $\overline{G}^{ex}$ and recovery and that hence it may be reasonably deduced that the changes observed in flotation recovery in such cases are related to other phenomena such as bubble-particle attachment.

REFERENCES

Bogdanov, O S, Hainman, V Y, Podnek, A K and Jarvis, N A, 1957. Investigation of the action of modifying agents in flotation. In *Progress in Mineral Dressing*. Stockholm: Transactions of the International Congress on Mineral Dressing, p 479.

Corin, K C and O'Connor, C T, 2014. A proposal to use excess Gibbs energy rather than HLB number as an indicator of the hydrophilic–liphophilic behavior of surfactants, *Minerals Engineering,* 58,17–21.

Davies, J T, 1957. Gas/Liquid and Liquid/Liquid Interfaces, in *Proceedings of the Second International Congress of Surface Activity*, Butterworths, London. 1, pp 426–438.

Fosu, S, Skinner, W and Zanin, M, 2015. Detachment of coarse composite sphalerite particles from bubbles in flotation: Influence of xanthate collector type and concentration, *Minerals Engineering,* 71, 73–84.

Fredenslund, A, Gmehling, J and Rasmussen, P, 1977. Vapor-liquid equilibria using UNIFAC: a group contribution method. *Elsevier Scientific Publishing Company*, Amsterdam, Oxford, New York.

Fuerstenau, D W, 1957. Correlation of contact angles, adsorption density, zeta potentials and flotation rate. *Transactions of the Metallurgical Society of AIME,* 208: 1365–1367.

Fuerstenau, M C, Harper, R W and Miller, J D, 1970. Hydroxamate vs fatty acid flotation of iron oxide. *Transactions of the Metallurgical Society of AIME,* 247: 1, 69.

Gerber, P and Soares, R P, 2010. Prediction of Infinite-Dilution Activity Coefficients Using UNIFAC and COSMO-SAC Variants. *Industrial & Engineering Chemistry Research,* 49, 16, 7488–7496.

Han, S, Nguyen, A V, Kim, K, Park, J and You, K, 2020. Measurements and analysis of xanthate chain length effect on bubble attachment to galena surfaces, *Minerals Engineering,* 159, 106651.

Harris, M C and O'Connor, C T, 2017. Characterization of frothers and their behavior using partial molar Excess Gibbs energy, *International Journal of Minerals Processing,* 158, 63–67.

Laskowski, J S, 2003. Fundamental properties of flotation frothers, in *Proceedings of the 22nd International Mineral Processing Congress,* Cape Town, South Africa, pp 788–797.

Marabini, A M, Ciriachi, M, Plescia, P and Barbaro, M, 2007. Chelating reagents for flotation, *Minerals Engineering,* 20, 1014–1025.

McFadzean, B, Castelyn, D G and O'Connor, C T, 2012. The effect of mixed thiol collectors on the flotation of galena, *Minerals Engineering,* 36–38, 211–208.

Nagaraj, D R and Ravishanker, S A, 2007. Flotation Reagents – A critical overview from an industry perspective, in *Froth flotation: A century of innovation* (M Fuerstenau, G Jameson and R-H Yoon, eds.) p 390 (The Society for Mining, Metallurgy, and Exploration Inc: Littleton).

O'Connor, C T, 2021. Investigating the use of excess Gibbs energy to predict the hydrophobicity of a mineral treated with a collector, *Minerals Engineering,* 160, 106692.

October, L L, Corin, K C, Manono, M M, Schreithofer, N and Wiese, J G, 2020. A fundamental study considering specific ion effects on the attachment of sulfide minerals to air bubbles, *Minerals Engineering,* 158, 106313.

Pienaar, D, Jordaan, T, McFadzean, B and O'Connor, C T, 2019. The synergistic interaction between dithiophosphate collectors and frothers at the air-water and sulphide mineral interface, *Minerals Engineering,* 138, 125–132.

Pugh, R J, 2007. The Physics and Chemistry of Frothers. in *Froth flotation: A century of innovation*. (M Fuerstenau, G Jameson and R-H Yoon, eds.) pp 359–382 (The Society for Mining, Metallurgy, and Exploration Inc: Littleton).

Sahoo, H, Rath, S, Das, B and Mishra, B, 2016. Flotation of quartz using ionic liquid collectors with different functional groups and varying chain lengths, *Minerals Engineering,* 95, 107–112.

Sandler, S I, 2006. *Chemical, Biochemical and Engineering Thermodynamics*. 4th Ed, John Wiley & Sons. Springer Series in Surface Sciences, 51.

van Oss, C J and Good, R J, 1988. On the mechanism of hydrophobic interactions, *Journal of Dispersion Science and Technology,* 9, 355–362.

Xiong, R, Sandler, S I and Burnett, R I, 2014. An Improvement to COSMO-SAC for Predicting Thermodynamic Properties, *IEC Research,* 53 (19) 8265.

Yang, X, Albijanic, B, Liu, G and Xhou, Y, 2018. Structure–activity relationship of xanthates with different hydrophobic groups in the flotation of pyrite, *Minerals Engineering,* 125, 155–164.

Zhang, W, Nesset, J E, Rao, R and Finch, J A, 2012. Characterising frothers through critical coalescence concentration (CCC) 95-Hydrophile-Lipophile balance (HLB) relationship, *Minerals,* 2, 208–227.

Comparison of bubble coalescence time and thin film balance techniques in studying the interaction of flotation reagents and salt

Y Pan[1], G Bournival[2] and S Ata[3]

1. AAusIMM, PhD student, School of Minerals and Energy Resources Engineering, University of New South Wales, Sydney NSW 2052. Email: yueyi.pan@unsw.edu.au
2. MAusIMM, Lecturer, School of Minerals and Energy Resources Engineering, University of New South Wales, Sydney NSW 2052. Email: g.bournival@unsw.edu.au
3. MAusIMM, Associate Professor, School of Minerals and Energy Resources Engineering, University of New South Wales, Sydney NSW 2052. Email: s.ata@unsw.edu.au

ABSTRACT

A custom-made set-up that measures bubble coalescence time and the thin film balance (TFB) technique were used to explore the role of residual xanthate (potassium amyl xanthate, PAX) and salt (NaCl) on the adsorption of two frothers (methyl isobutyl carbinol-MIBC, and di-propylene glycol-DPG) at the air-water interface. This paper is primarily focused on the comparison of these two techniques in studying the interaction between the flotation reagents and salt emphasizing their capabilities and limits. The results from the coalescence rig showed that the presence of PAX improved the stability of bubbles in both frother solutions and led to a bubble coalescence inhibition at 50–500 ppm DPG. These measures were compared with the results from the TFB. Findings from the TFB were overall in good agreement with the bubble coalescence time, but a higher stability level was observed in thin films under the same condition. The effect of salt on the frother and PAX mixture was also explored, and the results showed an adverse impact of the salt on the interaction of frother and PAX with both techniques. However, variations were found between them in some cases. The TFB is much more sensitive to the presence of dissolved gas and oil droplets.

INTRODUCTION

The stability of thin films and bubbles in surfactant solutions can be explored through various techniques. Bubble coalescence time, film lifetime and thickness are measured in order to demonstrate the adsorption efficiency of the surfactant at the air-water interface, and surfactant impact on bubble stability (Castro *et al*, 2012; Cho and Laskowski, 2002; Karakashev and Nguyen, 2007). In flotation practice, bubble stability plays an important role in the bubble-particle attachment; meanwhile, the property of thin liquid films trapped between the bubbles directly affects the bubble and foam stability.

The bubble coalescence time technique relies on the interaction of air bubbles. Two bubbles of similar size are generated at the tips of adjacent capillaries and brought together until they are in close contact. The time for the two bubbles to merge is referred to as coalescence time. Longer merging times mean higher bubble stability. The coalescence time is closely related to the adsorbed surfactant molecules on the bubble surface (Cho and Laskowski, 2002; Craig, 2004; Firouzi *et al*, 2015; Grau and Laskowski, 2006). The bubble coalescence studies related to flotation reagents, primarily focus on the frothers and salts, while other reagents (eg, collectors) are largely ignored. Pan *et al* (2021) found that the xanthate ions (PAX) can prolong the lifetime of bubbles in the MIBC solutions and cause significantly high bubble stability at certain concentrations.

The thin film balance technique (TFB) studies the thinning of the films formed between the two tips of a double concave drop, which is similar, if not identical, to the thin liquid film formed between two bubbles. The film properties such as film lifetime, equilibrium and rupture thickness, are highly sensitive to the presence of chemicals (Karakashev *et al*, 2008a; Manev and Pugh, 1992; Wang and Yoon, 2006). The technique is therefore used to investigate the kinetics of film thinning to get insights into foam stabilisation mechanism (Wang and Yoon, 2005). Few studies have investigated the xanthate effect on the film surfaces. Manev and Pugh (1992) studied the influence of potassium ethyl xanthate (KEX) on the non-ionic surfactant adsorption, ie Dowfroth 200 and polyoxypropylene alkyl ethers ($C_{12}(EO)_5$) at the air-water interface by measuring the equilibrium film thickness using a TFB found that KEX had a negative impact on the surfactant-adsorbed films.

The interactions among the collector and salt at the air-water interfaces are inevitable with the co-existence of reagents and salts in the flotation pulp. The authors have previously investigated the interaction among collector, salt, and frothers and their impact on the bubble stability via various techniques (Pan *et al*, 2021, 2022a, 2022b, 2022c). An extension of the previous work and using the same system, this study provides a close look at the findings from the bubble coalescence rig and TFB and assesses the capabilities of the techniques and the meaningfulness of the results they provide.

EXPERIMENTAL

Materials

Methyl isobutyl carbinol (MIBC) and Di Polypropylene Glycol (DPG) were used as frothers, provided by Aldrich (≥98 per cent) and Sigma–Aldrich (≥99 per cent), respectively. MIBC and DPG were selected to represent two frother families, ie aliphatic alcohols and polypropylene glycol with a molecular weight of 102 and 134 g mol^{-1}, respectively. The collector, potassium amyl xanthate (PAX) was supplied by Tokyo Chemical Industry (>97 per cent). All the testing solutions containing PAX were pH monitored and adjusted to 9 ± 0.5 using NaOH and HCl. A cleaning solution was used for the glassware cleaning. The Milli-Q water was utilised for preparing all solutions. The laboratory room temperature was maintained at 22 ± 1.5°C.

Bubble coalescence time measurement

The bubble coalescence time was measured by observing the coalescing process of bubble pairs generated from two adjacent capillaries (Ata, 2008). Figure 1 shows the experimental set-up. Bubbles of approximately 2 mm in diameter were generated at the tip of two stainless steel capillaries in a cubic quartz cell to avoid image distortion. The capillaries were connected to two independent micro-syringe and pump systems. The bubbles were brought together gradually using a stage positioner (T-LA28A, Zaber Technologies Inc) after 10 s aging time. The coalescing process was recorded using a high-speed camera (Fastcam APX RS, Photron) at capture rates of 50–500 frames per second depending on the time required for the coalescence in different solutions. The coalescence time was defined as the time interval from the point when bubble pairs were in contact to the point where rupture of the thin liquid film takes place.

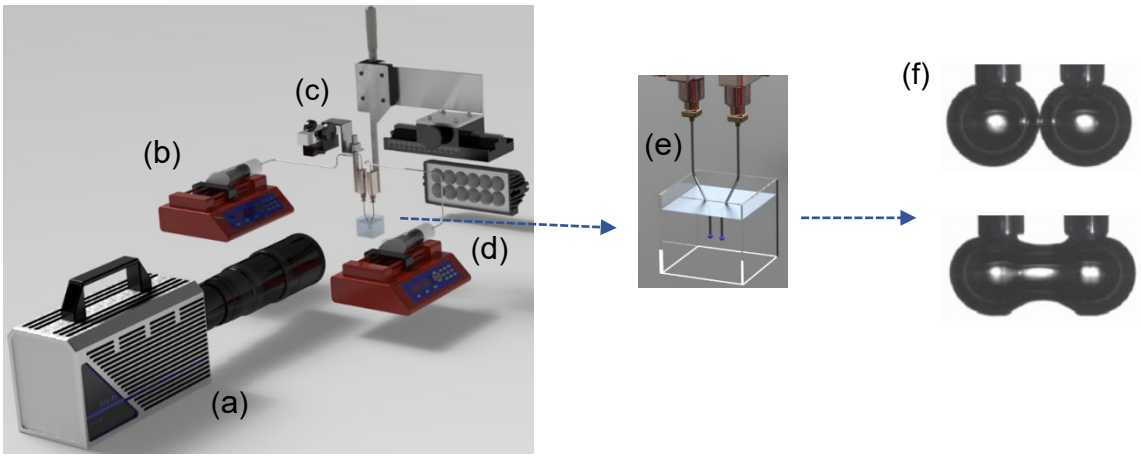

FIG 1 – Schematic of the bubble coalescence set-up: (a) CCD camera, (b) microsyringe pump, (c) stage positioners, (d) light source, (e) stainless steel capillary with bubbles generated, (f) a coalescing bubble pair.

The cleanliness of the quartz cell and capillaries was tested before taking any measurements. A coalescence time of less than 0.003 s in Milli-Q water was considered evidence of no contaminants. The lifetime of the bubbles in each solution was determined based on the average value of at least ten measurements.

Thin film measurement

The foam film was created in a Scheludko–Exerowa cell, as shown in Figure 2, where a horizontal foam film was generated.

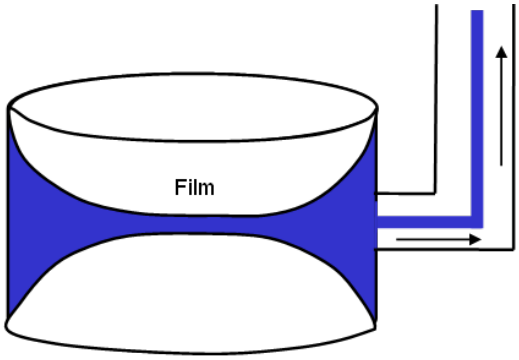

FIG 2 – Schematic diagram of Scheludko–Exerowa cell.

A droplet of the tested solution was placed inside the film holder and liquid was pumped out using an airtight micro-syringe to form a microscopic thin foam film. A small foam film was created aging for approximately 2 min to ensure the adsorption of surfactant on the film surface. The radius of the thin film was then adjusted with the micro-syringe to 200 ± 25 μm, at which the recording of the film thinning process was started.

RESULTS AND DISCUSSION

PAX impact on bubble and film stability in the frother solutions

The effect of PAX on the stability of bubbles and films created in two frother solutions (ie, MIBC and DPG) was previously investigated and reported by Pan *et al* (2021, 2022c). The concentration of PAX in the investigation was kept very low (1 ppm) to simulate the residual xanthate concentration experienced in flotation. In these studies, film and bubble stability behaviour is carefully analysed in terms of frother concentration, and possible mechanisms were provided. Here, the results of the two techniques are briefly presented and explained followed by a discussion on the comparison of the techniques emphasizing their capabilities and limits under controlled conditions.

Figure 3 presents the lifetime of thin films and bubbles generated in the MIBC solution in the absence and presence of 1 ppm PAX with respect to MIBC concentration. With the addition of 1 ppm PAX, the lifetime of bubbles in MIBC is substantially increased above 50 ppm, as clearly shown in the figure. Interestingly, a declining trend above 5×10^2 ppm is noticed in the MIBC/PAX mixture with rising MIBC concentrations, presumably due to the competitive adsorption between MIBC and PAX. Likewise, the stability of thin films in the MIBC/PAX solution strengthens with increasing MIBC concentration and the film becomes ultra-stable above 10 ppm MIBC. The observed ultra-stability of the MIBC/PAX system is likely related to the increasing electrostatic repulsion on the film surfaces. PAX may act as an electrolyte to enhance the MIBC adsorption as suggested by Manev and Pugh (1992).

From Figure 3, the improved bubble stability in the MIBC/PAX system is also observed in the thin film balance measurements with increasing MIBC concentration, but with a more drastic improvement. This is probably because of the difference between the measuring techniques, eg the approach speed and the radius of the contacting surface (Horn *et al*, 2011; Karakashev *et al*, 2008b). The approach speed in the bubble coalescence measurement refers to the bubble surface approach at a macroscopic distance, which is approximated by the capillary (holding the bubbles) moving speed. The approach speed of the film surface is very likely to be different from that of the bubble approaching speed during their contact on a microscopic scale. Though there is a lack of quantitative information on the film interface approach speed in the thin film balance measurements, the films in the Scheludko–Exerowa cell are formed at a slower and steadier rate which can lead to the variation in bubble stability level. Also, there are possible variations between the radius of thin films between the bubble pair in the coalescence rig and that in the TFB measurements. Consequently, the number

of surfactant molecules adsorbed on the film surface could be different, causing a varied stability level found in the two techniques.

On the other hand, the bubble stability in the MIBC/PAX solution exhibits a declining trend above 5×10^2 ppm MIBC, while the film stability at the corresponding conditions still establishes ultra-stability. With higher MIBC concentrations, the varied response of these two techniques indicates that the surfactant adsorption on the bubble surfaces is more disordered than that on the film surfaces. Given the contacting surfaces in these techniques, the lateral diffusion of the surfactant molecules may be more advantageous and stable during the surfactant adsorption on the film surfaces in the TFB measurement. In the bubble coalescence measurement, however, the vertical diffusion of the surfactant molecules on the contacting bubble surfaces may be influenced by gravity, causing unorganised and less efficient adsorption (Eriksson and Ljunggren, 1989; Wang and Yoon, 2005).

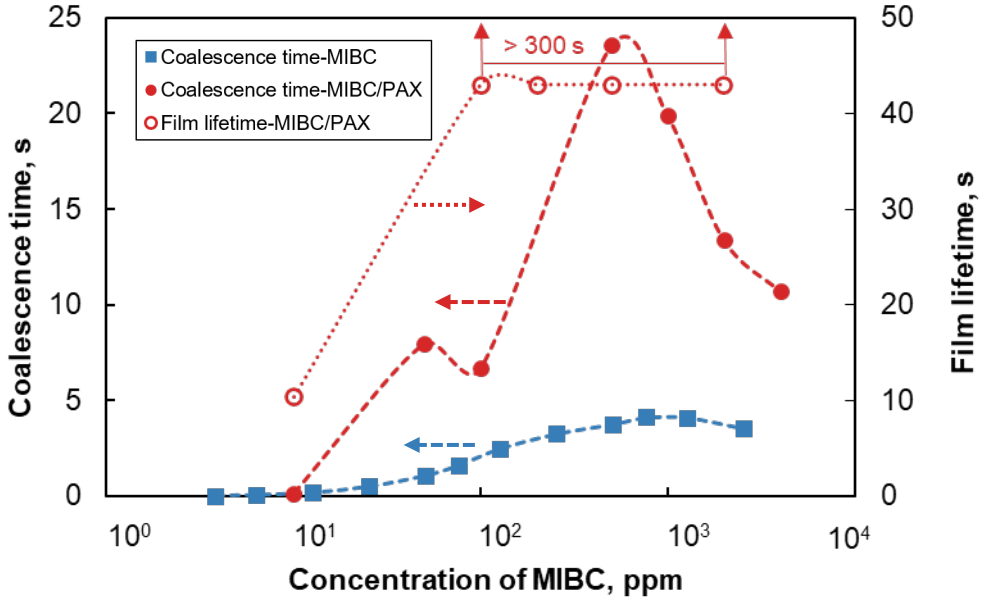

FIG 3 – Effect of MIBC concentration on the lifetime of bubbles and films in MIBC only and MIBC/PAX solutions. The film lifetime measured longer than 300 s over 50 – 2×10^3 ppm is illustrated with the upward arrows.

Figure 4 shows the lifetime of the bubbles and films in the DPG only and DPG/PAX mixture in terms of DPG concentration. From the figure, the bubble coalescence time in the DPG solutions increases steadily with increasing DPG concentrations. Surprisingly, the thin film lifetime is significantly promoted above 10 ppm, lasting over 300 s (indicated with an upward arrow in the figure). The rising concentration results in a higher surfactant coverage on the film surfaces, and hence higher film stability. However, the ultra-stability observed in the thin film study could barely be expected from the coalescence time results, since only meta stable bubbles were observed in coalescence time results under the same conditions. Factors, such as the approach speed of the two bubbles mentioned above, can affect the mobility of films, and hence the film and bubble stability (Horn *et al*, 2011; Wang and Qu, 2012). Moreover, the presence of impurities in the DPG solution (about 1 per cent) may result in more stable film surfaces. This suggests that the bubble coalescence time measurements are relatively less sensitive to impurities in the system.

The presence of 1 ppm PAX changes from the metastability of bubbles in the DPG solution to ultra-stability over the concentration range of 50 – 5×10^2 ppm DPG. For the thin film results, as shown in Figure 4, the film stability in the DPG/PAX mixture also illustrates an ultra-stable state, but from a lower frother concentration. Interestingly, results from both techniques show a decrease in stability above 2×10^3 ppm DPG. This result suggests that similar reagent molecule adsorption behaviour may occur at the contacting film surfaces between the thin film balance and bubble coalescence experiments, despite the differences (ie interface approach speed) between the two techniques. The film and bubble stability are strongly affected by the surfactant adsorption on the film surfaces. Bournival *et al* (2014) found that the elasticity at low surfactant concentrations can stabilise the

bubble surface and slow down the film thinning process, while the elasticity decreased at high concentrations, which explains the decrease in the film stability found at high DPG concentrations (2×10^3 ppm).

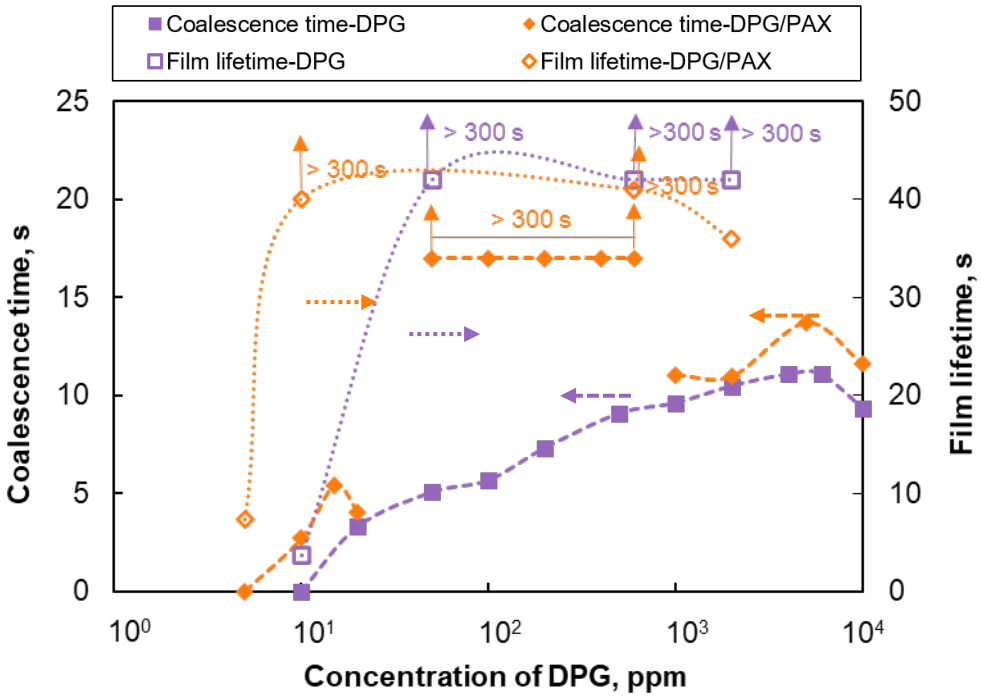

FIG 4 – Effect of DPG concentration on the lifetime of thin films and bubbles in DPG and DPG/PAX solutions. The lifetime of thin films and bubbles measured longer than 300 s is illustrated with the upward arrows.

PAX and salt impact on bubble and film stability of frothers

In the presence of salt, the stability of thin films and bubbles in the frother and PAX mixtures was also studied. The results from the thin film balance and coalescence time measurements are compared to establish the relationship between the two techniques. In the presence of NaCl, the ultra-stable films and bubbles formed in the MIBC/PAX solutions are largely dampened, shifting to a meta-stabile state, as shown in Figure 5. Additionally, both techniques show that a higher concentration of NaCl reduces the stability of bubbles and films in the DPG/PAX/NaCl system. The added NaCl screens the surface charge, which decreases the electrostatic repulsion between the film surfaces and induces cavitation as put forward by Pan *et al* (2022c).

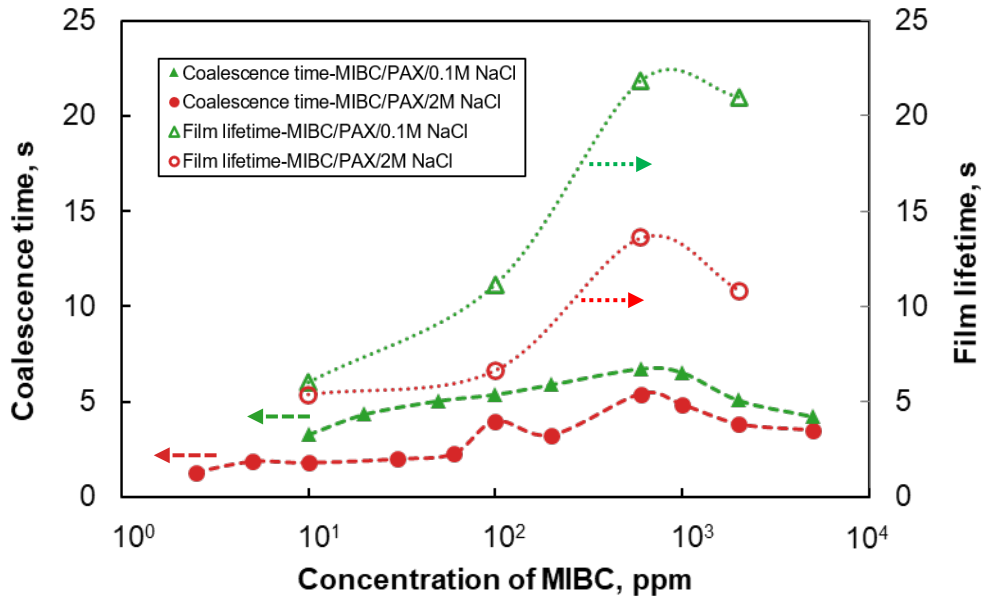

FIG 5 – The lifetime of thin films formed in the MIBC solution in the presence of 1 ppm PAX and NaCl with respect to MIBC concentration.

As seen in Figure 5, with both techniques, the stability of bubbles diminishes at high MIBC concentrations. In the case of 2 M NaCl, this decrease is due to the increase in dissolved gas that bridges the film surfaces, resulting in film rupture (Hermann *et al*, 1995; King, 2002; Qu *et al*, 2009; Weissenborn and Pugh, 1996). Furthermore, Pan *et al* (2022c) observed small bubbles during the TFB experiment in the MIBC/PAX/2 M NaCl solution at high MIBC concentrations. The observed bubbles could be MIBC droplets that are unable to dissolve in the mixture solution, which is also the likely cause of the decrease found in the bubble coalescence time measurements.

Figure 6 shows the lifetime of bubbles and films in the DPG/PAX/NaCl solutions as a function of DPG concentration. As seen, the bubble lifetime follows a steady increasing trend with increasing DPG concentrations. A higher concentration of salt (4 M) in the mixture is found to better stabilise the bubbles. As the presence of 4 M NaCl destabilises the film considerably and dominates the film stability in the DPG/PAX/NaCl system, it is difficult to acquire any trend with increasing DPG. Therefore, the highest NaCl concentration investigated is 2 M in the thin film balance measurements. Even with the addition of 2 M NaCl, the film rupture is faster; higher DPG concentrations in the DPG/PAX/NaCl system decrease the film lifetime further. Compared to the bubble coalescence results, there are contrary findings from the thin film with increasing NaCl concentrations in the DPG/PAX/NaCl solutions. This is more likely to be due to the presence of oil droplets and dissolved gas which may trigger the film rupture but might have less impact on the bubble coalescence time. This confirms that the thin film measurement is highly sensitive to the presence of any droplets or dissolved gas.

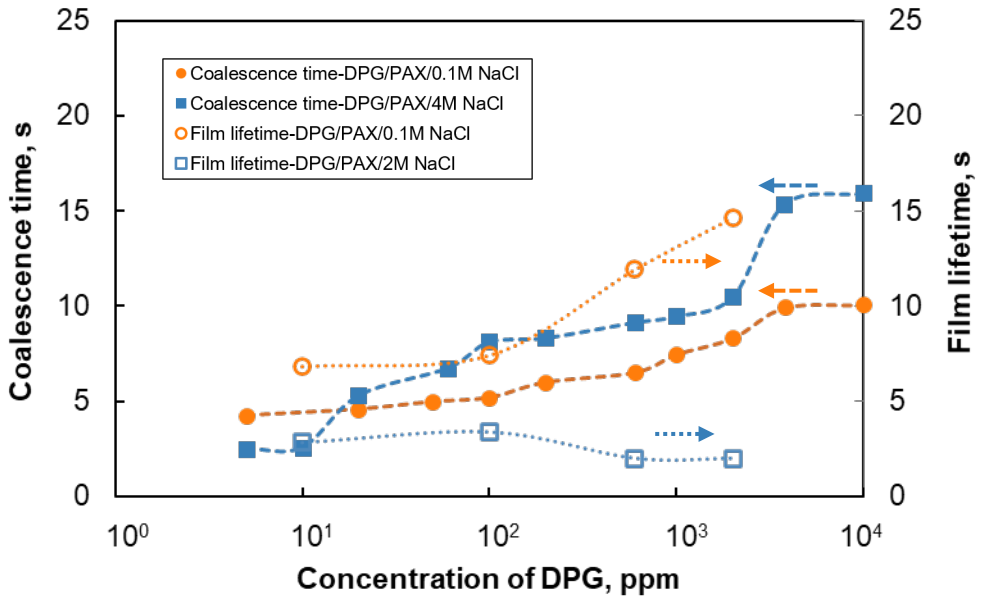

FIG 6 – The lifetime of thin films and bubbles formed in the DPG solution in the presence of 1 ppm PAX and NaCl as a function of DPG concentration.

CONCLUSIONS

The effect of xanthate collector (PAX) and NaCl on the stabilities of bubbles and films generated from two frother solutions (MIBC and DPG) was studied by the coalescence rig and thin film balance technique, respectively. The results show that the presence of PAX significantly improves the stability of bubbles in both frother solutions. With the addition of NaCl, the improved bubble stability found in the frother/PAX mixtures appears to be depressed. From the TFB experiments, the thin film stability demonstrates a similar trend to the bubble stability indicated by the bubble coalescence time. Variations between the bubble and thin film stability are found under some conditions. For example, with the DPG solutions, only metastability is observed in the bubble coalescence measurement, while ultra-stability in the thin film measurements. Additionally, the higher salt concentration in the DPG/PAX/NaCl system results in a contradictory findings between the two techniques. This is mainly because the thin film balance apparatus is more sensitive to the dissolved gas and oil droplets, which are mostly seen at high salt and surfactant concentrations. Factors such as the approach speed of the bubbles (or film) surfaces and the radius of contacting films can also lead to the difference in the results from these measurements. Overall, the synergistic effect of PAX and frother at the air-water interface is clearly shown, an important factor to consider when designing a reagent scheme for an ore type.

ACKNOWLEDGEMENTS

Yueyi Pan acknowledges financial support from the China Scholarship Council.

REFERENCES

Ata, S, 2008. Coalescence of bubbles covered by particles. *Langmuir, 24*(12), 6085–6091.

Bournival, G, Ata, S, Karakashev, S I and Jameson, G J, 2014. An investigation of bubble coalescence and post-rupture oscillation in non-ionic surfactant solutions using high-speed cinematography. *Journal of Colloid and Interface Science, 414*, 50–58.

Castro, S, Toledo, P and Laskowski, J, 2012. Foaming properties of flotation frothers at high electrolyte concentrations, in the *Water in Mineral Processing – Proceedings of the First International Symposium* (ed: J Drelich), pp 51–60, (SME).

Cho, Y S and Laskowski, J S, 2002. Bubble coalescence and its effect on dynamic foam stability. *The Canadian Journal of Chemical Engineering, 80*(2), 299–305.

Craig, V S, 2004. Bubble coalescence and specific-ion effects. *Current Opinion in Colloid & Interface Science, 9*(1–2), 178–184.

Eriksson, J C and Ljunggren, S, 1989. A molecular theory of the surface tension of surfactant solutions. *Colloids and Surfaces, 38*(1), 179–203.

Firouzi, M, Howes, T and Nguyen, A V, 2015. A quantitative review of the transition salt concentration for inhibiting bubble coalescence. *Advances in Colloid and Interface Science, 222*, 305–318.

Grau, R A and Laskowski, J S, 2006. Role of frothers in bubble generation and coalescence in a mechanical flotation cell. *Canadian Journal of Chemical Engineering, 84*(2), 170–182.

Hermann, C, Dewes, I and Schumpe, A, 1995. The estimation of gas solubilities in salt solutions. *Chemical Engineering Science, 50*(10), 1673–1675.

Horn, R G, Del Castillo, L A and Ohnishi, S, 2011. Coalescence map for bubbles in surfactant-free aqueous electrolyte solutions. *Advances in Colloid and Interface Science, 168*(1–2), 85–92.

Karakashev, S I and Nguyen, A V, 2007. Effect of sodium dodecyl sulphate and dodecanol mixtures on foam film drainage: Examining influence of surface rheology and intermolecular forces. *Colloids and Surfaces A: Physicochemical and Engineering Aspects, 293*(1–3), 229–240.

Karakashev, S I, Manev, E D, Tsekov, R and Nguyen, A V, 2008a. Effect of ionic surfactants on drainage and equilibrium thickness of emulsion films. *Journal of Colloid and Interface Science, 318*(2), 358–364.

Karakashev, S I, Nguyen, P T, Tsekov, R, Hampton, M A and Nguyen, A V, 2008b. Anomalous ion effects on rupture and lifetime of aqueous foam films formed from monovalent salt solutions up to saturation concentration. *Langmuir, 24*(20), 11587–11591.

King, A, 2002. Solubility of gases in micellar solutions, in *Encyclopedia of Surface and Colloid Science,* Vol. 4, pp 4749–4759, (CRC press).

Manev, E D and Pugh, R J, 1992. Drainage and equilibrium thickness of aqueous films containing nonionic frothers and xanthate flotation collector. *Journal of Colloid and Interface Science, 151*(2), 505–516.

Pan, Y, Bournival, G and Ata, S, 2021. The role of non-frothing reagents on bubble size and bubble stability. *Minerals Engineering, 161*, 106652.

Pan, Y, Bournival, G and Ata, S, 2022a. Foaming behaviour of frothers in the presence of PAX and salt. *Minerals Engineering, 178*, 107405.

Pan, Y, Bournival, G, Karakashev, S I, Yang, B, Wang, L and Ata, S, 2022b. Effect of electrolyte and flotation collector on foam films in the presence of frothers. Submitted to *Chemical Engineering Science*.

Pan, Y, Gresham, I, Bournival, G, Prescott, S and Ata, S, 2022c. Synergistic effect of frothers, collector and salt on bubble stability. *Powder Technology*, 117028.

Qu, X, Wang, L, Karakashev, S I and Nguyen, A V, 2009. Anomalous thickness variation of the foam films stabilized by weak non-ionic surfactants. *Journal of Colloid and Interface Science, 337*(2), 538–547.

Wang, L and Qu, X, 2012. Impact of interface approach velocity on bubble coalescence. *Minerals Engineering, 26*, 50–56.

Wang, L and Yoon, R-H, 2005. Hydrophobic forces in thin aqueous films and their role in film thinning. *Colloids and Surfaces A: Physicochemical and Engineering Aspects, 263*(1–3), 267–274.

Wang, L and Yoon, R-H, 2006. Stability of foams and froths in the presence of ionic and non-ionic surfactants. *Minerals Engineering, 19*(6–8), 539–547.

Weissenborn, P K and Pugh, R J, 1996. Surface tension of aqueous solutions of electrolytes: relationship with ion hydration, oxygen solubility, and bubble coalescence. *Journal of Colloid and Interface Science, 184*(2), 550–563.

Drag sensor and other tools for real-time monitoring of a flotation process

H Park[1] and L Wang[2]

1. Advance Queensland Research Fellow, The University of Queensland, Brisbane Qld 4067. Email: hangil.park@uq.edu.au
2. Senior Lecturer, The University of Queensland, Brisbane Qld 4067. Email: liguang.wang@uq.edu.au

ABSTRACT

Froth flotation is one of the most widely used beneficiation processes for fine and ultrafine coals and minerals. Maintaining optimal metallurgical performance in industrial flotation operation is still a challenging task owing to the lack of an effective tool to diagnose the flotation performance in real-time. For this purpose, a number of flotation performance monitoring systems with different working principles have been developed to provide instant feedback for process control and optimisation.

In this paper, for the first time, five different flotation performance monitoring systems were systematically compared through an on-site trial in a coking coal flotation plant in Queensland, Australia. The monitoring systems were used to measure (i) gas holdup, (ii) overflowing froth velocity, (iii) overflowing froth height, (iv) air recovery and (v) drag force exerted by overflowing froth, in an industrial flotation column and the outputs of these systems were collected simultaneously at a wide range of operating conditions.

For each monitoring system, the best regression model describing the correlation between the system output and the flotation performance was selected from various regression models (eg linear, quadratic, power-law and logarithmic) using the Akaike information criterion (AIC). A comparison of the coefficient of determination (R^2), residual sum of squares (RSS) and measuring accuracy at 95 per cent confidence level of the best regression models of these monitoring systems suggested that the drag sensor outperformed the other systems at a wide range of flotation operating conditions. The superior performance of the drag sensor was attributed to its distinctive design that enabled intimate sensing of variation of the overflowing froth properties. Furthermore, the drag sensor had the ability to monitor feed ash content variation when the other operation variables were set almost constant.

INTRODUCTION

Many flotation plants experience a large daily variation in flotation recovery, although a common goal is to maximise the flotation recovery while meeting the product quality requirement. The optimal flotation performance can be maintained only when the operational variables (eg frother dosage, collector dosage, airflow rate, froth depth, feed flow rate) are adjusted in a timely manner in response to the detected variation of the flotation performance. However, there is no diagnostic system to monitor the variation of the flotation recovery in-real time. Consequently, there is a pressing need to develop an effective diagnostic system to improve the eco-efficiency of the coal and mineral industries as the large daily fluctuation in recovery represents a loss of profit and the creation of additional environmental liability with the increased burden to the tailing proposal.

It is widely recognised in the flotation community that a good gas dispersion condition in the pulp zone is desirable for achieving a high flotation performance (Ahmed and Jameson, 1985; Gorain *et al*, 1998; Finch *et al*, 2000). Various gas dispersion parameters ranging from gas holdup (ε_g) to bubble surface area flux (S_b) have been proposed and correlated with flotation performance (Gorain *et al*, 1998; Finch *et al*, 2000; Nesset *et al*, 2006; Massinaei *et al*, 2009; López-Saucedo *et al*, 2012). Among these gas dispersion parameters, gas holdup measurement in the pulp zone is widely used to estimate the flotation performance in the industry due to the availability of a reliable measurement technique in the industrial environment (Finch *et al*, 2000; López-Saucedo *et al*, 2012).

The froth has not received much attention until recent years. A number of studies found that froth properties such as froth mobility, froth stability and froth rheology can also greatly affect the flotation performance (Cutting, Barber and Newton, 1986; Barbian, Ventura-Medina and Cilliers, 2003; Shi

and Zheng, 2003; Tsatouhas, Grano and Vera, 2006; Farrokhpay, 2012; Neethling and Brito-Parada, 2018). Research efforts were made to develop techniques to quantify froth stability, ranging from froth stability column (Barbian, Ventura-Medina and Cilliers, 2003) to electrical impedance (Hu, Ofori and Firth, 2009; Nissinen *et al*, 2014), but it was found that froth stability alone cannot predict the flotation performance effectively (Mehrabi, Mehrshad and Massinaei, 2014). Similarly, Runge *et al*, (2007) and Park, Bai and Wang (2022) reported that froth mobility can only be used as an auxiliary variable to indicate the flotation performance.

Recent research progress suggests that air recovery, defined as the fraction of air entering the flotation cell that overflows the launder as unburst bubbles, has a strong correlation with the flotation performance (Barbian *et al*, 2007; Smith, Hadler and Cilliers, 2010; Hadler *et al*, 2012; Qu, Wang and Nguyen, 2013). Cilliers and co-workers found that the optimal flotation performance was achieved at the peak air recovery where the froth stability and mobility were optimally balanced (Barbian *et al*, 2007; Smith, Hadler and Cilliers, 2010; Hadler *et al*, 2012). The air recovery can be determined using the following equation:

$$\alpha = \frac{Q_{\text{overflow}}}{Q_{\text{in}}} = \frac{\lambda \cdot v_{\text{f}} \cdot h_{\text{lip}} l_{\text{lip}}}{Q_{\text{in}}} \quad (1)$$

where Q_{in} is the volumetric flow rate of air entering the cell, λ is the air fraction of the overflowing froth, v_{f} is the velocity of overflowing froth, h_{lip} is the froth height over the lip and l_{lip} is the lip length of the flotation cell. A laser distance metre and a froth camera (with associated image analysis software) can be used to measure h_{lip} and v_{f}, respectively, to determine α. The air recovery concept has yet to be widely applied in monitoring and controlling flotation despite its successful usage as a plant audit in the mineral industry (Smith, Hadler and Cilliers, 2010; Hadler *et al*, 2012).

In the present study, for the first time, the diagnostic performance of five different systems was evaluated through an on-site trial in a coking coal flotation plant in Queensland, Australia. Multiple tools were installed at an industrial column flotation cell to monitor (i) gas holdup, (ii) overflowing froth velocity, (ii) overflowing froth height, (iv) air recovery and (v) drag force exerted by overflowing froth. Outputs of these tools were collected simultaneously at a wide range of operating conditions (including and beyond normal conditions) by deliberately changing the aeration rate and frother dosage. The correlation between the flotation yield and the output of the five tools was compared overall the experimental conditions tested. Likewise, the correlation between the combustible recovery and the output of these tools were investigated. The same approach was applied to process only the experimental data that were obtained at the normal operating conditions, where the potential of using these tools to detect the variation of the ash content of the flotation feed was also examined.

METHOD AND EXPERIMENTAL

Approach

The test work was carried out in a coking coal preparation plant for five days at various aeration and frother dosing rates as shown in Table 1. At each experimental setting, the flotation feed, concentrate and tailing samples were simultaneously collected twice with a minimum 10 minute waiting period between the first and second sample collection (i..e, sample collection for Experiment Number *n*+1 was done at least 10 minutes after that of Experiment Number *n*, with *n* = 1, 3, 5, … or 15). The collected samples were transported to The University of Queensland to determine the ash content for assessing the flotation yield and combustible recovery.

TABLE 1

Operating conditions and flotation performance during the on-site test work.

Date	Exp. No.	Frother Dosage (mL/min)	Aeration (m^3/hr)	Yield (%)	R_{Comb} (%)	Product Ash (%)
Day 1	1	190	1699	59.0	80.6	7.1
	2	190	1700	52.1	76.9	6.8
	3	190	945	31.3	46.5	3.8
	4	190	941	17.5	25.9	3.5
Day 2	5	170	1687	43.2	71.5	8.1
	6	170	1697	44.1	75.3	7.9
	7	0*	1224	39.5	69.6	6.7
	8	0*	1196	40.9	69.6	6.2
Day 3	9	120	1694	44.8	74.1	6.8
	10	120	1704	41.2	71.1	6.9
	11	120	992	29.9	54.7	5.2
	12	120	997	26.4	47.2	6.1
Day 4	13	200	1690	49.9	76.7	5.8
	14	200	1687	50.8	77.7	5.8
Day 5	15	190	1721	53.5	80.1	6.6
	16	190	1693	53.8	80.5	6.7

* Site was experiencing overfrothing issue throughout the plant because of high residual frother concentration within the plant. As a result, the frother dosage was cut-off to 0 during the trial, but there was still a significant amount of froth overflowing.

Diagnostic systems

Multiple instruments were installed at an industrial column flotation cell to monitor (i) gas holdup, (ii) overflowing froth velocity, (iii) overflowing froth height, (iv) air recovery and (v) drag force exerted by overflowing froth.

The gas holdup in the pulp phase, ε_g, was measured using a differential pressure transmitter (EJX110A, Yokogawa), which was regularly calibrated by the site personnel. The gas holdup values obtained from the plant data acquisition system were used directly in the present work.

The overflowing froth velocity, v_f, was measured using a web camera (C930, Logitech). The web camera was installed above the column to record a video of the overflowing froth at 15 frames per second. The recorded video was analysed offline using Visofroth™ (OSC-4D, Metso) to determine the overflowing froth velocity, v_f.

The overflowing froth height, h_{lip}, was measured using a laser distance metre (DLS-C 15, Dimetix). The froth height at 5 cm (horizontal distance) away from the cell lip was measured with a default sampling rate. The acquired value was averaged every 5 seconds and then logged on the hard disk of a computer. Note that the laser distance device had no detectable destructive effect on froth stability as it had low incident laser power and illuminated intermittently.

Air recovery, α, was calculated using Equation 1 above. The volumetric flow rate of air entering the flotation column, Q_{in}, was obtained from the site instrumentation directly. The total lip length of the flotation cell, l_{lip}, was 45.23 m as determined from the dimensions of the internal and outer launders. The following assumptions were made while calculating the air recovery value:

- λ (air fraction of the overflowing froth) was assumed unity (Smith, Hadler and Cilliers, 2010; Hadler *et al*, 2012).
- The velocity of overflowing froth, v_{f}, was assumed to be same along the cell lip.

The values of v_{f}, h_{lip} and Q_{in} obtained over the time, when the flotation feed, concentrate and tailing samples from the flotation cell were collected, were respectively averaged and then used to compute the air recovery, α.

The drag force exerted by overflowing froth was measured by installing a cantilever beam with a 1 mm thickness as shown in Figure 1. The details of the working principle of the drag sensor can be found elsewhere (Park and Wang, 2021), so it is only described in brief here. When the drag sensor was immersed, it obstructs the froth movement and experiences a drag force. The amount of deflection of the cantilever beam (ie strain) was monitored by attaching the strain gauges on both sides of the cantilever beam.

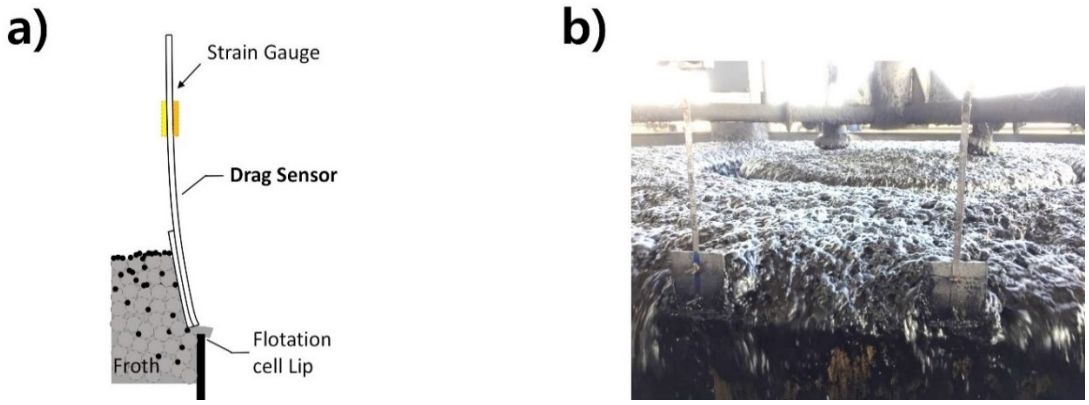

FIG 1 – The drag sensor: a) Side view, b) Drag sensors installed at an industrial-scale flotation column.

Regression analysis

A mean value of the output from each monitoring system during each sampling period was calculated and then analysed with the corresponding flotation yield or the combustible recovery. In the present study, five different equations listed in Table 2 were fit to the obtained data using the method of least squares. Among the five different models, the most suitable model with the lowest Akaike information criterion (AIC) value was selected as it considers both the goodness of fitting and the complexity of the model. The AIC value, $AICc$, was calculated using the following formula (Burnham and Anderson, 2002):

$$AICc = n \ln\left(\frac{\sum(y-\hat{y})^2}{n}\right) + \frac{2\,K\,(K+1)}{n-K-1} \quad (2)$$

where n is the number of samples, y is the observed value, $\hat{y}$ is the predicted value and K is the number of adjustable parameters in the model.

TABLE 2

List of regression models tested to describe the correlation between monitoring system output and the flotation performance.

Expression	Description	Equation	No. adjustable parameters
1	Linear	$Y = Ax + B$	2
2	Quadratic	$Y = Ax^2 + Bx + C$	3
3	Simple power law	$Y = Ax^B$	2
4	Complex power law	$Y = Ax^B + C$	3
5	Logarithmic law	$Y = A\ln(x) + B$	3

RESULTS AND DISCUSSION

Correlation with flotation yield

The diagnostic performance of five monitoring systems was examined over a wide range of aeration rate (940–1720 m^3/hr) and frother dosing rate (0–200 mL/min), where the clean coal yield and product ash content varied between 17.5 to 59.0 per cent and 3.5 to 8.1 per cent, respectively. Table 3 shows the best-fit-models with the calculated residual sum of squares (*RSS*), coefficient of determination (R^2) and Akaike information criterion ($AICc$) for the experimental data. It was found that Expressions 3, 3, 4, 1 and 1 (highlighted in bold in Table 3) were the most suitable model to describe the correlation between flotation yield and the output of the monitoring systems 1 to 5, respectively.

Figure 2 shows the data points of flotation yield versus the outputs from the monitoring systems. Strikingly, the drag sensor (Figure 2e) gave a very high R^2 value (ie 0.97) comparing to other systems whose R^2 value varied from 0.72 to 0.84. Furthermore, the drag sensor showed the narrowest prediction interval at a given output implying that the new drag sensor can diagnose the flotation yield the most sensitively and accurately.

The superior performance of the drag sensor can be attributed to its distinct design that enables physical contact with the overflowing froth and thus intimate sensing of the variations of the overflowing froth properties such as froth stability, froth mobility and froth viscosity (Park and Wang, 2021). It is likely that the drag sensor has captured a rather comprehensive set of information, including froth velocity, froth depth over the lip and froth viscosity (or solids loading).

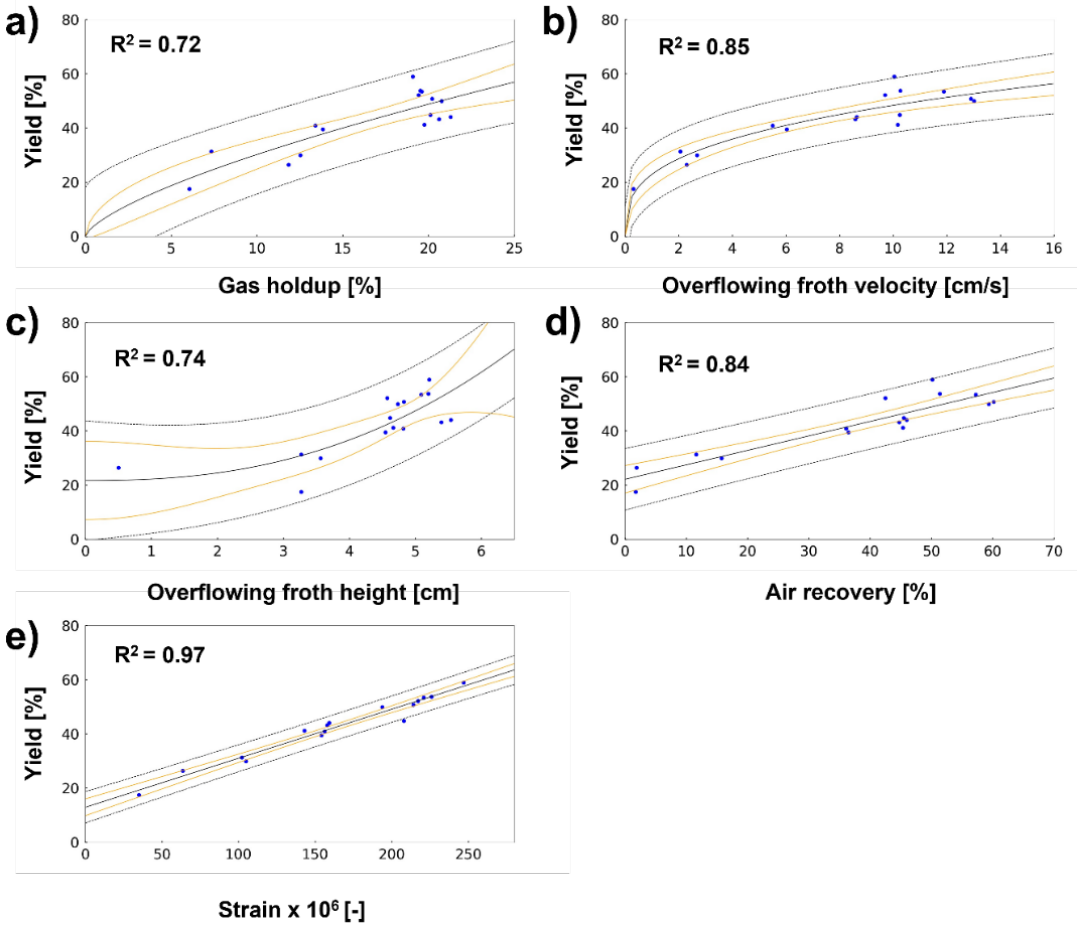

FIG 2 – Correlation between clean coal yield and the outputs from the five different monitoring systems overall the operating conditions tested. The monitoring systems respectively measure (a) gas holdup, (b) overflowing froth velocity, (c) overflowing froth height, (d) air recovery and (e) drag force exerted by overflowing froth. The lines represent best regression (black solid line), 95 per cent confidence interval (yellow solid) and prediction interval (black dashed). The R^2 values are those highlighted in bold in Table 3.

TABLE 3

Best fit models to describe the correlation between flotation yield, *Y* and output from each monitoring system.

Expression	Best-fit-model	*RSS*	R^2	*AICc*
System 1: Gas holdup				
1	$Y = 1.9x + 10$	586	0.70	58.5
2	$Y = -0.057x^2 + 3.5x + 0.63$	538	0.72	58.3
3	**$Y = 6.1x^{0.69}$**	**548**	**0.72**	**57.5**
4	$Y = 15x^{0.49} – 15$	546	0.72	58.5
5	$Y = 25 \ln(x) – 25$	557	0.71	57.7
System 2: Overflowing froth velocity				
1	$Y = 2.5x + 23$	362	0.81	50.9
2	$Y = -0.18x^2 + 5.0x + 18$	272	0.86	47.4
3	**$Y = 23x^{0.33}$**	**281**	**0.85**	**46.8**
4	$Y = 16x^{0.42} + 7.6$	277	0.86	47.7
5	$Y = 10 \ln(x) – 24$	364	0.81	50.9
System 3: Overflowing froth height				
1	$Y = 6.6x + 13$	911	0.53	65.6
2	$Y = 1.9x^2 – 5.3x + 27$	692	0.64	62.3
3	$Y = 16x^{0.67}$	1083	0.44	68.4
4	**$Y = 0.52x^{2.4} + 211$**	**600**	**0.74**	**58.0**
5	$Y = 11 \ln(x) + 27$	1289	0.33	71.1
System 4: Air recovery				
1	**$Y = 0.53x + 22$**	**326**	**0.84**	**47.8**
2	$Y = -0.0021x^2 + 0.66x + 21$	294	0.85	48.6
3	$Y = 16x^{0.28}$	304	0.81	50.7
4	$Y = 1.2x^{0.81} + 20$	279	0.85	48.6
5	$Y = 8.7 \ln(x) + 14$	367	0.77	54.3
System 5: Drag Sensor				
1	**$Y = 0.18x + 13$**	**66**	**0.97**	**23.7**
2	$Y = -0.000080x^2 + 0.20x + 12$	65	0.97	24.5
3	$Y = 1.7x^{0.63}$	71	0.96	24.9
4	$Y = 0.41x^{0.86} + 9.5$	64	0.97	24.3
5	$Y = 21 \ln(x) – 61$	167	0.91	38.5

Correlation with combustible recovery

During the five-day site trial, R_{comb} varied from 25.9 to 80.6 per cent. Similarly, five different regression models (listed in Table 2) were fit to the R_{comb} versus output of monitoring systems to find the most suitable model to describe the correlation. Table 4 shows that the quadratic model had the

smallest AIC value for all the monitoring systems tested, except System 2 (ie overflowing froth velocity) where the complex power-law model had the smallest AIC value.

TABLE 4

Best fit models to describe the correlation between R_{comb} and output from each monitoring system.

Expression	Best-fit-model	*RSS*	R^2	*AICc*
System 1: Gas holdup				
1	$R_{comb} = 2.9x + 20$	646	0.82	60.1
2	**$R_{comb} = -0.19x^2 + 8.3x - 13$**	**439**	**0.88**	**55.0**
3	$R_{comb} = 11x^{0.63}$	567	0.85	58.0
4	$R_{comb} = 900x^{0.038} - 930$	482	0.87	56.5
5	$R_{comb} = 38 \ln(x) - 36$	478	0.87	55.3
System 2: Overflowing froth velocity				
1	$R_{comb} = 3.4x + 4$	683	0.81	61.0
2	$R_{comb} = -0.44x^2 + 9.4x + 28$	168	0.95	39.6
3	$R_{comb} = 40x^{0.28}$	189	0.95	40.4
4	**$R_{comb} = 110x^{0.31-}67$**	**161**	**0.96**	**38.9**
5	$R_{comb} = 15 \ln(x) - 40$	182	0.95	39.8
System 3: Overflowing froth height				
1	$R_{comb} = 9.3x + 27$	1653	0.55	75.1
2	**$R_{comb} = 3.1x^2 - 10x + 48$**	**1083**	**0.70**	**69.4**
3	$R_{comb} = 35x^{0.46}$	2153	0.41	79.4
4	$R_{comb} = 0.60x^{2.6} + 38$	1182	0.68	70.8
5	$R_{comb} = 15 \ln(x) + 46$	2480	0.32	81.6
System 4: Air recovery				
1	$R_{comb} = 0.75x + 39$	453	0.88	54.4
2	**$R_{comb} = -0.011x^2 + 1.4x + 34$**	**300**	**0.92**	**48.9**
3	$R_{comb} = 29x^{0.25}$	361	0.90	50.8
4	$R_{comb} = 7.7x^{0.48} + 25$	328	0.91	50.3
5	$R_{comb} = 13 \ln(x) + 25$	465	0.87	54.8
System 5: Drag Sensor				
1	$R_{comb} = 0.24x + 29$	472	0.87	55.1
2	**$R_{comb} = -0.0012x^2 + 0.57x + 8.9$**	**186**	**0.95**	**41.3**
3	$R_{comb} = 5.6x^{0.49}$	281	0.92	46.8
4	$R_{comb} = 210x^{0.091} - 260$	211	0.94	43.3
5	$R_{comb} = 29 \ln(x) - 77$	210	0.94	42.1

Figure 3 shows the correlations between combustible recovery, R_{comb} and the outputs of monitoring systems. The output of the drag sensor (Figure 3e) had a strong positive correlation with R_{comb}, with the R^2 of the best quadratic fit being 0.95. The overflowing froth velocity (Figure 3b) had a comparable R^2 value (ie 0.96) while air recovery and gas holdup had slightly weaker correlations (R^2

= 0.92 and 0.88, respectively). Both drag sensor and overflowing froth velocity showed narrower prediction intervals at a given output compared to other monitoring systems, implying that drag sensor and overflowing froth velocity can be used to diagnose the combustible recovery more accurately than the other systems.

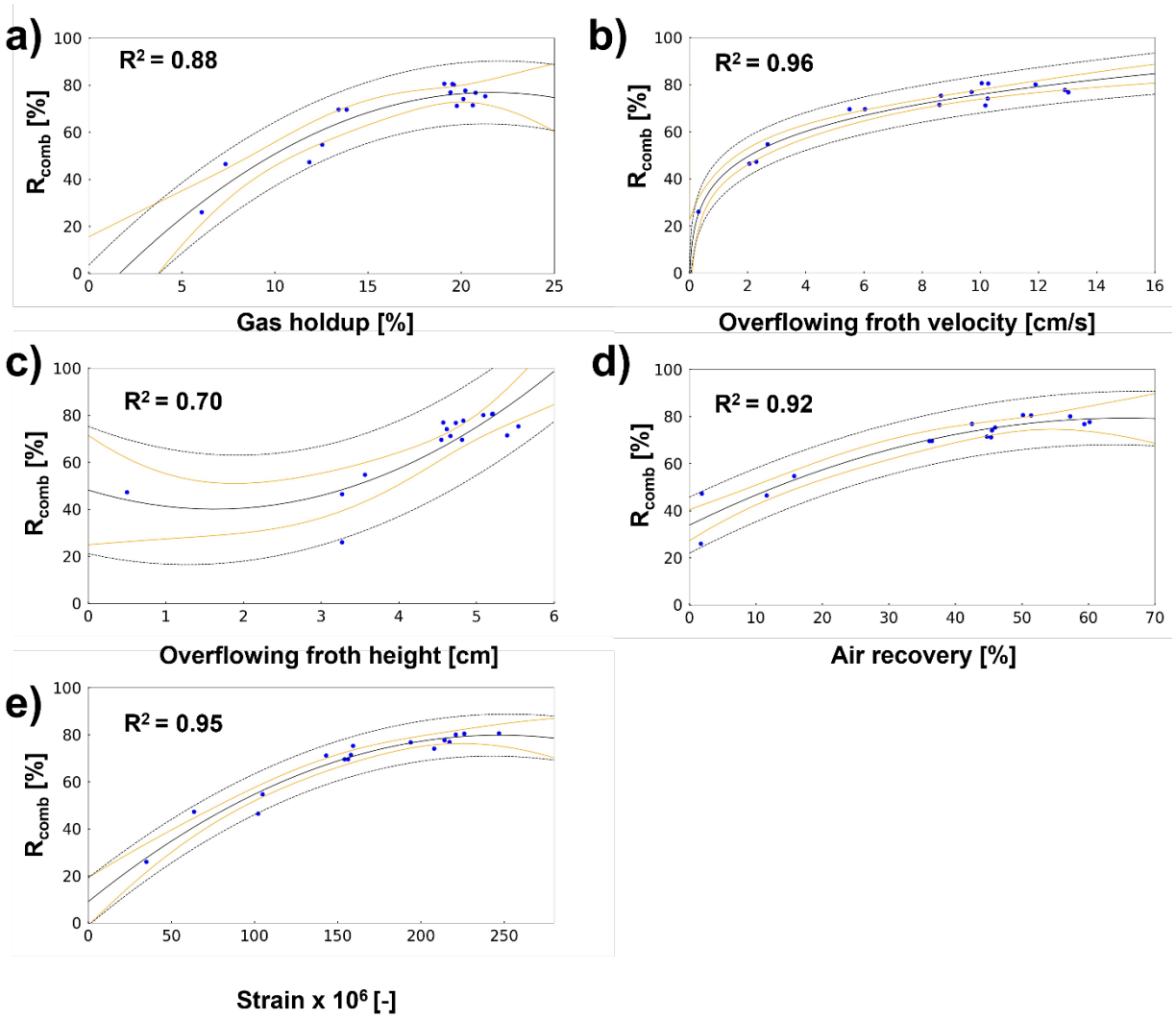

FIG 3 – Correlation between combustible recovery, R_{comb} and the outputs from the five different monitoring systems overall the operating conditions tested. The monitoring systems to measure (a) gas holdup, (b) overflowing froth velocity, (c) overflowing froth height, (d) air recovery and (e) drag force exerted by overflowing froth. The R^2 values are those highlighted in bold in Table 4.

Correlation with feed ash content at the normal operating conditions

Many coal flotation plants experience large daily variations in recovery due to variation in the feed quality but do not have real-time monitoring tools for process control and optimisation. The flotation performance is primarily governed by the flotation feed quality as long as the other flotation operating condition is set constant. In the present work, the possibility of the flotation performance monitoring systems to detect the variation of the ash content in the flotation feed was examined at the normal operation conditions (ie frother dosage at least 170 mL/min and aeration rate at approximately 1700 m^3/hr), with the measured feed ash contents falling in the range of 32.0 per cent – 46.0 per cent.

Table 5 shows the best-fit-models and calculated *RSS*, R^2 and *AICc*. It was found that the lowest AIC value was attained with expressions 5, 2, 2, 3 and 1 (highlighted in bold in Table 5) for the monitoring systems 1 to 5, respectively.

TABLE 5

Best fit models to describe the correlation between feed ash content, Ash_{feed} and output from each monitoring system.

Expression	Best-fit-model	*RSS*	R^2	*AICc*
System 1: Gas holdup				
1	$Ash_{feed} = 4.8x – 58$	34.3	0.75	14.0
2	$Ash_{feed} = 0.15x^2 - 1.1x – 0.56$	33.2	0.76	17.4
3	$Ash_{feed} = 0.027x^{2.4}$	34.5	0.76	13.9
4	$Ash_{feed} = 4.6x^{1.0} – 59$	33.0	0.76	17.3
5	**$Ash_{feed} = 100 \ln(x) – 260$**	**32.9**	**0.76**	**13.7**
System 2: Overflowing froth velocity				
1	$Ash_{feed} = -1.0x + 50$	114.2	0.17	23.7
2	**$Ash_{feed} = 1.6x^2 – 36x + 230$**	**34.5**	**0.75**	**17.7**
3	$Ash_{feed} = 80x^{-0.30}$	111.6	0.18	23.5
4	$Ash_{feed} = (2.6*10^{18})x^{-19}–37$	39.0	0.71	18.7
5	$Ash_{feed} = -12 \ln(x) + 67$	109.0	0.20	23.3
System 3: Overflowing froth height				
1	$Ash_{feed} = 6.7x + 5.0$	101.7	0.26	22.7
2	**$Ash_{feed} = 27x^2 – 270x + 690$**	**58.8**	**0.57**	**22.0**
3	$Ash_{feed} = 9.2x^{0.89}$	102.0	0.26	22.7
4	$Ash_{feed} = -260x^{-0.16} + 240$	104.1	0.24	26.5
5	$Ash_{feed} = 33 \ln(x) – 14$	103.8	0.24	22.9
System 4: Air recovery				
1	$Ash_{feed} = -0.19x + 49$	125.2	0.09	24.4
2	$Ash_{feed} = 0.031x^2–3.4x + 130$	119.0	0.13	27.6
3	**$Ash_{feed} = 110x^{-0.26}$**	**124.4**	**0.09**	**24.4**
4	$Ash_{feed} = 110x^{-0.27} + 2.1$	124.4	0.09	28.0
5	$Ash_{feed} = -9.9 \ln(x) + 78$	124.6	0.09	24.4
System 5: Drag Sensor				
1	**$Ash_{feed} = -0.13x + 66$**	**10.4**	**0.92**	**4.5**
2	$Ash_{feed} = -0.00023x^2–0.043x + 57$	10.2	0.93	7.9
3	$Ash_{feed} = 1100x^{-0.64}$	12.3	0.91	5.8
4	$Ash_{feed} = 400x^{-0.13} – 160$	11.5	0.92	8.9
5	$Ash_{feed} = -26 \ln(x) – 180$	11.4	0.92	5.2

Figure 4 shows only the drag sensor had a strong correlation (R^2 = 0.92) with the feed ash while other systems had low R^2 values. The narrow prediction interval of the drag sensor suggests that it could also be used to monitor feed ash content variation when other operation variables are set almost constant.

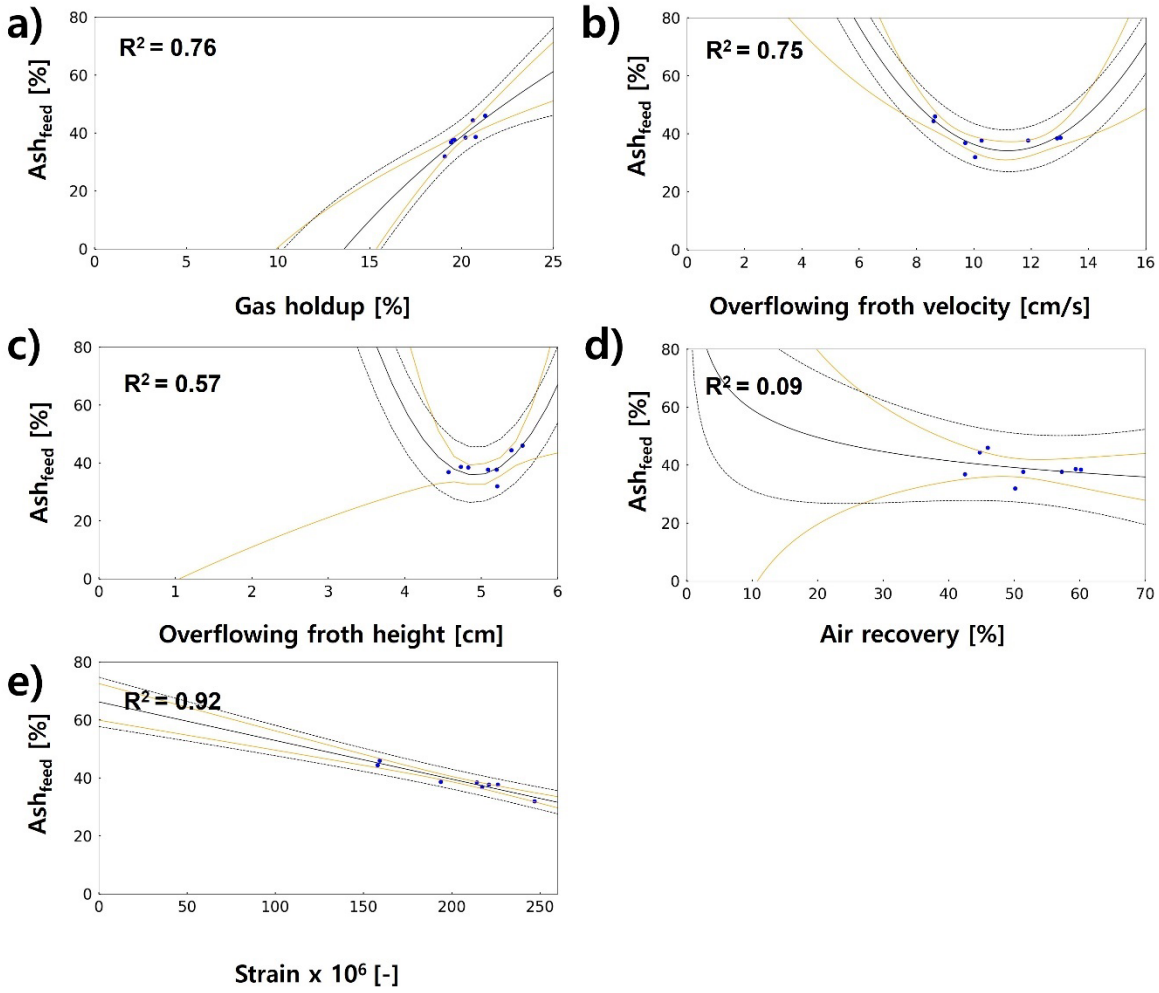

FIG 4 – Correlation between feed ash content and the outputs from the five different monitoring systems at the normal operating conditions. The monitoring systems to measure (a) gas holdup, (b) overflowing froth velocity, (c) overflowing froth height, (d) air recovery and (e) drag force exerted by overflowing froth. The R^2 values are those highlighted in bold in Table 5.

CONCLUSIONS

In the present study, five different flotation performance monitoring systems, measuring (i) gas holdup, (ii) overflowing froth velocity, (iii) overflowing froth height, (iv) air recovery and (v) drag force exerted by overflowing froth, were installed at a large industrial column flotation cell and its diagnosis ability was tested at a wide range of the flotation operation conditions by deliberately adjusting frother dosage and aeration rate.

It was found that the drag sensor outperformed the other systems for monitoring the clean coal yield (mass recovery). When monitoring the combustible recovery, the sensor performed similarly to the froth velocity measurement system but outperformed the other three systems. It was also found that the drag sensor, which was originally designed for flotation performance monitoring via monitoring the froth properties, enabled instant detection of the variation of the feed ash content when other operation conditions were set almost constant.

The present results suggest that the drag sensor can be used as a low-cost stand-alone device to help monitor flotation performance online and provide instant feedback for process optimisation and control.

ACKNOWLEDGEMENTS

The authors gratefully thank the financial support from the Australian Coal Industry's Research Program (ACARP Project C26012) and Changzhi Bai for experimental assistance. HP acknowledges the Queensland Government for an Industry Research Fellowship.

REFERENCES

Ahmed, N and Jameson, G J, 1985. The effect of bubble size on the rate of flotation of fine particles. *International journal of mineral processing*, 14(3), pp 195–215.

Barbian, N, Cilliers, J J, Morar, S H and Bradshaw, D J, 2007. Froth imaging, air recovery and bubble loading to describe flotation bank performance. *International Journal of Mineral Processing*, 84(1–4), pp 81–88.

Barbian, N, Ventura-Medina, E and Cilliers, J J, 2003. Dynamic froth stability in froth flotation. *Minerals Engineering*, 16(11), pp 1111–1116.

Burnham, K P and Anderson, D R, 2002. *Model Selection and Multimodel Inference: A Practical Information-Theoretic Approach*, pp 60–80 (Springer, New York).

Cutting, G W, Barber, S P and Newton, S, 1986. Effects of froth structure and mobility on the performance and simulation of continuously operated flotation cells. *International journal of mineral processing*, 16(1–2), pp 43–61.

Farrokhpay, S, 2012. The importance of rheology in mineral flotation: A review. *Minerals Engineering*, 36, pp 272–278.

Finch, J A, Xiao, J, Hardie, C and Gomez, C O, 2000. Gas dispersion properties: bubble surface area flux and gas holdup *Minerals engineering*, 13(4), pp 365–372.

Gorain, B K, Napier-Munn, T J, Franzidis, J P and Manlapig, E V, 1998. Studies on impeller type, impeller speed and air flow rate in an industrial scale flotation cell. Part 5: validation of k-Sb relationship and effect of froth depth. *Minerals Engineering*, 11(7), pp 615–626.

Hadler, K, Greyling, M, Plint, N and Cilliers, J J, 2012. The effect of froth depth on air recovery and flotation performance. *Minerals Engineering*, 36, pp 248–253.

Hu, S, Ofori, P and Firth, B, 2009. Monitoring of froth stability using electrical impedance spectroscopy. *International Journal of Mineral Processing*, 92(1–2), pp 15–21.

López-Saucedo, F, Uribe-Salas, A, Pérez-Garibay, R and Magallanes-Hernández, L, 2012. Gas dispersion in column flotation and its effect on recovery and grade. *Canadian Metallurgical Quarterly*, 51(2), pp 111–117.

Massinaei, M, Kolahdoozan, M, Noaparast, M, Oliazadeh, M, Yianatos, J, Shamsadini, R and Yarahmadi, M, 2009. Hydrodynamic and kinetic characterization of industrial columns in rougher circuit. *Minerals Engineering*, 22(4), pp 357–365.

Mehrabi, A, Mehrshad, N and Massinaei, M, 2014. Machine vision based monitoring of an industrial flotation cell in an iron flotation plant. *International Journal of Mineral Processing*, 133, pp 60–66.

Neethling, S J and Brito-Parada, P R, 2018. Predicting flotation behaviour–The interaction between froth stability and performance. *Minerals Engineering*, 120, pp 60–65.

Nesset, J E, Hernandez-Aguilar, J R, Acuna, C, Gomez, C O and Finch, J A, 2006. Some gas dispersion characteristics of mechanical flotation machines. *Minerals Engineering*, 19(6–8), pp 807–815.

Nissinen, A, Lehikoinen, A, Mononen, M, Lähteenmäki, S and Vauhkonen, M, 2014. Estimation of the bubble size and bubble loading in a flotation froth using electrical resistance tomography. *Minerals Engineering*, 69, pp 1–12.

Park, H and Wang, L, 2021. Industrial demonstration of a sensor for monitoring coal flotation. *Minerals Engineering*, 167, p 106884.

Park, H, Bai, C and Wang, L, 2022. A convolutional neural network for classification of froth mobility in an industrial flotation cell. *Mineral Processing and Extractive Metallurgy Review*, pp 1–9.

Qu, X, Wang, L and Nguyen, A V, 2013. Correlation of air recovery with froth stability and separation efficiency in coal flotation. *Minerals Engineering*, 41, pp 25–30.

Runge, K, McMaster, J, Wortley, M, La Rosa, D and Guyot, O, 2007, March. A correlation between Visiofroth™ measurements and the performance of a flotation cell. In *Ninth Mill Operators' Conference,* pp 19–21 (The Australasian Institute of Mining and Metallurgy: Melbourne)

Shi, F N and Zheng, X F, 2003. The rheology of flotation froths. *International Journal of Mineral Processing*, 69(1–4), pp 115–128.

Smith, C D, Hadler, K and Cilliers, J J, 2010. Flotation bank air addition and distribution for optimal performance. *Minerals Engineering*, 23(11–13), pp 1023–1029.

Tsatouhas, G, Grano, S R and Vera, M, 2006. Case studies on the performance and characterisation of the froth phase in industrial flotation circuits. *Minerals Engineering*, 19(6–8), pp 774–783.

Exploring two approaches for real-time measurement of frother concentration

H Park[1], Y Lee[2], Y Matviychuk[3], D J Holland[4] and L Wang[5]

1. Advance Queensland Research Fellow, The University of Queensland, Brisbane Qld 4072. Email: hangil.park@uq.edu.au
2. PhD student, University of Canterbury, Private Bag 4800, Christchurch 8140, New Zealand. Email: yejin.lee@pg.canterbury.ac.nz
3. Postdoctoral Research Fellow, University of Canterbury, Private Bag 4800, Christchurch 8140, New Zealand. Email: eugene.matviychuk@canterbury.ac.nz
4. Professor, University of Canterbury, Private Bag 4800, Christchurch 8140, New Zealand. Email: daniel.holland@canterbury.ac.nz
5. Senior Lecturer, The University of Queensland, Brisbane Qld 4072. Email: liguang.wang@uq.edu.au

ABSTRACT

Reuse of process water in mineral and coal flotation plants is widespread to effectively reduce freshwater consumption. However, the accumulation of the frother in the recycled process water is a growing problem as high remnant frother concentration often leads to undesirable overfrothing issues throughout the plants. Various approaches have been proposed by others to measure frother concentration, but none of them is used in flotation practice owing to the requirement of time-consuming sample preparation steps and/or specialist training to operate and maintain. There is a pressing need for the development of a simple and fast frother concentration measuring technique to avoid overfrothing issues and to optimise the flotation process.

The present paper presents two promising approaches to measuring frother concentration online.

The first approach measures the concentration of alcohol type frothers based on the host-guest interactions between frother molecules and a formulated liquid. This method is simple and fast as it only requires mixing the formulated liquid with the water sample for up to one minute. The potential of this approach was demonstrated by determination of the residual MIBC concentrations at different locations across a coal flotation plant.

The second approach measures frother concentration using a solid-phase extraction (SPE) process and a cryogen-free benchtop NMR spectrometer. Using this approach, both alcohol type and polyglycol type frother solutions can be analysed for concentration determination within 30 minutes. It has also been demonstrated that the concentration of individual frothers in a frother blend (ie MIBC and PPG425 in water) can be accurately analysed even in the presence of background chemicals. This technique has otential for real-time measurement of frother concentration as the whole process can be fully automated.

INTRODUCTION

The mining industry is consuming a large amount of water primarily for beneficiation of minerals and coals. Reuse of process water has become widespread, but recycling of the process water without caution entails undesirable accumulation of frother, which can cause overfrothing (‘froth out’) problems in pumps, sumps, thickeners, and even in a dense medium circuit. In order to prevent overfrothing problems, there is a pressing need for a simple and fast on-site frother concentration measurement technique.

Research efforts have been made to measure remanent frother concentration, ranging from colourimetric technique to gas holdup measurment (Fuerstenau, 1982; Lahey and Clarkson, 1999; Weber, Gomez and Finch, 2003; Gélinas and Finch, 2005; Zanin *et al,* 2009; Maldonado *et al,* 2010; Zangooi, Gomez, and Finch 2010, 2016; Zhang, Zhu, and Finch, 2013). None of these techniques is used on-site for daily operation due to poor repeatability (Lahey and Clarkson, 1999), interference from residual organic and inorganic contaminants (Weber, Gomez and Finch, 2003; Maldonado *et al,* 2010), requirement of time-consuming sample preparation steps (Gélinas and Finch, 2005; Zangooi, Gomez, and Finch 2010, 2016) and/or specialist training to operate and maintain the sensitive

analytical equipment (Zanin *et al,* 2009; Zhang, Zhu, and Finch, 2013). Many flotation plants, therefore, restrict frother dosage below a certain level to avoid the overfrothing problems, which causes a significant loss of yield and revenue (DeHart *et al,* 2016).

Over the past five years, the authors developed two approaches for frother concentration monitoring that can be used in daily flotation operations. Method 1 is based on the host-guest interactions between frother molecules and a formulated liquid (Park and Wang, 2018, 2021). Method 2 uses a solid phase extraction (SPE) process to selectively concentrate frother molecules and then analyse the frother concentration using a cryogen-free benchtop-NMR spectrometer (Lee *et al,* 2021, 2022). Both methods demonstrated high measuring accuracies even in the presence of residual organic and inorganic contaminants. More importantly, these two methods have potential as the whole process can be fully automated and does not require specialist skills to operate the instruments (ie UV-Vis spectrophotometer and benchtop NMR).

In the present study, these two methods are briefly described along with the research findings. The advantages and limitations are discussed and compared with those of the colourimetric method, which has been used for plant auditing in the last 20 years (Gélinas and Finch, 2005; Zangooi, Gomez and Finch 2010, 2016).

METHOD 1

Method 1 involves complexations between frother molecule and a formulated liquid. The formulated liquid mainly comprises pyrene and β-cyclodextrin (β-CD). It was found that when alcohol type frother is mixed with the formulated liquid, ternary complexes of frother, pyrene, and β-CD molecules are formed. The procedure is described in detail elsewhere for frother concentration measurement in coal flotation where methyl isobutyl carbinol (MIBC) is used as frother and diesel is used as collector (Park and Wang, 2018, 2021). In brief, the method involves spiking a known amount of MIBC and then mixing with α-cyclodextrin (α-CD) to suppress interference from the diesel. After that, the formulated liquid was added to yield a final solution (ie a mixture of the original water sample, α-CD, and the formulated liquid), which was shaken by hand a few times and then analysed with a UV-Vis spectrophotometer.

The concentration of frother in the original water sample can be determined by obtaining the UV-Vis spectrum of the final solution. Figure 1a shows the UV-Vis spectra of the final sample solution that was prepared by mixing the formulated liquid with a MIBC solution containing 0 to 20 ppm of MIBC. There is a sharp peak at 336 nm in the absence of MIBC, but increasing MIBC content in the sample would lead to a gradual increase in intensity of the peak at 339 nm as more ternary complexes would be formed. It was found that the change in the absorbance at 340 nm was proportional to the frother concentration in the sample solution (Figure 1b).

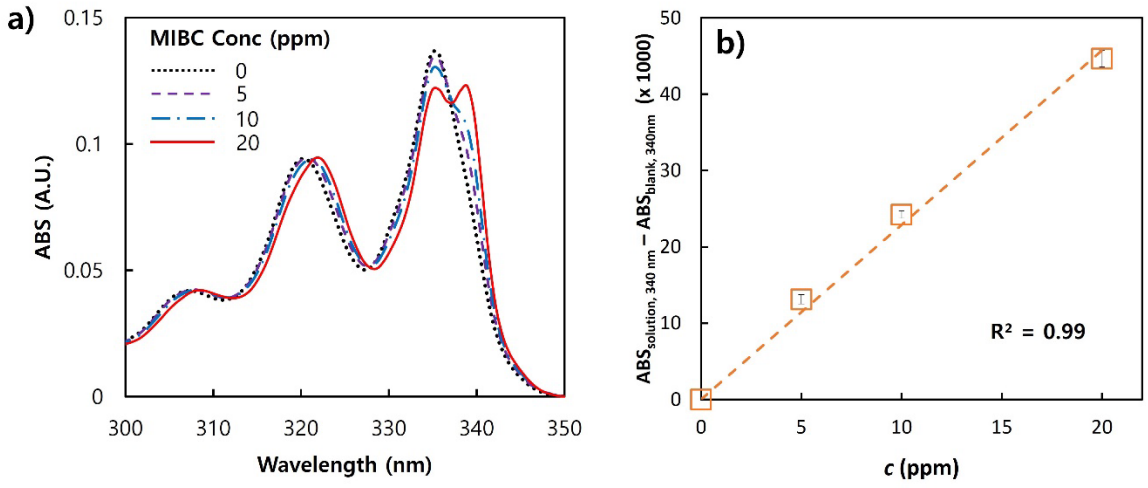

FIG 1 – (a) UV-Vis spectra of the final solution containing formulated liquid and MIBC standard solution. (b) Corrected absorbance at 340 nm versus MIBC concentration in the standard solution.

A plant survey was conducted using Method 1 to determine residual MIBC concentration distribution across a coking coal flotation plant in Queensland, Australia (Park and Wang, 2021). Figure 2 shows that the flotation feed stream prior to frother dosing contained 3.1 ppm of MIBC, indicating a considerable amount of MIBC was present in the process water returning to the flotation circuit. The MIBC concentrations in the flotation concentrate and tailing streams were around 4.2 ppm and 6.0 ppm, respectively. The partitioning of MIBC between the flotation concentrate and tailing, however, was not seemingly consistent with the dosed amount of MIBC in the flotation feed (ie 11–14 ppm). This might be due to adsorption of the MIBC molecules on the coal particles in the sampled slurry as there was up to two hours delay in filtration of the particles from these samples before being packed and transported for frother concentration measurement. The same figure shows that the remanent MIBC concentrations in the tailing thickener underflow and overflow streams were 5.5 and 4.8 ppm, respectively, while the return water dam contained 2.9 ppm MIBC. The results suggested that a considerable amount of residual MIBC was also present in the plant water circuit.

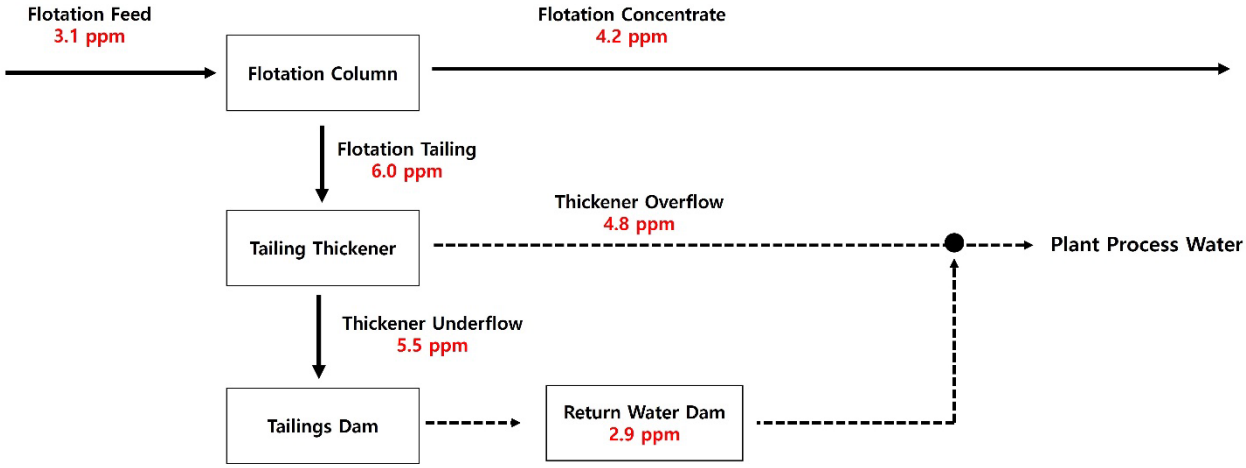

FIG 2 – Measured MIBC concentration (in ppm) at six different locations across a coking coal flotation plant in Queensland, Australia. Modified from Figure 7 in Park and Wang (2021).

METHOD 2

The SPE process was necessary in Method 2 to increase the frother concentration at least 100 times to make sure the concentration of the frother is well above the detection limit of the benchtop NMR spectrometer. The SPE process, described in detail in Lee *et al* (2021, 2022), started with loading 4 mL of methanol and then the same volume of aqueous HCl solution. After that, 1 L of the acidified sample was loaded to allow selective adsorption of the frother molecules on the cartridge. After loading the sample, the cartridge was dried for 10 minutes before being loaded with 4 mL of methanol to elute the adsorbed frother molecules. The eluent was then mixed with an internal standard (ie TMSP, 3-(Trimethylsiyl)propionic-2,2,3,3,-d4 acid sodium salts) with 1:1 v/v ratio to yield a final solution. The final solution was analysed with the NMR spectrometer. The acquired ^{1}H NMR spectrum was analysed using a quantum mechanical analysis model (Matviychuk *et al,* 2019, 2020) rather than the standard peak integration method as the characteristic peaks of the common frothers (ie MIBC and polypropylene glycol with an average molecular weight of 425 g/mol) and collectors (ie diesel and potassium ethyl xanthate) overlap between chemical shifts of 1.1–1.5 ppm as shown in Figure 3. It was found that the measured spectrum (blue solid line) matches well with the modelled one (red dashed line) even though the characteristic peaks of MIBC, polypropylene glycol with an average molecular weight of 425 g/mol (PPG425), and potassium ethyl xanthate (KEX) are overlapping each other (ie chemical shifts of 0.7–1.3 ppm for MIBC, 1.0–1.2 ppm for PPG425, and 1.2–1.5 ppm for KEX). The modelled NMR intensities of internal standard and frothers were used to calculate the frother concentration in the measured sample. The concentration in the original sample (before concentrating using the SPE process) was then determined from a calibration of the efficiency of the SPE process.

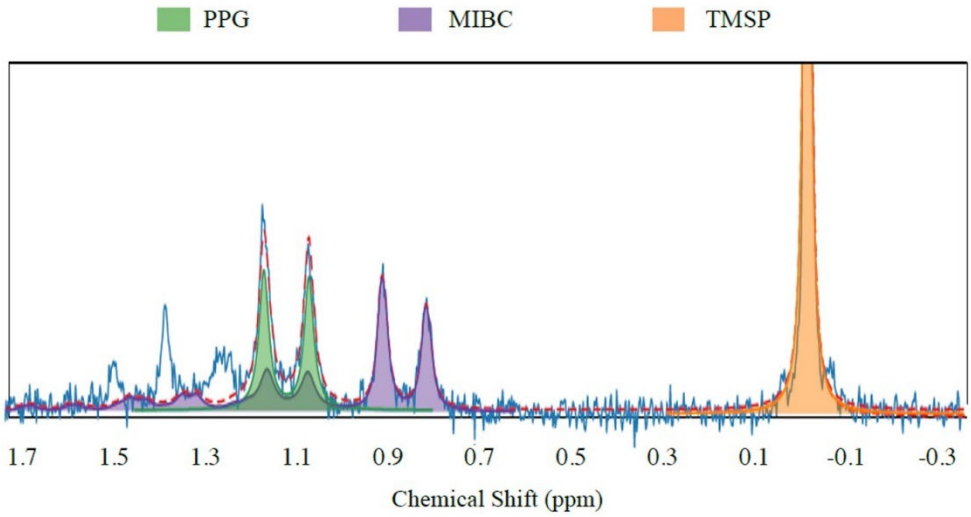

FIG 3 – ^{1}H NMR spectra of the final solution comprising internal standard and concentrated eluent. The original sample before the SPE process contained 5 mg/L of MIBC, 5 mg/L of PPG425, and 1 × 10^{-3} M KEX. The KEX was not fitted or quantified (blue peaks at around 1.3–1.5 ppm), but the presence of KEX does not influence the quantification of the other compounds singnificantly. Reproduced with permission from Lee *et al* (2022).

Figure 4 demonstrates that Method 2 can accurately quantify the concentrations of individual frothers in the MIBC-PPG45 blends within 30 minutes even in the presence of common contaminants encountered in flotation plants. The absolute error in estimation, $|c_{\text{sample}} - c_{\text{measured}}|$, was below 0.5 mg/L regardless of blending ratios and process water qualities.

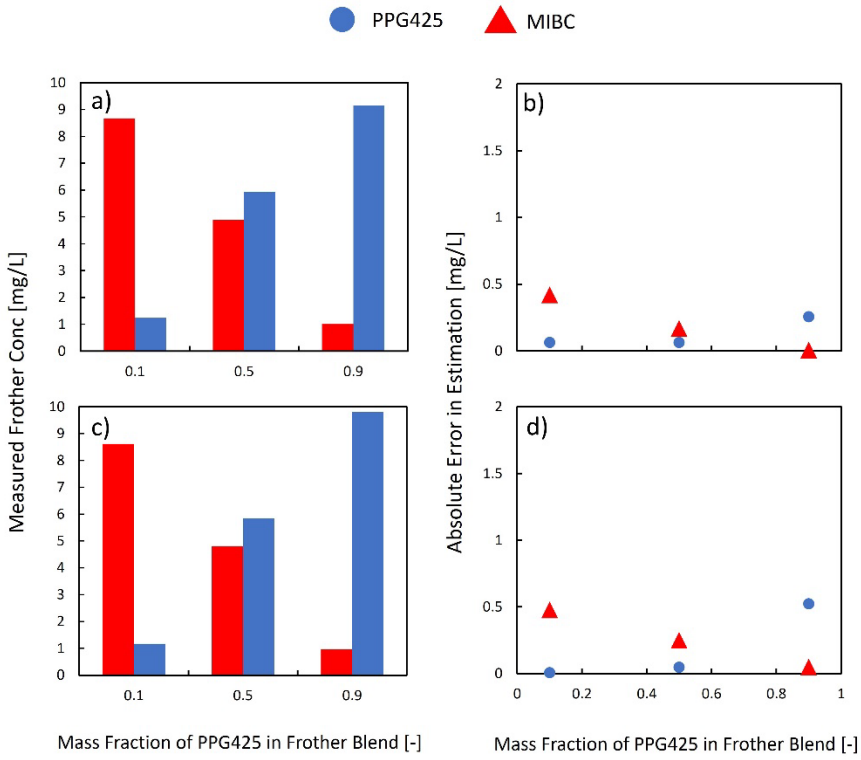

FIG 4 – Quantification of individual frothers in different simulated process water samples containing MIBC-PPG425 blends. Overall frother concentration was maintained at 10 mg/L while preparing the simulated process water from (a, b) coal flotation plants, and (c,d) mineral processing plants. The simulated process water from coal flotation plants contained background electrolytes and saturated concentration of diesel while the one from mineral processing plants contained background electrolytes and 1 × 10^{-3} M KEX. Reproduced with permission from Lee *et al,* 2022.

REMARKS ON AVAILABLE TECHNIQUES

Table 1 shows a summary of Methods 1 and 2 and the colourimetric method. The colourimetric method was selected for comparison as the usefulness of the technique has been demonstrated by multiple on-site testings (Gélinas and Finch, 2007; Zangooi, Gomez, and Finch 2010, 2017) and it has been used by multiple research groups. Method 1 is the simplest and fastest to detect frother. It has a potential as an in-plant frother concentration measurement tool because the whole process can be fully automated as it only involves sequential dosing and mixing of multiple reagents. Despite its distinctive advantages, the requirement of tight temperature control (ie ± 0.5°C or better) and the inability to detect PPG-type frothers are two major limitations.

Method 2, in contrast, is insensitive to frother type. More importantly, it can accurately detect individual frothers in frother blends without requiring any chemical reaction as it is based on NMR analysis. Method 2 also has a great potential for fully automated on-site frother measurement as there is a commercially available automated SPE system (Wagner *et al,* 2020). It was found that Method 2 is the most costly technique among these three methods as it requires a relatively expensive instrument (ie benchtop NMR and automated SPE process) and regular replacement of SPE cartridge.

The colourimetric method can also detect various types of frothers. The possibility of individual frother detection in the frother blend was also discussed by Gélinas and Finch (2005) even though it has not yet been demonstrated. The main disadvantage of the colourimetric method is the requirement of relatively time-consuming and complicated sample preparation steps, which limit automation of the colourimetric method for real-time frother detection. Furthermore, it generates a relatively large amount of toxic waste (ie concentrated sulfuric acid and chloroform) compared to the other two methods.

TABLE 1

Summary of three frother detection methods.

	Method 1	**Method 2**	**Colorimetric Method**
Step 1: Sample Preparation – Frother Extraction and Concentration			
Method	-	Solid Phase Extraction	Liquid-Liquid Extraction
Degree of concentration	-	>100 times	10 times
Reagent	-	HCl Methanol	NaCl Chloroform
Time	-	30 min	30 min
Step 2: Sample Preparation Step – Reaction			
Method	Host-Guest Complexation	Internal Standard Addition	Komarowsky Reaction
Reagent	α-CD β-CD Pyrene MIBC	TMSP	Sulfuric acid Salicyl-aldehyde
Time	<10 min including spiking known amount of MIBC, α-CD addition, and mixing with a formulated liquid (β-CD and Pyrene)	-	30 min including dehydration of frother molecule in Chloroform followed by the Komarowsky reaction

Step 3: Analysis			
Instrument	UV-Vis	Benchtop NMR	UV-Vis
Calibration Curve	Required	Not required, but R_{avg}, recovery of frother during the SPE process, needs to be known	Required
Performance			
Accuracy	$\pm$ 1.2 ppm	$\pm$ 0.5 ppm	$\pm$ 1.0 ppm
Remarks			
Advantages	1. Possibility of Automation 2. Relatively simple sample preparation step 3. Field testing completed	1. Ability to detect individual components in frother blend 2. Possibility of automation	1. Field testing completed 2. Confirmed by multiple research groups
Limitations	1. Inability to detect PPG type frother 2. Interference from background electrolyte and certain types of collector 3. Requirement of temperature control ($\pm$0.5°C)	1. Relatively expensive 2. Need information on the recovery of target frother during the SPE process 3. Field testing has not been conducted	1. Difficulty of automation due to requirement of complex sample preparation steps 2. Long sample preparation time 3. Generation of a large volume of waste toxic compound (ie chloroform)

CONCLUSIONS

Two potential methods for real-time measurement of remnant frother concentration on-site have been presented. The pros and cons of these two methods are compared with those of the colourimetric method, developed by Finch and co-workers.

The first approach, based on host-guest interactions, is a fast method to detect aliphatic alcohol type frother. As it only requires sequential dosing and mixing various reagents with the filtered slurry sample, it is the simplest method of all three considered in the present study. The suitability of on-site use of this method has been demonstrated by the determination of remnant MIBC concentration at different locations across a coking coal flotation plant. The whole process can be automated, so it has potential for online frother analysis in coal flotation plants.

The second approach uses a cryogen-free benchtop NMR spectrometer to detect alcohol and PPG type frothers, and the analysis can be done within 30 minutes. It does not involve any chemical reactions but requires the SPE process to selectively concentrate frother molecules from the filtered slurry sample. It can detect individual frother in a MIBC-PPG425 blend accurately regardless of blending ratios and water qualities. As a high-throughput automated SPE system is commercially available, the second approach is promising for on-site real-time frother analysis in a broad range of flotation operations.

The colourimetric method, which has been used in academic research for around 20 years, can accurately analyse various types of frothers without experiencing significant interference from the common contaminants encountered in the flotation plants. However, it is not yet suitable for online applications due to its low analysis rate and complicated sample preparation steps that require some degree of human intervention.

ACKNOWLEDGEMENTS

The authors gratefully thank the support from the Australian Coal Industry Research Program (ACARP Project C26012) and New Zealand Ministry of Business, Innovation and Employment (UOCX1502). HP acknowledges the Queensland Government for an Industry Research Fellowship.

REFERENCES

DeHart, R, Bethell, P, Luttrell, G, Kohmuench, J and Mankosa, M, 2016. Economic Benefits of a Deslime Flotation Circuit Using StackCell Technology at Patriot's Kanawha Eagle Coal Preparation Plant. in *XVIII International Coal Preparation Congress*, pp. 991–996 (Springer: Cham).

Fuerstenau, D W, 1982. Adsorption of frothers at coal/water interfaces. *Colloids and Surfaces*, 4(3): 213–227.

Gélinas, S and Finch, J A, 2005. Colorimetric determination of common industrial frothers. *Minerals Engineering*, 18(2): 263–266.

Gélinas, S and Finch, J A, 2007. Frother analysis: Some plant experiences. *Minerals Engineering*, 20(14): 1303–1308.

Lahey, A and Clarkson, C, 1999. Evaluation of residual frother from column flotation circuits, ACARP Report C6045

Lee, Y, Matviychuk, Y, Park, H, Wang, L and Holland, D J, 2021. Quantitative frother analysis on coal mine process water with a benchtop NMR spectrometer. *Journal of Magnetic Resonance*, 331: 107054.

Lee, Y, Park, H, Matviychuk, Y, Holland, D J and Wang, L, 2022. Frother concentration measurement with a benchtop NMR spectrometer. *Minerals Engineering*, 180: 107512.

Maldonado, M, Desbiens, A, Del Villar, R and Aguilera, R, 2010. On-line estimation of frother concentration for flotation processes. *Canadian Metallurgical Quarterly*, 49(4): 435–446.

Matviychuk, Y, Steimers, E, von Harbou, E and Holland, D J, 2020. Bayesian approach for automated quantitative analysis of benchtop NMR data. *Journal of Magnetic Resonance*, 319: 106814.

Matviychuk, Y, Yeo, J and Holland, D J, 2019. A field-invariant method for quantitative analysis with benchtop NMR. *Journal of Magnetic Resonance*, 298: 35–47.

Park, H and Wang, L, 2018. Determination of the concentration of MIBC in coking coal flotation. *Minerals Engineering*, 127: 74–80.

Park, H and Wang, L, 2021. Frother distribution in an industrial coal flotation circuit. *International Journal of Coal Preparation and Utilization*, 1–14.

Wagner, L, Zargar, M, Kalli, C, Fridjonsson, E O, Ling, N N, May, E F, Zhen, J and Johns, M L, 2020. Solid-Phase Extraction Nuclear Magnetic Resonance (SPE-NMR): Prototype Design, Development, and Automation. *Industrial & Engineering Chemistry Research*, 59(47): 20836–20844.

Weber, T, Gomez, C O and Finch, J A, 2003. A frother concentration meter, in *Proceedings of the 35th Annual Meeting of the Canadian Mineral Processors*, pp. 639–652. (Canadian Institute of Mining, Metallurgy and Petroleum: Ottawa)

Zangooi, A, Gomez, C O and Finch, J A, 2010. Frother analysis in industrial flotation cells. *Canadian Metallurgical Quarterly*, 49(4): 389–396.

Zangooi, A, Gomez, C O and Finch, J A, 2016. Frother analysis in flotation circuits: Refinement of a colorimetric technique. *Minerals Engineering*, 93: 41–49.

Zangooi, A, Gomez, C O and Finch, J A, 2017. Mapping frother distribution in industrial flotation circuits. *Minerals Engineering*, 113: 36–40.

Zanin, M, Wightman, E, Grano, S R and Franzidis, J P, 2009. Quantifying contributions to froth stability in porphyry copper plants. *International Journal of Mineral Processing*, 91(1–2): 19–27.

Zhang, W, Zhu, S and Finch, J A, 2013. Frother partitioning in dual-frother systems: Development of analytical technique. *International Journal of Mineral Processing*, 119: 75–82.

Synthesis of novel flotation collectors based on cardanol derivatives and its RAFT copolymers

T Perera[1], B Fan[2], T Hsia[3] and S Thang[4]

1. PhD candidate, Monash University, School of Chemistry, Clayton Vic 3800. Email: tammitage.perera@monash.edu
2. Research Fellow, Monash University, School of Chemistry, Clayton Vic 3800. Email: bo.fan@monash.edu
3. Research Fellow, Monash University, School of Chemistry, Clayton Vic 3800. Email: tina.hsia@monash.edu
4. Professor, Monash University, School of Chemistry, Clayton Vic 3800. Email: san.thang@monash.edu

ABSTRACT

The mining industry is currently focusing to develop and adopt sustainable collector chemistry that can efficiently recover valuable minerals from their natural state. However, a limited number of research can be seen on the design and synthesis of polymeric flotation collectors. The focal objective of this research is to synthesise a more effective polymeric collector with advanced architecture to utilise in the mineral processing industry. Reversible Addition-Fragmentation Chain Transfer (RAFT) co-polymers with cardanol derivatives have the potential to selectively trap valuable metals in the flotation process in a more efficient way. Cardanol exhibits amenability to chemical modification for making tailor-made monomers that can further produce polymers with high value.

The synthesis of a series of fit for purpose copolymers in this study was accomplished by RAFT polymerisation. The ability to design complex architecture is a significant advantage in engineering polymeric collectors by RAFT polymerisation. Initially, commercially available cardanol was converted to a cardanol based monomer and copolymerised with commercially available monomers to synthesise a series of novel cardanol based copolymers with predetermined molecular weights. The side groups of the copolymer were chemically modified to incorporate functionality that can be selectively adsorbed on the chalcopyrite surface.

INTRODUCTION

Froth flotation is one of the most unique, popular and effective operational processes for mineral beneficiation in the mineral industry. It is a process of selectively separating beneficial minerals from a mixture, by attaching relevant minerals to the froth or air bubbles that arise from the mixture. Today, froth flotation is the most widely used process in recovering valuable minerals via the separation of particles based on the differences in surface wettability. The common theme among various flotation cells, including mechanical cells, column cells and Jameson cells, is to introduce a particle suspension into an agitated and aerated vessel. Generally, a selective surfactant or a collector blends with the suspension, which preferentially attaches to the valuable mineral and renders the surface with hydrophobicity. The valuable particles can then attach to the bubbles introduced into the vessel. Subsequently, the particle-laden bubbles rise to the top of the suspension to form a froth, which discharges into a launder as mineral concentrate. Finally, the unwanted hydrophilic gangue, which cannot attach to the bubbles, settles at the bottom and is released into the waste stream (Moncayo-Riascos and Hoyos, 2017; Balaram, 2019). The froth flotation process depends on the variation of surface properties. It is achieved by the adsorption of selective collectors onto the desired mineral surfaces. In most cases, these collectors are made from petroleum and are not biodegradable. One of the significant by-products in the cashew industry is cashew nut shell liquid (CNSL). It is a unique natural source of phenol with a long unsaturated carbon chain (Caillol, 2018; Peungjitton *et al*, 2009). Cardanol is one of the major by-products of CNSL and due to its fascinating chemical structure, it can be used to synthesise bio-based collectors for froth flotation.

Cardanol is versatile starting material with great potential to replace the number of raw materials derived from fossil resources. With the presence of the C15 alkyl chain, the phenolic hydroxyl group and an aromatic ring, cardanol makes it an interesting starting material for synthesising various monomers and collectors. A limited number of studies have reported the development of polymeric

flotation collectors. The mining industry faces significant challenges in developing and adopting sustainable collector chemistry to effectively recover valued minerals from their natural state. A limited number of researchers have reported on the development of polymeric flotation collectors. RAFT copolymers could be an efficient solution to selectively trap metals in the flotation process.

Reversible Addition-Fragmentation Chain Transfer (RAFT) is a controlled living radical polymerisation invented by Moad, Rizzardo and Thang in the 1990s (Chiefari *et al*, 1998). The process is mediated by a RAFT agent (thiocarbonylthio compound) that revolutionised the scientific world in producing better polymers. RAFT polymerisation can produce block, star, and complex architectures of polymers that are useful for industrial and biomedical applications (Moad *et al*, 2009, 2013). This process has received enormous attention from the industry as its ability to further polymerise at the end of the reaction. The capability to regulate the molecular weight and dispersity of the targeted polymer is very useful in the synthesis of polymeric surfactants (Moad *et al*, 2009). The focal objective of this research is to synthesise more effective polymers to be utilised in the mineral processing industry. RAFT copolymers with cardanol moieties were explored to selectively bind chalcopyrite in a more efficient way.

RESULTS AND DISCUSSION

Four polymers with xanthate functionality [Poly(CA_A-*co*-X_A), Poly(CA_B-*co*-X_B), Poly(CA_C-*co*-X_C) and Poly(CA_D-*co*-X_D)] were synthesised by the RAFT polymerisation at pre-determined molecular weights ($M_{w,theo}$ 2500, 5000, 10 000 and 25 000 respectively). The hydrophilic and lipophilic components were kept at a roughly constant ratio. The chalcopyrite samples used in this study were purchased from Ward's Science. X-ray diffraction spectroscopy (Figure 1) confirmed the presence of silica and pyrite impurities in the chalcopyrite samples used.

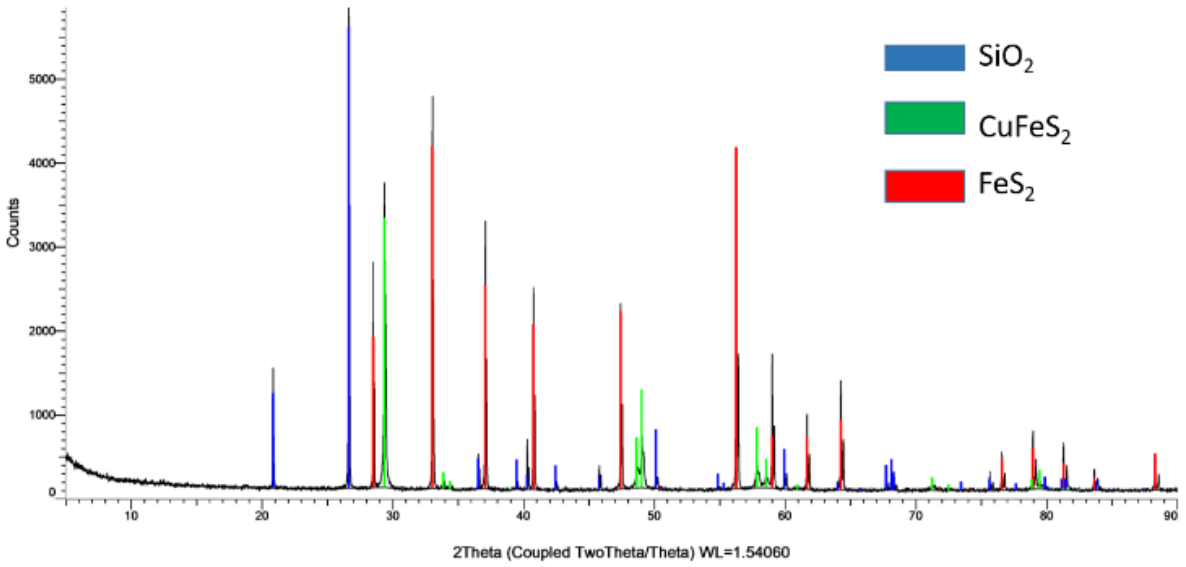

FIG 1 – XRD phase diagram of chalcopyrite obtained from the Ward's Science indicates the presence of silica and pyrite impurities.

The contact angle of the chalcopyrite surface was measured as a function of polymer concentration. The hydrophobicity of the chalcopyrite surface was assessed by measuring the static contact angle of 10 µl drops of water, using the sessile drop method and using a contact angle goniometer. Five measurements were made on each sample and the mean contact angle and standard deviation were reported. The wettability of chalcopyrite surfaces modified by Poly(CA_A-*co*-X_A), Poly(CA_B-*co*-X_B), Poly(CA_C-*co*-X_C) and Poly(CA_D-*co*-X_D) was investigated with polymer concentrations ranging from 50 to 500 ppm. All experiments were carried out in deionised water media. The pH of the medium was maintained at 9. The corresponding results are shown in Figure 2.

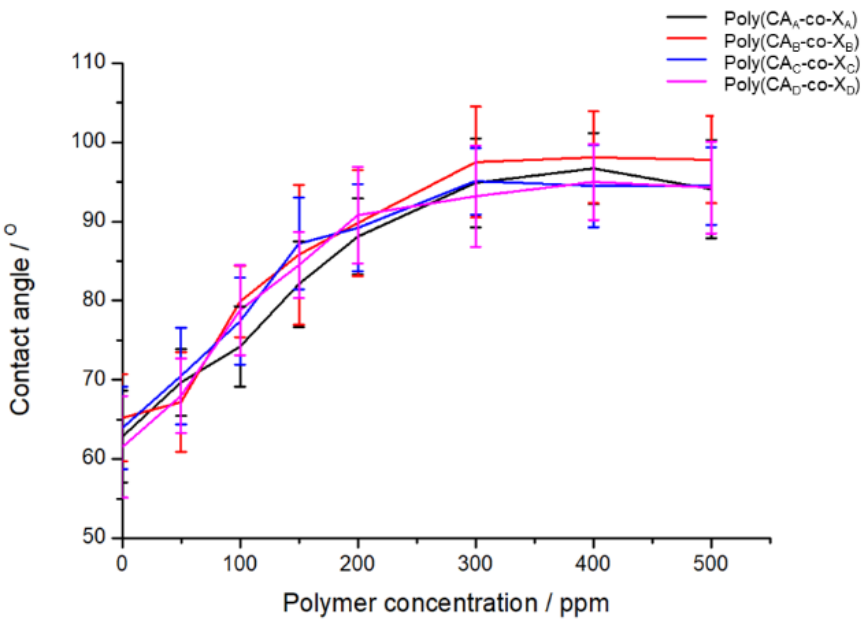

FIG 2 – Contact angle deviation of chalcopyrite surfaces at different polymer concentrations.

Results of these experiments show that the xanthate-functionalised Poly(CA$_A$-*co*-X$_A$), Poly(CA$_B$-*co*-X$_B$), Poly(CA$_C$-*co*-X$_C$) and Poly(CA$_D$-*co*-X$_D$) can effectively adhere to the surface of chalcopyrite, leading to a hydrophobic modification of its surface. As shown in Figure 2, the contact angle increased significantly in the presence of all four polymers and the contact angle increased with increasing polymer concentration. The increase in contact angle indicates the adsorption of polymeric collectors on the surface of chalcopyrite and the effectiveness of these collectors in increasing the hydrophobicity of its surface.

In these experiments, the minimum contact angle (polymer-free chalcopyrite surface) stayed between 61.5° and 65.2°, which is similar to the values reported in the literature (Muganda *et al*, 2011; Han *et al*, 2016; Bai *et al*, 2018). The contact angle remained consistent until the polymer was added. The hydrophobicity of the chalcopyrite surface increased significantly until it levelled off at 300 ppm of Poly(CA$_A$-*co*-X$_A$). The contact angle of the rest of the polymer-chalcopyrite surface also levelled off at 300 ppm. The achievement of the maximum contact angle on the chalcopyrite surface is shown by the flattening of the contact angle of the graph. This is in line with what would be expected for the other polymers, as the ratios of cardanyl acrylate and xanthate moieties are the same.

It is known that an increase in molecular weight increases the length of the polymer backbone, which contributes to the hydrophobic nature of the polymer. Results of this experiment show that the contact angle (93.2° ± 6.4°) readings for Poly (CA$_D$-*co*-X$_D$), the polymer with the highest molecular weight ($M_{w,theo}$ 25 000), are relatively lower than those for the lower molecular weight polymers. Furthermore, out of the five contact angle readings, the standard deviation was relatively high in Chalcopyrite-Poly(CA$_D$-*co*-X$_D$) system.

There are a number of factors that contribute to the contact angle of the chalcopyrite surface. Chau and co-workers (Chau *et al*, 2009) reported that surface roughness, heterogeneity and molecular interactions also contribute to the contact angle. Zhu and co-workers (Zhu *et al*, 2020) reported the increased flotation performance in their studies was based on the surface roughness and hydrophobicity of quartz surfaces. In this study, the chalcopyrite samples were polished by hand using a Saphir 520 polishing machine. As a result, it was difficult to maintain the surface roughness at a constant value over the entire surface, resulting in different roughness across the surface. Scratches on the surface during the polishing process resulted in different roughness on the metal surface. In addition, the polished chalcopyrite surface has different compositions, such as silica and pyrite, creating a heterogeneous surface. In addition, the XRD phase diagram of the chalcopyrite used for this experiment confirmed the presence of impurities. The synthetic polymeric collector targets sulfide minerals, such as chalcopyrite, while it does not bind to silica, resulting in a change in contact angle on the same surface.

Adsorption of the xanthates (-$OCS_2^-K^+$) on the chalcopyrite surface occurs through three pathways. These are chemisorption, physisorption or surface precipitation (Bowden and Young, 2016; Ahmadi *et al*, 2018). Bowden and co-workers (Bowden and Young, 2016) showed that chemisorption of xanthates on the surface of chalcopyrite would occur in the region where Cu_2S is formed after oxidation of the chalcopyrite surface. In this study, UV-Vis spectra were recorded in order to understand the interaction of Poly(CA_A-*co*-X_A), Poly(CA_B-*co*-X_B), Poly(CA_C-*co*-X_C) and Poly(CA_D-*co*-X_D) with chalcopyrite surfaces. As shown in Figure 3, there is a strong xanthate peak at 301 nm prior to the interaction of the polymer with the chalcopyrite surface. After interaction with chalcopyrite, the xanthate peak diminishes significantly. The depletion of the xanthate peak, therefore, indicates the adsorption of xanthate polymer on the surface of chalcopyrite.

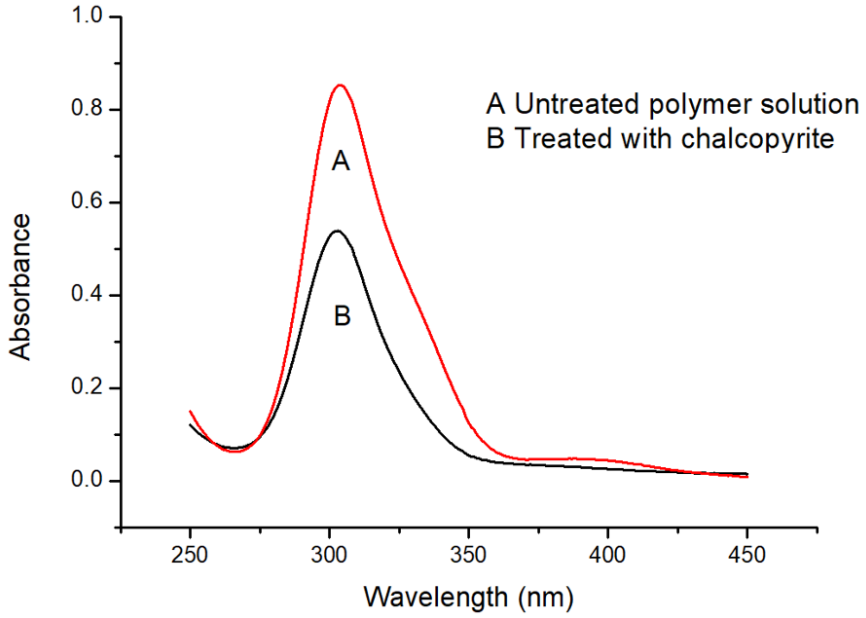

FIG 3 – UV-Visible spectra of Poly(CA_A-*co*-X_A) solution before and after interaction with the chalcopyrite. The absorbance was measured in 0.25 mg/ml polymer solution (A) and after treating the same solution with 1 g of chalcopyrite (B).

CONCLUSIONS

The results of the contact angles and UV-Visible spectroscopy studies show the adsorption of the fit for purpose polymers on the chalcopyrite surface and the hydrophobic modification of the chalcopyrite surface. These polymers were validated against chalcopyrite surfaces. In the forthcoming study, these polymers will be validated against other sulfide minerals such as galena, chalcocite, covellite and sphalerite. In addition, the flotation recoveries of the sulfide minerals need to be analysed against the chain length of the polymers.

ACKNOWLEDGEMENTS

The authors would like to thank the ARC Centre of Excellence for Enabling Eco-Efficient Beneficiation of Minerals, grant number CE200100009 for providing financial support for this research.

REFERENCES

Ahmadi, R, Ravanasa, E and Mirzapour, Y, 2018. Exploring mechanism of xanthate adsorptionon chalcopyrite surface: An atomic force microscopy study. *Journal of Mining and Environment,* 9, 1009–1018.

Bai, L, Liu, J, Han, Y, Jiang, K and Zhao, W, 2018. Effects of xanthate on flotation kinetics of chalcopyrite and talc. *Minerals,* 8, 369.

Balaram, V, 2019. Rare earth elements: A review of applications, occurrence, exploration, analysis, recycling, and environmental impact. *Geoscience Frontiers,* 10, 1285–1303.

Bowden, J and Young, C, 2016. Xanthate chemisorption at copper and chalcopyrite surfaces. *Journal of the Southern African Institute of Mining and Metallurgy,* 116, 503–508.

Caillol, S, 2018. Cardanol: A promising building block for biobased polymers and additives. *Current opinion in green and sustainable chemistry,* 14, 26–32.

Chau, T, Bruckard, W, Koh, P and Nguyen, A, 2009. A review of factors that affect contact angle and implications for flotation practice. *Advances in colloid and interface science,* 150, 106–115.

Chiefari, J, Chong, Y K, Ercole, F, Krstina, J, Jeffery, J, Le, T P, Mayadunne, R T A, Meijs, G F, Moad, C L, Moad, G, Rizzardo, E and Thang, S H, 1998. Living free-radical polymerization by Reversible Addition-Fragmentation Chain Transfer: The RAFT process. *Macromolecules* 31, 5559–5562.

Elizondo-Álvarez, M A, Uribe-Salas, A and Bello-Teodoro, S, 2021. Chemical stability of xanthates, dithiophosphinates and hydroxamic acids in aqueous solutions and their environmental implications. *Ecotoxicology and Environmental Safety,* 207, 111509.

Han, Y-X, Zhu, Y-M, Li, Y-J and Hao, L, 2016. Flotation behaviors and mechanisms of chalcopyrite and galena after cyanide treatment. *Transactions of Nonferrous Metals Society of China,* 26, 3245–3252.

Iwasaki, I and Cooke, S R, 1958. The decomposition of xanthate in acid solution. *Journal of the American Chemical Society,* 80, 285–288.

Moad, G, Rizzardo, E and Thang, S H, 2009. Living radical polymerization by the RAFT process–a second update. *Australian journal of chemistry,* 62, 1402–1472.

Moad, G, Rizzardo, E and Thang, S H, 2013. RAFT Polymerization and some of its applications. *Chemistry – An Asian J,* 8, 1634–1644.

Moncayo-Riascos, I and Hoyos, B A, 2017. Effect of collector molecular structure on the wettability of gold for froth flotation. *Applied Surface Science,* 420, 691–699.

Muganda, S, Zanin, M and Grano, S, 2011. Influence of particle size and contact angle on the flotation of chalcopyrite in a laboratory batch flotation cell. *International Journal of Mineral Processing,* 98, 150–162.

Peungjitton, P, Sangvanich, P, Pornpakakul, S, Petsom, A and Roengsumran, S, 2009. Sodium cardanol sulfonate surfactant from cashew nut shell liquid. *Journal of Surfactants and Detergents,* 12, 85–89.

Zhu, Z, Yin, W, Wang, D, Sun, H, Chen, K and Yang, B, 2020. The role of surface roughness in the wettability and floatability of quartz particles. *Applied Surface Science,* 527, 146799.

The synergistic interaction between hexanol and dithiophosphate at the air-water and galena-water interface

D Pienaar[1], B McFadzean[2] and C T O'Connor[3]

1. Post-doctoral Fellow, Centre for Minerals Research, Department of Chemical Engineering, University of Cape Town, Cape Town, 7701, South Africa. Email: pienaar.dandre@gmail.com
2. Associate Professor, Centre for Minerals Research, Department of Chemical Engineering, University of Cape Town, Cape Town, 7701, South Africa. Email: belinda.mcfadzean@uct.ac.za
3. Professor, Centre for Minerals Research, Department of Chemical Engineering, University of Cape Town, Cape Town, 7701, South Africa. Email: cyril.oconnor@uct.ac.za

ABSTRACT

Collector and frother molecules in sulfide mineral flotation are thought to have separate roles in the flotation process, where the collector selectively hydrophobizes the mineral surface and the frother adsorbs onto the bubble surface, inhibiting bubble coalescence. Molecular interactions have been observed between these molecules which allow them to co-adsorb at each of the respective interfaces, improving pulp phase recovery. This study investigated the molecular interactions between sodium diethyl dithiophosphate (SDEDTP) and hexanol, and the mechanism by which these interactions improve the recovery of galena.

In this study each of the respective interfaces were investigated for the adsorption of SDEDTP. The adsorption of SDEDTP on galena was measured by UV-Vis spectrophotometry and isothermal titration calorimetry. At the air-water interface foam stability and pulp bubble coalescence was used to quantitatively discern if there are interactions between SDEDTP and hexanol. Microflotation and induction time experiments were performed to determine the effect of SDEDTP, hexanol and their mixtures on mineral recovery and bubble-particle attachment. The results of all these tests were collated to determine if SDEDTP-hexanol mixtures synergistically improve sulfide mineral recovery.

It was found that SDEDTP reduced bubble coalescence in the pulp demonstrating activity at the air-water interface. Together SDEDTP and hexanol synergistically enhanced foam stability. This indicated that there are attractive molecular interactions between these reagents. Even though DTP did not adsorb onto galena, DTP-frother mixtures synergistically improved the recovery and attachment probability of this mineral. Adsorption studies with aeration showed that DTP in the presence of a frother transfers from the air-water interface to the galena mineral-water interface during bubble-particle collision. It was proposed that the transfer of hexanol through the thin film enhanced the kinetics of film thinning between the bubble and the particle by destabilising the thin film thus improving pulp phase mineral recovery.

INTRODUCTION

Reagents with dithiolate reactive headgroups have long been used as collectors in base metal sulfide (BMS) flotation. Xanthates are the most widely used of these reagents. Dialkyl dithiophosphates and dithiocarbamates are also frequently used, generally as co-collectors. Figure 1 shows the chemical structure of these collectors.

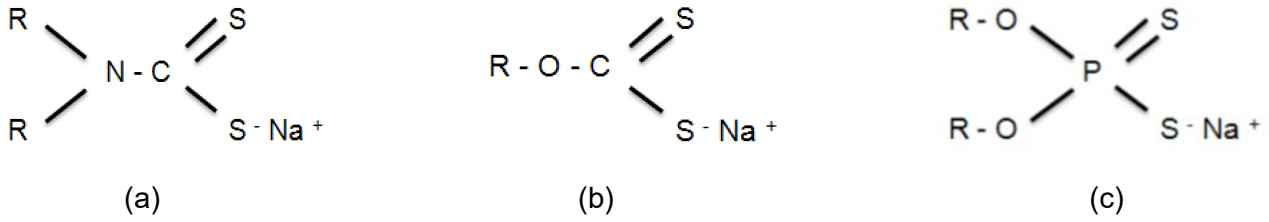

(a) (b) (c)

FIG 1 – Chemical structure of a) dithiocarbamate, b) xanthate, and c) dithiophosphate.

Of these three collectors, the dialkyl dithiophosphates (DTP) do not bond as strongly with the mineral surface due to the two electron-withdrawing oxygen atoms attached to the phosphorus atom (Lotter and Bradshaw, 2010). In contrast, dithiocarbamates (DTC) have electron donating properties

resulting in a higher electron density in the dithiol headgroup resulting in a stronger bond with the mineral surface. In this context xanthates are intermediate between DTP and DTC in terms of bonding strength.

Previous studies have shown that DTP may adsorb onto mineral surfaces depending on the experimental conditions. Nagaraj and Brinen (2001) have shown minimal adsorption of di(iso)butyl DTP (SDIBDTP) onto pyrite using TOF-SIMS whereas McFadzean and O'Connor (2014) have shown, using isothermal titration calorimetry and UV-vis spectroscopy, that there is essentially no adsorption of diethyl DTP onto galena. Petrus *et al* (2011) made similar observations with diethyl DTP on chalcopyrite and tennantite. All these experiments were conducted under basic pH conditions where it was shown that metal hydroxide species on the mineral surface reduce the amount of available adsorption sites, inhibiting the adsorption of DTP (Petrus *et al*, 2011). At acidic pH conditions greater adsorption of DTP onto the same minerals was observed (Güler and Hiçyilmaz, 2004; Petrus *et al*, 2011).

Notwithstanding these experimental results which indicate that diethyl DTP does not appear to adsorb onto sulfide mineral surfaces the addition of diethyl DTP has been shown to enhance the floatability of sulfide minerals (Manono *et al*, 2020; Kloppers *et al*, 2016; McFadzean, Mhlanga and O'Connor, 2013). This is particularly the case when DTP is added as a co-collector. Recently it has been shown, in microflotation tests, that when using diethyl DTP in the presence of a frother (hexanol) the flotation kinetics of galena is synergistically improved (Figure 2; Pienaar *et al*, 2019). This is of particular interest since it has been previously shown that SDEDTP showed no interaction at all with galena (McFadzean and O'Connor, 2014).

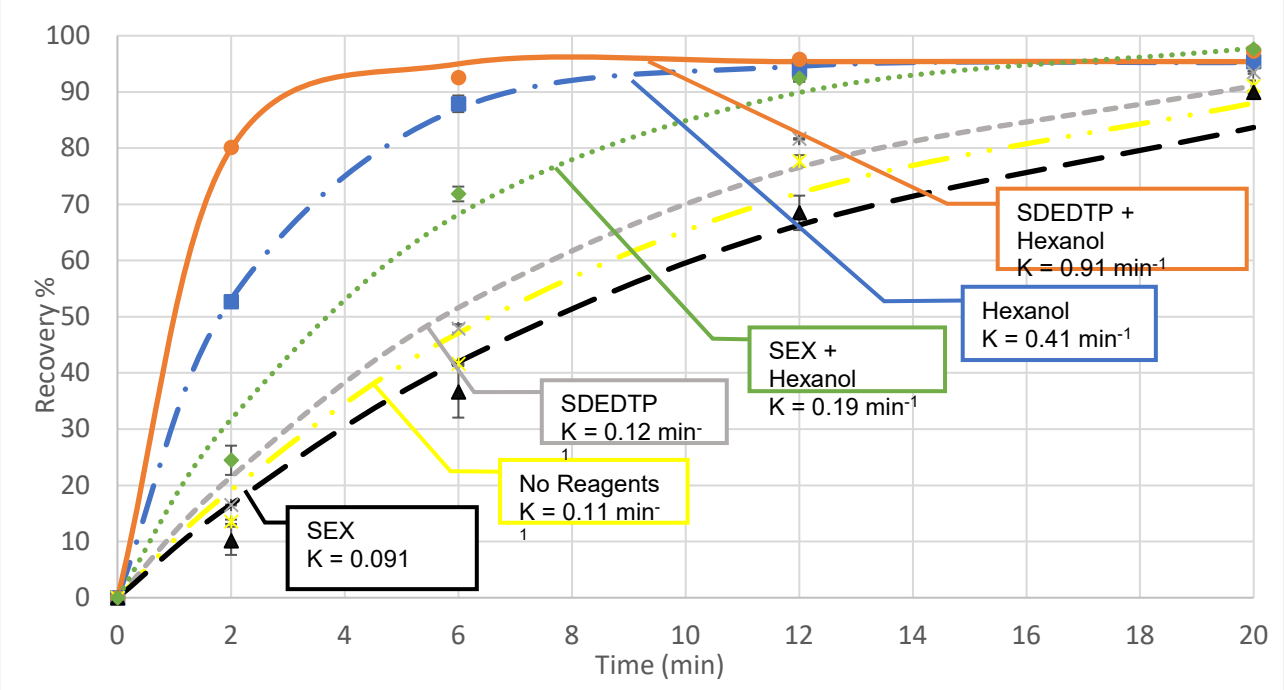

FIG 2 – Recovery of galena as a function of time at pH 9 using single reagents and reagent mixtures. Collectors are dosed at 50 per cent monolayer coverage and the frother is dosed so that the concentration is just above the CCC (Pienaar *et al,* 2019).

Interactions between collectors and frothers have been shown to synergistically increase pulp phase recovery and froth stability (Leja and Schulman, 1954). Surface active substances, similar to reagents that are used as collectors and frothers in flotation, are often used in mixtures. Molecular interactions between these mixtures frequently result in synergistic improvements in performance compared to the individual reagents (Rosen, 1986).

The main theory that attempts to explain how the molecular interactions between collectors and frothers synergistically improves mineral recovery and enhances froth stability is known as penetration theory and was proposed by Leja and Schulman (1954). This theory is based on diffuse mixed monolayers of collectors and frothers forming at the air-water and mineral water interface due

to the molecular interactions occurring between these molecules. When a particle collides with the bubble, the diffuse monolayers at the air-water and mineral-water interface can transfer from one interface to another. This increases the concentration of collector on the mineral surface, destabilising the thin film between the bubble and particle thus improving bubble-particle attachment kinetics and synergistically enhancing recovery and froth stability. In contrast to this theory, Lekki and Laskowski (1971) proposed that the frother molecules destabilise the thin film between the bubble and the particle during the attachment process due to the sparing solubility of frothers, specifically alcohols, in water.

Some authors (Fuerstenau, 2001; Yan, 2016; Wang and Miller, 2018) have found that amine-based collectors adsorb at the mineral surface during the bubble-particle collision process. Rao (2013, p 652) argued that the diffusion of the collector through the thin film between the bubble and the particle would not significantly influence the induction time but proposed that the presence of a second type of surfactant may significantly improve the induction time.

Since diethyl DTP does not adsorb onto the galena surface, it may be that the synergistic improvements in recovery can be ascribed to phenomena described above, *viz*. mainly that diethyl DTP interacts with hexanol at the air-water interface and that the reagents transfer from the air-water interface to the mineral-water interface during bubble-particle collision.

The present study has thus focused on investigating the effect of the addition of hexanol on factors such as the adsorption of the collectors at the mineral-water interface using standard adsorption tests and isothermal calorimetry as well the effect of hexanol addition on factors such as the bubble -particle attachment, foam stability and bubble coalescence in the pulp phase.

EXPERIMENTAL

Mineral preparation

The galena sample was obtained from Ward's Natural Science Establishment, Rochester, NY. The sample was received in chunks of 150 mm diameter. The sample was crushed to about 10 mm and then pulverised in a Sieb mill for 15 seconds and then dry sieved for 20 min on a shaker into three fractions, *viz*. -125+106 µm, -106+38 µm, -38 µm. Samples were stored under nitrogen at -30°C to minimise surface oxidation The sample was found to be very pure containing less than 1 per cent by mass impurities.

Reagents

The collectors used in this study were provided by AECI Mining Chemicals, South Africa. Sodium diethyl dithiophosphate (SDEDTP) was received in a high pH solution, which stabilises the dithiophosphate. GC analysis confirmed the purity of the SDEDTP at 96 per cent, with 4 per cent diethyl thiophosphate also present. Reagents were freshly prepared in a stock solution with deionised water.

Synthetic plant water (SPW) was used in all experiments. The composition of the synthetic plant water has been described previously (Pienaar *et al,* 2019). The pH at which the experiments were conducted was either 4 or 9. This was done by adjusting the solution's pH (after reagents and solids were added) with 0.1 M HCl or 0.1 M NaOH.

Adsorption studies

The isothermal titration calorimetry experiments were carried out in a TAM III isothermal titration microcalorimeter manufactured by TA Instruments, used in heat flow mode. The adsorption studies were carried isothermally and the amount of reagent which did not adsorb on the mineral was determined using UV spectroscopy. The procedure used in both of these sets of experiments has been described in detail elsewhere (McFadzean and O'Connor, 2014).

Adsorption tests were also performed in the presence of air-bubbles to determine if the collector transfers from the air-water interface to the mineral surface. Details of this experimental procedure can be found in Pienaar (2022).

Bubble coalescence tests

Frothers inhibit bubble coalescence at very low concentrations, which are typically employed in flotation. These concentrations are generally lower than the sensitivity of surface tension measurements to detect, which is why bubble size measurements were also carried out. The critical coalescence concentration (CCC) is known as the concentration at which coalescence is completely inhibited, and the bubble size is only controlled by sparger geometry (Cho and Laskowski, 2001).

Since the literature indicates that DTP is active at the air-water interface (Dai *et al*, 2001; Jordaan, 2018), CCC measurements were used to measure the activity of DTP at the concentrations that are used in flotation. Furthermore, the CCC of mixtures of collectors and frothers were used to observe if there were any observable synergistic interactions at these typical flotation concentrations.

Bubble size was measured using the Anglo Platinum Bubble Sizer (APBS), which is based on the McGill design described by Hernandez-Aguilar *et al* (2004). The entire system has been described elsewhere (Pienaar, 2022). The same concentrations of reagents were used in the bubble sizer as in the flotation cell.

Foam stability

Foam stability tests were conducted to observe if there are any synergistic interactions between collectors and frothers at the air-water interface at the concentrations typically used in flotation. Concentrations were chosen to be between 0.26 mM and 0.53 mM of collector or frother which corresponds to dosages between 50 and 100 g/ton at 35 per cent solids. The Bikerman (1973) test was used to determine the dynamic foam stability of the mixtures. The entire experimental procedure has been described elsewhere (Pienaar, 2022). In these tests the following relationship was used to determine the factor $\sum$ which represents the average amount of time that the gas is entrained in the foam (Barbian *et al,* 2003).

$$\sum = \frac{H_{max} * A}{Q}$$

where H_{max} is the maximum height the foam reaches, A is the cross-sectional area of the column, and Q is the volumetric flow rate of the air. All experiments were performed in triplicate.

Particle-bubble attachments tests

The Automated Contact Time Apparatus (ACTA) is used to determine the bubble-particle attachment probability under various chemical conditions and its use has been described in detail elsewhere (Aspiala *et al*, 2018). In the present studies mineral particles in the -125 + 106 µm size range were used to make up the particle bed. Before each experiment the particles were sonicated for 5 minutes, and then wet screened over a 106 µm screen to remove any fines. The particles were conditioned in 100 mL of deionised water, which was adjusted to pH 9. The same dosages for collector and frother was used as in the microflotation experiments.

RESULTS AND DISCUSSION

Adsorption tests

Table 1 shows the results of the adsorption tests using both SEX and SDEDTP. The amount adsorbed was determined by the difference between the original concentration of the reagent in the solution and its concentration after 20 minutes of contact with the galena. The mole percent of SDEDTP and SEX adsorbed onto galena at pH 9, with or without hexanol present, is shown. Collectors were dosed to cover 50 per cent of the mineral surface, and the frother was dosed at the CCC, the critical coalescence concentration. Most importantly to note is that, consistent with previous studies reported above, the relative amount of SDEDTP adsorbed onto the galena is negligibly low.

TABLE 1

Adsorption of SEX and SDEDTP onto galena in the presence and absence of hexanol.

	SEX	SEX + Hexanol	SDEDTP	SDEDTP + Hexanol
Collector adsorbed on galena (%)	96.4 ± 0.08	96.4 ± 0.05	~0	1.4 ± 0.89
Monolayer coverage (%)	48.2 ± 0.04	48.2 ± 0.03	~0	0.7 ± 0.45

Interestingly when these tests were carried out either in the presence or absence of aeration (Figure 3) it was found that in the case of aeration, the SDEDTP-hexanol mixture adsorption more than doubled. This is presumably due to the SDEDTP transferring from the air-water interface to the mineral-water interface in the presence of hexanol. These results indicated that the role of SDEDTP is at the air-water interface and that it there is an interaction with hexanol.

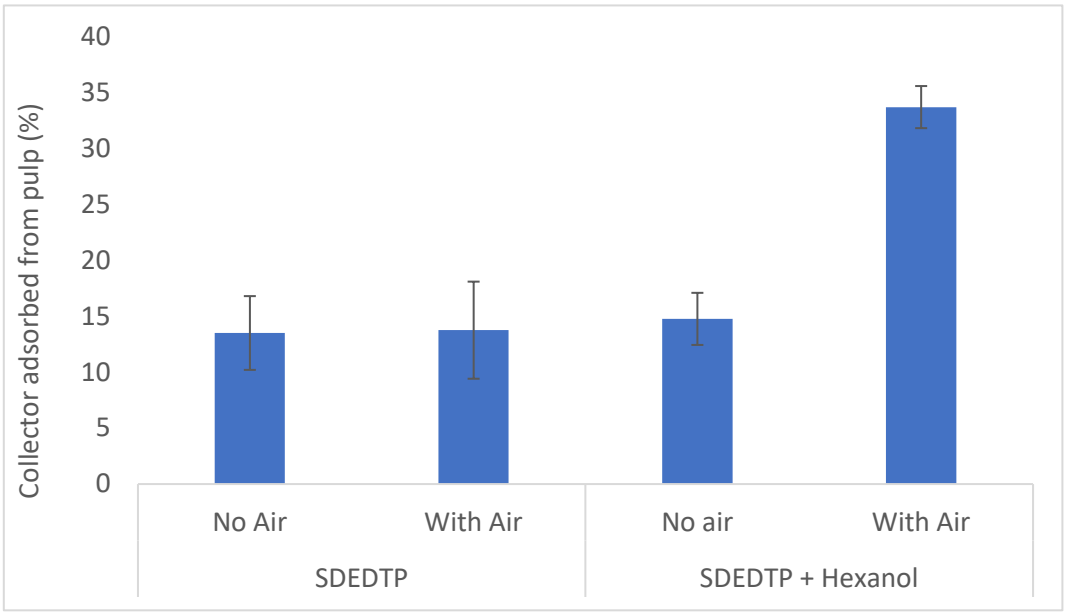

FIG 3 – The adsorption of SDEDTP onto galena at pH 9 with and without air.

Isothermal calorimetry tests

Figure 4 shows the results obtained in calorimetry experiments to determine the enthalpy of adsorption of SDEDTP onto galena in the presence and absence of hexanol at dosages equivalent to pseudo-monolayer surface coverages of 0.5 to 2. The highest enthalpy value was observed at the lowest coverage. As SDEDTP dosage increased, the value of the exotherm decreased and remained constant at around -5 kJ/mol. However, when hexanol is present there is a much lower enthalpy of adsorption which again is consistent with the fact that any increase in microflotation recovery is not due to some enhanced adsorption of the SDEDTP onto the galena. The values of the adsorption enthalpies are very low compared to those previously found for xanthate or dithiocarbamate collectors onto galena, which were in the region of -40 to -70 kJ/mol (McFadzean and O'Connor, 2014). This supports the contention that there is very little adsorption of SDEDTP onto the galena surface with or without the presence of hexanol.

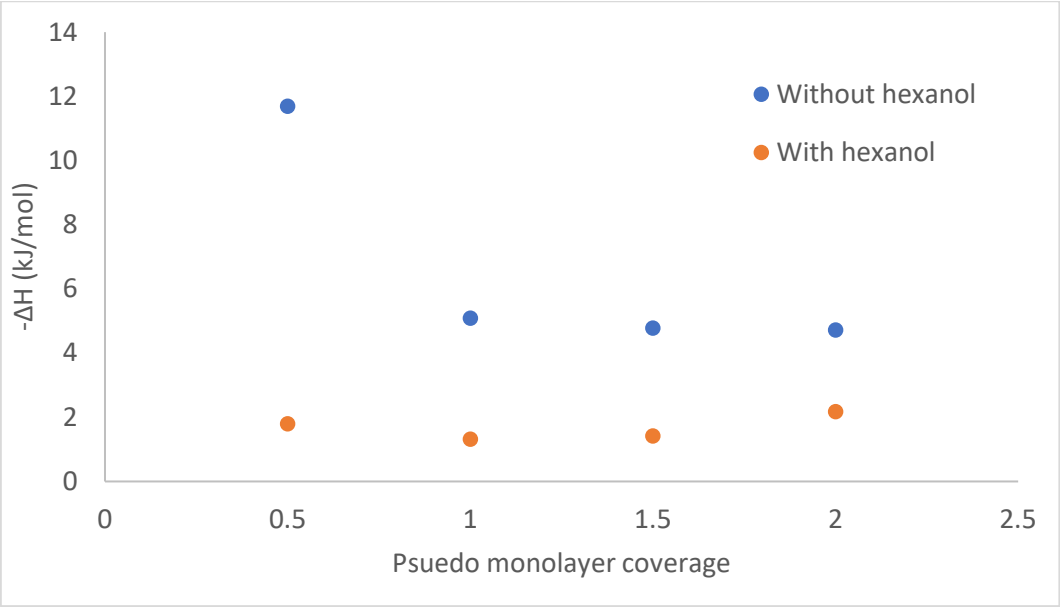

FIG 4 – The enthalpy of SDEDTP adsorption onto galena at pH 9 in the presence of hexanol and without hexanol as a function of surface area coverage.

Bubble coalescence tests

Figure 5 shows the Sauter mean bubble diameter as a function of surfactant concentration. The CCC95 value for hexanol was determined to be 10.2 ppm, which corresponds to the 11 ppm found by Zhang *et al* (2012). At concentrations as low as 3 ppm SDEDTP showed significant activity at the air-water interface, but compared to hexanol, SDEDTP reduced pulp bubble coalescence to a lesser extent.

The mixture of hexanol and SDEDTP did not show any synergistic effect. At concentrations lower than the CCC of hexanol, the pulp bubble size of the mixture followed a straight line, which was equivalent to the bubble size of the SDEDTP component (100 ppm). Even though interactions are not observed, there is clear evidence that SDEDTP is active at the air-water interface at very low concentrations.

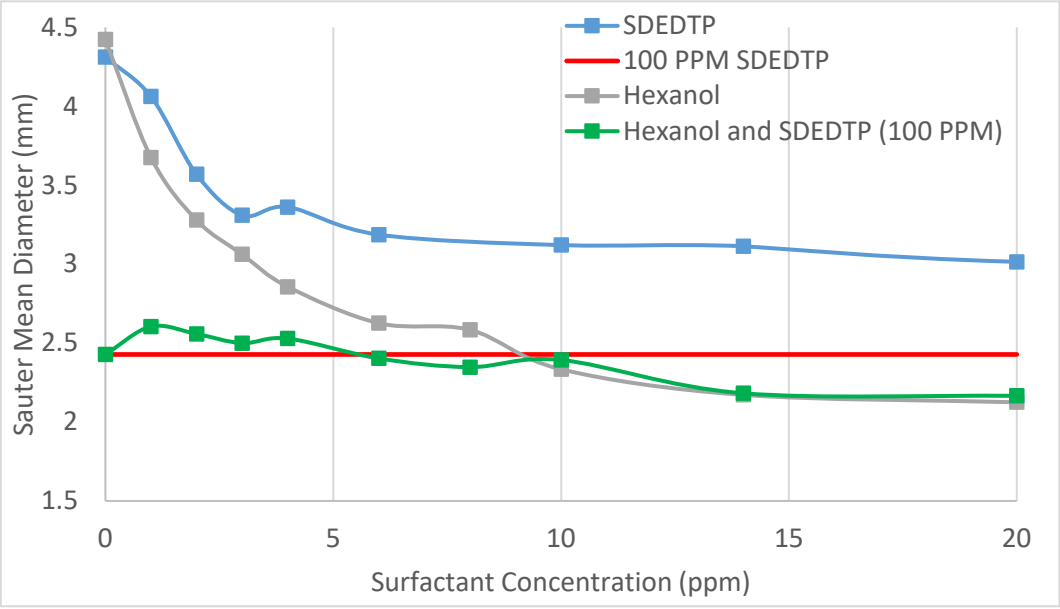

FIG 5 – Sauter mean diameter as a function of surfactant concentration for hexanol, SDEDTP, and their mixture.

Foam stability tests

Table 2 shows the indicators of dynamic foam stability, ∑, of a range of various thiol collectors mixed with hexanol, at different ratios and concentrations. The collectors used were diethyl, di n-butyl, di-iso-butyl DTP's and isobutyl xanthate. Three dosages of collector were used, *viz*. mole fractions of 0.5, 0.32 and 0.67. Foam stability tests were primarily performed as an indicator of collector activity at the air-water interface and its interaction with hexanol at the air-water interface.

TABLE 2

The dynamic foam stability factors of various thiol collector mixtures with hexanol, at different ratios and concentrations. Additive values represent the mixture stability factor calculated from single reagent experiments.

Mole fraction collector	0.5		0.32		0.67	
Total concentration of surfactants [mM]	0.52		0.79		0.79	
	Dynamic foam stability factor ∑ (s)					
Reagents	$\sum_{Calculated}$	$\sum_{Experimental}$	$\sum_{Calculated}$	$\sum_{Experimental}$	$\sum_{Calculated}$	$\sum_{Experimental}$
SDEDTP + Hexanol	1.96	1.51	5.67	1.85	1.96	4.04
SD(N)BDTP + Hexanol	1.91	1.35	5.61	2.36	2.02	4.04
SD(I)BDTP + Hexanol	2.36	3.93	6.06	5.95	2.36	5.05
SIBX + Hexanol	1.91	1.35	5.61	2.52	1.91	4.71

The calculated dynamic foam stability factor values were determined from single reagent experiments. The values were linearly combined as a function of the concentration of each reagent (weighted sum contribution). Comparing the calculated values to the experimental values serves as an indication of whether the surfactant mixtures additively, synergistically, or antagonistically affect the dynamic foam stability. The change in the dynamic foam stability factor values are shown in Table 3.

TABLE 3

The change in the dynamic foam stability factor ($\sum_{Experimental} - \sum_{Calculated}$) for the collector-hexanol mixtures as a function of mole percent of collector.

Mole fraction of collector	**Total surfactant concentration [mM]**	**SDEDTP**	**SD(N)BDTP**	**SD(I)BDTP**	**SIBX**
0.32	0.79	-3.81	-3.25	-0.11	-3.09
0.50	0.52	-0.45	-0.56	1.57	-0.56
0.67	0.79	2.08	2.02	2.69	2.80

It is clear that the increase in synergistic behaviour is driven by the increase in mole fraction of collector since there is a large difference between the 0.32 and 0.67 mole fractions at the same concentration of 0.79 mM. Interestingly, the collectors on their own formed negligible amounts of foam. Lower mole fractions of collector and higher mole fractions of hexanol produce an antagonistic response, where the difference between the experimental and calculated dynamic foam stability factor is negative.

These results show that there are definite interactions between diethyl DTP and hexanol at the air-water interface.

Particle-bubble attachment tests

Figure 6 shows the attachment probability measurements as determined using the ACTA procedure. These are determined as the ratio of the 396 bubble-particle attachment opportunities that actually resulted in attachment, to the total. With previous devices similar to the ACTA there are only ten bubble-particle attachment opportunities. Clearly the presence of hexanol with SDEDTP had a significant effect on the probability of galena particles attaching to bubbles. This is a most significant result in the context of the present investigation. Also shown in this figure are the respective masses of galena recovered in the automated contact time apparatus (ACTA) for each of reagent regimes. Clearly the presence of hexanol in the case of SDEDTP significantly increased the attachment probabilities and the mass of galena recovered. In the case of SEX this was not the case and the adsorption results showed that this cannot ascribed to a reduced adsorption of SEX onto the galena surface since the probability of attachment is hardly affected by the presence of hexanol. It may be surmised that the hexanol played a different role such as possibly inhibiting the adsorption of SEX onto the galena surface and thus reducing its recovery. Bubble size is controlled in the ACTA tests so the improvements in attachment probability cannot be ascribed to any bubble size effects.

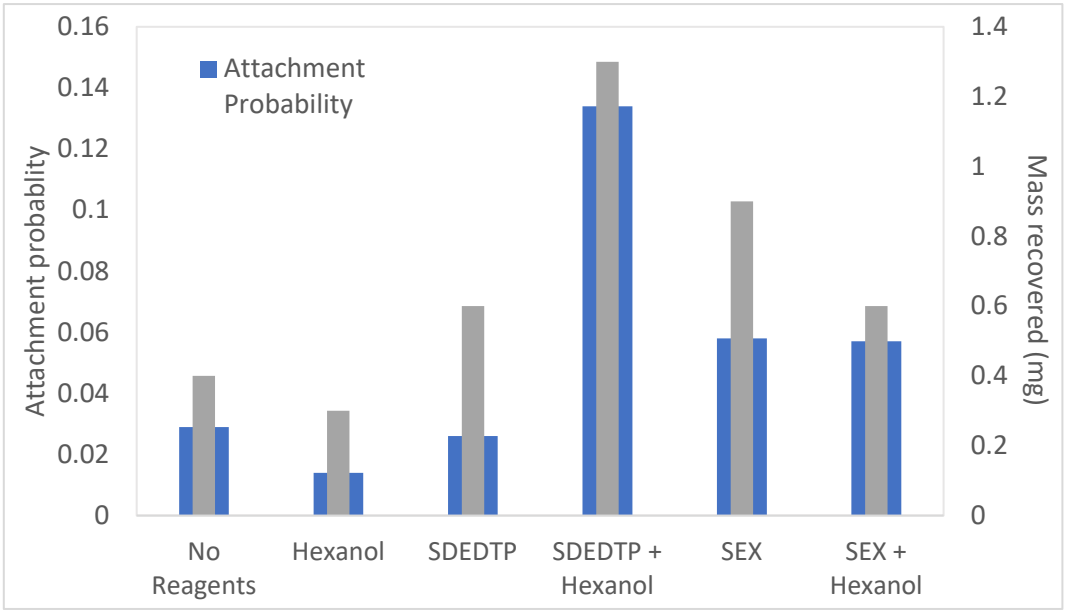

FIG 6 – Bubble-particle attachment probability and mass recovery of galena (pH 9) in the automated contact time apparatus. Collectors are dosed at 50 per cent monolayer coverage and the frother is dosed so that the concentration is just above the CCC. (Contact time = 20 ms).

Even though the synergistic effects of the SDEDTP-hexanol mixture are observed in energetically quiescent environments such as the ACTA and the microflotation cell where factors like the bubble-particle aggregate stability are not significantly impacted, it has been shown that in higher energy environments such as the batch flotation cell that SDEDTP in the presence of a frother attained high recoveries for galena – 89.0 per cent (McFadzean, Mhlanga and O'Connor, 2013). This indicates that this synergistic effect between SDEDTP and frothers may yield similar results in industry.

CONCLUSION

Previously is has been shown that the addition of hexanol to either SEX or SDEDTP in studying the flotation of galena in a microflotation cell had a major effect on the rate of flotation. This is especially interesting in the case of SDEDTP which is known to hardly adsorb onto the galena mineral particle but in the presence of hexanol the rate of flotation was shown to increase from 0.12 min^{-1} to 0.91 min^{-1}. Adsorption and calorimetry tests confirmed the fact that SDEDTP hardly adsorbs onto the galena, but in the presence of aeration and hexanol SDEDTP shows improved adsorption. Of particular interest to the current investigation was the fact that the probability of attachment of the

galena particle treated with DTP onto a bubble increased significantly in the presence of hexanol. The probability of attachment increased from ~0.025 to ~0.135 which is almost equivalent to the increased rate of flotation observed in the microflotation tests (Pienaar *et al,* 2019). These results strongly support the hypothesis that the role of the hexanol in this system is to influence the phenomenon of attachment of the mineral particle to the bubble. The role of SDEDTP in bubble-particle attachment is still not clear. Foam stability and adsorption tests under aeration indicates that there may be some complex interaction occurring between the SDEDTP and the hexanol at the interface. The interaction between the reagents and the adsorption mechanism may promote attachment of the mineral particle to the bubble. It is proposed that the transfer of hexanol through the thin film enhances the kinetics of film thinning between the bubble and the particle by destabilising the thin film thus improving pulp phase mineral recovery and rate of flotation.

ACKNOWLEDGEMENTS

The authors would like to acknowledge the South African Minerals to Metals Research Institute and the members of the Reagent Research Group, Anglo Platinum, Impala Platinum, and Lonmin for funding. Certain funding for this research was provided by the National Research Foundation of South Africa (South Africa) (NRF) [Grant number 103641] and Academy of Finland Mineral Resources and Material Substitution MISU program (Finland) – Protocol development for evaluation of water-saving alternatives in minerals processing – 'Bridging North to South' project. Any opinion, finding and conclusion or recommendation expressed in this material is that of the authors and the NRF does not accept any liability in this regard.

REFERENCES

Aspiala, M, Schreithofer, N and Serna-Guerrero, R, 2018. Automated contact time apparatus and measurement procedure for bubble-particle interaction analysis. *Minerals Engineering*. 121, 77–82.

Barbian, N, Ventura-Medina, E and Cilliers, J J, 2003. Dynamic froth stability in froth flotation. *Minerals Engineering*. 16(11):1111–1116.

Bikerman, J J, 1973. *Foams*, https://doi.org/10.1007/978–3-642–86734–7

Cho, Y S and Laskowski, J S, 2002. Effect of flotation frothers on bubble size and foam stability. *International Journal of Mineral Processing*, 64, 69–80.

Dai, Z, Bradshaw, D J and Harris, P J, 2001. Collector–frother interactions in chalcocite flotation. In: Finch, J A, Rao, S R, Huang, L, (Eds.), *Interactions in Mineral Processing. 40th Annual Conference of Metallurgists of COM*, Toronto, Canada

Fuerstenau, D, 2001. Excess nonequilibrium collector adsorption and flotation rates. *Mining, Metallurgy & Exploration*. 18(2):83–86. DOI: 10.1007/bf03402876.

Güler, T and Hiçyilmaz, C, 2004. Hydrophobicity of chalcopyrite with dithiophosphate and dithiophosphinate in electrochemically controlled condition. *Colloids and Surfaces A: Physicochemical and Engineering Aspects*. 235(1–3):11–15. DOI: 10.1016/j.colsurfa.2004.01.009.

Hernandez-Aguilar, J R, Coleman, R G, Gomez, C O and Finch, J A, 2004. A comparison between capillary and imaging techniques for sizing bubbles in flotation systems. *Minerals Engineering*, 17, 53–61.

Jordaan, T, 2018. *Investigating the role of dithiophosphate in the flotation of base metal sulfides*. MSc. University of Cape Town.

Kloppers, L, Maree, W, Oyekola, O and Hangone, G, 2016. Froth flotation of a Merensky Reef platinum bearing ore using mixtures of SIBX with a dithiophosphate and a dithiocarbamate. *Minerals Engineering*. 87:54–58. DOI: 10.1016/j.mineng.2015.12.003.

Leja, J and Schulman, J H, 1954. Flotation theory: molecular interactions between frothers and collectors at solid–liquid–air interfaces, *Trans. A I M E*, 199, pp. 221–228.

Lekki, J and Laskowski, J, 1971. On the dynamic effect of frother-collector joint action in flotation. *Transactions of the Institute of Mining and Metallurgy*. (80):174 – 179.

Lotter, N O and Bradshaw, D J, 2010. The formulation and use of mixed collectors in sulphide flotation. *Minerals Engineering*, 23(11–13), 945–951.

Manono, M, Matibidi, K, Otunniyi, I, Thubakgale, C, Corin, K and Wiese, J, 2020. The Behaviour of Mixtures of Sodium Iso-Butyl Xanthate and Sodium Di-Ethyl Dithiophosphate during the Flotation of a Cu-Ni-Pt Ore in Degrading Water Quality. *Minerals*. 10(2):123. DOI: 10.3390/min10020123.

McFadzean, B and O'Connor, C T, 2014. A thermochemical study of thiol collector surface reactions on galena. *Minerals Engineering*. 65, 54–60.

McFadzean, B, Mhlanga, S and O'Connor, C, 2013. The effect of thiol collector mixtures on the flotation of pyrite and galena. *Minerals Engineering*. 50–51:121–129. DOI: 10.1016/j.mineng.2013.06.018.

Nagaraj, D and Brinen, J, 2001. SIMS study of adsorption of collectors on pyrite. *International Journal of Mineral Processing*. 63, 45–57.

Petrus, H T B, Hirajima, T, Sasaki, K and Okamoto, H, 2011. Study of diethyl dithiophosphate adsorption on chalcopyrite and tennantite and varied pHs. *Journal of Mining Science*, 47(5), 695–702.

Pienaar, D, 2022. *The synergistic interaction between dithiophosphate and frothers at the air-water and mineral-water interface*. PhD. University of Cape Town

Pienaar, D, Jordaan, T, McFadzean, B and O'Connor, C T, 2019. The synergistic interaction between dithiophosphate collectors and frothers at the air-water and sulphide mineral interface, *Minerals Engineering*, 138 (2019) 125–132

Rao, S R, 2013. *Surface Chemistry of Froth Flotation: Volume 1 & Volume 2*. Springer Science & Business Media.

Rosen, M J, 1986. Phenomena in mixed surfactant systems. *ACS symposium series*. American Chemical Society Washington, DC.

Wang, X and Miller, J, 2018. Dodecyl amine adsorption at different interfaces during bubble attachment/detachment at a silica surface. *Physicochemical Problems of Mineral Processing*. 54.

Yan, H, 2016. *Collector transfer between bubble and particle collision*. MSc. University of British Columbia.

Zhang, W, Nesset, J, Rao, R and Finch, J, 2012. Characterizing Frothers through Critical Coalescence Concentration (CCC)95-Hydrophile-Lipophile Balance (HLB) Relationship. *Minerals*. 2(3):208–227. DOI: 10.3390/min2030208.

Investigating the floatability of sperrylite and its interactions with selected standard and novel collectors

S Pikinini[1], B McFadzean[2], C T O'Connor[3] and X Zhang[4]

1. PhD Candidate, Centre for Minerals Research, University of Cape Town, Rondebosch, Cape Town 7700. Email: PKNSEB001@myuct.ac.za
2. A/Professor, Centre for Minerals Research, University of Cape Town, Rondebosch, Cape Town 7700. Email: Belinda.mcfadzean@uct.ac.za
3. Professor, Centre for Minerals Research, University of Cape Town, Rondebosch, Cape Town 7700. Email: Cyril.OConnor@uct.ac.za
4. State Key Laboratory of Mineral Processing, BGRIMM Technology Group, Beijing 102600, China. Email: zhangxingrong@bgrimm.com

ABSTRACT

The Platreef in South Africa contains one of the world's largest reserves of platinum group elements. One of the major platinum group minerals (PGM) components in this ore is sperrylite ($PtAs_2$), which has been found to be slow floating compared to the other PGMs. In a study aimed at determining the reasons for the poor floatability of sperrylite and to improve its recovery, tests were carried out to determine the interactions of the mineral with a range of standard and novel collectors. Microflotation tests were carried out to determine the hydrophobicity of the minerals before and after adsorption of collectors. In addition, experiments were carried out to determine the enthalpy and extent of collector adsorption on the minerals and to investigate electrochemical interactions between sperrylite and selected standard collectors.

The results indicated that poor collector adsorption was the major cause for the poor floatability of sperrylite. Sperrylite had both poor natural (14.5 per cent) floatability and collector-induced flotation recoveries, the highest recovery of 26 per cent being observed using PNBX collector at pH 9. Moreover, the rest potential tests showed that the interaction of sperrylite with standard collectors such as xanthates was poor. The decrease in potential after the addition of the standard collectors ranged from 7.9 mV to 24.9 mV under alkaline conditions. Furthermore, sperrylite rest potentials remained unchanged with a change in pH from basic to acidic, indicating its resistance to surface alteration. Surface alteration of the minerals is key for the chemisorption of collectors to take place on the mineral surface. This was further emphasised by flotation recoveries at low pH, where only certain collectors responded positively to a decrease in pH and these were shown to have undergone a structural change. This work has highlighted the difficulties associated with sperrylite flotation and provides some direction for future research.

INTRODUCTION

Sperrylite, one of the PGM minerals recovered by the froth flotation of the Platreef PGM ores in South Africa, has been found to be slow floating compared to the other platinum group minerals (PGMs). As a result, fully liberated particles of the mineral have been found in the tailings streams of the Platreef concentrator. Sperrylite constitutes around 21 per cent of the Platreef ore, hence the need to improve its recovery (Shackleton *et al*, 2007; O'Connor and Shackleton, 2013). Xanthate collectors are used as the main collector and dithiophosphates as co-collectors to recover at least five PGM minerals at once. The reasons for the poor floatability of this mineral are still not clear and very few studies of the individual PGM minerals have been carried out to date. A study by Shackleton *et al* (2007), confirmed the poor floatability of sperrylite and also cited poor collector adsorption after detecting dixanthogen on all the minerals tested except sperrylite. Another study by Waterson *et al* (2016) cited that the surface topography of sperrylite made the Pt atoms fairly inaccessible, resulting in greater steric hindrances that could hinder collector adsorption. Moreover, the study indicated that the collector binding energy was lower than that of the OH^- ions making it difficult for the collector to displace the OH^- ions from the mineral under alkaline conditions. Also, a study by Shamaila and O'Connor (2008) using Platreef ore, showed that the rate constants and flotation recoveries of the arsenides were lower than that of the tellurides. Electrochemical and in situ Raman spectroscopic studies carried out by Vermaak *et al* (2007) indicated that the hydrophobicity of sperrylite increased

with an increase in potential. The potential controlled contact angle measurements, in the presence of ethyl xanthate, gave the highest contact angle of 54° at a potential of 400 mV (vs SHE). The above studies were not conclusive and some of them were dependent on the quality of the synthetic samples produced.

The present study attempts to establish the reasons for the poor floatability of sperrylite with the aim of improving its recovery. The interactions of the mineral with standard and some novel collectors were determined in order to shed light on the hydrophobicity and surface characteristics of sperrylite.

EXPERIMENTAL

The experimental work involved the synthesis of the sperrylite mineral since it could not be found in nature in quantities that are sufficient to conduct the tests. The microflotation tests were then carried out to determine the natural and collector-induced hydrophobicity of the mineral. Additional tests were also carried out to further understand the interaction of sperrylite with different collectors.

Mineral synthesis

Stoichiometric amounts of sponge Pt, of purity 99.95 per cent, and As were weighed and placed into a silica ampoule. The tube was evacuated for 24 hours, and the tube was then sealed by heating with an oxy-propane gas flame. The sealed tube was then placed into a vertical tube furnace and sintered according to the following program. The sample was heated to 800°C at a rate of 2.5°C/min and then the temperature held at 800°C for 84 hours. After being slowly cooled to 400°C at a rate of 0.5°C/min the sample was held at 400°C for 24 hours after which it was cooled to room temperature at a rate of 0.4°C/min. The mineral samples were ground and sintered for a second time to avoid the presence of free platinum.

Microflotation tests

The UCT microflotation system was used to determine the hydrophobicity of sperrylite (Bradshaw and O'Connor, 1996). Synthetic plant water (SPW) with ionic strength of 4.84E-2 M was used in this study. The composition of SPW has been described elsewhere (Pienaar *et al*, 2019). Hydrochloric acid (HCl) and sodium hydroxide (NaOH) were used as pH modifiers throughout the tests to adjust the pulp pH. 10 per cent sodium hypochlorite (NaClO) was used to modify the Eh of the pulp from 168 mV to 660 mV. MIBC was used as a frother and was dosed at 20 ppm, which is above the critical coalescence concentration (Cho and Laskowski, 2002).

Standard thiol collectors commonly used on PGM concentrators, potassium normal butyl xanthate (PNBX), sodium normal butyl dithiocarbamate (SNBDTC) and sodium di-normal butyl dithiophosphate (SNDBDTP), were selected for this study. Novel collectors were synthesised by BGRIMM Technology in Beijing. The structures and names of the synthesized collectors are shown in Figure 1.

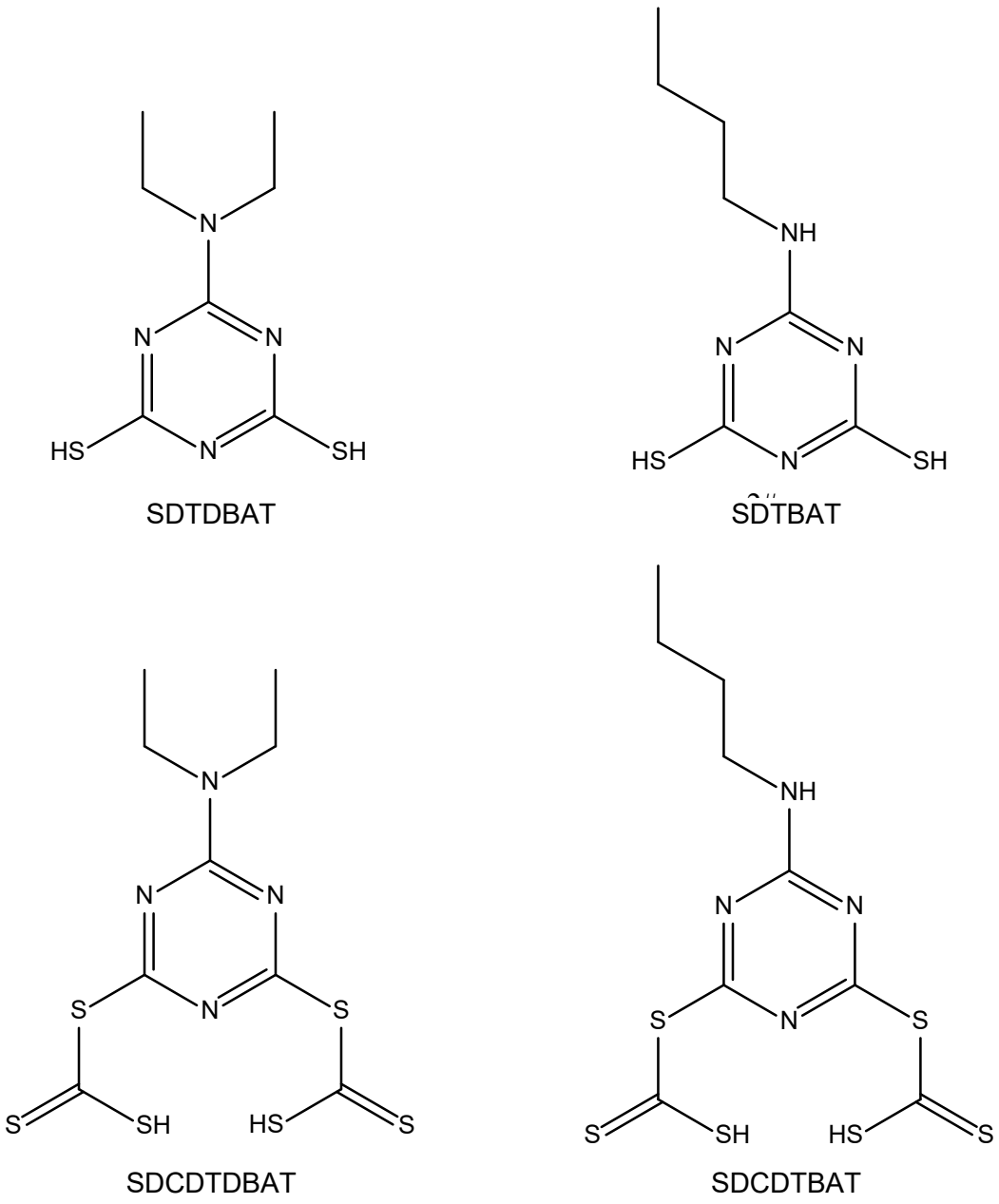

FIG 1 – Structure of novel collectors synthesised.
2,6-dithio-4-di-butylamino-1,3,4-triazine (SDTDBAT),
2,6-dithio-4-butylamino-1,3,4-triazine (SDTBAT),
2,6-dicarbonodithioate-4-di-butylamino-1,3,5-triazine (SDCDTDBAT), and
2,6-dicarbonodithioate-4-butylamino-1,3,5-triazine (SDCDTBAT).

A 2 g mineral sample, of a size fraction of -106 + 38 µm, was placed in a beaker with 50 ml of plant water or distilled water and sonicated for 5 minutes to fully disperse all the particles in the sample. The calculated collector dosage aimed at achieving a particular pseudo-layer coverage based on the BET analysis results, was added and the slurry was then conditioned for 10 minutes while stirring at a constant rate using a magnetic stirrer. The pH was constantly adjusted to the required pH during the conditioning period because a decrease in the pH was observed with all the minerals. Air was introduced at a constant airflow rate of 8 ml/min and the concentrates were collected at cumulative times of 2, 6, 12 and 20-minutes. Table 1 shows the results for the reproducibility tests on sperrylite which gave relative standard errors on cumulative recoveries of below 5 per cent except for the first concentrate that had the relative standard error of 14.5 per cent. The relative standard error of the first concentrate was higher since it is more difficult to obtain small relative standard errors when the recovered sample masses are so small. It was not possible to carry out all sperrylite tests in duplicate due to the limited quantity of mineral available and the cost of synthesizing the samples.

TABLE 1

Collectorless recovery of sperrylite at pH 9, with relative standard error.

Time (mins)	Run 1	Run 2	Average Recovery (%)	Relative Standard Error (%)
0	0	0	0	0
2	3.1	4.2	3.7	14.52
6	7.5	7.5	7.5	0.63
12	11.6	10.9	11.3	3.11
20	14.5	14.5	14.5	0.06

Adsorption tests

The difference between the absorbance spectra of the collectors in 50 ml of distilled water before and after adding the mineral was used to calculate the amount of collector adsorbed on the mineral surface. The appropriate absorbance peak was chosen for each collector that corresponded to their absorbance maxima. Collector dosage equivalent approximately to one pseudo-monolayer was used and the pH of the pulp was adjusted to either pH 9 or pH 4 as required throughout the conditioning period of 5 minutes. The absorbance of a reference sample of sperrylite in water was subtracted from the collector-sperrylite sample absorbance to account for any absorbance on the sperrylite.

Rest potential tests

The rest/open circuit potentials of the minerals were measured using a Gamry Instruments Reference 600^{TM} Potentiostat/Galvanostat/Zero Resistance Ammeter (G). A detailed explanation for the electrochemistry equipment set-up used for the rest potential measurements has been given by Tadie (2015) and Dzinza (2018). The natural sperrylite electrode was sourced from the nickel ore deposit of the Sudbury Basin in Ontario Canada. A buffer solution of pH 9.5 was made up of 0.05 M sodium tetraborate ($Na_2B_4O_4$) in a solution of 0.1 M sodium sulfate ($NaSO_4$) which was added as an electrolyte. Potassium hydrogen tartrate ($KHC_4H_4O_6$), with a purity of 97.5 per cent, was used to make a pH 3.5 buffer solution. All the buffer solutions used for the rest potential tests were made using deionised water.

The silver/silver chloride (Ag/AgCl) reference electrode and the sperrylite working electrode, were immersed into 450 ml of the buffer solution contained in a 25 ± 1°C temperature-controlled reaction vessel. The system was run under open circuit for 600 seconds before adding the collector and another 600 seconds after adding the collector. The potential reading at 600 seconds was taken as the rest potential of the minerals, while the reading at 1200 seconds was taken as the final rest potential of the mineral. The collector dosage of 6.24×10^{-4} M was maintained throughout all the runs. The standard deviations of the sperrylite rest potentials were also calculated from the average rest potentials determined for each collector run and the rest potentials were found to be quite reproducible as they ranged from ±7.2 mV to ± 10.7 mV.

Isothermal titration calorimetry tests

Isothermal titration calorimetry tests were carried out to measure the adsorption enthalpies at 25°C using the TAM III isothermal titration microcalorimeter. This technique measures the heat consumed or released during a reaction of the minerals with a given ligand. The sperrylite sample of mass 0.2 ± 0.0005 g was weighed into a stainless steel ampoule and 0.7 ml of distilled water was added into each ampoule and sonicated for 3 minutes to disperse the slurry. It was not possible to control and adjust the pH of the slurry after loading the ampoules into the titration channel, hence all the tests were carried out at the natural pH of the slurry, that was around 6.3. The ampoules were loaded into the calorimeter and the titration syringe was loaded with the collector solution. Time was given for the machine to stabilise and full calibration of the machine against a known power input was carried out before each run. The instrument was programmed to add 2 µL of the collector every hour once

the selected conditions were met. The 2 µL collector solution was precalculated based on the BET results to cover 0.25 pseudo-monolayers of the mineral surface. Ten titrations that amounted to 2.5 pseudo-monolayers collector coverage were carried out for each run.

The area under the peaks that resulted from the mineral-collector interactions were integrated to obtain the specific enthalpies of adsorption per injection. Heats of dilution per injection of a collector were also carried out for each collector and subtracted from the mineral-collector heats of adsorption. In this study, data from 4 titrations that amounted to 1 pseudo-monolayer collector coverage heats of adsorption were calculated and reported. A more detailed methodology and information on the isothermal titration calorimetry tests have been extensively described by McFadzean and O'Connor (2014); Taguta *et al* (2017); Taguta (2015). Tests were carried out in duplicate and results obtained show that the relative standard error was less than 10 per cent.

RESULTS

Mineral characterisation

The synthetic sperrylite was characterised by X-Ray Diffraction (XRD) and Scanning Electron Microscope (SEM) to confirm the composition of the mineral. The Rietveld refinement for synthetic sperrylite showed that 87 per cent sperrylite was formed with 12 per cent arsenolite and 1 per cent platinum. Figure 2 shows the backscattered electron (BSE) micrograph of the -106 + 38 µm synthetic sperrylite sample and its respective spectra. The energy dispersive spectroscopy (EDS) results confirmed that the sample consists mostly of sperrylite, which is the required phase (Table 1). The elemental compositions and the BSE micrograph shows tiny specks of free platinum (less than 20 µm), mostly locked within the larger sperrylite particles. Smaller particles in the micrograph do not contain any free platinum.

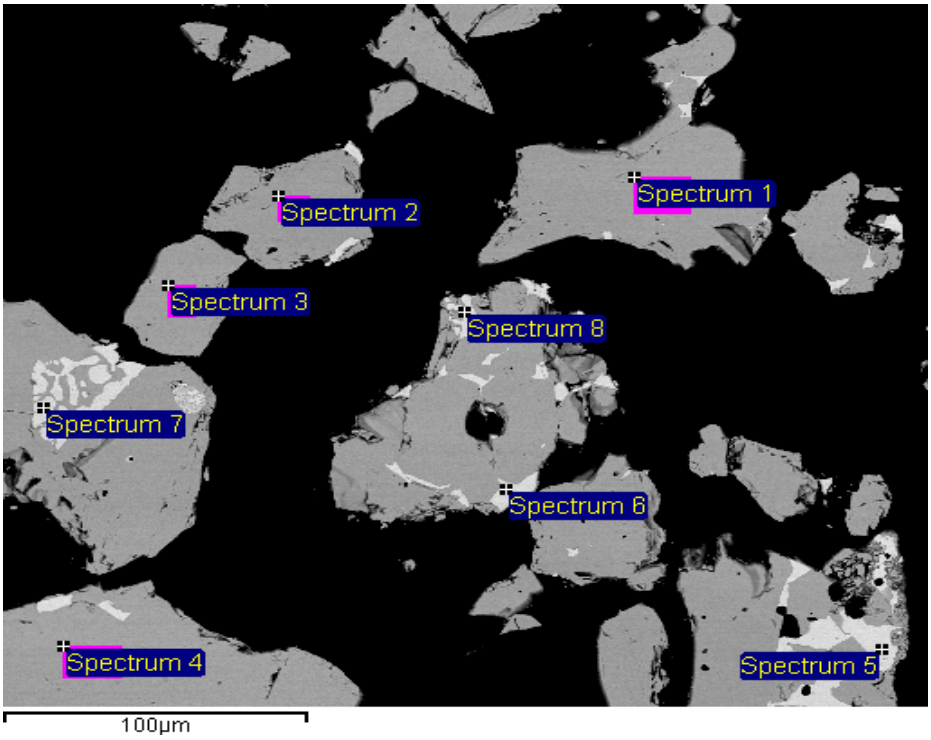

FIG 2 – BSE micrograph of synthetic sperrylite of size fraction, -106 + 38 µm.

Figure 3 shows the Back Scattered Electron (BSE) micrograph of the natural sperrylite electrode and the respective spectra (1 and 2). The Energy Dispersive Spectroscopy (EDS) results (Table 3) for the natural sperrylite electrode show that the mounted mineral pieces are homogenous and had the composition of 100 per cent $PtAs_2$. Spectrum 3 shows a crack between the 2 sperrylite mineral pieces that were mounted on the electrode, hence it does not contain any Pt and As. The average Pt:As ratio from the electroprobe analysis was 1.33, which is very close to the theoretical value and it could be concluded that the sperrylite sample was almost completely pure.

TABLE 2

EDS results for synthetic sperrylite of size fraction, -106 + 38 µm. Each spectrum corresponds to a spectrum indicated in Figure 1 and the Pt/As ratio are calculated from the experimental data (SEM) and from theoretical molecular weight considerations (expected).

Spectrum	As (wt%)	Pt (wt%)	Pt/As Ratio from SEM	Pt/As Expected Ratio
Spectrum 1	42.38	57.62	1.36	1.3
Spectrum 2	42.81	57.19	1.34	1.3
Spectrum 3	43.08	56.92	1.32	1.3
Spectrum 4	42.83	57.17	1.33	1.3
Spectrum 5 to 8	-	98.34	-	1.3

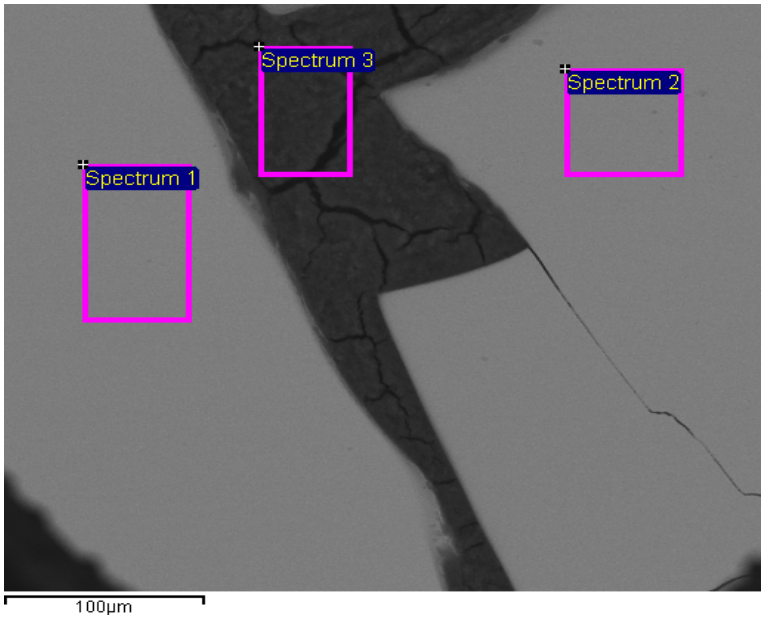

FIG 3 – BSE micrograph of the natural sperrylite electrode.

TABLE 3

EDS results of the natural sperrylite electrode. Each spectrum corresponds to a spectrum indicated in Figure 2 and the Pt/As ratio are calculated from the experimental data (SEM) and from theoretical molecular weight considerations (expected).

Spectrum	As (wt%)	Pt (wt%)	Pt/As Ratio from SEM	Pt/As Expected Ratio
Spectrum 1	42.17	57.83	1.37	1.3
Spectrum 2	43.91	56.09	1.28	1.3

Microflotation

The first set of tests were done under standard conditions of pH 9 in synthetic plant water. The collector types that were used were the standard thiol collectors found on many PGM concentrators. Dosage was maintained at 1 monolayer coverage based on the BET analysis results and collector chain length was maintained consistent, using the butyl chain. Table 1 showed that the tests results had good reproducibility giving the relative standard errors of 14.5 per cent, 0.6 per cent, 3.1 per cent and 0.06 per cent for the concentrates collected at 2, 6, 12 and 20-minute intervals respectively. The standard deviation error bars on the collectorless recovery at pH 9 represent the average standard deviations expected for each result, of 0.75 per cent, 0.07 per cent, 0.5 per cent and 0.01 per cent for the concentrates collected at 2, 6, 12 and 20-minute intervals respectively.

Sperrylite recovery, under these conditions, in the absence of a collector was 14.5 per cent (Figure 4) and indicates that the mineral has a poor natural flotation response. Adding the standard collectors at the equivalent of 1 pseudo-monolayer coverage resulted in little improvement in the mineral recovery, the recoveries being: PNBX (26.0 per cent) >SNBDTC (24.3 per cent) >SNDBDTP (23.3 per cent) >SIBX (19.9 per cent). It is worth noting that PNBX gave a recovery of 6 per cent greater than SIBX which is currently used as the preferred collector in the PGM concentrators. Generally, sperrylite showed a poor flotation response even after adding the standard collectors under alkaline conditions.

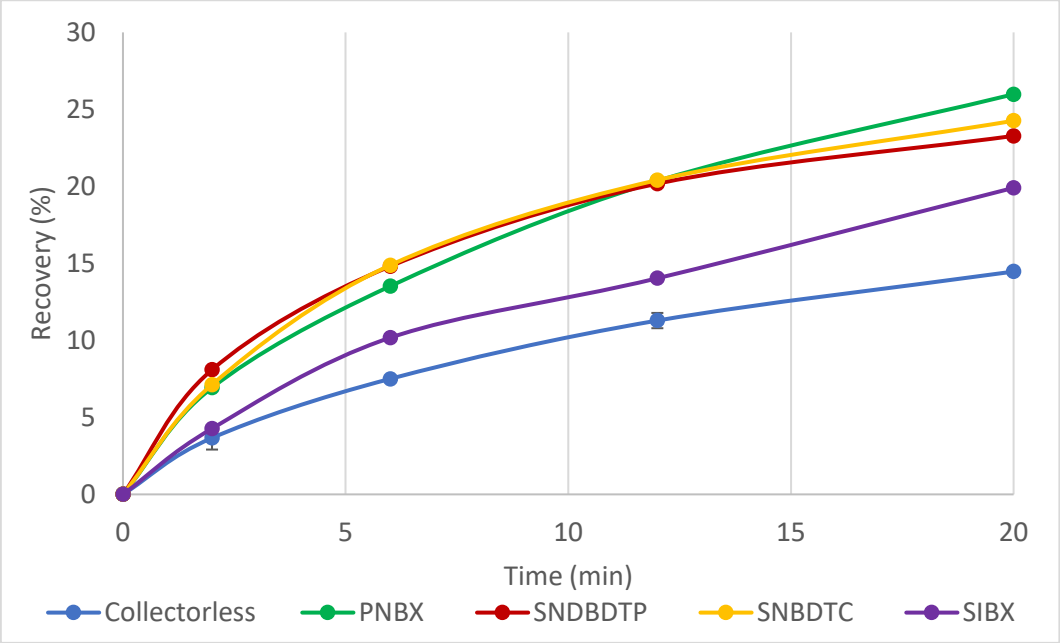

FIG 4 – Microflotation recovery-time graphs of sperrylite with no reagent and standard collectors at pH 9 in synthetic plant water, I = 4.84E-2 M and 20 ppm MIBC frother.

Novel collectors

A set of novel collectors were synthesised based on the use of nitrogen linking atoms that would enhance their electron-donating properties and result in stronger binding energy with sperrylite. The cumulative recoveries after 20 minutes flotation time of collectorless and standard collector tests, *viz*. PNBX, SIBX, SNDBDTP and SNBDTC, are shown in Figure 5 for comparison. Novel collectors SDTBAT and SDCDTDBAT, did not improve the recoveries of sperrylite beyond its natural floatability. In fact, SDTDBAT, and SDCDTBAT were less efficient and had recoveries lower than the collectorless recovery. The novel collectors did not offer any flotation recovery benefit to sperrylite at pH 9, even though they gave higher binding energies as indicated by the isothermal titration calorimetry results (Figure 14).

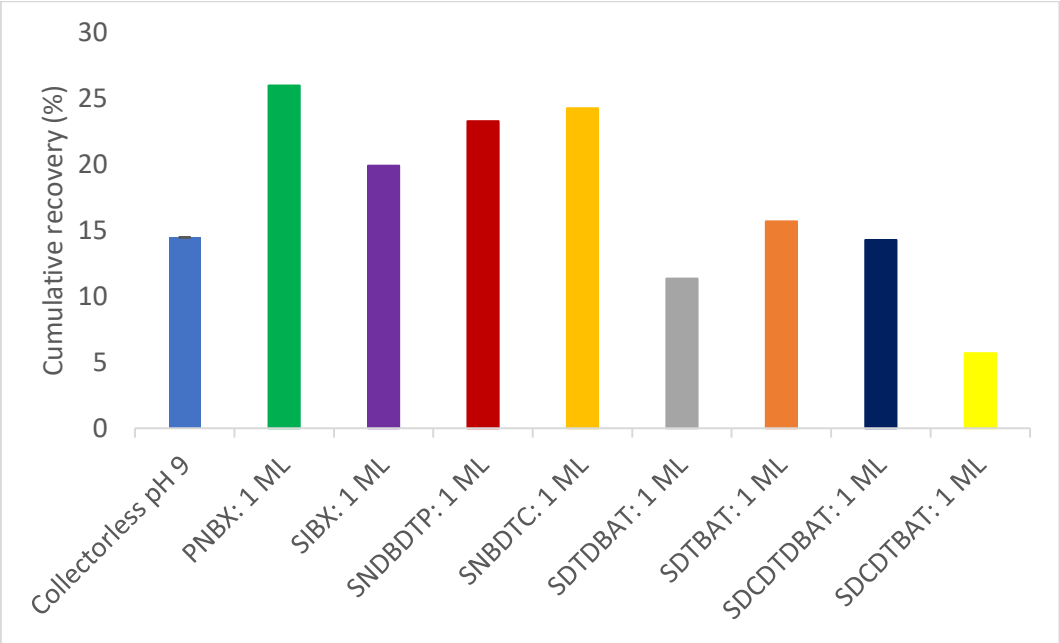

FIG 5 – Final cumulative flotation recoveries of sperrylite after 30 min with no reagent and novel collectors and how they compare to standard collectors, at pH 9 in synthetic plant water of ionic strength, Ionic strength = 4.84E-2 M and 20 ppm MIBC frother.

Effect of pH

The effect of the pH was investigated, by carrying out the flotation tests at pH 4 in synthetic plant water. It was hypothesized that the hydroxide species formed on the mineral surface at high pH inhibited collector adsorption which resulted in poor recoveries. Figure 6 shows cumulative recoveries of selected collectors at 20 minutes flotation time for pH 4 and pH 9, for comparison. Flotation at pH 4 resulted in improved recoveries in the case of SNBDTC, SDTBAT and SDCDTDBAT to 48.5 per cent, 41.7 per cent, and 23.3 per cent respectively (compared to 24.3 per cent, 15.7 per cent, and 14.3 per cent at pH 9). However, the recovery of PNBX remained unchanged even at low pH. A slight improvement in the collectorless recovery was also seen at pH 4, confirming the poor natural floatability of the mineral.

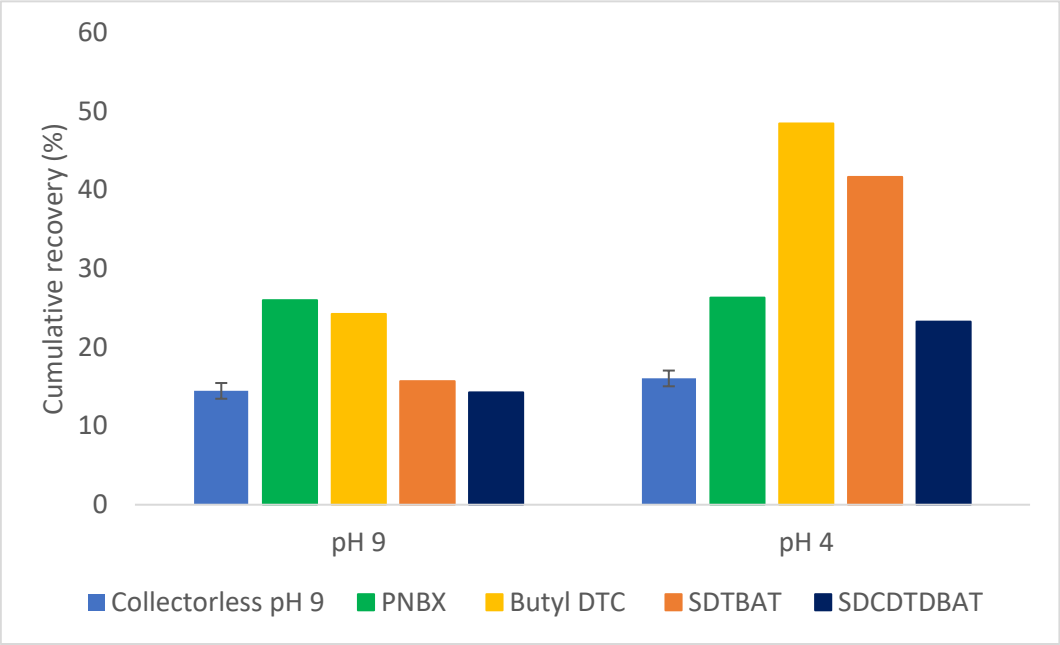

FIG 6 – Effect of pH on the final cumulative microflotation recoveries of sperrylite with standard and novel collectors, in synthetic plant water, I = 4.84E-2 M and 20 ppm MIBC frother.

Increased collector dosage

In an attempt to increase the flotation recovery of sperrylite, tests at higher collector dosages were carried out and the results are presented in Figure 7. It was hypothesized that increasing the collector dosage of the thiol collectors could lead to improved recoveries, as observed with pyrite and potassium amyl xanthate (PAX) (Fuerstenau *et al*, 1968). However, increasing the collector dosage of PNBX to 3, 5 and 10 equivalent pseudo-monolayers, in fact, reduced the recovery to 16.2 per cent, 10.9 per cent, and 15.7 per cent respectively. Adding SNBDTC and SNDBDTP at 10 monolayers did not result in any improvement in the recovery of sperrylite. The highest improvement, *viz*. to 45.4 per cent, was obtained after adding the equivalent of 30 pseudo-monolayers of SNBDTC. This is equivalent to a dosage of 4421 g/t of the pure mineral. This would obviously be much lower under plant conditions where the sperrylite is typically only present at less than 1 g/t.

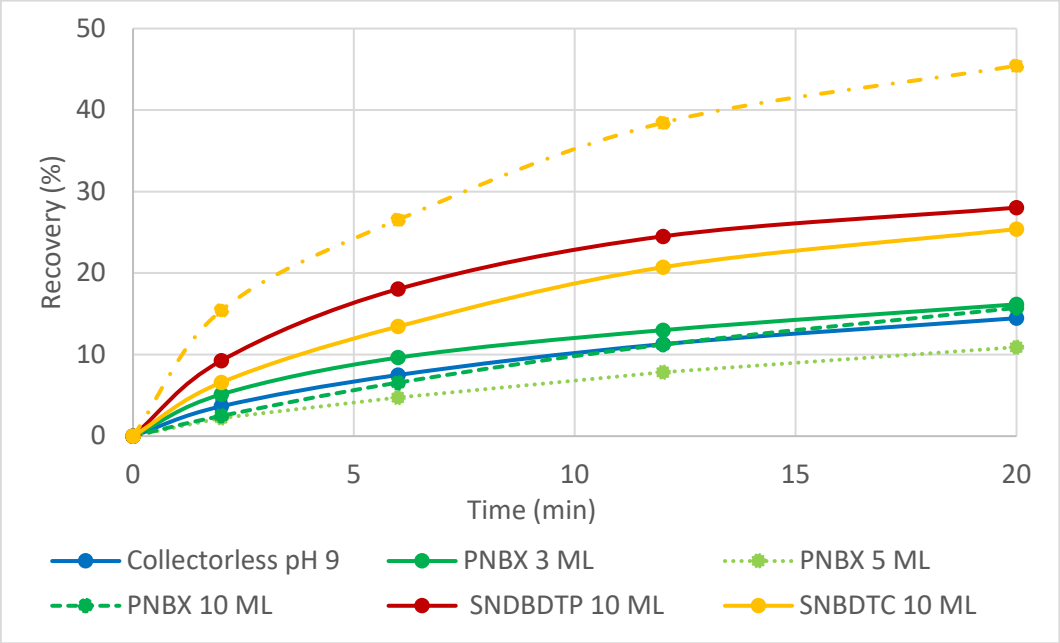

FIG 7 – Microflotation recovery-time graphs of sperrylite with standard collectors at 3, 5, 10, and 30 pseudo-monolayer (ML) dosages at pH 9 in synthetic plant water, Ionic strength = 4.84E-2 M and 20 ppm MIBC frother.

Effect of Eh

An investigation into the effect of increasing Eh at pH 9 on flotation recovery was carried out since it had been suggested by Vermaak *et al* (2007) that an increase in Eh would improve xanthate collector adsorption onto sperrylite. Increasing the pulp Eh from the natural Eh (160 mV) to 660 mV, in fact, depressed the recovery of sperrylite by 14.4 per cent, which is slightly less than the case for collectorless flotation (Figure 8). The collector used was PNBX and other conditions were standard.

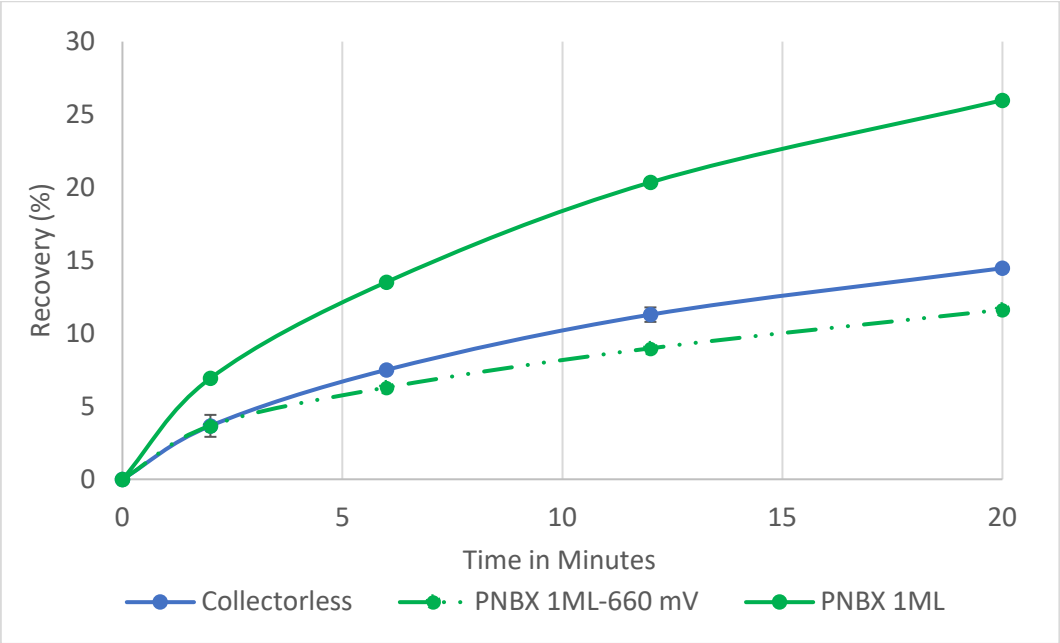

FIG 8 – Effect of increasing the pulp Eh from natural Eh to 660 mV on the recovery of sperrylite with PNBX collector, at pH 9 in synthetic plant water, I = 4.84E-2 M and 20 ppm MIBC frother.

Collector adsorption

UV-Vis spectrophotometry was used to determine the amount of standard and novel collectors adsorbed at pH 9, and to relate these results to the results obtained in the tests for flotation recovery of sperrylite. Essentially the difference between the starting concentration and that after adsorption for 10 minutes was measured. Figure 9 shows that there was minimal adsorption by all collectors at pH 9 with the exception of SNBDTC that had about 51.4 per cent adsorption. These results correlate with the poor flotation recoveries obtained when using these collectors. SNBDTC was the only collector that had an appreciable extent of adsorption onto the sperrylite surface at pH 9. However, this did not translate to an increase in flotation recovery as shown in Figure 8. The adsorption of SNDBDTP was not conclusive (NC) since there was overlap of the reference spectra with the collector sample at the wavelength of interest. The novel collectors were hardly adsorbed onto sperrylite, with the highest adsorption density of 1.9 per cent for the SDTDBAT collector.

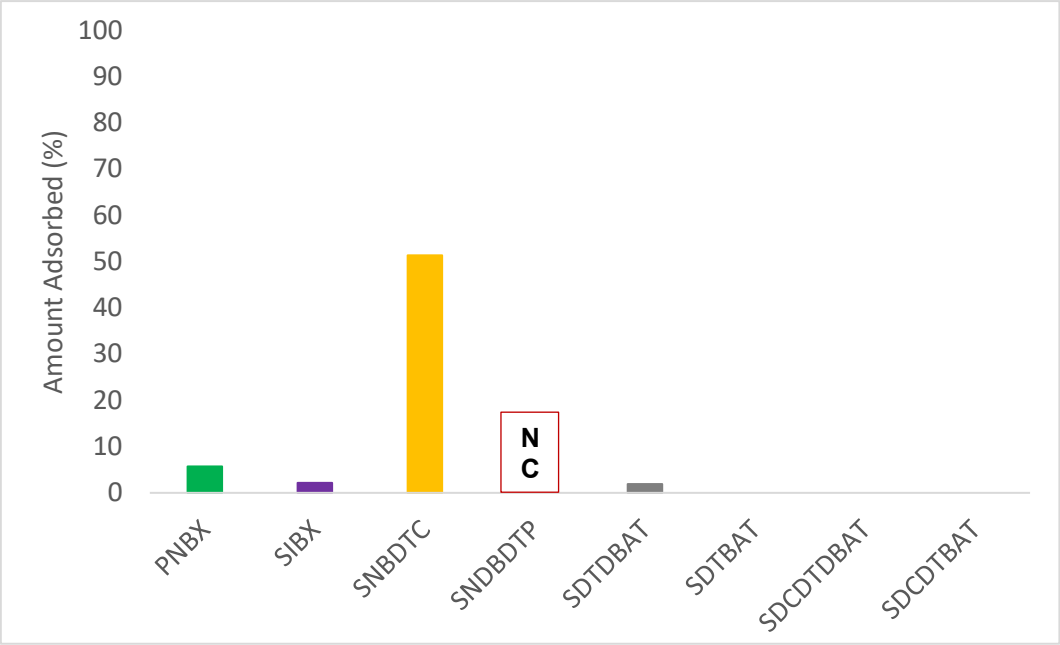

FIG 9 – Amount of standard and novel collectors adsorbed on sperrylite, at 1 pseudo – monolayer coverage dosage, at pH 9, in distilled water. NC = not conclusive.

Figure 10 shows the amount of thiol and novel collectors adsorbed under acidic conditions. PNBX and the novel collectors were adsorbed to a greater extent at pH 4 than pH 9 while SNBDTC was adsorbed to a lesser extent under acidic conditions. The increase in the amount of collectors adsorbed correlate well with the flotation recoveries obtained under acidic conditions except for PNBX and to a lesser extent SNBDTC.

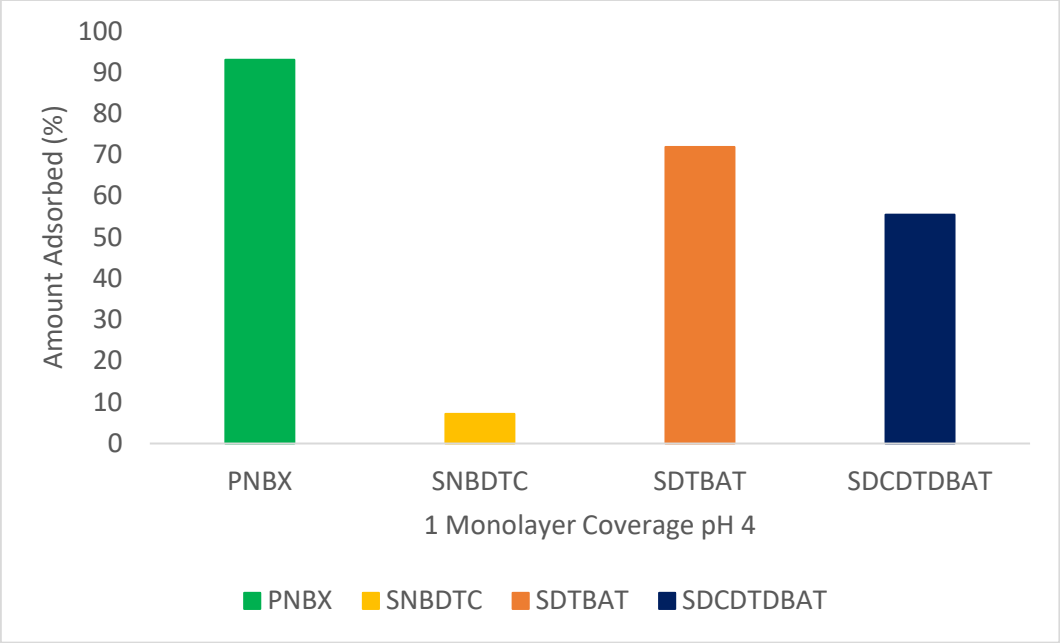

FIG 10 – Amount of standard and novel collectors adsorbed on sperrylite, at 1 pseudo-monolayer coverage dosage, at pH 4, in distilled water.

It was found that the UV-Vis spectra of certain of the collectors was different at pH 9 and pH 4. Figure 11 shows the change in the spectra of SNBDTC and SDCDTDBAT collectors with change in pH. There is a decrease in the primary peaks of SNBDTC and SDCDTDBAT at 285 nm and 269 nm, respectively, and an increase the absorption in the UV range towards 200 nm. This indicates that these collectors have undergone a structural change at low pH.

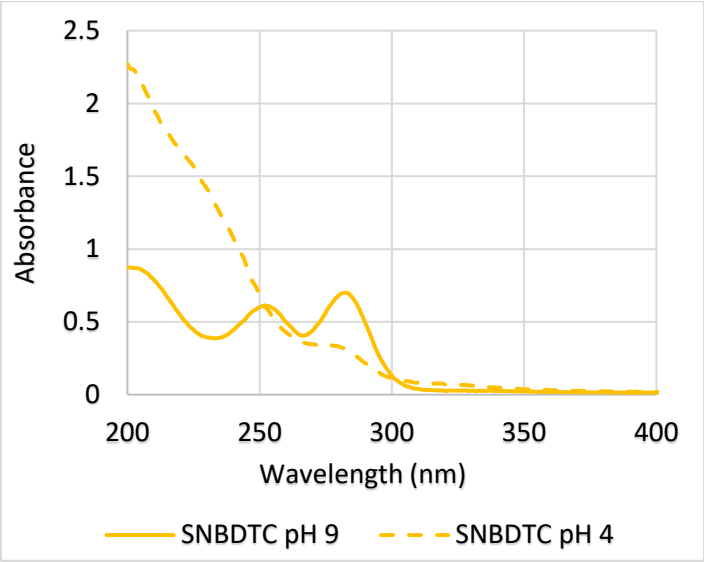

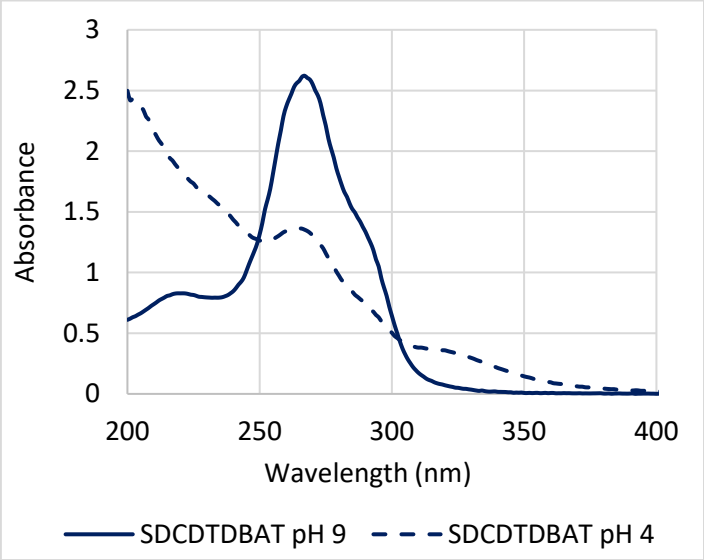

FIG 11 – A comparison of the SNBDTC and SDCDTDBAT UV-Vis spectra at pH 9 and pH 4.

Rest potential measurements

The average rest potential of the natural sperrylite from the plotted data before adding the collectors at 600 seconds was 233.7 ± 7.2 mV (Figure 12). The mineral showed very little interaction with all the collectors as indicated by the small decrease in potential after adding the collectors. The order for the extent of interaction as indicated by the decrease in rest potential: SNBDTC (24.9 mV) >PNBX (17.6 mV) >SNDBDTP (7.9 mV). Despite the minimal interaction of the mineral with the collectors, the results suggest that, if anything, dithiolates are the most likely species to form on the mineral surface.

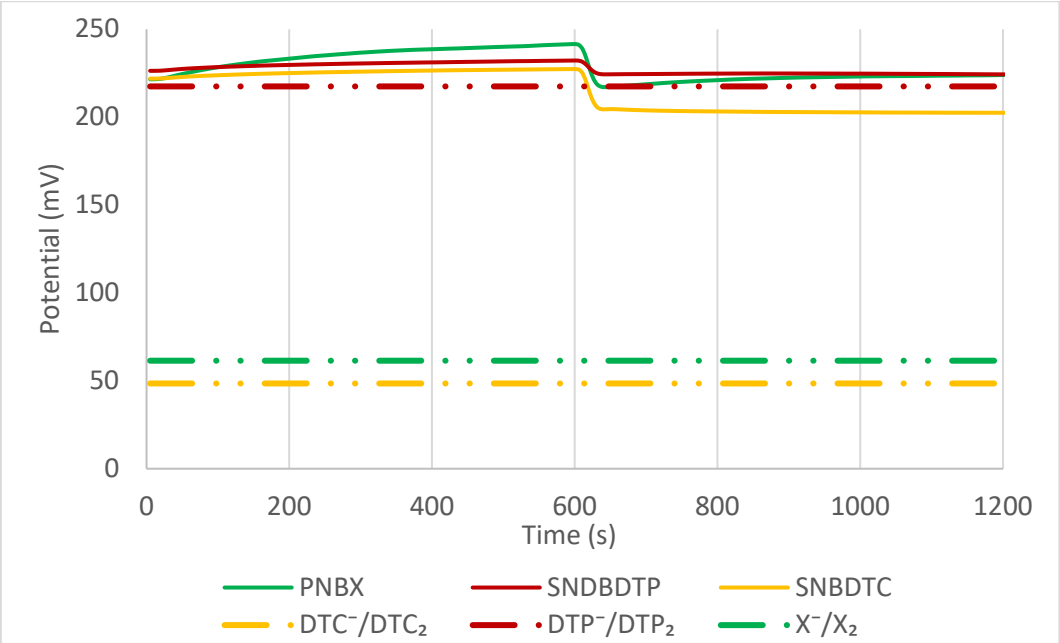

FIG 12 – Rest potential results of natural sperrylite in the absence and presence of standard collectors, after 600 seconds, at pH 9.5 The dotted lines indicate the oxidation potential of the standard collectors.

The interactions of the natural sperrylite electrode with the thiol collectors at pH 3.5 is shown in Figure 13. The average rest potential of the natural sperrylite before adding the collectors at 600 seconds was 243.7 ± 10.7 mV. It is worth noting that there was only a slight increase of 10 mV in the rest potential of sperrylite under acidic conditions. This increase is within the calculated standard deviation of the rest potentials at pH 3.5 and pH 9.5 and it can be concluded that the sperrylite surface remained unaltered at these different pHs. The mineral showed a marked increase in the extent of interaction upon addition of the collectors compared to higher pHs. PNBX and SNBDTC reacted to a far greater extent compared to SNDBDTP. In this case, a change in the order of interaction as indicated by the decrease in rest potential was observed as opposed to what was observed at pH 9.5, where PNBX had the greater extent of interaction as opposed to SNBDTC: PNBX (126 mV) >SNBDTC (107 mV) >SNDBDTP (44.4 mV). Dithiolates were expected to form with PNBX and SNBDTC. However, due to the high oxidation potential of SNDBDTP, it is suggested that, if anything, the metal thiolate will be formed with sperrylite.

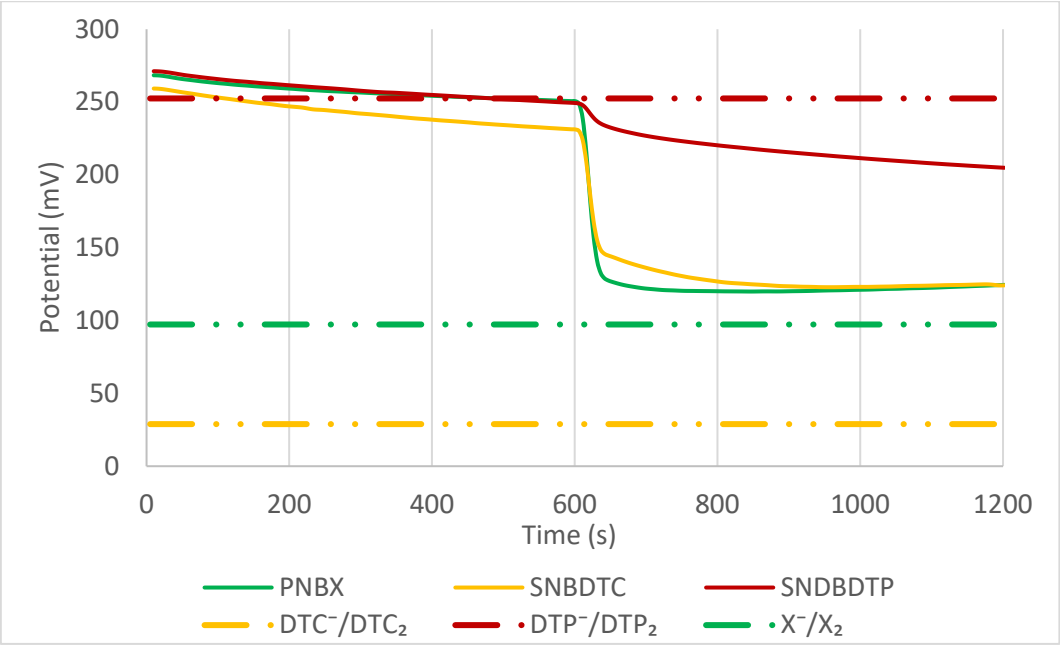

FIG 13 – Rest potential results of natural sperrylite in the absence and presence of standard collectors, after 600 seconds, at pH 3.5 The dotted lines indicate the oxidation potentials of the standard collectors.

Isothermal titration calorimetry

The isothermal titration calorimetry results showed that the collectors with the nitrogen linking atoms, *viz*. SNBDTC and the novel collectors, gave the higher binding energies compared to PNBX and SNDBDTP (Figure 14). Also, all the novel collectors gave higher binding energies compared to the standard collectors but that did not correspond to the amount of collector adsorbed onto the mineral nor on the flotation recoveries. The SNDBDTP collector gave a very low heat of adsorption and this seems to be consistent with its minimal extent of interaction as observed during the rest potential tests.

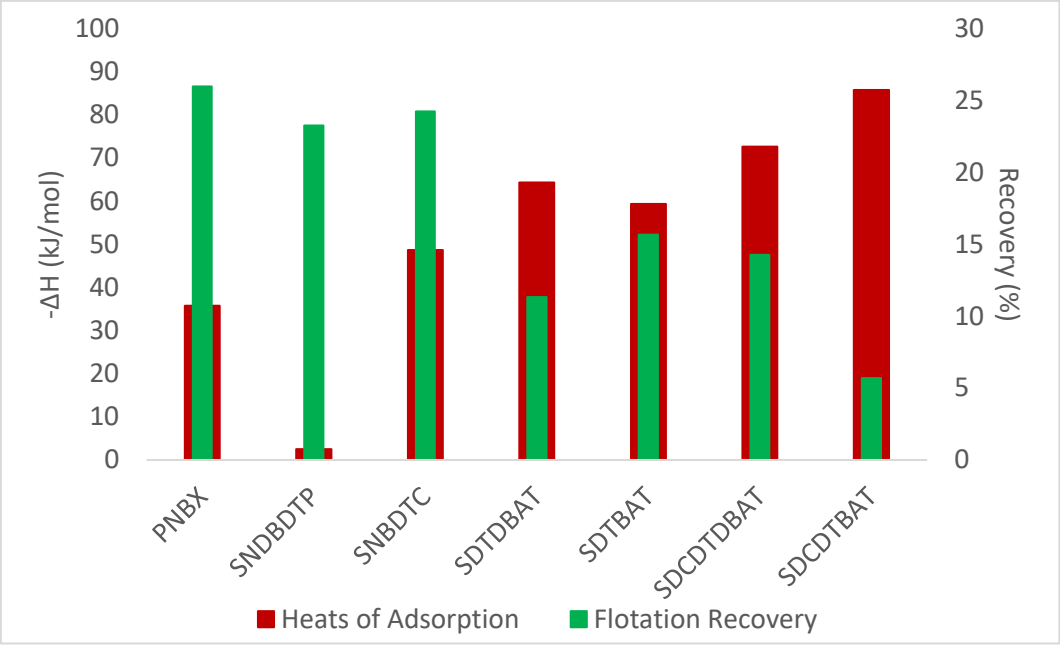

FIG 14 – Heats of adsorption of sperrylite at 1 pseudo-monolayer coverage using novel collectors and how they compare to standard collectors, at natural pH of 6.3, in distilled water. In addition, the microflotation recoveries of sperrylite with standard and novel collectors at pH 9 in synthetic plant water, Ionic strength = 4.84E-2 M and 20 ppm MIBC frother.

DISCUSSION

The characterisation tests using the XRD and EDS analysis indicated that the synthetic sperrylite had a purity of 87 per cent and the natural sperrylite electrode was homogenous and ~100 per cent sperrylite. The EDS analysis results showed that the sample was fairly homogenous and that the mineral consists of mostly sperrylite. The presence of arsenolite on the surface of the particles is most likely to have had no impact on the flotation and adsorption results. Arsenolite dissolves in water to form arsenous acid (H_3AsO_3) and its solubility in water is 37 g/L at 20°C (Nielsen and Larsen, 2014). Free platinum specks (less than 20 µm) were seen in the core of a few -106 + 38 µm size fraction in Figure 2 and most of them were locked within the particles of around 100 µm, which would not have greatly affected the floatability of the mineral. The floatability of the mineral samples is mainly determined by its surface properties. Most of the raw platinum and arsenic particles were successfully converted to sperrylite using the low temperature sintering process, where the reagents were heated below the melting temperature of sperrylite. Free platinum specks were also noted in the work of Shackleton *et al* (2007) were they resulted in a higher recovery of those samples compared to samples where less free platinum was observed. This was not the case in this study where floatability of the sperrylite was very low. In addition, it was shown that a naturally sourced sperrylite electrode behaved in the same way as a synthetic mineral electrode. This supports the contention that the amount and liberation of the free platinum in these samples had very little effect on their response and that the response of the synthetic sperrylite can be assumed to be similar to that of natural sperrylite.

The microflotation test results using the standard collectors revealed that sperrylite had poor natural and collector-induced floatabilities. The highest recovery obtained was 26 per cent with PNBX. The adsorption tests revealed that poor collector adsorption was the major cause for the poor flotation recoveries of sperrylite, hence there was little improvement in the recoveries after adding the collectors. The adsorption results showed that the xanthate collectors, PNBX (5.7 per cent) and SIBX (2.2 per cent) were poorly adsorbed on sperrylite. Even though, SNBDTC was adsorbed to a greater extent (51.4 per cent), that did not translate to improved recoveries. The extent of interaction of sperrylite with the collectors during the rest potential tests confirmed that the extent of interaction between collectors and sperrylite was very low This also suggests that, even though the SNBDTC was shown to adsorb onto the sperrylite, this was not an electrochemical interaction and may be a physisorption interaction at these pH's. These results confirm that there is indeed very little interaction that takes place between sperrylite and the tested standard collectors. This finding is key in giving insight into the poor flotation response of sperrylite. Large increases in collector concentration were required to produce any positive effects in flotation recovery and these were most noticeable for the SNBDTC.

Similar results were found in the flotation tests with the novel collectors. These revealed that poor collector adsorption (between 0 per cent to 1.2 per cent) is what led to the poor recovery of sperrylite (between 5.7 per cent and 15.7 per cent). The minimal adsorption could also have been caused by the steric hindrance posed by the ring collector structures, even though they gave higher binding energies as opposed to the PNBX collector as shown by the isothermal titration calorimetry results.

The effect of pH was also investigated by carrying out tests under acidic conditions. A decrease in pH reduces the competitive adsorption between the collectors and the OH^- ions. A study by Waterson *et al* (2016) that indicated that the binding energy of OH^- with sperrylite was higher than that of the ethyl xanthate collector. Improved interaction of the mineral with different collectors was observed as opposed to alkaline conditions. PNBX adsorption improved from 5.71 per cent at basic conditions to 93.1 per cent at acidic conditions. However, this improvement in adsorption density of the collector did not translate into an improved recovery at pH 4. This indicates that, even though the xanthate collectors may adsorb on the sperrylite mineral surface, the resultant hydrophobicity is not sufficient to allow bubble-particle attachment. An improvement in the recovery of sperrylite with SNBDTC, SDTBAT and SDCDTDBAT by 24.2 per cent, 26 per cent and 9 per cent respectively was noted. This could be attributed to improved collector adsorption for SDTBAT and SDCDTDBAT collectors at pH 4. On the contrary, the adsorption of the SNBDTC was reduced from 51.4 per cent to 7.19 per cent at pH 4 and does not correspond with the improved recovery. Interestingly, the UV-Vis spectra of SNBDTC and SDTBAT and SDCDTDBAT collectors indicate that the structure of the collectors have changed under acidic conditions. It is not clear what the altered structure would be,

other than the protonated version of basic structures. It is expected that these molecules will have high pKa values, which are associated to the electron-donating linking atoms in the collectors. The opposite is true for the PNBX and SNDBDTP collectors which possess oxygen, electron-withdrawing linking atoms and have low pKa values, making the collector molecules acidic (Rao, 2004). For example, the reported pKa values of PNBX, sodium normal diethyl dithiocarbamate (SNDEDTC) and SNDEDTP are 2.23 (Hayashi *et al*, 1984), 7.5 (Raju and Forsling, 1991) and ~0 (Rao, 2004) respectively. The pKa values for the novel collectors were not determined in this study, but it is expected to be in a similar range to the SNBDTC pKa. Studies have shown that the decomposition of xanthate collector takes place below the pH of 2 as reflected by the decrease in the pyrite recoveries of pyrite below the pH 2 (Leppinen, 1990; Fuerstenau *et al*, 2007). From the results it can be seen that pH is not the major cause for poor floatability of sperrylite, where the highest recovery of 48 per cent was obtained with SNBDTC.

The calorimetric data showed that there was some fairly substantial interaction between the collectors and the sperrylite surface. The novel cyclic collectors produced heats of interaction more negative than -60 kJ/mol, which is similar to, or greater than those seen previously for base metal sulfide-collector interaction (Taguta *et al,* 2017). This interaction is substantiated by the extent of adsorption of these collectors at lower pH's, which was between 55 and 90 per cent for the PNBX and cyclic collectors. Due to the difficulty in controlling pH within the calorimeter, it is not possible to make a direct comparison between results at either pH 9 or 4, since the actual pH in the calorimeter is somewhere in between these two pH's. Nonetheless, the extent of interaction, which was confirmed by adsorption and rest potential data, did not extend to a marked increase in flotation performance as noted previously.

The rest potential results showed that there was almost no change in surface potential of sperrylite from basic to acidic conditions. This is an indication that sperrylite is resistant to surface alteration and remained unoxidised under alkaline conditions. Studies have revealed that surface oxidation could either aid or be the cause of the poor floatability of minerals, depending on the extent of oxidation. Hence, this study has suggested that there is not extensive surface oxidation which causes the poor floatability of sperrylite under alkaline conditions. However, there was a greater extent of interaction with all the collectors under acidic conditions as opposed to alkaline conditions. This observation also corresponds with the extent of collector adsorption observed at pH 4 with the exception of SNBDTC. Sperrylite seems to exhibit refractory characteristics and since froth flotation is mainly dependent on the surface alteration of the mineral, improving the recovery of sperrylite by chemical means will be challenging. A study by Mwase (2016) confirmed that sperrylite leached slowly with cyanide and cyanide-ferricyanide lixiviants, suggesting the refractory nature of the mineral. This reveals the difficulty experienced in trying to break the Pt-As bonds, resulting in the poor dissolution of platinum.

Increasing the pulp Eh from 168 mV to 660 mV had a depressing effect on sperrylite. The recovery of sperrylite at a high Eh of 660 mV with PNBX was 11.6 per cent compared to 26 per cent at an Eh of 168 mV. This result contradicted electrochemical and Raman spectroscopic studies carried out by Vermaak *et al* (2007) that concluded that the hydrophobicity of sperrylite should increase with an increase in potential. The electrochemical contact angle measurements, in the presence of ethyl xanthate, gave the highest contact angle of 54° at a potential of 400 mV (vs SHE). These authors found that the surfaces of sperrylite were hydrophilic at low potentials, with contact angles of 0° at potentials of 200 mV and below. They noted the formation of dixanthogen bands at higher Eh's. However, the current study, conducted under standard flotation conditions of collector concentration, shows that raising the pulp potential does not improve flotation recovery. This shows that the sperrylite mineral surface cannot catalyse the oxidation of xanthate under normal flotation conditions. In addition, the surface potential of sperrylite was less than 300 mV under both alkaline and acidic conditions. This casts doubt on the prediction of the formation of dithiolates, which was made from the rest potential data. Hence, the rest potential measurements are not always consistent with the surface analysis results seen from previous studies

CONCLUSIONS

The results in this study indicate that the major reason for the poor floatability of sperrylite is that it is naturally hydrophilic and had a poor interaction with the standard and the tested novel collectors.

Furthermore, the mineral also showed some resistance to surface alteration as seen in the rest potential results, which remained unchanged under alkaline and acidic conditions. The electrochemistry results showed that chemisorption of the xanthate collectors, which involves an exchange of electrons between the collector and the acceptor on the mineral surface, did not take place on the sperrylite surface at pH 9. The adsorption of certain collectors and the recovery of sperrylite were improved at lower pH. However, this may be due to the transformation of collector species at low pH rather than an alteration in mineral surface, since the improvement was only noticed for collectors whose structure underwent change at low pH. PNBX, which did not undergo a structural change at low pH's, showed no difference in recovery despite the 93.1 per cent adsorption of the collector at pH 4. This study has shown the challenges inherent in the flotation recovery of sperrylite and highlighted some areas of potential interest in ongoing research.

ACKNOWLEDGEMENTS

The authors acknowledge the funding received from the South African Department of Science and Innovation and the UCT Hydrometallurgy Research Group for providing the natural sperrylite electrode.

REFERENCES

Bradshaw, D J, O'Connor, C T, 1996. Measurement of the sub-processes of bubble loading in flotation. *Minerals Engineering*, 9 (4) 443–448.

Cho, Y S and Laskowski, J S, 2002. Effect of flotation frothers on bubble size and foam stability. *International Journal of Mineral Processing*, 64, 69–80.

Dzinza, L, 2018. *An investigation into the effect of potential modifiers on the flotation of a copper sulphide ore*. Masters Thesis, University of Cape Town, Faculty of Engineering and the Built Environment, Chemical Engineering Department, Cape Town, South Africa.

Fuerstenau, M C, Jameson, G and Yoon, R, 2007. *Froth flotation, A century of Innovation,* Society for Mining, Metallurgy and Exploration Inc, Englewood, CO.

Fuerstenau, M C, Kuhn, M C and Elgillani, D A, 1968. The role of dixanthogen in xanthate flotation of pyrite, *Society for Mining, Metallurgy & Exploration Transaction*, pp. 148–156.

Hayashi, Y, Sasaki, K, Inomata, S and Yanagidani, T, 1984. Acid dissociation constants of alkyl xanthic acids and formation constants of cadmium (II) and zinc (II) xanthato complexes in 1:1 v/v H2 DMF Medium, *The Chemical Society of Japan*, 57 (11), pp. 3074–3076.

Leppinen, J O, 1990. FTIR and flotation investigation of the adsorption of ethyl xanthate on activated and non-activated sulphide mineral, *International Journal of Mineral Processing*, 30 (3–4), pp. 245–263.

McFadzean, B and O'Connor, C T, 2014. A thermochemical study of thiol collector surface reactions on galena. *Minerals Engineering*, 65, 54–60.

Mwase, J M, 2016. An investigation of cyanide-based heap leaching for extracting precious metals from Platreef ore. PhD Thesis, University of Cape Town, Faculty of Engineering and the Built Environment, Chemical Engineering Department, Cape Town, South Africa.

Nielsen, E and Larsen C J, 2014. Arsenic, inorganic and soluble salts. The Danish Environmental Protection Agency, Denmark.

O'Connor, C T and Shackleton, N J, 2013. Investigations into the recovery of Platinum Group Minerals from the Platreef ore of the Bushveld Complex of South Africa. *Platinum Metals Rev,* 57(4), 302–309.

Pienaar, D, Jordaan, T, McFadzean, B and O'Connor, C T, 2019. The synergistic interaction between dithiophosphate collectors and frothers at the air-water and sulphide mineral interface. *Minerals Engineering*, 138, 125–132.

Raju, B G and Forsling, W, 1991. Adsorption mechanism of diethyl dithiocarbamate on covellite, cuprite and tenorite. *Colloids and Surfaces*, 60, pp. 53–69.

Rao, S R, 2004. *Surface Chemistry of Froth Flotation Volume 2: Reagents and Mechanisms*, Kluwer Academic/Plenum Publishers, New York.

Shackleton, N J, Malysiak, V and O'Connor, C T, 2007. Surface characteristics and flotation behaviour of platinum and palladium arsenides. *International Journal of Mineral Processing*, 85(1–3), 25–40. https://doi.org/10.1016/j.minpro.2007.08.002

Shamaila, S and O'Connor, C T, 2008. The role of synthetic minerals in determining the relative flotation behaviour of Platreef PGE tellurides and arsenides. Min*erals Engineering*, 21 899–904.

Tadie, M, 2015. *An electrochemical investigation of Platinum Group Minerals*. PhD Thesis, University of Cape Town, Faculty of Engineering and the Built Environment, Chemical Engineering Department, Cape Town, South Africa.

Taguta, J, 2015. *The thermochemical behaviour of thiol collectors and collector mixtures with sulphide minerals*. Masters Thesis, University of Cape Town, Faculty of Engineering and the Built Environment, Chemical Engineering Department, Cape Town, South Africa.

Taguta, J, O'Connor, C T and Mcfadzean, B, 2017. The effect of the alkyl chain length and ligand type of thiol collectors on the heat of adsorption and floatability of sulphide minerals. *Minerals Engineering*, *110*(August), 145–152. https://doi.org/10.1016/j.mineng.2017.04.021

Vermaak, M K G, Pistorius, P C and Venter, J A, 2007. Fundamental electrochemical and Raman spectroscopic investigations of the flotation behaviour of $PtAs_2$. *Minerals Engineering*, 20(12), 1153–1158. https://doi.org/10.1016/j.mineng.2007.04.004

Waterson, C N, Tasker, P A, Farinato, R, Nagaraj, D R, Shackleton, N, Morrison, C A, 2016. A computational and experimental study on the binding of dithio ligands to sperrylite, pentlandite and platinum. *The Journal of Physical Chemistry*, 120, 22476–22488.

Impact of hydrophobic particles on the classification of flotation frothers

Y Saavedra Moreno[1], G Bournival[2] and S Ata[3]

1. PhD Candidate, School of Minerals and Energy Resources Engineering, University of New South Wales, NSW 2052. Email: y.saavedramoreno@unsw.edu.au
2. Senior Research Associate, School of Minerals and Energy Resources Engineering, University of New South Wales, NSW 2052. Email: g.bournival@unsw.edu.au
3. Associate Professor, School of Minerals and Energy Resources Engineering, University of New South Wales, NSW 2052. Email: s.ata@unsw.edu.au

ABSTRACT

Flotation frothers are heteropolar molecules that are preferentially adsorbed at the bubble interface to enhance the flotation performance by promoting the formation of small and stable bubbles. Frothers have different characteristics that can be used to classify them. A classification framework has been recently presented by Saavedra Moreno *et al* (2022) to classify non-ionic frothers by conducting a principal component analysis (PCA) and a hierarchical clustering analysis (HCA). However, for the purpose of the present research, only five frother characteristics, including molecular weight (MW), hydrophile–lipophile balance (HLB), critical coalescence concentration (CCC), the minimum Sauter mean diameter (D_L), and foam stability index (DFI) were used in the PCA and HCA. All those characteristics were evaluated for a two-phase system in the absence of particles. Realising the important role that particles play in froth stability and behaviour, the effect of hydrophobic particles on the presented frother classification framework was investigated in this study. Four frothers with different characteristics, methyl isobutyl carbinol (MIBC), 1-pentanol, tri (propylene glycol) (TPG), and tri (propylene glycol) methyl ether (TPM), were chosen. The experiments were carried out in the presence and absence of silica particles esterified with 1-pentanol. It was evident that the results for 1-pentanol, TPM, MIBC, and TPG in the three-phase system agreed well with the frother classification presented for the two-phase system as frothers were clustered in the same groups. The findings from this research support the use of the frother classification system presented in two-phase system to select a specific frother for a particular application without the necessity of conducting laborious experiments in a three-phase system.

INTRODUCTION

Flotation performances are controlled by the use of chemical reagents. Frothers are heteropolar compounds with a hydrophilic group and a hydrocarbon chain (Wills and Finch, 2016). They are used in flotation primarily to generate air bubbles (Finch *et al*, 2008; Grau and Laskowski, 2006), aid gas dispersion (Quinn *et al*, 2007), and improve the stability of the froth (Laskowski *et al*, 2003b), that is critical to maintaining flotation performance.

Frothers can be classified based on numerical values. For instance, they can be grouped based on the hydrophilic-lipophilic balance number (HLB). The molecular weight (MW) could be used in conjunction with the HLB values to offer an indication of how a frother could behave in a two-phase and a three-phase system (Laskowski, 1993; Laskowski, 2004; Huang *et al*, 2019; Pugh, 2000; Gredelj *et al*, 2009). The minimum Sauter mean diameter (D_L), which is the limiting bubble size at the critical coalescence concentration (CCC) value, is another parameter that has been used to characterise frothers, finding that D_L increases as the number of hydrocarbon groups (*n*) and the number of propylene oxide groups (*m*) increase (Zhang, 2012). However, the study aimed only to group the frothers based on the relationship between D_L and frother structure with no intention to present a comprehensive classification framework. Other researchers have selected the characteristics such as CCC and MW to group frothers. The CCC versus HLB is another trend that has been presented for classification by assessing the capacity of a frother to inhibit bubble coalescence. Furthermore, foam stability has also been used to characterise frothers based on the foam produced under dynamic and static conditions. Perhaps the most used method to study flotation foams is the Bikerman test, in which gas is bubbled into a surfactant solution (Blute *et al*, 2009; Karakashev *et al*, 2012; Harris and O'Connor, 2017; Saavedra Moreno *et al*, 2021, 2020). The

dynamic foamability index (DFI), which was introduced by Małysa *et al* (1987), is another foam stability parameter to characterise frothers. Laskowski *et al* (2003a) have presented a binary frother classification by studying the DFI-CCC relationship, reporting that high DFI values and low CCC values are characteristics of a powerful frother that generate stable foam under dynamic conditions and can inhibit coalescence. In a more recent study, frothers were characterised by foaminess, coalescence time and oscillation of bubbles, and detachment of particles (Chipfunhu *et al*, 2019). However, the results presented by these authors aimed to only assess the flotation performance given by these frothers, and a frother classification was not attempted. It is worth noting that no studies have attempted to classify frothers using more than three characteristics and assessing the importance of these characteristics in a more meaningful frother classification system.

In a recent publication, the authors presented a statistical analysis to classify non-ionic frothers in a two-phase system based on seven frother characteristics (Saavedra Moreno *et al*, 2022). A principal component analysis (PCA) and a hierarchical cluster analysis (HCA) were conducted, clustering the frothers into four groups, in which Group 1 consisted of the most powerful frothers that produced stable foams, and Group 4 was composed of the weakest frothers with two transition categories. The aim of the present study is to assess how well the frother classification system in a two-phase system translates to the three-phase system.

METHODOLOGY

Experimental methodology

In a typical experiment for the dynamic foam stability, esterified silica particles at 20 wt per cent were added into a beaker together with 150 ml of frother solution and mixed properly before pouring into the column. The column used for the three-phase system was the same column used for two – phase system; however, a variable speed motor was fitted to maintain the particles in suspension as illustrated in Figure 1. More details of the experimental set-up and conditions can be found in the recent publications of Saavedra Moreno *et al* (2021) and Saavedra Moreno *et al* (2021).

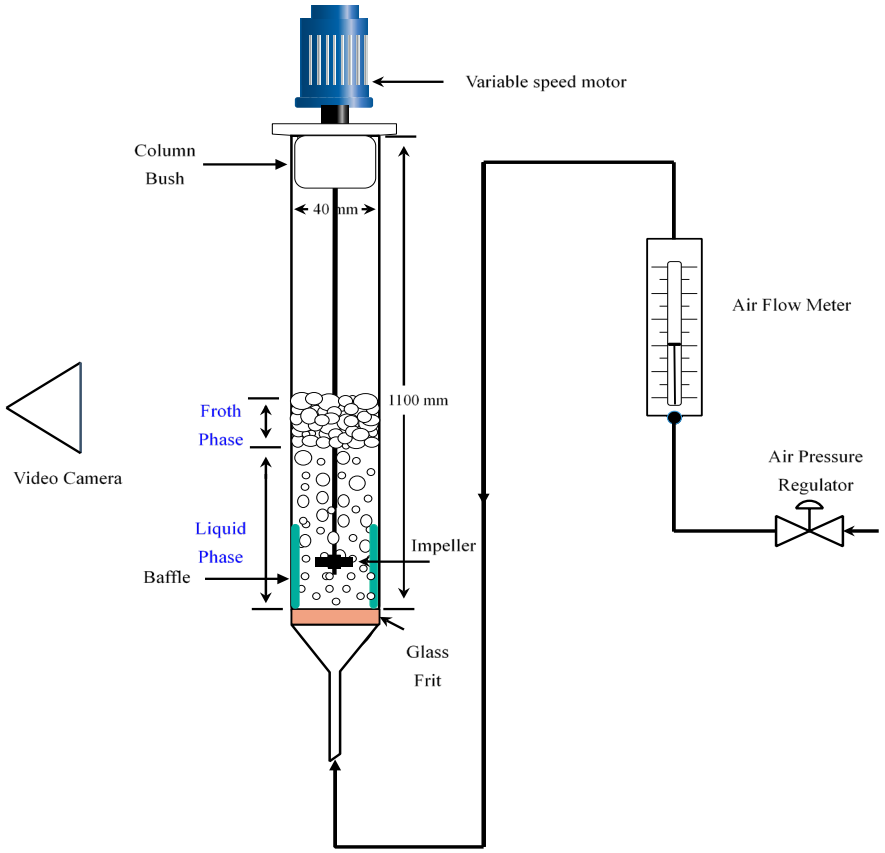

FIG 1 – Schematic representation of the column used for three-phase experiments.

A stainless-steel impeller with a diameter of 4 mm was encapsulated into a stainless-steel tube to eliminate any motion caused by the impeller in the froth phase. The two ends of the tube were sealed with Polytetrafluoroethylene (PTFE) bushes. A PTFE four-blade impeller was screwed to the bottom of the impeller. A column bush made from PTFE was fitted at the top of the column to maintain the impeller in the centre of the column. It is important to mention that the column bush had 16 perforated holes of 5 mm diameter to replicate the same conditions of an open column used for the two-phase experiments. In all the three-phase experiments, the produced froth never reached a height closed to the top column bush. A circular baffle with a 55 mm height was fitted at the bottom of the column to ensure all particles were maintained in suspension as seen in Figure 1 and there was not any swirling flow. The air was injected through the frit, starting at an air flow rate of 0.1 L min^{-1} (0.14 cm s^{-1}). Sufficient time, between 1 to 4 minutes, was allowed for the foam to reach an equilibrium height. The foam height was measured once the foam had reached the maximum height. In all the experiments, the air flow rate was increased progressively from 0.1 L min^{-1} (0.14 cm s^{-1}) to 4.0 L min^{-1} (5.42 cm s^{-1}).

Statistical analysis

Principal component analysis

The principal component technique transforms the correlated variables chosen into uncorrelated variables, referred to as principal components, which are linear combinations of the original variables. Each principal component correlates with a variable that is referred to as loading, and a sample or an observation and it has a factor score in each principal component, which is calculated as a linear combination of the original variable and the loading value (Abdi and Williams, 2010). All the transformations of the variables to principal components. In the present study, PCA was applied in a search of the correlation structure between each frother and the frother characteristics presented in Table 1. The five frother characteristics, including MW, HLB, CCC, D_L, and DFI were selected. The values of the frother characteristics are summarised in Table 1. The statistical software R was used for the principal component analysis. The function `prcomp()` in R was used for this analysis and the variables were standardised to have each variable with equal importance independently of the variable values and an equal range value. The standardisation of the variables was done by dividing the difference between the variable values and the arithmetic mean of the variable values by the standard deviation of the values.

Hierarchical cluster analysis

The hierarchical clustering analysis (HCA) was implemented on the principal components to group frothers based on similarities and present a frother classification. This clustering analysis is commonly presented in a dendrogram. In the HCA, the Euclidean distance, which is the square distance between the coordinates of two frothers (Bandyopadhyay and Saha, 2012), was selected as the distance method. Ward's method measures the distance between clusters. This method is based on the criterion of classical sum-of-squares, generating clusters that minimise the total variance (Murtagh and Legendre, 2014). For the HCA, a function in Rstudio called `hclust ()` was used as it performs the hierarchical cluster analysis using the first three principal components for clustering the frothers. The HCA assigned a high value to frothers that were similar in order to firstly group them (Ben-Hur and Guyon, 2003). The initial groups were clustered based on their similarities. As the similarities decreased, the subgroups were merged into a single cluster.

TABLE 1

Summary of numerical values of molecular weight (MW), hydrophile–lipophile balance (HLB), critical coalescence concentration at which bubble size is reduced by 95 per cent (CCC), the minimum Sauter mean diameter (DL), and dynamic foam stability index (DFI) values for all tested frothers. DFI* is the dynamic foamability index obtained from the literature.

No	Frother	MW	HLB	CCC	DL	DFI s dm^3 $mmol^{-1}$	DFI* s dm^3 $mmol^{-1}$
1	1-butanol	74.12	7.00	0.688	0.880	0.23	1.34[a]
2	1-pentanol	88.15	6.53	0.230	0.920	0.98	5.52[a]
3	2-pentanol	88.15	6.53	0.276	0.910	1.09	
4	3-pentanol	88.15	6.53	0.379	0.930	1.06	
5	1-hexanol	102.17	6.05	0.088	1.000	3.78	33.78[a]
6	MIBC	102.17	6.00	0.082	0.990	6.93	36.99[b]
7	1-octanol	130.23	5.10	0.051	1.150	37.74	79.34[a]
8	DPG	134.17	9.25	0.404	0.710	0.43	
9	TPG	192.25	9.12	0.175	0.690	2.10	
10	PPG425	425.00	8.62	0.014	0.740	582.25	
11	PPG725	725.00	8.00	0.010	0.790	422.10	
12	PPG1000	1000.00	7.37	0.008	0.880	564.86	
13	PM	90.12	8.28	0.447	0.840	0.10	5.70[b]
14	DPM	148.20	8.13	0.167	0.830	3.52	35.0[b]
15	TPM	206.28	7.98	0.070	0.890	43.91	196.0[b]
16	AeroFroth 70	102.00	4.13	0.0818	1.170	6.85	
17	AeroFroth 65	425.00	11.9	0.016	1.340	699.68	
18	OrePrep F-507	447.00	14.40	0.008	1.290	532.19	
19	1-pentanol (150 ml)	88.15	6.53	0.230	0.920	0.89	
20	1-pentanol (150 ml+particles)	88.15	6.53	0.230	0.920	1.18	
21	MIBC (150 ml)	102.17	6.00	0.082	0.990	2.91	
22	MIBC (150 ml+particles)	102.17	6.00	0.082	0.990	9.94	
23	TPM (150 ml)	206.28	7.98	0.070	0.890	3.53	
24	TPM (150 ml+particles)	206.28	7.98	0.070	0.890	22.14	
25	TPG (150 ml)	192.25	9.12	0.175	0.690	1.26	
26	TPG (150 ml+particles)	192.25	9.12	0.175	0.690	10.07	

[a]Sweet *et al* (1997), [b]Laskowski *et al* (2003a).

RESULTS

Principal component analysis

The loadings, the variance, and the cumulative variance for all five principal components are summarised in Table 2. The loadings were the coefficients in the linear combinations, and they ranged from 0.0 to 0.74, indicating that the larger the magnitude of the loading value, the more

important that variable in the principal component. The PCA indicated that the first principal component already explained 51.23 per cent of the variance, and the addition of the second and third principal components explained 89.6 per cent of the variance in the data set. This means that PCA could reduce the dimensionality of variables from five variables to only three principal components.

TABLE 2

Loadings on the five principal components of the original variables.

Variables	Loadings with original variables				
	PC1	**PC2**	**PC3**	**PC4**	**PC5**
MW	0.54	-0.21	0.37	-0.43	-0.59
HLB	0.37	-0.49	-0.58	0.49	-0.21
CCC	-0.42	-0.41	-0.47	-0.66	-0.05
DL	0.22	0.74	-0.55	-0.19	-0.27
DFI	0.59	-0.06	-0.10	-0.32	0.73
Variance	51.23	23.12	15.25	8.742	1.66
Cumulative variance	51.23	74.35	89.6	98.34	100

For instance, PC1 was strongly linked with all variables (loading values greater than 0.30), except with D_L that had a loading value of 0.22. DFI and MW, presented the largest loading values, indicating the importance of the foam stability properties and molecular weight over the other considered variables. PC2 represented only 23.12 per cent of the variance and it was positively correlated with D_L, which had the highest loading value on PC2, 0.74. The HLB and D_L variables had the largest contribution to PC3; however, PC3 only represented a 15.25 per cent variance contribution.

To interpret the results of the PCA, the score of each frother in the coordinate system of the first three principal components is presented in Figures 2 and 3. The linear combination of the original variable selected in the PCA for the first principal components are given in Equations 1, 2, and 3. The coefficient in the equations were the loading values presented in Table 2. In Figure 2, it can be seen four main regions, in which Region 1 was situated at a negative value for PC1 and a positive value for PC2. Most of the aliphatic alcohol frothers were situated in this region. Moreover, it is shown that 1-pentanol in a two-phase system (frother No 2 and 19 as referred in Table 2) is located at the same positions as 1-pentanol in the presence of particles. The same results were found for MIBC, indicating that aliphatic alcohols frothers in a two-phase and three-phase system showed the same position in the PC1 versus PC2. Region 2 was formed by two commercial frothers, AeroFroth 65 and OrePrep F-507. As can be seen, these frothers were on the positive side of PC1 and PC2. The DFI, MW, and HLB have the largest positive loading values on the principal component 1 (PC1) suggesting that the frothers in Region 3 are the most powerful frothers to produce a stable foam under dynamic conditions. The final region, Region 4, is located at the negative value for PC1 and PC2, and contained frothers from different families. The other two frothers, TPM and TPG, that were tested in the presence of particles, also had the same position as TPM and TPG in the absence of particles, see PC1 versus PC2 graph shown in Figure 2. The findings suggest that the two-phase system to classify frothers can be used without the need of doing experiments in the presence of particles.

$$\mathbf{PC1} = 0.54MW + 0.37HLB - 0.42CCC + 0.22D_L + 0.59DFI \quad (1)$$

$$\mathbf{PC2} = -0.21MW - 0.49HLB - 0.41CCC + 0.74D_L - 0.06DFI \quad (2)$$

$$\mathbf{PC3} = 0.37MW - 0.58HLB - 0.47CCC - 0.55D_L - 0.10DFI \quad (3)$$

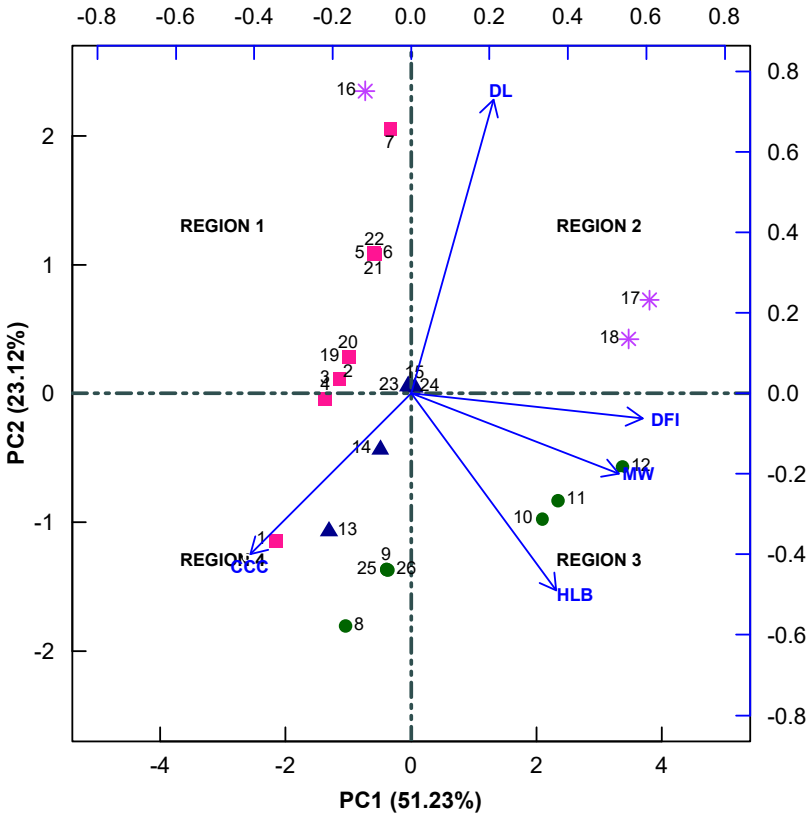

FIG 2 – Principal component 1 (PC1) versus principal component 2 (PC2). The score of each frother on PC1 and PC2 are shown by symbols, (■) aliphatic alcohols, (●) polypropylene glycols, (▲) propylene glycol methyl ethers, and (✳) commercial frothers.

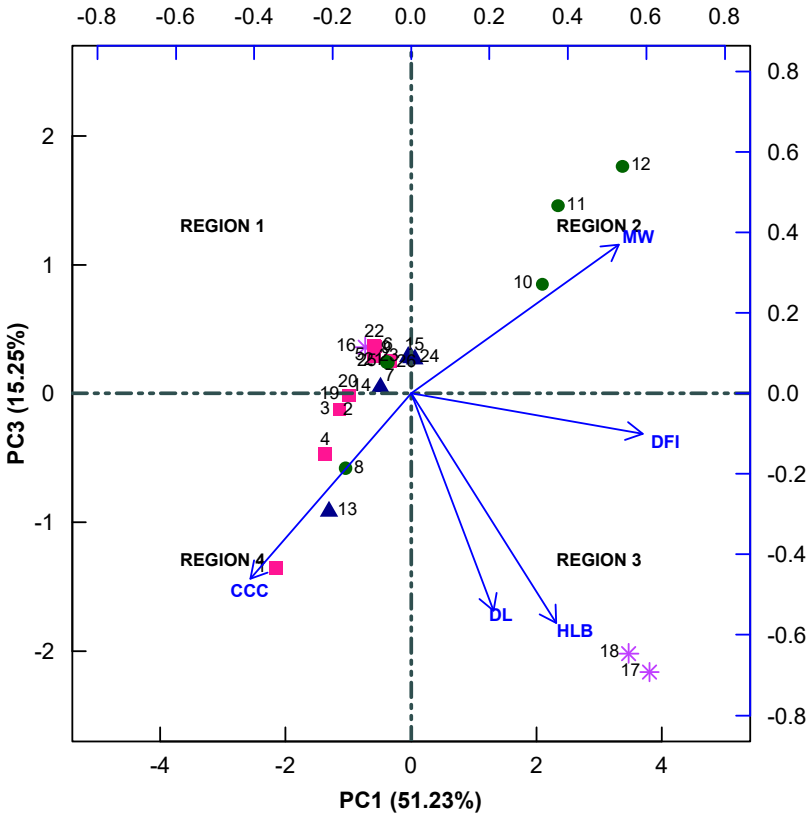

FIG 3 – Principal component 1 (PC1) versus principal component 3 (PC3). The score of each frother on PC1 and PC2 are shown by symbols, (■) aliphatic alcohols, (●) polypropylene glycols, (▲) propylene glycol methyl ethers, and (✳) commercial frothers.

To complement the PCA results, Figure 3 was presented to show the score in the first and third principal components, PC1 and PC3, respectively. Like Figure 2, the frothers were classified into four regions; however, PC1 versus PC3 tend to cluster a few different frothers in Region 1 and Region 4 compared with those regions using PC1 versus PC2. It should be highlighted that HLB showed the highest negative loading values on PC3, which also indicated that OrePrep F-507 and AeroFroth 65 were the most selective frothers as the HLB values were high. The molecular weight had a positive loading value on PC3, indicating that the frothers in Region 2 were powerful frothers, presumably due to the high molecular weight. As found in Figure 2, the frothers tested in the absence and presence of particles had the same position in PC1 and PC3, confirming that the proposed frother classification system in a two-phase system translates well to the three-phase system as frothers were clustered in the same groups.

Classification framework

Figure 4 presents the dendrogram using the first three principal components for all the 26 frothers. It is observed that frothers were grouped into four main groups. It is important to mention that the only variable value that was changed for the PCA and HCA was the dynamic froth stability (DFI). When comparing the dynamic foam stability, it is observed that 1-pentanol, which was classified as a weaker frother (Group 4) due to the high CCC value and small DFI value, was positively affected by the presence of particles reporting a slightly higher DFI value but still grouped as a weaker frother. It is evident that the results for 1-pentanol, TPM, MIBC, and TPG in the three-phase system agree well with the frother classification presented for the two-phase system, as frothers were clustered in the same groups. Moreover, there was not a major impact of the initial volume solution that was considered for the dynamic foam stability experiments on the frother classification. Therefore, these findings support the use of the classification system presented for a two-phase system by Saavedra Moreno *et al* (2022) to select a specific frother for a particular application without the necessity of conducting laborious experiments in a three-phase system.

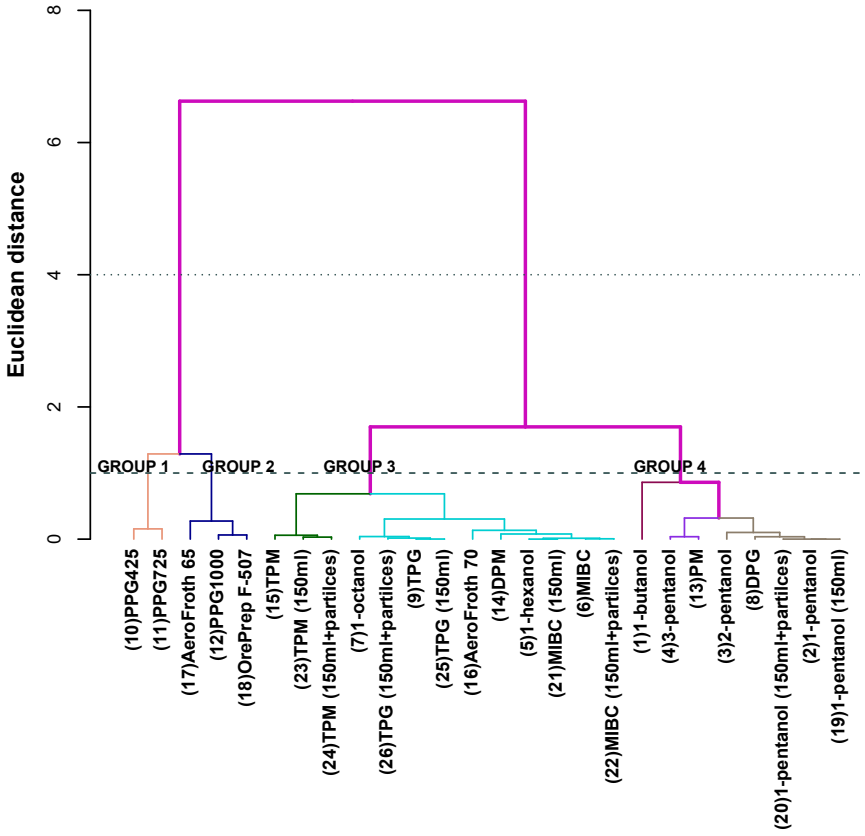

FIG 4 – Hierarchical clustering for all tested frothers using the first three principal components. At a Euclidean distance of 1, frothers were clustered into four groups, in which frothers in the further right-hand side group were more selective with high values of CCC and small values of foam stability (DFI).

Practical implications

The practicality of the results of this research suggests that in a two-phase system, the stability of the foam under dynamic conditions is correlated to the frother type, however, it would be different in a flotation process as it was shown in the present study that hydrophobic particles could affect the frothing properties of the frothers, especially for TPG. In terms of froth stability, the three-phase system (in the presence of particles) showed a similar frother ranking to the two-phase system (with particles), except that among the four tested frothers, TPG behaved as a more powerful frother in a three-phase system than MIBC as it had a higher DFI value (as shown in Table 1). Whereas MIBC appears to become a less effective frother in the presence of particles, it produced a more stable foam under dynamic conditions in a two-phase system than TPG. An explanation of this result could be that MIBC is adsorbed onto the surface of the particles causing a depletion of the frother concentration in the solution; however, it is believed that the frother adsorbed on the surface of particles may be transported to the surface of the bubble improving the bubble stability (Bournival *et al*, 2015). The adsorption of MIBC on coal particles has been well documented in previous studies (Aston *et al*, 1989; Fuerstenau, 1982). In a three-phase system, a powerful frother like TPM, which produced a stable froth in dynamic conditions, could be more suitable in the flotation of coarse particles as it may provide a more stable froth that would support their higher mass (Laskowski, 2004). By contrast, a weaker frother in terms of the frothing capacity such as 1-pentanol could be suitable for the flotation of fine and relatively more hydrophobic particles, such as coal particles. A weaker frother could help to control the froth stability challenges associated to a significant amount of fine particles in the flotation circuit. Previous research conducted by Gupta *et al* (2007) showed MIBC as a frother with poor froth stability and high selective properties for fine particles (<75 μm), highlighting the high reduction of ash content in the flotation of coal.

CONCLUSIONS

In terms of froth stability under dynamic conditions, the three-phase system (in the presence of particles) showed a similar frother ranking to the two-phase system (in the absence of particles), except that TPG behaved as a more powerful frother in a three-phase system than MIBC. In the three-phase system, the dynamic froth stability results aligned with the frother classification for frothers in two-phase system. Therefore, the frother classification presented in a two-phase system could be used as a guideline to choose frothers based on the desired characteristics, without the need to test the frother in a three-phase system.

REFERENCES

Abdi, H and Williams, L J, 2010. Principal component analysis. *Wiley interdisciplinary reviews: computational statistics,* 2, 433–459.

Aston, J, Lane, J and Healy, T, 1989. The solution and interfacial chemistry of nonionic surfactants used in coal flotation. *Mineral Procesing and Extractive Metallurgy Review,* 5, 229–256.

Bandyopadhyay, S and Saha, S, 2012. 'Similarity measures', *Unsupervised classification: similarity measures, classical and metaheuristic approaches and applications*, Springer Science and Business Media, pp. 59–73.

Ben-Hur, A and Guyon, I, 2003. 'Detecting stable clusters using principal component analysis', *In:* Brownstein, M J and Kohodursky, A, (eds.) *In Functional Genomics: Methods and Protocols,* Springer, pp. 159–182.

Blute, I, Pugh, R J, van de Pas, J and Callaghan, I, 2009. Industrial manufactured silica nanoparticle sols. 2: Surface tension, particle concentration, foam generation and stability. *Colloids and Surfaces A: Physicochemical and Engineering Aspects,* 337, 127–135.

Bournival, G, de Oliveira e Souza, L, Ata, S and Wanless, E J, 2015. Effect of alcohol frothing agents on the coalescence of bubbles coated with hydrophobized silica particles. *Chemical Engineering Science,* 131, 1–11.

Chipfunhu, D, Bournival, G, Dickie, S and Ata, S, 2019. Performance characterisation of new frothers for sulphide mineral flotation. *Minerals Engineering,* 131, 272–279.

Finch, J A, Nesset, J E and Acuña, C, 2008. Role of frother on bubble production and behaviour in flotation. *Minerals Engineering,* 21, 949–957.

Fuerstenau, D, 1982. Adsorption of frothers at coal/water interfaces. *Colloids and surfaces,* 4, 213–227.

Grau, R A and Laskowski, J S, 2006. Role of frothers in bubble generation and coalescence in a mechanical flotation cell. *The Canadian Journal of Chemical Engineering,* 84, 170–182.

Gredelj, S, Zanin, M and Grano, S, 2009. Selective flotation of carbon in the Pb–Zn carbonaceous sulphide ores of Century Mine, Zinifex. *Minerals Engineering,* 22, 279–288.

Gupta, A K, Banerjee, P, Mishra, A and Satish, P, 2007. Effect of alcohol and polyglycol ether frothers on foam stability, bubble size and coal flotation. *International Journal of Mineral Processing,* 82, 126–137.

Harris, M C and O'Connor, C T, 2017. Characterization of frothers and their behavior using partial molar Excess Gibbs energy. *International Journal of Mineral Processing,* 158, 63–67.

Huang, Q, Yang, X and Honaker, R Q, 2019. Evaluation of frother types for improved flotation recovery and selectivity. *Minerals,* 9, 1–17.

Karakashev, S I, Georgiev, P and Balashev, K, 2012. Foam production–ratio between foaminess and rate of foam decay. *Journal of Colloid and Interface Science,* 379, 144–147.

Laskowski, J S, 2004. Testing flotation frothers. *Physicochemical Problems of Mineral Processing,* 38, 13–22.

Laskowski, J S, Cho, Y S and Ding, K, 2003b. Effect of frothers on bubble size and foam stability in potash ore flotation systems. *The Canadian Journal of Chemical Engineering,* 81, 63–69.

Laskowski, J, 1993. Frothers and flotation froth. *Mineral Processing and Extractive Metallurgy Review,* 12, 61–89.

Laskowski, J, Tlhone, T, Williams, P and Ding, K, 2003a. Fundamental properties of the polyoxypropylene alkyl ether flotation frothers. *International Journal of Mineral Processing,* 72, 289–299.

Małysa, E, Małysa, K and Czarnecki, J, 1987. A method of comparison of the frothing and collecting properties of frothers. *Colloids and Surfaces,* 23, 29–39.

Murtagh, F and Legendre, P, 2014. Ward's hierarchical agglomerative clustering method: which algorithms implement Ward's criterion? *Journal of classification,* 31, 274–295.

Pugh, R, 2000. Non-ionic polyethylene oxide frothers in graphite flotation. *Minerals Engineering,* 13, 151–162.

Quinn, J, Kracht, W, Gomez, C, Gagnon, C and Finch, J, 2007. Comparing the effect of salts and frother (MIBC) on gas dispersion and froth properties. *Minerals Engineering,* 20, 1296–1302.

Saavedra Moreno, Y, Bournival, G and Ata, S, 2020. Comparing the froth stability of two-phase and three-phase systems for various frother types. *Proceedings of the XXX International Mineral Processing Congress*, South Africa.

Saavedra Moreno, Y, Bournival, G and Ata, S, 2021. Foam stability of flotation frothers under dynamic and static conditions. *Separation and Purification Technology,* 274, 1–12.

Saavedra Moreno, Y, Bournival, G and Ata, S, 2022. Classification of flotation frothers–A statistical approach. *Chemical Engineering Science,* 248, 117252.

Sweet, C, van Hoogstraten, J, Harris, M and Laskowski, J, 1997. The effect of frothers on bubble size and frothability of aqueous solutions. In: Finch, J A, Rao, S and Holubec, I, (eds.), *Processing of complex ores: mineral processing and the environment*, Sudbury, Canada, pp. 235–245.

Wills, B A and Finch, J A, 2016. 'Froth flotation', *Wills' Mineral Processing Technology: An introduction to the practical aspects of ore treatment and mineral recovery,* 8th edn, Elsevier Science and Technology Books, pp. 265–380.

Zhang, W, 2012. *Frothers and Frother Blends: A Structure—Function Study,* PhD Thesis, Department of Mining and Materials Engineering, McGill University (Canada). 150 p.

Towards a model-informed process control strategy for coal flotation in a Jameson Cell

J S Siong[1], A J Morrison[2], J Wang[3], M Yahyaei[4] and K Runge[5]

1. PhD Candidate, Sustainable Minerals Institute, The University of Queensland, Brisbane Qld 4068. Email: j.siong@uq.edu.au
2. Senior Research Fellow, Sustainable Minerals Institute, The University of Queensland, Brisbane Qld 4068. Email: angus.morrison@uq.edu.au
3. Postdoctoral Research Fellow, Sustainable Minerals Institute, The University of Queensland, Brisbane Qld 4068. Email: j.wang30@uq.edu.au
4. Associate Professor, Sustainable Minerals Institute, The University of Queensland, Brisbane Qld 4068. Email: m.yahyaei@uq.edu.au
5. Associate Professor, Sustainable Minerals Institute, The University of Queensland, Brisbane Qld 4068. Email: k.runge@uq.edu.au

ABSTRACT

The flotation cells used to upgrade ultrafine metallurgical coal (-250 µm) are usually poorly controlled leading to unnecessary loss of combustibles from the flotation system. This is mainly because coal flotation cells are typically controlled for process stability rather than optimisation of flotation performance. This is especially true for a flotation device commonly used in coal applications in Australia – the Jameson Cell. This then provides an opportunity to improve the flotation performance by shifting from a stabilising control strategy to a proactive optimising control strategy. For an optimising control strategy, the control system will require a means of relating and then measuring in real-time, the effect of changing operating conditions on the coal flotation performance. Hence, the major aim of this work is to propose a possible model-informed process control strategy that could be used for real-time performance optimisation. In this study, industrial site work was conducted on an industrial-scaled Jameson Cell at a Coal Handling and Preparation Plant (CHPP) in Central Queensland, Australia where superficial gas velocity was controlled to six different levels. At the same time, other process variables such as froth depth and flotation feed properties were measured. The empirical models developed from this study suggested that combustible recovery is a function of superficial gas velocity, froth depth, feed solid content and feed ash content and that a peak in combustible recovery existed as a function of superficial gas velocity. This led to the development of a model-informed control strategy that aimed to maximise the combustible recovery by determining and then operating the cell at the superficial gas velocity at which the peak occurs. This peak superficial gas velocity was found to be only a function of feed solid content. Based on these findings it would seem possible to operate a Jameson cell at peak performance by online measurement of feed solid content, prediction of the optimum superficial gas velocity and stabilising control to maintain operation at that superficial gas velocity set point. The development of this model-informed control strategy can serve as a basis for the development of a more sophisticated model-predictive control (MPC) system. However, more work will need to be done to improve the predictivity of the combustible recovery model by measuring and modelling performance over a wider range of operating conditions.

INTRODUCTION

A typical metallurgical coal preparation and handling plant (CHPP) usually contains several parallel circuits that clean coal based on targeted size ranges. Ultrafine coal (-250 µm) that accounts for approximately 20 per cent of the raw coal feeding a plant, is usually upgraded using froth flotation (Mackinnon and Swanson, 2010). A commonly used flotation cell to treat ultrafine coals in Australia is the Jameson Cell. The Jameson Cell has gained its popularity due to its simplicity of operation and ease of maintenance. It contains no moving parts and achieves multi-pass flotation operation with a small footprint (Huynh *et al*, 2014). Unlike the mechanical cell, it does not contain an impeller, instead, it contains downcomers to generate fine bubbles between 200 to 1000 µm in size. Smaller bubbles have an increased surface area to volume ratio and this increases their carrying capacity. A detailed explanation of the operating principles of a Jameson Cell are discussed by a number of

authors including Atkinson *et al* (1993), Jameson (1995), Evans *et al* (1995), Harbort *et al* (2003), Cowburn *et al* (2005), Pokrajcic *et al* (2005) and Huynh *et al* (2013).

The Jameson cell usually employs a stabilising control strategy where a specific operating variable such as froth depth, is controlled to a pre-determined set point. A change in the set point will only be made by the operator when the flotation performance is observed to be significantly changed (Huynh *et al*, 2013). Since the flotation system is controlled for process stability rather than based on actual performance which would be affected by various uncontrolled process variables such as coal feed properties and water properties, its flotation performance is often just good but not optimal.

There is thus an opportunity to improve the flotation performance of a Jameson Cell operating in a coal application by shifting from a stabilising control system to an optimising control system. One of the widely used multivariate control algorithms for optimising control systems is the model-predictive control (MPC) system. The MPC is a proactive system which allows for the effects of a change in process variable on the flotation performance to be measured in real-time and then a responsive change is made to the set points of the operating variables to achieve the targeted optimal flotation performance, for instance, maximising combustible recovery.

Process variables associated with the Jameson Cell

The major process variables that can affect the coal flotation performance of a Jameson Cell includes the air-to-pulp ratio (APR), froth depth, reagent dosage, wash water rate and flotation feed properties such as feed solid content and feed ash content.

Air-to-pulp ratio (APR) is the volumetric fraction of air in the slurry fed into the Jameson Cell. It directly affects the amount of air injected into the system and thus affects the gas hold-up and flow regime within the downcomer. This in turns, causes an effect to the turbulence generated at the region near to the downcomer outlet (Sahbaz *et al*, 2012). As it is difficult to vary feed flow and feed properties to the Jameson cell as it is controlled by the performance of upstream processes and its internal recycle mechanism used to maintain a constant slurry feed pressure, in this work, the APR is varied by varying the volumetric air flow rate. In order to generalise the volumetric air flow rate and eliminate the effect of the diameter of the flotation cell, volumetric flow rate is converted to superficial gas velocity.

Superficial gas velocity (J_g) is the upward rising velocity of air bubbles in a specific flotation cell. It can directly influence the flotation kinetics and thus is closely linked to the rate of concentrate production (Atkinson *et al*, 1993; Mohanty and Honakeri, 1999; Harbort and Alexander, 2006). In a Jameson cell, J_g can be obtained using Equation 1 where the cross-sectional area of the riser tank is the area normal to the froth flow direction, excluding the area occupied by the downcomers.

$$J_g\ (cm/s) = \frac{Downcomer\ volumetric\ air\ rate\ (cm^3/s)}{Cross-sectional\ area\ of\ riser\ tank(cm^2)} \quad (1)$$

Froth depth is the distance between the pulp-froth interface and the cell lip. In Jameson cells, shallow froth depths of less than 100 mm result in higher combustible recovery but also high ash product content (Atkinson *et al*, 1993). Shallow froth results in less bubble coalescence and particle drop back but also less drainage of entrained particles. Atkinson *et al* (1993) also reported that a froth depth of above 200 mm did not significantly affect the flotation performance of the Jameson Cell. This, however, was a trend that needs further verification. It is also likely that the impact of froth depth will be a function of cell design considerations (eg cell diameter) and interactive effects with other parameters such as gas rate.

Traditionally, frother concentration plays a major role in reducing bubble size within the pulp phase due to its ability to prevent bubble coalescence. In the froth phase, it reduces bubble bursting and bubble coalescence and can improve froth mobility which reduces particle drop back. In a Jameson Cell, the effect of frother concentration on the bubble size and hence, the overall flotation performance is similar to that of other conventional flotation cells. Osborne *et al* (2013) reported that in a metallurgical coal operation using a Jameson Cell, an increase in frother concentration was found to have dramatically increased the combustible recovery. They concluded that this was because an increase in frother concentration had increased the carrying capacity of the flotation cell

by preventing coalescence of bubbles and thus providing more bubble surface area available for coal particle attachment.

Flotation control based on froth structure and characteristics

In an industrial flotation application, it is not uncommon for the operators to control the flotation performance by visual inspection of froth structure and characteristics. Over the years, machine vision technologies such as JKFrothCam and Metso's VisioFroth have been developed to obtain online froth characteristics for implementation into a more advanced process control system (Holtham and Nguyen, 2002; Runge *et al*, 2007; Supomo *et al*, 2008; Jahedsaravani *et al*, 2014; Massinaei *et al*, 2019). However, since characteristics such as froth colour, froth bubble size, and froth texture are highly dependent on environmental factors, they have proved difficult to correlate with performance. Advanced process control systems have thus usually centred around the use of froth overflowing velocity (Morar *et al*, 2012; Jahedsaravani *et al*, 2016).

A common control strategy is to use froth overflowing velocity to control mass pull, as discussed in Supomo *et al* (2008). Froth overflowing velocity was measured, and froth depth was adjusted to achieve the desired mass pull. This control strategy assumes that froth velocity can provide a direct measure of mass pull (Runge *et al*, 2007; Morar *et al*, 2012). However, this is not as always true because the mass pull rate for a given velocity is also dependent on bubble loading and the entrainment of solids between the bubbles (Baas *et al*, 2007).

A control system that optimises the flotation process will require a means of relating, and then measuring in real-time, the effect of changing operating conditions on the coal flotation performance. However, to date, there is a lack of tools and measurement methods to provide real-time flotation performance estimates (ie combustible recovery and flotation concentrate ash content). Moreover, there is also a lack of a comprehensive models that relate the effects of operating variables to the performance of an industrial-scaled Jameson cell. This limits the understanding of the extent to which the operating variables should be altered to achieve the targeted flotation performance and also whether a change in the operating variable actually led to an improvement in the flotation performance in real-time. Hence, this work aims to determine how the coal flotation performance of a Jameson Cell are affected by process variables and to propose possible model-informed control strategies that could be used for real-time performance optimisation. This would provide a baseline of knowledge for the future development of a model-predictive control (MPC) system.

MATERIALS AND METHODS

The industrial site work for this study was performed on a Coal Handling and Preparation Plant (CHPP) in Central Queensland, Australia. This CHPP processes two coal types of different ranks and in this paper, these coal types will be labelled as high and low rank coal.

Coal feed properties

The two coal types can be distinguished by their ash content and particle size distributions. Figure 1a shows that the lower rank coal contains a higher feed ash content than higher rank coal. Figure 1b shows that the lower rank coal contained more fines (-125 µm) material than the higher rank coal type. The data shown on these graphs were measured in the feed to the Jameson cell during the industrial site work as the two coal types were processed through the CHPP.

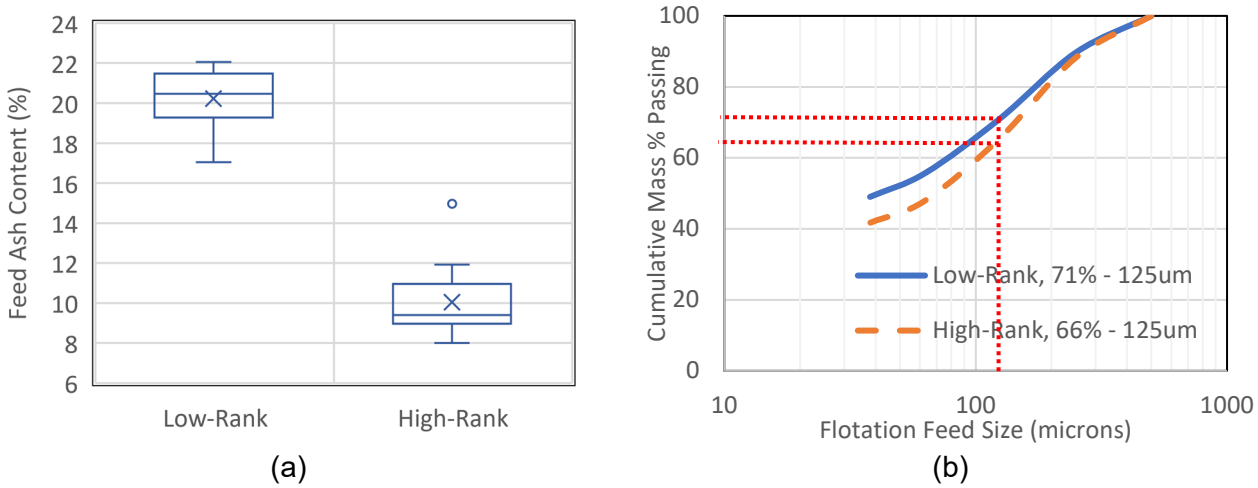

FIG 1 – (a) Box and Whisker's plot denoting variation in feed ash content; and (b) Particle size distribution of the two coal types.

It was initially assumed that data collected for the two coal types would need to be analysed separately. During data analysis, however, it was found that the differences in coal rank could be accounted for by their difference in ash content and particle size distribution, parameters that even exhibited a continuum even within the one coal type. It was possible to develop only one model to represent the Jameson cell behaviour and performance that was independent of coal rank.

Experimental work program

The flotation circuit used in the CHPP receives the ultrafine feed from the overflow of the upstream classifying cyclones. This classifier overflow is sent to a primary flotation circuit consisting of two parallel banks of three J5000/10 Jameson cells. The tailings from the two primary banks are sent to two B6500/24 Jameson Cells in the secondary flotation circuit. The experimental work of this study was conducted in one of the J5000/10 Jameson cells within the primary circuit. This cell was fitted with 10 downcomers, a riser tank and two launders – an inner and outer launder. Conducting experiments in the primary circuit has the advantage that there are no upstream flotation cells to affect the characteristics of the flotation feed and thus upstream disturbance is minimised.

In this project, only the supplied air rate set point was varied. Other variables such as frother dosage, wash water flow rate and froth depth, were kept constant by the plant control system. The effect of supplied air rate on the flotation behaviour was investigated at six different levels – 500, 600, 700, 800, 900 and 1000 m^3/h. A total of 31 runs were conducted with 15 runs conducted using low rank coal and 16 runs conducted using high rank coal.

During each experimental run, several measurements were made. These measurements can be categorised as relating to cell operating conditions or cell performance. The first category comprises of the operating conditions for the flotation cell that includes froth depth and superficial gas velocity. Froth depth is the distance between pulp-froth interface and the flotation lip (as shown in Figure 2a). Froth depth was measured using a manual ball float whereas superficial gas velocity was obtained using the gas rate recorded by the existing Plant Information (PI) system.

The second category includes measurements that enables the calculation of the flotation cell's performance. The rate of concentrate discharge was determined by measuring the time required for the concentrate to fill a sample cutter. This rate of concentrate was collected at three different position of a Jameson Cell as shown in Figure 2b. At the same time, samples were also collected from the recirculated feed and tailings stream of the flotation cell. These samples were sent to an industrial lab to obtain solid content, particle size distributions, overall ash content and ash content by size.

It was not possible to collect a fresh flotation feed sample (ie prior to the internal recirculated tail) from this Jameson cell. Therefore, the flotation performance analysed is the recovery across a single pass of the Jameson cell and not the overall performance from the Jameson unit where tailings are

recirculated and have multiple opportunities for recovery. A major assumption is that the single pass recovery and its driver is similar to the overall flotation performance of the Jameson unit.

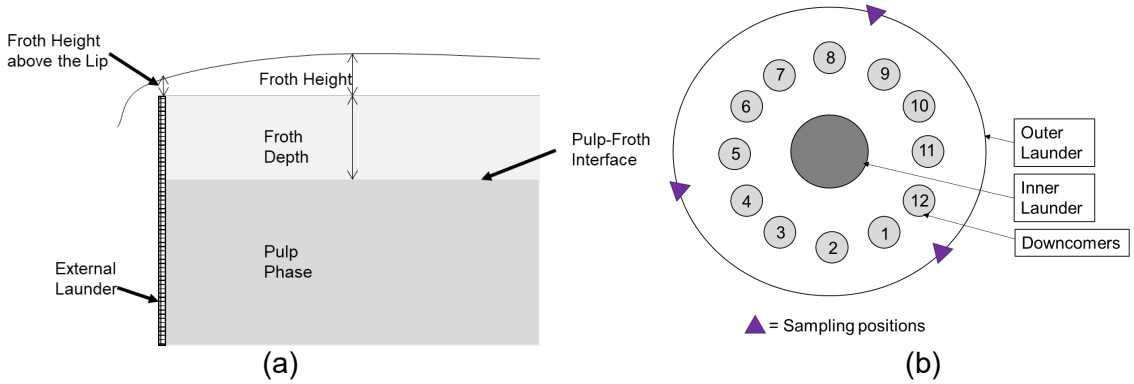

FIG 2 – (a) Schematic of zones of a flotation cell (b) Sampling positions around the outer launder of the selected Jameson cell.

During data analysis, all of the experimental data collected in category 2 were balanced within Microsoft Excel using the SOLVER function. Mass balancing utilises the least square criterion to simultaneously adjust the stream information to establish the mass split ratio to concentrate and provide a consistent set of stream data that satisfies the input stream = output stream criterion. Mass balancing provides a consistent set of information and also provides the 'best' estimate of the flotation performance with the highest likelihood of representing the truth (Napier-Munn, 2014).

Calculating flotation cell performance

Using the mass balanced data, the coal flotation performance of the Jameson Cell can be calculated. Coal flotation performance can be characterised using four major performance indicators – combustible recovery, product yield, ash rejection and product ash content.

Combustible recovery is the proportion of feed coal particles that are recovered into the product concentrate stream. It can be obtained by dividing the mass balanced flow of coal to the concentrate by the coal flow rate in the feed. Product yield is similar to the combustible recovery but it is essentially the overall solids recovery. It can be obtained by dividing the mass balanced concentrate solid flow rate by the feed solid flow rate. Product ash content is the mass balanced concentrate ash flow rate divided by the concentrate solids flow rate. Finally, ash rejection, $(1 - R_{Ash})$ is the ratio of feed ash rejected to the tailings stream and can be calculated using the following equation:

$$(1 - R_{Ash}) = \frac{Tailings\ ash\ flowrate}{Feed\ ash\ flowrate} \quad (2)$$

This paper will concentrate and report only the results pertaining to the combustible recovery. This is because the industrial site at which the work was performed aims to maximise the amount of combustibles recovered during flotation. Ash rejection is of importance but because the ash content of the coal product from flotation is relatively low compared to the other circuits in the CHPP, it is not considered a target for process control at the site of interest.

Empirical model development procedure

The stepwise regression algorithm of MATLAB® was used to develop multiple regression models to relate flotation performance with the process variables measured. Table 1 lists the process variables that were considered to have the potential to affect performance and the range over which they varied during the site work. Of these predictors, only supplied air rate was directly controlled while froth depth, reagent dosage, feed solid content, feed ash content and feed P80 were allowed to vary in response to changes in the supplied air rate and the performance of the upstream circuit. As mentioned, instead of using supplied air rate as a predictor for the regression analysis, superficial gas velocity (range) derived from the supplied air rate was used to normalise the rising velocity of bubbles from the surface area of the flotation cell available.

TABLE 1

A summary of the operating ranges of the process variables involved in the regression modelling.

Predictors	Units	Minimum	Maximum
Superficial gas velocity	cm/s	0.76	1.62
Froth depth	mm	28.0	138
Frother dosage	mL/min	485	501
Collector dosage	mL/min	202	255
Feed solid content	%	3.66	9.92
Feed ash content	%	8.01	22.1
Feed P80	μm	164	219

For the development of the performance model, all the process variables as listed in Table 1 were tested for its significance to combustible recovery. Stepwise regression analysis was performed to remove process variables that were not significant to the model (ie p-value greater than 0.05 for their highest order term or crossed-term). The insignificant variables were removed from the model. Besides that, the model development process also includes removing the outlying data points using standard statistical regression analysis methods and performed the standard model fitness test to finally arrive to a robust and statistically significant model as shown in Equation 3.

However, to maximise the statistical power of the empirical model, all of the available data points were used to build it and none were left to test the predictive power of the model. Instead, the 'Monte Carlo Simulation' or 'Bootstrapping' method described by Napier-Munn (2014) was used to obtain the 95 per cent confidence interval of the model prediction. This method generates 1000 random values based on the mean and standard deviation of the residuals generated from the initial model developed. This list of 1000 random values were then added to the response variable (ie combustible recovery) to create a matrix containing 1000 different response variables varying based on the mean and standard deviation of residuals. The regenerated response data were then used to generate 1000 different models giving 1000 different model coefficients and adjusted response values for each variable (Napier-Munn, 2014). These adjusted response values were then analysed to calculate the 95 per cent confidence interval.

RESULTS AND DISCUSSIONS

Empirical relationship between combustible recovery and process variables

The empirical model that best related the effect of process variables to the combustible recovery achieved in the Jameson Cell was found to be:

$$R_c = -68.4 + 0.44d_f + 93.0J_g - 7.15F_{solid} + 10.1F_{Ash} - 0.03d_fF_{Ash} + 18.9J_gF_{solid} - 1.19F_{solid}F_{Ash} - 82.7\,{J_g}^2 \quad (3)$$

where R_c is the combustible recovery (%), d_f is the froth depth (mm), Jg is the superficial gas velocity (cm/s), F_{solid} is feed solid content and F_{Ash} is feed ash content.

The model developed was statistically significant (p-value of 1.51×10^{-5}), with combustible recovery found to be a function of froth depth, superficial gas velocity, feed solid content and feed ash content. The model can also explain the bulk of the variations in the calculated combustible recovery evidenced by its high adjusted R^2 of 0.792. Feed P80 (ie 80 per cent of the feed passing size), was measured but dropped out from the model during the stepwise regression analysis procedure. This implies that overall P80 was not a significant variable affecting combustible recovery over the range it varied during the experimental campaign.

Table 2 details the model coefficients and the statistical significance of each model term. 'Standard Error' of the coefficients is an estimate of the standard deviation of the respective coefficient and the

'p-value' is a measure of the significance of the model terms. A model term with a p-value below 0.05 (ie 5.0×10^{-2}) means that it significantly affects the response, with 95 per cent confidence.

TABLE 2

Model terms and coefficients with their respective statistical significance for the model developed to predict combustible recovery

Model Terms	Model Coefficient	Standard Error	p-value
Intercept	-68.4	50.9	1.08×10^{-1}
d_f	0.44	0.14	5.04×10^{-3}
J_g	93.0	1.70	1.08×10^{-1}
F_{solid}	-7.15	-1.64	1.21×10^{-1}
F_{Ash}	10.1	4.93	1.52×10^{-4}
$d_f F_{Ash}$	-0.03	-2.83	1.21×10^{-2}
$J_g F_{solid}$	18.9	5.39	5.99×10^{-5}
$F_{solid} F_{Ash}$	-1.19	-4.90	1.61×10^{-4}
${J_g}^2$	-82.7	-3.44	3.34×10^{-3}

In order to investigate the individual effects of the various process variables on combustible recovery, an 'adjusted response plot' was constructed for superficial gas velocity. Figure 3a show the adjusted response plot for superficial gas velocity which describes the relationship between the fitted combustible recovery with a single predictor while averaging out the contributions of other process variables.

Figure 3a illustrated that that superficial gas velocity has a quadratic relationship with combustible recovery and there exists a peak in combustible recovery. This peak suggests that there is a specific superficial gas velocity that can maximise the recovery of combustibles for a given froth depth, feed solid content and feed ash content. This aligns with the observation found by Qu *et al* (2013) in lab-scaled mechanical coal flotation tests. It also aligns with research performed in metalliferous flotation by researchers such as Hadler and Cilliers (2009) who have observed a peak in sulfide mineral recovery with air rate in conventional flotation cells. This peak in combustible recovery observed as a function of superficial gas velocity implies that it is possible to maximise the combustible recovery by operating at the superficial gas velocity that gave the peak.

Most of the datapoints of superficial gas velocity also lies within the pink shaded region which represents the 95 per cent confidence interval obtained using the 'bootstrapping' method. The 95 per cent confidence interval was also shown to be relatively narrow which means that there is confidence that a peak in combustible recovery does indeed exist as a function of superficial gas velocity.

Figure 3a showed the overall response of superficial gas velocity on combustible recovery but in order to investigate the effect of the paired interactions between the variables and superficial gas velocity, the model was used to calculate combustible recovery for a range of superficial gas velocities at different froth depth, feed solid content and ash content, respectively, with all other variables kept constant at their mean value. This gives the plots of predicted combustible recovery as a function of superficial gas velocity, as shown in Figure 3b to 3d. Figure 3b to 3d illustrated that all the plots still exhibit a quadratic relationship between combustible recovery and superficial gas velocity.

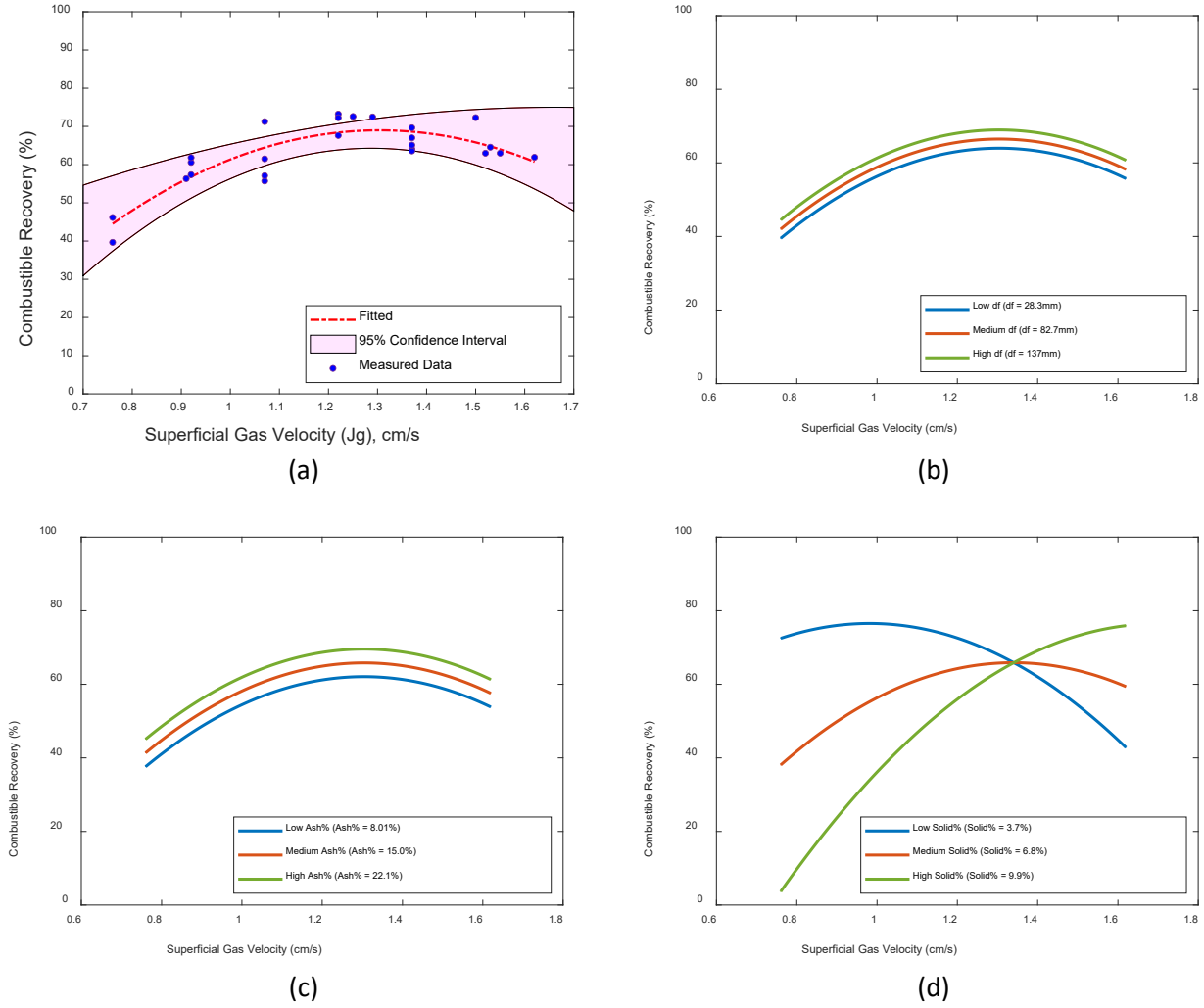

FIG 3 – (a) Adjusted combustible recovery response plot for superficial gas velocity; Predicted combustible recovery for a range of superficial gas velocity at low, medium and high; (b) froth depth at mean feed solid and ash content; (c) feed ash content at mean froth depth and feed solid content; (d) feed solid content at mean froth depth and feed ash content.

Figure 3b and 3c showed that varying froth depth and feed ash content changes the magnitude of the peak in combustible recovery, without changing the superficial gas velocity at which that peak occurs. Figure 3d showed that varying feed solid content can affect both the magnitude of the peak in combustible recovery as well as the superficial gas velocity at which it occurs. Hence, to enable a control strategy, it is important to understand how the feed solid content affects the superficial gas velocity at which the peak in combustible recovery occurs.

Simulations were performed to further investigate the interactive effects of the process variables and their effects on the peak combustible recovery with superficial gas velocity. For the simulations, combustible recovery was calculated for different combinations of froth depth, feed solid content, feed ash content for a range of different superficial gas velocity values using the developed regression model. All of these process variables were varied within the operating ranges tested for this study (as listed in Table 1). The superficial gas velocity values that led to the maxima in combustible recovery were then extracted for each combination of process variables.

$$J_{g,peak} = 0.11\, F_{solid} + 0.56 \quad (4)$$

where $J_{g,peak}$ is the J_g to attain peak in combustible recovery and F_{solid} is the feed solid content.

The superficial gas velocity required to attain a peak in combustible recovery was found to be a linear function of feed solid content. This linear function can be represented by Equation 4. The relationship

between the peak superficial gas velocity and feed solid content simulated at all combinations of froth depth and feed ash content is shown in Figure 4.

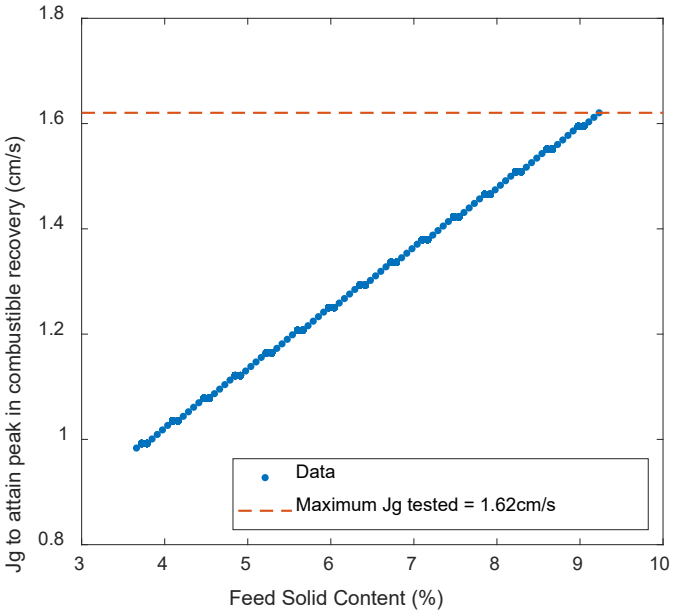

FIG 4 – Peak Superficial Gas velocity ($J_{g,\,peak}$) versus feed solid content for model regression simulations which involved varying feed solid content, froth depth and feed ash content.

Model-informed process control strategy

As outlined earlier, the coal flotation circuit of a CHPP is usually operated stably but not optimally, resulting in a significant amount of liberated combustibles lost to the tailings stream. This is mostly because a coal flotation cell usually employs a stabilising control system, as shown in Figure 5. The stabilising control is a passive approach where the operating variables are controlled to a specific pre-determined set point, and control action only applied when the process deviates from the set point. The flotation process is subject to a number of disturbances such as coal feed properties and water properties and these variations can result in a flotation cell requiring a change in set point to maintain optimum performance. Therefore, under certain conditions, operating the flotation cell at fixed set points results in suboptimal performance.

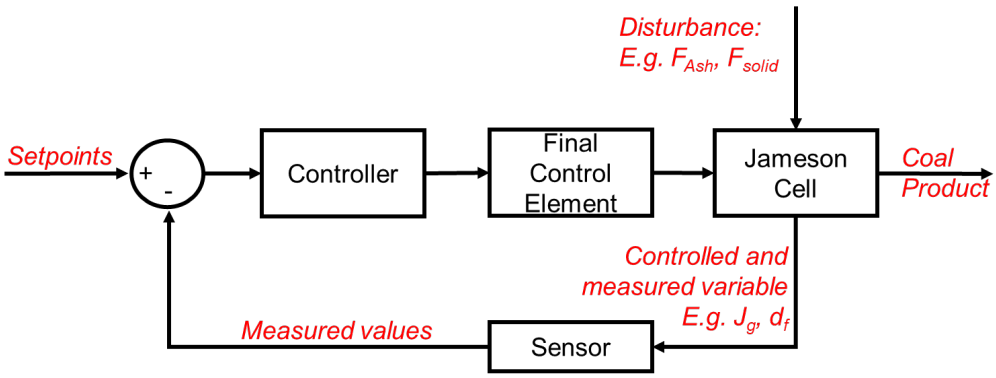

FIG 5 – Process stabilising feedback control.

On the other hand, the Model-informed process control (MiPC), instead of stabilising the process, provides direction for optimising the process, which can then be used to adjust the set point of the stabilising process control loop. The MiPC is a proactive system that uses process models to predict performance and determine the respective set points of the operating variables required to achieve the targeted performance (García *et al*, 1989).

The empirical model described above can be used as the basis for a combustible recovery – maximising MiPC for the Jameson cell based on ensuring the optimal superficial gas velocity for a

given feed coal. Since the combustible recovery-maximising gas velocity is independent of froth depth and feed ash content, as shown in Figure 3b to 3d, the linear relationship between J_g to achieve peak in combustible recovery, with feed solid content given in Equation 4 is sufficient in selecting the optimal superficial gas velocity. Figure 6 shows this MiPC diagrammatically.

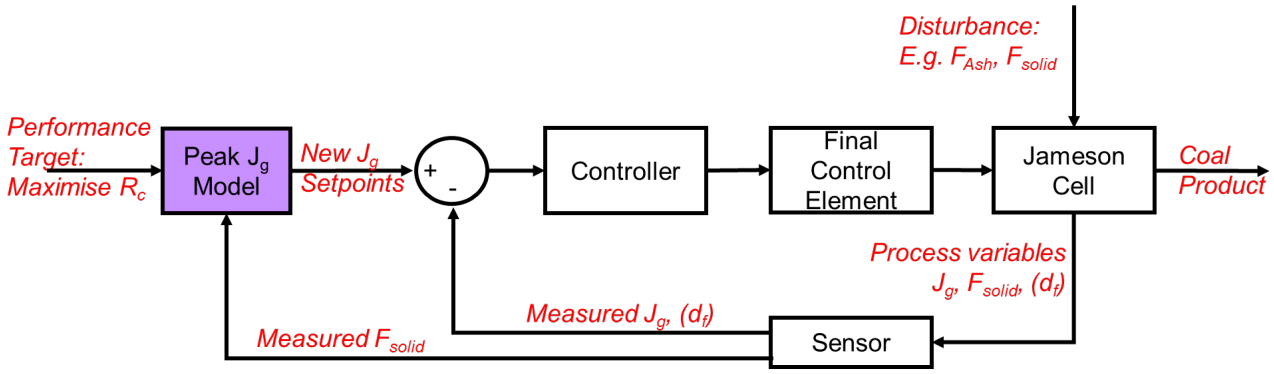

FIG 6 – Proposed model-informed process control (MiPC) strategy.

The MiPC shown in Figure 6 requires a measure of the feed solid concentration. This can come either from real-time densitometer measurements or from an estimate of a typical feed solid content based on historical process-monitoring surveys or mass balances. Air flow rate that gives superficial gas velocity (J_g) can be measured using differential pressure transmitters (Shean and Cilliers, 2011). The measured (or estimated) feed solid content will be inserted into the 'Peak J_g Model' represented using Equation 4 to determine the J_g needed to attain a peak in combustible recovery. This new J_g set point will be fed to the existing J_g stabilising control system where the new set point will be compared against the measured J_g to obtain an error for the process controller to stabilise the control system with this new J_g set point.

This interim control strategy is simple where it does not require the full variable measurement for the combustible recovery model (Equation 3). However, the empirical relationships may be specific to the single Jameson Cell and the coal types investigated. The empirical relationships can also only be considered valid within the ranges tested for the various process variables (Table 1). Moreover, in this work, only superficial gas velocity was controlled to the specific set point to obtain the empirical relationship of combustible recovery. Other variables such as froth depth were not controlled but still varied within the experimental program. Hence, for this interim control strategy, it is recommended to keep the set point of froth depth to the usual operating froth depth of 100 mm. This set point of froth depth was also recommended based on Atkinson *et al* (1993)'s study where a froth depth of less than 100 mm can result in higher combustible recovery. It may also be the case that the variation in froth depth achieved in the test program was interactively coupled with the air rate employed in the cell and an independent effect of froth depth on performance may differ from that observed in this data set.

It is therefore recommended that more work be done to determine the explicit effects of froth depth, flotation reagents and other variables on combustible recovery to improve the predictivity of the regression models. More work is also required to investigate whether the form of relationship observed in this Jameson Cell study would be similar in other Jameson cells or other flotation cells employed in coal flotation plants. The efficacy of this interim control strategy will also need to be tested to determine whether the difference in combustible recovery for using an online feed solid content measurement (measured using densitometer) and an estimated feed solid content value (from historical data).

CONCLUSIONS

In this study, a regression model to predict combustible coal recovery in a Jameson cell was developed and was a function of superficial gas velocity, froth depth, feed solid content and feed ash content. The model developed was statistically significant and was able to explain about 80 per cent of the variation in the measured combustible recovery. The model was also able to predict

performance for the two distinctly different coals that had been processed through the CHPP during the course of the experimental campaign.

An analysis of the regression model demonstrated that a peak in combustible recovery existed as a function of superficial gas velocity (J_g). It was also found that the superficial gas velocity required to attain maximum combustible recovery was independent of the froth depth and feed ash content measurements but was linearly correlated with feed percent solids. The higher the feed percent solids, the higher the superficial gas velocity required to achieve maximum recovery of coal in the flotation cell.

It is proposed that better performance can be achieved from a Jameson cell by implementing a model informed process control (MiPC) strategy that operates the cell at the superficial gas velocity that optimises combustible recovery. Since the J_g required to obtain the peak in combustible recovery was found to be only a function in feed solid content, the new J_g set point can be predicted based only on a feed solids concentration measurement. Once the peak Jg is established, a stabilising control strategy can be implemented to maintain cell operation at that air rate.

The regression model developed in this study, however, was obtained from data collected by controlling for superficial gas velocity only. Froth depth was not able to be explicitly controlled and other variables may affect performance as well. It is recommended that more work be performed to investigate the effects of other process variables. The aim would be to determine the applicability of the developed control strategy over a greater range of process variables as well as to improve the accuracy of the prediction of the regression model. More work will also need to be done to validate whether the form of the empirical relationships observed in this study would apply in other Jameson Cell applications and when operating using alternative types of flotation cell. Finally, the efficacy of this control strategy will also need to be tested to determine whether an estimated measurement of feed solid content was sufficient to maximise the combustible recovery. This will determine whether it is necessary to introduce a sensor for online feed solid content measurement. The work performed to date, however, has provided valuable insight into the potential form of a fully automated model-predictive control (MPC) system to optimise Jameson cell operation.

ACKNOWLEDGEMENTS

The authors would like to acknowledge the financial support from the Australian Coal Association Research Program (ACARP). The author's gratitude also extends to the host site for the assistance and financial support provided during the industrial work.

REFERENCES

Atkinson, B W, Conway, C J and Jameson, G J, 1993. Fundamentals of Jameson Cell Operation Including Size-Yield Response. In: J J Davies (ed.) *Sixth Australian Coal Preparation Conference*, Australian Coal Praparation Society.

Baas, D, Hille, S and Karageorgos, J, 2007. Improved Flotation Process Control at Newcrest's Telfer Operation. *Ninth Mill Operators' Conference Proceedings 2007* (The Australasian Institute of Mining and Metallurgy: Melbourne).

Cowburn, J S, Bourke, S and Hill, B, 2005. Design Developments of the Jameson Cell. *Centenary of Flotation 2005 Symposium,* Brisbane.

Evans, G M, Atkinson, B W and Jameson, G J, 1995. The Jameson Cell. In: K A Matis and M Dekker (eds.) *Flotation Science and Technology.* New York.

García, C E, Prett, D M and Morari, M, 1989. Model predictive control: Theory and practice—A survey. *Automatica,* 25, 335–348.

Hadler, K and Cilliers, J J, 2009. The relationship between the peak in air recovery and flotation bank performance. *Minerals Engineering,* 22, 451–455.

Harbort, G and Alexander, D, 2006. Gas dispersion measurements in coal flotation cells. *International Seminar on Mineral Processing Technology*, India. 254–264.

Harbort, G, Manlapig, E V, de Bono, S and Monaghan, A J, 2003. Air and fluid dynamics within a Jameson Cell downcomer and its implications for bubble-particle contact in flotation. In: L L D J Bradshaw (ed.) *XXII International Mineral Processing Congress*. 715–724.

Holtham, P N and Nguyen, K K, 2002. On-line analysis of froth surface in coal and mineral flotation using JKFrothCam. *International Journal of Mineral Processing,* 64, 163–180.

Huynh, L T N, Kohli, I, Osborne, D, Waal, H D and Walstra, C, 2013. Design and performance aspects of coal flotation – experiences with the Jameson Cell. Southern African Coal Processing Society Inernational Coal Conference, July 23 - 25 July 2013 Graceland, South Africa.

Huynh, L, Kohli, I and Osborne, D G, 2014. Busting The Myths of Flotation in The Australian Coal Industry. In: G Sherritt (ed.) *15th Australian Coal Preparation Conference – Continuing excellence in coal preparation,* Australian Coal Preparation Society Limited.

Jahedsaravani, A, Marhaban, M H and Massinaei, M, 2014. Prediction of the metallurgical performances of a batch flotation system by image analysis and neural networks. *Minerals Engineering,* 69, 137–145.

Jahedsaravani, A, Marhaban, M H, Massinaei, M, Saripan, M I and Noor, S B M, 2016. Froth-based modeling and control of a batch flotation process. *International Journal of Mineral Processing,* 146, 90–96.

Jameson, G J, 1995. Bubbly Flows and The Plunging Jet Flotation Column. *Twelfth Australasian Fluid Mechanics Conference.* The Unversity of Sydney, Australia.

Mackinnon, W L A and Swanson, A R, 2010. Strategies for Washing Australian Coals. *International Journal of Coal Preparation and Utilization,* 30, 69–82.

Massinaei, M, Jahedsaravani, A, Taheri, E and Khalilpour, J, 2019. Machine vision based monitoring and analysis of a coal column flotation circuit. *Powder Technology,* 343, 330–341.

Mohanty, M K and Honakeri, R Q, 1999. Performance optimization of Jameson flotation technology for fine coal cleaning. *Minerals Engineering,* 12, 367–381.

Morar, S H, Harris, M C and Bradshaw, D J, 2012. The use of machine vision to predict flotation performance. *Minerals engineering,* 36–38, 31–36.

Napier-Munn, T, 2014. Statistical methods for mineral engineers: how to design experiments and analyse data, Julius Kruttschnitt Mineral Research Centre.

Osborne, D, Huynh, L, Kohli, I, Young, M and Mercuri, F, 2013. Two decades of Jameson Cell installations in coal. *In:* G Özbayoğlu and A İ Arol (eds.) *XVII International Coal Preparation Congress*, Turkey.

Pokrajcic, Z, Harbort, G, Lawson, V and Reemeyer, L, 2005. Applications of the Jameson Cell at the head of base metal flotation circuits. Centenary of Flotation Symposium (The Australasian Institute of Mining and Metallurgy: Melbourne).

Qu, X, Wang, L and Nguyen, A V, 2013. Correlation of air recovery with froth stability and separation efficiency in coal flotation. *Minerals Engineering,* 41, 25–30.

Runge, K, McMaster, J, Wortley, M, Rosa, D L and Guyot, O, 2007. A Correlation Between Visiofroth^{TM} Measurements and Performance of a Flotation Cell. *Ninth Mill Operators' Conference Proceedings* (The Australasian Institute of Mining and Metallurgy: Melbourne).

Sahbaz, O, Ucar, A and Oteyaka, B, 2012. Effect of APR on Flotation in the Jameson Cell and Determining the Contact Angle. *XIII International Mineral Processing Symposium*, Turkey. Department of Mining Engineering, 375–381.

Shean, B J and Cilliers, J J, 2011. A review of froth flotation control. *International Journal of Mineral Processing,* 100, 57–71.

Supomo, A, Yap, E, Zheng, X, Banini, G, Mosher, J and Partanen, A, 2008. PT Freeport Indonesia's mass-pull control strategy for rougher flotation. *Minerals Engineering,* 21, 808–816.

Effect of sodium sulfite on flotation behaviour of bornite and tennantite

G P W Suyantara[1], T Hirajima[2], H Miki[3], K Sasaki[4], Y Tanaka[5] and Y Aoki[6]

1. Specially Appointed Assistant Professor, Department of Earth Resources Engineering – Kyushu University, Fukuoka, Japan, 819–0395. Email: pandhe@mine.kyushu-u.ac.jp
2. Emeritus Professor, Department of Earth Resources Engineering – Kyushu University, Fukuoka, Japan, 819–0395. Email: hirajima@mine.kyushu-u.ac.jp
3. Associate Professor, Department of Earth Resources Engineering – Kyushu University, Fukuoka, Japan, 819–0395. Email: miki@mine.kyushu-u.ac.jp
4. Professor, Department of Earth Resources Engineering – Kyushu University, Fukuoka, Japan, 819–0395. Email: miki@mine.kyushu-u.ac.jp
5. Metallurgist, Sumitomo Metal Mining Co., Ltd., Ehime, Japan, 792–0002. Email: yoshiyuki.tanaka.u8@smm-g.com
6. Metallurgist, Sumitomo Metal Mining Co., Ltd., Ehime, Japan, 792–0002. Email: yuji.aoki.m3@smm-g.com

ABSTRACT

The effect of sodium sulfite (Na_2SO_3) on the flotation behaviour of bornite and tennantite is reported in this work. Flotation tests were performed using pure minerals of bornite and tennantite under various concentrations of sodium sulfite at pH 9. The flotation results indicated that sodium sulfite exhibited a depressing effect on the floatability of bornite in the presence of 0.1 mM PAX. However, tennantite remained floatable after the addition of sodium sulfite in the presence of 0.1 mM PAX. The flotation tests using mixed bornite and tennantite confirmed the flotation results of single minerals. Surface characterisation using X-ray photoelectron spectroscopy (XPS) was performed to explain the flotation results. A mechanism is proposed based on the XPS analysis results.

INTRODUCTION

Recently, the separation of arsenic-bearing copper minerals and copper sulfide minerals has been an important issue owing to the increasing arsenic grade from the major copper mines (Schwartz *et al,* 2017). The inorganic arsenic in the copper ores poses a significant danger to the health and environment (Chatterjee *et al,* 1995; Mandal and Suzuki, 2002). Furthermore, there is a high penalty imposed by the smelters for processing a copper concentrate containing arsenic of more than 0.2 per cent, reducing the economic value of the copper concentrate (Biswas *et al,* 1994).

Tennantite ($Cu_{12}As_4S_{13}$), the most common arsenic-bearing copper mineral, is usually associated with copper sulfide minerals such as chalcopyrite ($CuFeS_2$) and bornite (Cu_5FeS_4). The separation of chalcopyrite and tennantite by flotation has been reported by various studies (Fornasiero *et al,* 2001; Petrus *et al,* 2014, 2012; Suyantara *et al,* 2020). However, there is a limited study on the separation of bornite and tennantite. A previous study investigates the effect of sodium sulfite (Na_2SO_3) on the floatability of chalcopyrite and enargite (Suyantara *et al,* 2021). They found that selective flotation of chalcopyrite and enargite was possible by Na_2SO_3 treatment. However, the effect of Na_2SO_3 on the flotation behaviour of bornite and tennantite has been not investigated. Therefore, this study mainly focuses on the investigation of the effect of Na_2SO_3 on the floatability of bornite and tennantite. The surface properties of both minerals were examined by using X-ray photoelectron spectroscopy.

MATERIALS AND METHODS

Materials

Bornite from Pinal Country (Arizona, USA) and tennantite from Tsumeb Mine (Tsumeb, Namibia) were used in this study. Both minerals were hand sorted, ground using a mortar and pestle, and screened passing a 38-micron screener. Industrial grade of potassium amyl xanthate (PAX) was supplied by Sumitomo Metal Mining Co., Ltd., (Tokyo, Japan) and used as a collector. Analytical grade of sodium sulfite (Na_2SO_3) as a depressant and industrial grade of pine oil as a frother were purchased from Wako Chemical Industries, Ltd., (Tokyo, Japan).

Flotation tests

Flotation tests of single and mixed minerals were carried out in this study. A mineral suspension with a pulp density of 0.33 per cent (ie 0.6 g mineral/180 mL ultrapure water) was prepared. The mineral suspension was treated with 0.1 mM PAX aqueous solution for 3 min. Na_2SO_3 treatment was then performed by adding a certain amount of Na_2SO_3 powder into the suspension. The Na_2SO_3 treatment was performed for 10 min. Finally, pine oil (102 ppm) was then added and the pH was controlled for 2 min. The pH of the mineral suspension was controlled at pH 9 throughout the mineral treatments by adding potassium hydroxide (KOH) or hydrochloric acid (HCl).

After the mineral treatments, the flotation tests were performed using a Partridge and Smith glass cell (Suyantara *et al,* 2018). The mineral suspension was transferred into the flotation cell and the flotation test was started by injecting 20 mL/min of nitrogen gas. The froth was collected for 6 min. The tailing and froth fractions were filtered, dried in an oven at 105°C for 12 h. The flotation recoveries of single and mixed minerals were calculated based on the recovery of the metal in the froth fraction (Semoto *et al,* 2021; Suyantara *et al,* 2020).

X-ray photoelectron spectroscopy (XPS) analysis

Surface characterisation using XPS was performed to investigate the effect of Na_2SO_3 treatment on the chemical species on the surface of bornite and tennantite. The mineral powders were treated with 5 mM PAX and 10 mM Na_2SO_3 for 3 and 10 min, respectively. The pH was controlled at pH 9 during the mineral treatment. After the treatment, the mineral suspension was filtered, dried under a vacuum. The XPS analysis was performed using AXIS 165 (Shimadzu-Kratos Co., Ltd., Manchester, United Kingdom) and Al Kα X-ray source at 1486.6 eV and 105 W. The survey and narrow scans were performed. The collected spectra were calibrated based on the binding energy of C 1s at 284.6 eV. Casa XPS software was used to deconvolute the collected spectra.

RESULTS AND DISCUSSION

Flotation tests

Figure 1 shows the effect of Na_2SO_3 on the recovery of bornite and tennantite in the single and mixed minerals systems. Figure 1a shows that both bornite and tennantite had a recovery of more than 80 per cent in the presence of 0.1 mM PAX and the absence of Na_2SO_3 at pH 9. The recovery of bornite gradually decreased with an increase in the concentration of Na_2SO_3 at pH 9. For instance, the recovery of bornite decreased from 87 per cent to 25 per cent after the addition of 1 mM Na_2SO_3. On the other hand, recovery of tennantite remained high after being treated with various concentrations of Na_2SO_3. This flotation result indicates that Na_2SO_3 exhibited a selective depression effect on the recovery of bornite.

The flotation result presented in Figure 1a suggests that selective flotation of bornite and tennantite might be possible by applying Na_2SO_3 treatment in the presence of PAX at pH 9. Flotation of mixed minerals was performed to test this result. Figure 1b shows that the selective flotation of bornite and tennantite was obtained in 0.1 mM PAX without the addition of Na_2SO_3 at pH 9. The recoveries of bornite and tennantite were 19 per cent and 70 per cent, respectively, in the absence of Na_2SO_3. This phenomenon was not observed in the flotation of both minerals in the single mineral system (Figure 1a). Therefore, the selective flotation result is likely caused by the interaction of both minerals in adsorbing PAX. The previous study indicates that tennantite adsorbed PAX more rapidly compared to that of bornite (Suyantara *et al,* 2020). There is a possibility that the interaction between bornite and tennantite enhanced the selective adsorption of PAX between these minerals. However, this argumentation requires further investigation in future studies.

The effect of Na_2SO_3 treatment enhanced the selective flotation of bornite and tennantite. The recovery of bornite decreased to 13 per cent after the addition of 0.5 and 1 mM Na_2SO_3. On the other hand, recovery of tennantite slightly increased from 68 per cent to 72 per cent and 74 per cent after the addition of 0.5 and 1 mM Na_2SO_3, respectively. The Newton efficiency results calculated using Equation (1) indicate that the addition of Na_2SO_3 enhanced the separation between bornite and tennantite. For instance, the addition of 1 mM Na_2SO_3 improved the Newton efficiency by 10 per cent

to 60 per cent. This flotation result demonstrates that separation of bornite and tennantite is possible by flotation after the Na_2SO_3 treatment in the presence of PAX at pH 9.

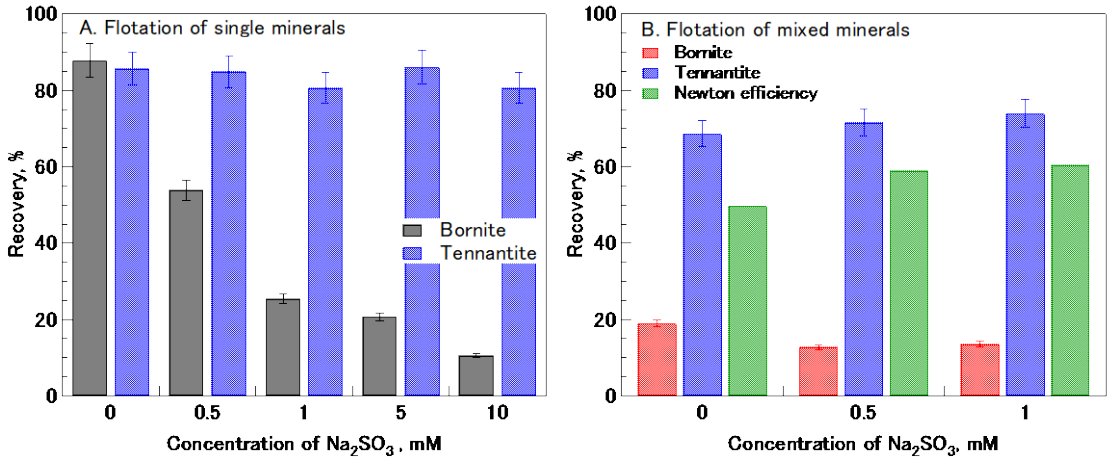

FIG 1 – Effect of Na_2SO_3 on recovery of bornite and tennantite in 0.1 mM PAX at pH 9.

XPS analysis

XPS analysis results indicate that the Cu 2p, Fe 2p, and As 3d spectra were slightly affected by the Na_2SO_3 treatment. Therefore, the S 2p spectra of bornite and tennantite are presented in this study to explain the selective flotation behaviour of both minerals after the Na_2SO_3 treatment. Figure 2 shows the S 2p spectra of bornite and tennantite after being treated with 10 mM Na_2SO_3, 5 mM PAX, and a mixture of 10 mM Na_2SO_3 and 5 mM PAX. The S 2p spectrum of bornite at pH 9 could be best fitted by four Gaussian-Lorentzian functions located at 161.0 eV, 162.4 eV,164.3 eV, and 167.5 eV. These binding energies are corresponded to monosulfide (S^{2-}) of bornite, disulfide (S_2^{2-}), polysulfide (S_n^{2-}), and sulfate (SO_4^{2-}) species, respectively. Similar species were observed on the surface of bornite after being treated with 10 mM Na_2SO_3. In the presence of 5 mM PAX, the sulfate peak disappeared on the bornite surface followed by the appearance of a new peak located at 162.0 eV. This new peak is assigned to the adsorbed amyl xanthate on the bornite surface. The Na_2SO_3 treatment in the presence of PAX produced a sulfate species on the bornite surface and reduced the peak intensity of adsorbed amyl xanthate.

Figure 2b shows that the S 2p spectrum of untreated tennantite at pH 9 can be deconvoluted by three Gaussian-Lorentzian functions located at 161.6 eV, 162.4 eV, and 167.9 eV. The peak located at 161.6 eV and 162.4 eV are attributed to monosulfide of tennantite and disulfide. The peak located at 167.9 eV corresponds to sulfate species. The intensity of the sulfate peak slightly increased after the addition of 10 mM Na_2SO_3. Meanwhile, there were no sulfate species identified on the surface of tennantite after the PAX treatment both with and without the addition of Na_2SO_3. The adsorption of PAX on the surface of tennantite is confirmed by the appearance of a peak located at 162.0 eV which is attributed to amyl xanthate.

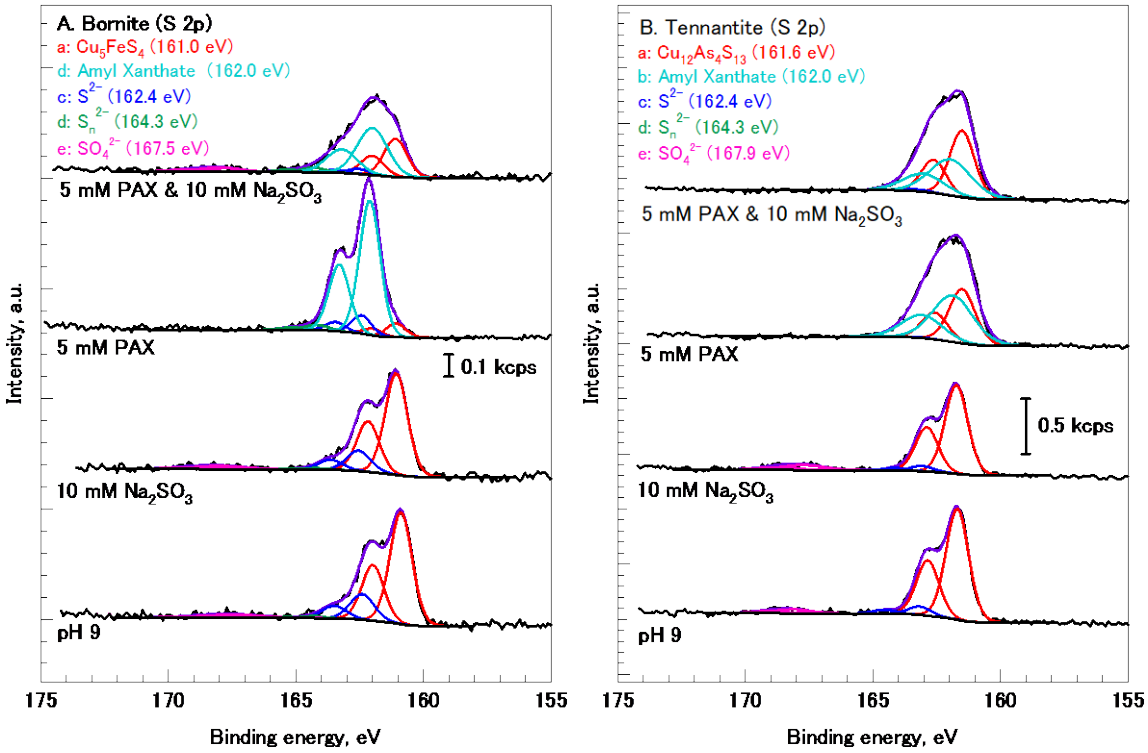

FIG 2 – S 2p spectra of bornite and tennantite after being treated with 10 mM Na_2SO_3, 5 mM PAX, and a mixture of 5 mM PAX and 10 mM Na_2SO_3 at pH 9.

Proposed mechanism

A surface mechanism is then proposed based on these XPS analysis results to explain the flotation behaviour of bornite and tennantite. The depressing effect of Na_2SO_3 on the floatability of bornite is likely caused by the formation of hydrophilic sulfate species as shown by Equation (1) and the removal of adsorbed PAX on the surface of bornite. The action of Na_2SO_3 on producing sulfate and reducing the concentration of adsorbed PAX could reduce the surface hydrophobicity of bornite, thus lowering its floatability. This argument is in agreement with previous studies that reported the detrimental effect of sulfate species on the floatability of chalcopyrite and enargite (Semoto *et al,* 2021; Suyantara *et al,* 2021, 2020).

$$SO_3^{2-} + \frac{1}{2}O_2 \rightarrow SO_4^{2-} \quad (1)$$

On the other hand, the absence of sulfate species on the tennantite surface is likely the main reason for its high floatability after the Na_2SO_3 treatment in the presence of PAX. Although Figure 2b indicates that the adsorbed PAX on the tennantite surface is slightly decreased after the Na_2SO_3 treatment, the concentration of adsorbed PAX is sufficient to render the surface hydrophobic in the absence of hydrophilic sulfate species. Therefore, the recovery of tennantite remained high after the Na_2SO_3 treatment in the presence of PAX.

CONCLUSIONS

The effect of Na_2SO_3 on the floatability of bornite and tennantite in the presence of PAX is investigated in this study. Flotation tests show that Na_2SO_3 exhibited a detrimental effect on the floatability of bornite. The main reason for the depression of bornite is the ability of Na_2SO_3 to produce hydrophilic sulfate species on the surface of bornite. In addition, Na_2SO_3 reduced the adsorbed PAX on the surface of bornite thus reducing its surface hydrophobicity. A similar effect of Na_2SO_3 on reducing the adsorbed PAX was observed on tennantite. However, there were no sulfate species formed on the surface of tennantite, thus tennantite remained floatable. The mixed flotation tests demonstrated that selective flotation of bornite and tennantite is possible by applying Na_2SO_3 treatment in the presence of PAX.

ACKNOWLEDGEMENTS

This study was supported by Sumitomo Metal Mining Co., Ltd., – Japan, Japan Oil, Gas, and Metals National Corporation (JOGMEC) – Japan, and a Grant-in-Aid for Science Research (JSPS KAKENHI) from the Japan Society for the Promotion of Science (JSPS) – Japan [Grant numbers JP19H02659 and JP19K22156]. We thank Yuta Orii for his support during the data collection for the micro flotation tests.

REFERENCES

Biswas, A K and Davenport, W G, 1994. *Extractive Metallurgy of Copper*, third edition. Oxford: Pergamon Press.

Chatterjee, A, Das, D, Mandal, B K, Chowdhury, T R, Samanta, G and Chakraborti, D, 1995. Arsenic in ground water in six districts of West Bengal, India: the biggest arsenic calamity in the world. Part I. Arsenic species in drinking water and urine of the affected people. *Analyst* 120(3): p.643–650.

Fornasiero, D, Fullston, D, Li, C and Ralston, J, 2001. Separation of enargite and tennantite from non-arsenic copper sulfide minerals by selective oxidation or dissolution. *International Journal of Mineral Processing* 61(2): p.109–119.

Mandal, B K and Suzuki, K T, 2002. Arsenic round the world: a review. *Talanta* 58(1): p.201–235.

Petrus, H T B M, Hirajima, T, Sasaki, K and Okamoto, H, 2012. Effects of sodium thiosulphate on chalcopyrite and tennantite: An insight for alternative separation technique. *International Journal of Mineral Processing* 102–103: p.116–123.

Petrus, H T B M, Hirajima, T, Sasaki, K and Okamoto, H, 2014. Separation mechanism of tennantite and chalcopyrite with flotation after oxidation using oxygen. In *IMPC 2014 – 27th International Mineral Processing Congress*, Santiago, Chile.

Schwartz, D M, Omaynikova, V Y and Stocker, S K, 2017. Environmental Benefits of the CESL Process for the Treatment of High-Arsenic Copper Concentrates. In *Hydroprocess-ICMSE*, Santiago, Chile: Gecamin Digital Publications Available at: http://www.gecaminpublications.com/hydroprocess-icmse2017/ [Accessed December 23, 2019].

Semoto, Y, Suyantara, G P W, Miki, H, Sasaki, K, Hirajima, T, Tanaka, Y, Aoki, Y and Ura, K, 2021. Effect of Sodium Metabisulfite on Selective Flotation of Chalcopyrite and Molybdenite. *Minerals* 11(12): p.1377.

Suyantara, G P W, Hirajima, T, Miki, H and Sasaki, K, 2018. Floatability of molybdenite and chalcopyrite in artificial seawater. *Minerals Engineering* 115: p.117–130.

Suyantara, G P W, Hirajima, T, Miki, H, Sasaki, K, Kuroiwa, S and Aoki, Y, 2020. Effect of H_2O_2 and potassium amyl xanthate on separation of enargite and tennantite from chalcopyrite and bornite using flotation. *Minerals Engineering* 152: p.106371.

Suyantara, G P W, Hirajima, T, Miki, H, Sasaki, K, Kuroiwa, S and Aoki, Y, 2021. Effect of Na_2SO_3 on the floatability of chalcopyrite and enargite. *Minerals Engineering* 173: p.107222.

Evaluation of the impact of modifying froth launders in an industrial flotation bank using novel flotation models

P Vallejos[1], J Yianatos[2], R Grau[3] and A Yáñez[4]

1. Researcher, Universidad Técnica Federico Santa María, Valparaíso, Chile. Email: paulina.vallejos@usm.cl.
2. Professor, Universidad Técnica Federico Santa María, Valparaíso, Chile. Email: juan.yianatos@usm.cl.
3. Director of R&D, Metso Outotec, Pori, Finland. Email: rodrigo.grau@mogroup.com.
4. Senior Manager, Metso Outotec, Espoo, Finland. Email: alejandro.yanez@mogroup.com.

ABSTRACT

In flotation cells, especially in large flotation units, froth management is a crucial variable that should be considered during the design phase or optimised to improve the performance of existing flotation circuits.

This paper presents a simulation evaluation of the effect of launder design on the metallurgical performance of an industrial flotation circuit consisting of five TankCell® e630 (630 m^3) cells in a Cu rougher duty. This analysis was carried out using a new industrial simulator, which was built on a wide database collected from many industrial concentrators. This tool is currently incorporated into HSC Chemistry® software and allows evaluation of the effect of launder design on mineral froth recovery, water recovery, entrainment, and other variables to be quantified.

The industrial flotation circuit was evaluated under different launder design scenarios, considering an actual flotation circuit that includes TankCell® e630 cells for calibration and as a reference (baseline). Firstly, two different designs were evaluated in the full circuit: a standard launder design and a new launder technology. It was found that the new launder technology enabled improvement of the mineral recovery along the circuit, mainly for coarse particles, due to the improvement in froth mineral recovery.

Next, the partial upgrade of the launder design along the circuit was analysed. Thus, the new launder technology was evaluated in the first and the last two cells of the bank. The results showed that upgrading the launders in different cells along the circuit delivered an increase in the final recovery with respect to the baseline, with a partial impact on the concentrate grade. However, these changes are less than those when evaluating the full upgrade scenario. A partial launder upgrade either in the first or last two cells of the bank showed similar final recoveries, but the latter enabled a slightly higher concentrate grade (about 1 per cent higher) to be achieved.

Finally, the evaluation of launder design using the industrial simulator made it possible to estimate its effect on variables that are not commonly obtained from plant surveys, including froth recovery per particle size, collection recovery per particle size and liberation, gangue entrainment and bubble loading grade.

INTRODUCTION

Industrial flotation circuits have seen a significant increase in mechanical cell sizes, and now many plants or expansions are fully equipped with 300 m^3 cells all over the world. Additionally, in recent years, larger cells of over 500 m^3 and 600 m^3 are being incorporated into new projects (Mattsson *et al*, 2017; Grau *et al*, 2018; Neethling *et al*, 2019). The new circuits with large cells have reported many advantages, eg lower consumption of specific energy, simpler circuits to operate with a lower number of cells, smaller footprint, and better control. However, new challenges arise to achieve the required recovery of the target cells. The main constraint in large cells is related to the decrease in froth recovery, which is strongly dependent on the longer froth transport distances and normally becomes the bottleneck of the system. To overcome this problem, new cell designs are required regarding the improvement of the froth transport together with the proper selection of operating conditions and control strategies. With this aim, Coleman (2009) has carried out research on launder design, and Brito-Parada and Cilliers (2012) have addressed the problem of launder configuration for improving froth transport. Grau *et al* (2019) have shown the improvement in flotation cell

performance after reducing the froth area in a flotation cell of 300 m^3 in operation at Atalaya copper concentrator, Spain. Additionally, Seaman *et al* (2021) have shown the optimisation of the existing rougher cells of 200 m^3 at Red Chris concentrator in Canada, where the installation of concentric launders to reduce the froth transport distance, together with a rougher control strategy, enabled improved cell recovery. Similarly, Bermudez *et al* (2021) have presented the results from launder retrofits with a new centre launder on the last three cells in the rougher circuit with 300 m^3 cells at Hudbay Constancia concentrator, Peru. Metallurgical recovery improvements of 0.70 per cent and 1.40 per cent in Cu and Mo, respectively, were reported. Additionally, Corona *et al* (2021) have described the effect of launder configuration on froth surface area (FSA) at different tank cell volumes.

Recently, Bermudez *et al* (2022) have presented the metallurgical results after installing a set of centre launder retrofits on the last three tank cells in one of the parallel rougher flotation rows with 300 m^3 cells at Copperton, USA. The results showed significant improvements in copper and molybdenum flotation recoveries throughout the rougher circuit.

Some studies have been conducted in industrial flotation circuits focused on the measurements and correlation of variables such as froth discharge velocity and top of the froth grades to correlate with the metallurgical performance (Yianatos *et al*, 2016). However, despite the advances in basic and applied research, there is still a lack of industrial data for flotation characterisation. In this sense, the main objective of this work is to present the evaluation of large industrial flotation cells (630 m^3), analysing froth launder arrangements to improve the froth transport into the concentrate. Thus, the effect was evaluated of changing the design of the launders in the full circuit, and a partial modification in the first two and the last two cells. For this purpose, an alternative launder design was simulated in four different scenarios, using new models implemented in the HSC® Chemistry simulator to evaluate metallurgical performance. Evaluation of other variables such as collection recovery, froth recovery, gangue entrainment and bubble loading grade along the flotation bank, allowed evaluation of different alternatives to improve the flotation bank performance.

The experimental testing for the simulator calibration was performed in the rougher banks of Buenavista del Cobre (BVC) concentrator in Mexico, which includes TankCell® e630 cells at the beginning of the rougher circuit (Grau *et al*, 2018).

METHODOLOGY

Evaluation of new launder designs in flotation cells

Two launder designs were evaluated in a simulated flotation bank consisting of five TankCell® e630 cells: a standard launder, shown in Figure 1a, corresponding to a double internal launder (Grau *et al*, 2019), and a new launder technology (upgrade), shown in Figure 1b.

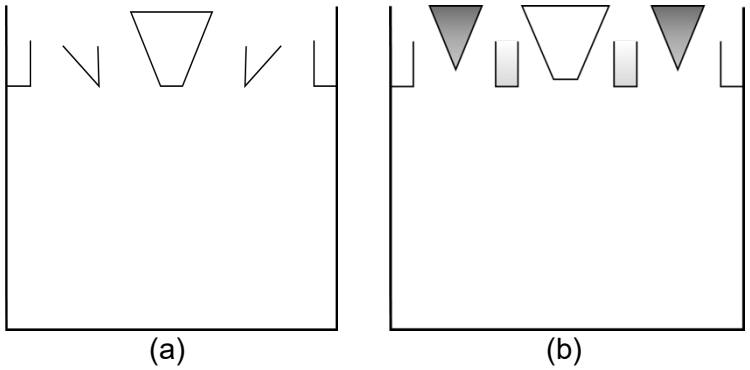

FIG 1 – Launder designs for TankCell® e630 cell: (a) standard launder (baseline) and (b) new launder technology (upgrade).

The new launder technology includes an adjustable froth crowder and centre launder, complementing the internal peripherical launder and the original froth crowder. The main objective of this launder design is to reduce the froth surface area and increases the overflow launder lip, enabling improved mineral transport in froth and increased froth recovery. The adjustable froth

crowder and the centre launder are highlighted in grey in Figure 1b. The centre launder is located between the froth crowder and the adjustable crowder.

Simulation of different scenarios for an industrial flotation circuit

Scenarios

Four scenarios were simulated to evaluate the metallurgical performance after changing the launder design in the flotation cells of a bank consisting of five TankCell® e630 cells. The first scenario corresponds to the baseline, concerning the full circuit with standard launders (without upgrade). Then, full and partial launder upgrades were evaluated.

The simulator was able to show the differences between the scenarios with respect to recovery, concentrate grade and internal variables such as froth recovery, entrainment, bubble loading grade and other variables.

The scenarios are:

1. Full circuit with standard launders (baseline).
2. Full circuit with new launder technology (upgrade).
3. New launder technology in the two first cells of the bank.
4. New launder technology in the two last cells of the bank.

Industrial flotation simulator to predict metallurgical performance

The industrial flotation simulator used in this study was developed from a wide database gathered from industrial sampling surveys performed at different flotation plants. This simulator includes the operating conditions, cell design and feed characteristics as input variables and allows the calculation of the metallurgical behaviour of each cell along a flotation bank (Yianatos *et al*, 2020). This tool is currently implemented in the HSC Chemistry software (Metso Outotec, 2022). The implementation process of this tool has been described earlier by Betancourt *et al* (2021).

The flotation simulator considers the sequential calculation of each single cell in series, assuming a two-zone system: collection and froth (Finch and Dobby, 1990; Yianatos *et al*, 2008). The feed minerals are characterised in terms of size-by-liberation classes.

The collection zone was characterised using a perfect mixing plus bypass flow model, based on actual residence time distribution measurements (per particle size) at industrial circuits using the radioactive tracer technique (Yianatos *et al*, 2016). To characterise the kinetics, a single rate constant (k) and a maximum recovery (Rmax) per size-by-liberation class were considered. In addition, the froth recovery was modelled as a function of four variables: froth stability, which depends on the solid flow rate entering the froth by true flotation; the launder design; the froth residence time; and the particle size. This model was built using a wide database on froth recoveries measured at different industrial plants. Froth recoveries from 40 per cent to 90 per cent were found in flotation plants and were used to calibrate the model.

The mineral recovery by entrainment (valuable and gangue) in each cell was estimated in terms of water recovery and particle settling velocity (Wang *et al*, 2016). The froth water recovery was represented as a function of solid froth recovery, froth depth and air flow rate, while the water entering the interface was considered as a function of gas holdup, air flow rate, pulp density and solid content.

The paper presented by Yianatos *et al* (2020) describes in more detail the models used to build the flotation simulator. Additionally, some case studies analysed with the industrial simulator have been presented in Vallejos *et al* (2020a, 2020b, 2021) and Betancourt *et al* (2021).

The industrial flotation simulator can represent the effect of both operating conditions and cell design characteristics on recovery and concentrate grade. According to the models and structure of the simulator, specific variables such as launder design were included in the simulator, which is an innovative topic in this type of tool and allows the study of the effect of the froth transport distance to the discharge lip on the metallurgical performance in industrial cells.

Simulation based on an actual industrial flotation circuit

Description of the industrial flotation circuit

This study is based on Buenavista del Cobre (BVC) mine Concentrator 1. BVC is a copper-molybdenum mine located in northern Mexico. Concentrator 1, processing 86 kt/d, has two parallel grinding-flotation sections known as section 1 and section 2. Both sections consist of three bulk (Cu and Mo) rougher flotation lines, and the rougher concentrate is transferred to a regrinding stage followed by two cleaning stages that produce a final bulk Cu-Mo concentrate.

In 2018, a TankCell® e630 cell was installed as the first cell in each existing rougher stage of sections 1 and 2. The implementation was recommended and reported by Grau *et al* (2018) based on a process assessment performed by personnel from Buenavista del Cobre and Outotec in 2015 to improve metallurgical performance.

Metallurgical surveys at BVC concentrator

The simulation study reported in this work is based on multiple sampling campaigns conducted around the TankCell® e630 flotation cells (Figure 2). The feed and tail samples were collected from automatic cutters, while the concentrate samples were cut manually at the end of the TankCell® e630 cell concentrate pipe.

FIG 2 – Schematic image of TankCell e630 and the flotation cell at BVC concentrator (Grau *et al*, 2018).

The products of four sampling rounds were combined and analysed size by size, and the results were mass balanced to obtain metallurgical performance per size class. Additionally, mineralogical information (microscopy) on the feed samples of BVC concentrator was available, including minerals distribution and mineral liberation (polished section).

Operating conditions such as grade, tonnage and solid content in feed, air flow rate, froth depth and pH were monitored through sampling surveys.

The average operating conditions of the TankCell® e630 cell observed in the sampling surveys were used as input variables for the simulation study. Froth depths of 25 cm and a gas flow rate of 55 m^3/min were considered for the four simulated scenarios. The operating conditions were set as input variables for each cell of the flotation bank, consisting of five TankCell® e630 units.

Table 1 shows the feed characteristics of BVC in terms of distribution of valuable mineral in size-by-liberation classes, total mass distribution and feed Cu grade per size class. Additionally, the flotation feed was composed of 78 per cent chalcopyrite, 17 per cent secondary Cu sulfides and 5 per cent tennantite.

TABLE 1

Feed characteristics of BVC cell used to carry out the scenario simulations.

	Valuable mass fraction (%)			Total mass fraction (%)	Cu grade (%)
	Liberation class (%)				
Particle size (µm)	**< 20**	**20–80**	**> 80**		
+106 (coarse)	20.7	32.2	47.1	36.5	0.40
+45 -106 (intermediate)	2.5	17.6	79.9	18.2	0.79
-45 (fine)	0.4	4.6	95.0	45.3	0.49

RESULTS AND DISCUSSION

Calibration of the metallurgical response predicted by the industrial simulator

The response predicted by the simulator was calibrated using the information from the sampling surveys performed at the BVC concentrator.

Figure 3 shows the recovery and concentrate grade for the TankCell® e630 cell, including measured and predicted data. Good agreement between the measured and simulated data can be observed.

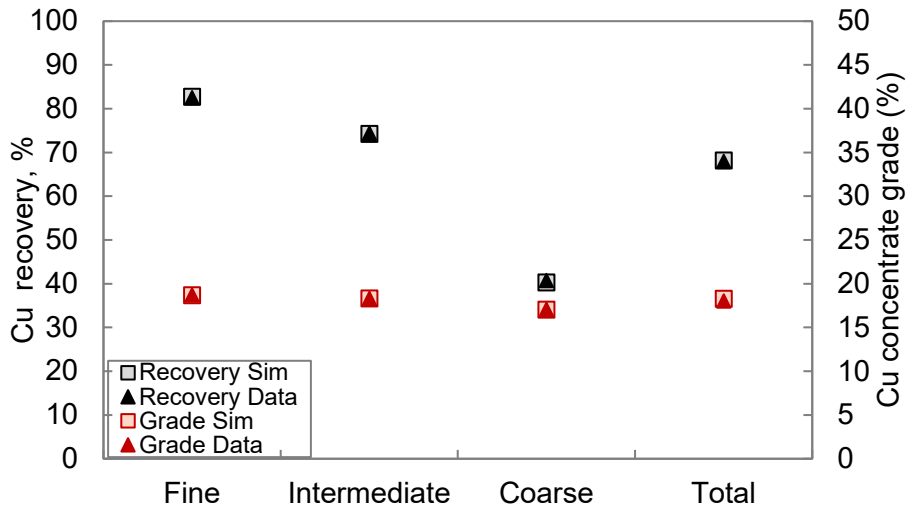

FIG 3 – Comparison between measured and simulated data: Cu recovery and concentrate grade.

Moreover, Suhonen *et al* (2019) earlier estimated the froth recovery in the TankCell® e630 cell at the BVC concentrator. Figure 4 shows the froth recovery for three froth depths. It was found that froth recovery decreased from 69 per cent to 47 per cent when the froth depth increased from 14 cm to 26 cm. Then, from the simulation study presented in this work, the froth recovery of the TankCell® e630 cell was predicted using the industrial simulator (at a froth depth of 25 cm, Table 1) and is shown with a red point in Figure 4. This plant value is in good agreement with the correlation shown for froth recovery versus froth depth. It should be noticed that the froth recovery model used in the industrial simulator was built and validated from a wide database of measurements performed at several industrial plants. Therefore, these results validate the estimation performed by Suhonen *et al* (2019) as well as strengthening the froth recovery model in the simulator.

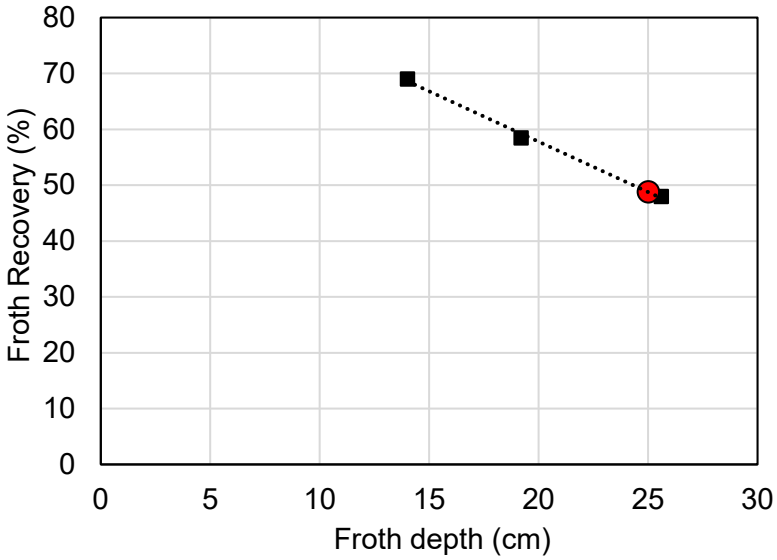

FIG 4 – Validation of froth recovery estimation in the TankCell® e630 flotation cell (Suhonen *et al*, 2019).

Comparison of different scenarios after launder upgrade

The four scenarios were compared with each other in terms of recovery and concentrate grade. Other variables such as froth and collection recovery, as well as gangue entrainment, water recovery and bubble loading grade were also analysed in this study.

Effect on Cu recovery

Figure 5a shows the simulated final Cu recovery per particle size class for each scenario. The results showed a higher final recovery for the full upgrade scenario, where the differences are more significant for coarse particles (+106 µm). The scenarios with launder upgrade in the first two cells and in the last two cells of the bank did not show any significant differences in recovery. Only a slight difference in recovery can be observed for the coarse class. In general, all the scenarios including a launder upgrade enabled improved recovery with respect to the original scenario (baseline).

Since coarse particles (+106 µm) are more affected by the launder upgrade, Figure 5b shows the simulated recovery profiles of this class for the four scenarios to illustrate the cell-to-cell recovery along the bank.

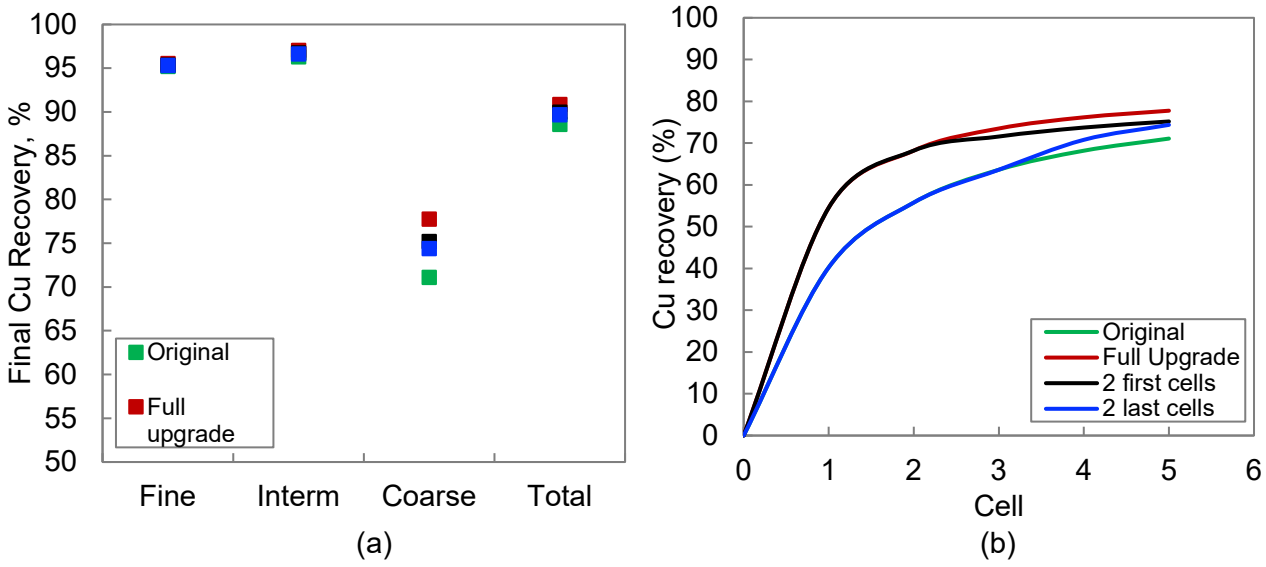

FIG 5 – Cu recovery results for the four scenarios: (a) final Cu recovery per particle size class; and (b) recovery profiles for coarse particles (+106 µm).

Figure 6a shows the simulated froth recovery along the bank for the four scenarios. When the launder upgrade was evaluated, it was found that froth recovery increased from 49 per cent to 76 per cent in the first cell. In the last cell, the froth recovery increased from 36 per cent to 52 per cent. Comparing the original and the full upgrade scenarios, an increase in froth recovery can be observed in all the cells along the bank. For the other two scenarios (partial launder upgrade), the effect of the launder upgrade in the first or last two cells on froth recovery is clearly noticeable.

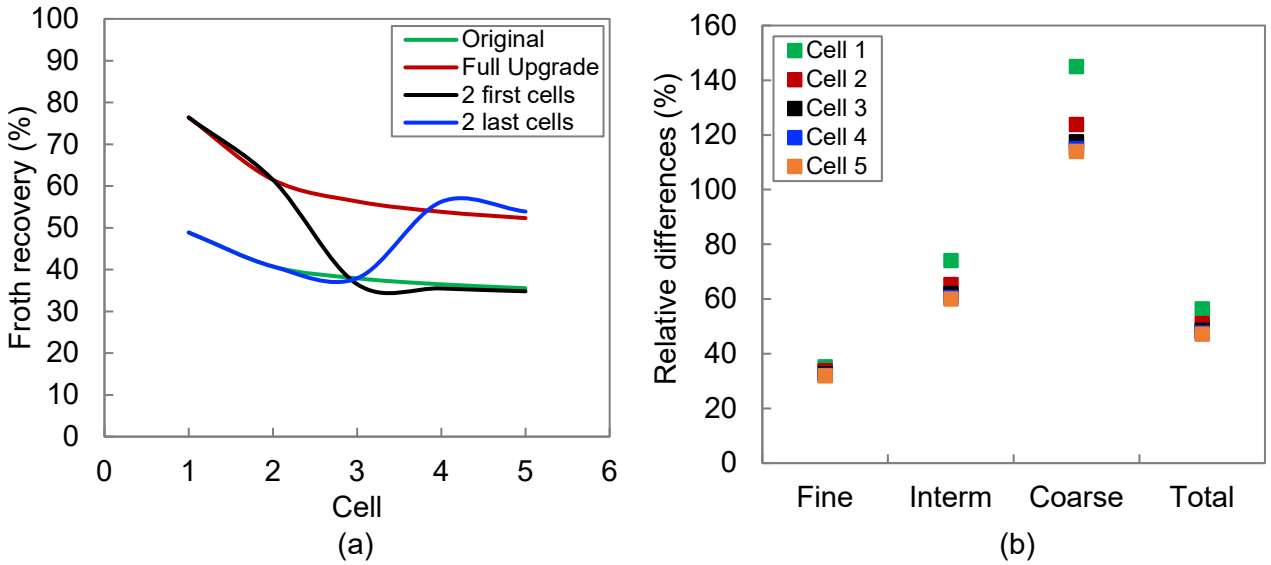

FIG 6 – (a) Froth recovery along the bank for the four scenarios and (b) relative differences in froth recovery between standard and upgraded launders per particle size class.

It should be noted that when froth recovery is improved in the first two cells because of the launder upgrade (third scenario), the froth recovery in the next cells is slightly lower than in the original scenario (equivalent cell characteristics). This occurs because the increase in recovery of the first cells decreases the mineral grade fed to the next cells, which strongly affects the collected mineral grade and flow rate, and therefore, the froth stability.

Figure 6b shows the relative differences in froth recovery between standard and new launders per particle size class and per cell along the bank. This is equivalent to comparing the cell-to-cell results between the first and the second scenario (baseline versus full upgrade). The relative values were calculated as the difference between the froth recovery for the upgrade condition and for the standard condition, with respect to the latter.

The results showed that the main impact of the launder upgrade is on coarse particles, improving froth recovery by more than 140 per cent (relative) in the first cell. This corresponds to an increase in froth recovery from 18.5 per cent to 45.3 per cent. In cells 2 to 5, the improvement in froth recovery is approximately 110–120 per cent (relative).

Figure 7a shows the simulated collection recovery along the bank for the four scenarios. The collection recovery decreased along the bank for all the scenarios, as expected, because of the mineral depletion along the bank (Figure 10). Figure 7a also shows lower collection recoveries along the bank for the second scenario (full upgrade) with respect to the baseline. This occurs because the increase in froth recovery (due to the launder upgrade) decreases the amount of valuable mineral dropping back to the collection zone. Thus, the mineral entering the collection zone (fresh feed + drop-back) has poorer characteristics and, therefore, decreases the collection recovery. For the two scenarios with the partial launder upgrade (third and fourth scenarios), the effect of improved froth recoveries in the first or last two cells on collection recovery can be seen clearly. The comparison of the four scenarios was performed considering the same gas flow rate, and therefore, the same superficial gas rate (J_G) at collection level, as indicated in Table 1.

Figure 7b shows the collection recovery per size-by-liberation class in the first cell of the original scenario. It can be observed that the collection recovery strongly increases when the liberation increases, mainly from the less liberated (<20 per cent lib.) to intermediate class (20–80 per cent

lib.). Particle size also has an effect on collection recovery, which increases while the particle size decreases; however, this effect is slight and less significant than that of liberation.

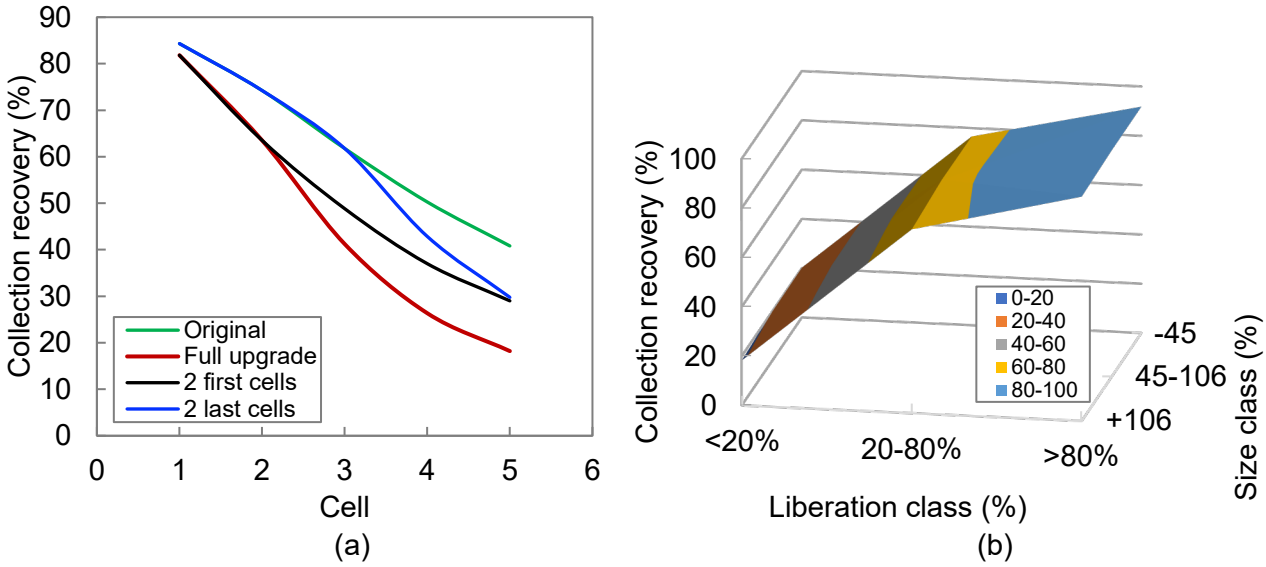

FIG 7 – (a) Collection recovery along the bank for the four scenarios and (b) collection recovery per particle size and liberation class (first cell, original circuit).

It is also noteworthy that the collection recovery in each size-by-liberation class does not significantly change for the other scenarios or the other cells along the bank. The main change is related to the mass distribution of minerals fed to each cell per size-by-liberation class, which significantly varies along the bank and when implementing a launder upgrade.

Effect on Cu concentrate grade

Figure 8a shows the simulated Cu concentrate grade of the bank per particle size class for each scenario. The highest concentrate grades are observed for the original scenario, and the differences are greater for fine particles (-45 µm). The scenarios with a partial launder upgrade (third and fourth scenarios) did not show any significant differences in the cumulative concentrate grade, but a launder upgrade in the last two cells enabled an approx. 1 per cent higher total grade to be reached. In general, all the scenarios including a launder upgrade showed lower concentrate grades than the original scenario (baseline). However, considering that the flotation bank corresponds to a rougher operation, a decrease in concentrate grade (and an increase in mass pull) should not cause significant operating problems, provided that the cleaning circuit has enough capacity to process the increment inflow rate.

Since the cumulative concentrate grade of fine particles (-45 µm) is more affected by the launder upgrade, Figure 8b shows the simulated cumulative grade profiles of fine particles for the four scenarios. This allows us to observe the behaviour of the cell-to-cell cumulative concentrate grade along the bank and the effect of a full and partial launder upgrade. The more significant decrease in concentrate grade for fine particles is due to the increase in gangue entrainment (Figure 9), promoted by the improved froth stability given by the new launders.

Figure 9 shows the simulated gangue entrainment flow rate along the bank for the four scenarios. The results showed that the gangue entrainment is considerably higher for the second scenario compared to the original one (full upgrade) in all cells. For the scenarios with a partial launder upgrade, gangue entrainment is significantly higher in the cells with the new launder. The trends observed in Figure 9 show a clear relationship with the profiles of Figure 8b, ie cells with a higher gangue entrainment have lower concentrate grades.

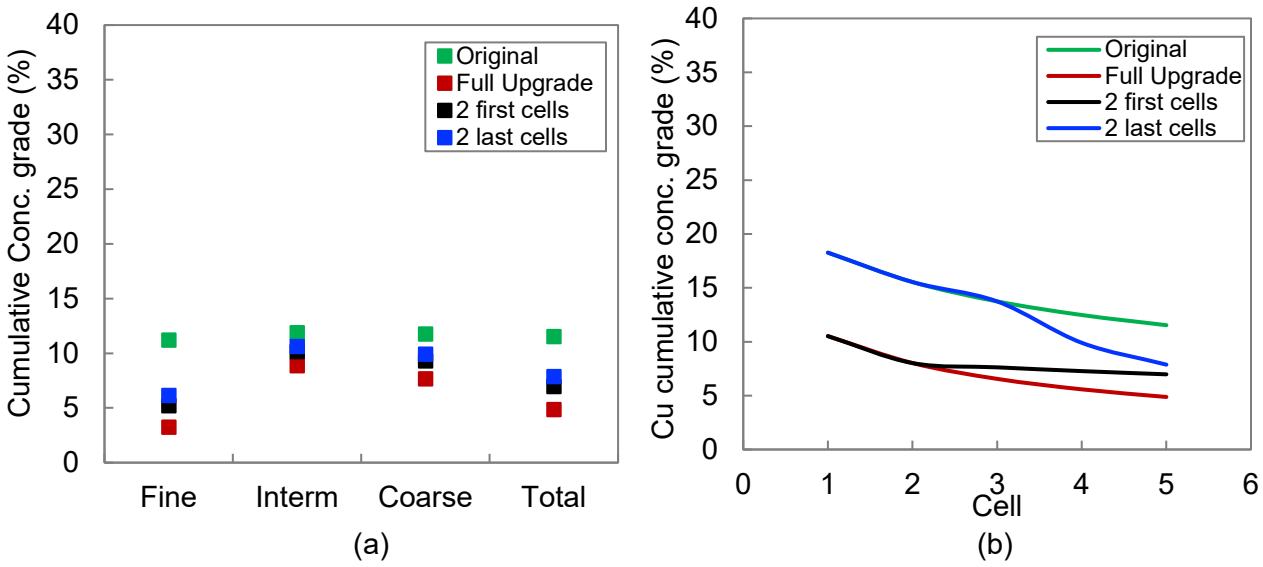

FIG 8 – Cu concentrate grade results for the four scenarios: (a) cumulative Cu concentrate grade per particle size class and (b) concentrate grade profiles for fine particles (-45 µm).

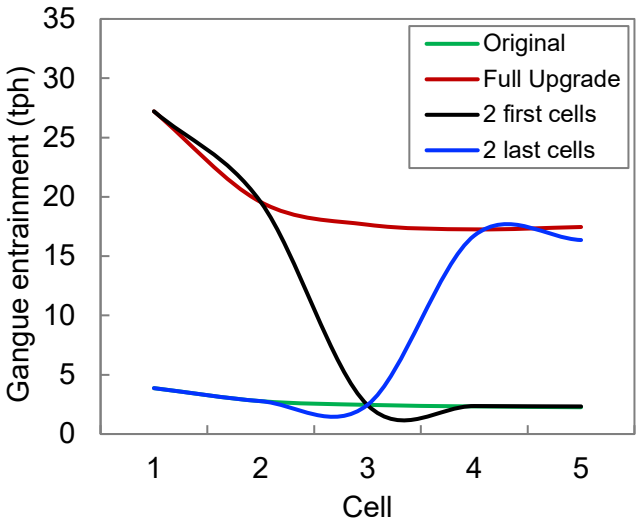

FIG 9 – Gangue entrainment along the bank for the four scenarios.

On the other hand, Table 2 shows the simulated froth water recovery along the bank for the four scenarios. This variable is directly related to froth mineral recovery and is also affected by the launder upgrade. Thus, the increase in gangue entrainment is caused by an increase in froth water recovery. The data presented in Table 2 shows the same trends along the bank as those in Figure 9 for gangue entrainment.

TABLE 2

Froth water recovery along the bank for the four scenarios.

Cell	Original	Full upgrade	2 first cells	2 first cells
1	10.7	29.7	29.7	10.7
2	8.9	23.9	23.9	8.9
3	8.3	21.9	8.0	8.3
4	8.0	20.9	7.7	21.8
5	7.8	20.3	7.6	20.9

Figure 10 shows the simulated bubble loading grade (collected minerals) along the bank for the four scenarios. The bubble loading grade decreased along the bank for all the scenarios, representing mineral depletion along the bank. However, the results showed lower grades in all cells for the full upgrade scenario compared to the original scenario. This occurs because the increase in total recovery along the bank, due to the launder upgrade in the whole bank, decreases the mineral grade fed to the collection zone of the cells, affecting the collected mineral grade.

The effect of the partial launder upgrade (third and fourth scenarios) can be clearly observed, reaching similar values in the last cell of the bank.

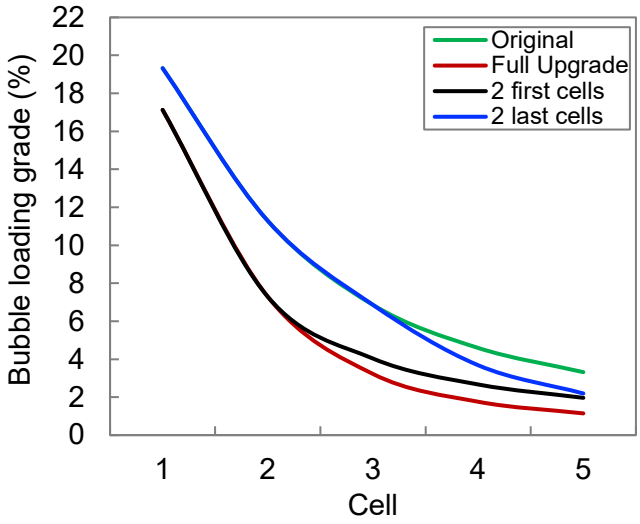

FIG 10 – Bubble loading grade along the bank for the four scenarios.

CONCLUSIONS

The industrial simulator allowed the evaluation of the metallurgical performance of a flotation bank under different scenarios with a full and partial launder upgrade. The study baseline was built with data from an actual industrial plant (Buenavista del Cobre, México), which enabled suitable calibration of the simulator prediction. Additionally, a previous froth recovery estimation of the first cell at Buenavista del Cobre was consistent with and validated by the industrial simulator.

The simulation results showed that either a partial or a full launder upgrade would improve recovery with respect to the original scenario (baseline). However, the highest final recovery was observed for the full upgrade of the bank. On the other hand, a partial launder upgrade either in the first or last two cells of the bank showed similar final recoveries. A launder upgrade would enable improved recovery, mainly of coarse particles.

The increase in total recovery when evaluating the launder upgrade is due to the increase in froth recovery in each cell, resulting from the improvement in froth stability and the decrease in froth transport distance. Froth recovery increased from 49 per cent to 76 per cent in the first cell and from 36 per cent to 52 per cent in the last cell according to the launder upgrade evaluation (with respect to the baseline). The main impact of the launder upgrade was on coarse particles, which improved froth recovery by more than 140 per cent (relative) in the first cell.

Furthermore, the results showed that either a partial or a full launder upgrade decreased the concentrate grade, because of the increase in gangue entrainment. Thus, fine particles (-45 µm) were more affected. The full upgrade scenario showed the lowest concentrate grades. A partial launder upgrade in the last two cells enabled a slightly higher concentrate grade to be reached than an upgrade in the first two cells (about 1 per cent higher). However, considering that the flotation bank corresponds to a rougher operation, a decrease in concentrate grade (and an increase in mass pull) should not cause significant operating problems, provided that the cleaning circuit has sufficient capacity to process the increment inflow rate.

It should be noted that the conditions for each scenario were not optimised along the bank, but the results show the potential and flexibility of using different launder designs in a flotation bank, as well as the strengths of the new flotation models.

Finally, the industrial simulator allowed evaluation of variables that are not usually included in the currently available simulation systems. Thus, variables such as size-by-liberation collection recovery, water recovery, gangue entrainment and bubble loading grade were characterised along the bank by the industrial simulator for each scenario. This tool enables the evaluation of a wide range of modifications in flotation cells, related to volume and launder configuration. As well as the launder designs evaluated in this study, other launder designs available for flotation cells can be evaluated to choose the right configuration to reach the desired metallurgical performance, which can be an increase in recovery, grade, or selectivity.

ACKNOWLEDGEMENTS

The authors are grateful to the Agencia Nacional de Investigación y Desarrollo (ANID), FONDECYT Project 1201335 and Universidad Técnica Federico Santa María for providing funding for process modelling and control research. Additionally, we would like to thank Grupo México, Buenavista del Cobre, for allowing this collaborative work to be published.

REFERENCES

Bermudez, G, Amelunxen, P, Medina, M, Taylor, M, Dube, R, 2021. Copper and molybdenum recovery increased by upgrading flotation cells with center launders at Hudbay Constancia. *SME Annual Meeting*, March 1–5, 2021, USA.

Bermudez, G, Perkins, T, Sorensen, R, Smith, C, Bartsch, L, Moyo, J, Dube, R and Brändström, M, 2022. Froth launder modification in 300 m^3 flotation cells at Kennecott Copperton concentrator. *SME Annual Meeting*, February 27 – March 02, 2022, Salt Lake City, USA.

Betancourt, D, Izart, C, Vallejos, P, Yianatos, J, Grau, R and Yañez, A, 2021. Development of a new tool for industrial flotation modelling and simulation, *in Proceedings of Procemin-Geomet 2021*, Santiago, Chile.

Brito-Parada, P and Cilliers, J, 2012. Experimental and numerical studies of launder configurations in a two-phase flotation system. *Minerals Engineering*, 36–38:119–125.

Coleman, R, 2009. Flotation cells: selecting the correct concentrate launder design. *Filtration and Separation*, 46(6):36–37.

Corona, M, Bermudez, G, Dube, R and Jalili, A, 2021. Recent advances in flotation cell froth management. CIM Virtual Convention and Expo. Westmount: CIM Journal.

Finch, J A and Dobby, G S, 1990. Column flotation (1st ed.). Pergamon.

Grau, R, Davoise, D, Yañez, A and López, A, 2019. Optimizing the froth area of large mechanical flotation cells, *in Proceedings of Procemin-Geomet 2019*, Santiago, Chile.

Grau, R, Tapia, J, Yáñez, A, Hicks, M, Chavira, J, Muro, G and Romero, J, 2018. Improving Buenavista del Cobre Flotation Performance with Outotec TankCell® e630 Technology, *in Proceedings of Procemin-Geomet 2018*, Santiago, Chile.

Mattsson, T, Grau, R, Rinne, A and Maksimianen, T, 2017. Hydrodynamic and metallurgical performance of large TankCell® flotation cell in comparison to smaller cells, *in Proceedings of Flotation'17*, Cape Town, South Africa.

Metso Outotec, 2022. HSC Chemistry® software, March 18th, 2022. Available from <https://www.mogroup.com/portfolio/hsc-chemistry/> [Accessed: 13 April 2022].

Neethling, S J, Brito-Parada, P R, Hadler, K and Cilliers, J, 2019. The transition from first to zero order flotation kinetics and its implications for the efficiency of large flotation cells. *Minerals Engineering*, 132:149–161.

Seaman, D R, Li, K, Lamson, G, Seaman, B A and Adams, M H, 2021. Overcoming rougher residence time limitations in the rougher flotation bank at Red Chris Mine, *in Proceedings of 15th Mill Operators Conference 2021*, Brisbane, Australia.

Suhonen, J, Grau, R, Yáñez, A, Miettinen, T, Tapia, A and Mattsson, T, 2019. Performance of TankCell® 630 at Buenavista del Cobre Cu-Mo concentrator, *in Proceedings of Flotation'19*, Cape Town, South Africa.

Vallejos, P, Yianatos, J, Grau, R and Yañez, A, 2020a. Evaluation of flotation circuits design using a novel approach, *Minerals Engineering*, Article 106591.

Vallejos, P, Yianatos, J, Grau, R and Yañez, A, 2020b. Effect of mineral feed characteristics on industrial flotation circuits performance by simulating mineralogical and operational changes, in Proceedings of IMPC 2020, Cape Town, South Africa.

Vallejos, P, Yianatos, J, Grau, R, Yañez, A, López, A and Davoise, D, 2021. Improving metallurgical performance in an industrial flotation bank by upgrading the first cell design, in Proceedings of Procemin-Geomet 2021, Santiago, Chile.

Wang, L, Runge, K, Peng, Y, and Vos, C, 2016. An empirical model for the degree of entrainment in froth flotation based on particle size and density. *Minerals Engineering*, 98:187–193.

Yianatos, J, Bergh, L, Vinnett, L, Panire, I, and Iriarte, V, 2016. Correlation between the top of froth grade and the operational variables in rougher flotation circuits. *Minerals Engineering*, 99:151–157.

Yianatos, J, Moys, M, Contreras, F and Villanueva, A, 2008. Froth recovery of industrial flotation cells. *Minerals Engineering*, 21(12–14):817–825.

Yianatos, J, Vallejos, P, Grau, R and Yañez, A, 2020. New approach for flotation process modelling and simulation. *Minerals Engineering*, 156, Article 106482.

Separation of graphite from cathode materials in spent lithium-ion batteries using flotation technology

L Verdugo[1], A Hoadley[2], L Zhang[3], B Etschmann[4], W Bruckard[5] and J M Menacho[6]

1. PhD Student, Monash University, Melbourne Vic 3800. Email: luis.verdugo@monash.edu
2. Assoc. Professor, Monash University, Melbourne Vic 3800. Email: andrew.hoadley@monash.edu
3. Assoc. Professor, Monash University, Melbourne Vic 3800. Email: lian.zhang@monash.edu
4. Research Officer, Monash University, Melbourne Vic 3800. Email: barbara.etschmann@monash.edu
5. Research Group Leader, CSIRO, Melbourne Vic 3169. Email: warren.bruckard@csiro.au
6. General Manager, De Re Metallica Ing. SpA, Santiago, Chile, 8581151. Email: jorge.menacho@drm.cl

INTRODUCTION

Since the introduction of Lithium-Ion Batteries (LIBs) in 1991, the market for lithium-ion cells has been driven by the high demand for portable electronic devices and more recently for batteries for the electric car industry. It is expected to grow rapidly to reach 2600 GWh globally by 2030 (US Government, Office of Energy Efficiency and Renewable Energy, 2021). However, there is a desperate need to recycle LIBs to recover valuable cathode materials and graphite. For this reason, several physical and chemical recycling technologies have been proposed to recover these materials from spent batteries. Amongst these, froth flotation technology is a potential cost-effective technology for separation of the graphite fraction from the lithium oxide components due to the natural hydrophobicity of graphite and density difference between graphite and cathode materials (Folayan *et al*, 2021).

In a typical electrochemical unit, the anode (graphite) and cathode materials represent 22 per cent and 31 per cent of the total weight in the battery (Jacoby, 2019). Graphite, with a particle size distribution between 10–20 μm, is fixed on the copper anode surface using an organic binder such as polyvinylidene fluoride (PVDF) (Vuorilehto, 2018). On the cathode unit, the lithium metal oxides with a particle size distribution between 1–17 μm (Zhang *et al*, 2022) are fixed on the aluminium current collector surface also using a similar organic. Untreated, this binder generates problems in the separation of these materials due to agglomeration of cathode materials and graphite. This is illustrated in the following image (Figure 1) taken for a mixed electrode material (fraction minus 38 μm) using SEM microscopy.

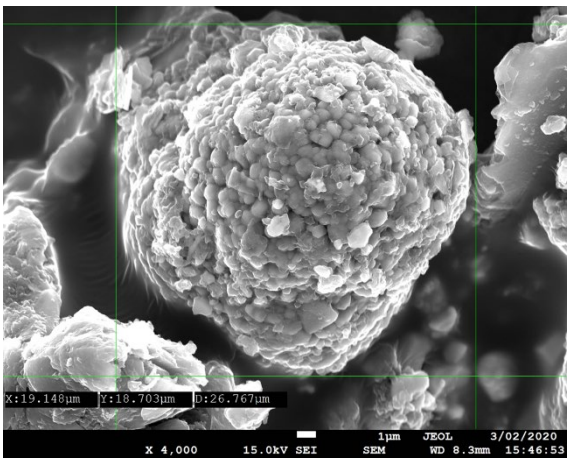

FIG 1 – Electron Micrograph of Agglomeration of Cathode Particles with Organic Binder and Anode Material (image taken by the author of this article).

The importance of the PVDF binder removal is a key aspect in treating the spent battery material. Different pre-treatment techniques such as roasting at high temperature between 500°C–700°C in an inert atmosphere such as nitrogen or argon are known to decompose these organic coatings

(Hanisch *et al*, 2015). Other techniques include the use of organic solvents such as N-Methyl-2-Pyrrolidone (NMP) or Dimethylformamide (DMF) which dissolve the organic coating thus providing an exposed metal oxide surface (He *et al*, 2021).

Another relevant factor is the particle size, which plays an important role in the separation of anode – cathode by flotation. Ultrafine oxide materials (particles with a size <10 μm) have a low probability of collision between particles and bubbles (Trahar and Warren, 1976). However, they still tend to be found in the concentrate, because they are entrained due to their small size (Shahbazi, Rezai and Koleini, 2010). This phenomenon is mainly controlled by the water recovery rate which is linearly correlated with the recovery of oxide materials (Jowett, 1966; Sajjad and Otsuki, 2022).

Several works have been reported using flotation as an efficient technique for separation of graphite from lithium metal oxides (LMO). Many report a high-grade of lithium metal oxides ranging between 50 per cent to 95 per cent in tailings and graphite grades between 80 per cent to 90 per cent in concentrates, depending on processing conditions and number of flotation stages (Yu *et al*, 2018; Liu *et al,* 2020). All these works involved testing industrial electrode materials which are not fully liberated (Vanderbruggen *et al*, 2021), due to the binder employed in the agglomeration of graphite and lithium metal oxides particles.

In this paper, the separation behaviour of anode and cathode materials in a synthetic mixture of graphite and NMC-111 and using a commercial spent lithium ion battery based on NMC-111 technology is explored. This analysis includes the study of different processing conditions in a single batch flotation stage with the aim to maximise the graphite recovery in concentrates and maximise the recovery of lithium metal oxides in tailings.

EXPERIMENTAL

In these experiments synthetic mixtures of electrode materials and real electrode materials taken from a spent commercial lithium-ion battery based on NMC-111 ($LiNi_{0.33}Mn_{0.33}Co_{0.33}O_2$) technology were used in the flotation experiments. Given the heterogeneous nature of LIBs, a full characterisation analysis was carried out on feed materials. These analyses include particle size analysis, scanning electron microscopy, X-ray diffraction, X-ray fluorescence, chemical analysis, contact angle analysis, thermogravimetric analysis and mineral liberation analysis (MLA), both before and after high temperature roasting.

The spent electrode materials, were roasted under nitrogen atmosphere (2 L/min) at 600°C for 2 h in a laboratory furnace, in order to remove the organic binder in samples.

Batch flotation trials were conducted in a 0.5 L Denver cell using air as carrier gas at 180 L/h equivalent to 1.05 cm/s as superficial gas rate, and using a mixing speed of 900 rev/min, in order to minimise the hydrodynamic effect in the entrainment degree of these oxides in the graphite concentrates. The solid content in slurries was 13 per cent w/w for all experiments and the reagents used were 0.1 M NaOH, used as pH modifier, and kerosene, (reagent grade, Sigma-Aldrich, Australia), as collector for graphite in some of the experiments.

The electrode materials used in these experiments were pure graphite (>99.9 per cent purity, particle size 100 per cent -20 μm, Sigma-Aldrich, Australia) and lithium nickel manganese cobalt oxide ($LiNi_{0.33}Mn_{0.33}Co_{0.33}O_2$), NMC-111, (>99.00 per cent purity, D_{50} = 7.5 μm, MSE supplies, USA) and the anode and cathode material were taken from a spent lithium ion battery model JH3 from LG Chem and provided by Envirostream Australia Pty Ltd. The frothers evaluated in this study were 2-Octanol, 97 per cent purity, supplied by Sigma-Aldrich Australia, 4-Methyl-2-pentanol (MIBC) reagent grade, 98 per cent purity, supplied by Sigma-Aldrich, Australia and Aerofroth® 88, (2-Ethylhexanol, >99 per cent purity), supplied by Solvay Australia. Regarding the dosages of collector and frother used in these experiments these were 350 g/t and 30 mg/L respectively. The flotation products were characterised using X-ray diffraction analysis and elemental analysis (CHNS analysis) used to measure the composition of total carbon assumed as graphite. Then, based on these results, elemental recoveries were calculated and flotation kinetics and grade/recovery data determined.

RESULTS

Characterisation results for the commercial battery electrode material before roasting, indicated a high agglomeration degree according SEM and MLA analyses with a content of carbon in cathode material between 5–6 per cent C, indicating the presence of the organic binder. After roasting, the organic content was reduced (down to 0.70 per cent C) in samples with a particle size 100 per cent -38 µm, indicating significant binder removal, even though SEM and MLA analyses indicated a persistent agglomeration. Additionally, contact angle analyses confirmed changes in contact angle values for cathode material when this material was roasted, indicating a beneficial effect of roasting in terms of imparting hydrophilicity.

Regarding flotation experiments, these were divided in two parts. The first part relates to experiments using synthetic mixtures of graphite and lithium nickel manganese cobalt oxide ($LiNi_{0.33}Mn_{0.33}Co_{0.33}O_2$, NMC-111) in a ratio 47 per cent for graphite and 53 per cent for NMC-111. Flotation results at pH 12 indicated a good separation efficiency (81.40 per cent) with a low entrainment degree of oxides in the graphite concentrates using the reagent Aerofroth® 88, where the cumulative recovery for graphite and NMC-111 at 8 minutes of flotation were 97.75 per cent and 16.35 per cent respectively.

Applying the same processing conditions used for the synthetic mixtures, the second set of experiments were conducted using real electrode materials which were roasted before processing. The feed grade for these materials was 38.16 per cent graphite and 61.84 per cent NMC-111 respectively. Flotation results at 8 min of flotation, indicated cumulative recoveries for graphite and NMC-111 of 94.44 per cent and 14.02 per cent respectively. High-grades of graphite (80.61 per cent) were obtained in concentrates with lower NMC-111 grades (19.39 per cent). In tailings the grades of graphite and NMC-111 were 11.20 per cent and 88.80 per cent respectively. These results indicate that the use of roasting is effective in terms of binder removal for cathode materials. The last statement is validated when the flotation kinetics (cumulative recovery versus time) of synthetic mixtures of graphite and NMC-111 is compared with the flotation kinetics of commercial materials. This is shown in Figure 2.

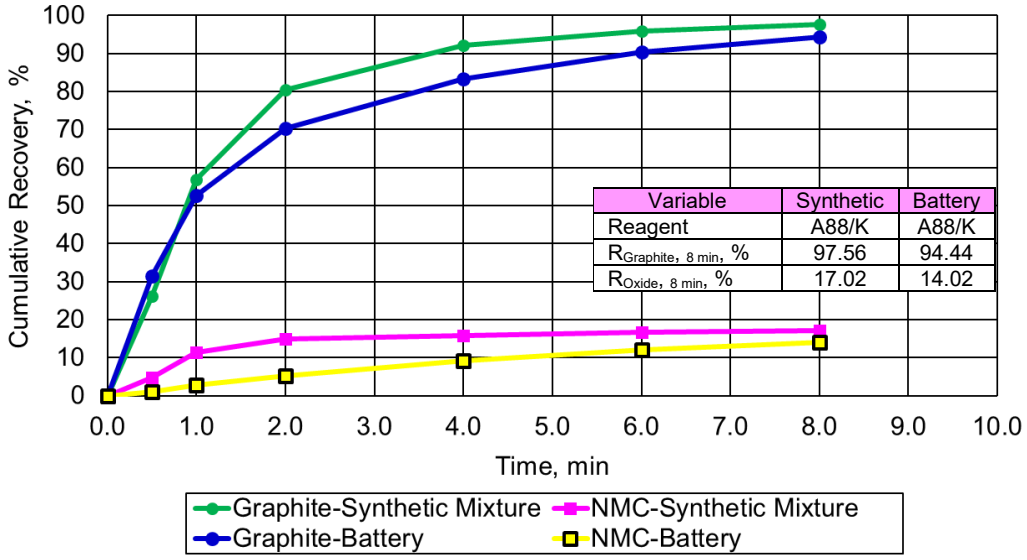

FIG 2 – Flotation Kinetics of Graphite and NMC-111 for each Experiment.

ACKNOWLEDGEMENTS

The authors would like to acknowledge The Chilean National Agency for Research and Development, (ANID), for the financial support given to this research through a PhD scholarship, Monash University for the development of this research work, the flotation equipment was purchased under the support of the Australian Research Council for Dr Lian Zhang, project number: IH170100009, Dr Igor Ametov from Solvay Australia for the reagent Aerofroth®-88, and CSIRO Mineral Resources and De Re Metallica Ing. for their technical support during this work.

REFERENCES

Folayan, T, Lipson, A, Durham, J, Pinegar, H, Liu, D, Pan, L, 2021. Direct Recycling of Blended Cathode Materials by Froth Flotation, *Energy Technology*, 9, 10, 2100468.

Hanisch, C, Loellhoeffel, T, Diekmann, J, Markley, K, Haselrieder, W, Kwade, A, 2015. Recycling of Lithium-Ion Batteries: A Novel Method to Separate Coating and Foil of Electrodes, *Journal of Cleaner Production*, 108, Part A, 301–311.

He, Y, Yuan, X, Zhang, G, Wang, H, Zhang, T, Xie, W, Li, L, 2021. A Critical Review of Current Technologies for The Liberation of Electrode Materials from Foils in The Recycling Process of Spent Lithium-Ion Batteries, *Science of The Total Environment*, 766, 142382.

Jacoby, M, July 15, 2019. It's Time to Get Serious About Recycling Lithium-Ion Batteries, Chemical and Engineering News, 97, 28, Available online: https://cen.acs.org/materials/energy-storage/time-serious-recycling-lithium/97/i28 (accessed on 23 March 2022).

Jowett, A, 1966. Gangue mineral contamination of froth, *Brit. Chem. Engng*, 11:330–333.

Liu, J, Wang, H, Hu, T, Bai, X, Wang, S, Xie, W, Hao, J, He, Y, 2020. Recovery of LiCoO2 and graphite from spent lithium-ion batteries by cryogenic grinding and froth flotation, *Minerals Engineering*, 148, 106223.

Sajjad, M, Otsuki, 2022, A Correlation between Flotation and Rheology of Fine Particle Suspensions, *Metals*, 12, 270.

Shahbazi, B, Rezai, B, Koleini, S, 2010. Bubble–Particle Collision and Attachment Probability on Fine Particles Flotation, *Chemical Engineering and Processing: Process Intensification*, 49, Issue 6, 622–627.

Trahar, W, Warren, L, 1976. The Flotability of Very Fine Particles – A Review, *International Journal of Mineral Processing*, 3, Issue 2, 103–131.

US Government, Office of Energy Efficiency and Renewable Energy, June 2021. National Blue Print for Lithium Batteries 2021–2030, Executive Summary, Available online: https://www.energy.gov/sites/default/files/2021–06/FCAB%20National%20Blueprint%20Lithium%20Batteries%200621_0.pdf (accessed on 16 March 2022).

Vanderbruggen, A, Gugala, E, Blannin, R, Bachmann, K, Serna-Guerrero, R, Rudolph, M, 2021. Automated Mineralogy as a Novel Approach for the Compositional and Textural Characterization of Spent Lithium-Ion Batteries, *Minerals Engineering*, 169, 106924.

Vuorilehto, K, 2018. Materials and function, in: R Korthauer (eds) *Lithium-Ion Batteries: Basics and Applications*, Springer: Berlin-Heidelberg.

Yu, J, He, Y, Ge, Z, Li, H, Xie, W, Wang, S, 2018. A promising physical method for recovery of LiCoO2 and graphite from spent lithium-ion batteries: Grinding flotation, *Separation and Purification Technology*, 190, 45–52.

Zhang, J, Qiao, J, Sun, K, Wang, Z, 2022. Balancing Particle Properties for Practical Lithium-Bon Batteries, *Particuology*, 61, 18–29.

New reagents for beneficiation of lithium ores

T Walsh[1] and S R Mudnuru[2]

1. Application and Development Chemist, Clariant Oil and Mining Services, Lara Vic 3212. Email: Tim.Walsh@clariant.com
2. Global Technology Manager – Decarbonization Minerals, Clariant Gulf FZE LLC, Dubai UAE 2326. Email: M.SureshRaju@clariant.com

ABSTRACT

The development of lithium-ion batteries, coupled with the global trend towards electrification of transportation, has led to a dramatic increase in the demand for lithium. The production of lithium from hard rock ores is increasing, and flotation has proved to be an effective means for the beneficiation of many pegmatitic lithium ores. Clariant Mining Solutions has developed a range of novel collectors for the flotation of spodumene and other lithium ores, and this paper presents examples of some of the most recent developments.

Fatty acids are the typical collectors for lithium flotation, however the grade and recovery achieved with these collectors is often below the desired level. There are also some significant drawbacks associated with the use of fatty acid collectors, such as the formation of calcium soaps which give rise to filtration problems and the need for acid washing.

Several FLOTINOR products have been developed as alternatives to fatty acids. These products offer equivalent or better metallurgical performance at significantly lower dosages than fatty acids. This offers benefits to the flotation circuit as well as potentially reducing the issues associated with downstream processing of the concentrate.

INTRODUCTION

Lithium is an important element in the world economy, with applications as diverse as glass and ceramics, lubricating greases and polymer synthesis (Martin *et al*, 2017). Recently, the development of rechargeable lithium-ion batteries, coupled with the global trend towards electrification of the transportation fleet, has led to a dramatic increase in the demand for lithium (Kavanagh *et al*, 2018). In addition to the production of lithium from brines, the production of lithium from hard rock ores is increasing, and flotation has proved to be an effective means for the beneficiation of many pegmatitic lithium ores (Tadesse *et al*, 2019).

Fatty acids are the typical collectors used for lithium flotation (Sousa *et al*, 2019). However, the grade and recovery achieved with fatty acid collectors is often below the desired level, which means that there is room for significant improvement (Xu *et al*, 2016). There are also some significant disadvantages associated with the use of fatty acid collectors, such as the formation of calcium and magnesium soaps which give rise to filtration problems and the need for acid washing of filter screens.

Clariant Mining Solutions has developed a range of novel collectors for the flotation of spodumene and other lithium ores. In the beneficiation of spodumene ores, Clariant's FLOTINOR anionic collectors are effective for the direct flotation of spodumene at neutral or alkaline pH.

RESULTS AND DISCUSSION

Spodumene rougher flotation

Spodumene Rougher Flotation tests were performed, to compare standard fatty acid to FLOTINOR 10339 (Figures 1 and 2). The results indicate that FLOTINOR 10339 is able to achieve the same grade at half the dose of standard fatty acid (Figure 1). For example, at 1000 g/t of fatty acid, the grade achieved is 3.5 per cent lithium oxide, whereas for FLOTINOR 10339, at a dosage of 500 g/t, we achieved a grade of 3.7 per cent lithium oxide.

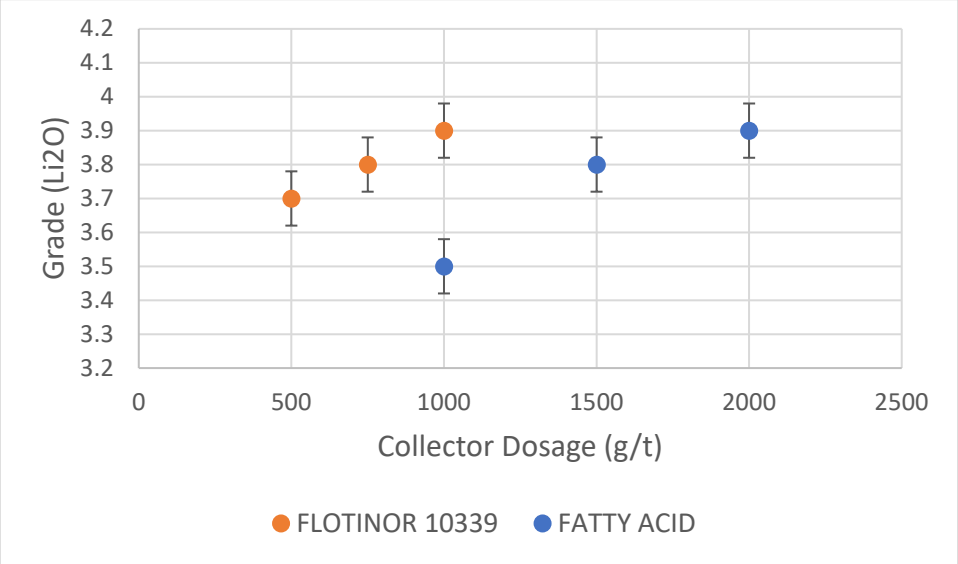

FIG 1 – Rougher test – grade versus collector dosage.

The Lithium Rougher recovery results indicate that FLOTINOR 10339 is able to achieve a higher recovery than standard fatty acid, at half the dosage (Figure 2). For example, at 1500 g/t fatty acid, the lithium recovery is 90 per cent. Whereas for FLOTINOR 10339, at 750 g/t, the recovery was 92 per cent.

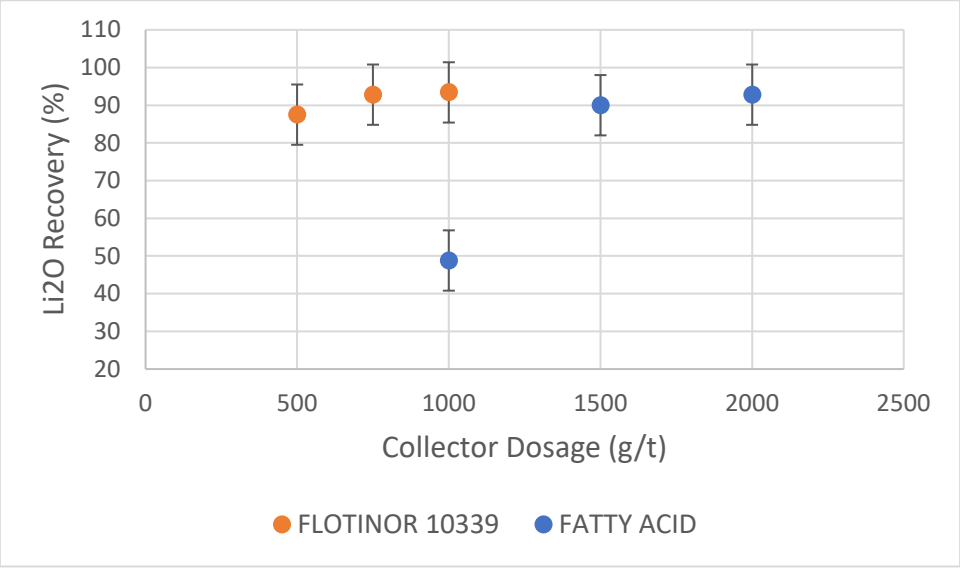

FIG 2 – Rougher test – recovery versus collector dosage.

Spodumene rougher and cleaner test

Spodumene Rougher and Cleaner tests were performed to compare fatty acid with FLOTINOR 10381 (Figures 3 and 4). Although there is some variability in the results, FLOTINOR 10381 can achieve a grade of approximately 6 per cent, which is higher than the fatty acid grade of approximately 5.5 per cent (Figure 3). This indicates that FLOTINOR 10381 is more selective against gangue minerals than fatty acid.

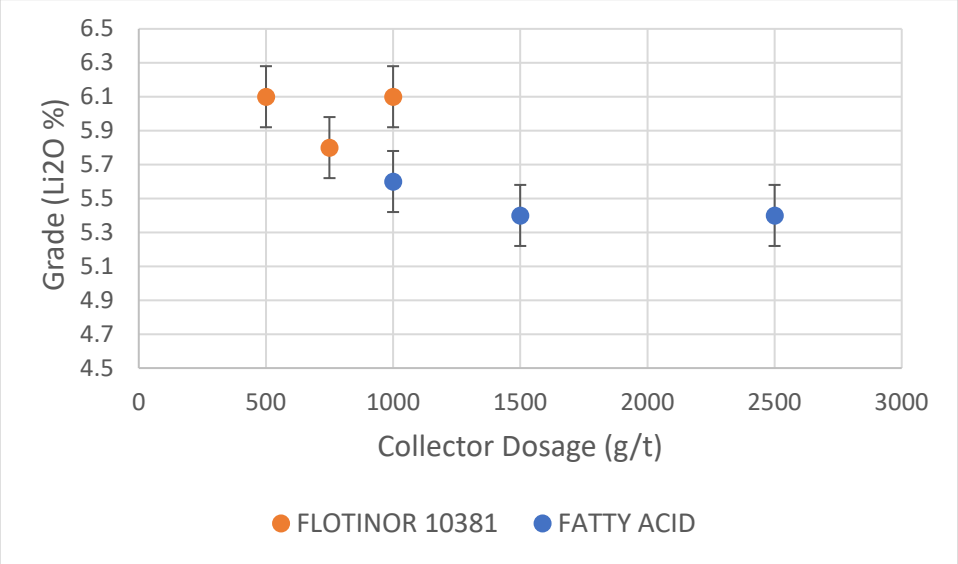

FIG 3 – Rougher and cleaner test – grade versus collector dosage.

FLOTINOR 10381 also gave a higher recovery than fatty acid at all dosage points (Figure 4). For example, at 2500 g/t fatty acid, the recovery is 80 per cent, whereas for FLOTINOR 10381 at 1000 g/t, the recovery is 85 per cent.

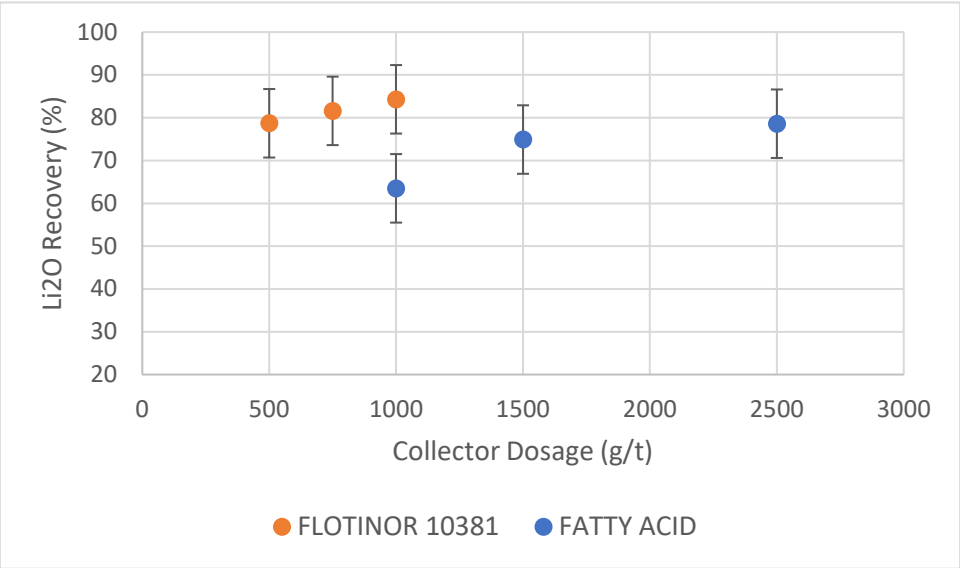

FIG 4 – Rougher and cleaner test – recovery versus collector dosage.

METHODS

In both cases, standard conditions were used as supplied by the relevant mines. Long conditioning times were used in order to adequately disperse the collector in the pulp.

Rougher test

The ore was crushed to -3.35 mm and split into 1.3 kg lots. For each flotation test the sample was ground to a P80 of 150 µm and deslimed in a 600 × 140 mm cylindrical column. After mixing in the column and allowing the slurry to settle for a predetermined time the top 525 mm of slimes pulp was decanted off. The remaining coarse settled pulp was transferred to a 2L Agitair cell. The pulp was conditioned for 10 min at 1000 rev/min with the required amount of collector and 1.2 ml of 8 per cent soda ash solution. Three rougher cons were collected at 30 second, 1 min and 1 min intervals. Lithium assays were performed at an external laboratory by peroxide fusion and ICP-AES.

Rougher and cleaner test

The ore was crushed to -3.35 mm and split into 1.3 kg lots. For each flotation test the sample was ground to a P80 of 150 µm and deslimed in a 600 × 140 mm cylindrical column. After mixing in the column and allowing the slurry to settle for a pre-determined time the top 525 mm of slimes pulp was decanted off. The remaining coarse settled pulp was transferred to a 2L Agitair cell. The pulp was conditioned for 10 min at 1000 rev/min with the required amount of collector and 1.2 ml of 8 per cent soda ash solution.

Rougher flotation was 3 min followed by a 3 min cleaner flotation. Lithium assays were performed at an external laboratory by peroxide fusion and ICP-AES.

CONCLUSIONS

Several FLOTINOR products for Lithium ores have been developed that deliver an equal or better grade and recovery of lithium compared to fatty acid at half the dose. Apart from the improved metallurgical performance, the lower dose of FLOTINOR products could reduce or the need for downstream acid washing processes that are often required when using fatty acids. There is also a potential for improve filtration performance.

REFERENCES

Kavanagh, L, Keohane, J, Cabellos, G G, Lloyd, A and Cleary, J, 2018. Global Lithium Sources – Industrial Use and Future in the Electric Vehicle Industry: A Review. *Resources*, 7(3), 57.

Martin, G, Rentsch, L, Höck, M and Bertaua, M, 2017. Lithium market research – global supply, future demand and price development. *Energy Storage Materials*, 6, 171–179.

Sousa, R, Ramos, V, Guedes, A, de Sousa, A B, Noronha, F and Leite, M M, 2019. Flotation of lithium ores to obtain high-grade Li_2O concentrates. Are there any mineralogical limitations? *International Journal of Mining, Materials, and Metallurgical Engineering (IJMME)*, 5, 7–18.

Tadesse, B, Makue, F, Albijanic, B and Dyer, L, 2019. The beneficiation of lithium minerals from hard rock ores: A review. *Minerals Engineering*, 131, 170–184.

Xu, L, Hu, Y, Wu, H, Tian, J, Liu, J, Gao, Z and Wang, L, 2016. Surface crystal chemistry of spodumene with different size fractions and implications for flotation. *Separation and Purification Technology*, 169, 33–42.

Improving flotation hydrodynamics to maximise nickel recovery from tailings

P Wang[1], S Parkes[2], M Yvon[3] and K P Galvin[4]

1. Research Associate, ARC Centre of Excellence for Enabling Eco-Efficient Beneficiation of Minerals, Newcastle Institute for Energy and Resources, University of Newcastle, Callaghan NSW 2308. Email: peipei.wang@newcastle.edu.au
2. PhD Student, ARC Centre of Excellence for Enabling Eco-Efficient Beneficiation of Minerals, Newcastle Institute for Energy and Resources, University of Newcastle, Callaghan NSW 2308. Email: Sian.Parkes@uon.edu.au
3. PhD Student, ARC Centre of Excellence for Enabling Eco-Efficient Beneficiation of Minerals, Newcastle Institute for Energy and Resources, University of Newcastle, Callaghan NSW 2308. Email: MeollaEsther.Yvon@uon.edu.au
4. Laureate Professor, ARC Centre of Excellence for Enabling Eco-Efficient Beneficiation of Minerals, Newcastle Institute for Energy and Resources, University of Newcastle, Callaghan NSW 2308. Email: kevin.galvin@newcastle.edu.au

INTRODUCTION

Mineral liberation is critical to maximise the grade and recovery of nickel, however this objective is challenged considerably by the poor flotation kinetics, especially that of ultrafine particles (Kelebek and Tukel, 2018; Multani and Waters, 2019). High recoveries demand long cell residence times and hence a large flotation capital expenditure (Wills and Finch, 2016). However, this leads to excessive entrainment of gangue minerals, thus negating efforts to depress its recovery.

This study aimed to investigate new hydrodynamic approaches to improve nickel flotation, focusing primarily on unrecovered nickel from a Western Australian tailings stream. Mechanical cell flotation experiments were conducted to understand the flotation kinetics, covering different size ranges. A novel Reflux Flotation Cell (RFC) was also used to improve the nickel recovery and reject the silicates. Future work aimed at applying the RFC to different size portions is also outlined.

METHODOLOGY, RESULTS AND DISCUSSION

The flotation experiments were firstly conducted using a 3 L mechanical cell at a pulp density of 13 per cent. 24 ppm of methyl isobutyl carbinol (MIBC) frother was maintained in the slurry and the wash water to ensure a stable froth, pH was adjusted to 10.5 and the air rate was adjusted to 0.34−0.68 cm/s. The nickel grade of the feed samples was 0.20 per cent, and this full-size feed (0–300 μm) was wet split into fine particles (-20 μm) and coarser particles (+20 μm). The nickel grade of the fine particles and coarser particles were 0.53 per cent and 0.14 per cent, respectively.

For the full-size feed and coarser particle feed, a three-stage mechanical cell flotation experiment was used, ie after the first stage of flotation, the overflow product was returned to the mechanical cell and floated again; this was repeated twice to eliminate entrainment and enhance the product grade. The flotation time of each stage was set at 5 minutes. For the coarser particles, the final product, after the three-stages of flotation, was analysed. For the flotation of the full-size range, re-flotation led to negligible improvement in the grade, hence the product from the first stage was analysed. For the fine particle feed, only one stage of flotation was used, with a 12 minutes flotation time.

The overall flotation performance is summarised in Table 1. It is shown that the highest product grade (0.68 per cent) was achieved for the fine particle flotation, while the highest upgrade (3.71) was achieved for the coarser particle flotation. For the coarser particle flotation, the product grade is 0.52 per cent, which is close to the product grade for the fine (0.68 per cent) and full-size range (0.56 per cent). The recovery of the coarser particles is 56.6 per cent, significantly higher than the flotation recovery over the full-size range. In the flotation of the coarser particles there is relatively little SiO_2 (0.73 per cent) to contend with, compared to the level within the fine size range (7.69 per cent) and overall size range (7.26 per cent).

TABLE 1

Overall comparison of mechanical cell flotation experiments with different size ranges.

Feed	Ni grade (%)	SiO_2 grade (%)	Ni Recovery (%)	Upgrade
Full-size range	0.56	7.26	30.8	2.81
Fine particles	0.68	7.69	21.2	1.28
Coarser particles	0.52	0.73	56.6	3.71

A separate set of experiments was conducted on the full size using a pseudo-continuous closed-loop RFC approach, with both the product and reject streams returned to the feed tank, which is ideal for relatively small samples and allowing a continuous feed. The RFC system consists of a vertical flotation section with a downcomer, and a system of parallel inclined channels below, which prevents bubble entrainment into the tailings, thus allowing independent control of the product liquid flux. The feed and gas enter via the downcomer and wash water is introduced via a plenum chamber located above the vertical section. The initial pulp density was ~10 per cent with both feed and wash water fluxes fixed at 0.62 cm/s. The gas flux was 1.25 cm/s and the product liquid flux was 0.21 cm/s, rendering a bias flux of 0.42 cm/s. The pH and MIBC were the same as for the mechanical cell flotation. Reject and product samples were taken simultaneously for analysis.

Table 2 compares the flotation performance of the mechanical cell and RFC. Overall, the RFC produces a higher nickel recovery (49.5 per cent) than that of the mechanical cell (30.8 per cent). The effective plug-flow feed flux of the mechanical cell experiments (theoretical basis from Parkes *et al*, 2022) was ~12 cm/(5 min × 60 s/min) =0.04 cm/s, a factor of more than 15 times lower than that of the feed fluxes used in the RFC (assuming the same recovery). The nickel grade and upgrade from the RFC are close to those from the mechanical cell which, considering the relatively high feed fluxes used, are significant. The product from the RFC contained a much lower SiO_2 grade (1.93 per cent) than that from the mechanical cell (7.26 per cent).

It is apparent from the mechanical cell tests that the presence of the fine particles impedes the overall flotation performance. Interestingly, the performance of the RFC on the overall feed was nearly as high as the performance of the mechanical cell on the coarser feed. It is anticipated however, that even better RFC performance could be achieved in the RFC by processing the fine and coarser portions separately.

TABLE 2

Overall comparison of flotation performance using mechanical cell and RFC.

	Ni grade (%)	SiO_2 grade (%)	Recovery (%)	Upgrade
Mechanical cell	0.56	7.26	30.8	2.81
RFC	0.52	1.93	49.5	2.60

CONCLUSIONS AND FUTURE WORK

Experimental results showed significant improvement in flotation kinetics through separate processing of the ultrafines, leading to more effective recovery of the coarser particles. Future options considered will include the use of the Graviton, a high-speed centrifugal device, to achieve fast desliming of the tailings at 20 μm, followed by application of the RFC on both portions. These advantages include the enhanced kinetics and capacity. Importantly, the system operates with a concentrated bubbly zone, and a strong counter-current bias flux to eliminate fine gangue entrainment. Ultimately, the aim is to outline the benefits achieved through these novel approaches to efficiently extract low-grade nickel ore.

ACKNOWLEDGEMENTS

The authors acknowledge the funding support from the Australian Research Council for the ARC Centre of Excellence for Enabling Eco-Efficient Beneficiation of Minerals, grant number CE200100009.

REFERENCES

Kelebek, S and Tukel, C, 2018. Separation of nickeliferous hexagonal pyrrhotite from pentlandite in Ni-Cu sulphide ores: Recovery by size performance. *Miner. Eng*. 125, 223–230.

Multani, R S and Waters, K E, 2019. Flotation recovery–by–size comparison of pyrrhotite superstructures with and without depressants. *Miner. Eng*. 130, 92–100.

Parkes, S, Wang, P and Galvin, K P, 2022. Investigating the System Flotation Kinetics of Fine Chalcopyrite in a REFLUX^{TM} Flotation Cell using a Standardised Flotation Cell Reference Method. *Miner. Eng*. 178, 107411.

Wills, B A and Finch, J A, 2016. *Will's Mineral Processing Technology: An Introduction to the Practical Aspects of Ore Treatment and Mineral Recovery*. Butterworth – Heinemann (Elsevier), Amsterdam.

Gold telluride synthesis and flotation

K Ward[1], B Tadesse[2] and L G Dyer[3]

1. PhD student, Western Australian School of Mines, Curtin University, Kalgoorlie WA 6430. Email: kylie.ward1@postgrad.curtin.edu.au
2. Senior Lecturer, Western Australian School of Mines, Curtin University, Kalgoorlie WA 6430. Email: bogale.tadesse@curtin.edu.au
3. Discipline Lead – Metallurgical Engineering, Western Australian School of Mines, Curtin University, Kalgoorlie WA 6430. Email: laurence.dyer@curtin.edu.au

INTRODUCTION

The Golden Mile ore deposit in Western Australia is one of the largest gold telluride deposits in the world. Approximately 20 per cent of the contained gold in the deposit is present as gold telluride minerals, the most prevalent being calaverite ($AuTe_2$) and petzite (Ag_3AuTe_2). Telluride mineralogy in the Golden Mile orebody is fine grained and complex having formed due to hydrothermal deposition in the late paragenetic sequence. Nineteen tellurium bearing minerals have been identified including gold and silver as well as mercury, lead and nickel tellurides (Shackleton, Spry and Bateman, 2003).

Extensive work has been completed on the flotation of gold, gold-silver alloys and gold ores however there is a lack of information detailing the difference between flotation of native gold and individual gold minerals (Dunne, 2016). Studies on the flotation behaviour of gold ores have focused primarily on the flotation of free gold and refractory sulfides (Teague, Van Deventer and Swaminathan, 1999).

Telluride minerals have been shown to be naturally floatable both in the laboratory and on an industrial scale using only a frothing agent (Johnston, 1933; Colbert, 1980). Laboratory flotation test work conducted as early as 1926 discovered that there was no difficulty in the flotation of Kalgoorlie ores with xanthate to produce a bulk gold and pyrite concentrate stating, ‘ores containing tellurides of gold and silver offer no difficulties since these minerals are even more amenable to flotation than pyrite’ (Winter and Moore, 1926).

Preliminary single mineral studies have previously been conducted on calaverite and sylvanite with the results indicating unoptimised mineral recoveries of up to 67 per cent when using copper sulfate and xanthate (Padmanaban and Lawson, 1991; Lu and Lawson, 1994). These studies did not examine the impact of pyrite depressants, process water or the presence of any surface products. A study conducted by (Yan and Hariyasa, 1997) examined the impact of collector type, collector dosage and pH on a high-grade Kalgoorlie telluride ore. The study found telluride minerals float readily with the addition of frother only however flotation rate and overall recovery is improved by the addition of xanthates. Copper sulfate was found to have a variable result when used as an activator.

The separation of a telluride concentrate to recover tellurium, improve gold recovery and reduce costs has been considered by operations in Kalgoorlie (Kleeman, 1963) however has never been successfully implemented. Test work conducted in the 1960s at laboratory and pilot scale indicated a separation of tellurides from pyrite was possible utilising lime and cyanide (Field, 1963). A similar circuit to recover a telluride concentrate from pyrite was operated at the Wright-Hargreaves Mine in Canada to maximise gold recovery during the 1950s (Singh, 1956). Detailed records of operating conditions for both circuits are not available.

In order to achieve a separation of gold tellurides from pyrite a fundamental understanding of the flotation performance of gold telluride minerals is required. The separation of telluride minerals from pyrite in a reverse flotation process will require the depression of previously floated, copper activated pyrite. The flotation response for telluride minerals under the conditions required to depress pyrite is largely unknown due to the lack of fundamental studies on telluride minerals and data from historical operating plants.

Isolating naturally occurring gold and silver telluride minerals from ores in significant quantity is a difficult and impractical task. Telluride minerals obtained from flotation plant concentrates are undesirable due to surface alteration by flotation reagents. Previous studies on platinum tellurides

have shown that flotation performance of tested synthetic telluride minerals was adequate when compared with that for natural ores (Shamaila and O'Connor, 2008).

Previous studies that have included the synthesis of gold and silver tellurides have documented the process to take up to four weeks to achieve a homogenous product (Echmaeva and Osadchii, 2009; Deschênes *et al*, 2006; Padmanaban and Lawson, 1991). This study demonstrates that a homogenous product can be synthesised without the need for long annealing stages. The modified procedure incorporates the use of multiple grinding and compression stages with short heat treatments enabling a final product to be prepared in a few days. Calaverite ($AuTe_2$), petzite (Ag_3AuTe_2) and hessite (Ag_2Te) have been prepared successfully using this method.

This study utilises a micro flotation column to conduct single mineral flotation test work. Initial results for test work conducted utilising synthesised gold and silver tellurides are discussed.

ACKNOWLEDGEMENTS

Financial support from the Australian Government Research Training Program and Mineral Research Institute of Western Australia (MRIWA) is gratefully acknowledged.

REFERENCES

Colbert, P, 1980. Gold ore treatment at Emperor Gold Mining Co. Ltd, Vatukoula, Fiji. *Mining and Metallurgical Practices in Australasia,* J T Woodcock (ed.), 492–494.

Deschênes, G, Pratt, A, Fulton, M and Guo, H, 2006. Kinetics and mechanism of leaching synthetic calaverite in cyanide solutions. *Minerals and Metallurgical Processing,* 23, 133–138.

Dunne, R, 2016. Flotation of gold and gold-bearing ores. *Gold Ore Processing.* Elsevier.

Echmaeva, E A and Osadchii, E G, 2009. Determination of the thermodynamic properties of compounds in the Ag-Au-Se and Ag-Au-Te systems by the EMF method. *Geology of Ore Deposits,* 51, 247–258.

Field, T D, 1963. Selective treatment of tellurides contribution by North Kalgurli (1912) Ltd. Symposium on Selective Treatment of Tellurides 1962.

Johnston, W, 1933. Tellurides: Problem or alibi? *Eng. Min. J,* 134, 333.

Kleeman, C M, 1963. Introduction – Tellurium. Symposium on Selective Treatment of Tellurides 1962. 3.

Lu, Z and Lawson, F, 1994. Metallurgical properties of synthetic sylvanite. AusIMM Proceedings (Australia). 89–93 (The Australasian Institute of Mining and Metallurgy: Melbourne).

Padmanaban, V and Lawson, F, 1991. Metallurgical properties of synthetic calaverite. The AusIMM proceedings. 31–37 (The Australasian Institute of Mining and Metallurgy: Melbourne).

Shackleton, J M, Spry, P G and Bateman, R, 2003. Telluride mineralogy of the Golden Mile deposit, Kalgoorlie, Western Australia. *Canadian Mineralogist,* 41, 1503–1524.

Shamaila, S and O'Connor, C T, 2008. The role of synthetic minerals in determining the relative flotation behaviour of Platreef PGE tellurides and arsenides. *Minerals Engineering,* 21, 899–904.

Singh, S, 1956. Selective grinding auriferous pyrite at the Wright-Hargreaves Mine Ltd. *Camborne School of Mines Magazine,* 56, 56–58.

Teague, A J, Van Deventer, J S J and Swaminathan, C, 1999. A conceptual model for gold flotation. *Minerals Engineering,* 12, 1001–1019.

Winter, A S and Moore, B H, 1926. Flotation of Pyritic Gold Ores With Special Reference to the Sulpho-Telluride Ores of Kalgoorlie. Perth: WA School of Mines.

Yan, D S and Hariyasa, 1997. Selective flotation of pyrite and gold tellurides. *Minerals Engineering,* 10, 327–337.

Passivation effect of immobilised ferric (hydroxy-)xanthate upon calcium/magnesium precipitates on the pyrite depression in alkaline conditions

J Xue[1], S Ishida[2], S Fuchida[3], Y Aoki[4], H Shimada[5], T Suwa[6] and C Tokoro[7,8]

1. Ph D Student, Graduate School of Creative Science and Engineering, Waseda University, Tokyo 169–8555, Japan. Email: xuejifeng@toki.waseda.jp
2. Master Student, Graduate School of Creative Science and Engineering, Waseda University, Tokyo 169–8555, Japan. Email: ksnzng28@asagi.waseda.jp
3. Assistant Professor, Faculty of Science and Engineering, Waseda University, Tokyo 169–8555, Japan. Email: sfuchida@aoni.waseda.jp
4. Senior Metallurgist, Sumitomo Metal Mining, Company Limited, Ehime 792–8555, Japan. Email: yuji.aoki.m3@smm-g.com
5. Metallurgist, Sumitomo Metal Mining, Company Limited, Ehime 792–8555, Japan. Email: hiromasa.shimada.w8@smm-g.com
6. Metallurgist, Sumitomo Metal Mining, Company Limited, Tokyo 105–8716, Japan. Email: takahiro.suwa.t7@smm-g.com
7. Professor, Faculty of Science and Engineering, Waseda University, Tokyo 169–8555, Japan. Email: tokoro@waseda.jp
8. Professor, Faculty of Engineering, The University of Tokyo, Tokyo 113–8656, Japan. Email: tokoro@sys.t.u-tokyo.ac.jp

ABSTRACT

Pyrite depression with prolonged pre-conditioning treatment in high salinity water has attracted much of researchers' interest in recent years considering the increased utilisation of multiple stage flotation, closed water circuits, clay minerals, and sea water in flotation plants. In this study, the role of calcium (Ca)/magnesium (Mg) precipitates in stabilising the dissociative ferric hydroxy-xanthate (FHX), and its effect on modifying the balance of hydrophobic/hydrophilic species on the pyrite surface were primarily investigated. The total amount of extractable Fe-bearing species on pyrite concentrates and tailings after floatability test was quantitively determined using ethylenediaminetetraacetic acid (EDTA) extraction tests combined with inductively coupled plasma optical emission spectroscopy (ICP-OES). A more evident accumulation of extracted-Fe in pyrite concentrates rather than it in pyrite tailings was observed at both pH 9 and 10.5 when pyrite was pre-conditioned in Ca/Mg-bearing solutions for 360 min. Fourier transform infrared (FTIR) spectroscopy showed the main xanthate derivatives changed from di-xanthogen (1155 cm^{-1}) to FHX (1167 cm^{-1}) on the oxidised pyrite samples that were preconditioned in Ca/Mg-bearing solutions. Scanning electron microscopy-energy dispersive spectrometry (SEM-EDS) suggested the preferential accumulation of FHX upon secondary Ca/Mg-bearing precipitates as reflected by the higher Fe/S ratio together with the decrease of O element herein after xanthate conditioning. Although the hydrophilic secondary Ca/Mg/Fe-bearing minerals on the pyrite surface generally deteriorate pyrite's floatability, the upper section of these secondary hydrophilic aggregates is partially covered by FHX alongside with further multilayer-adsorbed di-xanthogen. The precipitated Ca/Mg-bearing precipitates promotes the immobilisation of dissociated FHX derived from the reaction among iron oxyhydroxides and xanthate anions upon the localised secondary Ca/Mg/Fe-bearing minerals via acid–base complexation. Therefore, this phenomenon alleviates the hydrophilic modification of secondary Ca/Mg/Fe-bearing minerals to pyrite considering the immobilised FHX upon localised precipitates shows a slight hydrophobicity, and meanwhile, the upper FHX benefits the multilayer adsorption of di-xanthogen via the interaction among their inner hydrophobic alkyl chains.

INTRODUCTION

Pyrite is regarded as a gangue mineral in metal sulfides flotation due to its negative effect on the environment and lower economic value (Owusu *et al*, 2015; Bai *et al*, 2019). Commonly, increasing pre-conditioning time to enhance pyrite depression in alkaline conditions is available (Owusu *et al*, 2015). In recent years, considering the scarcity of fresh water, carrying out the flotation process using process water, high salinity water and even, using sea water has attracted the attention of

several researchers all over the world (Ikumapayi *et al*, 2012; Hirajima *et al*, 2016). In this process, Ca^{2+} and Mg^{2+} are two of representative metal cations that can precipitate on metal sulfides surface and deteriorate the floatability of metal sulfides flotation in alkaline conditions, while their depression effect was also observed to be more efficient when the pH is greater than 8.5 and 10, respectively, and their concentrates around 1×10^{-3} mol/L (Hirajima *et al*, 2016; Chen *et al*, 2020).

Xanthate-derived collectors are traditional and economic collectors used for metal sulfides flotation (Leppinen, 1990). The formation of di-xanthogen via the electrochemical reaction among xanthate anions and oxygen on metal sulfides' surface is widely accepted as controlling metal sulfides flotation (Smart *et al*, 2003; Mu, Peng and Lauten, 2016). Furthermore, Xanthate-derived collectors can react with ferric species like Fe^{3+}, $Fe(OH)_3$ and FeOOH, and form dissociative FHX such as $Fe(OH)_2X$ and $Fe(OH)X_2$ (X: Xanthate) when pH > 6 (Wang, Forssberg and Bolin, 1989; Smart *et al*, 2003). The role of slightly hydrophobic metal xanthate absorbing on metal sulfides flotation cannot be neglected (Goh *et al*, 2006, 2008). Wang, Forssberg and Bolin (1989), Leppinen (1990) and Jiang *et al* (1998) confirmed the stable existence of FHX at pH 8–11 within pe value of around -5.0–5.0 in the Fe-xanthate-H_2O thermodynamic system. On the other hand, Paredes, Acuña and Toledo (2019) assumed the height elevation of the highest peak of the pyrite surface morphology observed from atomic force microscope (AFM) after xanthate conditioning was contributed by the ferric amyl xanthate accumulation on the upper structure of Ca/Mg-bearing precipitates. Meanwhile, Zhang *et al* (2021) reported the higher loading capacity of potassium butyl xanthate (KBX) on the high-iron (Fe content: 1.14–16.18 wt. per cent) sphalerites after $Ca(OH)_2$ rather than NaOH regulating, while they indicated the adsorption of $CaOH^+$ leads to a more positive sphalerite surface and benefits to the adsorption of xanthate anions. However, the oily aggregation of di-xanthogen/FHX on oxidised pyrite surface as well as the obvious increase of S and Fe elements alongside with the decrease of elemental O on the site of colloidal secondary minerals after adding potassium ethyl xanthate (KEX) into the oxidation system, have been observed and determined via SEM-EDS analysis (Smart *et al*, 2003). Especially, in Ca/Mg-bearing solutions, the stabilisation effect of Ca/Mg hydroxy species on iron hydroxy species has also been reported, which may also influence the immobilisation of dissociative FHX from bulk solution via acid–base complexation among Ca/Mg/Fe hydroxy groups (Liu and Zhang, 2000; Mermillod-Blondin *et al*, 2005; Xue *et al*, 2022). As the adsorbed FHX negatively influences pyrite surface hydrophilicity, its immobilisation status regarding the potential enhancement by Ca/Mg-bearing precipitates on the pyrite surface should be discussed considering the chemical similarity between FHX and ferric hydroxy species.

This study was established to clarify the role of immobilised FHX in modifying the surface hydrophilicity of pyrite regarding the existence of Ca/Mg-bearing precipitates herein. For this purpose, surface characterisation was conducted and elaborated as the quantitative determination of iron bearing species on pyrite surface will be beneficial to understand the accumulation characteristics of FHX on pyrite surface in Ca/Mg-free and Ca/Mg-bearing solutions. The FTIR analysis combining with SEM-EDS analysis aimed at verifying the relationship among Ca/Mg-bearing precipitates and reprecipitation of FHX. This study will be useful to grasp the various performance of secondary precipitates in modifying the surface hydrophilicity of pyrite.

EXPERIMENTAL

Materials

Pyrite samples were obtained from Hanaoka Mine, Akita. Anhydrous $CaCl_2$ and $MgCl_2$, 4-methyl-2-pentanol (foaming agent), potassium bromide (KBr) powder, 1 mol/L, 5 mol/L HCl, 1 mol/L NaOH, 50 per cent (w/v) NaOH, acetone and 0.2 mol/L EDTA were purchased from Wako Pure Chemical Industries (Osaka, Japan). Potassium amyl xanthate (PAX; >97 per cent of the purity) was purchased from Tokyo Chemical Industry (Tokyo, Japan).

Pre-conditioning and flotation separation

0.5 g of clean pyrite samples (pre-washed by 5 mol/L HCl that preheated to 80°C then an acetone–water mixture of 1:1 volume then dried in vacuum for 12 h) were added in 0.1 L of prepared solution in a 0.25-L plastic beaker. In Ca/Mg-bearing solutions, 2.5×10^{-2} mol/L Ca^{2+} (100 ppm) or 4.1×10^{-2} mol/L Mg^{2+} (100 ppm) was set as the concentration of the Ca/Mg resource. During the entirety of

the reactions, the pH condition was maintained within ±0.2 of the initial pH values (9 and 10.5, respectively). After magnetic stirring at 700 rev/min and 25°C for specified minutes, each suspension was mixed with 1×10^{-3} L of 2.5 mol/L PAX solution for another 10 min of conditioning. Subsequently, each suspension was filtered using 0.1-μm mixed cellulose filter paper and the solid residue was freeze-dried separately before the surface characterisation test.

For the flotation separation of each pyrite sample, the same suspensions (after PAX conditioning) were mixed with 1×10^{-5} L of 4-methyl-2-pentanol for 1 min, respectively. Each mixture (0.1 L) was then transferred into a Hallimond tube with air purging (1.2×10^{-2} m^3/h) while the flotation time was fixed at 2 min (Xue *et al*, 2022). The concentrates and tailings were separately collected and filtered using a 0.1-μm mixed cellulose filter paper and the solid residue was freeze-dried.

Surface characterisation

EDTA extraction test

Each EDTA extraction test was conducted by blending 0.5 g concentrates/tailings and 4×10^{-2} L of 0.2 mol/L EDTA solution in an enclosed 5×10^{-2}-L plastic jar. After agitation at 300 rev/min for 1 h (pH = 7.5 ± 0.2), each suspension was filtered on 0.1-μm mixed cellulose filter paper and the extractable Fe in the filtrate was analysed by inductively coupled plasma optical emission spectroscopy with 0.02 ppm of detection limit (ICP-OES; Agilent 5100; Agilent, Santa Clara, CA, USA).

FTIR analysis

The chemical bonding forms of PAX powder, PAX-loaded ferrihydrite, pristine pyrite and PAX-loaded pyrite were determined by a Fourier transform infrared (FTIR; Spectrum One, Perkin-Elmer Inc., Massachusetts, American) spectrometer. The samples were prepared by mixing 80 mg KBr powder and 10 mg pyrite sample followed with tableting, then the test tablet was placed directly on the optic window. Meanwhile, a pure KBr powder tablet was applied for the background subtraction of FTIR analysis. The analysis was conducted from 4000 to 400 cm^{-1} using 32 scans with a resolution of 4 cm^{-1}.

SEM-EDS analysis

A thermal field emission scanning electron microscope (FE-SEM; JSM-6500F, JEOL, Tokyo, Japan) equipped with an energy dispersive spectrometer (EDS; JED-2300F, JEOL) was used to investigate the morphology and elemental distribution of pyrite surface. The accelerating voltage of the scanning electron microscope was set to 15 kV under the secondary electron model.

RESULTS and DISCUSSION

The EDTA extraction results were summarised in Table 1. After preconditioning in Ca/Mg-free solutions, a lower amount of extracted-Fe on the pyrite concentrates was confirmed, when compared with the one on pyrite tailings (ie 0.078 mg/g pyrite versus 0.139 mg/g pyrite at pH 9, and 0.102 mg/g pyrite versus 0.172 mg/g pyrite at pH 10.5, respectively). However, the tendency is just the opposite when pyrite preconditioning in Ca/Mg-bearing solutions especially in Mg-bearing solutions was employed (ie 1.278 mg/g pyrite versus 0.715 mg/g pyrite at pH 9, and 2.262 mg/g pyrite versus 0.953 mg/g pyrite at pH 10.5, respectively). The Ca/Mg-bearing precipitates on the pyrite surface can promote the reprecipitation of iron oxyhydroxides via acid–base complexation among Ca/Mg/Fe hydroxy groups herein (Fuchida *et al*, 2022; Xue *et al*, 2022). The interaction among iron hydroxy and Ca^{2+}/Mg^{2+} in alkaline conditions can be described as following Equations 1 and 2 (Cowan, Zachara and Resch, 1991; Liu and Zhang, 2000):

$$Ca^{2+} + Fe\text{-}OH + H_2O \rightarrow Fe\text{-}O\text{-}CaOH^+ + 2H^+ \quad (1)$$

$$Ca^{2+} + Fe\text{-}OH \rightarrow Fe\text{-}O\text{-}Ca^+ + 2H^+ \quad (2)$$

Moreover, KEX showed a ‘clean effect’ to iron oxyhydroxides by forming dissociative $Fe(OH)_2EX$ when the pH is over 9 (Smart *et al*, 2003). Combined with the EDTA extraction results, it could be speculated that the acid–base complexation among Ca/Mg hydroxy species and iron hydroxy species is also present in immobilising FHX on pyrite surface by Ca/Mg hydroxy species. The

oxidised pyrite surface first reacts with xanthate then forms dissociative FHX. The acid–base complexation among iron hydroxy groups in FHX and iron oxyhydroxides is faint, while the surface extracted-Fe merely performs in the form of iron oxyhydroxides that are positively related to pyrite depression. However, in Ca/Mg-bearing solution, the pyrite particles that immobilise more FHX via the acid–base complexation among Ca/Mg/Fe hydroxy species (which in turn cause further multilayer adsorption of di-xanthogen), are more hydrophobic and easier to float as concentrates.

TABLE 1

Concentration of surface extracted-Fe (mg/g pyrite) from pyrite concentrates and tailings after 360 min preconditioning in selected conditions.

Preconditioning environments		**Surface extracted Fe (mg/g pyrite)**
Ca/Mg-free solutions	pH 9, concentrates	0.078
	pH 9, tailings	0.139
	pH 10.5, concentrates	0.102
	pH 10.5, tailings	0.172
Ca-bearing solutions (2.5×10^{-2} mol/L Ca^{2+})	pH 9, concentrates	0.308
	pH 9, tailings	0.245
	pH 10.5, concentrates	1.304
	pH 10.5, tailings	1.212
Mg-bearing solutions (4.1×10^{-2} mol/L Mg^{2+})	pH 9, concentrates	1.278
	pH 9, tailings	0.715
	pH 10.5, concentrates	2.262
	pH 10.5, tailings	0.953

To determine the adsorption forms of xanthate-derived species on pyrite surface under different pre-conditioning status, the FTIR spectra of pyrite surfaces were all compiled in Figure 1. The peaks at 1380.2 cm^{-1} are contributed by metal-sulfur coordination, while the peak at 1135.6 cm^{-1} is due to the C-O-C symmetric stretching in xanthate anion as exhibited in Figure 1a (Leppinen, 1990; Zhang *et al*, 2013). Also, the peak at 1154.3 cm^{-1} (C-O-C symmetric stretching in di-xanthogen) was observed on the surface of PAX-loaded ferrihydrite, which indicated di-xanthogen was dominated on the surface of iron oxyhydroxides without the evident immobilisation of FHX. Similarly, the presence of di-xanthogen was also confirmed as the main adsorption form on oxidised pyrite surface after pre-conditioning in Ca/Mg-free solutions as reflected in Figure 1b. However, when pre-conditioning in Ca/Mg-bearing solutions, pyrite surface exhibited an evident migration of peaks from 1155.0 cm^{-1} to 1167.0 cm^{-1} (C-O-C symmetric stretching in metal xanthate structure), which were found on oxidised pyrite surface as reflected in Figure 1c and 1d (Zhang *et al*, 2013). With the prolonged pre-conditioning (360 min) of pyrite in Ca/Mg-bearing solutions, the more abundant accumulation of iron oxyhydroxides as well as the formation and immobilisation of FHX on the surface of pyrite, may change the dominance of xanthate derived species. Meanwhile, the corresponding elevation of peaks at 1380.2 cm^{-1} were also more evident on pyrite surface after pre-conditioning in Ca/Mg bearing solutions. The more remarkable accumulation of FHX thus further supported the EDTA-extraction results and the passivation effect of immobilised FHX on pyrite depression.

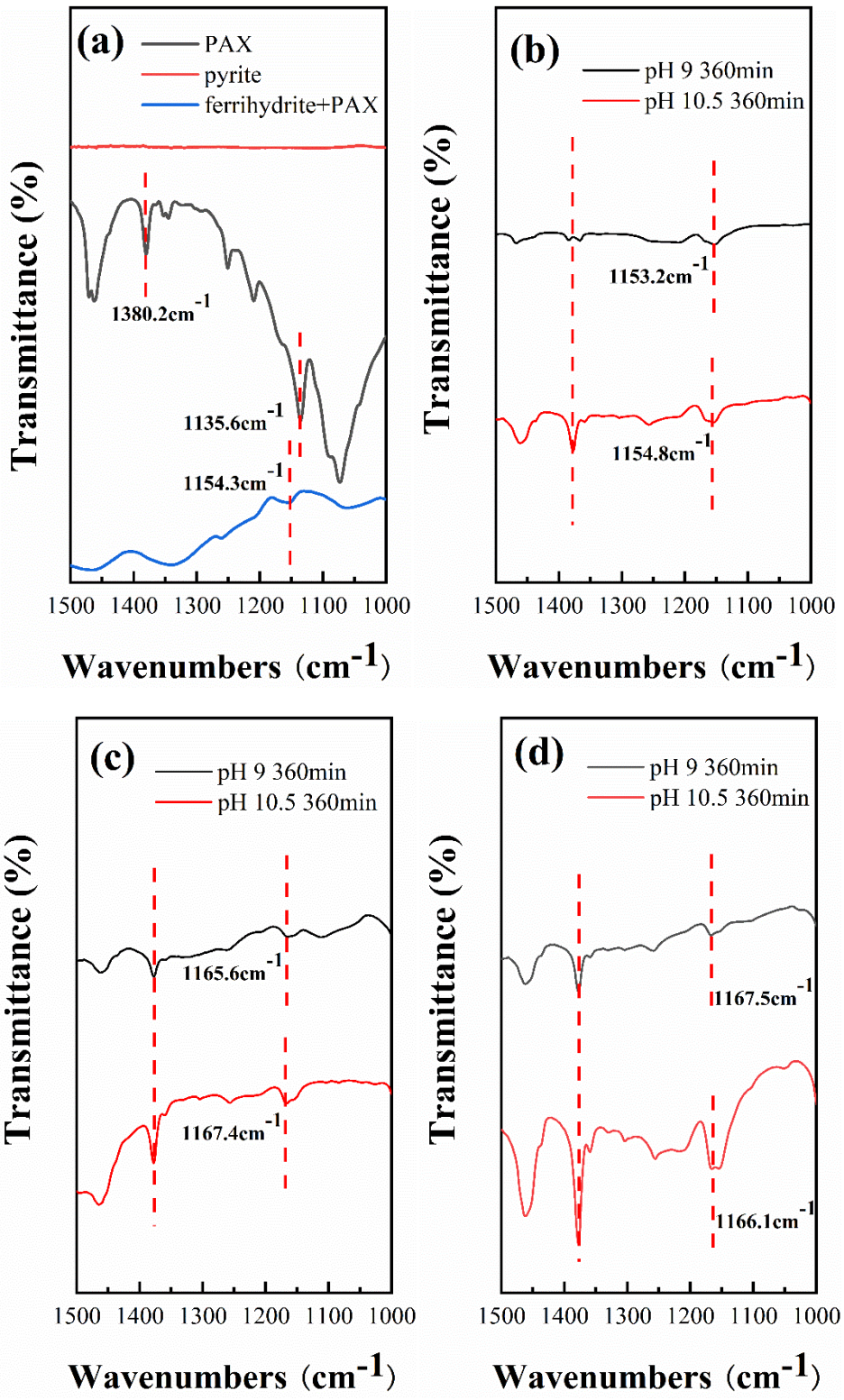

FIG 1 – FTIR spectra of samples surface: PAX, pristine pyrite and PAX-loaded ferrihydrite (a), pyrite after pre-conditioning in Ca/Mg free solution (b), pyrite after pre-conditioning in 0.0025 mol/m^3 $CaCl_2$ solution (c), pyrite after pre-conditioning in 0.041 mol/m^3 $MgCl_2$ solution (d).

To primarily and specifically investigate the distribution of xanthate derivates on pyrite surface considering its high correlation with Ca/Mg-bearing precipitates, a SEM-EDS analysis was performed by referring to the method developed by Smart *et al* (2003). Figure 2 reflected the localised pillar-structure Ca/Mg/Fe-bearing precipitates still maintained on the pyrite surface with the addition of PAX, while it is merely the partial dissolution of secondary precipitates (Wang, Forssberg and Bolin, 1989). From the semiquantitative determination of selected elements listed in Tables 2 and 3, upon the secondary minerals found on the oxidised pyrite surface, the Fe/S ratio is slightly

higher after xanthate treatment. Meanwhile, the increase of Fe and S accompanied with the decrease of O regarding their atomic ratio may be attributed to the partial dissolution of iron oxyhydroxides by xanthate, and the subsequent immobilisation of FHX upon the Ca/Mg/Fe-bearing precipitates. Consequently, the more abundant iron oxyhydroxides herein may deteriorate the surface hydrophilicity of oxidised pyrite in the presence of xanthate, while the more FHX on a pyrite particle leads to improved flotation recovery which is supported by the EDTA extraction results in Table 1.

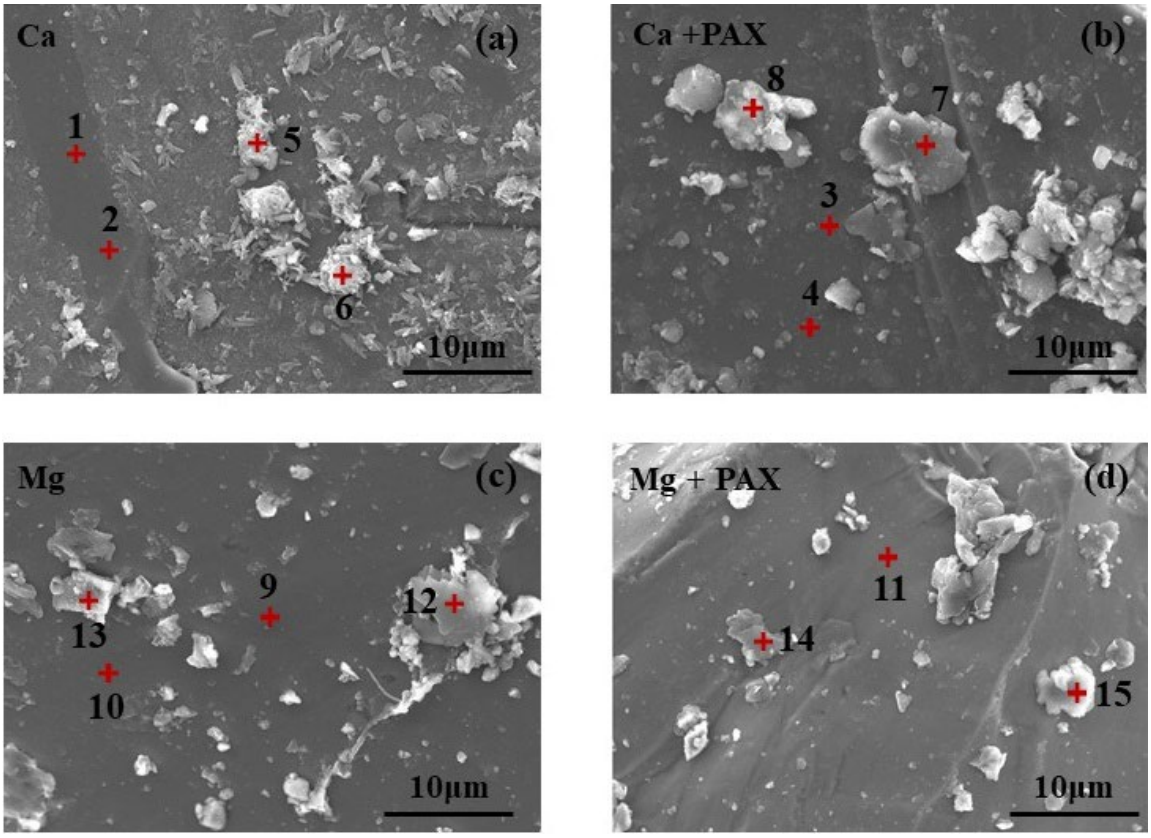

FIG 2 – SEM images of oxidised pyrite surface oxidised in 0.025 mol/m^3 Ca solution (a), 0.025 mol/m^3 Ca with 0.005 mol/m^3 PAX solution (b), 0.041 mol/m^3 Mg solution (c), and 0.041 mol/m^3 Mg with 0.025 mol/m^3 PAX solution (d). Conditions: 180 min Ca/Mg preconditioning + 10 min PAX conditioning, pH 10.5.

TABLE 2

Atomic ratio of Ca, Fe, S, O, C and Fe/S by EDS points analysis on the oxidised pyrite surface from SEM observation results in Figure 2a and 2b.

Point	Atomic ratio (%)					
	Ca	Fe	S	O	C	Fe/S
1	0.06	23.7	33.6	-	42.7	0.704
2	-	24.1	34.2	-	41.7	0.706
3	0.09	25.1	35.9	1.83	37.1	0.699
4	0.10	24.3	34.3	1.10	40.2	0.707
5	8.22	15.5	21.9	17.4	37.0	0.705
6	8.21	16.8	23.5	10.5	40.9	0.714
7	6.04	19.3	26.5	9.84	38.4	0.728
8	6.35	20.3	27.7	9.58	36.1	0.731

TABLE 3

Atomic ratio of Mg, Fe, S, O, C and Fe/S by EDS points analysis on the oxidised pyrite surface from SEM observation results in Figure 2c and 2d.

Point	Atomic ratio (%)					
	Mg	Fe	S	O	C	Fe/S
9	0.11	24.8	35.7	2.52	36.9	0.693
10	0.30	22.0	31.4	2.16	44.1	0.699
11	0.29	25.4	36.2	2.81	35.3	0.700
12	8.31	15.6	18.9	21.3	35.9	0.824
13	8.81	11.6	15.1	33.0	31.5	0.766
14	6.25	16.3	19.8	14.1	43.6	0.819
15	7.32	16.4	18.6	26.3	31.4	0.882

CONCLUSIONS

In this study, EDTA extraction results suggested the Ca/Mg-bearing precipitates may promote hydrophobic Fe-bearing species formation on pyrite particles. Further FTIR analysis verified accumulation of FHX on the oxidised pyrite samples that were preconditioned in Ca/Mg-bearing solutions. Combined with our previous research about acid–base complexation among Ca/Mg/Fe hydroxy groups, SEM-EDS analysis provided a perspective that the immobilisation of FHX also favoured Ca/Mg-bearing precipitates. The dissociative FHX was believed to form from the reaction among xanthate anions and iron oxyhydroxides. Consequently, the higher Fe/S ratio as well as the lower O element ratio upon Ca/Mg-bearing precipitates after xanthate treatment may be due to the partial substitution of iron oxyhydroxides for FHX. The pyrite particles with more FHX coverage facilitates the multilayer adsorption of di-xanthogen herein, and their depression effect by hydrophilic Ca/Mg/Fe-bearing precipitates could be passivated. This study preliminarily indicated the prolonged preconditioning of pyrite in Ca/Mg-bearing solutions not only promotes the hydrophilic substance accumulation upon its surface. However, the accumulation of hydrophobic FHX benefited from the immobilisation effect by Ca/Mg-bearing precipitates which also plays an important role in passivating the pyrite depression induced by hydrophilic Ca/Mg/Fe-bearing precipitates.

ACKNOWLEDGEMENTS

The authors are grateful to the Kagami Memorial Research Institute for Materials Science and Technology, Waseda University, for the assistance with FE-SEM-EDS and FTIR analysis. The authors also gratefully acknowledge the financial support of the China Scholarship Council.

REFERENCES

Bai, S, Yu, P, Li, C, Wen, S and Ding, Z, 2019. Depression of pyrite in a low-alkaline medium with added calcium hypochlorite: Experiment, visual MINTEQ models, XPS and ToF–SIMS studies, *Minerals Engineering,* 141:105853.

Chen, Y, Zhang, G, Shi, Q, Yang, S, Liu, D and Wang, M, 2020. Utilisation of trisodium phosphate to eliminate the adverse effect of Mg^{2+} on the flotation of pyrite, *Minerals Engineering,* 150:106281.

Cowan, C E, Zachara, J M and Resch, C T, 1991. Cadmium adsorption on iron oxides in the presence of alkaline-earth elements, *Environmental science and technology,* 25(3):437–446.

Fuchida, S, Xue, J, Ishida, S and Tokoro, C, 2022. Kinetic investigation of initial oxidative dissolution of pyrite in alkaline media (pH 9–12) and influence of Ca and Mg: a fundamental study for pyrite depression in froth flotation, *Journal of Sustainable Metallurgy*, 1–10.

Goh, S W, Buckley, A N, Gong, B, Woods, R, Lamb, R N, Fan, L J and Yang, Y W, 2008. Thiolate layers on metal sulfides characterised by XPS, ToF-SIMS and NEXAFS spectroscopy, *Minerals Engineering,* 21(12–14):1026–1037.

Goh, S W, Buckley, A N, Lamb, R N and Woods, R, 2006. The ability of static secondary ion mass spectrometry to discriminate submonolayer from multilayer adsorption of thiol collectors, *Minerals engineering,* 19(6–8):571–581.

Hirajima, T, Suyantara, G P W, Ichikawa, O, Elmahdy, A M, Miki, H and Sasaki, K, 2016. Effect of Mg^{2+} and Ca^{2+} as divalent seawater cations on the floatability of molybdenite and chalcopyrite, *Minerals Engineering,* 96:83–93.

Ikumapayi, F, Makitalo, M, Johansson, B and Rao, K H, 2012. Recycling of process water in sulphide flotation: Effect of calcium and sulphate ions on flotation of galena, *Minerals Engineering,* 39:77–88.

Jiang, C L, Wang, X H, Parekh, B K and Leonard, J W, 1998. The surface and solution chemistry of pyrite flotation with xanthate in the presence of iron ions, *Colloids and Surfaces A: Physicochemical and Engineering Aspects,* 136(1–2):51–62.

Leppinen, J O, 1990. FTIR and flotation investigation of the adsorption of ethyl xanthate on activated and non-activated sulfide minerals, *International Journal of Mineral Processing,* 30(3–4):245–263.

Liu, Q and Zhang, Y, 2000. Effect of calcium ions and citric acid on the flotation separation of chalcopyrite from galena using dextrin, *Minerals Engineering,* 13(13):1405–1416.

Mermillod-Blondin, R, Kongolo, M, De Donato, P, Benzaazoua, M, Barres, O, Bussière, B and Aubertin, M, 2005. Pyrite flotation with xanthate under alkaline conditions-application to environmental desulfurization. *In Centenary of flotation symposium,* pp 683–692 (The Australasian Institute of Mining and Metallurgy: Melbourne).

Mu, Y, Peng, Y and Lauten, R A, 2016. The depression of pyrite in selective flotation by different reagent systems–A Literature review, *Minerals Engineering,* 96:143–156.

Owusu, C, Fornasiero, D, Addai-Mensah, J and Zanin, M, 2015. Influence of pulp aeration on the flotation of chalcopyrite with xanthate in chalcopyrite/pyrite mixtures, *International Journal of Mineral Processing,* 134:50–57.

Paredes, Á, Acuña, S M and Toledo, P G, 2019. AFM Study of Pyrite Oxidation and Xanthate Adsorption in the Presence of Seawater Salts, *Metals,* 9(11):1177.

Smart, R S, Amarantidis, J, Skinner, W M, Prestidge, C A, La Vanier, L and Grano, S R, 2003. Surface analytical studies of oxidation and collector adsorption in sulfide mineral flotation, in *Solid-Liquid Interfaces: Macroscopic Phenomena—Microscopic Understanding* (ed: Wandelt, K and Thurgate, S), pp 3–62 (Springer-Verlag: Berlin).

Wang, X, Forssberg, K E and Bolin, N J, 1989. Thermodynamic calculations on iron-containing sulphide mineral flotation systems, I. The stability of iron-xanthates, *International journal of mineral processing,* 27(1–2):1–19.

Xue, J, Fuchida, S, Ishida, S and Tokoro, C, 2022. Insight on exogenous calcium/magnesium in weakening pyrite floatability with prolonged pre-oxidation: localized and concomitant secondary minerals and their depression characteristics, *Minerals*, 12(2), 115.

Zhang, S, Deng, Z, Xie, X and Tong, X, 2021. Study on the depression mechanism of calcium on the flotation of high-iron sphalerite under a high-alkalinity environment, *Minerals Engineering,* 160:106700.

Zhang, Y, Cao, Z, Cao, Y and Sun, C, 2013. FTIR studies of xanthate adsorption on chalcopyrite, pentlandite and pyrite surfaces, *Journal of Molecular Structure,* 1048:434–440.

Parametric study of flotation with acoustic sound

B Yang[1], C Y Ng[2] and L Wang[3]

1. PhD Candidate, The University of Queensland, Brisbane Qld 4072.
   Email: bingyu.yang@uq.edu.au
2. Post-doctoral Research Fellow, The University of Queensland, Brisbane Qld 4072.
   Email: ng.chunyong92@gmail.com
3. Senior Lecturer, The University of Queensland, Brisbane Qld 4072.
   Email: liguang.wang@uq.edu.au

ABSTRACT

Flotation process intensification is often achieved through changing chemical reagent scheme or flotation machine or both, which likely brings a hefty burden to the flotation plants in terms of capital or operating expenditure. A novel approach to flotation process intensification is the use of acoustic sound, which has been demonstrated to be effective in improving the flotation of various mineral systems with different type of flotation cells. This approach was based on the dynamic stabilisation effect of acoustic sound on the flotation froth. The present work aims to understand the influence of various experimental conditions on the effectiveness of the approach. First, the effects of sound frequency and amplitude were studied with column flotation of silica particles. Results showed that the flotation performance was improved only within a certain range of frequencies and above certain amplitude. The study was then extended to the mechanical flotation of quartz particles with various size ranges and at two solids concentrations. With sound, the recoveries of different size fractions within the range of 20–212 μm were all increased. In particular, the recovery of 150–212 μm particles was increased from 0 per cent to approximately 25 per cent, demonstrating the potential for extending the upper limit of particle size in flotation by using acoustic sound. Furthermore, mechanical flotation of chalcopyrite particles at various collector dosages (50–150 g/t) was carried out with and without sound. Results showed that the increment of the final flotation recovery was increased with sound at different collector dosages. Overall, acoustic sound has the potential to be used as an effective and versatile method for flotation process intensification.

INTRODUCTION

Froth flotation is a physicochemical process to separate valuable minerals from gangue particles, which has been successfully used on the industrial scale for more than a century. Over the years, numerous efforts have been made to optimise the flotation efficiency, but it remains an issue as to how to improve flotation efficiency in a cheap, simple and unified way. One apparent reason is that the separation process involves a wide range of factors such as particle properties, bubble size and fluid flow condition. Three aspects are considered to improve the flotation system, including equipment, chemistry, and operating conditions (Kawatra, 2011).

The flotation performance is determined by the complex bubble-particle interactions both in the pulp phase and froth phase (Neethling and Brito-Parada, 2018). The froth phase stability can influence the water drainage and overall recovery. Constantly coalescing and bursting of the bubbles will affect the froth recovery due to the bubble-particle detachment (Ata, 2009). Increasing froth dosage to enhance the froth stability has been widely used; however, overly stable froth discharged from the flotation cell could be a problem for downstream processing (Laskowski *et al*, 2007; Stevenson and Lambert, 2012). Therefore, using a non-chemical method to locally stabilise froth within the flotation cell is desirable.

Recent studies show that applying certain frequency and amplitude sound to a flotation system could improve the flotation rate which was linked to the improvement of froth stability (Ng, Park and Wang, 2020, 2021). These studies suggest that using acoustic sound could improve flotation performance without having over-frothing issues, which provide a potential way to improve flotation efficiency by retrofitting existing flotation machines.

Relatively few studies have been conducted to examine the factors affecting flotation with acoustic sound in a comprehensive manner. The present paper discusses the effects of various operating

variables such as sound frequency and amplitude, collector dosage, and particle size and type on mineral flotation in column flotation or mechanical flotation.

EXPERIMENTAL

Materials

Quartz particles (silica >99.6 per cent pure) with 80 per cent passing sizes of 43.4 μm and 80 μm were purchased from Sibelco Australia. The latter quartz particles were sieved into six different size fractions (-20 μm, 20–38 μm, 38–75 μm, 75–106 μm, 106–150 μm, and 150–212 μm). Chalcopyrite (98 per cent pure) was obtained from GEO discoveries. For quartz flotation, 3-(2-Ethylhexyloxy) propylamine (EHPA, >98.0 per cent pure, TCI Chemicals, Japan) was used as flotation frother and collector, which was neutralised by acetic acid (>99.0 per cent pure, Sigma-Aldrich, USA) at a molar ratio of 1:4.5. For chalcopyrite flotation, sodium ethyl-xanthate (Quantum Chemicals, Australia) and MIBC (98 per cent purity, Sigma-Aldrich, USA) were used as the collector and frother, respectively. Sodium hydroxide and hydrochloride acid solutions (1 per cent) were prepared as the pH modifier. Brisbane tap water was used for all experiments.

Experimental set-up

A Column with an inner diameter of 5 cm and height of 150 cm was used for the quartz flotation. A loudspeaker (Fx-10, Visaton) that was positioned 12 cm higher than the column cell lip, and an amplifier (PA935N, InterM) were used to adjust the sound frequency and amplitude. To minimise the sound dissipation, a sound concentrating tube was connected to the speaker.

A 1.5 L bottom-driven mechanical flotation cell with 11 cm of length, 11 cm of width, and 14.5 cm of height was used for flotation of the sieved quartz and chalcopyrite, respectively. An audio system comprising an underwater loudspeaker (13A22, Billionsound Technology), an amplifier (SA-155, REALISTIC), and a computer was used. The underwater speaker was placed 0.5 cm above the rotor.

All the flotation tests were done in batch mode.

Flotation procedures

Column flotation with quartz

A quartz sample with an 80 per cent passing size of 43.4 μm was used in column flotation. Feed slurry with 5 per cent wt solids content was conditioned with 500 g/t EHPA in a feed sump for 2 min, and the agitation speed of the sump was 450 rev/min. Then the air supply was turned on giving a superficial velocity of 1.2 cm/s, and the feed slurry was fed into the column with a volumetric rate of 1.2 L/min. Both concentrate and tailing streams were recycled back to the feed sump for a certain period of time (at least twice the pulp residence time) until the froth depth stabilised at 15 cm. The pulp residence time was 5 min. Followed by turning on the sound at tested frequency and amplitude for 2 min. Then five concentrates were collected (without being recycled back to the feed sump) for 1, 2, 3.5, 5 and 7 min, respectively, and between concentrate collections the pulp-froth was manually raised by lifting a level control bucket. The blank tests were conducted without turning on the sound.

Mechanical cell flotation with sieved quartz

A quartz sample with 80 per cent passing sizes of 80 μm was sieved into six subsamples with different size ranges. Each of these subsample was fed to the mechanical cell to understand the effect of particle size on flotation performance with and without sound. The flotation feed slurry was 1.2 L in volume with a solids content of 5 per cent wt or 20 wt per cent fully mixed at an agitation speed of 1200 rev/min for 1 min. After that, the slurry was conditioned with EHPA (at 25 g/t, 50 g/t, 200 g/t, 400 g/t, or 600 g/t) for 3 min at 750 rev/min, followed by placing the underwater speaker into the tank, switching on the air at a superficial velocity of 0.61 $cm \cdot s^{-1}$, and then turning on the sound at 375 Hz and 77 dB. Five concentrations were collected at 10 s, 30 s, 60 s, 60 s and 180 s by scarping the froth every 15 s, except for the first concentration which was 10 s. Make-up water was added into the cell constantly to maintain the pulp level.

Mechanical cell flotation with chalcopyrite

The crushed chalcopyrite sample (65 g) was wet grinded to achieve an 80 per cent passing size of 45 µm. Mill discharge was introduced to the mechanical flotation cell, and water was added to make a 1.3 L slurry with a solids content of 5 per cent wt. Sodium ethyl xanthate was dropped into the flotation cell and the slurry was conditioned for 3 min with a superficial velocity of 0.61 cm/s before adding 20 ppm MIBC to condition for another 1 min. Total collector used in the flotation was 50 g/t, 75 g/t, 100 g/t, 125 g/t or 150 g/t. Flotation pH was maintained at 10 by adding pH modifiers (1 per cent NaOH or 1 per cent HCl solution). Concentrates were collected for 1 min, 2 min, 3 min, 3 min and 6 min, respectively, by scraping the froth every 15 s. Make-up water was used to maintain the pulp level.

RESULTS AND DISCUSSION

Effect of acoustic sound on column flotation

By fitting the experimental data of column flotation to the classical first-order model, flotation rate constant K and maximum recovery R_{max} were obtained. The results showed that at the specific sound frequency and amplitude, flotation performance could be improved.

Figure 1a shows that when keeping sound amplitude at 125 dB, higher K and R_{max} values were observed at 350 and 400 Hz compared with the blank tests. For example, the rate constant increased from 0.20/min in the blank test to 0.33/min in the test with 350 Hz and 125 dB sound, and the increases were statistically significant based on the one-tailed t-test of two-sample assuming equal variances. Figure 1b shows that with sound at 110, 120, and 125 dB while maintaining the sound frequency at 350 Hz, the K and R_{max} values were higher than their counterparts without sound.

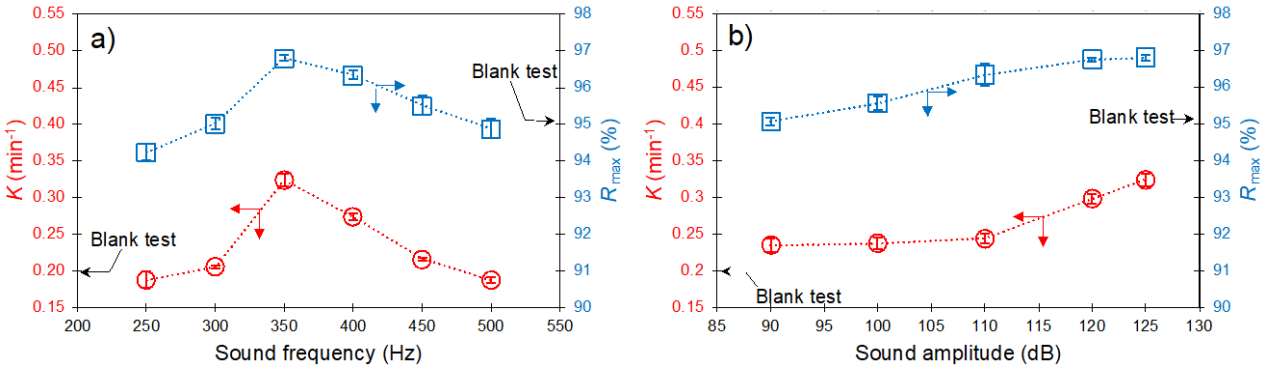

FIG 1 – Flotation rate constant (K) and maximum recovery (R_{max}) of quartz particles as a function of: (a) sound frequency and (b) sound amplitude. Collector (EHPA) dosage and superficial velocity were 500 g/t and 1.2 cm/s, respectively. The black arrows represent the rate constant and maximum recovery obtained from the blank test (without sound). The error bars represent one standard error obtained from at least three independent experimental runs.

Effect of acoustic sound on mechanical cell

Figure 2 shows the final flotation recovery as a function of particle size without and with acoustic sound at solids contents of 5 wt per cent and 20 wt per cent in the mechanical cell. The results indicate that for each feed solids content tested, at particle size coarser than 20 µm, final flotation recoveries were improved by applying acoustic sound. For fine particles (20–38 µm), intermediate particles (38–75 µm, 75–106 µm, 106–150 µm) and relatively coarse particles (150–212 µm particles), the flotation recovery increased from 89.0 per cent to 96.6 per cent, 89.0 per cent to 96.6 per cent, 87.7 per cent to 93.9 per cent, 83.0 per cent to 94.0 per cent and 0 to 25.1 per cent, respectively. These improvements were statistically significant as confirmed by the one-tailed t-test of two-sample equal variance, with each p-value being less than 0.05. However, for both solids content tested, no statistical difference was observed for the ultra-fine particles (<20 µm).

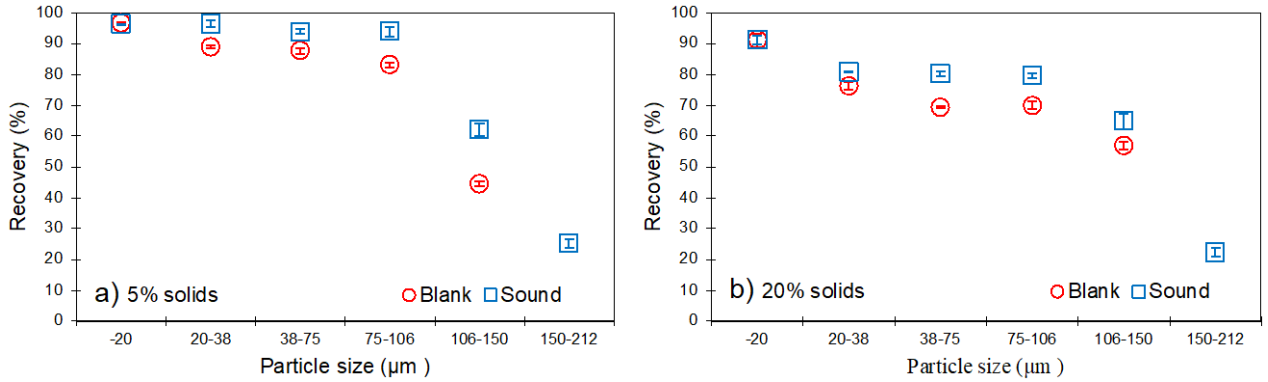

FIG 2 – Comparison of the flotation performance of quartz particle between the tests with and without acoustic sound at two feed solids contents: (a) 5 per cent and (b) 20 per cent. Collector (EHPA) dosage and superficial velocity were 400 g/t and 0.61 cm/s, respectively. The error bars represent one standard error obtained from at least two independent experimental runs. Adapted from Yang *et al* (2022).

Figure 3a illustrates the results for 38–75 μm samples at a feed solids content of 20 per cent. As shown, at a given reagent dosage ranging from 25 g/t to 400 g/t, the final flotation recovery with sound (375 Hz and 77 dB) was higher than that obtained without sound. Specifically, at a low EHPA dosage (25 g/t), the recovery was 41.0 per cent without sound, while the recovery with sound was 59.5 per cent. In contrast, at 600 g/t there was no statistically significant difference in the final recovery between with sound and without sound.

Figure 3b shows the relative recovery increments resulting from turning on the sound at various EHPA dosages. The relative increase decreased significantly from low to high dosages of EHPA. The highest increment was obtained at 25 g/t which was 45.0 per cent, followed by 14.0 per cent at 50 g/t. With further increasing EHPA dosage to 200 g/t and 400 g/t, the recovery increments were similar, being 6.8 per cent and 7.8 per cent, respectively. At 600 g/t, there was no recovery increment.

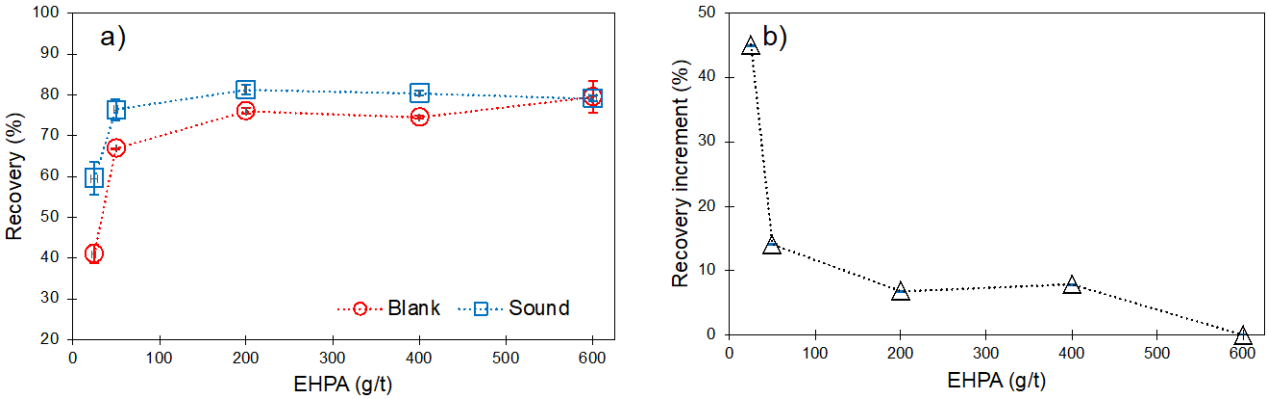

FIG 3 – (a) Comparison of the flotation performance of quartz particles at different collector (EHPA) dosages with and without acoustic sound and (b) flotation recovery increment. Particle size was 38–75 μm, feed solids content was 20 per cent, and superficial air velocity was 0.61 cm/s. The error bars represent one standard error obtained from two independent experimental runs. Adapted from Yang *et al* (2022).

Figure 4a shows the final flotation recovery of chalcopyrite as a function of collector dosage with and without sound. The chalcopyrite recovery increased with sodium ethyl xanthate dosage under both conditions. In the absence of acoustic sound (375 Hz and 77 dB), at 50 g/t sodium ethyl xanthate the final recovery was 18.1 per cent. However, when applying the sound to the flotation system the final recovery reached 27.4 per cent at the same collector dosage, suggesting that acoustic sound could help reduce the reagent consumption required to obtain a target recovery. At the other four tested dosages, the final flotation recovery increased by at least 6 per cent in the presence of acoustic sound. Figure 4b shows the final recovery increments resulting from applying the acoustic

sound. Lower recovery increments were observed at higher collector dosage, similar to what is shown in Figure 3b.

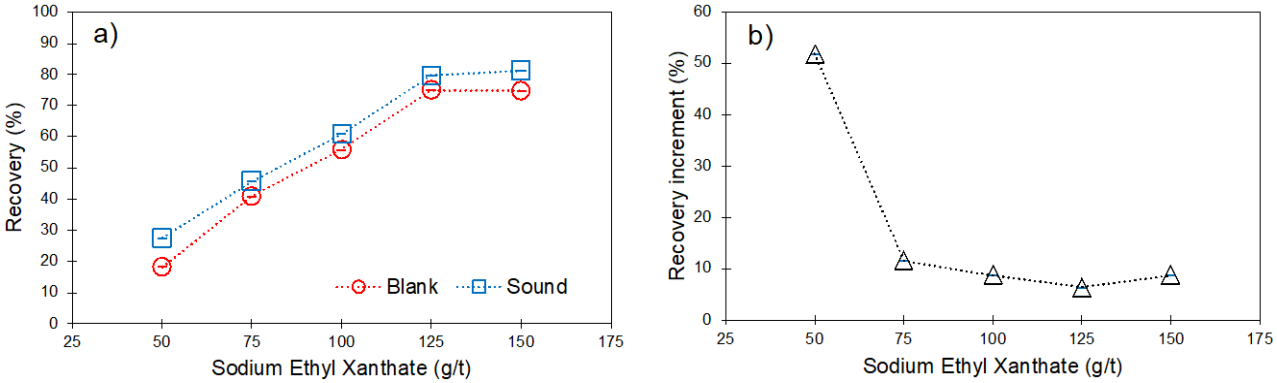

FIG 4 – (a) Final recoveries of chalcopyrite particles at different sodium ethyl xanthate dosages, with and without acoustic sound and (b) flotation recovery increment. The superficial air velocity was 0.61 cm/s, and the feed solids content was 5 per cent.

Possible mechanisms for the flotation performance improvement

Froth stability can be assessed by measuring the water recovery (Tao *et al*, 2000; Wiese *et al*, 2011). In the column flotation for quartz, the highest water recovery was measured at 350 Hz and 125 dB, where the peak flotation rate constant and maximum final recovery was also obtained. This finding suggested that the improvement of the flotation performance could be attributed to the increased froth stability induced by acoustic sound.

When turning on the sound at 350 Hz and 125 dB, smaller and more uniformed bubbles were observed in the column flotation, and the pulp-froth interface was lifted by approximately 1.0 cm. These observations indicated that applying acoustic sound in a flotation system could increase gas holdup. Fan and Cui (2005) also reported that a slower bubble rising velocity was detected in the field with sound than in the field without sound. Another study conducted by Stoev *et al* (1992) also proposed that bubbles pre-treated by sound would rise more slowly, which could improve the pulp aeration.

A relatively low flotation recovery of coarse particles can be attributed to the unstable froth phase, which makes coarse particles constantly drop back to the pulp phase (Ata and Jameson, 2013; Tabosa, Runge and Duffy, 2013). Inducing the acoustic sound to improve froth stability could help with overcoming this limitation. Figure 2 shows that flotation recoveries with a broad range of particle size increased with applying the sound, at either feed solids content tested. The increase in the recovery was remarkable for coarse particles (150–212 μm), so use of low-frequency sound can be a potential approach for increasing the grind size and thus decreasing upstream comminution cost, which often constitutes the major operating cost for a flotation plant in operation.

Both Figures 3 and 4 demonstrate that when keeping the same operation conditions, using acoustic sound could reach the same flotation recovery when a smaller reagent dosage was applied. For instance, the final flotation recovery obtained at 50 g/t EHPA with sound was comparable with the result collected at 200 g/t EHPA without sound (see Figure 3a). Furthermore, the experiments for quartz and chalcopyrite indicate that sound has the potential to improve flotation recovery of minerals of different type.

In the present work (at laboratory scale), the input power of the underwater speaker was merely 10 W. If this technology is scalable and the specific power input remains low in industrial flotation operations, use of underwater loudspeakers will be a simple and cheap approach for improving the efficiency of existing flotation machines.

CONCLUSIONS

Flotation tests of quartz and chalcopyrite particles were conducted either in the column or mechanical cell at a laboratory scale and in batch mode. Several flotation parameters were considered in this study, including sound frequency and amplitude, mineral type, particle size, feed

solids content, and collector dosage. The results showed that at certain frequencies and amplitudes, acoustic sound could improve the flotation performance for both quartz and chalcopyrite particles. The improvement of flotation performance by sound was seen over a broad range of particle sizes from 20 to 212 μm, irrespective of the solids content tested. In particular, the recovery of 150–212 μm particles was increased from 0 per cent to approximately 25 per cent. The study provides a potential approach for extending the upper size limit in the flotation process. Overall, low-frequency sound has the potential to be used as a versatile method for improving flotation efficiency.

REFERENCES

Ata, S and Jameson, G J, 2013. Recovery of coarse particles in the froth phase-A case study. *Minerals Engineering*. Elsevier, 45, pp. 121–127. doi: 10.1016/j.mineng.2013.02.006.

Ata, S, 2009. The detachment of particles from coalescing bubble pairs. *Journal of colloid and interface science*, 338(2), pp. 558–565.

Fan, J M and Cui, Z, 2005. Effect of acoustic standing wave in a bubble column. Industrial and engineering chemistry research. *American Chemical Society*, 44(17), pp. 7010–7018. doi: 10.1021/ie050125i.

Kawatra, S K, 2011. Fundamental Principles of Froth Flotation. In: P Darling (ed.), *SME Mining Engineering Handbook*, vol. 2, 3rd edition, Society for Mining Metallurgy and Exploration, Littleton, CO, pp. 1517–1531.

Laskowski, J S, Luttrell, G H, Arnold, B J, 2007. Part 3: Flotation chemistry, coal flotation. In: Fuerstenau, M C, Jameson, G J, Yoon, R-H (Eds), *Froth Flotation: A Century of Innovation* SME, pp. 611–634.

Neethling, S J and Brito-Parada, P R, 2018. Predicting flotation behaviour – The interaction between froth stability and performance, *Minerals Engineering*, 120(December 2017), pp. 60–65. doi: 10.1016/j.mineng.2018.02.002.

Ng, C Y, Park, H and Wang, L, 2020. The potential of acoustic sound to improve flotation kinetics. *Minerals Engineering*. Elsevier, 154(April), p. 106413. doi: 10.1016/j.mineng.2020.106413.

Ng, C Y, Park, H and Wang, L, 2021. Improvement of coal flotation by exposure of the froth to acoustic sound. *Minerals Engineering*. Elsevier, 168(December 2020), p. 106920. doi: 10.1016/j.mineng.2021.106920.

Stevenson, P, Lambert, N W A, 2012. Chapter 11: Froth phase phenomena in flotation. In: Stevenson, P. (Ed.), *Foam Engineering: Fundamentals and Applications*. John Wiley and Sons, pp. 242–244.

Stoev, St, Kuzev, L, Metodiev, M and Djendova, Sht, 1992. Vibroacoustic Improvements of Froth Flotation. In Mavros, P and Matis, K A (eds) *Innovations in Flotation Technology*. Dordrecht: Springer Netherlands, pp. 383–407. doi: 10.1007/978–94–011–2658–8_19.

Tabosa, E, Runge, K and Duffy, K, 2013. Strategies for increasing coarse particle flotation in conventional flotation cells. *Sixth International Flotation Conference (Flotation '13)*, (August 2015), pp. 18–21.

Tao, D, Luttrell, G, Yoon, R-H, 2000. A parametric study of froth stability and its effect on column flotation of fine particles. *Int. J Miner. Process*. 59 (1), 25–43.

Wiese, J, Harris, P, Bradshaw, D, 2011. The effect of the reagent suite on froth stability in laboratory scale batch flotation tests. *Miner. Eng*. 24 (9), 995–1003.

Yang, B, Ng, C Y and Wang, L, 2022. Mechanical flotation of mineral particles with an underwater speaker. *Mineral Processing and Extractive Metallurgy Review*. doi: 10.1080/08827508.2022.2058938

Characterisation of mineral flotation along industrial circuits using mineralogical analysis

J Yianatos[1], P Vallejos[2], M Rodriguez[3] and J Cortinez[4]

1. Professor, Universidad Técnica Federico Santa María, Valparaiso, Chile.
   Email: juan.yianatos@usm.cl
2. Researcher, Universidad Técnica Federico Santa María, Valparaiso, Chile.
   Email: paulina.vallejos@usm.cl:
3. Metallurgy and Process Control Manager, Doña Inés de Collahuasi Mining Company, Chile.
   Email: marodrigm@collahuasi.cl:
4. Senior Metallurgist, Doña Inés de Collahuasi Mining Company, Chile.
   Email: jfcortinez@collahuasi.cl.

ABSTRACT

Nowadays, one of the main problems in current flotation plants and new projects is the significant decrease in feed grades and changes in the mineral composition, which has an important effect on the mineral liberation and associations. Additionally, flotation plants usually operate with feed throughput higher than the original design, which has a significant impact on the feed particle size. All these conditions affect metallurgical performance, and must be evaluated and addressed, by improving control strategies for banks optimisation. For this purpose, the flotation of valuable minerals along the circuits requires better understanding, considering the compromise between performance and selectivity in flotation circuits.

This paper presents a characterisation of the different minerals recovered along industrial flotation circuits. Plant sampling campaigns, performed in a copper industrial concentrator in Chile, provided the data for the study. Two rougher flotation banks consisting of cells of 130 m^3 and 300 m^3 were analysed. All the samples from the industrial surveys were analysed by screening and mineralogy, and the mineral recovery along the circuits was evaluated per particle size class, liberation class, type of associations, and others. Additionally, operating data on froth depth profiles complemented the evaluation of the mineral composition of concentrate streams, along the circuit.

The results allowed for identifying and quantifying the main factors that affect the copper recovery and concentrate grade along the flotation banks. It was found that minerals with liberation lower than 50 per cent have a significant impact on the recovery. On the other hand, the decrease in the Cu grade in concentrates along the flotation circuits is mainly due to the relative increase of middling minerals (less liberated), non-valuable floatable minerals, such as free pyrite, and gangue entrainment. The characterisation of the gangue entrainment flow rate along the flotation banks showed a strong relationship with froth depth, which becomes more critical towards the last cells of the banks.

INTRODUCTION

At present, the industrial flotation processes face several challenges such as treatment of minerals that are more complex, lower feed grades and larger particle sizes that means lower liberation. This finally decreases the recovery of fine and coarser particles, also decreasing the concentrate grades.

Another critical issue is the water constraints because the use of continental water has been gradually limited or eliminated. The water constraint relates to the increase in the global water demand and environmental changes due to the global warming. For this reason, the alternative use of sea water is now a common practice in several plants all over the world, as either sea water or desalted water. The plant metallurgical performance depends on the water quality (ionic strength) and will vary for each type of minerals and conditioning.

The impact of the ionic strength on minerals flotation is well known, and it shows that industrial flotation requires a certain ionic strength for optimal performance. The industrial flotation operations at large scale typically operates with recycled water, which combined with fresh water, or make up water, to feed the flotation process. Recycle water normally contains a certain number of ions, which depends on the feed fresh water and the type of ore that can be partially dissolved during the flotation

process, and finally reaches an equilibrium for each operation. Le *et al* (2020) illustrate this point studying the water quality changes by effect of dissolved solids and water recirculation.

Li *et al* (2018) studied the effect of some ions in batch flotation and showed that for copper sulfide flotation, chlorides such as NaCl, KCl, $CaCl_2$, have a positive influence on the adsorption of SBX on the chalcopyrite surface, increasing the mineral recovery, while $MgCl_2$ and $CaCl_2$ decreased the recovery. Le *et al* (2020) reported that the presence of Na^+, Cl^- and Ca^{+2} shows a tendency to inhibit the bubble coalescence in addition to the frother effect.

In terms of reagents addition, Hassanzadeh (2016) showed that a proper distribution of reagents along the bank increases the final copper grade and recovery, due to the excess of reagent consumption in fine particles, which limited the surface coverage and recovery of coarse particles. This practice applies in some industrial concentrator plants.

Other studies based on the 'touch of froth' methodology have shown that the grade of the minerals collected by true flotation, or bubble-particle aggregate formation, along industrial flotation banks, does not change significantly with the operating conditions that affects the physical separation, such as the gas rate and froth depth (Sadr-Kazemi and Cilliers, 2000; Hadler, 2006). Thus, the evolution of the type and grade of collected minerals along a flotation bank will depend mainly on the feed mineralogy and reagents conditioning, while manipulated variables will affect the mass pull and entrainment, affecting the final concentrate grade and recovery.

Regarding the flotation circuits optimisation, Jowett and Sutherland (1985) stated that the potential usefulness of optimising criteria was prevented because of the lack of case data which could be used for a numerical simulation and optimisation of a complex circuit. By that time, these authors claim that a detailed evaluation of the mineralogical matrix of streams within the circuit would be required, but the available techniques were either too laborious or technically too difficult to obtain the necessary data. By that time, some researchers, eg Miller *et al* (1982) reported instruments under development based on QEM*SEM image analysis to solve the data acquisition problem. Now, the image analysis has reached a good reliable level and different commercial instruments are available for analysis, which has allowed for having periodic mineralogical information of the main streams in many plants all over the world.

To improve the flotation metallurgical performance in plant circuits, more robust data and enhanced control strategies are required. Chemical and mineralogical data are fundamental for improving the knowledge of the minerals collected and its transport into the concentrate, along the flotation banks, which will allow the selection of the optimal profiles of manipulated variables and reagent dosage to improve the recovery of fine and coarser particles.

In this way, planning the future flotation operation requires a careful analysis of the future minerals, considering their physical and mineralogical characteristics, as well as the type of water makeup that will be available. On the other hand, the actual flotation process characterisation in terms of kinetics and mineralogical analysis, including size and liberation classes, will contribute to the process knowledge to improve the industrial flotation models and to predict the future operations under different minerals associations and water quality.

In this work, overall sampling campaigns were performed at Compañía Minera Doña Inés de Collahuasi, Chile, to advance in the process knowledge in terms of mineralogy and operating conditions, to face the future challenges of the plant that includes minerals that are more complex, increase in plant capacity and changes in water quality.

METHODOLOGY

Sampling surveys were carried out in two rougher flotation banks at an industrial concentrator in Chile. The surveys included chemical and mineralogical analysis in all streams (feed, concentrates and tails), to characterise the mineral behaviour cell-to-cell along the banks. Thus, recovery per mineral species, particle size and liberation class, as well as concentrates composition and gangue entrainment characterisation were analysed along the banks.

Sampling surveys at an industrial concentrator

Three overall sampling campaigns were carried out at Compañía Minera Doña Inés de Collahuasi (CMDIC) concentrator, located on the high plateau of the Atacama Desert, Chile, at 4.400 masl. This concentrator consists of a rougher stage with nine flotation rows in parallel: 5 rows with 9 cells of 130 m^3 each and 4 rows with 6 cells of 300 m^3 each. The rougher concentrate is processed in a regrinding stage, whose product is sent to a first cleaner stage, consisting of five parallel rows: 3 rows with 3 cells of 160 m^3 and 2 rows with 4 and 3 cells of 130 m^3 each. The first cleaner concentrate is sent to a second cleaner composed of 10 flotation columns. The first cleaner tail is sent to a scavenger stage, which has five parallel rows: 3 rows with 6 cells of 160 m^3 each and 2 rows with 4 and 5 cells of 130 m^3 each. The scavenger concentrate is sent back to the regrinding stage, while the scavenger tail is combined with the rougher tail and form the final tail. The second cleaner tail is sent to another stage, consisting of two Jameson cells. The Jameson cells tail is sent back to the first cleaner. The Jameson cells concentrate, and the second cleaner concentrate are combined and correspond to the final Cu-Mo concentrate.

The study reported in this work was focused on the rougher stage of CMDIC concentrator. Two flotation banks were analysed: a rougher bank with 9 cells of 130 m^3 (Figure 1) and another with 6 cells of 300 m^3 (Figure 2). It must be noticed that each flotation bank is fed from different grinding lines, therefore, the two feed streams do not have the same characteristics.

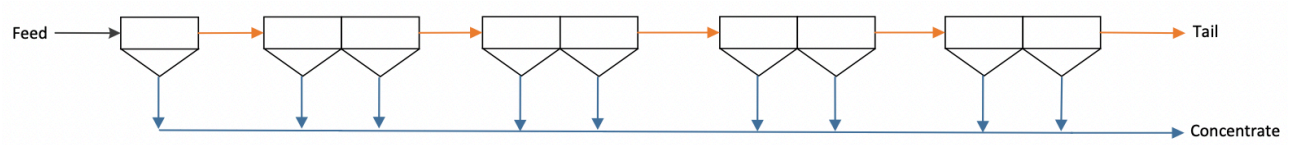

FIG 1 – Flotation bank A (9 cells of 130 m^3) at CMDIC concentrator.

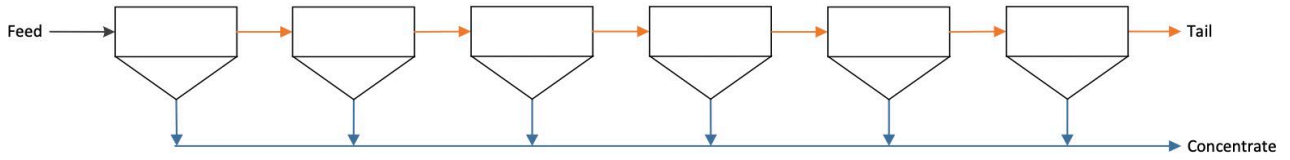

FIG 2 – Flotation bank B (6 cells of 300 m^3) at CMDIC concentrator.

The surveys included the sampling of feed, concentrates and tails streams of each cell in both flotation banks. The feed samples were collected from automatic cutters, while the concentrate and tails samples were manually cut on the overflow lip and at the bottom of each cell (near the tail outlet), respectively.

Feed characterisation from chemical and mineralogical analysis

All samples collected from the sampling surveys were submitted to chemical analysis and some of them to mineralogical analysis. Tables 1–4 show the characterisation of the feed samples from banks A and B.

Table 1 shows the feed characteristics for banks A (nine 130 m^3 cells) and B (six 300 m^3 cells) observed during the sampling surveys. This data represents the average of each variable during the sampling time. It can be observed that bank A has lower tonnage, lower Cu and Mo grades and finer particle size (P_{80}). The solid content is similar in both feed streams, about 30 per cent.

Table 2 shows the mass distribution of minerals in feed streams of banks A and B. Bank B showed a higher content of Cu sulfides and pyrite, which is consistent with the higher Cu and Fe grades showed in Table 1, respectively. Additionally, bank B has also a higher content of clays.

The total Cu sulfides presented in Table 2 are composed of different minerals, which are detailed in Table 3. Both feed streams have a similar Cu sulfide distribution and are mainly composed of chalcopyrite.

Table 4 shows the mass distribution of Cu sulfides per liberation class for bank A and B. The total mass of Cu sulfides was divided into five liberation classes: free (>95 per cent lib.), liberated

(>80 per cent lib.), middling (>50 per cent lib.), sub-middling (>20 per cent lib.) and locked (<20 per cent lib.). Data shows that the Cu sulfides mass is contained mainly in the free liberation class for both streams. In general, a similar liberation distribution in feed was observed for both banks.

TABLE 1

Feed characteristics for banks A and B.

	Bank A	**Bank B**
Tonnage (t/h)	518	1251
Solid content (%)	30.5	29.8
Particle size, P_{80} (µm)	121	189
Cu grade (%)	1.21	1.99
Mo grade (ppm)	262	338
Fe grade (%)	3.7	4.8

TABLE 2

Minerals distribution in feed of banks A and B.

	Bank A	**Bank B**
Cu Sulfides (%)	3.3	5.0
Pyrite (%)	5.3	6.2
Molybdenite (ppm)	438	565
Clays (%)	5.6	6.1

TABLE 3

Cu sulfides distribution in feed of banks A and B.

	Bank A	**Bank B**
Chalcopyrite	92.5	91.2
Bornite	5.7	5.3
Chalcocite	1.5	3.5
Other Sulfides	0.30	0.04

TABLE 4

Cu sulfides distribution per liberation class in feed of banks A and B.

	Bank A	**Bank B**
Free (>95%)	75.6	74.3
Liberated (>80%)	8.6	10.6
Middling (>50%)	4.7	5.6
Sub-Middling (>20%)	4.5	3.7
Locked (<20%)	6.7	5.8

RESULTS AND DISCUSSION

Flotation kinetic results

Figure 3 shows the recovery profiles of Cu, Mo, and Fe along the bank A (Figure 3a) and bank B (Figure 3b). The results show final Cu recoveries of 88.7 per cent and 94.4 per cent in bank A and

B, with concentrate grades of 16.4 per cent and 17.7 per cent, respectively. Mo recovery reached 64.1 per cent in bank A and 81.5 per cent in bank B, with concentrate grades of 0.26 per cent in both banks. Finally, Fe recoveries of 60.0 per cent and 65.0 per cent were observed in bank A and B, with concentrate grades of 34.1 per cent and 29.1 per cent, respectively. The mass recovery was 6.6 per cent in bank A and 10.7 in bank B.

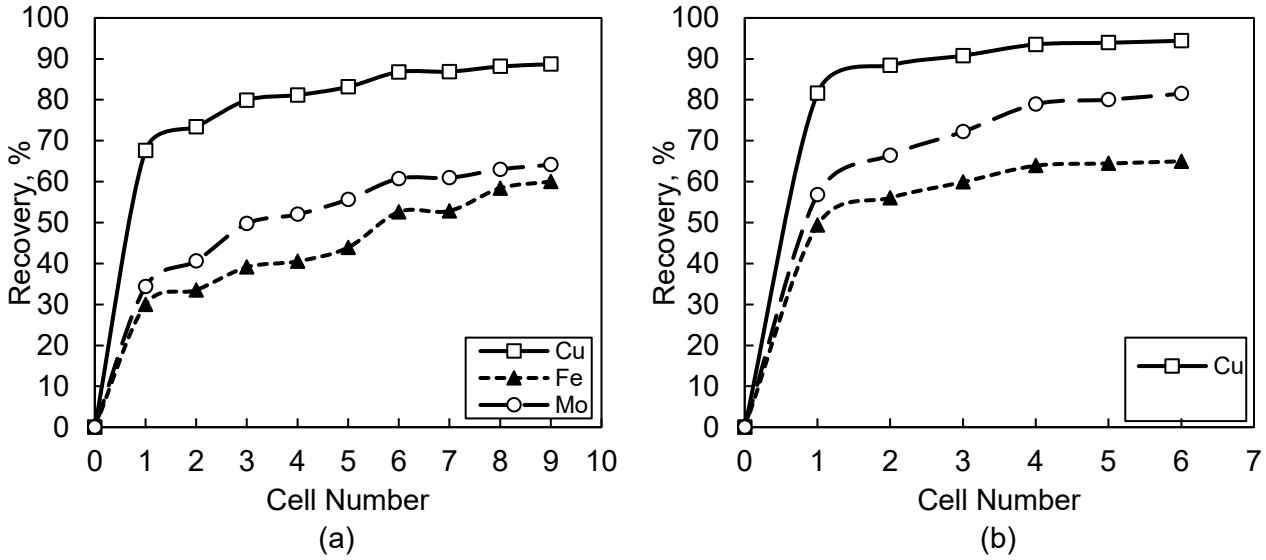

FIG 3 – Recovery profiles for Cu, Mo, and Fe: (a) Bank A and (b) Bank B.

The mineralogical analysis allowed for evaluating the recovery profiles of the main mineral presented in banks A and B, as shown in Figure 4a and 4b, respectively. It was found that bank B showed a higher final recovery of Cu sulfides and molybdenite, compared to bank A, which is partially due to the higher feed grades showed in Table 2. These differences can also be attributed to the different operating conditions and cell design of the banks. Additionally, clays and insoluble recoveries were also higher in bank B. On the other hand, bank A showed a higher pyrite recovery, which increases along the bank, although the pyrite grade in feed is lower than in bank B.

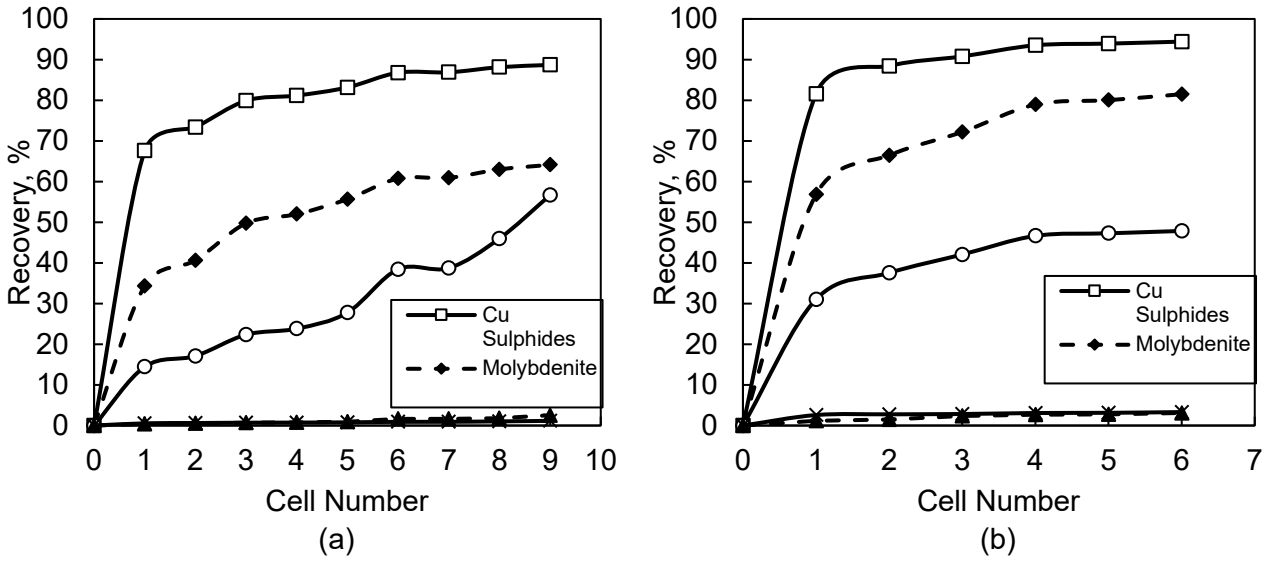

FIG 4 – Recovery profiles for the main minerals: (a) Bank A and (b) Bank B.

Characterisation of minerals flotation along the rougher banks

Characterisation of Cu recovery per particle size and liberation

Figure 5 shows Cu recovery profiles per particle size class for banks A and B. It can be observed that coarse particles (+150 µm) have a slower kinetic, whose difference is more significant in bank A. Particles finer than 150 µm do not show significant differences in recovery.

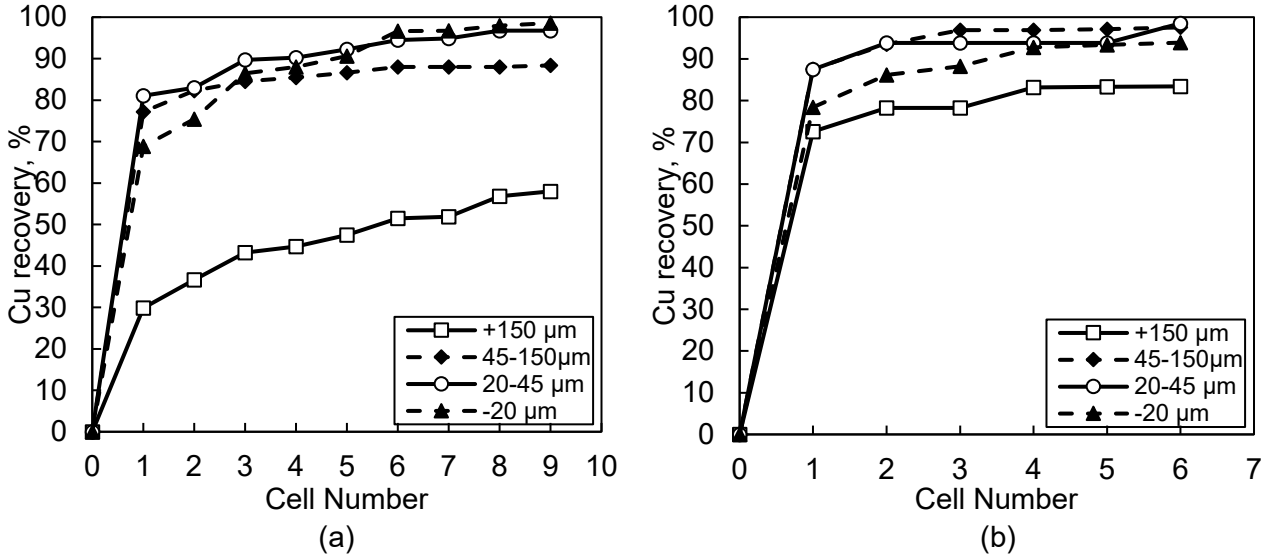

FIG 5 – Cu recovery profiles per particle size class: (a) Bank A and (b) Bank B.

In general, the results shows that bank B allowed for recovering coarser particles than bank A. It can occur because of the differences in operating conditions used in each bank and the different design and volume of the flotation cells (bank A, 130 m^3 versus bank B, 300 m^3). Cells in bank B have shorter froth transport distances than those in bank A, which favours the recovery of coarser particles. The effect of shortening froth transport distances by modifying launders configuration on the metallurgical performance has been evaluated in some simulation studies (Vallejos *et al*, 2020, 2021a), as well as in plant studies (Grau *et al*, 2019; Bermudez *et al*, 2021, 2022; Seaman *et al*, 2021), where similar results have been observed.

Figure 6 shows Cu recovery profiles per liberation class for banks A and B. Recovery gradually increases when liberation increases, whose trend was observed in both banks. However, bank B allowed for recovering more locked particles than bank A. This is consistent with the results from Figure 5, because less liberated particles commonly correspond to coarser particles, as well as liberated particles are generally related to finer particles.

It should be mentioned that the kinetics curves of Figure 6 are more separated from each other than those observed in Figure 5 for recovery per particle size class. Thus, liberation causes a more significant effect on recovery. Similar trends were observed in another flotation plant in Chile, whose results were presented by Vallejos *et al* (2018).

Figure 7 shows the final Cu recovery of banks A and B as a function of particle size (Figure 7a) and liberation (Figure 7b). The curves of recovery per particle size class follow the expected trend, where recovery decreases for finer and coarser particles (commonly called ‘Elephant curve’). It can be clearly observed that bank B is more efficient in recovering coarser particles, while bank A allowed for reaching a higher recovery of ultrafine particles.

The recovery curves per liberation class in Figure 7b show an increase from less to more liberated particles. An apparent linear relationship between recovery and liberation of particles >20 per cent lib. was observed for both banks. This is consistent with results observed in previous studies, at laboratory and plant scales, where recovery was characterised per particle size and liberation (Welsby *et al*, 2010; Vianna, 2004; Savassi, 2006) and whose data was analysed and modelled by

Vallejos *et al* (2021b). Additionally, recovery in each liberation class is similar for bank A and bank B, except for the locked class, where bank B reaches a higher recovery.

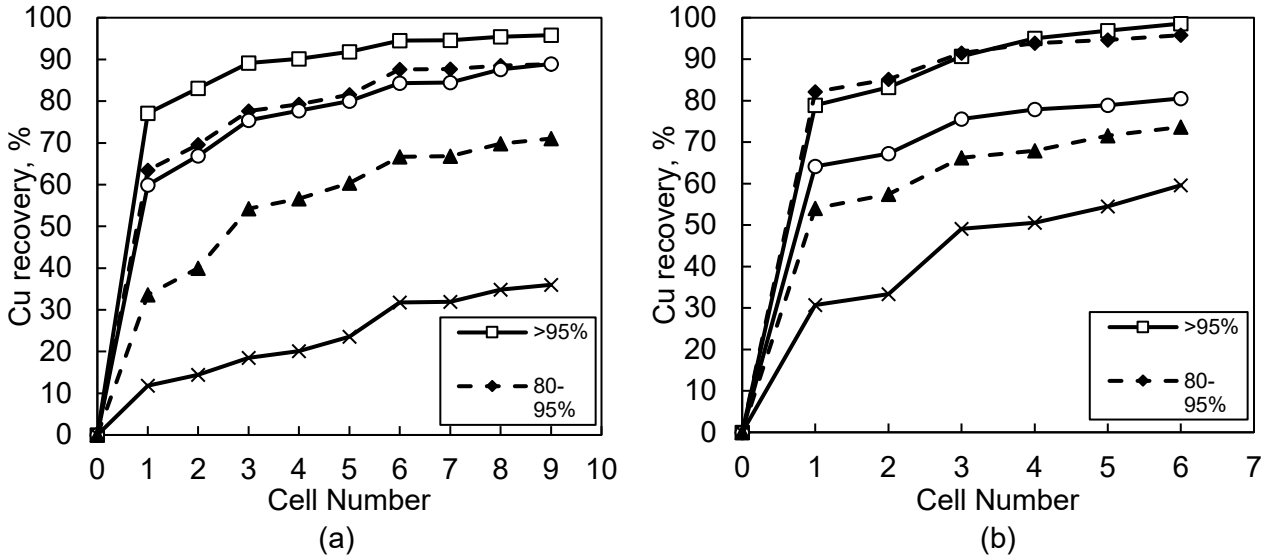

FIG 6 – Cu recovery profiles per liberation class: (a) Bank A and (b) Bank B.

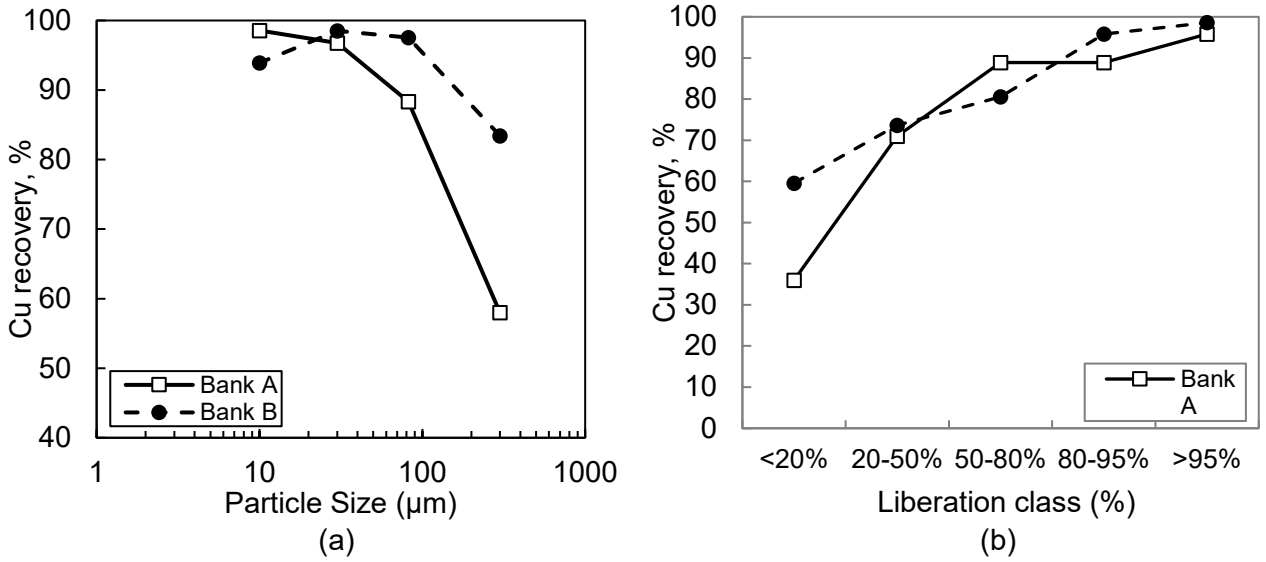

FIG 7 – Final Cu recovery of banks A and B versus.: (a) Particle size and (b) liberation class.

Characterisation of minerals in concentrate streams

Figure 8 shows the mineral content in the concentrate streams along the bank A and bank B (Figures 8a and 8b, respectively). The results show a strong decrease in the content of Cu sulfides towards the end of the banks, which is due to the valuable mineral depletion along the bank. Additionally, an increase in the content of pyrite and insoluble was observed along the banks. However, bank A presented a higher content of pyrite along the bank, while bank B had a higher content of insoluble. In other words, bank B achieved a better selective depression of pyrite, while bank A showed a better gangue entrainment control (analysed later in Figure 12).

Figure 9 shows the content of total Cu sulfides per liberation class in the concentrate streams along the bank A (Figure 9a) and bank B (Figure 9b). It was found that the relative content of free Cu sulfides (>95 per cent) in concentrates decreases along the banks, while the content of middling and locked particles increases.

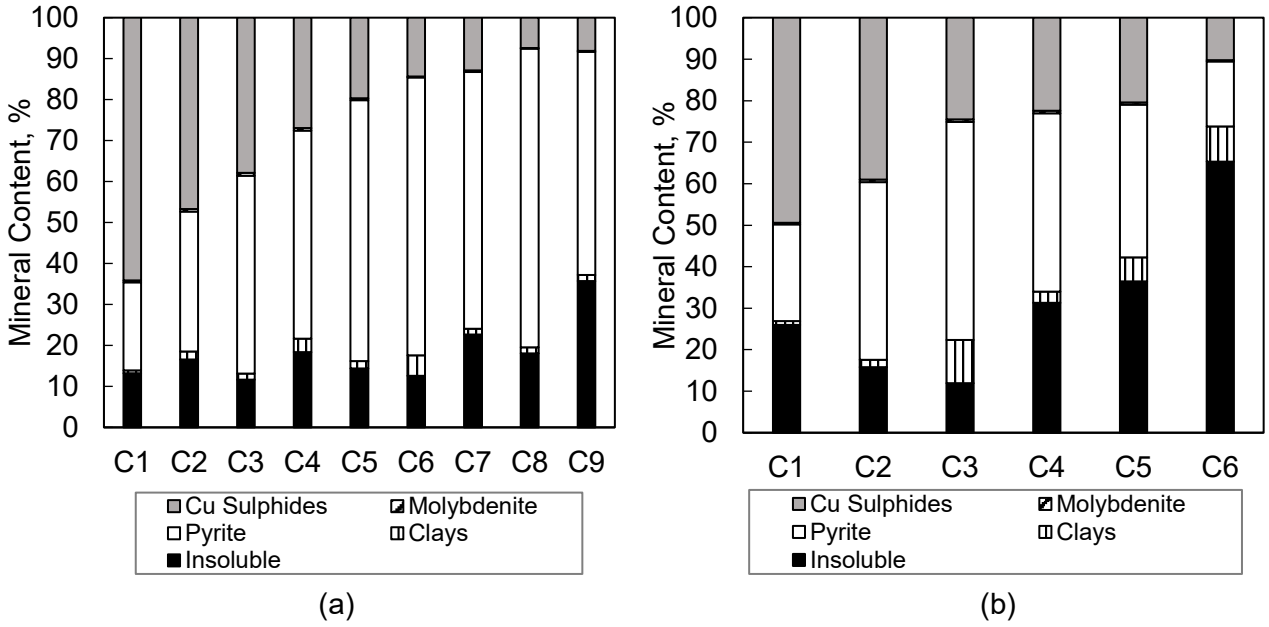

FIG 8 – Content of minerals in concentrate streams along the banks: (a) Bank A and (b) Bank B.

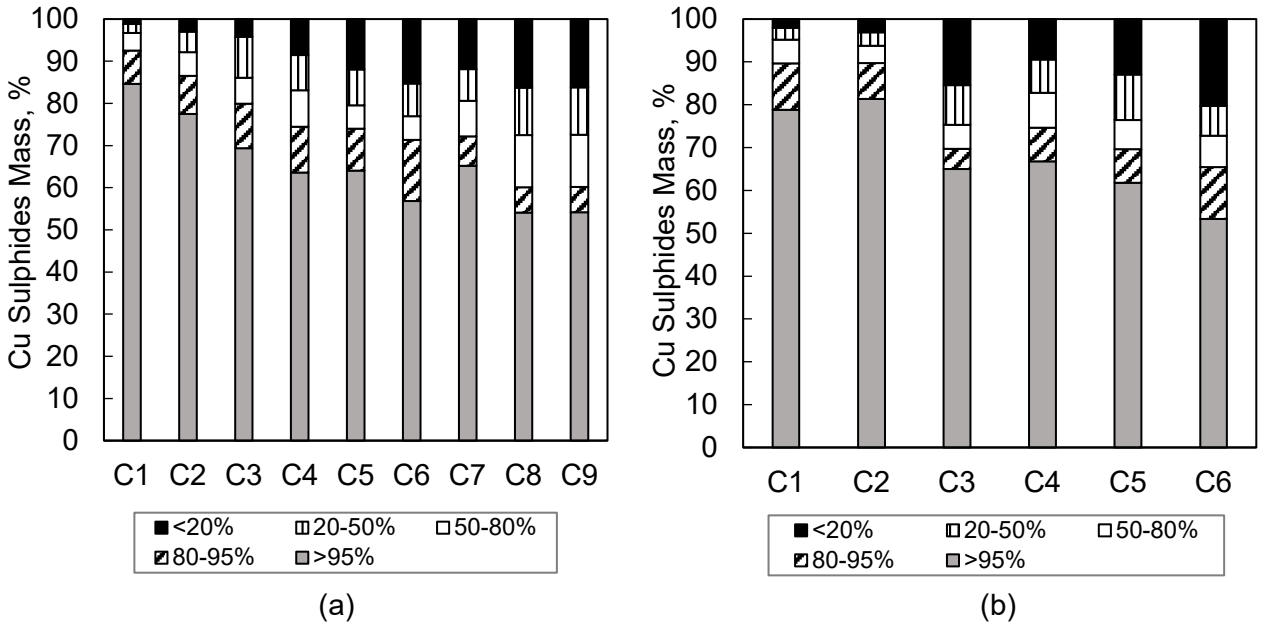

FIG 9 – Content of Cu sulfides per liberation class in concentrate streams in: (a) Bank A and (b) Bank B.

The most significant increase in the Cu sulfides content between the first and the last cells of the banks was observed for locked particles. This occur because free, liberated, and part of the middling particles are recovered in the first cells and are depleted throughout the banks. Then, the relative content of locked particles fed to the last cells of the bank is higher. Additionally, locked particles are more difficult to be recovered by true flotation because they have low exposed surface area, and longer residence times are required. Vallejos and Yianatos (2021) reported similar results from another Cu concentrator with 130 m^3 and 250 m^3 cells.

Figure 10 shows the content of Cu sulfides per association type in the concentrate streams of bank A and bank B (Figures 10a and 10b, respectively). The results show that most of the Cu sulfides are free in the concentrates of both banks, which can be also visualised in Figure 9. Additionally, a similar part of the Cu sulfides is associated with gangue or is a complex association, which increase along the bank as the content of free Cu sulfides decreases. Similar trends were observed for both banks.

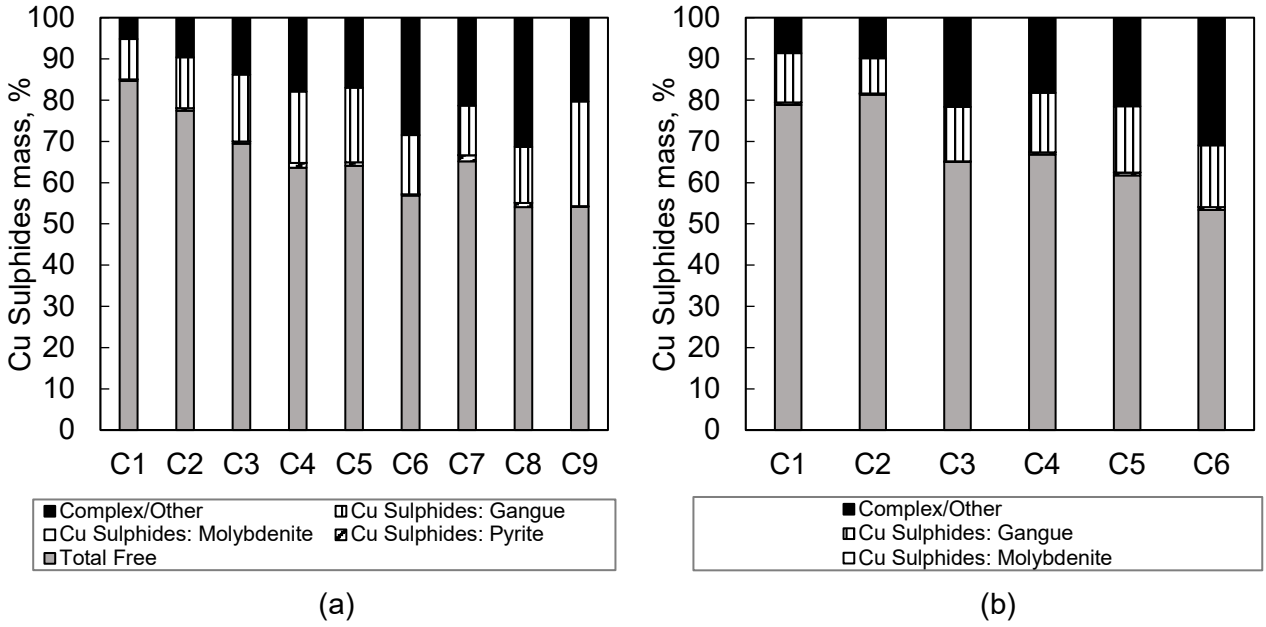

FIG 10 – Content of Cu sulfides per association type in concentrate streams in: (a) Bank A and (b) Bank B.

It must be noticed that the association of Cu sulfides with pyrite is quite low. Thus, it was observed that pyrite recovered into the concentrates is free or in association with gangue. Therefore, this mineral is partially activated and being mainly recovered by true flotation. Similar results about pyrite flotation in an industrial concentrator was studied by Yianatos *et al* (2014).

Figure 11 shows the content of free and middling minerals in concentrate streams for bank A (Figure 11a) and bank B (Figure 11b). The mineral content in the concentrate streams along the banks was analysed based on four groups of minerals: free Cu sulfides, free pyrite, middling (composed of pyrite, Cu sulfides and insoluble associations) and free insoluble (gangue entrainment), which are the main components of concentrates samples. The results from bank A and bank B show a decrease in the content of free Cu sulfides, and an increase in middling particles along the banks. Additionally, the content of free pyrite increased significantly along bank A, while it had a parabolic behaviour in bank B, with a greater contribution of middling and insoluble minerals in the last cells. With respect to the free insoluble, that represent the gangue entrainment, no significant content was observed along the bank A. However, bank B showed a higher content of free insoluble along the bank and particularly in the last cells, which is consistent with data from Figure 8.

The results show that the decrease in the concentrate Cu grades along the flotation banks is mainly due to the recovery of middling minerals and free pyrite, and to a lesser extent, to free insoluble.

Characterisation of gangue entrainment

Figure 12 shows the free insoluble content and froth depth profiles along bank A and bank B (Figures 12a and 12b, respectively). The froth depth in each cell was manually measured along the banks A and B.

The results showed the behaviour of gangue entrainment along the banks, which is more significant for bank B, and the relationship with the froth depth in each cell along the banks. A strong relationship was observed, where the free insoluble content increases when froth depth decreases. This trend is more notable for bank A.

It was observed that froth depth become critical to regulate the gangue entrainment, especially in the last cells of the flotation banks, to keep a suitable selectivity of the flotation process. Other operating variables, such as gas flow rate are also important to control the gangue entrainment.

These results show the imperative requirement of keeping a proper calibration of the level sensors, since the experience from other concentrators showed significant differences (up to 50–100 per cent)

when comparing the automatic data acquisition versus a simple manual measurement used for calibration. The same is relevant for the gas flow rate sensors related to the periodic calibration at the local pressure.

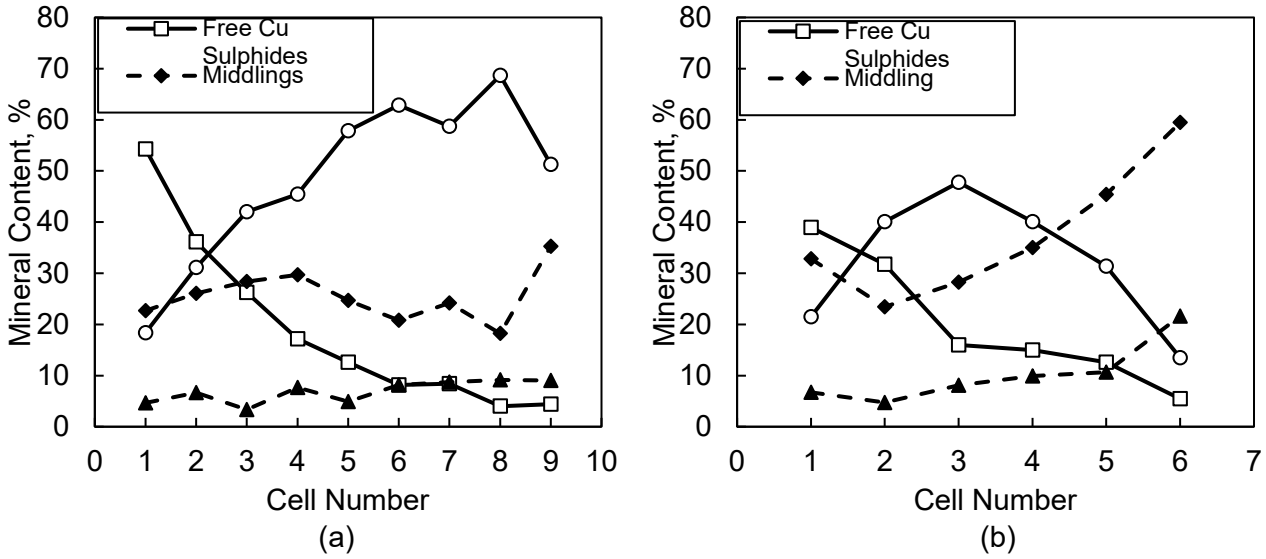

FIG 11 – Content of free and middling minerals in concentrate streams in: (a) Bank A and (b) Bank B.

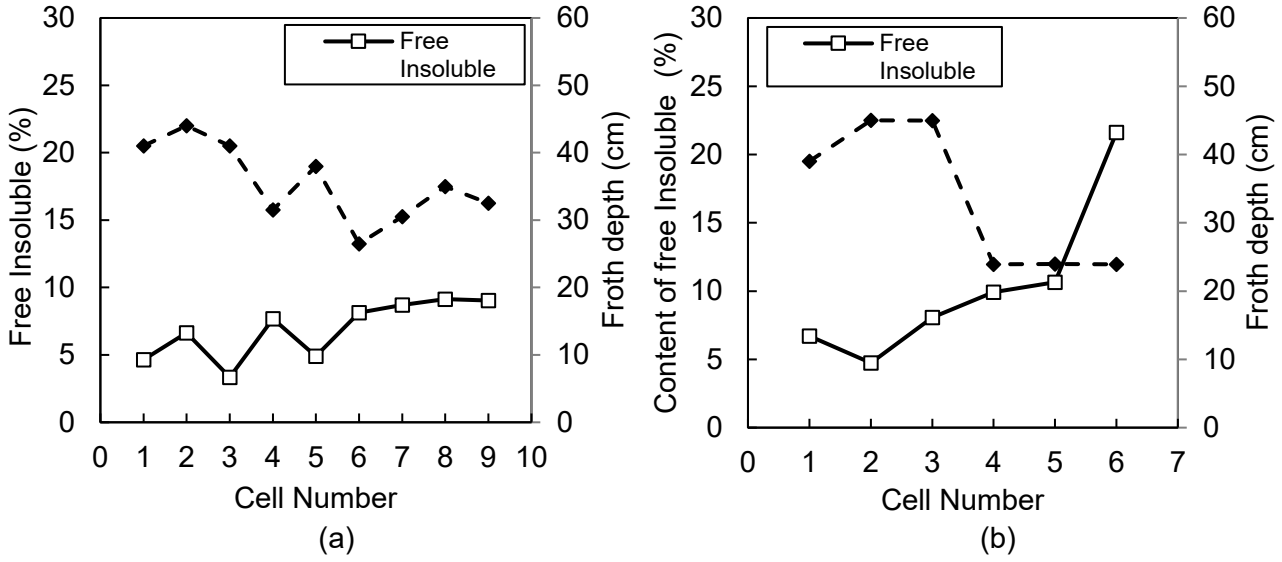

FIG 12 – Free insoluble in concentrate streams and froth depth along: (a) Bank A and (b) Bank B.

CONCLUSIONS

Two flotation rougher banks with cells of 130 m^3 and 300 m^3 at CMDIC concentrator were characterised, including recovery per mineral species, particle size and liberation class, as well as concentrates composition and gangue entrainment along the banks.

The results from both banks showed that recovery per particle size class followed the common trend, where recovery decreases for finer and coarser particles. It was observed that bank B (six 300 m^3 cells) was more efficient in recovering coarser and locked particles, because cells have shorter froth transport distances, while bank A (nine 130 m^3 cells) allowed for reaching a higher recovery of ultrafine particles, which can be associated with operating conditions.

On the other hand, recovery per liberation class showed an apparent linear increase from sub-middling to free particles in both banks. These results validated the relationships observed in

previous studies at laboratory and industrial scale. It was found that changes in liberation caused a more significant effect on recovery than particle size.

The characterisation of concentrate streams along the banks showed a strong decrease in the content of Cu sulfides towards the end of the banks, due to the valuable mineral depletion, while the content of pyrite and insoluble increased. It was observed that bank B achieved a better selective depression of pyrite, while bank A showed a better gangue entrainment control.

It was found that most of the Cu sulfides are free (>95 per cent) in the concentrates and decreases along the banks, while the content of middling and locked particles increases. This occur because free, liberated, and part of the middling particles are recovered in the first cells and are depleted throughout the banks. Additionally, a lower part of the Cu sulfides was associated with gangue or was in a complex association, which increases along the bank as the content of free Cu sulfides decreases.

The results showed that the pyrite recovered into the concentrates is free or in association with gangue. Therefore, this mineral is partially activated and is mainly recovered by true flotation (particularly for bank A).

It was observed that the decrease in the concentrate Cu grades along the flotation banks was mainly due to the recovery of middling minerals and free pyrite, and to a lesser extent, to free insoluble.

Finally, the results showed an increase in gangue entrainment throughout the banks, which was more significant for bank B. In addition, a strong relationship between the gangue entrainment and froth depth, was observed. Therefore, froth depth, and other variables such as gas flow rate, become critical to regulate the gangue entrainment, especially in the last cells of the flotation banks, to keep a suitable selectivity of the flotation process.

ACKNOWLEDGEMENTS

The authors are grateful to Agencia Nacional de Investigación y Desarrollo (ANID), FONDECYT Project 1201335, and Universidad Técnica Federico Santa María for providing funding for process modelling and control research. Additionally, the authors would like to thank Compañía Minera Doña Inés de Collahuasi for providing access to the plant and support for the sampling campaigns.

REFERENCES

Bermudez, G, Amelunxen, P, Medina, M, Taylor, M, Dube, R, 2021. Copper and molybdenum recovery increased by upgrading flotation cells with center launders at Hudbay Constancia. *SME Annual Meeting*, March 1–5, 2021, USA.

Bermudez, G, Perkins, T, Sorensen, R, Smith, C, Bartsch, L, Moyo, J, Dube, R and Brändström, M, 2022. Froth launder modification in 300 m^3 flotation cells at Kennecott Copperton concentrator. *SME Annual Meeting*, February 27 – March 02, 2022, Salt Lake City, USA.

Grau, R, Davoise, D, Yañez, A and López, A, 2019. Optimizing the froth area of large mechanical flotation cells, *in Proceedings Procemin-Geomet 2019*, Santiago, Chile.

Hadler, K, 2006. 'Down the bank froth stability and flotation performance'. PhD Thesis, University of Manchester, UK.

Hassanzadeh, A, 2016. Recovery improvement of coarse particles by stage addition of reagents in industrial copper flotation circuit. *Journal of Dispersion Science and Technology*. doi:10.1080/01932691.2016.1164061.

Jowett, A and Sutherland, D N, 1985. Some theoretical aspects of optimizing complex mineral separation systems. *International Journal of Mineral Processing*, 14(2):85–109.

Le, T M K, Schreithofer, N, Dahl, O, 2020. Dissolution test protocol for estimating water quality changes in minerals processing plants operating with closed water circulation. *Minerals*, 10(8):653.

Li, Y, Li, W, Wei, Z, Xiao, Q, Lartey, C, Li, Y and Song, S, 2018. The influence of common chlorides on the adsorption of sbx on chalcopyrite surface during flotation process. Mineral Processing and Extractive Metallurgy Review. doi:10.1080/08827508.2018.1497625.

Miller, P R, Reid, A F and Zuiderwyk, M A, 1982. QEM*SEM image analysis in the determination of modal assays, mineral associations, and mineral liberation, *in Proceedings XIV IMPC 1982*, Toronto.

Sadr-Kazemi, N, and Cilliers, J J, 2000. A technique for measuring flotation bubble shell thickness and concentration. *Minerals Engineering*, 13(7):773–76.

Savassi, O N, 2006. Estimating the recovery of size-liberation classes in industrial flotation cells: A simple technique for minimizing the propagation of the experimental error. *International Journal of Mineral Processing*, 78:85–92.

Seaman, D R, Li, K, Lamson, G, Seaman, B A and Adams, M H, 2021. Overcoming rougher residence time limitations in the rougher flotation bank at Red Chris Mine, *in Proceedings 15th Mill Operators Conference 2021* (The Australasian Institute of Mining and Metallurgy: Melbourne).

Vallejos, P and Yianatos, J, 2021. Analysis of Industrial Flotation Circuits Using Top-of-froth and Concentrate Mineralogy. *Mineral Processing and Extractive Metallurgy Review*, 42(7):511–520.

Vallejos, P, Yianatos, J, Grau, R and Yañez, A, 2020. Evaluation of flotation circuits design using a novel approach, *Minerals Engineering*, Article 106591.

Vallejos, P, Yianatos, J, Grau, R, Yañez, A, López, A and Davoise, D, 2021a. Improving metallurgical performance in an industrial flotation bank by upgrading the first cell design, in *Proceedings Procemin-Geomet 2021*, Santiago, Chile.

Vallejos, P, Yianatos, J, Vinnett, L, 2021b. A Model Structure for Size-by-Liberation Recoveries in Flotation. *Minerals*, 11:194.

Vallejos, P, Yianatos, J, Vinnett, L, Bergh, L, 2018. Characterization of the industrial flotation process based on size-liberation relationships. *Minerals Engineering*, 121:189–195.

Vianna, S M S M, 2004. 'The Effect of Particle Size, Collector Coverage and Liberation on the Floatability of Galena Particles in an Ore'. PhD thesis, Department of Mining, Minerals and Materials Engineering, The University of Queensland, Brisbane, Australia.

Welsby, S D D, Vianna, S M S M, Franzidis, J P, 2010. Assigning physical significance to floatability components. *International Journal of Mineral Processing*, 97:59–67.

Yianatos, J, Carrasco, C, Vinnett, L, Rojas, I, 2014. Pyrite recovery mechanisms in rougher flotation circuits. *Minerals Engineering*, 66–68:197–201.

Pulp rheology of fine mineral flotation – a review

Q Zhang[1], A Liu[2], X Wang[2] and W Peng[2]

1. Professor, Guizhou Academy of Sciences, Guiyang 550001, China. Email: zq6736@163.com
2. Guizhou Academy of Sciences, Guiyang 550001, China.

ABSTRACT

Pulp rheology plays a critical role in fine mineral flotation. Yield stress and apparent viscosity are two important rheological parameters affecting mineral flotation recovery. In this paper, the concept of pulp rheology and its measuring method are presented. The main factors, such as particle size, pulp concentration, mineral types, pulp temperature, inorganic salts, that affect the pulp rheology are systematically reviewed, and then followed by the discussion of the relationship between pulp rheological properties and flotation performance. Generally, high pulp apparent viscosity and yield stress values have been found to have an adverse effect on flotation recovery. In addition, due to the hetero-coagulation between the valuable mineral and gangue mineral, the pulp of mixed ore shows higher viscosity than that of the single mineral slurry. This paper is expected to provide some references for the efficient upgrading of low-grade and complex ores from the perspective of pulp rheology.

INTRODUCTION

Rheology is a science that studies the flow and deformation behaviour of materials. It is a new interdisciplinary subject among physics, chemistry, mechanics, biology and engineering technology. According to the different rheological properties of fluids, fluids can be divided into Newtonian fluids and non-Newtonian fluids. Figure 1 shows five typical rheograms representing the Newtonian and the non-Newtonian behaviours including dilatant, plastic, pseudoplastic and Bingham (Mewis and Wagner, 2012). Pulp is a solid suspension composed of mineral particles with different particle size and surface properties, flotation reagent and aqueous solution. In flotation, mineral slurries made of good quality ores often display a Newtonian behaviour, whereas complex and low-grade ore slurries normally exhibit a pseudoplastic or Bingham behaviour (Farrokhpay, 2012). The influence of pulp rheology on mineral flotation process has attracted the attention of scholars at home and abroad. Relevant researches conducted show that yield stress and apparent viscosity are two important rheological parameters affecting mineral flotation recovery (Wang and Li, 2020). Yield stress represents the stress at which a material begins to deform plastically, and the apparent viscosity measures the resistance of a material to gradual deformation by shear stress (Bakkera *et al*, 2009).

The Herschel–Bulkley model is widely used in flotation rheology characterisation, which is given as (Tadros, 2010):

$$\tau = \tau_0 + K\gamma^n \quad (1)$$

where τ and τ_o are the shear stress and yield stress, respectively. γ represents the shear rate, K and n are the parameters representing the flow index and consistency index, respectively. When flow index is lower than 1, the fluid material behaves as pseudoplastic or plastic flow. If flow index is greater than 1, the material is dilatant flow. When n is 1, the viscosity of the fluid material is constant, suggesting a Newtonian flow or Bingham flow.

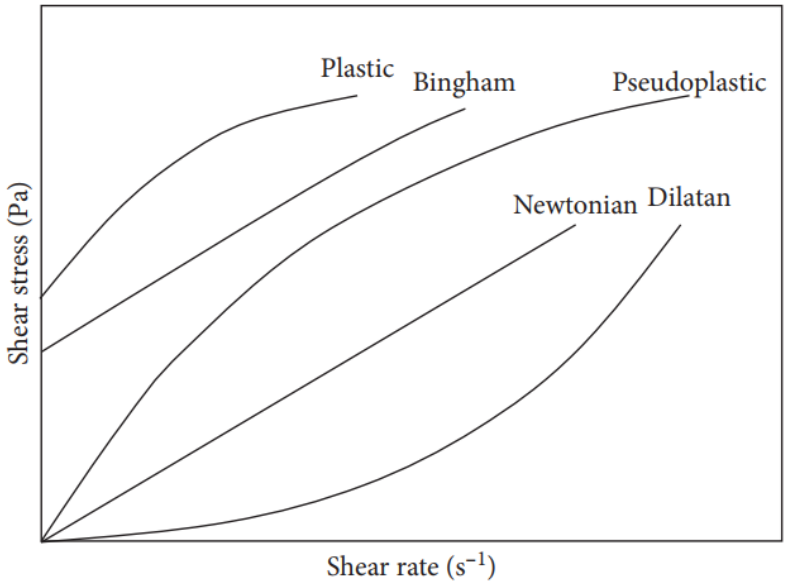

FIG 1 – Schematic diagram of shear rate as a function of shear stress for different fluids (Farrokhpay, 2012).

The apparent viscosity of the mineral slurry was calculated using the rheological data on the shear rate versus shear stress curve shown in Figure 2a by the following equation:

$$\eta = \tau/D \quad (2)$$

Where η is the apparent viscosity (Pa·s^{-1}), τ is the shear stress (Pa) and D is the shear rate (s^{-1}). The apparent viscosity of mineral pulp at 100 s^{-1} was selected to evaluate its rheological properties because 100 s^{-1} was usually regarded as a common shear condition near the impeller in industrial flotation cells (Ralston *et al*, 2007).

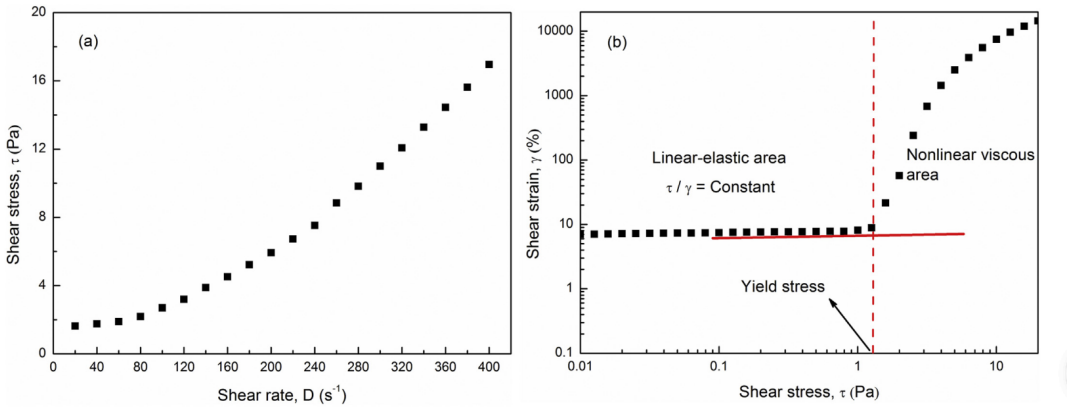

FIG 2 – The rheological curves: (a) shear rate versus shear stress curve; (b) shear stress versus shear strain curve; of the common mineral slurry (Chen *et al*, 2019).

The yield stress of the pulp was obtained from the shear stress versus shear strain curve as shown in Figure 2b. The shear stress value at the yield point where the sharp changes in shear strain occurred was regarded as the yield stress of the pulp. The yield point was calculated at the end point of the linear-elastic area region, where 5 per cent or bigger changes in shear strain were observed. The whole rheology curve was therefore divided into linear-elastic and nonlinear viscous region. It was assumed that the new-work structure caused by the particle interactions in mineral slurry could maintain its structure in the linear-elastic region and was destroyed in the nonlinear viscous region under external shear stress. The values of the points are the mean values of the three individual measurements repeated in the experiment (Chen *et al*, 2019).

MEASUREMENTS OF PULP RHEOLOGY

Various set-ups such as capillary viscometers, vibrating sphere viscometers and rotational rheometers have been used to measure pulp rheology, among which, the rotational rheometer has ascendancy over the other set-ups because it can be operated at a specific shear rate in addition to the ease of completing measurements and data analysis. Rotational rheometers generally include the relative rotation about a common axis of one of three geometries: concentric cylinder, cone and plate, or parallel plates (see Figure 3). The one with the concentric cylinder geometry (Figure 3a) has been widely applied for measurement of pulp rheology.

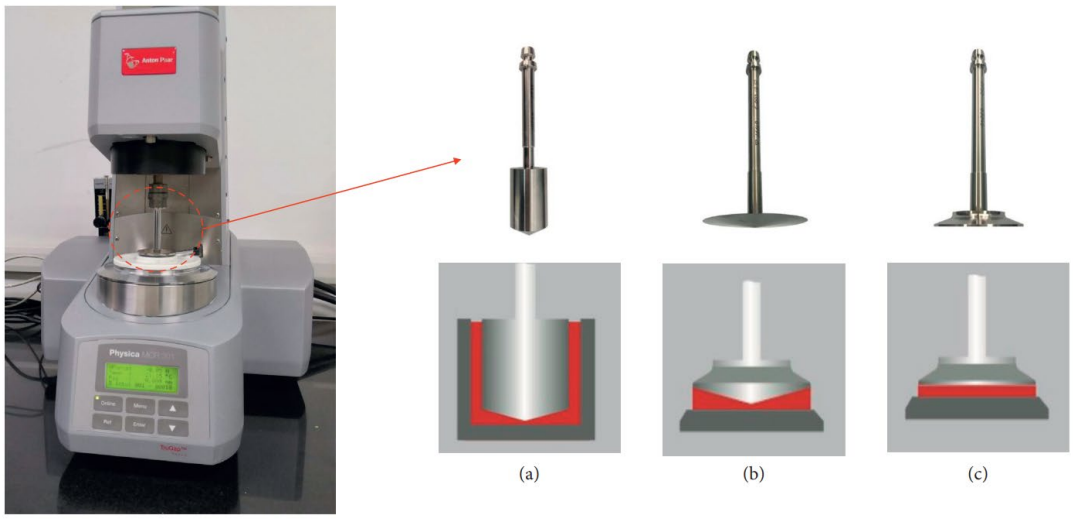

FIG 3 – Basic geometries for the rotational rheometer: (a) concentric cylinder; (b) cone and plate; (c) parallel plate.

The rheology measurement for pulps made of good quality ores has been a challenge because this type of pulps is generally of low viscosity, being Newtonian or very close to Newtonian. However, in most flotation operations, pulps made of high-quality ores are not expected to cause detrimental rheological effects on flotation performance. For low-grade and complex ores, pulp rheology measurement becomes particularly critical. It can produce a highly viscous pulp. Researchers have demonstrated that consistent measurement for this type of pulps can be obtained using the bob and cup style rheometer.

RHEOLOGY OF FLOTATION PULP

In recent years, more and more researches have been made on flotation from the perspective of pulp rheology. The study of pulp rheology has involved the typical sulfide ore (Muster and Prestidge, 1995; Prestidge, 1997), oxidised ore (Zhou *et al*, 2001), clay mineral (Papo *et al*, 2002), coal slime (Boylu *et al*, 2004). The results showed that many factors can affect the rheological properties of pulp, and those factors interfere with each other (He *et al*, 2006). In the actual flotation process, a variety of factors need to be taken into considerations in order to obtain the appropriate rheological properties of pulp. The main factors include: ore properties (mineral composition (Burdukova *et al*, 2008), particle size distribution (He *et al*, 2004; Tari *et al*, 1999), mineral surface properties), flotation reagents (reagent dosage, pH value (Ding and Pacek, 2008)), operating factors (such as pulp concentration and temperature) and flotation machine characteristics (structure and properties of flotation machine, stirring strength, aeration capacity, bubble size etc) (Mueller *et al*, 2010). This paper reviews the change law of rheological properties such as viscosity, yield stress and viscoelasticity of pulp caused by the difference of mineral particle size and surface properties in pulp fluid. And it reveals the interaction, aggregation and dispersion behaviour of mineral particles in pulp, so as to provide a basis for the study of grinding, stirring, flotation and other processes.

Effect of mineral particle size on rheological properties of pulp

The particle size of mineral has a great influence on the rheology of pulp. Generally, the apparent viscosity of the pulp increases as particle size decreases. Figure 4 shows the apparent viscosity of

a gold ore slurry with high clay contents as a function of particle size, particle size effect became notable when the pulp solids concentration exceeded 25 wt. per cent, and the apparent viscosity of the mineral suspension increased with decreasing particle size. This clearly shows that the apparent viscosity is affected by particle size and pulp solid concentration (Farrokhpay *et al*, 2013). Das *et al* (2011) evaluated the influence of mineralogy and particle size on the viscosity of high concentration slurry, and found that the slurry containing fine particles has higher viscosity and poor rheology. Mixing montmorillonite with some pure minerals can improve the rheological properties of slurry.

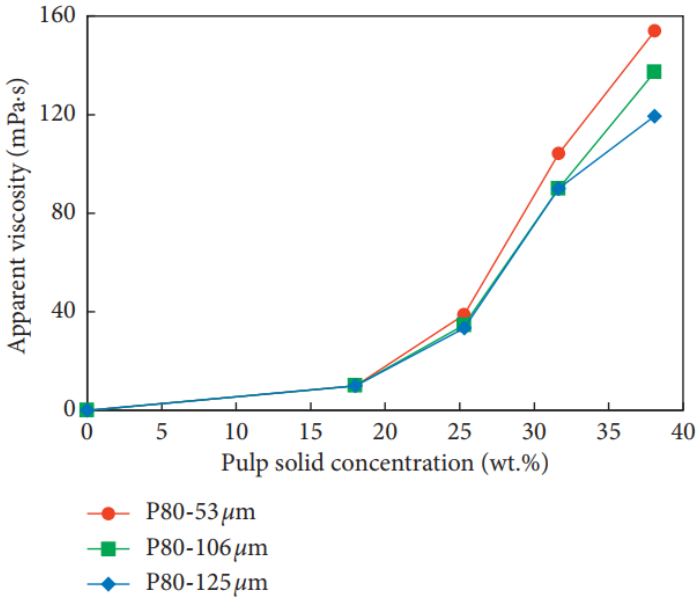

FIG 4 – Apparent viscosity of the ore as a function of pulp density for different P80 values (Farrokhpay *et al*, 2013).

Effect of pulp concentration on rheological properties

The pulp concentration is the main factor affecting the rheology of mineral suspensions (Mueller *et al*, 2010). With the increase of solid particle concentration in the pulp, the number of particles per unit volume increases, the distance between particles decreases, and the interaction force increases. The internal friction during relative movement increases, which hinders the interlayer movement of the pulp, resulting in the increase of pulp apparent viscosity and poor rheology. As shown in Figure 5, when the feed solid concentration is higher than 25 vol. per cent, a discernible increase in the apparent viscosity of the feed samples could be observed. This would result in rheological complexities in the separation process. In mineral flotation, the pulp solid concentration generally ranges from 5 wt. per cent to 40 wt. per cent, with an upper-bound concentration of about 50 wt. per cent. The results show that a low concentration pulp displays a Newtonian behaviour, and a high concentration pulp is typically non-Newtonian exhibiting a pseudoplastic or Bingham behaviour, which could cause deleterious rheological effect on flotation (Becker *et al*, 2013; He *et al*, 2004).

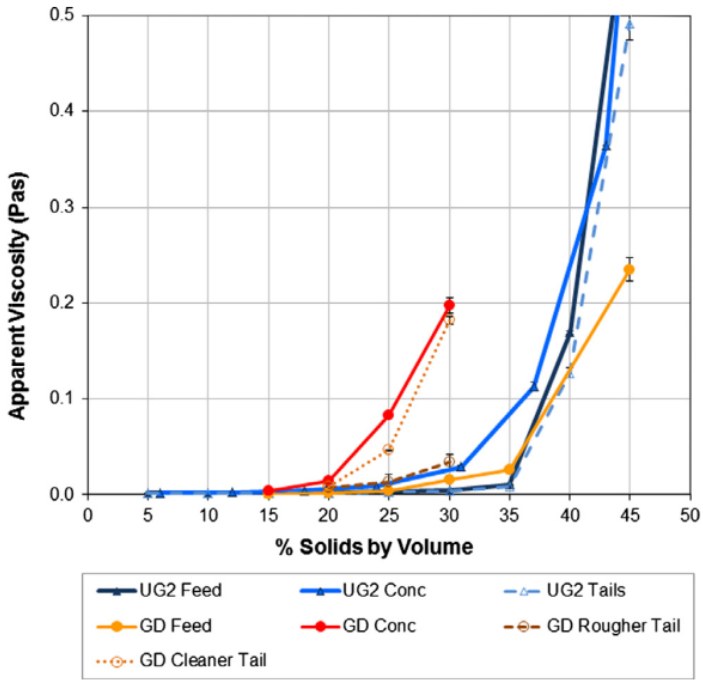

FIG 5 – The comparison of the apparent viscosity of the UG2 and Great Dyke flotation samples at different solid concentrations (Becker *et al*, 2013).

Qi *et al* (2013) found that the rheology of bauxite slurry deteriorates with the increase of solid content. When the solid content is lower than 1050 g/L, the pulp is a Bingham fluid; when the solid content is higher than 1050 g/L, it is transformed into power-law fluid, and the yield stress of pulp increases sharply. When studying the influence of surfactants on the fluidity of bauxite beneficiation tailings, Liu *et al* (2009) found that the bauxite tailings have fine particle size with irregular morphology, and the pulp belongs to pseudoplastic fluid. With the increase of concentration, the pulp viscosity increases, and meanwhile the consistency coefficient and rheological index also increase. This indicates that with the increase of tailings concentration, the interaction between particles increases, and thus strengthens the network structure of pulp.

Effect of mineral types on rheological properties of pulp

Research shows that the pulp rheology is affected by the mineral composition in pulp, especially the clay minerals. Clay minerals with layered structure have a significant impact on the rheology of pulp. Zhang and Peng (2015) studied the effect of clay minerals on pulp rheology and the flotation of copper and gold minerals. It was found that clay minerals modified the pulp rheology depending on the type of clay minerals present. Bentonite, a 2:1 structured clay mineral increased pulp viscosity more significantly than kaolinite, a 1:1 structured clay mineral, and poorly crystallised kaolinite increased pulp viscosity more than well crystallised kaolinite.

Figure 6 presents the difference in the Bingham viscosity of different clay minerals that usually exist in real ores. Clearly, the rheological behaviour of flotation pulps is closely associated with mineral type, and phyllosilicate minerals, particularly swelling clays and serpentine minerals, can result in higher viscosities compared with nonphyllosilicate minerals such as quartz (Ndlovu *et al*, 2014).

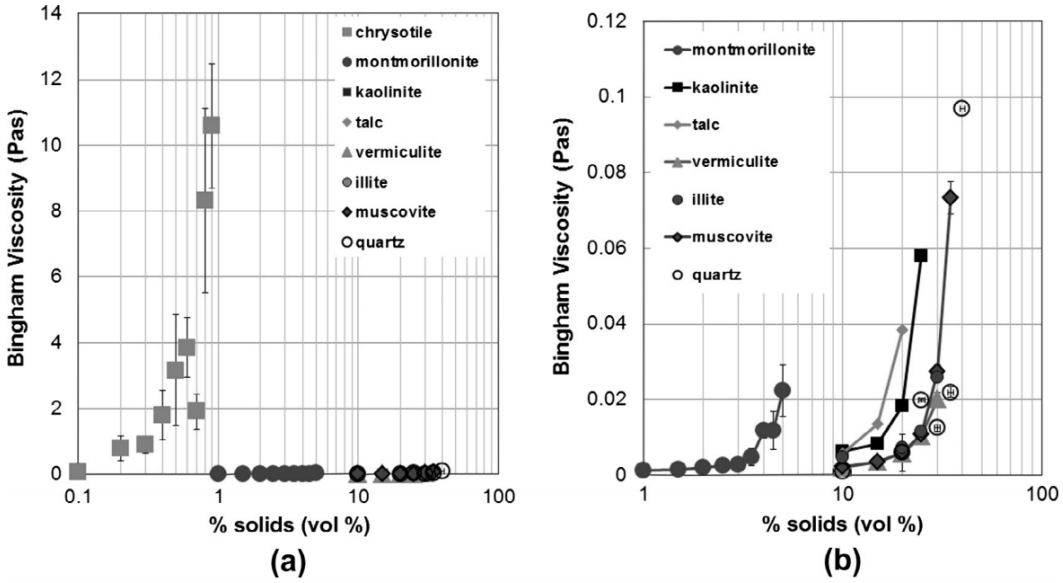

FIG 6 – A comparison of the Bingham viscosities of phyllosilicate group minerals (Ndlovu *et al*, 2014).

Hu *et al* (2020) studied the effect of serpentine on chalcopyrite slurry rheology and flotation, the results show that increasing the serpentine concentration can increase the apparent viscosity of mixed ore pulp, resulting in an increase in the foam entrainment of serpentine and the MgO content in concentrate.

Basnayaka *et al* (2017) investigated the influence of kaolin and bentonite clays on the flotation of gold-bearing pyrite. They observed that bentonite clay reduced the pyrite recovery, and modified the pulp rheology more than kaolin did. The addition of Ca^{2+} ions to the pulp containing bentonite improved the pyrite flotation recovery by its ability to modify the rheological characteristics. In addition, the rheological characteristics such as the flow index and the consistency index affected the flotation performance as the former indicates the extent of movement of bubbles and particles within flotation pulp. Such finding suggests the possibility of using the rheological measures to monitor the changes in the flotation performance in routine plant operations.

Chen *et al* (2017) investigated the effect of amorphous silica on pulp rheology and copper flotation. The results showed that found that the presence of amorphous silica increased the pulp viscosity more significantly than quartz. And low percentage of amorphous silica had little influence on copper recovery, and causing a significant increase in mass recovery, and decrease in copper grade.

Effect of temperature on rheological properties of pulp

Pulp temperature is an important factor affecting flotation index. Temperature will not only affect the adsorption of reagent on the mineral surface, but also significantly change the rheological properties of pulp. With the increase of temperature, the irregular thermal movement of liquid molecules and dispersed particles will intensify. When the intermolecular force decreases, the dispersion will become better, and the viscosity of pulp will decrease. MacCarthy *et al* (2016) studied the acid leaching mechanisms and rheological behaviour of a low-grade saprolitic nickel laterite ore. They found that the slurries displayed time-dependent, non-Newtonian, shear thinning rheological behaviour. The pulp viscosities and shear yield stresses were generally greater at lower than at higher temperature (Figure 7). Qi *et al* (2013) found that the viscosity of the bauxite pulp increases with the increase of temperature. The reason may be that the increase of temperature could promote kaolinite to form amorphous sodium silicate slag. And the increase of temperature promotes the alkali solution to dissociate large particles into small particles.

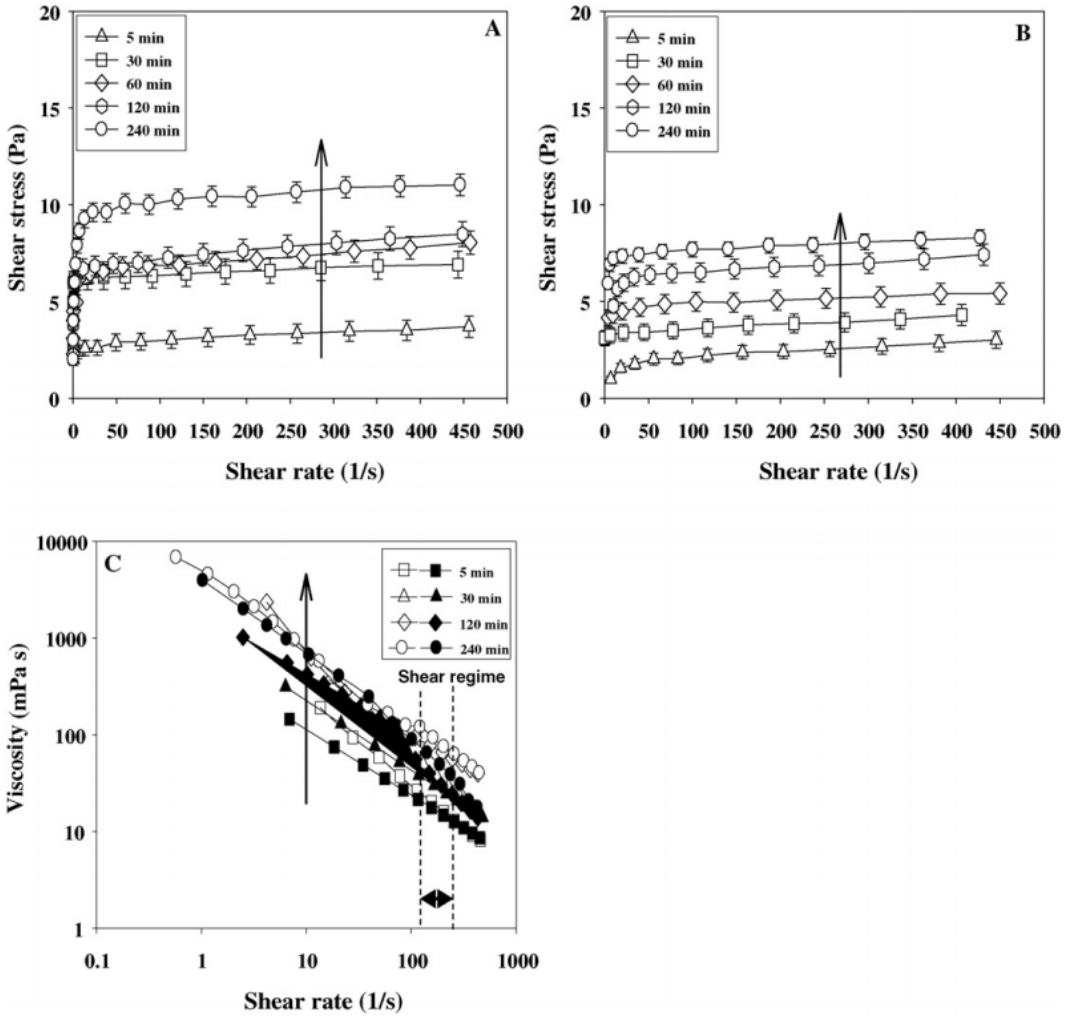

FIG 7 – Shear stress versus shear rate flow curves at 70°C (A) and 95°C (B) and variation of apparent viscosities with shear rate (C) at 70°C (unfilled) and 95°C.

Effect of inorganic salts on rheological properties of pulp

The addition of inorganic salt will neutralise the charge on the particle surface, compress the double electrode layer and reduce the electrostatic repulsion between particles, agglomerate the dispersed particles, and then affect the pulp rheology (Gustafsson *et al*, 2000; Mosa *et al*, 2008). Li *et al* (2016) studied the influence of NaCl on coal slime flotation and rheological properties of slurry. The results showed that the addition of NaCl reduced the surface potential of coal particles, weakened the electrostatic repulsion between coal particles and between coal particles and bubbles, and then promoted the agglomeration between particles. With the increase of NaCl concentration, the viscosity and the apparent particle size of the slurry increase gradually. It accelerates the coalescing of the coal particles, makes the flotation froth more stable, and thus improving the recovery rate of the combustible body of the slime. Ding *et al* (2007) studied the effects of different kinds of inorganic salts on the rheology of iron oxide suspension, and found that the counter ions with high number have stronger agglomeration effect on particles than those with low number, and the apparent viscosity of suspension is large. Yang *et al* (2005) found that the viscosity of montmorillonite suspension increases with the increase of NaCl concentration, because the addition of NaCl can compress the double electrode layer between montmorillonite lamellae and form an unstable network structure, resulting in the increase of viscosity. Yu *et al* (2020) found that both calcium ion and sodium hexametaphosphate could reduce the viscosity and yield stress of serpentine pulp and disperse serpentine particles. When there is a certain amount of calcium ion in serpentine pulp, the addition of sodium hexametaphosphate has little effect on the yield stress and viscosity of serpentine pulp.

EFFECT OF PULP RHEOLOGY ON FLOTATION

The pulp rheological behaviour plays a critical role in effective flotation of fine minerals. Generally, high pulp apparent viscosity and yield stress values have a detrimental effect on flotation recovery. With the increase of apparent viscosity and yield stress, a corresponding decrease in the recovery will appear. Besides, due to the hetero-coagulation between the valuable mineral and gangue mineral, the pulp of mixed ore shows higher viscosity than that of the single mineral slurry.

Wang *et al* (2020) found that fine minerals could change the pulp rheology and affect the pyrite recovery. The apparent viscosity of the mixed ores slurry increased with the addition of fine diaspore (FDIA), kaolinite and illite, and the pyrite recovery decreased in varying degrees. The addition of pyrophyllite had a significant deteriorating effect on flotation. When the addition of pyrophyllite was 5 wt. per cent, the pyrite recovery was reduced to 49.2 per cent (Figure 8). Pyrophyllite affected pyrite recovery not only by the rheological behaviour of the pulp, but also by because pyrophyllite was adsorbed on the surface of pyrite and diaspore, and thus producing hetero-aggregation. Generally, the order in which the reduction of pyrite recovery was affected by the additions of fine minerals was pyrophyllite > FDIA > kaolinite > illite.

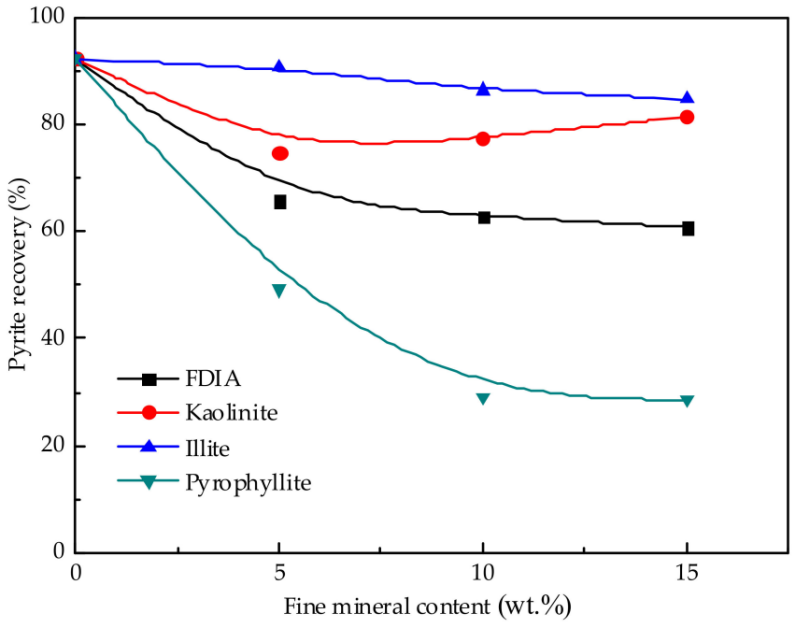

FIG 8 – Effect of different fine mineral additions on pyrite recovery.

Patra *et al* (2012) investigated the effect of pulp rheological behaviour on selective separation of Ni minerals from fibrous serpentine ores. With an increase in the pulp fibre (chrysotile and nylon) content, an increase in the pulp yield stress values and a corresponding decrease in the Copper recovery were found. Notably, pulp was immovable when the copper ore contained more than either 6 per cent of chrysotile or 2 per cent of nylon fibres. Increase in the pulp yield stress values is considered to be due to the entanglement of fibres, which further leads to the formation of fibre networks in the pulp. The height, texture, and consistency of the froth phase were observed to be different with increases in the pulp yield stress values.

Chen *et al* (2019) found that when quartz and fluorite particles were mixed in water, the yield stress of the mixed mineral slurry was much higher than that of the single mineral slurry, demonstrating a strong hetero-coagulation between the two minerals. The flotation performance of the fine fluorite particles with different degree of hetero-coagulation was tested. They observed a detrimental effect on the fluorite flotation, showing that the flotation recovery and flotation rate decreased (Figure 9). It was found that the hetero-coagulation deteriorated the fine fluorite flotation by forming strong network structures that could interfere with the rising processes of the bubbles carrying valuable mineral particles.

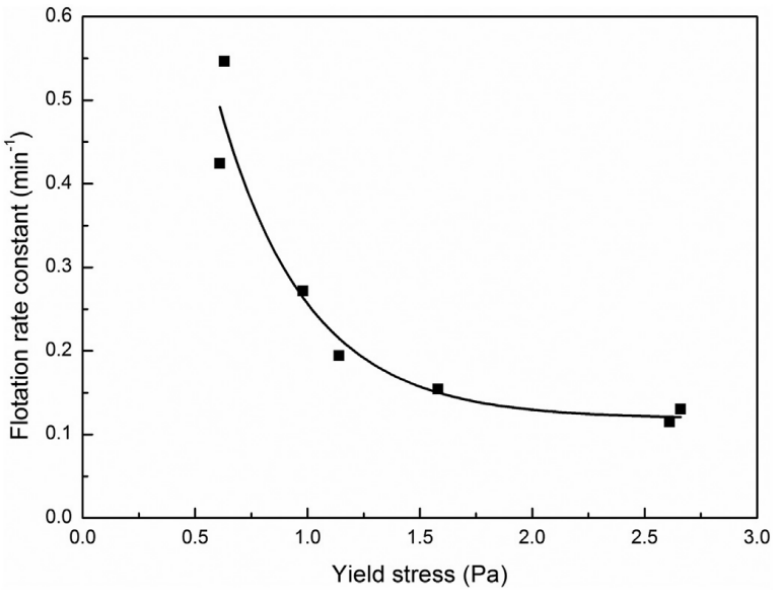

FIG 9 – Fluorite flotation rate constant as a function of the yield stress of flotation pulp.

Liu *et al* (2021) investigated the detrimental influences of serpentine on Cu-Ni sulfide flotation through rheology studies. They found that the hetero-coagulation was not the only factor affecting the flotation of Cu-Ni sulfide containing serpentine, high pulp viscosity could also worsen that. However, with the addition of coarse garnet particles (-104 + 44 μm), the pulp yield stress decreased remarkably, illustrating that the hetero-coagulation between sulfide and serpentine was limited. Furthermore, pulp viscosity also decreased obviously, and the synthetic actions improved Cu-Ni sulfide flotation. Micro-flotation and batch flotation results verified that the Ni recovery in concentrate increased significantly with a remarkable decrease in SiO_2 content after adding garnet (Figure 10).

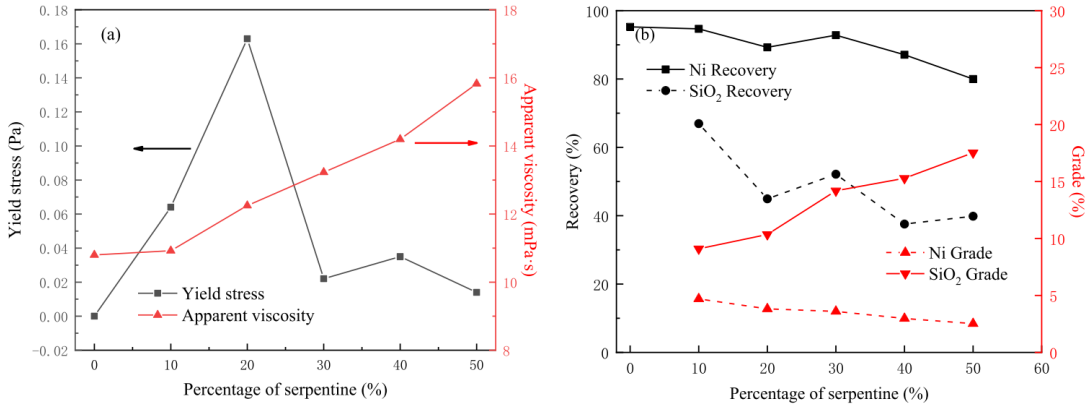

FIG 10 – Effect of the percentage of serpentine on (a) rheological behaviours and (b) flotation performance of mixed minerals in the presence of PBX with a total pulp concentration of 20 wt. per cent (Liu *et al*, 2021).

Zhang and Peng (2015) found that the pulp rheology modified by clay minerals was strongly correlated with copper and gold flotation. The higher pulp viscosity corresponded to the lower copper recovery. While high pulp viscosity was related to the decreased gold flotation, slightly increased pulp viscosity by clay minerals enhanced gold flotation.

Not all the flotation recovery decreases with an increase in pulp viscosity. A slightly viscous pulp is also beneficial to coarse particle flotation. Xu *et al* (2012) found an increased recovery of coarse hydrophobic quartz particles when adding glycerol to increase the medium viscosity. Discernible change was found in the pulp viscosity, from 0.9 mPa·s in water to 7.6 mPa·s in a 50 per cent glycerol/water mixture. When pulp viscosity increased, a more stable bubble-particle aggregate was

formed, leading to the increase in the quartz recovery. Therefore, using a proper viscous pulp is recommended for the flotation of either coarse particles or precious metals.

CONCLUSIONS

This paper reviews the pulp rheology in mineral flotation. It reveals that the pulp rheology plays a critical role in fine mineral flotation. The rotational rheometer has been widely used to measure the yield stress and apparent viscosity.

1. The main factor that affects the pulp rheology includes particle size, pulp concentration, mineral types, pulp temperature and inorganic salts. The fine particle or high concentration of the pulp shows high apparent viscosity, but the addition of inorganic and high temperature can decrease the pulp apparent viscosity, besides the pulp rheology is affected by the clay minerals.
2. There is a close relationship between pulp rheology and flotation performance. Generally, high pulp apparent viscosity and yield stress values have a detrimental effect on flotation recovery. In addition, due to the hetero-coagulation between the valuable mineral and gangue mineral, the pulp of mixed ore shows higher viscosity than that of the single mineral slurry.
3. The addition of coarse garnet particles would remarkably decrease the pulp yield stress and viscosity, so as to increase the flotation recovery of valuable mineral and decrease the impurity content.

ACKNOWLEDGEMENTS

This research was funded by the National Natural Science Foundation of China (52164018).

REFERENCES

Bakkera, C W, Meyer, C J and Deglona, D A, 2009. Numerical modelling of non-newtonian slurry in a mechanical flotation cell. *Minerals Engineering*, 22(11): 944–950.

Basnayaka, L, Subasinghe, N and Albijanic, B, 2017. Influence of clays on the slurry rheology and flotation of a pyritic gold ore. *Applied Clay Science*, 136: 230–238.

Becker, M, Yorath, G, Ndlovu, B, Harris, M, Deglon, D and Franzidis, J P, 2013. A rheological investigation of the behaviour of two Southern African platinum ores. *Minerals Engineering*, 49: 92–97.

Boylu, F, Dinçer, H and Ateşok, G, 2004. Effect of coal particle size distribution, volume fraction and rank on the rheology of coal-water slurries. *Fuel Processing Technology*, 85(4): 241–250.

Burdukova, E, Becker, M, Ndlovu, B, Mokgethi, B and Deglon, D A, 2008. Relationship between slurry rheology and its mineralogical content, I*nt Minerals Processing Congress. Proceedings of 24th International Minerals Processing Congress,* Beijing, pp. 2169–2178

Chen, W, Chen, Y, Bu, X Z, Long, T, Zhang, G F, Chen, F F, Liu, R Z, Jia, K and Song, Y H, 2019. Rheological investigations on the hetero-coagulation between the fine fluorite and quartz under fluorite flotation-related conditions. *Powder Technology*, 354: 423–431.

Chen, X M, Hadde, E, Liu, S Q and Peng, Y J, 2017. The effect of amorphous silica on pulp rheology and copper flotation. *Minerals Engineering*, 113: 41–46.

Das, G K, Kelly, N and Muir, D M, 2011. Rheological behaviour of lateritic smectite ore slurries. *Minerals Engineering*, 24(7): 594–602.

Ding, P and Pacek, A W, 2008. Effect of pH on deagglomeration and rheology/morphology of aqueous suspensions of goethite nanopowder. *Journal of Colloid and Interface Science*, 325(1): 165–172.

Ding, S Q, Zhang, Y F and Xu, J R, 2007. A study on the rheo-parameters of coagulated Fe_2O_3 suspensions. *Journal of University of Science and Technology of Suzhou (Engineering and Technology),* 20(4): 44–47.

Farrokhpay, S, 2012. The importance of rheology in mineral flotation: A review. *Minerals Engineering*, 36–38: 272–278.

Farrokhpay, S, Bradshaw, D and Dunne, R, 2013. Rheological investigation of the flotation performance of a high clay containing gold ore from Carlin trend, *Proceedings of the 5th World Gold 2013 Conference: Challenges in Gold Mining*, (The Australasian Institute of Mining and Metallurgy: Melbourne).

Gustafsson, J, Mikkola, P, Jokinen, M and Rosenholm, J B, 2000. The influence of pH and NaCl on the zeta potential and rheology of anatase dispersions. *Colloids & Surfaces A Physicochemical & Engineering Aspects*, 175(3): 349–359.

He, M Z, Wang, Y M and Forssberg, E, 2004. Slurry rheology in wet ultrafine grinding of industrial minerals: a review. *Powder Technology*, 147(1–3): 94–112.

He, M Z, Wang, Y M and Forssberg, E, 2006. Parameter studies on the rheology of limestone slurries. *International Journal of Mineral Processing*, 78(2): 63–77.

Hu, J C, Yu, X G, Shi, Q, Bing, X L and Luo, Q Y, 2020. Effect of serpentine content on rheological properties and flotation of pulp. *Metal Mine*(12): 125–129.

Li, G S, Deng, L J, Cao, Y J and Ran, J C, 2016. Effects of NaCl on coal flotation and its mechanism. *Journal of China University of Mining and Technology*, 45(5): 1038–1042.

Liu, D Z, Zhang, G F and Gao, Y W, 2021. New perceptions into the detrimental influences of serpentine on Cu-Ni sulfide flotation through rheology studies and improved the separation by applying garnet. *Minerals Engineering*, 171: 107110.

Liu, G H, Huang, Y J, Zhang, M, Li, X B, Peng, Z H and Zhou, Q S, 2009. Influence of Surfactants on the Rheological Properties of Bauxite Tailings. *Mining and Metallurgical Engineering*, 29(2): 25–28.

MacCarthy, J, Nosrati, A, Skinner, W and Addai-Mensah, J, 2016. Atmospheric acid leaching mechanisms and kinetics and rheological studies of a low grade saprolitic nickel laterite ore. *Hydrometallurgy*, 160: 26–37.

Mewis, J and Wagner, N J, 2012. *Colloidal Suspension Rheology*. Cambridge University Press, New York.

Mosa, E S, Saleh, A H M, Taha, T and El-Molla, A M, 2008. Effect of chemical additives on flow characteristics of coal slurries. *Physicochemical Problems of Mineral Processing*, 42: 107–118.

Mueller, S, Llewellin, E W and Mader, H M, 2010. The rheology of suspensions of solid particles. *Proceedings of the Royal Society A: Mathematical, Physical and Engineering Sciences*, 466: 1201–1228.

Muster, T H and Prestidge, C A, 1995. Rheological investigations of sulphide mineral slurries. *Minerals Engineering*, 8(12): 1541–1555.

Ndlovu, B, Forbes, E, Farrokhpay, S, Becker, M, Bradshaw, D and Deglon, D, 2014. A preliminary rheological classification of phyllosilicate group minerals. *Minerals Engineering*, 55: 190–200.

Papo, A, Piani, L and Ricceri, R, 2002. Sodium tripolyphosphate and polyphosphate as dispersing agents for kaolin suspensions: rheological characterization. *Colloids and Surfaces A: Physicochemical and Engineering Aspects*, 201(1–3): 219–230.

Patra, P, Bhambhani, T, Nagaraj, D R and Somasundaran, P, 2012. Impact of pulp rheological behavior on selective separation of Ni minerals from fibrous serpentine ores. *Colloids and Surfaces A: Physicochemical and Engineering Aspects*, 411: 24–26.

Prestidge, C A, 1997. Rheological investigations of ultrafine galena particle slurries under flotation-related conditions. *International Journal of Mineral Processing*, 51(1): 241–254.

Qi, L J, Gu, S Q and Yin, Z L, 2013. Research on rheology of gibbsite-boehmite bauxite slurry. *Mining and Metallurgical Engineering*, 33(5): 101–105.

Ralston, J, Fornasiero, D, Grano, S, Duan, J and Akroyd, T, 2007. Reducing uncertainty in mineral flotation-flotation rate constant prediction for particles in an operating plant ore. *International Journal of Mineral Processing*, 84: 89–98.

Tadros, T F, 2010. *Rheology of Dispersions: Principles and Applications*. Wiley-VCH.

Tari, G, Ferreira, J M F and Fonseca, A T, 1999. Influence of particle size and particle size distribution on drying–shrinkage behaviour of alumina slip cast bodies. *Ceramics International*, 25(6): 577–580.

Wang, C, Zhang, Q, Mao, S and Qin, S H, 2020. Effects of fine minerals on pulp rheology and the flotation of diaspore and pyrite mixed ores. *Minerals*, 10(1): 60.

Wang, L and Li, C, 2020. A brief review of pulp and froth rheology in mineral flotation. *Journal of Chemistry*, 2020: 1–16.

Xu, D, Ametov, I and Grano, S R, 2012. Quantifying rheological and fine particle attachment contributions to coarse particle recovery in flotation. *Minerals Engineering*, 39: 89–98.

Yang, J T, Fan, H, Bu, Z Y and Li, B G, 2005. Swelling behavior of montmorillonite, rheological behavior of montmorillonite aqueous suspension and blend of suspension and emulsion. *Journal of the Chinese Ceramic Society*, 33(12): 1457–1463.

Yu, X G, Hu, J C and Shi, Q, 2020. Effects of calcium ion and sodium hexametaphosphate on slurry rheology. *Non-Metallic Mines*, 43(4): 24–27.

Zhang, M and Peng, Y J, 2015. Effect of clay minerals on pulp rheology and the flotation of copper and gold minerals. *Minerals Engineering*, 70: 8–13.

Zhou, Z, Scales, P J and Boger, D V, 2001. Chemical and physical control of the rheology of concentrated metal oxide suspensions. *Chemical Engineering Science*, 56(9): 2901–2920.

Advances in mineral processing – pre-concentration and waste rejection

Pre-concentration by screening – a cost-effective approach to testing and evaluation

N Clarke[1] and A Barros[2]

1. Principal Consultant, Imtech Pty Ltd, Perth WA 6009. Email: imtech@ozemail.com.au
2. Professional Senior de Metalurgia, Minera de Cobre Quebradona, Medellin, Colombia. Email: abarros@AngloGoldAshanti.com

ABSTRACT

Preconcentration of run-of-mine subgrade and marginal ore by screening has the potential to substantially improve the economics of mining, particularly for large, low-grade orebodies, and to reduce environmental impacts. It has recently been the subject of a major research effort by a joint public-private research body, CRCORE. Yet despite this, there appears to have been only one fully commercial installation, at Bougainville Copper Limited in the late 1980s. Two reasons for the limited application are that not all ores have suitable properties and the economics of all pre-concentration processes on low-grade materials are highly sensitive to the precise balance of mass and value recovery and to the pre-concentration process cost, including materials handling. These factors make it imperative to have good test data on the process response of feedstock across the orebody. Collecting that data presents major challenges, which differ for green and brownfields operations.

This paper first discusses the approach to preliminary evaluation developed by CRCORE, which relies on testing of coarse rejects or drill chips available from exploration drilling programs. This method is an efficient first step in evaluating an orebody which is deemed geologically to be potentially amenable to screen upgrading, but it does have limitations and must be followed by larger scale work. A suite of methods have been developed by the authors as a result of test work since the 1990s on several projects, supplemented by published data, which aim to provide statistically robust data at lower cost than large scale bulk sampling tests.

For greenfields projects, the upgrade response measured on material crushed to -53 mm has been found to correlate closely with ROM ore, with no scale-up required for material with upgrade responses in the range of commercial interest. Large diameter whole drill core, such as PQ, is expected to be suitable for this method. As drilling such core is costly, the aim should be to establish relationships between upgrade performance and proxy measurements such as multi-element chemical or hyperspectral analyses. This approach was successful at the Gramalote gold project in Colombia. The method is not applicable for ores with thick vein material comparable with the crush size, but such material is not suitable for upgrading by screening and would be eliminated by the preliminary testing.

For brownfields projects where blasted material can be sampled, the upgrade response can be accurately measured by sampling only the finer fraction of the ore, selecting a top size which represents 30–50 per cent or more of the ROM size distribution. This is likely to be between 50 and 100 mm. The much finer size compared with the full ROM ore greatly reduces the sample mass required to achieve a given intrinsic sampling error and enables sample preparation to be undertaken with large-scale laboratory equipment rather than mobile crushing plant. The accuracy of the method can be improved by measuring the approximate mass of oversize rejected during sampling. Some ores do show a systematic deviation from the assumed model fit which results in this method slightly underestimating the upgrade response, and it would therefore still be recommended to take one or two full bulk samples to confirm results before a final investment decision.

INTRODUCTION

There has been increasing interest in recent years in methods of pre-concentrating ore by rejecting waste at coarse sizes, as reducing head grades have increased the amount of material to be processed. For much of the 20th century the main response to lower grades was increasing process plant throughput and using larger equipment, including mine trucks, tumbling mills and flotation cells. Carrasco *et al* (2014) showed that between 1960 and 2000 available mine truck payload increased from 35 t to 380 t, or more than ten times, leaving little scope for further cost reduction by this

approach. The disposal of large quantities of fine process tailings with acceptable safety standards is increasingly difficult and costly (ICMM, 2021) and for large new mines in arid areas such as Western Australia, sourcing sufficient water at acceptable cost can be as critical as finding the orebody itself.

Pre-concentrating low-grade ore or mineralised waste by screening is a simple process that has the potential to markedly improve production economics. The process was operated at large scale (6000 t/h) at Bougainville Copper Limited (BCL) from January 1987 until mine closure in 1989 (Burns and Grimes, 1986). Run-of-mine (ROM) material that would otherwise have been categorised as waste was screened at 31–50 mm, recovering 60–70 per cent of the copper into 30–40 per cent of the feed mass in screen undersize, with an upgrade factor of about 1.8. Low-grade ore was also screened and upgraded. Overall, the same quantity of material was fed to the process plant but with higher grade and higher resource recovery.

A cooperative research centre was established in 2010 in Brisbane, Australia with the task of Optimising Ore Extraction (CRCORE) and a major focus was pre-concentration by screening, potentially enhanced by coarser blasting of waste (Rutter, 2017). CRCORE subsequently assisted with major trials at:

- Newcrest's Telfer mine in Western Australia (Bowman and Bearman, 2014).
- Anglo American's Los Broncos mine in Chile (Keeney *et al,* 2020).
- AngloGold Ashanti's Gramalote project in Colombia (Clarke *et al,* 2020).
- Sumitomo's Minera San Cristóbal mine in Bolivia (Adair *et al,* 2019).

In all of these cases, some ore types upgraded as effectively as the amenable ores at BCL but of the three operating plants, only San Cristóbal is known to have continued to operate screening plant for some time after the trials. Bowman and Bearman (2014) noted that it may be difficult to achieve the potential benefits when retrofitting screen upgrading to a brownfields operation and greenfields applications may be more promising. Another factor critically affecting economics of all pre-concentration processes is that additional costs are incurred for materials handling and additional processing, whilst some values are lost to the reject stream. Superficially attractive processes often prove to be uneconomic on further analysis. It is thus essential to have a reliable means of predicting upgrade performance in the planning stage for any pre-concentration project, and mapping it across the orebody.

PREDICTING PERFORMANCE FROM COARSE REJECTS

A key outcome of the work by CRCORE was the development of a relatively low-cost method to identify orebodies potentially amenable to upgrading by screening (CRCORE, 2014). The method relies on the fact that diamond drill core from mine exploration programs is usually split using a diamond saw, then the entire mass of half the core crushed to typically <3 mm, and a subsample pulverised and assayed. The remaining <3 mm material, termed the 'coarse rejects,' is stored and can be made available for further testing. Where reverse-circulation (RC) drilling is used, chips of similar size are also generated and stored and may be used instead.

The evaluation involves taking representative samples of coarse rejects for typically about 100 drill intercepts initially and screening to produce four or five size fractions. Where possible screen sizes are chosen to ensure a minimum of 10 per cent and a maximum of 30 per cent mass in each fraction (Adair *et al,* 2019) and the sample mass is selected to provide sufficient for assay in all fractions.

The cumulative metal and mass recoveries to undersize are calculated. Results can be presented either as plots of metal recovery versus mass recovery or an 'Upgrade Factor' (UF) can be calculated by dividing metal recovery by mass recovery and plotting against mass recovery (all as cumulative values). The product grade at any point on the curve is the feed grade multiplied by UF. Although the shape of the relationship varies with different ores, a good linear regression fit can generally be obtained by plotting the log of the UF against log cumulative mass recovery (BoBo *et al,* 2020). Since UF is 1 when 100 per cent of the feed reports to undersize, the log:log relationship can be forced through the point 0:0 and the constant is zero. The slope of the regression line then represents the comparative strength of the upgrade response. The best possible response is 100 per cent recovery

of values to undersize at all mass pulls, which gives a maximum slope of -1. Multiplying the slope by -200 gives a Ranking Response (RR) number, which thus varies between 0 and 200 if upgrading to the fines occurs or could theoretically vary down to -200 where an ore upgrades into the oversize.

The approach is illustrated in Figure 1 using data from work on the Gramalote deposit (Clarke *et al,* 2020) and from the Los Bronces deposit (CRCORE, 2014). The data from the Los Bronces drill hole closely follows the log-log relationship, but the Gramalote data shows what has been termed a 'bird-wing' effect, where the response is strong at coarser sizes but relatively weaker at finer. This is seen most clearly when the data is plotted as metal versus mass recovery, in Figure 1a. The reason for this effect is thought to be that gold at Gramalote is strongly associated with pyrite and the average pyrite grain size is 2 mm, coarser than the crush size for the coarse rejects. However, this limitation is not relevant to upgrading at industrial sizes.

Despite this bird-wing effect and the occurrence of some samples which upgraded to the coarse fractions, overall the Gramalote ore samples had an average RR about 90, well above the RR 80 which CRCORE regarded as indicating a strong potential for pre-concentration by screening alone, without additional manipulation such as selective blasting. A conceptual study showed that this process had the potential to add substantial value to the Gramalote project and justified a further extensive study (Clarke *et al,* 2020).

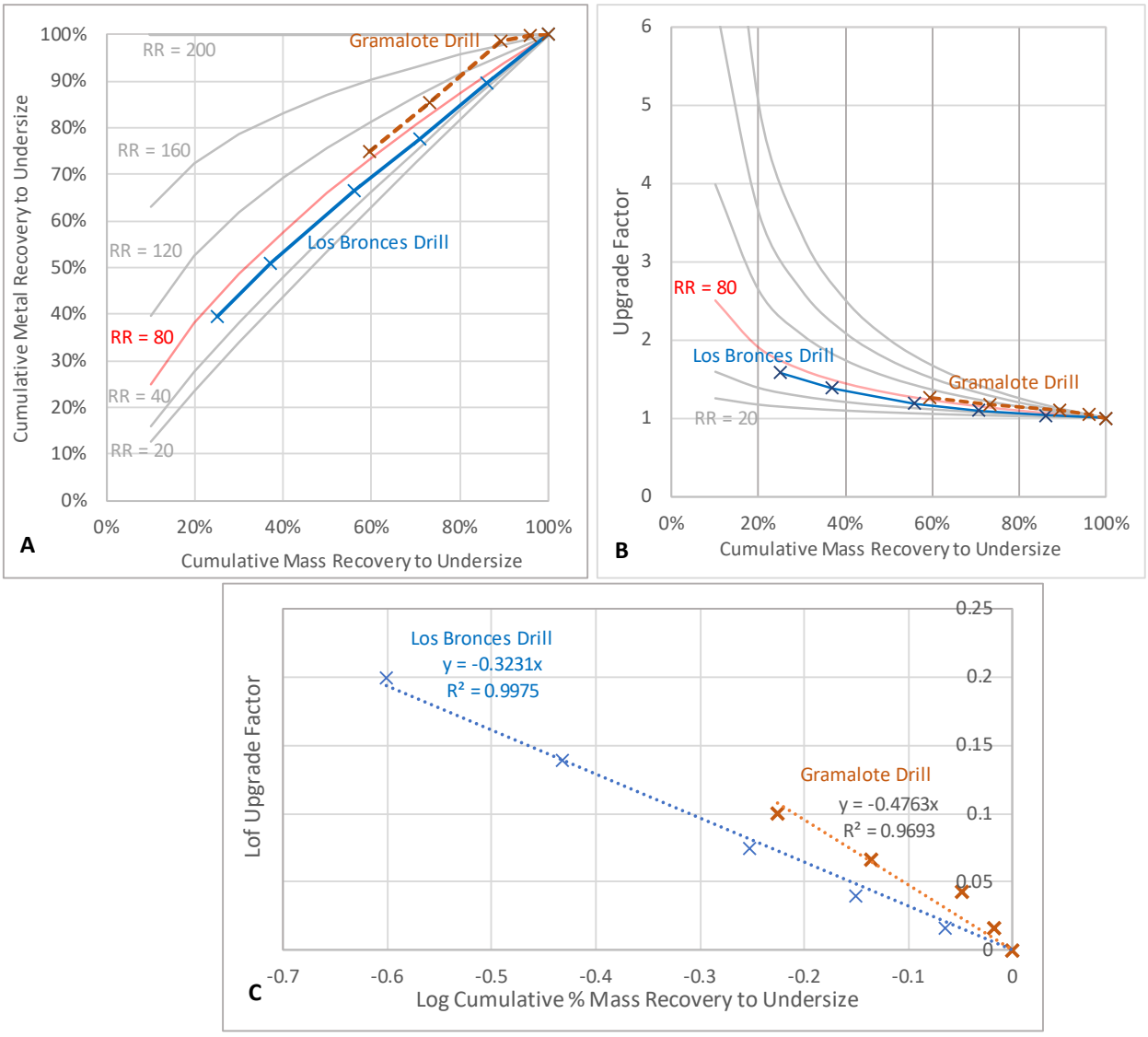

Los Bronces Diamond Drill Data						Gramalote Diamond Drill Data DD59					
Sieve	Mass	Cu	Cum % to U/S		Upgrade	Sieve	Mass	Au	Cum % to U/S		Upgrade
mm	g	%	Mass	Metal	Factor	mm	g	g/t	Mass	Metal	Factor
2.36	152	0.37	86%	90%	1.038	1.70	284	0.013	96%	100%	1.040
1.70	170	0.37	71%	78%	1.096	1.18	454	0.029	89%	99%	1.105
1.18	164	0.36	56%	66%	1.189	0.60	1106	0.150	73%	85%	1.167
0.60	208	0.39	37%	51%	1.379	0.30	944	0.139	59%	75%	
0.30	132	0.46	25%	40%	1.583	-0.30	4092	0.230			
-0.30	276	0.76	0%	0%							
Total	1102	0.48				Total	6880	0.183			
Slope RR					-0.323 65	Slope RR					-0.476 95

Los Bronces data extracted from TR#080, 2014

FIG 1 – Example data calculation and presentation for analysis of diamond drill coarse rejects.

The Los Bronces raw drill hole data generally did not meet the RR 80 benchmark, but large-scale trials proceeded to investigate the full suite of Grade Engineering® techniques which includes methods of enhancing the natural response (Keeney *et al,* 2020).

Although testing of coarse rejects has been established by CRCORE as a useful technique for identifying orebodies or ore types potentially amenable to upgrading, the resulting upgrade response does not equate directly to the response on ROM ore and has to be scaled. This is illustrated in Figure 2 with Figure 2a showing data from the Gramalote project (Clarke *et al,* 2020) while Figure 2b shows published data for a copper porphyry mine (Carrasco *et al,* 2014).

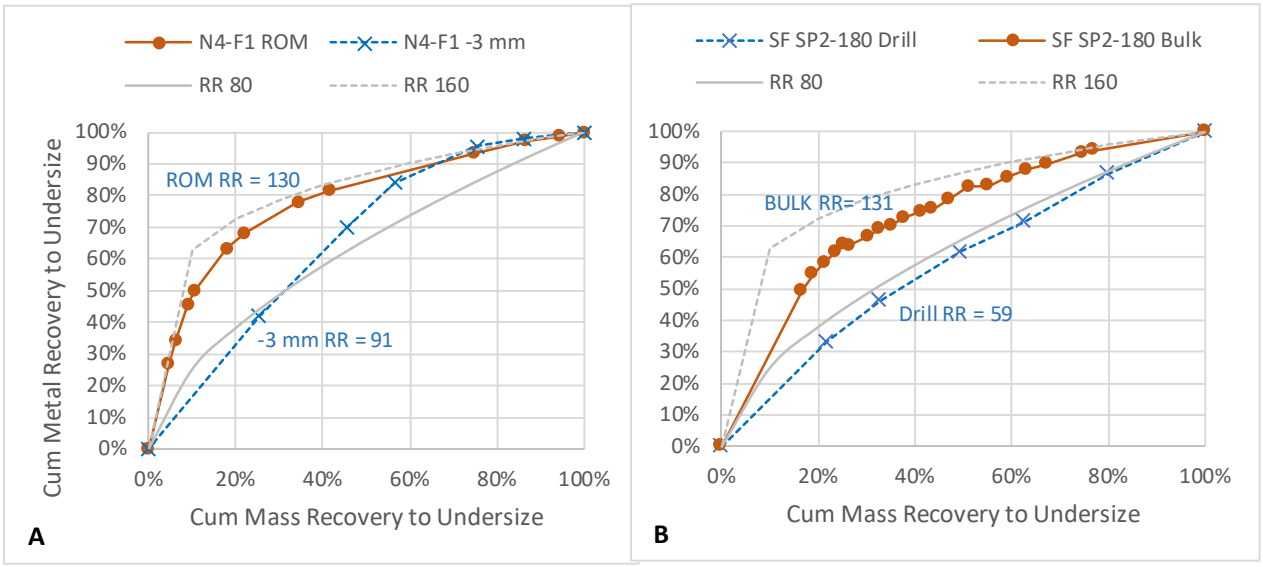

FIG 2 – Comparison of upgrade responses on ROM and -3 mm crushed ore for two deposits.

In these examples there is a large difference between the upgrade response on ROM ore (brown) and -3 mm crushed material (blue) for both ores. At a typical mass pull of 40 per cent, the difference on Gramalote ore is 80 per cent gold recovery on ROM ore versus 62 per cent on -3 mm crushed material, which is economically very substantial. The difference is not constant but varies with ore type and mass pull.

In Figure 2b the nominal -3 mm material is from crushed drill core while 'Bulk' is from testing of a sample of ROM ore. In Figure 2a however, both samples were derived from the same bulk ore sample mined from an underground adit. During testing for the Gramalote project, 18 bulk samples of about 17 t each were taken from the adit. Six cross-cuts were mined, located along the adit so as to provide good spatial and head grade coverage of the main orebody. At each cross-cut, three successive 1.6 m cuts were taken, thus providing a measure of short-range variability. Twelve of the samples were tested as received and also at three crush sizes. The finest crush size used the same final crushing procedure as used on diamond core. A progressive crushing technique was used, so all crushed products derived from the same head sample, thus eliminating the effect of sampling errors at ROM size. The overall sampling error for the coarsest fractions was estimated as ±10 per cent (Clarke *et al,* 2020). Figure 2a above shows that the -3 mm products showed the same 'bird-wing' effect as seen in the crushed drill core.

Figure 3 compares the upgrade response in the -3 mm and ROM materials for all samples. For this purpose, the gold recovery at 40 per cent mass pull to undersize has been read from manually fitted curves, as this allows a better fit to the -3 mm data than the log-log fit. A mass pull of 40 per cent is a likely operating point for Gramalote ores. Figure 3 shows that the average response estimated from the -3 mm material is a useful predictor of the **average** response of ROM ore but provides no information on variability.

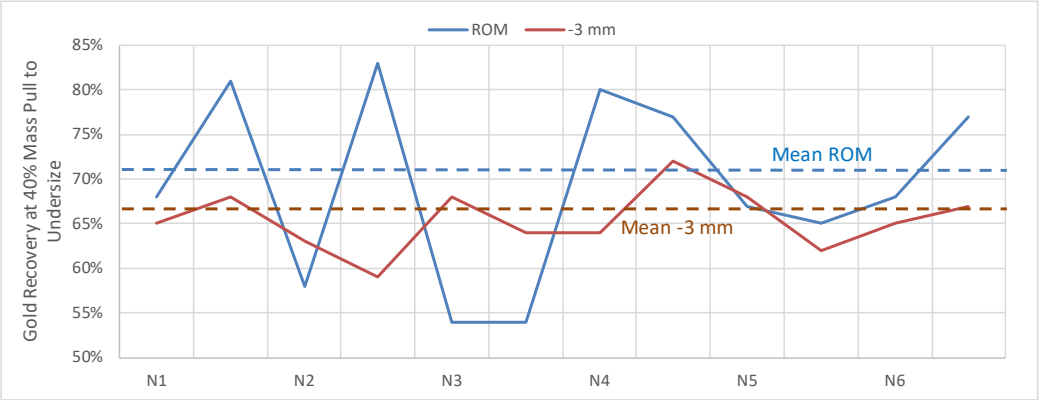

FIG 3 – Upgrade response in ROM and -3 mm material at six cross-cuts along an adit at Gramalote.

CORE BREAKAGE EVALUATION

The potential for pre-concentration by screening is entirely dependent on the way the ore breaks. Explosive blasting breaks ore by two mechanisms: breakage due to tensile waves which will tend to occur along planes of weakness and breakage in the pulverised zone close to the charge (Bauer and Crosby, 1990). In the pulverised zone softer minerals are preferentially broken which results in the practically universal upgrading of values in the fines for sulfide bearing ores. However, although the metal grades in the fines can be high, the mass of material involved is often small and by itself does not represent an economic opportunity. This was found to be the case, for example, in a preliminary study of the potential for screen pre-concentration at the Sunrise Dam mine of AngloGold Ashanti (Clarke, 2014).

For the cases discussed in this paper, economic opportunities for screen pre-concentration arise when:

- metal values are strongly vein-associated with minimal values disseminated through the rock matrix; and
- breakage occurs along mineralised fracture planes, or veinlets, which are more frequent in higher grade ore.

In such ores, higher grade material breaks finer (Burns and Grimes, 1986). A small-scale study was carried out at Gramalote (Clarke *et al,* 2020) to better understand breakage patterns in core and the approach is strongly recommended to ensure results of subsequent larger-scale programs are correctly interpreted and indeed worthwhile. It involved selecting 6 × 1 m lengths of core covering all the key alteration types, measuring and photographing veins or fractures and vein spacing and breaking with controlled hammer blows of increasing force while the core lengths were supported by the ends only. The process continued until all material was less than 50 mm (a typical pre-concentration separation size). The products were sorted into three categories: preferentially broken along mineralised planes, randomly broken and thick high quartz veins.

The work showed that not all veins were planes of weakness and some low and medium grade ore with average vein spacing about 50 mm nonetheless broke randomly with no upgraded fraction. Thick quartz veins could result in gold reporting preferentially to oversize. The overall strong upgrade response to the fines in this test resulted from one piece of core with only five fractures/m, but for which preferential breakage of the fractured section resulted in pieces assaying 9 g/t and carrying 90 per cent of the gold, while the randomly broken material assayed 0.1 g/t.

Coarse assay rejects at -3 mm cannot carry information on the effects of vein spacing, continuity and fracture resistance which affect large scale upgrading results. Crushing to -3 mm does however result in preferential crushing of softer vein material versus the rock matrix and therefore measures the amount of vein associated values and the potential for upgrading. Where vein material is hard, reverse upgrading will be observed. Where the values are vein associated but the veins do not break readily, fine crushing may overstate the full-scale upgrade potential whereas when veins break readily fine crushing will understate the potential.

Coarser crush sizes may correlate better with upgrade potential but as will be discussed below, it is likely that the crush size needs to be larger than the vein thickness, and probably than the average vein spacing, to achieve reliable results.

PREDICTING UPGRADE PERFORMANCE FROM CRUSHED DRILL CORE

It has been shown above that analyses of -3 mm coarse rejects provide a good preliminary indication of orebody amenability to preconcentration by screening, but do not directly measure upgrade potential or variability. For greenfields projects another method of evaluation based on drill core is essential.

The initial study into pre-concentration by screening at BCL involved taking 134 haul-truckloads of 140 t ore each from all accessible ore zones and subsampling by conveyor cuts or fractional shovelling to produce 1.5–2 t subsamples. The samples were screened at sizes from 152.4 to 12.7 mm and each fraction was stage crushed and split to produce 200 g samples of -1 mm material for assay (Burns and Grimes, 1986). The Bougainville ores were naturally highly fractured, with 95 per cent passing 150 mm in ROM ore (Paki and Koginmo, 1988), thus reducing sample preparation costs and intrinsic sampling errors. To enable prediction of upgrade performance in future ore sources, a diamond drilling campaign was completed. A short tumbling test was developed, testing 3 m lengths of drill core taken from every 30 m. The process was designed to break the ore along major weaknesses and so simulate the effect of blasting. Unfortunately, no details of the core diameter or test conditions used were published. To calibrate the drill core results, a hole was drilled through two mining benches and bulk samples taken from around the holes. Both tumbled core and the bulk sample were screened at 31.75 mm, resulting in similar masses to undersize at 34.5 per cent for core and 32.5 per cent for the bulk sample. Both copper and gold recovery to the undersize were substantially higher for the bulk sample, at 64 per cent versus 59 per cent for copper and 67 versus 60 per cent for gold. For planning purposes the drill core results were scaled up by the difference.

Gramalote project

For the Gramalote project, as discussed above, bulk samples were mined from six cross-cuts along an exploration adit. Of the three successive 17 t cuts at each of the six locations, two processed the full 17 t using a progressive crushing approach that resulted in upgrade curves at ROM, -53, -24 and -3 mm crush sizes. The third cut was used for a preliminary program which processed a 1 t subsample at two sizes, ROM and -53 mm, again using a progressive crushing approach. The preliminary program was intended to provide an early indication of feasibility as well as detailed sampling error and particle size information which could be used to design the full program. In practice, the results of the preliminary program were not significantly different to the results of the subsequent more comprehensive testing.

There were several reasons for testing at different crushed sizes, but one was to investigate if crushed drill core could be used to measure upgrade response and map it across the orebody. The results at -3 mm would be ideal but the limitations were discussed above. Next preferred would be a nominal 24 mm crush size as it is achievable with half-core of typical routine diameter (eg NQ or NTW), but -53 mm would be feasible, albeit quite costly, using purpose drilled whole PQ or HTW core.

Figure 4 shows the relationship between the RR values on crushed material and on ROM ore, with ROM ore on the X-axis and Crushed Products on the Y-axis. It shows that RR values on -53 mm material (blue) are strongly correlated with ROM material, with a correlation coefficient (R^2) of 0.93. The grey line shows a 1:1 relationship for comparison and the responses on ROM and crushed material are practically identical above RR 100, but on lower response ores the -53 mm crushed material slightly overestimates the ROM response. In practice it is the higher response ores which would justify installation of screening.

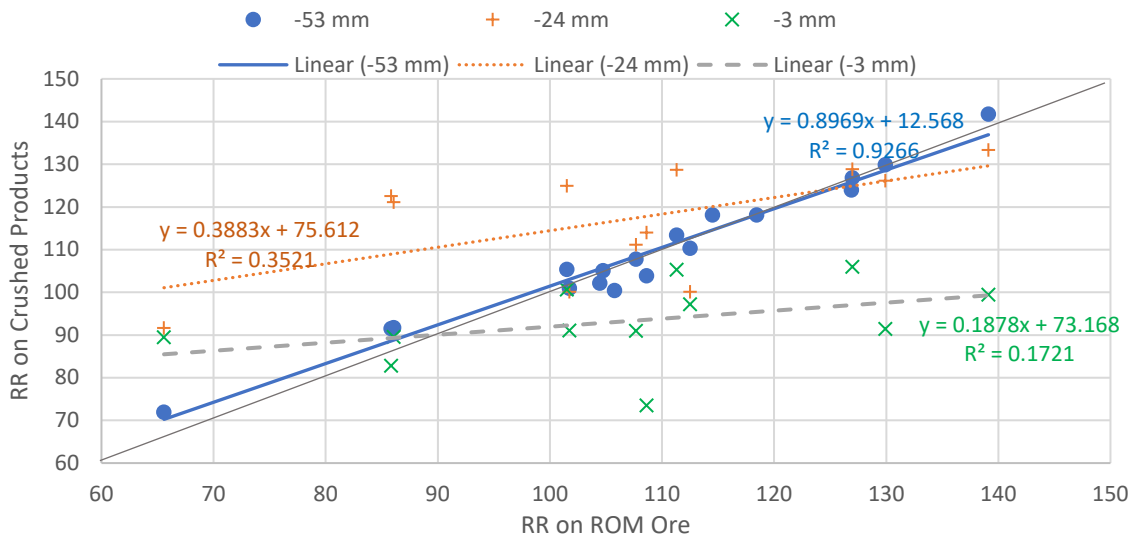

FIG 4 – Ranking responses for ROM and crushed Gramalote samples.

The RR values on crushed -24 mm material (brown) correlate poorly with the ROM ore, with R^2 0.35. The relationship is far from 1:1 so presents the same problem as coarse rejects, that the results require calibration by tests at coarser sizes over a range of ores with different responses. Crushing to -24 mm does substantially improve the upgrade response on lower response ores, as seen to a much lesser extent with crushing to -53 mm, but the improvement would not justify the cost of crushing.

The RR values on -3 mm crushed material confirm the lack of a relationship with ROM ore that was seen in Figure 3, with R^2 0.17. The fine crush size reduces the upgrade response across all ores except for the single sample with ROM RR<70.

Gold recoveries at 40 per cent mass pull have also been read from manually fitted curves for all samples and are shown in Table 1.

TABLE 1

Mean gold recoveries at 40 per cent mass pull to undersize.

	Au Recovery %			
	ROM	**Crush**	**P(T<=t) 2-tail**	**No. of pairs**
Crushed -53 mm	70.2	70.6	0.51	18
Crushed -24 mm	69.3	74.7	0.03	12
Crushed -3 mm	69.3	65.4	0.24	12

Table 1 shows that at 40 per cent mass recovery the gold recovery on nominal -53 mm crushed material is only 0.4 per cent higher than on ROM ore and this difference is not statistically significant using a paired t-test at 95 per cent confidence interval. Crushing to -24 mm does significantly increase average recovery, by 5.4 per cent, and crushing to -3 mm reduces average recovery by 3.9 per cent, which is however not statistically significant.

Los Bronces

Test work at the Los Bronces mine also explored the effect of crushing on upgrade response (Keeney *et al,* 2020) using pilot plant test work at tonnage scale. There was no significant effect from crushing over the range from 200 mm to 37.5 mm. Three ore samples were tested and were subject to a progressive crushing procedure with all size fractions derived from a single head sample. The samples were sourced from an open pit, but it was assumed upgrading would be practiced on primary crushed ore or finer, hence the coarsest size examined simulated primary crushing

to -200 mm. This work supports the conclusion that crushed material down to 37.5 mm can be used to evaluate the upgrade response of ore.

Kalgoorlie Consolidated Gold Mines

A major investigation into preconcentrating by screening was carried out at Kalgoorlie Consolidated Gold Mines (KCGM) in 1992–1993 (Clarke, 1993). The project started because three samples of -100 mm material taken from subgrade material dumps for heap leach test work had much higher grades than expected from block modelling. It was considered that the high-grades could either be due to natural upgrading in the finer fractions, or imprecision in modelling and material routing. In either case, there was a large potential financial benefit from an investigation. The test program included processing one entire nominal 10 000 t subgrade block through the small Paringa plant; processing 15 samples of -100 mm material through a purpose-constructed 1 t/h Mini-screening and crushing plant; for each of three blocks from the 15, processing four replicate subsamples of 130–200 t each through a mobile crushing and screening plant and then processing selected products from that plant through the Mini-plant; and finally testing an additional eight selected subgrade samples through the Mini-plant.

The final conclusion from the project was that although 19 of the 26 samples tested did upgrade to the fines, in no case was pre-concentration by screening more profitable than direct treatment. However, the project led to the development of much useful knowledge for future screen upgrading studies and to improved methods for block delineation and hence material allocation.

For the three blocks treated through the mobile crushing plant, all samples were first passed over a 100 mm grizzly and the oversize and undersize were separately crushed and sampled. Sample masses were determined by a weightometer, by bucket counts and by stockpile survey. The most reliable procedure was found to be the survey. The crushing plant consisted of a primary jaw crusher followed by a screen in closed-circuit with a cone crusher. The final product was about 80 per cent passing 11 mm. Four replicate subsamples were taken of this product for both oversize and undersize for each of the four replicate subsamples from each block. Each subsample was assayed in duplicate for a total of 64 assays for each oversize and undersize product, so the degree of upgrading into the -100 mm fraction could be measured and the errors could also be assessed.

For all three blocks, separate samples of uncrushed -100 mm material had previously been sized and assayed using the Mini-plant, so the ROM upgrade response curve could be determined. Additionally, for all three blocks the -11 mm crushed product was sized and assayed and for two of the blocks the primary crusher product was sized and assayed. Thus, upgrade responses were measured on material crushed to 80 per cent passing 70 mm and 11 mm. The upgrade responses are reported in Figure 5 using the CRCORE method of calculation.

The RR determined on -100 mm ROM material will be discussed in a later section. Figure 5 shows however that for KCGM ores RR values from neither primary crushed nor fine crushed material correlate with RR values determined from ROM ore. The average value on fine crushed ore does provide an indication of the average value on ROM ore but provides no information on block-by-block variations. This is similar to the situation with -3 mm crushed material on Gramalote ores. The size-by-size data on primary crushed ore is very erratic, as can be seen by comparing results for samples A and B but it nonetheless appears that crushing has suppressed the block-by-block variation in response.

The results from KCGM do not negate the concept of estimating RR from suitably crushed drill core, but they do show the importance of preliminary coarse reject and core breakage studies to understand the nature of the ore and its amenability to screen upgrading before undertaking larger scale work. Figure 5 shows the low upgrade response of fine crushed ore, averaging RR 27, which would have ruled out further work had the preliminary evaluation techniques discussed above been available at that time.

Block	RR Calculated from:					
	ROM	ROM	Primary Crushed			Fine
	All	-100 mm	Mean	A	B	Crushed
140217 #1	48	56	ND			26
15004	30	37	3	10	-6	38
150021 #4	22	43	3	14	-14	17
Mean	33	45	3	12	-10	27
P(T<=t) 2 tail	NA	0.12	0.11	0.23	0.01	0.55

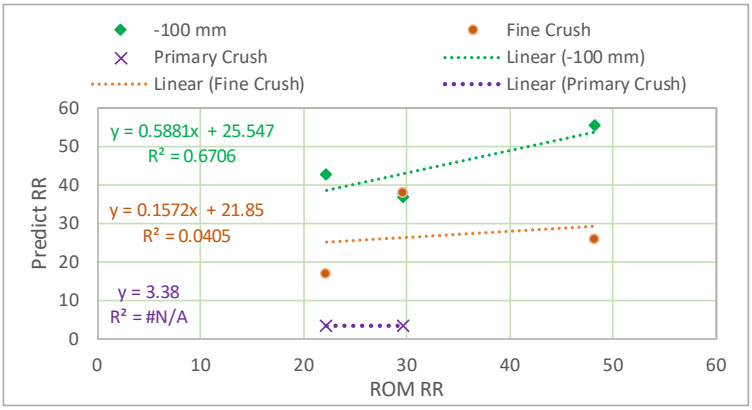

FIG 5 – Effect of crushing on upgrade response rank for KCGM subgrade ore.

ROM ORE TESTING – A LOWER COST PROCEDURE

For a brownfields project some bulk samples should be tested as part of an evaluation of pre-concentration by screening. However, in practice it is very difficult to carry out a ROM bulk sampling program and achieve reliable and reproducible results as the usually coarse size distribution requires large samples. The problem is exacerbated for gold ores containing either coarse gold grains or large gold clusters. In these circumstances investigations become primarily an exercise in reducing sample errors to the point where it is possible to draw conclusions. However, it was discovered during the investigation at KCGM (Clarke, 1993), discussed above, that the upgrade response measured on the -100 mm fraction of ROM ore appeared to be a close estimate of the response on ROM ore, probably within the accuracy of the ROM estimate. This approach has since been tested on data from three other orebodies:

- Underground ore from various shafts operated by Gold Mines of Kalgoorlie in the 1950s.
- Published data from BCL.
- Gramalote.

In all these cases full ROM samples were taken, sized and assayed. From the data, the upgrade response has been determined for the full ROM data and for various undersize fractions. For this paper the upgrade responses have been re-calculated using the CRCORE RR curve fit.

KCGM data

For KCGM open pit ore, the data is shown in Figure 5. Based on three ore samples treated through an industrial mobile crushing and screening plant, with sizing of the -100 mm material through a Mini-plant, the RR for the -100 mm material averaged 45 compared to the ROM material 33. The difference is not statistically significant. A regression analysis showed a useful correlation coefficient (R^2) of 0.67. Although this is not statistically significant, with only three data points, it led to the subsequent investigations. The 95 per cent passing size for the ROM material averaged 1260 mm and for the -100 mm fraction it averaged 93 mm. The -100 mm fraction contained 30–40 per cent of the weight in the full ROM size distribution.

The sampling theory of Gy is widely accepted for estimating sampling errors. The original form of this equation (Pitard, 1989) predicted that the sampling error was proportional to the cube of the coarsest (95 per cent passing) particle size and used a fixed liberation factor based on the ratio of the gold grain size to the particle size. Experience showed that this equation greatly overestimated actual errors on gold ores. For the test work at KCGM the estimation of sample error was based on the estimated maximum particle grade for the respective product:

$$\sigma_{FE}^2 = \left(\frac{1}{M_s} - \frac{1}{M_L}\right) \times d^3 \times f \times g \times \left(\frac{a_{max}}{a_L} - 1\right) \times RD^1)$$

Where:

σ_{FE}^2 is the fundamental sampling variance

M_s is the sample mass (g)

M_L is the lot mass (g)

d is the particle diameter in cm, taken as the 95 per cent passing size

f is the shape factor (f × d^3 = volume)

g is the size distribution factor, which corrects top size to average size

a_{max} is the maximum particle grade (decimal fraction) of mineral for particles of diameter d

a_L is the lot grade as a decimal fraction of mineral

$RD^1 = \frac{RD_{Au} \times RD_g}{RD_g \times a_{max} + RD_{Au} \times (1 - a_{max})}$ which is the density of a particle at maximum grade

Where:

RD_{Au} is the relative density of gold

RD_g is the relative density of gangue

In this equation the sampling variance is still proportional to the cube of the particle diameter but is moderated by the reduction in maximum particle grade in coarser products. It is impractical to exactly determine the maximum grade of 1 m lumps in ROM ore and so the maximum grade was estimated from the measured coefficient of variation of replicate assays at finer sizes, using a hierarchical analysis of variance. It was found that there was a good relationship between particle size and maximum particle grade, of the form:

$$Log_{10}(a_{max}) = 4.33 - 1.77 \times log_{10}(d)$$

for which $R^2 = 0.63$

Extrapolating above 200 mm using this relationship, the estimated maximum particle grade for the top size in ROM ore is 4.2 g/t. In the -100 mm fraction it is 421 g/t. The total quantity of ROM ore treated in the mobile plant for each block was about 500 t while the Mini-plant treated 4–5 t of the -100 mm ROM fraction. With these quantities, the estimated coefficient of variation on the head grades, based on maximum particle grades, is ±7 per cent for ROM ore and ±13 per cent for the -100 mm fraction. The error on the -100 mm fraction could be reduced to 7 per cent by treating 20 t samples, or just 4 per cent of the tonnage to be treated at ROM size for the same error. Moreover, whereas large scale on-site equipment is needed to establish the grade of ROM ore, -100 mm material can be processed at some commercial testing laboratories. Of course, the actual sample size that needs to be tested depends on the ore characteristics.

Gold mines of Kalgoorlie data

During the course of the investigation at KCGM some reports dating from 1955 were located, which investigated the variation of gold grade with particle size in underground ores at Gold Mines of Kalgoorlie (GMK) (Coles, 1955). At that time, it was the practice to take grab samples, literally a hand-full, from every underground truck and reconcile with plant recovered grade. The samples were taken only from the fines. Up to 1952 agreement was good but after that time underground sampling showed erratic high-grades which were not reflected in plant recovered grade. The problem correlated with increasing amounts of telluride rich gold ore. As tellurides are soft, it was thought they might report preferentially to the fines. Two initial rounds of test work were carried out which confirmed that high-grade friable material did preferentially report to the fines. A more extensive investigation was then carried out, taking 16 full 1 t truckloads from eight different shafts in the GMK stable and sizing and assaying the size fractions using eight repeat samples for every size fraction. The largest screen used was a rectangular 125 × 63 mm and this retained an average of 42 per cent of the mass but varying from 17–80 per cent for the different sources. The ore was slabby and the top size in a truck with 57 per cent oversize was measured as about 125 × 70 × 63 mm, indicating a narrow size range for the oversize material.

The Response Ranking for both the ROM material (total truck contents) and the -63 mm fractions are shown in Figure 6.

	Response Rank		Corr Coeff R^2		%<63 mm
	ROM	-63 mm	ROM	-63 mm	
Oroya 15L 1505 Stope	65	66	1.00	1.00	42.9
Oroya 6L 617 Stope	14	40	0.57	0.99	58.7
Iron Duke 9L Sec 22 OHW	10	12	0.87	0.86	82.5
Iron Duke 13L Hinchcliffe	7	26	0.37	0.98	61.7
Paringa S Shaft 1000L (a)	70	66	1.00	1.00	43.9
Paringa S Shaft 1000L (b)	105	80	0.98	0.99	48.6
NNB 4L 623 Series	36	32	0.98	0.91	20.1
NNB 7L 1160 Sec	47	58	0.99	0.97	47.7
Perseverance 9L LVN	36	17	0.93	0.94	63.8
Perseverance 22L Bell Stope	6	3	0.80	0.75	53.3
Enterprise 17L Sec 9-10 N	3	0	0.93	0.14	65.6
Enterprise 22L Greenhill	15	-15	0.46	0.54	40.8
Hainault 6L 606 Stope	35	36	0.99	0.98	85.7
Hainalt 5L Bin bulk	17	23	0.84	0.92	72.1
South Kalgurli 4L 310 Stope	27	26	0.98	0.98	73.9
S Kalgurli 2180L 8 N Stope	44	43	0.97	0.95	64.6
Mean	34	32			57.9
Probability (T<=t) two tail	0.70				

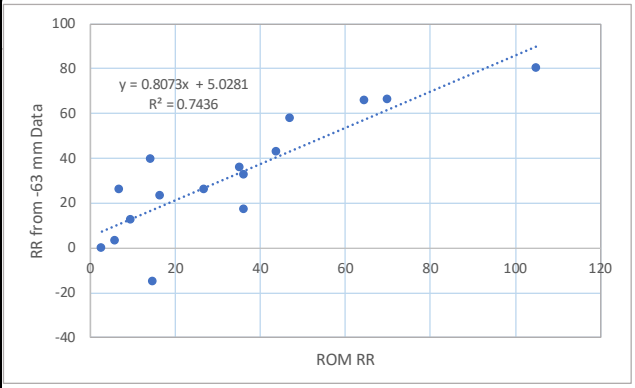

FIG 6 – Response Rankings for Run-of-Mine and -63 mm material from 16 mine trucks at GMK.

There is no significant difference between the average RR_{ROM} and RR_{-63}, which are 34 and 32 respectively. The two are also highly correlated, with R^2 0.74, which is statistically highly significant. Figure 6 also shows the correlation coefficients for the individual log-log fits used to derive RR values. In four of the six cases where the RR values differ substantially for the ROM and -100 mm fraction (highlighted in yellow), the correlation coefficient on the RR estimate for the ROM ore is low. Thus, the main factor reducing the correlation between RR_{ROM} and RR_{-63} is probably sampling errors on the oversize in the ROM ore.

Bougainville Copper Limited data

The investigation into pre-concentration by screening at BCL was discussed above. Burns and Grimes (1986) reported average size by grade and size analysis data for two ore types with a good upgrade response. The data has been extracted from the graphs and used to calculate RR values for ROM ore and for various size fractions of ROM ore. The 95 per cent passing size for ROM ore is about 150 mm, which is quite fine for open pit ore due to the highly fractured nature of the deposit, also key to the good upgrade response. The results are summarised in Table 2.

TABLE 2

Response rankings for Bougainville Copper Limited ROM ore and fractions.

	Response Rankings				Corr Coeff R^2 for RR Estimate				% Undersize		
	ROM	-152 mm	-76.2 mm	-50.8 mm	ROM	-152 mm	-76.2 mm	-50.8 mm	-152 mm	-76.2 mm	-50.8 mm
Gold											
BCL KD	115	114	109	111	1.00	1.00	1.00	1.00	98%	75%	53%
BCL PS	128	126	127	127	1.00	1.00	1.00	1.00	94%	73%	53%
Mean	122	120	118	119							
Copper											
BCL KD	88	86	82	84	1.00	1.00	1.00	1.00	98%	75%	53%
BCL PS	121	118	118	117	1.00	1.00	1.00	1.00	94%	73%	53%
Mean	104	102	100	100							

Table 2 shows very close agreement between RR values calculated from ROM ore and all size fractions. It is notable that the BCL results give a practically perfect correlation in the plots of data used to estimate RR, which doubtless contributes to the good correlations between RR for the ROM ore and size fractions. The RR values estimated from the -50.8 mm fractions are the best to compare with the other sites as the undersize in this fraction is 53 per cent of the ROM sample.

Gramalote data

Data from the Gramalote project has also been used to investigate the relationship between the upgrade response of ROM ore and of the -53 and -106 mm size fractions. The calculated RR values are shown in Table 3.

TABLE 3

Upgrade responses for Gramalote ROM ore, -50 and -100 mm fractions.

	Response Rankings					Mass% of ROM	
	ROM	-106 mm	Sim ROM -106 mm	-53 mm	Sim ROM -53 mm	-106 mm	-50 mm
N1F1	111	105	106	107	108	59	36
N2F1	86	88	89	89	89	61	42
N3F1	66	64	65	62	61	58	34
N4F1	130	126	130	114	127	75	42
N5F1	102	98	103	95	102	78	50
N6F1	102	96	99	89	94	69	51
N1F2	113	102	106	82	84	78	45
N2F2	109	97	102	69	67	44	27
N3F2	86	95	96	98	101	91	60
N4F2	139	140	143	136	142	82	43
N5F2	108	103	106	96	101	89	64
N6F2	127	125	127	117	124	72	54
N1F3	105	105	106	104	101	67	37
N2F3	106	102	107	103	113	73	45
N3F3	104	100	103	96	101	87	61
N4F3	115	109	100	117	103	82	52
N5F3	118	116	118	118	123	91	70
N6F3	127	123	127	119	118	87	60
Mean	108	105	107	101	103	75	48
t-test prob. chance		0.0104	0.3716	0.0132	0.3708		
Slope		1.001	0.970	0.737	0.745		
Intercept		3.08	4.30	34.25	28.38		
R^2		0.96	0.95	0.78	0.89		

Table 3 shows that RR_{ROM} and RR_{-106} correlate closely, with R^2 0.96. Moreover, the relationship is practically 1:1 with no scale-up factor required although the small difference is statistically significant due to the consistency of the data. This is perhaps not surprising however as on average 75 per cent of the ROM ore was in the -106 mm fraction, so a better comparison with a typical open pit situation may be the -53 mm ROM fraction, which carries 48 per cent of the mass on average. In this case the correlation coefficient is 0.78 and the mean RR for the set is 101 versus 108 calculated from the ROM ore. This is still a strong relationship, but it is worth examining why the RR from the -53 and -106 mm fractions underestimates the true RR for most samples. Sample N2F2 may be taken as an example.

GRT-N2-F2				
Sieve Held, mm	Cum % Pass	Au g/t	Au % Pass	UF
+175	100		100	1.00
175	82.1	0.01	97.04	1.18
125	65.7	0.02	92.08	1.40
75	44.0	0.02	85.63	1.95
53	28.9	0.06	72.96	2.52
39.8	18.7	0.12	56.33	3.02
23.8	11.6	0.19	38.87	3.34
19.8	10.1	0.17	35.41	3.51
12.3	7.5	0.14	30.50	4.09
9.8	6.4	0.18	27.99	4.35
4.7	4.9	0.22	23.58	4.81
2.8	3.4	0.31	17.22	5.11
-2.8	0.0	0.39	0.00	
Total		0.08		

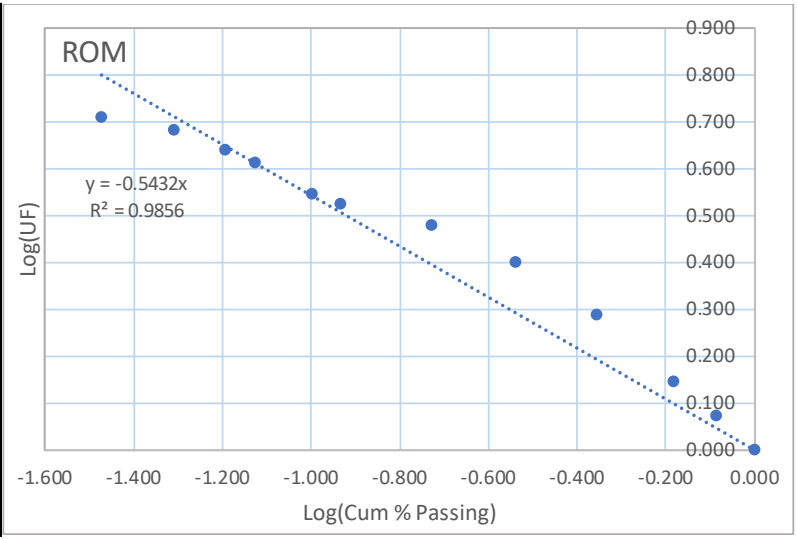

FIG 7 – Size-assay distribution for Gramalote ROM sample N2F2 and RR estimation plot.

Figure 7 shows the variation in gold grade with particle size and the resulting log Cum per cent Passing versus log UF plot. The data table in Figure 7 shows a sharp decline in the gold grades above 40 mm, which results in a systematic deviation above the line for the first five points in the log-log plot. This systematic deviation also means that the log-log curve fit underestimates the benefits of upgrading by screening at mass pulls of around 40 per cent. For that reason, evaluation of screen upgrading for the Gramalote pre-feasibility study was based on plots of raw data, not the mathematical curve fit (Clarke *et al,* 2020). There is no way to overcome this problem without the additional cost of sampling the top-size material, but as can be seen in Table 3 the impact is effectively some additional conservatism in the economic evaluation.

It is possible to improve the correlation with RR_{ROM}, particularly for the -53 mm fraction, by reconstructing an approximate ROM sizing. This refinement of the method requires that the mass percentage of the +50 mm material is measured during sampling, but not the assays. The geometric mean size of the +50 mm material also needs to be approximately known, which can be determined using image analysis. The work would be most economically carried out by a small excavator or backhoe fitted with a sieve bucket and weighing instrumentation. The largest rocks may exceed the machine's capacity and are pushed aside and counted. The remainder of the material is weighed in the sieve bucket then sieved with the undersize being collected in a skip-bin or bulk bags. The oversize is discarded. The undersize is subsequently also weighed, then sent to a sample processing plant for screening, then crushing and subsampling of the individual size fractions. The assay of the +50 mm material is estimated by plotting the known size fraction grades against the geometric mean fraction size and extrapolating using a power curve (or other suitable form) to the mean size of the +50 mm material. Table 3 shows the results, labelled Sim ROM -106 mm and Sim ROM -53 mm. There is little benefit from applying the approach to the -106 mm material, but for the -53 mm it improves both the estimate of average RR and the correlation with ROM material with only a small amount of extra effort. The method could equally well be applied at an intermediate size, such as 75 mm.

EFFECT OF PARTICLE SIZE ON SEPARATION SIZE

An important question when designing a screen pre-concentration plant for a greenfields project is whether the optimum separation size remains the same with scale-up to ROM material, or the mass pull remains the same. If the separation size is controlled by vein spacing, that would suggest that the separation size should remain the same and the mass pull vary. However, both the Gramalote and Los Bronces test work shows that the RR value remains the same over a range of coarse crush sizes. This implies that it is the optimum mass pull that remains the same and the separation size that varies. Nonetheless, it would be wise to allow for some fine-tuning of the separation size in any greenfields plant design. The BCL data does not provide any guidance on this question as the 80 per cent passing size of ROM ore was fine, at about 90 mm, and the drill core was tested by tumbling rather than crushing and resulted in a similar separation size on core and ROM ore.

CONCLUSIONS

The results of the studies reported here show that size-by-assay studies of the coarse rejects from drill core, or RC drill chips, are a cost-effective means of determining whether an orebody is potentially amenable to pre-concentration by screening. The results do not however correlate with variable responses across the orebody and must be calibrated by large scale test work. The reason is that fine crushing measures the proportion of metallic values which is vein associated rather than disseminated, but suppresses all information on vein thickness, spacing or breakage characteristics. A study of the breakage characteristics of drill core selected to cover all major alteration types is a low-cost way to supplement the coarse reject information and guide subsequent studies. Pre-concentration by screening is likely to be effective when high-grade sections of core break relatively finely (eg <50 mm) to produce high-grade particles while lower grade sections break randomly to produce larger and lower grade particles. If a substantial proportion of the values is in veins which are thick compared to a likely separation size, then screening is unlikely to result in consistent upgrading. High values in thick and hard quartz veins are likely to result in upgrading to the coarser fractions.

It is advantageous to evaluate pre-concentration as part of a greenfields project design as this allows for mine planning and plant location to be optimised for the entire process. However, greenfields projects may have little or no access to bulk samples and planning must be based on drill core. It has been shown for two projects evaluated that the upgrade response measured on coarse crushed drill core correlated very well with the response of blasted ROM ore with little or no scale-up factor required. A third project (BCL) required a scale-up factor to be established by bulk sampling (but used tumbling rather than crushing) while for a fourth project (KCGM) the upgrade response of crushed ore did not correlate with ROM ore. The reason in this last case is likely to be that the gold at KCGM occurred in veins which were thick compared to the crushed sizes used and so the response was suppressed. Application of the preliminary evaluation techniques developed since that work was done would have shown that the KCGM ore was not amenable to upgrading.

The cost of large diameter core drilling for upgrading studies across a deposit would be large. However, for Gramalote it was shown that the upgrade response could be correlated with chemical or hyperspectral databased on a moderate number of samples (Clarke *et al,* 2020; Guerrero *et al,* 2020) and then proxy data used to map the response in more detail.

For a brownfields site, the most effective means of study is sampling material from operating benches. However, sampling the full ROM size distribution is costly and difficult due to the typically large top-size, consequent large sample masses required to control intrinsic sampling errors and the cost of processing that coarse material. Test work at four sites has shown that instead of sampling the entire size range, samples can be taken only of the -100 mm material, or finer depending on the ROM top size. This can greatly reduce the sample size required for a given accuracy, in one case by a factor of 25 times. The samples can also be screened and prepared for assay using equipment available at larger commercial testing laboratories. All four sites showed a strong correlation between the upgrade response of selected size fractions and the ROM ore. It has also been shown that the correlation can be improved by measuring the oversize and undersize fraction weights at the time of sampling and deriving a simulated ROM distribution. This can be done with relatively little extra effort. For the Gramalote project the upgrade response measured from finer size fractions is biased a little low, due to the coarsest fractions having consistently lower grades than expected from the modelled relationship. However, the difference is not enough to materially change the economics and provides some additional conservatism.

Although the methods described here will greatly reduce the cost of studies for either green or brownfield projects, while providing high quality data, in all cases it is likely that at least one ROM bulk sample would need to be sourced and tested before proceeding with final approval and engineering. It is also recommended that any screening plant should be designed to allow some flexibility in the separation size in operation.

ACKNOWLEDGEMENTS

The work reported here has involved many people, but the guidance and encouragement of Doug Halbe at Kalgoorlie Consolidated Gold Mines was key to the successful completion of that project.

The assistance of Eugenio Gatto of Northern Star Resources Ltd, current owners of KCGM, in reviewing the paper and giving permission to publish the KCGM and GMK data is gratefully acknowledged. The Gramalote upgrading by screening project could not have happened without the support and encouragement over many years of V Chamberlain and R Sanhueza and the hard work of the on-site teams. Approval by AngloGold Ashanti, B2Gold and the Gramalote JV to publish the Gramalote data is gratefully acknowledged.

REFERENCES

Adair, B, Keeney, L, King, D and Scott, M, 2019. Gangue rejection in practice – the implementation of Grade Engineering® at the Minera San Cristóbal Site, in *Physical Separation '19*. (Minerals Engineering International, Falmouth, Cornwall.)

Bauer, A and Crosby, W A, 1990. Blasting*, in Surface Mining, 2nd Edn, ed B Kennedy*, pp 540–583. (SME, Littleton, Colorado).

BoBo, T, La Rosa, D and Cameron, P, 2020. Preconcentration in the pit – size matters, in *Preconcentration Digital Conference* (The Australasian Institute of Mining and Metallurgy: Melbourne).

Bowman, D and Bearman, R, 2014. Coarse waste rejection through size based separation, *Minerals Engineering,* http://dx.doi.org/10.1016/j.mineng.2013.12.018

Burns, R and Grimes, A, 1986. The application of pre-concentration by screening at Bougainville Copper Limited, *in Proceedings AusIMM Development Symposium, Madang, Papua New Guinea.*

Carrasco, C, Keeney, L and Walters, S, 2014. Development of geometallurgical laboratory tests to characterize metal preconcentration by size, *in Proceedings XXVII International Mineral Processing Congress, Santiago* (Gecamin Digital Publications).

Clarke, N, 1993. Final report on upgrading by screening project, internal report Kalgoorlie Consolidated Gold Mines, December.

Clarke, N, 2014. Testwork on pre-concentration by screening at Sunrise Dam, internal report, AngloGold Ashanti, Australia.

Clarke, N, Barros, A, Hunt, J and Keeney, L, 2020. Grade engineering at Gramalote gold deposit, Colombia: an example of industry-research collaboration, Part 1, in *Preconcentration Digital Conference* (AusIMM, Melbourne).

Coles, E, 1955. Sampling and assaying investigation, Technical Report Number 8, Gold Mines of Kalgoorlie (Aust) Limited.

CRCORE, 2014. P1A-052 A review of preferential grade by size deportment data analysis procedures and comparative ranking methods, Technical Report TR#080, Brisbane Australia, CRCORE. Available from https://www.crcore.org.au/news/publications/technical-report-tr080. Accessed 18th February 2022.

Guerrero, N, Hunt, J, Clarke, N, Barros, A and Keeney, L, 2020. Grade engineering at Gramalote gold deposit, Colombia: an example of industry-research collaboration, Part 2, in *Proceedings of the Preconcentration Digital Conference 2020,* pp 409-415 (The Australasian Institute of Mining and Metallurgy: Melbourne).

ICMM, 2021. *Tailings Management: Good Practice Guide*, Introduction (International Council on Mining and Metals, London).

Keeney, L, Beaton, N, Scott, M, D, la Rosa, E, Amini, J, Rutter and Faramarzi, F, 2020. The integration of mine-to-mill and grade engineering at Anglo American's Los Broncos Mine using IES, in *Preconcentration Digital Conference* (The Australasian Institute of Mining and Metallurgy: Melbourne).

Paki, O K and Koginmo, V I, 1988. Crushing and screening operations at Bougainville Copper Limited, in *Third Mill Operators Conference, May 1988* (The Australasian Institute of Mining and Metallurgy: Melbourne).

Pitard, F, 1989. *Pierre Gy's sampling theory and sampling practice, Volume I, Heterogeneity and sampling*, 2nd edn, pp 166–167 (CRC Press, Florida).

Rutter, J, 2017. Grade Engineering and GE View: Cooperative Research Centre for Optimising Resource Extraction (CRCORE) White Paper, Brisbane, Australia.

Development of a new beneficiation plant for recovery of iron and apatite concentrates through wet tailing dams

A Dehghani Ahmadabadi[1], A H Baladastian[2], R Hejazi[3], M Saghaeian[4] and V Sheikhzadeh[5]

1. Senior Process Engineer, Fakoor Sanat Tehran Company (FSTCO), Tehran, Iran. 1586633118. Email: dehghani@fstco.com
2. Process Engineer, Fakoor Sanat Tehran Company (FSTCO), Tehran, Iran. 1586633118. Email: Baladastian@fstco.com
3. R&D Manager, Fakoor Sanat Tehran Company (FSTCO), Tehran, Iran. 1586633118. Email: Hejazi@fstco.com
4. Technical Chairman, Fakoor Sanat Tehran Company (FSTCO), Tehran, Iran. 1586633118. Email: Saghaeian@fstco.com
5. Managing Director, Fakoor Sanat Tehran Company (FSTCO), Tehran, Iran. 1586633118. Email: Sheikhzadeh@fstco.com

ABSTRACT

With the declining of high-quality hematite and magnetite iron ore reserves and the increasing accumulation of material resulting from mining and beneficiation operations that appear as low-quality depots and discharged materials in tailing dams, the necessity of recycling these reserves is increasingly becoming a critical demand. The Chadormalu iron ore mine is among the largest deposits of magnetite-hematite iron ore in Iran. In this mine, the total wet processing tails accumulated in tailing dams are over 92 Mt containing 25–40 per cent Fe. Laboratory and pilot tests on tailing samples led to the design and implementation of the Chadormalu Tailing Recovery plant (CTR) with a unique process circuit in Iran. In the CTR plant, after three steps of re-pulping with spiral classifiers and sanding machines, the underflow is concentrated by two stages of WMIMS and produces 64 per cent Fe grade magnetite concentrate. The tailings of the drums are mixed together and introduced into the hematite recovery section, including two stages of VPHGMS separators, and 60 per cent Fe grade hematite concentrate is produced. This plant has been in operation for over ten years with a total yield of 18.93 per cent. Due to changes in the materials extracted through new tailing dams, the quality of the final concentrate dramatically dropped to 56.36 per cent Fe and 0.79 per cent P; therefore, applying reverse flotation and removing phosphorus from the final concentrate was inevitable. By using this approach, upgrading of the concentrate to 63.01 per cent Fe and 0.05 per cent P was obtained. Furthermore, regarding the high amount of phosphorus in the tailing streams, direct flotation has been designed to produce apatite concentrate as a by-product stream through a flotation system comprising series banks of Rougher, Cleaner, and Re-Cleaners flotation cells. Hence based on the results, at optimum conditions, a final apatite concentrate with a yield of 15.78 per cent and 14.06 per cent P could be achieved. Successful implementation of this project has led to the production of magnetite-hematite and apatite concentrates with annual capacities of 250 000 and 45 000 t, together with total yields of 11.59 per cent and 6.19 per cent (includes de-sliming of apatite flotation feed), respectively.

INTRODUCTION

The Chadormalu iron ore mine is located in Yazd province and has a total reserve of 400 Mt with an average iron grade of 55.2 per cent and a phosphorus content of 0.94 per cent. The predominant abundance of iron ore components in this mine includes magnetite and hematite minerals. The production of iron ore concentrate with a capacity of about 10 Mt/a is carried out through five processing plants operating in parallel. Due to the accumulation of wet tailings of the factory's production lines since 1997 in the tailings dams, the accumulated tailings reserve in the old dams is equal to 10.5 Mt and for the new dams is approximately equal to 82 Mt. Figure 1 shows the location of the old and new tailings dams of the five concentrate production lines of the Chadormalu iron ore complex.

FIG 1 – Location of old and new tailings dams to accumulate wet tailings from the Chadormalu iron ore processing lines.

Preliminary studies conducted by the Fakoor Sanat Tehran Company (FSTCO) on the old tailing dams showed that the average Fe grade of accumulated tailings is about 40 per cent (range 35–45 per cent) and for the new tailing dams is in the range of 25–30 per cent. Hematite, martite, and magnetite minerals are also the main iron minerals of those dams. Therefore, in the first stage of factory construction, the potential of recycling concentrate from tailings accumulated in the old tailings dams (due to the higher attractiveness for investment and construction of the factory) was examined by FSTCO through laboratory and pilot tests. With the successful implementation of this plant in 2012, which was launched as two separate sections for the recovery of magnetic concentrate and hematite concentrate, the waste recovery process related to the old dams is still in operation. Dahe has addressed this process in a number of articles (Dahe, 2009, 2011). Simultaneously with the depletion of accumulated tailings in the old dams, issues related to the reuse of tailings of the new dams from 2021 were raised.

Due to differences in grade characteristics and weaker upgrading properties of the new tailing dam samples, reprocessing tests of the samples revealed that in the current circuit of the plant, optimisation of the magnetic separation sections and addition of reverse flotation to remove impurities (especially phosphorus) should be on the agenda (Baladastian *et al*, 2020; Nunes *et al*, 2012; Pereira and Papini, 2015; Santana *et al,* 2008). In addition, due to the presence of large amounts of apatite minerals in the output tailings stream of the plant, the extraction program of the apatite concentrate by direct flotation after a de-sliming operation on the flotation feed was also assessed for the processing circuit of the plant (Baladastian *et al*, 2020). Thus, during the operation of the plant for a period of ten years, a combined iron ore concentrate with a cumulative tonnage of 1.97 Mt, an average Fe grade of 63.91 per cent, and a total yield of 18.93 per cent from the old tailings dams has been produced. In addition, it is expected that by modifying the plant process circuit, it will be possible to recover the accumulated materials in Chadormalu's new tailing dams and, consequently, to produce magnetite-hematite iron ore concentrate and an apatite concentrate. Therefore, the annual production plan of 250 000 t of iron ore concentrate and 45 000 t of apatite concentrate will be investigated with the required amendments.

In this article, a brief overview of the basic principles of the Chadormalu Tailing Recovery Plant (CTR) design, product specifications during ten years of operation, as well as validation tests based on changing the grade specifications for new tailings dam samples, and requirements for improvements and modifications to the plant are discussed.

DESIGN OF CHADORMALU TAILING RECOVERY PLANT

The design and construction of the CTR plant were carried out in 2010 by FST Company. In order to design the processing circuit, after preparing the sampling plan for different parts of the tailing dams, the sampling operation was performed by drilling holes with an auger drill. According to the plant operations plan, these tailings dams have been accumulated in several different sections since 1996. Some of these tailings dams are filled in an irregular fashion (Dam 1, 2, 3, 4, 5 and Pool 1, 2), and some of them are systematically filled with tailings (A, B, C, D, E, F, G). Figure 2 (top-left) shows a schematic of the location of different dams and sampling points. In addition, Figure 2 (top-right and bottom) presents the output results of geostatistical studies on samples taken from different pits, which led to the formation of iron grade classification patterns in the different dams.

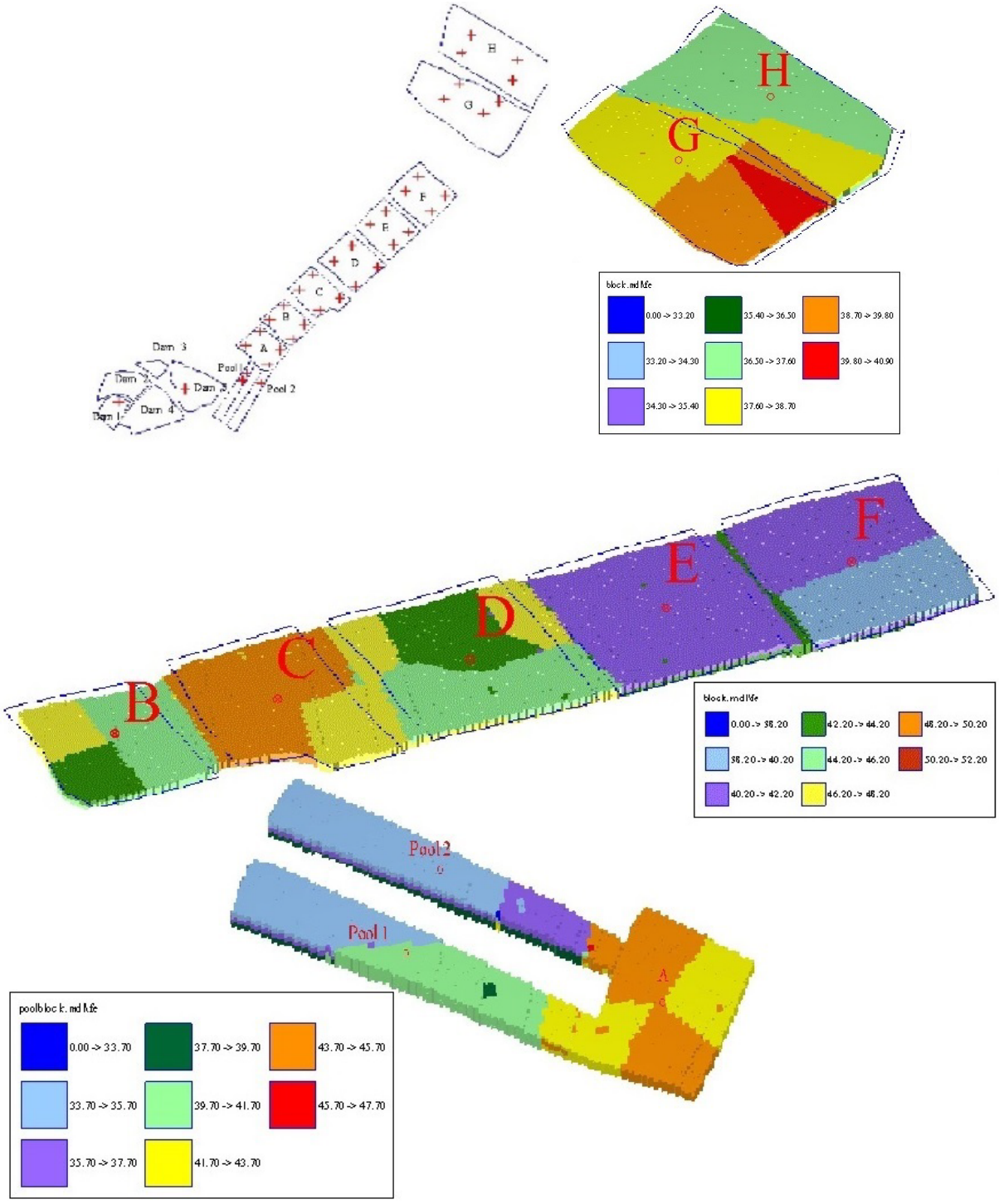

FIG 2 – Location of sampling points from different sections of old tailings dams (left) and geostatistical results of iron grade classification for tailings reserves in different dams (right).

Determination of the grade characteristics, including Fe and FeO, as well as the magnetic separation behaviour of different samples by laboratory and pilot tests, showed that the plant production process should include two different phases of production comprising magnetite concentrate and hematite concentrate. Accordingly, the first part of the plant consists of a three-stage circuit of spiral classifiers that convert the materials extracted from the tailing dams into a slurry pulp and separates the sand particles from the feed samples. To complete the coarse particle removal process, the output stream of the classifiers is passed through rotary screens, and then this output with a d_{80} grain size of 60 microns is fed to the two stages of 3800 Gauss magnetic separators acting as rougher and cleaner. The output concentrate from the cleaner separator is the final magnetite concentrate with 64 per cent Fe grade and 8 per cent yield. After being mixed, the tailings of the two separation steps are sent to the Vertical Ring and Pulsation High Gradient Magnetic Separators (VPHGMS) section (as a rougher and cleaner circuit) to extract hematite concentrate. The output of the second separator has a 60 per cent Fe grade and 12 per cent yield as hematite concentrate. At the end of the process, the final magnetite and hematite concentrates produced by each part of the plant are sent to a thickener to mix and increase the solids percentage, and pressure filters dewater the thickener underflow to reduce the moisture content below 8 per cent. Therefore, the main parts of the plant and its major equipment are as follows:

- Magnetite recovery plant:
  - Pulp making: three stages of spiral classifiers and rotary screens.
  - Concentration: two stages of 3800 Gauss drum separators.
- Hematite recovery plant:
  - Concentration: two stages of 10 000 Gauss VPHGMS separators.
  - Thickening: thickener for water recovery from magnetite and hematite concentrate streams.
  - Dewatering: vertical press filtration of magnetite-hematite concentrate.
  - Thickening: thickener for water recovery from tailing streams.

INVESTIGATION OF PLANT CHANGES BASED ON SAMPLES FROM NEW TAILING DAMS

Due to the difference in the quality characteristics of the tailings accumulated in the new tailings dams and planning to produce concentrate from them, sampling was conducted from different parts of the dams, and laboratory studies were accomplished as follows:

- Performing wet magnetic separation experiments as rougher and cleaner using MIMS 3800 Gauss separators (magnetite recovery).
- Conduct rougher and cleaner VPHGMS separation tests (hematite recovery).
- Perform reverse flotation tests to remove phosphorus from the combined concentrate.
- De-sliming of the tailing stream for removal of particles smaller than 15 microns.
- Conduct direct flotation tests to recover apatite concentrate.

Investigation of physical and chemical characteristics of the sample

Chemical specifications and the particle size distribution of the sample representing the new tailings dams used in the experiments are shown in Table 1.

TABLE 1

Results of chemical analysis and sieve analysis of samples prepared from the new tailings dams for validation tests.

Chemical specifications		PSD Specifications	
Fe (%)	27.57		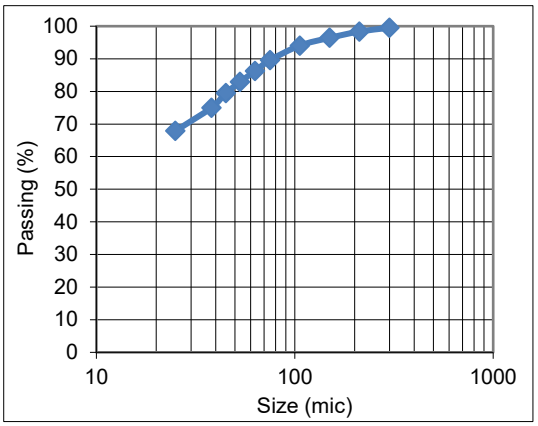
FeO (%)	2.88	d_{100}<500 micron	
P_2O_5 (%)	6.87		
SiO_2	19.30		
Al_2O_3 (%)	4.07		
CaO (%)	14.92	d_{97}=168 micron	
MgO (%)	3.64		
K_2O (%)	0.47		
Na_2O (%)	1.01	d_{80}=46 micron	
TiO_2 (%)	0.49		
SO_3 (%)	0.79		
LOI (%)	8.49		

Evaluation of optimal test results for the production of iron ore concentrate

Two-stage rougher and cleaner magnetic separation experiments were conducted to produce magnetic concentrate using wet medium intensity (3800 Gauss) drum separators under different conditions to obtain the optimal operating state, leading to the production of 58.50 per cent Fe grade concentrate with 5.20 per cent total yield. Next, the drum tailings were mixed and tested to produce hematite concentrate using two stages of the VPHGMS separator at 10 000 and 7000 Gauss field intensities. The output of these experiments was a 55.34 per cent Fe grade hematite concentrate and 11.48 per cent overall yield. By mixing the magnetite and hematite concentrates in each stage, a product with a Fe grade of 56.36 per cent and a phosphorus content of 0.79 per cent was obtained, which does not have suitable quality specifications for sale. Therefore, a reverse flotation process was utilised to remove the maximum amount of impurities, increase the Fe content, and reduce the phosphorus content of the concentrate. Experiments were performed under various operating conditions, including the combined use of sodium carbonate and caustic soda as a pH regulator, sodium silicate as a dispersant, and a 50 per cent Alke and Dirol mixture (with a chemical structure similar to the group of fatty acids) as a collector. The results of the optimal test selected for use in the plant circuit included the production of a concentrate with Fe grade 63.01 per cent and a yield of 72.07 per cent with a phosphorus content of 0.05 per cent. The complete results for the optimal tests performed to produce the final iron ore concentrate with the desired quality characteristics for sale are described in Table 2.

TABLE 2

Results of magnetic separation and reverse flotation tests of the sample representing the new tailings dams to produce a composite iron ore concentrate.

Stage	Product	Yield (%)	Fe (%)	Fe $_{rec}$ (%)	P (%)	SiO_2 (%)
Feed Spec.		100.00	27.57	100.00	3.00	19.3
MIMS (Rougher)	Conc.	6.05	56.09	12.19	--	--
	Tail	93.95	25.84	87.81	--	--
MIMS (Cleaner)	Conc.	85.91	58.50	89.60	0.50	2.95
	Tail	14.09	41.40	10.40	--	--
Total MIMS Stages	Mag-Conc.	5.20	58.50	11.03	0.50	2.95
	Tail	94.80	25.98	88.97	3.13	19.57
VPHGMS Feed Spec.		100.00	25.98	100.00	3.13	19.57
VPHGMS 10000 (Rougher)	Conc.	25.50	50.00	49.08	--	--
	Tail	74.50	17.76	50.92	--	--
VPHGMS 7000 (Cleaner)	Conc.	45.00	55.34	49.81	0.92	6.03
	Tail	55.00	45.63	50.19	--	--
Total VPHGMS Stages	Hem-Conc.	11.48	55.34	24.44	0.92	6.03
	Tail	88.53	22.17	75.56	3.42	21.33
Mixed Mag and Hem Concentrate Spec.		16.08	56.36	32.78	0.79	5.06
Phosphors Reverse Flotation	Conc.	72.07	63.01	80.57	0.05	5.06
	Tail	27.93	39.20	19.43	2.69	5.07
Final Iron Concentrate		11.59	63.01	26.37	0.05	5.06
Final Tailing		88.41	23.04	73.63	--	--

Evaluation of optimal test results for the production of apatite concentrate

Production of apatite concentrate was performed on a mixed tailing sample from the VPHGMS separators with a phosphorus content of 2.44 per cent. Due to the very fine grain size of the sample and in order to enhance flotation performance, a de-sliming operation was conducted using a hydrocyclone with a cut size of 15 microns to eliminate ultrafine particles from the input of the flotation system. Based on this, 53.29 per cent by weight of the sample as fine particles entered the overflow section with a 1.78 per cent phosphorus grade and were withdrawn from the test circuit. Even though the hydrocyclone underflow was 46.71 per cent by weight of the sample, its phosphorus content was 3.25 per cent, implying 62.22 per cent recovery of the sample's total phosphorus reported to the underflow section. Direct flotation experiments of apatite mineral were carried out at a constant solids content of 25 per cent and under various operating conditions, including different amounts of sodium silicate as a dispersant and Apirol C as a collector at a pH optimal range of about 10 by sodium carbonate and caustic soda mixture. In addition, since the utilised collector is from the group of fatty acids and has suitable frothing properties, frother reagents were not used to stabilise the froth stream. After flotation tests (in the form of rougher and three cleaner stages) under various conditions, the optimal test result resulted in the production of apatite concentrate with a phosphorus grade of 14.06 per cent, a yield of 15.78 per cent, and Fe grade of 1.92 per cent. For these optimal conditions, sodium silicate and collector consumption were 600 and 300 g/t, respectively. Finally, Table 3 shows the complete outcomes of the optimal flotation tests conducted to generate apatite concentrate from the tailings output of the electromagnetic separators.

TABLE 3

Results of direct flotation tests of the tailings sample output from the magnetic separation circuit to deliver apatite concentrate.

Test Stage	Time	Product	Yield (%)		P (%)	$P_{rec.}$ (%)		Fe (%)	SiO_2 (%)
	Min		Stage	Total		Stage	Total		
Rougher	40	Conc.	32.16	15.02	9.35	92.49	43.20	9.75	4.55
		Tail	67.84	31.69	0.36	7.51	3.51	26.93	30.33
Cleaner 1	11	Conc.	73.63	11.06	11.46	90.29	39.01	4.13	2.16
		Tail	26.37	3.96	3.44	9.71	7.70	25.43	11.22
Cleaner 2	7	Conc.	81.61	9.03	12.73	90.63	35.35	2.60	1.47
		Tail	18.39	2.03	5.84	9.37	11.36	10.93	5.23
Cleaner 3	4	Conc.	81.66	7.37	14.06	90.19	31.88	1.92	1.00
		Tail	18.34	1.66	6.81	9.81	14.83	5.61	3.58
Total Results	62	Final Conc.	15.78	7.37	14.06	68.26	31.88	1.92	1.00
		Final Tail	84.22	39.34	1.22	31.74	14.83	25.05	25.98
Feed: Hydrocyclone Underflow			100.0	46.71	3.25	100.0	46.71	21.31	22.04

PROCESS CHANGES OF FACTORY FLOW DIAGRAM

The initial plant flow diagram, according to the beneficiating behaviour of the samples from the old tailings dams, involves three consecutive stages of pulp making and discarding of coarse particles with two stages of magnetic separation of medium intensity (magnetite concentrate production) and two stages of electromagnetic separation (production of hematite concentrate) as shown in Figure 3 (old circuit). Due to changes in the quality characteristics of tailings accumulated in the new dams and disparities in concentrating characteristics and the objective of delivering apatite concentrate, process adaptions in the plant circuit were critical. Therefore, after conducting redesign studies and choosing the optimal conditions, the adaptation of the plant circuit was developed and implemented for the newly defined goals. The schematic of the flow diagram of the new plant is displayed in Figure 3 (new circuit). Hence, it can be stated that circuit modifications have been done in two ways: raising the number of existing equipment items to sustain and elevate the plant's production capacity and adding new equipment to enhance the quality of iron ore concentrate and delivering a by-product of apatite concentrate.

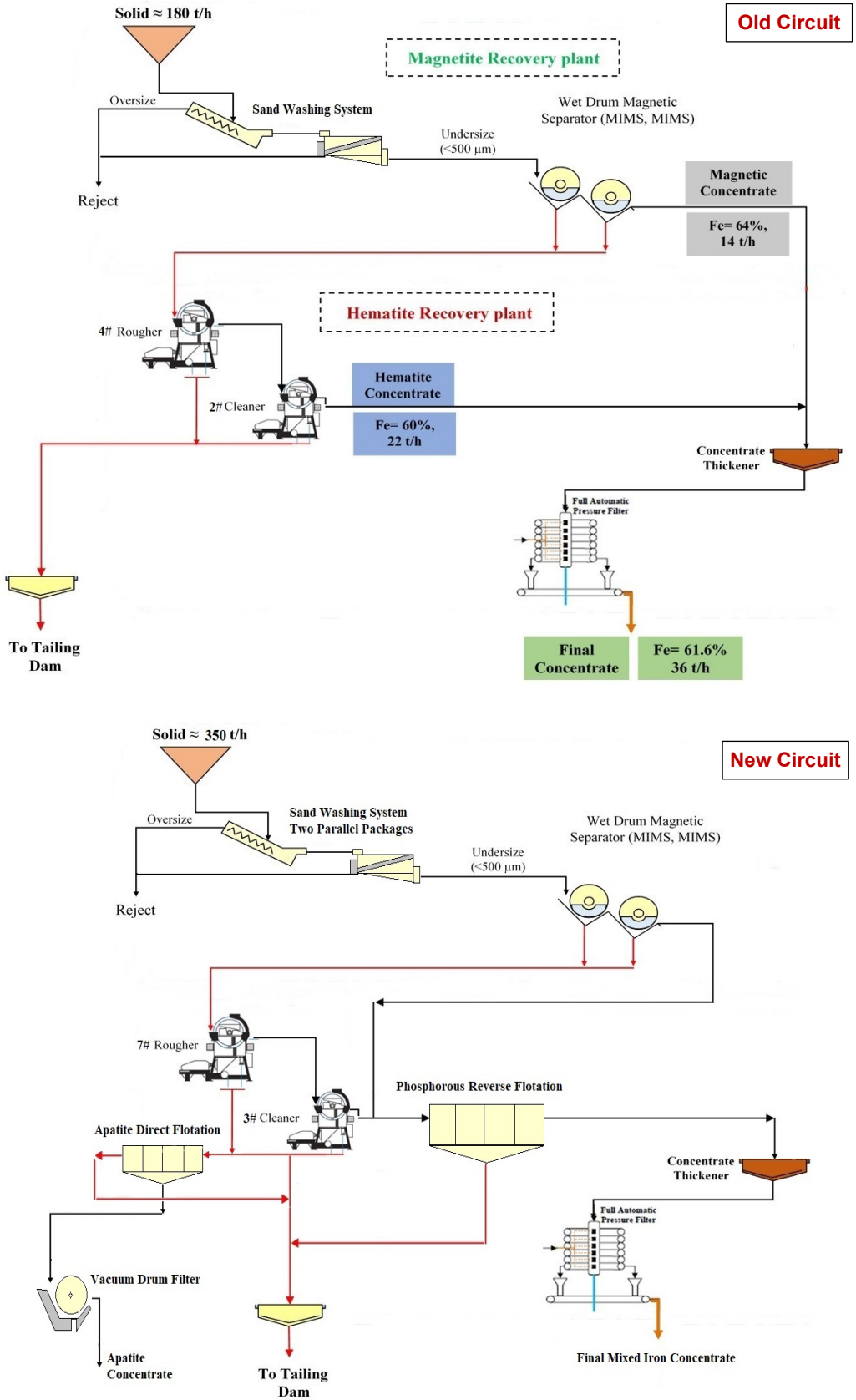

FIG 3 – Old and new process flow diagrams of the concentrate extraction plan from Chadormalu tailing dams.

CONCLUSION

The Chadormalu Iron Ore Recovery Plant (CTR) was launched in 2012 as the first plant in Iran to produce concentrate from tailings accumulated in the Chadormalu Iron Ore Complex tailing dams.

These dams were divided into two types of old dams (with high Fe content) and the new ones (with low Fe grade), and initial technical and economic studies were conducted on the samples from the old dams. By performing sampling programs and acquiring grade information from different points, simulation and preparation of geostatistical models for assessing Fe grade-Stock reserve were conducted. In addition, by conducting Davis Tube magnetic separation experiments, upgrading models based on Yield-Fe grade graphs for the concentrate produced were organised. Then, laboratory and pilot scale magnetic separation studies were executed using wet medium and high intensity magnetic separators. An integrated circuit utilising both types of equipment to produce combined magnetite-hematite concentrate was considered the optimal design. Accordingly, the plant has a feed capacity of 180 t/h and a production capacity of 36 t/h of blended iron ore concentrate with Fe grade 61.6 per cent and a yield of 20 per cent. A review of the plant's ten year production reports demonstrates that during this period about 10.41 Mt of iron ore tailings with a grade of 41.01 per cent Fe were fed to the plant, and the total production of concentrate was equal to 1.97 Mt with a Fe grade of 63.91 per cent. Consequently, the plant's total production yield during these ten years was 18.93 per cent.

Simultaneously with the start of targeting new tailing dams for concentrate production and due to differences in the grade specifications of these dams, re-sampling operations and validation tests of plant performance were investigated. Pilot experiments based on the current design of the plant indicated that it was not possible to produce concentrate with the desired Fe grade for sale in target markets and hence upgrading methods should be added. Accordingly, due to the high amounts of phosphorus as a disturbing element, reverse flotation experiments were conducted to remove phosphorus from the magnetic concentrate sample under various conditions, and, based on the optimal conditions, it was found that the production of flotation concentrate with Fe grade 63.01 per cent and phosphorus content 0.05 per cent with a total yield of 11.59 per cent was possible. Finally, based on the goal of maintaining capacity and improving the quality of the product, the plant circuit contained an increased number of pulp-making equipment and electromagnetic separators with the addition of a flotation circuit. In this way, it was possible to feed the plant at 350 t/h and deliver at least 35 t/h (taking into account the 15 per cent drop in production) of iron ore concentrate with desirable quality characteristics. In addition, due to the high levels of phosphorus in the non-magnetic tailings of the plant, a direct flotation circuit to produce apatite concentrate was also put on the agenda, and the results of the optimal tests revealed that it was possible to produce apatite concentrate with a phosphorus content of 14.06 per cent and total yield of 13.24 per cent. Therefore, in the new plan for the plant, the secondary target of annual production of 45 000 t of apatite concentrate with apatite content of 32.27 per cent was included.

ACKNOWLEDGEMENT

To carry out technical and economic studies of the project, the authors of the article thank and appreciate the support of the CEO of Fakoor Sanat Tehran Company (FSTCO), Mr. Mohammad Vahid Sheikhzadeh.

REFERENCES

Baladastian, A H, Dehghani, A A, Hejazi, R, Saghaeian, M, Sheikhzadeh, V, 2020. Investigation of apatite reverse flotation process to improve quality of ultrafine hematite concentrate – FST Hematite Tailing Recovery Plant, in *Proceedings IMPC 2020*.

Dahe, X, 2009. Application of SLon magnetic separators in modernising the An Shan Oxidised Iron Ore Processing Industry, in *Proceedings Iron Ore Conference 2009*, pp 223–229 (The Australasian Institute of Mining and Metallurgy: Melbourne).

Dahe, X, 2011. The Integrative Technology of SLon Magnetic Separator and Centrifugal Separator for Processing Oxidised Iron Ores, in *Proceedings Iron Ore Conference 2011*, pp 367–372 (The Australasian Institute of Mining and Metallurgy: Melbourne).

Nunes, A P L, Pinto, C L L, Valadão, G E S, Viana, P R M, 2012. Floatability studies of wavellite and preliminary results on phosphorus removal from a Brazilian iron ore by froth flotation, *Minerals Engineering*, 39:206–212.

Pereira, A C, Papini, R M, 2015. Processes for phosphorus removal from iron ore – a review. *REM: R. Esc. Minas, Ouro Pret*, 68(3):331–335.

Santana, R C, Farense, A C C, Fortes, M C B, Ataide, C H, Barrozo, A S M, 2008. Influence of particle size and reagent dosage on the performance of apatite flotation, *Separation and Purification Technology* 64:8–15.

The study of applying dry cobbing pre-concentration and its impact on concentrator efficiency and pit optimisation – Yogi BIF magnetite iron ore mine

R Hejazi[1], M Saghaeian[2] and V Sheikhzadeh[3]

1. R&D Manager, Fakoor Sanat Tehran Company, Tehran, Iran. Email: hejazi@fstco.com
2. R&D Deputy, Fakoor Sanat Tehran Company, Tehran, Iran. Email: saghaeian@fstco.com
3. Managing Director, Fakoor Sanat Tehran Company, Tehran, Iran. Email: sheikhzadeh@fstco.com

ABSTRACT

Mining dilution is one of the most important factors affecting the economy of mining projects. Instead of quantifying dilution in mining studies, it is common to assume a general dilution such as 5 per cent for massive deposits. Dilution increases the operating costs in the plant by increasing the tonnage of material to be milled. It prolongs the mine life by reducing plant's effective capacity. It also reduces the feed grade. In most cases, lower feed grade means lower plant recovery. Dilution also increases the cut-off grade, which in turn reduces the overall ore utilisation of a mine. In this study has been investigated applying pre-concentration by dry magnetic separation for decreasing of dilution impact on reserve estimation and open pit design in low-grade iron ore mine. Based on the preliminary open pit design and assumption 3 per cent as dilution factor, the mineable ore in life-of-mine (measured + indicated) has been estimated with Fe = 25 per cent, SiO_2 = 49.7 per cent. Based on the experimental test work on the ore, by dry low intensity magnetic separation of dry HPGR product grinding circuit, it is possible to remove diluted waste material and liberated gangue before concentrate plant, so that around 34 per cent rejected and Fe grade increase from 25 per cent to 33 per cent and by weight recovery 66 per cent. The results of the test work showed that this methodology could decrease largely the impact of dilution in the feed to the plant. It also slightly effect on the reducing of dilution factor impact for open pit design and optimisation and leads to increase the mineable tonnage in the low-grade magnetite iron ore mine.

INTRODUCTION

The quality of iron ore deposits has deteriorated worldwide as a result of long-term mining (Tsutomu *et al,* 2015). The beneficiation of low-grade iron ores has received many attentions in the recent years due to the depletion of high-grade iron ore reserves and the raising demand around the world for steelmaking (Behnamfard and Khaphaje, 2019). In order to make the treatment of low-grade deposits economically viable, large quantities of rock need to be mined and processed. The associated infrastructure costs (power, water supply, accommodation and support services, waste storage) result in a substantial penalty on the project, from both capital and operating cost perspectives (Foggiatto *et al,* 2014).

One of the most important issues in low – grade deposit is cut-off grade that is simply a grade used to assign the destination of material mined; leave in place, sending to mineral processing plant or send it to waste disposal dump (Narrei and Osanloo, 2015). Mining dilution is also other important factors affecting the economy of mining projects. Dilution increases the operating costs in the mill by increasing the tonnage of material to be milled. In addition to its direct impact on short-term income of a mine, dilution causes significant changes in other factors that on the long-term reduce the overall value of the project (Ebrahimi and Eng, 2013).

Pre-concentration aims to remove diluted waste and gangue material at as coarse a particle size and as early in the process as possible. This increases the grade of ore proceeding to the next stage of processing and may significantly reduce energy consumption and processing costs (Duffy *et al,* 2015). The pre-concentration is could be to reduce dilution impact especially in low-grade iron ore mine. It is very vital and its effects on amount mineable reserve and cut-off grade. In this study has been investigated effect of one stage cobbing magnetic separation on the dilution factor and optimisation pit of Yogi BIF magnetite iron ore resource. The primary source of iron for the Yogi deposit is a magnetite-rich BIF, which forms a steeply dipping. The overall iron content is

around 25 per cent, based on RC and diamond drilling assays. The magnetite-rich BIF is tight to folded and trends north–south for approximately 27 km on the tenements, capping ridges and low hills (Hejazi *et al,* 2018). Cobbing magnetic separation test work has been done in different product of crushing and dry grinding circuit and also by several drum magnetic separator consist of c dry grinding HPGR product (k99~4 mm, k99~1.4 mm). Based on the test results and economical grade of the feed to the beneficiation plant, it has been specified optimum dilution factor and cut-off grade for optimisation pit.

DEFINITION and PROBLEM

Definition

Dilution means the barren material that is mixed with the ore during the mining operation and is extracted with ore. This material along to the ore are sent to the processing plant. This is resulted to increase tonnage of ore and also decreasing its grade. Dilution can be specified as the ratio of the tone of waste mined and sent to the mill to the total tonnage of ore and waste combined that are milled. It usually expressed in percent format.

Dilution happens in two different areas. Sometimes within an ore block there are waste inclusions or low-grade pockets of ore that cannot be extracted alone and are mined with the mining block. This is called internal dilution. Internal dilution is difficult if not impossible to avoid. In BIF magnetite iron ore mine, the amount of internal dilution is relatively high. Lithology and grade distribution are important factors in internal dilution. Other dilution is called external dilution that is related to the waste outside of the orebody that is extracted during the extracting of ore block. This dilution is depend on geology, shape of orebody, drilling and blasting techniques, scale of operation and equipment size. External dilution that can be controlled using proper equipment and mining practices. Figure 1 illustrates internal and external dilution in a bench of an open pit mine (Ebrahimi and Eng, 2013).

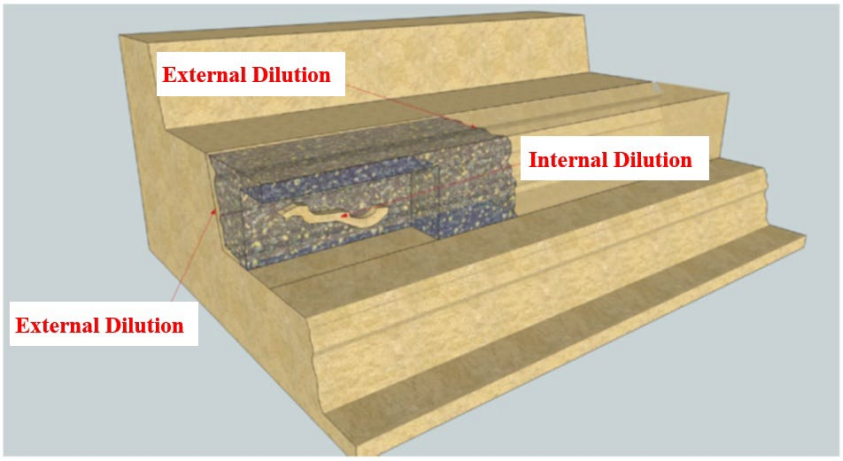

FIG 1 – Different types of dilution (Maxam Fundacion, 2018).

Problem

One of the main consequences of dilution is the reduction of mill feed grade. Lower feed grade means less income. For marginal grade ore, dilution may reduce the grades to a degree that it becomes uneconomic to be processed, in other words dilution may turn an ore block to waste.

Due to dilution, energy and materials that are used in the processing plant to treat the waste portion of the feed are wasted. As a result, the mill unit operating cost increases directly by the amount of the dilution factor (Ebrahimi and Eng, 2013).

Occupying part of the processing capacity by sending waste rocks to the plant prolongs mine life. As a result it delays cashing the value of mineable resource on time as planned. A longer mine life obviously lowers the net present value (NPV) and internal rate of return (IRR).

EXPERIMENTAL

Study area

The studied district of Yogi is located approximately 430 km north-east of Perth in the Yalgoo Greenstone in the Yilgarn Craton, Western Australia and 233 km east of the Geraldton port. Banded iron formations (BIF) magnetite are primary iron source of the Yogi project that is situated as arc deep inclined body named Yogi Mine. The deposit is variable weathered but predominately situated as band of magnetite-quartz with mafic amphibolite in-depth. Presence of two iron oxides is interpreted as due to gradual oxidation of magnetite rich ore. Consequently, hematite-enriched BIF transformed to magnetite-enriched BIF in shallow depths (>40 m). Moreover, presence of iron and cummingtonite rich silicates indicate reversible transformation of BIF that shows a slight differed chemical specifications in fresh to weathered BIF.

Material

A representative sample of Yogi deposit BIF magnetite iron ore by weight 1000 kg from diamond cores was obtained for studies from different depth of the deposit that consist of fresh magnetite iron ore and waste. In order to study effect of the pre-concentration on internal and external dilution, two samples A, B have been prepared. The sample A was consisted of fresh magnetite iron ore and sample B consist of fresh rock and waste. The each samples were crushed to less than 4 mm and then thoroughly mixed separately and representative sample was drawn by conning and quartering method for different characterisation, mineralogical and dry magnetic separation studies. The completed chemical and physical analysis of the each sample and different size fractions obtained from the size analysis studies were determined. The closed size fractions for experimental studies were prepared by stage crushing in laboratory jaw and roll crusher.

Quantitative mineralogy

Table 1 illustrates quantitative mineralogy measured for the core sample of fresh rock. The modal mineralogical show Magnetite and Quartz as the two main mineral species present in the samples. Olivine/Pyroxene is secondary gangue.

TABLE 1

Quantitative mineralogy of the core sample of fresh rock.

Mineral	Mineral formula	Mass per cent (%)
Magnetite	Fe_3O_4	28.15
Quartz	SiO_2	48.24
Olivine/Pyroxene	$(Mg, Fe)_2SiO_4/(Mg, Fe)_2Si_2O_6$	19.15
Amphibole	$Ca_2(Mg, Fe)_5Si_8O_{22}(OH)_2$	1.95
Carbonate	$CaCO_3$ and $CaFe(CO_3)_2$	1.84
Biotite/Phlogopite	$K(Mg, Fe)_2AlSi_3)_{10}(OH, F)_2$	0.15
others	--	0.52

As to be expected, magnetite is the main source of iron in the sample, to the near exclusion of any other mineral phase detected in these samples. More than 98 per cent deportment of Fe is related to magnetite.

Chemical analysis

Chemical analysis of the prepared sample A and B are as Table 2.

TABLE 2

Head assay analysis.

Sample ID	Fe (%)	SiO_2 (%)	Al_2O_3 (%)	CaO (%)	P (%)	S (%)	MgO (%)	Fe_3O_4 (%)
Sample A	25.81	50.55	2.43	1.61	0.049	0.064	1.81	28.15
Sample B	23.92	53.41	3.15	1.76	0.050	0.10	1.91	25.31

Pilot-scale dry magnetic drum separator

Two pilot-scale dry LIMS and MIMS drum magnetic separator with filed intensity 1100 and 2700 gauss were used for the studies, respectively. It has adjustable drum speed for effective separation of gangue and magnetic material. The different sized material was prepared by stage crushing in a laboratory roll crusher of different set gaps followed by screening at the desired size. The effect of particle size on magnetic separation was studied using different sizes of iron ore of minus 4 mm and minus 1.4 mm. The objective of the study was to achieve better grade and recovery with respect to iron values at any of the sizes.

RESULTS AND DISCUSSION

This section presents and discusses results for the effect of pre-concentration by dry magnetic separator on decreasing dilution effect and results of resource estimation for Yogi low-grade iron ore deposit.

Resource estimation

Table 3 presents resource of total model for various cut-off grades of iron. According to open pit considerations, the amount of mineral resource in elevation level of 110 m that is equal to depth of 250 m was calculated by five iron cut-off grade of 15, 20, 22, 24 and 26 per cent. As indicated, mineral resource is equal to 416 Mt with mean grade of 25.27 per cent with consideration of Fe cut-off grade = 20 per cent.

TABLE 3

The amount of mineral resource in five Fe cut-off grade level.

Depth (m)	Elevation (m)	Cut-off grade Fe (%)	Tonnage (Mt)	Average of Fe (%)	Average of SiO_2 (%)
250	110	15	526.7	23.67	50.3
		20	416	25.27	49.70
		22	358	25.96	49.40
		24	282	26.73	49.03
		26	163	27.97	48.37

Dry magnetic separation test

Table 4 illustrates the results of the dry low and medium intensity magnetic separator. As it can be seen, for sample A and by one dry LIMS magnetic separation on minus 4 mm grain size and linear speed 1.5 m/s, the iron grade of the feed increased from 25.81 per cent to 33.44 per cent and by weigh recovery 65.96 per cent. Regarding the sample B, it could be produced a pre-concentrate with iron grade 33.35 per cent and by weight recovery 59.35 per cent after crushing to less than 1.4 mm and one stage dry LIMS magnetic separation with linear speed 2.5 m/s. The produced dry tailing has also iron grade less than 10 per cent that is liberated gangue and waste material.

TABLE 4

The results of dry magnetic separation tests.

Test No.	Sample	Size (mm)	Intensity (gauss)	Speed (m/s)	Wt. (%)	Fe (%)	Fe-rec. (%)
1	Type A	1.4	1100	2.5	62.36	34.15	82.51
2		1.4	2700	2.5	69.03	32.96	88.15
3		4.0	1100	1.5	65.96	33.44	85.46
4		4.0	2700	1.5	74.15	31.36	90.10
5	Type B	1.4	1100	2.5	59.35	33.35	82.75
6		1.4	3800	2.5	71.23	30.25	90.08
7		4.0	1100	1.5	67.14	31.15	87.43
8		4.0	3800	1.5	74.13	29.31	90.81

Optimisation results (without pre-concentration)

In order to determine mineable mineral resource, economic block model of the mine was made and optimisation of final pit limit was performed to maximise net present value (NPV) by mine strategic optimisation software.

Optimisation of final pit limit was performed based on aforementioned parameters, assumptions, and latest topography data using mine optimisation software. Based on the optimisation results, the amount of mineable resource inside the optimum pit is 367 Mt with stripping ratio of 1.5:1. Moreover, mean Fe grade is 25.5 per cent that fulfil grade limits of the plant.

Effect of pre-concentration on optimisation results

Based on the results in two type samples of the Yogi iron ore deposit, iron ore pre-concentration has the potential to improve resource tonnage by reducing the cut-off grade and improving iron grade of the feed. More iron ore content can be extracted while the processing plant treats less tonnage at higher feed iron grade.

As mentioned, the main scenario has a Fe cut-off grade of 20 per cent delivering 367 Mt of mineable ore to the processing plant with an average grade of 25 per cent Fe. With the inclusion of dry magnetic separation pre-concentration, the cut-off grade is reduced to 15 per cent. The resulting average grade of mined ore is reduced to 23.67 per cent Fe and with resource tonnage 526.7 Mt.

Based on the new optimisation results and consideration of new parameters as Table 5, the amount of mineable resource inside the optimum pit is 400 Mt with stripping ratio of 1.3:1. Moreover, mean Fe grade to the plant is 25.6 per cent.

TABLE 5

Modified parameters used for pit optimisation (with consideration pre-concentration).

Parameters	Value	Unit
Pre-concentration Cost	1.25	AU$/t Concentrate
Pre-conc. Weight Rec.	60%	%
Technical Cut-off	15%	% (Fe)

Without pre-concentration	With pre-concentration
Fe Cut-off grade= 20 per cent	Fe Cut-off grade= 15 per cent
Average Fe grade= 25.67 per cent	Average Fe grade= 23.67 per cent

Resource tonnage= 416 Mt	Resource tonnage= 526.7 Mt
Mineable tonnage= 366.8 Mt	Mineable tonnage= 400 Mt
Feed Fe grade to the plant= 25 per cent	Feed Fe grade to the plant= 25.6 per cent

Effect of pre-concentration on increasing production of the plant

The test work showed at existing process flow diagram of the plant with fixed capacity, dry pre-concentration has the potential to modify the plant feed and increase the production capacity. Production and profit will increase with consideration pre-concentration, and the amount of ore treated (and associated costs and energy) per tonne of product is reduced. According to below mentioned items, high level Net Present Value (NPV) analysis suggests that incorporating a pre concentration plant to upgrade the feed grade to 33 per cent Fe grade for the project may improve the NPV over the life-of-mine.

Without pre-concentration	With pre-concentration
Feed Fe grade to the plant= 25 per cent	Fresh Feed Fe grade= 25 per cent
Concentrate weight recovery= 27 per cent	Feed Fe grade after pre-concentration= 33 per cent
Annual feed to the plant= 18.51 Mt	Annual feed to plant= 15.15 Mt
Annual concentrate tone= 5 Mt	Annual concentrate tone= 5 Mt
Fe of final concentrate= 65–66 per cent	Fe of final concentrate= 65–66 per cent

CONCLUSIONS

The aim of consideration of dry pre-concentration by dry magnetic separation in Yogi iron ore deposit is to remove liberated waste and gangue material that is related to the internal or external dilution, before energy and cost intensive downstream processing and handling. Lower tonnage of ore are processed per ton of iron concentrate, reducing the costs, energy and water consumption per ton of concentrate. Dry pre-concentration has the potential to improve the profitability and reduce the environmental. According to this this study, the below results are concluded by inclusion dry-pre-concentration in the Yogi iron ore project:

- Decreasing Fe cut-off grade from 20 to 15 per cent and increasing resource tonnage from 416 to 526 Mt.
- Increasing mineable tonnage of deposit from 367 Mt to more than 400 Mt with average Fe grade 25 per cent.
- Decreasing feed to the plant from 18.51 Mt to 15.15 Mt.
- Increasing the lifetime of the Yogi iron ore deposit.
- Decreasing the capital and operating cost accordingly.

ACKNOWLEDGEMENTS

The authors would like to thank from management and personnel of FST Company and its R&D Test Centre, FIJV Company and KMCE Consulting for comprehensive supporting for this research paper.

REFERENCES

Behnamfard, A and Khaphaje, E, 2019. Beneficiation of a low-grade iron ore by combination of wet low-intensity magnetic separation and reverse flotation methods. *Journal of Mining and Environment*, 10(1), pp. 197–212.

Duffy, K A, Valery, W, Jankoic, A and Holtham, P, 2015. Bulk ore sorting for pre-concentration: what, how, and why?. *PROCEMIN, 2015*, p. 11.

Ebrahimi, A and Eng, P, 2013. The importance of dilution factor for open pit mining projects. In *Proceedings of the 23rd World Mining Congress.*

Foggiatto, B, Bueno, M, Lane, G, McLean, E and Chandramohan, R, 2014. The economics of large scale ore sorting. In *Proceedings of the XXVII International Mineral Processing Congress IMPC*, pp 20–24.

Hejazi, R, Ahadi, M, Tavousi, M, Asghari, O, Saghaeian, M and Barreiro, R, 2018. Improved magnetic separation testing for geometallurgical modelling of BIF magnetite deposit – Australia, Yogi mine. In *Proceedings of XXIX International Mineral Processing Congress*, Russia.

Maxam Fundacion, 2018. Blasting solutions and dilution control.

Narrei, S and Osanloo, M, 2015. Optimum cut-off grade's calculation in open pit mines with regard to reducing the undesirable environmental impacts, *Journal of Mining, Reclamation and Environment*, 29(3):226–242.

Tsutomu, N, Norihito, Y, Takeshi, F and Yuta, T, 2015. Beneficiation plants and pelletizing plants for utilizing low grade iron ore. *KOBELCO Technology Review*, no. 33.

Pre-concentration – more than bulk ore sorting

L Pyle[1], W Valery[2], P Holtham[3] and K Duffy[4]

1. Minerals Processing Engineer, Hatch, Brisbane Qld 4000. Email: lindon.pyle@hatch.com
2. Global Director–Consulting and Technology, Hatch, Brisbane Qld 4000. Email: walter.valery@hatch.com
3. Senior Consultant, Hatch, Brisbane Qld 4000. Email: peter.holtham@hatch.com
4. Senior Process Engineer, Hatch, Brisbane Qld 4000. Email: kristy.duffy@hatch.com

ABSTRACT

The mining industry is becoming increasingly focused on pre-concentration due to its potential economic and environmental benefits, particularly for the more complex, low-grade, high throughput operations now being developed. Advances in technology have seen bulk ore sorting (BOS) trialled at several operations. However, BOS should not be seen as a 'silver bullet', it can offer significant benefits, but only under the right conditions. Deposits with interspersed mineralogy or disseminated, fine-grained minerals can be difficult for BOS. Large batches of barren or low-grade material are required for BOS to be effective.

Hatch has recently completed several studies for clients who believed that bulk sorting was the most suitable pre-concentration technique for their operation, based only on an assumed sorter recovery or on laboratory trials of the chosen sensor. However, minimal consideration had been given to the heterogeneity of the deposit, the achievable separation batch size or sensor repeatability.

Evaluation of BOS needs to consider both heterogeneity and sensor suitability. The valuable or gangue mineral must be present in such a way that it can be separated effectively in the large bulk sorting batch sizes, without competing minerals or changing ore characteristics affecting the metal upgrade or recovery. Also, the sensor chosen must be able to detect either the valuable mineral, a proxy for the valuable mineral, or a gangue mineral for rejection with sufficient accuracy and precision (repeatability).

This paper presents three recent case studies, emphasizing markers which indicated that bulk sorting was unsuitable for the project whilst highlighting the pre-concentration technologies which were applicable (including particle sorting, and coarse particle gravity separation). The modelling methodology, equipment sizing and forward work plans developed to verify these alternative solutions are also presented, demonstrating the key factors contributing to a thorough scoping assessment.

INTRODUCTION

The value of pre-concentration is being increasingly recognised for both brownfield expansions (targeting increased metal production within existing throughput constraints), and greenfield projects seeking opportunities to minimise CAPEX, OPEX and reduce the production of fine wet tailings, as part of a suite of technologies that will enable more eco and resource efficient processing (Duffy *et al*, 2015b; Adair *et al*, 2020). This interest is evidenced by the launch of the inaugural AusIMM Preconcentration Digital Conference in 2020.

Several technologies exist that can be used for pre-concentration, as shown in Figure 1. Selective mining applies an appropriate grade control block size to minimise dilution and can be coupled with selective blasting which involves the application of less blasting energy in waste sections to produce coarser fragmentation of waste, and higher blasting energy in ore sections to produce finer fragmentation of ore.

Pre-screening exploits the natural deportment of valuable mineralisation into finer size fractions following breakage, to reject a coarse, barren oversize.

FIG 1 – Summary of technologies available for pre-concentration.

Sensor based sorting uses sensing technologies such as prompt gamma neutron activated analysis (PGNAA/PFTNA), magnetic resonance (MR), X-ray transmission (XRT) and X-ray fluorescence (XRF) to measure element or mineral concentrations. Bulk ore sorting involves the measurement and separation of batches of ore (either on a conveyor or in a shovel bucket), while particle sorting involves measurement and separation of individual particles. Bulk and particle sorting can also be used in combination, with bulk sorting followed by scavenging of bulk rejects using particle sorting.

Gravity concentration uses density differences between valuable and gangue minerals at a coarse size to produce a concentrate either by jigging or dense medium separation (DMS).

Coarse particle flotation involves recovery of partially liberated valuable mineral particles following coarse primary grinding (with a P_{80} of around 600 µm). The idea is to liberate the gangue and reject barren material at a coarse size, rather than having to grind the entire feed to the fine size required for complete liberation of the valuable mineral.

There is a growing interest in bulk ore sorting (BOS) due to the potential for significant energy and cost savings as well as environmental benefits, with site trials being undertaken at operations worldwide, such as the deployment of PGNAA and XRF sensors at the Anglo American Mogalakwena PGE mine (Scott *et al,* 2020) and MR trials for copper sorting at the Cozamin mine (Beal and Singh, 2020). Ore and waste material can be separated at high throughput, close to the mine (where in situ heterogeneity is at a maximum), with minimal operating costs and without requiring significant changes to downstream circuits. However, successful bulk ore sorting requires the appropriate sensor selection to detect a valuable (or gangue) element/mineral with sufficient accuracy; and sufficient heterogeneity *in situ* and after mining to enable effective separation (Duffy *et al,* 2015a).

USING GEOSTATISTICS TO EVALUATE DEPOSIT AMENABILITY TO BULK ORE SORTING

Effective bulk ore sorting is dependent upon sensor selection and the presence of heterogeneity both *in situ*, and after mining, that enables large volumes of material to be designated as ore or waste. Several approaches to quantify the *in situ* heterogeneity of orebodies have been presented in literature, including the use of fractals or examination of grade variation along composite drill hole lengths. Although ‘down-the-hole’ analysis provides an initial indicator of grade variation and can be used to support further detailed analysis, linear variability from drill core lengths is not representative of the variability of grade in three dimensions. Different degrees of variability can be observed in different directions (anisotropy) depending on how the deposit is formed. Both methods fail to consider the impact of mining, load and haul, ROM stockpiling and crushing activities on how the *in situ* heterogeneity translates to an on-belt grade variation for bulk ore sorting.

Mineral deposit grades are spatially correlated, which has a direct impact on variances within a block or parcel of ore. Classical statistics consider random and independent variables, so cannot adequately assess grade variability in a deposit, whereas geostatistics considers the spatial relationship between variables. In mineral resource estimation, the initial data is derived from

diamond drill core or reverse circulation cuttings, which represents a small sample volume relative to the volume to be mined. The volume considered is also known as the support size in geostatistical terms, and as the support becomes larger and samples are composited to a larger scale the distribution of grade will become less variable (Harding and Deutsch, 2019).

In geostatistics, the covariance or variogram describes the degree of spatial dependence of a variable. The variogram consists of three key components, the nugget effect, range (distance in which variables are dependent) and the sill, as shown in Figure 2. To encompass the spatial relationship and variability in different directions, 3D variograms are modelled using an ellipsoid (also shown in Figure 2). Thus, providing a much more representative estimate of variability for the deposit considering anisotropy.

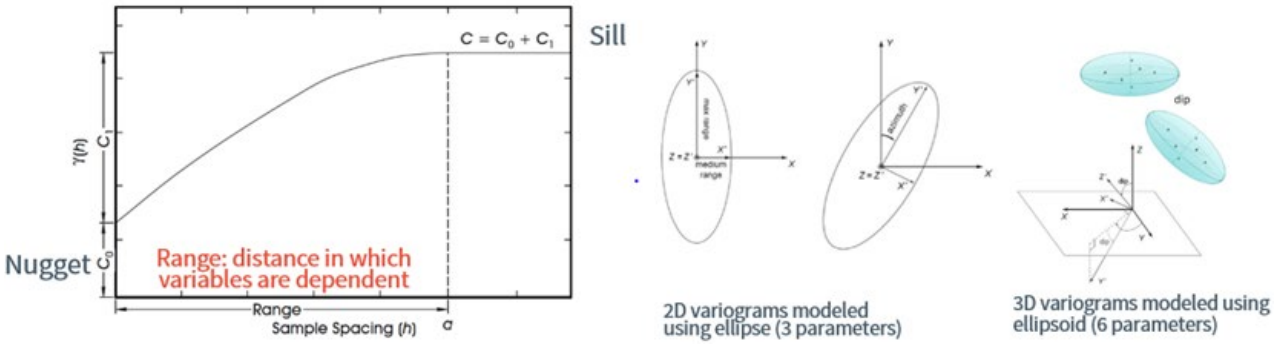

FIG 2 – Estimating 3D variability with geostatistics.

Geostatistics can be used to evaluate the grade variation at different scales (different batch or block sizes) by calculating the dispersion variance. Dispersion variance is used to quantify the dispersion of the variable (in this case grade) as a function of the geometry and size of the domain. The dispersion variance, D^2, increases for smaller block sizes as the variability is averaged (or smoothed) when moving to larger blocks (a change of support), as shown in Figure 3.

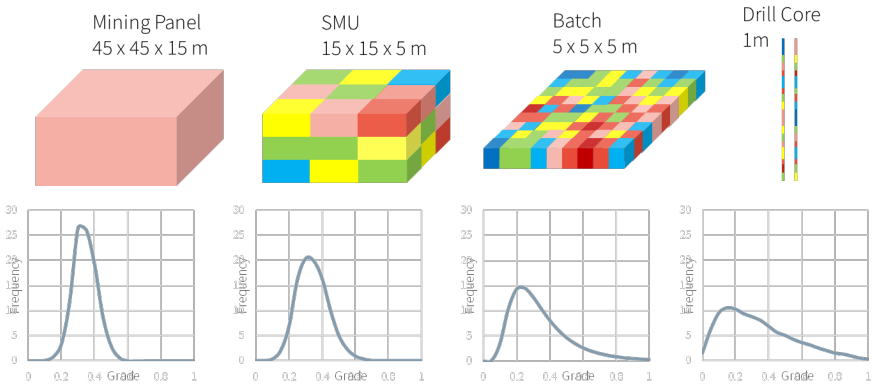

FIG 3 – Distribution of grade variability at different block/support sizes.

The dispersion variance of smaller blocks or parcels *v* (ie a small support), inside a larger region/support, *V*, is the difference between the average variogram values (Gammabar) calculated on *V* and *v* (Brooker, 1991), shown numerically in Equation 1.

$$D^2(v,V) = \bar{\gamma}(V,V) - \bar{\gamma}(v,v) \quad (1)$$

Gammabar ($\bar{\gamma}$) in the above equation is calculated as the average of all possible vector pairs (head and tail) of grades over the range of the variogram. These pairs are set using a lag distance, where both ends of the vector sit within the mining block V. This sum is conducted for all pairs in all three axis directions, which is the critical step that allows this method to consider variation in three dimensions. The Gammabar calculation is repeated for the smaller batch size, v, within the larger V, to obtain two different values as inputs to Equation 1 (Isaaks and Srivastava, 1989).

To evaluate the potential for bulk ore sorting, it is important that the selection of the batch and block sizes v and V consider the mining method. The small v represents the smallest scale at which heterogeneity is maintained for sorting. It should be selected to compensate for the loss of *in situ* heterogeneity through the mining process to represent grade variation as seen on the conveyor belt, for example 5 × 5 × 5 m batches. The large V is determined by the mining block size – for existing operations this can be the grade control block model (eg 10 × 10 × 10 m), or it may be even larger for greenfield projects eg the selective mining unit or mining panel size. The greater variation of the smaller block grades (compared to the larger mining blocks) determines the amount of material that could be rejected by the bulk sorter that would otherwise form part of the plant feed due to grade averaging within the larger mining blocks. The block size selection and dispersion variance calculation methodology has been published by Valery *et al* (2016) and Reple *et al* (2018) as a case study evaluating the Phu Kham operation.

In summary, to quantify the variation in grade and thus potential benefits of batch ore sorting on each ore domain, the authors follow a five-step process:

1. Obtain the semi variogram function for the valuable element and ore domain/lithologies in the deposit. Each variogram should include three sets of data (sill and ranges in each direction).
2. Calculate Gammabar (average variogram value) between all head and tail pairs (grades) within the large mining block V, summing vectors in each of the three semi-variogram directions. Repeat this calculation for the small volume v.
3. Calculate dispersion variance, D^2 as Gammabar (V) minus Gammabar (v).
4. With each large mining block size V having a known average grade (via methods such as kriging, the grade control model or using the domain average grade), the distribution of grades inside the large block V when it is sorted in the small batch v can be constructed.
5. Apply the grade distribution to all small v batch portions inside V, the grade and tonnage values using the batch volume and ore specific gravity can be calculated and tonnage-grade curves plotted, which shows the mass of material rejected as an increasing cut-off grade is applied.

CASE STUDIES

The three case studies below summarise recent projects conducted by the authors to assess pre-concentration technologies. In each case, bulk ore sorting was evaluated but was determined to be suboptimal for the application and alternative strategies were recommended. These cases are presented to highlight different factors that affected bulk ore sorting suitability. Case 1 describes a greenfield, underground porphyry copper ore, Case 2 an open pit copper-cobalt operation processing marginal stockpiles, while Case 3 presents an analysis of bulk ore sorting for a greenfield open pit gold project.

Case study 1 – underground porphyry copper ore

This study involved evaluation of potential pre-concentration routes for a greenfield porphyry copper project, with the copper occurring predominantly as disseminated covellite and pyrite-covellite veinlets. The proposed mining method was block caving, feeding a conventional SABC circuit followed by flotation to produce separate copper and pyrite concentrates. Initially bulk ore sorting appeared to offer significant potential as the low selectivity mining method would inevitably introduce large amounts of barren and low-grade material into the plant feed. Significant CAPEX savings were anticipated from rejecting a portion of the feed, thereby reducing the size of the concentrator. Coarse gangue rejection was expected to help alleviate challenges faced by the project in obtaining approval for wet tailings disposal.

Bulk ore sorting facilitates more accurate implementation of the selected cut-off grade, and the optimum cut-off grade will be dependent on the economics, mining methods, and downstream processing. In the case of block caving, there is very little scope for grade control in the mining operation; everything within the cave is mined which includes internal dilution and dilution from the cave walls and roof. Bulk sorting may be the only way for a caving operation to have some control for the implementation of cut-off grade.

However, the use of block caving poses significant challenges for successful bulk ore sorting. The disseminated nature of the orebody will limit the ability of BOS to reject totally barren batches of material. In addition, combining crushed ore underground from many drawpoints onto a single surface transfer conveyor will significantly reduce the *in situ* heterogeneity. Therefore, Hatch evaluated BOS alongside alternative pre-concentration technologies including screening, DMS, particle sorting and coarse particle flotation to determine which options were viable for further study.

To overcome the lack of deposit-specific data, an estimated primary crusher product PSD was generated based on data from a comparable underground block caving Cu operation. The Cu distribution in this stream was then calculated using the technique described by Bazin *et al* (1994). This approach has been shown to be valid for many other projects (Runge, Tabosa and Holtham (2014). More recently, Ehrig *et al* (2020) showed the Bazin relationship holding for a given ore over two separate size ranges, 3–200 mm and 13–150 µm. It is acknowledged that this technique cannot be used to estimate assay distributions to coarse fractions from flotation feed (cyclone overflow) samples due to the bias introduced through cycloning and density effect. Ideally, in an operating plant, coarser samples of SAG mill feed or secondary crusher product would be available for calculation of the ROM assay, however in greenfield projects crushed drill core may be the coarsest size by assay data source available.

Assay by size data for <1 mm crushed drill core samples from the project orebody was used as input to this Bazin analysis in order to estimate the Cu distribution in the primary crusher product PSD, as shown in Figure 4.

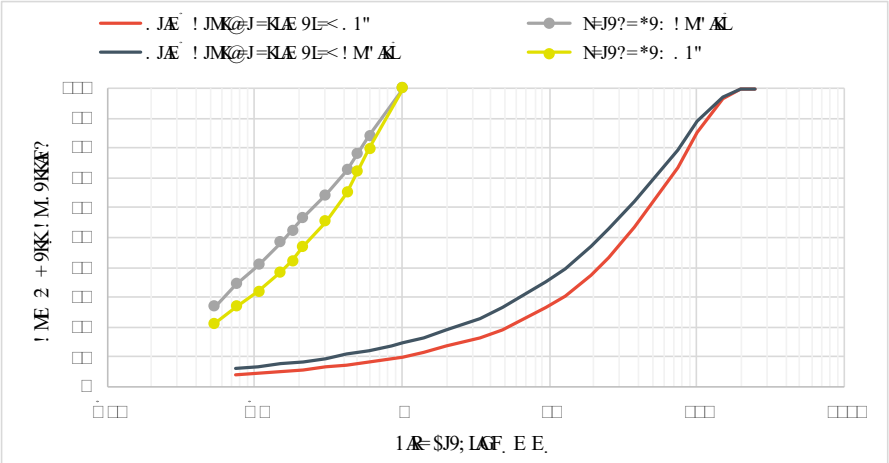

FIG 4 – Overall primary crusher product mass and estimated copper distribution with laboratory data.

The data in Figure 4 was initially used to assess the potential for pre-concentration by pre-screening. By varying screen aperture size, mass and metal recovery curves to undersize were produced. Results from three domains in the orebody are shown in Figure 5 compared with published examples from the literature. In contrast to the published studies, which showed recoveries up to 83 per cent Cu in 60 per cent of the mass, this case study showed only 65–70 per cent Cu recovery depending on the domain being processed. The results are much closer to the parity line compared with the published data indicating a low potential for upgrade by screening alone.

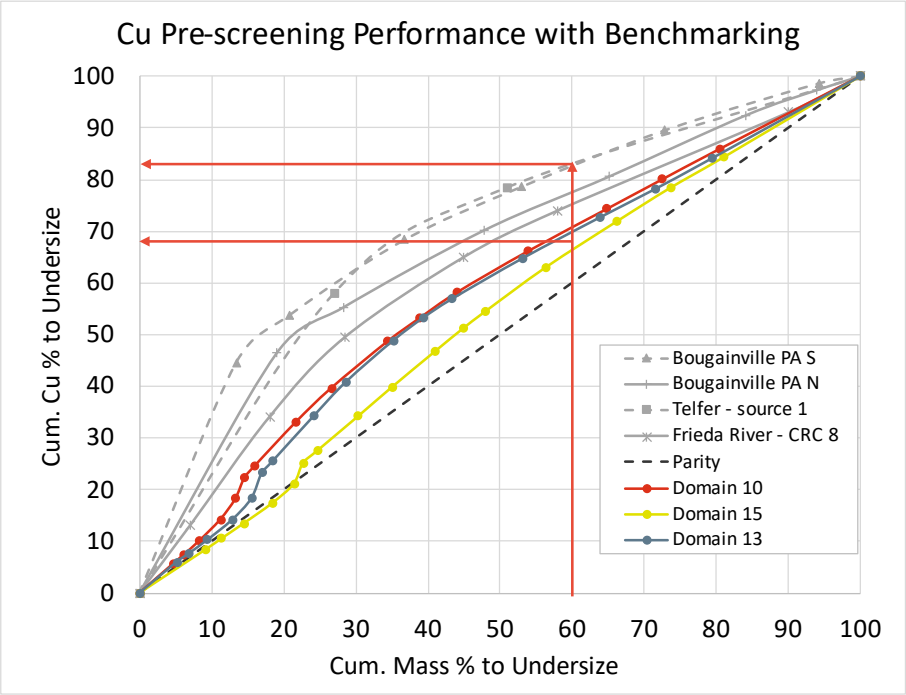

FIG 5 – Pre-screening benchmark cases and case study cumulative mass per copper curves.

The amenability of the deposit to BOS was analysed using the geostatistical approach outlined earlier based on variograms from resource definition drill holes. Whilst the batch size that can be measured by a sensor on a conveyor may be only 10–40 t (depending on measurement time), a block of this size cannot be mined without mixing with adjacent blocks, and in the case of a caving operation, also mixing with material extracted from other drawpoints. Therefore, the size of the small block used in the dispersion variance calculations should be larger than the batch size that will be measured by the sorter to account for this dilution. However, it is difficult to know what an appropriate size for v should be, as there is no actual data to validate models and assess the degree of mixing. A small block size, v, of 3 × 3 × 3 m has been used in this analysis, representing approximately 80 t to account for mixing before the bulk sorter. The large block size, V, was taken as 45 × 45 × 15 m based on the block size of the geological model. The grade variation of these small blocks within the larger mining blocks of 45 × 45 × 15 m was then calculated. By applying a progressive cut-off grade to the smaller blocks, cumulative mass and metal recovery curves for bulk ore sorting were generated. At the proposed sorter cut-off grade of 0.5 per cent Cu, 93 per cent of the copper could be recovered in 85 per cent of the mass, achieving a plant feed grade upgrade ratio of 1.1.

As the scope for BOS in this project seemed limited, alternative methods such as particle sorting were examined that allow for separation on an individual particle basis and reduce the impact of mixing during the mining process.

Compared to other alternatives, particle sorting requires significant additional material handling and crushing to produce the narrow feed size range required for sorting. Both coarse (45–135 mm) and fine (15–45 mm) sorting circuits were proposed to meet design requirements of a 1:3 ratio of smallest: largest particle in the sorting feed stream. In this case, the +135 mm and -15 mm streams report direct to the plant, however this should be evaluated on a case-by-case basis depending on metal deportment by size. Sorter throughput is highest when processing coarser particles, thus careful selection of sorting fractions in consultation with vendors is necessary to balance sorter performance and accuracy against capital cost. Penetrative XRT sorting technology was recommended for this application due to the presence of copper within sulfide minerals that can be identified based on their density differential from gangue.

No particle sorting test work was available to inform the study, thus data from published sorter performance treating copper sulfide ores was used to provide a range of expected performances, (Figure 6). Particle sorting performance is strongly dependent on ore type, mineralisation, liberation and of course sensor type, so it is recommended that initial sighter test work is performed on the main ore domains to obtain performance values. Initial test work is often carried out by suppliers for

little or no cost and allows a significant improvement in the study outcomes to be delivered, even at a concept level.

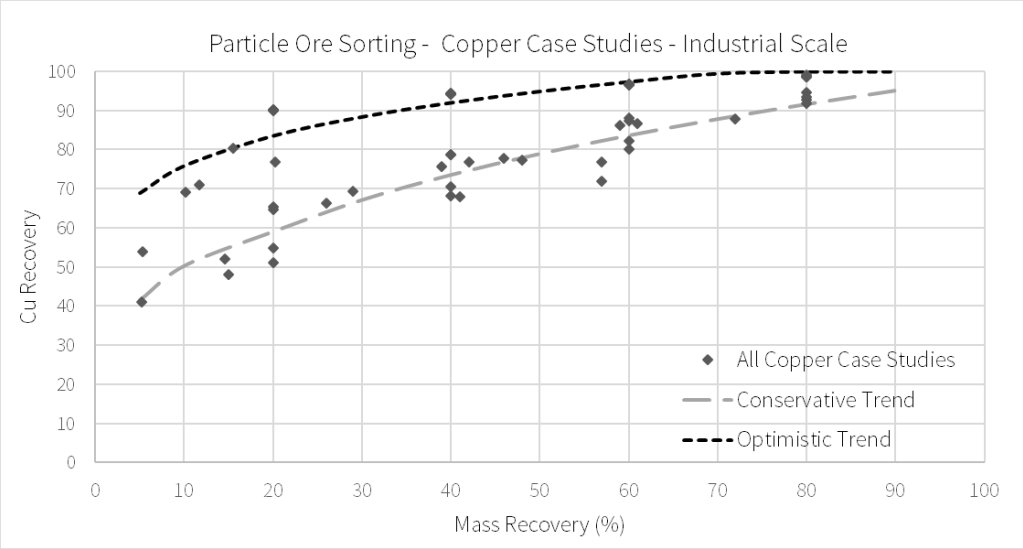

FIG 6 – Case studies of industrial scale Cu particle ore sorting with fitted trendlines.

Gravity concentration via jigging and DMS were also evaluated as part of this project. With the simplicity, lower operating and capital cost of jigging, a trade-off against the improved upgrade and shaper separation performance of DMS.

Examination of the dominant copper and gangue minerals in the deposit identified a potential pre-concentration opportunity. There are distinct density differences between the primary quartz and alunite gangue (S.G ~2.7) and the denser sulfides (covellite and pyrite S.G ~4.7). However, separation of perfectly liberated minerals, is not achievable. To estimate more realistic mass and Cu recovery values, drill core data with mineralogical composition at 4 m intervals was used to calculate the specific gravity of each length (Figure 7). By applying a progressive density cut point to the drill core, the resulting Cu recovery and mass rejection was predicted. With an accurate gravity separation method such as DMS, a sharp separation at an S.G of 2.7 could recover 94 per cent Cu whilst rejecting 31 per cent of the mass (Figure 7). This application would clearly have to be verified through more extensive test work, however it revealed potential that would otherwise have been overlooked if bulk ore sorting was the focus to the exclusion of all other pre-concentration methods.

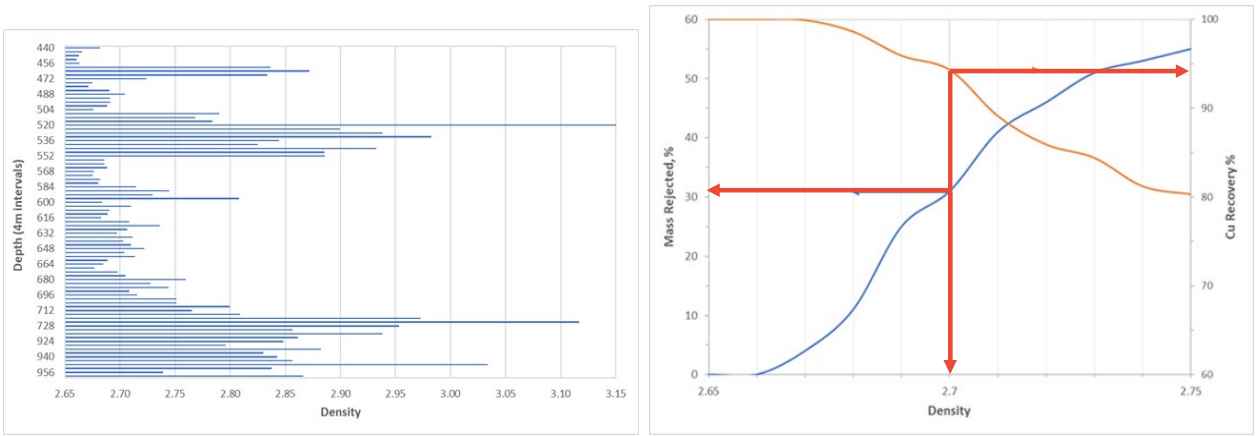

FIG 7 – Density variation down the drill hole (left) and resulting Cu recovery and mass rejection (right).

Furthermore, whilst mixing would occur during mining by block caving, pre-concentration methods that separate individual particles (like DMS and particle sorting) are not affected by the mixing during mining which affects the performance of BOS due to the separation of batches of material. Therefore,

a higher upgrade can be achieved (if suitable ore characteristics exist), but with the trade-off of higher cost and lower throughput than BOS.

Finally, the use of coarse particle flotation cells for pre-concentration further downstream than the above alternatives was investigated. If liberation and heterogeneity limit the applicability of other pre concentration options, coarse particle flotation may still be viable. It may also be used in combination with other pre-concentration options for further energy and cost savings. If flotation could be performed at a P_{80} of 300–500 µm rather than 100 µm, the potential energy savings in comminution would be around 30–50 per cent. Coarser grind sizes also have the potential to significantly reduce operating costs for power and grinding media. They also result in coarser tailings streams creating certain operational advantages and cost reductions at sites that incorporate sand embarkments, tailings filtration or paste backfill.

The flotation of coarser particles within conventional mechanical cells is typically limited by turbulence that causes bubble-particle detachment in the pulp phase or drop back from the froth phase of heavier particles. This is further exacerbated by the poor liberation of coarse particles in the 150–200 µm range which reduces the strength and amount of bubble-particle contact.

The limitations of conventional flotation machines can be overcome through the utilisation of a fluidised-bed flotation machine specifically engineered for the selective recovery of feeds containing very coarse particles. In this study, the Eriez HydroFloat separator was assessed, as it is the only coarse particle flotation technology commercially available and recently applied on an industrial scale to base metals in a tailings scavenging duty (Vollert *et al,* 2019). By using a quiescent, aerated fluidised bed, the turbulence commonly found in a mixed-tank contacting environment is greatly minimised. As a result, delicate bubble-coarse particle aggregates are more likely to report to the concentrate without disruption. The absence of a continuous froth phase minimises drop back that can occur at the pulp/froth interface. Furthermore, the HydroFloat operates most effectively with a feed tailored to a narrow size range, typically this is a top to bottom size ratio of 5:1.

Two applications of coarse particle flotation (CPF) technology are widely known in industry – the coarse gangue rejection (CGR) flow sheet and the tails scavenging flow sheet. Tails scavenging duty applies a CPF circuit to the final flotation tails stream to target metal losses in coarser size fractions eg >150 µm. In this duty the primary aim is improved recovery, which justifies the installation of the CPF circuit, with a secondary benefit being the potential to increase circuit throughput without the requirement to install additional grinding power to maintain the optimal flotation grindsize. In a coarse gangue rejection flow sheet, CPF technology is fed from grinding cyclone underflow to produce a coarse low-grade concentrate and a coarse barren tail. A comparison of these two circuits based on test work and plant data at the Cozamin Cu-Pb-Zn-Ag operation published by Regino *et al* (2020) found that the CGR flow sheet allowed 30 per cent of final tails to be removed in this coarse barren fraction, reducing the size of the tailings storage facility and pumping requirements. Furthermore, the capacity of the flotation circuit could be reduced by 40 per cent compared to a conventional plant flow sheet. By coarsening the grinding circuit product size to produce suitable feed PSD, grinding power requirements are reduced, compared to grinding the entire plant feed to a conventional flotation feed size, with an expected power reduction of 29–50 per cent, and in a greenfield application this would also reduce plant footprint and civil/structural costs. There are currently no CGR circuits operating in base metals, as the tighter integration of HydroFloat with the plant flow sheet poses a significant risk to profitability and operability dependant on CPF technology. However, in the context of pre-concentration, with a focus on gangue rejection at coarser size fractions prior to conventional processing, this flow sheet offers the most significant benefits.

Installation of CPF within the primary grinding circuit was proposed in this case study to reject coarse gangue ahead of the main flotation circuit. The comminution circuit feed would be ground coarser than the current target grind size P_{80} of 180 µm, with grinding circuit product (cyclone overflow) classified using screens and cyclones, or a combination of these technologies, to prepare the feed to both fine (conventional) and coarse particle flotation stages. The fines of the classification stage would feed the proposed rougher flotation bank and the coarser stream would feed a fluidised bed coarse particle flotation cell. The coarse flotation concentrate would require further grinding and cleaning to produce a final concentrate and would, therefore be sent to the proposed rougher scavenger concentrate regrind ball mill. Coarse flotation tail would be rejected and combined with rougher-scavenger tail to form the final tail.

Pilot test work has shown that a fluidised bed cell could recover up to 70 per cent of composite sulfide particles between 300–600 µm with a sulfide liberation greater than 15 per cent, and that this would increase to >90 per cent recovery of sulfides in finer fractions (Vollert *et al,* 2019). Previous studies by Hatch, for a copper ore, also show that HydroFloat cell recovery could be maintained above 90 per cent for particle sizes up to 425 µm for copper sulfides with less than 10 per cent liberated present in the HydroFloat concentrate (Valery *et al,* 2020).

In the absence of laboratory HydroFloat test work to model the circuit performance, liberation data was analysed as an indicator of performance. QEMSCAN mineral liberation data showing the distribution and liberation by size of sulfide (covellite, enargite and pyrite) particles in test work samples was used to provide an indicator of potential performance. The analysis suggested that approximately 96 per cent of sulfides below 450 µm had more than 15 per cent surface liberation and thus were amenable to recovery by coarse particle flotation (Figure 8 left).

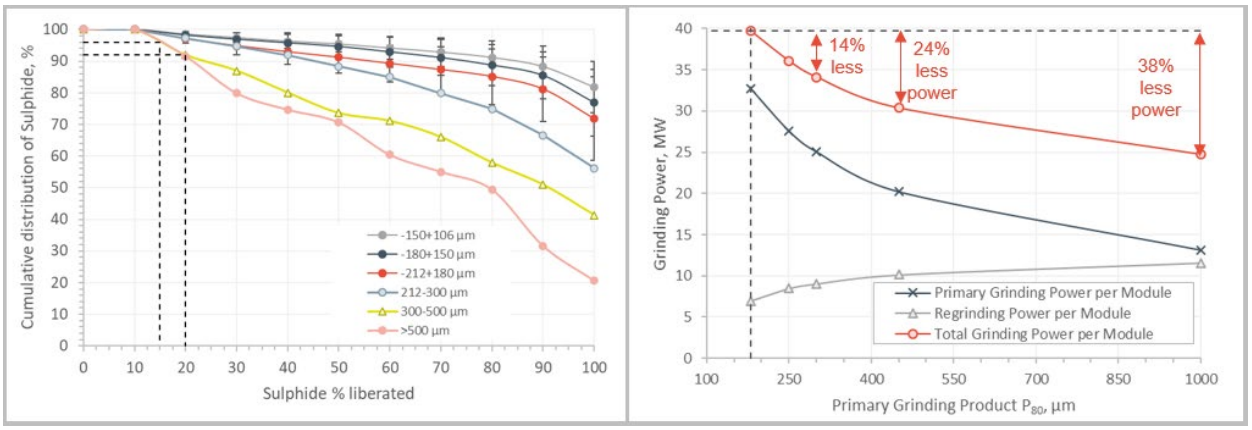

FIG 8 – Cumulative distribution of sulfides (covellite, enargite and pyrite) by degree of liberation (left), and simulated grinding power as a function of primary grinding product P_{80} (right).

Preliminary simulations and power-based calculations were used to estimate the impact of coarse flotation on the overall grinding energy for different primary grind sizes. Power based methodology can be used to calculate the total SAG – ball mill circuit comminution energy requirements as well as the increase in regrind power consumption that occurs as a result of regrinding the coarse HydroFloat concentrate prior to cleaning. This allows the total grinding power to be calculated for a fixed throughput and specific energy input requirements based on ore characteristics, feed size and product sizes. Figure 8 (right) shows the result of this calculation, with a significant reduction in primary grinding power when moving from the original target grind size P_{80} of 180 µm to 425 µm established as suitable for coarse ore flotation. Despite the increase in regrind energy consumption, the total power consumption decreases by 24 per cent which is a significant saving. In addition, CAPEX savings from smaller mill sizes as well as a reduction in footprint and civil/structural costs would be significant.

A summary of the performance of the pre-concentration routes assessed during the study is presented in Figure 9. Coarse particle flotation is not shown, as it appears later in the flow sheet than the other pre-concentration options. The potential benefits are not expected to be as significant and do not translate easily onto a mass-metal curve. However, if dissemination and liberation limits the applicability of other pre-concentration options, the potential to reduce energy consumption and increase throughput with coarse particle flotation is significant.

This low-grade porphyry deposit is a good target for pre-concentration due to its large size and thus large volumes of barren dilution material which could potentially be rejected prior to downstream processing. However, the ore may be finely disseminated and experience significant mixing during mining, limiting the upgrade potential of BOS which separates large batches of material. By considering all pre-concentration options, alternative opportunities such as gravity concentration via DMS were defined that would not have been apparent if BOS was the exclusive focus.

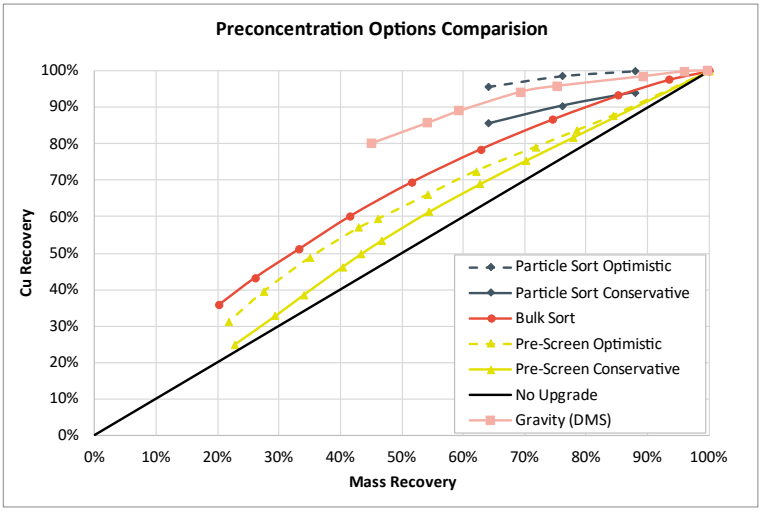

FIG 9 – Comparison of mass and metal recovery curves for preconcentration routes.

Case study 2 – bulk ore sorting of low-grade copper-cobalt stockpiles

In this project, the client had a significant volume of stockpiles to be reprocessed, built from marginal material accumulated throughout the life-of-mine (LOM). The stockpiles consisted of oxide and sulfide minerals including malachite, carrolite and chalcopyrite, with gangue primarily composed of dolomite, magnesite and quartz. The initial project scope was to assess the suitability of bulk ore sorting to treat the four largest copper containing stockpiles and also as a proof-of-concept for application to the client's other operations.

There were several issues that significantly limited the potential for BOS in this scenario. An initial study undertaken by the company considered three scenarios for the Cu and Co grades within these stockpiles. However, an assumed sorter recovery of 90 per cent was used when predicting the copper ore accepted for downstream processing. This value was assumed with no consideration for the ability of the bulk ore sorting system to clearly distinguish ore and waste batches within the piles. The stockpiles were built from marginal material ranging from 0.6–1.5 per cent Cu (with all lower grade material sent to waste during mining) thus the grade variation available to achieve this assumed recovery was significantly limited.

The second area of concern was the competing requirements for the proposed BOS system. Cu and Co both contribute significantly to the overall profitability of the operation; however assay data from stockpile samples (and historical mine data) suggested there was no clear correlation between Cu and Co grades, thus rejecting material based on Cu grade alone has the potential to reject material high in Co. This also has a significant effect on the sensor types that would be suitable for BOS, for example although magnetic resonance sensors are extremely well suited to detecting chalcopyrite, they are unable to detect oxide minerals or cobalt. Alternate sensors, such as PGNAA which determine the full elemental composition of a material, would be required to assess both Cu and Co grade. Further discussions with the client subsequently indicated that the consumption and cost of sulfuric acid used in the downstream oxide leaching circuit was a significant factor in plant profitability, to the extent that even high Cu/Co grade batches would be unprofitable to process if they also contained significant amounts of acid consuming gangue (GAC) – mainly dolomite.

Assay results from 70 very small (20 kg) samples across the stockpiles were assessed to examine the variation in Cu/Co grade and acid consumption and illustrate the impact of multiple cut-off decision drivers for this operation. As shown in Figure 10, sorting based only on Cu grade would discard much of the Co and likewise a sort considering only Co grade would discard much of the Cu (red shaded areas are the reject fractions for the assay samples). Furthermore, a sort based on acid consumption would discard much of both the Cu and Co.

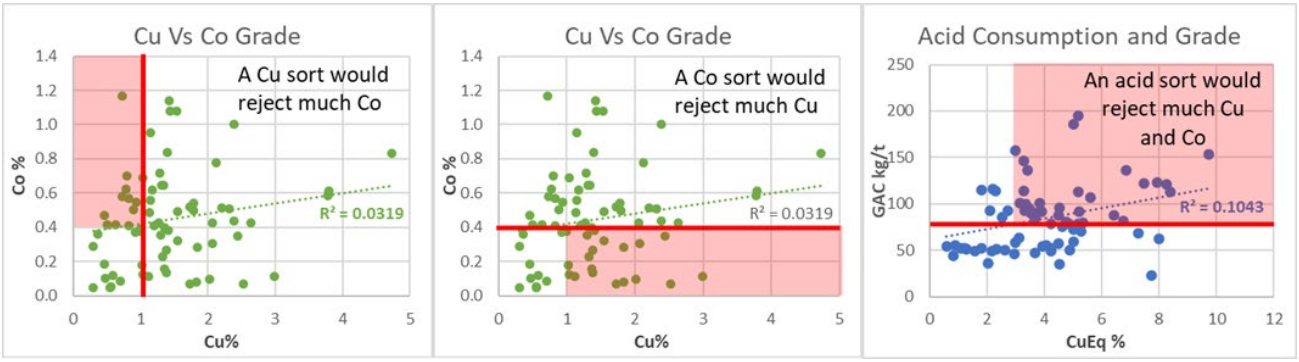

FIG 10 – Impact of competing factors on bulk sorting performance.

Two methods were considered to address this issue, firstly sorting using a combined set of rules that would require Cu and Co grades to be above the cut-off threshold (expressed as a Cu equivalent based on the price difference between Cu and Co):

$$\text{Cu Eq} = \text{Cu\%} + \text{Co\%} \times 6 \text{ (For example, for 1\% Cu and 0.5\% Co, Cu Eq} = 4\%)$$

Rules such as the following could then be applied:

If Cu Eq <4% = Discard

If Cu Eq >6% and Acid cons >60 kg/t = Discard

If Cu Eq >6% and Acid cons <60 kg/t = Accept

Secondly, calculation of a batch value, using historical regressions from plant data to relate the measured grade of Ca or CaO to plant acid consumption and subtracting this cost from the contained metal value:

$$Batch\,Value = Contained\,Value\,(Cu\ grade\ x\ price + Co\ grade\ x\ price) - Acid\ Cost\,(acid\ consumption\ x\ price)$$

To demonstrate the potential performance of a rules-based sorting algorithm, a series of sorting scenarios with different cut-off requirements were applied to the 70 stockpile samples with assay data used to calculate an accept or reject decision. Various rules were applied to assess the improvement in performance by scaling the accepted acid consumption based on the contained metal (contained value), ie higher contained value batches justify higher acid processing costs. These scenarios use the Cu equivalent approach as discussed earlier. The best case achieved minor upgrades of ~1.2 and 1.1 for Co and Cu, respectively and ~10 per cent reduction in acid consumption, recovering 78 and 72 per cent of the Cu and Co in 66 per cent of the mass. Other scenarios achieved a higher degree of acid consuming material rejection; however, the Cu/Co losses were unacceptable.

The analysis provided insight into the issues faced when multiple competing performance drivers impact the sorting decision. However, the assay samples represent 20 kg batches only and a further reduction in performance would be expected when considering full-scale sorting batches due to mixing and homogenisation.

The third factor which affected the suitability of bulk ore sorting for this project is the considerable mixing and homogenisation that occurs during stockpile formation and reclaiming, which will reduce the grade variability. In order to model the change in variability, the grade control block model for the mine (which in this case had a fine resolution: 5 × 5 × 2.5 m) was used as a baseline, along with topography surveys and truck dispatch data, to build block models for copper of the four stockpiles. Figure 11 shows the resulting tonnage and grade curves. Solid lines represent the in situ material (from grade control), and dashed lines show the material properties once stockpiled. If a sorting cut-off grade of 1 per cent Cu was applied to the in situ material, approximately 15 Mt would be above cut-off grade, and this mass has a grade of 1.3 per cent Cu, as shown by the red arrows. However, if the same 1 per cent sorter cut-off grade was applied to the stockpiled material, only 10 Mt would be above this cut-off, and the material would have a lower grade of only 1.08 per cent Cu.

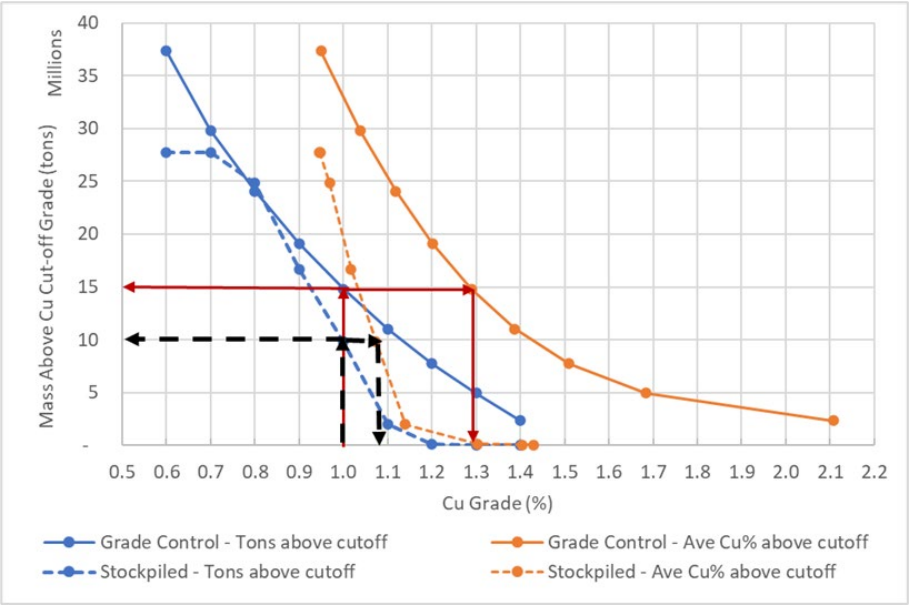

FIG 11 – Comparison of Cu grade and tonnage curves for in situ and stockpiled material.

The stockpile block models were only populated with data for copper, not cobalt, thus in order to estimate the impact of stockpiling on cobalt variability and sorter performance an alternative approach was required. The grade control blocks with copper grade between 0.6 and 1.5 per cent Cu were selected as the blocks sent to the marginal stockpiles. The *in situ* cobalt grade distribution in these selected blocks was modelled, then the standard deviation of the modelled grade distribution was reduced by a factor to account for the homogenisation of building and reclaiming the stockpiles. This homogeneity factor is related to the number of layers of the stockpile, assumed to be ten layers in this case.

The homogenisation factor is an empirical measure of the reduction in variability within stockpiles and can be used to quantify the degree of homogenisation from different stockpile designs (De Wet, 1994; Schofield, 1980).

$$H_f = \frac{S_{in}}{S_{out}} = k \times \sqrt{N}$$

H_f = homogenisation factor

S_{in} = standard deviation of input (mined material – stockpile feed)

S_{out} = standard deviation of output (reclaimed stockpile product)

k = parameter in range of 0.5–0.7

N = number of stockpile layers

In past projects conducted by the authors grade standard deviation has been reduced between two to four times through the stockpiling and reclaim process, depending on the number of stockpile layers, significantly limiting the opportunity for bulk ore sorting.

Monte Carlo simulations were performed to randomly extract the blocks from the stockpile and create the cobalt grade distribution accounting for the homogeneity effect when reclaiming the material, as there was no spatial information regarding the blocks in the stockpile. The tonnages and cobalt grades were calculated for each cobalt grade interval (block) so that the stockpile potential upgrade and recovery for a cobalt bulk sort could be evaluated. The cobalt bulk sort final result in Figure 12 is more promising than the copper bulk sort, which is a function of the in situ grade distribution and mineralisation types. It is clear that while some improvement could be achieved for Co with a mass recovery of 60 per cent recovering ~75 per cent Co, when both elements are considered in a combined reject or accept decision the ability to reject barren mass is limited.

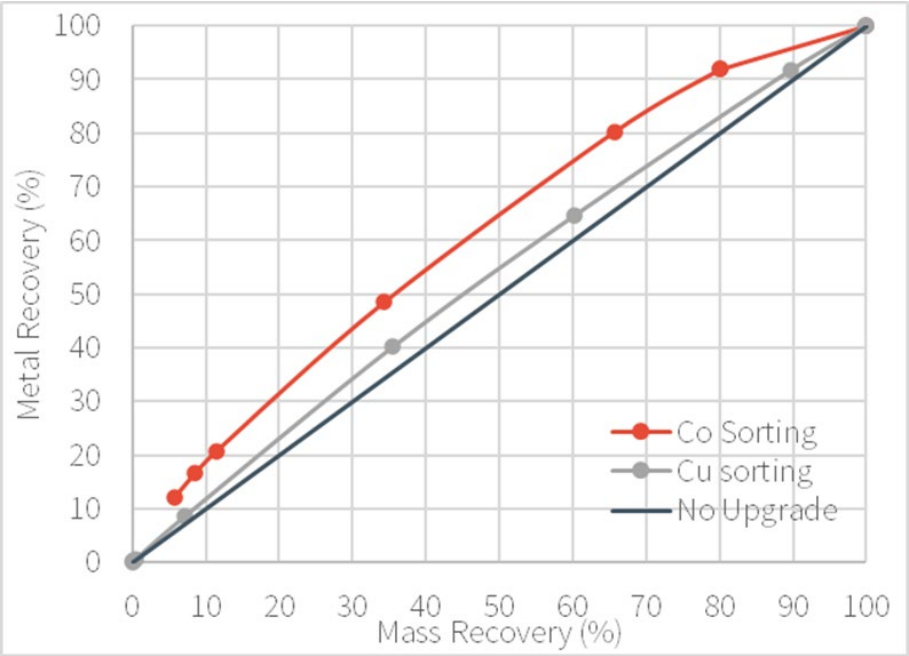

FIG 12 – Overall Cu and Co BOS performance.

Alternative methods of pre-concentration were also proposed for this project, including screening, particle sorting and DMS. These act on individual particles rather than batches, eliminating the issues arising from homogenisation and competing sorting factors. However, particle size analysis indicated that a significant mass of ROM material was -10 mm which typically bypasses some pre-concentration processes. With no assay data available for this fine fraction, the optimal destination (direct to plant feed or reject stockpiles) could not be selected. The destination of this stream is a key factor in determining the size of the pre-concentration plant and CAPEX requirements to supply the existing process plant at its design capacity. This is illustrated by the concept level CAPEX developed for this project in Figure 13. This estimate was developed based on the requirement to produce 250 t/h of pre-concentration product to feed the downstream plant, with major equipment scaled from past project estimates using the six-tenths rule, and lang factors applied to calculate direct and indirect costs. Options where the fine stream is rejected to waste stockpiles required a significantly higher feed rate and larger equipment sizes, which would make the capital cost prohibitive. Due to their complexity, options such as particle sorting which require additional infrastructure and crushing stages prior to separation have higher CAPEX (~US$ 27 million) and OPEX costs than technologies like BOS (~US$ 14 million in this study). More detailed techno-economic analysis of pre-concentration options conducted by (Pyle *et al*, 2020) identified that the overall net present value (NPV) of these projects is strongly affected by the feed grade upgrade (and mass rejection) that can be achieved, thus, a successful application of pre-concentration must be suited to both the orebody mineralogy/liberation and provide financial benefits in terms of NPV and payback periods.

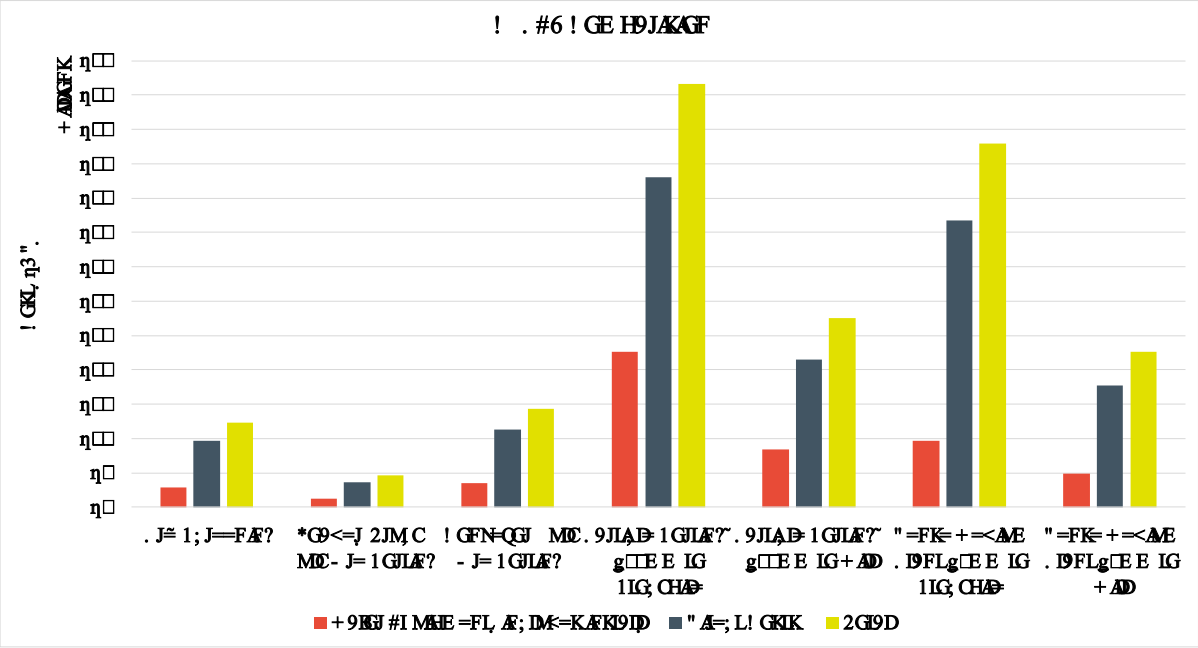

FIG 13 – Concept level CAPEX for pre-concentration circuits producing 250 t/h product in this case study.

Case study 3 – open pit gold project

The third case study is from a greenfield open pit gold project, processing a low-grade deposit at 0.87 g/t Au with a throughput of 1800 t/h. The aim was to utilise BOS as a low CAPEX option to treat low-grade ore comprising one of three domains in the plant feed. This would upgrade the mill feed to reduce CAPEX for an equivalent gold production and reduce mill footprint in the heavily layout constrained site. Hatch was engaged to review previous bulk ore sorting test work and performance assumptions, and propose alternative BOS circuit designs, including in-pit sensing and diversion, shovel-based sorting, traditional conveyor-based sorting arrangements and combined bulk and particle sorting to ‘clean’ the accepts stream or ‘scavenge’ the rejects. Three areas of concern were identified in this project that would limit BOS performance and would be observed in similar applications.

Prior test work had been conducted with sensor suppliers to examine the potential for direct gold measurement using PGNAA (which is a significant development) as well as measurement via proxy elements. Measurement for Au correlated reasonably well with lab fire assay results (Figure 14 left), which initially suggested that direct Au measurement could be feasible. However, these measurements were obtained with a 1-hour sensing time, and upon further investigation, the repeatability of these results raised significant concerns. As per the repeatability measurements in Figure 14 right, shorter measurement durations of 20 and especially 2 minutes resulted in significant scatter in the grade readings obtained compared to the lab assay value, across various samples. In order to exploit the deposit heterogeneity, sorting should operate in the range of 30 secs – 2 min batches. Thus, at a feed grade of 0.87 g/t, the 2-minute result variation observed here would make direct Au measurement using PGNAA unfeasible due to the lack of precision, resulting in mischaracterised batches of ore to waste and vice versa.

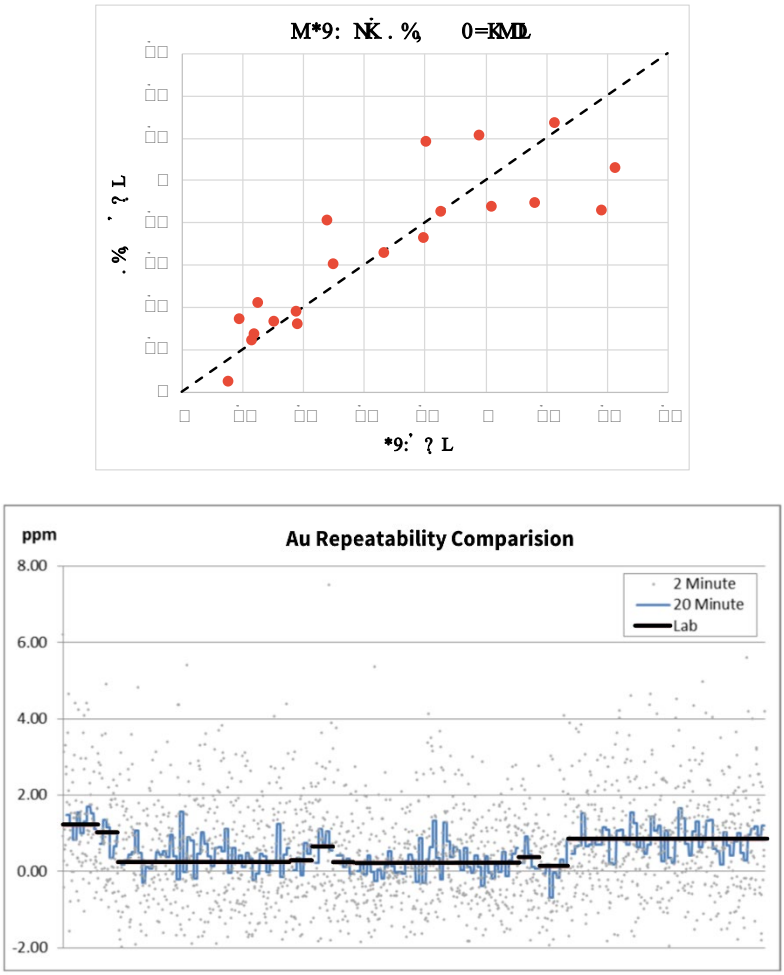

FIG 14 – PGNAA sensor versus lab measurement (left) and repeatability (right).

A second method proposed for bulk sorting at this deposit was the use of proxy elements based on 3000 ICP elemental data sets including Si, Mg, Al, Ca, Fe and K as predictors of gold grade. The deposit contains three distinct ore domains as follows:

- Geomet 1: Rich quartz vein with higher gold grade.
- Geomet 2: Altered granitoid with higher gold grade.
- Geomet 3: Tonalite with disseminated pyrite and lower gold grade.

The three geometallurgically different domains each required a separate proxy model, (currently based on around 1000 ICP data sets each) and model regressions yielded R^2 values of 0.22 to 0.57, indicating the equations were a poor predictor of actual Au grade. Although further work was recommended to obtain additional elemental data sets to improve these models, the issue of sorting three different domains remains. Geomet 3, comprising 60 per cent of the deposit, is the primary domain intended for BOS to exploit the lower grade nature of this material (half the grade of Geomet 1 and 2) and thus the potential for upgrade with major mass rejection. However, the three domains cannot be mined independently due to the proposed open pit mining method and the distribution of domains throughout the deposit. Thus, extremely stringent grade control block models and truck scheduling would be required to ensure only domain 3 ore is directed to the sorter, with domains 1 and 2 bypassing direct to the plant. In addition, for mixed domain areas of the pits, the sorter would have to be configured to select between different proxy relationships based on the batch of ore being processed.

The final limitation with BOS in this project was the initial methodology used to assess heterogeneity and therefore the potential mass rejection and Au recovery values. The initial analysis used composited drill core lengths of 1.5 m up to 4.4 m to represent the volume of ore seen by the sorter on a conveyor up to sorting of ore batches in a truck. The grade from this length was extrapolated

into a cube and then each cube could be accepted or rejected with the application of a sorter cut-off grade. However, there are several significant issues with this method that overestimate the performance as follows:

1. Mining methods are typically horizontal in nature, and the variability along a length of drill core in 1 dimension vertically is not reflective of the 3D variability of batches of ore extracted by excavator buckets
2. Mixing during blasting, load and haul and materials handling was not considered in the analysis and would significantly reduce heterogeneity
3. The smallest scale at which heterogeneity can be maintained is the size of the excavator bucket which is used to extract the blasted material (29 m^3 for this project) due to the mixing that occurs during mining. Attempting to calculate recovery at smaller scales from either drill core lengths or batch sizes passing through the BOS sensor will overestimate the mass rejection and upgrade that can be achieved.

To show the impact of using composite drill core lengths to estimate mass and gold recoveries for BOS (if Au could be directly measured), the authors compared the method used by the client to results from geostatistical analysis. Three variograms from zones of high, mid and low-grade material were used for geostatistical analysis. The mass and metal recoveries were obtained using the dispersion variance calculation described earlier in this paper, using the mine block model size and loading/hauling equipment sizes to estimate the impact on heterogeneity and thus BOS performance. The strength of this approach is two-fold; firstly, by calculating Gammabar (the average variogram) for both mining block (V) and sorter batch (v) sizes using all three directions of the semi-variogram, the variation in grade in three dimensions is captured. This enables a horizontal grade variation to be captured in the formation of some deposit. Furthermore, it prevents overestimation of BOS potential, for example where vein style mineralisation might result in significant assay variation over 10 or 20 metres of drill core, whereas the mining process which progresses horizontally through a bench wouldn't excavate the variability in this direction. Secondly, by selecting the small batch size based on the mining method eg excavator bucket size and truck tray volume, the dilution and mixing introduced through mining to be considered in the BOS performance calculation, preventing an overoptimistic result compared to down the hole compositing which does not capture this aspect.

For this case study, previous down the hole analysis had been used to calculate gold recovery from BOS and using an exponential equation $\left(Rec = 100 \times 1 - e^{-\frac{k}{100 \times Mass\ Pull}}\right)$, mass-metal recovery curves were fitted to the down the hole analysis result by varying the k value from 3.7 to 9.6. This change theoretically approximated sorting performance at different sorting batch sizes from a 12 m bench to 1.5 m pod on a conveyor. Figure 15 presents the combined mass and metal recovery curves for both methods of analysis, showing the down the hole analysis would indicate metal recoveries of 70–80 per cent in only 30 per cent of the mass, whereas the more rigorous geostatistical approach indicated only 50 per cent Au recovery in the same 30 per cent mass yield.

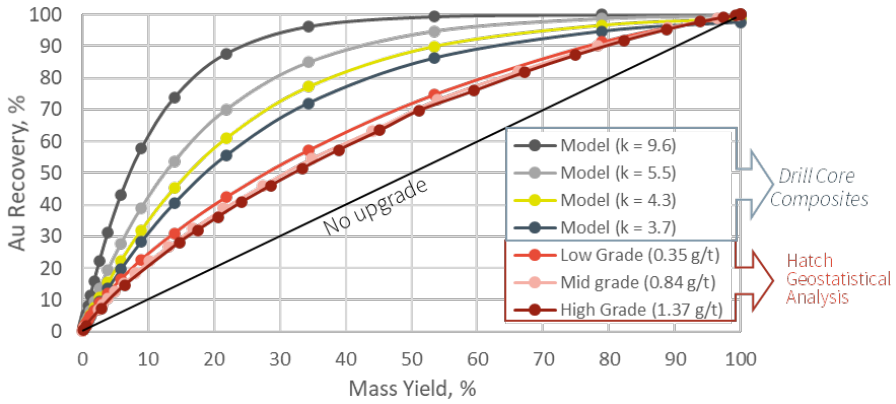

FIG 15 – Mass and gold recovery curves for drill core composites compared to geostatistical analysis.

CONCLUSIONS

This paper has presented several recent projects examining the application and benefits of pre-concentration technologies. Bulk ore sorting was a particular focus for these studies due to its relative simplicity, ability to process material directly after mining with no further crushing or screening required upfront and lower CAPEX, OPEX and simplified layout requirements compared to other alternative pre-concentration technologies.

Three case studies were drawn from a variety of operations and commodities to highlight key factors or requirements for the successful implementation of bulk ore sorting. In these cases, one or even multiple instances of the following issues limited successful BOS application:

- Heterogeneity – suitable heterogeneity needs to be present in the deposit in situ and maintained through the mining process to enable effective separation at a truck, shovel or conveyor batch scale depending on the sorting technology being applied. A geostatistical approach is one of the most rigorous ways to quantify grade variation, because it allows for variation in three dimensions to be considered in the analysis and the selection of small v sorting batch size accounts for mixing in the excavation, load and haul stages to establish the grade variation as seen on the conveyor.
- Sensor suitability – all potential valuable or waste elements should be evaluated for sorting to determine which established bulk sorting sensors such as PGNAA/PFTNA, MR or XRF could be applied. Sometimes unconventional approaches may be required to target a gangue element or mineral, or a proxy mineral or element, if direct measurement of the valuable element, such as gold, is unfeasible.
- Mineralogy and liberation – consideration should be given to the value of all elements in the deposit and their recovery via BOS. In some applications, such as the Cu/Co case study, the correlations between valuable minerals may directly impact sorting performance, different elements may not be measurable using the same sensor or disseminated minerals may limit the upgrade potential.

A successful scoping study should consider bulk ore sorting alongside all the other potential technologies to determine which options can deliver a successful pre-concentration outcome. By investing in initial test work using minimal sample masses as part of the scoping level study, the value delivered through these assessments can be significantly improved by delivering orebody specific results, mass balances and CAPEX estimates. BOS certainly has an important role to play in the future of mining and minerals processing, however operations, vendors and consultants need to be aware there are other pre-concentration options which may be more suitable than BOS.

These studies are presented to support future successful applications of bulk ore sorting for the right deposit type with suitable heterogeneity. The selection of the optimum pre-concentration route needs to be evaluated considering the deposit characteristics and in an integrated analysis with mining and downstream processing. These technical aspects also need to align with positive financial metrics. Mining and processing teams cannot operate independently, as maximum benefits from BOS will only be obtained when a shift in mining practices is made to retain in situ heterogeneity as much as possible as opposed to blending it out.

REFERENCES

Adair, B, Revell, R, King, D and Keeney, L, 2020. A ‘no tailings dam future’ – preconcentration strategies ‘down the sizes and across the value chain’, presented at the *Preconcentration Digital Conference*, November 2020, pp. 5–17 (The Australasian Institute of Mining and Metallurgy: Melbourne).

Bazin, C, Grant, R, Cooper, M and Tessier, R, 1994. A method to predict metallurgical performances as a function of fineness of grind. *Minerals engineering*. 1994, Vol 7, Num 10, pp 1243–1251.

Beal, C and Singh, S, 2020. Improved mining recovery with bulk ore sorting and MR technology, Preconcentration Digital Conference 2020 (The Australasian Institute of Mining and Metallurgy: Melbourne).

Brooker, P, 1991. *A geostatistical primer*. World Scientific.

De Wet, N, 1994. *Homogenizing/blending in South Africa – an update*. 14(1), p. 93.

Duffy, K, Valery, W, Jankovic, A and Holtham, P, 2015a. Integrating Bulk Ore Sorting into a Mining Operation to Maximise Profitability, in *Proceedings of MetPlant 2015*, pp. 273–287 (The Australasian Institute of Mining and Metallurgy: Melbourne).

Duffy, K, Valery, W, Jankovic, A and Holtham, P, 2015b. Resource Efficient Mining Processes of Tomorrow, in *Proceedings of the Third International Future Mining Conference*, pp. 227–238 (The Australasian Institute of Mining and Metallurgy: Melbourne).

Ehrig, K, Liebezeit, V, Macmillan, E, Li, Y, Pewkliang, B and Smith, M, 2020. Preconcentration via waste rejection based on fragment size – Olympic Dam Case Study. in *Proceedings of the Preconcentration Digital Conference 2020*, pp. 336–344. (The Australasian Institute of Mining and Metallurgy: Melbourne).

Harding, B and Deutsch, C, 2019. Change of Support and the Volume Variance Relation. [Online] Available at: https://geostatisticslessons.com/lessons/changeofsupport

Isaaks, E and Srivastava, M, 1989. *An Introduction To Applied Geostatistics*. New York: Oxford University Press.

Pyle, L, Valery, W, Holtham, P and Duffy, K, 2020. Techno-economic comparison of pre-concentration options for a Ag-Pb-Zn deposit. Cape Town, XXX International Mineral Processing Congress.

Regino, R, Wong, H, Lopez, O, Adams, K, Hobert, B and Wasmund, W, 2020. A Comparison of Two Circuit Applications for Implementation of Coarse Particle Flotation. Conference of Metallurgists 2020.

Reple, A, Chieregati, A C, Valery, W and Prati, F, 2018. Bulk ore sorting cut-off estimation methodology: Phu Kham Mine case study. *Minerals Engineering*, 4, Volume 149, pp. 105498–105501.

Runge, K, Tabosa, E and Holtham, P, 2014. Integrated Optimisation of Grinding and Flotation Circuits, in *Proceedings of the 12th AusIMM Mill Operators Conference* (The Australasian Institute of Mining and Metallurgy: Melbourne).

Schofield, C, 1980. *Homogenisation/Blending Systems Design and Control for Minerals Processing*. TransTech Publications.

Scott, M, Rutter, J, du Plessis, J and Alexander, D, 2020. Operational deployment of sensor technologies for bulk ore sorting at Mogalakwena PGE Mine. Preconcentration Digital Conference 2020 (The Australasian Institute of Mining and Metallurgy: Melbourne).

Valery, W, Duffy, K, Holtham, P, Tabosa, E, Andrade, B, 2020. Conducting comprehensive evaluations of preconcentration options. in *Proceedings of the Preconcentration Digital Conference 2020*, pp. 345–355 (The Australasian Institute of Mining and Metallurgy: Melbourne).

Valery, W, Duffy, K, Prati, F, Reple, A, Holtham, P and Walker, P 2016. Evaluation of Bulk Ore Sorting for Pre-concentration of Copper Ore at PanAust Phu Kham Operation. in *Proceedings of the 24th World Mining Congress - Mining in a World of Innovation*, Rio de Janeiro, Brazilian Mining Association, pp. 145–154.

Vollert, L, Akerstrom, B, Seaman, B and Kohmuench, J, 2019. Newcrest's industry first application of Eriez HydroFloat technology for copper recovery from tailings at Cadia Valley Operations. in *Proceedings of the* 58th Conference of Metallurgists hosting the International Copper Conference, British Columbia.

Towards grade engineering using X-ray microtomography

F Reyes[1], K Barbosa[2], C Evans[3], V Jokovic[4] and G Wilkie[5]

1. Research Fellow, The University of Queensland, Sustainable Minerals Institute, Julius Kruttschnitt Mineral Research Centre, Brisbane Qld 4068. Email: f.reyes@uq.edu.au
2. Postdoctoral Research Fellow, The University of Queensland, Sustainable Minerals Institute, Julius Kruttschnitt Mineral Research Centre, Brisbane Qld 4068. Email: k.barbosa@uq.edu.au
3. Senior Research Fellow, The University of Queensland, Sustainable Minerals Institute, Julius Kruttschnitt Mineral Research Centre, Brisbane Qld 4068. Email: c.evans@uq.edu.au
4. Senior Research Fellow, The University of Queensland, Sustainable Minerals Institute, Julius Kruttschnitt Mineral Research Centre, Brisbane Qld 4068. Email: v.jokovic@uq.edu.au
5. Research Manager, The Cooperative Research Centre focused on Optimising Resource Extraction-CRC ORE, Kenmore Qld 4069. Email: g.wilkie@crcore.org.au

ABSTRACT

The idea behind Grade Engineering is to exploit the natural heterogeneity of an orebody (spatial, temporal) in order to divert low-value waste out of the mining value chain. Essentially, this involves rejecting material at relatively coarse particle sizes (10 mm to 200 mm). However, lack of knowledge about the inherent particle grade distributions in these coarse particle size ranges limits the opportunities for optimisation. Particle grade distributions are essential for quantifying and modelling gangue liberation and yield curves. These curves can then be used to predict the mass and value flows that will go towards the accept and the reject streams.

Particle grade distribution information for particles coarser than 10 mm can be collected based on chemical assays of sufficient number of individual particles. However, for smaller particles (1 mm to 9 mm), a significantly larger number of particles is required for assays. Moreover, in some cases, the mass of individual particles is smaller than the minimum mass required for chemical assaying. Also, other quantification techniques such as automated mineralogy, eg Mineral Liberation Analysis (MLA), require extended measurement times to analyse statistically representative numbers of particles at these size ranges.

This work investigates the use of 3D X-ray microtomography to fill this quantification gap at these size ranges (1 mm to 9 mm). In-house image processing algorithms are used to estimate the mineral/metal content in each particle. Particle grade distributions, as well as density distributions, are thus produced without a minimum mass requirement and with each scan providing information about tens to hundreds of particles at a time.

Mineralogical data from MLA analysis, of finer size ranges, is used to inform X-ray microtomography, so a simpler 3D mineral map can be obtained using the image intensity. Chemical assay information of the scanned samples is used to validate and correct the mineral phase segmentation.

INTRODUCTION

The fundamental idea of Grade Engineering as articulated by the Australian Government's Cooperative Research Centre for Optimising Resource Extraction (CRC ORE) is to exploit the natural heterogeneity of an orebody (spatial, temporal or particle) in order to divert low-value waste out of the mining value chain prior to expensive and environmentally deleterious comminution and processing unit operations. This involves rejecting material at relatively coarse particle sizes (typically 10 mm to 200 mm in size) prior to fine crushing and SAG milling. A significant challenge to overcome when working at these coarse particle sizes is that very little is known about the inherent particle grade distributions that are present in these coarse particle size ranges. Particle grade distributions are necessary for measuring and modelling gangue liberation and yield curves that can predict mass and value flows going to accept and reject streams.

Two major reasons contributing to this challenge are the amount of material (number of particles) that needs to be sampled as well as analysed at these coarse particle sizes, and the general lack of analytical and modelling techniques that can, cost-effectively, measure and analyse the liberation characteristics at these coarse particle sizes. By contrast, fine particle liberation measurements, for

particles below 1 mm, have been routinely captured for over three decades using process mineralogy tools such as Mineral Liberation Analysis (MLA) and/or Quantitative Evaluation of Material by Scanning Electron Microscopy (QEMSCAN) (Fandrich *et al*, 2007).

Works by Wilkie (2016) and Scott (2018) have made significant inroads into the challenge of quantifying particle grade distributions at coarse particle sizes. These works have shown that some porphyry copper and gold deposits exhibit well-behaved lognormal particle grade distributions. It means that these distributions can be used to model, with high confidence, yield curves for the ore's sortability and to understand the comminution process and the mineral liberation at coarse particle sizes. Furthermore, these distributions can be generated with analysis of, as little as, 40 to 100 particles per size fraction as shown in Figure 1.

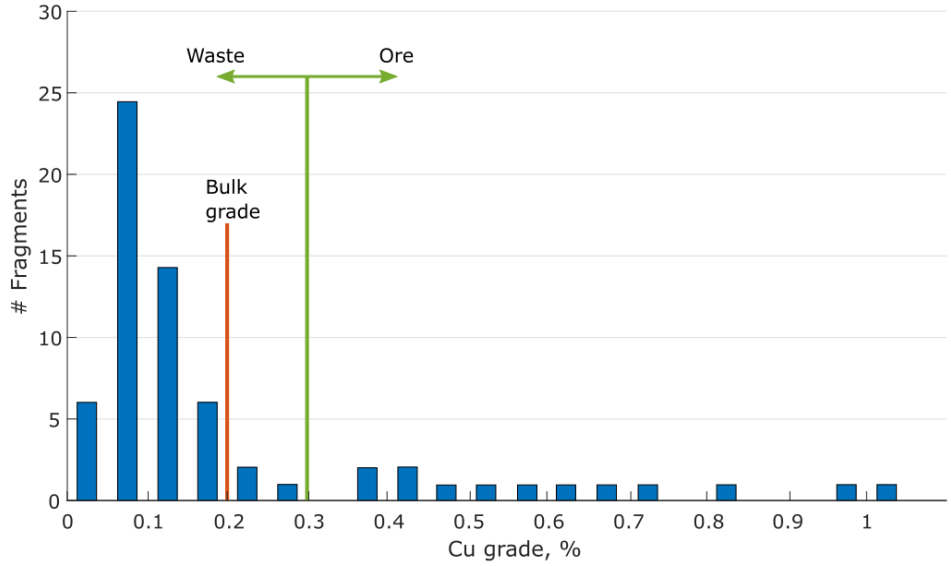

FIG 1 – Particle grade distribution of a copper ore with underlying low particle statistics (adapted from Wilkie, 2016).

The next challenge is to extend the methodology introduced by Wilkie (2016) to finer particle sizes. Particle grade distribution information for particles coarser than 10 mm can be collected based on chemical assays. However, for smaller particles (1 mm to 9 mm), either a significant larger number of particles is required for statistical robustness or the mass of individual particles is below the minimum mass required for chemical assays. These two limitations restrict chemical assaying and MLA/QEMSCAN analyses to be used as the analytical tool to develop particle grade distributions at these smaller size fractions.

The main aim of this work is to use 3D X-ray microtomography (XMT) to characterise coarse ore feeds at smaller sizes that cannot be analysed by traditional methods in order to measure at which particle size the gangue material starts to be fully liberated. It is expected that the gangue material liberates at much coarser sizes than valuable minerals, sizes at which the traditional MLA method would not be practical to use. Information about the gangue liberation size and particle grade distributions are important for early coarse gangue rejection processes.

METHODOLOGY

Sample preparation and acquisition

A porphyry copper ore from a Chilean mine was used for this work. Approximately 10 kg of material was sized using a fourth-root of two sieve series. Representative samples from ten size classes were analysed using 3D X-ray micro-Tomography (XMT). The representative sample for each size class was placed in a 20 mm diameter cylindrical sample holder and scanned using a Zeiss Xradia 520 Versa at 20.9 micron/voxel resolution. The settings for the XMT are summarised in Table 1.

TABLE 1

XMT acquisition settings.

Parameter	Value	Unit
Voltage	80	kV
Current	87	mA
Exposure time	1.5	s
Voxel size	20.9	microns
Number of projections	1018	-
Filter	No filter	-

The number of scans and total number of analysed particles per size fraction is presented in Table 2. Note that for finer size fractions one scan translates into more than a thousand particles scanned in the field of view. This means robust statistics with little sample preparation and scanning time, in contrast with MLA analysis (Evans and Napier-Munn, 2013). Also note that the material from the -3.35 + 2.8 mm particle size range was not analysed; this decision was made because the initial XTM scanning of coarse, middle and fine particles has indicated that this size fraction was not important as the gangue liberation size. Thus, early results informed which size fractions were not essential for capturing the characteristics of the ore and/or which ones required fewer scans.

TABLE 2

Number of particles analysed per size fraction analysed by X-ray 3D tomograph.

Size fraction (mm)	Number of tomography measurements	Number of particles analysed
-8 + 6.7	11	125
-6.7 + 5.6	8	131
-5.6 + 4.75	3	84
-4.75 + 4.0	4	178
-4.0 + 3.35	4	368
-2.8 + 2.36	2	453
-2.36 + 2.0	1	409
-2.0 + 1.7	2	1341
-1.7 + 1.4	1	1123
-1.4 + 1.18	2	3806

Image processing

As particles are simply packed in the sample holder, the reconstructed volume (Figure 2) has to be post-processed in order to distinguish particles from one another (Figure 3). A moments thresholding algorithm (Glasbey, 1993) is used to segment the particles from the air phase and a marker-based watershed algorithm (Mesa *et al*, 2022) is used to separate the particles. The unique label number is assigned to each particle that allows for its size, density and mineral content to be quantified and logged.

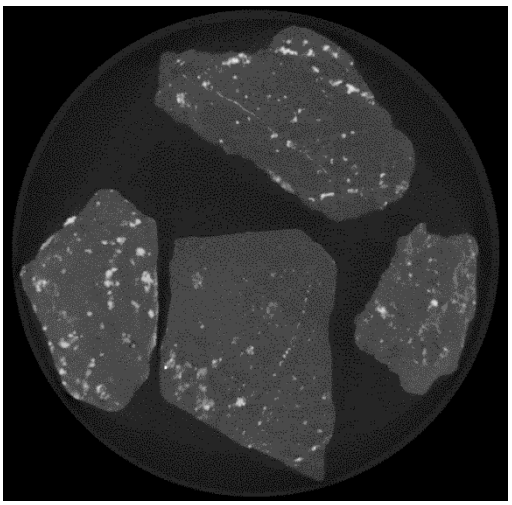

FIG 2 – A cross-section of the 3D XMT image of particles in the -8 + 6.7 mm size range.

FIG 3 – A cross-section of segmented 3D XMT image where each particle is segmented and assigned a unique label number.

Mineral identification

The MLA analysis of the ore indicates that the main gangue minerals are quartz, albite and siderite and the main sulfide minerals are pyrite and chalcopyrite, as shown in Table 3. These minerals are then grouped according to the expected brightness in the XMT image, and these final groups are also shown in Table 3.

TABLE 3

Main minerals present, as obtained from MLA analyses of finer size fractions.

Mineral	%wt	Phase group
Albite	37.49	Quartz
Sericite (muscovite + illite)	19.18	Quartz
Quartz	15.14	Quartz
Siderite	8.12	Carbonates
Pyrite	4.34	Pyrite
Chalcopyrite	2.36	Chalcopyrite
Other	13.37	-

Each pixel value from the XMT scans was classified based on defined threshold values as one of the following phase groups: background, quartz, carbonates, pyrite and chalcopyrite as shown in Figure 4a. The initial threshold values were determined by using the National Institute of Standards and Technology database of X-ray attenuation for different materials (Berger *et al*, 2010). The attenuation is related to pixel brightness and can be used to segment the different mineral phases in the particles (Figure 4b). In order to keep pixel values consistent from one scan to another, mineral standards (quartz, pyrite and gold fragments) were introduced to each of the scanners. Then thresholds values for each phase were detected using:

- A Maximum Entropy algorithm to segment sulfides (pyrite and chalcopyrite) from the gangue minerals using Kapur *et al* (1985).
- Carbonates, which sit in-between sulfides and quartz were segmented manually, using visual inspection of their shape and the information about quartz and sulfide known threshold values (Figure 4b).
- Copper minerals, which were segmented from sulfide minerals using a modified version of the Maximum Entropy algorithm that looks for a local maximum after the known sulfide value (global maximum).

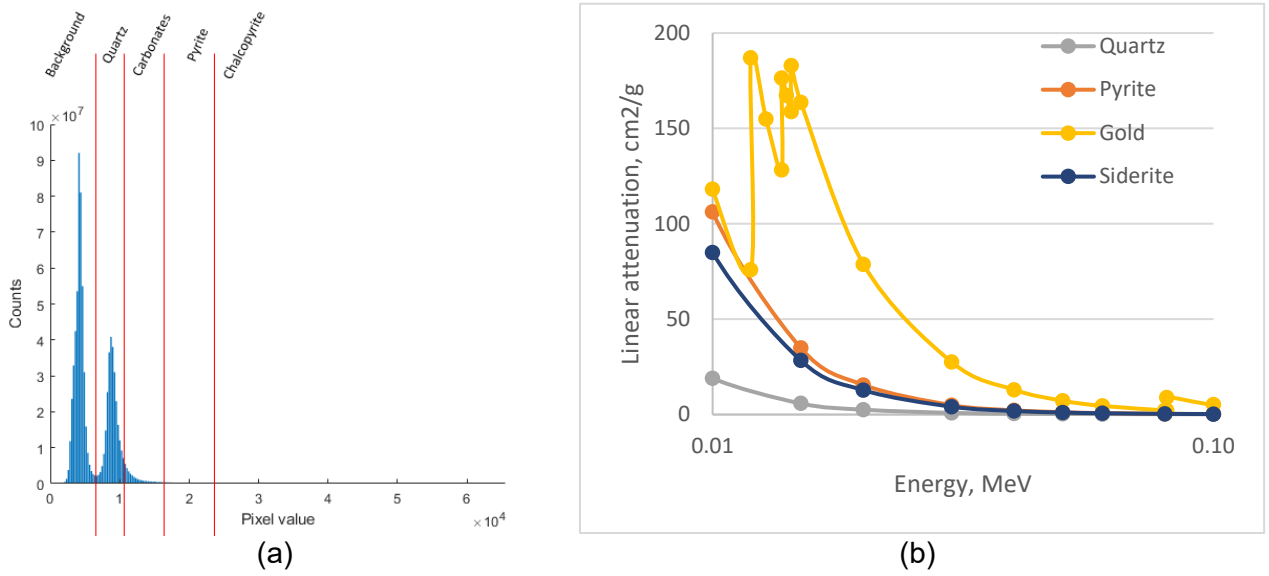

FIG 4 – (a) Example of pixel value histogram of a scanned sample where distinct peaks identify the phase groups, (b) theoretical attenuation of different minerals.

Particle quantification

After particle separation and mineral phase identification, a 3D image of each particle now consists of a collection of pixels with only five possible values (air, quartz, carbonates, pyrite and chalcopyrite). For each particle, based on the total number of pixels for each of these phases and using the known densities of quartz, siderite, pyrite and chalcopyrite, the mass, volume and density is calculated and logged. In this way, the particle grade distributions for each mineral group can be obtained.

A subset of the scanned samples was sent for chemical assaying to determine metal content on the bulk sample. The percent metal detected by the elemental analyses was then compared against the XMT analyses and the threshold values used in the analysis were adjusted to improve the XMT estimates.

RESULTS AND DISCUSSION

The first step is to check the particle separation algorithm, because the watershed-based algorithms can suffer from over-segmentation due to the irregular shape of the objects (Wang *et al*, 2015). This

check is performed by plotting the particle size distribution for each of the scanned size fractions, as shown in Figure 5. If the particle separation algorithm was correctly segmented, the quantified particle size distribution for all the particle sizes will match the upper and lower sieve series. Any mistake during the segmentation should result in the particle size distribution containing a significant amount of finer or coarser particles; this was not the case in Figure 5.

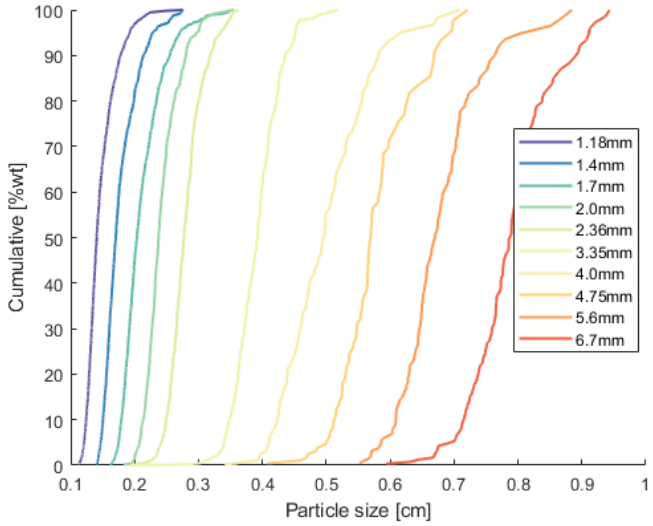

FIG 5 – Particle size distributions obtained from the XMT; the labels show the lower sieve limit for each size fraction (eg 6.7 mm indicates -8 mm + 6.7 mm).

As mentioned before, a subset of the scanned sample was sent for chemical assaying, determining their copper content. This metal content is compared against the metal content value predicted by XMT (Figure 6a). The threshold values were adjusted to minimise the discrepancy between the copper values determined by chemical assaying and the updated copper content values estimated based on the XMT analysis (Figure 6b).

Based on the results in Figure 6, it can be concluded that the XMT can accurately measure the copper content in the analysed samples.

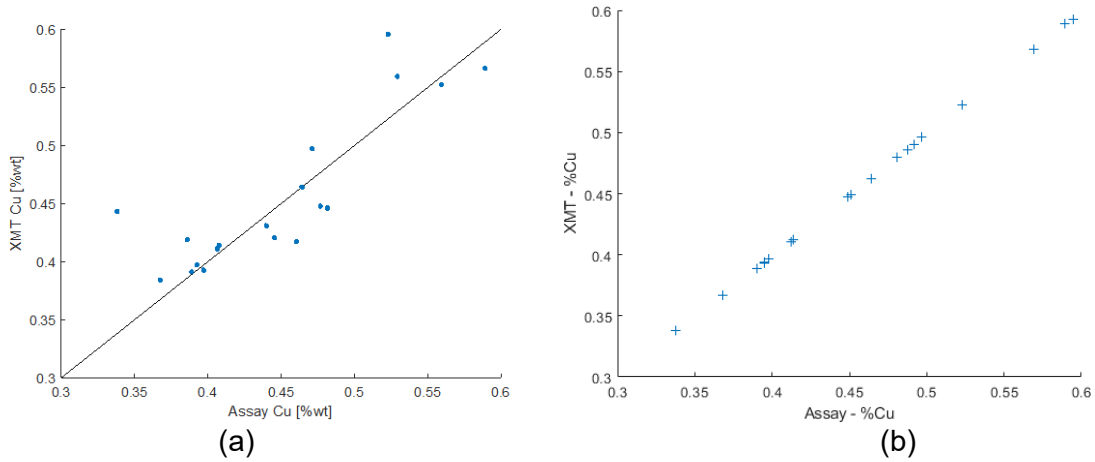

FIG 6 – (a) Comparison of XMT and chemical assay values for the copper content of each scanned volume. (b) Comparison after threshold correction.

After calculating the amount (volume and mass) for each mineral phase for each particle, the mineral liberation can be estimated for a given particle. Also, after analysis of all particles, the mineral liberation distributions can be obtained for each size fraction.

The information about the liberation of chalcopyrite is presented in Figure 7. These results indicated that the liberated gangue particles (the particles within the 0–0.01 per cent liberation category in Figure 7) are present in all analysed size fractions. As expected, the proportion of gangue particles

increases for the smaller particles. The results also show that the group of liberated gangue particles is dominant (40–50 per cent of material) for the particles below 4.75 mm; this could be an indicator of the start of the gangue liberation process.

The presence of high-grade particles was noticed for the particles below 1.7 mm. As the particles become smaller (1.18 mm particles), evidence of a bi-modal mineral liberation distribution is observed.

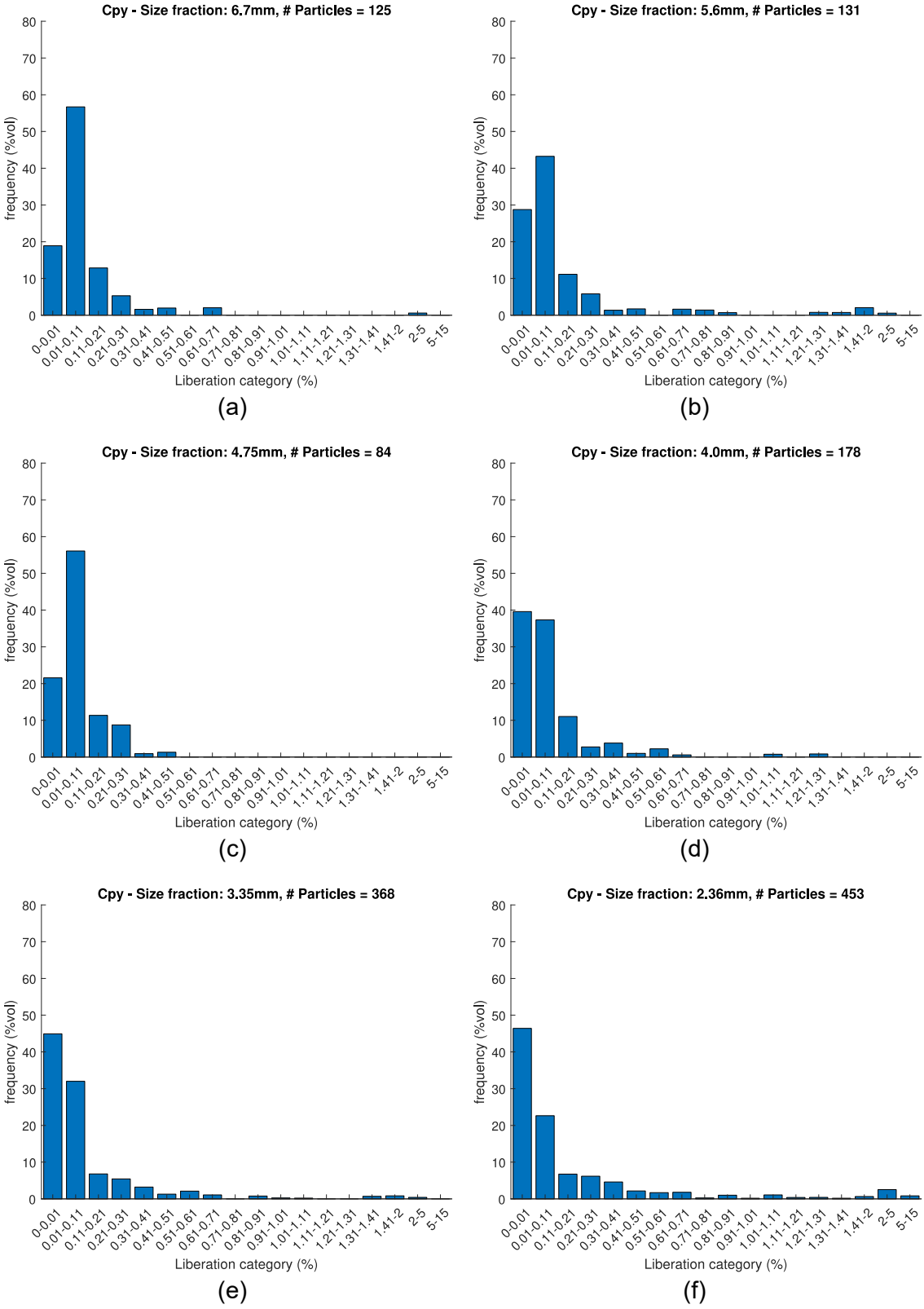

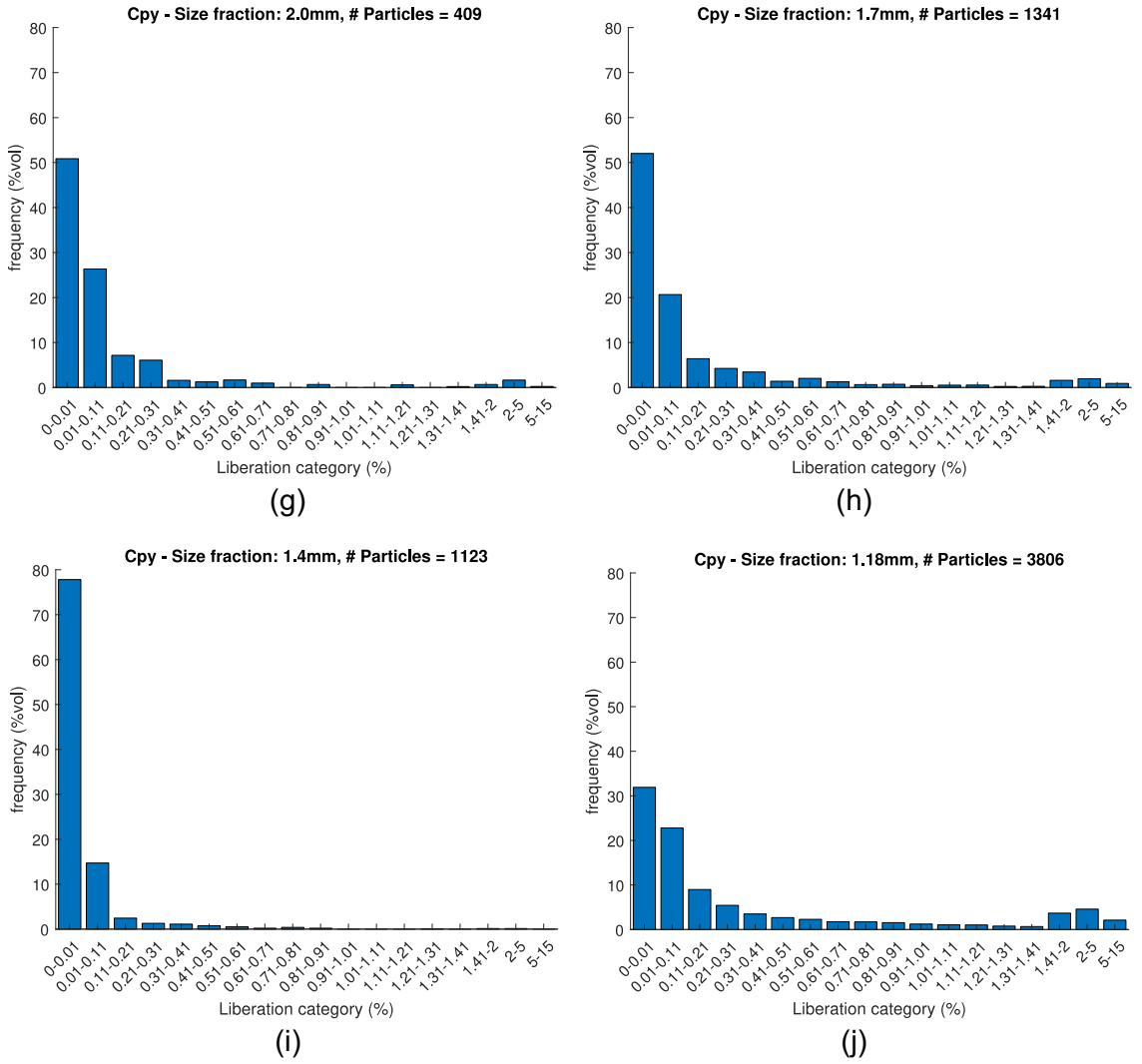

FIG 7 – (a) to (j) Chalcopyrite content particle distribution at different size fractions, from +6.7 mm to +1.18 mm, as in Table 2.

CONCLUSIONS AND DISCUSSION

The results presented in this work show that X-ray microtomography is an appropriate method to accurately measure copper content in particles from the -6.7 + 1.18 mm size range. Therefore, this method can be used to detect the gangue particles and measure the degree of mineral/gangue liberation for each analysed ore particle.

It is recommended to validate this method for particles finer than 1.18 mm, where traditionally MLA analysis is used.

- This work demonstrates that the gangue material liberates at much coarser sizes (about a few millimetres larger) than valuable minerals for the analysed samples.

ACKNOWLEDGEMENTS

The study was conducted with funding from the Australian Government's Cooperative Research Centre (CRC) for Optimising Resource Extraction, CRCORE P1–017 Project. The authors acknowledge and appreciate CRCORE's support of this work.

REFERENCES

Berger, M J, Hubbell, J H, Seltzer, S M, Chang, J, Coursey, J S, Sukumar, R, Zucker, D S, Olsen, 2010. XCOM: Photon Cross-sections Database. NIST Standard Reference Database 8 (XGAM).

Evans, C L, and Napier-Munn, T J, 2013. Estimating error in measurements of mineral grain size distribution. *Minerals Engineering,* 52, 198–203.

Fandrich, R, Gu, Y, Burrows, D, and Moeller, K, 2007. Modern SEM-based mineral liberation analysis. *International Journal of Mineral Processing*, 84(1–4), 310–320.

Glasbey, C A, 1993. An analysis of histogram-based thresholding algorithms. CVGIP: *Graphical Models and Image Processing*, 55, 532–537.

Kapur, J N, Sahoo, P K and Wong, A C K, 1985. A New Method for Gray-Level Picture Thresholding Using the Entropy of the Histogram, *Graphical Models and Image Processing*, 29(3): 273–285.

Mesa, D, Quintanilla, P, and Reyes, F, 2022. Bubble Analyser — An open-source software for bubble size measurement using image analysis. *Minerals Engineering*, 180, 107497.

Scott, M, 2018. Reducing Water, Energy and Emissions through Grade Engineering®. *Mine Excellence 2018–3rd International Seminar of Operational Excellence in Mining*, 21–23 March 2018, Santiago, Chile

Wang, Y, Lin, C L, Miller, J D, 2015. Improved 3D image segmentation for X-ray tomographic analysis of packed particle beds. *Minerals Engineering*, 83, 185–191.

Wilkie, G J, 2016. Rapid Assessment of the Sorting Potential of Copper Porphyry Ores through Modelling of Textures and Grade Distributions. The University of Queensland.

Advances in mineral processing – solid-liquid separation

Two-fluid modelling of mineral tailing sedimentation and consolidation

N I K Ekanayake[1], S Hassan[2], S P Usher[3], D J E Harvie[4] and A D Stickland[5]

1. Research Fellow, ARC Centre of Excellence for Enabling Eco-Efficient Beneficiation of Minerals, Department of Chemical Engineering, The University of Melbourne, Vic 3010. Email: nilanka.ekanayake@unimelb.edu.au
2. PhD Candidate, ARC Centre of Excellence for Enabling Eco-Efficient Beneficiation of Minerals, Department of Chemical Engineering, The University of Melbourne, Vic 3010. Email: sajid@student.unimelb.edu.au
3. Research Fellow, ARC Centre of Excellence for Enabling Eco-Efficient Beneficiation of Minerals, Department of Chemical Engineering, The University of Melbourne, Vic 3010. Email: spusher@unimelb.edu.au
4. Associate Professor, Department of Chemical Engineering, The University of Melbourne, Vic 3010. Email: dharvie@unimelb.edu.au
5. Senior Lecturer, ARC Centre of Excellence for Enabling Eco-Efficient Beneficiation of Minerals, Department of Chemical Engineering, The University of Melbourne, Vic 3010. Email: stad@unimelb.edu.au

INTRODUCTION

Dewatering mineral tailings is a responsible tailing management strategy in the mining industry that improves the stability of mineral tailing storage facilities by producing dry and stackable tailings. Further, this process increases water productivity and minimises power requirements for tailing transport. Equipment that operates under gravity, such as thickeners and clarifiers, is commonly employed in separating liquid and concentrating mineral slurries. From a physical point of view, sedimentation and consolidation are the two mechanisms that drive the solid-liquid separation in the gravity settling process. Sedimentation is the process of suspended particles settling, whereas consolidation is the compaction of the solid bed under its own weight or due to an applied force.

During sedimentation, the interaction between the solid and liquid phase is due to the drag force acting on the particles. A hindered settling function, $R(\phi)$, that depends on solid volume fraction (ϕ) is used to modify the slip velocity of settling particles accounting for surrounding particles. The transition between sedimentation and consolidation is characterised by the gel point. It is the critical volume fraction that the structure of the suspension changes from individual particles suspended in a fluid to a porous network of particles filled with fluid. The solid network can withstand normal stress and resist compression until the normal stress exceeds a critical pressure. This critical pressure, commonly known as the compressive yield stress $P_y(\phi)$, increases with solid volume fraction. Therefore, networks with high solid volume fractions can support a higher compression force.

While the classical dewatering theory of Buscall and White (1987) is a powerful tool that has been widely used to model the above dewatering phenomenon, limitations mainly associated with its one-dimensional nature impede the applicability of the theory to many real solid-liquid separation units as they typically involve multi-dimensional (ie 2D, 3D) flow. This work outlines a numerical framework that generalises classical dewatering theory to incorporate shear forces, suspension rheology, and multi-dimensional phenomena to address the limitations outlined above. For this, a two-fluid Eulerian framework that accounts for multi-particle effects and is based on a volume averaging technique is utilised together with material-dependent hindered settling, $R(\phi)$, and compressive yield stress $P_y(\phi)$, functions for mineral tailing suspensions. Implementation is via the *arb* multiphysics finite volume code (Harvie, 2010). Note that both solid and liquid phases of the suspension are treated as incompressible continuum phases, and for each phase, mass and momentum conversation equations are solved.

In this study, we chose a calcium carbonate suspension as a model system to investigate the sedimentation and consolidation behaviour of mineral tailings. Settling tests experiments are performed in settling columns with large column diameters to minimise wall effects. Complementary numerical simulations are performed in a 2D Cartesian geometry that represents an infinite domain size in the horizontal direction, thus neglecting any wall effects. No-slip and no-flux boundary conditions are used for the top and bottom walls and a fixed pressure condition is used at the top

wall. A structured, refined mesh with 4000 cells is chosen to satisfactorily represent the fluid–bed interface dynamic. Transient simulations are performed, and the model predictions are validated against the experimental batch sedimentation results for two specific suspension types.

RESULTS AND DISCUSSION

Simulation results for gravity settling of two calcium carbonate suspensions with different particle sizes and the corresponding experimental results are analysed here. The properties and initial conditions of the suspensions are listed in Table 1.

TABLE 1

Properties of calcium carbonate suspensions prepared using different particle sizes from Omya Australia Pty Ltd called Omyacarb 40 and Omyacarb 2.

Suspension name	Particle size Sauter diameter – d_{32} (μm)	Initial bulk concentration (v/v)	Initial suspension height (m)
Omyacarb 40	12.5	0.0761	0.30
Omyacarb 2	2.5	0.1000	0.28

Figure 1 shows both the experimental and numerical results for the variation of interface height between the clear fluid and suspension (h) with time (t) during batch sedimentation. Overall, the numerical simulations predict the interface height variation with time for both suspensions reasonably well. This validates the closure equations developed for $R(\phi)$ and $P_y(\phi)$ as well as the two-fluid framework model employed. A faster settling rate or otherwise a steep gradient of dh/dt is observed for suspensions with large particles (Omyacarb 40) both numerically and experimentally. After around 5000 s, Omyacarb 40 reaches its steady-state condition with the interface height settling at 0.051 m. In contrast, Omyacarb 2 suspension exhibits transient settling even after 40 000 s. For nearly similar bulk concentrations and initial solid loading, both numerical and experimental data suggest that the final bed height of small particles (Omyacarb 2) is twice the final bed height for large particles (Omyacarb 40) due to differences in the gel point.

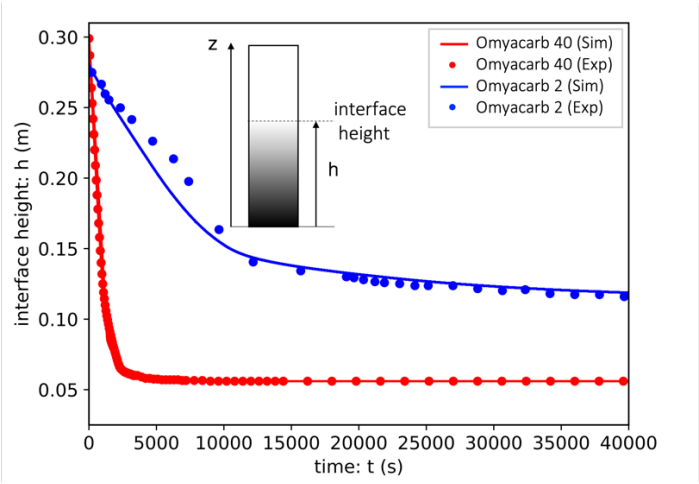

FIG 1 – Variation of clear fluid-suspension interface height with time for Omyacarb 40 (large particles) and Omyacarb 2 (small particles) calcium carbonate suspensions.

Figure 2 shows the simulated concentration profiles for different time intervals for the Omyacarb 40 suspension. Up to 2000 s, the suspension zone between the top and bottom interface shows a uniform solid fraction equal to the initial bulk concentration. The zone below the lower interface, representing the sediment zone, shows non-uniform solid distributions. Around 1400 s, the top and bottom interfaces meet, leaving only a clear fluid zone and a sediment zone. After this time, the sediment height slowly decreases and stabilises to a steady state profile.

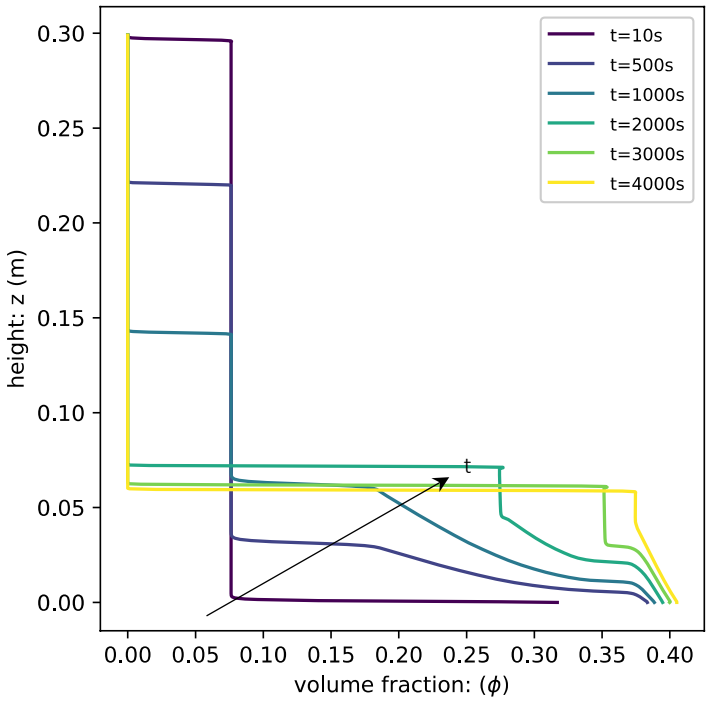

FIG 2 – Simulated vertical profiles of solid volume fraction at different time intervals for Omyacarb 40 suspension.

CONCLUSIONS AND FUTURE WORK

Sedimentation and consolidation due to the self-weight of suspension are modelled within a generalised two-fluid framework for synthetic mineral tailing suspensions. An integrated numerical and experimental approach is used to predict the material-dependent closure equations required for the two-fluid model. This work demonstrates the possibility of modelling multi-dimensional solid-liquid separation problems based on measured phenomenological properties. In the context of model validation, having accurate experimental measurements of concentration profiles would benefit in improving the compressive yield stress function. Future work will consider the partitioning mixture shear stresses between solid and liquid phases to account the plastic shear rheology present in mineral tailings.

ACKNOWLEDGEMENTS

Support from the Australian Research Council for the ARC Centre of Excellence for Enabling Eco-Efficient Beneficiation of Minerals, grant number CE200100009 is gratefully acknowledged. One of the authors (SH) acknowledges the support from the Research Training Program Scholarship through The University of Melbourne. The authors report no conflict of interest.

REFERENCES

Buscall, R, and White, L R, 1987. The consolidation of concentrated suspensions. Part 1 – The theory of sedimentation. *Journal of the Chemical Society, Faraday Transactions 1: Physical Chemistry in Condensed Phases*, 83(3):873–891.2.

Harvie, D J E, 2010. An implicit finite volume method for arbitrary transport equations. *ANZIAM Journal*, 52:C1126-C1145.

Determination of apparatus parameters affecting the filterability of iron ore tailing by the laboratory filter press device

N Esmaeili[1], A Dehghani Ahmadabadi[2], R Hejazi[3], M Saghaeian[4], and V Sheikhzadeh[5]

1. Process Engineer, Fakoor Sanat Tehran Company, Tehran, Iran, 1586633118. Email: N.esmaeili@fstco.com
2. Senior Process Engineer, Fakoor Sanat Tehran Company, Tehran, Iran, 1586633118. Email: Dehghani@fstco.com
3. R&D Manager, Fakoor Sanat Tehran Company, Tehran, Iran, 1586633118. Email: Hejazi@fstco.com
4. Technical Chairman, Fakoor Sanat Tehran Company, Tehran, Iran, 1586633118. Email: Saghaeian@fstco.com
5. Managing Director, Fakoor Sanat Tehran Company, Tehran, Iran, 1586633118. Email: Sheikhzadeh@fstco.com

ABSTRACT

The need to use wet methods to process most minerals makes the mineral processing industry very water-dependent. On the other hand, water scarcity, especially in arid areas, is a significant threat to the mining industry's future. Therefore, prevention of unnecessary water loss and efficient water recovery methods are more considered by the beneficiation plants. In this research, the apparatus parameters comprising feeding pressure, chamber thickness, and time and pressure of the air blowing stage were selected to investigate their influences on the filterability of wet tailing related to the Paya Foolad processing plant located in Yazd province, Iran. The chamber thickness at three different levels (33, 43, and 53 mm), feeding pressure at three different levels including 7, 10, and 13 bar, and air blowing at the pressures of 8, 10, and 12 bar were studied by the full factorial of design expert method which 3^3 or 27 experiments were designed. To investigate the effect of air blowing time, the filtrate was weighed during the air blowing stage of all tests, and then moisture content was calculated. Experiments results showed that the minimum moisture content of filter cake with a value of 16.38 per cent was obtained from the test conditions, including the chamber thickness of 33 mm, feeding pressure of 13 bar, air blowing pressure of 12 bar, and air blowing time of 120 seconds. The filtration capacity of this test was 0.19 t/m^{2}h. Also, the maximum filtration capacity with a value of 0.247 t/m^{2}h was achieved from the test conditions with the chamber thickness of 43 mm, feeding pressure of 13 bar, and without air blowing stage. The filter cake moisture of this test was 20.68 per cent.

INTRODUCTION

Water scarcity for processing, space and topography limitation of wet tailing disposal, severe environmental impacts such as soil and water pollution, dam structure failure, and acid mine drainage, have made the tailing management of processing plants critical (Mamghaderi, Gharebaghi, Noparast, 2018; Gomes, De Tomi, Assis, 2016; Nguyen *et al*, 2021). In the last five decades, 63 major tailings dam failures have been reported worldwide, which is thought-provoking. Each failure event causes extensive damage to the local environment and, in catastrophic cases, has resulted in the loss of human life (Owen *et al*, 2020). For example, the disastrous failure of the tailings dam of the Brumadinho iron mine in Brazil happened on 25 January 2019, and killed 259 people. Millions of tons of hazardous mining waste spread to the Paraopeba River, which had detrimental effects on the local community's livelihood and the living environment of aquatic species. This failure and similar incidents in other countries, such as Canada, China, the Philippines, and Italy, have highlighted the need to transform conventional tailings dams into low-risk and well-monitored disposal methods such as dry stacking or co-disposal (Nguyen *et al*, 2021).

To ensure safe tailings management and prevent unnecessary water loss, efficient water recovery methods have been more considered by the beneficiation plants (Gomes, De Tomi, Assis, 2016). Dewatering of wet tailing is an essential part of mineral processing circuits (Dash *et al*, 2011; Mamghaderi *et al*, 2021). In mineral processing plants, dewatering is carried out using different equipment comprising dewatering screens, thickeners, centrifuges, vacuum filters, and pressure

filters, which decreases the moisture content of product and tailings (Hakkinen, Ekberg, 2009). To recycle a significant amount of water and to reduce the volume of the disposed tailings, the filtration process of the iron ore tailings is done with the filter press equipment (Frankle *et al*, 2022; Dias *et al*, 2003). Usage for finer particles, elimination or reduction of drying, high capacity, automatic operation, filter cloth management, and filter cake washing are the other main advantages of this equipment (Townsend, 2003).

Filtered tailings enable sustainable water use and intelligent tailings management. Eliminating wet tailings dams and the reuse of process water minimise environmental impact, cut complexity and help miners attain a social license to operate (FLSmidth, 2020).

This paper describes the tests performed by a laboratory-scale filter press device to determine the effects of apparatus parameters, including feeding pressure, chamber thickness, air blowing pressure, and air blowing time, to design a water recovery unit for the Paya Foolad beneficiation plant.

MATERIAL AND METHODS

Sample analysis

Slurry sample was taken from the underflow of the tailing's thickener of the Paya Foolad processing plant, located in Yazd province, Iran. After preparation, sample characterisation was studied. Wet sieving and cyclosizer analysis, pycnometer, and chemical analysis were done to specify the size distribution, true density, and elemental compound of the sample, one by one. The determined true density was 3.00 g/cm^3. Also, Table 1 shows the chemical specifications with sieving and cyclosizer analysis results.

TABLE 1

The chemical assays and size analysis of iron ore tailing.

Chemical specifications (%)		**Size distribution**	
		Grain size (µm)	**Passing (%)**
Fe_{total}	12.60	300	98.51
FeO	3.15	212	94.66
SiO_2	28.78	150	88.26
Al_2O_3	3.81	106	81.74
MgO	16.54	75	72.55
CaO	10.85	63	68.38
K_2O	0.64	53	65.25
MnO	0.12	45	60.72
Na_2O	0.80	38	57.73
P_2O_5	0.17	25	50.19
SO_3	11.43	21	47.00
TiO_2	0.22	15	40.91
LOI	0.94	11	35.39

Experiments

Filtration experiments were performed using a laboratory bench-scale membrane chamber filter press set-up with a filter area of 207.64 cm^2. The employed filter cloth was the same type of clothes that are used for iron ore tailing dewatering at the other plants of FST Company. For feeding slurry

sample to filter press, a high-pressure feeding mixer was utilised that can provide feeding pressure up to 13 bar. The slurry solid percent of all tests was adjusted to 50 per cent w/w.

The tests were aimed to determine and optimise the apparatus parameters influencing the iron ore tailing filterability. As one of the most critical parameters, the chamber thickness was investigated at three different levels, including 33, 43, and 53 mm. Furthermore, feeding pressure was studied at 7, 10, and 13 bar levels.

Air blowing is the most energy-intensive phase of the filtration cycle, and blowing time should be minimised (Townsend, 2003). The air blowing pressure was checked at three levels, consisting of 8, 10, and 12 bar. To determine the effect of air blowing time on the moisture content of filter cake, the filtrate was weighed during the blowing time, and moisture content was calculated.

The following equations were used to calculate moisture content and filtration capacity:

$$M = \frac{m_{wet} - m_{dry}}{m_{wet}} \times 100 \quad (1)$$

$$FC = \frac{36 \times m_{dry}}{T \times A} \quad (2)$$

$$T = T_{Feeding} + T_{Squeezing} + T_{Air\ Blowing} + T_{Technical} \quad (3)$$

Where M is the moisture content of cake (%), m_{wet} is the wet cake weight (g), m_{dry} is the dry cake weight (g), FC is the filtration capacity (t/m^2.h), T is the filtration cycle time (s), A is the filter area (cm^2), $T_{Feeding}$ is the feeding stage time (s), $T_{Squeezing}$ is the time of pressing the filter cake with diaphragm or membrane (s), $T_{Air\ Blowing}$ is the air blowing stage time (s), $T_{Technical}$ is a parameter for industrial equipment that includes the times of closing and opening filter plates, cake discharge, cloth washing etc (s) (Sparks, 2011). In this research, the technical time was assumed to be 5 minutes and the squeezing time was 0 (zero).

RESULT AND DISCUSSION

The effect of chamber thickness

Increasing the thickness of the chamber usually increases filtration capacity or throughput and decreases investment and operating costs, but due to the increment of the cake thickness, it changes specific cake resistance, moisture content, and cake density. So, it is necessary to identify optimal chamber thickness.

Based on Figure 1, it can be seen that the moisture content of the cake rises with increasing the chamber thickness, but at first, the filtration capacity goes up with increasing chamber thickness, and then it declines. The reason for this issue is to grow up the feeding time and reduce the cake density because of climbing the cake resistance formed in the chamber thickness of 53 mm.

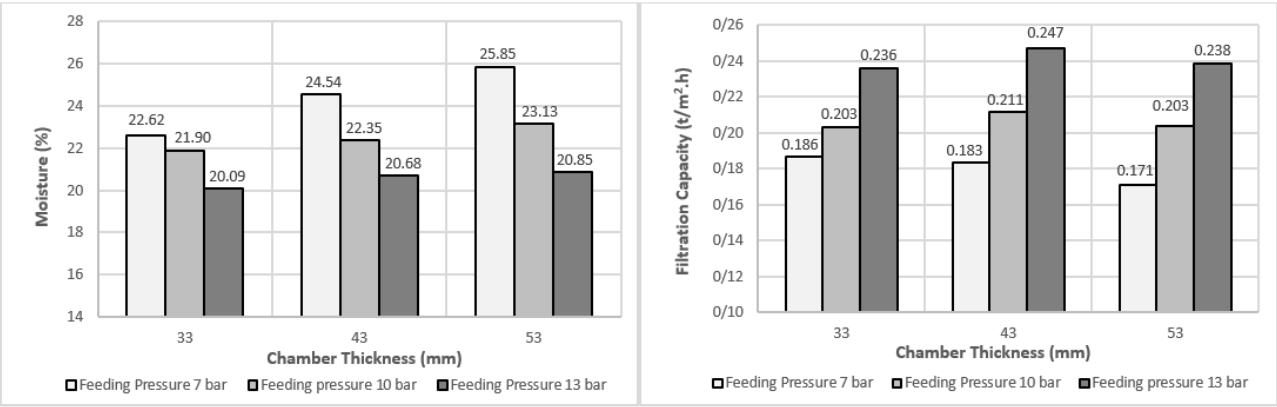

(a) (b)

FIG 1 – Effect of feeding pressure and chamber thickness on (a) moisture content of cake and (b) filtration capacity, without air blowing stage.

The effect of feeding pressure

Pressing produces cakes that are uniform in thickness and consistency and avoids cake cracking (Townsend, 2003). It can be done with high-pressure slurry pumping or squeezing stage in the membrane-chamber filter press. When a high-pressure slurry pump is used, the cake density is increased, and it helps to enhance the filtration capacity.

In Figure 1, the changes in filter cake moisture and filtration capacity in conjunction with increasing feeding pressure can also be seen. It indicates that when the feeding pressure goes up, the moisture content of the cake decreases, and the filtration capacity increases. The observed increase in the filtration capacity is due to a reduction in feeding time and an enhancement in cake density. The decrement in moisture content is related to the squeezing of the cake as a result of high-pressure slurry pumping.

Also, it seems that there is an interaction between chamber thickness and feeding pressure so that by increasing the thickness of the chamber at 7 bar feeding pressure, the filtration capacity is always reduced, while for higher feeding pressures this trend is different. It is probably owing to the growth of cake resistance by raising the cake thickness and the inability of the feeding pressure of 7 bar to fill the chamber and increase the filter cake density. Figure 2a indicates variation in the dry filter cake density versus the different chamber thicknesses and feeding pressures. The filter cake that is produced through the feeding pressure of 7 bar and the chamber thickness of 53 mm is illustrated in Figure 2b. It is clear that the feeding pressure of 7 bar could not fill the chamber plate with 53 mm thickness.

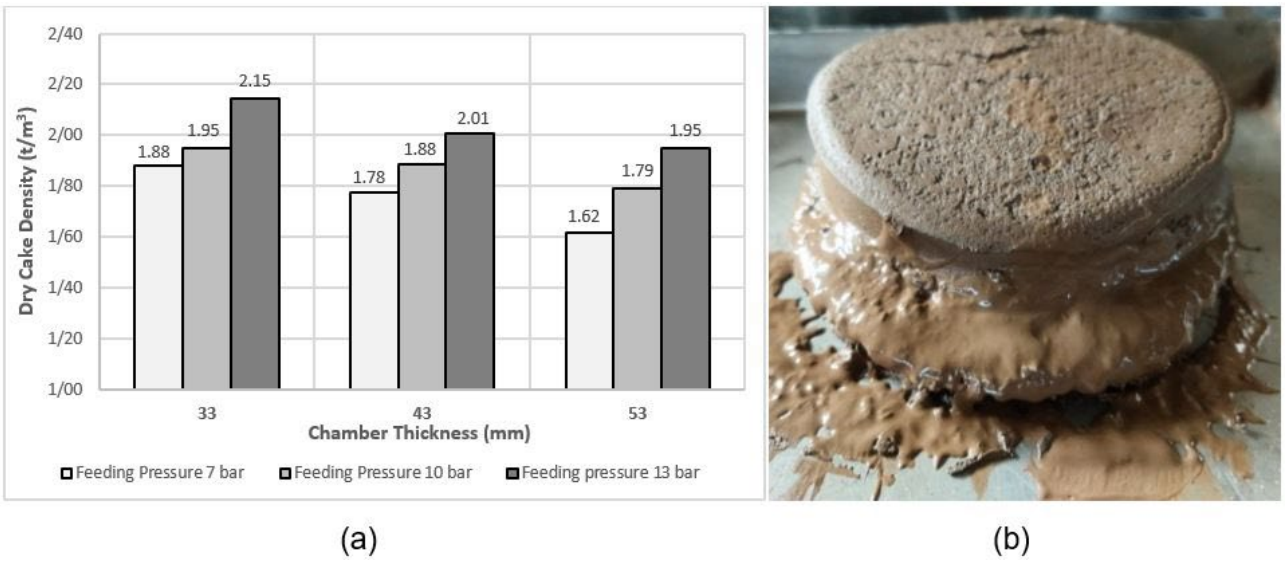

FIG 2 – (a) Effect of feeding pressure and chamber thickness on dry filter cake density, (b) The filter cake that is formed with the feeding pressure of 7 bar and the chamber thickness of 53 mm.

The effect of air blowing pressure at different times

In the air blowing stage, compressed air passes through the filter cake to effect final drying to target moisture. Although increasing the air blowing time lessens the filtration capacity. Figure 3 shows the effect of air blowing pressure and time on the moisture reduction of the filter cake that is formed with different conditions of feeding pressure and chamber thickness. As can be seen for all conditions of cake formation, the air blowing pressure of 12 bar and air blowing time of 120 seconds had the maximum influence on the moisture reduction. Also, it seems that by increasing of the level in relation to both parameters (air blowing time and pressure), the moisture content will continue to decline, but it should be noted that by the level growth of these parameters, investment costs will also increase.

Figure 4a and Figure 4b specify the moisture content of filter cakes and the filtration capacity respectively, when the air blowing was applied. This figure reveals that the minimum moisture content of 16.38 per cent for the filter cake has been achieved from the cake formation condition of 33 mm chamber thickness and the feeding pressure of 13 bar. In addition, the maximum filtration

capacity by an average of 0.204 t/m^{2}h has been obtained at both conditions of the chamber thicknesses 43 and 53 mm with the feeding pressure of 13 bar.

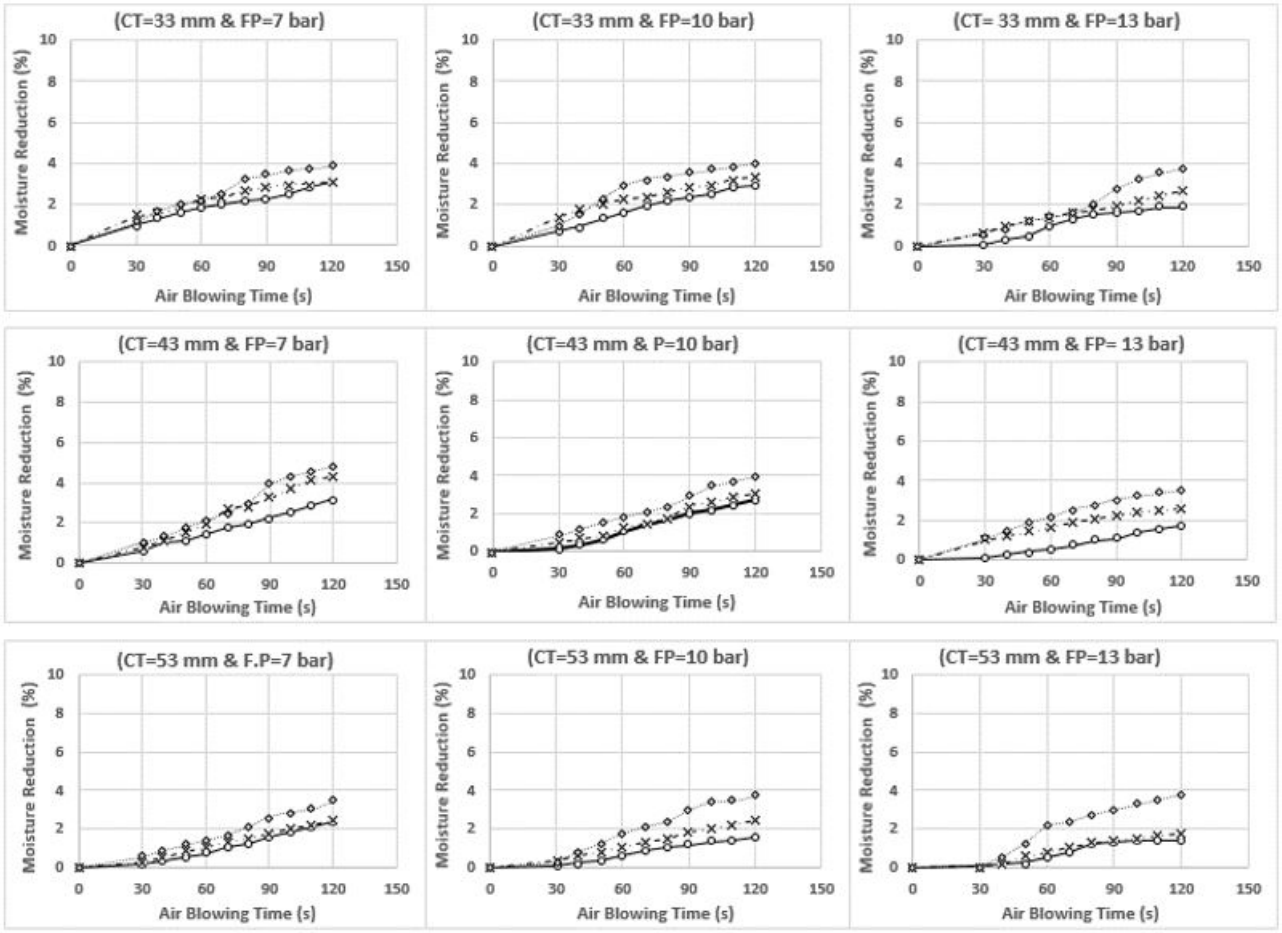

FIG 3 – Effect of air blowing pressure and time on the moisture reduction of the filter cake formed with the different conditions (CT= cake thickness and FP= feeding pressure).

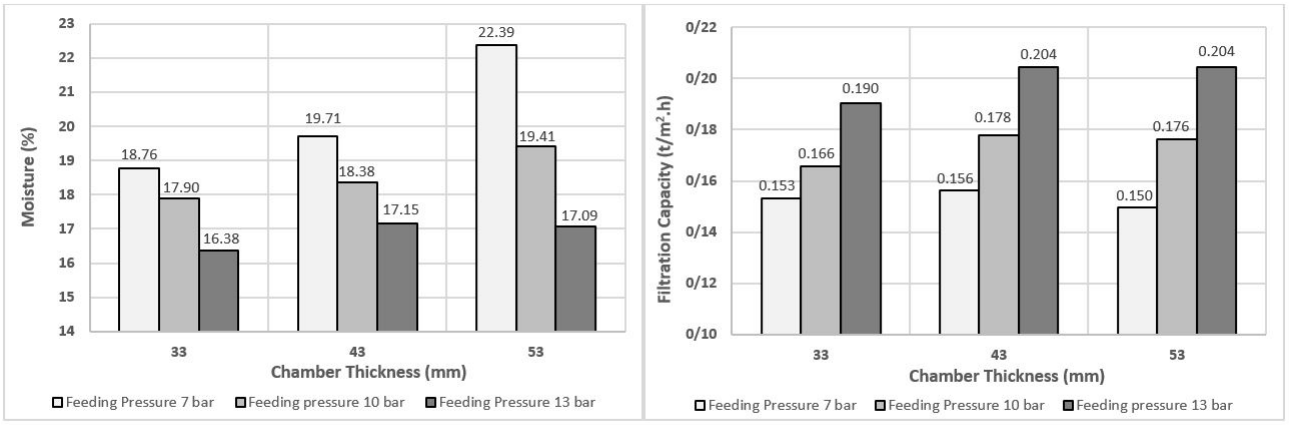

(a) (b)

FIG 4 – Effect of feeding pressure and chamber thickness on (a) moisture content of cake and (b) filtration capacity, with 120-second air blowing at the pressure of 12 bar.

A comparison between Figure 1 and Figure 4 displays that moisture was mostly reduced when the air blowing stage was done but also filtration capacity was decreased. In addition, it can be seen that the filtration capacity difference between the chamber thickness of 53 and 43 mm, especially at the feeding pressure of 13 bar, has disappeared. That is due to the superiority of the total time increasing influence related to the filtration cycle versus the effect of cake density after the air blowing stage was applied.

CONCLUSIONS

This study aimed to determine the effects of four main apparatus parameters of filter press, including feeding pressure, chamber thickness, air blowing time, and air blowing pressure, on the filterability of tailings of iron ore processing plant by a laboratory-bench scale membrane-chamber filter press set-up. According to the achieved results, the moisture content of filter cake was raised by increasing the chamber thickness because the cake resistance grows as cake thickness increases. But the filtration capacity was increased at first and then was reduced. It was due to lowering the cake density and boosting the feeding time for higher chamber thicknesses.

The results also showed that by going up the feeding pressure, the moisture content of filter cake was decreased, and the filtration capacity was increased. The reasons were identified as increasing the cake density and decreasing the feeding time, respectively. The results of filtration tests with the air blowing stage indicate that the moisture content of the cake and the filtration capacity were reduced. So, the higher air blowing pressure, the higher rate of moisture reduction was gained.

Based on the results of the tests, the minimum cake moisture with a value of 16.38 per cent was obtained for the test conditions comprising 33 mm chamber thickness, feeding pressure of 13 bar, 12 bar air blowing pressure, and air blowing time of 120 seconds. The maximum filtration capacity with a value of 0.247 t/m^2h was achieved from conditions of 43 mm chamber thickness, feeding pressure of 13 bar, and without air blowing stage.

ACKNOWLEDGEMENTS

The authors would like to thank from management and personnel of FST Company and its R&D test centre, especially Mr. Ali Sheikhzadeh and Mr. Reza Abedini for comprehensively supporting this research project.

REFERENCES

Dash, M, Dwari, R K, Biswal, S K, Reddy, P S R, Chattopadhyyay, P, Mishra, B K, 2011. Studies on the effect of flocculant adsorption on the dewatering of iron ore tailings, *Chemical Engineering Journal*, Volume 173, Issue 2, pp 318–325.

Dias, C L P, Valadao, G E S, Araujo, A C, Peres, A E C, Amarante, S C, 2003. The effect of reagents on ultrafine iron ore vacuum filtration, *Filtration & Separation, Elsevier Advanced Technology*, Volume 40, Issue 5, pp 36–39.

FLSmidth, 2020. Sustainability Report.

Frankle, B, Morsch, P, Kessler, C, Sok, T, Gleib, M, Hermann, N, 2022. Iron Ore Tailings Dewatering: Measurement of Adhesion and Cohesion for Filter Press Operation, *Journal of Sustainable Dewatering and Tailing Disposal in Mineral Industry*, Volume 14, Issue 6, 3424.

Gomes, R B, De Tomi, G, Assis, P S, 2016. Iron ore tailings dry stacking in Pau Branco mine, Brazil, *Journal of Materials Research and Technology*, Volume 5, Issue 4, pp 339–344.

Hakkinen, A, Ekberg, B, 2009. Dewatering of iron ore slurry by a ceramic vacuum disc filter, in *9th International Conference on Chemical and Process Engineering*, Volume 17, pp 1431–1436.

Mamghaderi, H, Aghababaei, S, Garabaghi, M, Noaparast, M, Albijanic, B, Rezaei, A, 2021. Investigation on the effects of chemical pretreatment on the iron ore tailing dewatering, *Journal of Colloids and Surfaces A: Physicochemical and Engineering Aspects*, Volume 226, 126855.

Mamghaderi, H, Gharabaghi, M, Noaparast, M, 2018. Optimization of role of physical parameters in the filtration processing with focus on the fluid flow from pore, *Journal of Minerals Engineering*, Volume 122, pp 220–226.

Nguyen, C V, Nguyen, A V, Doi, A, Dinh, E, Nguyen, T V, Ejtemaei, M, Osborne, D, 2021. Advanced solid-liquid separation for dewatering fine coal tailings by combining chemical reagents and solid bowl centrifugation, *Journal of Separation and Purification Technology*, Volume 259, 118172.

Owen, J R, Kemp, D, Lebre, E, Svobodova, K, Murillo, G P, 2020. Catastrophic tailings dam failures and disaster risk disclosure, *International Journal of Disaster Risk Reduction*, Volume 42, 101361.

Sparks, T, 2011. *Solid-Liquid Filtration A user's guide to minimizing cost & environmental impact, maximizing quality & productivity*, Elsevier.

Townsend, I, 2003. Automatic pressure filtration in mining and metallurgy, *Journal of Materials Research and Technology*, Volume 16, Issue 2, pp 165–173.

Effect of fine particles on the dewaterability of bimodal mixtures

S Hassan[1], N I K Ekanayake[2], S P Usher[3], P J Scales[4], R J Batterham[5] and A D Stickland[6]

1. PhD Candidate, ARC Centre of Excellence for Enabling Eco-Efficient Beneficiation of Minerals, Department of Chemical Engineering, The University of Melbourne, Victoria 3010. Email: sajid@student.unimelb.edu.au
2. Research Fellow, ARC Centre of Excellence for Enabling Eco-Efficient Beneficiation of Minerals, Department of Chemical Engineering, The University of Melbourne, Victoria 3010. Email: nilanka.ekanayake@unimelb.edu.au
3. Research Fellow, ARC Centre of Excellence for Enabling Eco-Efficient Beneficiation of Minerals, Department of Chemical Engineering, The University of Melbourne, Victoria 3010. Email: spusher@unimelb.edu.au
4. Emeritus Professor, ARC Centre of Excellence for Enabling Eco-Efficient Beneficiation of Minerals, Department of Chemical Engineering, The University of Melbourne, Victoria 3010. Email: peterjs@unimelb.edu.au
5. Kernot Professor of Engineering, ARC Centre of Excellence for Enabling Eco-Efficient Beneficiation of Minerals, Department of Chemical Engineering, The University of Melbourne, Victoria 3010. Email: r.batterham@unimelb.edu.au
6. Senior Lecturer, ARC Centre of Excellence for Enabling Eco-Efficient Beneficiation of Minerals, Department of Chemical Engineering, The University of Melbourne, Victoria 3010. Email: stad@unimelb.edu.au

ABSTRACT

Mineral tailings often contain a continuum of particles from coarse to fine, where the latter is less than 10 μm in diameter. There is increased pressure for greater dewatering of tailings, for both water recovery and to create safer storage impoundments. The dewatering process can increase the solid concentration by either using gravitational forces (thickeners), centrifugal forces (centrifuges), or applied pressure (filters), all of which are limited by the solids concentration dependent rate and equilibrium extent of dewatering. There is a move to the use of filters as the final dewatering step at many mine sites, however, quantification of the true differences in dewatering between tailings samples is often seen as requiring expensive pilot scale work. Previous work has examined the effect of fine particles on shear rheology and the gel point or free settling concentration of the tailings. A validated method of comparing the dewatering of samples in filtration in a quantitative manner is demonstrated herein for a particulate mixture where the proportion of fine particles in the mixture is varied systematically. Although the particulate system does not cover the size range of all tailings systems, the methodology represents a generic laboratory based approach to the quantification of the differences in dewatering between particulate suspensions in filtration.

The work used two different particle sizes of a model mineral, calcium carbonate, with Sauter mean diameters of 12 μm and 2.1 μm, to produce bimodal mixtures of coarse and fine particles. These sizes were mixed in different proportions, and suspension characterisation was performed using compressional rheology and shear rheology. Sedimentation and pressure filtration tests were performed to produce a data set of fundamental dewatering (compressional rheology) parameters across a large range of solids weight fraction. The effect of fine particle ratio on the dewaterability of bimodal mixtures was assessed for a range of bulk weight fractions. Its impact on filtration process performance was then evaluated using validated filter press modelling.

INTRODUCTION

Mineral tailings are the non-economic waste product from the extraction of valuable minerals that can account for >99 per cent of the total tonnage of ore processed (Adiansyah *et al*, 2015). This makes the mining industry the largest producer of waste, with an estimated global volume of 8.85 Bt of tailings from all different minerals and metals production (Baker *et al*, 2020). The traditional way of storing this waste is nominally as wet tailings in large dams. The dams are often referred to as tailings storage facilities (TSF). Every year on average, at least two tailings dam failures occur (Jones and Boger, 2012), resulting in significant (sometimes of order billions of dollars) human, environmental and economic costs.

The demand for minerals is growing and along with a trend towards production from lower-grade ores (Batterham, 2011; Wang *et al*, 2014), the volume of tailings is also increasing. To increase the solids concentration of the tailings, thickening has been the industry standard but for fine tailings that are not free draining, further dewatering is needed to achieve a geotechnically safe product. For some systems, particularly high clay systems, this may not be attainable even after high pressure filtration, but a method that quantifies the limitations in a consistent and repeatable manner is still lacking. To determine the dewatering characteristics of tailings and quantitatively compare dewatering differences to a fixed moisture content, a robust theoretical framework is required, along with experimental suspension characterisation of the relevant dewatering parameters of the mineral tailing of interest. To this end, our laboratory uses the compressional rheology framework first reported by Buscall and White (1987) and looks to compare the dewatering differences between samples using a self-consistent filtration modelling approach that first validates the experimental dewatering parameters and then uses the same framework for scenario modelling to compare performance (Skinner *et al*, 2015).

Mineral tailings usually contain a varying particle size distribution from coarse to fine (the latter being nominally defined as <10 μm) particles and are often, because of mineralogy, bimodal mixtures. To demonstrate the dewaterability comparison method, two different sizes of calcium carbonate were used to produce model tailings of fine and coarse particles with the capacity to systematically vary the level of fines. The sample was not chosen based on a typical tailings mineralogy but to be reproducible from batch to batch in terms of particle size and have a constant surface potential interaction with changing particle size. This allows the effect of particle size to be studied in a systematic fashion, in isolation of changes in surface chemistry. Material characterisation was performed for different mixtures of fine and coarse particles using compressional and shear rheology approaches, quantifying the effect of fine particles on the compressibility, permeability and shear yield properties. The dewatering parameters from this characterisation were then validated (Skinner *et al*, 2015) (not shown here) and used in a numerical model of a filter press to predict the filtration time and solids throughput for different cake solids, allowing dewaterability comparison. In this instance, one of the comparators was the equivalent filter area required for different levels of fines.

THEORY

Compressional rheology

The theoretical framework of compressional rheology introduced by Buscall and White (1987) was used in this study to perform characterisation of calcium carbonate suspensions to find dewatering properties across a wide range of solids volume fraction, ϕ. The dewatering rate and extent for a suspension are dependent upon multiple factors such as the applied pressure force, particle-particle interaction and viscous drag force between the particles and the liquid. The framework defines the gel point of a suspension, ϕ_g, as the minimum solids volume fraction at which particles can form a self-supporting structure. For a suspension to reach higher solids concentrations, pressures need to be applied that exceed the compressive yield stress, $P_y(\phi)$. This parameter is defined as the resistance of suspension to consolidation due to the interparticle network strength. The hindered settling rate, $R(\phi)$, determines the rate of dewatering and this depends on the hydrodynamic interactions between the fluid and the particles (Landman and White, 1994).

To obtain the key material properties, $P_y(\phi)$ and $R(\phi)$, a combination of batch sedimentation and pressure filtration tests were used. To describe the compressive yield stress and hindered settling function for the full range of solids concentration and serve as a descriptor of these parameters for modelling, the following empirical constitutive equations (Usher *et al*, 2013) were used:

$$P_y(\phi) = \begin{cases} 0 \; for \; \phi < \phi_g \\ P_{y1}(\phi) = \left(\frac{a_1(\phi_{cp1}-\phi)(b_1+\phi-\phi_{g1})}{\phi-\phi_{g1}}\right)^{-k_1} \; for \; \phi_g < \phi_p \\ P_{y2}(\phi) = \left(\frac{a_2(\phi_{cp2}-\phi)(b_2+\phi-\phi_{g2})}{\phi-\phi_{g2}}\right)^{-k_2} \; for \; \phi_p < \phi_{cp} \end{cases} \quad (1)$$

$$R(\phi) = r_a\left(\phi - r_g\right)^{r_n} + r_b \quad (2)$$

where a_1, a_2, b_1, b_2, ϕ_{g1}, ϕ_{g2}, ϕ_p, ϕ_{cp1}, ϕ_{cp2}, k_1, k_2, r_a, r_b, r_g and r_n are the fitting parameters obtained experimentally, and ϕ_{cp} is the solids volume fraction at close packing.

Shear rheology

For a material to flow, a minimum shear stress needs to be exerted on the material, commonly characterised as the shear yield stress. A vane in a cup method was introduced by Nguyen and Boger (1983) to calculate the shear yield stress. Using this method, a four-bladed vane was fully submerged into the suspension and was rotated at 0.2 rev/min to obtain the maximum torque, T_{max}. The torque was then converted to shear yield stress, τ_y, using Equation 3.

$$\tau_y = \frac{T_{max}}{K} \tag{3}$$

The vane constant, K, depends on the dimensions of the vane and is defined in Equation 4. The height and diameter of the vane are referred to as H_v and D_v respectively.

$$K = \frac{\pi D_v^3}{2}\left(\frac{H_v}{D_v} + \frac{1}{3}\right) \tag{4}$$

MATERIALS AND METHODS

Two different sizes of calcium carbonate (Omyacarb 1 and 40, Omya Australia) were used to represent fine and coarse particles. A 0.01 M KNO_3 electrolyte solution was prepared using Milli-Q water and was added to the Omya powders to obtain a solids weight fraction of 54 wt per cent. A mixture containing 70 wt per cent Omya40 and 30 wt per cent Omya1 solids was also prepared. These suspensions were mixed for 24 hrs to ensure homogeneity. The pH of the suspensions was 8.4 ± 0.1. The particle size distribution of the suspensions was measured using a Malvern Mastersizer 3000 with the results shown in Figure 1. The Sauter mean diameter, d_s, of Omya1 and Omya40 were 2.1 μm and 12 μm respectively. The mixture of Omya40 (0.7), Omya1 (0.3) had a d_s of 5.2 μm.

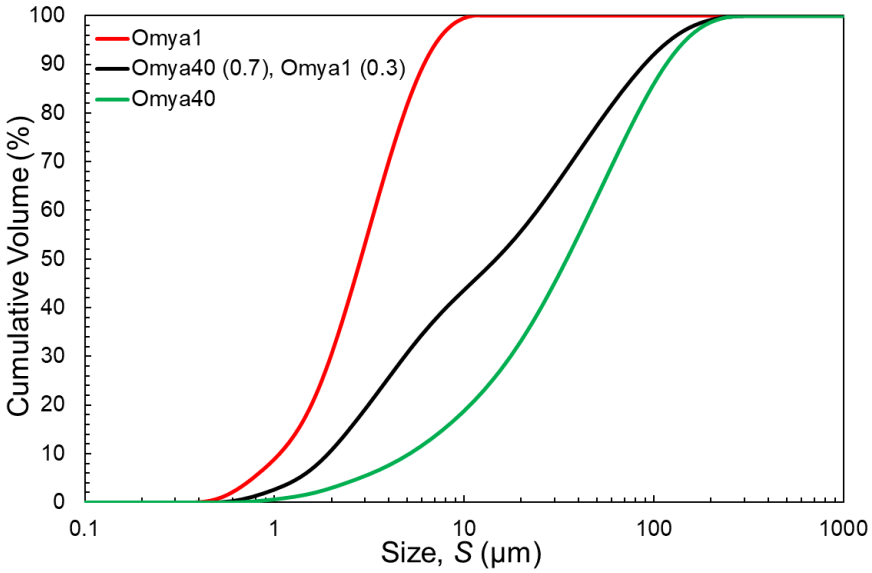

FIG 1 – Cumulative particle size distribution of Omyacarb suspensions.

The material characterisation using compressional rheology (Buscall and White, 1987) was performed through two different techniques. The compressive yield stress, $P_y(\phi)$, and hindered settling function, $R(\phi)$, for suspensions at low solids volume fraction were obtained through a batch sedimentation technique (Lester *et al*, 2005) while a stepped pressure filtration method was used for suspensions at solids concentrations above the gel point (de Kretser *et al*, 2001; Usher *et al*, 2001). The pressures chosen were 20, 40, 80, 150, 300 and 600 kPa.

For the compressibility filtration tests, each set pressure was applied to the sample until there was no more filtrate, after which it stepped to the next pressure. For the permeability filtration tests, each

set pressure was applied to obtain the linear slope of *t versus* V^2 in the cake formation region, where *t* is the time and *V* is the specific filtrate volume. Combining the results from both the tests gave the material characterisation properties of $P_y(\phi)$ and $R(\phi)$ for the full range of the solid's weight fraction. The shear yield stress was measured from the peak stress at constant rate flow start-up using the vane in a cup method (Nguyen and Boger, 1983). Re-prediction of the stepped pressure data was performed to validate the efficacy of the dewatering parameter extraction using the method of Skinner *et al* (2015).

RESULTS AND DISCUSSION

The results obtained from both the sedimentation and filtration tests were first combined to give the compressive yield stress, $P_y(x)$, across the whole range of solids concentrations. The results are presented in Figure 2 in terms of weight fraction, *x*, instead of volume fraction (ϕ). The data at higher solids weight fraction are from filtration testing while the data at lower solids weight fraction are from sedimentation testing. For a certain $P_y(x)$, Omya1 reaches a much lower equilibrium solids weight fraction when compared with Omya40. This indicates that the extent of dewatering for Omya40 is higher. Omya40 suspensions can reach up to 82.20 wt per cent for a $P_y(x)$ of 600 kPa compared to 75.25 wt per cent of Omya1 at the same pressure. The gel point is where the compressive yield stress is zero and it was calculated as 42.58 wt per cent and 62.66 wt per cent for Omya1 and Omya40 respectively. For the mixture, the gel point was found to be 58.29 wt per cent and the solids weight fraction reached 85.47 wt per cent at 600 kPa. At lower pressures, the extent of dewatering is lower than the pure Omya40 suspension. However, above 100 kPa, the mixture shows a better dewatering extent as at higher pressures, the finer particles are forced into the interstitial gaps of the coarser particles, increasing the solids concentration.

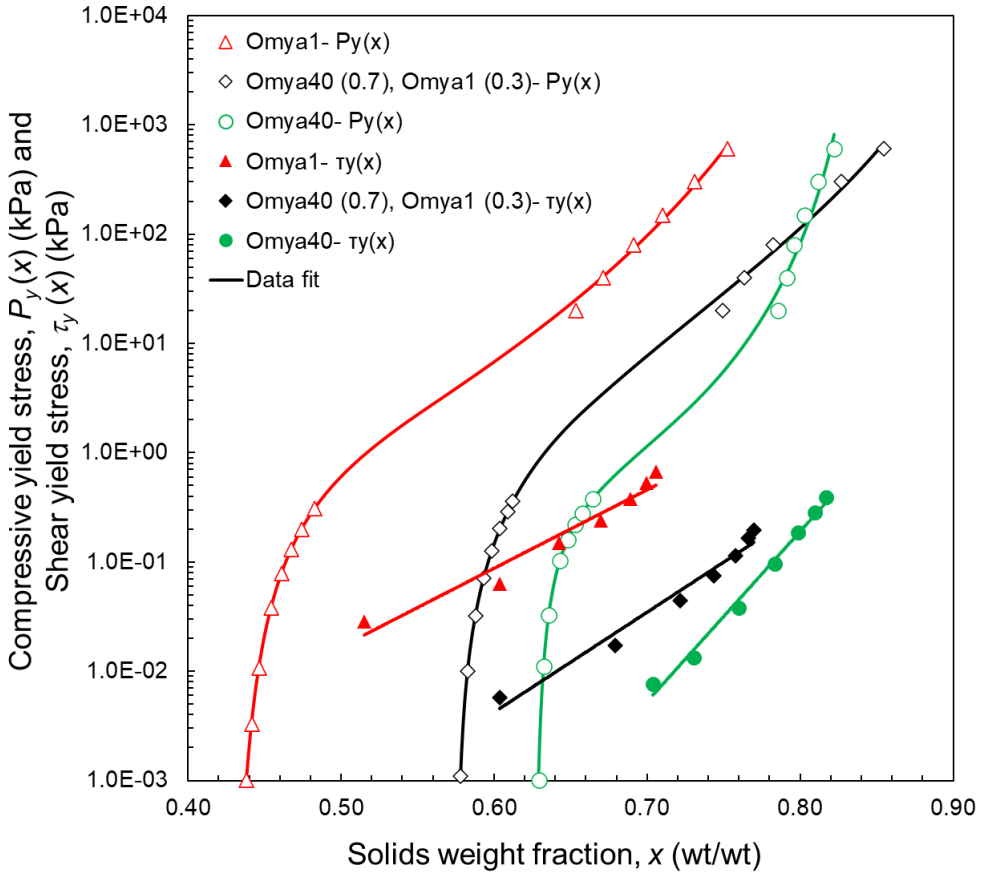

FIG 2 – Compressive and shear yield stress curves of Omyacarb suspensions.

Figure 2 also shows the shear yield stress, τ_y, as a function of solids weight fraction, *x*. The smaller sized particles in Omya1 suspensions have a higher surface area per unit volume which causes the shear yield stress to be higher compared to Omya40. Hence, the presence of Omya1 particles in the mixture produces a higher shear yield stress for a given solids weight fraction. Comparing the shear

to the compressive yield stress shows that the shear yield stress for the Omya suspensions is up to three orders of magnitude lower. This indicates that incorporating shear into dewatering operations has the potential to improve the dewatering process (Höfgen *et al*, 2019, 2020).

Figure 3 shows the hindered settling function, *R(x)*. For a given cake solids weight fraction, Omya1 has a much higher hindered settling rate (by 1–2 orders of magnitude) compared to Omya40. As the permeability is inversely proportional to the hindered settling function, the permeability of Omya40 is thus higher than Omya1. Therefore, the Omya40 suspension will be much faster to dewater. Smaller sized particles present in Omya1 create more resistance to flow, resulting in a lower permeability. With the presence of 30 per cent fines in the mixture, the permeability was reduced by up to 1 order of magnitude compared to the Omya40 suspension.

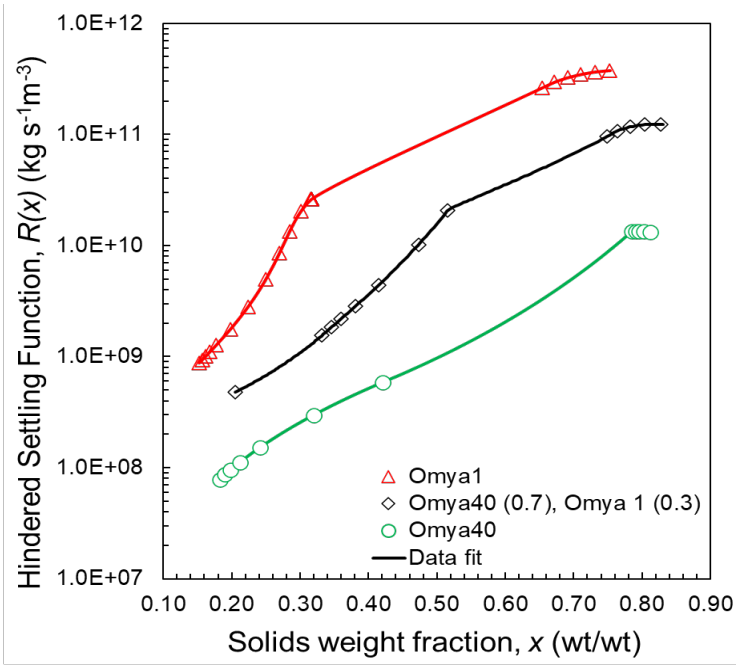

FIG 3 – Hindered settling function of Omyacarb suspensions.

A fixed cavity plate and frame filter numerical model (Stickland *et al*, 2006) was used to predict the average specific solids throughput, x_0<*Q*>, against the average cake solids, x_F, for the suspensions fed to a filter. The results of the model are shown in Figure 4. It was assumed that the fill pressure of the system was 600 kPa, the initial height of the suspension, h_0, was 1.5 cm (that is, the filter chamber was $2h_0$ = 3 cm), the initial solids concentration, x_0, was 23 wt per cent, the handling time, t_H, was 300 secs, and the membrane resistance, R_m, was negligible. For Omya1, the solids throughput increases and reaches a maximum, after which it decreases with increasing cake solids. For Omya40, as the filtration time is quicker than the handling time, the throughput increases with increasing cake solids. In short, the filtration becomes limited by the filter cake permeability for Omya1 under the specified conditions, whereas the throughput is dominated by the time taken to open the press, drop the cake and re-start the process for the Omya40 (Stickland *et al*, 2016). For the mixture, although there is potential to reach higher solids at higher pressures, the presence of the fine particles also means the filtration behaviour is filter cake permeability limited, similar to but not to the same extent as for the Omya1 suspension.

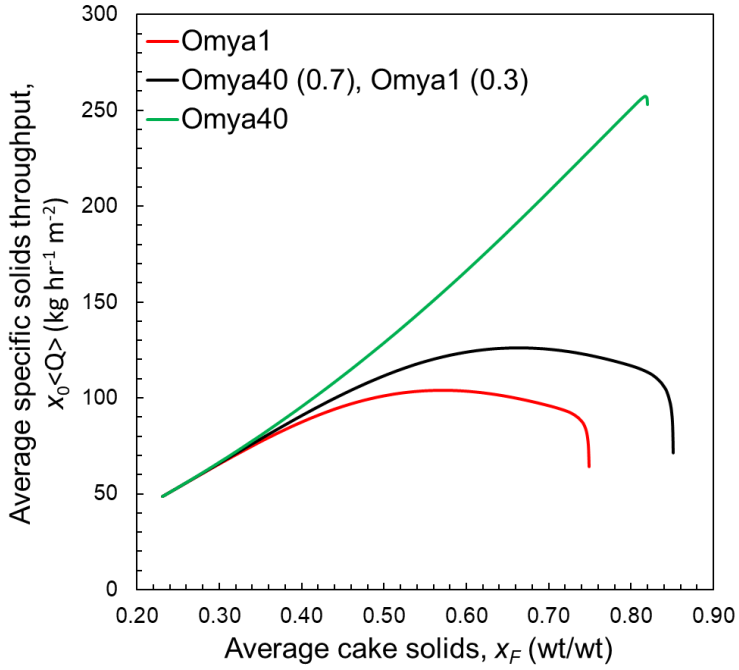

FIG 4 – Specific solids throughput prediction of Omyacarb suspensions using the plate and frame filter model.

Using the model, the filtration area was calculated for a feed suspension at x_0 = 23 wt per cent to reach a final average cake solids of x_F = 73 wt per cent. The data is presented in Figure 5. It is interesting to note that the strong dependence of the filter area required on the particle size when the surface chemistry of the system is held constant.

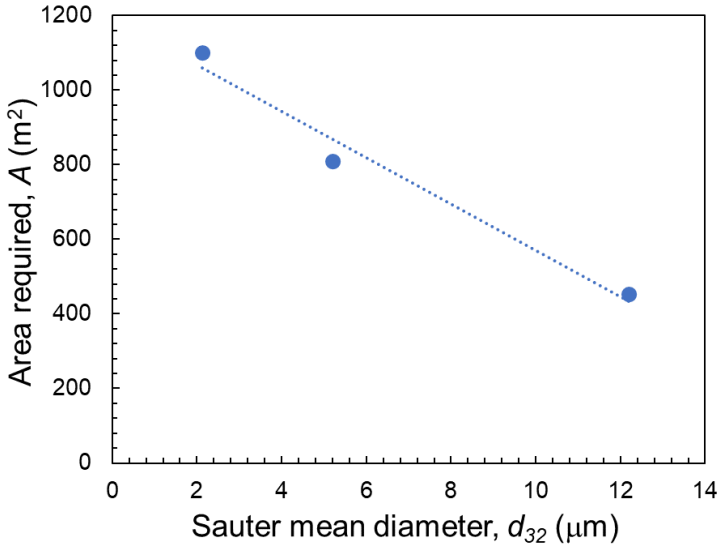

FIG 5 – Plate and frame filter area required as a function of sauter mean diameter for 100 t/hr throughput of Omyacarb suspensions at x_0 = 23 wt per cent to reach x_F = 73 wt per cent.

CONCLUSIONS

A dewatering characterisation was performed for two size fractions of calcium carbonate to represent fine and coarse particles in mineral tailings. Using a mixture of these components gives the flexibility to represent a wide range of mineral tailings (in particle size terms, not mineralogy), allowing the effect of adding finer particles in particle mixtures to be fully quantified without changing surface chemistry. The simple case study demonstrates how changes in the extent and rate of dewatering and differences between samples can be quantified and how filtration conditions can become limiting as the proportion of finer particles increases.

A numerical model of fixed cavity plate and frame filtration was used to predict the filtration time and filtration area required to process 100 t/hr solids throughput. Depending on the finer particles present in tailings, this model can be used to quantitatively compare different samples as well as predict the plate and frame filter size required along with the optimum solids throughput to achieve certain final cake moisture.

Consistent with previous work, the shear yield stress of the suspensions was observed to be up to three orders of magnitude lower than the compressive yield stress. The data indicate the potential of introducing shear into filtration devices, whilst applying pressure, to improve the rate and potentially the extent of dewatering. Devices that can exploit this behaviour are now being trialled (Höfgen *et al*, 2019).

ACKNOWLEDGEMENTS

This project is funded by the Australian Research Council through the ARC Centre of Excellence for Enabling Eco-Efficient Beneficiation of Minerals, grant number CE200100009. S. Hassan is also the recipient of a Research Training Program Scholarship through The University of Melbourne.

REFERENCES

Adiansyah, J S, Rosano, M, Vink, S and Keir, G, 2015. A framework for a sustainable approach to mine tailings management: disposal strategies. *Journal of Cleaner Production,* 108, 1050–1062.

Baker, E, Davies, M, Fourie, A, Mudd, G and Thygesen, K, 2020. Towards zero harm – a compendium of papers prepared for the global tailings review. *Chapter II-mine tailings facilities: overview and industry trends*.

Batterham, R, 2011. Trends in comminution driven by energy. *Advanced Powder Technology,* 22, 138–140.

Buscall, R and White, L R, 1987. The consolidation of concentrated suspensions. Part 1 – The theory of sedimentation. *Journal of the Chemical Society, Faraday Transactions 1: Physical Chemistry in Condensed Phases,* 83, 873–891.

De Kretser, R G, Usher, S P, Scales, P J, Boger, D V and Landman, K A, 2001. Rapid filtration measurement of dewatering design and optimization parameters, *AIChE Journal,* 47, pp. 1758–1769.

Höfgen, E, Collini, D, Batterham, R J, Scales, P J and Stickland, A D, 2019. High pressure dewatering rolls: Comparison of a novel prototype to existing industrial technology. *Chemical Engineering Science,* 205, 106–120.

Höfgen, E, Teo, H-E, Scales, P J and Stickland, A D, 2020. Vane-in-a-Filter and Vane-under-Compressional-Loading: novel methods for the characterisation of combined shear and compression. *Rheologica Acta,* 59, 349–363.

Jones, H and Boger, D V, 2012. Sustainability and Waste Management in the Resource Industries. *Industrial and Engineering Chemistry Research,* 51, 10057–10065.

Landman, K A and White, L R, 1994. Solid/liquid separation of flocculated suspensions. *Advances in Colloid and Interface Science,* 51, 175–246.

Lester, D R, Usher, S and Scales, P J, 2005. Estimation of the hindered settling function R(ϕ) from batch settling tests, *Aiche Journal,* 51, pp. 1158–1168.

Nguyen, Q D and Boger, D V, 1983. Yield Stress Measurement for Concentrated Suspensions. *Journal of Rheology,* 27, 321–349.

Skinner, S J, Studer, L J, Dixon, D R, Hillis, P, Rees, C A, Wall, R C, Cavalida, R G, Usher, S P, Stickland, A D and Scales, P J, 2015. Quantification of wastewater sludge dewatering. *Water Research,* 82, 2–13.

Stickland, A D, De Kretser, R G, Scales, P J, Usher, S P, Hillis, P and Tillotson, M R, 2006. Numerical modelling of fixed-cavity plate-and-frame filtration: Formulation, validation and optimisation. *Chemical Engineering Science,* 61, 3818–3829.

Stickland, A, Irvin, E, Skinner, S, Scales, P, Hawkey, A and Kaswalder, F, 2016. Filter Press Performance for Fast-Filtering Compressible Suspensions. *Chemical Engineering and Technology,* 39, 409–416.

Usher, S P, De Kretser, R G and Scales, P J, 2001. Validation of a new filtration technique for dewaterability characterization, *AIChE Journal,* 47, pp. 1561–1570.

Usher, S P, Studer, L J, Wall, R C and Scales, P J, 2013. Characterisation of dewaterability from equilibrium and transient centrifugation test data. *Chemical Engineering Science,* 93, 277–291.

Wang, C, Harbottle, D, Liu, Q and Xu, Z, 2014. Current state of fine mineral tailings treatment: A critical review on theory and practice. *Minerals Engineering,* 58, 113–131.

Quantifying the effects of clay on dewatering in mineral tailings

Y Luo[1], N I K Ekanayake[2], N Amini[3], S P Usher[4], E Moon[5], K P Hapgood[6], P J Scales[7] and A D Stickland[8]

1. PhD Candidate, ARC Centre of Excellence for Enabling Eco-Efficient Beneficiation of Minerals, Department of Chemical Engineering, The University of Melbourne, Vic 3010. Email: yuxuanl7@student.unimelb.edu.au
2. Research Fellow, ARC Centre of Excellence for Enabling Eco-Efficient Beneficiation of Minerals, Department of Chemical Engineering, The University of Melbourne, Vic 3010. Email: nekanayake@student.unimelb.edu.au
3. Research Fellow, ARC Centre of Excellence for Enabling Eco-Efficient Beneficiation of Minerals, Faculty of Science, Engineering and Built Environment (SEBE), Deakin University, Vic 3216. Email: negin.a@deakin.edu.au
4. Research Fellow, ARC Centre of Excellence for Enabling Eco-Efficient Beneficiation of Minerals, Department of Chemical Engineering, The University of Melbourne, Vic 3010. Email: spusher@unimelb.edu.au
5. Senior Lecturer, ARC Centre of Excellence for Enabling Eco-Efficient Beneficiation of Minerals, Faculty of Science, Engineering and Built Environment (SEBE), Deakin University, Vic 3216. Email: ellen.moon@deakin.edu.au
6. Professor, ARC Centre of Excellence for Enabling Eco-Efficient Beneficiation of Minerals, Swinburne University of Technology, Vic 3216. Email: khapgood@swin.edu.au
7. Emeritus Professor, ARC Centre of Excellence for Enabling Eco-Efficient Beneficiation of Minerals, Department of Chemical Engineering, The University of Melbourne, Vic 3010. Email: peterjs@unimelb.edu.au
8. Senior Lecturer, ARC Centre of Excellence for Enabling Eco-Efficient Beneficiation of Minerals, Department of Chemical Engineering, The University of Melbourne, Vic 3010. Email: stad@unimelb.edu.au

INTRODUCTION

Clay and clay minerals are commonly found in mineral orebodies and increasingly show negative impacts in processing operations. The amount of clay usually varies with location across the orebody. This not only causes poor performance but large and often unpredictable process variabilities. As such, the presence of clay in the ore negatively impacts most unit operations, including comminution, concentrating (ie flotation), separations, dewatering and tailings management.

The main issue with clays is their high aspect ratio, which causes a low density in particulate aggregates (large occluded volume) and higher suspension viscosities at any given solids concentration. As a result, achieving low moisture content tailings is made difficult, leading to higher water use per tonne of ore and a larger and less geotechnically stable tailings storage volume (Chryss, 2017).

In this study, the effect of clay in mineral tailings is explored and quantified using a comprehensive dewaterability analysis (de Kretser *et al,* 2001). Batch sedimentation and pressure filtration methods were implemented for measuring the compressibility and permeability over a range of solids concentrations and at varying proportions of clay. The variation in clay content of tailings was simulated using a combination of fine calcium carbonate (Omyacarb 10 from Omya Australia Pty Ltd) with D[3,2] of 6.6 μm and varying proportions of kaolinite (ASP200 Kaolin from BASF) with D[3,2] of 1.9 μm. The dewatering properties of these simulated tailings were measured and then used in models of thickening and filtration (Usher and Scales, 2005; Stickland *et al,* 2006). This combination of experimental characterisation and modelling allows changes in clay addition to be systematically quantified in terms of dewatering throughput and degree of dewatering (final moisture content).

RESULTS

Four simulated tailing suspensions were prepared in this study, these being pure Omyacarb 10, pure Kaolin, and mixtures of Omyacarb 10 with 10 per cent and 20 per cent Kaolin. The dewaterability of

the samples was then characterised using stepped-pressure filtration testing (de Kretser *et al,* 2001) and batch sedimentation testing (Lester *et al,* 2005) The equilibrium extent of consolidation or compressive strength, $P_y(x)$, and solid-liquid drag or hindered settling, $R(x)$, results are presented in Figure 1a and 1b, respectively.

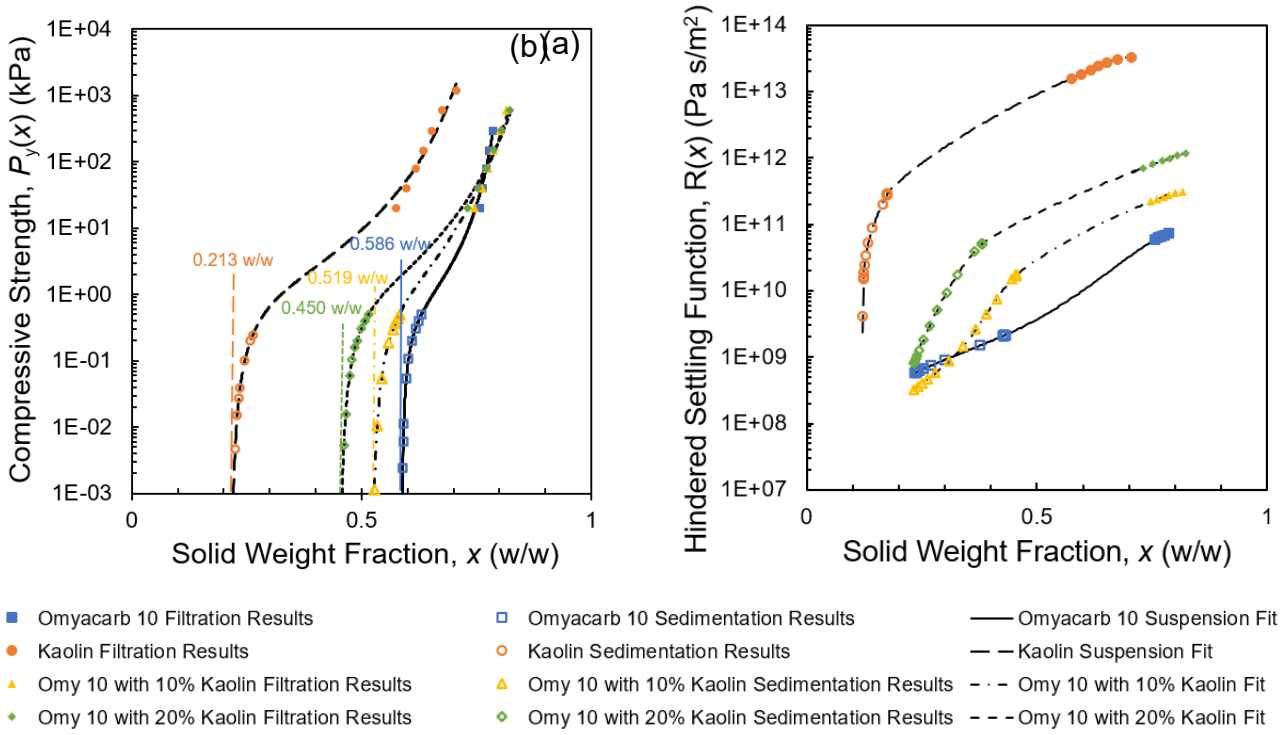

FIG 1 – (a) Compressive strength and (b) hindered settling function for Kaolin and Omyacarb 10 simulated tailings.

The results in Figure 1(a) demonstrate that the addition of clay to the Omyacarb 10 suspension causes a decrease in the gel point (the concentration with zero strength) from 0.586 w/w to 0.519 w/w and 0.450 w/w with 10 per cent and 20 per cent kaolin respectively. This is due to the increased specific surface area, non-spherical shape and increased inter-particle interaction of the clay. However, additions of these amounts of clay did not affect the high-pressure dewatering extent, suggesting the clay may be filling interstices of the Omyacarb. The Kaolin only suspension, on the other hand, has a much lower gel point (0.213 w/w) and higher compressive strength at all solid weight fractions compared to the other suspensions. Figure 1(b) shows that, as the concentration of Kaolin increases, the hindered settling function increases dramatically, which means the tailings are less permeable with increasing clay content.

To quantify the real change in dewaterability between the samples, a fixed-cavity filter press model (Stickland *et al,* 2006) was used to predict the filter area and the filtration time required to filter a suspension with a known feed concentration x_0 to a fixed final average cake concentration x_F. Both the filter area and the filtration time increase exponentially with clay content. Figure 2 (a) shows with the presence of kaolin, the average solid throughput per membrane area decreased significantly where Figure 2(b)shows that to achieve x_F = 0.72 w/w with capacity at 100 t/h, the filter area required for the pure Omyacarb 10, 10 per cent and 20 per cent kaolin suspensions are 750, 1730 and 4749 m^2, respectively. While the filtration time was 237 s for the pure Omyacarb 10 suspension, this increases to 959 s with 10 per cent Kaolin followed by 3150 s with 20 per cent Kaolin. The pure Kaolin suspension is unable to reach 0.72 w/w at the test pressure due to it's high compressive strength. To achieve just a solid weight fraction of 0.64 w/w would require a filter area of 43 657 m^2.

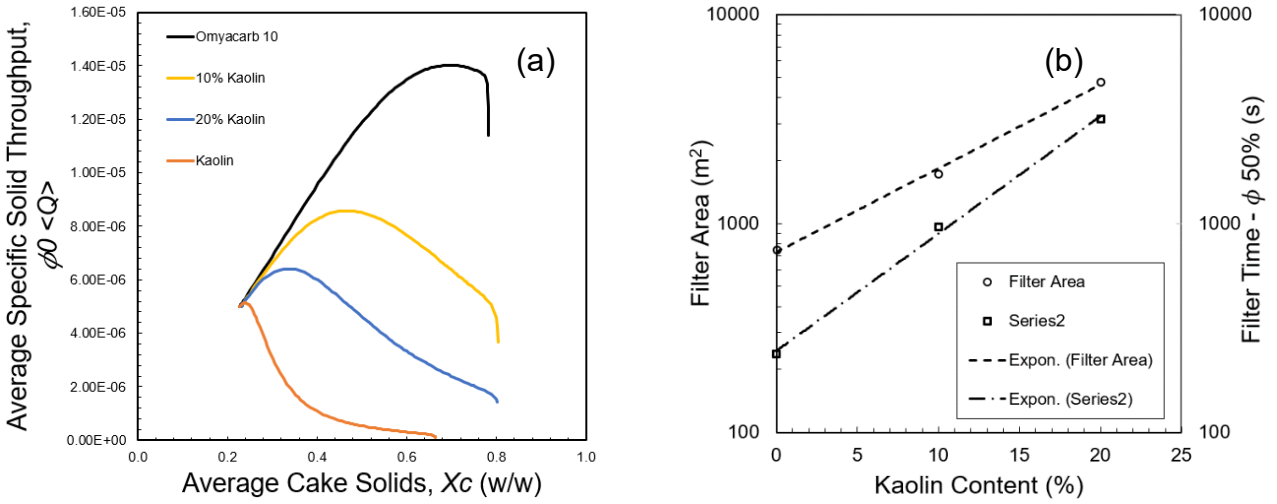

FIG 2 – Model predictions of (a) Solid Throughput per Membrane Area and (b) Filter Area and Filtration Time to achieve a final solid weight fraction of x_F = 0.72 w/w for different kaolin content: Initial Solid Weight Fraction (x_0 = 0.22) w/w, Fill Pressure (ΔP_F = 300 kPa), Membrane Resistance (R_m = 0), Total Handling Time (t_H = 300 s).

CONCLUSION

This work provides a methodology to quantify the changes in dewatering behaviour due to the presence of clay. Increasing clay content in tailings decreases the gel point and the permeability. As a result, larger filter size and a longer filtration time are required, which increases the cost of the dewatering process.

ACKNOWLEDGEMENT

This project is funded by the Australian Research Council through the ARC Centre of Excellence for Enabling Eco-Efficient Beneficiation of Minerals, grant number CE200100009. Y Luo is supported by a University of Melbourne Research Scholarship.

REFERENCES

Chryss, A, 2017. *Effects of Clay in Tailings Handling and Storage*, Cambridge University Press, Cambridge: 381–399.

De Kretser, R G, Usher, S P, Scales, P J, Boger, D V and Landman, K A, 2001. Rapid filtration measurement of dewatering design and optimization parameters. *Aiche Journal* 47(8): 1758–1769.

Lester, D R, Usher, S P and Scales, P J, 2005. Estimation of the Hindered Settling Function R (Φ) from batch-settling tests. *Aiche Journal* 51(4): 1158–1168.

Stickland, A D, De Kretser, R G, Scales, P J, Usher, S P, Hillis, P and Tillotson, M R, 2006. Numerical modelling of fixed-cavity plate-and-frame filtration: formulation, validation and optimisation. *Chemical Engineering Science* 61(12): 3818–3829.

Usher, S P and Scales, P J, 2005. Steady state thickener modelling from the compressive yield stress and hindered settling function. *Chemical Engineering Journal* 111(2–3): 253–261.

Computational simulation of particle agglomeration in a shear flow

Y Z Qian[1], S P Usher[2], A Alexiadis[3], P J Scales[4] and A D Stickland[5]

1. PhD Candidate, ARC Centre of Excellence for Enabling Eco-Efficient Beneficiation of Minerals, Department of Chemical Engineering, The University of Melbourne, Vic 3010.
   Email: yunzhouq@student.unimelb.edu.au;
   School of Chemical Engineering, The University of Birmingham, Birmingham B15 2TT UK.
   Email: yyq004@student.bham.ac.uk
2. Research Fellow, ARC Centre of Excellence for Enabling Eco-Efficient Beneficiation of Minerals, Department of Chemical Engineering, The University of Melbourne, Vic 3010.
   Email: spusher@unimelb.edu.au
3. Reader, School of Chemical Engineering, The University of Birmingham, Birmingham B15 2TT UK. Email: a.alexiadis@bham.ac.uk
4. Emeritus Professor, ARC Centre of Excellence for Enabling Eco-Efficient Beneficiation of Minerals, Department of Chemical Engineering, The University of Melbourne, Vic 3010.
   Email: peterjs@unimelb.edu.au
5. Senior Lecturer, ARC Centre of Excellence for Enabling Eco-Efficient Beneficiation of Minerals, Department of Chemical Engineering, The University of Melbourne, Vic 3010.
   Email: stad@unimelb.edu.au

INTRODUCTION

Particle agglomeration exists in a variety of natural and industrial flow problems. Particle dispersion in the atmosphere, atmospheric ice crystals agglomeration during snowflake forming, and pollution removal in aquatic systems through sediment deposition are some examples in nature. Particle agglomeration is also involved extensively in the industry, for instance, treatment of sewage, ash collection from combustion burners, flame generation of nanoparticles, and fine particle removal in gas cyclones. Specifically, in the mining industry, particle aggregation in solid-liquid separation plays an important role in accelerating slurry dewatering and thus improving the performance of thickening and filtration operations (Fernando Concha, 2014; Usher, Spehar and Scales, 2009). Therefore, it is indispensable, for optimising particulate processing, to have a deep understanding of particle agglomeration.

According to many experimental investigations, the number of particles in an aggregate typically varies as an exponential function of radius of gyration of aggregates, where the exponent of the function is referred as aggregates' fractal dimension (Adachi and Ooi, 1990; Liu *et al*, 1990; Jiang and Logan, 1991). The fractal dimension's value is determined by the mechanism through which the aggregate was generated and the stage at which it was formed. Typical values of fractal dimension are in the range of roughly from 1.5 to 3.0 (Brasil *et al*, 2001). The fractal dimension influences the aggregate's material characteristics, such as its elastic and shear moduli (Shih *et al*, 1990; Narine and Marangoni, 1999a; 1999b). The force network of aggregate is affected by its fractal structure, which impacts the shear stress required to cause aggregate fragmentation (Kobayashi, Adachi and Ooi, 1999; Higashitani, Iimura and Sanda, 2001; Bache, 2004; Scurati, Feke and Manas-Zloczower, 2005; Wengeler and Nirschl, 2007).

A Eulerian–Lagrangian approach was recently employed by certain investigators (Chen, Li and Marshall, 2019; Chen and Li, 2020; Ruan, Chen and Li, 2020; van Wachem *et al*, 2020; Yao and Capecelatro, 2021) to explore agglomeration as well as deagglomeration in both turbulent and laminar flows. In these studies, only momentum transfer between the solid and fluid phases was taken into account, not the physical existence of particles in the fluid (particles are "invisible" to the flow). In this research, to describe all fluid-fluid, fluid-particle, and inter-particle interactions that exist in the system, two discrete particle methods, Smoothed Particle Hydrodynamics (SPH) (Liu and Liu, 2003) and Discrete Element Method (DEM) (Bićanić, 2007) are combined. Rahmat *et al* (2020) adopted this novel SPH-DEM approach; however, an inappropriately basic description of inter-particle interaction was used in their study. To improve this, here, one common used adhesion contact model, the Derjaguin–Muller–Toporov (DMT) (Derjaguin, Muller and Toporov, 1975) or Johnson–Kendall–Roberts (JKR) (Johnson *et al*, 1971) model is chosen. Furthermore, this proposed numerical tool is used to examine the influence of different important parameters on particle

aggregate structure, such as the Adhesion number *Ad*, which quantifies the interparticle attraction, and Reynolds number *Re*, which quantifies the influence of hydrodynamics. This investigation has the potential not only to more comprehensively and accurately understand particle aggregate structures, but also to provide engineering guidance for optimising dewatering processes.

RESULTS AND DISCUSSION

In the simulations using this novel SPH-DEM approach, after early increase, the average aggregate size approaches a stable size. This steady-state size is acquired after the number of particles in average aggregate reaches a plateau. Based on whether shear or adhesion prevails, or if both mechanisms are at work, this steady state can be achieved in three different ways. When shear dominates, the first occurs. The surface energy of the particles is low and there are almost no aggregates. Even when minor aggregates create, hydrodynamic forces easily break them apart. At steady state, this results in a large number of dispersed elementary particles. When adhesion dominates, the second occurs. Aggregates do not grow any more once they've cleared the whole nearby region where there aren't any more particles to cluster together. Within the flow domain, this results in branched aggregates. When both shear and adhesion are at work, the final occurs. Aggregation and fragment approach a dynamic equilibrium and the average aggregate size remains constant, but the forms vary from squished spheres to strings of elementary particles. Figure 1 presents some aggregates creating in a particle dilute suspension for different Reynolds (*Re*) and Adhesion (*Ad*) numbers. At large *Ad*, adhesion forces are dominant, and aggregation prevails. At small *Ad*, particles tend not to adhere to each other, resulting in highly dispersed systems.

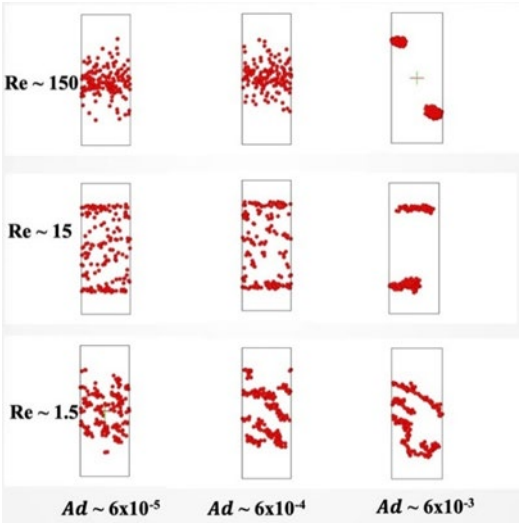

FIG 1 – Steady-state structures of particle aggregates in plane for different Reynolds numbers and adhesion numbers in a dilute particle suspension.

CONCLUSIONS

A novel SPH-DEM model is proposed in this study to investigate the effect of Reynolds and Adhesion numbers on particle agglomeration suspended in a simple shear flow. Depending on different Reynolds and Adhesion numbers, aggregates come in a variety of morphologies, ranging from lengthy thread-like structures to compact spheroids. Once Reynolds and Adhesion numbers are known, this information can rapidly identify the agglomeration type.

This research also offers an approach that would be used to investigate a wide range of inter-particle interactions. The proposed method can be extended to additional adhesion models (apart from JKR or DMT model) or greater ranges of *Re* and *Ad* if necessary.

ACKNOWLEDGEMENTS

The authors thank the University of Melbourne and the University of Birmingham for the Priestley PhD Scholarship. Infrastructure and personnel associated with the work were funded by the ARC Centre of Excellence for Enabling Eco-Efficient Beneficiation of Minerals, grant number CE200100009.

REFERENCES

Adachi, Y and Ooi, S, 1990. Geometrical structure of a floc. *Journal of Colloid and Interface Science*, 135(2), pp. 374–384. https://doi.org/10.1016/0021–9797(90)90007-B.

Bache, D H, 2004. Floc rupture and turbulence: a framework for analysis. *Chemical Engineering Science*, 59(12), pp. 2521–2534. https://doi.org/10.1016/j.ces.2004.01.055.

Bićanić, N, 2007. Discrete Element Methods. In: *Encyclopedia of Computational Mechanics*. [online] John Wiley & Sons, Ltd. https://doi.org/10.1002/0470091355.ecm006.pub2.

Brasil, A M, Farias, T L, Carvalho, M G and Koylu, U O, 2001. Numerical characterization of the morphology of aggregated particles. *Journal of Aerosol Science*, 32(4), pp. 489–508. https://doi.org/10.1016/S0021–8502(00)00097–5.

Chen, S and Li, S, 2020. Collision-induced breakage of agglomerates in homogenous isotropic turbulence laden with adhesive particles. *Journal of Fluid Mechanics*, [online] 902. https://doi.org/10.1017/jfm.2020.582.

Chen, S, Li, S and Marshall, J S, 2019. Exponential scaling in early-stage agglomeration of adhesive particles in turbulence. *Physical Review Fluids*, 4(2), p. 024304. https://doi.org/10.1103/PhysRevFluids.4.024304.

Derjaguin, B V, Muller, V M and Toporov, Y P, 1975. Effect of contact deformations on the adhesion of particles. *Journal of Colloid and interface science*, *53*(2), pp. 314–326.

Fernando Concha, A, 2014. *Solid-liquid separation in the mining industry*, pp. 6–7, Springer.

Higashitani, K, Iimura, K and Sanda, H, 2001. Simulation of deformation and breakup of large aggregates in flows of viscous fluids. *Chemical Engineering Science*, 56(9), pp. 2927–2938. https://doi.org/10.1016/S0009–2509(00)00477–2.

Jiang, Q and Logan, B E, 1991. Fractal dimensions of aggregates determined from steady-state size distributions. *Environmental Science & Technology*, 25(12), pp. 2031–2038. https://doi.org/10.1021/es00024a007.

Johnson, K L, Kendall, K, Roberts, A D and Tabor, D, 1971. Surface energy and the contact of elastic solids. *Proceedings of the Royal Society of London. A. Mathematical and Physical Sciences*, 324(1558), pp. 301–313. https://doi.org/10.1098/rspa.1971.0141.

Kobayashi, M, Adachi, Y and Ooi, S, 1999. Breakup of Fractal Flocs in a Turbulent Flow. *Langmuir*, 15(13), pp. 4351–4356. https://doi.org/10.1021/la980763o.

Liu, G-R and Liu, M B, 2003. *Smoothed particle hydrodynamics: a meshfree particle method*. World scientific.

Liu, J, Shih, W Y, Sarikaya, M and Aksay, I A, 1990. Fractal colloidal aggregates with finite interparticle interactions: Energy dependence of the fractal dimension. *Physical Review A*, 41(6), pp. 3206–3213. https://doi.org/10.1103/PhysRevA.41.3206.

Narine, S S and Marangoni, A G, 1999a. Fractal nature of fat crystal networks. *Physical Review E*, 59(2), pp. 1908–1920. https://doi.org/10.1103/PhysRevE.59.1908.

Narine, S S and Marangoni, A G, 1999b. Mechanical and structural model of fractal networks of fat crystals at low deformations. *Physical Review E*, 60(6), pp. 6991–7000. https://doi.org/10.1103/PhysRevE.60.6991.

Rahmat, A, Weston, D, Madden, D, Usher, S, Barigou, M and Alexiadis, A, 2020. Modeling the agglomeration of settling particles in a dewatering process. *Physics of Fluids*, 32(12), p. 123314. https://doi.org/10.1063/5.0029213.

Ruan, X, Chen, S and Li, S, 2020. Structural evolution and breakage of dense agglomerates in shear flow and Taylor-Green vortex. *Chemical Engineering Science*, 211, p. 115261. https://doi.org/10.1016/j.ces.2019.115261.

Scurati, A, Feke, D L and Manas-Zloczower, I, 2005. Analysis of the kinetics of agglomerate erosion in simple shear flows. *Chemical Engineering Science*, 60(23), pp .6564–6573. https://doi.org/10.1016/j.ces.2005.05.059.

Shih, W-H, Shih, W Y, Kim, S-I, Liu, J and Aksay, I A, 1990. Scaling behavior of the elastic properties of colloidal gels. *Physical Review A*, 42(8), pp. 4772–4779. https://doi.org/10.1103/PhysRevA.42.4772.

Usher, S P, Spehar, R and Scales, P J, 2009. Theoretical analysis of aggregate densification: Impact on thickener performance. *Chemical Engineering Journal*, 151(1), pp. 202–208. https://doi.org/10.1016/j.cej.2009.02.027.

van Wachem, B, Thalberg, K, Nguyen, D, Martin de Juan, L, Remmelgas, J and Niklasson-Bjorn, I, 2020. Analysis, modelling and simulation of the fragmentation of agglomerates. *Chemical Engineering Science*, 227, p. 115944. https://doi.org/10.1016/j.ces.2020.115944.

Wengeler, R and Nirschl, H, 2007. Turbulent hydrodynamic stress induced dispersion and fragmentation of nanoscale agglomerates. *Journal of Colloid and Interface Science*, 306(2), pp. 262–273. https://doi.org/10.1016/j.jcis.2006.10.065.

Yao, Y and Capecelatro, J, 2021. Deagglomeration of cohesive particles by turbulence. *Journal of Fluid Mechanics*, [online] 911. https://doi.org/10.1017/jfm.2020.1020.

Influence of pre-aggregation of fines on binder agglomeration

C A Thomas[1,5], P J Scales[2,5], K P Galvin[3,5] and G V Franks[4,5]

1. Research Fellow, Chemical Engineering, The University of Melbourne, Vic 3010. Email: casey.thomas@unimelb.edu.au
2. Professor, Chemical Engineering, The University of Melbourne, Vic 3010. Email: peterjs@unimelb.edu.au
3. Laureate Professor, Chemical Engineering, The University of Newcastle, NSW 2308. Email: kevin.galvin@newcastle.edu.au
4. Professor, Chemical Engineering, The University of Melbourne, Vic 3010. Email: gvfranks@unimelb.edu.au
5. ARC Centre of Excellence for Enabling Eco-Efficient Beneficiation of Minerals.

INTRODUCTION

It is increasingly important to recover fine valuable particles (<20 μm) from ores due to declining ore grades. The applicability of the common recovery technique, froth flotation, is reduced due to size limitations (Fuerstenau *et al*, 2007; Trahar and Warren, 1976). Froth flotation works to exploit the hydrophobicity of the mineral surface, allowing for the valuable material to attach to the rising air bubbles, and be concentrated and recovered in the froth layer. Notably, the particle surface must exhibit sufficient hydrophobicity, as well as collide with the rising air bubble to be transported to the froth, leaving the majority of the aqueous phase and unwanted solid material behind. Fine particles within this size range are difficult to recover with froth flotation, as they have lower probability to collide with a rising air bubble (Crawford and Ralston, 1988; Trahar, 1981). For particles that do have collision with the air bubbles, they have insufficient inertia to penetrate through the air-liquid interface at the bubble surface, due to their small size.

Oil agglomeration has been studied as an additional solution to the issues that arise with fines flotation, whereby the spreading of oil over the particle surface initiates some aggregation of the material into larger structures (Capes and Darcovich, 1984; Mehrotra *et al*, 1983). Specifically, the oleophilicity/hydrophobicity of the material needs to be considered for this method, and major downfall of this method is due to oil costs. In order to address the oil requirements and thus high cost, van Netten *et al* (2017). have formulated a high-internal-phase (HIP) water-in-oil emulsion, which allows for the properties of the oil for agglomeration to be retained but replaced the majority of the bulk with inexpensive aqueous solution. It has been shown to selectively target hydrophobic particles from a mixed suspension of hydrophobic and hydrophilic particles in an aqueous solution (van Netten *et al*, 2017). Through the use of a high-shear environment, and thus turbulent mixing, the HIP emulsion, otherwise known as binder, ensures the rapid adhesion of the hydrophobic material to the small emulsion droplet interfaces. These surfaces thus readily coalesce and allow for the agglomeration of the hydrophobic particles, resulting in a solid-liquid separation from the remainder of the aqueous solution, recovering the valuable material.

Pre-aggregation of particles is also an alternate solution to the recovery of fine mineral particles, as the resultant agglomerates of particles are now in the size range whereby collision probability and inertia is sufficient for attachment to the air bubbles (Miettinen *et al*, 2010). Additionally, the oil agglomeration method is suitable for materials which already exhibit sufficient hydrophobicity for the spreading of the oil on the solid-liquid interface, yet the recovery/removal of some hydrophilic materials may also be required. Thus, the pre-aggregation of the particles can both tune the hydrophobicity of the surface, as well as potentially reduce the required binder dosage for separation due to lower surface area of the aggregates compared to individual particles. This will further reduce the costs owing to the concentration of oil present within the binder. Furthermore, interest into novel reagents for increased recovery of minerals is growing. One example is a temperature responsive polymer for targeted switching of mineral hydrophobicity as a response to environmental conditions (Ng *et al*, 2015). Such polymers, whilst increasing the recovery of the mineral, in comparison to conventional, commercial reagents, also introduce further costs into the process.

The aim of this work is to compare the amount of binder required for aggregated particles to the unaggregated primary particles. It is expected the aggregated particles will require less binder due

to the lower surface area. Both conventional poly acrylamide flocculants and novel temperature responsive flocculants based on poly (N-isopropyl acrylamide) will be investigated.

METHODOLOGY

The binder, a 5 wt per cent oil and 95 wt per cent aqueous emulsion was made with 2.5 wt per cent sorbitan monooleate and 2.5 wt per cent dodecane and the aqueous solution included 3 wt per cent NaCl. This ratio of organic to aqueous phases was found to give the most optimal oil dosages by van Netten *et al* (2017) previously. Both silica and talc particles, with average particle size within the fines range, less than 20 μm, have been observed to determine and compare the efficacy of pre-aggregation studies to the efficiency of the previously studied binder recovery.

Pre-aggregation studies of the particles (60 g) were completed with both cetyltrimethylammonium bromide (CTAB) and poly(N-isopropylacrylamide) (PNIPAM) at various concentrations in a Waring variable speed blender, with 500 mL of water, at 2000 rev/min for 60 seconds. Experiments were completed at room temperature and above the lower critical solution temperature (LCST) of the responsive polymer. Post particle conditioning phase, varying masses of the binder were added to the slurry and the blender speed increased to 22 000 rev/min for 7 seconds, to ensure the delivery of the oil to the agglomerate surfaces. Subsequently, the agglomerates were thoroughly washing and separated from the aqueous phase and any unrecovered particles using a 150 μm screen. This screen was chosen as the aperture size exceeds the top size of the particles studied. The two samples (retained on the screen, and the underflow) were dried in an oven held at 100°C in pre-weighed trays until completely dry. The mass of both sample streams were determined, allowing the recovery to calculated and thus the efficiency of both the binder and pre-aggregation of the particles to be determined.

PRELIMINARY FINDINGS

The agglomeration and recovery of chemically-hydrophobized particles using a previously studied emulsion binder was confirmed and compared to the behaviour of naturally hydrophobic particles. It was corroborated that agglomeration is achievable with the low oil concentrations as required for the process to be cost-efficient for implementation into industry. Additionally, it is expected that introducing the pre-aggregation of the particles prior to binder addition allowed for an increase in particle size, and thus decrease in surface area to volume ratio, further reducing the oil requirements for solid-liquid separation to occur. The influence of temperature, both above and below the LCST of the responsive polymer, were examined and the recovery efficacy was analysed with consideration to both the costs of the oil and novel reagents utilised.

ACKNOWLEDGEMENTS

The authors acknowledge the funding support from the Australian Research Council for the ARC Centre of Excellence for Enabling Eco-Efficient Beneficiation of Minerals, Grant Number CE200100009.

REFERENCES

Capes, C E and Darcovich, K. (1984). A survey of oil agglomeration in wet fine coal processing. *Powder Technology, 40*(1), 43–52. doi:https://doi.org/10.1016/0032–5910(84)85054–8

Crawford, R and Ralston, J J. (1988). The influence of particle size and contact angle in mineral flotation. *International Journal of Mineral Processing, 23*(1–2), 1–24.

Fuerstenau, M C, Jameson, G J and Yoon, R H. (2007). *Froth Flotation: A Century of Innovation*: Society for Mining, Metallurgy, and Exploration.

Mehrotra, V P, Sastry, K V S and Morey, B W. (1983). Review of oil agglomeration techniques for processing of fine coals. *International Journal of Mineral Processing, 11*(3), 175–201. doi:https://doi.org/10.1016/0301–7516(83)90025-X

Miettinen, T, Ralston, J and Fornasiero, D. (2010). The limits of fine particle flotation. *Minerals Engineering, 23*(5), 420–437. doi:https://doi.org/10.1016/j.mineng.2009.12.006

Ng, W S, Sonsie, R, Forbes, E and Franks, G V. (2015). Flocculation/flotation of hematite fines with anionic temperature-responsive polymer acting as a selective flocculant and collector. *Minerals Engineering, 77*, 64–71. doi:https://doi.org/10.1016/j.mineng.2015.02.013

Trahar, W J and Warren, L J. (1976). The flotability of very fine particles – A review. *International Journal of Mineral Processing, 3*(2), 103–131. doi:https://doi.org/10.1016/0301–7516(76)90029–6

Trahar, W J. (1981). A rational interpretation of the role of particle size in flotation. *International Journal of Mineral Processing, 8*(4), 289–327. doi:https://doi.org/10.1016/0301–7516(81)90019–3

van Netten, K, Borrow, D J and Galvin, K P. (2017). Fast Agglomeration of Ultrafine Hydrophobic Particles Using a High-Internal-Phase Emulsion Binder Comprising Permeable Hydrophobic Films. *Industrial & Engineering Chemistry Research, 56*(38), 10658–10666. doi:10.1021/acs.iecr.7b02215

Modelling the performance of high-pressure dewatering rolls

S P Usher[1], S Hassan[2], N I K Ekanayake[3], A D Stickland[4], P J Scales[5] and R J Batterham[6]

1. Research Fellow, ARC Centre of Excellence for Enabling Eco-Efficient Beneficiation of Minerals, Department of Chemical Engineering, The University of Melbourne, Vic 3010. Email: spusher@unimelb.edu.au
2. PhD Candidate, ARC Centre of Excellence for Enabling Eco-Efficient Beneficiation of Minerals, Department of Chemical Engineering, The University of Melbourne, Vic 3010. Email: sajid@student.unimelb.edu.au
3. Research Fellow, ARC Centre of Excellence for Enabling Eco-Efficient Beneficiation of Minerals, Department of Chemical Engineering, The University of Melbourne, Vic 3010. Email: nilanka.ekanayake@unimelb.edu.au
4. Senior Lecturer, ARC Centre of Excellence for Enabling Eco-Efficient Beneficiation of Minerals, Department of Chemical Engineering, The University of Melbourne, Vic 3010. Email: stad@unimelb.edu.au
5. Emeritus Professor, ARC Centre of Excellence for Enabling Eco-Efficient Beneficiation of Minerals, Department of Chemical Engineering, The University of Melbourne, Vic 3010. Email: peterjs@unimelb.edu.au
6. Kernot Professor of Engineering, ARC Centre of Excellence for Enabling Eco-Efficient Beneficiation of Minerals, Department of Chemical Engineering, The University of Melbourne, Vic 3010. Email: r.batterham@unimelb.edu.au

INTRODUCTION

The dewatering of slurries can be a bottleneck in mineral processing operations whether separating process intermediates, final products or mineral tailings. Continuous processes such as gravity thickening, centrifugation, belt filtration, rotary drum and disk filtration are preferred over batch processes for achieving high solids throughputs and water recovery rates. However, these high throughput processes can be limited in the output solids concentration achieved and are not optimum for very fine materials. High-pressure dewatering rolls have the potential to maximise the output solids concentration with high throughput by combining shear, compression and vacuum. A demonstration device has been trialled at The University of Melbourne incorporating two semi-permeable concentric cylinders rotating under vacuum with slurry fed into the gap (Höfgen *et al,* 2019). This presentation outlines the modelling of the continuous rolls system using 1D dewatering theory to predict the influence of varying process parameters on dewatering performance.

THEORY

Modelling of the continuous rolls system is a complex three-dimensional process involving shear and compressional rheology, but can be simplified to a 2D process as shown in the diagram in Figure 1. Ignoring the shear flows, the filter cake thickness can be described in 1D as a function of roller angle, which is proportional to the cake formation time. Thus, the system can be modelled using 1D dewatering theory. The material properties used to describe the dewatering, as described by Landman and White (1994), are the compressive yield stress, $P_y(\phi)$ which quantifies the solids volume fraction, ϕ, to which a material can be compressed for an applied compressive stress and the hindered settling function, $R(\phi)$, which quantifies the resistance to the flow of fluid through the solids network structure. The hindered settling function is inversely related to permeability. In filtration systems where gravity is not significant, $P_y(\phi)$ and $R(\phi)$ can be combined into a single term known as the solids diffusivity, $D(\phi)$. Modelling 1D filtration theory reduces the flux-diffusion equation that describes the system to a simpler diffusion equation, albeit with a moving boundary condition. Stickland *et al* (2006) developed a numerical algorithm to solve this equation for standard filtration systems, but can be adapted to high-pressure dewatering rolls as well.

Filtration on the high-pressure dewatering rolls involves filter cake formation under constant pressure vacuum as the cylinders rotate, followed by cake compression once the filter cakes meet. The dewatering in a high-pressure dewatering roller system can be divided into two stages as illustrated in Figure 1.

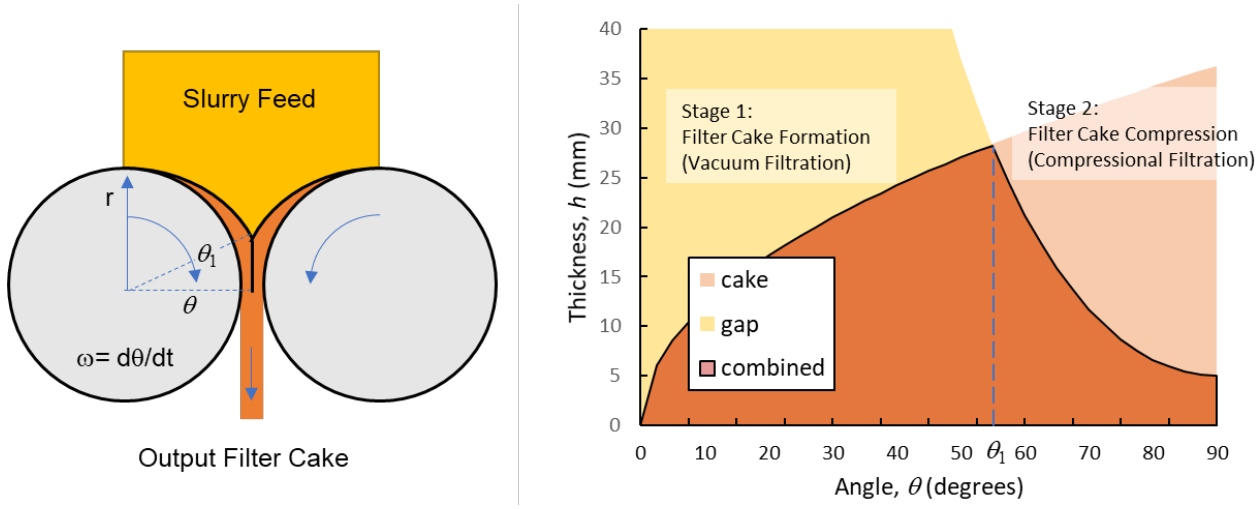

FIG 1 – Simplification of cylindrical dewatering rolls to one-dimensional geometry.

Stage 1 – Filter cake formation

The first part involves constant pressure vacuum filtration of the slurry at the initial solids concentration as the rollers rotate inwards under vacuum. The operation is similar to rotary vacuum filtration (Usher, 2002; Stickland *et al,* 2011). Assuming negligible membrane resistance, the average solids concentration of the filter cake is expected to be constant, in accordance with Darcy's law and as demonstrated through a similarity solution by Landman and White (1997).

Stage 2 – Filter cake compression

The second stage begins when the filter cakes converge and transmit additional stress (both compressive and shear). If all of the stress contributes to compression with effectively no shear, the effective filtration pressure is increased and the maximum possible dewatering is determined through a simple material balance dictated by the roller gap as a function of rotation angle with maximum compression at 90 degrees where the rollers converge to a minimum gap. Alternatively, there might be virtually no more dewatering if the less consolidated portions are fully displaced through shear as the filter cakes converge. The real answer is in between these limits, where operational data can enable insights into how dewatering potential can be maximised.

PROCESS MODELLING

The impact of varying process parameters on dewatering performance has been modelled to predict the influence of cylinder rotation speed, feed solids concentration, vacuum pressure and the mechanically applied compressive stress between the cylinders. The modelling predicts the trade-off between rotation speed, solids throughput, water recovery rates and output solids concentration. Figure 2 provides a demonstrative modelling output example, where during Stage 1 – filter cake formation, the average filter cake solids concentration is constant and then during stage 2 – filter cake compression, the average filter cake solids concentration can increase significantly during as the rollers converge.

The predictions are compared with trial data, not just to validate the modelling, but also to identify operational regimes that enable enhanced dewatering relative to predictions through combined shear and compression in the nip between the two cylinders.

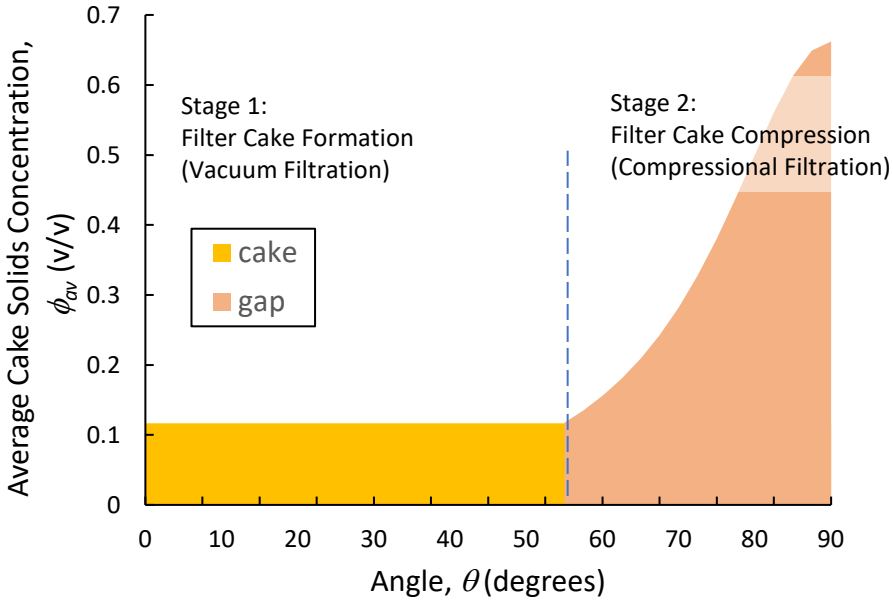

FIG 2 – High-pressure dewatering rolls performance modelling.

CONCLUSIONS

The dewatering of slurries can be a bottleneck in mineral processing operations, but process modelling indicates that high-pressure dewatering rolls can potentially enhance the extent of dewatering while maintaining throughput in a continuous process. The development of a model that can predict performance based on fundamental material properties of compressibility and permeability enables the identification of optimal process conditions and equipment sizing for full-scale application.

ACKNOWLEDGEMENTS

Support from the Australian Research Council for the ARC Centre of Excellence for Enabling Eco-Efficient Beneficiation of Minerals, grant number CE200100009 is gratefully acknowledged. S Hassan is supported by a Research Training Program Scholarship through The University of Melbourne. Declaration of Interests: The authors report no conflict of interest.

REFERENCES

Höfgen, E, Collini, D, Batterham, R J, Scales, P J and Stickland, A D, 2019. High pressure dewatering rolls: Comparison of a novel prototype to existing industrial technology. *Chemical Engineering Science,* 205: 106–120.

Landman, K A and White, L R, 1994. Solid/liquid separation of flocculated suspensions. *Advances in Colloid and Interface Science,* 51: 175–246.

Landman, K A and White, L R, 1997. Predicting filtration time and maximizing throughput in a pressure filter. *AIChE J.* 43(12): 3147–3160.

Stickland, A D, de Kretser, R G, Scales, P J, Usher, S P, Hillis, P and Tillotson, M R, 2006. Numerical modelling of fixed-cavity plate-and-frame filtration: Formulation, validation and optimisation. *Chem. Eng. Sci,* 61: 3818–3829.

Stickland, A D, White, L R and Scales, P J, 2011. Models of rotary vacuum drum and disc filters for flocculated suspensions. *AIChE J.* 57 (4): 951–961.

Usher, S P, 2002. Suspension dewatering: Characterisation and optimisation. *Department of Chemical Engineering*, The University of Melbourne: 347.

Evaluation of filter cake by microcomputed tomography

F Zhang[1], G Bournival[1], H L Ramandi[1] and S Ata[2]

1. School of Minerals and Energy Resources Engineering, University of New South Wales, Sydney NSW 2052.
2. School of Minerals and Energy Resources Engineering, University of New South Wales, Sydney NSW 2052. Email: s.ata@unsw.edu.au

ABSTRACT

Many coal processing plants have adopted water recycling schemes in the process of coal beneficiation. Water recycling reduces the costs and environmental impacts, however, the soluble mineral salts in the coal, associated minerals, and the source of the water pose a new problem of increased salinity in the process water. Although the effects of inorganic electrolytes on coal flotation, settling, and product quality have been discussed in previous studies, the interactions between process water chemistry and the flocculants are not well understood. The present work investigates the coal product filter cake characteristics by using micro-computed tomography (μCT). Experiments were carried out by using a coal flotation product and a customised vacuum filtration set-up. The samples were conditioned by varying some key parameters, including inorganic salt concentration, and flocculant dosage, and filtered under a constant 40 kPa vacuum. The filter cakes obtained from the vacuum filtration were scanned by μCT and the reconstructed 3D image of the cakes was analysed. The 2-phase and 3-phase image segmentation techniques were applied, and the porosity results suggested that filter cake formed from lower salinity slurry consists of a significant amount of subresolution pores, especially at the top-and the mid-section. Meanwhile, the proportion of the subresolution pores of the filter cake was found to significantly decrease when salt concentration was increased. Some correlations between μCT results and filtration results were established and a possible salt – flocculant – coal interaction was proposed.

INTRODUCTION

Vacuum filtration is a commonly adopted practice in many coal processing plants for dewatering coal products (Osborne, 2013). During filtration, the particles deposit on a filter medium, usually a filter cloth, and form a porous filter cake. The moisture entrained in the product from the previous beneficiation process is then removed through the connected pores within the filter cake. The product moisture is strictly controlled for the operations in power stations and blast furnaces, and it is also a major parameter in product price determination. An increased product moisture was found to be closely related to a decrease in the net calorific value (Mao *et al*, 2020) and an increase in ash (Parekh, 2009). Furthermore, the saltwater retained in the product, which is commonly seen in many processing plants (Bournival *et al*, 2021; Wang *et al*, 2014), has been found to affect the coking properties of metallurgical coals (Zhang *et al*, 2019a). Such negative impacts can cause a significant reduction in the product price. For example, a 1 per cent increase in moisture in 3 Mt coal products is estimated to cause a loss of up to US$300 000 (Tao *et al*, 2000a).

It has been well established that the structure of the cake can be a critical factor in the filtration kinetics and filter cake properties, and it is largely affected by the slurry materials that form the cake. For example, the structure of a filter cake is strongly dependent on the size of the particles (Zhuo *et al*, 2020) with a decrease in particle size causing an increase in pore shape irregularity and tortuosity whilst the permeability and the porosity of the cake decrease. Other studies suggested that the particle size distribution of the solids is directly related to the specific cake resistance (Ofori *et al*, 2012; Thapa *et al*, 2009). Cakes that consist of a large fraction of fine particles were found to have increased specific cake resistance, and the increase in specific cake resistance can subsequentially cause a decrease in filtration rate and final cake moisture (Kakwani *et al*, 1985; Gong *et al*, 2013). Chemical modifications have been applied to the filtration process to alter the particle size distribution by adding reagents such as flocculants. Previous studies have shown that the use of flocculants can improve the moisture removal in fine coal filtration (Singh, 1997; Sung and Turian, 1994; Tao *et al*, 2000a; Eraydin, 2009). The enhancement in moisture removal was attributed to the increased pore radius due to the aggregation of particles and formation of the bigger sized flocs (Sung and Turian, 1994; Patwardhan *et al*, 2006; Tao *et al*, 2003), hence the specific cake resistance is reduced (Ofori

et al, 2012; Thapa *et al*, 2009; Hogg, 2000; Alam *et al*, 2011; Besra *et al*, 1998). The pore size distribution is also closely related to the particle size. The pore size distribution of a filter cakes formed from slurries that contains finer particles was found to be smaller in general in comparison with the pore size in filter cakes formed with coarser particles (Khazaie *et al*, 2022). Similarly, the use of aggregating reagents, such as flocculant and coagulant, was found to result in bigger pores in filter cakes (Hu *et al*, 2020; Tao *et al*, 1999). Dissolved inorganic salts in the process water were also found to have an aggregating effect on coal particles (Bournival *et al*, 2021; Wang *et al*, 2014, Wang and Peng, 2014). The inorganic electrolytes in the process water can cause compression of the electrical double layers around coal particles, enhancing the particle – particle attractions and thus forming aggregates with larger sizes and a faster settling rate (Li *et al*, 2021; Zhang *et al*, 2019b). Although not much work has been done regarding the effect of salts on filter cake structure and filtration kinetics, it is reasonable to assume that the effect would be somewhat similar to that of flocculants and coagulants. It is also one of the research interests of the present study, in which process water salinity was considered to be an impactful factor of filtration kinetics and filter cake structure.

The techniques used for investigating the filter cake structure have advanced drastically in recent years. Most of the filtration studies (Pham, 2021; Li *et al*, 2021) have employed Darcy's law (Darcy, 1856) and the Carman–Kozeny Equations (Kozeny, 1927; Carman, 1937) (Equations 1–3) for filter cake property analysis.

$$\frac{t}{V} = \frac{\alpha \mu c}{2A^2 \Delta P} V + \frac{R\mu}{A\Delta P} \tag{1}$$

$$K = \frac{Q\mu L}{A\Delta P} \tag{2}$$

$$S^2 = \frac{\varepsilon^2}{K_0 K(1-\varepsilon)} \tag{3}$$

The filtration curves, usually plotted as filtrate volume versus time, are first fitted into Equation (1), the gradients and the intercept of Equation (1) are then used for calculating the specific cake resistance, α, and the medium resistance, R. The permeability of the cake, K, is a function of the flow rate, Q, and the specific surface area of the cake, S, is a function of the permeability The other parameters such as the fluid viscosity, μ, solid concentration, c, cross-sectional area of the cake, A, pressure drop across the cake, ΔP, and the porosity, ε, are measured during experiments, and a value of 5 is used for fixed bed for the Kozeny constant, K_0. Many significant parameters, such as the specific cake resistance, specific cake surface area, cake permeability, and medium resistance, are calculated from these equations and served as the theoretical basis for many studies (Li *et al*, 2021; Feng *et al*, 2020; Fan *et al*, 2015). However, despite the significance of these studies, the understanding of the filter cake structure and its impactful factors are still limited. The cake-forming dynamics were only observable by using optical techniques incorporated with image processing techniques. Furthermore, investigations of the cake structure build-up at different stages of filtration were almost impossible because of the difficulty in analysing the cake sample mid-filtration and post-filtration. Fortunately, advances in technology enabled researchers to use modern techniques, such as micro-computed tomography (*μ*CT) (Feng *et al*, 2020), scanning electron microscopy (SEM) (Chang-Sheng *et al*, 2006), and nuclear magnetic resonance (NMR) (Hu *et al*, 2020), which provides more insights on the structure of the cake. Out of these techniques, the use of *μ*CT in filter cake studies have been widely acknowledged due to its nondestructive nature and relatively high accuracy. The *μ*CT technique was originally established for medical uses. It utilises the attenuation of X-ray radiations of sample materials. The differences in the attenuation coefficient from different sample materials are recorded and processed to generate 2D images of the sample object. These 2D images are then stacked and thus a 3D image of the sample object is reconstructed. While *μ*CT was exclusively used for examinations of human body parts like bones and organs, it was later found to be applicable to coal (Kemp, 1929). Several studies (Mathews *et al*, 2017; Yao *et al*, 2009; Wang *et al*, 2019) have demonstrated the advantages of using of *μ*CT imaging technique for coal investigations with some specifically focused on coal filter cakes (Hu *et al*, 2020; Feng *et al*, 2020).

In *μ*CT imaging, high-resolution images are always preferable as they provide less error. From the images, direct flow simulations and feature analysis can be accurately achieved (Blunt *et al*, 2013; Shah *et al*, 2016; Da Wang *et al*, 2021). However, high-resolution *μ*CT images, even though

achievable with currently available technology, are usually downsampled to suit the computational resources available to most users for processing and modelling. Nonetheless, the segmentation of low-resolution images can cause a significant error due to the uncertainty near pore-grain boundaries (Saxena *et al*, 2017). The recognition of pores in *μ*CT imaging is dependent on the image resolution and the type of material examined (Baveye *et al*, 2017). Sollins and Radulovich (1988) reported that the porosity in their tropical soil samples was mostly made of pores with diameters less than 5 μm, making the pore characterisation much more complex and bringing inaccuracy in porosity estimation. Churchman and Payne (1983) reported that a *μ*CT image with a resolution of 10 μm is too large for recognising the pores in clayey and clay-loam soils. However, there are usually voxels with intermediate intensity gradients that is neither below the void intensity gradient nor above the solid intensity gradient. The intermediate intensity gradients suggest that the voxels contain partially void features, which requires further processing of the voxel, to create a partial volume of the voxel based on the intensity gradient of the voxel (Ramandi *et al*, 2016; Sheppard *et al*, 2004; Schlüter *et al*, 2014). It has been proposed that the pores in *μ*CT images can be categorised as resolved pores and subresolution pores (Soulaine *et al*, 2016). To incorporate the subresolution pore phase, the attribution of porosity to a subresolution pore utilises Equations 4–6 (Lin *et al*, 2016). The total porosity, $\emptyset_{total}$, is calculated by combining the subresolution porosity, $\emptyset_{sub}$, and the resolved porosity, $\emptyset_{resolved}$. The subresolution porosity is calculated by multiplying the number of voxels counted as the sub – resolution phase, V_{sub}, by the subresolution porosity value, $\widetilde{\emptyset}_{sub}$, which is determined based on the grey intensity gradient during image segmentation, the value is always less than 1. The resolved porosity, $\emptyset_{resolved}$, is calculated by multiplying the number of voxels in the resolved pore phase, $V_{resolved}$, by the resolved porosity value, $\widetilde{\emptyset}_{resolved}$, which equals to 1.

$$\emptyset_{total} = \emptyset_{sub} + \emptyset_{resolved} \tag{4}$$

$$\emptyset_{sub} = \widetilde{\emptyset}_{sub} V_{sub} \tag{5}$$

$$\emptyset_{resolved} = \widetilde{\emptyset}_{resolved} V_{resolved} \tag{6}$$

The evolution of the image segmentation technique, from 2-phase (pore phase and solid phase) to 3-phase (resolved pore phase, subresolution pore phase, and solid phase) has enabled the faster and more accurate processing of lower resolution *μ*CT images. Further development has also included the fourth phase by separating the solid phase into the coal phase and minerals phase, but it is not the research interest of the present work.

The present work investigates the effect of slurry salinity on filter cake structure by using the *μ*CT imaging technique. Some preliminary filtration experiments were conducted, and the filter cake structures were evaluated with *μ*CT imaging. The scanned images were segmented by using 2-phase and 3-phase segmentation techniques for result comparison. The segmented images were reconstructed into 3D images and analysed for structural changes of the filter cake. The aim of the present work is to establish relationships between process water quality, filtration kinetics, and filter cake structure by correlating the filtration results and the *μ*CT imaging results. The novel approach adopted in this study is expected to lay the foundation for future works using the *μ*CT technique in filtration investigations.

MATERIALS AND METHODOLOGY

Sample characterisation

All samples used in the present study were received from an Australian coal processing plant. The sample used in the present work was a flotation product collected from a site treating a high-rank metallurgical coal. The particle size distribution (PSD) and ash analysis of the sample are shown in Table 1.

TABLE 1

Coal sample particle size distribution and ash analysis.

Size class (μm)	PSD (%)	Ash (%)
-20	26.1	8.75
+ 20 -45	15.2	5.76
+ 45 -63	8.5	5.74
+ 63 -125	20.9	4.53
+ 125 -250	18.9	3.43
+ 250 -300	1.9	4.29
+ 300 -500	2.0	4.87

The present study employs NaCl to control the salinity of the slurry and an anionic flocculant, SNF FloPAM AN923SH, which is currently being used in the specific coal processing plant where the sample came from. The slurry pH was controlled by adding pH modifiers, $NaHCO_3$ and H_2SO_4 for acidity and alkalinity, respectively. A 200 g slurry was prepared (5 per cent solid concentration), and the salt concentration and the slurry pH were adjusted to the desired level prior to each filtration test.

Filtration experiments

Filtration experiments were carried out using a customised filtration unit as shown in Figure 1. A Büchner funnel with a perforated filter disc was used and the filtrate was collected into a filter flask. The filtrate mass was constantly monitored by a loadcell under the flask, and the real-time filtrate mass data was recorded on a computer at 1 Hz. The slurry salinity was changed by adding a NaCl solution to the slurry. A low flocculant dosage was used for the comparison of structural differences using high and low salt concentrations. The experimental conditions are shown in Table 2. The filtration was driven by a constant vacuum pressure of 40 kPa.

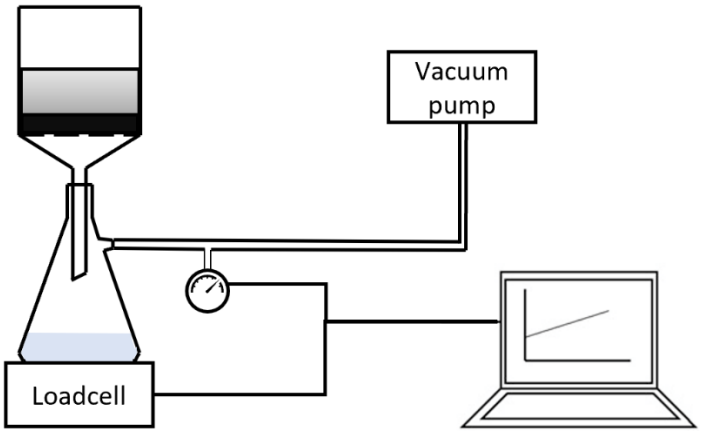

FIG 1 – Illustration of filtration set-up.

TABLE 2

Filtration conditions for μCT imaging.

Sample	pH	Salt (M)	Flocculant (g/t)
a	8.5	0.002	0
b	8.5	0.002	50
c	8.5	0.2	50

*μ*CT scanning and image analysis

The filter cake samples were collected using a 10 mm ID transparent Perspex tube placed on the filter paper before the slurry was poured into the funnel. The tube and the filter paper underneath were removed and formed the sample for scanning. The filter cake samples were scanned using a HeliScan MicroCT scanner where the X-ray source voltage was set to 60 keV. The samples prepared were 10 × 10 mm^2 in the cross-sectional area and cake thickness ranged from 6.38 mm to 7.23 mm. The scanned data was then reconstructed as 2D image slices first and stacked as 3D images. Three regions of interest (ROI) on the 3D images were selected across the cake height (top, middle, and bottom sections) from each filter cake sample image. The dimension of each ROI was set to 278 × 278 × 278 voxels (2 × 2 × 2 mm^3) with each voxel having a physical size of 7.23 × 7.23 × 7.23 μm^3. The raw images were smoothed by applying filters in the image processing software. First, an anisotropic diffusion filter was applied to improve phase separation and denoising, then the unsharp mask filter was applied to enhance image contrast. The pore structure contained the resolved pore phase and subresolution pore phase. The segmentation of these phases was conducted by using the Mango image processing software. An example of the 2-phase segmentation and 3-phase segmentation is shown in Figure 2. The segmented images were then visualised in 3D and the cake porosity was analysed by using Thermo Fisher Scientific's Avizo software.

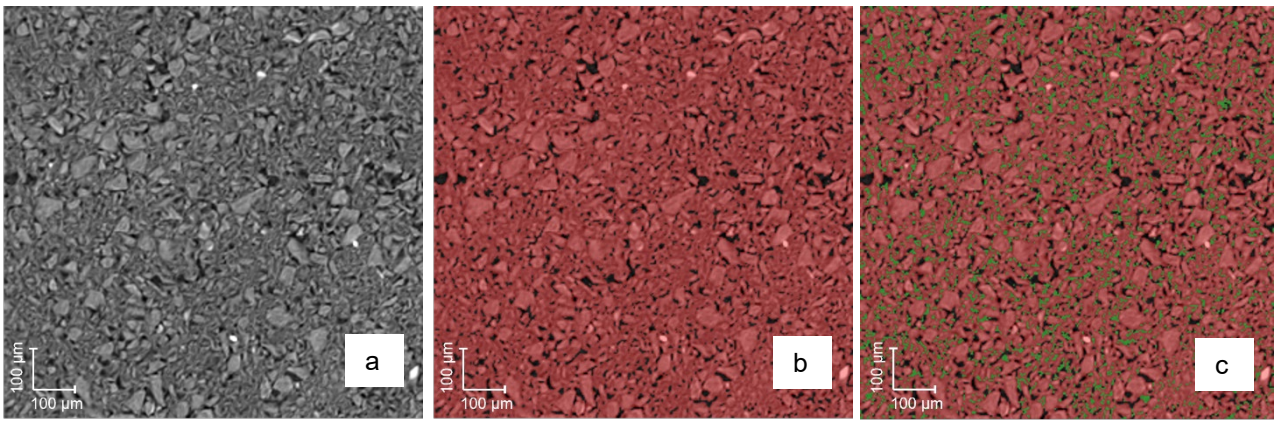

FIG 2 – Sample images of (a) smoothened original grey scale image, (b) 2-phase segmented image, and (c) 3-phase segmented image. The black colour represents the pore phase in (b) and resolved pore phase in (c); the red colour represents the solid phase in (b), and the green colour represents the subresolved pore phase in (c).

RESULTS AND DISCUSSION

Image segmentation: 2-phase versus 3-phase

The 3-phase segmentation technique requires the user to set two intensity thresholds, the 'void/solid threshold' and the 'subresolution void/solid threshold'. It is essentially a two-step segmentation technique that first separates the 'confirmed void' from the image, which is labelled as 'resolved pores'; then the remainder of the unlabelled image goes through an additional segmentation to separate the 'confirmed solid' from the image. The remaining unlabelled image is lastly labelled as the 'subresolution pores'. With the 2-phase segmentation, because only one intensity thresholds were involved to separate the solid and void phases, the segmentation either include or exclude the voxels with intermediate intensities, resulting in either under- or over-counting of the pore volume.

A comparison of porosity results from the 2-phase segmentation and the 3-phase segmentation at the mid-section from each sample can be found in Table 3. There is a significant difference in porosity results between the 2-phase and 3-phase segmentations. It appears that when there are more subresolution voids in the image, the porosity analysis from the 2-phase segmentation images showed a greater divergence from that of a 3-phase segmented image. On the other hand, the 2-phase segmentation showed similar results as the 3-phase segmented image when the image contains more resolved pores. The reason to the overestimation of the porosity with the 2-phase segmentation is because the voxels with intermediate intensities were considered as 'resolved'

pores. Therefore, the pore volume that was attributed to these voxels were completely ‘void’ and the porosity analysis showed an overestimation of the porosity. On the other hand, the 3-phase segmentation was able to provide more accurate results because the volume was considered partially ‘void’, the proportion of the void volume was attributed by the algorithm introduced in the previous section.

TABLE 3

Porosity comparison of images obtained from 3-phase segmentation and 2-phase segmentation (data analysed from mid-section ROIs of each sample).

	3-phase porosity (%)			2-phase porosity (%) (Including intermediate intensities)
	Resolved	Sub – resolution	Total	
a	8.11	6.80	14.91	18.52
b	7.95	8.19	16.14	19.48
c	17.70	2.01	19.71	20.69

Similarly, if the 2-phase segmentation was configured to avoid the selection of the voxels with intermediate intensities, the porosity will result in underestimation of the porosity, because only the resolved pores will be attributed to a void volume. Therefore, for the sake of result accuracy and consistency, the 3-phase segmentation was adopted for image segmentation for all result analysis in the later sections in this paper.

Structural changes across cake height

The μCT image analysis shows that the porosity generally increases from the top to the bottom of the filter cake sample. The porosity of both the resolved and the subresolution pore phases was analysed. A sample image of the selected ROIs from each filter cake sample and the distribution of pores across the cake height are presented in Figure 3. Both the subresolution porosity and the resolved porosity were affected by the slurry salt concentration and the flocculant dosage. When slurry salinity was low (0.002 M NaCl, samples a and b), increasing the flocculant dosage to 50 g/t mostly increased the subresolution porosity at the top of the cake. While the porosity in mid-cake section remained unaffected by the addition of flocculant, the bottom section of the cake contains less subresolution pores when flocculant dosage was increased.

By comparing the resolved and subresolution porosities of samples b and c in Figure 3, it was found that increasing the slurry salinity did not significantly affect the total porosity of the cake on any selected section. However, the proportion of the resolved porosity significantly increased. It is evident that the porosities of sample b at the top – and the mid – sections were mainly contributed by the increase in the subresolution porosity, while the porosities of the selected sections on sample c were mainly resolved porosity. The results suggest that when the slurry salinity was increased, there was more larger pores but less fine pores. The image analysis results correlate well with the observations during filtration, where increasing the slurry salinity and reduced the filtration time. The reduced filtration time indicates that the filter cake has less specific resistance that allowed easier liquid flows.

	ROI image	Porosity distribution
a	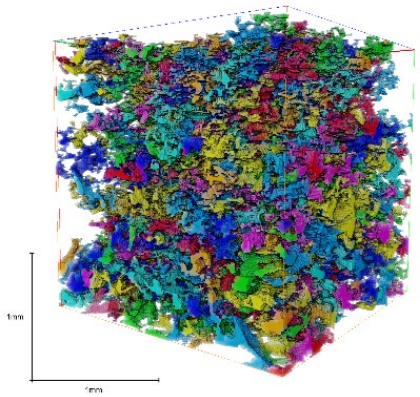	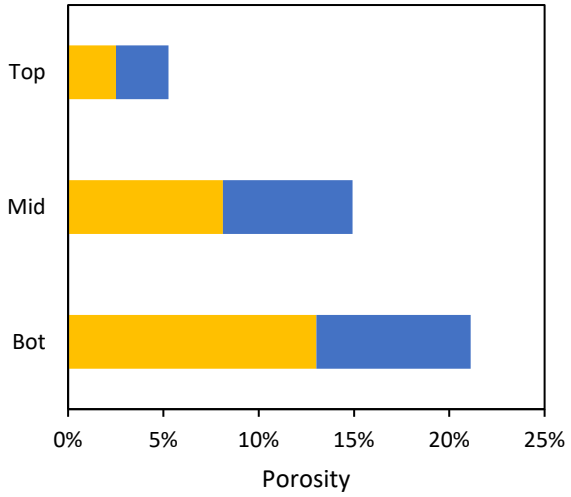
b	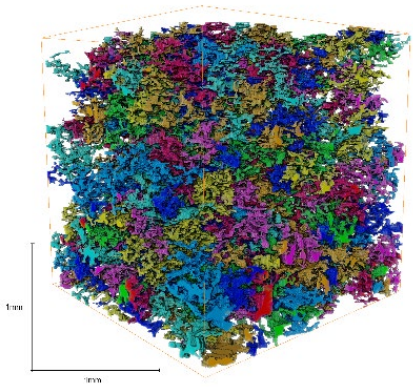	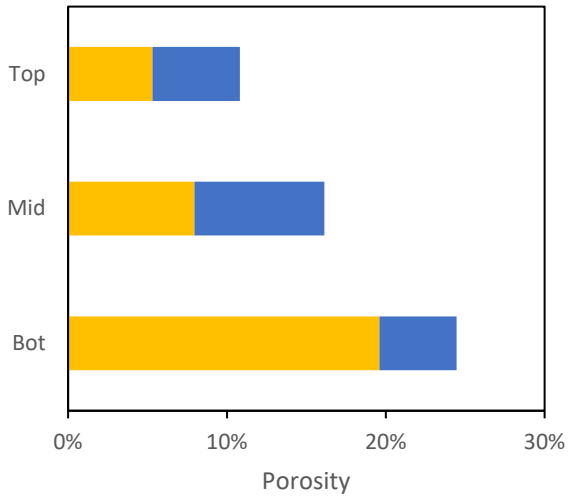
c	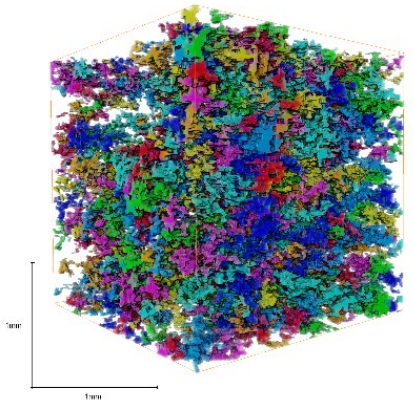	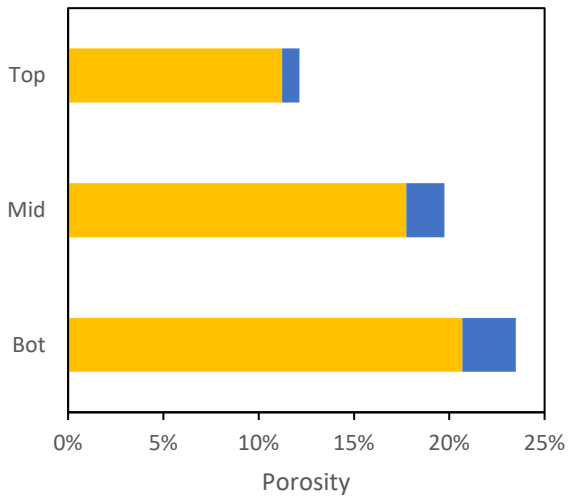

FIG 3 – Sample image of ROIs and the resolved porosity (yellow) and subresolved porosity (blue) at different cake height (image scale: 1 mm).

The filtration results were analysed using Equations 1–3 to calculate the specific cake resistance and the permeability while the moisture of each cake sample was calculated after drying. The results shown in Figure 4 suggest that increasing either the flocculant dosage or the slurry salinity can reduce the specific cake resistance, improving the cake permeability, and subsequently reducing the cake moisture. The filtration results seem to correlate well with the *μ*CT results, where the larger resolved pores might play a more dominant role on the filtration kinetics. It might be possible that the increase in flocculant dosage might cause more and larger sized flocs to form. These flocs settle faster at the bottom of the funnel at the beginning of filtration, creating a more porous and permeable bottom layer, hence allowing better filtration performance. The increased porosity contributed to the increases in the widths of the water channels, also known as capillary radius (Parekh, 2009). Such increase was previously found to be beneficial to allow easier displacement of liquid through void spaces (Tao *et al*, 2000b). Thus, because of the increased capillary radius, an increased permeability and a decreased cake moisture were observed. In general, the filtration rate decreases over filtration time, which is due to the build-up of specific cake resistance as the cake thickness increases (Wakeman and Tarleton, 2005; Tien *et al*, 1997; Iritani, 2013). During the cake build-up process, the particles deposit in the existing pores as they travel along the liquid stream. Eventually, some pores and channels are partly or completely filled, resulting in dead-end pores, smaller pores, and poorer pore connectivity (Ho and Zydney, 2000). However, under the effect of flocculation, it is likely that pores are too small such that flocs do not fill them, subsequently they are left open and available for liquid to travel through. In addition, it has been studied elsewhere (Bournival and Ata, 2021; Wang and Peng, 2014) that the salt in process water can result in compression of electrical double layers around coal particles, hence enhancing the agglomeration of particles. Such an effect was found to be enhancing the froth flotation yield, as well as accelerating the settling process (Wang *et al*, 2014; Zhang *et al*, 2019b). It might be possible that the agglomerated particles settle in a similar manner to flocs, hence allowing a faster filtration rate and less fine pores. Nonetheless, although the mechanism proposed here seems possible, confirmative work needs to be carried out in the future to gain more insights.

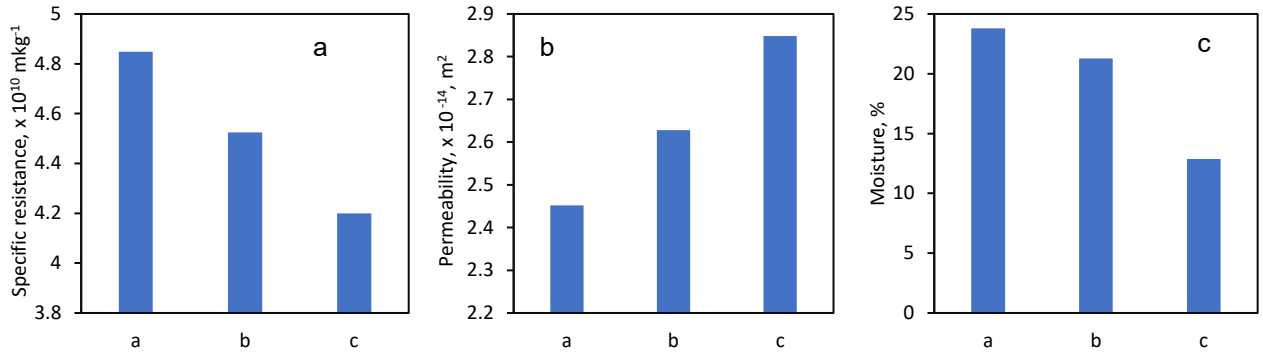

FIG 4 – Comparison of (a) specific cake resistance and (b) permeability (c) moisture of the filter cake samples.

CONCLUSIONS

The effects of slurry salinity and flocculation on filter cake structure has been investigated by using the *μ*CT technique. The slurry conditions were found to affect the deposition of particles/flocs as the cake is building up. As a result, the structure of the filter cake was changed and so was the filtration kinetics. The comparison of the 2-phase and 3-phase segmentation techniques suggested that for the lower resolution images, the 3-phase segmentation provides higher accuracy and more details of the cake porosity. The filtration results correlated well with the porosity results from *μ*CT imaging. Both slurry salinity and flocculation were found to have positive impacts on the filtration performance, improving the permeability of the cake. Furthermore, the image analysis suggested that the improvement might be contributed mainly by the increases in the larger sized resolved pores, and the effects of the subresolution pores on the filtration kinetics might not be as significant. Although the work presented here is still preliminary and focuses on limited number of factors, the present work shows the applicability of the *μ*CT technique in coal filtration studies and the advanced information it can provide.

ACKNOWLEDGEMENTS

The authors would like to thank the Australian Coal Association Research Program (ACARP) for supporting this project and providing the industrial samples for experiments.

REFERENCES

Alam, N, Ozdemir, O, Hampton, M A and Nguyen, A V, 2011. Dewatering of coal plant tailings: Flocculation followed by filtration. *Fuel,* 90, 26–35.

Baveye, P C, Pot, V and Garnier, P, 2017. Accounting for sub-resolution pores in models of water and solute transport in soils based on computed tomography images: are we there yet? *Journal of hydrology,* 555, 253–256.

Besra, L, Singh, B, Reddy, P and Sengupta, D, 1998. Influence of surfactants on filter cake parameters during vacuum filtration of flocculated iron ore sludge. *Powder technology,* 96, 240–247.

Blunt, M J, Bijeljic, B, Dong, H, Gharbi, O, Iglauer, S, Mostaghimi, P, Paluszny, A and Pentland, C, 2013. Pore-scale imaging and modelling. *Advances in Water resources,* 51, 197–216.

Bournival, G and Ata, S, 2021. The impact of water salinity and its interaction with flotation reagents on the quality of coal flotation products. *Journal of Cleaner Production*, 129519.

Bournival, G, Zhang, F and Ata, S, 2021. Coal Flotation in Saline Water: Effects of Electrolytes on Interfaces and Industrial Practice. *Mineral Processing and Extractive Metallurgy Review,* 42, 53–73.

Carman, P C, 1937. Fluid flow through granular beds. *Trans. Inst. Chem. Eng,* 15, 150–166.

Chang-Sheng, S, Guang-Yuan, X and Yue-Qiu, Z, 2006. Study of the inner structure of fine coal filter cake. *Journal of China University of Mining and Technology (English Edition),* 1.

Churchman, G and Payne, D, 1983. Mercury intrusion porosimetry of some New Zealand soils in relation to clay mineralogy and texture. *Journal of soil science,* 34, 437–451.

Da Wang, Y, Blunt, M J, Armstrong, R T and Mostaghimi, P, 2021. Deep learning in pore scale imaging and modeling. *Earth-Science Reviews,* 215, 103555.

Darcy, H, 1856. *Les fontaines publiques de la ville de Dijon: exposition et application*, Victor Dalmont.

Eraydin, M K, 2009. *Scale-up of using novel dewatering aids.* Virginia Tech.

Fan, Y, Dong, X and Li, H, 2015. Dewatering effect of fine coal slurry and filter cake structure based on particle characteristics. *Vacuum,* 114, 54–57.

Feng, Z, Dong, X, Fan, Y, Li, H, Dong, Y, Ma, X and Chen, R, 2020. Use of X-ray microtomography to quantitatively characterize the pore structure of three-dimensional filter cakes. *Minerals Engineering,* 152, 106275.

Gong, G-Q, Zhang, Y-J and Xie, G-Y, 2013. Study of the compacting process model of fine clean coal dewatering by filter pressing. *Journal of China University of Mining and Technology*, 06.

Ho, C-C and Zydney, A L, 2000. A combined pore blockage and cake filtration model for protein fouling during microfiltration. *Journal of colloid and interface science,* 232, 389–399.

Hogg, R, 2000. Flocculation and dewatering. *International Journal of Mineral Processing,* 58, 223–236.

Hu, P, Liang, L, Xie, G, Zhou, S and Peng, Y, 2020. Effect of slurry conditioning on flocculant-aided filtration of coal tailings studied by low-field nuclear magnetic resonance and X-ray micro-tomography. *International Journal of Mining Science and Technology,* 30, 859–864.

Iritani, E, 2013. A Review on Modeling of Pore-Blocking Behaviors of Membranes During Pressurized Membrane Filtration. *Drying technology,* 31, 146–162.

Kakwani, R M, Gala, H B, Chiang, S H, Klinzing, G E and Tierney, J W, 1985. Dewatering of fine coal — micrographic analysis of filter cake structure. *Powder Technology,* 41, 239–250.

Kemp, C N, 1929. XIV.—The X-Ray Examination of Coal Sections.(Preliminary Note.). *Proceedings of the Royal Society of Edinburgh,* 48, 167–179.

Khazaie, A, Mazarji, M, Samali, B, Osborne, D, Minkina, T, Sushkova, S, Mandzhieva, S and Soldatov, A, 2022. A Review on Coagulation/Flocculation in Dewatering of Coal Slurry. *Water,* 14, 918.

Kozeny, J, 1927. Uber kapillare leitung der wasser in boden. *Royal Academy of Science, Vienna, Proc. Class I,* 136, 271–306.

Li, Y, Chen, Y, Xia, W and Xie, G, 2021. Filtration of kaolinite and coal mixture suspension: Settling behavior and filter cake structure analysis. *Powder Technology,* 381, 122–128.

Lin, Q, Al-Khulaifi, Y, Blunt, M J and Bijeljic, B, 2016. Quantification of sub-resolution porosity in carbonate rocks by applying high-salinity contrast brine using X-ray microtomography differential imaging. *Advances in Water Resources,* 96, 306–322.

Mao, Y, Xia, W, Xie, G and Peng, Y, 2020. Rapid detection of the total moisture content of coal fine by low-field nuclear magnetic resonance. *Measurement,* 155, 107564.

Mathews, J P, Campbell, Q P, Xu, H and Halleck, P, 2017. A review of the application of X-ray computed tomography to the study of coal. *Fuel,* 209, 10–24.

Ofori, P, Nguyen, A V, Firth, B, Mcnally, C and Hampton, M A, 2012. The role of surface interaction forces and mixing in enhanced dewatering of coal preparation tailings. *Fuel,* 97, 262–268.

Osborne, D, 2013. *The Coal Handbook: Towards Cleaner Production: Volume 2: Coal Utilisation*, Elsevier.

Parekh, B, 2009. Dewatering of fine coal and refuse slurries-problems and possibilities. *Procedia Earth and Planetary Science,* 1, 621–626.

Patwardhan, A, Chugh, Y, Arnold, B and Terblanche, A, 2006. Dewatering ultrafine clean coal in a TH filter press. *Coal Preparation,* 26, 33–54.

Pham, T H, 2021. *Experimental investigation on crack formation in filter cakes with wide particle size distribution.* PhD, Technische Universität Bergakademie Freiberg.

Ramandi, H L, Mostaghimi, P, Armstrong, R T, Saadatfar, M and Pinczewski, W V, 2016. Porosity and permeability characterization of coal: a micro-computed tomography study. *International Journal of Coal Geology,* 154–155, 57–68.

Saxena, N, Hofmann, R, Alpak, F O, Dietderich, J, Hunter, S and Day-Stirrat, R J, 2017. Effect of image segmentation and voxel size on micro-CT computed effective transport and elastic properties. *Marine and Petroleum Geology,* 86, 972–990.

Schlüter, S, Sheppard, A, Brown, K and Wildenschild, D, 2014. Image processing of multiphase images obtained via X-ray microtomography: a review. *Water Resources Research,* 50, 3615–3639.

Shah, S, Gray, F, Crawshaw, J and Boek, E, 2016. Micro-computed tomography pore-scale study of flow in porous media: Effect of voxel resolution. *Advances in water resources,* 95, 276–287.

Sheppard, A P, Sok, R M and Averdunk, H, 2004. Techniques for image enhancement and segmentation of tomographic images of porous materials. *Physica A: Statistical mechanics and its applications,* 339, 145–151.

Singh, B, 1997. The influence of surface phenomena on the dewatering of fine clean coal. *Filtration and separation,* 34, 159–163.

Sollins, P and Radulovich, R, 1988. Effects of soil physical structure on solute transport in a weathered tropical soil. *Soil Science Society of America Journal,* 52, 1168–1173.

Soulaine, C, Gjetvaj, F, Garing, C, Roman, S, Russian, A, Gouze, P and Tchelepi, H A, 2016. The impact of sub-resolution porosity of X-ray microtomography images on the permeability. *Transport in porous media,* 113, 227–243.

Sung, D-J and Turian, R M, 1994. Chemically enhanced filtration and dewatering of narrow-sized coal particles. *Separations Technology,* 4, 130–143.

Tao, D, Groppo, J and Parekh, B, 1999. Effects of polymers and metal ions on vacuum filtration of fine coal. *Coal Perparation,* 20, 207–225.

Tao, D, Groppo, J and Parekh, B, 2000a. Enhanced ultrafine coal dewatering using flocculation filtration processes. *Minerals Engineering,* 13, 163–171.

Tao, D, Groppo, J and Parekhm, B, 2000b. Effects of vacuum filtration parameters on ultrafine coal dewatering. *Coal Perparation,* 21, 315–335.

Tao, D, Parekh, B, Liu, J and Chen, S, 2003. An investigation on dewatering kinetics of ultrafine coal. *International journal of mineral processing,* 70, 235–249.

Thapa, K B, Qi, Y and Hoadley, A F A, 2009. Interaction of polyelectrolyte with digested sewage sludge and lignite in sludge dewatering. *Colloids and Surfaces A: Physicochemical and Engineering Aspects,* 334, 66–73.

Tien, C, Bai, R and Ramarao, B, 1997. Analysis of cake growth in cake filtration: Effect of fine particle retention. *AIChE journal,* 43, 33–44.

Wakeman, R and Tarleton, S, 2005. *Solid/liquid separation: principles of industrial filtration*, Elsevier.

Wang, B and Peng, Y, 2014. The effect of saline water on mineral flotation – A critical review. *Minerals Engineering,* 66–68, 13–24.

Wang, B, Peng, Y and Vink, S, 2014. Effect of saline water on the flotation of fine and coarse coal particles in the presence of clay minerals. *Minerals Engineering,* 66–68, 145–151.

Wang, G, Shen, J, Liu, S, Jiang, C and Qin, X, 2019. Three-dimensional modeling and analysis of macro-pore structure of coal using combined X-ray CT imaging and fractal theory. *International Journal of Rock Mechanics and Mining Sciences,* 123, 104082.

Yao, Y, Liu, D, Che, Y, Tang, D, Tang, S and Huang, W, 2009. Non-destructive characterization of coal samples from China using microfocus X-ray computed tomography. *International Journal of Coal Geology,* 80, 113–123.

Zhang, F, Bournival, G and Ata, S, 2019a. The influence of process water chemistry on coal thermoplastic properties. *Powder Technology,* 345, 468–477.

Zhang, N, Chen, X, Nicholson, T and Peng, Y, 2019b. The effect of saline water on the settling of coal slurry and coal froth. *Powder Technology,* 344, 161–168.

Zhuo, Q, Liu, W, Xu, H and Wang, D, 2020. Effect of particle size distribution on filter cake pore structure and coal slurry dewatering process. *International Journal of Coal Preparation and Utilization*, 1–16.

Future operations – future mineral processing plants

Stirred milling design – incorporating the IsaMill™ into the Jameson Concentrator

I Gurnett[1], A Swann[2], G Stieper[3] and L Collier[4]

1. Senior Metallurgist, Glencore Technology, Brisbane Qld 4006.
   Email: ion.gurnett@glencore.com.au
2. Senior Metallurgist, Glencore Technology, Brisbane Qld 4006.
   Email: andrew.swann@glencore.com.au
3. Technology Manager, Glencore Technology, Brisbane Qld 4006.
   Email: Glenn.Stieper@glencore.com.au
4. Principal Mechanical Engineer, Glencore Technology, Brisbane Qld 4006.
   Email: lance.collier@glencore.com.au

ABSTRACT

In 2021, Glencore Technology unveiled the Jameson Concentrator and announced the Ozernoye (due for commissioning in 2022) and New Britannia Projects (commissioned Q4 2021). As part of the Ozernoye project, a conventional circuit consisting of flotation tank cells coupled with a vertical regrind mill was compared to a Jameson Concentrator. The Jameson Concentrator replaced the entirety of the conventional flotation equipment with Jameson Cells, with the M20 000 IsaMill™ as the selected regrind mill. Selecting the Jameson Concentrator design for Ozernoye reduced the footprint to less than 50 per cent of the conventional circuit, with a key saving to the project lowering the building height by 15 m. Reduced power demand and maintenance spares resulted in operating cost savings 50 per cent lower than a conventional circuit. This Jameson Concentrator design has been implemented before and is deemed low risk in the industry. The success of this design has previously been seen at the Philex Concentrator in 1996 and most recently at Hudbay's New Britannia installation in 2021.

This paper addresses the strong influence of test work in the design process of the IsaMill™. The IsaMill™ design in the Jameson Concentrator was based on test work principles that allow for an accurate 1:1 scale up. This paper explores how the M20 000 in particular, and IsaMills™ in general, are designed and developed for commercial installation. Particular focus will be on test work sample size, the accuracy of scale-up, the appropriateness of test work, the impact on grinding media selection (on mill efficiency and OPEX), understanding the effect of viscosity, and the influence of particle size measurement techniques when analysing the results.

INTRODUCTION

In 2021, Glencore Technology unveiled the Jameson Concentrator with the announcement of the Ozernoye Project, due for commissioning in late 2022. A conventional circuit consisting of flotation tank cells coupled with a vertical regrind mill was compared to a Jameson Concentrator during the feasibility study. This comparison led to selection of the Jameson Concentrator, which replaced the entirety of the conventional flotation equipment with Jameson Cells, with the M20 000 IsaMill™ as the selected regrind mill. Selecting the Jameson Concentrator design for Ozernoye reduced the footprint to less than 50 per cent of the conventional circuit, lowered the building height by approximately 15 m, reduced the power demand (due to less equipment), and reduced maintenance spares. This results in an operating cost saving of roughly 50 per cent of that of a conventional circuit.

This paper aims to highlight the benefits of the Jameson Concentrator and how the M20 000 IsaMill™ with its new reduced footprint design fits into this circuit, and aims to address some of the intricacies that are involved in setting up the regrind signature plots and the importance of various parameters (eg media size, same size, density etc) on the mill sizing.

WHAT IS THE JAMESON CONCENTRATOR?

The Jameson Concentrator is a product that was launched in 2021 that incorporates both the Jameson Cell and IsaMill™ (if regrind is required) into the full flotation/regrind circuit. This was developed to address performance inefficiencies, high costs and large carbon footprints seen within conventional circuit designs. Conventional circuits typically result in larger physical footprints and

high circuit volumes, because conventional circuit sizing is based on the residence time to achieve the required recoveries. By design, the Jameson Cell does not incorporate residence time into the design process due to the intense mixing in the downcomer forcing collisions between bubble and particle and eliminating short-circuiting. By removing the residence time constraint, cell sizing becomes dependent only on carrying capacity and volumetric flow. The result is an overall smaller footprint and less equipment to achieve an equivalent duty.

With Jameson Cell designs having a 15–60 per cent recycle for process stability, the circuit can absorb high variations in throughput rates and feed grades (assuming it's not carrying capacity-constrained). This, in turn, allows for the ability to absorb changes in feed mineralogy where other technologies struggle. The fast kinetics from the collisions within the downcomer enables the ability to target liberated minerals and scalp off a final concentrate, which significantly reduces the footprint of downstream equipment, increases process stability and reduces the circuit complexity.

Ultimately, selecting a circuit consisting only of Jameson Cells, with 35+ years of proven successes, has enabled a design with significantly reduced footprint and circuit inventory. By reducing the size of the circuit and having fewer moving parts (no compressors or agitators required), there are significant savings in both the CAPEX and OPEX while reducing the overall complexity of the circuit (fewer flotation units and stages which reduces recirculating loads). These benefits drove the decision to select the Jameson Concentrator for the Ozernoye Project. The Jameson Concentrator design was previously executed at the Philex Concentrator in 1996 (Harbourt *et al,* 1997). The most recent success at Hudbay's New Britannia installation was commissioned in 2021, demonstrating and proving the concept that reduces any process risks.

To help demonstrate some of these benefits, Figure 1 is an example showing the effective footprint reduction you would expect with a Jameson Concentrator for a ~1400 t/h Copper Nickel Concentrator. Seventy-six conventional cells have been replaced with 18 Jameson Cells with two M3000 IsaMills. This equates to a footprint reduction of greater than 50 per cent and a noticeable reduction in height due to no lifting constraints for agitators during maintenance.

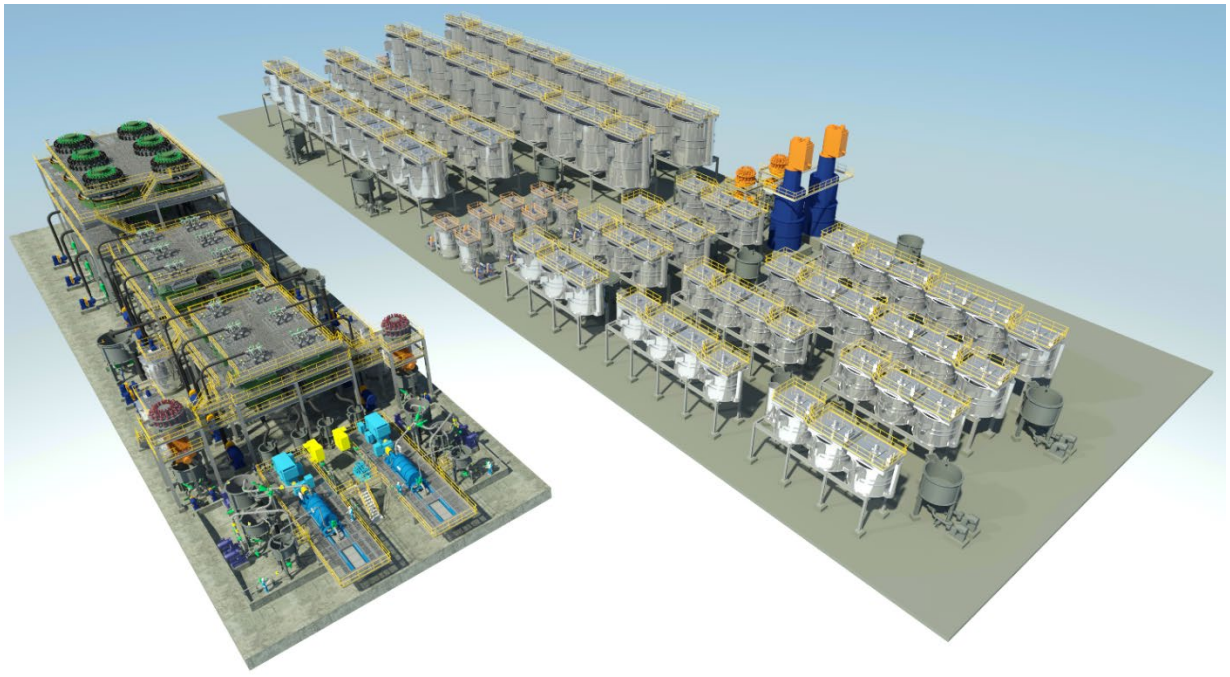

FIG 1 – Copper-Nickel concentrator comparison.

THE DEVELOPMENT OF THE REDUCED FOOTPRINT M20 000

In 2020 Glencore Technology recognised that an IsaMill™ needed to be developed that could treat higher volumetric throughput rates whilst remaining cost-effective in terms of OPEX (eg shipping of parts and maintenance spares). To satisfy this criterion, the M20 000 was developed with a 5 MW motor. Three of these IsaMill™ designs will be installed and commissioned as part of the Ozernoye project from late 2022 to early 2023.

The new IsaMill™ design is a significant improvement over the taller, more capital-intensive designs of the pre-2020 period. It was recognised after engaging with industry; there was room to optimise and reduce the cost to the end client. Therefore, the IsaMill™ layout was re-designed to the 'reduced footprint plant' version (Figure 2). The main changes to the design are as follows (Gurnett *et al,* 2021b):

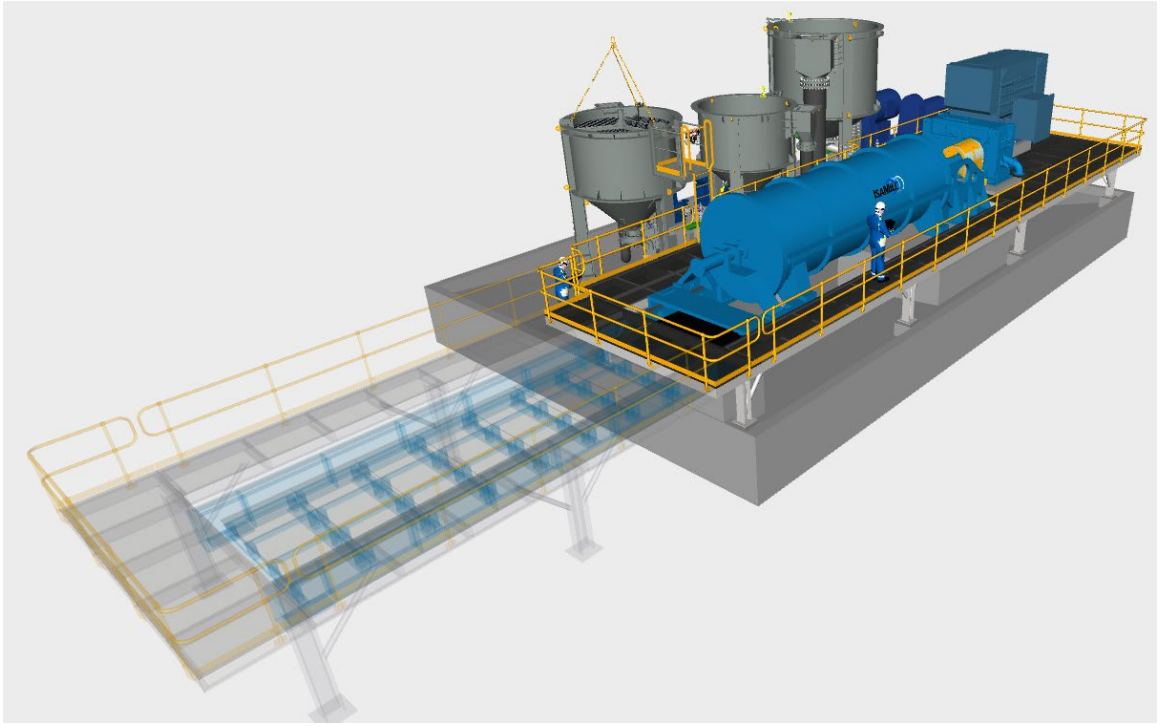

FIG 2 – 3D Model of the M20 000 IsaMill™.

- The media hopper has been repositioned from under the IsaMill™ to the side. Due to the backpressure created from the rotor, it was possible to utilise this action to pump media out of the IsaMill™ to a media storage tank/hopper during its maintenance shutdown sequence rather than discharging to the hopper below the IsaMill™.
- The fixed rails are now optional (depending on layout and maintenance requirements), as now a removable rails structure allows for the option to reduce the footprint and allow for an additional maintenance service area when the mill is in operation.
- The IsaMill™ can utilise gland water injected directly into the plant's main supply, which eliminates the need for a gland water tank and corresponding pumps.
- The IsaCharger™ water can be directly supplied from the plant process water; this eliminates the need for an IsaCharger™ water tank and corresponding pumps.
- The overall costs have been reduced by changing several valves with alternative designs.
- Moving the Oil Lubrication Systems (OLS) to the side of the IsaMill™ and allowing for a gravity return (which dictates the height of the plant).

TEST WORK

The IsaMill™ is fundamentally sized on two different factors; volumetric flow and specific energy. Both items are key to mass and heat balances. While volumetric flow is quite simple to derive, the specific energy is an intricate number from the IsaMill™ Signature Plot, which is conducted on an M4 IsaMill™ (Figure 3).

The IsaMill™ Signature Plot test is widely accepted as the industry standard for specific energy determination performed by accredited laboratories worldwide. It is known for the highly accurate 1:1 scale-up, with numerous previously published examples (eg Stirring the Pot: A New Direction for IsaMilling by Barns and Curry, 2006).

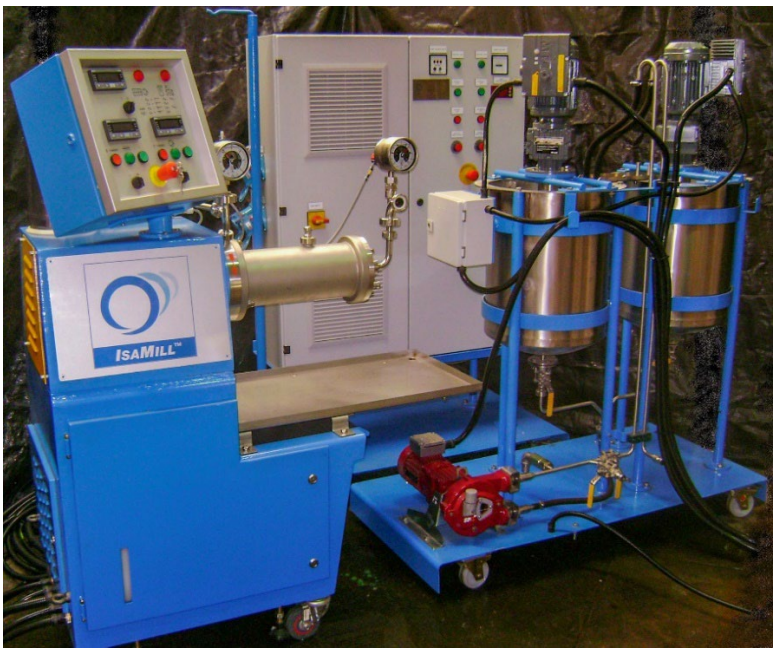

FIG 3 – M4 IsaMill in which Signature Plots are conducted in the laboratory (Gurnett *et al,* 2021a).

While the test is an industry standard, there are many intricacies involved with setting up the test. This paper aims to help explain the conditions behind the test and why they are so important within the design process of the IsaMill™. Noticeable ramifications can affect the mill sizing if the Signature Plot is done incorrectly. The following sections aim to provide an understanding of why the test is designed the way it is.

Sample size

One of the biggest concerns raised by clients with the Signature Plot tests is that accumulating 15 kg of material for a greenfield site is an arduous and expensive exercise. The common question raised is 'why can't smaller masses be used'? This mass requirement is to ensure there is sufficient material to allow the test to achieve a steady state and produce accurate and repeatable results. Previous publications showed that for a stirred milling test to achieve steady state, there must be sufficient sample to replace the mill voidage volume at least 3–4 times (Larson *et al,* 2011). This stipulation avoids hold-up of coarse particles, which causes serious underestimation of energy in the range of 30–50 per cent.

Figure 4 demonstrates this sample mass requirement quite clearly. A standard Signature Plot (dark blue) was conducted on an operating gold plant (3.5 SG feed). To validate the test conditions, the plant feed was surveyed (red dot). The graph shows that the plant feed falls on the Signature Plot line demonstrating the suitability of the Signature Plot relationship for predicting operating plant data – enabling direct scale-up from the Signature Plot test to full plant conditions.

To demonstrate the impact of insufficient sample material and how this results in reporting undersized specific energy, a 5 kg sample was run through the Signature Plot procedure. The results of this are shown in Figure 4 (light blue line). This reduced sample mass produced a Signature Plot relationship for the tested material below the initial test. By aligning the plant sampled feed point with the revised energy plot, the outcome is an estimation of grinding energy approximately 30–40 per cent lower. This underestimation of the energy requirement is simply from not having sufficient mass in the sample and not allowing the test process to come to a steady state within the mill.

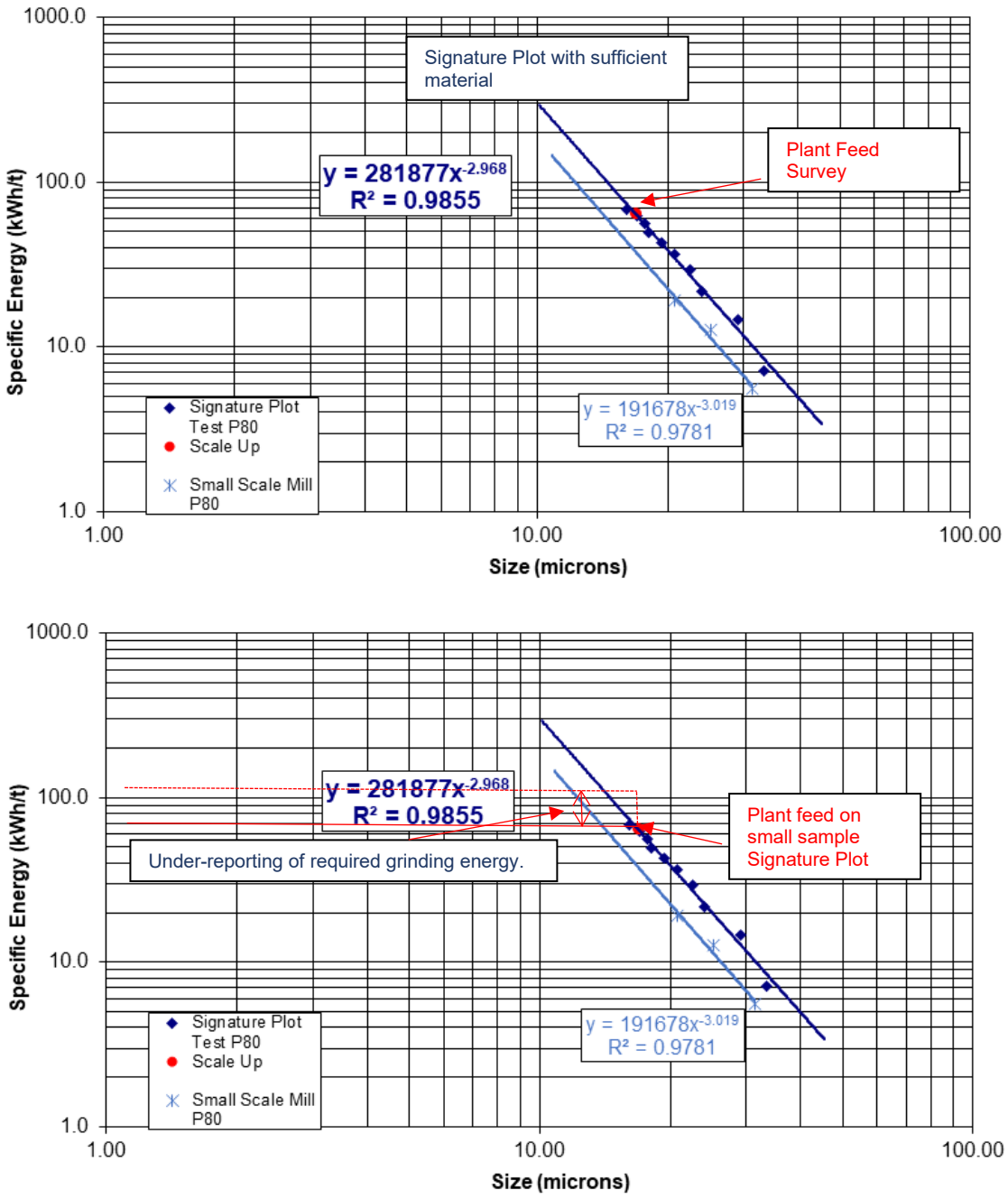

FIG 4 – Comparative scale-up Signature Plot with a small mass sample (Gurnett *et al,* 2021a).

This underestimation in specific energy from the 5 kg test is expected when comparing the ratio of sample mass (undergoing the test) to the void volume of the mill.

A mathematical demonstration of this is provided in Table 1. The data shows the effect of SG and required sample sizes within a standard M4 (4L) IsaMill™. As shown, with the range of nominated SG of the material, between 13.4 to 22.4 kg is required to achieve sufficient material turnover in the mill to meet steady-state conditions. As the mill's volume increases, the underestimation effect will be further exaggerated unless more feed sample mass is available.

TABLE 1

Explanation of sample requirements for the IsaMill™ to achieve steady state.

Media volume @100%, L	3.4		
Media volume @74%, L	2.5		
Void space between packed beads,%	24		
Total available void space inside mill, L	1.5		
Volume of void space in between beads, L	0.6		
Void space in mill not occupied by media, L	0.9		
SG of solids in the sample	3.0	4.0	5.0
Volume of solids to reach steady state (3x), L	4.5	4.5	4.5
Minimum mass of sample required, kg	13.5	18.0	22.5

Based on the example above, a 5 kg sample (at a SG of 3.0) will provide sufficient material only for a single full pass, not reaching steady-state conditions. The inability to reach steady-state conditions will result in the coarse material inherently retained within the stirred mill, incorrectly influencing the specific energy plot. Without reaching steady-state conditions, this will always result in underreporting of the energy required.

Glencore Technology has investigated small sample test trials for the last 25 years using its M4 IsaMill, unfortunately without much success in this field. While it is a challenge, Glencore Technology has not given up on this quest and continues to seek solutions with smaller sample mass. However, it is worth highlighting the recent development of the Ellison Test (Johnston, 2014).

The authors note that the results of the Ellison tests are becoming commonplace in initial concept studies and their inclusion in NI 43–101 disclosure reports (Standards of Disclosure for Minerals Projects – Canadian Securities Administrators). At a high level, the Ellison test can utilise an 800 g sample to provide results accurate at +/– 35 per cent (Johnston, 2014) and can be used as an indicator of the magnitude of power you will need, eg 10 v 20 kWh/t. However, to guarantee the 1:1 scale up, the Signature Plot is still required to be conducted in the design process as the project proceeds.

Importance of sample selection

Glencore Technology has a Signature Plot database that can be used in the absence of any sample/site-specific test work. The database contains hundreds of tests conducted on various ore types and minerals. When Signature Plot test work is conducted on a sample, the full sample is treated through an M4 IsaMill™ to produce a Signature Plot representative of that material type.

Generally, Signature Plots are undertaken on a sample of material generated from an upstream separation process, commonly froth flotation at a laboratory or pilot scale. It is challenging to duplicate the cyclone separation with such material quantities to prepare a feed to the IsaMill™ similar to an open-loop circuit (feed from a cyclone underflow). Attempting this would result in a test that may not be reliably scalable to full plant conditions.

In some brownfield applications, it is possible to conduct a Signature Plot on the ‘direct feed’ from a classification stage, assuming it can be sampled correctly. There are numerous applications in pre-leach grind duties where this has been conducted.

A common misunderstanding within the industry is the scale-up of the Signature Plot to full plant sizes where the mill may be installed in either a closed or open-loop circuit. A simplified example of these is shown in Figure 5.

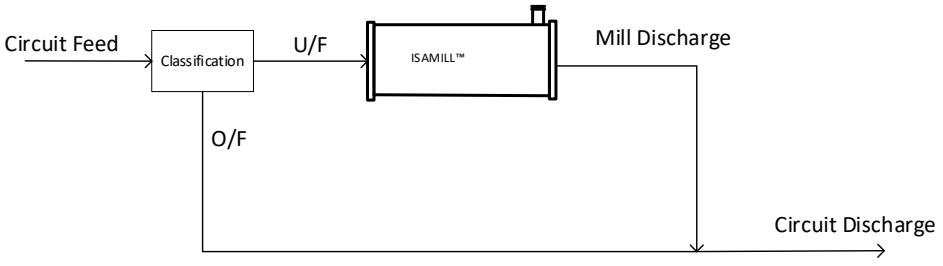

Simplified Open Loop Circuit

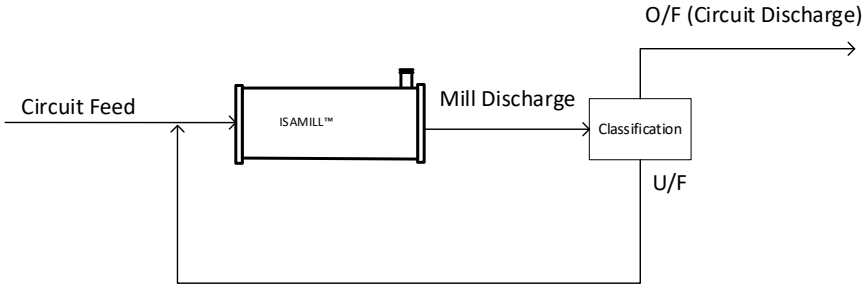

Simplified Closed Loop Circuit

FIG 5 – Simplified IsaMill™ operating circuits.

In open-loop circuits with cyclone classification of the feed, the coarser material will report to the IsaMill™ at a reduced tonnage rate (compared to the circuit feed). The trade-off is that the cyclone underflow will require more energy input (per unit mass) as the material is coarser, albeit at lower mass rates. This is more simply explained in Figure 6 (selected data points have been exaggerated for clarity of explanation) for an open-loop circuit.

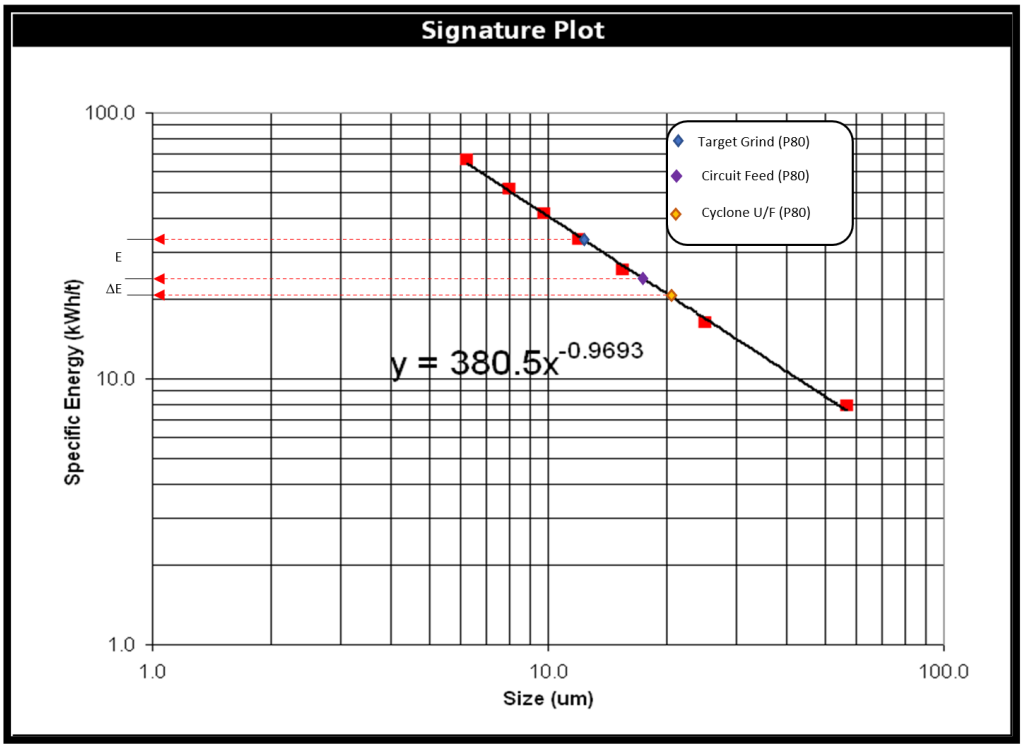

FIG 6 – Signature Plot application to cyclone classification of the feed.

Based on the successful scale-up of many applications in open loop circuits, the following relationship holds:

$$E \times T_{circuit} \approx (E + \Delta E) \times T_{CycloneUF}$$

Where:

E	= circuit specific energy, duty based on circuit feed to target grind size [kWh/t]
ΔE	= specific energy, additional duty based on reducing the coarser cyclone underflow to the circuit feed size [kWh/t]
$T_{circuit}$	= circuit solids throughput [dry t/h]
$T_{cyclone\ UF}$	= classification underflow solids throughput [dry t/h]

In a closed-loop circuit, the 'fresh feed' will be consistent with the open-loop (same circuit fresh feed); however, the specific feed rate to the mill will increase with the circulating load from the cyclone stage. Fine material circulating back from the cyclones does not impact the overall energy requirements as this material will preferentially bypass the grinding zones within the mill. However, the IsaMill™ will preferentially treat the coarse fraction within the feed due to the internal classification within the mill.

The scale-up from 'circuit feed' samples in the Signature Plot database has reliably been used to demonstrate that the specific energy requirements for the target grinding conditions are independent of the open or closed configuration. Sizing of the IsaMill™ is therefore done based on appropriate sample selection applied to the circuit 'fresh feed'.

In practice, it is helpful to consider the Signature Plot profile as a 'circuit' specific energy that will be valid for either open or closed-loop applications.

This relationship was beneficial during the design development of the Ozernoye Project, as the mill was then fixed in size based on the Signature Plot and fine grinding plant capacity. Plant design progression that required both open and closed loops evaluation did not impact the final mill sizing. This allowed certainty of mill size to progress through the unit's fabrication, plant footprint, and mill grind performance early in the project.

Bond Work versus IsaMill™ signature plot

Often Glencore Technology is requested to use Bond work indices for IsaMill™ sizings, mainly when expensive test work campaigns have already been completed without considering appropriate fine grinding test work. There are several issues with applying the Bond work test results to fine grinding. Glencore Technology has recognised several fatal flaws when applying these results under 100 microns to the IsaMill™.

Bond's theory (Figure 7) proposes an exponential energy curve with a constant power of -0.5. While this is a good approximation down to 100 µm, below this the exponent varies significantly among particularly different ores. The Bond Work Index relationship will then underestimate energy requirements at fine sizes.

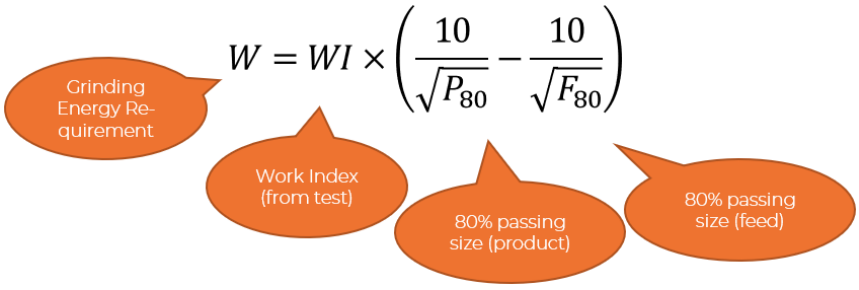

FIG 7 – Bond Work Index equation.

When comparing both test work and full-scale operational differences between a stirred grinding mill and a ball mill, this logically makes sense, as the Bond test has different media sizes, ball and ore trajectories, and ball-particle/ball-shell interactions. Additionally, the Bond test uses plant feed, not regrind circuit feed, with the material characteristics between a concentrate and a circuit feed being significantly different.

Impact of ceramic media selection

Grinding media has a significant effect on IsaMill™ efficiency and OPEX. Selecting correct media will result in substantial improvements in specific energy; conversely, choosing incorrect media has a detrimental impact on mill performance. Multiple variables impact grinding efficiency, critically media size, media SG and condition of the media itself. To demonstrate the effect of these criteria, the Signature Plots in Figures 8 and 9 illustrate the impact of media size and SG selection.

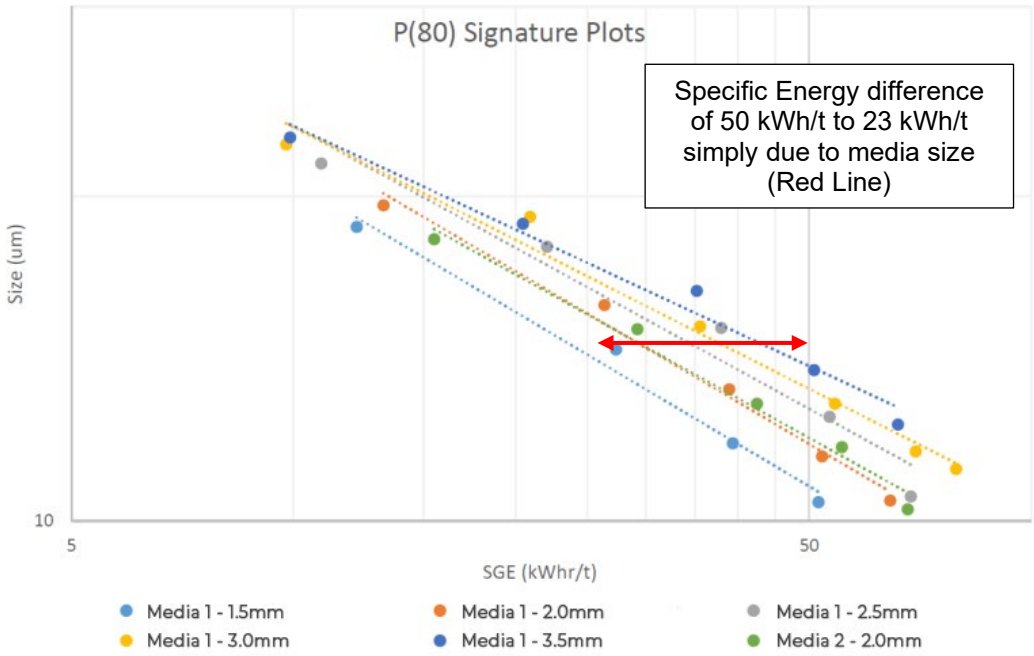

FIG 8 – Effect of media size on milling efficiency (Gurnett *et al,* 2021a).

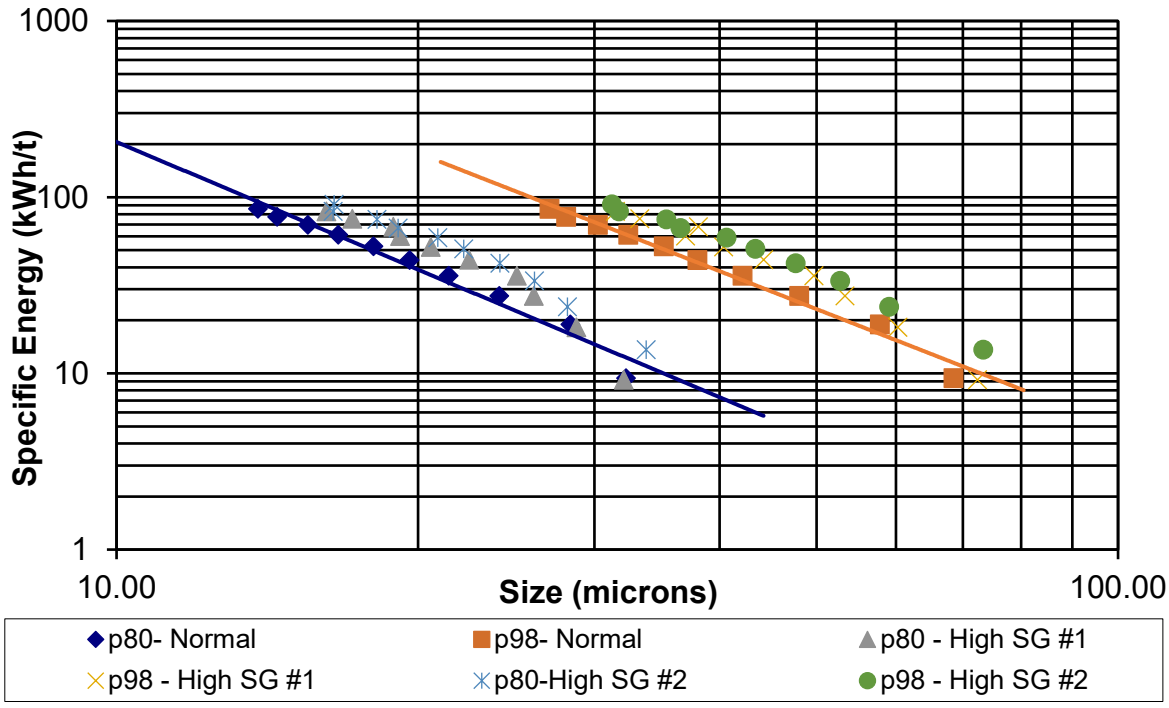

FIG 9 – Normalised Signature Plot – 3.7 SG media versus 4.5 SG media (Gurnett *et al,* 2021a).

When media is normally selected, it must provide sufficient energy to break the coarsest particles in the feed at the same rate as they enter the IsaMill™, utilising a reduction ratio ($F_{80} \div P_{80}$) of less than 8 per media type (diameter range ie 1.5 mm, 2.0 mm, 2.5 mm etc). This is the minimum requirement

with room for efficiency improvements when the media is optimised correctly. As demonstrated in Figure 8, in a trial undertaken at a gold mining operation, an energy variation of 23 kWh/t was observed when increasing media size (diameter) from 1.5 mm to 3.5 mm.

With more ceramic media suppliers supplying into the market, there has been a notable uptake in available types of media. One of the most apparent trends of late has been the introduction of higher SG media, particularly in the vertical mill market. In horizontal milling configurations, such as the IsaMill™, the higher SG media was found to be inefficient whilst causing accelerated wear of the internal components.

In Figure 9, this relationship is demonstrated with 4.5 SG media (High SG). This media was run multiple times for repeatability against the normal (3.7 to 3.8 SG) media typically used in an IsaMill™. Each trial of the High SG (4.5) media showed an average increase in specific energy of 20 per cent. The authors believe that the higher energy demand is attributed to the increased energy to move media. This additional energy only offsets a smaller portion of the extra energy imparted in the breakage mechanisms, resulting in an overall decrease in grinding efficiency.

In Figure 10, Glencore Technology obtained the 2020 cost of ceramic media for different densities from a well-known media supplier. To model the impact of SG selection on operating expenditure, the yearly cost for ceramic media was estimated for a mill operating at 2.5 MW and a typical media consumption rate of 12 g/kWh. The difference between selecting 3.7 SG media over 4.5 SG media could theoretically result in OPEX savings every two years, roughly equivalent to the cost of a single M10 000 IsaMill™.

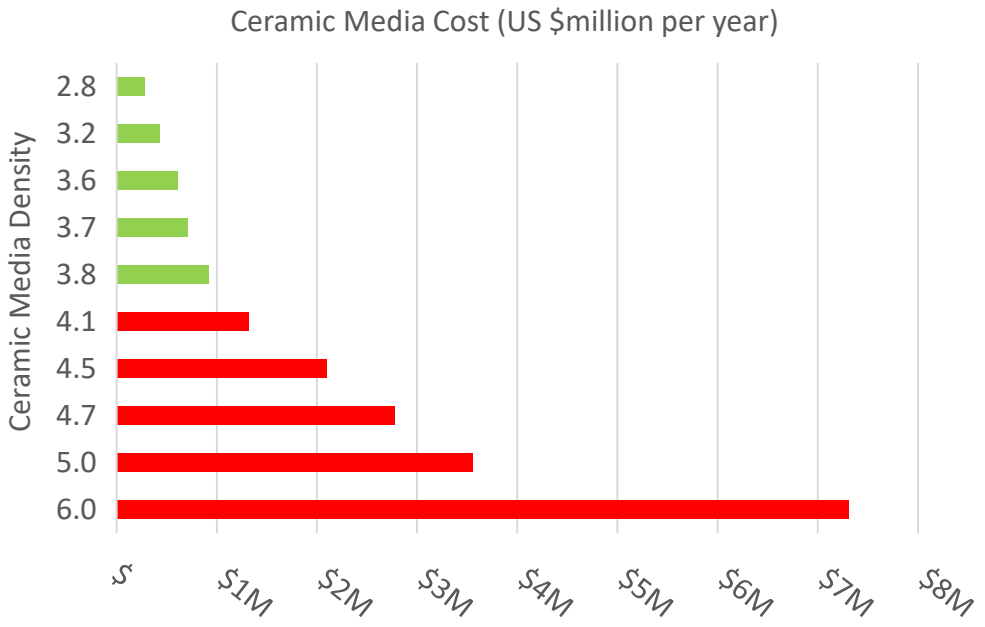

FIG 10 – Comparative costs for different media SGs (Gurnett *et al,* 2021a).

While it is known stirred vertical mills have been utilising higher SG media to address the challenge of media retention within the mills, the benefits to the horizontal IsaMill™, through its ability to use low SG media, are not adequately appreciated. The use of 3.7–3.8 SG media substantially reduces the operating cost for the IsaMill™ and makes it the ideal selection for Jameson Concentrator designs.

Understanding the effect of viscosity

When the IsaMill™ Signature Plot test is undertaken, it is conducted with a feed condition of 18 to 20 per cent solids (v/v). The purpose of this is to limit the viscosity impacts on grinding efficiency. As the density (per centv/v solids) increases and the material progressively grinds finer, it increases the likelihood of viscosity impacts arising from the increased exposed surface area. This can cause the charge to ‘lock-up’ and turn into a viscous mass exhibiting as a rotating plug of material and media rather than the desired highly agitated, turbulent grinding environment. This is evidenced by

a significant and rapid drop in the IsaMill™ power draw, a decrease in feed pressure and an increase in the Coarse Size Index (CSI) ratio (P98:P90 ratio).

The high viscosity can push the IsaMill™ into a situation where it will start to be overcharged as a result (the media top-up system responds to the drop in power draw by adding grinding media) and can potentially lead to heavily accelerated internal component wear rates. Therefore, to mitigate this issue, Glencore Technology designs the IsaMills™ to operate at 20 per cent solids (v/v). As the Signature Plot is designed to replicate the full-scale mill performance, density has to be controlled in the test work phase. The relationship between density/viscosity and efficiency has been outlined in the M4 test work in Figure 11.

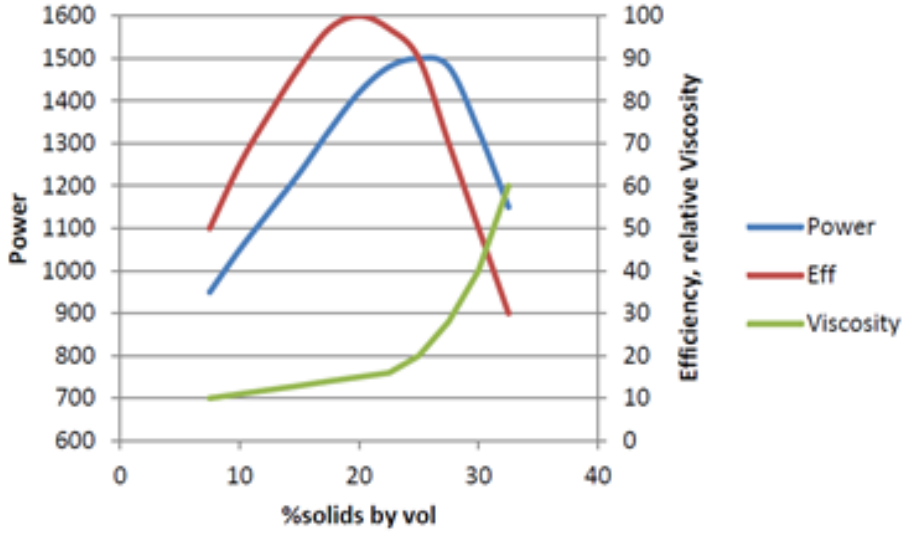

FIG 11 – Effect of density on the grinding efficiency within the IsaMill™ (Gurnett *et al,* 2021a).

Influence of particle size measurement techniques

Due to the fundamental principles on which laser particle-size-analysis units (eg Malvern Mastersizers) work, they generally report a coarser result compared with a screen sizing method. This is because laser sizers utilise an 'equivalent sphere' method. They measure the volume of non-spherical particles, calculate the diameter of an equivalent sphere, and use this as the particle diameter for the Particle Size Distribution (PSD) calculations (Malvern, 2014). In Figure 12, an example of how shape influences the design is seen when a 100 µm long, 20 µm wide particle could potentially pass through a 21 µm aperture screen but would measure as a 39 µm particle in the Malvern laser sizer.

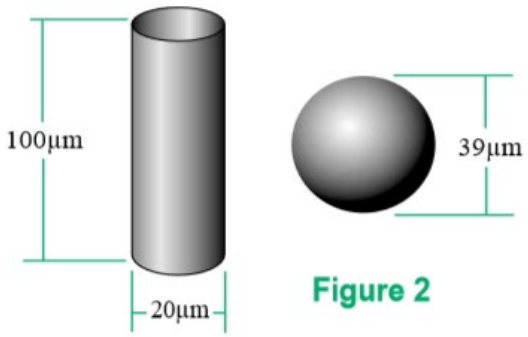

FIG 12 – Effect of particle shape on sizing (Malvern, 2014).

Therefore, if a sample has lots of non-spherical particles, eg micaceous silicates, the 'coarseness' of the Malvern compared to screen sizing results will be exaggerated. The effect should theoretically be reduced as the particles are ground through more IsaMill™ passes and increasingly become spherical. This feeds the design process when scale-up of the regrind mills is undertaken; the same method of sizing analysis needs to be used as in the test work. It is up to the test work coordinator to decide which particle sizing method the laboratory should use.

THE FUTURE

While the Jameson Concentrator is a step forward in concentrator design, there are still design improvements being undertaken. It has been recognised (particularly in colder climates) that the size of the structure for the concentrator (roof and height of the building) could be optimised.

Glencore Technology is currently developing an ERM-Less design, which is removal of the External Recycle Mechanism (ERM) that sits below the Jameson Cell. This new design will allow the installation height of the Jameson Cell B series to be significantly reduced. This reduced height Jameson Cell complements the horizontal milling capabilities of the IsaMill™ and should dramatically reduce capital costs through reduced building height/volumes, structural supports and crane requirements. Figure 13 demonstrates the achievable height saving for the B8500/12 Jameson Cell.

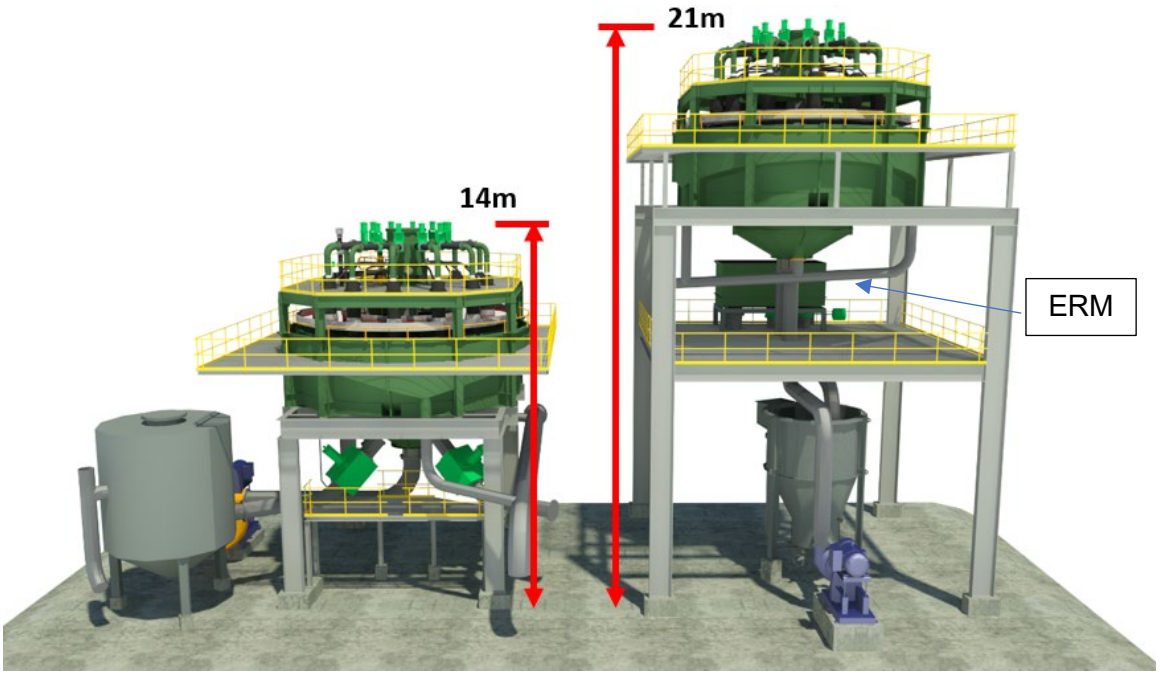

FIG 13 – New B8500/12 ERM-Less design.

While there are opportunities for further layout optimisation, there is also scope to increase the processing applications of the IsaMill™. When the IsaMill™ was first introduced to the market in the late 1990s, the target grind size was in the sub-10-micron range, as this was the specific need of Mount Isa Mines and McArthur River Mining at the time. The IsaMill™ quickly became a market leader in ultra-fine grinding. When ceramic media were introduced, improved efficiencies were achieved in the IsaMill™ (Curry and Clermont, 2005). As more ceramic media suppliers have entered the market, this has driven costs down and allowed larger media to be developed.

Current test work conducted on the IsaMill™ has demonstrated that the mill can operate with a feed of 400 microns (P_{80}) and top size of 1 mm using 6 mm media. Ceramic media in the range up to 14 mm is now commercially available, effectively meaning that the IsaMill™ theoretically can operate in the secondary/tertiary milling space.

This further enhances the scope of the Jameson Concentrator to offer greater value through improved capital and operating cost savings. Research and Development programs in this field are currently underway.

CONCLUSION

The author intends that this paper provide some guidance on the Signature Plot conditions and the importance of test variables' influence on obtaining a 1:1 scale up on specific energy. Underestimating energy requirements can lead to bottlenecking in new designs. As grades decline and liberation becomes more complex and critical, understanding your stirred mill and its ability to achieve a desired grind size is fundamental for project success. The IsaMill™ is the preferred stirred

mill choice in the Jameson Concentrator, as it is a mature low risk technology that repeatedly achieves the desired performance from reliable test work.

REFERENCES

Barns, K and Curry, D, 2006. Stirring the Pot: A New Direction for IsaMilling, *Ultrafine Grinding* 06.

Curry, C and Clermont, B, 2005. Improving the Efficiency of Fine Grinding—Developments in Ceramic Media Technology, Paper presented at the Randol Conference.

Gurnett, I, De Waal, H and Stieper, G, 2021b. The IsaMill™ – 25 years of Stirred Milling. CIM 2021 Convention, May 3–6, Vancouver BC, Canada.

Gurnett, I, Stieper, G and Price, A, 2021a. IsaMill and Jameson Cell: Technology for the Future Short Course Presented at CIM 2021, at Vancouver, Canada on 29 April, 2021.

Harbourt, G, Murphy, A and Budod, A, 1997. Jameson Cell developments at Philex Mining Corporation, in *Proceedings 6th AusIMM Mill Operators Conference* (The Australasian Institute of Mining and Metallurgy: Melbourne).

Johnston, H E, 2014. Development of the Bench Scale IsaMill Signature Plot Test: Introducing the Eliason Test.

Larson, M, Anderson, G, Morrison, R and Young, M, 2011. Regrind Mills: Challenges of Scaleup. SME Annual Meeting. Denver, Colorado, USA.

Malvern, 2014. Basic principles of particle size analysis [online]. Available from: <https://www.atascientific.com.au/wp-content/uploads/2017/02/AN020710-Basic-Principles-Particle-Size-Analysis.pdf> [Accessed: 18 March 2022].

Future (and present) trends in flotation circuit design

L Pyle[1], E Tabosa[2], S Vianna[3], S Sinclair[4] and W Valery[5]

1. Minerals Processing Engineer, Hatch, Brisbane Qld 4000. Email: lindon.pyle@hatch.com
2. Senior Process Engineer, Hatch, Brisbane Qld 4000. Email: erico.tabosa@hatch.com
3. Senior Process Engineer, Hatch, Brisbane Qld 4000. Email: sergio.vianna@hatch.com
4. Minerals Processing Consultant, Hatch, Brisbane Qld 4000. Email: steven.sinclair@hatch.com
5. Global Director–Consulting and Technology, Hatch, Brisbane Qld 4000. Email: walter.valery@hatch.com

ABSTRACT

The conventional approach to flotation circuit design has undergone a number of developments in the past decade. The need to maximise recovery and value when processing low-grade orebodies at high throughput presents a number of challenges. For example, improving both fine and coarse particle recovery, footprint and layout constraints, as well as managing CAPEX/OPEX, are driving innovations in cell selection, design, sizing and duty.

Economies of scale have traditionally been achieved by the installation of large mechanical cells with volumes over 600 m^3 to meet residence time requirements for high-capacity plants. However, in these large cells performance and flotation efficiency are compromised. Reduced mixing, turbulence, dead zones, greater froth travel distance to the concentrate launder plus increased chance of particle detachment back into the pulp phase limit their effectiveness.

Hatch has completed concept studies, feasibility and detailed engineering designs for several flotation technologies which are setting new standards for circuit design and performance. This paper describes the piloting, modelling, and engineering required to install the largest Jameson Cell developed for a rougher-scalping duty, as well as evaluation of Jameson Cells not only in cleaner stages (their traditional use) but also in pre-flotation and scalping duties. The paper also covers engineering design of coarse particle flotation circuits, including experience with conceptual studies, test work and detailed design to apply the Eriez HydroFloat™ to coarse tailings scavenging.

Finally, the evaluation and application of small footprint and fast flotation kinetics cells such as Eriez StackCell®s, Woodgrove Staged Flotation Reactor (SFR) and Direct Flotation Reactor (DFR) is discussed.

INTRODUCTION

Flotation machine manufacturers have historically focused on increasing cell size, with cell volumes increasing from 100 to over 680 cubic metres in the past 20 years. This increase has been driven mainly by the desire for fewer, high-capacity cells, resulting in a simplified plant layout and reduced maintenance. An overall decline in orebody head grades has also resulted in higher plant throughput, and thus larger equipment sizes, to maintain metal production. Unfortunately, larger cells require increased energy input to maintain particles in suspension. The increased energy input results in greater turbulence which is a major contributor to the loss in recovery of coarse particles. Likewise, the size and reduced number of cells in series can result in an increase in bypass or short-circuiting of material; with a detrimental effect on the slow floating mineral particles (ie fines). Although larger mechanical cells reduce flotation circuit footprint compared to smaller volume alternatives, the fact remains that tank cell circuits still occupy a significant area, which can be a challenge for layout constrained sites eg in mountainous regions. They also require significant investment in civil/structural design and foundations to support the large masses, often at height to enable gravity flows.

Large cells are more energy efficient in that the total energy per unit volume is reduced, however, high specific energy input is required to improve the flotation kinetics of fine and/or slow-floating particles. Larger cells are more difficult to sample representatively and inspect, impacting their ability to be run optimally. Management of froth transport parameters can also be challenging, with smaller numbers of large cells experiencing significant step-change in concentrate mass and mass pull down the bank, meaning that each cell must be assessed individually for lip loading and froth carrying

capacity with tailored launder configurations and froth crowding. Finally, with the need to process more complex orebodies, combined with the coarse and fine particle recovery optimisation challenges mentioned above, tank cell circuits often involve one or more recirculating streams to improve recovery. However, this is a suboptimal arrangement, mixing streams of different particle classes or sizes (or floatability) means that it is often challenging to optimise the circuit to target improved recovery of a particular size-by-mineral class.

Over the last 10 years, the industry has seen the development of several new types of flotation cells, applying fundamental flotation principles to address the issues identified above, such as pneumatic cells with froth wash water for improved fines recovery and entrainment reduction, fluidised bed cells and energy efficient stage flotation cells. Furthermore, some new cell designs have occurred recently that are yet to be readily applied in industry but offer significant potential, such as the Jord International's NovaCell and FLSmidth Reflux Flotation Cell

This paper will examine the potential that various flotation technologies offer for improving both fine and coarse particle recovery, meeting footprint and layout constraints, as well as managing CAPEX/OPEX, and increasing constraints on energy and water consumption. Three key areas will be discussed including pneumatic cells, such as the Jameson Cell being applied in rougher/rougher-scalper duties for Cu/Au and Au operations. Secondly, the design and modelling of coarse particle flotation circuits based on recent Hatch projects in concept, PFS and Detailed Design/Execution project phases will be examined. Finally, opportunities for energy-efficient, small footprint cells, particularly for increasing rougher capacity in brownfields expansion projects will be detailed. These experiences will be used to highlight the authors expectations for future flotation circuit design trends, some of which are already occurring today.

NEW TECHNOLOGIES FOR FLOTATION CIRCUIT DESIGN

Manufacturers of conventional flotation cells continue to refine the design of their rotor-stator mechanisms for improved fine and coarse particle flotation. These improved designs aim to improve solids suspension, gas dispersion and bubble-particle attachment. Some examples of impeller-stator mechanisms are the nextSTEP™ of FLSmidth and FloatForce of Metso:Outotec. These mechanisms can also be retrofitted to existing flotation cells. For finer particles, a mechanism one size smaller than normally selected can be used at higher speed. For coarse particles, a larger mechanism at lower speed will provide sufficient mixing while minimising high turbulence.

Alternative technologies have been developed with the goal of providing more efficient flotation, including multi-chamber mechanical machines supplied by Eriez (StackCell®) and Woodgrove (Staged Flotation Reactor, SFR, and Direct Flotation Reactor, DFR). These devices build on the concept of focused energy input to enhance fine particle and relatively coarse particle (DFR) recovery as well as improving flotation kinetics. This novel approach decouples the particle contacting and collection zone within the cell from the froth phase separation zone. As a result, overall unit size can be reduced while maintaining the same capacity and metallurgical performance. It is worth mentioning that these flotation machines are not sized based on residence time. The implications of this step-change in technology are numerous and include a significant reduction in energy consumption (>40 per cent) as well as reductions in plant height, footprint and foundation loads of greater than fifty percent. One notable installation of these cell types is the Woodgrove SFR cells installed for the BHP Spence Growth Option concentrator project which involves 78 SRF cells for both Cu and Mo flotation as the operation transitions from oxide to sulfide processing (Heffernan, 2018). This circuit commenced operation in May 2022 and had a 50 per cent reduced footprint and 60 per cent lower energy consumption compared to a conventional tank cell circuit of similar capacity (BHP, 2022).

Another alternative technology that provides more efficient flotation is pneumatic flotation, examples include the Jameson, Concorde, Imhoflot and Reflux flotation cells. These cells do not use an impeller like mechanical cells. Rather, the air and pulp are mixed in a continuous stream of high fluid velocity through a downcomer or venturi to disperse the air into fine bubbles and maintain particle suspension. Froth wash water is often used to enhance concentrate grade, minimising recovery by entrainment. There has been a growing application of these types of cells, not only in cleaner stages (their traditional use) but also in pre-flotation and scalping duties (Hassanzadeh *et al,* 2022).

The authors have recently been involved in the evaluation and detailed design of circuit expansion options involving the addition of Jameson Cells in rougher-scalper duty to gold operations in Russia and Cu-Au concentrator in Australia. Glencore Technology has recently launched the Jameson Concentrator, a flexible combination of Jameson Cell and IsaMill technology that can comprise an entire flotation circuit (roughing, scavenging and cleaning stages) as well as regrinding. This approach uses fast kinetics Jameson Cells with adjustments to wash water, froth depth and vacuum pressure to operate the cell effectively in all duties and significantly reduce plant footprint and energy consumption (Harbort, 2019). A full Jameson Cell concentrator is installed at Hudbay' s New Britannia Cu/Au operation in Canada and in the near future another flotation circuit comprising solely of Jameson Cells will be installed at the Ozernoye lead/zinc greenfield in Russia, with the authors being involved in the initial phases of the development of the latter.

There is also an increasing demand for coarse particle flotation as this would lead to a reduction in energy demand in preceding comminution stages and increase production rates. For example, if flotation could be performed at a P_{80} of 300 µm rather than 100 µm, the potential energy savings in comminution would be around 30–50 per cent. Coarser grind sizes also have the potential to significantly reduce operating costs for power and grinding media. They also result in coarser tailings streams creating certain operational advantages and cost reductions at sites that incorporate sand embarkments (dry stacking), tailings filtration or paste backfill.

The reduction in recovery for coarse particles is often attributed to detachment due to excessive turbulence within conventional mechanical flotation cells. Poor liberation can also create challenges when treating coarse particles. The low degree of liberation for particles coarser than 150 µm can reduce the strength of bubble/particle aggregates. This condition reinforces the need for a non-turbulent flotation environment to maximise coarse particle flotation (Kohmuench *et al,* 2018). The limitations of conventional flotation machines can be overcome through the utilisation of a fluidised-bed flotation machine specifically engineered for the selective recovery of feeds containing very coarse particles. The HydroFloat™ separator, designed in the early 2000s, and initially used in industrial minerals applications, addresses the limitations of traditional flotation systems (Kohmuench *et al*, 2001). By using a quiescent, aerated fluidised bed, the turbulence commonly found in a mixed-tank contacting environment is greatly minimised. As a result, delicate bubble-particle aggregates are more likely to report to the concentrate without disruption. The absence of a continuous froth phase minimises drop back that can occur at the pulp/froth interface (Kohmuench *et al*, 2018). Furthermore, the HydroFloat™ operates most effectively with a feed tailored to a narrow size range, typically this is a top to bottom size ratio of 5:1, requiring effective feed preparation circuit design as detailed later in this paper. The NovaCell™, by Jord International is a recently commercialised cell that uses a combination of feed injection via a downcomer and froth phase for fine particle recovery with a fluidised bed zone to simultaneously enable the recovery of coarse particles in a single flotation device.

The diagram shown in Figure 1 highlights the main alternative flotation technologies and recent developments in flotation in orange.

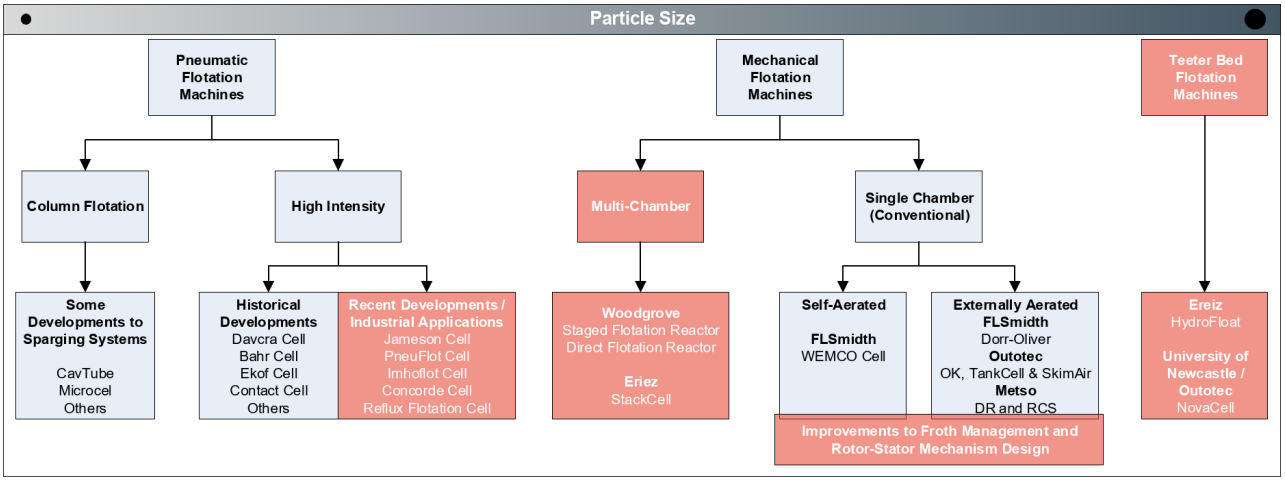

FIG 1 – Flotation machine types.

With the suite of alternative flotation technologies available, the authors recognise that one area for continued development is the laboratory test work required to simulate cell performance and its translation to modelling. Batch and locked cycle test procedures for predicting mechanical cell and circuit performance are well-established and conducted by laboratories, companies and universities worldwide. These are generally accepted as predictors of any mechanical tank cell performance, independent of designs specific to each vendor. The same cannot be said for the suite of alternative and emerging technologies. Some laboratory scale procedures exist, such as three-stage dilution test for Jameson Cells, but generally vendor specific piloting is required to produce performance data for modelling (eg grade-recovery curves versus mass pull). This poses challenges for greenfield projects, where test work is often performed using drill core samples and insufficient sample is available to conduct a suite of pilot tests. It also compromises brownfield projects which may be schedule or logistics constrained and thus do not have sufficient time to organise site piloting of three or four different cell types.

JAMESON CELLS FOR NEW DUTIES

Pneumatic flotation machines were among the first machines used in flotation. However, with the advent of mechanical subaeration cells, the use of pneumatic flotation machines declined significantly (Harbort, 2019). There are several design types of pneumatic flotation cells. Although a variety of aerators, pulp feed arrangements, and separating vessel designs exist, the applied principles and fundamental design remain unchanged. Jameson Cells have traditionally been utilised in a cleaning duty due to their ability to produce high-grade concentrates and improved fines recovery minimising losses to slimes (Hassanzadeh *et al*, 2022).

The first example of Jameson Cells in a roughing duty was at the Philex Cu/Au mine in the Philippines, which progressively transitioned their existing tank cell circuit to a complete Jameson Cell circuit (Roughers, Scavenger, Cleaner, Recleaner and Cleaner-Scavenger) in 1996 (Harbort *et al*, 1997).

Recently, the authors have been involved in optimisation projects and engineering studies to install Jameson Cells in a rougher duty for Au and Cu operations, including the development of the new Z-series cell for increased capacity.

Hatch progressed Rougher Jameson Cell design and installation through Concept, PFS, FS and Detailed Design phases for an Australian Cu-Au operation who wanted to address flotation recovery losses as part of a plant expansion. Early study phases analysed flotation circuit survey data and mass balance results which showed that the distribution of solids, gold and copper below 20 µm in the final tailings were 18 per cent, 35 per cent, and 20 per cent, respectively. This was a significant imbalance, with the majority of gold and copper minerals occurring in well-liberated particles. Various options were considered to improve the recovery of these fine and ultrafine gold and copper particles which are currently lost to tailings, especially in the rougher-scavenger bank. Preliminary modelling was used to identify the most promising alternatives. The Jameson Cell in a rougher-scalper duty was shown to produce a higher Au and Cu recovery and grade, due to the generation of a fine average bubble size (0.5 mm), low turbulence (no rotor) and the presence of froth washing water. The recovery effect is expected to be particularly pronounced in the fines/ultrafine particle size range (<20 µm).

A pilot program using an L500/1 cell, comprising 55 tests, was undertaken to determine the expected performance of the Jameson Cell in rougher-scalper duty. Results from the Jameson Cell piloting showed that:

- A fraction of the copper mineral particles (eg chalcopyrite) in the feed were sufficiently liberated at the current grind size P_{80} of 140 µm to allow a final grade concentrate to be produced without further grinding (for liberation improvement).
- Froth washing water in the Jameson cell significantly reduced the recovery of gangue minerals by entrainment, resulting in a substantial improvement in copper concentrate grade up to 28–30 per cent Cu.

The grade/recovery curves from pilot testing with and without froth washing are plotted in Figure 2. The Jameson Cell can be operated with froth washing turned on to produce a final concentrate

('scalping' mode), or off to operate in 'standard' roughing mode. In the latter, unit Cu recovery (up to 80 per cent) is greater than what is typically achieved in a single mechanical cell due to the attributes of the Jameson Cell technology (no short-circuiting, finer bubble size – 0.3–0.6 mm, and high mixing intensity). Due to the potential for future variation in ore characteristics, including variation in the liberation characteristics of the ore, and potential increased in the penalty element fluorine, the option to send Jameson Cell concentrate to regrind and cleaner circuit is maintained (ie rougher duty).

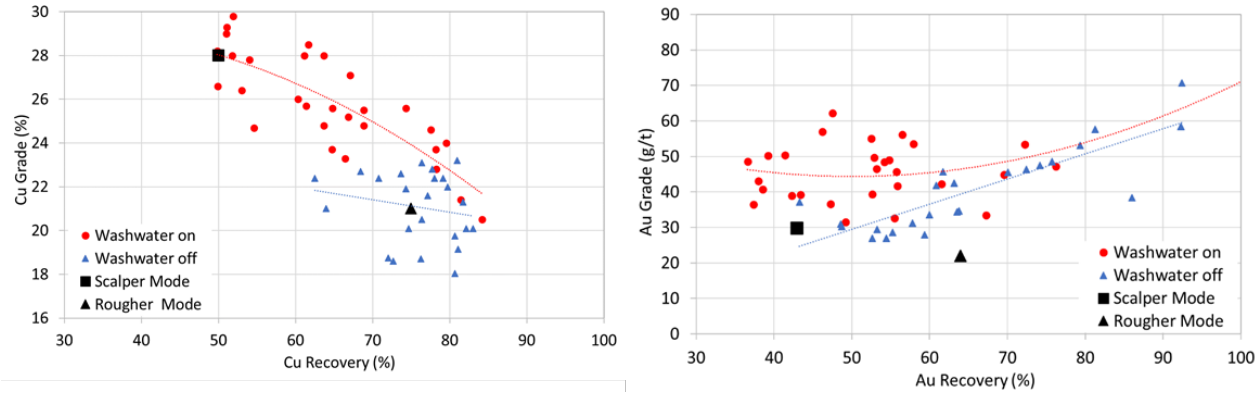

FIG 2 – Pilot L500 Jameson Cell grade-recovery curve for Cu (left) and Au (right) with Rougher and Scalper design points.

Two mass balances were produced during this project for equipment design and capacity checks utilising JKSimFloat to model mass and volume flows and cell performance, as shown in Figure 3. Flotation recovery will be a strong function of the circuit arrangement, flotation bank residence times, ore floatability and cell operating parameters. Flotation modelling is a great tool for simulating these various interactive effects. Hatch uses floatability component models where the stream floatability is represented by a multi-component floatability distribution and the rate constants of these components are a function of the cell operating conditions, ore properties particle size, mineral association/liberation and pulp chemistry.

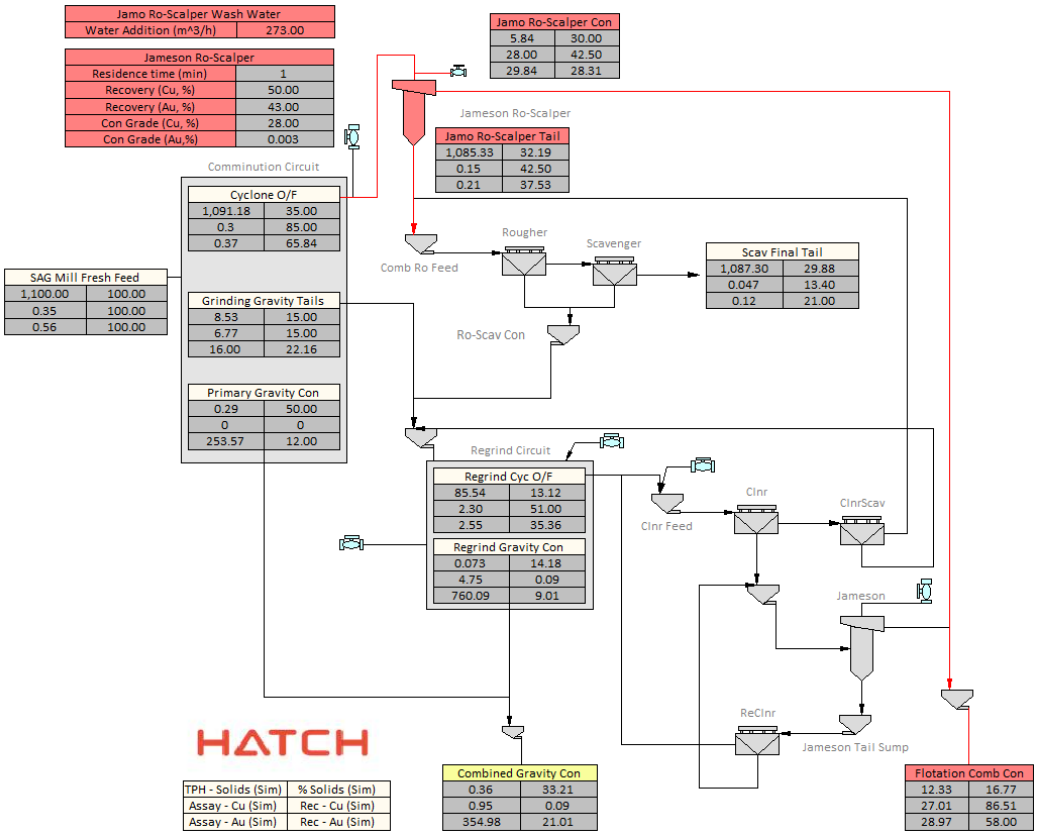

FIG 3 – JKSimFloat model for upgraded flotation circuit with Rougher-Scalper Jameson Cell.

The overall recovery (R) of each mineral in each flotation bank is a function of the recovery of each of its components (R_i) weighted according to the proportion of each component in the bank feed, as shown in Equation 1 (Savassi, 1998; Runge *et al*, 2001). Thus, flotation recovery is also a function of the proportion of each component in the flotation feed (m_i).

$$R = \sum_{i=1}^{n} m_i \cdot \frac{C\, k_i^{batch}\, \tau\, (1-R_w)+ENT\, R_w}{(1+C\, k_i^{batch}\, \tau\,)(1-R_w)+ENT\, R_w} \quad (1)$$

Where: C is the scale-up factor to account for differences in cell operation between the full-scale cell in comparison to the batch laboratory flotation cell, k_i^{batch} is the flotation rate of each floatability component (i) achieved in the batch laboratory flotation test performed using standard operating conditions, R_W is water recovery, *ENT* is the degree of entrainment and τ is the residence time.

There is no widely accepted model for Jameson cells available and their metallurgical performance is often scaled up from laboratory (dilution batch flotation tests) and/or pilot plant testing by assuming fixed values for metal recovery, concentrate grade and concentrate percent solids. With the growing application of these types of cells, not only in cleaner stages (their traditional use) but also in pre-flotation and scalping duties, there is a need to predict performance more accurately for circuit design and optimisation. The authors use a new approach to simulate Jameson Cell performance and its applicability has been demonstrated in different operations. This methodology has been previously published by Tabosa *et al* (2020).

Jameson cell design performance targets from the piloting campaign were established as follows:

- **Jameson Rougher**: 75 per cent Cu recovery at 21 per cent Cu grade (Cu enrichment ratio of 70), 1.1 per cent concentrate mass pull, 40 per cent w/w concentrate solids concentration with no wash water addition.
- **Jameson Rougher-Scalper**: 50 per cent Cu recovery at 28 per cent Cu grade (Cu enrichment ratio of 93.3), 0.5 per cent concentrate mass pull, 30 per cent w/w concentrate solids concentration with 273 m^3/h wash water addition.

When using fixed recovery and mass split values to simulate Jameson Cells, the product streams (concentrates and tailings) will have the same floatability distribution as the feed. This will result in unrealistic performance of the overall circuit and limits the simulations that can be performed (for example, changes in circuit reconfiguration). For more accurate simulations, it is necessary to predict the floatability distribution of the products of the Jameson Cell. A simplification to the floatability component model is used to better assess the separability of a Jameson cell in a flow sheet. The effect of residence time can be removed by assuming a fixed and short residence time of one minute in Equation 1. This simplified floatability component model allows the floatability of the feed to the Jameson cell to be redistributed, producing different floatability distributions in the concentrate and tailings streams and accounting for the impact on downstream rougher-scavenger tank cell performance. Expected ore floatability of the Jameson Rougher and Jameson Rougher-Scalper tail streams (ie new fresh feed to the existing rougher bank of mechanical cells) are compared with ore floatability characteristics of the original cyclone overflow feeding flotation in Figure 4. A slower copper and gold flotation kinetics stream are expected to be feeding the existing rougher bank of mechanical cells for both Rougher and Rougher-Scalper scenarios, with the increased mass pull for the rougher scenario having the larger effect on tailings floatability as expected. The flotation piloting and modelling approach utilised here allowed a single large Jameson Cell to maintain circuit recovery despite an ~30 per cent increase in throughput, which severely impacted residence time in the rougher-scavenger bank. Moreover, the use of this alternative technology targeted specific fine Cu-Au losses and provided an option to relieve the overloaded cleaner circuit through effective use of wash water, minimising entrainment and enabling a final concentrate grade product to be produced.

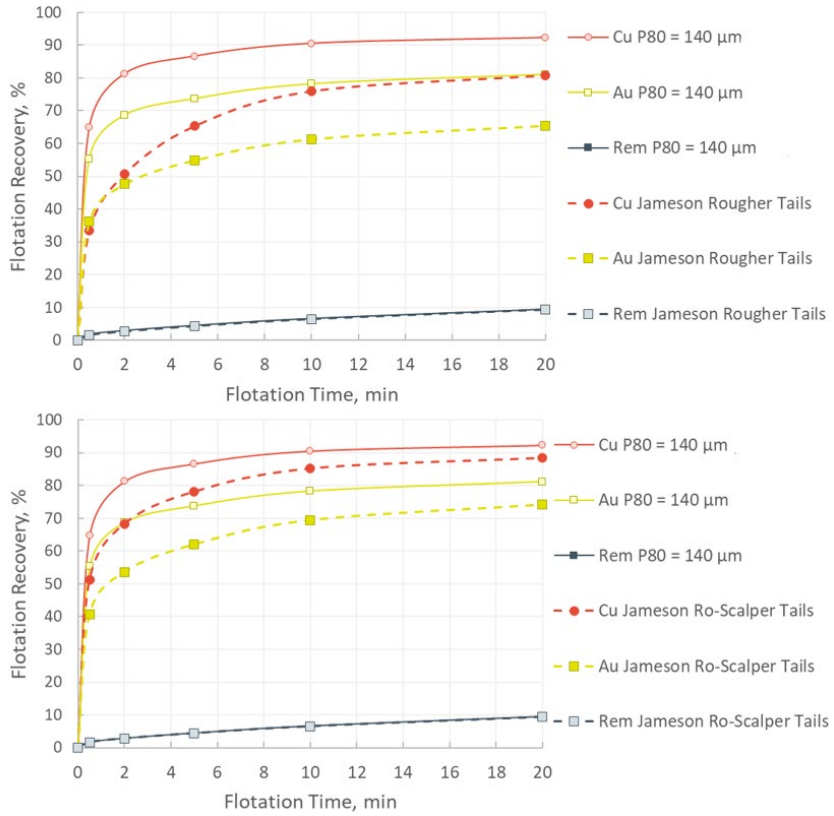

FIG 4 – Cu, Au and Remainder floatability characteristics for flotation circuit feed and Jameson Rougher (top) and Rougher-Scalper (bottom) tails.

Although the application of a Jameson Cell has been presented in the above analysis, cells such as the Imhoflot G-cell offer similar potential, as shown by comparison test work analysed by the authors for a Russian gold operation, where grade-recovery curves were produced for both cell types operating side by side in rougher-scalper and cleaner duties (Figure 5).

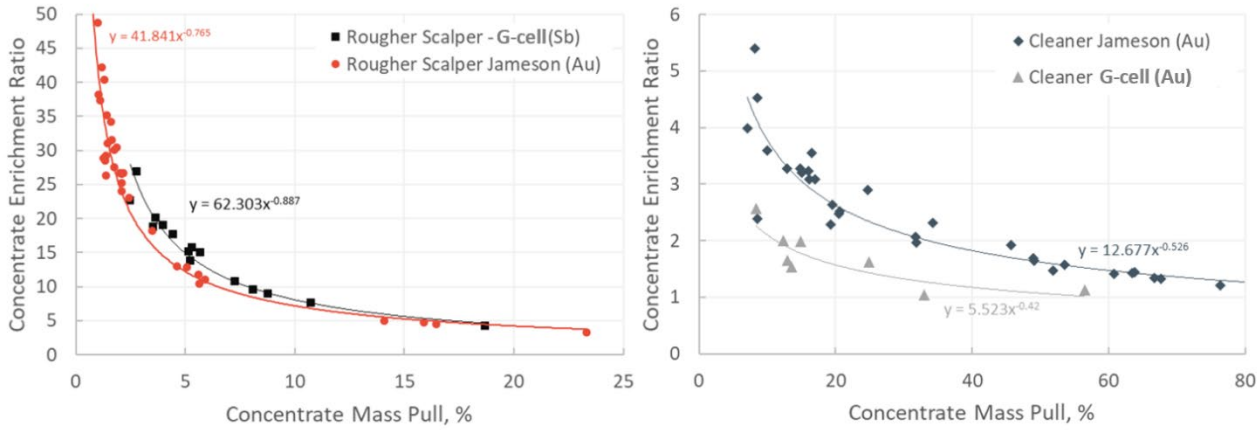

FIG 5 – Jameson Cell and Imhoflot G-cell pilot test rig mass pull verses enrichment curves.

Pilot trials of the G-cell at the Kazzinc Altyntau Kokshetau operation in Kazakhstan further demonstrated the success of pneumatic cells in alternate duties – specifically the cyclone overflow stream. The 8 Mt/a gold concentrator includes crushing, grinding and coarse gold recovery via flash flotation and gravity concentration prior to flotation. The conventional tank cell circuit operates with a feed grade of 0.81 g/t Au and has a final tailings grade of 0.47 g/t, with size-by-size analysis indicating 65 per cent of Au losses were in the <38 µm fraction (Hoang *et al,* 2022). Size by size pilot unit performance indicates that in this duty it was possible to recover up to 66–69 per cent of the gold in <20 and 38 µm fractions after reagent and cell parameter optimisation (Figure 6). Significantly, across the nine test conditions an average concentrate grade of 19.9 g/t Au was

obtained, compared to the existing circuit final concentrate grade of 25–30 g/t achieved with two cleaning stages.

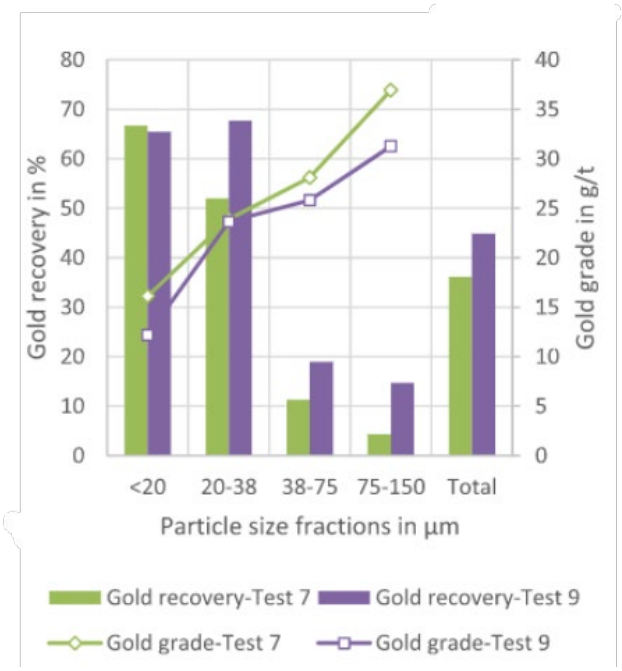

FIG 6 – Imhoflot pilot G-cell Au recovery by size and concentrate grade with optimised reagent addition (reproduced from Hoang *et al*, 2022).

Overall, the various piloting and modelling results above support the theory that Jameson Cells, and similar pneumatic flotation cell types have significant potential for new, scalping duties at the head of flotation banks, where they can effectively recover fast floating, fine or well-liberated valuable minerals and also relieve capacity constraints in the downstream circuit.

COARSE PARTICLE FLOTATION CIRCUITS

Increasing throughput with fixed installed comminution energy or increasing grind size as a strategy to reduce comminution energy consumption can result in coarsening of flotation feed size and a reduction in particle liberation and recovery (Fosu *et al*, 2015).

Coarse particles require intensive stirring energy to suspend them and have a lower probability of particle bubble attachment due to poor liberation. In addition, the high-shear environment of a conventional flotation cell results in a higher rate of bubble particle detachment. The results is a higher representation in the tailings of a conventional flotation cell (Whitworth *et al*, 2022).

One technology suitable to recover coarse particles is fluidised bed flotation where the flotation cell contains a bed of particles as well as and up flow of fluidising water. Eriez' HydroFloat™ and Jord International's NovaCell™ fluidised bed flotation units are currently used for coarse particle flotation (Whitworth *et al*, 2022).

The Eriez HydroFloat™ cell combines hindered teeter-bed of fluidised solids with the injection of small air bubbles. to float coarse particles from a reagentised fines deficient feed. The unit contains three sections, an upper freeboard section, a middle separation section and the lower dewatering cone (Kohmuench *et al*, 2018).

Brownfield installations of Eriez HydroFloat™ units have been predominantly used in a scavenger duty where there is a lower risk to the existing facility. The use of coarse particle flotation technologies within the primary grinding circuit to concentrate valuable coarse mineral particles or to remove well-liberated gangue minerals in base and precious metals is still in early stages despite its promising potential.

The Jord International's NovaCell™ is an emerging coarse particle flotation technology with a cell containing a fluidised-bed and a disengagement zone. The feed is combined with a recycle stream

and enters via a downcomer to the top of the disengagement zone and falls counter-currently downwards where it then forms the fluidised bed. In contrast with Eriez HydroFloat™, the NovaCell™ does not require a tailored narrow feed size distribution. Furthermore, the NovaCell™ produces both a coarse particle concentrate and a fines stream containing froth concentrate (Jameson and Emer, 2019).

There is no widely accepted model for the Eriez HydroFloat™ available, and metallurgical performance is often scaled-up from laboratory HydroFloat™ tests and/or pilot plant testing by assuming fixed values for metal recovery by size, mass recovery by size and concentrate percent solids.

Mineralogical and liberation analyses of the HydroFloat™ test work feed, concentrate and tailings streams by size can be used to determine the distribution and recovery of valuable minerals by exposure surface area. This will indicate the class of mineral particles which have a higher probability to be recovered to concentrate.

Laboratory flotation testing on the HydroFloat™ concentrate at various regrind sizes (P_{80}) can provide key circuit design information such as target grind size, concentrate grade, tailings grade and mass recovery. This information feeds into the flow sheet development and influences where the HydroFloat™ concentrate and tailings products will be directed into the new or existing circuit.

The HydroFloat™ concentrate contains limited fine, comprised predominantly of gangue minerals which can be harder than the plant feed. There are limited HydroFloat™ concentrate regrind installations available for benchmarking in the development of new operations with the reliance of test work for specific energy determination. To quantify the specific energy requirement to achieve a target grind size there are a number of vendor and non-vendor tests are available including:

- Levin standard test (Non-Vendor)
- Levin modified test with 19 mm media (Non-Vendor)
- Bond test (Non-Vendor)
- Metso:Outotec Jar Mill test (Vendor)
- Nippon Eirich Tower mill (Vendor)

The authors have been involved in several projects where non-vendor testing was conducted in parallel to vendor testing to reduce risk and reliance on the vendor tests for material with limited historical benchmarking.

Hatch has worked on coarse particle flotation circuit design and installation through PFS, FS and Detailed Design Engineering phases for an Australian Cu-Au operation who wanted to address flotation recovery losses as part of a plant expansion. Early study phases analysed flotation circuit survey data and mass balance results showed that on average 45 per cent of copper loss to tails was coarser than 106 µm, and of these particles, the majority displayed low surface exposure of copper sulfides.

Technology trade-off analysis was conducted for the selection coarse particle flotation flow sheets for circuit modelling. Several options of pre-classification were identified for further analysis with a common downstream flow sheet selected that included coarse particle flotation, dewatering cyclones and concentrate regrind followed by a cleaner Jameson cell. The dedicated HydroFloat concentrate treatment equipment was selected to maximise liberation and minimise the load on the existing cleaning circuit.

The coarse particle flotation concentrate is reground to 38 µm in a Vertimill™ operating in closed circuit with a cluster of regrind cyclones. The inclusion of the concentrate regrind and cleaner Jameson Cell in the flow sheet allowed a high-grade low mass concentrate stream to be directed to the cleaner circuit and the lower grade Jameson tailings stream to be returned to the head of rougher circuit.

Several coarse particle flotation circuit mass balances were produced during this project for equipment design and capacity checks utilising Limn to model Cu, Au and gangue by size, mass and volume flows and cell performance, as shown in Figure 7. Circuit recovery and concentrate

grade will be a function of the circuit configuration and performance including the pre-classification recovery-by-size, ore floatability, HydroFloat™ cell operating parameters, concentrate mass, regrind mill size and Jameson Cell operating parameters.

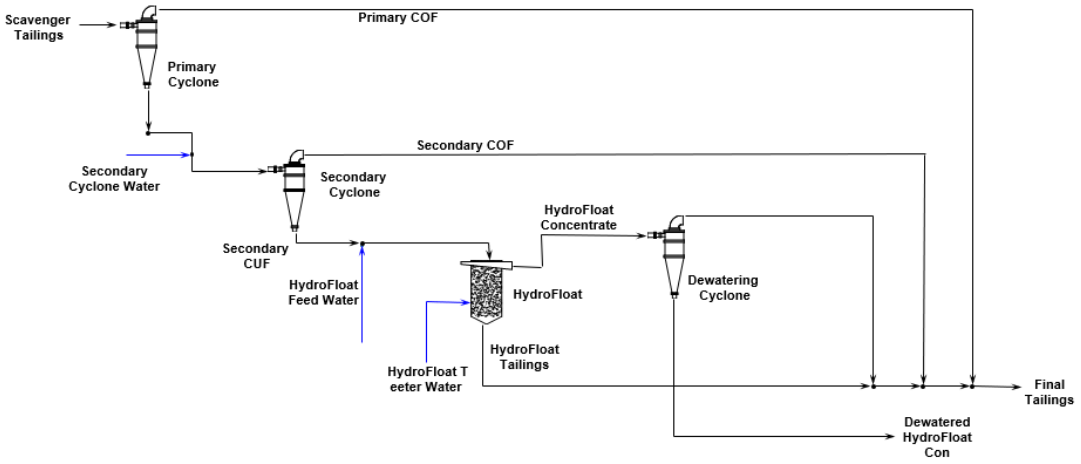

FIG 7 – Coarse Particle Flotation Limn Flow sheet.

Preliminary simulations of the proposed flow sheet configurations were conducted using the plant flotation model with the additional of the coarse particle flotation circuit (Table 1).

- **Simulation 1**: **Single Stage Cyclones**. A single stage cyclone pre-classification circuit ahead of the HydroFloat™. The single cyclone stage had the lowest classification efficiency with larger mass flows require to maximise the recovery of coarse material to coarse particle flotation.
- **Simulation 2**: **Two Stage Cyclones**. A two-stage cyclone pre-classification circuit ahead of the HydroFloat™. The dual stage has an improved classification efficiency relative to a single cyclone stage.
- **Simulation 3**: **Crossflow™ Classifiers**. A pre-classification circuit containing a cyclone stage followed by Crossflow™ classifiers ahead of the HydroFloat™. The Crossflow™ classifier classification circuit provided the highest classification efficiency of the classification options. However, this option has high process water consumption (+50 per cent) relative to the other options.

Table 1

Simulation results of the coarse particle flotation circuit.

Parameter	Base Case	Simulation 1	Simulation 2
Rougher-scavenger tails, t/h	2392	2518	2497
Dewatered coarse particle flotation concentrate, t/h	-	127	106
Dewatered coarse particle flotation concentrate Cu grade,%	-	0.46	0.5
Dewatered coarse particle flotation concentrate Au grade, g/t	-	0.97	1.05
Cu grade in final tail,%	0.079	0.65	0.66
Au grade in final tails, g/t	0.15	0.12	0.12
Cu flotation recovery,%	77.6	81.7	81.3
Au flotation recovery,%	70.0	75.8	75.2
Change in Cu recovery,%(Delta)		+4.1	+3.7
Change in Au recovery,%(Delta)		+5.8	+5.2

A preliminary trade-off study was conducted to further reduce the number of options, with the single and dual stage cyclone pre-classification options chosen for further simulation and preliminary engineering. Additional simulations were conducted to identify the most promising circuit flow sheets, equipment sizes and circuit configurations to allow coarse, lean composite Cu and Au sulfide bearing mineral particles to be scavenged and recovered.

The dual cyclone option was identified as the option that provided the optimum balance between operability, maintainability, CAPEX and recovery. A dual stage cyclone classification was selected for the pre classification circuit to progress to feasibility and detailed engineering design. The upgraded flotation circuit with coarse particle flotation was modelled in JKSimFloat using inputs from the coarse particle flotation circuit Limn model. The JKSimFloat circuit flow sheet is shown in Figure 8.

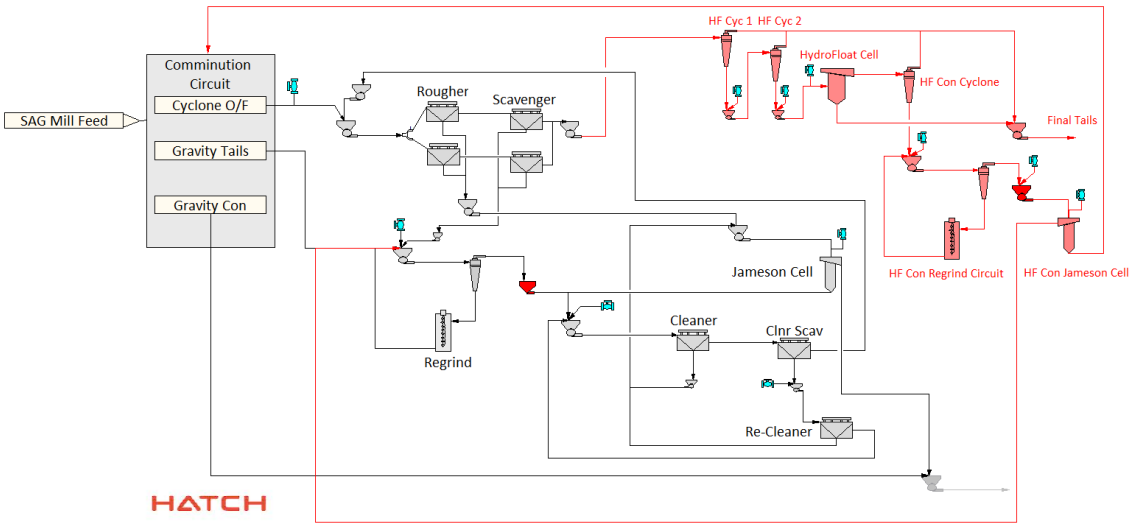

FIG 8 – JKSimFloat model for upgraded flotation circuit with Coarse Particle Flotation Circuit.

With each of the pre coarse particle flotation classification circuits investigated, the imperfect classification resulted in a portion of the fine material reporting to coarse particle flotation feed. Fine particles reporting to the HydroFloat™ feed will be hydraulically carried to the concentrate by entrainment through the continuous overflow of teeter water over the lip of the concentrate launder. The circuit included deslime/dewatering cyclones ahead of the regrind circuit to remove the low-grade fines. The majority of the fine material reporting to the concentrate results in HydroFloat™ tailings comprising mostly of coarse particles, with challenging material properties including high abrasiveness and poor particle suspension. To aid the slurry material properties the flow sheet combined the fines containing dewatering cyclone overflow and the two pre-classification cyclone overflow streams with the HydroFloat™ tails in the launder prior to the tailings hopper.

Material properties of the HydroFloat™ tailings and high process water demand of the coarse particle flotation circuit in combination with upstream and downstream equipment availabilities were also a consideration in the inclusion of bypasses in the overall flow sheet design. The flow sheet was designed with cyclone overflow recycles in the pre-classification circuit to enable the cyclone feed pumps to continue to run with minimal additional process water during start-up, shutdown or if the feed to the coarse particle flotation circuit is bypassed. A recycle of the coarse particle flotation tailings was included in the flow sheet to enable to coarse particle flotation circuit to be recycled for a short time if there was downstream limitations. The coarse particle flotation circuit tailings reported to the existing tailings thickener to maximise the recovery of process water.

ENERGY-EFFICIENT AND SMALL FOOTPRINT FLOTATION CELLS

Flotation optimisation has traditionally been focused on grade and recovery performance improvements. However, with the growing need for energy efficiency and the dramatic increase in flotation cell size in recent years it is worth considering how well energy is utilised within flotation cells. In conventional mechanical flotation cells a certain amount of energy is required to meet the basic requirements for flotation (air dispersion, solids suspension and particle-bubble collision and

attachment). Tabosa *et al* (2016) have shown that flotation rate in the collection zone and the fraction of the cell with higher turbulence increases as more of the power drawn by the impeller is dissipated as shear in the impeller-stator region. They have shown that recovery improved for conditions that increase the volume of the highly turbulent zone and thus achieve high local energy dissipation near the impeller. This ensures more efficient use of the energy imparted to the impeller and should promote higher collision rates. However, improvements in the collection zone may not translate to an increase in overall recovery unless improvements to the froth phase are implemented to minimise the detrimental effect of turbulence on the froth zone recovery. Ideally, bubble-particle collision/attachment and the froth separation could be considerably optimised if carried out in separate units.

New mechanical flotation cell technologies such as these supplied by Eriez's StackCell® (Figure 9) and Woodgrove (SFR – Staged Flotation Reactor and DFR – Direct Flotation Reactor, Figure 10) decouples the particle-bubble collection zone within the cell from the froth phase separation process. These alternatives have been developed with the goal of providing more efficient flotation using separate chambers for particle-bubble collision and for froth separation. These devices build on the concept of focused energy input to enhance fine particle and relatively coarse particle (DFR) recovery as well as improving flotation kinetics. Similarly to high-intensity pneumatic flotation cells (eg Jameson, PneuFloat and Imhoflot G-cells), these technologies provide a high intensity contained reactor zone where fine bubbles are generated and intensely mixed with feed pulp before discharging into a quiescent separation chamber. The difference, however, is that the high intensity energy in these devices is generated by moving parts (ie impeller) rather than by injection of air under high-pressure or air induced by vacuum in the aerator of high-intensity pneumatic flotation cells (Hassanzadeh *et al*, 2022).

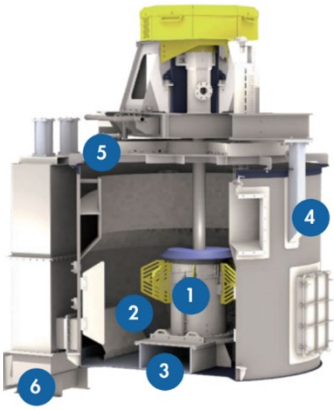

FIG 9 – Eriez StackCell®: 1. collection chamber, 2. separation chamber, 3. feed inlet, 4. froth, 5. wash water system, 6. tailings discharge (Eriez, 2022).

FIG 10 – Woodgrove Staged Flotation Reactor (left) and Direct Flotation Reactors (right) (Nelson and Lelinski, 2019; Woodgrove Technologies, 2022).

The Staged Flotation Reactor (SFR) is a flotation cell comprising three separate stages: particle collection, bubble disengagement and froth recovery (Figure 10). By decoupling the three processes, the SFR aims to optimise each of the three processes separately. The rotor in the particle collection chamber (tank) is designed to provide localised high energy input through a high shear impeller zone leading to high particle-bubble collision/attachment (ie high collection efficiency). The second tank purpose is to deaerate the slurry (bubble disengagement) and rapid recovery froth to the lauder minimising froth drop back. The third tank or froth recovery unit uses wash water and high solids flux. It is worth noting that the principle of operation of the Woodgrove Technologies Staged Flotation Reactor (SFR) is very similar to Eriez StackCell®s (see Figure 9). Some significant installations of SFR units in copper concentrators are BHP-Billiton's Spence and Tech Resources Limited 's Quebrada Blanca 2 in Chile, which combines FLSmidth 600 m^3 nextStep cells in rougher duty with SFR(s) in cleaner-duty. The development of the Staged Flotation Reactor was followed by the Direct Flotation Reactor (DFR) – a flotation cell which operates without the froth phase. The complete DFR unit is pressurised and has low footprint due to the lack of the froth phase. According to Woodgrove Technologies the main advantages of the SFR and DFR cells include reduced power/air consumption, reduced footprint, reduced installation and infrastructure costs (eg DFR units can be installed on the same level) (Moore, 2021). Unfortunately, at the time this paper is written, technical information on the metallurgical performance of Woodgrove Technologies cells or industrial flotation circuits comprising only SFR and/or DFR units in public domain is scant or almost inexistent. This certainly affects the confidence of engineering and mining companies to embrace this type of cells in large throughput concentrators (eg rougher duty).

The authors of this paper have been evaluating the metallurgical performance of these alternative flotation technologies in greenfield and brownfield optimisation and expansion at concept, pre-feasibility, and feasibility level projects. In brownfield expansion projects, for example, available footprint is often an issue and alternative solutions to installing conventional mechanical flotation cells need to be evaluated to deliver the equivalent capacity and eliminate the need for constructing additional building for new flotation equipment.

Furthermore, overall unit size can be reduced while maintaining the same (or higher) capacity and metallurgical performance. The implications of this step-change in technology are numerous and include a significant reduction in energy consumption (>40 per cent) as well as reductions in plant height, footprint and foundation loads of greater than fifty percent.

Seaman *et al* (2021), for example, have looked at alternatives to overcome rougher residence time and footprint limitations in the rougher flotation bank at Red Chris Mine, Canada. Additional 600 m^3 of rougher capacity was required and they considered SFR/DFR and StackCell technologies. Jameson cells were also considered for this duty. They demonstrated that Eriez StackCell®s have superior kinetic performance compared to conventional mechanical tank cells, with flotation rates for copper and gold bearing minerals being at least four times faster compared to the plant cells. They have also shown that the required rougher volume increase of 600 m^3 to overcome rougher residence time limitations can be fulfilled by 25 per cent of this volume using two 75 m^3 StackCell®s with Hatch completing PFS engineering to fit these cells inside the existing process building.

The authors of this paper have also conducted a trade-off study between the Staged Flotation Reactor (SFR) and Direct Flotation Reactor (DFR) for the cleaner scalper of a North American copper-gold concentrator as part of the flotation expansion project. The flow sheet investigated for the scope of this trade-off is presented in Figure 11, which presents a clear depiction of the new unit operation within the existing processing circuit. The SFR or DFR were tested in cleaner-scalper duty taking primary high-grade regrind cyclone overflow. The regrind cyclone overflow consists of freshly reground rougher concentrate. The SFR or DFR concentrate is sent directly to final concentrate while the tailings will either feed the existing 1st cleaners or bypass directly into the 1st cleaner tailings.

Pilot-scale test work was performed by taking a bleed from the regrind cyclone overflow under 3-pass and 4-pass scenarios to evaluate the use of 3 or 4 SFR or DFR units in series. However, the pilot-scale test work for the SFR and DFR were conducted three years apart; therefore, the ore parameters feeding the mill during these two campaigns were subject to the ore conditions from the mine. The SFR campaign processed lower copper grade than the DFR campaigns, but both campaigns had similar gold feed grade.

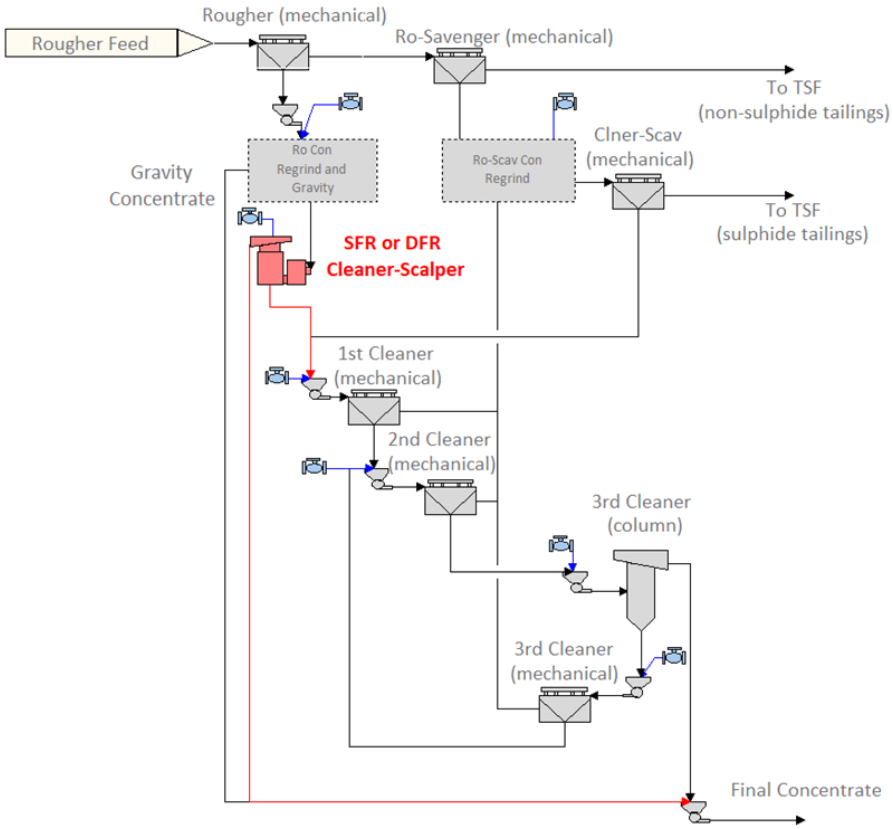

FIG 11 – Simplified Flotation Flow sheet of a Cu/Au operation.

Figure 12 shows the best pilot-scale testing results of the SFR and DFR units (with 3 and 4 passes). It can be clearly seen that the SFR had a superior metallurgical performance than the DFR units for Au and Cu recovery and enrichment ratio. For example, at 8 per cent mass pull the SFR and DFR Cu recoveries sit around 90 per cent and 65 per cent, respectively. Regarding the SFR and DRF Cu versus Au recoveries, Figure 12 clearly shows that most of the data points of the SFR sit above 80 per cent Cu and 50 per cent Au recovery. In contrast, most of the data points for the DFR testing sit above 60 per cent Cu and 40 per cent Au recovery. And finally, regarding Cu and Au enrichment ratio (or selectivity) versus mass pull the SFR units again outclassed the DFR units with enrichment ratios above 12 and 8 for Cu and Au versus above 6 for Cu and 4 for Au for the SFR units.

The SFR processed feed with a much higher pyrite to chalcopyrite ratio than the DFR. Both SFR and DFR banks (three units in series) can be installed within the existing processing plant constraints. The SFR bank and the required auxiliaries take an area of approximately 126 m^2, whereas the DFR bank only take about 68 m^2 area. Besides the smaller foundation area that DFR requires, this option also takes less vertical space since all the DFR cells are on the same level and no equipment needs to be elevated. Capital costs of the DFR cells were also around 8 per cent lower than the SFR cells, with OPEX of the DFR being slightly lower than the SFR.

Although the DFR requires a smaller footprint and no elevation, the SFR cell outperformed the DFR during the pilot-scale testing in cleaner-scavenger duty. In addition, there are currently more industrial installations of SFR than DFR processing similar Cu/Au ore types in cleaner-scalper duty. Therefore, installing three SFR units to increase cleaner circuit capacity and also to improve the flotation circuit metallurgical performance was the preferable option.

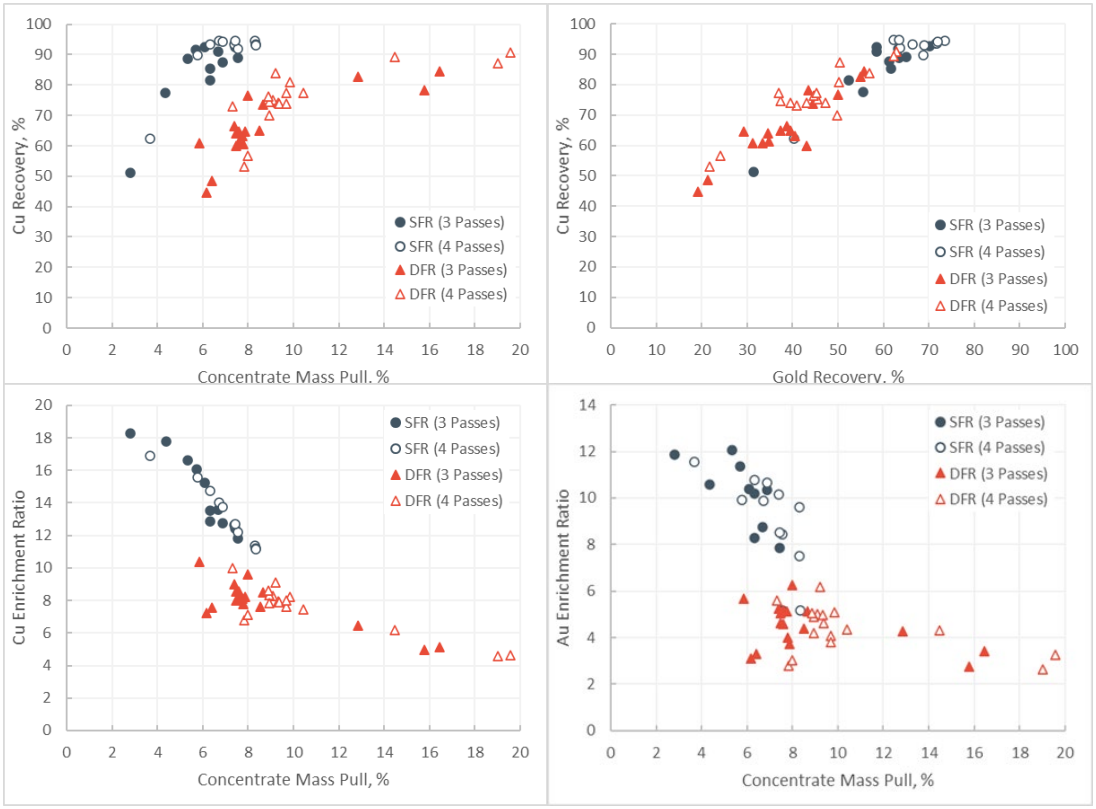

FIG 12 – SFR and DFR pilot metallurgical performance in a Cu/Au operation.

CONCLUSION

The mining industry faces multiple challenges such as processing low-grade, mineralogically complex orebodies, reductions in energy consumption and carbon emissions, water scarcity/quality, environmental, social and governance issues etc. At the same time, the demand for metals like copper, iron, cobalt, lithium and nickel is projected to reach its peak by 2050 (Watari *et al*, 2020).

Traditionally, flotation circuits design, equipment sizing and selection are performed based on laboratory and/or plant-scale test work (eg kinetics and locked-cycle tests) complemented by detailed mineral/liberation characterisation and personal experience (benchmarking data). Software packages such JKSimFloat, SysCAD, HSC Chemistry, METSIM and Limn are largely used to perform mass balance, in model development and simulation. However, there is a strong need to incorporate financial analysis modules (revenue maximisation or cost minimisation) on the flotation software packages.

The future of flotation circuit design will incorporate different cell types such as mechanical with or without froth wash water, pneumatic (eg Jameson, Columns) and hybrid cells (eg Reflux Flotation Cell, HydroFloat, NovaCell) in brownfield and greenfield projects in conventional and, more importantly, in non-conventional applications such as coarse gangue removal (pre-concentration) prior to flotation using flotation devices like the Eriez HydroFloat™ or Jord International's NovaCell™. In addition, in large throughput base and precious metals circuits, flotation machines such as Glencore Technology Jameson cells, Eriez StackCell®s and Woodgrove Direct/Stage flotation reactors will likely have to be scaled-up to process high solids flow rates (eg First Quantum Cu/Mo Panama, Anglo American Cu/Mo Los Bronces operations) if operated in rougher duty. In precious and base metals coarsening the feed to flotation to a P_{80} in excess to 200 µm is likely to become more prevalent to minimise energy consumption, carbon emissions, and to reduce costs and/or risks of downstream processes like thickening, filtration, tailings management, etc.

Flotation will continue to be a powerful and versatile concentration method in the foreseen future. And, flotation circuit design, equipment selection and sizing will keep adapting to tackle the current and future mining challenges. This will require engineering companies working closely with mining

companies, flotation equipment manufacturers, reagent suppliers, Universities and Technology centres.

REFERENCES

BHP, 2022, May 13. BHP inaugurates a new copper concentrator in Spence which will allow the operation to be extended by 50 years. Retrieved from https://www.bhp.com/news/articles/2022/05/bhp-inaugurates-a-new-copper-concentrator-in-spence

Eriez, 2022. StackCell flotation, accessed April 2022, https://www.eriez.com/NA/EN/Flotation/StackCell-Flotation.htm

Fosu, S, Awatey, B, Skinner, W, Zanin, M, 2015. Flotation of coarse composite particles in mechanical cell vs. the fluidised-bed separator (The HydroFloat™), *Miner. Eng*. 77, 137–149, https://doi.org/10.1016/j.mineng.2015.03.011

Harbort, G J, Murphy, A S, Budod, A, 1997. Jameson cell developments at Philex Mining Corporation, In: *Proceedings of 6th AusIMM Mill Operators' Conference*, pp 105–114 (The Australasian Institute of Mining and Metallurgy: Melbourne).

Harbort, G, 2019. Pneumatic Flotation, in *SME Mineral Processing & Extractive Metallurgy Handbook*, R Dunne, S Kawatra and C Young (eds.), SME, 2019.

Hassanzadeh, A, Safari, M, Hoang, D, Koshas, H, Albijanic, B, Kowalczuk, P B, 2022. Technological assessments on recent developments in fine and coarse particle flotation systems, *Minerals Engineering*, 180, https://doi.org/10.1016/j.mineng.2022.107509

Heffernan, V, 2018. A staged start-up – The journey to successful scale-up for Woodgrove Technologies' innovative three-stage flotation reactor, *CIM Magazine*, 13(3).

Hoang, D, Imhof, R, Sambrook, T, Bakulin, A, Murzabekov, K, Abubakirov, B, Rudolph, M, 2022. Recovery of fine gold loss to tailings using advanced reactor pneumatic flotation Imhoflot™. *Minerals Engineering*, 107649. Retrieved from https://doi.org/10.1016/j.mineng.2022.107649

Jameson, G J, Emer, C, 2019. Coarse chalcopyrite recovery in a universal froth flotation machine. *Minerals Engineering*, 134, 118–133.

Kohmuench, J, Luttrell, G, Mankosa, M, 2001. Coarse particle concentration using the hydrofloat separator. *Miner. Metall. Process*, 18 (2), 61–67.

Kohmuench, J, Mankosa, M, Thanasekaran, H, Hobert, A, 2018. Improving coarse particle flotation using the HydroFloat™ (raising the trunk of the elephant curve), *Miner. Eng*, 121, pp 137–145. https://doi.org/10.1016/j.mineng.2018.03.004

Moore, P, 2021. Flotation Factors. *International Mining magazine*, October 2021, 36–45.

Nelson, M and Lelinski, D, 2019. Mechanical Flotation, in *SME Mineral Processing & Extractive Metallurgy Handbook*, R Dunne, S Kawatra and C Young (eds.), SME, 2019.

Runge, K C, Dunglison, M E, Manlapig, E V and Franzidis, J P, 2001. Floatability component modelling a powerful tool for flotation circuit diagnosis. *Proceedings Fourth International Symposium on Fundamentals of Minerals Processing*, CIM, 93–107.

Savassi, O, 1998. Direct estimation of entrainment and the froth recovery of attached particles in industrial flotation cells, PhD. Thesis, University of Queensland.

Seaman, D, Li, K, Lamson, G, Seaman, B A, Adams, M H, 2021. Overcoming rougher residence time limitations in the rougher flotation bank at Red Chris Mine. In: *Proceedings of 15th AusIMM Mill Operators' Conference*, 193–207 (The Australasian Institute of Mining and Metallurgy: Melbourne).

Tabosa, E, Runge, K, Holtham, P, 2016. The effect of cell hydrodynamics on flotation performance, *International Journal of Mineral Processing*, 156 (2016) 99–107.

Tabosa, E, Vianna, S, Valery, W, Duffy, K, Holtham, P, Pyle, L and Andrade, B, 2020. Modelling Pneumatic Flotation Cells for Circuit Design and Optimization, *IMPC 2020 Congress Proceedings*, pp 3081–3091, Cape Town, South Africa: International Mineral Processing Congress.

Watari, T, Nansai, K, Nakajima, K, 2020. Review of critical metal dynamics to 2050 for 48 elements, *Resources, Conservation And Recycling*, 155:104669, doi:10.1016/j.resconrec.2019.104669

Whitworth, A, Forbes, E, Verster, I, Jokovic, V, Awatey, B, Parbhakar-Fox, A, 2022. Review on advances in mineral processing technologies suitable for critical metal recovery from mining and processing wastes, *Cleaner Engineering and Technology,* Vol 7, https://doi.org/10.1016/j.clet.2022.100451

Woodgrove Technologies, 2022. Woodgrove direct flotation reactor, accessed April 2022, http://www.woodgrovetech.com/direct-flotation-reactor/

Electrically-enhanced supersonic shock wave reactors for sustainable mining

J S J van Deventer[1]

1. Director, Zeobond Pty Ltd, Highett Vic 3190. Email: jannie@zeobond.com

INTRODUCTION

Most comminution machines use compressive forces to fracture particles, even when it is known that tensile fracture is more effective. The reason is that it is not straightforward to design a device that places particles in a sufficiently intense tensile field that causes fracture. What is not widely known, is that the energy of fracture reduces even more when particles are placed in an electric field. Little has been published on the effect of electric fields on chemical reactions and changes in material properties. It is well known that pulsed high voltage systems induce particle fracture by generating plasma within the material (Andres, 1995). In contrast, the low voltage, high current system proposed here for particle fracture have not been reported. Hydrodynamic cavitation devices producing shock waves have been used in mineral processing (Ross, Singh and Pillay, 2019), but without the application of an electric field. Reactor designs using supersonic shock waves have been used for petrochemical processing (Knowlen, Mattick and Stevens, 2015), but the combination with an electric field (Lansell, Keating and Lowe, 2017) is rare. This paper presents potential applications of electrically-enhanced supersonic shock wave (EESS) reactors in the mining industry with the aim to enhance sustainability.

ROLE OF ELECTRIC FIELDS

Most research on the effect of electric fields on chemical reactions has focused on heterogeneous catalysis (Tsiplakides and Balomenou, 2009). Despite all this work, controversy remains about the nature of the enhancing effect, which may be one or two orders of magnitude. A key finding is that catalytic reactions proceed not just at a higher rate in the presence of an electric field, but also at a lower temperature, which places less demand on construction materials. The literature is conclusive that Joule heating caused by the electric field plays a minor role in enhancing reactions. It has also been concluded that a modulated electric field can significantly decrease the activation energy of catalytic reactions. Depending on the direction of an electric field, the dissociation energy of chemical bonds may be weakened substantially (Mata *et al,* 2009). Moreover, metals like gold may melt under ambient conditions in the presence of an electric field through the increase in entropy (De Knoop *et al,* 2018). Therefore, it is possible to drive the Gibbs free energy lower by an increase in entropy induced by an electric field, rather than an increase in temperature as is used in most conventional reaction systems.

The integration of an electric field in a supersonic shock wave reactor is an engineering challenge. For example, catalytic electrode materials are subjected to high wear conditions and may foul easily. Moreover, the feeding of particulate material without using slurry systems into a high-pressure reactor requires special technology.

APPLICATIONS

Zeobond and partners have demonstrated that a 10 tonne per hour EESS reactor can be used for (a) energy-efficient comminution of rock, (b) reduction of oxide and sulfide minerals to metal powders, (c) gasification of carbonaceous waste such as used tyres to syngas for electricity generation, and (d) production of cement from various source materials. The gas-solid EESS reactor is volumetrically scalable, which suggests that scale-up risk is low up to 100 tonnes per hour, although it has not yet been demonstrated. Potential applications in the mining industry are obvious for the recycling of waste, the reduction in energy consumption and less transportation of goods to remote sites. Zeobond's current focus is on the production of highly reactive supplementary cementitious materials (SCM) from waste with low reactivity. The EESS reactor has the capability to rapidly cool down products through a venturi nozzle, hence preserving their glassy state instead of forming unreactive crystalline products. EESS reactors could potentially produce reactive SCM from mine tailings and reduce the demand for expensive Portland cement in backfill.

Much has been written about the detection and recovery of unassayable precious metals occurring as nanoparticles (NP) (Helmy *et al,* 2013; Van Deventer, 2013). These NPs may be refractory to chemical attack (Mettela *et al,* 2018) or may occur as oxide clusters. Preliminary tests using a pilot slurry EESS reactor has demonstrated that the assayable grade of several gold ores and tailings could be increased significantly. It was also demonstrated that this 'additional' gold is economically recoverable by conventional carbon-in-leach cyanidation as well as thiosulfate leaching. EESS processing increased the liberation of preg-robbing carbon in some ores, but such carbon could be removed effectively by froth flotation or could be treated by blinding agents. The EESS reactor is not just liberating and transforming these NPs, but it is also aggregating the NPs into recoverable, metallic gold.

REFERENCES

Andres, U, 1995. Electrical disintegration of rock, *Miner. Process. Extract. Metall. Rev*, 14:87–110.

De Knoop, L, Juhani Kuisma, M, Löfgren, J, Lodewijks, K, Thuvander, M, Erhart, P, Dmitriev, A and Olsson, E, 2018. Electric-field-controlled reversible order-disorder switching of a metal tip surface, *Physical Review Materials*, 2(8):085006.

Helmy, H M, Ballhaus, C, Fonseca, R O C, Wirth, R, Nagel, T and Tredoux, M, 2013. Noble metal nanoclusters and nanoparticles precede mineral formation in magmatic sulphide melts, *Nature Communications*, 4:2405.

Knowlen, C, Mattick, A T and Stevens, C J, 2015. Supersonic shockwave reactors, and associated systems and methods, *PCT patent application* WO 2015/077335 A2.

Lansell, P, Keating, W and Lowe, D, 2017. Systems and methods for processing solid materials using shockwaves produced in a supersonic gaseous vortex, *US Patent* 9724703B2.

Mata, I, Molins, E, Alkorta, I and Espinosa, E, 2009. Effect of an external electric field on the dissociation energy and the electron density properties: The case of the hydrogen bonded dimer HF···HF*, *J Chem Phys*, 130:044104.

Mettela, G, Kouser, S, Sow, C, Pantelides, S T and Kulkarni, G U, 2018. Nobler than the noblest: noncubic gold microcrystallites, *Angewandte Chemie*, 57(29):9018–9022.

Ross, V, Singh, A and Pillay, K, 2019. Improved flotation of PGM tailings with a high-shear hydrodynamic cavitation device, *Minerals Engineering*, 137:133–139.

Tsiplakides, D and Balomenou, S, 2009. Milestones and perspectives in electrochemically promoted catalysis, *Catalysis Today*, 146: 312–318.

Van Deventer, J S J, 2013. The precious metals we prefer to ignore, *Minerals Engineering*, 53:266–275.

Future operations – maximising separation at coarse particle sizes

Enhancing grade engineering outcomes with precise breakage

R Lage[1], V Jokovic[2], C Antonio[3] and R Morrison[4]

1. PhD candidate, The University of Queensland, Sustainable Minerals Institute, Julius Kruttschnitt Mineral Research Centre, Brisbane Qld 4068. Email: r.lage@uq.edu.com
2. Senior Research Fellow, The University of Queensland, Sustainable Minerals Institute, Julius Kruttschnitt Mineral Research Centre, Brisbane Qld 4068. Email: v.jokovic@uq.edu.au
3. Senior Research Fellow, The University of Queensland, Sustainable Minerals Institute, Julius Kruttschnitt Mineral Research Centre, Brisbane Qld 4068. Email: c.antonio@uq.edu.au
4. Honorary Professor, The University of Queensland, Sustainable Minerals Institute, Julius Kruttschnitt Mineral Research Centre, Brisbane Qld 4068. Email: r.morrison@uq.edu.au

ABSTRACT

The decline of ore head grades has resulted in higher energy usage and increased production of waste in mining operations. Therefore, the mining industry is continually searching for innovation in the face of the growth in demand for mineral resources and sustainable development. One of the proposed solutions is to utilise the natural behaviour of some ores where mineralisation preferentially deports to certain size fractions after breakage. This behaviour can be utilised to enable early coarse gangue rejection and reduce the amount of material sent to further stages of mineral processing operations, thus decreasing energy consumption and improving energy efficiency. The Cooperative Research Centre for Optimising Resource Extraction's (CRC ORE) Grade Engineering® methodology utilises this approach to remove uneconomic material at the early stages of mineral processing using conventional breakage and sizing. It is hypothesised that this approach could be further improved by utilising breakage technologies that can deliver more controlled breakage. The Vertical Shaft Impactor (VSI) crusher was identified to be such a technology that could be utilised to control and promote selective breakage of particles by changing its parameter settings. This study investigates the influence of device settings including throughput and rotor design on single and multiple particle breakage, on metal deportment and coarse gangue rejection, in a laboratory-scale VSI unit. Additionally, these results are compared with the grade by size deportment promoted by a laboratory-scale jaw crusher device. The results demonstrated that, in some scenarios, there is a potential to use VSI to enhance the concentration of minerals into fines compared to a traditional crushing method.

INTRODUCTION

In order to meet the demand for metals, the mining industry has to increase the mining of low-grade deposits. However, this strategy increases the generation of mineable waste, tonnage required for processing to produce metals (Carrasco, 2017), and energy use. Most of the energy in mineral processing operations is consumed by comminution circuits, which are energy inefficient. To ensure sustainable development in this scenario, the mineral processing industry seeks technologies to increase efficiency.

Early coarse gangue rejection technologies can potentially increase the productivity and efficiency of metal units (Bearman, 2013; Bowman and Bearman, 2014; Carrasco, 2017; Johnson, 2018). Coarse gangue rejection is based on the principle that some ores deport mineralisation preferentially in specific size fractions after breakage, as observed by Bearman (2013), Carrasco (2013), and Bérubé and Marchand (1984). The process is based on the selective or preferential breakage of a crack to branch through mineral grains more often in one mineral compared to the others (Figure 1). Thus, the preferentially broken mineral occurs in the fine size fractions after the individual events of fracture (King and Schneider, 1998).

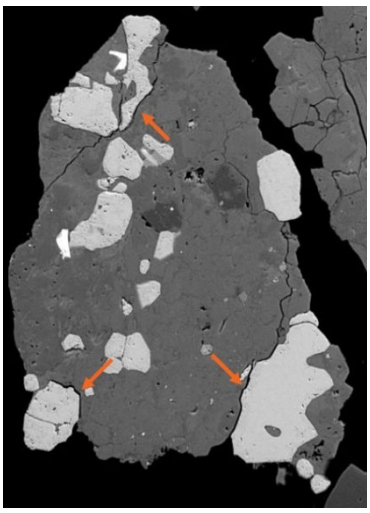

FIG 1 – Selective breakage and mineral grains (King, 2001, cited in Revell, 2018).

The preferential deportment can be used for the rejection of coarse gangue particles and improvement of the feed stream grade in traditional mineral processing circuits through pre-concentration. Pre-concentration utilises a range of techniques such as screening and automatic sorting after blasting and crushing to separate ore and gangue through size-by-size deportment differences (Napier-Munn, 2015). Based on this principle, CRC ORE developed the Grade Engineering (GE) system to assess and optimise the use of early coarse gangue rejection. GE combines ore properties with separation technologies, analysing the net value to reject lower grade material in present circuits of mine plans (Walters, 2017).

Material properties and breakage methods can influence selective liberation since different equipment types result in different applications of stress. Thus, GE outcomes can potentially be enhanced by the breakage method. Impact load promotes more pre-concentration compared with other types of loads (Stepanov *et al,* 1991; Hesse and Lieberwirth, 2018). Therefore, equipment that preferentially breaks particles by impact can potentially improve grade by size deportment.

Impact breakage is an important mechanism present in the size reduction process of the VSI crusher together with surface breakage. Moreover, the specific comminution energy applied to particles in VSI crushers is more controlled compared with conventional crushers such as jaw crushers whose breakage is influenced by the size and shape of particles processed. Consequently, VSI crushers potentially improve preferential deportment.

VSI operates by rock material being fed through a feed hopper, falling vertically into the rotor that is spinning at high speeds, where particles are accelerated by centrifugal force. The particles are then ejected from the rotor against stationary anvils, crossing an environment of flying debris that transit in the chamber, as illustrated in Figure 2.

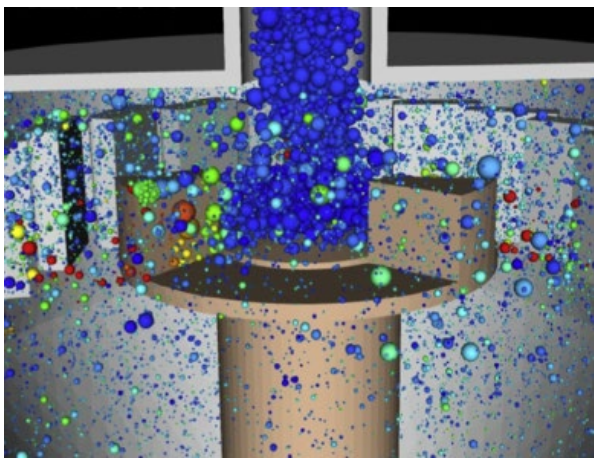

FIG 2 – Simulation of a VSI, in which particles are being thrown against anvils from the rotor (Sinnott and Cleary, 2015).

VSI settings possibly influence metal deportment and coarse gangue rejection. These include the rotor design, throughput, and single or multiple particle breakage since they affect particle breakage. These factors are investigated using a laboratory-scale VSI crusher and compared with the grade by size department achieved using a laboratory-scale jaw crusher. The results of this work contribute to the understanding of the potential of VSIs to improve grade by size deportment compared with a traditional crushing method.

MATERIALS AND METHODS

Two low-grade sulfide ores (Ore A and Ore B) from a silver, lead, and zinc mining operation were used in this study, identified as Ore A and Ore B Both ores were provided as 1500 kg SAG feed samples that were sized using a $\sqrt{2}$ sieve series (75 mm to 6.7 mm) and weighed. From each size fraction, subsamples were selected using a rotary splitter and sent for assaying later.

The laboratory-scale VSI is a small unit consisting of a hopper covered by a lid, a rotor, and a chamber. Figure 3 shows a Rocky® simulation of the VSI interior design. The main components of the laboratory-scale jaw crusher are a feed and a discharge chute, controls for gap adjustment, a product collection bin and start-stop controls for operation. The laboratory-scale VSI unit used had a maximum feed top size of <12 mm which limited the feed size that could be used in this study. The feed size range for the testing was -11.2 + 6.7 mm.

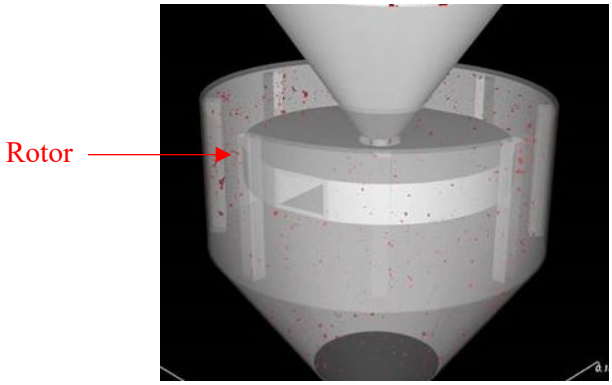

FIG 3 – Interior design of the laboratory-scale VSI – Rocky® simulation.

The breakage products of a VSI and jaw crusher were compared using the t_{10} parameter. t_{10} is defined as the percentage of product that passes one-tenth of the initial particle size and relates to the energy required for particle breakage in Equation 1 (Napier-Munn *et al,* 1996):

$$t_{10} = A\left(1 - e^{-b*E_{cs}}\right) \quad (1)$$

where:

E_{cs} Specific comminution energy (kWh/t)

A and b ore parameters related to impact breakage

Low t_{10} values can be linked to low energy applied to the material and an increased likelihood of providing only sufficient energy to promote selective breakage. During selective breakage, valuable minerals tend to deposit into the fines and a size fraction was necessary to differentiate coarse and fine material. Consequently, a t_{10} of 15 per cent was selected to compare the test results between the VSI and jaw crusher, where material retained on the nominated sieves was considered coarse and material passing through was considered as fines. For each initial size fraction tested, a different sieve was utilised according to the t_{10}.

The VSI testing conditions involved 18 experiments for Ore A and 12 experiments for Ore B, using:

- One rotor speed
- Two size fractions (-11.2 + 9.5 mm and -8 + 6.7 mm)
- Two different flow rates (low throughput and high throughput)

- Two different rotor lengths (short rotor and long rotor).

The low throughput test utilised approximately 1 kg of material at 1 kg per minute. The high throughput test was roughly 4 kg of material at 40 kg per minute. The long and short rotors measured 27 cm and 17 cm in length, respectively. The VSI speed was adjusted for both rotors' lengths to achieve a t_{10} of approximately 15 per cent. The speed is based on the results of the rock breakage characterisation of Ore A and Ore B using the Julius Kruttschnitt Rotary Breakage Tester (JKRBT). The JKRBT and VSI have similar operating principles, thus the VSI tip speed was based on the JKRBT tip speed required to produce a t_{10} of 15 per cent using both ores. The average E_{cs} using VSI for Ore A was 0.57 ± 0.02 kWh/t and for Ore B was 0.58 ± 0.02 kWh/t. Each test was repeated three times.

A full factorial design with three repeats was selected for each size fraction and Table 1 summarises the factors, high and low levels, and notations for each test. The product of the -11.2 + 9.5 mm material was split into two after sieving: one part containing passing 1.18 mm and another part containing +1.18 mm material. The product of -8 + 6.7 mm samples was split into materials below finer and coarser than 850 µm.

TABLE 1

Parameters and notation of VSI testing.

Factor	Level	Notation
Short rotor	170 mm (length)	SR
Long rotor	270 mm (length)	LR
Low throughput	1 kg/min	LT
High throughput	44 kg/min	HT

The laboratory-scale jaw crusher tests utilised 1 kg batch samples of the -8 + 6.7 mm (Ore A) and the -11.2 + 9.5 mm (Ore B). Before the crushing tests, trials were run to adjust the crusher close size settings (CSS) to achieve a t_{10} of 15 per cent for each size fraction. At the end of the trials, a CSS for Ore A and Ore B of approximately 2 mm was chosen for a throw of roughly 7 mm. After setting the crusher gap, three repeat runs for each sample were undertaken and the broken material was sized using the screen sizes shown in Table 2.

TABLE 2

Screen sizes of crushing test for Ore A and Ore B.

Ore A	Ore B
9.5 mm	6.7 mm
6.7 mm	4.75 mm
4.75 mm	3.35 mm
3.35 mm	1.7 mm
1.7 mm	0.85 mm
1.18 mm	-

Representative samples from each test from both equipment were obtained for characterisation using a portable handheld XRF (pXRF). A subset of the samples was selected for laboratory assaying and the results were compared with the pXRF results for calibration of the device.

RESULTS AND DISCUSSION

The Figure 4 shows the comparison between pXRF readings and chemical assaying results after calibration. The results demonstrate that pXRF is a suitable method for the analysis of Ag, Pb, and Zn in the samples.

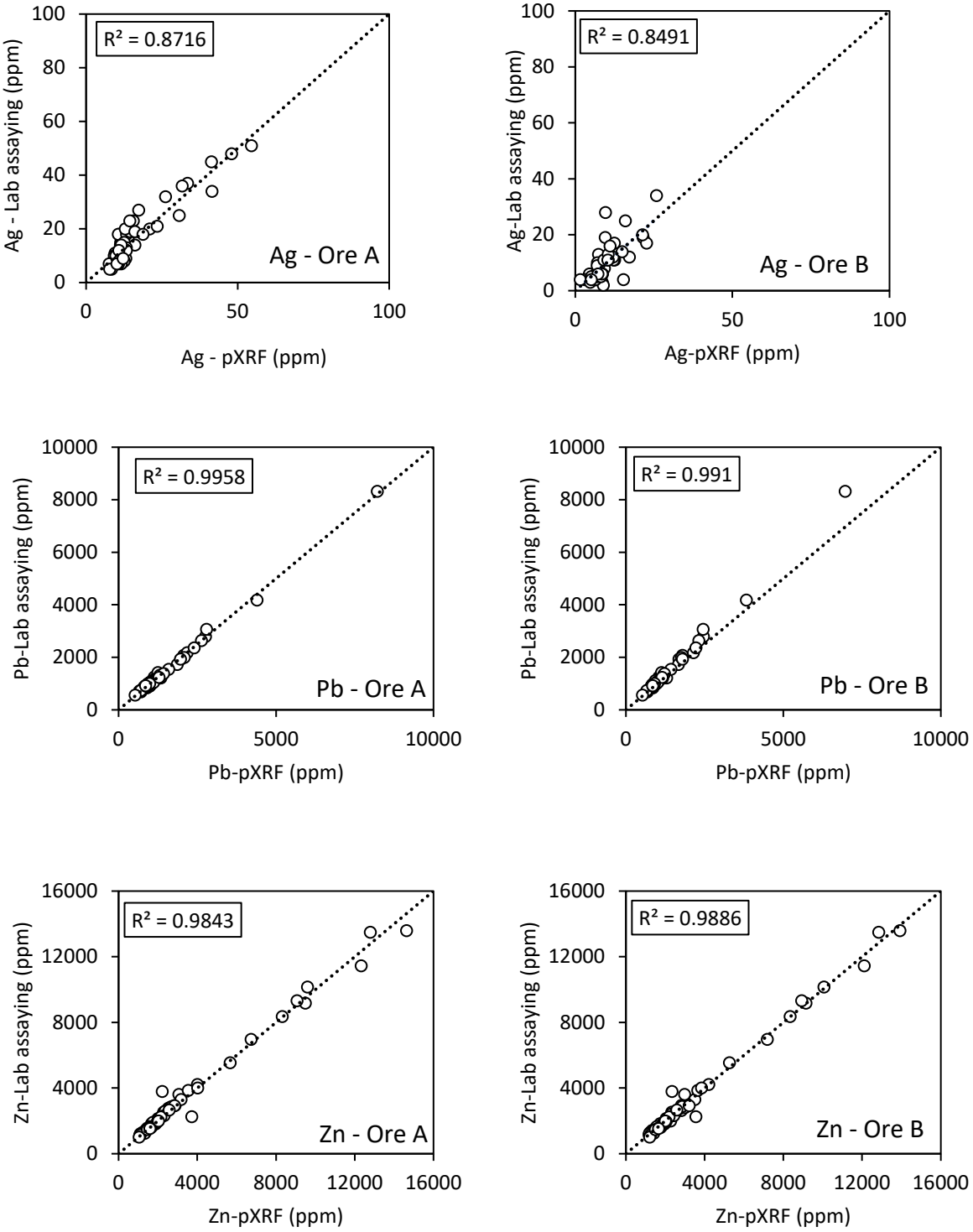

FIG 4 – pXRF versus ICP results of Ore A and Ore B.

An analysis of grade deportment by size of the bulk as-received samples for Ore A and Ore B was undertaken by plotting the screen undersize mass recovery versus cumulative metal recovery, as illustrated in Figure 5. This figure shows the potential of preferential Ag, Pb, and Zn deportment by size for Ore A and Ore B in the size range of -75 + 6.7 mm. The reference line represents no preferential deportment.

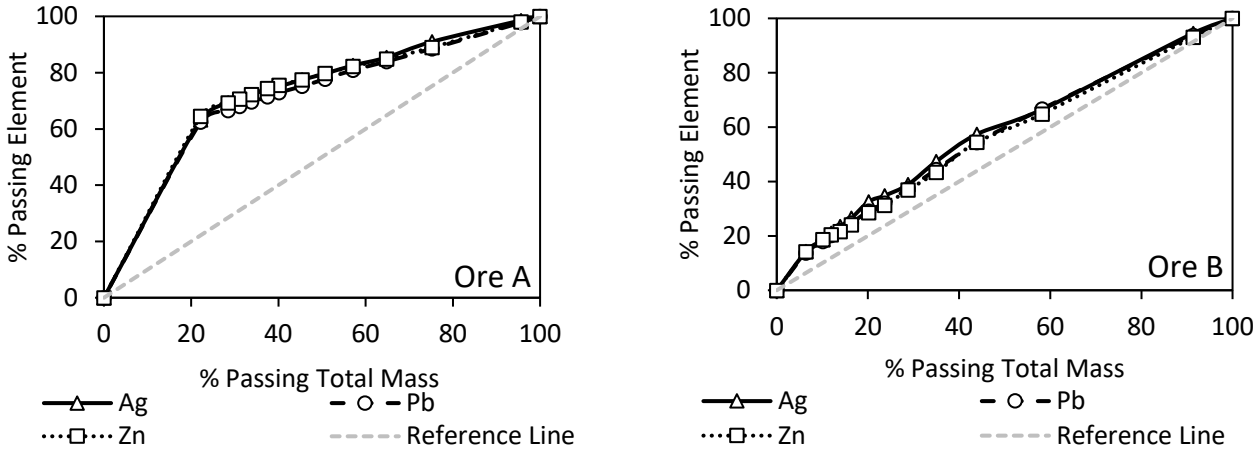

FIG 5 – Ore A and Ore B percentage passing of mass and Ag, Pb and Zn in the -75 + 6.7 mm size range.

The results indicate that over 60 per cent of the silver mass is in fines (20 per cent of the total mass) in Ore A, which is more amenable to early coarse gangue rejection compared to Ore B This is more apparent in Figures 6, 7 and 8 where the percentage of mineral deportment by size is shown for Ag, Zn and Pb respectively. In Ore A, most of the metals are concentrated in the material below 6.7 mm. However, in Ore B the metal content is more distributed across the coarse sizes fractions with most metals existing in the -75 + 53 mm size fraction. In the case of Ore A, the fine material that represents 25 per cent of the mass and contains nearly 65 per cent of the metals can be removed by simple screening leaving coarse material that could be rejected, resulting in potential coarse gangue rejection. Conversely, only 35 per cent of the metals are deposited into 25 per cent of the fines for Ore B Nevertheless, the particle size distribution of the bulk samples in Figure 9 shows that Ore A is finer than Ore B This can explain the higher amenability of Ore A for pre-concentration compared to Ore B.

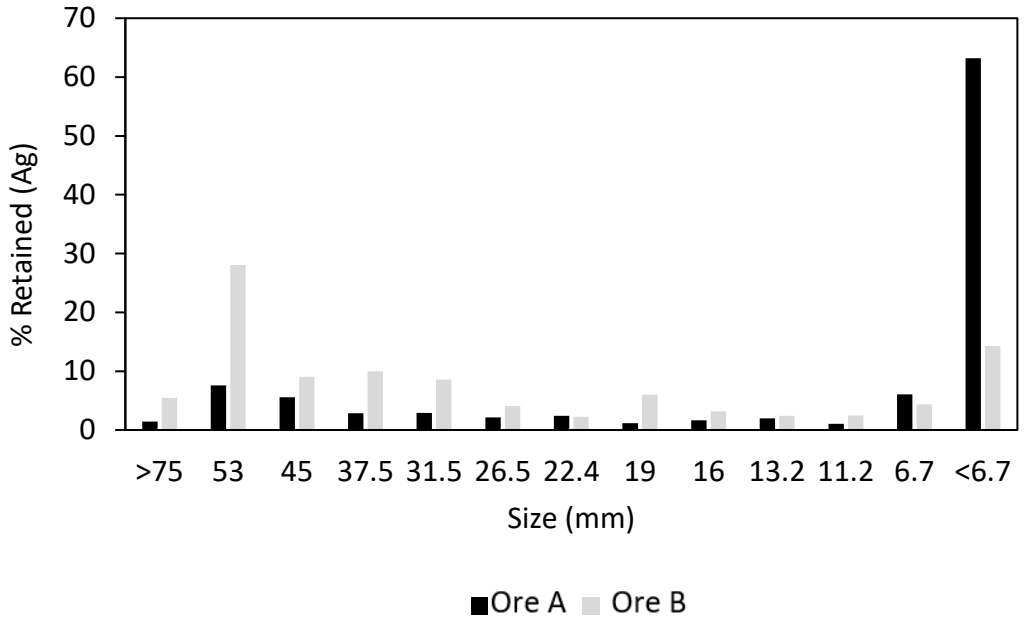

FIG 6 – Percentage silver retained in each size fraction for Ore A and Ore B.

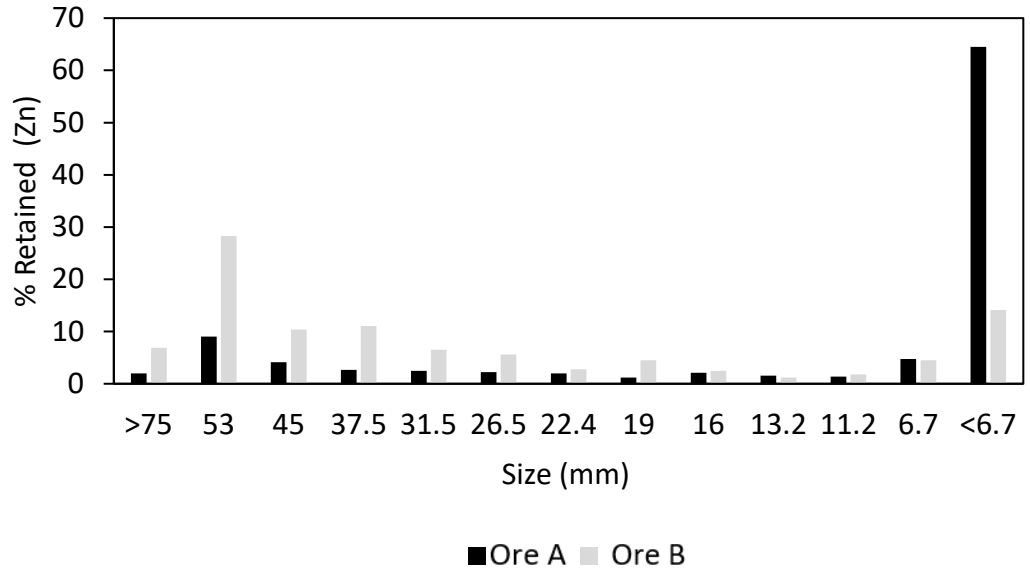

FIG 7 – Percentage zinc retained in each size fraction for Ore A and Ore B.

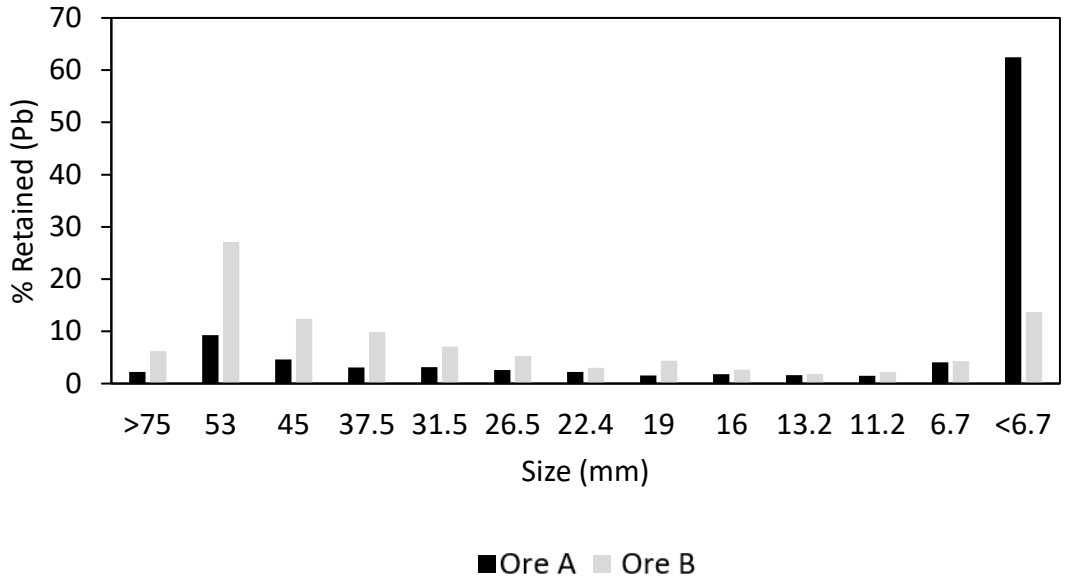

FIG 8 – Percentage lead retained in each size fraction for Ore A and Ore B.

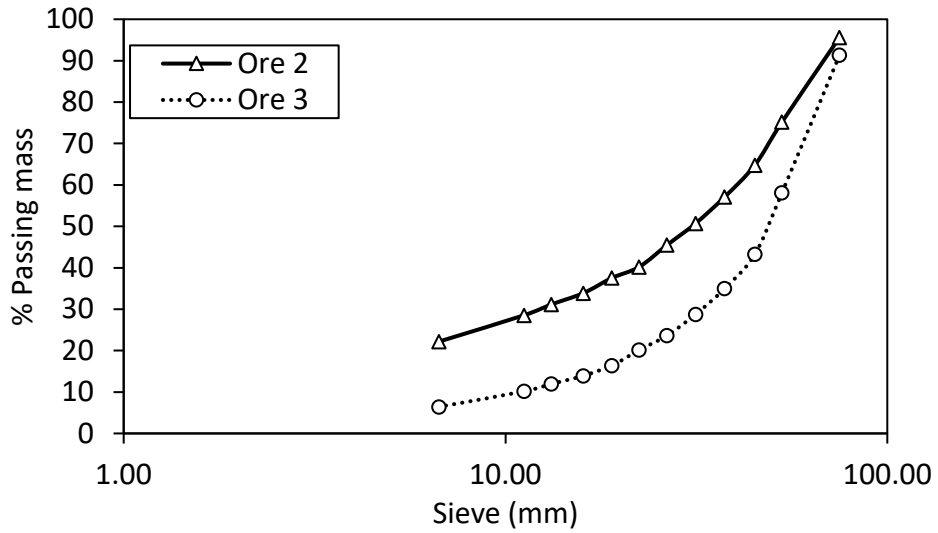

FIG 9 – Particle size distribution of bulk as-received Ore A and Ore B with 95 per cent confidence interval.

Comparison of metal deportment by size results for Jaw Crusher and VSI

VSI and jaw crusher breakage mechanisms and stress events that they impart on rock particles are different. However, the particle size distributions shown in Figure 10 show that their products' t_{10} were similar. The mass and silver recovery for the VSI and crushing tests of Ore A at -8 + 6.7 mm feed size in Figure 11 indicate that silver recovery at a 20 per cent mass recovery is higher for the VSI crusher compared to the jaw crusher. This is potentially related to the more precisely controlled breakage mechanisms inside the VSI chamber. The effect of different VSI throughputs (SR-HT versus SR-LT) in metal deportment was insignificant in this scenario.

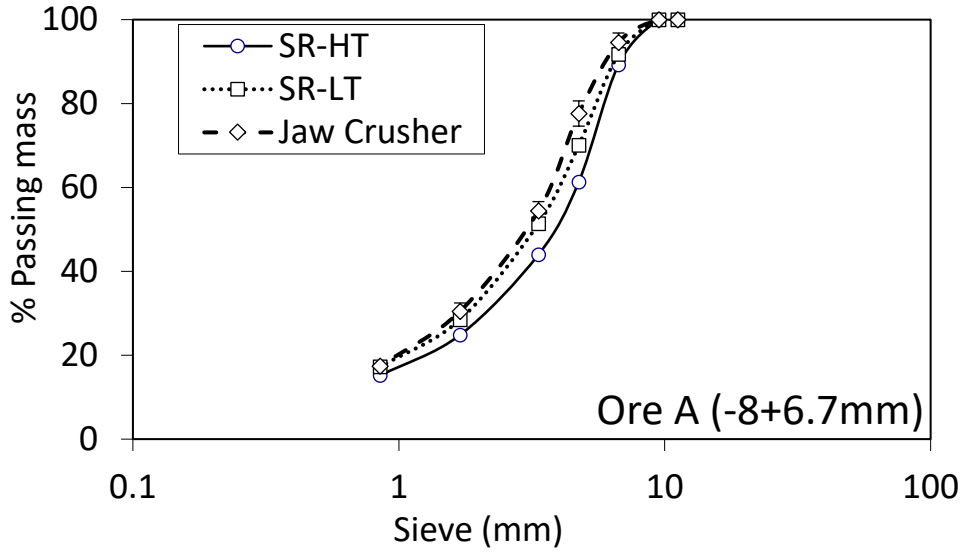

FIG 10 – Particle size distribution Ore A -8 + 6.7 mm feed size for the VSI and crushing test with 95 per cent confidence interval.

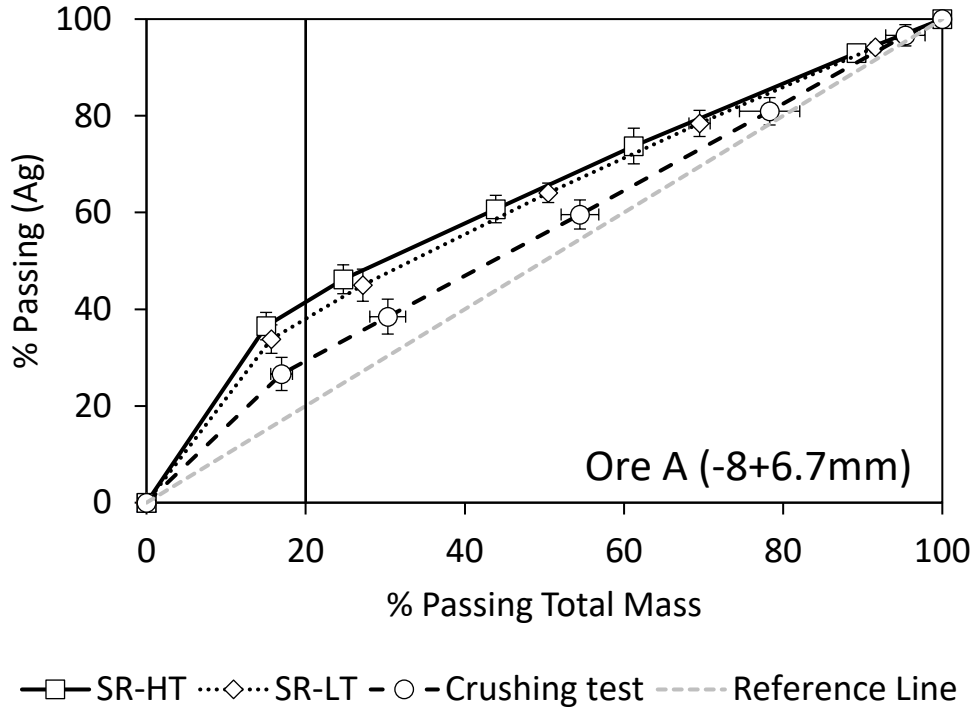

FIG 11 – Ag recovery versus mass recovery for Ore A (-8 mm + 6.7 mm) with 95 per cent confidence interval.

The zinc recovery versus mass recovery curves for Ore B for -11.2 + 9.5 mm are presented in Figure 12. Zinc recoveries at 20 per cent mass recovery are higher for the VSI than for the jaw crusher. Above 60 per cent mass recovery, the zinc recoveries achieved by the VSI test for Ore B were similar to the jaw crusher results. This can be related to the poor amenability for selective breakage of Ore B as shown in Figure 5.

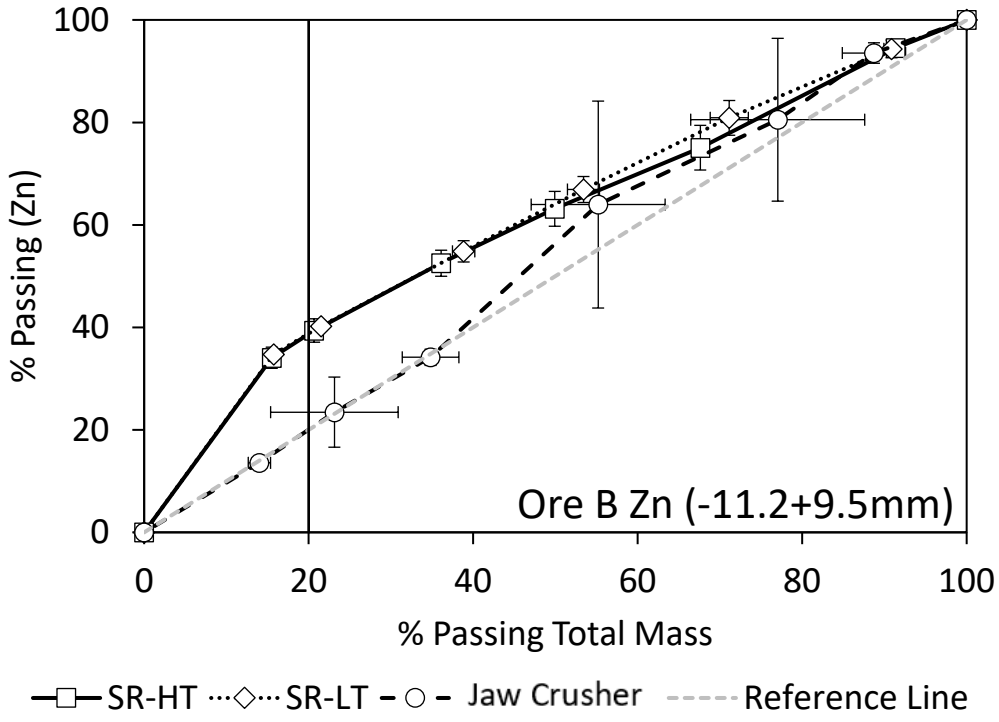

FIG 12 – Ore B percentage passing of mass and Zn of -11.2 + 9.5 mm initial size fraction with 95 per cent confidence interval.

To validate the results, the metal recovery at 20 per cent mass cumulative passing was calculated using a cubic spline interpolation. Then, a paired t-test was conducted at 95 per cent confidence interval for the VSI and jaw crusher results, where the null hypothesis considered that both equipment produce similar results. Considering a significance level of 0.05, the p-values in Table 3 reject the null hypothesis since they are lower than 0.05, indicating a difference in metal deportment.

TABLE 3

P-values of t-test between VSI and crushing test.

	Ore A -8 + 6.7 mm	**Ore B -11.2 + 9.5 mm**
Test	**Ag**	**Zn**
SR-HT	0.026	0.017
SR-LT	0.028	0.016

To demonstrate that the higher metal recoveries achieved during the VSI testing were not caused by different mass pulls (mass recoveries), the particle size distribution of the material from the VSI and jaw crusher tests were compared.

Based on Figure 10, the Ore A material that was broken using the jaw crusher produced more fines than the VSI at the same feed particle size. The size distribution suggests that a higher metal deportment achieved with the VSI is partially associated with less mass deported into the fines compared to the jaw crusher and, consequently, more coarser gangue can be rejected using the VSI It should be noted that the analysis was conducted based on the fine end of the curves.

Influence of VSI parameters on the ore response

The VSI promoted higher metal deportment compared to the jaw crusher in the scenarios analysed so far. However, VSI parameters such as rotor design, throughput and the feed size fraction may also affect the deportment of the valuable minerals into the fines. The influence of the VSI test settings on the cumulative metal recovery was compared at 40 per cent cumulative mass passing for silver and at 20 per cent for lead and zinc. The mass pulls were selected based on the minimum

mass required to potentially generate a significant difference in grade response between the VSI and jaw crusher tests. The percentage of metal passing for each experiment was calculated using cubic spline interpolation. The analysis of factors was then conducted using Stepwise Regression in Minitab® 2019 since this regression method is useful in identifying meaningful predictors. Essentially, the process requires removing and adding predictors individually until two conditions are satisfied:

- All variables in the model have P-values less than the specified alpha.
- All variables not in the model have P-values greater than the specified alpha.

The Stepwise Regression of Ore A and Ore B was conducted using an alpha of 0.05 following a hierarchical model, where lower-order parameters related to high-order parameters are considered in the model. In this method, the model analyses all factors and their interactions, considering lower orders (A, B and C) to higher orders (A*B*C). Table 4 shows the main outcomes of the analysis. The regression analysis for Ore A was conducted after removing a test that presented a large residual. Regression equations for Pb for Ore A and Zn for Ore B were not included since no terms analysed entered the model.

TABLE 4

Stepwise regression analysis of Ore A and Ore B at 0.05 alpha – Hierarchical model.

Ore	Metal	Regression Equation	R^2 (adj)	P-value of terms
Ore A	Zn	% Passing Zn = 0.40 + 0.08*Rotor(SR)	22.28%	0.032
	Ag	% Passing Ag = 0.53 + 0.06*Rotor(SR) – 0.06*Throughput(LT)	33.61%	0.017 (Rotor) 0.016 (Throughput)
Ore B	Pb	% Passing Pb = 0.30 + 0.05*Feed Size(-8 + 6.7)	58.94%	0.004
	Ag	% Passing Zn = 0.35 + 0.04*Feed Size(-8 + 6.7)	35.89%	0.040

The regression equations show that VSI parameters are significant to the responses for Zn and Ag of Ore A, whilst Ore B metal recovery is only affected by the feed size. This behaviour can be related to the higher natural amenability to pre-concentration of Ore A as compared to Ore B Variations in the VSI setting conditions cause grade by size enhancement variations in an ore that shows a predisposition to pre-concentration and it appears that Ore B is insensitive to these changes. The equations for Zn and Ag for Ore A suggest that the short rotor was able to increase metal recovery and a lower throughput decreased the response in the tests. The trend is illustrated in Figure 13. This could be explained by the increased rock-to-rock interactions due to the higher population of particles inside the VSI chamber at high throughputs or short rotor settings that improve mineral concentration into the fines. A short rotor increases the probability of particle interaction since it creates a larger gap between the rotor aperture and the VSI chamber, accommodating more flying debris. The probability is also higher using a higher throughput setting.

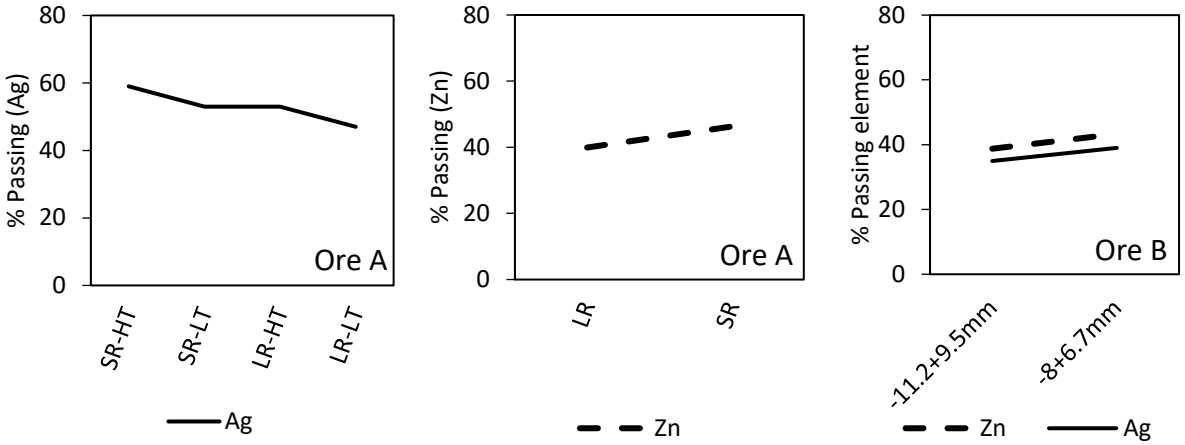

FIG 13 – Percentage passing comparison of elements according to experimental factors for VSI tests using Ore A and Ore B.

To investigate this behaviour, the particle size distribution of the short and long rotors was compared at high throughput for Ore A The results, shown in Figure 14, indicate that the short rotor is generating material with a slightly finer product size distribution than the long rotor for the same feed size. The results suggest that a wider gap between the rotor and anvils increases the number of particles in suspension inside the VSI chamber and consequently the probability of collisions between the debris. These collisions or interactions can be related to the removal of additional mineralisation from the particles' surface and a higher concentration of valuable metals into the fines for this ore. Further analysis of the particle size distribution was conducted utilising the t_n-size family, from t_5 to t_{40}. For a feed size of -11.2 + 9.5 mm, the t_5 is equal to the percentage of mass passing the one-fifth of the initial size fraction or 2.06 mm in this case. The mass of material passing a certain t_n-size was compared using a paired t-test that considered the null hypothesis that there is no difference in the mass passing. In the majority of the cases, the difference in the mass passing was significant and a different amount of mass was reported to the selected size fraction Table 5.

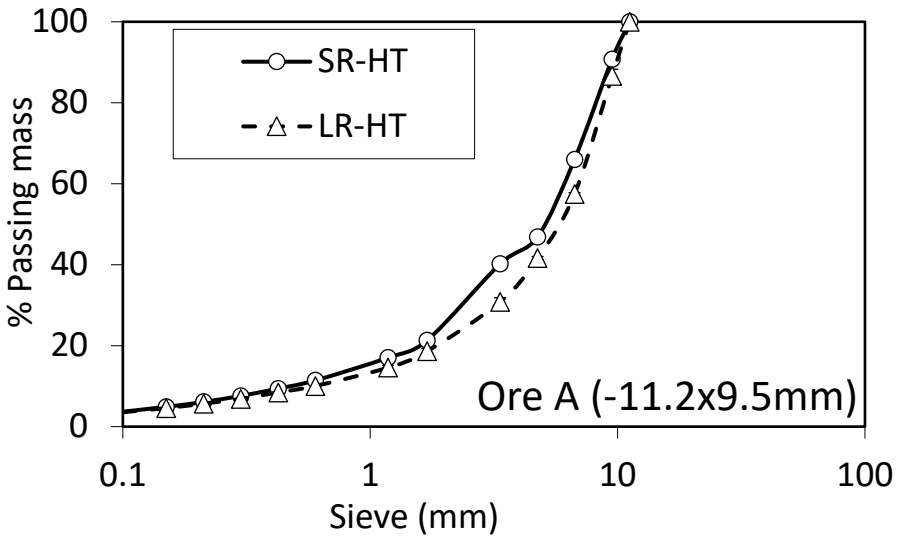

FIG 14 – Particle size distribution of SR-HT and LR-HT of Ore A for -11.2 + 9.5 mm feed size with 95 per cent confidence interval.

TABLE 5

t-test comparing the percentage of mass passing at the t_n size for SR-HT and LR-HT of Ore A - 11.2 + 9.5 mm feed size.

t_n-size family	Size fraction (mm)	P-value
5	2.06	0.001
10	1.03	0.013
20	0.52	0.070
30	0.34	0.030
40	0.26	0.046

CONCLUSIONS

The grade by size deportment of Ore A and Ore B was analysed after breakage using a laboratory-scale jaw crusher and a laboratory-scale VSI More metal was recovered at a similar mass pull using the VSI compared to the jaw crusher, indicating its potential as a device to improve metal deportment into the fines. A comparison of the VSI operating parameters indicated that running at high throughputs resulted in the enhancement of the response to pre-concentration. This is an indication that improvements in grade by size deportment can benefit from the breakage that occurs when multiple particles are interacting rapidly with each other, similar to what occurs inside a VSI chamber. The use of a short rotor, as opposed to a long rotor, also improved this behaviour for some of the elements analysed. This was attributed to the increased amounts of particles that are suspended in the VSI chamber when the short rotor was used. Greater rock-to-rock interaction is promoted resulting in and there is an increase in ore response. However, the investigation also suggests that the response is ore and size-dependent, requiring individual evaluation of the use of the technique. The results demonstrate that the grade by size deportment of some ores can potentially be further improved by increasing the interaction of particles inside the VSI For the ores that naturally concentrate valuable minerals into the fines after breakage, improvements in pre-concentration amenability could significantly decrease the amount of material required to be processed in a mining circuit.

ACKNOWLEDGEMENTS

The authors would like to thank the Australian Government's Cooperative Research Centre for Optimising Resource Extraction (CRC ORE) for sponsoring the project. CRC ORE is part of the Australian Government's CRC Program, which is made possible through the investment and ongoing support of the Australian Government. The CRC Program supports industry-led collaborations between industry, researchers, and the community.

REFERENCES

Bearman, R A, 2013. Step change in the context of comminution. *Minerals Engineering* 43–44: 2–11.

Bérubé, M A and Marchand, J C, 1984. Evolution of the mineral liberation characteristics of an iron ore undergoing grinding. *International Journal of Mineral Processing* 13(3): 223–237.

Bowman, D J and Bearman, R A, 2014. Coarse waste rejection through size based separation. *Minerals Engineering* 62: 102–110.

Carrasco, C E, 2013. *Development of geometallurgical tests to identify, rank, and predict preferential coarse size by size Au deportment to support feed preconcentration at Telfer Au-Cu mine, Newcrest Western Australia*. A thesis for the degree of Master of Philosophy at The University of Queensland.

Carrasco, C E, 2017. *Integrated Assessment to Quantify Size-Based Grade Engineering Operating Strategies and Economic Impacts*. Doctor of Philosophy Thesis, The University of Queensland.

Hesse, M and Lieberwirth, H, 2018. Influencing Parameters of the Selective Comminution at Impact Load. XXIX International Mineral Processing Congress, Moscow, Russia.

Johnson, N W, 2018. Existing opportunities for increasing metallurgical and energy efficiencies in concentrators. *Minerals Engineering* 118: 62–77.

King, R P and Schneider, C L, 1998. Mineral liberation and the batch communition equation. *Minerals Engineering* 11(12): 1143–1160.

Napier-Munn, T J, Morrell, S, Morrinson, R and Kojovic, T, 1996. *Mineral Comminution Circuits: Their Operation and Optimisation*. Indooroopilly, Qld, Julius Kruttschnitt Mineral Research Centre.

Napier-Munn, T, 2015. Is progress in energy-efficient comminution doomed? *Minerals Engineering* 73: 1–6.

Revell, P, 2018. Aligning an applied research & innovation program with industry needs. Annual CRC ORE Assembly. Brisbane, Australia.

Sinnott, M D and Cleary, P W, 2015. Simulation of particle flows and breakage in crushers using DEM: Part 2 – Impact crushers. *Minerals Engineering* 74: 163–177.

Stepanov, A L, Shinkorenko, S F, Frolov, A V and Kochetkov, P A, 1991. Selective comminution of two-component mineral mixtures. *Journal of Mining Science* 27(3): 202–207.

Walters, S G, 2017. Driving Productivity by Increasing Feed Quality Through Application of Innovative Grade Engineering® Technologies. *Tenth International Mining Geology Conference* (The Australasian Institute of Mining and Metallurgy: Melbourne).

Improving mill throughputs, with coarse and fine particle flotation in the NovaCell™

S Morgan[1] and G J Jameson[2]

1. Technology Manger – Flotation, Jord International Pty Ltd, St Leonards NSW 2065. Email: smorgan@jord.com.au
2. Laureate Professor, Centre for Multiphase Processes, University of Newcastle, NSW 2308. Email: graeme.jameson@newcastle.edu.au

ABSTRACT

It is well known that the head grades of valuable mineral deposits are declining. To satisfy the global demand for metals, mine throughput rates must increase to maintain production, whilst improving the efficiency of conventional mining and processing techniques. Although there've been improvements in all areas of mining, processing plants have increased in size needing more capital investment, whilst consuming a greater amount of energy and water. One example of this, would be mechanical flotation cells with mixing mechanisms. These cells have increased in volume from 3 m^3 to 680 m^3, to accommodate higher volumetric flow rates being processed through the circuit. In addition, the flotation circuits have increased in complexity to accommodate low-grade feed material and produce saleable concentrates.

In the coming years, these deposits will likely decline further in valuable minerals and the mining industry will face significant challenges to process even higher throughputs economically and manage their environmental impact. Thus, new sustainable technologies are needed to meet these objectives.

The NovaCell™, invented by Laureate Professor Graeme Jameson, has been developed to deliver step changes in process efficiency and to optimise current processing practices. Its novel configuration produces the ideal hydrodynamic conditions for both coarse and fine particle flotation recovery. It recovers valuable particles from 1 µm to 1 mm at least, depending on the ore liberation characteristics. Operators can achieve higher mineral recoveries, at a coarser grind size than current technologies can deliver. Thus, milling energy and efficiency requirements are alleviated. In addition, the coarser grind size improves water recovery from the tailings stream. When the NovaCell™ is included in the circuit, it has the ability to improve plant profitability and reduce the environmental impact of mining.

This paper presents circuit simulations of a Semi-Autogenous Ball mill Crusher (SABC) circuit where the NovaCell™ technology treats various streams to recover metal and reject gangue at a coarse grind size. The results will compare the mill throughput rates and energy consumption of the baseline and modified circuits for a porphyry copper ore. In addition, the paper will present NovaCell™ recovery-by-size results for copper, at the simulated feed grind sizes to predict the plant metal recovery performance for the modified circuit configuration.

INTRODUCTION

It is well known that the head grades of valuable mineral deposits are declining. To satisfy the global demand for metals, mine throughput rates must increase to maintain production, whilst improving the efficiency of conventional mining and processing techniques. Although there've been improvements in all areas of mining, processing plants have increased in size needing more capital investment, whilst consuming a greater amount of energy and water. One example of this, would be mechanical flotation cells with mixing mechanisms. These cells have increased in volume from 3 m^3 to 680 m^3, to accommodate higher volumetric flow rates being processed through the circuit.

In the coming years, these deposits will likely decline further in valuable minerals and the mining industry will face significant challenges to process even higher throughputs economically and manage their environmental impact. Thus, new sustainable technologies are needed to deliver step changes in process efficiency and to optimise current processing practices. The NovaCell™, invented by Laureate Professor Graeme Jameson, has been developed to improve current mining practices in four main areas:

- To enable lower energy input circuits, by selectively recovering valuable minerals at a coarser grind size.
- To increase the recovery of valuable minerals across the full-size distribution in simple and flexible circuits.
- To reduce water consumption and dust creation through early waste rejection at a coarse particle size.
- To minimise the size of tailings dams through facilitating dry tailings disposal technologies.

The NovaCell™ has a novel configuration, which produces the best hydrodynamic conditions for both fine and coarse particle flotation recovery. Feed material entering the NovaCell™, is distributed across downcomers where particles and tiny bubbles collide in the high-shear zone ideal for fine and ultrafine particle recovery. Material exiting the downcomers enters the fluidised bed, where partially loaded bubbles surround particles in a low-shear environment ideal for coarse particle recovery. Both fine and coarse valuable minerals rise in the NovaCell™ and are collected as two separate streams. A high-grade flotation concentrate is collected at top of the cell, whilst coarser valuable particles that may detach are collected in an inverted cone. The coarse valuables can then be recovered by a separation device, such as a cyclone or screen for further processing.

Jameson and Emer (2019) found that for porphyry copper ore, the NovaCell™ in batch testing obtained 100 per cent recovery at large sizes up to 300 µm. In coal, Jameson *et al* (2020) demonstrated that the NovaCell™ successfully recovered high-grade coal particles with a top size of 2 mm, in batch and continuous mode. These papers demonstrate that the novel configuration produces the ideal hydrodynamic conditions for both coarse and fine particle flotation recovery. The NovaCell™ top view and plant 3D model is shown in Figure 1.

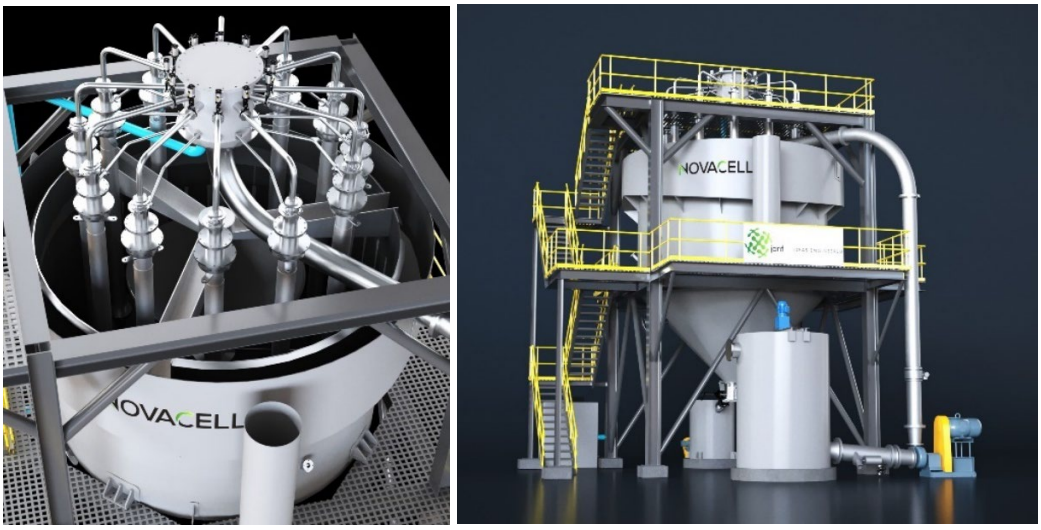

FIG 1 – NovaCell™ top view (left) and plant 3D model (right).

In this paper, we investigate the effect of throughput rates on the flotation feed P_{80} using several milling circuit configurations. We start with the Semi-Autogenous Ball mill Crusher (SABC) as a baseline comminution circuit, operating at a throughput of 1000 t/h (dry) solids. In Comminution Circuit 1, the feed rate is increased to 1600 t/h (dry) solids. In Comminution Circuit 2, the SABC model is modified to include a NovaCell™ taking feed particles at top size of 600 µm. The NovaCell™ is rejecting coarse waste material at this point and tailings exits the circuit as part of the final tailings, bypassing the flotation circuit. Comminution Circuits 3 and 4 show further configurations. Experiments are described in which a laboratory NovaCell™ was used to float a low-grade porphyry copper ore at a top feed size of 600 µm. The recovery by size data are used as inputs to the various circuit configurations to predict the metallurgical performance.

OPERATING AT HIGHER THROUGHPUTS RATES WITH THE NOVACELL™

In mining, operating at higher than nameplate throughput rates can occur for various reasons. The most common causes are related to declining ore grades and an increase in commodity prices. Declining ore grades mean that the extracted ore from the deposit produces a lower-than-design feed grade and there is less valuable mineral per tonne of ore processed. For example, Mudd and Jowitt (2018) considered global copper trends and discovered that the average ore grade in copper production has been declining over time. Thus, there is growing need for copper processing plants to operate at higher throughput rates to achieve the desired metal production.

An increase in commodity prices occurs when there is a greater demand for metals. This can be caused by a decrease in supply and/or customers increasing their consumption rate. The World Bank (2020) predicted that the transition to low-carbon technologies will accelerate the global demand for copper over the next 25 years. Thus, mine operators will want to capitalise on these higher prices and maximise throughput rates to increase revenue and profitability.

To understand how the NovaCell™ would assist mine operators achieve higher throughput rates, Jord first investigated the effect of higher throughput rates on existing comminution circuits. It is expected that at higher throughput rates, feed material with similar ore 'hardness' characteristics would produce a coarser particle size distribution to the flotation circuit. Generally, this is reported as the cyclone overflow mass 80th percentile size (P_{80}), or % passing a particular mesh size.

To quantify this effect, Jord used JKSimMet circuit models to understand the change in the flotation feed P_{80} values at higher throughput rates. Once these P_{80} values were determined, flotation test work with the NovaCell™ laboratory test unit was conducted at the equivalent grind sizes.

JKSimMet model development and simulations

The first model, Comminution Circuit 1 comprised a Semi-Autogenous (SAG) mill in closed circuit with a screen and pebble crusher. The pebble crusher closed side setting was 12 mm and the re-circulating load was approximately 25 per cent. The SAG mill screen undersize fed a Ball mill in closed circuit with a hydrocyclone. The Ball mill re-circulating load was approximately 250 per cent. The hydrocyclone overflow stream was the feed stream to the flotation plant. The comminution circuit is commonly known as a SABC milling circuit design and is generally considered a baseline flow sheet for porphyry copper deposits. Figure 2 presents the process schematic of the Comminution Circuit 1 developed in JKSimMet for a throughput rate of 1600 t/h (dry) solids.

The second model, Comminution Circuit 2 was comprised of a modified SABC milling circuit. The Ball mill was still in closed circuit with the hydrocyclone, however a NovaCell™ unit was added between the hydrocyclone and Ball mill. The hydrocyclone underflow was screened and the –600 µm material fed the NovaCell™. The NovaCell™ product entered the Ball mill for further mineral liberation. The hydrocyclone overflow remained the feed stream to the flotation plant. The objective of the circuit was to remove the coarse waste material prior to downstream processing. Thus, the NovaCell™ coarse tailing stream bypassed the flotation circuit and formed part of the final tailings. Figure 3 presents the process schematic of the Comminution Circuit 2 developed in JKSimMet for a throughput rate of 1600 t/h (dry) solids.

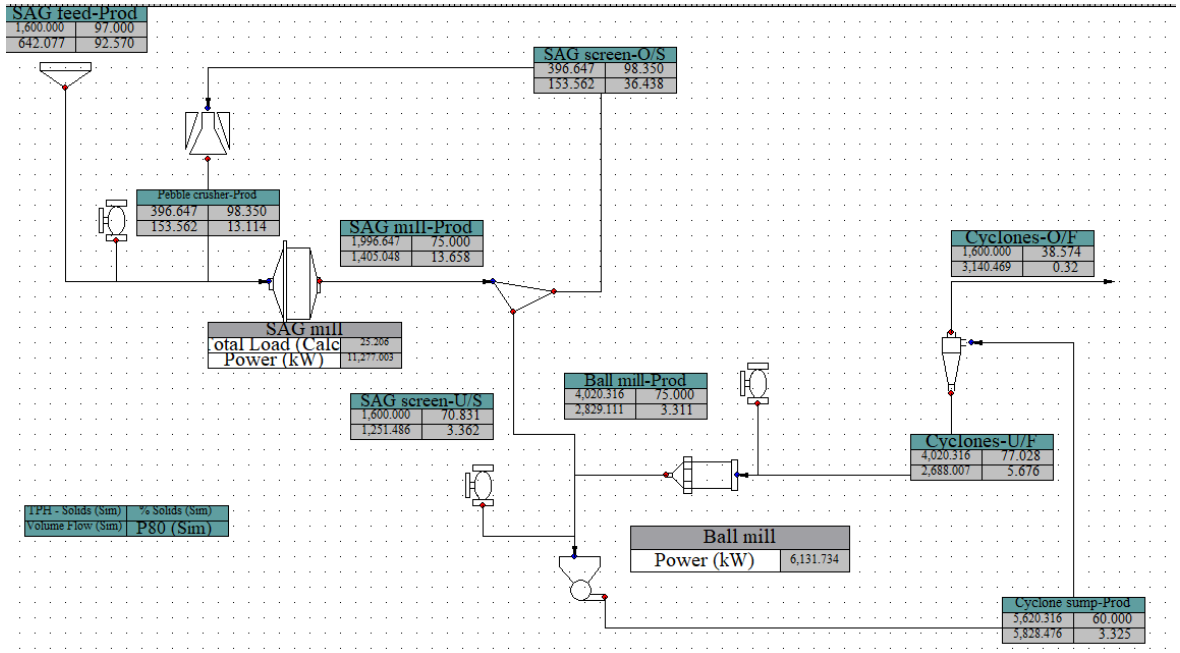

FIG 2 – JKSimMet process schematic of Comminution Circuit 1, at 1600 t/h (dry) solids.

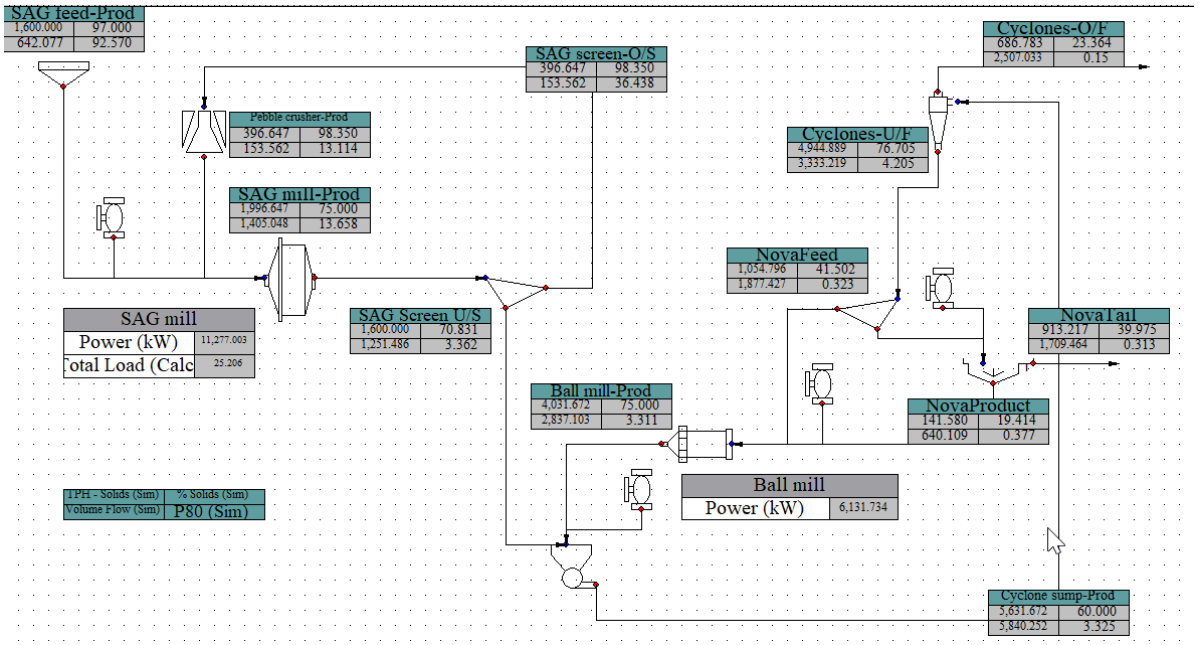

FIG 3 – JKSimMet process schematic of Comminution Circuit 2, at 1600 t/h (dry) solids.

The third model, Comminution Circuit 3 also comprised of a modified SABC milling circuit. The Ball mill discharge material was screened and the – 600 µm material fed the NovaCell™. The NovaCell™ product was re-circulated to the Ball mill via the hydrocyclone. The NovaCell™ coarse tailing stream bypassed the flotation circuit and formed part of the final tailings. Thus, like Comminution Circuit 2, the coarse waste material was removed prior to downstream processing. Figure 4 presents the process schematic of the Comminution Circuit 3 developed in JKSimMet for a throughput rate of 1600 t/h (dry) solids.

The fourth model, Comminution Circuit 4 also investigated a modified SABC milling circuit. The SAG mill discharge material was screened and the – 600 µm material fed the NovaCell™. The NovaCell™ product was re-circulated to the Ball mill via the hydrocyclone. Like Comminution Circuit 2 and 3, the NovaCell™ tail comprised of coarse waste material that was rejected ahead of downstream processing. Figure 5 presents the process schematic of the Comminution Circuit 4 developed in JKSimMet for a throughput rate of 1600 t/h (dry) solids.

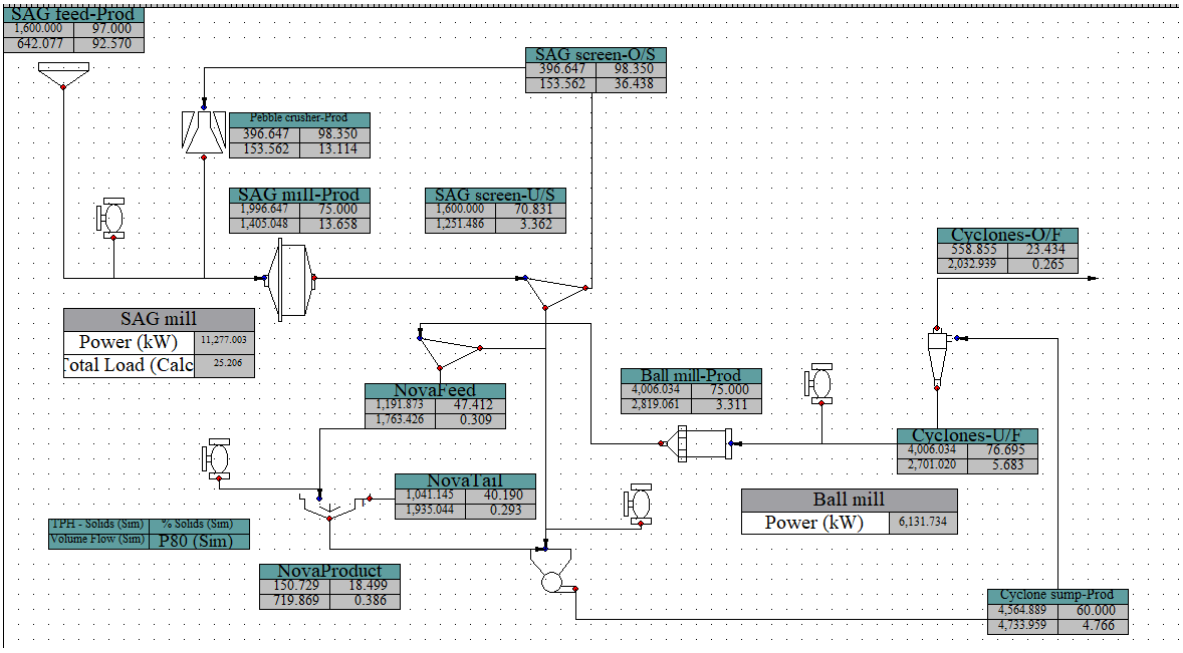

FIG 4 – JKSimMet process schematic of Comminution Circuit 3, at 1600 t/h (dry) solids.

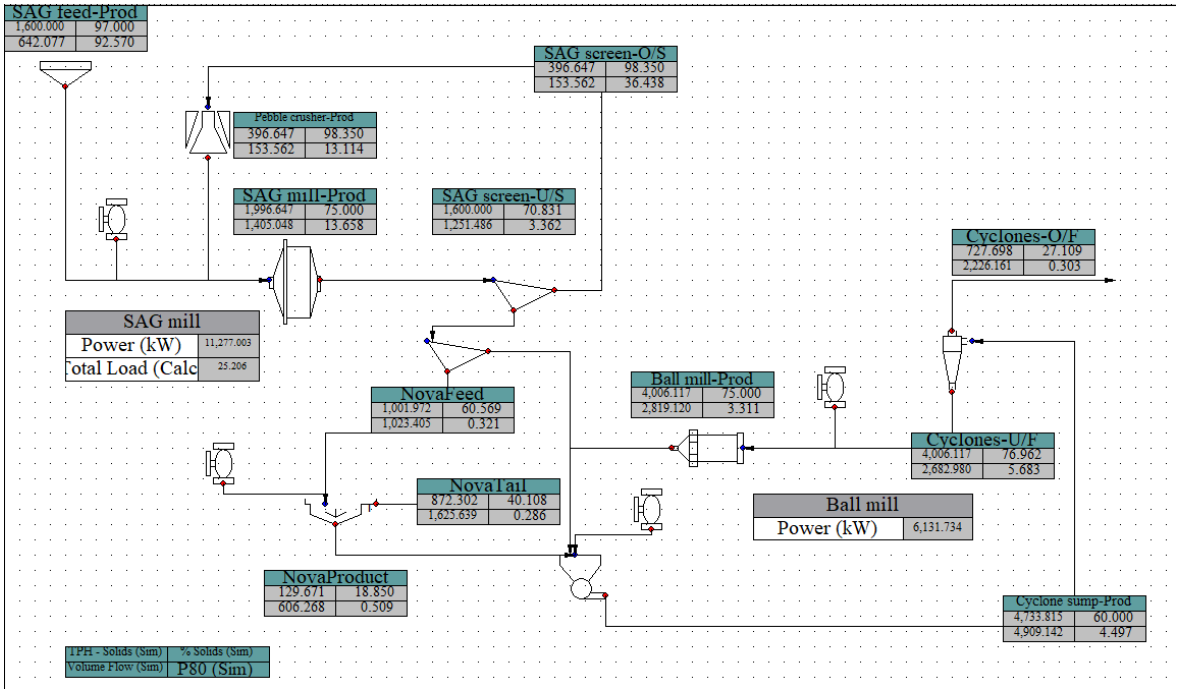

FIG 5 – JKSimMet process schematic of Comminution Circuit 4, at 1600 t/h (dry) solids.

Table 1 details the JKSimMet model comminution circuit key parameters used in all the JKSimMet models. The SAG mill, Ball mill and pebble crusher dimensions were kept unchanged. Thus, the simulations predict the performance of an existing operation ramping up the throughput rates, without making equipment changes to the comminution circuit.

TABLE 1

JKSimMet comminution circuit key parameters.

Key Parameters	SAG Mill	Ball Mill
Axb	45	
Bond Work Index (kWh/t)	15	
Ore SG (t/m3)	2.7	
Internal Diameter (m)	10.30	5.92
Length (m)	5.25	8.53
Total load (%)	25	40
Pebble Crusher (mm)	12	n/a

The impact breakage parameters A and b would be obtained from results of JK Drop Weight Testing. The values used in the simulation, Axb = 45 and Bond Work Index = 15 kWh/t, represents an ore of 'medium' hardness and grindability.

In the Comminution Circuit 2, 3 and 4, the NovaCell™ is represented as a 'dummy' thickener. The NovaCell™ tailings is at the top of the thickener and NovaCell™ product at the bottom. The NovaCell™ 'model' is a simple Whiten efficiency curve which represents the percentage of each size fraction recovered to the product stream (Napier-Munn *et al*, 1996). The shape of the curve is controlled by parameters that would otherwise be determined from laboratory-scale NovaCell™ test work data, namely the particle size distributions of the NovaCell™ feed, tailings and product. The parameters used in the model are shown in Table 2. For the purposes of these simulations, a 'typical' size-by-recovery curve was used to define the shape of the NovaCell™ efficiency curve model.

TABLE 2

NovaCell™ key parameters.

Fines Split to Fine product (%)	6.0
Sharpness of Efficient Curve – Alpha	15.0
Initial Dip in Efficient Curve – Beta	6.32
Corrected d50 (MM)	1.16

JKSimMet simulation results

In the simulation modelling, the base case scenario targeted a typical cyclone overflow P_{80} of 150 µm. The selected throughput represented a mid-tier operation at 1000 t/h (dry) solids, approximately 8.0 Mt per annum (Mt/a). Comminution Circuit 1 scenario, represented the base case flow sheet, however the throughput rate was increased to 1600 t/h (dry) solids, approximately 13.0 Mt/a. To accommodate the higher throughput rate with the existing equipment, the SAG mill operating conditions ie ball load, critical speed, grate open area and pebble port size were all modified. These represent typical strategies adopted by operations to achieve throughput rate increases, should coarsened grind targets be deemed acceptable.

For the Comminution Circuit 2, 3 and 4 scenarios, the increased throughput rate of 1600 t/h (dry) solids was kept constant, and the process flow sheets previously described in Figures 3, 4 and 5 were adopted. It should be noted that in all the scenarios the pebble crusher and Ball mill circuit re-circulating loads were retained at approximately 25 per cent and 250 per cent, respectively. The comminution circuit simulated parameters and results for the scenarios investigated are presented in Table 3.

TABLE 3

Comminution circuit simulated parameters and results.

	Base Case	Circuit 1	Circuit 2	Circuit 3	Circuit 4
Plant Feed Throughput (tph)	1000	1600	1600	1600	1600
SAG Mill					
Ball load (%)	11	15	15	15	15
Critical Speed (%)	75	78	78	78	78
Grate Open Area	0.07	0.10	0.10	0.10	0.10
Pebble Port Size (mm)	45	63	63	63	63
Screen (mm)	10	15	15	15	15
Re-circulating Load (%)	24	25	25	25	25
Power Draw (kW)	9395	11 277	11 277	11 277	11 277
Ball Mill					
Ball Load (%)	40	40	40	40	40
Critical Speed (%)	74	74	74	74	74
Discharge Rate (tph)	2526	4020	4032	4006	4006
Power Draw (kW)	6132	6132	6132	6132	6132
NovaCell™ Plant					
Coarse Waste Rejected (tph)	0	0	913	1041	872
Conventional Float Circuit					
Throughput Rate (tph)	1000	1600	687	559	728
Feed P_{80} (µm)	150	320	150	265	303

The simulation results for the comminution circuits indicated the following:

- In Comminution Circuit 1, for a 60 per cent increase in throughput rate at 1600 t/h (dry) solids, the cyclone overflow coarsens from P_{80} 150 µm to a P_{80} of 320 µm. The SAG mill modifications resulted in an increase in power draw to 11 277 kW. This represented a 12 per cent increase in the total power draw, which may not be possible in practice if this is beyond the capacity of the installed motor. In addition, the volumetric flow rate to the flotation circuit increased by 60 per cent. Thus, the flotation circuit would need new flotation equipment to accommodate for the coarser feed material and higher throughput rates, including additional regrind milling capacity.
- In Comminution Circuit 2, for throughput rate of 1600 t/h (dry) solids, the cyclone overflow remains at a P_{80} of 150 µm. Likewise, the SAG mill power draw increases by 12 per cent which could be a constraint if this is beyond the motor capacity. However, the key difference is that with the NovaCell™ treating the cyclone underflow material, the system rejected 57 per cent of the plant feed as coarse tailings. As a result, the volumetric flow rate to the flotation circuit decreases by 31 per cent. Thus, the existing flotation circuit could be used ‘as is’ without additional equipment.
- In Comminution Circuit 3, the total power draw was the same as Circuit 2. For a throughput rate of 1600 t/h (dry) solids, with NovaCell™ treating the Ball mill discharge material, the system rejected 65 per cent of the plant feed as coarse tailings. Although this was higher than the Circuit 2 simulation, the cyclone overflow coarsened to a P_{80} of 265 µm.

- In Comminution Circuit 4, the total power draw was the same as Circuit 2 and 3. For a throughput rate of 1600 t/h (dry) solids, with NovaCell™ treating the SAG mill discharge material, the system rejected 55 per cent of the plant feed as coarse tailings. The cyclone overflow coarsened significantly to a P_{80} of 303 µm.

In general, the JKSimMet simulations confirmed that with some modifications to the existing SABC milling circuit, it is possible to operate at 60 per cent higher throughputs rates. However, in the Comminution Circuit 1, 3 and 4, the consequence would be a coarser flotation feed material at P_{80} of 320 µm, 265 µm and 303 µm, respectively.

In most base metal operations, the rougher/scavenger circuit includes conventional float cells ie aerated tank cells with mixing impellers. Lynch *et al*, (1981) showed that for conventional industrial float cells the valuable mineral recovery in the coarse (+150 µm) size classes, is significantly lower than the intermediate size classes. Thus, if there is a greater proportion of valuable minerals in the coarser size fractions, we can expect lower metal recoveries from conventional float cells.

In Comminution Circuit 1, we also noted that the volumetric flow rate to the flotation circuit would increase by 60 per cent. Given that the float circuit has a fixed volumetric capacity, as the throughput rate increases the available residence time to recover these valuable minerals decreases. Depending on the ore properties, the change in circuit residence time can have a significant effect on the metallurgical performance of the circuit. Thus, additional flotation equipment would need to be added to recover coarse valuable particles and increase the overall flotation residence time.

In Comminution Circuit 2, the NovaCell™ included in the modified SABC milling circuit, enabled the flotation feed grind size to remain the same at a P_{80} of 150 µm. In addition, the volumetric flow rate to the flotation circuit reduced by 31 per cent. Thus, for the higher throughput rate, it would be expected that the overall plant metallurgical recovery in the existing float circuit would remain the same or improve, with no added copper losses to the tailing storage facility (TSF). In Comminution Circuit 3 and 4, it was expected that the coarser flotation feed size would result in lower copper recoveries in the conventional flotation circuit. Thus, of the modified SABC milling circuits investigated, Comminution Circuit 2 was selected as the best circuit configuration for coarse waste rejection.

In all the simulated scenarios, successfully operating at higher throughput rates with the existing milling equipment is highly dependent on new flotation technologies, like the NovaCell™, being able to recover valuable minerals at coarser flotation feed grind sizes in the P_{80} range of 300 to 350 µm. Thus, the next step was to investigate the NovaCell™ metallurgical performance at these flotation feed grind sizes.

NovaCell™ Laboratory Test work

To investigate the NovaCell™ metallurgical performance, laboratory test work was conducted on ore material from an operating mine with a low-grade porphyry copper deposit. The site was selected because the mineralogy indicated sufficient mineral liberation at a coarse grind size.

At the operating mine, the target flotation feed size is a P_{80} of 150 µm, and the rougher/scavenger circuit has aerated tank cells with mixing impellers. The average copper recovery to the final product is 90 per cent, at an average grade of 25 per cent Cu. Thus, for the NovaCell™ to be a viable option, the results needed to indicate equivalent copper recoveries but at significantly coarser grind sizes of P_{80} of 300 to 350 µm.

NovaCell™ experimental set-up

The NovaCell™ testing was conducted on run-of-mine (ROM) material sampled ahead of the comminution circuit. Upon receipt, the material was crushed to a top size of 600 µm with a jaw crusher. The sample feed grade was 0.47 per cent Cu, and the crushed material indicated a P_{80} of 420 µm. The whole sample, consisting of particles in the range 0 to 600 µm, was used as the feed material for the NovaCell™ batch experiments. The copper deportment in the sample feed is shown in Figure 6.

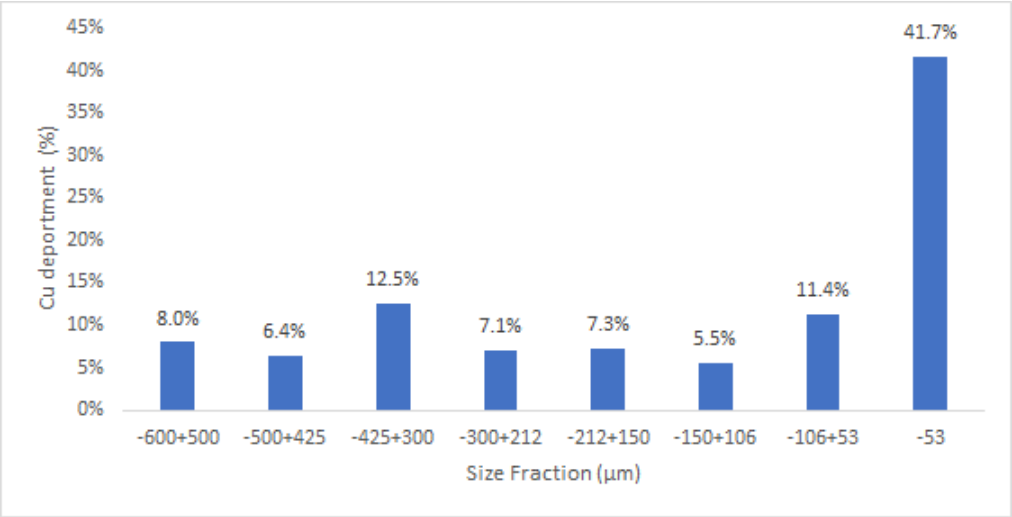

FIG 6 – Copper deportment in the NovaCell™ feed sample.

The results indicated that 41 per cent of the copper was in the +150 µm size factions, and 59 per cent in the -150 µm size factions. Thus, the NovaCell™ needed to achieve good recovery-by-size results across the full particle size distribution to achieve copper recovery performance of 90 per cent or better.

The NovaCell™ batch laboratory set-up is shown in Figure 7. It comprised of a column with an internal diameter of 100 mm, and a height of 1600 mm. A single downcomer with a diameter of 20 mm was inserted in the centre of the column. The screen mesh size was 425 µm.

At the beginning of the experiment, the sample mass was placed in the NovaCell™, and reagents were added and circulated for 10 minutes. Potassium amyl xanthate (PAX) was used at 80 g/t as collector. A mixture of MIBC and Dowfroth 250 was used as frother, at a concentration in the pulp of 20 ppm. NaHS was added as required, to keep the Eh at – 82 mV throughout the test. The pH was maintained at 8.9. After the 10 minute conditioning period, the air supply was opened and the flow rate was set and maintained at a constant value using a mass flow metre, to give a superficial velocity (J_g) of 1.2 cm/s in the column. The froth depth was 350 mm. Make-up water dosed with frother and collector was used to keep the liquid level constant during the batch tests.

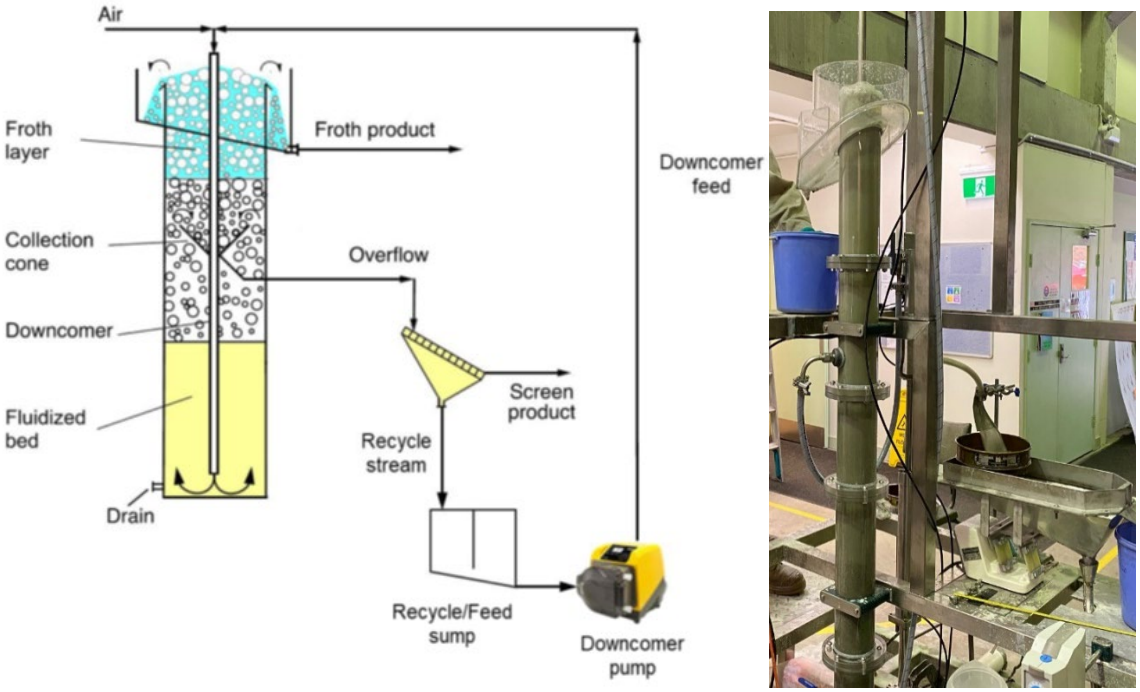

FIG 7 – NovaCell™ laboratory scale schematic (left) and batch test unit (right).

The purpose of the test was to measure the ultimate recovery of copper in the feed. Thus, samples of the concentrates were taken over the first 26 minutes of flotation. Thereafter, additional MIBC was added, and flotation continued for a further 14 minutes. At the end of the test, three products were produced. The accumulated froth concentrate 1, accumulated froth concentrate 2 and accumulated screen concentrate. The contents of the cell were also collected and analysed as tails.

The samples of the feed, products and tails were dried and weighed, and screened into 8 size fractions of top size 600, 500, 425, 300, 212, 150, 106 and 53 µm. The samples were ground to <75 µm in a ring mill, digested in acid and analysed for copper using ICP-MS. Standards were included in every run.

NovaCell™ test work results

The data for the mass fractions, the assays and calculated copper distributions on a unsized basis are shown in Table 4. The NovaCell™ product was the sum of froth concentrate 1, froth concentrate 2 and screen oversize.

TABLE 4

NovaCell™ results unsized basis (P_{80} of 420 µm).

	Mass pull (%)	**Copper assay (% cu)**	**Copper distribution (%)**
NovaCell™ Feed	100	0.47	100.0
(a) Froth concentrate 1	5.7	6.74	80.5
(b) Froth concentrate 2	1.7	0.68	2.4
(c) Screen Oversize	3.4	0.91	6.6
NovaCell™ Product (a)+(b)+(c)	10.8	3.94	89.5
NovaCell™ Tails	89.2	0.06	10.5

For a flotation grind size P_{80} of 420 µm, the NovaCell™ results indicated a copper recovery of 89.5 per cent, at a product grade of 3.94 per cent Cu. The copper recovery was split across the three product streams *viz*. froth concentrate 1, froth concentrate 2 and screen oversize. Froth concentrate 1 indicated the highest copper recovery of 80.5 per cent. Froth concentrate 2 indicated the lowest copper recovery of 2.4 per cent. The screen oversize indicated a copper recovery of 6.6 per cent.

The overall mass pull to the NovaCell™ product was 10.8 per cent, and the tailings fraction was 89.2 per cent of the feed. Thus, by grinding to a top size of 600 µm, the gangue rejection was almost 90 per cent of the feed. It should be noted that the froth concentrate 2 mass pull of 1.7 per cent was similar to the copper recovery at 2.4 per cent. Thus, the results suggest that after 26 minutes of flotation (froth concentrate 1) there is very little mineral selectively. It is recommended that kinetic rate and reagent optimisation test work be conducted to determine the required NovaCell™ residence time. Based on the current results, it is expected that the overall rougher/scavenger residence time would be less than 26 minutes.

The NovaCell™ batch test was conducted to maximise copper recovery and reject gangue. Thus, a high product grade was not expected. The NovaCell™ individual product grades of the froth concentrate 1, froth concentrate 2 and screen oversize were 6.74 per cent Cu, 0.68 per cent Cu and 0.91 per cent Cu, respectively. The NovaCell™ combined product grade was 3.94 per cent Cu. The NovaCell™ product streams will require further mineral liberation in the regrind circuit together with flotation cleaning to produce a saleable copper product. This approach is currently being adopted on-site where the rougher and scavenger product streams feed an existing regrind milling circuit.

The NovaCell™ copper recovery-by-size results for the combined NovaCell™ product and three individual product streams are presented in Figure 8.

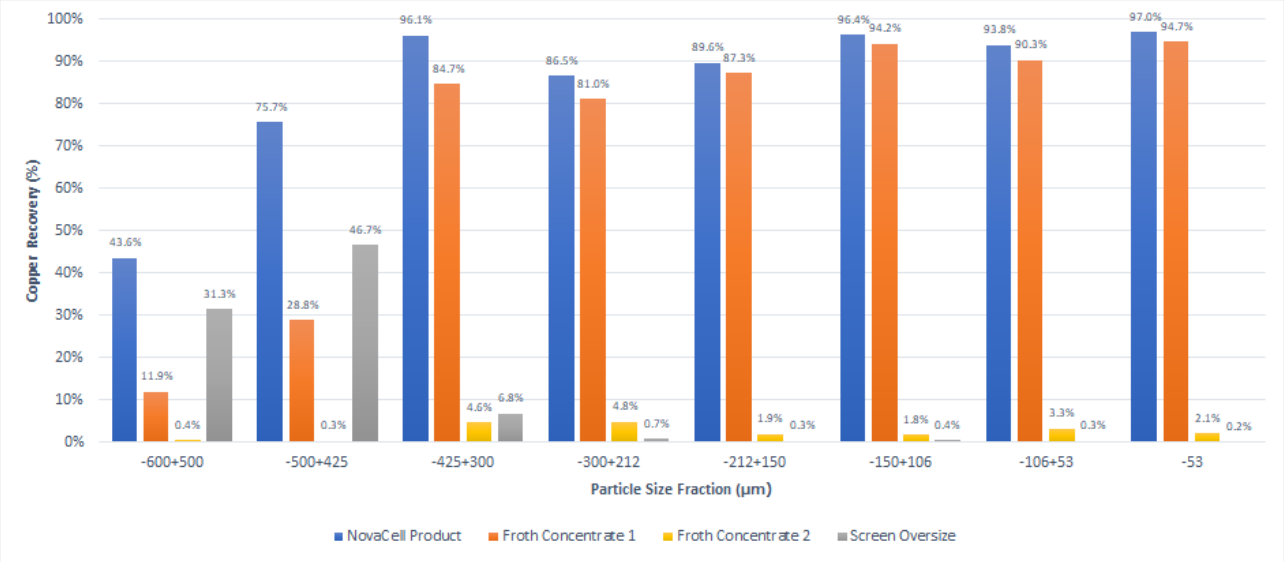

FIG 8 – NovaCell™ product copper recovery by-size results.

The results indicated copper recoveries across the full particle size distribution. In the -150 µm size band, copper recoveries above 90 per cent were achieved. In the -425+150 µm size band, copper recoveries above 85 per cent were achieved. In the -500+425 µm size band, the copper recoveries were lower but still above 75 per cent. In the -600+500 µm size band, the copper recoveries were the lowest at 44 per cent. This is likely caused by the valuable minerals being encapsulated by gangue particles or having minimal mineral surface liberation. It is expected that different mineralogy's would contribute to large variations in the recovery of this size range across different ore types. Those with coarsely-liberating minerals could be expected to exhibit higher recoveries in this size range, and this remains an area of ongoing test work.

A comparison of the individual product streams indicates coarse valuable particles in both the froth concentrate and screen products. For example, in the -600+500 µm size band, 12 per cent of the copper recovery reported to the froth concentrate and the remaining 31 per cent was recovered over the screen. Thus, the results indicate that the NovaCell™ technology is capable of recovering coarse valuable particles whilst still maintaining a froth layer for mineral selectivity. In the -425 µm size bands, majority of the copper recovery reported to the froth concentrate because the screen selected has a mesh size of 425 µm. Particles below 425 µm collected in the screen oversize were the result of blinding caused by insufficient washing.

It was interesting to understand the difference between the valuable particles recovered to the froth and screen oversize, especially in the coarse size fractions. Thus, the concentrate assay divided by the feed assay for each size fraction was calculated to determine the copper upgrade ratio. The NovaCell™ copper upgrade ratio by-size results for the combined NovaCell™ product and three individual product streams are presented in Figure 9.

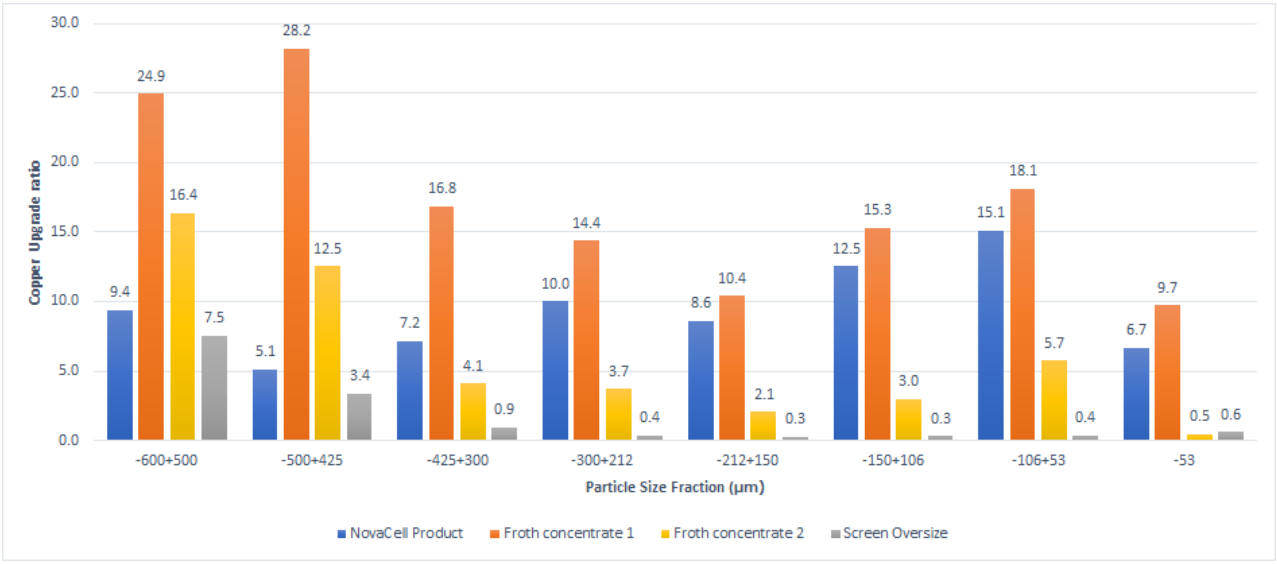

FIG 9 – NovaCell™ product copper upgrade ratio by-size results.

The results indicate that the froth concentrates had a higher copper upgrade ratio than the screen oversize product. Thus, the results suggest that the valuable particles recovered to the froth concentrate were more mineral rich than the valuable particles recovered to the screen oversize. It was hypothesized that the more mineral rich particles likely had a greater degree of mineral surface liberation. This then promoted better attachment to bubbles and recovery to the froth concentrate. The valuable particles recovered over the screen had a weaker attachment to bubbles and likely had less mineral surface liberation. Note, the differences in the mineral richness of the NovaCell™ products also allows for circuit flexibility. In some cases, the froth concentrate and screen oversize products may be treated separately depending on their product grade. The NovaCell™ combined product upgrade ratio was 8.4.

Using the NovaCell™ laboratory test data, it is possible to predict the recovery at lower top sizes, by successively distributing mass and copper from coarser size fractions to the smaller size fractions. This process delivers essentially a cumulative behaviour up to a designated top size. For example, in the -600+500 µm size band, the feed represents 14.7 per cent of the total, and there are corresponding masses in froth concentrate 1, froth concentrate 2, screen oversize and tails. Similarly, the copper distribution in this size band is 8 per cent of the total.

We now assume that the material in the coarsest size band is figuratively ground, so it no longer exists, and the top size band is now -500+425 µm. The total solids and copper masses in the -600+500 µm fraction are distributed among the remaining size bands, in proportion to the contribution made by each size band to the overall mass and copper recoveries in all classes from 0 to 500 µm. By repeating the process step by step from each size band to the next finer size band, the resulting mass and copper for a set of diminishing top sizes of grind are calculated. The overall effect is to progressively reduce the top grind size so all the masses end up in the -53 µm size band at 97 per cent copper recovery.

The total mass of the samples is conserved, so the overall mass pull remains at 10.8 per cent. The copper mass in the feed is also conserved. The grade is not conserved, but for any sample, it can be calculated from the corresponding copper assays and total mass values. The results of the calculations are shown in Table 5.

TABLE 5

NovaCell™ copper recovery and grade as a function of grind size.

Top grind size (µm)	P_{80} (µm)	Cu recovery (%)	Con grade (% cu)	Tailings grade (% cu)
600	420	89.5	3.94	0.06
500	350	93.5	4.12	0.03
425	298	94.7	4.18	0.03
300	210	94.9	4.07	0.03
212	148	95.7	3.94	0.02
150	105	96.3	3.90	0.02
106	74	96.3	3.71	0.02
53	37	97.0	3.17	0.02

The results indicate that when the -600+500 µm size band is redistributed, the overall recovery increases to 93.5 per cent. It continues to rise as further relatively coarse fractions are figuratively crushed and redistributed. The average enrichment ratio is 8.2. The tailings grades are essentially 'throwaway tails' and the feed grade is maintained at 0.47 per cent Cu.

In general, the laboratory results indicated that at coarse flotation feed sizes ie P_{80} of 300 µm to 350 µm, the NovaCell™ achieved copper recoveries higher than the current plant performance. Thus, the next step was to use both the simulation and laboratory results, to predict the plant metallurgical performance at higher throughput rates with the NovaCell™ added to the circuit.

NovaCell™ predicted metallurgical performance

The NovaCell™ can be added to the milling or flotation circuit to support higher throughput rates, in a number of configurations.

NovaCell™ in coarse flotation rougher duty

To investigate the potential metallurgical benefits in the flotation circuit, the simulated results from Comminution Circuit 1 were used. The SABC milling circuit at a throughput rate of 1600 t/h (dry) solids produced a feed to the flotation circuit of P_{80} of 320 µm. The NovaCell™ installed at the head of the conventional flotation circuit would operate in a rougher duty. The NovaCell™ tails would be pumped to the existing float circuit for additional metallurgical recovery. It is expected that the upgraded flotation circuit would have sufficient residence time for the higher throughput rate.

The NovaCell™ product streams would combine with the other circuit concentrates, and feed the regrind milling circuit for mineral liberation. The throughput rate and feed P_{80} to the regrind mill will increase and it has been assumed that regrind mill could be modified to maintain the product P_{80} to the cleaner circuit. Thus, the cleaner tails losses are expected to be the same. The final plant tailings material will be coarser and the dewatering rate of the material is expected to improve. The tailings thickener will need to be studied to understand whether equipment upgrades are required in this area. The proposed circuit configuration is illustrated in Figure 10.

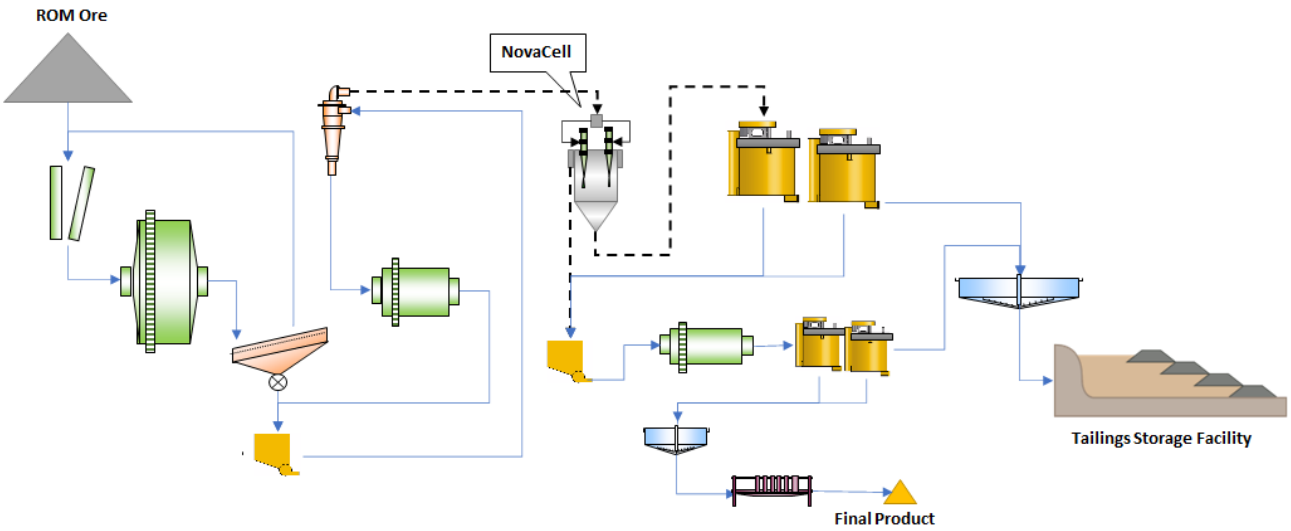

FIG 10 – NovaCell™ in coarse flotation rougher duty.

To predict the NovaCell™ metallurgical performance in the coarse flotation rougher duty, the laboratory results for a P_{80} of 300 µm were used, as detailed in Table 5. The results suggest that the NovaCell™ would achieve a copper recovery of 95 per cent, at a concentrate grade of 4.2 per cent Cu. If we assume a similar copper upgrade ratio and metal losses in the cleaner circuit, then the copper recovery would be 92 per cent to the final product, at a concentrate grade of 25 per cent Cu. Table 6, details the existing plant performance versus the predicted performance when the NovaCell™ is added to the flotation circuit.

The results indicate that with the NovaCell™ in a rougher duty, the existing SABC milling circuit could operate at 60 per cent higher throughput rates and achieve an overall copper recovery to the final product higher than the existing circuit. For a plant availability of 92 per cent and feed grade of 0.47 per cent Cu, the NovaCell™ would increase the copper tonnes to the final product by 64 per cent. It should be noted that the material pumped to the tailing storage facility (TSF) would also increase by 60 per cent.

TABLE 6

Existing circuit versus NovaCell™ added to flotation circuit

	Throughput Rate (dry tph)	Flotation Feed P_{80} (µm)	Total Power Draw (kW)	Product Copper Recovery (%)	Product Copper Tonnes (yearly)	Tailings to TSF (dry tph)
Baseline	1000	150	15 527	90	34 090	900
NovaCell™ added to flotation circuit	1 600	320	17 409	92	55 757	1440
% Change	60% Increase	113% Increase	12% Increase	2% Increase	64% Increase	60% Increase

NovaCell™ in coarse waste rejection

To investigate the potential metallurgical benefits in the milling circuit, the simulated results from Comminution Circuit 2 were used. The modified SABC milling circuit at a throughput rate of 1600 t/h (dry) solids produced a feed to the flotation circuit of P_{80} of 150 µm. In addition, the throughput rate to the flotation circuit reduced by 31 per cent. Thus, the NovaCell™ installed in the milling circuit ensured that no additional equipment was required in the existing flotation and regrind milling circuits.

The NovaCell™ installed between the primary and secondary grinding circuits, would receive part of the cyclone underflow stream at a feed P_{80} of 323 µm (due to the screen immediately prior to the NovaCell™, as per Figure 3). The NovaCell™ tails would be coarse waste material and would bypass

the flotation circuit and exit the circuit. These coarse tailings are likely to be free draining and would be suitable for dry tailings disposal. Thus, it is expected that this material would not be pumped to the TSF. The NovaCell™ product streams would feed the Ball mill for mineral liberation. The proposed circuit configuration is presented in Figure 11.

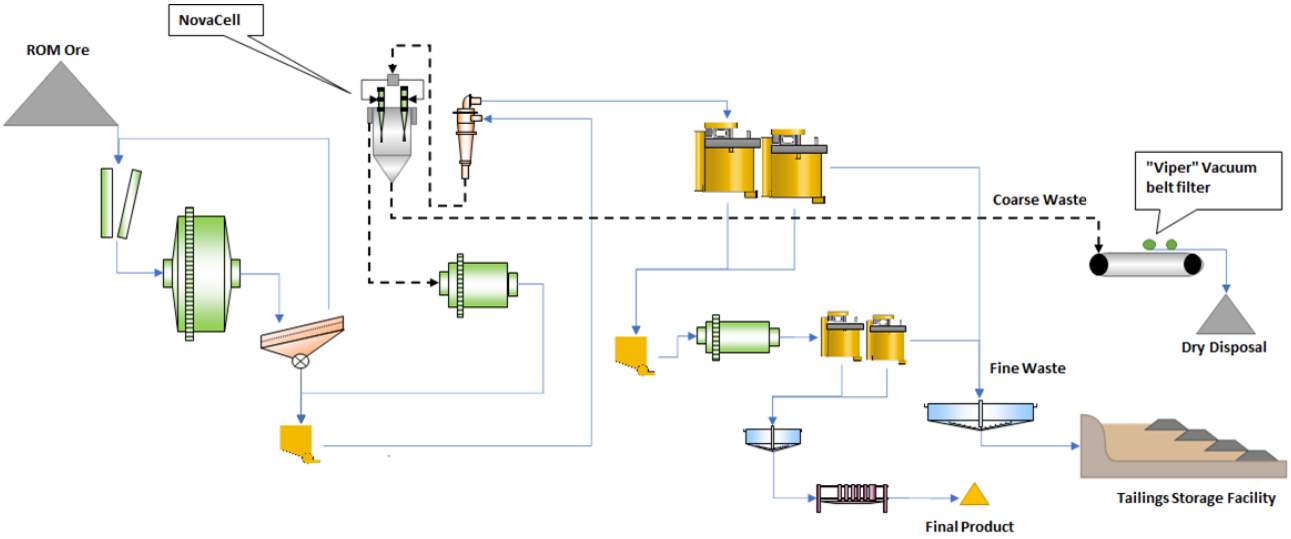

FIG 11 – NovaCell™ in coarse waste rejection.

To predict the NovaCell™ metallurgical performance in the waste rejection duty, the laboratory results for a P_{80} of 300 µm were used, as detailed in Table 5. The results suggest that the NovaCell™ would achieve a copper recovery of 95 per cent, at a concentrate grade of 4.2 per cent Cu. Thus, the coarse waste rejection stream would have 5 per cent Cu losses. We can expect that some of the copper lost in this stream to have also been lost in the conventional flotation circuit at a feed P_{80} of 150 µm. In addition, the conventional flotation circuit will have more flotation residence time by treating a lower volumetric flow rate. Thus, being conservative we have estimated the copper recovery to be 90 per cent to the final product, at a concentrate grade of 25 per cent Cu.

Table 7, details the existing plant performance versus the predicted performance when the NovaCell™ is added to the milling circuit.

TABLE 7

Existing circuit versus NovaCell™ added to milling circuit.

	Throughput Rate (dry tph)	**Flotation Feed P_{80} (µm)**	**Total Power Draw (kW)**	**Product Copper Recovery (%)**	**Product Copper Tonnes (yearly)**	**Tailings to TSF (dry tph)**
Baseline	1000	150	15 527	90	34 090	900
NovaCell™ added to milling circuit	1600	150	17 409	90	54 545	617
% Change	60% Increase	No change	12% Increase	No change	60% Increase	31% Decrease

The results indicate that with the NovaCell™ improving coarse waste rejection, the modified SABC milling circuit could operate at 60 per cent higher throughput rates. The overall copper recovery to the final product would remain the same. However, for a plant availability of 92 per cent and feed grade of 0.47 per cent Cu, the NovaCell™ would still increase the copper tonnes to the final product by 60 per cent. Another advantage of the NovaCell™ circuit, is that the amount of tailings material sent to the TSF would decrease by 31 per cent, even at the higher throughput rate. This has two environmental benefits for the plant operation. Firstly, less material would be entering the TSF

improving the overall water recovery and life of the storage facility. Secondly, less metal ions would be entering the TSF reducing the potential harmful effects of acid mine drainage.

In summary, for both the circuit configurations investigated, the NovaCell™ added to the circuit enabled 60 per cent higher throughput rates and significantly increased the copper tonnes to the final product by up to 64 per cent.

CONCLUSIONS

The JKSimMet results indicated that 60 per cent higher throughput rates can be achieved by incorporating a NovaCell™ flotation unit into rougher and comminution circuits. If the SABC circuit is not modified, as in Comminution Circuit 1, the flotation feed will coarsen significantly to P_{80} of 320 µm. If the SABC milling circuit is modified to include coarse waste rejection, it is possible to maintain the flotation feed at a typical grind size ie P_{80} of 150 µm. However, the location of the NovaCell™ in the modified SABC circuit influences the flotation feed grind size. Comminution Circuit 2, with the NovaCell™ treating part of the cyclone underflow, indicated the best circuit performance in terms of both flotation feed grind size and coarse waste rejection. For all the simulations conducted, the results indicated that flotation technology capable of efficiently recovering coarse valuable minerals would be needed in the circuit to maintain efficient copper metallurgical performance.

For the low-grade porphyry copper deposit investigated, the laboratory results indicated that at relatively coarse flotation feed sizes *viz* P_{80} of 300 µm to 350 µm, the NovaCell™ achieved copper recoveries higher than the current plant performance. Coarse valuable particles were recovered to both the froth and screen products, with the froth product being of higher concentrate grade. The NovaCell™ combined product indicated a copper upgrade ratio typical of conventional float cells in similar duties.

The JKSimMet simulation and laboratory results were used to predict the plant metallurgical performance at 60 per cent higher throughput rates with the NovaCell™ added to the milling or flotation circuit. The NovaCell™ in a coarse rougher duty ahead of conventional flotation cells indicated a 64 per cent increase in the copper tonnes to the final product. The NovaCell™ in a coarse waste rejection duty between the primary and secondary grinding mills indicated a 60 per cent increase in the copper tonnes to the final product. There were also environmental benefits predicted for the waste rejection circuit. At the higher throughput rate, the waste material pumped to the tailings storage facility (TSF) decreased by 31 per cent, improving the circuit's water recovery and the life of the storage facility.

It is recommended that the proposed NovaCell™ milling and flotation circuit configurations be further investigated at pilot scale to quantify the benefits for different ore types. The results will also assist in the metallurgical and commercial justification of the NovaCell™ technology for plant throughput expansions. Similar pilot campaigns have been scheduled and the results are expected to be discussed in future papers.

It is also recommended that the NovaCell™ be considered for new base metal deposits, especially porphyry copper deposits. JKSimMet simulations have indicated that for similar throughput rates, the NovaCell™ in the modified SABC circuit reduces energy consumption by 34 per cent and waste to the TSF by 57 per cent, when compared to traditional mining practices. As a result, the NovaCell™ adopted in future mining operations would significantly reduce CO_2 emissions and water consumption without compromising metal recovery. An added benefit of the early waste rejection, would be a reduction in the downstream milling and flotation equipment requirements. In summary, the NovaCell™ added to new process flow sheets has the potential to make a step change in mining operations, by lowering capital expenditure, reducing plant footprints, minimising energy and water consumption whilst still maintaining high levels of metal revenue.

ACKNOWLEDGEMENTS

The authors would like to acknowledge Lonn Cooper, Joshua Sovechles and Kitty Tang from Hunter Process Technologies (HPT) for their assistance in conducting the NovaCell™ laboratory test work. We would also like to thank Tim Vizcarra from JKTech for his guidance and feedback during the JKSimMet simulations.

The authors acknowledge the funding support from the Australian Research Council for the ARC Centre of Excellence for Enabling Eco-Efficient Beneficiation of Minerals, grant number CE200100009.

REFERENCES

Jameson, G J and Emer, C, 2019. Coarse chalcopyrite recovery in a universal froth flotation machine. *Minerals Engineering* 134, 118–133.

Jameson, G J, Cooper, L, Tang, K K and Emer, C, 2020. Flotation of coarse coal particles in a fluidized bed: The effect of clusters. *Minerals Engineering* 146, 2–13.

Lynch, A, Johnson, N, Manlapig, E and Thorne, C, 1981. *Mineral and Coal Flotation Circuits: Their Simulation and Control*. Amsterdam: Elsevier Publishing.

Mudd, G and Jowitt, S, 2018. 'Growing Global Copper Resources, Reserves and Production: Discovery Is Not the Only Control on Supply'. *Economic Geology*, 113(6), p. 1235–1267.

Napier-Munn, T J, Morrell, S, Morrison, R D and Kojovic, T, 1996. Mineral comminution circuits — their operation and optimisation. Julius Kruttschnitt Mineral Research Centre, Brisbane, Australia.

The World Bank, 2020. Climate Smart Mining – Minerals for Climate Action. [Online]. Available at: https://www.worldbank.org/en/topic/extractiveindustries/brief/climate-smart-mining-minerals-for-climate-action

EdgeFrag – an edge computing framework for on-site ore fragmentation analysis using deep convolutional neural networks

A Ray[1], A Swain[2], S Rani[3], C Bhaumik[4] and T Chakravarty[5]

1. Embedded Devices and Intelligent Systems, TCS Research, Kolkata, 700156, India. Email: ray.arindam@tcs.com
2. Embedded Devices and Intelligent Systems, TCS Research, Kolkata, 700156, India. Email: swain.amit@tcs.com
3. Embedded Devices and Intelligent Systems, TCS Research, Kolkata, 700156, India. Email: smriti.rani@tcs.com
4. Embedded Devices and Intelligent Systems, TCS Research, Kolkata, 700156, India. Email: c.bhaumik@tcs.com
5. Embedded Devices and Intelligent Systems, TCS Research, Kolkata, 700156, India. Email: tapas.chakravarty@tcs.com

ABSTRACT

In a typical Mine to Mill pipeline, the feed size distribution of run-of-mine (ROM) ore has a significant impact on the efficiency of downstream mineral processing operations. Previously, several image processing techniques based on adaptive thresholding, filtering, and watershed algorithm were used to conduct fragmentation analysis of ore materials. However, these algorithms were susceptible to issues originating from the overlapping of ore aggregates and dynamic changes in illumination, thus affecting the segmentation accuracy. Deep learning approaches provide an additional advantage in this scenario where these dynamic variations can be captured, and an environment agnostic model can be trained. These again pose challenges as deep learning models incur a large memory footprint and computational overhead. The current work attempts to address both of these key issues for on-site particle size analysis. A state-of-the-art deep neural network – Nuclear Segmentation Tool (NuSeT) has been used. NuSeT employs an ensemble of Convolutional Neural Networks (CNNs), followed by a Region Proposal Network (RPN). This helps to delineate the boundaries between the overlapping regions. This network has been trained on a data set consisting of 1200 lab-scale images of different rock aggregates, their manually annotated ground-truth labels, and 300 synthetically generated noisy images having diverse morphological features. The trained model has been compressed using model optimisation tools to generate a lightweight model, without a significant drop in segmentation accuracy. The pre-trained model reported a segmentation dice loss of 0.13 and an F1-score of 0.95. The optimised model was tested on various edge devices, and it resulted in a three-fold improvement in inference time as compared to the base model.

INTRODUCTION

Mineral industry requires continuous production and processing of ore to meet stringent profitability targets. In this production focused industry, even a slight improvement in the cycle time of unit operations or efficacious material handling can impact annual production figures. A crucial aspect of the mining value chain is fragmentation analysis or size inspection of ore materials. Ma *et al* (2020) pointed out that in autogenous (AG) mills, the optimum feed must contain sufficient coarse lumps to act as grinding media, thereby impacting the power consumption and throughput of mills.

On-site fragmentation analysis using vision sensors necessitates two primary requirements – image segmentation accuracy and real-time inferencing capabilities of the system. In the context of accuracy, ore image segmentation poses a unique set of problems such as overlapping ore particles, fuzziness in the image due to uneven lighting, dust and several other factors. Traditionally, commercial systems have used classical image processing techniques. In addition to them being unsuitable for segmenting overlapping boundaries, they heavily depend on manual optimisation thus rendering them unsuitable for online analysis.

To address this gap, this paper leverages the analogy between rock fragmentation and biomedical cell nuclei segmentation. Nuclei segmentation presents itself with a very similar set of challenges like ambiguity in boundary assignment, and low signal-to-noise ratio (SNR) due to uneven illumination. Therefore, a state-of-the-art deep learning (DL) segmentation framework Nuclear

Segmentation Tool (NuSeT), used by Yang *et al* (2020) has been used in the training process of this work. NuSeT reduces false positives and achieves superior performance in segmenting densely packed particles. Additionally, the current paper addresses the problem of large processing time associated with Convolutional Neural Networks (CNNs) by using a model optimisation framework (OpenVINO) to provide the necessary speed-up required for real-time inferencing.

The three primary contributions of this work are:

- Improving accuracy of coarse particle segmentation by domain transformation of the NuSeT framework and training it on a lab-scale data set of ore images.
- Data augmentation and generation of synthetic data to make the data set more realistic.
- Trained model optimisation to make it lightweight and suitable for use in on-device and on-site inferencing.

PREVIOUS WORK

The practise of ore fragmentation analysis has witnessed several transformations, starting from traditional methods like visual inspection and manual sieve analysis to online ore imaging systems. Today, we have sophisticated vision systems which can be mounted atop conveyor belts to perform complex image processing tasks. With the tremendous growth in the field of artificial intelligence and computer vision, now the research hotspot has shifted to addressing challenges in the ore image processing pipeline. Suprunenko (2020) developed an ore segmentation framework using a standalone U-Net based deep learning algorithm. Following this, several other works have explored U-Net and its derivative networks for solving the task of overlapping ore segmentation – however the data used in the same reflected minimal overlap of particles. Ma *et al* (2020) presented a unique approach of classifying the ore image segmentation task into empty belt, fine and coarse segmentation tasks in the first layer. Following up with this initial classifier, they had separate algorithms to tackle each of these tasks. Liu *et al* (2020) suggested a combination of U-Net and Res U-Net deep learning networks to perform accurate segmentation of ore particles. Huang *et al* (2020) used transfer learning approach on a Mask R-CNN pre-trained model which was trained on the well-known COCO data set and a customised data set of manually annotated ore particles. The additional contribution here was the morphological analyses of the results based on a standard template of pre-defined shapes and sizes.

Most of the above-mentioned works addressed the problem of training and validation accuracy improvement in the context of ore image segmentation. Yet, the real problem of deploying such high footprint networks on embedded devices remains open in this context. Gadosey *et al* (2020) and Vaze *et al* (2020) pointed out the cost of using CNNs and resulting slow CPU inference times due to numerous parameters and floating-point operations. In this paper, we attempt to address this problem by using an optimised model which is not only able to accurately segment overlapping ore particles but does the same with minimal on-device inference time. The current work jointly addresses the issue of precise ore segmentation and optimising the generated model without significant drop in the model accuracy.

METHODOLOGY

NuSeT is used as the backbone deep network for segmentation of ore particles. The entire network is constructed to detect and compensate multifarious lighting conditions for segmenting cell nuclei from a densely populated environment. Physically, this work operates on images taken from a vision sensor positioned vertically above the conveyor, to get a top view of the ore structures placed on the same. Before feeding the input images to the network, some preprocessing tasks are performed as highlighted below.

- Preprocessing: The input images are resized to a height of 240 pixels and a width of 320 pixels. Such a size is chosen to preserve the characteristics of the ore structures, while not overwhelming the downstream network with extended inferencing times. The 3 channel (red, green, blue) data is next converted to a grey scale intensity map following the convention:

$$I_{(i,j)} = 0.2989R_{(i,j)} + 0.587G_{(i,j)} + 0.114B_{(i,j)}$$

Here, $I_{(i,j)}$ is the intensity at the $(i,j)^{th}$ pixel coordinate, while $R_{(i,j)}$, $G_{(i,j)}$ and $B_{(i,j)}$ are the intensities for the red, green and blue channels at the same location. Consequently, the brightness of the generated grey scale image is adjusted by a factor of K to make it suitable for feeding into the network.

The preprocessed image is then fed to the deep network. The overall pipeline for the network is illustrated in Figure 1 and consists of:

- U-Net: U-Net (Ronneberger *et al*, 2015) presents a deep learning architecture based on reusing contextual information from layers in the network. As indicated in Figure 1, it makes use of convolutional layers followed by max-pooling layers in the contracting part of the network (the left arc of the U-structure) and convolutional layers followed by upsampling layers (the right arc of the U-structure). The large number of feature channels on the upsampling part and the depth of the structure allows for the transfer of rich context information to the corresponding higher resolution layers.

  Following the NuSeT architecture, two U-Nets are used to achieve ore segmentation. The entire image is first normalised (*whole-norm* in NuSeT terminology) – this mitigates image intensity differences and contributes towards better learning and improvement of network performance. Usually, images are normalised by removing the intensity computed from all its pixels in a given data set (Yang *et al*, 2020). This, however, might cause varying levels of normalisation for individual image instances, especially if they have significant intensity differences. Thus, normalisation of the whole image data addresses this issue, but simultaneously creates intensity differences in images with smaller regions of varying ore densities. Additionally, this normalisation performs poorly in images affected with varying levels of illumination. To alleviate this problem, a two-step normalisation approach is adopted. Firstly, the background and foreground are separated from the whole-normalised image using a U-Net. The detected foreground is further normalised (*foreground-norm* in NuSeT terminology) and passed through a second U-Net of the same depth to distinguish between the ore fragments themselves. Adoption of such a two-layered system allows for better segmentation results, as the foreground normalised images have better resistance to imperfect lighting conditions (low SNRs).

- Region Proposal Network (RPN): RPN (Ren *et al*, 2015) is a shallow network that predicts object bounding boxes. It internally uses a classifier that determines the probability of a proposal containing the target object and a regressor that regresses the coordinates of the same. The final bounding boxes for a detected object are usually determined using Non-Max Suppression (NMS) on the proposed regions. To improve accuracy in images with significant ore size differences, the original RPN architecture is modified to use bounding boxes based on the mean ore size for each image. Additionally, instead of training the U-Net and the RPN separately, the feature extraction part of RPN is reused with the lowest layer of the U-Net to avoid higher memory costs and longer training time. In this way, a RPN is used to achieve separation of instances of various overlapping ore structures.

- Watershed algorithm: The output of the second U-Net and information from the RPN are combined to distinguish between closely spaced particles in the image using the established watershed algorithm. In this work, the RPN outputs serve as markers on the U-Net segmented images, thereby achieving effective segmentation and crisp boundary detection even for closely spaced and overlapping ore particles.

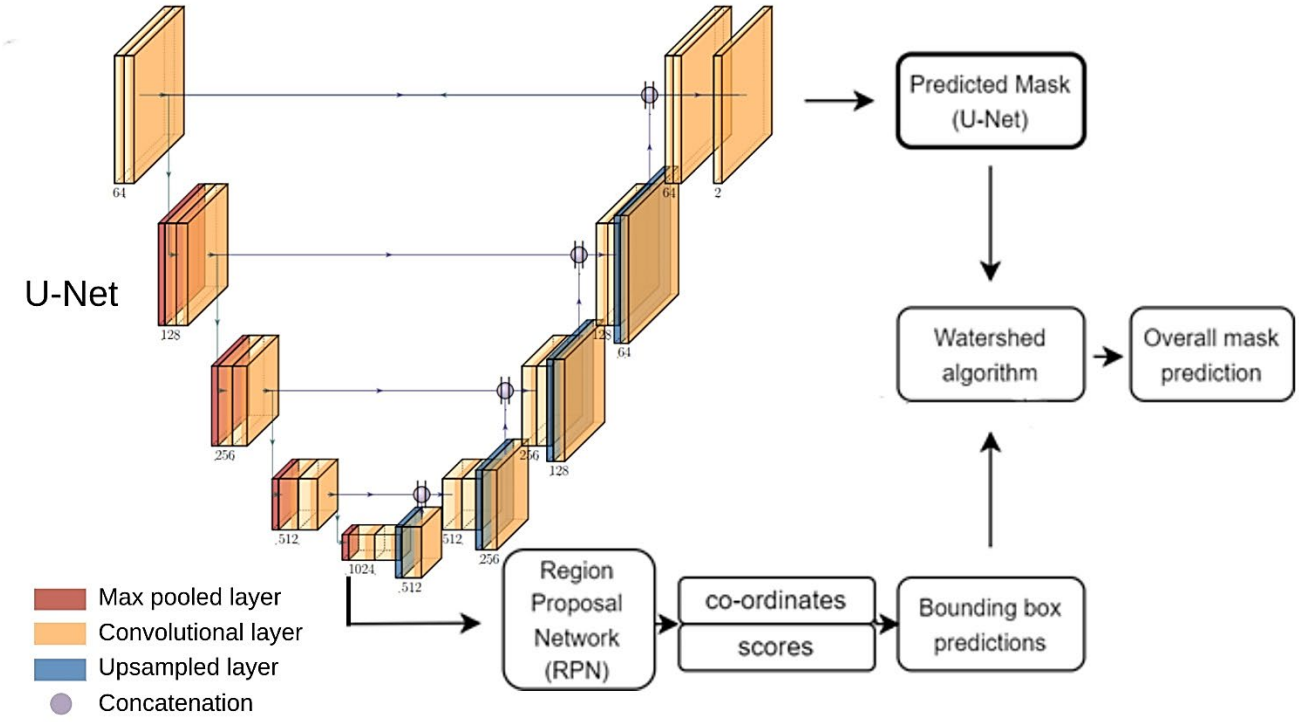

FIG 1 – Model architecture for the proposed system. The underlying U-Net is highlighted and the flow of data through the other layers are also illustrated.

Model Optimisation

CNNs have been widely adopted for discovering intricate structures and learning deep underlying features in large data sets. One might achieve a good accuracy using these networks, but they are over parameterised. This manifests in form of large memory footprint and poor inference times. The task of deploying a CNN based network for a time-critical inferencing task such as online ore segmentation atop conveyor belts becomes challenging. We aim to generate a compressed form of our network, for use in low-power and resource constrained edge systems. Hence, we optimise our model using Intel's OpenVINO framework (Zunin, 2021). Several operations such as pruning and quantisation are performed, which results in a smaller sized model. These results are evaluated in terms of the improvement in inferencing accuracy and processing time.

Data Augmentation

To create a robust model, data augmentation techniques such as random orientation, mirror flipping, rotation and scaling with random morphological features are applied on the training images. Additionally, several synthetic ore images are generated and perturbed randomly to improve the richness of the data set and prevent overfitting. Such synthetic images are exposed to Gaussian noise, salt and pepper noise, Gaussian blurring and overlapping number of ore particles. The binary masks for such synthetic images were created as well and erosion is used to demarcate between overlapping ore particles. A 4:1 ratio of real images to synthetic images is taken.

Evaluation Metrics

To evaluate the performance of the model, the following performance metrics are adopted: mean Intersection over Union (IoU), Root Mean Square Error (RMSE), and F1.

The mean IoU, F1 scores and RMSE values are calculated respectively using the following expressions:

$$Mean\ IoU = \frac{1}{N_{cls}} \sum_{k=0}^{N_{cls}} \frac{TP_k}{TP_k + FN_k + FP_k}$$

$$F1 = \frac{1}{N_{cls}} \sum_{k=0}^{N_{cls}} \frac{2TP_k}{2TP_k + FN_k + FP_k}$$

$$RMSE = \sqrt{\frac{1}{N_{px}} \sum_{i} (y_i - y_{ipred})^2}$$

Here, for a single image, TP, FP, TN and FN denote the pixel-level counts of true positive, false positive, true negative and false negative. N_{cls} is the number of possible classes of prediction for a pixel (in this work N_{cls} = 2, for the foreground and the background). The number of pixels in the image is given by N_{px}. y_i and $y_{i,pred}$ denote the value of the i^{th} pixel in the ground truth mask and predicted binary mask respectively. The average metrics of all images in the data set are obtained from the pixel level metrics over the entire data set of images.

EXPERIMENTATION AND RESULTS

The lab-scale data set prepared for this work consists of 1200 images, along with 300 augmented images for a total of 1500 images. The training to validation split was in the ratio of 80:20. The learning rate was 0.00005 and Adam optimiser was used with a batch size of 64. The entire system was trained end-to-end for 100 epochs on a platform with a NVIDIA Quadro GPU and an Intel Xeon processor. Figure 2 shows the results of the created segmentation system. The output of the two U-Nets can also be seen in Figure 2b. It is observed that segmentation is carried out with a high degree of precision, even in cases where the input image has low resolution, is noisy and has overlapping ore particles. Table 1 summarises the metrics reported by our model. It is seen that the mean IoU is above 90 per cent and the final F1 score above 0.95, indicating highly effective segmentation.

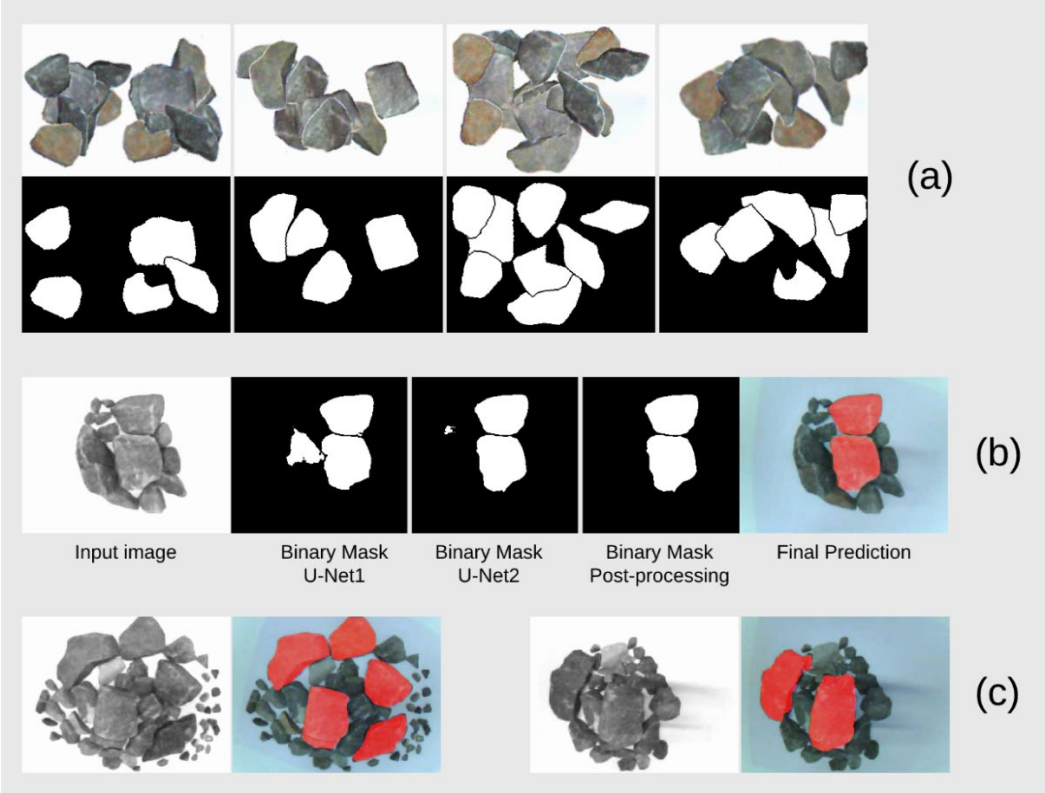

FIG 2 – Ore segmentation results. (a) highlights the synthetic data set generated. Top images are synthetic images created, and bottom images denote their corresponding binary masks. (b) showcases the outputs at various stages of the pipeline. (c) denotes sample input images and generated output masks.

TABLE 1

End-to-end performance metrics for the test set.

Model metric	Value
Mean IoU	0.91
F1	0.95
RMSE	0.016

The final U-Net dice loss (Yang *et al*, 2020) and cross-entropy loss were 0.13 and 0.04 respectively. The sum total of the RPN classifier and regressor loss was 0.1. Thus, the U-Net and the RPN working simultaneously can effectively demarcate between closely packed ores. Moreover, features generated at the lowest layer of the U-Net can be used to advantageously train the RPN. The reported values in Table 1 fall significantly when synthetic images are excluded from the training set. This ensures that the model does not overfit and can generalise well. Table 2 captures the improvement obtained in terms of inference time improvement on several hardware when convolutional layers are accelerated using the Intel OpenVINO framework. It is seen that the model performs appreciably fast even on a portable single board computer (Raspberry Pi v4), when coupled with Intel's Neural Compute Stick 2 (NCS2) module. The inference times mentioned below are reported for a single image as fed to the network.

TABLE 2

Model inference time comparison on various hardware.

Hardware used	Inference time
CPU: Intel Atom	1.6s (baseline)
SBC + Intel NCS2	0.57s
CPU: Intel Xeon	0.47s

CONCLUSION

Based on the results and findings of this work, the following conclusions can be summarised in relation to the proposed approach of using an optimised NuSeT model for on-device ore fragmentation analysis:

- This paper adopted the NuSeT deep learning network to address the problem of densely stacked ore particles. NuSeT, which a model developed for the purpose of biomedical cell nuclei segmentation, was re-trained on a lab-scale data set of ore images. The trained segmentation model achieved good performance in delineating the edges of overlapped or particles and isolating the coarse particles. With a mean IoU over 90 per cent and a F1 score over 0.95, the trained model exhibits excellent accuracy and performance.
- By establishing a custom data set of 1200 images with around 300 synthetically augmented images, the training data reflects the robustness of the model to perform in realistic and challenging field scenarios.
- The trained model was optimised without significant drop in accuracy. The final optimised model exhibited three hold improvement in the inference time as well experienced minimal loss ie final U-Net dice loss of 0.13 and cross-entropy loss 0.04.

The proposed edge computing framework has strong relevance for utility in belt ore segmentation use-cases. It must be noted that a binary segmentation task has been attempted as part of this paper. This enables fragmentation analysis mainly from the perspective of separating the coarser materials from a mixed distribution of ore. As a future work, the full-scale fragmentation analysis on the same data set using a multi-class segmentation framework has been envisaged.

REFERENCES

Gadosey, P K, Li, Y, Agyekum, E A, Zhang, T, Liu, Z, Yamak, P T and Essaf, F, 2020. Sd-unet: Stripping down u-net for segmentation of biomedical images on platforms with low computational budgets. *Diagnostics*, 10(2), p. 110.

Huang, H, Luo, J, Tutumluer, E, Hart, J M and Stolba, A J, 2020. Automated segmentation and morphological analyses of stockpile aggregate images using deep convolutional neural networks. *Transportation Research Record*, 2674(10), pp. 285–298.

Liu, X, Zhang, Y, Jing, H, Wang, L and Zhao, S, 2020. Ore image segmentation method using U-Net and Res_Unet convolutional networks. *RSC Advances*, 10(16), pp. 9396–9406.

Ma, X, Zhang, P, Man, X and Ou, L, 2020. A new belt ore image segmentation method based on the convolutional neural network and the image-processing technology. *Minerals*, *10*(12), p. 1115.

Ren, S, He, K, Girshick, R and Sun, J, 2015. Faster r-cnn: Towards real-time object detection with region proposal networks. *Advances in neural information processing systems*, 28.

Ronneberger, O, Fischer, P and Brox, T, 2015, October. U-net: Convolutional networks for biomedical image segmentation. In *International Conference on Medical image computing and computer-assisted intervention* (pp. 234–241). Springer, Cham.

Suprunenko, V V, 2020, November. Ore particles segmentation using deep learning methods. In *Journal of Physics: Conference Series* (Vol. 1679, No. 4, p. 042089). IOP Publishing.

Vaze, S, Xie, W and Namburete, A I, 2020. Low-memory CNNs enabling real-time ultrasound segmentation towards mobile deployment. *IEEE Journal of Biomedical and Health Informatics*, 24(4), pp. 1059–1069.

Yang, L, Ghosh, R P, Franklin, J M, Chen, S, You, C, Narayan, R R, Melcher, M L and Liphardt, J T, 2020. NuSeT: A deep learning tool for reliably separating and analyzing crowded cells. *PLoS computational biology*, *16*(9), p. e1008193.

Zunin, V V, 2021, September. Intel OpenVINO Toolkit for Computer Vision: Object Detection and Semantic Segmentation. In *2021 International Russian Automation Conference (RusAutoCon)* (pp. 847–851). IEEE.

Optimisation of a laboratory Hydrofloat™ separator in the coarse particle flotation of a PGM-bearing Platreef ore

J Taguta[1], M Safari[2], V Govender[3] and D Chettyt[4]

1. Chief Engineer, Mintek, Praegville, Randburg, 2194, Johannesburg.
   Email: jestost@mintek.co.za
2. Principal Engineer, Mintek, Praegville, Randburg, 2194, Johannesburg.
   Email: mehdis@mintek.co.za
3. Senior Scientist, Mintek, Praegville, Randburg, 2194, Johannesburg.
   Email: veruskag@mintek.co.za
4. Head of Mineral Science, Mintek, Praegville, Randburg, 2194, Johannesburg.
   Email: deshc@mintek.co.za

ABSTRACT

Coarse particle flotation (CPF) is one of the strategies to reduce energy consumption into comminution. CPF recovers coarse particles with low liberation requirements and also rejects coarse barren waste upfront resulting in reduced downstream processing requirements. However, the HF has not yet been applied in PGM flotation. In this paper, the amenability of the Platreef ore to CPF using the HydrofloatTM technology developed by Eriez was investigated. Extensive flotation test work coupled with mineralogical analysis of feed and selected flotation products was conducted to optimise the primary grind and the hydrodynamic parameters, ie bed-level, air and water rates in the flotation of coarse Platreef ore feed using the HF separator. The results showed that the Platreef ore is amenable to coarse particle flotation using the HydrofloatTM technology. The results demonstrated that the HF separator achieved high recovery efficiencies across the 150–300 microns size fraction. The HF separator achieved relatively lower recoveries of the sub 150 µm showing that the hydrodynamic conditions prevailing in the HF separator favour recovery of coarse and not fine particles. Mineralogical analysis showed that all the liberated PGMs were recovered in the concentrate as there were no liberated PGMs in the tailings. 85.3 vol per cent of PGMs identified in the concentrate were associated with BMS attached to silicate or oxide gangue particles. Most of the PGMs attached to or locked within silicate or oxide gangue reported to the tailings. It was found that an increase in bed height, water rate and air flow rate resulted in an increase in PGMs recovery to a maximum. A further increase in the hydrodynamic parameters resulted in a decline in the PGMs recovery. The practical implications of the findings on the modification of existing circuits or design of novel flow sheets for the processing of the Platreef ores are discussed.

INTRODUCTION

South Africa supplies almost 80 per cent of the world platinum group elements (PGE) demands contributing significantly to the economy of the country because of a massive resource deposit called the Bushveld Complex, BC. The PGEs are extracted from three mineralised horizons namely the Merensky, UG2 and Plat reefs. The Platreef ore is considered the hardest ore requiring relatively high energy input in the comminution stage compared to its UG2 and Merensky counterparts. The hardness of the Platreef ore is attributed to a high serpentine content. Flotation efficiency of the Platreef ore is hugely dependent on liberation as some PGMs are completely enclosed in gangue silicates cannot be floated, hence the need to grind finer to 80 per cent passing 75 µm to liberate the PGMs and BMS. The conventional comminution circuits, comprising of a cone crusher, high pressure grinding roll and ball mill, targeting a primary grind of 80 per cent passing 75 µm are energy intensive as the finer the product size, the higher the energy consumption rate (Mwale *et al,* 2005). Research has shown that 70–75 per cent of the total electrical energy in most mineral processing plant is consumed by the comminution process (Musa and Morrison, 2009). Apart from the high energy consumption, grinding finer generates fines which are difficult to recover using conventional mechanical flotation cells. Fine grinding also lead to the sliming of PGMs and BMS resulting in losses. Some PGM operations implement staged grinding utilising complex Mill Float, Mill, Float circuits (MF2) or Mill Float, Mill, Float Mill Float circuits (MF3) circuits in order to prevent overgrinding which leads to the sliming of PGMs and BMS. A number of PGM concentrators use implement flash

flotation to recover liberated coarse PGMs and BMS in the hydrocyclone underflow before recycling them back to the mill.

Conventional flotation machine challenges in BMS and PGMs

Conventional sulfide flotation machines are typically limited to a particle size range of 10–100 µm due to inherent constraints created by the pulp and froth phases (Jameson, 2010). This phenomenon is depicted in well-recognised 'elephant curve' shown in Figure 1.

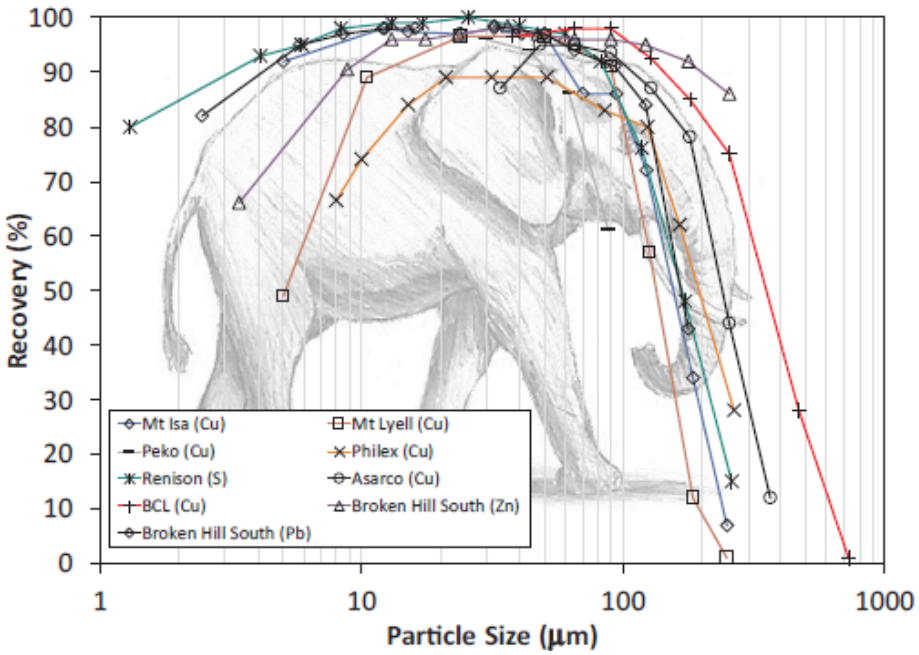

FIG 1 – Recovery as a function of particle size for conventional industrial flotation system (Lynch *et al,* 1981).

Figure 1 shows that particles outside the critical range of 10–100 µm are typically lost in most flotation concentrators as a result of the inherent constraints associated with conventional mechanical cells. The decline in the recovery of coarse particles (>100 µm) is attributed to many reasons including poor liberation (Schulze, 1977), low carrying capacity of bubbles (Paiva and Rubio, 2016) and detachment of bubble-particle aggregates due to high turbulence (Jameson, Nguyen, and Seher, 2007). The poor recovery of fines (<10 µm) is attributed to low collision efficiencies with relatively large bubbles (Trahar and Warren, 1976). The fines are slow-floating and thus require longer residence times, high turbulence and relatively higher collector dosages due to high particle surface area. Fines are also highly reactive and susceptible to oxidation rendering them difficult to recover by flotation.

As orebodies are becoming increasingly low-grade and mineralogically complex, huge flotation capacity is required to achieve high concentrator throughput. However, huge conventional mechanical flotation cells require high energy input due to mechanical agitation to keep particles in suspension. Rinne and Peltola (2008), in a study of the cost breakdown of large flotation cells, established that about 68 per cent of the cells' total operating cost is attributed to energy consumption.

Coarse particle flotation using the Hydrofloat technology

The conventional strategy to increase energy efficiency in comminution has mostly been the application of more energy efficient equipment technologies eg autogenous grinding (AG), HPGR, IsaMill, HIG mill etc (Pokrajcic *et al,* 2009). Another strategy to increase energy efficiency is coarse ore upgrading which has many benefits including reduced energy consumption that goes into crushing and grinding (comminution), coarse gangue rejection and increased plant throughput. However, it should be noted that grinding coarser affects liberation and particle size of the valuable minerals. The inherent limitations associated with the conventional flotation machines to recover

coarse particles can be overcome by new technologies such Eriez's Hydrofloat™ technology which is specifically designed for coarse particle flotation. The HF utilises fluidised-bed flotation specifically designed for the selective recovery of feeds containing very coarse particles. The HF operates without a rotating impeller as particle suspension is achieved by the smooth and hindered settling conditions of the particles rather than by the turbulent conditions of the traditional flotation cell. The quiescent environment prevailing in the HF provides low turbulence, enhanced bubble-particle contacting and increased particle residence time. The elimination of the froth phase also promotes the recovery of coarse particles. Based on extensive literature review, the performance of the HF separator depends on the physical particle properties (particle density, particle size distribution), ore properties (mineralogy, liberation and texture), hydrodynamic conditions (superficial air and water flow rates, bed height etc) and chemical conditions (reagent types, dosages etc).

The HF technology has been successfully applied in the coarse flotation of industrial minerals in which particles coarser than 3 mm can be recovered at industrial scale. Recent studies also showed that the HF is capable of coarse upgrading of sulfide ores at laboratory and pilot scales. Paiva and Rubio (2016) demonstrated that the HF achieved higher recoveries of classified, coarse fractions of -297+210 μm and +297 μm than conventional flotation (CF) for a copper sulfide mineral as an example of a difficult-to-liberate ore at laboratory scale. Miller *et al* (2016) showed that the HF was able to recover metalliferous values at a grind size much coarser than that treated in industrial concentrators during the flotation of a low-grade gold ore. Miller *et al* (2016), using high resolution X-ray microtomography (HRXMT), showed that the HF recovered nearly 100 per cent of the 0.850 × 0.500 mm composite particles containing as little as 1 per cent surface exposure of sulfide mineral in scavenging applications. They further showed that tailings contained virtually no particles containing more than 1.5 per cent exposed sulfide grain surface area. Fosu *et al* (2015) concluded that the HF outperformed the CF for the upper particle size of about 500 mm during the flotation of model synthetic composites of quartz in lead borate matrix with simple and locking texture at laboratory scale. Awatey *et al* (2013) showed that the recovery of coarse sphalerite using the HF increased with increasing bed-level, superficial water and gas flow rates. They also demonstrated that there exist thresholds for each operating parameter above which recovery started to decrease. They also established that the HF outperformed the CF for the recovery of the +425 mm sphalerite particles. Awatey *et al* (2014) found that the critical contact angle required to float coarse sphalerite particles in CF was higher than in HF, and increased as particle size increased for the flotation of sphalerite (0.250–1.180 mm) at laboratory scale. The HF was found to outperform the CF at the same particle size and contact angle of the coarse sphalerite particles.

The application of the HF technology in the PGM industry has potential to improve energy and metallurgical efficiencies as well as concentrator capacity. Specifically, coarse ore grinding would avert undesirable generation of fines and sliming of PGMs and BMS due to overgrinding. Coarse PGM ore flotation using the HF would overcome challenges associated with the recovery of fines highlighted earlier on. This study investigated the amenability of the PGM-bearing Platreef ore to treatment by the HF technology. This study also aimed to determine the optimum hydrodynamic conditions for operating the HF for the flotation of a PGM-bearing Platreef ore. This paper also analysed comparative performances of the HF and the conventional flotation on a PGM-bearing Platreef ore.

EXPERIMENTAL PROCEDURES

Sample preparation

The Platreef ore from the Bushveld complex in South Africa was investigated in this study. One tonne of material was crushed to 100 per cent -1.7 mm using a cone crusher. The crushed sample was then dry milled for 40 minutes using a ball mill utilising high chrome media in 30 kg batches. After milling, all the milled samples were blended and homogenised to prepare one composite, and was dry screened using 106 μm and +300 μm sieves to produce 106–300 μm size fraction. The -106 μm material was removed to minimise the effect of hydraulic entrainment. 500 g subsamples were removed from each size fraction for mineralogical and chemical analysis.

Particle size distribution

The particle size distribution (PSD) of the 106–300 µm size fraction was characterised and the results are presented in Figure 2 and Table 1.

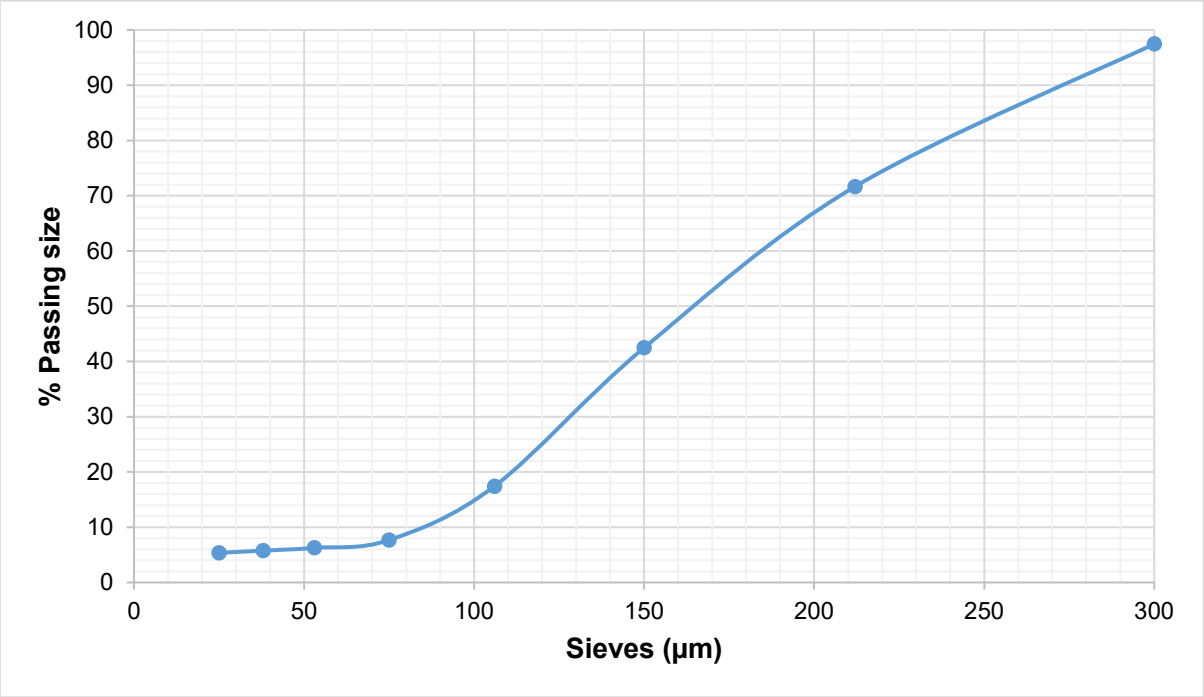

FIG 2 – PSD of the of the 106–300 µm size fraction.

TABLE 1

PSD of the of the 106–300 µm size fraction.

Particle size range (µm)	% passing 150 µm	% passing 106 µm	% passing 25 µm
106–300	43	17	5.4

The presence of the -106 µm size fraction is due to the inefficiency associated with the dry screening method.

Ore chemistry

Subsamples were also removed from each size fraction for chemical and mineralogical analysis. Chemical analysis was conducted on the subsamples using fire assay methods for the PGMs (Pt, Pd and Au) assays, ICP OES for base metal sulfides and LECO for total S. The head grades of the ore presented in Table 2 show that the ore had ~2.59 g/t 3E, 0.08 per cent Cu and 0.16 per cent Ni.

TABLE 2

Head grades of the Platreef ore.

PGMs	Cu	Ni	Fe	Total S
(g/t)	(%)	(%)	(%)	(%)
2.59	0.08	0.16	6.39	0.28

Size by assay

A 1 kg subsample was removed from the milled composite sample for size by assay determination (SBA). The subsample was wet screened at 25 µm. The screen undersize was dried and weighed while the oversize was dried and subjected to sizing using a root two sieve series from 300 µm. The

masses retained on each screen were weighed to determine a full-size distribution. The SBA and mass distribution data are shown in Table 3.

TABLE 3

SBA and mass distribution data of the milled composite sample.

Sieve size (µm)	Mass (g)	Mass (%)	Grade			Mass distribution (%)		
			3E	Cu	Ni	3E	Cu	Ni
+300	6.72	2.3	2.59	0.063	0.1	5.9	0.1	0.2
-300+212	68.31	23.2	2.36	0.062	0.093	54.7	1.4	2.2
-212+150	81.77	27.7	1.75	0.073	0.099	48.6	2.0	2.7
-150+106	76.83	26.1	1.62	0.11	0.1	42.2	2.9	2.6
-106	61.07	20.7	2.67	0.22	0.14	55.3	4.6	2.9
Total	**294.7**	**100.0**						

The results show that the PGMs and BMS were deported in both the fine (-106 µm) and coarse size fractions (+106–300 µm). It is clear that for the coarse particle size fraction, the coarser the particle the higher the 3E grade while an opposite trend was observed for the Cu. There was no variability in the in the Ni grades across the coarse particle size fraction. From a flow sheet design perspective, it should be feasible to upgrade the Platreef ore using coarse particle flotation technologies such as the Hydrofloat™ technology. Furthermore, a split feed would be required with the fine size fraction (-106 µm) floated using the conventional flotation machines. The results further show that by removing the -106 µm particle size fraction, 73 per cent, 59 per cent and 73 per cent of the 3E, Cu and Ni were retained in the coarse particle size fraction.

Mineralogy

Mineralogical analysis was conducted on the feed, concentrate and tailings samples using automated scanning electron microscopy, a Mineral Liberation Analyser and quantitative X-ray diffraction by Rietveld refinement methods. PGM, BMS and gangue specific attributes were extracted from mapped particles in the screened feed, the concentrate and tails samples, whereas QXRD determined bulk modal mineralogy in the concentrate and tails.

BMS search

Pentlandite was the major BMS species present followed by pyrrhotite and chalcopyrite. Approximately 12 mass per cent of pyrite was present. Galena and millerite were present in trace amounts (~0.1 mass per cent). The majority of pyrite, pyrrhotite, pentlandite, chalcopyrite, galena and millerite grains were fine grained and reported to the 0–75 µm grain size class. Pentlandite, pyrite and pyrrhotite were moderately liberated with more than 71 per cent better than 80 per cent liberated. Chalcopyrite and galena were moderately liberated with more than 60 per cent better than 80 per cent liberated. The majority of BMS minerals were liberated and minor to trace amounts associated with gangue and other BMS mineral phases.

PGM search

PGE-tellurides were the dominant PGM species comprising ~62.1 vol per cent followed by PGE-sulfides, PGE-arsenides and trace amounts of PGE-alloys. Approximately 15.9 vol per cent of PGMs reported to the 0–3 µm size class, ~45.9 vol per cent of PGMs to the 3–6 µm size class, ~12.5 vol per cent of PGMs to the 6–9 µm size class and ~25.7 vol per cent of PGMs to the 9–12 µm size class. The ore had poor liberation with ~4.5 vol per cent of PGMs being fully liberated. 31.2 vol per cent of the PGMs were associated with the BMS (chalcopyrite, pentlandite, pyrrhotite and pyrite). The majority of PGMs identified in the sample were associated with enstatite, chlorite, diopside magnetite plagioclase quartz, hornblende and mica.

Flotation tests and procedure

Hydrofloat feed preparation and tests

10 kg material was pulped at 77 per cent solids density and conditioned in an 88 L rotating drum to prepare feed for the HF tests. Sodium isobutyl xanthate (SIBX), a sulfide collector was dosed at 120 g/t (unoptimised dosage) and conditioned for 2 minutes. All the flotation reagents were prepared at 1 per cent strength. The conditioned pulp was slowly fed to the HF separator using a vibrating over-head feeder which to discharge the feed material from the top of the separator. A frother, Senfroth 522, was pumped continuously into the water line at a flow rate of 3.98 L/h. Three hydrodynamic parameters, *viz*: bed height, air flow rate, superficial water rate were investigated with only one parameter being varied at a time. For the baseline test, air flow rate (AFR), water flow rate (WFR) and bed height (BH) were set at 2.5 L/h, 2.5 L/h and 28.8 cm, respectively. The concentrate was collected into a settling tank and allowed to settle. The tailings were also discharged at the end of each test. Both the concentrate and the tailings samples were dried, screened into different size fractions for chemical analysis. Flotation tests were conducted in duplicates for reproducibility of mass pulls. Mass pulls were compared and tests which deviated by at least 5 per cent were rejected and repeated to ensure reproducibility.

RESULTS AND DISCUSSION

This section presents results on the effect of hydrodynamic conditions on the performance of the Hydrofloat separator.

Optimisation of hydrodynamic parameters

The +106–300 µm size fraction was used for test work aimed to optimise of the HF separator's hydrodynamic parameters.

Effect of bed height on the HF separator performance

The effect of bed height on the performance of the HF separator was investigated and the results are shown in Table 4 and Figure 3 which show that an increase in bed height resulted in an increase in PGM recovery to a maximum.

TABLE 4

Effect of bed height on the performance of the HF separator in the treatment of the Platreef ore (AFR = 2.5 L/h; WFR = 2.5 L/h).

Bed height (cm)	MP (%)	Recovery (%)		
		3E	Cu	Ni
28.8	17.8	71.8	59.6	59.1
32.5	16.5	84.5	55.8	35.1
35.0	22.3	79.3	69.7	65.7

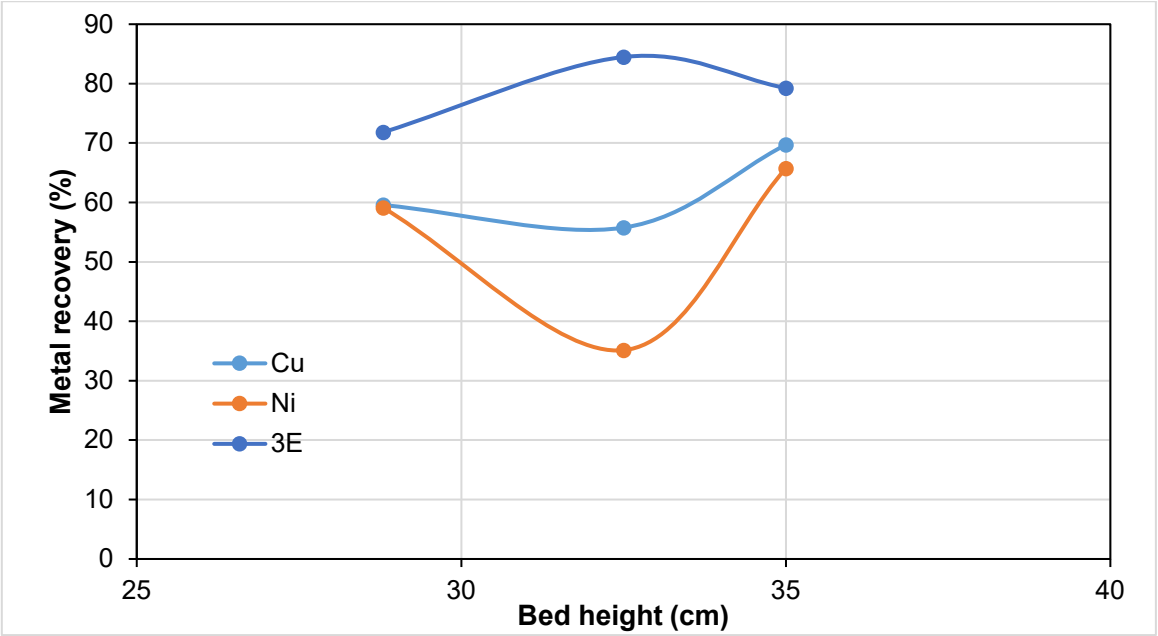

FIG 3 – Effect of bed height on 3E, Cu and Ni recoveries (AFR = 2.5 L/h; WFR = 2.5 L/h).

A further increase in bed height resulted in a drop in the PGM recovery. The opposite was observed for Ni and Cu. The effect of bed height on the grade of PGMs and BMS was minimal. The results agree with Awatey *et al* (2013) who demonstrated that the recovery of coarse sphalerite using the HF increased with the superficial air flow rate and that there exists a threshold for the air flow rate above which recovery started to decrease. The optimum bed height of 32.5 cm was selected for subsequent test work.

There is an optimum bed height at which flotation of the PGMs flotation recovery for coarse particles is maximum, below or above which recovery begins to decrease. This observation suggests that the travel distance between the top of the bed to the overflow lip for the bubble-particle aggregate plays a very vital role in the recovery of coarse particles. The longer the travel distance, the higher the probability of the coarse and heavy particles accumulating, penetrating and settling to the bottom of the separation chamber. The drop in recovery as the bed height increases above the optimum bed height may be due to the proximity of the feed system to the of the teeter bed which may be inducing localised turbulence or increasing the probability of detachment of coarse particles by injecting feed directly into the teeter bed instead of the quiescent zone above the fluidised zone. The drop in recovery as the bed height increases below the optimum bed height may be due the long distance between the feed system and the teeter bed which may increase the probability of detachment of coarse particles.

Effect of water rate

The effect of water rate on the performance of the HF separator was investigated and the results are shown in Table 5 and Figure 4.

TABLE 5

Effect of water flow rate on the performance of the HF separator in the treatment of the Platreef ore (AFR = 2.5 L/h; BH = 32.5 cm).

Water rate (L/h)	MP (%)	Recovery (%)		
		3E	Cu	Ni
1.5	23.9	55.0	54.8	45.1
2.5	17.8	71.8	59.6	59.1
3.5	27.8	59.0	41.9	59.6
5.0	52.7	46.5	40.9	31.3

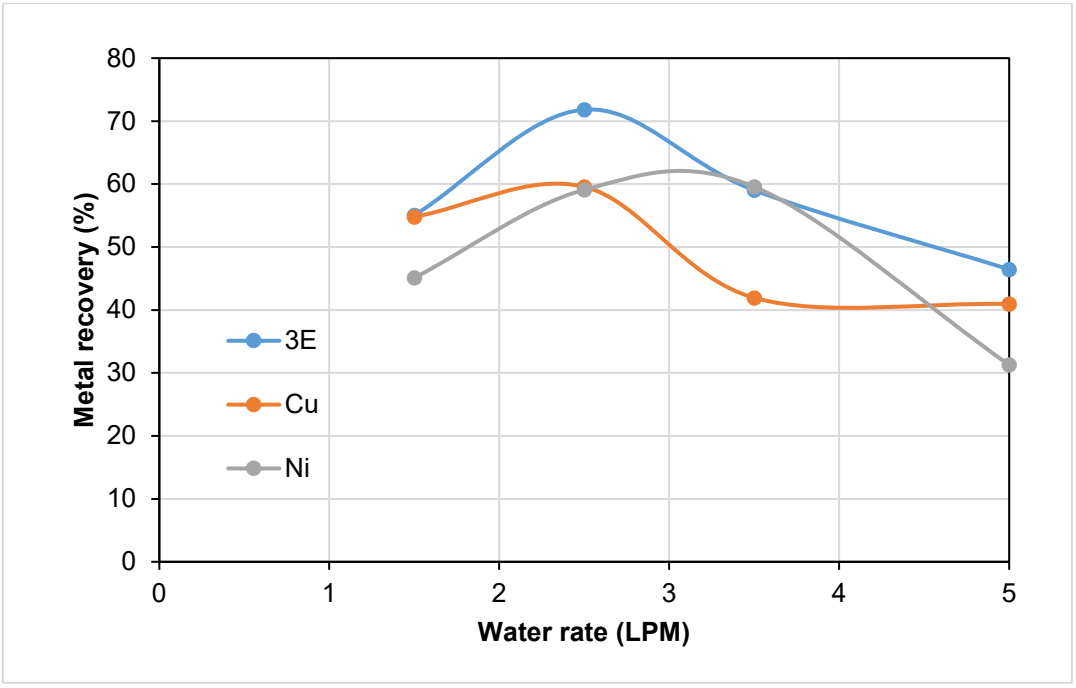

FIG 4 – Effect of water rate on 3E, Cu and Ni recoveries (AFR = 2.5 L/h; BH = 32.5 cm).

Four water flow rates were investigated, *viz*: 1.5, 2.5, 3.5 and 5.0 L/h. The bed height and air flow rate were maintained constant at 32.5 cm and 2.5 L/h, respectively. The results show that an increase in water rate resulted in an increase in PGM and BMS recoveries to a maximum. A further increase in water rate resulted in a drop in the PGM and BMS recoveries. The results agree with Awatey *et al* (2013) who showed that the recovery of coarse sphalerite using the HF increased with the superficial water rate and that there exists a threshold for the water flow rate above which recovery started to decrease. The optimum water rate of 2.5 L/h was therefore selected for subsequent test work. The Hydrofloat separator is designed to operate under quiescent conditions. It is therefore critical to minimise or control any condition that has the potential of generating high turbulence in the HF. At excessively high-water flow rates beyond the optimum, turbulence is generated within the fluidised bed which causes bubble–particles aggregates that were successfully attached to detach, hence they fall back into the bed and in this case recovery will drop.

Effect of superficial air flow rate

The effect of superficial air flow rate on the performance of the HF separator was investigated and the results are shown in Table 6 and Figure 5.

TABLE 6

Effect of air flow rate on the performance of the HF separator performance (WFR = 2.5 L/h; BH = 32.5 cm).

Air flow rate (L/h)	MP (%)	3E	Cu	Ni
1.0	21.7	68.7	51.3	52.3
2.5	17.8	71.8	59.6	59.1
4.0	37.5	58.6	51.0	46.6

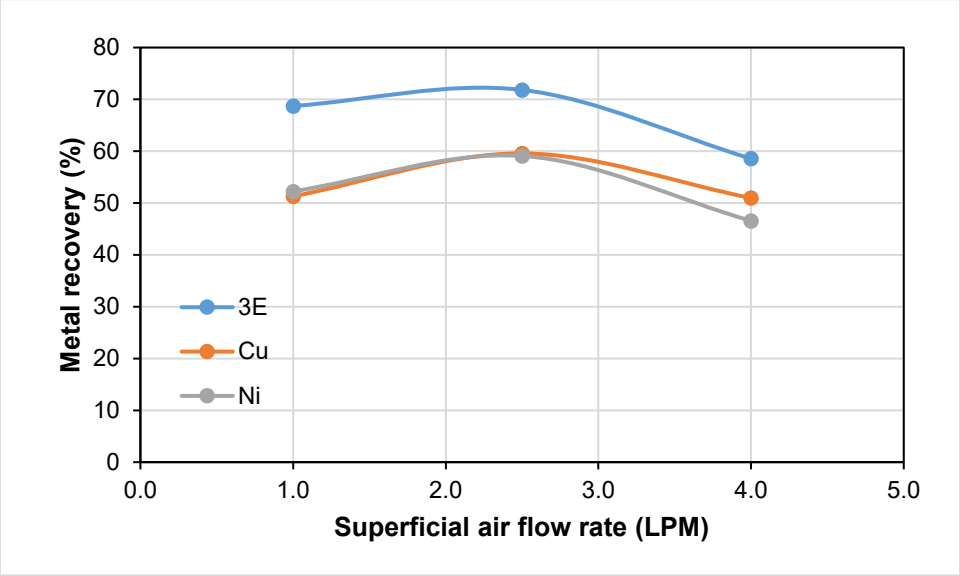

FIG 5 – Effect of air flow rate on 3E, Cu and Ni recoveries (WFR = 2.5 L/h; BH = 32.5 cm).

Three air flow rates were investigated, *viz*: 1.0, 2.5 and 4.0 L/h. The bed height and water flow rate were maintained constant at 32.5 cm and 2.5 L/h, respectively. The results show that an increase in the air flow rate resulted in an increase in PGM and BMS recoveries to a maximum. A further increase in the air flow rate resulted in a drop in the PGM and BMS recoveries. The optimum air flow rate was therefore 2.5 L/h. Similar results were obtained by Awatey *et al* (2013) during the flotation of coarse sphalerite using the HF separator.

The air flow interestingly was the parameter that had great influence on the recovery of particles. It is expected from the theory that by increasing the air flow rate, the gas holdup in the cell will increase; thereby increasing the probability of bubble–particle collision and attachment. Coarse particles are best floated in the presence of large volumes of finely divided bubbles. Finely divided bubbles attach more readily to hydrophobic sites on the particles which aids in the formation of bubble–particle clusters which increases their buoyancy for easy lift-up. When the air flow rate increases the bubble sizes are expected to consequently increase. This effect is thoroughly explained in Gontijo (2009). Another experimental observation was that when the gas rate was increased above 2.5 L/min, a certain degree of turbulence was created within the cell that could cause some bubble–particle aggregates to breakdown and fall back into the bed. Gas rates above a certain threshold creates turbulence and hence losses.

Recovery by size information for optimised test

Recoveries by size were characterised for the optimised HF test to assess the contribution of different narrow sizes classes to the overall recoveries. The recovery by size data is presented in Figure 6.

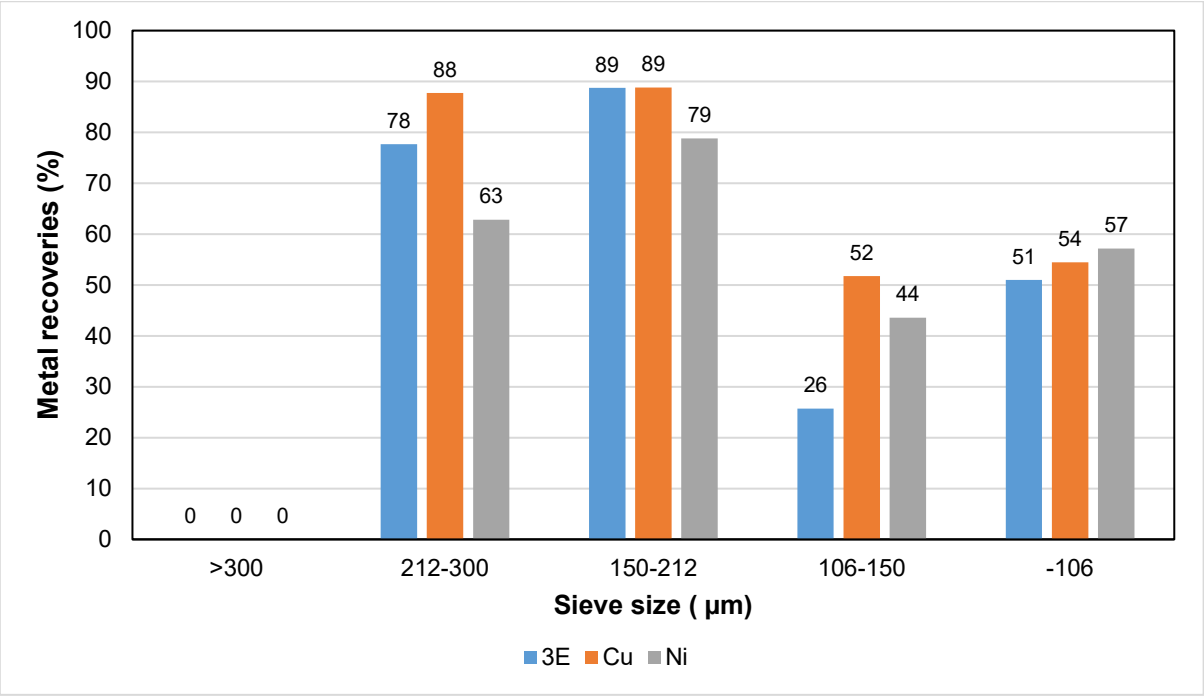

FIG 6 – 3E, Cu, Ni and Fe recovery by size range for the 106–300 µm (BH = 32.5 cm; WFR = 2.5 L/h; BH = 32.5 cm).

The results showed that the HF was not able to recover particles coarser than 300 microns for the conditions used. The feed had 2.5 per cent of the +300 µm material which did not report to the concentrate. Instead, this coarse material was lost to the tailings. The PSD of the tailings showed that it contained 4 per cent of the +300 µm material. The results show that the highest 3E, Cu and Ni recoveries were observed for the 150–212 µm followed by the 212–300 µm particle size ranges. The results demonstrate that the HF achieved high recovery efficiencies across the 150–300 microns size fraction.

It is clear that the HF separator achieved relatively lower recoveries of the sub 150 µm. These results show that the hydrodynamic conditions prevailing in the HF separator favour recovery of coarse and not fine particles. This suggest that the conditions prevailing in the separator promotes coarse particle flotation (+150 µm) and not fine particle flotation (-150 µm). Finer particles would require high energy input, maybe higher collector dosages and deeper froth depth, all these conditions do not exist with the HF environment. The same applies to particles coarser than 300 µm. The implication of this finding is that the sub 150 µm material should be removed from the HF feed material. Thus, the cut should be coarsened from 106 µm used in this study to 150 µm. Furthermore, the top size of the feed to the HF unit should be 300 µm. Therefore, rigorous classification of the HF feed is necessary to achieve high recoveries of the valuable minerals.

Characterisation of flotation products

Concentrates and tailings PSDs

The PSDs of the concentrates and tailings generated from the optimisation tests were characterised and the results are presented in Figure 7.

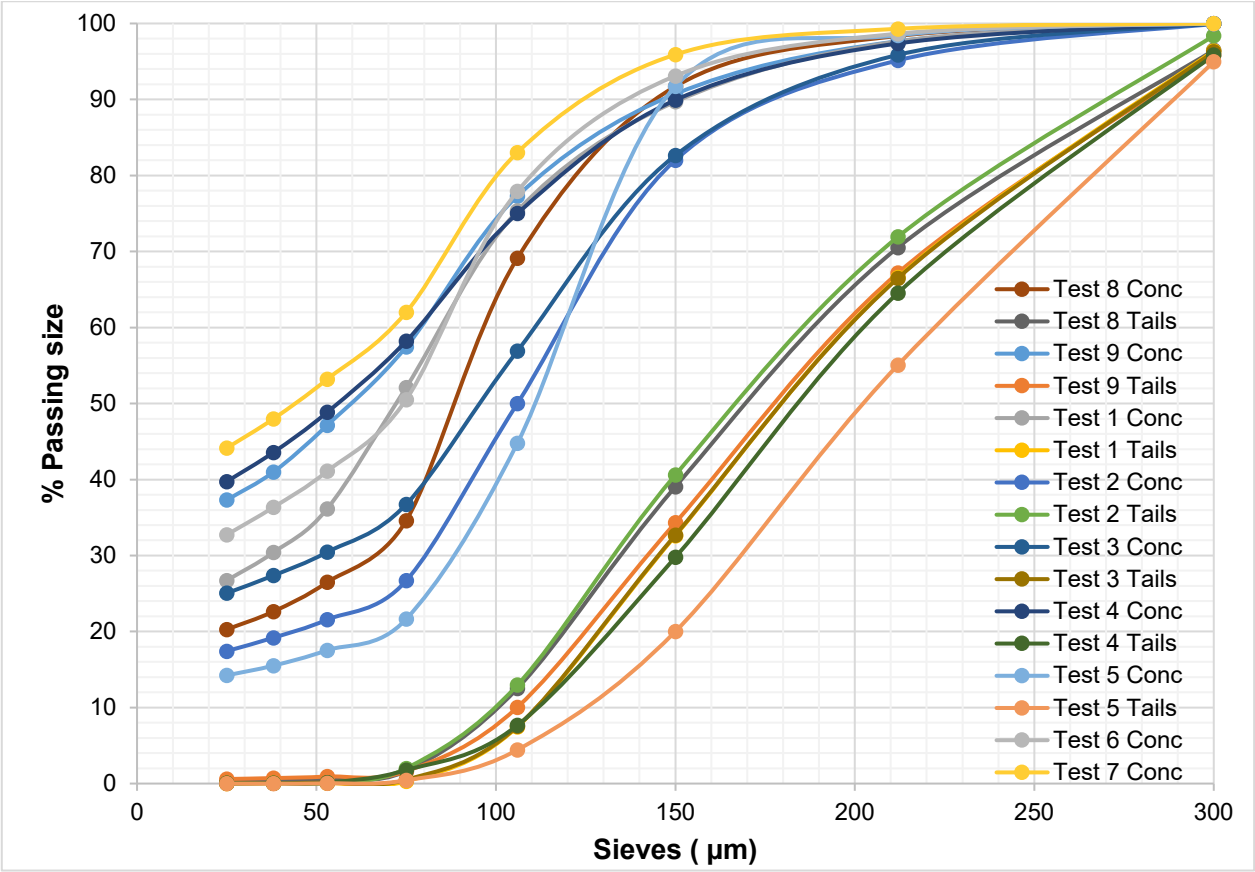

FIG 7 – PSDs of all the HF tests flotation products.

The results show that the HF separator preferentially recovered finer particles than coarse particles. The coarse particles reported to the tailings. Furthermore, the results show that no particles coarser than 300 µm reported to the concentrate. It should be however noted that the feed material contained a small proportion of the -106 µm, averaging at around 17 per cent. Particles finer than 106 µm are reported to be recovered by entrainment instead of true flotation during coarse particle flotation using the HF separator.

Concentrate and tailings mineralogy

Mineralogical analysis of the concentrate and tailings was conducted and the mode of occurrence of the PGMs is shown in Table 7.

TABLE 7

PGM mode of occurrence in the concentrate and tailings.

Liberation characteristic	PGM Vol (%)	
	Concentrate	Tailings
Liberated PGMs	7.1	0
PGMs associated with liberated BMS (Base Metal Sulfides)	1.0	1
PGMs associated with BMS locked in silicate or oxide gangue particles	0.6	0
PGMs attached to silicate or oxide gangue particles	2.4	9.8
PGMs associated with BMS attached to silicate or oxide gangue particles	85.2	60.7
PGMs locked within silicate or oxide gangue particles	3.7	28.6
	100	**100**

Mineralogical analysis showed that all the liberated PGMs were recovered in the concentrate as there were no liberated PGMs in the tailings. 85.3 vol per cent of PGMs identified in the concentrate were associated with BMS attached to silicate or oxide gangue particles. Most of the PGMs attached to or locked within silicate or oxide gangue reported to the tailings. Grain size distributions of the PGMs showed that most of the PGMs in the concentrate were coarser than those in the tailings. It is clear that the HF separator was therefore able to recover all the liberated PGMs as well as most of the PGMs that were associated with BMS. Furthermore, the HF was not able to recover most of the PGMs that were attached to or locked within silicate or oxide gangue particles.

Future research work

In South Africa, PGMs are extracted from three mineralised horizons namely, the Merensky, Upper Group 2 (UG2) and Platreef. This study has demonstrated that the Platreef ore is amenable to CPF using the HF technology. It is therefore recommended that ore variability test work be conducted to also investigate the amenability of the UG2 and Merensky ores to CPF using the HF technology. It is hypothesized that the hydrodynamic and chemical conditions will be function of the ore types. This is because the three reefs (Platreef, UG2 and Merensky) are mineralogically different as depicted in Figure 8.

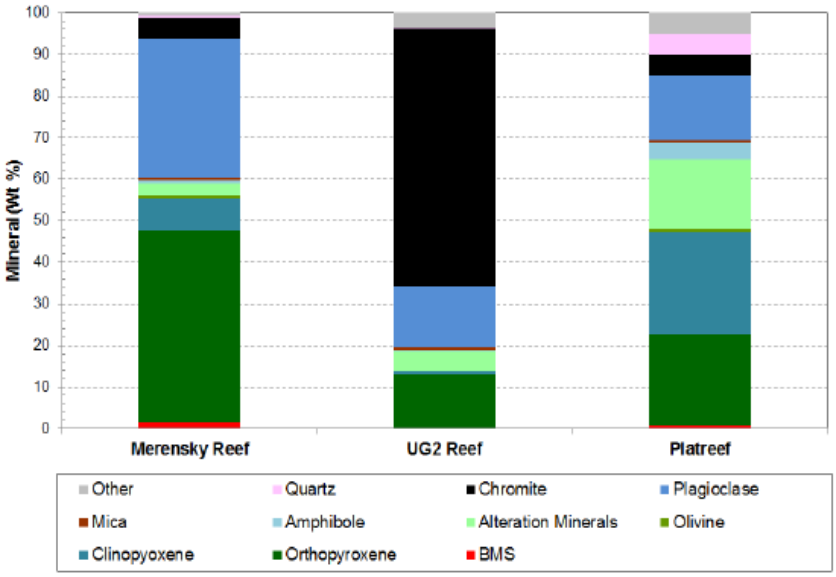

FIG 8 – Major gangue minerals contained in the different Bushveld complex orebodies (Schouwstra *et al,* 2010).

The UG2 consists predominantly of the dense chromite gangue while the Merensky and Platreef ores consist predominantly of less dense silicate minerals. The relative density of Merensky ore is 3.2 g/cm^3, Platreef ore is 3.1 g/cm^3 and that of UG2 ore is 4.3 g/cm^3 (Von Gruenenwaldt, 1977). Consequently, processing the UG2 ores using the HF technology may require relatively higher AFR and WFR to achieve a fluidisation bed required for superior flotation performance. The UG2 ore is classified as a 'hard' to 'very hard' ore (due to the high chromite content) requiring relatively high energy input in the comminution stage to liberate the ore. Apart from the high energy consumption, another challenge encountered in UG2 ore processing using the conventional flow sheet (Figure 1) is that fine grinding required to liberate PGMs inadvertently generates fine chromite which entrains easily into the concentrate during flotation. Chromite grades exceeding 3 per cent in the concentrate attracts financial penalty from downstream smelting operators. Coarse particle flotation of the UG2 ore using the HF technology may overcome the challenges of fine chromite entrainment.

In conventional flow sheets, the UG2 orebody is processed for its PGM content and the fine chromite reports to the tailings as gangue mineral. However, chromite is considered as a valuable resource in the production of ferrochrome. South Africa is the world's largest producer of ferrochrome and supplies it to most of the global stainless steel producers. This shows that there is a demand for this chromite and every opportunity should be utilised to match this demand. There is currently a lot of

research work to design and optimise technologies and processes to recover fine chromite from historic and current chrome tailings dumps. Another advantage of using CPF to process the UG2 ore is that the coarse chromite tailings becomes another revenue stream for the mines.

The Merensky and UG2 reefs have been exploited for decades and mining in some locations has reached a critical point, such that many mining houses are finding it expensive to expand at depth. Some mining houses are on the verge of closing their operations while some are shifting their attention to low-grade PGE reefs eg the UG1, MG and LG reefs. Processing these low-grade PGM reefs using conventional flow sheet is energy intensive due to the need for fine grinding to liberate the valuable minerals and the huge flotation capacity to achieve high concentrator throughput. This study demonstrated that the HF technology has low liberation requirements in PGM processing making it attractive for the CPF of the low-grade PGM resources. There is therefore need to develop novel flow sheets utilising the HF technology for the CPF of the low-grade PGM resources to increase plant throughput, reduce plant footprint as well as improve energy and metallurgical efficiency. The HF technology has potential to not only revolutionise the PGM industry but also extend the life-of-mine (LOM) for PGM mines in South Africa.

CONCLUSIONS

This study investigated the amenability of the Platreef ore to coarse particle flotation using the Hydrofloat^{TM} technology developed by Eriez was investigated. Extensive flotation test work was conducted to optimise the primary grind and the hydrodynamic parameters, ie bed-level, air and water rates in the flotation of coarse Platreef ore feed using the HF separator.

The results showed that the Platreef ore is amenable to coarse particle flotation using the Hydrofloat^{TM} technology. Mineralogical analysis showed that all the liberated PGMs were recovered in the concentrate as there were no liberated PGMs in the tailings. 85.3 vol per cent of PGMs identified in the concentrate were associated with BMS attached to silicate or oxide gangue particles. Most of the PGMs attached to or locked within silicate or oxide gangue reported to the tailings. The optimum bed-level, superficial water and air rates were established. An increase in bed height, water rate and air flow rate resulted in an increase in PGMs recovery to a maximum. A further increase in the hydrodynamic parameters resulted in a decline in the PGMs recovery. Similar trends observed for copper and nickel. The practical implications of the findings on the modification of existing circuits or design of novel flow sheets for the processing of the Platreef ores are discussed.

ACKNOWLEDGEMENTS

The authors wish to acknowledge the financial and technical support of Mintek and approval to publish the results.

REFERENCES

Awatey, B, Thanasekaran, H, Kohmuench, J N, Skinner, W, Zanin, M, 2014. Critical contact angle for coarse sphalerite flotation in a fluidised-bed separator vs. a mechanically agitated cell. *Miner. Eng.* 60, 51–59.

Awatey, B, Thanasekaran, H, Kohmuench, J, Skinner, W, Zanin, M, 2013. Optimization of operating parameters for coarse sphalerite flotation in the HydroFloat^{TM} fluidised-bed separator. *Miner. Eng.* 50–51, 99–105.

Fosu, S, Awatey, B, Skinner, W, Zanin, M, 2015. Flotation of coarse composite particles in mechanical cell vs. the fluidised-bed separator (The HydroFloat^{TM}). *Miner. Eng.* 77, 137–149.

Gontijo, C, 2009. Coarse particle flotation, PhD Thesis, University of South Australia.

Jameson, G J, 2010. New directions in flotation machine design, *Miner. Eng*. 23, 835–841.

Jameson, G J, Nguyen, A V and Seher, A, 2007. The flotation of fine and coarse particles. In N Fuerstenau, G Jameson, and R-H Yoon (eds.), *Froth flotation – A century of innovation,* pp 339–372. Littleton, Colorado, USA: SME.

Lynch, A J, Johnson, N W, Manlapig, E V and Thorne, C G, 1981. *Mineral and Coal Flotation Circuits: Their Simulation and Control*. Elsevier Publishing, Amsterdam, 291 p.

Miller, J D, Lin, C L, Wang, Y, Mankosa, M J, Kohmuench, J N and Luttrell, G H, 2016. Significance of exposed grain surface area in coarse particle flotation of low-grade gold ore with the Hydrofloat^{TM} technology. *Proceedings of the XXVIII International Mineral Processing Congress*, September 11–15, Quebec City, Canada.

Musa, F and Morrison, R, 2009. A more sustainable approach to assessing comminution efficiency, *Miner. Eng.* 22, 593–601.

Mwale, A H, Musonge, P and Fraser, D D, 2005. The influence of particle size on energy consumption and water recovery in comminution and dewatering systems, *Miner. Eng.* 18, 915–926.

Paiva, M and Rubio, J, 2016. Factors affecting the floto-elutriation process efficiency of a copper sulfide mineral. *Min. Eng.* 86, 59–65.

Pokrajcic, Z, Morrison, R, Johnson, N W, 2009. Designing for a reduced carbon footprint at greenfield and operating comminution plants. In: Malhotra, D, Taylor, P, Spiller, E, LeVier, M. (Eds.), *Recent Advances in Mineral Processing Plant Design, Society for Mining, Metallurgy and Exploration: Littleton, USA*, pp. 560–570.

Rinne, A, and Peltola, A, 2008. On lifetime costs of flotation operations, *Miner. Eng.* 21, 846–850.

Schouwstra, R, Kinloch, E, Lee, A, 2010. A short geological review of the Bushveld Complex. *Platin. Met. Rev*. 44, 33.

Schulze, H J, 1977. New theoretical and experimental investigations on stability of bubble/particle aggregates in flotation: A theory on the upper particle size of floatability. *International Journal of Mineral Processing,* 4, 241–258.

Trahar, W J, and Warren, L J, 1976. The floatability of very fine particles – A review. *International Journal of Mineral Processing,* 3(2), 103–131.

Von Gruenenwaldt, G, 1977. The mineral resources of the Bushveld Complex. *Mineral Science and Engineering*, 9(2):83–96.

Future operations – mine-to-mill integration

The end of the rainbow – real time direct gold analysis in run-of-mine ore at Newcrest's Telfer mine using GEOSCAN analysis

L A Balzan[1], A de Paor[2], A Doorgapershad[3] and W Futcher[4]

1. Chief Technology Officer, Scantech International Pty Ltd, Camden Park SA 5038. Email: l.balzan@scantech.com.au
2. Geology Superintendent, Newcrest, Telfer, WA. Email: angela.dePaor2@newcrest.com.au
3. Chief Geologist, Newcrest, Telfer WA. Email: ashok.doorgapershar@newcrest.com.au
4. Senior Metallurgist, Newcrest, Melbourne Vic 3000. Email: William.futcher@newcrest.com.au

ABSTRACT

Over the last decade, the minerals industry has continued to adopt new technologies to benefit the measurement and control of a variety of processes. Real time elemental analysis has been an important technological advance to give immediate feedback on material grades and problematic components for processing. Due to its presence in very low concentrations, measurement of gold in ore has not been considered possible for real time analysis. However, as advances continue to be made in analysis technology, an opportunity to determine if gold could be directly measured in ore presented itself, with Newcrest and Scantech undertaking a research project to characterise, test and verify gold analysis using Scantech's high specification GEOSCAN PGNAA analyser, ultimately resulting in a GEOSCAN installed and successfully functioning at Newcrest's Telfer gold mine. Through its work with a variety of different commodity producers, Scantech has been able to adapt the GEOSCAN to provide real time analysis for phosphorus, sulfur, chromium, nickel, cadmium and mercury. Even notoriously difficult to measure elements like lithium and platinum have become realities. It stands to reason that gold presented the next frontier, with keen and vital support from Newcrest to ensure this reality.

This paper outlines the process, including factory characterisation of gold using a pure sample, initial test work and results at Cadia Mine using measurement of gold by proxy and direct measurement, and finally the commissioning and verification of direct gold analysis at Telfer. The paper details the steps involved, and presents recent results achieved on-site, including ongoing verification and calibration work. The implications of direct measurement for low concentrations of gold in ore and future research into the technique conclude the paper.

INTRODUCTION

Throughout the ages, gold has occupied a special place among metals. Current commodity prices ensure that this remains the case. In the world of real time analysis, direct measurement of gold presented significant challenges due to its low concentration in ore. While numerous other industries have been able to benefit from achieving real time compositional analysis, the same has not been possible for measuring gold. Scantech's GEOSCAN elemental analyser utilises a technique known as prompt gamma neutron activation analysis (PGNAA), which allows for the representative and independent direct measurement of elements in conveyed flows. The data can be used for making process control decisions based on the data, whether this is feed-forward control, feedback control, metal accounting, or otherwise. The technology has been well established in industries such as cement (Harris *et al*, 2005) and iron ore (Matthews and du Toit, 2011) for decades, with newer commodities such as copper (Arena and McTiernan, 2011; Balzan *et al*, 2017), lead zinc (Patel, 2014), phosphate (Balzan and Kalicinski, 2019) and more being developed in recent times. In all cases, the process for evaluating new elements for analysis follows a similar path, where the elemental PGNAA response is characterised and then tested on real material samples. The analysis technique responds differently for different elements, based on the properties of the elemental nuclei, with some elements responding better than others. Gold had been predicted to have an excellent response to the technique, however difficulties in the characterisation step rendered the element elusive for online analysis on conveyed ore flows. In recent years, advances had been made to measure otherwise difficult elements of interest, including elements such as mercury which are typically present at low concentrations, lithium which has a challenging response to the technique,

and even platinum, which is both challenging and at low concentrations. Successes in these industries prompted significant interest to examine the possibilities for measuring gold.

To address the problem Scantech and Newcrest established a research project to explore direct gold measurement. The opportunity to characterise, test and verify the direct measurement of gold using Scantech's high specification GEOSCAN PGNAA analyser became apparent, and a test program was set-up ultimately resulting in a GEOSCAN installed and successfully functioning at Newcrest's Telfer gold mine. This paper outlines the process for the development of the GEOSCAN GOLD and its successful deployment at Telfer. A brief summary of the equipment technology is provided, as well as a description of Telfer's operations. The development of gold measurement capabilities is provided, including factory characterisation of gold using a pure sample, initial test work and results at Newcrest's Cadia Mine using measurement of gold by proxy and direct measurement, and finally the commissioning and verification of direct gold analysis at Telfer. The paper details the steps involved, and presents recent results achieved on-site, including ongoing verification and calibration work. The implications of direct measurement for low concentrations of gold in ore and future research into the technique conclude the paper.

HOW THE GEOSCAN WORKS

The GEOSCAN on belt analyser utilises thermal neutron capture technology to determine the elemental composition of conveyed bulk materials in real-time. A Californium-252 radioactive source located within the instrument below the belt generates a flux of neutrons, which are then absorbed by the conveyed material as it passes through the tunnel of the GEOSCAN. The neutrons are captured by the nuclei of the atoms in the material flowing on the belt, and gamma-rays are instantaneously produced at specific energies for each element. The gamma-ray spectrum is captured by an array of high performance detectors located at the top of the GEOSCAN, where Scantech's signal processing algorithms resolve the signal into a set of individual elemental results.

The measurement technique is completely penetrative allowing for analysis of the full material stream, and entire bed-depth and belt-width. It is also independent of ore mineralogy, particle size, and belt speed, thereby allowing for fully representative analysis of the conveyed material. Since all material is analysed continuously, the GEOSCAN does not suffer from sampling errors, such as if any of the top surface only measurement techniques were used. Results are produced for a suite of elements calibrated for the specific requirements of the particular application, which can vary from installation to installation, and is tailored to account for variation due to changes in the belt load and material composition.

Additionally, through-belt moisture (TBM) analysis systems, utilising a microwave transmission measurement technique to directly measure the moisture content of the conveyed material, are installed alongside the majority of GEOSCANs providing both elemental and moisture results. The TBM has undergone scrutiny for use within the iron ore industry, and has become widely accepted for its high level of accuracy (Balzan and Harris, 2015) in this and the majority of commodities in the minerals industry.

Results from the GEOSCAN and TBM are exported to the plant control system typically every two minutes in the majority of installations. This analysis period has been traditionally selected as it allows for sufficient time for reliable and repeatable results while minimising inherent randomness from radioactive decay. In the majority of cases, this analysis period is also fast enough to provide results that can be acted upon in downstream process control (feed-forward control) or upstream material management (feedback control) as required.

NEWCREST TELFER OPERATIONS

Telfer gold mine was founded in 1972, with ownership by Newcrest since 1990. It is located in the Great Sandy Desert of Western Australia, around 400 km from Port Hedland. It is comprised of the Main Dome and West Dome open pits and an underground mine, producing both gold and copper. It has a dual train comminution circuit, flotation and cyanide circuits producing both gold doré and copper-gold concentrates. The concentrates are trucked to Port Hedland and exported to various smelters. The gold doré is refined at the Perth Mint.

The mine operates with a fly-in fly-out workforce, and has agreements with the local Martu people, the traditional owners of the land surrounding the Telfer gold mine. Newcrest supports the indigenous population providing support, training, employment and contracting for the local people. Telfer is also committed to environmental programs to ensure ongoing sustainability, particularly in its management and recovery of cyanide in the gold processing plant.

GOLD RESPONSE CHARACTERISATION

In order to produce effective analysis of an element, the response of the particular element needs to be characterised inside the GEOSCAN. Historical research has characterised pure elemental responses for PGNAA analysis (Lone *et al*, 1981), providing a theoretical basis for characterisation, however an empirical baseline must be established inside the equipment and tested on real material to be fully developed. This process requires the testing of a sufficiently large and well-defined sample of the element to be tested inside a GEOSCAN. This process allows for all the nuances of the physics of measurement to be properly considered in development of an elemental response. The physics of measurement is unique to the GEOSCAN and while it has a basis in the theoretical PGNAA response, all analysers that utilise this analysis technique will have a different response. This implies that the response characterisation developed in this test work applies specifically to Scantech's GEOSCAN and does not apply at all to any other PGNAA equipment. The results obtained and discussed in this paper therefore cannot be generalised.

To develop the response characterisation for gold, a pure and well-defined sample of gold was obtained for testing. Through discussions and its relationship with Newcrest, Scantech was able to obtain a sample of pure gold beads from Newcrest. Newcrest participated in the characterisation program with Scantech, where the pure gold was analysed in a number of scenarios inside a GEOSCAN in Scantech's factory in Adelaide, Australia. The sample was analysed multiple times, with varying background materials to obtain a full understanding and measurement response for pure gold. Figures 1 and 2 show the gold sample used for testing and the sample in the GEOSCAN respectively.

FIG 1 – 1.003 kg sample of pure gold from Newcrest.

FIG 2 – Gold sample presented to GEOSCAN in Scantech's factory.

Following the pure response measurements, the data was processed to develop a gold response that could then be utilised for measurement of gold in material that passes through the GEOSCAN's analysis tunnel. The response was integrated into Scantech's proprietary analysis algorithms, and subsequently tested on a wide range of samples. Samples of varying materials and varying gold concentrations were presented to the factory GEOSCAN for analysis, with the results subsequently compared to laboratory analysis for the samples. Test results are shown in Figure 3. The initial testing demonstrated excellent correlation between laboratory and GEOSCAN results, and became the stage gate for proceeding to deployment at a real world site for further testing and analysis.

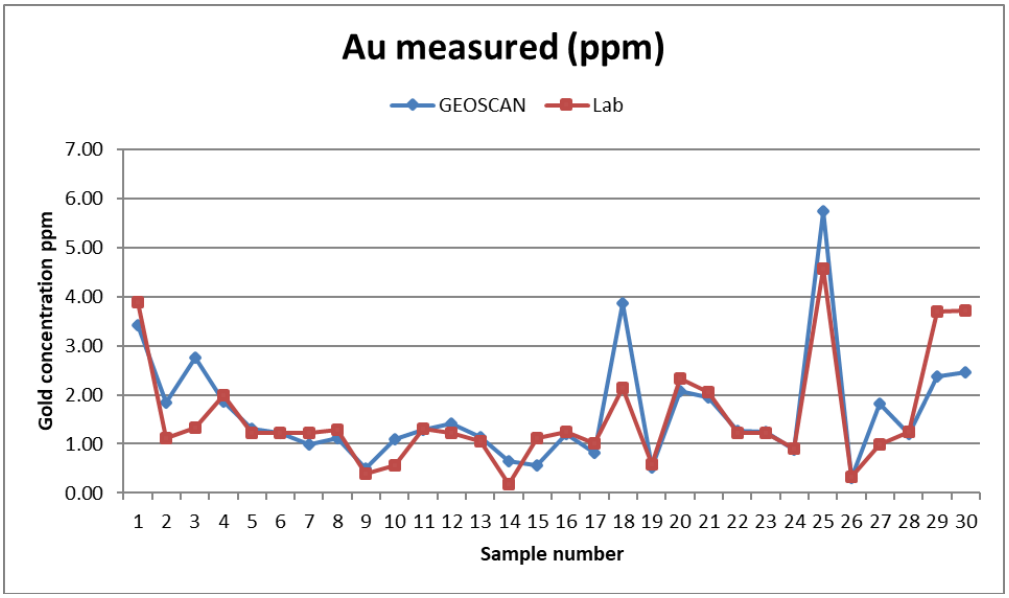

FIG 3 – GEOSCAN (blue) and laboratory (red) analysis for gold in the factory sample testing program.

INITIAL RESULTS FROM CADIA

The gold response developed in the test work described above was installed on Newcrest's GEOSCAN installed at the Cadia mine. The Cadia installation had been set-up to provide primarily rapid analysis of copper grade, as well as other elements, with results being reported every 30 seconds to the plant. The copper and other elements formed part of a standard, high specification GEOSCAN installation, where the intention was to use the GEOSCAN and other analysers for classification and potentially diversion of the material. It was known that the Cadia deposit included gold at low concentrations, and since the GEOSCAN had already been installed and was working successfully, it followed logically to test the newly developed gold characterisation models on Cadia's material.

Cadia's gold concentration was observed to share reasonable correlation to copper and sulfur, with both elements already calibrated and working on the GEOSCAN. It was determined to undertake two tests for gold measurement, with one being the direct measurement using the characterisation model, and the second being using a correlation model based on the measurement of copper and sulfur. Both systems would operate in parallel.

Samples of the conveyed flow were obtained, and a comparison made between the laboratory analysis of the samples and results from the GEOSCAN. As well as the usual suite of elements for analysis, gold was included in the laboratory assay data. By making multiple subsamples, sampling error was observed and established a baseline for performance comparison. A number of calibration curves were set-up to assess gold analysis performance by proxy measurement of copper and sulfur, as well as the direct measurement from the GEOSCAN. The process involved determining a suitable analysis period for the GEOSCAN to integrate over for the direct gold measurement. Due to the low concentration of gold in the ore, the counting statistics for direct gold measurement were significantly different to the statistics of the far-more abundant elements of copper and sulfur and others. While it was possible to maintain 30-second analysis periods for copper and sulfur, and thus for the proxy measurement of gold, it was found that longer measurement periods of 5 to 10 minutes were

required for the direct measurement of gold to ensure that measurement repeatability was within the expected bounds determined by the duplicate sampling process.

Table 1 shows the performance results for copper, sulfur, proxy-gold and direct gold measurement. To assess performance, the root mean square deviation (RMSD) is calculated between the set of laboratory results and corresponding GEOSCAN results. The correlation of the two data sets is also calculated. Figures 4–7 show the comparison of laboratory analysis and GEOSCAN analysis for these four elemental responses.

TABLE 1

Performance results between laboratory and GEOSCAN analysis for copper, sulfur, calculated gold and directly measured gold.

	Cu%	S%	$Au_{calculated}$ ppm	$Au_{measured}$ ppm
RMSD	0.02	0.06	0.39	0.36
Correlation	0.92	0.82	0.65	0.86

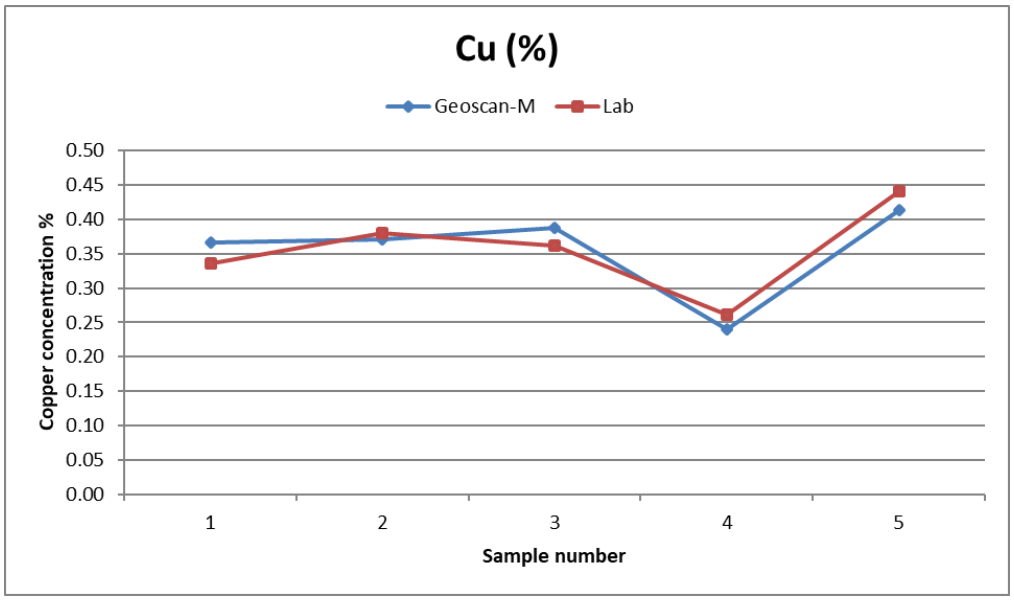

FIG 4 – GEOSCAN (blue) and laboratory (red) trend for copper.

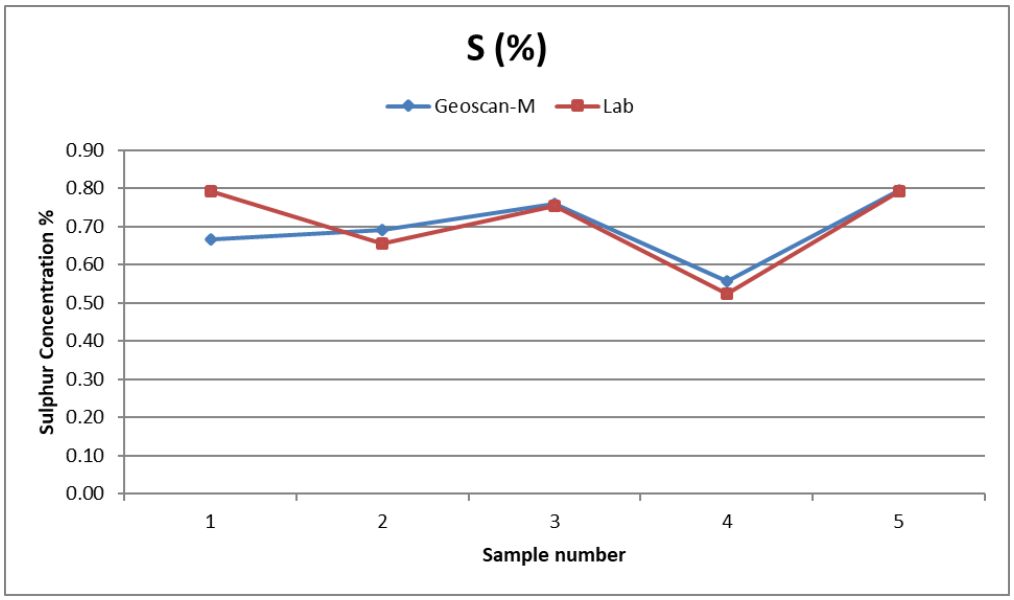

FIG 5 – GEOSCAN (blue) and laboratory (red) trend for sulfur.

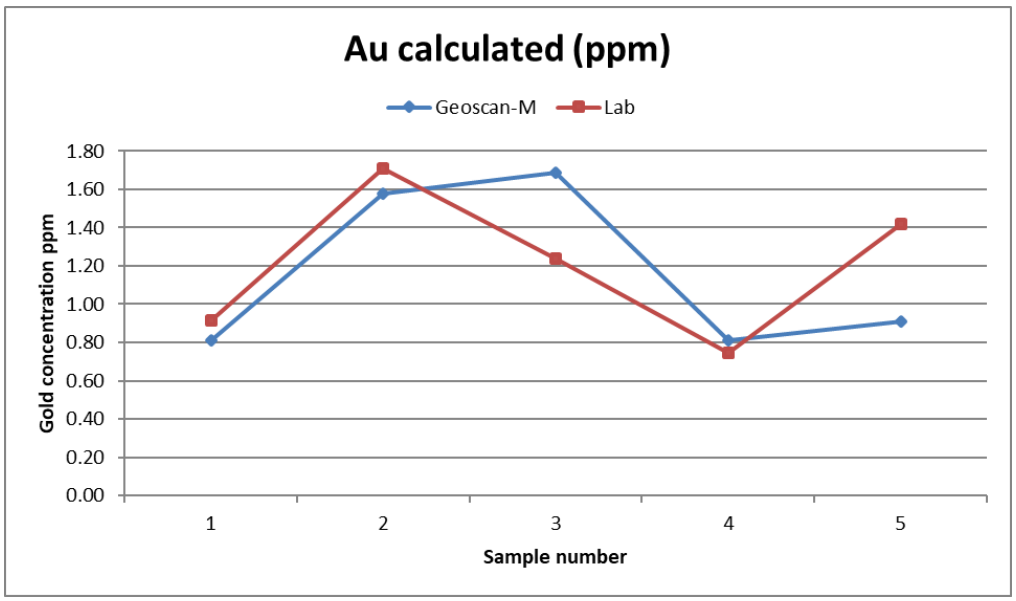

FIG 6 – GEOSCAN (blue) and laboratory (red) trend for calculated gold.

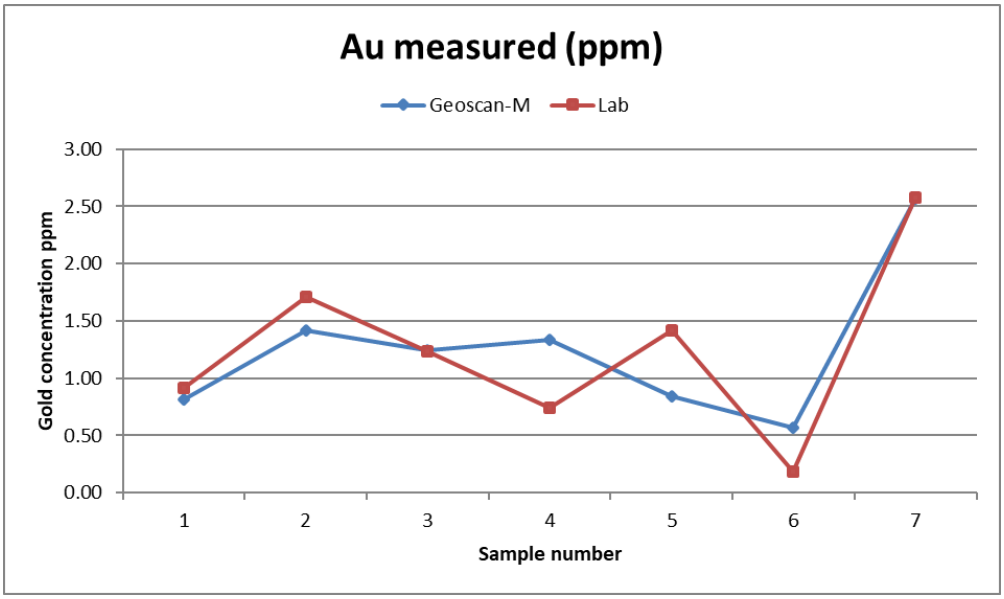

FIG 7 – GEOSCAN (blue) and laboratory (red) trend for directly measured gold.

Note that the directly measured gold response has an additional two data points. The five samples used for calibration and determination of the main calibration of elements shown in Figures 4–6 were collected previously, with the newly developed gold response retrospectively applied to this sample data. An additional two sample points were collected to verify the gold response, as shown in Figure 7. The two additional points were used in the performance calculations shown in Table 1. The performance for direct measurement is in line with what was obtained through proxy measurement, with a key difference being that the direct measurement does not depend on the validity and robustness of the proxy model, and therefore can respond to actual differences in gold concentration rather than relying on an underlying relationship.

As can be seen, the response for directly measured gold is improved compared to the proxy-measurement, with both improved RMSD performance and better correlation. In addition to the improved robustness of direct measurement over relying on an approximated model, the direct measurement offers a clear advantage. These results were used to justify the next stage of installation and testing a GEOSCAN at Telfer gold mine, as discussed in the following section.

RESULTS FROM DIRECT GOLD MEASUREMENT AT TELFER

Following the test results from Cadia, a GEOSCAN was purchased for installation at Telfer in 2019, with the equipment commissioned throughout 2020. The gold analysis module was fully calibrated by the start of 2021.

Telfer does not have a correlation between copper or sulfur and gold, and thus relies only on the direct measurement of gold by the GEOSCAN. The characterisation and verification work at Cadia suggested a good response would be expected, despite significant differences in the orebodies. Since the GEOSCAN's elemental response is independent for different elements, differences in the ore were not expected to impact on the GEOSCAN's performance.

The GEOSCAN was calibrated to provide elemental results on seven elements plus moisture. The elemental results include directly measured gold every 10 minutes, silver every 10 minutes, and copper, sulfur, iron, nickel, cobalt and moisture every 30 seconds. Since there is no clear underlying model for the calculation of gold based on other elemental responses, only the directly measured gold results are reported.

As for the Cadia results, a summary of performance for the key elements of gold, silver, copper and sulfur is shown in Table 2, where RMSD and correlation for the elements is shown. Figures 8–11 show these same results.

TABLE 2

Performance results between laboratory and GEOSCAN analysis for gold, silver, copper and sulfur.

	Au ppm	Ag ppm	Cu%	S%
RMSD	1.19	1.34	0.12	0.70
Correlation	0.30	0.26	0.80	0.82

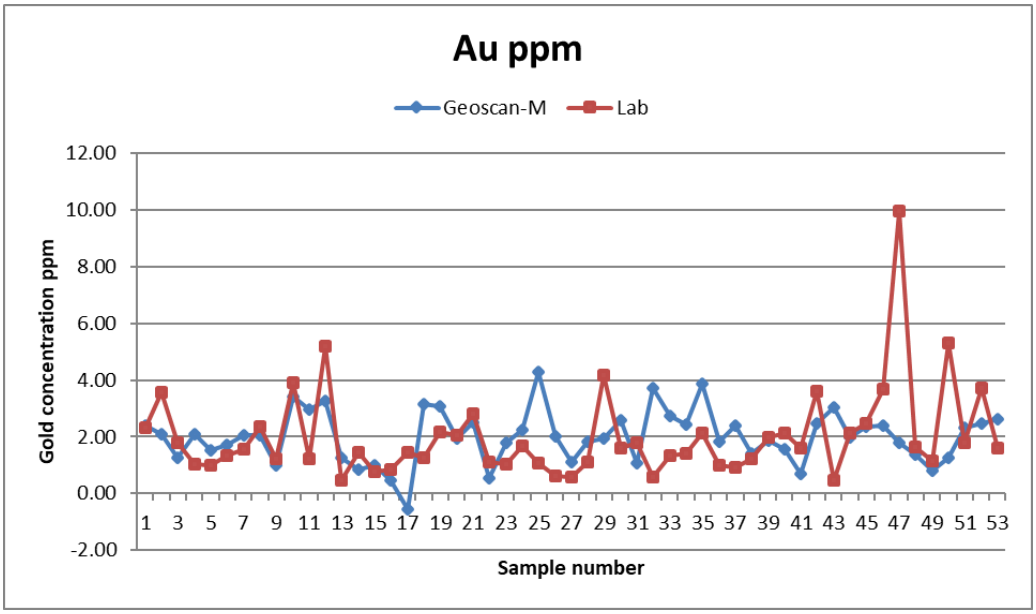

FIG 8 – GEOSCAN (blue) and laboratory (red) trend for gold.

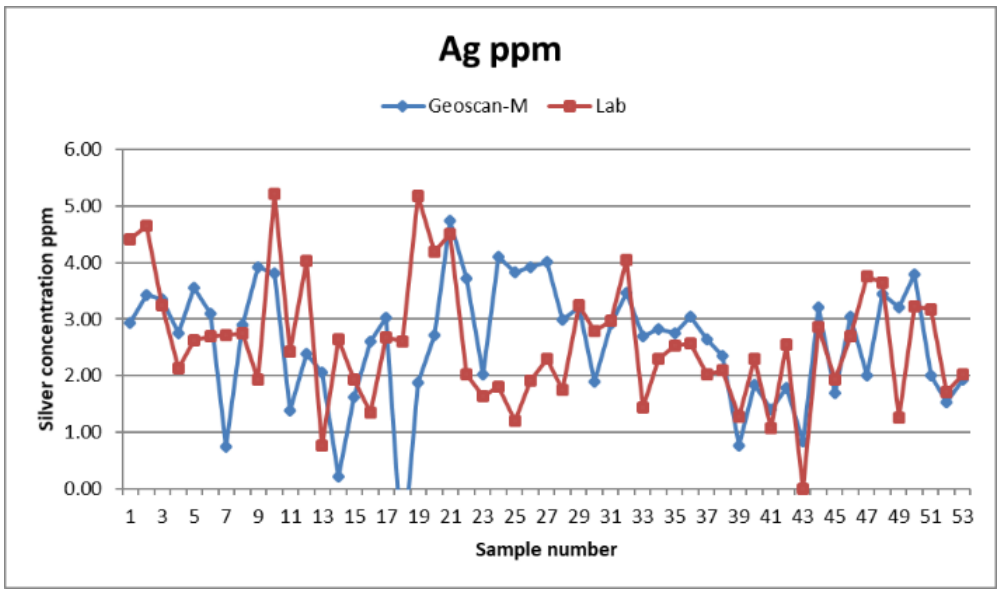

FIG 9 – GEOSCAN (blue) and laboratory (red) trend for silver.

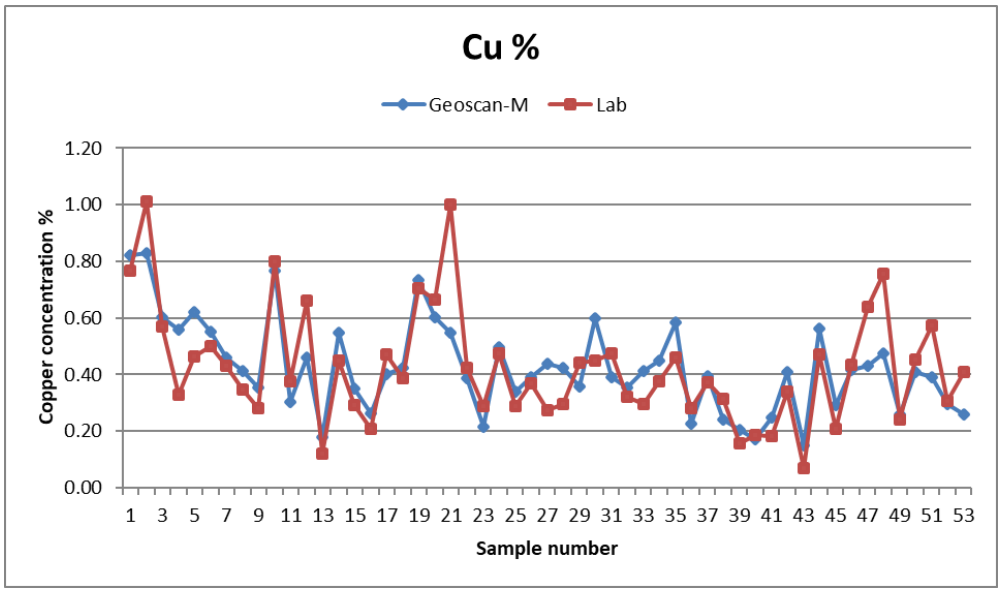

FIG 10 – GEOSCAN (blue) and laboratory (red) trend for copper.

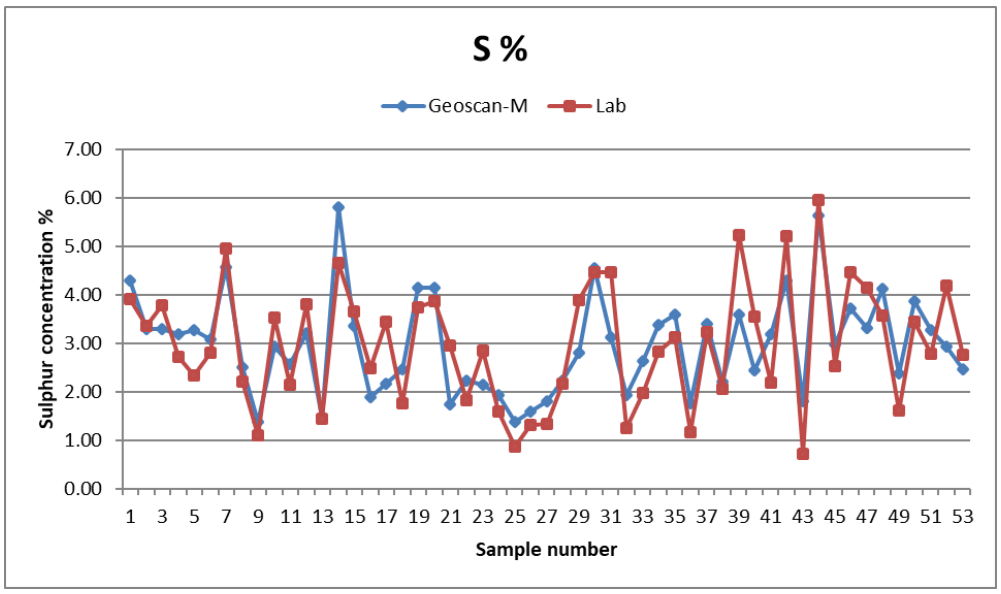

FIG 11 – GEOSCAN (blue) and laboratory (red) trend for sulfur.

It is noted that there are some gold results where the GEOSCAN and laboratory analyses do not agree. As explained previously, representative sampling for gold can be challenging due to the high nugget effect of gold in ore. It is expected that there is a reasonable possibility for large sampling errors to be present in laboratory data as a result, which can lead to over or under reporting of gold concentration. In such cases, because the GEOSCAN is observing all material continuously, it therefore does not suffer from sampling error, and it can highlight potential discrepancies in metal accounting in such situations. Further clarification and verification of such situations is the subject of future work, as briefly discussed in the following section.

The results for direct gold measurement across the larger sample set available at Telfer validates the measurement technique and confirms that the GEOSCAN can provide effective accurate direct measurement of gold in ore, even at typically low concentrations when considering the magnitude of sampling errors, as discussed above.

FUTURE RESEARCH

Further refinement of the calibration is expected as more knowledge is obtained about the ore being analysed. Sample data is routinely collected within Scantech's recommended calibration verification period, and is consolidated to ensure calibration optimality into the future.

It has been observed that gold ore sample collection suffers from high sampling error due to the nugget effect of gold distribution in deposits. Subsamples of collected samples show widely varying gold content, indicating potential issues in making comparisons between the laboratory analysis and GEOSCAN analysis, which does not contain any sampling error. To help ensure this, Scantech is exploring methodologies where the gold concentration can be modified and varied in a controlled way. It is evaluating the potential for utilising known standardised samples to help create a calibration baseline model that can be further fine-tuned with on-site calibration samples.

Additionally, a wide variety of gold producers and mines are undertaking installation of the GEOSCAN to provide direct measurement of gold in real time. As the technology becomes more established in the industry, it is expected that more producers will attempt to exploit the benefits gained by Newcrest Telfer with its installation.

CONCLUSIONS

This paper has described the development of direct measurement of gold capability using Scantech's high-specification GEOSCAN on belt analyser, and presented case study results from Newcrest's Telfer mine. A description of the analysis technology has been provided, as well as a summary of Telfer's operations. The methodology for the gold analysis capability has been described, together with an explanation of the test program and outcomes from deployment at the Cadia mine. The positive results observed at this test site led to the installation of the GEOSCAN at the Telfer mine and the development of direct measurement of gold in ore at this site. The paper has presented the results observed following the commissioning and calibration of the GEOSCAN at Telfer. The results have validated the test work undertaken at Scantech's factory and at the Cadia mine. In addition to direct gold analysis, other key elements are reported. A brief summary of future research and development for gold analysis concludes the paper.

REFERENCES

Arena, T and McTiernan, J, 2011. On-belt analysis at Sepon copper operation. *Proceedings MetPlant 2011*, pp 527–535 (The Australasian Institute of Mining and Metallurgy: Melbourne).

Balzan, L A and Kalicinski, M, 2019. GEOSCAN-M Use For Process Improvement in Phosphate Plants. 'SYMPHOS 2019', *5th International Symposium on Innovation and Technology in the Phosphate Industry*. Procedia Engineering.

Balzan, L A, Harris, A R and Bauk, Z, 2017. Faster analysis: recent advances in GEOSCAN on-belt analysis techniques allowing for rapid real-time measurement of minerals. *Proceedings of COM2017 Conference of Metallurgists.* Canadian Institute of Mining, Metallurgy and Petroleum.

Balzan, L and Harris, A, 2015. Real-time through-belt moisture analysis for iron ore, *Proceedings of the Iron Ore Conference 2015*, pp 539–542 (The Australasian Institute of Mining and Metallurgy: Melbourne).

Harris, A, Smith, K and Rossi, F, 2005. On-belt analysis breakthrough. *International Cement Review*. Oct 2005, pp 62–66.

Lone, M A, Leavitt, R A and Harrison, D A, 1981. Prompt gamma rays from thermal-neutron capture, *Atomic Data and Nuclear Data Tables*, Vol. 26, No. 6, November 1981.

Matthews, D and du Toit, T, 2011. Real-time online analysis of iron, validation of material stockpiles and roll out for overall elemental balance as observed in the Khumani Iron Ore Mine South Africa. *Proceedings Iron Ore 2011*, pp 297–305 (The Australasian Institute of Mining and Metallurgy: Melbourne).

Patel, M, 2014. On-belt elemental analysis of lead-zinc ores using prompt gamma neutron activation analysis. *Proceedings XXVII International Mineral Processing Congress 2014*. Gecamin: Santiago, Chile, chapter 17.

Scenario-based evaluation of potential value chain gains using Integrated Extraction Simulator – Mt Keith Nickel West case study

F Faramarzi[1], E Amini[2], L Bolden[3], N Beaton[4] and E Koh[4]

1. Metallurgist, CRCORE, Pullenvale Qld 4069.
2. Manager – Technical Services, Orica, Windsor Qld 4030. Email: eiman.amini@orica.com
3. Principal Technology, BHP, Perth WA 6000.
4. Senior Manager – IES, Orica, Windsor Qld 4030.

ABSTRACT

In the early 1990s, engineers found that the interconnected nature of mining and minerals processing provided an opportunity to unlock additional value by breaking from the established practice of silo-based cost minimisation to focusing on maximising profit across the value chain. The key lays in leveraging blast intensity for improved productivity in the plant. The approach of 'Mine to Mill' was thus formalised as an operating strategy aiming to maximise overall profitability through integrated value chain optimisation and having since provided many documented cases of sites achieving productivity gains between 0–20 per cent.

This study determines whether implementing a Mine to Mill strategy to reduce SAG mill feed particles size could increase value at the operation. The Integrated Extraction Simulator (IES) was used as a tool for technical evaluating and quantifying the respective value. First, a base case flow sheet of the Mt Keith Operations was developed in IES that included the configuration of the value chain constraints to reflect the actual operational performance. Two blast patterns, standard and intense, were used in combination with four target final comminution product sizes (P_{80}) of 170, 187 (actual), 200, and 230 µm to provide eight scenarios for evaluation. Each scenario was then simulated with the resulting throughputs and recoveries used to determine associated 'Net Incomes'. The IES simulation results indicated that using Mine to Mill strategy by maintaining the target size (P_{80}) at 200 µm, improved economic performance by 8.6 per cent relative to the base case. Further, even Mine to Mill strategy was adopted without maintaining the target grind size the economy performance increased by 3.4 per cent for the given time frame that the simulations were conducted for.

The study used a method for identifying the significant value that can be unlocked by a site without deploying Capex to upgrade the plant. The developed approach facilitates domain or block model-based economic evaluations to quantify the opportunity of applying practical methodologies such as Mine to Mill over the life of an asset.

INTRODUCTION

Blasting establishes the initial ore fragmentation that is subsequently reduced in downstream processes such as crushing and milling (Valery *et al*, 2001; Morell and Valery, 2001). The interconnected nature of blasting and minerals processing offered an opportunity to shift from traditional isolated optimisation strategies to value-based, integrated approaches considering the blast fragmentation variation impact on the process performance. This methodology known since early 1990s as 'Mine to Mill' focuses on boosting blast powder factor through changes to blast design and explosives to reduce top size and generate more fine material. Such distributions often pass through the first grinding stage rapidly because of reduced amount of intermediate-sized material (25–50 mm) which builds the load in the SAG/AG mills and are difficult to break.

Process simulation is an established approach for design and optimisation that assists with exploring feasibility and impact of change(s) on process performance through analysis of 'what if' scenarios. Over the past decades, it has been a standard practice to configure flow sheets in simulation structures such as IES (Amini *et al*, 2020), JKSimMet® (Morrison and Richardson, 2002), MODSIM (King, 1990), and SysCAD (Stepto *et al*, 1990), with a range of equipment models incorporated in them. An initiative of a flow sheet is to represent the state of the process. Consistent data should be collected sufficiently to develop a base-case flow sheet. These data are sourced from site plant surveys, laboratory experiments, value chain instrumentation, resource block models, technical and design reports. However, a flow sheet which represents a narrow time frame will lose its fidelity over

time due to frequent ore and plant operation variations within a mine lifespan. In general, data collection through surveys is often a costly option, nonetheless, an alternative might be considering operational data, namely 'Process Information (PI)' which are stored in the control system historians. Some challenges with PI data have been inconsistency, redundancy, unreliable instrument readouts (Lishchuk *et al*, 2020; Hodouin, and Everell, 1980) and large variations (with unknown sources and amounts).

There are numerous examples in the literature, some of which are quantifying the effect of Mine to Mill (Kanchibotla *et al,* 1999; Grundstrom *et al,* 2001; Hart *et al,* 2001; Scott *et al,* 2002; Burger *et al,* 2006; Jankovic *et al,* 2004; Diaz *et al,* 2015; Kanchibotla *et al,* 2015), ore competence variability (Faramarzi *et al*, 2019) or using Grade Engineering® techniques to modify mill feed particle size distribution with upgraded undersize fractions (Carrasco *et al,* 2017; Scott and Amini, 2020). More recently, fine-tuning methodology was developed and validated to generate high fidelity flow sheets using mine data historians which aims to represent more realistically the equipment capacity and performance across the value chain. In this regard, data-driven, fine-tuned flow sheets were developed in IES (Amini and Beaton, 2020), which were used to evaluate optimal scenarios by considering feed size, introduction of Grade Engineering® material and product size as variables. The simulation outcomes were then used for scale-up and strategic planning purposes for the operations (Amini *et al,* 2020). Application of such base case flow sheets which were fine-tuned based on operational data was extended to other concentrators, which are most useful for everyday scenario-based analyses, process control and optimisation.

Referring to a previous Mine to Mill study reported by Clark and Scott (2002), utilising intense blasting at Mt Keith lead to reduced kWh/t which was accompanied by 7.0 per cent increase in mill throughput. In this paper, Integrated Extraction Simulator (IES) was used to develop an integrated flow sheet of Mt Keith value chain based on PI data of 44 processed stockpiles, where the model includes drill-and-blast, crushing, milling and flotation units with the capability to manage multi-variable simulations. It was aimed to quantify the impact of drill-and-blast practice and comminution process final grind size on the downstream process performance and the operation's economy. The aim of this paper is to document the Mt Keith Operations case study that have conducted by Cooperative Research Centre for Optimising Resource Extraction (CRC ORE). The potential for making beneficial and low-risk changes across the value chain is demonstrated by developing fully integrated, fine-tunned flow sheets. These flow sheets are most useful to *quantify and manage the potential value* generated by the intense blasting of ore and final grind size control to be implemented in the day-to-day mine operation strategies.

METHODOLOGY

Five stages are completed to develop a base case flow sheet for Mt Keith Operation which are explained in details in the following sections.

Drill-and-blast information were explored along with PI data from 44 processed stockpiles between April 2017 and May 2020 to determine most implemented and also the practical range for the drill-and-blast practice at the site. The considered simulation scenarios were defined with the aim to quantify value before and after perusing a Mine to Mill strategy for several operational conditions. It should be noted that few assumptions made in this project are outlined in this section as well.

Data collection, curation, and analysis

In general, the data collected for developing IES-based flow sheets is sourced from field and plant surveys, updated or obsolete process flow sheets, laboratory experiments, block models, operational data, technical and design reports, site personnel. Hence, it is a wide range, however, the information required can be categorised into two groups based on their application:

- *The data set that is vital to develop a value chain flow sheet:* This type of information is mainly used in the incorporated unit models (eg blast fragmentation, grinding, classification and separation models). The latest schematic of the process flow sheet is necessary because it provides details on the number and type of the equipment used and how the material is distributed through the whole process.

- *The data set that is vital to generate a base case flow sheet and keep it tuned over time:* The operational data or 'PI data' is in this category because the aim of such data – informed, value chain flow sheets would be to predict the future based on the recorded history. Depending on the project objectives, this data can be represented in different sequential time frames (minutely, hourly, daily, monthly etc) and obviously the smaller the scale the larger variation is expected. It is obvious that following timely change of initiatives such as orebody, operational strategies, and market, it becomes necessary to update and re-tune the flow sheet with latest data inputs.

It should be noted that not all the information collected is useful. The key objective of data curation and analysis is preparing *relevant* and *reliable* data which are aligned with the equipment models parameters requirements and the process response. For this purpose, useful data should be discriminated from the redundant and then being presented in appropriate number, format, size, and units. In this process it is also important to account for misinformation as well as disinformation. The former considers vital data which are missed or not available and the later refers to unexpected information, ie unreliable instrument readouts. Analysis of data is an essential step which also engages technical and analytical knowledge of individuals, eg engineers, data analytics specialists. This includes running several basic tests to ensure *consistency* of the data by establishing relevant correlations between different values eg to explore how throughout is correlated to ore hardness or recovery is influenced by mineralogy.

Base case flow sheet configuration

A well-configured flow sheet is a start point to develop a data-driven base case for a value chain. The goal at this stage would be to zero or minimise the difference between the actual (operational data) and simulated values as much as possible. To configure a flow sheet is to illustrate different process units, how they are connected, and define the ore properties that are being processed. The latest schematic of process units and streams is the first step to configure a value chain flow sheet. An initiative of a flow sheet is to represent the state of the process. A set of consistent data should be collected sufficiently which can be sourced from site and plant surveys, laboratory experiments, value chain instrumentation, and technical reports to develop a base-case flow sheet. The flow sheet configured should be consistent with the PI data in a way that key pieces of information are attributed to its origin. Generally, design characteristics of the units/equipment used in the flow sheet are inserted at the 'flow sheet configuration' stage. The operational data provides 'actual' values which should be predicted accurately through simulation. Key inputs sourced from the operational data are rock mass properties (uniaxial compressive strength, Young's modulus, mean *in situ* block size), density, throughput, feed size distribution, ore density, ore breakage characteristics (A, b, ta and BWi), SAG mill percent solids and fractional speed, elemental analysis and recovery.

In this case study, the Integrated Extraction Simulator (IES) was used to generate an integrated base case flow sheet of the Mt Keith Operations. IES is a cloud-based simulation and optimisation platform, mainly designed to predict and optimise mining value chain performance while effectively integrating different units of operation including drill-and-blast, crushing, grinding, and flotation. The most frequently used blast patterns and explosive were used as inputs to the blast fragmentation model with respect to drill-and-blast design parameters. The most used blast fragmentation models are incorporated into IES such as the original Kuz-Ram (Cunningham, 2005) and Crushed Zone Model (CZM) where the later was used as it provides a better estimation of blast-induced fines (Kanchibotla *et al,* 1999).

Two levels of blast intensity were considered in this case study, defined as Standard and Intense between which only burden and spacing differs. This study includes 44 stockpiles which were processed between April 2017 and May 2020, with the drilling geometry of B × S = 7 × 8 m as the most used blast pattern, called the 'standard blast' and B × S = 5 × 6 m have been used rarely as the most 'intense blast'. Figure 1 shows the IES-based flow sheet for the Mt Keith Operations. As shown, the process circuit at Mt Keith Operations contains two SAG mills (with inside liners diameter and length of 9.50 × 9.15 m), separately in closed circuit with a screen and a hydrocyclone cluster which reports to three ball mills. Each ball mill is in closed-circuit with hydrocyclone classification. Based on the data of 44 processed stockpiles, the comminution circuit generates a feed size between 163 and 222 µm for the flotation stage. It is worth noting the volumetric filling was

21.2 per cent for SAG mill 1 and 22.2 per cent for SAG mill 2 where SAG mills 1 and 2 were charged with 16.1 per cent 16.9 per cent grinding steel balls and both SAG mills were operating at 74 per cent of its critical speed which was constant.

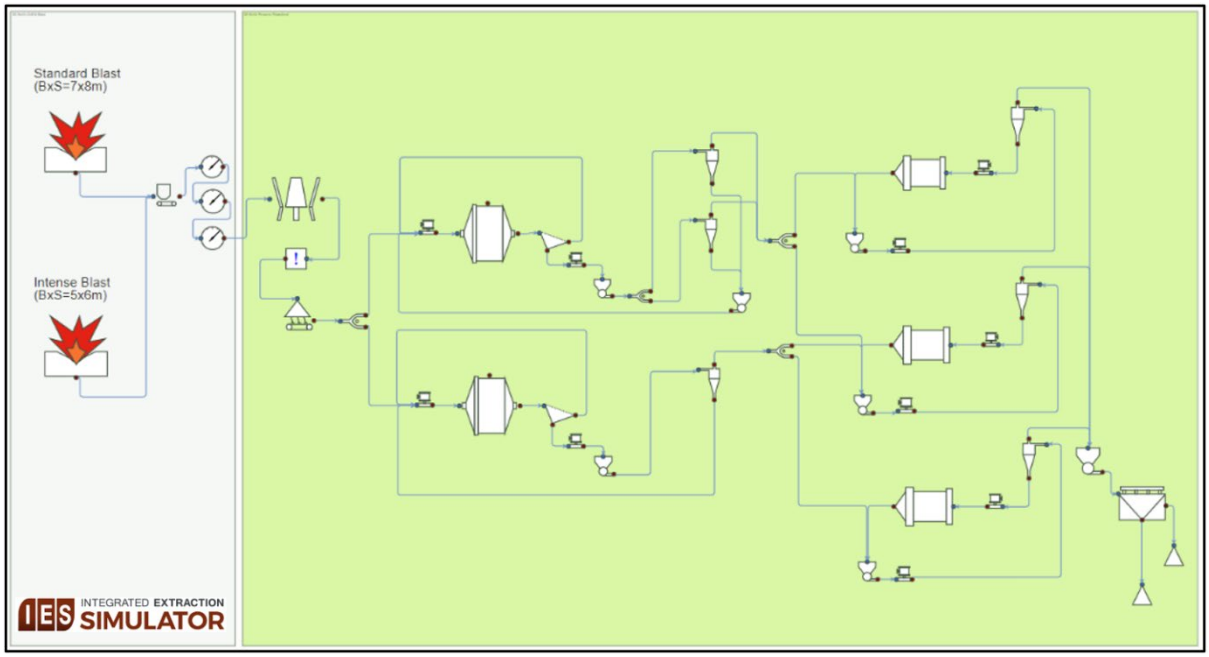

FIG 1 – Mt Keith Operations flow sheet.

Base case model development

The application of an integrated base case of Mt Keith Operations was to quantify potential performance and economic improvements for several grind sizes if a Mine to Mill strategy was adopted. The base case flow sheet represents average of a set of operational data including 44 stockpiles, hence model fidelity depends on whether variations in the ore type and operational conditions remain in the range of the data it is developed based upon. Only six processed stockpiles out of 44 had ore breakage characteristics test work results available, where the average of these attributes was used for establishing the base case model (Table 1).

TABLE 1

Ore breakage properties essential to modelling and simulation in IES.

Stockpile	A	b	A×b	ta	BWi (kWh/t)
D073	72.7	0.7	51	0.51	31.7
A059	72.6	0.76	55	0.55	31.7
B079	74	0.74	55	0.55	31.8
C084	76.2	0.68	52	0.52	31.8
A060	78	0.65	51	0.51	31.2
Average	75.1	0.67	50	0.51	31.5

The P_{80} size range of the 44 stockpiles varies between 163 and 222 µm, and the base case fails to compensate such a wide range. However, the base case should represent process performance under different product sizes because this variable is used as a constraint in the constraint manager. This necessitates using a multistate manner by inserting appropriate D50 cyclone model parameters for the given cyclone product 80 per cent passing size (P_{80}) in the simulations. Based on the operational data of the six stockpiles, a correlation was found between the throughput and P_{80} (Figure 2). An empirical model was developed to dynamically calibrates D50 of the cyclone model based on the target grind size (P_{80}) which are shown in Figure 3. These predictive models are used

to estimate D50 values for being used in the Mt Keith IES-based flow sheet for any target P_{80} size. It should be noted that the integrated model developed supports P_{80} sizes between 163 and 230 µm which covers a wide range of operational P_{80} at Mt Keith Operations.

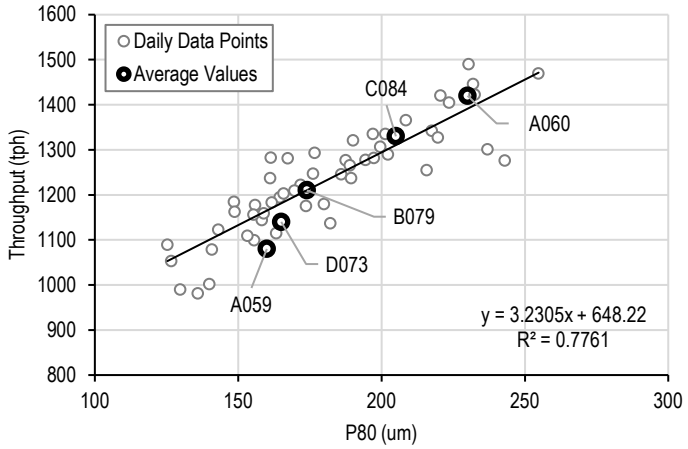

FIG 2 – Correlation between throughput and P_{80} – stockpiles A059, D073, B079, C084 and A060.

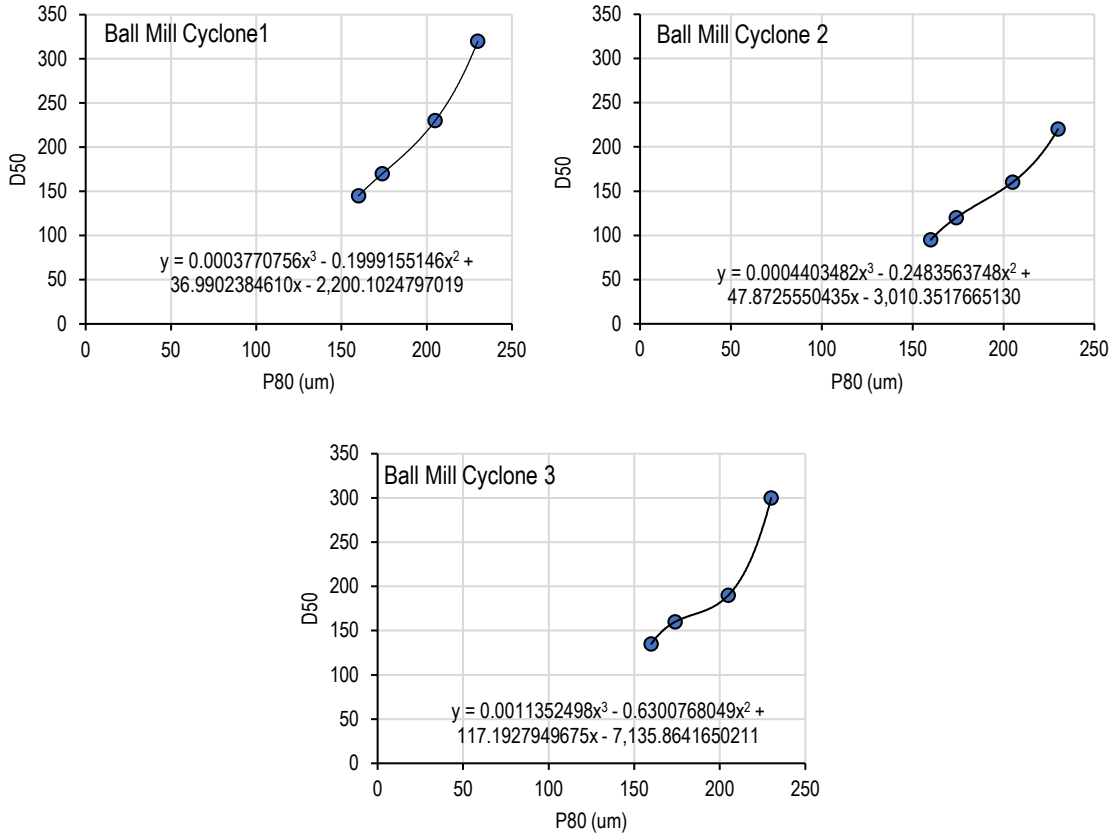

FIG 3 – Predictive models for D50 at different sizes for the three ball mill cyclones.

The 44 data sets were ranked based on the final product size (P_{80}) from small to large and then five data sets were chosen between the minimum and maximum P_{80} sizes which are 163, 173, 186, 200 and 222 µm as shown in Table 2. The predictive models given in Figure 3 were used to estimate D50 of each cyclone at an assigned P_{80}. This data set was used to evaluate reliability of the base case for presenting the state of the process.

TABLE 2

Operational data of five out of 44 stockpiles and size-based D50 estimates.

No.	Feed Ni (%)	Feed S (%)	Feed Talc (%)	Con Ni (%)	TPH (t/h)	Rec (%)	P_{80} (µm)	Cyc1 D50	Cyc2 D50	Cyc3 D50
1	0.757	1.057	0.500	21.4	1267	71.8	163	151	101	143
2	0.657	0.600	0.633	20.7	1300	65.7	173	169	119	159
3	0.612	0.824	1.486	19.2	1361	60.6	186	189	135	169
4	0.650	0.987	0.100	19.5	1390	69.9	200	219	153	182
5	0.592	0.923	0.180	17.2	1403	64.0	222	284	195	248

The results from the base case integrated model confirms existence of an acceptable agreement between the observed and predicted for the throughput and recovery (Figure 4). The base case flow sheet was used to proceed with evaluating several scenarios for potential process improvement through simulation.

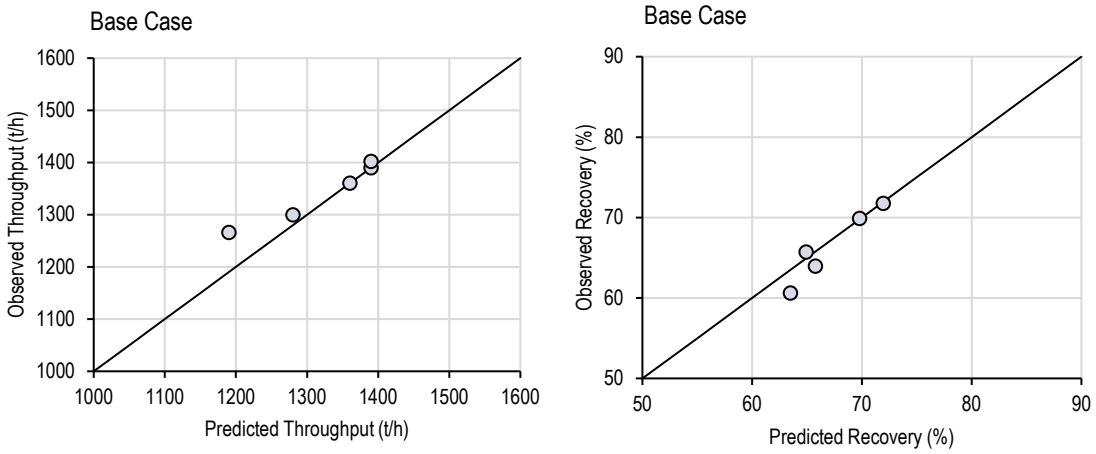

FIG 4 – Agreement between observed and predicted throughput (left) and recovery (right) – five stockpiles.

Simulation scenarios

For this study eight scenarios were considered which includes standard and intense blasting designs each of which accounts for four final product grind sizes (P_{80}) of 170, 187, 200, and 230 µm. There are assumptions related to ore breakage variability and likely impact of ore dilution after intense blasting which are addressed and might be considered in future studies.

Considerations

Two levels of blast intensity were considered as part of the scenarios, labelled standard and intense. Based on the drill-and-blast data, the most common geometry used for blasting was B × S = 7 × 8 m and B × S = 5 × 6 m was the tightest blasthole pattern, which were considered for standard and intense blasting practices. Table 3 gives details of the blast designs considered for this case study and their predicted muck pile size distributions are illustrated in Figure 5.

TABLE 3

Databased blast design information used for simulation.

Description	Standard Blast	Intense Blast
Blasthole Diameter (mm)	251	251
Burden (m)	7.0	5.0
Spacing (m)	8.0	6.0
Bench Height (m)	12.0	12.0
Blasthole Length (m)	13.5	13.5
Column Charge Length (m)	8.0	8.9
Explosive per Blasthole (kg)	494.8	550.5
Relative Weight Strength of Explosive	77.0	77.0
Explosive Density (g/cm^3)	1.25	1.25
Velocity of Detonation (m/sec)	5800	5800
Powder Factor (kg/m^3)	0.74	1.53
Specific Drilling (m/m^3)	0.020	0.038

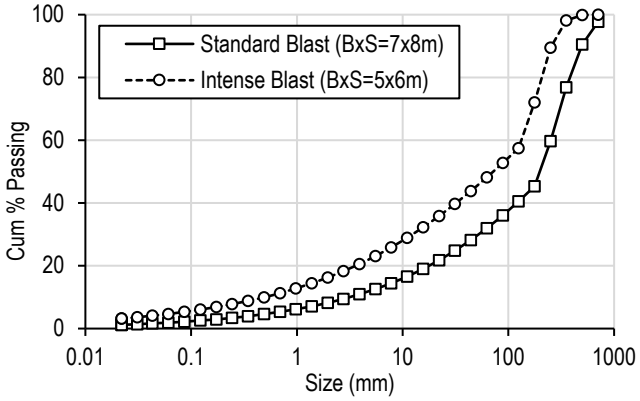

FIG 5 – Predicted muck pile size distributions of considered blast designs.

Eight simulation scenarios which were considered for being performed for 44 stockpiles, which account for the interaction between the upstream (drill-and-blast) and downstream (target product P_{80} size) constrains (Figure 6). The objective is to compare potential outcomes of the standard and intense blasting strategies under four conditions of the ball milling constraint, 'product P_{80} size'.

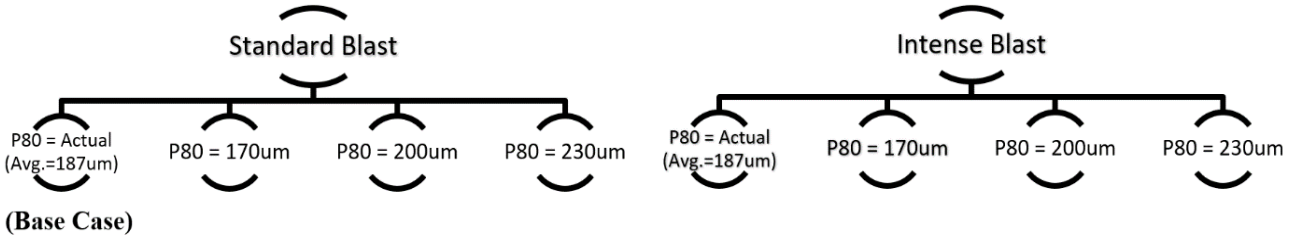

FIG 6 – Simulation scenarios.

The economic impact of Mine to Mill is quantified based on actual product grind size (P_{80}) sourced from the operational data collected from 44 processed stockpiles. Simulations were conducted for these stockpiles at four levels of product grind sizes (P_{80}) which are the main constraints in the IES simulations.

Assumptions

The simulation and value evaluation studies include two assumptions as follows:

- Firstly, ore comminution properties (A, b, ta and BWi) are assumed the same for all the stockpiles: A change in ore comminution properties will impact the performance of subsequent process units such as grinding and flotation. The available ore comminution properties (A, b, ta and BWi) shown in Table 1 did not have significant variation that could influence the process performance. This study did not consider the impact of ore competence variability and it is assumed that ore comminution property is the same for all the stockpiles.
- Secondly, the possible impact of ore dilution due to intense blasting is not considered in value quantification: Implementing more intense blasts will elevate risk of blast-induced undesirable side effects such as backbreak, ground vibration, airblast and flyrock as well as dilution which imposes additional expenses for taking appropriate mitigation measures and control strategies. However, ore dilution for increased blast intensity has been reported before (Eshun and Dzigbordi, 2016; Esen *et al,* 2007; Engmann *et al,* 2013), which can directly impact value across the chain through ore loss and disposal of waste or less valuable material to the mill. This undesirable phenomenon can be measured by blast movement monitoring systems and be controlled/mitigated by tuning blast design parameters (ie timing, pattern, and distribution of explosives energy etc). This study does not consider ore loss and dilution impact for lack of measurements in this area.

Value quantification

Value can be expressed as the difference between the Net Income earned from changing the status quo into a different operating strategy. A finer blast fragmentation will be at the cost of increased drilling and blasting expenses, however, a finer feed may improve SAG milling throughput capacity and eventually production rate that compensates the blasting cost which need to be quantified.

Three elements of costs were defined to calculate the blast cost:

- Drilling cost (A$/m).
- Explosives cost (A$/tonne of explosive).
- Other blasting costs (A$/hole) for the drill-and-blast expenses.

Based on CRC ORE's database, an average cost of drill-and-blast in Australian mines is A$16/m for drilling holes, A$1000/t of explosive, and A$35/hole for other blasting costs in form of detonators, boosters, delays, tie ins, and other fixed costs. Accordingly, the drill-and-blast cost per tonne of rock was A$0.40 for standard and A$0.80 for intense blasting scenarios.

Processing cost per milled tonnage of ore (A$/t) and cost per tonne of Ni in Concentrate at Mt Keith operation were used for quantifying relative changes in profitability. The income was then calculated based on the Ni price at the time of study which was A$20 190/t. Accordingly, the Net Income per stockpile was calculated using the costs and nickel price mentioned above for the simulated scenarios.

However, because of strict confidentiality considerations, in this paper financials are presented in terms of percent change relative to the base case. The details on the calculations are given below:

- Drill and Blast Cost per Stockpile (A$):

$$\text{Total Stockpile Tonnage (t)} \times \text{Blasting Cost per Tonne of Rock (A\$/t)} \quad (1)$$

- Milling Cost (A$/hr):

$$\text{Processing Cost per Tonnage of Ore Milled (A\$/t)} \times \text{Average Throughput of the Stockpile (t/h)} \quad (2)$$

- Processing Cost (A$/hr):

$$\text{Processing Cost per Tonne of Ni in Concentrate (A\$/Ni t)} \times \text{Metal Yield from the Stockpile (t/h)} \quad (3)$$

- Metal Yield (t/hr):

$$\text{Ni in Feed (\%)} \times \text{Recovery (\%)} \times \text{Throughput (t/h)} \quad (4)$$

- Total Milling Cost (A$):

$$\text{Milling Cost (A\$/h)} \times \text{Number of Hours to Process the Stockpile (h)} \quad (5)$$

- Total Processing Cost (A$):

$$\text{Processing Cost (A\$/h)} \times \text{Number of Hours to Process the Stockpile (h)} \quad (6)$$

- Total Cost (A$):

$$\text{Drill \& Blast Cost per Stockpile (A\$)} + \text{Total Processing Cost (A\$)} \quad (7)$$

- Income per Stockpile (A$):

$$\text{Metal Yield (t/h)} \times \text{Number of Hours to Process the Stockpile (h)} \times \text{Ni Price per Tonne (A\$/t)} \quad (8)$$

- Net Income per Stockpile (A$):

$$\text{Income per Stockpile (A\$)} - \text{Total Cost (A\$)} \quad (9)$$

- Relative Net Income (%):

$$100 \times (\text{Intense Blast Income (A\$)} - \text{Standard Blast Income (A\$)}) / \text{Standard Blast Income (A\$)} \quad (10)$$

RESULTS AND DISCUSIONS

In this study, the impact of changes in drill-and-blast practice on downstream was quantified through simulating several scenarios by using a fine-tuned flow sheet of Mt Keith Operations in IES – which counted in the effect of final product P_{80} size. Accordingly, generated variations in process performance (ie throughput and recovery) which are induced by a changed drill-and-blast design were monitored. This provides a quantitative description of process performance under multitude of operational conditions and how upstream and downstream processes may interact and impact the 'Net Income'. This section centres on presenting such results and developing a discussion on technical and economic aspects of the simulated scenarios.

Quantifying process performance at actual and three simulated P_{80} sizes

The first set of simulations uses the base case flow sheet with the aim to estimate process performance at actual P_{80} sizes for the standard and intense blasting practices. To speed up the analysis, a regression model was required to be developed between throughput and P_{80} based on the simulations, which assists with predicting the throughput for different actual P_{80} sizes. For this purpose, the five data sets (see Table 2) were selected which cover a wide range of P_{80} values observed in the stockpiles to be simulated in IES (shown in Table 3).

Two series of simulations (total of 10) were done on the data set to cover Standard and Intense scenarios. The throughput results obtained from those simulations were used to develop two interpolative models to expand the data to the 44 stockpiles. The models are given in Figure 7. It should be noted that Ni recovery was simulated in IES using the feed characteristics for each stockpile.

The results are given in Table 4, which suggest a potential improvement between 6–9 per cent at P_{80} size constraints (163, 173, 186, 200 and 222 µm) which were assigned based on actual data for the intense blasting strategy.

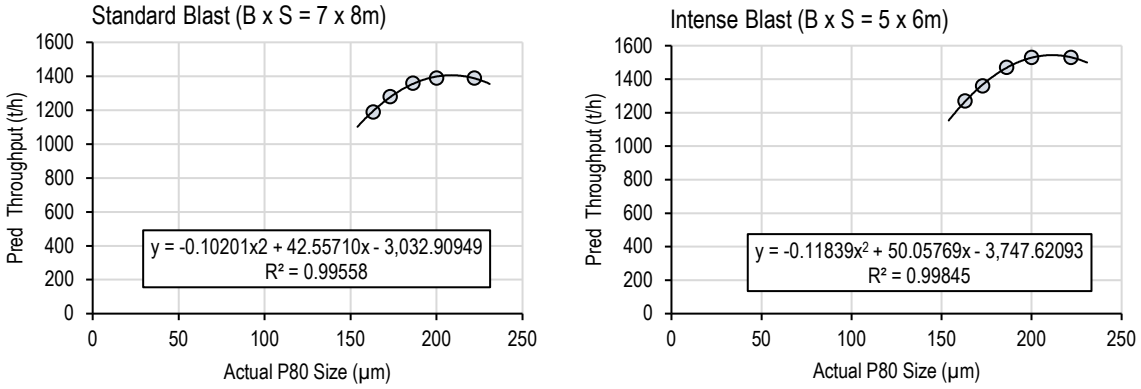

FIG 7 – Predictive models for throughput based on actual P_{80} size.

TABLE 4

IES simulation results for the selected data sets

No	Standard Blasting (7 × 8 m)			Intense Blasting (5 × 6 m)			Improvement (%)
	IES Throughput (t/h)	IES P_{80} (µm)	IES Recovery (%)	IES Throughput (t/h)	IES P_{80} (µm)	IES Recovery (%)	
1	1190	163.0	72.0	1270	163.0	72.0	6.0
2	1280	172.9	64.9	1360	172.8	64.9	6.0
3	1360	186.2	63.5	1470	186.0	63.5	7.0
4	1390	199.9	69.8	1530	199.9	69.8	9.0
5	1390	221.9	65.8	1530	221.8	65.8	9.0

To examine the fidelity of the whole modelling process, IES flow sheet in conjunction with the model developed were used to predict the throughput and recovery for all the 44 stockpiles for different sizes given in the operational data. The agreement between observed and predicted values is plotted for throughput and recovery for 44 stockpiles is given in Figure 8. It should be noted that fidelity of such a fine-tuned flow sheet is expected to lie within and satisfy the range of data captured by the 44 stockpiles, specifically P_{80} sizes. Deviating from the simulation range may deteriorate the accuracy of those predictions gradually.

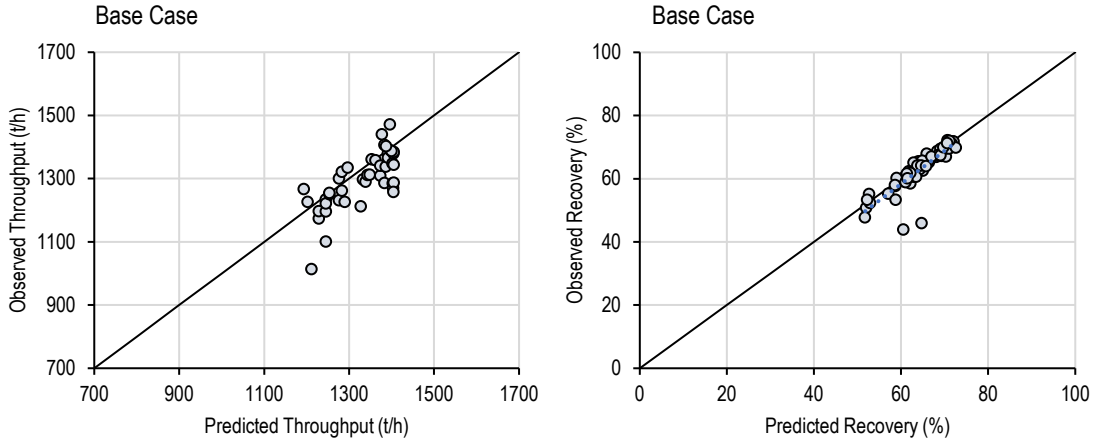

FIG 8 – Agreement between observed and predicted throughput (left) and recovery (right) – 44 stockpiles.

The Mt Keith Operations IES-based flow sheet was used for the 44 individual stockpiles for predicting the throughput and recovery for comparing two blasting practices, namely standard (B × S = 7 × 8 m) and intense (B × S = 5 × 6 m). A comparison of Standard with Intense blasting strategies was conducted through simulations for the 44 set of operational data with different P_{80} sizes (ranging between 163–222 µm).

Figure 9 compares required time (hrs) to process each stockpile for standard-actual P_{80} and intense-actual P_{80}. The results show that the time required to process the 44 stockpiles could be reduced from 9504 to 8789 hrs, where the difference is equivalent to 715 hours.

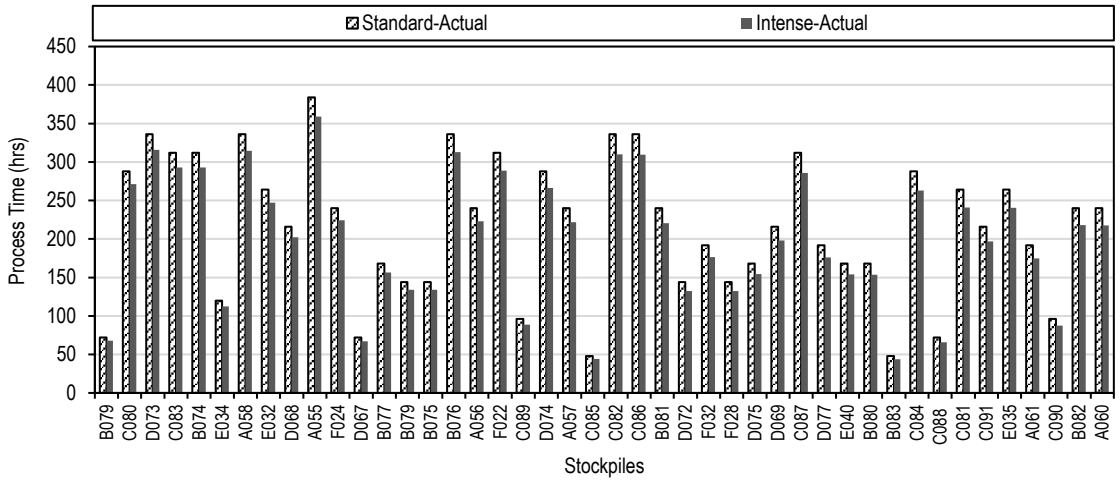

FIG 9 – Processing time per stockpile for the standard and intense drill-and-blast scenarios.

The potential Ni metal yield for each of the stockpiles was calculated using Equation 4 based on the Ni per cent recovery and simulated throughput for standard and intense blasting scenarios. It was aimed to quantify how metal yield may change if the drill-and-blast practice shifts from the standard and intense blast designs. The results of analysis suggested that 6.1–10.3 per cent improvement in the metal yield could be attained for individual stockpiles if a Mine to Mill strategy had been adopted. In other words, the intense blasting practice reduced the time to process the stockpiles. Implementing an intense blasting practice required about 52 per cent increase in powder factor and 46 per cent more in drilling.

In the second set of simulations, three levels of P_{80} sizes were used as constraints as 170, 200 and 230 µm and these constraints were tested for the standard and intense blasting practices. Simulations were conducted under the constraints highlighted in Figure 6. A neural network flotation model was adapted and tested using the flotation plant PI data and the production laboratory daily recovery reports. The elemental grades of Ni, S and Talc as well as the final grind size are the input parameters to the Mt Keith flotation model which was used to simulate the recovery for 44 stockpiles. The results of these simulations (total of 264) suggested that with an intense blasting constant P_{80} strategy in place, at P_{80} = 170 µm, the metal yield improved by 3.2 per cent and at P_{80} sizes of 200 and 230 µm it increased by 10.1 per cent.

The results suggest that the fine P_{80} size of 170 µm diminishes potential benefits of Mine to Mill strategy in consequence of a higher SAG mill throughput because the ball milling circuit capacity is the bottleneck in particular at this P_{80}, which expectedly exceeds the maximum capacity of circulating load. Additionally, metal recovery notably reduced in response to poor performance of the flotation process as it was observed in the PI data. On the other side, for both P_{80} sizes of 200 and 230 µm, the simulated scenarios per stockpile confirms potential benefits of intense blasting as a useful strategy for improving the throughput and metal yield rates up to 9.0 per cent. Referring to the average and sum of the metal yield values for the 44 stockpiles, indicated that a P_{80} size of 200 µm delivers the highest metal yield compared to the P_{80} size '230 µm'. This implies that the optimal P_{80} is around 200 µm which results in the highest performance outcomes if a Mine to Mill approach being adopted.

Quantifying profitability

The percent of saveable processing cost estimated per stockpile is given in Figure 10. The left Y-axis of the graph represents the processing cost relative to the base case which potentially could be saved by each stockpile if a Mine to Mill strategy had been implemented, while the right Y-axis indicates the total tonnage processed per stockpile. Analysis of 44 processed stockpiles showed an intense blasting practice potentially could reduce the cost of processing for the given stockpiles by X per cent which varies within the range of 4.0 to 8.0 per cent for each stockpile. This was achieved by reducing the time required for processing each of the studied stockpiles (comparing *Standard-Actual* and *Intense-Actual*).

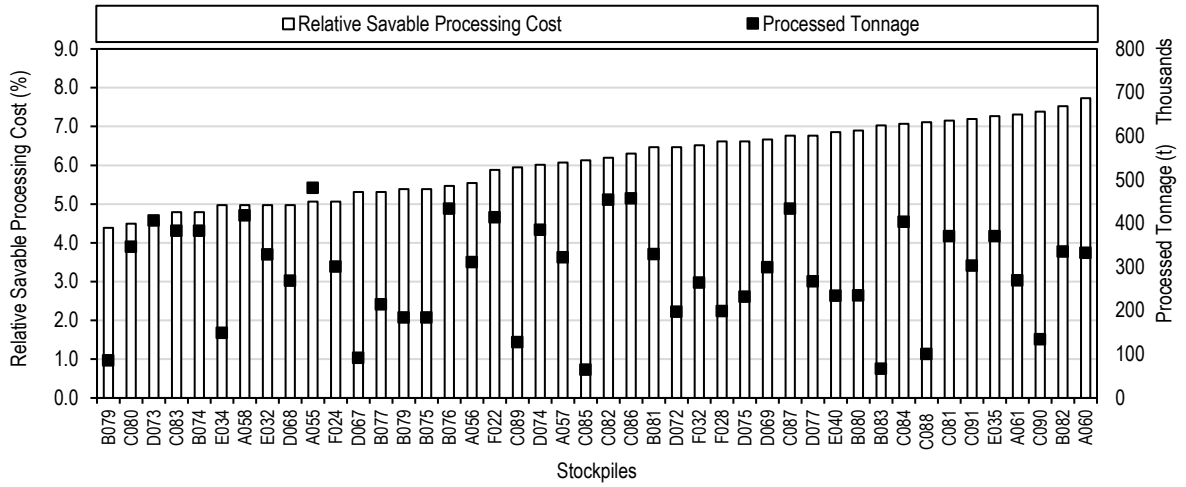

FIG 10 – Potential saveable cost relative to the base case for each stockpile if intense blasting was used.

Figure 11 shows the Net Income ratio of each simulation scenario relative to the Standard-Actual scenario (base case), suggesting that a Mine to Mill strategy can potentially increase the Net Income by increasing the actual grind size (P_{80}). Accordingly, the results imply that for the processed stockpiles between 2017 and 2020, maintaining the P_{80} at 200 µm might result in the highest economic gains (in operation costs saving) up to 8.58 per cent relative to the base case if the Mine to Mill strategy had been adopted. Considering Mine to Mill strategy without maintaining the grind size, using actual grind size in the operational data, resulted in +3.42 per cent increase in the Net Income. This could be achieved by reducing the processing cost per stockpile with spending less time for processing each stockpile (refer to Figure 9). This analysis is done by considering the mine could have kept up with the higher processing throughput rates showed in Figure 10 by utilising the current equipment efficiently.

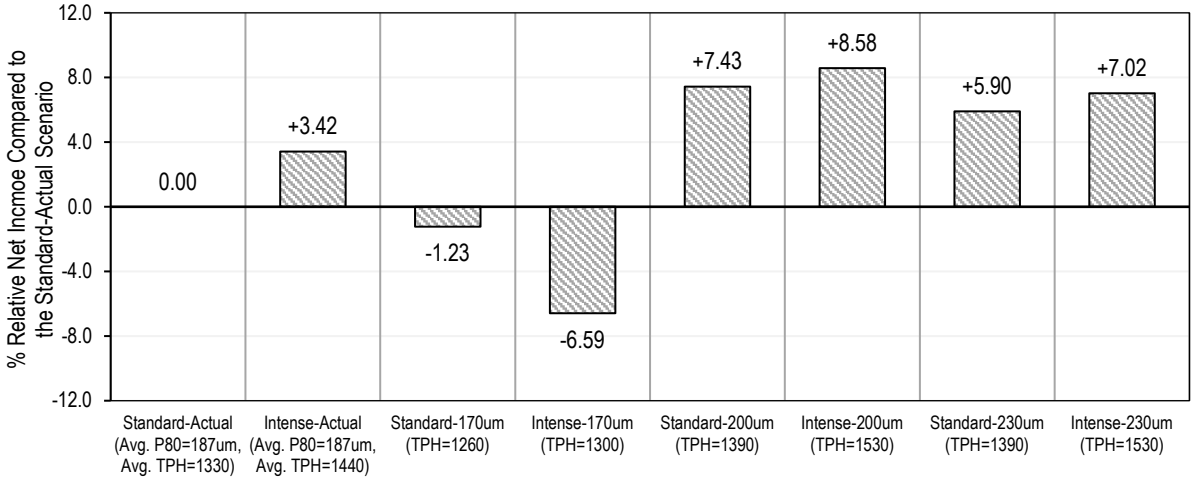

FIG 11 – Percent of relative Net Income change of different scenarios compared to the base case.

CONCLUSIONS AND RECOMMENDATIONS

In this paper, a fine-tuned flow sheet was developed in IES for the BHP's Nickel concentrator 'Mt Keith Nickel West', located in Western Australia. The study considered Mine to Mill approach to evaluate the improvement potentials and impediments towards an optimal operational strategy in presence of the process constraints. Two feasible levels of blasting intensity were compared and their impact on the downstream process performance as well as profitability was quantified through simulating eight scenarios in IES. The conclusions are as follows:

- Development of fine-tuned flow sheets offers new opportunities to minerals industry to take advantage of large on-site-generated data and effectively use it for making strategic decisions relating to production, control, and optimisation. Additionally, such models can keep their fidelity if changes in the ore type and operational conditions remain in the range of the data they are developed based upon. Nonetheless, accuracy and precision of current modelling approach can be improved through attaining a better knowledge of sources of errors and quantifying them, if possible.
- The results imply that perusing a Mine to Mill strategy can improve the SAG milling performance at Mt Keith Operations in a range between 6–9 per cent as the proportion of subgrate material (Approximately <47 mm) in the feed rises about 35 per cent, which speeds up of the grinding rate at this stage. This improved rate is reasonably aligned with the value (7.0 per cent improvement in throughput) reported by Clark and Scott (2002). However, depending on the target grind size P_{80}, a higher SAG mill throughput might not align with the ball milling circuit capacity and specific attention should be given to the energy balance between the SAG and ball milling circuits.
- An economic evaluation methodology was developed in this study for quantifying the value generated across the operation based on available information at the mine data historians. An important part of this methodology which should be highlighted relies on capturing operational constraints from the PI data and effectively integrating them into the process flow sheet.
- Analysis of outcomes indicates that maintaining the product P_{80} at 200 µm could result in up to +8.58 per cent relative to the base case – if the Mine to Mill strategy had been adopted to the 44 processed stockpiles. This scenario should be achievable in the real-world because of the high level of constraint management and fidelity in the IES flow sheet. However, it should be noted that this level of improvement may not be achievable for the whole orebody as its inherent characteristics and the degree of heterogeneity change through the life-of-mine. Therefore, it is recommended to extend this study to a domain-based or block model-based evaluation of potential value opportunity, which in turn will allow the value improvement to be quantified for the life-of-mine.

It should be noted that the presented outcomes are specific to the stockpiles for which the case study was developed based on, and this study assumptions do not necessarily represent current or future performance of Mt Keith Operations. As ore properties changes over time, future investigation is required to quantify potential risks and opportunities to assess and improve performance across the value chain.

ACKNOWLEDGEMENT

The authors would like to thank BHP's Mt Keith Nickel West Operations and CRC ORE for support and providing resources for this case study. Also, we acknowledge the contributions made by Mr. Percy Madrid at early stages of this project. CRC ORE is part of the Australian Government's CRC Program, which is made possible through the investment and ongoing support of the Australian Government. The CRC Program supports industry-led collaborations between industry, researchers, and the community.

REFERENCES

Amini, E and N Beaton, N, 2020. Development of mine operation value chain flowsheets fine-tuned and constraint based on the process information (PI) data to evaluate proposed operation strategies and ore pre-treatment technologies, in *Preconcentration Digital Conference 2020* (The Australasian Institute of Mining and Metallurgy: Melbourne).

Amini, E, Becerra, M, Bachmann, T, Beaton, N and Shapland, G, 2020. Development and Reconciliation of a Mine Operation Value Chain Flowsheet in IES to Enable Grade Engineering and Process Mass Simulations for Scale-up and Strategic Planning Analysis. *Mining, Metallurgy & Exploration*, 2020: p. 1–10.

Burger, B, McCaffery, K, Jankovic, A, Valery, W and McGaffin, I, 2006. Batu Hijau model for throughput forecast, mining and milling optimisation and expansion studies. *Advances in comminution*, 2006: p. 461–479.

Carrasco, C, Keeney, L, Napier-Munn, T J, Bode, P, 2017. Unlocking additional value by optimising comminution strategies to process Grade Engineering® streams. *Minerals Engineering*, 2017. 103–104: p. 2–10.

Clark, D and Scott, A, 2002. Milling throughput improvements at Mt Keith Operations. in WMC Resources Limited, Institute for International Research (IRR) Mine to Mill Conference, Perth, August. 2002.

Cunningham, C, 2005. The Kuz-Ram fragmentation model–20 years on, in *Brighton Conference Proceedings,* European Federation of Explosives Engineers, England.

Diaz, R, Mamani, H, Valery, W, Jankovic, A, Valle, R, Duffy, K A, 2015. Diagnosis of process health, its treatment and improvement to maximise plant throughput at goldfields Cerro Corona, in *SAG 2015 Conference Proceedings*. Vancouver, 2015.

Engmann, E, Ako, S, Bisiaux, B, Rogers, W and Kanchibotla, S, 2013. Measurement and modelling of blast movement to reduce ore losses and dilution at Ahafo Gold Mine in Ghana. *Ghana Mining Journal*, 2013. 14: p. 27–36.

Esen, S, La Rosa, D, Dance, A, Valery, W, Jankovic, A, 2007. Integration and optimisation of blasting and comminution processes, in *EXPLO conference 2007* (The Australasian Institute of Mining and Metallurgy: Melbourne).

Eshun, P A and Dzigbordi, K A, 2016. Control of ore loss and dilution at AngloGold Ashanti, Iduapriem mine using blast movement monitoring system. *Ghana Mining Journal*, 2016. 16(1): p. 49–59.

Faramarzi, F, Kanchibotla, S S and Morrison, R, 2019. Simulating the impact of ore competence variability on process performance – Case study of a large copper mine, in *SAG Conference 2019,* Vancouver, Canada.

Grundstrom, C, Jakovic, A, Kanchibotla, S S, Thornton, D M, 2001. Blast fragmentation for maximising the sag mill throughput at Porgera Gold Mine. in *Proceedings of the Annual Conference on Explosives and Blasting Technique 2001,* ISEE; 1999.

Hart, S, Valery, W, Clements, B, Reed, M, Song, M and Dunne, R, 2001. Optimisation of the Cadia Hill SAG mill circuit, in *SAG Conference 2001*.

Hodouin, D and Everell, M D, 1980. A hierarchical procedure for adjustment and material balancing of mineral processes data, *International Journal of Mineral Processing 1980,* 7(2): p. 91–116.

Jankovic, A, Valery, W and Davis, E, 2004. Cement grinding optimisation. *Minerals Engineering*, 2004. 17(11–12): p. 1075–1081.

Kanchibotla, S S, Valery, W and Morrell, S, 1999. Modelling fines in blast fragmentation and its impact on crushing and grinding, in *Explo '99–A conference on rock breaking* (The Australasian Institute of Mining and Metallurgy: Melbourne).

Kanchibotla, S, Musunuri, A and Kojovic, T, 2015. Stochastic modelling to assess the impact of ore variability on grinding circuit performance, in *SAG Conference 2015,* Vancouver, Canada.

King, R, 1990. Simulation—the modern cost-effective way to solve crusher circuit processing problems, *International Journal of Mineral Processing*, 1990. 29(3–4): p. 249–265.

Lishchuk, V, Koch, P H, Ghorbani, Y, Butcher, A, 2020. Towards integrated geometallurgical approach: Critical review of current practices and future trends, *Minerals Engineering*, 2020. 145: p. 106072.

Morrell, S and Valery, W, 2001. Influence of feed size on AG/SAG mill performance, *SAG2001*, Vancouver, BC, Canada, 2001: p. 203–214.

Morrison, R and Richardson, J, 2002. JKSimMet: A simulator for analysis, optimisation and design of comminution circuits. 2002.

Scott, A, Morrell, S and Clark, D, 2002. Tracking and Quantifying Value from 'Mine to Mill' Improvement, in *Proc Value Tracking Symposium*, Brisbane, Australia. 2002.

Scott, M and Amini, E, 2020. Quantifying economic and environmental impacts of preconcentration, in *Preconcentration, Conference 2020* (The Australasian Institute of Mining and Metallurgy: Melbourne).

Stepto, W D, Cilliers, B C and Glen, B, 1990. Application of dynamic process simulation. *SACAC Symposium*, May (MINTEK, Johannesburg), 1990.

Valery, W, Morrell, S, Kojovic, T and Kanchibolta, S, 2001. Modelling and simulation techniques applied for optimisation of mine to mill operations and case studies.

Techno-economic modelling of comminution circuit options

J J Hanhiniemi[1,2] and M S Powell[3]

1. MAusIMM, PhD Candidate, University of Queensland, SMI-JKMRC, Brisbane Qld 4068. Email: jeremy.hanhiniemi@uqconnect.edu.au
2. Head of Engineering, Weir Minerals, Artarmon NSW 2064. Email: jeremy.hanhiniemi@mail.weir
3. FAusIMM, Emeritus Professor, University of Queensland, SMI-JKMRC, Brisbane Qld 4068. Email: malcolm.powell@uq.edu.au

ABSTRACT

An overview of a techno-economic model for comminution processes for metalliferous ores is presented which illuminates the interplay between circuit design, machine design, ore characteristics, operating choices, blending and subsequent financial performance. This was developed to improved financial optimisation of existing plants and improved capital budgeting decisions. Existing financial models lack the technical depth and detail needed to accurately capture certain technical responses important to the financial outcome, such as nonlinear responses in blending of ore components, different responses of Unit Operations to particle size distribution, coarse and fine end blast fragmentation, classification performance, and the interplay between Unit Processes. Existing technical models lack some capability needed for financial modelling, such as broad integration, blend response, consumable use, bottleneck identification and constraints.

This paper describes a multi-component techno-economic model for comminution including blasting. It employs scenario analysis and simulation to predict marginal cash flow results from upgrades or design changes, operating choices, and ore properties. A marginal cash flow financial architecture is developed to facilitate analysis of only the comminution process, independent of others. Only Unit Processes which have a sensitive marginal cash flow response to, or technical bearing on, changes in comminution are analysed. These include drilling, blasting, crushing, grinding, classification, and separation response.

The modelling developed is demonstrated at Cortez Gold Mine. To test if the modelling can yield financial outcomes with improved fidelity and utility, several scenarios are simulated and compared using both these methods developed and existing techno-economic modelling. Comparisons between the results and the utility of the two modelling approaches is then conducted. It is demonstrated the differences in marginal Net Present Value (NPV) results are profound, and considerable utility is achieved in the new, detailed methods used. It is therefore recommended that techno-economic studies employ the methods developed and described here.

INTRODUCTION

There is an interrelationship between ore characteristics, machine and process design, and resulting cash flow from processing a unit of mineralised material. This paper summaries a Techno-Economic model of the comminution process, that separates characteristics of the ore, and the processing design and operation, independently, so that it can be applied generally across sites. This is then applied to a case study site, Cortez gold mine that operates an SABC circuit. The techno-economic architecture of the model is illustrated in Figure 1.

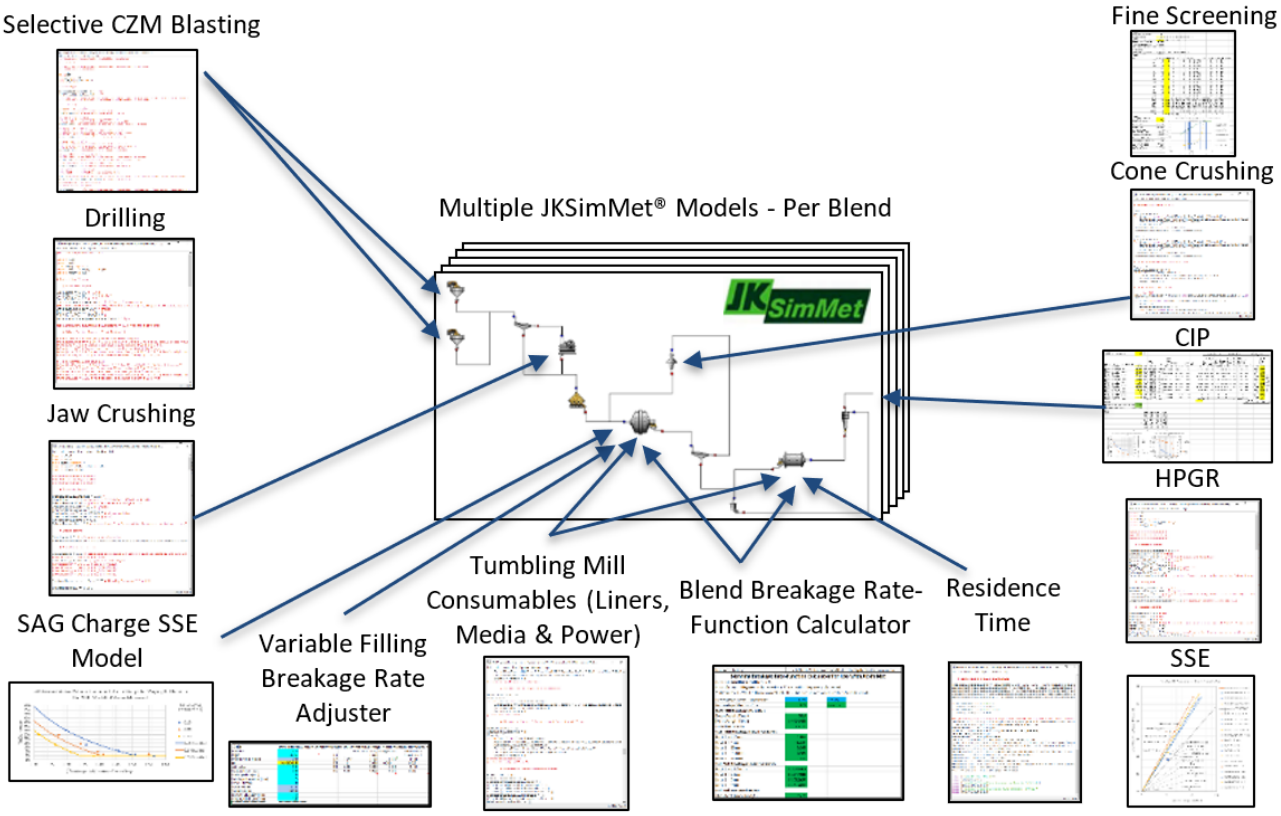

FIG 1 – Technical architecture.

In the centre are multiple JKSimMet® flow sheets, one per blend increment, and these form the basis of the wider modelling. The Variable Rates AG/SAG model and the Perfect Mixing Ball Mill models are employed here (Grimes and Keenan, 2015). A full simulation is provided from multiple blast designs to recovery responses. An external blast design model based on the Crushed Zone Model described by Kanchibotla *et al* (2001) has been coded and integrated. This model is better able to capture fines generation as compared to Kuz-Ram, and it allows for selective blasting. An external drilling model is also provided. A Jaw crusher model was also developed to supplement the JKSimMet® model.

Enhancements were made to tumbling mill modelling. A blend model was developed to provide response to blending in the SAG and ball mills as described in Hanhiniemi and Powell (2022). Further, SAG mill variable filling after Morrell (2001) was integrated, as was a residence time model to constrain the ball mill from overfilling based on the work of Shi (2016). For the SAG this is called the 'Variable Blend and Rates Model', and for the ball mill the 'Variable Blend Residence Constrained Perfect Mixing Model'.

Size Specific Energy (SSE) calculations, as described in Ballantyne *et al* (2015a, 2015b), are performed across the circuit to verify scenarios. As SAG charge composition impacts specific energy requirements, a 'SAG Charge Composition SSE Model' was developed to provide an indication of the reasonableness of simulated results with varying charge composition as also described in Hanhiniemi and Powell (2022). A tumbling mill consumables model was developed to supplement the SAG and ball mill models; in this media consumption and lifter-liner life is modelled mechanistically, as described in Hanhiniemi and Powell (2019).

A Carbon in Pulp (CIP) model is developed based and extending upon de Andrade Lima and Hodouin (2005), which is used to calculate recovery and its response to comminution circuit design. Finally a fine screen model after Bosman *et al* (2019) is also incorporated.

The technical modelling described above provides the inputs into the economic model, the overall architecture of which is presented in Figure 2. Again, multiple JKSimMet® models for various blends inform the financial model. Drill and blast, crushing (jaw and cone), primary SAG grinding, secondary ball mill grinding, and HPGR operating and unit costs models were developed. In addition, capital costs are determined for all upgrade scenarios considered. Overall, all these models inform the

marginal NPV, which calculates the present value of the marginal cash flows for all scenarios considered against a baseline circuit design and operation. This included considerations such as blend, strip ratio, grade, price, unit and capital costs. The marginal NPV can be thought of as sum of the additional or lost cash flows from implementing the upgrade as compared to continuing to operate per the baseline case, discounted to a present value over some defined period. It is a measure of the value of the upgrade, and the calculated period in this case was taken to be 5 years.

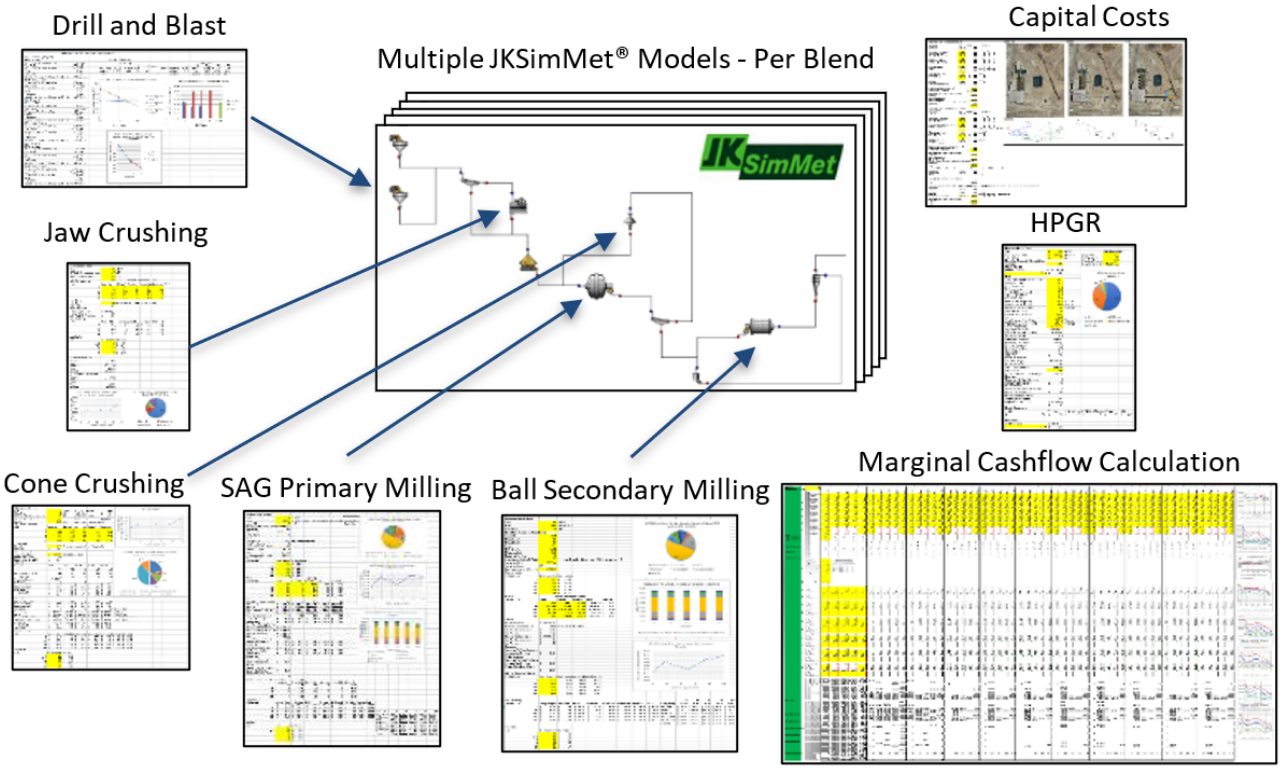

FIG 2 – Economic architecture.

Another economic performance measure is the before tax operating cash flow per ton or ore processed. This is the sum of the revenue less the cost of processing a ton of ore (including mining the required waste) and is a good measure of financial performance of the scenario when compared to a baseline. It is also presented as it indicates how upgrade scenarios can either increase or decrease the value of the ore.

ENHANCEMENTS ON EXISTING TECHNO-ECONOMIC MODELS

The new methods developed (or extensions made) in this new approach include:

- SAG and ball mill blend response.
- Mechanistic media and liner wear modelling.
- CIP leach modelling.
- Crusher volumetric constraint, force limits and wear.
- SAG charge composition SSE modelling.
- Bottleneck/constraint capture.
- Full particle size distributions calculated throughout the circuit.

Numerous other methods available were integrated into this Techno-Economic modelling, that are not typically incorporated. This included the following:

- Shi Ball Mill residence time constraint.
- JKMRC Crushed Zone Model Blasting.

- SSE constraint validation of simulations.
- Morrell (2001) SAG Filling Breakage Rate adjustment for variable SAG filling.
- Fine Screening.

Economic modelling includes the development of a marginal cash flow architecture which can isolate comminution circuit economics from other considerations. It is based on Activity Based Costing, and separation of Period costs. Cost models are also developed as previously described. There is also considerable integration and scripting required for both models developed in this research, and from existing literature. This includes 4400 lines of Python® language coding. The wide integration of modelling from drilling to separation response has also allowed for the evaluation of widely different upgrade or operating choices, and Mine-to-Mill blasting evaluation.

The methods used in this Techno-Economic model ('Detailed Methods') are compared with those which are termed, 'Existing Methods', defined by some of the characteristics below:

- Kuz-Ram blasting without a crushed zone.
- Single size (P80) modelling of crushing and grinding.
- Reduction ratio and Work Index (WI) based crushing.
- Linear blending response based on WI.
- Assumed power balance in comminution stages and utilisation.
- WI based throughput.
- Basic Unit Cost models (eg constant media consumption per ton assumed).

For each case study the detailed modelling is calibrated to a measured baseline, and then used to predict alternate upgrade scenarios. This is then repeated for these same scenarios using existing modelling. The difference between the two methods is analysed to see if a significant difference is achieved, and the fidelity of each is compared.

'DETAILED METHODS' MODELLING APPROACH

How each Unit Process from drilling to leach is modelled in the 'Detailed Methods' developed in this research is now briefly described.

Flow sheet development for blending and scenario analysis

Many simulators are single component, including JKSimMet®, however their flow sheets can be designed to allow some Unit Operations to be modelled in a multicomponent way. In this work, multiple feeders were used to represent different blast design fragmentations. The flow sheet was also set-up with splitters to adjust blend. Multicomponent crushing was modelled by employing multiple crusher models, one per component, to represent a single physical crusher. To support scenario analysis, the scenarios to be considered where included in the one flow sheet upfront by designing it so different upgrade options could be switched on and off. This greatly reduced the complexity when a flow sheet per blend increment was required. Figure 4 shows this flow sheet design for multicomponent crushing, different blast designs by component, and for blending. Figure 10 shows this also, and further how various upgrade options for a given case study can be included together, for an example scenario and blend.

Drilling and blasting

A drill cycle time calculation is used to determine available production rate (Gokhale, 2011). This responds to blast design, drill characteristics and rock properties. A cost model was also developed which also responds to blast design and drill type. An example is shown in Figure 3 of calculated drill Unit Costs, with blast designs and ore properties described later.

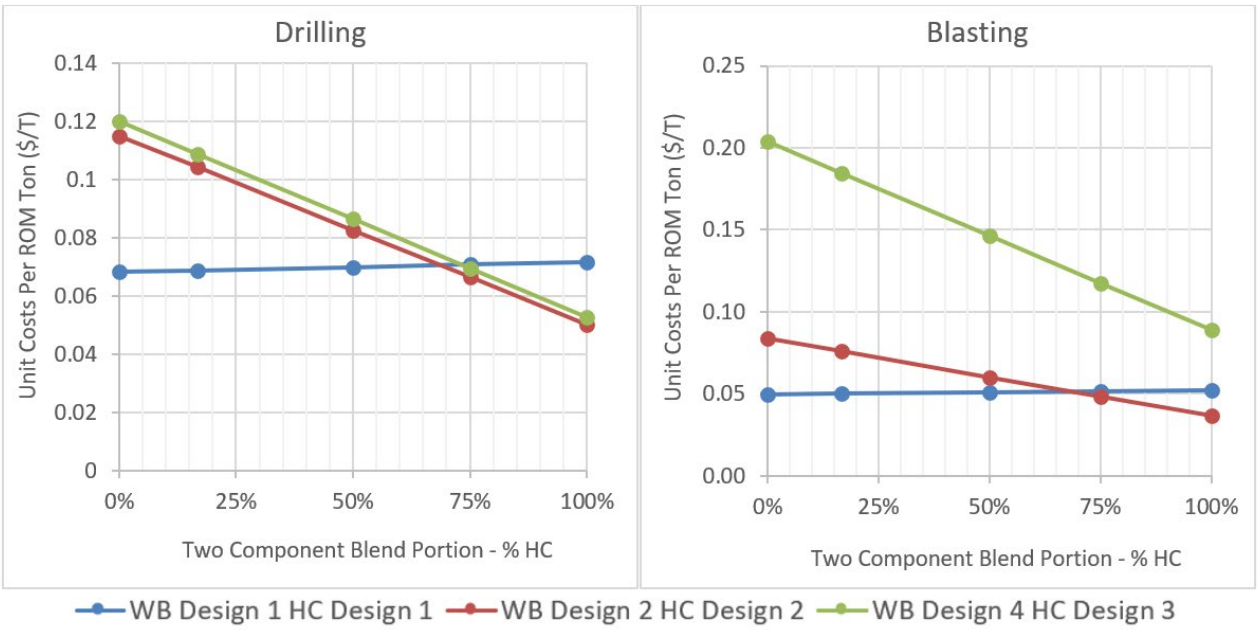

FIG 3 – Drilling and blasting unit costs versus blend for blast design scenarios – ore.

Unit Costs are calculated per component to represent selective blasting. For blast Particle Size Distribution (PSD) the single hole CZM is used to predict the Run-of-mine (ROM) size distribution as described in Kanchibotla *et al* (2001), JKMRC (1998, 2002). This CZM method is used as it has improved fines modelling over the Kuz-Ram model by fitting two distributions, one to the coarse zone and another to the crushed zone, and was conducted per waste and ore component. Model fitting is achieved via image analysis along with primary crushed product survey and crusher modelling, Rock Quality Designation (RQD), and ore characterisation tests. A procedure was developed for model fitting the bast and primary crushing together. Blasting costs are based on an *in situ* rate per kilogram of explosive, and as illustrated in Figure 3 the resulting Unit Costs for blasting vary with blast design and explosive type used (Design 4 and 3 employed high Velocity of Detonation Emulsion blends to promote the generation of fines). Figure 4 shows how multiple blast designs and blends of two ore components were fed into the overall model, achieving the modelling of selective blasting.

Jaw and cone crushing

For Jaw and Cone crusher modelling the JKSimMet® process model is extended to include constraint, consumables, response to blending and Unit Cost calculation. Starting with constraints three parts are included:

- Volumetric limits based on Rose and English (1967) for Jaws and Evertsson (2000) for cone crushers.
- Forcing limits are based on reduction ratio and limits on% fines in the feed.
- Power based on Andersen and Whiten crusher model (Napier-Munn *et al*, 1996).

For consumables, liner wear is established based on calibration with measured life based on crusher feed tons processed. Power costs are obviously determined by the Andersen Whiten power model. To achieve this, separate crushers are modelled by component to represent a single physical crusher as illustrated in Figure 4. Finally Operating and Unit Costs can be determined by combining power, liner, overhaul, maintenance, and operating costs. Overhaul costs on all equipment were estimated using the method described by Runge (1998).

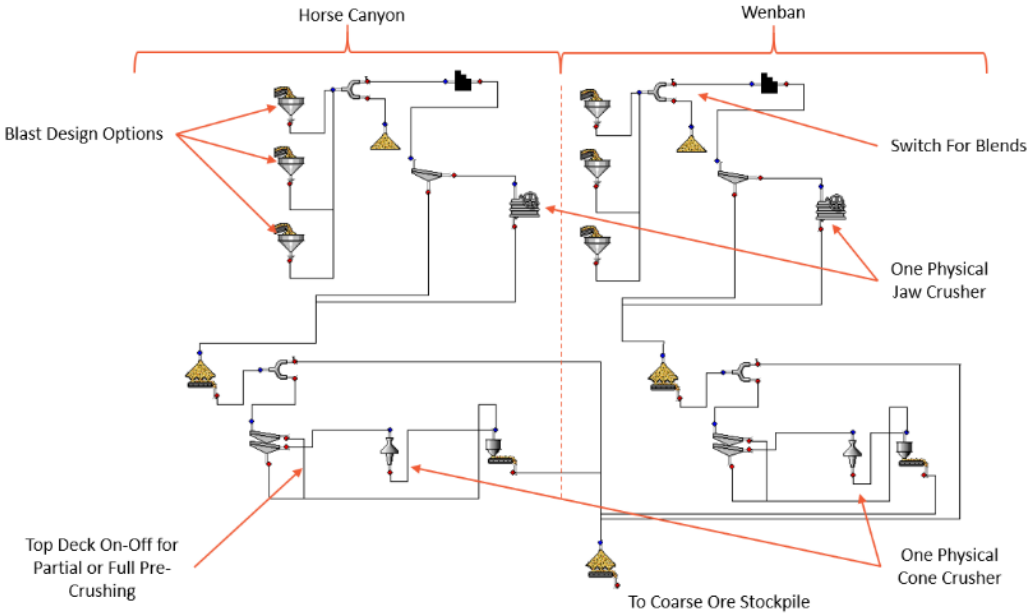

FIG 4 – Modelling approach for selective blasting designs, multicomponent crushing options, and blending.

SAG and ball milling

A 'Variable Blend and Rates' model was developed for SAG mills which extends upon the JKSimMet® Variable Rates Model. Similarly, a 'Variable Blend Residence Constrained Perfect Mixing' Ball Mill model was also developed, also extending upon the existing JKSimMet® model. These models are used in conjunction with JKSimMet® while employing an external, 'Breakage Rate and Function Calculator', the input to which is the blend proportion and each ores' characteristics. The work of Shi (2016) is also incorporated into the Ball Mill to constrain unrealistic simulations where overfilling would be occurring.

The newly developed modelling approach captures non-linearity of blend responses, occurring from changing ore competence-by-size, feed size distribution, and ore characteristics between the blend components. Constraint modelling also using SSE is employed, and a SAG Charge SSE Model was developed and applied to indicate likely increases in SSE known to occur in charge compositions with a low proportion of ore and high media fractions (Powell *et al*, 2015). Charge weight constraints are also applied based on total and media filling. The overall SAG and ball mill circuit modelling approach is described in detail in Hanhiniemi and Powell (2022).

Mill consumables

Operating costs of the SAG and ball mills was modelled via detailed technical models of consumables including media, liners, and power. Media and lifter-liner life and consumption is modelled based off the mechanistic model described in Hanhiniemi and Powell (2019). This mechanistic model requires calibration of two wear constants, for lifters and media, to a given ore type or blend. Once calibrated the model then responds to revised operating conditions – including for example ore filling, media filling, and speed – with varying media consumption and liner lives. Power costs are determined based on Morell's power model. Having established the consumables rates the unit costs can be determined while also including maintenance, operating, overhaul and slurry pumping costs for SAG and ball mill circuits.

Carbon in pulp circuit

CIP modelling developed in this research was based of the dissolution rate equation of Gold in solids, and the Cyanide consumption rate equations by de Andrade Lima and Hodouin (2005):

$$-\frac{d[Au]_S}{dt} = -r_{Au} = k_{Au}\left([Au]_S - [Au]_{s,\infty}\right)^{\alpha}[CN^-]^{\beta}[O_2]^{\gamma} \; and \; k_{Au} = k_{Au_1} - k_{Au_2}\bar{d}^{\theta}$$

$$-\frac{d[CN^-]}{dt} = -r_{CN^-} = k_{CN^-}[CN^-]^{\eta} \; and \; k_{CN^-} = \frac{k_{CN^-_1}}{\bar{d}^{\phi} - k_{CN^-_2}}$$

The residual concentration of valuables at infinite leach time from de Andrade Lima and Hodouin (2005) was modified for varying feed grade based off a simple conception of liberation and is of the form below:

$$[Au]_{s,\infty} = [Au]_{Feed}k_{D,\infty}(1 - k_{B,\infty}e^{k_{C,\infty}\bar{d}})$$

The rate equations used above are all functions of size, *d*, suited to capture recovery response with changes in the comminution circuit. Rate equations for carbon loading was also incorporated from literature (de Andrade Lima, 2007; Stange, 1991) and integrated into the modelling. Mass balances are then calculated for each CIP cell for aqueous cyanide, gold in solids, and aqueous and carbon phases. An Evolutionary Solver is used for gold concentrations in solution and in carbon by minimise error sum of squares against conservation of mass of components in all cells. Example results are provided in the Figure 9 showing gold in solids and aqueous phase, cyanide concentration, and carbon load in tanks.

For constrains, carbon feed rate and maximum carbon loading is included, and cell number and volume captures reducing recovery with increasing throughput. Ore characterisation is achieved via batch gold dissolution and separate cyanide consumption tests at varying controlled [CN-],[O_2], and size. Operating and Unit Costs can be estimated as specific cyanide addition and oxygen concentration are included allowing estimation of reagent and power cost.

CASE STUDY – CORTEZ MINE

Having described the method, it will now be applied to the case study – Cortez Gold Mine. It is an open cut gold mine with SABC circuit followed by CIP leaching illustrated in Figure 7. Two major ore components are mined together in the active pits – Horse Canyon (HC) and Wenban (Wb). Horse Canyon has an *Axb* 83.5 and a Bond Ball Mill Work Index (BBWI) of 17.1 kW/t. Wenban has an *Axb* 74.3 and a BBWI of 11.6 kW/t. Horse Canyon has a finer ROM distribution than Wenban, is softer in the larger size fractions, but harder in the finer fractions than Wenban. This is illustrated by the lower *Axb* for Wenban indicating higher competence, with the Horse Canyon then having a markedly higher BBWI. These varying competence-by-size features of the ores had a significant impact on the entire case study, via the blend response where synergies between the ores were found to improve overall circuit performance with controlled blending. This was implemented by the site to improve overall throughput without any capital expenditure (Ntiamoah *et al*, 2020). The ROM fragmentation of each is shown in Figure 5.

FIG 5 – Image of ROM stockpiles – Horse Canyon (left) and Wenban (right).

Blasting and primary crushing

Image analysis was performed on Wenban and Horse Canyon ROM, and combined crusher-grizzly product was surveyed for each ore. Calibration of the blast and jaw crusher modelling was complete per component using these measurements, drill core RQD data, crusher and grizzly details, and ore

Drop Weight and Compression Test results. This is complicated by the CZM model having coarse and fine fraction curves to fit and a fitting methodology was developed. Parity plots for both Wenban and Horse Canyon measured and modelled ROM and stockpile products showed reasonable results. These distributions are illustrated in Figure 6.

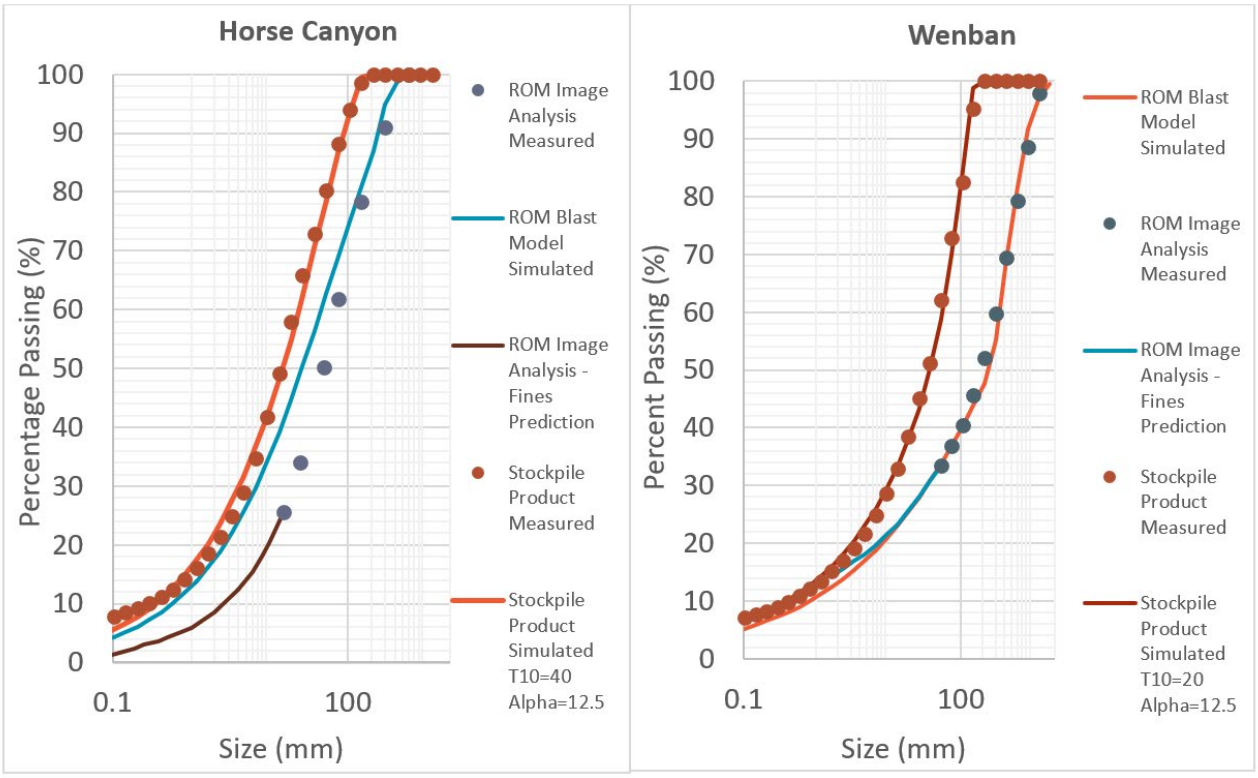

FIG 6 – Measured and model fitted stockpile product and ROM PSD – Horse Canyon (left) and Wenban (right).

Grinding circuit

Two full surveys were taken of the circuit for Wenban and Horse Canyon including crash stop and grind out, with surveyed streams shown in Figure 7 by the stars. Three further snapshot surveys were taken of controlled blends of the two components. For snapshot survey mill fillings, a soft sensor developed at the JKMRC for online mill filling estimation was used, which employs trunnion bearing oil pressure and temperature measurement to estimate fillings once calibrated to the full surveys (Hilden *et al*, 2020; Apelt *et al*, 2001). These five surveys were 0, 17, 50, 75 and 100 per cent Horse Canyon. These were mass balanced and model fitted and achieved convergence and were very successful.

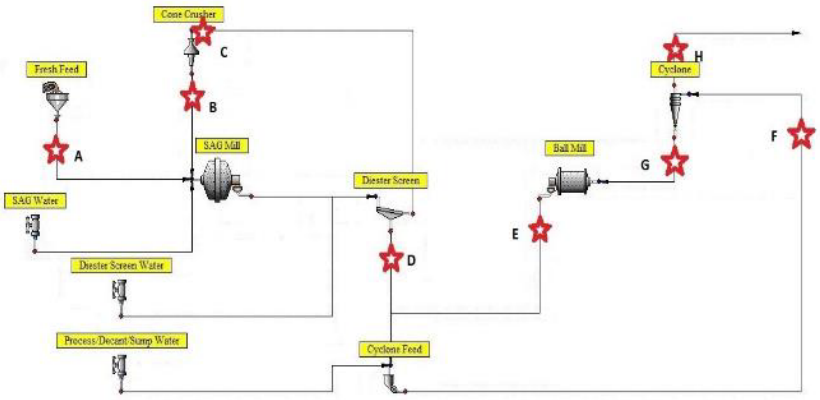

FIG 7 – Baseline circuit design and survey locations.

Mill consumables

The consumable model calibration is now described. SAG lifter wear was measured on-site, and this data along with the unworn design was used to calibrate the lifter/liner wear model, illustrated in Figure 8. A basic liner wear model was also developed.

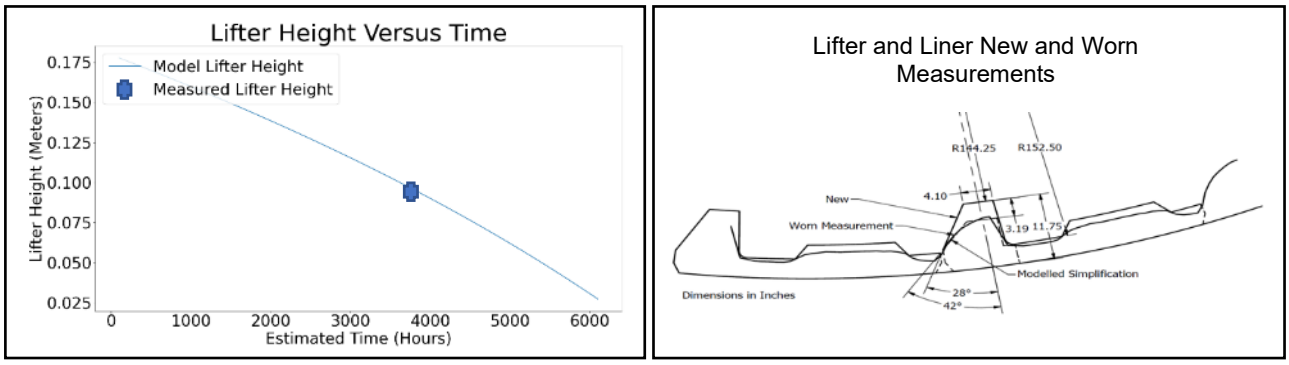

FIG 8 – Modelled and measured SAG liner wear.

The media wear model was also calibrated using a longitudinal record of media addition, Process Information (PI) data, and the Morrell power model (Morrell, 1993). The power model was used to estimate filling. Thus, the parameters required for the mechanistic wear model were established including speed, media filling etc. This calibration was performed at monthly increments, for two mostly constant blends. The resulting calibrated *k* value is a single parameter estimating the wear characteristics of the media-ore blend interaction (Hanhiniemi and Powell, 2019), and this was established by averaging the results over the longitudinal study, for both the ball and SAG mill.

Cip circuit calibration

As the specific batch gold dissolution and separate cyanide consumption tests were not available at the time, typical rate equation coefficients were used from literature from other gold ores for the modelling. The resulting modelled recoveries were compared to measured results in the baseline case, including the grind size, throughput, and circuit details, and were in good agreement. Thus, the same coefficients were used in scenario analysis. For cost modelling, as cyanide addition rates and oxygen concentrations were not altered, Unit Costs in this case study were assumed constant from the baseline. Figure 9 shows an example result of concentrations per tank.

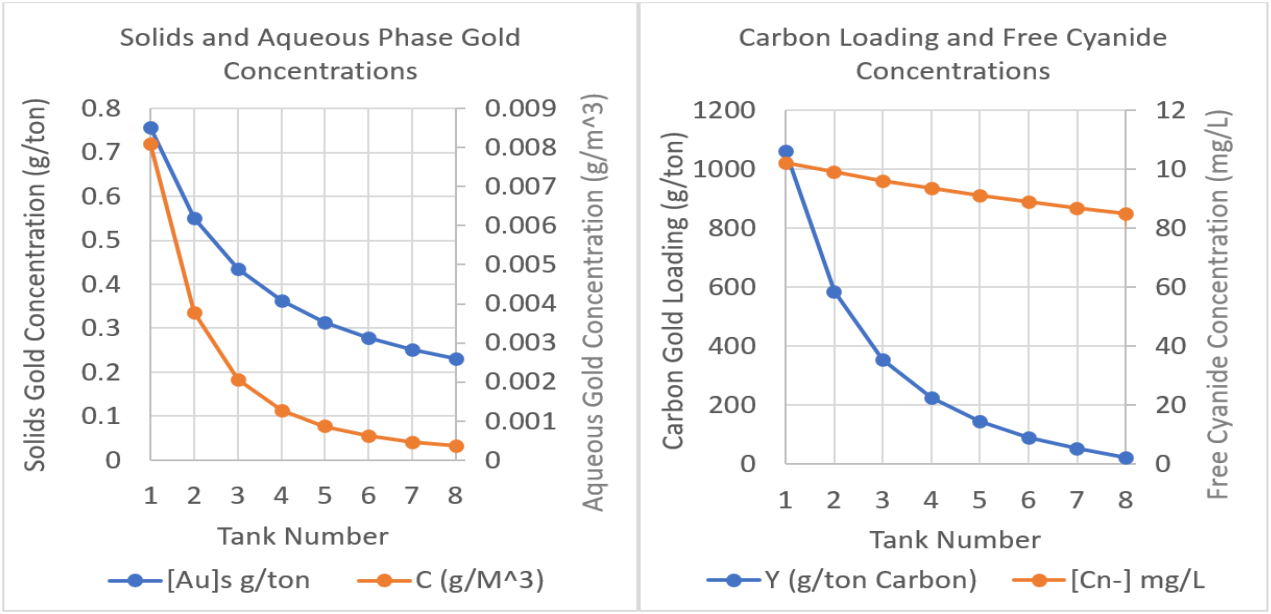

FIG 9 – Example modelled CIP circuit solids and aqueous gold concentration, carbon loading, and free cyanide concentration versus tank.

Overall simulator

Having calibrated the blasting, crushing, grinding, classification and CIP circuit an overall flow sheet for each blend and scenario was developed. This overall simulator also built-in the upgrade scenarios to be analysed in advance which are described in the next section. One example of the 25 simulations (five blends for each of the five cases – the Baseline Simulation and four upgrade scenarios) is illustrated in the Figure 10.

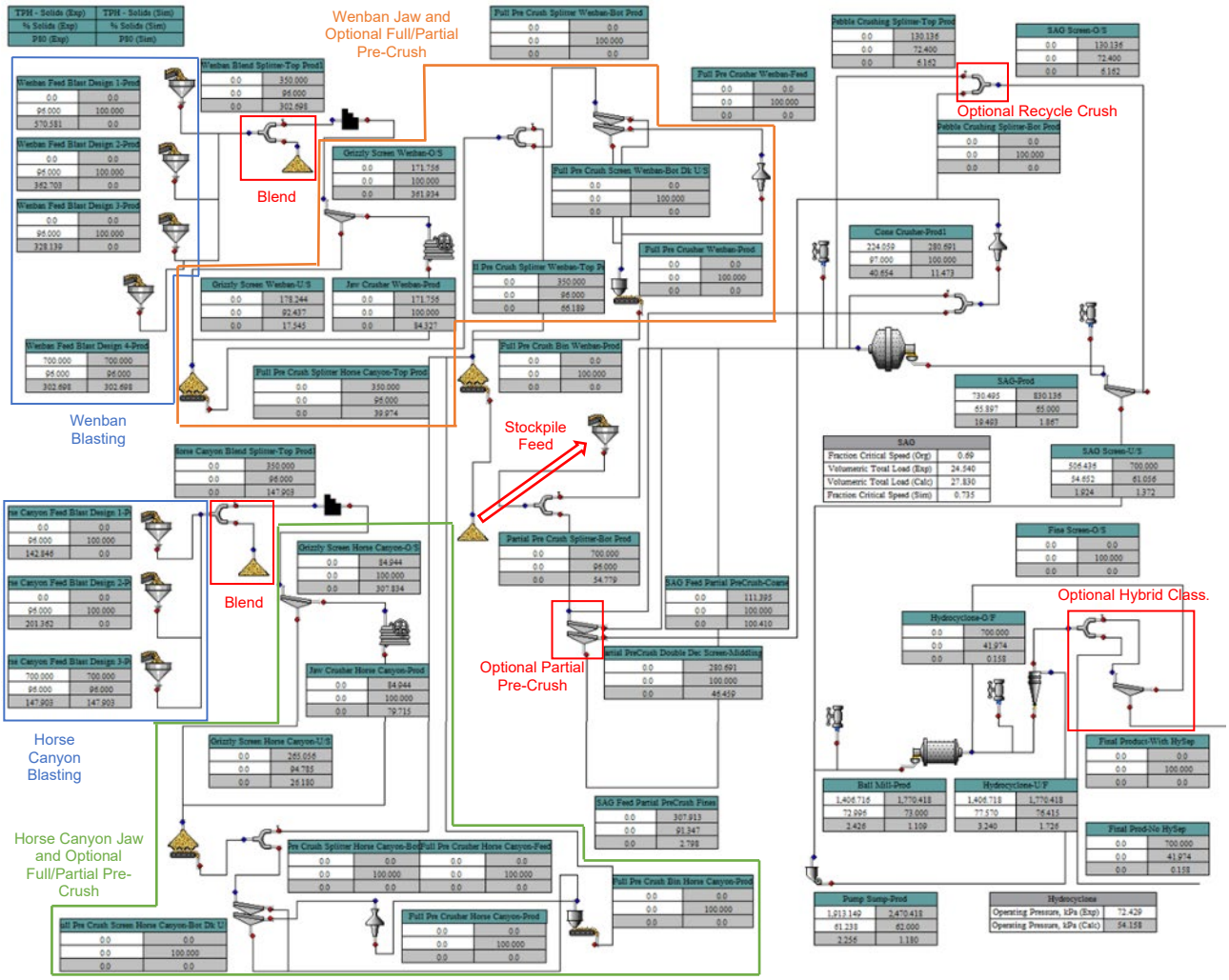

FIG 10 – Layout for multiple scenario assessment – Scenario 2 shown – 50 per cent Horse Canyon.

SCENARIO ANALYSIS OF UPGRADE OPTIONS

The overall simulator, as illustrated in Figure 10, was then used to model the following four scenarios. Note that these hypothetical scenarios are those of the authors', they do not indicate any plans or expansions by the site, and do not use actual mine plans, grades, or recovery results in determining financial results.

Scenario 1

Scenario 1's strategy was to employ full pre-crushing. A finer Wenban (WB) blast distribution was used as some material was too large, and a coarser Horse Canyon (HC) blast design was used as the rock quality was poor and the jaw and pre-crusher could tolerate a coarser feed. The media filling was increased in the SAG to operate as a Barely Autogenous Grinding (BAG) mill which is common in full pre-crush applications because of the finer feed. The SAG ball size was reduced. All scenarios reduced the jaw crusher CSS and grizzly aperture to 4 inches. A larger number of hydrocyclones

were employed and a coarser cut was targeted with vortex finder and spigot changes due to the relatively flat recovery curve with size.

Scenario 2

Scenario 2 employed an alternate pre-crushing design called partial pre-crushing where the problematic critical size is taken out as a middling steam and crushed, whereas the coarse stream is not crushed and is fed to the SAG to act as media. It also included selective blasting with a high intensity blast design including emulsion explosive with high Velocity of Detonation (VOD) to promote fines generation especially for the competent in the fines Horse Canyon. This was to debottleneck the ball mill with blends of increased Horse Canyon. SAG filling was increased, supported by the good composition provided by partial pre-crushing. Again, a larger number of hydrocyclones were employed and a coarser cut targeted with vortex finder and spigot changes with the relatively flat recovery-size curve.

Scenario 3

Scenario 3's strategy was to provide a low capital cost scenario. A finer WB and coarser HC blast design was employed which was the same design as Scenario 1. To reduce capital costs pre-crushing was not used. SAG filling was increased via grate design. The recycle crusher performance was improved to that expected from data across sites, but it remained the same size. Similar hydrocyclone changes were made.

Scenario 4

Scenario 4's strategy involved reducing the overall generation of material below the size required for liberation, and to comminute more in blasting and less in crushing and grinding. This was achieved by the same high intensity blast design in Scenario 2. No pre-crushing was employed, and SAG filling was increased with grate design. To reduce overgrinding of the fines, 'hybrid classification' using a hydrocyclone and fine screen was employed to sharpen the cut in classification in the ball mill circuit. This involved hydrocyclone modifications to produce a coarse cut, and then the use of fine screens to treat the hydrocyclone overflow. Screen underflow was the grinding circuit product, and overflow returned to the mill.

All flow sheets for these scenarios are shown in Figure 11.

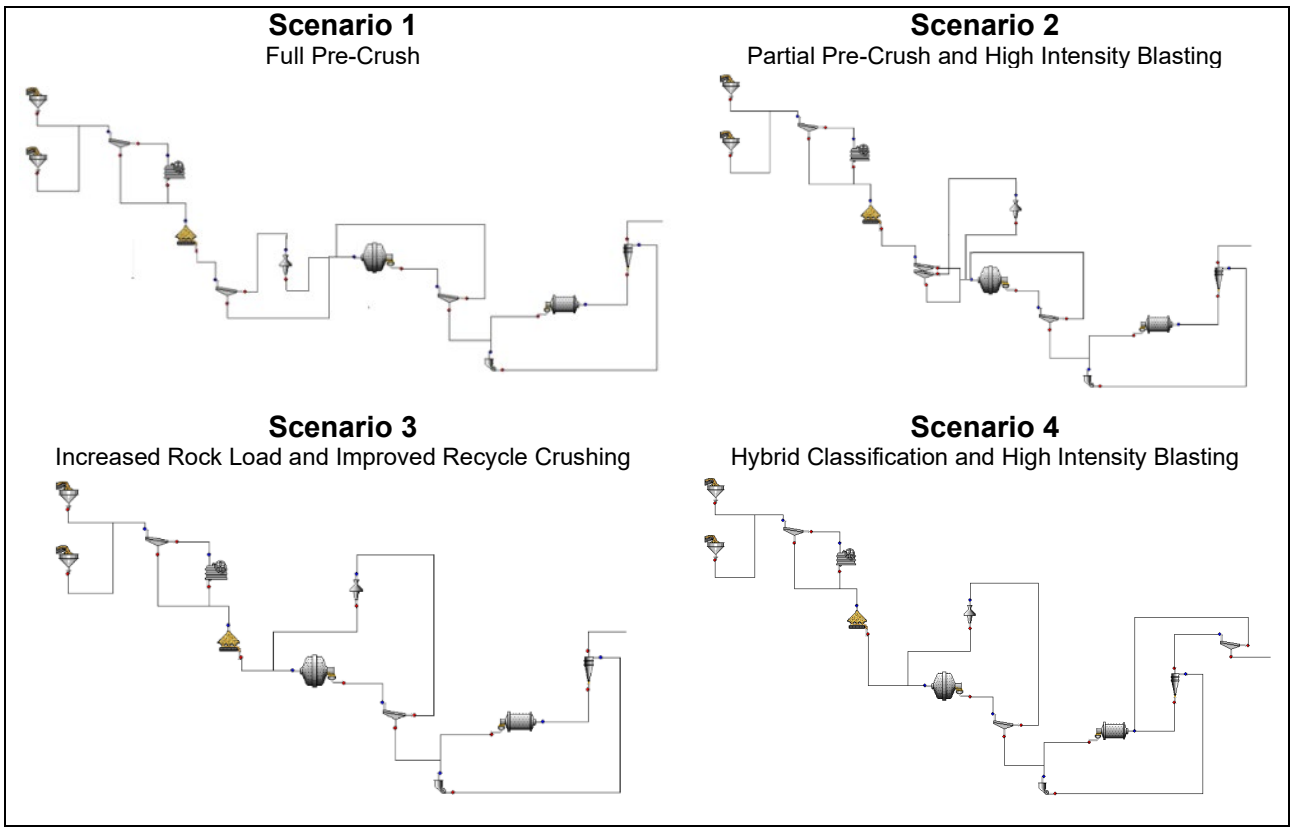

FIG 11 – Scenario flow sheets.

CASE STUDY RESULTS

Having calibrate the techno-economic models developed in this work, and simulated various potential upgrade scenarios, the outcomes are now presented. The interplay been ore component, circuit and equipment design and operation, and financial results can be seen. Figure 12 shows the throughput versus blend and scenario for the methods in this paper, 'Detailed Methods' (DM), and for 'Existing Methods' (EM) as previously described. Sensitivity Analysis was performed for an assumed throughput uncertainty of ±5 per cent as shown in the error bars, and this was carried through all technical and financial results. While Existing Methods don't predict product sizes, the same sizes were set from the Detailed Methods to provide direct comparison. Recovery modelling was also applied using the same methods.

Throughput

For Scenario 1, DM indicates no additional throughput for Horse Canyon, and only increase capital and operating costs. EM generally underpredict the performance with Wenban ore, and overpredict performance with Horse Canyon. This is as expected because the EM are unable to capture different breakage resistance and rates at different particle sizes in an ore component, and different size distribution-based constraints. They cannot model the emptying of the SAG mill and associated underutilisation of power. Compared to Wenban, Horse Canyon is softer in larger particle sizes, but is harder in the fine sizes. For this reason, it is ball mill constrained, and does not benefit much from the pre-crushing scenario compared to Wenban with little gains seen over the baseline. Wenban on the other hand was constrained by the recycle pebble crusher during the survey. The removal of pebble size material in the pre-crushing scenario greatly improves its performance in the SAG circuit, and it had a low BBWI and is processed at a high rate in the ball mill, yielding a marked improvement in throughput in Scenario 1 over the baseline. These effects are not captured by the EM, which predict less difference in throughput with blend.

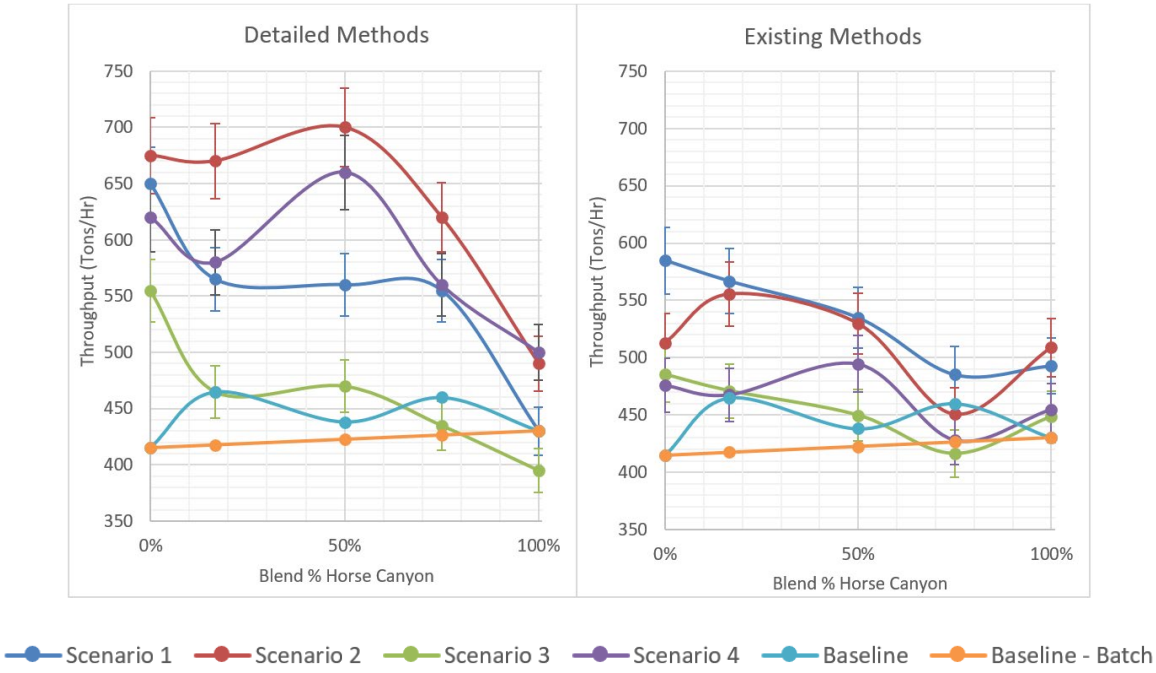

FIG 12 – Throughput versus blend and scenario – detailed and existing methods.

The EM most reliably predicts Scenario 1 of all cases, as this employs a blast design close to the original, and less significant departures occur between both approaches with respect to P80 size and size distribution overall.

Comparing Scenario 1 and 2 in Figure 12, the DM show a significant difference in performance with Scenario 2 providing higher throughput. It has a stronger nonlinear response with blend due to composition in the SAG mill. The EM also shown cannot discern the advantage of Scenario 2 over Scenario 1 in terms of throughput – and generally indicate erroneously Scenario 1 is the better upgrade. Again, EM cannot capture the mill filling and power utilisation improvement from bi-modal SAG feed preparation that improves Scenario 2 over 1, and EM cannot respond nonlinearly to blend. The benefit from fines generation in Scenario 2 blasting is underpredicted. with Kuz-Ram unable to model fines accurately. EMs also overpredict the performance on HC for the same reasons described above in Scenario 1.

The EM predict a much lower throughput in Scenario 2 and 4 than DM. This is because the single size blast model employed cannot predict the impact of increased fines generation with high intensity blasting. Scenario 2 promotes better throughput in pure Horse Canyon due to autogenous grinding in the SAG mill with improved composition, along with the fines generated in high intensity blasting using high VOD emulsion explosive and larger diameter blastholes.

The EM have a more linear response to blend. The high throughputs with synergistic blending in the DM for scenarios which contain a controlled SAG charge composition (Scenario 2 and 4) are not captured by the EM.

Scenario 3 achieves improvement in WB due to higher blast intensity and improve recycle crusher operation and SAG operation changes, but little improvement in other blends. EM fail to capture these improvements with a smaller improvement shown in Wenban.

DM in Scenario 4 indicate a good SAG composition promoting high throughput especially in middle bends, and overall improvement with high intensity blasting. Its performance in Horse Canyon is very good – even outperforming Scenario 2 which employs the same blast design – and this is due to hybrid classification which reduces overgrinding of this highly competent-in-the-fines ore. However, Figure 12 shows EM do not predict any significant improvement over the baseline due to their inability to predict fines generation in the blast, and failure to capture reduction in overgrinding in the ball milling with hybrid classification (due to a lack of full modelling of the particle size distribution).

Note that when constant product sizes are assumed in the EM, which would be the case when they are not set equal for comparison purposes with DM sizes as EM do not predict product size, the

response to blend is linear. EM fail to capture the non-linearity with blend, and this is the case in all scenarios. For further detail and verification of the Detailed Methods ability to capture response with blending and charge composition in the grinding mills, as referenced above, refer to Hanhiniemi and Powell (2022).

Unit costs

The individual Unit Costs versus blend are illustrated in Figure 13 for the DM. There are no nonlinear effects in drilling and blasting, however there are in all other unit processes. In drilling and blasting, Wenban rich blends have a higher cost due to the smaller burdens and spacings, and Scenarios 2 and 4 have higher costs due to higher intensity blasting and the use of more expensive emulsion explosive.

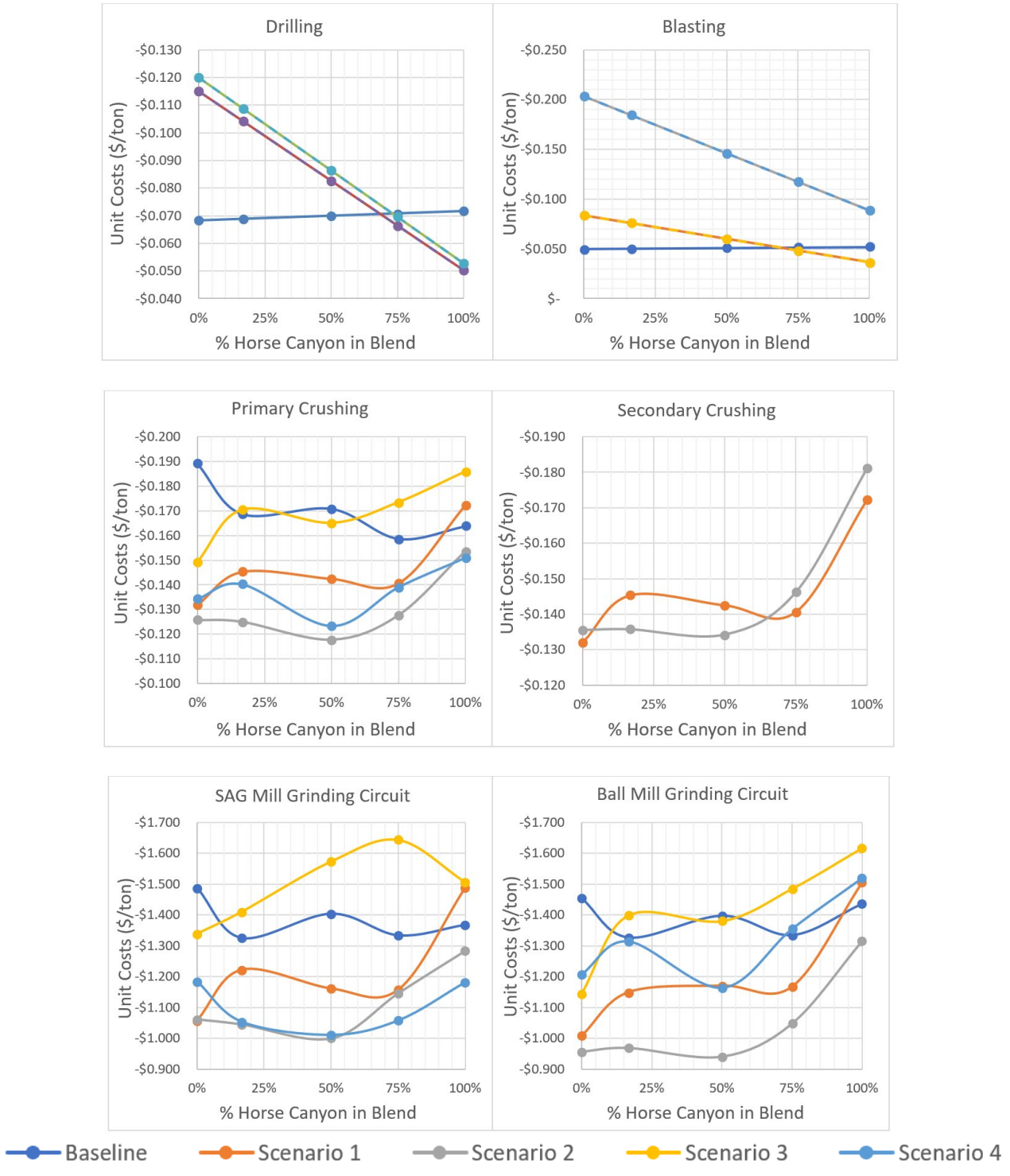

FIG 13 – Unit costs versus scenario and blend – detailed methods.

In crushing and grinding, Scenario 2 and 4 Unit Costs are dish shaped due to the improvements in throughput with synergistic blending. Note this is not prominent in the EM, where they were also higher due to the failure to capture blast design improvements in throughput.

Marginal NPV and operating cash flow

The marginal NPV for detailed and existing methods is presented here under constant metal price, term, strip ratio, discount rate, and grade. Note that these conditions, while reasonable for typical operations, do not closely represent those of the Cortez operation. The results for a five year term are repeated below. Differences between EM and DM were found to be profound, as illustrated in Figure 14.

For DM high intensity blast and partial pre-crush (Scenario 2) is high performing across all blends and is the second-best scenario for HC due to SAG charge composition and blast design promoting fines generation. Scenario 4 is also high performing and provides the best results for HC ore that benefits little from pre-crushing. Scenario 4 performs well on HC as it also avoids overgrinding of the highly competent-in-the-fines Horse Canyon, and the blast design promotes fines. Negative values occur in some upgrades and blends (eg full pre-crush Scenario 1 applied with Horse Canyon incurs added capital and operating costs but with no gain). Scenario 1 offers an improvement in all blends except Horse Canyon. Batch process without blending or the ore components results in a significant loss in value even with no other changes (note here feed grade of components were similar, for dissimilar grades the result may vary due to recovery effects). The best upgrade depends on ore blend and mine plan. The bars show the sensitivity analysis results for ±5 per cent throughput uncertainty.

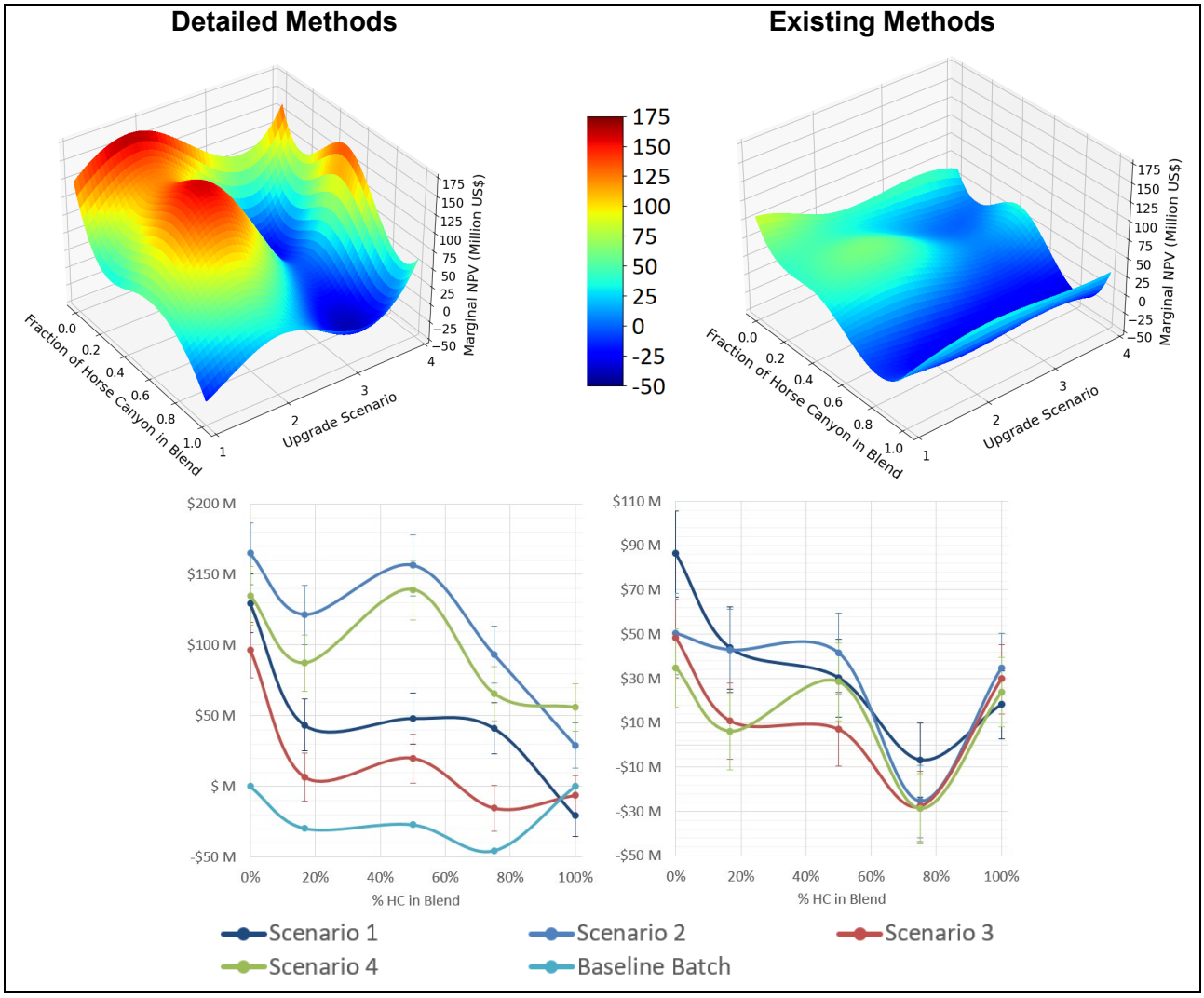

FIG 14 – 5 year marginal NPV versus blend and scenario – detailed and existing methods.

Comparing marginal NPV with throughput in DM, throughput is a strong predictor of economic performance rank among scenarios but not always a proxy. Scenario 1 has higher throughput in WB, but lower marginal NPV compared to Scenario 4 due to high costs of full pre-crush and BAG operation.

In EM the marginal NPV is grossly underestimated from the high intensity blasting cases. Little difference is capture between scenarios and response with blend is also linear – varying nonlinearly only due to product size being applying consistently in DM and EM. Scenario 2 clearly outperforms 1 in DM; however, EM shows little differentiation.

Operating cash flow per ton of ore

The before tax operating cash flow per ton of ore is shown in Figure 15, again at constant gold price, strip ratio, and grade. This can be thought of as the value of each ton of ore. In DM the value of the ore responds with blend and scenario, in EM however there is little response between scenarios, and the response with blend is more linear. The DM allows for clearer delineation of scenarios which can be implemented to increase the value of the ore, including Scenario 2 and 4. In EM no delineation between scenarios can be made outside this ±5 per cent throughput uncertainty in 0 per cent, 17 per cent and 75 per cent HC blends. In DM the delineation is more significant, with higher value scenarios identified in every blend even under the throughput uncertainty applied.

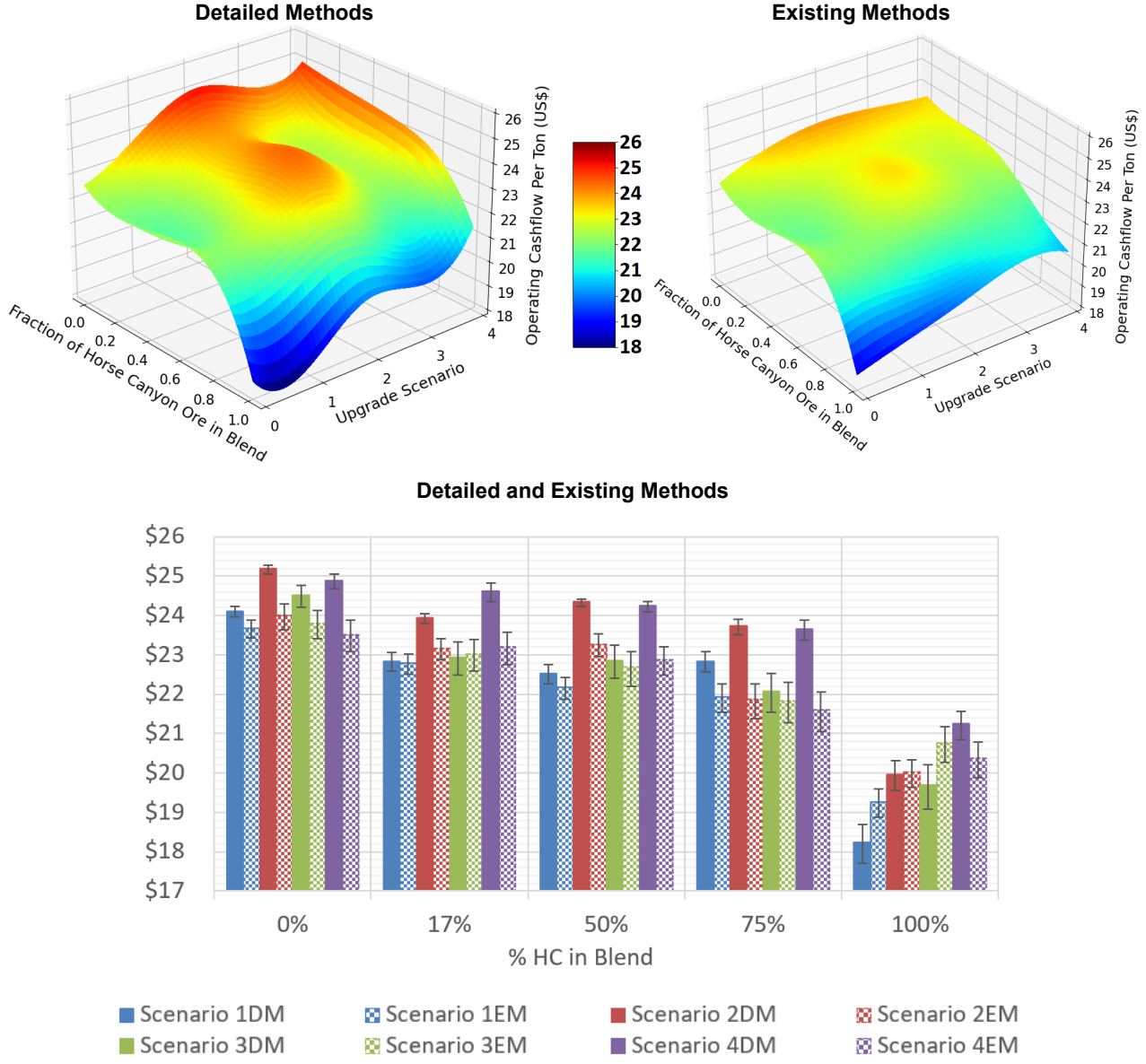

FIG 15 – Operating cash flow per ton versus scenario and blend – detailed (DM) and existing methods (EM).

Circuit upgrade and blending with varying ore competence-by-size

Comparing Scenario 3 and 1 directly examines the performance of full pre-crushing with varying blend characteristics, as the blast designs are the same. Horse Canyon is soft in the coarse sizes, but more competent than Wenban in fine sizes. Figure 12 Detailed Methods show full pre-crushing of the Wenban rich blends improves throughput, but with full Horse Canyon no improvement is achieved, as its soft-in-the-coarse material is easily broken down in the SAG mill without pre-crushing and it is ball mill constrained. The SAG mill composition in Scenario 3 assists improvements in middle blends, as some coarse material improved mill filling and autogenous grinding over Scenario 1, which however still produces a higher throughput. In Existing Methods these effects are not captured, and Scenario 1 is shown to have a better throughput than 3 with Horse Canyon, and response with blend is much more linear.

Per Figure 14 the consequence of these varying competence-by-size effects are that full pre-crushing either diminishes or adds no value (NPV) for Horse Canyon. For Wenban and 50:50 blends no value is created over Scenario 3 either, due to the loss of SAG mill charge composition narrowing the difference in throughput, and due to the additional costs of pre-crushing. For Operational Cash flow Per Ton (Figure 15), there's no difference between Scenario 1 and 3 outside the assumed uncertainty on throughput for 0 per cent, 17 per cent and 50 per cent, with a small improvement in 75 per cent HC with full pre-crushing. For Horse Canyon the pre-crushing upgrade reduces the value of the ore compared to Scenario 3.

As shown in Figure 14 value was created with blending, as opposed to batch processing, due to synergistic blending performance resulting from competence-by-size effects.

Comparing hybrid classification with partial pre-crushing

Comparing Scenario 4 and 2 examines the performance of partial pre-crushing versus hybrid classification. For throughput, partial pre-crushing improved performance at 17 per cent and 75 per cent HC with other blends having equal performance to Hybrid classification when including uncertainty. Considering operating cash flow per ton or ore, Hybrid Classification outperformed partial pre-crushing at 17 per cent and 100 per cent HC, with other blends being equal under the uncertainty. It was found that reduced overgrinding was achieved with hybrid Hydrocyclone-Fine Screen classification at little additional Unit Cost, which explains the improved performance especially considering 100 per cent HC which tended to be ball mill limited due to its competent-in-the-fines characterisation. Thus, hybrid classification improved the value of the ore over partial pre-crushing for some blends, which itself was an improvement on full pre-crushing. Both scenarios had the same marginal NPV when throughput uncertainty is included.

Existing Methods did not identify any difference in the operating cash flow per ton, and erroneously predicted the partial pre-crushing would outperform the hybrid classification scenario throughput at 100 per cent HC due to a failure to respond to competence-by-size characteristics in Scenario 2, and classification improvements in Scenario 4.

Hybrid classification and high intensity blasting performance

Comparing Scenario 4 and 3 examines the effectiveness of hybrid classification combined with high intensity blasting. When including the throughput uncertainty, Detailed Methods show the hybrid classification and high intensity blasting scenario yields improvements in operation cash flow per ton in all blends except Wenban, whereas Existing Methods show no difference. Also shown in Detailed Methods are significant improvement across all blends in marginal NPV (5 year) achieved with the hybrid classification and high intensity blasting scenario over that achieved with Scenario 3, whereas Existing Methods show no improvements in any blend (except for Wenban where throughput uncertainties just overlap). Existing Methods also show no improvement in throughput for any blend considering assumed uncertainty, whereas Detailed Methods show significant improvement across all blends for Scenario 4 over Scenario 3. This indicates that Hybrid Classification with high intensity blasting improves the value of the operation. Existing Methods fail to capture this due to a lack of response to improved classification. This lack of response is due to a failure to model full PSD throughout the circuit, and an inability to capture a reduction in overgrinding in the ball mill circuit with hybrid classification. Existing Methods also lack response to improved fines generation in the blast, again due to modelling based on a single P80 size.

Full pre-crushing versus partial pre-crushing

The performance of full pre-crushing (Scenario 1) versus partial (Scenario 2) will now be compared. Unfortunately, these cases did not employ the same blast designs to allow a more direct comparison, with Scenario 2 employing a higher intensity blast design and a different explosive (emulsion). Insights can still be gained however, by comparing these scenarios and the differences between existing and detail methods.

Detailed Methods show a significant difference in performance with Scenario 2 providing higher throughput, and this remains the case for all blends except Wenban when the uncertainty is included. A stronger nonlinear response with blend is present in Scenario 2 due to a good composition in the SAG mill being achieved allowing for the synergistic blending performance identified in measurement to manifest. The Existing Methods cannot discern the advantage of Scenario 2 over Scenario 1 in terms of throughput, with no difference identified considering the uncertainty except for Wenban where Scenario 1 provides higher throughput. Existing Methods cannot respond nonlinearly to blend, and the fines generation in Scenario 2 blasting is underpredicted by the unmodified Kuz-Ram modelling. Existing Methods also fails to identify the SAG mill ore emptying that occurs in full pre-crushing, and overpredicts the performance of HC.

The SAG Composition SSE Model was also employed to validate the JKSimMet® results. It indicated that Scenario 1's performance was likely overestimated as comparted to Scenario 2, due to JKSimMet®'s inability to respond to SAG inefficiencies that occur with low ore volumetric proportions in the charge. This is further described in Hanhiniemi and Powell (2022).

Note that when constant product sizes are assumed, which would be the case in the use of Existing Methods as size is not predicted, the EM response to blend is linear. Existing Methods fail to capture the non-linearity with blend.

CONCLUSIONS

In conclusion a techno-economic model of comminution in metalliferous mines has been developed and summarised in this paper, which is able to capture the interplay between ore characterisation, blending, machine and process design and operating choices, and resulting financial performance. The generalised approach was then demonstrated with application to a case study site. Scenario analysis of potential upgrade options was then conducted employing the modelling introduced. This was then repeated using methods typically employed for techno-economic assessment, referred to as Existing Methods.

The results of the new and existing methods were then compared. It was established that improved fidelity and utility was achieved with the new methods, including:

- Detailed Methods captured synergistic blending effects arising from varying competence-by-size and nonlinearity of blending of ore types. Existing Methods failed to capture this
- Detailed Methods captured and responded to changes in the fines generation know to occur with alterations in blast design, whereas the Existing Methods had unrealistic fine size distributions and insufficient response
- Detailed Methods were able to capture and respond to SAG/Ball bottleneck changes with blend and feed distribution. They also captured responses in SAG mill ore-media composition and associated impacts on transfer size, power utilisation, and cost know to occur. The Existing Methods failed to do this with the same fidelity
- Unit Costs in the Detailed Methods were shown to respond differently to Existing Methods because of throughput differences, and with operating conditions of the equipment. An example includes SAG mill media and liner life response in the Detailed Methods with operating conditions. These changes were not captured in Existing Methods
- Existing Methods failed to capture the benefits from changes in particle size distribution, such as the sharper classification achieved in Hybrid Classification. The benefits of these were however captured in the Detailed Methods through modelling full particle size distributions throughout the circuit, which also supported constraint and bottleneck identification

These differences in the fidelity and response between the two methods was demonstrated to have a profound impact on upgrade choice, marginal NPVs, and operating cash flow per ton, with the Detailed Methods providing improved understanding of the techno-economic performance of upgrade or operational choices.

It was also demonstrated that a comprehensive techno-economic model of the comminution process allowed for comparison of very different upgrade choices, such as hybrid classification and high intensity blasting versus pre-crushing. Wide integration of Unit Processes supported holistic assessments to be made, such as in drilling and blasting trade-offs with crushing and grinding in 'Mine-to-Mill' studies. The higher level of detail was generally applied across this modelling approach; in some sites specific variables will be significant to performance, and in others those same variables may not, but the detailed modelling provides for a response when required. Technical modelling was also improved by capturing constraints and consumable response. Novel circuit designs including partial mid-size crushing and hybrid classification showed promise and should be considered as potential upgrades. Modelling indicated high intensity blasting was high performing financially.

Finally, having observed how these new methods can provide improved utility and fidelity of techno-economic performance, it is worthy to note the wider impact on mine planning. In this study the mine plan was fixed, however with some scenarios showing an improved ore value, it is envisaged that this improved modelling could have a further increased impact and value when its results are iterated back into the mine planning process. These new methods should be employed in the financial optimisation of existing plants, and for improved capital budgeting decisions.

ACKNOWLEDGEMENTS

The authors would like to thank those also involved in the survey including Dr Marko Hilden, Dr Vlad Jokovic, the Nevada Gold Mines Cortez team and the JKMRC. Nevada Gold Mines is also thanked for their permission to publish. This work was supported by the Australian Government Research Training Program.

REFERENCES

Apelt, T A, Asprey, S P and Thornhill, N F, 2001. Inferential measurement of SAG mill parameters. *Minerals engineering,* 14, 575–591.

Ballantyne, G, Mainza, A and Powell, M, 2015a. Using comminution energy intensity curves to assess efficiency of gold processing circuits. *World Gold.*

Ballantyne, G, Peukert, W and Powell, M, 2015b. Size specific energy (SSE)-Energy required to generate minus 75 micron material. *International Journal of Mineral Processing,* 136, 2–6.

Bosman, J, Morgan, P and Cunningham, R, 2019. Estimating Ultra Fine Screening Performance And Efficiency. *SAG Conference.* Vancouver.

De Andrade Lima, L R P and Hodouin, D, 2005. A lumped kinetic model for gold ore cyanidation. *Hydrometallurgy,* 79, 121–137.

De Andrade Lima, L R P, 2007. Dynamic simulation of the carbon-in-pulp and carbon-in-leach processes. *Braz. J Chem. Eng,* 24, 623–635.

Evertsson, C, 2000. Cone Crusher Performance.

Gokhale, B V, 2011. *Rotary drilling and blasting in large surface mines*, Boca Raton, Fla.

Grimes, A and Keenan, C, 2015. JKSimMet Version 6.1 User Manual. In: R Lasker (ed.) *Steady State Mineral Processing Simulator.* JKTech Pty Ltd.

Hanhiniemi, J and Powell, M, 2019. Techno-Economic Modelling of Tumbling Mills: Economic Design and Operation. *International Semi-Autogenous Grinding and High Pressure Grinding Roll Technology,* 2019 Vancouver.

Hanhiniemi, J and Powell, M, 2022. Multicomponent Modelling of Ore Blending in Grinding Circuits: A New Model and Case Study. *Proceedings of the International Mineral Processing Council Asia-Pacific*, pp. 135–152 (The Australasian Institute of Mining and Metallurgy: Melbourne).

Hilden, M, Reyes, F and Yahyaei, M, 2020. The JKMRC Mill Filling Prediction Tool. Available: https://www.youtube.com/watch?v=2633RWfz_sc [Accessed: 9/6/2021].

JKMRC, 1998. Optimisation of Mine Fragmentation For Downstream Processing AMIRA Project P483.

JKMRC, 2002. Optimisation of Mine Fragmentation For Downstream Processing AMIRA Project P483A.

Kanchibotla, S, Walter, V and Morrell, S, 2001. Modelling Fines in Blast Fragmentation and Its Impact on Crushing and Grinding.

Morrell, S, 1993. *The Prediction of Power Draw in Wet Tumbling Mills.* University of Queensland.

Morrell, S, 2001. Modelling of the Load-Throughput Response of AG/SAG Mills. *AMIRA P9M Project Fourth Progress Report.* Julius Kruttschnitt Mineral Research Centre.

Napier-Munn, T J, Morrell, S, Morrison, R D and Kojovic, T, 1996. *Mineral comminution circuits: their operation and optimisation*, Julius Kruttschnitt Mineral Research Centre.

Ntiamoah, K, Rader, L, Yalcin, E, Powell, M, Jokovic, V, Hilden, M and Hanhiniemi, J, 2020. The influence of ore blending on mill throughput – Cortez mine case study. *Nevada Mineral Processing Division Conference.* Reno.

Powell, M S, Mainza, A N, Hilden, M and Yahyaei, M, 2015. Full Pre-Crush To SAG Mills – The Case For Changing This Practice. *SAG Conference, 2015* Vancouver.

Rose, H E and English, J E, 1967. Theoretical Analysis of the Performance of Jaw Crushers. *Institution of Mining and Metallurgy*, 32–43.

Runge, I R, 1998. *Mining Economics and Strategy*, Littleton: SME.

Shi, F, 2016. An overfilling indicator for wet overflow ball mills. *Minerals engineering,* 95, 146–154.

Stange, W, 1991. The optimization of the CIP process using mathematical and economic models. *Minerals engineering,* 4, 1279–1295.

Mine-to-Mill optimisation at Mont Wright

J Hill[1], R Ouellet[2], R Deslias[3], I K Kapinga[4], P O Devin[5], H Achache[6], W Valery[7], R Hayashida[8], T Farmer[9], B Bonfils[10] and K Duffy[11]

1. Director Mining Services, ArcelorMittal Exploitation minière Canada, Fermont (Québec) G0G 1J0, Canada. Email: jonathan.hill@arcelormittal.com
2. Drill and Blast Engineer, ArcelorMittal Exploitation minière Canada, Fermont (Québec) G0G 1J0, Canada. Email: raphael.ouellet@arcelormittal.com
3. Drill and Blast Junior Engineer, ArcelorMittal Exploitation minière Canada, Fermont (Québec) G0G 1J0, Canada. Email: romainjacky.deslias@arcelormittal.com
4. Geotechnical Engineer, ArcelorMittal Exploitation minière Canada, Fermont (Québec) G0G 1J0, Canada. Email: iriskalala.kapinga@arcelormittal.com
5. Head of Process Department, ArcelorMittal Exploitation minière Canada, Fermont (Québec) G0G 1J0, Canada. Email: pierolivier.devin@arcelormittal.com
6. Principal Process Engineer, ArcelorMittal Exploitation minière Canada, Fermont (Québec) G0G 1J0, Canada. Email: hamza.achache@arcelormittal.com
7. Global Director – Consulting and Technology, Hatch, Brisbane Qld 4000. Email: walter.valery@hatch.com
8. Senior Consultant Drill and Blast, Hatch, Belo Horizonte MG 30360–740, Brazil. Email: rodrigo.hayashida@hatch.com
9. Mining Engineer, Hatch, Brisbane Qld 4000. Email: thomas.farmer@hatch.com
10. Comminution Consultant, Hatch, Brisbane Qld 4000. Email: benjamin.bonfils@hatch.com
11. Senior Process Engineer, Hatch, Brisbane Qld 4000. Email: kristy.duffy@hatch.com

ABSTRACT

In 2019, ArcelorMittal Exploitation Minière (AMEM) and Hatch conducted a Mine-to-Mill (M2M) integration and optimisation project at Mont Wright (MW) iron ore complex in Canada. The aim was to increase production with little or no capital expenditure. In 2020 and 2021, the recommendations resulting from the M2M project were implemented by MW with assistance and refinement from Hatch.

Throughout the M2M project, site-specific models of the mine and plant (blast fragmentation, crushing, grinding, gravity separation) were developed and calibrated based on historical data, and audits and surveys carried out by MW and Hatch personnel. The models were integrated and used to simulate and determine optimised strategies across the entire value chain from the mine through to the plant, to increase production while minimising overall costs. Optimisation strategies were trialled and refined during implementation, accounting for the limitations encountered in the mine and plant.

During the project, ore domains were defined based on rock structure and strength, and blasting guidelines were developed for each to improve Run-of-mine (RoM) fragmentation for production blasts across multiple pits and reduce feed variability. Crushing and grinding simulations were conducted to assess the impact of finer RoM fragmentation and to optimise operating strategies for the finer feed. Simulations indicated an expected throughput increase of 7 to 26 per cent for the different grinding lines depending on the ore domain. One of the main recommendations in the plant was conversion of Mill 7 from Autogenous (AG) to Semi-Autogenous (SAG) grinding to fully utilise the available power, capitalising on the finer fragmentation from the mine and increasing throughput.

Implementation of the new operating strategies began in late 2020, including additional ore characterisation, refinement of domain definition, establishment of updated blasting guidelines to accommodate operational constraints, and conversion of Mill 7 to SAG (12 per cent ball charge). A composite (rubber/steel) mill liner design was also investigated to allow a higher ball charge in Mill 7. Throughput improvements of up to 10 per cent (overall, for all ore types) have been achieved to date and further benefits are expected when the refinements to blasting guidelines and all recommended M2M operating strategies are fully implemented.

INTRODUCTION

The AMEM MW iron ore complex is located in Quebec, Canada. The truck and shovel open pit mining across multiple pits feeds ore to a processing plant consisting of crushing, grinding, and gravity concentration. The processing plant currently consists of two gyratory crushers, six 32-foot AG mills and one 36-foot SAG mill in closed circuit with two stages of screening. The screen undersize is processed in three stages of spiral separation: rougher, cleaner, and re-cleaner.

In 2019, AMEM and Hatch conducted a M2M integration and optimisation project at MW, aiming to increase production with little or no capital expenditure. Hatch's approach to M2M integration and optimisation involves a structured methodology involving ore characterisation, detailed audits and surveys, model development, and integrated simulations to develop optimisation strategies (Valery, Duffy and Jankovic, 2019). All components are integrated to assess the impact of changes in each area across the entire value chain. Hatch specialists have implemented this structured approach to M2M at many sites around the world to improve production and minimise overall costs (Valery and Samuel, 2012; Valery *et al*, 2016, 2018a, 2018b, 2019; Valery, Duffy and Jankovic, 2019; Valle and Duffy*,* 2014; Tokarenko *et al*, 2017; Evangelista *et al*, 2021). This methodology is tailored to each operation, accounting for the specific conditions and limitations present.

Site-specific models of the mine and plant (blasting, crushing, grinding, and gravity separation) were developed and calibrated based on historical data and surveys carried out by MW and Hatch personnel. The models were integrated and used to assess impacts and benefits downstream in the plant from changes made in the mine and determine optimised strategies from mine to plant to increase production while minimising overall costs. Ore domains were defined based on the varying ore characteristics on-site, drill and blast guidelines were developed to account for these characteristics, and recommendations were provided for adjustments in plant operating strategies to maximise production. The recommendations from this project were implemented in 2020 and 2021, resulting in increased iron ore concentrate production.

METHODOLOGY

To successfully conduct the M2M project, the entire operation was investigated to form a strong understanding of the conditions, constraints, and any potential for improvement (Duffy and Valery, 2017; Valery, Duffy and Jankovic*,* 2019). *In situ* ore characteristics such as strength, structure, and mineralogy influence the performance of blasting and downstream processing. Therefore, a strong understanding of the ore characteristics is required to determine their impact on each stage of mining and processing, and the interactions between stages.

Existing ore characterisation, mining, and processing practices were reviewed, samples were collected for characterisation and breakage testing, audits were conducted of drill and blast operations, and a full plant survey was carried out. Surveys were conducted in the plant with ore fed from audited blast polygons to form a link between the ore properties and the resulting outcomes in terms of blast fragmentation and downstream processing performance. All the collected data was used in conjunction with the historical operating data and Hatch's extensive industrial database to develop the site-specific models, which were then used in simulations to evaluate opportunities for improvements in the mine and plant.

Ore domains were defined based on the range of rock strength and structure present across the multiple pits at MW. The Hatch blast fragmentation model was calibrated to the known conditions of an audited blast and used to define optimised blast designs for each of these ore domains to improve fragmentation for downstream processes (Valery *et al,* 2007, 2001; Isokangas *et al,* 2012; Bonfils *et al,* 2021). Integrated simulations were carried out with crushing and grinding models to assess the impacts of finer RoM fragmentation and to optimise operating strategies in the plant.

RESULTS AND DISCUSSION

Ore characterisation

The existing ore characterisation at MW focused on lithological descriptions of the rock mass and was being used to develop blasting criteria to provide sufficient size reduction for loading efficiency, equipment handling, and crusher feed constraints. However, the efficiency and throughput of

downstream comminution circuits can be improved by producing an optimised particle size distribution in the mine for plant feed, which depends on the operating mode of the comminution circuit (AG or SAG). The optimised RoM fragmentation for the AG and SAG mills was investigated in the M2M project, accounting for the coarse fragmentation impacting load and haul and crushing (influenced by rock structure) and the fine fragmentation impacting grinding (influenced by rock strength).

A large amount of ore characterisation data was already available, including geotechnical test results on drill core samples, joint and discontinuity mapping using photogrammetry, Point Load Testing (PLT) data, and laboratory rock strength tests including Uniaxial Compressive Strength (UCS). In terms of comminution testing, only a limited number of JK Drop Weight Testing (DWT) results were available. These comminution breakage characterisation tests are used in developing the comminution models in integrated analysis with the blast fragmentation model to optimise fragmentation.

By understanding the ore properties considering the impact of hardness in terms of not only blast fragmentation, but also comminution energy requirements, the overall operation can be optimised in terms of production while minimising overall costs. More energy is applied in harder and more structurally massive ores to alleviate the energy requirements downstream, while less blasting energy is applied in softer or more naturally fractured domains where the energy is not required for downstream performance improvements.

To assess the current conditions on-site in terms of ore characteristics, as well as to measure the specific properties encountered during the audits and surveys in the mine and plant, additional samples were collected by Hatch for testing. This included PLT to determine the Point Load Index (PLi, Is50), SMC testing to determine Drop Weight Index (DWi) and the Axb parameter, and Bond Ball Mill testing to determine the Bond Ball Work Index (BBWi). Hatch recommended that additional ore characterisation was conducted to map the deposit spatially in terms of strength and structure, at a higher resolution to inform blast design. PLT was recommended to determine rock strength, as this is a fast, low-cost method to collect a large number of samples that can be tested on-site, and correlated with other hardness and breakage parameters such as UCS and Axb. In terms of rock structure, Hatch recommended the use of photogrammetry for structural analysis, which was already implemented on-site at MW for the purposes of geotechnical stability assessments. Photogrammetric methods enable a fine resolution of structural data to be analysed, at a local level that influences coarse blast fragmentation in addition to global structural conditions impacting wall conditions and stability.

Ore domains were initially defined during the M2M project based on the range of rock strength and structure present across all ore sources at MW. These were later refined during implementation as further characterisation was conducted by MW personnel. This provided an overview of the variability in strength and structure within each active pit on-site. Rock strength and structure both varied significantly depending on region or location across the multiple pits on-site. A summary of the refined ore domain definitions in terms of strength and structure is shown in Figure 1.

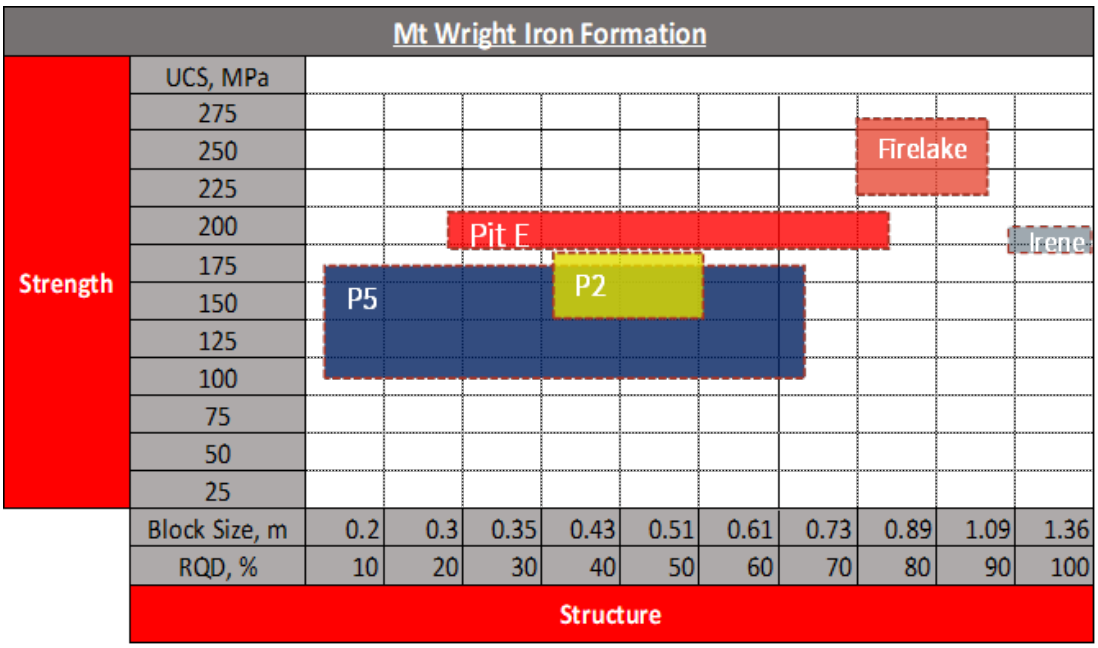

FIG 1 – Ore domain definition at Mont Wright.

Fragmentation and drill and blast optimisation

Optimisation of blasting requires accurate measurement of the resulting fragmentation. Blast fragmentation was measured using image analysis with SPLIT Desktop™ (Split) of photos collected at post blast muck piles, as well as trucks dumping RoM ore to the primary crushers. All image analysis systems used for measuring fragmentation cannot accurately measure fines content (-10 mm), as this material is often below the surface of muck piles, and is too small to be defined accurately by software delineation in the analysis. To overcome this, Hatch and MW conducted a calibration of the fines using sieved material from a primary crusher product belt cut sample. As the primary crusher acts mostly on the coarse particles in the feed, the content of fines in the primary crusher product provides a good indication of the fines generated during blasting.

A large degree of blast fragmentation variability was observed across all MW pits from the calibrated fragmentation measurements. The mean fragmentation for the trucks dumping RoM ore to the primary crusher during the survey, as well as the envelope describing the variability in fragmentation for the audit is shown in Figure 2. This fragmentation analysis was conducted on a representative sample of trucks dumping to the crusher, however for this small subset of all trucks loaded from the audited blast polygon, variations in the blast 80 per cent passing size (P80) and fines content (-10 mm) of up to 300 mm and over 20 per cent respectively were observed. This indicated the potential to improve downstream performance and stability by tailoring the blast design to both the strength and structure of the ore. With the application of different blast intensities for each domain according to the *in situ* characteristics, the variation in resulting fragmentation can be minimised.

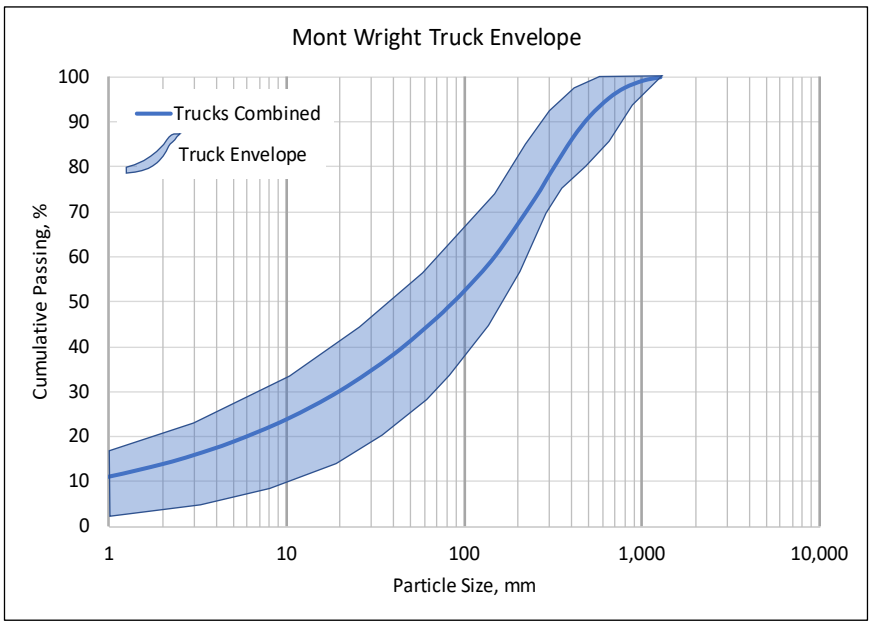

FIG 2 – Mean fragmentation and envelope of variability for trucks dumping to the primary crusher.

This measured fragmentation was used to calibrate the blast fragmentation model, alongside the measured ore characteristics and audited blast polygon conditions. The Hatch Blast Fragmentation Model is sensitive to the ore characteristics and their variability, explosive properties and performance, and blast design and implementation. Following model calibration, base cases were developed for each of the defined ore domains, based on the typical blasting practices on-site at the time. The blast fragmentation model was then used to simulate changes in blast design for each ore domain and determine optimum fragmentation for each of the different ore types.

The optimised blast guidelines developed and proposed for MW specify an appropriate level of blast energy for each ore type, with more energy applied in the harder and blockier domains, and less energy in the softer, more naturally jointed and fractured domains. A summary of the improved fragmentation from the initial blast guidelines for each domain in comparison to the audited base case RoM fragmentation is shown in Figure 3.

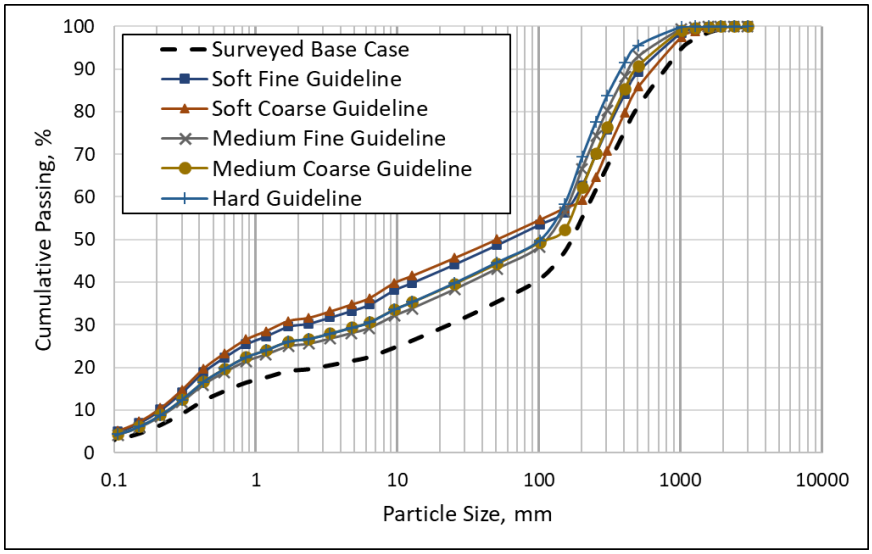

FIG 3 – Comparison of base case blast fragmentation with guideline blast fragmentation in each domain.

By applying the required blast energy to each domain, fragmentation variability can be reduced, and downstream processing performance improved. This can be carried out while avoiding excessive costs and potential damage in the mine that could occur by indiscriminately increasing blast intensity

across the entire operation. Blast intensity was increased using a combination of increasing charge length with a reduction in stemming length, as well as tightening the drilling pattern.

The blast model was further validated and updated during implementation of recommendations and optimisation strategies in 2021. An example of the measured fragmentation for one of the audited trial blasts during implementation compared with the simulated fragmentation is provided in Figure 4. The validation blasts showed a good match between the simulated and measured fragmentation, however some inconsistency was observed in the coarse fragmentation and top-size. The measured fragmentation for some trial blasts was finer than the predicted fragmentation from the model simulations. This was most likely due to the very good implementation practices on-site, as well as more limited variability in rock structure than initially modelled.

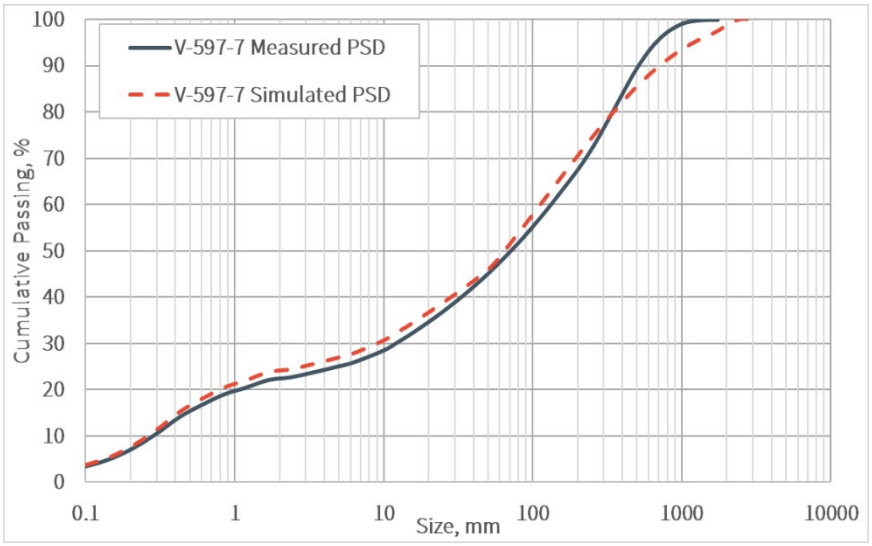

FIG 4 – Comparison of measured and simulated fragmentation for guideline trial blast.

During implementation, limitations in the mine were encountered, including minimum drilling spacing to enable safe and effective manoeuvring of drill rigs and explosive loading equipment. For each of the three typical drill diameters used on-site for production blasting (203 mm, 254 mm, 349 mm), a different limit in terms of burden and spacing was applicable. These constraints were accounted for in updated and refined blasting guidelines, and as a result, the blast intensity that could be implemented in each domain had to be adjusted.

During the M2M project, the base case blast intensity in terms of powder factor was approximately 1.0 kg/m^3. Following the initial M2M project, blast intensities varied across the defined ore domains in the range of around 1.0 to 2.2 kg/m^3 depending on the strength and structure of each domain. Following the trial blasts and identification of the drilling limitations, the updated guidelines for the refined ore domains had a range of powder factor between 1.1 and 1.8 kg/m^3. The limitations resulted in a decrease in the maximum blast intensity that was able to be safely and consistently implemented. However, following the validation trial blasts, it was found that significant improvements in fragmentation could still be gained with the refined blast guidelines.

Integration and process optimisation

For process optimisation, AG and SAG milling each benefit from a different feed size distribution, and so the ideal feed conditions will be dependent on the operation of the grinding circuits. However, both methods of comminution benefit from an increase in the content of -10 mm fine material. To determine the optimum feed size distribution for each mode of operation, site-specific models of crushing, grinding, and gravity concentration were developed from detailed plant surveys and historical data. JKSimMet was used to develop mechanistic models using machine parameters and ore properties, and calibrated to the measured survey data collected during the M2M project. These were integrated with the blast fragmentation model to identify opportunities for optimisation in the plant. Crushing and grinding simulations were carried out to assess the impacts of finer RoM fragmentation and to optimise operating strategies for this feed.

With the implementation of blasting guidelines and the finer RoM feed, throughput was simulated to increase in the range of 0–8 per cent depending on the ore domain, with greater benefits simulated in the harder and more structurally massive domains. The finer RoM fragmentation from the implementation of the blasting guidelines would also allow the primary crusher to be operated with a finer gap setting to provide a finer mill feed, further increasing mill throughput. Simulations indicated the finer mill feed would further increase throughput by about 2–5 per cent. The increase in throughput is dependent on which ore domain is being fed, and to which grinding line/mill. The plant during the M2M project was arranged in seven parallel lines, with Lines 1 to 6 each consisting of a 32-foot AG mill in closed circuit with two stages of screening, treating around 1200 t/h of primary crusher product. Line 7 consists of a 36-foot AG mill with the same screening arrangement, treating around 2800–3200 t/h.

Historical operating data was provided for analysis during the M2M project, and the typical power draw for Mill 7 for the period from October 2018 to February 2019 is shown in Figure 5. It can be seen that the installed power (14.9 MW) was being reached less than 1 per cent of the time. At the time, all mills were operating fully autogenously, and mill power was not being fully utilised in Line 7 and Line 4.

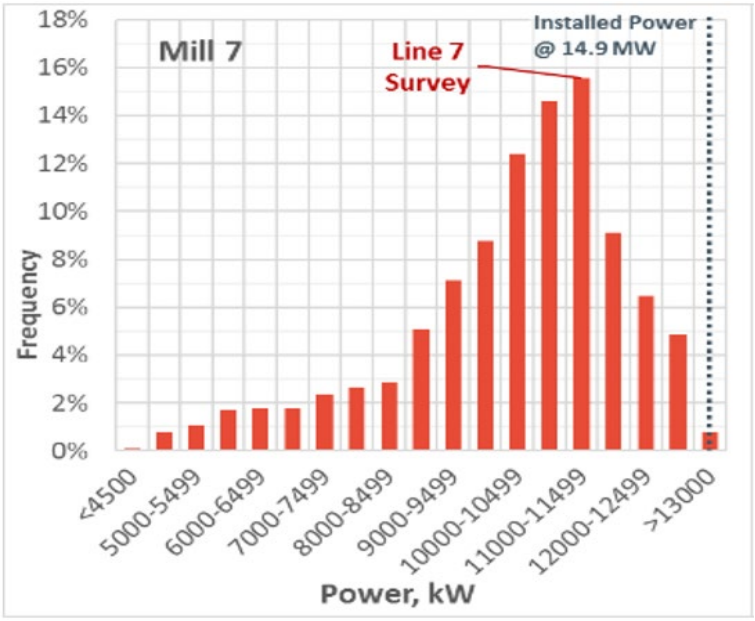

FIG 5 – Power draw in Mill 7 (AG) for October 2018 to February 2019.

The grinding lines were near the limit of achievable power consumption in AG operation, and to utilise the available power, grinding media was required. To achieve greater increases in throughput without significant capital expenditure, Hatch recommended that AMEM convert the current AG mills with available power to SAG mill operation to fully utilise the available power. Power calculations indicated that 15 per cent balls could be added to Mill 7, and 10 per cent added to Mill 4, based on the available installed power. Additionally, it is critical sized material (in the size range of 40–60 mm) that builds up in the mill load and limits the throughput in SAG and AG mills. For MW, further size reduction of this critical size material was best achieved by means introducing steel grinding media.

While AG mills require a different feed size distribution to SAG mills to maximise throughput, both modes of operation benefit from the increased production of fines (-10 mm) by the drill and blast optimisation and recommended drill and blast guidelines (Kanchibotla *et al,* 1998; Kanchibotla, Valery Jnr and Morrell, 1999; Grundstrom *et al*, 2001; Valery *et al*, 2007: Valery, Duffy and Jankovic, 2019). Following the update of the blasting guidelines, integrated blasting, crushing, and grinding simulations estimated throughput increases of 7 to 26 per cent for the different grinding lines depending on the different ore types. A summary of the simulated increase in throughput for Line 7 for each domain, depending on the implementation of recommendations in shown in Figure 6.

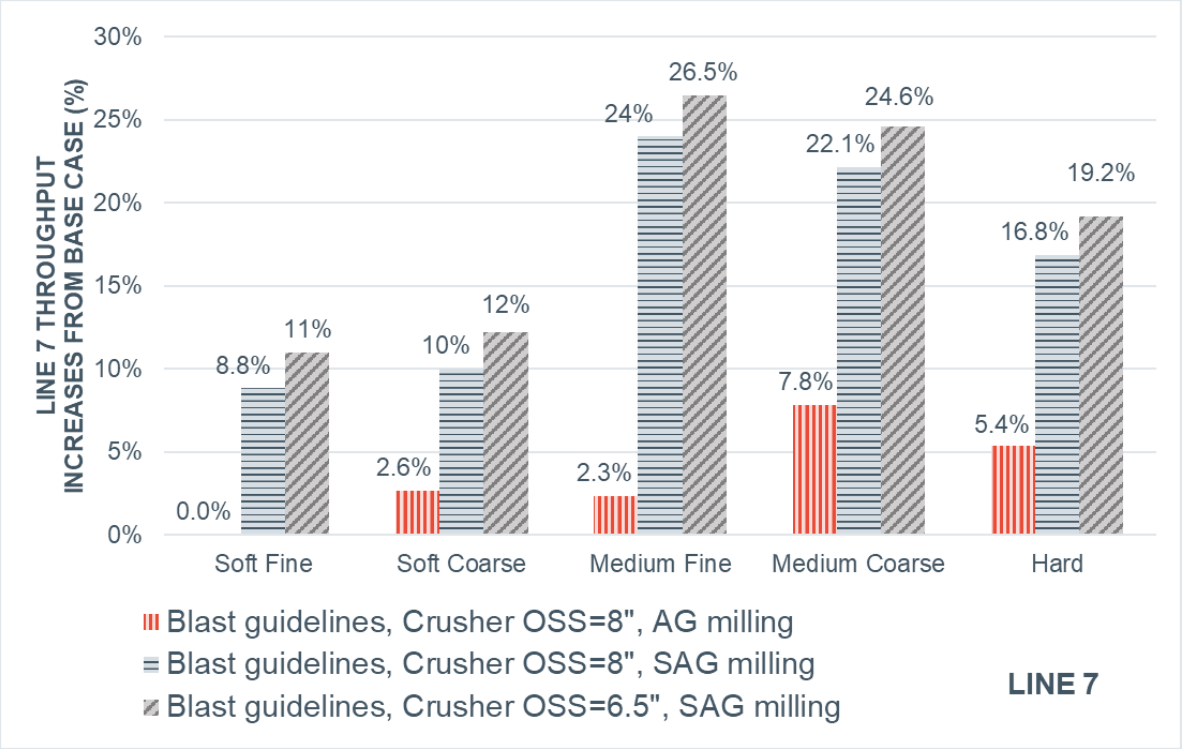

FIG 6 – Simulated increase in throughput for Line 7 depending on ore domain and change in operation.

Throughput improvements for each line were calculated on a weighted average basis, accounting for the proportion of feed in each of the defined ore domains. For Lines 1–6, a throughput increase of almost 5 per cent was simulated for the finer mill feed resulting from implementation of blasting guidelines and tighter primary crusher gap. For Line 7, the finer mill feed should increase throughput by about 6 per cent, with AG to SAG conversion providing an additional 14 per cent increase in throughput.

In late 2020, Line 7 was successfully converted to SAG milling with 12 per cent ball charge resulting in an increase in throughput of about 10 per cent. A higher ball charge of 15 per cent was originally recommended but could not be achieved due to the mill weight causing the bearing pressure limitation to be exceeded. Therefore, an alternative composite liner design has been investigated for Line 7 to reduce the mass of the liners compared to existing steel liners. The reduction in liner weight will enable ball charge to be increased to the recommended 15 per cent making use of available power without exceeding bearing pressure constraints and further increasing throughput.

Line 4 is currently still operating as an AG mill but will be converted to SAG milling in 2022 following adjustment of the liner design to suit SAG mill mode of operation.

CONCLUSIONS AND ONGOING WORK

The M2M optimisation project identified integrated strategies in the mine and plant to increase throughput by 7 to 26 per cent (depending on the processing lines and ore types) with minimal capital expenditure. Implementation of the recommended operating strategies started in late 2020, including further ore characterisation, refinement of ore characterisation and definition of domains, adjustment of blasting guidelines, and conversion of Line 7 to SAG (with 12 per cent ball charge). Throughput increases of up to 10 per cent overall, for all ore types, have been achieved to date and further benefits are expected when the refined blasting guidelines and all recommended operating strategies are fully implemented.

As an extension of the M2M optimisation, a throughput forecast has also been developed, integrating the ore properties, mine plan and schedule, blast fragmentation and comminution models. This model will be used to accurately predict future throughput, provide advance notice of the impact of changes in ore characteristics, and assist with strategic long-term planning.

REFERENCES

Bonfils, B, Valery, W, Jankovic, A, Duffy, K, Tabosa, E and Holtham, P, 2021. Multi-component Mine-to-Mill Optimization Applied to Iron and Gold Ores. *Mill Operators Conference 2021*, Brisbane, Queensland.

Duffy, K and Valery, W, 2017. It's not just about more explosives. *CIM Magazine*, December 2017.

Evangelista, G, Moreira, A, Moura, F, Souza, I, Resende, F, Henrique, P, Corsini, J, Ribeiro, A, Valery, W, Valle, R, Hayashida, R and Plasencia, C, 2021. Integrated Optimisation of Drill and Blast and Comminution Processes at Lundin Mining – Chapada. *Procemin 2021, 17th International Conference on Mineral Processing and Geometallurgy*.

Grundstrom, C, Kanchibotla, S, Jankovic, A and Thortnton, D, 2001. Blast Fragmentation for Maximising the Grinding Circuit Throughput at Porgera Gold Mine, *Proceedings of the 27th Annual Conference on Explosives and Blasting Technique*, pp 250–258.

Isokangas, E, Valery, W, Jankovic, A and Sonmez, B, 2012. Using process integration and optimisation to provide integrated process solutions for mining operations, from mine to mill. *XXVI International Mineral Processing Congress*, New Delhi, India.

Kanchibotla, S S, Morrell, S, Valery Jnr, W and O'Laughlin, P, 1998. Exploring the Effect of Blast Design on SAG Mill Throughput at KCGM. Paper presented at the Mine to Mill Conference, in Brisbane, Australia, October, 1998.

Kanchibotla, S S, Valery Jnr, W and Morrell, S, 1999. Modelling fines in blast fragmentation and its impact on crushing and grinding. *Explo'99 Conference*, Kalgoorlie, WA.

Tokarenko, A, Timofeyev, I, Kilin, S, Valery, W, Valle, R, Duffy, K and Yelkin, I, 2017. Increasing Production at Polyus Gold Blagodatnoye with Holistic Optimization from Mine-to-Plant. *Procemin 2017: 13th International Mineral Processing Conference*, Santiago, Chile, 4–6 October 2017.

Valery, W and Samuel, M, 2012. Mine to mill mastery – Antamina boosts throughput for hard ores with support from Metso PTI. *CIM Magazine*, November, 2012, 7(7):44–46.

Valery, W, Duffy, K and Jankovic, A, 2019. Mine-to-Mill Optimization, in *SME Mineral Processing and Extractive Metallurgy Handbook* (R Dunne, S Kawatra and C Young, eds), SME, 2019.

Valery, W, Duffy, K, Faveere, R, Hayashida, R, Jankovic, A, Tabosa, E and Yelkin, I, 2018b. Improving profitability, sustainability and the overall operating efficiency from Mine to Process in Russian operations. in *Proceedings of the XXIX International Mineral Processing Congress – IMPC 2018*, Moscow, Russia.

Valery, W, Duffy, K, Valle, R, Hayashida, R, Jankovic, A, Holtham, P, Tabosa, E and Andrade, B, 2019. An Optimization Journey: from Blasting, Dry AG Milling to Regrind HPGR and Everything in Between. *Procemin 2019: 14th International Mineral Processing Conference*.

Valery, W, Jankovic, A, La Rosa, D, Dance, A, Esen, S and Colacioppo, J, 2007. Process integration and optimisation from mine-to-mill. *Proceedings of the International Seminar on Mineral Processing Technology*, India. pp. 577–581.

Valery, W, Morrell, S, Kovovic, T and Kanchibotla, S, 2001. Modelling and simulation techniques applied for optimisation of mine to mill operations and case studies. Presented at VI Southern Hemisphere Conference on Minerals Technology, in Rio de Janeiro, Brazil, 27–30 May.

Valery, W, Valle, R, Duffy, K, Jankovic, A and Tabosa, E, 2016. Complete Optimisation from Mine-to-Mill to Maximise Profitability [Комплексная оптимизация параметров горных работ и технологических операций для повышения рентабельности производства]. *Zoloto I Technologii*, Russia, June 2016, 2(32):62–67.

Valery, W, Valle, R, Jankovic, A, Hayashida, R, Duffy, K, Holtham, P, Tabosa, E and Vianna, S, 2018a. Integrated optimization of mining and minerals processing operations. *Procemin 2018: 14th International Mineral Processing Conference*, Santiago, Chile, 28–30 November 2018.

Valle, R and Duffy, K, 2014. Full Process Integration and Optimization of Blasting and Comminution Operations at Cerro Corona. Presented at the International Mining Conference and Expo, Las Vegas, 23–25 September.

From drill to mill – measure while drilling for rock characterisation in comminution

C Paredes[1] and V Jokovic[2]

1. Senior Mining Engineer, Eltirus, Brisbane Qld 4000. Email: constanza.paredes@eltirus.com
2. Senior Research Fellow, Julius Kruttschnitt Mineral Research Centre, University of Queensland, Brisbane Qld 4068. Email: vjokovic@uq.edu.au

ABSTRACT

Some production blasthole drilling rigs are capable of measuring and storing various operational parameters while operating (Measuring While Drilling data-MWD). There are a number of examples from the literature where MWD data is used to predict rock properties such as lithology, strength and fractures.

However, the effective application of MWD data for predicting comminution performance has not been proven; this could be due to either the influence of processes which exist between drilling and milling (eg blasting, stockpiling, crushing etc) or lack of correlation between MWD and plant performance.

Ore comminution tests estimate ore breakage parameters that can be used to predict plant performance. Therefore, this study investigates the links between the MWD data acquired in laboratory and ore breakage parameters. In total, six rock types were tested with a wide range of rock strength. Showing the correlation between MWD data and ore characterisation parameters would open a path forward to the implementation of MWD predictions of plant performance in full-scale plants.

INTRODUCTION

Measure while drilling for rock mass characterisation

The Mine to Mill value chain involves a series of complex inter-dependent processes, each one sensitive to a range of rock mass properties. A good understanding of rock mass properties that control the breakage, separation and transportation behaviour is critical to design and maintain a sustainable, efficient, and profitable operation. Traditional rock mass characterisation is based in geotechnical testing of expensive exploration cores. However, Measure-While-Drilling could provide a characterisation that is integrated with the mining process, providing a higher density of samples at a lower cost, as well as rock mass indicators based on the actual rock response to the breakage process during drilling.

Measure-While-Drilling is a process of measuring and recording of drilling machine parameters while operating. For open pit rotary drills, the standard records associated with MWD are rotary speed (N), torque (T), pull-down force (W) and rate of penetration (ROP). The current state of drill rig and GPS technology allows for records of MWD parameters to be accurately located in space, captured at the open pit bench and transmitted in real-time to a database computer. The research has shown that this data can be used to detect rock type, strength, and rock mass structures (Hatherly *et al*, 2015; Manzoor *et al*, 2020; Rai *et al*, 2015) but the industry has been slow to implement these advances. The extension of MWD strength indicators towards the prediction of rock comminution performance has been proposed and modelled (Araya *et al*, 2015; Eloranta, 2003; Paredes, Jokovic, and Kanchibotla, 2018; Simkus and Dance, 1998). However, no study has shown a definite correlation between MWD and comminution parameters.

MWD Indicators of rock strength

The study of breakage mechanics during drilling was initiated by the need for the development of new techniques for efficient drilling in the oil industry (Meador, 2009). Drill rig and drill bit design studies looked for rock properties that influence the mechanics of rock breakage at the contact between the bit and the rock to improve drilling efficiency (Somerton, 1959). This has provided the background for a scientific approach to characterising rock strength using MWD data. Teale (1965)

studied the kinematics of drills and introduced the concept of specific energy of drilling (SE_d) as the mechanical work done to excavate a unit volume of rock; the value of SE_d for rotary tricone drills is given by Equation 1.

$$SE_d = \frac{W}{A_B} + \frac{2\pi}{A_B}\frac{NT}{ROP} \quad (1)$$

Where:

SE_d	Mechanical specific energy of drilling [Pa]
W	Pull-down force [N]
N	Rotary speed [Hz]
T	Torque [Nm]
AB	Blasthole area [m^2]
ROP	Rate of penetration [m/s]

The value of SE_d is typically expressed in units of MPa, but the actual physical quantity measured is the energy developed by the forces produced by the drill motors by volume of rock drilled. Teale (1965) showed that in optimal drilling conditions, the value of SE_d could be used as an indicator of rock strength (UCS). Multiple studies have employed SE_d to estimate rock strength in open pit mining (Araya *et al*, 2015; Dupriest and Koederitz, 2005; Jain and Singh, 1993) but only a few studies have employed the minimum specific energy as the rock strength indicator.

The rock strength indicators that combine the four key MWD variables (ROP, T, N and W) have been proposed for open pit mining from engineering correlations and site-specific studies. Leighton (1982) and Lebel (1984) employed the Rock Quality Index (RQI) derived from MWD data to estimate rock strength to optimise blasting. Rabia (1985) defended the use of empirical correlations of MWD data to rock strength over the use of the specific energy for site-specific purposes. Furthermore, Peck (1986) developed the first site-based study where data recorded by drill rig on-board computers was employed to characterise rock strength.

Linear multivariate regressions models based on MWD data or a combination of MWD and other sources of information have been employed in case studies for rock recognition, blast optimisation and excavation stability analysis. The introduction of artificial intelligence technologies and advanced statistical tools have provided a new way of producing models that predict strength or rock type from MWD data (Beattie, 2009; Kadkhodaie-Ilkhchi *et al*, 2010; Vezhapparambu, Eidsvik, and Ellefmo, 2018). While multivariate regression and artificial intelligence models can provide a highly accurate prediction of rock strength for a particular site, no general law linking MWD data to rock properties can be inferred from them. This is because the physical phenomena underlying the correlations found in the models tend to be overlooked in this approach.

MWD Indicators of rock mass structures

The presence of a void or open fracture within the rock can generate sharp changes in the values of MWD data (Barr and Brown, 1983), such as a spike in the rate of penetration and a drop in Torque. The detection of individual fractures using these changes in the MWD profiles has varying degrees of success, because of their dependency on the rock type and orientation of the fracture (Khorzoughi *et al*, 2018). Besides, the ability of MWD data to produce a fracturing index is constrained by the sampling interval (van Oosterhout, 2016).

Schunnesson (1996) showed that the RQD of the rock in tunnelling could be estimated from the variability of the torque and rate of penetration signals. This concept initiated an area of MWD-related research that is focused at estimating the fracturing and damage indicators which are important for underground mining and tunnelling (Navarro *et al*, 2018; van Eldert *et al*, 2018).

MWD Indicators of rock mass comminution properties

The concept of using MWD indicators to predict comminution performance in open pit mining was first introduced by Simkus and Dance (1998). In their study, they incorporated aspects of MWD, material tracking and comminution performance at Highland Valley Copper, currently operating

under Teck. The authors describe the plan to incorporate MWD into process prediction, but the results of the site trial were not published. The concept was later re-introduced at another operation run by Teck (Carmen de Andacollo Mine) by Araya *et al* (2015). The full scale trial aimed to use the specific energy of drilling combined with the crusher and mill parameters to predict SAG circuit specific energy and plant throughput was published by Galvez (2017). Although no significant correlation or trend can be found between SE_d and comminution properties of rock or plant throughput, the author indicates that the value of SE_d can be incorporated in a multivariate regression to predict plant throughput with a significant p-value.

A study aiming to correlate a MWD-based strength indicator to rock breakage properties in crushing and grinding was developed by Park and Kim (2020) using sandstone and limestone specimens at a laboratory setting. The selected strength indicator is a modified penetration rate that is scaled by pull-down force, rotation speed and torque on a rock-type base. While the models developed have limited statistical significance and are developed in a narrow range of rock strength, the study highlights the potential of MWD data for predicting comminution properties of rock.

Ore breakage characterisation using JKRBT

Over the last few decades, the JKMRC has been characterising the ore samples using Drop Weight Tester and more recently using JK Rotary Breakage Tester (JKRBT). The amount of breakage is modelled using a single parameter, t_{10}, which represent the cumulative percent passing $1/10^{th}$ of the initial material size. As expected, the t_{10} is dependent on the specific comminution energy, E_{cs}, used during the breakage and this relationship can be modelled by:

$$t_{10} = A * \left(1 - e^{-bE_{cs}}\right) \quad (2)$$

The parameters A and b are fitted values and are used by many mineral processing engineers in their simulation to estimate the SAG comminution circuit throughput. The product A×b has also been used as an indicator of ore hardness, where values below 30 indicate competent rocks.

For a small amount of sample, A and b values can be estimated based on testing of only one size fraction (-11.2+9.5 mm), and that test is known as JKRBTLite test.

The A and b parameters are designed to simulate the performance of the ore in a SAG mill, and the relationship between the A×b parameter and impact resistance is nonlinear. These characteristics can complicate the process of building a linear model that relates the A×b to MWD data. For example, the Sandstone specimens, with A×b values ranging from 132 to 206, is not expected to induce a large change in the energy utilised in a SAG circuit, if all other SAG parameters are kept constant. In contrast, a change of A×b parameter from 20 to 60 has a significant impact on SAG mill energy consumption.

The effective application of MWD data for predicting comminution performance has not been proven; this could be due to either the influence of processes that exist between drilling and milling (eg blasting, stockpiling, crushing etc) or lack of correlation between MWD and plant performance. In order to exclude the later, this study investigates the links between the MWD data acquired in the laboratory and the A×b ore breakage parameter.

EXPERIMENTAL METHOD

Experimental design

For this study, six rock types were selected to represent a broad range of rock hardness/strength from sandstone (softer) to basalt (competent) as presented in Table 1. Several rock samples from each rock type were used in testing. The samples ranged from 35 × 35 × 30 cm to 50 × 50 × 50 cm in size. In order to secure the samples during the drilling, rocks had to be set in concrete blocks, as shown in Figure 1.

TABLE 1

Rock types and specimens in drilling program.

Rock type	Code	Origin	Expected strength	Number of rock samples
Sandstone	SST	Helidon Quarry, Qld	Low	4
CHOP	CHOP	Gold Mine, U.S.A	Medium-low	4
Pipeline	PPL	Gold Mine, U.S.A	Medium-high	3
Porphyry	TN	Copper Mine, Peru	Medium-high	4
Basalt	BAS	Bromelton Quarry, Qld	High-very high	4

FIG 1 – Concrete block with four rock samples prepared for drilling.

The authors assume that concrete blocks provide similar confinement conditions to all the rock samples, and if there is an influence of the concrete on the MWD data, it would be the same to every rock sample. Thus, any correlation between MWD and rock properties observed in the laboratory should not be influenced by the concrete blocks. The relationship between MWD data and ore characterisation parameters at laboratory scale testing will not be the same for *in situ* rock, but the findings of this study can provide a path forward to the potential use of MWD data in predictions of plant performance.

Several holes were drilled on each rock sample, and to avoid biases, the order in which the drilling proceeded was randomised. A factorial experiment with two factors (pulldown force and rotational speed), at three levels for each factor was designed for each rock type, following the procedure detailed in Napier-Munn (2014). An example of the pull-down force and drill speed used during the drilling is presented in Table 2.

TABLE 2

Drilling parameters for drilling a rock type.

Speed, N [rev/min]	Pull-down force, W [kN]		
	25	**40**	**60**
80	Hole 1	Hole 2	Hole 3
100	Hole 4	Holes 5&10	Hole 6
120	Hole 7	Hole 8	Hole 9

Laboratory drilling experiments

The drilling experiments were conducted on a full-sized drill rig able to drill in rotary and rotary percussion modes. A tungsten carbide rotary tricone manufactured by Glinik was used in the drilling program to obtain MWD data for 8–10 holes on each rock type, including a repeat set for sandstone rock. The drill rig was operated with a size NQ rod connected to the tricone through a custom-made adaptor. The tricone had a $2^{15}/_{16}$ inch diameter and was classified as 613Y in the IADC classification, designed for drilling medium strength rocks.

The first 1–2 cm of drilling was performed following a collaring regime where the rotary speed and pulldown force were reduced. Holes were then drilled at constant nominal N and W to the maximum depth allowed by the rock sample, ranging from 10 to 35 cm in length. During the drilling, four MWD parameters were recorded; displacement, torque, pull-down force and drill speed. All parameters, except rotary speed, were sampled at 1000 Hz sampling rate; rotary speed was sampled at 10 Hz sampling rate. Based on drill displacement and time, the rate of penetration rate (ROP) was calculated.

After drilling, the rocks were removed from the concrete block and crushed using a laboratory crusher at the JKMRC pilot plant to produce rock particles of suitable size for JKRBTLite test. Based on this test, the A×b parameter was established for each rock sample.

PROCESSING AND ANALYSIS OF MWD DATA

Signal processing

An example of all MWD data recorder during drilling a hole is presented in Figure 2. The rate of penetration in Figure 2 shows a spike during the first few seconds, while the drill bit is travelling through the collar (already drilled) and a pre-weakened section and then remains stable. In this case, the pull-down was maintained constant at 37 kN along the entire hole, but the rotary speed was not stable between 330 and 440 seconds (the first few centimetres of drilling). While the information on this time interval represents valid drilling records in almost its entirety, the actual final time interval to be considered in the analysis is between 440 and 560 seconds, when the rotary speed and pull-down force remained relatively constant. If the pull-down force and rotary speed are constant, then the average and standard deviation of the dependant variables are expected to depend only on rock properties.

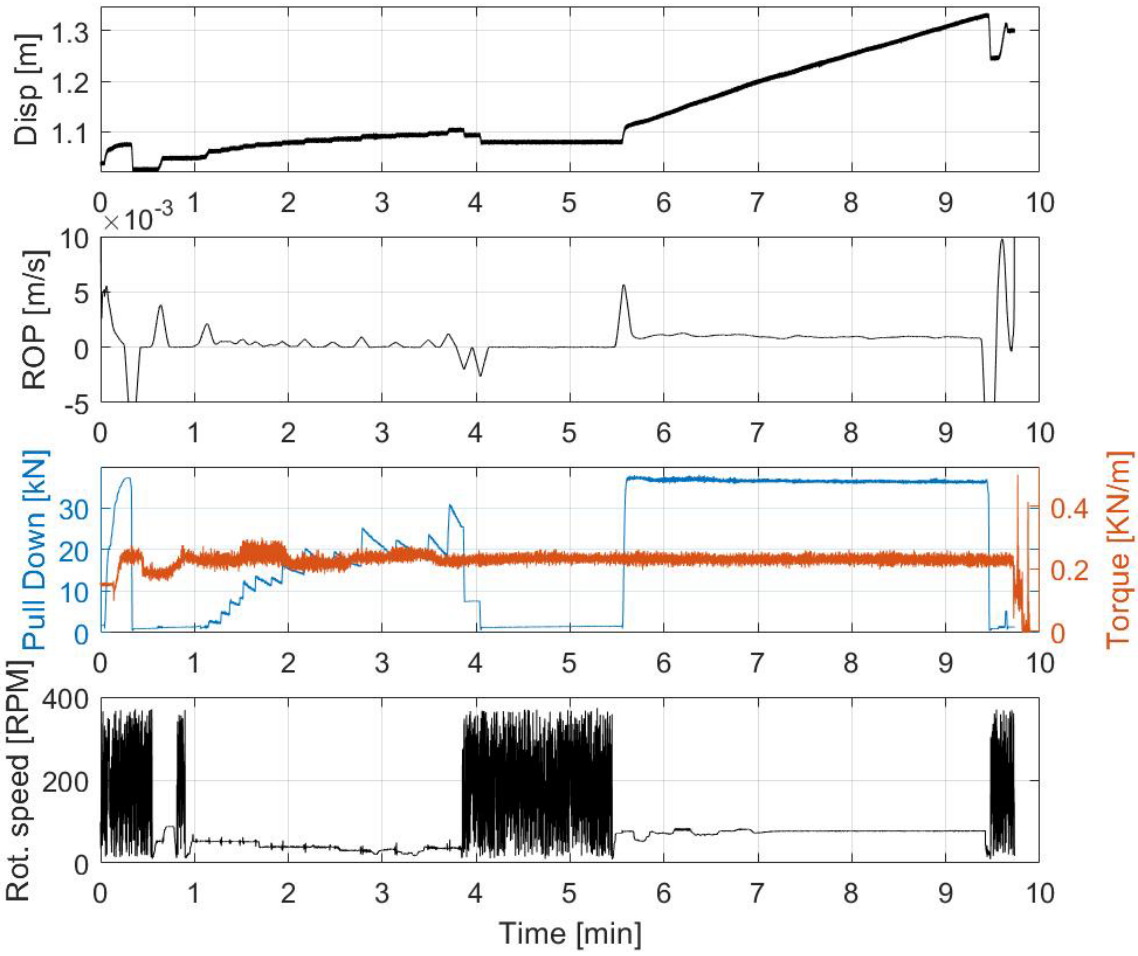

FIG 2 – Complete (unfiltered) MWD data set for Basalt drilled at pulldown force of 35 kN and speed 75 rev/min.

A more systematic approach to determine the period of stable rotary speed was provided by Cooley and Tukey (1965), who were using a Fourier Fast Transform (FFT) analysis to observe the frequencies of vibration in the Torque signal. Therefore, the final time-window to extract drilling data was selected by identifying a'stable drilling section' as an interval of time defined by the following criteria:

- Stable pull-down force, close to the target pull-down set by the drilling program.
- Stable rotary speed and pull-down force, within 10 per cent of the target set by the drilling program.
- Positive rate of penetration.
- Stable power spectrum (FFT) of the torque signal.

An example of the vibration pattern of the torque signal observed on a Basalt Specimen is presented in Figure 3. The first section of the rotary speed signal shows the control of the speed was not accurate and changes approximately match the changes in torque. The noise in the Torque signal is masking the general trend; however, the effect is more evident on the spectrogram plot, where each change in rotary speed induces a change in the frequency of the peaks in the spectrogram until a stable regime is reached.

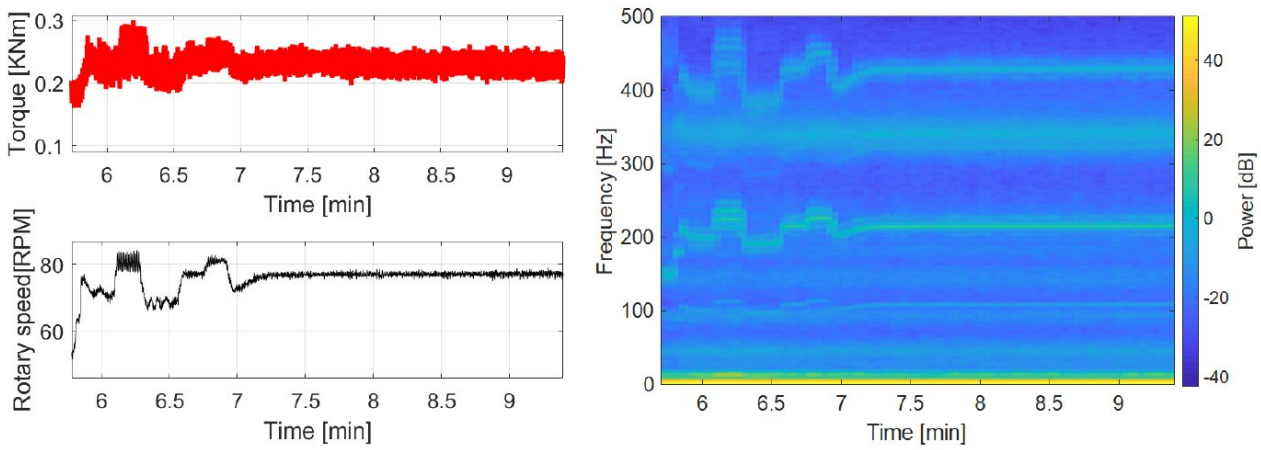

FIG 3 – Torque and rotary speed signal (left) and the spectrogram of the torque signal (right).

As previously mentioned, the spectrogram of the torque signal contains a number of peaks that are correlated to the rotary speed. During a stable drilling section, these peaks are located at specific frequencies. This was observed for all drilling holes. The position (frequency), the height and the half-width (as displayed in Figure 4) of three dominant peaks were used in further analysis. It is expected that information about these peaks will vary across rock types.

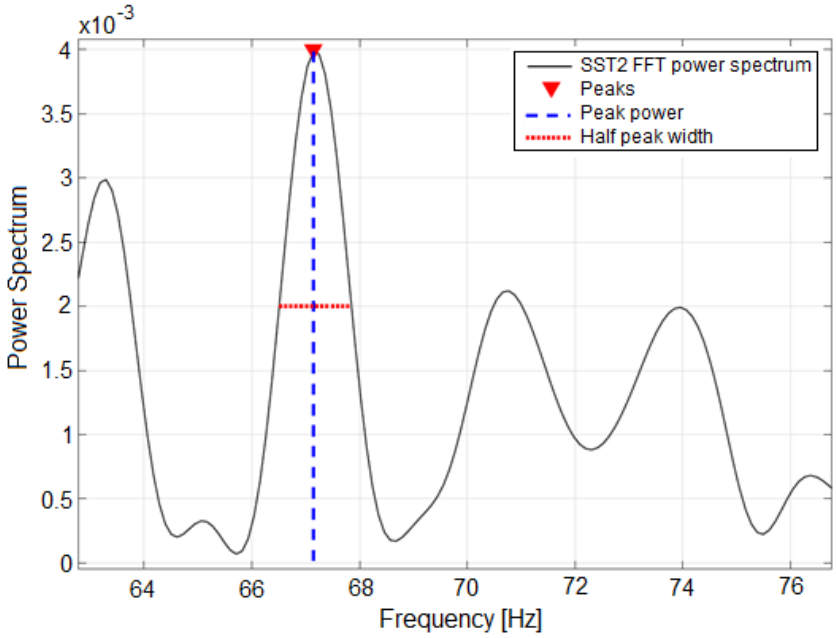

FIG 4 – One of the dominant peaks in the frequency spectrum of torque signal recorded during stable drilling conditions in a Sandstone Specimen.

RESULTS AND DISCUSSION

Table 3 presents the average pull-down, rotary speed, ROP and torque and values of A×b for each rock sample. The intensity (peak power multiplied by the half peak width) of the three largest peaks of the Torque signal is also shown as these values will be used in the modelling section. The experimental error for the measured A×b can be estimated from the A×b values for basalt rocks as this material has been used at the standard material to measure the experimental error in Drop Weight test due to the homogeneity of the deposit (Stark *et al*, 2008). The confidence interval for A×b using t-student distribution is ±2.2.

TABLE 3

Average values of MWD data and A×b for each rock sample.

Rock sample	Holes	Average MWD data				Torque Peaks Intensity			A×b
		Speed, N [rev/min]	Pull down force, W [kN]	ROP [mm/s]	Torque, T [Nm]	I1 [db·Hz]	I2 [db·Hz]	I3 [db·Hz]	
BAS-A	4,5,8	62	43	1.3	213	2.4	0.6	0.8	25
BAS-B	2,6	45	53	1.2	200	1.9	0.7	0.3	28
BAS-C	1,3,9	47	49	1.5	209	1.7	0.4	0.4	29
BAS-D	7,10	66	42	1.2	226	2.7	0.5	0.8	28
CHOP-A	3,4	96	46	4.0	334	50.4	3.8	2.0	69
CHOP-B	5,8,9	116	48	5.7	427	45.6	10.0	2.3	52
CHOP-C	1,2	91	41	4.1	325	65.4	1.4	1.0	67
CHOP-D	6,7,10	110	46	4.2	361	44.0	9.3	1.2	47
PPL-A	1,3,10	95	46	4.4	314	52.1	9.8	5.5	25
PPL-B	4,5,9	106	44	5.2	314	32.6	6.6	1.3	33
PPL-C	2,6,7,8	108	46	5.9	340	51.0	5.6	1.2	30
SST-A	2,4,6,7,8	105	42	7.5	329	14.5	1.7	0.6	139
SST-B	1,3,5,9,10	98	42	6.9	308	5.2	0.8	0.2	141
SST-C	3,5,6,8,9 (repeats)	104	48	8.4	365	7.0	3.4	1.1	132
SST-D	1,2,4,7,10 (repeats)	98	34	4.7	295	8.0	2.1	0.8	206
TN-A	2	40	46	0.8	238	0.1	0.1	0.2	42
TN-B	3,7	64	47	1.3	263	2.7	0.2	0.2	35
TN-C	5,6	62	52	1.6	289	1.0	0.7	0.6	27
TN-D	1,4,8	62	40	1.4	246	0.7	0.4	0.1	28
TS-A	7,8,9	80	45	1.7	275	1.7	1.1	0.4	35
TS-B	5,6	54	34	1.7	205	5.6	1.3	0.3	32
TS-C	2,4	50	42	1.2	201	0.3	0.1	0.1	32
TS-D	1,3	40	48	1.4	191	0.4	0.5	0.0	34

Modelling the A×b parameter using a novel approach to MWD data

Due to the nonlinear correlation between the A×b and the specific comminution energy of the SAG circuit, a generalised linear regression model (GLM) was used to predict A×b based on MWD data. It was assumed that the A×b has a gamma distribution.

Several combinations of variables were tested in the GLM. For example, the intensities for the second and third peak of FFT signal were normalised by the intensity of the first peak and the reciprocal of all MWD variables and variability of the parameters were tested for significance. The stepwise regression analysis was conducted to remove the parameters that are not statistically significant. The best regression model is presented by Equation 3.

$$(A \times \mathrm{b})^{-\frac{3}{2}} = 0.02 - \frac{0.2}{W} - \frac{0.21}{N} - 4 \cdot 10^{-4} I_1 + 7 \cdot 10^{-4} I_2 - 2 \cdot 10^{-5} I_3 \cdot T + 322 \frac{ROP_{rawSD}}{ROP} + 0.9 \cdot ROP_{rawSD}\, I_3 + 4 \cdot 10^{-6} I_1^2 - 4 \cdot 10^{-5} I_2^2 \quad (3)$$

Where the parameters are:

W	Pull-down force in [kN]
N	Rotation speed in [rev/min]
ROP_{rawSD}	Standard deviation of raw ROP signal in [m/s]
I_1	Intensity of peak 1 in [dbHz]
I_2	Intensity of peak 2 in [dbHz]
I_3	Intensity of peak 3 in [dbHz]

Equation 3 describes the generalised linear regression model with an estimated dispersion (the equivalent measure to RMSE for a GLM) of 0.0146. The p-values of all factors range from $1.5 \cdot 10^{-10}$ to $3.2 \cdot 10^{-3}$. A stepwise regression analysis indicated that the variability of ROP (ROPrawSD) is more significant in the A×b regression than the ROP.

Using this model, the A×b values were predicted based on MWD data for all 67 holes. The measured and predicted values of A×b are presented in Figure 5. The confidence intervals for predicted A×b values are also included in Figure 5. These intervals are larger for higher A×b values. For example, for predicted A×b of 24, the 95 per cent confidence interval is [20.26, 33.97] whereas for A×b of 60, the same interval is [43.5, 117.4].

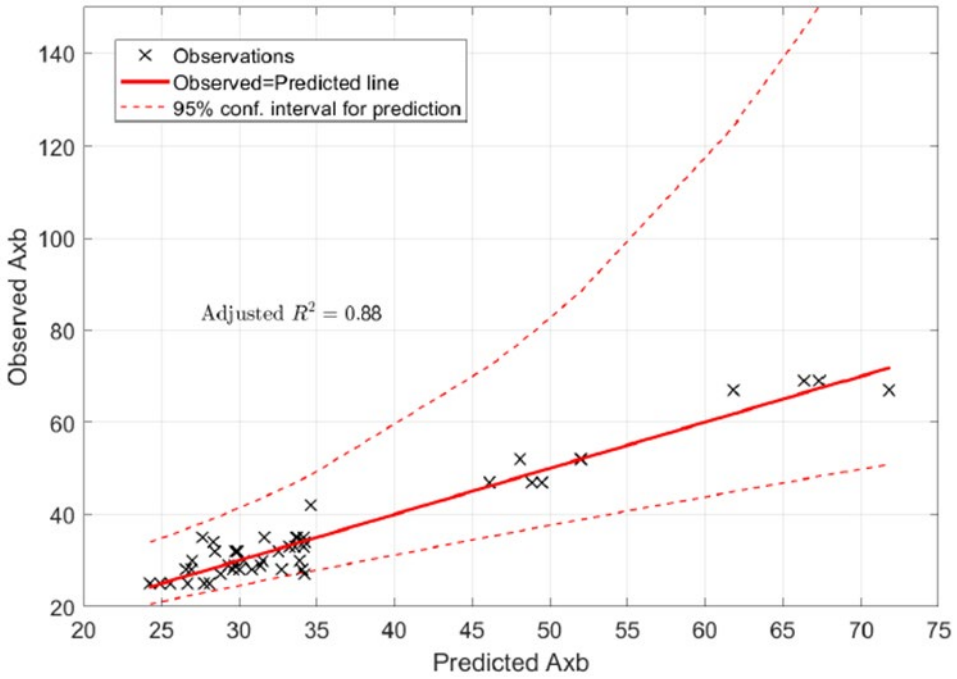

FIG 5 – A×b values predicted by GLM model versus measured A×b values.

Although some data in Figure 5 are clustered, the adjusted R^2 value of 0.88 indicates that the proposed model predicts A×b values reasonably well. Based on this, it can be concluded that there is a correlation between the MWD data acquired in the laboratory and the A×b ore breakage parameter.

CONCLUSIONS

This study investigates the links between the MWD data acquired in the laboratory and the A×b ore breakage parameter. Six rock types with a wide range of rock strength were tested. In total, 67 holes were drill using the rotary tricone drilling in laboratory, and rock samples were characterised using JKRBLite test.

A generalised linear regression model (GLM) was used to predict A×b value based on MWD data (pull-down force, rotation speed, Standard deviation of the raw rate of penetration, torque and FFT of torque signal). The adjusted R^2 value of 0.91 indicate that the proposed model predicts A×b values

reasonably well; therefore, there is a correlation between the MWD data acquired in the laboratory and the A×b ore breakage parameter. The correlation between MWD data and ore characterisation parameters at laboratory scale testing provides a path forward to the potential use of MWD data in predictions of plant performance.

ACKNOWLEDGEMENTS

The authors would like to thank the University of Queensland and Sustainable Mineral Institute for the financial support for this study. The authors would also like to acknowledge the help of Chris Lear during the experimental drilling program and Dr. Sarma Kanchibotla for his support to this research.

REFERENCES

Araya, V, Jeraldo, C, Bennett, D, Torres, G and Aravena, J, 2015. Drill Specific Energy at Teck Carmen de Andacollo. Paper presented at the XIV Congreso Geologico Chileno, La Serena, Chile.

Barr, M V and Brown, E T, 1983. A site exploration trial using instrumented horizontal drilling. Paper presented at the 5th ISRM Congress.

Beattie, N, 2009. Monitoring-While-Drilling for Open-Pit Mining in a Hard Rock Environment: An Investigation of Pattern Recognition Techniques Applied to Rock Identification, Masters thesis, Queen's University Kingston, Ontario, Canada.

Cooley, J W and Tukey, J W, 1965. An Algorithm for the Machine Calculation of Complex Fourier Series. *Mathematics of Computation*, 19(90), 297–301. doi: 10.2307/2003354.

Dupriest, F E and Koederitz, W L, 2005. Maximizing Drill Rates with Real-Time Surveillance of Mechanical Specific Energy. Paper presented at the SPE/IADC Drilling Conference, Amsterdam.

Eloranta, J, 2003. Characterization of the pre and post blast environments. Paper presented at the The annual Conference on Explosives and Blasting Technique.

Galvez, N, 2017. Estudio de la energía específica de perforación de pozos de tronadura como predictor de tratamiento en corto plazo en Compañía Teck Carmen de Andacollo. (Ingeniero Civil Metalúrgico), Universidad Tecnica Federico Santa María.

Hatherly, P, Leung, R, Scheding, S and Robinson, D, 2015. Drill monitoring results reveal geological conditions in blasthole drilling. *International Journal of Rock Mechanics and Mining Sciences*, 78, 144–154. doi: http://dx.doi.org/10.1016/j.ijrmms.2015.05.006.

Jain, A K and Singh, D P, 1993. Specific Energy as a Criterion for Drillability of Rocks – a Laboratory Study. *Geotechnical Instrumentation and Monitoring in Open Pit and Underground Mining*, 253–263.

Kadkhodaie-Ilkhchi, A, Monteiro, S T, Ramos, F and Hatherly, P, 2010. Rock Recognition From MWD Data: A Comparative Study of Boosting, Neural Networks, and Fuzzy Logic. *IEEE Geoscience and Remote Sensing Letters*, 7(4), 680–684. doi: 10.1109/Lgrs.2010.2046312.

Khorzoughi, M B, Hall, R and Apel, D, 2018. Rock fracture density characterization using measurement while drilling (MWD) techniques, *International Journal of Mining Science and Technology*, 28(6):859–864.

Lebel, J R G, 1984. An investigation to evaluate the relationship between rock quality index (RQI) and powder factor for surface mining. (Master of Applied Science Text), The University of british Columbia, Vancouver, Canada. Retrieved from https://open.library.ubc.ca/collections/831/items/1.0081071.

Leighton, J C, 1982. Development of a correlation between rotary drill performance and controlled blasting powder factors, Retrieved from https://open.library.ubc.ca/collections/831/items/1.0095103.

Manzoor, S, Liaghat, S, Gustafson, A, Johansson, D and Schunnesson, H J E G, 2020. Establishing relationships between structural data from close-range terrestrial digital photogrammetry and measurement while drilling data. 267, 105480.

Meador, R A, 2009. Logging-While-Drilling A Story Of Dreams, Accomplishments, And Bright Futures. Paper presented at the SPWLA 50th Annual Logging Symposium, The Woodlands, Texas.

Napier-Munn, T, 2014. Statistical Methods for Mineral Engineers - How to Design Experiments and Analyse Data: Julius Kruttschnitt Mineral Research Centre.

Navarro, J, Sanchidrián, J A, Segarra, P, Castedo, R, Costamagna, E and López, L M, 2018. Detection of potential overbreak zones in tunnel blasting from MWD data. *Tunnelling and Underground Space Technology*, 82, 504–516. doi: https://doi.org/10.1016/j.tust.2018.08.060.

Paredes, C, Jokovic, V and Kanchibotla, S, 2018. Prediction of run of mine particle size distribution and grinding circuit performance using blast hole drilling data. Paper presented at the 12th International Symposium on Rock Fragmentation by Blasting.

Park, J and Kim, K, 2020. Use of drilling performance to improve rock-breakage efficiencies: A part of mine-to-mill optimization studies in a hard-rock mine, *International Journal of Mining Science and Technology*.

Peck, J P, 1986. Application of drill monitoring to rock mass characterization. (Master of Engineering), McGill University.

Rabia, H, 1985. Specific Energy as a Criterion for Bit Selection. *Journal of Petroleum Technology*, 37(8), 1225–1229.

Rai, P, Schunesson, H, Lindqvist, P A and Kumar, U, 2015. An Overview on Measurement-While-Drilling Technique and its Scope in Excavation Industry. *Journal of The Institution of Engineers (India): Series D*, 96(1), 57–66. doi: 10.1007/s40033–014–0054–4.

Schunnesson, H, 1996. RQD predictions based on drill performance parameters. *Tunnelling and Underground Space Technology*, 11(3), 7. doi: 10.1016/0886–7798(96)00024–7.

Simkus, R and Dance, A, 1998. Tracking Hardness and Size: Measuring and Monitoring ROM Ore Properties at Highland Valley Copper. Paper presented at the AusIMM Mine to Mill Conference (The Australasian Institute of Mining and Metallurgy: Melbourne).

Somerton, W H, 1959. A laboratory study of rock breakage by rotary drilling. *Journal of Petroleum Technology*, 2016, 6.

Stark, S, Perkins, T and Napier-Munn, T J, 2008. JK drop weight parameters – a statistical analysis of their accuracy and precision, and the effect on SAG mill comminution circuit simulation, in *Proceedings of MetPlant 2008 Conference* (The Australasian Institute of Mining and Metallurgy: Melbourne).

Teale, R, 1965. The concept of specific energy in rock drilling. *International Journal of Rock Mechanics and Mining Sciences and Geomechanics Abstracts*, 2(1), 57–73. doi: http://dx.doi.org/10.1016/0148–9062(65)90022–7.

van Eldert, J, Schunnesson, H, Johansson, D and Saiang, D, 2018. Measurement While Drilling (MWD) technology for blasting damage calculation. Paper presented at the 12th International Symposium on Rock Fragmentation by Blasting, FragBlast12.

van Oosterhout, D, 2016. Use of MWD data for detecting discontinuities.

Vezhapparambu, V S, Eidsvik, J and Ellefmo, S L J M, 2018. Rock classification using multivariate analysis of measurement while drilling data: Towards a better sampling strategy. 8(9), 384.

Strategic and tactical mine planning considering value chain performance for maximised profitability

R Smith[1], F Faramarzi[2] and C Poblete[3]

1. Global GEOVIA Services Director, Dassault Systèmes, Brisbane Qld 4000.
   Email: ralph.smith@3ds.com
2. Global Senior Mining Industry Consultant, Dassault Systèmes, Brisbane Qld 4000.
   Email: farhad.faramarzi@3ds.com
3. GEOVIA R&D Apps Portfolio Senior Manager, Dassault Systèmes, Santiago, Chile.
   Email: cristian.poblete@3ds.com

ABSTRACT

In the minerals industry, 'value' is the difference between the expected revenue derived from saleable minerals and the costs required to liberate them from gangue. In the early 1990s, it was found that the interconnected nature of mining and minerals processing provides an opportunity to unlock additional value by breaking from the established practice of silo-based cost minimisation to focusing on maximising profit across the value chain. The approach of 'Mine-to-Mill' was thus formalised as an operating strategy aiming to improve profitability through leveraging blast intensity for increased milling throughput. However, today the mining sector not only has to deal with more complex orebodies at lower grades, but there is also an accelerating need to develop sustainable capabilities and continuously upgrade its practice for addressing other challenges; of the intensified global demand for commodities, limited resources, market volatility and also new environmental and social regulations/responsibilities. Therefore, this level of sophistication necessitates innovative solutions for effective response to changed situations, hence setting real-time optimising strategies towards risk mitigation and value maximisation.

The constant challenge for any mining operation whichs to align strategic and tactical objectives. Strategic Mine Planning is a long-range production planning which aims at maximising the value from the exploitation of an ore deposit, while Tactical Mine Planning focuses on short-range plans to maintain operational viability. With recent advances in technology and data analytics, there is an opportunity to integrate key mining and processing stages. That is, integrating existing isolated mine production planning and optimisation strategies with the downstream KPIs, assessing performance through scenario-based simulations, and then dynamically re-optimising production plans for maximised profitability across the value chain over the mine lifespan.

This paper offers a methodological framework for integrating mine production planning and downstream process performance. A 'Holistic Model of Mine Optimisation' is conceptualised, which relies on GEOVIA's capabilities ranging from mineral resources modelling, design and planning to simulating process plants through evaluation of 'what-if' scenarios. A case was exemplified for a Cu-Ag-Ag deposit, and the potential impact of implementing Mine-to-Mill improvement strategies was quantified at a strategic level through simulating several scenarios. Improvement ranges of three key variables of mining rate, milling rate and Cu recovery were considered for analyses which were based on several reported Mine-to-Mill projects. The results implied the potential to improve the Net Present Value (NPV) by 15 per cent without deploying Capex only through maintaining Mine-to-Mill optimisation strategies. This approach offers sustainable solutions for unlocking the potential for improving the NPV over life-of-mine for green – and brownfield projects through practicing Mine-to-Mill basics, which essentially would assist with better decision-making by aligning optimisation objectives across the value chain. The developed approach is proposed, case examples presented, and implications discussed.

INTRODUCTION

From the early 1900s, mining and processing have been operated as separate silos. The former was focused on producing ore at a required rate and cut-off grade. The latter's objective was to process ore as provided by the upstream. However, the realities of mining and processing confirm a series of interconnected and sequential stages aiming at removal, transportation and size reduction of ores for liberating valuable minerals from the gangue. This interconnected nature of the minerals industry

motivated a paradigm shift from silo-oriented optimisation strategies to value-based, integrated approaches. The new paradigm demands optimal contribution of each stage towards maximising overall value across the value chain rather than realising silos' distinct objectives – widely known as 'Mine-to-Mill' since the the early 1990s. Recognition of the importance of drill-and-blast as the first step in comminution, let to the approach aiming at manipulation of blast designs to produce more appropriate mill feed size distributions for improved grinding capacity. The Mine-to-Mill approach is now widely implemented in the mining industry across the globe, with documented productivity gains in the range of 5–20 per cent (Burger *et al*, 2006; Hart *et al*, 2001; Kanchibotla *et al*, 1999; Scott *et al*, 2002; Valery *et al*, 2019). From the mining perspective, drill-and-blast is an excavation method for exploiting an ore deposit rather than tailoring feed size distribution for increased milling throughput. The mining stage is mainly concerned with '*in time* extraction and transportation' of certain volumes of material within a time frame, which has to be executed in sequence following a 'mining plan'. The time frame defines the nature and hence key objectives of mine planning strategies, commonly known as 'Strategic' for long-range and 'Tactical' for short- and medium-range planning.

Today, the mining sector is confronting new challenges in dealing with more complex ore deposits at lower grades and the elaboration of social and environmental concerns, limiting the effectiveness of conventional strategies if not nullify. Therefore, the next generation of Mine-to-Mill should adapt the emerging techniques and technologies in field measurement, ore characterisation, data analytics, advanced control systems, ore pre-concentration, blending strategies, valourisation of low-grade dumps, waste management, modelling and simulation in a more sophisticated and inclusive manner. This offers new opportunities to further improve downstream gains by leveraging more variables and allows for effective integration of mining and processing stages. With this proviso in mind, application of Mine-to-Mill should not be limited to downstream gains, but also could be deterministic in Strategic and Tactical Mine Planning. That is, the development of stochastic analysis to quantify Mine-to-Mill impacts at strategic and tactical levels, which are deterministic in achieving economic and strategic targets of mining companies.

Optimisation is a continuous and data-driven endeavour for mining projects, which materialises when maximum profitability is achieved across the value chain. The measures for an optimised operation frequently change with an update of information on resource properties and market initiatives, which ultimately determine the expansion or contraction of mining projects. Therefore, in the presence of large uncertainties, integrated modelling solutions would accelerate the real-time alignment of upstream and downstream objectives more interactively. Simulation is an established approach for exploring the feasibility and impact of 'change(s)' on Key Performance Indicators (KPIs) through analysis of 'what if' scenarios. Scenario-based analysis has been widely used in mining and processing with exemplified applications in optimising upstream (Godoy, 2018; Morales *et al*, 2019; Poblete *et al*, 2016b; Rimélé *et al*, 2020; Smith *et al*, 2021) and downstream (Carrasco *et al*, 2016; Faramarzi *et al*, 2018, 2019; Grundstrom *et al*, 2001; Kanchibotla *et al*, 1999; Scott *et al*, 2002) KPIs. Accordingly, this study reviews several Mine-to-Mill case studies in the Asia Pacific region with the aim to establish linkages between KPIs of mining and processing disciplines at a strategic level and improve our understanding of their interdependence through analysis of scenarios. A few published works have highlighted the interdependence of mine planning and processing, but without quantifying the impacts on strategic and tactical measures. In this respect, a well-structured study was conducted at the Mount Isa lead-zinc to explore the flotation performance of ore sourced from key mining domains (Munro, 1986; Young *et al*, 1997). This resulted in adopting a pre-concentration strategy to reject some ore from the mine plan, which lowered the tonnage of ore being mined and processed. Moreover, Bye (2011) documented case studies mainly centred on spatially modelling and applying geo-metallurgical/geo-technical attributes and discussed potential benefits to mine planning and economic optimisation. He pointed out the significance of ore variability on mine valuation, production schedule and economic gains. In an example, Bye (2011) employed a geo-metallurgical model to gain further value from geo-metallurgical initiatives by incorporating them into block models to show the impact of ore variability on the mine plan and identified high-risk periods to optimise the mine schedule.

In this paper, we document proof of concept of an outcome-based solution developed at GEOVIA Dassault Systèmes, which expectedly assists the minerals industry with improved operational viability and sustainability. The proposed solution extends the application of conventional 'Mine-to-

Mill' to the mine planning space. A scenario-based example is developed in the context of Mine-to-Mill based on considered case studies, demonstrating the potential for unlocking additional value for the whole mine lifespan by using the most-trusted software package in Strategic Mine Planning GEOVIA Whittle™.

STRATEGIC VERSUS TACTICAL

In mine planning, Strategic and Tactical encapsulate objectives to be achieved at certain timespans over the life-of-mine (LOM).

Strategic Mine Planning aims at capturing maximum potential value from the exploitation of an ore deposit on an annual time scale, generally expressible in Net Present Value (NPV).

Tactical Mine Planning aims at ensuring viability and sustainability of the strategic planning at an operational level on monthly or even weekly scales. Therefore, it tracks and measures operational performance regarding its alignment with strategy, and corrective action is taken when required to minimise the gap between planned versus actual practice.

In the context of Mine-to-Mill optimisation, with extending its application to the realm of mine planning, we propose approaches as follows:

- Strategic Mine-to-Mill
- Tactical Mine-to-Mill

Strategic Mine-to-Mill aims at considering and quantifying potential gains from applying Mine-to-Mill optimisation strategies in long-term, for capturing maximum economic potential of ore reserves. The key objective would be to establish linkages between strategic KPIs of a mining project (eg NPV, IRR, and LOM) and performance improvement possibilities in the downstream. This level of integration allows for a more realistic assessment of overall value by harmonising upstream and downstream activities at a strategic level.

Tactical Mine-to-Mill centres on the realisation of Strategic Mine-to-Mill by implementing Mine-to-Mill optimisation strategies in a sustainable manner. In general, Tactical Mine-to-Mill applies conventional Mine-to-Mill strategies to maximise profitability across the value chain by improving process performance (eg throughput, target product size, recovery) and to ensure objectives of the Strategic Mine-to-Mill are fulfilled.

Overall, the conceptualised Strategic and Tactical Mine-to-Mill approaches aim to integrate key stages exploration, mining and processing and interrogate their interdependence through simulating 'what-if' scenarios. To further explain, achieving objectives of Strategic Mine-to-Mill depends on downstream gains and accounts for reliability the '*block model*' used for development of a strategic mine plan. Therefore, the extent of exploration activities, resource modelling and estimation and mine design considerations are respected. The representativeness of the block model improves during the LOM through continuous accumulation of orebody knowledge, which assists with fine-tuning adopted strategies for optimal outcomes. The Tactical Mine-to-Mill uses the block model for delivering short- and medium-range schedules. It engages drill-and-blast progress, haulage system, blending strategies, destination and flow of materials of different types. The Tactical Mine-to-Mill takes place at an operational level, not only accounts for blasting outcomes (ie muck pile fragmentation and ore loss/dilution) but also it engages timing and characteristics of material flow across the value chain – which should assist with *ore/waste tracking* most useful for ore feed quality and waste management.

WHERE ARE OPPORTUNITIES?

Mine-to-Mill optimisation is a well-established technique with a range of applications for improvement and optimisation of process performance. It effectively leverages the drill-and-blast practice to influence downstream stages' performance by implementing blast-induced changes to ore feed size distribution (Morrell and Valery, 2001), breakage, and physical properties (Michaux and Djordjevic, 2005). These then translate into changes in crushing and screening performance (Kojovic *et al*, 1995), AG/SAG mill throughput (Hart *et al*, 2001; Nielsen and Kristiansen, 1995), and flotation. Several examples are but are not limited to the influence of blast fragmentation on crushing and

screening performance (Kojovic *et al*, 1995), and AG/SAG mill throughput (Dance, 2001; Michaux and Djordjevic, 2005; Morrell and Valery, 2001; Nielsen and Kristiansen, 1995) and flotation (Valery *et al*, 2019). However, as exemplified in this paper, the Strategic and Tactical Mine-to-Mill aims at real-time re-scale of mining and processing activities for optimal outcomes in response to large uncertainties introducible to most operations.

A more advanced Mine-to-Mill strategy should incorporate key processing parameters into the mine planning for improved '*productivity*' of the whole value chain (mineral reserve-to-metal) over LOM rather than boosted '*production*' (ie mill throughput) gains maximised value, ie NPV. This approach would further support the sustainability of green- and brownfield mining projects via operational leverages, as further explained below.

- Project risk mitigation options at strategic and tactical levels:

  To de-risk mining projects, it is necessary that the interaction between key stages across the value chain being captured in a quantitative manner. This allows for the short and long-term development of tailored strategies for scaling mining and processing activities which most reflects on orebody characteristics, hence mitigates 'unknown' risks associated with CAPEX and OPEX. Embedding Mine-to-Mill possibilities into Strategic and Tactical Mine Planning procedures is a dynamic approach which aims at estimating value over LOM in real-time, so corrective actions are taken when required for minimising the gap between planned versus actual practice or improvement strategies implemented when the opportunity is recognised.

- Improving sustainability at the operational level:

  As aforementioned, Strategic and Tactical Mine Planning leaves the door open to improvement opportunities which is critical to the sustainability of current and future mining operations. There is no limit to confronting challenges to the mining sector, which can limit the effectiveness of conventional strategies if not nullify. Strategic and Tactical Mine-to-Mill has to account for the integration of emerging technologies towards risk mitigation and value maximisation. As mining operations adapt the emerging techniques and technologies in practice, surveying and data analytics, automation and control systems in a more sophisticated manner; then the influence of such changes/improvements has to be reflected at a strategic and tactical level over LOM. That is, expressing value as a dynamic measure *'in practice'*, so it requires re-evaluation for best representing the economic status of a project.

- Harmonising upstream and downstream activities:

  The upstream activities are mainly concerned with removal of *in-situ* rock volumes in sequence, and then depending on transferring them to different destinations based on their value (ie grade/metal content). The key objective of downstream activities is to extract value from the material provided by the upstream, which may not necessarily result in maximum profitability. However, the question is:

  - What if, we tailor/scale the upstream activities eg planning, blasting, loading and haulage to provide the downstream with the material, which gains optimal *productivity* across the value chain?

  This obviously requires tuning conventional mine plans to account for new considerations and establish harmony between the mining and processing stages in short, medium and long-terms. It is important to note that the heterogeneous nature of orebodies introduces large uncertainties into all quantitative evaluations, design, and predictions (Faramarzi *et al*, 2020). The extent of the variability of ore changes across the value chain, and hence its impact. A better understanding of the flow of material of different types from the pit to the process plant should assist with better 'waste/ore tracking' for ore feed quality and variability management. More importantly, it helps quantify the impact of ore-induced operational variations (ie production bottlenecks or poor productivity) on the viability of mining projects in different timespans.

- Waste management and valourisation:

  Commodity price volatility is an ever-present and influential factor in decision-making at both strategic and tactical (or operational) levels, which ultimately determine expansion or

contraction of mining projects. Strategic Mine-to-Mill might provide a better understanding of 'value volatility' over LOM. The development of stochastic analysis for price changes and accordingly estimating contingencies for difficult periods, or potential gains from the valourisation of 'low-grade' material. This area requires further investigation and development of robust techniques in future because appropriate management of waste/low-grade materials is critical to the sustainability of green- and brownfield mining projects.

MINE-TO-MILL CASE STUDIES IN ASIA PACIFIC REGION

Review of selected case studies

The Mine-to-Mill approach has been implemented at many mining operations worldwide, showing that the capacity and efficiency of crushing and grinding processes are significantly influenced by run-of-mine (ROM) size distribution, which is driven by the blasting. Through modelling and simulation, McKee *et al* (1995) indicated the potential for 20 per cent higher grinding capacity achievable by tailoring the blast-induced PSD. The practice has resulted in billions of dollars of additional value to the minerals industry since 1990s, mainly achieved through increased throughput. Many of these are documented, and operational improvements gained are reported. In this section, we review several Mine-to-Mill optimisation projects commissioned in the Asia Pacific region across gold, copper, lead and zinc commodities. Each project offers exclusive lessons to learn depending on their considerations and characteristics, providing a better understanding of possibilities if embedded in the mine planning context.

Case Study #1 – Cadia Hill Gold Mine, Australia

The Cadia Hill concentrator was commissioned in July 1998, aiming at processing 2065 t/h of monzonite ore, giving an annual processing rate of 17 Mtpa. Hart *et al* (2001) reported a range of strategies for SAG mill capacity debottlenecking and improving overall performance of Cadia Hill comminution circuit – one of which strategies was Mine-to-Mill optimisation. A reduction in SAG mill feed size F80 to 70 mm increased throughput between 10–15 per cent. Accordingly, the powder factor increased from the standard 0.8 to 1.2 kg/m^3 for improved fragmentation, which resulted in a 10 per cent higher throughput by improving the SAG feed rate from 2270 to 2505 t/h. More intense blasting by tightening the drill pattern (Burden × Spacing) produced more 'fines', visually evident during the trial and confirmed by lower pebble recycle rates. A finer PSD from intense blasting increased SAG mill power draw but resulted in overall lower specific power consumption.

Case Study #2 – Porgera Gold Mine, Papua New Guinea

Progeria Joint Venture and Dyno Nobel identified the SAG mill as a production bottleneck, in particular when milling hornblende diorite (Lam *et al*, 2001). The Mine-to-Mill project centred on optimising blast design for improving the milling rate by altering the feed size distribution. For this purpose, the blasting powder factor was increased from the standard 0.24 to 0.38 kg/t, which reduced SAG feed P50 from 75 to 35 mm. Thus, the finer feed boosted the SAG milling rate from 673 to 774 t/h, which equals a 15 per cent increase in SAG milling throughput.

Case Study #3 – Ernest Henry Copper-Gold Mine, Australia

The Ernest Henry Mine concentrator, commissioned in August 1997, with a nominal throughput rate of 1200 t/h. Strohmayr and Valery (2001) conducted an extensive optimisation program which included filed surveys, ore characterisation, blast fragmentation modelling, comminution modelling and simulations. In this Mine-to-Mill project, alternative blast designs in conjunction with a closer crusher gap (from 130 to 115 mm) improved SAG mill throughput. More intense blasting provided more favourable feed size distributions as the amount of fines (below 10 mm) in the feed increased from 18.6 per cent (standard blast practice) to 21.4 per cent in blast designs with higher powder factors. The study confirmed the potential to increase mill throughput to 12 per cent by altering the blast designs and primary crusher gap (Strohmayr and Valery, 2001).

Case Study #4 – KC Gold Mine, Australia

The KC Gold Mine (KCGM) treats ore from the Super Pit at Kalgoorlie. Kanchibotla *et al* (1998) explored the interdependence between fragmentation size distribution from blasting and SAG mill throughput. Standard blast design with powder factor of 0.58 kg/m^3 compared to modified designs with powder factors of 0.66 (Design 1) and 0.96 kg/m^3 (Design 2). The simulations indicated that the SAG mill feed rate of 1250 t/h from standard blasting could be improved up to 1480 t/h, which equals 18.4 per cent higher milling capacity. This study argued possible pitfalls of intense blasting from the dilution viewpoint and more importantly highlighted the need for the energy balance between the SAG and ball milling circuits as well as loss of recovery for a changed final grind size.

Case Study #5 – Batu Hijau Copper-Gold Mine, Indonesia

The key objective of commencing Mine-to-Mill at the Batu Hijau Copper-Gold operation was to modify blasts for improved SAG mill throughput (Burger *et al*, 2006; McCaffery, 2006). For different zones of the orebody, regression models were developed to predict throughput separately for 16 domains. In addition to grinding capacity, it was recognised that a domain-based blasting strategy should also improve loading rates through fragmentation top size reduction. Between 2006 and 2011, extensive orebody characterisation allowed for improvement of blasting and mill throughput predictive models and coding mill throughput predictive equations into the mine block model, which was used for short and long-term production planning based on mill throughput prediction to ±2.0 per cent accuracy.

Productivity gains of 10 per cent for loading rates in the pit and 10–15 per cent increases in SAG mill throughput for individual ore domains were reported. The Sandsloot mine is another example where a modified blasting strategy was deployed for improving operational performance (Bye, 2006). Loading rate and milling performance were monitored at this mine between 2001 and 2003, which demonstrated a significant impact of powder factor on these KPIs by 18 per cent improvement in average milling rate, and 13 per cent increase in average instantaneous load rate (ore and waste).

Case Study #6 – Mount Isa Lead and Zinc Mine, Australia

The case study of Mount Isa Lead and Zinc Mine demonstrates benefits from applying integrated mining and processing strategies in a different space through cut-off grade control for improved flotation performance (Young *et al*, 1997). It was noticed that determination of ore cut-off grade without accounting for flotation performance of ore from different sources in the mine results in poor prediction. Recognising the interconnected nature of mining stages, a new strategy was adopted to establish the link between head grades of each ore type, concentrate grades, recovery as well as capital and operating costs for each mined ore resource. Because of alignment of the mining practice with downstream objectives, 30 per cent of the 'low-value' ore was removed from the mine schedule, which reduced operating costs, while improved recovery of silver, lead and zinc by 5.0 per cent, 5.0 per cent and 2.0 per cent, respectively.

Implications from the case studies

Numerous Mine-to-Mill case studies at mining operations across the globe provide a reliable base from which to integrate and harmonise the upstream and downstream stages for maximised controllability and, therefore value. The literature does not reflect long-term outcomes of implementing Mine-to-Mill at the operations – if the changes were sustained for a while. However, the authors believe that Mine-to-Mill strategies determined at a specific time frame, need continuous re-visit because of the thin line between profit and loss in mining industry.

The review of selected case studies commissioned in the Asia Pacific region, provides a base for the proof of concept by indicating improvement potentials. The conventional Mine-to-Mill studies imply the potential to improve milling capacity by 20 per cent (from intense blasting), productivity gains of 10 per cent for loading rates in the pit (from intense blasting) and metal recovery up to 5 per cent (from ore feed quality management). These values vary by site; however, in this paper, we use the values to quantify the impact of such improvements over LOM at strategic and tactical levels. The authors acknowledge that there are other improving techniques such as coarse flotation and Grade Engineering®, application of novel explosives etc, which can significantly enhance profitability and sustainability of mining operations. In this paper, we mainly focused on conventional

Mine-to-Mill leverages; however, there is no limit for applying other technologies to improve the overall practice, all of which are well-settled within the Mine-to-Mill optimisation context developed in the early 1990s.

METHODOLOGY

The Strategic Mine-to-Mill optimisation comprises several strategic steps required for unlocking maximum potential economic gains from an ore reserve. The term 'strategic' in this concept aims at aligning the steps with the strategic objectives of the project (Figure 1).

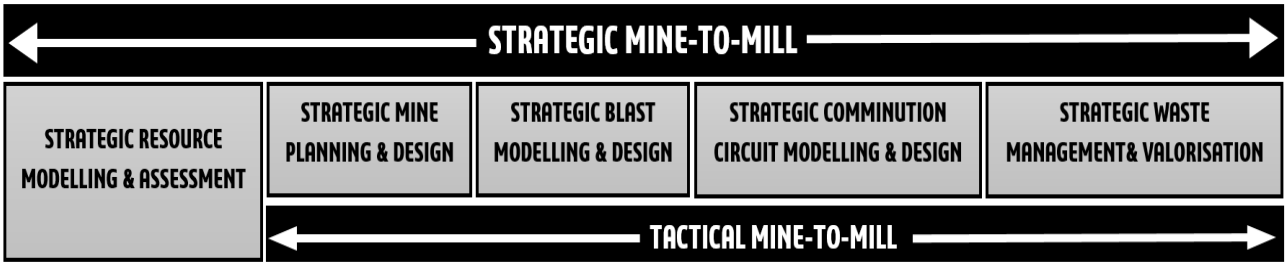

FIG 1 – Strategic Mine-to-Mill and involved stages.

Key requirements of applying any Mine-to-Mill optimisation are as follows:

- Data acquisition across the value chain:

  Data collection, curation, analysis, and interpretation are important parts of any quantitative evaluation, and Mine-to-Mill has been no exception. For the diverse nature of mining stages in practice, a wide range of information has to be analysed in order to quantify the interaction between them, which also necessitates effective communication between people of different disciplines/specialisations across the value chain.

- Access to reliable software packages for modelling and evaluation:

  There are numerous technologies available in the industry ranging from simple to sophisticated, which assist specialists in their everyday decision-makings. GEOVIA Dassault Systèmes software capabilities (with over 17 000 active users) covers geology modelling, resource estimation and mine design (GEOVIA Surpac™), Strategic Mine Planning (GEOVIA Whittle™), Tactical Mine Planning and scheduling (GEOVIA MineSched™). For simulation purposes, simulation process automation and design optimisation solutions (SIMULIA and CATIA Products) provide a reliable base for integrating and optimising all mining stages through the development of 'what-if' scenarios. In blasting and processing fields, the JKSimBlast® and JKSimMet® software packages developed by Julius Kruttschnitt Mineral Research Centre, The University of Queensland, are among the most widely-used products in the field, which have been used for decades in Mine-to-Mill projects worldwide. It is evident that applying Mine-to-Mill at strategic and tactical levels requires suitable tools and technologies critical to each stage. In this paper, an outcome-based solution is proposed based on some of the most industry-trusted software packages available in the minerals industry. Today with the fast progress of technology in computation, measurement, data analytics and simulation areas, it is expected that more sophisticated technologies are being developed for modelling, simulating and controlling all stages of ore resource exploitation on platforms in a real-time manner.

Data requirement

To develop a holistic model of a mining operation, representative data has to be collected sufficiently across the value chain. Availability and representativeness of data is critical to modelling and process design. A detailed data-related discussion is beyond the scope of this paper, and could be found elsewhere (Hustrulid and Kuchta, 1995; Napier-Munn, 2014; Napier-Munn *et al*, 1996). However, the nature of data requirements is briefly addressed here. In general, the data required for Strategic Mine-to-Mill can be categorised depending on its applicability:

- *The data required for Strategic Resource Modelling and Assessment*:

  Resource estimations underpin multi-million-dollar investment decisions made by mining companies, strategic decisions along with financial, social and environmental considerations. Geological databases acquired from drill holes are the most common set of data used for Strategic Resource Modelling and Assessment. The information from drill holes describes the location of the drill hole collar, the maximum depth of the hole and whether a linear or curved hole trace will be calculated when retrieving the hole. This information combined with data acquired from topographic surveys and characterisation test works conducted on retrieved cores (eg assays, geological, geotechnical and chemical properties of deposit at different subsurface spatial coordinates) are used to describe an orebody. An outcome of this stage is a block model, which describes orebodies properties, eg shape, volume and characteristics through size cubes or cuboids. A block model is critical to all quantitative evaluations in most mining operations, where upstream and downstream data such as mining, blasting and metallurgical data can be coded into it to describe impact of mined blocks on operational performances. GEOVIA Surpac™ is one of the world's most popular software, supporting open pit and underground operations and exploration projects.

- *The data required for Strategic Mine Planning and Design*:

  The resource block model is the data library, which is used for mine planning and design at strategic and tactical levels. A wide-range of information is utilised at this stage, which covers topographic surveys, rock mass and ore geological, mechanical, metallurgical characterisations, mining and processing capacity, elements prices, and costs imposed across the value chain over LOM.

- *The data required for Strategic Blast Modelling and Design*:

  The essential task to break rock down into a specific size fraction starts at the very beginning by drilling and blasting operations and continues by subjecting ore to a series of breakage processes through comminution machines. This proceeds to the point where particles meet appropriate size criteria for being treated in a beneficiation process. Strategic Blast Modelling and Design aims at optimal overall productivity, which is reachable if design criteria are aligned with a project's strategic objectives. The key data required for this practice could be described as pre-blast and post-blast. Key pre-blast information required is rock mass properties, explosives properties, operational and safety considerations. Post-blast data are but not limited to fragmentation size distribution, backbreak, ground vibration, noise, flyrock, movement and ore dilution, dust and Nox emissions.

- *The data required for Strategic Comminution Circuit Modelling and Design*:

  To model a process plant is to configure a flow sheet, which illustrates units and their interaction. An initiative of a flow sheet is to model the state of the process. Irrespective of simulation structures, to develop a 'base-case' model, consistent data has to be collected sufficiently, which can be sourced from site and plant surveys, laboratory experiments, value chain instrumentation, technical reports etc. Today, some industry-trusted examples of simulating packages are JKSimMet® (Morrison and Richardson, 2002), MODSIM (King, 1990), SysCAD (Stepto *et al*, 1990) and MolyCop Tools (Silva *et al*, 2015) with a range of useable unit models incorporated in them. Reliable comminution circuit modelling and design is a strategic step towards harmonising upstream and downstream activities and is critical to project economics. The data should be sourced from plant surveys; nonetheless, an alternative might be considering the operational history of the plant, namely 'historic or operational data'. Common data is a requirement of this stage but not limited to the units/equipment design and operational characteristics, ore properties (eg A, b, ta, SPI, BWi, density, grade, mineralogy), flow characteristics through streams (eg mass flow, percent solids, size distributions), operational considerations (eg power draws, mill fractional speed, screen sizes, hydrocylones pressure, target size), and KPIs (eg throughput, recovery).

- *The data required for Strategic Waste Management and Valourisation*:

  Developing a plan for managing current and future waste/low-grade material should be part of any strategic decision-making. In addition to ore physical, mechanical, metallurgical and

chemical properties, it would be worth creating a data set including the location of dumped materials of different kinds by deploying GPS-based and survey techniques, or even track of material by implanting RFIDs. Such information should assist with generating new block models of waste dumps for future modelling and assessment practices.

- *The data required for continuously improving accuracy and precision of strategic stages*:

  Finally models of mining and processing activities developed based on operational data represent a narrow time frame and will lose their fidelity over time due to frequent variations introducible within a mine life cycle. The fidelity of a model can be assessed by comparing the degree of agreement between actual and predicted values where an error is given as a quantitative measure of the discrepancy. For the models representing operational stages a 'mean absolute error' within ±10 per cent is desirable. As a measure of precision, the Relative Error (RE) expresses magnitude of error relative to the measured/actual value, which reads:

$$Relative\ Error(\%) = 100 \times \frac{(Measured\ Value - Predicted\ Value)}{Measured\ Value} \quad (1)$$

  Upon collecting more descriptive data by integrating and using more accurate measurement systems and sensors into mining and processing stages, a more detailed description of an orebody can be generated. This should assist decision-makers with considering unseen aspects of their plans, refine, improve or even re-define their strategic and tactical objectives.

It is important to note that not all the information collected is useful. The key objective of data curation and analysis is preparing 'relevant' and 'reliable' data. For this purpose, useful data should be discriminated from the redundant and presented in an appropriate number, format, size and units. In this process, it is also important to account for misinformation as well as disinformation. The former considers vital data missed or unavailable, and the latter refers to 'unexpected' information, ie unreliable instrument readouts. Analysis of data is an essential step, which also engages technical and analytical knowledge of individuals, eg engineers, data analytics specialists. This includes running several basic tests to ensure 'consistency' of the data by establishing relevant correlations between different values eg ore properties and KPIs. Additionally, when developing a base-case model, specifically a 'process plant' if using a software package eg JKSimMet®, it is vital to check if the data available aligns with the unit models requirements. For example, the common breakage test in most South American operations is SAG Power Index, namely SPI (Starkey *et al*, 1994), however, this index is not useable in the JKMRC AG/SAG mill model (Morrell and Morrison, 1989) as the model requires A, b (ore competence indices) and ta (ore abrasion index) values from the JK Drop Weight Test (JKDWT) (Napier-Munn *et al*, 1996). Therefore, relevant test works should be conducted, or the values should be estimated based on available indices using established correlations. As these breakage tests are extensively used, it has been a common practice for metallurgists developing correlations between the SPI and JKDWT breakage indices.

In summary, because of the very diverse nature of data generated across the mining value chain, data preparation for modelling such activities would engage multiple disciplines of geologists, geotechnical, exploration specialists, mining, blasting and process engineers, and well as data scientists. Within the context of mine planning, Couzens (1979) advised that it is 'vital to keep our objectives clearly defined while realising that we are dealing with estimates of grade, projections of geology, and guesses about economics – *we must be open to change and communicate'*.

Software packages

Strategic resource modelling, assessment and mine design – GEOVIA Surpac™

The software supports to open pit and underground operations and exploration projects in more than 120 countries. Key capabilities of GEOVIA Surpac™ are drill hole data management, geological and block modelling, resource estimation; geo-statistics, drill-and-blast and mine design.

Strategic mine planning – GEOVIA Whittle™

The software is used to evaluate the financial viability and the optimal open pit mining strategy for a deposit. It is a commercially trusted tool applied in scoping, feasibility, life-of-mine scheduling, and ongoing re-evaluation of mine plans throughout the production phase. GEOVIA Whittle™ aims at

optimal scenarios through provides the capability to consider key mining, processing, geological, geotechnical and financial considerations into any analysis at an annual timescale over LOM.

Tactical mine planning – GEOVIA MineSched™

The software provides scheduling to improve productivity for surface and underground mines of all sizes and types. GEOVIA MineSched™ aims at realisation of a strategic mine plan by taking into account operational details at monthly and weekly timescales over LOM. Tactical Mine Planning is the chain loop that facilitates harmonising the upstream and downstream stages through integration. The tool provides seamless capabilities in short- and medium-term mine scheduling by accounting for the strategic mine plan considerations, grade control, blasting sequence, haulage system, mining and processing capacities, and tracking different types of materials. It allows for the development of constraint-based scenario analysis to reach optimal and feasible alternatives, which de-risk realisation of strategic objectives.

Blasting and mineral processing – JKSimBlast®, JKSimMet® and MolyCop Tools®

JKSimBlast® is a user-friendly tool for drill-and-blast design and predicting muck pile PSD based on blast fragmentation models such as the original Kuz-Ram (Cunningham, 2005) and Crushed Zone Model (CZM). It is proven that the Kuz-Ram model underestimates the amount of fines (-25 mm) in the ROM PSD (Comeau, 2018), which significantly affects the downstream processes of crushing, grinding and flotation. Therefore, the CZM developed by JKMRC is a suitable alternative when estimating the contribution of smaller size fractions is of prime importance, specifically for Mine-to-Mill optimisation purposes because the model provides a more realistic estimation of blast-induced fines (Kanchibotla *et al*, 1999). In mineral processing, software packages such as eg JKSimMet® and MolyCop Tools® might be used for developing reliable base-case flow sheets of process plant. For example, JKSimMet® is software for comminution circuit mass balancing, modelling and simulating, which benefits from a wide range of validated comminution and separation models developed by the JKMRC (Napier-Munn *et al*, 1996).

Design of experiment

Design of experiments consists of carrying out a set of tests that allow the generation of results, which, when analysed, provide objective evidence to study the behaviour of a process, in this case Mine-to-Mill optimisation process.

The objective is quantify and analyse the influence of applying Mine-to-Mill optimisation at strategic and tactical levels – so it centres on overall value maximisation, ie Net Present Value, 'NPV'. The Net present value is the present value of the cash flows at the required rate of return of a project compared to your initial investment. In other words, it considers the 'Time Value of Money' in the assessment of an investment opportunity. Thus, near future cash flows are worth more today than distant future cash flows. The equation for NPV reads as follows (Fisher, 1930):

$$NPV = \sum_{t=1}^{n} \frac{R_t}{(1+k)^t} - C \tag{2}$$

Where C is initial capital investment, R is cash flow per period, k is the discount rate and t represents time. Another economic indicator is the Internal Rate of Return, 'IRR' which is used in financial analysis to estimate the profitability of the potential investment. IRR is a discount rate that makes the NPV of all cash flows equal to zero in a discounted cash flow analysis. In general, the higher IRR is, the more desirable an investment is to make.

In this paper, we propose an example based on implications from conventional Mine-to-Mill projects, which demonstrates the potential application of the GEOVIA Surpac™, Whittle™ and MineSched™ in the implementation of 'Strategic Mine-to-Mill' and 'Tactical Mine-to-Mill' approaches, which are conceptualised at GEOVIA Dassault Systèmes in 2021, and introduced in this paper.

The considerations and assumptions of this study are:

- The JKSimBlast® and JKSimMet® software packages are not used for the modelling nor for the analyses given in this paper. However, base-case models of downstream processes are

critical for linking and harmonising the upstream and downstream activities in an interactive manner. That is, GEOVIA Whittle™ (Strategic Mine Planning software package) is fed by downstream KPIs generated from a base-case model of a process plant, which assists with integrating the upstream and downstream KPIs, and quantify their interactions.

- This study does not consider ore loss and dilution in value quantification. However, intense blasting generally limits control over the outcomes. It increases the risk of undesirable side effects such as backbreak, ground vibration, air-blast and flyrock, and dilution, which imposes additional expenses for taking appropriate mitigation measures and control strategies. However, ore dilution is the phenomenon, which may result in a remarkable loss of value as reported before (Engmann *et al*, 2013; Esen *et al*, 2007; Eshun and Dzigbordi, 2016). It can directly affect the overall value through ore loss and disposal of waste or less valuable material to the mill. In this space, blast movement modelling and monitoring systems assist with tuning blast design parameters (ie timing, pattern, explosives properties and distribution of blast energy etc) for reduced ore loss.
- Review of several implemented Mine-to-Mill projects in Asia Pacific region implies performance improvement opportunity of up to 20 per cent in milling capacity, 10 per cent in loading rate, and 5.0 per cent in recovery. The values are used to quantitatively taking into account impact of such Mine-to-Mill induced results on strategic and tactical mine plans. Accordingly, What if scenarios will be considered in ±20 per cent, ±10 per cent and ±5 per cent for milling rate, mining rate and recovery, respectively.
- Pre-concentration in mining aims to manipulate ore feed quality by removing low value gangue material prior to the comminution process. Pre-concentration requires a suite of well-established techniques and technologies being utilised to exploit differences in physical and chemical properties of an ore to separate valuable minerals from gangue. Thus, depending on ore characteristics, a technique based on size, gravity, conductivity, competence, magnetic susceptibility, thermal reactivity etc, can assist with feed upgrade prior to energy-intensive size reduction stages – and should be used as an optimising leverage for next generation Mine-to-Mill projects. GEOVIA Whittle™ allows for grade control (improving ore feed quality) for both the pit and process plant. Accordingly, the impact of adopting an ore pre-concentration strategy on the strategic outcomes is quantified, and discussed.
- Metal (copper, gold and silver) price and selling costs are assumed constant over LOM.
- In this paper, a constant financial model is used for estimating mining and processing costs. Because of confidentiality considerations, details of financial models used cannot be shared. However, it is worth noting that implementing Mine-to-Mill practices generally results in more than doubled drill-and-blast costs, while saving money by improving loading and haulage efficiency and even safety. On the processing side, an intense blasting practice potentially could reduce the cost of processing for a given ore type by reducing the process time. To reflect such changes in cash flow across the value chain, it is required to develop *sophisticated financial models* by tracking changes over a significant timespan, which is an area of future investigation in Strategic Mine-to-Mill planning and optimisation.

Base-case development

A block model of copper-gold-silver deposit with two dominant rock types is used for developing a base-case model for quantifying the impact of downstream changes on overall value, NPV. For this purpose, GEOVIA Whittle™ was used to integrate mining throughput with downstream KPIs of mill throughput and recovery, which are the focus of this paper. It is also worth highlighting that this study specifically deals with mining production rate, process throughput and recovery as the three key KPIs that were frequently considered in previous Mine-to-Mill projects. However, these KPIs are significantly determined by geology, mineralogy and geo-mechanical properties of orebodies and quantifying the impact of such variables on mine plans is beyond the scope of this article. It is worth adding that it benefits from the 'Throughput Factor' as a useful leverage to account for the milling rate of different rock types (influenced by ore competence and feed PSD), which makes it most appropriate for Mine-to-Mill investigations. Operational constraints/considerations can be set to account for likely bottlenecks between mining and processing for any given period. Furthermore,

GEOVIA Whittle™ allows for accounting variable values for different times for any given input eg mining and milling rates, recovery, financial variables and grade targets as business objectives and hence adopted strategies may require refining changes over time (See Figure 2).

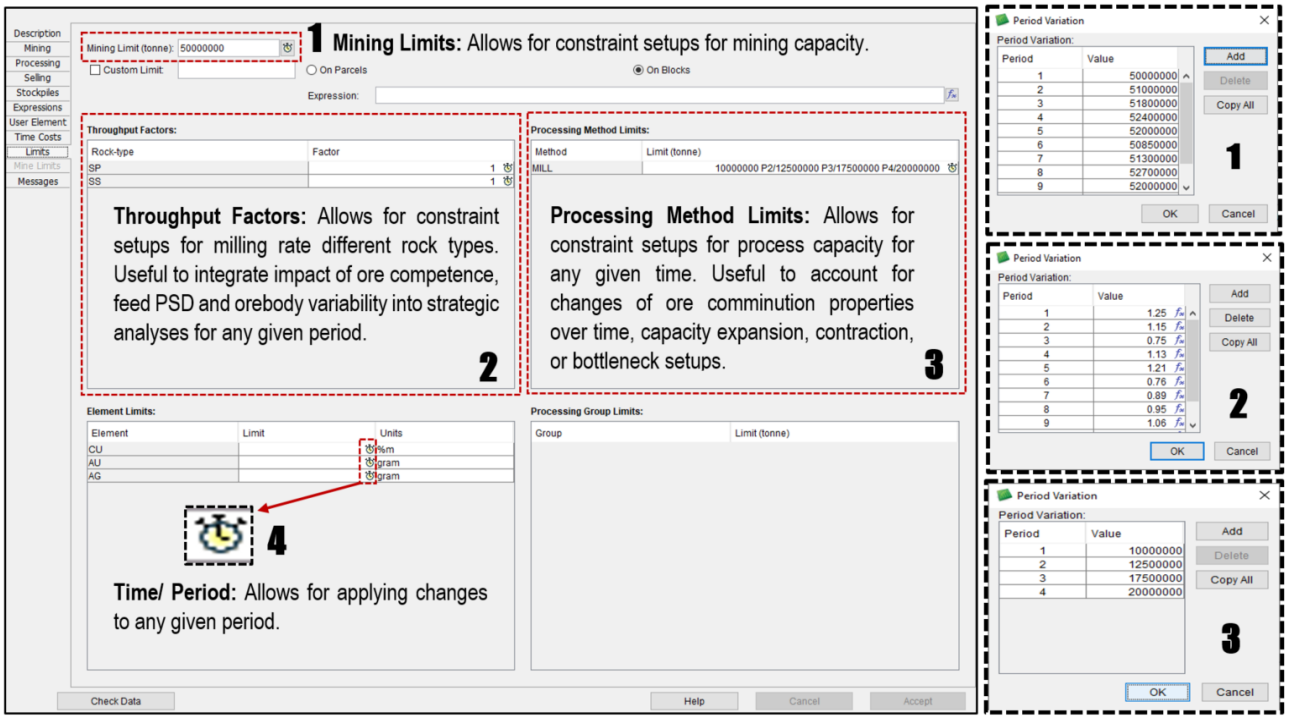

FIG 2 – Mining and processing constraints set-up interface – GEOVIA Whittle™.

The optimal pushbacks were selected through the 'directional mining' approach, which evaluates profitability through testing several mining starting points. That is, depending on orebody shape and distribution of grade within it, adopting an appropriate starting point will impact NPV as it controls 'metal yield' from any part of an orebody over time. Poblete (2016a) comprehensively describe the approach, and then estimated its influence on NPV.

In this study, we tested directions of North (0°), North-east (45°), East (90°), South-east (135°), South (180°), South-west (225°), West (270°) and North-west (315°), out of which the 'East' alternative resulted into the best outcome compared to the others.

The 3D Lerchs-Grossmann algorithm is used for pit optimisation, which accounts for block values, mining precedence and is capable of fining 3D outline with the highest possible value. For the Scheduling practice, GEOVIA Whittle™ benefits from Milawa algorithm, which combines feasible schedules into careful economic forecasting for improved NPV. Details on Lerchs-Grossmann and Milawa algorithms are beyond this paper's scope and is comprehended elsewhere (Lerchs, 1965). Figure 3 showing mining directional and phases (pushbacks) optimised for Cu-Au-Ag deposit.

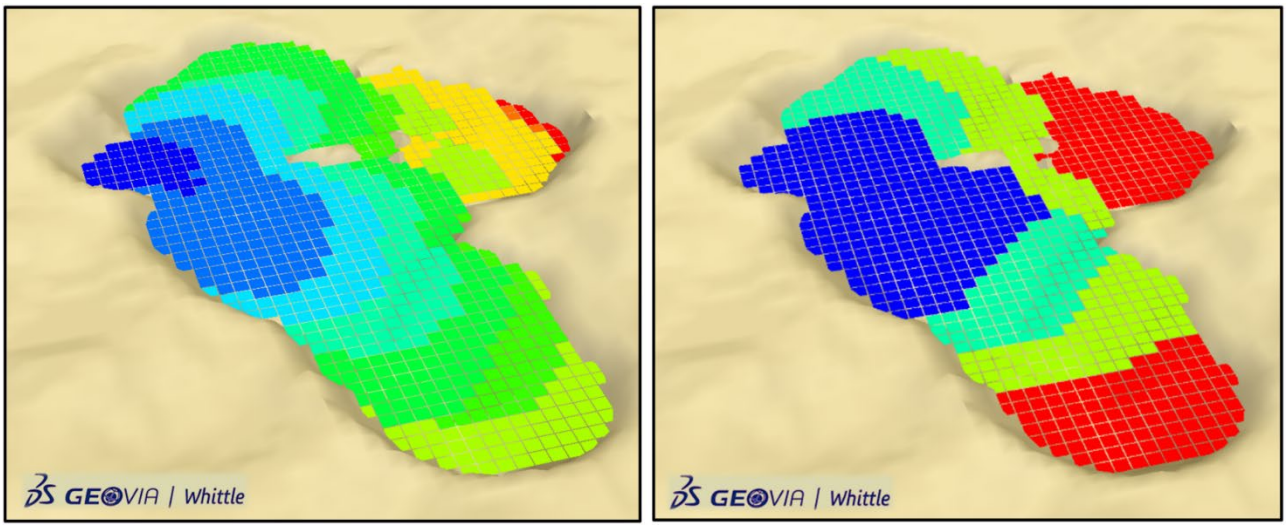

FIG 3 – Pit expansion towards East using directional mining approach (Left) and the four optimal mining phase (pushbacks) selected for scheduling purposes (right) – GEOVIA Whittle™

The pushbacks should satisfy mining and processing constraints, and produce the highest NPV from moving volumes of earth in sequence. Figure 4 shows the base-case schedule which illustrates the amount of material of different type and their destination over 17 years of mine life. Failure to provide enough ore feed results in decreased profitability, therefore strategies like having stockpiles for compensating ore feed shortage for difficult periods are helpful to maintain productivity over LOM and ensure production balance between the upstream and downstream stages.

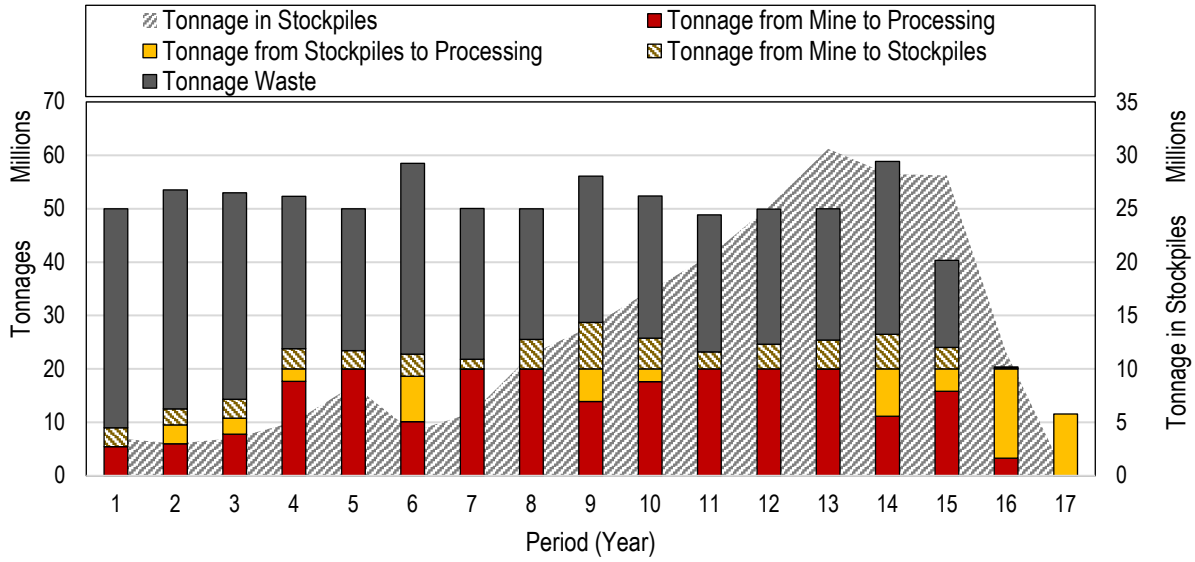

FIG 4 – Strategic scheduling: material movement over LOM, Base-Case

Figure 5 shows the scheduling for tonnage removal from each pushback. Obviously, in the 17th year of LOM, removed tonnages from the pit is zero, indicating that the ore reserve is fully exploited. The ore feed required by the process in the last two years of LOM (years 16th and 17th) is provided by the stockpiles.

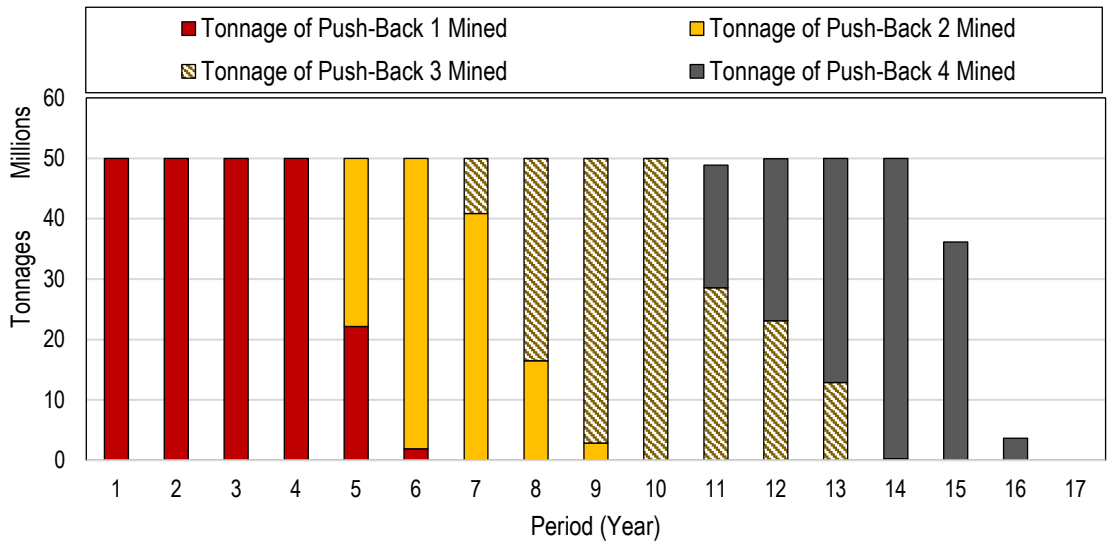

FIG 5 – Strategic scheduling: tonnage of pushbacks mined over LOM, Base-Case.

Scenario-based simulations

Three key areas of improvement by adopting a Mine-to-Mill approach are mining rate, milling rate and recovery. Based on documented values from reviewed case studies, the variation of values by 10 per cent, 20 per cent and 5 per cent were considered improvement opportunities compared to the base case. However, a poor drill-and-blast practice can be deleterious and limit value. Therefore, sensitivity analysis of individual key variables (26 scenarios) and combinations of them (8 scenarios) were conducted in the context of Mine-to-Mill.

Table 1 provides further details on development of scenario-based simulation runs for sensitivity analysis of individual key variables by using GEOVIA Whittle™.

TABLE 1

Ranges and levels of key variables used in GEOVIA Whittle™ (26 scenarios).

Description	Variation	Scenarios	Unit	Minimum	Base-case	Maximum
Mining Capacity/Rate	± 10.0% @ 2.5% Levels	8	t/h	5137	5708	6279
			t/d	123 288	136 986	150 685
Milling Capacity/Rate	± 20.0% @ 5.0% Levels	8	t/h	1826	2283	2740
			t/d	43 836	54 795	65 753
Cu Recovery	± 5.0% @ 1.0% Levels	10	%	78	83	88

Four scenarios were considered for evaluating potential losses and gains from optimising key variables of mining and milling rates as well as recovery in a Mine-to-Mill context:

- Scenario 27: Mining Rate = -10%, Milling Rate = -20%, Cu Recovery = -5%
- Scenario 28: Mining Rate = -5%, Milling Rate = -10%, Cu Recovery = -2.5%
- Scenario 29: Mining Rate = +5%, Milling Rate = +10%, Cu Recovery = +2.5%
- Scenario 30: Mining Rate = +10%, Milling Rate = +20%, Cu Recovery = +5%

Four additional scenarios were assessed with only accounting for the mining and milling rates, and assuming Cu recovery is constant:

- Scenario 31: Mining Rate = -10%, Milling Rate = -20%, Cu Recovery = 0.0%
- Scenario 32: Mining Rate = -5%, Milling Rate = -10%, Cu Recovery = 0.0%

- Scenario 33: Mining Rate = +5%, Milling Rate = +10%, Cu Recovery = 0.0%
- Scenario 34: Mining Rate = +10%, Milling Rate = +20%, Cu Recovery = 0.0%

RESULTS, ANALYSIS AND DISCUSSION

Three areas of potential gain from implementing changes in drill-and-blast practice were studied and their impact on NPV was quantified by simulating several scenarios using the Strategic Mine Planning and Optimisation software package, GEOVIA Whittle™. Accordingly, generated variations in overall value were recorded. This provides a quantitative figure of potential gains from Strategic Mine-to-Mill under several operational conditions, and how upstream and downstream processes may interact; hence NPV is impacted. This section centres on presenting such results and developing a discussion on the technical and economic aspects of the simulated scenarios.

For a given example of Cu-Au-Ag deposit, three key variables of mining rate, milling rate and recovery were analysed to quantify their impact at a strategic level. The range of variation for each variable was adopted from several Mine-to-Mill case studies in Asia Pacific region.

Figure 6 provides a brief summary of how implementing Mine-to-Mill optimisation strategies potentially changes the Net Present Value, NPV in the long-term without deploying CAPEX. In the context of Mine-to-Mill and its improvement potentials, the simulation outcomes suggest recovery and mining rate as the most effective leverages the overall value and then the milling rate. It is important to note how failure in maintain optimal mining and milling practices (here blast-induced impact on the downstream stages) may diminish profitability over life-of-mine.

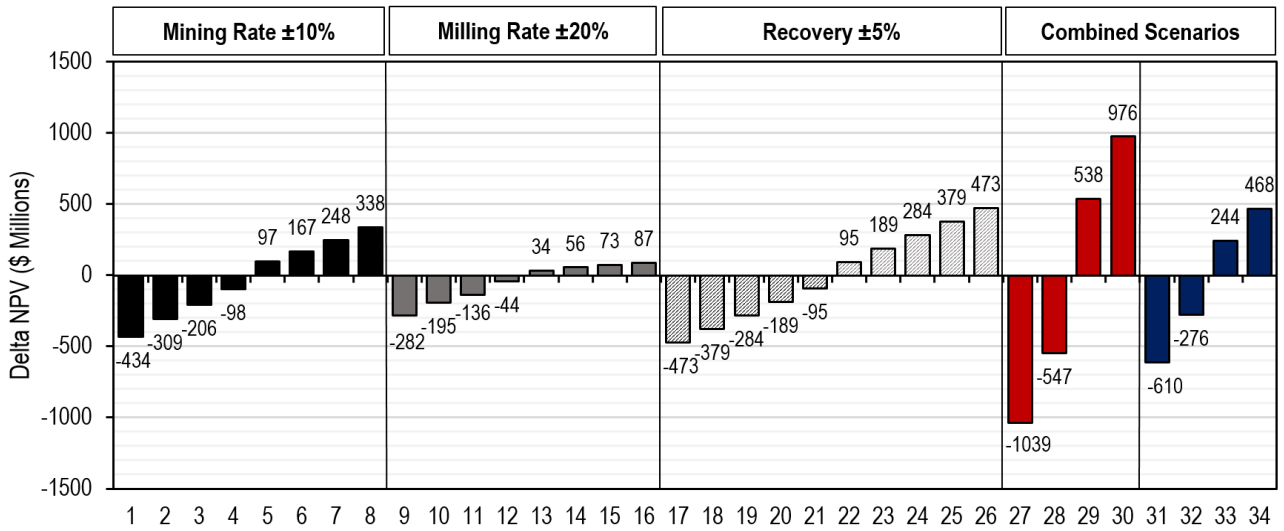

FIG 6 – NPV changes compared to the base-case NPV for all considered scenarios.

The results of simulated scenarios are given in Figure 7 for individual variables. Figure 8 and Table 2 summarise the results for the combined scenarios, which account for potential improvements or decrease of mining rate, milling rate and recovery at the same time, indicating extreme possibilities for potential gains and losses.

As it is implied in Figure 7, for the given example, 10 per cent improvement in *mining rate/capacity* through '*implementing and maintaining*' quality drill-and-blast practices over life-of-mine can translate into approximately 6.0 per cent increase in the NPV, while failure to move earth volumes in sequence may impose a loss of 9.0 per cent in NPV over LOM. Mining rate changes resulted in ±5.0 per cent.changes in IRR. Increases in mining capacity should generally be accompanied by a reduction in costs due to economy of scale. However, if the original fleet is maintained and this improvement is associated with improved performance of load-and-haul operation as a result of a finer muck pile fragmentation (eg if the shovels were the bottleneck for mining and any improvement in their performance results in shorter waiting times for trucks), it should imply an extra cost also associated with the mine cost, specifically associated with drill-and-blast costs – this additional cost should cushion the increase in value. On the other hand, the increase in this mining capacity offers

the possibility of providing better quality ore available over time, to be sent to the process plant, and postponing the lower quality material by sending it to the stockpile, which would contemplate its re-handling costs.

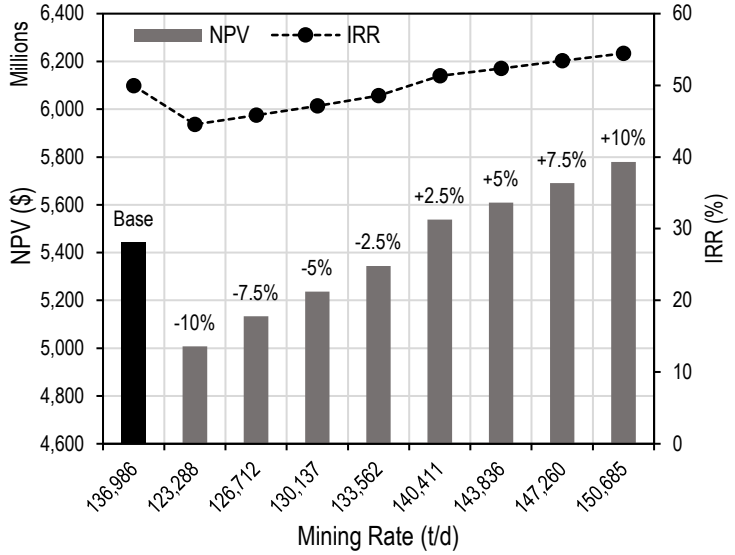

Run #	Mining Rate (t/d)	NPV ($M)	IRR (%)	Mine Life (y)
Base	136 986	5442	49.92	16.58
1	123 288	5007	44.55	17.28
2	126 712	5133	45.83	17.00
3	130 137	5236	47.14	16.76
4	133 562	5344	48.55	16.69
5	140 411	5539	51.31	16.46
6	143 836	5609	52.37	16.40
7	147 260	5690	53.42	16.35
8	150 685	5779	54.46	16.30

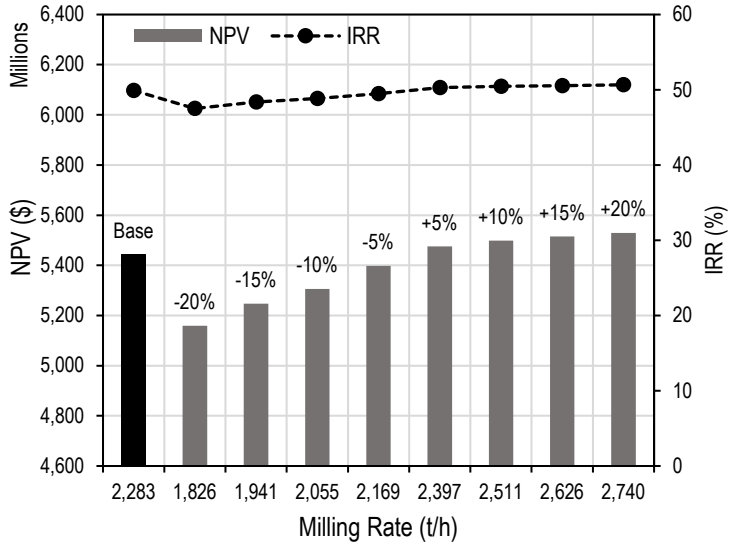

Run #	Milling Rate (t/h)	NPV ($M)	IRR (%)	Mine Life (y)
Base	2283	5442	49.92	16.58
9	1826	5160	47.51	19.89
10	1941	5247	48.39	18.89
11	2055	5306	48.86	18.01
12	2169	5398	49.5	17.22
13	2397	5476	50.28	16.08
14	2511	5498	50.46	15.66
15	2626	5515	50.56	15.37
16	2740	5529	50.66	15.29

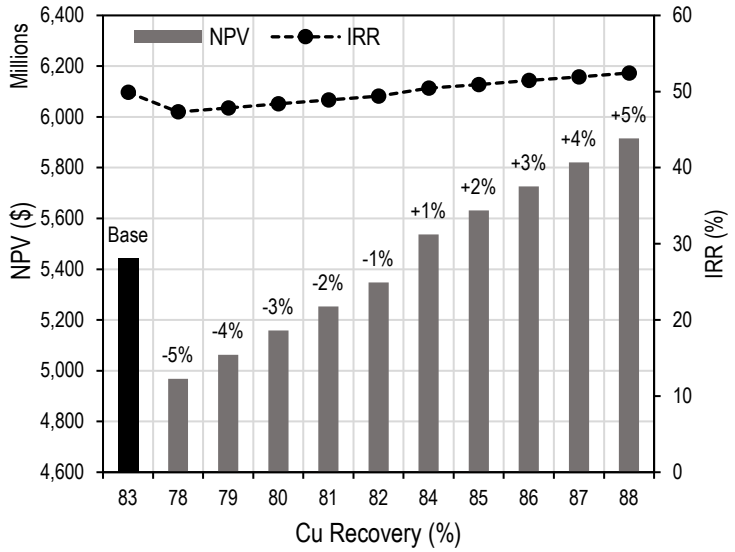

Run #	Recovery Cu (%)	NPV ($M)	IRR (%)	Mine Life (y)
Base	83	5442	49.92	16.58
17	78	4969	47.32	16.58
18	79	5063	47.85	16.58
19	80	5158	48.37	16.58
20	81	5253	48.89	16.58
21	82	5347	49.4	16.58
22	84	5537	50.43	16.58
23	85	5631	50.93	16.58
24	86	5726	51.44	16.58
25	87	5821	51.94	16.58
26	88	5915	52.44	16.58

FIG 7 – Results of sensitivity analysis of individual key variables by using GEOVIA Whittle™.

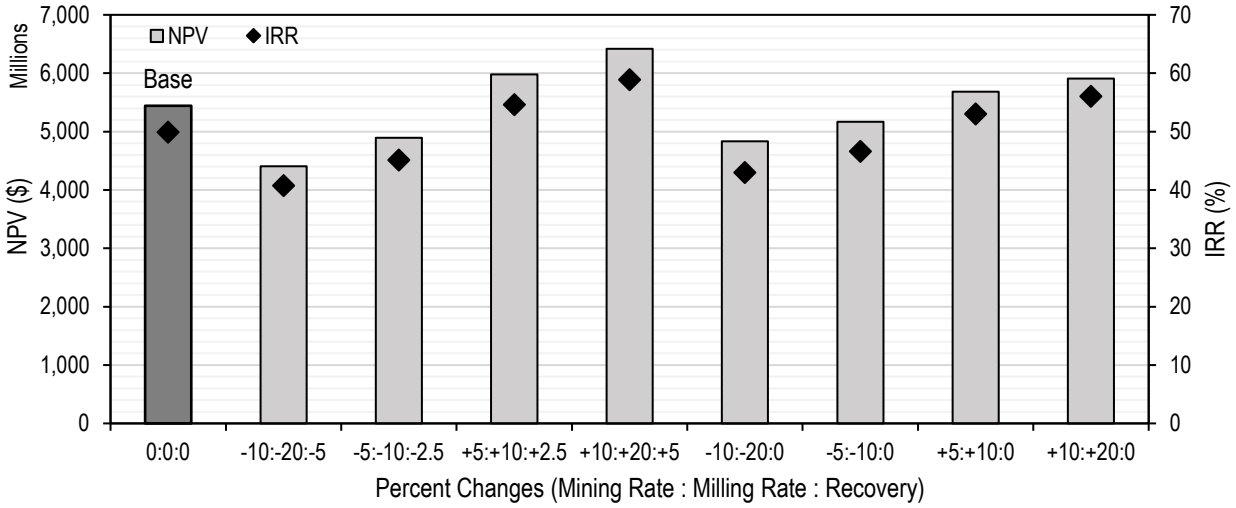

FIG 8 – Results of sensitivity analysis of combinations of key variables by using GEOVIA Whittle™.

TABLE 2

Details of simulated scenarios for combinations of key variables.

Run #	% Changes (M:M:R)	Mining Rate (t/d)	Milling Rate (t/h)	Recovery Cu (%)	NPV ($M)	ΔNPV ($M)	Relative NPV Changes (%)	IRR (%)	Mine Life (y)
Base	0:0:0	136 986	2283	83	5442	0	0.0	49.92	16.58
27	-10:-20:-5	123 288	1826	78	4403	-1039	-23.6	40.77	20.21
28	-5:-10:-2.5	130 137	2055	80	4894	-548	-11.2	45.17	18.14
29	+5:+10:+2.5	143 836	2511	86	5980	538	9.0	54.66	15.36
30	+10:+20:+5	150 685	2740	88	6418	976	15.2	58.91	14.30
31	-10:-20:0	123 288	1826	83	4832	-610	-12.6	43.00	20.20
32	-5:-10:0	130 137	2055	83	5166	-276	-5.3	46.61	18.14
33	+5:+10:0	143 836	2511	83	5686	244	4.3	53.04	15.36
34	+10:+20:0	150 685	2740	83	5910	468	7.9	56.06	14.30

NOTE: **M**ining Rate: **M**illing Rate: **R**ecovery = (M:M:R)

The *milling rate/capacity* suggests the potential to impact the NPV between -6.0 per cent and +2.0 per cent, which its dollar equivalence range would be -$282 M and +$87 M (See Figure 7). The process plant is generally the bottleneck of the value chain, so its limit determines the metal yield, and hence cash flow. It is worth noting that conventional Mine-to-Mill optimisation mainly aims to improve the milling throughput by performing high-energy blasts to tailor ore feed PSD in favour of SAG milling (generate more <10 mm fines). However, it is of prime importance to ensure power balance between the SAG and ball milling stages. The finer fragmentation feed may result in overloading the ball mill-cyclone circuit, and consequently impose pressure on circulating load – limiting throughput. For such operational scenarios, enlarging cyclone cut size (Product P80) might reduce circulating load – however, the impact on recovery should be evaluated. As expected, the milling rate is most effective on life-of-mine in longer term if milling rate improvements could be maintained.

The Cu *recovery* directly accounts for metal yield/saleable product, and the result suggest dramatic influence of recovery on NPV over life-of-mine. In this example, ±5.0 per cent changes in recovery resulted in NPV varying between -10 per cent and +8.0 per cent, equivalent to half a billion dollar in 17 years of operation (See Figure 7). The simulation scenario indicate 1.0 per cent change in recovery means $95 M over LOM, which is $5.6 M per annum for the given example – which highlights importance of applying grade control and ore loss reduction strategies across the value chain.

Applying a Mine-to-Mill optimisation approach at strategic level, should aim at delivering operational improvements. Not only limited to milling throughput, but also in mining rate as well as recovery. Figure 8 and Table 2 show the results of scenarios that account for Mine-to-Mill gains in three key areas of production with varying degrees/percentages. Compared to the conventional Strategic Mine Planning (Base-Case), the results suggest the potential to improve NPV up to $976 M over 14 year life-of-mine, by adopting a Mine-to-Mill at a strategic level without the need to deploy additional CAPEX. However, poor performance of mining, milling and beneficiation stages may be associated with risk of diminishing NPV by $1.039 B over an extended LOM of 20 years.

It is important to note that Strategic Mine-to-Mill optimisation can only be realised in the presence of tactical plans. The tactical plans are tailored to deliver improvements at an operational level. With respect to the significant influence of metal yield/recovery on NPV, proper grade control and ore loss reduction strategies should be considered across the value chain to manage grade variability and maintain recovery over time with the objective to maximise orebody utilisation. This requires several techniques, including measurement and analytics, Strategic Geological Modelling, blast movement monitoring and control for reduced ore dilution, ore pre-concentration and blending, comminution and classification. Exploring the results of all scenarios, highlights that maximised profitability is only achievable if the ore reserve is efficiently utilised in sequence and maintaining quality practices in mining, milling and flotation over LOM. With For this purpose, operational KPIs should be optimised and continuously improved over time, following development of new solutions, technologies and techniques (ie Mine-to-Mill approach) and their long-term impact being described quantitatively. At an operational level, Tactical Mine-to-Mill aim at realising strategic objectives through plans of implementation in medium- and short-term time frames.

An area of interest for future work should be integrating energy consumption estimates into strategic LOM evaluations, specifically the amount used at the downstream stage. To further discuss the matter of importance, Cohen (1983) estimates that 30–50 per cent of total plant power draw, and up to 70 per cent for hard ores is consumed by comminution. In minerals industry, energy is not consumed to best possible advantage in the comminution equipment and efficiency is only of the order of 0.1–2 per cent considering the energy required to generate new surface area relative to mechanical energy input (Fuerstenau and Abouzeid, 2002; Tromans, 2008). It has been identified that power efficiency for crushers varies between 70–80 per cent compared with single particle breakage in a drop weight tester (Morrell *et al*, 1992), while the value for ball mills and SAG mill is about 30 per cent and 40 per cent, respectively (Musa and Morrison, 2009). It was noted by Tromans (2008) that the limiting energy efficiency under compression varies between 5–10 per cent depending on the value of Poisson's ratio and under the uniaxial tension does not exceed 66 per cent. He argued that efficiencies of 5–10 per cent will not be achievable in practice, because the strain energy within a considerable region of a compressed particle makes no contribution to the fracture process and dissipates in forms of heat and kinetic. Thus, understanding fundamental limitations inherent in mechanical breakage of rock is the key to explore more efficient alternatives (Napier-Munn, 2015). Measuring the extent of competence variability within an ore domain should help to more accurately scale the size of quipment, estimate required energy and also better understand the nature of observed variation in the mill performance whether it is ore-induced or has an operational/technical origin. As an example, the Extended Drop Weight Testing (EXDWT) approach allows to consider particles pre-breakage physical properties, eg mass, density, dimension, orientation, colour, roundness, textural features etc, and investigate their possible link to particles competence based on the concept of 't_n-family per particle'. This capability offers the potential for the first time to account for more sources of variation, thus more closely estimate the true competence heterogeneity within a sample of ore (Faramarzi, 2020; Faramarzi *et al*, 2020). Overall, energy consumption is important to the mining industry and is likely to become more so because of increasing expense, as well as new regulatory and market interventions (Napier-Munn, 2015), therefore estimating energy usage at a strategic level should be beneficial in decision-making and establishing more sustainable alternatives for efficient utilisation ore reserves.

This study, specifically underlined the NPV improvement potential that could be achieved only by quality, value-driven drill-and-blast practices within Mine-to-Mill. Although blasting plays a deterministic, proven role in improving downstream performances; for best utilisation of an ore reserve, innovative techniques should be applied across the value chain, backed by more

sophisticated financial models which could effectively reflect economic consequence of changes over life-of-mine.

CONCLUSIONS

The Strategic Mine-to-Mill optimisation as conceptualised in this paper, centres on long-term impact of adopting and maintaining optimisation strategies. Application of Mine-to-Mill at strategic and tactical levels would suggest opportunities for a step change improvement in the controllability of mining and processing performances, and substantially improved economics of operations.

In this paper, the potential impact of adopting Mine-to-Mill improvement strategies on the Net Present Value (NPV) was estimated for a Cu-Au-Ag deposit. Three key variables of mining, milling, and recovery rates were analysed within potential ranges for performance improvement, reported from Mine-to-Mill studies.

For the given case study, analysis of outcomes indicates that, maintaining value-driven strategies could result in up to +15 per cent higher NPV relative to the base-base. Although, recovery was found to be the most influential variable on NPV (by 8.0 per cent); however, based on the results, only mining and milling performance improvements through blasting could generate 7.9 per cent more value relative to the base-case. It is concluded that developing such analyses at a strategic level and integrating operational possibilities into calculations should assist with better understanding of potential gains and losses quantitatively. This would also be useful for establishing more robust risk management strategies in presence of uncertainties (ie commodity price, ore property) introducible over LOM. It is concluded that sustainable ore reserve utilisation is achievable if upstream and downstream activities becoming '*mutually informative*' and their KPIs shared in real-time for harmonising activities for maximised overall value. Future study should focus on addition of more levels of sophistication, some would be as follows:

- S*tochastic analysis of the impact of ore variability at a strategic level*: Although, ore variability is frequently debated as a major source of uncertainty in process performance, most of the current ore testing methods do not capture the variability within ore samples and process performance. Predictions are based on using average values for ore characteristics. It is required to use ore characterisation approaches which are designed for measuring the extent of variability inherent to the orebodies (ie mineralogical, textural and breakage characteristics of orebodies as key drivers to process performance KPIs such as recovery and throughput) and estimate the extent of ore-induced operational variability. This should assist with developing more realistic plans at the Tactical Mine-to-Mill stage in light of diagnosing likely bottlenecks across the value chain over LOM as ore properties change, although this remains a focus of future work.
- *Development of 'more' sophisticated financial models for value-chain studies*: While it is helpful to integrate Mine-to-Mill into strategic considerations, it is equally important to develop sophisticated financial models which can reflect on implemented changes.
- *Accounting for the impact of ore loss/dilution in long-term analyses:* High-energy blasting generally limits control over the outcomes, therefore might be associated with risk of ore loss through dilution. Blast-induced ore dilution is the phenomenon that can directly affect the overall value, NPV over time, and performance by feeding the mill with less valuable material. While it is important to reflect on ore dilution at a strategic level, it is also critical to set-up risk mitigation measures through blast movement modelling and monitoring systems for tuning blast design parameters (ie timing, pattern, explosives properties and distribution of blast energy etc) for reduced ore loss.
- *Application of operational history of the plant, namely 'historic or operational data':* Process plant historian (PI) data are indicative of the state of a process (commonly used for tactical/operational evaluations), but some challenges with 'operational' (PI) data have been inconsistency, redundancy, unreliable instrument readouts and large variations (with unknown sources and amounts). However, careful curation and analysis of PI data could assist with providing insightful information on process performance, constraints and bottlenecks. This would assist with developing strategic evaluations as well as risk assessment in light of operational constraints.

ACKNOWLEDGEMENTS

The authors would like to acknowledge Dassault Systèmes for sponsoring this work, which made it possible for the authors to present this paper at IMPC Asia Pacific 2022. Dassault Systèmes provides software solutions that allow customers to create innovative new products and services using virtual experiences and enables business and people with 3DEXPERIENCE universes where they can imagine sustainable innovations capable of harmonising product, nature, and life. The IMPC Council and AusIMM are sincerely acknowledged, for their effort in putting the IMPC Asia Pacific 2022 conference together in Australia.

REFERENCES

Burger, B, McCaffery, K, Jankovic, A, Valery, W and McGaffin, I, 2006. Batu Hijau model for throughput forecast, mining and milling optimisation and expansion studies. *SME 2006 Conference*, St. Louis, USA.

Bye, A, 2006. The strategic and tactical value of a 3D geotechnical model for mining optimization, Anglo Platinum, Sandsloot open pit. *Journal of the Southern African Institute of Mining and Metallurgy*, 106(2), 97–104.

Bye, A, 2011. Case studies demonstrating value from geometallurgy initiatives. *GeoMet 2011–1st AusIMM International Geometallurgy Conference 2011*.

Carrasco, C, Keeney, L, Scott, M and Napier-Munn, T, 2016. Value driven methodology to assess risk and operating robustness for grade engineering strategies by means of stochastic optimisation. *Minerals Engineering*, 99, 76–88.

Cohen, H, 1983. Energy usage in mineral processing. *Institution of Mining and Metallurgy Transactions*, 92.

Comeau, W, 2018. Explosive energy partitioning and fragment size measurement—Importance of the correct evaluation of fines in blasted rock. In *Measurement of Blast Fragmentation,* pp. 237–240. Routledge.

Couzens, T R, 1979. Aspects of production planning: Operating layout and phase plans. *Open Pit Mine Planning and Design* (JT Crawford and W A Hustrulid, eds.), pp 217–232.

Cunningham, C, 2005. The Kuz-Ram fragmentation model–20 years on. *Brighton conference proceedings*.

Dance, A, 2001. Benefits of mine-mill integration. *Intelligence in a Materials World, Proceedings of the Third International Conference on Intelligent Processing and Manufacturing of Materials*.

Engmann, E, Ako, S, Bisiaux, B, Rogers, W and Kanchibotla, S, 2013. Measurement and modelling of blast movement to reduce ore losses and dilution at Ahafo Gold Mine in Ghana. *Ghana Mining Journal*, 14, 27–36.

Esen, S, La Rosa, D, Dance, A, Valery, W and Jankovic, A, 2007. Integration and optimisation of blasting and comminution processes. *EXPLO conference*.

Eshun, P A and Dzigbordi, K A, 2016. Control of ore loss and dilution at AngloGold Ashanti, Iduapriem mine using blast movement monitoring system. *Ghana Mining Journal*, 16(1), 49–59.

Faramarzi, F, 2020. The measurement of variability in ore competence and its impact on process performance. The University of Queensland.

Faramarzi, F, Jokovic, V, Morrison, R and Kanchibotla, S S, 2018. Quantifying variability of ore breakage by impact–Implications for SAG mill performance. *Minerals Engineering*, 127, 81–89.

Faramarzi, F, Kanchibotla, S S and Morrison, R, 2019. Simulating the impact of ore competence variability on process performance – Case study of a large copper mine. *SAG Conference*, Vancouver, Canada.

Faramarzi, F, Napier-Munn, T, Morrison, R and Kanchibotla, S S, 2020. The extended drop weight testing approach–What it reveals. *Minerals Engineering*, 157, 106550.

Fisher, I, 1930. *Theory of interest: as determined by impatience to spend income and opportunity to invest it*, Augustusm Kelly Publishers, Clifton.

Fuerstenau, D and Abouzeid, A-Z, 2002. The energy efficiency of ball milling in comminution. *International Journal of Mineral Processing*, 67(1), 161–185.

Godoy, M, 2018. A risk analysis based framework for strategic mine planning and design—Method and application. In *Advances in Applied Strategic Mine Planning,* pp. 75–90. Springer.

Grundstrom, C, Kanchibotla, S, Jankovich, A, Thornton, D and Pacific, D D N A, 2001. Blast fragmentation for maximising the sag mill throughput at Porgera Gold Mine. *Proceedings of the annual conference on explosives and blasting technique.*

Hart, S, Valery, W, Clements, B, Reed, M, Song, M and Dunne, R, 2001. Optimisation of the Cadia Hill SAG mill circuit. *SAG Conference*.

Hustrulid, W and Kuchta, M, 1995. Open pit mine planning and design. Volume 1-Fundamentals.

Kanchibotla, S S, Valery, W and Morrell, S, 1999. Modelling fines in blast fragmentation and its impact on crushing and grinding. *Explo '99–A conference on rock breaking* (The Australasian Institute of Mining and Metallurgy: Melbourne).

Kanchibotla, S, Morrell, S, Valery, W and O'Loughlin, P, 1998. Exploring the effect of blast design on SAG mill throughput, *KCGM Mine to mill conference*.

King, R, 1990. Simulation—the modern cost-effective way to solve crusher circuit processing problems. *International Journal of Mineral Processing*, 29(3–4), 249–265.

Kojovic, T, Michaux, S and McKenzie, C, 1995. Impact of blast fragmentation on crushing and screening operations in quarrying. *Proceedings of the EXPLO 1995 Conference*, Brisbane, Qld.

Lam, M, Jankovic, A, Valery, W and Kanchibotla, S, 2001. Maximising sag mill throughput at porgera gold mine by optimising blast fragmentation.

Lerchs, H, 1965. Optimum design of open-pit mines. *Trans CIM*, 68, 17–24.

McCaffery, K, 2006. Batu Hijau-Controlled Mine Blasting and Blending to Optimize Process Production at Batu Hijau. *Proc. SAG 2006*.

McKee, D, Chitombo, G and Morrell, S, 1995. The relationship between fragmentation in mining and comminution circuit throughput. *Minerals Engineering*, 8(11), 1265–1274.

Michaux, S and Djordjevic, N, 2005. Influence of explosive energy on the strength of the rock fragments and SAG mill throughput. *Minerals Engineering*, 18(4), 439–448.

Morales, N, Seguel, S, Cáceres, A, Jélvez, E and Alarcón, M, 2019. Incorporation of geometallurgical attributes and geological uncertainty into long-term open-pit mine planning. *Minerals*, 9(2), 108.

Morrell, S and Morrison, R, 1989. Ore charge, ball load and material flow effects on an energy based SAG mill model. *Proceedings Advances in Autogenous and SAG Technology*, 697–712.

Morrell, S and Valery, W, 2001. Influence of feed size on AG/SAG mill performance. *SAG2001*, Vancouver, BC, Canada, 203–214.

Morrell, S, Napier-Munn, T and Andersen, J, 1992. The prediction of power draw in comminution machines. *1992 SME Annual Meeting*.

Morrison, R and Richardson, J, 2002. JKSimMet: A simulator for analysis, optimisation and design of comminution circuits.

Munro, P, 1986. Commissioning and operation of the 800 t/h heavy medium cyclone plant at Mount Isa Mines Ltd. *Transactions-Institution of mining and metallurgy. Section C Mineral processing and extractive metallurgy*, 95(12), 229–230.

Musa, F and Morrison, R, 2009. A more sustainable approach to assessing comminution efficiency. *Minerals Engineering*, 22(7), 593–601. https://doi.org/https://doi.org/10.1016/j.mineng.2009.04.004

Napier-Munn, T J, 2014. Statistical methods for mineral engineers-How to design experiments and analyse data (Vol. 5). Julius Kruttschnitt Mineral Research Centre.

Napier-Munn, T J, 2015. Is progress in energy-efficient comminution doomed? *Minerals Engineering*, 73(Supplement C), 1–6. https://doi.org/https://doi.org/10.1016/j.mineng.2014.06.009

Napier-Munn, T J, Morrell, S, Morrison, R D and Kojovic, T, 1996. Mineral comminution circuits: their operation and optimisation (Vol. 2). Julius Kruttschnitt Mineral Research Centre, University of Queensland.

Nielsen, K and Kristiansen, J, 1995. Can blasting enhance the grindability of ores? *Transactions of the Institution of Mining and Metallurgy*, Section A, 104.

Poblete, C G M, Romero, J and Fuentes, D, 2016a. Impact of the starting point and of the direction of open pit exploitation on the mining plan. *Sixth International Conference on Innovation in Mine Operations*, Santiago, Chile.

Poblete, C, González, M, Romero, J, Fuentes, D and Abdrashitova, O, 2016b. Use of Robust Design Methodology for the Production Scale Definition in Open Pit Mining. *Proceedings Ninth AusIMM Open Pit Operators Conference*.

Rimélé, A, Dimitrakopoulos, R and Gamache, M, 2020. A dynamic stochastic programming approach for open-pit mine planning with geological and commodity price uncertainty. *Resources Policy*, 65, 101570.

Scott, A, Morrell, S and Clark, D, 2002. Tracking and quantifying value from 'mine to mill'improvement. *Proc. Value Tracking Symposium*, Brisbane, Australia.

Silva, A C, Silva, E M S and Silva, J A d O, 2015. Ball Mill Simulation with Moly-Cop Tools. *2015-Sustainable Industrial Processing Summit*.

Smith, R D R, Poblete, C, Romero, J and Van Der Hout, N, 2021. Using design of experiments to improve strategic mine planning, *Life of Mine Conference*, Brisbane, Australia.

Starkey, J, Dobby, G and Kosick, G, 1994. A new tool for SAG hardness testing. *Proceedings of the 26th Canadian Mineral Processors Annual Meeting*, Ottawa, ON, Canada.

Stepto, W D, Cilliers, B C and Glen, B, 1990. Application of dynamic process simulation. *SACAC Symp*, May (MINTEK, Johannesburg).

Strohmayr, S and Valery, W, 2001. SAG mill circuit optimisation at Ernest Henry Mining. *Proceedings of the SAG 2001 Conference*, Vancouver, BC, Canada.

Tromans, D, 2008. Mineral comminution: Energy efficiency considerations. *Minerals Engineering*, 21(8), 613–620. https://doi.org/http://dx.doi.org/10.1016/j.mineng.2007.12.003

Valery, W, Duffy, K and Jankovic, A, 2019. Mine to Mill optimization. *SME mineral processing and extractive metallurgy handbook*, 335–343.

Young, M, Pease, J, Johnson, N and Munro, P, 1997. Developments in milling practice at the lead/zinc concentrator of Mount Isa Mines Limited from 1990. *AusIMM Sixth Mill Operators Conference*, Madang, Papua New Guinea.

Development of a three-dimensional model for simulating stockpiles and bins with size segregation

Z Ye[1], M Hilden[2] and M Yahyaei[3]

1. PhD Candidate, Julius Kruttschnitt Minerals Research Centre, The University of Queensland, Brisbane Qld 4068. Email: ziming.y@qq.com
2. Senior Research Fellow, Julius Kruttschnitt Minerals Research Centre, The University of Queensland, Brisbane Qld 4068. Email: m.hilden@uq.edu.au
3. Associate Professor, Julius Kruttschnitt Minerals Research Centre, The University of Queensland, Brisbane Qld 4068. Email: m.yahyaei@uq.edu.au

ABSTRACT

Stockpiles and bins play an important role in the overall performance of mineral processing plants. However, at both the plant design stage and during process optimisation, stockpiles and materials handling facilities do not receive as much attention as comminution and classification units. Size segregation is a common issue in most granular storage systems. The size distribution range for stockpiles is very wide in the mining industry and when fine and coarse particles segregate, this can create fluctuations and cause processing units to receive uneven feeds. The size segregation in material handling and storage impacts the performance of the downstream equipment and circuits. Modelling this problem can improve the understanding of size segregation and provide information for operating the comminution circuit. Therefore, a three-dimensional dynamic stockpile/bin model has been developed at the Julius Kruttschnitt Mineral Research Centre (JKMRC), which can simulate the dynamic response of a stockpile or bin. A Continuous Cellular Automata was developed, dividing the volume of the bin/stockpile into a three-dimensional grid of cells. Each cell contains an independent set of properties that are tracked throughout the simulation. Size segregation during material flow and trajectory segregation from the conveyor are incorporated into the model. The variation in the stockpile/bin surface profile and size distribution of feeders under the stockpile/bin can be predicted. The model structure and validation are discussed in this paper. The industrial validation shows how the stockpile/bin model can be applied in the industry, leading to improved stockpile/bin design. The three-dimensional dynamic stockpile/bin model can contribute to control of the comminution circuit because different operational strategies can be run using the model. This study demonstrates how size segregation is included in the dynamic stockpile/bin model and shows the importance of modelling materials handling and storage for process control and optimisation. The stockpile/bin model will connect the mine and the primary crusher to the grinding circuit, which is expected to enhance the understanding of process control of materials handling and storage, and Mine to Mill optimisation.

INTRODUCTION

Granular flow, mixing and segregation are topics of intense research because of their impacts on downstream processes and product quality in many industries. In mining, segregation occurs throughout the whole process, from the load and haul to waste disposal. This issue significantly impacts plant performance when it occurs in coarse ore stockpiles during the filling and discharging processes (Benito *et al*, 2013). Most mine sites use large coarse ore stockpiles or bins as a buffer between the mine or primary crushers and the processing plant, thus decoupling these processes. However, stockpiles and materials handling facilities do not receive as much attention as comminution and classification units at the plant design stage and process control.

The term segregation refers to the process whereby particles tend to become less well mixed with respect to properties such as size, density, shape, surface roughness, presence and amount of clays, or moisture content. It is an important phenomenon affecting many granular processes in industries such as mining, aggregates, chemicals, food processing and pharmaceuticals (Williams, 1990). Segregation occurs in many parts of the mining process, including blasting, caving, and extraction; however, the direct impact on plant performance occurs when binned or stockpiled ores are segregated upon discharging (Enstad and Mosby, 1998). Particle characteristics are not the only factors that influence material segregation: the feed rate, the bin geometry and the filling angle are

also critical parameters to be considered (Combarros *et al*, 2014; Yu and Saxén, 2014). However, particle size is usually considered to be the most important (Combarros *et al*, 2014; Wu and Baeyens, 1998).

Descriptions of the mechanisms driving segregation are provided by Enstad and Mosby (1998), (Tang and Puri, 2004), Bridgwater (1994) and De Silva *et al* (2000). Schulze (2008) observes that 'the processes of segregation are complex and thus cannot be predicted quantitatively'. Thirteen mechanisms are listed by De Silva *et al* (2000): trajectory, air current, rolling, sieving, impact, embedding, angle of repose, push-away, displacement, percolation, fluidisation, agglomeration and concentration-driven displacement. The mechanisms dominating stockpile segregation in most cases are listed below in Figure 1.

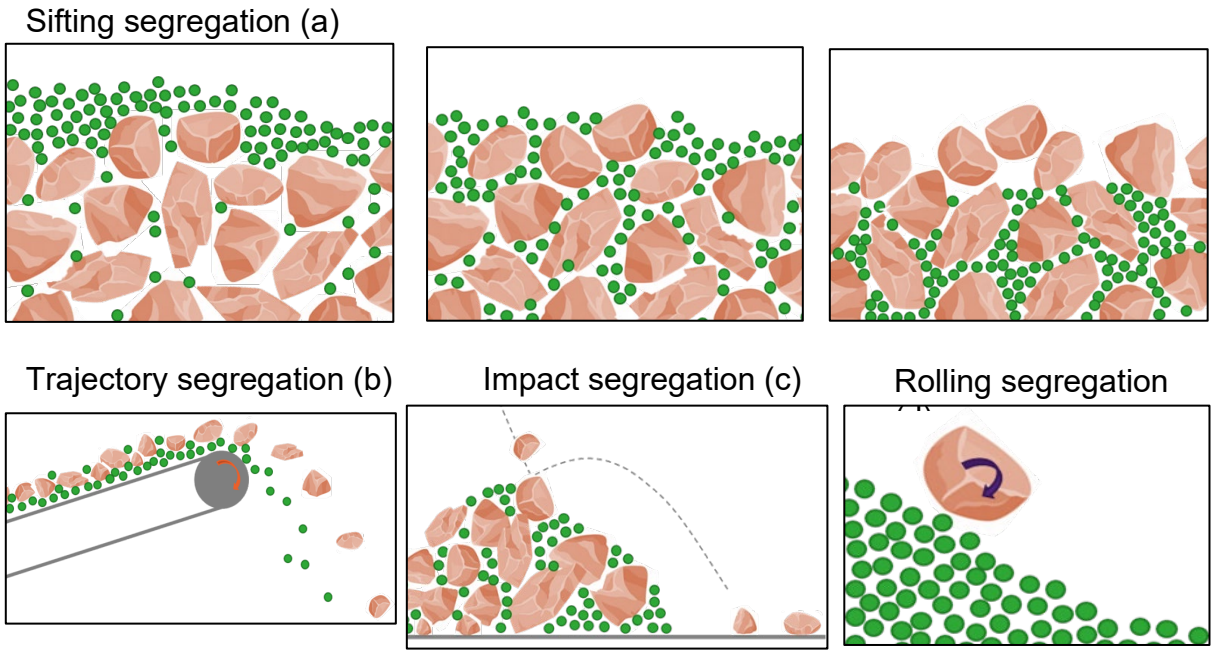

FIG 1 – Different size segregation mechanisms in stockpiles

Size segregation in materials handling and storage causes fluctuations in the particle size distribution that then impacts the performance of the downstream equipment and processes. Dynamic models of materials handling and storage incorporating size segregation are necessary to understand how variations affect the output, which can provide useful information to the operators.

The Continuous Cellular Automata (CCA) method is used for the model developed in this paper because of the need to create a sufficiently fast and practical model for use in dynamic simulation. CCA discretises the stockpile or bin into a 3D grid of cells. In contrast to the Discrete Element Method (DEM) where each particle is simulated independently and particles can potentially interact with distant particles through force chains, CCA simulates cells each containing a large number of particles with perhaps several bulk properties; and interactions in each time step are only with immediate neighbouring cells. Compared with other simulation methods, such as the discrete element model, CCA is a less accurate/less physical representation of the system, but it is considerably faster. The details of the model structure are described in the following section.

The dynamic stockpile/bin dynamic model accounts for the varying flow of material onto the stockpile or bin and the flow drawn from the base of the pile or bin. A size segregation model accounts for size segregation during material flow and a trajectory segregation model to account for the size segregation induced by the feed conveyor. The variation in the stockpile/bin surface profile and size distribution of feeders under the stockpile/bin can be predicted. The model structure and method are discussed in this paper along with validation results, which will provide insights to develop improved stockpile/bin designs. The three-dimensional dynamic stockpile/bin model can therefore have practical application in stockpile/bin design, comminution process control and optimisation (Ye *et al*, 2021).

METHODOLOGY

Figure 2 outlines the methodology for researching the size segregation of a stockpile/bin. The laboratory experiments have important connections with the two other sections. The experimental design is outlined by Ye *et al* (2019), including the ore preparation, the device design and the method used to collect the samples. The result of the laboratory experiments can contribute to the model fitting and calibration for predicting the industrial-scale behaviour. For validating the model, the industrial data is significant, and the variation of the industrial data can show the dynamics of the industrial behaviour. The industrial data has been collected and analysed (Yahyaei *et al*, 2021) and it was used for model validation. This paper focuses on the stockpile/bin model structure and method and the industrial validations show the feasibility and application of the model.

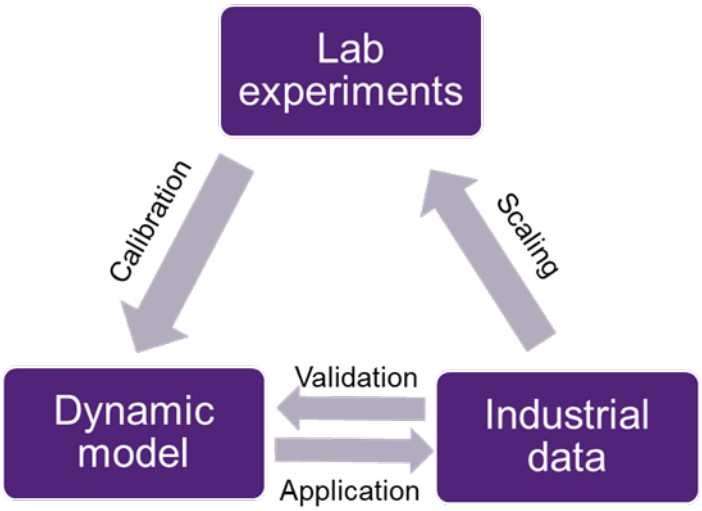

FIG 2 – The relationship of main aspects of this research.

Dynamic stockpile/bin model method

The Continuous Cellular Automata (CCA) method allows for the division of the stockpile/bin into a 3D grid of cells according to the resolution defined by the user. The model evolves over time: at each time step, the model calculates a sequence of basic interactions:

1. **Feeding** ore to the stockpile or bin.
2. **Discharging** ore from the base of the stockpile or bin.
3. **Migration** of voids to the surface.
4. **Surface-flow** to maintain the angle of repose.

This sequence is repeated at each time-step and the details of each step are explained in the following sections. The model does not at present have the capability to model dozers pushing ore from outside of stockpile into the drawdown zones.

Feeding; discharging and migration

In the three-dimensional model, each cell in the grid is characterised by several properties. Minimally, these properties include the fractional filling, the characteristic size (P80) of the particles and a state parameter. The ‘state’ describes its interaction behaviour, whether it is a full cell, a surface cell or an empty cell. During the feeding process, an increment of material representing a fraction of a cell volume is added to selected surface cells at every time-step. The trajectory segregation from the conveyor has been added into the model to decide which surface cells receive material. In the discharging process, at every time-step, an increment of ore may be removed from the drawpoint cells at the base of the stockpile. The number and location of discharge points can be defined according to the stockpile feeder design. The amount discharged (t/h) from each operating feeder depends on the speed of the feeders. When the cell at the discharge point becomes empty, a void or ‘hole’ is created at the base of the pile. Of the nine cells adjoining this cell from above, a random full cell is selected to drop into the hole: the probability of selection is given by a probability map as

shown in Figure 3, which is commonly used in CA models (Castro *et al*, 2009; Kozicki and Tejchman, 2005). Castro *et al* (2009) proposed that the probability should be inversely proportional to the distance from the hole to the upper cell. This implies probabilities for the centre, pc = 0.163; edges, pl = 0.115; and diagonals, pd = 0.094; based on the relative distances between the centre-points of these cells and the centre-point of the void. This event re-fills the empty drawpoint cell and creates a new void in the next level up, which in turn is filled from the level above that, initiating an immediate migration of the void to the surface. Near the top, when the migrating cell has a surface cell above it, the surface cell drops vertically and terminates the migration chain. The discharge event thereby creates a random 'path' for the hole migration as illustrated in Figure 3. Continuous drawdown will result in an inverted cone shaped hole above the discharge points.

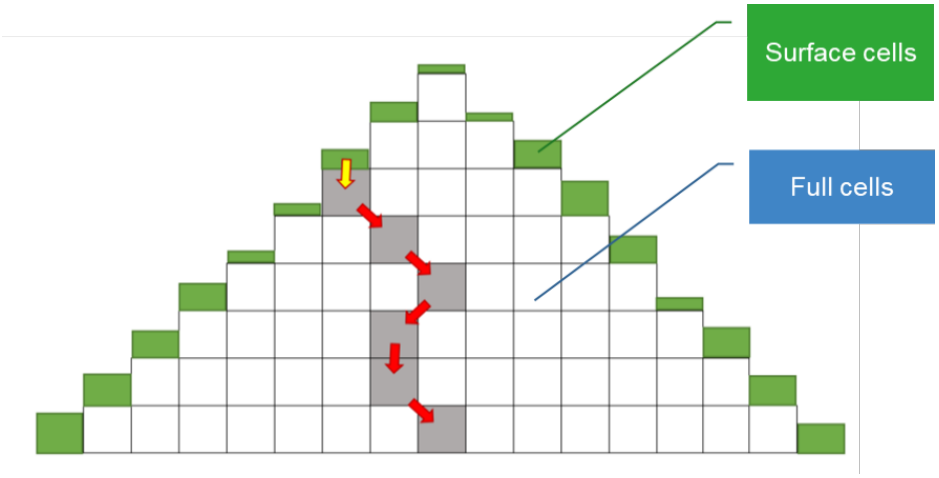

FIG 3 – An example of random materials flow from the surface to the bottom of a stockpile.

Surface flow with size segregation

The feeding and discharge mechanisms alter the surface profile, hence surface flow needs to be calculated to allow materials to flow to the neighbouring columns when the height difference exceeds a slope threshold defined by the angle of repose (AoR). A constant angle of repose implies that the maximum height difference between adjacent stable columns is the same over the entire pile; however, the AoR could also be made a function of the particle size in the local surface cell. The Moore (1964) neighbourhood method is used in the stockpile/bin model for materials flow in this paper. The method compares the height of all eight neighbour columns in the four cardinal directions (N-S-E-W) and the four ordinal (diagonal) directions (NW-NE-SW-SE), except at the edges of the stockpile. The height threshold of materials flow to or from the four ordinal columns is $\sqrt{2}$ times the threshold in the cardinal directions. In this way, the stockpile forms an 8-sided pyramid.

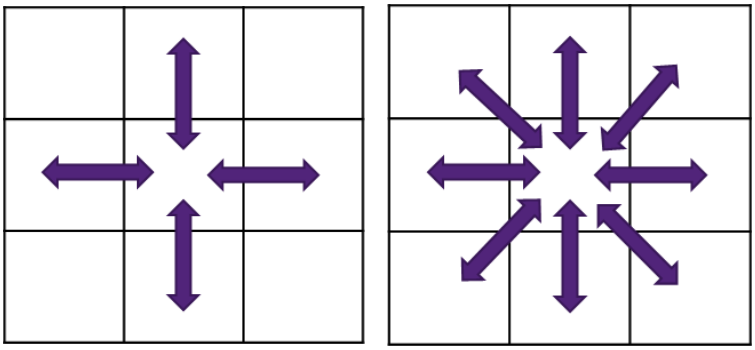

FIG 4 – Two kinds of materials flow between columns: Von Neumann method (left) and Moore method (right)

During the surface flow events, materials flow from the higher column to the lower column. An asynchronous calculation with a stochastic updating scheme (Ingerson and Buvel, 1984) has been used in the development of this model. This means that for each time-step, the order for calculating each column is randomised, and as the flow amount between each pair of columns is calculated, the

heights of the columns are updated immediately. Hence, potentially, materials can flow further than one adjacent cell within the same time-step. This differs from the synchronous calculation more commonly used in CA simulations, where column heights are updated simultaneously at the end of the time-step.

For particle size to be adequately incorporated into the stockpile model, the effect of size segregation needs to be included. Firstly, a segregation function is required. Functions for bidisperse or binary mixtures have been developed in this model development. P50 or P80 values can represent the size distribution of each cell. Dolgunin and Ukolov (1995) mixture function (as below) was added into the model when materials flow to the neighbouring column. These describe the small particle flux, F^s, as a function of the concentration of small particles in the mixture, ϕ^s, and a segregation rate parameter, S, which can control the segregation degree.

$$F^s{}_{Dolgunin\ \&\ Ukolov} = -S.\phi^s(1-\phi^s)$$

The segregation model is applied to all surface flow events in the model. At any time when a volume, V, flows from one column to another, 2V of material from the higher column is mixed and then divided into segregated coarse and segregated fines fractions according to the segregation function. The coarse portion will move to the low column and the fines portion will remain on the high column as illustrated in Figure 5. A similar approach is used in the modelling of trajectory segregation such that coarse ore is thrown further by the conveyor. The segregation function is applied to divide the feed from the conveyor into two equal parts while in flight. Both parts then settle on the surface of the pile in adjacent columns: the coarse part further from the conveyor and the fine part nearer to the conveyor.

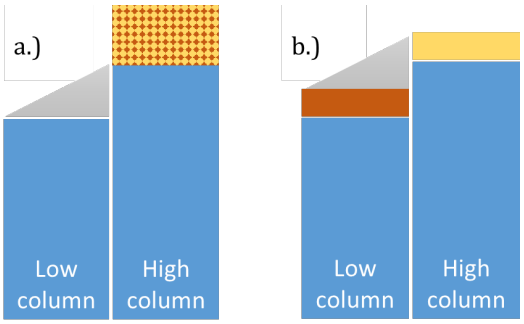

FIG 5 – Flow of material from a high to a low column. Particles in the high column are segregated. The coarse fraction flows to the low column (a) and the fine fraction remains (b).

By this method, the particle size is included in each cell and each cell contains an independent set of properties. In contrast to basic or discrete CA where each cell contains an integer state parameter, the CCA approach differs by allowing each cell to contain both integer and continuous variables (Gosálvez *et al*, 2009). As noted above, each cell contains the state, the filling level, and the characteristic particle size. This can be expanded to include other attributes such as composition (grade), density, hardness etc, and be linked to mine production data. These properties can then be tracked over time.

SIMULATION RESULTS AND VALIDATION

The stockpile/bin model is used to predict the flow behaviour of an industrial stockpile including the stockpile height variation and particle size distribution of the feeders under the stockpile. Making use of size distribution data measured for the industrial stockpile, scaled laboratory piles were constructed and the experimental results were used to fit the segregation parameter in the model. MATLAB was used as the programming platform as it is easy to code and debug, and it has a very large database of built-in functions, as well as data analysis and visualisation tools.

The industrial stockpile is fed from an inclined conveyor handling primary crusher product and the stockpile discharges via eight apron feeders onto two parallel conveyors feeding two SAG mills. Due to size segregation in the stockpile, the two SAG mills receive unequal size distributions, which impacts the performance of the comminution circuit. The maximum capacity of the industrial stockpile which is used for the model validation is 550 000 tons. The diameter of the industrial stockpile is over

100 metres, and the particles have a top size of 250 mm. Industrial data for the stockpile was collected over a period of 57 days at a resolution of 5 minutes. The contents of the simulated pile were initialised using about 4 days of data with the simulated discharge feeders turned off until the stockpile height matched the observed height at the start of the simulation window. The data for running the simulation include the fixed inputs, the dynamic data for the inputs and the dynamic data for the outputs. The fixed inputs are from the stockpile design, including the location of the conveyor; the location of the feeders under the stockpile; the angle of repose; and the segregation parameter from the model fitting. The dynamic inputs of the stockpile were updated at every time-step in the model, including the feed rate; the feed size distribution (F80); the discharge rate and the feeders' speed. The dynamic outputs for the simulation results include the stockpile height and the particle size distribution at each of the discharge feeders.

Stockpile height variation

The stockpile evolves with every time-step. Figure 6 illustrates the stockpile surface profile and height of each column at different times during the simulation, incorporating the P80 of each cell. The change in the shape of the stockpile over time depends on the filling and discharge rates. When using the eight-neighbour (Moore) algorithm for surface flow, the shape of the stockpile forms an 8-sided pyramid. The shape and the height of the stockpile can be observed from the simulation results.

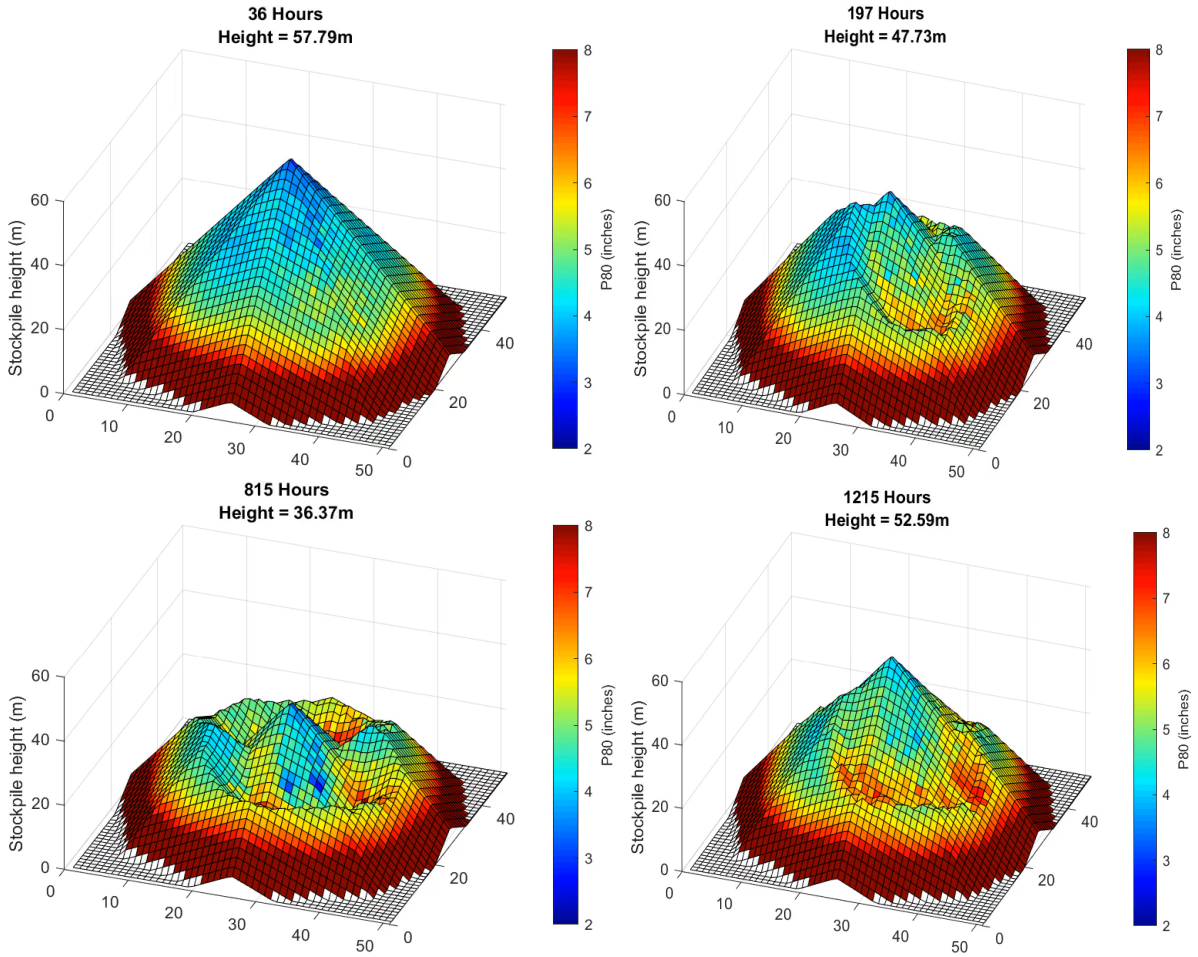

FIG 6 – The variation of the industrial stockpile height and P80 of each cell during the simulation.

The stockpile heights from simulations and industrial data from a height sensor offset from the centre of the stockpile were compared. The stockpile heights from the industrial sensor and the simulation over 57 days are shown in Figure 7, demonstrating good agreement. Moreover, while the physical height sensor can measure the height at one point, however, the highest point of the stockpile is not always in the centre, and it varies with time based on how to operate the stockpile. The stockpile

model can infer the complete stockpile surface profile, which can further be analysed to estimate additional information including total and live stockpile volumes.

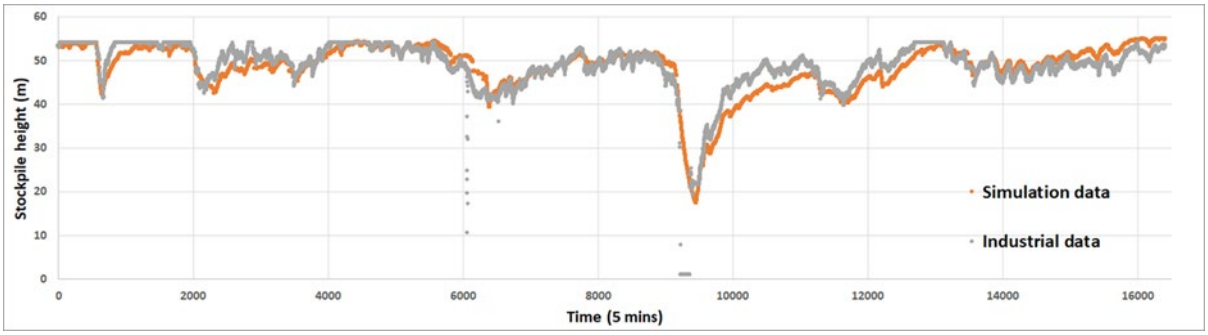

FIG 7 – Comparison of measured and simulated stockpile heights.

Particle size distribution

Based on the modelling method, the P80 of each cell and column in the stockpile can be recorded throughout the simulation (seeing Figure 6). The particle size distribution changes when the stockpile is feeding and discharging. A 2D example in Figure 8 shows the P80 of each cell in a cross-section through the centre of the stockpile. This example clearly demonstrates the size segregation in the stockpile: the edge of the stockpile has more coarse particles, and the centre of the stockpile has finer particles. According to the location of the feeders and how the operators run these feeders, the P80 of the different cells and columns of the stockpile will change with time. It can be observed that the stagnant regions near the bottom are coarser than the top cells. Zones of both coarse and fine particles can form in parts of the pile due to size segregation and the flow patterns induced by the discharge feeders. Moreover, each cell has a characteristic P80 value which can change with time during the simulation. This information of the P80 of each column and each cell within the stockpile cannot be reliably sampled from an industrial stockpile.

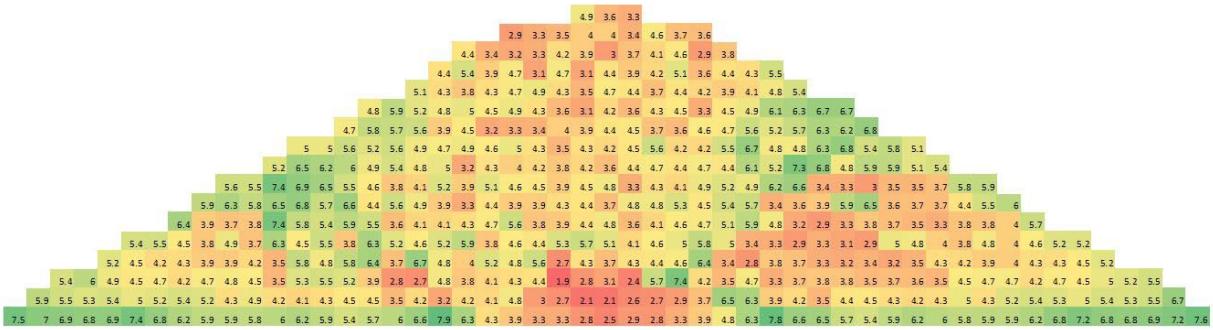

FIG 8 – The P80 (inches) of each cell in the centre of the stockpile.

The average P80 on the two reclaim conveyors under the stockpile are listed in Table 1. Over this 57 day analysis period, the simulated results closely match the industrial results. In the simulation, the particles in line 1 are coarser than in line 2 after including the feed conveyor trajectory segregation, because the coarse particles on the top of the stockpile feed conveyor land closer to line 1. The variations in the P80 values of the two lines over 57 days are shown in Figure 9. The trends in the variation of the industrial data and the simulation results are similar, which indicates that the stockpile model is useful for estimating the variation of the particle size distribution. However, the industrial data (especially of line 2) has additional variability that the stockpile model is not able to predict, which might be due to the periodic operation of dozers and a mobile crusher which discharges onto the pile near line 2.

TABLE 1

Comparison of the average P80 of line 1 and line 2

Average number	Line 1	Line 2
Industrial P80 (inch)	4.4	4.0
Model P80 (inch)	4.3	3.9

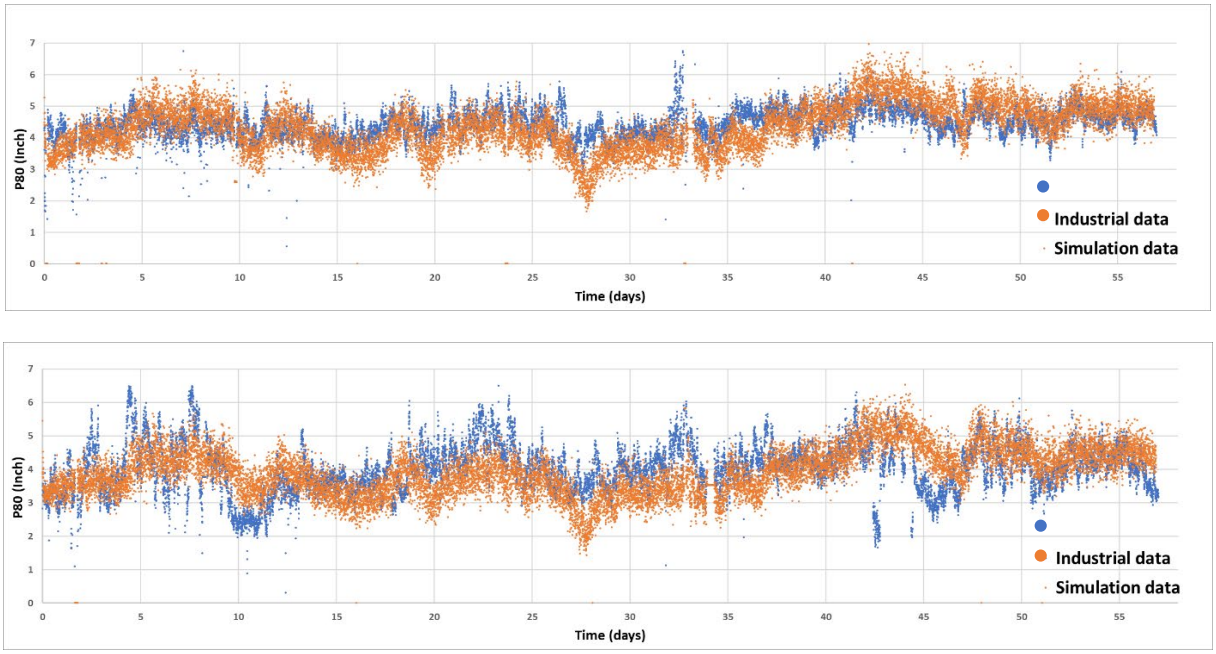

FIG 9 – The variations in the P80 values of line 1 (top) and line 2 (bottom) over 57 days.

CONCLUSION

The development in this paper of a 3D stockpile/bin model based on the Continuous Cellular Automata (CCA) method appears to be the first time that a dynamic 3D CCA-based stockpile model has incorporated size segregation and mass-flow discharge. These mechanisms are considered essential to model the behaviour of real stockpiles and to track ore flow-through the pile. The application of the model to an industrial stockpile shows that the methodology captures the dynamic behaviour of real stockpiles with sufficient accuracy to predict the product size and surface profile; and that the model can calculate faster than real-time. Although the model was only tested on historical data, the obvious application is in process control as a soft sensor. Integration of the model into a plant control system would be beneficial for the optimisation of SAG mill operating parameters and maximise power draw and throughput. The model also has utility for evaluating various stockpile design configurations which have previously only been feasible using physical scale models.

This study makes several practical contributions to understanding how the temporary storage of segregating granular materials in stockpiles and bins can be modelled. Modelling ore storage with size segregation is an important problem in minerals processing where stockpiles and bins are large and often poorly utilised. Storing granular materials is also a significant problem in other industries. While much more research is required, this study has demonstrated how segregation behaviour can be characterised and included within a dynamic model suitable for the design and simulation of ore stockpiles of the type widely used in the mining industry. This new capability has several implications for the discipline. The model also fills gaps in the optimisation of the mineral processing circuit by connecting the mine and the primary crusher to the grinding circuit, which is expected to enhance the performance of advanced process control, including Mine to Mill and geometallurgical optimisation.

ACKNOWLEDGEMENTS

This work is based on research supported by the Advanced Process Prediction and Control Group at the Julius Kruttschnitt Mineral Research Centre. The authors would like to thank the University of Queensland, Sustainable Minerals Institute and Julius Kruttschnitt Mineral Research Centre (SMI-JKMRC) for their support.

REFERENCES

Benito, J G, Ippolito, I and Vidales, A M, 2013. Novel aspects on the segregation in quasi 2D piles. *Powder Technology,* 234:123–131.

Bridgwater, J, 1994. Mixing and Segregation Mechanisms in Particle Flow, In *Granular Matter: An Interdisciplinary Approach* (A Mehta, ed.), Springer, New York, pp. 161–193.

Castro, R L, Gonzalez, F and Arancibia, E, 2009. Development of a gravity flow numerical model for the evaluation of drawpoint spacing for block/panel caving. *Journal of the Southern African Institute of Mining and Metallurgy*, 109(7), 393–400.

Combarros, M, Feise, H J, Zetzener, H and Kwade, A, 2014. Segregation of particulate solids: Experiments and DEM simulations. *Particuology*, 12(Supplement C), 25–32.

De Silva, S R, Dyrøy, A and Enstad, G G, 2000. *Segregation mechanisms and their quantification using segregation testers*. Springer Netherlands, Dordrecht, pp. 11–29.

Dolgunin, V N and Ukolov, A A, 1995. Segregation modeling of particle rapid gravity flow. *Powder Technology*, 83(2), 95–103.

Enstad, G G and Mosby, J, 1998. *Segregation of particulate solid in silos*. London, UK.

Gosálvez, M A, Xing, Y, Sato, K and Nieminen, R M, 2009. Discrete and continuous cellular automata for the simulation of propagating surfaces. *Sensors and Actuators A: Physical*, 155(1), 98–112.

Ingerson, T E and Buvel, R L, 1984. Structure in asynchronous cellular automata. *Physica D: Nonlinear Phenomena*, 10(1–2), 59–68.

Kozicki, J and Tejchman, J, 2005. Application of a cellular automaton to simulations of granular flow in silos. *Granular Matter*, 7(1), 45–54.

Moore, E F, 1964 *Sequential machines: Selected papers*. Addison-Wesley Longman Ltd, Redwood City, CA, USA.

Schulze, D, 2008. *Powders and bulk solids. Behaviour, characterization, storage and flow*. Springer, 22.

Tang, P and Puri, V M, 2004. Methods for Minimizing Segregation: A Review. *Particulate Science and Technology*, 22(4), 321–337.

Williams, J C, 1990. Mixing and segregation in powders. *Principles of Powder Technology*, 71–90.

Wu, S Y and Baeyens, J, 1998. Segregation by size difference in gas fluidized beds. *Powder Technology*, 98(2), 139–150.

Yahyaei, M, Ye, Z, Hilden, M, Ruitz, E A and Gavelan, Z, 2021. Investigating the size segregation of stockpile at MMG's Las Bambas and its impact on performance of SAG mills, In *Mill Operators 2021*, Brisbane, Australia.

Ye, Z, Yahyaei, M and Hilden, M, 2021. Application of a Three-Dimensional Dynamic Stockpile Model for Process Optimisation, In *Conference: Procemin – Geomet 2021*, Santiago, Chile.

Ye, Z, Yahyaei, M, Hilden, M and Powell, M A, 2019. Development of a laboratory test to quantify the size segregation in stockpiles, In *16th European Symposium on Comminution & Classification* UK.

Yu, Y and Saxén, H, 2014. Segregation behavior of particles in a top hopper of a blast furnace. *Powder Technology*, 262 (Supplement C), 233–241.

Future operations – modelling and ‘big data’ utilisation

Detection of ball mill overloading using dynamic time warping

N Adhikari[1], G Forbes[2], M Hilden[3] and M Yahyaei[4]

1. PhD Student, Sustainable Minerals Institute (SMI), University of Queensland (UQ), Brisbane Qld 4067. Email: n.adhikari@uq.edu.au
2. Senior Research Fellow, SMI, UQ, Brisbane Qld 4068. Email: g.forbes@uq.edu.au
3. Senior Research Fellow, SMI, UQ, Brisbane Qld 4068. Email: m.hilden@uq.edu.au
4. Associate Professor, SMI, UQ, Brisbane Qld 4068. Email: m.yahyaei@uq.edu.au

ABSTRACT

Avoiding ball mill overloading is crucial for the stable operation of a grinding circuit. Although many studies have discussed the importance of detecting ball mill overloading, limited research has been conducted to date. This paper demonstrates a novel approach to quantifying ball mill overloading using historical operational data combined with data analytics. Patterns of gradually increasing mill load and decreasing power draw are an indication of ball mill overloading. The multivariate dynamic time warping (DTW) algorithm is used to detect these patterns in the data. The identified patterns, along with the fuzzy logic model, are then used to generate a likelihood score for ball mill overloading. The fuzzy logic model incorporates insights from data and process expert knowledge to increase the prediction accuracy of the proposed methodology. The combination of global and local constraints of DTW such as Sakoe-Chiba, Itakura parallelogram, step patterns, and open-end are investigated for various normalisation techniques with varying series lengths. The analysis of production data from the Semi-Autogenous Grinding (SAG) Mill, Ball Mill, and Pebble Crushing (SABC) circuit, suggests that coarse materials in the SAG mill feed are the likely cause of the ball mill overloading, which in turn results in a coarse product in the cyclone overflow. The statistical comparison of cyclone P_{80} is performed with the one-way ANOVA with a 95 per cent confidence level and found that the mean values of cyclone P_{80} for the various states of overloading are statistically different.

INTRODUCTION

Ball mill overloading

The identification and quantification of ball mill overloading is of great significance when operating the mill as it affects the comminution circuit performance. Ball mill overloading can occur due to excessive circulating load causing a build-up in the volume of slurry in the mill, or it can be due to an accumulation of coarse solids with a low breakage rate accumulating in the mill. When ball mill overloading occurs, the following phenomena are often noticed in the circuit: mill load increases, power draw gradually decreases, circulating load increases due to an increase in mass flow rate, sump level rises, and pump speed increases despite the normal operation in the SAG mill (Arbiter, 1991; McClure and Gopaluni, 2015). Due to higher circulating load and mill filling, the ball mill does not sufficiently grind out materials. Consequently, coarser materials report to the cyclone overflow, which may affect flotation performance in terms of grade, recovery, or tailing volume. Additionally, if the mill discharge does not have a screen, then balls inside the mills are more likely to flush out due to the rise of mill filling.

To resolve the overloading issue, operators will typically reduce or stop the circuit feed for a certain period until the mill recovers. This results in a reduction in the throughput and hence the production of metal. Therefore, the early detection of possible ball mill overloading is important for optimising a key performance indicator (KPI) of business by optimising the grinding circuit performance.

Ball mill overloading identification

The ability to warn of incipient ball mill overloading is crucial for effective process control so that corrective action can take place according to the bottleneck in the circuit. Unfortunately, few models have been developed that can identify or predict the ball mill overloading. The existing empirical power draw model (Napier-Munn *et al*, 1996) and perfect mixing ball mill model (Whiten, 1976; Napier-Munn *et al*, 1996) do not directly model ball mill overloading events. However, the power model predicts that power draw reaches a peak with filling and excessive filling continues to

decrease power draw due to the increasing weight of the slurry pool (Soleymani, Fooladi and Rezaeizadeh, 2016). The ball mill model predicts a peak in breakage rates with respect to particle size, hence a coarsening of mill feed results in the rapid further accumulation of coarser particles in the circuit.

Several studies have investigated the identification of ball mill overloading. Lo *et al* (1987) experimentally determined the incipient overloading conditions of a ball mill. Their study found that overload occurs in the following scenarios: for the particular feed rate when the mill filling continuously increases and power starts to decrease; when the mill filling is greater than about 50 per cent; and for a lower feed rate when percent solids is high and coarser feed. The feed characteristics such as feed size and feed rate to the ball mill, the mill filling, and power draw are explicitly used to predict overloading conditions, while the SAG mill performance and circulating load in the circuit are excluded from their analysis. Their approach can be difficult to apply online because it requires a measured feed size distribution to the ball mill.

Shi (2016) developed a mechanistic overfilling indicator for wet overflow ball mills based on the slurry residence time inside the mill. The methodology determines the overfilling threshold using the residence time established from an analysis of industrial ball mill survey data. However, the methodology does not use power draw or mill weight but requires prior knowledge of ball filling as well as slurry flow rate as inputs to a geometry-based model which can estimate the slurry filling in real-time.

On the other hand, Espinoza *et al* (1995) designed a clustering-based soft sensor model to detect ball mill overloading. The clustering technique applied in their work was initially proposed by Ginsberg (1992). The methodology applies a threshold to the power draw to differentiate between normal operation and several overloading categories. However, the methodology does not use an estimate of the mill load or bearing pressure measurement.

Recent case studies by Powell *et al* (2021) have identified that ball mill overloading in SABC circuits is often caused by a coarser discharge from the SAG mill due to operating the circuits at higher throughputs. In particular, pebble crushers are responsible for increasing the proportion of particles slightly smaller than the discharge trommel or screen but have a low breakage rate in the ball mill (Powell *et al*, 2021). They suggest that other possible factors may be the cause of the overloading, namely, a higher feed rate, too fine a target grind size, too coarse a feed, the top size of feed is too large, and a build-up of recirculating loads due to insufficient cyclone classification. Their study found that the corrective action undertaken to address the ball mill overloading problem creates an opportunity to improve the milling efficiency by 5 per cent. Some of these corrective actions include adjusting the aperture of the screen to control the coarser product of the SAG mill, adjusting the closed side setting of the pebble crusher in order to grind to a fine size, and using the appropriate ball size. Bypassing the feed to the pebble crusher, especially for less competent ore can also overcome ball mill overloading issues if the SAG mill can take more feed (Powell, Evertsson and Mainza, 2019).

Arbiter (1991) assumed that breakage effectiveness decreases in the larger diameter ball mill due to a decrease of rotational flow over the pulp feed flow, causing a lower residence and grinding time of the materials. However, he suggested that the grinding effectiveness can be improved by increasing the mill speed which increases the frequency of impacts. Arbiter (1991) suggested that by correctly adjusting the pulp axial velocity for a given aspect ratio (ratio of the mill length to diameter), one can mitigate the overloading risk and proposed an axial flow velocity of 0.072 m/s to identify overloading onset. However, Powell *et al* (2021) argue that many ball mills with significantly higher axial velocities perform well.

Although theoretical and experimental methods have been undertaken to understand and determine the ball mill overloading, methods incorporating data analytics in the production data less common in the published literature. However, machine learning has been applied to detect the SAG mill overloading using principal component analysis (McClure, 2013); support vector machines (McClure and Gopaluni, 2015); and artificial neural networks (Keaton, Wood and Schaffer, 2002; Gallello, 2021).

This study proposes that time-series patterns of simultaneously decreasing power and increasing bearing pressure (or load cell reading) in the historical plant data can be utilised to identify potential

ball mill overloading scenarios. The scenarios as shown in Figure 1 when the ball mill power draw starts further decreasing while the mill load (the bearing pressure) increases due to solid concentration inside the mill is an indication of the ball mill overloading. Although Powell *et al* (2021) mentioned that an increase in circulating load and a decrease in power is the clearest indication of ball mill overloading, the patterns in the circulating load is not used to identify the overloading in this work. This is because the circulating load contains more noise than bearing pressure or load cell. To identify these patterns in the data, the Dynamic Time Warping (DTW) algorithm (Velichko and Zagoruyko, 1970; Sakoe and Chiba, 1978) is utilised. DTW shows promising results in identifying the pattern in the time series data (Berndt and Clifford, 1994). Further, the fuzzy logic for multiple criteria decision-making (Carlsson and Fuller, 1996; Kahraman and Cagri Tolga, 2009) has been applied in order to make a systematic and rational decision whilst categorising the various degrees of overloading.

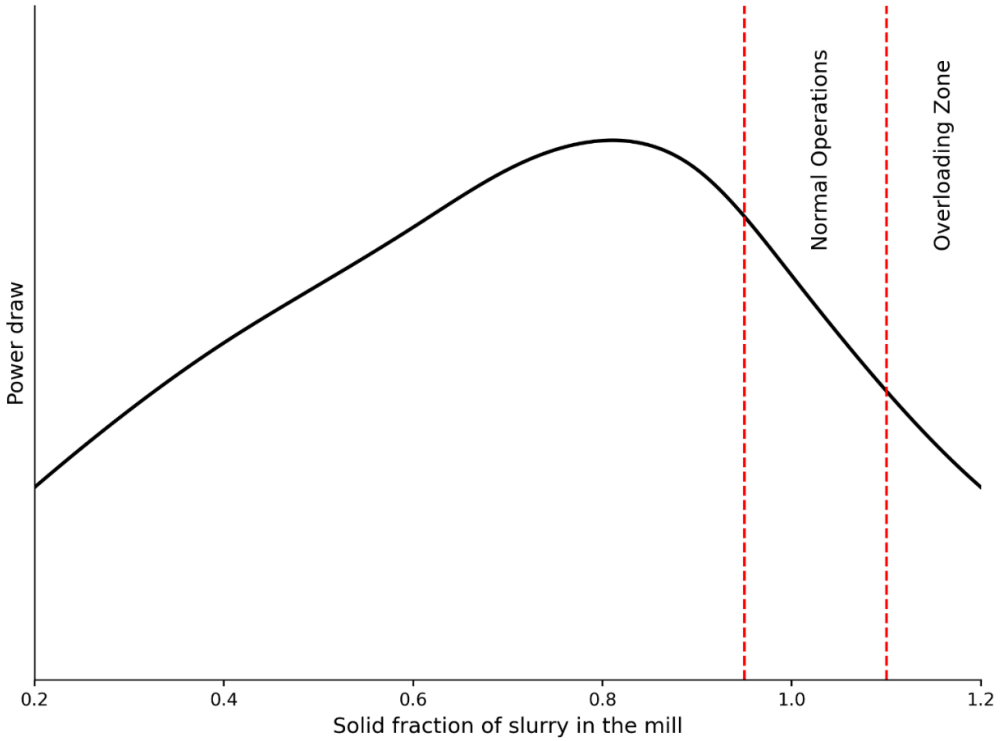

FIG 1 – Schematic graph of the power draw versus the solid fraction of slurry in the mill based on our knowledge of ball mill operation and power draw model (Morrell, 1996).

The concept implemented in this work is based on fuzzy sets (Zadeh, 1965) and the fuzzy classification of continuous variables (Ruspini, 1969). The fuzzy concept has been used in this work because DTW is capable of identifying the downtrend of the ball mill power draw. However, it is unable to determine the dropping of the power draw due to the restarting of the motor after interruptions (Mirosevic and Maljkovic, 2015). The decision boundaries of the fuzzy logic generated using the distribution of the data are further guided by process expert knowledge. While further strengthening the decision of the overloading conditions, the overloading score is ranked on a percentile scale rather than a binary scale.

Dynamic time warping algorithm

The DTW algorithm is popular for comparing time series data. The algorithm can stretch or compress series while aligning an element between two time series so that a distance measure between the series is minimised. The algorithm was first developed in the 1970s for word and voice recognition (Velichko and Zagoruyko, 1970; Sakoe and Chiba, 1978). Since then, it has been employed in numerous domains: bioprocess monitoring (Gollmer and Posten, 1996); biomedical informatics (Tormene *et al*, 2008; Yuan *et al*, 2011); and space physics (Laperre, Amaya and Lapenta, 2020). Examples of the applications of DTW include finding the best alignment and estimating time shift (Yuan *et al*, 2011); measuring similarity between original and forecast series to evaluate the model

(Laperre, Amaya and Lapenta, 2020); measuring similarity on highly correlated multivariate data (Bankó and Abonyi, 2012); and finding patterns (Berndt and Clifford, 1994).

Although the algorithm is popular in other domains, most of the applications of DTW in minerals processing are relatively recent. The DTW algorithm has been applied in the mineral processing industry: to compare coal flotation yield-ash curves (Bournival and Ata, 2021); to recognise operating modes in iron ore sintering process data (Du *et al*, 2020); to analyse and prioritise control system alarms in flotation plant (Hu *et al*, 2015); to detect anomalies in feeding data for an industrial cone crusher (Liu *et al*, 2022); and to track ore flow-through coarse ore stockpiles (Glesson, 2020). The major possibilities of the DTW algorithm in the mineral processing industry are the identification of the patterns in time series data, calculating residence time, and calculating time shifts between stream measurements.

The DTW algorithm has been modified to various variants due to the interest in enhancing performance power when implementing it into various domains (Salvador and Chan, 2007; Niennattrakul and Ratanamahatana, 2009; Al-Naymat, Chawla and Taheri, 2012; Mueen and Keogh, 2016; Zhang *et al*, 2017). Most of them are available in the open-source programming languages R and Python (Giorgino, 2009).

A variety of constraints can be used in the algorithm. These have been extensively researched (Itakura, 1975; Sakoe and Chiba, 1978; Salvador and Chan, 2007;; Al-Naymat, Chawla and Taheri, 2012). The algorithm has a number of global and local constraints, such as the Sakoe-Chiba band, Itakura parallelogram, and step patterns. Constraint plays an important role in speeding up the DTW as it reduces the search space of the possible alignment. Salvador and Chan (2007) emphasize that constraint is one of the techniques to speed up DTW. Also, the constraint can greatly impact the resultant match between two signals. Hence, in this work, constraints are imposed to achieve better matching between signals. The Sakoe-Chiba band (Sakoe and Chiba, 1978) and Itakura parallelogram (Itakura, 1975) are two commonly used global constraints. Among these two global constraints, the Sakoe-Chiba band is found to be widely used by researchers. This may be due to its compatibility with a local constraint such as step patterns (Tormene *et al*, 2008). The warping window width is the main parameter of the Sakoe-Chiba band constraint. The role of the warping window parameter is to constrain the warping path moving along the diagonal. The DTW distance is equivalent to Euclidean distance when the warping window width is equal to one (Keogh and Ratanamahatana, 2005).

Aims

The main aim of this study is to identify ball mill overloading from the historical operational data. The identification of the simultaneous occurrence of increasing trend of bearing pressure and decreasing trend of motor power is utilised to identify multiple occurrences of similar events such as the ball mill overloading in the data. The findings will help to a better understanding of the factors associated with ball mill overloading that can be utilised to take preventive actions in the processing plant.

METHOD AND MATERIALS

The framework

The methodology applied in this work has been completed in three stages. Firstly, the published literature is reviewed in order to understand the various scenarios that have resulted in ball mill overloading. This is then further applied to define the parameters of DTW, namely slope and length of the reference signals, length of the sliding windows, and the decision boundaries of the fuzzy criterion. Secondly, the overloading scenarios determined in the data are validated with the knowledge discovered through the literature review. Finally, some knowledge is generated from the analytical insights of the overloading. The conceptual framework is visualised in Figure 2. The domain knowledge has been applied in the various stages of the procedure to guide the methodology properly.

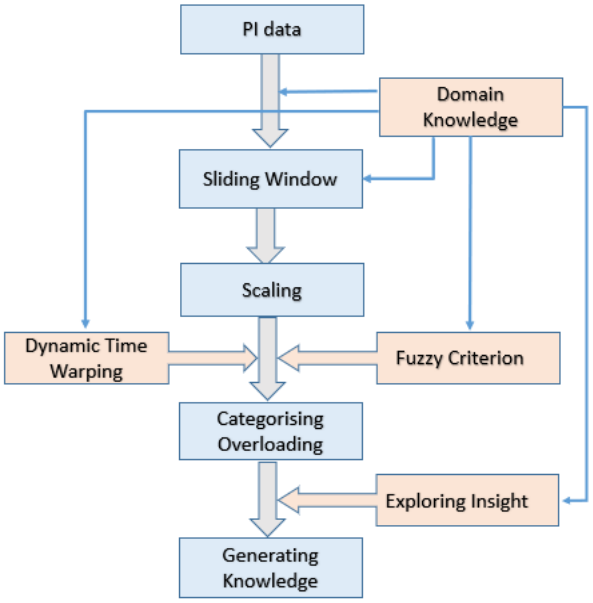

FIG 2 – Conceptual framework of the identification of the ball mill overloading in PI data.

Industrial data

This study analysed a year's worth of historical data with two minutes resolution from a gold processing plant. The data set contains the process information of a typical SABC circuit. The following information is included in the data set: feed size and feed rate to the SAG mill, percent solids, water addition, bearing pressure, power draw and speed of the SAG and ball mill, size distribution cyclone overflow, flow rate to the cyclone, number of the operating cyclone, power draw, pebble size and feed rate to crusher. Histograms of some of these variables is shown in Figure 3. The visualisation omits outliers to better illustrate the distributions within the normal operating range.

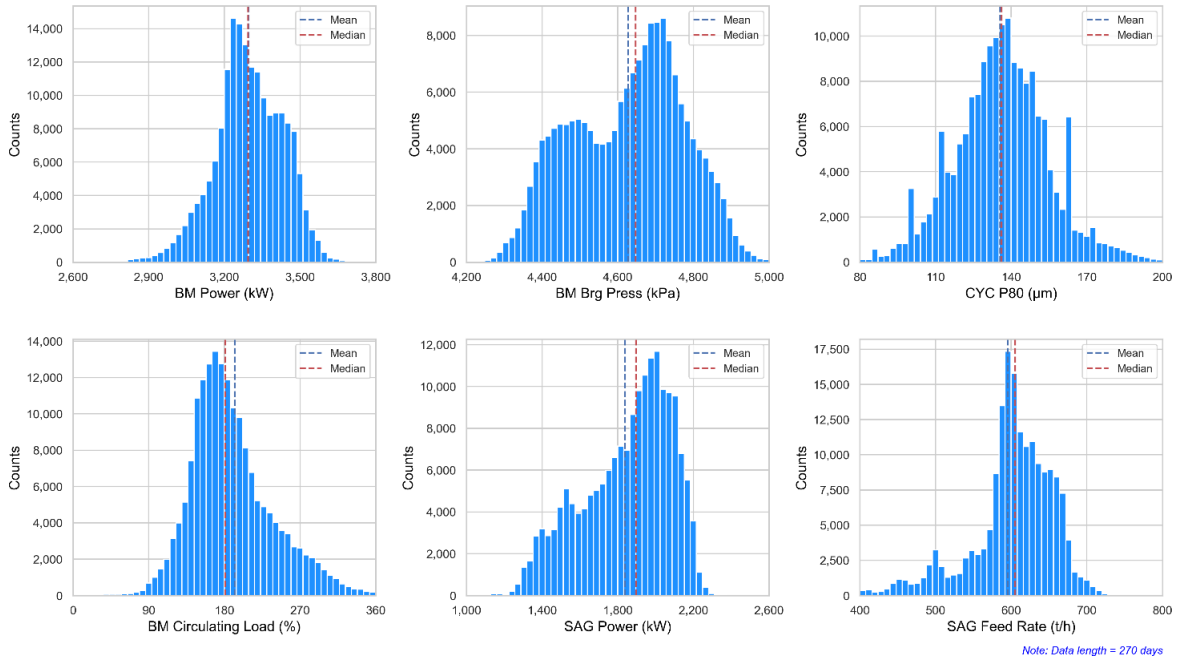

FIG 3 – Distribution of key process variables.

Sensor faults and errors may result in poor quality of data, for example, if sensors experience drift or suffer damage (Pothina and Ganguli, 2020). Hence, the reliability of the data is checked with the help of other variables. Some basic data cleaning is also required, including renaming columns for universal understanding, removing missing rows and columns, converting data to metric systems

from other unit systems, and adding new calculated variables such as circulating load and pebble generation ratio.

Reference signals and slope identification

Powell *et al* (2021) found that the ball mill power dropped by an average of 100 kW when overloading occurred over around 30 minutes. Arbiter (1991) suggested that overloading usually lasts around 20 minutes. Hence after observing the resolution and patterns of ramping up of bearing pressure and ramping down of power in the data, two reference signals each ten instances (20 minutes) in length for a 100 kW decrement in power and a 100 kPa increment in bearing pressure are defined. These reference signals are then used to find similar patterns of 100 kW drop in power when 100 kPa increase in bearing pressure within a 20-minute interval (ten instances) has been identified.

Figure 4 demonstrates the reference signals that are created with these assumptions. They are specific power and bearing pressure values. However, the DTW algorithm identifies similar patterns in the data set based on the values of the test and reference signals.

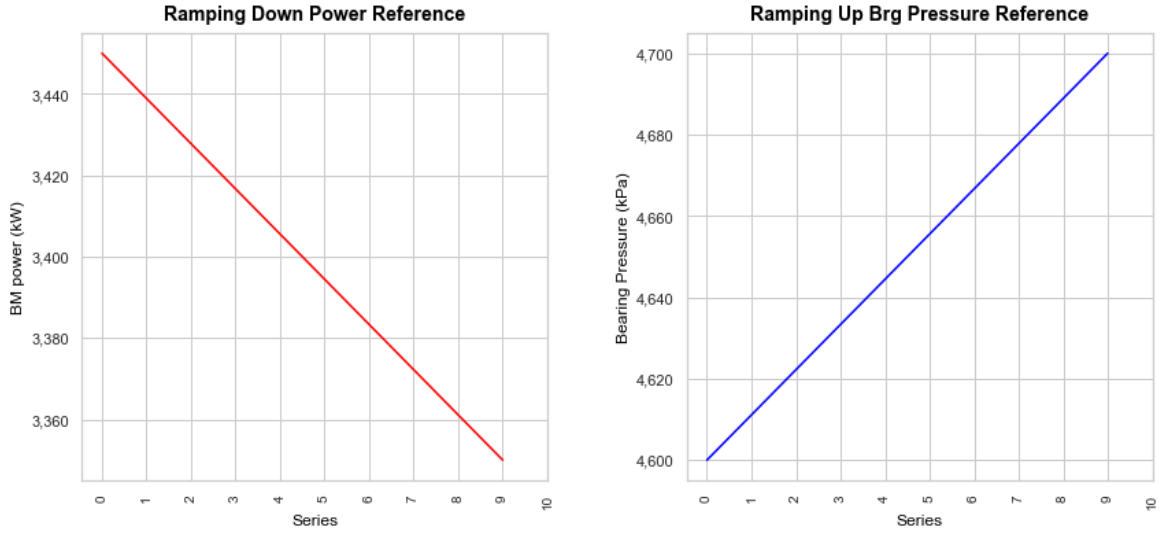

FIG 4 – Reference signals.

Sliding window

The sliding window concept is applied in this work for two main purposes. Firstly, to make the reference and test signals equal in length. The advantages of having identical lengths are discussed later. Secondly, to ensure all of the patterns in the data are captured by the algorithm. Figure 5 is an example of the process of sliding windows for window size ten and step size three. At every iteration, the window moves by three units until the window reaches the end point of the series.

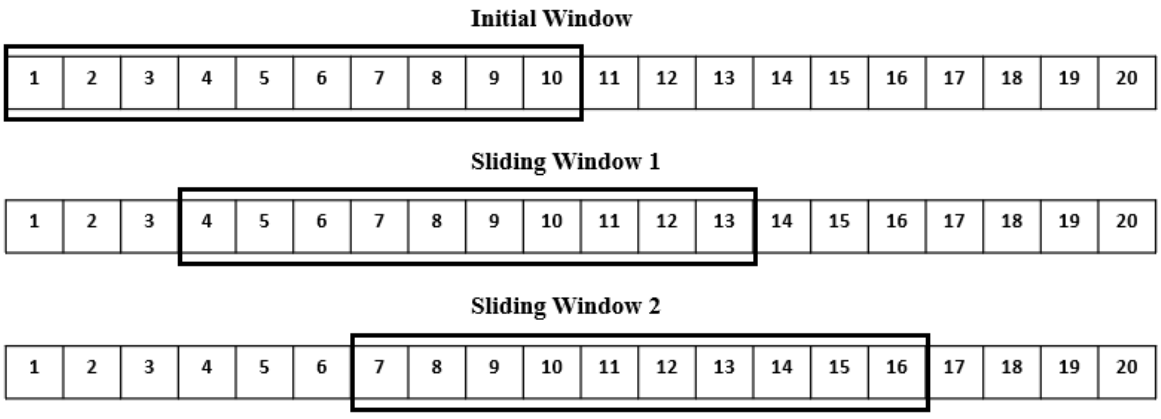

FIG 5 – Concept of a sliding window. Reconstructed from Hota *et al* (2017).

The DTW in this study aims to identify similar patterns in the variables in the PI data to that of reference signals. The length of the sliding window is considered equal to the length of the reference signal of 20 minutes (ten samples for our data set). The same length enables the global and local constraints to be effectively applied to the DTW algorithm. To correctly account for the patterns within two window widths, the step size is considered as three instances (six minutes interval), which is about one-third of the sliding window. This means that the sliding window is moved by only three samples in each iteration.

Scaling data

The performance of the DTW is investigated against the normalisation or standardisation techniques. The formula for standardisation is expressed as:

$$z = \frac{x-\mu}{\sigma} \tag{1}$$

Where, μ is the mean value, σ is the standard deviation, and z is the standardised score of the x.

It is found that the standardisation technique does not perform well in matching the patterns in the data set. For instance, while normalising the data with the standardisation technique, the reference signal of down ramping of motor power (~ 3500 kW) perfectly matches the patterns in the dead zone (~ 0 kW) of motor power while the expected match should be above 2000 kW. The details are shown in Figure 6.

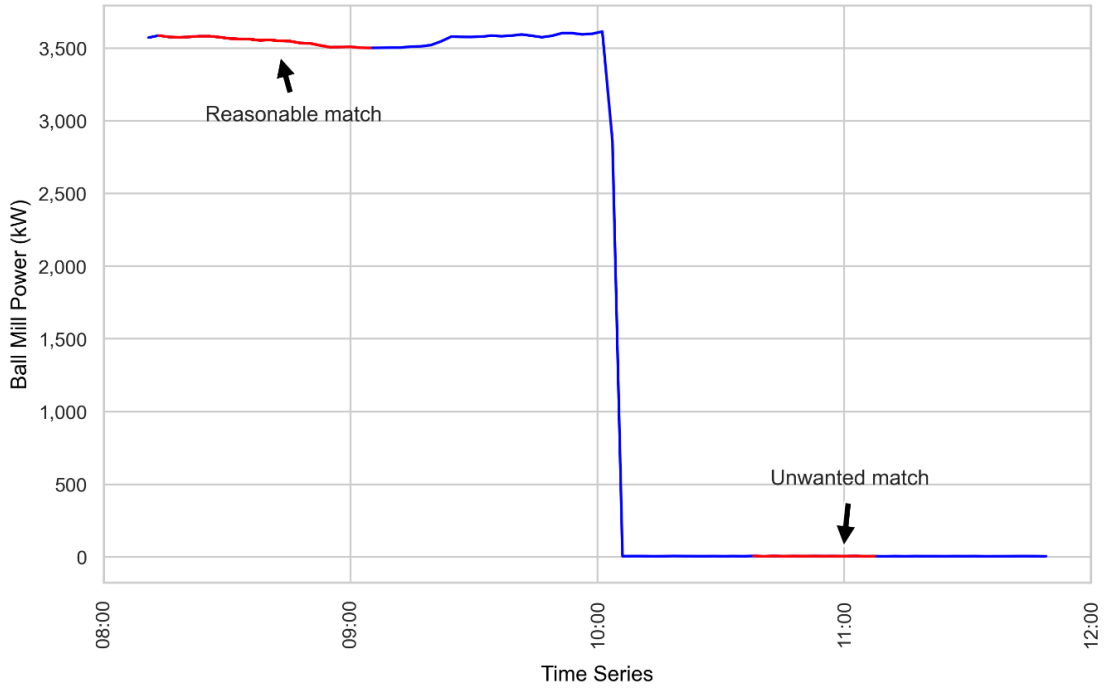

FIG 6 – Matching of down ramping signals using DTW.

To resolve the normalisation problem, a technique of scaling the data has been devised. The technique resets series to start at zero by subtracting the series by the first instance of the series so that reference and test signals are identical at the start of the series. The scaling is performed for each variable separately due to large differences in values between the variables. The formula of the proposed scaling technique is presented below.

$$x = x_1, x_2, \ldots., x_n \tag{2}$$

$$S = x_1 \tag{3}$$

$$y = (x_1 - S), (x_2 - S), \ldots., (x_n - S) \tag{4}$$

Where, x is an original series, S is an offset, and y is a series after scaling.

DTW algorithm

In this study, the DTW-Python library developed by Giorgino (2009) has been applied to calculate the DTW distance while the results are visualised with the modified functions. The example of the plot used to observe the warping path and alignment is shown in Figure 7. The left-hand side heatmap plot, along with the blue line, shows the warping path when matching two signals, while the right-hand side plot visualises the matched points in both time series. The test signals refer to the actual time series from the data for a sliding window. To find the optimum matches between two signals, the warping path is constraining to move along the diagonal, the details of the constraints are discussed later.

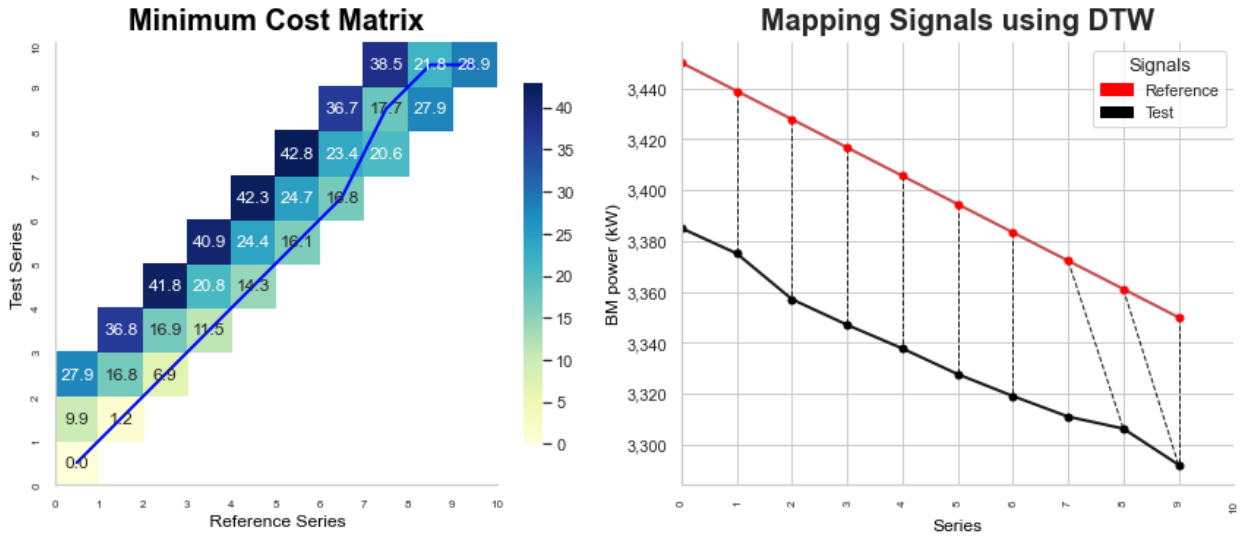

FIG 7 – Visualisation of warping path and matching points between two signals.

Constraint used in DTW

The global constraint Sakoe-Chiba band has been applied in this work because of its ability to apply the local constraint such as step patterns simultaneously. The step pattern allows the flexibility of the algorithm not to match the end point of the test series with reference signals. For instance, the beginning point of the test signal is not matched with the reference signal in the mapping signals visualisation in Figure 7. The warping window width, a parameter of the Sakoe-Chiba Band, is set to 10 per cent of the series length as suggested in the literature (Niennattrakul and Ratanamahatana, 2009).

Among three different types of step patterns such as asymmetry, symmetry1, and symmetry2, the asymmetry step patterns have been applied in this work to optimise the warping path within a global constraint of the Sakoe-Chiba Band. The asymmetric step patterns guarantee the warping path to be single-valued. It constrains to match each element of the reference signals exactly once which can be observed in Figure 7. More details about the constraints used are found in the paper published by Tormene *et al* (2008).

Due to the restriction of the asymmetry step pattern, one point of the reference signals may not be matched with multiple points of the test signal. Also, the warping path is constrained not to move along the vertical y-axis. The formula used to calculate the minimum cost matrix when using the asymmetry step pattern is:

$$Minimum\ cost\ (i,j)\ =\ min\left[c\ (i-1,j), c\ (i-1,j-1), c\ (i-1,j-2)\right]\ +\ D\ (i,j) \qquad (5)$$

Where i and j are indices of the reference and test series respectively. c is the cost while D is the Euclidean distance between i and j.

Fuzzy logic

A fuzzy logic algorithm is created using the variables that may indicate possible ball mill overloading. The important variables are DTW distance measured on motor power and bearing pressure of ball mill, ball mill circulating load, and SAG mill feed rate. These variables are identified using the

literature on ball mill overloading discussed in the previous section. Hence, the fuzzy algorithm reflects the factors that influence ball mill overloading, such as power drops due to an increase in mill load, higher circulating load in the ball mill circuit, and higher feed rate to the SAG mill. Firstly, the rank score values from one to four are calculated for every instance of the important variables using threshold values. The threshold is determined using the distribution of the data as shown in Figure 3, along with process expert knowledge. If v is the rank score variable of a variable u, then, the rank score for an instance of a variable is defined as:

$$v_i = \begin{cases} 1 \; if \; u_i \; is \; less \; likely \; cause \; of \; overloading \\ 2 \; if \; u_i \; is \; moderately \; less \; likely \; cause \; of \; overloading \\ 3 \; if \; u_i \; is \; moderately \; high \; likely \; cause \; of \; overloading \\ 4 \; if \; u_i \; is \; highly \; likely \; cause \; of \; overloading \end{cases} \tag{6}$$

$$\forall \; i \; (length \; of \; data) = 1, 2, \ldots, n$$

Where, u_i and v_i is the i^{th} instances (values) of a variable u and v respectively.

Secondly, the average percentile score is calculated using the rank scores of these variables. Mathematically,

$$Average \; percentile \; score = \frac{Sum \; of \; scores \; of \; important \; variables \; in \; a \; row}{Total \; possible \; score} \times 100\% \tag{7}$$

Finally, the percentile ranked score is converted into three different categories of the overloading such as probable, overload, and start-up effect. The percentile overloading score from 45 per cent to 65 per cent is categorised as probable, and that of 65 per cent and above is defined as overloading. In contrast, the start-up effect is characterised an event with a more than 45 per cent percentile score that happens within 50 minutes following a major stoppage. The distribution of the overloading score shown in Figure 8 is used to define the overloading rank from the percentile score. The distribution has only included the instances that have overloading scores between 0 and 100 which represents less than ten percent of the total data. The remaining data returns a negative score due to penalty for zero likelihood of overloading. The stabilisation time of the mill after a major shutdown is 50 minutes based on the patterns in the data and prior knowledge of the process.

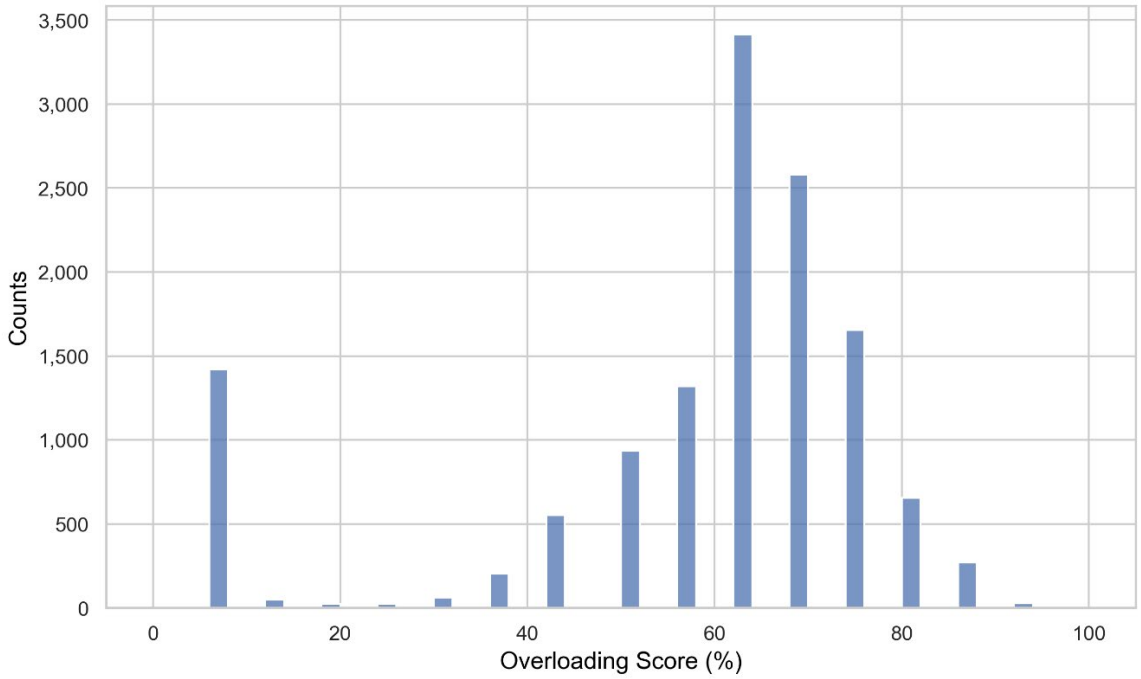

FIG 8 – Distribution of the ball mill overloading score for the instances that have scores between 0 and 100.

RESULTS AND DISCUSSION

Ball mill overloading scenarios

The methodology shows promising results in terms of identifying the timestamps (observations) in the time series of the PI data when ball mill power decreases and bearing pressure increases. The red coloured marking in the time series shown in Figure 9 corresponds to the simultaneous occurrences of the ramping up trends of bearing pressure and ramping down trends of motor power. The magnified plots has been shown in Figure 15 in the Appendix. The trends identified in the time series are further utilised to identify the ball mill overloading. It is interesting to note that all these identified trends are not always overloading. Hence further classification is required.

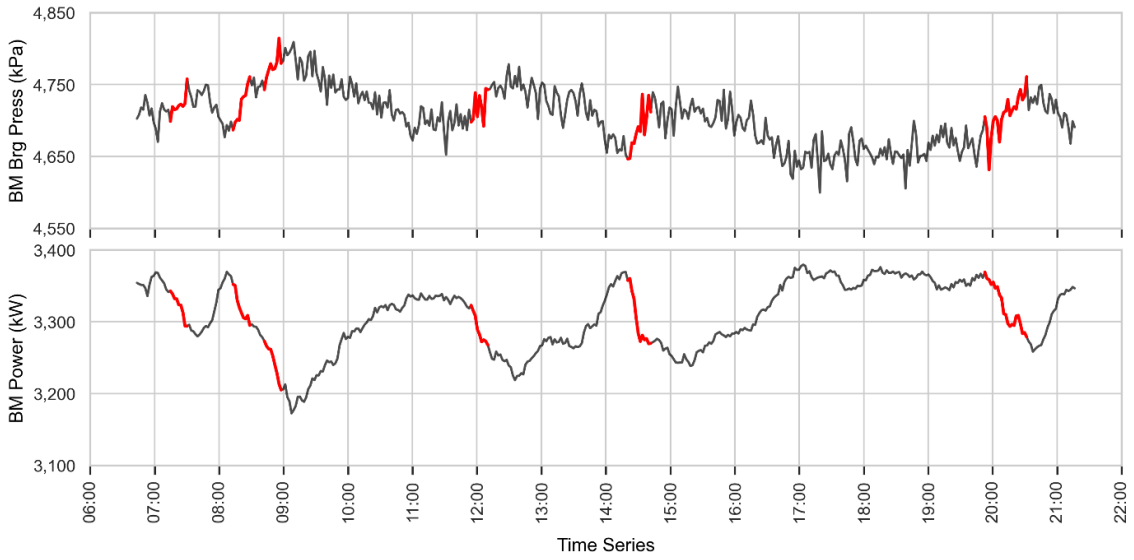

FIG 9 – Identification of patterns in the time series using DTW.

The start-up effect in the ball mill may have similar patterns of simultaneously increasing mill load and decreasing power draw. However, bearing pressure readings could be abnormal due to additional hydraulic pressure being applied to achieve hydraulic lift during start-up, hence bearing pressure at this time cannot be directly compared with readings during normal operation. The green colour markers in the visualisation, as shown in Figure 10 identify the start-up effect. An additional case is shown in Figure 14 in the Appendix. The study also observed that it takes almost 50 to 60 minutes to stabilise the operations when a major shutdown occurs in the plant. Hence, the fuzzy system has been used to distinguish the start-up effect from the overloading event.

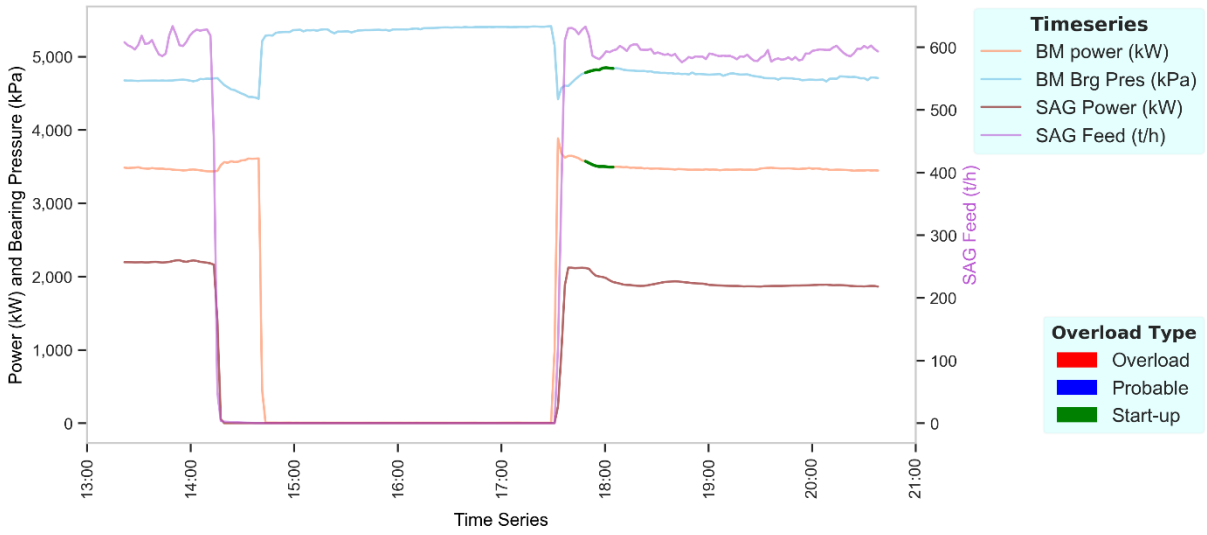

FIG 10 – Ball mill overloading detection in PI data.

Figure 11 shows a group of violin plots for key indicative process variables categorised by different types of overloading. A violin plot is a hybrid of kernel density and box plots where the white dot in the centre is the median and the thick bar in the centre is the interquartile range. The almost equivalent shape of violin plots for a variable reflects that overloading categories have a similar distribution. The position of the median and the interquartile range are found to be different across various states of overloading. It is observed that the overloading condition is associated with a decrease in power draw, an increase in the mill load in the form of bearing pressure, and an increase in circulating load. These observations are consistent with the literature and gives us confidence that the proposed methodology works well to identify the overloading conditions.

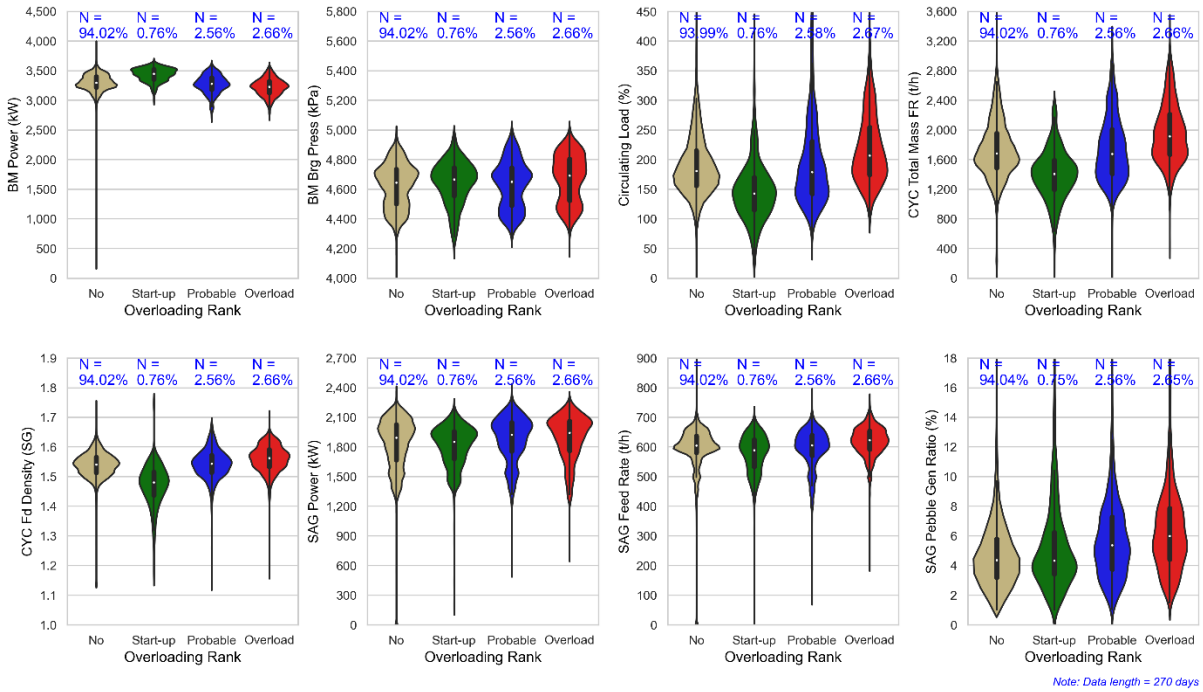

FIG 11 – Ball mill overloading scenarios observed in the data.

Other performance indicators such as cyclone mass flow rate and cyclone feed density vary in a manner similar to that of circulating load. This is to be expected because these variables are highly correlated. The ball mill overloading appears to be affected by the performance of the SAG mill, with overloading being associated with higher SAG feed rate, power, and pebble generation. This suggests that a coarser product from the SAG may be responsible for the ball mill overloading for this processing plant.

It is observed that the pebble generation has increased during ball mill overloading. To validate the visual indication in the violin plot, a one-way ANOVA test has been performed to test whether the SAG mill pebble generation ratio for the classes of overloading rank is statistically significant. The p values for all the multi-class test cases are found to be less than 0.05. This means we have enough evidence to reject the null hypothesis for a 5 per cent level of significance. Therefore, it is concluded that there are significant differences in SAG mill pebble generation ratios for the various overloading ranks. Details of the statistical tests can be found in the Appendix.

Ball mill overloading detection

The segments of the different degrees of the overloading, along with the time series of the various significant variables during overloading, are visualised in Figure 12. The time series is visualised with a dual y-axis. The left-hand side y-axis is used for the ball mill power, the bearing pressure, and the SAG mill power, while the right-hand side is used for feed rate, circulating load, and cyclone P_{80}. The red, blue, and green colour segments on the time series of the power draw and bearing pressure represents the different degrees of the overloading identified using fuzzy logic.

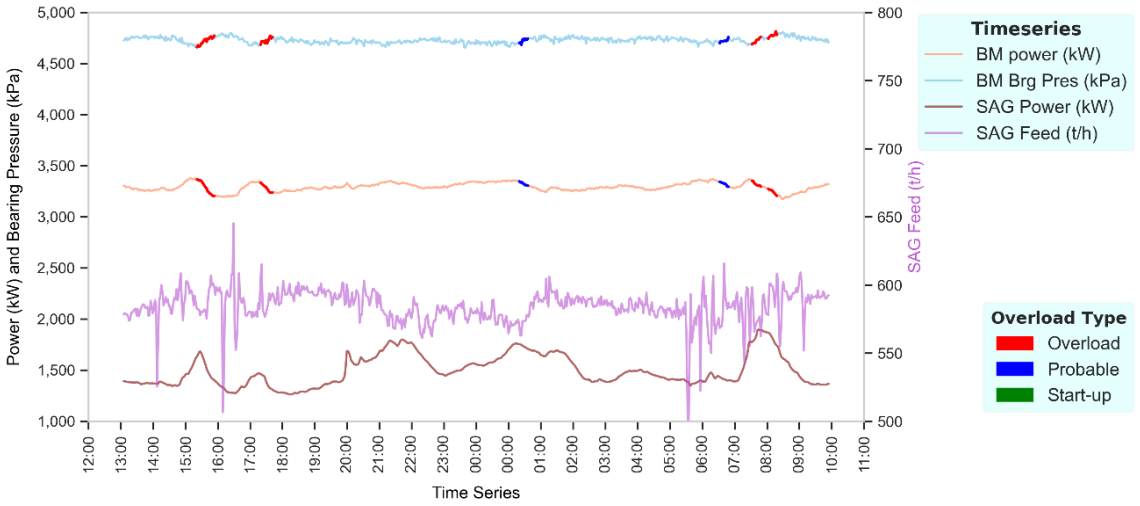

FIG 12 – Ball mill overloading detection in PI data with other influence variables.

Consequences of ball mill overloading

The study observed a similar consequence of overloading as discussed in the literature, namely the increase of coarser materials reporting to the cyclone overflow. This is shown in Figure 13. The ball mill start-up generates relatively fine materials compared to other scenarios. This is because the operator usually adds more water to the circuit when starting operations of the grinding circuit after a major shutdown. The additional water increases the slurry level in the mill until the materials are transported from the SAG mill feed end to the ball mill. It also helps to stabilise the circuit performance and minimises equipment damage. Hence, soon after the operation starts, a larger proportion of water comes out from the cyclone overflow, which may contain fine materials. The probable overloading conditions are associated with overloading with less degree of confidence which is also responsible for the coarse grinding.

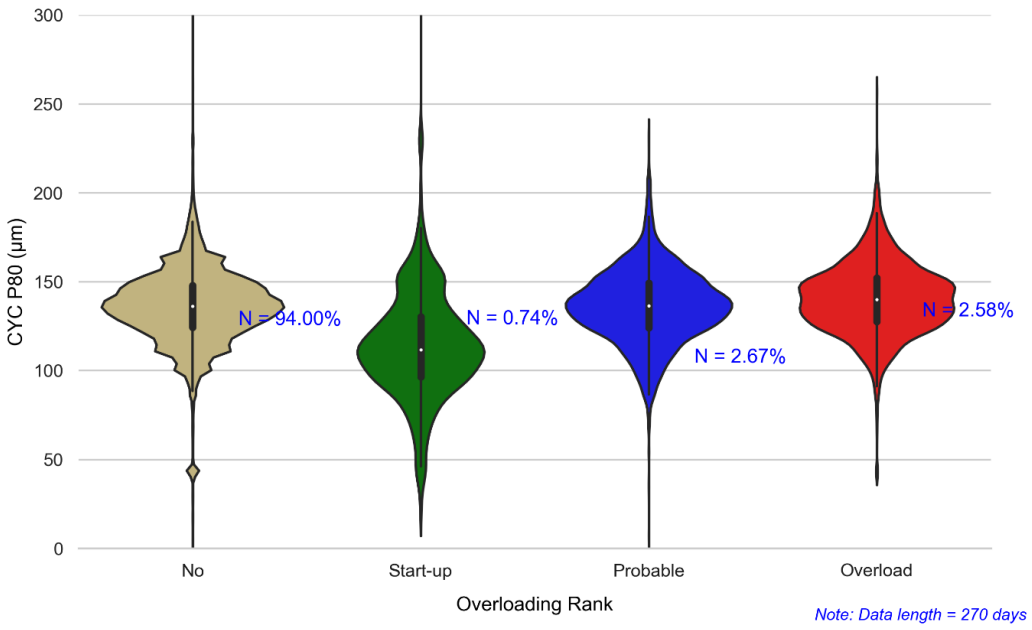

FIG 13 – Consequences of ball mill overloading on cyclone P_{80}.

Statistical tests have been conducted to test whether the value of cyclone P_{80} for different classes of overloading rank is significant. The p values for all the multi-class test cases are found to be less than 0.05. That means we have enough evidence to reject the null hypothesis for a 5 per cent level of significance. Therefore, it is concluded that there are significant differences in cyclone P_{80} for the various overloading ranks. One can argue that the finer or coarser product in the cyclone overflow is due to other conditions in the circuit, such as variation of ore types or variation of operating

conditions of equipment in the circuit. However, further study may be required to draw a solid conclusion from the results as the data does not have the label of overloading. The label of the overloading refers to the actual overloading categories that can be presented as a variable in the data.

CONCLUSIONS

The application of Dynamic Time Warping has been shown to be able to identify ball mill overloading in the historical operational data. The results show that DTW is effective in identifying the patterns of a decrease in power and an increase in bearing pressure simultaneously in the data in various scenarios. The operational conditions associated with the ball mill overloading scenarios are also discussed. The study found that the generation of pebbles is significantly higher during the overloading and that the overloading may result in a coarser cyclone overflow. The statistical comparison is performed with the one-way ANOVA with a 95 per cent confidence level. Hence, the identification of the ball mill overloading in this study can be useful to understand its causes and consequences. In future work, the proposed methodology can be used to label the data, which in turn can be used to develop a predictive model to predict the overloading in the online environment.

The degree of accuracy of the overloading could not be determined as the data does not have a label of the events (ground truth). However, to increase confidence in the results, the ranking scores of the overloading have been introduced using fuzzy logic. Apart from fuzzy logic decision boundaries, it is found that the parameters of the algorithm (global and local constraints), data resolution, data normalisation method, window length, and slope of the reference signals play an important role while detecting patterns. The results and performance of the algorithm can be improved if the training data has a label of the overloading events.

The decision boundary of the fuzzy logic has been manually set based on insights from data as well as the processing knowledge. Further work is required to automatically update the decision boundaries of the fuzzy logic directly from data. The impact of the resolution (timestamps interval) of the time series data on DTW performance has yet to be investigated and will be the focus of future work.

ACKNOWLEDGEMENTS

The authors would like to acknowledge The University of Queensland for supporting this research through the Higher Degree Research Scholarship and Karen Holtham for the editorial review of this document.

REFERENCES

Al-Naymat, G, Chawla, S and Taheri, J, 2012. SparseDTW: a novel approach to speed up dynamic time warping. *2009 Australasian Data Mining* [Online], 101. [Accessed December].

Arbiter, N, 1991. Dimensionality in ball mill dynamics. *Mining, Metallurgy & Exploration,* 8, 77–81.

Bankó, Z and Abonyi, J, 2012. Correlation based dynamic time warping of multivariate time series. *Expert Systems with Applications,* 39, 12814–12823.

Berndt, D J and Clifford, J, 1994. Using dynamic time warping to find patterns in time series. KDD Workshop, Seattle, WA, USA:, 359–370.

Bournival, G and Ata, S, 2021. An evaluation of the Australian coal flotation standards. *Minerals,* 11, 550.

Carlsson, C and Fuller, R, 1996. Fuzzy multiple criteria decision making: Recent developments. *Fuzzy Sets and Systems,* 78, 139–153.

Du, S, Wu, M, Chen, L, Cao, W and Pedrycz, W, 2020. Operating mode recognition of iron ore sintering process based on the clustering of time series data. *Control Engineering Practice,* 96.

Espinoza, P A, Gonzalez, G D, Casali, A and Ardiles, C, 1995. Design of soft-sensors using cluster techniques. International Mineral Processing Congress, October 1995 San Francisco. 22–27.

Gallello, D, 2021. *Artificial intelligence applied to mill optimization* [Online]. Control Engineering. Available: https://www.controleng.com/articles/artificial-intelligence-applied-to-mill-optimization/ [Accessed Jan 2022].

Ginsberg, D W, 1992. *Cluster analysis for mineral processing applications.* Doctor of Philosophy, The University of Queensland, School of Engineering.

Giorgino, T, 2009. Computing and visualizing dynamic time warping alignments in R: the dtw package. *Journal of Statistical Software,* 31, 1–24.

Glesson, D, 2020. *DataCloud bridging the mining industry's data divide* [Online]. International Mining. Available: https://im-mining.com/2020/08/20/datacloud-bridging-mining-industrys-data-divide/ [Accessed Jan 2022].

Gollmer, K and Posten, C, 1996. Supervision of bioprocesses using a dynamic time warping algorithm. *Control Engineering Practice,* 4, 1287–1295.

Hu, W, Afzal, M S, Brandt, G, Lau, E, Chen, T and Shah, S L, 2015. An application of advanced alarm management tools to an oil sand extraction plant. *IFAC-PapersOnLine,* 48, 641–646.

Itakura, F, 1975. Minimum prediction residual principle applied to speech recognition. *IEEE Transactions on Acoustics, Speech and Signal Processing,* 23, 67–72.

Kahraman, C and Cagri Tolga, A, 2009. An alternative ranking approach and its usage in multi-criteria decision-making. *International Journal of Computational Intelligence Systems,* 2, 219–235.

Keaton, M, Wood, M and Schaffer, M, 2002. Application at Ok Tedi Mining of a neural network model within the expert system for SAG mill control. Canadian Mineral Processors Conference, 2002 Ottawa, Canada. 21–23.

Keogh, E and Ratanamahatana, C A, 2005. Exact indexing of dynamic time warping. *Knowledge and Information Systems,* 7, 358–386.

Laperre, B, Amaya, J and Lapenta, G, 2020. Dynamic time warping as a new evaluation for dst forecast with machine learning. *Frontiers in Astronomy and Space Sciences,* 7, 39.

Liu, Q, Song, B, Ding, X and Qin, S J, 2022. Fault diagnosis of dynamic processes with reconstruction and magnitude profile estimation for an industrial application. *Control Engineering Practice,* 121.

Lo, Y C, Rogovin, Z, Herbst, J A and Lee, K, 1987. Detection and prediction of overload conditions in ball mill grinding. *Mining, Metallurgy & Exploration,* 4, 214–217.

McClure, K S and Gopaluni, R B, 2015. Overload detection in semi-autogenous grinding: a nonlinear process monitoring approach. *IFAC-PapersOnLine,* 48, 960–965.

McClure, K S, 2013. *Algorithm for nonlinear process monitoring and controller performance recovery with an application to semi-autogenous grinding.* Doctoral of Philosophy, University of British Columbia.

Mirosevic, M and Maljkovic, Z, 2015. Effect of sudden change load on isolated electrical grid. *International Conference on Electrical Systems for Aircraft, Railway, Ship Propulsion and Road Vehicles.* Aachen, Germany: IEEE,

Morrell, S, 1996. Power draw of wet tumbling mills and its relationship to charge dynamics – Part 2: An empirical approach to modelling of mill power draw. *Transactions of the Institutions of Mining and Metallurgy, Section C: Mineral Processing and Extractive Metallurgy,* 105, C54-C59.

Mueen, A and Keogh, E, 2016. Extracting optimal performance from dynamic time warping. *Proceedings of the 22nd ACM SIGKDD International Conference on Knowledge Discovery and Data Mining* [Online].

Napier-Munn, T J, Morrell, S, Morrison, R D and Kojovic, T, 1996. *Mineral comminution circuits: their operation and optimisation,* Indooroopilly, Qld, Julius Kruttschnitt Mineral Research Centre.

Niennattrakul, V and Ratanamahatana, C A, 2009. Learning DTW global constraint for time series classification.

Pothina, R and Ganguli, R, 2020. Detection of subtle sensor errors in mineral processing circuits using data-mining techniques. *Mining, Metallurgy & Exploration,* 37, 399–414.

Powell, M S, Evertsson, C and Mainza, A, 2019. Redesigning SAG mill recycle crusher operation. SAG Conference, September 2019 Vancouver, Canada.

Powell, M S, Yahyaei, M, Mainza, A and Tavares, L M, 2021. The endemic issue of ball mill overload in SABC circuits. *Mill Operators Conference.* Brisbane.

Ruspini, E H, 1969. A new approach to clustering. *Information and Control,* 15, 22–32.

Sakoe, H and Chiba, S, 1978. Dynamic programming algorithm optimisation for spoken word recognition. *IEEE Transactions on Acoustics, Speech and Signal Processing,* 26, 43–49.

Salvador, S and Chan, P, 2007. FastDTW: Toward accurate dynamic time warping in linear time and space. *Intelligent Data Analysis,* 11, 561–580.

Shi, F, 2016. An overfilling indicator for wet overflow ball mills. *Minerals Engineering,* 95, 146–154.

Soleymani, M M, Fooladi, M and Rezaeizadeh, M, 2016. Experimental investigation of the power draw of tumbling mills in wet grinding. *Proceedings of the Institution of Mechanical Engineers. Part C, Journal of mechanical engineering science* [Online], 230.

Tormene, P, Giorgino, T, Quaglini, S and Stefanelli, M, 2008. Matching incomplete time series with dynamic time warping: an algorithm and an application to post-stroke rehabilitation. *Artificial Intelligence in Medicine,* 45, 11–34.

Velichko, V M and Zagoruyko, N G, 1970. Automatic recognition of 200 words. *International Journal of Man-Machine Studies,* 2, 223–234.

Whiten, W J, 1976. Ball mill simulation using small calculators. *Australasian Institute of Mining and Metallurgy,* 258, 47–53.

Yuan, Y, Chen, Y-P P, Ni, S, Xu, A G, Tang, L, Vingron, M, Somel, M and Khaitovich, P, 2011. Development and application of a modified dynamic time warping algorithm (DTW-S) to analyses of primate brain expression time series. *BMC Bioinformatics,* 12, 347–347.

Zadeh, L A, 1965. Fuzzy sets. *Information and Control,* 8, 338–353.

Zhang, Z, Tavenard, R, Bailly, A, Tang, X, Tang, P and Corpetti, T, 2017. Dynamic time warping under limited warping path length. *Information Sciences,* 393, 91–107.

APPENDIX

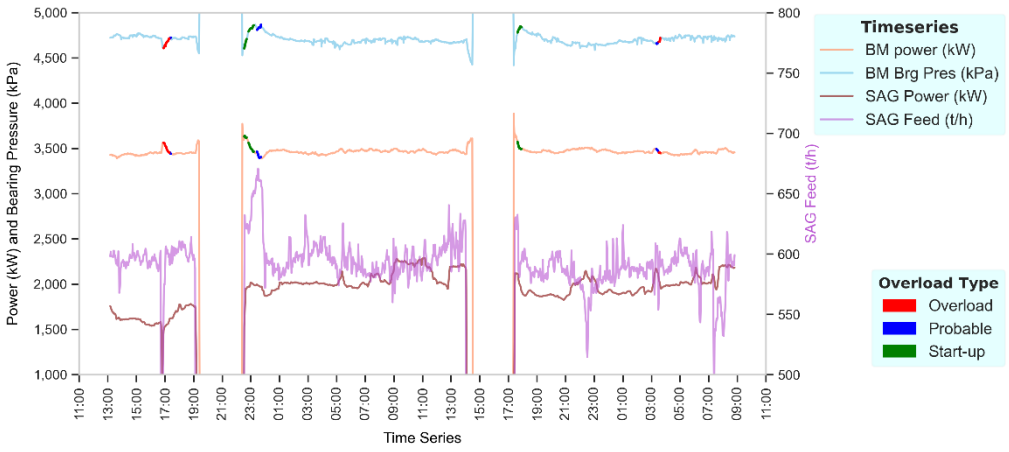

FIG 14 – An extended plot of the start-up effect detection shown in Figure 10.

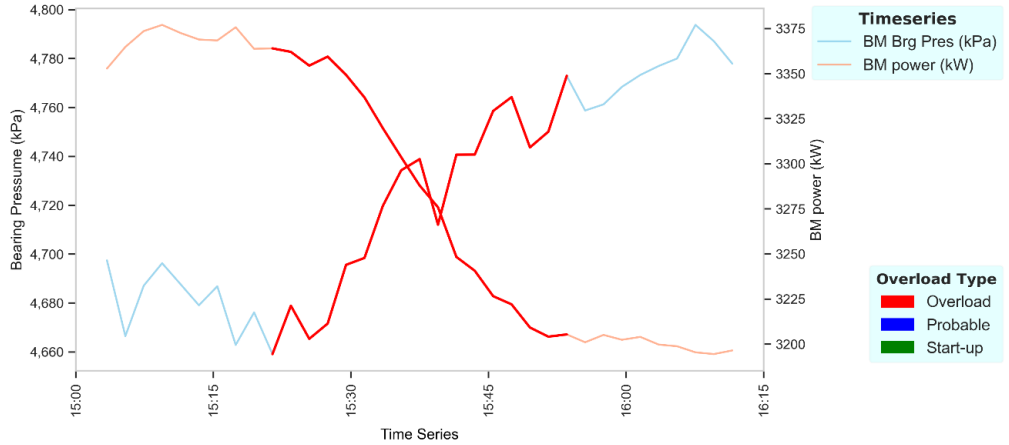

FIG 15 – The magnified plot of the identification of an increasing pattern of bearing pressure and decreasing pattern of power.

Statistical tests to see whether the SAG mill pebble generation ratio and cyclone P_{80} for the ball mill overloading ranks are significant

The following hypotheses are formulated to test whether the values of variables are significant across various overloading ranks.

- Null Hypothesis:

  mean values of the variable corresponding to different overloading ranks are equals.

- Alternative Hypothesis:

  mean values of the variable corresponding to different overloading ranks are different.

Case 1 – Output of one-way ANOVA test for the SAG mill pebble generation ratio against ball mill overloading classes

Interpretation

The p values obtained from the ANOVA analysis that is presented in Tables 1 and 2 are less than 0.05 which means we do have enough evidence to reject the null hypothesis for a 5 per cent level of significance. Therefore, it is concluded that there are significant differences in SAG mill pebble generation ratios for the various overloading ranks.

TABLE 1

Test results of one-way ANOVA for the SAG mill pebble generation ratio.

	Sum Square	Degree of Freedom	F-statistics	p-value
C (Overload Rank)	1.419	3.000	258.296	0.000
Residual	332.508	181640.000		

TABLE 2

Multi classes test of the SAG mill pebble generation ratio.

Group 1	Group 2	Diff	Lower	Upper	q-value	p-value
No	Start-up	0.006	0.004	0.008	11.780	0.001
No	Yes	0.018	0.017	0.019	68.225	0.001
No	Probable	0.011	0.010	0.012	41.214	0.001
Start-up	Yes	0.012	0.010	0.014	22.059	0.001
Start-up	Probable	0.005	0.003	0.007	9.399	0.001
Yes	Probable	0.007	0.006	0.008	18.900	0.001

Case 2 – Output of one-way ANOVA test for cyclone P_{80} against ball mill overloading classes

Interpretation

The p values obtained from ANOVA analysis that is presented in Tables 3 and 4 are less than 0.05 which means we do have enough evidence to reject the null hypothesis for a 5 per cent level of significance. Therefore, it is concluded that there are significant differences in cyclone P_{80} for the various overloading ranks.

TABLE 3

Test results of one-way ANOVA for the SAG mill pebble generation ratio.

	Sum Square	Degree of Freedom	F-statistics	p-value
C (Overload Rank)	7.943 × 10^5	3.000	258.296	0.000
Residual	1.350 × 10^8	188633.000		

TABLE 4

Multi classes test for cyclone P_{80}.

Group 1	Group 2	Diff	Lower	Upper	q-value	p-value
No	Start-up	22.727	21.049	24.406	49.183	0.001
No	Yes	3.711	2.809	4.613	14.943	0.001
No	Probable	0.965	0.051	1.878	3.838	0.034
Start-up	Yes	26.434	24.544	28.333	50707	0.001
Start-up	Probable	23.691	21.792	25.591	45.316	0.001
Yes	Probable	2.747	1.480	1.013	7.881	0.001

Net metal production maximisation in the digital era

O A Bascur[1]

1. Principal, OSB Digital, LLC, The Woodlands, TX 77381. Email: osvaldo@osbdigit.com

ABSTRACT

Ores are becoming extremely variable with mineralogy and hardness disturbing the integrated crushing, grinding, flotation, and thickening processes. The current mining, comminution and flotation sensors provide large amounts of data for process optimisation. To augment the operational knowledge for proactive actions for improving the performance of the integrated rock processing complexes, we need to add the right process knowledge context and operational modes.

Without these proper operational contexts in place, the results are unmanaged downtime, process troubles, maintenance interruptions, and unmet production schedules. By measuring operational modes and managing these unproductive times (trouble times), people can find new ways of improving profitability and efficiency of the plant. The inFORMAtion (FORMA = SHAPE) created by the real-time analytics enables us to calculate the metal recovery in real time and to develop predictive analytic models to secure the best operating conditions based on the type of ore currently mined. Using the latest advanced analytics, machine learning, big data analytics tools and cloud computing enables the creation of new workflows and collaboration between mining, concentrator plants, and the enterprise, including services providers.

Machine learning pervades our culture in a multitude of ways, from medical diagnosis and data management to speech synthesis and search engines. The novel approach of using machine-learning techniques coupled with dynamic process models in grinding, such as Dynamill™ and Dynaflote™, a new operational integrated process model is realised and implemented.

These days of remote operations utilising the capability to integrate mining operations from drilling to product delivery is an industry boon. With mines in inconvenient, out-of-the-way locations, people can now work from home, remotely supporting operations and staying safe and healthy during these challenging times. Today, subject matter experts (SMEs) can increase productivity by developing predictive models to classify the operating conditions owing to large variations in ores, catching the hidden production, energy, and water losses by ore type and unmeasured disturbances. People call this a ‘follow the money’ strategy, the ability to survive and adapt to these unforeseen forcing factors affecting the communities and support.

The application of a digital plan twin to mining, mineral processing and extractive metallurgical process using advanced analytics tools is presented here.

INTRODUCTION

The declining supplies of high-grade ores and increasing consumption of mineral and metal products have demanded higher operational efficiencies with minimum capital investments. The economic efficiency is maximised by manipulating the grinding and flotation circuits along the grade/recovery curve relationship. To achieve such technical and economic objectives, improved stabilisation of the grinding and flotation circuits is required. It is known that grinding circuits represent the largest consumption of electrical power and water in mineral processing (Wills and Finch, 2016).

Currently the major road block in the Digital Transformation is the cultural change that it is required and adapting to new ways for Business Process Workflows using Cloud Computing. Critical problems are the difficulties in integrating the silos (Mine, Mill, Maintenance, Engineering, Environmental and Safety) (Bascur, 2020a). Currently each person or area has their own version of the truth using spreadsheet to get the operation data (as DARK data) without a Subject Matter Expert (SME) validating, classification and aggregation of the real time operation data.

This paper presents a summary for maximising metal production using the latest cloud computing tools to solve operational problems in a different way by using real time series operational data and adding the right type of dynamic models. The knowledge embedded in the dynamic process models augments the value of the raw data by reducing the number of KPIS to a handful set to manage a

metallurgical complex. The additional details are documented in a recent book (Dunne, 2019; Bascur, 2019, 2020a, 2020b; Bascur and Gorrie, 2021).

NET METAL PRODUCTION RATE MAXIMISATION

Figure 1 shows the Net Production Rate (NMPR), Metal Recovery around the optimal grind subject to operational constraints.

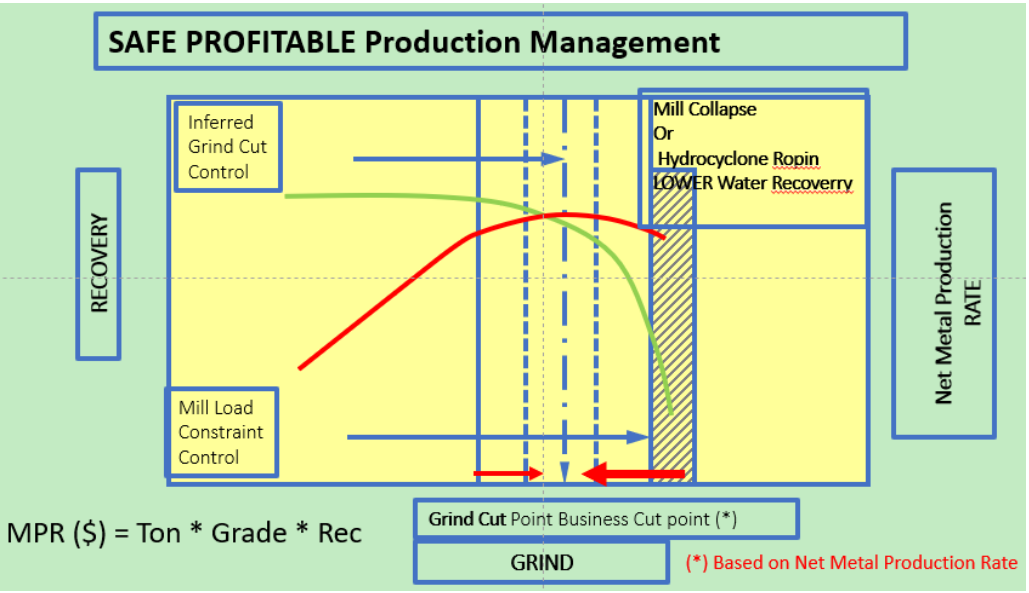

FIG 1 – Tonnage, feed grade and recovery optimisation and particle size and process constraints (Bascur, 2020a).

The optimal economic milling rate can be obtained by finding the maximum profit in terms of tonnage for a given ore grade there is a unique milling rate to provide the grind size that will yield maximum profit under certain economic conditions. As expected, the curves in Figure 1 are not unique and are changing constantly (Bascur, 1990). Thus, the information must be handled on a timely basis in a real time information system. The computer system will in turn provide for adapting values of the moving constraints and set points. This is known as online adaptive decision-making or control.

Digital twins for mineral processing plants

Today digital technologies enable to build a digital twin using an object data model with advanced analytics. A digital twin is a digital representation of a physical object or system, a virtual replica of physical devices that can be used to run simulations before actual devices are built and deployed (Shaw and Frülinger, 2019).

Integrating physical processes and computer systems is the challenge presented by the as the digital twin senses the state of the physical system and transform the time-series data into information and applies decisions and actions for management and controls. A road map to tackle these issues in described in Bascur (2020a).

The industrial IoT (IIOT is an enabling technology of Digital Twins, DT, providing the networking infrastructure, calculations for each of the plant units to sense, alert and interact smoothly between each other.

Gartner included DT as top strategy technology trend number 4 for 2018 (among the top 10 trends) that will contribute to the intelligent digital portfolio, that is integration of things, services, content and people. The DT can help optimise physical asset performance through efficient predictive and preventive maintenance operations, thus reducing overall maintenance costs and downtime (Bascur, 2020a). It can act as a tool for predictive analysis, evaluating the performance of the plant production, identifying potential bottlenecks (hidden losses), assessing asset utilisation and minimising operating costs (Rasheed, San and Kvamsdal, 2020). We will present a strategy to build a digital twin in four steps with a fifth which is for the continuous improvement of the living plant.

Building a digital twin is complex, and there is as yet no standardised platform for doing so (Sierla *et al*, 2022). These new techniques, that has been implemented in several industries, requires top access to historical database and the transformation of real time series into information. It is paramount to understand all process involved that debottleneck the plant, the integration of the planning targets with the real time cost which enables the estimation of the maximum profit while avoiding operation and equipment constraints in the plant. The maximisation of production is integrated with an asset reliability and prescriptive maintenance. For a mineral processing plant a digital twin looks like Figure 2.

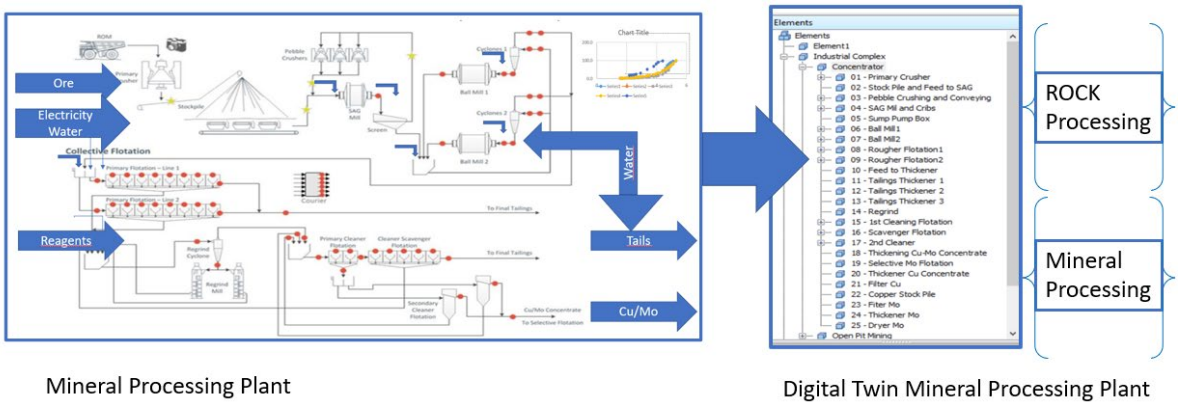

FIG 2 – Digital twin into a digital object-oriented database (Bascur and Gorrie, 2021).

In practice, the recovery curves for the plant are calculated in real time using the gross error detector algorithm as part of a Digital Twin Digital Operational model (Bascur, 2020a). Seeq Workbench tool is used by process people to clean, calculate and contextualise data, view and work with the model results. Seeq has the capabilities to treat real time series filter data to obtain the best process predictive models using least squares regression and Python based algorithms (Kelleher *et al*, 2015; Raschka, 2015; Brunton and Kutz, 2019). Seeq Organiser simplifies the presentation of the results in dashboard in a clear succinct form for collaboration and further socialisation of the possibilities of improvement (Seeq, 2020).

In practice, the recovery curves for the plant are now calculated in real time using the gross error detector algorithm as part of a Digital Twin Digital Operational model (Bascur, 2019). The market conditions can be entered to establish a profit index to determine the optimal tonnage based on laboratory calculated recoveries. Having this information on hand, the only problem is to maintain the desired size cut–liberation–tonnage triad. This translates into finding a method that will absorb the disturbances that the grinding circuit is subject to, and to estimate the constraints and adequate indices for profitable

The steps to implement an operational model for maximisation of metal production is to create an object-oriented database of the mineral processing plant with the online identification of the operating states of all the units in the chain supply. These enables to choose the running ok time to run the predictive models and to push closer to the process and equipment constraints. Second the hidden the losses are captured and the losses are estimated for people, to realise the losses due to violating process constraints. The third step is getting a predictive model of the key KPI's for the plant and to understand which variables are available to push to the constraints toward the goal of maximising the net metal production rate.

Transforming real time data and operational events into information and knowledge

The collection and contextualisation of real-time data is essential to provide input to more sophisticated offline predictive analytics and data analysis tools. Aggregating asset and time context to the data and operational state of the data allows significant production events to be processed automatically, storing needed information at the desired level of detail.

Figure 3 shows the transformation of the Mineral Processing Plant into a Digital Twin build using a unit object building block which contains is a set of instruction to identify the operating states and to

calculate the critical production, energy, water and recovery metrics. This unit model and algorithm simplifies the semantic to access easily all process variables for further analysis, cleansing, aggregation and predictive modelling. Seeq Workbench advanced analytics tool is used by process people to clean, calculate and contextualise data, view and work with the model results. Seeq Organiser simplifies the presentation of the results in dashboard in a clear succinct form for collaboration and further socialisation of the possibilities of improvement (Seeq, 2020). This novel process workflow leads to the creation of valuable information which be further improved using machine learning tools starting with cleansed gridded data sets, develop models and operationalise the findings. There is total transparency my maintaining a journal of each step in the data transformation. Once the Digital Twin is created the synergy to democratise the data usage by people happens. A dynamic least squares regression method is used in developing all models (Brunton and Kutz, 2019).

Phyton has become the engineering tool for process engineers (Albrecht, 2021; Buenemann, 2021; Rasheed *et* al, 2021). The reader can also find great examples in (Raschka, 2015; Ericson *et al*, 2016; Kelleher *et al*, 2015).

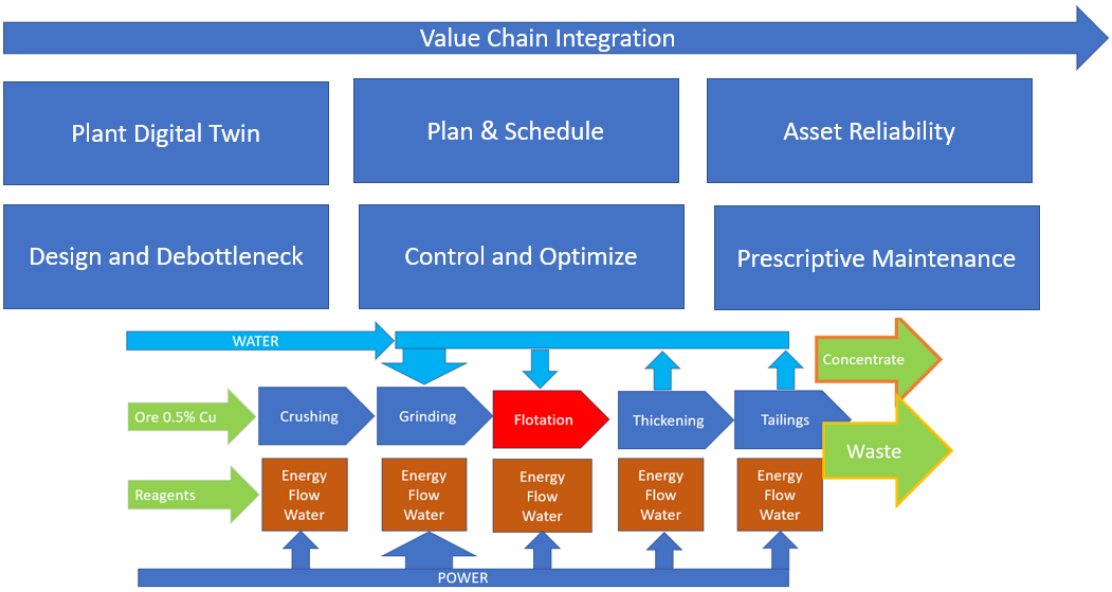

FIG 3 – Digital twin plant to represent the plant and optimisation (Bascur, 2019).

Digital twin hidden process constraints and production losses

The follow the money approach described by (Plourde *et al*, 2017) has been used in this paper. Figure 4 shows the copper recovery versus grind cut and NMPR versus Grind Cut and the same key variables versus the cyclone feed % solids. As such, the critical constraints for maximising the overall production rate are the cyclone feed % solids due to the nonlinearity of the viscosity versus % solids. This variable correlates very well with the particle size P80. In this work we use the full-size distribution of the SAG Mill feed and the Ball Mills cyclone overflow particle size distribution (PSD). These size distributions are modelled using the Gaudin Schumann (GS) particle size model to obtained the particle size distribution shape characterised by the M parameter of the GS Model (F3(d) = (d/DMAX)^M. As such, the optimal throughput is obtained based on the ball mills the process constraints identified. Figure 4 shows that if the % solids to cyclones goes above 68 per cent both the Metal Recovery and the NMPR decrease. These curves are changing all the time due to the ore variability from the mine and the predictive model need to be running in real time to be adjusted due the large ore type changes processing lower grade ores. The rheological characteristics of the ore are a critical aspect in creating a digital twin model. The viscosity relationships between particle size distribution, % solids, mineral density have been reported by Bascur (1991) and Shi, Napier-Munn and Asomah (2010), and adopted into dynamic grinding simulator by Bascur and Herbst (1985) and later improved by Bascur and Junge (2015).

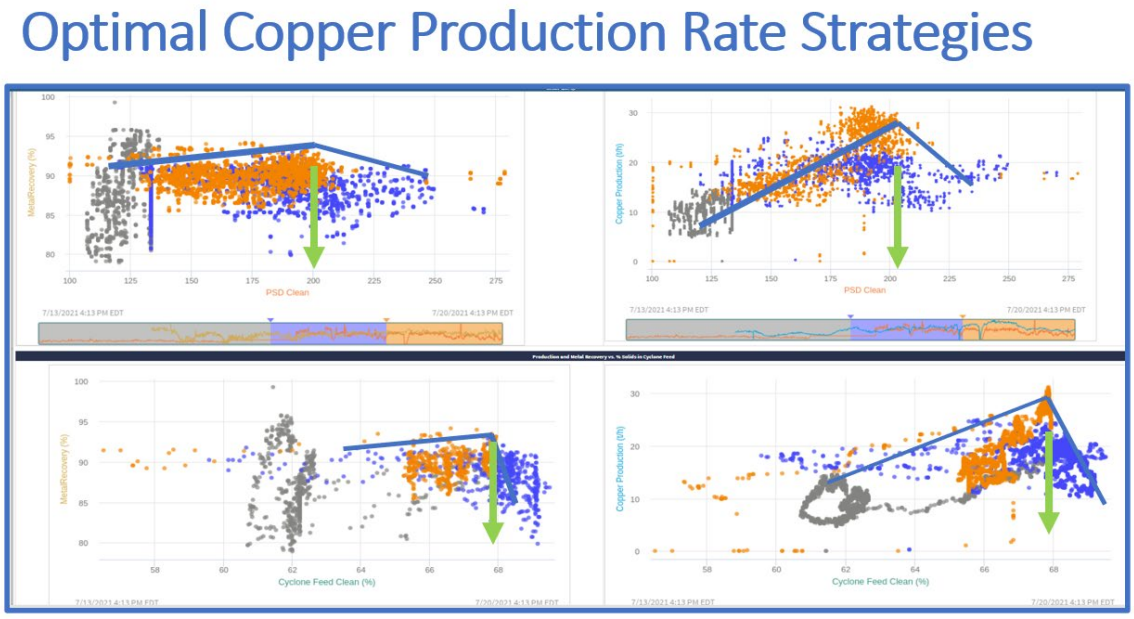

FIG 4 – Metal Recovery, Production Rate versus P80 and cyclone feed % solids (Bascur, 2020b).

This is reality of today low-grade ores mineral processing plant (high consumption of electricity and water). As such the Digital Twin Model consider the energy and water input for each section of the plant and keeps close account of the specific energy and water usage. For operational event where the desired operating conditions is not met a trouble-time event is generated to access the hidden losses in the whole plant (Bascur, 2019).

Figure 5 shows the operational events captured automatically from the PI System converted into Seeq capsules to be able to run the performance calculations to estimates the production, electricity and water hidden losses for the whole plant. The real time series data is processed together with the operating modes and capsules to have insights and information to create and validate the predictive models. As such, having a good estimate of the losses which are caused by a process unit not performing as it should according to economic plant schedule. The capabilities of integrating raw data (Dark data) with operational events in the SEEQ environment are the key features that enables to perform these calculations and to develop sound predictive models for any set of operating data and ore types running. The characterisation of the orebody is a must to classify the operating regimes which bring a higher value to the plant economics.

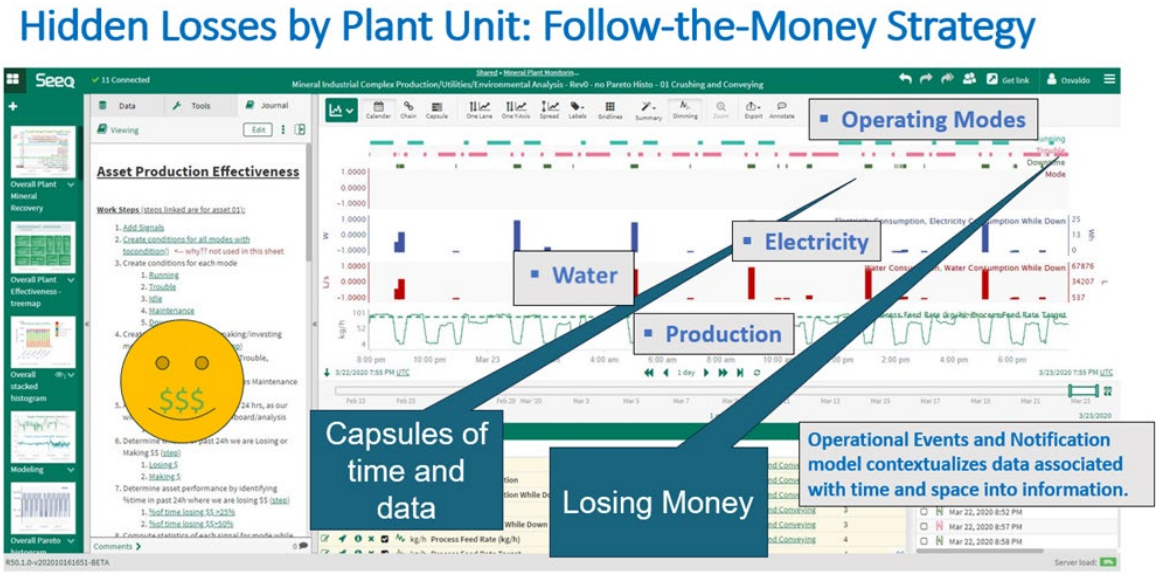

FIG 5 – Hidden losses by plant area Follow the Money Approach.

RESULTS AND DISCUSSION

Top priority is to maintain the desired throughput with the right cut size and the particle size distribution shape (PSDS) for maximising the rougher flotation recovery and water recovery for the large tailing effluents generated in low-grade ores processing. The dynamical grinding and classification phenomenological models are described in the literature (Pate and Herbst, 1983; Bascur and Herbst, 1985; Bascur *et al*, 1986; Herbst and Pate, 1998; Bascur and Junge, 2015).

Integrated grinding/flotation model for P80 and particle size distribution shape optimisation

Figure 6 shows the Dynamill model using real plant data and SEEQ Predictive analytics model results calculations displayed in PI Vision tool. The data used is cleansed and filter using the SEEQ Advanced analytics engine. It uses the size distribution particle size distribution of the output of the stockpile, all the process flows, level, pressure, load sensors, and the Outotec PSI particle size analyser time series data placed of the output of the Hydrocyclone overflow. The Dynamill Hydrocyclone equations are used to model the cyclone behaviour and to predict the cyclone overflow and underflow streams in real time to have the estimates to close the pulp and water mass balances around the grinding and classification circuits.

At the bottom of Figure 6 shows the Digital Twin Plant Grind Cut model using SEEQ Advanced Predictive Model development environment (Seeq, 2020). The raw data is cleansed according to Running OK operating mode prior to use in the least squares' regression model. This operational state is calculated for each of the Unit involved in the model creation using the PI System Analytics in real time. As such, the process models are created using the operational mode when the process units are in production. The least squares minimisation algorithm (Brunton and Kutz, 2019) provides a predictive model is very robust and provide a measure of the key variables to improve the active process control strategy. In addition, DYNAMILL™, the Dynamic Grinding/Classification model provides the full mass balance of the circuit to maintain the right pulp density in the hydrocyclones bank. As discussed, the sump water addition is the critical manipulated to maintain the cyclone hydrodynamics performing correctly. The SAG-Sump-Cyclones – Ball Mills Dynamic Grinding on line model provides a strategy to avoid cyclone roping performing a predictive alert to maintain the right hydrodynamic performance of the hydrocyclones (Bascur and Junge, 2015). A pulp suspension model is used to predict the viscosity of the pulp to avoid violating the mill transport dynamic and the pulp fed to the cyclones (Bascur, 1991).

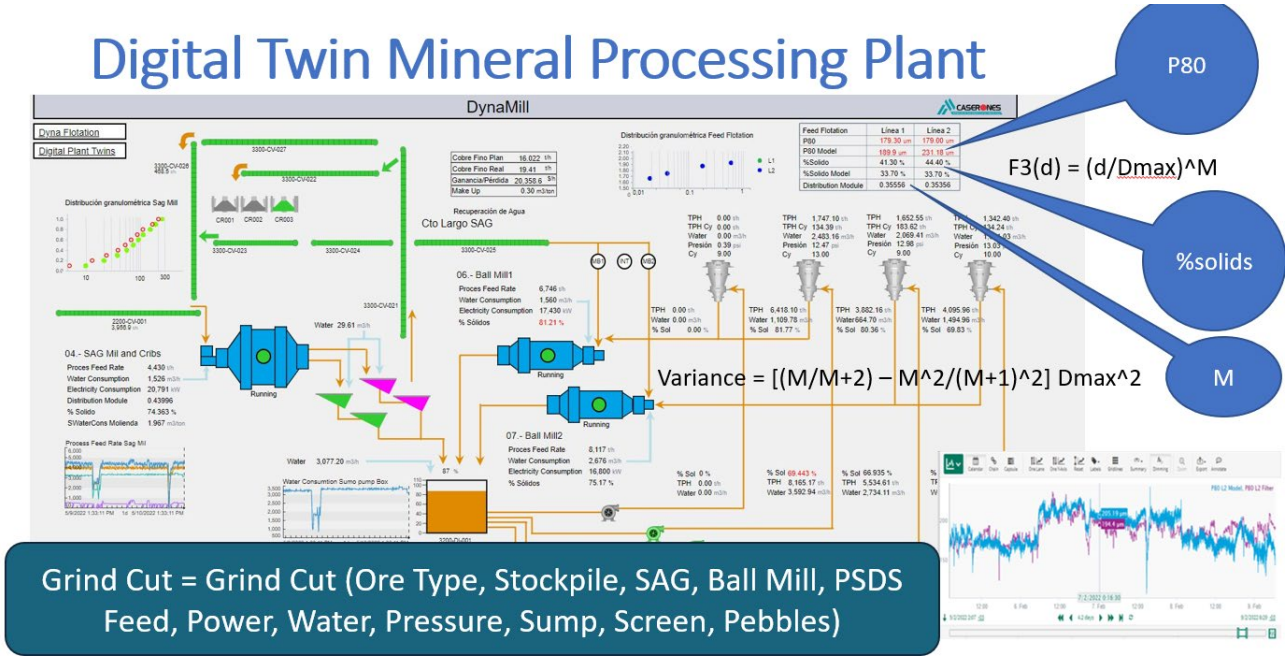

FIG 6 – Digital Twin Plant – grinding P80 and M predictive models.

Figure 7 shows the grinding raw data, virtual sensors augmented data using process models and performance calculations, target variables and controller variables.

Grinding Model output P80 and M

Inputs	Virtual Sensors	Target Variables	Control Variables
SAG Feed Flow Rate	% Solids Cyclone O'	Cyclone Feed % solids	Overflow % Solids
Feed % Solids	% Solids Cyclone U'	Feed Water Addition	P80
Feed PH	% Solids SAG Mill	Sump Water Addition	PSDS or M Gaudin
Sump Pulp Level	% Solids Mills	Sump Pulp Level	Mill Loads
Water Flow Rates	Viscosity estimates	% Solids Mills	Mill % Solids
Particle Size P80	PSD Shape	Pump Speeds	% Solids U
Particle Size M	Mill Load estimates	SAG Mill Flow Rate	
Number of Cyclones		Sump Water Addition	
Mill Weights		SAG Mill Feed Water	
Water/Feed Ratio		BM 1 Water Addition	
Pumps Amps		BM 2 Water Addition	
Mill Powers			Process Constraints

FIG 7 – Grinding input, virtual sensors, target and controlled variables.

Each flotation cell is modelled individually to characterise its hydrodynamic conditions in the pulp and the dart valves are manipulated to keep the air hold up profile (Bascur and Herbst, 1982; Bascur 2013). DYNAFLOTE is the most advanced Dynamic Flotation Operating Model including the Pulp and Froth phase hydrodynamics subprocesses to predict the attachment and detachment in the pulp, and the entrainment and drainage subprocess of species in the froth phase (Fuerstenau, 1999) shown in Figure 8. The hydrodynamics of the flotation cell is optimised using the Air Holdup Model to define the best flotation bank level, turbulence and air profiles to maximise the NMPR. The water separation models are based on a unified solid liquid model (Bascur, 1991).

Dynamic Flotation Model

Bascur and Herbst, 1982. Collaboration University of Utah and UC Berkeley

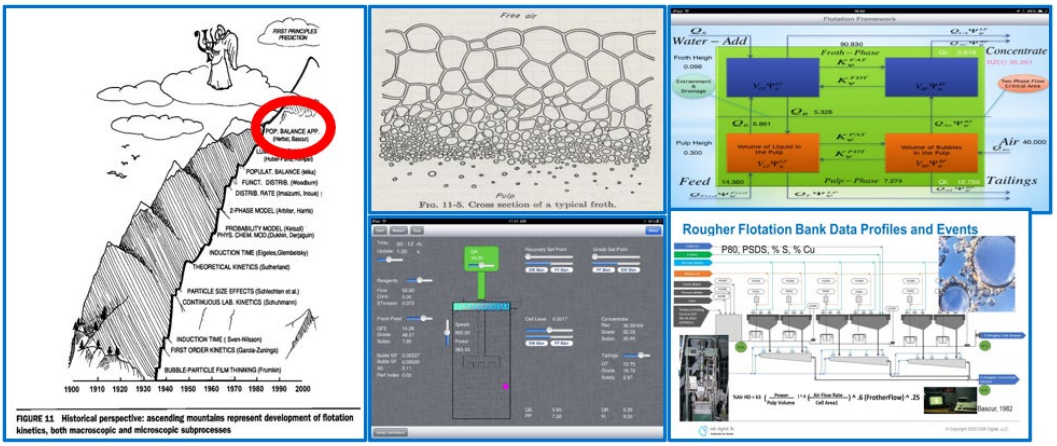

Source: D.W. Fuerstenau, "The Froth Flotation Century," *Advances in Flotation Technology*, ed. B.K. Parek and J.D. Miller (Englewood, CO: SME, 1999), pp. 3-21.

FIG 8 – Dynamic Flotation Model based on continuity equation and flotation hydrodynamics.

Figure 9 shows a typical rougher flotation bank with the current instrumentation to measure the hydrodynamics state of the each of the flotation units. As such, with have the pulp level, dart valve

position, froth height, bubbles sizes, colour and movement, the amperage of the motor for the impeller, the air flow rate, the collector addition flow rate, process flow rate to the bank, the frother flow rate and addition point, % solids in the feed and in the tails, chemical X-rays assays in the feed, concentrate and tailings. All this data is cleansed and classify prior to doing one line mass balances and creating predictive analytics models using the analytics tools of the PI System and Seeq advanced analytics.

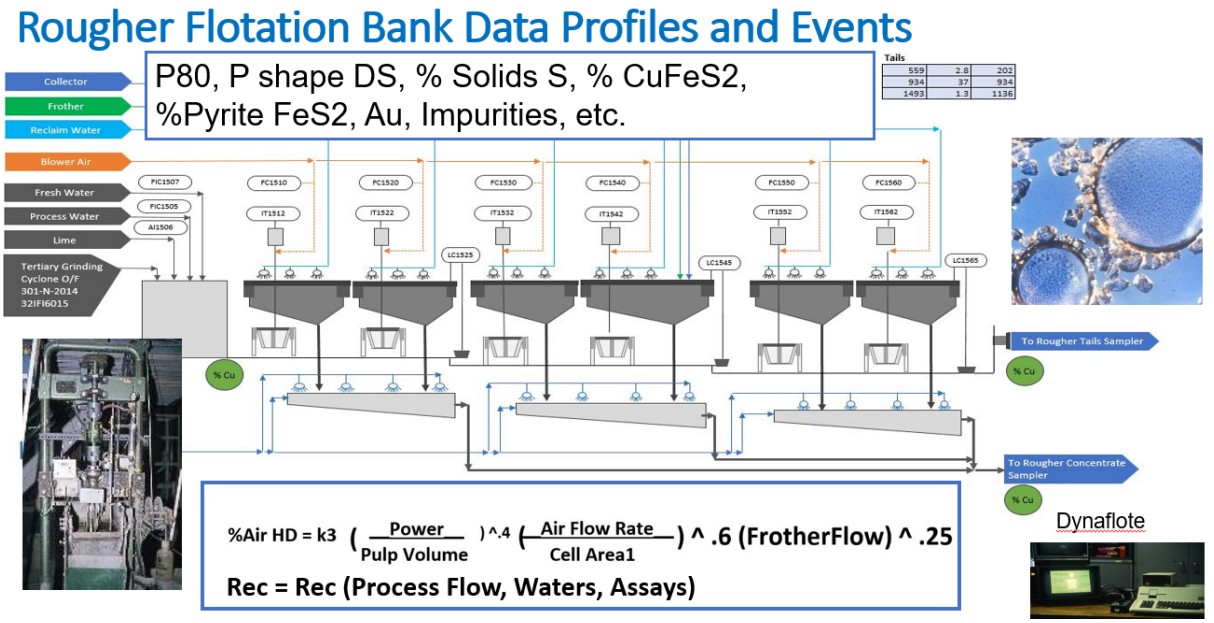

FIG 9 – Rougher Flotation Bank with the key measurements used to calibrate the model.

Maximisation of the Net Copper Production (NMPR)

A real time mass balance is performed using the predictive algorithm to estimate the flotation recovery, concentrate metal mass and tailing metal mass flow rate on line. The Net Metal Production Rate is calculated in real time. The Copper Production (TPH) (NMPR) model integrate the SAG Mill/Ball Mills and Flotation Banks to find the optimal Mill Production Flow rate which maximise the NMPR. Figure 10 shows the excellent predictive model which is used to mode all the variable within the proper range. The model is continuously correlated to adapt to the different type of ores and mineralogical composition.

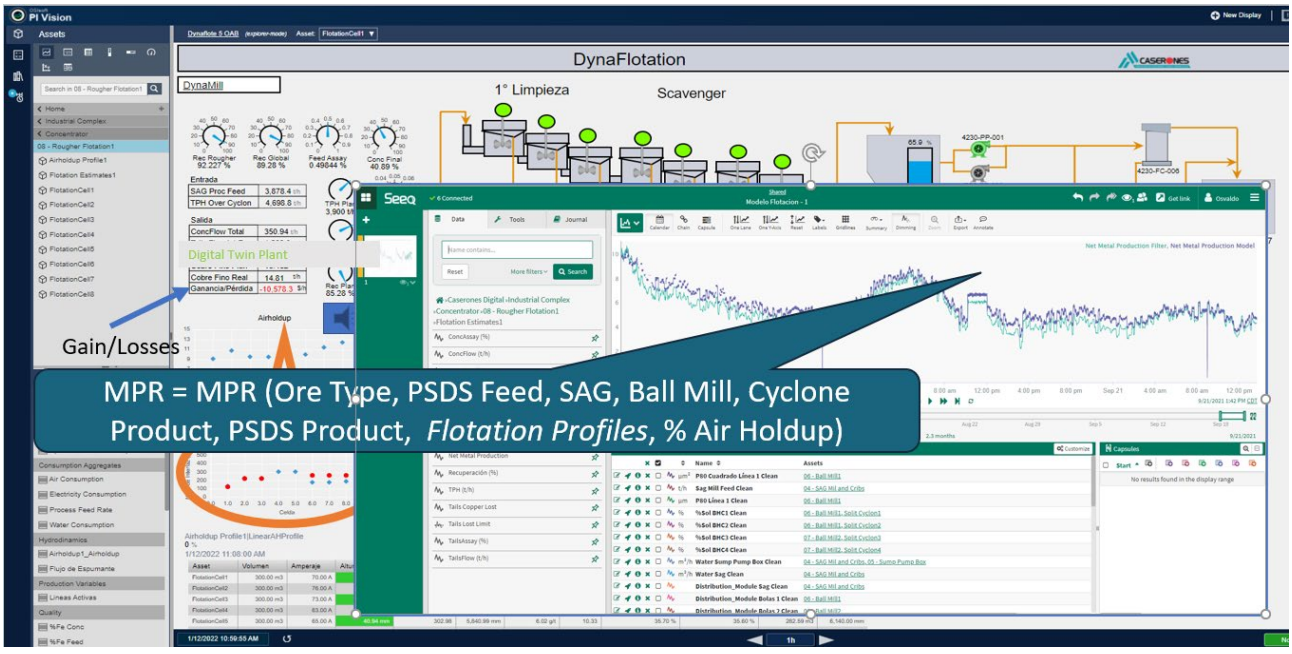

FIG 10 – Digital Twin Plant – copper production TPH actual versus predicted.

Figure 11 shows the operational and augmented variables based on the phenomenological model to consider in creating a predictive model using machine learning tool. The disturbances, manipulated and observed variables are used to find the best set of operating condition for a given ore type.

Rougher Flotation Metal Production Rate

Inputs	Virtual Sensors	Target Variables	Control Variables
SAG Feed Flow Rate	P80 Estimate	Cyclone Feed % solids	Recovery
Silo Inventory Level	PSD Shapes (M) estimates	Feed Water Addition	Metal Production Rate
Feed % Cu	Mill Load estimates	Sump Water Addition	PSDS M O'
Cells Pulp Levels	Metal Production Rate	Sump Pulp Level	Mill Loads
Water Flow Rates	Rougher Flotation Recovery	% Solids Mills	Mill % Solids
Particle Size P80's	Cell Air Holdups	SAG Mill Flow Rate	% Solids U
Particle Size M's	Cell Level Profile	# of Cyclones	Concentrate % Cu
Cells Frother Flow Rate	Air velocity estimate	SAG Mill Feed Water	
Air Flowrate	Bubble Size estimate	BM 1 Water Addition	
Water/Feed Ratio	Air Holdup Profile	BM 2 Water Addition	
Cells Amps		Feed % Cu	
% Cu Concentrate and Tails		Tails % Cu	Process Constraints

FIG 11 – Rougher flotation inputs, virtual sensors, target and controlled variables.

Figure 12 shows the results of running a least squares multivariable regression with a filtered and classified operational events set of real time series data. Figure 12 shows the grinding flotation net metal production rate model parameters statistics. The R squared for the model is 95 per cent showing a good fit of the selected operating and augmented variables selected to model this important plant KPI.

Parameters and Model

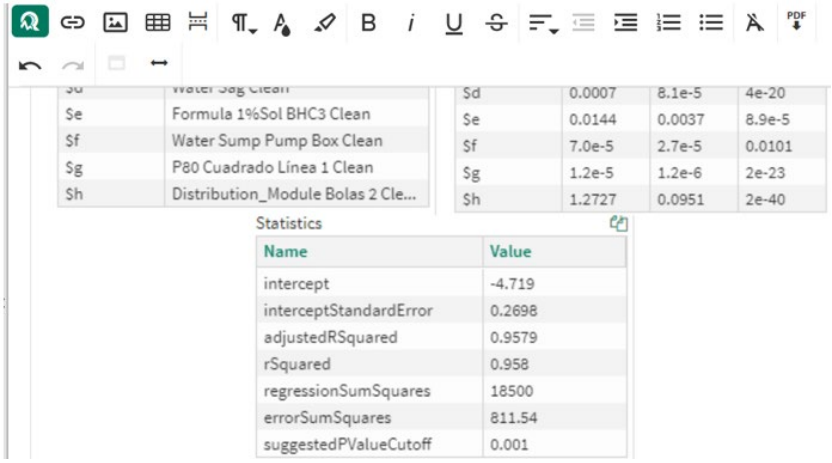

FIG 12 – Grinding/flotation net metal production rate model parameters statistics.

We have discussed the importance of provide the best grinding product in Rougher Flotation to liberate the valuable mineral and minimise the metal losses in the tails. In a concentrator, for lower grade ores, 99 per cent of the contained solids will report to the Rougher Flotation tailings and the thickeners feed. Therefore, having the **right size distribution shape** during grinding assists in having the best settling rates of flocculated particles in the hydrocyclones coarse tailing solids separation and fines particles high-capacity thickeners. The two important controls of a thickener are related to the properties of the thickener feed and underflow. For example, the presence of very fine

clays particles in the feed greatly affects the thickener settling velocity and an appropriate flocculant, and automatic flocculation dosage, is necessary. The principal property of the underflow is the solid concentration which is properly controlled by maintaining defined level of the sediment in the thickener by manipulating the underflow rate.

Figure 13 shows the excellent fit that models the water recovery from the gravity separation and three high-rate thickeners using the least squares model with real time data cleansed, filtered and classified for each operating mode.

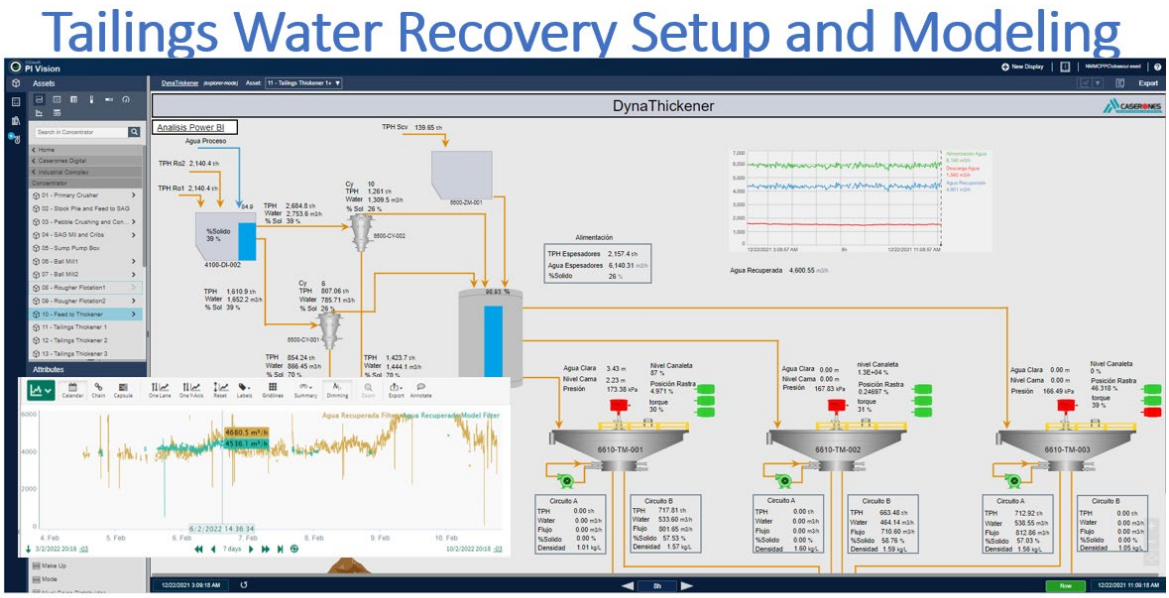

FIG 13 – Grinding/flotation net metal production rate model parameters statistics.

Having Real Time Process Predictive Analytics Models for Grinding/Flotation and Water Recovery on the tailings thickeners enable to predict all the critical process variables and to avoid process constraint'. It gives the latitude to move the manipulated variables available to drive the process plant towards the best Net Metal Production Rate based to the optimal mill throughput, the current ore feed grade and the metal recovery estimated from the flotation banks mass balances in real time from the X-ray's analysers.

The Mineral Processing digital twin includes the tailings water recovery of the fines and coarse particles tailing impoundment areas as shown in Figure 14. It was found that right PDS provides higher water recovery for optimizing the grinding process. Water availability is a huge constraint in the higher Andes.

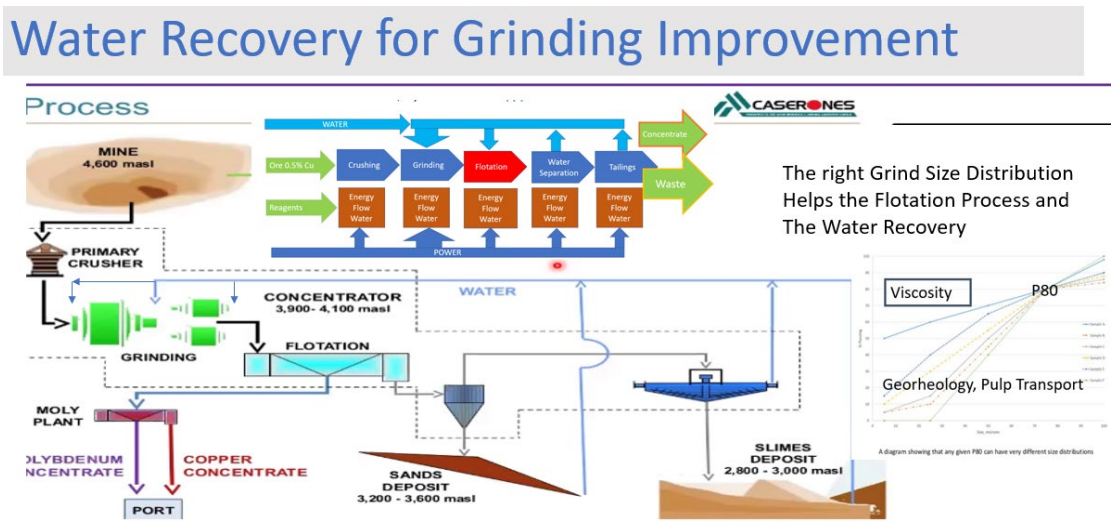

FIG 14 – Sands deposit and slimes deposit water recovery for use in grinding.

BIG DATA OVERALL PRODUCTION EFFECTIVENESS

The amount of the data generated in large mineral processing plant is very large. The transformation of the raw data with the operating events for each created a huge set of information. This extremely valuable of set of operating aggregated data by unit operational mode provide insights that enables to look at the Overall Production Effectiveness (OPE) of the plant in term of the production, efficiency and asset availability. The operational information shows the production, electricity and water consumption for each of the units in the value chain. As such, enabling us to identify the process bottlenecks and the hidden losses when the units in the plants are not running synchronised or running below the production plan. This type of operating data analysis is used to look for large impact on water and electricity due to lower grades orebody. It shows what is the overall throughput that enables to maximise the metal production and associate the electricity and water costs. It also shows the effects of any unit in downtime while operating for a month or a season. Figure 15 shows the many dimensions that the mineral processing plant will have to access the production, electricity and water consumption based on an integrated view of all units working at the same operating mode or not.

Microsoft has developed these new tools that take the pre-processed data generated in a data historian such as the PI System. The PI System is configured with the digital plant model which can automatically generated the operating mode to generate the right aggregation of all variables for each unit to be able to perform the multidimensional analysis using the Power BI in your desktop or running in the Cloud.

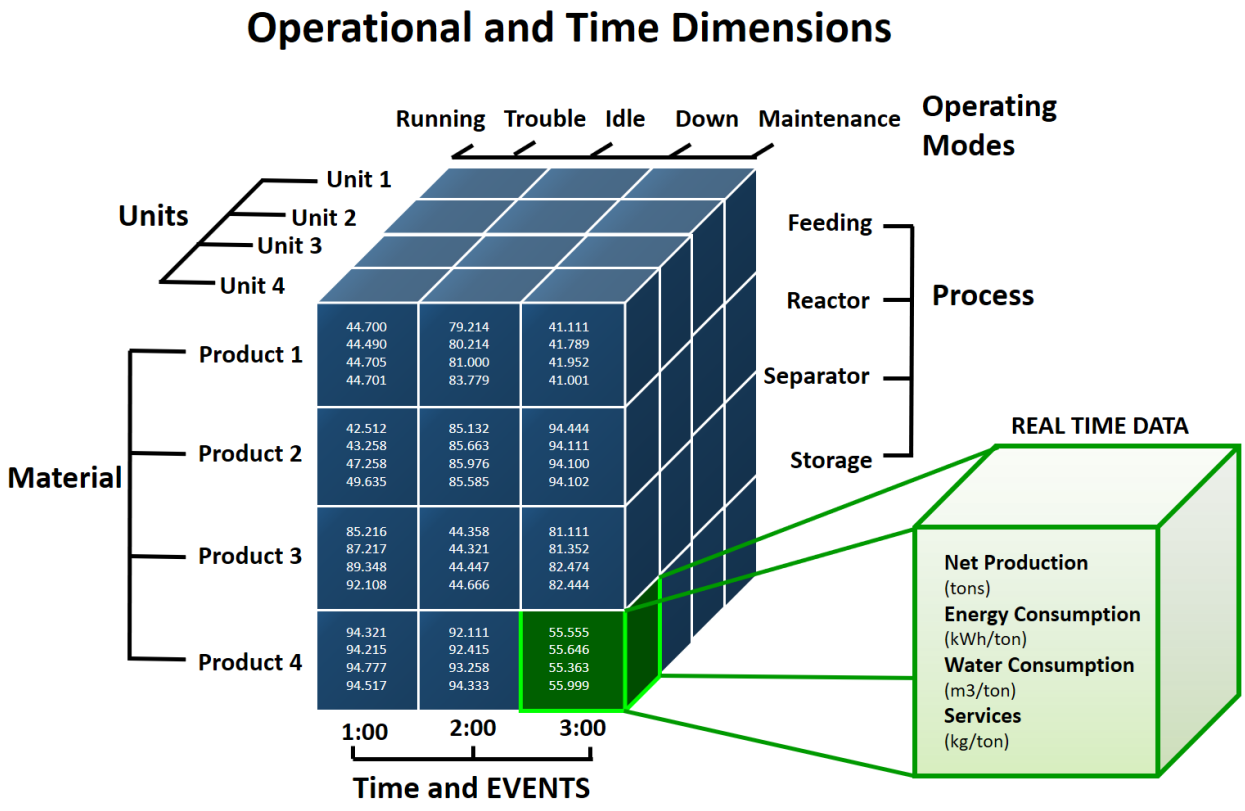

FIG 15 – Operating and time dimensions for the data aggregation and analysis.

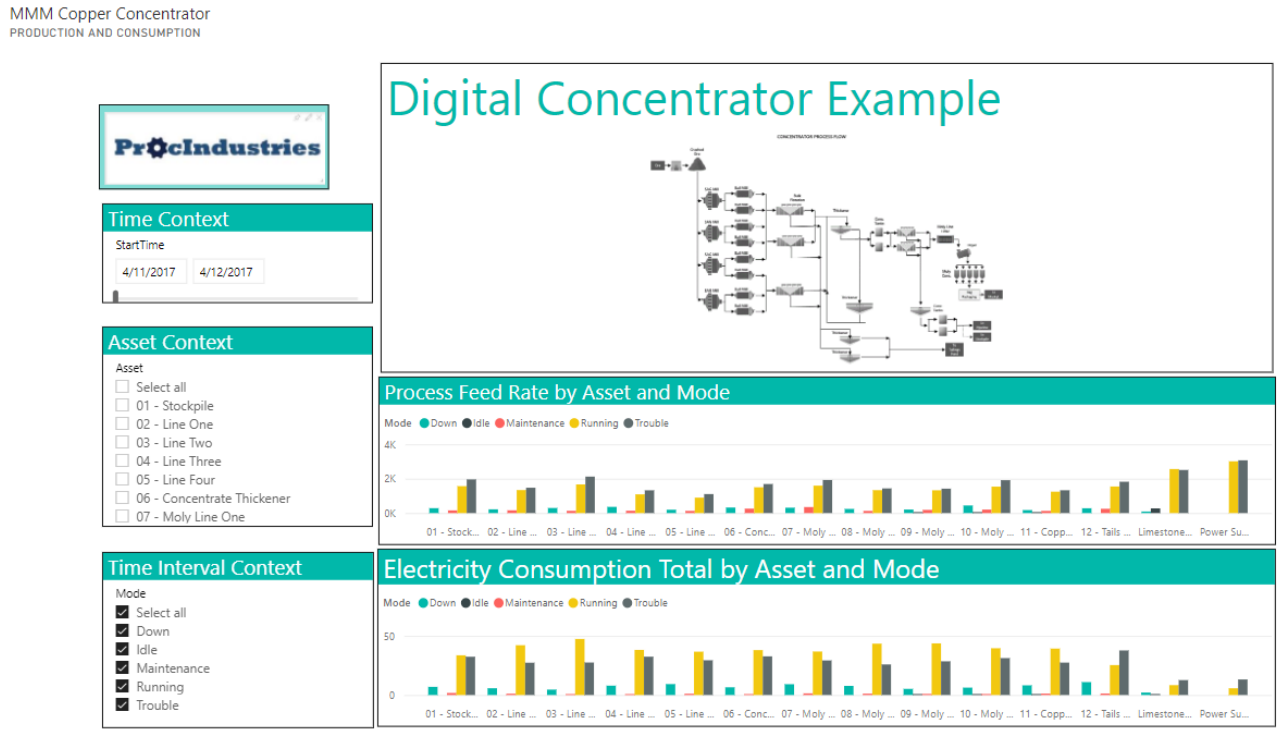

(a)

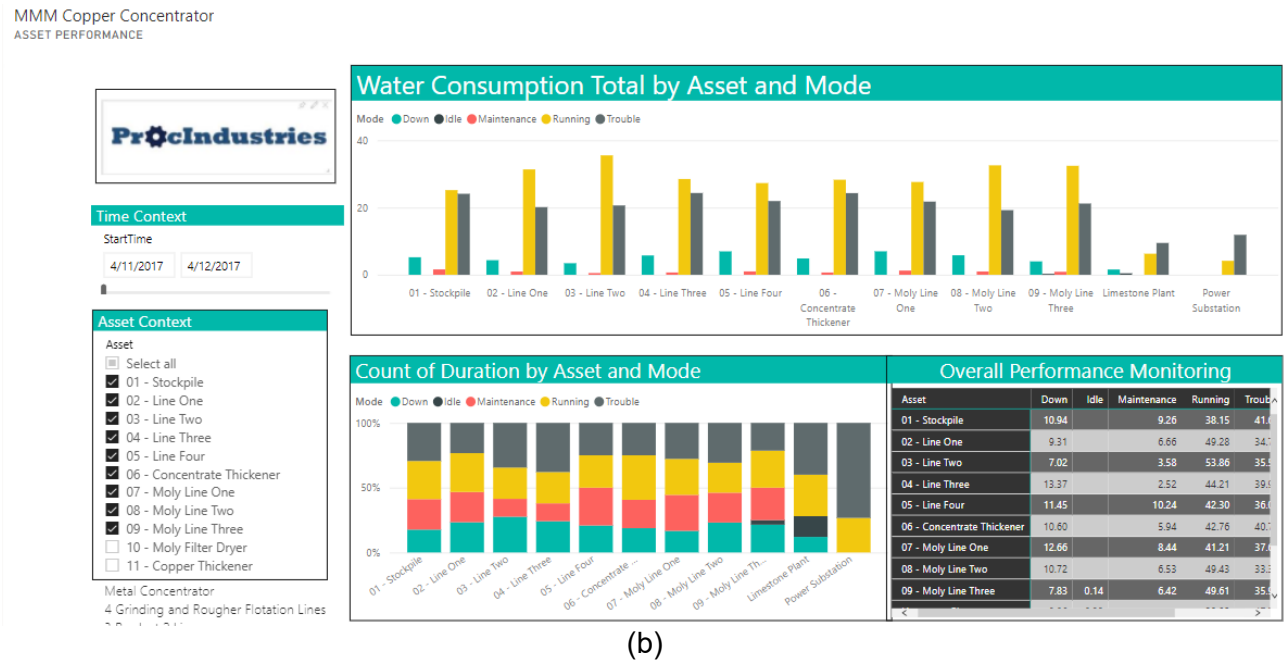

(b)

FIG 16 – Operating and time dimensions for the data aggregation and analysis.

Figure 16a shows an example of an analysis for a typical large low-grade ore plant. The first display shows the results for the analysis of the process feed rate for each unit over time and characterise by the operating time of the each of the unit. These operating times are the events generated depending on how the process unit is doing according the economic schedule of the whole plant. Running OK, In Troubles, Down, Idle or in Maintenance operating mode.

Figure 16b display shows the water consumption pareto chart by unit for the selected period on time based on the operating conditions. It also shows the overall plant production effectiveness calculating the percentage of time for each unit in Running according to the economic schedule, out the plan due to a process constraint, down because of unknown stoppage, or during a schedule maintenance period. As such, the plant manager and maintenance can see the effects of pushing the plan and not doing the right preventive maintenance. The condition-based maintenance and

equipment health prediction are also included in the process unit object model to predict the time that the unit might break. Figure 3 shows the many parts of the Digital twin and advanced analytics which are used to optimise a process plant.

As such the key results of implementing such a strategy using the advanced analytics capabilities in the cloud are:

- Reduce Variances between Production Schedule and Real Executed Results.
- Cleanse data and add missing Information for Management.
- Augment data into information using engineering knowledge.
- Chose new KPIs for the Digital Age (Real Time Metrics).
- Effective Communications and Improve Decision Support.
- Avoid Hidden Production Losses and Equipment Failures.
- Innovate with new business processes using the CLOUD.
- Digital Disruption promotes Dynamic Performance Management.

CONCLUSIONS

The maximisation of the copper recovery and production rates provides a new way to process low-grades ores which have much less profit margins that traditional grade ore models. The capability to continuously follow the money an optimal mill throughput is continuously adapted to maximise the NMPR and the hybrid models in the grinding with the rheo-metallurgical estimates to avoid the operating hydrodynamics constraints in the Mill, Cyclones Feed, Underflow and Overflows (Plourde *et al*, 2017; Bascur and Soudek, 2019; Steyn, Bascur, Gorain, 2018).

The key takeaways in implementing a Digital Twin Plant are:

- Digital transformation is a journey.
- Data can be transformed into inFORMAtion by users at the desired degree of detail.
- Increase the visibility of the unknown.
- SEEQ Advanced Analytics offers dynamic decision support for the mining complex.
- Integrate operations, and systems can be used in a practical way.
- Adapt your organisation with a new team.
- Improve operational efficiency and sustainability.

It was proven that early and continued participation of plant personnel and management is essential for successful integration of different sections into overall process decision support. The synergy of a robust historian with modern self-advanced analytics tools allows the transformation of raw data into valuable information for timely decision-making.

ACKNOWLEDGEMENTS

The author acknowledges the support of OSB Digital, Seeq and the team at Lumina copper to carry out the research, design and configuration of the Digital Twin.

REFERENCES

Albrecht, J, 2021, Step into the Digital Age with Python, CEP, September, pp. 47–53.

Bascur, O A and Gorrie, T, 2021. Maximizing Copper Recovery using Digital Twins with Predictive Analytics, *Procemin Geomet 2021 Proceedings, 17th International Conference on Mineral Processing and Geometallurgy,* www.gecamin.cl/procemin.geomet

Bascur, O A and Herbst, J A, 1982, Dynamic Modeling of Flotation with a View Towards Automatic Control, XIV IMPC Proceedings, Toronto, CA, www.onemine.org

Bascur, O A and Junge, P A, 2015. Dynamill, Dynaflote and Optimill iPad Apps, Apple Store, CA.

Bascur, O A and Soudek, A, 2019. Grinding and Flotation Optimization Using Operational Intelligence, *Mining, Metallurgy & Exploration*, 36, SME Springer, CO. pp. 139–149, www.onemine.org

Bascur, O A, 1990. Profit-Based grinding controls, *Minerals and Metallurgical Processing*, February, SME, CO. pp. 9–15, www.onemine.org

Bascur, O A, 1991, A unified Solid Liquid Separation Framework, *Fluid Particle Separation Journal*, 4, pp. 117–122.

Bascur, O A, 2013. A dynamic flotation framework for performance management, C Young and G Luttrell, *Separation Technologies for Minerals, Coal and Earth Resources*, SME, Englewood, CO. pp. 40–45. www.onemine.org

Bascur, O A, 2019. Process Control and Operational Intelligence, In: Chapter 2.6, SME Mineral Processing and Extractive Metallurgy SME Handbook, SME, Englewood, CO. www.smenet.org, https://books.google.com/books?id=4hKGDwAAQBAJ&q=process+control&source=gbs_word_cloud_r&cad=4#v=snippet&q=process%20control&f=false

Bascur, O A, 2020a. Digital Transformation in the Process Industries: A Road Map, in press, CRC Press, Boca Raton, FL. https://youtu.be/ck3QmNpoiiE, https://www.amazon.com/-/e/B07XV5HXX9

Bascur, O A, 2020b, Digital Transformation Mining Plants, 7th International Congress on Automation in Mining, Gecamin, Santiago, www.gecamin.cl

Bascur, O A, and Herbst, J A, 1985. Dynamic Simulators for Training Personnel in the Control of Grinding/Flotation Systems, IFAC Symposium on Automation for Mineral Resource Development (The Australasian Institute of Mining and Metallurgy: Melbourne).

Bascur, O A, Freeh, E J, and Herbst, J A, 1986. Dynamic Simulation and Estimation of Industrial Grinding Circuit Control Characteristics, *ISA Transactions*, Vol. 15, N0. 2, pp. 77–84.

Brunton, S L and Kutz, J N, 2019. Data-Driven Science and Engineering, Machine Learning, Dynamical Systems, and Control, 2nd Edition, Cambridge University Press. UK.

Buenemann, A, 2021. Scaling Machine Learning for the Manufacturing Masses, Control Engineering, September, Control Engineering, Scaling machine learning for the manufacturing masses.

Dunne, R, 2019. SME Mineral Processing and Extractive Metallurgy, SME, CO. www.smenet.org

Ericson, G, Martens, J, and Rohm, W A, 2016. What is Azure Machine Learning Studio?, Microsoft Azure, https://docs.microsoft.com/en-us/azure/machine-learning/studio/what-is-ml-studio

Fuerstenau, D W, 1999. The Froth Flotation Century, SME, CO. pp. 3–21, www.onemine.org

Herbst, J A and Pate, W T, 1998. Dynamic Simulation of Size Reduction Operations from Mine to Mill, No. 4, pp. 243–248 (The Australasian Institute of Mining and Metallurgy: Melbourne).

Kelleher, J D, Namee, B M and D'Arcy, A, 2015. Fundamentals of Machine Learning for Predictive Analytics, The MIT Press, Cambridge, Massachusetts.

Pate, W T and Herbst, J A, 1983. Dynamic Estimation of Unmeasured Variables in an Industrial Grinding Circuit Using a Kalman Filter, Preprint # 83–124, SME Annual Meeting, Atlanta.

Plourde, M, Bascur, O A, Paquet, S and Gervais, D, 2017. Digital innovation in modern engineering and operational excellence. Presented at the 2017 SME Annual Conference and Expo, Denver, February 19–22.

Raschka, S, 2015. *Python Machine Learning*, Packt Publishing, Birmingham, UK.

Rasheed, A, San, O and Kvamsdal, 2020. Digital Twin: Values, Challenges and Enablers, IEEE Access 8, 21980–22012. https://doi.org/10.11019/ACCESS.2020.2970143.

Seeq, 2020. Seeq Workbench, Organizer and Data Lab, Seattle, WA, www.seeq.com

Shaw, K and Frülinger, J, 2019. What is a digital twin and why it's important to IoT Network World, Jan 31, 2019 10:07 am PST 2019.

Shi, F N, Napier-Munn, T J and Asomah, I K, 2010. Rheological Effects in Grinding and Classification, *Min. Pro. Met. Rev*, Vol. 20, PP 123–131.

Sierla, S, Azangoo, M, Rainio, K, Papakonstantinou, N, Fay, A, Honkanaa, Vyatkin, V, 2022. Roadmap to semi-automatic generation of digital twins for brownfield process plants, *Journal of Industrial Information Integration*, 27 100282 https//doi.org/10.1016/j.jii.2021.100282

Steyn, J, Bascur, O A, Gorain, B, 2018. Metallurgy Analytics, *Mining Engineering*, SME, pp.18–29.

Wills, B A and Finch, J A, 2016. *Mineral processing technology* (8th edition), Elsevier Ltd.

Development of a user-friendly R platform for optimising mineral processing

B Ben Said[1], L Pereira[2], T Saeed[3], D Huu Hoang[2], N Kupka[2], R Tolosana-Delgado[2] and M Rudolph[2]

1. Helmholtz-Institute Freiberg for Resource Technology, Helmholtz-Zentrum Dresden-Rossendorf, Chemnitzer Str. 40, 09599 Freiberg, Germany. Email: b.ben-said@hzdr.de
2. Helmholtz-Institute Freiberg for Resource Technology, Helmholtz-Zentrum Dresden-Rossendorf, Chemnitzer Str. 40, 09599 Freiberg, Germany.
3. Institute of Mechanical Process Engineering and Mineral Processing, TU Bergakademie Freiberg, 09599 Freiberg, Germany.

ABSTRACT

An open-source and user-friendly platform for design of experiments in the context of mineral processing operations is introduced. No specific knowledge of programming languages is required for using the platform. Depending on the user needs, the platform suggests the optimal experimental strategy with a minimum number of runs required. Different types of experimental designs such as screening, full factorial and central composite designs are currently available and more approaches will be added at a later stage. In this contribution, we illustrate how the platform can be used to optimise a laboratory flotation experiment with six factors. Besides, the automatically generated graphs serve to illustrate the interactions between variables and their importance for understanding and forecasting the process. The platform provides reliable and robust results enabling a better understanding of the process.

INTRODUCTION

The mining industry is constantly seeking to optimise the economic and environmental standards of its operations. The increasing complexity of orebodies to be mined poses challenges to the efficiency of mineral processing operations – efforts are required to assure these operations can be optimised for a better grade and yield of mineral concentrates, as well as a reduction in energy and resource requirements (Evans *et al*, 2009). Most importantly, these efforts should consider the properties of ores and their relation to the process parameters to be optimised. Within this context, statistical design of experiments (DoE) has gained importance and is increasingly used in both industry and research.

Nevertheless, most DoE platforms belong to commercial software packages, or the limited open access options require extensive background knowledge from the user in different fields (eg programming languages). We propose here an open source and user-friendly platform embedded in a workflow for the use of DoE in the context of mineral processing operations. The proposed workflow enables its use even by those that are not familiar with the topic. In this contribution, we apply the proposed workflow to optimise a laboratory flotation experiment with six factors. Results are illustrated with the open-source platform.

DESIGN OF EXPERIMENTS AND PLATFORM WORKFLOW

Design of experiments

Design of experiments (DoE) is a statistical technique to gain insight into a process by quantifying the effect of process variables on the measured process response. In addition, it serves to get statistically validated relationships between these process variables with minimal number of experiments. DoE is widely used for optimisation tasks (Durakovic, 2017). The different types of DOE allow us to investigate and optimise the process under study with an efficient and methodical way of working.

Proposed DoE workflow

Figure 1 displays the DoE workflow proposed in this work and integrated in the open source platform. The workflow is subdivided into three different phases: (1) screening, (2) investigation and modelling, and (3) verification and optimisation. These phases are explained in the following subsections.

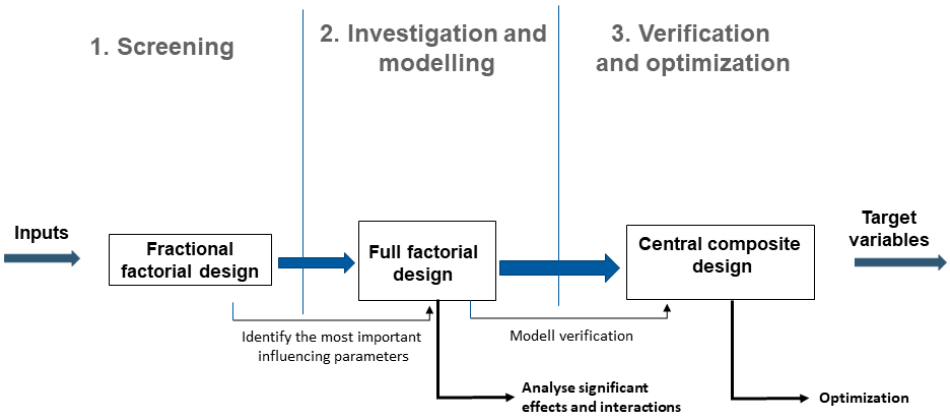

FIG 1 – Methodology and approach to the platform.

Screening

As the name suggests, the screening phase serves to screen out process parameters that are not significant to the response variable. The most common design type used for screening purposes and thus implemented in the platform is the fractional factorial design (Durakovic, 2017). This design is used when a high number of process parameters must be investigated, which would make the use of full factorial design too costly and time-consuming. In this type of design, a fraction of the total runs from a full factorial design is taken.

Since only part of the experimental volume is covered in the screening phase, some effects are confounded (ie the impacts of two or more variables cannot be disentangled), resulting in a loss of resolution. Resolution describe how far the effects in a fractional factorial design are aliased (Durakovic, 2017). More information about the resolution of a DoE can be found in (Jankovic, Chaudhary and Goia, 2021). If the users wish to optimise the process using a fractional factorial design of experiments, they will incur in the risk that it may lead to incorrect results. That risk can be compensated if the user has sufficient knowledge about the process to neglect the interaction effects (Gunst and Mason, 2009).

Investigation and modelling

After screening out the irrelevant process parameters, a full-factorial DoE is conducted in the investigation/modelling phase with the remaining parameters. The goal is to test each individual combination of the independent process parameters and their effects on the response variables. The full factorial design estimates linear and two-factor interaction effects. At this stage, the process is investigated for its main effects and all interactions. To visualise the results, the user can choose between three types of diagrams:

- the Pareto diagram, which shows the magnitude of the effects from the largest to the smallest effect.
- the main effects diagram, which is the effect of one of process parameters on the response variable, ignoring the effects of all other process parameters.
- and the interaction diagram, which shows how the main effects interact with each other.

By adding centre points to the design, it is possible to check whether there is a curvature in the assumed model. This check is important for the determination of the most accurate predictions possible.

Proceeding with the modelling phase, a model assumption must be made. The user can choose between three assumptions: linear, interaction or full second-order model. Several tools are available to identify the most appropriate model assumption for a specific case. Here we use three types of residual plots (Best and Wolf, 2014). First, plotting the model residuals against the order of observation allows to check whether temporal or spatial co-dependencies between the experiments are influencing the results. A non-random pattern hints at a lack of independence. Second, the variance of the residuals is examined to ensure that they are homogeneous by plotting the residuals against the fitted values. The variance of the residuals should be uniform overall predicted values,

an assumption known as homoskedasticity. If the plot shows a pattern, then the variances are not consistent and this assumption is not fulfilled. Third, a Q-Q plot is used to check if the residuals are normally distributed. In the ideal case, this plot should show a straight line. Inversely, the more the plotted points deviate from a straight diagonal line, the less likely it is that the model residuals follows a normal distribution.

The last stage is to check linearity by plotting the surface of the assumed model and the measured points. In this way, it is possible to ascertain how the measured points fit the assumed model. In this case, the centre-point has special relevance since it provides information about the curvature (or lack of) of the model. The fitting function of the corresponding model is created with a multiple (linear or nonlinear) regression.

Verification and optimisation

Central composite designs are extensions of the factorial experimental designs. They are composed of a partial factorial or full factorial experimental design and a so-called CCD star with a central experiment whose extreme settings go beyond those of the factorial experimental design. A central composite experimental design is suitable for studying quadratic relations (Ahn, 2015).

To ensure a minimum number of experiments and maximum flexibility for the user, the central composite design composes our workflow as part of the verification of the assumed model in the case of a second-order model assumption. It is assumed that the full factorial experimental design with centre points already performed is sufficiently ample to estimate curvature effects. Instead of running the full star point subset with its associated replicates, the user can run it only partly and compare it to the assumed model. Next, if desired, the full star point subset can be used to improve the model. In this case, three types of verification are provided:

1. Specific verification. This sort of verification is appropriate when the user is interested in further investigating a part of the experimental volume and to be sure that the adopted model fits well in this experimental volume. Here the user has the choice to investigate the volume near the centre, at the borders or outside the experimental area. The last option is very valuable if the user not only wants to verify the model, but also wants to check whether the model is suitable for larger experimental areas without having to create a completely new experimental plan.
2. Advanced verification. This type of verification is applicable when the user wants to validate the model in the entire experimental volume. Even though this type of verification is time-consuming, it is the most reliable available.
3. Simple verification. This option is only suitable if no curvatures were detected in the investigation phase (and therefore a linear or interaction model is used). It consists of measuring the point with the optimal parameter settings and comparing the results obtained with the numerically determined optimum.

Further improvements foreseen to our workflow (which will consequently be implemented in the open source tool) will allow users to select their own verification points and design their own verification plan.

Once the model is established and verified, the process can be numerically optimised in various contexts. In our platform, the Hooke-Jeeves algorithm and Lagrange method are used for single, multivariate and constrained optimisation. The three types of optimisation differ according to the optimisation objectives and process specifications as illustrated in the section *Model verification and optimisation*.

The open source platform was programmed in R mainly using the ‘shiny’ package (Chang *et al*, 2021), allowing to generate web-based user interfaces. This strategy allows to provide users access to the proposed DoE workflow without any programming knowledge required. The platform can be accessed in (Ben Said *et al*, 2022).

Table 1 compiles all packages used to construct the platform.

TABLE 1

Used R packages in the platform.

Package	Purpose
shiny (Chang *et al*, 2021) shinydashboard (Chang and Borges Ribeiro, 2021)	Create the web app platform
shinyhelper (Chris, 2019)	Help files
FrF2 (Groemping, 2014)	Create and analyse fractional and full factorial designs
DoE.wrapper (Groemping, 2020)	Create and analyse central composite designs
pid (Dunn, 2018)	Pareto charts
plotly (Sievert, 2020)	Contour and surface plots, with some interactivity
pracma (Werner, 2021)	Numerical response optimisation
dfoptim (Varadhan, Borchers and Bechard, 2020)	Constrained optimisation
dplyr (Wickham *et al*, 2021) plyr (Wickham, 2011)	Data handling
stats (R Team, 2021)	Statistical calculations (core R package, no installation required)

CASE STUDY

The case study investigated here deals with the optimisation of scheelite recovery with froth-flotation from a low-grade ore. The feed ore contains 0.5 per cent scheelite, 1.1 per cent calcite and about 55 per cent quartz. The response variables selected for this optimisation study are scheelite grade, scheelite recovery and mass pull.

Colloidal silica, a new depressant, is used to increase the selectivity between scheelite and semi-soluble salt type minerals. Three types of colloidal silica are investigated on laboratory scale: standard (stdCS), aluminate-modified and silane-modified silica. All colloidal silica types were supplied by Akzo Nobel. Four process parameters were investigated besides the colloidal silica types: pH, collector dosage, frother dosage and colloidal silica dosage. The collector used is sodium oleate, pH modifiers are hydrochloric acid and sodium hydroxide, frother is 4-Methyl-2-pentanol (MIBC). These reagents were supplied by Carl Roth GmbH and Alfa Aesar.

Next, the results obtained with the proposed workflow are presented and discussed. All illustrations were generated in the open source platform and all experiments were repeated two times.

Screening

Our focus in this phase is to determine the most important main effects. Since we had no previous knowledge about possible two-way interactions between the process parameters studied, we selected the fractional factorial design with resolution 4. The experimental design, which is carried out individually for each of the three colloidal silica types, is shown in Figure 2. The correlation table at the bottom right of Figure 2 shows the correlation between the main effects and the two interaction effects. Since there is no correlation (at resolution >=4), the entire table is highlighted in blue, corresponding to zero correlation.

Design plan

Download

run.no	pH	NaOl.dosage	MIBC.dosage	CS.dosage
1	8.00	100.00	20.00	100.00
2	10.00	100.00	50.00	100.00
3	10.00	400.00	50.00	500.00
4	10.00	400.00	20.00	100.00
5	10.00	100.00	20.00	500.00
6	8.00	400.00	20.00	500.00
7	8.00	400.00	50.00	100.00
8	8.00	100.00	50.00	500.00
9	9.00	250.00	35.00	300.00
10	10.00	400.00	20.00	100.00
11	8.00	400.00	50.00	100.00
12	10.00	100.00	50.00	100.00
13	8.00	100.00	50.00	500.00
14	8.00	100.00	20.00	100.00
15	10.00	400.00	50.00	500.00
16	10.00	100.00	20.00	500.00
17	8.00	400.00	20.00	500.00
18	9.00	250.00	35.00	300.00

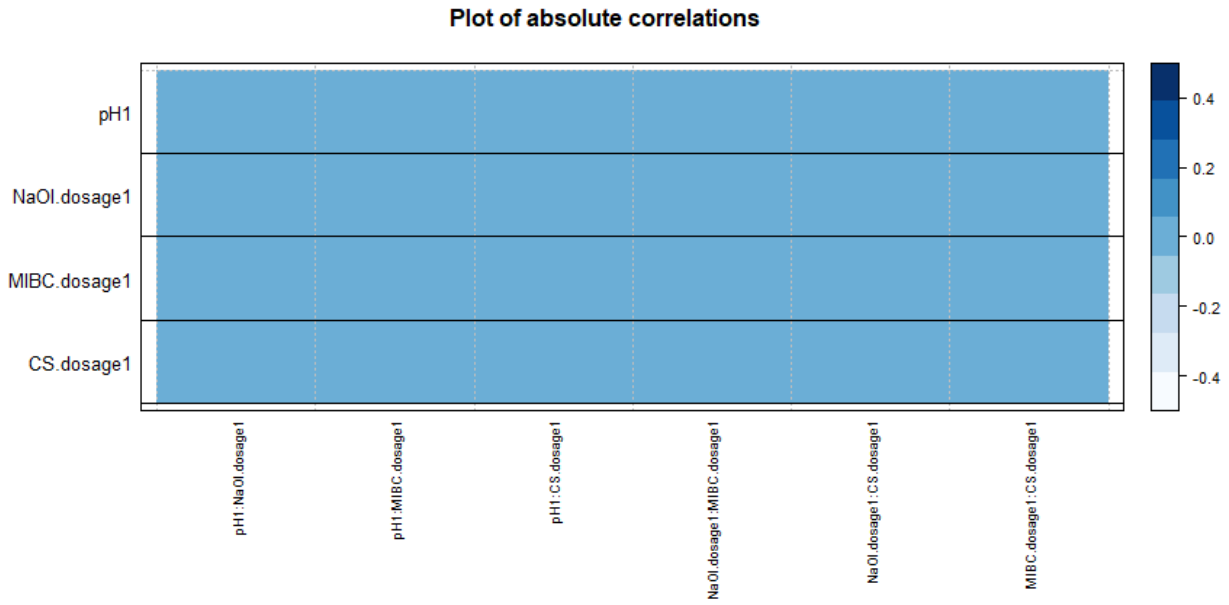

FIG 2 – Creation of the fractional factorial design in the 'Generate' tab.

All experiments were conducted at the Helmholtz Institute Freiberg for resource technology with 500 g of ore at 33 per cent pulp density in a Magotteaux® bottom-driven flotation cell. Each had only a rougher stage, lasted seven minutes and involved three concentrates with a 5 sec scraping rate, 450 min^{-1} impeller speed and an air flow rate of 5 L/min. All samples were split and analysed with a Bruker S1 Titan 600 handheld X-ray fluorescent (XRF) instrument at the Helmholtz Institute Freiberg

for resource technology. The calibration of the instrument was carried out with samples analysed by ALS Global®.

The screening phase results for the three colloidal silica modifications are shown in Figure 3 as pareto charts indicating the magnitude (absolute value) and importance of the effects. Process parameter sodium oleate dosage is the most important regarding scheelite grade and mass pull, and parameter pH is the most important regarding scheelite recovery. Given the importance of collector dosage and pH, these are kept for the investigation phase.

Even thought, colloidal silica (CS) dosage is only significant for some response variables (Scheelite grade and mass pull using stdCS modified with silane as depressant), the aim of this study is to evaluate colloidal silica as a new depressant in scheelite flotation. Thus, we opted to keep Colloidal Silica dosage as a process parameter and to extend the investigated area in the Investigation phase. In addition, a significant difference is observed between the three stdCS modifications in terms of scheelite grade and recovery. On the one hand, the silane-modified colloidal silica provides the highest scheelite grade and recovery. On the other hand, standard colloidal silica is of interest from an economic point of view. Therefore, we decided to keep these two types of CS for proceeding to the investigation phase.

From the Pareto charts it is easy to recognise that the MIBC dosage plays a minor role on the response variables, with the exception of the scheelite grade using stdCS and aluminate-modified stdCS as depressant. Therefore, we decided to omit the MIBC dosage for the following investigations.

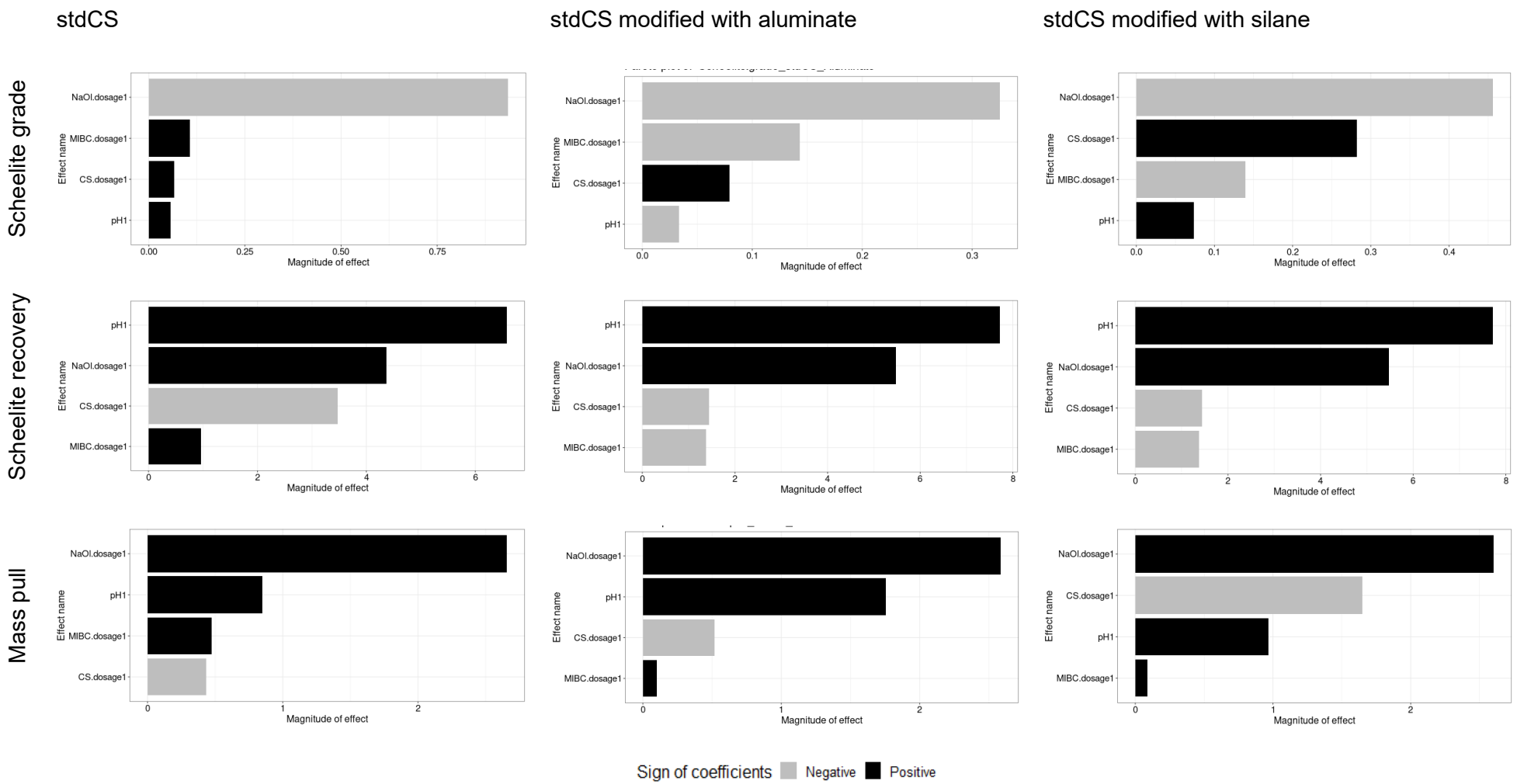

FIG 3 – Pareto charts of the screening phase for the target variables (scheelite grade, scheelite recovery, and mass pull) for the three types of sodium stabilised colloidal silica (stdCS).

Investigation and modelling

For the sake of saving space, the presentation and discussion of results will focus solely in scheelite grade as response variable. Other response variables will be evaluated again in in the section *Model verification and optimisation*. In the investigation phase, the user is not limited to investigate the process parameters used in the screening phase. On the contrary, findings that arise from the screening phase should be implemented on the following phases to assure the best optimisation route. Here, we introduce the specific surface area of the colloidal silica as a process parameter.

The specific surface area of colloidal silica was investigated in the range of 250 to 500 m^2/g. The implementation of centre-points can be problematic in some cases, especially when dealing with discrete variables, or when the implementation of the centre point of a parameter is not possible due to technical/mechanical constraints. For this study, two centre-point issues exist: colloidal silica with the mean specific surface area/particle size is not available and colloidal silica modifications are discrete variables.

The DoE approach is flexible enough to address these issues. For each type of colloidal silica (standard or silane-modified with associated specific surface area/particle size), a full-factorial plan is created that includes centre points with varying pH, collector dosage and dosage of colloidal silica. After the experiments have been carried out, the plans are combined into a full-factorial plan without centre points and the modification and specific surface area/particle size are added as parameters to investigate the effects of all process parameters. Overall, 72 tests are required with this approach. which is almost the same number of experiments (74) that would be required conventionally.

Since no main effects or interactions are confounded, the effects in the pareto charts can be investigated separately. From the Pareto diagram (Figure 4) it can be concluded that the silane modification and the specific surface area have an insignificant positive effect on the target variable.

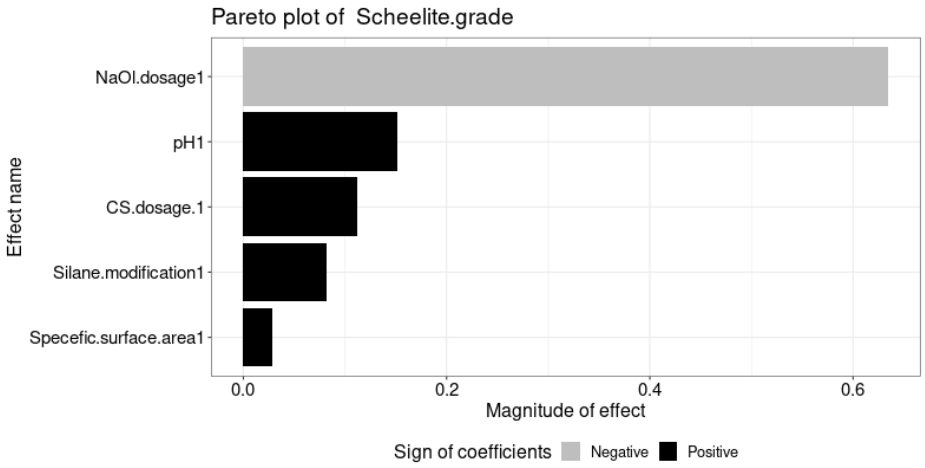

FIG 4 – Pareto charts of the investigation phase for the target variables scheelite grade.

From a scientific point of view, these results provide a basis for further fundamental research using atomic force microscopy, in particular to understand the effects of silane modification and specific surface area. Since the standard colloidal silica is more cost efficient, it is decided to only keep it for further investigations. The variation of higher specific surface area is used to establish and validate the corresponding model.

Figure 5 shows the different residual plots for the different model assumptions possible, all based on scheelite grade. From the plot of the residuals, it is evident that an interaction model is not applicable to this case study. That is because the residuals seem to not be randomly dispersed in the ‘residuals versus order of observation’ and ‘residuals versus fitted values’ plots. The choice of model assumption is then restricted between the linear and two-order model. A linearity check with display of the surface plot with the measured centre points shows that the two-order model would be the better model assumption. In this case, a specific or an advanced verification will be required to verify the estimated curvature.

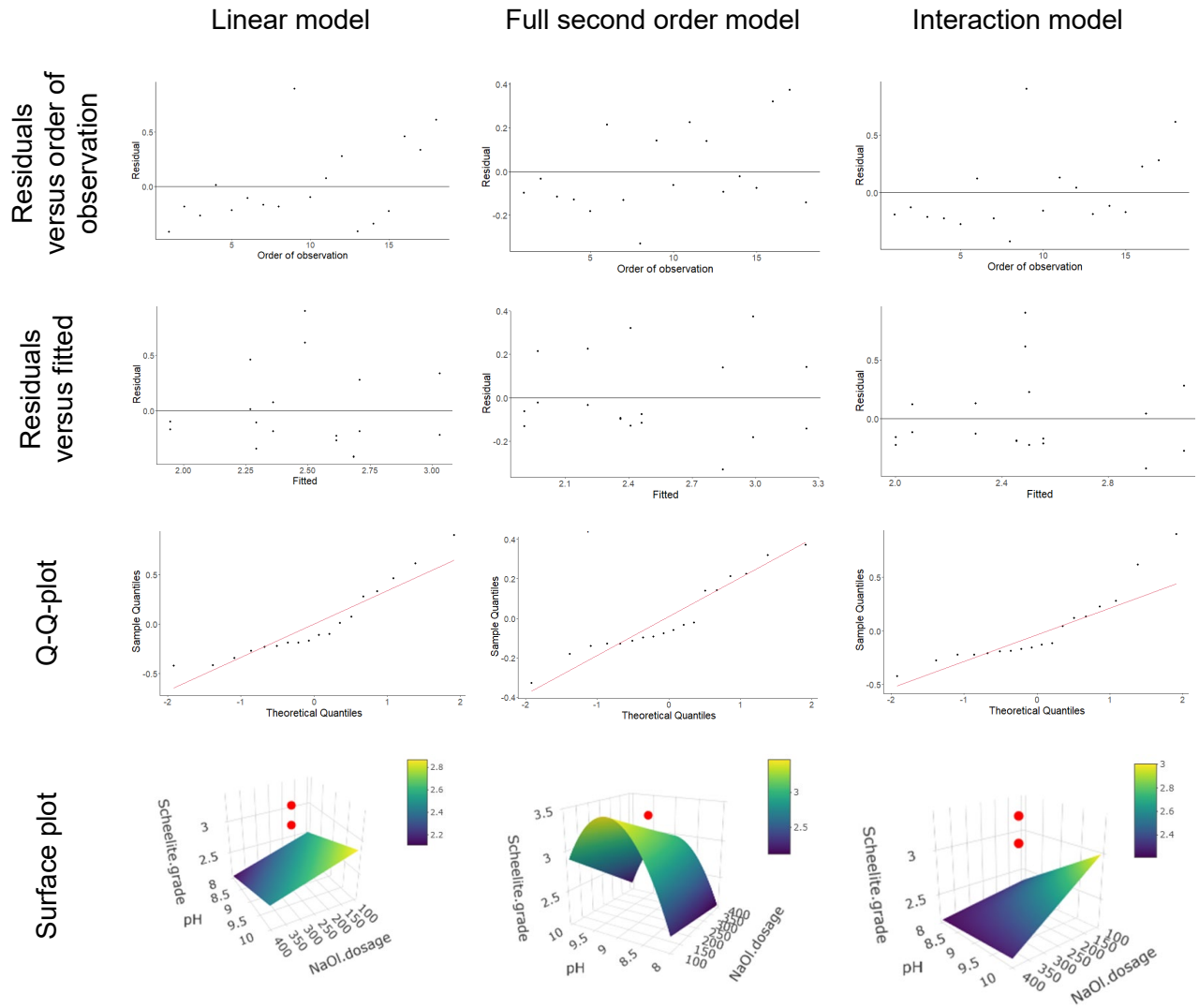

FIG 5 – Residuals and surface plots for the model assumption for scheelite grade.

Model verification and optimisation

Currently, a visual assessment of the fit of the verification points is required to evaluate the viability of the assumption chosen. The measured verification points are plotted together with the surface plot of the assumed model for the response variable (Figure 6). In the studied case, a specific verification point was tested at the border of the investigated area. The implementation of the verification points shows a curvature along the axis of the process parameter CS dosage, which could not be modelled by the full factorial design carried out in the investigation phase. Therefore, the verification points were implemented in the model.

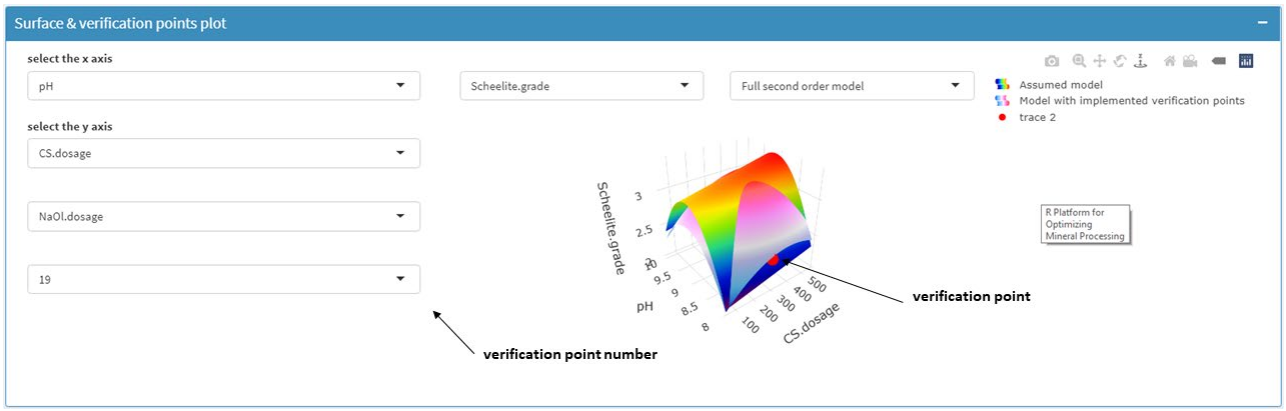

FIG 6 – Performed specific verification with implementation of the verification points in the model.

Now that the model is verified, the process can be optimised. In many cases, mineral beneficiation investigations are not only interested in a single response variable, but would rather consider several response variables of particular importance. These can be, for example, grade and recovery in mineral separation processes. Furthermore, the target variables and their optimisation can vary across the process stages. In industrial beneficiation plants, for example, different separation stages target specific process outcomes. For example, rougher and scavenger stages target maximum yield, while cleaner stages target specific metal grades that satisfy product specifications. Multi-response optimisation allows us to take this aspect into account by optimising two response variables simultaneously.

One option for multi-response optimisation is to assign specific coefficients to each response variable, according to its importance to the process, thus constructing a cost function. Other multi-response optimisation option is the so-called constrained optimisation, where one response variable is optimised while a second one only has to remain in an admissibility region. An example is the minimisation of energy consumption in grinding processes for obtaining a certain particle size distribution, since particle size distribution must be kept at specific intervals to assure the efficiency of the subsequent mineral separation processes. The results of single response, multi response and constrained optimisation for this case study are shown in Figure 7.

Optimisation type	**Optimisation goal**
Single response optimisation	Maximise scheelite grade
Multi response optimisation	Rougher stage: maximise scheelite grade and recovery with the scheelite recovery twice more important than scheelite grade
Constrained optimisation	Maximise mass pull for a specific scheelite grade

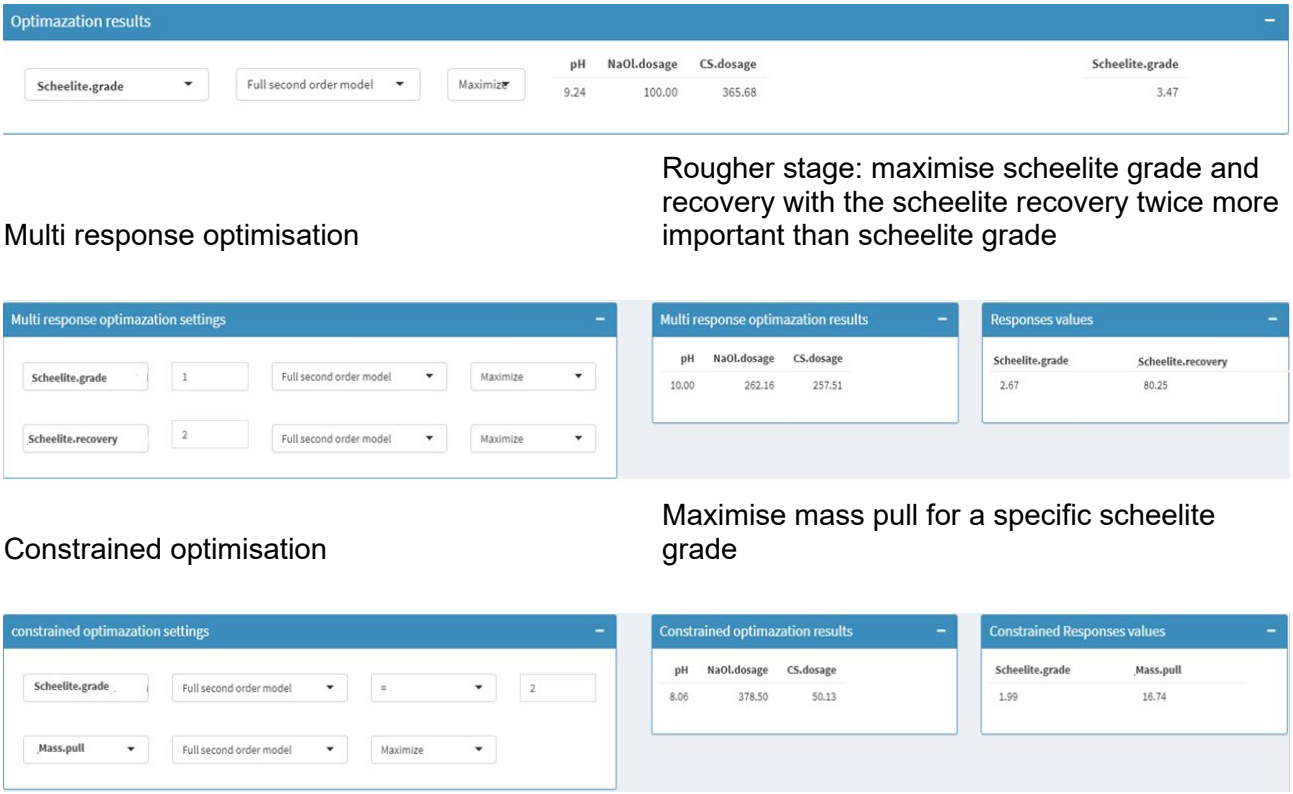

FIG 7 – Single response, multi response and constrained optimisation performed in the Tab ‘Optimisation.

The optimum scheelite grade is 3.47 per cent with parameter settings of pH 9.24, NaOl dosage of 100 g/t and CS dosage of 366 g/t. When scheelite recovery is additionally considered with an importance ratio compared to scheelite grade of 2/1, the optimal NaOl dosage increases to 262 g/t and the optimal CS dosage decreases to 258 g/t which agrees with the observed main effects of the process variables on the response variables. With these parameter settings, a scheelite recovery of 80 per cent and a scheelite grade of 2.67 per cent are achieved. In addition, a maximum mass pull of approximately 17 per cent is achieved when a scheelite content of 2 per cent is desired.

CONCLUSIONS

The workflow introduced in this contribution allows for the application of design of experiments without extensive prior knowledge required. While most techniques applied in here are already described in text books and available across different software, this work introduces a concise DoE workflow that is freely available in an open source web platform. Even though this is a well-defined workflow on a robust methodology, users still have the flexibility to conduct their research according to their specific needs, constrains, and objectives. In addition, the workflow and platform are designed specifically for raw materials separation processes.

Nevertheless, these tools do not serve as a replacement for the theoretical and technical knowledge required for the process under investigation. It is rather an accompanying tool for performing investigation and optimisation tasks, in research or industrial environments, in a robust way, while also minimising time and resources required for these investigations. The platform will be under constant development, always taking into consideration the needs of mineral processing. The next planned improvements, besides those already mentioned along the manuscript, are the implementation of D-Optimal designs and the application of statistics-based guidance for users.

A case study for the selective flotation of scheelite from a low-grade ore containing semi-soluble salt type minerals was used in here to illustrate the workflow. In the case study, not only the feasibility of using colloidal silica as a depressant in scheelite flotation was investigated, but also the importance of pH, collector and frother dosages, as well as colloidal silica specific surface area to this process. Finally, the optimal process parameter settings were determined at laboratory scale.

The results obtained will serve as basis for future industrial transfer. In addition, they will also be used for fundamental studies using atomic force microscopy, in particular to understand the effects of the type of modification and specific surface on the surface chemistry of the minerals studied.

ACKNOWLEDGEMENTS

The authors would like to thank colleagues at Nouryon (formerly AkzoNobel Surface Chemistry, Sweden) for providing flotation reagents. The authors are also very grateful to Wolfram Bergbau and Hütten AG for providing the scheelite ore. This paper was written thanks to the financial support of the CoSiFlot project (03THWSN006). Said project has received funding from ‘WIPANO – Knowledge and Technology Transfer through Patents and Standards’ program.

REFERENCES

Ahn, H, 2015. Central Composite Design for the Experiments with Replicate Runs at Factorial and Axial Points, *Industrial Engineering, Management Science and Applications 2015*.

Ben Said, B, Pereira, L, Tolosana-Delgado, R and Rudolph, M, 2022. A user-friendly R Platform for Optimizing Mineral Processing, https://hifgeomet.shinyapps.io/Optimization_Tool/

Best, H and Wolf, C, 2014. *The SAGE Handbook of Regression Analysis and Causal Inference*, SAGE Publications Ltd.

Chang, W and Borges Ribeiro, B, 2021. shinydashboard: Create Dashboards with ‘Shiny’. R package version 0.7.2 https://CRAN.R-project.org/package=shinydashboard

Chang, W, Cheng, J, Allaire, J, Sievert, C, Schloerke, B, Yihui Xie, Allen, J, Mcpherson, J, Dipert, A and Borges, B, 2021. shiny: Web Application Framework for R. R package version 1.6.0 https://CRAN.R-project.org/package=shiny

Chris, M-T, 2019. shinyhelper: Easily Add Markdown Help Files to ‘shiny’ App Elements. R package version 0.3.2 https://CRAN.R-project.org/package=shinyhelper

Dunn, K, 2018. pid: Process Improvement using Data. R package version 0.50 https://CRAN.R-project.org/package=pid

Durakovic, B, 2017. Design of experiments application, concepts, examples: State of the art. *Periodicals of* Engineering *and Natural Sciences (PEN),* 5.

Evans, C, Coulter, B, Wightman, E and Burrows, A, 2009. Improving Energy Efficiency Across Mineral Processing and Smelting Operations – A New Approach. *SDIMI Conference.*

Groemping, U, 2014. Package for Creating and Analyzing Fractional Factorial 2-Level Designs. http://www.jstatsoft.org/v56/i01/

Groemping, U, 2020. DoE.wrapper: Wrapper Package for Design of Experiments Functionality. R package version 0.11 https://CRAN.R-project.org/package=DoE.wrapper

Gunst, R F and Mason, R L, 2009. Fractional factorial design. *WIREs Computational Statistics,* 1, 234–244.

Jankovic, A, Chaudhary, G and Goia, F, 2021. Designing the design of experiments (DOE) – An investigation on the influence of different factorial designs on the characterization of complex systems. *Energy and Buildings,* 250.

R Team, 2021. R: A Language and Environment for Statistical Computing. https://www.R-project.org/

Sievert, C, 2020. Interactive Web-Based Data Visualization with R, plotly, and shiny. https://plotly-r.com

Varadhan, R, Borchers, H W and Bechard, V, 2020. dfoptim: Derivative-Free Optimization. R package version 2020.10–1 https://CRAN.R-project.org/package=dfoptim

Werner, B H, 2021. pracma: Practical Numerical Math Functions. R package version 2.3.6 https://CRAN.R-project.org/package=pracma

Wickham, H, 2011. The Split-Apply-Combine Strategy for Data Analysis. http://www.jstatsoft.org/v40/i01/

Wickham, H, Romain, F, Lionel, H and Kirill, M, 2021. dplyr: A Grammar of Data Manipulation. R package version 1.0.7 https://CRAN.R-project.org/package=dplyr

Multidimensional separation and characterisation of particulate samples with focus on mineral raw materials

R Ditscherlein[1], T Buchwald[2], E Schach[3], M Buchmann[4] and U A Peuker[2]

1. Institute of Mechanical Process Engineering and Mineral Processing, Technische Universität Bergakademie Freiberg, Agricolastraße 1, D-09599 Freiberg, Germany. Email: ralf.ditscherlein@mvtat.tu-freiberg.de
2. Institute of Mechanical Process Engineering and Mineral Processing, Technische Universität Bergakademie Freiberg, Agricolastraße 1, D-09599 Freiberg, Germany.
3. Helmholtz Institute Freiberg for Resource Technology, D-09599 Freiberg, Germany. Email: e.schach@hzdr.de
4. Institute of Low-Carbon Industrial Processes, German Aerospace Center, Walther-Pauer-Straße 5, 03046 Cottbus. Email: markus.buchmann@dlr.de

INTRODUCTION

En route towards a sustainable circular economy, the multidimensional understanding of separation processes and related characterisation methods represents an interdisciplinary challenge involving various scientific areas, eg geology, metallurgy, and the overall umbrella of data science. Modern measurement methods, working either in 2D (eg SEM-based mineral liberation analysis (Buchmann *et al,* 2020) dynamic image analysis) or 3D (eg X-ray tomography (Ditscherlein *et al*, 2022a), are capable of capturing a huge variety of particle–discrete information. This enables a specific and highly resolved characterisation of the whole process flow chain, while also requiring in-depth data processing and a deep understanding of the physical measurement system, in order to extract relevant information (Schach *et al*, 2019).

We present such a workflow from the separation experiment to the creation of an accessible multidimensional data visualisation based on the different particle–discrete data sets. 'Particle–discrete' here means that each characteristic parameter is available on the level of the single particle, so that information regarding composition, physical and/or geometric properties are available for each particle of the data set individually. This allows the calculation of multiple shape and size statistics. With such a property vector being available for each particle, it is now possible to analyse correlations between the different parameters and derive multidimensional separation functions.

EXAMPLE 1 – PARTICLE SIZE VERSUS PARTICLE SHAPE

Considering the data shown in Figure 1, where a particle–discrete data set is plotted with respect to two properties, particle diameter and aspect ratio. The two parameters show a very distinct correlation when plotted in 2D, while the marginal cumulative distribution functions (CDFs) appear to be ordinary CDFs, which in fact can each be approximated well by a Weibull distribution function. In two dimensions, the cumulative distribution function may be defined analogous to the 1D case:

$$Q_r(x_i, y_j) = P(x < x_i, y < y_j) \tag{1}$$

where x and y may be any parameters that can be measured or inferred from a measurement, like aspect ratio and volume–equivalent particle diameter, respectively. The index r denotes the quantity with the discrete measurements are weighted, most commonly simply by index (number–based or non–weighted, $r = 0$) or by weight/volume ($r = 3$).

The marginal distribution is deducted from the two-dimensional CDF by integration over one of the two parameters, ie either x or y.

$$Q_r(x) = \int_{y_{min}}^{y_{max}} Q_r(x, y)\, dy \tag{2}$$

The probability density function (PDF) is now defined via the cumulative distribution function for the 2D case as:

$$q_r(x_i, y_j) = \frac{\mathrm{d}^2}{\mathrm{d}x\mathrm{d}y} Q_r(x_i, y_i) \tag{3}$$

The PDF for the data introduced in Figure 1 is shown in Figure 2. As was the case with the CDF, the marginal PDFs do not give any information about the highly correlated nature of the two parameters in the 2D space.

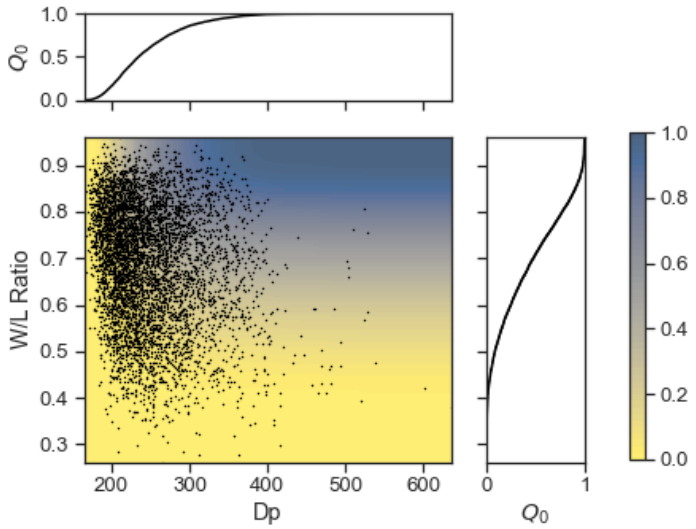

FIG 1 – Representation of a particle–discrete data set, showing the particle diameter of the volume–equivalent sphere (Dp) and the width–to–length ratio (W/L Ratio). The 2D CDF is displayed as a colour gradient from 0.0 (yellow) to blue (1.0). The number–based CDFs of the marginal statistics (Dp and W/L Ratio) are plotted over the respective axis.

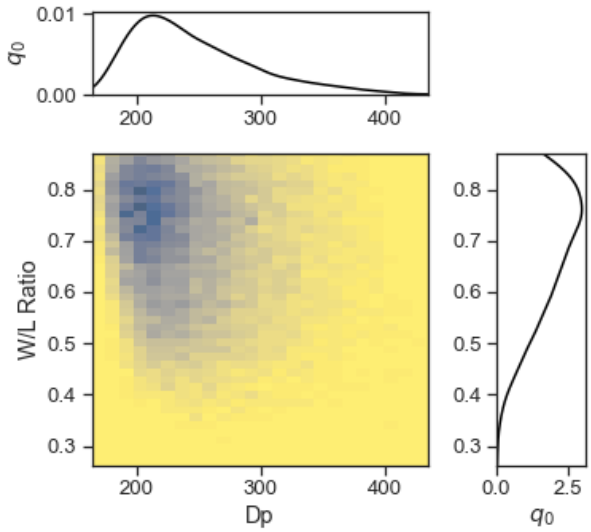

FIG 2 – The particle–discrete data set of Figure 1 as a 2D, normalised histogram with 50 × 50 bins. The marginal PDFs are shown over the respective axes.

On almost any device built to classify particles according to a certain parameter, be it particle size, particle shape, density, ore content, magnetisation etc, the resulting separation function is not simply be correlated with the target parameter, but with other parameters as well. For example, in sieving, while particle width is the primary parameter due to which particles are separated, particle shape will also play a role, depending the kind of sieving apparatus and parameters of operation. While the particle size may be the parameter of relevance in a product's specification, the description of the multidimensional separation becomes increasingly important in order to understand how a product stream behaves in an industrial flow sheet.

If the particle collective of Figure 2 as feed stream is now separated according to particle size *and* shape, the resulting coarse and fine fractions may look like the plots given in Figure 3. Here, as above, the information about the complex correlation of particle size and aspect ratio in the 2D space is not contained in the marginal probability density functions.

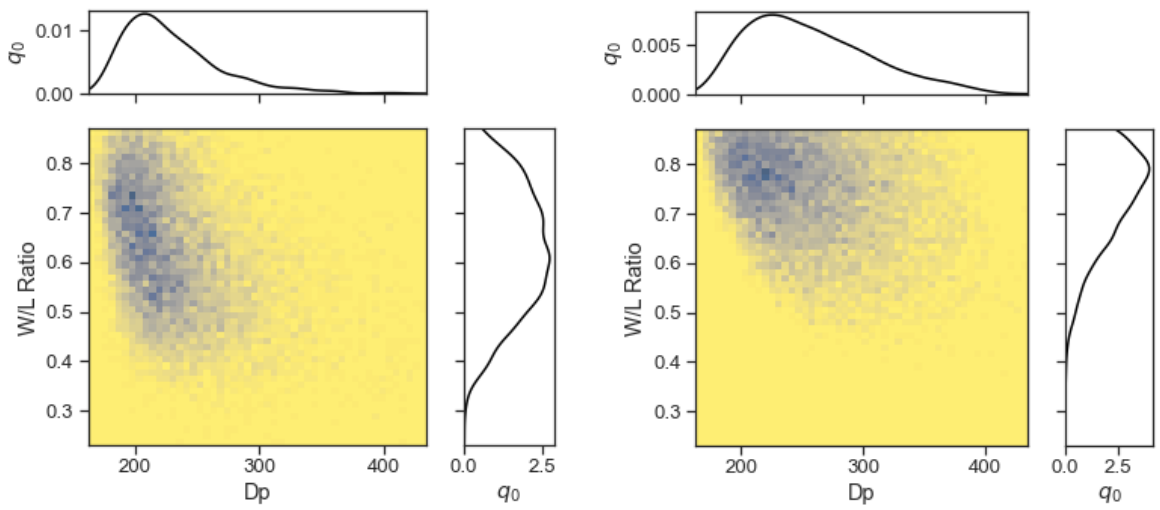

FIG 3 – Fine (left) and coarse fractions (right) of the data set of Figure 2. The particles have been classified according to both particle size and shape, resulting in a separation in 2D space which cannot be inferred from the marginal PDFs.

The multi-dimensional, in this case 2D, separation function can now be calculated from the data contained in the probability density distributions of coarse fraction and feed, if the coarse fraction is regarded as the product stream.

$$T_r(x,y) = v_{r,\text{product}} \cdot \frac{q_{r,\text{coarse}}(x,y)}{q_{r,\text{feed}}(x,y)} \tag{4}$$

in which $v_{r,\text{product}}$ is the yield of the product, for example index–based:

$$v_{0,\text{product}} = \frac{N_{\text{coarse}}}{N_{\text{feed}}} \tag{5}$$

so that, for a separation into two streams:

$$q_{r,\text{feed}}(x,y) = v_{r,\text{product}} \cdot q_{r,\text{product}}(x,y) + v_{r,\text{waste}} \cdot q_{r,\text{waste}}(x,y) \tag{6}$$

The separation function that can be calculated for the shown example is plotted in Figure 4. The separation function is highly correlated in the given 2D space, which leads to interesting shapes for the marginal separation functions of the two particle characteristics, size (Dp) and shape (W/L Ratio). Both marginal separation functions never reach 100 per cent, while the area of full separation ($T(x,y)$ = 1.0) is clearly visible in the 2D plot. The marginal separation function of particle size also has a clear fish hook, where a minimum is reached at only T_{Dp} = 45 per cent. While these phenomena often lead to speculations as to their origins, the treatment via multidimensional separation functions gives a very intuitive graphical explanation.

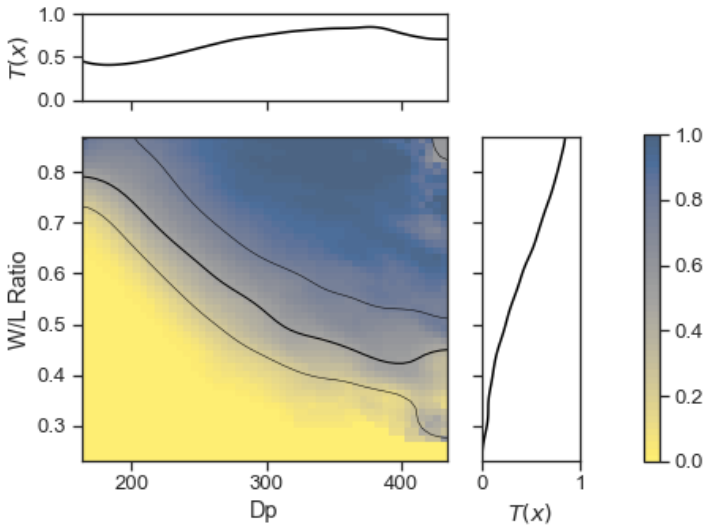

FIG 4 – Separation function for the feed and coarse streams of Figures 2 and 3, which was calculated according to Equation 3. The lines denote the percentiles T_{25}, T_{50} and T_{75}.

EXAMPLE 2 – PARTICLE SIZE VERSUS IRON-OXIDE CONTENT

The multidimensional approach can be also used for material specific separation processes in mineral processing, eg by regarding size and material content at the two decisive parameters determining the separation process. In a case study the separation of a skarn ore with a dry magnetic drum has been investigated using MLA-information to acquire the two-dimensional particle-discrete data (see Figure 5).

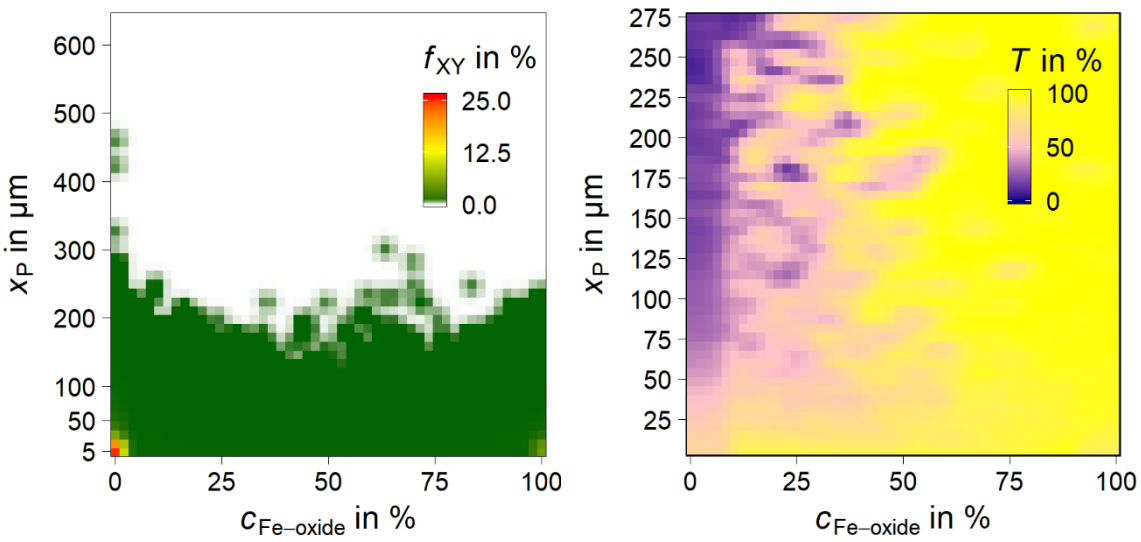

FIG 5 – Case study in mineral processing – magnetic separation of a skarn ore with different Fe-content in the particles. fXY is the superimposed probability density distribution of particle property X and Y, which is in this case the concentration of iron-oxide and the particle size, respectively.

Looking at the two-dimensional separation function, it can be concluded that there is a minimum content for the Fe oxides below which a clear depletion of the particles off the magnetic product results. Above 75 µm, the separation behaviour is mainly independent of the particle size. Above a Fe-oxide content of approx. 10 per cent within the individual particles, these are enriched in the magnetic product stream. However, a relatively wide transition range is shown, which illustrates a poor separation efficiency for this property. Below approx. 75 µm, the values of the separation function $T(x_p, c_{Fe-oxide})$ decrease significantly and there is an unselective enrichment in the magnetic product stream with respect to the particle property Fe oxides content. This can partly be explained by the design of the magnetic drum separator, since smaller particles adhere, eg due to

van-der-Waals forces more strongly to the drum and are thus already discharged into the magnetic product with lower Fe oxide contents.

If the proposed workflow to acquire particle discrete data sets and to use them to generate multidimensional separation functions is supplemented by an adapted particle sample preparation strategy, which prevents particle-particle contacts, the application of highly efficient image processing workflows (eg machine learning algorithms) and the optimal integration of supporting correlative measurements (eg energy-dispersive X-ray spectroscopy in case of MLA) is clearly simplified (Ditscherlein *et al*, 2020). The resulting data can then easily be utilised and exchanged in an interdisciplinary manner as we briefly show on the example of a particle database concept (Ditscherlein *et al*, 2022b).

REFERENCES

Buchmann *et al*, 2020. *Minerals Engineering,* 150, 106284.

Ditscherlein *et al*, 2020. *Microscopy and Microanalysis*, 26, 676–688.

Ditscherlein *et al*, 2022a. *Powder Technology,* 395, 235–242.

Ditscherlein *et al*, 2022b. *Microscopy and Microanalysis*, 28, 350–360.

Schach *et al*, 2019. *Minerals Engineering,* 137, 78–86.

Opportunities and challenges in the move towards data-driven and dry lab approaches in the mineral industry

Y Ghorbani[1], S E Zhang[2], J E Bourdeau[3], G T Nwaila[4] and J Rosenkranz[5]

1. Associate Professor, Minerals and Metallurgical Engineering, Luleå University of Technology, Luleå, Sweden, SE-97187. Email: yousef.ghorbani@ltu.se
2. Research Scientist, Geological Survey of Canada, Ottawa, Canada, K1A 0E8. Email: ezhan053@uottawa.ca
3. Research Scientist, Geological Survey of Canada, Ottawa, Canada, K1A 0E8. Email: bourdeau.julie.e@gmail.com
4. Director, Wits Mining Institute (WMI), University of the Witwatersrand, Johannesburg, South Africa, 2050 Wits. Email: glen.nwaila@wits.ac.za
5. Professor, Minerals and Metallurgical Engineering, Luleå University of Technology, Luleå, Sweden, SE-97187. Email: jan.rosenkranz@ltu.se

ABSTRACT

The amount of data in the mineral industry continues to increase and the desire to innovate using data, especially big data remains insatiable. We call this the data-innovation gap, which could be addressed through our concept of the dry laboratory. In other disciplines and industries, the rise of structured and sometimes sandboxed innovation and experimentation centres has been in response to addressing the data-innovation gap. We observe and reason that in a data-driven environment, the ability to optimally generate and utilise data for many realms in the mineral industry including research, development, business operations, education and strategic planning either is, or will become essential. In this paper, the concept, opportunity, and the necessity for a move towards data-centric and dry laboratory approaches in the mineral industry are assessed. We argue that the dry laboratory provides the ideal environment to host, utilise and generate data, in a manner that sandboxes the risks and provides the industry and other stakeholders with the rewards of innovation and experimentation. We introduce key components of the mineral value chain in a framework that would enable the establishment of dry laboratories in the mineral industry, while simultaneously examining the components from both academia and industry perspectives.

INTRODUCTION

Modern mineral value chains are complex and transcend individual business processes or stages. Gated stages (silos) traditionally compartmentalise the risks and data. This is counterproductive for the global optimisation of the value chain. Siloed data is hard to link or fuse, difficult to access and while the quality of the data pertaining to a specific process may be sufficient to meet its needs, such data may not meet the quality needs of modern uses, such as data repurposing. The mining industry is under pressure to innovate core business operations to address challenges such as: (a) declining ore grades; (b) increasing ore complexity; (c) rising environmental, social and governance (ESG) requirements; and (d) rising desire for national self-sufficiency (Sánchez and Hartlieb, 2020). This is particularly crucial for critical raw materials (or CRMs). Achieving mineral value chain-wide optimisation necessitates a system-level, integrated approach that prioritises data generation and usage. For this purpose, we propose a data-centric laboratory (dry lab) that serves as a hub for linking businesses, data and geoscientists, mineral engineering and institutions, by providing a dedicated workspace for data-centric activities. Although pioneers in the industry exist (see for instance the Vale experience; Vale, 2018), no framework is available for such a concept. The success of dry labs in some disciplines has created dedicated subfields, such as computational physics and chemistry, bioinformatics and electrical engineering, and even policy and governance (eg Policy Horizons USA, Wellstead and Nguyen, 2020).

Integrated approaches necessitate a systems view of the processes involved, effective communication between subsystems, and substantial use of data (Lotter, 2011; Aasly and Ellefmo, 2014; Philander and Rozendaal, 2014; Lund and Lamberg, 2014; Lund *et al*, 2015; Ding *et al*, 2017; Dominy *et al*, 2018; Nwaila *et al*, 2020; Lishchuk *et al*, 2020; Ghorbani *et al*, 2021a, 2021b, 2022; Pan *et al*, 2022). The mineral industry produces sizable and big data through geoscientific surveys,

mining, mineral processing, and metal/mineral production. The evolution of information and communication technology (ICT) has facilitated data generation, which is likely to continue with the further deployment of sensor networks and online sensors. The modern ICT landscape in terms of global coverage, bandwidth and flexibility continues to offer untapped potential in real-time data generation, transport, collection and usage. This technological transition coincides with the industry's erosion of profit margins due to the aforementioned challenges. Despite this situation, the mining industry can be unenthusiastic to adapt new technologies and data. Data-centric technologies are potential solutions that can reshape the entire mining landscape (Ghorbani *et al*, 2021a, 2022). There are attempts to embrace modernised data usage and big data (eg Mkhabela and Manzi, 2017 and references therein; Sehoole *et al*, 2020), although the overwhelming practice remains legacy technology. For example, considerable amounts of data are dominantly stored in cold storage (McCoy and Auret, 2019; Ghorbani *et al*, 2021a, 2022) and big data management (Bascur, 2020; Qi, 2020) is yet to be considered and incorporated, despite such data being a key unifying component for system-level analyses. In contrast, Amazon, Meta (Facebook) and Google demonstrate the potential of data-mining to gather, process and transform data, in order to extract insights to pursue business objectives (Russell, 2014).

We define the dry lab as a dedicated and common workspace to facilitate data-centric activities in a manner that integrates and leverages multidisciplinary data from all stages of the mineral value chain. Experimentation in a dry lab is performed using data, mathematics, statistics, simulations, visualisations, analytics, machine learning and artificial intelligence. Dry labs generally do not overlap with wet labs, which focus on physical experimentation rather than data or digital experimentation. We assess driving factors behind dry labs and propose key components of a framework that would enable the establishment of dry labs in the mineral industry. Our proposed framework components include: computers and algorithms; data, storage and access; ICT infrastructure and sensors; data and geo-scientists and engineers; data (and ICT) management and governance; and an operational and financial model (Figure 1).

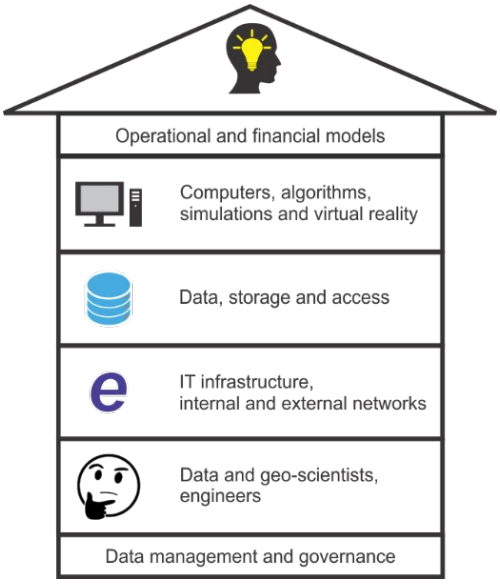

FIG 1 – Proposed framework components of dry labs. The key components are organised in horizontal blocks.

DRIVING FACTORS TOWARDS DRY LAB AND DATA-DRIVEN APPROACHES

Digital transformation in the mineral industry

Powerful computers and sensors continue to benefit the mineral industry. For example: (1) the use of computers to automate the processing and interpretation of 3D seismic surveys (Mkhabela and Manzi, 2017 and references therein; Sehoole *et al*, 2020); and (2) materials science and computer-aided design that promote innovation in mineral processing and extractive metallurgy devices (Anderson *et al*, 2014); (3) enhanced instrumentation of production plants for process control and modelling. The drive to improve industrial efficiency and performance resulted in various creative

technology-based approaches (Massinaei and Doostmohammadi, 2010; Makokha and Moys, 2012; Jahedsaravani *et al*, 2014, 2016). However, significant hindrances have been encountered, such as the quality and quantity of data in metallurgical plants, inseparable metallurgical and metal accounting and irregular data collection (Gaylard *et al*, 2009; Ghorbani *et al*, 2020a, 2022; Qi, 2020; Bascur, 2020).

Based on the use of data, we identify a hierarchy of data reliance within the engineering and sciences based on its historical progression and dependency relationships:

1. Fundamental data generation activities, such as experimentation and observation.
2. In-discipline data analysis, modelling and interpretation, including statistical analysis.
3. Computational modelling, such as fluid dynamics and stochastic modelling.
4. Interdisciplinary data analytics, including predictive modelling using artificial intelligence, data science and machine learning.

Lower levels of data reliance are prerequisites of higher levels. Fundamental data generation feeds analysis and modelling, which extend into computational modelling. Finally, the desire to integrate and repurpose data, as well as to engineer new data resulted in data analytics and data science. It is fascinating that numerical computing predates the rise of computing power; for example, humans handled discretised workloads to numerically determine the yield of the first atomic bombs (Atomic Heritage Foundation, 2017). Similarly, artificial intelligence research predates its modern deployment by decades (Samuel, 1959; Bascur, 2020). Past instances that resemble dry labs exist but primarily relied on computational methods to solve problems that were difficult or impossible to study experimentally (eg Callaway, 2020).

Relative to other sciences, geoscience is more abductive (a probable conclusion from what is known) instead of deductive and inductive (Kleinhans *et al*, 2005). Scientific abduction is used to reconstruct multiple probable models that concord with incomplete evidence, of which some models may be useful. Rapidly testing models with data is effective to find solutions to the challenges facing the mineral industry. Data-centric approaches including data-driven modelling have been used to address challenges within the mineral industry, such as: computer modelling for frothing control in flotation (Quintanilla *et al*, 2021); machine learning-based modelling for mineral processing (McCoy and Auret, 2019); and, automation systems for industrial processes and minerals engineering (Jämsä-Jounela, 2019).

The challenges around the use of data (eg accessibility and quality) would be adequately addressed in a data-centric setting. To foster innovation and experimentation, we argue that dry labs are essential as they:

1. Isolate risks from businesses (sandboxing) and focus on solutions that are generally useful and unrestricted by business barriers (eg intellectual property rights).
2. Leverage data, algorithms and computation in a centralised manner and attract talents to the mining sector (eg data scientists).
3. Provide data-driven services and products.
4. Centralise resources and planning to maximise the probability of data-centric innovations.

Current approaches, sources and types of data, the fate of data and costs

Within dry labs, many types of data would be encountered. We provide a hierarchical categorisation scheme that divides data into legacy and operational (Figure 2), based on the data's current usage. Operational data is currently being used for its original purpose; otherwise, the data is legacy, such as historical surveys, assays, technical process records, business process and labour utilisation records. Legacy data is repurpose-able to derive additional insights through improvements to methods of data usage, for example, through re-analyses of seismic data (eg Manzi *et al*, 2015; Sehoole *et al*, 2020) and repurposing data for analytics (Nwaila *et al*, 2020; Ghorbani *et al*, 2021a, 2022; Zhang *et al*, 2021). In some cases, legacy data combined with predictive modelling and simulation has proven to be efficient in deciphering complex interaction of minerals and reagents eg understanding multistage flotation processes (Quintanilla *et al*, 2021).

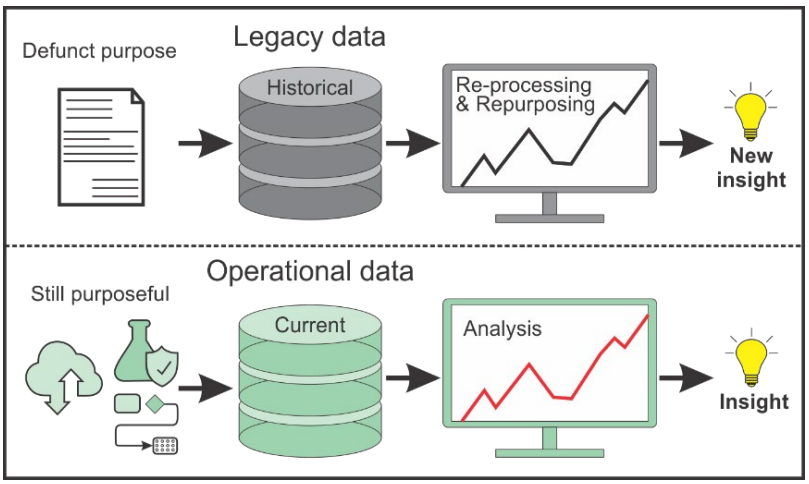

FIG 2 – Categories of data and their utilisation. Legacy data is defined as data that is currently no longer being used, whereas operational data is still being used for the purpose that it was generated for.

By origin, each type of data can be further divided into primarily: (1) scientific and engineering data that capture information, typically regarding physical processes; and (2) business data such as labour usage, financial status and commodity pricing. While other types of data exist, we restrict our discussion to around (1) and (2). Data in category (1) is often gathered through formal methodology and may be complex, such as mass balances, chemical assays or reaction kinetics. This type of data is useful for simulation of physical and plant processes. In the past, metallurgical experiments that produce data regarding reaction kinetics, such as wet simulations of reactor vessels have generated a wealth of data in category (1) and mainly of a legacy type by proportion. Such data has been used with success in understanding large-scale patterns in extractive metallurgy and the insights are valuable to processing plant design (Chakraborti, 2021; Ghorbani *et al*, 2021a, 2022; Soofastaei, 2021). Synthetic data (eg simulation-derived data) belongs to category (1) and is both useful (Nwaila *et al*, 2021) and already dry lab-based. Business transaction data in category (2) can be useful for plant optimisation, production planning and business intelligence (Nwaila *et al*, 2020; Ghorbani *et al*, 2021a, 2022).

Wet and dry labs

Laboratories are spaces that centralise resources such as equipment, infrastructure, management and materials to enable experimentation (Bertholf, 2017). Increasing levels of scientific reduction has resulted in instruments that are capable of probing increasingly finer details of reality, which has been driving the evolution of wet labs. Dry labs are driven by a system consideration of data. Where there is sufficient data generation and usage, wet and dry labs are complimentary. For some disciplines, this had resulted in interdependent and interconnected dry and wet labs (eg the CERN (https://home.cern/), MAX IV (https://www.maxiv.lu.se/) and Diamond Light Source (https://www.diamond.ac.uk/Home.html)). However, these spaces are non-interchangeable and have functionally distinct purposes and design considerations. The data-centric nature of dry labs ensures that by design, they are able to effectively use data to generate valuable insights, in addition to being able to generate targeted data for further investigation (Ghorbani *et al*, 2021a, 2022).

Driving factors

Drivers for dry labs primarily exist along three key domains – data, sensors and computation. In general, increasing dimensionality, density and quantity of data due to improved instrumentation and sensors have resulted in a proportionate need for computational power and talent. The latter need resulted in the rise of data management, governance and analytics companies, which exist to tackle client data needs. We view this as a stop-gap solution, as the cost associated with such services are high and the availability of geoscientists and geoscience-competent data scientists will likely be a key differentiator between existing multipurpose consulting and advisory companies and dry labs (see Ghorbani *et al*, 2022 for details).

Transformation towards a layered operating model

Digital computing, sensors and data (DCSD) are the three main components of modern data-driven techniques by forming a feedback loop that is self-improving. Sensors generate data, which is analysed using computers and algorithms, which subsequently promotes the development and deployment of sensors, physical and virtual (also called soft-sensors). Many drivers of the dry labs' concept (Ghorbani *et al*, 2020b, 2022) are technologies that invariably encompass DCSD. A traditional operational model (Figure 3) does not explicitly consider the positive feedback nature of DCSD systems.

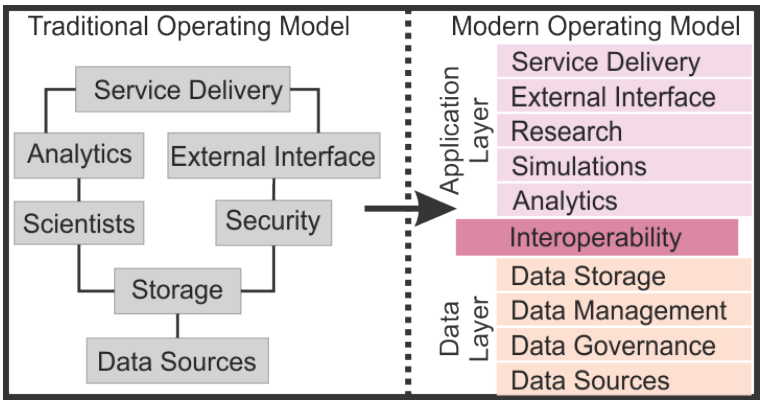

FIG 3 – Comparison of the traditional and a modified dry lab operating model. The modern operating model delineates layers of functionality (eg data layer) that can be formalised and are interoperable.

Modern DCSD deployments are capable of generating high bandwidth, quality, dimensionality and quantities of data that inspired the industry 4.0 concept (Indri *et al*, 2018), which proposes corresponding changes in the manner that the data and technologies are perceived, governed, managed and utilised. The ability to access, comprehend, process, analyse, protect and share and leverage modern data for insight generation have necessitated the creation of data and ICT management and governance functions within the enterprise setting. This is highly relevant to dry labs, because data is a core asset that requires a management and governance system. In this view, dry lab personnel are data consumers and contributors (DAMA International, 2017). For big data, the considerations centre around the notion of architecture, which is broadly a formalised approach to ingest, process and analyse such data. Such issues are being studied in the modern context (Yan *et al*, 2017; Indri *et al*, 2018; Bousdekis and Mentzas, 2021; Hinojosa-Palafox *et al*, 2021). Big data capability should be considered at the design phase of an operating model, because, ironically, the threshold to big data is lower for dry labs that are less capable of handling big data.

We propose a modified digital operating model for dry labs based on the industry 4.0 concept (Figure 3). In this model, the explicit delineation of layers of functionality enables structured laboratory development across layers in a compartmentalised manner. The bottommost layer contains data generation, storage, quality control and assurance and security processes. The governance aspect is intended to facilitate the management and usage aspects, through a clear view of roles and responsibilities (eg data consumer, data contributor, data owner/trustee, data steward, data custodian, DAMA International, 2017). In the topmost layer, the data is consumed to perform a variety of tasks, such as simulations, analytics, research and service delivery (Figure 3). An external interface bridges lab ICT components with the outside to exchange information and data, such as through data portals, web interfaces, cloud access and pipelines. Interoperability refers to interoperability of data, ICT and cross-domain interoperability (Hosseini and Dixon, 2016; eg for geographical information systems data, see ESRI, 2020). This ensures that the data and systems are usable by all data roles across levels and that data can be repurposed (eg Allen *et al*, 2013; Vercruysse *et al*, 2019). In addition, this layer enables service delivery, as it permits the translation of data and standards to client specifications. In traditional operating models, the data layer is generally unnecessary as the amount of data per source is comparatively low and its application is

typically discipline-specific and project-centred, and therefore, not usually cross-disciplinary and intended for repurposing or reuse (eg not data science-specific). In a data-centric environment, cross-disciplinary uses of data are common and data consumers are mostly data specialists, who are seldom geoscientists (eg Asamoah *et al*, 2020). Therefore, in dry labs, there is an explicit need for data repositories, catalogues and streams, containing many types of linkable or mergeable data (Qudrat-Ullah and Panthallor, 2021). To achieve interoperability in retroactive implementation is impractical (Gallagher *et al*, 2004). The ICT needs for pre-digital laboratories are centred around the delivery of information and services (eg Bertholf, 2017). In dry labs, ICT should be centred around the delivery of databased products and usage of data. Model implementation depends on capacity.

THE REQUIRED RESOURCES FOR DATA-CENTRIC DRY LABS

Dry labs require resources that are different to wet labs. The difference consists of a combination of technology, people and culture, data governance and management, and a suitable financial and operational model.

Technology

Key technologies must be present within dry labs to enable their core functionality, which include computing equipment, data storage devices and ICT infrastructure. Where the dry labs are expected to simulate aspects of the mineral processing in the industry, instrumentation and automation of processes is also important and should be designed to mimic processes in the mineral industry (Jämsä-Jounela, 2019). The ICT requirements (eg of bandwidth) depend on the nature of the dry lab. Cloud computing environments may be alternatives to local computing and may facilitate the adoption of digital solutions, as it may be easier for the industry to adopt the cloud than to build infrastructure. Another benefit of cloud computing is its flexibility, expandability and high availability (Sether, 2016). Cloud computing necessitates a loss of control and unfavourable cost-benefit analysis in smaller deployments. Local data storage is unavoidable if there are substantial amounts of data generated within a laboratory that requires intermediate storage, for example, for quality control and assurance purposes before their integration into a data repository or for training.

The design of the infrastructure must be flexible and adequate. Both ‘centralised’ and ‘decentralised’ ICT infrastructure systems (Sulankivi, 2004) may be applicable. Rapid and high-bandwidth access to key data sets that are routinely used in a dry lab would require localised ICT infrastructures. However, this set-up is not ideal for cloud computing or interfacing with external centralised ICT infrastructures, for which, remote data access and storage is better suited. Remotely hosted data benefits from cloud computing, such as through the use of Delta Lakes (Armbrust *et al*, 2020). As many tasks within dry labs do not require on-site presence, remote access capabilities for laboratory staff members may be an important factor (Manalu *et al*, 2020; Gupta *et al*, 2021). In this case, decentralised ICT infrastructure may be a requirement.

Effective use of exiting knowledge in the mineral industry

Knowledge in the mineral industry can be combined with data-driven approaches to improve the usefulness of models (eg knowledge-informed neural networks or one-shot learning). In dry labs, knowledge is important to understand business context, potential, and limitations of its processes (Hinojosa-Palafox *et al*, 2021; Pan *et al*, 2022). Legacy and operational data (Figure 2) contain valuable information regarding relationships between feed characteristics and performance indicators, which provide indirect knowledge of the structure and/or composition of the feed sources (Ghorbani *et al*, 2020a, 2021a, 2022). Operational data could be combined with analytics to yield insights and knowledge to drive improvement in plant performance (Jahedsaravani *et al*, 2016). Short-term knowledge can be leveraged to deliver just-in-time feedback to plants and long-term knowledge can guide the design and enhancement of plants. The knowledge gained from legacy data can benefit future operations by providing improved metrics to screen and assess complex ore treatments and empower cost reductions in the operation and design of mineral processing plants (Ghorbani *et al*, 2021a, 2022). In addition, knowledge-driven data gathering can be used for both scientific and data-driven purposes, as their generation methodology can explicitly account for the needs of scientific hypothesis testing. This is even more important for academic and regulatory purposes.

People and culture

Data literate and motivated talents are the key to dry labs (Asamoah *et al*, 2020). Dry labs may recruit trans-disciplinary experts (computational scientists, data scientists and engineers, and analysts, Figure 4), in addition to subject matter experts (eg geoscientists, mineral industry engineers and technicians). The technical requirements for management may be high and multidisciplinary (Humphreys, 2015). Staff and client interoperability depends on information exchange (Figure 4). Services of the dry lab must minimally adhere to some standards around data and information, for which, education and training is necessary. For this purpose, the dry lab plays both enabling and benefactor roles.

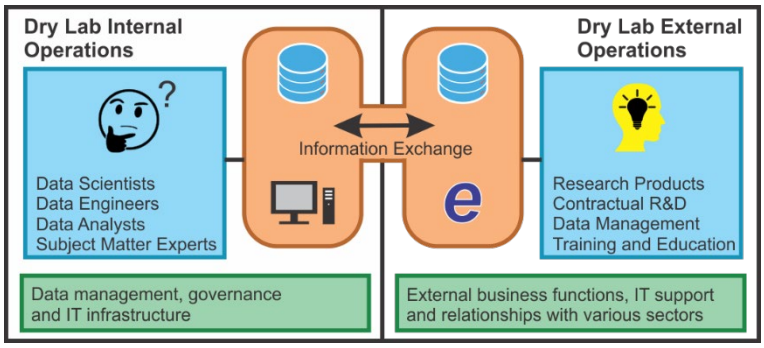

FIG 4 – Internal and external dry lab operations and their interactions.

Data-driven geoscience and mineral engineering education and open data

Geoscientific data is expensive (eg compared with commerce) (Dramsch, 2020), and often sparsely sampled, because it is primarily limited by resources and opportunity. As such, data-driven techniques are infrequently used but increasing in popularity (Qudrat-Ullah and Panthallor, 2021). This can result in a shortage of trans-disciplinary experts who are also geoscience literate, which must be addressed for effective recruitment for dry labs (Asamoah *et al*, 2020). Dry labs can build substantial capacity, for instance, by contributing open data (which also promotes reproducibility and replicability), cross-training and educating data-specialists or geoscientists. This also helps to mitigate undesirable effects of only using private data in the industry. Open geoscientific data already exists, such as Geoscan hosted by Natural Resources Canada (a Canadian governmental department) and some academic journals are focused on data sharing and reuse (eg Tedersoo *et al*, 2021). Open data portals present a useful model for breaking through siloed data with an additional effect of promoting data volunteers and citizen data scientists. Dry labs can also lower the cost of data in geosciences (Dramsch, 2020) through the development of cheaper sensors, methods and more capable algorithms. An excellent example is the proliferation of wide-spectrum sensors, which has made remote sensing the cheapest form of reconnaissance (Ghorbani *et al*, 2021a, 2021b, 2022). Similarly, dry labs can evolve, reinvent and repurpose instrumentation and processes toward cost reduction and automation.

Simulation-based training and learning

In the last decades, virtual reality (VR) and augmented reality (AR) evolved (Amin *et al*, 2013; Ritter *et al*, 2018) and became available to consumers (Cipresso *et al*, 2018). Their modern origin can be traced to Ivan Sutherland, who proposed a system that mimics observable reality (Sutherland, 1965). Such systems employ interactive perceptual engagement similar to that in video games, by providing a depiction of an environment and bidirectional interactivity, which occurs over human-machine interfaces (Biocca, 1997; Lombard and Ditton, 1997; Loomis *et al*, 1999; Biocca *et al*, 2001; Bailenson *et al*, 2006; Skalski and Tamborini, 2007; Andersen and Thorpe, 2009; Slater, 2009; Sundar *et al*, 2010; Amin *et al*, 2013; Ritter *et al*, 2018). AR is a form of VR in the sense that augmentation of perception is layered on physical reality (Cipresso *et al*, 2018). Their ability to replicate physical detail and stimuli has enabled flight, military and surgical training, architectural design, maintenance, entertainment and education (Cipresso *et al*, 2018 and references therein). However, the cost of dedicated systems is exorbitantly high, which is not the case with consumer systems (Aslam *et al*, 2019) that are still well-suited to training and learning (Castelvecchi, 2016).

The benefits of VR – and AR-based training include reduction of energy consumption, improved mineral recovery and improved process efficiency (McCoy and Auret, 2019).

It is possible to also use such systems to navigate reality, such as underground mines and mineral processing plants. In this usage, VR seamlessly transition into virtual presence devices, both of which are probably key for the rise of human-supervised or -audited automation in the mineral industry (Phacharoen and Akatimagool, 2020). Since these systems require considerable environmental data and research and development power, most of which centre around creating a representation of the environment being simulated, dry labs are excellent hosts.

Unlike older plants, some modern ones produce machine-readable data (Chen *et al*, 2017). Application of digital twins in the mineral industry have seen significant advances in recent years. Essentially, a digital twin is a digital carbon replica of plant processes, where variables can be changed to determine their upstream and downstream impacts (Sierla *et al*, 2021) while isolating the risks. Where used in this manner, digital twins have already been demonstrated to be effective in system optimisation (Rasheed *et al*, 2020). Examples of digital twins include (Leonida, 2018): (a) Andritz IDEAS Digital Twin, which is a widely accepted simulation tool for minerals processing operations in steady state; (b) Petra Datascience MAXTA, which uses the mill as the best laboratory from the mine plan to the plant to track materials, and perform block-by-block classification of behaviour characteristics, which allows operators to gain insight into the plant's performance; (c) GE Digital Mine, which allows operators access to a comprehensive system for analysing data and making informed decisions; and (d) Metallurgical Systems by Met Systems, which uses tags within the local historian to monitor processing in real time and model the process response. There are several documented deployments of digital twins (Goodall, 2020), such as: (a) the Ban Houayxai gold mine, where Petra Datascience integrated mine planning with mineral processing; and (b) using virtual instrumentation to increase efficiency at OceanaGold Haile, which was published by Andritz. These practices fit perfectly within dry labs. For example, 3D plant models and simulations can be produced in a dry lab by leveraging digital twin capabilities (Erdos *et al*, 2015; Sierla *et al*, 2021). This can be achieved using a point cloud obtained by LiDAR scanning. To identify certain component types (eg tank or pump), component attributes (eg tank width, height, and location of nozzles), 3D locations, and connections between components, the point cloud can be segmented and classified using segmentation and machine learning (eg pipes, cables or wires) to facilitate digital twinning (Allegra *et al* 2006; Sierla *et al*, 2021). Dry labs can also provide leadership in the design of a digital architecture for the mineral industry, select appropriate technologies, and integrate them in a controlled environment.

Gamification in training

Gamification is a process where game-like elements are added to tasks (Walz, 2015), which can be a way to improve technology engagement (Rai and Beck, 2017; Feeney, 2017) by leveraging human psychological needs, for example, to socialise, learn, compete achieve and seek closure (Kapp, 2012; Lieberoth, 2015). Where used ethically, gamification can build motivation and facilitate digital transformation. This approach is also what makes AR systems useful, as a mechanism to provide feedback and correction, as well as rewards. Live feedback is also beneficial for learning and engagement since studies show that receivers of feedback tend to be more successful and satisfied (eg Di Serio *et al*, 2013; Wilson *et al*, 2020; Bergamo *et al*, 2022). Dry labs can offer gamification as a service, such as designing effective training programs with skill progression and mastery. This could be especially useful in communicating abstract or difficult concepts like mineral deposit development or recognition of hazards (Eiter *et al*, 2018).

Data governance and management

The purpose of a dry lab should guide the design of ICT, governance and management systems (Treder, 2020) to ensure that these are fit-for-purpose. This ensures that data and ICT are appropriately handled through formalised roles, responsibilities, policies and guidelines, which creates laboratory standards around data and practices (DAMA International, 2017 and eg Fleckenstein and Fellows, 2018). A minimum level of ICT infrastructure would likely include: networks; data storage systems; data catalogues, profiling and quality inspection tools; and access provisioning. Useful starting principles could be the FAIR principle (Wilkinson *et al*, 2016), which states that data should be findable, accessible, interoperable and reusable. The existence and size

of a governance structure depend on the size of the dry lab and whether it is embedded inside another structure, such as an institution. Where greater governance is absent, dry labs may establish a governance structure (Kuiler, 2019). The management of data in a laboratory setting roughly breaks down into two key lines: management of systems and infrastructure and of data assets such as data repositories and streams (Mahanti, 2021). Lab management may require two different skillsets that may be mapped to laboratory technicians, engineers, and system – and/or data-analysts and data scientists.

Operational and financial models

To ensure sustainability of dry labs, a key component is a viable operational and financial model. The operational model refers to both the internal operations and the service model. Internal operations of a laboratory include the organisational structure and laboratory strategic design. The service model includes the interaction between the internal operations and clients (van der Aalst *et al*, 2021). For dry labs, some of the structure of wet labs can be incorporated with data-centric adaptations. A suitable financial model is impossible to establish at the moment, as the data-centric market within geoscience and metallurgy is in its infancy. In smaller labs, computers may be cheaper than analytical instruments and typically require less upkeep (Pourbafrani *et al*, 2020). We offer two scenarios. In one, if dry lab running costs including staff salaries are substantially higher than those of wet labs, then outputs of dry labs must be correspondingly more expensive. Taken to the extreme, if costs are too high to perform non-profit research, then dependence on the existence of a parent institution is unavoidable or dry labs would be restricted to performing high profit research. This seems to be the case for most data analytics companies (Reisert *et al*, 2018). In the reverse scenario, the costs are sufficiently low to permit dry labs to produce non-profit or low-profit products, such as academic papers, patents and prototypes.

SUMMARY AND OUTLOOK

The amount of data and the desire to use digital systems such as VR and AR warrant further examinations into a cohesive workspace that facilitates data-centric innovation and experimentation. The establishment of such workspaces, which we refer to as dry labs, would enable a sandboxed environment (buffered between private and public interests and specifically encouraged to undertake risks that would be unacceptable in private industries or impractical in academia) that maximises the use of data-centric techniques (Figure 5). Dry labs in our conception would serve as hubs that link together businesses, institutions and other laboratories (eg wet labs) and would primarily conduct data analytics, predictive modelling, simulations, sensor and algorithm design, method development, and education. With the increasing data-innovation gap, we imagine that dry labs will become inevitable within the mineral industry, following the footstep of wet labs.

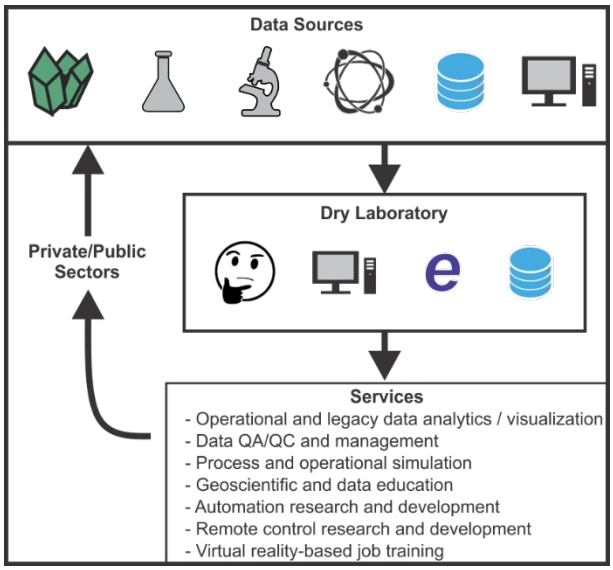

FIG 5 – Functional depiction of a dry lab, including its potential client services.

ACKNOWLEDGEMENTS

This project was funded by the Centre for Advanced Mining and Metallurgy (CAMM), a strategic research environment established at Luleå University of Technology, which is in turn funded by the Swedish government.

REFERENCES

Aasly, K and Ellefmo, S, 2014. Geometallurgy applied to industrial minerals operations, *Mineralproduksjon*, 5: A21–A34.

Allegra, D, Gallo, G, Inzerillo, L, Lombardo, M, Milotta, F L M, Santagati, C and Stanco, F, 2006. Low-cost handheld 3D scanning for architectural elements acquisition, in *Proceeding of the STAG: Smart Tools and Apps in Computer Graphics*, pp 127–131.

Allen, D K, Karanasios, S and Norman, A, 2013. Information sharing and interoperability: the case of major incident management. *Eur J Inf Sys*, 23:418–432.

Amin, H J, Aziz, K, Halamek, L P and Veran, T N, 2013. Simulation-based learning combined with debriefing: trainers satisfaction with a new approach to training the trainers to teach neonatal resuscitation. *BMC Res Notes*, 6:251.

Andersen, S M and Thorpe, J S, 2009. An if–thEN theory of personality: significant others and the relational self, *J Res Pers*, 43:163–170.

Anderson, C, Dunne, R and Uhrie, J, 2014. *Mineral processing and extractive metallurgy: 100 years of innovation*, 696 p (Society for Mining Metallurgy and Exploration (SME): Englewood).

Armbrust, M, Das, T, Sun, L, Yavuz, B, Zhu, S, Murthy, M, Torres, J, van Hovell, H, Ionescu, A, Łuszczak, A, Świtakowski, M, Szafrański, M, Li, X, Ueshin, T, Mokhtar, M, Boncz, P, Ghodsi, A, Paranjpye, S, Senster, P, Xin, R and Zaharia, M, 2020. Delta lake: high-performance ACID table storage over cloud object stores, in *Proceedings of the VLDB Endowment*, 13, pp 3411–3424.

Asamoah, D A, Doran, D and Schiller, S, 2020. Interdisciplinarity in Data Science Pedagogy: A Foundational Design, *J Comput Inf Sys*, 60:370–377.

Aslam, S, Ahsan, M, Hannan, S, Hamza, M, Jaffery, M, 2019. Development of a software based PIC24F series microcontroller educational trainer, in *International Conference on Engineering and Emerging Technologies (ICEET)* (Pakistan).

Atomic Heritage Foundation, 2017. The human computers of Los Alamos [online], *National Museum of Nuclear Science & History*. Available from: <https://www.atomicheritage.org/history/human-computers-los-alamos> [Accessed: 4 August 2021].

Bailenson, J N, Yee, N, Merget, D and Schroeder, R, 2006. The effect of behavioural realism and form realism of real-time avatar faces on verbal disclosure, nonverbal disclosure, emotion recognition, and copresence in dyadic interaction, *Presence*, 15:359–372.

Bascur, O A, 2020. *Digital Transformation for the Process Industries: A Roadmap*, 320 p (CRC Press).

Bergamo, P A D S, Streng, E S, Carvalho, M A D, Rosenkranz, J and Ghorbani, Y, 2022. Simulation-based training and learning: A review on technology-enhanced education for the minerals industry, *Miner Eng*.

Bertholf, R L, 2017. Laboratory Structure and Function, in *Clinical Core Laboratory Testing* (eds: R Molinaro, C McCudden, M Bonhomme, A Saenger), pp. 1–23 (Springer: Boston).

Biocca, F, 1997. The cyborg's dilemma: progressive embodiment in virtual environments, *J Comput Mediat Commun* 3:JCMC324.

Biocca, F, Harms, C and Gregg, J, 2001. The networked minds measure of social presence: pilot test of the factor structure and concurrent validity, in *4th Annual International Workshop on Presence*, pp. 1–9. (Philadelphia).

Bousdekis, A and Mentzas, G, 2021. Enterprise Integration and Interoperability for Big Data-Driven Processes in the Frame of Industry 4.0, *Front Big Data*, 4:644651.

Callaway, E, 2020. 'It will change everything': DeepMind's AI makes gigantic leap in solving protein structures, *Nature*, 588:203–204.

Castelvecchi, D, 2016. Low-cost headsets boost virtual reality's lab appeal, *Nature*, 533:153–154.

Chakraborti, S, 2021. Application of big data, solution to mining analytics [online]. Available from: <https://www.wipro.com/natural-resources/application-of-big-data-solution-to-mining-analytics/> [Accessed: 21 December 2021].

Chen, B, Wan, J, Shu, L, Li, P, Mukherjee, M and Yin, B, 2017. Smart factory of Industry 4.0: key technologies, application case, and challenges, *IEEE Access*, 6:6505–6519.

Cipresso, P, Chicchi Giglioli, I-A, Raya, M A and Riva, G, 2018. The past, present, and future of virtual and augmented reality research: A network and cluster analysis of the literature, *Front Psychol*, 9:2086.

DAMA International, 2017. *DAMA-DMBOK: Data Management Body of Knowledge*, 590 p, second ed. (Technics Publications, Basking Ridge: New Jersey).

Di Serio, Á, Ibáñez, M B and Kloos, C D, 2013. Impact of an augmented reality system on students' motivation for a visual art course, *Comput Educ*, 68:586–596.

Ding, J, Yang, C and Chai, T, 2017. Recent progress on data-based optimisation for mineral processing plants, *Eng*, 3:183–187.

Dominy, S, O'Connor, L, Parbhakar-Fox, A, Glass, H and Purevgerel, S, 2018. Geometallurgy – A route to more resilient mine operations, *Min*, 8:560.

Dramsch, J S, 2020. 70 years of machine learning in geoscience in review, in *Advances in Geophysics* (eds: B Moseley, L Krischer), volume 61, pp 1–55 (Elsevier).

Eiter, B M, Bellanca, J L, Helfrich, W., Orr, T J, Hrica, J, Macdonald, B and Navoyski, J, 2018. Recognizing mine site hazards: Identifying differences in hazard recognition ability for experienced and new mineworkers, in *Advances in Human Factors in Simulation and Modeling: Advances in Intelligent Systems and Computing* (ed: D. Cassenti), volume 591 (Springer).

Erdos, G, Nakano, T, Horváth, G, Nonaka, Y and Váncza, J, 2015. Recognition of complex engineering objects from large-scale point clouds, *CIRP Ann Manuf Technol*, 64(1):165–168.

ESRI, 2020. ESRI support for open geospatial platforms. ESRI White paper. ESRI, California, pp 37.

Feeney, R, 2017. Old tricks are the best tricks: Repurposing programmed instruction in the mobile digital age, *Perform Improv Q*, 56:6–17.

Fleckenstein, M and Fellows L, 2018. Data Governance, in *Modern Data Strategy* (Springer).

Gaylard, P G, Morrison, R D, Randolph, N G, Wortley, C M G and Beck, R D, 2009. Extending the application of the AMIRA P754 code of practice for metal accounting, in *Proceedings of the 5th Base Metals Conference, Kasane, Botswana* (Southern African Institute of Mining and Metallurgy: Johannesburg).

Ghorbani, Y, Nwaila, G T and Chrisa, M, 2020a. Systematic framework toward a highly reliable approach in metal accounting, *Miner Process Extr Metall Rev*, 1–15.

Ghorbani, Y, Nwaila, G T, Zhang, S E and Hay, M P, 2021a. Repurposing legacy metallurgical data part II: Case studies of plant performance optimisation and process simulation, *Min Eng*, 160:106667.

Ghorbani, Y, Nwaila, G T, Zhang, S E and Rosenkranz, J, 2021b. Rethinking mineral processing and extractive metallurgy approaches to ensure a sustainable supply of high-tech and critical raw materials, in: *Rare Metal Technology 2021: The Minerals, Metals & Materials Series* (eds: G Azimi, T Ouchi, K Forsberg, H Kim, S Alam, A A Baba, N R Neelameggham) (Springer).

Ghorbani, Y, Nwaila, G T, Zhang, S E, Hay, M P, Bam, L C and Guntoro, P-I, 2020b. Repurposing legacy metallurgical data Part I: A move toward dry labs and data bank, *Min Eng*, 159:106646.

Ghorbani, Y, Zhang, S E, Nwaila, G T and Bourdeau, J E, 2022. Framework components for data-centric dry laboratories in the mineral industry: A path to science-and-technology-led innovation, *Extr Ind Soc*, 101089.

Gupta, R, Srivastava, P, Sharma, S and Alrasheedi, M, 2021. Leveraging big data to accelerate supply chain management in Covid-19, in *The big data-driven digital economy: artificial and computational intelligence: Studies in Computational Intelligence* (ed: A M A Musleh Al-Sartawi), Volume 974 (Springer).

Hinojosa-Palafox, E A, Rodríguez-Elías, O M, Hoyo-Montaño, J A, Pacheco-Ramírez, J H and Nieto-Jalil, J M, 2021. An analytics environment architecture for industrial cyber-physical systems Big Data solutions, *Sensors*, 21(13):4282.

Hosseini, M and Dixon, B E, 2016. Syntactic interoperability and the role of standards, in *Health Information Exchange* (ed: B E Dixon). (Academic Press).

Humphreys, D, 2015. An industry transformed, in *The remaking of the mining industry* (Palgrave Macmillan: London).

Indri, M, Grau, A and Ruderman, M, 2018. Guest editorial special section on recent trends and developments in industry 4.0 motivated robotic solutions, *IEEE Trans Industr Inform*, 14:1677–1680.

Jahedsaravani, A, Marhaban, M H and Massinaei, M, 2014. Prediction of the metallurgical performances of a batch flotation system by image analysis and neural networks, *Miner Eng*, 69:137–145.

Jahedsaravani, A, Marhaban, M H, Massinaei, M, Saripan, M I and Noor, S B M, 2016. Froth-based modeling and control of a batch flotation process, *Int J Miner Process*, 146:90–96.

Jämsä-Jounela, S-L, 2019. Future automation systems in context of process systems and minerals engineering, *IFAC-PapersOnLine*, 52:403–408.

Kapp, K M, 2012. *The gamification of learning and instruction: Game-based methods and strategies for training and education* (Pfeiffer: San Francisco).

Kleinhans, M G, Buskes, C J J and de Regt, H W, 2005. Terra Incognita: Explanation and reduction in Earth Science, *Int Stud Philos Sci*, 19(3):289–317.

Kuiler, E W, 2019. Data Governance, in *Encyclopedia of Big Data* (eds: L. Schintler, C. McNeely) (Springer).

Leonida, C, 2018. The Intelligent guide to: digital twins in mining [online]. *Intelligent Miner*. Available from: <https://theintelligentminer.com/2018/12/29/digital-twins-in-mining/> [Accessed: 14 December 2021].

Lieberoth, A, 2015. Shallow gamification, testing psychological effects of framing an activity as a game, *Games Cult*, 10:229–248.

Lishchuk, V, Koch, P-H, Ghorbani, Y and Butcher, A R, 2020. Towards integrated geometallurgical approach: Critical review of current practices and future trends, *Miner Eng*, 145:106072.

Lombard, M and Ditton, T, 1997. At the heart of it all: the concept of presence, *J Comput Mediat Commun*, 3.

Loomis, J M, Blascovich, J J and Beall, A C, 1999. Immersive virtual environment technology as a basic research tool in psychology, *Behav Res Methods Instr Comput*, 31:557–564.

Lund, C and Lamberg, P, 2014. Geometallurgy–A tool for better resource efficiency, *Eur Geol Mag*, 37:39–43.

Lund, C, Lamberg, P and Lindberg, T, 2015. Development of a geometallurgical framework to quantify mineral textures for process prediction, *Miner Eng*, 82:61–77.

Mahanti, R, 2021. Corporate governance subdisciplines, data, and data governance, in *Data Governance and Compliance* (Springer).

Makokha, A B and Moys, M H, 2012. Multivariate approach to on-line prediction of in-mill slurry density and ball load volume based on direct ball and slurry sensor data, *Miner Eng*, 26:13–23.

Manalu, E P S, Muditomo, A, Adriana, D, Trisnowati, Y, Kesuma, Z P and Dwiyani, R H, 2020. Role of information technology for successful responses to Covid-19 pandemic, in *International Conference on Information Management and Technology (ICIMTech)*, pp 415–420.

Manzi, M, Cooper, G, Malehmir, A, Durrheim, R and Nkosi, Z, 2015. Integrated interpretation of 3D seismic data to enhance the detection of the gold-bearing reef: Mponeng Gold mine, Witwatersrand Basin (South Africa), *Geophys Prospect*, 63:881–902.

Massinaei, M and Doostmohammadi, R, 2010. Modeling of bubble surface area flux in an industrial rougher column using artificial neural network and statistical techniques, *Miner Eng*, 23:83–90.

McCoy, J T and Auret, L, 2019. Machine learning applications in minerals processing: A review, *Min Eng*, 132:95–109.

Mkhabela, M and Manzi, M S D, 2017. Detection of potential methane gas pathways in deep South African gold mines, *J Geophys Eng*, 14:960–974.

Nwaila, G T, Ghorbani, Y, Becker, M, Frimmel, H E, Petersen, J and Zhang, S, 2020. Geometallurgical approach for implications of ore blending on cyanide leaching and adsorption behaviour of Witwatersrand gold ores, South Africa, *Nat Resour Res*, 29:1007–1030.

Nwaila, G T, Zhang, S E, Tolmay, L C K and Frimmel, H E, 2021. Algorithmic optimization of an underground Witwatersrand-Type gold mine plan, *Nat Resour Res*, 30:1175–1197.

Pan, I, Mason, L R and Matar, O K, 2022. Data-centric Engineering: integrating simulation, machine learning and statistics. Challenges and opportunities, *Chem Eng Sci*, 249:117271.

Phacharoen, E and Akatimagool, S, 2020. Improvement of in-company trainers' competencies using simulation-based training for EEC electronics industries, in *The Impact of the 4th Industrial Revolution on Engineering Education* (eds: M Auer, H Hortsch, P Sethakul) (ICL 2019 Advances in Intelligent Systems and Computing: Springer).

Philander, C and Rozendaal, A, 2014. A process mineralogy approach to geometallurgical model refinement for the Namakwa Sands heavy minerals operations, west coast of South Africa, *Miner Eng*, 65:9–16.

Pourbafrani, M, van Zelst, S J and van der Aalst, W M P, 2020. Supporting decisions in production line processes by combining process mining and system dynamics, in *IHSI 2020* (eds: T Ahram, W Karwowski, A Vergnano, F Leali, R Taiar) AISC, volume 1131, pp 461–467 (Springer).

Qi, C-C, 2020. Big data management in the mining industry, *Int J Miner Metall Mater*, 27:131–139.

Qudrat-Ullah, H and Panthallor, P N, 2021. Integrated and advanced information systems in LSOPM operations, in *Operational Sustainability in the Mining Industry. Asset Analytics (Performance and Safety Management)* (Springer: Singapore).

Quintanilla, P J, Neethling, S J and Brito-Parada, P R, 2021. Modelling for froth flotation control: A review, *Min Eng*, 162:106718.

Rai, V and Beck, L B, 2017. Play and learn: Serious games in breaking informational barriers in residential solar energy adoption in the United States, *Energy Res Soc Sci*, 27:70–77.

Rasheed, A, San, O and Kvamsdal, T, 2020. Digital twin: values, challenges and enablers from a modeling perspective, *IEEE Access*, 8:21980–22012.

Reisert, C, Zelt S and Wacker J, 2018. How to move from paper to impact in business process management: The journey of SAP, in *Business Process Management Cases. Management for Professionals* (eds: J vom Brocke, J Mendling) (Springer).

Ritter, E M, Taylor, Z A, Wolf, K R, Franklin, B R, Placek, S B, Korndorffer Jr J R and Gardner, A K, 2018. Simulation-based mastery learning for endoscopy using the endoscopy training system: a strategy to improve endoscopic skills and prepare for the fundamentals of endoscopic surgery (FES) manual skills exam, *Surg Endosc*, 32:413–420.

Russell, M A, 2014. Mining the social web, 2nd edition, 448 p (O'Reilly Media).

Samuel, A L, 1959. Some studies in machine learning using the game of checkers. *IBM J Res Dev*, 3:210–229.

Sánchez, F and Hartlieb, P, 2020. Innovation in the mining industry: Technological trends and a case study of the challenges of disruptive innovation, *Min Metall Explor*, 37:1385–1399.

Sehoole, L, Manzi, M S D, Zhang, S E and Bourdeau, J E, 2020. An innovative seismic and statistical approach to understand 3D magmatic structures and ore deposits in the western Bushveld Complex, South Africa, *Ore Geol Rev*, 103784.

Sether, A, 2016. Cloud Computing Benefits [online]. Available from: <https://ssrn.com/abstract=2781593> [Accessed: 27 October, 2021].

Sierla, S, Azangoo, M, Rainio, K, Papakonstantinou, N, Fay, A, Honkamaa, P and Vyatkin, V, 2021. Roadmap to semi-automatic generation of digital twins for brownfield process plants, *J Ind Inf Integr*, 100282.

Skalski, P and Tamborini, R, 2007. The role of social presence in interactive agent-based persuasion, *Media Psychol*, 10:385–413.

Slater, M, 2009. Place illusion and plausibility can lead to realistic behaviour in immersive virtual environments, *Philos Trans R Soc Lond (B) Biol Sci*, 364:3549–3557.

Soofastaei, A, 2021. *Data analytics applied to the mining industry* (CRC Press).

Sulankivi, K, 2004. Benefits of centralized digital information management in multipartner projects. *ICT con*, 9:35–63.

Sundar, S S, Xu, Q and Bellur, S, 2010. Designing interactivity in media interfaces: a communications perspective, in *Proceedings of the SIGCHI Conference on Human Factors in Computing Systems*, pp 2247–2256 (Boston).

Sutherland, I E, 1965. The ultimate display, in *Multimedia: from Wagner to virtual reality* (eds: R. Packer, K. Jordan) (New York).

Tedersoo, L, Küngas, R, Oras, E, Köster, K, Eenmaa, H, Leijen, A, Pedaste, M, Raju, M, Astapova, A, Lukner, H, Kogermann, K and Sepp, T, 2021. Data sharing practices and data availability upon request differ across scientific disciplines, *Sci Data*, 8:1–11.

Treder, M, 2020. Data Governance, in *The Chief Data Officer management handbook* (Apress: California).

Vale, 2018. Digital Lab: understanding the new technologies coming to Vale [online]. *Vale*. Available from: <http://www.vale.com/brasil/EN/aboutvale/news/Pages/novas-tecnologias-chegando-a-vale.aspx> [Accessed: 12 December 2021].

van der Aalst, W M P, Brockhoff T, Ghahfarokhi A F, Pourbafrani M, Uysal M S and van Zelst S J, 2021. Removing operational friction using process mining: Challenges provided by the internet of production (IoP), in *Data Management Technologies and Applications* (eds: S Hammoudi, C Quix, J Bernardino), DATA 2020. Communications in Computer and Information Science, volume 1446. (Springer).

Vercruysse, K, Dawson, D A and Wright, N, 2019. Interoperability: A conceptual framework to bridge the gap between multifunctional and multisystem urban flood management, *J Flood Risk Manag*, 12:e12535.

Walz, S, 2015. The gameful world: Approaches, issues, applications, 31 p. (MICT Press).

Wellstead, A M and Nguyen, S, 2020. The Rise of Policy Innovation Labs: A Catalog of Policy Innovation in the United States. Available from: <http://dx.doi.org/10.2139/ssrn.3513548> [Accessed 14 September, 2021].

Wilkinson, M D, Dumontier, M, Aalbersberg, I J, Appleton, G, Axton, M, Baak, A, Blomberg, N, Boiten, J W, da Silva Santos, L B, Bourne, P E, Bouwman, J, Brookes, A J, Clark, T, Crosas, M, Dillo, I, Dumon, O, Edmunds, S, Evelo, C T, Finkers, R, Gonzalez-Beltran, A and Mons, B, 2016. The FAIR Guiding Principles for scientific data management and stewardship, *Sci Data*, 3:160018.

Wilson, L P, Brown L D, Reed R and Burgess J L, 2020. Gamification of hazards recognition in mining with a tabletop card game, in *Advances in Simulation and Digital Human Modeling* (eds: D Cassenti, S Scataglini, S Rajulu, J Wright), AHFE 2020. Advances in Intelligent Systems and Computing, volume 1206 (Springer).

Yan, J, Meng, Y, Lu, L, Li, L, 2017. Industrial Big Data in an Industry 4.0 Environment: Challenges, Schemes, and Applications for Predictive Maintenance, *IEEE Access*, 5:23484–23491.

Zhang, S E, Nwaila, G T, Tolmay, L, Frimmel, H E, Bourdeau, J E, 2021. Integration of machine learning algorithms with Gompertz Curves and Kriging to estimate resources in gold deposits, *Nat Resour Res*, 30(1):39–56.

Quantitative assessment of separation quality, using neural networks and multivariate stochastic modelling

T Kirstein[1], O Furat[2], T Leißner[3], K Bachmann[4], U A Peuker[5] and V Schmidt[6]

1. PhD Student, Ulm University, Ulm Baden-Württemberg 89081. Email: tom.kirstein@uni-ulm.de
2. PhD Student, Ulm University, Ulm Baden-Württemberg 89081. Email: orkun.furat@uni-ulm.de
3. Senior Scientist, TU Bergakademie Freiberg, Freiberg Saxony 09599. Email: Thomas.Leissner@mvtat.tu-freiberg.de
4. Senior Scientist, Helmholtz-Zentrum Dresden-Rossendorf, Dresden Saxony 01328. Email: k.bachmann@hzdr.de
5. Professor, TU Bergakademie Freiberg, Freiberg Saxony 09599. Email: urs.peuker@mvtat.tu-freiberg.de
6. Professor, Ulm University, Ulm Baden-Württemberg 89081. Email: volker.schmidt@uni-ulm.de

INTRODUCTION

Separation processes are an essential step in many process engineering applications in the field of particle technology. For example, in order to enrich minerals in a targeted manner, ores are typically crushed, classified, and sorted such that high-grades are achieved with a high recovery at the same time. To describe and optimise the processes, the influence of particle properties on the process result has to be investigated. In this study, magnetic separation processes are considered which are, for example, used to separate various mineral components of interest from crushed ores. During such separation processes, the more a particle is magnetized by a magnetic field, the greater is its likelihood of being discharged into the magnetic product. However, the particles resulting from a preceding crushing process are often compounds of multiple minerals, ie they are composite particles. Each mineral component within such a composite particle contributes according to its volume fraction and its material-specific magnetizability to the magnetizability of the particle and thus to its separation behaviour, see Leißner *et al* (2016). In addition to the magnetization properties of particles, the separation success depends on further particle properties, such as the size and shape of particles, which can be characterized by a large number of descriptors, see Bagheri *et al* (2015). The general goal of the present study is to develop a method that takes such influencing factors into account in order to reliably and comprehensively quantify the separation success. For describing separation processes as completely as possible, the influencing particle properties must first be quantified. However, especially with regard to particle morphology, this is only feasible to a limited extent when using methods of two-dimensional (2D) microscopic imaging and the stereological approach, see Chiu *et al* (2013). Thus, a three-dimensional (3D) description of particles is required which provides both the 3D particle morphology and texture as well as the mineralogical particle composition. For example, this is possible by using a combination of computed tomography (CT) and 2D scanning electron microscopy/energy dispersive spectroscopy (SEM-EDS), see Reyes *et al* (2017).

In the present work, such 2D and 3D image data is leveraged to design a fully parametric stochastic model to determine joint probability distributions of particle size/shape/textural/compositional descriptors–allowing for the estimation and interpretable characterization of high-dimensional interdependencies of particle descriptors. By comparing such stochastic characterizations of feed and concentrate material, insight into particle separation behaviour is gained. An overview of the workflow is given in Figure 1. The usability of the method is exemplarily demonstrated in the extraction of zinnwaldite-rich particles from a feed material that consists of four main silicate components. Note that, while the considered particle system is composed of particles with volume equivalent diameters of 40–200 µm, the presented methodology can be analogously applied to other size ranges, assuming the provided CT image data is sufficiently well resolved with an adequate field of view.

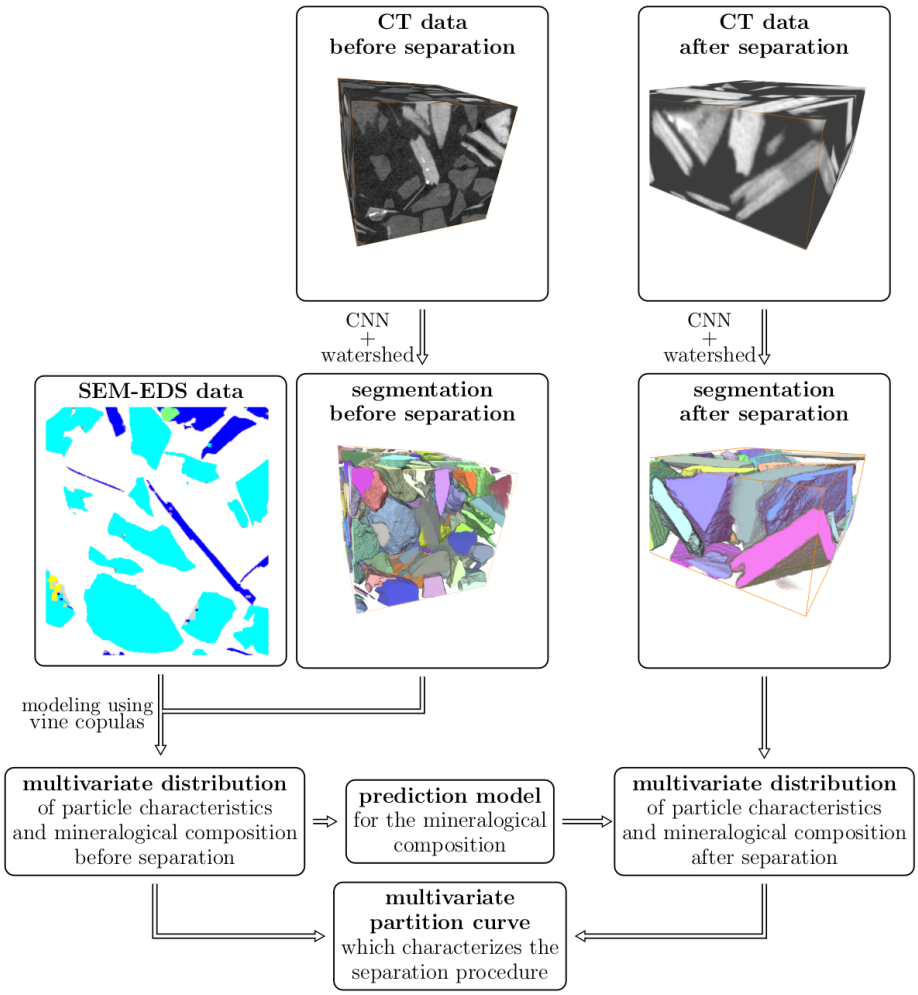

FIG 1 – Schematic illustration of the presented workflow for quantitative assessment of separation quality if SEM-EDS data is not available for the concentrate material.

SEGMENTATION OF CT IMAGE DATA

In order to describe the particle system before and after separation using multivariate probability distributions of their size, shape, and textural descriptors, individual particles must first be identified in CT image data of feed and concentrate materials, respectively. Therefore, an image segmentation procedure is used that partitions CT image data into a background region and regions which correspond to individual particles. A modified version of the convolutional neural network described in Çiçek *et al* (2016) is chosen to achieve a 3D segmentation of the image data while requiring a small amount of hand labelling for training purposes. In this case study, three annotated slices were sufficient for network training. In the resulting segmentation maps, particles are separated from each other, however, particle shapes and sizes may still be inaccurate. Therefore, a marker-based watershed algorithm is used subsequently, where the regions identified by the neural network are utilised as initial regions (ie markers) for the region growth performed by the watershed algorithm, see Furat *et al* (2022) for a detailed description of the image segmentation procedure.

MULTIVARIATE STOCHASTIC MODELLING OF PARTICLE DESCRIPTORS

Particle descriptors characterizing the size, shape, and texture of particles can be computed from the particle-wise segmented CT image data. Additionally, the mineralogical composition of particles and the modelling thereof are of great interest. In order to obtain such information, which is not provided by the CT data, correlated phase-wise segmented SEM-EDS slices are utilised. In total, seven particle descriptors, including the zinnwaldite volume fraction, are considered, allowing for a detailed characterization of particles. Since the separation behaviour is influenced by a multitude of particle descriptors, their interdependencies must be considered. This is done by estimating the joint seven-variate probability distribution, however, estimating such a joint probability distribution is a

challenging task. Non-parametric estimation methods, such as kernel density estimators, are prone to overfitting in high-dimensional applications. In this case study, multivariate probability distributions of particle descriptors are determined using parametric vine copulas, see Joe (2014) for more details. Besides the efficient characterization of the considered particle system, the resulting multivariate probability distribution can be used as a prediction model for the mineralogical composition, as depicted in Figure 2. More precisely, by considering conditional probability distributions a particle's zinnwaldite volume fraction can be estimated from its size, shape, and textural descriptors (which are determined from the CT image data), allowing for the mineralogical characterization of particles that do not intersect with a SEM-EDS slice. The feasibility of this approach is demonstrated in Furat *et al* (2022). By fitting multivariate probability distributions to the data of particle descriptors in the feed and concentrate materials, the so-called Tromp function, which describes the likelihood that a particle in the feed ends up in the concentrate, can be computed to evaluate the separation process, see Schach *et al* (2019). In particular, this allows for the quantitative assessment of separation quality in relation to particle size and shape properties, and additionally, the separation outcome can be predicted for different feed materials prior to the application of the separation process.

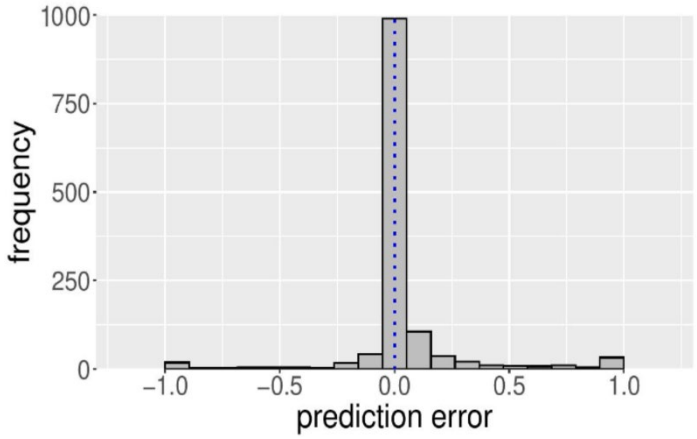

FIG 2 – Histogram of the prediction error when estimating the zinnwaldite volume fraction using vine copulas.

REFERENCES

Bagheri, G H, Bonadonna, C, Manzella, I, and Vonlanthen, P, 2015. On the characterization of size and shape of irregular particles, in *Powder Technology*, 270:141–153.

Chiu, S, Stoyan, D, Kendall, W S, and Mecke, J, 2013. *Stochastic Geometry and Its Applications* (J. Wiley and Sons).

Çiçek, Ö, Abdulkadir, A, Lienkamp, S S., Brox, T and Ronneberger, O, 2016. 3D U-net: Learning dense volumetric segmentation from sparse annotation, in *Medical Image Computing and Computer-Assisted Intervention*, 424–432.

Furat, O, Kirstein, T, Leißner, K, Bachmann, K, Gutzmer, J, Peuker, U A and Schmidt, V, (2022). Prediction of mineralogical particle composition using CT data and R-vine copulas (submitted).

Joe, H, 2014. *Dependence Modeling with Copulas* (CRC Press).

Leißner, T, Bachmann, K, Gutzmer, J, and Peuker, U A, (2016). MLA-based partition curves for magnetic separation, in *Minerals Engineering*, 94:94–103.

Reyes, F, Lin, Q, Udoudo, O, Dodds, C, Lee, P D and Neethling, S J, 2017. Calibrated X-ray micro-tomography for mineral ore quantification, in *Minerals Engineering*, 110:122–130.

Schach, E, Buchmann, M, Tolosana-Delgade, R, Leißner, T, Kern, M, van den Boogaart, K G, Rudolph, M and Peuker, U. A, 2019. Multidimensional characterization of separation processes–Part 1: Introducing kernel methods and entropy in the context of mineral processing using SEM-based image analysis, in *Minerals Engineering*, 137:78–86.

The effect of head lifter bars on an AG mill discharge system using coupled DEM SPH simulations

V Murariu[1]

1. Principal Scientist, Metso Outotec USA, Inc., York, PA-17402.
   Email: vasile.murariu@mogroup.com

ABSTRACT

The performance of the discharge system of a 32-foot Autogenous Mill is investigated using Metso Minerals Inc. Discrete Element Method (DEM) coupled with Smoothed Particle Hydrodynamics (SPH) code. The simulations were carried out on three different pulp lifter designs including radial, curved and twin chamber. The main goal of the numerical investigation is to quantify the effect of the head lifter bars placed inside the discharge cone on the performance of the discharge system. Two sets of simulations were run on each pulp lifter design with and without head lifter bars. Several key performance parameters were computed and compared including: discharge rates for solids and slurry, hold-up amounts in the pans for solids and slurry and flowing rates of the solids and slurry through the grates in both directions (from inside the mill into the pans and from the pans back into the mill). The head lifter bars proved to have a clear effect on the discharge system performance on all three pulp lifter designs.

INTRODUCTION

Grinding Mills constitute, still, the main equipment in mineral processing for size reduction of the ores. Their performance depends on many factors that includes both design and operational parameters. In many mills, the broken ore inside the mills is removed by a system of discharge grates that allows the smaller rocks to leave the mill. At the same time, very fine particles are carried with the water and discharged easily through the grates. The entire process of breaking of the ore, its movement along the mill from feed end to the discharge end and the transport of the fine ore through the grates is a very complex and very difficult process to model or simulate in its entirety. A model of a full-scale mill should include the breakage of the rocks, the coupling between solids and water and a very large number of particles. Due to its complexity, simplified models have been developed using population balance approaches (Herbst, Lo and Rajamani, 1985; Morrell, 2004) that relies on plant data and experimental tests to estimate breakage characteristics of the ore.

Over the last 20 years new techniques were developed to model the granular flow of solids rocks and their interactions. Such a technique is the Discrete Element Method (DEM) (Campbell, 1997) that is a numerical algorithm that solves the equation of motions of every particle at every time step by computing the forces acting on the particles. Early models of the ball mills (Mishra and Rajamani, 1992, 1994) and (Rajamani and Mishra, 1996) for SAG mills were mainly in 2D and were used to predict the charge motion. 3D models of slices of grinding mills were used to investigate the charge motion (Herbst and Nordell, 2001; Cleary, 2001). Full 3D models of a Hardinge pilot scale SAG mill were developed by Cleary (2004, 2009) and Morrison and Cleary (2008).

These models were using just rocks without the presence of slurry. Slurry has an important role in the transport of the fine solids and influences the breakage and the dynamics of the ore inside the mill. A numerical method that is often used to simulate the slurry flow is the Smoothed Particle Hydrodynamics (SPH) (Monaghan, 1992, 1994, 2005). One-way coupled DEM + SPH model for a SAG mill was introduced by Cleary, Sinnott and Morrison (2006). Fully coupled models off mills were given by Cleary, Hilton and Sinnott (2017).

The discharge system of a grinding mill can be considered as two distinct processes. The first process consists of the presentation of the slurry and ore to the grate, and subsequently the flow-through the grates into the pans. The second process is the discharge of the slurry and solids from the pans. Both processes have great potential in limiting the discharge rate and therefore the mill throughput. Coupled DEM + SPH model of the second process has been reported by Lichter *et al* (2011) and Ciutina and Soriano (2014). DEM model of the flow-through the grate and discharge system of just rocks has been presented by Gutierrez *et al* (2018) and Asakpo, Heath and Chaffer

(2018). These last two papers presented the effect of different pulp lifter designs on the discharge efficiency.

This paper is also analysing the effect of the presence or absence of the inner lifter bars inside the discharge head on the discharge performance of a AG mill, but the simulation is using DEM coupled with SPH method. The simulations of three different pulp lifters designs, namely: radial, curved and twin chamber with and without the head lifter bars are compared in terms of discharge rates, hold-up in the pans and flow rates through grates in both directions. The grates design is kept unchanged between these configurations in order to evaluate only the effect of the head lifter bars on the discharge efficiency.

NUMERICAL MODELS

The simulations of the mill discharge systems described in this paper were carried out using a coupled DEM+SPH in-house software. The two distinct numerical models used are the Discrete Element Method (DEM) and Smoothed Particle Hydrodynamics (SPH).

DEM is a numerical technique in which the motion and the interactions of a large number of solid discrete particles are computing using Newton's laws of motion. This method solves the equations of motion of each particle at every time step by evaluating the sum of the force acting upon the particle. The interactions between particles are modelled as a linear spring-dashpot that allows particles to overlap. The dashpot makes the collision dissipate energy during contact.

The SPH method is well described by Monaghan (1992, 1994) and consists in obtaining an approximate solution of the Navier-Stokes equation of fluid dynamics by replacing the fluid with a set of discrete particles. These particles interact with each other through pressure and viscous forces. Each particle interacts to varying degrees with its neighbours based on the distance between them and a so-called kernel function which depends on the distance between fluid particles.

VALIDATION OF THE MODEL

The model has been validated by running a simulation of a 32-foot diameter AG mill discharge for which audit data was available. The mill had 36 pans and a radial design for the pulp lifters. The grates had an opening of 3.75 in and the total open area of the grates for the whole discharge was 9619 in^2. The rotational speed for the mill was 76 per cent of critical speed or 10.4 rev/min. The simulation has used the discharge system comprised of the grates, pulp lifter, discharge cone, cover and trunnion and 0.5 m slice of the mill attached to the discharge system. The mill slice includes the liners with the proper profile as per the mill design.

The audit data that will be used for the validation of the model is presented in Table 1.

TABLE 1

Audit data for the AG mill used in the validation of the model.

Mill Speed (% CS)	Discharge Rates		Mill filling (%)	Solids% by w/w (wt%)
	Solids (t/h)	Water (m^3/h)		
76	1056	330	33	78

Based on the audit data and the mill design, a model of the mill has been created using Metso ProSim plant simulator. The model has been used to estimate the size distribution of the charge inside the mill slice. The size distribution calculated from ProSim has been used to fill the slice with solids and SPH particles corresponding to the operating conditions of the mill. The minimum size for the DEM particles used in the simulation was 19 mm.

The simulation has been run at the beginning with the grates blinded in order to allow the solid particle and SPH fluid particles to settle and to reach the charge shape. After that, the grates were opened, and the simulation has run until a steady state has been reached. During simulation, valuable information has been collected including:

- discharge flow rates for solids and water.

- flow rates of solids and water through the grates in both directions, inwards (from pans back into the mill) and outwards (from inside the mill into the pans).
- mass hold-up in pans for solids and water.

The steady state condition was achieved when:

- the hold-ups have reached a constant mass for both solids and water.
- the mass balance has been reached. The mass balance criteria was considered reached when the difference between the outwards and inwards flow rates through the grates is close to the discharge flow rate at the trunnion end.

The simulations have shown that in most cases the steady state has been reached after 35 seconds or about six revolutions.

The results from the validation run are shown in Figure 1. The graphs present the time dependency of the discharge rates, hold-ups in the pans and the flow rates through the grates inwards and outwards for both solids and water.

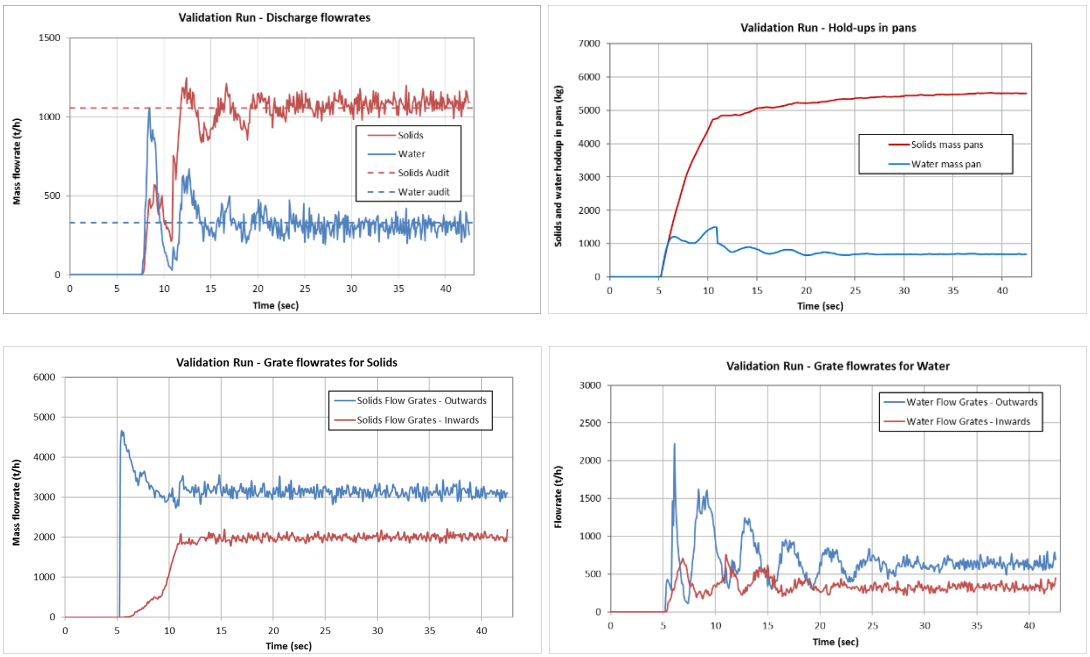

FIG 1 – Simulation results from the validation run.

The first graph on the top-left shows the discharge rates (solid lines) and the audit data (dotted lines). The results from the simulations are very close to the plant data. The second plot on the top-right presents the mass of solids and water recirculated in the pans. It can be easily noticed that the amount of solids recirculated in the pans is larger than the one for the water. Also, both plots have reached a plateau after 35 seconds (which corresponds to almost six revolutions of the mill) meaning that the simulation has reached the steady state. An efficient discharge system should have these two lines as low as possible. Even more, a higher recirculation of the solids and water in pans will increase the wear of the lifters and pans reducing the life of the discharge system.

The last two plots at the bottom show the flow rates through the grates in both directions inwards (from pans back into the mill) and outwards (from inside the mill into the pans). Both plots also show a peak in the discharge rates outwards right after five seconds which corresponds to the moment when the grates are opened. The difference between the blue and red lines in these two plots represents the net transport of the solids and water through the grates. A good discharge system should have a net transport as large as possible and even more important the inwards flow rate as lower as possible. Table 2 below summarise the results presented in Figure 1.

TABLE 2

Audit data and the simulation results from the validation run.

Discharge Rates				Hold-up		Net Transport Flow rate	
Solids Audit (t/h)	**Solids Sim (t/h)**	**Water Audit (t/h)**	**Water Sim (t/h)**	**Solids (kg)**	**Water (kg)**	**Solids (t/h)**	**Water (t/h)**
1056	1092	330	311	5511	682	1098	310

As it was mentioned earlier, another way to check whether the steady state has been reached is by comparing the net flow rates through the grates with the discharge rates at the trunnion end. Table 2 above shows that the net transport through the grates is very close to the discharge rates for both solids and water which is an indication of the steady state been achieved.

The plots presented in Figure 1 are very useful when different discharge systems are compared in terms of their efficiency or recirculation of the solids and water in the pans. Any design changes performed on a discharge system, such as: grates open area, aperture of the grates, arrangements of the grates, pan lifter designs, pans height, angle of the discharge cone etc, will change the appearance of these plots and will allow quantifying the effect of these changes on the performance of the discharge end.

In the next section such a comparison is carried out on three different pan design lifters, namely: radial, curved and twin chamber.

COMPARISON OF DIFFERENT PULP LIFTER DESIGNS WITH AND WITHOUT INNER LIFTER BARS

The comparison of the three different pan lifter designs was performed on a slightly modified version of the AG mill used during the validation process. The rotational speed has been kept unchanged at 76 per cent CS. The only design changes that have been made to the mill used in the validation process are:

- A new grate design with several more opening of 3.5 in and 2.0 in apertures.
- A larger total open area of 13 950 in^2 which represents an increase of 45 per cent from the validation design.
- The length of some of the lifter bars has been increased.
- Each design has been built in two versions, one with the inside lifter bars and one without inside bars.

The three designs are shown in Figure 2. In Figure 3 the designs with and without inside lifter bars for the radial design is also shown.

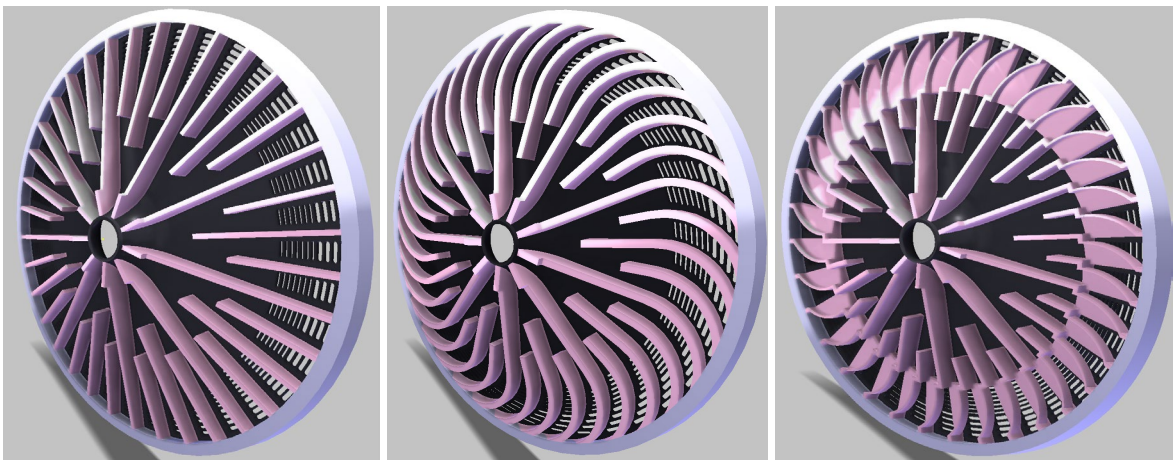

FIG 2 – Designs of the three discharge systems used for the performance comparison.

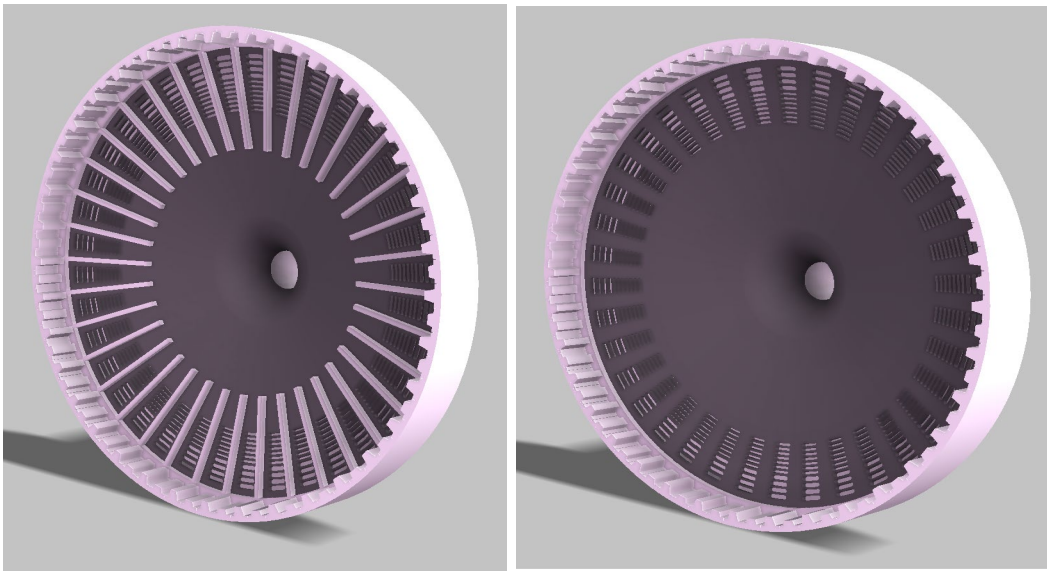

FIG 3 – Designs of the radial discharge systems with and without inner lifter bars.

All three discharge systems have the same grate design, the same open area and very similar radial arrangements of the grates. By doing so, the only thing that is changed between the three designs is the pulp lifters. The simulations were run in a similar way to the validation run. The 0.5 m mill slice is filled with solids and water while the grates openings are blinded. The simulation runs for more than a revolution to allow the particles and water to settle and to create the kidney shape of the charge. At that moment, the grates are opened, and the solids and water start to flow out of the mill into the pans and then discharged through the trunnion. New solids and water are added into the slice in order to keep the filling of the slice as close as possible to the required 33 per cent filling by volume. The simulation runs for about six revolutions long enough so that the steady state is reached. Once the simulation has reached the steady state, the post-processing of the output data takes place.

SIMULATION RESULTS FOR THE RADIAL PULP LIFTERS DESIGN

Two snapshots of the simulations for the radial pulp lifters design with and without head lifter bars taken at steady state are shown in Figure 4. The image shows clearly that this particular design of the lifters and grates leads to an increased amount of solids being recirculated in the pans. Comparing the design with head lifter bars (on the left) with the one without head lifter bars (on the right) one can notice that the design without head lifters shows more ore recirculated in the pans. This visual observation could be verified when the results are presented below in Figure 5.

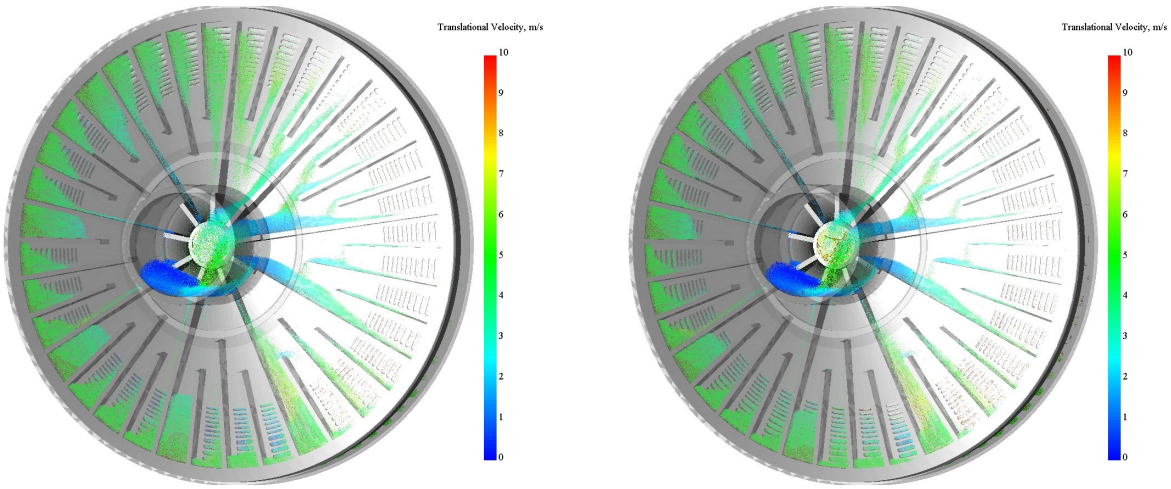

FIG 4 – Snapshots of the radial design simulations without and with head lifter bars.

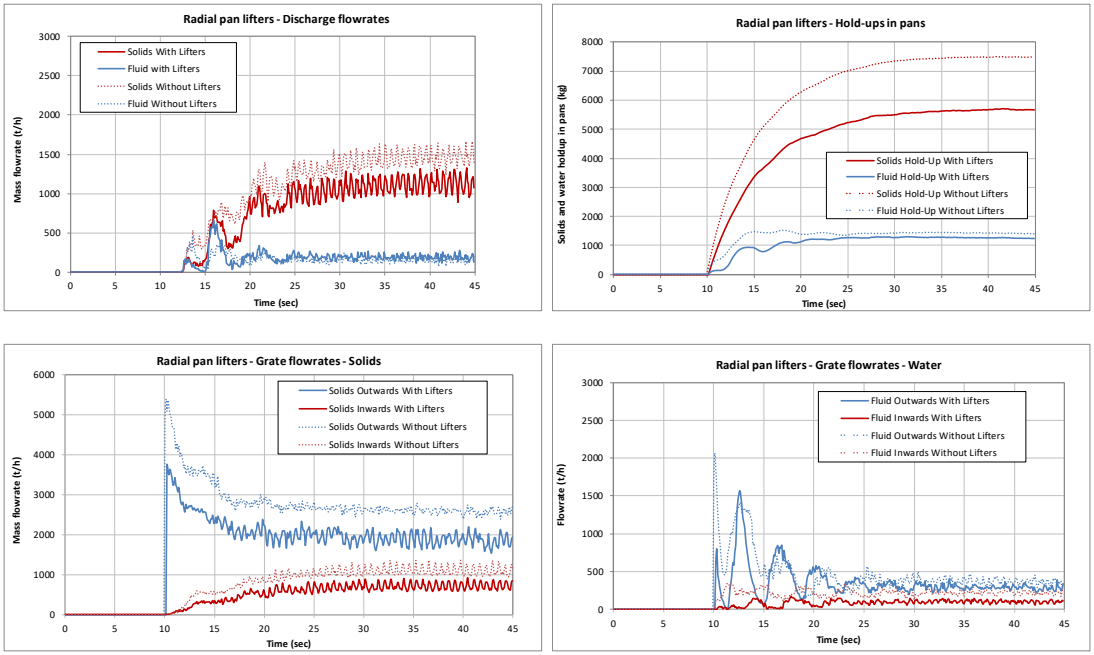

FIG 5 – Results for the radial pulp lifter designs with (solid lines) and without (dot lines) head lifter bars.

On the plots shown below and throughout the whole paper, the solid lines are for the case with the head lifter bars, while the dot lines are for the case without head lifter bars. The term ‘fluid’ used in the plots’ legend refers to water (slurry without fine solid particles).

The graphs confirm what we have already noticed by visually inspecting the two snapshots from the simulations. The radial design without head lifters discharges more solids and has a larger amount of solids held-up in the pans. The discharge of the fluid and the transport through the grates seem to be not affected by the presence or absence of the head lifter bars. The increase in discharge rates of the solids is achieved mainly by an increase in the amount of solids passing through the grates (bottom-left plot above).

The averaged flow rates calculated after the steady state has been reached are shown in Table 3 for both cases with head lifters (W) and without head lifters (W/O). The table also shows the Net Transport Flow rate which represents the difference between the outwards and inwards flows through the grates. At steady state the discharge rates (calculated at the trunnion end) should be very close to the Net Transport Flow rate through the grates.

TABLE 3

Averaged flow rates and hold-ups for the radial pulp lifter design for both cases: with (W) and without (W/O) head lifters.

Discharge Rates				Hold-Up				Net Transport				% Solids		Slice Filling	
Solids (t/h)		Water (t/h)		Solids (kg)		Water (kg)		Solids (t/h)		Water (t/h)		w/w		%	
W/O	W	W/O	W	W/O	W	W/O	W	W/O	W	W/O	W	W/O	W	W/O	W
1467	1124	152	190	7490	5673	1436	1239	1480	1118	141	177	90.6	85.5	27.1	31.7

The results from the radial pulp lifter design shows that the discharge is quite efficient in discharging the solids, but it has a problem discharging the water. The low discharge rates for the water can be explained by the fact that a large amount of water is sent back into the mill through the grates. On top of that, there is a large mass of solids held-up in the pans that will contribute to an excessive wear of the lifter bars and bottom of the pans. Most probably this design will create a slurry pool inside the mill.

SIMULATION RESULTS FOR THE CURVED PULP LIFTERS DESIGN

The second design simulated was the curved pulp lifters design. In order to keep the grates' design unchanged from the radial design, some of the grates were shifted to accommodate for the curved lifters. The shifting of the grates was done so that the radial distribution of the grates openings does not differ too much from the radial one. By doing this, the effect of the grates on the performed comparison is minimised. Two snapshots of the simulations with and without head lifter bars are shown in Figure 6. The results for the curved lifters are presented in Figure 7 and the averaged flow rates in Table 4. In order to compare the three different designs, the scale of the Y-axis of the plots has been kept the same between the designs.

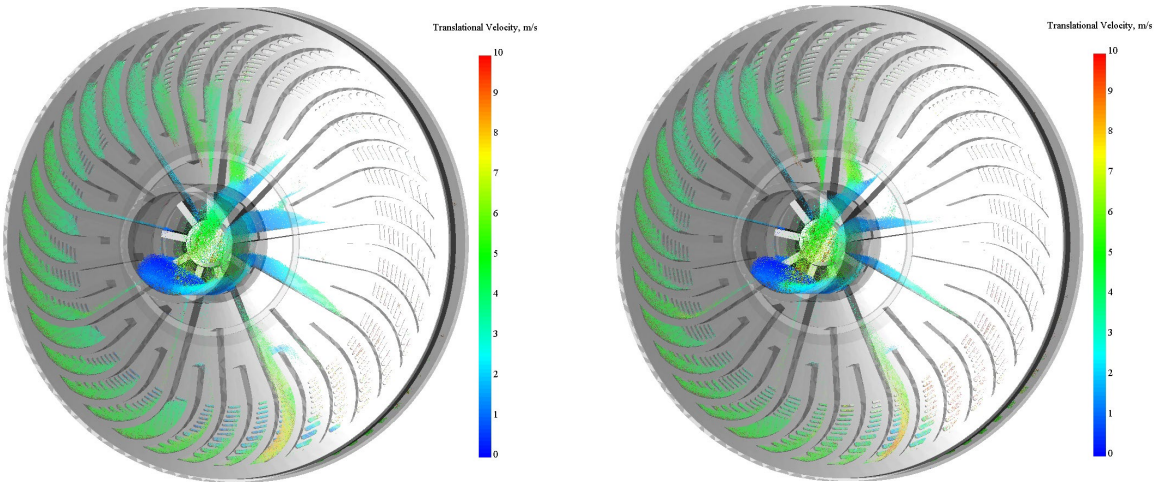

FIG 6 – Snapshots of the curved lifters simulations without and with head lifter bars.

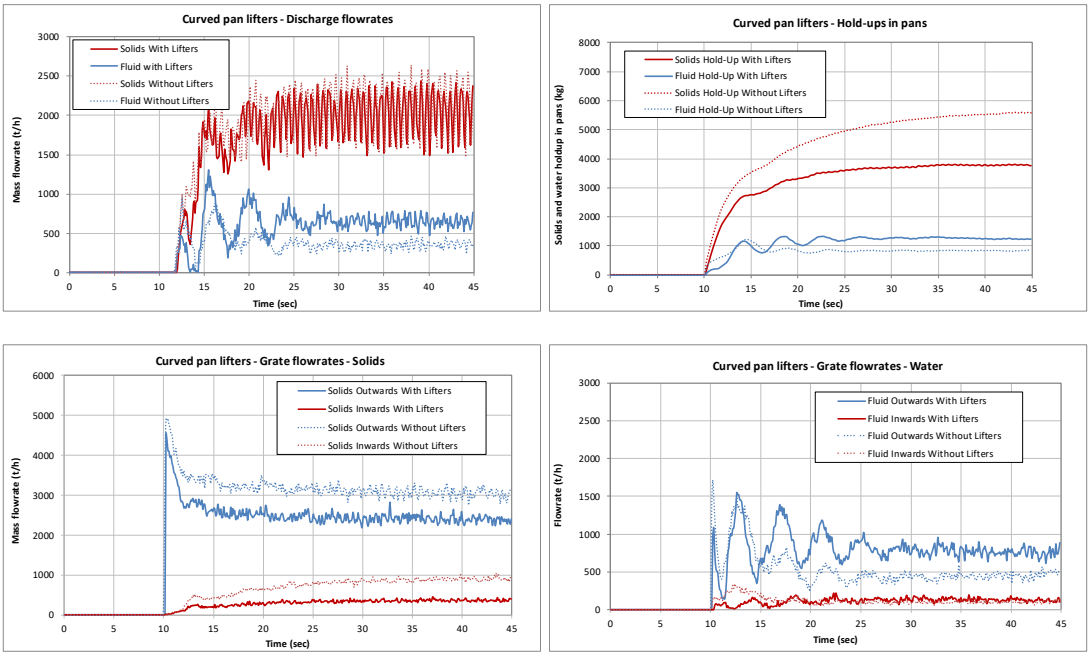

FIG 7 – Results for the curved pulp lifter designs with (solid lines) and without (dot lines) head lifter bars.

TABLE 4

Averaged flow rates and hold-ups for the curved pulp lifter design for both cases: with (W) and without (W/O) head lifters.

Discharge Rates				Hold-Up				Net Transport				% Solids		Slice Filling	
Solids (t/h)		Water (t/h)		Solids (kg)		Water (kg)		Solids (t/h)		Water (t/h)		w/w		%	
W/O	W	W/O	W	W/O	W	W/O	W	W/O	W	W/O	W	W/O	W	W/O	W
2101	2021	361	636	5590	3773	831	1246	2108	2029	385	628	85.3	76.1	28.4	32.1

The curved design shows a significant improvement from the radial design. Regarding the presence or absence of the head lifter bars, there is clear indication that these lifter bars have an influence on the performance of the curved design, especially on the slurry discharge. The solids discharge seems unchanged, while the slurry discharge shows a significant increase in the discharge rates when the lifter bars are present. The increase in the slurry discharge rate is mainly due to an increase in the slurry passing through the grates into the pans accompanied by almost the same flow back into the mill as per the design without lifter bars. The hold-ups of solids in the pans are larger for the design without lifter bars, while the slurry hold-up is slightly larger for the design with lifter bars.

SIMULATION RESULTS FOR THE TWIN CHAMBER PULP LIFTERS DESIGN

The third design used for the comparison is a novel design proposed several years ago. The twin chamber design was developed to minimise the occurrence of flow-back and recirculation of the ore in the pans. The ore and the slurry passed through the grates is quickly moved into an adjacent chamber that is not in touch with the grates thus eliminating the chance of solids and slurry to flow back into the mill through the grates. A similar design with the added chamber has been created for this simulation while the grates design and their arrangements has been kept the same as for the previous two designs. A snapshot of the simulation is shown in Figure 8.

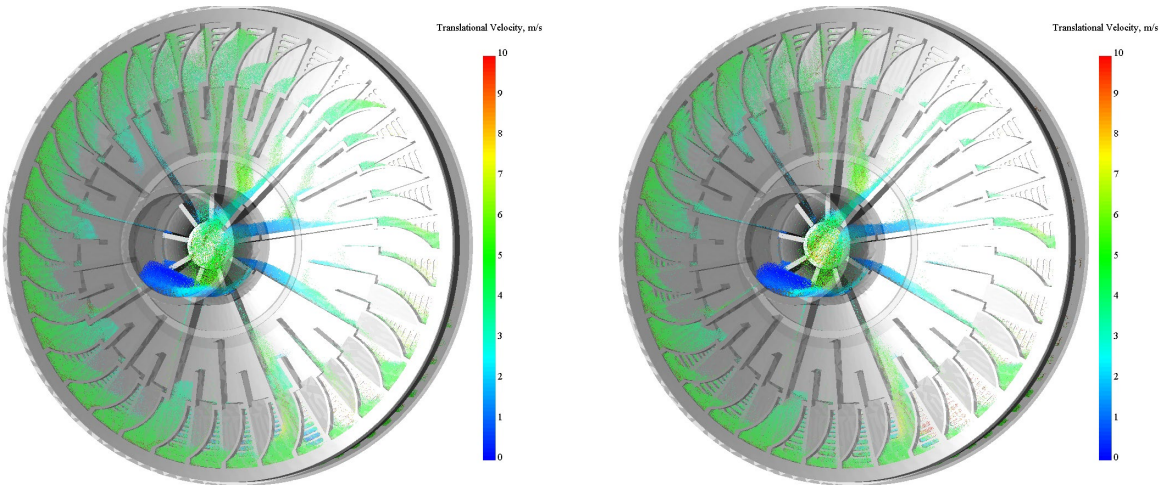

FIG 8 – Snap-shots of the twin chamber simulations without and with head lifter bars.

The results of the simulations are depicted in Figure 9 in a similar manner with four plots showing the flow rates and hold-ups of solids and water. The average flow rates calculated at steady state are shown in Table 5.

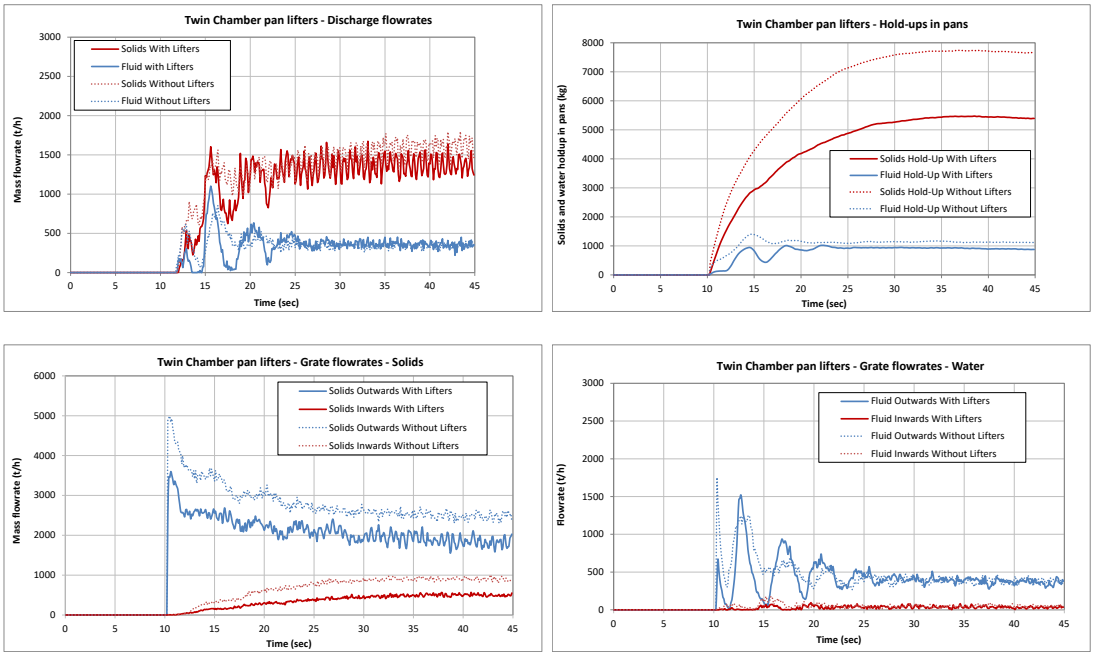

FIG 9 – Results for the twin chamber designs with (solid lines) and without (dot lines) head lifter bars.

TABLE 5

Averaged flow rates and hold-ups for the twin chamber pulp lifter design for both cases: with (W) and without (W/O) head lifters.

Discharge Rates				**Hold-Up**				**Net Transport**				**% Solids**		**Slice Filling**	
Solids (t/h)		**Water (t/h)**		**Solids (kg)**		**Water (kg)**		**Solids (t/h)**		**Water (t/h)**		**w/w**		**%**	
W/O	W	W/O	W	W/O	W	W/O	W	W/O	W	W/O	W	W/O	W	W/O	W
1602	1371	344	355	7703	5438	1129	904	1587	1355	331	339	82.3	79.4	26.7	31.7

The twin chamber design shows overall improvements over the radial design but cannot surpass the efficiency of the curved design. Comparing the performance of the twin chamber designs with and without head lifter bars it can be noticed that there is no difference in the discharge rates for the slurry. The design without lifter bars discharges more solids than the design without lifter bars, but this is accompanied by an increase in the hold-up of solids and slurry in the pans.

The Tables 6 and 7 summarise the results from all six simulations for an easier comparison of the designs. It must be mentioned here that the comparison between these designs is valid for this particular mill design, this discharge grate open area and grate arrangements, this discharge end design and these mill operating parameters. In a different mill design, under different operational conditions, the results might be different. The main goal of this paper was to present the capability of the software as a design tool and how it can be used to design and compare different discharge systems. It must be also highlighted here the importance of the validation and the calibration of the model before any design changes are investigated.

TABLE 6

Comparison of the results for all three designs – Solids.

Design	Discharge Rates (t/h)		Hold-up (kg)		Net Transport (t/h)	
	W/O	W	W/O	W	W/O	W
Radial	1467	1124 (-23%)	7490	5673 (-24%)	1480	1118
Curved	2101	2021 (-4%)	5590	3773 (-33%)	2108	2029
Twin Chamber	1601	1371 (-14%)	7703	5438 (-29%)	1587	1354

TABLE 7

Comparison of the results for all three designs – Water.

Design	Discharge Rates (t/h)		Hold-up (kg)		Net Transport (t/h)	
	W/O	W	W/O	W	W/O	W
Radial	152	190 (+25%)	1436	1239 (-16%)	141	177
Curved	361	636 (+76%)	831	1246 (+50%)	385	628
Twin Chamber	344	355 (+3%)	1129	904 (-20%)	331	339

The table is also showing (in brackets) the changes of the flow rates and hold-ups as a percentage of the design without head lifters. Any decrease in value from the design without head lifters is shown in red while the increases are shown in green. There are two interesting conclusions from the table above:

1. The presence of the head lifter bars reduces the amount of solids discharged by the mill. The reduction in discharge rates for the solids is accompanied by a reduction in the amount of solids hold-up. The curved design is less affected by the presence of the lifter bars with only 4 per cent decrease in solids discharge rates. However, this slight decrease in discharge rates of the solids for the curved design is accompanied by a large decrease in the solids hold-up in the pans.
2. Regarding the effect of the head lifter bars on the slurry discharge, the effect is opposed to the solids. This time, the presence of the head lifter bars increases the slurry discharge rates and is also accompanied by a reduction in the slurry hold-up in the pans. The exception is again the curved design. The slurry discharge rate for the curved design with head lifter bars is increased by 76 per cent compared to the design without lifter bars. This increase is accompanied by an increase in the slurry hold-up of 50 per cent.

One other important characteristic of the discharge system that can be compared between these three designs is related to the efficiency of the grates, more precisely the passing of the ore and

water through the grates in both directions. The flow rates in and out through the grates are shown in Tables 8 and 9 for solids and water, respectively. The tables also include the percentage change from the design without the head lifters.

TABLE 8

Flow-through grates rates – Solids.

Design	Flow Rates – Inwards (t/h)		Flow Rates – Outwards (kg)	
	W/O	W	W/O	W
Radial	1108	737 (-33%)	2588	1855 (-28%)
Curved	918	361 (-61%)	3025	2390 (-21%)
Twin Chamber	905	501 (-45%)	2492	1856 (-26%)

TABLE 9

Flow-through grates rates – Water.

Design	Flow Rates – Inwards (t/h)		Flow Rates – Outwards (kg)	
	W/O	W	W/O	W
Radial	221	103 (-53%)	363	280 (-23%)
Curved	112	127 (13%)	497	755 (52%)
Twin Chamber	51	34 (-33%)	382	373 (-2%)

The results show that the presence of the head lifter bars reduces the flow of solids through the grates in both directions. For the slurry, we have again the curved design that behaves differently than the other two designs. The curved design with head lifter bars has a significant increased amount of slurry flowing out and slightly increased amount flowing back into the mill. The twin chamber, with its novel design (designed to reduce the amount of slurry flowing back into the mill) is behaving as expected in terms of slurry flow-through the grates. The amount of slurry flowing back into the mill for the twin chamber design is a lot smaller than the other two designs.

WEAR PATTERNS COMPARISON BETWEEN THE DESIGNS

The simulations can also determine the areas of high wear which are a good indication of how different parts of the discharge system will wear under mill running conditions. Figure 10 shows the wear patters for all three designs taken at the same time of 33 seconds after the grates were opened.

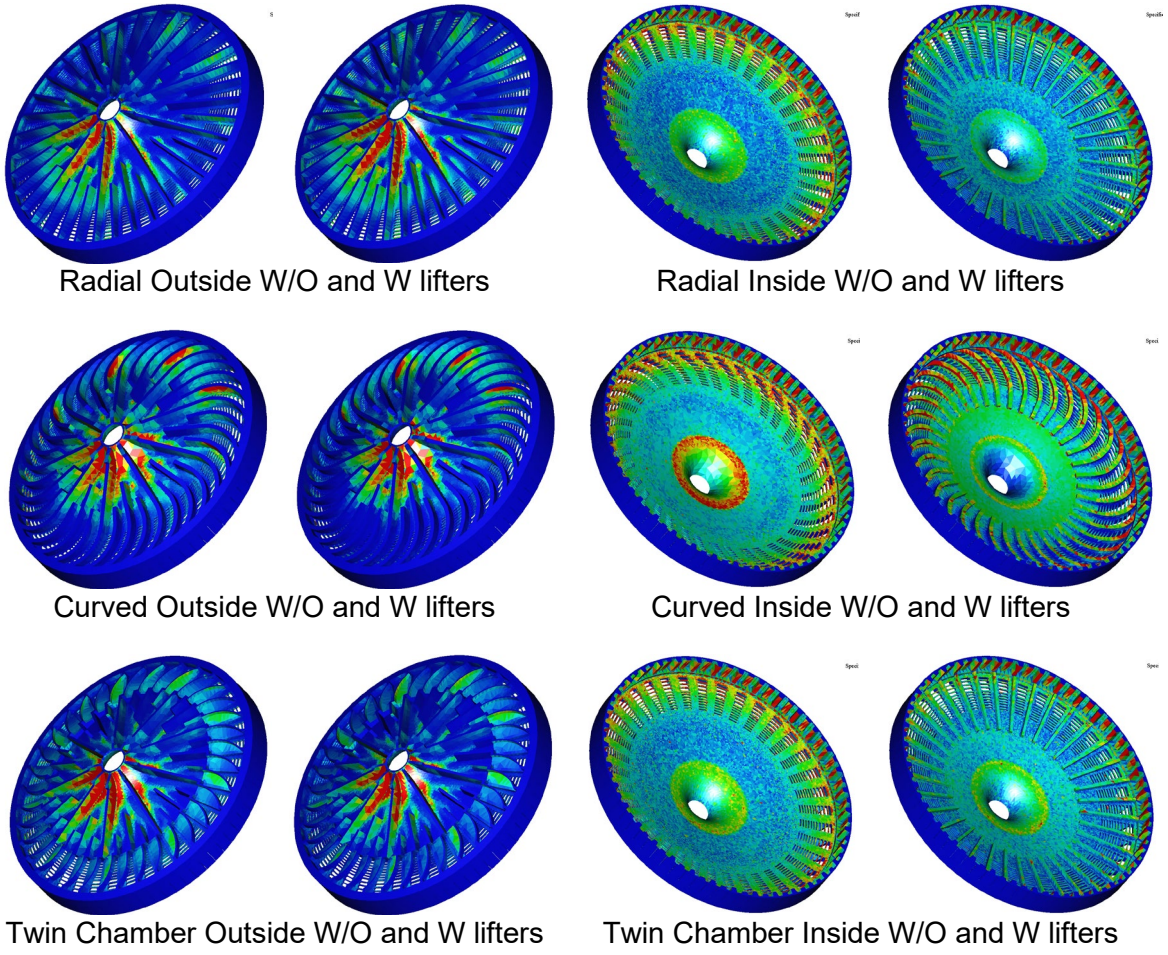

FIG 10 – Wear patterns for the three designs.

The wear patterns show high wear in the area of the cone discharge for all three designs, with the radial design showing less wear in that area than the other two. At the same time, the radial design has a discharge rate lower than the other two. The curved design wears around the cone discharge area almost similarly to the twin chamber design, but the curved design is discharging a lot more ore than the twin chamber. The curved design is also exhibiting a higher wear area every fourth curved lifter which corresponds to the longest pan lifters. This high wear area for the curved design is consistent with the recirculation of the ore in the pans. The twin chamber design also shows some wear on the surface of every fourth wedge adjacent to the longest pan lifter. The cause of the wear is due to the same fact namely, the recirculation of the ore in the pans along the longest lifter bars.

Regarding the effect of the head lifter bars, there is clear evidence that the designs without the lifter bars show more wear inside the head, especially at the grates level. The inside of the grates is wearing at a faster rate when the lifter bars are not present. The reason for that is that the lifter bars lift the ore which then slides along the lifter bars and drops back into the mill. If the lifter bars are not present, then the ore spends most of its time at the bottom of the head increasing the wear of the grates. Also, the curved design without the head lifter bars exhibits a higher wear inside the head around the discharge cone, which is not shown on the other two designs. However, the curved design with the head lifter bars shows excessive wear of the head lifter bars, in contrast with the other two where this kind of wear is not present.

CONCLUSIONS

This paper presents a DEM+SPH model of the mill discharge system including a slice of the mill and flow-through the grates of solids and water. The model has been validated against a 32’ AG mill and then used on a slightly modified discharge system to compare three different pan lifter designs. The comparison between the three designs was carried out on very similar grates design and mill slice,

the only changes were related to the pan lifters configuration and the presence or absence of the head lifter bars.

The model runs until the system reaches a steady state that it is checked two-folds. Firstly, by comparing the net flow rates of solids and water through the grates with the discharge rates at the trunnion end. Secondly, by following the amount of solids and water held-up in the pans. At steady state, the hold-up reaches a plateau for both solids and water. The steady state is usually reached after six revolutions of the mill.

The simulations prove that the head lifter bars have definitely an effect on the discharge rates, on the net flow of the ore and slurry through the grates, and on the wear patterns.

The model can extract very useful information regarding the discharge rates, the net flow-through the grates, the hold-ups in the pans and the recirculation rates back into the mill for both solids and water. The information obtained after the simulation has reached steady state could be successfully used to compare different designs and investigate how changes made to the grates or the pan lifters would affect the performance of the discharge system. Wear patterns could also be computed from the simulations allowing for improvements to be made in areas that show high wear.

For the best results, the model must be validated against existing plant data before attempts to quantify how different design changes will affect the performance of the mill discharge system.

REFERENCES

Asakpo, E, Heath, A R and Chaffer, S, 2018. Results from Installing Turbo Pulp Lifter (TPL) in Ahafo SAG Mill, paper presented to Comminution 2018 Conference, Cape Town, 16–19 April.

Campbell, C S, 1997. Computer Simulation of Powder Flows, in *Powder Technology Handbook,* (ed: Gotoh), pp 777–793, (Dekker: New York).

Ciutina, S and Soriano, R J, 2014. Curved Pulp lifters – can they save energy?, paper presented to 12th AusIMM Mill Operators' Conference (The Australasian Institute of Mining and Metallurgy: Melbourne).

Cleary, P W, 2001. Recent advances in DEM modelling of tumbling mills, *Minerals Engineering,* 14: 1295–1319.

Cleary, P W, 2004. Large scale industrial DEM modelling, *Engineering Computations,* 21: 169–204.

Cleary, P W, 2009. Industrial particle flow modelling using DEM, *Engineering Computations,* 26(6): 698–743.

Cleary, P W, Hilton, J E and Sinnott, M D, 2017. Modelling of industrial particle and multiphase flows, *Powder Technology,* 314: 232–252.

Cleary, P W, Sinnott, M D and Morrison, R D, 2006. Prediction of slurry transport in SAG mills using SPH fluid flow in a dynamic DEM based porous media, *Minerals Engineering,* 19: 1517–1527.

Gutierrez, A, Ahues, D, Gonzalez, F and Merino, P, 2018. Simulation of material transport in a SAG mill with different geometric lifter and pulp lifter attributes using DEM, *Mining, Metallurgy & Exploration,* 36(2): 431–440.

Herbst, J A and Nordell, L, 2001. Optimization of the design of sag mill internals using high fidelity simulation, in *Proceedings SAG 2001* (ed: A Barratt and M Mular), pp 150–164.

Herbst, J A, Lo, Y C and Rajamani, K, 1985. Population balance model predictions of the performance of large diameter mills, *Minerals and Metallurgy Process,* 2(2): 114–120.

Lichter, J K, Suazo, M, Noriega, R and Murariu, V, 2011. The application of Multiphysics models for the design of mill discharge system, in *Proceedings SAG 2011* (ed: K Major, B Flintoff, B Klein and K McLeod), Vancouver, Canada.

Mishra, B K and Rajamani, R J, 1992. The discrete element method for the simulation of ball mills, *Applied Mathematical Modelling,* 16: 598–604.

Mishra, B K and Rajamani, R K, 1994. Simulation of charge motion in ball mills. Part 1: experimental verification, *International Journal of Mineral Processing,* 40: 171–186.

Monaghan, J J, 1992. Smooth Particle hydrodynamics, *Annual Review of Astronomy and Astrophysics,* 30: 543–574.

Monaghan, J J, 1994. Simulating free surface flow with SPH, *Journal of Computational Physics,* 110: 399–406.

Monaghan, J J, 2005. Smoothed particle hydrodynamics, *Reports on progress in physics,* 68: 1703–1759.

Morrell, S, 2004. A new autogenous and semi-autogenous mill model for scale-up design and optimization, *Minerals Engineering,* 17: 437–445.

Morrison, R D and Cleary, P W, 2008. Towards a virtual comminution machine, *Minerals Engineering,* 21: 770–781.

Rajamani, R K and Mishra, B K, 1996. Dynamics of ball and rock charge in SAG mills, in *Proceedings SAG 1996*, (University of British Columbia).

Plant operational strategy with metallurgical digital twin

A Remes[1], M Hultgren[2], J Kortelainen[3] and J Moilanen[4]

1. Technology Advisor, Metso Outotec Finland Oy, Espoo FI-02230.
   Email: antti.remes@mogroup.com
2. Senior specialist, Metso Outotec Finland Oy, Pori FI-28101.
   Email: matias.hultgren@mogroup.com
3. Simulation Specialist, Metso Outotec Finland Oy, Espoo FI-02230.
   Email: johanna.kortelainen@mogroup.com
4. Director – Digital Solutions, Metso Outotec Finland Oy, Espoo FI-02230.
   Email: jari.moilanen@mogroup.com

INTRODUCTION

A step change in productivity for mining companies is achievable by using existing data as a resource. Bringing the data together from various systems and applying it for process simulations and advanced analytics help in managing the variability of the process. These digital twin technologies create new insights into metallurgical processes and give an opportunity to optimise operations over the full production value chain.

DESIGN CRITERIAS

Expectations for the metallurgical digital twins

Sustainability is at the forefront of industry discussion and a top priority right now. By solving resource efficiencies and emission footprints with accurate models, the digital twin technologies enable sustainable and economical operations. Recipe matching to variable ore types allows for significant savings in energy, water, and chemicals per produced tonne of product. The process simulation allows operations to efficiently use resources in an optimal way while considering both the impacts and constraints. The performance feedback from the operations and plant information hub allows for the opportunity to better understand how the processes interact and influence each other. With the ability to test run any process configuration and operating strategy before execution, the risk of environmental, financial or safety issues are greatly mitigated. This increased knowledge allows for better decision-planning within the plant.

Unbiased process models critical for reliable operation

Critical for the usefulness of process simulation models and digital twins for online monitoring and future scenario predictions is unbiased reliability of the underlying process models. Typical reasons why the simulation models may get biased are changes in the process operating state that, at worst, invalidate the calibration of the models. These changes may be slow, as in the case of equipment wear, changes in ore characteristics, seasonal fluctuation of ambient temperature or quality of process water. Alternatively, the changes may be abrupt because of sudden changes in the ore feed or key equipment planned or unplanned shutdowns.

Unbiased models for digital twins can be achieved with automated adaptation and learning from online sensors and process history data. A specific model parameter adaptation algorithm minimises any sudden modelling errors and drifting divergence (Figure 1). The model itself is based on first-principle equations, equipment dimensions and flow sheets in dynamic mode. Exactly similar models are used in plant design and equipment dimensioning, but in static mode. For example, in flotation, for digital twin dynamic model adaptation online elemental assays are continuously applied to detect changes in the ore floatability, and as a result the automated system adapts flotation kinetic rates of minerals. Model parameter adaptation methods, like gradient-based, can be computationally intensive. Here in adaptation, the proper first-principle model is used in conjunction with a surrogate model. The surrogate is formed between the model parameters and the resulting modelling error cost function. The parameter optimisation iterates efficiently both fast-surrogate and the globally-robust first-principle models with plant data.

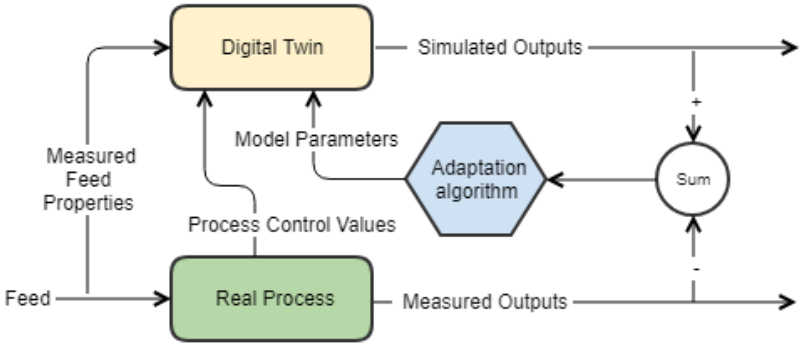

FIG 1 – Principle of automated model adaptation of a digital twin.

Connectivity to the plant data

Metallurgical digital twin connectivity is designed to comply with requirements for each plant and corporate IT policies. The digital twin application runs in the cloud. Typically, plant data from DCS is accessed with pipeline of on-site OPC server, data routing I/O service software and firewalls (Figure 2). Cloud-end connectivity is handled with an IoT Hub of the cloud. User web log-in authentication utilises standardised cloud technologies.

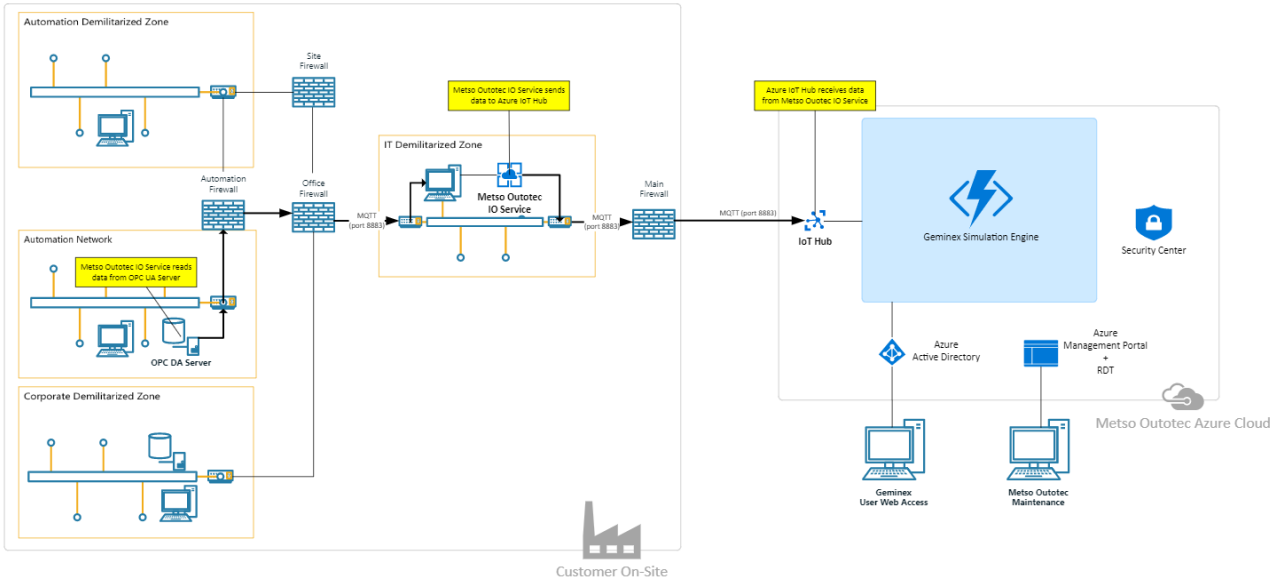

FIG 2 – Schematic architecture of a cyber secure connection from the edge to cloud.

The cloud application runs the plant dynamic model in simulation engines. The simulation models are well established minerals processing, hydro – and pyrometallurgical dynamic first-principle models implemented with HSC simulation platform. The engines are capable to run both in real-time monitoring mode and for fast-forward predictive scenarios, started from any operating time of the plant.

PRACTICAL IMPLEMENTATION

Implementation of a digital twin

Typical implementation of metallurgical digital twin is split in phases. In the first phase, a static model of the operation is created with actual process flow sheet. Attention at this phase is on defining the process connections and mass balances with related process performance data that form the basis for the process model. Typically, the data is readily available from process test campaigns, and the data can be used when validated for current process flow sheet.

In the second phase, the static process model is converted dynamic with equipment hold-ups to allow for time dependent simulations. At third phase, the created simulation model is connected with

live plant data for effective model adaptation. The focus on data connectivity is in establishing a cyber secure one-way communication link using industry standards and best IoT practises that accommodate to existing modern infrastructure for Information (IT) and Operational Technologies (OT).

Key parameters for seamless operation

Digital twin is used for plant optimisation on a daily basis. It is seamlessly integrated with APC process optimisers, seeking the optimal set points for them. For example, the varying feed ore, constraints, and equipment availabilities implies varying plant optimal operating regions. Digital twin predictions will give a set of alternative operating targets and finds optimum further for each process area APCs. Finally, for example in flotation, the control actions are made into froth speed, aeration, levels and reagent dosages.

Importance of user experience

User experience and user interfaces play a key role in practical implementation of any digital twins for plant daily operation. Good practice is to have a flow sheet as a basis for presenting the results. The plant flow sheet is similar to that in process automation systems, but focuses mainly on operational information, minimising process control related items (Figure 3). Instead, vast amounts of soft-sensor data and enriched information based on the dynamic model and analytics are available.

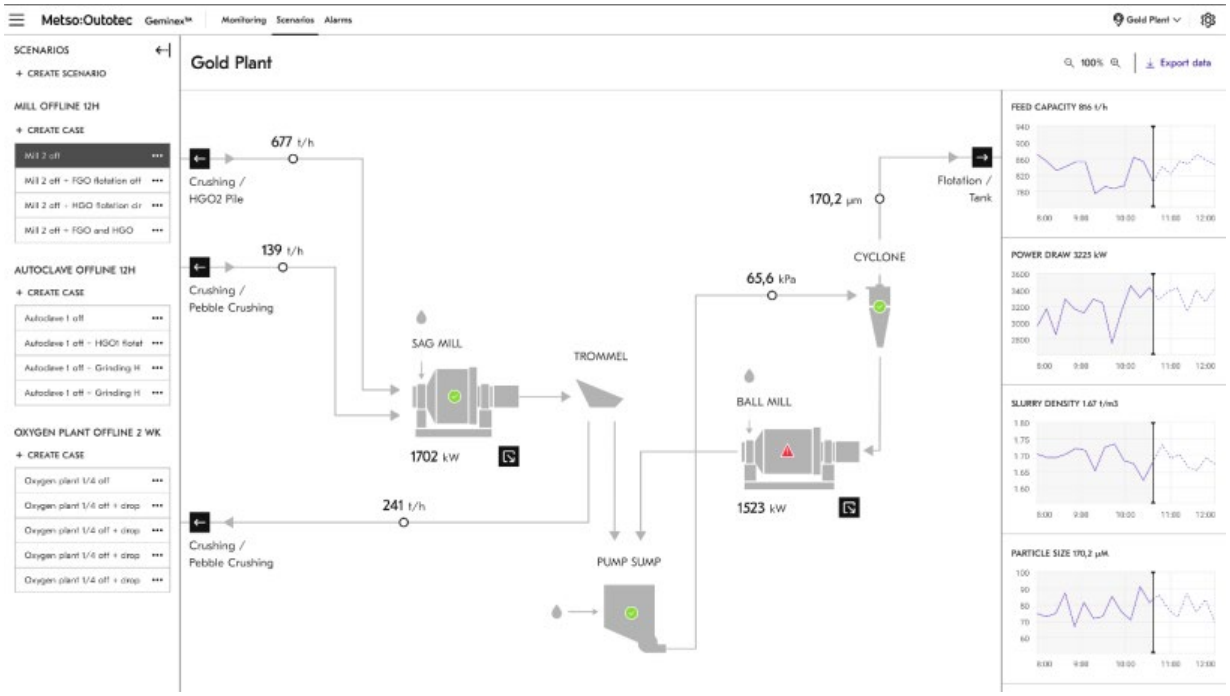

FIG 3 – Example of an operator view to a metallurgical digital twin.

ROADMAP FOR BENEFITS

Case example at a gold concentrator

Example case of a gold concentrator starts building the metallurgical digital twin for a sulfide flotation consisting of static and dynamic models for flotation with live data connection for the digital twin. Essential for setting up the metallurgical digital twin is to discover and plan in advance how the digital twin will be used by the plant operator, metallurgist, and production planning teams. This facilitates the implementation of the digital twin with the right focus and creates commitment of the teams. Figure 4 shows an outcome of a facilitated workshop before development of a digital twin to identify the expected benefits of the metallurgical twin. Cross departmental contribution from different organisational levels highlights multiple sources of benefits to the operations.

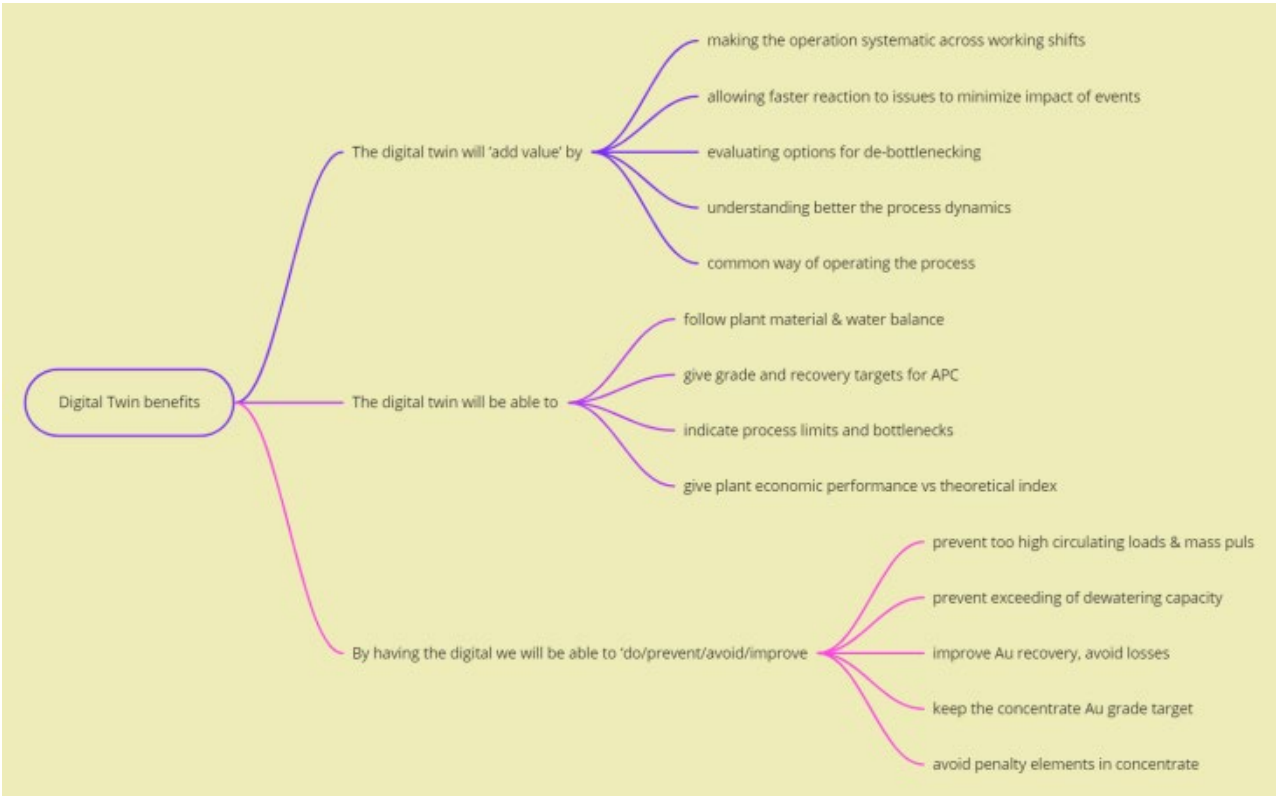

FIG 4 – Identified benefits of a metallurgical digital twin for a gold concentrator.

Information flow from digital twin to advanced process control (APC)

Achieving the aspired benefits of metallurgical twin requires a clear view on how the information from the twin will be used in plant operations. This needs to be elaborated in workshops with the users of the digital twin to identify possible missing links. Figure 5 illustrates a logical flow of information from the process inputs to the digital twin and further to control actions in the flotation circuit developed in the example case.

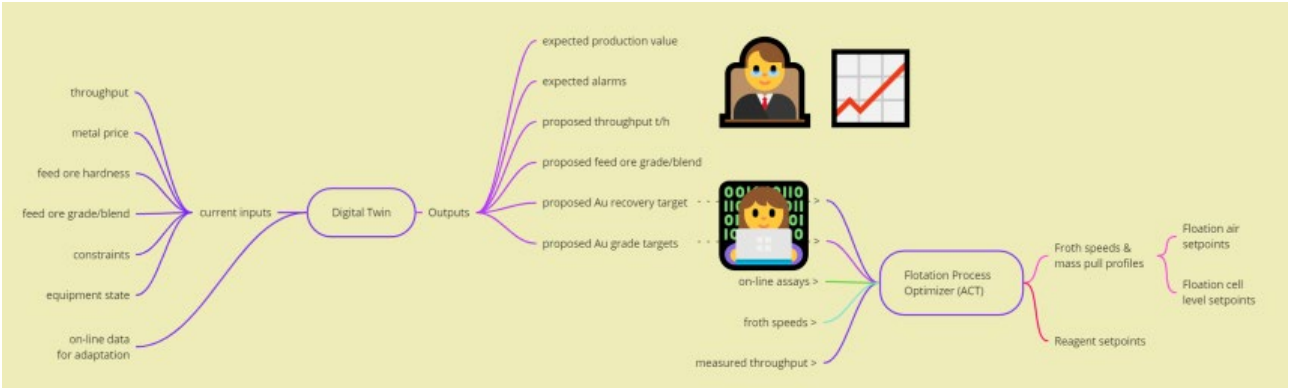

FIG 5 – Information flow from inputs to outputs with digital twin.

CONCLUSION

Typical key drivers for the digital transformation and implementation of digital twins relate to increasing operational productivity, uplifting the ore grade, recovery, and process throughput. Digital twins contribute to these by allowing operations to make decisions based on complete oversight of material flow and blends.

Furthermore, a key contributor for successful digital twin project ensuring long-term gain from modern technology, was recognised that the development needs to be end user directed, rather than developer driven. Also, strong backbone was identified to originate from long-term development by

the technology supplier, realised to end users by subject-matter industry technology transfer and training.

For the future, metallurgical digital twins have clear potential to help the mining industry fight the climate change by reducing their carbon and environmental footprint. Future processing plants require more resilience for energy, water and materials. Development of modern technologies to address this resilience requires high level of control and optimisation of the full operation, provided by the metallurgical digital twins. In addition, the future trend is towards autonomous operations, for example, at remote locations and to increase safety of the people and environment. Eventually these imply that processing plants require functions of metallurgical digital twins for targeting autonomous operation with situational awareness and view to operational future.

Assessment of rare earth elements recovery potential from inactive tailing storage facilities in Western Australia

S K Sarker[1], N Haque[2], W Bruckard[2] and B K Pramanik[3]

1. RMIT University, Melbourne Vic 3001. Email:
2. CSIRO Mineral Resources, Clayton South, Melbourne Vic 3169.
3. RMIT University, Melbourne Vic 3001.

ABSTRACT

There are over 60 000 mine sites considered abandoned in Australia. More than 23 000 such sites are located in Western Australia alone. These abandoned mine sites are the known cause of significant environmental, public health, and safety issues. Mine tailings, generally stored in tailings storage facilities (TSFs), are the main source of these issues. However, some selective TSFs are increasingly being considered a potential secondary source of critical minerals. In Western Australia, there are 653 inactive TSFs reported. The objective of this study was to identify the potential TSFs for rare earth elements (REEs) recovery using satellite images and a companion matrix of the host metals. This study used Google Earth Pro. for visual inspection of the satellite images. This study identified six inactive TSFs with major product iron, which is the host of the companion of some REEs. Among the identified TSFs, the TSF with ID 475 had the highest area coverage of 5.02 km^2, which ranked 1st in relative potential in terms of the volume of tailings available for reprocessing. The highest 418 inactive TSFs were found with a major product of gold which has no companionality with REEs in the matrix. Similarly, other major products of the TSFs had little to no companionality of REEs in the matrix. Moreover, the amount of recoverable REEs from the identified TSF is subject to the concentration of the elements in tailings, which can only be known after conducting a detailed characterisation of the tailings sample. Based on the characterisation results, a flow sheet comprising selective processes for liberating the REEs can be developed after lab-scale experiments.

INTRODUCTION

Australian mining industry is one of the major contributors to the national economy, and its contribution was over 10 per cent of the total GDP during the fiscal year 2019–2020 (Australia – Country Commercial Guide, 2021). However, mining operations have left a huge footprint on the country's landscape due to mainly abandoned or neglected mine sites. Studies have found that there are 95 320 hard rock mine sites in Australia, of which the majority (about 90 per cent), are not active (Werner *et al*, 2020). About 70 per cent of these inactive mine sites in Australia are considered abandoned or neglected. The Australian state of Western Australia (WA) is home to the largest number of neglected mine sites which are estimated to be over 20 000 (Werner *et al*, 2020). Many of these neglected mine sites produced tailings during the processing of ores to extract metals, and the tailings were stored on-site in the tailings storage facilities (TSFs). The WA has reported about 1000 TSFs in a database of mines and minerals called MINDEX (https://minedex.dmirs.wa.gov.au).

The TSFs are considered to be the most environmentally polluting part of the mining operations. This is due to the fact that mine tailings are currently the largest volume of waste materials in the world. Importantly, it is not the only issue of degradation of the land area occupied by the huge volume of tailings, but the tailings also produce highly acidic water rich in heavy metals called acid mine drainage (AMD). The AMD has been labelled by the United Nations (UN) as 'the second biggest problem facing the world after global warming'. However, the TSFs are increasingly being considered to be a potential secondary source of some metals considered critical by many countries. The list of critical minerals for the major economies of the world includes, among others, rare earth elements (REEs), cobalt (Co), and lithium (Li). These are also included in the list of critical minerals for Australia. Due to having strategic importance of these critical minerals, they have been referred to as strategically important critical minerals (SICMs) in a study by Sarker *et al* (2022a).

The REEs are among the most important critical minerals due to their unique properties, which make them suitable for emerging technologies such as modern electronics and climate change abating industries such as electric vehicles, wind power, and solar energy. The REEs are mainly produced

from primary deposits. However, declining ore grades in primary deposits have led to the exploration of waste and by-products as secondary sources including coal fly ash (Sarker *et al*, 2022b) and mine tailings (Tunsu *et al*, 2020). The mine tailings, in particular, have attracted a lot of attention from the scientific community recently mainly because of the amount of tailings available for processing and their environmental impacts. Several studies have demonstrated that old mine tailings could be processed to recover the REEs (Peelman *et al*, 2018; Tunsu *et al*, 2020; Vaughan *et al*, 2021). Apart from the tailings of REEs mine sites, some iron-bearing tailings are also the host of the REEs. A number of studies have used tailings from iron mine sites to recover REEs (Frietsch and Perdahl, 1995; Abaka-Wood *et al*, 2019; Moran-Palacios *et al*, 2019). The findings suggest that the tailings from iron mines are worth of investigating for REEs recovery. It is also evident from the companion matrix (Figure 1) which shows that more than 50 per cent of some of the REEs (Ce, Nd, Pr and La) are produced as the by-products of iron. In practice, the REEs produced as the by-products at the mine sites were rarely recovered due to a little to no economic significance, and they ended up in the TSFs. Importantly, their concentrations in old and historic TSFs are like to be higher due to less efficient recovery processes used. This increases the recovery potential of REEs from old and historic TSFs.

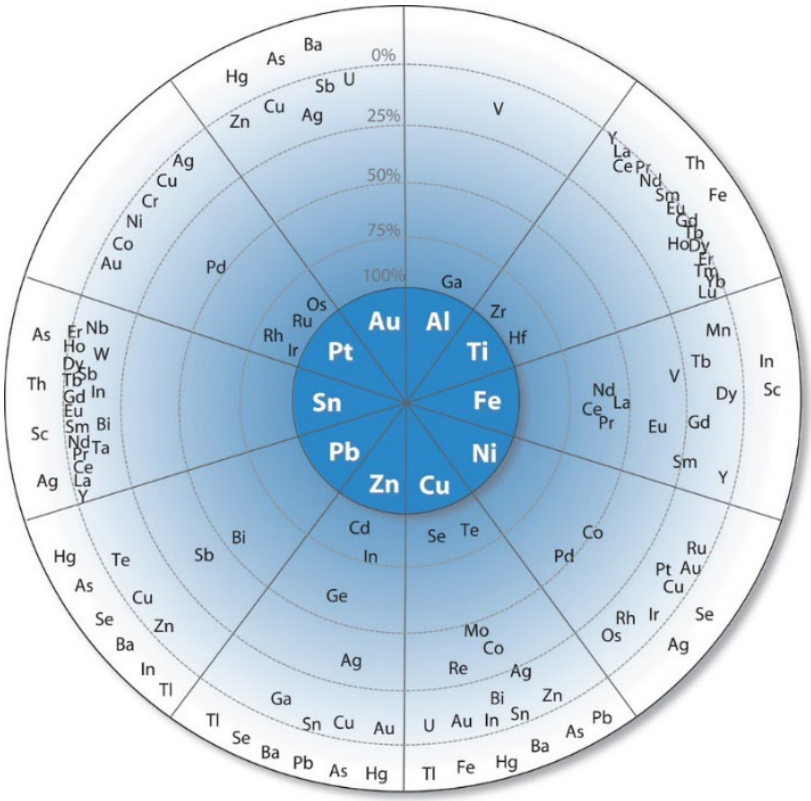

FIG 1 – Companionality matrix based on the production of host metals (inner circle) and companion metals (outer circles). Adopted from Nassar *et al* (2015).

The objective of this study was to identify the inactive TSFs of iron mine sites in WA. The assessment consisted of identifying the TSFs of iron-bearing tailings using a publicly available data set of TSFs of WA.

MATERIALS AND METHODS

The publicly available database of metals and minerals of WA called MINEDEX was used to identify the TSFs containing tailings from iron mines. This study used the data sets validated by Sarker *et al* (2022c) for visual inspection in satellite images and the companionality matrix developed by Nassar *et al* (2015) (Figure 1) to identify the host metals exploited as the major commodities of TSFs. In this study, TSFs with the major commodity of iron was separated from other major commodities. Using the data set, the TSFs were categorised according to their major commodities exploited (Table 1).

TABLE 1

Inactive TSFs in WA according to the major commodities and their companion elements with greater or equal to 50 per cent companionality (Nassar *et al*, 2015).

Major host commodities exploited	Number of inactive TSFs	Companion metals with 50% Companionality
Gold (Au)	418	none
Silver (Ag)	201	not a host in the matrix
Nickel (Ni)	37	Pd, Co
Cobalt (Co)	25	not a host in the matrix
Zircon (Zr)	16	not a host in the matrix
Copper (Cu)	10	Se, Te
Zink (Zn)	7	Cd, In, Ge
Lead (Pb)	6	Bi, Sb
Iron (Fe)	6	Nd, Ce, Pr, La

RESULTS AND DISCUSSION

Among the 539 inactive TSFs in WA, six were identified with a major commodity of iron (Table 1). Although six TSFs were identified, the TSFs with ID 67 and ID 296 were found to represent a single TSF in satellite image with an area coverage of 0.13 km^2. This made total TSFs down to five. An approximate area covered by each TSF was calculated in satellite images in Google Earth Pro. The area coverage was considered in this study to be the main element for assessing the relative potential for REEs recovery in terms of the volume of tailings available for reprocessing. This is because estimation of the volume of the tailings in the TSFs using the elevation feature of Google Earth would give unrealistic results due to the fact that the depth of the TSFs cannot be known from the satellite images. This study found the TSF with ID 475 had the largest area with a land coverage of 5.02 km^2 by a cluster of TSFs. This made the TSF to rank 1st in the relative area coverage ranking with the highest amount of tailings available for potential recovery of some REEs from this TSF. The other TSFs with relative ranking for the potential recoverable amount of REEs in ascending order are 273, 272, 67 and 296, and 517 (Table 2).

TABLE 2

Potential TSFs for REEs recovery in WA.

TSFs' ID	Name	Coordinates Latitude Longitude	Major commodities exploited	Approximate Area of the TSFs (sq.km)	Relative Ranking
67 and 296	Cockatoo Island	-16.1008 123.625	Fe	0.13	4
272	Tom Price/Rio Tinto	-22.716 117.802	Fe	0.63	3
273	Tom Price/Rio Tinto	-22.723 117.803	Fe	0.88	2
475	East Pilbara Iron Ore/FMG (clusters of TSFs)	-22.3272 119.391	Fe	5.02	1
517	Iron Bridge	-21.2421 119.059	Fe	0.1	5

Identifying the TSF using the companionality matrix is a fundamental step toward finding the potential TSFs from a large number of TSFs. Therefore, it needs to be supplemented with a detailed characterisation of the tailings before any tangible decision on moving forward to the next steps for REEs recovery can be made. The detailed characterisation should seek to find out the particle size

of the tailings, minerals type, mineral liberation and mineral locking, and concentration of the REEs. The next steps generally involve beneficiation for enhancing the grade of REEs in tailings followed by extraction processes to selectively separate the REEs. Depending on the geochemical and mineralogical properties of the tailings and the types of REEs present in the tailings, both beneficiation and extraction processes can be worked out. Generally, the beneficiation process includes any or a combination of gravity separation, magnetic separation, and froth flotation. The concentrate produced from the beneficiation then undergoes complex extraction processes of hydrometallurgy or biohydrometallurgy. The hydrometallurgical processes may include acid leaching of the concentrate followed by solvent extraction of the leached solution to separate REEs. The hydrometallurgical processes are chemical-intensive. On the other hand, the biohydrometallurgical methods which use micro-organisms to convert metals to soluble forms are considered environmentally friendly (Sarker *et al*, 2022b).

CONCLUSIONS

This study has demonstrated that some inactive TSFs in Western Australia may have the potential for REEs recovery based on the companion matrix of the host metals. Though this study is limited to an assessment of the companion matrix of the host metals, the findings could be taken as a preliminary result that can be validated by further studies on detailed characterisation of tailings from the TSFs and lab-scale experiments on the recovery of REEs by beneficiation followed by hydrometallurgical or bio-hydrometallurgical processes.

ACKNOWLEDGEMENTS

We would like to acknowledge The Commonwealth Scientific and Industrial Research Organisation (CSIRO) and RMIT University for funding this research.

REFERENCES

Abaka-Wood, G B, Zanin, M, Addai-Mensah, J, Skinner, W, 2019. Recovery of rare earth elements minerals from iron oxide–silicate rich tailings – Part 1: Magnetic separation, *Minerals Engineering*, 136, 50–61.

Australia – Country Commercial Guide, 2021. https://www.trade.gov/knowledge-product/exporting-australia-market-overview (accessed on 15/4/2022).

Frietsch, R and Perdahl, J-A, 1995. Rare earth elements in apatite and magnetite in Kiruna-type iron ores and some other iron ore types, *Ore Geology Reviews*, 9, (6), 489–510.

Moran-Palacios, H, Ortega-Fernandez, F, Lopez-Castaño, R, Alvarez-Cabal, J V, 2019. The Potential of Iron Ore Tailings as Secondary Deposits of Rare Earths. *Applied Sciences*, 9, 2913.

Nassar, N T, Graedel, T E, Harper, E M, 2015. By-product metals are technologically essential but have problematic supply. *Science Advances*, 1 (3), e1400180.

Peelman, S, Kooijman, D, Sietsma, J, Yang, Y, 2018. Hydrometallurgical Recovery of Rare Earth Elements from Mine Tailings and WEEE. *Journal of Sustainable Metallurgy*, 4, 367–377.

Sarker, S K, Haque, N, Bhuiyan, M, Bruckard, W, Pramanik, B K, 2022a. Recovery of strategically important critical minerals from mine tailings, *Journal of Environmental Chemical Engineering*, 10 (3),107622.

Sarker, S K, Haque, N, Bruckard, W, Bhuiyan, M, Pramanik, B K, 2022c. Development of a geospatial database of tailing storage facilities in Australia using satellite images, *Chemosphere*, 303 (2), 135139.

Sarker, S K, Sultana, S, Haque, N, Hughes, A E, Bruckard, W, Pramanik, BK, 2022b. Rare earth elements recovery from secondary sources, in *Environmental Technologies to Treat Rare Earth Elements Pollution: Principles and Engineering* by A Sinharoy and P N L Lens (Eds.), Chapter 5, 115–129.

Tunsu, C, Menard, Y, Eriksen, D Ø, Ekberg, C, Petranikova, M, 2020. Recovery of critical materials from mine tailings: A comparative study of the solvent extraction of rare earths using acidic, solvating and mixed extractant systems. *Journal of Cleaner Production*, 218, 425–437.

Vaughan, J, Tungpalan, K, Parbhakar-Fox, A, Fu, W, Gagen, E J, Nkrumah, P N, Southam, G, van der Ent, A, Erskine, P D, Gow, P, Valenta, R, 2021. Toward Closing a Loophole: Recovering Rare Earth Elements from Uranium Metallurgical Process Tailings. *The Journal of The Minerals, Metals and Materials Society*, 73, 39–53.

Werner, T T, Bach, P M, Yellishetty, M, Amirpoorsaeed, F, Walsh, S, Miller, A, Roach, M, Schnapp, A, Solly, P, Tan, Y, Lewis, C, Hudson, E, Heberling, K, Richards, T, Chia, H C, Truong, M, Gupta, T, Wu, X, 2020. A geospatial database for effective mine rehabilitation in Australia. *Minerals*, 10 (745).

SPH modelling-based SAG mill pulp lifter design improvement at Tritton mine and its performance on grinding circuit

N S Weerasekara[1], J J Hanhiniemi[2], T Rivett[3], J Heo[4], P Erepan[5], J Barrow[6] and S Hayes[7]

1. Principal Engineer, Weir Minerals Australia, Artarmon NSW 2064. Email: nirmal.weerasekara@mail.weir
2. MAusIMM, Head of Engineering, Weir Minerals, Artarmon NSW 2064. Email: jeremy.hanhiniemi@mail.weir
3. Area Manager, Weir Minerals Australia, Parkes NSW 2870. Email: thomas.rivett@mail.weir
4. Process Engineer, Weir Minerals Australia, Eight Mile Plains Qld 4113. Email: jun.heo@mail.weir
5. Senior Processing Engineer, Aeris Resources – Tritton Operations, Hermidale 2831 NSW. Email: perepan@aerisresources.com.au
6. Processing Manager, Aeris Resources – Tritton Operations, Hermidale 2831 NSW. Email: jbarrow@aerisresources.com.au
7. Graduate Process Engineer, Aeris Resources – Tritton Operations, Hermidale 2831 NSW. Email: shayes@aerisresources.com.au

ABSTRACT

In a modern concentrator plant, the semi-autogenous grinding (SAG) mill still plays an important part and is one of the highest capitally intensive pieces of equipment on-site. It also attracts a significant proportion of the operational cost, including electricity, grinding media and wearing mill internal parts like liners, lifters and pulp lifters. Whilst the shell, drive train and foundations represent very 'lumpy' capital investments the replaceable wear components can be customised for site-specific conditions. Therefore, it's vital that these wearing mill internal parts, during their life inside the mill, deliver maximum performance. An optimally designed and operating SAG mill, that delivers the best performance, carries majority of the grinding load off from the secondary and tertiary grinding equipment like ball mills and fine grinding mills.

Over the last two of years, Aeris Resources Tritton Copper Mine Operation, Australia, undertook a considerable amount of work to improve the performance of SAG mill internals, which in turn led to improved grinding performance. Smoothed particle hydrodynamics (SPH) was used in gaining detailed insight into complex flow behaviour in applications/components like pulp lifters, along with Discrete Element Modelling (DEM) for SAG mill liner/lifter for mill charge trajectories. These understandings were then used to build a computational framework for modelling industrial pulp lifters and to investigate unique problems associated with their design and performance.

This paper will present the design optimisation of the Tritton SAG mill pulp lifters using SPH along with other mill internals. Then it will investigate the SAG mill performance using plant historic data and site survey data combined with process modelling tools including JKSimMet®. This paper will further investigate the impact of this unit equipment improvement on the overall grinding circuit performance, its benefits thus far, and potential for further ongoing improvements elsewhere in the grinding circuit including other potential upgrades.

INTRODUCTION

Plant operators have always sought to obtain better performance from their grinding circuits. To that end, reviewing plant performance using plant survey data, historic operating data, ore property data along with simulation tools will lead to a deeper understanding of the process and assists in identifying opportunities to improve plant performance. These improvements could come in the form of improved plant operating philosophies to improvement in equipment design.

Given that SAG mills are a work horse in modern plant, SAG mill optimisation is particularly important, poor liner design has a detrimental effect on milling performance and on liner life, (Powell, 1991). As an unoptimised SAG mill can potentially lead to reduced throughput capacity, inefficient power utilisation, accelerated wears, slurry pooling, and loss of valuable materials through poor separation and overgrinding, to name a few issues. This results in a loss of revenue and increased

operational costs. Reduced milling efficiency can result in excess power usage and decreased recovery of the valuable minerals. Excess wear results in exorbitant materials costs, and excessive downtime which reduces mill availability and impacts on plant throughput (Powell *et al,* 2006). Therefore, optimising SAG mill internal plays an important part.

The great power of simulation as an optimisation and indeed design tools, is its ability to explore many different scenarios quickly and efficiently – the 'what if?' questions (Napier-Munn *et al,* 1996). This enables greater confidence and lends support for the application of a design for improved performance in terms of maximised throughput with optimum product size. The combination of new tools with a more rigorous approach to understanding the interaction of mill liners with overall mill performance and economics, forms the basis of an integrated approach to liner management (Powell *et al,* 2012).

Some previous work has been carried out in computational modelling of pulp lifter sections using DEM (Alkac, 2011; Rajamani *et al,* 2011; Rajamani, 2007) and SPH (Cleary *et al,* 2006). These modelling exercises concentrated on the flow though the grate only, rather than on the flow in the pulp lifter chamber. Limited work has being presented in terms of using CFD and coupled CFD–DEM to give a more realistic simulation of the interaction of the fluids and solids in the slurry (Weerasekara and Powell*,* 2014). Furthermore, There are dozens of papers in the proceedings of the SAG conference series that attest to issues with process design (for example SAG06, 2006; SAG11, 2011) and subsequent more recent ones (Weerasekara *et al,* 2013), but lot of them lacks the linkage between the computation modelling and overall process modelling that links/validate with plant performance data. In this work an attempt has been made to utilise these tools to improve design.

Tritton Copper Mine, owned by Aeris Resources, is located approximately 65 km west of Nyngan in New South Wales, Australia. Copper ore has been processed through the Tritton concentrator since commissioning in late 2004. The plant is currently treating 220 t/h of ore from two different mines with a feed grade of approximately 1.67 per cent Cu (Erceg and Hooper, 2015). The current objective is to increase the overall throughput while maintaining the target P_{80} of 75 µm. The flotation circuit achieves 94.5 per cent recovery at a grade of 20.5 per cent Cu, which Tritton is aiming to improve. With that objective Tritton were looking at different options.

The concentrator utilises a single stage of crushing followed by a 1500 kW SAG mill, closed circuit ball mill, and two parallel closed-circuit Verti-Mills each closed with Cavex® cyclones to produce a flotation feed of P_{80} 75 µm at 220 t/h. Primary flotation concentrate is also reground prior to additional flotation cleaning to produce a saleable product which is dewatered and railed to port (Figure 1).

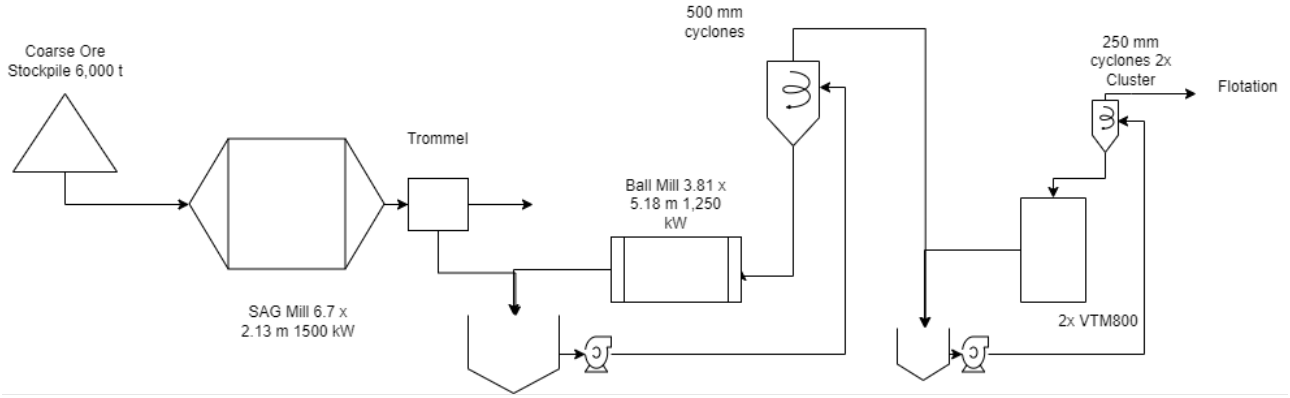

FIG 1 – Tritton grinding circuit simplified flow sheet.

Expansion of mining activities (including satellite pits) in 2018 brought a renewed focus on the throughput at the concentrator. Tritton were looking at different options and were primarily interested in those that did not require any major capital investment. Given that the SAG mill is the workhorse of the plant, increasing its performance became the main focus. Consequently, an opportunity was identified to improve grinding performance through mill internals design including increasing the discharge grate size and/or open area, and pulp chamber design changes. To this end, detailed DEM and SPH was carried out in reviewing the design. The modelling facilitated the opportunity to investigate how the capacity of the pulp lifters could be increased, enabling increased throughput.

Additionally, an increased open area with smaller apertures was achieved on the discharge grates (Weerasekara and Town, 2019). This paper attempts to quantify process performance, predicted using DEM and SPH, through process data and quantify the impact of these changes after all grate and pulp lifters were updated to the new design in early 2022.

SPH and DEM MODELLING – SAG MILL INTERNAL REVIEW AND MODIFICATIONS

As a first stage of mill internal review, shell lifter and liner design were reviewed using DEM modelling (RockyDEM, 2017). The lifters were optimised to minimise overthrow for a typical operating filling level (Figure 2) of the Tritton SAG mill. This work formed the basis and guide for the next stages of optimisation of the mill internals, which is the review of the mill discharge components.

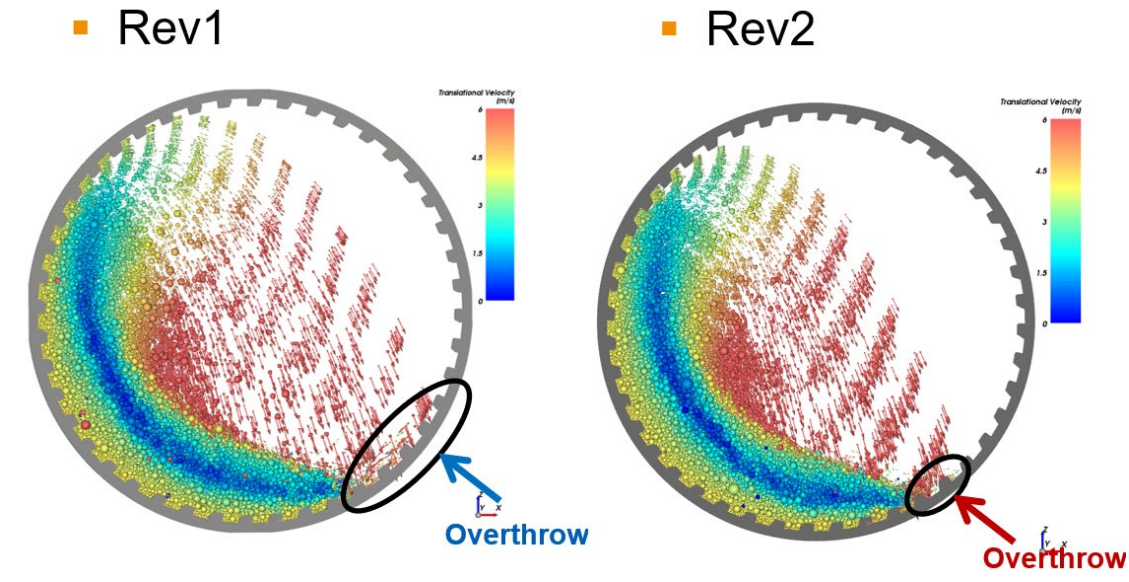

FIG 2 – Shell liner DEM modelling for two different lifter/liner geometric revisions.

The pulp discharge mechanism, consisting of a grate and pulp lifter arrangement, is an integral component of AG/SAG mills. The grate retains over-size particles in the mill charge. The mixture passing through the grate consists of coarse and finer particle products, generated due to the grinding process in the mill. In the text, the term 'slurry' is referring to this mixture. The pulp lifters transport the slurry, which has passed through grate apertures, into the discharge trunnion (Figure 3).

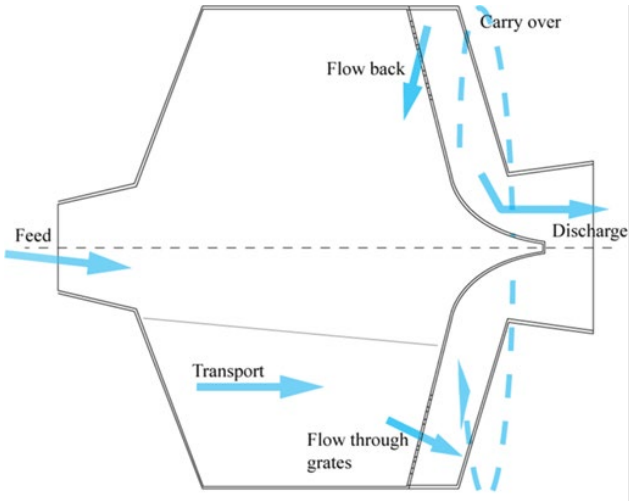

FIG 3 – Graphical representation of the slurry transport in an AG/SAG mill (Weerasekara and Powell, 2014).

Understanding and visualisation of the flow dynamics through grates and pulp lifter chambers for each potential arrangement is needed to assess its performance, and subsequently identifying bottlenecks and inefficiencies. This visualisation plays an important part in design optimisation, but is a challenging task in an operational mill. Therefore, one must rely on computational modelling techniques like DEM, computational fluid dynamics (CFD) or SPH with the aid of plant operational data.

This work looks at optimising pulp lifter design using SPH at Tritton mines' SAG mill with the view of increasing throughput and optimising wear (Figure 4). SPH simulations, with the aid of DEM simulation, characterises the flow dynamics in the pulp lifter system. However, this application requires excessive computation time/power for a fully three-dimensional simulation. For more details of the modelling work, the reader is referred to Weerasekara and Town (2019).

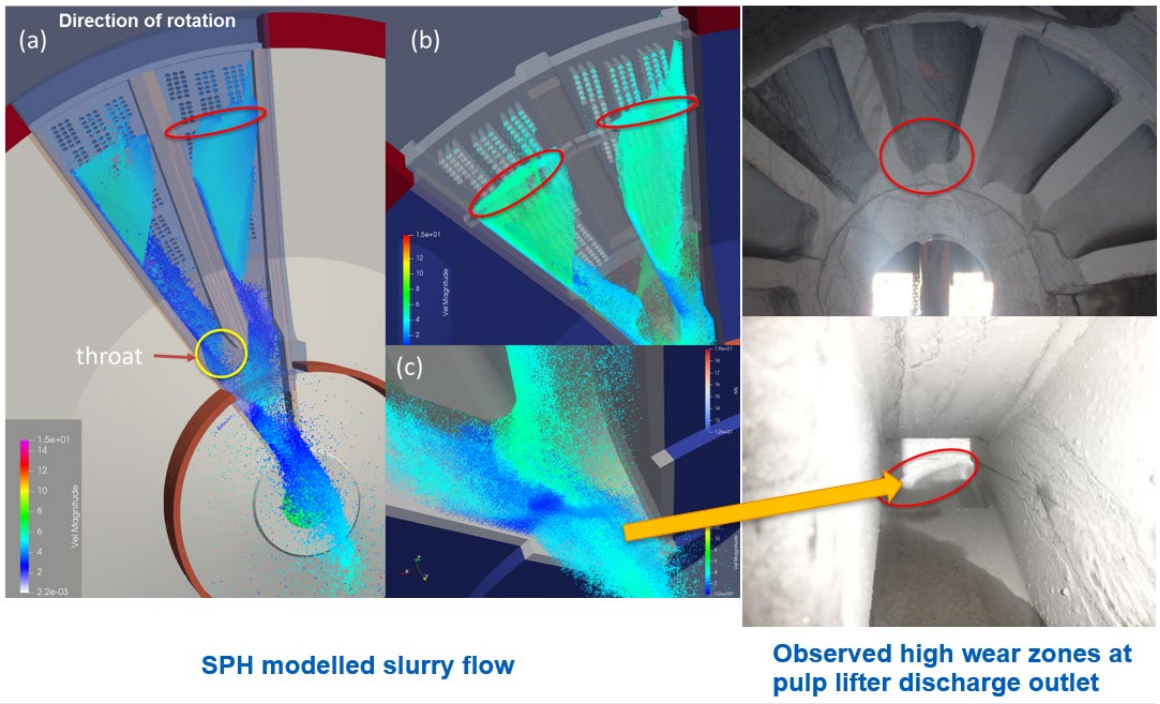

FIG 4 – Comparison of SPH modelled slurry flow wear observed on-site (Weerasekara and Town, 2019).

The modelling showed high wear zones at the pulp lifter discharge outlet. In the incumbent design, with the rotation of the mill, slurry was not being discharged effectively and the aggressive recirculation was causing localised wear (Figure 4). To combat this, a threefold approach was proposed: increase the open area in each panel by 1.1 per cent, widen the throat of each pulp lifter by 39 per cent and optimise the reinforcement bar to facilitate improved flow in the chamber without compromising structural strength. These changes would result in quicker discharge of slurry and reduction in slurry returning with the rotation of the mill, while achieving increased throughput.

The design work involved in SAG internals was documented in detail in Weerasekara and Town (2019), which led to the following design changes on-site: the lifters and liners were changed as an initial stage, the open area of the grates was increased from 10.73 per cent to 11.83 per cent, the grate aperture was decreased, and the pulp lifters were modified.

These design changes were targeted to increase throughput by reducing flow back and carryover (as described in Figure 3). Removal of fines with water from the mill reduces overgrinding allowing more ore to be processed for a given energy input. The modelling predicted that modifying the grate plate and pulp lifter design would lead to a decrease in recirculation (slurry carry-over) by 24 per cent and increase slurry filling by 10 per cent, leading to a potential increase in overall throughput of approximately 8 per cent. The Weir Minerals mill specialists continue to work in partnership with Tritton to implement these improvements.

As part of new design implementation on-site, trials were in place at Tritton:

- In 2019, the site initially installed six new-design trial grate plates, with notable improvement in P_{80}, which has the capacity to reach a throughput capability of 250 t/h.
- In the second stage of trial, the site increased the number of new-design trial grate plates to 11, keeping 11 of standard design. This helped in relieving the load off the ball mill.
- In the third stage, the number of new-design trial grate plates was increased to 16, which resulted in further improvement in P_{80}, with the capacity to reach throughput capability of 250 t/h.
- Site installed new-design pulp lifters recently.

SOME OBSERVATIONS OVER TIME ON-SITE DUE TO THESE CHANGES

Overthrow was highlighted in the original DEM work and confirmed from mill inspections. When a mill is overthrowing, particles strike the lifters and liners rather than landing at the toe of the charge. Following the initial DEM work and upgrading mill lifters and liners, the operation of the SAG mill was also changed to operate at a filling of about 24 per cent at all times. This operational change has resulted in SAG mill reline campaigns going from 12 weeks to 16 weeks. No attempt has been made in this work to separate the effect of this operational change from the effects of the grate and pulp lifter changes.

Note that an additional benefit of the site focus on the SAG mill was the elimination of a premature failure mode on the cyclone feed pumps. Prior to the improvement works, large grinding media was reporting to the cyclone feed pump. Improved structural integrity of the mill grates, sealing the hole in the centre of the discharge end and replacing the trommel increased the service life of the pump from 600 to 2000 hours (without any change in impeller design or materials of construction).

JKSIMMET® MODELLING – SAG MILL PERFORMANCE REVIEW

Over the course of this exercise, several plant surveys were carried out before and after new design upgrades to the SAG mill with the aim of reviewing and assessing the performance. The SAG Mill performance was reviewed using JKSimMet® (Figure 5), using three independent surveys around the SAG mill so far. The first survey was executed around 2016/2017 before the implementation of the grate design changes. This survey became the basis for the design review of the pulp system using DEM and SPH. Then a mini-survey was carried out in late 2021 after implementing the grate design changes only. Then another mini-survey was performed after the pulp lifter installation in early 2022 (this includes the new grate design). Each survey data set was mass-balanced and then model-fitted separately. The model-fitted parameters were then assessed and analysed. This data was used to update and improve the overall simulation for the site.

New design upgrade to the SAG mill

The SAG mill performance was first characterised by the breakage rates in the mill. The breakage rate was fitted with respect to the particle size distribution (PSD) observed in each survey. The calculated breakage rate/function was then used to simulate the mill with respect to changes in variables such as feed rate, feed PSD, and slurry density in the mill.

As a first step, fitted breakage rates using survey data before and after the new grate design (modification) were compared (Figure 6). The fitted breakage rates from the mini-survey data largely follow the typical trend observed in SAG mills (Figure 7). A typical breakage rate range is also plotted in Figure 8 for reference. These rate curves exhibit a characteristic shape, where the coarser breakage rates relate to abrasive breakage and the breakage rates around the finer particles relates to predominately impact breakage, similar to coarse ball milling (Morrell and Morrison, 1996). A dip around the 40 mm mark due to ‘critical size’ particles is accurately represented in the 2021 mini-survey results compared to the survey data collected in 2016/2017. This is clearly seen in Figure 6 below. This can be attributed to improved SAG mill performance. The plot of the breakage rates from 2021 mini-survey results (after the grate design modifications) are in close alignment with typical SAB mill breakage rate plots. However, the 2016/2017 survey results show unusual breakage rates which could be representing suboptimal performance before any optimisation work.

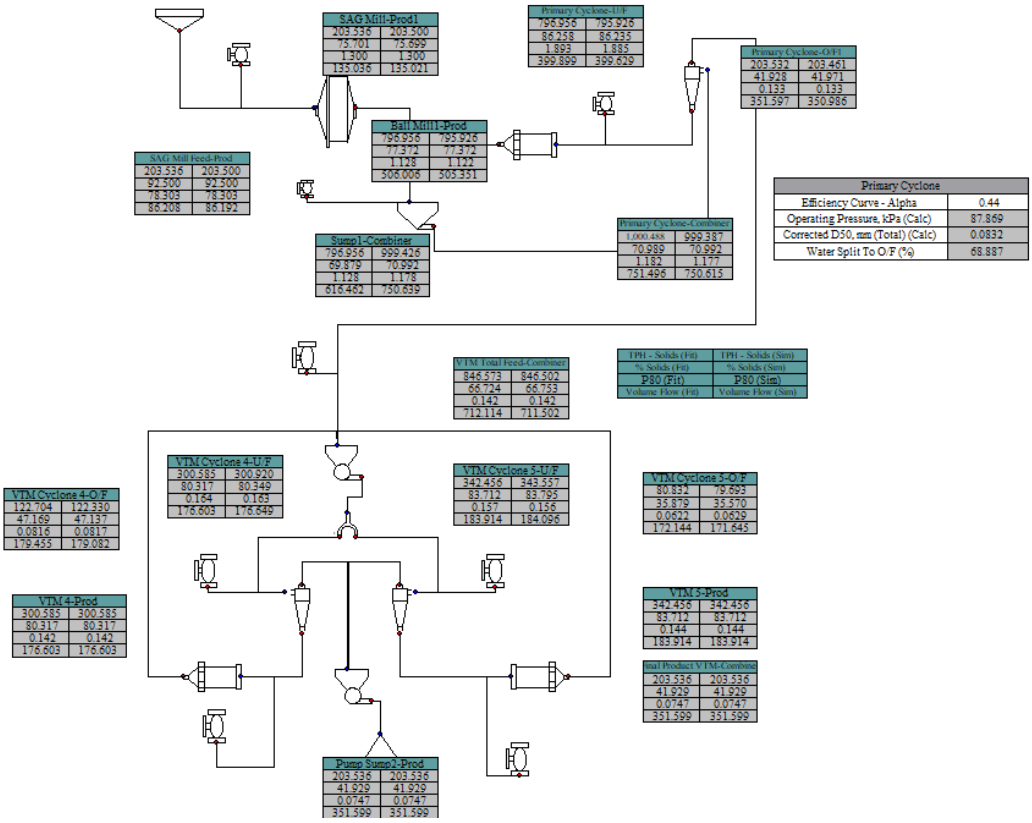

FIG 5 – Baseline model flow sheet.

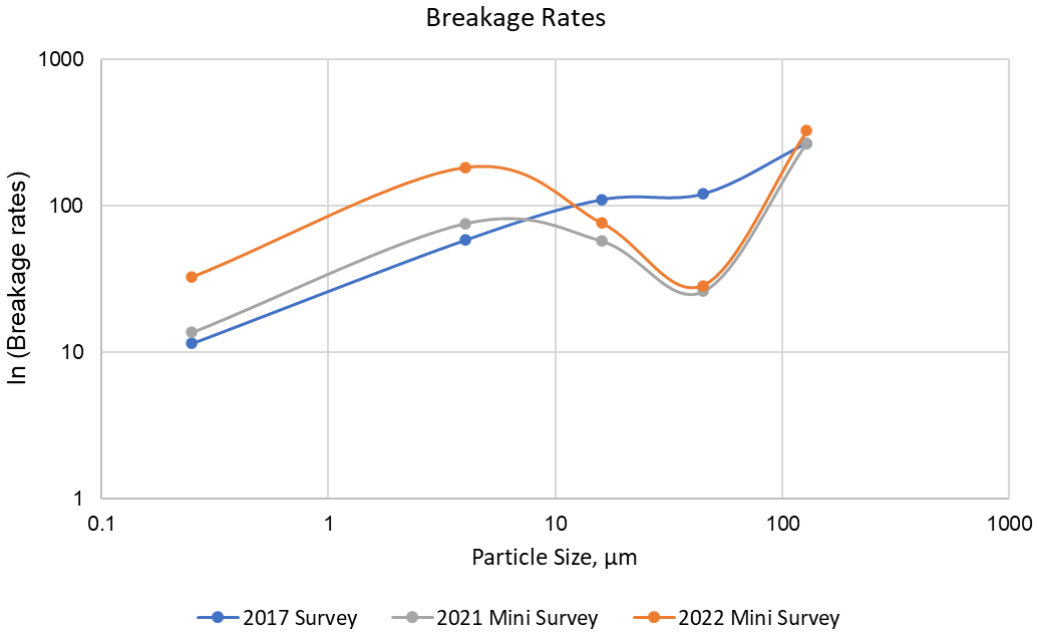

FIG 6 – Breakage rates.

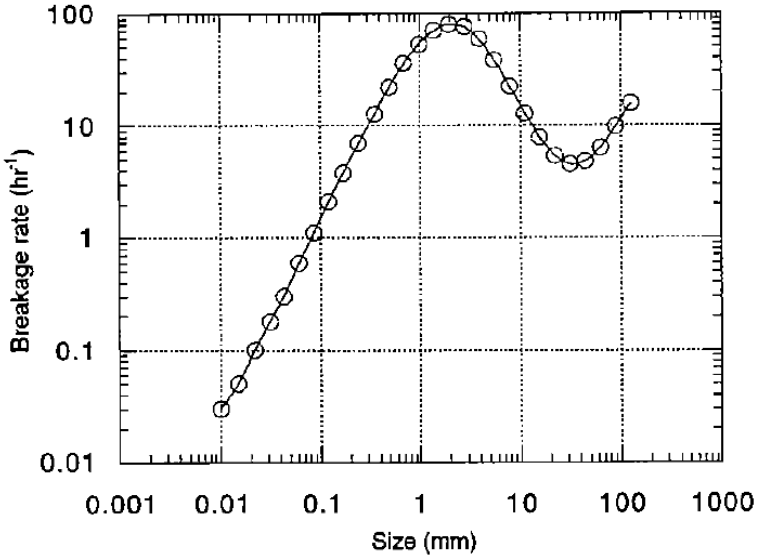

FIG 7 – An example of a breakage rate distribution (Napier-Munn *et al,* 1996).

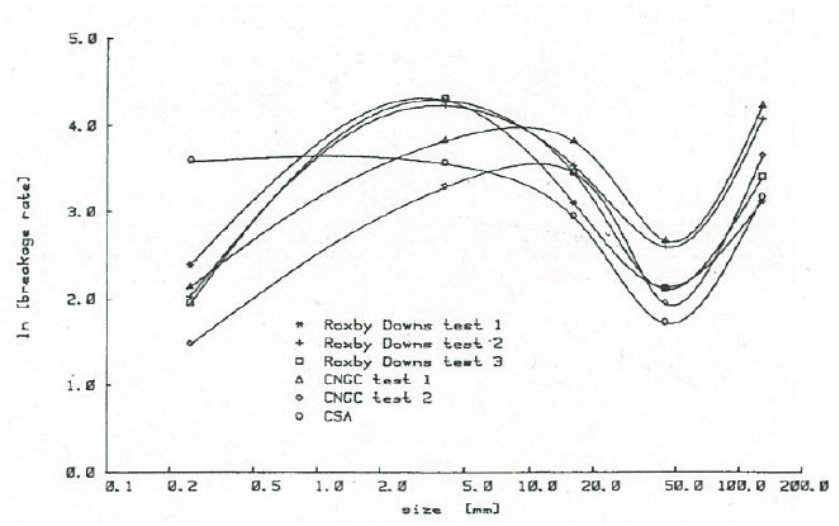

FIG 8 – Typical breakage rates (JKSimMet, 2014).

The breakage rates fitted from the recent survey data (2021) are close to typical breakage rates from several published surveyed sites. Given this, there is more confidence on the surveying practice and fitting result obtained here than in the previous survey. Further, it can be seen that the fine size rates have increased – as would be expected from the higher charge filling and improved autogenous grinding performance. This was likely achieved by the optimisation of the SAG mill internals and process operations. The new fitted rates from the 2021 survey will be used to update the models developed in JKSimMet® for more accurate results when processing the upcoming ore deposit.

To further review the process benefits around the performance of the SAG mill, the historical data of before and after the new grate upgrade were analysed and plotted as mill power versus throughput (Figure 9). Due to the change in the competencies of the ore treated during this period, the throughput could not be pushed higher than 230 t/h. Despite using more competent ore, it shows the power utilisation is in a similar range (Figures 9 and 10) The historic power draw data shows that the SAG mill operates at around 1420 kW, which is 95 per cent of the install power (1500 kW). Furthermore, when comparing the average SAG mill discharge P_{80}, it has come down to 1.03 mm in 2021 from 1.27 mm during 2016/2017 survey period. This shows that the mill is now capable of finer grinding and can process higher throughputs whilst maintaining a manageable power draw. This is not withstanding variations of ore feed size and competence, which are unknown.

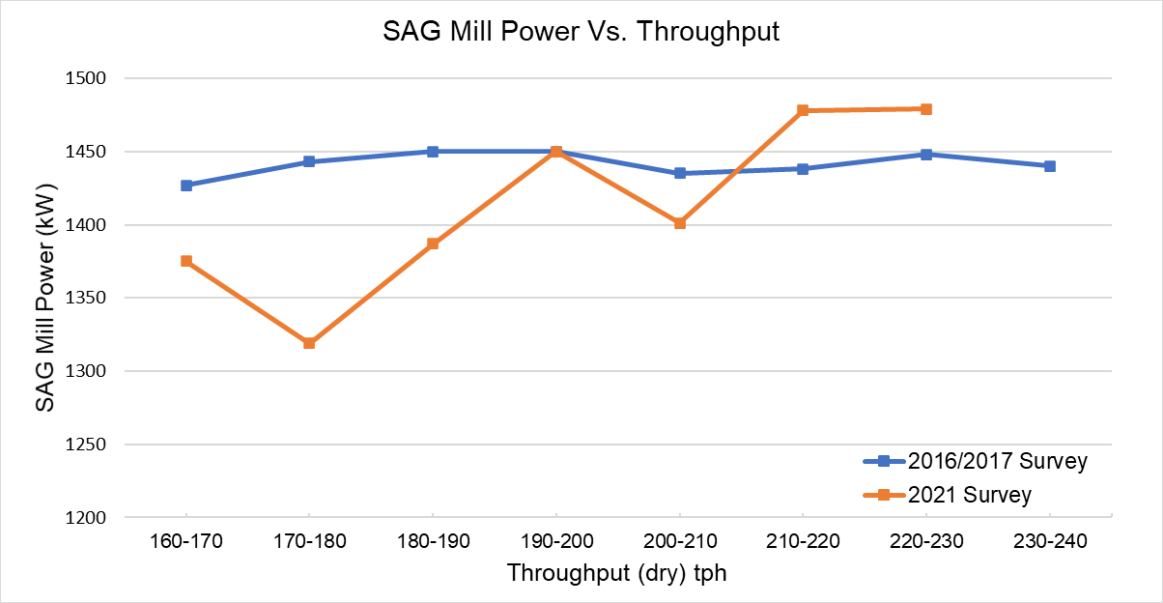

FIG 9 – Power versus throughput before and after new grates 2016/2017 Survey (before grate design changes) versus 2021 Survey (after grate design changes).

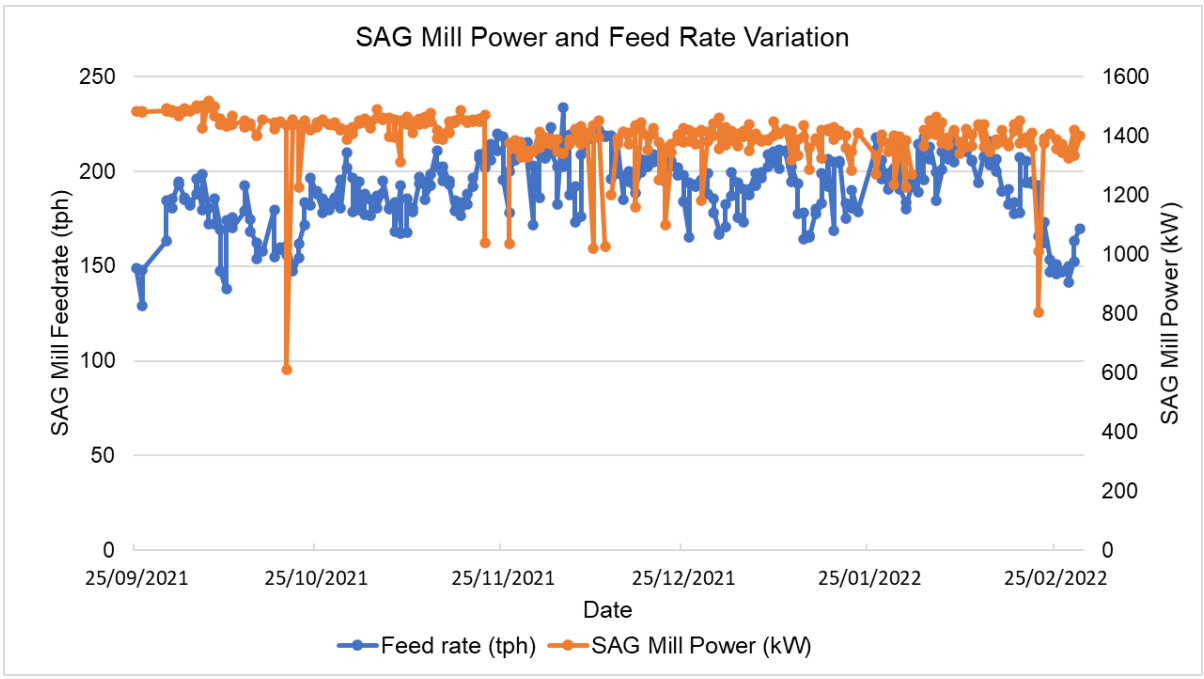

FIG 10 – Historical throughput (dry) and power data after new grates (2021 Survey).

SAG mill grinding efficiency

Table 1 below compares the specific energies and the operating work indices for both the 2021 survey and 2016/2017 survey data sets. The operating work index is defined as the total energy required to breakdown the ore per tonne in the mill (Wills and Finch, 2015). It can be utilised in quantifying potential improvements in grinding efficiency by comparing the operating work indices between the two survey results. A decrease in the operating work index implies that grinding efficiency has increased, as it requires less energy to breakdown the ore, assuming constant ore properties.

The 2021 survey data set showed a 11 per cent reduction in the operating work index compared to the 2016/2017 survey result. The reduction in the operating work index indicates or could be attributed to higher grinding efficiency during the 2021 survey. This was likely achieved by improved grinding, from increased ore filling and power utilisation, with the updated mill internals and grate changes.

TABLE 1

Estimated milling duty.

	2016/2017 Survey	2021 Survey	2022 Survey
Specific Energy (kWh/t)	7.13	6.91	8.68
Operating Work Index (kWh/t)	28.07	25.24	19.96

Potential future circuit upgrade scenario

The site has undertaken the study of the new orebody from the Budgerygar ore deposit. This new ore is expected to be available for processing on-site in upcoming years. The SMC results from test work executed at JKTech indicated some changes in the ore properties compared to the existing ore. The Budgerygar ore displays softer ore characteristics, as seen in the comparison of SMC test results in Table 2. Table 3 provides a key as to the relative hardness of the Axb and Ta parameters.

TABLE 2

SMC test results.

Sample	DWi (kWh/m^3)	DWi* (%)	Mia (kWh/t)	Mih (kWh/t)	Mic (kWh/t)	A	b	Axb	SG	Ta
Budgerygar Ore	4.7	25	12.3	8.5	4.4	50.8	1.35	68.58	3.22	0.55
Current Ore	5.1	30	14.4	10.1	5.2	61.5	0.93	57.20	2.92	0.51

TABLE 3

Resistance to impact breakage – SMC.

Relative hardness	Very hard	Hard	Moderate hard	Medium	Moderate soft	Soft	Very soft
Axb	<30	<30–38	38–43	43–56	56–67	67–127	>127
Ta	<0.24	0.24–0.35	0.35–0.41	0.41–0.54	0.54–0.65	0.65–1.38	>1.38

To prepare for the upcoming Budgerygar ore, Tritton requested a study to be carried out to assess the effects of the Budgerygar ore on the overall plant response and the performance of the circuit. This work was done by simulating the base case model (based on the 2016/2017 survey data) with the updated ore parameters obtained from the SMC test work and updated breakage rates from the recent survey conducted in 2021 for the SAG mill. In addition, the effects of the pulp lifter changes will be captured and analysed at a later stage, when the data is received.

As predicted, the results indicate that the change in ore properties had significant effects on the transfer sizes in various streams and grinding stages which can be seen in Table 4. This highlights the need to employ simulation for planning the processing of new ores, and to conduct circuit optimisations including transfer sizes, grinding and classification performance. Therefore, a series of circuit upgrade scenarios are currently being reviewed as part of the optimisation study in partnership with Tritton mines.

TABLE 4

Budgerygar ore simulation transfer sizes.

		SAG mill feed (mm)	SAG mill discharge (mm)	Ball mill feed (mm)	Ball mill product (mm)
Underground Tritton and Murrawombie Open Pit Ore blend	2017 survey – prior to optimisations	78	1.3	1.89	1.13
Underground Tritton and Murrawombie Open Pit Ore blend	2021 survey results – after grate design changes	56	1.031	TBD	TBD
Budgerygar Ore	Based on 2017 survey model parameters	56	1.06	0.69	0.53

CONCLUSIONS

The objective of this work was to identify the process benefits of the improved SAG internal design changes, informed via SPH and DEM modelling work, recently installed in the primary grinding circuit at Tritton. This work focuses on improving wear life, improving cut size/transfer sizes between major pieces of equipment, and improving overall grinding and classification efficiency.

The modifications in the SAG mill design included:

- Pulp lifter design.
- Increased open area fraction of the grates.
- Decreased grate aperture sizes.

The process modelling tool, JKSimMet®, was utilised to determine the process benefits using independent survey data at each stage of the installation (before the grate design changes, after the grate design changes, after the installation of the modified pulp lifters) provided to Weir.

Through optimisation of the mill internals, the survey data indicated that the site achieved:

- Improved energy utilisation by 11 per cent (Lowered Bond Work Index, increased throughput).
- Improved grinding efficiency (Improved Operating Work Index from 28.07 to 25.24 kWh/t).
- Improved breakage rates/function that best reflects the typical SAG mill breakage rates compared to 2016/2017 survey data.
- Potential increase in throughput capacity to about 250 tph (which requires more data for validation).

A further evaluation of the plant was performed using the ore characterisation data of the Budgerygar ore deposit. This detailed analysis will continue to be used to simulate various scenarios via JKSimMet®, to continue ongoing process optimisation of the overall circuit, continuing collaboration with Tritton.

ACKNOWLEDGEMENTS

The authors would like to thank Tritton Copper Mine for supporting and implementing the outcome of this work and permission to publish the article. Special appreciation is extended to Peter Erepan, Jamie Barrow and operating, maintenance and metallurgy personnel from Tritton. Authors would like to thank Sharon Lo proofreading this document. Also, thanks to Grant Payseno, Mill Systems Engineer from Weir Minerals for his continued help.

REFERENCES

Alkac, D, 2011. Modeling flow in pulp lifter channels of grinding mills with computational fluid dynamics. In: *Metallurgical Engineering*. University of Utah.

Cleary, P W, Sinnott, M D and Morrison, R D, 2006. Prediction of slurry transport in SAG mills using SPH fluid flow in a dynamic DEM based porous media, *Minerals Engineering,* 19(15), pp. 1517–1527.

Erceg, M and Hooper, B, 2015. The Tritton copper mine, New South Wales: new understanding of the deposit and its potential from mining of this blind discovery.

JKSimMet, 2014. User manual and training course materials.

Morrell, S and Morrison, R D, 1996. AG and SAG mill circuit selection and design by simulation. In A L Mular, D J Barratt and D A Knight (Eds.), *International autogenous and semi-autogenous grinding technology,* vol 2, pp 769–790. Vancouver: University of British Columbia, Department of Mining and Mineral Process Engineering.

Napier-Munn, T J, Morrell, S, Morrison, R D and Kojovic, T, 1996. *Mineral Comminution Circuits – Their Operation and Optimisation*. JKMRC, University of Queensland, Brisbane, Australia.

Powell, M S, 1991. The effect of liner design on the motion of the outer grinding media in a rotary mill. *International Journal Mineral Processing* 31: 163–193.

Powell, M S, Hilden, M M, Weerasekara, N S, Yahyaei, M, Toor, P, Franke, J and Bird, M, 2012. A more holistic view of mill liner management, *Proceedings of the 11th Mill Operators Conference*, pp 95–104 (The Australasian Institute of Mining and Metallurgy: Melbourne).

Powell, M S, Smit, I, Rdziszewski, P, Cleary, P, Rattray, B, Eriksson, K and Schaeffer, L, 2006. The selection and design of Mill Liners, in *Advances in Comminution*, pp 331–376.

Rajamani, R K, 2007. Simulation of charge transport in the pulp lifter of a semi autogenous grinding mill. In: DEM 07, Brisbane, Australia.

Rajamani, R, Alkac, D, Delgadillo, J, Kumar, P, Page, D, Fillion, M and Pelletier, S, 2011. Pulp-lifter flow modeling study in a pilot scale mill and application to plant scale mills. In: Major, K, Flintoff, B, Klein, B, McLeod, K (Eds.), SAG2011 *Proceedings of the International Autogenous and Semiautogenous Grinding Technology 2011*, CIM.

RockyDEM, 2017. RockyDEM Technical manual, ESSS Rocky.

SAG06, 2006. Mular *et al,* (Eds.), *Proceedings of the International Autogenous and Semiautogenous Grinding Technology 2006*, CIM.

SAG11, 2011. K Major, B Flintoff, B Klein, K McLeod (Eds.), *Proceedings of the International Autogenous and Semiautogenous Grinding Technology 2011*, CIM.

Weerasekara, N S and Powell, M S, 2014. Performance characterisation of AG/SAG mill pulp lifters using CFD techniques, *Minerals Engineering*, 63:118–124.

Weerasekara, N S and Town, S, 2019. Optimising pulp lifter design using SPH Simulation: Tritton story, In: *Proceedings of the International Autogenous and Semiautogenous Grinding Technology 2019*, CIM.

Weerasekara, N S, Powell, M S, Cleary, P W, Tavares, L M, Evertsson, M, Morrison, R D, Quist, J and Carvalho, R M, 2013. The contribution of DEM to the science of comminution, *Powder Technology*, 248:3–24.

Wills, B A and Finch, J A, 2015. *Wills' Mineral Processing Technology* (Eighth Edition). Montréal: Butterworth-Heinemann.

BP neural network based on MIV algorithm and its application in phosphate ore flotation index prediction

Y J Wu[1], Q Zhang[2,3,4] and S W Huang[5]

1. Postgraduate, Guizhou University, Guiyang China 550025. Email: 1061671870@qq.com
2. Professor, Guizhou Academy of Sciences, Guiyang China 550025. Email: zq6736@163.com
3. Professor, National and Local Joint Engineering Laboratory for Efficient Utilization of Superior Mineral Resources in Karst Area, Guiyang China 550025.
4. Professor, Guizhou Key Laboratory for Comprehensive Utilization of Nonmetal Mineral Resources, Guiyang China 550025.
5. Professor, College of Land Resources Engineering, Kunming University of Science and Technology, Kunming China 650093. Email: 594770837@qq.com

ABSTRACT

In the flotation process, flotation index detection is an important means to reflect the flotation process index and improve the flotation process and efficiency. Aiming at the difficulty of flotation index detection, a prediction method combining mean impact value (MIV) algorithm and BP neural network is proposed in this paper. First of all, based on the flotation mechanism of the knowledge and experience to determine fineness of grind, pulp density, flotation time, dosage of collector and acidic wastewater, the rotor speed, a total of six parameters as the basis of forecast flotation index, and through the single factor experiment and orthogonal experiment to study the effect of related variables on the flotation indexes, then through the MIV algorithm select appropriate input variables of neural network model are set-up, Finally, the prediction model of phosphate ore flotation index is established by BP neural network. The effectiveness and feasibility of the proposed method will verified by subsequent experiments.

INTRODUCTION

In recent years, with the rapid development of industrial and agricultural modernisation, the demand for phosphate resources is also increasing year by year, and the high quality phosphate ore that can be directly used is increasingly exhausted. Therefore, the processing of middle and low-grade phosphate rock and its effective utilisation plays an important role in the development of phosphate rock resources in China (Zhang *et al*, 2017). According to statistics, China's phosphate mineral reserves are relatively rich. As of 2019, China's phosphate mineral reserves are about 3.3 billion tons. Due to the long production cycle of phosphate ore flotation process, there are some problems in the intermediate flotation process, such as high coupling and variety of factors affecting the flotation results (Xue and Zhang, 2019). In order to monitor the change of flotation index and improve the yield of phosphate rock, it is very important to accurately predict the result of flotation index.

In the past, there are mainly two ways to predict the actual flotation indexes: one is to predict the flotation indexes through the on-site workers' long-term experience for many years; the other is to predict the flotation indexes based on the flotation theory or through a large number of experimental data under certain conditions. However, it is difficult to describe a complex production system(like this) by means of simple manual observation or linear control.

At present, soft sensor technology has been widely used in mining, mineral processing, coal-fired power generation and other process industries (Sun *et al*, 2021). Literature studied the influence of flotation time, reagent concentration and pulp pH value on ion flotation to remove Zn, compared the accuracy of Zn prediction by neural network model using genetic algorithm and multiple linear regression model, and the results showed that the accuracy of neural network prediction model was higher. The research of prediction model shows that pH value and flotation time of pulp has great influence on zinc ion removal rate (Hoseinia *et al*, 2020). Literature demonstrates the forecasting performance of flotation reagent dosage forecasting model established by BP neural network and generalised regression neural network through experiments, and points out that BP neural network has higher accuracy in flotation reagent dosage prediction (Yang *et al*, 2020). Literature the neural network combining principal component analysis, chaotic ant colony algorithm and least square method is used to predict the economic indicators in the flotation process. By comparing with the

principal component analytic-BP neural network model, the prediction accuracy of this model is improved by 1.8 per cent (Zhang *et al,* 2016). Literature takes inflating volume, ore feeding concentration, grade, particle size and reagent flow as control variables of the soft sensor model, and concentrate grade and recovery as output variables, and establishes a feedforward neural network model based on particle swarm optimisation algorithm and gravitational search algorithm (Wang and Han*,* 2015). In literature, BP neural network model was established by collecting experimental data through orthogonal test, and the agent system was optimised by BP neural network model to simulate the change rule under the action of different agents. In addition, the optimised agent system could reduce the dosage of agents while keeping the flotation index unchanged (Zhang *et al,* 2018).

As a new field of intelligent control research in recent decades, neural network system is a highly nonlinear dynamic system combining artificial intelligence, dynamic model, nonlinear system and other disciplines. It has the advantages of strong adaptability, strong robustness and strong parallel processing ability. Although neural network control is a black box model and is not good at expressing knowledge, it has strong self-applicability, self-organisation and learning ability and can approximate arbitrary complex nonlinear mapping to analyse the dynamic characteristics of the control system. In today's intelligent industrial production, neural network control in intelligent control, information data processing, prediction and other fields have been a large number of applications. In this context, neural network control technology in the flotation process has been paid more and more attention.

FLOTATION PROCESS AND PREDICTION MODEL DESIGN

Due to the complexity of flotation process, there are a lot of influencing factors and external disturbing factors. It is particularly important to choose the control variables for flotation index prediction (Popli *et al*, 2018). This paper studies the influence factors of reverse flotation process of phosphate ore in the flotation process. Based on the study of flotation mechanism and experience, six parameters including grinding fineness, amount of collector, amount of pH regulator, pulp concentration, rotor speed and flotation time were used as the basis for predicting flotation indexes.

Considering the different factors under the same conditions on the concentrate flotation grade and recovery of P_2O_5 different degree of influence, so the flotation efficiency as the orthogonal test of the investigation index, so as to analyse the overall effect of each factor on the flotation index.

Criterion formula of flotation efficiency:

$$E_h = \frac{\varepsilon - \gamma}{1 - \frac{\alpha}{\beta_m}} \quad (1)$$

Where: ε is concentrate recovery, γ is fine mineral rate, α is raw ore grade, β_m is collophanite single mineral theoretical grade (42.06 per cent).

The training input data of neural network are single factor test data and orthogonal test data of grinding fineness, collector dosage, pH regulator dosage, pulp concentration, rotor speed and flotation time, and the flotation efficiency calculated after each single factor test and orthogonal test is output. The number of training samples is 50 groups.

There were 25 groups of single factor tests. In the single factor test, the slurry concentration was 27 per cent, the adjusting agent dosage was 0.2 m^3/t, the collector dosage was 750 g/t, flotation time was 4 min, rotor speed was 2000 rev/min and grinding fineness was 73.8 per cent. Perform the single factor test as shown in Table 1.

TABLE 1

Single factor flotation test.

Pulp density (%)	Adjuster Dosage (m^3/t)	Collector dosage (g/t)	Flotation time (min)	The rotor speed (rev/min)	Grinding fineness (%)
23	0.05	300	0.5	1600	64.4
27	0.1	450	1	1800	73.9
31	0.15	600	1.5	2000	77.8
35	0.2	750	2	2200	82.5
38	0.25	900	4	2400	92.4

Then 25 groups of training samples were orthogonal test with six factors and five levels. The orthogonal test was carried out by changing the grinding fineness, the amount of collector, the amount of pH regulator, pulp concentration, rotor speed and flotation time. as shown in Table 2.

TABLE 2

Orthogonal flotation test.

	Factors	Level				
		1	2	3	4	5
A	Pulp density (%)	23	27	31	35	38
B	Adjuster Dosage (m^3/t)	0.05	0.1	0.15	0.2	0.25
C	Collector dosage (g/t)	300	450	600	750	900
D	Flotation time (min)	0.5	1	1.5	2	4
E	The rotor speed (r/min)	1600	1800	2000	2200	2400
F	Grinding fineness (%)	64.4	73.9	77.8	82.5	92.4

AVERAGE INFLUENCE VALUE ALGORITHM

Average influence value algorithm

When considering the establishment of neural network model, the selection of input variables is particularly important for the establishment of accurate model. If there are too many input variables, the structure of the model will become complicated and the training time of neural network will be increased. Similarly, too many variables will lead to over-fitting phenomenon in the training process, while too few input variables will lead to under-fitting phenomenon, which will decrease the accuracy of the model. In order to select appropriate input variables, Dombi *et al* (1995) proposed to use mean impact value (MIV) to reflect the changes of weight parameters in the established neural network, so as to better evaluate the correlation of various variables in the neural network. The specific screening process is shown in Figure 1.

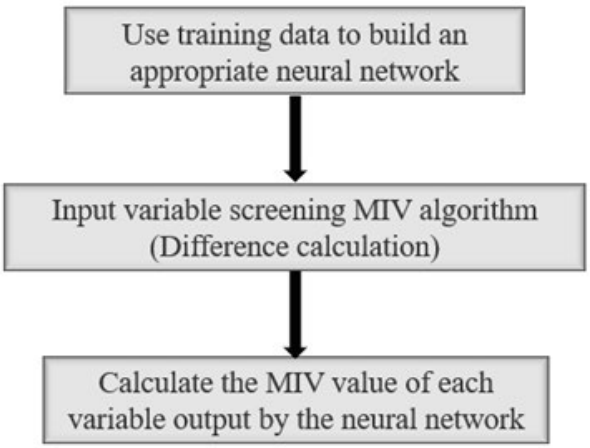

FIG 1 – Flow chart of variable screening.

Mean impact value (MIV) algorithm is to increase or decrease each input variable in a certain proportion, and input the increased or decreased variable into the neural network model again, and then express the responsiveness of the relevant input variable to the model through MIV value. The absolute value of its MIV value represents the influence degree of the input variable on the model, and the sign represents the direction of the correlation of the input variable. Its specific calculation is as follows:

1. Train n input variables and m training samples on the neural network to obtain the appropriate neural network structure, and then increase or decrease the input variable P in the training sample by 10 per cent in order to obtain two new training samples P_1 and P_2.
2. The new training samples P_1 and P_2 were predicted by the established neural network model, and the results were recorded as P_1^1 and P_2^2.
3. Calculate the difference between P_1^1 and P_2^2, and the result can be expressed as the influence value of the i-th input variable on the output result $V_{iv(j)}$.
4. V_{imp} is averaged according to the number of training samples N, and the obtained value represents the average influence value of the input variable on the output of the neural network $V_{miv(j)}$.

$$V_{miv(j)} = \frac{1}{m}\sum_j^m V_{iv(j)} \quad \text{(j=1,2,3,…,n)} \tag{2}$$

Rank according to the absolute value of MIV calculated by the model, and analyse the influence degree of correlation of each input variable according to the order of rank. According to the importance of each input variable, select the variable that has little influence on the output, so as to realise the selection of input parameters.

BP neural network model

BP neural network is a forward neural network propagating according to the direction of error, which is mainly composed of input layer, hidden layer and output layer. Because of its strong nonlinear mapping ability, self-learning and self-adaptability, it has always been a hot spot in the field of neural network research and application. The number of input nodes of BP neural network is its input dimension, and the number of output nodes is its output dimension. The number of hidden layer nodes can be determined according to the complexity of practical problems.

In this paper, the input variables are grinding fineness, collector dosage, pH regulator dosage, pulp concentration, rotor speed and flotation time, and the flotation efficiency is taken as the output variable. According to the structure of the neural network, the constructed neural network has six input nodes and one output node. At present, the empirical formula is generally adopted to select the number of hidden layer nodes:

$$b = \sqrt{n+m} + a \tag{3}$$

Where, b is the number of nodes at the hidden layer, n is the number of input nodes, m is the number of output nodes, and a is the constant of [1,10].

The neural network model in this paper adopts a double hidden layer, with a node number of 10–6-1. Its transfer function is divided into tansig and logsig. Considering its slow convergence speed, the training function trainLM is adopted. The number of iterations is 1000, and the root mean square error is 0.001, and the learning rate is 0.01. When training the neural network model, it is not necessary to separate the test data set from the training data set for the small size of the data set. The advantages of this algorithm are the linear combination of minimising weights and generating proper network squared errors and good generalisation (Nuri *et al*, 2017). Therefore, 50 groups of data are selected as training samples of neural network, and 50 groups are test samples of neural network.

The neural network after parameter setting is trained, and the training results are shown in Figure 2.

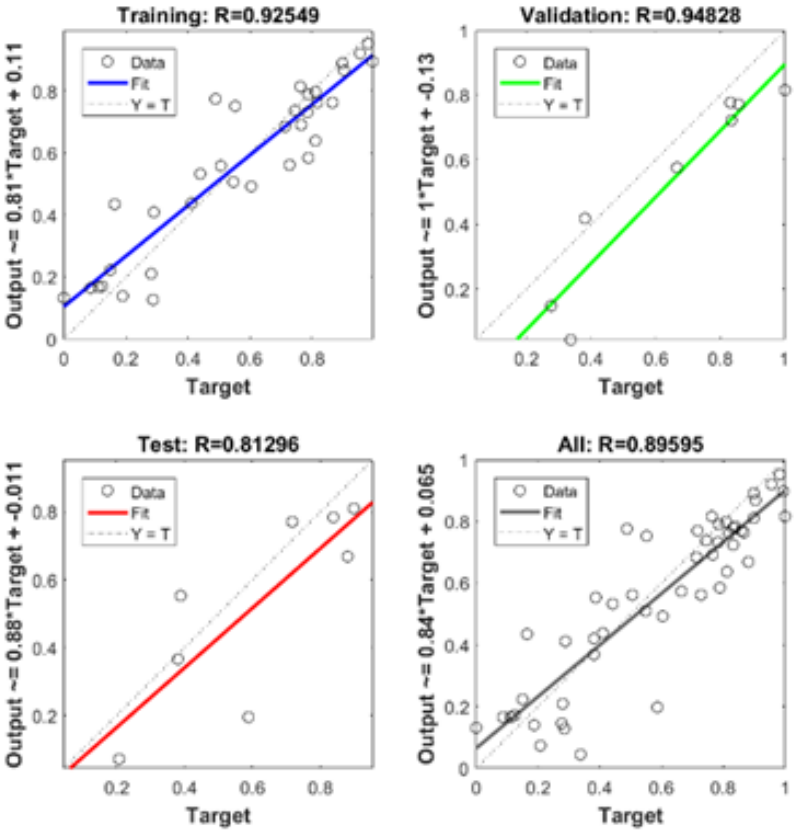

FIG 2 – Training results.

As can be seen from Figure 3, although the mean square error of BP neural network training can reach 10^{-3}, which has a certain fitting effect, there is still a large error between its predicted value and test value. Next, we need to use MIV algorithm to screen variables for further transformation of BP neural network.

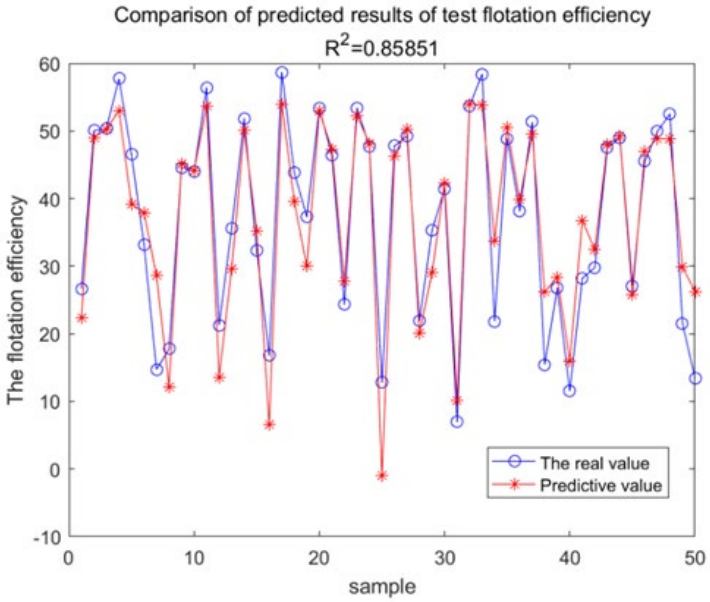

FIG 3 – Comparison between predicted value and tested value of BP neural network.

Screening results based on MIV-BP neural network model

MIV screening results

The prediction results of each input variable obtained by MIV-BP neural network are shown in Table 3. The analysis shows that flotation time has the greatest influence on flotation efficiency, and its MIV value is 3.6813. The other influencing degrees on flotation efficiency are the dosage of pH regulator, pulp concentration, collector dosage, rotor speed and grinding fineness in sequence. According to the analysis of the result after screening, it is helpful to improve the accuracy of prediction model by selecting the variable with greater influence as the input variable of neural network. After screening, factors with MIV value greater than 1.5 were selected as input variables, including flotation time, dosage of pH regulator, pulp concentration and dosage of collector.

TABLE 3

Comparison of MIV values of input variables.

The input variable	The flotation efficiency	
	MIV value	The sorting
Adjuster Dosage	2.5167	2
Grinding fineness	-0.7781	6
Collector dosage	1.6529	4
Pulp density	– 1.7692	3
Flotation time	3.6813	1
The rotor speed	-0.9860	5

Network training

The structure of the neural network after variable screening by MIV algorithm is 4–10–6-1, where the transfer function from the input layer to the hidden layer is tansig, the transfer function from the hidden layer to the output layer is logsig, and the training function of its model is traingdm. Application of ANN with validation and training data sets as a unique ones. The MiV-BP neural network is trained and tested according to the above operations, and the results are as shown in Figures 4 and 5.

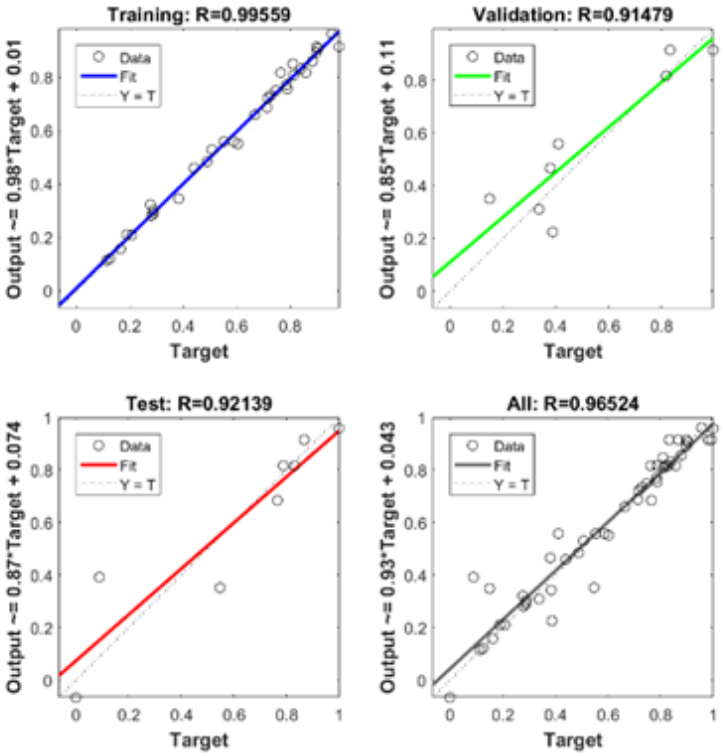

FIG 4 – MiV-BP neural network training results.

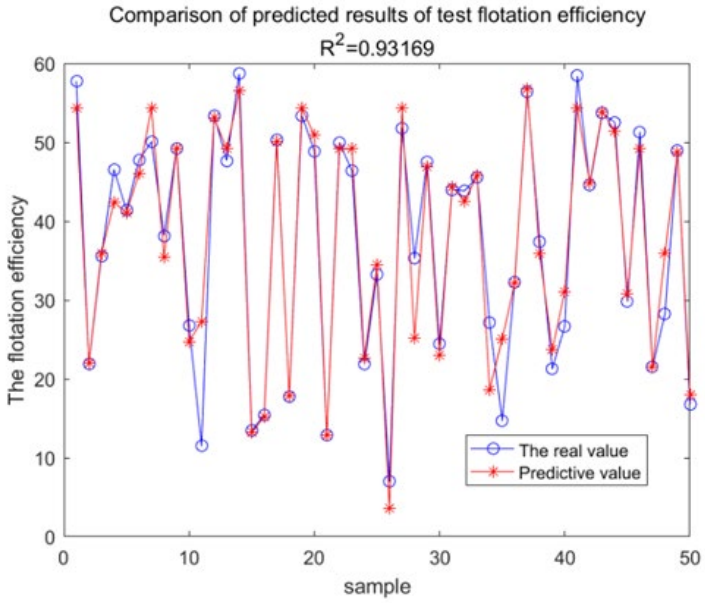

FIG 5 – Comparison of MiV-BP neural network predicted value and tested value.

In order to better test the forecasting performance of the model, absolute error, relative error, mean square error (MSE) and coefficient of determination (R^2) were selected as the evaluation indexes of the model prediction. The results of the two models are shown in Table 4.

TABLE 4

Comparison of network prediction model results.

The model name	Absolute error		The relative error (%)		MSE	R^2
	Max	Min	Max	Min		
BP	13.8821	0.0559	1.0755	0.0011	31.1949	0.8585
MIV-BP	15.7357	0.0208	1.3356	0.0009	14.9620	0.9317

As can be seen from Table 4, compared with the BP neural network model, the MIV-BP neural network model not only has a simpler model structure, but also has a lower MSE value and a higher R^2 value because it can effectively screen input variables, indicating that the prediction results are closer to the real value.

CONCLUSIONS

1. The effects of grinding fineness, collector dosage, pH regulator dosage, pulp concentration, rotor speed and flotation time on flotation efficiency were studied by MIV screening algorithm. Among them, the flotation time has the greatest influence on flotation efficiency, and its MIV value is 3.6813. The other influencing degrees in flotation efficiency are the dosage of pH regulator, pulp concentration, collector dosage, rotor speed and grinding fineness in order.
2. The accuracy and fitting of the BP neural network established by single factor and orthogonal experiment is low after training and testing. The MIV variable screening method is used to optimise the model and finally obtain the MIV-BP neural network model. Compared with the BP neural network model, the prediction accuracy of the model is higher and the fitting degree is better.

ACKNOWLEDGEMENTS

This work was financially supported by the National Key R&D Program of China (No. 2018YFE0110300).

REFERENCES

Dombi, G W P, Nandi, P M, Saxe, J M M, Ledgerwood, A M M and Lucas, C E M, 1995. Prediction of Rib Fracture Injury Outcome by an Artificial Neural Network. *Journal of Trauma and Acute Care Surgery*, 39(5): 206–208.

Hoseinia, F S, Rezai, B, Kowsari, E and Safari, M, 2020. A hybrid neural network/genetic algorithm to predict Zn(II) removal by ion flotation. *Separation science and technology,* 55(6): 1197–1206.

Nuri, O S, Allahkarami, E, Irannajad, M and Abdollahzadeh, A, 2017. Estimation of selectivity index and separation efficiency of copper flotation process using ANN model. *Geosystem Engineering*, 20(1): 41–50.

Popli, K, Afacan, A, Liu, Q and Prasad, V, 2018. Development of online soft sensors and dynamic fundamental model-based process monitoring for complex sulfide ore flotation. *Minerals Engineering*, 124: 10–27.

Sun, J, Meng, X, Qiao, J F, 2021. Soft measurement of main steam Flow based on MIV-RBF neural network. *Control engineering*, 1–6.

Wang, J, Han, S, 2015. Feed-Forward Neural Network Soft-Sensor Modeling of Flotation Process Based on Particle Swarm Optimization and Gravitational Search Algorithm. *Computational Intelligence and Neuroscience*, 1–10.

Xue, K, Zhang, R, Y, 2019. Research progress on distribution and metallogenic characteristics of phosphate ore resources in China. *Journal of minerals*, 39(01): 7–14.

Yang, X H, Zheng, C, Wang, H X, 2020. Research on flotation dosage forecasting model. *Coal preparation technology* (01): 87–90.

Zhang, L, Yang, H H, Feng, A S and Tan, X M, 2017. Development and utilization status and market analysis of global phosphate resources. *Mineral protection and utilization,* (05): 105–112.

Zhang, Y, Wang, X D, 2018. Optimization of flotation reagent system based on orthogonal test and BP artificial neural network. *Non-ferrous Metals (Mineral processing part),* (2): 99–102.

Zhang, Y, Zhu, J, 2016. Economic and technical index prediction of flotation process based on chaotic ant colony neural network. *Journal of Shanghai Jiaotong University*, 50(06): 975–979.

Modelling particle aggregation by coupled CFD-DEM method

L Zeng[1], E Goudeli[2] and G V Franks[3]

1. PhD Student, Chemical Engineering, ARC Centre of Excellence for Enabling Eco-efficient Beneficiation of Minerals, The University of Melbourne, Parkville Vic 3010. Email: lequanz@student.unimelb.edu.au
2. Lecturer, Chemical Engineering, ARC Centre of Excellence for Enabling Eco-efficient Beneficiation of Minerals, The University of Melbourne, Parkville Vic 3010. Email: eirini.goudeli@unimelb.edu.au
3. Professor, Chemical Engineering, ARC Centre of Excellence for Enabling Eco-efficient Beneficiation of Minerals, The University of Melbourne, Parkville Vic 3010. Email: gvfranks@unimelb.edu.au

INTRODUCTION

Particle aggregation and dispersion in suspension are important in the mineral industry as the particle characteristics (eg size, structure and shape) highly influence product grade and recovery and process efficiency (Franks, 2005). For instance, the size of aggregates determines which valuable minerals can be collected in froth flotation (Trahar and Warren, 1976); the filtration process usually prefers a strong but porous structure for the aggregates (Zhou and Franks, 2006). Aggregate size and structure are usually controlled by altering the pH, adding surface modifiers, such as polymers or salt, or applying shear forces to the suspension (Franks and Zhou, 2010). Especially, shear forces applied to the suspension can increase the probability of collision between primary particles, which induces particle aggregation in suspension (Hunter, 2001). Although much research has focused on aggregate dynamics in the suspension experimentally, the mechanisms are still not fully understood due to the difficulties of observing aggregate behaviour over very short time scales in a microscopic level. Computer simulations are becoming imperative to study particle and aggregate dynamics as they enable observation of particles and aggregates in suspensions without interference (Kushimoto *et al*, 2020).

In the first stage of this work, Computational Fluid Dynamics (CFD) coupled with Discrete Element Method (DEM) were applied to investigate the effect of simple shear on the aggregation of alumina particles by accounting for particle-particle (surface, contact and collision forces) and particle-fluid interactions (hydrodynamic forces), as well as the motion of particles and fluid. Some structural characteristics (fractal dimension, average size and size distribution) of the aggregates after aggregation are quantified in the post-processing analysis.

THEORY

The governing equations for coupled CFD-DEM method are discussed below.

The DEM is used to describe the motion of particles and the forces acting on them, which include the translational (Equation 1) and rotational motion (Equation 2), respectively (Cundall and Strack, 1979):

$$m_i \frac{d^2}{dt^2} \boldsymbol{x_i} = \sum \boldsymbol{F} = \boldsymbol{F_{i,n}} + \boldsymbol{F_{i,t}} + \boldsymbol{F_{i,f}} + \boldsymbol{F_{i,b}} \quad (1)$$

$$I_i \frac{d}{dt} \boldsymbol{\omega_i} = \boldsymbol{r_{i,c}} \times \boldsymbol{F_{i,t}} + \boldsymbol{T_{i,r}} \quad (2)$$

where m_i is the particle mass, t is the time, $\boldsymbol{x_i}$ denotes the position vector of particle *i*, $\sum \boldsymbol{F}$ denotes the vector of the sum of forces applied on particle *i*, $\boldsymbol{F_{i,n}}$ represents the normal particle interaction forces, $\boldsymbol{F_{i,t}}$ is the tangential particle interaction forces, $\boldsymbol{F_{i,f}}$ is the particle-fluid interaction forces, and $\boldsymbol{F_{i,b}}$ is the sum of all other body forces of particles (eg gravity, van der Waals attraction and electrical double layer repulsion), I_i is the moment of inertia for a solid spherical particle, $\boldsymbol{\omega_i}$ is the rotational velocity, $\boldsymbol{r_{i,c}}$ is the radius, and $\boldsymbol{T_{i,r}}$ represents the rolling friction torque.

The CFD is used in the simulation to describe the motion of fluid. Equation 3 describes the continuity of fluid, while Equation 4 illustrates the motion of fluid, respectively (Kloss *et al*, 2012):

$$\frac{\partial \alpha_f}{\partial t} + \nabla \cdot (\alpha_f \boldsymbol{u_f}) = 0 \tag{3}$$

$$\frac{\partial (\alpha_f \boldsymbol{u_f})}{\partial t} + \nabla \cdot (\alpha_f \boldsymbol{u_f} \boldsymbol{u_f}) = -\alpha_f \nabla \frac{p}{\rho_f} - \boldsymbol{R_{pf}} + \nabla \cdot \boldsymbol{\tau} \tag{4}$$

where α_f is fluid volume fraction, $\boldsymbol{u_f}$ is the velocity of fluid, p is pressure, ρ_f is the density of fluid, $\boldsymbol{R_{pf}}$ is the momentum exchange with the particles, and $\boldsymbol{\tau}$ is the stress tensor.

PRELIMINARY RESULTS

We had 2500 alumina particles with initial size 1.5 μm and solid volume fraction of 3.5 v% that were simulated at pH = 9, under a shear rate of 1000 s^{-1} in a 0.05 mm side length Couette cubic flow cell. Figure 1 shows the snapshots of the formed particle aggregates at (a) 0, (b) 0.02 and (c) 0.2 s. The initially spherical primary particles aggregate quickly under shear leading to the formation of small, compact aggregates (at 0.02 s) that grow further, forming larger fractal-like aggregates (at 0.2 s).

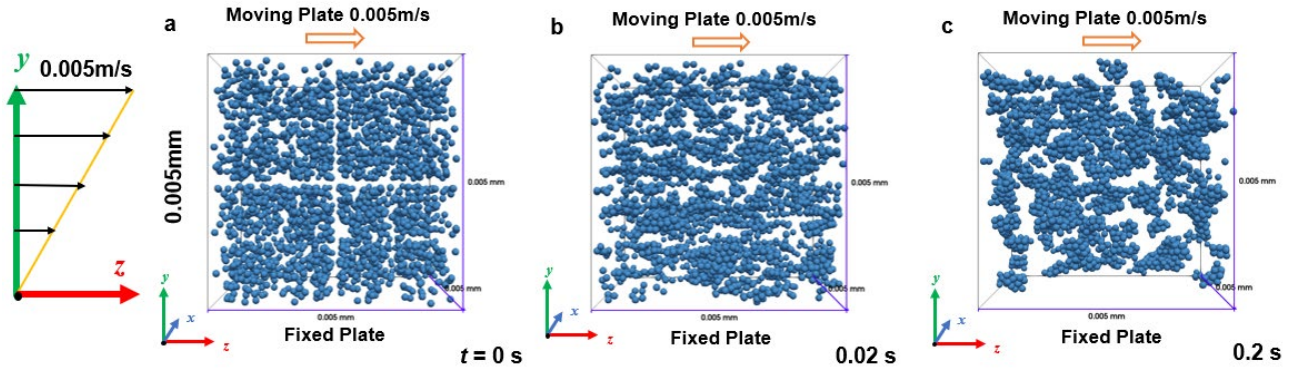

FIG 1 – Snapshots of 1.5 microns alumina particles under constant shear rate of 1000 s^{-1} at pH = 9 in a 0.05 mm side length of Couette flow cell at (a) 0, (b) 0.02, and (c) 0.2 s with initial volume fraction of 3.5 v%.

Some structural characteristics of aggregates after the simulations have been determined in the post-processing. Steady state properties are established after about 0.06 s. The aggregate size distribution, once steady state has been established, has been found to closely match the experimental distribution and that predicted by Kushimoto *et al* (2020). The temporal evolution of the average size, number of aggregates, average number of particles in each aggregate and fractal dimension as a function of time have been characterised. Aggregates consisting of more than ten primary particles attain an asymptotic fractal dimension of 2.2.

CONCLUSIONS

- The alumina aggregate size distributions determined in the simulations are qualitatively and quantitatively aligned with the simulations and experimental results presented in Kushimoto *et al* (2020) for similar sized particles (1 μm).
- Particle aggregation takes place quickly (within 0.06 s) at shear rate of 1000 s^{-1} leading to on average ten particles per aggregate, an average equivalent diameter of 7.5 μm and fractal dimension of 2.2.

ACKNOWLEDGEMENTS

A/Prof. Gabriel da Silva is gratefully acknowledged. Thanks to The University of Melbourne and Australian Research Council (ARC) Centre of Excellence (CoE) for Enabling Eco-Efficient Beneficiation of Minerals Grant No. CE200100009 for offering research funds and scholarships for this project. This research was supported by The University of Melbourne's Research Computing Services and the Petascale Campus Initiative.

REFERENCES

Cundall, P A and Strack, O D L, 1979. A discrete numerical model for granular assemblies. *Géotechnique,* 29, 47–65.

Franks, G V and Zhou, Y, 2010. Relationship between aggregate and sediment bed properties: Influence of inter-particle adhesion. *Advanced Powder Technology,* 21, 362–373.

Franks, G V, 2005. Innovative Applications of Controlled Particle Interactions. *Chemical Engineering Research and Design,* 83, 937–946.

Hunter, R J, 2001. Foundations of colloid science.

Kloss, C, Goniva, C, König, A, Amberger, S and Pirker, S, 2012. Models, algorithms and validation for opensource DEM and CFD-DEM. *Progress in Computational Fluid Dynamics,* 12, 140–152.

Kushimoto, K, Ishihara, S, Pinches, S, Sesso, M L, Usher, S P, Franks, G V and Kano, J, 2020. Development of a method for determining the maximum van der Waals force to analyze dispersion and aggregation of particles in a suspension. *Advanced Powder Technology,* 31, 2267–2275.

Trahar, W J and Warren, L J, 1976. The flotability of very fine particles — A review. *International Journal of Mineral Processing,* 3, 103–131.

Zhou, Y and Franks, G V, 2006. Flocculation Mechanism Induced by Cationic Polymers Investigated by Light Scattering. *Langmuir,* 22, 6775–6786.

First-principles calculation of the effect of substitution of Ca for Mn on the bond formation and atomic activity of rhodochrosite crystals

J Q Zhang[1] and Q Zhang[2,3,4]

1. Postgraduate, Guizhou University, 550025, China. Email: zjq824824@163.com
2. Professor, Guizhou Academy of Sciences, 550001, China. Email: zq6736@163.com
3. Professor, National and Local Joint Laboratory of Engineering for Effective Utilization of Regional Mineral Resources from Karst Areas, Guiyang 550025, China.
4. Professor, Guizhou Key Lab of Comprehensive Utilization of Nonmetallic Mineral Resources, Guiyang 550025, China.

ABSTRACT

Rhodochrosite from different sources has a certain degree of impurity defects and the substitution of impurity elements, such as calcium, magnesium, iron, copper, and zinc for manganese in rhodochrosite greatly affects the beneficiation performance of rhodochrosite. The first-principles method in computational chemistry was used to study the effects of impurity element substitution of Mn on the bonding between atoms and atomic activity of rhodochrosite crystals. The calculation of the substitution energy of different impurity atoms shows that the selected impurity atoms of Ca, Mg, and Fe can spontaneously replace the Mn atoms in the rhodochrosite, and the impurity atoms that are most likely to be substituted are selected for analysis. The Band Structure, Density of States, and Mulliken Population of the rhodochrosite crystal before and after the Ca substitution are calculated, and the bonding characteristics and electronic structure are analysed. The internal bonding characteristics and the electronic structure changes of the rhodochrosite crystal the Ca substitution were studied. The results show that the Mn3d orbitals and O2p orbitals are the most active, and the bonding between Mn and O atoms near the Fermi level is stronger. Ca substitution leads to a more stable crystal structure of rhodochrosite. The Ca substitution makes the Fermi level move upward, and a new energy level formed by the Ca4s orbital is generated at the bottom of the valence band. The impact of Ca substitution on the beneficiation performance of rhodochrosite was discussed.

INTRODUCTION

Rhodochrosite ($MnCO_3$) has become one of the main sources of manganese resources. More than 90 per cent of the manganese ore resources in China belong to low-grade poor manganese ore, with complex composition and finely disseminated particles (Zhou *et al*, 2015). Because of its importance in the metallurgical industry, manganese is considered one of my country's national industrial strategic resources (Kirchmeyer and Reuter, 2005; Zhang and Cheng, 2007). To meet the market demand of the manganese in the future, it is of great practical significance to efficiently process low-grade rhodochrosite ores. Flotation is one of the most effective methods to increase the recovery rate of fine-grained low-grade rhodochrosite (Luo *et al*, 2018).

In practical production, the floatability of rhodochrosite is poor, resulting in rhodochrosite flotation cannot be used in industrial practice. The low flotation efficiency of rhodochrosite is closely related to its crystal and electronic structure. The electronic structure determines the crystal properties of minerals, which are closely related to the surface properties, which directly affect the flotation efficiency. Starting from the crystal structure of rhodochrosite, it is very important to explore the electronic structure of rhodochrosite crystal to clarify the influence of the internal crystal structure of minerals on flotation. Rhodochrosite has a triangular crystal structure. In nature, rhodochrosite has a variable chemical composition, and manganese is often replaced by calcium, magnesium, iron, copper, and zinc (He *et al*, 2020). The substitution of impurity elements for manganese greatly affects the flotation performance of rhodochrosite. Due to the diversity of conditions and environments in the process of mineral formation, rhodochrosite from different sources has a certain degree of impurity defects. To explore the effect of element substitution on rhodochrosite crystals, this paper selects the Ca atom substitution with the highest content in rhodochrosite minerals. According to literature statistics, there are few studies on the flotation of rhodochrosite. However, there has been a lot of research on the crystal structure using density functional theory. He *et al*

(2020) analysed the influence of the substitution of impurity atoms in the rhodochrosite crystal on the properties of rhodochrosite crystals and believed that the impurity substitution improved the electrochemical properties of rhodochrosite. Jiang *et al* (2017) used density functional theory (DFT) to study the electronic structure of fluorite crystals containing rare earth (Ce, Th, U, and Y) impurities. The results show that the doping of impurity atoms makes the Fermi level High-energy direction transfer makes fluorite easier to accept electrons, and the incorporation of impurities enhances the reactivity of fluorite and oleic acid. Chen *et al* (2011) used density functional theory (DFT) to systematically study the electronic structure of natural galena containing ten typical impurities. The calculation results show that impurities change the electronic properties of galena, including lattice parameters, semiconductor types, Fermi energy levels, state density and band gap width. The results show that the flotation properties of galena vary with impurity atoms. So it is feasible to use density functional theory to study the basic properties of rhodochrosite.

In this paper, Density Functional Theory is used to study the effect of substitution of Ca for Mn atoms in rhodochrosite on the crystal structure of rhodochrosite. The Band Structure, Density of States, and Mulliken Population are used to influence the electrons of rhodochrosite before and after the substitution of impurity atoms. The electronic structure, bond formation, and bond strength were studied. The research on the substitution of the Ca atom, the impurity atom with the largest content in rhodochrosite, helps us explain the reasons for the low flotation efficiency in the process of rhodochrosite flotation, helps us understand the flotation mechanism, and provides theoretical guidance for flotation practice. It lays the foundation for the follow-up study on the changes in the surface properties of rhodochrosite before and after the impurity substitution. The internal structure of rhodochrosite crystals and the properties of bonding have been studied, which is of great significance for understanding the properties of rhodochrosite and lays a foundation for the subsequent exploration of the rhodochrosite flotation mechanism.

THEORETICAL MODELS AND METHODOLOGY

The calculation in this study is based on the DFT and completed by the CASTEP module (Milman *et al*, 2010) of Materialstudio software. The adopted rhodochrosite crystal structure (Graf, 1961) is shown in Figure 1a, and the cell parameters are a = b = 4.7771 Ångstrom, c = 15.664 Ångstrom, α = β = 90 degree, γ = 120 degree. The crystal structure geometry optimisation process of rhodochrosite includes exchange-correlation functional (Yanai *et al*, 2004), energy cut-off (Parker *et al*, 2006), and k-point (Monkhorst and Pack, 1976). BFGS algorithm (Pfrommer *et al*, 1997) was used to optimise the crystal structure. The interaction between electron and ion nucleus is described by ultra-soft pseudopotential (Vanderbilt, 1990). The geometric optimisation is set according to the following convergence accuracy: the convergence accuracy of maximum force, maximum stress, and maximum displacement are set to 0.1 electron volt per ampere, 0.2e9 pascal, and 0.005 Ångstrom. The total energy and the convergence precision of SCF are set to 5.0e-5 electron volt per atom and 2.0e-6 electron volt per atom. All atomic orbitals involved in the calculation are $C2s^2 2p^2$, $O2s^2 2p^4$, $Mn3d^5 4s^2$, $Ca3s^2 3p^6 4s^2$.

By optimising the cut-off energy, Brillouin zone K point, and exchange-correlation function, select cut-off energy as 440 electron volt, Brillouin zone K point as 2 × 2 × 3, exchange-correlation function as GGA-PBESOL, the optimisation resulting crystal structure is shown in Figure 1b. The unit cell parameters are a = b = 4.807624 Ångstrom, c = 15.667713 Ångstrom, α = β = 90 degree, γ = 120 degree. The unit cell parameter error after crystal structure optimisation is change in a = 0.64 per cent, change in c = 0.02 per cent, the error is within 1 per cent, and the optimised crystal structure can be used for calculation.

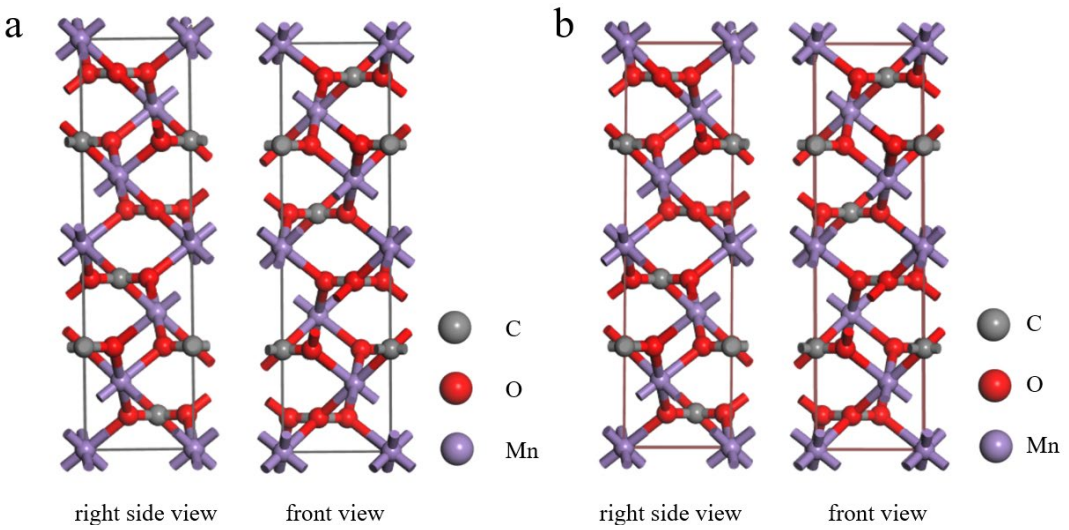

FIG 1 – (a) The original configuration; and (b) the optimised crystal structure of rhodochrosite crystals.

ANALYSIS OF THE ELECTRONIC STRUCTURE OF RHODOCHROSITE CRYSTAL

Analysis of rhodochrosite energy structure

From the energy band diagram of rhodochrosite crystal (Figure 2) we can find that the electron band structure of rhodochrosite is divided into five energy intervals between -25 electron volt and 9 electron volt. The valence band between -25 electron volt and -23 electron volt is mainly composed of O2s and C2s orbitals. The O2p orbital also contributes to some extent, but the contribution is small, and there is a small amount of Mn3d orbital contribution. The valence band between -22 electron volt and -20 electron volt is mainly composed of O2s and C2p orbitals, with a small contribution from O2p and Mn3d orbitals. The valence band between -11 electron volt and -2.4 electron volt is mainly composed of O2p and C2p orbitals, and O2s and C2s orbitals also contribute to some extent. The valence bands below the top of the valence bands in the range of 0 electron volt to -2.4 electron volt are mainly composed of Mn3d and O2p orbitals. The conduction band energy levels are mainly composed of Mn3d and O2p orbitals. The highest point of the valence band and the lowest point of the conduction band are not in the same Brillouin region, which is an indirect bandgap semiconductor.

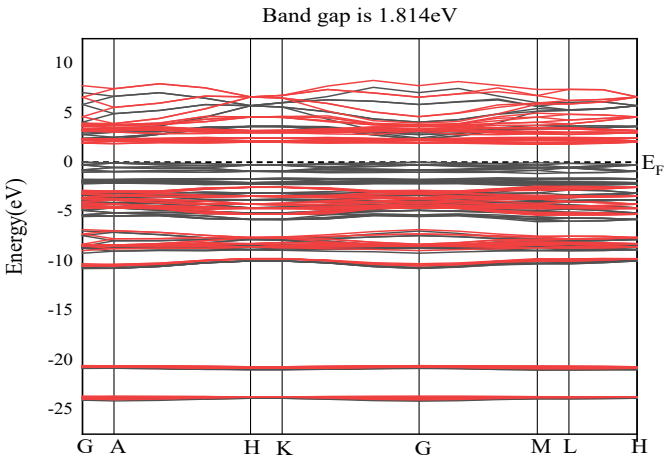

FIG 2 – Energy band diagram of rhodochrosite crystal.

The energy band structure can reflect the direction of electron transfer. Electrons flow from high energy levels to low energy levels. The high energy level orbital has reducibility, while the low energy level orbital has oxidation (Chen, 2015). On the band diagram, the lower the energy level, the more

stable it is. It can be seen from the band diagram of rhodochrosite that Mn3d and O2p are the most active atomic orbitals in rhododendron.

In metallic conductors, almost all important physical phenomena occur at the Fermi level, and electrons and orbitals far away from the Fermi level do not participate in the reaction (Ren, 2006). It can be seen from the density of states diagram of single orbitals that Mn3d is the main contribution near the Fermi level, and O atoms also contribute to a certain extent. Therefore, the electrochemical properties of rhodochrosite are mainly caused by manganese atoms and an oxygen atom. Because of the crystal field, the Mn3d orbital of the manganese atom is divided into two parts. Therefore, the Mn3d orbital is intermittently distributed in the valence band and conduction band. It can be seen from the density of states of each orbit that there are relatively strong resonance peaks in Mn3d orbit and O2p orbit near -1 electron volt and 3 electron volt, indicating that the bonding between Mn atom and oxygen atom is strong near the Fermi level. In the bonding process, the reaction activity of the oxygen atom is also relatively high.

Analysis of rhodochrosite crystal the density of states

The density of states is one of the most important parameters describing the state of electronic motion in solid physics. The quantum calculation method used in the CASTEP module of the Material Studio software underestimates the Fermi level when calculating the density of states (Chen, 2015). Due to the underestimation of the Fermi level, the curve on the density of states diagram is slightly different from the curve on the energy band diagram. But it does not affect the analysis of atom bonding and atom reactivity.

As shown in Figure 3b, the density of states peak formed by the O2s orbital in zone I corresponds to the bonding σ orbital formed between two oxygen atoms, and the orbital width is 1.7 electron volt. The density of states peak formed by O2s orbital in zone II is the anti-bond σ* orbital formed between two oxygen atoms, and the orbital width of the anti-bond σ* orbital formed between two oxygen atoms is 1.8 electron volt. The degree of bonding and anti-bonding cleavage of O2s orbital is small. The greater the degree of splitting between the bonding orbital and the anti-bonding orbital, the greater the strength of the corresponding bond, and the smaller the degree of splitting between the bonding orbital and the anti-bonding orbital, the smaller the strength of the corresponding bond. Therefore, the strength of the O-O the bond formed between the O2s orbitals in zone I and zone II is relatively small. In zone III, O2p orbitals and O2s orbitals ‘resonate’ obviously, O2s orbitals and O2p orbitals form σ bonds, and the bonding orbital width is 2.12 electron volt. In zone IV, O2s orbitals and O2p orbitals form anti-bonded σ* orbitals, The anti-bond orbital width is 2.12 electron volt. The degree of the bond-anti-bond split is small. In zone V, O atom pairs are formed by O2p orbitals to form σ bonds. The bonds below the Fermi level are obvious, and the bonds above the Fermi level are weak. The relative size of the bond action needs to be combined with the Mulliken bond population value to determine.

It can be seen in Figure 3c that the corresponding density of states peaks of O2s orbital and C2s orbital in the zone I are the bonding σ orbitals formed between C and O atoms, and the bonding orbital width is 1.7 electron volt. In zone II, the O2s orbital and the C2p orbital ‘resonate’ obviously, forming a bonded σ orbital, and the O2s orbital and the C2p orbital state density overlap to a large extent. The O2s orbital state density peak span is large and the delocalisation is strong, indicating that the O2s orbital has a strong bonding effect. To show that the bond strength between C-O needs to be judged by combining the bond length and the size of the Mulliken bond population. In zone III, O2p orbitals and C2s orbitals form bonding σ orbitals. In zone IV, O2p orbitals and C2p orbitals form bonding σ orbitals. In zone V, that is, in the valence band near the Fermi level, the orbital contribution of C atoms is very small, indicating that the orbital effect of C atoms is very small, which shows that the activity of C atoms is small. In the VI area, the O2p orbital and the C2p orbital overlap to a large extent, but the C2p orbital is the main one. Since the electronegativity of the O atom is greater than that of the C atom, the O2p orbital and the C2p form an anti-bond in the VI area σ* orbit.

As shown in Figure 3d, the bonding orbitals of Mn atoms are mainly near the Fermi level, indicating that the reactivity of Mn atoms is relatively high. In the density of states diagram, the bonding effect between O-Mn in zone I is very weak. In zone II, O2p orbitals are dominant, and O2p orbitals are highly electronegative, forming bond σ orbitals with Mn3d orbitals. But the degree of overlap is small, and the effect of the O2p orbital and Mn3d orbital is small. In zone III, the contribution of Mn3d

orbitals is greater, and the Mn3d orbitals and O2p orbitals near the Fermi level form anti-bonding σ* orbitals; in zone IV, the bond formation between O-Mn is similar to that in zone III Nature. It can be seen from Figure 3 that the Mn3d orbital has no substantial bond-antibonding cleavage. The essential reason is the symmetry and energy mismatch of the orbital.

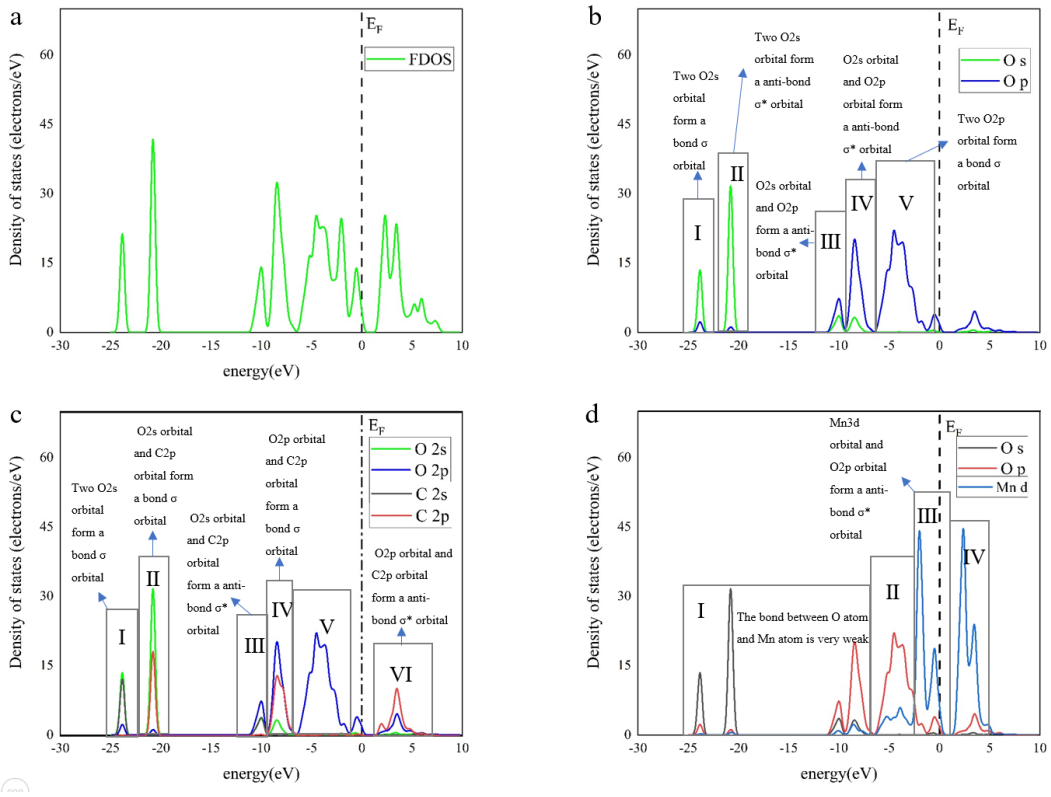

FIG 3 – Rhodochrosite bonding state density map, (a) is rhodochrosite total state density map, (b) is rhodochrosite oxygen atom bonding state density map, (c) is rhodochrosite C and O atom bonding state density map, (d) is Rhodochrosite O and Mn atom bonding state density diagram.

Analysis of rhodochrosite Mulliken population

Mulliken population (Mulliken, 2004) can quantitatively describe the electron transfer, bonding characteristics, and the contribution of the corresponding orbital of C, O, and Mn atoms in rhodochrosite crystal. The Mulliken charge populations of atoms in rhodochrosite crystal are listed in Table 1. Rhodochrosite crystal Mulliken bond population is listed in Table 2.

TABLE 1

Mulliken charge populations of atoms in rhodochrosite crystal.

Mulliken Populations					
Species	orbit			Total number of valence electrons	charge (e)
	s	p	d		
C	0.88	2.45	0.00	3.33	-0.67
O	1.79	4.81	0.00	6.60	0.60
Mn	0.27	0.27	5.29	5.83	-7.17

TABLE 2

Mulliken bond population of atoms in rhodochrosite crystals.

Bond	Population	Length (Ångstrom)
C-O	0.88	1.29961
O-Mn	0.19	2.20229
O-O (1)	-0.21	2.96362
O-O (2)	-0.02	2.96362

The C2s orbital exhibits electron-loss characteristics, losing 1.12 electrons, and the C2p orbital exhibits electronic characteristics, obtaining 0.45 electrons. In general, the C atom exhibits electron-loss characteristics, losing 0.67 electrons. O2s orbital exhibits weak electron-loss characteristics, losing 0.21 electrons, O2p orbital exhibits electronic characteristics, obtaining 0.81 electrons, and O atoms exhibit electronic characteristics, obtaining 0.6 electrons. The Mn4s orbital loses 1.73 electrons, the Mn3p orbital loses 5.73 electrons, and the Mn3d orbital loses 0.29 electrons. Generally speaking, the lost electrons are 7.17 electrons. The analysis from the perspective of electron gains and losses shows that in rhodochrosite, the most reactive Mn atom is consistent with the previous analysis results of the energy band diagram and the density of states diagram. Combining the energy band diagram and the density of states diagram analysis, we can find the most reactive Mn3d orbital in the single-orbital density diagram of Mn, but in the atomic population analysis, the data show that the 3p orbital of the Mn atom loses the most electrons, causing this the reason for this phenomenon may be that after the Mn atom participates in the reaction, its internal electrons are rearranged. A part of the electrons in the Mn4s orbital transitions to the 3d orbital and the other part is transferred to other atoms to participate in bonding.

The Mulliken bond population value reflects the bond strength between atoms. The value is between 0 and 1. The closer to 1 the stronger the covalency, and the closer to 0 the stronger the ionicity (Mayer, 2010). It can be seen from Table 2 that the Mulliken population values of C-O and O-Mn bonds are 0.88, 0.19. The O-O bond in crystal has two different population values of -0.21 (O-O(1)) and -0.02 (O-O(2)) respectively, It is indicated that the covalency between C-O bonds is strong, and the bond population of O-O is less than zero. It shows that there is a weak anti-bonding effect between O-O bonds, and the bond population of some O-O bonds are close to zero, indicating that some O atoms are in non-bonded form. The bond can be known from the bond length. The bond strengths of C-O, O-Mn, and O-O satisfy C-O>O-Mn>O-O, and the Mulliken bond population between C-O is 0.88, indicating that the C-O bond in rhodochrosite has strong covalent properties. The bond length between C-O is 1.29961 Ångstrom, so the C-O bond is stronger than other bonds in rhodochrosite and is not easy to break. It has been reported that in carbonate minerals, C atoms in the anion $CO3^{2-}$ bond with sp2 hybrid orbital, and C atoms and O atoms are connected by a C-O single bond and are the same. The eight electrons around C atoms are evenly distributed by three O atoms, and each O atom occupies eight thirds electrons. Because the average shared electron of the C-O single bond in carbonate increases, the bond length is relatively short. The O-O bond has a

longer bond length and a weak bond strength, which is consistent with the previous analysis of the density of states. Therefore, O-Mn and O-O bonds are easier to break. It can be seen from the above analysis that in the process of crushing and grinding rhodochrosite, O-Mn bonds and O-O bonds are relatively easy to break, so Mn and O atoms are more likely to produce unsaturated fractured formation, so O and Mn sites are easy to break. It is exposed on the fracture surface, and the O sites and Mn sites have strong reactivity.

THE EFFECT OF REPLACING MN WITH CA ON THE ELECTRONIC STRUCTURE OF RHODOCHROSITE CRYSTAL

Defect formation energy of impurity atoms in rhodochrosite

To explore whether the substitution of impurity atoms in rhodochrosite crystals can occur spontaneously and the degree of difficulty of substitution, the degree of difficulty of impurity atoms replacing Mn to form lattice defects is judged by calculating the defect formation energy. Defect formation energy refers to the energy required to form defects in mineral crystals. The formula for calculating defect formation energy is (Iori *et al*, 2007):

$$\Delta E = E_{defect}^{total} + E_x - E_{perfect}^{total} - E_{impurity} \quad (1)$$

E_{defect}^{total} is the total energy of minerals containing defects. $E_{perfect}^{total}$ is the total energy of minerals. E_x and $E_{impurity}$ are the energy of metal atoms and impurity atoms. When the defect formation can be positive, it generally means that the defect cannot proceed spontaneously. Defect formation energy mainly considers the relative size of various defects, to determine the degree of difficulty of defect formation in the crystal (Chen, 2012).

Rhodochrosite usually contains elements such as Ca, Mg, Fe, etc. The substitution energies of the three elements are obtained by substituting the impurities in the rhodochrosite crystals as shown in Table 3.

TABLE 3

Substitution energy of different impurity atoms in rhodochrosite.

	$E_{perfect}$ per electron volt	E_{defect} per electron volt	E_x per electron volt	$E_{impurity}$ per electron volt	△E per electron volt
Fe	-12668.1755	-12878.0856	-645.5426	-854.7574	-0.6953
Ca	-12668.1755	-13022.6028	-645.5426	-997.4503	-2.5196
Mg	-12667.1755	-12993.2524	-644.5426	-969.7940	-0.8255

It can be seen from the magnitude of the substitution energy that the crystal defects of rhodochrosite formed by the substitution of Ca, Mg, and Fe elements can proceed spontaneously, and the element Ca is the easiest to proceed spontaneously, followed by the elements Mg and Fe. This paper selects the most easily replaced Ca atoms of Mn in rhodochrosite to study the lattice defects of rhodochrosite.

The effect of replacing Mn with Ca on the bonding and electronic structure of rhodochrosite crystal

Analysis of rhodochrosite energy band after Ca replaced Mn

The crystal structure of rhodochrosite after Ca substitution is shown in Figure 4. After the Mn atoms in the rhodochrosite crystals are replaced by Ca atoms, the energy band structure has changed significantly. The energy band diagram of rhodochrosite crystal after Ca substitution is shown in Figure 5. The forbidden bandwidth is changed from 1.814 electron volt to 1.906 electron volt. Compared with rhodochrosite crystals, the valence band electrons need to transition to the conduction band. Energy increases. Taking the Fermi level (E_F) as the energy zero point, Ca substitution moves the Fermi level upward. The direction of electron transfer is from high energy level to low energy level. The high energy level orbit is reductive, and the low orbit energy level is

oxidising. Compared with pure rhodochrosite crystals, the conduction band energy level is reduced, and the rhodochrosite crystals replaced by Ca are more stable. Due to the introduction of impurity Ca atoms, the density of states of adjacent O atoms has changed. The contribution of O2s orbitals between -22 electron volt and -20 electron volt is reduced, but the contribution of O2p orbitals in the conduction band is increased, and there is a new density of states peak; compared with ideal rhodochrosite crystals, the density of states peaks of the Mn3d orbital in the valence band and conduction band is reduced, and the degree of reduction of the density of states peaks in the valence band is more obvious. This is mainly because the density of states peaks in the valence band The lack of an Mn atom reduces the contribution of the Mn3d orbital; due to the substitution of Ca atoms, a new energy level formed by the Ca4s orbital is generated at the bottom of the valence band, so the rhodochrosite crystal becomes more stable after the replacement of Ca.

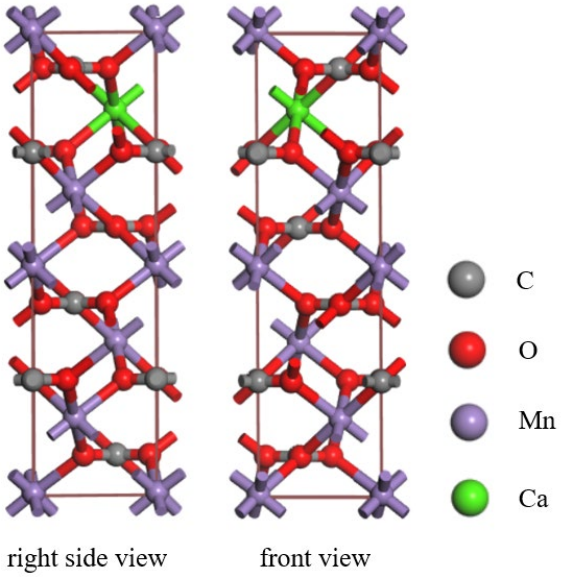

FIG 4 – Crystal structure of rhodochrosite after Ca substitution.

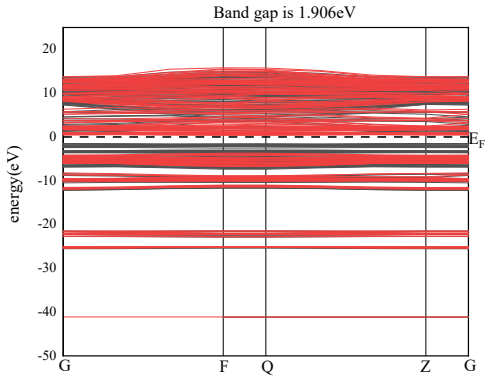

FIG 5 – Energy band diagram of rhodochrosite crystal after Ca substitution.

Analysis of the density of states map of rhodochrosite after replacing Mn with Ca

As shown in Figure 6a, it can be seen from the total density of states diagram that, except for a new energy level formed at the bottom of the valence band, there is no obvious change in the valence band, and the density of states peak in the conduction band has strong fluctuations. This is the Mn3p after the replacement of Ca. The change of the orbit.

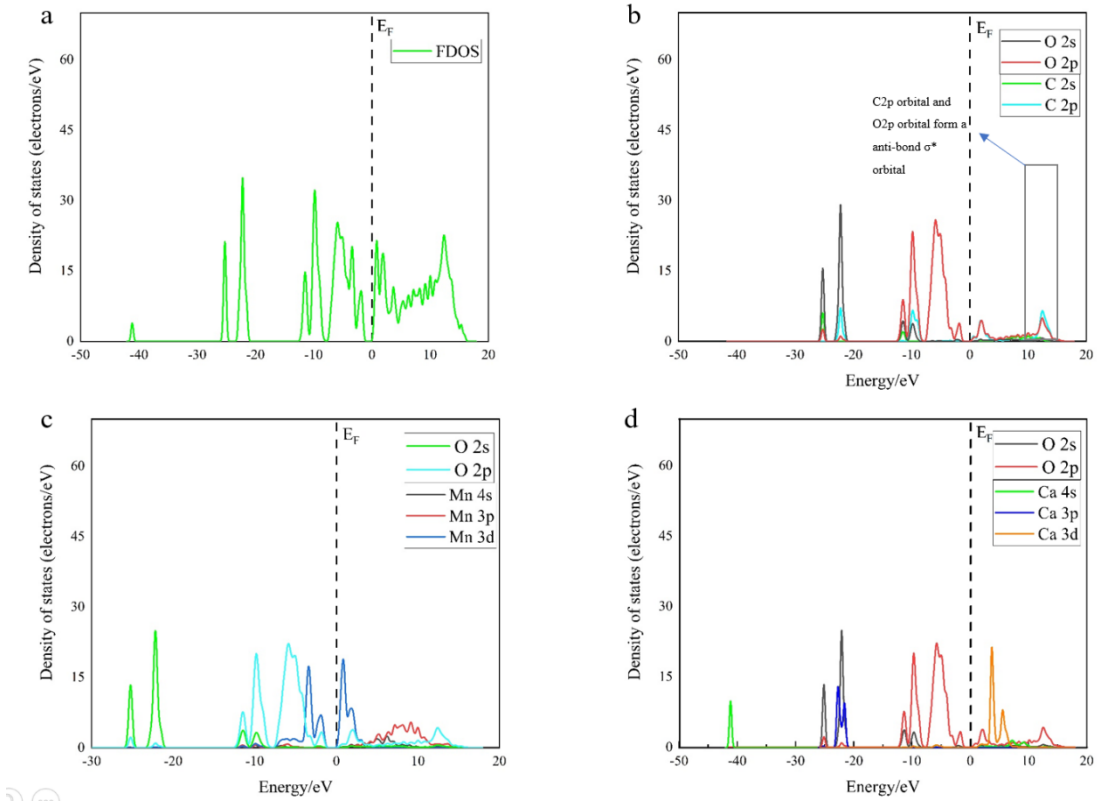

FIG 6 – Rhodochrosite bonding state density map after Ca substitution, (a) is the total density of states of rhodochrosite after Ca substitution, (b) is the bond state density map of rhodochrosite oxygen atom after Ca substitution, (c) is Ca substitution Density diagram of bonding states of C and O atoms in rhodochrosite, (d) is the density diagram of bonding states of O and Mn atoms in rhodochrosite after Ca substitution).

As shown in Figure 6b, comparing the unsubstituted rhodochrosite crystals, it can be found that after Ca substitution, the difference in the bonding of C and O atoms in the valence band is small, but the density of states peak of the C2p orbital in the conduction band is higher than that of the O2p orbital, and The 'resonance' phenomenon is obvious, but the electronegativity of O atoms is greater than that of C atoms, so the C2p orbitals and O2p orbitals form anti-bonding σ* orbitals in the conduction band after the substitution.

As shown in Figures 6c and 6d, that the Ca-O atom bonding state density diagram of the rhodochrosite crystal after Ca substitution, it can be seen that the 'resonance' phenomenon of the density of states peak between the Ca and O atoms is not obvious, and the substitution site of the Ca atom is in the bulk phase. For Mn atoms, comparing the bonding state density between O-Mn before substitution, it can be found that the 'resonance' phenomenon of Ca-O bonding state density after substitution is reduced, which indicates that after Ca atoms replace Mn atoms, they become The bond effect is reduced, and the specific bond strength needs to be determined by the bond length of the O-Mn bond and O-Ca bond before and after the substitution.

It can be seen from the bond state density diagram of the O-Mn atom in the rhodochrosite crystal after the Ca substitution that the 'resonance' phenomenon between the Mn3d orbital and the O2s and O2p orbitals is not significantly changed after the Ca substitution. The bonding between O atoms and Mn atoms in the manganese ore crystal has no major influence.

Analysis of Mulliken population of rhodochrosite after replacing Mn with Ca

Table 4 shows the Mulliken population of rhodochrosite atoms after Ca substitution. Comparing the atomic Mulliken population values before and after the Ca substitution, the degree of change before and after the C atom takes the band is not large. The C1 and C5 atoms near the substituted Ca site lose 0.01 more electrons than before the substitution, and the distance from the Ca substitution site is longer. The far C atom loses 0.01 electrons less than before the substitution. O1, O4, O7, O11,

O14, and O17 atoms closer to the Ca site get 0.04 more electrons than the unsubstituted, and the other O atoms have more get 0.01 electrons. The 4s orbital electron of the Ca atom leaps into the 3d orbital, which causes the 3d orbital of the Ca atom to get 0.49 electrons. During the bonding process, part of the electrons in the 4s orbital jumps to the 4d orbital, and some electrons are transferred to other atoms, the Ca3s orbital. It exhibits weak electron-gaining characteristics, gaining 0.11 electrons. In general, Ca atoms show electron-loss characteristics, losing 1.39 electrons. The number of lost electrons of Mn atoms decreases after Ca substitution. From the above analysis, it can be seen that the electron-gaining characteristics of O atoms increase, the electron-losing characteristics of metal elements and C atoms decrease, the oxidability decreases, and the reducibility increases.

TABLE 4

Mulliken population of rhodochrosite atoms after Ca substitution.

Atomic Populations (Mulliken)					
Atomic number	**s**	**p**	**d**	**Total**	**Charge (e)**
C1, C5	0.88	2.44	0.00	3.32	0.68
C2, C3, C4, C6	0.89	2.45	0.00	3.34	0.66
O1, O4, O7, O11, O14, O17	1.8	4.85	0.00	6.64	-0.64
O2, O3, O5, O6, O8, O9, O10, O12, O13, O15, O16, O18	1.8	4.81	0.00	6.61	-0.61
Ca1	2.11	6.01	0.49	8.61	1.39
Mn1, Mn2	0.28	0.27	5.30	5.85	1.15
Mn3, Mn4, Mn5	0.29	0.27	5.28	5.84	1.16

Through the analysis of the Mulliken bond population of the rhodochrosite crystals after the Ca substitution, the bonds in the rhodochrosite crystals after the Ca substitution are divided into five types as shown in Table 5. Through analysis, it is concluded that there is no significant change in the bond population value between the C-O bonds after the replacement of Ca. It shows that Ca substitution has little effect on the covalency between C-O bonds, and Ca substitution has little effect on the bond length of C-O bonds, which can be approximately ignored. The bond length of the O-Mn bond near the Ca site decreases, and the bond length of the O-Mn bond far away from the Ca site increases. The bond length of the O-O (3) bond after Ca substitution is significantly reduced, indicating that the O-O bond after substitution is more stable than before. The O-Ca bond formed after Ca substitution is longer than that of the O-Mn bond before substitution. The bond population of the O-Ca bond is less than that of the O-Mn bond, and the ionicity of the O-Ca bond is more important. It is more ionic than the O-Mn bond. From the above analysis, it can be seen that the bond near the Ca site after the Ca substitution becomes more stable than before the substitution, and the bond far away from the Ca site becomes weaker than before the substitution.

TABLE 5

Mulliken bond population of atoms in rhodochrosite mono cells after Ca substitution.

Bond	**Population**	**Length (Å)**
C-O	0.86 ~ 0.88	1.30
O-Ca	0.10	2.35
O-O(1)	-0.02 ~ -0.01	2.95 ~ 2.99
O-O(2)	-0.02	2.95

O-O(3)	-0.22 ~ -0.21	2.25 ~ 2.26

CONCLUSION

First-principles calculations are used to analyse the crystals before and after the replacement of rhodochrosite Ca, and the bonding between the atoms in the rhodochrosite is analysed by the density of states and Mulliken population. Through the energy band structure, the density of states diagram and Mulliken population analysis of the changes in the atomic activity of the rhodochrosite crystals before and after the Ca substitution and the stability of the bonds, the following conclusions are drawn.

1. Through the energy band analysis of the rhodochrosite crystals, it is concluded that the highest point of the valence band and the lowest point of the conduction band are not at the same high symmetry point in the Brillouin zone, which is an indirect bandgap semiconductor. Among the atomic orbitals in rhodochrosite, Mn3d and O2p orbitals are the most active. The bonding between Mn and O atoms near the Fermi level is stronger.
2. The O-O the bond population is less than zero, indicating that there is a weak anti-bonding effect between O-O bonds, and the bond population of some O-O bonds are close to zero, indicating that some O atoms are non-bonded. The orbital effect of the C atom is very small, which shows that the activity of the C atom is relatively small. The contribution of Mn3d orbital is relatively large. The Mn3d orbital and O2p orbital near the Fermi level form an anti-bonded σ* orbital. In the analysis of atomic population, the data shows that the 3p orbital of the Mn atom loses the most electrons, which leads to this phenomenon. The reason may be that after the Mn atom participates in the reaction, its internal electrons are rearranged, and part of the electrons in the Mn4s orbital transitions to the 3d orbital, and the other part is transferred to other atoms to participate in bonding. In the process of crushing and grinding rhodochrosite, O-Mn, and O-O bonds are relatively easy to break, so Mn atoms and O atoms are more likely to produce unsaturated fractured structures, so O sites and Mn sites are easily exposed on the fracture surface, and the O site and Mn site have strong reactivity.
3. Rhodochrosite crystal defects formed by the substitution of Ca, Mg, and Fe elements can proceed spontaneously, and the Ca element is the easiest to proceed spontaneously, followed by Mg and Fe elements.
4. Rhodochrosite crystals after Ca substitution are more stable. After Ca substitution, the electron-gaining characteristics of O atoms increase, and the electron-losing characteristics of metal elements and C atoms decrease. For mineral crystals, the oxidising property decreases, and the reducibility increases.

ACKNOWLEDGEMENTS

The authors gratefully acknowledge the financial support of National Key RandD Program of China (No. 2018YFC1903500)

REFERENCES

Chen, J, Lei, W, Ye, C and Jin, G. (2011). A DFT study of the effect of natural impurities on the electronic structure of galena. *International Journal of Mineral Processing*, 98 (3–4), 132–136.

Chen, J. (2012). *Principles of the flotation of sulphide minerals bearing lattice defects*, Central South University Press Changsha, China.

Chen, J. (2015). *The Solid Physics of Sulphide Minerals Flotation*, Central South University Press: Changsha, China.

Graf, D L. (1961). *Crystallographic tables for the rhombohedral carbonates*.

He, G, Li, K, Guo, T, Li, S, Huang, C and Zeng, Q. (2020). First-principles calculations of electronic structure of rhodochrosite with impurity. *Physicochemical Problems of Mineral Processing*, 56.

Iori, F, Degoli, E, Magri, R, Marri, I, Cantele, G, Ninno, D, ... Ossicini, S. (2007). Engineering silicon nanocrystals: Theoretical study of the effect of codoping with boron and phosphorus. *Physical Review B Condensed Matter*, 76.

Jiang, W, Gao, Z, Sun, W, Gao, J and Hu, Y. (2017). A density functional theory study on the effect of lattice impurities on the electronic structures and reactivity of fluorite. *Minerals*, 7 (9), 160.

Kirchmeyer, S and Reuter, K. (2005). Scientific importance, properties and growing applications of poly (3, 4-ethylenedioxythiophene). *Journal of Materials Chemistry*, 15 (21), 2077–2088.

Luo, N, Wei, D Z, Shen, Y B, Liu, W G and Gao, S L. (2018). Effect of calcium ion on the separation of rhodochrosite and calcite. *Journal of Materials Research and Technology*, 7 (1), 96–101.

Mayer, I. (2010). Bond order and valence: Relations to Mulliken's population analysis. *International Journal of Quantum Chemistry*, 26 (1), 151–154.

Milman, V, Refson, K, Clark, S, Pickard, C, Yates, J, Gao, S-P, ... Segall, M. (2010). Electron and vibrational spectroscopies using DFT, plane waves and pseudopotentials: CASTEP implementation. *Journal of Molecular Structure: THEOCHEM*, 954 (1–3), 22–35.

Monkhorst, H J and Pack, J D. (1976). Special points for Brillouin-zone integrations. *Physical review. B, Condensed matter*, 13 (12), 5188–5192.

Mulliken, R S. (2004). Electronic Population Analysis on LCAO–MO Molecular Wave Functions. I. *Journal of Chemical Physics*, 23 (10), 1841–1846.

Parker, J S, Doherty, B, Taylor, K T, Schultz, K D, Blaga, C I and Dimauro, L F. (2006). High-Energy Cutoff in the Spectrum of Strong-Field Nonsequential Double Ionization. *Physical Review Letters*, 96 (13), 133001.

Pfrommer, B G, Côté, M, Louie, S G and Cohen, M L. (1997). Relaxation of crystals with the quasi-Newton method. *Journal of Computational Physics,* 131 (1), 233–240.

Ren, S Y. (2006). *Electronic states in crystals of finite size: quantum confinement of Bloch waves*, Springer.

Vanderbilt, D. (1990). Soft self-consistent pseudopotentials in a generalized eigenvalue formalism. *Physical Review B Condensed Matter*, 41 (11), 7892.

Yanai, T, Tew, D P and Handy, N C. (2004). A new hybrid exchange-correlation functional using the Coulomb-attenuating method (CAM-B3LYP). *Chemical Physics Letters*, 393 (1–3), 51–57.

Zhang, W and Cheng, C Y. (2007). Manganese metallurgy review. Part I: Leaching of ores/secondary materials and recovery of electrolytic/chemical manganese dioxide. *Hydrometallurgy*, 89 (3–4), 137–159.

Zhou, F, Yan, C, Wang, H, Sun, Q, Wang, Q and Alshameri, A. (2015). Flotation behavior of four C18 hydroxamic acids as collectors of rhodochrosite. *Minerals Engineering*, 78, 15–20.

Future operations – net zero emissions

Influence of quarry assets on aggregate products' environmental impact – can we continue to omit it?

C Lee[1], P Muren[2], G Asbjörnsson[3], E Hulthén[4] and M Evertsson[5]

1. PhD Student, Chalmers University of Technology, Gothenburg 41322, Sweden. Email: leec@chalmers.se:
2. Senior Advisor, NCC Industry AB, Solna 17080, Sweden. Email: per.muren@ncc.se
3. Assistant Professor, Chalmers University of Technology, Gothenburg 41322, Sweden. Email: gauti@chalmers.se:
4. Associate Professor, Chalmers University of Technology, Gothenburg 41322, Sweden. Email: erik.hulthen@chalmers.se:
5. Professor, Chalmers University of Technology, Gothenburg 41322, Sweden. Email: magnus.evertsson@chalmers.se

ABSTRACT

Demands for transparent environmental data concerning the products we consume is growing. One way of providing such information that is gaining popularity is through Environmental Product Declarations (EPDs). These are standardised documents based on data collected from a Life Cycle Assessment (LCA) of the product in question, starting from the raw material extraction. This makes extraction industries key in ensuring specific data is available for downstream products. Most frequently, EPDs focus on one year of production data emitting any environmental burdens associated with the set-up or extended life cycle of the production facility. For aggregate production, this leads to the omission of environmental burdens from assets or capital goods in the form of equipment and buildings on-site, beyond that of yearly operational and maintenance inputs. This study aims to evaluate the influence of said assets on the overall environmental burden associated with aggregate products, to determine if the influence is in fact nominal and can be excluded, or if more work should be done to include assets in assessments. The study conducts an LCA at a crushed rock aggregate production plant in Western Sweden, to estimate the significance of asset related burdens on the products' environmental impact in 13 impact categories including climate change. Three scenarios are analysed, and results show that at current estimates for Reference Service Lives (RSLs) for assets, a significant impact is seen for two impact categories: climate change and resource use. To reduce the impact of assets to below the significance threshold, increasing the RSL, improving machine utilisation, and investigating downstream systems that can improve resource use are recommended.

INTRODUCTION

After the release of the sixth Assessment Report on Climate Change from the IPCC in August 2021, urgency has once again been placed on shifting swiftly away from 'business as normal' if we want to limit temperature rises across the planet (Intergovernmental Panel on Climate Change (IPCC), 2021). Climate change is not the only sustainability issue in focus in the next decade, however, with the UN's Sustainable Development Goals (SDGs) highlighting 17 interdisciplinary areas for improvement through 169 individual targets (United Nations (UN), 2015). To contribute to these calls to action, industries across the globe will need to improve their environmental sustainability.

With sustainability becoming a commonplace term, more people are seeking definitions to what defines sustainability. One way to add clarity to discussions surrounding sustainability is to provide metrics in the three aspects, or pillars, of sustainability: economic, environmental, and social concerns (Dewulf and Van Langenhove, 2005). Dozens of different methodologies have been developed to provide metrics on sustainability with varying aspects in focus. According to Angelakoglou and Gaidajis (2015), categories of environmental assessment methods include: material and energy flow analyses (eg Ecological Footprint), Environmental Accounting (eg Cost-Benefit Analysis), and Life Cycle Assessments (eg Environmental Product Declarations).

Among aggregate producers, methods based on Life Cycle Assessment (LCA) have been growing in popularity in recent years, particularly for producing Environmental Product Declarations (EPDs) (Papadopoulou, 2021). This is linked to the implementation of the Construction Products Regulation

in 2013 by the EU Commission where EPDs were named for use as sustainability assessments when available (European Parliament, 2011). Since then, the number of EPDs for construction products has grown dramatically (Andersson, 2022) and is likely to continue, with other building certificate schemes also promoting EPDs including LEED (Leadership in Energy and Environmental Design), BREEAM (Building Research Establishment Environmental Assessment Method) and Green Star.

Despite the life cycle of assets being highlighted as an integral system in assessing the environmental impact of aggregates from a life cycle perspective by Blengini *et al* (2012), current standards do not require the inclusion of environmental burdens from assets (also referred to as capital goods, infrastructure, or capital equipment) beyond that of yearly operational and maintenance inputs (Svensk Standard (SIS), 2010, 2019). Some LCA studies on aggregates have sited issues in finding reliable data for assets leading to their deliberate exclusion (Rosado *et al*, 2017), others have only considered the performance of specific equipment (Ghanbari *et al*, 2018; Jullien *et al*, 2012) and some do not consider assets at all (Bendouma *et al*, 2020; Martinez-Arguelles *et al*, 2019). A recent study by Segura-Salazar and Tavares (2021) is the first LCA study on aggregate production from hard rock to include impacts from infrastructure to the best of the authors knowledge. The study showed infrastructure made notable contributions to impact categories of human toxicity and mineral resources use with minor contributions to climate change, freshwater ecotoxicity, fossil and nuclear energy use, and water scarcity. Furthermore, a recent study for two mines in Europe by Lai *et al* (2021) showed significant contributions from infrastructure for an underground fluorspar mine while only minimal contributions for an open pit iron ore mine, highlighting variability across mining practises and the need for clarity for practitioners on when assets are likely to be nominal inputs. These recent contributions raise questions for aggregate producers as to whether assets should be included in the scope of LCA studies, or if contributions are negligible.

This study aims to contribute key insights into the inclusion of assets in LCA studies for aggregate producers to better understand the role they play in environmental impact for aggregate products and help provide guidance for the industry. To achieve this, the study uses a case study of a hard rock aggregate production plant in Western Sweden to model the contribution of assets using an attributional LCA.

METHODOLOGY

The LCA case study was conducted at a hard rock aggregate quarry located at Skälebräcke in the west of Sweden, operated by NCC Industry AB for the production year of 2020. The quarry was first granted a permit for the extraction of approximately 8 000 000 t of raw material in 2004 and had extracted around 50 per cent of this by 2019. The LCA follows methodological guidelines given by ISO standards 14001:2006 and 14040:2006 (Svensk Standard (SIS), 2006b, 2006a) for an attributional LCA for accounting purposes (Michael *et al*, 2018), and uses GaBi LCA software with the connected GaBi databases for data relating to background systems and emission factors in foreground systems. The characterisation model used for impact categories is in line with the EN 15804:2012 +A2:2019 standard (Svensk Standard (SIS), 2019) from here on referred to as EN 15804.

Goal and scope

The goal for the study is to gain understanding of the influence that background systems related to assets have on the environmental impact of aggregate products in attributional LCA studies to aid future decision-making at a micro (plant) scale. Conclusions can also aid in the development of a specific Product Category Rules (PCR) to provide clearer guidance on where system boundaries should be drawn for aggregate products in the production of EPDs. The functional unit used is one t of aggregate product at the plant gate. The system boundary for foreground systems has been set from raw material extraction (cradle) to the gate of the factory where products are ready for distribution to customers (gate) with key production processes shown in Figure 1. For background systems, the system boundary includes raw material extraction, manufacturing, and transportation based on generic data. Flows related to maintenance are limited to those activities occurring in the reference year.

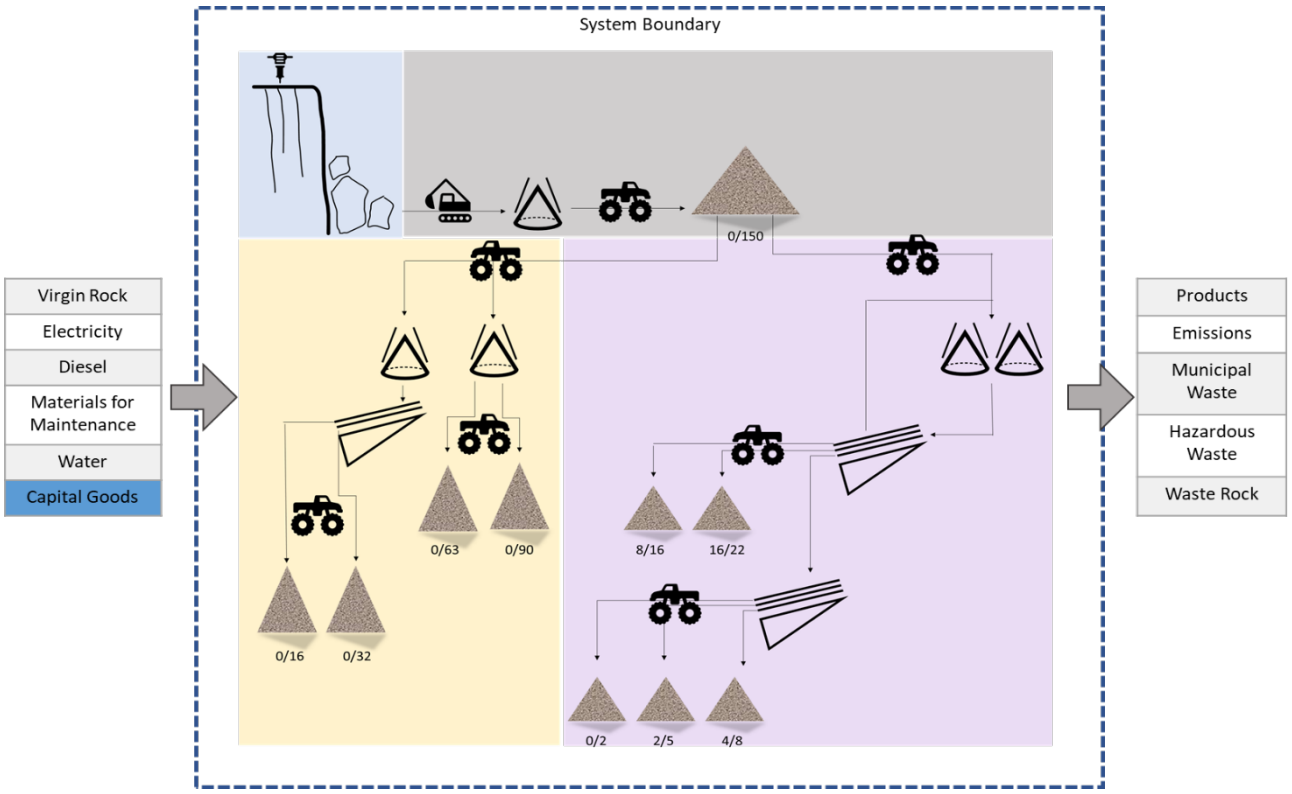

FIG 1 – Simplified flow sheet of processes included in the system boundary for the cradle to gate LCA study of Skälebräcke quarry with key flows in and out of the system. Activities in light blue represent Blasting and Drilling; grey represents Primary Crushing; yellow represents Secondary Crushing and Screening; and purple Tertiary Crushing and Screening. Loading and Hauling activities are represented by the vehicle symbols and occur within all phases of operation. Flows marked in blue are adjusted in the three different scenarios considered.

Due to a lack of data on consumption within different processes, flows are modelled in a black box approach for the key life cycle stages in the production highlighted in Figure 1. Fuel consumption for primary and secondary crushing has been monitored collectively. To allow for a distinction between these stages, fuel consumption has been divided evenly between the crushing equipment in these stages before being inputted into the models.

A cut-off point of 10 per cent of utilised time is used for assets at the plant to exclude some equipment which is used at multiple sites. For maintenance related flows, a weight cut-off criteria of 2000 kg is used for non-hazardous materials and a more sensitive cut-off criteria of 100 kg is used for hazardous material flows. The system boundary includes upstream activities but does not extend to downstream activities.

To understand the influence of assets on the overall impact, three scenarios are investigated. The different scenarios are described as:

- Scenario A: baseline scenario. Yearly maintenance related flows and fuel consumption for assets are considered but no background systems from outside the one-year reference period are included. This scenario represents current practice among producers for EPDs.
- Scenario B: inclusion of assets. Background systems for assets considering current Reference Service Life (RSL) values, as estimated by the Plant Manager for a quarry environment, are included. An RSL of 40 years for production machinery (crushers and screens) and buildings on-site, and 15 years for yellow machinery (wheel loaders, excavators etc) is applied.
- Scenario C: inclusion of assets using shortened RSL values. Background systems for assets are included assuming an RSL at half the estimated values applied in Scenario B (ie 20 years for production machinery and buildings, and 7.5 years for yellow machinery).

The list of assets considered in scenarios B and C for the study are given in Table 1.

TABLE 1

Capital goods at Skälebräcke included in scenarios B and C.

Production machinery and buildings	Yellow machinery
1 × jaw crusher	3 × wheel loaders
2 × spider crusher	1 × tractor
2 × cone crusher	2 × excavator
3 × screeners	
1 × office building	
1 × storage building	

As over ten different products are produced at the plant, products have been congregated into three separate groups which have been based on their associated crushing stages, where Product Group 1 (PG1) refers to aggregates produced after one crushing stage shown in grey in Figure 1; Product Group 2 (PG2) represents aggregates produced in a secondary crushing phase highlighted in yellow in Figure 1; and Product Group 3 (PG3) indicates the finest products produced on-site that have gone through the crushing phase shown in purple in Figure 1. Results are then given per product group. Results are also divided between the three different scenarios examined. Thirteen different impact categories are examined including three subdivisions of climate change to distinguish between fossil, biogenic, and land use and land use change as defined by the EN 15804 characterisation model based on the Environmental Footprint (EF) methodology.

RESULTS

Results for the 13 categories for each scenario and product group are shown in Table 2. The results are significantly higher for PG2 and PG3 compared to PG1 reflecting the large impact of subsequent crushing stages.

To further understand the significance of different results for the 13 impact categories examined, the results have been normalised using the global normalisation factor per person from the EF methodology (Sala *et al*, 2017). The normalised results for the three scenarios investigated are displayed in Figure 2 for the 13 impact categories analysed and divided by the product groups. These results indicate that climate change, eutrophication, photochemical ozone formation, and fossil resource use are the more significant areas of concern for the plant from a global perspective. The scale of these impacts is small; however, it is important to emphasize that results have been reported per product (one t) rather than the total for the site.

TABLE 2

Environmental impact per product group for 13 impact categories analysed in the three different scenarios examined per product group (PG).

Environmental Impact Category (EN15804+A2)	Scenario A			Scenario B			Scenario C		
	PG1	**PG2**	**PG3**	**PG1**	**PG2**	**PG3**	**PG1**	**PG2**	**PG3**
Climate Change – total (kg CO_2 eq.)	2.48 E+00	4.34 E+00	4.26 E+00	2.50 E+00	4.42 E+00	4.38 E+00	2.53 E+00	4.50 E+00	4.49 E+00
Climate Change, fossil (kg CO_2 eq.)	*2.45 E+00*	*4.30 E+00*	*4.22 E+00*	*2.48 E+00*	*4.39 E+00*	*4.34 E+00*	*2.51 E+00*	*4.47 E+00*	*4.46 E+00*
Climate Change, biogenic (kg CO_2 eq.)	*1.13 E-02*	*8.60 E-03*	*8.72 E-03*	*8.98 E-03*	*6.35 E-03*	*6.51 E-03*	*6.68 E-03*	*4.11 E-03*	*4.30 E-03*
Climate Change, land use and land use change (kg CO_2 eq.)	*1.64 E-02*	*3.18 E-02*	*3.11 E-02*	*1.64 E-02*	*3.18 E-02*	*3.12 E-02*	*1.65 E-02*	*3.19 E-02*	*3.13 E-02*
Ozone depletion (kg CFC-11 eq.)	2.08 E-10	2.08 E-10	2.08 E-10	2.08 E-10	2.08 E-10	2.08 E-10	2.08 E-10	2.08 E-10	2.08 E-10
Acidification (Mole of H+ eq.)	2.68 E-02	4.78 E-02	4.69 E-02	2.69 E-02	4.80 E-02	4.72 E-02	2.70 E-02	4.82 E-02	4.75 E-02
Eutrophication, freshwater (kg P eq.)	6.38 E-06	1.20 E-05	1.17 E-05	6.48 E-06	1.21 E-05	1.19 E-05	6.57 E-06	1.23 E-05	1.21 E-05
Eutrophication, marine (kg N eq.)	1.26 E-02	2.32 E-02	2.27 E-02	1.26 E-02	2.32 E-02	2.28 E-02	1.26 E-02	2.33 E-02	2.28 E-02
Eutrophication, terrestrial (Mole of N eq.)	1.46 E-01	2.63 E-01	2.58 E-01	1.47 E-01	2.64 E-01	2.59 E-01	1.47 E-01	2.64 E-01	2.60 E-01
Photochemical ozone formation, human health (kg NMVOC eq.)	3.49 E-02	6.55 E-02	6.42 E-02	3.49 E-02	6.57 E-02	6.44 E-02	3.50 E-02	6.59 E-02	6.46 E-02
Resource use, mineral and metals (kg Sb eq.)	7.18 E-07	8.84 E-07	8.77 E-07	7.88 E-07	9.59 E-07	9.54 E-07	8.59 E-07	1.03 E-06	1.03 E-06
Resource use, fossils (MJ)	3.24 E+01	5.74 E+01	5.63 E+01	3.27 E+01	5.82 E+01	5.74 E+01	3.30 E+01	5.90 E+01	5.85 E+01
Water use (m^3 world equiv.)	1.42 E-01	1.60 E-01	1.59 E-01	1.43 E-01	1.60 E-01	1.59 E-01	1.43 E-01	1.61 E-01	1.60 E-01

To gain insight about the influence on environmental impact of assets at the plant, the percentage change for each impact category in Scenarios B and C are given in relation to the baseline Scenario A and are given in Table 3. The largest differences between scenarios can be seen in resource use and climate change. Large decreases are seen in emissions related to biogenic carbon within the climate change category, likely due to the inclusion of wood in the buildings on-site acting as carbon sinks. Although the percentage change is significant, the significance of this category overall is low, as can be noted from Figure 2.

To determine whether these results are significant, the criteria given in ISO 14044 is used where a contribution of over 2.5 per cent to the environmental impact is deemed significant. Climate change and resource use for PG3 show the largest differences between scenarios and so have been further analysed per life cycle stage. The contribution of each life cycle stage for these two categories is given in Figure 3. The overall contribution to climate change was 2.7 per cent, accounting for the smallest contribution from a life cycle, bar maintenance which contributed 0.7 per cent. This makes assets a significant contributor while maintenance was below the significance threshold.

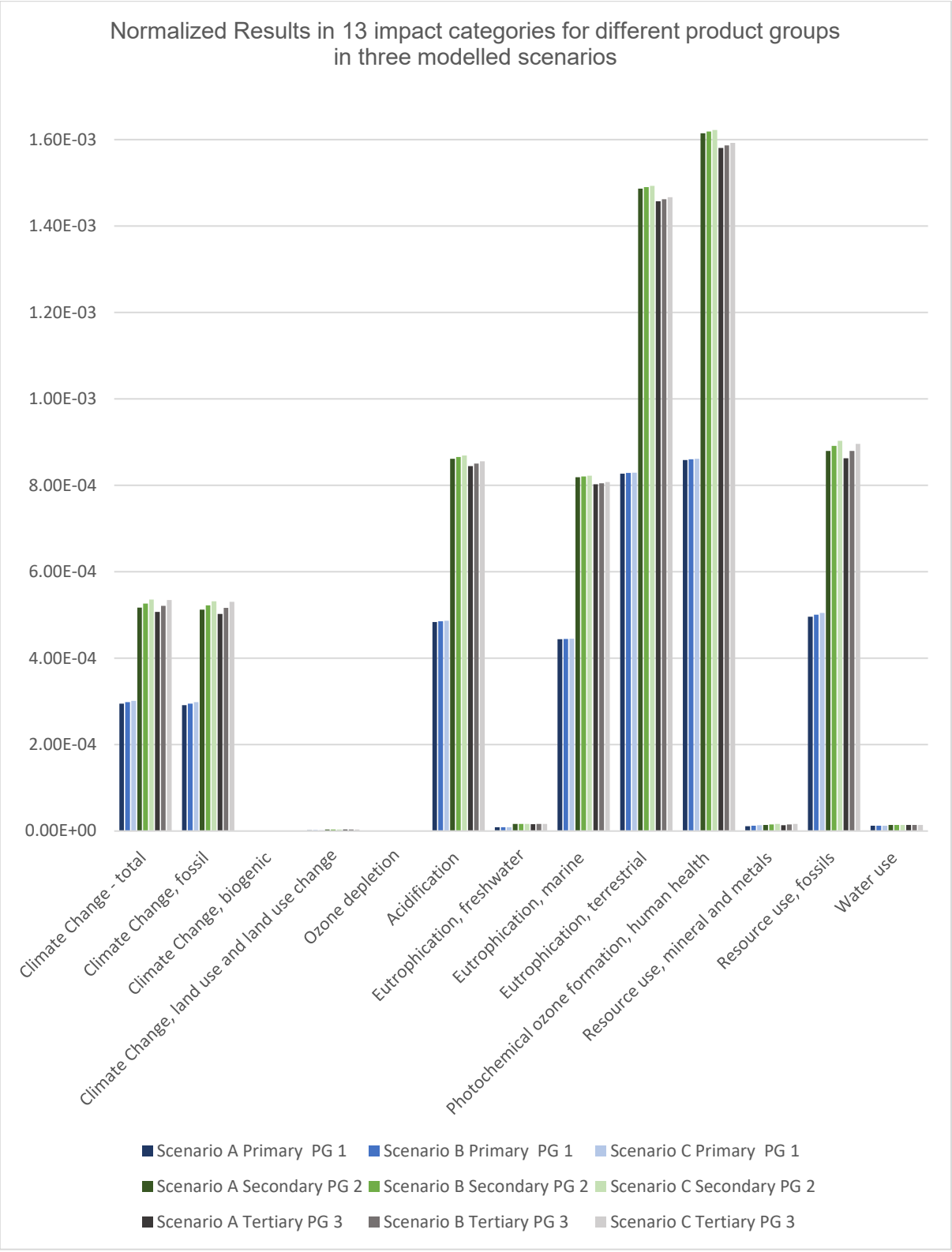

FIG 2 – Normalised results for 13 environmental impact categories examined per product group at Skälebräcke quarry. Results are given per tonne of product produced. Scenario A represents a baseline scenario, Scenario B represents a scenario where assets are considered in the overall impact, and Scenario C represents a scenario where assets have a shortened RSL.

TABLE 3

Percentage change for different scenarios compared to the baseline scenario A for 11 key impact categories given in EN15804. Scenario A represents a baseline scenario (assets excluded), Scenario B represents a scenario where assets are considered in the overall impact, and Scenario C represents a scenario where assets have a shortened RSL. Shading indicates level of change (green for positive change and red for negative change).

Environmental Impact Category (EN15804+A2)	Scenario B			Scenario C		
	PG 1	PG 2	PG 3	PG 1	PG 2	PG 3
Climate Change – total (kg CO_2 eq.)	1%	2%	3%	2%	4%	5%
Climate Change, fossil (kg CO_2 eq.)	*1%*	*2%*	*3%*	*2%*	*4%*	*5%*
Climate Change, biogenic (kg CO_2 eq.)	*-20%*	*-26%*	*-25%*	*-40%*	*-52%*	*-50%*
Climate Change, land use and land use change (kg CO_2 eq.)	*0%*	*0%*	*0%*	*0%*	*0%*	*1%*
Ozone depletion (kg CFC-11 eq.)	0%	0%	0%	0%	0%	0%
Acidification (Mole of H+ eq.)	0%	0%	1%	1%	1%	1%
Eutrophication, freshwater (kg P eq.)	1%	1%	2%	3%	2%	3%
Eutrophication, marine (kg N eq.)	0%	0%	0%	0%	0%	1%
Eutrophication, terrestrial (Mole of N eq.)	0%	0%	0%	0%	0%	1%
Photochemical ozone formation, human health (kg NMVOC eq.)	0%	0%	0%	0%	0%	1%
Resource use, mineral and metals (kg Sb eq.)	10%	8%	9%	19%	16%	17%
Resource use, fossils (MJ)	1%	1%	2%	2%	3%	4%
Water use (m^3 world equiv.)	0%	0%	0%	1%	1%	1%

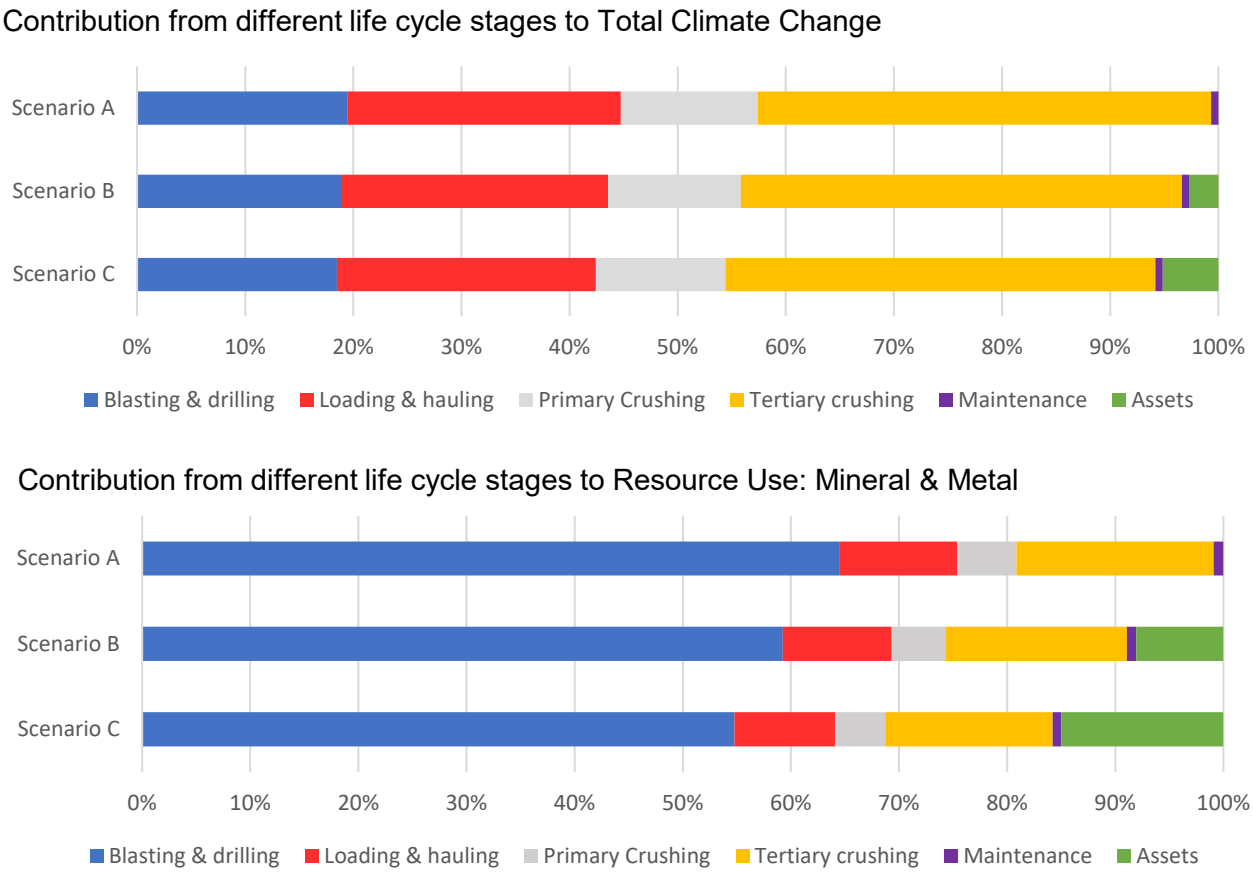

FIG 3 – Contribution of different life cycle stages to Total Climate Change and Resource Use of minerals and metals per tonne product produced in group 3. Scenario A represents a baseline scenario (assets excluded), Scenario B represents a scenario where assets are considered in the overall impact, and Scenario C represents a scenario where assets have a shortened RSL.

For resource use of metals and minerals, assets contributed 8.1 per cent to the impact category making it the fourth largest causal life cycle stage after blasting and drilling, loading and hauling, and tertiary crushing, and crossing the significance threshold. Maintenance had a low impact in this category; however, the reference year had no metal purchases for replacement parts which is unusual (Asbjörnsson *et al*, 2018). The overall significance of this category is also low when considering the normalised scores seen in Figure 2.

DISCUSSION

The results from this study indicate that assets are a significant contributor to the environmental impact from aggregate production at current estimated RSLs in quarries for two of the impact categories examined: climate change and resource use. Looking closer at the climate change category, the impact of assets was only significant for PG3. This could indicate an underutilisation of crushing equipment for finer products, as a similar amount of equipment is needed to produce significantly less product. Further investigation to see if aggregate producers can increase the utilisation of crushers for finer products to reduce this impact is encouraged.

Despite the resource use category having a low significance overall when considering the normalised values, contributions from assets were significant for all product groups.

Maintenance made insignificant contributions in both categories examined per life cycle stage and can raise questions as to whether it is necessary to include impacts associated with this activity in LCAs conducted by aggregate producers. As previously mentioned, there were no metal replacement purchases during the reference year which is unusual for aggregate plants (Asbjörnsson *et al*, 2018). Assuming two t of replacement steel parts during the year increases the contribution of this category to 9.1 per cent for resource use, crossing the significance threshold.

The use of a 2000 kg cut-off point for non-hazardous materials may have excluded some key purchases for this activity and a lower cut-off point is encouraged in future studies. It is, therefore, recommended that maintenance is still included in future studies despite its low significance in this study and consideration to metal wear parts should be taken when deciding cut-off points.

Including assets in future studies requires more data collection, particularly for background systems related to the assets themselves, which is already a challenge for producers (Lee *et al*, 2022). To reduce the contribution of assets below the significance threshold to justify excluding assets in the future, actions can be taken to increase the RSL for assets and improve utilisation of crushing equipment associated with products produced in smaller quantities. Investigation into the inclusion of downstream systems for assets where recycling is utilised could also see a reduction in impact for resource use.

Assets have a direct influence on daily running conditions, for example, fuel consumption which has a larger contribution to the results than that of the assets itself. When considering the replacement of assets earlier than their expected RSL, environmental improvements from energy savings should outweigh the increased impact from assets to be justified from an environmental perspective. This can be significant as quarries look to switching to electrified equipment.

The case study has investigated one operation for aggregate production from crushed rock in Sweden. Differences between aggregates produced from other sources should be investigated separately to account for any significant differences in the production processes used.

CONCLUSION

This study has evaluated the contribution to environmental impact per product from assets at an aggregate production plant in Sweden. The results of this case study show that assets do have a significant contribution to two impact categories investigated: climate change and resource use. To reduce the contribution below the significance threshold, increasing the RSL, improving utilisation of crushing equipment for smaller product fractions, and inclusion of downstream systems, for example recycling for improved resource use, should be considered. It is important to consider that the impact from assets is much smaller than that from fuel consumption which is directly linked to some equipment assets. When considering switching equipment out to more efficient alternatives before the expected RSL is reached, savings should outweigh any increases in impact from the reduced RSL, like those seen in Scenario C in this study.

ACKNOWLEDGEMENTS

The data used was collected for the master thesis conducted by Christina Lee at the University of Gothenburg within the MSc. Environmental program. Our thanks are extended to all those who supported that process and the staff at NCC Industry AB who aided in the data collection.

REFERENCES

Andersson, J, 2022. Construction LCA's 2022 Guide to Environmental Product Declarations (EPD) (Online). https://constructionlca.co.uk/. Available: https://constructionlca.co.uk/ (Accessed 27/02/2022).

Angelakoglou, K and Gaidajis, G, 2015. A review of methods contributing to the assessment of the environmental sustainability of industrial systems. *Journal of Cleaner Production*, 108, 725–747.

Asbjörnsson, G, Hulthén, E and Evertsson, C, 2018. Comminution process modelling from a sustainability perspective. *Comminution 18–11th International Comminution Symposium*, 2018. 1–9.

Bendouma, S, Serradj, T and Vapur, H, 2020. A case study of the life cycle impact of limestone quarrying on the environment. *International Journal of Global Warming*, 22, 432–447.

Blengini, G A, Garbarino, E, Šolar, S, Shields, D J, Hámor, T, Vinai, R and Agioutantis, Z, 2012. Life Cycle Assessment guidelines for the sustainable production and recycling of aggregates: the Sustainable Aggregates Resource Management project (SARMa). *Journal of Cleaner Production*, 27, 177–181.

Dewulf, J and Van Langenhove, H, 2005. Integrating industrial ecology principles into a set of environmental sustainability indicators for technology assessment. *Resources, Conservation and Recycling*, 43, 419–432.

European Parliament, COTEU, 2011. Regulation (EU) No 305/2011 of the European Parliament and of the Council of 9 March 2011 laying down harmonised conditions for the marketing of construction products and repealing Council Directive 89/106/EEC Text with EEA relevance.

Ghanbari, M, Abbasi, A M and Ravanshadnia, M, 2018. Production of natural and recycled aggregates: the environmental impacts of energy consumption and CO_2 emissions. *Journal of Material Cycles and Waste Management*, 20, 810–822.

Intergovernmental Panel on Climate Change (IPCC), 2021. Summary for Policymakers. In: *Climate Change 2021: The Physical Science Basis*. Contribution of Working Group I to the Sixth Assessment Report of the Intergovernmental Panel on Climate Change (ed: Masson-Delmotte, V, P Zhai, A Pirani, S L Connors, C Péan, S Berger, N Caud, Y Chen, L Goldfarb, M I Gomis, M and Huang, K L, E Lonnoy, J B R Matthews, T K Maycock, T Waterfield, O Yelekçi, R Yu AND B Zhou). Cambridge University Press.

Jullien, A, Proust, C, Martaud, T, Rayssac, E and Ropert, C, 2012. Variability in the environmental impacts of aggregate production. *Resources, Conservation and Recycling*, 62, 1–13.

Lai, F, Beylot, A, Navarro, R, Schimek, P, Hartlieb, P, Johansson, D, Segarra, P, Amor, C and Villeneuve, J. 2021. The environmental performance of mining operations: Comparison of alternative mining solutions in a life cycle perspective. *Journal of Cleaner Production*, 315, 128030.

Lee, C, Papadopoulou, P, Asbjörnsson, G, Hulthén, E and Evertsson, M, 2022. Understanding Current Challenges in Evaluating Environmental Impacts for Aggregate Producers through a Case Study in Western Sweden. *Sustainability*, 14, 1200.

Martinez-Arguelles, G, Acosta, M P, Dugarte, M and Fuentes, L, 2019. Life Cycle Assessment of Natural and Recycled Concrete Aggregate Production for Road Pavements Applications in the Northern Region of Colombia: Case Study. *Transportation Research Record*, 2673, 397–406.

Michael, Z H, Ralph, K R and Stig Irving, O, 2018. *Life Cycle Assessment: Theory and Practice*, Cham, Springer.

Papadopoulou, P, 2021. Towards a pre-verified EPD tool with simulation capabilities for the aggregates industry. Chalmers tekniska högskola.

Rosado, L P, Vitale, P, Penteado, C S G and Arena, U, 2017. Life cycle assessment of natural and mixed recycled aggregate production in Brazil. *Journal of Cleaner Production*, 151, 634–642.

Sala, S, Crenna, E, Secchi, M and Pant, R, 2017. *Global normalisation factors for the Environmental Footprint and Life Cycle Assessment*, Luxembourg, Publications Office of the European Union.

Segura-Salazar, J and Tavares, L M, 2021. A life cycle-based, sustainability-driven innovation approach in the minerals industry: Application to a large-scale granitic quarry in Rio de Janeiro. *Minerals Engineering*, 172, 107149.

Svensk Standard (SIS), 2006a. Environmental management – Life cycle assessment – Principles and framework (ISO 14040:2006). SIS database.

Svensk Standard (SIS), 2006b. Environmental management – Life cycle assessment – Requirements and guidelines (ISO 14044:2006). SIS database.

Svensk Standard (SIS), 2010. Environmental labels and declarations – Type III environmental declarations – Principles and procedures (ISO 14025:2006). SIS database.

Svensk Standard (SIS), 2019. Sustainability of construction works – Environmental product declarations – Core rules for the product category of construction products (EN 15804:2012+A2:2019). SIS database.

United Nations (UN), 2015. The 17 Goals (Online). Available: https://sdgs.un.org/goals (Accessed 14/06/2021).

Future operations – waste processing and sustainable operation

Using automated mineralogy to simulate metal removal from silicomanganese slag

H Apaza Blanco[1], M Dadé[2], R Akhanchi[3], S Lafon[4] and T Riegler[5]

1. Mineral Processing Engineer, Eramet Ideas, Trappes 78190, France. Email: helene.apazablanco@eramet.com
2. Research and Development Engineer, Eramet Ideas, Trappes 78190, France. Email: mickael.dade@eramet.com
3. Technician, Eramet Ideas, Trappes 78190, France. Email: rachid.akhanchi@eramet.com
4. Senior Technician, Eramet Ideas, Trappes 78190, France. Email: sebastien.lafon@eramet.com
5. Senior Scientist, Eramet Ideas, Trappes 78190, France. Email: thomas.riegler@eramet.com

ABSTRACT

In the light of upsurge of waste generation in Europe, governments are taking measures to promote the development of recycling activities with the aim to enact a no-waste policy in a foreseeable future. In this context, steel slag valourisation has been intensively studied since the last decade and has been found to be a low-carbon substitution of ordinary Portland cement. Eramet Norway Kvinesdal plant operates an electric arc furnace (EAF) to produce silicomanganese (SiMn) alloys with a metal particle content in the slag around 5 wt per cent. Therefore, the ability to selectively remove metal particles present as droplets within the silicate glass constrains the possible usages of the slag. The purpose of this study is to understand the impact of the comminution scheme on the texture and morphology of metal particles and its implication for removal from the slag through gravity separation. Two samples grinded under different parameters were studied using an automated mineralogical analyser (QEMSCAN®) to characterise the size, density, and liberation of the mineral phases. In addition, metal particles recovery tests were performed using a laboratory scale shaking table and the results were compared to a process mineralogy methodology. Shaking table separation, which is based on the particle size distribution, density, and the shape factor of particles, allows to remove a large part (70–77 per cent recovery for a 20 per cent yield) of metal particles however the finest are still present with the silicate particles. The process modelling, based on the combination of density and size, are in good agreement with these experimental results. Further work could assess the effect of particle shape on separation efficiency to better control the process and improve the overall metal recovery.

INTRODUCTION

Metallurgical slag recycling has received much attention in recent years as a result of stricter waste reduction policies, and the promotion of circular economy making of slags potential by-products of metallurgical operations. Extensive studies on ground granulated blast furnace slag have managed to integrate this new component into cement standard as a low-carbon substituent (Özbay *et al,* 2016). However, most of the Electric Arc Furnace (EAF) slags are currently recycled for low-value applications, such as coarse aggregates, and only a few studies have investigated high added value routes (Kumar *et al,* 2013; Frias *et al,* 2006). To enable new applications, comminution and purification of the slag constitute mandatory steps in where eco-efficiency (eg with reduced water, power consumption) must be considered. This study is part of the GREENY (GRinding Energy EfficiencY) project which focuses on developing a reuse route for the Silicomanganese (SiMn) slag produced in Kvinesdal plant (Norway) using modelling tools to predict the energy consumed during the comminution step (Lindroos *et al,* 2021). SiMn is a key product resulting from the manganese metallurgy process and its refining generates between 1 and 1.5 tonne of slag per tonne of alloy produced (Hunsbedt, 2019). The Kvinesdal processing plant, produces an annual output of 180 kt of silicomanganese through three moderns 30 MW smelting electric arc furnaces.

Slag up-grading has been investigated using both magnetic separation and gravity separation (Shen and Forssberg, 2003). However, contribution of the comminution process remains unsatisfactory as many studies are only reporting liberation size when choosing a comminution scheme. It is widely recognised that selecting an adequate comminution scheme represent an easy way to increase the eco-efficiency of a high energy intensity process (Napier-Munn, 2015). This study attempts to jointly

evaluate both the comminution and the separation steps with the combination of modelling and physical separation tests using a shaking table. According to Sivamohan and Forssberg (1985) size, density and shape are the main parameters dictating particles movement during shaking table separation. One way to acquire such data is to run gravity separation tests but alternative methods, developed by Grobler and Bosman and based on process mineralogy, have shown to provide a fastest way to collect data (Grobler and Bosman, 2010; Pascoe *et al,* 2007).

The present work presents a detailed mineralogical analysis conducted using an automated mineralogical analyser (QEMSCAN®) on the crushed material prior to the shaking table tests. The shaking table test results were compared with three simulations and the use of classifier taking into account the following physical properties of particles: mass, density, and a combination of density and size.

MATERIAL AND METHODS

Silicomanganese slag composition and comminution process

The Kvinesdal slag typical composition is ranging from: 3 to 6 wt per cent Mn, 20 to 21 wt per cent Si, 7 to 9 wt per cent Al, 13 to 16 wt per cent Ca and 4 to 6 wt per cent Mg. The silicomanganese slag provided by the plant was then shipped to Metso:Outotec R&D facilities (Finland) to be comminuted. Two types of technology were used in series: a cone crusher (MX^{TM} series) and a vertical shaft impactor (BARMAC® series), both designed by Metso:Outotec. Single use of vertical shaft impactor has successfully led to substantial energy savings for several applications (Numbi and Xia, 2016). The present work is focused on two different tests. The first sample test, called T4, has been taken after a first crushing step using the cone crusher in a closed loop whereas the second (T9) has been sampled after a second comminution step (BARMAC®). Both materials were dry screened at 2 mm and the undersized fractions sent to Eramet Ideas facilities (France). Those fractions were divided into subsamples using a riffle splitter or rotary divider. Chemical compositions were determined by X-ray fluorescence (WD-XRF) on fused borate beads are given in Table 1 for each sample.

TABLE 1

Chemical compositions determined by XRF.

Sample	Chemical elements (wt.%)							
	Mg	Mn	Si	Ba	K	Fe	Ca	Al
T4	5.12	6.40	21.00	0.54	0.90	0.42	15.40	9.35
T9	4.69	6.52	21.70	0.53	0.70	0.48	16.70	7.92

Shaking table test

Gravity (jigging, tabling) and magnetic separation techniques have been widely used for recovery of metal from slags especially on iron and steel industries due to their high capacity and low operation cost (Sripiya and Murty, 2004; Shen and Forssberg, 2003). Considering the size of the material three type of separation were suitable: gravity enhanced separator, spiral concentrator and shaking table.

On the present study, both samples were processed using a simple and reliable gravity processing technique: a shaking table. Shaking table was chosen because of its high precision, easy adjustment, and low-quantity requirement. A standard Holman-Wilfley model 800 shaking table with a riffle pattern adapted to fine sand was used. Shaking table operational parameters are reported in Table 2. The stroke speed was set at 300 rev/min for each test. Flow rates from wash water and repulping water were measured using a volumetric flowmeter. To increase separation efficiency and keep a ratio between upper and lower particle size around three, only the sieved fraction 100–500 µm was processed. Three tests with several end elevation angle, table tilts and wash water flow rate conditions were performed for both materials. Only the best tests (T4E2 and T9E2), based on yield recovery curves, were chosen for the mineralogical analyses and the subsequent comparisons.

TABLE 2

Operational parameters of shaking table tests.

Material	Test Id	End elevation (°)	Table tilt (°)	Repulping water (L/min)	Feed solid concentration (%)	Wash water (L/min)	Total water (L/min)	Feed flow rate (kg/h)
T4	E1	0.85	2.60	3.6	7	13.5	17.1	15.9
T4	E2	0.95	3.00	3.6	6	14.1	17.7	15.0
T4	E4	0.90	2.55	4.0	6	8.7	12.7	14.8
T9	E1	0.90	2.60	5.8	4	8.4	14.2	13.9
T9	E2	1.05	2.80	5.8	5	12.5	18.3	17.7
T9	E3	1.25	2.85	5.6	4	9.2	14.8	14.2

Automated mineralogy and process mineralogy

T4E2 and T9E2 samples, collected from the initial state and after shaking table step, were sampled for automated mineralogical analyses (Pascoe *et al,* 2007; Grobler and Bosman, 2010). Due to the drastic change of mass, size and density of particles depending on the phase nature, a further aspect of sample preparation has been addressed. To be representative of samples in two-dimensional and mitigate the problem of density segregation, a specific sample preparation protocol was used (Figure 1).

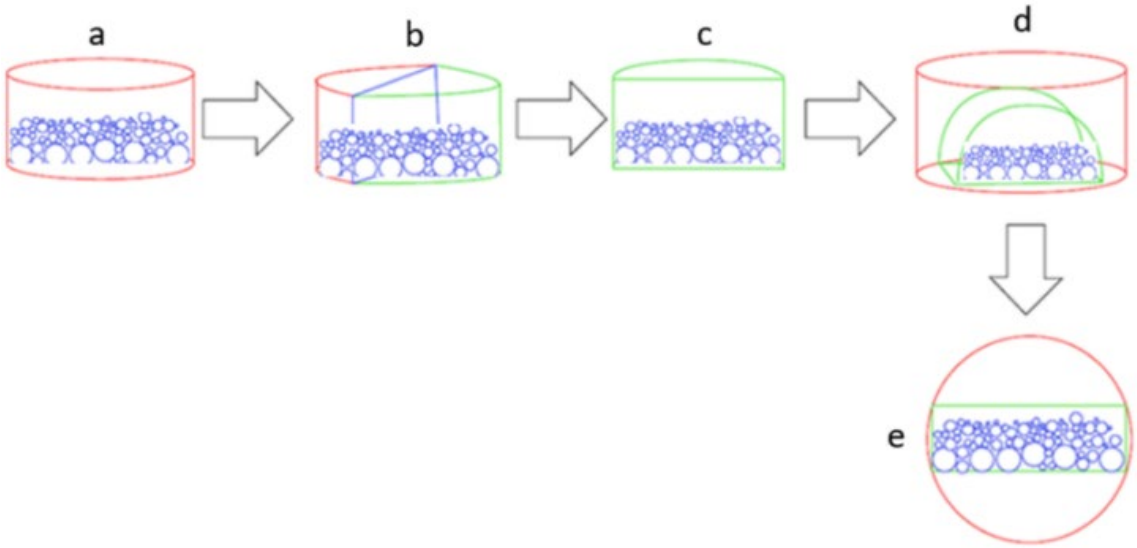

FIG 1 – Resin embedding methodology to avoid density and size segregation.

First, samples are embedded in an epoxy resin (a). When the resin has set, the sample is cut vertically in half (b and c) and embedded one more time in epoxy resin with the cut face down (d). Then, the granulometric distribution of slag and SiMn particles is covered in a polished section (e). Struers RotoForce-3 and RotoPol-31 devices were used to polish samples. First, silicon carbide papers <5 µm were used before to finish the preparation with diamond polishing suspension on a cloth <1 µm size.

Data acquired from the QEMSCAN® system were performed on the FEI 650 scanning electron microscope equipped with two Bruker 30 mm^2 EDS detector at an acceleration tension of 25 kV and a beam current of 10 nA. X-ray signal mineralogical interpretation was performed using a database constrained with X-ray diffraction, scanning electron microscopy and electron microprobe analyser *in situ* chemical composition of the various identified phases. The material was then classified using three different model: particle density, particle mass and a combination of density and size of particle as proposed by Fitzpatrick *et al* (2016). Size and density fraction were carefully chosen on iDiscover software depending on the sample. Those fractions were used to simulate a separation product based on particle size and density distributions.

Yield and mineralogical composition of each fraction were extracted to plot cumulated recovery/yield curves. For the density and mass models, the cumulated recovery was built using cumulated values in ascending order of respectively densities or mass fractions defined before. For the combination of their density and size, each fraction was assigned a rank based on the following equation (Fitzpatrick *et al,* 2016) where fraction size and density were standardised. Model factor a, b and c were adjusted to fit the experimental values. Then, results were cumulated in an ascending order of rank.

$$rank_{i,j} = size_i^a + b \times density_j^c$$

Those three simulated curves based on the different model were fitted using JMP® statistical software using the formula below. Model parameters a, b, c and r are adjusted using a Gauss-Newton algorithm. Each modelled curve is subsequently compared to the fitted experimental curve using the least square method.

$$Recovery\ (yield) = a + b \times r^{yield} + c \times yield$$

RESULTS AND DISCUSSION

Previous studies indicate that both density and size should be considered to model gravity separation response. As reported by Fitzpatrick *et al* (2016), a shaking table model could be developed using only quantitative mineralogy analysis, showing a reasonable prediction of the grade recovery on a synthetic ore. The present work focused on testing this aforementioned methodology as well as simpler and faster methods on secondary raw material. Each modelling attempt was compared to the recovery/yield curves obtained from mineralogical analyses of the tabling products for T9E2 and T4E2.

Assay reconciliation

QEMSCAN® data interpretation requires a QA/QC validation performed by the comparison between the bulk chemical composition interpreted from QEMSCAN® and XRF chemical analyses (Figure 2). This aims to assess the accuracy of the mineralogical database and ensure good confidence in the interpreted modal mineralogy. A good agreement can be observed for both samples (Figure 2). Some deviations from the ideal 1:1 line can be observed for each sample, in particular for Al, Mg and Mn chemical elements. This discrepancy could be due to the global chemistry given for glaucochroite phase on the QEMSCAN® database, and some degree of solid solution in the silicate glass challenging to take into consideration. Furthermore, silicate glasses, generally identified by K content, are not indexed in our QEMSCAN® database.

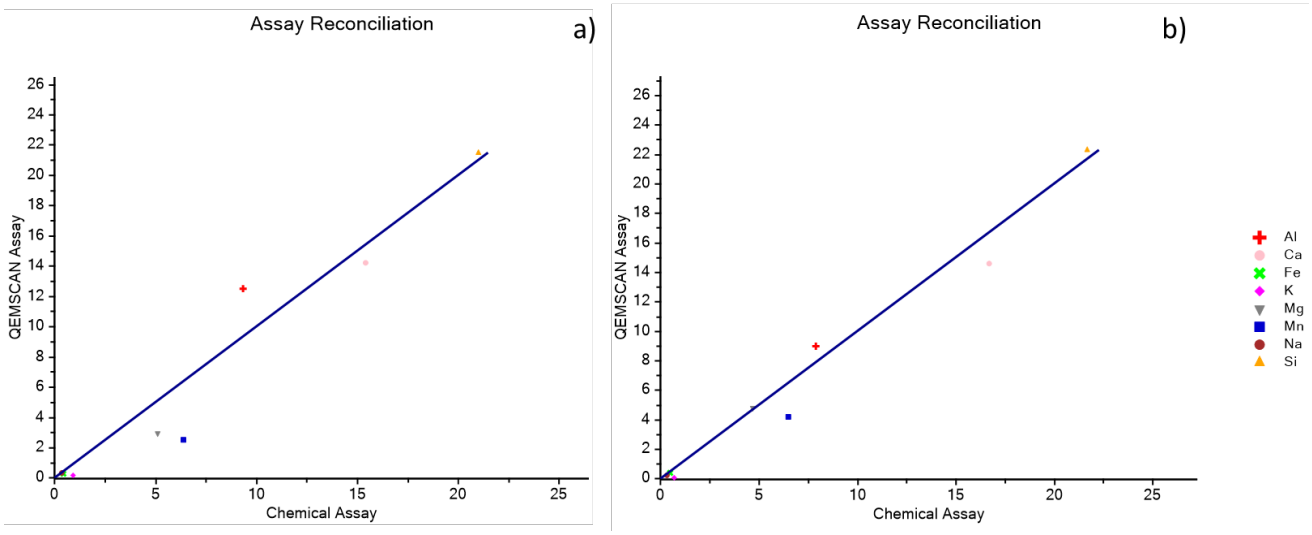

FIG 2 – Assay reconciliation between QEMSCAN® and chemical analyses for samples T4 (a) and T9 (b).

Slag mineralogy

Figure 3 illustrates the diversity of morphology, size and micro-texture of comminuted Kvinesdal slag particles from T4 (a) and T9 (b) before separation tests. In a first instance, the density and size segregation mentioned before is well illustrated. Then, it can be observed most of particles identified are associated to silicates slag have chemical composition in agreement with wollastonite ($CaSiO_3$) and glaucochroite ($CaMnSiO_4$). Modal compositions are of 44 per cent of wollastonite and 48 per cent of glaucochroite for T4 and 65 per cent of wollastonite and 25 per cent of glaucochroite for T9. These high temperature mineral phases are thought to be formed during the pyrometallurgical process of SiMn production. Quartz and other minor silicate phases are also indexed in a very low quantity (from 1 per cent to 2 per cent), therefore they will be considered negligeable in the present study. For each sample silicon carbide were observed through some slag particles but more important, micrometre size Mn-rich particles, possibly pure metal, trapped inside silicate slag, have been observed using scanning electron microscopy and were also identified and indexed by the QEMSCAN® system.

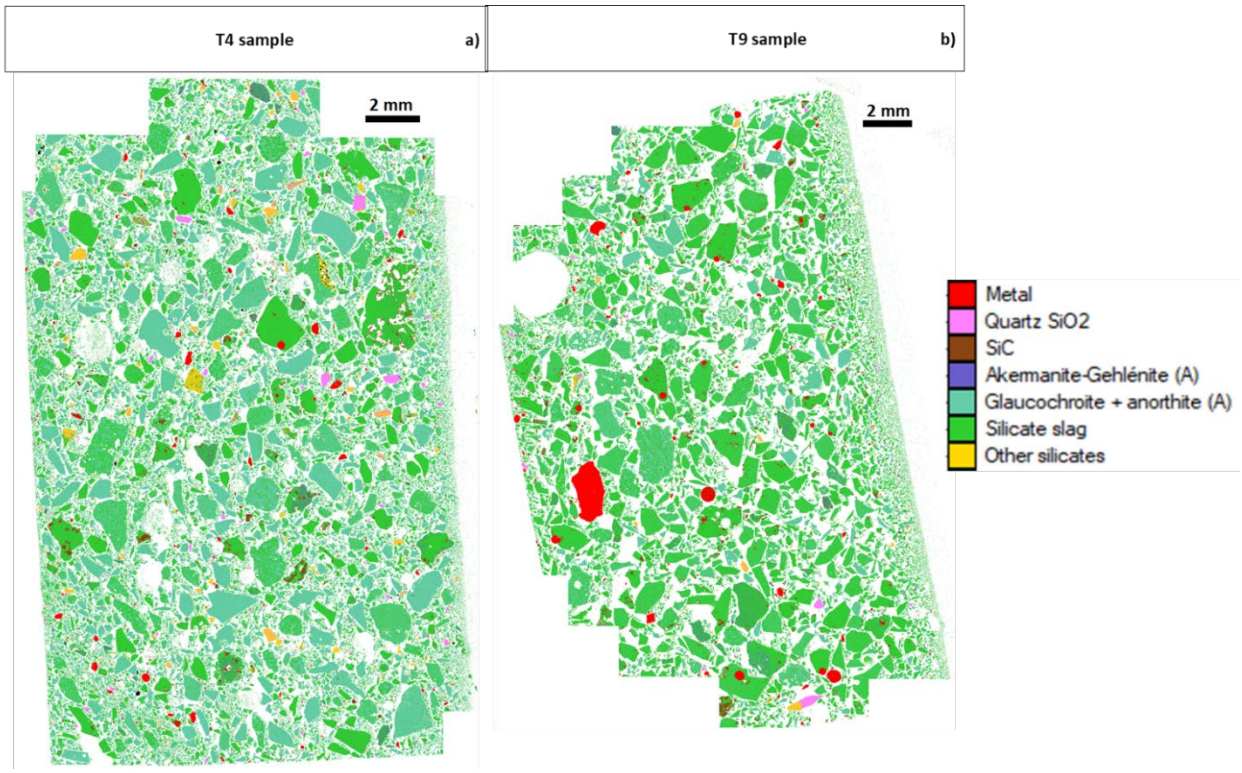

FIG 3 – QEMSCAN interpreted mineralogical maps of samples T4 (a) and T9 (b), as-received from the comminution tests.

In addition, two types of Fe-rich silicomanganese were identified: Brownleeite (SiMn) and Mavlyanovite (Mn_5Si_3). For the ease of reader and further data processing both phases of different Si:Mn ratio where merge in a single category classified in the 'Metal' group.

Particle size distribution of both samples is included from 15 µm to 1488 µm and from 15 µm to 1645 µm respectively for T4 and T9. All particles which have a lower size than 100 µm are considered as ultrafine and non-recovered particles and then, were removed using a sieve in this study.

In addition to the morphology and size of metal particles, the main parameter to consider is the liberation. In our approach, the liberation principle is based on the texturally associated phases. The percent of liberation is estimated using the 2D sections of the studied particles, neglecting the 3D particles shape. The high number of analysed particles will allow to transform 2D information into 3D by a stereological algorithm included in the iDiscover software. Data exploration revealed that metal particles can be considered well liberated with 61 per cent and 58 per cent liberation reported for T4 and T9 samples, respectively. Therefore, these liberated particles could be recovered using physical

properties such as density. Indeed, the density of silicomanganese metal is from 6000–8700 kg.m^{-3}, respectively for mavlyanovite and brownleeite, against 3000 kg.m^{-3} for silicate slags.

Physical separation results

One of the most efficient and practical way to recover valuable elements using their density and size is the shaking table. This is particularly true for particle set displaying a narrow size distribution range. Therefore, T4 and T9 samples were preprocessed by wet sieving from 100 µm to 500 µm to feed the shaking table.

As illustrated in Figure 4, a concentrate of metal particles (in red) is obtained despite some remaining silicate slag (in green). Some well liberated metal particles were observed on the middlings whereas a low amount of silicomanganese particles is still present inside the tailings fraction. These results are also in agreement with the colour of the various streams observed on the shaking table deck during the tests.

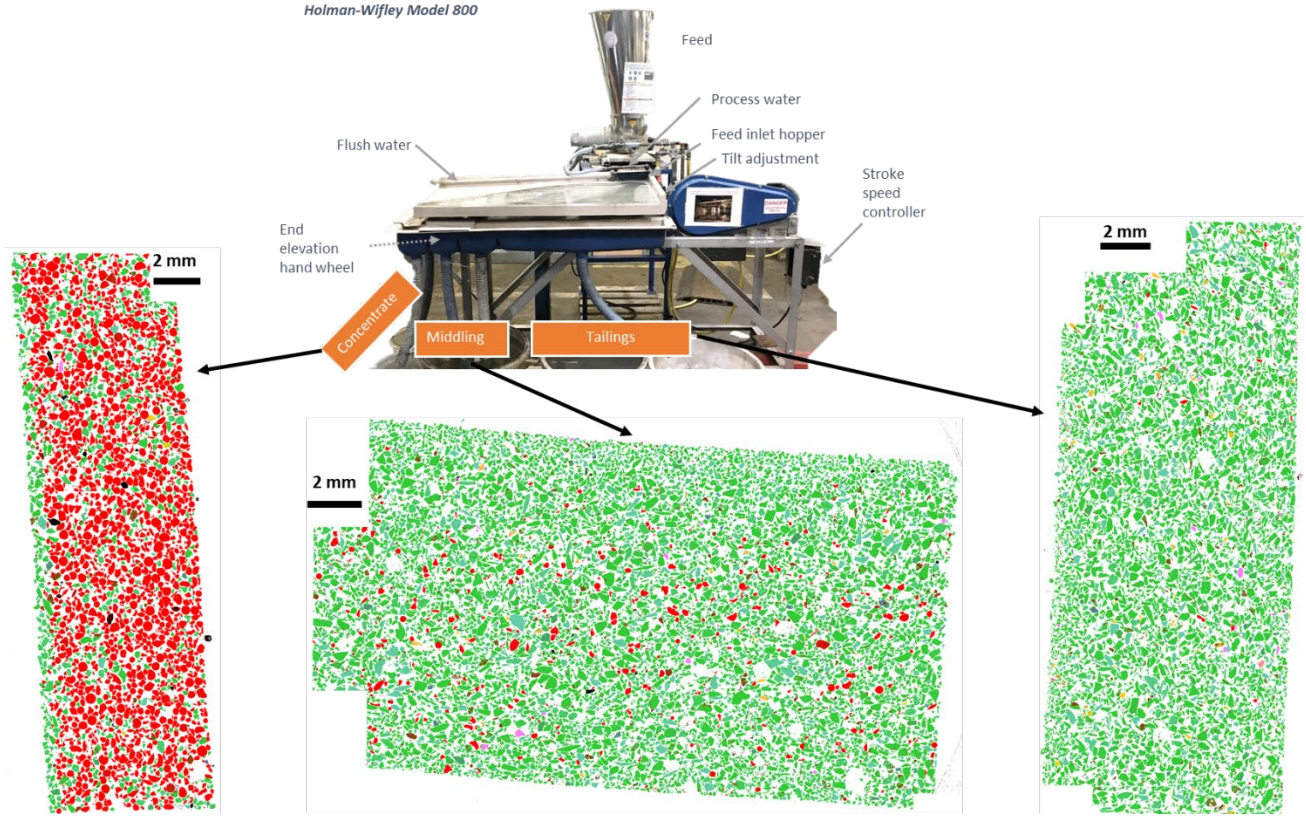

FIG 4 – Picture of shaking table and illustration of metal recovery for T9 sample.

A more detailed analyse of the tailings fraction, reveals that the mesh size of perfect spherical metal particles is about 160 µm, compared to the middlings and concentrate samples which are respectively about 160 µm and about 240 µm. This difference of mesh size could explain the metal particles occurring inside the tailings fraction by a size effect predominant over the density properties. Particle size distributions for T9 and T4 are almost identical from 100 µm to 500 µm (Figure 5). However, a slight difference between both samples can be observed on the density distribution curves from 2800 kg.m^{-3} to 3400 kg.m^{-3}. Indeed, the density curve increases sharply for the T4 compared to the T9. As gravity separation depends both on density and particle size, this density variation could get an effect on the physical separation occurring for T4 compared to the T9 sample.

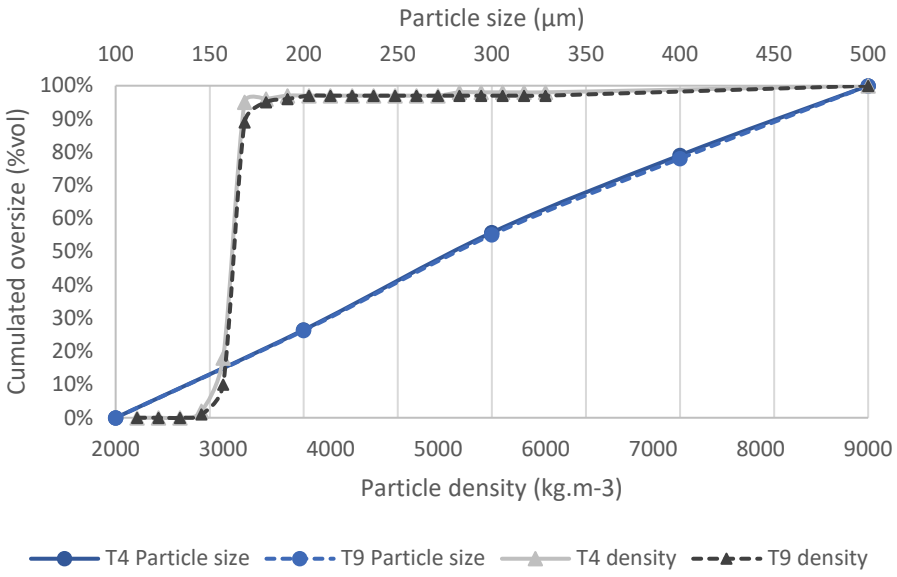

FIG 5 – Size and density classes for T4 and T9.

Mineral composition and yield of each class (mass, density and combination of size and density) are then extracted from iDiscover software to build the Figure 6, which depicts the cumulated recovery as a function of cumulated yield of the heavy product for each classification. Metal recovery of experimental tests is ranging from 69 per cent for T9E2 to 77 per cent for T4E2 for a yield set at 20 per cent. Those results are consistent with the highest liberation found previously on T4 sample. To simulate the experimental curve obtained after shaking table tests, three classifications were used: particle mass, particle density and combination of size and density of particles. It should be noted that some fractions in the studied model were containing only a few particles which could affect the representativity of the mineralogical composition.

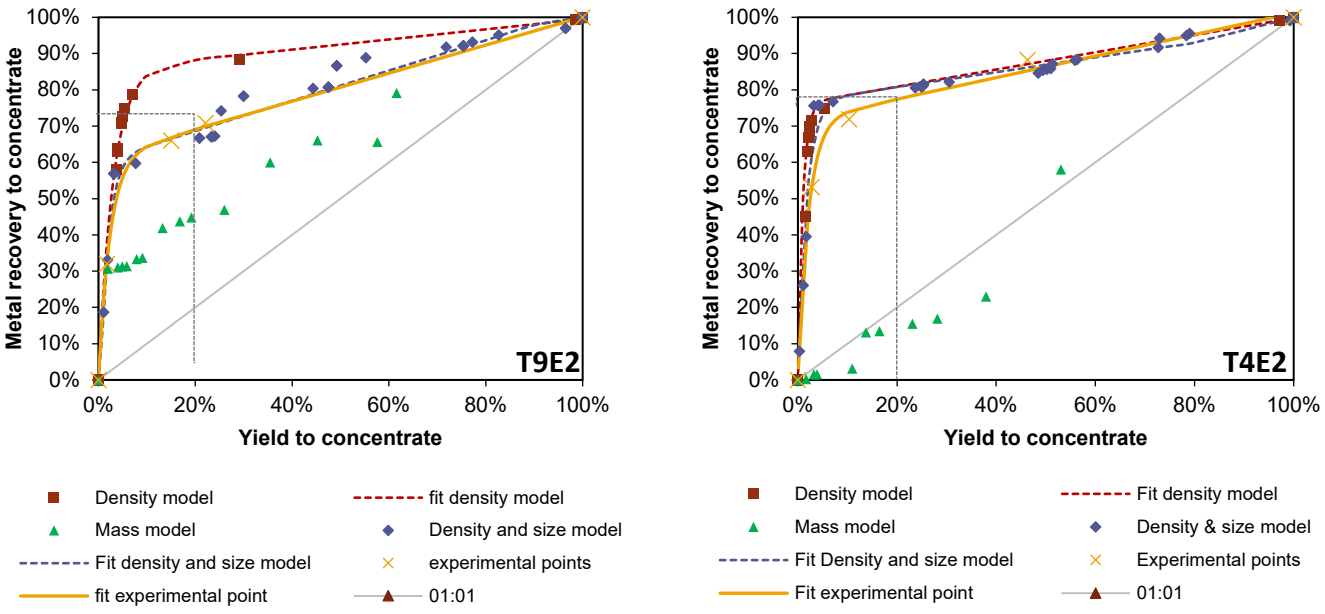

FIG 6 – Recovery / yield curve simulated using three model (density, mass, combination of density and size) and experimental curves.

The simplest attempt consisted in reproducing a perfect sink and float analysis by using only the particle density as classifier. Modelling results are significantly different between both samples. For

T9E2, the density model curve is largely (≈ 20 per cent) over the experimental results whereas for T4E2 the results are essentially equivalent.

The use of particle mass classifier, which should reflect both size and density effect, was poorly correlated with experimental data and highly dispersed as can be seen in the Figure 6. It can be noted that for T4E2, most of the simulated points are below the non-separation curve (represented in light grey) which is not consistent with experimental and expected results.

Then, simulated values from the density and size model are more dispersed than the ones simulated from density only, but they are close to the experimental data with correlation coefficients above 0.97 for both set of experimental data. Those results are consistent with the one obtained on synthetic ore by Fitzpatrick *et al* (2016). As highlighted by the density distribution and liberation, T4E2 separation seems to be mainly governed by density.

T4 and T9 has been sampled in two different point of the comminution process which has led to distinct mineralogical and morphological characteristics. The first sample T4 has gone through successive crushing step in a close loop circuit which resulted in a higher liberation of metal particles and to a separation mainly governed by density. For the second sample, T9, the sample was taken after a vertical shaft impactor after an open classification circuit which led to a liberation slightly different than the T4 sample. The physical separation is less efficient after a shaft impactor step compared to multiple cone crusher step.

CONCLUSIONS

Prior work has documented methods to upgrade Silicomanganese slag using both magnetic and gravity separation steps. To achieve mineral liberation an efficient comminution step is necessary prior those operations. Several studies (eg, Napier-Munn, 2015) point out that optimising the target and the comminution process is one way to reduce energy consumption. A method to simulate results from an automated mineralogy analyser acquired by the QEMSCAN® system has been developed by Fitzpatrick *et al* (2016) on a synthetic ore. However, those studies have not been tested on not perfectly liberated ore resulting from different type of grinding which can led to differences in liberation, particle shape and particle size distribution.

In this study, three models, including the model mentioned previously, were tested for secondary raw material gravity separation and highlight the implication of these models results into the development of a comminution flow sheet. It was found that the model developed by Fitzpatrick *et al* (2016) was the most reliable with a correlation coefficient between the two fitted curves above 0.97 and applicable to both materials tested, even if a density-only model seems applicable for sufficiently liberated sample. Overall, gravity separation enables a metal recovery in the concentrate between 69 and 77 per cent for a 20 per cent yield. This study therefore tends to confirm a fast method to simulate gravity separation results based on QEMSCAN® analyses. It should provide an assessment of comminution performance associated with separation results. However, some limitations are worth noting such as the number of particles on each fraction and the number of experiments used to confront models. Future works should therefore include more samples taken at various comminution stage. Furthermore, the particle shape aspect should be taken into account in the modelling of shaking table tests.

ACKNOWLEDGEMENTS

This activity has received funding from the European Institute of Innovation and Technology (EIT), a body of the European Union, under the Horizon 2020, the EU Framework Program for Research and Innovation. This work is part of a project called GREENY (Grinding Energy EfficiencY) that focuses on increasing the energy efficiency of comminution and enabling the beneficiation of difficult to process secondary raw materials. The authors would like to thank Eramet Norway for providing SiMn slag samples. Metso:Outotec for their work on comminution, and the other partners (VTT, Luleå and Freiberg) for their support. The authors are also grateful to the members of the Eramet Ideas technical team for their support.

REFERENCES

Fitzpatrick, R, Hegarty, P, Ghorbani, Y and Rollinson, G, 2016. Quantitative mineralogy for improved modelling of shaking tables. *IMPC 2016: XXVIII International Mineral Processing Congress Proceedings*.

Frias, M, Sánchez de Rojas, I, Santamaría, J and Rodrígez, C, 2006. Recycling of silicomanganese slag as pozzolanic material in Portland cements: Basic and engineering properties. *Cement and Concrete Research*, 36(3), pp. 487–491.

Grobler, J D and Bosman, J B, 2010. Spiral concentrator modelling using Qemscan® particle mineral analysis. *Physical Beneficiation 2010 Conference*.

Hunsbedt, L, 2019. Silico-manganese slag – a versatile by-product from Eramet Norway. *Global Slag Conference 2019*.

Kumar, S, García-Triñanes, P, Teixeira-Pinto, A and Bao, M, 2013. Development of alkali activated cement from mechanically activated silico-manganese (SiMn) slag. *Cement and concrete Composites*, 40, pp. 7–13.

Lindroos, M, Andersson, T, Laukkanen, A, Suarez, L, Kajberg, J, Jonsen, P, Terva, J and Kallio, M, 2021. Micromechanical and multi-scale modeling of manganese containing slag comminution in the design of energy efficient secondary raw material beneficiation processes. *Minerals Engineering*, Volume 170, p. 106995.

Napier-Munn, T, 2015. Is progress in energy-efficient comminution doomed?. *Minerals Engineering*, Volume 73, pp. 1–6.

Numbi, B P and Xia, X, 2016. Optimal energy control of a crushing process based on vertical shaft impactor. *Applied Energy*, Volume 162, pp. 1653–1661.

Özbay, E, Erdemir, M and Halil İbrahim, D, 2016. Utilization and efficiency of ground granulated blast furnace slag on concrete properties – A review. *Construction and Building Materials*, Volume 105, pp. 423–434.

Pascoe, R D, Power, M R and Simpson, B, 2007. QEMSCAN analysis as a tool for improved understanding. *Minerals Engineering*, Volume 20, pp. 487–495.

Shen, H and Forssberg, E, 2003. An Overview of recovery of metals from slags. *Waste Management*, 23, pp. 933–949.

Sivamohan, R and Forssberg, E, 1985. Principles of tabling. *International Journal of Mineral Processing*, Volume 15, pp. 281–285.

Sripiya, R and Murty, C, 2004. Recovery of metal from slag/mixed metal generated in ferroalloy plants – a case study. *Int. J Miner. Process*, 75, pp. 123–124.

Modelling of water quality impact on flotation performance and potential of improvement – case of a Cu-Ni flotation plant

E Braak[1], P Wavrer[2], B Musuku[3], M A De Ville D'Avray[4], O Mdere[5] and S Brochot[6]

1. Process Engineer, CASPEO, Orléans France. Email: e.braak@caspeo.net
2. Process Engineer, CASPEO, Orléans France. Email: p.wavrer@caspeo.net
3. Chief Metallurgist, Boliden Kevitsa Mine, Petkula Finland.
   Email: benjamin.musuku@boliden.com
4. Process Engineer, CASPEO, Orléans France. Email: ma.devilledavray@caspeo.net
5. Process Engineer, CASPEO, Orléans France. Email: o.mdere@caspeo.net
6. Company Director, CASPEO, Orléans France. Email: s.brochot@caspeo.net

ABSTRACT

Water management is a key strategic driver of mineral processing plant operations. Its importance keeps increasing along with global economic and environmental concerns, leading to the need of reusing process waters within plants. To address this issue in the frame of the European project ITERAMS, a prototype model of flotation plant that accounts for impact of water quality on process performance was developed as a tool to simulate recycling scenarios. It gathers modelling tasks to provide insight in water impacted/involved operation: flotation and water treatment unit operations. The chosen technologies for water treatment are Dissolved Air Flotation (DAF) for fines removal and Ion Exchange Resins (IER) for sulfate removal. The influence of water quality upon flotation is assessed via the determination of empirical laws of kinetics variation depending on water composition, using the first order kinetic model with ultimate recovery. These unit models were first developed separately with specific focus. They were then adapted and integrated into a global plant model, calibrated with plant survey and lab experiment data. The obtained model simulates an industrial Cu-Ni flotation plant. It gives plant behaviour trends depending on the water treatment implementation. The presented case illustrates the importance not to limit the study of water impact on process performance to lab or pilot scale survey, but to integrate their results into a plant scale model to predict behaviour which cannot be easily deduced from the experimental work only. Building this prototype also enabled to highlight the main weaknesses of the modelling approach and to suggest improvement opportunities to enhance the reliability of the simulator results. The paper describes the model structure and the method for calibration using a mix of plant and lab data. It presents the main results of the performed simulations.

INTRODUCTION

Water is a required utility for a mineral processing plant facility, both as a transportation media and reaction medium, with requirement of several m^3 of water per ton of processed ore. The general decrease of orebody head grades leads to larger amounts of ore to process, and consequently larger water consumption. On a global water-saving trend, the recycling of process water is gaining importance, but this recirculation can impact plant performance. As an alternative or a previous step before expensive plant trials, computer simulation enables assessing different water management strategies through testing of alternative circuits, optimising design and evaluating process economics. This paper presents the modelling approach to create a flotation plant model that accounts for issues related to water management (influence on process, and associated water treatment units to remedy the problems encountered), and its implementation to build a simulator for an industrial Cu-Ni flotation plant.

The simulator was developed in the frame of the European Union H2020 project ITERAMS, and relies on experimental results obtained by the project partners. These results are briefly recalled and referred to when published. Building the simulator required three main steps:

- First, a sampling campaign was carried out to evaluate the plant performances and provide reference mass balance for model calibration via data reconciliation.
- Then each operation required to build the global plant model was specifically developed and calibrated. For water treatment, the selected technologies were Dissolved Air Flotation (DAF)

for fines removal and Ion Exchange Resins (IER) for sulfate removal. Regarding mineral processing focus was made on flotation. This is a complex process that involves numerous parameters and phenomena. Understanding its dependence on water quality has been, and still is, a great research issue (Rao and Finch, 1989; Levay, Smart and Skinner, 2001; Michaux, Rudolph and Reuter, 2018). The retained approach is empiric, at the expense of a more theoretical approach based on first principles that would be hardly implemented. It consisted, using the classical first order kinetic model, in determining the variation of kinetics depending on water quality based on batch test series.

- These unit blocks were then integrated in a global plant model. Based on the reconciled reference data from sampling campaign and the equipment characteristics, the flotation kinetics were calibrated for each stage of the plant to provide the finalised plant simulator.

Several scenarios were then assessed to estimate the potential for plant operation upgrading with the implementation of water treatment solutions. The main limitations and improvement perspectives of the model are also discussed.

CASE STUDY AND SAMPLING CAMPAIGNS

Kevitsa (Finland) plant operates over a Cu-Ni-PGE deposit. The concentrator employs a sequential Cu-Ni flotation circuit. The tailings from the Ni circuit are then further floated to separate the low and high sulfur tailings, the latter being specifically stored in a dedicated pond to limit the risk of acid mine drainage (Musuku, Muzinda and Lumsden, 2016). Water is reused with important recycling rate, ranging from 86 to 97 per cent (Muzinda and Schreitofer, 2018). The presented simulator is restricted to the Cu-Ni flotation circuits, and to the monitoring of Cu and Ni metals. A global sampling campaign was conducted to provide raw data in order to establish a consistent mass balance of the plant via data reconciliation. The sampling strategy is summarised in Figure 1.

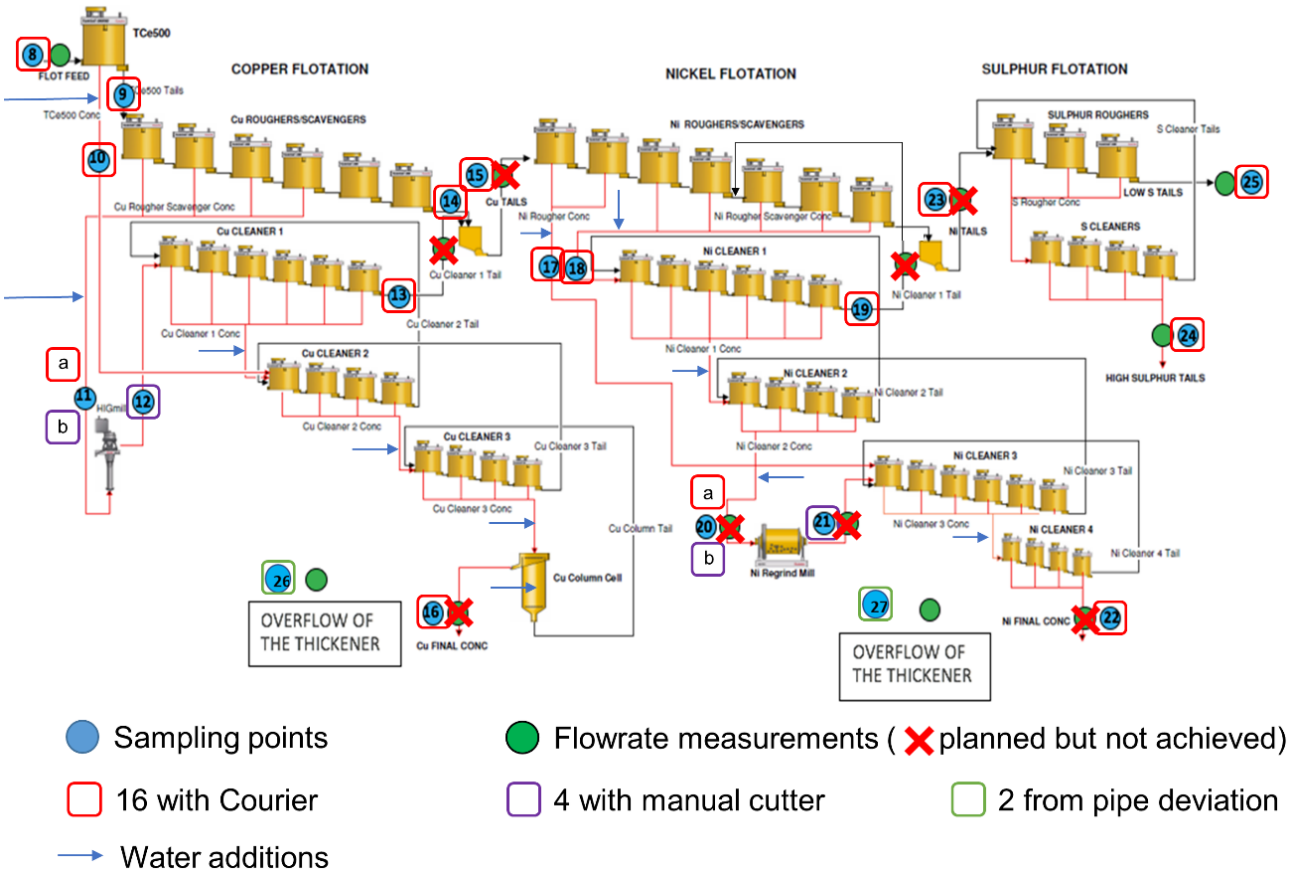

FIG 1 – General flow sheet and sampling strategy.

Most of the streams were sampled with the automatic sampler associated with the Courier© system, used in manual mode. Else, samples were taken from pipe derivation or with a manual cutter. Water

is added on some parts of the flotation circuits to adjust the solids content, these additions are represented by blue arrows.

Duplicate samples were systematically taken into two separate buckets: one for liquid analysis and one for solids analysis. For solids analysis, raw pulp samples are weighed, dried in an oven at 90°C and weighed again to estimate the pulp water content (and solids content). The obtained dry solids are then split and analysed via X-ray fluorescence for Cu, Ni, S, Fe, Mg and Ca contents. The solid specific gravity, which is used for calculation, is supposed to be 3.15 for all the streams. Problems of confidence in water component analyses were outlined by project partners in charge of this task (Le *et al*, 2020). Most water samples considered in this study were plant waters characterised by a high instability, and the results of the study showed that the methodology for the evaluation of mining effluents for environmental purposes, usually used to control the fulfilling of environmental regulations, is not suitable for evaluating process waters recirculated in the mineral processing plants.

Three flow rate measurements are available: for *flotation feed* (8), *low sulfur tails* (24) and *high sulfur tails* (25). No flow measurements are available for water addition streams, the considered data are then an estimate from a balance provided by the plant staff.

Data reconciliation was performed with the USIM^{TM} PAC software. The lack of reliable quantitative and qualitative data regarding water flows led to the abandonment of considering water composition for the balance reconciliation, and water is thus balanced only quantitatively.

As rather few flow measurements are available, most solid mass flow rates are estimated with the 2-outputs formula. If the calculated split ratios are close to each other for all components, their mean value is taken. Else, the one corresponding to the metal treated by the flotation circuit is taken as it is certainly the most accurate.

Reconciliation problems could occur because of missing data, which can require many calculations and lead to less redundancy, and also because of inaccurate data initialisation. The chosen strategy is thus to firstly reconcile for solids and liquid at the same time on a simplified flow sheet (one node per flotation circuit), with setting higher confidence in solids data and flow rate measurements. This enabled to introduce redundancy with the liquid flow estimates on one hand, and the solid content measurements on the other hand, and to improve the estimate of water additions per flotation circuit. The results of this first balance calculation were used as raw data for the calculation of the detailed balance of each flotation circuit. Calculated values for the 'boundary streams' (for *example flotation feed* (8), *Cu tails* (15) and *Cu final conc* (16) for Cu flotation circuit) are fixed. Some simplifications are made on each circuit flow sheet because of the lack of sampling points and measurements (mostly grouping of cleaner stages). Hence, as the reconciled data give information for a less detailed flow sheet than the general one (Figure 1), which is close to the one that is used for the plant simulator, assumptions are needed to complete the data set for calibration, as detailed in section *Global model*.

This reconciled balance still provides general plant performance. Regarding the water usage, water additions on flotation circuits represent 797.8 m^3/h with 15.9 per cent for Cu flotation circuit. With a water flow rate of 1592.6 m^3/h on flotation feed, the total water consumption is 2390.4 m^3/h (~35 per cent for flotation ~65 per cent for grinding), and the global consumption is 2.59 m^3/t_{ore} (ore feed rate of 922.3 t/h).

MODELLING APPROACH

Water treatment

The objective of the water treatment models is to size the treatment units depending on the quality of the input water, the expected output quality, and the quantities to be treated. These models also calculate the required quantities of reagents, the energy consumption and the effluent flow rates to be treated, which are parameters to consider in the overall evaluation of the water treatment scenarios.

Dissolved air flotation

Dissolved Air Flotation (DAF) is a process for the removal of suspended solids or water immiscible liquids (oils and greases). Air is dissolved in water under pressure (~4–6 bars), which is then released to atmospheric pressure. This pressure reduction allows to generate microbubbles which agglomerate with the particles to be eliminated to form aggregates with an average density lower than that of water. The process is usually preceded by a coagulation-flocculation step to produce flocs with properties that favour aggregation with the air bubbles. The DAF itself is divided into two stages: the water to be treated first enters a contact zone in which it is mixed with the air-saturated water. The bubble-floc aggregates created in this contact zone then pass into the separation zone, where the hydraulic load is lower. These aggregates are separated from the water by flotation and recovered in the foam which is scraped off the top of the tank.

Several configurations exist for pressurisation. In most of the plants the pressurised water is a part of the clarified water stream that is recirculated, but it is also possible to directly pressurise the effluent that must be treated. Only the first configuration will be considered here, with the recirculation rate being one of the important operating and sizing parameters. Only rectangular configuration is considered for flotation tank.

The modelling is based on design consideration. It is adapted from Haarhoff and van Vuuren (1993), who provide guidelines and reference values for DAF wastewater treatment plant design. The model is based on one of the main design criteria: the target air concentration in the contact zone (set to 8 mg/L). From saturator parameters (pressure – 5 bars, efficiency – 90 per cent) and temperature, mass balance and Henry law enable to calculate the recirculation rate. Other design constraints are set, such as acceptable flow rate per unit, length/width ratio of the separation zone and hydraulic loading in contact and separation zones. The model deduces from these inputs the equipment dimensions, the required number of units, and operating parameters, such as retention time in the contact zone. These values can then be checked against conventional design criteria, such as those provided by Edzwald (2010).

The performance of the treatment (per cent of removed components) is directly set depending on the experimental results. Reagent addition for precipitation and coagulation-flocculation are managed with concentration regulators, with respective target concentrations of 1 g and 70 g per cubic metre of treated water. A study from Nijhuis Water Technology (Long, Broeders and Menkveld, 2016), an industrial DAF supplier, is taken as reference point for the calculation of the energy consumption of the process. The specific energy consumption is considered to decrease linearly with flow rate, from 0.069 kWh/m^3 at 100 m^3/h, to 0.037 kWh/m^3 at 1500 m^3/h.

Ion exchange resins

Ion Exchange Resins (IER) are frequently used as a separation, purification or decontamination process. The applications of the process are varied, ranging from water softening and purification to uranium concentration. The process operates in semi-continuous mode. When used for decontamination, the water to be treated is pumped through the column and the concentration at the outlet is continuously monitored. When the concentration (or the average concentration) of the purified water reaches a limit value, the resins must be regenerated. During regeneration, the flow to be treated must either be redirected to another column in operation, stored in a buffer tank waiting next adsorption cycle, or not treated as bypassing the installation.

The process is modelled as an adsorption column. It is controlled by monitoring the variation of the output concentration as a function of time, providing the so-called ‘breakthrough curves’, which characterise the performance of the process. These curves typically have an S-shaped appearance (Figure 2), and several models mathematically equivalent to the sigmoid curve but expressed in different ways are frequently found in the literature (Chu, 2020): the Adams-Bohart, the Yoon-Nelson and the Thomas models. The Thomas model was chosen in this study, for which the breakthrough curve is given by the following equation:

$$\frac{c(t)}{c_0} = \frac{1}{1 + exp\left[-c_0 k_{th}\left(t - \frac{qm}{c_0 Q}\right)\right]}$$

Where:

$c(t)$	is the concentration at the output at time t (mg/L)
c_0	is the concentration at the input (mg/L)
t	is the time from the beginning of the adsorption cycle (s)
k_{th}	is the adsorption kinetic constant (L/mg.s)
q	is the adsorption capacity of the resin (mg/g)
m	is the mass of resins in the column (g)
Q	is the input flow rate (L/s)

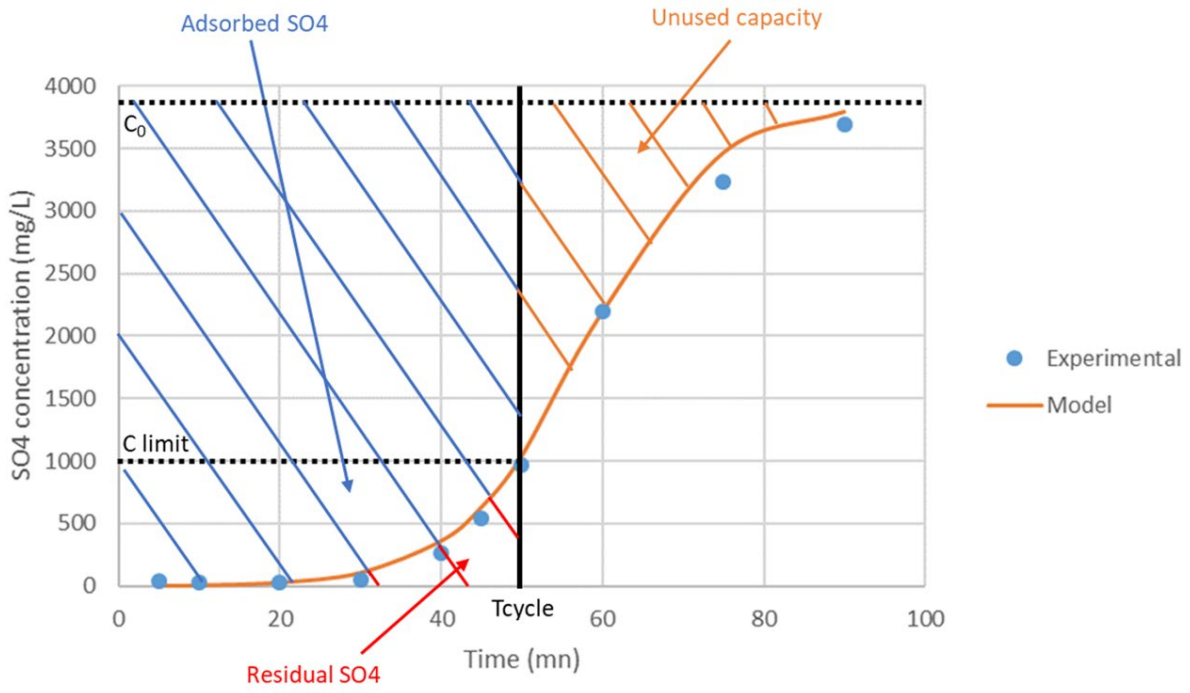

FIG 2 – Modelling and integration on a breakthrough curve (synthetic wastewater).

In the frame of the ITERAMS project, IER were chosen as a means for specifically treating sulfates. These sulfates induce problems of scaling in the pipes due to the precipitation of gypsum, as observed on another site studied in the project where high concentrations of sulfates are reached (>2000 mg/L). The first experimental tests were performed on synthetic water with a high sulfate load (Can *et al*, 2020). The calibrated Thomas model is in good agreement with these experimental results (Figure 2). Calibration on synthetic loaded water (input at 3860 mg/L) gives 51.56 mg/g and 2.74×10^{-5} L/mg.min for q and k_{th} respectively. The same type of experimentation was carried out using Kevitsa process waters (Ekmekçi, 2020, personal communication). The adjustment of the model parameters gives values of the same order of magnitude, respectively 46.36 mg/g and 7.44×10^{-5} L/mg.min for q and k_{th}, with lower sulfate concentrations (~ 500 mg/L).

Thomas model, thus allowing to simulate the performance of a column via the prediction of the breakthrough curve, has been integrated into a more global model which simulates a bank of n columns operating in parallel. Each column is considered to be operating full time, with n-1 columns simultaneously in the adsorption phase, treating water, while the remaining column is in the regeneration phase. If only one column is used, then it is bypassed during its regeneration phase. The model calculates the performance (output concentration) as a function of the sizing parameters (number of columns, quantity of resins per column), the properties of the resins (capacity), the reaction parameters (kinetic constant) and the operating parameters (flow rate). When the output concentration reaches a defined limit concentration (average or gross), the adsorption cycle ends as the resins must be regenerated. Since the process operates in semi-continuous mode and the plant simulation is performed in steady state, the average output concentration is estimated by integrating

the residual amount over one cycle (integral in red in Figure 2), which is then distributed evenly over the cycle time to simulate a pseudo-continuous mode:

$$Residual\ SO_4\ per\ unit\ time = \frac{Q}{t_{cycle}} \int_0^{t_{cycle}} c(t)dt$$

The amount of adsorbed component is the complement of c(t) to c_0 (integral in blue in Figure 2):

$$Adsorbed\ SO_4\ per\ unit\ time = \frac{Q}{t_{cycle}} \int_0^{t_{cycle}} \big(c_0 - c(t)\big)dt$$

The energy requirement for pumping through the columns, depending on the input flow rate, is estimated using FLUIDFLOW© software, assuming that a column is a fixed bed filled with 1 mm diameter spherical beads, with a particle void fraction of 0.26.

Flotation

The flotation modelling approach is semi-empiric. It is based on the first order kinetic model with two populations (floating and no-floating), for which the recovery is provided by the hereunder equation:

$$R(t) = R_\infty\big(1 - e^{-kt}\big)$$

The aim is to determine the variations of the model parameters, namely ultimate recovery R_∞ and flotation kinetic k, as a function of the water composition. A general assumption made to build the global model is that water quality mostly impacts flotation behaviour through kinetic constant rather than ultimate recovery. The modelling task resumed to determine the kinetic variation depending on the concentration of the water components, some dissolved (*dis* subscript) and some in colloidal fine particles (*sol* subscript):

$$k = f([SO_{4\,dis}], [Mg_{dis}], [Si_{dis}], [Si_{sol}], [Fe_{sol}]\dots)$$

GLOBAL MODEL

The global model gathering the described modelling blocks was developed with USIM™ PAC software, which is a platform for steady-state mineral processing simulation. The modelling process is divided into several steps:

- Flow sheet drawing: description of the process in terms of successive unit operations and material streams.
- Phase model: description of the material handled by the plant. It can include solid phase (minerals, size classes, floating populations), water phase (components), reagents …
- Initialisation of the input streams.
- Calibration of the mathematical models for each unit operation.

The model can then be used to run simulations and analyse their results.

Main hypothesis

The retained flow sheet for the Kevitsa plant simulator is adapted from the general one presented previously in section *Case study and sampling campaign* and is described on Figure 3. The main difference is that Ni rougher/scavenger bank is split in two stages, to manage the recirculation from Ni cleaner 1, and that the final sulfur flotation is not considered.

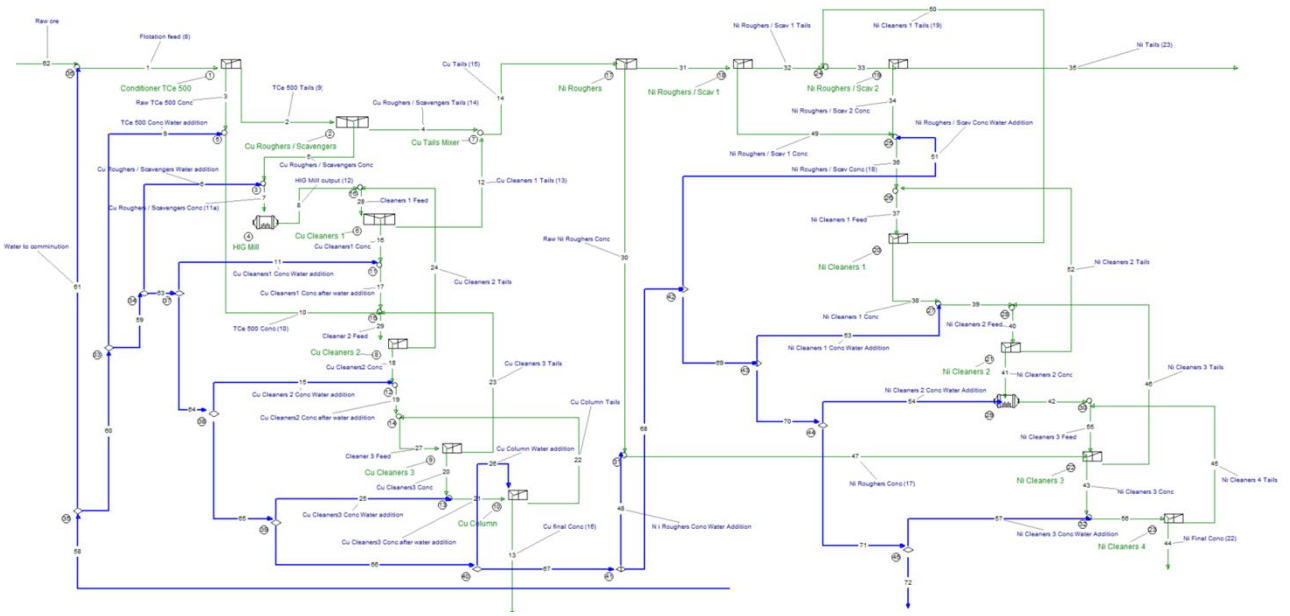

FIG 3 – Flow sheet used for Kevitsa plant simulator.

This flow sheet includes each flotation stage and goes in a finer granularity than the flow sheets considered for data reconciliation. Assumptions are thus required for flotation stages for which no data are available. They are described hereafter.

Regarding the material description, two different approaches are possible for solid phase composition: in terms of metals or minerals. Although the analyses performed during the survey provide metal contents, it is more realistic to consider minerals for flotation simulation. To do so, the mass balance obtained from data reconciliation is transposed from metal to mineral balance, assuming a mineralogical model based on the mineralogical composition of the feeding ore provided by plant staff for the day of the survey. For example, cubanite and chalcopyrite are the main minerals bearing Cu. As there is no measurement allowing to know their relative content in the material along the process, except in the ore for the plant feed, it is better to manage a pseudo-mineral which is an average of both, its Cu content of 28.97 per cent being calculated from their relative content in the feed and their respective content of Cu. Assuming only these minerals are Cu bearing, the pseudo-mineral content can be deduced from the ore Cu content. This transposition from metal to mineral composition is necessary to consider the deportment of the other elements constituting those minerals, which are following the same kinetics, and which have not to be accounted as gangue mineral components. The gangue recovery would be overestimated if only metals are considered, which would then impact kinetics estimation.

Similarly, a Ni pseudo-mineral is considered, but it needs a particular handling because of its depression in the Cu circuit. To account for that, the Ni pseudo-mineral is split into two pseudo-mineral subpopulations: one which is floating in the Cu and Ni circuits (named ‘Ni min flot Cu’) and the other which is floating in the Ni circuit only (named ‘Ni min depr Cu’). The latter being activated in Ni circuit (null kinetics in Cu circuit, not-null in Ni circuit). The amount of floating ‘Ni min flot Cu’ was initialised to represent 14.62 per cent of total Ni.

Figure 4 sums up how the ore and the water are described in the simulator phase model.

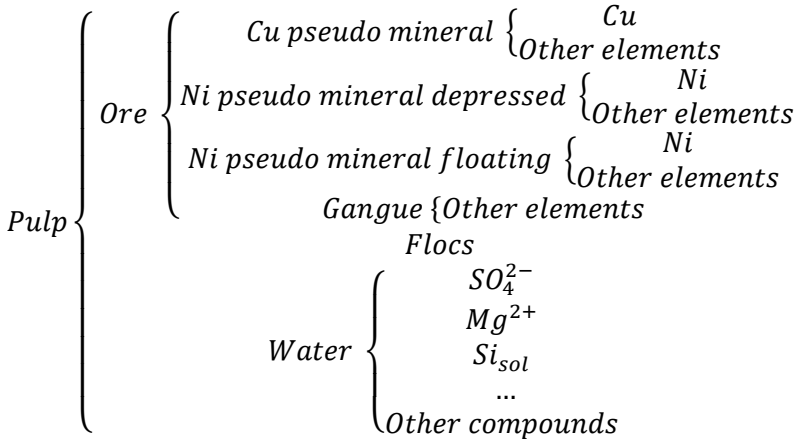

FIG 4 – Phase model for material description in simulations.

As neither size distribution nor composition per size class was measured, the model only considers an overall recovery of minerals within the full size range. As no information was available on the relative flotation kinetics for Cu-and Ni-bearing minerals, it is assumed they float with the same speed than their associated pseudo-mineral.

As mentioned previously, a general assumption made to build this model is that water quality mostly impacts flotation behaviour through kinetic constant rather than ultimate recovery. This latter directly corresponds to the proportion of floating population in the retained model. The ultimate recovery of a given pseudo-mineral is thus initialised in the feed stream and is not further impacted by water quality. The following values are considered for this initialisation:

Cu: 88.34%.

'Ni min flot Cu': 100%.

'Ni min depr Cu': 60.66%.

Gangue: 3.42%.

The residence time being proportional to the volume of slurry in the cells, the proportion of the cell volume occupied by slurry must be considered. The same operational volume proportion is assumed for every flotation cell, regardless of its location in the circuit. With an operation level between 85 and 90 per cent, and gas hold-up between 5 and 10 per cent, an 85 per cent effective volume percentage is used. Due to lack of data, the Cu flotation column is modelled as a conventional flotation cell for simplification.

Some assumptions are also required to manage the water repartitions and complete the reconciled material balance:

- The impact of water quality on froth structure and water recovery in the froth is not assessed in the model. The water recovery in the froth is set to a fixed value, when available from plant surveys.
- When not available, it is estimated from the range of pulp density targeted on flotation stages: with target values between 1.2 and 1.3 kg/L, and considering a solid specific gravity of 3.15, a corresponding range of solid content of 24.4–33.8 per cent is calculated. The solid content is thus assumed to be 25 per cent on every cleaner concentrate.
- The level of details for water addition is higher in the simulation flow sheet than in the most detailed flow sheet considered for data reconciliation. From the latter, the 'global' streams of water addition are split following the proportions given by the raw values provided by the plant staff.

The distribution of water is simply managed by derivation from a distribution line with a flow rate slightly higher to the global water consumption of the circuits, the amount of water added corresponding to the reference mass balance.

Reference case calibration

The aim of this step is to set the kinetic parameters of each mineral for each flotation stage in a way that the calibrated model would provide a simulated mass balance as close as possible to the target mass balance. The target mass balance consists of the reconciled mass balance, adapted to the selected phase model, which is deduced from the transposed mineral balance as previously described. It is completed with calculations for flotation subpopulations, which are required only for rougher and scavenger tails of each circuit, knowing that 100 per cent of the ore in the concentrate belong to the floating subpopulation.

The kinetics are directly adjusted, when possible, ie when only one stage is studied at a time. When several stages must be simultaneously calibrated (because of recycling from one to another), the supervisor function of USIM^{TM} PAC is used. This feature enables to run several simulations by varying selected parameters and monitor selected simulation outputs as sensors. The set of parameters can iteratively be affined until a satisfying result is obtained compared to the target mass balance.

The assumptions about kinetics and the order of stage calibration steps are summed up hereunder:

- Cu circuit:
  - Same kinetic parameters used for rougher and rougher/scavenger tanks concerning Ni pseudo-mineral ('Ni min flot Cu').
  - Same kinetic parameters used for cleaners 2–3 tanks and column concerning Cu pseudo-mineral, Ni pseudo-mineral ('Ni min flot Cu') and gangue minerals.
  - Calibration of the models for rougher (adjustment), rougher/scavenger (adjustment), cleaners 1–2–3 + column (supervision).
- Ni circuit:
  - Same kinetic parameters for cleaners 3–4 tanks concerning Cu pseudo-mineral, Ni pseudo-mineral (both 'Ni min flot Cu' and 'Ni min depr Cu') and gangue minerals.
  - Calibration of the models for rougher (adjustment), rougher/scavenger 1–2 (supervision), cleaners 1–2–3–4 (supervision).

After calibration of all unit operation models, the full flotation flow sheet has been simulated and compared to the material balance based on reconciled data obtained from plan survey results.

Determination of relationship between flotation kinetics and water quality

The influence of water composition on flotation kinetics is modelled using the results from water treatment studies including pilot plant tests coupled with batch flotation tests performed during the experimental part of the project. Detailed experimental results were shared internally in the project, both for DAF (Saari, 2020, personal communication) and IER (Ekmekçi, 2020, personal communication) test series. DAF studies have been presented by Jansson, Saari and Musuku (2020), results of IER tests have been published for another plant studied in the project (Özturk and Ekmekçi, 2020).

Sequential flotation test series were carried out with raw process waters and treated waters. The considered tested waters are:

- For IER: raw process water (PW1) and treated process water at different time (PW1–30 min and PW1–120 min).
- For DAF: process water (PW), Ni thickener overflow (Ni Th) and Cu thickener overflow (Cu Th), raw (DAF In) and treated (DAF out).

The water component concentration range corresponding to the different flotation tests is summed up in Table 1.

TABLE 1

Water composition: component concentration ranges (mg/L). *dis* for dissolved and *sol* for colloidal solid components.

	SO_4 dis	Mg dis	Si dis	Ni dis	S_2O_3 dis	Mg sol	Si sol	Ni sol	Cu sol	Fe sol
Min (mg/L)	0.1	49.6	5.34	0.05	2.5	0	0	0	0.1	0.4
Max (mg/L)	780	91.7	7.64	0.34	24	21.1	9.97	1.25	12	12

The overall flotation protocol is nearly the same for both test series and is described in Table 2. Sulfur flotation circuit was not included for IER series.

TABLE 2

Sequential batch test protocol as reference flotation test.

Flotation stage	Batch test protocol
Cu flotation circuit	2 min conditioning 5 min flotation 5 min flotation
Ni flotation circuit	2 min conditioning 7.5 min flotation 2 min conditioning 12.5 min flotation
Sulfur flotation circuit	1 min conditioning 5 min flotation

These tests were analysed as follows, separately for both test series:

- The flotation of Cu is estimated only from Cu flotation circuit stages. First, every batch test is calibrated on the two points of that stage (at 5 and 10 min) giving the two parameters of the flotation model: $R\infty$ and k. Then the maximal value obtained for $R\infty$ is set to all the experiments and k fitted again. It is assumed that Cu flotation behaviour is similar for Cu and Ni circuit stages.
- The behaviour of Ni during flotation is assessed separately for Cu and Ni flotation circuit stages. For Ni in Cu stage the method is the same as for Cu. The difficulty of analysing sequential flotation tests is that the material feeding the Ni circuit stage depends on the upstream performances of the Cu circuit stage. In these tests, Ni recovery on Cu circuit stage is very much higher than observed in the plant. Indeed, the sequential flotation test mainly represents rougher and scavenger stages, not cleaners, and Ni is not much specifically depressed. It is thus difficult to compare batch tests between them as the feeding material of Ni circuit stages is different from one test to another. It is assumed that the floated Ni at the Cu circuit stage should have been partially depressed, and that most Ni should have reported to the feed of Ni circuit stage. The amount of Ni reporting to the Cu concentrate is estimated using the recovery of Ni in the Cu circuit from the reconciled balance of the plant. The Ni reporting to Ni circuit feed is assumed to float rapidly. The fitting of kinetic model is thus done considering the flotation time and recoveries (from which the estimated Ni reported to Cu concentrate is deduced) at Ni circuit stage. The fitting is done first to determine the common $R\infty$ and the k parameter is then readjusted.
- The flotation behaviour of gangue is supposed to be the same for the whole circuit and is estimated in the same way than Cu but considering the five floated samples.

To enable the comparison between both test series, the kinetics are not considered by their absolute value but by their relative value to a reference kinetic constant (the one for the process water for the considered test series). The obtained results are summed up in Table 3.

TABLE 3 – Relative flotation kinetics. PW stands for Process Water and Th for Thickener.

Test	k/k_{ref} Cu	k/k_{ref} Ni Cu circuit	k/k_{ref} Ni Ni circuit	k/k_{ref} Gangue
PW1	1.000	1.000	1.000	1.000
PW1–30 min	0.210	0.296	0.282	0.526
PW1–120 min	0.791	0.546	0.428	0.872
PW DAF In	1.000	1.000	1.000	1.000
PW DAF Out	1.444	1.721	1.291	1.038
Ni Th DAF In	1.544	1.537	1.366	0.693
Ni Th DAF Out	1.271	1.356	1.296	0.706
Cu Th DAF In	1.584	1.278	0.713	0.778
Cu Th DAF Out	1.721	1.530	1.215	0.972

The variation of kinetic constant with the composition of water is fitted with the following law:

$$\frac{k}{k_{ref}} = a_0 + a_1[SO_{4\,dis}] + a_2[SO_{4\,dis}]^2 + a_3[Mg_{dis}] + a_4[Si_{dis}] + a_5[Ni_{dis}] + a_6[Si_{sol}] + a_7[Fe_{sol}]$$

These laws are clearly purely empirical, without physical meaning, with a large number of parameters that could lead to underdetermination of the system. Further work would be needed to provide a more generalised and predictive mathematical function as a first step. This identification of more critical parameters would then guide towards the identification of the physico-chemical mechanisms in action and deduction of phenomenological model. Nevertheless, the model as it stands provides good fitting of the previously calculated kinetics for the experimental trials and is considered sufficient to provide overall trends in the impact of water treatment on plant performance.

SIMULATION RESULTS

Two simulations were first performed, for process water with (PW tr) and without (PW) treatment (Table 4). The water treatments applied were sequentially DAF and IER. IER alone may require pre-treatment, notably to remove suspended organic matter. It is assumed that DAF ensures this pre-treatment. The water flow entering the plant is equal to 2400 m^3/h, as estimated on the reconciled balance. The selected PW composition is the one of PW DAF In, with an adapted sulfate concentration of 620 mg/L (between the process water concentrations of the two test runs, 580 and 656 mg/L for IER and DAF test series respectively). The target composition of PW tr is the one of PW DAF Out, with a sulfate concentration lowered to 500 mg/L (570 mg/L reachable if only DAF would be applied).

TABLE 4

Composition of waters used in simulations (mg/L). *dis* for dissolved and *sol* for colloidal solid components.

	SO_4 dis	Mg dis	Si dis	Ni dis	S_2O_3 dis	Si sol	Ni sol	Cu sol	Fe sol
PW	620	91.7	7.64	0.05	18	6.36	1.25	3.48	6.5
PW tr	500	49.6	7.16	0.025	5	5.84	0.075	0.1	2.4

The DAF treats the entire water stream, while IER only a portion (930 m^3/h, representing 38.75 per cent) as the sulfate load is rather low compared to the target concentration.

From the composition of the water entering the plant, the kinetic constants are adjusted according to the variation laws previously determined, for each mineral and each circuit (Table 5). These coefficients are applied to the kinetic constants of the reference case to obtain the model corresponding to each stage. The flotation kinetics increase for each mineral and remain stable for the gangue, suggesting an overall improvement in plant performance.

TABLE 5

Coefficient of variation of flotation kinetics.

	k/k_{ref} Cu	**k/k_{ref} Ni Cu circuit**	**k/k_{ref} Ni Ni circuit**	**k/k_{ref} Gangue**
PW	0.998	0.983	0.976	0.999
PW tr	1.395	1.602	1.137	1.008

This first set of simulations showed a significant impact of water treatment on Ni flotation, mainly in the Cu circuit. As described in the previous sections, the modelling of Ni flotation is more complex as less information is available for the model to properly account for Ni depression behaviour. The model might not integrate well this impact and the influence of water quality could have been overestimated. It is therefore decided to carry out an additional simulation with a limiting case where Ni depression prevails and the influence of water composition on the Ni flotation is totally neglected for the Cu circuit (setting k/k_{ref} = 1 for Ni minerals).

The obtained results are summed up in Tables 6 and 7 respectively for Cu and Ni. The results are presented as increments compared to the reference case (without water treatment) simulation results.

TABLE 6

Simulation results regarding Cu.

	With treatment	**With treatment Ni depression predominant in Cu circuit**
Recovery in Cu Concentrate (%)	+ 5.2	+ 5.1
Grade in Cu Concentrate (%)	- 1.27	+ 0.09
Recovery in Ni Concentrate (%)	- 4.0	- 3.9
Grade in Ni Concentrate (%)	- 0.92	- 0.98
Overall recovery (%)	+ 1.2	+ 1.2

TABLE 7

Simulation results regarding Ni.

	With treatment	**With treatment Ni depression predominant in Cu circuit**
Recovery in Cu Concentrate (%)	+ 4.9	+ 0.1
Grade in Cu Concentrate (%)	+ 1.11	- 0.04
Recovery in Ni Concentrate (%)	- 3.7	+ 1.0
Grade in Ni Concentrate (%)	+ 0.13	+ 0.37
Overall recovery (%)	+ 1.1	+ 1.1

The increase in flotation kinetics deduced from the pilot tests induces an increase in the overall recovery for both Ni and Cu in the plant simulation, respectively around 1.1 and 1.2 per cent. But this is potentially associated with a loss of selectivity: in the scenario for which the impact of water on Ni flotation in the Cu circuit is not neglected, more Cu is recovered in the Cu concentrate, but a significant part of the additional Ni recovery is in the Cu concentrate. This leads to a decrease in Cu grade in the Cu concentrate, and a decrease in Ni recovery in the Ni concentrate. This is critical because the Ni recovered in the Cu concentrate is considered as lost since smelters do not pay for it (Muzinda and Schreitofer, 2018).

Qualitatively, the model predicts the trend of overall increase in recovery, but quantitatively, the actual values must fall somewhere in between the two cases: one where the recovery of Ni in the Cu concentrate is likely overestimated, and water treatment has a negative impact, and the other where the variation in this recovery is neglected and water treatment may have a positive impact. The question remains as to where this most likely mass balance lies, with further research needed to make the model more reliable.

The model also provides data for estimating the costs associated with water treatment, which must also be considered in the overall evaluation of the scenarios. With a capacity of 1500 m^3/h per unit, the DAF treatment requires two units, each with an energy consumption of 0.044 kWh/m^3 of treated water. The IER treatment is sized considering the following column dimensions: 2 m height and 3 m diameter, containing 11 660 kg of resins. Six columns are required. The adsorption cycle time is estimated at about 22 h. With a flow rate of 186 m^3/h through the columns in operation, the pressure drop calculated with FLUIDFLOW© is 0.9 bar and the corresponding required pumping power is estimated at 5.99 kW, which represents, integrated over an adsorption-regeneration cycle, 0.033 kWh/m^3 of treated water. The additional operating cost induced by water treatment, expressed per metric ton of processed ore, and assuming a water consumption of 2.59 m^3/t_{ore}, are the following:

- Energy: 0.147 kWh/t_{ore} (respectively 0.114 and 0.033 kWh/t_{ore} for DAF and IER)
- Coagulant: 181.3 g/t_{ore}
- Flocculant: 2.59 g/t_{ore}

PERSPECTIVES

Taking advantage of the issues encountered during the development of the plant model, the following improvements are suggested, grouped by modelling task:

- Flotation:
  - *General considerations – more detailed experiments*. To go further than the simplification assuming the same flotation behaviour for the different minerals bearing the recovered metal, minerals should be monitored instead of metals. Chemical or mineralogical analysis per size class on batch flotation tests would allow to set size dependent flotation laws and have a finer understanding of the impact of water quality associated to the impact of regrinding. Combined with the water recovery in the froth, this could allow a better estimation of the relative contributions of true flotation versus entrainment.
  - *Water management.* Integrating the impact of water composition on froth properties (stability, depth), which in turn impacts mineral and water recoveries in the froth, would enhance the model predictivity. This is also important regarding water quality: if some water with a very different composition is added to a concentrate for solid content regulation, the composition of the mixed water can be predicted more reliably, and thus also its impact on downstream stages.
- Water treatment:
  - *More detailed understanding of water treatment impact*. When pre-treatment steps are necessary (coagulation-flocculation for DAF), evaluating their specific impact on the composition of water would be preferable to model the process with finer granularity. The example of DAF provides an interesting link with the phase model step required for global modelling, which highlights the importance of describing the material on an appropriate way. During coagulation/flocculation, the dissolved compounds are transferred from liquid to

solid. They therefore no longer appear in the liquid, but may still have an impact on flotation, which cannot be evaluated if their new 'form' (flocs) is not monitored on the flotation test series (here turbidity could have served as a proxy).

- *Impact of the overdosed water treatment reagent in flotation*. Some reagents could be required for suitable water treatment unit, either directly on its operation or to adjust its water output quality: coagulant/flocculant for DAF, pH correction after IER. These reagents could remain on the treated water, in their direct form if overdosed, or on a modified form if untreated (such as flocs for DAF as previously mentioned). Both could impact flotation. In the present case, this impact is directly integrated in the test (they could be present on various extent but are not measured nor characterised): by testing treated water on a batch flotation test, a global impact of water quality can be seen. But the specific impact of these reagents cannot be estimated, and this would be an enhancement of the experimental protocol to consider them as parameters to monitor.

The case study presented in this paper corresponds to a long loop recycling scenario: water is recycled from the tailings pond and treated, providing the same process water distributed throughout the flotation plant, with a given quality that may not be optimal for the circuit into which the water is reinjected. In this case, the recycling of process water may induce the recycling of reagents promoting Ni flotation on the Cu circuit, which is not desirable because it may lead to a loss of selectivity. An alternative solution would be to consider a specific water recirculation within the main circuits of the flotation plant, which would correspond to a short loop recycling scenario. This configuration would have two advantages: to recycle water with the corresponding reagents to the redistribution circuit, and to avoid introducing these reagents into a circuit where they would have a negative impact on performance.

These two kinds of approaches are summarised on the conceptual flow sheets of Figure 5 for long loop water recycling from final tailings and Figure 6 for short loop water recycling from intermediate solid/liquid separation stages.

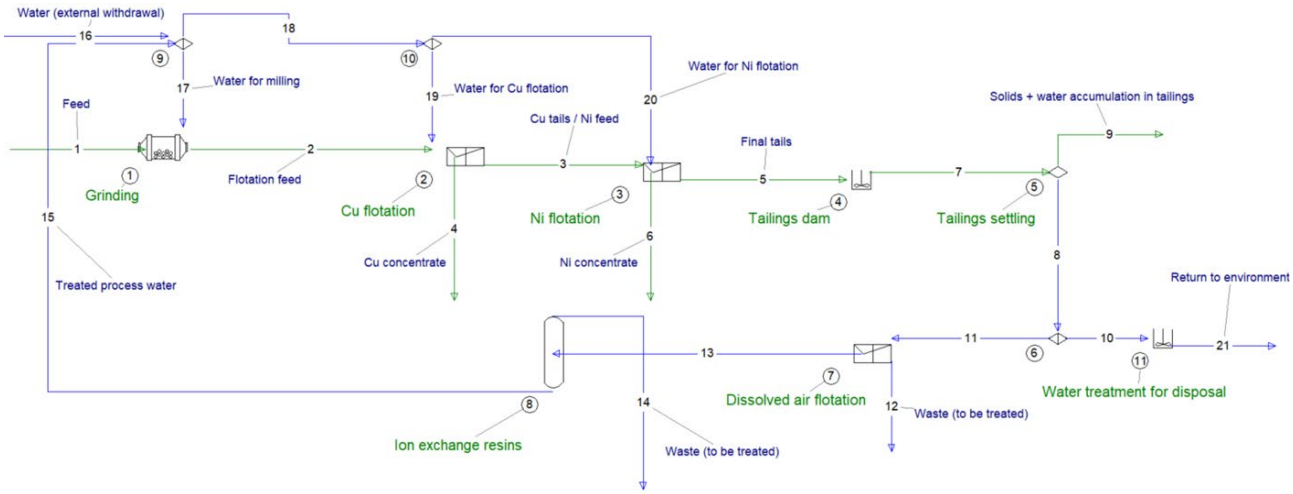

FIG 5 – Long loop water recycling, from tailings.

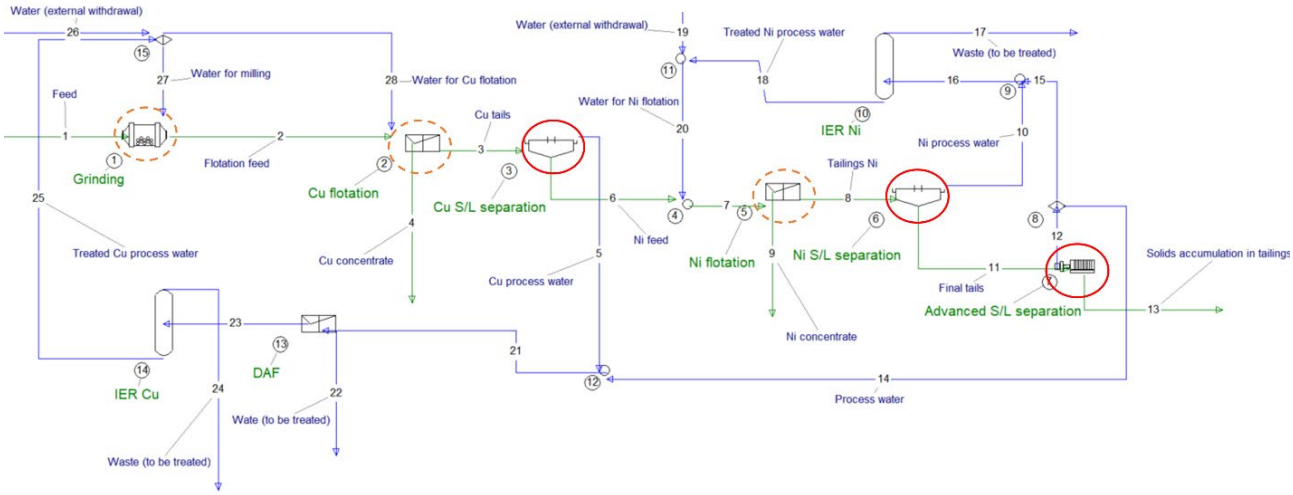

FIG 6 – Short loop water recycling.

To enable these recycling in the short-loop type scenarios, the addition of solid/liquid separation processes into the flow sheet is required (circled in red in Figure 6), such as thickener and filter press. In addition, a more thorough understanding of water reactivity would be required to address these types of scenarios. Indeed, in the long loop recycling scenario, the dissolution of the ore in the flotation circuit has been neglected, the assumption is made that it mainly occurs in the tailings pond. But if all the water is recycled, dissolution would occur within the circuit (this could be during both the grinding and flotation stages, circled in dotted orange in Figure 6), and without any treatment, the dissolved components would accumulate over time. It would be necessary to account for this dissolution rate within the plant to allow proper sizing of the required water treatment units.

CONCLUSIONS

A prototype model that simulates the impact of water quality on a flotation process plant has been built in three main steps: measurement campaigns in the plant and establishment of material balances, modelling of the process units involved or impacted by water management (water treatment and flotation) and integration into a global full-scale model.

Although there is uncertainty associated with the quantitative results of this model given the required assumptions, it does provide qualitative trends. The performed simulations predict an overall increase in recovery for both Ni and Cu, potentially associated with a loss of selectivity, with a significant portion of Ni passing into the Cu concentrate when recirculating water treatment operations are incorporated. Additional research remains necessary to confirm the suggested plant behaviour and to exploit the potential of the model. The presented case also well illustrates the importance of the systemic approach adopted with the integration of the unit operations in the global plant simulator: while the experimental results could suggest a general improvement of the performances, the simulated trend at the plant scale is not so clear-cut. It reveals some behaviours that would not be intuitive, and difficult to anticipate from the sole laboratory or pilot tests.

ACKNOWLEDGEMENTS

This research received funding from the European Union H2020 program under grant agreement no. 730480, ITERAMS project.

The authors would like to acknowledge Boliden Kevitsa Mine for their technical support.

REFERENCES

Can, I B, Biçak, O, Özçelik, S, Can, M and Ekmekçi, Z, 2020. Sulphate removal from flotation process water using ion-exchange resin column system, *Minerals*, 2020(10):655.

Chu, K H, 2020. Breakthrough curve analysis by simplistic models on fixed bed adsorption: In defense of the century-old Bohart-Adams model, *Chemical Engineering Journal*, 380:122513.

Edzwald, J K, 2010. Dissolved air flotation and me, *Water Research* 44:2077–2106.

Haarhoff, J and van Vuuren, L, 1993. A South African Design Guide for Dissolved Air Flotation. Water Research Commission, Pretoria, South Africa.

Jansson, K, Saari, E and Musuku, B, 2020. The process water quality effect on the flotation recovery of sulphide ore. *Gecamin water congress 2020* 12–16 October.

Le, T M K, Miettinen, H, Bomberg, M, Schreithofer, N and Dahl, O, 2020. Challenges in the assessment of mining process water quality, *Minerals*, 2020(10):940.

Levay, G, Smart, R S C and Skinner, W M, 2001. The impact of water quality on flotation performance, *The Journal of South African Institute of Mining and Metallurgy* 101(2):69–75.

Long, H, Broeders, E and Menkveld, H W H, 2016. Applying real-time pollution control to reduce chemical costs and energy usage for DAF. *Proceedings of the Water Environment Federation* 2016(12):3227–3234.

Michaux, B, Rudolph, M and Reuter, M A, 2018. Challenges in predicting the role of water chemistry in flotation through simulation with an emphasis on the influence of electrolytes, *Minerals Engineering* 125:252–264

Musuku, B, Muzinda, I and Lumsden, B, 2016. Cu-Ni processing improvements at First Quantum's Kevitsa mine, *Minerals Engineering* 88:9–17.

Muzinda, I and Schreithofer, N, 2018. Water quality effects on flotation: Impacts and control of residual xanthates, *Minerals Engineering* 125:34–41.

Özturk, Y and Ekmekçi, Z E, 2020. Removal of sulfate ions from process water by ion exchange resins. *Minerals Engineering* 159:106613.

Rao, S R and Finch, J A, 1989. A review of water re-use in flotation, *Minerals Engineering* 2:65–85.

Toward increasing fit-for-purpose water supply for mineral processing operations in the Western Australian Goldfields – potential sources and treatment

N Mbedzi[1] and L G Dyer[2]

1. Research Fellow, WA School of Mines: Minerals, Energy and Chemical Engineering, Curtin University, Kalgoorlie WA 6430. Email: n.mbedzi@curtin.edu.au
2. Discipline Lead, Metallurgical Engineering, WA School of Mines: Minerals, Energy and Chemical Engineering, Curtin University, Kalgoorlie WA 6430. Email: laurence.dyer@curtin.edu.au

INTRODUCTION

Water usage in the Mining and Mineral Processing is significant globally, but far more so in Mining precincts such as Western Australia. Due to limited fit-for-purpose supply, water is a limiting factor to further economic development and diversification in regions such as the WA goldfields. Mineral processing operations in the region currently source water from supplies ranging from scheme water to hypersaline groundwater.

Contaminated water streams have varied impacts on unit operations' efficacy and efficiency, and thus the required quality differs between processes. This ranges from the performance of flotation operations, metal extraction and recovery, reagent consumption and equipment maintenance.

Various water treatment methods, including precipitation, ion exchange, adsorption, and membrane filtration, are used for water softening, that is, the removal of Ca^{2+} and Mg^{2+} ions. The choice of the processing method to use in water treatment is influenced by various factors such as the cost, water quality requirements, process' selectivity, discharge regulations and disposal requirements.

Membrane filtration is an established technology, especially in the food industry (Van der Horst *et al*, 1995; Nguyen *et al*, 2003; Bouchoux *et al*, 2005). Membrane filtration is a separation technique whereby a semi-permeable barrier separates a solution into two phases, a concentrate and a permeate by selectively allowing the passage of components. The separation of the components is dependent on the physical and or chemical properties of the components and the membrane. It is also gaining attention as an alternative promising processing technology in the treatment of wastewaters for recycling, reuse, and to some extent for metal recovery from complex streams (Van der Merwe, 1998; Ricci *et al*, 2015; Aguiar *et al*, 2016; Amaral *et al*, 2018). Membrane filtration consists mainly of four non-equilibrium pressure-driven processes: microfiltration (MF), ultrafiltration (UF), nanofiltration (NF) and reverse osmosis (RO) classified based on pore size.

There has been increased research interest in the viability of using NF in wastewater treatment in recent years (Ricci *et al*, 2015; Aguiar *et al*, 2016; Amaral *et al*, 2018). NF is an intermediate process between UF and RO, presenting separation characteristics of both processes (Mulder and Mulder, 1996). NF offers high selectivity for divalent ions, especially Ca^{2+} and Mg^{2+}, multivalent anions such as SO_4^{2-} and CO_3^{2-} (Van der Merwe, 1998) and organic solutes; high permeate fluxes; and low retention rate of monovalent ions such as Na^+ and Cl^-. For example, in a study by Feini *et al* (2008), comparing the performance of NF and RO membranes in metal effluent treatment, more than 95 per cent rejection of Ca^{2+}, Mg^{2+} and SO_4^{2-} ions was reported and was comparable to the rejections reported from RO at the same operating pressure range of 0.6 to 2.2 MPa. The rejection for organics was slightly lower in NF, as well as the rejection rates for monovalent ions Na^+ and Cl^- ranging from 30 to 50 per cent compared to 75 to 80 per cent in RO. The distinguished selectivity between divalent and monovalent ions demonstrated by NF membranes makes them better suited for processing wastewaters from mining operations.

The use of membrane filtration, especially NF and RO in desalination and wastewater treatment in supplementing water supply, produces brines rich in Ca^{2+}, Mg^{2+}, Na^+, Cl^- and SO_4^{2-} ions, amongst many other species. As desalination is becoming prominent, it is paramount that the reuse and valourisation of the brines is considered a priority in order to alleviate the environmental impact of membrane technology and maximise water utilisation. Brine valourisation will significantly improve the two well-known conventional methods for brine waste management: zero liquid discharge (ZLD)

and volume reduction, by giving the brines an added value as they will be used as raw materials to produce other by-products.

There are several studies on the feasibility of extracting calcium and magnesium by-products from brines by precipitation for economic gain and as a waste mitigation strategy (Drioli *et al*, 2004; Reig *et al*, 2016; Lalia and Hashaikeh, 2021; Lalia *et al*, 2021). The upstream removal of calcium from the brines is considered a priority to inhibit scaling caused by the precipitation of calcium salts, especially gypsum and calcium carbonates. However, most studies are increasingly interested in an integrated system for the selective and sequential removal of calcium, magnesium and sodium salts.

Of increasing interest is the use of carbonates, and in consideration of the growing interest by scientists in carbon capture and storage (CCS) to alleviate greenhouse gas accumulation in the atmosphere, the brines from desalination and hypersaline water treatment could be used as a readily available source of the necessary metal ions, Mg^{2+} and Ca^{2+} ions, for CCS. This could be cost-effective since there is no need for mineral dissolution at supercritical CO_2 and concentrated acids used to generate Ca^{2+} and Mg^{2+} rich solutions in direct and indirect carbonation in geological formations, respectively.

This study has shown the successful application of precipitation to remove Ca and Mg from synthetic brines as both their hydroxides and carbonates. The degree of recovery, selectivity, crystallinity and solid-liquid handling properties were noted to vary significantly between the two precipitating agents (Figure 1). A staged recovery would be effective in producing multiple products of different composition based on the equilibria of the two metals. Thereby, the cost of production as well as the purity and value of the various potential products must be considered when selecting the most appropriate system.

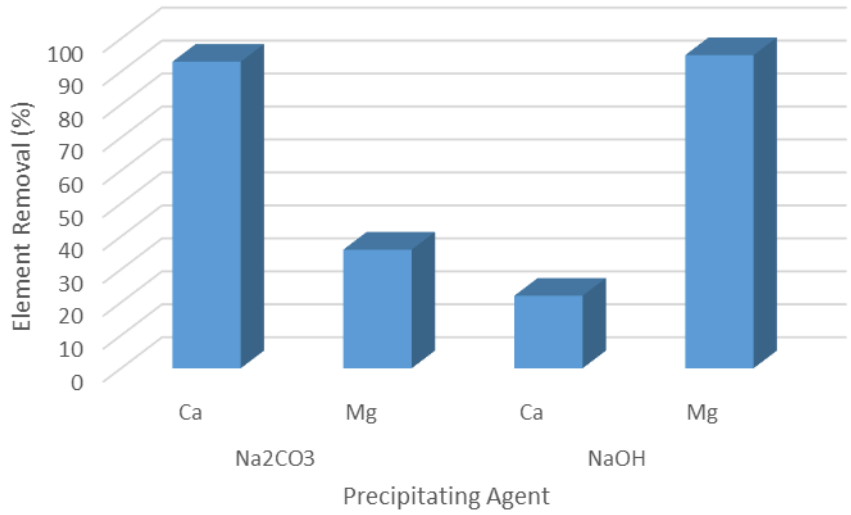

FIG 1 – Extent of precipitation of Ca and Mg with sub-stoichiometric addition of the precipitating agents.

Precipitation is a promising method for producing by-products from concentrate streams and returning a much greater proportion of the water for utilisation.

ACKNOWLEDGEMENTS

Financial support from the Western Australian Government's Department of Primary Industry and Regional Development (DPIRD) through the Regional Economic Development Grant Program is gratefully acknowledged. As is the contribution of CRC ORE ltd. and the partnership with the Goldfields Esperance Development Commission (GEDC) and Ecotechnol.

REFERENCES

Aguiar, A O, Andrade, L H, Ricci, B C, Pires, W L, Miranda, G A and Amaral, M C, 2016. Gold acid mine drainage treatment by membrane separation processes: An evaluation of the main operational conditions. *Separation and Purification Technology,* 170, 360–369.

Amaral, M C, Grossi, L B, Ramos, R L, Ricci, B C and Andrade, L H, 2018. Integrated UF–NF–RO route for gold mining effluent treatment: From bench-scale to pilot-scale. *Desalination,* 440, 111–121.

Bouchoux, A, Roux-De Balmann, H and Lutin, F, 2005. Nanofiltration of glucose and sodium lactate solutions: variations of retention between single-and mixed-solute solutions. *Journal of Membrane Science,* 258, 123–132.

Drioli, E, Curcio, E, Criscuoli, A and Di Profio, G, 2004. Integrated system for recovery of CaCO3, NaCl and MgSO4· 7H2O from nanofiltration retentate. *Journal of Membrane Science,* 239, 27–38.

Feini, L, Zhang, G, Qin, M and Zhang, H, 2008. Performance of nanofiltration and reverse osmosis membranes in metal effluent treatment. *Chinese Journal of Chemical Engineering,* 16, 441–445.

Lalia, B S and Hashaikeh, R, 2021. Electrochemical precipitation to reduce waste brine salinity. *Desalination,* 498, 114796.

Lalia, B S, Khalil, A and Hashaikeh, R, 2021. Selective electrochemical separation and recovery of calcium and magnesium from brine. *Separation and Purification Technology,* 264, 118416.

Mulder, M and Mulder, J, 1996. *Basic principles of membrane technology*, Springer Science & Business Media.

Nguyen, M, Reynolds, N and Vigneswaran, S, 2003. By-product recovery from cottage cheese production by nanofiltration. *Journal of Cleaner production,* 11, 803–807.

Reig, M, Casas, S, Gibert, O, Valderrama, C and Cortina, J, 2016. Integration of nanofiltration and bipolar electrodialysis for valorization of seawater desalination brines: Production of drinking and waste water treatment chemicals. *Desalination,* 382, 13–20.

Ricci, B C, Ferreira, C D, Aguiar, A O and Amaral, M C, 2015. Integration of nanofiltration and reverse osmosis for metal separation and sulfuric acid recovery from gold mining effluent. *Separation and purification technology,* 154, 11–21.

Salvato, J A, Nemerow, N L and Agardy, F J, 2003. *Environmental engineering*, John Wiley & Sons.

Van Der Horst, H, Timmer, J, Robbertsen, T and Leenders, J, 1995. Use of nanofiltration for concentration and demineralization in the dairy industry: Model for mass transport. *Journal of Membrane Science,* 104, 205–218.

Van Der Merwe, I, 1998. Application of nanofiltration in metal recovery. *Journal of the Southern African Institute of Mining and Metallurgy,* 98, 339–341.

Sorting of lithium-ion battery components

A Kaas[1], T Lyon[2], C Wilke[3] and U A Peuker[4]

1. Research Associate, Institute of mechanical process engineering and mineral processing – Technical University Freiberg, Agricolastr. 1, 09599 Freiberg, Germany. Email: Alexandra.Kaas@mvtat.tu-freiberg.de
2. Research Associate, Institute of mechanical process engineering and mineral processing – Technical University Freiberg, Agricolastr. 1, 09599 Freiberg, Germany. Email: Tony.Lyon@mvtat.tu-freiberg.de
3. Research Associate, Institute of mechanical process engineering and mineral processing – Technical University Freiberg, Agricolastr. 1, 09599 Freiberg, Germany. Email: Christian.Wilke@mvtat.tu-freiberg.de
4. Professor, Institute of mechanical process engineering and mineral processing – Technical University Freiberg, Agricolastr. 1, 09599 Freiberg, Germany. Email: Urs.Peuker@mvtat.tu-freiberg.de

ABSTRACT

The intention of the recycling of lithium ion batteries (LIB) is to regain valuable materials, for instance graphite, aluminium, copper, cobalt, nickel, or lithium, and close the material cycle to preserve natural resources. During the recycling chain different mechanical processes take place intending to gain pure products which can be reused. One important stage following comminution is the separation of the different materials.

In terms of separation two main groups can be distinguished: classifying and sorting. In this paper the focus lies on the sorting ie the separation based on characteristic physical properties like density or shape. Prior to the separation the material has to be fully liberated. After liberation some materials can already be separated in single-origin materials while others need to undergo further treatment.

During the mechanical processing of LIB, a comminution product with the different battery components is generated. For instance, the separator foil, electrodes and housing material. Now the components can be separated by using various methods, eg density, magnetic separation or flotation. Flow sorting, as part of density separation can use either air (eg zig-zag-air-classifier) or water (hydro-separator) as medium. In a first flow sorting step during the moderate temperature route of LIB recycling the zig-zag-air-classifier separates cell housing, separator foil and electrodes due to their different settling velocities, using higher and lower air stream velocities. Separator foil and cell housing can be further processed and purified by using for instance eddy current or magnetic separation. However, separation of the two types of electrodes is challenging as they show the same settling velocity and can therefore not directly be separated with the flow sorting and need to undergo further treatment to delaminate them from the active material.

After stressing the electrodes again, the foils are mostly delaminated and compacted, and the active material can be screened off. As a result, two products are generated: current collector foils and black mass. As the settling velocity is a function of size, shape and density the second comminution step is very important for the flow sorting process. The compacting during the second comminution reduces the influence of the size and shape on the sorting process and the separation is mainly affected by the density difference of copper and aluminium. The goal of the second flow sorting step (either by zig-zag air classifying or hydro-upstream sorting) is to obtain the two metals as concentrates which can be smelted in order to be reused. Moreover, the black mass can then be further processed using flotation to separate eg graphite or by magnetic sorting to separate ferrous components.

The sorting of LIB faces different challenges as the material compound contains a lot of valuable components which should be finally available in single types in order to enable further processing. The influences underlying the separation, such as shape, size and density, play a decisive role. It is important to alter the particles of the materials in such a way that separation is technically and economically possible.

INTRODUCTION

It is impossible to imagine our modern society without Lithium Ion Batteries (LIB). They are used for stationary energy storage, in information technologies, electrically powered vehicles and serval portable applications. Furthermore, the number of LIB will continuously increase in the future as they play a significant role to reduce global warming (Pinegar and Smith, 2020).

However, the resources for the battery production are unevenly distributed geostrategically and will run out in the coming years. For this reason, battery materials should be circulated in a closed loop during their life cycle (Friedrich, Träger *et al,* 2012; Zhao, 2017; Windisch-Kern, Gerold *et al,* 2022). That's why recycling is so important and has to be improved in yield and quality.

Different process schemes of LIB recycling are already established worldwide (Werner, Peuker *et al,* 2020). The processes can be differentiated in a chemical, thermal and/or mechanical treatment. Moreover, recycling means to separate the different components from each other to generate new usable raw materials and achieve a closed loop. In the case of the mechanical processing the material compounds have to be liberated through different mechanisms like cutting or impact stress. This is essential in order to separate downstream the liberated materials according to their physical properties using various processes. In this way, it is possible to produce various concentrates that can be used as highly enriched input materials for subsequent, eg metallurgical, processes.

PRETREATMENT – MECHANICAL LIBERATION OF COMPONENTS USING CRUSHING AND MILLING

LIBs are complex material compounds consisting of different valuable materials like copper and aluminium as electrode foils and nickel, manganese and cobalt in the cathode coating. Mechanical processes breakup the compounds and liberate the materials. This allows not only the enrichment using separation mechanisms, but also reduces the particle size, which enables easier handling of the particulate material. (Vezzini, 2014; Chagnes and Swiatowska, 2015; Wuschke, Jäckel *et al,* 2019a; Pinegar and Smith, 2020).

Especially in LIB recycling, not all goals can be achieved with a single stressing step. So crushing, ie shredding is applied as initial step to achieve a size reduction, that the resulting battery fragments can be easier supplied to a second milling step to fully liberate the components (Wuschke, Jäckel *et al,* 2019b). For the first crushing of LIB shearing, tearing and for pouch cells also cutting are applied as stress modes (Werner, Peuker *et al,* 2020).

The second liberation step, milling, is done in order to decoat the current collector foils from the active material. The literature states out that milling is mainly applied for decoating, delamination or pulverisation (Gaines, 2014) by using stress modes like impact stress, shearing and/or bending. The milling process results in selective comminution of brittle coating materials and deformation of ductile metal foils. Therefore, grinding tools like hammers, impact pins or plates combined with designs such as profiled wear surfaces, trapezoidal riffle sieves or sieve rings are used. Applying operating speeds of 50–140 m/s shear and bend stresses interact in order to achieve objectives regarding size, shape and degree of deformation, decoating and liberation of the product particles.

SORTING OF LIB-MATERIALS

Sorting is subdivided according to the mechanisms of action used to separate the starting materials into different concentrates. For the sorting of LIB-components, gravimetric, magnetic, eddy current and wettability (flotation) sorting are primarily used (Werner, Peuker *et al,* 2020). This will be discussed in more detail below.

Gravity separation

Zig-zag-air classifier

In a Zig-zag (ZZ)-air classifier, the particles are separated due to their settling velocity. Here particle properties play an important role as the settling velocity is a function of size, shape and density. The main component of a ZZ classifier is a characteristic segmented channel. The variety in design of the channel is broad and can be adapted to the separation task by adopting eg the number of stages,

the stage angle or the width of the segments. In secondary material processing the particle size ranges from 5–50 mm (Kaas, Mütze *et al,* 2022). A ZZ classifier operates with an air flow from bottom to top forming vortex rolls beneath the edges of the channel due to the shape of the channel. At every stage a cross-flow sorting of particles takes place (Friedrichs and Tomas, 1996). Hence, the ZZ classifier is a series of cross-flow separators achieving a high separation efficiency (Senden 1979; Rosenbrand, 1986; Tomas and Gröger, 2000).

Due to the different shape and size generated in crushing it is possible that particles with high density difference can have the same trajectories (same settling velocities) (Veit and Bernardes, 2015). Hence, the degree of liberation plays an important role for this sorting device. For LIB recycling ZZ classifiers are used to fractionate the separator foils and other thin plastic foils at lower air velocities (1.5–2.5 m/s). In a further separation step electrode foils are enriched as light fraction and housing material as heavy fraction (Chagnes and Swiatowska, 2015; Wuschke, Jäckel *et al,* 2019a). In other sorting steps it is even possible to separate the electrode foils from each other. Depending on the pretreatment, foils can be compacted and delaminated in one milling step to generate suitable particle properties (size and shape) for the separation in the ZZ classifier (Figure 1).

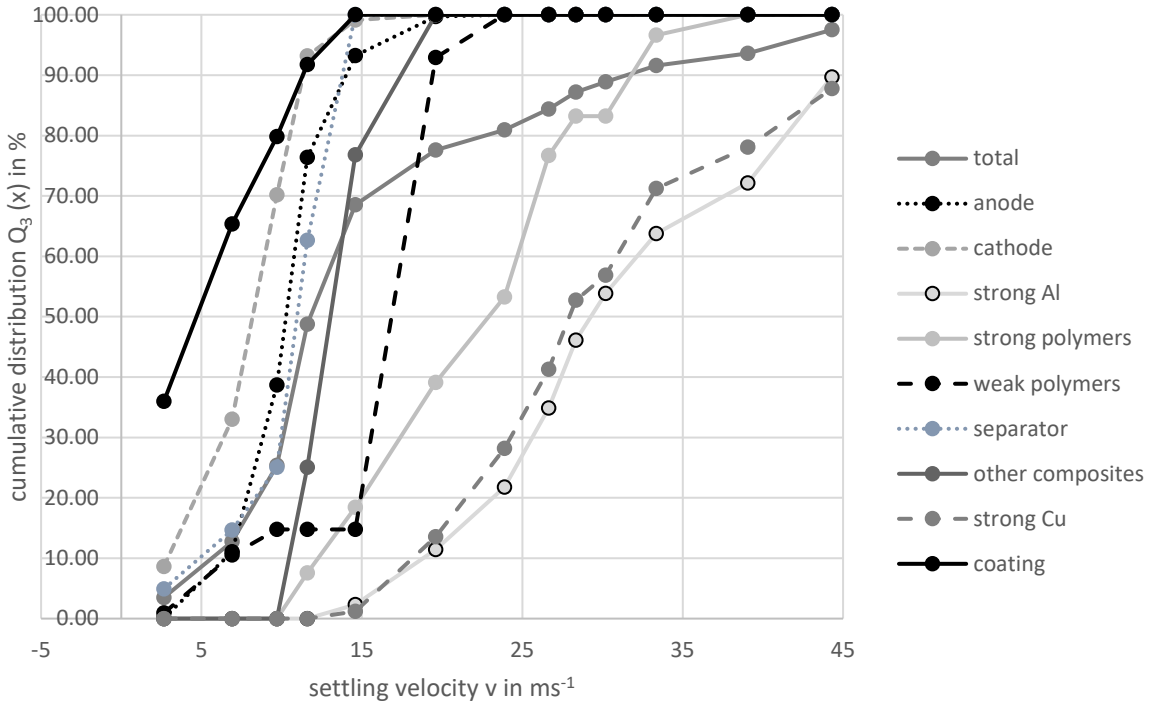

FIG 1 – Settling velocity of battery components after the first crushing.

Another effect, which is due to the irregular shape of the particles in secondary raw material processing is that they have an irregular trajectory and their settling velocity is very difficult or impossible to predict. Therefore, the values determined mostly by experimental procedure are referred to as quasi-stationary settling velocities.

Hydro-upstream-sorting

Gravitational sorting uses the particle density as separation feature, the process is additionally influenced by shape and size. Using water as separation medium the influence is not as dominant as in a ZZ air classifier. In hydro-upstream-sorting particles are fed into a column which is filled with water. By fluidisation of the water the particles are dispersed and separated due to their density in rising product (low density) and descending product (higher density) (Böhme, 1989). For LIB recycling, hydro-sorting can be used for the separation of electrode foils after delamination and compaction. Here better results, eg a higher separation sharpness, are achieved than in ZZ classifier sorting (Figure 1). However, a general problem of wet media processes is the drying of the material afterwards and the required treatment of process water (Tomas, Gröger *et al,* 1999). Figure 2 shows a Fuerstenau-2-diagram comparing the sorting results of a ZZ classifier and an experimental hydro-

upstream sorting for the same sample of decoated electrode foils. For this purpose, the output of the specifically lighter aluminium foil in the rising material is plotted on the ordinate axis and the output of the specifically heavier copper foil in the rising material is plotted on the abscissa axis. The larger the enclosed area between the graph and the theoretical splitting line (black), the better is the sorting of the materials.

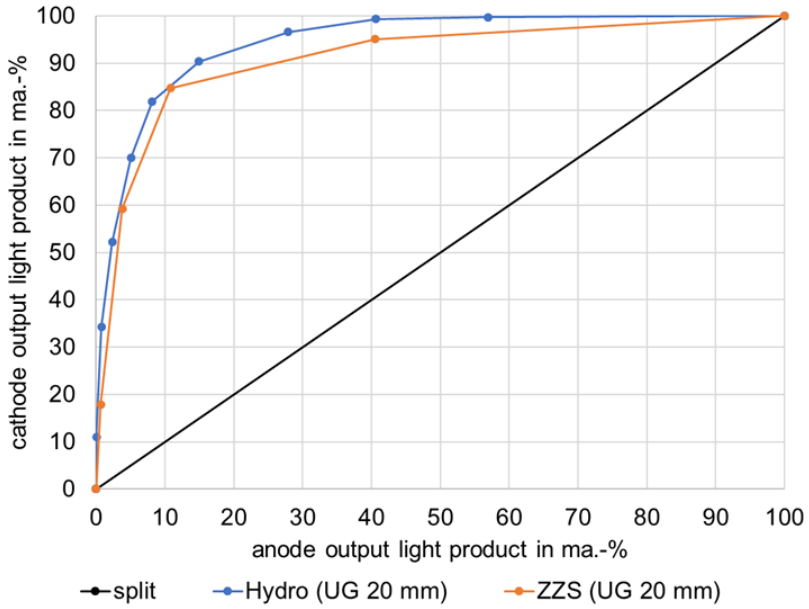

FIG 2 – Separation of electrode foils using ZZ-classifier (ZZS) and hydro-upstream-sorting (Hydro).

Centrifugal concentrators

In order to separated cathode and anode active material from each other after delamination, gravity is insufficient due to the small particle sizes. The separation method is applied either under wet or dry conditions which depends on the further treatment.

In dry applications a spiral airflow is used. Hence, the heavy or coarse particle are transported to the outer circumference by centrifugal forces acting at a higher level, where they can be discharged continuously or discontinuously. The lighter particles move through a cage wheel to the centre of the spiral and are discharged. Since the influence of size can also affect the separation by density, pre-treatment to generate a uniform particle size, eg by grinding and sieving, is important. In wet applications a cylindrical-conical drum is used which is rotating around a vertical axis and water streams up from bottom to top forming a macro-vortex. The principle of operation is the same to dry conditions. Hence, light particles are carried out with the water from the centre of cyclone whereas heavy particle enrich at the walls of the vessel. However, this principle is mainly used to remove heavy impurities which make up less than 1 per cent of the material (Wills and Finch, 2015).

Magnetic separation

In magnetic separation sorting is done due to the magnetic susceptibility of the particles which are separated in magnetic and non-magnetic components. The devices can be categorised as follows in Table 1 (Schubert, 2012; Wuschke, Jäckel *et al,* 2019a):

TABLE 1

Categorisation of magnetic separation (Schubert, 2012).

Intensity of magnetic field	Type of particle displacement	Type of magnets
Low gradient High gradient	Retention Lift-out Deflection sorting	Permanent magnets Electro magnets

As in other sorting principles the separation is influenced by other particle properties. Here the particle volume is affecting the resulting magnetic forces which is why the design and technology of the device has to be adjusted.

Overhead separators and drum separators are operating continuously under dry conditions with a high intensity. In LIB recycling those separators are used to separate casing fragments and peripheral materials as well as screws. Hence, steel components are recovered and further treatment equipment is protected against wear. Especially with these separators, which work according to the lift-out principle, the particle shape also has a large influence, as this essentially determines the flight path. In contrast, matrix magnetic separators are applied for wet and dry applications (Ellis and Montenegro, 2019) for particles smaller than 1 mm. Those particles are mainly components of the black mass for which matrix separators are used in wet conditions. Here a magnetic cathode concentrate and a non-magnetic anode concentrate are produced. The separation of coating materials (black mass) show better results than sorting current collector materials (aluminium and copper) using magnetic forces (Arnberger, 2016).

Eddy current separation

Using eddy currents, components are separated due to their electrical conductivity (Schubert, 2012). In this sorting process, non-ferrous metals are selectively separated by inducing eddy currents in electrically conductive particles. The induced magnetic field in the particles opposes the excitation field, resulting in a repulsive force effect (Lorentz force). This ensures the separation (Laufs, Gallenkemper *et al,* 2010). The deflecting Lorentz force depends on the physical properties of the particles (shape, size, electrical resistance, material density of the material to be separated) and the induced magnetic field (strength, range, frequency) (Schubert, 2012). A size range of 5–150 mm (Nickel, 2013; Baron, Behnsen *et al,* 2017) is mainly used for this sorting method. Here, the separation of non-metallic materials (polymers) and non-ferrous metals (copper and aluminium) takes place. The process is influenced by the shape and wall-thickness of the material which may prevent a higher separation efficiency (Lin, Fan *et al,* 2003). Eddy current separation can be applied to process the heavy product containing the LIB-housing (Figure 3).

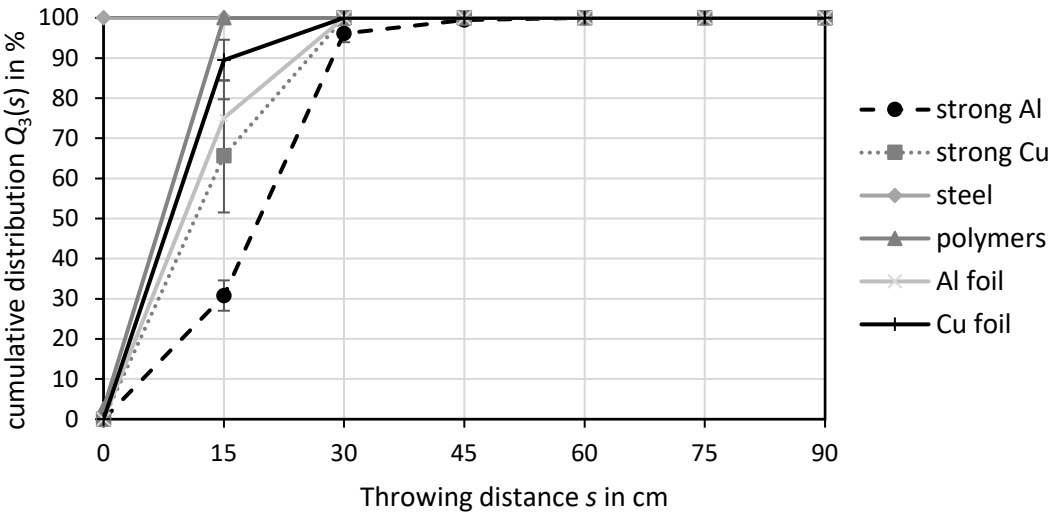

FIG 3 – Throwing distance of housing components.

Flotation

This physicochemical separation process uses the different wettability (Schubert and Bischofberger, 1996, 1998; Schubert, 2005, 2007, 2008) of particles to separate them. Before the actual sorting process takes place, the particles have to be ground to a size of 50–500 µm. The particles are then suspended and conditioned with the addition of reagents. Bubbles are generated by adding air and thus grain-bubble impacts are realised. After the grain-bubble aggregate have risen and the foam has been removed, the foam product is further processed. Reagents such as collectors, frothers, pushers and aerators are used depending on the requirements and serve to control the hydrophobicity.

Flotation plays an important role in the preparation of the black mass in the context of LIB recycling. The active materials of the anode and cathode, graphite and lithium metal oxides, are to be recovered in this way. Graphite is naturally hydrophobic thus recovered in the froth product and the cathode material is hydrophilic and should remain as flotation residue (Zhan, Oldenburg *et al,* 2018; Larouche, Tedjar *et al,* 2020). However, the system is influenced by remaining electrode additives like polyvinylidene fluoride binder, carbon black, or organic solvents from the electrolyte (Vanderbruggen, Gugala *et al,* 2021). Moreover, the preprocessing, ie degree of liberation regarding metal foils, and wettability of the particles, influences the separation efficiency. Currently, the research focus is on finding suitable reagents (eg paraffin) (Larouche, Tedjar *et al,* 2020; Sommerville, Shaw-Stewart *et al,* 2020) and depollution strategies to remove binder and organic solvents (Vanderbruggen, 2021).

Summary and outlook

Mechanical processing technology offers many tools to effectively process LIB. In the process, material concentrates can be produced that represent highly enriched starting materials for the subsequent cleaning processes. As a result, these processes can be operated more economically and higher recycling rates can be achieved.

Due to the different property functions of the various battery types, the processes must be individually adapted. More standardised batteries would enable a more economical implementation of the recycling processes.

However, as new batteries are constantly being researched to increase their performance and safety, and new designs are thus created and new materials are applied, there will continue to be a great need for research on the processing of batteries in the future.

ACKNOWLEDGEMENTS

The presented contents are based on a project funded by the German Federal Ministry of Education and Research under the grant number 03XP0337, 03XP0354AE, 03XP0246C. The authors are responsible for the con-tents of this publication.

REFERENCES

Arnberger, A, 2016. Entwicklung eines ganzheitlichen Recyclingkonzeptes für Traktionsbatterien basierend auf Lithium-Ionen-Batterien, University of Leoben.

Baron, M, Behnsen, A, Bidlingmaier, W, Cimatoribus, C, Clauß, D, Dornbusch, H, Eckstein, K, Escalante, N, Faulstich, M and Feil, A, 2017. *Einführung in die Kreislaufwirtschaft: Planung--Recht--Verfahren*, Springer-Verlag.

Böhme, S, 1989. Zur Stromtrennung zerkleinerter metallischer Sekundärrohstoffe. *Freiberger Forschungsheft*. Leipzig, Germany, Deutscher Verlag für Grundstoffindustrie. 785.

Chagnes, A and Swiatowska, J, 2015. *Lithium process chemistry: Resources, extraction, batteries, and recycling*, Elsevier.

Ellis, T W and Montenegro, J A, 2019. Magnetic Separation of electrochemical cell materials. RSR Technologies Inc. US Patent US10046334B2.

Friedrich, B, Träger, T and Weyhe, R, 2012. *Recyclingtechnologien am Beispiel Batterien*. *Proceedings 25th Aachener Kolloquium Abfallwirtschaft*, Forum M, Aachen, Germany.

Friedrichs, J and Tomas, J, 1996. Aerosortierung von Bauschutt. *Arbeits-und Ergebnisbericht des Sonderforschungsbereiches* 385: 197–250.

Gaines, L, 2014. The future of automotive lithium-ion battery recycling: Charting a sustainable course. *Sustainable Materials and Technologies* 1: 2–7.

Kaas, A, Mütze, T and Peuker, U, 2022. Review on Zigzag Air Classifier. *Processes* 10(4): 764.

Larouche, F, Tedjar, F, Amouzegar, K, Houlachi, G, Bouchard, P, Demopoulos, G and Zaghib, K, 2020. Progress and status of hydrometallurgical and direct recycling of Li-ion batteries and beyond. *Materials* 13(3): 801.

Laufs, P, Gallenkemper, B, Pretz, T and Rettenberger, G, 2010. *Einführung in die Abfallwirtschaft*, Springer-Verlag.

Lin, J-R, Fan, C, Chang, I and Shiu, J, 2003. Clean process of recovering metals from waste lithium ion batteries, Google Patents.

Nickel, W, 2013. *Recycling-Handbuch: Strategien—Technologien—Produkte*, Springer-Verlag.

Pinegar, H and Smith, Y R, 2020. Recycling of end-of-life lithium-ion batteries, Part II: Laboratory-scale research developments in mechanical, thermal, and leaching treatments. *Journal of Sustainable Metallurgy* 6(1): 142–160.

Rosenbrand, G G, 1986. The separation performance and capacity of zigzag air classifiers at high particle feed rates. Eindhoven, University Eindhoven.

Schubert, H and Bischofberger, C, 1996. Zu den Mikroprozessen Blasenzerteilen und Korn-Blase-Haftung in mechanischen Flotationsapparaten sowie Konsequenzen für die Massstabsübertragung der Makroprozesse. *Aufbereitungs-Technik* 37(5): 193–202.

Schubert, H and Bischofberger, C, 1998. On the microprocesses air dispersion and particle-bubble attachment in flotation machines as well as consequences for the scale-up of macroprocesses. *International Journal of Mineral Processing* 52(4): 245–259.

Schubert, H, 2005. Nanobubbles, hydrophobic effect, heterocoagulation and hydrodynamics in flotation. *International Journal of Mineral Processing* 78(1): 11–21.

Schubert, H, 2007. Zur optimalen Hydrodynamik der Fein-und Feinstkornflotation. *Aufbereitungs Technik-Mineral Processing* 48(7): 30–47.

Schubert, H, 2008. On the optimization of hydrodynamics in fine particle flotation. *Minerals Engineering* 21(12–14): 930–936.

Schubert, H, 2012. *Handbuch der mechanischen Verfahrenstechnik*. Hoboken, NJ, USA, John Wiley & Sons.

Senden, M M G, 1979. Stochastic models for individual particle behavior in straight and zig zag air classifiers, Eindhoven, Netherlands.

Sommerville, R, Shaw-Stewart, J, Goodship, V, Rowson, N and Kendrick, E, 2020. A review of physical processes used in the safe recycling of lithium ion batteries. *Sustainable Materials and Technologies* 25: e00197.

Tomas, J and Gröger, T, 2000. Assessment of multistage turbulent cross-flow aeroseparation of building rubble. *Developments in Mineral Processing*, Elsevier. 13: C7–34-C37–43.

Tomas, J, Gröger, T, Küchler, C and Friedrichs, J, 1999. Abtrennen von Wertstoffen aus Bauschutt. *Chemie Ingenieur Technik* 71(6): 637–642.

Vanderbruggen, A, 2021. *Recovery of graphite from spent lithium ion batteries*. Proceedings of International Battery Recycling Conference, Salzburg, Austria.

Vanderbruggen, A, Gugala, E, Blannin, R, Bachmann, K, Serna-Guerrero, R and Rudolph, M, 2021. Automated mineralogy as a novel approach for the compositional and textural characterization of spent lithium-ion batteries. *Minerals Engineering* 169: 106924.

Veit, H M and Bernardes, A M, 2015. Electronic waste: generation and management. *Electronic waste*, Springer: 3–12.

Vezzini, A, 2014. Manufacturers, materials and recycling technologies. *Lithium-Ion Batteries*, Elsevier: 529–551.

Werner, D, Mütze, T and Peuker, U, 2020. Recycling chain for spent lithium-ion batteries. *Metals* 10(3): 316.

Wills, B A and Finch, J A, 2015. *Wills' mineral processing technology: an introduction to the practical aspects of ore treatment and mineral recovery*. Oxford, UK, Butterworth-Heinemann.

Windisch-Kern, S, Gerold, E, Nigl, T, Jandric, A, Altendorfer, M, Rutrecht, B, Scherhaufer, S, Raupenstrauch, H, Pomberger, R and Antrekowitsch, H, 2022. Recycling chains for lithium-ion batteries: A critical examination of current challenges, opportunities and process dependencies. *Waste Management* 138: 125–139.

Wuschke, L, Jäckel, H, Gellner, M and Peuker, U, 2019b. *Comminution Of Li-Ion Traction Batteries*. Proceedings of European Symposium on Comminution and Classification, Gothenborg, Sweden.

Wuschke, L, Jäckel, H, Leißner, T and Peuker, U, 2019a. Crushing of large Li-ion battery cells. *Waste Management* 85: 317–326.

Zhan, R, *et al*. 2018. Recovery of active cathode materials from lithium-ion batteries using froth flotation. *Sustainable Materials and Technologies* 17: e00062.

Zhao, G, 2017. Resource utilization and harmless treatment of power batteries. *Reuse and Recycling of Lithium-Ion Power Batteries* (G Zhao Ed), pp 335–378.

Influence of silica fume on interfacial transition zone of concrete prepared by red mud–cement

X H Li[1,3,4] and Q Zhang[2,3,4]

1. Senior Experimentalist, Mining College, Guizhou University, Guiyang 550025, China. Email: xhli1@gzu.edu.cn
2. Professor, Guizhou Academy of Sciences, Guiyang 550001, Guizhou, China. Email: zq6736@163.com
3. Professor, National and Local Joint Laboratory of Engineering for Effective Utilization of Regional Mineral Resources from Karst Areas, Guiyang 550025, China.
4. Professor, Guizhou Key Lab of Comprehensive Utilization of Nonmetallic Mineral Resources, Guiyang 550025, China.

ABSTRACT

Red mud (RM) is an insoluble industrial waste after extracting alumina from bauxite. RM is still mainly treated by storage or landfill at present, which not only occupies land resources, but also causes environmental pollution to our water and soil. The application of RM in concrete proposed has been one of the effective ways to absorb a large amount of RM. Nevertheless, RM – cement concrete still shows such problems as low mechanical properties and industrial application difficulty. In this paper, silica fume (SF) was used as mineral admixture to study SF on the mechanical properties and Interfacial Transition Zone (ITZ) structure of RM – cement. The findings showed that the SF had high water demand and resulting in low water-binder ratio near the ITZ. CH crystals near the ITZ could not get enough water to form coarse crystals. Meanwhile, the active SiO_2 content of the silica was high and the C-S-H gel was formed by reacting with the CH crystals, filling the ITZ. and reducing the pore size near the ITZ.

INTRODUCTION

Cement is an important powdered hydraulic inorganic cementitious material, which has been widely used in the construction industry. CO_2 emissions in cement industry account for 5 per cent of the current human-made CO_2 emissions (Kim *et al*, 2016) and excessive CO_2 emissions will lead to global warming and destroy the ecology (Nabavi-Pelesaraei *et al*, 2017). Given that the sustainable development of resources and low carbon emissions are advocated, the preparation of concrete with solid industrial waste with certain pozzolanic activity as mineral admixture is found to be of some help to reduce the amount of cement. Compared with ordinary cement concrete, the early reaction degree and strength of concrete containing mineral compound are lower (Rao, Sravana and Rao, 2016). However, mineral admixture could improve the workability, durability and mechanical properties of concrete (Türkmen, Gül and Çelik, 2008). The admixture can not only fill and absorb $Ca(OH)_2$(CH), but also increase the viscosity of the paste. The concrete paste mixed with active mixture has good water retention and difficult to secrete water, which can effectively prevent the formation of water sac and the enrichment of CH and thus improving the mechanical properties to a certain extent (Mehta and Ashish, 2020).

The development of industrialisation has produced a huge demand for raw materials, resulting in the accumulation of a large number of industrial solid wastes. Industrial solid wastes not only occupy land resources and pollute the environment, but also restrict the development of enterprises and waste resources. The harmless and resource utilisation of industrial solid waste could be conducive to the reduction of industrial solid waste. Therefore, compared with the traditional mineral admixture, industrial solid waste as an admixture will have a good prospect. At present, industrial applications have been realised, such as fly ash (Singh, 2018), yellow phosphorus slag (Wang, Huang and Wang, 2018), blast furnace slag (Zhou, Deng and Liu, 2017) and so on. Red mud (RM) is a large amount of solid waste produced by bauxite industry after the production of alumina (Krivenko *et al*, 2017), whose coagulant activity is weak and the direct mixing of concrete mainly plays a filling role. But RM can optimise the structure of Interfacial Transition Zone (ITZ) in concrete to a certain extent and thus improving the reduction of interface crack width (Li and Zhang, 2022). Silica fume (SF) is a by-product of ferroalloy smelting ferrosilicon and industrial silicon (Wang *et al*, 2021). Because SF is

formed by air oxidation and condensation precipitation of SiO_2 and Silicon gas produced in electric furnace. With its pozzolanic reactivity, SF has found its wide application as active admixture. Adding a certain amount of SF to concrete can highly improve the strength, compactness and durability of concrete (Jun, Kim and Kim, 2019). In this paper, SF was proposed as mineral admixture with aim of studying the effect of SF on the ITZ between RM and cement concrete. It was expected to provide some insights for further optimising the performance of RM-cement concrete.

EXPERIMENTAL MATERIALS AND METHODS

Raw materials

The RM was collected from an Alumina plant in Guiyang, China. It was crushed into powder as the test material. The cement used was ordinary Portland cement. Table 1 shows that the content of SF used was more than 90 per cent, with a small amount of CaO, Al_2O_3, Fe_2O_3, MgO and so on. XRD of SF is shown in Figure 1. There is a significant widening peak in the range of 15–35°, indicating that the content of amorphous components in SF is high. The diffraction peaks of crystalline phase minerals are few, indicating that SF has high potential hydration gellation activity. The results of laser particle size analysis are shown in Figure 2. The average particle size of SF is 66.71 μm and 75 per cent particles are concentrated below 72.84 μm.

Two kinds of aggregate (standard sand and dolomite aggregate) were used in this experiment. Standard sand was produced according to 'The Chinese national standard GB/T17671–1999' and the SiO_2 content is more than 96 per cent. The particle size distribution of standard sand is as follows: +2 mm, -2~1.6 mm, -1.6~1.0 mm, -1.0~0.5 mm, -0.5~0.16 mm, -0.16~0.08 mm, respectively account for 0 per cent, 6.9 per cent, 27.3 per cent, 34.3 per cent, 19.4 per cent and 11.5 per cent. Dolomite aggregate was collected from Guiyang surrounding construction sand factory.

TABLE 1

Results of multi-element analysis of SF.

Chemical elements/%	SiO_2	CaO	Al_2O_3	TiO_2	Fe_2O_3	MgO	K_2O	Na_2O	P_2O_5
SF	92.30	0.30	0.36	-	0.08	0.60	-	0.90	-
Cement	20.08	60.65	4.61	0.55	3.36	1.98	0.54	0.85	0.22

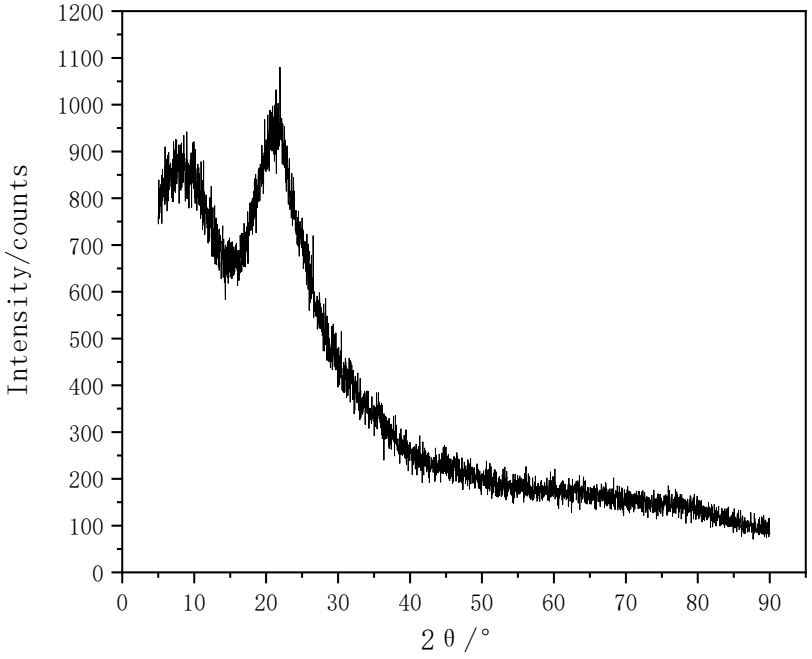

FIG 1 – XRD pattern of SF.

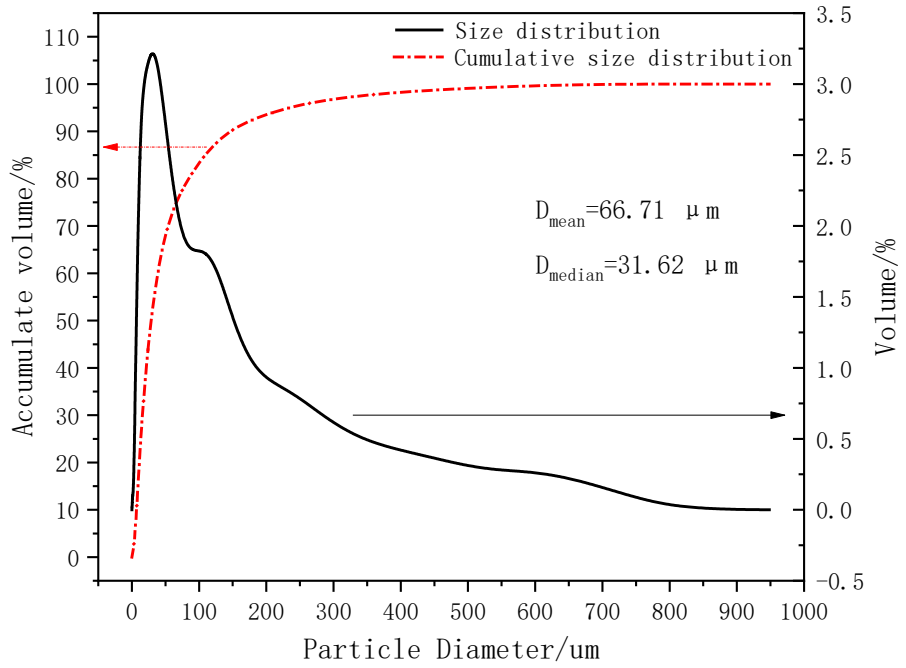

FIG 2 – Particle size distribution of SF.

Specimen preparation and experimental methods

Procedures of specimen preparation

In order to eliminate, to the maximum extent, the interference of other materials (such as coarse aggregate) on the study results of the ITZ, the concrete specimen prepared were relatively simple mortar blocks according to the national standard GB/T-17671-1999 (cement mortar strength test method (ISO method)). The test configuration is shown in Table 2. The mixed mixture was placed into a concrete mould (a three-way probe with a size of 40 mm × 40 mm × 160 mm) and three specimens of the same size were cast. The curing conditions of specimens were as follows: humidity >90 per cent, temperature 20±1°C.

TABLE 2

Composition ratio of RM-SF-cement concrete.

Specimen number	RM proportion /%	RM content /g	SF proportion /%	Cement proportion /%	SF content /g	Cement content /g	Aggregate (standard sand) /g	Water /mL
S-1	10.00	45.00	0.00	90.00	0.00	405.00	1350.00	225.00
S-2			9.00	81.00	40.50	364.50		225.00
S-3			18.00	72.00	81.00	324.00		245.00
S-4			27.00	63.00	121.50	283.50		265.00
S-5			36.00	54.00	162.00	243.00		285.00
S-6			45.00	45.00	202.50	202.50		305.00
S-7			54.00	36.00	243.00	162.00		325.00
S-8			63.00	27.00	283.50	121.50		345.00
S-9			72.00	18.00	324.00	81.00		365.00
S-10			81.00	9.00	364.50	40.50		385.00
S-11			90.00	0.00	405.00	0.00		405.00

Mechanics performance testing

Compressive strength and flexural strength were used to characterise the mechanical properties of concrete. Yaw-300b microcomputer controlled compression and flexural testing machine were used to test the compression and flexural strength of the concrete specimen through ISO method. Three parallel concrete specimen were prepared for each test, with the final test results being taken for the average of the test results (there were three parallel test samples and six parallel test samples in terms of flexural strength).

Microporous structure testing

The microporous size and microporous distribution of ITZ in concrete were studied by (AutoPore 9510). Specimen preparation process are as follows. After specimen were cured for 28 days, 20 g representative particles with ITZ were selected from the centre part of the broken specimen and then soaked in ethanol for 48 hours to stop hydration. The sample was placed in an oven (50°C) to dry until constant weight appeared. During the measurement, each sample was tested twice. The pore was modelled as a cylindrical channel using washburn-Laplace law. The test pressure P and the radius of the cylinder were expressed by the following formula: $P = 2\sigma\cos\theta/r$ (An, Hui-Mi and Sao-Jeng, 2011), P is mercury injection pressure (Pa), σ is mercury surface tension (N/m), θ is mercury contact angle (rad), r is the equivalent diameter of the invasion hole (m).

Microporous structure testing

The concrete specimen prepared in 2.2.1 was crushed after curing for 28 days and the particles in the middle part were taken. The aggregate of the particles was separated from the cementitious material by gently tapping with a metal hammer. The side area of the cementitious material linked to the aggregate was tested by X-ray diffractometer (SmartLab 9KW). Test parameters were as follows: copper target, tube voltage 45 kV, tube current 100 mA, scanning step size 0.02°, measuring range (2θ) 5–90°, scanning rate 5°/min.

Hydration heat testing

Hydration heat of cementitious materials and mineral admixtures were tested by microcalorimeter (C80). The specimen was 40 mg with as much water (3 mL) as possible. The temperature program was set as 20°C to 30°C, 0.5°C/min and 4300 min from 30°C to 30°C.

EXPERIMENTAL RESULTS AND DISCUSSION

Effect of SF on mechanical properties of RM-cement concrete

The test results of SF on mechanical properties of RM-cement concrete were shown in Figure 3. The effects of different amounts of SF mixed with RM-cement on the flexural and compressive strength of concrete were found to be basically the same. When the content of RM was 10 per cent, the bending strength and compressive strength increased at first and then decreased with the increase of SF content. When the content of SF is 18.00 per cent, the compressive and flexural strength reached to the maximum. Therefore, the appropriate amount of SF was suggested to be 18.00 per cent. When the content of SF exceeds 72.00 per cent, the concrete with a curing age of seven days lost its compressive and flexural strength. The particle size of SF was small and easily soluble in water, which led to a great increase in water demand of composite cementitious materials. Therefore, under the same conditions, the viscosity of slurry was high and the workability of mortar decreases. When the amount of SF in concrete was too large, the water involved in the pozzolanic reaction of SF decreased under the condition of the same water consumption and thus leading to insufficient pozzolanic reaction. Such would be neither conducive to the improvement of concrete strength, nor keep mechanical properties.

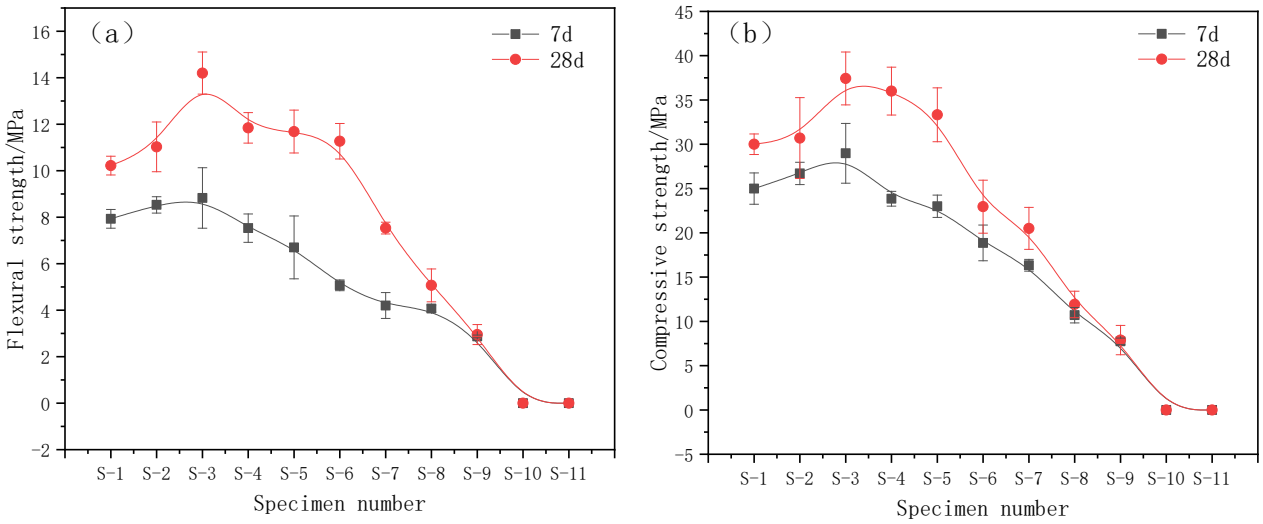

FIG 3 – Influence of different mixing amount SF and RM on flexural and compressive strength of concrete (a: flexural strength; b: compressive strength).

Effect of SF on pore size distribution of ITZ of RM-cement concrete

The mixing ratio with better mechanical properties was selected as cementing material (RM: SF: cement was 10:18:72). The blank test cementitious material ratio (RM: cement was 10:90) and dolomite was selected as aggregate. Sample number format is similar to 5.1, namely 10RM-18G-722-C, 10RM-90P-C. The prepared concrete was crushed after curing for 28 days and the particles containing ITZs were put into anhydrous ethanol for 48 h to stop the hydration reaction. After the samples were dried, the pore size and pore size distribution were tested by MIP method. Table 3 shows the test results of the porosity and the pore size of ITZ in concrete with SF, RM and cement composite cementification material. Figure 4 shows the cumulative pore size and pore size distribution curve of the ITZ.

TABLE 3

Test results of porosity and pore size of concrete.

Specimen number	Specimen weight/g	Hg weight/g	Bulk density /(g•mL^{-1})	Total intrusion volume/ (mL•g^{-1})	Average pore diameter (4V/A) /nm	Median pore diameter (volume)/nm
10RM-90P-C	3.29	60.47	2.33	0.04	17.50	50.70
10RM-18G-72P-C	3.96	73.54	2.17	0.07	9.70	13.90

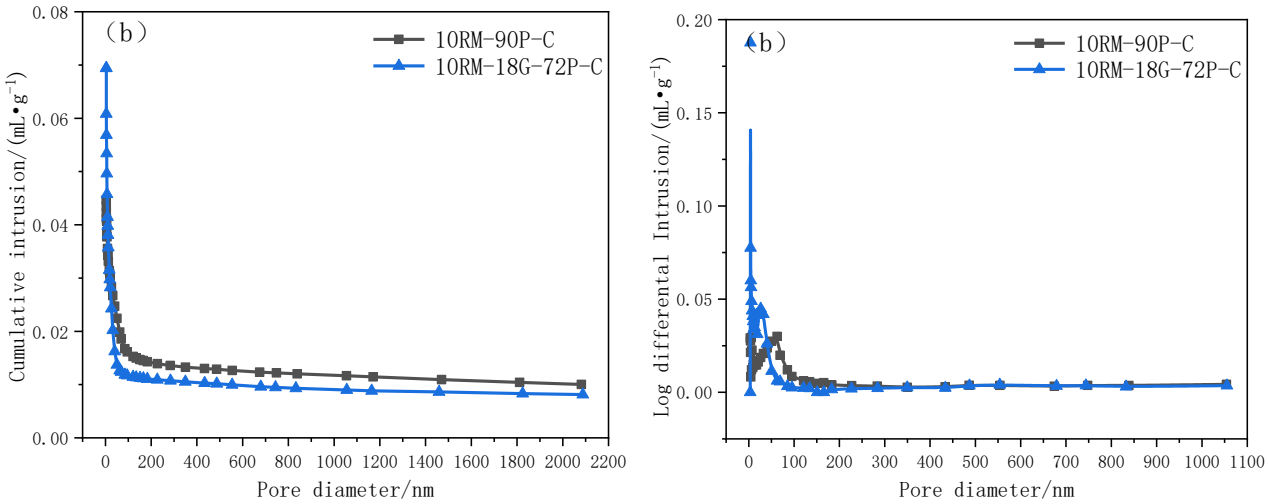

FIG 4 – Test results of pore size of ITZ in concrete (left: cumulative pore size; right: Aperture distribution).

As can be seen from Table 3, compared with RM-cement composite cementing material, the average pore diameter and median pore diameter of SF-RM-cement composite cementing material are smaller. It can be seen from Figure 4 that the cumulative pore diameter and pore size distribution of ITZ in concrete of SF-RM-cement composite cementing material are better than that of RM-cement composite cementing material. Therefore, SF has a good optimisation effect on the ITZ of concrete. Wollastonite requires a large amount of water, which can effectively absorb a large amount of residual water when added into concrete and thus resulting in a low water-binder ratio near the ITZ and poor growth of CH crystals. And it was difficult to form coarse crystals and low porosity would appear. Conversely, the low void ratio limits the growth space of CH crystals and thus leading to further densification of the ITZ. In addition, the reaction between active SiO_2 and CH in SF further reduced the CH content (the reaction formula is as follows) (Chen *et al*, 2010) and the product C-S-H gel was generated to fill the porous area near the ITZ.

From the perspective of pore size, SF mixing can effectively reduce the ITZ porosity of RM-cement concrete and reduce the micropore size.

Effect of SF on phase composition of ITZ in RM-cement concrete

Due to the side wall effect and micro-area bleeding effect at the early hydration stage, the water-binder ratio at the ITZ of the aggregate/cementing material is large, the hydration reaction is sufficient and the calcium hydroxide crystal is coarse (Chen *et al*, 2012). Therefore, the phase composition of the interface area is quite different from that of the matrix. Based on the previous research results, the pore size distribution of concrete interface prepared by the SF-RM-cement composite gelled material is quite different from that of the pure cement. Mineral admixtures have a certain influence on the composition of the concrete interface area. XRD micro zone test was used to study the phase composition of the ITZ in concrete. The test results are shown in Figure 5. The strong water absorption of SF leads to a small water-binder ratio in the ITZ, which makes it difficult to form coarse CH crystal. The highly active SF reacted with CH to form C-S-H gel (Equations 1 and 2) and thus resulting in the reduction of CH crystals in the ITZ. The calcite peaks are obvious, which may be caused by carbonisation reaction caused by long contact time with air during storage. The calcite peak of 10RM-90p is slightly stronger, which also indicates that more CH is generated in the ITZ of 10RM-90P.

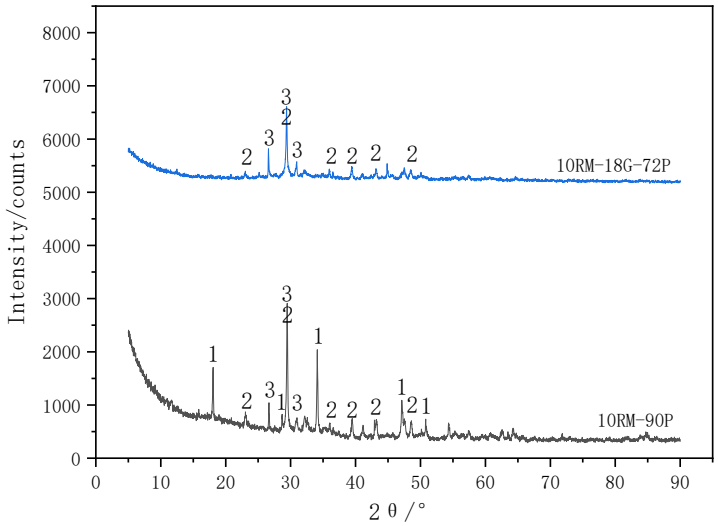

FIG 5 – XRD test results of ITZ in concrete (1 – Portlandite; 2 – Calcite; 3 – calcium silicate hydrate).

$$\equiv Si\text{-}O\text{-}Si\equiv + H\text{-}OH \rightarrow \equiv Si\text{-}OH \text{(slower response)} \quad (1)$$

$$\equiv Si\text{-}OH + Ca(OH)2 \rightarrow C\text{-}S\text{-}H \quad (2)$$

Hydration heat testing of composite cementitious materials

From the whole hydration process, the hydration reaction of cement is an exothermic process and its heat release and rate are related to mineral composition. The hydration heat thus, reflected its hydration process. Ordinary Portland cement. RM and SF were respectively treated with sufficient water (3 mL) at 30°C for about 40 mg to test the heat exchange process. The hydration heat release rate curve and hydration heat release curve are shown in Figure 6. At the initial stage, the heat release rate of SF and RM were lower than that of cement and the total heat release was also lower than that of cement, indicating that compared with cement, there were fewer substances in SF and RM that can participate in hydration reaction to form gel. Their gelling activity is lower than that of cement. The hydration heat release of RM is very low. Except for an obvious exothermic peak in the initial period, the exothermic rate curve is smooth in other reaction time, indicating that the gelling activity of RM is very low and the filling effect is mainly exerted by the direct mixing concrete (Su and Li, 2021). There is a large exothermic peak of SF after the second exothermic peak of cement, which is mainly caused by the reaction of a large amount of active glassy SiO_2 with water to form silica-rich gel.

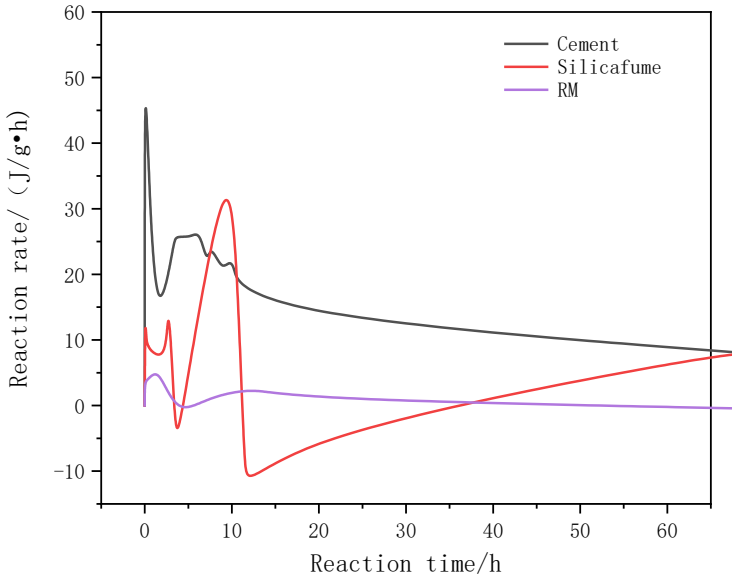

FIG 6 – Heat release rate curve of raw material hydration at the temperature of 30°C.

CONCLUSIONS

- The effects of different amounts of SF mixed with RM-cement on the flexural and compressive strength of concrete are basically the same. When the content of RM is 10 per cent and by adding the content of SF, the flexural and compressive strength were found to increase at first and then decrease gradually. The appropriate content of SF in RM-cement concrete was proposed to be 18.00 per cent.
- The addition of SF to concrete could effectively absorb a large amount of residual water, leading to low water-binder ratio near the ITZ, poor growth of CH crystals. And it was difficult to form coarse crystals and thus appeared low porosity. Low void ratio limits the space for the growth of CH crystals and resulting in further densification of the ITZ.
- Compared with cement, the heat release rate of SF and RM at the initial stage was found to be lower than that of cement and the total heat release was also lower than that of cement. The reaction between active SiO_2 and CH in SF further reduced the content of CH. The product C-S-H gel was formed to fill the porous area near the ITZ.

ACKNOWLEDGEMENTS

This work was financially supported by the National Key R&D Program of China (2018YFC1903500).

REFERENCES

An, C, Hui-Mi, H and Sao-Jeng, C, 2011. Properties of Concrete Incorporating Bed Ash from Circulating Fluidized Bed Combustion and Ground Granulates Blast-furnace Slag. *Journal of Wuhan University of Technology. Materials science edition*, 26(2), 348–354.

Chen, J, Zhao, B, Wang, X, Zhang, Q and Wang, L, 2010. Cemented backfilling performance of yellow phosphorus slag. *University of Science and Technology Beijing*, 17(1), 121–126.

Chen, Z, Yang, L F, Xu, F and Feng, Q G, 2012. A New Method for Measuring the Length of ITZ on Concrete Section by Digital Image Processing Technique. *Applied Mechanics and Materials*, 256–259, 2359–2362.

Jun, Y, Kim, J H and Kim, T, 2019. Hydration of Calcium Sulfoaluminate-Based Binder Incorporating Red Mud and Silica Fume. *Applied Sciences*, 9(11), 2270.

Kim, J, Park, W, Jang, Y, Kim, S, Kim, S, Nam, Y, Kim, D and Rokugo, K, 2016. Mechanical Properties of Energy Efficient Concretes Made with Binary, Ternary and Quaternary Cementitious Blends of Fly Ash, Blast Furnace Slag and Silica Fume. *International Journal of Concrete Structures and Materials*, 10(3), 97–108.

Krivenko, P, Kovalchuk, O, Pasko, A, Croymans, T, Hult, M, Lutter, G, Vandevenne, N, Schreurs, S and Schroeyers, W, 2017. Development of alkali activated cements and concrete mixture design with high volumes of red mud. *Construction and Building Materials*, 151,819–826.

Li, X and Zhang, Q, 2022. Influence behavior of phosphorus slag and fly ash on the interface transition zone in concrete prepared by cement-red mud. *Journal of Building Engineering*, 49,104017. 10.1016/j.jobe.2022.104017

Mehta, A and Ashish, D K, 2020. Silica fume and waste glass in cement concrete production: A review. *Journal of Building Engineering*, 29, 100888.

Nabavi-Pelesaraei, A, Bayat, R, Hosseinzadeh-Bandbafha, H, Afrasyabi, H and Berrada, A, 2017. Prognostication of energy use and environmental impacts for recycle system of municipal solid waste management. *Journal of Cleaner Production*, 154(15), 602–613.

Rao, S K, Sravana, P and Rao, T C, 2016. Abrasion resistance and mechanical properties of Roller Compacted Concrete with GGBS, *Construction and Building Materials*, 114, 925–933.

Singh, N, 2018. Fly Ash-Based Geopolymer Binder: A Future Construction Material. *Minerals (Basel)*, 8(7), 299.

Su, Z and Li, X, 2021. Study on Preparation and Interfacial Transition Zone Microstructure of Red Mud-Yellow Phosphorus Slag-Cement Concrete. *Materials*, 14(11), 2768.

Türkmen, O, Gül, R and Çelik, C, 2008. A Taguchi approach for investigation of some physical properties of concrete produced from mineral admixtures. *Building and Environment*, 43(6), 1127–1137.

Wang, L, Jin, M, Wu, Y, Zhou, Y and Tang, S, 2021. Hydration, shrinkage, pore structure and fractal dimension of silica fume modified low heat Portland cement-based materials. *Construction and Building Materials*, 272, 121952.

Wang, Q, Huang, Z and Wang, D, 2018. Influence of high-volume electric furnace nickel slag and phosphorous slag on the properties of massive concrete. *Journal of Thermal Analysis and Calorimetry*, 131(2), 873–885.

Zhou, Y, Deng, H and Liu, J, 2017. Rational Utilization of Fine Unclassified Tailings and Activated Blast Furnace Slag with High Calcium. *Minerals*, 7(4), 48.

Occurrence mechanism of phosphorus impurities in phosphogypsum – an insight from density functional theory calculations

X B Li[1,3,4], Q Zhang[2,3,4] and L J Li[3,4,5]

1. Doctor, Mining College, Guizhou University, Guiyang 550025, China. Email: xbli3@gzu.edu.cn
2. Professor, Guizhou Academy of Sciences, Guiyang 550001, China. Email: zq6736@163.com
3. Professor, National & Local Joint Laboratory of Engineering for Effective Utilization of Regional Mineral Resources from Karst Areas, Guiyang 550025, China.
4. Professor, Guizhou Key Lab of Comprehensive Utilization of Nonmetallic Mineral Resources, Guiyang 550025, China.
5. Doctor, Mining College, Guizhou University, Guiyang 550025, China.

ABSTRACT

Phosphogypsum (PG) is a harmful industrial waste from the production of phosphoric acid. The main composition of PG is calcium sulfate dihydrate ($CaSO_4·2H_2O$), but it contains various impurities such as phosphate, fluoride and organic matters. Among which, the phosphorus impurity is the most unfavourable factor for affect its resource utilisation. Unfortunately, the existing form of phosphorus in PG is unclear. In this paper, the occurrence mechanism of phosphorus impurity in PG was studied by density functional theory calculations. The results show that HPO_4^{2-} can replace SO_4^{2-} into dihydrate gypsum lattice to form a stable configuration, H forms a covalent bond with O, both H and P are in the state of electron loss, and O present the state of getting the electron, it's mostly from the P orbital. In HPO_4^{2-}, the H-O bond density is mainly contributed by the O2p orbital. H1s orbital and O2p orbital have obvious resonance phenomenon at -10–0 eV, and there is s, p orbital hybridisation. When using $H_2PO_4^-$ to replace SO_4^{2-} of dihydrate gypsum, $H_2PO_4^-$ has an H atom that is hard to bond with O atom, indicating that $H_2PO_4^-$ can't stably exist in the crystal structure of dihydrate gypsum, so it can't replace SO_4^{2-} into the crystal lattice of dihydrate gypsum. Therefore, the phosphorus impurities mainly replace SO_4^{2-} with HPO_4^{2-} into the dihydrate gypsum lattice to form co-crystallised phosphorus ($CaHPO_4·2H_2O$).

INTRODUCTION

Phosphogypsum is a large amount of industrial solid waste discharged during the production of wet-process phosphoric acid, and is also an important renewable gypsum resource (Cánovas *et al*, 2018). According to statistics, about five tons of phosphogypsum are produced for every one ton of phosphoric acid, and about 280 Mt of phosphogypsum are produced every year in the world (Islam *et al*, 2017; Tayibi *et al*, 2009). In 2019, the production of phosphogypsum in China was 75 Mt, and the comprehensive utilisation rate was 40 per cent (Ye, 2020). The main component of phosphogypsum is dihydrous gypsum ($CaSO_4·2H_2O$), in addition, it also contains harmful impurities such as phosphorus, fluorine and organic matter (Nizevičienė *et al*, 2018). Due to the complex composition of phosphogypsum and more impurities, its utilisation is difficult and the comprehensive utilisation rate is low. At present, the storage treatment is mainly adopted, which not only takes up a lot of land resources, but also contains soluble phosphorus, fluorine and other substances that will cause pollution to the surrounding environment, which is an important factor for the sustainable development of phosphorus chemical industry (Rashad, 2017; Yang *et al*, 2016). In 2006, the State Environmental Protection Administration first identified phosphogypsum as hazardous solid waste; In 2018, Guizhou Province proposed to fully implement the 'production based on use' of phosphogypsum, to achieve the balance between production and consumption of phosphogypsum, and strive for zero new heap; In 2019, the Ministry of Ecology and Environment issued the implementation plan of the special investigation and rectification of 'three phosphorus' in the Yangtze River, try to use about two years to basically figure out the base number of 'three phosphorus' industries, and focusing on solving prominent ecological and environmental problems such as heavy pollution, high risk and serious violations of laws and regulations in the 'three phosphorus' industries. Therefore, how to accelerate the resource utilisation of phosphogypsum is the focus of current research.

The impurities in phosphogypsum are the key to its resource utilisation. Due to the nature of phosphate ore and the production process of phosphoric acid, the morphology and content of impurities in phosphogypsum are different. The main impurities in phosphogypsum include phosphoric acid and its salt, fluoride and organic matter. In addition, the wet-process phosphoric acid production process also results in the accumulation of heavy metals and radioactive elements in phosphogypsum. Among them, phosphorus is the most important factor affecting the performance of phosphogypsum, it exists in three forms: soluble phosphorus, eutectic phosphorus and insoluble phosphorus, and soluble phosphorus (H_3PO_4, $H_2PO_4^-$, HPO_4^{2-}) has the greatest effect (Rashad, 2017; Huang *et al*, 2016). The soluble phosphorus is converted into $Ca_3(PO_4)_2$ precipitated in the hydration process of gypsum, and covers the surface of semi-hydrated gypsum crystal. As a result, the setting time of building gypsum is significantly prolonged, the structure is loose and the strength is reduced, limits its application in the field of construction. Eutectic phosphorus ($CaHPO_4{\cdot}2H_2O$) is formed by HPO_4^{2-} substituting part of SO_4^{2-} into the dihydrate gypsum lattice (Ölmez and Yilmaz, 1988; Yang, 2008). $CaHPO_4{\cdot}2H_2O$ and $CaSO_4{\cdot}_2H_2O$ both belong to monoclinic system with similar lattice constants, and they are easy to form solid solution. The effect of eutectic phosphorus on the properties of phosphogypsum is similar to that of soluble phosphorus (Zhang *et al*, 2015). Insoluble phosphorus mainly exists in the form of $Ca_3(PO_4)_2$ in the unreacted apatite, which has little effect on the performance of phosphogypsum.

In conclusion, the forms of phosphorus in phosphogypsum are complex. Although there are many studies on phosphorus impurities in phosphogypsum, there are few reports on the occurrence forms of phosphorus impurities in phosphogypsum from the microscopic perspective based on density functional theory. Therefore, in this paper, CASTEP module in MS 8.0 software was used to study the substitution of SO_4^{4-} in dihydrate gypsum by PO_4^{3-}, HPO_4^{2-} and $H_2PO_4^-$, and analysed substitution cell parameters, substitution energy, Mulliken population, density of states etc, so as to determine the form of phosphorus impurity in dihydrate gypsum.

CALCULATION METHOD

Based on the first principles of density functional theory, the CASTEP module in MS 8.0 software was used to complete all the simulation and calculation. The crystal structure of dihydrate gypsum is selected from the American Mineralogist crystal Structure Database (AMCSD) (Figure 1). Crystal structure of dihydrate gypsum is a combination of Ca^{2+} and SO_4^{2-}, which is a layered lattice structure formed by alternating layers of water molecules and layers perpendicular to the strong axis (010) and parallel to the plane, and the interior of the ion binding layer is the binding force produced by the interaction of positive and negative ions; The lattice constants of dihydrate gypsum are a = 5.679 Å,b = 15.200 Å,c = 6.522 Å,α = γ = 90°, β = 118.430°, space group C2/C. On the basis of optimisation of commutative correlation functional, truncation energy and billrouin region K-point, based on these conditions, the cell parameters of gypsum dihydrate were calculated, the error between the calculated and experimental values of dihydrate gypsum cell parameters is less than one per cent (Table 1). On the basis of phase optimisation of dihydrate gypsum, PO_4^{3-}, HPO_4^{2-} and $H_2PO_4^-$ were used to replace SO_4^{2-} in dihydrate gypsum to construct the crystal model of phosphorus doped dihydrate gypsum (Table 1: b–d). Analysis of electronic structure of doped gypsum dihydrate includes density of states, substitution energy, Mulliken population analysis and so on.

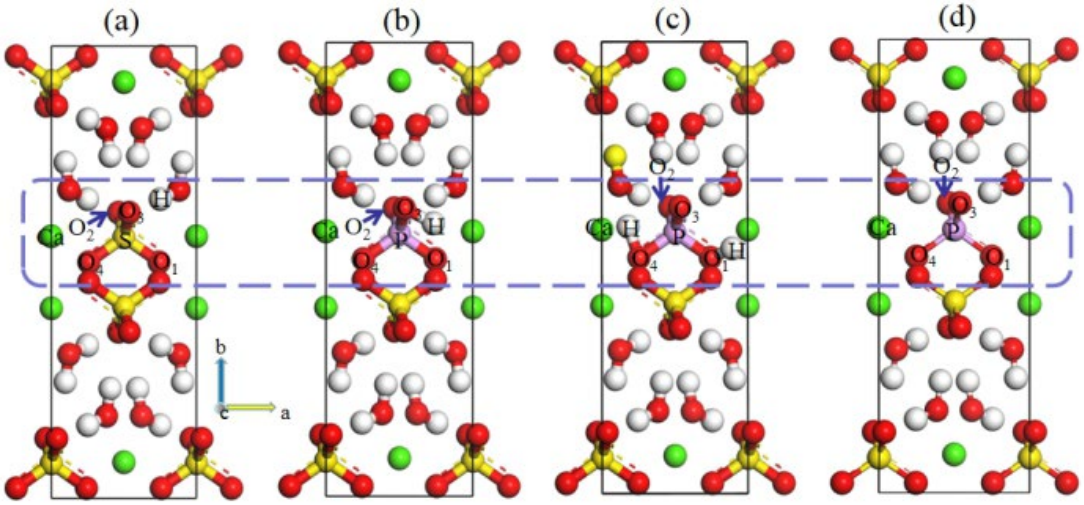

FIG 1 – Crystal structure model of dihydrate gypsum and phosphorus doped dihydrate gypsum: (a) Dihydrate gypsum structure model; (b) The model of HPO_4^{2-} replacing SO_4^{2-} in dihydrate structure gypsum; (c) The model of $H_2PO_4^-$ replacing SO_4^{2-} in dihydrate structure gypsum; (d) The model of PO_4^{3-} replacing SO_4^{2-} in dihydrate structure gypsum.

TABLE 1

Error analysis between calculated and experimental values of lattice constants of dihydrate gypsum.

The value	Crystal cell parameters/Å			β/°	error/%		
	a	b	c		a	b	c
Calculated value	5.659	15.096	6.504	117.941°	-0.32	-0.73	-0.37
Experimental value	5.679	15.202	6.522	118.430°			

RESULTS AND DISCUSSION

H-O and P-O sites of PO_4^{3-} HPO_4^{2-} and $H_2PO_4^-$

PO_4^{3-} contains four O atoms (O_1, O_2, O_3, O_4). When PO_4^{3-} replaces SO_4^{2-}, no H combines to O, But H can combine with any of the four O atoms to form HPO_4^{2-} (H-O_1, H-O_2, H-O3, H-O_4), therefore, there are four different orientations after the replacement of SO_4^{2-} by HPO_4^{2-} (Figure 2) and six different orientations after the replacement of SO_4^{2-} by $H_2PO_4^-$ (Figure 3). The distance between H and O of different orientations is calculated (Table 2). Similarly, when these three substitution processes occur, P will combine with any of the four O atoms to form (P-O_1, P-O_2, P-O_3, P-O_4) (Table 3). After PO_4^{3-} replaces SO_4^{2-}, the cell diagram is basically consistent with (Figure 1d), and the positions of each element are basically unchanged.

TABLE 2

The distance of different H-O sites in dihydrate gypsum doped with HPO_4^{2-} and $H_2PO_4^-$.

HPO_4^{2-}	H-O distance		$H_2PO_4^-$	Longer H-O distance		Shorter H-O distance	
(a)	$H\text{-}O_1$	0.993	(e)	$H\text{-}O_3$	2.715	$H\text{-}O_1$	1.018
(b)	$H\text{-}O_2$	1.010	(f)	$H\text{-}O_1$	2.295	$H\text{-}O_4$	1.255
(c)	$H\text{-}O_3$	1.010	(g)	$H\text{-}O_2$	1.915	$H\text{-}O_1$	1.015
(d)	$H\text{-}O_4$	1.015	(h)	$H\text{-}O_2$	2.130	$H\text{-}O_3$	0.995
			(i)	$H\text{-}O_4$	3.025	$H\text{-}O_3$	1.000
			(j)	$H\text{-}O_4$	2.998	$H\text{-}O_2$	0.991

TABLE 3

The distance of different P-O sites in diaqueous gypsum doped with PO_4^{3-},HPO_4^{2-} and $H_2PO_4^-$.

Ion species	Number	The distance between P and the O sites			
		$P\text{-}O_1$	$P\text{-}O_2$	$P\text{-}O_3$	$P\text{-}O_4$
PO_4^3		1.547	1.547	1.552	1.552
HPO_4^{2-}	(a)	1.671	1.526	1.532	1.529
	(b)	1.523	1.647	1.554	1.522
	(c)	1.524	1.551	1.638	1.531
	(d)	1.520	1.520	1.541	1.640
$H_2PO_4^-$	(e)	1.635	1.548	1.539	1.522
	(f)	1.614	1.549	1.544	1.532
	(g)	1.637	1.549	1.539	1.522
	(h)	1.543	1.566	1.677	1.556
	(i)	1.526	1.561	1.618	1.526
	(j)	1.552	1.683	1.584	1.546

According to Figure 2 and Table 3, the lengths of all P-O bonds (Table 3) are in the range of 1.520 ~ 1.677 Å, and within the sum of covalent radii (covalent bond length 1.100 Å) and O (covalent bond length 0.730 Å) is (1.830 Å), indicating that after the substitution of SO_4^{2-} by PO_4^{3-}, HPO_4^{2-} and $H_2PO_4^-$, Both P and O are bonded.

According to (Table 2), after the substitution of SO_4^{2-} by HPO_4^{2-}, the H-O bond length ranges from 0.993 to 1.015 Å, which is close to the sum of the covalent radius (1.050 Å) of H (0.320 Å covalent bond length) and O (0.730 Å covalent bond length), that means H can bond with O; after $H_2PO_4^-$ replaces SO_4^{2-}, the distance between H and O changes greatly, the distance between longer H-O is between 1.915 ~ 3.025 Å, the short H-O distance is between 0.995 ~ 1.255 Å. Query the periodic table of ion radius: Sum of the atomic radii of the bond between H and O, the bond lengths of covalent bond and ionic bond are 0.980 Å, 1.050 Å and 1.720 Å respectively, indicating that there is an H in $H_2PO_4^-$ that is difficult to bond with O, and the other H can bond with O. In addition, we need to analyse whether unbonded H is bonded to other adjacent atoms in the dihydrate gypsum lattice, the bond between the two H's is 0.640 Å, the sum of the atomic radius and the length of the ionic bond formed by H and Ca is 2.060 Å and 1.310 Å respectively, the distance between unbonded H and the nearest O, H and Ca is 1.740 Å, 0.957 Å and 2.382 Å respectively, all distances are greater than the length of the bonds that can be produced, indicating that $H_2PO_4^-$ can't exist stably in the crystal structure of dihydrogypsum, so it can't replace SO_4^{2-} into the crystal lattice of dihydrogypsum.

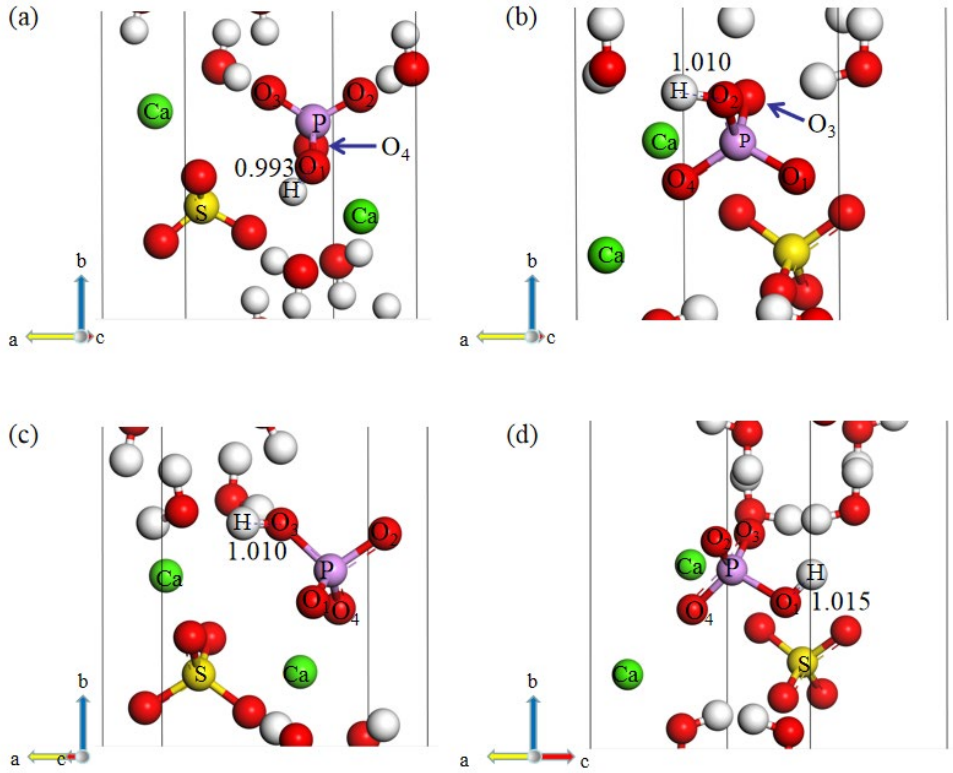

FIG 2 – Local schematic diagram of four different hydrogen sites where HPO_4^{2-} replaces SO_4^{2-}.

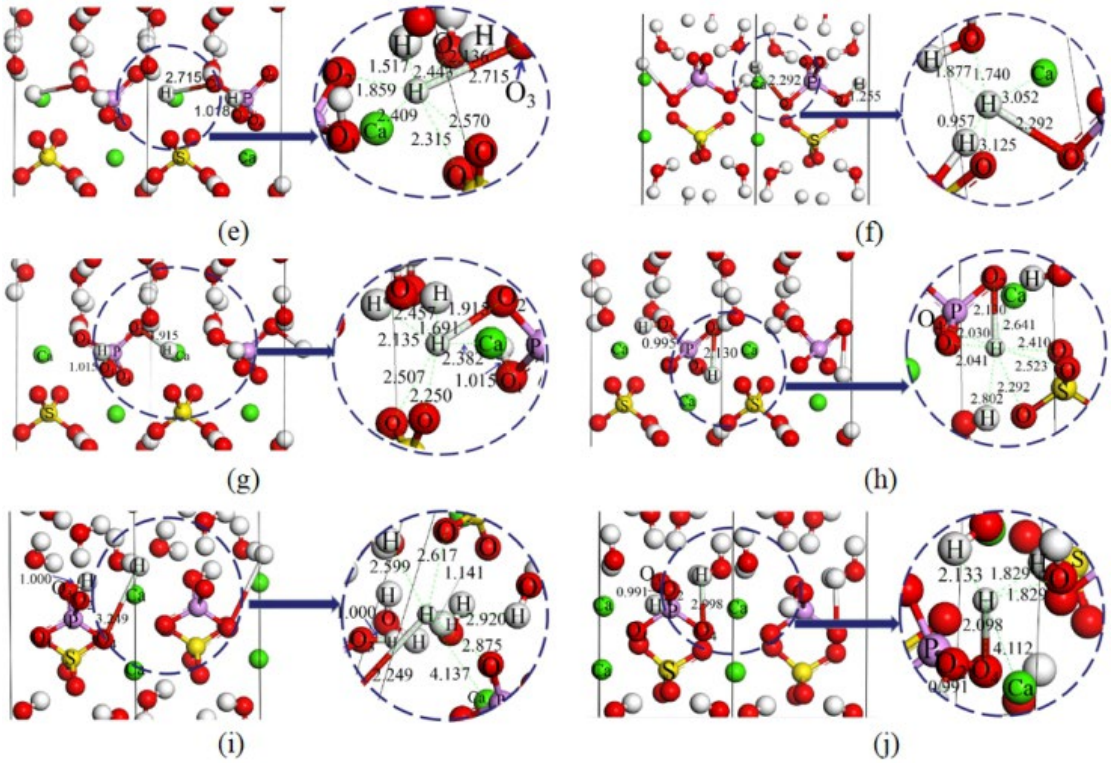

FIG 3 – Local sketches of six different hydrogen sites where $H_2PO_4^-$ replaces SO_4^{2-}.

Cell parameter analysis

Compared with the experimental values of lattice constants of dihydrate gypsum, the changes of crystal cell parameters of the optimised dihydrate gypsum after SO_4^{2-} was replaced by PO_4^{3-}, HPO_4^{2-} and $H_2PO_4^-$ were analysed (Table 4).

TABLE 4

The changes of crystal cell parameters of dihydrate gypsum after replacing SO_4^{2-} with PO_4^{3-}, HPO_4^{2-} and $H_2PO_4^-$.

Ion species	Number	a		b		c		α		β		γ	
		Calculated value	Change rate	Calculated value	Change rate	Calculated value	Change rate	Calculated value	Change rate	Calculated value	Change rate	Calculated value	Change rate
PO_4^{3-}	/	5.67	0.14	15.05	-0.29	6.51	0.11	90.00	0.00	117.62	-0.27	90.00	0.00
HPO_4^{2-}	(a)	5.67	0.13	15.09	-0.07	6.49	-0.2	89.46	-0.60	117.41	-0.45	90.56	0.63
	(b)	5.68	0.44	15.17	0.46	6.37	-2.09	89.68	-0.36	117.12	-0.70	90.09	0.10
	(c)	5.71	0.86	15.14	0.31	6.41	-1.43	90.02	0.03	116.75	-1.01	90.67	0.75
	(d)	5.62	-0.66	15.05	-0.28	6.57	0.97	89.66	-0.38	117.55	-0.33	89.71	-0.32
$H_2PO_4^-$	(e)	5.64	-0.27	15.06	-0.21	6.66	2.46	90.50	0.56	118.00	0.05	90.60	0.67
	(f)	5.64	-0.33	15.08	-0.08	6.57	1.00	90.22	0.24	117.70	-0.21	89.74	-0.28
	(g)	5.62	-0.70	15.14	0.30	6.64	2.11	90.35	0.39	117.81	-0.11	90.62	0.68
	(h)	5.70	0.82	15.15	0.37	6.52	-0.07	89.94	-0.07	116.89	-0.89	90.81	0.90
	(i)	5.64	-0.37	15.45	2.37	6.39	-1.71	85.56	-4.94	116.71	-1.04	90.37	0.41
	(j)	5.74	1.40	15.10	0.03	6.41	-1.41	91.09	1.28	118.48	0.49	88.73	-1.41

According to (Table 4), compared with the experimental value, after replacing SO_4^{2-} with PO_4^{3-}, the cell parameters of dihydrate gypsum changed little, but since the electricity price of PO_4^{3-} is different from that of SO_4^{2-}, an H+ still needs to be added to PO_4^{3-} to reach the balance of electricity price. So PO_4^{3-} can't directly replace SO_4^{2-} into the dihydrate gypsum lattice. After doping HPO_4^{2-} and $H_2PO_4^-$, the change rates of alarm parameters of dihydrate gypsum at different hydrogen sites are all less than 2.5 per cent, (a) the change of cell parameters after position substitution is the smallest, and the absolute value is much less than 2.5 per cent.

Substitutive energy calculation

In dihydrous gypsum, PO_4^{3-}, HPO_4^{2-} and $H_2PO_4^-$ replace SO_4^{2-} with many different sites, and the chemical environment around different sites is quite different. When P is replaced by S in dihydrous gypsum lattice, the degree of difficulties of substitution is different due to the different H sites, and the substitution mechanism is complicated. In essence, there is an energy change in the process of P doping in dihydrate gypsum. Therefore, the degree of ease with which substitution occurs can be measured by the change in energy during the doping process (doping energy or substitution energy).

Hydrogen phosphate replaces the sulfate group in dihydrate gypsum, and the corresponding substitution energy is defined as follows:

$$\Delta E = E_{defect}^{total} + E_{SO_4{}^{2-}} - E_{perfect}^{total} - E_{impurity}$$

E_{defect}^{total} and $E_{perfect}^{total}$ respectively represent the total energy of the phosphate-doped dihydrate gypsum, E_S and $E_{impurity}$ are the energies of sulfur atom and impurity atom respectively, in which the impurity atom includes phosphorus atom and hydrogen atom (in which the substitution energy of PO_4^{3-} is calculated without H). Theoretically, a negative value of ΔE means that the substitution process can occur, and the larger the absolute value, the easier the defect is to form in the lattice. According to the order of the absolute value of ΔE, we can determine the degree to which defects can form in mineral crystals.

Substitutions at different sites of the three ions are shown in (Table 5). In general, the absolute value of substitution energy (ΔE) from large to small is PO_4^{3-} >HPO_4^{2-}> $H_2PO_4^-$. Then the cell structure after PO_4^{3-} substitution is the most stable, the absolute value of ΔE of HPO_4^{2-} is higher than that of ΔE of $H_2PO_4^-$, so the structure is more stable.

TABLE 5

Energy changes after replacement of SO_4^{2-} by PO_4^{3-}, HPO_4^{2-} and $H_2PO_4^-$.

Ion species	Number	E_{defect}^{total}	$E_{SO_4^{2-}}$	$E_{perfect}^{total}$	$E_{impurity}$	ΔE
PO_4^{3-}	/	-15984.66	-2019.04	-16067.71	-1921.80	-14.18
HPO_4^{2-}	(a)	-16002.89	-2019.04	-16067.71	-1940.47	-13.74
	(b)	-16003.25	-2019.04	-16067.71	-1940.47	-14.11
	(c)	-16002.95	-2019.04	-16067.71	-1940.47	-13.81
	(d)	-16003.08	-2019.04	-16067.71	-1940.47	-13.94
$H_2PO_4^-$	(e)	-16015.51	-2019.04	-16067.71	-1958.83	-8.00
	(f)	-16015.78	-2019.04	-16067.71	-1958.83	-8.27
	(g)	-16015.51	-2019.04	-16067.71	-1958.83	-8.00
	(h)	-16015.49	-2019.04	-16067.71	-1958.83	-7.98
	(i)	-15984.66	-2019.04	-16067.71	-1958.83	-8.56
	(j)	-16002.89	-2019.04	-16067.71	-1958.83	-7.80

In the result of single hydrogen doping, the magnitude order of the absolute value of substitution energy is: (b)> (d)> (c)> (a), the absolute value of ΔE of (b) is the largest, which is -14.11 eV. It can be seen that the O_2 site represented by (b) is the most ideal site for single H doping, and the energy after HPO_4^{2-} substitution is the lowest and the structure is the most stable; in the result of two hydrogen doping, the magnitude order of the absolute value of substitution energy is: (i)> (f)> (e)> (g)> (h)> (j), it can be seen from Table 2 that $H_2PO_4^-$ can't stably replace SO_4^{2-} into the dihydrate gypsum lattice, so does not represent the two optimal sites for hydrogen doping.

Mulliken population analysis

Mulliken charge population indicates that the overlapping charge between atoms reflects the strength of the covalent bond formed between atoms. The larger the overlapping population between atoms is, the covalent bond exists between atoms; the smaller the overlapping population is, the no chemical bond or ionic bond exists between atoms. Tables 6 and 7 shows the different O sites of SO_4^{2-} in dihydrate gypsum doped with H, and the Mulliken charge population in which P substituted S in SO_4^{2-}. As can be seen from Table 6, when HPO_4^{2-} replaces SO_4^{2-} in dihydrate gypsum, the doped H and P are in the state of electron loss, H loses electrons (0.44 ~ 0.46 e), P loses electrons (2.29 ~ 2.31 e). In total, the outermost s and p orbitals each lost about 1.1 to 1.2 e. O is presented as an electron, and the number of electrons is 0.96 e or 0.97 e, mainly from the P orbital. As can be seen from Table 7, when the two H in the assumed $H_2PO_4^-$ exist in dihydrate gypsum, the bonding H-O site represents elements that gain and lose electrons similar to those in the substitution of HPO_4^{2-} for SO_4^{2-}, which has similar effects on its microscopic electron shell, and the properties of the corresponding elements are also consistent.

TABLE 6

Charge populations of H and P doped at each O site in HPO_4^{2-} substituted SO_4^{2-}.

Atomic		Orbital				Valence electrons	Electrons	Valence shell
		s	p	d	f			
(a)	H	0.54	0.00	0.00	0.00	0.54	0.46	$1s^1$
	O	1.84	5.12	0.00	0.00	6.97	-0.97	$2s^22p^4$
	P	0.89	1.82	0.00	0.00	2.71	2.29	$3s^23p^3$
(b)	H	0.54	0.00	0.00	0.00	0.54	0.46	$1s^1$
	O	1.83	5.14	0.00	0.00	6.97	-0.97	$2s^22p^4$
	P	0.88	1.82	0.00	0.00	2.70	2.30	$3s^23p^3$
(c)	H	0.56	0.00	0.00	0.00	0.56	0.44	$1s^1$
	O	1.82	5.14	0.00	0.00	6.96	-0.96	$2s^22p^4$
	P	0.88	1.81	0.00	0.00	2.69	2.31	$3s^23p^3$
(d)	H	0.56	0.00	0.00	0.00	0.56	0.44	$1s^1$
	O	1.84	5.13	0.00	0.00	6.97	-0.97	$2s^22p^4$
	P	0.88	1.81	0.00	0.00	2.70	2.30	$3s^23p^3$

TABLE 7

Charge populations of bonded H and P and corresponding O sites incorporated in $H_2PO_4^-$ substituted SO_4^{2-}.

Atomic		Orbital				Valence electrons	Electrons	Valence shell
		s	p	d	f			
(e)	H	0.56	0.00	0.00	0.00	0.56	0.44	$1s^1$
	O	1.84	5.13	0.00	0.00	6.97	-0.97	$2s^22p^4$
	P	0.88	1.81	0.00	0.00	2.69	2.31	$3s^23p^3$
(f)	H	0.86	0.00	0.00	0.00	0.86	0.14	$1s^1$
	O	1.87	5.02	0.00	0.00	6.89	-0.89	$2s^22p^4$
	P	0.88	1.81	0.00	0.00	2.69	2.31	$3s^23p^3$
(g)	H	0.56	0.00	0.00	0.00	0.56	0.44	$1s^1$
	O	1.84	5.13	0.00	0.00	6.97	-0.97	$2s^22p^4$
	P	0.89	1.81	0.00	0.00	2.69	2.31	$3s^23p^3$
(h)	H	0.56	0.00	0.00	0.00	0.56	0.44	$1s^1$
	O	1.82	5.12	0.00	0.00	6.94	-0.94	$2s^22p^4$
	P	0.93	1.91	0.00	0.00	2.84	2.16	$3s^23p^3$
(i)	H	0.53	0.00	0.00	0.00	0.53	0.47	$1s^1$
	O	1.82	5.16	0.00	0.00	6.99	-0.99	$2s^22p^4$
	P	0.88	1.81	0.00	0.00	2.70	2.30	$3s^23p^3$
(j)	H	0.54	0.00	0.00	0.00	0.54	0.46	$1s^1$
	O	1.84	5.09	0.00	0.00	6.94	-0.94	$2s^22p^4$
	P	0.94	1.94	0.00	0.00	2.88	2.12	$3s^23p^3$

Mulliken bond population can reflect the doping of H at different O sites of SO_4^{2-}, and the bonding strength and the corresponding bond length when P substituted S in SO_4^{2-}. By analysing the population of Mulliken bond, we can judge the stability of the combination of the corresponding elements at each point, and compare it with the substitution energy, so as to judge the difficulty of various forms of phosphorus in the dihydrate gypsum lattice. As shown in Table 8, when HPO_4^{2-} replaces SO_4^{2-}, the populations of Mulliken bonds formed by H-O and P-O were close to each other, and H-O_1 bond had the highest population (0.55) and the shortest bond length, indicating that H-O_1 bond showed stronger covalence and stronger effect; compared with the interactions between P and O at different sites, P-O_3 has the highest bond population, showing stronger covalence and stronger interaction.

TABLE 8

Mulliken bond populations of H-O and P-O after SO_4^{2-} was replaced by HPO_4^{2-} and $H_2PO_4^-$.

Ion species	Number	Mulliken bond population	
		H-O	P-O
HPO_4^{2-}	(a)	0.55	0.37
	(b)	0.51	0.40
	(c)	0.52	0.41
	(d)	0.52	0.40
$H_2PO_4^-$	(e)	0.51	0.42
	(f)	0.27	0.46
	(g)	0.52	0.42
	(h)	0.54	0.41
	(i)	0.52	0.43
	(j)	0.53	0.37

When $H_2PO_4^-$ replaces SO_4^{2-}, the population of Mulliken bond at the H and O sites of bonding has certain fluctuation. but the bond population and bond length of P and O sites were similar to the data when HPO_4^{2-} replaced SO_4^{2-}. indicating that one H in $H_2PO_4^-$ had little effect on the bond formation of the other H.

Density of states analysis

The density of states is the number of electronic states corresponding to a unit of energy (ΔE), which projects the energy band over the energy range, then can get the total density of the system. Bonding molecular orbitals are mainly the atomic orbital of a more electronegative atom mixed with the contribution of another less electronegative atomic orbital; anti-bonding molecular orbitals are mainly composed of atomic orbitals of less electronegative atoms, and some of them are contributed by more electronegative atomic orbitals. To judge the bonding and antibonding properties, it is necessary to give the state density of corresponding valence electron orbitals of corresponding atoms, namely, partial-wave density of states (PDOS). By analysing the ‘resonance’ of PDOS, the bonding characteristics are determined. Bonding density of H-O in gypsum cell dihydrate after SO_4^{2-} substituted by HPO_4^{2-} (Figure 4).

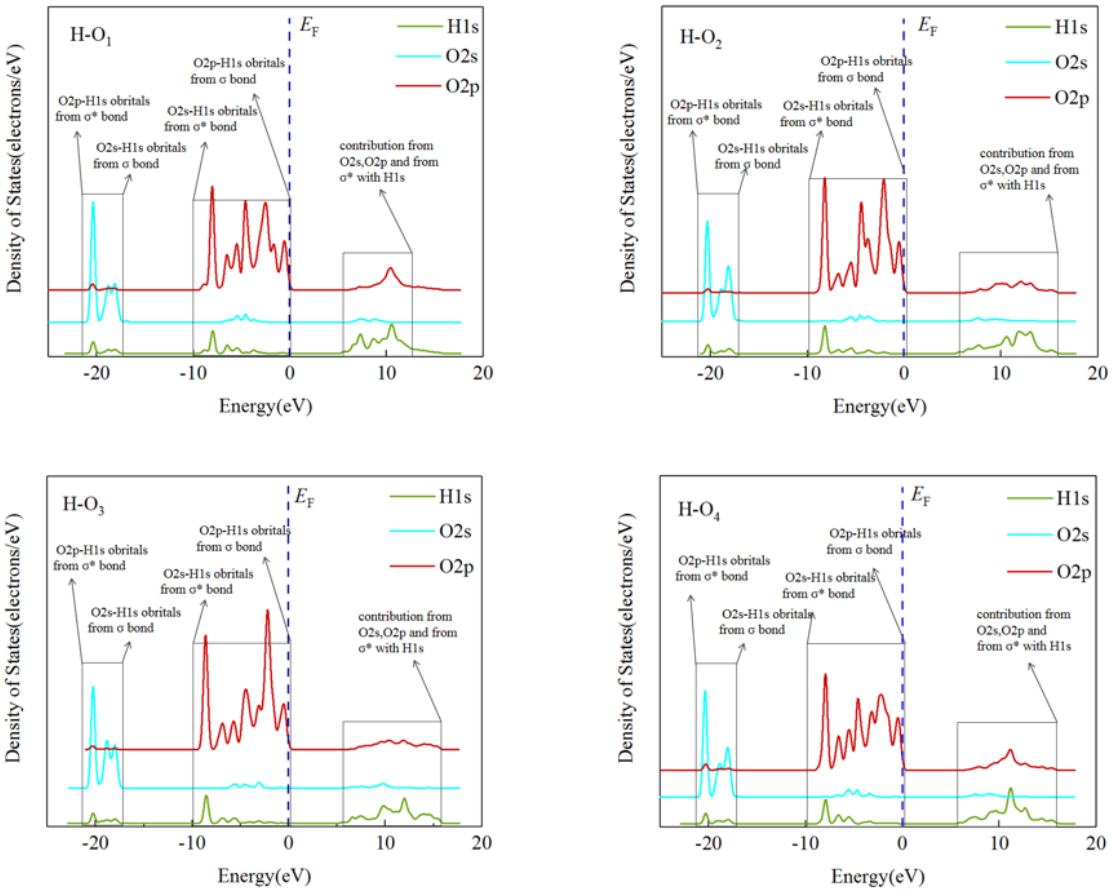

FIG 4 – Bonding density of H-O_1, H-O_2, H-O_3 and H-O_4 in gypsum cell dihydrate after SO_4^{2-} was replaced by HPO_4^{2-}.

According to Figure 4, near the Fermi level, the H-O bond density in HPO_4^{2-} is mainly contributed by the O2p orbital, H1s channels and O2p orbitals produce obvious 'resonance' phenomenon at -10 ~ 0 eV, s and p orbital hybridisation, indicating that O and H bond in this range, and H bond with O_1, O_2, O_3 and O_4 atoms is basically the same type. The O2s and H1s orbitals form σ bonds at -20 ~ -15 eV, and the O2p and H1s orbitals form σ* antibonding in this range. The O2p and H1s form σ bonds in the range of -10 ~ 0eV, and O2s and H1s form σ* antibonding in the range of -10 ~ 0eV; the O2s, O2p and H1s form σ* antibonding at 5 ~ 15eV. Due to the large degree of crack between σ bonding and antibonding, the corresponding H-O bond is stronger, and the σ bond and σ* bond contribute more to the bond strength. H-O mainly forms covalent bonds (the population of Mulliken bond is about 0.51~0.55). Therefore, the bond is generally not easy to break.

CONCLUSIONS

1. The electrovalence of PO_4^{3-} and SO_4^{2-} is different, PO_4^{3-} can't directly replace SO_4^{2-} into the dihydrate gypsum lattice; the P and O of both HPO_4^{2-} and $H_2PO_4^-$ are bonded; HPO_4^{2-} can replace SO_4^{2-} in dihydrate gypsum to form a stable configuration, after doping with HPO_4^{2-}, the cell parameters of dihydrate gypsum have little change, and the H-O bond length is close to the sum of the covalent radius of H and O, indicating that H and O can form covalent bond; after $H_2PO_4^-$ replaces SO_4^{2-}, the distance between H and O changes greatly. One H in $H_2PO_4^-$ is difficult to bond with O, while the other H can bond with O, indicating that $H_2PO_4^-$ can't stably exist in the crystal structure of dihydrate gypsum, so it can't replace SO_4^{2-} into the crystal lattice of dihydrate gypsum.
2. When HPO_4^{2-} replaces SO_4^{2-} in dihydrate gypsum, both H and P show electron loss. The s and P orbitals in the outermost shell of P each lose 1.1 ~ 1.2 e. O shows electron state, mainly P orbital gain; the Mulliken bond populations of H-O and P-O formed by the doped H and different O sites were close, and H-O bond showed strong covalence.

3. Near the Fermi level, H-O bond density in HPO_4^{2-} is mainly contributed by the O2p orbital, and H1s orbital and O2p orbital have obvious ‘resonance’ phenomenon at -10 ~ 0 eV, and s and p orbital hybridisation exists.

ACKNOWLEDGEMENTS

This research was funded by the National Natural Science Foundation of China (U1812402).

REFERENCES

Cánovas, C R, Macías, F, Pérez-López, R, Basallote, M D and Millán-Becerro, R, 2018. Valorization of wastes from the fertilizer industry: Current status and future trends. *J Clean. Prod*. 174, 678–690.

Huang, Z H, Luo, K B and Li, H P, 2016. Types of impurity in phosphogypsum and the method of removing impurity research review. *Bulletin of the Chinese Ceramic Society* 35 (5), 1504–1508.

Islam, G M S, Chowdhury, F H, Raihan, M T, Amit, S K S and Islam, M R, 2017. Effect of phosphogypsum on the properties of Portland cement. *Procedia Engineering* 171, 744–751.

Nizevičienė, D, Vaičiukynienė, D, Michalik, B, Bonczyk, M, Vaitkevičius, V and Jusas, V, 2018. The treatment of phosphogypsum with zeolite to use it in binding material. *Constr. Build. Mater*. 180, 134–142.

Ölmez, H and Yilmaz, V T, 1988. Infrared study on the refinement of phosphogypsum for cements. *Cement Concrete Res*. 18 (3), 449–454.

Rashad, A M, 2017. Phosphogypsum as a construction material. *J Clean. Prod*. 166, 732–743.

Tayibi, H, Choura, M, López, F A, Alguacil, F J and López-Delgado, A, 2009. Environmental impact and management of phosphogypsum. *J Environ. Manage*. 90 (8), 2377–2386.

Yang, L, Zhang, Y S and Yan, Y, 2016. Utilization of original phosphogypsum as raw material for the preparation of self-leveling mortar. *J Clean. Prod*. 127, 204–213.

Yang, M, 2008. Effect of impurities on the properties of phosphogypsum with different forms, Chongqing University.

Ye, X D, 2020. Status and situation analysis of phosphogypsum utilization in China in 2019. *Phosphate & Compound Fertilizer* 35 (7), 1–3.

Zhang, R, Li, Y J, Liu, J, Zhao, Y Y and Jiang, Y D, 2015. Utilization of phosphogypsum and treatment of the impure elements. *Conservation and Utilization of Mineral Resources* (2), 50–54.

Solvent extraction of lithium with orgranophosphinic acid

J Lu[1], K Mumford[2] and G Stevens[3]

1. PhD Candidate, The University of Melbourne, Melbourne Vic 3010.
   Email: junnanl@student.unimelb.edu.au
2. Associate Professor, The University of Melbourne, Melbourne Vic 3010.
   Email: mumfordk@unimelb.edu.au
3. Emeritus Laureate Professor, The University of Melbourne, Melbourne Vic 3010.
   Email: gstevens@unimelb.edu.au

ABSTRACT

Due to the rapid growth of green energy storage and electric vehicles, the supply chain of critical metals required for lithium-ion batteries is under pressure. Circular economies provide promising relief whereby the end-of-life lithium-ion batteries are recycled to manufacture new batteries. The current solvent extraction based recycling process typically focuses on cobalt and nickel recovery, and lithium is left in the raffinate for subsequent precipitation and purification. This study aims to utilise solvent extraction for lithium recovery, with lower costs.

Solvent extraction is a mature technology for Co and Ni separation. It is also a competitive separation technology for primary lithium resource. It has the higher throughput compared to other separation technologies such as precipitation, ion exchange or membrane technologies. The cost of recycling can be reduced if the same solvent can be used to retrieve all metals in one step.

In preliminary tests, it was found that the extraction behaviour of lithium is different from other metals (Lu *et al*, 2021). At the higher pH, with excess extractant, the single stage extraction efficiency of lithium was capped. Conventional linear slope analysis (LSA) cannot describe the lithium extraction. In the present study, equilibrium status iteration (ESI) was applied to determine the equilibrium constant and the stoichiometric ratio of the polynuclear compounds extracted (Figure 1).

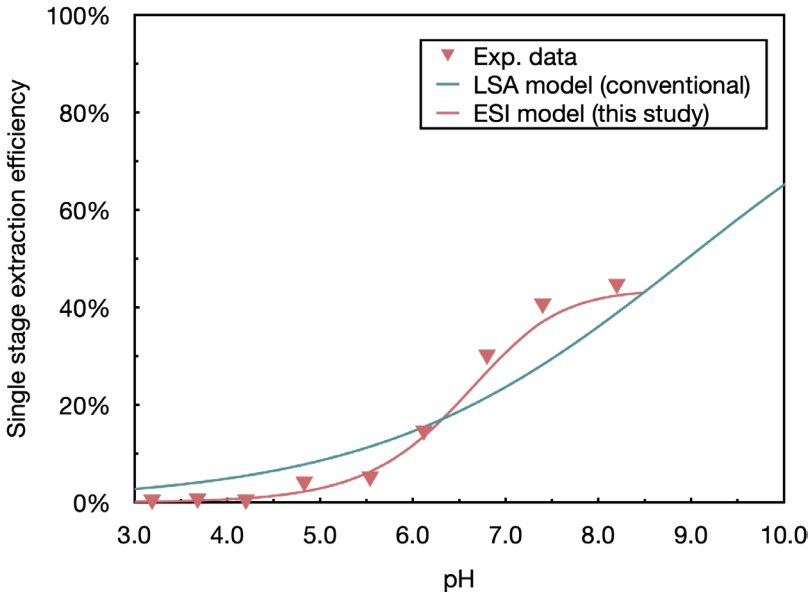

FIG 1 – Comparison: fitting the experimental data with the LSA and the ESI.

This description of the lithium extraction mechanism facilitates the preliminary tests required to design a separation unit. As shown in Figure 2, ESI can predict the heterogenous equilibrium in various conditions (Lu *et al*, 2021). The operating condition, to extract lithium from the lithium-ion batteries black mass leachate, can be optimised with the model. This new process offers an opportunity to recycle Ni Co and Li in a single process.

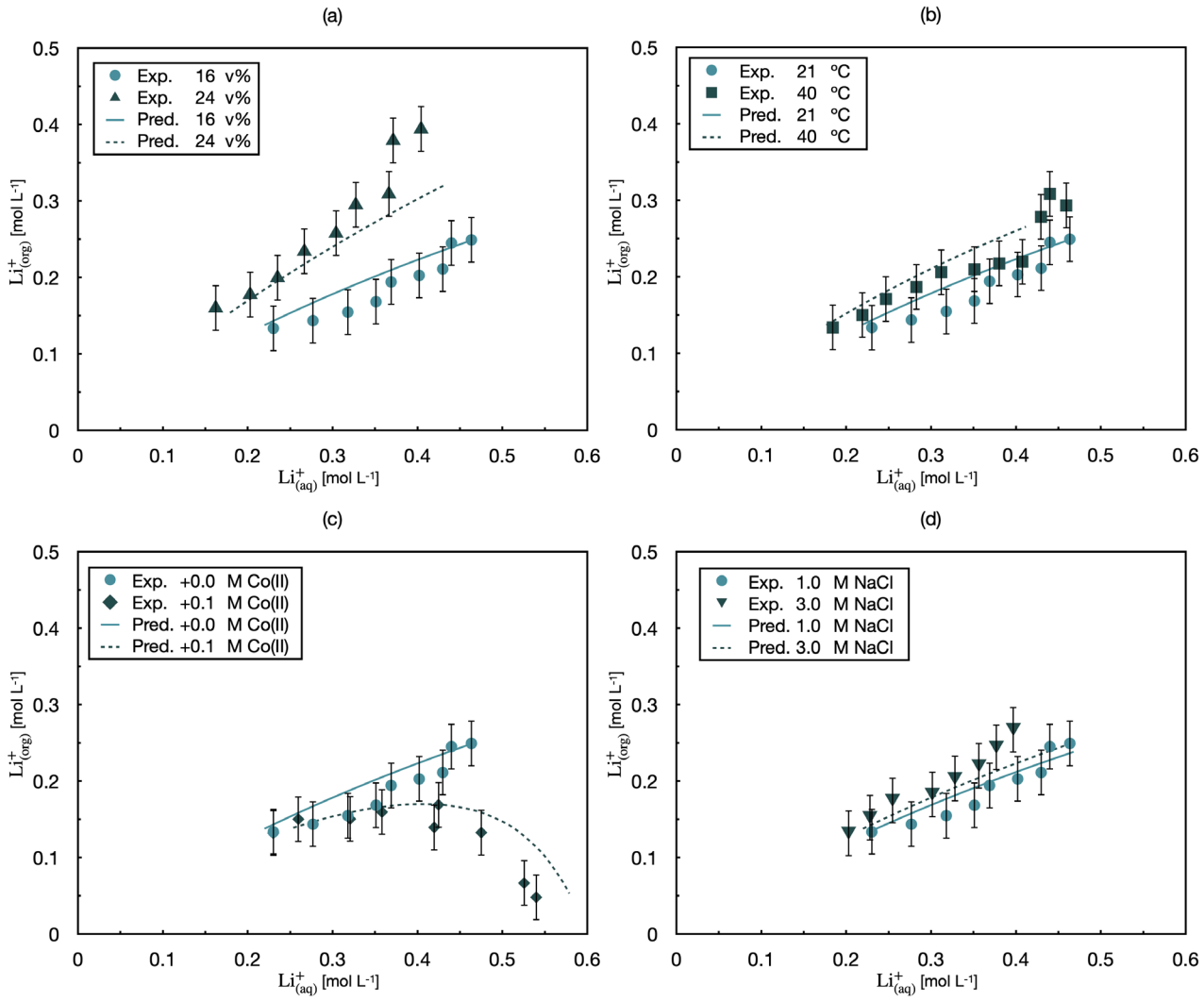

FIG 2 – Isothermal results of extracting lithium with Cyanex/272/tributyl phosphate/kerosene at various operating conditions. (Curves represent the model prediction, while the data points show the experimental validation. All isotherm tests were controlled at the same pH of 8.0 ± 0.1, and different O/A ratios. Results of 16v% Cyanex 272, 21°C, with 0.0 mol L^{-1} Co(II) and 1 mol L^{-1} NaCl was set as the benchmark. Operating conditions are also adjusted at different (a) Cyanex 272 concentrations (16 v%/24 v%), (b) temperatures (21°C/40°C), (c) Co(II) concentrations (0.0 mol L^{-1}/0.1 mol L^{-1}), (d) Ionic strengths (1 mol L^{-1} NaCl/3 mol L^{-1} NaCl)).

The closed collaboration is also an opportunity to Australia. Australis is large exporter of battery raw materials. By having a more collaborated Australian battery value chain, Australian batteries can be cheaper, more sustainable, and more competitive in the global market.

ACKNOWLEDGEMENTS

The content of this presentation is a part of the PhD program, under the supervision of the Assoc. Prof. Kathryn Mumford, and the Emeritus Laureate Prof. Geoff Stevens. Here I would like to express my greatest appreciation for their consistent professional advice in the study. In addition, I would like to appreciate the inspiring conversations with my group members from the Advanced Separation Group, including Dr. April Li, and Ms. Jiyizhe Zhang. Also, I would like to thank the Envirostream Australia Pty Ltd for sending the black mass sample, as well as the effort in facilitating the onshore lithium-ion battery recycling in Australia.

REFERENCES

Lu, J, Stevens, G W and Mumford, K A, 2021. Development of heterogeneous equilibrium model for lithium solvent extraction using organophosphinic acid. *Separation and Purification Technology, 276*, 119307.

Recent advances in recycling and utilisation of metallurgical dusts from steel industry

L Lu[1] and H Han[2]

1. Senior Principal Research Scientist, CSIRO Mineral Resources, Technology Court, Pullenvale Qld 4069. Email: Liming.Lu@csiro.au
2. Research Scientist, CSIRO Mineral Resources, Technology Court, Pullenvale Qld 4069. Email: Hongliang.Han@csiro.au

ABSTRACT

With the rapid development of steel industry, the global annual crude steel production has reached 1950.5 Mt in 2021. However, crude steel production is also accompanied by a large amount of solid wastes, wastewater and flue gases. Metallurgical dusts include solid wastes from BF, BOF, EAF and other operations in the steel works and are important by-products of the steelmaking industry, accounting for approximately 10 per cent of the crude steel production. As most of these dusts contain harmful heavy metals and hazardous organic compounds, simple release of them as landfilling materials will cause serious environmental problems. In addition, these dusts often contain valuable elements such as iron, carbon, calcium, zinc, lead, etc. Therefore, it is desirable to recover the valuables from these dusts in a judicious manner.

In view of the potential economic and environmental benefits, it is of particular importance to develop appropriate approaches for recycling and utilisation of the metallurgical dusts. Direct recycling in full or partly through the iron and steel making process was extensively tested. While there appeared to be some economical merits in plant trials, direct recycling has also introduced some challenges, such as contamination of liquid steel by undesirable elements and increased energy consumption. Furthermore, these dusts are generated in large quantities and vary vastly in chemical composition, such as harmful elements. Therefore, it is extremely important to establish the scope of the problems associated with recovering the valuable elements from different wastes while evaluating and developing recycling and utilisation technologies. This paper first discusses the characteristics of these metallurgical dusts, then reviews and comments on the recent technological advances in recycling and utilisation these dusts through pyrometallurgical processes.

INTRODUCTION

In the past 20 years, the world crude steel production has increased rapidly from 850.1 Mt in 2000 to 1950.5 Mt in 2021, mostly due to the rapid expansion in steel production in China. However, the steel production is inevitably accompanied by a large amount of solid wastes (metallurgical dusts and slag), as well as wastewater and gas which has posed a great threat to both environment and human health (Mo *et al*, 2015; Gomes *et al*, 2016; Pan *et al*, 2016; Sharma *et al*, 2017). About 650–700 kg solid wastes in BF-BOF route and 200–250 kg solid wastes in EAF route are generated for every tonne of steel produced. Metallurgical dusts are one of the important solid wastes and by-products of the steelmaking industry with output accounting for about 10 per cent of the crude steel production (Dutra *et al*, 2006; Lin *et al*, 2017). The composition of these dusts varies widely depending on the composition of input materials. As metallurgical dusts often contain harmful heavy metals and organic compounds, they can be categorized as hazardous wastes, which makes them difficult to store and transport (Lis *et al*, 2015).

For disposal of solid wastes, landfilling offers a simple solution (Donald and Pickles, 1996). However, metallurgical dusts usually contain valuable elements such as iron, carbon, zinc, lead etc, which can be recovered and reused in a judicious manner. Therefore, any simple disposal of these dusts is becoming less attractive, which not only causes accumulation of heavy metals and other hazards in the groundwater and soil under the impact of rain, posing harm to animals and plants as well as human, but also results in a waste of resources as valuable elements such as zinc and iron are not recovered.

It is hence of great importance to develop appropriate approaches for the treatment of metallurgical dusts in view of the potential economic and environmental benefits. Many technologies have been

proposed and tested for the recycling and utilisation of metallurgical dusts, however most of these technologies are still in the laboratory and pilot experiment stage. Hydrometallurgical processes are often thought to be most energy efficient, however have shown a poor overall efficiency when applied for recycling of the metallurgical dusts due to their quantities and varieties. In addition, the hydrometallurgical processes generate a large amount of secondary waste materials while recycling the primary wastes. Therefore, pyrometallurgical processes may present significant potentials for recycling and utilisation of metallurgical dusts. Direct recycling and utilisation of metallurgical dusts in full or part through pyrometallurgical processes has been extensively trialled by the steel industry and has showed some economical merits in some plant trials (Jensen and Wolf, 1997; Sasamoto and Fujisawa, 1997; Schmitt *et al*, 1997; Lopez and Lopez-Delgado, 2002; Southwick, 2010). However, there are also some problems associated with direct recycling, such as deterioration of steel quality, high energy consumption due to recirculation of zinc, K etc, unknown effect of enrichment of other heavy metals, etc.

This paper first discusses the characteristics of typical metallurgical dusts, and then reviews and comments on the recent technological advances in recycling and utilisation through pyrometallurgical process.

CHARACTERISTICS OF TYPICAL METALLURGICAL DUSTS

The characteristics of metallurgical dusts include chemical composition, mineral composition, particle size distribution etc and are important in selecting and determining suitable recycling processes.

BF dust

Blast furnace (BF) dust is a solid waste generated from the ironmaking plant. It is a brown or black powder with a particle diameter of 1–100 μm and 90 per cent below 50 μm (Vereš *et al*, 2012). It becomes claylike in the presence of moisture. The BF dust varies widely in chemical composition depending on the raw materials of ironmaking, including Fe, C, Zn, and other elements typically found in iron ores. Zinc is usually present in different zinc-bearing phases, such as zincite (ZnO), franklinite ($ZnFe_2O_4$) and zinc silicate (Zn_2SiO_4). In addition, the BF dust sample contains magnetite (Fe_3O_4), hematite (Fe_2O_3), wustite (FeO), and quartz (SiO_2).

BOF dust

BOF dust is collected by BOF (basic oxygen furnace) offgas cleaning equipment. The BOF dust sample presents a heterogeneous distribution of particle size with 50–80 per cent of particles below 10 μm (Vereš *et al*, 2015). Iron and zinc are the main elements in most of BOF dusts. Besides, the dust is also characterised by relatively high contents of Ca, Mg, Si and small amount of P. Zinc is typically in the form of zinc ferrite (franklinite, $ZnFe_2O_4$) and zinc oxide (zincite, ZnO), whereas iron is mainly in the form of franklinite and magnetite (Fe_3O_4).

EAF dust

Electric furnace dust (EAF) dust is collected EAF bag filter (Martins *et al*, 2008; Pickles, 2010). EAF dust is very fine, almost 99 per cent of the particles below 50 μm (Kukurugya *et al*, 2015). EAF dust contains about 24–45 per cent Fe and 8–33 per cent Zn. In addition, EAF dust also contains hazardous lead, chromium and cadmium. Five main minerals have been identified in the EAF dust and include ZnO, $ZnFe_2O_4$, Fe_3O_4, CaO and SiO_2 (Kukurugya *et al*, 2015).

REACTIONS IN PYROMETALLURGICAL PROCESSES

Pyrometallurgical processes involves carbothermic reduction and calcification to recover valuable metals such zinc, iron, lead etc from metallurgical dusts (Pan *et al*, 2016). The main reactions involved in pyrometallurgical processes are summarised in Table 1 (Lin *et al*, 2017). Zinc oxide, ferrous oxide, lead oxide, chromium trioxide and cadmium oxide can be reduced into metallic forms at relatively low temperatures (<1000°C). After reduction, zinc, lead and cadmium will evaporate and then be condensed, separated and recovered, while iron and chromium will be retained in the residue.

TABLE 1

Main reactions involved in the pyrometallurgical processes.

Reaction	A/J mol^{-1}	B/J mol^{-1}K^{-1}	Reaction temperature/°C	ΔH^{o}_{298}/kJ mol^{-1}
ZnO(s) + C(s) = Zn(g) + CO(g)	362944.64	-295.31	955.88	370.35
ZnFe2O4(s) + C(s) = Zn(g) + Fe(s) + CO(g)	855953.00	-804.09	791.35	872.19
PbO(s) + C(s) = Pb(l) + CO(g)	98050.00	-170.28	302.10	113.16
3Fe2O3(s) + C(s) = 2Fe3O4(s) + CO(g)	132495.49	-223.46	319.78	132.03
Fe3O4(s)+ C(s) = 3FeO(s) + CO(g)	197349.71	-203.55	696.39	209.38
FeO(s) + C(s) = Fe(s) + CO(g)	151872.55	-151.94	726.41	155.31
C + CO2(g) = 2CO(g)	171143.98	-174.76	706.16	172.47
ZnO(s) + CO(g) = Zn(g) + CO2(g)	191800.66	-120.55	1317.90	197.89
ZnFe2O4(s) + CO(g) = Zn(g) + Fe(s) + CO2(g)	174271.00	-108.64	1330.96	182.31
PbO(s) + CO(g) = Pb(l) + CO2(g)	-62076.00	-14.54	---	-59.31
3Fe2O3(s) + CO(g) = 2Fe3O4(s) + CO2(g)	-38648.00	-48.70	---	-40.40
Fe3O4(s)+ CO(g) = 3FeO(s) + CO2(g)	26206.00	-28.79	637.10	36.91
FeO(s) + CO(g) = Fe(s) + CO2(g)	-19288.00	22.85	570.96	-17.16
CrO3(s) + 3C(s) = Cr(s) + 3CO(g)	240039.35	-515.58	192.42	246.65
CdO(s) + C(s) = Cd(g) + CO(g)	251964.01	-288.92	598.94	260.26
CdO(s) + CO(g) = Cd(g) + CO2(g)	80820.00	-114.16	434.80	87.79
ZnFe2O4(s) + CaO(s) = Ca2Fe2O5(s) + ZnO(s)	-23199.00	-16.89	---	-27.54

RECYCLING AND UTILISATION PROCESSES

While the characteristics of metallurgical dusts are different, both BF, BOF dust and EAF dusts are high in Fe and Zn. Many pyrometallurgical processes have been developed or are under development to recover Zn and Fe.

RHF process

Figure 1 presents a schematic representation of the rotary hearth furnace process (RHF). The history of RHF ironmaking started in the mid-1960s with the development of the ‘Heat Fast’ process by Midrex. Since then, several RHF based ironmaking processes have been developed. These include Inmetco (Bleakney *et al*, 1998), Fastmet (Fuji *et al*, 2002; McClelland, 2002), Iron Dynamics (Lehtinen *et al*, 1999), DryIron (Apple *et al*, 2002; Daiga *et al*, 2002), and ITmk3 (Kobayashi *et al*, 2001; Tsuge *et al*, 2002). The differences among these RHF processes lie in the raw materials (iron ore or iron-containing wastes), type of agglomerate (pellets or briquettes), process temperature, and treatment of the product. Inside the RHF, the Zn and Fe bearing minerals are reduced quickly at temperatures of >1250°C. Up to 95 per cent of the zinc is removed from the pellets or briquettes as fume while the iron oxide in the pellets or briquettes is metallised to levels greater than 90 per cent metallic iron. Based on the success of the initial industrial operations, more than 15 units with the capacity of 60 000–500 000 tons of dust per year are now in operation, converting metallurgical dusts into valuable mineral resources.

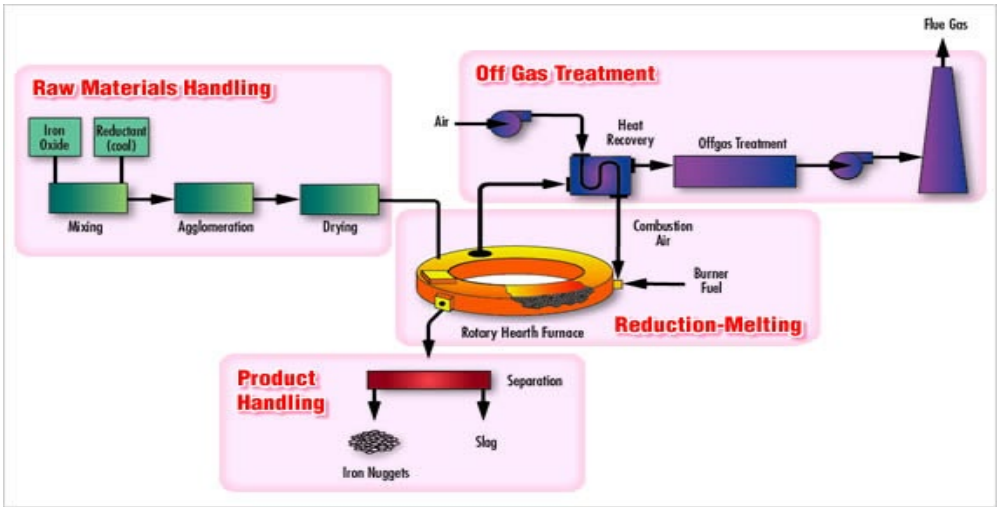

FIG 1 – Schematic representation of the RHF process (Ishikawa *et al*, 2008).

Waelz process

A schematic representation of the Waelz process is shown in Figure 2. The process involves treating zinc and iron containing metallurgical dusts with a carbon containing reducing agent/fuel, in a rotary kiln at 1000°C to 1500°C (Clay and Schoonraad, 1976). The kiln feed materials are typically pelletized before addition (Mager *et al*, 2000), and kiln size is typically 50 m long by 3.6 m internal diameter, with a rotation speed of around 1 rpm. The residence time is about 3–10 hours depending on the feed material (Mager *et al*, 2003). The Waelz process is considered to be a 'best available technology' for zinc recovery as the process has been adopted at industrial scale worldwide (Mager *et al*, 2000). As of 2014, the Waelz process is the preferred or most widely used process for zinc recovery of zinc from electric arc furnace dust (90 per cent) (Antrekowitsch *et al*, 2014). And more than 45 units with the capacity of 40 000–160 000 tons of dust per year are now in operation.

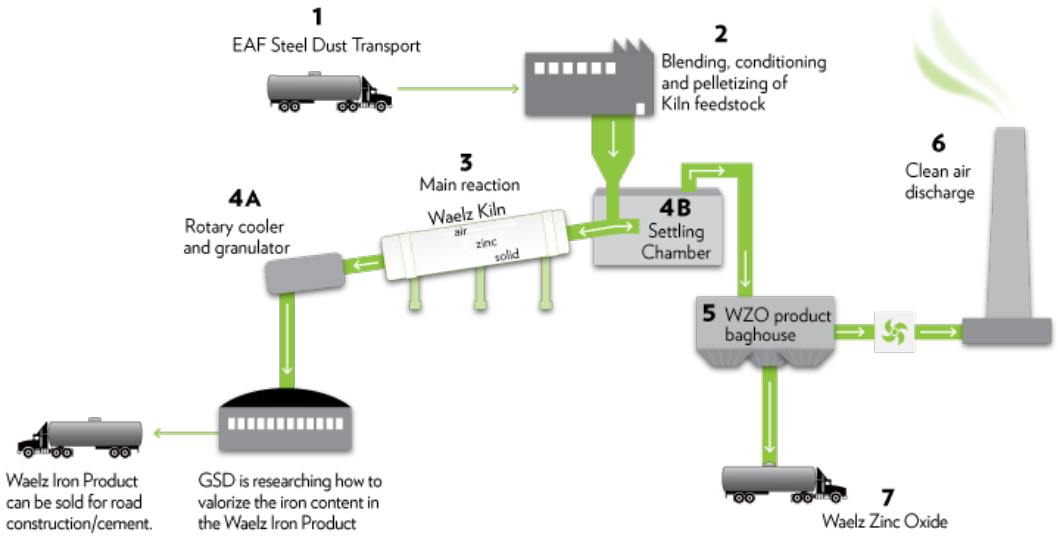

FIG 2 – Schematic representation of the Waelz process (GSD, 2018).

Oxicup process

Figure 3 presents a schematic representation of the Oxicup® process. In this process, waste oxides, BOF dust, BF dust, and mill scale are mixed with 15 per cent coke breeze and cement binder and formed as self-reducing bricks in a vibrating press. The bricks are stored for five days for curing and then charged, along with skulls and coke, in a shaft furnace (cupola) (MourÃO and Takano, 2003; Fisch and Kesseler, 2006; Holtzer *et al*, 2015). The proportion of the bricks in the charge could be up to 70 per cent, while the others are lumpy residues like pit scrap, skulls or zinc coated bales, etc. Inside the furnace, the material spends about 20 minutes in the temperature range between 1000°C and 1400°C (Kurunov, 2012). After that, hot metal, slag, and zinc-rich dust can be obtained. After

tests in a pilot plant in 1999 in Duisburg, Germany, the process was scaled up to a commercial installation in 2004 (Gudenau *et al*, 2005). Now more than five units with the handling capacity of 25–80 tons of dust per hour are in operation worldwide.

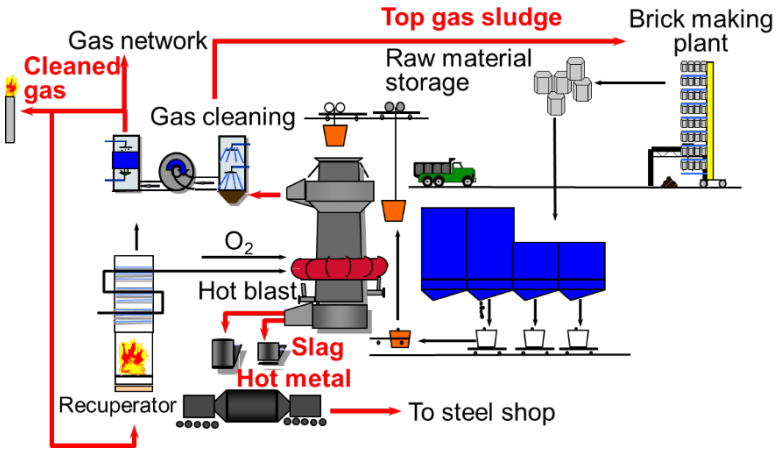

FIG 3 – Schematic representation of the Oxicup® process.

DK process

Figure 4 shows a schematic representation of the DK process. It was developed by Duisburger Kupferhutte and is basically a modified blast furnace ironmaking process producing pig iron and zinc (oxide) dust from blast furnace dusts, sludges and other wastes (Hillmann and Sassen, 2006). In the blast furnace, the iron oxides and zinc compounds in the sinter are gradually reduced as they descend. Thus, liquid pig iron is accumulated with liquid slag in the blast furnace hearth, while the dust with zinc contents between 65–68 per cent is collected from top gas (Sassen and Hillmann, 2011). DK Recycling and Roheisen GmbH is one of the largest recyclers of ferrous waste materials of the steel industry in the world, 500 000 tons waste materials recycled in the DK process every year.

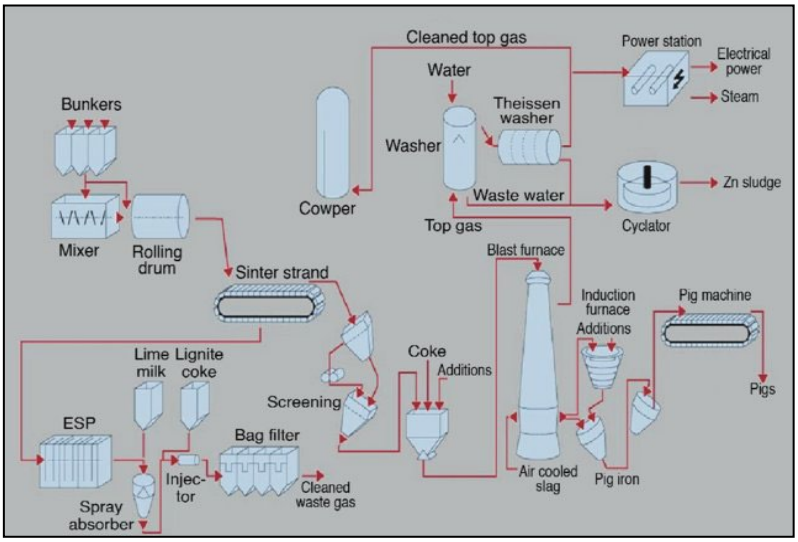

FIG 4 – Schematic representation of the DK process.

PRIMUS process

Figure 5 shows a schematic representation of the PRIMUS PROCES. It was developed by Paul Wurth, consisting of the combination of a multiple hearth furnace (MHF) and electric arc furnace (MF;) (Hansmann *et al*, 2000). The dusts (EAF dust, BF dust etc) are pelletised and fed with high-volatile coal into the MHF where drying, heating and reduction take place. This is followed by final reduction, carburisation and melting in a specially designed MF. Zinc and lead are transferred to the off-gas system and recovered as a marketable zinc oxide concentrate (Roth *et al*, 2001; Suetens

et al, 2014a, 2014b). Fe in the feed material is recovered as pig iron. The first industrial PRIMUS plant was commissioned in 2003 in Luxembourg and could treat around 60 000 tons of EAF dust and 15 000 tons of oily mill sludge per year (Guillaume *et al*, 2008). The second one has operated in Taiwan since 2009 and treats up to 100 000 tons of EAF dust and integrated steelmaking wastes per year.

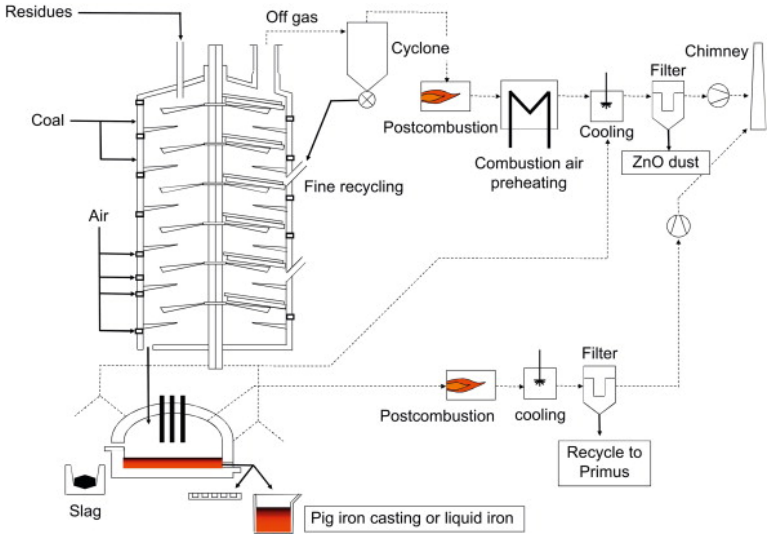

FIG 5 – Schematic representation of the PRIMUS® process.

RecoDust process

Figure 6 displays the process principle of the RecoDust process (Delfs *et al*, 2011a), a novel technology for the recycling of metallurgical dusts. This process can be divided into four steps. The slagging of the dust under reducing conditions happens in the first step. Due to the high process temperatures of up to 1900°C and the reducing conditions in the reaction vessel, the target volatile components are transferred into the gas phase while the other components report to liquid slag for recycling. In the second step, the flue gas from Step one undergoes a post combustion process, where the metallic zinc vapour is transferred into its solid oxide phase (Delfs *et al*, 2011b). Water also is added to provide a cooling effect on the flue gas, reducing its temperature from 1900 down to 800°C. Further cooling occurs from 800 down to 180°C in the third step, which makes flue gas cleaning with bag-filters possible. In the last step, the dust enriched with zinc oxide is separated from the flue gas using bag-filters and collected. This process is still in the pilot plant status.

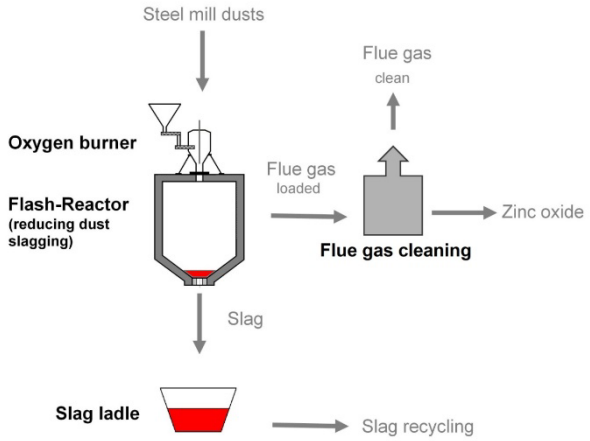

FIG 6 – Process principle of the RecoDust-Process.

LAMS Process

The LAMS Process (Lime Addition and Magnetic Separation Process) aims at recovering zinc oxide from the metallurgical dusts by addition of calcium carbonate (Itoh *et al*, 2008) or lime (Chairaksa-

Fujimoto *et al*, 2015). The LAMS Process consists of the reaction of metallurgical dusts with CaO followed by the adequate crushing and high gradient magnetic separation. In this process, most of lead and chloride are removed at temperatures below 900°C, whereas complete removal of fluorine occurred above 1000°C in the presence of calcium oxide (Chairaksa-Fujimoto *et al*, 2015, 2016).The by-product of this process, calcium ferrite, may be used in sintering process or dephosphorization during the process of steelmaking. This process has much better efficiency than the other process. Another benefit of this process is the preferential volatilisation of lead, chloride and fluorine in the metallurgical dusts (Chairaksa-Fujimoto *et al*, 2015).

Other processes

Besides the above processes, other alternative technologies such as Fluidized-Bed process (Yang *et al*, 2014, 2017), Induction Furnace process (Bratina and Lenti, 2008), Plasma Arc Fuming process (Goff and Denton, 2004), Flame Reactor Process (Pusateri *et al*, 1988), i-Meltor™ process (SMS, 2018), composite agglomeration process (Zhang *et al*, 2017), Pellets-Metallized Sintering Process (Chun and Zhu, 2015), Coke Breeze-less Sintering process (Nakano *et al*, 2000), heat treatment by PVC (Lee and Song, 2007) or plastic waste (Grabda *et al*, 2014) process etc, can also be used for recovering zinc and Fe from metallurgical dusts.

EVALUATION OF VARIOUS METALLURGICAL PROCESSES

The strengths and weaknesses of different pyrometallurgical processes are summarised in Table 2. The technologies like Waelz, RHF, Oxicup, DK, and PRIMUS processes are relatively mature for processing metallurgical dusts, however, they often suffer from several drawbacks, including large initial capital investment in equipment, great energy consumption and high shipping costs, etc. In addition, as mentioned above, the majority of the pyrometallurgical processes focus only on recovery of zinc, lead and iron from dusts in which other hazardous elements such as chlorine and chromium were not explored adequately (Bruckard *et al*, 2005; Lin *et al*, 2017). Finally the slag stream product of the pyrometallurgical processes is often a crude oxide which requires further treatment and thus additional input of energy (Suetens *et al*, 2014a).

TABLE 2

The strengths and weaknesses of different pyrometallurgical processes.

Process	Strengths	Weaknesses	Comments
Waelz	well-known, adaptable to changes in raw materials	high Zn content material needed, slag not always saleable	standard for EAF dust
RHF	well-known, good for Fe, Zn, Pb, Cd separation	high energy consumption for high metallisation, low quality DRI, mostly for BF charge	justified when landfill cost is expensive
Oxicup	flexible charge, production of hot metal, low emissions, low investment	Zn charge limited, high coke consumption	limited references
DK	flexible charge, production of hot metal	Zn charge limited, high coke consumption	works well under particular business condition
PRIMUS	flexible charge, 100% recycling rate, cheap reducing agent, production of hot metal	high energy consumption, especially electricity consumption	limited references
RecoDust	no additional solid reducing agent, flexible charge, dust input	high temperature, high energy consumption, low quality of slag	still in the pilot plant status
LAMS	low temperature, better efficiency, no additional solid reducing agent	high Zn content material needed, large addition of calcium carbonate or calcium oxide	still in the lab experiment status

CONCLUSIONS

While the characteristics of metallurgical dusts are different, most metallurgical dusts, such as BF, BOF dust, EAF dusts are characterised with high Fe and Zn contents. The principle aim of pyrometallurgical processing of metallurgical dusts is hence to recover valuable metals such zinc, iron, lead etc, from the dusts using carbothermic reduction and calcification. Many pyrometallurgical technologies have been developed and are being developed for processing metallurgical dusts, including Waelz, RHF, Oxicup, DK, PRIMUS and more. Some of these technologies have had industry applications, however the others are still at laboratory and pilot testing stages.

ACKNOWLEDGEMENTS

The authors would like to thank CSIRO Mineral Resources for permission to publish the paper and for the financial support of this work. Special thanks to reviewers for their valuable comments and improvements to the paper.

REFERENCES

Antrekowitsch, J, Steinlechner, S, Unger, A, Rösler, G, Pichler, C, Rumpold, R, 2014. *Zinc and Residue Recycling. Handbook of Recycling*, pp. 113–124.

Apple, R A, Powers, J G, Molnar, D A, 2002. Waste oxide reduction facility at rouge steel. *Ironmaking Conference Proceedings*. ISS, pp. 693–704.

Bleakney, R R, Hanewald, R H, Cingle III, G, 1998. Carbon steel waste recycling experience using the INMETCO process. *Steelmaking Conference Proceedings*. ISS, pp. 405–410.

Bratina, J E, Lenti, K M, 2008. PIZO furnace demonstration operation for processing EAF dust. *Iron and Steel Technology* 5, 118–122.

Bruckard, W J, Davey, K J, Rodopoulos, T, Woodcock, J T, Italiano, J, 2005. Water leaching and magnetic separation for decreasing the chloride level and upgrading the zinc content of EAF steelmaking baghouse dusts. *International Journal of Mineral Processing* 75, 1–20.

Chairaksa-Fujimoto, R, Inoue, Y, Umeda, N, Itoh, S, Nagasaka, T, 2015. New pyrometallurgical process of EAF dust treatment with CaO addition. *Int J Min Met Mater* 22, 788–797.

Chairaksa-Fujimoto, R, Maruyama, K, Miki, T, Nagasaka, T, 2016. The selective alkaline leaching of zinc oxide from Electric Arc Furnace dust pre-treated with calcium oxide. *Hydrometallurgy* 159, 120–125.

Chun, T, Zhu, D, 2015. New Process of Pellets-Metallized Sintering Process (PMSP) to Treat Zinc-Bearing Dust from Iron and Steel Company. *Metallurgical and Materials Transactions B* 46, 1–4.

Clay, J E, Schoonraad, G P, 1976. Treatment of zinc silicates by the Waelz Process. *Journal of the South African Institute of Mining and Metallurgy* 77, 11–14.

Daiga, V R, Horne, A, Thornton, J A, 2002. Steel mill waste processing on a rotary hearth furnace to recover valuable iron units. *Ironmaking Conference Proceedings*. ISS, pp. 655–665.

Delfs, N, Dobay, F M, Pilz, K, Raupenstrauch, H, 2011a. RecoDust – The Capabilities of Steel Mill Dust Recycling. *BHM* 156, 157–160.

Delfs, N, Geier, B, Raupenstrauch, H, 2011b. RecoDust – Capabilities for Processing of Steel-Mill Dusts. *2nd International Conference and Exhibition on Clean Technologies in the Steel Industry*, pp. 1–7.

Donald, J R, Pickles, C A, 1996. Reduction of electric arc furnace dust with solid iron powder. *Canadian Metallurgical Quarterly* 35, 255–267.

Dutra, A J B, Paiva, P R P, Tavares, L M, 2006. Alkaline leaching of zinc from electric arc furnace steel dust. *Minerals Engineering* 19, 478–485.

Fisch, T, Kesseler, K, 2006. Oxycup shaft furnace of ThyssenKrupp steel strategy for economic recycling of fine grained ferrous and carbonaceous residues. *Environmental Seminar*, pp. 90–98.

Fuji, K, Tanaka, H, Maki, T, 2002. Start-up operations report on the 2nd commercial FATMETR plant. *Ironmaking Conference Proceedings*. ISS, pp. 705–712.

Goff, T J, Denton, G M, 2004. Direct smelting of stainless steel plant dust. *Tenth International Ferroalloys Congress*, pp. 687–692.

Gomes, H I, Mayes, W M, Rogerson, M, Stewart, D I, Burke, I T, 2016. Alkaline residues and the environment: a review of impacts, management practices and opportunities. *Journal of Cleaner Production* 112, 3571–3582.

Grabda, M, Oleszek, S, Shibata, E, Nakamura, T, 2014. Study on simultaneous recycling of EAF dust and plastic waste containing TBBPA. *J Hazard Mater* 278, 25–33.

GSD, 2018. Waelz kiln technology. *Global Steel Dust*, http://www.globalsteeldust.com/waelz_kiln_technology.

Gudenau, H W, Senk, D, Wang, S W, Martins, K D, Stephany, C, 2005. Research in the reduction of iron ore agglomerates including coal and C-containing dust. *ISIJ International* 45, 603–608.

Guillaume, P, Devos, G, Roth, J L, 2008. Recycling residues into metals. *Millennium Steel*, 25–30.

Hansmann, T, Frieden, R, Solvi, M, Monai, J, 2000. Primus – a new process for the recycling of steelmaking by-products and the prereduction of iron ore. *Stahl und Eisen* 120, 49–53.

Hillmann, C, Sassen, K J, 2006. Solutions for dusts and sludges from the BOF process. *Stahl und Eisen* 126, S149-S156.

Holtzer, M, Kmita, A, Roczniak, A, 2015. The recycling of materials containing iron and zinc in the OxyCup process. *Archives of Foundry Engineering* 15, 126–130.

Ishikawa, H, Kopfle, J, McClelland, J, Ripke, J, 2008. Rotary hearth furnace technologies for iron ore and recycling applications. *Archives of Metallurgy and Materials* 53, 541–545.

Itoh, S, Tsubonie, A, Matsubae-Yokoyama, K, Nakajima, K, Nagasaka, T, 2008. New EAF Dust Treatment Process with the Aid of Strong Magnetic Field. *ISIJ International* 48, 1339–1344.

Jensen, J T, Wolf, K, 1997. Reduction of EAF dust emissions by injecting it into the furnace. *MPT Metallurgical Plant and Technology International* 20, 58.

Kobayashi, I, Tanigaki, Y, Uragami, A, 2001. A new process to produce iron directly from fine ore and coal. *Ironmaking Conference Proceedings*. ISS, pp. 649–657.

Kukurugya, F, Vindt, T, Havlík, T, 2015. Behavior of zinc, iron and calcium from electric arc furnace (EAF) dust in hydrometallurgical processing in sulfuric acid solutions: Thermodynamic and kinetic aspects. *Hydrometallurgy* 154, 20–32.

Kurunov, I F, 2012. Environmental Aspects of Industrial Technologies for Recycling Sludge and Dust That Contain Iron and Zinc. *Metallurgist* 55, 634–639.

Lee, G S, Song, Y J, 2007. Recycling EAF dust by heat treatment with PVC. *Minerals Engineering* 20, 739–746.

Lehtinen, L, Hansen, J, Rokop, N, 1999. Iron dynamics process: A new way to make iron. *AISE Steel Technology* 76, 37–39.

Lin, X, Peng, Z, Yan, J, Li, Z, Hwang, J-Y, Zhang, Y, Li, G, Jiang, T, 2017. Pyrometallurgical recycling of electric arc furnace dust. *Journal of Cleaner Production* 149, 1079–1100.

Lis, T, Nowacki, K, Zelichowska, M, Kania, H, 2015. Innovation in Metallurgical Waste Management. *Metalurgija* 54, 283–285.

Lopez, F, Lopez-Delgado, A, 2002. Enhancement of electric arc furnace dust by recycling to electric arc furnace. *J Environ Eng-Asce* 128, 1169–1174.

Mager, K, Meurer, U, Garcia-Egocheaga, B, Goicoechea, N, Rutten, J, Sagge, F, Simonetti, W, 2000. Recovery of Zinc Oxide from Secondary Raw Materials: New Developments of the Waelz Process. In: Stewart, D L, Stephens, R, Daley, J C. (Eds.), *Fourth International Symposium on Recycling of Metals and Engineered Materials*. TMS (The Minerals, Metals and Materials Society), pp. 329–344.

Mager, K, Meurer, U, Wirling, J, 2003. Minimizing dioxin and furan emissions during zinc dust recycle by the Waelz process. *JOM* 55, 20–25.

Martins, F M, dos Reis Neto, J M, da Cunha, C J, 2008. Mineral phases of weathered and recent electric arc furnace dust. *J Hazard Mater* 154, 417–425.

McClelland, J M, 2002. FASTMETR: Proven process for steel mill waste recovery. *Ironmaking Conference Proceedings*. ISS, pp. 667–682.

Mo, K H, Johnson Alengaram, U, Jumaat, M Z, Yap, S P, 2015. Feasibility study of high volume slag as cement replacement for sustainable structural lightweight oil palm shell concrete. *Journal of Cleaner Production* 91, 297–304.

MourÃO, M B, Takano, C, 2003. Self-Reducing Pellets for Ironmaking: Reaction Rate and Processing. *Mineral Processing and Extractive Metallurgy Review* 24, 183–202.

Nakano, M, Okada, T, Hasegawa, H, Sakakibara, M, 2000. Coke breeze-less sintering of BOF dust and its capability of dezincing. *ISIJ International* 40, 238–243.

Pan, H, Zhang, X, Wu, J, Zhang, Y, Lin, L, Yang, G, Deng, S, Li, L, Yu, X, Qi, H, Peng, H, 2016. Sustainability evaluation of a steel production system in China based on emergy. *Journal of Cleaner Production* 112, 1498–1509.

Pickles, C A, 2010. Thermodynamic modelling of the formation of zinc-manganese ferrite spinel in electric arc furnace dust. *J Hazard Mater* 179, 309–317.

Pusateri, J F, Bounds, C O, Lherbier, L W, 1988. Zinc Recovery via the Flame Reactor Process. *JOM* 40, 31–35.

Roth, J L, Frieden, R, Hansmann, T, Monai, J, Solvi, M, 2001. PRIMUS (R), a new process for recycling of by-products and producing virgin iron. *Revue De Metallurgie* 98, 987–996.

Sasamoto, H, Fujisawa, A, 1997. Behavior of zinc on dust recycling in EAF. *55th Electric Furnace Conference*, Chicago, Illinois, USA, pp. 123–125.

Sassen, K J, Hillmann, C, 2011. The DK process – for the recovery of iron and zinc from BOF dusts and sludges. *Steel Times International*, 17–18.

Schmitt, R, Kusik, C, O'Neil, R, Cowx, P, Schade, C, 1997. Minimizing electric arc furnace dust generation. *55th Electric Furnace Conference*, Chicago, Illinois, USA, pp. 567–581.

Sharma, N, Nurni, V N, Tathavadkar, V, Basu, S, 2017. A review on the generation of solid wastes and their utilization in Indian steel industries. *Mineral Processing and Extractive Metallurgy* 126, 54–61.

SMS, 2018. Residue recycling technology. *SMS Group*, https://www.sms-group.com/plants/all-plants/residue-recycling-technology/.

Southwick, L, 2010. Still no simple solution to processing EAF dust. *Steel Times International* 34, 43–45.

Suetens, T, Klaasen, B, Van Acker, K, Blanpain, B, 2014a. Comparison of electric arc furnace dust treatment technologies using exergy efficiency. *Journal of Cleaner Production* 65, 152–167.

Suetens, T, Van Acker, K, Blanpain, B, Mishra, B, Apelian, D, 2014b. Moving towards better recycling options for electric arc furnace dust. *JOM* 66, 1119–1121.

Tsuge, O, Kikuchi, S, Tokuda, K, Ito, S, Kobayashi, I, Uragami, A, 2002. Succesful iron nuggets production at Itmk3 pilot plant. *Ironmaking Conference Proceedings*. ISS, pp. 511–519.

Vereš, J, Lovás, M, Jakabský, Š, Šepelák, V, Hredzák, S, 2012. Characterization of blast furnace sludge and removal of zinc by microwave assisted extraction. *Hydrometallurgy* 129–130, 67–73.

Vereš, J, Šepelák, V, Hredzák, S, 2015. Chemical, mineralogical and morphological characterisation of basic oxygen furnace dust. *Mineral Processing and Extractive Metallurgy* 124, 1–8.

Yang, S, Liu, C, Gao, X, Li, J, 2014. Study on Dezincification and De-Lead of Blast Furnace Dust by Fluidized Reduction Experiment. Celebrating the Megascale: *Proceedings of the Extraction and Processing Division*. TMS (The Minerals, Metals and Materials Society), pp. 675–683.

Yang, S, Zhao, M, Li, J, Feng, J, Liu, Q, 2017. Removal of Zinc and Lead from Blast Furnace Dust in a Fluidized-Bed Roaster. *Journal of Sustainable Metallurgy* 3, 441–449.

Zhang, Y B, Liu, B B, Xiong, L, Li, G H, Jiang, T, 2017. Recycling of carbonaceous iron-bearing dusts from iron and steel plants by composite agglomeration process (CAP). *Ironmaking and Steelmaking* 44, 532–543.

Implementation of the water accounting framework at Tritton Copper Mine

S Lynch-Watson[1], R Powell[2], S Vink[3] and P Erepan[4]

1. Director – Process Optimisation and Labs, Metso Outotec Australia Ltd, Brisbane Qld 4009. Email: suzanne.lynch-watson@mogroup.com
2. Senior Consultant – Mining and Environment, Metso Outotec Australia Ltd, Brisbane Qld 4009. Email: roxana.powell@mogrouppartners.com
3. Principal Research Fellow, Centre for Water in the Minerals Industry at the Sustainable Minerals Institute, St Lucia Qld 4067. Email: s.vink@smi.uq.edu.au
4. Senior Processing Engineer – Aeris Resources – Tritton Operations, Hermidale NSW 2831. Email: perepan@aerisresources.com.au

INTRODUCTION

Water as a resource is becoming increasingly valuable with figures indicating that by 2025, approximately half of the world's population will be living in water-stressed areas (WHO, 2022). The pressure is on the mining industry to improve water management practices to ensure responsible use of this valuable resource. Demonstrating responsible water use can be the difference between having a social license to operate or not. According to a global survey of more than 350 companies conducted in 2021 by the Carbon Disclosure Project (CDP) (CDSB, 2021), the financial cost of water risks is US$301 billion, an estimated five times more than the cost of addressing those risks. In addition, demand from investors for companies to disclose their impacts on water security and demonstrate proactive measures to mitigate them is growing. The mining industry, identified as one of the top eight industrial water consumers, is directly affected by this investor pressure.

The water risks facing the mining sector were also highlighted in a study completed by the World Wildlife Fund for Nature (WWF, 2020; Morgan, 2020), which collected data from more than 3000 operating mine sites around the world. The study analysed the associated risks by commodity, geographical location, companies and river basins, and classified the risk according to regulatory requirements, physical damage posed by floods or water scarcity and reputational damage due to disasters. It concluded that these three categories pose significant risk to mining companies globally and are exacerbated in some regions due to spatial clustering. Figure 1 shows the results for the top ten at-risk countries with at least five mine sites, using a water risk scale of 1 to 5 and considering the different risk factors.

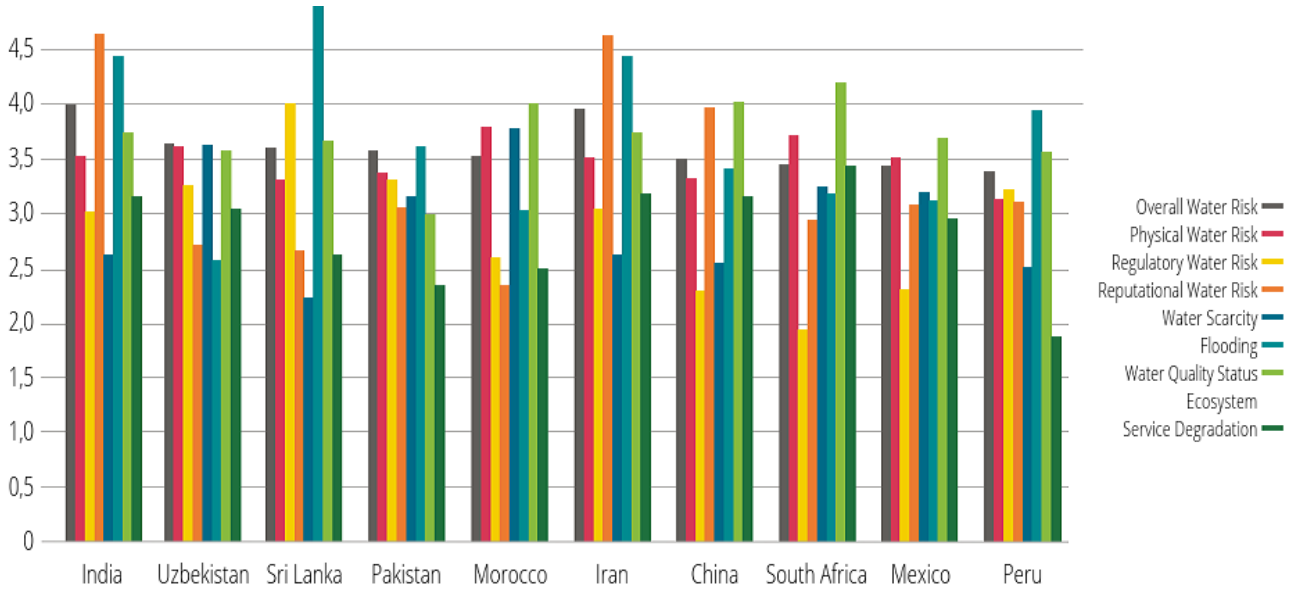

FIG 1 – Water risk category scores top ten countries (source: Morgan, 2020).

Clearly, the industry collectively can no longer afford to disregard the water risk associated with mining activities and must take more responsibility for accounting and management of this critical resource. There is no single global standard for defining best water management practice in the mining industry, but there are three methodologies currently in use most frequently, which provide guidance to operations for making improvements. An overview of the three approaches is provided in this paper, including their advantages and application. The Water Accounting Framework (WAF) developed by the Minerals Council of Australia (MCA) in conjunction with the University of Queensland (UQ) and industry collaborators (MCA, 2014), is the methodology applied in this case.

This paper explains the WAF methodology as well as the implementation at the Tritton Copper Mine, owned by Aeris Resources and located in New South Wales, Australia. Working collaboratively with site personnel, data was collected from various sources on-site and in the local region and then used to benchmark site water usage and identify opportunities for improvement. Challenges associated with data collection and analysis are described, and ways to improve these processes for future cases are identified. The benefits gained from implementing this framework are also presented.

Finally, a preview of the next steps is outlined, which will include developing a model of the operational system and running simulations to forecast water demand under various scenarios, which will help the operation to plan better and mitigate risk. Future planned work also includes simulating the impact of variable water quality on recovery and other processing variables.

OVERVIEW OF WATER EFFICIENCY STANDARDS AND METHODOLOGIES

During the past decade, several standards to report on water use and efficiency have been developed for the mining and other industries. One of the most well-known across different industries is the Global Reporting Initiative (GRI, 2018) which has achieved widespread acceptance amongst mining companies. The indicators resulting from this approach are widely reported at a corporate level as part of their sustainability reporting. Another well-known methodology is the Water Footprint Network (Hoekstra *et al*, 2011), which has been an important initiative in the food and agricultural industries, however with low acceptance in the mining industry (Danoucaras *et al*, 2013). The third approach is Water Accounting, which is in keeping with the global trend across many industries of using accounting as a key part of sustainable development and reporting (Godfrey and Chalmers, 2012). There are two water accounting approaches currently in use in the mining industry: the Water Accounting Framework and the Water Reporting Guide developed by the International Council on Mining and Metals (ICMM, 2021). Each of these reporting initiatives has established guidelines and published case studies for improving the effectiveness of water accounting and management in mining operations. Although the guidelines were developed separately, they have much in common and have aligned more closely in recent times to provide a more consistent and unified approach.

A comparison of the three common approaches used to report on water is shown in Table 1, where the differences and advantages of using the WAF methodology are indicated. In summary, not only does the water accounting approach provide a guideline for collecting, categorising, and assessing water flows across an operation, it also provides a means to benchmark the operation and ensures that the information and data collected is useful as inputs to other reporting standards.

The GRI is a means of providing a range of high-level metrics across various topics, useful for reporting at a corporate level. The strength of the water accounting approach is that it provides practical guidance at a site level for identifying and making improvements and for communicating the results, outcomes and plans to other stakeholders at various levels of reporting. The data collected can also be used as inputs to the GRI reporting metrics. The Water Footprint approach, although useful in other industries, is not widely used in mining.

TABLE 1

Summary of the comparison of the three water reporting approaches (source: Danoucaras *et al*, 2013).

Water Accounting Framework	Global reporting initiative	Water footprint
Role in sustainability initiatives: Provides definitions for consistent sustainability reporting. Can then provide numbers for other initiatives.	A snapshot of 30 environmental indicators covering areas such as water, materials, biodiversity, effluent and transport.	There is scope in the Water Footprint methodology to conduct a Water Footprint Sustainability Assessment.
Reuse and Recycling defined separately. Raw (new) water not included. Proportion against task demands.	Reuse/recycling synonymous. Rainwater is included. Proportion against site inputs.	Closest concept is that the water footprint should decrease as the site uses water more.
Inputs are listed with source categories.	Inputs are listed with source categories.	No equivalent.
Outputs are listed with destination categories.	Only discharge is reported.	Outputs that are not returned to the source catchment.

WATER ACCOUNTING FRAMEWORK

The development of the Water Accounting Framework began in 2005 as part of a strategic program led by the MCA, who engaged the Sustainable Minerals Institute (SMI) at UQ to 'develop a suite of metrics' to enable consistent reporting and benchmarking of water accounting and management practices. It came at a time when there was much focus on water, especially in Australia, with the National Water Initiative (MCA, 2014) water policy reform program simultaneously investing in the development of Water Accounting Frameworks and potentially, regulatory instruments. Additionally, the Bureau of Meteorology received additional powers under the Water Act 2007 to collect water information from anyone who held it. The chronological development of the WAF, including the development of its link to the Water Reporting of ICMM, is shown in Figure 2.

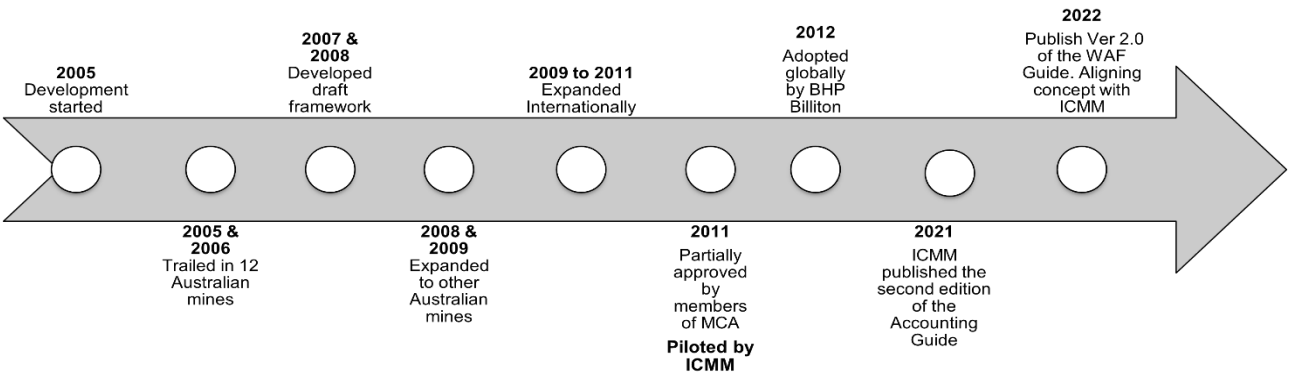

FIG 2 – Evolution of water accounting in mining.

Many mining companies, including BHP, Rio Tinto, Glencore and others, utilise all or part of the WAF methodology in their operations. A summary of the water accounting and management strategies currently in use by many of the global mining houses is shown in Table 2.

TABLE 2

Summary of the water management strategies of global mining houses.

Company	Water accounting/management strategy		
	MCA	ICMM	GRI standards
Anglo-American		Y	
BHP	Y	Y	Y
Barrick		Y	
Boliden		Y	
Codelco		Y	
First Quantum Minerals	Y		
Freeport McMoran	Y	Y	
Glencore	Y	Y	Y
Grupo Mexico		Y	Y
Industrias Peñoles SAB de CV		Y	
JSW			Y
Maaden Group		Y	Y
Norilsk Nickel		Y	
Rio Tinto	Y	Y	Y
Vale		Y	Y

The WAF methodology was developed specifically as a flexible and practical approach for water accounting and reporting in the minerals industry. It is intended to provide a standardised framework for measuring, benchmarking and assessing water usage across a mine site, and for communicating that in a consistent way.

A complete and updated description of the WAF, including a detailed presentation of the approach and definition of all terminology, has been recently published (MCA, 2022). The five key parts of the implementation of the WAF are: Scope, Data Collection, Applying WAF Concepts, Reports and Review. These are described below.

SCOPE: As with any structured methodology, the first critical step is to define the scope of the water account including the objectives and the boundary limits. The process of defining the scope should consider the nature and scale of the operation, including for example the stakeholders, intended audience, geographical limits, and surrounding water users. The scope definition is important in ensuring that the operational facility and the surrounding water systems are clearly defined.

- *Operational Facility*: this is fundamental to the goal of the WAF in providing a flexible, practical approach. The operational facility is a flexible term that allows companies to define the boundary of the system (‘system boundary’) over which the framework will be applied. It can include a mining operation with mining activities and processing plant only, or it can be extended to also include additional facilities, including smelting, leaching and port facilities.

DATA COLLECTION: While corporate water reporting is usually annual, collection of site data for operational management and accounting typically occurs on a range of intervals (daily, weekly, monthly or quarterly) depending on the nature of the data collected (ICMM, 2021). Challenges in data collection include lack of measured or metered flows and the need to use calculated or typical values as estimates. The accuracy of the account decreases with an increasing number of estimated values, but the process is important in highlighting gaps in data acquisition.

APPLYING WAF CONCEPTS: Some specific terms are used when applying the methodology, intended to provide a clear and structured way to simplify the operation, categorise flows and calculate metrics. Defining these clearly with respect to the specific operation is an important part of the implementation process.

Conceptual model: This model defines the relationship between the operational facility and surrounding environment, including the input and output flows across the system boundary. The relationship between the operational facility and the surrounding environment is show in Figure 3.

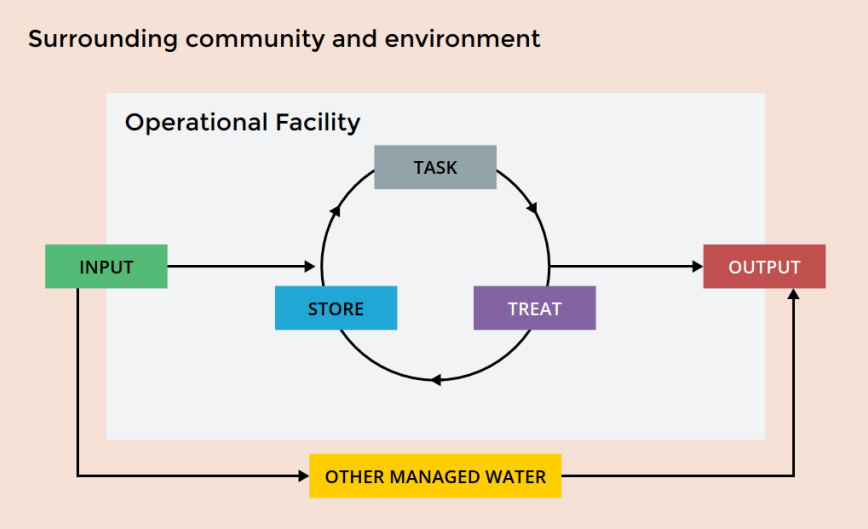

FIG 3 – Conceptual Model for WAF (source: MCA, 2022).

Operational Model: This is a model of the operational facility which describes the flows within it. Flows are between stores, tasks and treatment facilities.

- *Tasks*: A task is a set of operational activities that use water within the operational facility boundary. They can include the processing plant, auxiliary activities such as dust suppression, water used in the mine and others.
- *Stores:* These are water storage facilities or units within the operational facility. Within the WAF, stores are grouped according to two types: new water and mixed water.
- *New Water*: Describes water that has been actively withdrawn by the site from the environment (for example, borefields or rivers) or third parties, including municipal or industrial suppliers, to meet the operational water supply demand.
- *Worked Water*: Water that has previously been used by the site in an operational task.
- *Mixed Water*: A combination of new water and worked water.
- *Other Managed Water (OMW):* Water which is actively managed by the operation but does not enter the operational water system used to supply the operational water demand. This was formerly named by WAF as diversion.
- *Recycled/Reused Water*: Water that has been used in an operational task and is recovered and used again in an operational task, either without (reuse) or with (recycle) treatment.
- *Materiality of Flows:* A flow is judged to be 'material' if it is of sufficient volume or significance to influence the overall site water accounting report. Significance can include environmental impact, not just quantity. If omission of a water flow does not change any decisions on-site, then a flow is not considered material.

Water Quality: To achieve operational targets, minimise the risk of impact to receiving environments and realise opportunities to enhance the value of water by promoting circular management (ICMM, 2021), it is fundamental to understand and actively manage the range of water qualities present across the site. The inclusion of the water quality in the accounting and reporting process is included as part of both the WAF and ICMM accounting processes. The WAF uses three categories to classify

the water quality. In the case of ICMM reporting, there are only two categories since it does not separate out the flows classified in categories 1 and 2 according to the WAF approach.

Each flow entering (inputs) or leaving (outputs) the operational facility is assigned a water quality category from 1 (high quality water) to 3 (low quality water). The water quality categorisation in WAF is presented in Figure 4.

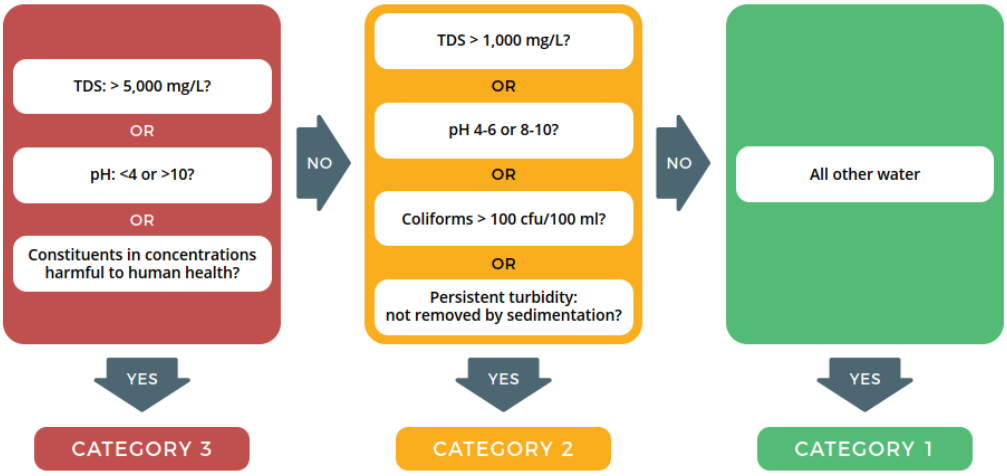

FIG 4 – Water Quality Categorisation in WAF (source: MCA, 2022).

REPORTS: Once the accounting part of the process has successfully consolidated and assessed the relevant water data across the operational facility, the information and findings must be clearly communicated to the relevant stakeholders regarding the water use of a site or company. The WAF reports can be used in this way and can also provide guidance for using WAF information to satisfy other reporting requirements. Four key statements make up the water account according to the WAF:

- *Contextual Statement:* This is an essential part of the WAF as it ensures accounts are directly relevant to the context in which a facility is operating. A contextual statement provides background information about the water resources of the operational facility as well as any conditions that have an impact on the management of those water resources.
- *Accuracy Statement:* This shows the respective proportions of each flow by volume which are measured, estimated or simulated, and the level of confidence for each number. This measure highlights where effort can be made to reduce the gaps in data acquisition to improve the accuracy of the balance and allow strategies for improvement to be developed.
- *Input–Output Statement:* This statement is a table presenting the flows between the environment and the boundary of the operational facility, including changes in water storage over the accounting period. It includes a list of inputs, outputs and OMW, with their associated water quality category. It is only possible to create this statement once the operational model for a system has been developed.
- *Statement of Operational Efficiencies:* This lists the total flows into the tasks, the volumes of reused and recycled water, and the resulting reuse and recycling efficiencies. The efficiencies are a measure of the proportion of reused and recycled flows in relation to the total flows into the tasks and are a useful benchmarking tool for comparison with other operations.

REVIEW: The final step is the review process. The data collection and analysis stages establish a baseline against which to measure improvements and to identify further opportunities for improved water management practices. When the review process is undertaken regularly, the WAF provides the basis for implementing and measuring continuous improvement initiatives.

In summary, the WAF is the first and more complete water accounting methodology and reporting tool for the mining industry. Since the scope of the approach is at the site level rather than corporate level, the use of the WAF opens opportunities to improve the water efficiency of mining sites. It also provides a valuable tool for the operation to take further control based on the standardised reporting outcomes which enable the site to measure performance against a common benchmark of the water

use in the mining industry. In addition, aside from the benefits of improved water accounting and management strategies, the implementation of this approach allows for the development of a model of the site water balance. The model can be used to run simulations forecasting water demand under various scenarios and enables operations to plan better and mitigate risk.

The application of the WAF is best explained using the Tritton Operation case study to demonstrate the implementation in practical terms.

TRITTON OPERATION CASE STUDY

The WAF methodology was implemented on-site at Tritton Copper Mine, located in Hermidale, New South Wales (NSW) within the Bogan Local Government Area. The work was initiated in early 2020 as a collaboration between Metso Outotec, the SMI and the Tritton Operation. The objective was to determine strategies for improving the efficiency of water usage across the operation and to find potential means of reducing the uncertainty and cost associated with reliance on regional water allocations.

Tritton is in a region characterised by a harsh climate in which the evaporation rate consistently exceeds precipitation. The primary source of water is distributed to the site via a buried pipeline that extracts water from the Macquarie River at Gunningbar Creek. The water usage is carefully metered and monitored as part of the NSW State Government legislation regarding water allocations. With low average rainfalls and high evaporation, the water allocations are critical in keeping communities and industries operating, hence the need for the government to manage closely.

The operation consists of two sites, Tritton and Girilambone. Girilambone is geographically separate from the main production site and includes mainly geological prospects with some minor mining and heap leaching activities. The Tritton site, the main operation, consists of an underground mine, processing plant, tailings facilities and other activities. The two locations have interlinked new water storage facilities and both rely on the same local supply.

Site visit and data collection

A four-day visit to site was conducted in March 2020. Site activities included meetings with operational management and staff, inspections, data collection and review of data with operations personnel. Some key decisions resulting from the site visit were:

- To establish that the data collected and utilised to perform the water balance and accounting assessment would use metre readings, production data, meteorological data and estimations based on-site conditions for the year 2019.
- To identify two potential operational facilities, including defining the system boundary for each. In each case, the respect site (Tritton and Girilambone) and associated activities were included within the operational facility.
- To determine that insufficient data was available related to the activities conducted at Girilambone. It was decided to focus only on Tritton, including its associated environment and activities, during this study. Apart from better data availability, the operational facility defined by the Tritton site represents the majority of water flows, including the consumption of new water, meaning that this operation is likely to provide more significant opportunities for improvement. Therefore, the remainder of the project only considered Tritton within the scope of the WAF implementation process.

The conceptual model of the Tritton site established that the system boundary included the underground mine, processing plant, paste plant, tailings facility and administration offices.

Operational model

The next step in the WAF approach is the development of an operational model. Within the operational model, internal flows between stores, tasks and treatment facilities are defined. The operational model forms the basis of the development of the overall water balance since the definition of each water flow enables values to be assigned based on measurements, calculations or estimations. This then enables the water accounting analysis to be conducted.

The operational model developed for the case study is as shown in Figure 5, including all inputs, outputs and OMW crossing the system boundary, and the flows between stores, tasks and treatment facilities inside the boundary.

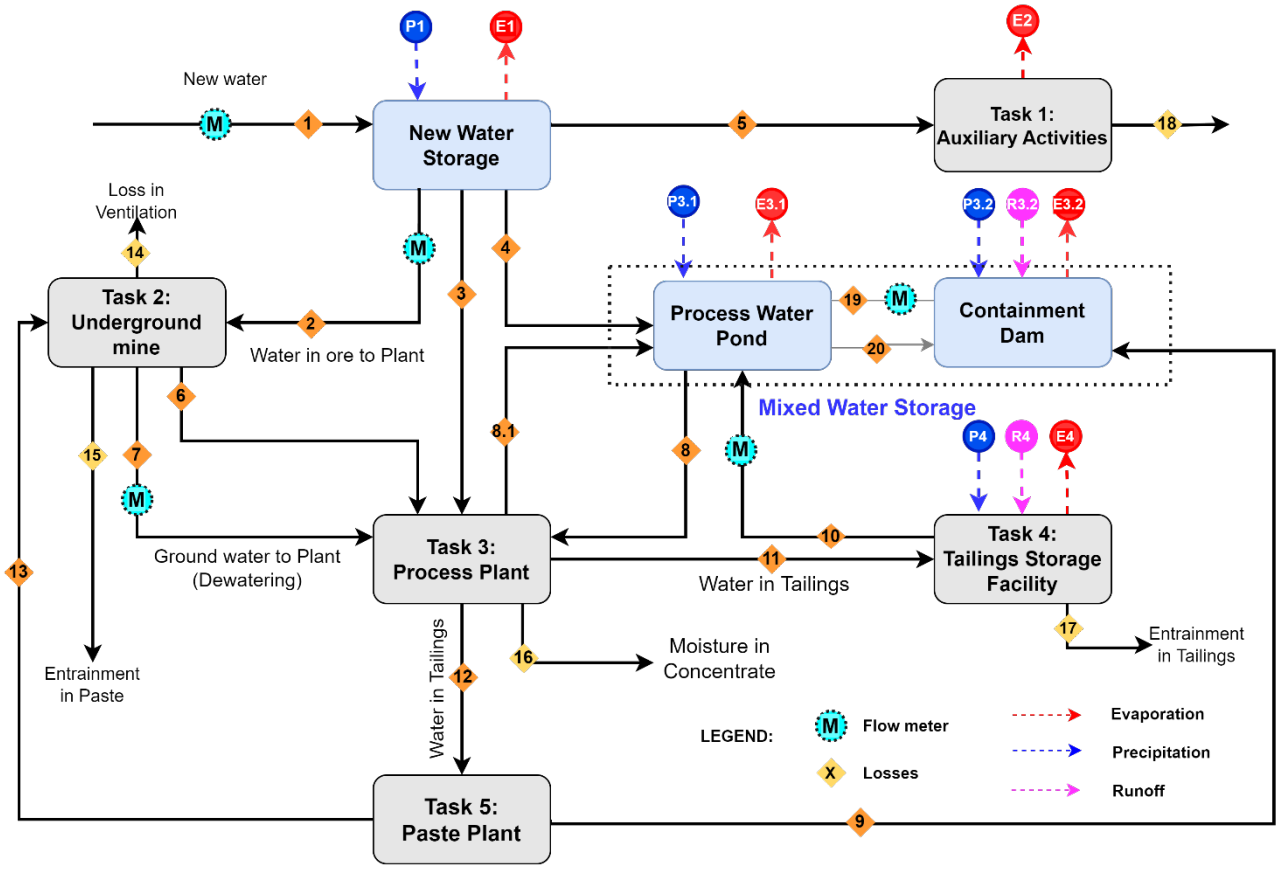

FIG 5 – Tritton Site Operational Model.

In terms of inputs and outputs, the most significant input to the system is the new water from Gunningbar Creek. Other inputs include precipitation, run-off, infiltration and water pumped from the underground mine. Outputs include water in the concentrate removed from site, evaporation, water used in auxiliary activities (dust suppression etc) and other losses. OMW can be discounted from this case since all the water that is managed by the operation enters the water system and is accounted for inside the system boundary.

The main store on-site is the new water storage facility, called New Water Storage, which receives the fresh (or new) water to site via the Girilambone site new water storage pond. This water is classified as Category 1 in terms of quality. The second water storage is the Mixed Water Storage which receives water from various sources, some of which are not measured. For this model, it is assumed that the mixed water includes water from the containment dam and process water pond. Other sources or users of mixed water are included as part of various tasks due to the flows being identified as immaterial, meaning that they do not significantly contribute to the water account.

The environmental pond is used by local fauna and is topped up with new water, which is unmeasured. As a result, this pond has been included within one of the tasks rather than as a store. In addition, there is a sedimentary pond next to the Tailings Storage Facility (TSF) which captures and stores run-off water from the catchment area during a rain event. This was also included as one of the tasks due to it being deemed not a material flow for the TSF and overall account. Water from this pond is pumped to the lagoon which is part of the TSF.

The five tasks identified on-site, as well as the activities and elements incorporated, are as follows:

Task 1: Auxiliary Activities including dust suppression, administration offices, environmental pond, wash bay and the cement batch plant. The only data available is the metre reading for the dust suppression. The other flows have all been estimated with very low confidence.

Task 2: Underground Mine including all activities related to the extraction of the ore from the underground mine.

Task 3: Processing Plant incorporating the entire processing plant, starting with the run-of-mine (ROM) and finishing with the concentrate and tailings.

Task 4: Tailings Storage Facility includes all activities related to the storage and recovery of processing water from the tailings dam. This task includes the sedimentary pond.

Task 5: Paste Plant including activities related to the production of paste. The production of paste requires a proportion of the tailings to be diverted to this plant to produce reinforcing material for underground work.

WATER ACCOUNTING REPORTING RESULTS

After the data collection process and the development of the operational model, the next step is to develop the four key statements, or standard metrics, used to benchmark the performance of the operation, provide insight into the accuracy of the measurements, and benchmark the operation in terms of its use and reuse of water on-site.

Contextual statement

The Tritton copper mine is located in a region characterised by semi-arid weather conditions and environment. Although two separate sites were identified within the same lease, the Tritton site is the only focus for the implementation of the WAF. The primary source of water for the operation is a regional dam which provides water to Tritton via a buried pipeline that extracts water from Gunningbar Creek, a tributary of the Macquarie River. The water is pumped first to the Girilambone new water pond and from there, it is pumped to the Tritton site new water pond via a buried pipeline where it is distributed primarily to the underground mine and processing plant as required.

The operation holds three water access licenses, with permits enabling extraction from specific locations in the local water system. Including supplementary water, the operation has a combined license of 931 ML of water annually. Three additional water access licenses enable water extraction from a local groundwater source up to 344 ML. The annual allocation from the NSW government is delivered at the beginning of each financial year, with any supplemental water acquired in the market.

The topography of the site is relatively level with natural slopes rarely exceeding 5 per cent. Gently undulating low hills surround the site, with soil types including moderately deep to pale red gravelly sandy clays and an earthy fabric and extensive coarse fragments throughout the profile. The soil appears moderately well-drained, although this varies with slope position. Some surface sealing and water repellence causes run-off even in minor storm events.

With a semi-arid climate, typically the summers are very hot and the winters relatively cool. The nearest town receives an average annual rainfall of 435 mm, with slight summer dominance. Potential evaporation, calculated using data from the nearest weather station in a larger regional town, averages 2025.9 mm per annum with distinct summer dominance. Average evaporation exceeds average rainfall in all months. The 100-year, 72-hour storm event equates to 2.87 mm/h or a total rainfall of 207 mm. An analysis of local rainfall data between 1896 and 2016 shows that the design storm event was exceeded three times.

The operation has Water Management Plans in place for both sites, as well as a Sediment Plan. As part of these plans, all areas surrounding the boundaries of each water system considered in this study have water diversions in place to prevent water from outside the defined sites from entering the system. The only water to cross the boundary of the primary system is as defined in the Input-Output Statement.

Input-output statement

The Input-Output summary for the Tritton site is included in Table 3.

TABLE 3

Tritton site input-output summary.

Input-Output	Element	Sub-element	Water Quality			Sub-Element Total (ML)	Accuracy (high, medium, low)			Note
			Category 1 (ML)	Category 2 (ML)	Category 3 (ML)		Measured	Estimated	Simulated	
Inputs	Surface Water	*Rivers and Creeks*	928.2			928.2	High			1
		Precipitation	186.4			186.4		Low		2
		Run-off		51.1		51.1		Low		2
	Groundwater	*Aquifer Interception*			1.2	1.2		High		1
		Bore Fields				0				
		Entrainment			51.7	51.7		High		3
	Sea Water	*Estuary*				0				
		Sea/Ocean				0				
	Third Party Water	*Contract/Municipal*				0				
		Wastewater				0				
	TOTAL INPUTS		**1114.6**	**51.1**	**52.9**	**1218.6**				
Outputs	Surface Water	*Discharge*				0				
		Environmental Flows				0				
	Groundwater	*Seepage*				0				
		Reinjection				0				
	Sea Water	*Discharge to Estuary*				0				
		Discharge to Sea/Ocean				0				
	Supply to Third Party					0				
	Other	*Evaporation from Stores*	398.0			398.0		Low		2

		Evaporation from Road Watering	24.0			24.0		High		4
		Entrainment, Tailings			343.1	343.1		Low		5
		Entrainment, Paste in Mine			186.1	186.1		Low		6
		Ventilation	246.0			246		Low		7
		Entrainment, Concentrate			12.3	12.3		High		3
		Discharges Auxiliary, Task			9.5	9.5		Low		8
	TOTAL OUTPUTS		**668.0**	**–**	**551.0**	**1219.0**				
Other Managed Water (OMW):										
Inputs	Surface Water	*Precipitation and Run-off*				0				
	Groundwater	*Aquifer Interception*				0				
	TOTAL DIVERSION INPUTS		**0**	**0**	**0**	**0**				
Outputs	Surface Water	*Discharge*				0				
	Groundwater	*Reinjection*				0				
	Other	*Evaporation*				0				
	TOTAL DIVERSION OUTPUTS		**0**	**0**	**0**	**0**				

Notes:

1. *This is a metered value obtained from production spreadsheet. It is a measured flow with high confidence in the value.*
2. *Sourced from Bureau of Meteorology. The flow is estimated with low confidence.*
3. *Calculated from production data with high confidence in the value.*
4. *This value assumes all water used for dust suppression evaporates. As dust suppression is metered, there is high confidence in this value.*
5. *Calculated from production data. The water entrainment and balance around the TSF is not yet well-understood. Hence there is low confidence in this value.*
6. *Calculated from production data. Water entrainment in the mine is not currently well-understood. Hence there is low confidence in this value.*
7. *Calculated with limited data. There is low confidence in this value.*
8. *This is the quantity of water required to balance the Auxiliary Activities task. The value has low confidence due to the low confidence in some of the other values.*

Inputs to the primary system consist mainly of the new water from Gunningbar Creek via a metered pipeline from the Girilambone site storage system, and other minor sources associated with precipitation and run-off. Dewatering from the mine is a minor metered input, measured with high confidence, which is diverted to the tailings thickener.

Regarding outputs from the system, it should be noted that there is no discharge of effluent to the natural system, therefore the outflow is defined by losses associated with production of concentrate, moisture in the product, evaporation, and entrainment in tailings and paste. Other minor losses are associated with auxiliary activities. Notably, the losses in ventilation could be more significant but estimates are based on the data available.

The overall summary of the water balance is shown in Table 4. This summary includes a breakdown of the water flows according to source and quality. The water has been classified into one of three categories as already defined, with Category 1 being the highest quality.

TABLE 4

Tritton site water balance summary.

Category	Category 1	Category 2	Category 3
Input summary by source and quality (ML/YR)			
Surface water	1115	51	0
Groundwater	0	0	53
Sea water	0	0	0
Third-party water	0	0	0
Output summary by destination and quality (ML/YR)			
Surface water	0	0	0
Groundwater	0	0	0
Sea water	0	0	0
Third-party water	0	0	0
Other	668	0	551
Change in storage (ML)		**0**	

The Input-Output statement is shown in Table 5.

TABLE 5

Tritton site input-output water balance statement.

Total inputs	1219	ML
Total outputs	1219	ML
Inputs–outputs	0	ML
Storage at start	0	ML
Storage at end	0	ML
Change of storage	0	ML

Accuracy statement

The Accuracy Statement, as shown in Table 6, indicates that 38 per cent of the flows for the Tritton site water balance are measured, all of which have been measured with high confidence. At the time of data collection, the metre for the tailings return was not reliable and so the flow was estimated. As this flow is important, calibration of the metre or the purchase of a new metre is recommended so that the data provided is correct and the accuracy of this statement is improved.

TABLE 6

Tritton site accuracy statement.

Flow types	Percent of all flows, %	Confidence (%)		
		High	Medium	Low
Measured	38	38	0	0
Estimated	62	4	0	58
Simulated	0	0	0	0
Total	100	42	0	58

No flows were simulated. The remaining 62 per cent of the flows on-site were estimated, most of them (58 per cent) with a low level of confidence. The most significant flows which have been estimated with low confidence are losses due to evaporation (398 ML), entrainment in the tailings (343 ML) and the losses from the ventilation system (246 ML). If more accurate calculation of these flows were possible, the accuracy statement would be much improved. As an example, calculating evaporation based on local conditions instead of having to use the evaporation data from the regional station located about 130 km from site would increase the confidence in this value and result in a significant improvement to the overall accuracy statement.

Statement of operational efficiencies

Considering all flow entering the tasks and the amount of water that has been recirculated, the proportion of water reuse is 68 per cent, as shown in Table 7. There is no measure of any recycled water streams on-site.

TABLE 7

Tritton site operational efficiencies.

Total flows into tasks (ML)	2784
Volume of reused water (ML)	1899
Reuse efficiency (%)	68
Volume of recycled water (ML)	0
Recycling efficiency (%)	0

OBSERVATIONS AND RECOMMENDATIONS

The following points summarise the outcomes, including recommendations, of the work done to date in implementing the WAF as part of this case study:

- The management of water on-site is shared by several departments, each responsible for reading and recording metre data and storing it in their own system. The process plant, environmental and mining departments conduct their own water monitoring and recording to varying degrees of detail. This varied approach is non-ideal in creating a single, consistent data set for the analysis, management and reporting of water use. A designated, multi-disciplinary team with a shared responsibility for implementing a centralised water management system including data collection procedures, calibration of instruments, data control and reporting, would help improve the quantity and quality of water data available, and hence improve water management practices overall.
- The requirement for new water, which is part of the annual water allocations, could potentially be reduced if a strategy is implemented to prioritise the use of this high-quality water for tasks which require it, including gland seals and water systems for equipment and cooling. Currently, new water taken from the nearby creek is transferred to the Tritton site via the new water storage facility on the Girilambone site. At the time of the site visit, the practice was to occasionally divert this water to the process water pond without consistent metering of this

flow. New water transfer to the process water system is justified if required to maintain process plant operation. However, consistent and reliable measurement of this flow will be helpful in justifying improvement initiatives based on economic and environmental drivers. Similarly, a cost-benefit analysis to potentially justify increasing the capacity of the Tritton site new water pond could reduce the cost associated with sending expensive, high-quality water to the containment pond when the Girilambone site new water storage facility is at capacity.

- Evaporation accounts for approximately 33 per cent of the water losses from site. This estimate is based on the available data, including the estimate of total water losses from the TSF of 61 per cent with most of the remaining 28 per cent due to entrainment. Significant evaporation losses are from the TSF and the containment dam. Accurate measurement of all losses due to evaporation would lead to a much-improved benchmark for the accuracy statement and more importantly, provide incentive to reduce these losses for better water management. One challenge is to quantify the relationship between the containment dam water level and its surface area, to enable the evaporation loss variation with dam level to be quantified. Measuring the dam level is an important part of the regular data collection on-site for water accounting.
- Two flows have been identified as key measurements which, if able to be collected with an increased level of confidence, will lead to an increase in the accuracy of the water accounting system. In addition, a measured flow has been identified as not critical to the water balance:
    - The metre measuring the water returning from the tailings facility into the processing pond located in the processing plant is measured using a metre which provided unreliable readings for the period of the study. The data from it was discarded. As this flow is important, calibration of the metre or the purchase of a new metre is recommended to increase the accuracy of the water accounting report.
    - The new water directly reporting from the Tritton site new water pond to the plant is an important flow which is currently unmeasured. This high-quality water is necessary for plant operation, reagent mixing for flotation and the ablution and cooling systems. The measurement of this flow is important to be able to identify better management strategies and better predict the annual water allocation requirements on-site.
    - Currently, there is a metered reading of the water which is transferred from the containment pond to the process water pond within the Tritton site mixed water system. For water accounting, this information is not relevant as it represents mixed water. It is not clear how this information is used, if at all, and the metre may be more suitable elsewhere.
- The estimated monthly water use data, together with historical weather data, could assist in predicting water allocation requirements throughout the year. To better quantify the monthly offer/demand, a regular system for recording critical water flow measurements could be implemented. This will help to improve the understanding of the offer/demand variation during the year which in turn would enable water management strategies to be improved so that new water is better utilised and excess water in storage, leading to increased losses to evaporation and storage facility overflows, is avoided.
- Water accounting results from this site, based on data collected in 2008, showed a reuse efficiency of 71 per cent, compared with reuse efficiencies of 78, 53 and 35 per cent for other mine sites in the same region. The Tritton Operation was one of the best at that time, and the current reuse efficiency of 68 per cent indicates that the operation has continued to manage water in a similar way. Potential strategies for increasing the reuse efficiency will be identified as part of the future scope of this work.

CONCLUSIONS AND FUTURE DEVELOPMENT

Case study learnings

The Tritton Operation case study and results confirm that the WAF provides a clear method and well-defined guidelines for collecting the required water data from an operation so that the metrics for water efficiency can be calculated in a flexible, generic, and easy-to-understand manner. The

adaptation of the approach to the GRI reporting methodology has not been demonstrated in this case study but the process involved in implementing the WAF means this is something which can be done as part of future projects, if GRI reporting is required.

Due to the versatility of the tool, it can be easily implemented in mining operations and can provide the information necessary for multiple reporting purposes including at the site and corporate levels. The results from this approach can be applied at the corporate level for interim reporting, but also for setting strategic targets and applying corrective measures in advance. The approach is also flexible in that the outcomes can be applied across the entire corporate portfolio, providing input to the strategic direction of all operations regardless of geographical location, country or commodity.

In this case study, the WAF methodology and reporting is applied at the operation level. Application at this level means that it can provide information which enables reporting outcomes to be translated into practical actions at the local site level to comply with water requirements and uses in the specific basin(s), taking the needs of the local environment and other stakeholders into account.

The outcomes from this case study have demonstrated that the data collection process, using the WAF methodology, was successful in defining the water system boundaries and developing a mass balance over that system. At an operational level, this data could be translated into the standard WAF reports to provide practical recommendations and actions for improving the water management strategies on-site and for increasing the efficient use of the resource.

The operational model developed for the case study defined the elements required to take account of all water uses on-site. It was then used as the basis for comparing results for operations in similar contexts and for integrating them for corporate purposes. It enabled a baseline of the operation to be established so that it could be used to benchmark performance and to define objectives and strategies for continuous improvement.

The results from this study were compared with information from previous reports, including information from other operations in the geographical region. The comparison provides an excellent base for classifying the operation in the geographical context. In this case, the existing information management was shown to be at a good level already. However, it also identified some gaps in the data collection and management processes, highlighting opportunities for improvement.

Holistically understanding the water system using this methodology permitted advice on improvements that the operation can implement with low or no cost. If the recommendations are implemented, it is possible to have a measured improvement in the reporting results.

Finally, it was proven that the WAF provides the foundation to create a holistic, standardised water account for a mining operation with the transparency necessary to enable input into different levels of decision-making and provide information for other reporting within the operation.

Future developments

This work is the first part of a project which will result in improved capability to understand, measure, manage and improve water use and reuse in mining operations, for best environmental and economic outcomes. Further work is already in progress, and more is planned.

The holistic water balance obtained using the WAF methodology provides the foundation for developing a software-based model tailored to the operation but following the structure of the WAF.

Once the model is developed, it can be used for various purposes. Firstly, the expected changes due to the recommendations already provided can be simulated to quantify the benefits and provide justification for any cost incurred. In addition, the model can simulate different scenarios based on these recommendations and choose the investment that has the most significant impact on the operation result.

These software-based models also open the possibility of simulating further scenarios; initially, this could concentrate on simulations to quantify the water required to meet the demand of the operation under various climactic and other scenarios which would enable the operation to better predict and manage water requirements in those cases.

In addition, the WAF differentiation on water quality opens the possibility for further development, starting with having a better understanding of the quality of the water flows available for different

tasks in the mining operation and effluent control. This classification of the water into three categories of quality makes it possible to utilise the properties of the water or water mix better.

Understanding the impact on recovery due to variations in water quality, through simulation and test work, will enable improved control of the water quality for optimal and stable recovery. Current losses in recovery, and resulting financial losses, due to variable water quality will be better understood and mitigated with this approach.

Using simulation of the recirculating water and the resulting changes in water chemistry in the processing plant, it will be possible to identify the point at which recirculation adversely impacts recovery. This will enable decisions to be made regarding blending of water to prevent recovery losses or treatment options to be investigated, including with economic justification.

Most cases which currently exist which have used the WAF have been in brownfield projects; however, it is possible to apply the same methodology in greenfield projects, which will be fundamental in the decision-making process for future projects.

ACKNOWLEDGEMENTS

The authors gratefully acknowledge:

- Personnel from Aeris Resources' Tritton Operation. Without their active and open participation and support, this project would not have been possible. Metso Outotec would especially like to thank management for permission in publishing this paper.
- The staff from SMI's Centre for Water in the Minerals Industry (CWiMI) for collaboration on this project, for the development of the fundamentals of the WAF for the mining industry, and for the support and training received before and during project implementation.
- The MCA for the vision required to promote and investigate the challenge of providing the industry with tools to manage water resources. The effort has established the Australian mining industry amongst the leaders internationally in providing tools to enable consistent reporting and continuous improvement for water management in the global mining industry.

REFERENCES

Climate Disclosure Standards Board (CDSB), 2021. Water risks: why investors care about sustainability [Online]. Available at: https://www.cdsb.net/natural-capital/1262/water-risks-why-investors-care-about-sustainability [Accessed: 26-3-2022].

Danoucaras, N, Woodley, A and Vink, S, 2013. Corporate sustainability reporting for water: Water footprint, global reporting initiative and the water accounting framework. Heliotopos, Greece, *Proceedings of the 6th International Conference on Sustainable Development in the Minerals Industry (SDIMI 2013)*.

Global Reporting Initiative (GRI), 2018. GRI Standard GRI 303: *Water and Effluents*, Amsterdam: Global Reporting Initiative.

Godfrey, J and Chalmers, K, 2012. *Water Accounting: International Approaches to Policy and Decision-making*. Online ed. Cheltenham; UK: Edward Elgar Publishing.

Hoekstra, A, Chapagain, A, Aldaya, M and Mesfin, M, 2011. *The Water Footprint Assessment Manual: Setting the Global Standard*. First ed. London, Washington: Eathscan.

International Council on Mining and Metals (ICMM), 2021. *Water Reporting: Good practice guide*, 2nd Edition, s.l.: International Council on Mining and Metals.

Mineral Council of Australia (MCA), 2014. *Water Accounting Framework for the Minerals Industry*, s.l.: Mineral Council of Australia.

Mineral Council of Australia (MCA), 2022. *Mineral Industry Water Accounting Framework*, User Guide, Version 2.0, s.l.: Mineral Council of Australia.

Morgan, A J, 2020. *An analysis of water risk in the mining sector-Water Risk Filter Research Series*, Vol 1, s.l.: WWF.

The World Wide Fund for Nature (WWF), 2020. Mining companies and commodities face significant water risks, warns WWF report. [Online] Available at: https://wwf.panda.org/wwf_news/?359211/Mining-companies-and-commodities-face-significant-water-risks-warns-WWF-report [Accessed 25 3 2022].

World Health Organization (WHO), 2022. World Water Day 2022: Groundwater, invisible but vital to health. [Online] Available at: https://www.who.int/news-room/feature-stories/detail/world-water-day-2022-groundwater-invisible-but-vital-to-health [Accessed 25 March 2022].

Flotation processing of fine chrome from UG2 platinum operations in South Africa

G Marape[1] and K Shame-Letsoalo[2]

1. Principal Engineer, Mintek, Randburg South Africa 2195. Email: getrudem@mintek.co.za
2. Engineer, Mintek, Randburg South Africa 2195. Email: kagisegos@mintek.co.za

ABSTRACT

South Africa holds over 70 per cent of world's total chrome reserves. Chromium is an important raw material for the production of stainless steel and ferrochrome alloys. This study investigated the flotation of fine chrome (15–20 per cent Cr_2O_3) from UG2 platinum operations tailings in South Africa. In South Africa, the upper group 2 (UG2) chromitite layer is found in the western and eastern limbs of the Bushveld Complex (BC), generally mined for extraction of Platinum group minerals (PGMs). Typical processing of run-of-mine (ROM) UG2 ore for PGMs entails crushing, mill-float 2 (MF2) circuit with interstage coarse chromite removal. This circuit generates final tailings that are rich in ultra-fine chromite (<80 per cent passing 75 µm), which is not recoverable by typical chromite recovery techniques such as gravity and magnetic separation. Recovery losses increase substantially at sizes finer than 75 µm as more than 50 per cent of chrome is dominated in this fraction. With millions of tonnes of historical and current tailings produced by primary platinum producers at 15–20 per cent Cr_2O_3, chrome ore producers are now focusing on the reprocessing of tailings to recover fine chrome.

Mintek has been involved in the flotation of fine podiform and stratiform chrome ores. Various process routes at varying dosages that could yield a final product at 40 per cent Cr_2O_3 and reasonable Cr_2O_3 recovery were tested. Many promising findings were made but the effect of gangue type and pH was not evaluated. This paper seeks to determine the effect of UG2 gangue type and pH on chromite flotation. Mineralogy of two UG2 tailings sourced from two different sites in Western limbs was compared as well as chromite recovery performance at three pH points, ie acidic and alkaline. Results showed that the success of fine chromite flotation in alkaline or acid conditions is dependent on the dominant gangue type present. A saleable chrome product of more than 40 per cent Cr_2O_3 could be achieved in an open circuit at up to more than 60 per cent recovery depending on the gangue type, pH and slimes content (-10 µm).

INTRODUCTION

South Africa possesses about 70–77 per cent of the world chromium reserves (Roskill Information Services, 2019; Mosiane, 2007). Chromium is an essential element and important raw material for the production of stainless steel and ferrochrome alloys (Murthy *et al*, 2011; Mosiane, 2007). China is the largest Ferrochrome and stainless steel producer and consumer of chrome ore in the world (Murthy *et al*, 2011; Mosiane, 2007). Over the years, China's ferrochrome market has been dependent on chrome ore imports from South Africa (Mosiane, 2007). In 2014, China imported about 61 per cent of chrome ore from South Africa (Phillippe, 2015). Podiform and stratiform deposits are the main commercial chromite deposits (Murthy *et al*, 2011). The Bushveld Igneous Complex located in South Africa is the main stratiform deposit. Kazakhstan chromite ore reserves are of the podiform type (Murthy *et al*, 2011). Podiform deposits are richer in chromium than stratiform deposits with a relatively high Cr:Fe ratio (Murthy *et al*, 2011).

In South Africa, the Bushveld Complex (BC) is the major source of chromite and MG, LG and UG2 reefs are beneficiated to provide the required feedstock. The UG-2 reef of the BC consists mainly of chromite, which can constitute up to 75 per cent by mass (Murthy *et al*, 2011). The exploitation of the UG2 reef for the recovery of PGMs provides potential for the recovery of fine chromite. Chromite can be recovered from primary or secondary PGM flotation tails. UG2 ore tailings previously regarded as waste, are now reprocessed to recover chrome ore which can be used by ferrochrome producers due to the rising demand for stainless steel (Murthy *et al*, 2011). It is reported that about 25 per cent of the mineral value is lost to slimes during the processing of ores (Murthy *et al*, 2011). Various gravity separation techniques such as Shaking table, Spiral concentrator and Reflux classifier have been tested to assess the amenability of interstage chrome removal by gravity

separation, ie recovery of chromite from UG2 primary flotation tails (Marape and Thiele, 2017). These techniques employed showed that a final saleable product grade >40 per cent Cr_2O_3 can be achieved. Recovery of fine chromite from UG2 secondary flotation tails by gravity separation has not been very successful since these tails are very fine (<100 µm). Gravity separation is less efficient when processing fine sized particles less than 75 µm (Murthy *et al*, 2011; Gupta and Yan, 2006). Flotation is a physico-chemical separation process that utilises the difference in surface properties of valuable minerals and unwanted gangue. Extensive studies have shown that flotation can upgrade particles up to 10 µm in size (Wills and Napier-Munn, 2006). Previously, various authors investigated the flotation of chromite fines from tailings (Gallios *et al*, 2007; Feng and Aldrich, 2004; Yigit, 1981; Guney *et al*, 1999). Gallios *et al* (2007) investigated fine chromite flotation from serpentine using sodium oleate (SO), sodium dodecyl sulfate (SDS) and cetyl trimethyl ammonium bromide (CTMAB) as a function of pH and modifiers. Results showed it is possible to selectively float chromite from serpentine using various reagent schemes. However, the success depends on pH, collectors and modifiers employed. Carboxymethyl cellulose (CMC) as a modifier was found to depress chromite in alkaline conditions while fluorosilic acid, cyclodextrin and ethylene diamine-tetraacetic acid (EDTA) activated chromite flotation in acidic and neutral pH values. Feng and Aldrich (2004) investigated cationic and anionic flotation of fine chromite (-100 µm) from western chrome mine in South Africa in columns. In the absence of a collector, point zero charge of chromite was found to be at pH 4. Addition of sodium dodecyl sulfate (SDS) caused zeta potential to shift more to the negative values while addition of cetyl trimethyl ammonium bromide (CTMAB) shifted zeta potential to the positive values. Chromite recovery of anionic flotation with SDS was the highest at pH 4 showing chromite surface is positive at pH <4. Chromite recovery of cationic flotation with CTMAB was the highest at pH 11 confirming CTMAB adsorped on negatively charged chromite surface. The authors further showed presence of dissolved $Al^{3+,}$ Fe^{2+}, Mg^{2+} and Cr^{3+} ions tends to change zeta potential of chromite as a function of pH affecting chromite flotation with both anionic and cationic collectors (Feng and Aldrich, 2004; Guney *et al*, 1999). To date it is not clear if the success of fine chromite flotation in alkaline or acid conditions is also dependent on the dominant gangue type present. This study investigated chromite flotation of two samples with varying major gangue to ascertain if similar reagent types and conditions will yield similar flotation performance.

EXPERIMENTAL PROCEDURE

Sample preparation for mineralogical analysis

As received sample A and sample B tailings from UG2 tailings were subjected to electron microprobe and particle tracking analyses to determine composition of sample, major gangue minerals and their liberation characteristics. Each sample was screened at various screen sizes in preparation for mineralogical analysis.

Mineral liberation Analysis (MLA)

The automated instrumentation used in this characterisation study was the Mineral Liberation Analyser (MLA). During a measurement, the MLA will generate an X-ray analysis for each grey level region within a particle. During the analysis, >10 000 particles per polished section/slab will be analysed and processed by the MLA. A larger number of particles aids in the acquisition of a statistically representative data set of the overall sample. Particle characterisation data pertaining to mineral types/compositions, particle size, density, weight percent of the particle population, area of particle, shape factor, circularity, and perimeter of each particle will be determined during offline processing. For purposes of this study, calculations were based on shape descriptors such as shape factor, circularity and equivalent circle diameter (ECD) will included in the overall data set. Bulk chemical assays of the as received sample were used to reconcile MLA data.

Electron microprobe analysis

Chrome-bearing minerals, as well as major gangue minerals were analysed by EMPA to determine the chemical composition of the particles. A maximum of 50 analysis points were probed.

Laboratory flotation tests

Sample preparation for laboratory flotation tests by desliming

Representative subsamples of as received sample A and sample B were deslimed at 10 µm, using a hydrocyclone. Tests were conducted at 100 kPa pressure and 20 per cent solids. Overflow and underflow streams from the test work were filtered, dried and subjected to particle size distribution and chemical analysis. The remaining underflow product was blended and split into 1 kg batches for flotation test work. As received samples, deslimed products were all submitted for standard ICP – OES chemical analysis to determine Cr_2O_3, FeO, MgO, Al_2O_3, SiO_2, CaO, TiO_2, V_2O_5 and MnO, in all samples.

Laboratory rougher flotation tests

Figure 1 and Table 1 show rougher rate flow sheet and conditions tested on deslimed and as is sample A and sample B. Tests were conducted to investigate the effect of desliming at 10 µm on chromite grade and recovery performance.

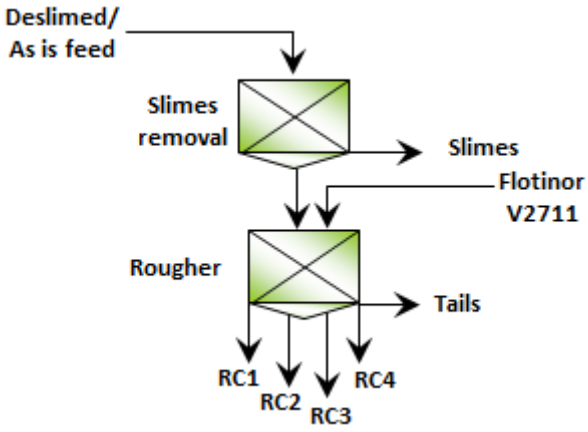

FIG 1 – Rougher rate flow sheet tested.

TABLE 1

Rougher rate test conditions.

Parameter/reagent	Sample A		Sample B
	As is	Deslimed	Deslimed
Dow 200 (g/t)	79	78	68
98% H_2SO_4 (g/t)	1510	1340	981
Flotinor V2711 collector (g/t)	840	279	250
Float time (min)	2	2	2
pH rougher	2.5	2.5	2.5

Four stage laboratory flotation tests

Figure 2 and Tables 2 to 3 show flotation flow sheet and test work conditions tested on sample A and sample B. Tests were conducted to assess if chromite from UG2 tailings can be upgraded to >40 per cent Cr_2O_3 in acidic and alkaline conditions.

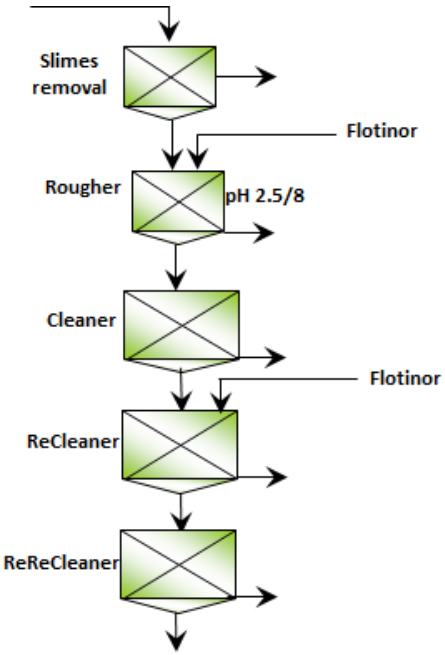

FIG 2 – Four stage flotation flow sheet tested.

TABLE 2

Flotation operating conditions employed.

Parameters	Operating conditions	Units
Cell volume	2	L
Stirrer/Impeller speed	1100	rev/min
Air flow rate	12.6	NL/min
Scraping interval	15	Seconds
Initial% Solids	~33	%

TABLE 3

Reagents and dosages added.

Reagent	Sample A		Sample B	
pH	2.5	8.3	2.5	8.3
Dow (g/t)	118	95	68	80
98% H_2SO_4 (g/t)	1340	-	980	-
Flotinor V2711(anionic collector)	310	-	190	-
CMR175 (Cationic collector)	-	280	-	220
Na_2SiO_3 (g/t)	340	70	105	50
NaOH (g/t)	-	80	-	70

Table 2 shows operating conditions employed during the test work. Reagents and dosages added are presented in Table 3. Cationic collector CMR175 was employed for flotation tests conducted in alkaline conditions while anionic collector flotinor V2711 was employed for flotation tests conducted in acidic conditions at pH 2.5.

Chemical analysis

All flotation products were dried, weighed and pulverised using the tungsten bowl. A standard ICP – OES method was used to analyse for Cr_2O_3,FeO, MgO, CaO and major gangue elements.

RESULTS AND DISCUSSION

This section presents and discusses the mineralogy, assay by size analysis and flotation results on sample A and sample B. Flotation results are discussed in terms of grade and recovery performance of chromite at various pH and reagents tested. Only optimum flotation results are presented.

Mineralogical analysis and head chemical analysis

Table 4 shows chemical analysis of sample A and sample B. Sample A was at 17.27 per cent Cr_2O_3 grade at 17.58 per cent FeO and 30.97 per cent SiO_2. Sample B was at a slightly lower 14.79 per cent FeO grade and higher 19.78 per cent Cr_2O_3.

TABLE 4

Head chemical analysis of as received sample A and sample B.

Sample ID	%Al_2O_3	%CaO	%Cr_2O_3	%FeO	%MgO	%MnO	%SiO_2	%TiO_2
Sample A	10.83	3.09	17.27	17.58	16.11	0.17	30.97	0.62
Sample B	15.64	3.79	19.78	14.79	13.19	0.15	29.09	0.35

Tables 5 and 6 show modal analysis of sample A and sample B. The two samples were dominated by chromite as expected but dominated by different gangue minerals. Orthopyroxene was the major gangue mineral in sample A and feldspar was the major gangue mineral in sample B. Both samples depicted high chromite and gangue minerals liberation (>90 per cent liberation) as expected, as the two samples are final UG2 tailings.

TABLE 5

Modal analysis of sample A.

Mineral name	Mass %	% Liberation
Chromite	44.5	99
Orthopyroxene	34.1	98
Plagioclase	8.9	97
Clinopyroxene	9.6	98
Other	2.9	>90
Total	100	

TABLE 6

Modal analysis of sample B.

Mineral name	Mass %	% Liberation
Quartz	0.4	91
Feldspar	24.9	93
Enstatite	18.7	90
Biotite	1.5	81
Serpentine	2.2	77
Chromite	50.5	93
Other Minerals	1.8	
Total	100	

Table 7 shows composition of chromite, orthopyroxene and plagioclase in sample A. Electron microprobe analysis revealed that average chromite composition of chromite contained 44 per cent Cr_2O_3. Chromite spinel contained 7.98 per cent MgO and 13.78 per cent Al_2O_3. Orthopyroxene and plagioclase identified at major gangue with orthopyroxene enriched in FeO at 12 per cent FeO.

TABLE 7

Composition of chromite, orthopyroxene and plagioclase in sample A.

Mineral name	%Cr_2O_3	%Fe_2O_3	%FeO	%MnO	%MgO	%Al_2O_3	%SiO_2	%CaO
Chromite	44.01	7.28	21.98	0.21	7.98	13.78	-	-
Orthopyroxene	0.62	-	12.29	-	3.44	0.28	57.34	0.36
Plagioclase	0.10	-	0.91	-	0.06	31.38	47.28	18.24

Chromite distribution by size

Figure 3 shows distribution, grade of chromite by size. Chromite is dominated in the -25 µm fine fraction. Sample A had 27 per cent -10 µm while sample B had 15 per cent -10 µm slimes. It was for this reason that the two samples were deslimed at 10 µm prior to flotation to reduce slimes. Slimes have a high surface area and result in high reagent consumption. Sample A is finer than sample B with more than 50 per cent of material finer than 25 µm.

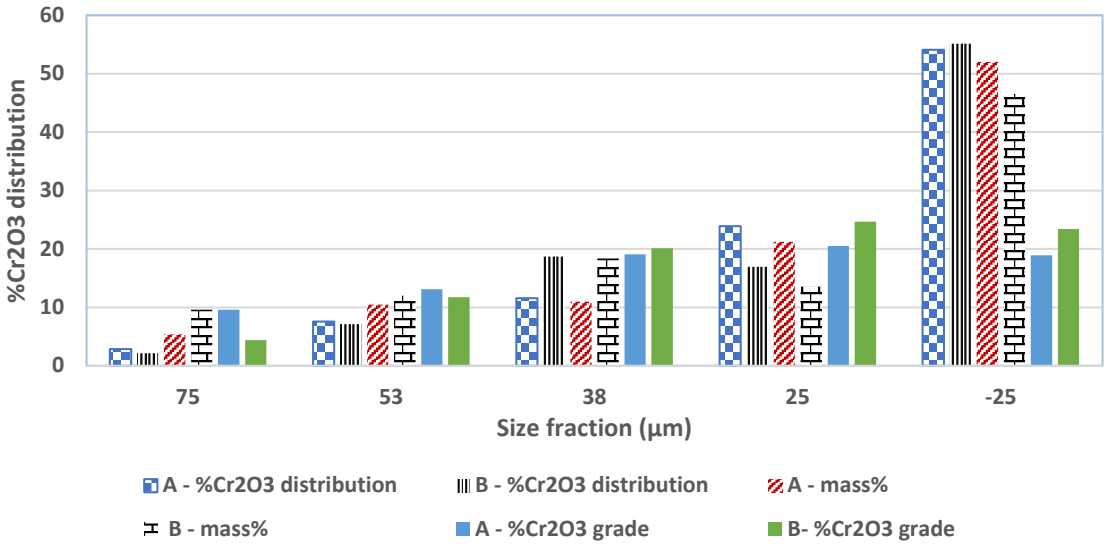

FIG 3 – Chromite distribution by size in sample A and sample B.

Flotation test results

Sample preparation by desliming

Sample A and sample B were deslimed at 10 µm to reduce slimes prior to flotation. Table 8 shows cutpoint, chromite grade and recovery of each stream for each sample. Mass reporting to overflow was higher for sample A as expected as it has a higher -10 µm resulting in higher per cent Cr_2O_3 losses. Other methods including flocculation are recommended to upgrade chromite lost to -10 µm. Desliming slightly upgrades chromite to underflow as depicted by slight chromite grade increase in the underflow.

TABLE 8

Deslimed U/F and O/F products.

Stream	Parameter	Sample A	Sample B
Hydrocyclone	D50c (µm)	10.34	10.00
U/F	Mass %	78.48	91.49
	$\%Cr_2O_3$	19.9	18.7
	%FeO	18.45	15.5
	$\%SiO_2$	31.8	30.2
	$\%Cr_2O_3$ recovery	83.44	91.73
	%FeO recovery	80.50	92.35
	$\%SiO_2$ recovery	76.46	91.21
O/F	Mass %	21.52	8.51
	$\%Cr_2O_3$	14.4	18.7
	%FeO	16.3	13.8
	$\%SiO_2$	35.7	31.3
	$\%Cr_2O_3$ recovery	16.56	8.27
	%FeO recovery	19.50	7.65
	$\%SiO_2$ recovery	23.54	8.79

Effect of desliming on flotation performance

Sample A and sample B were both subjected to rougher tests to assess the effect of upfront desliming at 10 µm on chromite flotation. Figure 4 shows chromite grade and recovery performance while Table 9 shows conditions and reagent dosages. Desliming improved chromite grade and recovery performance. Desliming reduced reagent consumption by more than 60 per cent. Sample B depicted a higher chromite grade and recovery performance. This could be related to the mineralogical differences between the two samples including remaining slimes finer than 10 µm.

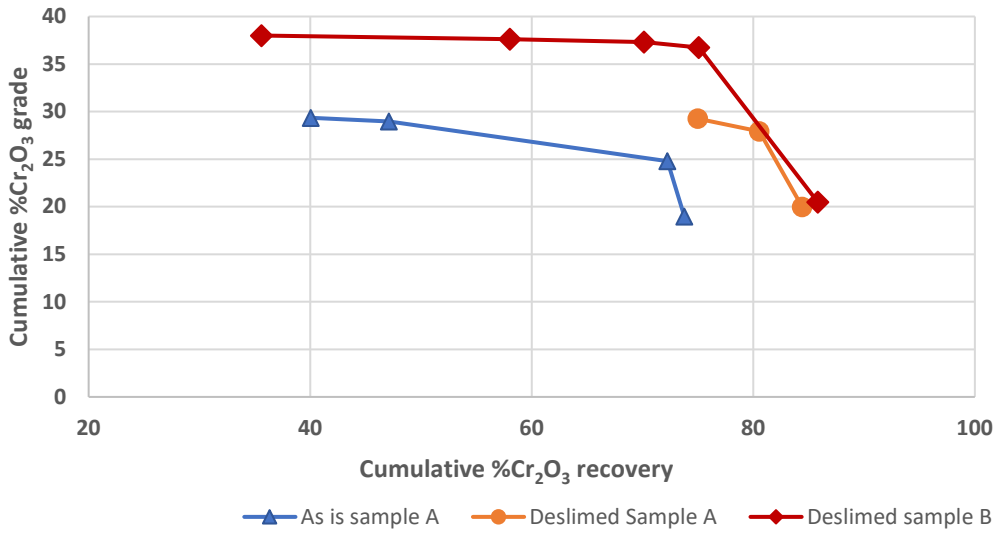

FIG 4 – Effect of desliming on rougher rate.

TABLE 9

Effect of desliming on rougher performance at pH 2.5.

Parameter/reagent	Sample A		Sample B
	As is	Deslimed	Deslimed
Dow 200 (g/t)	79	78	68
98% H_2SO_4 (g/t)	1510	1340	981
Flotinor V2711 collector (g/t)	830	269	250
% Cr_2O_3	29	29	40
% Mass yield	24	48	39
% Cr_2O_3 recovery	40	75	71
Float time (min)	2	2	2
pH rougher	2.5	2.5	2.5

Flotation performance at acidic and alkaline conditions

Various tests were conducted in acidic and alkaline conditions. Only optimum results are presented. With three cleaning stages chromite could be upgraded to 41.93 per cent Cr_2O_3 grade at 27.77 per cent Cr_2O_3 recovery. Sample B could however be upgraded to 42 per cent Cr_2O_3 at 61 per cent Cr_2O_3 recovery confirming chromite selectivity can be easily achieved in acidic conditions. Literature showed selectivity between chromite and typical silicates associated with chromite depends on zeta potential and pH (Wesseldijk *et al,* 1999; Siyuan *et al*, 2018). At pH of 2–2.5 chromite and gangue minerals olivine and pyroxene depict opposite zeta potential showing selectivity will be easily achieved at pH below 4 (Wesseldijk *et al,* 1999; Siyuan *et al*, 2018). Chromite performance differences between the two samples may be related to the mineralogical differences, head grade and remaining slimes.

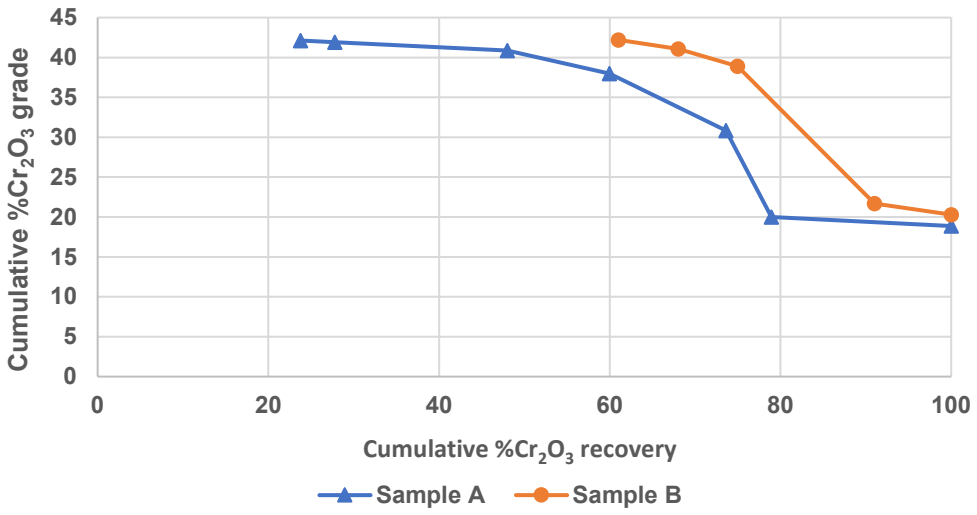

FIG 5 – Cumulative per cent Cr_2O_3 grade and recovery performance of sample A and B at pH 2.5.

Table 10 shows overall mass balance of sample A showing overall mass yield and per cent Cr_2O_3 recovery is determined by amount of -10 µm deslimed upfront. This confirms the need to investigate methods that can upgrade chromite lost to -10 µm such as flocculation.

TABLE 10

Overall sample A mass balance relative to feed.

Unit	Stream	Mass%	Cumulative Grade		Cumulative Recovery	
			Cr_2O_3	$\%SiO_2$	Cr_2O_3	$\%SiO_2$
As received	Feed $_{(head)\ calc}$	100	18.13	30.79	100	100
Desliming hydrocyclone	Underflow	70	18.87	30.85	72.86	70.14
	Overflow	30	16.4	30.65	27.14	29.86
Flotation	Flotation feed	70	18.87	30.85	72.86	70.14
	Slimes	17.83	15.60	33.70	15.34	19.51
	Rougher conc	31.53	30.84	15.08	53.64	15.44
	Rougher tails	20.64	3.41	52.50	3.88	35.19
	Cleaner Conc	20.85	37.98	5.90	43.69	3.99
	Cleaner Tails	10.68	16.90	33.00	9.96	11.45
	Recleaner Conc	15.51	40.87	2.35	34.97	1.19
	Recleaner tails	5.34	29.60	16.20	8.72	2.81
	RRCConc	8.75	41.93	0.86	20.23	0.25
	RCCTails	6.76	39.50	4.28	14.74	0.94
Final tails (O/F+Slimes+RT		68.47	12.28	38.03	46.36	84.56

Table 11 shows overall mass balance of sample B at pH 2.5 showing the overall mass yield and recovery is determined by slimes content removed by desliming.

TABLE 11

Overall mass balance of sample B in acidic conditions.

Stream	Mass%	Grade (%)		Recovery (%)	
		Cr_2O_3	SiO_2	Cr_2O_3	SiO_2
RCC	26.85	42.2	1.32	58.87	1.17
RCT	4.34	34.00	11.48	7.66	1.69
CC	31.19	41.06	2.78	66.54	2.86
CT	4.6	24.2	23.2	5.78	3.52
RC	35.79	38.89	5.4	72.32	6.38
RT	42.16	7.08	43.9	15.51	61.09
Slimes	13.54	12.3	38.4	8.61	17.16
Cyclone underflow	91.49	19.3	30.2	91.73	91.2
Cyclone overflow	8.51	18.7	31.3	8.27	8.8

Tables 12 and 13 show recovery of chromite from sample A and sample B in alkaline conditions at pH 8.3. Results show poor chromite selectivity in sample A but a good selectivity in sample B. Further tests were conducted on sample A at pH 10.5 though results have not been shared in this paper. Sample A depict poor selectivity in alkaline conditions. Based on literature this is related to orthopyroxene and chromite having the same zeta potential in alkaline conditions (Wesseldijk *et al,* 1999; Siyuan *et al*, 2018).

TABLE 12

Sample A chromite performance in alkaline conditions at pH 8.3.

Stage	Mass (%)	%Grade		%Recovery	
		Cr_2O_3	SiO_2	Cr_2O_3	SiO_2
Rougher Tails	59.88	11.56	39.56	37.58	76.65
Rougher Conc	40.12	28.65	17.98	62.42	23.35
Cleaner Tails	15.90	23.17	24.90	20.00	12.81
Cleaner Conc	24.22	32.25	13.44	42.41	10.53
Re. Cleaner Tails	4.87	24.24	23.55	6.41	3.71
Re. Cleaner Conc	19.35	34.26	10.90	36.00	6.82
Re.Re. Cleaner Tails	2.03	26.59	20.58	2.92	1.35
Re.Re. Cleaner Conc	8.96	36.32	8.30	17.67	2.41
Re.Re. Cleaner Conc2	5.04	34.93	10.05	9.56	1.64
Re.Re. Cleaner Conc3	3.33	32.38	13.27	5.85	1.43

TABLE 13

Sample B chromite performance in alkaline conditions at pH 8.3.

Stream	Mass%	Grade	Recovery
		Cr_2O_3	Cr_2O_3
RCC	26.85	42.92	59.87
RCT	4.34	36.38	8.20
CC	31.19	40.47	65.58
CT	4.6	20.58	4.92
RC	35.79	35.08	65.23
RT	42.16	3.7	8.10
Slimes	13.54	14.65	10.31
Cyclone underflow	91.49	19.3	91.73
Cyclone overflow	8.51	18.7	8.27

Table 13 shows chromite grade and recovery performance of sample B in alkaline conditions showing CMC175 employed was able to selectively recover chromite from associated gangue. Different cationic collectors and modifiers such as $CuSO_4$, $MgCl_2$ are recommended as per previous authors to investigate if they can reverse either chromite or orthopyroxene zeta potential to enhance selectivity in sample A (Wesseldijk *et al,* 1999; Siyuan *et al*, 2018).

CONCLUSIONS

This study investigated the recovery of fine chromite from UG2 tailings in South Africa. From this study it can be concluded that tailings from UG2 processing mines have varying gangue minerals and still contain substantial chromite that can be upgraded to a saleable 40 per cent Cr_2O_3 grade. Chromite selectivity is easily achieved in acidic conditions at pH 2.5. This was related to the zeta potential differences between chromite and associated gangue. In alkaline conditions, the presence of orthopyroxene as a major gangue possess a challenge in achieving selectivity. It is therefore recommended that other reagent types and modifiers should be tested to assess if the addition of a modifier can reverse chromite zeta potential in alkaline conditions.

REFERENCES

Feng, D and Aldrich, C, 2004. Recovery of Chromite fines from wastewater streams by column flotation. *Hydrometallurgy*, Vol. 72, pp. 319–325.

Gallios, G P, Deliyanni, E A, Peleka, E N and Matis, K A, 2007. Flotation of chromite and serpentine. *Separation and Purification*, Vol. 55, pp. 232–237.

Guney, A, Onal, G and Celik, M S, 1999. A new flowsheet for processing chromite fines by column flotation and the collector adsorption mechanism. *Minerals Engineering*, Vol. 12, pp 1041–1049.

Gupta, A and Yan, D S, 2006. *Minerals Processing Design and Operation*, Elsevier, Amsterdam, pp. 494–497.

Marape, G and Thiele, H, 2017. Recovery of chromite from UG2 primary rougher flotation tails. Mintek report.

Mosiane, M C, 2007. The impact of chrome ore exports on the local ferrochrome industry. Department of Mineral Resources. Directorate: Mineral Economics.

Murthy, Y R, Tripathy, S K and Kumar, C R, 2011. Chrome ore beneficiation challenges and opportunities. *Minerals Engineering*, Vol. 24, pp. 375–380.

Phillippe, R, 2015. Chrome makes it Stainless. *10th Asian Stainless Steel Conference*, Singapore. https://www.metalbulletin.com/events/download.ashx/document/speaker/7975/a0ID000000X0kINMAZ/Presentation Accessed [13 April 2019].

Roskill Information Services, 2019. Chromium markets suppressed with ongoing surplus ore supply. [Available online] https://www.globenewswire.com/news release/2019/06/19/1870969/0/en/Roskill-Chromium-markets-suppressed-with-ongoing-surplus-ore-supply.html [Accessed: 13 August 2020].

Siyuan, Y, Baohua, X, Lu, L and Li, C, 2018. Role of magnesium-bearing silicates in the flotation of pyrite in the presence of serpentine slimes, *Powder Technology*, vol. 332, pp. 1–7.

Wesseldijk, Q I, Reuter, M A, Bradshaw, D J and Harris, P J, 1999. Flotation behaviour of Chromite with respect to the beneficiation of UG2 ore. *Minerals Engineering*, Vol 12. Pp. 1177–1184.

Wills, B A and Napier-Munn, T J, 2006. *Magnetic and electrical separation*. Elsevier Science & Technology Books, pp. 353–372.

Yigit, E, 1981. Chromite Flotation. Mintek Technical Memorandum 15064.

Development and upcycling of sulfidic mining waste rock in alkali – activated materials with tackiness investigation

H Niu[1], Y Du[2], C Brumaud[3], P Kinnune[4], G Habert[5] and M Illikainen[6]

1. Doctoral student, Fibre and Particle Engineering Research Unit, University of Oulu, FI-90570, Oulu, Finland. Email: he.niu@oulu.fi
2. Doctoral student, Chair of Sustainable Construction, ETH Zürich, Zürich, Switzerland. Email: du@ibi.baug.ethz.ch
3. Postdoctoral researcher, Chair of Sustainable Construction, ETH Zürich, Zürich, Switzerland. Email: brumaud@ibi.baug.ethz.ch
4. Associate Professor, Fibre and Particle Engineering Research Unit, University of Oulu, FI-90570, Oulu, Finland. Email: paivo.kinnunen@oulu.fi
5. Professor, Chair of Sustainable Construction, ETH Zürich, Zürich, Switzerland. Email: habert@ibi.baug.ethz.ch
6. Professor, Fibre and Particle Engineering Research Unit, University of Oulu, FI-90570, Oulu, Finland. Email: mirja.illikainen@oulu.fi

ABSTRACT

Sulfidic mining wastes generated from mining processing such as mineral beneficiations and ore excavation possibly pose potential threats in environment and human activities due to the acid mine drainage and heavy metal leaching. It is essential to seek out alternative solutions to reprocess and repurpose those wastes rather than accumulating them in stockpiles or tailing impoundments.

Alkali-activated materials, sometimes equal to geopolymer (low calcium content), are three-dimensional frameworks by reacting aqueous alkali metal solutions with solid aluminosilicate powders. It facilitates the valourisation of potential secondary raw materials including mining waste rocks. Therefore, it is worthy to investigate the mining waste rock based geopolymer, thereby reducing the environmental impact and producing high value-added materials.

Mining waste rocks are received from Neves Corvo mine, Portugal, as raw materials for geopolymer preparation. Waste rock is not suitable for geopolymer production due to its chemically inert properties. However, mechanochemical activation using rod ball mill, was carried out to enhance the chemical reactivity in this study. Next, corresponding geopolymers were produced with different milling durations, that is 6 h, 12 h and 24 h. Different curing temperature were also investigated. Finally, 7-day compressive strength was measured to assess the mechanical performance of geopolymers. The tackiness properties of the waste rock-based geopolymer were evaluated. And tack test was performed with and without a Pentaethylenehexamine (PEHA) additive.

The results indicates that a longer milling duration led to a higher content of amorphous content. Sulfidic mining waste rock can be a potential candidate for alkali-activated materials after mechanochemical treatment. Curing regime has overwhelming effects on mechanical performance of final products. The introduction of PEHA can alter the rheological properties of the paste including altering sticky behaviour.

INTRODUCTION

Sulfidic waste rock is produced from mining sectors during the ore excavation. Waste rock is also a non-economical complex that is explored to access ores. The particle size of waste rock can vary from site to site, for instance, Smith *et al* (2013) investigated the Diavik waste rock project that the particle can range in mass from 5 kg to 10 kg. Sulfidic mining waste rock often contains sulfide minerals, which may lead to acid rock drainage if it was disposed without suitable treatments. To reduce the environmental impacts of waste rock, these dumps should be shaped appropriately. Especially, sulfidic waste rock needs to be covered to prevent sulfide oxidation after the mine closure (Brend, 2007). Backfill of crushed waste rock into goafs is widely used; however, the influence of particle size and compact behaviour needs to be carefully taken into consideration (Li *et al*, 2019). Cement paste backfill can be an alternative method, for contaminants can be stabilised in matrix (Coussy *et al*, 2012). Mining wastes are currently underutilised industrial side streams. They

possess potentially abundant aluminosilicate resources for cementitious materials manufacturing, including alkali-activated materials (Scrivener *et al*, 2018).

Alkali-activated materials are produced from reacting aluminosilicate-rich precursors with alkaline solutions, such as sodium silicate and sodium hydroxide solutions (Provis, 2013). The reaction of aluminosilicates with alkali solution are proposed by Duxson *et al* (2007) that amorphous aluminosilicate phases (metakaolin) can dissolve, reorganise, and polymerise further occurs to hardened samples. The preconditions can be concluded that the precursors have certain amounts of aluminosilicates which is also amorphous (chemically reactive) (Martins *et al*, 2021). Waste rock that based on aluminosilicates is potential candidate for producing alkali-activated materials.

It is essential to improve the chemical reactivity of mining waste rock for subsequent alkali activation. Thermal treatment has been widely used to improve the chemical reactivity of mining wastes. The most typical example of thermal treatment is the calcination of kaolin to produce metakaolin (Alonso and Palomo, 2001; Provis and Van Deventer, 2009). Other than thermal treatment, a potentially greener approach, mechanochemical treatment sheds some light on producing promising precursors for the alkali activation. MacKenzie *et al* (2008a) carried out the mechanochemical process rather than thermal treatment to enhance the chemical reactivity of 2:1-layered lattice aluminosilicates for alkali activation. It shows that vibratory disc mill for 15 min has the similar XRD pattern to that of ball milled for 60 h.

Stickiness has be a problem for alkali-activated materials while moulding these materials due to the sticky and viscous nature of alkali activators, effecting the workability (Nath and Sarker, 2012; Subramanian and Solaiyan, 2021). The sticky alkali-activated materials can sometimes clog the nozzle or attach to stainless steel moulds making it hard to demould and clean in the application of 3D printing. Tack test has been used to evaluate the stickiness in cement and food industry (Kawashima *et al*, 2014; Wang and Hartel, 2021).

In this paper, the potential of using sulfidic waste rock as secondary raw materials for producing alkali-activated materials were investigated. Mechanochemical activation was performed using a rod ball mill machine. The resulted waste rock-based alkali-activated materials are subjected to rheological test including oscillation measurements and tack test.

MATERIALS AND METHODS

Sulfidic mining waste rock (SWR) are received from Neves Corvo, Portugal. The chemical composition is shown in Table 1. About 7.3 Mt of waste rock is accumulated in Cerro do Lobo Tailings Management Facility over the period of 2010 to 2019. The fresh SWR is firstly jaw crushed with a Wedag jaw crusher and then double roller crushed utilising a Mesto Mineral Marcy roller crusher until a particle size lower than 1 mm. The subsequent mechanochemical activation (1 kg of SWR) was performed using a rod ball mill (TPR-D-950-V-FU-EH by Germatec, Germany) for 6 h, 12 h and 24 h with addition of 0.2 wt per cent grinding aid (Niu *et al*, 2021), which are named RB6h, RB12h and RB24h.

TABLE 1

Chemical composition of sulfidic waste rock by XRF spectroscopy.

Main component	SiO_2	Al_2O_3	CaO	MgO	K_2O	Fe_2O_3	SO_3	TiO_2	MnO	L.O.I.
(wt.%)	52.31	12.15	0.56	1.98	1.49	16.69	12.34	0.56	0.13	9.7

The alkali activator is prepared by mixing sodium silicate solution (VWR Chemicals, SiO_2: 26.5 per cent, Na_2O: 8 per cent, H_2O: 65.5 per cent) and sodium hydroxide pellets (VWR Chemicals, >97 per cent). Deionised water is used whenever it is required. The mix design is present in Table 2 (with liquid/solid = 0.35). The paste is produced by mixing rod ball mill treated SWR (70 g) with alkali activator using a shear mixer (IKA® WERKE) for 3 min at a rate of 700 rev/min. After pulling the paste in polyethylene moulds with a dimension of 20 mm (height) and 25 mm (diameter), a vibration machine (Vortex-Genie 2, Prolab Oy) is used to remove the air bubbles. The samples are demolded after curing in 23°C, 40°C, 60°C and 80°C oven for 24 h and continued curing until seven days for compressive strength test. The final geopolymers are dubbed RB6WRG, RB12WRG and

RB24WRG. Alkali-activated materials produced with raw waste rock are regarded as reference named as WRG.

TABLE 2

Mix design of rod ball milled samples for making corresponded alkali-activated materials.

Sample name	Na_2SiO_3 solution	NaOH	Extra water
RB6WRG	26.67 g	3.32 g	7.67 g
RB12WRG	-	-	-
RB24WRG	-	-	-

Particle size distribution (PSD) is determined using a laser diffraction particle size analyser (LS 13320, Beckman Coulter, Inc, Brea, CA, USA). X-ray diffraction analysis is subjected to a Rigaku SmartLab 4.5 kW, with the equipment parameters of Co source (40 kV and 135 mA) K_α ($K_{\alpha1}$ = 1.78892 Å; $K_{\alpha2}$ = 1.79278 Å; $K_{\alpha1/K\alpha2}$ = 0.5), scan rate of 3°/min and 0.02°/step. The phase identification is conducted using a PDXL2 Software Suite with an integrated PDF-4 (2019) database. 10 wt per cent rutile is introduced as internal standard to compare the crystalline intensity of each phase. Unconfined compressive strength is performed with a Zwick Roell 100 kN machine with a loading force of 2.4 kN/s until failure. Three parallel samples are prepared for each batch.

The tack test is performed using the Rheometer (Malvern Kinexus Lab plus). Serrated plate-plate geometry with a diameter of 40 mm is selected. The paste abovementioned is inserted between two paralleled serrated plates (40 mm in diameter) and pressed with a constant speed to reach a gap of 3 mm. To minimise the effect of ultimate memory, the paste is left 1 min for relaxing prior to starting the tack test. The evolution of normal force is recorded by lifting the upper plate with a velocity of 500 μm/s. A different pulling up speed was applied on RB12WRG to see the debonding process. In addition, RB12WRG is studied with and without chemical additive (1.6 wt per cent). Pentaethylenehexamine (PEHA, $C_{10}H_{28}N_6$, technical grade, Sigma-Aldrich) is utilised as the chemical additive.

RESULTS AND DISCUSSION

Mechanochemical activation of sulfidic waste rock

Mechanochemical activation of SWR is successful using a rod ball mill machine. The structure of certain minerals such as muscovite and clinochlore are disrupted which is revealed from XRD patterns in Figure 1a. The intensity of quartz and pyrite remains intact even after extending the milling duration to 24 h due to its stable structure and high crystallinity. It is obvious that the intensity of clinochlore and muscovite decreases with the incremental grinding time, in which RB24h expresses the amorphous feature, ie the peaks of 2:1-layered aluminosilicates are almost disappeared. The mechanism of mechanochemical activation of layered aluminosilicates has been studied previously (MacKenzie *et al*, 2008b; Niu *et al*, 2020). Those aluminosilicates are potential precursors for subsequent alkali activation when it reacts with alkali activators. To investigate the relationship between particle size distribution and amorphization, all the milled samples are subjected to particle size analyser Figure 1b. It significantly decreases the particle size after 6 h milling compared with raw waste rock. $D_{x(x=10,\ 50\ and\ 90)}$ reflects that the particle size of RB6h is nearly half of the size of original waste rock. When the grinding time increases, the particle size of RB6h and RB24h shows similarity but $D_{(50\ and\ 90)}$ of RB24h is slightly higher than that of RB12h. The results indicate that some particle agglomeration happened with prolonged milling time, but the amounts of smaller particles increase in terms of D_{10}. However, once the crystallinity is considered, it can be found that more amorphization occurred in RB24h with less particle size change. In our previous research, we found that the grinding aid could alter the structure of aluminosilicates and produce large amounts of irregularly shaped particles related to amorphous phases (Niu *et al*, 2021).

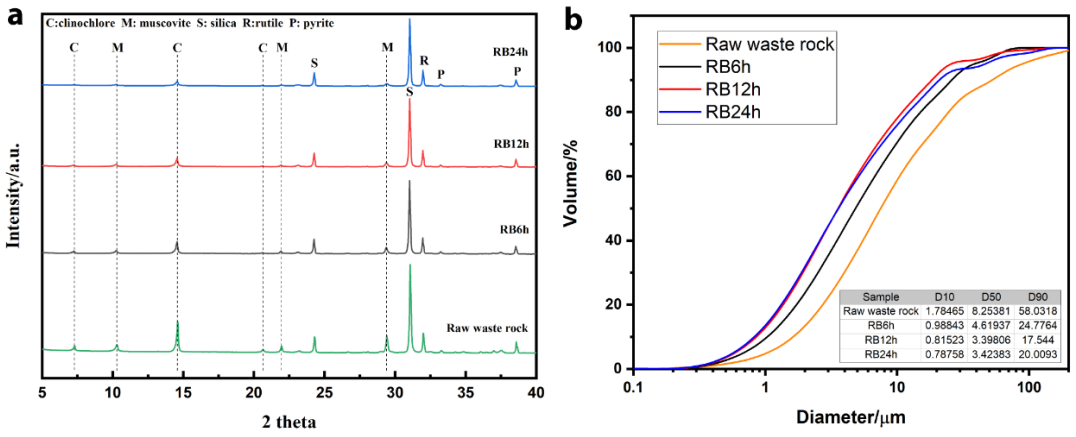

FIG 1 – XRD analysis (a) and particle size distribution (b) of rod ball milled samples with different time duration.

Alkali activation of sulfidic waste rock

The alkali-activated waste rock is prepared according to the recipe and the 7-day compressive strength of corresponding samples is presented in Figure 2. Most of the samples can be successfully demoulded after curing at certain temperature after 24 h, which means the reaction of alkali activation/geopolymerisation occurred, showing that a 3-dimensional aluminosilicate framework is formed. It is presumed that the aluminosilicate units are dissolved from amorphous phase of clinochlore and muscovite, thereafter, these units are reorganised and polymerised to condensed matrix (Duxson *et al*, 2007). The compressive strength of the final materials is increasing with the growing grinding time. Both RB12WRG and RB24WRG after curing under a temperature higher than 60°C have the suitable compressive strength for mining backfill (Cihangir *et al*, 2012). However, the volume expansion, shrinkage and long-term durability still need more research in the future.

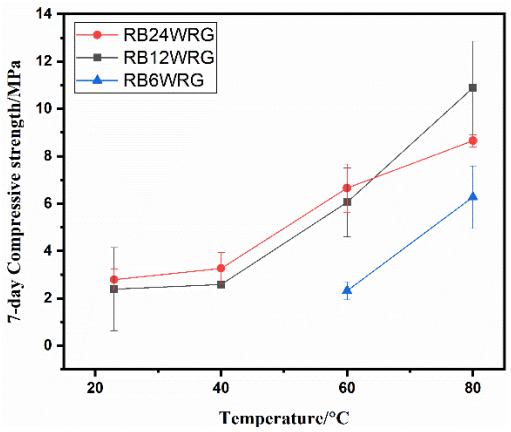

FIG 2 – Effect of curing temperatures on alkali-activated waste rock.

Figure 2 also shows the influence of curing temperature on the compressive strength of final alkali-activated materials. As for the sample prepared from RB6h, it is not possible to obtain hardened materials after curing under 23°C and 40°C while RB12h and RB24h can generate condense matrix with a lower compressive strength of 2.39 MPa and 2.79 MPa, respectively. A higher curing temperature results in a more favourable compressive strength. However, RB12WRG displays the highest compressive strength of more than 10 MPa at seventh day under 80°C which is higher than that of RB24WRG. It is mainly because of the high volume shrinkage due to the high temperature, leading to cracks and voids (Nasvi *et al*, 2012).

Tack test

Figure 3a displays the tack test of alkali-activated materials produced from mechanochemically treated SWR with different milling time. The curve shows that the normal force first increases to reach a peak force (F_{max}) and then decreases to a final plateau (Kaci *et al*, 2009). It requires a shorter

time to reach F_{max} with the increasing milling time of the precursors. It is interesting that the maximum F_{max} of pulling up can be varied with different milling time. Milling for 24 h can significantly decrease the tensile adhesive while 12 h treatment otherwise increases the adhesion, although the rupture process for both mixes almost complete equally. According to Meeten's research (2002), the yield stress has the relationship with F_{max}. When there is the same velocity applied, F_{max} is proportional to yield stress, therefore, 24 h milling samples possesses a similar yield stress as raw waste rock with more reactive property. Another interesting point is that the time for reaching Fmax decreases with the incremental grinding time, indicating the energy could dissipate faster within the pastes, in another word, which could reflect the pastes are getting more 'elastic' with the mechanochemical treatments.

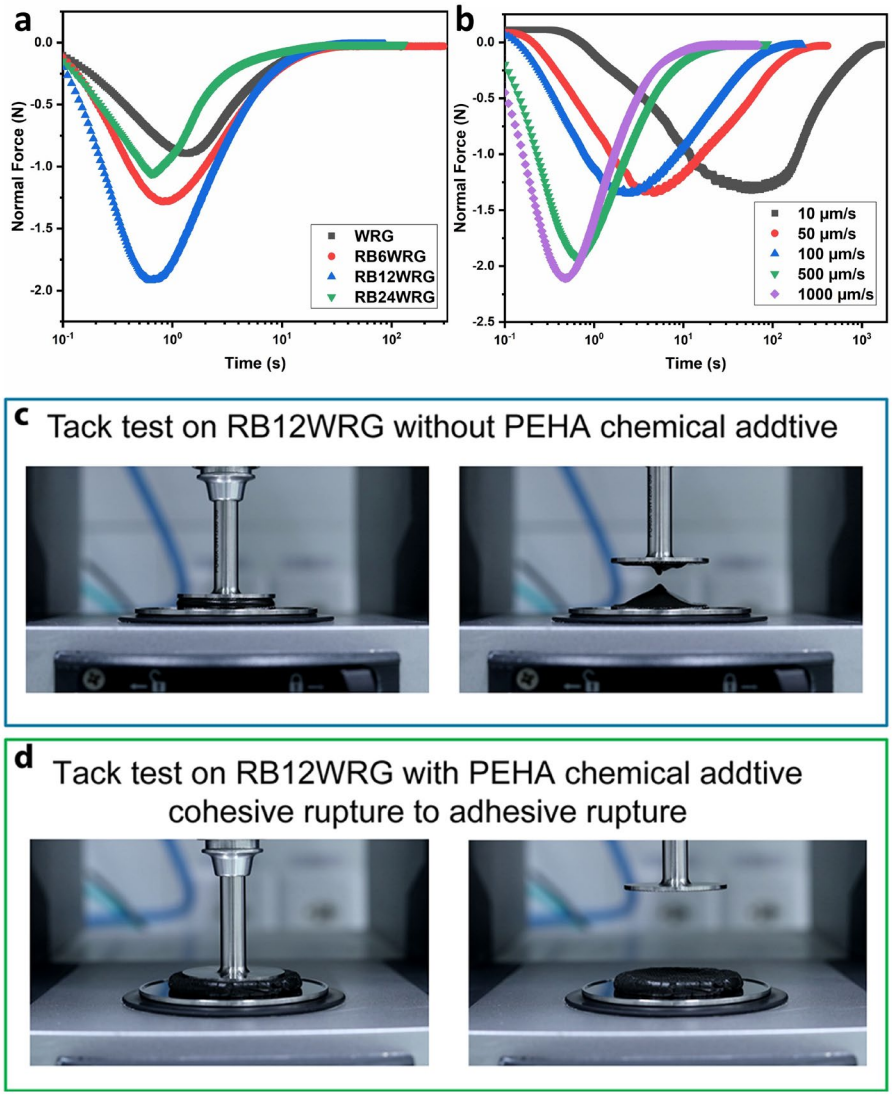

FIG 3 – Tack test of different geopolymer samples (a), different pulling up speed applied on RB12WRG (b), and tack test without (c) and with additives (d) of alkali-activated sulfidic waste rock.

Figure 3b shows the evolution of the pulling up force with time in terms of different stretching speeds on RB6WRG (with highest F_{max}). In a range of lower speeds, such as 10 to 100 µm/s, lead to a same F_{max} which means that the materials intrinsic adhesion is dominate the rupture behaviour independent with velocities. As for higher speeds of 500 and 1000 µm/s, it corresponds to a higher flow resistance other than materials intrinsic adhesion. Compared with cement samples, it shows a shorter time to reach the maximum value within a second when the speeds are higher than 500 µm/s (Bouras *et al*, 2019; Van Tien, 2014). To eliminate the effect of resistance to dynamic flow (Qian, 2017), F_{max} under 100 µm/s can be considered as the closest value to cohesion for RB6WRG (1.37 N). Further research is more interesting on performing velocity curve on all RBWRG materials.

The effect of PEHA addition on the stickiness of waste rock-based alkali-activated materials is presented in Figure 3c and 3d. Without chemical additive incorporated, the sample expresses cohesive rupture behaviour. The failure mode of tack test is changed to adhesive rupture once 1.6 wt per cent PEHA added, and the paste no longer glues to the upper plate. Cohesive rupture refers to the interaction inside the materials, whereas adhesive rupture happens at the interface between the materials and substrate/geometry (Fujii Yamagata, 2018). Reducing stickiness of aluminosilicate clays, such as kaolin and illite, has been reported that PEHA can be a potential anti-sticking chemical for the application of tunnelling (Zumsteg *et al*, 2014; Zumsteg and Puzrin, 2012). The relationship between PEHA and dissolved aluminosilicate units is still not clear at this stage. However, it can be assumed that long polymer chain of PEHA can attach to the surface of the mineral particles, forming a covering agent or lubricant in the waste rock intervals.

CONCLUSIONS

The sulfidic mine tailings are successfully used to prepare alkali-activated materials with good compressive strength after mechanochemical activation using a rod ball mill. More reactive amorphous phase which could facilitate the aluminosilicate dissolution process was formed after treatment. Furthermore, mechanochemical process can significantly affect the particle interaction leading to different tackiness behaviours.

PEHA as chemical additive can significantly reduce the adhesive behaviour between the substrate and alkali-activated materials for future application. Furthermore, it is expected to further investigate the optimum dosage amount of such chemical additive and principal mechanism between the interface of PEHA and alkali-activated materials. Evolution of pulling up force versus time with different polymer content will be performed in the future by using probe tack test with different stretching velocities.

ACKNOWLEDGEMENTS

This research is funded by the European Union's Framework Program for Research and Innovation Horizon 2020 under Grant Agreement No. 812580. (Project 'MSCA-ETN SULTAN', https://etn-sultan.eu). H.N would like to thank the financial support from of Oulun yliopiston tukisäätiö.

REFERENCES

Alonso, S, Palomo, A, 2001. Calorimetric study of alkaline activation of calcium hydroxide–metakaolin solid mixtures. *Cement and Concrete Research* 31, 25–30. https://doi.org/10.1016/S0008–8846(00)00435-X

Bouras, R, Mohand, C S H, Sonebi, M, 2019. Adhesion and rheology of joints fresh mortars. *Journal of Materials and Engineering Structures «JMES»* 6, 157–165.

Brend, L G, 2007. *Mine Wastes, Characterization, Treatment and Environmental Impacts*.

Cihangir, F, Ercikdi, B, Kesimal, A, Turan, A, Deveci, H, 2012. Utilisation of alkali-activated blast furnace slag in paste backfill of high-sulphide mill tailings: Effect of binder type and dosage. *Minerals Engineering* 30, 33–43. https://doi.org/10.1016/j.mineng.2012.01.009

Coussy, S, Benzaazoua, M, Blanc, D, Moszkowicz, P, Bussière, B, 2012. Assessment of arsenic immobilization in synthetically prepared cemented paste backfill specimens. *Journal of environmental management* 93, 10–21.

Duxson, P, Fernández-Jiménez, A, Provis, J L, Lukey, G C, Palomo, A, van Deventer, J S J, 2007. Geopolymer technology: the current state of the art. *Journal Materials Science* 42, 2917–2933. https://doi.org/10.1007/s10853–006–0637-z

Fujii Yamagata, A, 2018. Les propriétés adhésives et rhéologie interfaciale de mortiers colles.

Kaci, A, Bouras, R, Chaouche, M, Andreani, P.-A, Brossas, H, 2009. Adhesive and rheological properties of mortar joints. *Applied rheology* 19, 51970–1.

Kawashima, S, Chaouche, M, Corr, D J, Shah, S P, 2014. Influence of purified attapulgite clays on the adhesive properties of cement pastes as measured by the tack test. *Cement and Concrete Composites* 48, 35–41.

Li, M, Zhang, J, Song, W, Germain, D M, 2019. Recycling of crushed waste rock as backfilling material in coal mine: effects of particle size on compaction behaviours. *Environmental Science and Pollution Research* 26, 8789–8797. https://doi.org/10.1007/s11356–019–04379–9

MacKenzie, K J D, Komphanchai, S, Vagana, R, 2008a. Formation of inorganic polymers (geopolymers) from 2:1 layer lattice aluminosilicates. *Journal of the European Ceramic Society* 28, 177–181. https://doi.org/10.1016/j.jeurceramsoc.2007.06.004

MacKenzie, K J D, Komphanchai, S, Vagana, R, 2008b. Formation of inorganic polymers (geopolymers) from 2:1 layer lattice aluminosilicates. *Journal of the European Ceramic Society* 28, 177–181. https://doi.org/10.1016/j.jeurceramsoc.2007.06.004

Martins, N P, Srivastava, S, Simão, F V, Niu, H, Perumal, P, Snellings, R, Illikainen, M, Chambart, H, Habert, G, 2021. Exploring the Potential for Utilization of Medium and Highly Sulfidic Mine Tailings in Construction Materials: A Review. *Sustainability* 13. https://doi.org/10.3390/su132112150

Meeten, G, 2002. Constant-force squeeze flow of soft solids. *Rheologica acta* 41, 557–566.

Nasvi, M M, Gamage, R P, Jay, S, 2012. Geopolymer as well cement and the variation of its mechanical behavior with curing temperature. *Greenhouse gases: science and technology* 2, 46–58.

Nath, P, Sarker, P K, 2012. Geopolymer concrete for ambient curing condition. Presented at the *Proceedings of the Australasian structural engineering conference*, Perth, Australia, pp. 11–13.

Niu, H, Adrianto, L R, Escobar, A G, Zhukov, V, Perumal, P, Kauppi, J, Kinnunen, P, Illikainen, M, 2021. Potential of Mechanochemically Activated Sulfidic Mining Waste Rock for Alkali Activation. *Journal of Sustainable Metallurgy.* https://doi.org/10.1007/s40831–021–00466–9

Niu, H, Kinnunen, P, Sreenivasan, H, Adesanya, E, Illikainen, M, 2020. Structural collapse in phlogopite mica-rich mine tailings induced by mechanochemical treatment and implications to alkali activation potential. *Minerals Engineering* 151, 106331. https://doi.org/10.1016/j.mineng.2020.106331

Provis, J L, Van Deventer, J S J, 2009. Introduction to geopolymers, in: *Geopolymers*. Elsevier, pp. 1–11. https://doi.org/10.1533/9781845696382.1

Provis, J, 2013. *Alkali activated materials: state-of-the-art report*, RILEM TC 224-AAM Springer, New York.

Qian, Y, 2017. *Characterization of structural rebuilding and shear migration in cementitious materials in consideration of thixotropy*. Columbia University.

Scrivener, K L, John, V M, Gartner, E M, 2018. Eco-efficient cements: Potential economically viable solutions for a low-CO2 cement-based materials industry. *Cement and Concrete Research* 114, 2–26. https://doi.org/10.1016/j.cemconres.2018.03.015

Smith, L J D, Blowes, D W, Jambor, J L, Smith, L, Sego, D C, Neuner, M, 2013. The Diavik Waste Rock Project: Particle size distribution and sulfur characteristics of low-sulfide waste rock. *Applied Geochemistry* 36, 200–209. https://doi.org/10.1016/j.apgeochem.2013.05.006

Subramanian, N, Solaiyan, E, 2021. GGBFS & M-sand impact on workability and strength properties of fly-ash based geopolymer concrete. *Indian Journal of Engineering and Materials Sciences (IJEMS)* 27, 67–76.

Van Tien, P, 2014. Influence of re-dispersible powder on the properties of mortars. *Journal of Materials and Engineering Structures «JMES»* 1, 2–10.

Wang, R, Hartel, R W, 2021. Caramel stickiness: Effects of composition, rheology, and surface energy. *Journal of Food Engineering* 289, 110246.

Zumsteg, R, Plötze, M, Puzrin, A, 2014. Reduction of the clogging potential of clays: new chemical applications and novel quantification approaches. Presented at the *Bio-and Chemo-Mechanical Processes in Geotechnical Engineering: Géotechnique Symposium in Print 2013*, ICE Publishing, pp. 44–54.

Zumsteg, R, Puzrin, A M, 2012. Stickiness and adhesion of conditioned clay pastes. *Tunnelling and Underground Space Technology* 31, 86–96.

Water treatment methods for mineral processing operations

H A G Rodriguez[1], B Tadesse[2], B Albijanic[3] and L G Dyer[4]

1. Western Australian School of Mines, Curtin University, Kalgoorlie WA 6430. Email: h.guerraro@postgrad.curtin.edu.au
2. Western Australian School of Mines, Curtin University, Kalgoorlie WA 6430. Email: bogale.tadesse@curtin.edu.au
3. Western Australian School of Mines, Curtin University, Kalgoorlie WA 6430. Email: boris.albijanic@curtin.edu.au
4. Western Australian School of Mines, Curtin University, Kalgoorlie WA 6430. Email: laurence.dyer@curtin.edu.au

ABSTRACT

Limited freshwater availability, increasing competition for water among multiple users, cost of purification, corporate sustainability goals etc, are the main factors driving the minerals industry to focus on water quality and usage. Increasing water reuse and accessing alternative sources to freshwater for mineral processing, particularly in flotation, are potential strategies being implemented to improve water efficiency. In flotation, good water quality is needed to develop an appropriate reagent scheme and optimise operating conditions to maximise performance. High concentrations of dissolved ions in groundwater, sea water, or recycled water may alter the water structure, particle surface wettability, and colloidal interactions between bubbles and particles, negatively affecting mineral flotation. This paper aims to identify water treatment options that produce suitable water for flotation and other unit operations. In addition, it discusses the performance of nanofiltration membranes to have water with enough quality for the flotation of rare-earth minerals based on the ionic strength tolerance threshold at which impurities begin to impact the separation process.

This study found that two of the membranes used could reject more than 96 per cent of divalent cations and more than 76 per cent of sodium under the conditions of 12 bar of transmembrane pressure and 65 per cent of the recovery. It also was demonstrated that the lyotropic series of rejection agrees with the hydration energy and the salt diffusion coefficient of the different ions.

INTRODUCTION

The mineral processing sector consumes a considerable amount of water; for instance, processes that do not reuse water utilise between 1.9 to 3 m^3 of water per ton of ore processed (Bulut and Yenial, 2016). Water is used in a wide range of mining activities, and due to the environmental preoccupation and the lack of water, the industry has become aware of its responsibilities. It is constantly evaluating the best way to use water. The search for improvements in conservation and reuse increases the recycling and the use of lower quality water in different sections of the operation, such as groundwater or sea water, that usually contains high concentrations of ions and salts. At the same time, processes tend to be in areas where the demand of different industrial sectors are competing with the use of domestic water, or in areas where the access to water of quality is scarce and expensive for the operation due to the transportation costs (Di Feo *et al*, 2021).

Several mine sites in Australia have introduced saline water in their mineral processing practice. Base metal sulfide flotation plants at Mt Keith, Leinster, and the Kambalda Nickel Concentrator in Western Australia use bore water with high ionic strength. Saline water is used at KCGM and Kanowna Belle for sulfide (gold ore) flotation. Saline or sea water is also used in many other flotation plants worldwide, including copper plants in Chile, gold-rich copper ore processing plants in Indonesia, and base metal sulfides flotation in South Africa. In some cases (eg Kanowna Belle gold mine), the salinity of the water used in flotation can reach up to 200 000 mg/L, which is several times higher than that of sea water (Wang and Peng, 2014).

Multiple studies have reported the effect of electrolytic species dissolved in water on the flotation processes. The different impacts on the recovery of valuable minerals depend on the ore type and the physicochemical characteristics of the water. Generally, the flotation of copper sulfide minerals is positively impacted by the presence of high amounts of calcium and sulfate; however, in the case of lead-zinc sulfide minerals, the effect of high ions concentration seems to be dependent on the

mineralogy of the ore, the chemical composition of the water and the process itself with some study cases demonstrating enhance in the recovery. In contrast, the recovery in flotation is suppressed (Bulut and Yenial, 2016).

Flotation of phosphate minerals such as monazite, which is one of the primary sources for rare earth elements, is affected by bivalents cations such as Ca^{+2} and Mg^{+2} charging the surface of the mineral positively, causing the increase in the consumption of reagents (Derhy *et al*, 2020). For example, Zhang *et al* (2017) demonstrated that in the process of flotation of monazite with fatty acids as a collector, ions of $CaOH^{+}$ present in the water were attached by hydrogen bonding at the surface of the monazite, decreasing the hydrophobicity of the monazite, hence reducing its recovery. Salts and hardness in water are highly reactive, with fatty acids developing insoluble compounds resulting in loss of selectivity of the reagents, making froth flotation and tailing challenging management operations (Dos Santo *et al*, 2010; Ozkan and Acar, 2004). Keeping in mind the flotation of the ionic strength tolerance, a threshold at which ions in the water begin to impact the separation process has been defined. In an ongoing unpublished study at the Western Australia School of Mines, it has been identified that concentrations below 50 ppm for divalent cations (Ca, Mg) and below 500 ppm of sodium in water can be tolerated by the process without representing significant changes in recovery and grade.

Water is usually a significant concern in the mining industry in Australia and worldwide in general. It is becoming more relevant to find water treatment methods suitable for each operation financially viable considering the vast amount used in mineral processing operations. Currently, there are several treatment options involving physical, electro, and chemical processes that remove salts through a membrane or an ion exchange resin inducted by a specific current or precipitation of the ions as an insoluble salt.

Membrane separation methods such as reverse osmosis have been implemented in several processes because this method provides rates of remotion of dissolved species as high as 98 per cent (Wang *et al*, 2019). Many mineral processing operations do not require water of ultra-high quality, then; reverse osmosis becomes an overvalued option.

Waters rich in sulfate (>700 mg/L) and content of calcium higher than 100 mg/L is not recommended in this process because of the high scaling potential of $CaSO_4$ and all the expenses associated with the frequent membrane replacement (Bowell and Parshley, 2000). Reverse osmosis is an energy-intensive process, accounting for around 44 per cent of its cost. In countries like Australia, where the energy cost has a fundamental role in the industry, it becomes an appreciable portion of the processing expenses (Bajpayee *et al*, 2011). On the other side, a nanofiltration is an option that can provide enough water quality for mineral processing operations removing divalent under the proper membrane selection. In the specific conditions, some monovalent ions with less cost associated since this process are used lower transmembrane pressures than reverse osmosis (Deepti *et al*, 2020; Dach, 2009).

MATERIALS

The raw water for this study was provided from one of the bores at Mt Weld Mine operations, and ICP-MS determined the concentration of cations. The Ca, Mg, and Na concentration found in the raw water was 140, 167 and 1547 mg/L, respectively.

The filtration experiments were conducted in a pilot unit supplied by Ecotechnol Australia (Figure 1). This pilot unit was designed to test different UF and NF membranes under other conditions such as pressure and permeate recovery. The Ecotechnol rig is mainly composed of one feed tank of the volume of 0.1 m^3, a high-pressure booster pump which was used for the filtration and for the cleaning of the membrane, one pressure vessel housing on a standard 40” X4” membrane module with retractile end and feed caps allowing the change of membrane, a manual regulation valve on the concentrate line to adjust the pressure of operation and the permeate and concentrate lines which can be fitted as recirculation loop with the feed tank and an external scale to measure the weight of the desirable recovery of permeate.

FIG 1 – Ultrafiltration – Nanofiltration rig.

Three organic nanofiltrations (NF) membranes and one ultrafiltration (UF) membrane fabricated by different companies (Dow Filmtec and Membranes Development specialists (MDS) were studied. The nanofiltration membranes used are thin-film composite membranes NF90 and are characterised as tight nanofiltration membranes with relatively high sodium chloride rejection (>85 per cent). Table 1 shows the commercial names of the membranes and their correspondent suppliers as the primary polymer used for their fabrication.

TABLE 1

Commercial name and manufacturer of the NF and UF membranes.

Commercial name	Application	Manufacturer	Polymer
UF Ecotechnol	Ultrafiltration	MDS – Ecotechnol	Polyamide
NF90–4040	Nanofiltration	DOW Filmtec	Polyamide
4040 D Ecotechnol	Nanofiltration	MDS – Ecotechnol	Polyamide
4040 A Ecotechnol	Nanofiltration	MDS – Ecotechnol	Polyamide

EXPERIMENTAL TECHNIQUES

Before each experiment, the membranes were washed with caustic solid (0.2 per cent w/w) to restore the membrane's permeability. Each membrane was pressurised using deionised water at 4 bars for 30 min until the conductivity of the permeate was steady and similar to the initial deionised water.

As the raw water used in the experiments was obtained from one of the bores at Mt Weld mine, an ultrafiltration stage was required as pre-treatment to avoid nanofiltration membrane fouling. The nanofiltration experiments were carried out with three different nanofiltration membranes and an initial mass of 22 kg of ultra-filtrated bore water from the Mt Weld mine site. The concentrate was recirculated to the feed tank, and the permeate was collected and sampled at three different recoveries (15, 45 and 65 per cent). The feed pressure was adjusted for each test and was varied in the range of 8 to 20 bar. Additionally, the permeate flux and the ion's rejection were determined by measuring the permeate flow and the concentration of ions in the permeate.

RESULTS AND DISCUSSION

Hydraulic permeability

The hydraulic permeability (Lp) of the nanofiltration membranes tested was obtained from the slop of the fluxes obtained at different pressures, additionally from the x-intercept was determined the critical forces (Pc), which is the pressure when the transmembrane pressure is equal to osmotic pressure triggering the mobilisation of ions from the feed water to the concentrate.

It was found that the flux through the membranes is proportional to the transmembrane pressure (Figure 2) obeying the homogenous solution diffusion through the polymeric membrane model. That describes the proportionality of the water mass transfer flux and the pressure differential across the membrane. The permeate flux with the membranes NF90 4040 and 4040A starts at an applied pressure of 0.884 and 2.45 bar, respectively, while 4040D starts at 0.078 bar for the membrane. This indicates that the former membrane has the most expansive pore size, resulting in lower ions rejection. Membrane 4040A has the tightest pores and is more dependent on osmotic pressure, requiring more force to mobilise the feed through the membrane. Additionally, because of the differences in pore size between the membranes, the permeability of the membranes differs from one to another; as the pore size decrease, the ions in solution make the surface of the membrane more compact, reducing the permeability of the membranes.

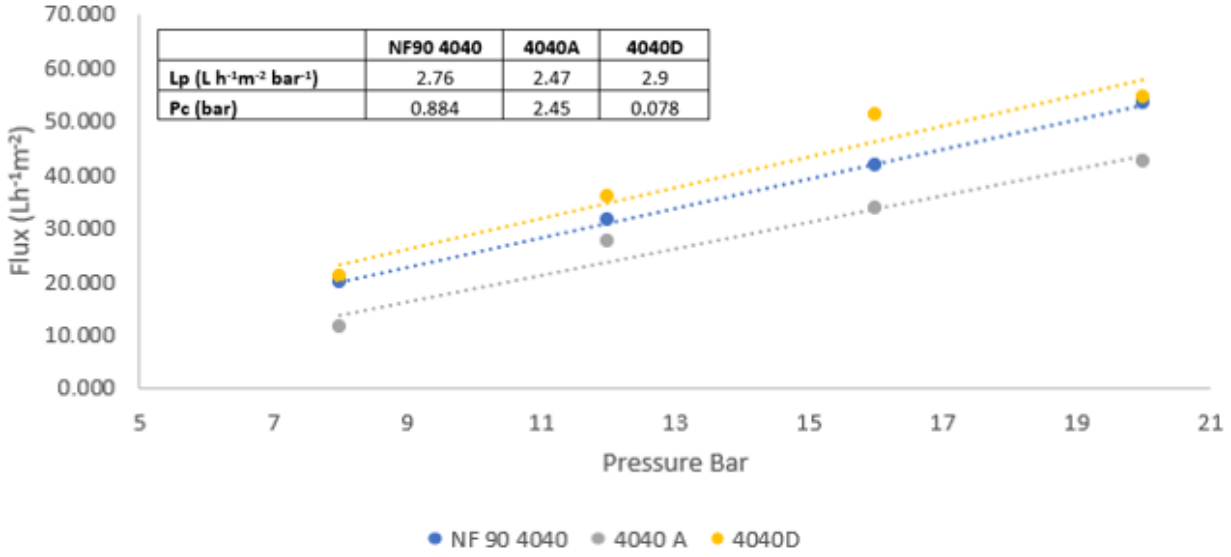

FIG 2 – Bore water Mt Weld mine flux as a function of pressure.

Rejection of cations

The three different membranes rejection of calcium, magnesium, and sodium was conducted in various conditions (Table 2). The pattern of denial is similar for the three membranes; as the transmembrane pressure increases, the ion rejection increase, which agrees with results reported by other researchers (Ahmad *et al,* 2004). It was observed that while the recovery increases, the membrane performance decreases. This is because the concentration returns to the feed stream, increasing the concentration of ions to be rejected, growing the ion driving force and changing membrane surface characteristics affecting the rejection of ions.

TABLE 2

Ion rejection as a function of pressure and recovery.

Pressure (bar)	Recpovery	Ca			Mg			Na		
		NF90 4040	4040A	4040D	NF90 4040	4040A	4040D	NF90 4040	4040A	4040D
8	15%	99%	88%	55%	99%	95%	74%	79%	82%	30%
	45%	98%	89%	50%	98%	93%	70%	76%	76%	26%
	65%	98%	80%	46%	98%	88%	67%	74%	61%	23%
12	15%	99%	97%	59%	99%	98%	76%	82%	91%	36%
	45%	98%	97%	57%	98%	97%	74%	78%	89%	35%
	65%	98%	96%	52%	98%	97%	71%	76%	86%	31%
16	15%	99%	97%	56%	99%	98%	74%	87%	90%	21%
	45%	99%	97%	53%	99%	97%	72%	83%	89%	19%
	65%	98%	96%	51%	99%	96%	70%	80%	86%	18%
20	15%	99%	97%	52%	99%	97%	68%	87%	90%	26%
	45%	98%	97%	53%	98%	97%	70%	83%	88%	24%
	65%	98%	96%	52%	98%	96%	69%	80%	86%	22%

Figure 3 shows the trend of ions rejection by the membranes 4040A and NF90 4040, which were the membranes with better performance. The rejection mechanisms with the membranes are driven by the membrane's pore size and the transmembrane pressure achieving the maximum rejection over 12 bar of pressure. The NF90 4040 has a high rejection of divalent ions from 8 bar of pressure applied. The surface of the NF90 4040 may be a slightly more negative charge than the 4040A facilitating the divalent ions rejection at lower pressures. In the case of sodium rejection, the low permeability and the tightest pores of the 4040A membrane plays a fundamental role in increasing sodium rejection.

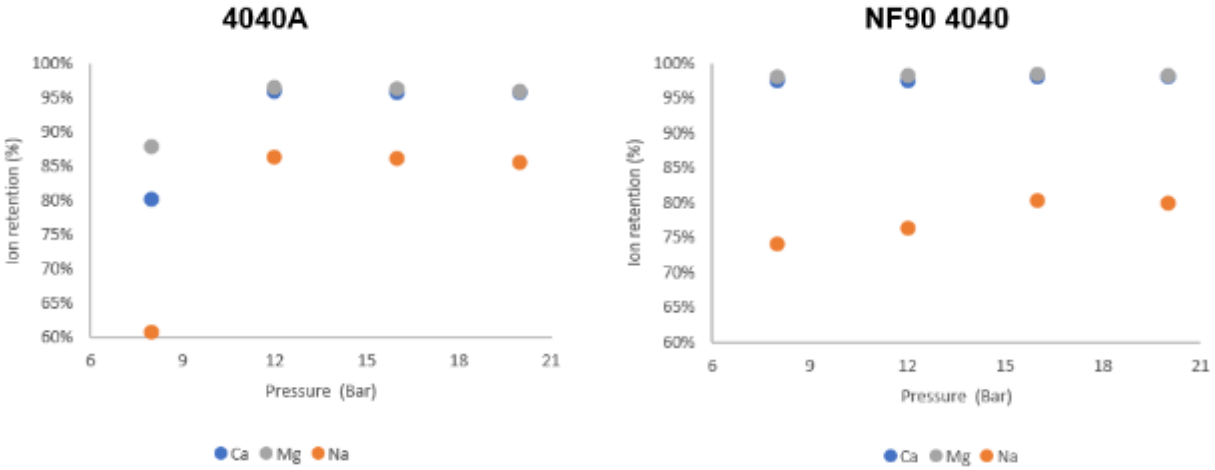

FIG 3 – Ion rejection at different pressure at 65 per cent recovery.

The 4040A and the NF90 4040 membranes have performed better than the 4040D membrane rejecting more than 95 per cent of the divalent ions (Ca^{+2}, Mg^{+2}) and more than 74 per cent of monovalent ions (Na^{+}) in all the pressure and recovery range evaluated. The former membrane has the largest pores showing low rejection of divalent ions (under 86 per cent) and monovalent ions (under 22 per cent) at the higher pressure and 65 per cent of the recovery.

The rejection of ions in this study obeys the lyotropic series of rejection by nanofiltration membranes, following the next order of rejection Mg^{+2}>Ca^{+2}>Na^{+}, suggesting that the divalent ions are rejected better than monovalent ions (Koyuncu *et al,* 2001). To validate the lyotropic series rejection of the membranes used, the empirical linear equation found by Wiesner and Aptel (1996), described the rejection as a function of pressure.

$$\frac{\Delta P}{R} = \frac{Z_2}{Z_1}\Delta P + \frac{1}{Z_1}$$

Where R is the rejection of the ion expected by the membrane at a determined pressure, z_1 and z_2 are constants for each ion and each membrane, in that order of ideas $z_{Mg}>z_{Ca}>$ a comparing each membrane. Table 3 shows the constants z_1 and z_2 of each ion in each membrane, which agrees with the expected lyotropic rejection series.

TABLE 3

Lyotropic constants for each ion in each membrane.

Constants	Ca^{+2}			Mg^{+2}			Na^{+}		
	4040D	4040A	NF90 4040	4040D	4040A	NF90 4040	4040D	4040A	NF90 4040
Z_1	0.37	0.47	12.18	3.61	1.03	51.02	0.04	0.20	0.70
Z_2	0.65	0.44	12.37	5.14	1.02	51.83	0.03	0.18	0.82

One of the main reasons for the order of ion rejection (Mg>Ca>Na) is because the differences in the hydration energy of each ion: 2018, 1548 and 407 kJ $mol^{-1,}$ respectively, which indicates that ions with high hydration energy will require more energy to push it through the pores of the membranes. In addition, added to the hydration energy, the salt diffusion coefficient of monovalent ions is higher than the calcium and magnesium (Ahmad *et al,* 2004).

CONCLUSIONS

Usually, mineral processing operations that require high water purity use methods such as reverse osmosis to remove the complex ions, with high energy consumption and high operational costs. Therefore, this study presents nanofiltration as an alternative method that, under the right conditions of operation and the right membrane can be applied as potential, which in comparison with reverse osmosis, uses low pressures and low operational costs. The nanofiltration membranes NF90 4040 and 4040A and4040D have been employed in a scale rig to study their performance to produce water with concentrations under the threshold of 50 mg/L of calcium and magnesium and 500 mg/L of sodium. It was found that the NF90 4040 and the 4040A membranes were able to produce a permeate with enough quality not to affect critical mineral processing operations such as the flotation of monazite. Also, it was found that both membranes (NF90 4040, 4040A) reject more than 96 per cent of calcium and magnesium and more than 76 per cent at pressures over 12 bar and recovery of 65 per cent. The results also show that the membrane 4040D did not perform well for the bore water used in the tests.

ACKNOWLEDGEMENTS

This study has been supported by Lynas and Minerals Research Institute of Western Australia through Master of Philosophy scholarship at Curtin University (Western Australian School of Mines)

REFERENCES

Ahmad, A, Ooi, B, Mohammad, A and Choudhury, J, 2004. Development of a highly hydrophilic nanofiltration membrane for desalination and water treatment. *Desalination,* 168, 215–221.

Bajpayee, A, Luo, T, Muto, A and Chen, G, 2011. Shallow temperature membrane-free desalination by directional solvent extraction. *Energy and environmental science,* 4, 1672–1675.

Bowell, R and Parshley, J, 2000. Sulphate and salt minerals: The problem of treating mine waste. *Mining environmental,* 11–13.

Bulut, G and Yenial, U, 2016. Effects of major ions in recycled water on sulphide minerals flotation. *Minerals and metallurgical processing,* 33 (3), 137–143.

Dach, H, 2009. Comparing nanofiltration and reverse osmosis processes for selective desalination of brackish water feeds. PhD thesis (unpublished) Engineering science, University D Angers.

Deepti, A, Sinha, P, Biswas. S, Sarkar, Bora, U and Purkait, M, 2020. Separation of chloride and sulphate ions from nanofiltration rejected wastewater of steel industry. *Journal of water process engineering,* 33, 101–108.

Derhy, M, Taha, Y, Hakkou, R and Benzaazoua, M, 2020. Review of the Main Factors Affecting the Flotation of Phosphate Ores. *Minerals,* 10, 1109.

Di Feo, A, Hill, C, Hart, B, Volchek, K, Morin, L and Demeres, A, 2021. The effects of water recycling on flotation at a North American concentrator. *Minerals Engineering,* 170.

Dos Santo, M, Santana, R, Capponi, F, Ataide, C and Barrozo, M, 2010. Effect of ionic species on the performance of apatite flotation. *Separation and purification technology,* 76 (1), 15–20.

Koyuncu, I, Yazgan, M, Topacik, D and Sarikaya, H, 2001. Evaluation of the low pressure RO and NF membranes for an alternative treatment of Buyukcekmece Lake. *Water Science and technology: Water supply,* 1(1), 107–115.

Ozkan, S, and Acar, A, 2004. Investigation of impact of water type on borate ore flotation. *Water research,* 38(7), 1773–1778.

Wang, B, and Peng, Y, 2014. The effect of saline water on mineral flotation – A critical review, *Minerals Engineering,* 66, 13–24.

Wang, Y, Guo, X, Bai, Y and Sun, X, 2019. Effective removal of calcium and magnesium sulfates from wastewater in the rare earth industry. *Royal society of chemistry*, 9, 33922–33930.

Wiesner, M and Aptel, P, 1996. *Mass Transport and Permeate Flux and Fouling in Pressure-Driven Processes. In: Water Treatment Membrane Handbook* (McGraw-HillCom: New York.)

Zhang, W, Honaker, R and Groppo, J, 2017. Flotation of monazite in the presence of calcite part I: Calcium ion effects on the adsorption of hydroxamic acid. *Minerals Engineering,* 100.

Mechanical recycling of Li-Ion batteries – processing challenges

C Wilke[1], A Kaas[2], T Lyon[3] and U A Peuker[4]

1. Research Associate, Institute of mechanical process engineering and mineral processing – Technical University Freiberg, Agricolastr. 1, 09599 Freiberg, Germany. Email: Christian.Wilke@mvtat.tu-freiberg.de
2. Research Associate, Institute of mechanical process engineering and mineral processing – Technical University Freiberg, Agricolastr. 1, 09599 Freiberg, Germany. Email: Alexandra.Kaas@mvtat.tu-freiberg.de
3. Research Associate, Institute of mechanical process engineering and mineral processing – Technical University Freiberg, Agricolastr. 1, 09599 Freiberg, Germany. Email: Tony.Lyon@mvtat.tu-freiberg.de
4. Professor, Institute of mechanical process engineering and mineral processing – Technical University Freiberg, Agricolastr. 1, 09599 Freiberg, Germany. Email: Urs.Peuker@mvtat.tu-freiberg.de

ABSTRACT

As part of global environmental protection measures, there is an increasing focus on decarbonisation. This also includes the use of electric motors as an alternative to combustion engines in the transport sector. This is accompanied by an increasing demand for high-performance batteries. The lithium-ion batteries (LIB) usually used require many valuable raw materials. In order to secure the demand for these raw materials in the long-term and globally, the batteries must be recycled, as this is the only way to close the material cycle.

The whole recycling chain includes different process technologies eg thermal, hydro – and pyrometallurgical or mechanical. This contribution will focus on the mechanical processing of the spent LIB. Prior to the mechanical treatment the LIBs are disassembled to cell level and have to be discharged in order to prevent an electrical hazard. In a first comminution step, the cells are cut up so that the contained solvents from the electrolyte can evaporate. It is important to remove the solvents as they are toxic and pose a fire hazard.

After drying the shredded material is screened to remove the so-called black mass (fraction <1 mm) which contains most of the electrode coating. The coarse fraction is sent to a two-stage air flow separation in which the heavy particles (plastics, steel, aluminium) of the cell housing and the separator foil are separated. The remaining fraction is a mixture of the current collector foils with residual coating and remaining impurities of separator foil and housing.

As the foils have a similar settling velocity due to their shape (thin and flat) and density (because of the remaining coating), they are stressed again to delaminate and compact them. After the stressing, the current collector foils get screened to take out another black mass fraction which contains the rest of the coating. The coarse fraction contains the foils which are separated in another flow sorting to produce an aluminium and a copper concentrate. All concentrates can be further processed in metallurgical processes. But higher material recycling rates can be generated through upstream mechanical processing.

During the process chain the recycling of LIB faces a number of challenges. Different hazards can occur due to the destroying of the electrochemical isolation. Moreover, some of the chemicals in the LIB are highly flammable and toxic. In addition to the hazards, LIBs are complex composites containing a lot of different value materials like graphite, plastics and different metals, which all need to be liberated and separated in a multiple-stage process chain.

INTRODUCTION

With increasing number of electric vehicles (EV) the demand of raw materials to produce the lithium-ion batteries (LIB) rises. The International Energy Agency (IAE) estimates the global EV stock to increase from 11 million in 2020 to 145–230 million vehicles in 2030 (Bibra *et al*, 2021). As the resources are limited and to a high amount imported into Europe, there is a need to recycle the batteries from used EV. Neef *et al* (2021) estimate for the European LIB production, that until

2040 more than 40 per cent of the cobalt demand and more than 15 per cent of the lithium, nickel and copper demand can be covered with recycling material. Also, the legal requirements regarding recycling rates are getting more stringent. The European legislature is currently discussing the targets for the future recycling rates. The current proposal of the European Commission states for the whole battery cell a recycling rate of 65 per cent by 2025 and 70 per cent by 2030. For the contained metals the proposed rates are 90 per cent by 2025 and 95 per cent by 2030 for nickel, cobalt and copper and 35 per cent by 2025 and 70 per cent by 2030 for lithium (European Commission, 2020). Chinas targets for the recovery rates are even higher, eg 98 per cent for cobalt, manganese and nickel and 85 per cent for lithium (Li *et al*, 2021).

LIB are complex material compounds. The cells contain two electrodes, a cathode and an anode. In between the electrodes is a separator foil, mostly Polyethylene (PE) and Polypropylene (PP), and a fluid electrolyte, consisting of solvents and a conductive salt. The cathode is made of an aluminium foil which is coated with an active material and a binder. This active material can eg be Lithium-Nickel-Manganese-Cobalt-Oxide (NMC) or Lithium-Nickel-Cobalt-Aluminium-Oxide (NCA). The anode consists of a copper foil coated most commonly with graphite and a binder. The two electrodes are folded or rolled into windings. Those windings are sometimes covered with a plastic foil and/or a stronger copper foil. To protect the windings against damage and moisture and to keep the electrolyte solvents inside, the windings are contained in housings made of aluminium or steel. Those housings can be prismatic or cylindric hard cases or soft pouches (Leuthner, 2013; Rothermel *et al*, 2018).

With pyrometallurgical processing it is possible to achieve the required recovery rates of 95 per cent for nickel, cobalt and copper (Brueckner *et al*, 2020). However due to the high temperature, organic components like plastics are decomposed and some of the metals (Al, Li and Mn) are oxidised and transferred to the slag phase. It is therefore difficult to achieve the overall recycling rates and it is not economically feasible to recover the required amount of lithium from the slag (Pinegar and Smith, 2019; Werner *et al*, 2020). Here lies the advantage of the mechanical processing at low temperatures. The plastic, copper and aluminium foils can be separated and sent to a further recycling process. In a subsequent hydrometallurgical treatment lithium and manganese can be recovered along with the cobalt and nickel.

However, the mechanical recycling faces other challenges. All the flammable and toxic components from the electrolyte, that would get decomposed in the high temperatures of the pyrometallurgical process, start to evaporate or to decompose once the cells are opened during comminution and need to be taken care of (Werner *et al*, 2020). Also, the binder is still intact and the coatings need to be separated by mechanical stress from the electrode foils so that the foils and the active materials can be recycled in the following process steps (Brueckner *et al*, 2020).

MECHANICAL PROCESSING

The mechanical processing starts with the pre-treatment of the batterie packs, modules or cells. The pre-treatment can include sorting, disassembling, discharging and thermal pre-treatment.

After the pre-treatment the batteries are crushed to liberate the materials. Subsequent to a drying stage the crushed material is screened to recover the active material and air flow sorted to recover the housing material and the separator foil. The remaining fraction, a mixture of the electrode foils, which is still partly coated with active materials, gets crushed again to liberate the remaining active material. The liberated active material is recovered in a second classification stage in the fine fraction. The coarse fraction is air flow sorted to separate the aluminium and copper foils from each other (Wuschke, 2018). The whole process and the products are displayed in Figure 1.

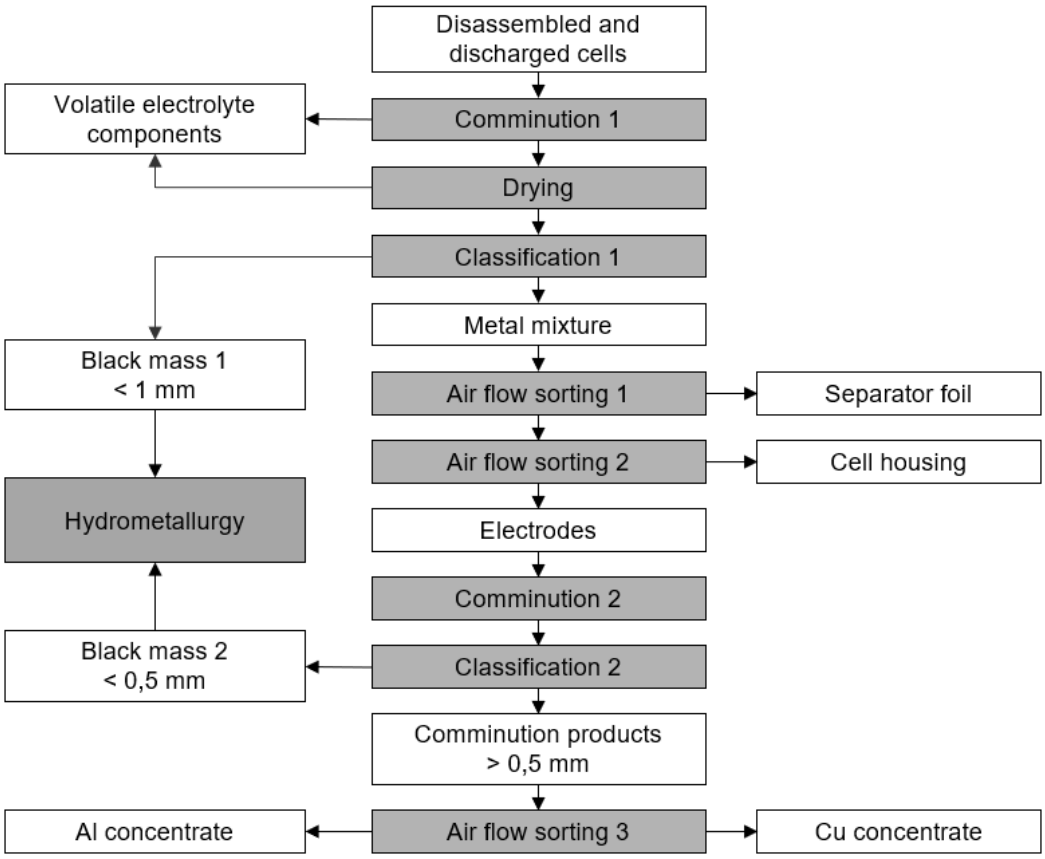

FIG 1 – Mechanical recycling process chain based on the process of the Technical University Freiberg (Wuschke, 2018).

Pre-treatment

Depending on the input material and the process design, different pre-treatment steps can be applied. Those include pre-sorting, disassembling, discharging and thermal treatment of the batterie packs, modules or cells.

Pre-sorting

As there is a big variety of LIB, they can be pre-sorted to improve the quality of the recycling products and to reduce the complexity of the downstream process. The batteries are either sorted by cell type or by cathode chemistry. Pre-sorting is especially important, if the LIB are mixed with other types of batteries like nickel–metal hydride (NiMH). The sorting is done either manually by hand-picking and visual detection or automated with different types of sensors like optical, X-ray or electromagnetic sensors (Larouche *et al*, 2020; Sziegoleit, 2013; Werner *et al*, 2020).

Disassembling

Depending on the size of the first comminution stage, the batterie packs need to be disassembled into modules or single cells to fit into the primary crusher/shredder. An advantage of the disassembly is, that the periphery components like housing, cooling system, battery management system can be sent to established recycling process like electronic waste recycling. Therefore, they do not get polluted if crushed together with the battery cells and the recycling efficiency is improved. It is also possible to reuse some of the components. The disadvantage of the disassembly is, that it is time-consuming and due to the large variety of battery systems not yet automated, which makes it a cost intensive process step, which also bears the dangers of the high voltage and energy density (Werner *et al*, 2020; Windisch-Kern *et al*, 2022).

Discharging

To reduce the risk of a thermal runaway, a self-accelerated exothermic reaction, during comminution, the batteries are discharged prior to crushing. This reduces the electrochemical energy inside the

cells and the reactions are less. Discharging is either done with an electric resistor or with a brine solution (Werner *et al*, 2020; Windisch-Kern *et al*, 2022).

Thermal treatment

To remove the electrolyte solvents and to decompose the conductive salt, the LIB can be pre-treated thermally at temperatures between 250 and 600°C under inert atmosphere. An advantage of a higher temperature is, that the polyvinylidene fluoride (PVDF) binder decomposes between 300–550°C, which improves the delamination of the electrode foils and improves also the hydrometallurgical process. The disadvantage arises from the energy demand, which grows with the treatment temperature applied (Georgi-Maschler *et al*, 2012; Larouche *et al*, 2020; Werner *et al*, 2022).

First comminution

The first process step of the mechanical recycling is the comminution. The batterie cells or modules are shredded to liberate the individual components to be able to sort them by material type. If the LIB were not thermally pre-treated, the crushing is either done under inert atmosphere with protective gas like nitrogen or under vacuum, so that the flammable gases are directly removed and the risk of fire or explosion is avoided (Brueckner *et al*, 2020). Alternatively, the crushing can also be done wet in water or a brine solution (Diekmann *et al*, 2018b) or the batteries can be deactivated in liquid nitrogen so that the crushing is done cryogenic (Vezzini, 2014).

As the batteries are composed of a mixture of metals and plastics, comminution by shearing, cutting and tearing needs to be applied (Werner *et al*, 2020). The crushing is therefore done with rotor shears (low speed shredder) and can be done either in one or in two stages (Diekmann *et al*, 2018b). The aim of the comminution is to liberate the electrode foils and the separator from the housing. Also some of the active material will already get de-coated from the electrode foils. Wuschke *et al* (2019) showed, that a grid with maximum openings of 30 mm should be applied after the crusher, to achieve a sufficient liberation for an effective separation.

During comminution the contained electrolyte solvents are set free and need to be recovered from the exhaust gas stream. A subsequent drying stage after the crushing is necessary for safe operation of the following process steps. It is important, that the drying is done at temperatures below the melting temperature of the contained plastics, so that no new compounds are created which would be difficult to separate (Werner *et al*, 2021). The thermal treatment also influences the de-coating behaviour of the foils, since the active material becomes more attached to the electrode foils (Wuschke, 2018). Figure 2 shows that with increasing pre-treatment temperature, higher forces are necessary to remove the coatings from the electrode foils.

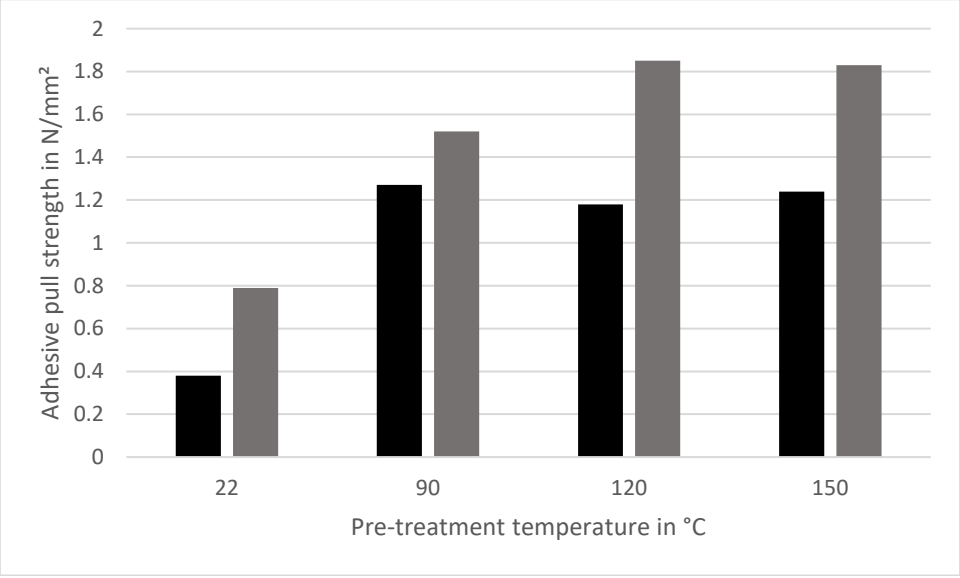

FIG 2 – Influence of the pre-treatment temperature on the adhesive strength of the coating of the electrode foils (Wuschke, 2018).

For instance, Stehmann *et al* (2018) applied drying temperatures between 80–120°C. The challenge in the drying stage is, that the conductive salt, lithium hexafluorophosphate ($LiPF_6$), starts to decompose at a temperature of around 60°C, if it gets in contact with aerial humidity. The decomposition releases highly toxic and corrosive hydrofluoric acid which needs to be removed from the exhaust gas (Diekmann *et al*, 2016).

First separation

After the comminution, the material is classified, to separate the liberated active material. In two consecutive air classification steps the housing materials and the separator foils are separated (cf. Figure 1). The order of the processing steps can vary. For instance, Diekmann *et al* (2018a) used the air classifier to separate the housing materials before the classification step. The second air classification, to take out the separator foil, was done after the second comminution. On the other hand Wuschke *et al* (2019) applied first the classification step followed by the two air classifications prior to the second crushing.

Classification

The aim of the classification is to separate the active material, that has been liberated from the electrode foils, into the fine fraction. The fine fraction is called black mass and contains the metal oxides of the cathode and the graphite of the anode together with the binders, the carbon black, the conductive salt and some of the low volatile solvents that did not evaporate. It also contains small particles of aluminium and copper from the current collector foils and iron particles from the housing. Those are defined as impurities as they are not wanted in the black mass (Diekmann *et al*, 2018a).

The classification is done with a vibrating screen and a mesh size of 0.5 mm (Diekmann *et al*, 2018a) or 1 mm (Wuschke, 2018). The selection of the mesh size depends on the desired recovery rate of the active material and on the acceptable amount of impurities. Peschel *et al* (2022) showed, that the coarser the size fraction, the higher are the amounts of copper and aluminium impurities.

Air classification

The air classification is done with a Zig-Zag-air classifier. The separation of a Zig-Zag classifier is based on the settling velocity of the particles due to their density difference. Particle size and shape also have an influence on the separation. Light particles are taken up by an air stream while heavy particles are falling down. The cut size of the Zig-Zag-classifier can be adjusted by the velocity of the air flow. In a first step, a light fraction, consisting of the separator and other thin plastic foils, is removed. The heavier material is sorted again in a second step to remove heavy housing materials like aluminium, steel and thicker plastic particles (Kaas *et al*, 2022). Figure 3 shows the remaining fraction, a mixture of the electrode foils, which is sent to a second comminution stage for further liberation (Diekmann *et al*, 2018a; Wuschke *et al*, 2016; Zhong *et al*, 2020).

FIG 3 – Electrode foil mixture after first Zig-Zag-air classification.

Second comminution

As the electrode foils are not completely decoated after the first comminution step, they need to be crushed again. Diekmann *et al* (2018a) showed, that with a second comminution, the yield of the active materials could be increased from 60 to 75 per cent. The comminution can be done eg with a hammer mill or a cutting mill. The second comminution has also the advantage, that the current collector foils are compacted. The higher compaction leads to a greater separation efficiency in the subsequent air sorting. The disadvantage of the second comminution is, that some of the foil material is milled too much and ends up in the black mass (Diekmann *et al*, 2018a; Wuschke *et al*, 2016).

Second separation

The electrode mixture from the second comminution step is screened again, to separate the liberated coating material. Afterwards the current collector foils are separated in a final air classifying step. Hereby the aluminium foil of the cathode goes to the light fraction and the copper foil of the anode goes to the heavy fraction (Bi *et al*, 2019). Wuschke (2018) showed, that the separation efficiency depends much on the second comminution. The better the compaction of the foils, the more precise is the cut in the air flow sorting. Model material of an anode foil after second comminution can be seen in Figure 4. As an alternative to the air classifying, also optical sorting or hydro upstream sorting can be applied (Diekmann *et al*, 2018a; Wuschke, 2018).

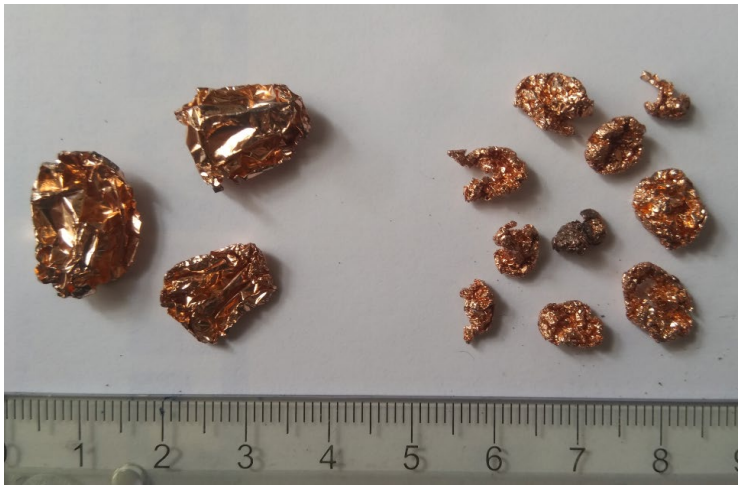

FIG 4 – Good (right) and poor (left) compacted anode foil particles.

Hydrometallurgy

The black mass, which is obtained at the two classification stages, is further treated in a hydrometallurgical process to recover the contained metals (Li, Co, Mn, Ni) from the cathode coating and the graphite from the anode as well as the lithium from the conductive salt. In the process, the black mass is first leached in eg sulfuric acid to dissolve the metals. The graphite remains as residue. After the leaching the dissolved metals are separated by solvent extraction and then recovered either by precipitation (Li and Mn) or electrowinning (Co, Ni) (Brueckner *et al*, 2020).

SUMMARY AND OUTLOOK

Compared to the pyrometallurgical processing, the mechanical treatment has the challenge, that the electrolyte solvents and the conductive salts are not deactivated and cause fire and health hazards. They need to be taken care of by thermal pre-treatment or by crushing either wet or under inert atmosphere. However, due to the demand of higher recycling rates, it is expected, that in the future the hydrometallurgical processing will be more commonly applied than the pyrometallurgical treatment, because it is better suited to recover the lithium. As for hydrometallurgical treatment, the active mass needs to be liberated from the cells, there is also an increasing demand for mechanical processing of LIB by crushing, classifying and sorting.

ACKNOWLEDGEMENTS

The presented contents are based on projects funded by the German Federal Ministry of Education and Research under the grant numbers 03XP0337, 03XP0354AE, 03XP0246C. The authors are responsible for the contents of this publication.

REFERENCES

Bi, H, Zhu, H, Zu, L, He, S, Gao, Y and Gao, S, 2019. Pneumatic separation and recycling of anode and cathode materials from spent lithium iron phosphate batteries. *Waste Management and Research,* 37, 374–385.

Bibra, E M, Connelly, E, Gorner, M, Lowans, C, Paoli, L, Tattini, J and Teter, J, 2021. Global EV Outlook 2021: Accelerating ambitions despite the pandemic. International Energy Agency.

Brueckner, L, Frank, J and Elwert, T, 2020. Industrial Recycling of Lithium-Ion Batteries – A Critical Review of Metallurgical Process Routes. *Metals,* 10.

Diekmann, J, Hanisch, C, Froböse, L, Schälicke, G, Loellhoeffel, T, Fölster, A-S and Kwade, A, 2016. Ecological Recycling of Lithium-Ion Batteries from Electric Vehicles with Focus on Mechanical Processes. *Journal of The Electrochemical Society,* 164, A6184-A6191.

Diekmann, J, Sander, S, Sellin, G and Kwade, A, 2018a. Material Separation. *In:* (A Kwade and J Diekmann, eds.) *Recycling of Lithium-Ion Batteries: The LithoRec Way.* Springer.

Diekmann, J, Sander, S, Sellin, G, Petermann, M and Kwade, A, 2018b. Crushing of Battery Modules and Cells. *In:* (A Kwade and J Diekmann, eds.) *Recycling of Lithium-Ion Batteries: The LithoRec Way.* Springer.

European Commission, 2020. Proposal for a Regulation of the European Parliament and of the Council concerning batteries and waste batteries, repealing Directive 2006/66/EC and amending Regulation (EU) No 2019/1020. *In: COM(2020) 798 final.* Brussels.

Georgi-Maschler, T, Friedrich, B, Weyhe, R, Heegn, H and Rutz, M, 2012. Development of a Recycling Process for Li-ion Batteries. *Journal of Power Sources,* 207, 173–182.

Kaas, A, Mütze, T and Peuker, U A, 2022. Review on Zigzag Air Classifier. *Processes,* 10, 764.

Larouche, F, Tedjar, F, Amouzegar, K, Houlachi, G, Bouchard, P, Demopoulos, G P and Zaghib, K, 2020. Progress and Status of Hydrometallurgical and Direct Recycling of Li-Ion Batteries and Beyond. *Materials,* 13.

Leuthner, S, 2013. Lithium-ion battery overview. *In:* (R Korthauer, ed.) *Lithium-Ion Batteries: Basics and Applications.* Berlin: Springer.

Li, W, Yang, M, Long, R, Mamaril, K and Chi, Y, 2021. Treatment of electric vehicle battery waste in China: A review of existing policies. *Journal of Environmental Engineering and Landscape Management,* 29, 111–122.

Neef, C, Schmaltz, T and Thielmann, A, 2021. Recycling von Lithium-Ionen Batterien: Chancen und Herausforderungen für den Maschinen – und Anlagenbau Karlsruhe: Fraunhofer-Institut für System – und Innovationsforschung ISI.

Peschel, C, Van Wickeren, S, Pribisch, Y, Naber, V, Werner, D M, Frankenstein, L, Horsthemke, F, Peuker, U A, Winter, M and Nowak, S, 2022. Comprehensive Characterization of Shredded Lithium-Ion Battery Recycling Material. *Chemistry A European Journal*.

Pinegar, H and Smith, Y R, 2019. Recycling of End-of-Life Lithium Ion Batteries, Part I: Commercial Processes. *Journal of Sustainable Metallurgy,* 5, 402–416.

Rothermel, S, Winter, M and Nowak, S, 2018. Background. *In:* (A Kwade and J Diekmann, eds.) *Recycling of Lithium-Ion Batteries: The LithoRec Way.* Springer.

Stehmann, F, Bradtmöller, C and Scholl, S, 2018. Separation of the Electrolyte – Thermal Drying. *In:* (A Kwade and J Diekmann, eds.) *Recycling of Lithium-Ion Batteries: The LithoRec Way.* Springer.

Sziegoleit, H, 2013. Sortierung von Gerätebatterien. *In:* (K J Thomé-Kozmiensky and D Goldmann, eds.) *Recycling und Rohstoffe – Band 6.* Neuruppin: TK Verlag Karl Thomé-Kozmiensky.

Vezzini, A, 2014. Manufacturers, Materials and Recycling Technologies. *In:* (G Pistoia, ed.) *Lithium-Ion Batteries: Advances and Applications.*

Werner, D M, Mütze, T and Peuker, U A, 2020. Recycling Chain for Spent Lithium-Ion Batteries. *Metals,* 10, 316–334.

Werner, D M, Mütze, T and Peuker, U A, 2021. Influence of cell opening methods on organic solvent removal during pretreatment in lithium-ion battery recycling. *Waste Management and Research*.

Werner, D M, Mütze, T and Peuker, U A, 2022. Influence of Cell Opening Methods on Electrolyte Removal during Processing in Lithium-Ion Battery Recycling. *Metals,* 12, 663.

Windisch-Kern, S, Gerold, E, Nigl, T, Jandric, A, Altendorfer, M, Rutrecht, B, Scherhaufer, S, Raupenstrauch, H, Pomberger, R, Antrekowitsch, H and Part, F, 2022. Recycling chains for lithium-ion batteries: A critical examination of current challenges, opportunities and process dependencies. *Waste Management,* 138, 125–139.

Wuschke, L, 2018. *Mechanische Aufbereitung von Lithium-Ionen-Batteriezellen.* PhD, TU Bergakademie Freiberg.

Wuschke, L, Jäckel, H-G, Borsdorff, D, Werner, D M, Peuker, U A and Gellner, M, 2016. Zur mechanischen Aufbereitung von Li-Ionen-Batterien. *BHM Berg – und Hüttenmännische Monatshefte* 161, 267–276.

Wuschke, L, Jäckel, H-G, Leißner, T and Peuker, U A, 2019. Crushing of large Li-ion battery cells. *Waste Management,* 85, 317–326.

Zhong, X, Liu, W, Han, J, Jiao, F, Zhu, H and Qin, W, 2020. Pneumatic separation for crushed spent lithium-ion batteries. *Waste Management,* 118, 331–340.

Industry challenges – ensuring a sustainable future

Mitigating disputes in mineral processing contracts

B W Atkinson[1]

1. FAusIMM(CP), Mediator and Expert Determiner, Engineering Contracts Mediation, Thornton NSW 2322. Email: bruce@basacon.com.au

ABSTRACT

Contracts involving process infrastructure are complex, involving design and integration, supply, construction, commissioning, proof-of-performance testing and operation. Expectation gaps frequently arise, and any resulting litigation can lead to a long, expensive, and stressful process. In the interim, the end user's requirements may remain unfulfilled, leading to loss of recovery and/or production.

Every reasonable effort must be deployed to minimise the opportunity for disputes. This requires a sharp focus on planning, broad-brush risk assessment, and formulation of the design basis and the resulting technical specifications. The proposed commercial terms and conditions must be properly integrated with the technical specifications. Competent tender assessment and contract formulation are critical.

There are almost always several unknowns and anticipated risks when it comes to a new or modified mineral processing facility. Facilities require careful integration of civil, structural, mechanical and electrical elements incorporating many different components. Sometimes material selection proves to be wrong despite the best of intentions. Regularly, the design envelope for ore to the process (particle size distribution and/or concentrations of values) do not quite meet the design intent. Sometimes there are issues regarding how representative a process stream sample may be. Regardless of how well process infrastructure is procured, disputes will arise.

At the end of an infrastructure acquisition, the Principal requires a robust facility that functions correctly, and the Vendor wants a good reference site to demonstrate its capability. When a dispute occurs, the parties to the contract need to be mindful of the 'big picture' and make sure they act to minimise all associated 'costs' including financial, delays, personnel stress, and ongoing unplanned draw on resources.

This paper summarises the key actions required to minimise the opportunities for disputes, and describes examples where mediation or expert determination may be employed to promptly and cheaply address process engineering disputes.

INTRODUCTION

Disputes frequently arise in the provision of process facilities and/or provision of individual items of process equipment. Such disputes commonly arise from factors including:

- Expectation gap(s) – different interpretations of scope.
- Communication failures – very common when critical personnel change during the course of a project, or when egos dominate.
- Late completion.
- Performance (capacity).
- Performance (product quality).
- Run-of-mine ore outside of design envelope.
- Premature failure or degradation.

Avoidance of disputes must always be the primary objective. Proper planning, design basis assessment, risk assessment, contract and project documentation, and project management all go a long way to minimising the opportunities for disputes.

Disputes cost time, money and personal stress and disruption. In addition, the more costly a dispute, the more that future insurance premiums may be affected. It is important to recognise that disputes

will happen, and to have an effective management regime for handling them. Sometimes, the parties are able to deal amicably and solve the issues themselves. However, in many cases personalities and egos dominate, and a more serious dispute escalates. That is the critical time in a dispute, and the prompt use of mediation and/or expert determination where appropriate, can save large amounts of personnel and financial resources.

Litigation (pursuit of legal rights) is always a very important 'fall-back' consideration. The threat of litigation provides the underlying incentive for parties to act reasonably. Legal rights arise from the contract(s) between the parties and any overriding statutory requirements. The outcomes of litigation are generally public if the matter carries through to court proceedings.

A critical aspect of dispute prevention is to focus on the nature of the contract(s) and to cover all anticipated outcomes, and their ramifications, within the contract(s).

However, it is virtually impossible to codify into a contract all of the possible outcomes, and the most appropriate manner in which to accommodate the subsequent impacts.

As a result, it is really important that parties to a contract have a means by which to deal with their interests, ie their 'needs' and to a lesser degree, 'wants'. It is very important to distinguish between a party's legal rights and their interests.

One option is to employ *mediation* as the first port of call to any dispute which cannot be readily handled by the parties themselves. Mediation is private and confidential. A mediator is a neutral facilitator who provides the parties a safe and confidential 'bubble' in which to discuss all pertinent aspects and work towards a solution which draws on the available resources of each party with the objective of working out a timely and achievable solution, rather than resorting to the adversarial pursuit of legal rights. Another option is *expert determination*.

When a serious dispute arises, insurers need to be notified. Many contracts call for mediation and/or expert determination as the first 'external' action in a dispute, but even if the contract does not call for either of those options, mediation or expert determination can (and should) be instigated subject to consent from the parties. Interestingly, litigation itself is often resolved using mediation, and so it is advantageous for all parties to try that as the first course of action, if for no other purpose than to narrow down and clarify a reduced list of matters subject to litigation.

This paper describes the key actions necessary to minimise the opportunity for process facility disputes.

MINIMISING THE OPPORTUNITIES FOR DISPUTES

The author has been involved in process engineering for 40 years. Based on his experience, Table 1 provides a summary of the critical factors which are necessary to apply in order to minimise the opportunities for disputes, or to minimise the ramifications of disputes.

TABLE 1

Dispute prevention project checklist.

Item	Requirement
Planning	No short cuts. Identify ground conditions (archaeological/indigenous, geotechnical). Quantify ore feedstock quality variation and availability, accounting for realistic levels of mining dilution and ore quality variation. Consider local ambient conditions (may impact upon feedstock and/or product storage and handling as well as personnel protection, materials selection, chemical types and strengths – eg efficacy of flotation, or freezing of reagents). Investigate services availability (power, water, communications, roads and delivery access etc). Identify construction needs (laydown space, craneage access, temporary services, construction staff availability, accommodation and travel etc).

	Identify external constraints and their time impacts (approvals, labour and skills availability). Identify environmental constraints (tailings handling, emissions controls including water, dust, contaminants, noise, odour, buffer requirements). Consider future capacity requirements (expansion allowances/modularity).
Risk Assessments generally	Ensure the attendance of appropriately experienced personnel with diverse experience. A lot of wasted effort, money, time and heartache can be avoided by leveraging off the experiences of others. Don't artificially limit the duration of risk assessments. Make sure they are comprehensive and competently facilitated.
Broad Brush Risk Assessment	Assess the project as a whole at an early stage, prior to specifications finalisation, to help inform the design and contract basis.
Design Basis	Make sure the design basis is really clear before the broader technical specifications are prepared. As well as specifying an hourly production rate, or similar, make sure the annualised throughput is well understood so that overall availability is properly factored.
Principal's Project Requirements (PPR)	Formulate specifications (PPR) as comprehensively as possible. That does not mean developing a detailed design, but instead means that the PPR must clearly and comprehensively define the inputs to, and required outputs of, the project, and any particular aspects that are really important to the Principal. The PPR must clearly describe the split of roles and responsibilities. The PPR must clearly describe the ramifications of anticipated problems and what needs to be achieved upon occurrence of foreseen issues. Make sure the scope of work and the battery limits are very clearly defined. Use drawings to help define battery limits. Include risk assessments (or similar) as a minimum: • detailed design phase: HAZOP/CHAIR 1/Safety in Design – pre-finalisation of design. • detailed design phase: CHAIR 2 – pre-construction. • commissioning (including cut-ins) – pre-commissioning. Include adequate time and resources for design review. Commission an independent peer review. Include explicit requirements, and detailed documentation, for training and refresher-training of Principal's staff.
Draft Contract (for distribution to potential vendors/tenderers)	Make sure the general conditions of contract (commercial terms and conditions) are properly integrated with the technical specifications. Avoid conflicting or ambiguous terminology. Use plain language. Ensure independent review to check that the words as written reflect what is required. (There are frequently instances of where an engineer may understand what the specification is likely to mean, but if the words are not clear and unambiguous, legal loopholes immediately arise). Make sure that the proof-of-performance (POP) testing requirements are practical and clearly documented including details as to *representative* sampling methodologies and durations, minimum sample volumes or masses, and analysis requirements. Seek specialist sampling design advice to avoid later arguments as to sample representivity. Clearly define any prerequisites of POP testing.

	Consider and specify how POP testing will be undertaken. For example, special arrangements may be necessary such as temporary instrumentation, and/or temporary process changes such as mild-steel or PE pipe spool sections to accommodate on-pipe flowmeters. Clearly define what constitutes successful testing ('acceptance'), and what happens in the event of unsuccessful testing outcomes. Include documentation that clearly lays out the consequences if the contract is not met, for example: • feed ore outside of design envelope. • product quality out of specification. • required capacity not achieved. • excessive operating costs (consumables and/or labour). • excessive maintenance requirements. • completion delayed (application of Liquidated Damages). Worked example calculations of contract price adjustments are particularly helpful to any subsequent contract interpretation. <u>Dispute procedures:</u> Clearly describe the valid form of a Notice of Dispute. Provide clear clauses to allow mediation and/or expert determination before litigation is initiated. Provide clear information as to the nominating authorities for mediator and/or expert determiner and make sure they are valid. For example, IEAust and AusIMM *do not* provide a nomination service.
Known unknowns (minimising variations)	Frequently, some parts of the contract will not be able to be fully defined at the time the contract is executed. For example, actual models of instrumentation or other equipment may change between design and procurement, or the Principal may wish to keep options open. For individual items such as instrumentation, valves or pumps, 'prime cost items' may be included in the contract which allows their actual cost to flow-through the contract on a transparent cost-basis without needing to apply variations. For larger portions of the work which are initially ill-defined, eg an online analysis 'system', the best approach is to use a 'provisional sum' for that portion of the Works, so that it may be flexibly handled within the contract, again without any need to resort to a variation. Variations put contract price and time at large, so they should be avoided to the extent practicable.
Tender evaluation, contract negotiation and formulation	Make sure that the vendor clearly demonstrates an understanding of the risks and that their mitigation options are realistic and appropriate. This goes hand-in-hand with demonstrating their relevant experience. Confirm that the Vendor's offer incorporates all of the Principal's non-negotiables (eg preferred equipment, ore feedstock design envelope, product quality and capacity) and that any non-conformances with the PPR and Draft Contract are very clearly documented, and not inconspicuous as qualifications or exclusions which could later be construed to be incorporated in the contract. Make sure that the vendor has the requisite corporate 'strength' and relevant insurances to be able to backup its guarantees. Make sure that the vendor's proposed subcontractors and suppliers are equally aware of the project requirements.

	Assess the vendor's proposed Program to make sure it is realistic and adequately accommodates external constraints, and the Principal's inputs and reviews, especially design reviews, risk assessments, witness and hold points.
Resulting contract – Communication	The required communication channels must be clear. Provide an environment whereby any party to the contract is able to raise concerns and problems immediately so as to mitigate their impact.
Continuity	Do everything possible to maintain the same team for the life of the project through to commissioning and at least the early phase of operation. This is critical to maintain execution of design intent. Evaluate the staff retention history of each vendor and procure access to a commitment for critical staff continuity (to the extent reasonably feasible). One example may be inclusion of a clause allowing the Principal to independently engage the services of a prior employee of the Contractor if that employee leaves the Contractor prior to Completion.
Time for Completion	Late completion is one of the most common causes of disputes. All parties to a contract need to be realistic upfront as to how much time is required to conduct the project properly. When projects are expedited to meet tight time frames, they invariably end up taking much longer due to the pressures and mistakes that subsequently arise.

PREFERRED DISPUTE RESOLUTION MECHANISMS

How does mediation work?

The first stage is that the parties must agree on an independent mediator, and that is usually handled by listing a nominating authority, eg The Resolution Institute or the Australian Disputes Centre, in the dispute resolution clause of the contract.

Litigation addresses legal rights. Very often, the legal rights of parties do not necessarily align with their interests (what they actually need or want). Parties are after solutions which enable them to move forward promptly. Litigation cannot offer that, since it is generally a long drawn-out, expensive, stressful and disruptive process.

Mediation is a private, informal and flexible, but carefully structured process whereby the mediator ensures that discussions are conducted in a respectful and productive fashion.

Mediation is conducted as an open discussion in a 'without prejudice' environment.

Mediations may be completed in just one day, although more complex matters may require multiple sessions. Brief pre-mediation introduction sessions are conducted between the mediator and each party individually to make sure they are familiar with the process that will be gone through during the mediation itself.

The mediator is a neutral party who facilitates meaningful discussion between the parties regarding their actual interests. During the mediation process, private sessions within each party or between any one party and the mediator are conducted as necessary to allow each party to 'check in' with progress and make sure they are comfortable with the conduct of the mediation.

A skilled mediator draws out all of the relevant issues that are important to each party, so that each party may appreciate all of the factors at play. Lasting solutions to disputes depend on all issues being addressed. The mediator does not offer advice nor make any decisions. The parties themselves are taken through a process whereby they drill into the real problems, large or small. The mediator facilitates the parties themselves to create options and agree upon outcomes that meet their needs. The mediator is a facilitator to flesh out the parties' mutual and individual concerns.

The mediation process is not necessarily based on the contract between the parties, but instead offers the opportunity for each party to explore what they actually need or desire, with the opportunity

for all parties to assist a feasible outcome. Parties to mediation are permitted to seek independent advice during a mediation, and generally have legal advisers in attendance.

Mediation is all about seeking workable compromise, at minimum cost, in minimum time, and with low resource consumption. Participants in a mediation process are more likely to be satisfied with a mediation process than with any more formal hearing-style process. In many cases, the outcome of a mediation is very positive for the parties since it preserves business relationships.

Parties entering mediation are required to sign an Agreement to Mediate. That Agreement requires:

- the parties to commit that any agreed outcomes of the mediation are enforceable.
- the parties to actively participate the mediation in a respectful manner.
- the parties to commit to strict confidentiality to the extent that the law allows.
- any matters discussed in mediation are subject to legal privilege, not to be used in any subsequent legal proceedings (other than enforcement of any agreed mediation outcome).

The mediator facilitates the outcomes of the mediation to be documented and signed by all parties at the conclusion of the mediation.

Mediation can be undertaken in person or online. Online options are often very attractive when the parties are geographically separated, which is often the case for mine site related contracts.

Where does expert determination fit in?

It is preferable that the dispute resolution clause in the contract lays out the procedure for expert determination, normally by reference to a published set of Expert Determination Rules. The nominating authority for the expert determiner also needs to be listed.

On occasions, parties to a dispute have unreconcilable differences regarding one or more key technical aspects. Such issues may be central to the dispute, or simply sideline issues which provide ongoing ‘fodder’ to the dispute.

Expert determination is a less known, but formal option for *privately* resolving confined issues that are in dispute. The parties jointly agree to appoint an independent expert in the field (for example, an appropriately qualified and experienced engineer or scientist with legal knowhow), who then independently reviews the facts of each element subject to dispute, and determines an outcome for each one of them.

Expert determination is based upon a separate contract between the parties and the expert. Such a contract may only be entered into if the original contract between the parties allows for it, or if the parties to the original contract separately consent to determination of the dispute by expert determination. The expert may only consider the scope of the dispute which is explicitly agreed to in the expert’s contract with the parties, unless both/all parties subsequently consent to any amendments. An expert determination is required to proceed in accordance with a pre-determined time frame, since one of its key benefits is expedient dispute resolution.

Critically, the participants agree beforehand to be bound by the decisions of the independent expert.

Expert determination is an effective way of resolving disputes which have limited substantial items of claim. The approach reduces the overall cost of the dispute in any event, because it avoids the costs of expert witnesses which would otherwise need to be engaged by each party independently. In other words, the cost of one expert determination removes the need to appoint expert witnesses for each party separately.

Apportionment of costs of mediation and expert determination

Costs are normally proportioned equally between the parties, but the parties can agree in advance to any cost-sharing arrangement.

EXAMPLE 1 – MEDIATION

Circumstances

The Contractor entered a Design and Construct contract for a mineral concentrator. When the construction was completed, and performance testing was undertaken, the flotation grade-recovery performance did not meet the performance guarantee requirements, even though 'on its face', the raw ore was within specification of head grade and particle size distribution.

Status prior to mediation

The Principal lodged a claim on the Contractor to make good the process, noting that the ore feed was within the raw ore feed envelope for all performance tests, such that the Contractor had no legal 'out' clause.

The Contractor nonetheless rejected the claim, counter-claiming that all aspects of the contract had been fulfilled, and that performance requirements could not be upheld due to the ore characteristics. The Contractor presented information showing that the actual ore characteristics displayed poorer liberation (geometallurgy) characteristics compared to the ore samples provided at the time of tender preparation.

Proceedings and outcome of mediation

The Principal could have proceeded with the prima-facie case, since in the contract, the raw ore was characterised only by a particle size range and a head grade range per size fraction. Had the legal case proceeded, it would have taken years, and even though it may have been ultimately 'successful' for the Principal, the consequential loss (not recoverable) in terms of lost product and revenue would have been extreme. Both the Principal and the Contractor were aware that despite the ore being within specification for the purposes of the contract, independent testing of the ore sampled during performance test found it to be less liberated than was originally anticipated.

The Principal's staff were not highly experienced in geometallurgy and mineral liberation, whereas the Contractor had specific investigative skills in that area. As a result of the mediation, it was agreed that the litigation could be set aside on the basis that:

- the Contractor would provide free metallurgical advice to the Principal, based on Mineral Liberation Analysis (MLA), as to what ground size distribution was required in order to achieve the required concentrate grade and recovery.
- the Principal would pay the Contractor, at full cost-recovery, to make the relevant changes to the concentrator which included increased pumping capacity for increased recirculation around the grinding circuit, and replacement of the existing bank of hydrocyclones.

The resulting outcomes included:

- the Contractor was able to advise on initial changes to concentrator operation (implemented within one month) which enabled target grade to be achieved, albeit at lower than budgeted throughput.
- further concentrator changes were implemented within six months, and the target grade and recovery were ultimately achieved.

EXAMPLE 2 – EXPERT DETERMINATION

Circumstances

A contract was entered for new flotation equipment in a mineral concentrator. The new equipment was very compact compared to the original equipment, offering space and operating cost (much lower installed power) advantages. The new equipment had been subjected to pilot-scale testing (in summer months as it happened) on-site to demonstrate its performance relative to existing equipment that needed to be replaced. The design basis (mean flotation residence time) was agreed in the contract.

The new equipment was commissioned in winter months, and the proof of performance testing failed marginally in terms of recovery at required grade. The ore was within specification in all respects. Flotation feed was tested at an independent laboratory and the required recovery was found to be achievable. However, the Respondent also found, through parallel testing, that flotation rate, and hence recovery, was particularly sensitive to the process water temperature. It was apparent that the higher energy and longer residence time of the pre-existing system was sufficient to raise the process water temperature and avoid the issue.

Status prior to mediation

Litigation was launched by the Claimant via a Statement of Claim. The Respondent lodged a counter-claim.

The claim and counter-claim each contained numerous elements, however there was single underlying issue which was the root of all argument, namely whether there was an implied term in the contract that the flotation system design accounted for variations in process water temperature, despite the fact that the Claimant had agreed to the design basis.

Expert determination approach

Both parties agreed to jointly appoint an expert determiner to assess whether the implied term existed. The parties pre-agreed that the expert determiner's outcome would be final and binding. The expert determiner was required to assess the technical and contractual information provided, and then make a written determination, including an explanation of the reasons.

Although this approach resulted in one party 'losing', it saved both parties a large quantum of legal costs, court costs and time in coming to a resolution which avoided subsequent years of litigation which would most likely have come to a similar outcome.

CONCLUSIONS

High quality and comprehensive technical specifications, which are properly integrated with commercial terms and conditions, combined with careful tender evaluation and Contractor selection, go a long way toward minimising the potential for crippling disputes when it comes to delivering process infrastructure.

However, there are almost *always unknowns and risks* when it comes to the design and planning of a process facility. Process facilities are highly complex, with numerous interactions. As a result, disputes arise.

Disputes need to be contemplated as an *integrated working element* of a project, rather than applying a 'head in the sand' approach hoping that the dispute resolution clauses in the contract will never be used. Recognising and accepting the potential for disputes, mediation and expert determination should be employed to expedite pragmatic resolution, preserve functional business relationships, and minimise the amount of disruption caused.

Experimental study of slag liquidus to recover metals from waste printed circuit boards (PCBs) using a pyrometallurgical route

M K Islam[1], M Somerville[2], M I Pownceby[3], J Tardio[4], N Haque[5] and S Bhargava[6]

1. Postgraduate Student, RMIT University, Melbourne Vic 3000. Email: s3737858@student.rmit.edu.au
2. Team Leader, CSIRO, Melbourne Vic 3168. Email: michael.somerville@csiro.au
3. Senior Principal Research Scientist, CSIRO, Melbourne Vic 3168. Email: mark.pownceby@csiro.au
4. Associate Professor, RMIT University, Melbourne Vic 3000. Email: james.tardio@rmit.edu.au
5. Principal Scientist, CSIRO, Melbourne Vic 3168. Email: nawshad.haque@csiro.au
6. Professor, RMIT University, Melbourne Vic 3000. Email: suresh.bhargava@rmit.edu.au

INTRODUCTION

Electronic waste (e-waste) is one of the fastest growing waste streams across the world with a global generation of more than 50 Mt every year (Forti *et al,* 2020). Rapid technical advancement together with growing demand for modern electronic and electrical equipment (EEE) is contributing to shortages of key metals and minerals. It is possible to recover these key metal components from waste electronics using conventional metallurgical processes. This secondary resource could therefore be an alternative to traditional mining and mineral processing of ore deposits and may provide environmental and economic benefits. Among EEE items mobile phones are one of the fastest growing electronic goods. Due to their relatively short lifespan mobile phones are disposed faster thus increasing the need for recovery and reuse of metals. Despite their smaller size and volume, mobile phones contain considerable amounts of precious metals, base metals, rare earths, and other critical metals mainly embedded in the PCBs. For example, gold content in e-waste PCBs ranges from 10–1600 ppm while gold is commercially being mined from the ores containing 3–5 ppm gold (Rao *et al,* 2020). On the other hand, dumping huge volume of wastes in landfills could cause environmental catastrophe with severe consequences on human health if these e-wastes are not handled properly.

Smelting PCBs requires high temperatures (above 1400°C) as the generated slags contain higher amounts of refractory oxides such as SiO_2, Al_2O_3 and CaO (Islam *et al,* 2021). In this regard, a suitable flux or combination of fluxes could reduce the liquidus temperature of slag system to assist separation of alloy and slag phases by smelting at relatively lower temperatures. This article describes the phase equilibria study of slag systems generated during smelting discarded PCBs with addition of fluxes (Na_2O, B_2O_3) to reduce the liquidus temperature of slags and thus minimise the energy consumption to recover value metals from PCBs.

EXPERIMENTAL METHOD AND RESULTS

The phase equilibria of the slag systems were studied using the well-known drop-quench method followed by Electron Probe Microanalysis (EPMA). Synthetic CaO-Al_2O_3-SiO_2 (CAS) slags relevant to PCB smelting were doped with 5–20 wt. per cent Na_2O and B_2O_3 separately to investigate the effect of these fluxing materials on the liquidus temperature and phase equilibria of the quaternary slags. The CAS slags doped with different amounts and types of fluxing material were wrapped with thin platinum foils and thermally equilibrated inside the hot zone of a vertical tube furnace at different temperatures. When the melt reached equilibrium, the slag containing capsules were dropped into the water-quenching bath underneath to rapidly quench. This way the high temperature structure of the slags was retained and subsequently analysed with Scanning Electron Microscopes (SEM) and EPMA. The primary phase of each slag was identified and the liquidus temperature of different slag compositions were determined using an iterative approach beginning from the temperature above to the temperature below the liquidus of a particular slag composition. The instrumental arrangement for the phase equilibria experiments is shown schematically in Figure 1.

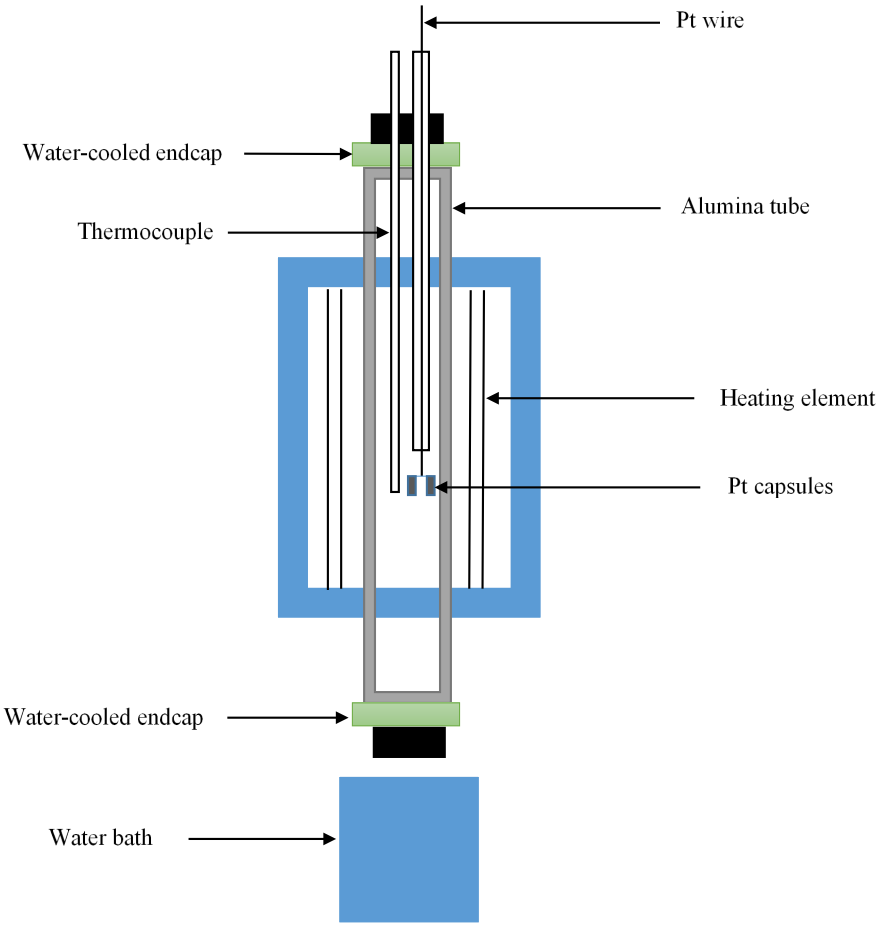

FIG 1 – Experimental set-up for phase equilibria study of slags.

Overall, the liquidus temperature of doped slags decreased with the increase of Na_2O and B_2O_3 contents although it increased when CAS slag was doped with Na_2O at CaO/SiO_2 (C/S) ratio of 1.0. In addition, B_2O_3 doping was more effective in reducing liquidus temperature compared to the similar level of Na_2O doping. Figure 2 shows the liquidus temperature of undoped and Na, B-doped slags. It was seen that liquidus dropped by 435°C to 900°C by doping 18.3 wt. per cent B_2O_3 within CAS slags of C/S ratio 1.0. Similarly, due to Na_2O doping the liquidus drops from 1335°C to the lowest 1110°C for 16.5 wt. per cent Na_2O with the CAS slag at C/S ratio 0.6. However, the liquidus temperature increased in case of Na_2O doping at C/S ratio 1.0 due to the primary phase field shifting from gehlenite ($2CaO.Al_2O_3.SiO_2$) to highly stable larnite ($2CaO.SiO_2$).

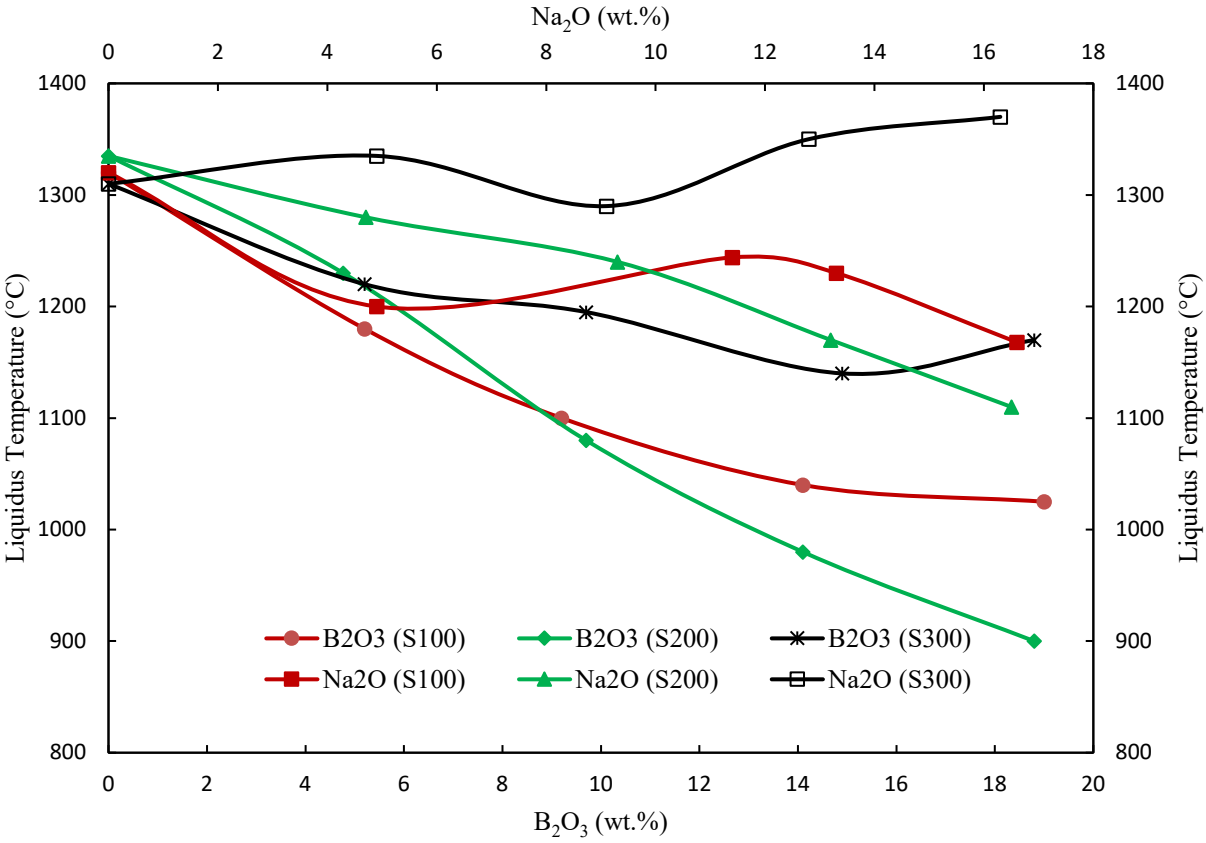

FIG 2 – Effect of Na_2O and B_2O_3 on the liquidus temperature of CaO-Al_2O_3-SiO_2 slags. S100, S200 and S300 indicate three slag series with C/S ratios of 0.3, 0.6 and 1.0 respectively.

The lower liquidus of slags by using flux will assist to design smelting operation at lower temperatures and provide flexibilities in operation. Additionally, the expected lower viscosity of these slags helps transport of metals through the slags by gravity thus increasing the recovery of metals from PCBs. The distribution of metals in different phases are currently under investigation using the knowledge of phase equilibria. This part of the hypothesis (optimum fluxing with Na_2O and or B_2O_3 would improve recovery rate of metals) can be tested with these proposed smelting experiments.

ACKNOWLEDGEMENTS

The authors are grateful to Tom Austin and the Materials Characterization Team of CSIRO Mineral resources for their support to run the experiments and analyse the samples.

REFERENCES

Forti, V, Balde, C P, Kuehr, R and Bel, G, 2020. The Global E-waste Monitor 2020: Quantities, flows and the circular economy potential.

Islam, M K, Somerville, M, Pownceby, M I, Tardio, J, Haque, N and Bhargava, S, 2021. Phase Equilibria Study of CaO-Al2O3-SiO2-Na2O Slags for Smelting Waste Printed Circuit Boards. *JOM*, 73(6), pp 1889–1898.

Rao, M D, Singh, K K, Morrison, C A and Love, J B, 2020. Challenges and opportunities in the recovery of gold from electronic waste. RSC Advances, 10(8), pp 4300–4309.

Tailings disposal improvement for a more sustainable clay processing plant

G G R Nogueira[1], M N Moraes[2], A M Garcia[3] and C F Matos[4]

1. Research Specialist, RHI Magnesita, Contagem, MG, Brazil 32210–190. Email: gustavo.nogueira@rhimagnesita.com
2. Head of Raw Materials and Basic Mixes R&D SAM, RHI Magnesita, Contagem, MG, Brazil 32210–190. Email: matheus.naves@rhimagnesita.com
3. Head of Production Other Minerals, RHI Magnesita, Contagem, MG, Brazil 32210–190. Email: andrey.garcia@rhimagnesita.com
4. Head of Quality, Process and Shipment, RHI Magnesita, Brumado, BA, 46100–000. Email: cassandro.matos@rhimagnesita.com

ABSTRACT

The refractory grade clay processing plant of RHI Magnesita, in Uberaba – Brazil, presents a circuit with two hydrocyclones in series with three centrifuges for coarse and fine quartz removal. The quartz sand tailings pulp with 30 per cent solids w/w is sent to tailings dams posing an environmental problem. Therefore, this study evaluates the installation of two spiral classifiers to process the plant tailings and stockpile it in a stable way, eliminating the need of tailings dam. Moreover, higher clay mass recovery and smaller make-up water usage can be achieved with the classifiers overflow recirculation to the processing plant. According to pilot tests performed, the proposed technology of spiral classifiers achieves good separation for the material and a stable sand pile, encouraging the execution of industrial trials. Similarly, the plant trial carried out with a leased equipment confirms the classifier suitability to the process, supporting the decision of building an industrial installation. The plant results after the spiral classifiers commissioning show 32 per cent reduction in solids tailing generation, consequently increasing the plant recovery. Additionally, there is a 60 per cent reduction in the make-up water consumption. On top of that, the sand tailings are disposed in stable piles instead of being sent to tailings dams. Thus, this study brings a new sustainability level to the clay plant. It is now running more efficiently, with higher yield, generating less residues as well as using less make up water from the environment. The tailing dams, that are not anymore required for the process, are under assessment for complete decommissioning.

INTRODUCTION

RHI Magnesita's Uberaba unit is located about 70 km from the city and is dedicated to the mining and processing of Al_2O_3-rich refractory clay in Minas Gerais state, Brazil. The raw clay lots are fed into the beneficiation plant to remove free silica from the clay, which is in the form of sandy quartz. With the removal of free silica, the Al_2O_3 content is increased so that it approaches the content required for refractory applications. The clay fed into the plant passes through a crusher to breakup the clay lumps formed, then goes to a sequence of agitators, where water is added, allowing the clay particles to detach themselves from the coarser particles, with this the coarse quartz settles and is intermittently discharged. Afterwards, it passes through a vibrating sieve whose main function is to retain organic material present in the clay, following to a battery of hydrocyclones and centrifuges that classify the clay and remove the remaining quartz. After processing, the material is pumped to drying yards and, when dry, is transported by truck to RHI Magnesita's Ponte Alta unit, where it is calcined and sintered in a rotary kiln.

In its conformation before the project, the plant tailings were generated in the form of pulp. The material was directed to sedimentation dams. However, this way of disposing the tailings generated a high operational dependence on the tailings dams. In addition, this configuration reduced the mass recovery and increased the plant's water consumption, since part of the clay was sent to the tailings due to process inefficiencies and these slurry tailings carried a large amount of water to the dams. Thus, this study evaluates alternatives to reduce the generation of pulp tailings in the processing unit.

According to Gupta and Yan (2016), mineral separation and classification of heavier and lighter particles as well as coarse and fine particles can be carried out in a wet or dry state. However, most

of them are performed in a liquid environment since it is more effective. This leads to large quantities of water being needed to process minerals. Wills and Napier-Munn, 2006, state that spiral classifiers are well suited for classification of coarse particles, being usually employed in dewatering and washing stages since they are easy to operate and are energy effective.

Tailings management is one of the major problems faced by mining industry nowadays. Water removal from tailings is of economic and environmental importance (Toprak and Altun, 2021). According to Sofra and Boger (2002), mining tailings must be disposed in ways that are both cost-effective and environmentally right. Additionally, there is a recognisable global trend in minimising water usage and storage in mining.

Since direct tailings disposal in rivers does not contain the waste material and brings inevitable interactions with the external environment (Franks *et al*, 2011), a good option to guarantee safe tailings management is dried disposal instead of the traditional slurry disposal (Gomes *et al*, 2016). Therefore, according to Das and Sarkar (2018), the mining industry is faced with a challenge of treating the tailings to recover the valuables and reduce its generation.

METHODOLOGY

The study was carried out in three stages, evaluation of alternatives and pilot tests, industrial test for technical validation and equipment sizing and, finally, the implementation of the solution in the industrial process.

Alternative evaluation and pilot tests

Seeking technical solutions, several technologies were surveyed, and two alternatives proved to be promising since they allowed the disposal of generated tailings in piles, being deeply studied. A research study was carried out to evaluate the alternative of spiral classifiers and paste thickening. Both processes would prepare the tailings for direct piling, instead of sedimentation dykes as was the previous situation.

Paste thickening was evaluated on a pilot scale and the results indicated technical feasibility. Using a pilot paste thickener, the processed tailings showed paste properties, validated by the Slump and Flume tests. The Slump test provides an indication of the stability of the pile and the Flume test measures the angle of repose of the suspension, indicating the area needed for the pile. However, this process would require a large area for stacking the material and would not decrease the generation of tailings.

The tailings disposal was also evaluated with a pilot scale spiral classifier, bringing good results of pile formation with the tailings formed and, in addition, a reduction in the generation of tailings from the plant, returning part of the material to the circuit to be reused. The spiral classifier uses the particle settling velocity property for its size separation. Thus, the coarser particles (sand), which are deleterious to the product, settle faster and are removed through the spiral movement of the equipment, forming a pile with the tailings containing low levels of moisture. The smaller particles (clay) do not settle easily and go to the equipment overflow together with the process water, in this way the clay and water, which would be lost, are returned to the production process. With these benefits, this technology was chosen to carry out industrial tests.

Industrial test

The industrial test took place in Uberaba using a single-thread spiral classifier. During the test, the best equipment inclination parameters were defined, as well as the ideal screw rotation that allowed the removal of the tailings, without generating disturbances in the classifier settling pool. The tests demonstrated the feasibility of the equipment, with the tailings pile being generated with a good repose angle and low residual moisture.

Solution implementation

Along with all auxiliary equipment, such as tanks, pumps and belt conveyor, the spiral classifiers were installed in Uberaba, as shown in Figure 1 with the new process flow chart.

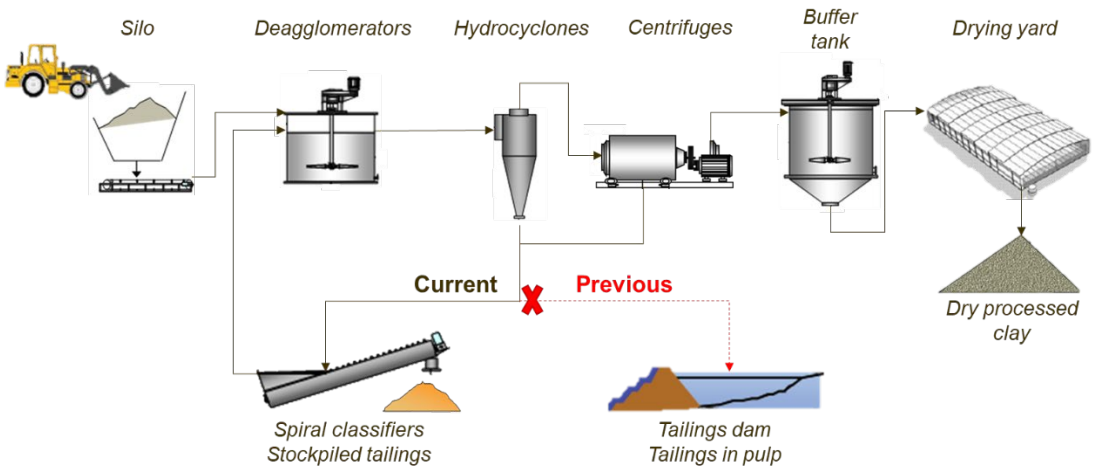

FIG 1 – Simplified flow chart with the implemented solution.

The classifiers were designed to receive the waste from the processing plant, separating the sandy part for disposal in pile, from the clay in pulp to return to the process, following the concept studied and validated in pilot and industrial scale tests.

RESULTS AND DISCUSSION

Both the pilot and industrial trials with the spiral classifier receiving the clay tailings produced good results in terms of the generated tailings consistency and useful clay recovery. Table 1 summarises the main results from these tests.

TABLE 1

Industrial trials results compared to pilot results using the screw classifier.

Analysed parameter	Pilot Trial	Industrial Trial
Feed solids concentration (%)	55	55
Quartz on overflow (%)	4.6	4.5
Underflow solids (%)	81	78
Yield (%)	41	56

From the results shown on Table 1, the industrial trial could replicate the pilot equipment results, with similar solids concentration on the underflow and quartz content on the overflow. The yield was higher in the industrial trial, but this value is strongly dependent on the quartz content from the feedstock, hence, was not an extra benefit of this process. The results of the industrial test confirmed the technical feasibility of the alternative, placing the tailings in piles and returning water and clay recovered in the classifiers to the circuit. The data obtained in this step were used for the design calculations and the equipment sizing.

The spiral classifiers were commissioned and, after the adjustments made to ensure the reliability of the process, it was possible to quantify that there was an increase of 32 per cent in the mass recovery of the plant, as can be seen in Figure 2.

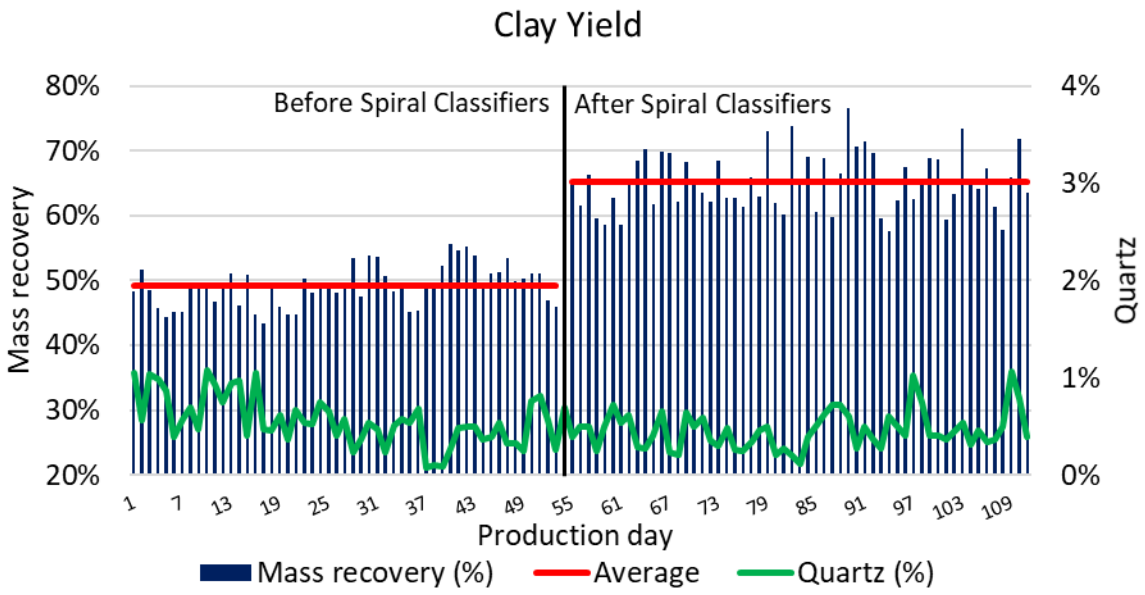

FIG 2 – Clay yield before and after study implementation.

This increase in yield did not compromise the quartz content – the major contaminant removed in the process – of the product, keeping the same levels as before the study implementation. All processing tailings is directed to the classifiers, reducing the generation of waste by 35 per cent, which is now stacked. In addition, 6.5 m³/h of water is recovered in the classifiers and returned to the process, reducing the need for new water from the beneficiation plant, which is very significant for a small plant. Therefore, the study carried out, through research and development of processes, pilot and industrial tests, and industrial application, managed to achieve the expected objective of reducing the tailings generated and dependence on the tailings dams.

CONCLUSIONS

The study carried out led to the addition of spiral classifiers to the circuit of the clay beneficiation plant in Uberaba. The generation of tailings in pulp, as occurred in the traditional circuit, was changed to a pile disposal, using spiral classifiers to recover clay and water for the process and dewater the sandy fraction that composes the tailings.

After installing the equipment in Uberaba, the measured gain in mass recovery was 32 per cent, increasing the useful life of the clay reserves.

The generation of tailings from hydrocyclones and centrifuges reduced its mass by 35 per cent and the disposal of tailings in piles resulted in a recirculation of 6.5 m³/h of water that previously accompanied the tailings to the sedimentation dams.

Therefore, the addition of classifiers to the beneficiation circuit showed excellent results for the Uberaba unit, leading to an increase in recovery and removing the great dependence on sedimentation dams that received the tailings in pulp with a high amount of water.

This fact strengthens RHI Magnesita's position in the global refractory market and supports the export of products originating from this unit. In addition, this important study reinforces the company's commitment to seek more sustainable ways of operating, with less use of natural resources, such as clay and water, and less generation of tailings, which, in addition, are now disposed of in piles, reducing the concern with tailings dams.

ACKNOWLEDGEMENTS

The authors are grateful to RHI Magnesita for the testing facility, samples, and permission to publish this work.

REFERENCES

Das, A, Sarkar, B, 2018. Advanced Gravity Concentration of Fine Particles: A Review, *Mineral Processing and Extractive Metallurgy Review*, 39:6, 359–394.

Franks, D M, Boger, D V, Cote, C M, Mulligan, D R, 2011. Sustainable development principles for the disposal of mining and mineral processing wastes, *Resources Policy*, 36, issue 2, p. 114–122.

Gomes, R B, Tomi, G, Assis, P S, 2016. Iron ore tailings dry stacking in Pau Branco mine, Brazil, *Journal of Materials Research and Technology*, Volume 5, Issue 4, Pages 339–344.

Gupta, A, Yan, D S, 2016. *Mineral processing design and operations: An introduction* (2nd ed.). Elsevier.

Sofra, F, Boger, D V, 2002. Environmental rheology for waste minimisation in the minerals industry, *Chemical Engineering Journal*, Volume 86, Issue 3, Pages 319–330.

Toprak, N A, Altun, O, 2021. Considering hydrocyclone operation for tailings dewatering purpose and its effects on product specifications of paste backfill operations, *Minerals Engineering*, Volume 173, 107176.

Wills, B A, Napier-Munn, T, 2006. *Wills' mineral processing technology: An introduction to the practical aspects of ore treatment and mineral recovery* (7th ed.). Elsevier; Butterworth-Heinemann.

Development of a general model for predicting the removal behaviour of harmful elements from acid mine drainage considering the processes of neutralisation, oxidation, and surface complex formation

Y Takaya[1], S Fuchida[2] and C Tokoro[3]

1. Associate Professor, University of Tokyo, Tokyo, 113–8656, Japan. Email: y-takaya@g.ecc.u-tokyo.ac.jp
2. Associate Professor, Tokyo University of Marine Science and Technology, Tokyo, 108–8477, Japan. Email: sfuc001@kaiyodai.ac.jp
3. Professor, Waseda University, Tokyo, 169–8555, Japan. Email: tokoro@waseda.jp

INTRODUCTION

Acid mine drainage (AMD) containing harmful metal elements such as lead (Pb), cadmium (Cd), and arsenic (As) is discharged from many mines around the world. Once AMD discharges into rivers, it can pollute the surrounding environment and cause serious social issues. Therefore, to establish the effective and low-cost treatment method of AMD is inevitable for protecting the environment and for making the sustainable future. Addition of neutralisers is common method to treat AMD, however the lower-cost method is required because AMD discharge may continue semi-permanent. Recently, passive treatment methods that utilise the natural process and energy are attracting much attentions. Among the passive treatment methods, open channel filled with neutraliser is most common due to its low technical difficulty and has already implemented in some mines (Ziemkiewicz *et al*, 1994). To encourage further implementation of open neutralising channel, we developed a geochemical simulation model that can accurately predict the efficiency of AMD treatment. Our model can be applied on any type of AMD and enables the optimal design of channels such as size and filling ratio of neutralisers.

METHODS

Limestone and PAdeCS, a commercial environmental remediation agent made from waste concrete sludge, were tested in our simulation. Limestone is composed mainly of calcite and is commonly used in passive treatment system (open limestone channel). PAdeCS is the environmental remediation agent provided by Nippon Concrete Industries Co., Ltd. and is composed mainly of portlandite. PAdeCS is produced from waste concrete sludge and has high alkaline content. The mineralogical compositions of our neutralisers were shown in Table 1. AMD composition is set to pH 3.6, Cd: 0.64 mg/L, Cu: 45 mg/L, Pb: 2.7 mg/L, and Zn: 61 mg/L based on the actual AMD from A mine in Japan.

TABLE 1

The mineral compositions of neutralisers and their specific surface area.

	Limestone		**PAdeCS**	
	Composition [mol/kg-rock]	**Specific surface area [cm^2/g]**	**mineral [mol/kg-rock]**	**Specific surface area [cm^2/g]**
Albite	-	-	0.0916	1.00
Annite	-	-	0.0252	1.00
Anorthite	-	-	0.305	1.00
Calcite	9.99	0.80	1.02	1.00
Gypsum	-	-	0.372	0.01
Phlogopite	-	-	0.0649	1.00
Portlandite	-	-	5.65	1.19
Quartz	-	-	1.83	1.00
Siderite	-	-	0.264	1.00

Geochemical simulation model was developed by using X1t, a built-in software of Geochemist's Workbench, a commercial geochemical modelling software (Bethke *et al*, 2021). In this model, the following equation (Equation 1) is used for the rate law of mineral dissolution, and the dissolution rate constant and the activation energy for each mineral were taken from Palandri and Kharaka (2004) and Raoof *et al* (2012).

$$R = k * A * M * (1 - \frac{IAP}{K}) \quad (1)$$

Where R is dissolution rate [mol/s], k is rate constant [mol/m^2/s], A is specific surface area [m^2/g], M is amount of neutraliser [g], IAP is ion activity product, and K is solubility product.

The model can reproduce the increase in pH and the precipitation of secondary minerals accompanied by the dissolution of neutraliser and can also reproduce the behaviour of harmful metal elements such as Cd, Cu, Pb, and Zn. Prior to conducting the simulations, neutralisation tests in laboratory were conducted with limestone and PAdeCS to determine the specific surface area of each constituent mineral. The determined specific surface area is also listed in Table 1.

In this study, we predicted the treatment of AMD within the combined channel of limestone and PAdeCS (Figure 1). The assumed channel consists of 12 m long limestone channel (former part) and 6 m long PAdeCS channel (latter part). The channel size was set to be 1 m wide and 0.5 m depth, and AMD flow rate was assumed to be 1.2 m^3/h. The filling ratio of limestone and PAdeCS were set at 50 per cent and 10 per cent, and the residence times were calculated to be 2.5 and 2.25 hrs, respectively. In our model, we divided 18 nodes (1 node = 1 m) along with the channel.

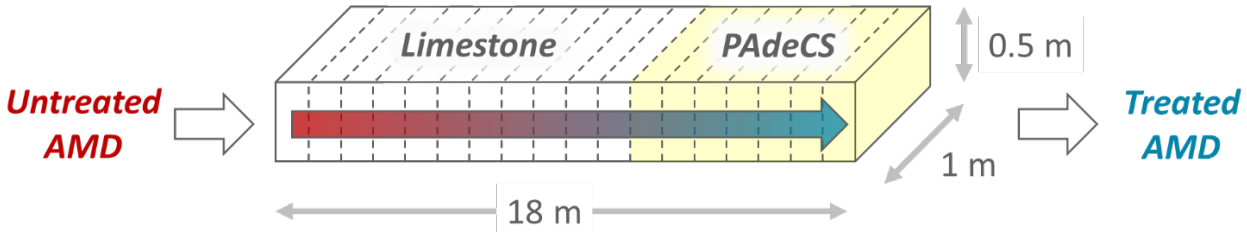

FIG 1 – Schematic diagram of the combined channel of limestone and PAdeCS.

RESULTS AND DISCUSSION

Figure 2 shows the pH and harmful element concentration changes of AMD along with the channel. pH of AMD increased to 6.21 at the end of limestone channel and to 11.38 after reaction with PAdeCS (Figure 2a). This result clearly indicated that the neutralisation potential of PAdeCS is very high. The concentrations of harmful metal elements decreased with increasing solution pH, the concentrations of Cu and Pb decreased under the effluent standards in Japan (Cu: 3 mg/L, Pb: 0.1 mg/L) only within the limestone channel (Figure 2b). Cd and Zn concentration were also successfully decreased under the standards (Cd: 0.03 mg/L, Zn: 2 mg/L) within the PAdeCS channel. All of these harmful elements were removed from AMD mainly as carbonate minerals ($CdCO_3$, $(Cu_2(CO_3)(OH)_2$, $PbCO_3$, $ZnCO_3$) because the enough amount of bicarbonate ions was supplied into the water via limestone dissolution. In addition to carbonates, Zn was also removed as silicate (Zn_2SiO_4).

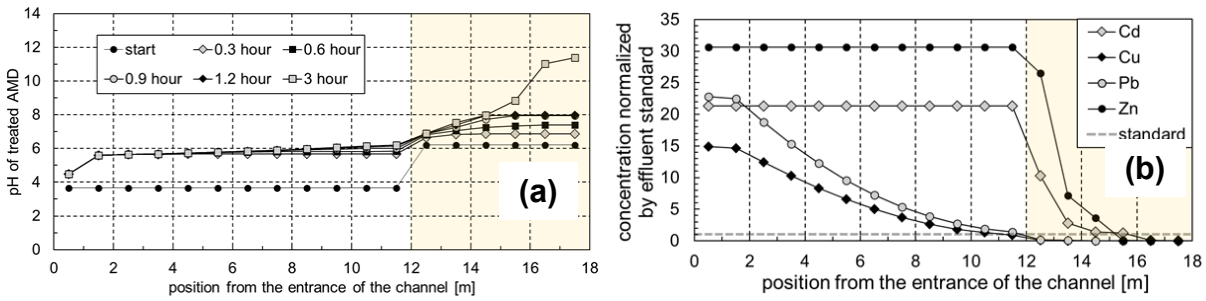

FIG 2 – AMD chemistry change within the combined open neutraliser channel: (a) pH; and (b) harmful element concentration.

In this calculation, ferrihydrite and birnessite were predicted to be formed by oxidation. Because these minerals have high surface complexation potential, we also conducted the simulation including a surface complex formation. In this calculation, CD-MUSIC (Charge Distribution Multi Site Complexation) model was applied. These minerals can be formed without neutralisation, we simulated only the oxidation of AMD solution. In this simulation, Fe and Mn concentration were set to 9.6 mg/L and 1.5 mg/L, respectively. As shown in Figure 3, harmful element removal by surface complexation was negligible for Cd, Cu, Pb, and Zn in this condition, but it was revealed that As is efficiently removed by ferrihydrite.

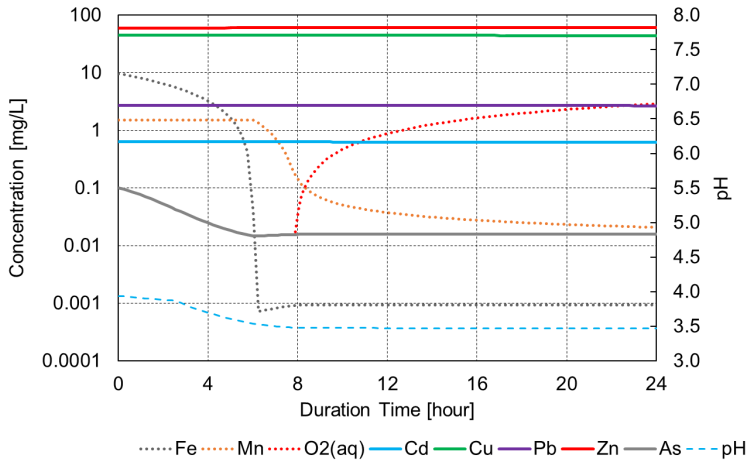

FIG 3 – AMD chemistry change with mineral precipitation and surface complexation by oxidation.

In this study, we developed a new geochemical model for predicting the efficiency of AMD treatment by open neutraliser channel. Our results show that Cu and Pb are preferentially removed in the limestone channel and that the additional treatment by PAdeCS is needed for Cd and Zn removal. We also found that the surface complexation has high potential for As removal. Our model can be easily applied on any type of AMDs, and therefore, can contribute the appropriate design of open neutraliser channel and also ensure the sustainable future by encouraging the implementation of passive treatment.

ACKNOWLEDGEMENTS

This study was partly conducted as a part of commissioned research with Japan Oil, Gas and Metals National Corporation (JOGMEC), and was also supported by Waseda Research Institute for Science and Engineering.

REFERENCES

Bethke, C M, Farrell, B and Sharifi, M, 2021. The Geochemist's Workbench Release 15: GWB Essentials Guide. Aqueous Solutions, LLC, Champagin, IL, 203 p.

Palandri, J L and Kharaka, Y K, 2004. A compilation of rate parameters of water-mineral interaction kinetics for application to geochemical modeling. Geological Survey Menlo Park CA.

Raoof, A, Nick, H M, Wolterbeek, T K T and Spiers, C J, 2012. Pore-scale modeling of reactive transport in wellbore cement under CO_2 storage conditions. *International Journal of Greenhouse Gas Control*, 11, S67-S77.

Ziemkiewicz, P F, Skousen, J G and Lovett, R, 1994. Open limestone channels for treating acid mine drainage: a new look at an old idea. *Green Lands*, 24(4), 36–41.

National mine waste assessment – pathways to an economically sustainable critical mineral industry in Australia

J P Thorne[1], Z Weng[2], G M Mudd[3], A Parbhakar-Fox[4], A Britt[5], K Bhowany[6], G Fraser[7] and H Degeling[8]

1. National Mine Waste Assessment Project Leader, Geoscience Australia, Canberra ACT 2906. Email: jane.thorne@ga.gov.au
2. Critical Mineral Specialist, Geoscience Australia and School of Engineering, RMIT University, Canberra ACT 2906. Email: zhehan.weng@ga.gov.au
3. Associate Professor, School of Engineering, RMIT University, Melbourne Vic 3000. Email: gavin.mudd@rmit.edu.au
4. Senior Research Fellow, Sustainable Minerals Institute, University of Queensland, Brisbane Qld 4072 Email: a.parbhakarfox@uq.edu.au
5. Director Mineral Resources Advice and Promotion, Geoscience Australia, Canberra ACT 2906. Email: allison.britt@ga.gov.au
6. Postdoctoral Research Fellow, Sustainable Minerals Institute, University of Queensland, Brisbane Qld 4072 Email: k.bhowany@uq.edu.au
7. Director Geochronology and Stratigraphy, Geoscience Australia, Canberra ACT 2906. Email: geoff.fraser@ga.gov.au
8. Director Minerals Geoscience, Geological Survey of Queensland, Brisbane Qld 4000 Email: helen.degeling@resources.qld.gov.au

INTRODUCTION

The global transition towards clean and sustainable technologies, transport and energy is highly dependent on reliable and expanded supply of critical minerals such as cobalt, lithium and rare earth elements. As a leading global mineral supplier, Australia has hundreds of active and historic mines and mineral processing operations with associated mine waste facilities. These potentially contain significant amounts of untapped resources of critical (and other) minerals with subsequent commercial and strategic opportunities for diversifying supply chains to meet growing demand, with superior environmental outcomes.

The concept of reprocessing waste material is not new. Successful reprocessing operations have reportedly lead to economic return and diversification for some companies (eg Kingston Resources Limited, 2022). However, little is known about the location, quantities and geochemical compositions of Australia's waste material. To date, most assessments for critical mineral potential from mine waste are either site-specific or limited to particular processing configurations.

As part of the Australian Government's $225 million Exploring for the Future program, led by Geoscience Australia in partnership with state and territory governments and universities, the National Mine Waste Assessment seeks to provide a comprehensive and consistent approach to assessing Australia's mine waste. A digital Atlas of Australian Mine Waste provides contemporary locational information at national scale and helps stakeholders identify new mineral opportunities. This work is enhanced by the addition of secondary prospectivity studies to examine the potential of mine waste for economic and responsible recovery of critical minerals, supported by the development of prospectivity modelling and economic assessment tools.

ATLAS OF AUSTRALIAN MINE WASTE

The recovery of raw materials from mineral deposits produces vast quantities of waste material such as waste rock, tailings and slag (Lottermoser, 2010). With Australia's long history in mining, this waste could contain considerable quantities of valuable critical minerals that were previously of limited economic interest. Realising this potential and understanding Australia's secondary prospectivity for critical minerals first requires a comprehensive understanding of its distribution across the nation.

To aid Australia's development as a reliable and responsible supplier of critical minerals, Geoscience Australia, the Royal Melbourne Institute of Technology and the University of Queensland, supported

by state and territory geological surveys, have created a national database of mine waste with accurate geospatial, geochemical and economic information about Australian mine waste facilities. This database is an extension of Geoscience Australia's OZMIN database, which describes Australian mineral deposits including geological, resource and production data (Ewers *et al*, 2000; Geoscience Australia, 2020), and includes new fields such as waste type, storage type and structural information, and usage status.

The Atlas of Australian Mine Waste delivers this information to stakeholders across government, industry and the broader community via an easily accessible digital platform. Where available, the atlas includes detailed geochemistry and mineral system resource potential and/or associated potential critical mineral endowment. Population of this information is being supported by a mine waste geochemical sampling and analysis campaign.

National Mine Waste geochemical sampling and analysis campaign

Detailed waste characterisation from a broad range of origins is required to identify economic opportunities and potential secondary recovery from Australia's mine waste. Accordingly, a national mine waste geochemical sampling and analysis campaign is underway by university partners at selected sites across Australia.

This campaign is identifying the chemical and mineralogical composition of samples, with a focus on the unrealised value of critical metals (eg Co, REE, In, W, Ga, Ge). The study includes mineralogy, heterogeneity and re-mobilisation of metals in the mine waste environment and contributes to our understanding of the genetic relationships between ore deposit types and critical metal content in mine wastes. The results are being used to assess factors that may contribute to the economic viability of reprocessing mine wastes to extract metals and will provide site-specific validation of predictive modelling.

In addition, this campaign aids the establishment of a standard for geochemical sampling. Assessing mine waste facilities for reprocessing is still in its infancy and a consensus in best-practice sampling for this purpose is lacking (Blannin *et al*, 2022). Incorporating knowledge of the original ore, processing, and depositional history of the tailings with carefully planned sampling designs and, complete chemical, mineralogical and textural characterisation is required to assess potential valorisation of the materials (Parbhakar-Fox *et al*, 2019; Blannin *et al*, 2022). This work will encourage robust assessment of Australian's mine waste sites and aid researchers in devising appropriate, site-specific sampling schemes to minimise uncertainty.

Prospectivity modelling and economic assessment

To understand the potential of Australia's mine waste as secondary sources of critical minerals, researchers will develop novel modelling to assess the economic viability of mine waste processing operations in Australia. Planned for future years, this work will de-risk and validate economic potential by evaluating specific tailings from related mineral system and deposit types with emerging processing technologies and adjustable by/co-product targets for enhancing Australia's role in the global critical mineral supply chain.

This work will provide pre-competitive information and can be used to benchmark economic assessments for tailings management and reprocessing options. The unique value propositions and technological capability being proposed here has been demonstrated by Geoscience Australia's 'Economic Fairways Mapper' and 'Hydrogen Economic Fairways Tool' (Walsh *et al*, 2020; 2021).

CONCLUSIONS

Mineral extraction from Australian mine waste is a key step towards growing Australia's responsible and sustainable mining industry and supports the priorities of the Australian Government's critical minerals strategy. The Atlas of Australian Mine Waste provides stakeholders with a detailed, accurate and contemporary assessment of the nation's potential secondary prospectivity for critical minerals. The national geochemical sampling and analysis campaign, and supporting prospectivity modelling and economic assessment, is unlocking Australia's mine waste potential and understanding of existing and future resource developments. The Exploring for the Future National

Mine Waste Assessment enhances Australia's capacity to meet growing global demand for critical minerals reliably and responsibly, while improving environmental outcomes and social licence.

ACKNOWLEDGEMENTS

Acknowledgements go to laboratory staff for assistance in sample preparation and analysis, to Australian state and territory geological surveys for their support and to the companies that have allowed access to their sites as part of this program. This extended abstract is published with the permission of the CEO of Geoscience Australia.

REFERENCES

Blannin, R, Frenzel, M, Tolosana-Delgado, R and Gutzmer, J, 2022. Towards a sampling protocol for the resource assessment of critical raw materials in tailings storage facilities, *Journal of Geochemical Exploration*, Vol 236, https://doi.org/10.1016/j.gexplo.2022.106974

Ewers, G R, Ryburn, R J, Hazell, M, Sedgmen, A, Bastrakov, E N and Black, J. 2000. OZMIN documentation: national mineral deposits dataset: version 3. Record 2000/018. Geoscience Australia, Canberra. http://pid.geoscience.gov.au/dataset/ga/33468

Geoscience Australia, 2020. Mineral Deposits and Mineral Resources WMS. Geoscience Australia, Canberra. http://pid.geoscience.gov.au/dataset/ga/144671

Kingston Resources Limited, 2022. Ramp-up of Gold Production at Mineral Hill, media announcement, 28 March, viewed 1 April 2022, https://kingstonresources.com.au/investor-centre/asx-announcements

Lottermoser, B G, 2010. *Mine Wastes: Characterization, Treatment and Environmental Impacts*. Springer Berlin Heidelberg. https://doi.org/10.1007/978–3–642–12419–8_1

Parbhakar-Fox, A, Gilmour, S, Fox, N and Olin, P, 2019. Geometallurgical Characterization of Non-Ferrous Historical Slag in Western Tasmania: Identifying Reprocessing Options. *Minerals* 9(7):415. https://doi.org/10.3390/min9070415

Walsh, S D C, Laura, E, Weng, Z, Wang, C, Joseph, M and Feitz, A, 2021. Evaluating the economic fairways for hydrogen production in Australia. *International Journal of Hydrogen Energy*, 46(73), 35985–35996. https://doi.org/10.1016/j.ijhydene.2021.08.142

Walsh, S, Northey, S A, Huston, D L, Yellishetty, M and Czarnota, K, 2020. Bluecap: a geospatial model to assess regional economic viability for mineral resource development. *Resources Policy* 66:101598. https://doi.org/10.1016/j.resourpol.2020.101598

Pumping sustainably – power and water consumption in mineral processing plants: *someone should care*

A Varghese[1,4], S Martins[2], E Lessing[3], G M Hassan[5] and A Karrech[6]

1. Business Development Manager – Pumps, Metso Outotec, Perth WA 6110.
   Email: alan.varghese@mogroup.com
2. Research and Development Engineer, Metso Outotec, Lachine Quebec H8S 2R9.
   Email: sudarshan.martins@mogroup.com
3. Vice President Engineering – Pumps, Metso Outotec, Espoo 02230.
   Email: evert.lessing@mogroup.com
4. PhD Student, University of Western Australia, Perth WA 6009.
   Email: alan.varghese@research.uwa.edu.au
5. Senior Lecturer, University of Western Australia, Perth WA 6009.
   Email: ghulam.hassan@uwa.edu.au
6. Associate Professor, University of Western Australia, Perth WA 6009.
   Email: ali.karrech@uwa.edu.au

ABSTRACT

Pumping sustainably stems from the recent Intergovernmental Panel on Climate Change (IPCC) report. In the mineral processing sector, comminution processes are attracting an increasing interest to achieve sustainability. Comminution accounts for 4 per cent of total global energy consumption. A typical mineral concentrator plant dedicates, on average, 50 per cent of the total concentrator energy to comminution processes. While pumps, the second most common machine in the world, are considered ancillary machines with small individual footprint – be it energy, cost, or water – their numbers greatly amplify their cumulative impact. Collectively, pumps account for 15 per cent of global consumption of the world's electricity, and on average mine site total pump-motor energy consumption is estimated to be 25–32 per cent.

Despite the abundant literature on pumps, no holistic review on their sustainable deployment has been found. Therefore, this paper investigates the energy and water consumption by pumps in mineral processing plants during three phases: the design phase, the installation and commissioning phase, and the mature operational phase. From the case studies – gold, copper, and iron ore operations – it is found that pumps consume 18–28 per cent of the plant energy and 7 per cent of the site water. Additionally considering pumps on an individual basis leads to short-term capital focus in the design phase and does not consider aggregated energy and water usage of all pumps. This leads to using conservative safety margins and not considering optimum selections to reduce power and water consumption. It is followed by evaluating the operating practices affecting efficiencies and providing recommendations. Furthermore, digitalisation as a means of efficient monitoring and performance tracking is also introduced. The functional performance of pumps is critical to each mineral processing plant and their overall analysis from the design, selection and operation can yield substantial savings and benefits. With the increasing awareness of climate change, a strong decarbonisation of the global economy, by continued emphasis on critically assessing methods and operations, is necessary.

INTRODUCTION

Mining and mineral processing represent some of humankind's earliest activities. Alongside agriculture, they have played a major role in the development of civilisation. Mining production has significantly grown over the years, with 2019 reporting 17.9 Bt of mining production globally, compared to 11.3 Bt and 9.6 Bt in 2000 and 1985 respectively (Reichl and Schatz, 2021). At present, China, USA, Russia, and Australia are the four biggest mining nations. The industry however faces various challenges such as decreasing ore grades, safety of workforce, rising energy costs, limited full operations overview, remote locations, value chain gaps, and climate change (Amponsah-Tawiah, Ntow and Mensah, 2016; Gunningham, 2008; James, 2014; Katz and Pietrobelli, 2018; Levesque, Millar and Paraszczak, 2014; Mudd, 2007, 2012, 2014; Shannon and Parker, 2020). Climate change is a long-term shift in weather, marked by changes in temperature, precipitation,

wind, snow cover etc (Environment and Climate Change Canada, 2022). Although many natural processes can cause climate change, the consensus is that, since the Industrial Revolution, human activity is the dominant cause of climate change observed today (IPCC, 2022b). In the assessed scenarios, limiting warming to around 1.5°C requires global greenhouse gas emissions to peak by 2025 at the latest, and be reduced by over 40 per cent by 2030 (IPCC, 2022a). Presently, as illustrated in Figure 1, this goal will not be met and more efforts are required. For mineral processing, climate change has direct effects on the industry, as summarised by Nelson and Schuchard (2010):

1. The supply of critical resources such as water and energy will face greater constraints.
2. The employee health and safety risks will increase, as rising temperatures correlate strongly with the risk of contracting a communicable disease or a heat-related injury, reducing worker productivity.
3. Obtaining and maintaining a social licence to operate will face greater challenges as industry competes with the community for resources.
4. Increased physical and non-physical risks will make project financing more difficult to secure.

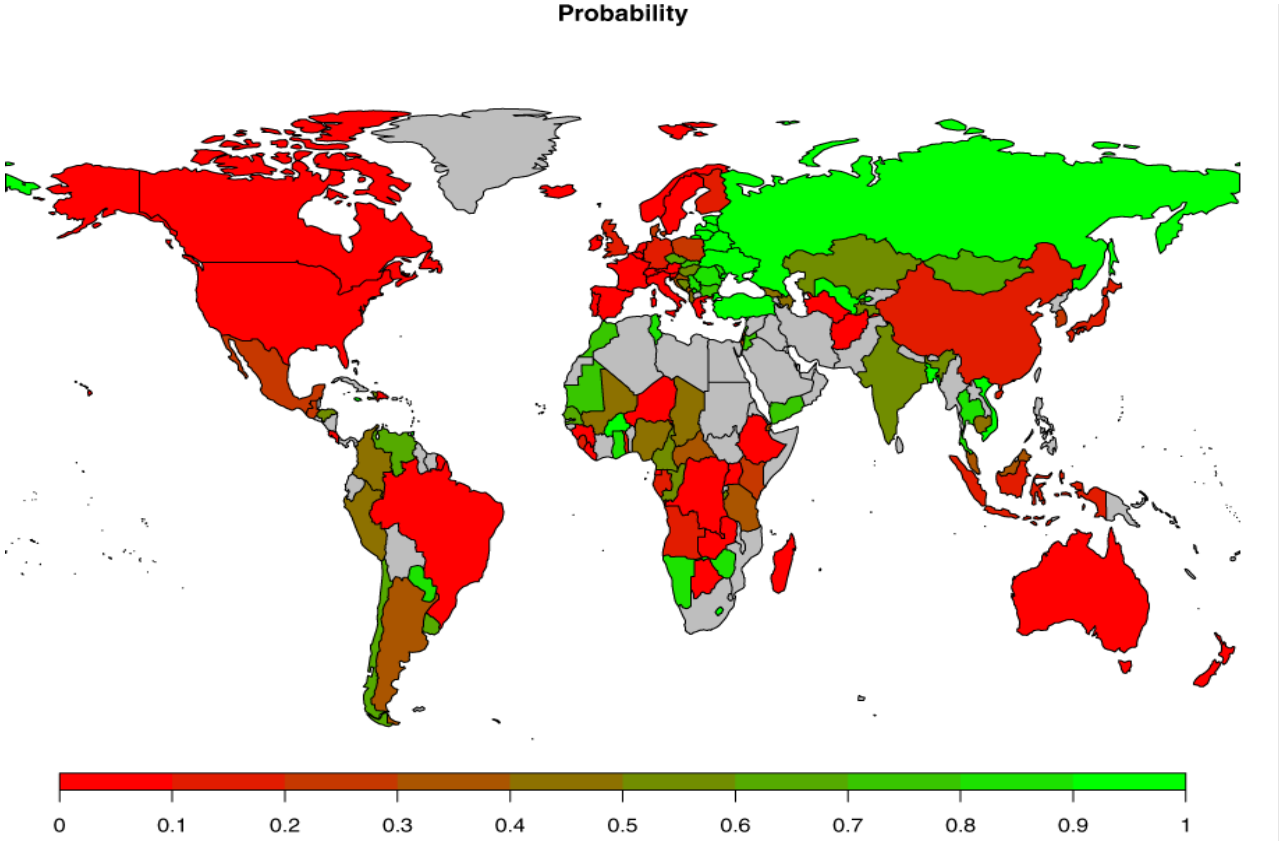

FIG 1 – Probability that countries achieve their Paris Agreement Goals according to their nationally determined contributions (NDCs) (Liu and Raftery, 2021).

In mineral processing, significant attention is provided to the comminution circuit for energy savings. Comminution accounts for about 4 per cent of total global energy consumption (Jeswiet and Szekeres, 2016). A typical mineral concentrator plant dedicates, on average, 50 per cent of the total concentrator energy to comminution processes. While pumps, the second most common machine in the world, are considered ancillary machines with small individual footprint – be it energy (CO_2), cost, or water – their numbers greatly amplify their cumulative impact. Large tonnages of slurry are pumped every year. For small and medium haul duties, pumping a slurry is more cost-effective than transporting it by conveyor belt or truck (McCain, 1981; Wilson *et al,* 2006). Centrifugal slurry pumps as shown in Figure 2a are capable of handling tough and abrasive duties. The pump's capability and robustness make it an essential part of modern mineral processing. Collectively, pumps account for 15 per cent of global consumption of the world's electricity, and on average mine site total pump-motor energy consumption is estimated to be 25–32 per cent (Jeswiet and Szekeres, 2016). Upon

comparison, in the water supply industry, the critical importance of efficient operation of large water pumps has been well recognised for a large number of years. For example, a study on pump efficiency monitoring and management at Melbourne water anticipated recommendations to carry out pump overhauls and improved pumping regimes were expected to yield energy savings in the order of 2–4 per cent which, equates to 3470 to 6940 MWh (Maddy *et al,* 2005). Similarly, study from Maurice and Ian (2001) summarised in Figure 2b, shows energy being the most dominant life cost of a typical pump-set in water and wastewater industry.

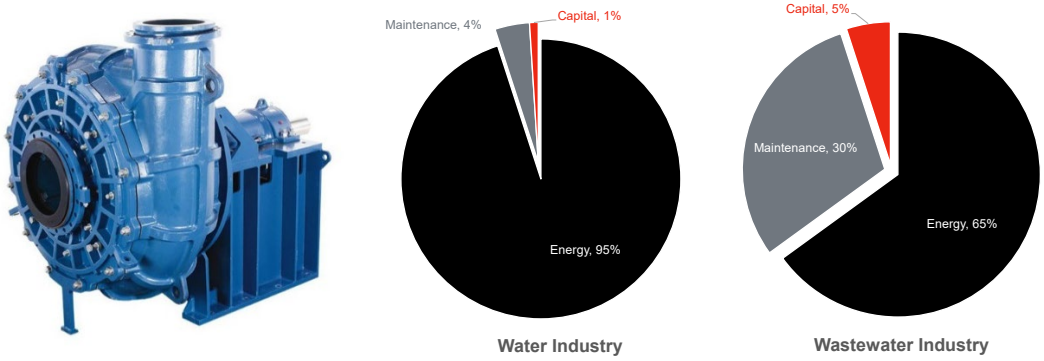

FIG 2 – (a) An example of centrifugal slurry pump (b) The whole life cost of typical water and wastewater industry pump set (Maurice and Ian, 2001).

Slurry pumps in contrast are smaller on average than large water supply industry pumps and much more plentiful on mineral concentrator sites. As the authors have indicated, this has hidden their combined contribution to overall power usage. There is of course some significant difference between water and slurry pumps in as much that slurry pumps have to deal with solid particles in the fluid, which for most part is water. The range of solids being pumped, their concentration, the solids specific gravity, hardness and shape can vary dramatically. In fact, the Hydraulic Institute (2016) defines four classes of slurry ranging from 1 for ‘Light’ to 4 for ‘Very Heavy’ slurry class. The impact of this various slurry classes on the wear of the wetted components of the pump ranges from pumps lasting potentially 18 months in the Light application to as low as a few weeks in the Very Heavy application. This of course has significant ramification on the whole life cost of a slurry pump. A preliminary guide based on Metso Outotec’s data is illustrated in Figure 3. The maintenance component reflects mostly the wear part contribution. From a sustainability point of view, it is therefore not sufficient to just consider the energy usage but also the overall usage of the wear material and by extension one could also consider the embodied energy in producing these wear parts. Another important point from the above is that there’s also a water cost. The question might rightfully be asked where this water usage comes from? Whilst water pumps by and large operate with mechanical seals to seal the pump shaft, this is not the case for slurry pumps. Due to the very arduous duty brought on by large solids content, slurry pumps by and large operate with water flushed gland seals to seal the pump shaft. General industry view is that mechanical seals are just not robust enough for slurry pumping.

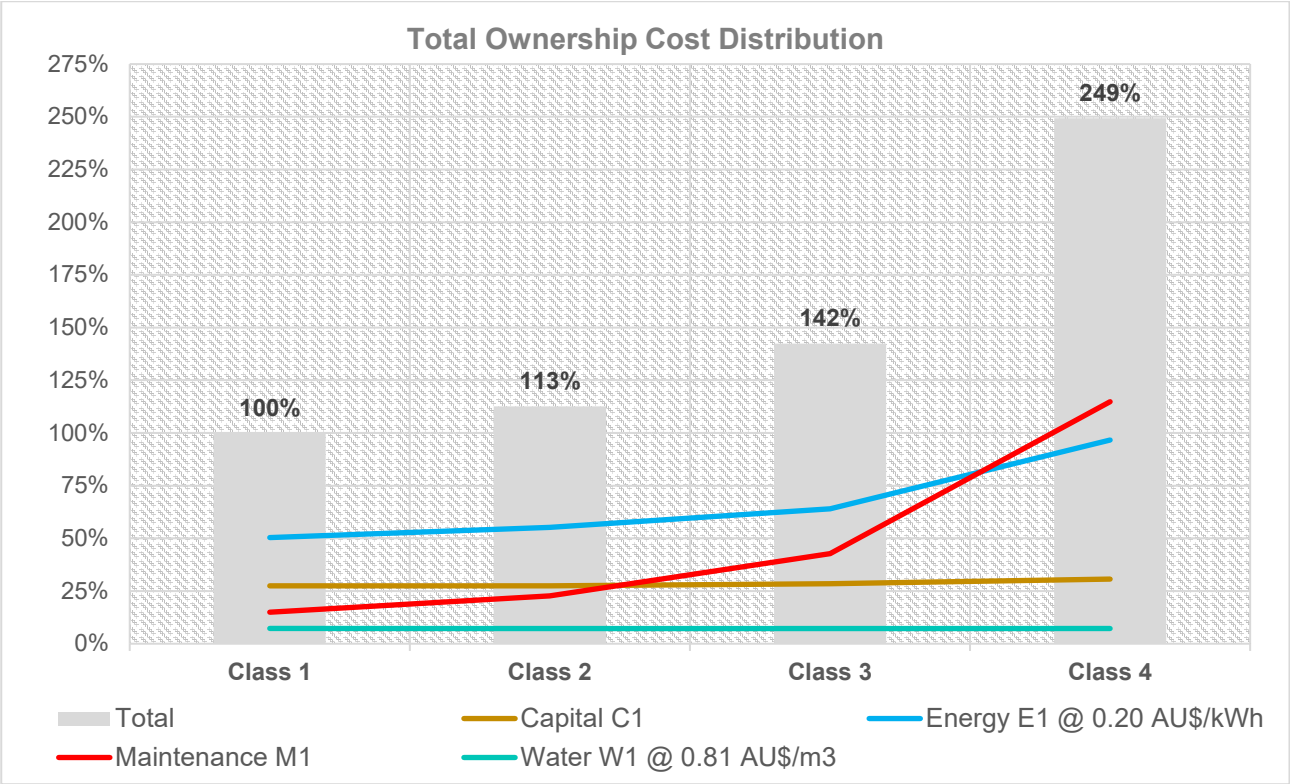

FIG 3 – Slurry pump total ownership cost distribution as per slurry class relative to class 1 as 100 per cent baseline.

Despite the abundant literature on pumps, no holistic review on their sustainable deployment has been found. Benchmarking energy usage in mining operations is challenging due to uniqueness of each mining operation (Pirouz *et al,* 2017). Water utilisation through pumping has received even less attention due to its indirect nature and small amount. This paper investigates the energy and water consumption by pumps in mineral processing plants using a life cycle approach consisting of three phases as illustrated in Figure 4. Investigation starts from the original pump design selection phase then proceeds to installation and commissioning phase with case examples from typical copper, magnetite and gold plants, and finally a detailed comparison of a pumping application when installed against its operational phase (five years later).

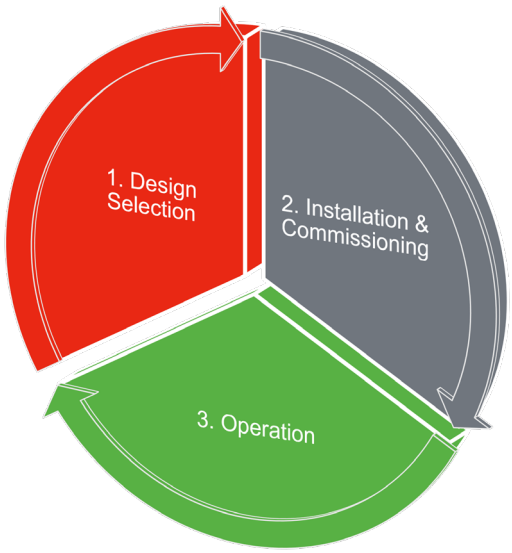

FIG 4 – Pump application life cycle consisting of three phases.

The objective is to quantify the sustainability footprint of pumps in mineral processing, and to understand the changes in the footprint throughout the phases of a pump's application life. To do so, the article is divided as follows: the first section outlines the methodology for data collection, the second section illustrates the results from the design selection phase, the installation and commissioning phase, followed by the operating phase. This section also includes discussions on the energy and water observations, with recommendations. Finally, with sustainability in mind, a number of conclusions are drawn.

METHODOLOGY

The initial aim was to obtain the relevant information and data through a detailed literature review. It became abundantly clear that there is an absolute lack of data and information available in the literature and a new plan had to be formulated. The alternative was to draw on the extensive Metso Outotec Plant Solution Business Line data. This was a partial solution as only a small number of sites had complete data sets. Moreover, the actual data of operational plants with respect to pump power and water usage was largely elusive.

Based on the above, the approach and goals were amended to better reflect actual data and information available:

1. Quantify how pumps in general are sized and selected and the relative impact it has on water usage and power requirements – fortunately, plenty of internal data was available for this.
2. Quantify power and water usage of pumps in a mineral concentrator based on initial design.
3. Quantify the difference between the design and actual power and water usage based on the set of available data
4. Make recommendation based on the findings above to optimise pump sizing and selection during the design phase or identify potential optimisation of current installed pumps.

To accomplish this, the following methodology presented in Figure 5 was conducted. For the first goal, the authors have collated global data of pump sizing carried out by both internal and external users over the last two years using Metso Outotec's proprietary PumpDim™ pump sizing and selection software. The aim of which was to select the most common pump for review. For the second goal, authors developed selection criteria to identify case examples for mineral concentrator plants in consultation with plant design engineers and operations teams within Metso Outotec. The selection criteria for case studies comprised of inclusions such as: (1) plants must be less than 15 years old; (2) plants can be in construction or operational phase; (3) focus must be on typical minerals concentrator plant like Copper, Gold etc; (4) cases must be from different regions or countries; and (5) information of pump applications must be available. Case examples where pumping applications falls in extreme ends such as limited volume of applications in dry hematite plants or high volume of applications in alumina refinery plants were excluded. For the third goal, a cyclone feed pump application was selected for review. Wherever possible, improvements were noted, quantified and recommendations were added. Later for validation purposes of improvements, two external design engineering companies and two operational sites were consulted. Similarly, feedback was discussed with original design engineering and operations team who provided the case examples.

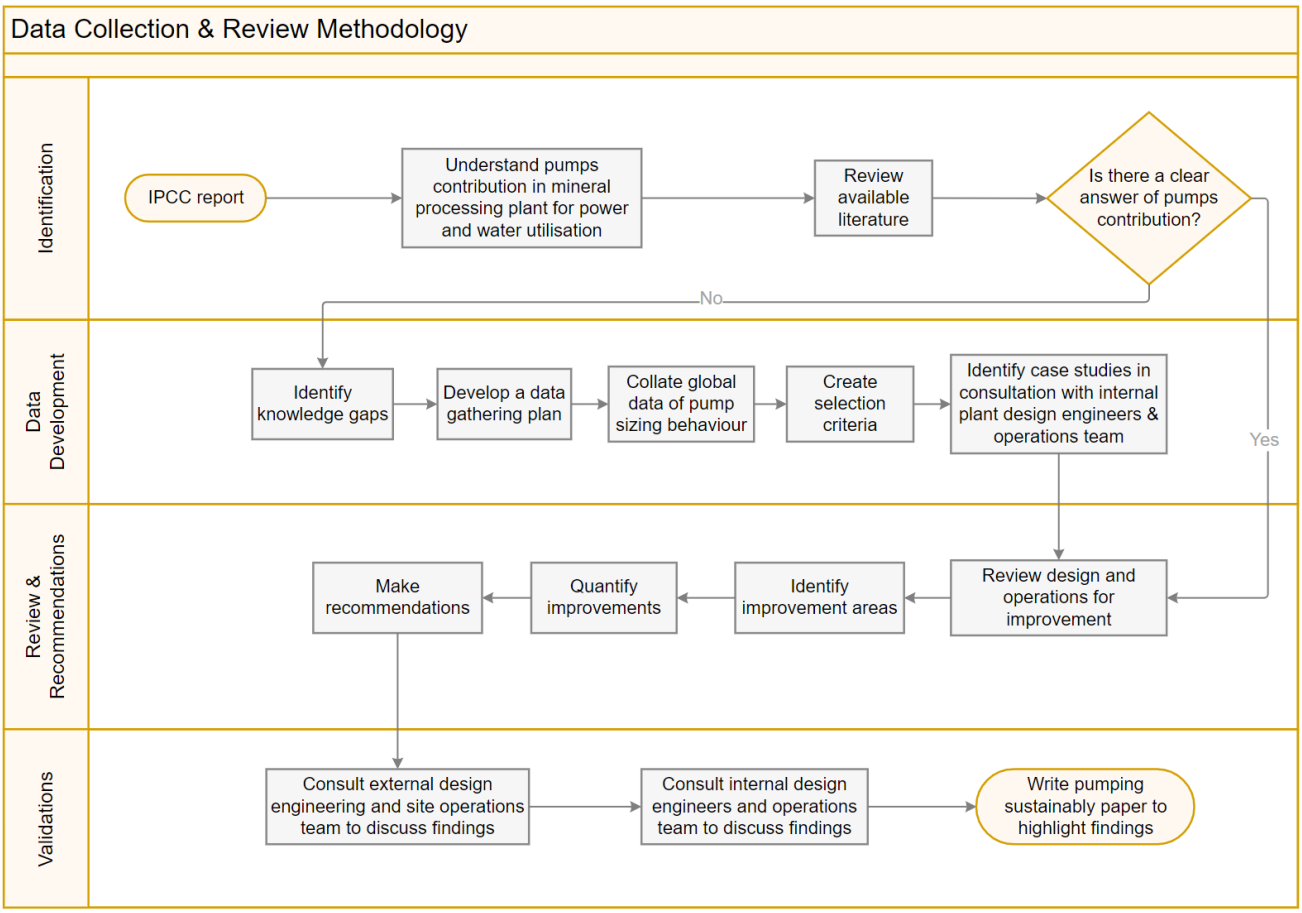

FIG 5 – Flow diagram of methodology.

RESULTS AND DISCUSSION

An analysis of the pump application life cycle is presented. It starts with phase 1, an analysis of slurry pump sizing behaviour – selecting a pump always begins with this step. Next, using examples of typical copper, magnetite iron and gold plants from the installation and commissioning (phase 2) helps in understanding the pumps contribution to the power and the water utilisation at site. Finally, a comparison of a slurry pump application between the installation and the mature operational stage (five years later) – phase 3 – is presented. These cases are explained below, with recommendations and limitations, with the goal of enhancing the understanding of new sizing, plant design, upgrades, and optimisation for pumps. As this is a life cycle view, improvements gleaned throughout drive the improvements of the next generation of pumps and aid development of sustainable future mineral processing plants.

Phase 1 – slurry pump sizing

Metso Outotec recently launched, PumpDim™, a cloud-based pump sizing and selection tool which has enabled easy data collection of global pump sizing by both internal and external resources. In total 43 561 sizing information, dating from 1 January 2020 to 30 March 2022 was analysed. The most common pump selected is the HM150 with 3077 sizings, representing 7 per cent of the total selections. This is followed by the HM200 and HM100 pumps, with 2491 and 2463 sizings respectively, contributing about 6 per cent each (Figure 6a). It is important to note that these sizings capture complete range of selections including initial scoping, budget quoting, installations, optimisation and verification purposes. Hence, representing a valuable snapshot of typical application where these pumps are eventually installed and operated. To give some perspective of where these pumps lie in the overall Metso Outotec offering, and by extension in the market, with reference to size of pump, comparison can be drawn by referring to best efficiency flows at an arbitrary 40 m of water head. Flows for the overall range varies from as low as 31 m^3/hr to as high as 12 250 m^3/hr, with the HM 100 at 160 m^3/hr, the HM 150 at 340 m^3/hr and the HM 200 at 600 m^3/hr it is therefore quite evident that they represent the smaller end of the scale.

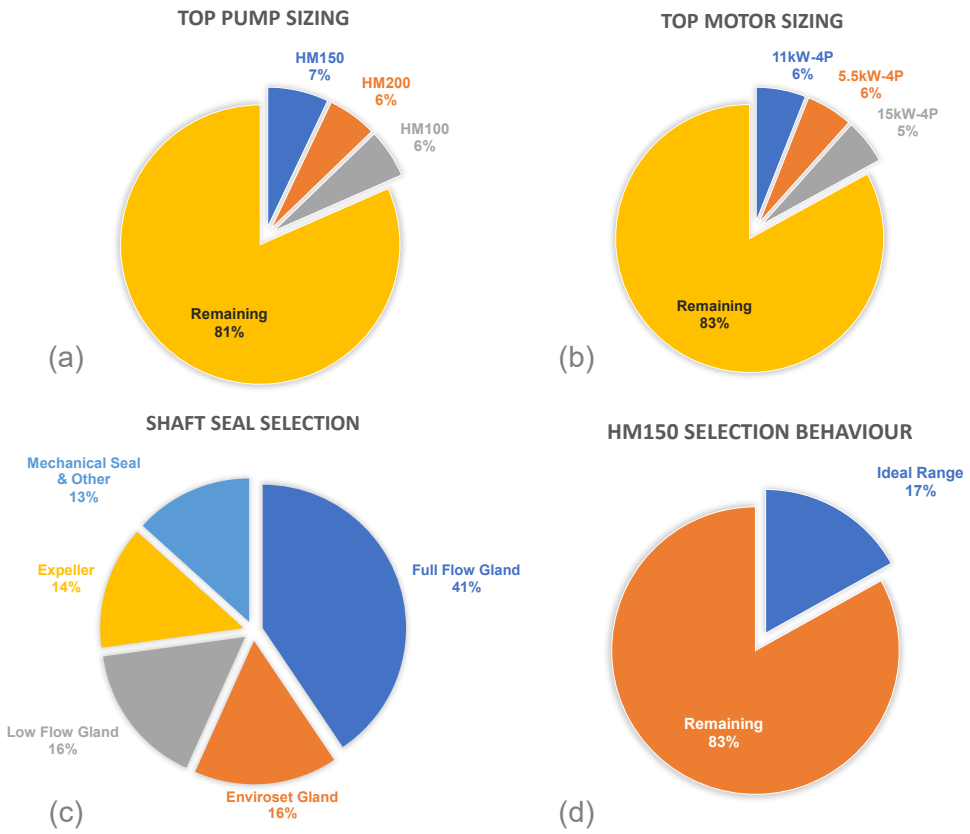

FIG 6 – Pie charts highlighting (a) top pump sizing (b) top motor sizing (c) distribution of shaft seal selection and (d) HM150 selection behaviour.

Given its popularity, the HM150 – a **H**eavy-Duty **M**etal slurry pump with a **150** mm suction – is selected for a detailed review. The number of sizings, as presented in Figure 7, indicate a large range of operating selections. Also indicated in Figure 7 is the Best Efficiency Line (BEL), reflecting the head and flow combination where the highest hydraulic efficiency (79 per cent) for this pump is achieved. Slurry pumps are very robust and can be operated over quite a large operating range. For instance, this specific pump, which is classed as a pump for highly abrasive duty, Service Class 3 as per the Hydraulic Institute (2016) can be operated in a Preferred Operating Range (POR) from 50–105 per cent of Best Efficiency Flow (QBEP). As one strays from the Best Efficiency Flow however it can be well understood that this not only negatively impacts power consumption but also affects wear. Based on Walker, Wells and Bodkin (1994) work they demonstrated that minimum wear occurs at 80 per cent of QBEP. Similarly, Sustainability Victoria (2015) states that a pump is generally considered oversized if it is not operated at or within 20 per cent of its BEP. With this as background the authors defined a ‘Ideal Operating Range’ of 80–100 per cent QBEP to reflect an optimal range within which both wear and power consumption is minimised. Only 17 per cent of selections fall in this ideal range (Figure 6d). The average selection behaviour highlights a slurry flow of 212 m^3/hr, 36 m head, 43 kW absorbed power, 70 per cent slurry efficiency and 72 per cent QBEP operation. Important to note here that pumping of slurries result in a derating of the head, flow and efficiency compared to using the same pump on water, which are based on empirical derived formulas.

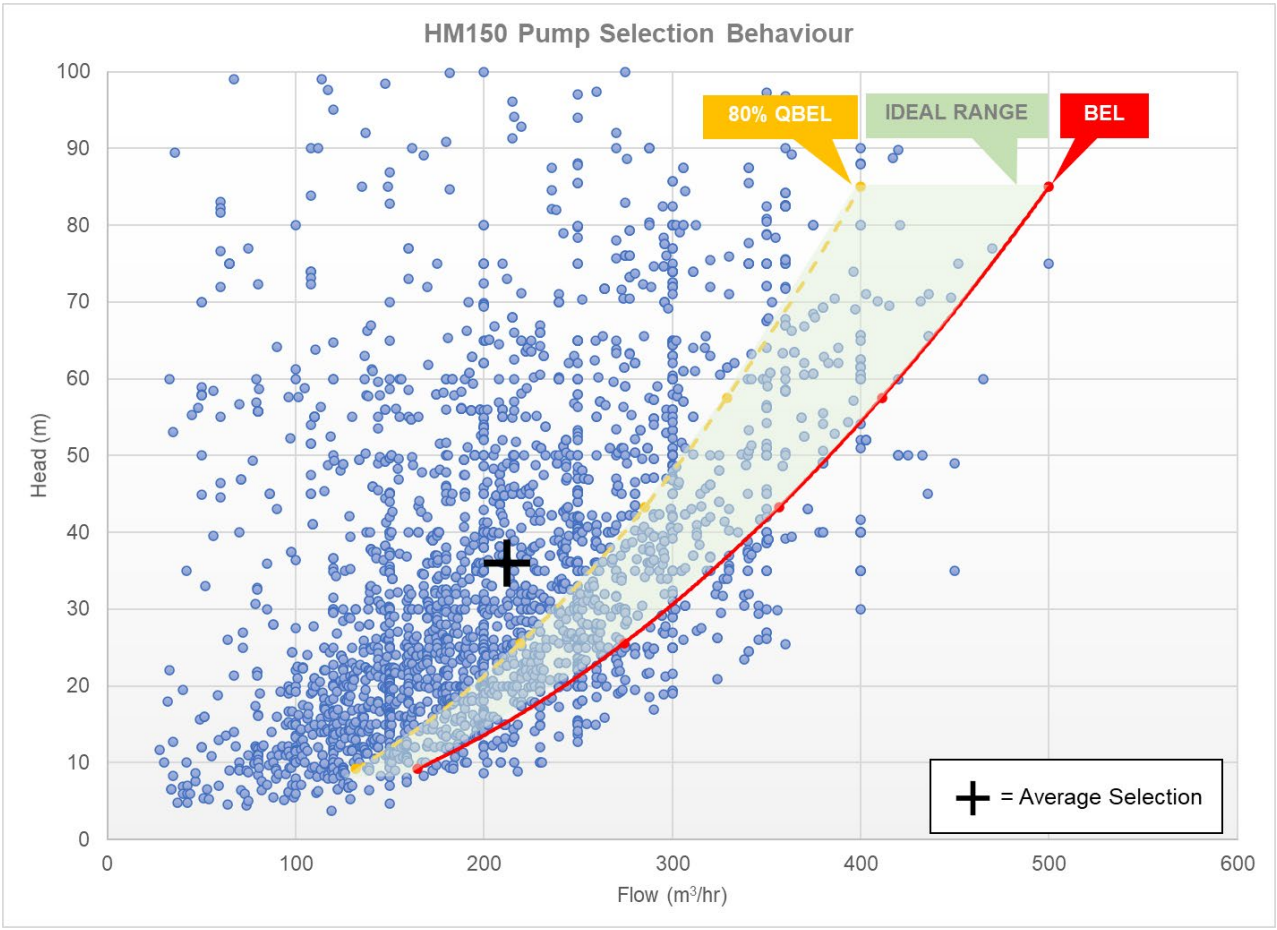

FIG 7 – HM150 slurry pump selection behaviour.

A review of 33 907 pump motor sizings have been conducted to understand power utilisation by pumps. It shows that 50 per cent selections were without variable frequency drives (VFD). The entire power base of the queries is 2.16 GW per annum. The most common sizing is a 11 kW, 4-pole motor with 2028 sizing queries (6 per cent of the total), followed by 5.5 kW and 15 kW with 1909 (5.6 per cent) and 1831 (5.4 per cent) of the sizings respectively (Figure 6b). Average power margin calculation is estimated as 58 per cent for motor greater than 5.5 kW, and 95 per cent for motors less than 5.5 kW. There are good reasons for having power margin on motors. Firstly, from a practical point of view, motors are available in defined sizes as per the suppliers and are not available in infinite number of sizes. It is therefore wise to choose the next largest size closest to the calculated capacity needed, which leads to some margin. In addition, as pointed out above slurry pumping involves derating based on well tried and tested empirical formulas but as this is not an exact science it is always good to include some safety margin, leading to some further power margin. Lastly inevitably sites do continuously chase throughput improvement and down the track having some margin for future improvement is a wise choice, adding yet again some power margin. Good practice however is to allow for on average, 20 per cent power margin over and above the calculated power needed.

Pumps use water in sealing of the shaft where it enters the case, the water has as main function to prevent ingress of dirt into the seal, reducing friction in the seal and cooling of the seal. Various types of seals have been developed over the years with the main defining factor the amount of water they consume to render the sealing function, except for the expeller seal. The most basic is the standard gland seal which design dates back to 1850s (Ridgway, 2010) and the most advanced is the mechanical seal with the first commercially successful seal being used on a centrifugal pump in 1928 (Buck Jr, nd; Ridgway, 2010). As generalisation a gland seal is much more basic in design, with much lower upfront cost but much higher water usage, compared to a mechanical seal which is more complex in design, higher upfront cost and has far lower water usage. Lastly there is also a dynamic seal, called an expeller seal as mentioned above. This is a dynamic seal type created by a rotating expeller which allows a dry seal whilst the pump is running. It does however come with higher energy

and wear cost as it is driven by the pump shaft and is exposed to the slurry. To understand water utilisation, a review of 28 667 pump sealing selections has been carried out. It indicates nearly 11 629, or 41 per cent, having full flow gland seal. This is followed by the Enviroset™ sealing and low flow gland seals, with 16 per cent for each. As the name indicates, low flow consumes less water than a full flow gland seal and in the same fashion the Enviroset™, a Metso Outotec proprietary gland seal consumes even lower water with on average 39 per cent less than the low flow and 69 per cent less than the full flow gland options. Overall, more than 70 per cent of the selected seals are a variant of the gland seal. Expeller seals are chosen 14 per cent of the time. The remaining selections are mechanical seals. These choices are summarised in Figure 6c. The total yearly water requirements for operating these pumps, in the worst case, are 219 million cubic metres. If the cost of water is approximately 0.81 AU$/$m^3$, the water requirement represents over 177 million dollars per annum.

Phase 2 – slurry pump installation and commissioning

Three standard mineral concentrator plants were selected for analysis: (i) a copper, (ii) a magnetite iron, and (iii) a gold plant. The copper plant consists of raw material storage, comminution, flotation, concentrate thickening, concentration filtration, tailings, reagent preparation and lime preparation areas. The total calculated power installed for the operation of the plant is 12.39 MW. Pumps contribute 21 per cent of the total installed power, with 2.56 MW. At over 8000 hours of operations – equivalent to a year, but excluding planned shutdowns – the pumps consume 20.5 GWh at a cost of AU$4.1 million. For Australia, the electricity emission factor for carbon dioxide is 0.97348 kg CO_2 per kWh (Ecoinvent, 2020). Therefore, for this plant, the pumps contribute 20 007 t of CO_2.

Similarly, the selected magnetite iron ore plant has crushing, conveying, stockpile feed and reclaim, two stage grinding, three stage separation, flotation, reagents, concentrate filtration, thickening, and tailings areas. The total power installed for the plant operation is 70.9 MW, with pumps contributing 12.7 MW or 18 per cent of the total. As in the last case, based on 8000 hours of operation, the pumps consume 102 GWh of energy, at a cost of AU$20.3 million, and produce 99 279 t of CO_2.

Finally, a standard gold plant, consisting of three-stage crushing, storage, grinding, flotation, thickening, filtration, acidulation, leaching and adsorption, elution and carbon regeneration, cyanide destruction, electrowinning, gold room, tailings and lime preparation, has been selected. This plant has information of both power and water utilisation. The total power installed for plant operation is 34.3 MW, with pumps drawing 9.5 MW or 28 per cent of the total. The pumps consume 75.7 GWh over the year, at a cost of AU$15.1 million and producing 73 662 t of CO_2. The water balance indicates 431 m^3/h of water for total plant, with pumps requiring 31 m^3/h (7 per cent) for sealing purposes. Pumps do not directly consume this water, rather it gets utilised in the process through sealing; any loses are due to friction, leakage or failures. Although this is applicable to the various types of seals – from full flow gland to double mechanical seals – the quantity of water requirement will vary. Moreover, the improper maintenance of seals results in considerable loss of water. Using same water cost estimate as above case, 0.81 AU$/$m^3$, pumps monopolise over $200 k of water per annum. Refer Tables 1 and 2 for summary of calculation for power and water utilisation on above plants respectively.

TABLE 1

Summary of installed power utilisation by pumps.

Concentrator plant		Copper	Iron	Gold
Power distribution		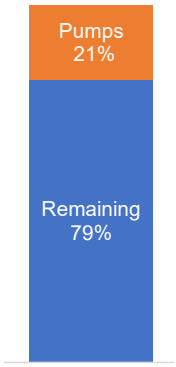		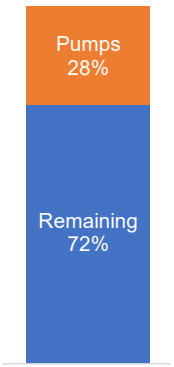
Total plant installed power	MW	12.4	70.9	34.3
Power installed for pumps	MW	2.6	12.7	9.5
Estimated plant annual operation	hours	8000	8000	8000
Energy consumed by pumps	GW/annum	20.8	101.6	76
Estimated cost of 1 kWh	AUD	$0.20	$0.20	$0.20
Electricity emission factor in Australia	kg CO_2/ kWh	0.97348	0.97348	0.97348
Pump carbon dioxide emission per annum	tonnes	20 007	99 279	73 662
Pump energy cost per annum	AUD	$4 110 560	$20 396 800	$15 133 920

TABLE 2

Summary of water utilisation by pumps.

Concentrator plant		Gold
Water distribution		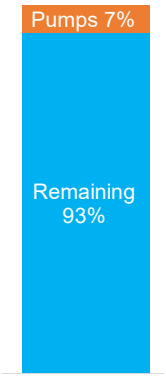
Total plant water	m^3/h	431
Water utilised by pumps	m^3/h	31
Estimated plant annual operation	hours	8000
Water consumed by pumps	m^3/annum	248 000
Estimated cost of water per cubic metre	AUD	$0.81
Pump water cost per annum	AUD	$200 880

Phase 3 – slurry pump, mature operation

For the final phase of application life cycle, a cyclone feed pump case example as presented in Figure 8 has been selected for detailed operational review. The operational phase of pump application commences once the pumps are installed and commissioned. Usually, on plants there is handover from EPC company (Engineering, Procurement and Construction) to the End-user (plant owner) looking after the operations. Generally, End-user personnel on-site involved for operating pumps are processing and maintenance team with support from engineering and other departments. During the operational phase, the pumps undergo various duty conditions depending on the operational regimes. From phase 1 pump selection, it is expected that the nominal duty condition will be the average duty condition during the operational period and the design max is the safety parameter added for future. With plants inevitably chasing throughput improvement as stated above, this operating envelope gets pushed. The focus being increased throughput traded off against increased conversion cost. Whilst energy increases definitely features in this calculation for larger operation units, especially comminution units eg grinding mills, ancillary equipment's energy increases are not generally scrutinised or considered with the same importance. This oversight can have quite a large impact however, as clearly demonstrated by Ballantyne (2019), where the author showed pumps, on average, add 1.6 kWh/t to comminution circuits.

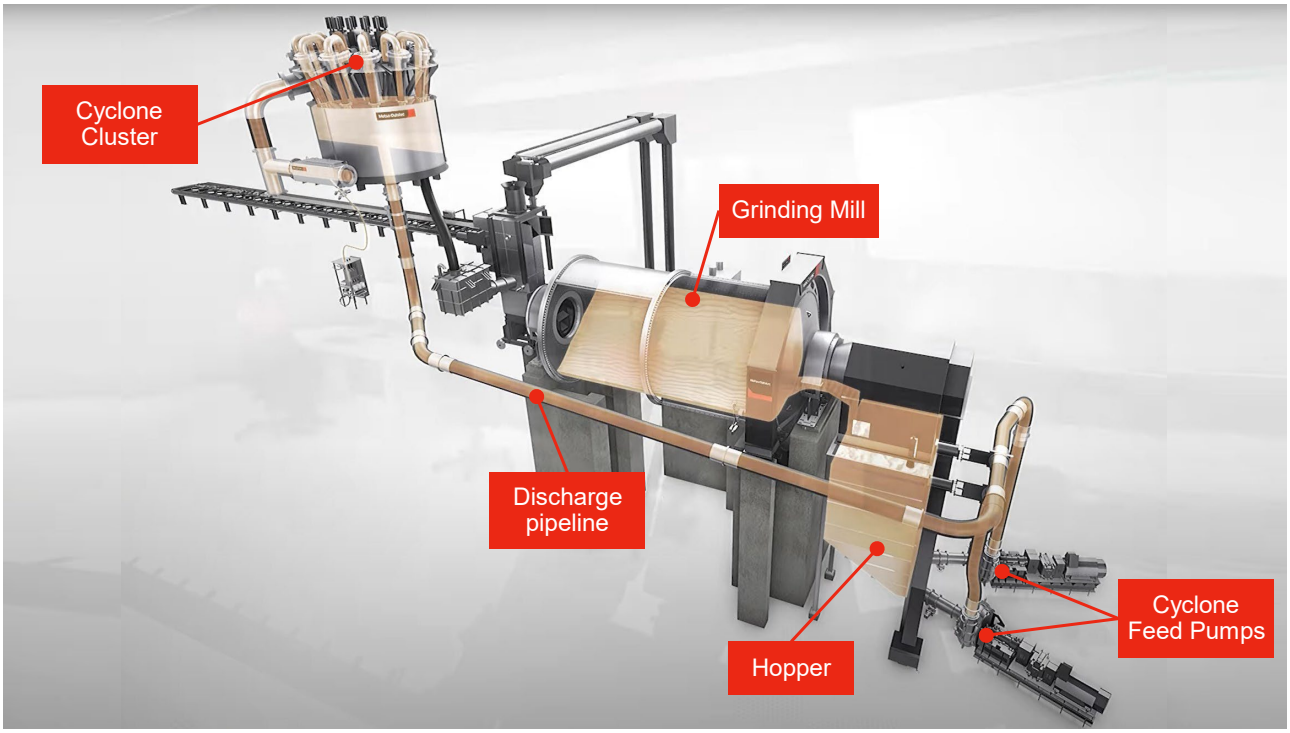

FIG 8 – Cyclone feed pump application in mill circuit.

In this case example, the data illustrated in Figure 9a shows original nominal and design max duty selection from phase 1 and 2, along with average duty and max duty five years later for the HM250 cyclone feed pump. It can be noted that over the period there has been a 42 per cent increase inflow, 19 per cent more concentration by weight and 17 per cent increase in slurry specific gravity. This results in an 85 per cent increase in absorbed power from original nominal selection to max duty five years later. This is at the brand new state of the hydraulics (impeller and casing). Wear can significantly contribute to the drop in efficiency resulting in higher power draw as well. Wear due to normal operation can contribute up to 25 per cent before it is replaced (Sustainability Victoria, 2015). The performance of the pump and corresponding life of both wet-end parts (due to wear) and bearing has significant impact. Experience shows that during operational stage, there is a significant focus on maintenance cost and availability aspects for this application being a Service Class 4, and generally the energy and water costs are overlooked. A total operating cost analysis using same estimate of 8000 hours operation in a year at cost of energy (AU$0.20 kW/h) and water (AU$0.81/m^3) is presented in Figure 9b. The life of wear part has also seen a decrease of 30 per cent by which

maintenance cost increases from both cost of new parts and labour. Cost of lost production is neglected as there is duty and standby pumps.

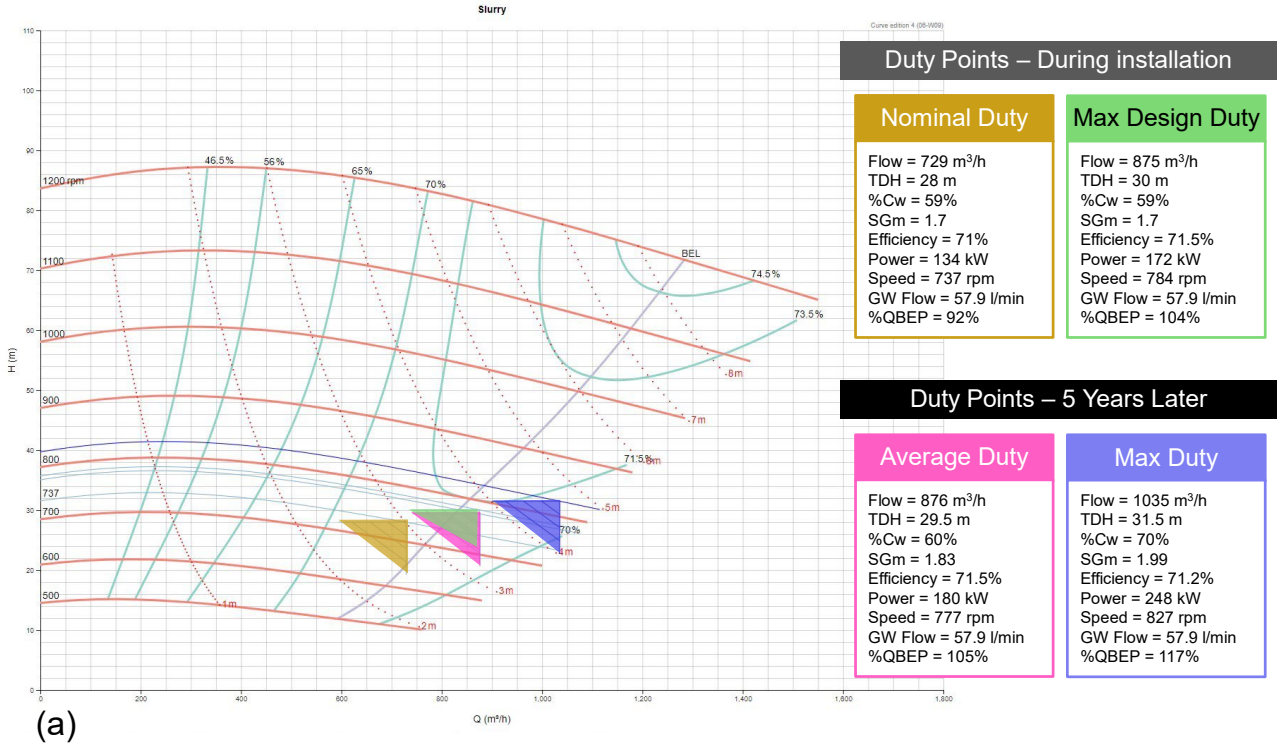

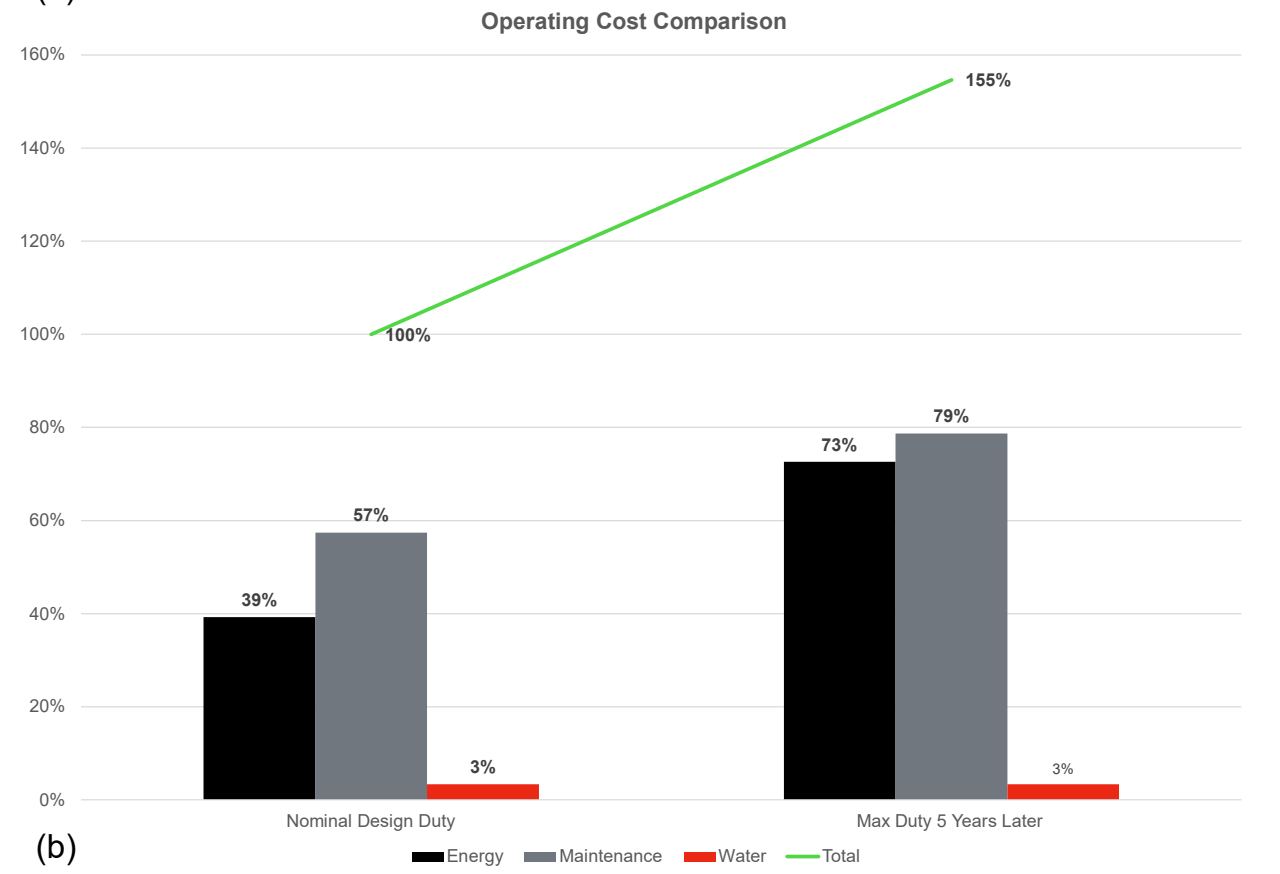

FIG 9 – Cyclone feed pump HM250 (a) slurry performance curve with duty points from design installation and five years later (b) operating cost comparison relative to normal design duty as 100 per cent baseline.

The result explains that there has been a 55 per cent increase in operating cost. Maintenance cost contributes the highest resulting from shorter life of wear parts from operating right of BEP

(117 per cent QBEP) and increased tonnages. It is important to note the relative increase in maintenance cost is only 37 per cent. However, when compared for energy the relative increase has been 85 per cent and standing in second on overall cost. This energy cost is normally not seen as it gets overlooked due to higher maintenance cost and availability of pump changes. The selection itself presents an undersized pump for the application and timely optimisation is needed to save energy and improve performance. Assuming, at an average 191 kW absorbed power by this pump per hour for five years results in 7437 t of CO_2 being produced. Water on the other hand has limited change as the pump requirement for gland water remains same. However, wear can significantly cause loss of water which may not be quantifiable but can be avoided using constant flow control valves. Another prominent observation is HM250 is a Service Class 3 pump operating at Class 4 duty. A specifically designed latest Class 4 pump like the MD Series of Mill Discharge Pump will be ideal for this application that will bring the maintenance cost down by longer lasting parts. Similarly, the adjustable side liner in MD pump with the higher efficiency impeller and Enviroset seal will promote savings in energy and water utilisation. It was noted that the MD series was not available during the original project five years ago. Upon closer observation, the authors note that, in most mine sites, Class 4 pumps do get considerable attention from the maintenance and operation team. This is due to higher frequency of parts changeout affecting availability of the plant, the maintenance cost of the replacement of parts, the labour cost, and complaints from associated team for additional tedious work from service interruptions. However, the pump-motor silently doubling the energy cost is not perceived as a concern as this does not affect anyone until alarms for high amperage or trips happen. If a Class 4 pump is not given enough attention from energy optimisation, then the condition of the other class of pumps, which are the majority in the plant, will be worse.

Power utilisation discussion

From Phase 1 above it is quite evident that oversizing of pumps is quite common with only 17 per cent falling in an ideal range with reference to power consumption. It is estimated, a better pump selection could save 3 per cent or 1.1 TWh/a of energy in 2015 (Reeves, 2001). Improvements in efficiency of pumping system can not only reduce energy costs but also reduce maintenance requirements, reduce greenhouse gas emissions and preserve natural resources (Sustainability Victoria, 2015). Studies indicate that many pumps do not operate at BEP, in fact average pumping efficiency in manufacturing plants can be less than 40 per cent (Creamer, 2014; Sustainability Victoria, 2015). Oversized pumps and use of throttle valve were identified as the two major contributors to the loss of efficiency.

In past couple of decades due to lower ore grades there has been a greater demand for increase on power size and efficiency of process machines to maintain a competitive plant throughput (Galarza, 2015). According to Creamer (2014), slurry pumps, process water pumps and dewatering pumps are at the heart of many processes and are often overlooked for energy savings potential as these pumps are embedded in this sophisticated process which are ultimate operational focus. This is quite evident from Phase 1 where the smaller pumps with consummately lower power needs make up far more of the overall sizings than the typically focused on big Mill discharge slurry pumps with their large, up to 3 MW drives. The findings of this report differ from the findings of authors Pirouz *et al* (2017), in which they identified slurry pumps account for an average of 10–15 per cent of total installed power. In Phase 2 of the report the authors findings are that although there is some spread depending on the commodity being processed pumps account for 18–28 per cent of plant installed power.

Several observations can be made from Figure 3. Firstly, a single pump type (Class 3, HM250) has been used that shows fairly constant capital cost. The HM250 was used for calculation to allow consistency with phase 3 and to focus on energy and water. Ideally, for Class 1 application the selection philosophy is to use a higher efficiency and low capital cost pump. Similarly, for Class 4 application a proper arduous duty pump like mill discharge is selected to reduce maintenance cost but can have relatively higher capital cost. Secondly, the total ownership cost can drastically change if the cost of electricity changes. Some areas may have cost-effective system such as hydropower that can produce low cost electricity while other areas can be diesel generated with premium energy cost. However, in addition to total ownership cost, the carbon dioxide emission needs to be closely looked into. This can also change as majority of slurry pumps operate on electric motor, but many dewatering pumps or mobile pumping applications have diesel generator drives that can further

impact carbon dioxide emissions. Figure 10 highlights changes to total ownership cost when cost of electricity is AU$0.05/kWh and AU$0.35/kWh respectively. Additionally, Figure 11a illustrates relative change to carbon dioxide emission for each class.

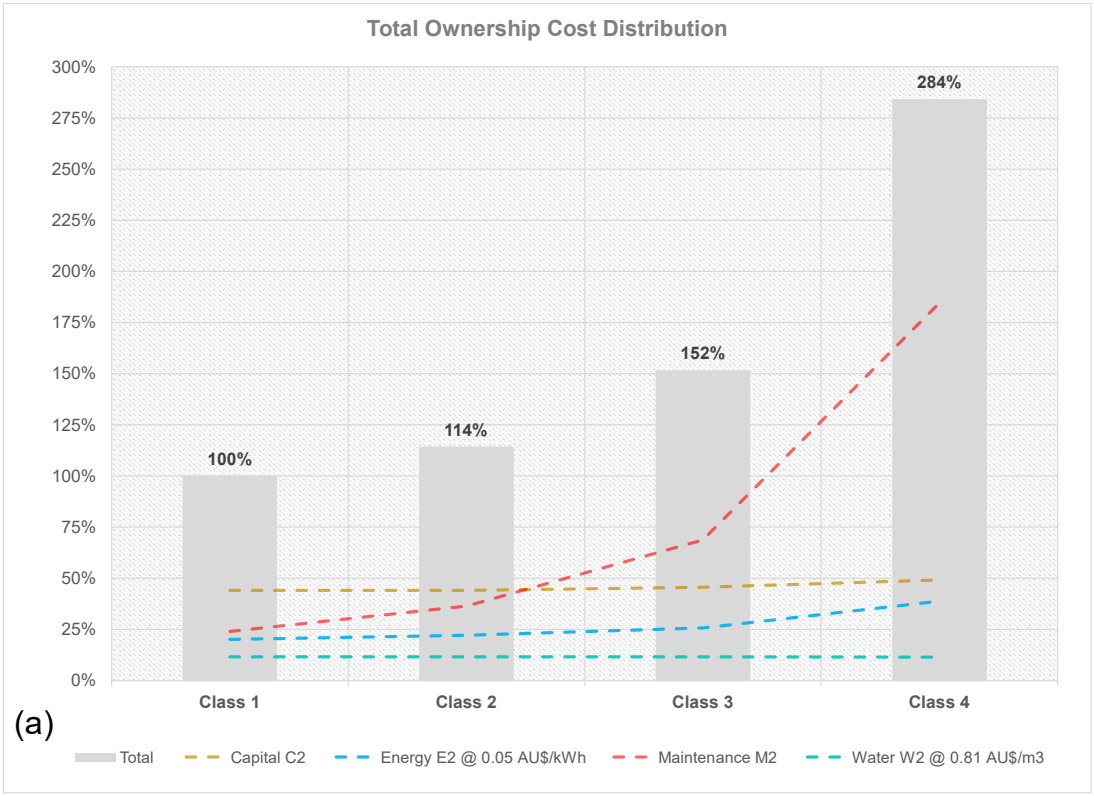

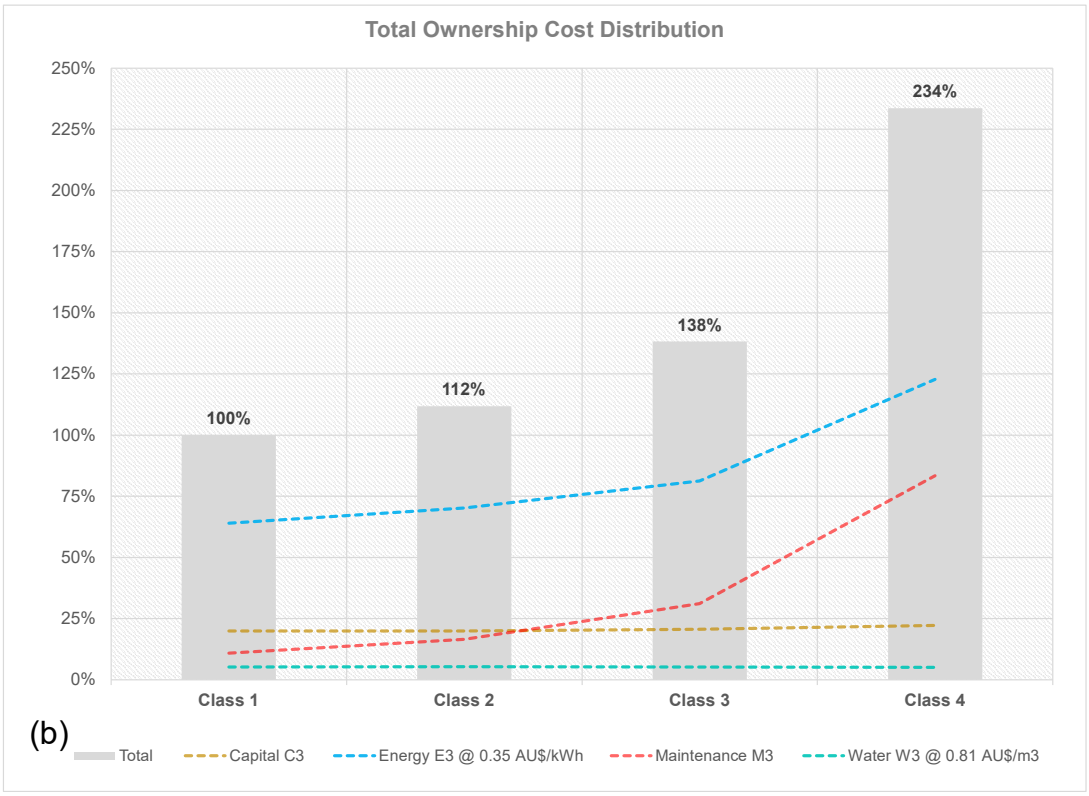

FIG 10 – Total ownership cost distribution as per slurry class relative to class 1 at 100 per cent baseline (a) with energy cost at AU$0.05/kWh; (b) with energy cost at AU$0.35/kWh.

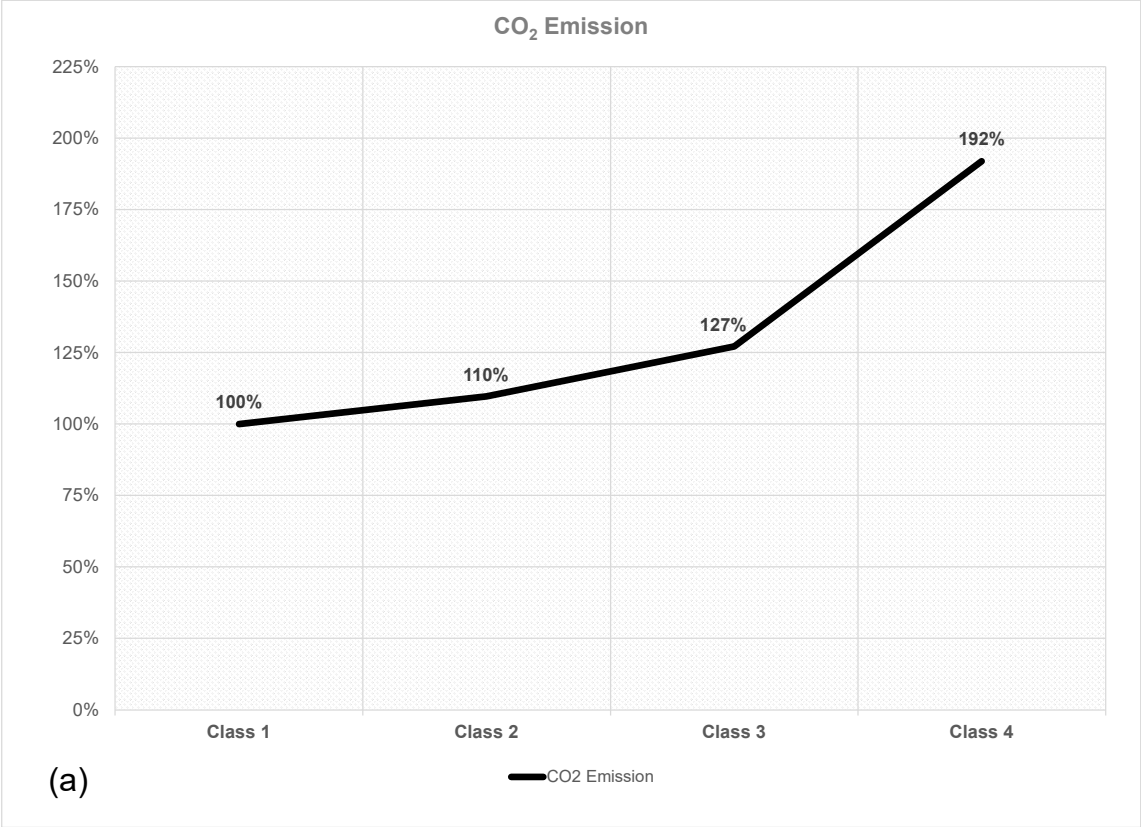

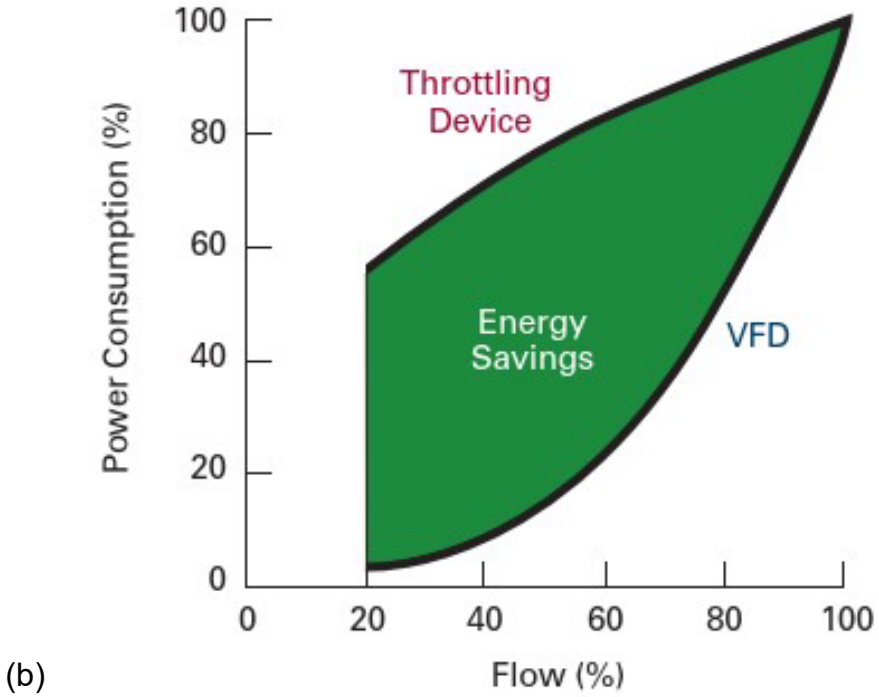

FIG 11 – (a) CO_2 emission per slurry service class (b) the amount of energy saved by using a Variable Frequency Drive versus a valve to control flow (Neuberger and Weston, 2012).

Slurry pumps are employed either in fixed flow or varied flow regimes to suit the process at hand. To account for the varied flow the use of throttling valves is employed in many applications. This is also true for the fixed flow pumps where higher throttled flow is used to allow for flow compensation as the pump wears. Running a higher flow pump with throttling valve translates into wasted energy that gets dissipated as heat. Instead, the use of variable speed drives allows for reducing the pump speed to compensate for any required flow change at a significant power saving as shown in Figure 11b.

From Phase 1 it is apparent that only 50 per cent of the sizings were made with a variable frequency drive with the rest being fixed speed. Whilst it is true that variable frequency drives have higher upfront cost compared to a simple fixed speed solution significant power savings can be made over the complete life of the pump not to mention significant savings in CO_2 emissions. Careful trade-off studies should therefore be undertaken. However, with low individual energy usage per pump and capital being the main driver during the initial engineering and construction phase, this frequently is not the case. Use of variable frequency drives in combination with motors has been increasing over the years due to many benefits such as soft start with minimum electrical utility disturbance (ie in rush current mitigation), full torque available at 0 speed for overload start-up with pulp solidification after long still stand period (superior to any other reduced voltage starting method), optimum and constant pump speed compared to across the line SCIM operation, flexible motor voltage and speed regardless of the power distribution voltage and frequency, and improve power factor (close to unitary) over the entire operating speed range (Galarza, 2015).

From Phase 1, we can further see that similarly to oversizing pumps, motors also tend to be significantly oversized. This stems from a 'better safe than sorry' mentality driven by fears about the inability to pump the slurry, brought on by wrong derating factors or incorrect slurry data being given to the designer. In addition, having spare capacity for future expansion and as has been pointed out gaps in available motor sizing from suppliers are other considerations. In this case bigger is not always better. The disadvantages of this significant oversizing are lower motor efficiency, lower power factor, higher motor cost, higher controller cost and higher installation cost (Csanyi, 2017). From a sustainability point of view, this is not a good outcome.

From Phase 3, it is noted that for one high profile application, the change in absorbed power over five year is 85 per cent. If similar consideration and upgrades are projected to the rest of the pumps, the energy usage can be significantly greater. Therefore, it is important to consider pumps holistically throughout the plant for efficient use and savings*:* if a Class 4 pump is not given enough attention from energy optimisation, then all other class pumps, which are the majority, will be silently growing in inefficiency, energy use, and increase in CO_2.

The main cause of climate change is the emission of greenhouse gases. The predominant source of these gases is human activity. In response, the 2015 Paris Agreement, a legally binding international treaty on climate change, was adopted by 196 parties. This can be achieved through the improvements in efficiency and through the transition to green energy.

Water utilisation discussion

From Phase 1 we can see that in general the less water efficient full flow gland seal is by far the preferred choice for sealing purposes. There is no dispute the simplicity of the design makes it extremely robust especially in the mineral processing environment. Even with severe wear of the sealing system, by maintaining sufficient water flow in most cases plants can limp through, albeit at significantly increased water consumption, to the next planned shutdown. This makes them extremely forgiving from an operational point of view compared to for example to a mechanical seal which if significantly worn will dictate an unplanned stoppage, endearing them to the operational crews. The question is at what water cost?

According to Delevingne *et al* (2020), as shown in Figure 12, 30–50 per cent of the production of copper, gold, iron, and zinc are located in zones subject to water shortages. The climate research points towards an increase in scarcity of water in these regions – the regions that are wet are becoming wetter, and the regions that are dry are becoming dryer (Famiglietti, 2019).

Water cost can vary significantly based on location and treatment. The authors have noted cost range from zero to US\$5/m^3 at lower end its mostly due to pumping energy while higher end is sophisticated water treatment plant such as reverse osmosis. This can affect the total ownership cost distribution as well, for consistency authors have used AU\$0.81/m^3.

As stated above, China, USA, Russia and Australia are the four biggest mining nations. Also, South America is home to a number of important mining installations. All are located in regions that will have water problems.

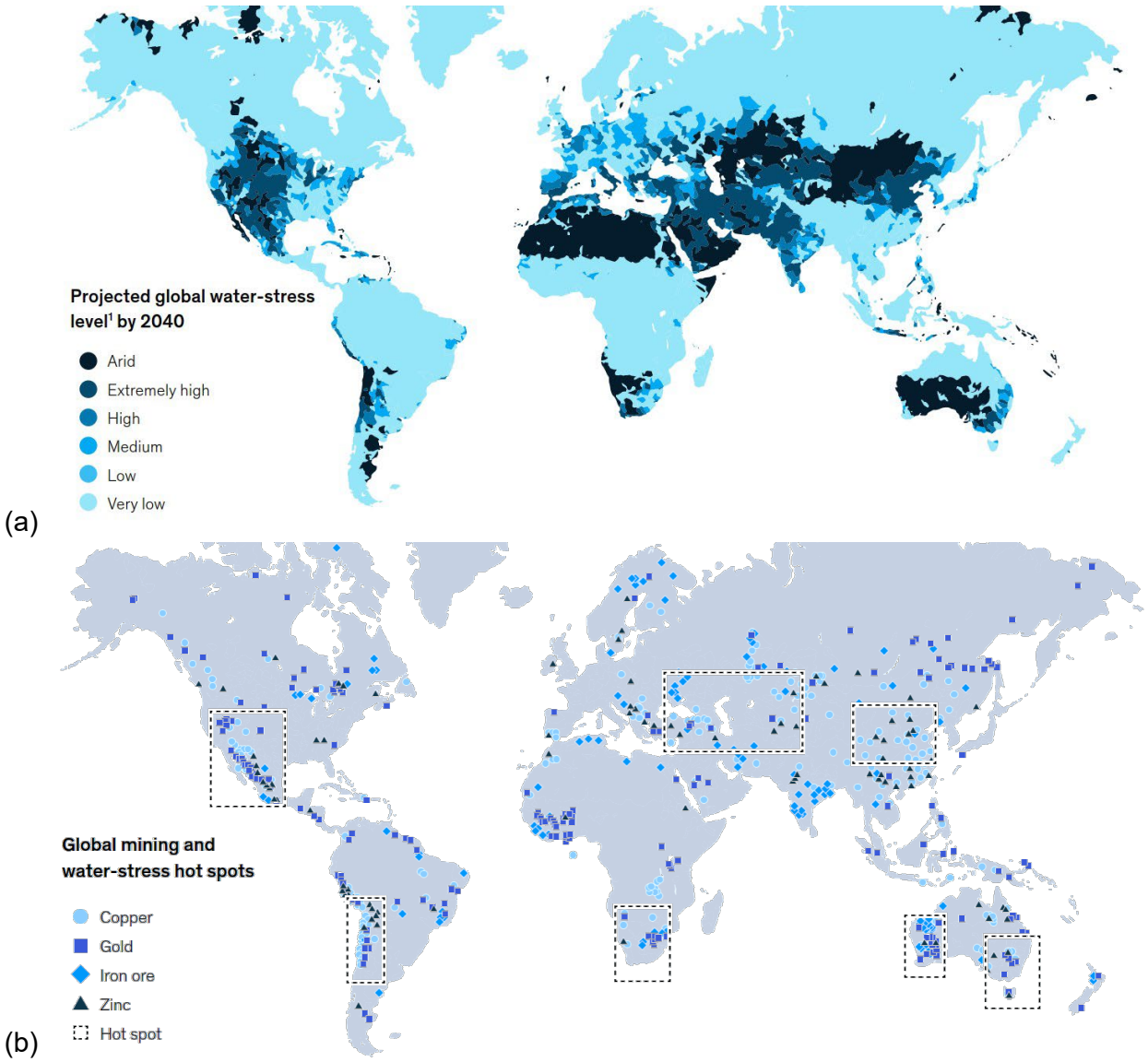

FIG 12 – (a) Global water stress, and (b) water stress and mining (Delevingne *et al,* 2020).

Recommendations

First and foremost, size matters – although small on individual basis, based on the large number of pumps employed on mine sites their aggregated power and water usage does matter. This needs to be *recognised* and much more attention needs to be paid during not only the plant design phase, but throughout the pumps' life cycle to optimise power and water usage.

By collecting data over the major phases of a pump's working life, recommendations can be made. The recommendations are meant to address the issues identified in the previous section. The recommendations are grouped by their nature.

Practical solutions

Recommendations for power reduction

Since the overall power draw of pumps is an important fraction of a plant's overall power draw, improving their efficiency or reducing the losses is advantageous. This can be achieved by:

1. Increasing the use of variable speed drives. This gives the operator some increased degree of freedom to keep the pump as optimal as possible given the process flow requirements.
2. Using high efficiency metal pumps for light duties. For this type of operation, they are an improvement over rubber pumps.

3. For water duties, use a water pump in lieu of slurry pumps. For this type of work, water pumps have a much better efficiency.
4. Using level-controlled sump pumps (descent slope designs).
5. Including additional elements when designing pumps, such as:
    - Limits to the total dynamic head in the design.
    - Using long radius bends instead of short radius bends.
    - Proper routing of pipes.
    - Improved water pump system design ie not all pumps running all the time.
6. Having a good hopper design. This is to avoid cavitation and other NPSH issues. This not only upsets process conditions but increases wear and reduce head and power leading to higher inefficiency.
7. Improving the pump finish by:
    - Decreasing the surface roughness.
    - Adding a surface protection.
8. Managing the wear through proper maintenance and operation.
9. Decreasing the tip speed. Increased speeds reduce the efficiency of the pump.
10. Shut off wastewater pumps when not in use.
11. Optimising the pump when it predominantly works outside its ideal conditions. This can include changing the impeller design, the motor, the piping, or the whole pump.
12. Regularly auditing the performance of the pump.
13. Scheduling pumps: only running certain pumps when needed.
14. Using direct drive pumps. Using V belt drives incurs and additional 7 per cent efficiency loss.
15. Adjusting the suction liner to touch. Field tests conducted at three different large slurry pump sites by Walker (2014) demonstrated that this adjustment to touch reduced the wear rate by 30–40 per cent, improved the flow rate up to 7 per cent, and the efficiency up to 3 points. This represents a significant saving in operating costs for a plant that adjusts diligently.

Recommendations for water utilisation

Although the impact on water is modest, if any sources of losses can be eliminated – within reason – they should be. It is the most sustainable solution, particularly in areas where water is becoming scarce. This can be achieved by:

1. Selecting the most water efficient seal, it will cost less in the long run.
2. Using gland seal water for thickener underflow dilution.
3. Having a dedicated mono pump for large slurry pumps (instead of a ring main).
4. Managing the wear, including that of the shaft sleeve, the packing, etc.
5. Scheduling adequate and regular maintenance.
6. Use constant flow control valves.
7. Reclaiming water from tailings.

Monitoring suggestion

As the adage goes, ‘you can’t control what you can’t measure’ (DeMarco, 1982). The data obtained for this study demonstrated that there is a significant gap in what can be measured and what is presently measured. This is especially true for the pump’s operational phase of the Pump Application Life Cycle where the authors really struggled to get any good verifiable data. There is much talk about Big Data, but this is definitely not the case with operational data availability on slurry pumps.

To really capitalise on the learnings through the Operational Phase, that then feeds into the Design Selection Phase, it is imperative that more effort is paid to get good verifiable data. The authors suggest that the trend of Digitalisation should be capitalised on to fill this gap, as a continual pump improvement model illustrated in Figure 13.

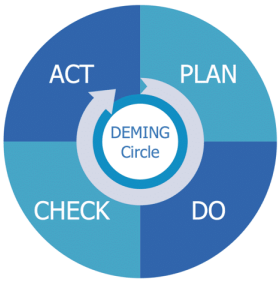

FIG 13 – Continual pump improvement model.

Digitalisation as an enabler

Digitalisation is a portmanteau word that has many meanings. Here, it is interpreted as the collection of data, its analysis and transformation into actionable insights – all occurring in the electronic realm, leveraging the power of modern digital systems. Digitisation is seen as a transformational change that will help the mining companies in reducing costs, improving business productivity, and transforming standard mining practices (Barnewold and Lottermoser, 2020). Examples are the autonomous haul truck, autonomous drill rigs, and heavy-haul long-distance trains. With this potential in mind, the following is suggested:

1. Add sensors such as slurry density instruments.
2. Consume as much of the data as possible. If you measure it, use it. The data is valuable enough for it to have been measured.
3. Define relevant metrics and derived quantities including:
   - Machine health metrics (drive, bearings, and seals).
   - Wear estimates.
   - Performance estimates.
   - Sustainability metrics.
4. Define a decision framework where action can be triggered by the actionable information. The actions are defined interventions meant to keep the pump at its best.
5. Assign champions for all the information, not just the information that relates to profit. Who is the custodian of the energy draw and the water use? Given the state of the climate, this may be the only morally defendable position: sustainability must be part or regular operations.

Recommendations for sustainability metrics

There are existing metrics for evaluating the health of mechanical systems and the pump performance. There are no published methods for estimating wear and sustainability in working pumps. The following metric is proposed to score the sustainability of pumps. It begins with some definitions.

At a given time, the operating state of the pump is defined as:

$$x(t) = \begin{cases} 0, when\ in\ maintenance\ at\ time\ t \\ 1, when\ in\ operation\ at\ time\ t \end{cases}$$

From this state, the availability A of the pump is the probability of finding the pump in a functional state.

$$A(t) = \Pr\left[x(t) = 1\right]$$

The assumption here is that wear drives most of the maintenance activities. Therefore, the availability can be used as a surrogate for wear. The water efficiency of the pump is a function of the volume of water lost to the seal (q) with respect to the total volumetric flow in the pump (Q).

$$\eta_{H_2O} = 1 - \frac{q}{Q}$$

Finally, the pump efficiency is a ratio between the hydraulic power generated and the power draw P. The hydraulic power is a product of the slurry density ρ, the gravitational constant g, the volumetric flow Q, and the head H.

$$\eta_P = \frac{\rho g Q H}{P}$$

Together, they give an indication of performance, energy efficiency, water waste, and wear (see Figure 14). In some sense, they touch on people, planet and profits (performance) – the definition of sustainability. These metrics must be regularly monitored, and appropriate action must be taken to keep them at their optimal.

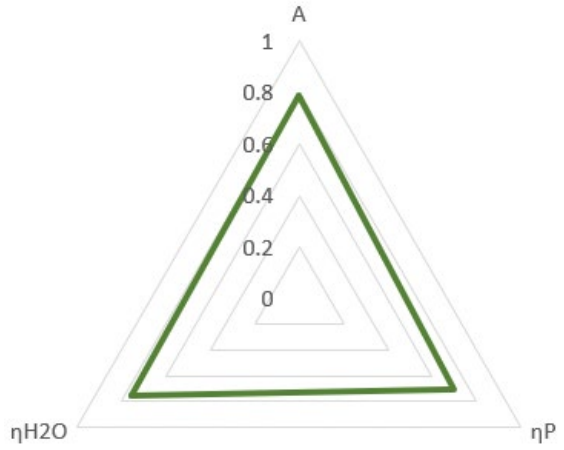

FIG 14 – The sustainability metrics.

CONCLUSIONS

Climate change will have a profound effect on human activity – mineral processing will not be spared. As the IPCC Chairman Hoesung Lee said, 'We are at a crossroads. The decisions we make now can secure a liveable future. We have the tools and know-how required to limit [the effects of] warming' (IPCC, 2022b). The implication is that all need to contribute at reducing greenhouse gas emissions and water consumption. This does not mean forgoing industry, just doing things better.

Mineral processing is an essential industry. It provides the raw materials that drive modern life and requires several specialised heavy machines to do its work. Although pumps are an essential to the operation of the mineral processing plant, they are often overlooked. However, the information presented here has demonstrated the importance of pumps. They consume approximately a quarter of the power and claim a tenth of the water. Therefore, some care as to how they are designed and used is important.

What is observed is that, when selecting a pump, some users do not consider performance to be king. Other reasons come into play, such as the physical footprint or the safety factor. These other considerations may push the end-user to sacrifice the optimal performance. Once installed, the motivation is to keep the pump working. It can consume whatever it needs, as long as it is working and performs. Consequently, performance data abounds. However, any query about quantifying water loss will likely go unanswered as it is not a performance metric. Finally, processing plants are dynamic – they change over time. Unsurprisingly, there is an evolution in the operation of the pump; how it was used the first day is often not how it is being used years later. This has a significant impact on the performance and the sustainability footprint of the pump.

Based on all phases in a pump's life, several observations can be made. Firstly, there are pragmatic actions that can be taken – they relate to seal choices, piping, variable/fixed drives, water, energy

use, etc. Also, there are gaps in the data. This needs to be corrected since partial information leads to uninformed decisions – a risky position to be in. As for the data that is collected, there is a need to transform it into information that can be acted upon. In the drive towards improved pumps, the information needs to be in the hands of someone who can act, be it the operator, the design engineer, etc.

One area everyone can act is sustainability. Not only does this relate to the environmental footprint of pumps in mineral processing, but in encompasses performance. This is a balanced approach but requires some additional thought. Digitalisation is seen as an enabler for sustainability and is the way forward.

ACKNOWLEDGEMENTS

The authors are grateful for the support from many individuals and organisations who have contributed to this research. In particular, Metso Outotec and the University of Western Australia for their collaboration. A number of colleagues from various Metso Outotec business units have contributed to the pumping sustainably initiative, namely Jimmy Löfgren for providing data on slurry pump selections and development on conceptual sustainability metrics, Buck Neo for preliminary sizing, the Plant Solutions team for providing case studies and recommendations from installations, and the Life Cycle Services team for reviewing operational issues. Additionally, the support by several engineering firms, mining companies, and pump manufacturers throughout the Asia-Pacific region for this initiative is greatly appreciated.

REFERENCES

Amponsah-Tawiah, K, Ntow, M A O and Mensah, J, 2016. 'Occupational Health and Safety Management and Turnover Intention in the Ghanaian Mining Sector', *Safety and health at work*, vol. 7, no. 1, pp. 12–17.

Ballantyne, G, 2019. Quantifying the additional energy consumed by ancillary equipment and embodied in grinding media in comminution circuits, in *SAG Conference*, Vancouver, Canada, 22–26 September, <https://www.ceecthefuture.org/media/downloads/11546–1-quantifying_the_additional_energy_consumed_by_ancillary_equipment_and_embodied_in_grinding_media_in_comminution_circuit.pdf>.

Barnewold, L and Lottermoser, B G, 2020. 'Identification of digital technologies and digitalisation trends in the mining industry', *International Journal of Mining Science and Technology*, vol. 30, no. 6, pp. 747–757.

Buck Jr, G S, nd. *History of Mechanical Seals*, SealFAQ, viewed on 9 April, 2022. <https://www.sealfaqs.com/?page_id=23>.

Creamer, J, 2014. 'Intelligent pump control contributes to significant energy savings in mining applications', Salt Lake City, Utah, 13–26 February, SME.

Csanyi, E, 2017. 'Why overmotoring an application is not such a good idea', viewed 4 April, 2022. <https://electrical-engineering-portal.com/overmotoring-application>.

Delevingne, L, Glazener, W, Grégoir, L and Henderson, K, 2020. 'Climate risk and decarbonization: What every mining CEO needs to know', viewed 2 April, 2022. <https://www.mckinsey.com/business-functions/sustainability/our-insights/climate-risk-and-decarbonization-what-every-mining-ceo-needs-to-know>.

DeMarco, T, 1982. *Controlling Software Projects: Management, Measurement and Estimation*, Yourdon Press, <https://books.google.com.au/books?id=y7AmAAAAMAAJ>.

Ecoinvent, 2020. 'Ecoinvent 3.7 country specific electricity emission factors', vol. 3.7.

Environment and Climate Change Canada, 2022. *Causes and effects of climate change*, Government of Canada, viewed 7 April, 2022. <https://www.canada.ca/en/environment-climate-change/services/climate-change/frequently-asked-questions.html>.

Famiglietti, J, 2019. 'A Map of the Future of Water', viewed 31 March, 2022. <https://www.pewtrusts.org/en/trend/archive/spring-2019/a-map-of-the-future-of-water>.

Galarza, L, 2015. 'Optimization of the Drive System for a Cyclone Feed Pump', Society for Mining, Metallurgy and Exploration.

Gunningham, N, 2008. 'Occupational Health and Safety, Worker Participation and the Mining Industry in a Changing World of Work', *Economic and industrial democracy*, vol. 29, no. 3, pp. 336–361.

Hydraulic Institute, 2016. *Rotodynamic Centrifugal Slurry Pumps for Nomenclature, Definitions, Applications, and Operation*, American National Standards Institute, Inc, USA.

IPCC, 2022a. *The evidence is clear: the time for action is now. We can halve emissions by 2030,* IPCC, <https://report.ipcc.ch/ar6wg3/pdf/IPCC_AR6_WGIII_PressRelease-English.pdf>.

IPCC, 2022b. ‘Summary for Policymakers’, in Climate Change 2022: Impacts, Adaptation, and Vulnerability. Contribution of Working Group II to the Sixth Assessment Report of the Intergovernmental Panel on Climate Change [H-O Pörtner, D C Roberts, M Tignor, E S Poloczanska, K Mintenbeck, A Alegría, M Craig, S Langsdorf, S Löschke, V Möller, A Okem and B Rama (eds.)], Cambridge University Press, In Press.

James, W, 2014. ‘Water scarcity and rising energy costs threaten mining industry’, *FT.com*.

Jeswiet, J and Szekeres, A, 2016. ‘Energy Consumption in Mining Comminution’, *Procedia CIRP*, vol. 48, pp. 140–145.

Katz, J and Pietrobelli, C, 2018. ‘Natural resource based growth, global value chains and domestic capabilities in the mining industry’, *Resources policy*, vol. 58, pp. 11–20.

Levesque, M, Millar, D and Paraszczak, J, 2014. ‘Energy and mining – the home truths’, *Journal of cleaner production*, vol. 84, pp. 233–255.

Liu, P R and Raftery, A E, 2021. ‘Country-based rate of emissions reductions should increase by 80% beyond nationally determined contributions to meet the 2°C target’, *Communications Earth and Environment*, vol. 2, no. 1, p. 29.

Maddy, P, Routley, R, Baxter, K, Chen, P and Lourensz, R, 2005. ‘Pump efficiency monitoring and management at Melbourne Water’, Schweppes Centre-Bendigo, 7th and 8th September.

Maurice, A Y and Ian, W, 2001. ‘Improving the energy efficiency of pumping systems’, *Journal of Water Supply: Research and Technology – AQUA*, vol. 50, no. 2, p. 101.

McCain, D L, 1981. ‘Slurry Transport System Operation – Introduction’, Society for Mining, Metallurgy and Exploration.

Mudd, G M, 2007. ‘Global trends in gold mining: Towards quantifying environmental and resource sustainability’, *Resources policy*, vol. 32, no. 1, pp. 42–56.

Mudd, G M, 2012. ‘Key trends in the resource sustainability of platinum group elements’, *Ore geology reviews*, vol. 46, pp. 106–117.

Mudd, G M, 2014. ‘The future of Yellowcake: A global assessment of uranium resources and mining’, *The Science of the total environment*, vol. 472, pp. 590–607.

Nelson, J and Schuchard, R, 2010. ‘Adapting to Climate Change: A Guide for the Mining Industry’, *BSR Briefs*, <https://www.bsr.org/reports/BSR_Climate_Adaptation_Issue_Brief_Mining.pdf>.

Neuberger, T and Weston, S B, 2012. ‘Variable frequency drives: energy savings for pumping applications’, *Industry Application IA04008002E*, <https://www.eaton.com/content/dam/eaton/markets/mining-metals-minerals/knowledge-center/white-paper/Variable-frequency-drives-energy-savings-for-pumping-applications.pdf>.

Pirouz, B, Javadi, S, Slatter, P, Zeller, M, Contasti, L and Pitis, C, 2017. ‘Energy Benchmarking of Slurry Pump Systems using the New Concept of Benchmark Energy Factor (BEF)’, Canadian Institute of Mining, Metallurgy and Petroleum.

Reeves, D, 2001. ‘Study on improving the energy efficiency of pumps’, <https://www.jacobalbertsen.dk/komposit/Darmstadtrapport.pdf>.

Reichl, C and Schatz, M, 2021. *World Mining Data, 2021*. Federal Ministry of Agriculture, Regions and Tourism, Vienna, <https://www.world-mining-data.info/wmd/downloads/PDF/WMD2021.pdf>.

Ridgway, N I, 2010. ‘Slurry pump gland seal three body wear and the influence of particle properties including hardness, size, fracture toughness and shape’, Doctor of Philosophy in Chemical Engineering thesis, University of Adelaide, Adelaide, <https://digital.library.adelaide.edu.au/dspace/handle/2440/63525>.

Shannon, H A and Parker, A W, 2020. ‘Evaluation of a Health Literacy Instrument Designed for the Mining Industry’, *Health literacy research and practice*, vol. 4, no. 2, pp. e84-e93.

Sustainability Victoria, 2015. *Energy Efficiency: Pumping Systems*, Pumps, Oversizing, Motor, Efficiency, Thermodynamic, Sustainability Victoria, Melbourne, Victoria.

Walker, C I, 2014. ‘Effect of throatbush adjustment on slurry pump operating costs’, *BHR Group – 19th International Conference on Hydrotransport 2014,* BHR Group Limited, pp. 103–115.

Walker, C I, Wells, P J and Bodkin, G C, 1994. *The effect of flow rate and solid particle size on the wear of centrifugal slurry pumps*, United States.

Wilson, K C, Addie, G R, Sellgren, A and Clift, R, 2006. *Slurry transport using centrifugal pumps*, Springer Science and Business Media.

Pathways to securing the skills pipeline in the resources sector

E Wightman[1], R Evans[2], C Rawson[3], E Lilford[4] and B Maybee[5]

1. Transformational Learning Group Lead, Sustainable Minerals Institute, University of Queensland, Brisbane Qld 4068. Email: e.wightman@uq.edu.au
2. Transformational Learning Principal, Sustainable Minerals Institute, University of Queensland, Brisbane Qld 4068. Email: robin.evans@uq.edu.au
3. Dean Learning and Teaching, Faculty of Science and Engineering, Curtin University, Perth WA 6102. Email: C.Rawson@curtin.edu.au
4. Associate Professor, Faculty of Science and Engineering, Curtin University, Perth WA 6102. Email: E.Lilford@curtin.edu.au
5. Associate Professor, Faculty of Science and Engineering, Curtin University, Perth WA 6102. Email: B.Maybee@curtin.edu.au

ABSTRACT

The mining industry is in the midst of a skills and knowledge shift, and workforce development is crucial to meet the economic, technical, societal and environmental challenges facing the sector. The Professional Certificate in the Foundations of Modern Mining (available on the edX platform), co-developed by the University of Queensland and Curtin University with support from the Minerals Council of Australia, addresses the recognised need to maintain a skills pipeline in the resources sector and to provide a potential pathway for a diverse range of learners into further study. It comprises six skill-building courses designed to consolidate and enhance the critical professional skills that will be needed to succeed in the resources sector. The creation of relevant, engaging material required collaboration with a wide group of people including: discipline experts, experienced learning designers, specialists in media production and graphic design as well as industry partners.

Each of the six courses has been through a piloting phase that included a cohort of industry participants (pilot-testers) with a diverse range of backgrounds from across the resources sector. The pilot-testers not only engaged with the online courses but also participated in regular focus group discussions that provided feedback to the course developers. The consultation process has been used extensively to refine the course materials and enhance the learner experience. This paper presents the outcomes from the piloting phase and highlights the potential of this pathway to not only cross-skill workers currently in the sector but also to re-skill workers who have never previously worked in mining.

WHAT ARE THE FOUNDATIONS OF MODERN MINING?

The mining industry faces imminent challenges in the recruitment of people with relevant, transferrable skills. The sector is experiencing a skills shift, from requirements for traditional hands-on skills, to a broader knowledge base and the so-called softer skills (Deloitte, 2019). With the vast majority of the workforce needed in the next five years already in employment, there is a well-publicised need to rapidly address their cross-skilling and re-skilling requirements. The Professional Certificate in the Foundations of Modern Mining (FoMM) was designed to provide learners with a thorough overview of the operational aspects of the modern minerals and mining sector. Within the context of the mining life cycle and its associated value chain, the content challenges them to consider how mining operates within the constraints of sustainability, a remote and dispersed workforce whose health, safety and wellness are paramount and, the use of digital technologies to transform operations in an increasingly technical and complex landscape.

The six courses that make up the Professional Certificate are as follows:

MINE1x The minerals and mining business provides an introduction to the mining sector through the lens of the value chain. It examines how companies and other stakeholders transform a mineral resource into a valuable product and other forms of capital.

MINE2x Minerals and mining in a sustainable world delves into the role of minerals in society, the history of the sustainable development agenda in the minerals industry and the emerging

focus on the relationship between mineral development and the Sustainable Development Goals.

MINE3x Operational foundations of mining provides an overview of the technical aspects of mining, including mining methods, mineral processing and downstream beneficiation activities, emphasising a systems perspective that highlights the opportunity for integration along the value chain.

MINE4x Leadership and diversity in mining explores the role of leadership within the mining sector, with an emphasis on incorporating diversity, leading technical teams and developing an innovation culture.

MINE5x Digital transformation of mining covers the applications of digital technology across the value chain, including automation and remote operations, exploring how this will transform the processes used and impact the nature of work and the skills required to operate successfully in the sector.

MINE6x Health, safety and wellness in mining articulates the key concepts in the management of health, safety and wellness in the mining workforces and communities, including the impact of new technologies and the importance of human factor considerations.

The overarching learning goals of the FoMM are to enable learners to:

1. Apply the lens of the value chain to review and critically analyse all aspects of the business of mining and its associated stakeholders.
2. Analyse the complexities of the life cycle of a mine through a systems approach from discovery to rehabilitation.
3. Explain how innovation has and will continue to impact the evolution of mining and business processes.
4. Create innovative solutions to contemporary problems in the mining sector.
5. Analyse how mining contributes to the sustainable development of society.
6. Distinguish and classify capabilities required across evolving roles and operating models within the mining sector.
7. Articulate the importance of an integrated organisational culture that delivers on safety, productivity and engagement.

PLANNING AND DEVELOPMENT

The course development, which included piloting of each of the six courses, was supported through the Minerals Council of Australia as part of their investment in ‘new university programs to create the professionals the modern mining sector needs’ (Constable, 2020). Teams from Curtin University and the University of Queensland worked collaboratively to co-create the courses with each institution taking the lead on three courses. Academics, learning designers and media specialists formed the core multidisciplinary team, which then engaged with an industry advisory group as well as a wider team of industry experts to confirm the overall program objectives and learning outcomes, and then to both plan and develop each course.

The planning phase served to ground the content in terms of the intended pool of learners as well as establish the framework for the quantum of learning to be delivered across the suite. The software delivery platform for the micro-credentials was chosen as edX, originally launched by MIT and Harvard, of which both Curtin University and The University of Queensland are chartered members. The platform hosts massive open online courses (MOOCs) that are available globally, including stackable options that provide pathways into higher education. With this being one of the goals of the FoMM, the six courses were designed to reflect the effort required for approximately 50 per cent of an Australian Graduate Certificate qualification. This meant that each was designed to contain approximately 20 hours of instructor-led content (videos, text, activities etc) and 20 hours of learner-led content (such as self-directed readings and assessment).

The MOOCs on the edX platform are available to leaners for free if they enrol in the audit stream. Leaners who pay a small fee can enrol as verified learners which allows access to the assessment material. Verified learners who successfully complete the assessment tasks on all six courses are then awarded the Professional Certificate. Verified learners are also able to continue to access the course materials beyond the course end date.

The development, or pilot-test, phase incorporated relatively short releases of each course, staggered over a period of approximately 12 months from August 2020 to September 2021. The purpose of these shorter releases (10–16 weeks, compared to the typical 10–12 months) was to quickly gather feedback on the content from learners, including a group of pilot tester learners specifically identified by the industry advisory group. In addition to collecting the standard analytics and survey data available directly from the platform, the pilot-testers were also regularly canvassed for feedback using facilitated focus groups with guided questions. The pilot-tester group included a total of 14 participants from a range of discipline areas including technical and non-technical specialisations, and included learners from the early stages of their career as well as more senior professionals in leadership roles.

OUTCOMES FROM THE PILOT PHASE

In total more than 2000 learners enrolled during the pilot-test phase, located in over 126 countries and covering every continent except Antarctica. Approximately 6 per cent of enrolled learners opted for the verified track with approximately half of the verified learners successfully completing the assessment requirements for the course.

Data from the online pre – and post-course surveys was used to help the course developers understand if the FoMM was meeting one of the intended purposes of cross-skilling workers currently in the sector or re-skilling workers who have never worked in the sector. The pre-course survey response rate was approximately 23 per cent, with close to 40 per cent of respondents having no previous experience in the sector, and with two-thirds taking the course to get skills in a new area or for employment opportunities. Those who were working in the sector were more likely to be early or mid-career with approximately half seeking new skills. The post-course evaluation survey response rate was much lower, however 85 per cent of respondents agreed that the course met the stated objectives.

The data gathered from pilot-testers during the focus groups was invaluable in assisting the course developers to fine-tune the course content. Two key themes consistently emerged:

- Learners underestimated the weekly time commitment required to complete the course work. All participants in the focus group were already engaged in full-time work, and therefore when combined with the shorter release time-frames for the pilot phase the consistent weekly effort required was often challenging. As the courses are released into the full self-paced offering, which is open for a much more extended period, the course teams will continue to monitor the learner experience to determine if this continues to be a concern.
- Learners particularly valued the industry input into the course content, including video content from a wide range of practicing industry professionals.

THE FUTURE

The data collected during the pilot-test phase of the program has provided clear signals about the reach and potential impact of this suite of micro-credentials in providing a skills pipeline for the resources sector. In addition to reaching those who are currently working outside the resources sector, the program has strong support within the sector. A number of mining companies have expressed their intention to incorporate some or all of these courses into their employee development programs. Recently, BHP supported the enrolment of 60 participants in their Australian 2021/2022 intern program into MINE2x as verified learners.

The course development team is also conscious of the need to maintain currency with the course content. Whilst the high-tempo course development phase is now complete, the core team remains in contact with the industry advisory group and discipline experts at both institutions to ensure that

course content remains relevant and engaging, with periodic updating of material to reflect current industry practice.

REFERENCES

Constable, T, 2020. Building skills for modern mining workforce, MCA media release, 17 February 2020.

Deloitte, 2019. The path to prosperity: why the future of work is human, Building the Lucky Country #7.

Industry challenges – processing

Improvements in overall copper recovery through CuSX-EW at BHP Olympic Dam

J A Aguirre Carrillo[1], B Nguyen[2] and T Thomson[3]

1. Senior Development Metallurgist, BHP – Olympic Dam, Olympic Dam SA 5725. Email: jose.aguirrecarrillo@bhp.com
2. Senior Production Support Metallurgist, BHP – Olympic Dam, Olympic Dam SA 5725. Email: bao.nguyen1@bhp.com
3. Principal Metallurgy Development, BHP – Olympic Dam, Olympic Dam SA 5725. Email: tim.thomson@bhp.com

ABSTRACT

The BHP Olympic Dam operation utilises Copper Solvent Extraction (CuSX) and Electrowinning (EW) to process copper from various by-product streams. A number of improvements focused on addressing reliability, operational and metallurgical issues were undertaken in the form of a continuous improvement program. This paper provides details of these various improvements and their subsequent contribution to process performance uplift. A new solvent extractant with increased copper selectivity showed less reagent degradation and less iron transfer to electrolyte. A review of the current operational strategy during circuit ramp up/down highlighted critical deviations that correlate to higher probabilities of dendritic growth in EW. A new filtration system was installed in EW in order to filter circulating electrolyte in three cells; this allowed for better capture of suspended solids across the tank house. SEM-EDS analysis showed colloidal silica, sericite and quartz, precipitated copper and iron sulfates, as well as lead oxide particles associated with lead spalling from the anodes. A new smoothing reagent in EW improved overall copper cathode quality. Finally, refurbishment of the rectiformer control system improved equipment reliability and stability. Together, this comprehensive development program has led to significant improvements in the current operation of the CuSX-EW circuit at Olympic Dam, providing an overall copper recovery improvement, an increase in EW current efficiency, a reduction in pre-strip rate and a significant reduction in the total number of recorded dendritic growth events.

INTRODUCTION

The BHP Olympic Dam (BHP-OD) operation in South Australia has the world's fourth largest copper resource (total resource grade of 0.88 per cent Cu). Additionally, the ore contains economic uranium, gold and silver values. The Olympic Dam operation uses grinding/milling, flotation, pyrometallurgy and hydrometallurgy to produce high-quality copper cathode, gold and silver bullion and uranium (SA Gov, 2011).

Copper is recovered at BHP-OD via two streams. Ore is crushed, milled and the copper sulfide-rich minerals are concentrated by flotation to the pyro metallurgical plant as part of the primary copper stream. The BHP-OD operation utilises a copper solvent extraction/electrowinning (CuSX/EW) plant to recover copper (Cu) from the secondary stream. This encompasses the following substreams: Flotation tailings; leached concentrate thickener overflow; flash furnace dust leach thickener overflow; refinery bleed stream and evaporation pond return liquor (EPRL).

The CuSX circuit is capable of processing up to 2500 m^3/h of Pregnant Leach Solution (PLS) through two parallel mixer-settler train arrangements. Downstream of the CuSX circuit, the EW plant receives filtered electrolyte that flows through 126 cells divided in 3 sections (42 cells each) with electric current supplied by 3 × 28 kA rectiformers (Figure 1).

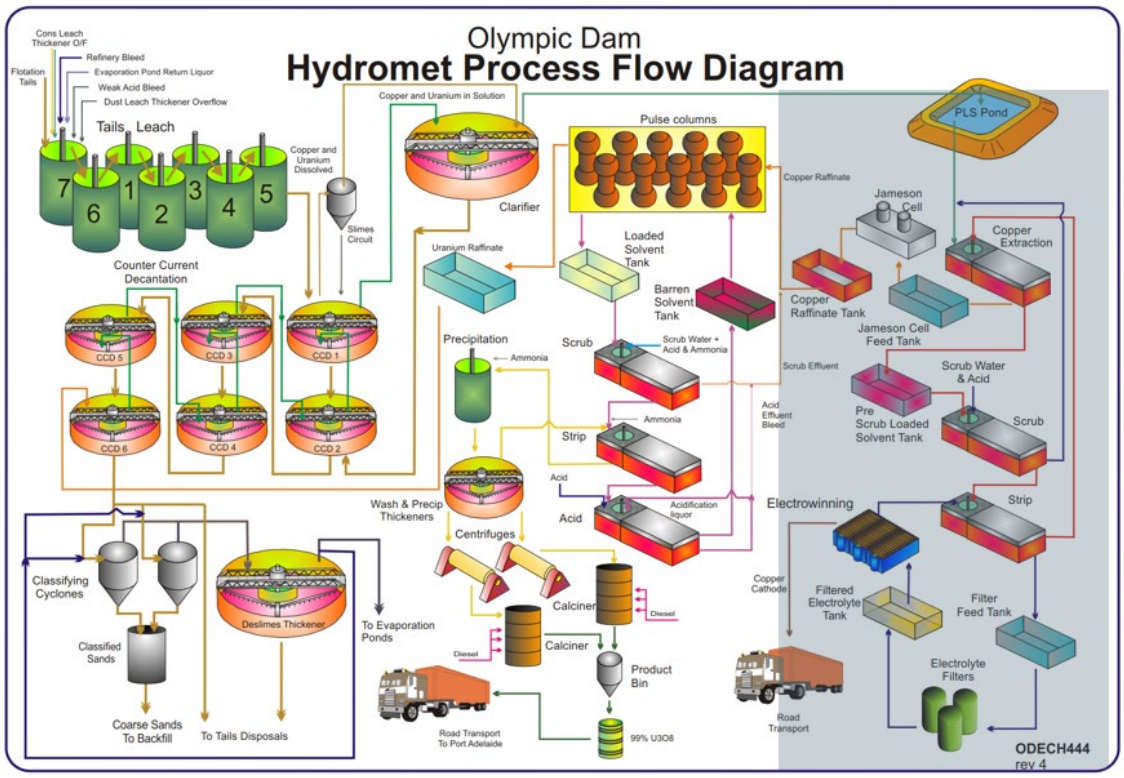

FIG 1 – Olympic Dam hydromet process flow diagram.

As part of the effect of the Global Financial Crisis in the mining industry, the business experienced an impact in available resources (operational and technical) and organisational changes that led to several challenges in resolving key production issues. The EW tank house experienced a gradual decline in performance across all key metrics, evidenced in a reduction of Current Efficiency (CE%) and overall EW copper production.

Two main production issues contributed to the aforementioned performance decline:

1. Pre-strip: Poor adhesion of the copper cathode deposit to the underlying 316 stainless steel blank mother plate lead to partial delamination of the cathode. Cathode would frequently prematurely self-strip from the mother-plate back into the cells (Figure 2), during transport to the Cathode Strip Machine (CSM) or in the cathode wash station prior to stripping. Depending on the pre-strip location, this caused an increase in electrical short circuits if the cathode falls within the cell; risk of dropped objects and hazard to operations personnel if cathode falls during crane operations and/or equipment downtime and manual operator intervention if the cathode falls within the CSM.
2. Dendritic growth: A sudden onset of field-oriented isolated crystals type (FI) copper growth, leading to needle like protrusions growing perpendicular to the cathode surface (Figure 3). Winand (1992) describes the FI copper crystal growth occurring from a lack of smoothing inhibition and high current density. Overtime, these needles (or internally referred to as ‘Christmas Tree Growth’ (CTG)) grow into complex coral like formations eventually ‘rounding off’ into globular nodules. These dendritic copper growths cause increased manual handling of pre-stripped plates, lead contamination in cathode, reduced copper output, accelerated equipment wear and tear, production delays and increased power costs due to shorting out the anodes.

FIG 2 – Example of copper cathode pre-strip in EW.

FIG 3 – Example of dendritic growth in EW.

IMPROVEMENT PROGRAM OVERVIEW

A concerted effort to uplift CuSX/EW performance was started with the intent to target and overcome specific safety, reliability, operational and metallurgical issues. The focus was on operational stability/discipline, reducing key driver variability, resolution of long-term asset issues and a technical program of work around diagnosing the potential root causes of dendritic growth. These improvements took place in both the CuSX and EW circuits. The summary of this work is highlighted below in Table 1.

TABLE 1

Summary of improvement program at BHP-OD CuSX-EW.

Focus areas	CuSX	EW
Focus on operational performance/discipline and reduction of known variability.	Reduction in oxime concentration to target levels resulting in less reagent consumption and losses. Implementation of a new solvent extractant, a recently developed reagent that provides higher Cu selectivity (BASF LIX® HS). This initiative resulted in less iron in loaded solvent samples and a reduction in electrolyte bleed rates. Changes in circuit ramp up and ramp down procedures in relation to key trigger points such as pregnant liquor solution (PLS) pond temperature, solids and silica concentration. Less dendritic growth events was evident in the EW tank house during recent ramp ups. Increased operational focus on maintaining mixer phase continuity in organic continuous to reduce the impacts of colloidal silica and solids. Implementation of routine shutdown cleanout strategies to remove jarosite, gypsum and precipitated solids enabling PLS flow rates to reach design specifications.	Salt and cobalt dosing upgrades to reduce concentration variation. Reinstatement of cell manifolds to improve electrolyte distribution. Change of sulfuric acid mist capture devices to reduce contamination potential in cathode. Installation of Idemin spacers to improve current distribution, currently executed in 1 out 3 EW sections. Reduction in amps variability through improved forecasting and focus on high current density (ie 200 A/m^2) in initial 24 hours of plating. Replacement of guar gum as smoothing agent with a polyacrylamide (BASF Magnafloc® 333) to improve reagent concentration stability and performance. Development of the leapfrog strategy to improve current efficiency in pre-strip impacted cells. Wax wheel reclaim system modifications to reduce wash water contaminants such as residual wax, polypropylene balls and copper sulfate.
Resolution of long-term asset issues.	Reinstatement of the filtered electrolyte tank. Maintenance and remediation program, and re-commissioning of the CuSX clay filter.	Replacement of the EW circulation tank, history of failures and plinth integrity concerns. Change in cathode plate strategy. Cessation of old strategy whereby EW would only get old Electrorefinery plates. Increase in operational discipline around replacement of old anodes during routine anode cleans. Cooling system to control electrolyte temperature within control limits during summer months and high shorting events. Improvements to rectiformers to increase equipment reliability. Due to aging equipment, a campaign was carried out to replace control cards in order to improve equipment uptime. A project for the total replacement of the rectiformers has been initiated.
Package of work around understanding dendritic growth drivers.		Laboratory trials using bulk sample of contaminated electrolyte and a small EW test cell. A big data analytics study using advanced analytics and machine learning to try and better identify hidden drivers in existing data. Plant scale trial of direct filtration of electrolyte prior to electrowinning. Different filtration media has been tested as a potential barrier of impurities transferred from CuSX.

IMPROVEMENTS IN COPPER SOLVENT EXTRACTION

Operational strategy – ramp up and ramp down

As highlighted previously, the copper supply to the CuSX/EW circuit is dynamic; any upstream process instability presents major operational challenges. As highlighted in Figure 4, dendritic growth events are intrinsically linked to the largest decreases in current efficiency (Figure 4a) and consequently higher pre-strip rate (Figure 4b). To address this problem, various technical investigations were undertaken to further diagnose the potential root causes for these dendritic growth events.

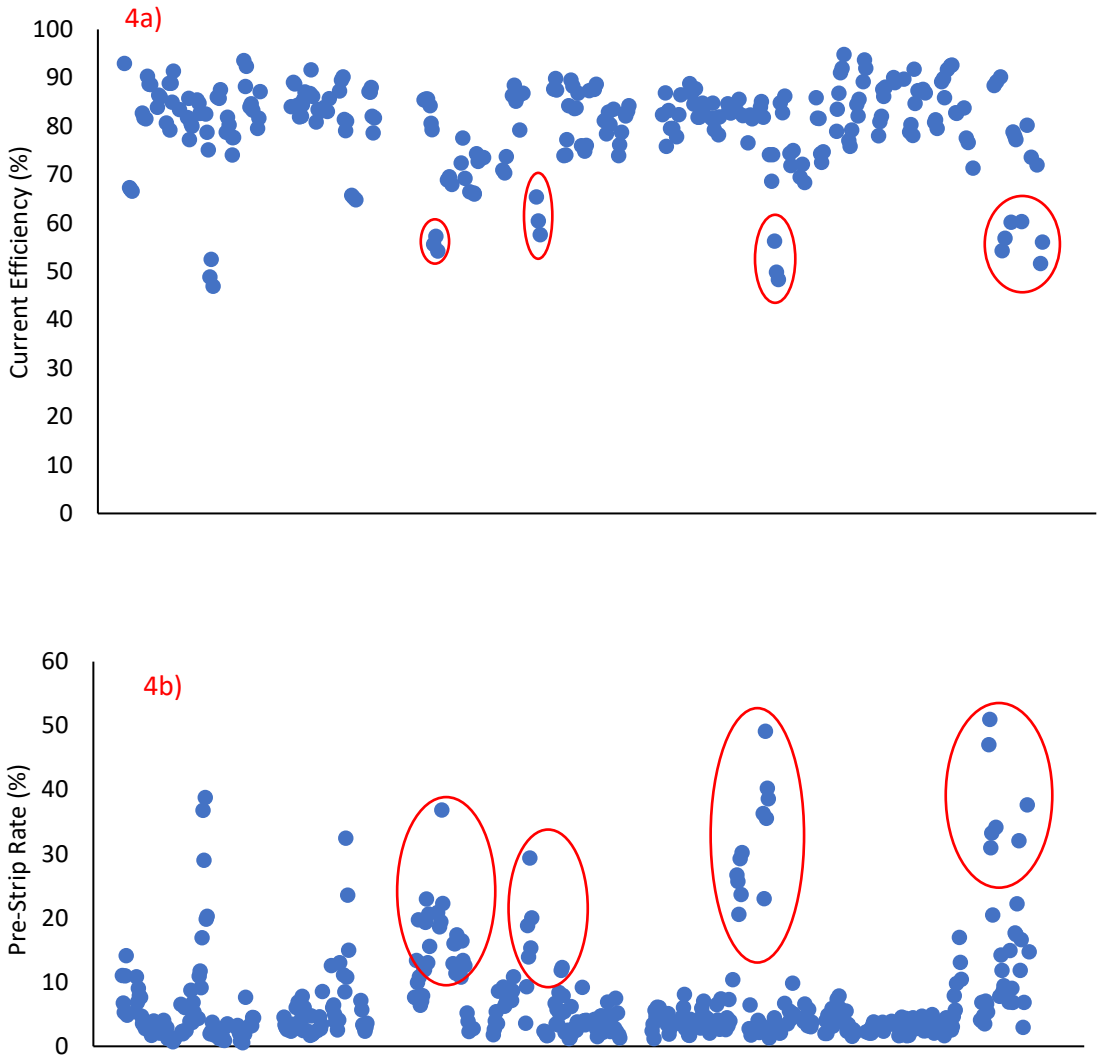

FIG 4 – (a) Olympic Dam Electrowinning Current Efficiency%; (b) Olympic Dam pre-strip rate% in Electrowinning. Circled in red is when the dendritic growth events occurred.

Through detailed analysis of previous dendritic growth events, a common set of upstream deviations were identified that led to a higher probability of dendritic growth event occurrence (Nguyen, 2021). The majority of these dendritic growth events occurred when the tails leach circuit was offline for an extended duration while the CuSX circuit remained online. The purpose of the tails leach circuit is to leach the uranium and copper minerals through the addition of sulfuric acid, sodium chlorate and steam through a series of agitated tanks. The tails leach slurry discharge provides the necessary heat transfer to the pregnant liquor solution and is the major source of seeding slimes for optimal flocculant operation and improved settling of total dissolved solids (TDS) in the clarification circuit. Slower phase disengagements often impacted by high total suspended solids and/or lower PLS pond

temperatures (Figure 5) have led to high aqueous entrainment in loaded solvent and undesirable increases in scrubbed solvent conductivity. These undesirable process conditions were found to be highly correlated to the dendritic growth events (Harris, 2020).

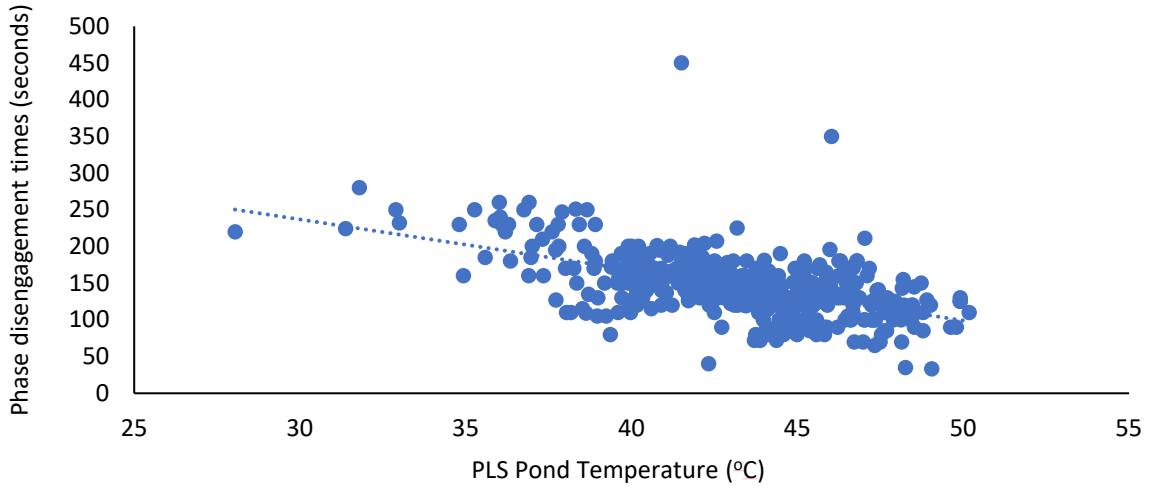

FIG 5 – Phase disengagement time versus PLS pond temperature.

A revision of the operational strategy and standardisation of ramp up and ramp down allowed better control of the key metrics that potentially contributed to the dendritic growth events. A reduction in dendritic growth events and improvement in overall process stability was seen (Figure 6).

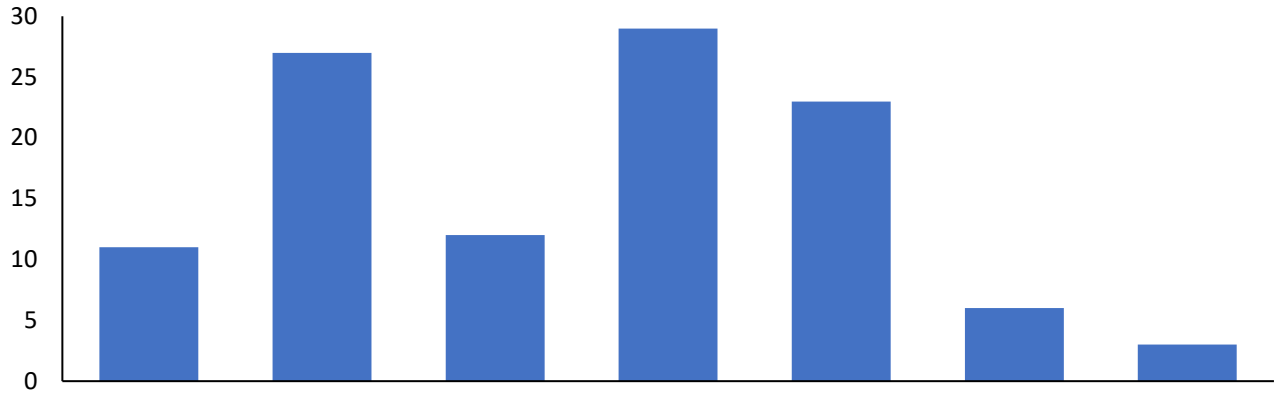

FIG 6 – Dendritic growth events at BHP Olympic Dam.

New extractant in CuSX

The CuSX circuit at Olympic Dam uses a chelating ligand to extract copper from the aqueous phase to the organic phase. It does so through a combination of aldoxime and ketoxime reagents. BHP SX reagent supplier, BASF, introduced a new reagent, LIX® HS as part of the formulation for the CuSX circuit and as replacement of LIX860-IC. After laboratory test work led by the supplier (Haig, Bender and Nisbett, 2018), it was evident that this new reagent:

- Required a much lower content of C12 aldoxime (LIX860-IC).
- Showed lower degradation rates when compared against existing reagents.
- Resulted in a higher copper selectivity over iron. LIX®HS has a selectivity higher than any current reagent (4000:1 at best).

The CuSX circuit carried out a gradual replacement of LIX860-IC (C12 Aldoxime) with LIX® HS (Initially called DP-HS-1011). In order to achieve the optimal reagent blend, the addition ratio

between aldoxime to ketoxime was determined experimentally to be 3:1 (Bui W, 2021). Furthermore, it was confirmed that LIX® HS indeed showed significantly less degradation, less than 3 per cent compared to 10–20 per cent of ketoxime (LIX84-IC) and 10–25 per cent of C12 aldoxime (LIX860-IC). Since July 2020, the presence of LIX® HS in the organic seemed to lower the degradation of ketoxime (LIX 84-IC) and increased the degradation of C12 aldoxime as evidenced in Figure 7.

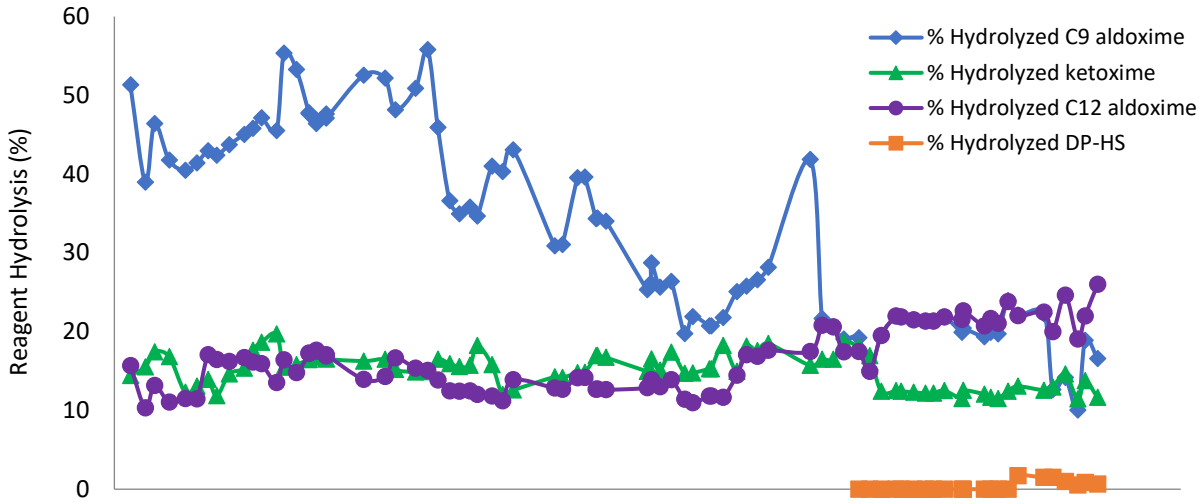

FIG 7 – CuSX Oxime degradation over time with changing reagent blend.

The chemical iron loading in the loaded solvent is highlighted in Figure 8. As observed, the iron loading trended downwards and a reduction in EW bleed rates was observed after the introduction of LIX® HS. This plant data agreed well with external lab analysis performed by BASF which highlights a higher copper loading in the loaded organic. A higher copper loading is preferential to lower chemically transferred iron and mitigate reagent acid catalysed degradation.

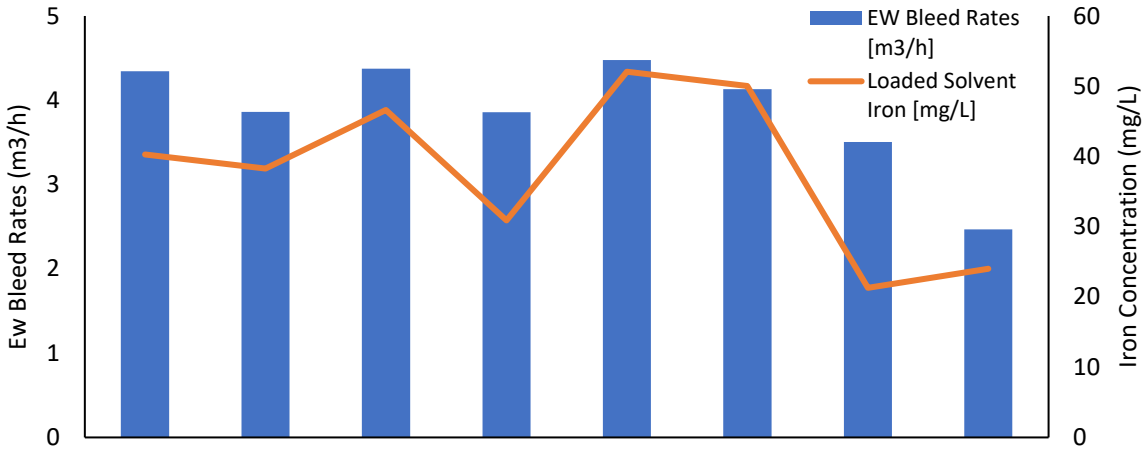

FIG 8 – Reduction in iron in loaded organic and EW bleed rates.

IMPROVEMENTS IN ELECTROWINNING

New smoothing reagent in EW

Historically, Olympic Dam EW circuit utilised guar (polysaccharides) as the smoothing agent used to produce smooth copper deposition and inhibit dendrite formation. With the aim of identifying a more stable and reliable option, various EW cathode smoothing agents were tested to determine a suitable alternative additive to mitigate dendritic growth.

There were two major types of additives tested; these are listed below:

1. Polysaccharides
    - Agent No. 1 (Guar gum) is known as a weak levelling agent and is also the conventional cathode smoothing additive used in the copper industry. Food grade Guar was currently used as a cathode-smoothing agent in the Olympic Dam's EW plant; it is dosed at a concentration of 350 g/t of Cu produced.
    - Agent No. 2 is produced in a very narrow range of molecular weight and highly homogeneous polymer from multistage purified natural raw material compared to the conventional Guar (Joshi, 2017).
    - Agent No. 3 is a modified polysaccharide smoothing agent, it is characterised as a low viscosity, highly soluble, non-ionic polymer.
2. Polyacrylamides (PAM) – are both levellers (helps produce smooth surface by inhibiting the growth of protrusions or edges) and current suppressors (Moats, Lumiya and Cui, 2015). They were primarily and originally designed to be used as a flocculant in the hydrometallurgy and water treatment industries.
    - Agent No. 4 is a non-ionic flocculant and dry polyacrylamide compound.
    - Agent No. 5 (BASF Magnafloc® 333) is a very high molecular weight, slightly anionic polyacrylamide flocculant supplied as a free flowing granular powder.

From lab based cell trials, PAM was deemed to be the most successful cathode smoothing agent in terms of nodulation-smoothing capabilities. BASF Magnafloc® 333 was selected as the preferred option. The results from PAM showed that apart from minor nodulations along the bottom edge, the cathode face was virtually free of nodulations and the plate was smooth to the touch throughout plating (Soriano, 2017). However, there was a primary concern on the pre-stripping/pre-opening that formed on the bottom left hand corner. In order to address the high pre-stripping observed during lab trials and the implementation of the new smoothing reagent at plant scale, a new dosing system was designed. This was installed with a low flow peristaltic pump together with a low flow detection flowmeter. As shown in Figure 9, the dosing rate of the smoothing agent has been adjusted and reduced to stable levels whilst pre-strip rates showed a favourable diminution.

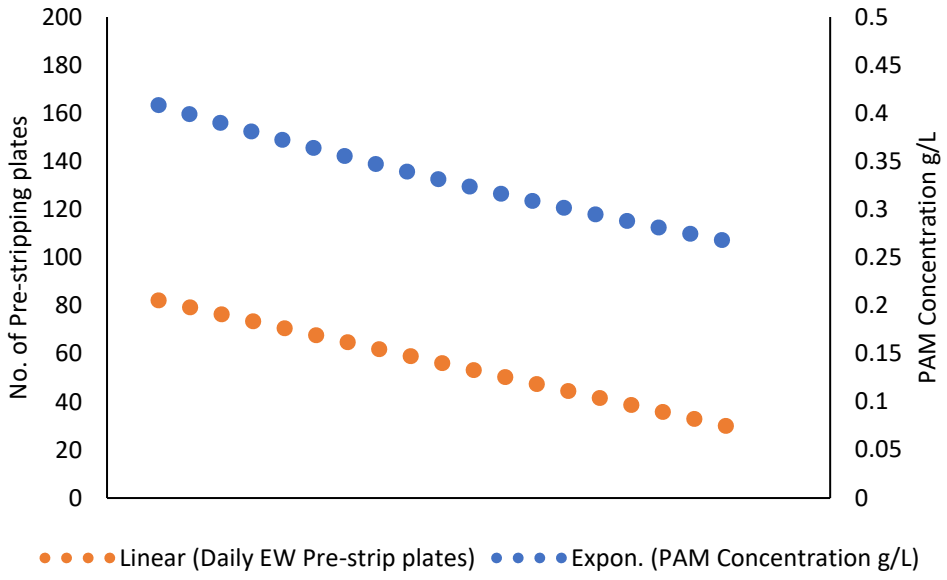

FIG 9 – Reduction in number of pre-stripping plates and Gradual reduction in smoothing agent in EW.

Anode verticality improvement – 'perfect cell trial'

The most expensive consumable in the electrowinning process is the power cost to produce copper cathode. The purpose of the tank house is to maximise its CE%. This is calculated from the actual

cathode harvested as a percentage of the theoretical copper plated over the same time period. The largest loss of CE% in the EW tank house is attributed to short circuits occurring between the anode and the cathode. While a large number of factors contribute to the nucleation and propagation of shorts, uneven spacing between the anodes and cathodes plays a significant role. The spacing of the anode and cathode at the top are well maintained by the insulator tabs. However, this may not be the case at the bottom as warped anodes or cathodes will reduce the spacing at the bottom resulting in the formation of a nodule, and in turn, propagating leading to a short circuit.

To address this problem in the OD EW tank house, a 'perfect cell' trial was conducted which consisted of 55 new lead alloy anodes, 54 new 316L stainless steel mother plates and a newly trialled Idemin anode spacers as shown in Figure 10. This was compared to 'control cells' of the section consisting of used mother plates, anodes and central button spacers. The advantages of the Idemin anode spacer were attributed to various factors including the difficulty to dislodge the spacer and its ability to stiffen the middle and bottom third of the anode thus reducing warping. This would significantly extend the usable life of the anodes.

FIG 10 – Optimised Rigidiser – RUO 2.0 stiffener.

In order to ensure that the new mother plates returned to the perfect cell during the trial period, a new stripping methodology was adopted for the trial period. Over four harvest cycles, the perfect cell CE% showed a statistically significant marked improvement of 5 per cent $\pm$ 1.8 per cent above the control cells as shown in Figure 11. Excellent copper quality was observed from the perfect cell. The anode spacers have now been installed in 1 out of 3 EW sections with overall improvements in CE% and reduction in pre-strip.

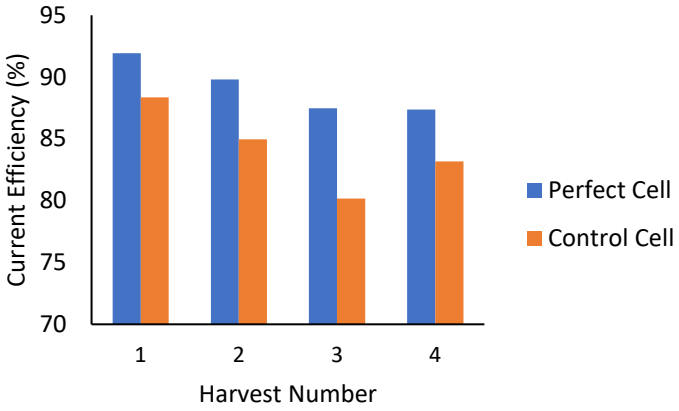

FIG 11 – CE% improvement for each harvest.

Electrowinning filtration skid

The purpose of the electrolyte filtration system trial was to determine the effectiveness of electrolyte filtration in improving electrolyte quality in order to mitigate dendritic growth on copper cathodes produced. The trial involved the use of three different types of filtration methods (cartridge, sock and sand) built on a standalone skid to assess benefits and downsides of the different filtration methods. Electrolyte feeding three cells was diverted to the skid via three-way valves in order to allow the electrolyte to be filtered through these different filters. The filtered electrolyte was returned back to the cells for copper plating. Each of the three filter types had both a duty and a standby arrangement. Once the differential pressure across the duty filter exceeded the high alarm limit indicating excessive build-up of solids across the filter, the standby filter was switched online and the duty filter offline. Switching between duty and standby filter was done through in-field manual valves. This could be done whilst the filter feed pump was in operation.

Due to the size of the filter media, the sock filter provided a practical method for further ultra-fine solids analysis. The filtrates from the socks filters were analysed under three scenarios: Unused filters, stable operation and post dendritic growth occurrence, in order to ascertain potential ultra-fine solid contributors to dendritic growth.

Unused filters

The three layers of unused filters were imaged through Scanning Electron Microscopy (SEM). Each layer is composed of a C or polymer C-H compound (SEM cannot detect H). Figure 12 shows inner and outer layer fibre sizes and ‘weave’ are the same; the middle layer contains smaller fibres and a tighter ‘weave’. The white specks on the inner and outer layer fibres consists of a Ca-oxide compound, believed to be deposited during the filter fabrication process

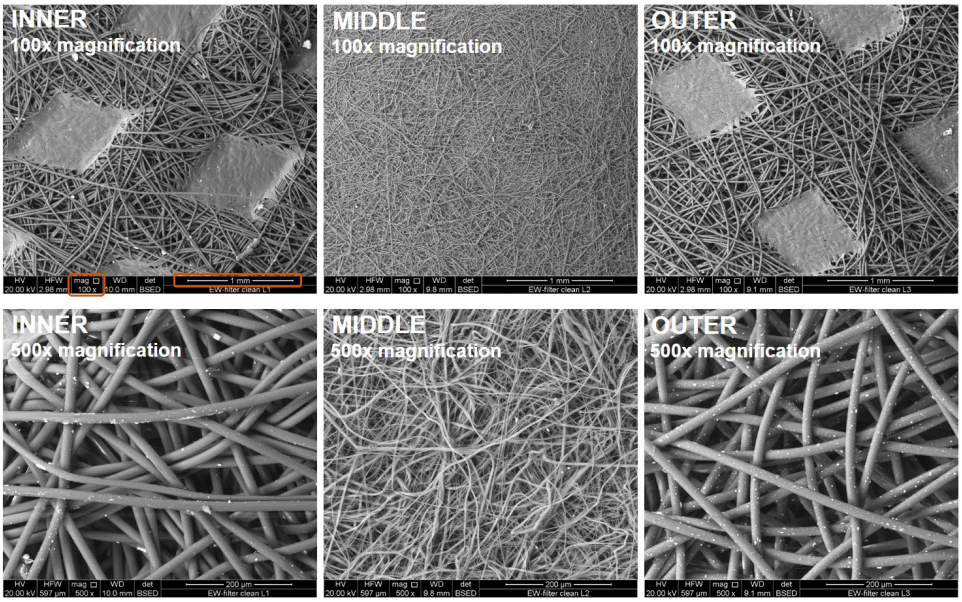

FIG 12 – Backscattered electron (BSE) imaging of unused filters.

Used filter – stable operation/no dendritic growth

Filter socks from a stable operation period were subject to SEM imaging. These samples corresponded to a time in EW operation when no dendritic growth occurred. Understanding and identifying the species present in a used filter helped to form a baseline of typical solids, so that future contaminants or undesired components could be detected and correlated to adverse dendritic growth events. The BSE imaging showed the occurrence of colloidal silica trapped by the filter fibres. The filter also showed the presence of crystalline copper and iron sulfates likely precipitated during drying of the filtrate material prior to imaging as shown in Figure 13.

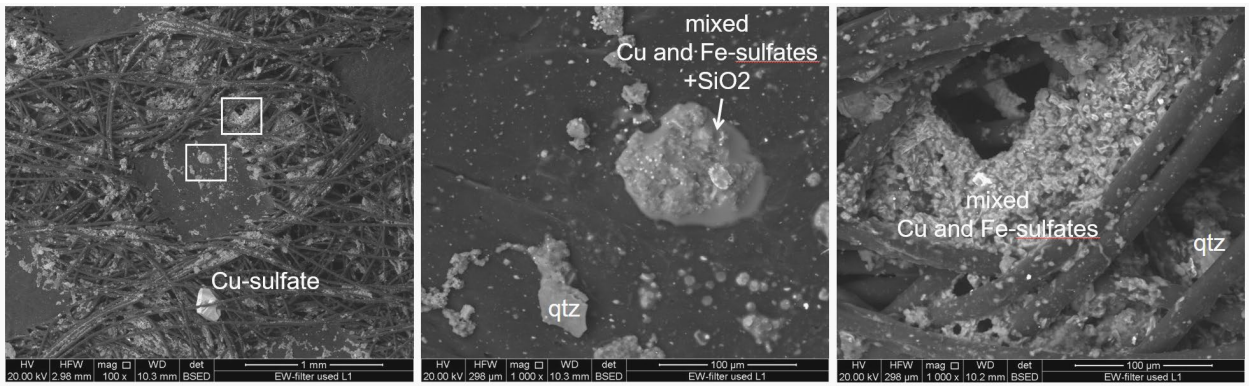

FIG 13 – BSE analysis of used filters (no dendritic growth).

Dendritic growth occurrence

After the detection of dendritic growth in Electrowinning, a new sock filter was immediately installed in order to capture the solids that might be contributing to the promotion of the event. The analysis was complemented by SEM-EDS of a number of cathode samples that were clearly impacted by dendrites. The cross-sections of the copper buttons were overlapped and compared against the respective rectiformer current, dosage of smoothing agent and chloride concentration in strong electrolyte. An applied current trend was then obtained for the total duration of the crop cycle and compared against the nature or morphology of the copper growth. Figure 14 shows noticeable changes in the rectiformer output, and hence current density affecting the crystal morphology. Sudden changes in electric current promote back reactions, which consists on the dissolution of copper that had already been deposited, causing cavities on the cathode surface. Around the time the rectiformer had multiple trips, there is a clear change in the size and morphology of the copper crystals. In this case, the nodules start to grow almost at the same time these changes occur in the rectiformer current.

FIG 14 – Cathode sample (Section E1 Middle).

The copper cathode samples were subjected to SEM-EDS to identify the elements and/or compounds. Special emphasis was given to the analysis of cavities where back reaction took place after high amperage fluctuations and where the deposition of foreign (undesired) elements occurred. This technique allowed the identification of lead oxide particles trapped within the copper, represented by the white particles in Figure 15. The cavities or hollow spaces formed throughout the copper deposition were easily filled with electrolyte and impurities, affecting the quality of the cathode and influencing the current density around the area; as a result, it is postulated that nodules are formed around these regions.

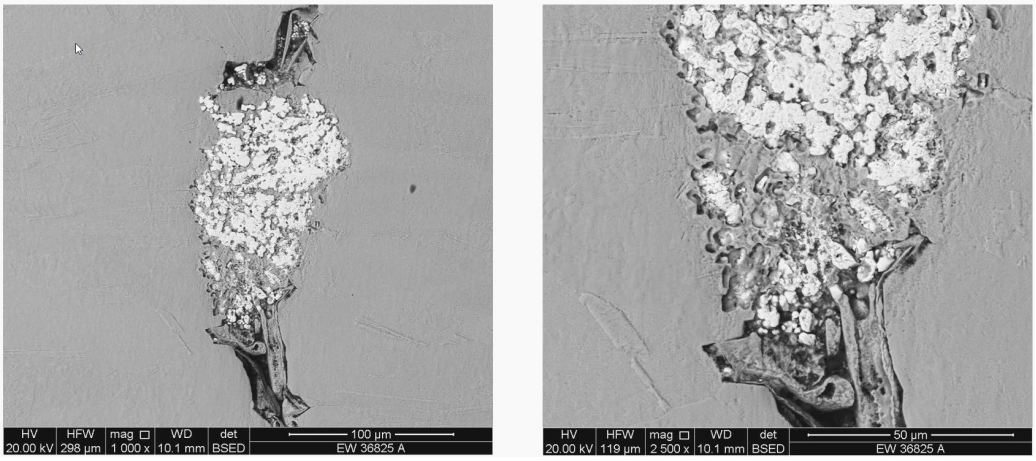

FIG 15 – SEM analysis of cathode sample (Section E1 South). White particles are lead oxide (PbO).

Sock filters layers analysis

Imaging of the filtrate from the filtration skid socks (4 and 10 micron) was conducted in order to characterise and understand the mineralogy of the material trapped during the dendritic growth event. The findings of the three different layers of the filter can be summarised as follows:

- The 10 micron inner and medium layers of the filter showed a high concentration of colloidal silica trapped through the fibres as evident in Figure 16. This soluble silica ('gel') promotes the clogging of filter fibres and assist with the capture of other type of solids. Copper and iron sulfates, which were mostly trapped by colloidal silica formations.
- The outer layer of the sock filter exposed the presence of lead oxide particles in a non-crystal structure and in a diverse range or particle sizes, as shown in Figure 17. The presence of lead suspended in electrolyte corresponds to the spalling effect of lead flakes from the anodes when exposed to drastic drops in current.

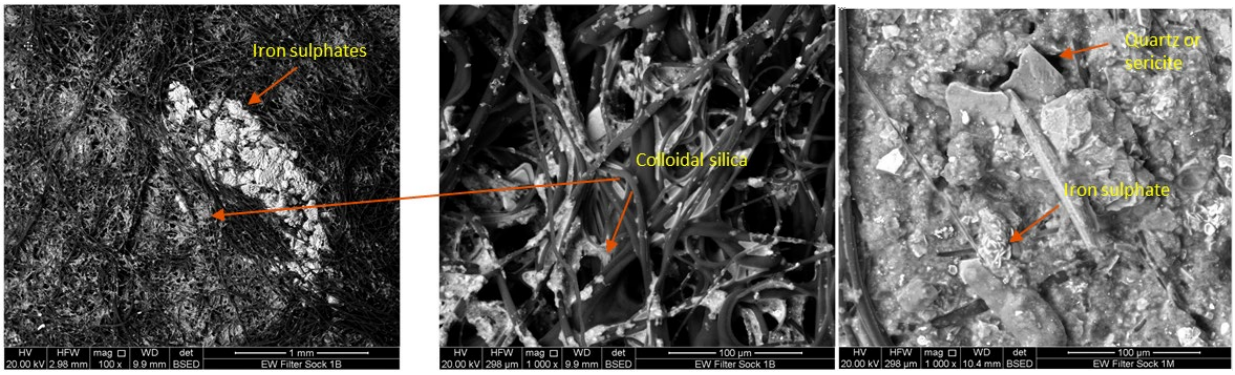

FIG 16 – Sock filter inner and medium layer from a dendritic growth event.

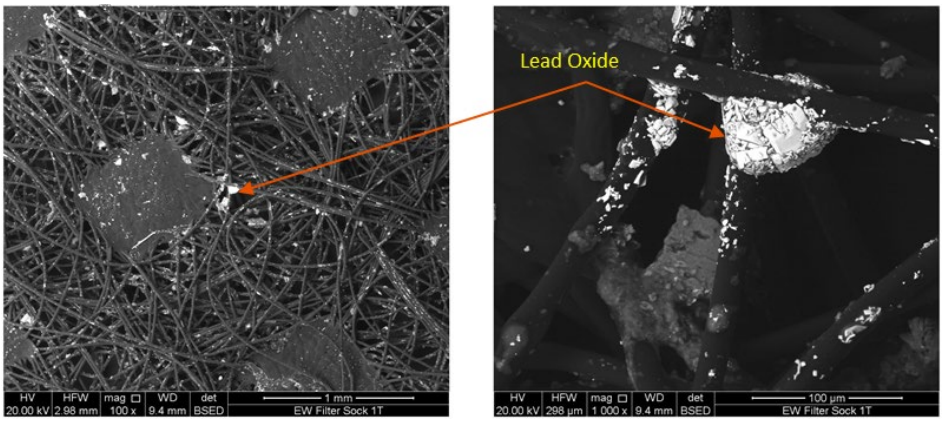

FIG 17 – Sock filter outer layer from a dendritic growth event.

Chemical characterisation (semi-quantitative) of filter residues

Elemental analysis through ICP-OES and ICP-MS of trapped residues on/in filter layers for this event showed an increased concentration of lead (Pb) with a range between 45 and 2714 ppm whilst the target for EW copper cathode for Pb is around 5 ppm. It also led to the conclusion that Cu is primarily precipitated as sulfates in the inner (first) layer of the filter sock and drops as the flow moves towards the outer layers.

Leap Frog strategy

Pre-strip copper within the EW cells causes shorting and a decrease in current efficiency. The shorts propagate over the growth cycle and will cause localised elevated heat spots around the copper cathode and electrolyte resulting in more pre-strip falling into the cells as shown in Figure 18. This would usually result in the section being taken offline for several days and require manual handling to remove the pre-strip copper. The other consequences of high pre-strip copper in the cells is that it can cause dead plates and double contacting of anodes and cathodes hanger bars on the bus bars potentially resulting in arcing. To resolve this problem, a collaborative effort between the technical and production teams identified a practical solution to reduce the number of shorts and slow down the acceleration of more pre-strip. The solution involved turning off the rectiformer for a short period, lifting a cell rack of anodes using a crane and using an insulated metallic bar to push the pre-strip copper onto the bottom of the cell. The process was repeated across each cell known as ‘leap frogging’. This helped ensure that most of the pre-strip copper would fall to bottom of the cell and not continue to short between the anode and cathode. The pre-strip copper lying at the bottom of the cells would dissolve over time during the electrolysis process. Figure 19 shows that after a leap frogging of one section, the CE% improved significantly in the next harvest. An operational procedure was created and this method has been adopted as a robust way to reduce shorts caused by pre-strip copper without incurring an extended shutdown.

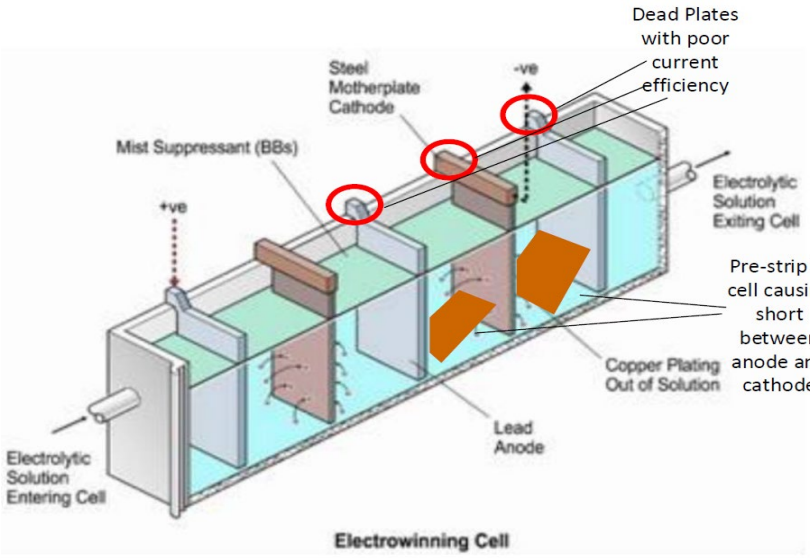

FIG 18 – Pre-strip inside of an EW cell.

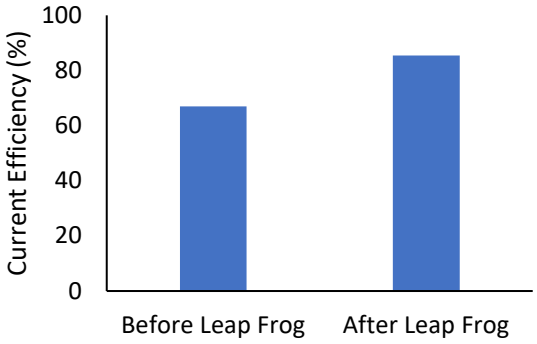

FIG 19 – Impact of Leap Frog in CE%.

Rectiformer improvements

The EW Rectiformers (RF) were past their serviceable life and have obsolete components; RF1 and RF2 are ~33+ years old whereas RF3 is ~29 years old. Rectiformer power failures are very common such that in one year, there was a cumulative 60+ recorded power failures for all three Rectiformers. Due to the age of the Rectiformers, the current technology does not have a diagnostic system, this results in significant downtime to troubleshoot and repair. The reliability and maintenance teams has implemented a series of improvements to help increase the availability of the rectiformers.

These improvements are summarised:

- Implementation of a programmable logic controller (PLC) to rectify the poor behaviour of the obsolete rectifier control cards and close the gap between the set point and the actual current.
- Finding an alternative original equipment manufacturer to produce the original obsolete control cards for spare parts.
- Replacing the whole set of the controller cards and unbalance protection relays.
- Review critical spares stock level for key devices such as silicon controlled rectifiers and fuses.
- Leveraging the internal electrical team's knowledge with the rectiformers and reduced reliance on third parties.

CONCLUSIONS

The overall Copper recovery through Copper Solvent Extraction and Electrowinning (CuSX/EW) at BHP Olympic Dam was increased by 15 per cent, which resulted in the highest EW Copper cathode production in the last 15 years. This is reflected by the improvement of key operational variables

such as an increase in 27 per cent of Copper transferred from CuSX to EW; an increase of 10 per cent in current efficiency in EW and a reduction of 74 per cent in the occurrence of dendritic growth events as shown in Figure 20.

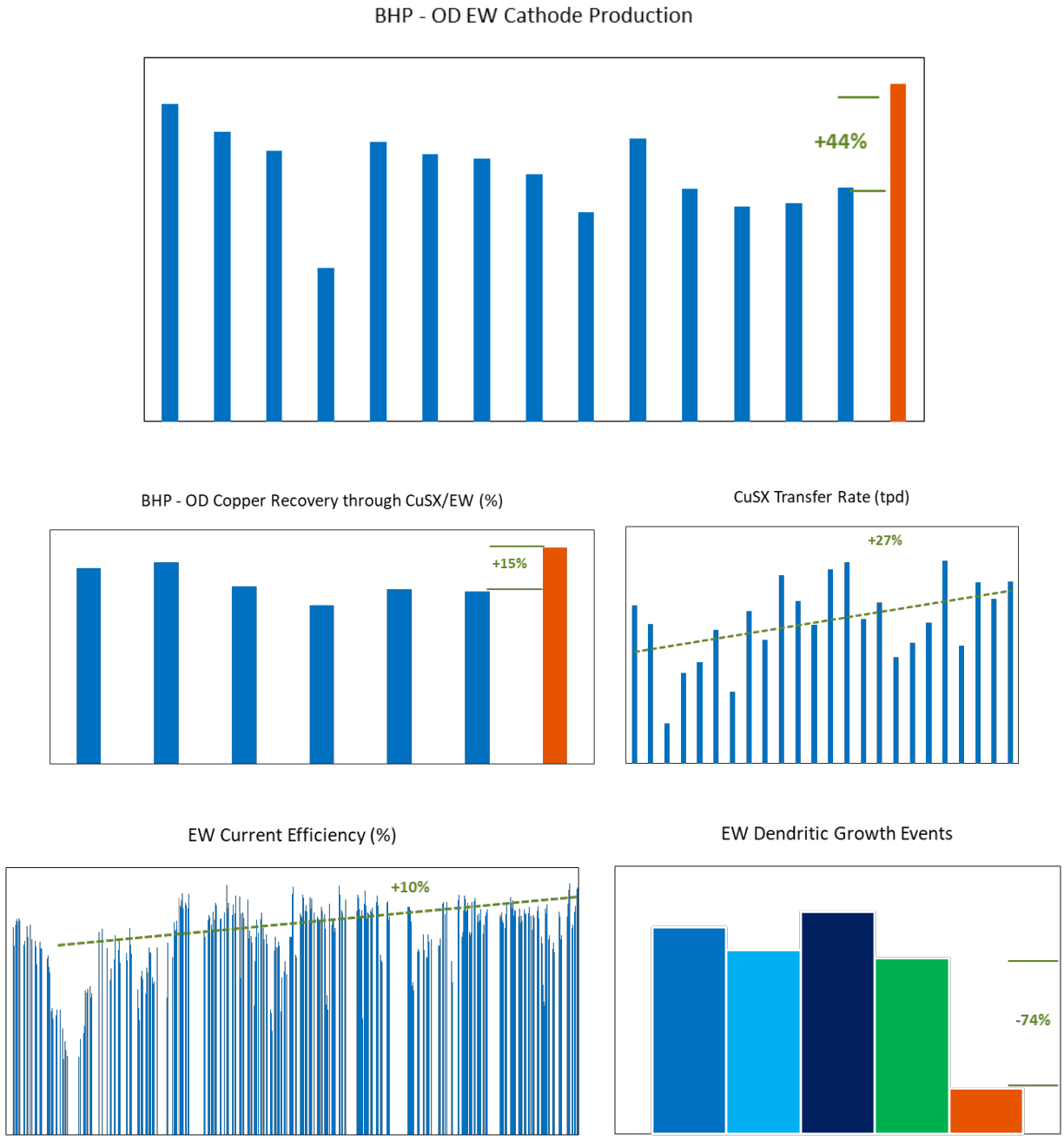

FIG 20 – Improvement in key operational variables across CuSX/EW at BHP Olympic Dam.

The standardisation of plant ramp up/down periods and the aim of reaching desirable process variables before increasing flows through CuSX/EW after a plant shutdown was a key factor to reduce the transport of impurities across the circuit that are believed to promote the occurrence of dendritic growth events.

In CuSX, an uplift in pipework cleaning contributed to the removal of jarosite and gypsum build-up that reduced the flow capacity across the circuit. The implementation of new extractant (BASF LIX-HS® improved copper transfer to solvent and lowered the rate of iron loading. As a result, a reduction in electrolyte bleed was evident.

Cathode pre-stripping in EW is caused by poor copper adhesion to the stainless steel mother-plate. Overdosing of smoothing reagents and the impact on the copper crystal growth can promote higher

metal internal stresses and copper delamination. The implementation of BASF Magnafloc® 333 as a new smoothing reagent improved the uniformity and appearance of plated copper and reagent concentration stability.

Anode verticality was improved in one third of the EW tank house in Olympic Dam by installing an anode spacer considerably decreased the number of shorts between cathode and anode and improved current density distribution throughout the mother plate.

Even though the implementation of a small-scale filtration skid has not resulted in the total mitigation of dendritic growth across the filtered cells, this equipment has been instrumental in the understanding of the type of solids that are transported across EW. Further, this has showed how spalled lead from anodes are deposited on the surface of the cathode during dendritic growth events and has assisted in the removal of impurities throughout the EW tank house given that the treated electrolyte eventually circulates through the entire circulation system.

It is imperative to implement a continuous improvement approach when it comes to resolving a decrease in plant performance that is impacted by a large set of different factors and plant conditions. Collaboration through a one-team philosophy, allowed metallurgical aspects to be reviewed and revised together with maintenance, operations and safety factors. This ultimately promoted a comprehensive overview of which causes that require attention and actions in their effective resolve.

ACKNOWLEDGEMENT

The authors wish to acknowledge BHP Olympic Dam Teams: Solvent Extraction and Electrowinning Operations; Technical Processing and Refinery; Maintenance Reliability, Maintenance Execution, Supply, Modifications and Operational Projects. Kathy Ehrig, BHP Olympic Dam Superintendent Geometallurgy. The authors also want to acknowledge the contribution and support provided by BASF.

REFERENCES

Bui, W, 2021. Interim report of DP-HS. BHP Technical Report.

Government of South Australia, 2011. Assessment Report – Environmental Impact Statement Olympic Dam Expansion.

Haig, P, Bender, J and Nisbett, A, 2018. 'CuSX Reagent for BHP OD Presentation'. BHP.

Harris, S, 2020. BHP Olympic Dam – Reducing Dendritic Growth. Consilium Technology.

Joshi, M, 2017. Vecosol FLW: Guar Smoothing Agent: Venus Colloids. Email.

Moats, M S, Lumiya, A and Cui, W, 2015. 'Examination of copper electrowinning smoothing agents. Part I: A review', *Minerals & Metallurgical Processing,* Vol. 33, No. 1.

Nguyen, B, 2021. FY21 & FY22 YTD Dendritic Growth Events. BHP Technical Report.

Soriano, I, 2017. Mini EW Test Cell Program – Wave 94145 – Improving the quality of EW Copper. BHP Technical Report.

Winand, R, 1992. Electrocrystallization – theory and applications, *Hydrometallurgy*, pp 567–598.

Role of reagents in achieving successful preflotation of organic carbon

T Bhambhani[1], G Sampayo[2], A Santana[3], I Ametov[4] and S Emery[5]

1. Principal Scientist, Solvay, Stamford, CT USA 06902. Email: tarun.bhambhani@solvay.com
2. Account Manager, Solvay, Tempe, AZ USA 85284. Email: gustavo.sampayo-reyes@solvay.com
3. Regional Technical Manager, Solvay, Tempe, AZ USA 85284. Email: alfredo.santana@solvay.com
4. Regional Technical Manager, Solvay, Baulkam Hills, NSW. Email: igor.ametov@solvay.com
5. Regional Sales Director, Solvay, Baulkam Hills, NSW. Email: stuart.emery@solvay.com

INTRODUCTION

Carbonaceous gangue mostly present as organic carbon (C_{org}) complicates processing of sulfide ores. C_{org} possesses sufficient naturally hydrophobic extended aromatic domains that leads to transport to the concentrate via 'true flotation', even in the absence of flotation collectors.

Downstream processing challenges are usually observed with concentrates containing substantial C_{org}, particularly smelter penalties and gold preg-robbing (Konieczny *et al,* 2013; Gupta, 2017; Afenya, 1991). C_{org} adsorbs reagents and increases the required dosages compared to sulfide ores that don't contain carbonaceous gangue (Gredelj, Zanin and Grano, 2009).

Separation of C_{org} from value and gangue minerals is complicated by complex mineral associations and the typically fine primary C_{org} grain size. Lastly, floating C_{org} frequently causes persistent, stable bubbles that impact the froth phase through a combination of froth phase crowding, stabilisation, and destabilisation effects (Wiese, Harris and Bradshaw, 2011; Lind, Tomlinson and Awmack, 2018). These frothing issues can slow flotation kinetics of value minerals, reduce recovery, force plants to operate with reduced air flow rates and increased froth depths in the flotation cells, contribute to operational variability, and reduce operator's ability to effectively control the process.

Strategies to manage C_{org} include preflotation prior to value mineral flotation, as well as depression of the C_{org}. Solvay has long articulated the holistic management of C_{org}, ie the strategies are not mutually exclusive (Jankolovits, Sampayo and Santana, 2020). In this document we focus on the preflotation strategy, specifically the role of C_{org} collectors and S depressants.

C_{org} preflotation results from rougher lab tests on a low-grade, coarse grained carbonaceous polymetallic feed are shown in Figure 1. The data shows that C_{org} collector AERO 736 leads to significantly lower Au recovery to the preflotation concentrate than the standard reagent scheme comprising frother only. Importantly, C_{org} recovery is equivalent in both cases. Also, the C_{org} flotation kinetics are not altered by the collector. Thus, the impact of this reagent must be through a different mechanism than those expected for C_{org} collectors. It is generally appreciated that entrainment is a prevalent mechanism for value losses to a preflotation concentrate (Gredelj, Zanin and Grano, 2009; Wiese, Harris and Bradshaw, 2011; Lind, Tomlinson and Awmack, 2018; Smith *et al,* 2008).

These data suggest that the C_{org} collector improves the froth properties such that Au entrainment is minimised. C_{org} gangue is known to stabilise the froth phase, leading to a persistent, voluminous froth that can hold significant water in the lamellae. Modification of the C_{org} surface using AERO 736 influences the behaviour of the C_{org} saturated froth. Such an impact of the reagent is not expected based on conventional mechanistic descriptions of C_{org} collectors.

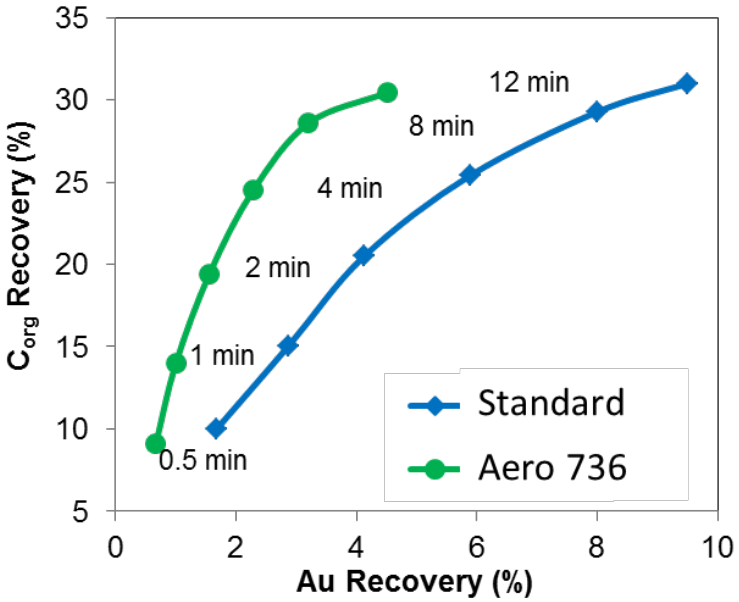

FIG 1 – C_{org} preflotation with two different preflotation reagent schemes on a low-grade, coarse grained carbonaceous polymetallic feed highlighting the froth modification mechanism in C_{org} collectors.

However, as noted in this example, separation in preflotation stages is less than perfect; in this case, the loss of Au is 4 per cent, but in some Pb and Zn operations where C_{org} is a problem, Pb, Zn and Ag losses can easily approach 5–10 per cent each; the amount is determined based the need to remove sufficient C_{org} so as to prevent downstream issues. The losses can be substantial and there is a need to minimise these losses to improve viability of the process. To this end, a useful approach is the depression of value sulfides and metallics in the preflotation cleaning stage, while floating the carbon. These values can then be resent to the value metal circuit recovery circuit. Figure 2 illustrates the operation of such a preflotation circuit.

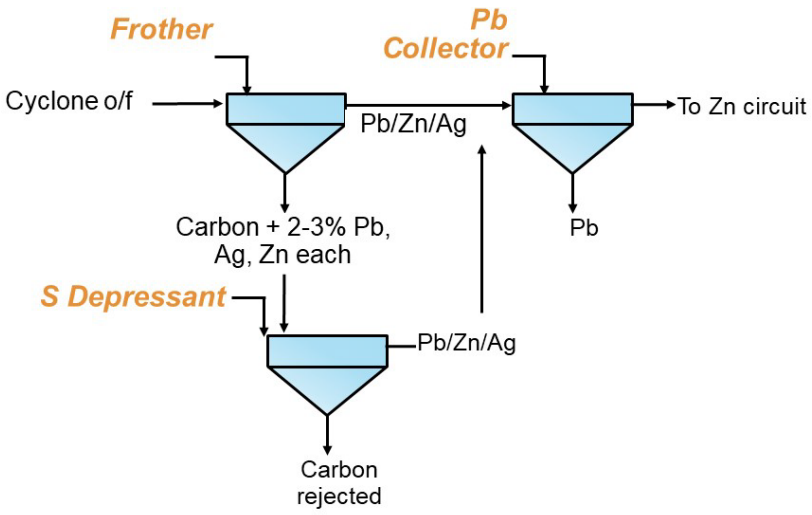

FIG 2 – Improved C_{org} preflotation circuit in a Pb-Zn-Ag plant.

Obviously, the liberation characteristics of the carbon must allow for this to work: all the C_{org} cannot be intimately associated with value minerals. Critical requirements of such depressants are: (a) the depressant does not depress the organic carbon, and (b) the depression is reversible, ie when the depressed value minerals are moved back to the sulfides/value minerals flotation stage, they can be 'reactivated' easily.

At Solvay, we have leveraged advances in chemistry to design novel sulfide depressants that meet the above criteria. Table 1 demonstrates the results using Solvay depressant A on an ore sample from a Pb/Zn mine in North America.

TABLE 1

Improved carbon preflotation circuit management using Sulfide Depressant A in the preflotation concentrate cleaning stage.

	Prefloat Rougher recoveries			**Prefloat Cleaner (Recoveries relative to cleaner feed)**			**Prefloat reject product (Relative to plant feed)**		
	C_{org} Rec (%)	**Pb Rec (%)**	**Zn Rec (%)**	**C_{org} Rec (%)**	**Pb Rec (%)**	**Zn Rec (%)**	**C_{org} Rec (%)**	**Pb Loss (%)**	**Zn Loss (%)**
C collector+ Frother only	35	10	12	73	70	90	25.6	7	11.0
With sulfide depressant A added	37	11	13	50	12	15	18.5	1.32	1.95

The outcomes demonstrate that in the rougher circuit, the use of the carbon collector results in a C_{org} recovery of approximately 35 per cent. Coming along with it (either via true flotation or entrainment) are 10 per cent Pb and 12 per cent Zn. Cleaning this preflotation concentrate results in flotation of practically all the C_{org} and most of the Pb and Zn (~70 per cent each). This translates to about 7 and 11 per cent loss of Pb and Zn to the preflotation concentrate. In contrast, the use of the sulfide and metallics depressant A results in a much more acceptable Pb and Zn loss (1–2 per cent each). Note that the overall C_{org} recovery did actually decrease with the use of sulfide depressant, from 25 per cent to 18.5 per cent. This is presumably related to intimate association between some of the C_{org} and value minerals, however even this much C_{org} removal is sufficient to enable the operations to achieve benefits in the downstream (Pb/Zn/Ag recovery) process. Also note that all the value minerals were reactivated with collector alone; these results are not included here for the sake of brevity.

It is thus possible to achieve material improvements in the preflotation of C_{org} through the use of novel collectors and value (sulfides and metallic) depressants.

REFERENCES

Afenya, P M, 1991. Treatment of Carbonaceous Refractory Gold Ores. *Miner. Eng.*, 4:1043–1055.

Gredelj, S, Zanin, M and Grano, S R, 2009. Selective flotation of carbon in the Pb–Zn carbonaceous sulphide ores of Century Mine, Zinifex. *Miner. Eng.*, *22*:279–288.

Gupta, N, 2017. Evaluation of graphite depressants in a poly-metallic sulfide flotation circuit. *Int. J. Mining Sci. Tech.*, *27*:285–292.

Jankolovits, J, Sampayo, G and Santana, A, 2020. Beyond Simple Mechanisms: A Meticulous Analysis of the Impact of Carbon Management Reagents in the Flotation of Carbonaceous Sulfide Ores. *Proceedings of the 2020 International Mineral Processing Congress*, Cape Town, South Africa.

Konieczny, A, Pawlos, W, Krzeminska, M, Kaleta, R and Kurzydlo, P, 2013. Evaluation of Organic Carbon Separation from Copper Ore by Pre-Flotation. *Physicochem. Probl. Miner. Process.*, *49*:189–201.

Lind, P J, Tomlinson, M A and Awmack, K, 2018. Organic Carbon Mitigation at Penasquito. In *50th Annual Canadian Mineral Processing Conference*: Ottowa, Ontario.

Smith, T, Lin, D, Lacouture, B and Anderson, G, 2008. Removal of Organic Carbon with a Jameson Cell at Red Dog Mine. In *40th Annual Canadian Mineral Processors Conference*: Ottowa, Canada. pp 333–346.

Wiese, J, Harris, P and Bradshaw, D, 2011. The effect of the reagent suite on froth stability in laboratory scale batch flotation tests. *Miner. Eng.*, *24*:995–1003.

Improving Buenavista del Cobre flotation performance with TankCell® e630 technology – a review after four years of industrial operation

R Grau[1], G Muro[2], A Yáñez[3], J Romero[4] and J Suhonen[5]

1. Director of R&D, Metso Outotec, Pori, Finland. Email: rodrigo.grau@mogroup.com
2. Plant Manager, Buenavista del Cobre, Grupo México, Cananea, Mexico.
3. Senior Manager, Metso Outotec, Espoo, Finland. Email: alejandro.yanez@mogroup.com
4. Key Account Manager, Metso Outotec, Hermosillo, Mexico. Email: jose.romero@mogroup.com
5. Technology Manager, Metso Outotec, Pori, Finland. Email: janne.suhonen@mogroup.com

ABSTRACT

The TankCell e630, with a nominal volume of 630 m^3, is the industry's largest, most proven mechanical flotation cell. The first TankCell® e630 flotation cells started operation at Buenavista del Cobre in 2018, which is a copper-molybdenum mine located in northern Mexico. The mine has two concentrators: Concentrator 1, in operation since 1986, currently processes approximately 86 000 metric tons of ore per day while Concentrator 2 is a modern concentrator, commissioned in 2016. In connection to a plant optimisation project, two 630 m^3 flotation cells were added in front of the bulk rougher circuit in Concentrator 1 to boost the metallurgical performance of the existing concentrator. They were selected based on a detailed evaluation conducted by a group of specialists from Buenavista del Cobre and Metso Outotec. This included a sampling campaign of the rougher flotation lines and simulation work to estimate the impact of adding new flotation units to the existing flow sheet. Some of the most important considerations were the plant layout constraints.

As part of the commissioning work and evaluation of TankCell® e630 flotation, the operational and metallurgical performance of both flotation cells, as well as the impact on overall recovery and concentrate grade, were monitored closely during the first year of operation. In addition, hydrodynamic conditions such as gas dispersion were measured, along with the mixing profiles.

In this paper, a summary of the metallurgical performance and a characterisation of the new technology is presented. More importantly, a detailed review is given of the last four years of continuous operation, taking a closer look at operating conditions such as variations in copper head grade, throughput, feed flow rate, grind size and solids content. Additionally, the operational and maintenance experience gained by the site team is presented.

INTRODUCTION

Grupo Mexico's Buenavista del Cobre is one of the largest copper mines in the world, with 525 000 metric tons of copper produced in 2021 (International Copper Study Group, 2021). The copper-molybdenum mine is located in the state of Sonora, Mexico and operates hydrometallurgical SX-EW plants to treat copper oxide ore while sulfide ore is processed in two flotation concentrators. Concentrator 1, which has been in operation since 1986 and Concentrator 2, with a design capacity for processing 100 kt of ore per day, which is a new plant design that started up in 2016. In this paper, the operation of Concentrator 1 is described in detail, since the first TankCell® e630 flotation cells were installed and started operation in this concentrator.

Concentrator 1 has been constantly increasing its throughput during the last years of operation, as shown in Figure 1. The current target is to reach and keep throughput values beyond 86 kt/d.

The ore is mined from an open pit from where it is sent to both concentrators. In Concentrator 1, the ore is crushed, and then fed to ten ball mills. The concentrator flow sheet, as shown in Figure 2, is divided into two parallel comminution-flotation sections, so that five ball mills feed each bulk rougher flotation section. The combined rougher concentrate is transferred to a common regrinding stage. The regrinding stage is normally operated with two or three ball mills depending on the operational and process requirements. The reground rougher concentrate is sent to two cleaner stages; the first cleaner stage is performed in columns and part of the concentrate produced in the columns is directed to a second cleaner stage, which is performed in mechanical flotation cells. This is in order to ensure that the target grades are achieved. The bulk concentrate (Cu-Mo) is then sent to a

thickener and from there to the molybdenum separation plant, where Cu and Mo concentrates are produced.

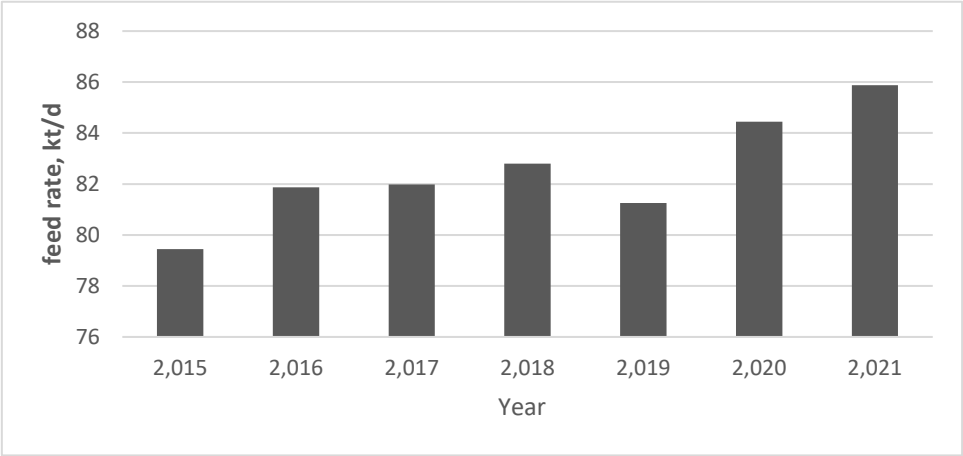

FIG 1 – Buenavista del Cobre, Concentrator 1, feed rate increase over the last seven years.

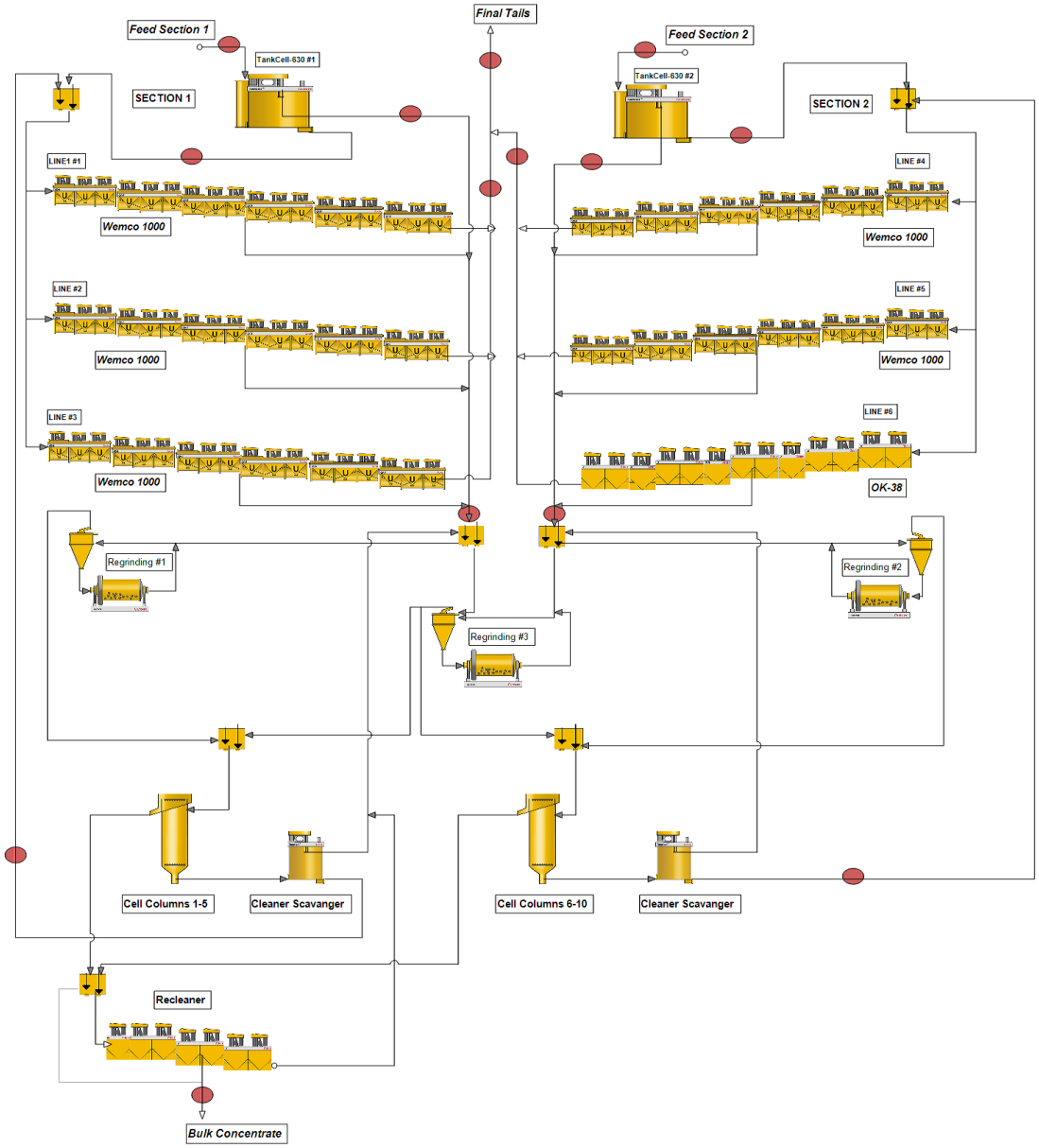

FIG 2 – Buenavista del Cobre 1, schematic diagram of the flotation circuit after the installation of the TankCell® e630 flotation cells. The red spots indicate the shift sampling points.

The tailings from the first cleaner stage are sent to a cleaner scavenger stage, which is performed in mechanical flotation cells. The cleaner scavenger concentrate is combined with the tailings from the second cleaner stage and sent back to the classification stage of the regrinding mills, whereas the tailings are normally sent back to the rougher flotation stage. Thus, both sections are normally operated by recirculating the cleaner scavenger tails (in a closed-loop system) unless there is a large increase in the recirculating load, in which case the cleaner scavenger tails are combined with the rougher tails. This event is often associated with an increase in the amount of pyrite in the ore.

ROUGHER FLOTATION

In 2018, two TankCell® e630 flotation cells were installed as first rougher cell of the two parallel flotation sections; the tails from these flotation cells are distributed into three flotation lines, as depicted in Figure 2. The section 1 rougher stage consists of three parallel lines of eighteen Wemco cells per line, each with a capacity of 1000 cubic feet in an arrangement of 3+3+3+3+3+3, so the total flotation capacity is approximately 1529 m^3.

The section 2 rougher stage also consists of three parallel lines, two of the lines equivalent to the flotation lines in section 1 and one line composed of thirteen Metso Outotec OK 38 cells with a net volume of 38 m^3 each in a configuration of 2+2+3+3+3, resulting in a total flotation capacity for the full section of approximately 1513 m^3. After upgrading the flotation stage, the rougher capacity was dramatically increased to a nominal capacity of approximately 2159 m^3 and 2143 m^3 for sections 1 and 2, respectively.

The recommendation for the increase in flotation capacity was the main outcome of a study conducted in 2015 (Miettinen and Bermudez, 2015). The study included a process survey and the development of a rougher flotation model to study the effect of increasing the feed rate to the concentrator. The findings of the simulation work indicated that the Cu and Mo recovery in the rougher stage would be increased by adding two TankCell® e630 flotation cells, even with an increase in the throughput of the concentrator. The size of the flotation cells and number of units were selected due to space (layout) constraints in the existing concentrator.

START-UP, OPERATION AND MAINTENANCE EXPERIENCE OF TANKCELL 630

The TankCell® e630 flotation units with a nominal volume of 630 m^3 at Buenavista del Cobre are described in detail (Grau *et al,* 2018) and are shown in Figure 3.

FIG 3 – TankCell® e630 flotation units: section 1 float cell to the right, installed outside the main concentrator building and section 2 float cell installed inside the main building.

The fresh slurry feed is transferred by gravitation to the feed box of each cell from the overflow of the cyclones. The concentrates from these two flotation cells gravitate into two common rougher

concentrate launders. In the case of the section 1 flotation unit, the tails gravitate into a distribution box, while the tails of the cell in section 2 are pumped to the distribution box. Two additional pumps were installed (one in operation and the other standby) for this project.

Both flotation cells were equipped with a variable-frequency drive so that the rotational speed of the rotor can be adjusted; the machines are equipped with the FloatForce® flotation mechanism. Dedicated centrifugal blowers are used to supply the flotation air to these units (two units in operation and one on standby). The internal froth collecting launder selected for these units is a double internal type, so it collects froth into two launders. A central froth crowder (froth cone) installed around the shaft promotes the radial movement of the froth towards the lip of the first internal launder, while the external part of this launder also acts as a crowder, promoting the movement of the froth towards the lip of the second peripherical launder.

With the aim of improving operational, process control, stabilisation, and optimisation experience, the two TankCell® e630 flotation units were equipped with an individual CellStation®, which is a local solution for controlling the air and pulp level in the flotation cell. The flotation cells were also equipped with FrothSense™ to monitor the velocity and other properties of the froth. Two types of sensor were installed to measure the pulp level, a traditional ball-float and LevelSense™, which is an alternative for measuring the level of the slurry-froth interphase by using electrical impedance. The cell has two dart valves to control the level of pulp. The air flow rate is measured via a mass flowmeter and controlled using an automatic air valve. The FrothSense™ system measures the velocity of the froth moving towards the lip of the flotation cell, and the velocity is adjusted by sending an external set point to the level controller and air flow rate controller, which is configured using an advance control tool (ACT). In the ACT application, priorities are assigned to the respective controllers and limits are assigned to each variable, ensuring robust and smooth control of the flotation unit.

The section 1 TankCell® e630 was started up on the 18 January 2018 at 20:00 local time. The cell was started up full of water and it was fed with the throughput coming from two grinding ball mills, ranging from 360 to 400 t/h, and reagent addition for Cu and Mo was also initiated. The cell was operated until the following morning, with a deep froth depth and at low Jg (0.5 cm/s). The intention was for the operating personnel to become familiar with the new flotation equipment. At 09:30, the throughput of one mill at a time was added to the feed of the TankCell® e630 every hour, once the product of the five mills had been directed to the flotation cells, the addition of reagents was adjusted, and the air flow rate was increased, and the froth level was decreased. The start-up of the cell in section 2 took place on the 1 March 2018, using a similar procedure. The operation of the new TankCell® e630 has since been reported to be simple and smooth. Due to the high level of instrumentation and with ACT in place, there has been very little requirement for the operator to interact with the cells even in the case of unexpected plant upsets for any reason. Moreover, in relation to the operation of the large cells, there was a report of an unexpected shutdown due to a blackout; it is worth pointing out that it was possible to restart the TankCell® e630 after six hours of blackout with the cell full of slurry.

The main operating parameters for both flotation cells are depicted in Table 1. It is important to mention that the power draw depends on many factors such as solids content, viscosity of the pulp, air flow rate, and mostly on the rotational speed and diameter of the flotation mechanism. The specific energy consumption of the TankCell® e630 flotation cells was found to be in the same range as that reported for TankCell® e300 (Morales *et al,* 2009). It should be noticed that in these two cases the grind size of the flotation feed was quite coarse, while the solids content in the case of the Buenavista del Cobre concentrator is higher.

TABLE 1

Main operating parameters of the large flotation cells.

Operating parameters	Range	Units
Residence time per cell	9.1–10.3	min
Air flow rate	30–35	N m^3/min
Froth depth, cm	25–30	cm
Specific power draw, float cell	0.63–0.68	kW/m^3
Specific power draw, Blower	0.18	kW m^3

Since start-up, the maintenance requirements of the TankCell® e630s have been minimal. After almost five months of continuous operation, the cell in section 1 was stopped and inspected for the first time in the middle of June 2018. Significantly, the wear parts including rotor, stator and dart valves did not show any sign of wear. The rotor and stator flotation mechanism of that cell was first replaced during the first quarter of 2022 after four years of continuous operation. The shutdown for wear parts replacement took 12 hours. This was preventive maintenance, due to the importance of the flotation cell in the performance of the concentrator, since no clear signs of the effect of wearing of the rotor/stator mechanism on flotation performance was observed. The Bond abrasion index for the ore processed in Buenavista del Cobre is in the range of 0.29. The Bond abrasion index is used as a measure of the relative abrasiveness of different rock materials on metals (Weiss, 1985). Even though there is no well-established relationship between the wear of a flotation mechanism and the Bond abrasion index, this index can be used to compare different ore types, so it is given here as a reference value. This was the first replacement of an original component of the flotation unit. The flotation mechanism of the TankCell® e630 in section 2 has not been replaced yet. The availability of the flotation circuit, according to the investigation of the authors of this paper, was found to reach 98 per cent.

CHARACTERISATION WORK OF THE NEW FLOTATION TECHNOLOGY

Gas dispersion measurements were conducted during the first year of operation of the flotation cells on two occasions. During the campaigns, the hydrodynamic properties of both cells were measured in terms of superficial gas velocity (Jg) profiles, gas hold-up, and bubble size reported as the Sauter mean diameter (d32). Additionally, several samples from different pulp depths from the launder lip were collected to analyse the mixing profiles in terms of particle size distribution and solids content. The measurement points for Jg and d32 are illustrated in Figure 4. Red dots indicate the measurement point for gas velocity and the yellow dot indicates the location where the bubble sizes were measured. The gas velocities and bubble sizes were measured approximately 80 cm below the froth-pulp interface.

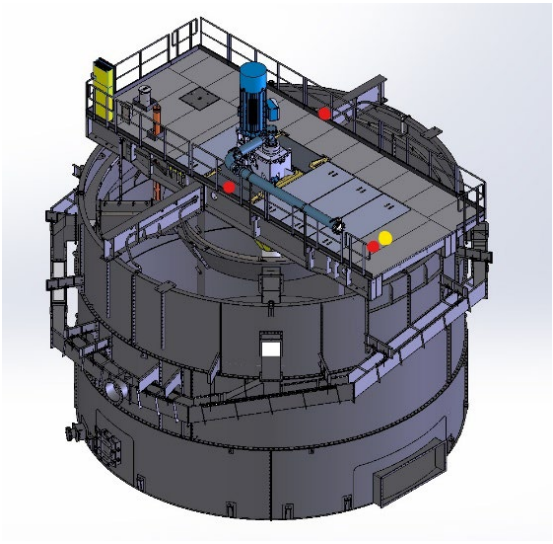

FIG 4 – Measurement points for gas dispersion characterisation.

The superficial gas velocities were measured using two plastic tubes, equipped with pressure sensors. The rate of increase in pressure inside the tubes can be converted to gas velocity. This approach is described in more detail by Gomez and Finch (2007). The gas holdup was measured by the technique described in detail by Tavera *et al* (2001). In this method, the gas holdup is calculated from the pressure difference between the tube ends (used for gas velocity measurements) and the slurry density. The density of the pulp between the probes should be known, and it is assumed that there is no accumulation of froth in the probes; nevertheless, the methodology has been proven to describe gas holdup accurately.

The bubble sizes and bubble size distributions were measured with a McGill University Bubble Viewer and Pixact imaging components and software. Bubble sizes were measured from the TankCell® e630 in both rougher sections. The McGill Bubble Viewer uses a plastic sampling tube to collect air bubbles from the pulp phase. The tube is partly immersed below the froth–pulp interface. The collected air bubbles are exposed to a high frequency camera system in the viewing chamber located in the upper part of the sampling tube. The chamber is filled with clean water which has levels of frother above CCC (critical coalescence concentration) after each measurement. This is done to avoid bubble coalescence.

The plastic tubes and their installation are shown together with the bubble size measurement device in Figure 5.

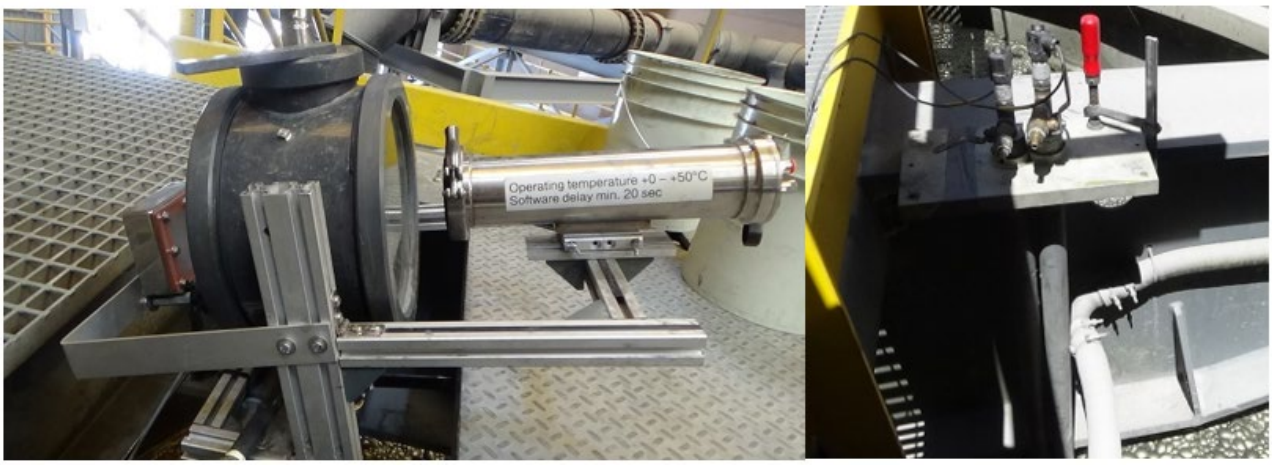

FIG 5 – Jg probe and McGill-Pixact system assembly.

The gas dispersion measurements are presented in Figure 6 (left) together with the results from measurements by Mattsson *et al* (2015a) conducted on the TankCell® e500. The data set including

flotation cells from 10 m^3 to 300 m^3 is according to Vinnet *et al* (2014). The correlation with the gas velocity is good despite the large range in cell sizes. The majority of the data fits within the error band of ±25 per cent. The model for bubble size estimation was further analysed by Vinnet *et al* (2014). It can be concluded that, within normal operating conditions (Jg between 0.5 and 1.5 cm/s), large flotation cells are capable of dispersing gas in a similar way to significantly smaller volume cells.

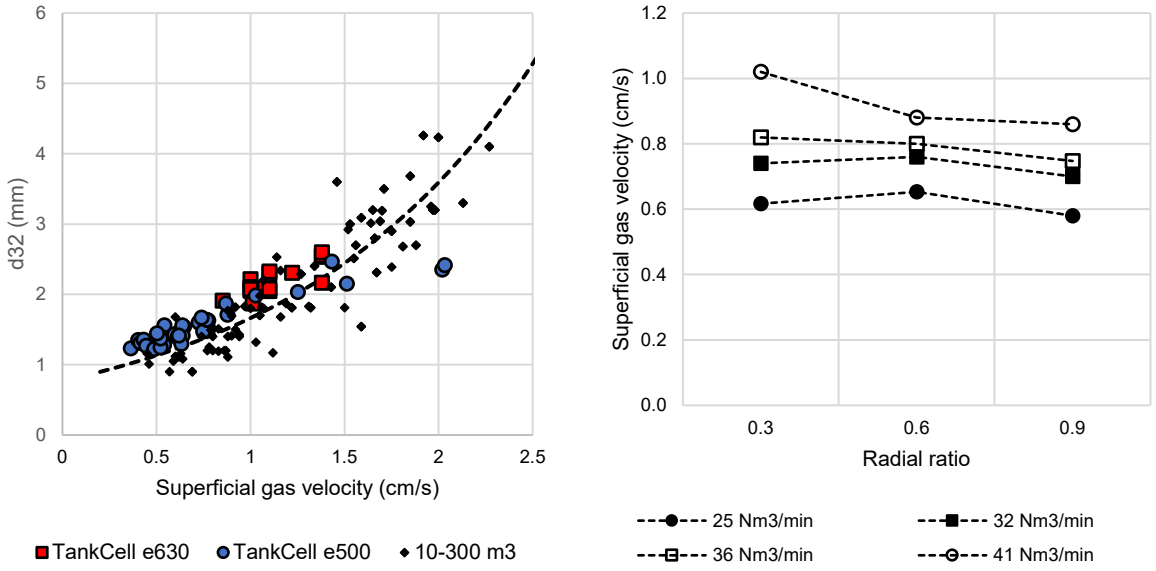

FIG 6 – Bubble size as a function of superficial gas velocity and TankCell® e630 gas velocity profile in section 2 as a function of radial ratio (0 corresponds to the rotor shaft).

As described earlier, the superficial gas velocities were measured from three locations to establish a gas velocity profile. Despite the large 11-metre internal diameter of TankCell® e630, the gas velocities at varying air flow rates seemed fairly stable. At a high air flow rate (41 Nm^3/min), the measured Jg value was slightly higher close to the rotor shaft.

The bubble surface area flux (Sb) has been proven to have a strong correlation with the flotation rate constant. The Sb values are presented in Figure 7 (right) together with results from similar campaigns conducted on the TankCell® e300 and TankCell® e500. The data from these campaigns has been presented earlier by Mattsson *et al* (2015a) and Grau, Nousiainen and Yanez (2014).

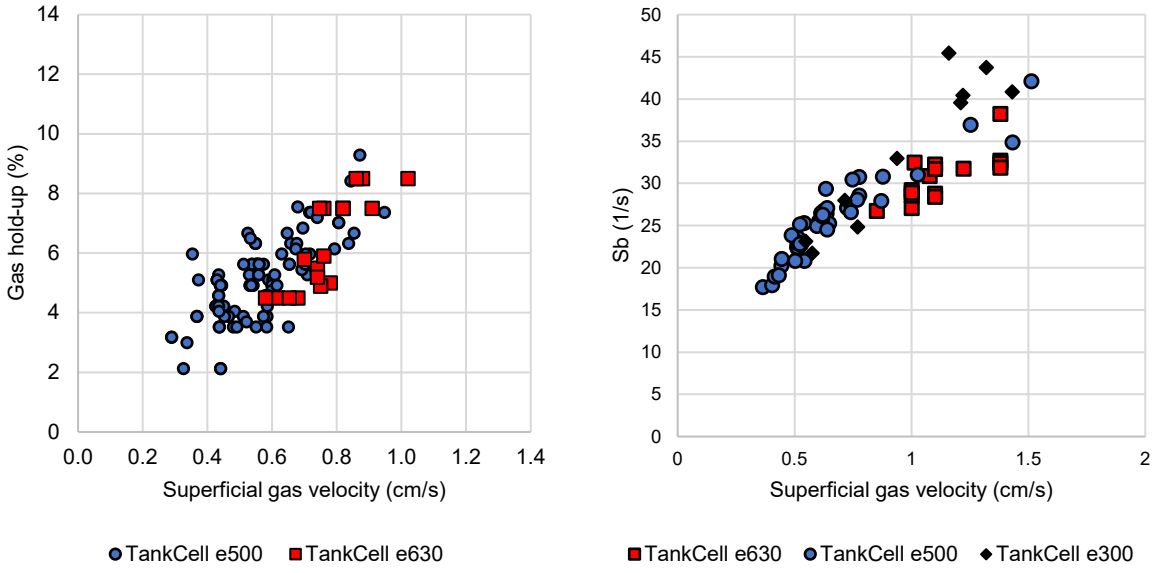

FIG 7 – Gas hold-up and bubble surface area flux as a function of gas velocity for different sizes of TankCell® units.

The relationship between gas velocity and gas holdup for TankCell® e500 and TankCell® e630 is also visualised in Figure 7 (left). As illustrated, the gas holdup values for e500 and e630 are fairly similar despite different measurement techniques. The results are very similar at low gas velocities, although there seems to be slightly more variation at gas velocities over 1 cm/s. However, the number of measurements at high gas velocities is also a lot lower than in the range 0.4–1 cm/s.

An air-operated double-diaphragm pump was used to collect samples from three different depths inside the cell (1.2, 2.2 and 4.4 m). The rotor speed during the sampling was set at a tip speed of 7.1 m/s. The results for the mixing profiles in terms of particle size (P80) and solids content are presented in Figure 8. As can be seen, near perfect mixing and complete homogeneity were achieved in both sections 1 and 2. This was achieved at a relatively coarse and rather high slurry density feed. Very similar results have been reported by Crosbie *et al* (2016) in a study on the TankCell® e500. According to Crosbie *et al* (2016), there was no sanding or significant loss of recovery at lower tip speeds (6 and 6.5 m/s). As the TankCell® e630 is equipped with a variable speed drive, it could therefore even be possible to operate the cells at a reduced tip speed without significant impact on metallurgical performance. However, this has not been investigated within the sampling campaigns conducted for this paper.

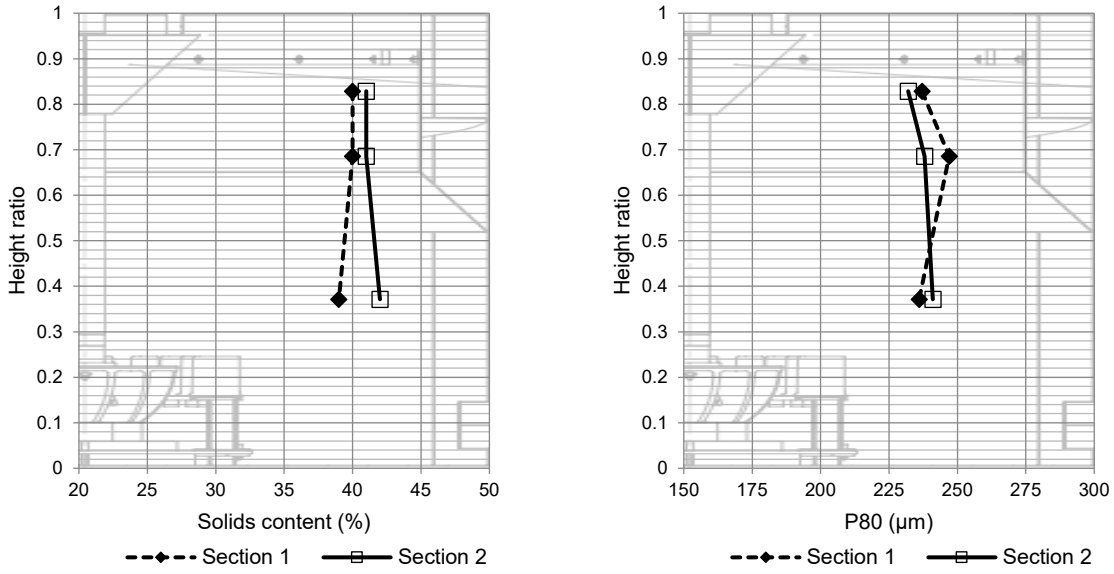

FIG 8 – Mixing profiles for solids % (left) and P80 (right).

ORE MINERALOGY

Since 2015, ore samples from Buenavista del Cobre have been periodically characterised at Metso Outotec Research Center with the focus on chemical and mineralogical properties. Overall, samples taken from 2015, 2016, 2018 and 2020 have been characterised in Table 2.

TABLE 2

Ore composition.

Composition of ore (wt.%)	2015	2016	2018	2020
Cu	0.62	0.7	0.45	0.56
Chalcopyrite	1.43	1.57	0.82	1.26
Secondary Cu sulfides	0.14	0.23	0.21	0.15
Pyrite	3.98	5.67	8.88	3.47

Over the years, the copper content has varied, but it was slightly lower in 2020 than in 2015 (0.62 per cent versus 0.56 per cent Cu). It is notable that the copper grade in the 2018 sample was only 0.45 per cent. Copper is carried mostly by chalcopyrite and to some extent by secondary copper sulfides, such as bornite and chalcopyrite. Although there is some variance in the copper-bearing mineral proportions, the ratio is stable. However, the amount of pyrite seems to vary from sample to sample significantly.

Additionally, the samples were analysed for the particle size distribution and the liberation degree of chalcopyrite. The grind sizes of samples have increased recently, which generally has a negative effect on the liberation of chalcopyrite, as shown in Figure 9.

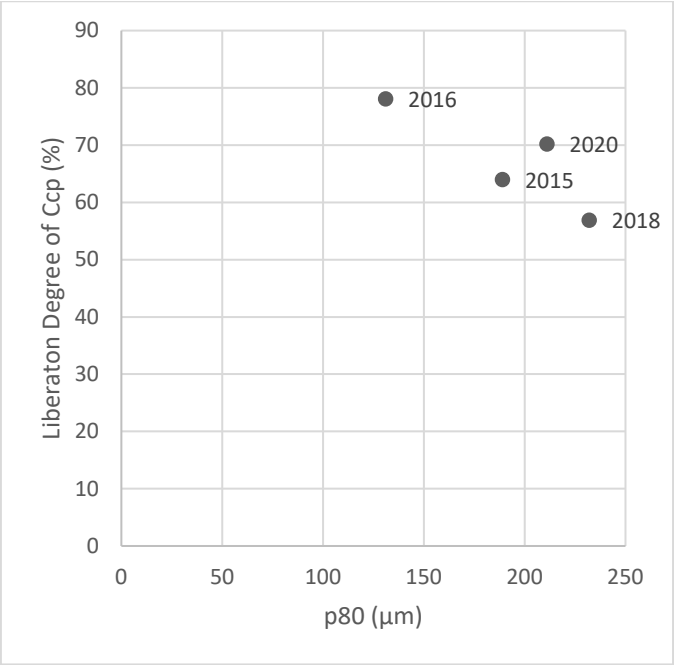

FIG 9 – Liberation degree of chalcopyrite (Ccp) versus grind size.

METALLURGICAL PERFORMANCE

The concentrator is operated in two shifts, day and night; during each shift, six sampling sets are collected. In other words, every two hours several streams are sampled by site personnel. Each process sample is analysed for Cu, Fe and Mo. In fact, during a day's operation, assays for a set of twelve sampling surveys are available. The collected samples are highlighted in Figure 2, and the types of samplers used are listed in Grau *et al* (2018).

The reagents used in rougher flotation can be described as follows: a moly collector or promoter which belongs to the family of hydrocarbons, the main collectors for Cu-bearing minerals belong to the family of thionocarbamates while an alcohol-based reagent is used as the frother. In rougher flotation, reagents are added in two locations, prior to or in the large flotation cells and in the distribution box where the feed is split into three parallel rougher lines.

During the first months of operation of both large flotation cells, the impact of operating parameters such as air flow rate, froth depth and rotor tip speed were evaluated by a team of specialists from Buenavista del Cobre and Metso Outotec. A series of process surveys were conducted which included collecting extra samples around the new flotation cells, as well as conducting hot flotation tests on the feed samples. The following procedure was always followed: after setting new operating parameters, at least four residence times of the TankCell® e630 were used before collecting samples. Each survey consisted of four rounds of sampling; the samples from different rounds were not composited – instead each sample, feed, concentrate and tails, so in total twelve samples were assayed individually for Cu, Fe, Mo and the solids content was also measured. The samples were collected using gravity samplers. The data obtained from each survey was reconciled and mass balanced using HSC Chemistry, software developed by Metso Outotec.

It was found that the cell from section 1 was able to produce higher Cu recoveries at lower grades. The measured recoveries were found to vary from 46 per cent to 68 per cent Cu recovery, whereas the concentrate grade produced was found to range from 8.8 per cent to 24 per cent. In the surveys conducted in the cell from section 2, it was found that the recovery varied from 36 per cent to 64 per cent while the concentrate grades varied from 17.8 per cent to 22.3 per cent. In terms of recovery, this is within the same range as reported for a TankCell® e300 tested at the Chuquicamata Cu Concentrator (Morales *et al,* 2009) The reasons for the difference in performance might be related to two sources: i) the addition point for the reagents in the case of section 1, which are added into the froth cone of the flotation cell, while in section 2, reagents are added to the cyclone overflow box and ii) the use of the FlowBooster™, this is an auxiliary agitator attached to the shaft of the cell in order to enhance hydrodynamic conditions (Grönstrand *et al,* 2006).

As an outcome of the analysis of the sampling surveys in addition to the knowhow of the concentrator staff on how the recovery of the rougher stage can be maximised, it was decided to choose selective flotation conditions. The aim was to produce high-grade rougher concentrates with the intention of retaining a significant amount of floatable material in the tailings so it could be efficiently recovered in the rougher mechanical cells further along the bank. This is an operational strategy used to improve the froth recovery of the last cells of a flotation bank by increasing the stability of the froth phase, Vallejos *et al* (2020) indicated that an increase in floatable minerals improves froth recovery because froth stability increases. This type of strategy can be used when there is enough flotation residence time in the flotation bank and there is a large number of flotation units. In other words, the performance of the complete bank is optimised to maximise overall Cu and Mo recovery. In addition, it was observed that rougher concentrate grade increased, see Table 4.

In Figure 10, the performance of the two TankCell® e630 flotation units is plotted as reconciled Cu recovery versus copper grade. The variation in grade and recovery can perhaps be explained by the variability of the operating conditions such as head grade, grind size, feed rate, liberation degree, ore mineralogy, reagents dosages, solids content and adjustments in flotation reagent dosages, etc. In other words, it seems that the first cell of the bank acts as the buffer of the full rougher bank. These types of variations are typical for the first cell in a flotation bank and this behaviour has been observed by the authors in other large flotation cells (Elgueta *et al,* 2009; Grau *et al,* 2019; Mattsson *et al,* 2015b).

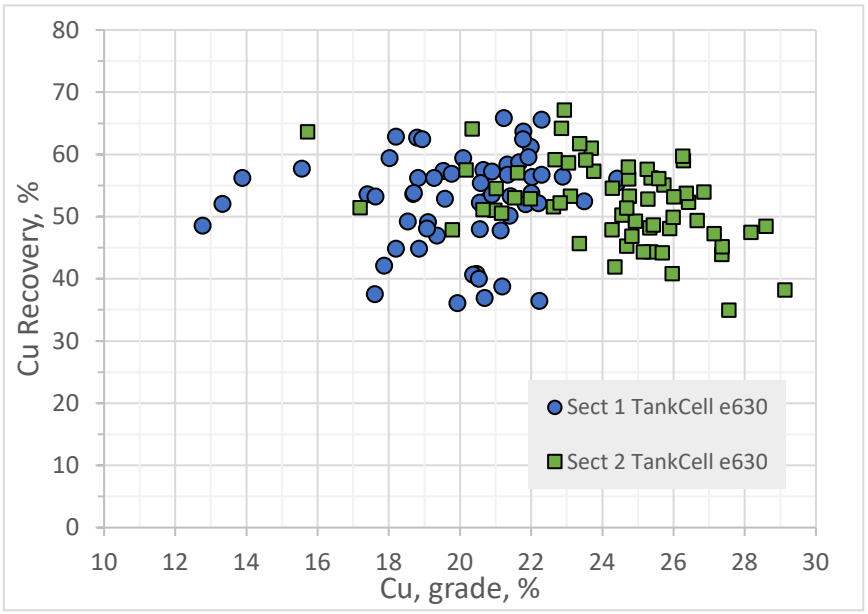

FIG 10 – Metallurgical performance of the TankCell® e630 flotation units.

From the several surveys conducted, the froth carry rate (FCR) and the lip load for these flotation cells can be calculated. These flotation parameters are used in the selection of flotation equipment (Bourke, 2005). In this case, the froth carry rate varied from 0.3 to 0.9 t/m^2 h with an average of 0.5 t/m^2 h, while the lip loading varied from 0.4 to 1.1 t/m h with an average of 0.6 t/m h. These values are in good agreement with the mean values reported by Coleman and Wong (2018) but are lower than the typical design range of 0.8 to 1.5 t/m^2 h for a rougher unit. Thus, it could perhaps be argued that these flotation units can be considered as a pre-rougher unit or scalping unit, rather than a rougher unit; the reason for this is the operating parameters selected for the operation and the enrichment ratios achieved that are higher than 30 on average.

It is also important to observe that the operating conditions have varied over the years, with the most relevant operating conditions shown in Table 3. In Figures 11 and 12, the impact of the operation is shown on these two flotation units in the overall performance of the concentrator. The data presented in these figures is the monthly average and it was calculated from the samples collected every two hours during each shift. The detailed analysis data per shift between November 2018 and December 2020 was unfortunately not available at the time of writing; instead, the annual average is presented later in this paper.

TABLE 3

Average operating conditions over various periods.

Operating parameters	2017 Sept–Dec	2018 Jan–Oct	2021 Jan–Dec
Grind size, µm	195	223	226
Solids content,%	39.7	38.0	40.4
Cu head grade,%	0.54	0.53	0.52
Fe head grade,%	3.1	3.5	3.0
Mo head grade,%	130	120	100

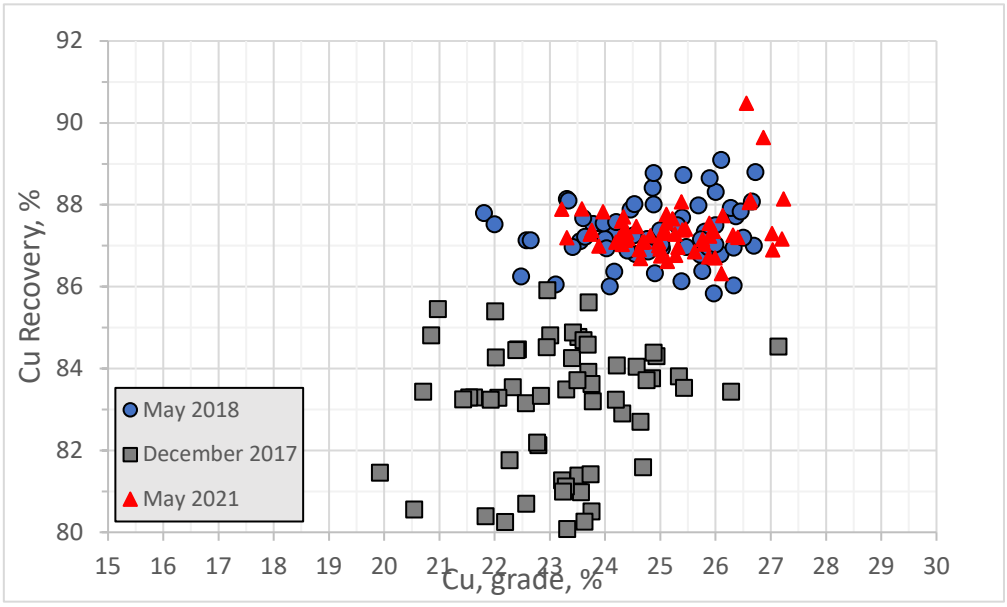

FIG 11 – Overall performance of BVC1, over three months: December 2017, May 2018 and May 2021.

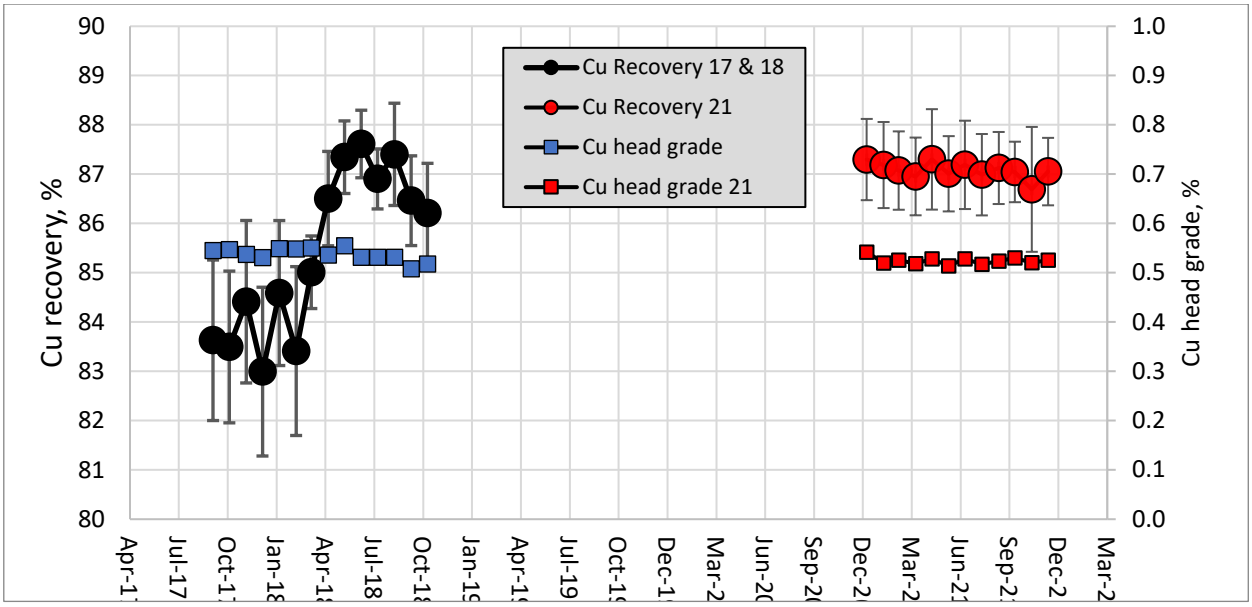

FIG 12 – Overall recovery of the bulk concentrator, Cu. The bars indicate the standard deviation of the month.

In April 2018, the overall recovery of the flotation circuit increased from values of approximately 83.6 per cent (last three months of 2017) to a recovery exceeding 86 per cent. During the following eight months of operation, the overall recovery was observed to reach values above 86 per cent, even exceeding 87 per cent Cu recovery during various months. The data presented in these two figures also indicates a reduction in the variation (standard deviations) in the overall recovery and overall Cu grade. It should also be mentioned that there seems to be an increase in the rougher concentrate Cu grade when comparing the performance before and after the upgrade in flotation capacity, see Table 3.

Regarding the monthly average recoveries during 2021, the overall performance is fairly stable, reaching recoveries of approximately 87 per cent over the whole year, with an average concentrate grade of 24.6 per cent Cu. During these four years of operation, no major modifications were introduced to the flotation circuit in terms of changes in the arrangement or modifications to the existing flotation equipment. Of course, a continuous optimisation has been made of the reagent dosages and of the type of reagent used in the flotation circuit. As a general trend, it can be mentioned that the consumption of reagents in collectors, frothers and lime has been reduced.

An important by-product of the concentrator is molybdenum concentrate. The overall recovery of this metal to the bulk concentrate is shown in Figure 13. It can be seen that the recovery of molybdenum seems to vary over a wider range; the last three months of 2017 reached a value of 57 per cent (recovery calculated based on assays), whereas after eight months of operation, in 2018, the average Mo recovery was approximately 60 per cent. The monthly recovery during 2021 reached a value of 62 per cent. It seems that the increment in Mo recovery is even larger than the increment in Cu recovery. This might be due to the fact that molybdenite usually presents slow flotation kinetics in the rougher stage, so an increase in flotation residence time has a positive impact on the recovery of this metal (Yianatos *et al,* 2012). A summary performance of the bulk concentrator over various period is shown in Table 4.

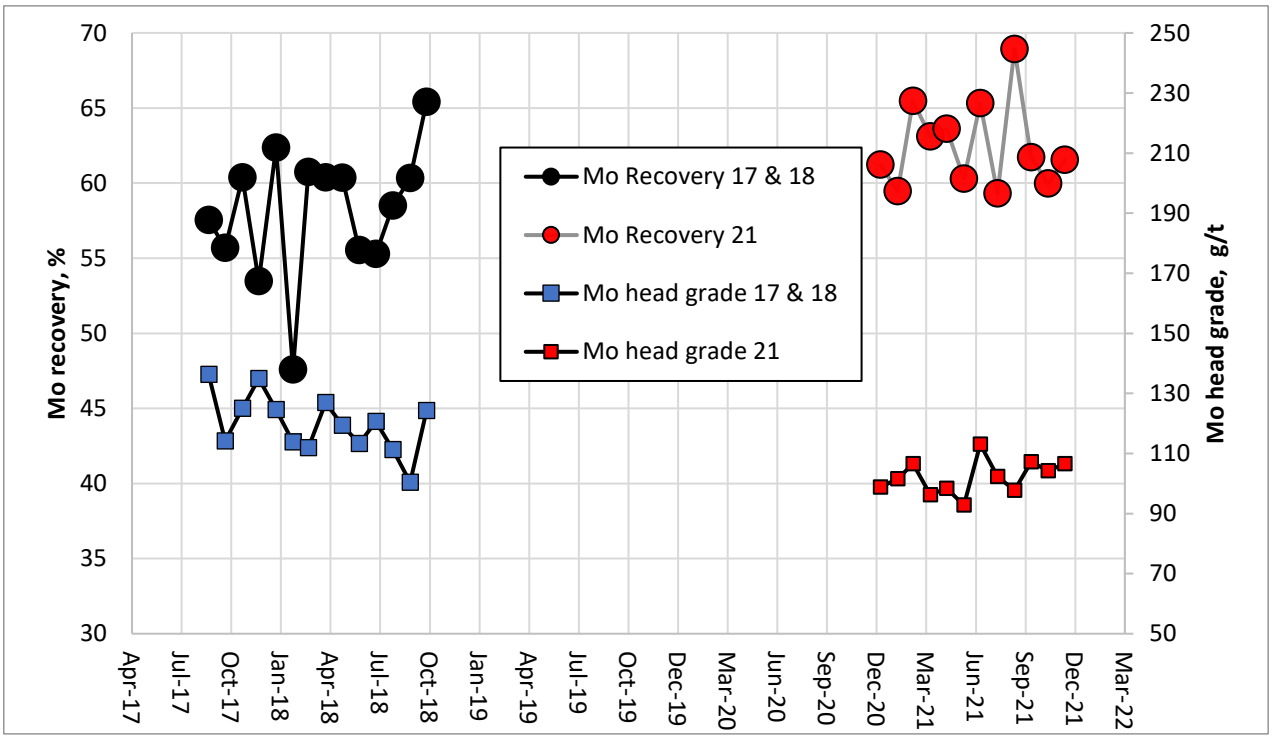

FIG 13 – Overall recovery of the bulk concentrator, Mo over various years.

TABLE 4

Summary of metallurgical performance over various periods, average values.

Operating parameters	2017 Sept–Dec	2018 Mar–Oct	2021 Jan–Dec
Overall Cu recovery,%	83.6	86.6	87.1
Overall Cu grade,%	23.2	24.3	24.5
Rougher Cu grade,%	8.8	10.0	10.5
Overall Mo recovery,%	57	60	62
Overall Mo grade,%	0.53	0.58	0.41

Finally, the overall recoveries over several years are presented in Figure 14. During 2018, a significant increase in recovery was achieved of 2.6 per cent units higher than the preceding year, despite the increase in feed rate and grind size. In 2019 and 2020, annual copper recoveries exceeded 86.5 per cent, while during 2021 the recovery reached values over 87 per cent, so there was a consistent total improved recovery of 3.5 per cent units compared to the plant performance before the addition of the new rougher capacity. It can be concluded that the implementation of these two large flotation cells has given the opportunity to operate the concentrator at a higher feed rate and enabled an increase in recovery to unprecedented values.

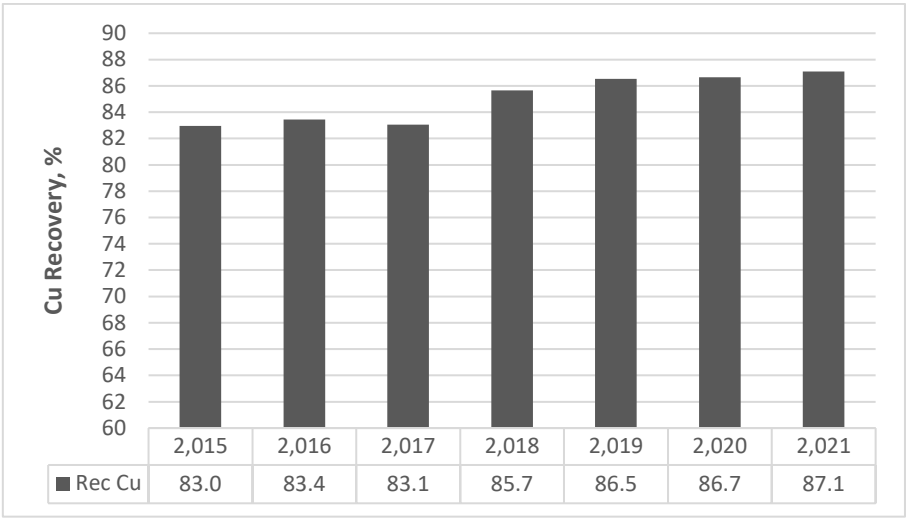

FIG 14 – Overall Cu recovery of the bulk concentrator, over seven years.

CONCLUSIONS

The following conclusions can be drawn from the four years of operation of the TankCell e630 flotation units:

1. A new flotation technology has been successfully introduced to the minerals processing industry. The first TankCell 630 cells, with a nominal volume exceeding 630 m^3, were successfully installed and commissioned in 2018 in a rougher copper application at the Buenavista del Cobre Mine, Mexico. The impact of the metallurgical performance of this large new flotation technology exceeded expectations already during the first months of operation, which has since been further confirmed and improved over the years of operation. This has had a positive and consistent impact on overall plant performance, allowing Buenavista del Cobre to reach recoveries of over 87 per cent Cu, even though the throughput and the grind size have increased.
2. Extensive flotation cell validation and characterisation work was conducted during the first year of operation with the aim of finding a better understanding of the subprocesses that occur inside the flotation cell. The equipment design and scale-up methodology that is used for these

large flotation cells was validated by gas dispersion, froth recovery, mixing profiles and power draw, amongst other measurements. Very good agreement was observed when benchmarking the TankCell® 630 measurements with those reported earlier for large flotation cells, including TankCell® e300 and TankCell® e500 cell sizes.

3. According to operator feedback, the flotation cells installed at Buenavista del Cobre, despite the size, are extremely easy to operate. The high level of automation and control implemented even further enhance the operational experience. From the maintenance point of view, this process equipment has been in continuous industrial operation for over four years without the need for replacing any original parts. Thus, it can be considered as a trouble-free and mature technology with very high availability, exceeding 98 per cent. The FloatForce® flotation mechanism was not replaced until after more than four years of operation due to wear, despite the abrasive environment.

ACKNOWLEDGEMENTS

The authors of this paper would like to acknowledge all the people that have participated in the design, installation, start-up, commissioning and validation of the first of Metso Outotec's largest operating flotation cells. The authors would also like to thank Buenavista del Cobre staff for their collaboration and work over all these years and for allowing this paper to be published.

REFERENCES

Bourke, P, 2005. Selecting flotation cells: how many and what size? *The AusIMM Bulletin May/June*, 47–48 (The Australasian Institute of Mining and Metallurgy: Melbourne).

Coleman, R and Wong, B, 2018. Flotation launder design and the measurement of critical froth transport parameters, paper presented to *14th AusIMM Mill Operator's Conference 2018* (The Australasian Institute of Mining and Metallurgy: Melbourne)..

Crosbie, R, Mattsson, T, Murphy, B and Maksimainen, T, 2016. Metallurgical performance of Outotec's e500 TankCell® at the Kevitsa Cu-Ni-PGE Concentrator, in *13th AusIMM Mill Operators' Conference*, pp. 127–134 (The Australasian Institute of Mining and Metallurgy: Melbourne).

Elgueta, H, Grau, R, Lamberg, P and Yañez, A, 2009. Statistical analysis of the operating performance of Outotec's TankCell® 300 flotation machine, in *Proceedings VI International Mineral Processing Seminar,* pp. 413–423 (Gecamin: Santiago).

Gomez, C O and Finch, J A, 2007. Gas dispersion measurements in flotation cells. *International Journal of Mineral Processing*, 84; 51–58.

Grau, R, Davoise, D, Yañez, A and López, A, 2019. Optimizing the froth area of large mechanical flotation cells, paper presented to *Procemin Geomet 2019, 15th International Mineral Processing Conference*, Santiago de Chile, 20–22 November.

Grau, R, Nousiainen, M and Yanez, A, 2014. Gas dispersion measurements in three Outotec flotation cells: TankCell 1, e300 and e500, in *Proceedings of the 27th International Mineral Processing Congress, IMPC,* p 197 chapter 5 vol 1.

Grau, R, Tapia J, Yañez, A, Hicks, M, Chavira, J, Muro, G and Romero, J, 2018. Improving Buenavista del Cobre flotation performance with Outotec TankCell® e630 technology, paper presented to *Procemin Geomet 14th International Mineral Processing Conference*, Santiago de Chile, 28–30 November.

Grönstrand, S, Niitti, T, Rinne, A, Turunen, J, 2006. Enhancement of flow dynamics of existing flotation cells. *In Proceedings of the Canadian Minerals Processors 38th Annual Operators Conference,* pp 403–422 (Canadian Institute of Mining: Ottawa).

International Copper Study Group 2021. *The World Copper Factbook 2021* [online]. [Accessed: 11th April 2022].

Mattsson, T, Grau R, Honkanen, M and Maksimainen, T, 2015a. Gas dispersion characterization campaign in Outotec TankCell® e500 at Kevitsa Cu-Ni-GE concentrator, paper presented to *Flotation 15*, Cape Town, 16–19 November.

Mattsson, T, Maksimainen, T, Muzinda, I, Lohilahti, J and Yanez, A, 2015b. Implementation of Outotec TankCell® e500 at FQML Kevitsa Cu-Ni-PGE concentrator, paper presented to *11th International Mineral Processing Conference*, Santiago, 21–23 October.

Miettinen, T, Bermudez, G, 2015. Buenavista del Cobre pre-assessment report, Metso Outotec Internal report.

Morales, P, Elgueta, H, Coddou, F, Ortiz, J, Pérez, C, Cortes, G, Grönstrand, S and Yañez, A, 2009. On hydrodynamic set-up of the TankCell® 300, paper presented to *Flotation 09*, Cape Town, 9–12 November.

Tavera, F, Escudero, R and Finch, 2001. Gas holdup in flotation columns: laboratory measurements, *International Journal of Mineral Processing,* 61: 23–40.

Vallejos, P, Yianatos, J, Grau, R and Yañez, A, 2020. Effect of mineral characteristics on industrial flotation circuits performance by simulating mineralogical and operational changes, in *Proceedings IMPC 2020: XXX International Mineral Processing Congress,* pp. 1692–1701 (IMPC and SAIMM: Cape Town).

Vinnet L, Yianatos, J and Alvarez, M, 2014. Gas dispersion measurements in mechanical flotation cells: Industrial experience in Chilean concentrators, *Minerals Engineering*, Vol. 57:12–15.

Weiss, N, 1985. *SME Mineral Processing Handbook*, vol 1, pp 25–27 (SME: New York).

Yianatos, Bergh, L, Vinnet L, Díaz, F and Torres, L, 2012. Metallurgical performance of the new flotation plant at Teck CDA, paper presented to *Procemin 2012*, Santiago de Chile, 21–23 November.

Magnetising roasting – magnetic separation technologies for maximum recovery and utilisation of refractory iron ore

H Han[1] and L Lu[2]

1. Research Scientist, CSIRO Mineral Resources, Technology Court, Pullenvale, QLD 4069. Email: Hongliang.Han@csiro.au
2. Senior Principal Research Scientist, CSIRO Mineral Resources, Technology Court, Pullenvale, QLD 4069. Email: Liming.Lu@csiro.au

ABSTRACT

With the rapid development of the steel industry in China, global iron ore resources of high quality are gradually being depleted. As a result, iron ore deposits of lower quality have been or are being developed to meet the market demand. However, these ores are often polymetallic with complex mineralogy, with Fe extremely hard to recover and utilise through conventional beneficiation technologies, which require clear liberation of coexisting minerals. Therefore, novel beneficiation flow sheets are urgently needed for upgrading these new types of refractory iron ores.

Magnetite has excellent magnetic susceptibility and can be readily separated from other non-magnetic minerals by magnetic separation. However, most of the ores currently being mined are predominantly comprised of weakly magnetic hematite and goethite. Therefore, in order to fully exploit the advantage of magnetic separation, the magnetic properties of weakly magnetic iron ores need to be modified. Fortunately, the magnetic susceptibility of iron ores can be improved through a process called magnetising roasting. During the magnetising roasting process, the weakly magnetic iron ores are converted into ferromagnetic magnetite or even metallic iron, which can be readily separated from gangue by magnetic separation. The magnetising roasting process is recognised as one of the most promising methods for upgrading refractory iron ore and has therefore received increasing attention. This paper focuses on the fundamental and laboratory research, industrial applications and future developments of these new beneficiation processes.

INTRODUCTION

In the past 20 years, the world iron and steel industry has experienced significant development and expansion due to rapid economic growth in China. This has resulted in a rapid increase in iron ore demand. The current supply of high-grade iron ores can no longer meet market needs. Low-grade deposits are therefore being developed and mined, and these types of iron ores may eventually become the main resources for iron and steelmaking. However, these low-grade iron ores must be upgraded to a suitable Fe grade and impurity level before being used by steel mills around the world due to their low-grade, fine grain size and complex mineralogy. Various beneficiation technologies (such as flotation, gravity separation etc) often upgrade the ores utilising their distinct physical or physicochemical properties without involving extensive pre-treatment apart from crushing and grinding. But due to the increasing complexity of the deposits, it is becoming increasingly difficult to achieve the required Fe grade at a high Fe recovery and low cost using these conventional technologies.

Magnetic separation technology plays an important role in upgrading these low-grade iron ores, because the magnetic separation process possesses the combined advantages of large capacity and low operating cost, as well as being environmentally friendly. However, most of the ores currently mined are contain high quantities of hematite and goethite (oxide ores) and siderite (carbonate ores), which are weakly magnetic. In order to exploit magnetic separation techniques, the magnetic properties of weakly magnetic iron ores need to be modified. Magnetising roasting is the most effective method to improve the magnetic susceptibility of iron ores. It involves the conversion of the weak magnetic iron minerals in an ore to their magnetic forms by subjecting the ore to the required atmosphere at elevated temperatures. The resulting ferromagnetic magnetite or metallic iron are then separated from the non-magnetic gangues by magnetic separation. Therefore, magnetising roasting – magnetic separation technology has received increasing attention and many variants of magnetising roasting processes have been developed for upgrading refractory iron ore. Compared with other conventional beneficiation methods, magnetising roasting – magnetic separation

technology is characterised by a high Fe grade product at high Fe recoveries and low production costs. This paper focuses on the fundamental, laboratory research, industrial applications and future developments of magnetising roasting – magnetic separation processes.

FUNDAMENTALS

Magnetising roasting – magnetic separation technology dates back to the nineteenth century, and probably earlier. Meyer (1963) gave a historical outline of the development of roasting furnaces since 1895; and Davis (1937) cited the magnetising reduction studies of W B Philips and C Jones which were published in 1890 and 1894, respectively (Uwadiale, 1992).

Magnetising roasting can be divided into reduction roasting, neutral roasting and oxidation roasting. Generally, reduction roasting is suitable for treating oxidised iron ores (hematite, goethite), neutral roasting for carbonate ores (siderite), and oxidation roasting for sulphide ores (eg pyrite).

Hematite and goethite

The conversion of hematite or goethite to magnetite or metallic iron at elevated temperatures can take place in the presence of both gaseous and solid reducing agents through the following possible reactions (Uwadiale, 1992):

$$3Fe_2O_3 + CO = 2Fe_3O_4 + CO_2 \quad (1)$$

$$Fe_3O_4 + CO = 3FeO + CO_2 \quad (2)$$

$$FeO + CO = Fe + CO_2 \quad (3)$$

$$3Fe_2O_3 + H_2 = 2Fe_3O_4 + H_2O \quad (4)$$

$$Fe_3O_4 + H_2 = 3FeO + H_2O \quad (5)$$

$$FeO + H_2 = Fe + H_2O \quad (6)$$

$$3Fe_2O_3 + C = 2Fe_3O_4 + CO \quad (7)$$

$$Fe_3O_4 + C = 3FeO + CO \quad (8)$$

$$FeO + C = Fe + CO \quad (9)$$

$$6Fe_2O_3 + C = 4Fe_3O_4 + CO_2 \quad (10)$$

$$2Fe_3O_4 + C = 6FeO + CO_2 \quad (11)$$

$$2FeO + C = 2Fe + CO_2 \quad (12)$$

Reactions 1 to 6 involve gaseous reducing agents and are often called indirect reduction while Reactions 7 to 12 use solid reducing agents and are called direct reduction. In the case of direct reduction, the carbon gasification reaction, or Boudouard reaction, below is believed to be the rate controlling step.

$$C + CO_2 = 2CO \quad (13)$$

Through the Boudouard reaction, CO_2 generated from the reactions is subsequently reduced to produce more CO (Flavio, 1992). Since the Boudouard reaction is an endothermic reaction, increasing temperature enables the Boudouard reaction to occur faster, resulting in a higher CO partial pressure and an accelerated magnetic reduction of hematite or goethite.

In addition, water can also react with the solid carbon through the following gasification reaction to produce H_2 and CO.

$$H_2O + C = H_2 + CO \quad (14)$$

This is also an endothermic reaction, where increasing temperature enables more rapid production of H_2 and CO. Therefore, the water formed in Reactions 4 to 6 is subsequently re-generated through Reaction 14 then further reacting with Fe oxide. In addition, the moisture in the solid reducing agent which is injected into the high-temperature reduction zone can promote the reduction reactions.

Hematite is known to be reduced in the following steps: $Fe_2O_3 \rightarrow Fe_3O_4 \rightarrow FeO \rightarrow Fe$. At temperatures below 570°C, the reduction leads to the formation of only magnetite and metallic Fe.

Below this temperature, wüstite (FeO) is unstable and decomposes eutectoidally into magnetite and metallic Fe. In magnetising operations, the formation of wüstite needs be avoided as it is only weakly magnetic. The following methods are typically used to control the degree of reduction and therefore the reduction products:

1. Control of the composition of the reducing gas. For example, at a CO_2:CO ratio of 9:1, it is possible to convert hematite to magnetite without formation of wüstite at a temperature of about 1200°C, whereas at the same temperature and with a CO_2:CO ratio of 1:9, metallic Fe is formed.
2. Control of the amount of reducing gas supplied to minimise the formation of weakly magnetic wüstite.

Goethite is first transformed to hematite through the following dehydroxylation reaction at temperatures below 371°C, which is then further reduced to magnetite or metallic iron as discussed above (Jang *et al,* 2014).

$$2\alpha\text{-}FeOOH = \alpha\text{-}Fe_2O_3 + H_2O \quad (15)$$

Siderite

The thermal decomposition of siderite is quite complex and depends on the roasting atmosphere. In a strong oxidising atmosphere (>21 per cent O_2), thermal decomposition of siderite occurred via the following steps: $FeCO_3 \rightarrow Fe_3O_4 \rightarrow \gamma\text{-}Fe_2O_3 \rightarrow \alpha\text{-}Fe_2O_3$ (Luo *et al,* 2016a). Siderite has self-magnetising characteristics, however, it is eventually fully oxidised to hematite. However, the decomposition product was found to be magnetite in a CO_2 atmosphere, and magnetite and wüstite in an inert atmosphere (Dhupe and Gokarn, 1990). According to Sun *et al* (2019), wüstite is first formed during the decomposition of siderite in an inert atmosphere by Equation 16, and finally oxidised to magnetite by Equation 17:

$$FeCO_3 = FeO + CO_2 \quad (16)$$

$$3FeO + CO_2 = Fe_3O_4 + CO \quad (17)$$

As wüstite is an intermediate phase, the overall decomposition of siderite in an inert atmosphere can be described by:

$$3FeCO_3 = Fe_3O_4 + CO + 2CO_2 \quad (18)$$

In an inert atmosphere, siderite transforms to magnetite, along with the formation of CO, which can then be used as a reducing agent. Therefore, simultaneous roasting of siderite and low-grade hematite ores has been proposed as a promising thermal beneficiation process (Yu *et al,* 2019) that requires no additional fossil fuel reducing agents and could represent a comparatively low carbon footprint process for thermal beneficiation. The co-roasting reaction of hematite and siderite is summarised below:

$$FeCO_3 + Fe_2O_3 = Fe_3O_4 + CO_2 \quad (19)$$

The Gibbs free energy of this reaction is negative at temperatures above 17°C, indicating the reaction is thermodynamically possible.

Pyrite

Under an oxidising atmosphere, pyrite is oxidised initially to pyrrhotite, and subsequently to magnetite via the following reactions:

$$7FeS_2 + 6O_2 = Fe_7S_8 + 6SO_2 \quad (20)$$

$$3Fe_7S_8 + 38O_2 = 7Fe_3O_4 + 24SO_2 \quad (21)$$

Due to the formation of SO_2, this is a typical process for producing sulphuric acid, with magnetite being a by-product of the process.

LABORATORY RESEARCH

As shown in Table 1, extensive magnetising roasting and magnetic separation laboratory studies have been conducted on refractory iron ores. The results have clearly demonstrated the feasibility and effectiveness of the method for upgrading refractory iron ores.

TABLE 1

Results of magnetising roasting and magnetic separation laboratory studies on refractory iron ores.

Ore type	Feed ore Fe content/%	Concentrate Fe content/%	Recovery/ %	Conditions	Source
Oolitic iron ore from Aswan, Egypt	45.2	59.6	~90.0	500°C for 20 min with 1.5 L/min H_2	Youssef and Morsi (1998)
Oolitic iron ore from Yunnan, China	44.6	60.2	85.9	Pre-calcination, 550°C for 10 min with a 1:4 mixture of CO and N_2	Zhou *et al* (2009)
Oolitic hematite from Hubei, China	43.8	57.0	83.8	800–900°C for 60–180 s in a gas mixture of 3–12% CO	Yu and Qi (2011)
Low-grade ore from Western Australia	50.7	63.2	60.1	700°C for 20 min at 2 L/min 50% CO and 50% CO_2 gas	Suthers *et al* (2014)
Oolitic hematite ore from China	46.3	58.4	84.0	650°C for 10s with a gas mixture of 40% H_2 and 60% N_2	Li *et al* (2015)
Hematite ore from Anshan, China	41.6	65.4	88.1	650°C in a gas mixture of 3.2 m^3/h H_2 and 4.8 m^3/h N_2 for 15 s	Yu *et al* (2018b)
Agbaja iron ore from Kogi, Nigeria	45.6	60.0	87.3	600°C for 60 min with mass ratio of coal to iron ore at 1:2	Uwadiale (1992)
Hematite and siderite from China	34.6	65.4	92.7	800°C for 8 min with 8% coal	Yu *et al* (2017)
Ooolitic hematite ore from China	49.0	55.6	83.8	800°C for 120 min using 20% coal and a 30 mm layer	Peng *et al* (2017)
Low-grade ore from Jharkhand, India	58.0	66.6	90.4	800°C for 30 min using 10% coal	Ravisankar *et al* (2019)
Limonite from Baotou, China	33.6	58.0	72.0	550°C for 30 min with 15% biomass	Zhang *et al* (2017)
Low-grade iron ore	51.6	64.0	76.0	950°C for 53 min with 3% activated charcoal	Rath *et al* (2014)
Low-grade iron ore	47.2	63.0	68.0	850°C for 90 min with ratio of blast furnace dust to iron ore at 0.4	Rath *et al* (2018)
Hematite and siderite ore from China	48.9 35.9	61.6	91.1	850°C for 20 min with ratio of siderite to hematite of 80:20	Chun *et al* (2015b)
Siderite ore from China	35.4	63.6	95.8	800°C for 15 min in neutral atmosphere using siderite particles 10–16 mm	He (2012)
Siderite from Shaanxi, China	25.0	59.6–59.4	72.0–73.7	700°C for 70 min in neutral atmosphere	Luo *et al* (2014)
Siderite from Shaanxi, China	21.4	58.2	79.4	800 or 850°C for 1 min in a weakly oxidising atmosphere of 1.05% O_2	Jiu *et al* (2008)
Siderite from China	---	59.1	89.9	750°C for 15 min in the piled state	Pang (2006)
Siderite from China	---	57.2	94.4	700°C for 3 min in the fluidised state	Pang (2006)
Siderite from China	37.3	62.6	89.2	550°C for 60 s at 0.5 m/s of 13.3% CO + 6.7% H_2+80% N_2	Zhao *et al* (2019)
Titanomagnetite ore	52.5	61.2	78.1	850°C for 1 hour with a mass ratio coke breeze to iron ore of 4:11	Jena *et al* (2015)
Iron ore tailings from Liaoning, China	17.4	61.3	88.2	800°C with 1% coal for 30 min	Li *et al* (2010)
Lead-zinc tailings from China	29.4	62.1	82.2	720°C with 7% coal for 30 min	Lei *et al* (2017)
Iron ore tailings from Liaoning, China	10.6	65.3	85.8	600°C for 20 s at a gas flow rate of 8 m^3/h (50% H_2 in N_2)	Li *et al* (2019)

Ore type	Feed ore Fe content/%	Concentrate Fe content/%	Recovery/ %	Conditions	Source
Pyrite cinder from China	45.6	66.2	73.3	700–800°C for 20 min with 300 kg/t pulverized coal injection	Zhu *et al* (2007)
Pyrite cinder from China	53.5	64.0	>90.0	750°C for 15 min using biochar	Fan *et al* (2015)
Ramin iron ore	---	84.0–95.7	93.0–95.7	1275°C for 15 min with excessive anthracite, bituminous coal, coke or charcoal	Weissberger and Zimmels (1983)
Oolitic iron ore from Hebei, China	47.7	92.5	90.8	1200°C for 60 min with 30% coal	Li *et al* (2011)
Antelope iron ore from Jilin, China	34.8	93.1	85.0	1275°C for 50 min at 30 mm layer with coal at twice amount required to reduce the iron in the ore	Li *et al* (2012)
Siderite from China	35.4	92.1	85.9	1050°C for 140 min at C/Fe=1.86 with 3% desulfuriser	Luo *et al* (2016b)
Titanomagnetite ore from Indonesian	51.9	91.8	88.5	1250°C for 60 min with 20% bituminous coal and 10% calcium fluoride	Gao (2016)
High-aluminium limonite ore from China	48.9	91.0	91.6	1050°C for 60 min with 12% sodium sulfate	Jiang *et al* (2010)
High-aluminium limonite ore from China	57.4	92.2	92.8	1050°C for 80 min with 16% coal and 9% sodium carbonate	Chun *et al* (2015a)
High-P oolitic hematite from China	49.0	92.7	92.5	1050°C for 120 min with excessive coal and 7.5% sodium sulfate, 1.5% borax	Li *et al* (2013)
High-P oolitic hematite from China	51.3	96.4	95.1	1250°C for 20 min and C/O of 1.0 with 8% CaO and 3% Na_2CO_3	Han *et al* (2015)
Bayan Obo ore from Inner Mongolia, China	32.2	91.6	93.2	1225°C for 30 min with the C/O molar ratio of 2.0	Gao *et al* (2010)
High-sulphur iron ore	---	80.0	---	1050°C for 4 hours at a lime:coal:ore mass ratio of 1.25:1.25:1	Khaki *et al* (2018)
Pyrite cinder from China	61.0	93.0	91.7	pre-oxidation with 5% borax at 1050°C for 10 min, reduction at 1050°C for 80 min with excessive amount of reducing agent	Long *et al* (2016)

INDUSTRIAL APPLICATIONS

Based on the laboratory research, various magnetising roasting processes have been designed and developed over the years. The common variants of the process including shaft furnace roasting, rotary kiln roasting and fluidised bed roasting, are compared and discussed below.

Shaft furnace roasting process

In the 1920s, Germany successfully built more than ten shaft furnace roasting and magnetic separation plants to process goethite and siderite ores, showing better efficiency than other beneficiation methods (Zhou, 2008). In early 1926, an industrial scale iron ore magnetising roasting shaft furnace was established in Anshan, China (Yu *et al,* 2019). The shaft furnace roasting – magnetic separation process has since become the major beneficiation method for processing refractory iron ores in China. At peak usage, China had more than 130 shaft furnaces, which processed about 13 Mt of iron ore per annum. Currently, only 44 shaft furnaces in JISCO (model: 100 m^3) are reported to remain in operation for roasting refractory specular hematite ores (Zhang, 2015).

In a shaft furnace, iron ore descends by gravity counter-current to the flow of reducing gas. The magnetising roasting process of iron ore can be divided into four steps from the top to the bottom of the furnace, namely, preheating, heating, reduction, and a cooling and discharge step, as shown in Figure 1 (Yu *et al,* 2019). The raw ores are gravity charged through a storage bin and a square funnel into the top of the furnace. The reducing gas is introduced at ambient temperature from the

bottom of the shaft furnace. In the preheating zone, the ores are first heated to 100–150°C by the ascending hot gas. The preheated coke oven gas and blast furnace gas are mixed with preheated air and burnt in the combustion chamber to generate a hot gas of the temperature in the range from 1050°C to 1150°C. The hot gas from the combustion chamber then flows up and heats the descending ores further to 700–850°C in the heating zone through convection, radiation, and conduction. In the reduction zone, the hot ores contact the ascending reducing gas, and are reduced by CO and H_2 to Fe_3O_4 at approximately 570°C. The partially reduced ores are loaded into a water-sealed pool to cool down before being discharged from the furnace and transferred to a grinding and magnetic separation plant by belt-conveyer machines.

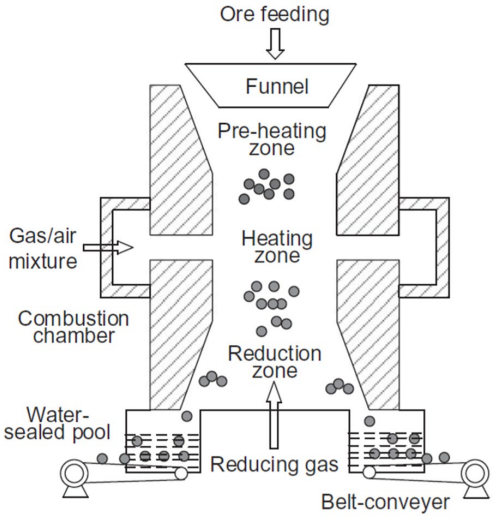

FIG 1 – Magnetising roasting process of iron ores in the shaft furnace (Yu *et al,* 2019).

Industrial applications indicate that the shaft furnace can only handle lump ore with a granularity of 15–75 mm to ensure the permeability of the shaft furnace. The production capacity of a typical shaft furnace is approximately 25 t/h with the residence time of the ore in the shaft furnace being up to 6–10 hours. As the partially reduced ore is chemically heterogeneous, the shaft furnace roasting process is often associated with low Fe recovery. Hence, the shaft furnace roasting process has been gradually replaced by other processes.

Rotary kiln roasting process

Unlike shaft furnaces, the rotary kiln is capable of processing iron ores with a granularity of less than 25 mm. Figure 2 illustrates the magnetising roasting process of iron ore in a rotary kiln.

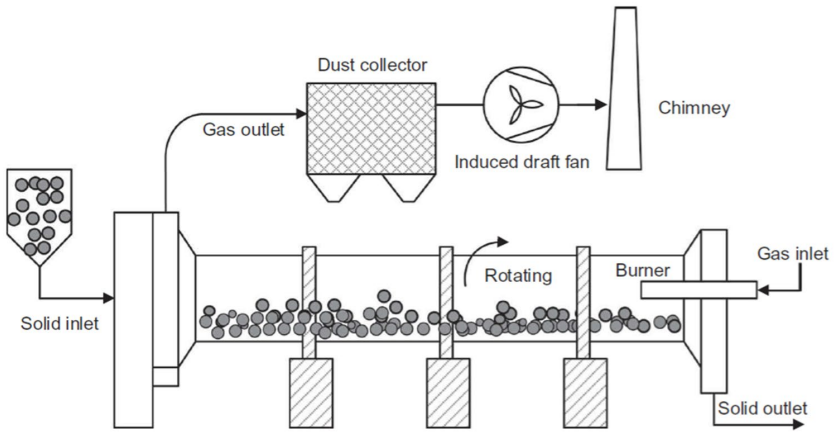

FIG 2 – Magnetising roasting process of iron ores in the rotary kiln (Yu *et al,* 2019).

Similar to the shaft furnace, the rotary kiln is divided into three zones from left to right: heating, reduction and cooling. The feed ore and solid reducing agent are charged in the kiln through a feeder

from one end of the furnace. With the help of slow rotation (0.4–1.0 rpm) of the rotary kiln and a slight inclination in the kiln, the iron ore particles move gradually towards the outlet end. They are first heated when contacting the counter flow of hot gas from the burner and then reduced to magnetite by solid reducing agents, such as coal, coke, biomass, etc. Finally, the roasted iron ore particles enter the cooling zone. The roasting temperature in a rotary kiln is usually up to 750–1000°C, and the iron ore particles generally reside in the furnace for 3–4 hours with an occupancy rate of 20–30 per cent. Due to the limitation in the length of the kiln body, the discharged roasted ore particles are often quite hot. Therefore, a cooling tube is sometimes installed at the discharge end of the kiln to further cool down the hot roasted ore particles to 50–70°C.

The rotary kiln process is used worldwide for the magnetising roasting of refractory ores, and it was proven capable of processing a wide range of ore types. In the former Soviet Union, 30 large-scale rotary kilns of ø 3.6 × 50 m with an annual processing capacity of 9 Mt of raw iron ores were established in central Siberia in the early 1960s for magnetising roasting low-grade iron ores (Meng, 2012). In Germany, four rotary kilns of ø 3.5 × 30 m were used for magnetising roasting low-grade iron ores (27 per cent Fe) using blast furnace off-gas as fuel. This process obtained an iron concentrate of 40.4 per cent Fe after roasting and magnetic separation (Sun, 2012). In the Czech Republic, four rotary kilns of ø 2.4 × 47.5 m were adopted to treat low-grade iron ores using blast furnace gas, coke oven gas or natural gas as fuel. An iron concentrate of 48–49 per cent Fe with a Fe recovery of 78–79 per cent was produced after magnetic separation (Yin *et al,* 2014). Recently, the rotary kiln process has been increasingly used in China (Yu *et al,* 2019).

Compared with the shaft furnace, rotary kilns show a better magnetising roasting performance. However, on average, they consume up to 60 kgce/t of raw iron ore, which is much higher than the 46 kgce/t of raw iron ore typically required by shaft furnaces. Furthermore, the formation of 'kiln rings' induced by the formation of low-melting substances, such as fayalite, during the roasting process, not only affects the product yield but also smooth furnace operation. Currently, the typical 'smooth-running' period for a rotary kiln (ie before maintenance is required) is only 30–75 days. Thus, high energy consumption and the formation of 'kiln rings' are still the main problems to be resolved to improve the rotary kiln magnetising roasting process.

Fluidised bed roasting process

In the fluidised bed roasting process, the iron ore particles are suspended by an upward flow of gas. Precise adjustment of the velocity of the gas flow to the particle size and the specific gravity of the ore is therefore required to make it possible to generate a floating mixture of gas and solid particles, which behaves almost like a liquid. The fluidising roasting process is reported to have some advantages over the other roasting technologies (Uwadiale, 1992; Yu *et al,* 2019), such as ease of control due to an absence of moving parts within the reactor, homogeneity of the roasted product, ability to handle fine particles, and high heat transfer and mass transfer efficiency, etc.

Since the 1950s, fluidised bed roasting has received increasing attention in the field of iron ore magnetising roasting, and much research has been conducted in the United Kingdom, the United States, Canada, Germany, France, Italy, China and other countries (Zhu and Li, 2014). Follonica, Italy, built the world's first fluidised magnetising roasting plant in 1964, which processed 1000 tons of pyrite per day to produce a 65 per cent Fe concentrate at a Fe recovery up to 95 per cent (Zhu and Li, 2014).

Development of the fluidised magnetising roasting process for refractory iron ores in China started in 1958 (Zhu and Li, 2014). Laboratory and pilot-scale experimental research has been conducted on refractory iron ores, such as Anshan hematite, Jiuquan siderite and specularite, Baotou Baiyun Ebo iron ore, etc. However, research on fluidised bed magnetising roasting has since stalled due to the sufficient supply of high-quality iron ores on the market.

As high quality iron ore resources are gradually being depleted, there is a renewed interest in the treatment of refractory iron ore by magnetising roasting. The fluidised magnetising roasting process is considered to be the most promising approach for handling weakly magnetic refractory iron ores due to its high roasting efficiency and low energy consumption. A variety of process variants, such as the multistage circulating fluidised bed magnetising roasting process, flash magnetising roasting

process and suspension magnetising roasting process have been studied and industrial scale facilities of these processes have been built in China (Yu *et al,* 2019).

Multistage circulating fluidised bed magnetising roasting process

This technology featured a low roasting temperature (about 450°C) and multiple stages of fluidised reduction magnetising roasting. An industry demonstration plant with an annual processing capacity of 100 000 tons of refractory iron ore was installed in 2008, and continuous and stable production was achieved in 2012. The demonstration plant further confirmed the laboratory and pilot test results that magnetising roasting can be achieved at a lower temperature of 450°C, which contributes to a lower energy consumption of only 36 kgce/t of raw iron ore (Zhu and Li, 2014). An iron ore concentrate of >57 per cent Fe was produced from a Yunnan limonite ore containing 33 per cent Fe with a Fe recovery rate of 93–95 per cent, and a tailings iron grade of <8 per cent.

Flash magnetising roasting process

Yu *et al* (2019) invented a new process of flash magnetising roasting for treating refractory iron ores of a fine particle size (<0.5 mm) reported in 2010. This process featured high reduction temperatures (750–950°C), low CO concentrations (<5 per cent) and short roasting times (5–60 s). As shown in Figure 3, the iron ore powder was preheated by the hot counter off-gas flow from the reactor via three cyclone stages. The hot combustion gas produced by the combustion of coal, converted hematite, goethite or siderite within the ore into magnetite rapidly, with the retention time of ore powder in the reactor estimated to be 5–60 s (Yu and Qi, 2011; Chen *et al,* 2017; Liu *et al,* 2017).

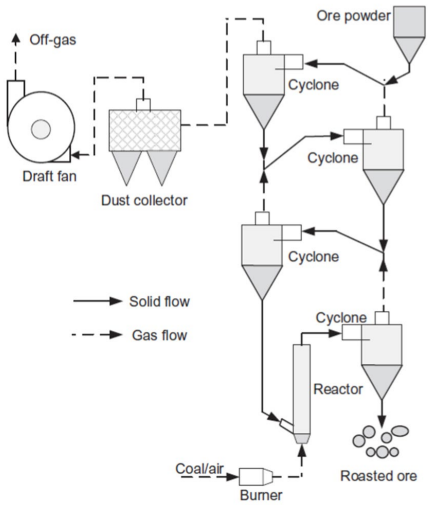

FIG 3 – Schematic of the flash magnetising roasting process (Yu *et al,* 2019).

Based on theoretical research and laboratory-scale experiments, an industrial scale testing facility of flash magnetising roasting with a capacity of handling 50 000 tons iron ores per year was built in 2012 (Chen *et al,* 2017). After achieving excellent results from continuous tests of a Hubei limonite ore, a flash magnetising roasting plant with a processing capacity of 600 000 tons of iron ores per year was completed at the end of 2015 in Hubei, China. This plant has operated continuously and reliably, and fully met the requirements of large-scale industrial production. An iron ore concentrate of 57.52 per cent Fe and 4.76 per cent SiO_2 was produced at a Fe recovery of 90.24 per cent from a Hubei limonite ore containing 32.52 per cent Fe. Furthermore, a low roasting energy consumption of only 31.22 kgce/t of raw iron ore was reported (Chen *et al,* 2017).

Suspension magnetising roasting process

An innovative suspension (fluidised) magnetising roasting process based on a technical route of heat-retaining reduction and re-oxidisation was proposed by Han *et al* (2015) and Yu *et al* (2018b, 2018c) for treating refractory iron ores in 2018. As shown in Figure 4, the feed ore powders (<0.8 mm) are preheated by a hot gas flow (about 700–900°C) originally from the combustion of natural gas, and then transported via a cyclone through a pneumatic carrier. The siderite and goethite in the ore powders are thermally decomposed or oxidised to hematite in the cyclone. The

newly formed hematite powders are then transferred into the reactor by gravity and react with the reducing gas CO or H_2 in the temperature range of 450–600°C to form magnetite. After magnetic reduction roasting, the mixture of reacting gas and artificial magnetite is transported to the cooler where the magnetite is re-oxidised to ferromagnetic maghemite (γ-Fe_2O_3) by air in the temperature range of 200–350°C. Meanwhile, the reacting gas travels into the heating furnace and reacts with the preheated air to heat the feed ore powders. Finally, the magnetic component of the roasted ore can be recovered by magnetic separation after being liberated from the gangue minerals.

Many pilot-scale suspension magnetising roasting and magnetic separation tests were conducted for the beneficiation of refractory iron ores (Yu *et al,* 2018a, 2018b, 2018c; Zhang *et al,* 2019). Excellent performance was achieved from pilot-scale tests, with iron grade increased to 60.2–66.8 per cent with a Fe recovery of 81.8–98.0 per cent by suspension magnetising roasting and magnetic separation.

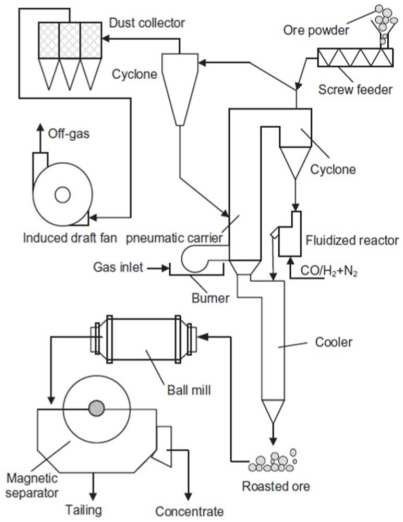

FIG 4 – Schematic of suspension magnetising roasting process (Yu *et al,* 2019).

Based on the pilot-scale tests, an industrial scale facility of suspension magnetising roasting with a processing capacity of 1.65 Mt of iron ores per year was built by JISCO (Yu *et al,* 2019). The facility went into production on 21 November 2020. This facility has operated reliably and met the key design specifications through a 1-year continuous campaign. An iron ore concentrate of >55 per cent Fe was produced from iron ore tailings containing 28–32 per cent Fe with a Fe recovery rate of >88 per cent.

Summary

Compared with the shaft furnace magnetising roasting process and the rotary kiln magnetising roasting process, the fluidised bed magnetising roasting processes, characterized by low energy consumption, high iron recovery, large processing capacity and longer maintenance cycles, represents the most promising approach for the beneficiation of refractory iron ores.

FUTURE DEVELOPMENT

Various magnetising roasting processes have achieved industrial application, but the products of these processes are all ferromagnetic magnetite. The direct production of metallic iron which can be readily used in steelmaking is a comparatively new alternative technology for utilising refractory iron ore. It can greatly reduce the energy consumption of the metallurgical process and reduce CO_2 emissions. However, these processes are still under laboratory and pilot-scale testing and have not yet reached a technical maturity level necessary for adoption by industry. Nevertheless, some of the direct reduction processes developed or being developed are believed to have the potentials for use in magnetising roasting and magnetic separation processes to produce metallic iron.

After systematically analysing the operating conditions, energy consumption, environmental impact and equipment investment, the following processes are considered to be adaptable to produce

metallic iron from refractory iron ore: coal-based rotary kiln, tunnel kiln, rotary hearth furnace, paired straight hearth furnace, flash ironmaking, etc. Among these processes, the rotary kiln, tunnel kiln and rotary hearth furnace have been industrialised for various alternative ironmaking processes, but adjustments are needed for their applications in refractory iron ore. However, the paired straight hearth furnace and flash ironmaking are still in the pilot-scale testing stage, such that more time is needed to achieve their industrial applications for refractory iron ore.

CONCLUSIONS

Magnetising roasting followed by magnetic separation is considered an effective method for the beneficiation of refractory iron ores. This technology has achieved wide industrial applications, such as shaft furnace roasting, rotary kiln roasting, and fluidised bed roasting. Among these processes, fluidised bed magnetising roasting is recognised as the most effective and promising technology due to its high reaction efficiency, low energy consumption and large processing capacity.

Production of metallic iron by magnetising roasting and magnetic separation provides a new alternative technical approach for utilising refractory iron ore. However, it is still under laboratory and pilot-scale testing and has not yet reached a technical maturity level necessary for adoption by industry.

ACKNOWLEDGEMENTS

The authors would like to thank CSIRO Mineral Resources for permission to publish the paper and for the financial support of this work. Special thanks to reviewers for their valuable comments and improvements to the paper.

REFERENCES

Chen, W, Yu, Y, Feng, Z, Lu, X, Zhao, Q and Liu, X, 2017. Six hundred thousand t/a refractory siderite flash magnetizing roasting complete sets technique and equipment. *Metal Mine* 3, 54–58.

Chun, T J, Long, H M and Li, J X, 2015a. Alumina-Iron Separation of High Alumina Iron Ore by Carbothermic Reduction and Magnetic Separation. *Separation Science and Technology* 50, 760–766.

Chun, T J, Zhu, D Q and Pan, J, 2015b. Simultaneously roasting and magnetic separation to treat low grade siderite and hematite ores. *Mineral Processing and Extractive Metallurgy Review* 36, 223–226.

Davis, E W, 1937. Magnetic Roasting of Iron Ore. Mines Experiment Station, University of Minnesota 13, 13–16.

Dhupe, A P and Gokarn, A N, 1990. Studies in the thermal decomposition of natural siderites in the presence of air. *International Journal of Mineral Processing* 28, 209–220.

Fan, X H, Deng, Q, Gan, M and Wang, H B, 2015. Effect of Biochar as Reductant on Magnetizing-roasting Behavior of Pyrite Cinder. *Journal of Iron and Steel Research, International* 22, 371–376.

Flavio, T D S, 1992. Thermodynamic aspects of the roasting processes in the pre-treatment of nickel ferrous garnierites. *Mineral Processing and Extractive Metallurgy Review* 9, 97–106.

Gao, E X, 2016. Mechanism of separating iron and titanium from beach titanomagnetite by using direct reduction – magnetic separation. University of Science and Technology Beijing.

Gao, P, Han, Y and Wu, H, 2010. Research on reduction-magnetic separation of Bayan Obo ore. *XXV International Mineral Processing Congress 2010*, pp. 1541–1547 (The Australasian Institute of Mining and Metallurgy: Melbourne).

Han, H L, Duan, D P, Yuan, P and Chen, S M, 2015. Recovery of metallic iron from high phosphorus oolitic hematite by carbothermic reduction and magnetic separation. *Ironmaking & Steelmaking* 42, 542–547.

He, W, 2012. The basic research on magnetizing roasting – magnetic separation of siderite. Central South University.

Jang, K, Nunna, V R M, Hapugoda, S, Nguyen, A V and Bruckard, W J, 2014. Chemical and mineral transformation of a low grade goethite ore by dehydroxylation, reduction roasting and magnetic separation. *Minerals Engineering* 60, 14–22.

Jena, M S, Tripathy, H K, Mohanty, J K, Mohanty, J N, Das, S K and Reddy, P S R, 2015. Roasting followed by magnetic separation: a process for beneficiation of titano-magnetite ore. *Separation Science and Technology* 50, 1221–1229.

Jiang, T, Liu, M D, Li, G H, Sun, N, Zeng, J H and Qiu, G Z, 2010. Novel process for treatment of high-aluminum limonite ore by reduction roasting with addition of sodium salts. *The Chinese Journal of Nonferrous Metals* 20, 565–571.

Jiu, S W, Xu, D L, Li, H, Song, H X and Zhang, L, 2008. An Investigation into Magnetization of Siderite Powder by Roasting in Suspension State. *Metal mine*, 33–35.

Khaki, J V, Shalchian, H, Rafsanjani-Abbasi, A and Alavifard, N, 2018. Recovery of iron from a high-sulfur and low-grade iron ore. *Thermochimica Acta* 662, 47–54.

Lei, C, Yan, B, Chen, T and Xiao, X M, 2017. Recovery of metals from the roasted lead-zinc tailings by magnetizing roasting followed by magnetic separation. *Journal of Cleaner Production* 158, 73–80.

Li, C, Sun, H, Bai, J and Li, L, 2010. Innovative methodology for comprehensive utilization of iron ore tailings part 1. The recovery of iron from iron ore tailings using magnetic separation after magnetizing roasting. *Journal of Hazardous Materials* 174, 71–77.

Li, G H, Zhang, S H, Rao, M J, Zhang, Y B and Jiang, T, 2013. Effects of sodium salts on reduction roasting and Fe–P separation of high-phosphorus oolitic hematite ore. *International Journal of Mineral Processing* 124, 26–34.

Li, K Q, Ni, W, Zhu, M, Zheng, M J and Li, Y, 2011. Iron Extraction from Oolitic Iron Ore by a Deep Reduction Process. *Journal of Iron and Steel Research, International* 18, 9–13.

Li, W B, Han, Y X, Liu, X, Shan, Y and Li, Y J, 2019. Effect of fluidized magnetizing roasting on iron recovery and transformation of weakly magnetic iron mineral phase in iron tailings. *Physicochemical Problems of Mineral Processing* 55, 906–916.

Li, Y J, Han, Y X, Zhu, Y M and Liu, J, 2012. Deep Reduction Tests of Antelope Iron Ore in Linjiang Area. *Journal of Northeastern University (Natural Science)* 33, 137–140.

Li, Y J, Wang, R, Han, Y X and Wei, X C, 2015. Phase transformation in suspension roasting of oolitic hematite ore. *Journal of Central South University* 22, 4560–4565.

Liu, X, Yu, Y, Hong, Z, Peng, Z, LI, J and Zhao, Q, 2017. Development and application of packaged technology for flash (fluidization) magnetizing roasting of refractory weakly magnetic iron ore. *Mining and Metallurgical Engineering* 37, 40–45.

Long, H, Chun, T, Di, Z, Wang, P, Meng, Q and Li, J, 2016. Preparation of Metallic Iron Powder from Pyrite Cinder by Carbothermic Reduction and Magnetic Separation. *Metals* 6, 88.

Luo, L Q, Zhang, J S, Gao, Y Y and Yu, Y F, 2014. Research on Dry Cooling Magnetic Roasting Technology for Siderite Ore. *Metal Mine*, 28–31.

Luo, Y H, Zhu, D Q, Pan, J and Zhou, X L, 2016a. Thermal decomposition behaviour and kinetics of Xinjiang siderite ore. *Mineral Processing and Extractive Metallurgy* 125, 17–25.

Luo, Y H, Zhu, D Q, Zhou, X L, Shi, B J and Zhang, F, 2016b. Coproduction of DRI Powder and Semi-coke from Siderite Ore and Low Rank Coal by Excessive Coal-based Direct Reduction in Rotary Kiln. *ISIJ International* 56, 78–87.

Meng, F D, 2012. Process and Mechanisms of Westen Hubei's Oolitic Hematite Ore Dressed by Reduction Roasting-Magnetic Separation. Wuhan University of Technology.

Meyer, K, 1963. The Lurgi Process of Magnetizing Roasting, a Possible Method of Processing Iron Ore. *Proceedings of the 6th International Mineral Processing Congress*, pp. 733–743.

Pang, Y L, 2006. The Research and Development of the Techniques for Siderite Powder Roasted and Magnetized in the State of Fluidization. Xi'an University of Architecture and Technology.

Peng, T, Gao, X, Li, Q, Xu, L, Luo, L and Xu, L, 2017. Phase transformation during roasting process and magnetic beneficiation of oolitic-iron ores. *Vacuum* 146, 63–73.

Rath, S S, Rao, D S, Tripathy, S K and Biswal, S K, 2018. Characterization vis-á-vis utilization of blast furnace flue dust in the roast reduction of banded iron ore. *Process Safety and Environmental Protection* 117, 232–244.

Rath, S S, Sahoo, H, Dhawan, N, Rao, D S, Das, B and Mishra, B K, 2014. Optimal recovery of iron values from a low grade iron ore using reduction roasting and magnetic separation. *Separation Science and Technology* 49, 1927–1936.

Ravisankar, V, Venugopal, R and Bhat, H, 2019. Investigation on beneficiation of goethite-rich iron ores using reduction roasting followed by magnetic separation. *Mineral Processing and Extractive Metallurgy* 128, 175–182.

Sun, B Q, 2012. Recent Advances in Beneficiation Technology of Complex Refractory Iron Ore. Sinosteel Maanshan General Institute of Mining Research.

Sun, Y S, Zhu, X R, Han, Y X and Li, Y J, 2019. Green magnetization roasting technology for refractory iron ore using siderite as a reductant. *Journal of Cleaner Production* 206, 40–50.

Suthers, S P, Nunna, V, Tripathi, A, Douglas, J and Hapugoda, S, 2014. Experimental study on the beneficiation of low-grade iron ore fines using hydrocyclone desliming, reduction roasting and magnetic separation. *Mineral Processing and Extractive Metallurgy* 123, 212–227.

Uwadiale, G G O O, 1992. Magnetizing reduction of iron ores. *Minerals Processing and Extractive Metallurgy Review* 11, 1–19.

Weissberger, S and Zimmels, Y, 1983. Studies on concentration and direct reduction of the Ramim iron ore. *International Journal of Mineral Processing* 11, 115–130.

Yin, W Z, Liu, L J, Liu, M B and Li, C, 2014. *Beneficiation Technology of Refractory Iron Ore.* Chemical Industry Press.

Youssef, M A and Morsi, M B, 1998. Reduction Roast and Magnetic Separation of Oxidized Iron Ores for the Production of Blast Furnace Feed. *Canadian Metallurgical Quarterly* 37, 419–428.

Yu, J W, Han, Y X, Li, Y J and Gao, P, 2019. Recent Advances in Magnetization Roasting of Refractory Iron Ores: A Technological Review in the Past Decade. *Mineral Processing and Extractive Metallurgy Review*.

Yu, J, Han, Y, Gao, P, Li, Y, Yuan, S and Li, W, 2018a. An innovative methodology for recycling iron from magnetic pre-concentrate of an iron ore tailing. *Physicochemical Problems of Mineral Processing* 54, 668–676.

Yu, J, Han, Y, Li, Y and Gao, P, 2017. Beneficiation of an iron ore fines by magnetization roasting and magnetic separation. *International Journal of Mineral Processing* 168, 102–108.

Yu, J, Han, Y, Li, Y and Gao, P, 2018b. Experimental study on utilization of crude concentrate from an Anshan-type hematite ore by suspension magnetization roasting-magnetic separation. *Journal of Central South University (Science and Technology)* 49, 771–778.

Yu, J, Han, Y, Li, Y and Gao, P, 2018c. Recovery and separation of iron from iron ore using innovative fluidized magnetization roasting and magnetic separation. *Journal of Mining and Metallurgy B: Metallurgy* 54, 21–27.

Yu, Y and Qi, C, 2011. Magnetizing roasting mechanism and effective ore dressing process for oolitic hematite ore. *Journal of Wuhan University of Technology – Materials Science Edition* 26, 176–181.

Zhang, K, Chen, X L, Guo, W C, Luo, H J, Gong, Z J, Li, B W and Wu, W F, 2017. Effects of biomass reducing agent on magnetic properties and phase transformation of Baotou low-grade limonite during magnetizing-roasting. *PLOS One* 12, 1–18.

Zhang, X L, Han, Y X, Sun, Y S and Li, Y J, 2019. Innovative utilization of refractory iron ore via suspension magnetization roasting: A pilot-scale study. *Powder Technology* 352, 16–24.

Zhang, Z, 2015. Process optimization on magnetic roasting of lump iron ore in shaft furnace. *China Metallurgy* 25, 11–14.

Zhao, Q, Xue, J L and Chen, W, 2019. Upgrading of iron concentrate by fluidized-bed magnetizing roasting of siderite to magnetite in CO–H2–N2 atmosphere. *Transactions of the Indian Institute of Metals* 72, 1381–1391.

Zhou, B, 2008. Roasting-Magnetic Separation and Direct Reduction of a Refractory Oolitic-Hematite Ore. Guangxi University.

Zhou, J, Zhu, Q, Wang, H and Ni, W, 2009. Magnetic roasting of an oolitic hematite and limonite ore in a fluidized bed reactor. *The Chinese Journal of Process Engineering* 9, 307–313.

Zhu, D Q, Li, J, Li, Q C, Pan, J, Xu, X F, Zhai, Y, Tang, Y Y and Cui, Y, 2007. Preparation of high quality magnetite concentrate from pyrite cinder by composite pellet reduction-roasting and magnetic-separation. *Chinese Journal of Nonferrous Metals* 17, 649–656.

Zhu, Q S and Li, H Z, 2014. Status quo and development prospect of magnetizing roasting via fluidized bed for low grade iron ore. *CIESC Journal* 65, 2437–2442.

Effects of sintering conditions on porosity, strength, and reducibility of hematite and magnetite tablets

I R Ignacio[1], G Brooks[2], M I Pownceby[3], M A Rhamdhani[4] and W J Rankin[5]

1. PhD candidate, Department of Mechanical and Product Design Engineering, Swinburne University of Technology, Hawthorn Vic 3122. Email: irosaignacio@swin.edu.au
2. Professor, Department of Mechanical and Product Design Engineering, Swinburne University of Technology, Hawthorn Vic 3122. Email: gbrooks@swin.edu.au
3. Senior Principal Research Scientist, CSIRO Mineral Resources, Clayton South Vic 3169. Email: mark.pownceby@csiro.au
4. Professor, Department of Mechanical and Product Design Engineering, Swinburne University of Technology, Hawthorn Vic 3122. Email: ARhamdhani@swin.edu.au
5. Adjunct Professor, Department of Mechanical and Product Design Engineering, Swinburne University of Technology, Hawthorn Vic 3122. Email: wjrankin@outlook.com

ABSTRACT

Iron ore sinter quality has a strong influence on the blast furnace productivity. Conventional wisdom says that the presence of the Silico-Ferrite-of-Calcium-and-Aluminium (SFCA) phases is crucial to maintaining sinter quality due to its reducibility. However, some new evidence suggests that porosity might be the main factor controlling reducibility, not mineralogy. This work aims to fundamentally understand the porosity of simple-sinter-systems, connecting it back to mineralogy, strength, and reducibility properties. Many factors can affect the final properties of a sinter. Therefore, the sintering conditions, such as temperature, atmosphere and holding time, were carefully selected. Thus, laboratory-scale experiments were conducted to simulate the sintering process by firing tablets of magnetite, hematite, lime and silica with varied compositions and under tightly controlled conditions. Posteriorly, the mineralogy of fired samples was observed using Scanning Electron Microscopy (SEM) and porosity was measured by the image analysis technique. Strength was determined using laboratory-scale tumble index (TI) equipment. Finally, the reducibility of samples was observed by the weight loss obtained after the reaction of the tablets under a reducing atmosphere of CO/N_2 (40 per cent and 60 per cent, respectively) at 950°C for 150 min in a scaled-down set-up. The results confirmed that highly reducible sinters can be produced without forming SCFA. However, it was also clear that reducibility is strongly linked to mineralogy. The best reducibility predictor was the mineralogy formed on the samples fired under lower maximum temperature (T_{max}) and lower holding times (t_{hold}). Furthermore, the porosity of the samples before reduction had a low influence on the reducibility of magnetite-containing samples compared to mineralogy.

INTRODUCTION

Iron ore sintering is the primary agglomeration method used by the ironmaking industry to convert iron ore fines (-6.3 mm) into a porous and strong material with improved metallurgical properties and suitable to feed the blast furnace. A continuous effort is made to increase the productivity of the blast furnace and, at the same time, reduce raw materials consumption, operation costs, and environmental impacts of the processes. One way to achieve that is to improve the quality of the sinter products.

For decades, sinter has been studied, and there is a consensus on what an ideal sinter should be to guarantee the desired performance. It is known that sinter mineralogy impacts enormously on the reducibility. Much attention has been given to the chemistry of those mineral phases; however, new evidence suggests that the textural side of mineralogy might play an important role in the performance of the sinter. It is still unclear how sinter texture is linked to permeability and porosity.

Many studies focused on the mineralogy, while others were dedicated to the sinter structure. It is known that the sinter must present high reducibility to facilitate the reduction reactions inside the blast furnace. However, iron ore sinter is formed by a complex combination of different mineral phases, each of them having its own level of reducibility and mechanical properties. Hematite, for instance, is the most reducible among the sinter phases, followed by the SFCA (Silico-ferrite of

Calcium and Aluminium) phases (being SFCA-I more reducible than SFCA), magnetite, olivines and, finally, fayalite (Pownceby and Clout, 2003; Biswas, 1981).

Over the years, researchers and practitioners have considered that the ideal sinter should be composed of unmelted hematite ore particles (+1 mm) (approximately 30 per cent) in a porous bonding matrix phase (approximately 70 per cent), comprised of the complex ferrite phase (SFCA), with only minor quantities of glass, magnetite, larnite or silicates (Clout, 1994; Pownceby and Clout, 2003). The consensus is that sintering should maximise the formation of the lower temperature platy SFCA-I and minimise the amount of prismatic SFCA (Clout, 1994). However, recent studies on pore structure and mineralogy of sinter have found surprising results, raising the question if sinter structure properties can overcome mineralogy when trying to obtain a good sinter.

Harvey *et al* (2019) conducted an experiment firing compact sinter analogues made from hematite ore (-1 mm in size) and fine (-5 μm) chemical reagents fluxes ($CaCO_3$, $MgCO_3$ and SiO_2), in a controlled gas atmosphere (N_2 and O_2, with $pO_2 = 5 \times 10^{-3}$), inside an infrared rapid heating furnace, to investigate the sintering conditions such as temperatures, holding time and cooling rate, on the reducibility of iron ore sinter. Reducibility (through Thermogravimetric Analysis) and porosity (through Mercury Intrusion and Nitrogen Pycnometry) tests were conducted on the fired samples. Results have shown that the degree of the reduction after 60 min (R_{60}) of samples fired at T_{max} = 1250°C and 1320°C have not changed much compared to the changes in the mineralogy. In other words, reducibility appears insensitive to the mineralogy. That is a shred of evidence that maybe structure influences more than mineralogy on sinter reducibility.

In a recent study, Purohit (2019) discovered a very reducible magnetite material while investigating new alternative processing routes for magnetite ores. In this study, lime-magnetite-pellets (LMPs) made from synthetic powders were fired in a horizontal tube resistance furnace under a reducing atmosphere of CO/CO_2, under various pO_2, at the temperatures of 850, 950 and 1050°C, for a wide range of heating times (5 to 720 min). Scaled-down reducibility tests showed that the fired LMPs presented reducibility similar to the industrial sinters. The above studies suggested that sinter with unusual mineralogy, high in magnetite, can still be attractive due to a favourable textural arrangement.

This work is part of a larger project investigating the relationship between the sinter mineralogy and porosity on important sinter properties, notably strength and reducibility, by developing a fundamental understanding of how porosity is created in simple-sinter-systems. The aims of this work are to:

- Create simple-sinter-system samples by combining magnetite fines, lime, and silica and fire them at different sintering conditions of temperatures and holding times. Hematite-containing samples were also created to serve as a comparison.
- Investigate the effects of the chemistry, maximum temperature, and holding time on porosity, reducibility, and strength of samples.
- Extend the analysis of porosity reported in Ignacio *et al* (2022) to include measurements of the reducibility and strength of the sinter samples.

EXPERIMENTAL

Sample preparation

Compressed tablets were made using high purity synthetic iron oxides, magnetite (<5 μm) and hematite (<5 μm), adding two types of fluxes, lime (<0.16 μm), and silica (<0.014 μm). This study opted for synthetic materials since their composition is closely controlled and easily reproduced.

Simple-sinter-systems were obtained by combining the powdered oxides in three different ways: pure iron oxides (Fe_2O_3 or Fe_3O_4), iron oxides (Fe_2O_3 or Fe_3O_4) plus lime (CaO), and finally, iron oxides (Fe_2O_3 or Fe_3O_4), plus lime (CaO) and silica (SiO_2). The basicity (ratio between CaO and SiO_2) was kept constant at approximately 2.0, which is the typical basicity used in iron ore sinters. Table 1 shows the compositions of the sinter tablets.

TABLE 1

Composition of sinter tablets (wt%).

Tablet	Fe_2O_3	Fe_3O_4	CaO	SiO_2	Basicity*
H	100	-	-	-	-
M	-	100	-	-	-
HL	95.0	-	5	-	-
ML	-	95.0	5	-	-
HLS	85	-	10	5	2.0
MLS	-	85.0	10	5	2.0

H = hematite, M = magnetite, HL = hematite + lime, ML = magnetite + lime, HLS = hematite + lime + silica and MLS = magnetite + lime + silica, *Basicity = CaO/SiO_2.

The chemicals were weighed using an electronic precision scale and mixed manually in a mortar and pestle under acetone for homogenisation. The amount of acetone used was enough to form a slurry to ensure the non-segregation of material. This slurry was then dried in an oven for 1 hour at 110°C and the mixing process was repeated. The dry powder blends were then pressed in a hydraulic press machine into 2.5 g (±0.05 g) tablets, using a stainless-steel die with 13 mm diameter. A constant compaction pressure of 4 t was applied for 2 minutes for all the samples.

Apparatus and sintering conditions

A horizontal tube resistance furnace (Nabertherm RHTH 120–300/18) with a molybdenum disilicide ($MoSi_2$) heating element was used to simulate the industrial sintering process. The furnace could operate up to 1800°C, with a maximum heating rate of 200°C/h. A temperature controller panel allowed programming the heating profiles of each experiment. A sacrificial alumina tube was placed inside the furnace to protect the main tube during operation and the ending flanges were circulated by water. Careful calibration of the furnace was carried out to guarantee the exact position and temperature difference of the hot zone.

Two samples were fired simultaneously to ensure that they were exposed to the same conditions inside the hot zone. An alumina rod with a boat attached to the end was used as a sample holder. A piece of nickel foil (99.96 per cent Ni) was placed in the base of the boat, which prevented the sample from reacting with the crucible during heating, thereby increasing its life and preventing alumina contamination of the sintered pellet. The foil was replaced every ten runs. Figure 1 shows the schematic of the horizontal furnace set-up.

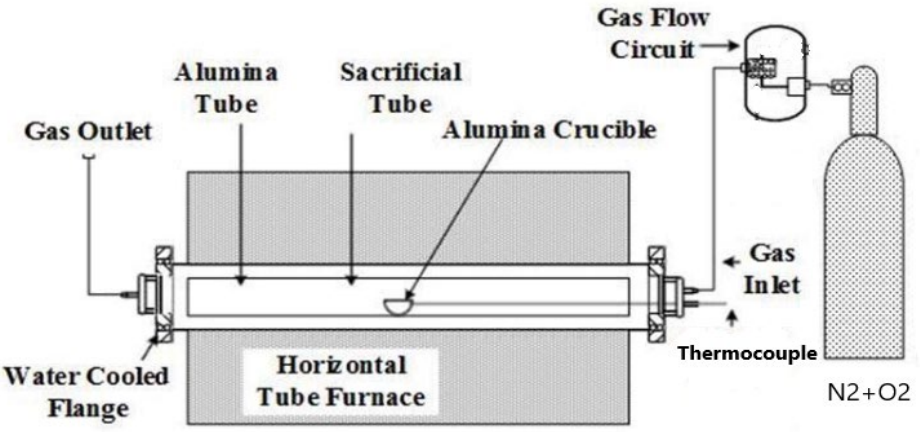

FIG 1 – Schematic representation of horizontal furnace set-up. Adapted from Purohit (2019).

The compacted tablets were fired under a controlled oxygen partial pressure (pO_2), held for a specific time (t_{hold}) under high temperature (T_{max}), and rapidly cooled, simulating the conditions of the flame front in actual sintering. Table 2 shows the firing conditions adopted in this study and how the

samples were identified. The temperatures, holding times and cooling techniques were based on what is observed in industrial sintering and in previous laboratory studies, such as in Hsieh and Whiteman (1989).

TABLE 2

Samples identification according to experimental conditions. XXX can be replaced by one of the six tablets identification H, HL, HLS, M, ML, and MLS, eg H001, HL001, HLS001, etc.

Sample No.	T_{max} (°C)	t_{hold} (min)
XXX 001	1350	4
XXX 002	1300	4
XXX 003	1250	4
XXX 004	1300	2
XXX 005	1300	6

A pre-mixed bottled gas containing 99.5 per cent N_2 and 0.5 per cent O_2 was used to control the furnace atmosphere. The mixed gas was injected into the furnace at a $pO_2 = 5\times10^{-3}$ atm, typical for iron ore sintering experiments (Pownceby and Clout, 2003; Harvey, 2020; Clout, 1994), and at a flow rate of 100 L/h, controlled by a gas flowmeter. This value for oxygen partial pressure is generally chosen for laboratory studies because it generates mineral assemblages and microstructures close to those observed in industrial iron ore sinters (Hsieh and Whiteman, 1989).

A total of 30 experiments were performed, with each sample composition being run in quadruplicate to provide enough material for subsequent analysis. Two pellets were used for strength measurements by the Tumble Index determination. As this is a destructive test, the broken pieces were used for posterior mineralogy characterisation (SEM, X-ray diffraction, and optical microscopy). One pellet was used for post-heating porosity measurements by Mercury Intrusion Pycnometry (MIP) and N_2 porosimetry, and the remaining pellet was used for the reducibility test. A complete study presenting all those results will be available in future publications.

ANALYSIS

Image analysis

The mineralogy of the samples was observed using Scanning Electron Microscopy (SEM). The sinter samples were prepared by roughly crushing the tablets, mounting a chip in resin before being plane ground and polished using an automated polisher. Finally, samples were coated with a thin layer (10 nm) of carbon to prevent electrostatic charging of the surface and promote a homogeneous emission of secondary electrons. Back Scattered Electron (BSE) photomicrographs were taken at different magnification. The SEM analyses were carried out at a high vacuum, a working distance of 10 mm, a high voltage of 15 kV, an emission current of 158 µA, a pressure of 1.1×10^{-6} Torr, and a gun pressure of 9.1×10^{-10} Torr.

The image analysis software OLYMPUS Stream Motion was used to analyse the images and to calculate the porosity of the samples. This technique calculates the area fraction (%) of the components using the threshold method to differentiate pores from the matrix by grey scale. The pores were considered as the dark spots on the images. Three images of each sample were taken from different areas on the sample surface and the average area fraction was calculated. The same technique was used in a previous publication by Ignacio *et al* (2022).

Strength

Strength was determined using laboratory-scale tumble index (TI) equipment. The same technique was used in previous studies (Ware, *et al,* 2013; Ware and Manuel, 2016; Clout and Manuel, 2003; Pownceby, *et al,* 2016) and consists of tumbling fired sinter tablets in pairs, for 8 min, inside a modified Bond Abrasion Tester. After that, the material is sieved, and the relative compact TI is given

as a percentage of the material retained at above 2 mm. A TI of 80 per cent is considered equivalent to a TI of 65 per cent in a sinter pot-grate test (Ware *et al,* 2013).

Reducibility

Reducibility was measured using a scaled-down technique due to the reduced size of the samples. A thermogravimetric analysis (TGA) set-up was used in this study, consisting of a vertical tube furnace (Eurotherm) with a control system, and a precision balance (FX-300i with 1 mg accuracy) placed at the top of the furnace measuring the weight loss of the sample during the reaction. The same set-up was used in previous work by Purohit (2019) and consists of placing a fired sample inside an alumina crucible held by a platinum wire basket and placed in the hot zone of the furnace. The furnace is sealed, and argon gas was purged to maintain a neutral atmosphere before and after each run. After a few minutes, the reducing atmosphere was created by purging a mixture of CO/N_2 (40 per cent and 60 per cent, respectively). The temperature for all tests was kept constant at 950°C, following the ISO 7215:2015 standard. The weight loss was recorded continuously every 0.125 sec using WinCT software for 150 min.

RESULTS AND DISCUSSION

Microstructural evolution and pore formation

Figure 2 shows the Back Scattered Electron (BSE) photomicrographs of selected magnetite-containing samples (M004, ML004 and MLS004), which were fired under a constant temperature of 1300°C for 6 min. It is possible to see the microstructural evolution and pore formation when lime and silica were added to the chemistry of those samples. All samples presented similar behaviour, pure iron oxide (magnetite or hematite) had low porosity, lime addition favoured the formation of pores, and lime+silica allowed the formation of more complex phases, such as calcium ferrites and calcium silicates. A more detailed discussion on the porosity of those samples is shown in the work of Ignacio *et al* (2022).

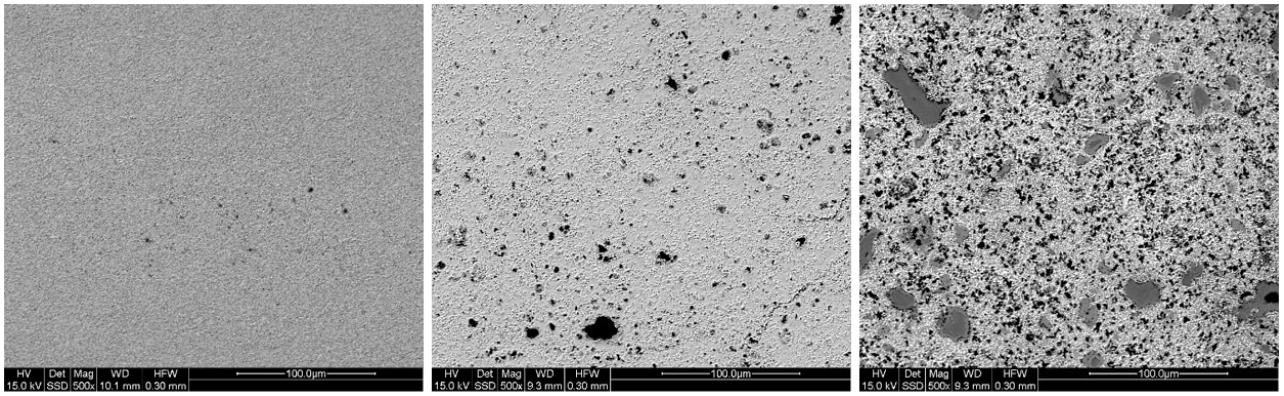

FIG 2 – BSE images showing the microstructural evolution and pore formation of fired magnetite-containing sinter samples under a constant temperature of 1300°C for 6 min.

Reducibility versus strength

Figure 3 shows the relationship between the weight loss (%) of the samples after reduction with the TI of samples pre-reduction. The weight loss is a strong indication that a sample presents good reducibility. As expected, hematite-containing samples presented higher reducibility than magnetite-containing samples for almost all the sintering conditions. Magnetite-containing samples fired at the highest temperature 1350°C for 4 min presented the lowest weight loss and, surprisingly, the same set of samples, when fired at lower temperature and time (1300°C for 2 min), showed the highest weight loss, indicating the highest reducibility (ML004 sample). The overall trend was an increase in reducibility with the decrease in T_{max} and t_{hold}, which confirms what was observed by Harvey *et al* (2019), where over-sintering led to poor reducibility of the sinter analogues.

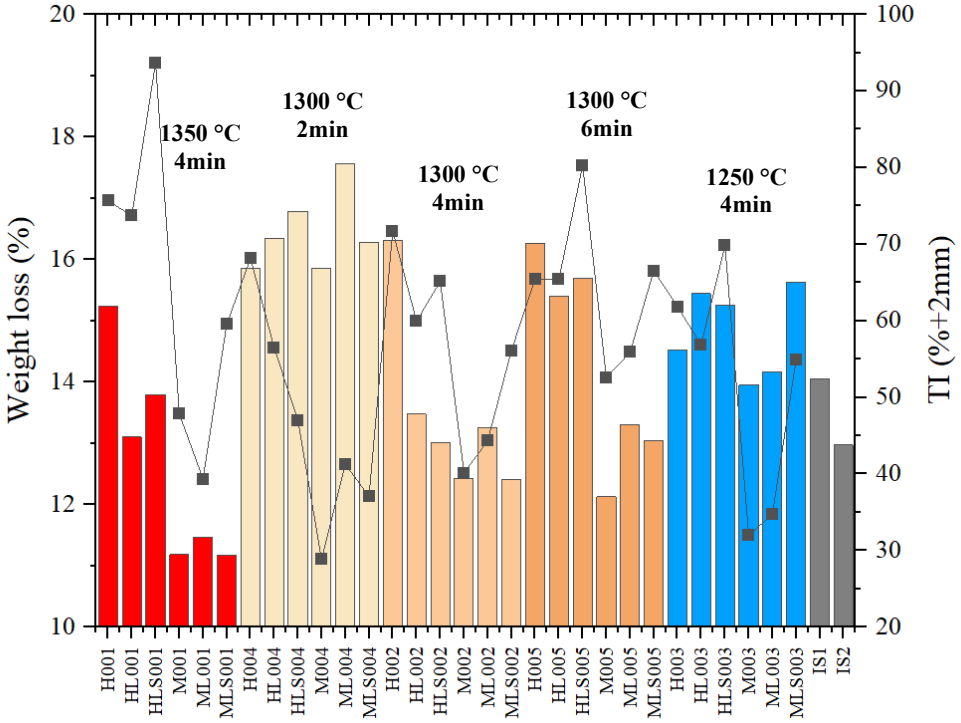

FIG 3 – Weight loss (%) and Tumble Index (%+2 mm) of fired sinter samples. The bars represent the weight loss of the samples, while the square dots represent the TI of the samples.

The TI shows a strong correlation with the chemistry and sintering conditions. Overall, magnetite-containing samples presented lower TI compared to the hematite-containing samples. The addition of silica, in general, increased the strength of the samples, reaching a maximum value of above 90 per cent TI for the HLS001 samples. The accepted strength value of 80 per cent was not achieved by the sinter analogues in this study, except for the samples HLS001 and HLS005 (with 93.69 per cent and 80.26 per cent TI, respectively).

The graph also shows the weight loss for two industrial sinters (named IS1 and IS2) for comparison. These samples were selected from two different industrial batches and presented similar basicity to the laboratory-made samples. A piece of sample weighing similarly to the laboratory-made samples was taken and reduced under the same conditions. The graph shows that many of the samples in this study presented higher reducibility when compared to the industrial sinters, which indicates that it is still possible to obtain reducible sinter, even if it does not contain SFCA.

Reducibility versus porosity

Figure 4 presents the weight loss (%) versus porosity (%) of all magnetite-containing samples preceding reduction reactions and the effects of T_{max} (Figure 4a) and t_{hold} (Figure 4b). Overall, the porosity of the samples before reduction had a lower influence on the reducibility of magnetite-containing samples. This suggests that the mineralogy obtained during the different sintering conditions had more impact on the reducibility of those samples. In this work, porosity was measured by image analysis of micrographs, considering only the 2D aspects of pores (these results were fully discussed at previous work Ignacio *et al* (2022)). Microporosity can affect reducibility due to the high pore surface area. However, to characterise microporosity, other porosity measurement techniques, such as Mercury Intrusion Porosimetry, will be carried out in future work.

As observed before, the addition of lime and lime+silica has impacted the porosity of magnetite samples. However, the same trend was not observed on the samples fired at 1300°C for 6 min, which had the porosity decline when lime and silica were added to the samples.

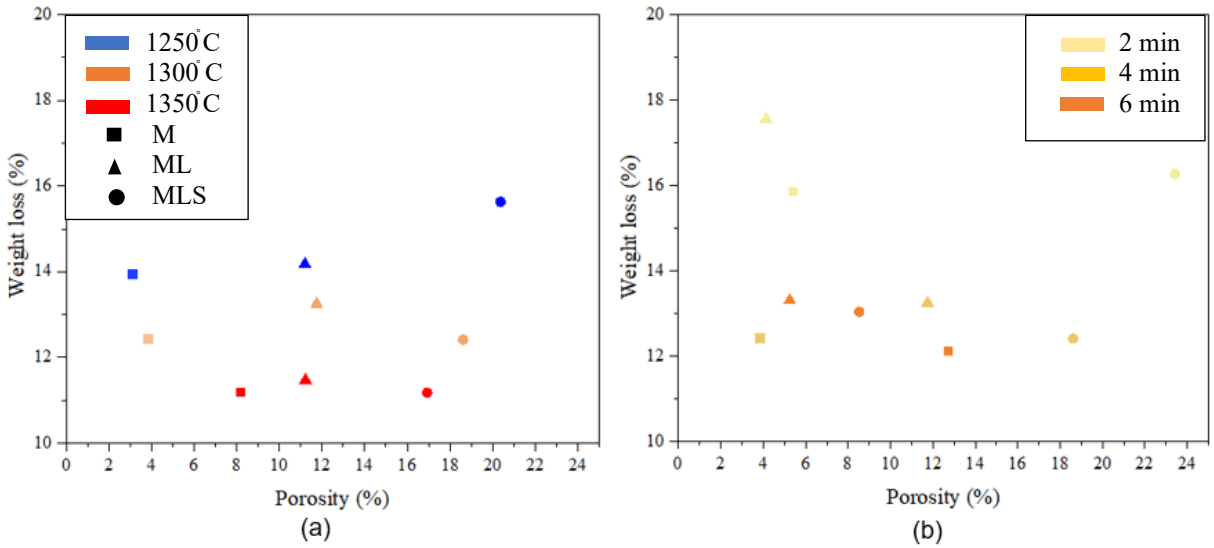

FIG 4 – Weight loss (%) versus porosity (%), pre-reduction reactions, for the magnetite-containing samples at (a) different T_{max} and (b) different t_{hold}.

CONCLUSIONS

Simple-sinter-systems were created by mixing magnetite and hematite with lime and silica and fired under different sintering conditions. The effects of the sintering conditions on porosity, strength and reducibility of those samples were investigated in this work. For that, laboratory-scale experimentation was used to simulate the sintering process and the reduction reactions happening in the blast furnace posteriorly.

In general, highly reducible sinters could be formed without forming SFCA. For example, magnetite lime sinters compared favourably with hematite lime sinters. Clearly, mineralogy and reducibility are closely linked but a lower maximum temperature (T_{max}) and lower holding times (t_{hold}) were also found to be favourable for increasing reducibility. Also, the porosity of the samples pre-reduction had a low influence on the reducibility of magnetite-containing samples compared to mineralogy. Mineralogy also affected the strength of those samples when lime and silica were added, forming complex phases. Further investigation needs to be done on the pore characteristics of those samples, particularly microporosity, as this plays an important role in reducibility and mechanical behaviour of sinter.

ACKNOWLEDGEMENTS

The authors acknowledge the Swinburne University of Technology and The Commonwealth Scientific and Industrial Research Organisation (CSIRO) for providing financial support for this research through the Australian Government Research Training Program (RTP) Scholarship and a CSIRO Ph.D. Top-up Scholarship.

REFERENCES

Biswas, A, 1981. Principles of Blast Furnace Ironmaking, Theory and Practice, pp 188–261.

Clout, J, M, F and Manuel, J, 2003. Fundamental investigations of differences in bonding mechanisms in iron ore sinter formed from magnetite concentrates and hematite ores, *Powder Technology*, 130:393–399.

Clout, J, M, F, 1994. Formation of key iron ore sinter phases from Hamersley fines: implications for ultra-fines chemistry and sinter formation, *CSIRO*, pp. 107.

Harvey, T, 2020. Influence of mineralogy and pore structure on the reducibility and strength of iron ore sinter, PhD Thesis, The University of Newcastle, Newcastle.

Harvey, T, O'Dea, D, Evans, G, M and Honeyands, T, 2019. Influence of sintering conditions on the reducibility of iron ore sinter analogues, in *Iron Ore Conference 2019*, pp 862–871.

Hsieh, L and Whiteman, J, A, 1989. Effect of oxygen potential on mineral formation in lime-fluxed iron ore sinter, *ISIJ International*, 29(8):625–634.

Ignacio, R, I, Brooks, G, Pownceby, M, I, Rhamdhani, M, A and Rankin, W, J, 2022. Porosity in iron ore sintering, in *Proceedings of the Iron and Steel Technology Conference 2022*, pp 1821–1830 (Association for Iron and Steel Technology: Pittsburgh).

ISO 7215:2015. Iron ores for blast furnace feedstocks – Determination of the reducibility by the final degree of reduction index (International Organization for Standardization).

Pownceby, M, I and Clout, J, M, F, 2003. Importance of fine ore chemical composition and high temperature phase relations: applications to iron ore sintering and pelletising, *Mineral Processing and Extractive Metallurgy*, 112(1):44–51.

Pownceby, M, I, Webster, N, A, S, Manuel, J, R, Ware, N, 2016. The influence of ore composition on sinter phase mineralogy and strength. *Transactions of the Institutions of Mining and Metallurgy, Section C: Mineral Processing and Extractive Metallurgy*, 125 (3):140–148.

Purohit, S, 2019. Alternative processing routes for magnetite ores, PhD Thesis, Swinburne University of Technology, Victoria.

Ware, N and Manuel, J, 2016. Fundamental nucleus assimilation behaviour of haematite and goethite containing ores in iron ore sintering, *Transactions of the Institutions of Mining and Metallurgy, Section C: Mineral Processing and Extractive Metallurgy,*125(3):149–155.

Ware, N, Manuel, J, R, Raynlyn, T and Lu, L, 2013. Melting behaviour of hematite and goethite fine ores and its potential impact on sinter quality, in *Iron Ore Conference 2013*, pp 485–486.

Quantitative 3D micrometallurgy for challenging ores

M A Knackstedt[1], L Knuefing[2], Y Zhang[3], N Francois[4] and R W Henley[5]

1. Director, ARC Training Centre for M3D Innovation, Australian National University, Canberra ACT 2600. Email: mark.knackstedt@anu.edu.au
2. Image Analyst and Trainer, ARC Training Centre for M3D Innovation, Australian National University, Canberra ACT 2600. Email: lydia.knuefing@anu.edu.au
3. Postdoctoral Fellow, ARC Training Centre for M3D Innovation, Australian National University, Canberra ACT 2600. Email: yulai.zhang@anu.edu.au
4. Fellow, ARC Training Centre for M3D Innovation, Australian National University, Canberra ACT 2600. Email: yulai.zhang@anu.edu.au
5. Honorary Professor, ARC Training Centre for M3D Innovation, Australian National University, Canberra ACT 2600. Email: richard.henley@anu.edu.au

ABSTRACT

The transition to net zero carbon poses challenges for the mining sector because of its demand for critical metals. Among these are copper, nickel, and cobalt for electric vehicles and batteries; as well as iron and aluminium for electricity transmission. In terms of metal requirement, copper is of major importance since, in addition to this new demand, its use continues to increase naturally by about 3 per cent per annum through modernising of the developing world. As with many industries, copper mining is facing increasing capital and operating costs. The reducing average metal grade and changing mineral processing requirements of newly-discovered ores add to these cost burdens; as does industry's response to environmental, social, and corporate governance (ESG) requirements. Comminution by crushing and grinding, and mineral separation are major cost factors in ore processing; but a detailed understanding of the mineralogy and microfabric of ores is not commonly applied in designing process flow sheets, even though feed characteristics are crucial to optimum flow sheet design and operation. Mitigation of mineralogy-associated costs requires accurate data on ore-mineral grain-size, shape, surface area as well as distribution and specific mineral associations.

X-ray micro-computed tomography (μCT) was developed in the petroleum sector to address similar scaling issues to those faced by the mining industry through micro-characterisation of reservoir properties. In our laboratory we have expanded from this sector into 3D micrometallurgical applications, through core-scanning and segmentation of X-ray tomography data. Data are obtained from drill core up to 15 cm in diameter, at a grain resolution of only a few microns. Results from some presently-operating major porphyry copper deposits are presented.

INTRODUCTION

Challenging ores, by definition, pose new problems for mineral liberation and concentration that may make or break the exploitation of a recognised mineral resource. Otherwise known as refractory ores, resolution of the challenges they provide has a history of driving technological advances in the mining industry (Wills and Finch, 2015). The challenges arise principally from particle and grain scales and the intricate relationships between ore and gangue minerals as well, of course, as grade in the mill feed. Until recently metallurgical approaches have relied substantially on physical methods for determination of these parameters alongside a range of microanalytical methods including scanning electron microscopy (SEM).

X-ray computed micro-tomography (X-ray μCT) is based on the simple principle of measuring the relative attenuation of an X-ray beam by different materials so that the internal distribution of phases (minerals, porosity, microporosity, fractures) may be precisely mapped bypassing the sample between an X-ray source and a detector in much the same way as for CT-scanning in hospitals. The potential of X-ray μCT to address the challenges posed by ore materials was recognised over thirty years ago (Miller *et al,* 1990). Continuing improvement in data acquisition and processing have rapidly advanced this scanning technology so that high resolution imaging techniques are now available to quantitatively tackle metallurgical problems (Godel, 2013; Wang and Miller, 2020). However, until recently the uptake of the technology in the mining sector has been quite slow, in part

because of rapid development of automated scanning electron methods of 2D mineral mapping in ore sections. The latter however are constrained by the steric effects that are inherent in two-dimensional surface measurements as well as on unconscious bias in selection of samples for sectioning. However, the challenges of new ore types and lower grades, together with requirements to achieve higher energy and cost efficiencies, demand that new approaches be trialled and integrated into geometallurgical analysis. In short there is a need for a quantum leap in the rapid acquisition, over a range of scales, of 3D statistical data for particles and grains in potential ore materials, including their sizes, shapes and surface areas in order to tune existing large scale processing methodologies and assess new opportunities.

In this paper we describe mining industry-focused applications of X-ray μCT under continued development at the National Laboratory for X-ray Micro Computed Tomography at the Australian National University. Over the last two decades a series of advanced techniques have been specifically developed for data-intensive applications in petroleum reservoir engineering (Arns *et al,* 2004; Dunsmuir *et al,* 1991) and carbon sequestration management (Andersson *et al,* 2013; Herring *et al,* 2014). These techniques included routines for exact integration of 2D into 3D X-ray CT data sets (Latham *et al,* 2008), time resolved studies of displacement (Oeren *et al,* 2019), reactive transport (Liu and Mostaghimi, 2018) and multiphase fluid movement in geological core material and upscaling of data from sample to resource scales. The laboratory also has developed X-ray μCT scanners capable of high-resolution imaging of, for example, PQ diamond drill core (up to 85 mm diameter) as well as crushed ore material at resolutions down to 1–2 microns. It has also commissioned a scanner for larger drill core up to 1 metre long and 200 mm in diameter as well as specialty scanners for tracking fluid flow-through rock material as may be required for development of *in situ* mineral recovery.

The combination of technologies and workflows that were developed under the heading of Digital Rock Technology (DRT) for the energy sector now provide a foundation for a highly integrated, multi-platform approach to geometallurgical problems and especially to the analysis of complex ore assemblages. In this paper we summarise two examples of the extension of DRT applied to porphyry copper rock material. The first demonstrates the ability of X-ray μCT to quantitatively resolve mineral phases such as bornite, pyrite and gold, and define key geometallurgical parameters such as grain size, shape and surface areas. Being a non-destructive methodology, this then releases the 3D image for targeted application of other determinative methods including compression and crushing tests for rock strength and mineral liberation as will be demonstrated in the second example.

X-ray μCT also allows imaging and quantification of three-dimensional void structures in geomaterials, opening up new avenues to improve our understanding and characterisation of the way fluids reside in and move through the subsurface in, for example, in situ mineral recovery. Pores and fractures larger than a few microns can be imaged directly, and void space at all scales can be measured by scanning samples in varying conditions of saturation. Such time series analyses can reveal the varying ways in which porosity is hosted by different rock components, and enable estimation of direction and degree of flow anisotropy and leaching potential of different samples.

DIGITAL ROCK TECHNOLOGY

X-ray μCT provides 3D quantitative digital imaging of the components of rock materials (spatial distributions of each mineral, fabric etc) in much the same way as medical CT scanning provides interactive 3D imaging of patients. It offers a natural and powerful extension to traditional petrographic analysis, as it allows observations and measurements to be extended into three dimensions. At its simplest, the data can be visualised to show the relative spatial distributions of different minerals, fabrics, and textures, all of which can be quantified.

We use an integrated multi-scale methodology incorporating 3D μCT imaging (see Figure 1) – all samples were imaged in 3D at the National Laboratory for X-ray Micro Computed Tomography (https://ctlab.anu.edu.au/) based at the Australian National University (ANU) using two different custom-built HeliScan μCT systems. Typically three tomographic images are obtained – first for a larger sample volume and then secondly a subset at higher resolution in a dry state and thirdly after saturation with X-ray contrast materials. Contrast agents are specifically designed to enhance imaging of the connected porosity/fractures, clay and other microporous phases within the rock.

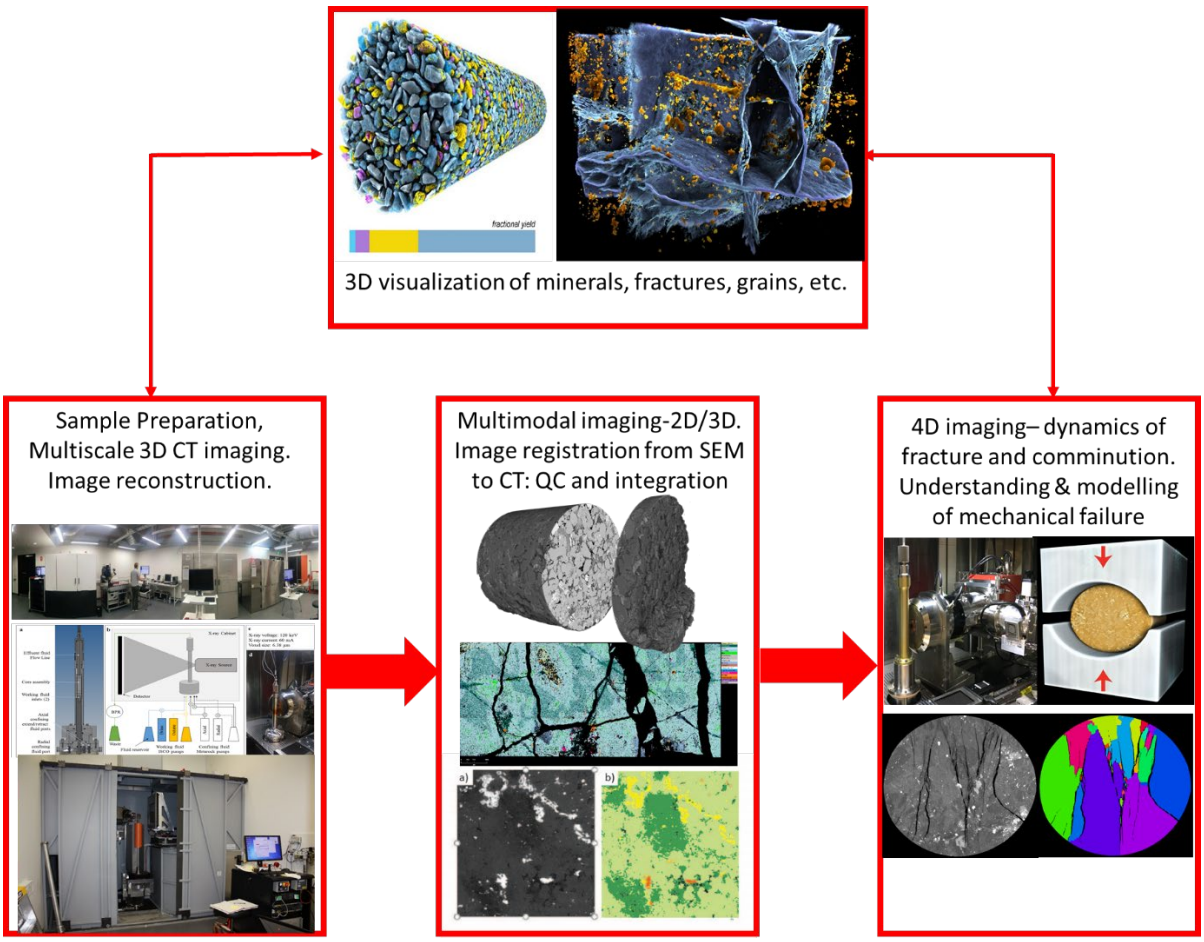

FIG 1 – Summary of imaging and analysis workflow undertaken at ANU Laboratories on core material.

Whereas traditional practice in the interpretation of X-ray μCT scan data has been to assign machine dependent attenuation ranges to specific minerals, we have developed precise methods for calibration by registering high resolution (5 micron) 2D SEM images from polished sections taken from the sample within the 3D field-of-view that was imaged (Sok *et al*, 2010). Segmentation into mineral populations is also archived by registering SEM-EDS (eg QEMSCAN™ or equivalent mineral maps) (Latham *et al*, 2008). X-ray μCT data for scanned samples may be used directly or as rendered data sets to provide interactive 3D visualisations using DRISHTI v.2.6.3 software (Limaye, 2012a).

The standard workflow undertaken on each sample is summarised in Figure 1. For ore materials we term this approach to analysis of ore materials as '*3D Micrometallurgy (3DM)'*, recognising that the technology provides unique quantitative data for the resolution of geometallurgical problems. We stress that X-ray μCT is not a 'plug-n-play' technology, but one that provides the foundation from which custom applications are spring-boarded for specific problems. Its use reduces the time and material costs associated with traditional mechanical and microanalysis based methods for estimating ore particle parameters and, as a digital record, enables integration and upscaling as required for large scale mining operations throughout the history of a mining operation.

X-ray μCT applications to porphyry Cu-Au deposits

Given that *porphyry copper* deposits supply more than 66 per cent of the current global production of copper (Singer, 2017), it is likely that they will remain the principal source of new copper into the future. These bulk tonnage deposits are bodies of highly fractured and altered rocks containing low-grades of Cu (<0.5 wt per cent Cu) along with Au, Ag, Mo and other recoverable metals. Future production will come from deposits greater than 1 Bt in scale that require major capitalisation for cave to super-cave underground production. In order to optimise production and mitigate risk, these

investments require orders of magnitude more definitive mineralogical and physical data than is undertaken in current practice.

As well as increasing the rate of discovery of new deposits, this places demands on extending the mineable resources in existing deposits. In turn this pushes the industry into the territories of lower grade reserves, more complex copper sulfide ore mineral assemblages and a requirement for deep high-cost mining operations. All of these introduce higher levels of risk, the mitigation of which comes through greater access to high resolution data at all scales in order to strengthen the modelling that underpins such highly capitalised developments.

Ore and gangue mineral distributions

The first example demonstrates the range of quantitative geometallurgical data obtained by non-destructive X-ray μCT scanning at a range of scales. Normally, in the industry, these data would be examined through traditional assay and 2D mineragraphic methods which, through steric effects, cannot provide fully quantitative data.

The scanned sample (Figure 2a) is from a porphyry copper in an early stage of assessment. It is a highly fractured and pervasively altered volcanic rock that contains disseminated and veinlet pyrite and Cu Fe sulfides. Its split core assay contains 0.13 wt per cent Cu and 1.6 g/t Au.

The X-ray μCT analysis commences with a reconnaissance scan of the whole sample. The scan resolution is 6.4 microns and Figure 2b shows one of the several thousand images each equivalent to a polished section. The distribution of sulfides is clear as well as their distinction from lower X-ray attenuation silicate gangue minerals.

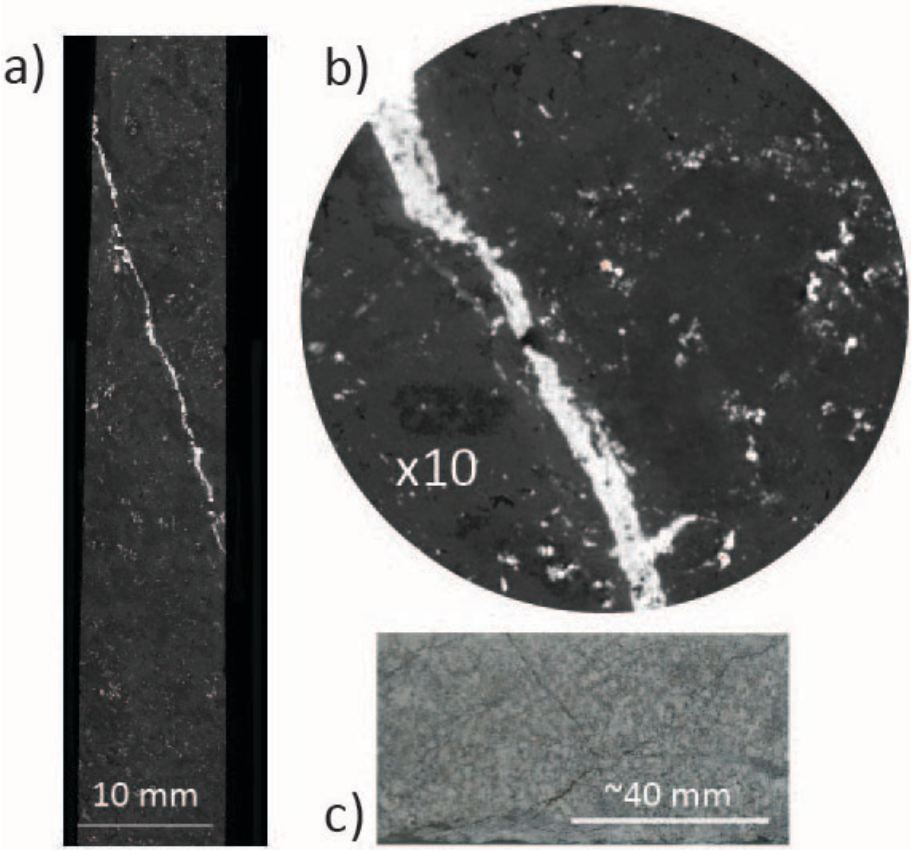

FIG 2 – Sample 1. (a) central vertical slice through the X-ray μCT scan at a voxel resolution of 6.4 microns. (b) enlargement of part of (a) showing the detail of sulfide veining and dissemination through the silicate rock matrix. (c) part of the original NQ half-core sample.

For this example, we scanned a 6 mm subcore of the sample, at a voxel resolution of 2.98 microns (μm) – ie each cube has a volume of 2.6×10^{-8} mm^3, in order to commence segmentation of phases and quantification of grain and particle distributions. Figure 3 provides a DRISHTI visualisation of these data. Such visualisation (Figure 3) clearly demonstrates how the intergranular space is infilled

by clay. It also shows how interrogation of the tomogram is achieved through visualisation techniques enabling side-by-side comparison of selected parts of the tomogram showing different mineral selections. Metallurgically this is important because it shows the irregular distribution of gold grains within the sample along with a much greater abundance of bornite than can be discerned from the 2D surface of a). This is an important stereological effect which further demonstrates the value of 3D imaging.

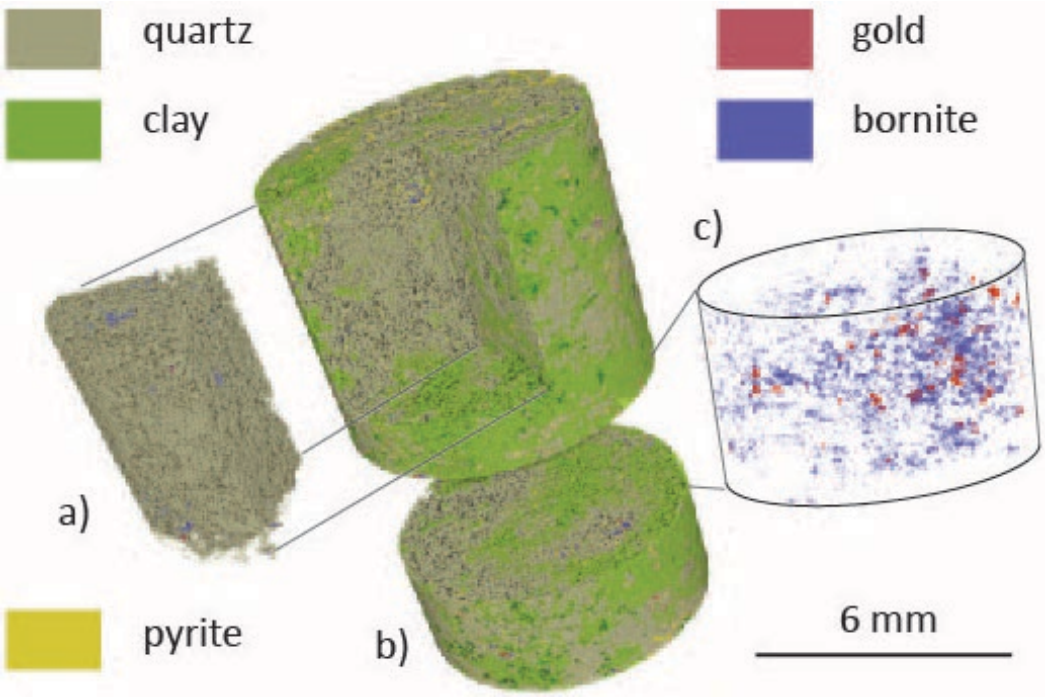

FIG 3 – This composite shows the digitised subcore of sample 1 expressed through DRISHTI visualisation software. These images are captured from on-screen live session manipulation of the 3D data to show the different mineral selections and viewpoints.

The real power of X-ray μCT scanned data lies, however, in its interrogation to provide quantitative data for mineral parameters such as grain size, surface area, mineralogy and mineral associations. The 3D scan contains more than 31×10^9 (31 billion) voxel cubes each of which may be *segmented* through its X-ray absorbance into mineral composition and effective density by registering high resolution backscattered SEM images into the tomogram and correlating with equivalent QEMSCAN™ mineral mapping. Figure 4 provides an example of the correlated mineral segmentation that is achieved. Here it is appropriate to note a frequently encountered issue with the presentation of X-ray μCT data in reports and publications is that it is commonly presented in a 2D format which is perceptibly indistinguishable from standard 2D mineragraphic images. To resolve this, scan data are analysed quantitatively as described below and the data can be provided for analysis through 3D visualisation software such as the DRISHTI package (Limaye, 2012b).

Following segmentation a variety of parametric data may be resolved. Table 1 shows the volume percent of each segmented phase. These data may be converted to weight percent values where we note that the weight percent Cu (0.134 per cent) matches the assay value for the analysed half core sample itself. This is a useful result that suggests the uniformity of mineralisation at different scales. Table 1 also shows the presence of 0.003 weight percent of dense phases based on a density of 14 g/cc. Based on assay values, these include gold or electrum, but may also contain some zircon. Dual energy scanning potentially separates the two, but for geometallurgical purposes in porphyry copper deposits their combined value is appropriate for liberation plant design.

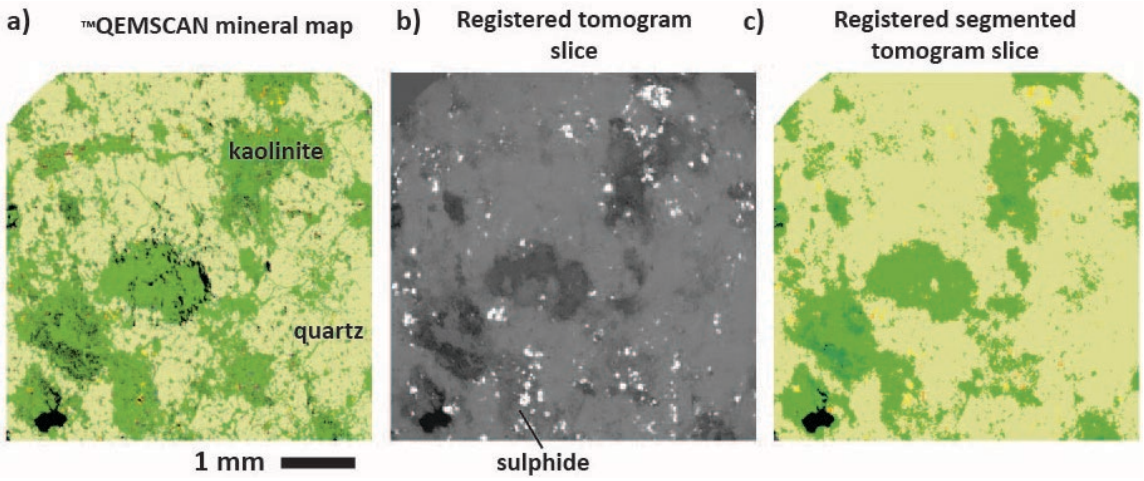

FIG 4 – Zoom segment of the tomogram of the sub-plug of sample 1, showing a QEMScan mineral map (left) from a polished section in the imaged volume, the same section within the 3D tomogram (middle) and the mineral segmentation derived from the 3D tomographic data (right).

TABLE 1

Volume (%) of segmented mineral phases and porosity in the subcore scan of sample 1.

Mineral	Volume, %	Density, g/cc	Wt %
Bornite	0.59	4.19	0.89
Pyrite	1.23	4.9	2.18
Quartz	4.69	2.65	61.92
Clay	32.51	2.9	34.05
Porous clay	0.87	2.8	0.88
Dense phases (gold, zircon)	0.02	14	0.08
Pores	0.10		

Grain size distributions

Segmentation also enables quantification of the properties of individual grains (eg size, shape, orientation) within the full 3D volume. Figure 5, for example, provides grain sizes for the bornite in the subcore of sample 1, and for the heavy minerals that have very high X-ray attenuation. The latter are here dominated by gold. These data are obtained as a range of equivalent spherical grain diameters as fitted numerically into each identified particle, and are presented as both cumulative grain size and binned grain size plots. These grain size data may be translated into surface areas based on their range of equivalent diameters, but this approach does not account for surface roughness. Roughness can be measured via a more complex multistep tomographic process.

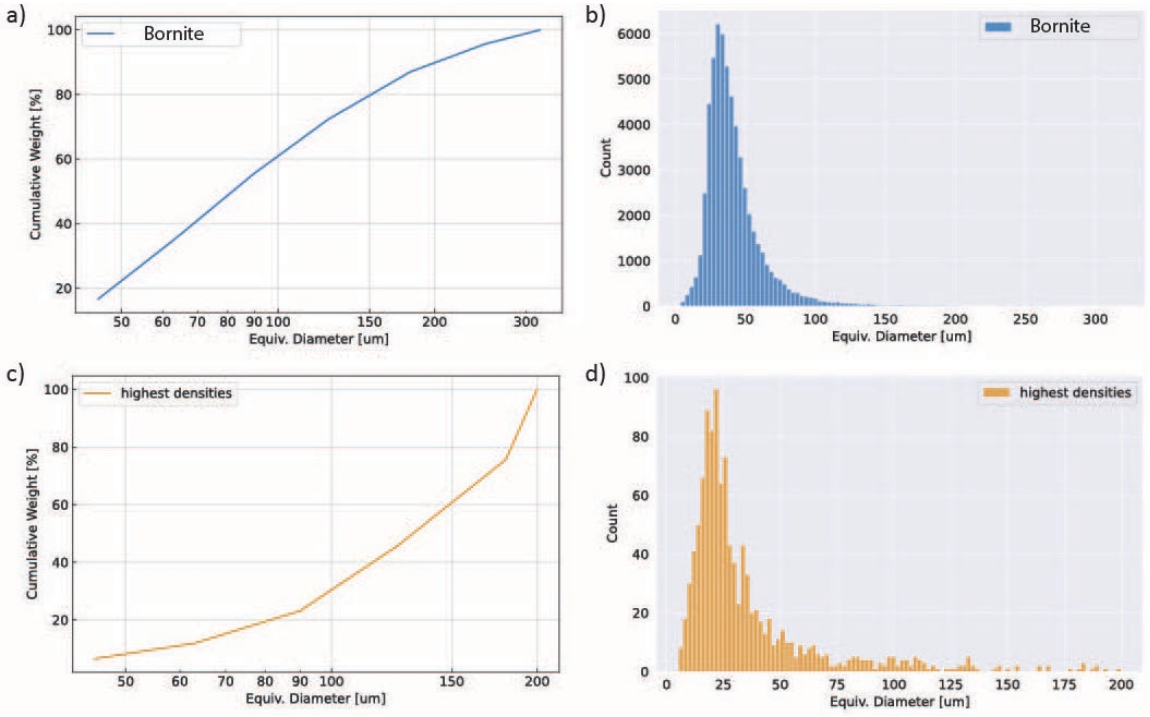

FIG 5 – Cumulative grain size and histograms for bornite (a and b), and for the high X-ray attenuation minerals, gold and zircon (c and d).

Mineral associations

We also investigated which minerals are in contact with the high-density grains by looking at adjacent voxels to the grain boundary as given by the mineral segmentation. These distributions are shown in Figure 6 for a) the bornite grains, and b) the heavy mineral grains that are predominantly gold. These data provide a quantitative guide to mineral liberation process design free of steric effects. Quartz is the dominant occluding phase for both bornite and for gold, which informs questions of crushing and grinding size. Improved recovery then depends upon methods for recovery from grains occluded by, for bornite, pyrite and for gold from both sulfides.

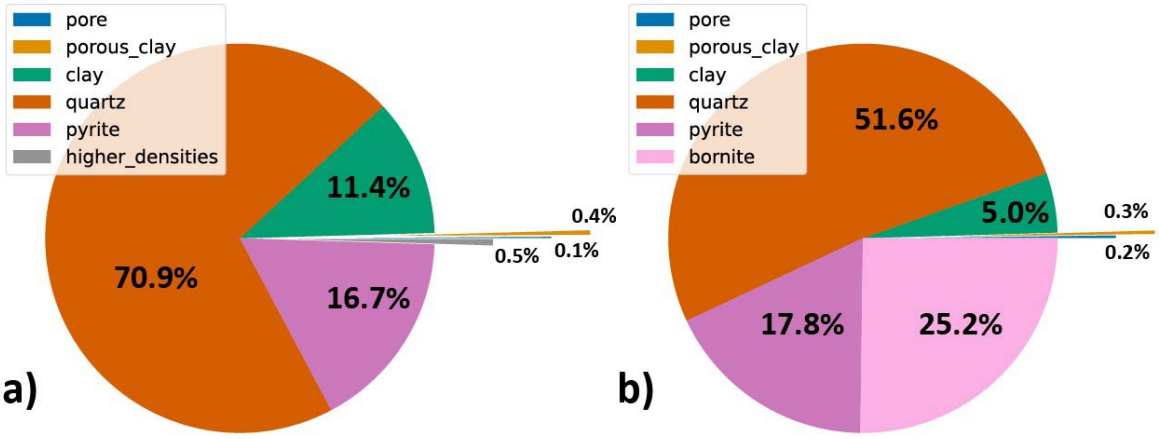

FIG 6 – Percentages of minerals in contact with a) bornite and b) high density minerals (principally gold).

Porosity mapping

Porosity occurs in rock materials over a wide range of scales down to submicron and nanoscales. The presence of microporosity decreases mineral density and hardness and so is a fundamental property of the rock mass processed through stages of crushing and comminution prior to froth flotation. It is also a property that underlies the relative friability of variably altered host rocks to mineralisation and therefore on mineral liberation consequent on crushing and comminution.

However, porosity measurement is not a standard practice in most metallurgical applications, but becomes central to the development of *in-situ* metal recovery operations.

Given this important role in rock material properties and mineral liberation, we have developed an advanced method to better identify and map porous voxels (Ghous *et al,* 2007; Knackstedt *et al,* 2007) in 3D down to submicron scales. In this method, a second tomogram is captured of the same material where the contrast of the porosity has been enhanced through the addition of a contrast agent (eg NaI or other doped brine) filling the connected pore space. The images are then brought into perfect geometric alignment, known as registration (Latham *et al,* 2008). This results in two exactly aligned tomograms, which due to the X-ray dense contrast brine used to enhance the saturated image, differ only in contrast of the connected pore space (see Figure 7a to 7b). Subtracting the dry tomogram from the saturated tomogram (Figure 7c) removes all influence of mineralogy and leaves only the brine response, both in the resolved pores as well as in the connected subresolution porosity. The grey scale value of the difference image is now linearly related to the amount of porosity represented by each voxel, with the end points given by fully open pores (100 per cent porous) and solid material (0 per cent porous). This porosity map allows us to accurately visualise all the connected porosity, which includes resolved and subresolution porosity.

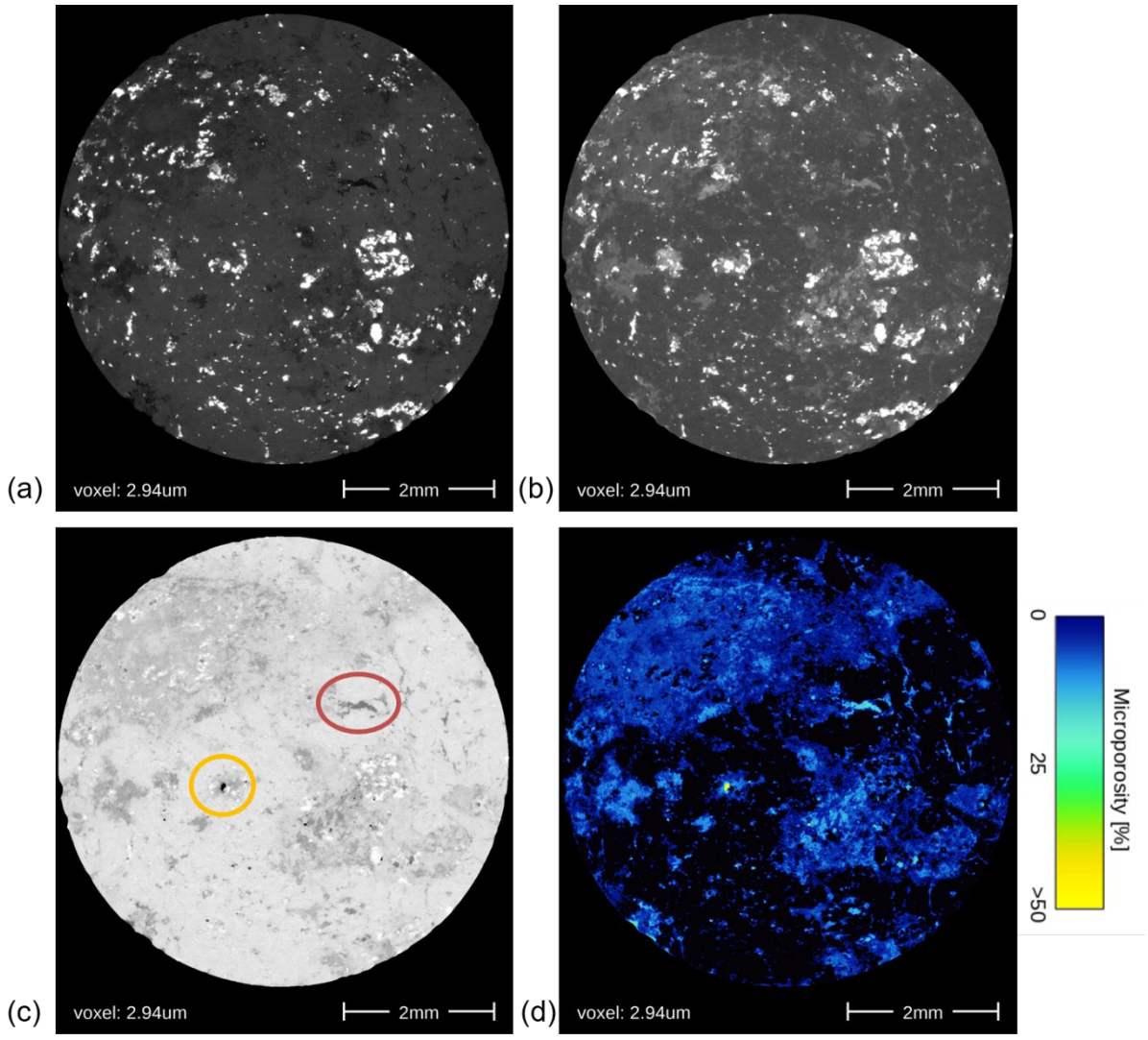

FIG 7 – Microporosity mapping in sample 1. (a) Slice through tomogram in dry state and (b) after saturation with attenuating fluid. (c) maps the difference in attenuation per voxel with an open pore highlighted in orange and a porous clay (local porosity ~ 30 per cent) highlighted by the red circle. (d) shows the extent of the connected porosity in a colour map. Most porosity is locally <5 per cent and is associated with submicron local features/cracks.

Figure 7d shows a colour map of the porosity distribution in the sample. Much of the porosity is <5 per cent locally, but coincides with the presence of copper sulfide minerals in the core. Quantification of the resolvable porosity from X-ray μCT scanning data is <0.1 per cent. Incorporating porosity from subresolution pores gives an estimate of 1.6 per cent.

Breakage and fracture development

Our laboratory has also developed the X-ray μCT capability of following fracture initiation and development through altered and mineralised rock material placed under stress (Francois, 2022a). Sample 2 is a chalcopyrite-mineralised altered volcanic rock from another porphyry copper deposit. Figure 8 is a 2D X-ray μCT slice through the tomogram of sample 2 after tensile fracturing in a Brazilian test. Investigation of the image provides detail (in 3D) of the relationship between induced fractures and chalcopyrite grains. This approach enables tracking and quantification of the proportion of sulfide mineral liberation that occurs during fracturing (Francois, 2022b) and can be adapted to track this proportion through stages of crushing and comminution. Image analysis of the tomogram shows that, for sample 2, 4.6 per cent of the total chalcopyrite has been liberated onto fractures as expressed in terms of the surface area of all the chalcopyrite grains giving a measure, in this case, of the liberation achieved by an initial fracture step.

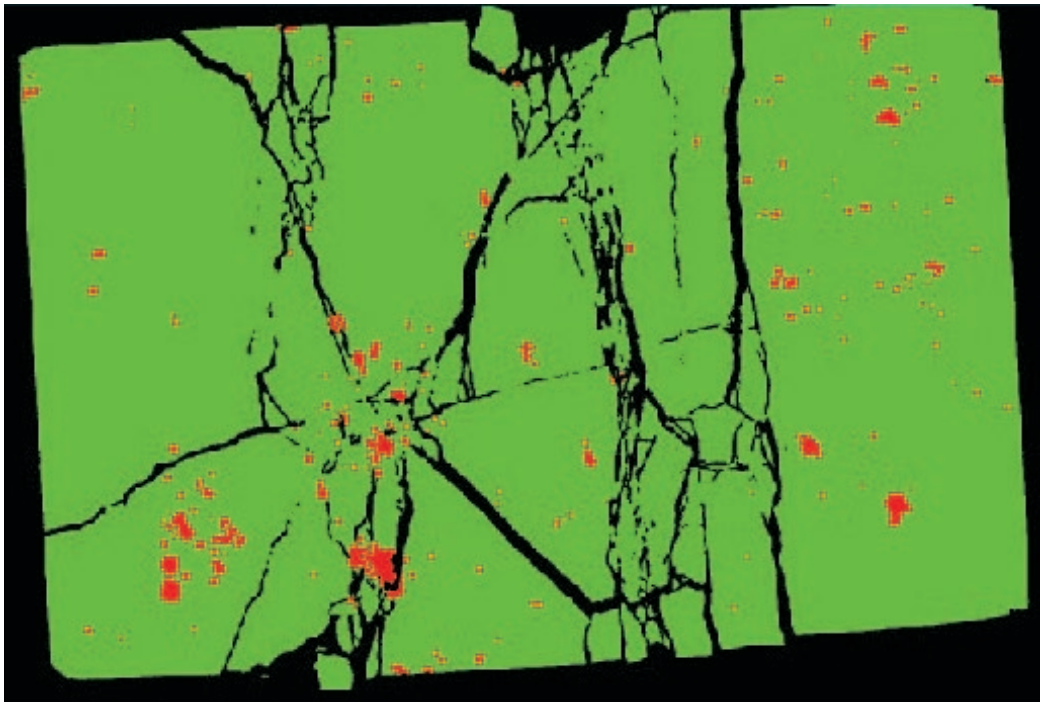

FIG 8 – A vertical slice of the segmented tomogram of the fractured disc of sample 2 showing the distribution of bornite relative to extensional fracturing. (black: fracture; red: copper sulfides; green: other minerals). The longer side is about 10 mm and the shorter is about 8 mm.

SUMMARY AND FUTURE DIRECTIONS

The combination of technologies and workflows that were developed under the heading of Digital Rock Technology (DRT) for the energy sector provides a foundation for a highly integrated, multi-platform approach to geometallurgical problems and especially to the analysis of complex ore assemblages. In this paper we have summarised two examples of the extension of DRT to porphyry copper rock material. The first demonstrates the ability of X-ray μCT to quantitatively resolve mineral phases such as bornite, pyrite and gold and define key geometallurgical parameters such as grain size and shape. X-ray μCT also allows imaging and quantification of the three-dimensional void structure in geomaterials, opening up new avenues to improve our understanding and characterisation of the way fluids reside in and move through the subsurface in, for example, *in situ* mineral recovery. Pores and fractures larger than a few microns can be mapped directly in core samples, and void space at all scales can be measured by scanning samples sequentially over different conditions of saturation. Such time series analyses can reveal the varying ways in which

porosity is hosted by different rock components, and enable estimation of direction and degree of flow anisotropy and leaching potential of different samples. Moreover, microporosity distribution has a fundamental effect on the hardness and fracturability of rock material, but has not previously been recognised as a key geomechanical parameter.

Being a non-destructive methodology, time resolved studies can also be undertaken on dissolution/leaching or mechanical tests, including compression and crushing tests for rock strength and mineral liberation as was demonstrated in the second example. The technology naturally allows extension to undertake dynamic studies of ore breakage and fragmentation (Francois, 2022b). In the latter studies, structural and mineralogical information can be directly compared to key features of the mechanical response of the ore and fracture pathways enabling one to enhance the understanding of breakage and comminution processes.

ACKNOWLEDGEMENTS

The authors would like to thank the Australian Research Council for support under the ARC Industrial Training Center for M3D Innovation and Michael Turner for image acquisition and core analysis work.

REFERENCES

Andersson, L, Herring, A, Newell, D, Carey, B and Wildenschild, D, 2013, High-resolution x-ray tomography imaging of supercritical CO2: Investigating capillary trapping under reservoir conditions and addressing wettability alteration. *AGU Fall Meeting Abstracts*, H41P-03.

Arns, C, Averdunk, H, Bauget, F, Sakellariou, A, Senden, T, Sheppard, A, Sok, R, Pinczewski, W and Knackstedt, M, 2004, Digital Core Laboratory: Analysis of reservoir core fragments from 3D images. *SPWLA 45th Annual Logging Symposium*: OnePetro.

Dunsmuir, J H, Ferguson, S, D'Amico, K and Stokes, J, 1991, X-ray microtomography: a new tool for the characterization of porous media. *SPE annual technical conference and exhibition*: OnePetro.

Francois, N, 2022a, A Versatile high-pressure apparatus for in situ microtomography in geomechanical investigations of rock failure. *Reviews of Scientific Instruments*.

Francois, N, Zhang, Y, Henley, R W, Kneufing, L, Cruikshank, R, Turner, M, Beeching, L, Limaye, A, Kingston, A, Saadatfar, M and Knackstedt, M, 2022b, In situ micro-tomography of the tensile fracture and fragmentation of copper ore (The Australasian Institute of Mining and Metallurgy: Melbourne).

Ghous, A, Senden, T J, Sok, R M, Sheppard, A P, Pinczewski, V W and Knackstedt, M A, 2007, 3D characterisation of microporosity in carbonate cores. *SPWLA Middle East Regional Symposium*: OnePetro.

Godel, B, 2013, High-resolution X-ray computed tomography and its application to ore deposits: From data acquisition to quantitative three-dimensional measurements with case studies from Ni-Cu-PGE deposits. *Economic Geology* 108, 2005–2019.

Herring, A L, Andersson, L, Newell, D, Carey, J and Wildenschild, D, 2014, Pore-scale observations of supercritical CO_2 drainage in Bentheimer sandstone by synchrotron x-ray imaging. *International Journal of Greenhouse Gas Control* 25, 93–101.

Latham, S, Varslot, T and Sheppard, A, 2008, Image registration: enhancing and calibrating X-ray micro-CT imaging. *Proc. of the Soc. Core Analysts, Abu Dhabi, UAE*, 1–12.

Limaye, A, 2012a, Drishti: a volume exploration and presentation tool. *Proc. SPIE, Developments in X-Ray Tomography VIII 8506.*

Limaye, A, 2012b, Drishti: a volume exploration and presentation tool. *Proc Spie* 8506, 85060X-85060X.

Liu, M and Mostaghimi, P, 2018, Reactive transport modelling in dual porosity media. *Chemical Engineering Science* 190, 436–442.

Miller, J, Lin, C and Cortes, A, 1990, A review of X-ray computed tomography and its applications in mineral processing. *Mineral Procesing and Extractive Metallurgy Review* 7, 1–18.

Oeren, P, Ruspini, L C, Saadatfar, M, Sok, R, Knackstedt, M and Herring, A, 2019, In-situ pore-scale imaging and image-based modelling of capillary trapping for geological storage of CO2. *International Journal of Greenhouse Gas Control* 87, 34–43.

Singer, D A, 2017, Future copper resources. *Ore Geology Reviews* 86, 271–279.

Sok, R, Knackstedt, M, Arns, C, Varlot, T, Ghous, A, Lathan, S and Sheppard, A, 2010. Pore Scale Characterisation of carbonates at multiple scales: Integration of Micro-CT, BSEM and FIBSEM. *Petrophysics*, 51(6). Paper Number SPWLA-2010-V51N6a1.

Wang, Y and Miller, J, 2020, Current developments and applications of micro-CT for the 3D analysis of multiphase mineral systems in geometallurgy. *Earth-Science Reviews* 211, 103406.

Wills, B A and Finch, J A, 2015, *Wills' mineral processing technology: an introduction to the practical aspects of ore treatment and mineral recovery*: Butterworth-Heinemann.

Large-scale flotation in operation – a case study on Cobre Panama

T Mattsson[1] and J Whyte[2]

1. Technology Manager, Metso Outotec, Espoo Finland, 02230.
   Email: toni.mattsson@mogroup.com
2. Technology Manager, Metso Outotec, Perth WA 6005. Email: jay.whyte@mogroup.com

ABSTRACT

As orebodies decrease in head grade, the need to treat greater tonnage continues, and will continue, to be a challenge for mineral processing plants. Additionally, producers must strive to remain economically viable – being mindful of both capital and operating costs to maintain sustainable growth of the company. Key considerations when designing such plants include power consumption, maintenance, footprint, installation and commissioning time, and the ability to accommodate varying head grades. The need for larger-scale beneficiation equipment arose from these requirements.

First Quantum Minerals' Cobre Panama operation is one of the world's largest copper mines opened in the last decade with a design throughput rate of 85 Mt/a, with future expansion plans for 100 Mt/a. The plant was commissioned in late 2018 and quickly achieved design throughput rates and recovery targets. For the rougher flotation duty, 28 × 630 m^3 Metso Outotec TankCells are employed in a four-bank configuration, along with a 300 m^3 Metso Outotec TankCell® cell at the head of each train to scalp off the fast-floating high-grade copper minerals. With respect to performance, both overall copper recoveries and equipment availability have been above targets to date.

This paper will discuss the installation and operational benefits of using large-scale flotation and the engineering challenges that were overcome during the design phase to develop these robust cells which have been able to accommodate variable throughput and ore head grade whilst delivering production profitability.

INTRODUCTION

Decreasing ore grades has driven the growing need to process large tonnages to ensure the economic viability of a project. With increasing throughputs, moving towards fewer larger equipment is the logical approach as it significantly reduces footprint, energy consumption, installation time, maintenance time, and allows for easier optimisation due to fewer equipment to operate.

Metso Outotec has been developing large-scale flotation cells since the 1970s to address increasing demand for larger equipment. Continuous research and development has allowed for the advancement to 100 m^3, 300 m^3, 500 m^3, and now 630 m^3 flotation cells. As of 2021, there is currently 85 TankCell® e630 successfully operating around the world in various applications. In this paper a case study from Cobre Panama operation is presented which is currently the biggest TankCell® e630 installation.

COBRE PANAMA OPERATION

The Cobre Panama Project, majority owned by First Quantum Minerals, is located approximately three hours West of Panamá City, in the Colón Province, Panamá. The orebody consist of several porphyry Cu-Au-Ag-Mo ore systems with key deposits located at Botija, Colina, Valle Grande and Balboa. The 3500 Mt of measured and indicated copper reserves are a low head grade, averaging 0.37 per cent. Chalcopyrite is the prominent mineral present with minor quantities of bornite and molybdenite found throughout.

The concentrator plant is capable of processing 85 Mt/a of ore with the capability to increase throughputs to 100 Mt/a. The Cobre Panama operation can produce more than 300 000 t of copper per annum along with gold, silver, and molybdenum.

Some of the largest mineral processing equipment is in operation at Cobre Panama due to the sheer size and complexity of the project. Metso Outotec supplied the majority of key equipment at the concentrator including 3 × MP2500 and 3 × MP1250 crushers, 2 × 40 ft 28MW SAG mills, 4 × 28 ft

22MW ball mills, 3 × 5MW regrind HIGmills™, various flotation TankCells® (630 m^3, 300 m^3, 200 m^3, and 100 m^3), 6 × High-Rate Thickeners, and 3 × Larox® PF filters.

Flotation circuit

The valuable chalcopyrite is recovered via froth flotation and has the option to pass through a separation circuit to separate out the molybdenite when present in high enough concentrations. Cobre Panama's rougher-scavenger circuit consist of four trains of seven TankCell® e630 flotation cells with a single TankCell® e300 placed at the front of each train to act as a scalper and recover the fast-floating chalcopyrite. Concentrate from these mechanical scalpers is then sent to a pneumatic flotation cell for further cleaning. Concentrate from the TankCell® e630s is combined with tailings from the first pneumatic cells and then sent to 3 × 5MW regrind HIGmills™ before being fed to the cleaner, cleaner scavenger, and re-cleaner circuit consisting of 8 × TankCell® e200s, 6 × TankCell® e300s, and 4 × TankCell® e100s respectively. Tailings of the re-cleaner is sent to a column that then produces a concentrate which is combined with the re-cleaner concentrate and coarse concentrate from the first pneumatic cell to produce a final concentrate. In Figure 1 pictures from the flotation section and Figure 2 the process flow diagram is presented.

FIG 1 – Cobre Panama is the first large scale greenfield copper operation designed and built with TankCell® e630 technology.

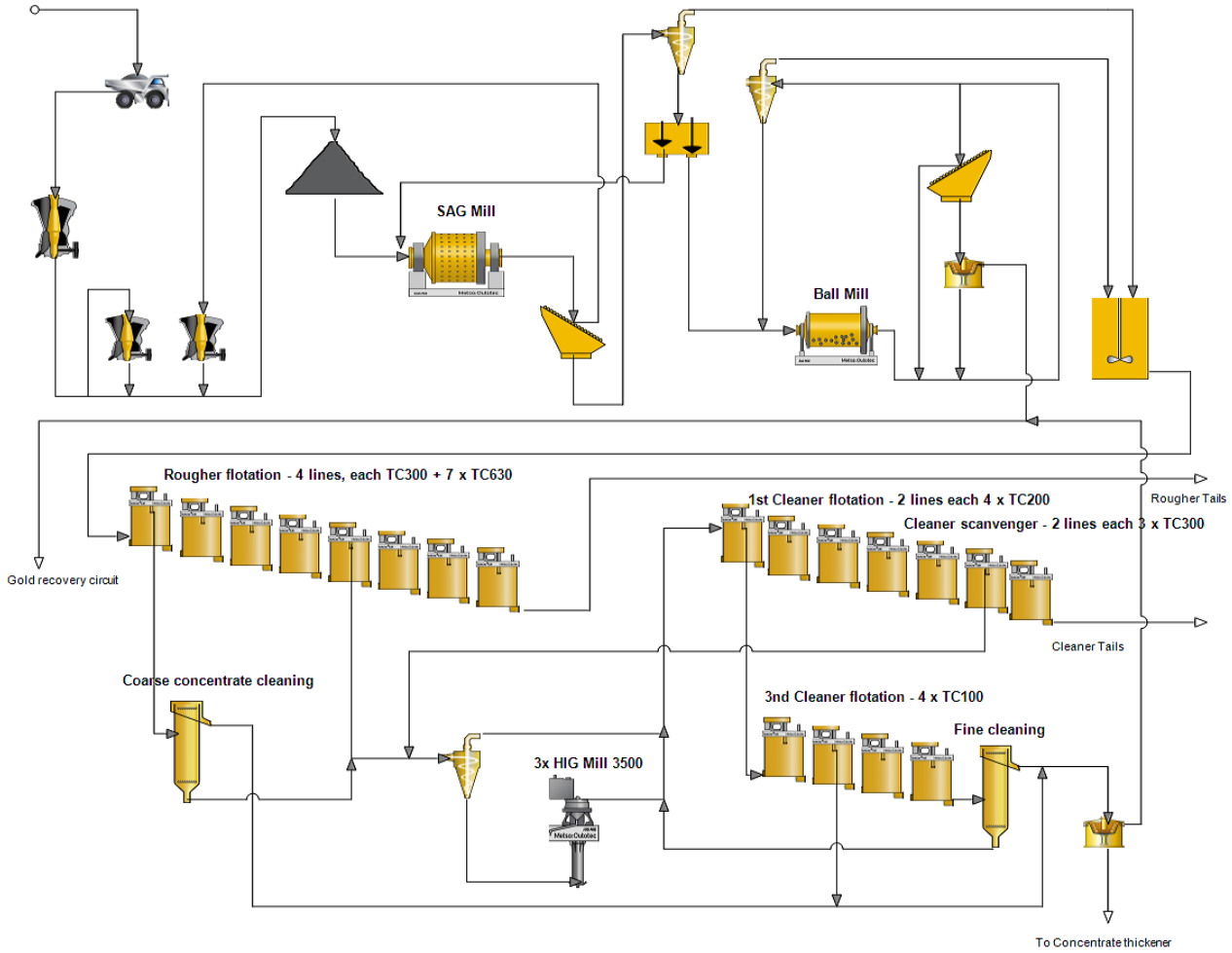

FIG 2 – Cobre Panama process flow diagram.

TankCell® e630 flotation cells in rougher and scavenger flotation duty

With the 28 TankCell® e630 flotation cells Cobre Panama is currently the world's largest TankCell® e630 installation and the first large scale greenfield Cu project which implemented flotation section using these 630 m^3 forced-air mechanical flotation cells. For the Cobre Panama project the single most important milestone to gain confidence to implement the project with the TankCell® e630 units was a successful first TankCell® e500 installation at Kevitsa Cu-Ni-PGE operation in October 2014, owned and operated then by First Quantum Minerals. Further confidence was gained from other TankCell® e630 installation which proved with the first TankCell® e500 installation that the large TankCell® flotation cells are energy efficient, provide high availability with minimal sanding, and equal metallurgical and gas dispersion performance than smaller well proven TankCell® flotation cells (Grau *et al,* 2018; Mattsson *et al,* 2015a, 2015b; Suhonen *et al,* 2019).

To ensure high froth recovery and adequate froth mobility of the cells the first two TankCell® e630 in each bank were configured with a unique double launder with radials and the next five cells with a centre launder. The double launder and centre launder are presented in detail in Figures 3 and 4, respectively.

The biggest advantage of these launder designs is the optimised froth surface area and reduced froth transport distance the donut launder located between the shaft and tank wall provides. The unique double launder design was a solution for the engineering challenge these large flotation cells with large diameter generated. The reduction of froth transport distance and froth surface area does promote high froth recovery, improved coarse particle recovery and improved froth stability.

In the project conventional mechanical flotation cell sizing procedure as well as scale-up factors were applied to ensure adequate residence time for the rougher flotation. It is considered that the TankCell® e630 provided for the project 5–10 per cent energy savings and 15–20 per cent footprint

savings against TankCell® e300 which is a 300 m^3 flotation cell and the most common size selected for large flotation circuits prior to the introduction of the TankCell® e500 and e630.

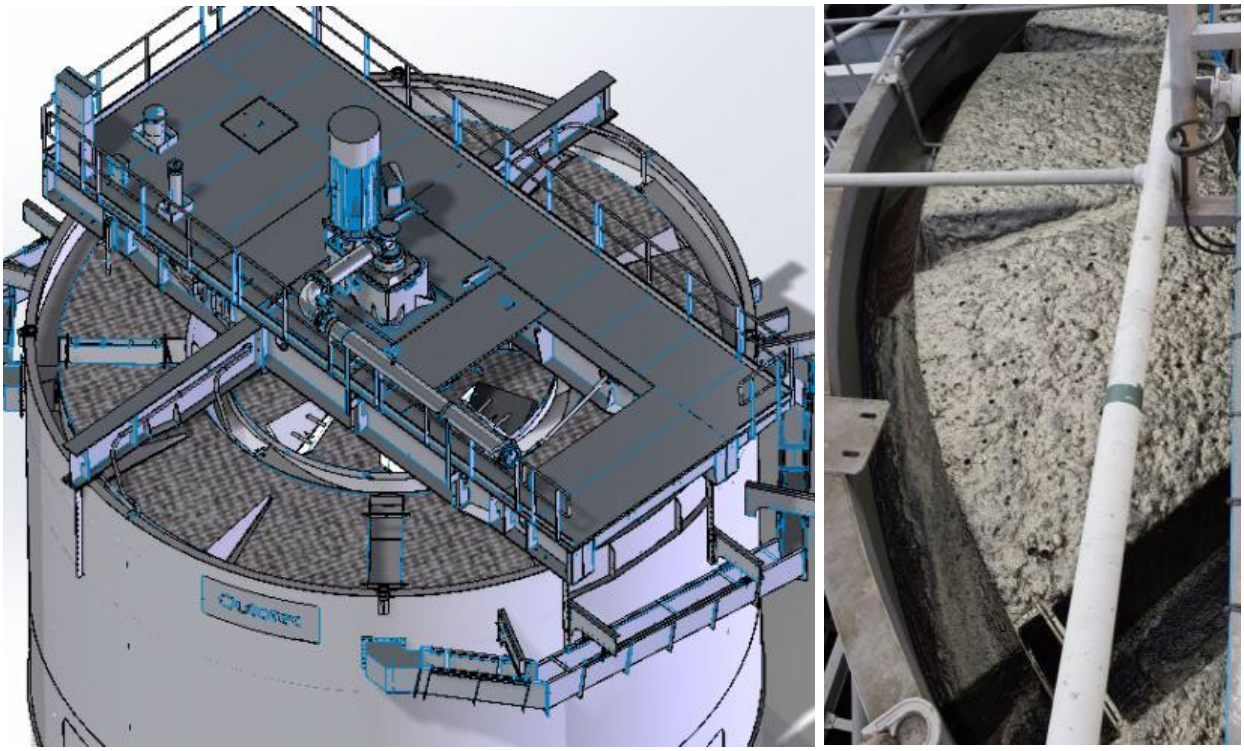

FIG 3 – Unique TankCell e630 double launder design with radial launders.

FIG 4 – TankCell e630 with a centre launder.

RESULTS AND DISCUSSION

First Quantum Mineral's self-performance approach with in-house technical expertise enabled Cobre Panama to achieve commercial production on 1 September 2019, only six months after first production. This achievement was an outcome of in-house project team developed over many years, use of external firms to provide specific expertise, coordination of project resources from development to commissioning to operation, and effective communication across the project (BMO, 2020, 2022).

The quick turnaround time from the first production to commercial production proves very successful implementation of the large-scale minerals processing equipment and shows that the TankCell® e630 provides high availability. Another confirmation of successful design, technology selection and implementation of the project is proven by the ore processed and achieved Cu recoveries during the year 2021, summarised in Figure 5. This figure shows stable production for all four quarters of the year and between 90 to 92 per cent Cu recovery.

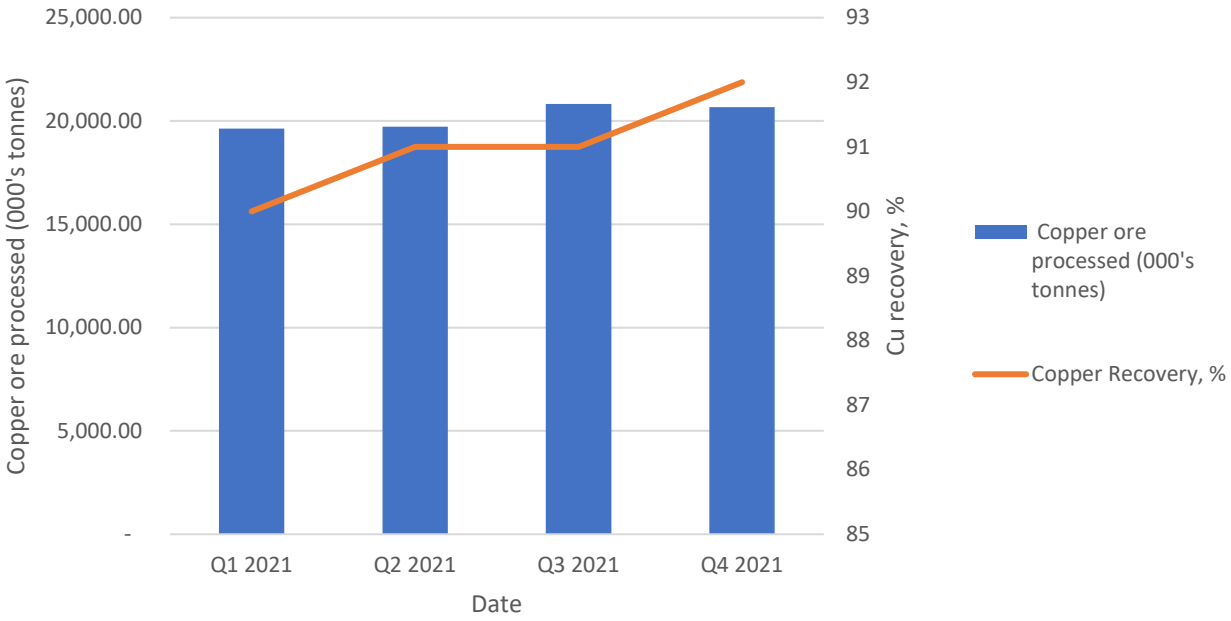

FIG 5 – Cobre Panama copper ore processed and Cu recovery (First Quantum Minerals, 2021, 2022).

During the year 2021 Cobre Panama exceeded their copper production guidance of 300 000–330 000 t of copper (First Quantum Minerals, 2021) with copper production of 331 000 t (First Quantum Minerals, 2022). This achievement is an outcome of successful mining and processing throughout the year as well as successful equipment selection and engineering prior project implementation.

CONCLUSIONS

From the Cobre Panama case study following conclusions can be drawn:

1. Rougher flotation performance exceeded expectations: The TankCell® e630 flotation cells enabled the project to meet and exceed the design copper production with energy and footprint savings.
2. Plant ramp-up achieved expectations: The equipment, including TankCell® e630, met the project requirements and design capacities were achieved confirming adequate equipment selection and sizing.
3. Six months to commercial production: Great teamwork and communication throughout the project enabled Cobre Panama to achieve commercial production in such a short span of time.

ACKNOWLEDGEMENTS

The authors would like to acknowledge all the teams involved in the design, installation and operation of these large scale cells at Cobre Panama. The authors would also like to thank First Quantum Minerals for their kind permission to publish this work.

REFERENCES

BMO, 2020. 29th Global Metals & Mining Conference; February 2020; https://s24.q4cdn.com/821689673/files/doc_presentations/2020/BMO-2020-february-Final.pdf

BMO, 2022. Global Metals & Mining Conference; February 2022; https://s24.q4cdn.com/821689673/files/doc_presentations/2022/BMO-Conference-Deck.pdf

First Quantum Minerals, 2021. Management's Discussion and Analysis – First quarter ended March 31, 2021, April 2021; https://s24.q4cdn.com/821689673/files/doc_financials/2021/Q1–2021-FQM-Management's-Discussion-Analysis-(FINAL).pdf

First Quantum Minerals, 2022. Management's Discussion and Analysis – Year ended December 31, 2021; February 2022; https://s24.q4cdn.com/821689673/files/doc_financials/2022/Q4–2021-FQM-Management's-Discussion-Analysis-FINAL.pdf

Grau, R, Tapia, J A, Yañez, A, Hicks, M, 2018. Improving Buenavista del Cobre Flotation Performance with Outotec TankCell® e630 Technology. *14th International Mineral Processing Conference, Procemin* 28–30 November, Santiago, Chile.

Mattsson, T, Grau, R, Honkanen, M and Maksimainen, T. 2015b. Gas Dispersion Characterization Campaign in Outotec TankCell® e500 at Kevitsa Cu-Ni-PGE Concentrator. *Flotation 2015 conference proceedings*.

Mattsson, T, Maksimainen, T, Muzinda, I, Lohilahti, J and Yanez, A, 2015a. Implementation of Outotec TankCell® e500 at FQML Kevitsa Cu-Ni-PGE concentrator. *Proceedings Procemin Conference*, Santiago Chile.

Suhonen, J, Grau, G, Yáñez, A, Miettinen, T, Tapia, A and Mattsson, T, 2019. Performance of TankCell® 630 at Buenavista del Cobre Cu-Mo concentrator. *Flotation 2019 conference proceedings*.

Real-time slurry mineralogy for process control

Y Van Haarlem[1], J O'Dwyer[2] and B Ganly[3]

1. Group Lead, CSIRO, Lucas Heights NSW 2234. Email: yves.vanhaarlem@csiro.au
2. Team Lead, CSIRO, Lucas Heights NSW 2234. Email: joel.odwyer@csiro.au
3. Team Lead, CSIRO, Urrbrae SA 5064. Email: Brianna.ganly@csiro.au

INTRODUCTION

In recent years there has been a strong drive in the mining and minerals processing industry to improve plant efficiency through real-time process optimisation and control. The major forces behind this are ever-reducing orebody grades in conjunction with rising operation costs and pressure to reduce the environmental impact of mining operations. Optimisation of the concentration process not only enables an increase in yield but also reduces economic and environmental costs through reductions in power, consumables and water usage.

A key factor in determining the efficiency of a mineral concentrator is the mineralogy of the process streams. Mineralogy has a strong influence on the behaviour of the processes involved in converting the raw feed ore into a concentrated product. Real-time knowledge of these minerals enables process control parameters to be adjusted in a systematic manner to optimise the process.

Many online measurement systems have been developed and deployed in processing plants that measure elemental concentrations in process streams. These systems use techniques such as X-ray fluorescence (XRF) and prompt gamma/neutron activation analysis (Smallbone, 1997; Lim and Sowerby, 2005). However, real-time measurement of mineralogy has proven to be more challenging. There are systems that measure mineralogy either directly (Roach *et al*, 2013) or indirectly (Kewe *et al*, 2014) but none have been adopted widely throughout the industry for various reasons. Magnetic resonance (MR) technology is proving to be a highly accurate method for analysing specific mineral phases, such as copper minerals (Bennett *et al*, 2009). However, it is limited to minerals that are amenable to the method and cannot be applied generally to all processing applications.

X-ray diffraction (XRD) is a method used to investigate the properties of crystalline materials and minerals. XRD has been used in laboratories since the early 20th century as the standard method to perform quantitative mineral phase analysis on samples of unknown composition. Accordingly, it has been widely adopted in the minerals processing industry to carry out routine assays of plant samples. The laboratory technique requires laborious sampling, preparation and analysis that can take hours or even days to complete. Therefore, the analysis cannot be used for real-time process control and optimisation since the plant conditions could have significantly digressed during the delay.

CSIRO has developed an online mineralogy and elemental slurry analyser that is capable of monitoring both mineral and metal content in real-time. The analyser is called the Mineral and Elemental Analyser (MEA) and combines XRD and XRF instruments into a single system that measures the process slurry directly without the need for sample preparation. In addition, the XRF analyser provides a measurement of the average particle size of the solids using CSIRO patented technology.

A photograph of the MEA analyser prototype described in this paper is shown in Figure 1. The MEA consists of an 80 L launder tank that accepts a subsampled slurry from the main process stream. The tank can accommodate a slurry flow rate of up to 100 L/min. The slurry in the tank is agitated using an overhead stirrer to ensure it remains homogeneously mixed. The total mass of sample measured in a 10-minute measurement cycle can be in the order of several hundred kilograms and therefore MEA provides a truly bulk measurement of the process stream composition. The X-ray systems are housed in the two cabinets mounted on either side of the launder tank.

FIG 1 – Photograph of the MEA with the main components labelled. The system consists of X-ray instrument enclosures that are mounted to an 80 L launder tank. The analyser has a footprint of approximately 2 m^2.

MEA can be used to improve the performance of most minerals processing operations, where accurate monitoring would enable real-time process control of circuits. In this paper, examples including copper sulfide, gold, and hard rock lithium ores will be given to illustrate some of the advantages MEA can provide.

ACKNOWLEDGEMENTS

The authors would like to acknowledge Jonathan Masters and Stephen Rainey for their invaluable contribution to the software, electrical and mechanical design of the MEA.

REFERENCES

Bennett, D W, Miljak, D G and Khachan, J, 2009. The Measurement of Chalcopyrite Content in Rocks and Slurries Using Magnetic Resonance, *Minerals Engineering*, 22, 9–10, pp. 821–825.

Kewe, T, Moffat, N, Strobos, P, van der Spuy, D, Paine, A P and Keet, K, 2014. Evaluation of the Blue Cube MQi Slurry Analyser for Application in an Advanced Control System for the Optimisation of a Gold Sulphide Flotation Circuit, *Proceedings of 12th AusIMM Mill Operators' Conference*, pp. 357–362 (The Australasian Institute of Mining and Metallurgy: Melbourne).

Lim, C S and Sowerby, B D, 2005. On-line Bulk Elemental Analysis in the Resources Industries Using Neutron-Gamma Techniques, *J. Radioana. Nucl. Chem.*, 264, 1, pp. 15–19.

Roach, G, Abernethy, D, O'Dwyer, J, Smith, M, Tickner, J and Van Haarlem, Y, 2013. Advanced Instrumentation for Analysis of Exploration, Mining and Process Materials, *Proceeding of World Gold*, pp. 277–282 (The Australasian Institute of Mining and Metallurgy: Melbourne).

Smallbone, A H, 1997. Automated on-line analysis for controlling industrial processes, *Pure Appl Chem*, 49, pp. 1609–1620.

Selective agglomeration of pentlandite using water-in-oil emulsion

M Yvon[1], P Wang[2] and K P Galvin[3]

1. PhD Student, ARC Centre of Excellence for Enabling Eco-Efficient Beneficiation of Minerals, Newcastle Institute for Energy and Resources, University of Newcastle, Callaghan NSW 2308. Email: meollaesther.yvon@uon.edu.au
2. Research Associate, ARC Centre of Excellence for Enabling Eco-Efficient Beneficiation of Minerals, Newcastle Institute for Energy and Resources, University of Newcastle, Callaghan NSW 2308. Email: peipei.wang@newcastle.edu.au
3. Laureate Professor, ARC Centre of Excellence for Enabling Eco-Efficient Beneficiation of Minerals, Newcastle Institute for energy and Resources, University of Newcastle, Callaghan NSW 2308. Email: kevin.galvin@newcastle.edu.au

INTRODUCTION

Falling ore grades coupled with an increase in demand for minerals has created a need for new separation techniques that can recover particles below the hydrodynamics limits of froth flotation. A novel ultrafast agglomeration technique that can selectively recover hydrophobic particles was recently developed. This novel binder can agglomerate and recover hydrophobic particles across a wide range of particles sizes, even ultrafines, in less than 7 s. The high internal phase water-in-oil emulsion binder consists of a network of tightly packed water droplets surrounded by a permeable thin layer of oil, bounded by the emulsifier sorbitan monooleate (SMO). The agglomeration of fine pentlandite, a nickel sulfide mineral, from a low-grade nickel tailings stream was investigated, and its performance compared to froth flotation. Different options to improve the agglomeration process are also discussed.

COMPARISON OF FLOTATION AND AGGLOMERATION

Mechanical cell flotation and agglomeration experiments were conducted using the -20 µm size fraction of a low-grade nickel scavenger tailings (NST) stream of a Cu-Ni sulfide flotation plant. The grade of nickel in this feed is 0.53 per cent. In order to maximise recovery, the fine size fractions were floated in a mechanical cell with a residence time of 12 min. Wash water (aqueous solution with 24 ppm of MIBC) was added to maintain the water level and minimise entrainment. The water-in-oil (W/O) emulsion was prepared as described in Borrow *et al* (2018) for the agglomeration experiments. After conditioning, varying amounts of the novel binder were added to the slurry via a syringe and agitated for 7 s at 22 000 rev/min. The slurry was then poured over a sieve to separate the product from the reject. The product and reject were dried and analysed. The results of the experiments are shown in Table 1.

TABLE 1

Technology comparison for nickel recovery from NST (-20 µm).

Beneficiation method	Nickel recovery (%)	Upgrade ratio
Flotation (12 min)	22	1.3
Agglomeration (7 sec)	43	1.6

The recovery of pentlandite is constrained by the slow kinetics of the flotation of the ultrafine particles in flotation. The long residence time required also increases the probability of gangue recovery by entrainment, hence the low upgrade. A ten-fold reduction in oil consumption and one order of magnitude reduction in agglomeration time can be achieved with the novel agglomeration process compared to pure oil agglomeration (van Netten *et al*, 2016). The permeability of the thin layers of oil and osmosis driving force created by the NaCl molecules in the novel binder reduce the hydrodynamic resistance (Deiuliis *et al*, 2021), resulting in higher nickel recoveries compared to flotation. However, the upgrade is quite low for both methods. The main gangue particles in the feed are non-magnesium silicates (27 wt per cent) and magnesium silicates (37 wt per cent). A slime coating can form on the valuable minerals due to the electrostatic attraction between the positively

charged pentlandite and negatively charged magnesium silicates particles (Feng *et al*, 2012), thereby affecting selectivity and recovery. Moreover, the poor selectivity in the agglomeration process can also be due to the interaction of the SMO in the novel binder with metal ions adsorbed on the surface of the gangue particles (Sahasrabudhe *et al*, 2021). The next section discusses different options investigated to optimise the recovery of pentlandite in the novel agglomeration process.

OPTIMISATION OF THE AGGLOMERATION PROCESS

Agglomeration experiments similar to the one described above were conducted on the -48 µm size fraction of a nickel rougher feed (NRF) stream of a Cu-Ni sulfide flotation plant. The grade of nickel in this feed is 2.7 wt per cent Ni. The results are shown in Figure 1.

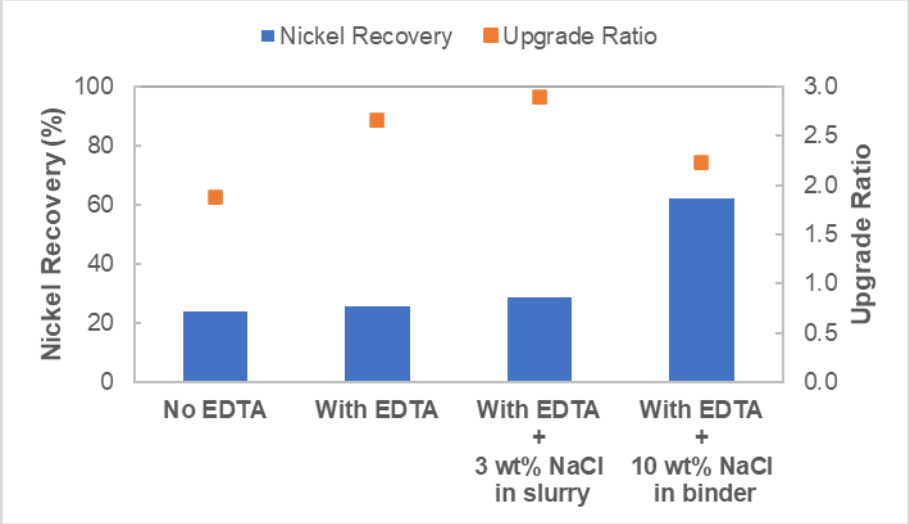

FIG 1 – Nickel recovery and upgrade ratio in agglomeration experiments at different conditions for NRF (-48 µm).

The feed used in the experiments was from a Cu-Ni sulfide flotation circuit and contained calcium ions that were added upstream in the process to depress the pentlandite and favour the chalcopyrite recovery. The feed was treated with 2×10^{-4} M ethylenediaminetetraacetic acid (EDTA) prior to agglomeration to remove adsorbed metal ions on the gangue particles and in turn prevent their agglomeration. The grade of the concentrate increased from 1.9 to 2.7 with EDTA treatment. Peng and Bradshaw (2012) showed that addition of electrolytes can minimise the coating of magnesium silicates slimes on the surface of pentlandite particles by compressing the electrical double layer, and thus reducing the electrostatic attraction between the oppositely charged particles. Therefore, 15 g (3 wt per cent) of NaCl was added to the slurry in the agglomeration experiment followed by EDTA treatment, resulting in a cleaner product with an upgrade ratio of 2.9. However, the use of EDTA and electrolyte addition increased the selectivity with only a slight increase in the nickel recovery (24 per cent to 29 per cent). The novel binder consisted of 95 per cent aqueous phase (3 per cent by weight NaCl) and 2.5 per cent kerosene and 2.5 per cent SMO. A positive osmotic driving force caused by the salt molecules in the binder is crucial to achieve very high recoveries in the agglomeration process (van Netten *et al*, 2017). The composition of the binder was modified by increasing the salt concentration to 10 per cent to increase the osmotic driving force as there are dissolved solids in the slurry. The change in the binder composition resulted in a recovery of 62 per cent and upgrade ratio of 2.23.

CONCLUSION

High nickel recoveries were achieved with the novel agglomeration process compared to flotation. The selectivity of the agglomeration process was improved by the addition of EDTA and electrolytes in the slurry. A binder composition with higher salt concentration proved beneficial in improving the nickel recovery. This paper aims to provide the fundamental knowledge for application of the novel

agglomeration process to solving the challenges associated with pentlandite recovery from low-grade complex sulfide ore rich in magnesium silicate gangue minerals.

ACKNOWLEDGEMENTS

The authors acknowledge the funding support from the Australian Research Council for the ARC Centre of Excellence for Enabling Eco-Efficient Beneficiation of Minerals, grant number CE200100009.

REFERENCES

Borrow, D J, Van Netten, K and Galvin, K P, 2018. Ultrafine Particle Recovery Using Thin Permeable Films. *Frontiers in chemistry,* 6, 220–220.

Deiuliis, G, Sahasrabudhe, G, Davis, R H and Galvin, K P, 2021. Water transport by osmosis through a high-internal-phase, water-in-oil emulsion. *Chemical engineering science,* 232.

Feng, B, Feng, Q and Lu, Y, 2012. A novel method to limit the detrimental effect of serpentine on the flotation of pentlandite. *International Journal of Mineral Processing,* 114–117, 11–13.

Peng, Y and Bradshaw, D, 2012. Mechanisms for the improved flotation of ultrafine pentlandite and its separation from lizardite in saline water. *Minerals Engineering,* 36–38, 284–290.

Sahasrabudhe, G, Deiuliis, G and Galvin, K P, 2021. Hydrophobization of minerals by sorbitan mono oleate (Span® 80): Selectivity of a novel agglomeration process. *Colloids and Surfaces A: Physicochemical and Engineering Aspects,* 630, 127460.

van Netten, K, Borrow, D J and Galvin, K P, 2017. Fast Agglomeration of Ultrafine Hydrophobic Particles Using a High-Internal-Phase Emulsion Binder Comprising Permeable Hydrophobic Films. *Industrial & engineering chemistry research,* 56, 10658–10666.

van Netten, K, Moreno-Atanasio, R and Galvin, K P, 2016. Selective agglomeration of fine coal using a water-in-oil emulsion. *Chemical Engineering Research and Design,* 110, 54–61.

AUTHOR INDEX